SCHOLARLY PUBLICATIONS

A CURRENT AWARENESS BULLETIN
OF RESEARCH OUTPUT

@DTU

(150th Edition)

JUNE 2025

BY: CENTRAL LIBRARY

DELHI TECHNOLOGICAL UNIVERSITY

(FORMERLY *DELHI COLLEGE OF ENGINEERING)*
GOVT. OF N.C.T. OF DELHI
SHAHBAD DAULATPUR, MAIN BAWANA ROAD
DELHI 110042

PREFACE

This is the **One Hundred Fifth** Issue of Current Awareness Bulletin started by Delhi Technological University, Central Library. The aim of the bulletin is to compile, preserve and disseminate information published by the faculty, students and alumni for mutual benefits. The bulletin also aims to propagate the intellectual contribution of Delhi Technological University (DTU) as a whole to the academia.

The bulletin contains information resources available in the internet in the form of articles, reports, presentations published in international journals, websites, etc. by the faculty and students of DTU. The publications of faculty and student which are not covered in this bulletin may be because of the reason that the full text either was not accessible or could not be searched by the search engine used by the library for this purpose.

The learned faculty and students are requested to provide their uncovered publications to the library either through email or in CD, etc. to make the bulletin more comprehensive.

This issue contains the information published during **June,2025**. The arrangement of the contents is alphabetical. The full text of the article which is either subscribed by the university or available in the web is provided in this bulletin.

Central Library

CONTENTS

1. An Integrated CNN-BiLSTM-Transformer Framework for Improved Anomaly Detection using Surveillance Videos, Sarfaraz Natha, 7***.1 Mohammad Siraj***, Fareed Ahmed, Majid Altamimi and Muslim Syed, Computer Technology and Applications, DTU

2. A Nature-Inspired Multi-Objective Gree nRouting Protocol for Iot-Enabled SDWSNs, ***3.Rohit Beniwal, 6.Nitesh Kumar***, Computer Science, DTU

3. A novel reciprocal linguistic cloud model and its integration with machine learning, ***6.Shweta Kalson, 3.Anjana Gupta***, Applied Maths, DTU

4. Attention-augmented squeeze-and-excitation enhanced mobile network for occluded facial expression recognition in resource-constrained environments, ***6.Ashi Agarwal,·3.Seba Susan***, IT, DTU

5. A simple 5D autonomous hyper chaotic system:dynamical analysis, synchronization via adaptive integral sliding modecontrol, andcircuit realization, Dinesh Khattar, ***3.Naokant Deo*** and ***6.Mukul Sirohi***, Applied Maths, DTU

6. An effective dual-droop control for voltage source converter-based multi-terminal DC system, ***6.Ashima Taneja, 3.Radheshyam Saha*** and ***3.1 Madhusudan Singh***, Electrical, DTU

7. Advancing Smart Farming with UAV-Based Deep Learning for Proactive Wheat Disease Management, ***8.Rohan Thakur, 8.Ronald Ekka, 8.Yash Kumar*** and ***3.Poornima Mittal***, ECE, DTU

8. A Review Of Chemical Recycling Pathways For Waste Polyurethane, ***6. Karnam Bharti***, ***3. Raminder Kaur***, Applied Chemistry, DTU

9. Adaptive WaterwheelPlant Optimization for Enhanced Region Selection in Robust Video Watermarking, ***6.Khushboo Chhikara*** & ***3.Manoj Kumar***, CSE, DTU

10. A STUDY OF KEY FACTORS DRIVING E-COMMERCE ADOPTION TO BOOST MSMES PERFORMANCE: AN ISM AND MICMAC ANALYSIS, ***6.Lavi Vats, 3.Ratnam Mishra***, Shekhar Tokas, USME, DTU

11. Advancing biofuel production through nanomaterials: a review of efficiency improvements, challenges, and future directions, Ashish Goyal, ***6.1Pradeep Kumar Meena***, Sagar Shelare and Sujeet Kumar, Mechanical, DTU

12. Ag@SnO2/g-C3N4T ernary Nano compositeas an Efficient Acetone Vapors Sensor, , ***6. Shivani Sangwan,6.Gagan Sharma, 6.Mohit Kumar,3.Deshraj Meena, 7.Yoshita Katiyar ,7.Anshika Goyal*** & ***3.Manish Jain***, A Physics, Chemistry, DTU

13. An IoT-Based Edge Computing Lossless Compression Approach for Enhancing Energy Efficiency in Networks, ***6.Mukesh Sahu & 3.Jeebananda Panda***, ECE, DTU

14. Assessment of Seismic Performance in Buildings with Plan Irregularities, ***8.Vipul Chandra*** and ***3.Hrishikesh Dubey***, Civil, DTU

15. Autonomous UAV Navigation and Mapping for Accurate Fruit Detection and Counting in Controlled Environments: Simulation and Real-World Validation, ***8.Kush Garg, 8..Nishant Chandna, 8.Somin Aggarwal, 8.Chirag Sehgal, 8.Arjun Gupta and 3.Prof. Rajesh Rohilla,*** Applied Mathematics, Mechanical, IT, CS, ECE, DTU

16. Assessment of Groundwater and Soil Contamination Due to Leachate Migration around Ghazipur Landfill: A Comprehensive Analysis Using WAWQI and SQI Models, ***6. Shraddha Sharma, 3.Geeta Singh*** & Gauhar Mehmood, ENVT. DTU

17. Breast Cancer Detection using T-gated Reconfigurable Field Effect Transistor-based Biosensor, ***6.Vijay Thakur, 3.Deva Nand***, Electrical and electronics, DTU

18. Compact planar UWB microstrip antenna with independently controllable dual notch bands, Subhajit Paul, ***7.1 SandeepRana***, Amit Ranjan Azad, Dalia Nandi and Akhilesh Mohan, ECE, DTU

19. Classifying Android Malware Categories through Dynamic System Calls Ranked via ReliefF***, 6.Yash Sharma and 3.Anshul Arora***, Applied Maths, DTU

20. Design of Dual Gate Mixer with Ambipolar Virtual Source Graphene Field Effect Transistor, ***6.Arjun Lal Kumawat, 3.Anukul Pandey*** and ***3.N.S.Raghava***, ECE, DTU

21. DynaMentA: Dynamic Prompt Engineering and Weighted Transformer Architecture for Mental Health Classification Using Social Media Data , Akshi Kumar, ***6.1 Aditi Sharma*** and ***7.1 Saurabh Raj Sangwan***, Computer Science, DTU

22. Design optimization of surface-inset type-PMSMusing scalarization and novel metaheuristic algorithm for two-post lift application, ***3.Monika Verma***, Electrical, DTU

23. Design of hybrid LMS-SOGI-basedphase-locked loop tested underadverse grid conditions, ***6.Oinam Lotika Devi*** and ***3.Alka Singh,*** Electrical, DTU

24. Devicemodelling andoptimization ofnewlead-free(NH4)3Sb2I9 perovskite solar cells by using SCAPS-1D software, ***6.Sumit Singh*** , ***6.Rahul Kundara*** and ***3.Sarita Baghel,*** Applied Physics, DTU

25. Design and Analysis of mm-Wave MIMO Antenna with a UWB AMC, ***6.Rohit Khandekar, 3.Deepika Sipal***, ECE,DTU

26. Disclosure without Engagement: An Empirical Review of Positionality Statements at FAccT, Hope Schroeder***, 8.Akshansh Pareek***, Solon Barocas, Design, DTU

27. Experimental and Numerical Investigations for Laser Bending of a Three-Ply Clad Sheet Metal, ***6. Praveen Kumar Singh, 3.Vijay Gautam***, Mechanical, DTU

28. Experimental and Numerical Analysis of Springback of AA1050-Fly Ash Green Composite Produced by Stir Casting Technique, ***6.1 Pankaj Kumar Sharma***, ***3.Vijay Gautam***, ***6.Subhajit Konar***, Vinita Bhardwaj, Amit Kumar Sharma, and Shashi Prakash Dwivedi, Mechanical, DTU

29. Enhancement of Wear Properties of Dissimilar SSDS 2507-IN718 Alloy Wall Via Ultrasonic Vibration Assisted Cold Metal Transfer Based Wire Arc Additive Manufacturing, ***3.Rajendra Prasad, 3.N. Yuvaraj, 3.Vipin*** and ***3.Qasim Murtaza,*** Mechanical, DTU

30. Enhancing Security and Scalability of IoMT Systems Using Blockchain: Addressing Key Challenges and Limitations, Harshit Kumar, Harsh Kumar, Harish***,*** ***6.Himanshu Nandanwar*** and ***3. Rahul Katarya,*** Computer Science, DTU

31. Establishment of measurement traceability of dielectric constant measurement using contact and non-contact methods, Satish, Rajendra S. Meena, ***8.1 Reva Singh***, Priyanka Jain, Joges C. Biswas, ECE, DTU

32. Effect of Interface Trap Charges on Improved Junctionless Nanowire Field Effect Transistor, ***6. Bharti, 3.Poornima Mittal***, ECE, DTU

33. Energy, exergy, energy matrices, exergoeconomic, and enviroeconomic (5E) analysis of active solar distiller using water loaded nanoparticles: A comparative study, Dharamveer Singh, Aakersh Chauhan, Ashok Kumar Yadav***, 3.S. Samsher***, and Ashish Dewangan Aqueel Ahmad, Mechanical, DTU

34. Energy Efficient Dynamic Logic based on TGDI Cell for Portable Electronics***, 6.Y. Parmar, 3.N. Pandey***, ECE, DTU

35. Gallium Nitride Gate-All-Around Macaroni Field Effect Transistor (GaN-GAA-MCFET): Biosensor for DNA detection, ***6.1 Shivani Yadav, 6.Vijay Thakur, 6.Aapurva Kaul,*** Amit Das, ***3.Sonam Rewari*** and ***3.Deva Nand***, ECE, DTU

36. Gig-economy integration: organizational development strategies for a f luid workforce, ***8.1 Uday Sai Garavandala,*** BBA, DTU

37. GIS- Based Landslide Susceptibility Mapping of Almora District in India: A Comparison of Different Techniques, ***6. Sandeep Panchal, 3. Amit Kr. Srivastava,*** Civil, DTU

38. Highly Sensitive Electrochemical Detection of Hydroquinone in Wastewater Using Ionic Liquid Grafted rGO-ZrO2 Nanohybrid-Based Conducting Paper, Mohd. Jamshaiya Raza, ***6.Owais Jalil***, Riyazuddeen, ***3.Devendra Kumar*** and Chandra Mouli Pandey, Applied Chemistry, DTU

39. HyperSwin: preventing deepfake proliferation with swin-efficient fusion in a hyperledger ecosystem***, 8.1Kartik Bindra, 8.Hitesh Gupta, 8.Devyansh Bhattacharya*** and ***3.Rahul Thakur,*** Computer Science, Mathematics, Physics, ECE, DTU

40. Investigating the performance vs. computational complexity tradeoff in cross-domain fire risk detection***, 6.Abhishek Verma, 3.Virender Ranga*** and ***3.Dinesh Kumar Vishwakarma***, IT, DTU

41. Investigation Temperature variation on DC and Analog performance of Gate Stack GNRFET using DFT-based atomic scale Modelling, ***6.Anshul, 3.Rishu Chaujar***, Applied Physics, DTU

42. Investigation of temperature-dependent performance degradation in AlGaN/InGaN/GaN HEMTs: Implications for device reliability and efficiency, Neda Ahmad, ***3.Sonam Rewari*** and Vandana Nath, ECE, DTU

43. Junctionless Spacer-Engineered SOI FinFET-Based Hydrogen Gas Sensor: Electrical Characterization and Sensitivity Analysis***, 6.Ayushi Lamba, 3.Rishu Chaujar*** and M. Jamal Deen, Applied Physics, ECE, DTU

44. Low leakage Schmitt trigger logic circuits design with improved noise immunity for energy-constrained applications, ***6.Bhawanand Jha***, Kirti Gupta and ***3.Rajeshwari Pandey***, ECE, DTU

45. Machine Learning-Driven Surrogate Modeling and Quantum Metaheuristics for Gurney Flap Optimization in Darrieus Wind Turbines, ***8.Subhrajit Roy, 8.Siddharth Joshi, 8.Vishal Jaiswal*** and ***3.Raj Kumar Singh***, Mechanical, DTU

46. Molecular docking and molecular dynamics simulation studies of thiazole-coumarin and thiazole-triazole conjugates against Mpro and ACE2 receptor for SARS COV-2***, 6.Deepak Mishra, 3.Ram Singh,*** Nupur S. Munjal, Naresh Kumar,· Prashant Kumar, ***3.Poonam*** and Sandeep Sharma, Applied Chemistry, DTU

47. Machine Learning-Driven Surrogate Modeling and Quantum Metaheuristics for Gurney Flap Optimization in Darrieus Wind Turbines, 8***.Subhrajit Roy, 8.Siddharth Joshi, 8.Vishal Jaiswal*** and ***3.Raj Kumar Singh***, Mechanical, DTU

48. Modeling of Multiport DC- DC Converter With Improved Fault- Tolerant Capability and Minimized Current Ripple Considering Circuit Parasitic, ***8.1.Rishabh Bansal 8.1Rushiv Bansal*** and ***3.Mayank Kumar***, Electrical Engg., DTU

49. ML-based prediction of scour depth around a cylindrical bridge pier: A comparative analysis of ANN, SVM, and Ensemble Trees, ***6.Geeta Devi, 3.Vijay Kaushik***, Civil, DTU

50. MoSWIN: Monkey Search Optimization and SWIN-based Flood Classification Architecture***, 6.Vinay Dubey, 3.Rahul Katarya,*** Computer Science, DTU

51. Model Predictive Control of Coal Fired Organic Rankine Cycle Systems, Zariro Manzungu , ***7.1 Victor Kuno***, Nano Science, DTU

52. Numerical simulation study of dispersive waves in presence of magnetic islands***, 6.NehaPathak,6.Jyoti, 3.Suresh C. Sharma*** and R.P. Sharma, Applied Physics, DTU

53. Numerical Simulation for Analog Performance Assessment of Vertically Stacked FeFinFET, ***6.Kajal Verma, 6.Yash Pathak*** & ***3.Rishu Chaujar,*** Applied Physics, DTU

54. On the Prediction of Temporal Dynamics of Turbulent Flows using a Hybrid Temporal Architecture (TurboNet), 8.Shubhanshu Rao, ***8.Subhrajit Roy, 8.Vishal Kumar Roy and 3.Raj Kumar Singh***, Mechanical, DTU

55. Optimization-based noise filtering among user-centric tweets to improve predictions in recommendation system ***6.Kirti Jain, 3.Rajni Jindal,*** Computer Science, DTU

56. Optimization, simultaneous saccharification and fermentation of Lemna minor using amylolytic cocktail produce from copra meal, ***6. Manjary Vyas, 3.Kriti Bhandari & 3.Jaigopal Sharma***, Biotechnology, DTU

57. Synthesisof Pyridazine- Based Scaffolds Using Electron Demand Diels–Alder (iEDDA) Reaction Possessing Promising Antimicrobial Activity, Ram Kumar, ***6.Deepak Gupta***,Yukta Yukta, Avneesh Mittal,Balaram Pani and Bholey Singh, Applied Chemistry, DTU

58. Studying Kangen Technology Dissemination in Indian Subcontinent: A Mathematical Modeling Framework, ***6.Saurabh Pandey, 3.Deepti Aggrawal***, USME, DTU

59. The Role of Databases in Cybersecurity and Threat Detection: Advancements through Spanner Graph Technology, ***8.1 Pushap Goyal***, Computer science, DTU

60. Tool geometry optimization for enhanced mechanical properties in friction stir welding of carbon steel, Anmol Bhatia, ***3.Reeta Wattal***, Rajeev Kumar, Anant Prakash Agrawal and Saurabh Dewangan, Mechanical, DTU

61. Tow-Thomas-Controlled Single-Phase Solar Powered Microgrids: Performance Evaluation in Grid-Tied and Standalone Operations, ***8.Madhur Agarwal, 8.Neeraj Bhardwaj, 8.Moksh Bashista, 3.Ankita Arora, 3.Shatakshi***, Electrical, DTU

62. Thumba (Citrullus colocyntis) seed oil: A sustainable source of renewable energy for biodiesel production, ***3.Amit Pal, 3.S S Kachhwaha, 3.S Maj***i and M K G Babu, Mechanical, DTU

63. The unique modified seesaw test (MST) instrument for the direct assessment of rock's tensile strength utilizing ring-shaped specimens, PARVEEN KUMAR, ***6.Srijan Srijan***, Vanita Aggarwal & Baljit Singh Walia, Civil, DTU

64. Triple-band perovskite based chiral metasurface biosensor with multi-functionalities, ***6.Vishakha Sharma,*** ***3.Yogita Kalra*** and ***3.Ravindra Kumar Sinha***, Applied Physics, DTU

65. Ultrasensitive Electrochemical Detection of EpCAM Antigen Based on Anti-EpCAM Conjugated With Highly Flexible Ag@Ti3C2Tx Modified Conducting Paper Platform,***6.Sweety, 6.Divya Hudda*** & ***3.Devendra Kumar***, A Chemistry, DTU

66. Unveiling the landscape fragmentation and its impact on land surface temperature using machine learning approach in Kolkata Metropolitan Area (India), Anik Saha, Sunil Saha,· Arijit Das,· Sudipta Mandal, ***3.Raju Sarkar*** &· Manob Das, Civil, DTU

67. Universal IoT-Enabled Smart Battery Charging Optimization: Leveraging AI, Automata Theory, and Real-Time Data for Enhanced Lifespan and Efficiency, ***8.1 Divyansh Arora*** , Ananya Goswami , Mritunjay Ranjan, Arif Md Sattar, Design, DTU

68. Voltage Angle Based Power System Inertia Estimation Using Synchrophasor Technology, ***6.Nitisha Sudhir Darwade, 3.S.T. Nagarajan***, Electrical, DTU

1. *Vice Chancellor*
2. *Pro Vice Chancellor*
3. *Faculty*
4. *Teaching-cum-Research Fellow*
5. *Asst. Librarian*
6. *Research Scholar*
7. *PG Scholar*
8. *Undergraduate Student*

1.1. *Ex Vice chancellor*
2.1. *Ex Pro Vice Chancellor*
3.1. *Ex Faculty*
4.1. *Alumni*
5.1 *Others*
6.1. *Ex Research Scholar*
7.1. *Ex PG Scholar*
8.1. *Ex Undergraduate Student*

Check for updates

Transactions on Emerging Telecommunications Technologies

WILEY

RESEARCH ARTICLE

A Nature-Inspired Multi-Objective Green Routing Protocol for Iot-Enabled SDWSNs

Rohit Beniwal | Nitesh Kumar

Department of Computer Science and Engineering, Delhi Technological University, New Delhi, India

Correspondence: Nitesh Kumar (nit.wadhera@gmail.com)

Received: 31 May 2024 | **Revised:** 13 December 2024 | **Accepted:** 24 May 2025

Funding: The authors received no specific funding for this work.

Keywords: clustering | green computing | internet of things | SDN | SDWSNs | wireless sensor networks

ABSTRACT

A smart city leverages technology and data to enhance the quality of life for its residents, improve urban services, and optimize resource management. The rapid rise in Internet of Things (IoT) devices has led to a significant surge in energy requirements, making energy optimization critical to mitigate this growing global demand. Clustering is a widely adopted technique to achieve energy optimization in IoT-enabled Software-Defined Wireless Sensor Networks (SDWSNs). In clustering, the network is divided into small groups, and a Cluster Head (CH) is chosen by a Control Station (CS) to forward data packets from sensing nodes. The role of CH is power-consuming as it aggregates data from its cluster and forwards it to CS; this may lead to hot-spot problems. Therefore, it is very important to select CH wisely. Hence, this article proposes an EO-C algorithm to address multiple objectives like hot-spot problems, network life, energy optimization, and reliability. EO-C aims to enhance energy efficiency in IoT-enabled SDWSNs by dynamically optimizing the selection process of CH using a novel fitness function based on residual energy, energy balance ratio, and alive node count. The simulation findings demonstrated that EO-C surpasses other SOA algorithms with an improvement in network lifespan ranging from 15.86% to 372.6%, showcasing its effectiveness across various scenarios. Additionally, EO-C exhibits robust scalability, effectively handling diverse node densities and deployment areas, making it a promising solution for sustainable IoT networks.

1 | Introduction

Today, the demand for IoT devices and their applications is rapidly increasing. Some of the applications of IoT-based networks include intelligent transit systems [1], industrial automation [2], healthcare [3], smart homes [4], intelligent farming [5, 6], environmental monitoring [7], etc. Due to their wide range of applications, IoT-based networks have become important in our everyday lives. At the heart of IoT devices lies their ability to make informed decisions based on data gathered through sensors or sensor networks. The growing IoT ecosystem demands the complex structure of Wireless Sensor Networks (WSN) [8]. WSN consists of sensor nodes that sense and route data but have limited connectivity, storage, and processing capabilities. Managing extensive IoT device networks, particularly in scenarios like WSNs operating in remote or inaccessible locations, poses significant challenges, including energy constraints, network scalability, network security [9], and data transmission reliability [10]. As WSN complexity grows, manual management and maintenance of dense networks become unfeasible in real-time. The SDWSNs address the constraints of standard WSNs by separating the data plane and control plane. The data plane

Abbreviations: IoT, internet of things; SDWSNs, software defined wireless sensor networks; WSN, wireless sensor networks.

© 2025 John Wiley & Sons Ltd.

collects and transmits data, while the control plane contains the device's operating logic. This separation makes it possible to update these devices remotely. Hence, it provides auto-control and monitoring capabilities in the network. SDWSNs replace conventional sensor nodes with Software Defined Sensor Nodes (SDSNs) [11] that automate network real-time monitoring and dynamic reconfiguration of SDSNs.

The integration of IoT with SDWSNs opened up a new world of possibilities. Recent studies [12, 13] show that the number of these devices is increasing exponentially due to their vast applications. These devices generally run on battery power or electricity; hence, energy conservation has become a major challenge in IoT-enabled SDWSNs. One effective solution to address this challenge is clustering [14]. In clustering, the network is divided into small clusters with a CH. Calculating the number of clusters required to transfer data to CS efficiently is a significant challenge in these networks [15]. The responsibility of CH is to collect the data from member nodes and forward it to CS. However, the role of the CH is highly energy-intensive, which can lead to uneven energy consumption across the network. This imbalance often causes a hot-spot issue, where certain CHs, due to their location, deplete their energy much faster than others. This issue not only disrupts network connectivity but also reduces the overall network lifespan. Therefore, selecting CHs strategically is crucial to maintaining energy balance, mitigating hot-spot problems, and enhancing network performance. In this research paper, we propose a new nature-inspired Equilibrium Optimization-based Clustering (EO-C) algorithm for energy-efficient routing in IoT-enabled SDWSNs. EO-C is based on the equilibrium optimizer algorithm [16]. EO-C intelligently selects CHs based on factors like energy, energy balance ratio, and alive nodes. The key contributions of the research paper are:

- This research work introduces an energy-efficient EO-C algorithm. The goal of this algorithm is to improve the network's life and mitigate the hot-spot problem.
- A novel fitness function is proposed, which is based on constraints such as total residual energy, energy balance ratio, and alive node count.
- EO-C dynamically selects the optimum cluster count based on network conditions.
- The performance of the EO-C algorithm is evaluated under various conditions to validate its effectiveness.
- The experimental study provided evidence that EO-C outperformed other state-of-the-art (SoA) methods

The paper is structured as outlined below: The literature review is discussed in Section 2, and Section 3 provides the preliminaries of the network and energy models used in this research article. The proposed model is discussed in Section 4. Section 5 covers performance analysis, encompassing simulation parameters, performance of EO-C, and comparative analysis. Section 6 concludes the research paper.

2 | Literature Survey

2.1 | Classical Approaches

In the realm of wireless sensor networks, energy efficiency and network longevity are critical factors that determine the viability and performance of these networks [17]. Prolonged network longevity directly impacts the network's ability to provide continuous data collection and monitoring over extended periods, which is essential for applications like environmental monitoring, healthcare, and industrial automation [18]. Clustering the network into small sub-networks with a CH is a way to improve network life and achieve energy efficiency. The Low-Energy Adaptive Clustering Hierarchy (LEACH) protocol, proposed by Heinzelman et al. [19], is one of the pioneering approaches in this domain and serves as a benchmark clustering algorithm. LEACH enhances the energy efficiency and lifetime of WSNs by selecting CHs based on a predetermined probability, thereby preventing the CHs from depleting energy too quickly. However, a limitation of LEACH is that it may repeatedly select the same CH, causing excessive energy drain for certain nodes. To address this limitation, Manjeshwar and Agrawal [20] proposed a Threshold-sensitive Energy-Efficient sensor Network (TEEN) protocol. Their research works also provided comprehensive insights into the trade-offs between TEEN and LEACH, particularly in terms of energy efficiency and network durability in different operating circumstances.

Younis and Fahmy [21] introduced a Hybrid Energy-Efficient Distributed clustering approach (HEED). HEED selects CH based on node proximity and residual energy. The simulation results show that HEED effectively extends the network lifespan. Muruganathan et al. [22] contributed to this discourse by presenting a centralized energy-efficient routing protocol named base station controlled dynamic clustering protocol. They extended the network life by distributing the energy dissipation equally among all the sensor nodes.

Chen et al. [23] introduced an unequal cluster-based routing protocol for WSNs specifically designed to address the energy imbalance issue. In their work, they proposed the formation of variable-size clusters, with node distance from the base station serves as a criterion for the selection of CH. The simulation result showed that unequal clustering can mitigate the hot-spot problem and enhance the network life. Haseeb et al. [24] proposed weighted energy-efficient clustering with a robust routing protocol, which optimizes the CH selection process by considering node energy, proximity to the base station, and local node density. Their approach increased the network lifespan at least by 12.3%. To address the hot-spot problem in WSN, an unequal fixed grid-based clustering algorithm was introduced by Singh et al. [25]. In their algorithm, unequal clusters were created to reduce the load on nodes closer to the BS while also preserving the energy of nodes located away from the BS. Results showed that the fixed grid-based approach improved energy efficiency, network lifespan, and load balancing in WSNs. One of the major challenges with these devices is the deployment of these devices

21613915, 2025, 6, Downloaded from https://onlinelibrary.wiley.com/doi/10.1002/ett.70199 by Delhi Technological University, Wiley Online Library on [26/06/2025]. See the Terms and Conditions (https://onlinelibrary.wiley.com/terms-and-conditions) on Wiley Online Library for rules of use; OA articles are governed by the applicable Creative Commons License

at remote locations, and this made it very difficult to manually update every device. Flauzac et al. [26] proposed a solution by integrating Software-Defined Networking (SDN) with Wireless Sensor Networks (WSNs) in IoT environments. They introduced the Software-Defined Networking Clustered Head (SDNCH) concept and also evaluated the effectiveness of SDN deployment in IoT clusters.

2.2 | Meta-Heuristics-Based Approaches

In this section, the application of various nature-inspired approaches in the domain of WSN or IoT-SDWSNs is discussed. As we discussed in the previous section, it is always efficient to divide WSN into clusters compared to the direct transmission method. But selecting CH is an NP-hard problem. This problem can be solved with the help of a meta-heuristic-based algorithm. Xiang et al. [27] presented an energy-efficient routing algorithm for SD-WSNs based on Particle Swarm Optimization (PSO) [28]. In their work, PSO was used to select the CH dynamically to optimize residual energy and transmission distance. Rao and Banka [29] introduced a modified version of the novel chemical reaction optimization algorithm to address the hot-spot problem. To optimize the network performance, they created smaller clusters near the base station and larger clusters for nodes that are far away from the base station. The results showed improved network lifetime, energy distribution, and packet delivery compared to SoA algorithms. Yogarajan and Revathi [30] presented an enhanced clustering and data collection algorithm for WSN using discrete ant lion optimization. Their approach optimizes cluster head selection by minimizing routing path length, which improves network lifetime, throughput, and energy efficiency. Agrawal et al. [31] proposed the Grey Wolf Optimizer-based Clustering algorithm (GWO-C). GWO-C focuses on CH selection to improve network lifetime and energy efficiency. To achieve this goal, they introduced an objective function based on sink distance, intra-cluster distance, residual energy, and CH balancing factor.

Mishra et al. [32] introduced the Energy Balanced Grey-Wolf Optimization (EBGWO) algorithm for green routing in SDWSNs. EBGWO enhances network lifespan and efficiency through optimized cluster head selection using CS to CHs distance, node residual energy, intra-cluster distance, and cluster size. It demonstrated superior performance in terms of residual energy, network lifespan, and throughput compared to the NW-PSO, PSO, and LEACH protocols. Abdulzahra et al. [33, 34] introduced various clustering and CH selection techniques for WSN-based IoT by integrating fuzzy logic and meta-heuristic methods. Their EFUCSS protocol employs fuzzy-based unequal clustering and sleep scheduling, achieving up to a 408.13% improvement in network lifespan. Similarly, their FONIC [35] protocol combines fuzzy logic with the Penguin Search Optimization Algorithm (PeSOA) to enhance CH selection based on fitness metrics like energy, centrality, and distance, outperforming protocols such as FIGWO and LEACH-PRO in packet delivery and longevity. Roberts et al. [36] introduced a dual-phased hybrid optimization framework combining Sailfish Optimization (SFO) and Spotted Hyena Optimization (SHO). This approach leverages SFO's rapid exploration for efficient CH selection and SHO's refined exploitation for routing optimization, achieving significant improvements in packet delivery ratio, energy efficiency, and network lifetime. Xiao et al. [37] presented BS-SCRM, a secure clustering routing method that integrates blockchain with a Whale Optimization Algorithm (WOA). BS-SCRM significantly enhances network security and efficiency, achieving a 24%–73% improvement in network lifetime under various attack scenarios.

WSN nodes near the CS or BS are often selected repeatedly, leading to the hot-spot problem, which can cause early network failure. To handle this issue, Jain et al. [38] presented a research paper based on Harris Hawk Optimization (HHO). They introduced the Harris Hawk Optimization using Unequal Clustering and Routing Algorithm (HHO-UCRA). The aim of HHO-UCRA is to improve WSN's efficiency by addressing the hotspot problem through unequal clustering. The method optimizes CH selection and routing by using a fitness function that considers neighbor node distance, sink distance, and energy ratio. Balasubramanian and Govindasamy [39] introduced the Energy-Aware Farmland Fertility Optimization-based Clustering Scheme (EAFFO) to extend the network lifespan. EAFFO optimizes the clustering using a novel fitness function based on the distance to neighbors, distance to the BS, and node energy.

2.3 | Major Challenges

After studying the literature, we recognized that the following are some of the important challenges that need to be addressed:

- **Network Life:** Extending the life of a network is a significant challenge in IoT-enabled SDWS networks. As the network is made up of a number of small devices, it is necessary to manage energy consumption at the nodes. Ensuring balanced energy consumption across the network not only helps prevent premature node failures but also maintains connectivity and overall network functionality for an extended period. Addressing this challenge is vital for achieving reliable and sustainable network operations.
- **Hot-Spot issue:** One of the major challenges in IoT-enabled SDWSNs is the hot-spot issue. This happens due to the uneven distribution of workload over the network. As nodes in high-traffic areas, or hot spots, are burdened with more data processing and transmission tasks, which leads to faster energy depletion and potentially disrupting network performance. Addressing this issue is critical to ensuring balanced energy consumption and prolonging the overall lifespan of the network.
- **Optimum number of clusters:** As direct transmission to the CS may lead to early failure of nodes, clustering provides an efficient method of communication in IoT-enabled SDWSNs. We can improve the efficacy of the network by dividing it into an optimum number of clusters.
- **Energy conservation:** As the number of IoT devices will increase exponentially in the coming years due to its vast applications. Although an individual IoT device consumes very little energy, but collectively their energy consumption is high. Therefore, it is necessary to minimize their energy consumption.
- **Reliability:** Reliability is one of the important issues in IoT-enabled SDWSNs. Sometimes, the failure of one node

21613915, 2025, 6, Downloaded from https://onlinelibrary.wiley.com/doi/10.1002/ett.70199 by Delhi Technological University, Wiley Online Library on [26/06/2025]. See the Terms and Conditions (https://onlinelibrary.wiley.com/terms-and-conditions) on Wiley Online Library for rules of use; OA articles are governed by the applicable Creative Commons License

may lead to the failure of the entire network. Therefore, it is a challenge for IoT-enabled SDWSNs to stay alive. Therefore, testing the proposed algorithm under various conditions is required to prove its reliability.

In this research paper, we propose a multi-objective green routing protocol (EO-C) for IoT-enabled SDWSNs. EO-C is inspired by the natural phenomenon of equilibrium. This method involves choosing CHs as an optimization problem, using the equilibrium optimizer [16] as its basis. We used a fitness function that considers three criteria to extend the network's lifespan: the distance between CHs and CS, the distance within clusters, and the residual energy of nodes.

3 | Preliminaries

This section presents the network model, energy model, and terminology used in the proposed algorithm.

3.1 | The Network Model

The network architecture of the IoT-enabled SDWSN is depicted in Figure 1. The integration of SDN principles in IoT introduced a groundbreaking element, particularly in the real-time modification of nodes within the network. Leveraging SDN, the network gains the capability to swiftly reconfigure and update nodes in real time, facilitating adaptive and responsive adjustments to evolving network conditions. This dynamic node management enhances the flexibility, scalability, and responsiveness of the IoT-enabled SDWSNs, ensuring an optimal and robust network infrastructure. In Figure 1, the IoT-enabled SDWSN architecture portrays the wireless connections of nodes with CS via CH. The network model is based on clustering to minimize energy consumption, where Normal Nodes (NN) monitor the environment and transmit sensory data to the cluster heads, aiding in data aggregation before transmission to the base station. The CH aggregates the data received from CN and forwards it to the CS. The task of CS is to collect data, select CH, and create clusters. Here are the assumptions regarding the network:

- All deployed nodes in the network architecture are homogeneous, possessing equivalent energy, computational capability, and data transmission range.
- $|IoT - SDWSNs| = |BS| \cup |CH| \cup |NN|$ and each device has identification number $I = 1, 2, 3 \ldots, i, \ldots, N$
- All the nodes CHs and SDSN are stationary.
- The CS is on external power.
- All nodes are deployed randomly in the area.
- Every node inside the SDWSNs has the capability to function in either sensing mode or communication mode.
- The task of SDSNs is to sense the assigned parameter and then communicate that data to CHs or Control Stations using wireless communication links. If the SDSN acts as a CH, it gathers the information from all the SDSNs in the cluster and then transmits it to the CS.
- Each SDSN is without GPS.

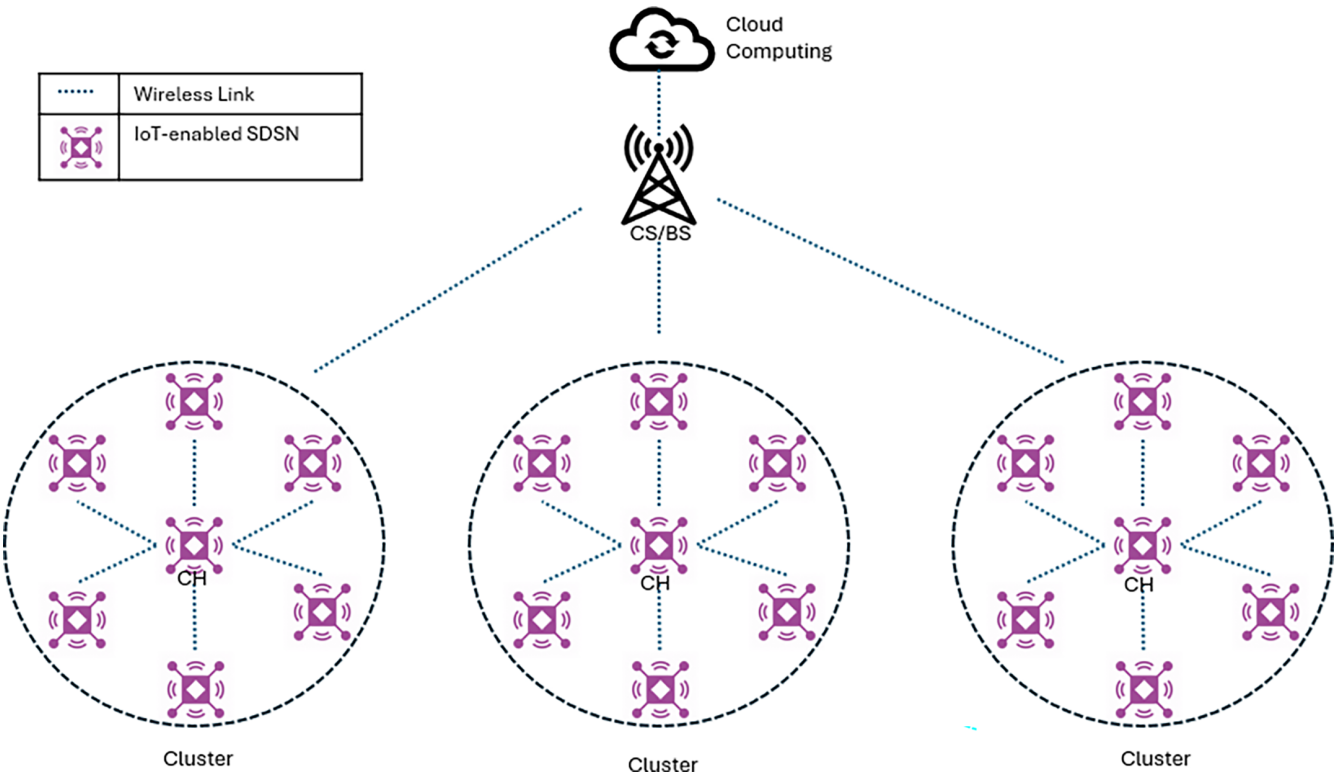


FIGURE 1 | An Illustration of an IoT-SDWSNs scenario with a CH and CS.

21613915, 2025, 6, Downloaded from https://onlinelibrary.wiley.com/doi/10.1002/ett.70199 by Delhi Technological University, Wiley Online Library on [26/06/2025]. See the Terms and Conditions (https://onlinelibrary.wiley.com/terms-and-conditions) on Wiley Online Library for rules of use; OA articles are governed by the applicable Creative Commons License

3.2 | The Energy Model

In this research paper, the energy model used for data communication is designed around the path attenuation model [40]. This model helps to estimate the energy required for transmitting data by considering how the signal weakens or loses strength as it travels over a distance. By incorporating the path attenuation model, the energy consumption for communication can be more accurately calculated, ensuring efficient use of resources in the network.

$$s(i,j) = \sqrt{(x_j - x_i)^2 - (y_j - y_i)^2} \tag{1}$$

Here,(x_i, y_i) and (x_j, y_j) is the location of transmitter and receiver, respectively. In addition, path loss may be compensated by using the power control mechanism. In this model, the free space model is applied if d is less than a threshold distance (s_{th}); else, the multi-path energy model gets employed. The energy consumption $E^{ij}_{SSDN_{TX}}$ for a general SSDN node to transmit k-bit data over distance (s) is calculated using the following Equation (2).

$$E_{SSDN_{TX}} = \begin{cases} k * E_{elec} + k * E_{mp} * s^4, & \text{for } s \geq s_{th}. \\ k * E_{elec} + k * E_{fs} * s^2, & \text{otherwise} \end{cases} \tag{2}$$

The energy consumption by the control node, $E_{CH_{TX}}$, for transmitting k-bits over distance, s, is calculated using Equation (3).

$$E_{CH_{TX}} = \begin{cases} k * (E_{elec} + E_{DA}) + k * E_{mp} * s^4, & \text{for } s \geq s_{th}. \\ k * (E_{elec} + E_{DA}) + k * E_{fs} * s^2, & \text{otherwise} \end{cases} \tag{3}$$

Where E_{DA} is the energy consumed in data aggregation by control nodes. The threshold distance s_{th} was calculated using Equation (4).

$$s_{th} = \sqrt{\frac{E_f}{E_m}} \tag{4}$$

Where E_f and E_m represent free space amplification energy and amplification energy for multi-path models, respectively.

4 | The Proposed Model

The Equilibrium Optimizer Clustering (EO-C) algorithm is discussed in this section. EO-C is based on the equilibrium optimizer algorithm by Faramarzi et al. [16]. The equilibrium optimizer algorithm is a meta-heuristic optimization method based on physics' fundamental principle of equilibrium. It is designed to identify the most favorable solution for a specific optimization problem by emulating the behavior of particles with different concentrations as they approach the state of equilibrium. By incorporating these principles, EO-C optimizes the clustering process in IoT-SDWSNs using the principle of exploration and exploitation within the framework of meta-heuristic optimization.

Algorithm 1 explains the pseudocode of the EO-C algorithm, which is structured into two main phases: initialization and optimization. Figure 2 illustrates the detailed flowchart of the EO-C algorithm, outlining its sequential workflow. The process begins with the initialization phase, where the network parameters, particle population, and the number of CHs are initialized randomly (explained in Subsection 4.1). Following this, the algorithm assigns initial fitness values and equilibrium candidates to the particles. In the optimization phase (explained in Subsection 4.2), the process begins by identifying the best CH candidate nodes using the Smallest Position Value (SPV) rule [41]. In the following step, the fitness of each particle is recalculated using the fitness function, which is explained in Subsection 4.3. The algorithm

ALGORITHM 1 | Equilibrium optimizer clustering.

Input: $Network\ Model,\ Nodes$
Output: $Optimal\ selection\ of\ CHs\&\ cluster\ count$

Initialize the particles and randomly initialize their concentrations using Equation (5)
Set $a_1 = 2$, $a_2 = 1$, and $GP = 0.5$
while $Itera < Max_{\text{iter}}$ **do**
  $n_{CH} = rand[min(5, ceil(alive * 0.1)), max(ceil(alive * 0.25), 1)]$
  for $i = 1$ to number of particles **do**
    $chList = SPV[n_{CH}, C_i]$
    Calculate the fitness of the i_{th} particle. $fit(C_i) = fitness(C_i, NetworkModel, n_{CH}, chList)$
    if $\text{fit}(C_i) < \text{fit}(C_{\text{eq1}})$ **then**
      $C_{\text{eq1}} = C_i$
      $\text{fit}(C_{\text{eq1}}) = \text{fit}(C_i)$
    else if $\text{fit}(C_i) > \text{fit}(C_{\text{eq1}})$ & $\text{fit}(C_i) < \text{fit}(C_{\text{eq2}})$ **then**
      $C_{\text{eq2}} = C_i$
      $\text{fit}(C_{\text{eq2}}) = \text{fit}(C_i)$
    else if $\text{fit}(C_i) > \text{fit}(C_{\text{eq1}})$ & $\text{fit}(C_i) > \text{fit}(C_{\text{eq2}})$ & $\text{fit}(C_i) < \text{fit}(C_{\text{eq3}})$ **then**
      $C_{\text{eq3}} = C_i$
      $\text{fit}(C_{\text{eq3}}) = \text{fit}(C_i)$
    else if $\text{fit}(C_i) > \text{fit}(C_{\text{eq1}})$ & $\text{fit}(C_i) > \text{fit}(C_{\text{eq2}})$ & $\text{fit}(C_i) > \text{fit}(C_{\text{eq3}})$ & $\text{fit}(C_i) < \text{fit}(C_{\text{eq4}})$ **then**
      $C_{\text{eq4}} = C_i$
      $\text{fit}(C_{\text{eq4}}) = \text{fit}(C_i)$
    end if
  end for
  $C_{\text{avg}} = (C_{\text{eq1}} + C_{\text{eq2}} + C_{\text{eq3}} + C_{\text{eq4}})/4$
  Find $C_{\text{pool,eq}}$ using Equation (7)
  if $Itera > 1$ **then**
    Find t using Equation (10)
    for $i = 1$ to number of particles **do**
      Choose one candidate from $C_{\text{pool,eq}}$ (randomly)
      Generate random vectors λ and r
      Generate vectors E using Equation (9)
      Generate vectors GCP using Equation (13)
      Generate vectors G_0 using Equation (12)
      Generate vectors G using Equation (11)
      Update C using Equation (8)
    end for
  end if
  $Itera = Itera + 1$
  $bestFitness = \text{fit}(C_{\text{eq1}})$
end while

21613915, 2025, 6, Downloaded from https://onlinelibrary.wiley.com/doi/10.1002/ett.70199 by Delhi Technological University, Wiley Online Library on [26/06/2025]. See the Terms and Conditions (https://onlinelibrary.wiley.com/terms-and-conditions) on Wiley Online Library for rules of use; OA articles are governed by the applicable Creative Commons License

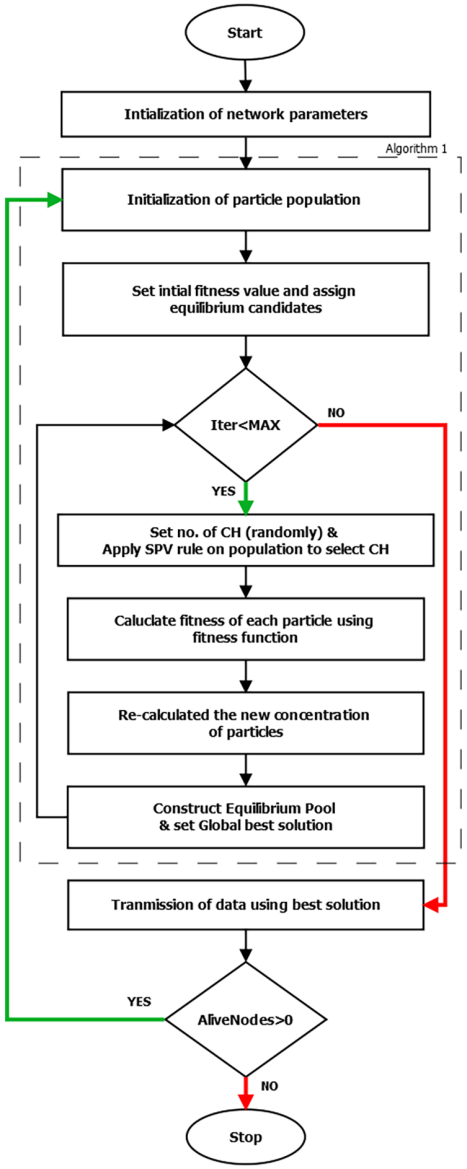


FIGURE 2 | EO-C flow chart.

subsequently updates the concentration of particles and constructs an equilibrium pool, selecting the global best solution to achieve optimization.

Once the global best solution is identified, the data transmission phase is executed using the best CH configuration. If nodes are alive, the process loops back to re-optimize and continue the transmission cycle; otherwise, the process terminates.

4.1 | The Initialization Phase

This phase starts with the initialization of n particles. The number of particles and the size of the search space define the initial particle concentrations. In the next step, the initial concentration of all n particles is randomly initialized with a uniform distribution across the search space using Equation (5).

$$C_i^{initial} = C_{\min} + rand * (C_{\max} - C_{\min}) \quad , for\ i = Natural\ Number\ upto\ n \tag{5}$$

C_i^{initial} denotes ith particle's initial concentration, where $rand$ is a random vector that lies within the [0, 1] range; $C_{\min}$ and $C_{\max}$ represents the minimal and maximum values of the dimensions. The number of particles in the population is represented by n.

4.2 | Optimization Phase

The equilibrium state refers to the ultimate convergence state of the algorithm [16], known as the global optimum. This phase is crucial for improving the algorithm's performance and convergence. The optimization process starts by entering into the main loop bounded by a maximum number of iterations, that is, (Max_{iter}). After entering the loop, it first randomly selects the number of clusters (n_{CH}) within a certain range based on the number of alive nodes using (6).

$$n_{\text{CH}} = \text{rand}\ [\min\ (5, \lceil \text{alive} \times 0.1 \rceil), \max\ (\lceil \text{alive} \times 0.25 \rceil, 1)] \tag{6}$$

where $alive$ is the total number of nodes with energy greater than 0.

During the second step, it calculates the fitness of each particle by executing the novel fitness function discussed in subsection 4.3. The particles are evaluated using the fitness function (fit) based on energy ratio, energy, and alive nodes. The third step starts with the creation of an equilibrium pool vector, $C_{pool,eq}$. During the initial stages of the optimization process, there is a lack of information regarding the equilibrium state. $C_{pool,eq}$ created using equation (7) by selecting the four best-so-far particles based on their fitness values $(C_{eq1}, C_{eq2}, C_{eq3}, C_{eq4})$ and arithmetic average (C_{avg}) of these four. The inclusion of these four candidates enhances the exploration capability, whereas the average candidate contributes to the exploitation aspect.

$$C_{\text{pool,eq}} = (C_{\text{eq1}}, C_{\text{eq2}}, C_{\text{eq3}}, C_{\text{eq4}}) \tag{7}$$

In the fourth step, the concentration for each particle is updated using Equation (8).

$$C = C_{\text{eq}} + (C - C_{\text{eq}}) * E + \frac{G}{\lambda V} * (1 - E) \tag{8}$$

Where $\lambda \sim [0, 1]$ is a random vector, and V is a unit vector. Here is a concise explanation of every element:

- **Equilibrium Component**: C_{eq}: The first term in Equation (8), C_{eq}, corresponds to the equilibrium concentration, serving as a reference point for the particle's concentration. It is calculated using Equation (7).
- **Exploration Component:** $(C - C_{\text{eq}}) * E$: The second term plays a crucial role in exploring the solution space globally, aiming to locate an optimum point. It emphasizes exploration by capitalizing on large concentration variations, such as the direct disparity between an equilibrium state and

21613915, 2025, 6, Downloaded from https://onlinelibrary.wiley.com/doi/10.1002/ett.70199 by Delhi Technological University, Wiley Online Library on [26/06/2025]. See the Terms and Conditions (https://onlinelibrary.wiley.com/terms-and-conditions) on Wiley Online Library for rules of use; OA articles are governed by the applicable Creative Commons License

a sampled particle. The exponential term, denoted as $\vec{E}$, is responsible for updating concentration and is calculated using the Equation (9).

$$\vec{E} = a_1 sign(\vec{r} - 0.5)\left[e^{-\vec{\lambda}t} - 1\right] \tag{9}$$

In Equation (9), the constant value a_1, specifically set to 2, represents the exploration capability. The second component, $sign(\vec{r} - 0.5)$, holds significant importance in determining both exploration and exploitation capabilities. Here, a random vector spanning a range of 0 to 1 is indicated by $sign(\vec{r})$. Using the Equation (10), the variable t is computed as a function of the iteration.

$$t = \left(1 - \frac{iter}{iterMax}\right)^{\left(a_2 \frac{iter}{iterMax}\right)} \tag{10}$$

In the given equation, $iter$ denotes the current iteration count, while $iterMax$ signifies the maximum iteration count in the optimization process. Furthermore, a_2 serves as a constant (typically set to 1), utilized to regulate the extent of exploitation capability.

- **Exploitation Component:** $\frac{G}{\lambda V} * (1 - E)$: Once a solution is identified, the third term fine-tunes the solution further. This term focuses on exploitation, leveraging minor concentration variations to enhance solution accuracy. It relies on generation rates, which are calculated using Equation (11) to navigate these subtle concentration changes effectively.

$$\vec{G} = \vec{G}_0.\vec{E} \tag{11}$$

Where $\vec{G}_0$ is the initial generation rate [16] and is calculated using the Equation (12).

$$G_0 = GCP * (C_{\text{eq}} - \lambda * C) \tag{12}$$

The generation rate control parameter, or GCP, is defined in Equation (13) as the generation term's potential contribution to the updating process.

$$GCP = \begin{cases} 0.5, & r_2 \geq GP. \\ 0, & else \end{cases} \tag{13}$$

Where $r1$ and $r2$ represent random numbers ranging from 0 to 1. The term Generation Probability (GP) represents the proportion of particles that used the generation term to update their states [16]. To achieve a balance between exploration and exploitation ($GP = 0.5$) is used [16]. This balance enables particles to explore the search space for better potential solutions while exploiting promising regions to effectively converge toward optimal solutions.

Finally, after updating the concentration of each particle, if the fitness of the updated particle is better than the old fitness value, the global best value is updated.

4.3 | Fitness Function

The fitness function is a foundational component of the EO-C algorithm, developed to optimize the selection of CHs in IoT-enabled SDWSNs. It addresses multiple objectives, including prolonging the network lifetime, mitigating the hot-spot problem, and maintaining energy efficiency across the network. The fitness function is mathematically formulated as:

$$\text{fitness} = \gamma \cdot f_1 + \delta \cdot f_2 + \eta \cdot f_3 \tag{14}$$

where f_1, f_2, and f_3 represent *total residual energy*, *energy balance ratio*, and *alive node count*, respectively. The weighting factors γ, δ, and η are used to balance the contribution of each criterion.

1. **Total Residual Energy (f_1):** The sustainability of the network significantly hinges upon the residual energy of its nodes. The Equation (15) gives the general formula for determining total residual energy, $E_{residual}$, which represents the first objective function f_1.

$$f_1 = E_{\text{totalCH}} + E_{\text{totalCommon}} \tag{15}$$

where E_{totalCH} and E_{totalNN} denote the residual energy of CH and normal nodes, respectively. By prioritizing configurations with higher residual energy, the fitness function ensures sustained operation of critical network components and extends the overall network lifespan. To determine the total remaining energy of the CH, whereas the calculation of the total residual energy of a normal node within the cluster is performed using Equation (17).

$$E_{\text{totalCH}} = \sum_{i=1}^{nCH} E^{iCS}_{CH_{TX}}(l, d) \tag{16}$$

The variables used in the calculation include nCH, which denotes the number of control nodes; l represents the number of bits; d, which indicates the distance between CH and CS; and $E^{iCS}_{CH_{TX}}$, which represents the residual energy in the ith node.

$$E_{\text{totalCommon}} = \sum_{j=1}^{nCHnNode} \sum_{i=1} E^{ij}_{SDSN_{TX}}(l, d_{i,j}) \tag{17}$$

Whereas the $d_{i,j}$ is the distance from the j^{th} CH and ith node; nNode rest of the nodes in the network excluding CH.

2. **Energy Balance Ratio:** Cluster heads typically perform more energy-intensive tasks such as data aggregation, coordination, and communication. If cluster heads have higher energy levels, they are more likely to remain stable and operational for a longer duration, enhancing the reliability and longevity of the network. To ensure the longevity of CH, we have considered the ratio of the average energy of selected CH to the average energy in normal nodes in the network, defined in Equation (18).

$$f_2 = \frac{E_{avg}(CH)}{E_{avg}(NN)} \tag{18}$$

This ratio provides a measure of the relative energy distribution between cluster heads and normal nodes within the cluster. A value greater than 1 indicates that, on average, cluster heads have more energy than normal nodes, which

21613915, 2025, 6, Downloaded from https://onlinelibrary.wiley.com/doi/10.1002/ett.70199 by Delhi Technological University, Wiley Online Library on [26/06/2025]. See the Terms and Conditions (https://onlinelibrary.wiley.com/terms-and-conditions) on Wiley Online Library for rules of use; OA articles are governed by the applicable Creative Commons License

potentially addresses the hot spot problem, where certain nodes become overburdened due to excessive energy consumption.

The average energy of CHs, $E_{avg}(CH)$, and the average energy of normal nodes, $E_{avg}(NN)$, is calculated using Equations (19) and (20) respectively.

$$E_{avg}(CH) = \frac{E_{\text{totalCH}}}{N_{CH}} \tag{19}$$

$$E_{avg}(NN) = \frac{E_{\text{totalCommon}}}{N_{NN}} \tag{20}$$

Where N_{CH} is the total number of CH in the network, and $E_{avg}(NN)$ represents normal nodes in the network.

3. **Total Alive Nodes:** The count of alive nodes provides a crucial metric for assessing the overall health and status of the network at any given time. Maintaining a higher number of alive nodes is essential for ensuring robust connectivity and uninterrupted data flow. The objective function f_3 encourages configurations that keep more nodes alive. Equation (21) is used to calculate the number of alive nodes in the network.

$$N_{\text{alive}} = \sum_{i=1}^{N} \text{countIF}(E_i(node) > 0) \tag{21}$$

Where $E_i(node)$ is the energy left in ith node.

By leveraging this fitness function, EO-C achieves optimal energy efficiency, longevity, and resilience, addressing both the hot-spot problem and overall network performance challenges.

5 | Result and Analysis

Table 1 provides an overview of the many factors associated with EO-C and IoT-enabled SDWSN, which form the basis for the performance analysis presented in this section using computer simulations. All experimental procedures were conducted using the MATLAB (version 2023a) software on an Intel i5 processor equipped with 8GB of RAM technology.

TABLE 1 | Parameters for testing.

Category	Parameter	Value
Network	Deployment area (m^2)	100×100
	CS (Position)	50,50
	Energy	0.5J per node
	No. of SDSNs	100
Application	Data Packet length	100 bits
	Broadcast packet size	25 bits
EO-C	Initial POP	20
	Iteration	100
	γ, δ, η	0.6, 0.2, 0.2

5.1 | Simulation Parameters

The behavior of SDWSNs nodes is simulated in a geographical area of 100m x100 m with a control station at the center using the testing settings listed in Table 1. A network of 100 nodes is deployed at random, as shown in Figure 3. An energy allocation of 0.5J is assigned to each node in the network.

The particle population was initialized using Equation (5) to generate their initial concentration. The search domain was configured as a multidimensional space, with particle concentration vectors confined to the range [−4, 4]. The population size and number of clusters play an important role in the optimization process. Both parameters are discussed below:

- **Optimal Population Size and Iterations count:** In order to determine the optimal number of particle populations and the minimum number of iterations, the fitness function was evaluated using various population sizes ranging from 5 to 50. The findings, illustrated in Figure 4, demonstrated that the optimal fitness value was achieved by setting the initial population size to 20 and imposing a maximum restriction of 100 iterations. The parameter configurations employed in this study effectively balanced the exploration and exploitation aspects within the search space, hence promoting efficient convergence toward optimal solutions.
- **The Optimal range of CH count:** In the proposed algorithm, the number of CH is not fixed; instead, the algorithm selects the best CH count based on network conditions. To determine the optimal range for CH count, we evaluated the EO-C with CH ranges of 5%, 10%, 15%, 20%, 25%, and 50%, as seen in Figure 5. The Figure 5 shows that the First Node Died (FND), Half Node Died (HND), and Last Node Died (LND) [42] metrics continually grow and reach a peak when the CH range is up to 25% of alive nodes; when the CH range is up to 50%, the performance of EO-C somewhat falls. Based on the previous observations, we may conclude that the optimal range for CH count is up to 25%.

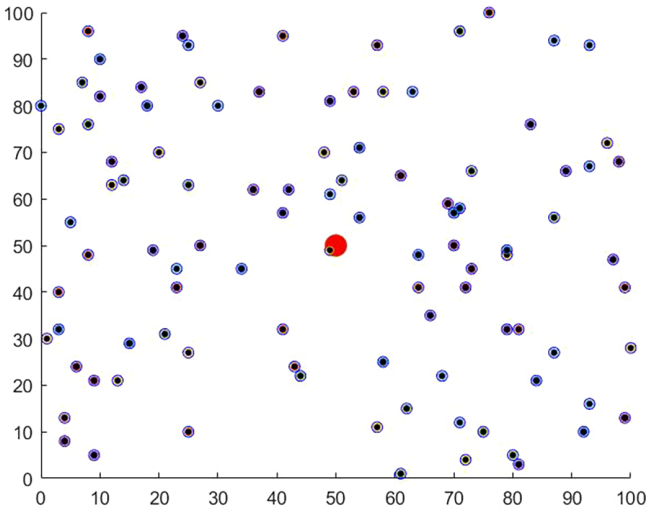


FIGURE 3 | Network scenario: Random deployment of 100 nodes in a 100 m×100 m area.

21613915, 2025, 6, Downloaded from https://onlinelibrary.wiley.com/doi/10.1002/ett.70199 by Delhi Technological University, Wiley Online Library on [26/06/2025]. See the Terms and Conditions (https://onlinelibrary.wiley.com/terms-and-conditions) on Wiley Online Library for rules of use; OA articles are governed by the applicable Creative Commons License

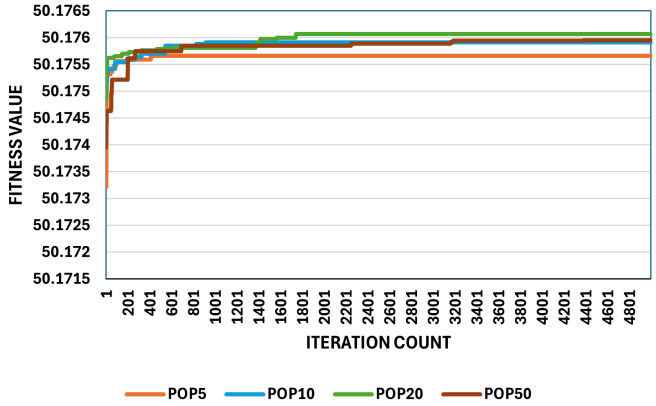


FIGURE 4 | Fitness of EO-C evaluated with various population sizes.

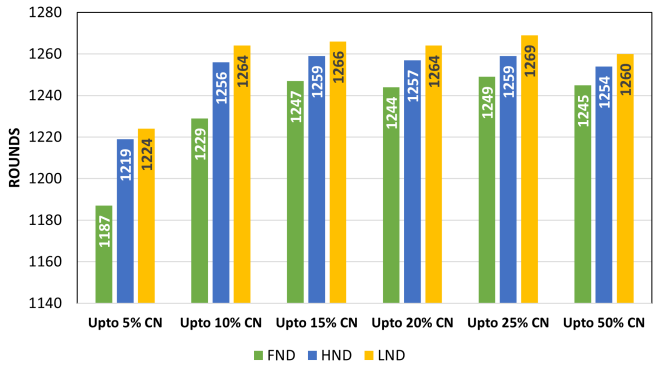


FIGURE 5 | Performance of EO-C with different ranges of CH count.

In subsequent experiments, a population size of 20 was selected, with an iteration limit of $iterMax = 100$. Additionally, the cluster head count was randomly chosen to be between 5% and 25% of the alive nodes.

5.2 | EO-C Performance Evaluation

In this sub-section, the performance of the EO-C algorithm under various conditions is examined.

- **Network Performance:** To test the network performance, 100 nodes are deployed in 100 m×100 m area with initial energy $100 \times 0.5J = 50J$ where each node is assigned $0.5J$ initial energy. As discussed in the preceding section, the CH count is capped at 25% of the total alive nodes. In EO-C, the cluster count varies dynamically with each round. Figure 6 shows that EO-C selects cluster numbers randomly based on fitness value. From the initial round until the 1260th round, the cluster count fluctuated between 16% and 25% of alive nodes and subsequently started decreasing from the 1261st round onward. The performance of EO-C is illustrated in Figure 7. The results demonstrate that the proposed algorithm sustained the transmission till the 1248th round. This delayed node failure demonstrates the proposed algorithm's robustness, as it lasted several rounds before experiencing the initial node failure at the 1249th round. Figure 8 depicts the total energy remaining in the network after each round, indicating a consistent and gradual energy decay. The proposed algorithm transmitted a total 29320 number of packets before exhausting their energy, which is shown below in Figure 9. The energy consumption analysis in Figure 10 reveals the distribution of energy usage among different activities within the network. The CH consumed the highest proportion of energy, accounting for 96.64% of the total 50 joules. Neighboring node communication (energyNN) utilized 3.51%, while energy aggregation (energyAgg) required only 0.0003%. These findings highlight the significant energy demands of the CH role, underscoring the importance of optimizing CH selection to enhance network energy efficiency. By addressing this imbalance, the proposed EO-C algorithm effectively mitigates energy hotspots and improves network lifespan, as demonstrated in the simulation results.

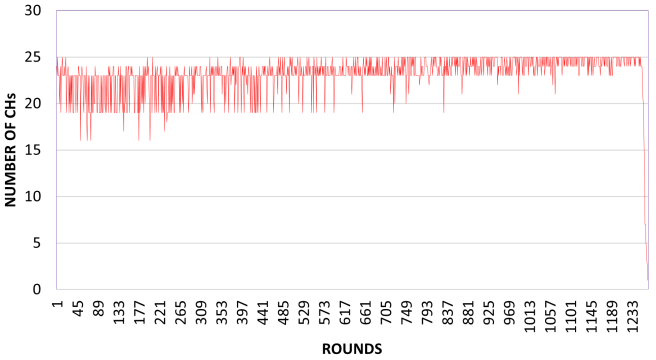


FIGURE 6 | Random number of CHs per round.

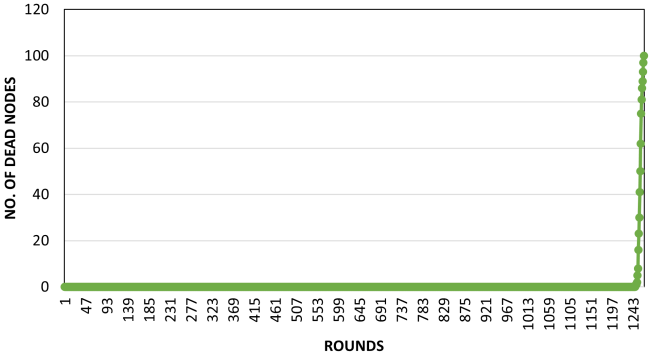


FIGURE 7 | Dead nodes per round.

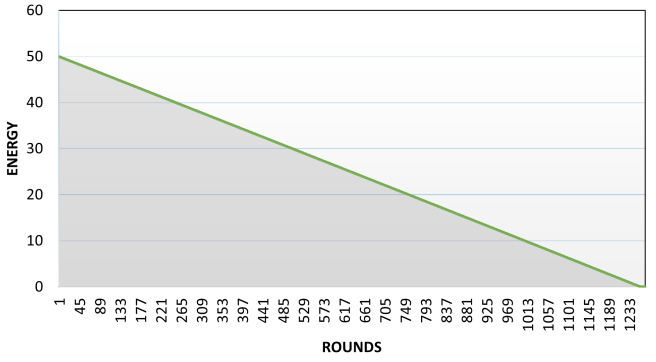


FIGURE 8 | Total network energy left per round.

21613915, 2025, 6, Downloaded from https://onlinelibrary.wiley.com/doi/10.1002/ett.70199 by Delhi Technological University, Wiley Online Library on [26/06/2025]. See the Terms and Conditions (https://onlinelibrary.wiley.com/terms-and-conditions) on Wiley Online Library for rules of use; OA articles are governed by the applicable Creative Commons License

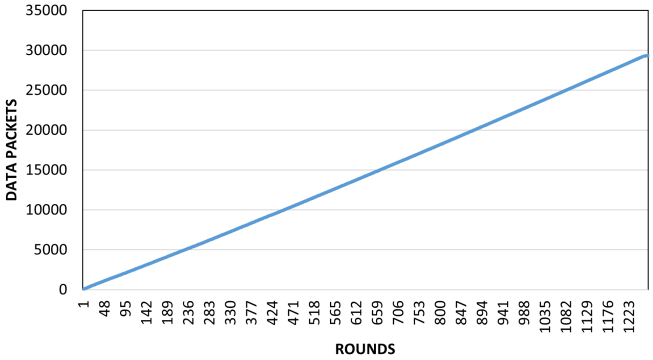


FIGURE 9 | Total data packet sent to CS per round.

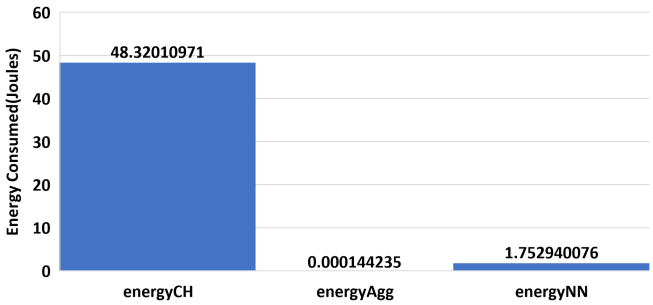


FIGURE 10 | Energy consumption by different phases.

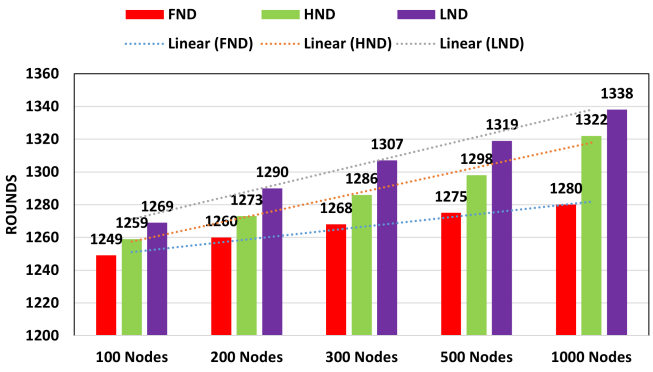


FIGURE 11 | Performance of EO-C with respect to various node densities.

- **Impact of Node Density:** To study the scalability and robustness of the proposed algorithm, we tested the EO-C algorithm with node density of 100, 200, 300, 500, and 1000 nodes in an area of 100 m×100 m. The Figure 11 shows the performance of the network in terms of the FND, HND, and LND. These metrics provide insights into the network's resilience and efficiency as node density changes. The results depict that, as the number of nodes increases, the performance of the network (in terms of FND, HND, and LND) shows an upward trend, peaking at 1000 nodes. This observation highlights the proposed algorithm's scalability, as it can effectively handle larger node populations while remaining robust and resilient. Furthermore, it emphasizes the algorithm's ability to adapt and optimize performance across varying node densities, an important aspect in real-world network deployments where node populations may fluctuate.

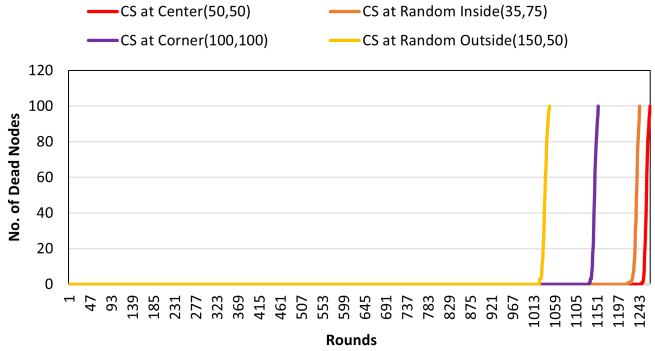


FIGURE 12 | Performance of EO-C with respect to various CS positions.

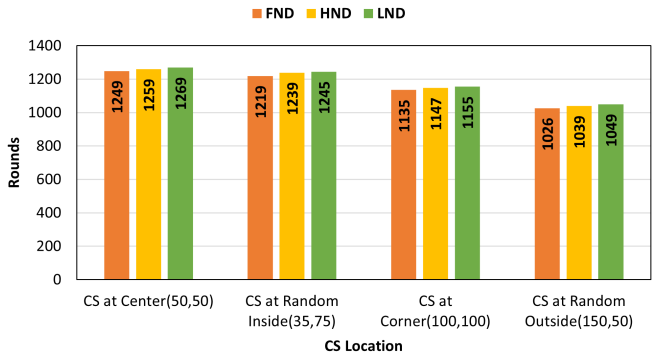


FIGURE 13 | FND, HND, and LND of EO-C network at various CS positions.

- **Impact of CS Location:** The control stations serve as central points for network management, data collection, and coordination. The location of CS has a great impact on network life. To test the performance of the proposed algorithm, we deployed 100 nodes in a 100 m×100 m area with the CS at the center location(50,50), random location(35,75) inside the deployment area, random location(50,150) outside the deployment area, and at the corner(100,100). From Figure 12, we can observe that the network performs best when the location of CS is at the center(50,50) and worst when CS is outside the deployment area, that is, location(50,150). This suggests that CS placement directly influences network performance, with central locations facilitating better network management and coordination. In Figure 13, metrics such as FND, HND, and LND exhibit minimal variation across all cases, with deviations ranging between 20 to 30 rounds. However, a clear trend emerges, network performance peaks when CS is located at the center, gradually declining as CS moves away from this optimal position, with the best performance observed at (50,50), followed by (35,75), (100,100), and worst at (50,150). By strategically locating CS, network designers can maximize efficiency and ensure robust operation, particularly in scenarios where network resources are limited.
- **Impact of area of deployment:** Understanding the effect of area on a network is critical for design, optimization,

21613915, 2025, 6, Downloaded from https://onlinelibrary.wiley.com/doi/10.1002/ett.70199 by Delhi Technological University, Wiley Online Library on [26/06/2025]. See the Terms and Conditions (https://onlinelibrary.wiley.com/terms-and-conditions) on Wiley Online Library for rules of use; OA articles are governed by the applicable Creative Commons License

and management. By considering the size of the deployment area, network planners can make informed decisions to address coverage, connectivity, resource allocation, scalability, and energy efficiency. To test the performance of EO-C in different coverage areas, we deployed 100 nodes in areas of sizes 100 m×100 m, 200 m×200 m, 300 m×300 m, 500 m×500 m, and 1000 m×1000 m. From Figures 14 and 15, we can observe that the performance of the network decreases as the area of deployment increases. Specifically, the EO-C algorithm performed best when the area is 100 m×100 m and worst when the area is 1000 m × 1000 m. Also, from Figure 15, we can observe a trend in FND and HND metrics. Both parameters experience a sharp decline as the deployment area increases. However, with LND, the value decreases gradually. FND for deployment areas 100 m×100 m, 200 m×200 m, 300 m×300 m, 500 m×500 m, and 1000 m×1000 m are 1249, 1032, 618, 119, and 6 rounds, respectively. This trend highlights the impact of deployment area size on network performance, with larger areas leading to quicker exhaustion of network resources and, consequently, earlier node failures.

5.3 | Comparative Analysis

In this section, we evaluate the simulation results of EO-C in comparison to several SoA algorithms, including LEACH [19], GWO-C [31], EBGWO [32], and EAFFO [39]. EO-C is configured using all parameters listed in Table 1. To evaluate the effectiveness of each algorithm, we consider performance metrics such as FND, HND, LND, residual energy, and the number of data packets sent to the CS.

The Table 2 and Figure 16 provide a comparison of performance metrics (FND, HND, & LND) for various algorithms, including EO-C, EAFFO, EB-GWO, GWO-C, and LEACH. The performance of EO-C surpasses that of other SoA algorithms across all metrics. EO-C records 1249 for FND, 1259 for HND, and 1269 for LND. In Figure 17, the number of dead nodes is plotted against the number of rounds. The results show that FND for EO-C, EAFFO, EB-GWO, GWO-C, and LEACH at 1249, 998, 1078, 538, and 270, respectively. EO-C exhibits a notable enhancement in network lifespan for periodic data collection when compared to several other algorithms. Although the network life span is high in EAFFO, that is, 2062, but EO-C outperforms EAFFO

TABLE 2 | Comparison of performance metrics.

Algorithms	FND	HND	LND
LEACH	270	447	662
GWO-C	538	1195	1377
EB-GWO	1078	1258	1303
EAFFO	998	1466	2062
EO-C	1249	1259	1269

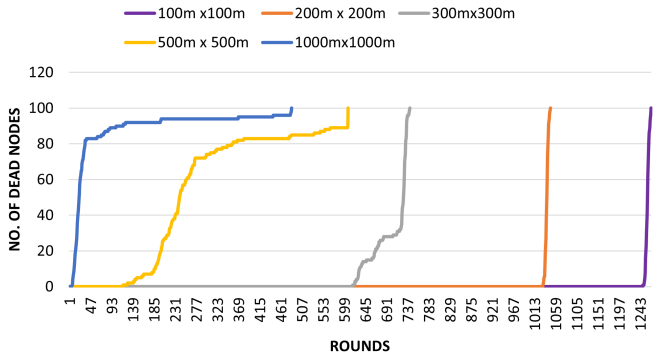


FIGURE 14 | Performance of EO-C in different deployment area sizes.

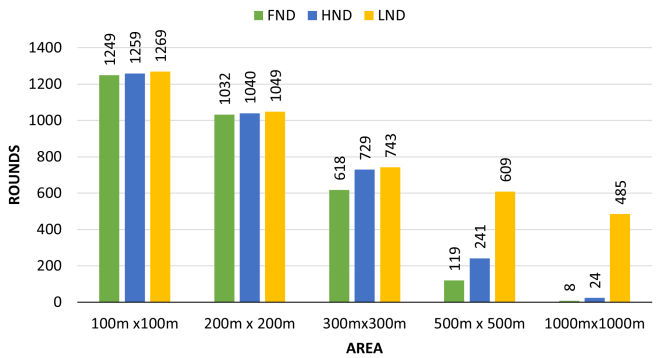


FIGURE 15 | Impact of deployment area size on FND, HND, and LND of the EO-C algorithm.

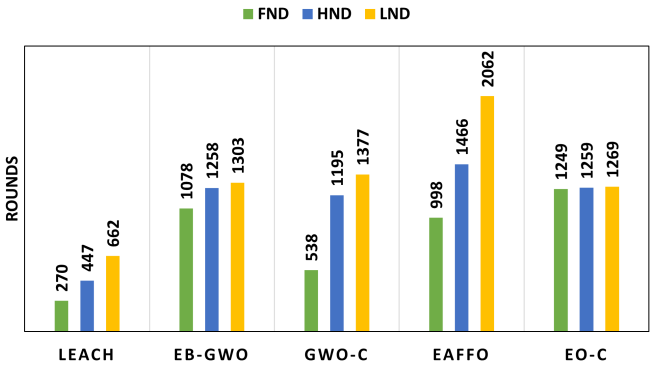


FIGURE 16 | Comparison of FND, HND, and LND of EO-C with SoA algorithm.

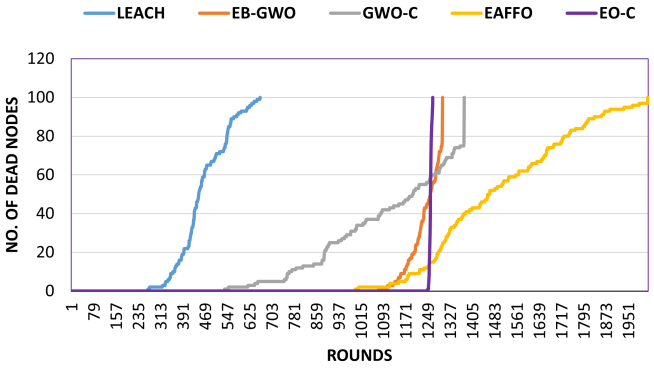


FIGURE 17 | Dead node comparison of EO-C with SoA algorithms.

21613915, 2025, 6, Downloaded from https://onlinelibrary.wiley.com/doi/10.1002/ett.70199 by Delhi Technological University, Wiley Online Library on [26/06/2025]. See the Terms and Conditions (https://onlinelibrary.wiley.com/terms-and-conditions) on Wiley Online Library for rules of use; OA articles are governed by the applicable Creative Commons License

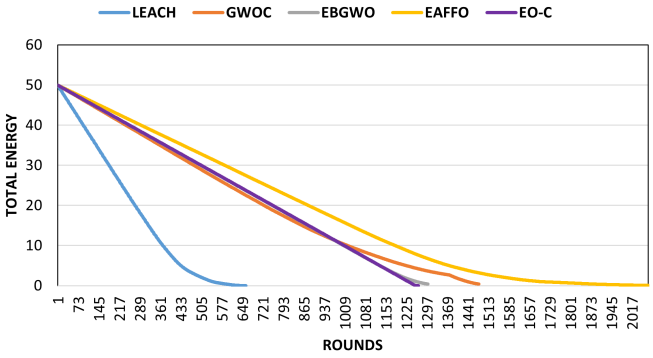


FIGURE 18 | Comparison of energy decay in EO-C with SoA algorithm.

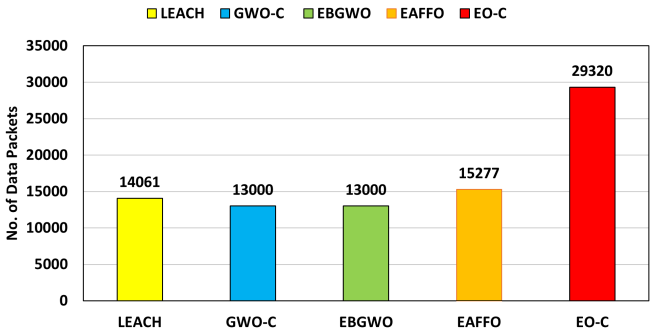


FIGURE 19 | Comparison of data packets sent to CS in EO-C with SoA algorithm.

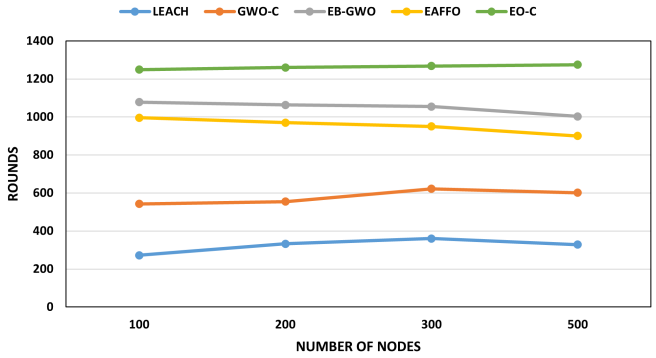


FIGURE 20 | Comparison of performance of EO-C with SoA algorithm with respect to node density.

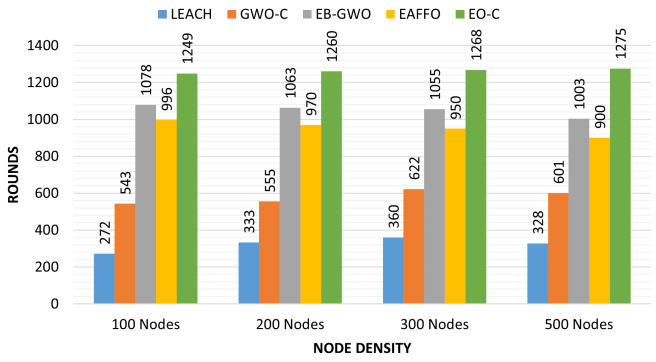


FIGURE 21 | Comparison of EO-C with SoA algorithm with respect to FND vs. node density.

in terms of FND by more than 25.15%. Moreover, EO-C outperforms LEACH, GWO-C, and EB-GWO, increasing network lifespan by over 362.6%, 132.15%, and 15.86%, respectively. Since EO-C exhibits the longest time to FND happened, these findings highlight EO-C's effectiveness in mitigating the hot spot problem, as well as its potential as an effective strategy for improving network longevity in the context of periodic data collection.

Figure 18 shows the network's residual energy per round. The graph shows a steady energy decline, which is important because it allows the algorithm to maintain network stability, with nodes failing only in the final 5% of rounds. This characteristic is especially important in scenarios where the failure of a single node might endanger the entire network.

Figure 19 illustrates the comparison of various SoA with the EO-C algorithm. The graph demonstrates that EO-C outperforms the EAFFO, EB-GWO, GWO-C, and LEACH algorithms in terms of data transmission volume, with 29320 data packets, which is 108.5% higher than LEACH.

To compare the robustness & the scalability of the proposed algorithm with SoA like EAFFO, EB-GWO, GWO-C, and LEACH. We tested our algorithm with 100, 200, 300, and 500 nodes in 100 m × 100 m area of deployment, as shown in Figures 20 and 21. From the analysis of the results depicted in the graph, it is evident that EO-C outperforms all the SOA algorithms across all tested network sizes. EO-C's ability to maintain superior performance as network size increases demonstrates its effectiveness in handling larger-scale deployments and resilience to scalability challenges. Thus, based on these findings, EO-C appears to be a promising solution for robust and scalable IoT-enabled SDWSNs applications.

5.3.1 | Mitigating Hot-Spot Problems

The simulation results highlight EO-C's superior performance in mitigating the hot-spot problem compared to SoA algorithms. EO-C achieved a FND metric of 1249 rounds, significantly outperforming LEACH (270 rounds), GWO-C (538 rounds), EAFFO (998 rounds), and EB-GWO (1078 rounds). This demonstrates that EO-C effectively prevents premature energy depletion in nodes near the base station by dynamically balancing energy consumption across the network. Furthermore, the energy decay analysis (Figure 18) demonstrates that EO-C promotes a gradual reduction in energy levels, ensuring that nodes in critical regions retain sufficient energy to prolong the network's lifespan. This balanced energy consumption effectively minimizes the formation of energy hotspots, enhancing the network's reliability, stability, and overall performance.

These results confirm EO-C's capability to alleviate hotspot issues, making it a robust and energy-efficient solution for IoT-enabled SDWSN applications, where network longevity and resilience are critical.

21613915, 2025, 6, Downloaded from https://onlinelibrary.wiley.com/doi/10.1002/ett.70199 by Delhi Technological University, Wiley Online Library on [26/06/2025]. See the Terms and Conditions (https://onlinelibrary.wiley.com/terms-and-conditions) on Wiley Online Library for rules of use; OA articles are governed by the applicable Creative Commons License

TABLE 3 | Pairwise t-test results between EO-C and other methods.

Comparison	t-statistic	*p*-value	Effect size (Cohen's d)	95% CI	Significance
LEACH vs EO-C	48.698	5.03×10^{-9}	6.12	[942.57, 1017.93]	Statistically significant
GWO-C vs EO-C	34.975	3.64×10^{-8}	5.23	[680.94, 819.06]	Statistically significant
EB-GWO vs EO-C	12.380	1.70×10^{-5}	2.78	[183.27, 274.73]	Statistically significant
EAFFO vs EO-C	14.667	6.31×10^{-6}	3.12	[224.86, 275.14]	Statistically significant

5.3.2 | Statistical Validation

To evaluate the performance of EO-C in comparison to other methods (LEACH, GWO-C, EB-GWO, and EAFFO), a pairwise t-test was conducted. The results (shown in Table 3) revealed statistically significant differences in performance between EO-C and SoA algorithms.

1. **LEACH vs EO-C:** EO-C significantly outperformed LEACH with a large t-statistic ($t = 48.698$) and an extremely low *p*-value ($p = 5.03 \times 10^{-9}$). The effect size (Cohen's $d = 6.12$) indicates a substantial difference, while the 95% confidence interval ([942.57, 1017.93]) confirms consistent performance gains.
2. **GWO-C vs EO-C:** A strong performance advantage was observed for EO-C, with a t-statistic of $t = 34.975$ and a *p*-value ($p = 3.64 \times 10^{-8}$). The effect size (Cohen's $d = 5.23$) reflects a substantial difference, supported by the confidence interval ([680.94, 819.06]).
3. **EB-GWO vs EO-C:** EO-C showed significant improvement over EB-GWO, evidenced by a t-statistic of $t = 12.380$ and a *p*-value ($p = 1.70 \times 10^{-5}$). The effect size (Cohen's $d = 2.78$) highlights a meaningful difference, with a confidence interval of [183.27, 274.73].
4. **EAFFO vs EO-C:** EO-C also outperformed EAFFO, with a t-statistic of $t = 14.667$ and a *p*-value ($p = 6.31 \times 10^{-6}$). The effect size (Cohen's $d = 3.12$) indicates a large difference, and the confidence interval ([224.86, 275.14]) reinforces the result.

The results strongly support the effectiveness of EO-C in achieving energy-efficient operation, delaying node failures, and sustaining network operations for longer durations. These findings highlight EO-C's potential for critical applications such as environmental monitoring, disaster management, and IoT-based systems.

6 | Conclusion & Future Scope

In this research article, we proposed and evaluated an equilibrium optimizer clustering algorithm. EO-C is based on an equilibrium optimizer algorithm and is designed to address the energy conservation, optimum CH selection, optimum CH count selection, and hot spot problem in IoT-enabled SDWSNs. EO-C addresses these challenges with the help of a dynamic CH count and a novel fitness function based on total residual energy, energy balance ratio, and total number of alive nodes in the network. Further, the performance of EO-C under various conditions is compared with several SoA algorithms, including EAFFO, EB-GWO, GWO-C, and LEACH. The results indicate that the EO-C outperforms other SoA algorithms in terms of network longevity, resilience, scalability, and coverage. The simulation results demonstrate that the proposed algorithm shows improvement ranging from 15.9% to 372.6% when compared with EAFFO, EB-GWO, GWO-C, and LEACH.

Although EO-C has shown promising results, its performance is tested under a controlled environment through simulations, which may not adequately represent the complexities of real-world scenarios. Future work shall focus on testing the performance of this algorithm in real-world scenarios. EO-C was designed and tested for stationary nodes only, limiting its applicability in dynamic scenarios like networks with mobile nodes or mobile CS [43]. Future work shall extend the algorithm to accommodate mobility, enabling it to perform effectively in environments with mobile nodes, such as vehicular networks or mobile IoT applications. Overall, EO-C has the potential to significantly improve the reliability and efficiency of IoT applications in various domains, including smart cities, environmental monitoring, and industrial automation.

Data Availability Statement

The data underlying this article will be shared on reasonable request to the corresponding author.

References

1. L. Kang, A. Sarker, and H. Shen, "Velocity Optimization of Pure Electric Vehicles With Traffic Dynamics and Driving Safety Considerations," *ACM Transactions on Internet of Things* 2, no. 1 (2021): 1–24, https://doi.org/10.1145/3433678.

2. M. Safi, S. Dadkhah, F. Shoeleh, H. Mahdikhani, H. Molyneaux, and A. A. Ghorbani, "A Survey on IoT Profiling, Fingerprinting, and Identification," *ACM Transactions on Internet of Things* 3, no. 4 (2022): 1–39, https://doi.org/10.1145/3539736.

3. A. I. Siam, M. A. El-Affendi, A. Abou Elazm, et al., "Portable and Real-Time IoT-Based Healthcare Monitoring System for Daily Medical Applications," *IEEE Transactions on Computational Social Systems* 10, no. 4 (2023): 1629–1641.

4. S. Constantinou, A. Konstantinidis, P. K. Chrysanthis, and D. Zeinalipour-Yazti, "Green Planning of Iot Home Automation Workflows in Smart Buildings," *ACM Transactions on Internet of Things* 3, no. 4 (2022): 1–30, https://doi.org/10.1145/3549549.

5. R. Karthiga, C. L. Brindha Devi, R. Janaki, C. Gayathri, V. Samuthira Pandi, and D. Shobana, "Iot Farm: A Robust Methodology Design to Support Smart Agricultural System Using Internet of Things With Intelligent

21613915, 2025, 6, Downloaded from https://onlinelibrary.wiley.com/doi/10.1002/ett.70199 by Delhi Technological University, Wiley Online Library on [26/06/2025]. See the Terms and Conditions (https://onlinelibrary.wiley.com/terms-and-conditions) on Wiley Online Library for rules of use; OA articles are governed by the applicable Creative Commons License

Sensors Association," in *Proceedings of the 2023 7th International Conference on Electronics, Communication and Aerospace Technology (ICECA)* (IEEE, 2023), 1332–1337.

6. A. K. M. Al-Qurabat, "A Lightweight Huffman-Based Differential Encoding Lossless Compression Technique in IoT for Smart Agriculture," *International Journal of Computing and Digital Systems* 11, no. 1 (2022): 9–18.

7. B. Singh Anurag, S. Jha, D. Sonkamble Archishmati, Z. M. Ustad, and R. Shukla Akash, "A Review on Various Methods Employed to Measure Air Quality in the Vicinity Using Internet of Things," in *Proceedings of the 2023 5th Biennial International Conference on Nascent Technologies in Engineering (ICNTE)* (IEEE, 2023), 1–6.

8. R. Beniwal and N. Kumar, "Energy Optimized Artificial Hummingbird Algorithm for Routing in IoT-Based Software-Defined Wsn," *International Journal of Communication Systems* 37, no. 8 (2024): e5748, https://doi.org/10.1002/dac.5748.

9. M. Karthikeyan, D. Manimegalai, and K. RajaGopal, "Firefly Algorithm-Based WSN-IoT Security Enhancement With Machine Learning for Intrusion Detection," *Scientific Reports* 14, no. 231 (2024): 1–15.

10. J. Liu, K. Lu, X. Cai, and M. N. Murthi, "Regenerative Cooperative Diversity With Path Selection and Equal Power Consumption in Wireless Networks," *IEEE Transactions on Wireless Communications* 8, no. 8 (2009): 3926–3932, https://doi.org/10.1109/TWC.2009.081030.

11. T. Luo, H.-P. Tan, and T. Q. S. Quek, "Sensor Openflow: Enabling Software-Defined Wireless Sensor Networks," *IEEE Communications Letters* 16, no. 11 (2012): 1896–1899.

12. European Commission, "The Next-Generation Internet of Things: A European Perspective," (2023), https://digital-strategy.ec.europa.eu/en/policies/next-generation-internet-things.

13. Statista Research Department, "Internet of Things (IoT) - Number of Connected Devices Worldwide From 2019 to 2030," (2024), https://www.statista.com/statistics/1183457/iot-connected-devices-worldwide/.

14. X. Fernando and G. Lăzăroiu, "Spectrum Sensing, Clustering Algorithms, and Energy-Harvesting Technology for Cognitive-Radio-Based Internet-of-Things Networks," *Sensors* 23, no. 18 (2023): 1–19.

15. M. Kingston Roberts, P. Ramasamy, and F. Dahan, "An Innovative Approach for Cluster Head Selection and Energy Optimization in Wireless Sensor Networks Using Zebra Fish and Sea Horse Optimization Techniques," *Journal of Industrial Information Integration* 41 (2024): 100642.

16. A. Faramarzi, M. Heidarinejad, B. Stephens, and S. Mirjalili, "Equilibrium Optimizer: A Novel Optimization Algorithm," *Knowledge-Based Systems* 191 (2020): 105190.

17. M. Esmaeeli and S. A. H. Ghahroudi, "Improving Energy Efficiency Using a New Game Theory Algorithm for Wireless Sensor Networks," *International Journal of Computer Applications* 136, no. 12 (2016): 1–4.

18. M. Andronie, G. Lăzăroiu, M. Iatagan, C. Uță, R. Ștefănescu, and M. CocoȘatu, "Artificial Intelligence-Based Decision-Making Algorithms, Internet of Things Sensing Networks, and Deep Learning-Assisted Smart Process Management in Cyber-Physical Production Systems," *Electronics* 10, no. 20 (2021): 2497.

19. W. R. Heinzelman, A. Chandrakasan, and H. Balakrishnan, "Energy-Efficient Communication Protocol for Wireless Microsensor Networks," in *Proceedings of the 33rd Annual Hawaii International Conference on System Sciences*, vol. 2 (IEEE, 2000), 10.

20. A. Manjeshwar and D. P. Agrawal, "Teen: A Routing Protocol for Enhanced Efficiency in Wireless Sensor Networks," in *Proceedings 15th International Parallel and Distributed Processing Symposium*, vol. 2001 (IPDPS, 2001), 2009–2015.

21. O. Younis and S. Fahmy, "Heed: A Hybrid, Energy-Efficient, Distributed Clustering Approach for Ad Hoc Sensor Networks," *IEEE Transactions on Mobile Computing* 3, no. 4 (2004): 366–379.

22. S. D. Muruganathan, D. C. F. Ma, R. I. Bhasin, and A. O. Fapojuwo, "A Centralized Energy-Efficient Routing Protocol for Wireless Sensor Networks," *IEEE Communications Magazine* 43, no. 3 (2005): S8–S13.

23. G. Chen, C. Li, M. Ye, and J. Wu, "An Unequal Cluster-Based Routing Protocol in Wireless Sensor Networks," *Wireless Networks* 15, no. 2 (2009): 193–207, https://doi.org/10.1007/s11276-007-0035-8.

24. K. Haseeb, K. A. Bakar, A. Ahmed, T. Darwish, and I. Ahmed, "Wecrr: Weighted Energy-Efficient Clustering With Robust Routing for Wireless Sensor Networks," *Wireless Personal Communications* 97, no. 1 (2017): 695–721, https://doi.org/10.1007/s11277-017-4532-5.

25. S. K. Singh, P. Kumar, and J. P. Singh, "An Energy Efficient Protocol to Mitigate Hot Spot Problem Using Unequal Clustering in Wsn," *Wireless Personal Communications* 101, no. 2 (2018): 799–827, https://doi.org/10.1007/s11277-018-5716-3.

26. O. Flauzac, C. Gonzalez, and F. Nolot, "Developing a Distributed Software Defined Networking Testbed for Iot," *Procedia Computer Science* 83 (2016): 680–684.

27. W. Xiang, N. Wang, and Y. Zhou, "An Energy-Efficient Routing Algorithm for Software-Defined Wireless Sensor Networks," *IEEE Sensors Journal* 16, no. 20 (2016): 7393–7400.

28. J. Kennedy and R. Eberhart, "Particle Swarm Optimization," in *Proceedings of ICNN'95 - International Conference on Neural Networks*, vol. 4 (IEEE, 1995), 1942–1948.

29. P. C. S. Rao and H. Banka, "Novel Chemical Reaction Optimization Based Unequal Clustering and Routing Algorithms for Wireless Sensor Networks," *Wireless Networks* 23, no. 3 (2017): 759–778, https://doi.org/10.1007/s11276-015-1148-0.

30. G. Yogarajan and T. Revathi, "Improved Cluster Based Data Gathering Using Ant Lion Optimization in Wireless Sensor Networks," *Wireless Personal Communications* 98, no. 3 (2018): 2711–2731, https://doi.org/10.1007/s11277-017-4996-3.

31. D. Agrawal, M. H. W. Qureshi, P. Pincha, et al., "Gwo-c: Grey Wolf Optimizer-Based Clustering Scheme for Wsns," *International Journal of Communication Systems* 33, no. 8 (2020): e4344, https://doi.org/10.1002/dac.4344.

32. P. Mishra, N. Kumar, and W. W. Godfrey, "A Meta-Heuristic-Based Green-Routing Algorithm in Software-Defined Wireless Sensor Network," in *Proceedings of the 2021 6th International Conference on Inventive Computation Technologies (ICICT)* (IEEE, 2021), 36–41.

33. A. M. K. Abdulzahra and A. K. M. Al-Qurabat, "A Clustering Approach Based on Fuzzy C-Means in Wireless Sensor Networks for IoT Applications," *Karbala International Journal of Modern Science* 8, no. 4 (2022): 2.

34. A. M. K. Abdulzahra, A. K. M. Al-Qurabat, and S. A. Abdulzahra, "Optimizing Energy Consumption in WSN-Based IoT Using Unequal Clustering and Sleep Scheduling Methods," *Internet of Things* 22 (2023): 100765.

35. S. A. Abdulzahra and A. K. M. Al-Qurabat, "Fonic: An Energy-Conscious Fuzzy-Based Optimized Nature-Inspired Clustering Technique for Iot Networks," *Journal of Supercomputing* 80, no. 1 (2024): 19845–19897.

36. M. K. Roberts, J. Thangavel, and H. Aldawsari, "An Improved Dual-Phased Meta-Heuristic Optimization-Based Framework for Energy-Efficient Cluster-Based Routing in Wireless Sensor Networks," *Alexandria Engineering Journal* 101 (2024): 306–317.

37. J. Xiao, C. Li, Z. Li, and J. Zhou, "Bs-Scrm: A Novel Approach to Secure Wireless Sensor Networks via Blockchain and Swarm Intelligence Techniques," *Scientific Reports* 14, no. 9709 (2024): 1–14.

21613915, 2025, 6, Downloaded from https://onlinelibrary.wiley.com/doi/10.1002/ett.70199 by Delhi Technological University, Wiley Online Library on [26/06/2025]. See the Terms and Conditions (https://onlinelibrary.wiley.com/terms-and-conditions) on Wiley Online Library for rules of use; OA articles are governed by the applicable Creative Commons License

38. D. Jain, P. K. Shukla, and S. Varma, "Energy Efficient Architecture for Mitigating the Hot-Spot Problem in Wireless Sensor Networks," *Journal of Ambient Intelligence and Humanized Computing* 14, no. 8 (2023): 10587–10604, https://doi.org/10.1007/s12652-022-03711-5.

39. D. Lubin Balasubramanian and V. Govindasamy, "Energy Aware Farmland Fertility Optimization Based Clustering Scheme for Wireless Sensor Networks," *Microprocessors and Microsystems* 97 (2023): 104759.

40. N. Kumar and R. Beniwal, "A Multi-Constrained Green Routing Protocol for IoT-Based Software-Defined WSN," *Concurrency and Computation: Practice and Experience* 36, no. 28 (2024): e8306, https://doi.org/10.1002/cpe.8306.

41. F. Tasgetiren, A. Chen, G. Gencyilmaz, and S. Gattoufi, *Smallest Position Value Approach* (Springer, 2009), 121–138, https://doi.org/10.1007/978-3-540-92151-6_5.

42. M. J. Handy, M. Haase, and D. Timmermann, "Low Energy Adaptive Clustering Hierarchy With Deterministic Cluster-Head Selection," in *Proceedings of the 4th International Workshop on Mobile and Wireless Communications Network* (IEEE, 2002), 368–372.

43. H. M. Lateef and A. K. M. Al-Qurabat, "An Overview of Using Mobile Sink Strategies to Provide Sustainable Energy in Wireless Sensor Networks," *International Journal of Computing and Digital Systems* 16, no. 1 (2024): 797–812.

21613915, 2025, 6, Downloaded from https://onlinelibrary.wiley.com/doi/10.1002/ett.70199 by Delhi Technological University, Wiley Online Library on [26/06/2025]. See the Terms and Conditions (https://onlinelibrary.wiley.com/terms-and-conditions) on Wiley Online Library for rules of use; OA articles are governed by the applicable Creative Commons License

The Journal of Supercomputing (2025) 81:979
https://doi.org/10.1007/s11227-025-07428-y

A novel reciprocal linguistic cloud model and its integration with machine learning

Shweta Kalson[1] · **Anjana Gupta**[1]

Accepted: 10 May 2025
© The Author(s), under exclusive licence to Springer Science+Business Media, LLC, part of Springer Nature 2025

Abstract
Challenges become more intricate in uncertain environments, mainly when human subjective evaluations play a crucial role. Cloud models offer a powerful framework for managing complex situations by describing the transformation between qualitative and quantitative knowledge, addressing uncertainty through randomness and fuzziness. This research proposes a novel Reciprocal Linguistic Cloud Model based on a reciprocal linguistic term set to facilitate the transition between reciprocal linguistic variables and clouds, enabling the construction of cloud descriptors. Further, a generalized reciprocal linguistic scale function is introduced. A Cloud Model scale is constructed, integrating a relative importance scale with the proposed reciprocal linguistic scale function. A real-time application is presented to explore uncertainty in human decision-making in criminal analysis. We integrate machine learning algorithms to analyse crimes in India and to predict future crime rates under uncertainty. Further, a comparative analysis demonstrates the superiority of our proposed research model.

Keywords Cloud model scale · Reciprocal linguistic term set · Reciprocal linguistic cloud model · Decision-making · Machine learning · Crime analysis

1 Introduction

Traditional methods of system analysis and computer simulation are conventionally adept at handling numerical data with precision. However, they encounter significant challenges when attempting to capture the intricate complexities and uncertainties

✉ Shweta Kalson
shwetakalson_2k22phdam02@dtu.ac.in

✉ Anjana Gupta
anjanagupta@dce.ac.in

[1] Department of Applied Mathematics, Delhi Technological University, New Delhi 110042, Delhi, India

Published online: 06 June 2025

inherent in human thought processes and decision-making. These methods often fall short in adequately representing the nuances of human cognition, which involve subjective evaluations, emotional influences, and varying degrees of uncertainty. The linguistic variable was proposed by L.A. Zadeh [1] in the year 1975 to express the challenges faced by decision-makers while using articial or natural languages. The theory 'Computing with Words (CWW)' is an approach that involves replacing numerical values with words in computational and reasoning tasks, which offers a more intuitive approach to problem-solving tasks. This paradigm shift allows for a more expressive representation of data and facilitates a deeper understanding of complex phenomena. Since its introduction, there has been extensive research on the use of linguistic variables in numerous applications [2–4]. Emerging as a crucial component in decision-making processes, Multi-Criteria Decision-Making (MCDM) serves as a fundamental framework in addressing complex decision scenarios. As a result, linguistic descriptors are preferred over other descriptors when dealing with MCDM problems. The cloud model was first presented by Li et al. [5, 6] in 2007. They proposed a new cognitive model called the cloud model and introduced a language concept that is expressed by the cloud model and contains uncertainty, specifically randomness, fuzziness, and the correlation between them. Three numerical descriptors are used by the cloud models to define linguistic concepts: HE (hyper-entropy), EN (entropy), and EX (expectation). The integration of linguistic variables with cloud models provides an effective technique for dealing with the uncertainties and complexity inherent in decision-making. This is especially useful in MCDM scenarios, where the qualitative character of linguistic variables, along with cloud models ability to convert between numerical information and qualitative concepts, provides decision-makers with a varied and effective tool-kit. By leveraging linguistic decision-making based on cloud models, decision-makers can navigate the intricacies of MCDM problems and arrive at more informed and realistic decisions. To address the complexities of human thought, linguistic decision-making is employed, bringing decision-makers closer to reality. Thus, the cloud model provides a way to overcome the inherent uncertainties in the decision-making process.

Various MCDM techniques have been examined so far, including the Analytic Hierarchy Process (AHP), Technique for Order of Preference by Similarity to Ideal Solution (TOPSIS), and Simple Additive Weighting (SAW) [7, 8]. In the 1970s, [9, 10] R. W. Saaty constructed a technique to measure with ratio scales called the Analytic Hierarchy Process. Since its introduction, the Analytic Hierarchy Process (AHP) approach has found extensive uses in many problem areas, including crime analysis and prevention ([11]), safety risk assessment ([12, 13]), etc. Many methods were created to tackle inconsistencies in the AHP process ([14–20]). Deng et al. [21] and Xie et al. [22] formulated a Cloud model-Analytic Hierarchy Process (CM-AHP) algorithm. The former builds on the Fuzzy Cloud Membership Function (FCMF) and investigates its use in risk assessment. At the same time, the latter presents the cloud model to define the uncertainty of the evaluation indexes. The improved AHP-cloud model was presented by Dai et al. [23] in 2022 to present a basic assessment cloud map for the stability and safety associated with the uranium tailing dam. In the follow-up research, many scholars have been dedicated to examining the CM-AHP method; Zheng et al. [24] in their study combined the cloud model (CM) theory

with the analytic hierarchy process (AHP) for the cloud evaluation of mental load state, Yan et al. [25] proposed the relative importance scale with the cloud model and explored its application in landslide susceptibility analyses. Furthermore, Yang et al. [26] proposed a realistic MCDM approach that utilizes the Delphi feedback method, the normal Cloud model, and group decision-making techniques to address the fuzziness and uncertainty of individual judgements. Anjali et al. [27, 28] introduced Shannon entropy-based backward cloud model and Dynamic Cloud Model based on Decision Field Theory to enhance model accuracy and decision-making in cloud models. Although in existing literature, Wang et al. [29] established a linguistic assessment scale capable of converting linguistic assessment information, encompassing any linguistic term set of odd labels, into numerical assessment values. However, a significant research gap has been identified. The scale introduced by Wang et al. in that paper does not incorporate the utilization of linguistic information of the type 1/n to n. Another problem identified is that it is only applicable to additive linguistic data. Based on this analysis, we introduce a new scale LSF called reciprocal linguistic scale function (RLSF), which incorporates the linguistic term sets of the type 1/n to n and caters to reciprocal linguistic term sets (RLTS). Further, a particular case of our introduced RLTS is the exploration of Saaty's relative importance scale (that is, 1/9 to 9). Using this illustrative example, we construct a new cloud model scale for Saaty's relative importance scale within the realm of linguistic approaches, particularly regarding its integration with the cloud model. A summary of key innovations and advantages of the proposed model compared with existing linguistic cloud models is given in Table 1.

The severity of a crime is subjective, as different offences are often perceived with varying degrees of seriousness and the conduct of a criminal involves the actions and behaviours exhibited by an individual engaged in unlawful activities or prohibited behaviour, often characterized by the violation of legal statutes or ethical norms. In India, the National Crime Records Bureau (NCRB) is essential to the gathering, processing, and sharing information about crimes. Crime in India is broadly classified into Cognizable Crime and Non-Cognizable Crime. Cognizable Crimes in India are those that the police can directly investigate without requiring a magistrate's permission. These crimes are broadly classified into IPC (Indian Penal Code) crimes and SLL (Special and Local Laws) crimes. The police station in charge can initiate investigations into cognizable crimes without seeking orders from a magistrate, impacting law enforcement's efficiency and the judicial process. This distinction in classification empowers the police department to take swift actions in cases of cognizable crimes, contributing to the maintenance of law and order in India. The NCRB has published crime rates in terms of crime per lakh people for suitable comparison. This is a more realistic representation of the state's law and order situation than absolute figures that ignore a state's size. Additionally, the NCRB has separated statistics on crimes such as murder, kidnapping and abduction, crimes against women, children, and senior citizens, and offences against property, as illustrated in Table 2.

Until now, numerous machine learning methods have been used to evaluate crime data such as in [33], the authors concluded that Random Forest Regression (RFR) relatively best fits the data while comparing with Decision tree

Table 1 A summary of key innovations and advantages of the proposed model compared with existing linguistic cloud models

Paper	Proposed model	Reciprocal linguistic model	Criminal behaviour analysis	Integration of cloud model with machine learning	Scale used
[30]	Unbalanced trapezoidal cloud (UTC) model	No	No	No	0 to 2n ($n \in N^+$)
[29]	Balanced linguistic cloud model	No	No	No	−n to n
[3]	Unbalanced 2-tuple linguistic model	No	No	No	2^{-n} to 2^m scale (n, $m \in N$)
[25]	Hybrid AHP-NFR-CM-ASIMG	No	No	No	Saaty's nine-scale
[22]	Cloud-Analytic Hierarchy Process (Cloud-AHP) algorithm	No	No	No	Saaty's relative importance (1/9 to 9) scale
[31]	Asymmetric Trapezoidal Cloud (ATC) model	No	No	No	0 to n
[32]	Probabilistic unbalanced linguistic cloud (PULC)	No	No	No	2^{-n} to 2^m scale (n, $m \in N$)
Current paper	Reciprocal linguistic cloud model (RLCM)	Yes	Yes	Yes	$1/n$ to n

Table 2 Various crime categories as classified by the NCRB

Crime categories	Description	Unit of measure
Murder	An act with three key elements: intentional harm, knowledge of fatal consequences, and intent to kill or cause deadly harm.	Crime rate
Crimes against women	Defined as physical, sexual, and emotional offences, including rape, assault, dowry death, domestic violence, stalking, and trafficking.	Crime rate
Kidnapping and abduction	An act involving unlawfully taking or detaining a person, often for ransom or exploitation.	Crime rate
Crimes against children	An act including child abuse, sexual exploitation, trafficking, child pornography, and violence.	Crime rate
Crimes against senior citizens	An act including murder, kidnapping, robbery, cheating, and breach of trust against senior citizens.	Crime rate
Offences against property	An act including burglary, theft, robbery, dacoity, criminal trespass, and arson.	Crime rate

regression (DTR) and Support vector regression (SVR), [34] proposes a novel Particle Swarm-Cuckoo Search (PS-CS) model that is a reliable instrument for forecasting crime rates using various ML algorithms, [35] illustrates the idea of utilizing machine learning techniques to anticipate juvenile delinquency caused by drug addiction and many more [36–38]. As various offences are frequently viewed as having differing degrees of gravity, the seriousness of a crime is subjective. Therefore, it becomes crucial to assign weights to different criminal acts based on human perception. In uncertain circumstances, challenges grow more complex, especially when human subjective judgements are important. Our work analyses these crimes employing a comprehensive methodology. Up until now, a lot of study has gone into combining the cloud model with linguistic phrases to examine different applications, including hotel selection [30], evaluation of industrial sewage discharge [31], investment return [3], teacher evaluation [39], etc. We investigate a case study to examine a practical application of our proposed methodology: Crime in India. Existing crime analysis literature has overlooked the weightage assignment to the gravity or severity associated with different crimes. Instead, all crimes are uniformly treated when total crime occurrences are calculated. Our research provides a framework for assigning varying degrees of weightage to crimes based on human decision-making processes, enhancing the accuracy and depth of crime analysis efforts. Our study aims to catalyze a paradigm shift in how crime is perceived, analysed, and addressed in India, ultimately contributing to more effective law enforcement strategies and societal interventions. For the analysis, secondary data was sourced from the 'Crime in India' report spanning the years 2018–2022 [40]. Since supervised regression algorithms such as Decision Tree, Random Forest, KNN, and Linear Regression are meant to predict continuous numerical values and require labelled data where each instance in the dataset is linked to a corresponding target variable, we believe these algorithms best fit our model. As shown in Fig. 1, the proposed system comprises data gathering, pre-processing, building a prediction model, training the dataset via cross-validation and testing, and comparing algorithms.

This study makes the following noteworthy contributions:

- To bridge the research gap, this article presents a reciprocal linguistic cloud model utilizing a reciprocal LT set with lower computational costs than existing computational models. The suggested model reduces complexity in terms of time and space and maximizes accuracy.



Fig. 1 Dataflow

- A technique grounded in the 3σ principle is presented for evaluating the entropy and hyper-entropy of the reciprocal cloud model. The definitions of entropy and hyper-entropy in this context differ from those outlined in [29], as they are based on reciprocal linguistic data.
- We propose a cloud model scale inspired by the classical Satty scale. Unlike the relative importance scale outlined in [25], our approach utilizes a reciprocal linguistic scale function, distinguishing it significantly.
- Utilizing the proposed framework of generalized reciprocal linguistic cloud and CM-AHP, our study devises a comparative method for ranking different criteria.
- The theoretical approach discussed above is integrated with machine learning to solve practical and real-life difficulties. Using our proposed method, we introduce an approach to evaluate the severity of crimes through human decision-making. Additionally, we leverage regression algorithms such as linear regression, KNN, Random Forest, and Decision Tree to forecast and mitigate potential criminal activities.

The subsequent sections of this paper are organized as follows: Sect. 2 establishes the foundational prerequisites for our proposed work. In Sect. 3, we unveil a novel linguistic scale function, transforming a reciprocal linguistic term set into a cloud and a new cloud model scale is proposed. Section 4 provides a comprehensive overview of our proposed research methodology. Section 5 undertakes an in-depth case study analysing Crime in India. Subsequently, Sect. 6 offers an extensive comparative analysis of our proposed methodology with other existing methods. Finally, Sect. 7 encapsulates the paper's conclusion.

Before further discussion, Table 3 introduces common abbreviations used throughout this article.

2 Preliminaries

Here, we provide some foundations of Linguistic Term Sets (LTS) and Linguistic Scale Function (LSF), and some basic concepts of the Cloud model.

2.1 Linguistic term set and linguistic scale function

Definition 1 [41, 42] Consider a finite LTS $Q = \{q_i \mid i = 0, 1, \ldots, 2\tau\}, \tau \in N$, where a linguistic variable is represented by q_i, and it satisfies the following conditions.

1. Consider an ordered set: $q_i > q_j$, if $i > j$.
2. The operator of negation exists: $q_i = \text{neg}(q_j)$, where $i + j = 2\tau$.
3. If $i \geq j$, then the max operator is $\max\{q_i, q_j\} = q_i$.
4. If $i \geq j$, then the min operator is $\min\{q_i, q_j\} = q_j$.

Table 3 Abbreviations used throughout the paper

Abbreviation	Definition	Explanation
DM	Decision-maker	Anyone who participates in the decision-making process
MCDM	Multi-Criteria Decision-Making	Challenges related to decision-making incorporating multiple criteria
RLSF	Reciprocal Linguistic Scale Function	A mapping from multiplicative reciprocal linguistic terms to numerical values
Ex	Expectation	The mathematical concept of the expected value of the cloud droplets
En	Entropy	Quantifies the level of uncertainty associated with a qualitative idea.
He	Hyper-entropy	The level of uncertainty in entropy
LSF	Linguistic Scale Function	A mapping function that assigns numerical values to linguistic terms
LT	Linguistic Term	A term characterized by values expressed in natural or artificial language, rather than numerical quantities
CM	Cloud Model	Transformation from qualitative to quantitative
AHP	Analytic Hierarchy Process	A technique to measure with ratio scales
CM-AHP	Cloud Model-Analytic Hierarchy Process	–
WCM	Weight Cloud Model	Uncertainty associated with the weight of each indicator
K_i	Reciprocal linguistic term	Notation of reciprocal linguistic term
ζ_i	A numerical value corresponding to K_i	Belongs to the interval [1/n,n]
s	Linguistic Scale Function (LSF)	A function that maps K_i *to* ζ_i
PCM	Pair-wise comparison matrix	–
$\hat{s}$	Score	Score corresponding to a cloud

Definition 2 [41, 42] The linguistic scale function g, given an LTS $Q = \{q_0, q_1, \ldots, q_\tau, \ldots, q_{2\tau}\}$, is a strictly monotonically increasing function from q_i to θ_i, where $g : q_i \to \theta_i, q_i \in Q, \theta_i \in [0, 1]$, and $\theta_0 < \theta_1 < \ldots < \theta_{2\tau}$.

Case 1: Given a uniformly distributed LTS

$$G_1 : g_1(q_i) = \theta_i = i/2\tau.$$

Case 2: Given a non-uniformly distributed LTS with the distances between two consecutive linguistic terms from the middle of the LTS to each end are increasing.

$$G_2 : g_2(q_i) = \theta_i = \begin{cases} \frac{\beta^\tau - \beta^{\tau - i}}{2\beta^\tau - 2}, & \text{if } 0 \le i \le \tau \\ \frac{\beta^\tau + \beta^{i-\tau} - 2}{2\beta^\tau - 2}, & \text{if } \tau < i \le 2\tau \end{cases},$$

where β represents the scale parameter. The previous studies have proposed experimental methods for determining the value of β within the interval [1.36,1.4] [4].

Case 3: Inspired by Case 2, given a non-uniformly distributed LTS with decreasing distance between two consecutive LTS from the middle

$$G_3 : g_3(q_i) = \theta_i = \begin{cases} \frac{\beta^i - 1}{2\beta^\tau - 2}, & \text{if } 0 \le i \le \tau \\ \frac{2\beta^\tau - \beta^{2\tau - i} - 1}{2\beta^\tau - 2}, & \text{if } \tau < i \le 2\tau \end{cases}.$$

2.2 Fundamental concepts of a cloud model

Definition 3 [5, 6] Let T be a qualitative concept over a universe of discourse $U = \{u\}$ and $x \in U$ is a random representation of the concept T, and $\mu_T(x) \in [0, 1]$ is the certainty level of x belonging to T corresponding to a random number exhibiting steady tendency. Therefore, the distribution of x within the universe U can be conceptualized as a 'cloud', with x referred to as a 'cloud drop', which satisfies $x \sim N(Ex, En'^2)$, $En' \sim N(En, He^2)$, and the certainty degree of x belonging to concept T satisfies

$$y = e^{-\frac{(x-Ex)^2}{2(En')^2}},$$

then the distribution of x within the universe U is termed a 'normal cloud'. Here,

- The symbol Ex denotes the mathematical concept of the expected value of the cloud droplets.
- Entropy, denoted as En, quantifies the level of uncertainty associated with a qualitative idea.
- Hyper-entropy, denoted as He, refers to the level of uncertainty in entropy, represented by En.

Definition 4 [6, 29] For a cloud drop (x, y), its contribution to concept T is quantified by the score function $s = xy$. With the numerical characteristics and implementation of a forward normal cloud generator, n cloud drops $\langle (x_1, y_1), (x_2, y_2), \ldots, (x_n, y_n) \rangle$ can be generated. The estimated $\hat{s}$ of cloud Y is determined as follows:

$$\hat{s}(Y) = \frac{1}{n} \sum_{i=1}^{n} x_i y_i. \tag{1}$$

In the context of two clouds denoted as Y_1 and Y_2, if $\hat{s}(Y_1) \geqslant \hat{s}(Y_2)$, then $Y_1 \geqslant Y_2$.

Considering the numerical characteristics (Ex, En, He) of a cloud, the forward cloud generator can be described as the following algorithm [6, 29]:

Algorithm 1 Forward normal cloud generator CG (Ex,En,He,n)

1: **Input:** three parameters Ex, En, He and the number of cloud drops n.
2: **Output:** n cloud drops and their certainty degree.
3: Generate a random number En_i' that follows a normal distribution, where the expected value is En and the variance is He^2.
4: Generate a random number x_i that follows a normal distribution, with an expected value of Ex and a variance of En_i'.
5: Evaluate $y_i = e^{-\frac{(x_i - Ex)^2}{2(En')^2}}$.
6: x_i represents a droplet in the universe, whereas y_i denotes the level of certainty that x_i belongs to the concept T.
7: Continue executing steps $3 - 6$ repeatedly until a total of n cloud droplets have been produced.

2.3 Rules governing different cloud operations

Given two Clouds Y_1 and Y_2, featuring digital characters $Y_1(Ex_1, En_1, He_1)$ and $Y_2(Ex_2, En_2, He_2)$, respectively, the results of arithmetic operations for Y_1 and Y_2, along with the outcome of the power operation for Y_1, collectively compose the Cloud Y characterized by $Y(Ex, En, He)$. The operational rules are outlined in Table 4 [6]. The concepts of Y_1 and Y_2 need to coexist within the same universe of

Table 4 Cloud operations [6]

Operator	Ex	En	He
$+$	$Ex_1 + Ex_2$	$\sqrt{En_1^2 + En_2^2}$	$\sqrt{He_1^2 + He_2^2}$
$-$	$Ex_1 - Ex_2$	$\sqrt{En_1^2 + En_2^2}$	$\sqrt{He_1^2 + He_2^2}$
$\times$	$Ex_1 \times Ex_2$	$\lvert Ex_1 \times Ex_2 \rvert \times \sqrt{\left(\frac{En_1}{Ex_1}\right)^2 + \left(\frac{En_2}{Ex_2}\right)^2}$	$\lvert Ex_1 \times Ex_2 \rvert \times \sqrt{\left(\frac{He_1}{Ex_1}\right)^2 + \left(\frac{He_2}{Ex_2}\right)^2}$
$\div$	$\frac{Ex_1}{Ex_2}$	$\left\lvert \frac{Ex_1}{Ex_2} \right\rvert \times \sqrt{\left(\frac{En_1}{Ex_1}\right)^2 + \left(\frac{En_2}{Ex_2}\right)^2}$	$\left\lvert \frac{Ex_1}{Ex_2} \right\rvert \times \sqrt{\left(\frac{He_1}{Ex_1}\right)^2 + \left(\frac{He_2}{Ex_2}\right)^2}$
$\wedge m$	Ex_1^m	$\sqrt{m} \times Ex_1^{m-1} \times En_1$	$\sqrt{m} \times Ex_1^{m-1} \times He_1$

discourse to ensure meaningful Cloud operations in the algorithm. The Cloud algebraic operations simplify into algorithms when both the entropy and hyper-entropy of either Cloud are zero.

Wang introduced a technique for generating five clouds based on the golden ratio, as outlined in [43]. However, this method is constrained by a significant limitation: It can solely handle linguistic term sets comprising five labels. To address this constraint, Wang et al., as discussed in [29], proposed a linguistic assessment scale capable of facilitating the conversion between clouds and linguistic variables across any linguistic term set with an odd number of labels, rather than just sets of five labels. However, it is important to note that this method does not incorporate the scale of the type (1/n to n) completely, which is a significant limitation. In the next section, we present an approach for converting linguistic variables of the kind (1/n to n) into clouds with an odd number of labels.

3 Proposed methodology

In this section, we present a reciprocal linguistic scale function, a new index scale, and a reciprocal scale (ranging from 1/n to n) designed to convert reciprocal linguistic variables (RLV) into a cloud.

Definition 5 Let K_i be a reciprocal linguistic variable in a reciprocal linguistic term set

$$K = \left\{ K_i \mid i = \frac{1}{n}, \ldots, 1, \ldots, n \right\}, \forall \ \ n \in N^*$$

Consider a reciprocal linguistic scale function 's' that maps

$$K_i \ to \ \zeta_i (i = \frac{1}{n}, \ldots, 1, \ldots, n)$$

that is expressed as follows:

$$s : K_i \rightarrow \zeta_i \quad (i = 1/n, \ldots, 1, \ldots, n)$$

$$\zeta_i = \begin{cases} (\frac{t^g - t^{g-i}}{2t^g - 2}) \frac{1}{log_g(n)} & (\frac{1}{n} \leqslant i < 1), \\ \frac{t^g + t^i - 2}{2t^g - 2} & (1 < i \leqslant n), \end{cases}$$

here $g = max(i)$ and $\zeta_i \in [0, 1]$ and $\zeta_{1/n} < \ldots < \zeta_1 < \ldots < \zeta_n$ is a numeric value and is monotonically increasing, and we take logarithm to the base g. The parameter 't' can be determined through experimental investigations. A previous study indicates that the value of 't' is likely to fall within the range of [1.36, 1.4], based on insights from numerous experimental studies [4]. A detailed exploration and discussion on the behaviour and selection of parameter 't' are presented in the Appendix.

Next, we prove the following theorem to formulate specific properties of the reciprocal linguistic scale function.

Theorem 1 Based on the reciprocal linguistic scale function (RLSF), the following properties hold:

1. If $\frac{1}{n} \leq i < 1$, then $0 \leq \zeta_i < \frac{1}{2\log_g(n)}$
2. If $1 < i \leq n$, then $\frac{1}{2} < \zeta_i \leq 1$

3.1 Method for transformation between reciprocal linguistic variables and clouds

This paper introduces a method of generating $(2n-1)$ clouds for all $n \in N^*$. The cloud generation procedure is represented as follows:

Algorithm 2 Reciprocal Linguistic Cloud model (RLCM)

Let $K_i \in K$ corresponds to Cloud $Y_i(Ex_i, En_i, He_i)$, of which the generation procedures are shown as follows:

Steps:

1. Evaluate ζ_i. Map K_i to ζ_i using Definition 5.

2. Evaluate Ex_i.

$Ex_i = X_{\min} + \zeta_i(X_{\max} - X_{\min})$.

3. Evaluate En_i.

Using the 3σ principle of the normal distribution curve, we can estimate En_i' as follows: $3En_i' = \max\{X_{\max} - Ex_i, Ex_i - X_{\min}\}$. Let us consider a cloud drop (x, y), where $x \sim N(Ex_i, En_i'^2)$.

$$En_i' = \begin{cases} \frac{(1-\zeta_i)(X_{\max}-X_{\min})}{3} & 1/n \leqslant i \leqslant 1 \\ \frac{\zeta_i(X_{\max}-X_{\min})}{3} & 1 < i \leqslant n \end{cases}$$

$$En_{i-1} = En_i = \begin{cases} \frac{(\zeta_{|n-1|}+\zeta_{|n|}+\zeta_{|n|})(X_{\max}-X_{\min})}{9} & 1 < i \leqslant n \\ \frac{(\zeta_i+2\zeta_{i+1})(X_{\max}-X_{\min})}{9} & i = 1 \end{cases}.$$

4. Evaluate He_i.

As $En_i' \sim N(En_i, He_i^2)$, satisfying the 3σ principle of the normal distribution curve we have the hyper-entropy as

$He_{i-1} = He_i = \frac{(En'^{+} - En_i)}{3}$,

where $En'^{+} = \max_k\{En_k'\}$.

3.2 Illustrative example

Following this, we provide a practical illustration to further explain the previously discussed methodology. When we put n = 9 in Definition 5 we get Thomas L. Saaty's scale [9], that is,

$$\left[\frac{1}{9}, \frac{1}{8}, \frac{1}{7}, \frac{1}{6}, \frac{1}{5}, \frac{1}{4}, \frac{1}{3}, \frac{1}{2}, 1, 2, 3, 4, 5, 6, 7, 8, 9\right]$$

This scale is essential for assessing the relative importance or preference of elements within the decision hierarchy and employs numbers between 1/9 and 9 to indicate the relative importance of various factors, we developed a Cloud model scale. This scale is based on Saaty's relative importance scale, CM, and linguistic decision-making theory to evaluate the capabilities of DMs.

Consider the universe $\left[X_{\min}, X_{\max}\right] = [1/9, 9]$ and let the RLTS be given as Table 5. The following describes the process by which reciprocal linguistic variables are converted to clouds:

1. Setting $t = 1.4$, the value for $\zeta_i (i = 1/9, 1/7, \ldots, 1, 3, 5, \ldots, 9)$ can be computed as

$$\zeta_{1/9} = 0.0193, \zeta_{1/7} = 0.0247, \zeta_{1/5} = 0.0342,$$
$$\zeta_{1/3} = 0.0557, \zeta_1 = 0.5102, \zeta_3 = 0.5444,$$
$$\zeta_5 = 0.6113, \zeta_7 = 0.7426, \zeta_9 = 1$$

2. $$Ex_{1/9} = 0.2825, Ex_{1/7} = 0.3303, Ex_{1/5} = 0.4151,$$
$$Ex_{1/3} = 0.6066, Ex_1 = 4.6460, Ex_3 = 4.9498$$
$$Ex_5 = 5.5453, Ex_7 = 6.7124, Ex_9 = 9$$

3. $$En'_{1/9} = 2.9058, En'_{1/7} = 2.8899, En'_{1/5} = 2.8616,$$
$$En'_{1/3} = 2.7978, En'_1 = 1.4513, En'_3 = 1.6129,$$
$$En'_5 = 1.8114, En'_7 = 2.2004, En'_9 = 2.9630$$

Table 5 Saaty's scale

Reciprocal scale	Linguistic term
$K_{1/9}$	Extremely significant
$K_{1/7}$	Very strongly significant
$K_{1/5}$	Strongly significant
$K_{1/3}$	Moderately significant
K_1	Equally significant
K_3	Moderately significant
K_5	Strongly significant
K_7	Very strongly significant
K_9	Extremely significant

Assume intermediate values for $K_{1/8}$, $K_{1/6}$, $K_{1/4}$, $K_{1/2}$, K_2, K_4, K_6, and K_8 between the two adjacent judgements

$$En_{1/9} = 2.8147, En_{1/7} = 2.1248, En_{1/5} = 1.7728,$$
$$En_{1/3} = 1.5932, En_1 = 1.5398, En_3 = 1.5932,$$
4. $En_5 = 1.7728, En_7 = 2.1248, En_9 = 2.8147$

$$He_{1/9} = 0.0494, He_{1/7} = 0.2794, He_{1/5} = 0.3967,$$
$$He_{1/3} = 0.4566, He_1 = 0.4744, He_3 = 0.4566$$
5. $He_5 = 0.3967, He_7 = 0.2794, He_9 = 0.0494$

As described by the reciprocal linguistic terms, the Cloud model scale is presented in Table 6. Figure 2 displays a graphical representation of the nine clouds. Figure 2a represents the clouds that correspond to the cloud model scale, while Fig. 2b represents the clouds that include intermediate values in the scale, that is $K_{1/8}, K_{1/6}, K_{1/4}, K_{1/2}, K_2, K_4, K_6, K_8$, between the two adjacent judgements.

3.3 Graphical analysis of the cloud model scale with uncertainty

The selection of the Cloud model for representing uncertainties is rooted in its notable conformity with human subjective cognition. Uncertainties within the Cloud model display a distinct pattern, with the highest uncertainty observed in the central region (waist) and diminishing towards the upper and lower boundaries. The areas of least uncertainty closely align with the expected value and the two endpoints. However, it is in the waist where uncertainty reaches its peak, indicating a lower level of confidence in these regions, a phenomenon that resonates with human subjective knowledge.

According to the '3σ' rule, we can obtain the upper and lower primary MFs of a Cloud (Ex, En, He) as follows [26].

$$\begin{cases} y_{\text{upper}} = e^{-\frac{(x-Ex)^2}{2(En+3He)^2}} \\ y_{\text{lower}} = e^{-\frac{(x-Ex)^2}{2(En-3He)^2}}. \end{cases} \tag{2}$$

$$y_{\text{diff}} = y_{\text{upper}} - y_{\text{lower}} = e^{-\frac{(x-Ex)^2}{2(En+3He)^2}} - e^{-\frac{(x-Ex)^2}{2(En-3He)^2}}. \tag{3}$$

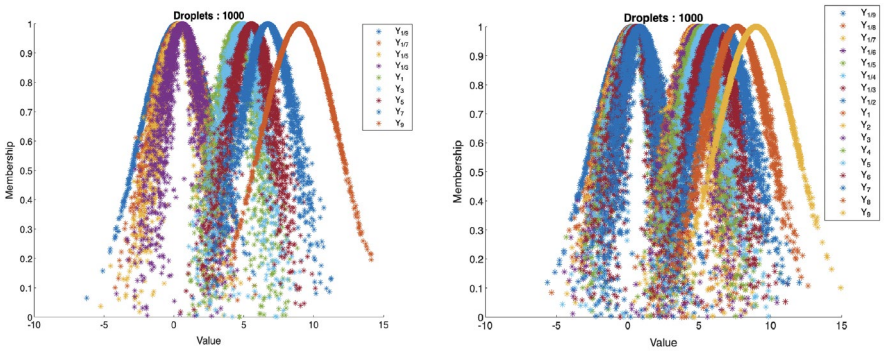
Next, using equation (3), the extremum points of uncertainty are given as

$$x_{\text{extremum}} = Ex \pm 2\sigma_1\sigma_2\sqrt{\frac{\ln\sigma_1 - \ln\sigma_2}{\sigma_1^2 - \sigma_2^2}}, \tag{4}$$

where $\sigma_1 = En + 3He$ and $\sigma_2 = En - 3He$. The difference function reflects the uncertainties.

Table 6 Cloud model scale

Relative importance	CM scale for K_i	Definition	Explanation
1	$Y_1 = (4.6460, 1.5398, 0.4744)$	Equally significant	Two activities i and j are equally significant to the objective
3	$Y_3 = (4.9498, 1.5932, 0.4566)$	Moderately significant	An activity i is slightly more significant over another activity j
5	$Y_5 = (5.5453, 1.7728, 0.3967)$	Strongly significant	An activity i strongly significant over another activity j
7	$Y_7 = (6.7124, 2.1248, 0.2794)$	Very strongly significant	An activity i is very strongly significant over another activity j
9	$Y_9 = (9, 2.8147, 0.0494)$	Extremely significant	An activity i is extremely significant over another activity j
1/3	$Y_{1/3} = (0.6066, 1.5932, 0.4566)$	Moderately significant	An activity j is slightly more significant over another activity i
1/5	$Y_{1/5} = (0.4151, 1.7728, 0.3967)$	Strongly significant	An activity j strongly significant over another activity i
1/7	$Y_{1/7} = (0.3303, 2.1248, 0.2794)$	Very strongly significant	An activity j is very strongly significant over another activity i
1/9	$Y_{1/9} = (0.2825, 2.8147, 0.0494)$	Extremely significant	An activity j is extremely significant over another activity i



(a) Cloud model scale (b) Including intermediate values

Fig. 2 Clouds corresponding to the cloud model scale

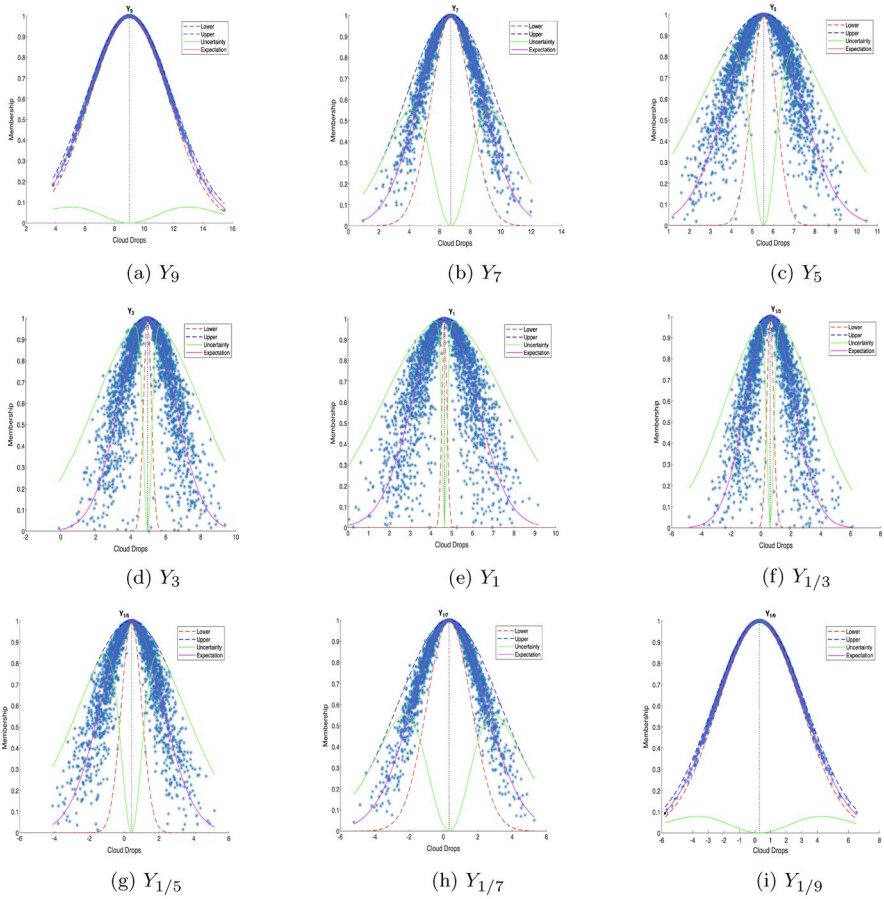
4 Research model

Consider a Multi-Criteria Decision-Making (MCDM) problem with m criteria $C = \{c_1, c_2, \ldots, c_m\}$ and t decision-makers $D = \{d_1, d_2, \ldots, d_t\}$. The assessment information for criterion C_j provided by decision-maker d_k $(k = 1, 2, \ldots, t)$ is denoted as a_{ij}^k, where the information takes the form of a reciprocal linguistic variable derived from a set of reciprocal linguistic terms $K = \{K_i \mid i = 1/n, \ldots, 1, \ldots, n, n \in N^*\}$. Then, the pair-wise comparison matrix given by decision-maker d_k is represented as $A^k = \left(a_{ij}^k\right)_{m\times m}$. This section introduces a method for determining the ranking of the criteria.

The decision-making process is outlined as the following steps:

1. Obtain the PCM corresponding to each DM d_k.

$$\begin{bmatrix} 1 & a_{12} & a_{13} & \cdots & a_{1(n-1)} & a_{1n} \\ \frac{1}{a_{12}} & 1 & a_{23} & \cdots & a_{2(n-1)} & a_{2n} \\ \frac{1}{a_{13}} & \frac{1}{a_{23}} & 1 & \cdots & a_{3(n-1)} & a_{3n} \\ \vdots & \vdots & \vdots & \ddots & \vdots & \vdots \\ \frac{1}{a_{1(n-1)}} & \frac{1}{a_{2(n-1)}} & \frac{1}{a_{3(n-1)}} & \cdots & 1 & a_{n(n-1)} \\ \frac{1}{a_{1n}} & \frac{1}{a_{2n}} & \frac{1}{a_{3n}} & \cdots & \frac{1}{a_{n(n-1)}} & 1 \end{bmatrix}$$



(a) Y_9 (b) Y_7 (c) Y_5

(d) Y_3 (e) Y_1 (f) $Y_{1/3}$

(g) $Y_{1/5}$ (h) $Y_{1/7}$ (i) $Y_{1/9}$

Fig. 3 As depicted in Fig. 3, the graphical representation vividly illustrates the relationship between uncertainty and DM's confidence in an MCDM problem. The graphical representation distinctly reveals that uncertainty is minimal when the DM selects 9 and 1/9, signifying a significant increase in the DM's confidence during decision-making. Conversely, as the DM's decision approaches 1, uncertainty peaks in this region, highlighting a maximal level of ambiguity. However, as the decision trajectory progresses towards 1/9, uncertainty subsequently diminishes once again. The nine clouds corresponding to the Cloud model scale with uncertainty

The diagonal elements are 1, as each criterion is perfectly comparable to itself.

2. Consistency check to prevent inconsistency in the PCM, it is crucial to use the consistency ratio to evaluate the matrix's consistency. The consistency ratio is expressed as follows:

$$\mathrm{CR} = \frac{\lambda_{\max} - \mathrm{m}}{(\mathrm{m}-1)RI},$$

Table 7 Random index

m	1	2	3	4	5	6	7	8	9	10	11	12
RI	0	0	0.58	0.9	1.12	1.24	1.32	1.14	1.45	1.49	1.52	1.54

where $\lambda_{\max}$ is the maximum characteristic root; m is the order of PCM; and RI can be obtained from Table 7.

3. Apply the transformation between reciprocal linguistic variables and clouds as described in Sect. 3 to transform the decision-making data into clouds. The transformed judgement matrix ($C_{m\times m}$) is established as follows:

$$C_{\mathrm{m\times m}} = \begin{pmatrix} C_{11}(Ex_{11}, En_{11}, He_{11}) & C_{12}(Ex_{12}, En_{12}, He_{12}) & \cdots & C_{1m}(Ex_{1m}, En_{1m}, He_{1m}) \\ C_{21}(Ex_{21}, En_{21}, He_{21}) & C_{22}(Ex_{22}, En_{22}, He_{22}) & \cdots & C_{2m}(Ex_{2m}, En_{2m}, He_{2m}) \\ \vdots & \vdots & \ddots & \vdots \\ C_{m1}(Ex_{m1}, En_{m1}, He_{m1}) & C_{m2}(Ex_{m2}, En_{m2}, He_{m2}) & \cdots & C_{mm}(Ex_{mm}, En_{mm}, He_{mm}) \end{pmatrix}.$$

Next we obtain the WCM's by employing the CM-AHP algorithm [22].

4. Take product of each row of the judgement matrix

$$Ex_i = \prod_{j=1}^{n} Ex_{ij}$$

$$En_i = \prod_{j=1}^{n} Ex_{ij} \sqrt{\sum_{j=1}^{n} \left(\frac{En_{ij}}{Ex_{ij}}\right)^2}$$

$$He_i = \prod_{j=1}^{n} Ex_{ij} \sqrt{\sum_{j=1}^{n} \left(\frac{He_{ij}}{Ex_{ij}}\right)^2}$$

5. Taking nth roots

$$Ex_i' = \sqrt[n]{Ex_i}$$

$$En_i' = \sqrt{\frac{1}{n}} \cdot \left(Ex_i\right)^{\frac{1}{n}-1} \cdot En_i$$

$$He_i' = \sqrt{\frac{1}{n}} \cdot \left(Ex_i\right)^{\frac{1}{n}-1} \cdot He_i$$

6. Parameters are combined according to the AHP formula

$$\sum_{i=1}^{n} Ex_i' = Ex_1' + Ex_2' + \cdots + Ex_i'$$
$$\sum_{i=1}^{n} En_i' = \sqrt{\left(En_1'\right)^2 + \left(En_2'\right)^2 + \cdots + \left(En_i'\right)^2}$$
$$\sum_{i=1}^{n} He_i' = \sqrt{\left(He_1'\right)^2 + \left(He_2'\right)^2 + \cdots + \left(He_i'\right)^2}$$

7. Normalizing

$$W\left(Ex_i\right) = \frac{Ex_i'}{\sum_{i=1}^{n} Ex_i'}$$
$$W\left(En_i\right) = \frac{Ex_i'}{\sum_{i=1}^{n} Ex_i'} \cdot \sqrt{\left(\frac{En_i'}{Ex_i'}\right)^2 + \left(\frac{\sum_{i=1}^{n} En_i'}{\sum_{i=1}^{n} Ex_i'}\right)^2}$$
$$W\left(He_i\right) = \frac{Ex_i'}{\sum_{i=1}^{n} Ex_i'} \cdot \sqrt{\left(\frac{He_i'}{Ex_i'}\right)^2 + \left(\frac{\sum_{i=1}^{n} He_i'}{\sum_{i=1}^{n} Ex_i'}\right)^2}$$

8. Aggregation step Subsequently, we apply the Synthetic Cloud Aggregation algorithm [26] to combine the clouds $Y_i\left(Ex_i, En_i, Ee_i\right)$. Suppose we have n clouds $Y_i\left(Ex_i, En_i, He_i\right)$, indexed by $i = 1, \ldots, n$, all within the same universe of discourse U. The synthetic cloud $Y_s\left(Ex_s, En_s, He_s\right)$ is defined as follows:

$$\begin{cases} Ex_s = \frac{1}{n}\sum_{i=1}^{n} Ex_i \\ En_s = \frac{1}{6}\left[\max_i\left\{Ex_i + 3En_i\right\} - \min_j\left\{Ex_j - 3En_j\right\}\right] \\ He_s = \frac{1}{n}\sum_{i=1}^{n} He_i \end{cases}$$

9. Rank the Criteria. Determine the score $\widehat{s}\left(Y_s\right)$ corresponding to each aggregated cloud Y_s using Eq. 1. Then, rank the criteria in accordance with the sequence of $\widehat{s}\left(Y_s\right)$.

Here, we present the pseudo-code for the proposed model to analyse uncertainty.

Algorithm 2 Analysing uncertainty

Steps:

1. Evaluate ζ_i. Map K_i to ζ_i using Definition 5.

2. Evaluate Ex_i.
$$Ex_i = X_{\min} + \zeta_i \left(X_{\max} - X_{\min}\right).$$

3. Evaluate En_i.
Using the 3σ principle of the normal distribution curve, we can estimate En'_i as follows: $3En'_i = \max\{X_{\max} - Ex_i, Ex_i - X_{\min}\}$. Let us consider a cloud drop (x, y), where $x \sim N\left(Ex_i, En'^2_i\right)$.
$$En'_i = \begin{cases} \frac{(1-\zeta_i)(X_{\max}-X_{\min})}{3} & 1/n \leqslant i \leqslant 1 \\ \frac{\zeta_i(X_{\max}-X_{\min})}{3} & 1 < i \leqslant n \end{cases}$$
$$En_{i^{-1}} = En_i = \begin{cases} \frac{\left(\zeta_{|n-1|}+\zeta_{|n|}+\zeta_{|n|}\right)(X_{\max}-X_{\min})}{9} & 1 < i \leqslant n \\ \frac{(\zeta_i+2\zeta_{i+1})(X_{\max}-X_{\min})}{9} & i = 1 \end{cases}.$$

4. Evaluate He_i.
As $En'_i \sim N\left(En_i, He_i^2\right)$, satisfying the 3σ principle of the normal distribution curve we have the hyper-entropy as
$$He_{i^{-1}} = He_i = \frac{(En'^{+} - En_i)}{3},$$
where $En'^{+} = \max_k\{En'_k\}$.

5 Application example

Decision-making in crime analysis and prevention is a multifaceted process shaped by numerous factors and uncertainties. Although numerous machine learning models are employed for predicting and forecasting crimes, they generally depend exclusively on data, neglecting the importance of subjective perspectives. Currently, there is a growing trend towards integrating subjective and objective approaches to tackle practical challenges. Objective data alone may not fully capture the complexities of a situation. Therefore, combining subjective opinions with objective methods for systematic analysis leads to more reliable evaluation outcomes than straightforward machine learning techniques. Given the broad scope of interpretations surrounding the term ‘crime’, which often varies among individuals, we sought subjective insights from legal professionals and educators in academic institutions such as colleges. The survey included a diverse set of respondents, comprising 58% male, 40% female, and 2% identifying as other. The majority (86%) were between 18 and 25 years old, followed by 9% in the 26 and 33 age group, 3% in the 34 and 40 range, and 3% aged 40 and above. Further, following a consistency check, 32.8% of the subjective data responses were validated as reliable and included in the analysis. This diverse collection of perspectives authentically represents public opinion. This study delves into the complexities of decision-making by analysing both objective data from India’s National Crime Records Bureau (NCRB) [40] and subjective data obtained through surveys. Our aim is to understand how decision-makers perceive and respond to

various criminal activities, as well as to assess the severity of each crime. Utilizing the extensive dataset from the NCRB, this study employs a multidisciplinary approach. Drawing upon principles from criminology, cloud model theory, and data science, we investigate patterns, trends, and correlations within the dataset using advanced analytical techniques. Our goal is to uncover the underlying uncertainties in decision-making processes, thereby providing nuanced insights into the complexities of crime analysis and prevention. A flowchart for implementing our proposed research model is illustrated in Fig. 4.

Analysing uncertainty in human decision-making

In this section, we employ our suggested approach that focuses on different crime categories at the national level, as illustrated in Table 2, and provide a weight to their severity based on collective public opinion. To provide suitable weights or scores to various crime categories, we utilized the RLTS as shown in Table 5. In addition, we integrated the cloud model scale to effectively capture and handle the inherent uncertainty, randomness, and fuzziness in the opinions of the DM. Following this, we applied the CM-AHP to rigorously assess and check for any inconsistencies in the DM's judgements, ensuring accurate weight assignments. We conducted a survey using Saaty's relative importance scale to assess DM's perceptions of crime severity. Each DM is asked to rate the seriousness or gravity of the six selected criminal activities. From the collected data, we constructed reciprocal 6×6 PCM for the six crimes above. This subjective assessment provides valuable insights into DM's thought processes and priorities. We analyse the survey responses and the NCRB data to identify correlations and trends. We aim to assess the alignment between perceived severity and actual crime rates by comparing DM's perceptions with objective crime data. Next, we obtain the upper triangular matrices corresponding to each DM DMd_k

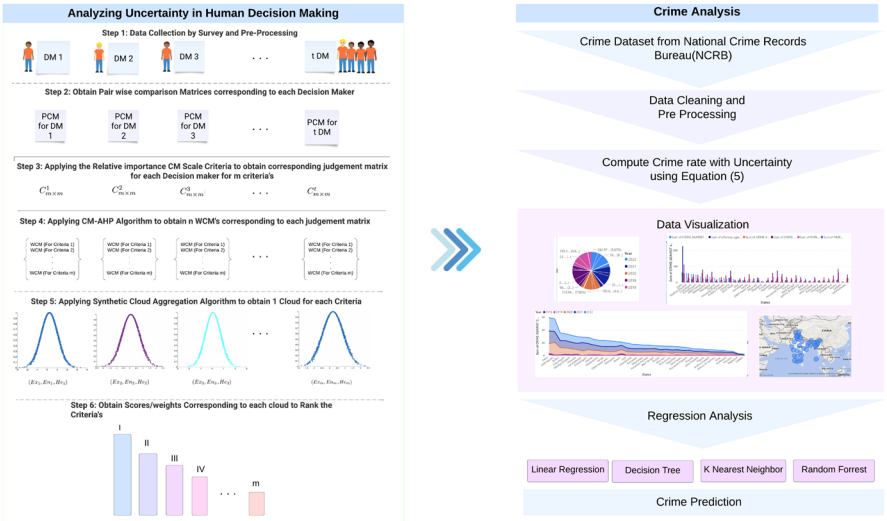


Fig. 4 Flowchart implementing our proposed research model

Algorithm 3 Analysing Uncertainty

Input: Survey data collected from decision makers
Output: Ranked Assessment of m criterions
for (n, data) **do**
    create_upper_triangular_matrix
    return matrix
end for
for each matrix Check_AHP_Consistency(matrix) **do**
    if consistency_ratio < 0.25 **then**
        Select DM matrix
        return DM matrix
    end if
end for
for each DM matrix **do**
    Process_Judgement_Matrix(DM matrix)
    for entry in DM matrix **do**
        if cell value is 'Cloud model Scale' **then** ▷ from table 6
            Set each a_{ij} to $Y_i(Ex_i, En_i, He_i)$
        end if
    end for
end for
Procedure CM-AHP
Output: WCM's corresponding to each criterion
for each datapoint **do**
    Compute Ex_i, En_i, He_i ▷ using Step 4
    Compute Ex'_i, En'_i, He'_i ▷ using Step 5
    Combining parameters ▷ using Step 6
    Compute $W(Ex_i), W(En_i), W(He_i)$ ▷ using Step 7
end for
Procedure Process_Synthetic_Aggregated_clouds(WCM's)
Output: Ranked assessment
for cloud $Y_i(Ex_i, En_i, He_i)$ **do**
    Evaluate $Y_s(Ex_s, En_s, He_s)$ ▷ using Step 8
    Calculate overall score $\widehat{s}(Y_s)$
end for
return Ranking

where Murder (*M*), Kidnapping & Abduction (*K_A*), Crime against women (*C_W*), Crime against children (*C_C*), Offences against property (*O_P*), Crime against senior citizens (*C_SC*), a_{ij} represents the Saaty's scale value for the criterion i compared to criterion j, the diagonal elements are all 1, as each criterion is perfectly comparable to itself.

Step 1. The PCM's of the ability corresponding to each DM established as follows: PCM for DM 1, DM 2, DM 3, ...t^{th} DM.

$$\begin{bmatrix} 1 & 9 & 1 & 1 & 9 & 5 \\ 1/9 & 1 & 1/9 & 1/3 & 1 & 1 \\ 1 & 9 & 1 & 1 & 5 & 1 \\ 1 & 3 & 1 & 1 & 3 & 3 \\ 1/9 & 1 & 1/5 & 1/3 & 1 & 1/5 \\ 1/5 & 1 & 1 & 1/3 & 5 & 1 \end{bmatrix}, \begin{bmatrix} 1 & 5 & 1 & 1 & 9 & 1 \\ 1/5 & 1 & 1/7 & 1/7 & 7 & 1/7 \\ 1 & 7 & 1 & 1 & 5 & 1 \\ 1 & 7 & 1 & 1 & 7 & 1 \\ 1/9 & 1/7 & 1/5 & 1/7 & 1 & 1/7 \\ 1 & 7 & 1 & 1 & 7 & 1 \end{bmatrix},$$

$$\begin{bmatrix} 1 & 1 & 1 & 1 & 1 & 1 \\ 1 & 1 & 1/3 & 1/5 & 1 & 1/7 \\ 1 & 3 & 1 & 1 & 3 & 1 \\ 1 & 5 & 1 & 1 & 3 & 1 \\ 1 & 1 & 1/3 & 1/3 & 1 & 1/7 \\ 1 & 7 & 1 & 1 & 7 & 1 \end{bmatrix}, \ldots, \begin{bmatrix} 1 & 5 & 3 & 3 & 9 & 3 \\ 1/5 & 1 & 1/5 & 1/5 & 7 & 1/7 \\ 1/3 & 5 & 1 & 1 & 7 & 1/3 \\ 1/3 & 5 & 1 & 1 & 7 & 1/3 \\ 1/9 & 1/7 & 1/7 & 1/7 & 1 & 1/9 \\ 1/3 & 7 & 3 & 3 & 9 & 1 \end{bmatrix}.$$

Step 2. Consistency check

We perform consistency checks on the responses provided by the DM (in the form of PCM) to ensure accuracy and consistency.

Step 3. Using our proposed cloud model scale, we obtain the cloud comparison matrices for the respective DM's with consistent responses as $C^1_{6\times6}, C^2_{6\times6}, C^3_{6\times6} \ldots C^t_{6\times6}$.

$C^1_{6\times6}$=

$$\begin{bmatrix} (4.6460, 1.5398, 0.4744) & (9, 2.8147, 0.0494) & (4.6460, 1.5398, 0.4744) & (4.6460, 1.5398, 0.4744) \\ (9, 2.8147, 0.0494) & (5.5453, 1.7728, 0.3967) & (0.2825, 2.8147, 0.0494) & (4.6460, 1.5398, 0.4744) \\ (0.2825, 2.8147, 0.0494) & (0.6066, 1.5932, 0.4566) & (4.6460, 1.5398, 0.4744) & (4.6460, 1.5398, 0.4744) \\ (4.6460, 1.5398, 0.4744) & (9, 2.8147, 0.0494) & (4.6460, 1.5398, 0.4744) & (4.6460, 1.5398, 0.4744) \\ (5.5453, 1.7728, 0.3967) & (4.6460, 1.5398, 0.4744) & (4.6460, 1.5398, 0.4744) & (4.9498, 1.5932, 0.4566) \\ (4.6460, 1.5398, 0.4744) & (4.6460, 1.5398, 0.4744) & (4.9498, 1.5932, 0.4566) & (4.9498, 1.5932, 0.4566) \\ (0.2825, 2.8147, 0.0494) & (4.6460, 1.5398, 0.4744) & (0.4151, 1.7728, 0.3967) & (0.6066, 1.5932, 0.4566) \\ (4.6460, 1.5398, 0.4744) & (0.4151, 1.7728, 0.3967) & (0.4151, 1.7728, 0.3967) & (4.6460, 1.5398, 0.4744) \\ (4.6460, 1.5398, 0.4744) & (0.6066, 1.5932, 0.4566) & (5.5453, 1.7728, 0.3967) & (4.6460, 1.5398, 0.4744) \end{bmatrix},$$

$C^2_{6\times6}$=

$$\begin{bmatrix} (4.646, 1.5398, 0.4744) & (5.5453, 1.7728, 0.3967) & (4.646, 1.5398, 0.4744) & (4.646, 1.5398, 0.4744) \\ (9, 2.8147, 0.0494) & (4.646, 1.5398, 0.4744) & (0.4151, 1.7728, 0.3967) & (4.646, 1.5398, 0.4744) \\ (0.3303, 2.1248, 0.2794) & (0.3303, 2.1248, 0.2794) & (6.7124, 2.1248, 0.2794) & (0.3303, 2.1248, 0.2794) \\ (4.646, 1.5398, 0.4744) & (6.7124, 2.1248, 0.2794) & (4.646, 1.5398, 0.4744) & (4.6460, 1.5398, 0.4744) \\ (5.5453, 1.7728, 0.3967) & (4.6460, 1.5398, 0.4744) & (4.646, 1.5398, 0.4744) & (6.7124, 2.1248, 0.2794) \\ (4.6460, 1.5398, 0.4744) & (4.646, 1.5398, 0.4744) & (6.7124, 2.1248, 0.2794) & (4.6460, 1.5398, 0.4744) \\ (0.2825, 2.8147, 0.0494) & (0.3303, 2.1248, 0.2794) & (0.4151, 1.7728, 0.3967) & (0.3303, 2.1248, 0.2794) \\ (4.646, 1.5398, 0.4744) & (0.3303, 2.1248, 0.2794) & (4.646, 1.5398, 0.4744) & (6.7124, 2.1248, 0.2794) \\ (4.646, 1.5398, 0.4744) & (4.646, 1.5398, 0.4744) & (6.7124, 2.1248, 0.2794) & (4.646, 1.5398, 0.4744) \end{bmatrix},$$

$$C^3_{6\times6}=$$

$$\begin{bmatrix}
(4.646,1.5398,0.4744) & (4.646,1.5398,0.4744) & (4.646,1.5398,0.4744) & (4.646,1.5398,0.4744) & (4.646,1.5398,0.4744) & (4.646,1.5398,0.4744)\\
(4.646,1.5398,0.4744) & (4.646,1.5398,0.4744) & (0.6066,1.5932,0.4566) & (0.4151,1.7728,0.3967) & (4.6460,1.5398,0.4744) & (0.3303,2.1248,0.2794)\\
(4.646,1.5398,0.4744) & (4.9498,1.5932,0.4566) & (4.646,1.5398,0.4744) & (4.6460,1.5398,0.4744) & (4.9498,1.5932,0.4566) & (4.6460,1.5398,0.4744)\\
(4.646,1.5398,0.4744) & (5.5453,1.7728,0.3967) & (4.6460,1.5398,0.4744) & (4.646,1.5398,0.4744) & (4.9498,1.5932,0.4566) & (4.6460,1.5398,0.4744)\\
(4.646,1.5398,0.4744) & (4.6460,1.5398,0.4744) & (0.6066,1.5932,0.4566) & (0.6066,1.5932,0.4566) & (4.646,1.5398,0.4744) & (0.3303,2.1248,0.2794)\\
(4.646,1.5398,0.4744) & (6.7124,2.1248,0.2794) & (4.646,1.5398,0.4744) & (4.646,1.5398,0.4744) & (6.7124,2.1248,0.2794) & (4.646,1.5398,0.4744)
\end{bmatrix},$$

$$\vdots$$

$$C^t_{6\times6}=$$

$$\begin{bmatrix}
(4.646,1.5398,0.4744) & (5.5453,1.7728,0.3967) & (4.9498,1.5932,0.4566) & (4.9498,1.5932,0.4566)\\
(9,2.8147,0.0494) & (4.9498,1.5932,0.4566) & (0.4151,1.7728,0.3967) & (4.646,1.5398,0.4744)\\
(0.4151,1.7728,0.3967) & (0.4151,1.7728,0.3967) & (6.7124,2.1248,0.2794) & (0.3303,2.1248,0.2794)\\
(0.6066,1.5932,0.4566) & (5.5453,1.7728,0.3967) & (4.646,1.5398,0.4744) & (4.6460,1.5398,0.4744)\\
(6.7124,2.1248,0.2794) & (0.6066,1.5932,0.4566) & (0.6066,1.5932,0.4566) & (5.5453,1.7728,0.3967)\\
(4.6460,1.5398,0.4744) & (4.646,1.5398,0.4744) & (6.7124,2.1248,0.2794) & (0.6066,1.5932,0.4566)\\
(0.2825,2.8147,0.0494) & (0.3303,2.1248,0.2794) & (0.3303,2.1248,0.2794) & (0.3303,2.1248,0.2794)\\
(4.646,1.5398,0.4744) & (0.2825,2.8147,0.0494) & (0.6066,1.5932,0.4566) & (6.7124,2.1248,0.2794)\\
(4.9498,1.5932,0.4566) & (4.9498,1.5932,0.4566) & (9,2.8147,0.0494) & (4.646,1.5398,0.4744)
\end{bmatrix}.$$

Further, **Steps 4, 5, 6, 7** use the CM-AHP algorithm for DM 1 as shown in Table 8, we get the weight cloud models (WCM's) for all the 6 Criminal activities, namely: Murder, Kidnapping and abduction, Crime against women, Crime against children, Offences against property, and crime against Senior citizens. Table 9 gives us the WCM's for t decision-makers.

Step 8. We apply the synthetic cloud aggregation algorithm to obtain aggregated clouds for each criminal activity as presented in Table 10. Figures 5 and 6 give us a graphical representation of the obtained aggregated clouds for each criminal activity.

Table 8 CM-AHP method for DM1

Step 4: The product of each row of the judgement matrix						
Ex_i	45,044.2	4.8551	23,252.7044	12,161.6391	0.6373	140.0232
En_i	35,676.9480	69.6446	18,592.8650	9731.7146	7.6175	708.0708
He_i	8600.7759	3.9411	5033.2730	2898.6159	0.9965	172.4306
Step 5: nth roots						
Ex'_i	5.9649	1.3013	5.3425	4.7955	0.9277	2.2788
En'_i	1.9288	7.6205	1.7440	1.5666	4.5268	4.7044
He'_i	0.4650	0.4312	0.4721	0.4666	0.5922	1.1456
Step 6: Parameters combined						
$\sum_{i=1}^{n} Ex'_i$	20.6106					
$\sum_{i=1}^{n} En'_i$	10.4838					
$\sum_{i=1}^{n} He'_i$	1.5830					
Step 7: Normalization						
$W(Ex_i)$	0.2894	0.0631	0.2592	0.2327	0.0450	0.1106
$W(En_i)$	0.1744	0.3711	0.1567	0.1407	0.2208	0.2351
$W(He_i)$	0.0317	0.0215	0.0303	0.0288	0.0289	0.0562

Table 9 Clouds corresponding to decision-makers for all six criminal activities

	M			*K_A*			*C_W*			*C_C*			*O_P*			*C_SC*		
	Ex	En	He	Ex	En	He	Ex	En	He	Ex	En	He	Ex	En	He	Ex	En	He
DM 1	0.342	0.221	0.055	0.059	0.238	0.045	0.160	0.262	0.073	0.160	0.262	0.074	0.030	0.222	0.018	0.248	0.309	0.085
DM 2	0.068	0.268	0.040	0.027	0.199	0.014	0.282	0.151	0.031	0.282	0.151	0.031	0.071	0.217	0.048	0.268	0.144	0.031
DM 3	0.307	0.270	0.034	0.056	0.397	0.009	0.184	0.358	0.074	0.147	0.612	0.020	0.023	0.182	0.013	0.283	0.249	0.032
DM 4	0.102	0.594	0.013	0.034	0.280	0.005	0.291	0.223	0.024	0.291	0.223	0.024	0.027	0.178	0.008	0.261	0.199	0.024
DM 5	0.049	0.319	0.024	0.141	0.303	0.072	0.347	0.234	0.042	0.353	0.238	0.042	0.027	0.199	0.017	0.082	0.322	0.048
DM 6	0.295	0.180	0.040	0.044	0.229	0.031	0.301	0.184	0.040	0.204	0.250	0.068	0.026	0.202	0.014	0.131	0.336	0.074
DM 7	0.173	0.327	0.071	0.077	0.355	0.039	0.315	0.235	0.039	0.248	0.186	0.035	0.024	0.188	0.012	0.163	0.444	0.060
DM 8	0.125	0.401	0.067	0.047	0.210	0.035	0.203	0.254	0.068	0.306	0.202	0.040	0.044	0.254	0.028	0.276	0.183	0.039
DM 9	0.052	0.253	0.037	0.144	0.367	0.082	0.343	0.229	0.048	0.332	0.222	0.047	0.089	0.324	0.059	0.042	0.165	0.033
DM 10	0.167	0.059	0.018	0.167	0.059	0.018	0.167	0.059	0.018	0.167	0.059	0.018	0.167	0.059	0.018	0.167	0.059	0.018
DM 11	0.289	0.174	0.031	0.063	0.371	0.022	0.259	0.156	0.030	0.233	0.141	0.029	0.045	0.221	0.029	0.111	0.235	0.056
DM 12	0.272	0.153	0.041	0.262	0.148	0.041	0.122	0.258	0.063	0.093	0.179	0.051	0.130	0.209	0.059	0.121	0.255	0.062
DM 13	0.287	0.177	0.041	0.146	0.237	0.066	0.299	0.184	0.041	0.194	0.358	0.080	0.046	0.245	0.033	0.028	0.165	0.022
DM 14	0.163	0.296	0.067	0.047	0.189	0.036	0.252	0.129	0.031	0.252	0.129	0.031	0.027	0.142	0.022	0.259	0.134	0.032
DM 15	0.239	0.104	0.025	0.039	0.193	0.028	0.228	0.099	0.024	0.236	0.102	0.024	0.023	0.148	0.017	0.235	0.102	0.024
DM 16	0.380	0.331	0.062	0.059	0.239	0.045	0.154	0.341	0.080	0.154	0.341	0.080	0.033	0.211	0.024	0.221	0.609	0.084
DM 17	0.150	0.322	0.079	0.061	0.234	0.045	0.325	0.215	0.056	0.159	0.263	0.074	0.064	0.208	0.048	0.241	0.302	0.084
DM 18	0.103	0.350	0.064	0.051	0.295	0.032	0.329	0.2398	0.044	0.351	0.253	0.046	0.038	0.163	0.032	0.128	0.414	0.069
DM 19	0.074	0.411	0.037	0.045	0.262	0.029	0.362	0.259	0.043	0.294	0.211	0.038	0.029	0.178	0.022	0.196	0.369	0.080
DM 20	0.195	0.361	0.081	0.049	0.266	0.033	0.290	0.184	0.042	0.281	0.179	0.041	0.027	0.182	0.019	0.158	0.257	0.071
DM 21	0.086	0.478	0.044	0.049	0.304	0.031	0.258	0.349	0.088	0.396	0.329	0.060	0.035	0.218	0.024	0.176	0.387	0.091
DM 22	0.218	0.418	0.093	0.131	0.425	0.072	0.092	0.258	0.060	0.138	0.302	0.073	0.335	0.269	0.059	0.086	0.269	0.060
DM 23	0.082	0.416	0.040	0.047	0.274	0.030	0.196	0.549	0.073	0.192	0.538	0.072	0.080	0.319	0.048	0.403	0.399	0.053

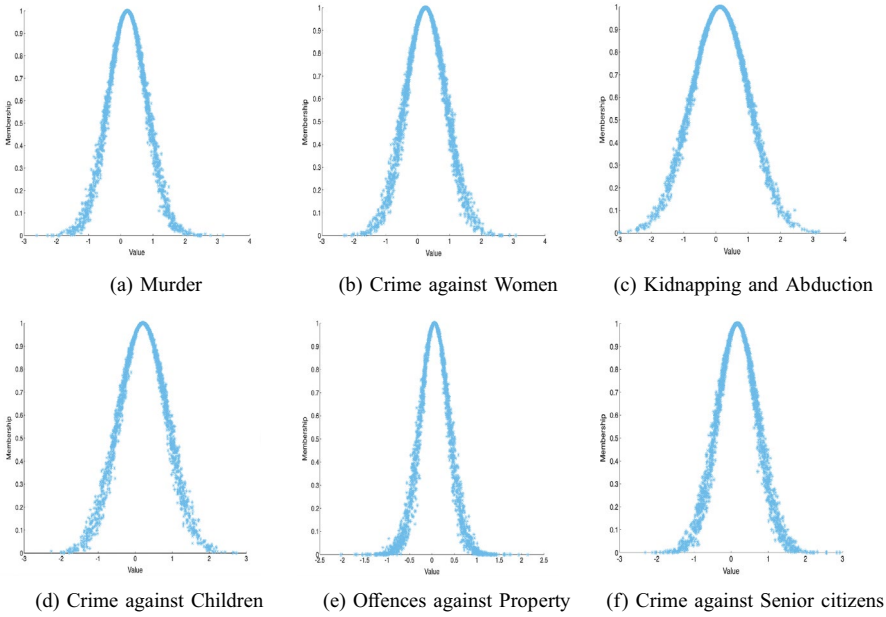
Table 9 (continued)

	M			*K_A*			*C_W*			*C_C*			*O_P*			*C_SC*		
	Ex	En	He	Ex	En	He	Ex	En	He	Ex	En	He	Ex	En	He	Ex	En	He
⋮	⋮	⋮	⋮	⋮	⋮	⋮	⋮	⋮	⋮	⋮	⋮	⋮	⋮	⋮	⋮	⋮	⋮	⋮
DM 63	0.1701	0.4602	0.0626	0.0460	0.2072	0.0343	0.2644	0.1749	0.0353	0.1824	0.2285	0.0608	0.0291	0.1671	0.0224	0.3079	0.2029	0.0380

where Murder (M), Kidnapping & Abduction (*K_A*), Crime against women (*C_W*), Crime against children (*C_C*), Offences against property (*O_P*), and Crime against senior citizens (*C_SC*)

Table 10 Synthetic aggregated clouds corresponding to different criminal activities

Murder	(0.2011, 0.6014, 0.0449)
Kidnapping & Abduction	(0.1259, 0.9003, 0.0419)
Crime against Women	(0.2453, 0.6435, 0.0533)
Crime against Children	(0.2068, 0.6524, 0.0503)
Offences against Property	(0.0551, 0.3176, 0.0322)
Crime against Senior citizens	(0.1659, 0.5394, 0.0474)

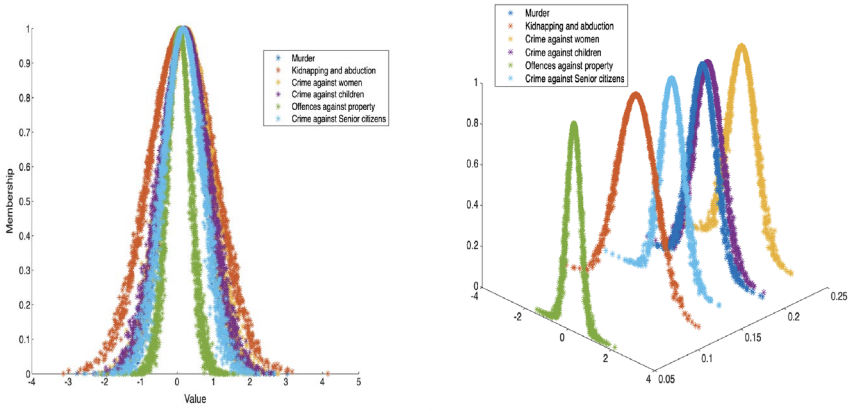


(a) Murder (b) Crime against Women (c) Kidnapping and Abduction

(d) Crime against Children (e) Offences against Property (f) Crime against Senior citizens

Fig. 5 Synthetic aggregated clouds associated with each crime

Step 9. We calculate scores for each cloud corresponding to criminal activities and rank the crimes by considering the degree of severity associated with each crime as detailed in Table 11; crime against Women is consistently regarded as more severe than other crimes by all decision-makers. The decision-makers' assessments reveal varying degrees of certainty in their evaluations. These rankings not only reflect the perceived severity but also capture the nuances of uncertainty inherent in the decision-making process among individuals.



(a) Synthetic aggregated clouds (b) 3D view of the aggregated clouds

Fig. 6 Synthetic aggregated Clouds corresponding to different criminal activities for t decision-makers

Table 11 Scores calculated for all crimes according to all the consistent DM's

Criminal activity	Scores	Ranking
Murder	0.1158	III
Kidnapping and abduction	0.1007	IV
Crime against Women	0.1496	I
Crime against Children	0.1323	II
Offences against Property	0.0259	VI
Crime against Senior Citizens	0.1004	V

Crime Analysis

In this section, we utilize the scores derived from our proposed methodology to examine the data gathered by the NCRB. The Crime in India report clearly states, 'The severity or nature of the offence has not been given any weightage. All offences have been uniformly considered when calculating the overall crime rate for a particular state [40]'. Our proposed methodology gives us a way of assigning weight to each crime by collective public opinion on the degree of severity associated with each crime.

5.1 Data collection and pre-processing

The 'Crime in India' report pertains to crime data collected for the calendar year spanning from 1 January to 31 December of every year. In our analysis, we will look at the crime rates of State/UT over 5 years, that is, 2018–2022. This data collection process involves seeking clarifications from various states, Union Territories, and Central Agencies. Our analysis will focus on the annual data for 'Crime in India', which is provided by 36 states and Union Territories (UTs) to the National Crime Records Bureau (NCRB). The NCRB thoroughly reviews this

data for any discrepancies or inconsistencies. If found, the NCRB communicates them to the respective State or UT for verification. Once final data is received from all states and UTs, including data from major metropolitan cities, the NCRB compiles an all-India crime report. Following international standards, the Bureau applies the 'Principal Offence Rule' for crime counting, meaning that each criminal incident is recorded as a single crime based on the most serious offence. If many offences are registered in a single FIR case, only the most heinous crime, i.e. the one that attracts maximum punishment, will be considered as a counting unit [40]. Crime is a complex phenomenon that cannot be attributed to a single cause. Multiple factors, such as socialization, economic conditions, demographic characteristics, and institutional factors, contribute to criminal behaviour. By addressing the complex and multifaceted causes of criminal behaviour, societies can work towards creating a safer and more just environment for all individuals. Using the crime rate from the NCRB Data and incorporating our proposed methodology, we analyse the Crime Rate with Uncertainty for each state corresponding to each criminal activity.

The Crime Rate with Uncertainty has been calculated as shown:

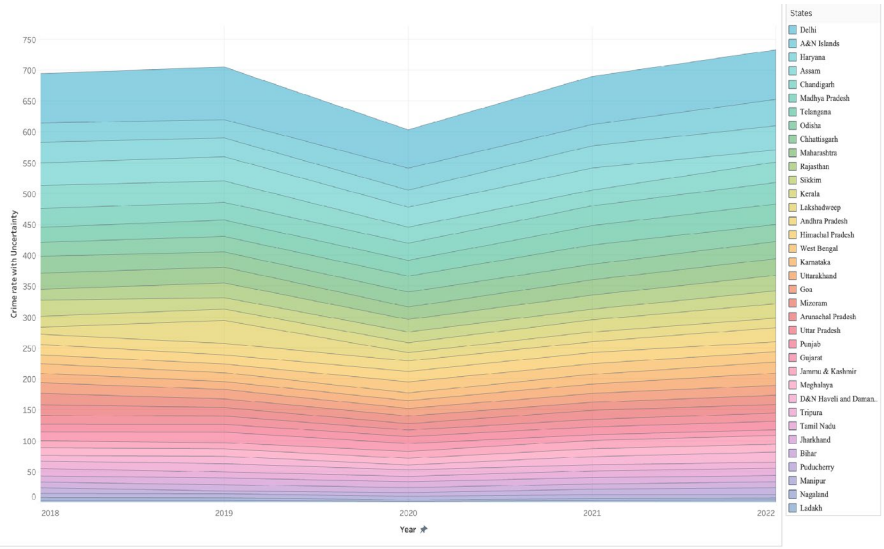
$$\text{Crime Rate with Uncertainty} = \frac{N}{n * P} \sum_{i=1}^{n} x_i y_i, \tag{5}$$

Where n is the number of cloud drops,(x_i, y_i) are the cloud drops corresponding to a Cloud Y, N is the number of criminal incidences, and P is the projected population per lakh.

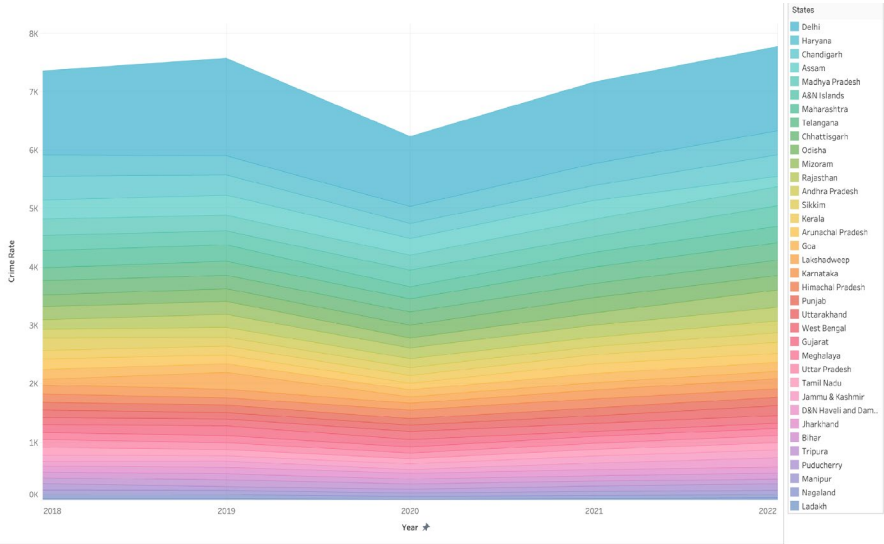
Figure 7 illustrates a time-series analysis of crime rates across different states from 2018 to 2022. Figure 7a and 7b compares crime rates with and without considering uncertainty, respectively. The alteration in state rankings becomes apparent after the application of weighting. Previously, A&N Islands held the third position in Fig. 7b. However, upon factoring in uncertainty, it ascended in the ranking due to its high rates of crime against women and children, which are the most heavily weighted crimes. Meanwhile, Delhi's ranking remained consistent as the most severe.

5.2 Visualization of data

Data visualization entails representing information and data graphically. By presenting data visually, patterns, trends, and relationships within the data can be identified more readily than through textual or tabular formats. Effective data visualization is essential for conveying insights and findings from data analysis clearly and compellingly. Through Power BI and Tableau, our analysis aims to visualize the Crime Rate with Uncertainty of different states/Union Territories corresponding to other crimes. Our study reflects decision-makers opinions on the severity of each crime incorporated with actual crime data. Figure 8 gives us a heatmap representation of the data. This heatmap visually represents crime rates across different states from 2018 to 2022, with varying colours indicating the magnitude of crime rates. The darker colours correspond to increased crime rates, while lighter colours signify lower crime



(a) Timeseries graph on Crime Rate with Uncertainty



(b) Timeseries graph on Crime Rate without Uncertainty

Fig. 7 Visualization of crime rates across various states

rates. States that stand out with exceptionally high or low crime rates compared to others can be identified as outliers. These outliers may require special attention for targeted interventions.

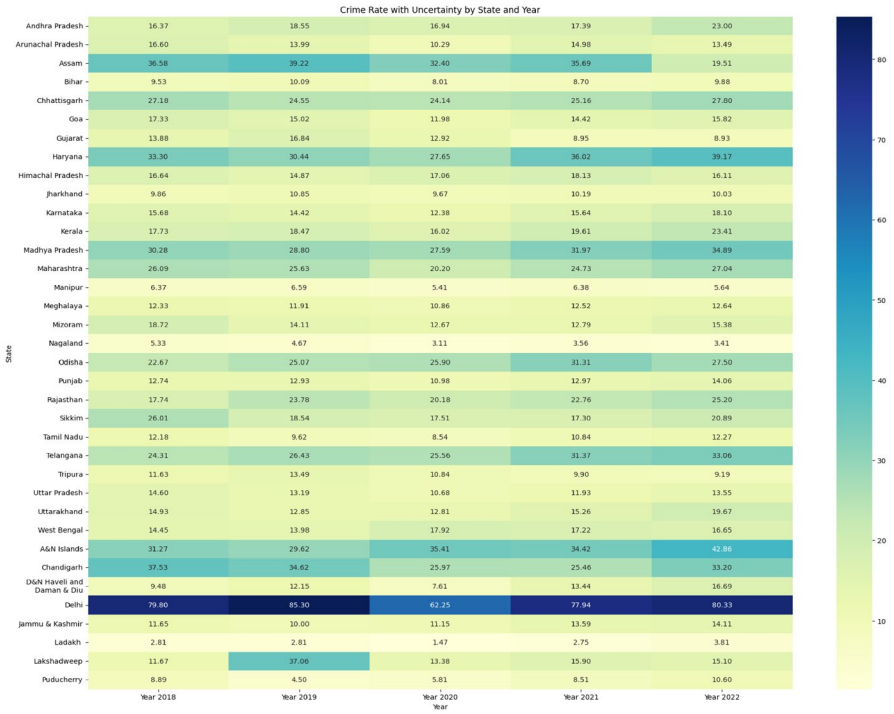


Fig. 8 Heatmap visualization of Crime Rate with Uncertainty by state and year

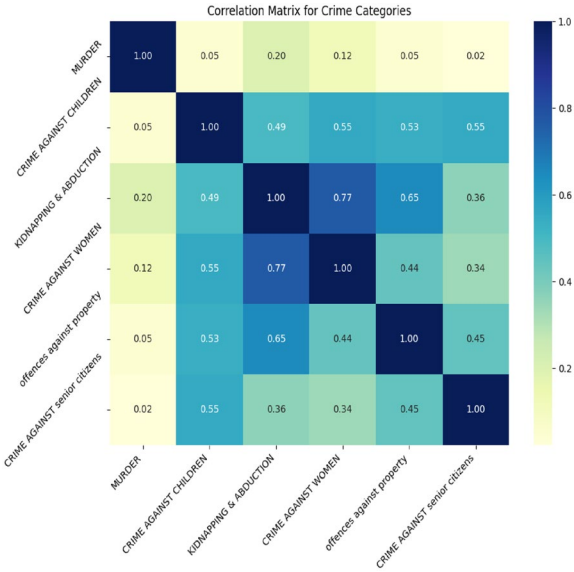


Fig. 9 Correlation matrix for crime categories

Figure 9 shows a correlation matrix represented as a heatmap. The correlation coefficients among variables are presented in a correlation matrix. Each cell in the matrix displays the correlation between two variables. A high correlation near one between two variables indicates a solid association between them. Conversely, a correlation near 0 indicates the absence of a linear relationship between the variables. The numbers in each cell represent the Pearson correlation coefficient between the variables. For example, the correlation between 'Offences against Property' and 'Crime against senior citizens' is 0.45, suggesting a moderate positive relationship. It is useful for identifying relationships between different types of crimes. For instance, if two types of crimes have a high positive correlation, it suggests that they increase or decrease together, which could be useful for law enforcement and public policy.

5.3 Trends in crime rates with uncertainty over the years

This section analyses trends or patterns in the crime rates from 2018 to 2022. Let's start by visualizing the overall trend of each type of crime across all states from 2018 to 2022. Figure 10 shows the average crime rate for each type of crime across all states over the years.

The crime against women and children shows notably higher rates, indicating prevalent issues in these areas. Kidnapping and abduction also register high variability and rates across states. In contrast, murder and crimes against senior citizens are relatively lower but still present concerns. Property offences show moderate levels but with noticeable peaks in certain regions. This visualization underscores the critical areas where law enforcement and social services need to focus their efforts to address and mitigate these crimes effectively.

5.4 Analysing crime using machine learning

Machine learning (ML) is an area of artificial intelligence focused on creating and analysing statistical algorithms capable of learning from data, generalizing to new

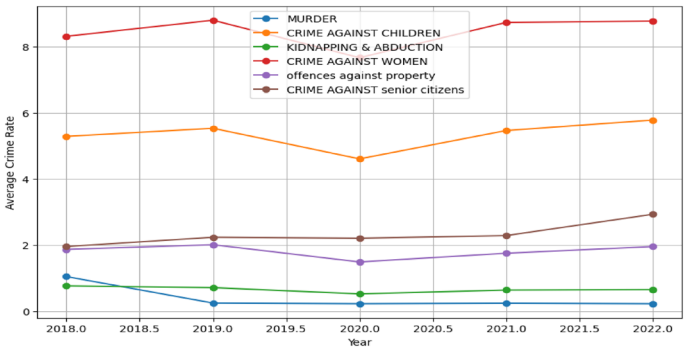


Fig. 10 Trends in Crime Rates with Uncertainty from 2018 to 2022

Table 12 List of parameters for hyperparameter tuning

Regression models	Hyperparameters	Search type
Random Forest Regressor	n_estimators: [50, 100, 200]; max_depth: [None, 10, 20]; min_samples_split: [2, 5, 10]	GridSearchCV
Decision Tree Regressor	max_depth: [None, 5, 10, 20]; min_samples_split: [2, 5, 10]	GridSearchCV
KNN Regressor	n_neighbors: [3, 5, 10]; weights: ['uniform', 'distance']	GridSearchCV
Linear Regression	fit_intercept: [True, False]	GridSearchCV

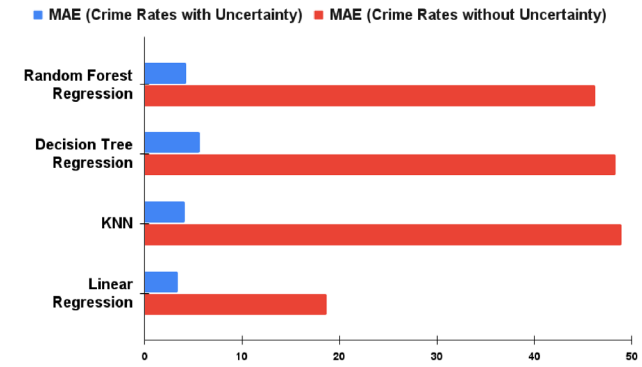
Table 13 Mean Absolute Error (MAE) and R^2 score obtained for crime rates with and without uncertainty using different regression models

	Crime Rates with Uncertainty		Crime Rates without Uncertainty	
Regression Algorithm	MAE	R^2 **Score**	MAE	R^2 **Score**
Random Forest Regression	4.30	0.70	46.29	0.70
Decision Tree Regression	5.69	0.61	48.32	0.67
KNN	4.08	0.74	48.92	0.67
Linear Regression	**3.44**	**0.80**	**18.69**	**0.81**

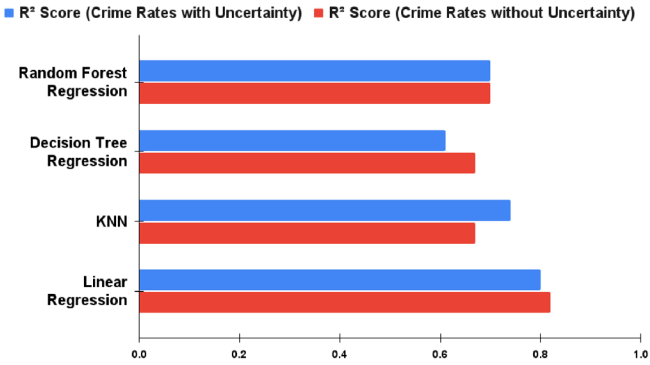
data, and executing tasks without explicit programming instructions [44]. Supervised learning algorithms construct a mathematical model using a dataset comprising input and corresponding output values. This dataset, termed training data, comprises multiple training examples, each consisting of one or more inputs and the desired output, referred to as a supervisory signal. Within the mathematical model, each training example is depicted as an array or vector, often referred to as a feature vector. In contrast, the training data itself is represented as a matrix. By iteratively optimizing an objective function, supervised learning algorithms acquire a function capable of predicting output for new inputs [38, 45]. This section focuses on supervised learning utilizing algorithms such as linear regression, random forest regressor, k-nearest neighbours (KNN) regressor, and decision tree regressor. These models encompass distinct regression techniques, offering a well-rounded comparison while maintaining analytical clarity and computational efficiency. Python is the programming language employed for building and training predictive models within this context. The libraries used are Sci-Kit Learn with Pandas, NumPy, and Matplotlib. To ensure accurate comparison, the same dataset is employed across all experiments.

5.4.1 Results and discussion

We used 'pandas' for data manipulation and 'sklearn' for various machine learning tasks. Cross-validation is executed utilizing the }*cross_validate*′ function from *sklearn.model_selection* library. The aforementioned algorithmic approaches employed to develop regression models, were then optimized using extensive



(a) Mean Absolute Error (MAE)



(b) R-Squared Score

Fig. 11 Comparison of predicted crime rates with and without uncertainty per 100k population using Mean Absolute Error (MAE) and R-Squared score

hyperparameter tuning via GridSearchCV as illustrated in Table 12. The measures for evaluation of the models are Mean Absolute Error (MAE) and R^2_score. Then, we look at the dataset for missing values. If there are any missing values, a warning message will be shown. This step is very important because missing data can affect model performance and thus must be addressed before further analysis.

We have fivefold cross-validation, dividing the dataset into five almost equal sections. In each iteration of this cross-validation process, one subset becomes the test set while the other four subsets are used in training a model. Each fold works as a test set once that operation is repeated five times. Performance measures such as MAE (Mean Absolute Error) and R-squared (R^2) scores are determined for each iteration and then averaged to better evaluate how well the model works. A

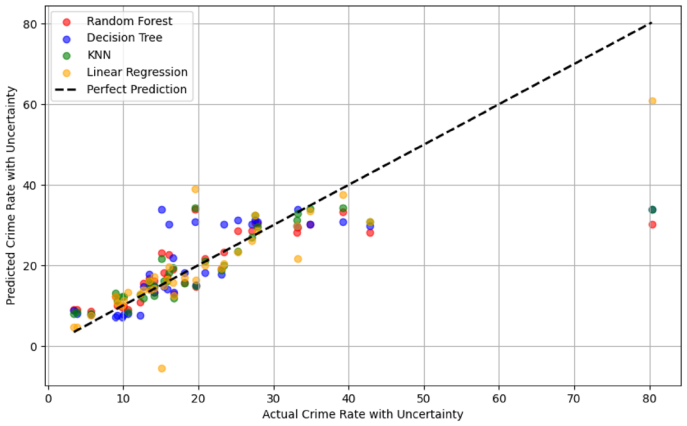
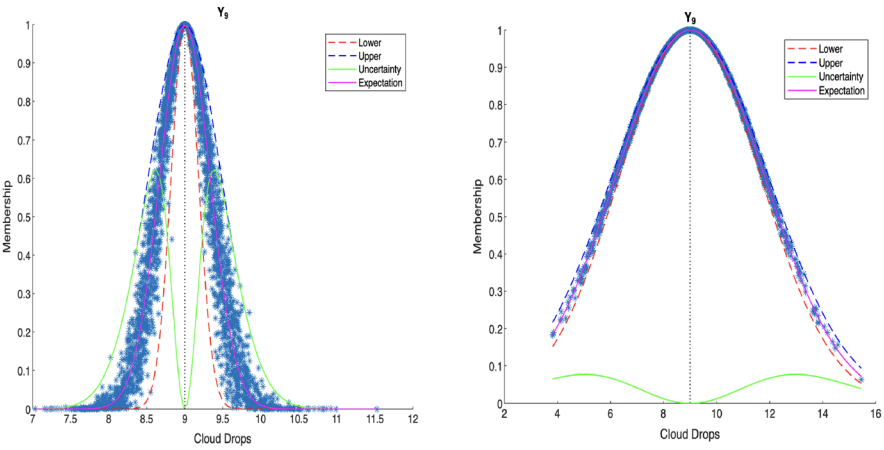


Fig. 12 Actual vs predicted Crime rates with Uncertainty for different regression models

comprehensive analysis of the regression models developed to predict crime rates with and without uncertainty is illustrated in Table 13. Further, Fig. 11 compares predicted crime rates with and without uncertainty per 100k population following mean absolute error (MAE) and R-squared score. The results indicate that incorporating uncertainty significantly improves crime rate predictions, as evident from the lower Mean Absolute Error (MAE) across all models. Linear Regression performs the best, achieving the lowest MAE and highest R^2 score. Models trained with uncertainty consistently yield better accuracy, demonstrating that accounting for uncertainty enhances predictive reliability.

In Fig. 12, we observe actual vs predicted crime rates for k-nearest neighbours (KNN), decision tree regressor, and random forest regressor. Using cross-validation with regression algorithms provides a reliable approach to assess models performance by training and validating it on multiple subsets of data thus avoiding the risk of overfitting and giving more accurate estimate of how well the model generalizes to unknown data. It ensures that the model's performance is not overly sensitive to the specific training-test split of the dataset and allows for the optimization of hyperparameters, leading to improved model performance and employing a fivefold cross-validation approach, wherein 80% of the data is utilized for training purposes. At the same time, the remaining 20% is allocated for testing. This partition cycles over the fivefold, guaranteeing that each fold takes a turn as the test set. This technique offers a more extensive perspective on the model's performance across several subsets of the data, hence minimizing the possibility of a biased or unrepresentative division. The final metrics reported for each model are averages from the five iterations, offering a more reliable estimate of the overall performance.



(a) $Y_9(9, 0.33, 0.05)$ (b) Y_9 by Our proposed method

Fig. 13 Comparing uncertainty in Cloud Y_9 as given by Yan et al. [25] and our proposed model (RLCM)

6 Comparative analysis

Here, we provide an in-depth analysis to validate the effectiveness of our proposed reciprocal linguistic cloud model. To demonstrate its superiority, we comprehensively compare findings from the previous studies, specifically those referenced in [25].

The key distinction lies in how the information is represented and the method used for evaluation to address decision-making challenges. Yan et al. [25] established a Relative Importance CM Scale, grounded in CM theory and the conventional AHP index scale, to assess individual Decision-Makers' (DM) abilities. In their model, the uncertainty is quantified using fixed values for entropy (EN) and hyper-entropy (HE), which restricts the model's flexibility and adaptability across diverse decision-making contexts. Compared with the studies of Yan et al. [25], the work presented in our paper has various advantages. Our paper employs a linguistic approach to scrutinize the inherent uncertainty in Multiple Criteria Group Decision-Making (MCGDM) problems related to DM's abilities to analyse various criteria. A graphical comparison reveals that Fig. 13a, which illustrates the cloud from Yan et al. with an expectation (EX) of 9, entropy (EN) of 0.33, and hyper-entropy

Table 14 Computation complexity of the defined methodology

Step	Complexity
ζ_i	$\mathcal{O}(n)$
Ex_i	$\mathcal{O}(n)$
En_i	$\mathcal{O}(n)$
He_i	$\mathcal{O}(n)$

(HE) of 0.05, exhibits higher uncertainty than the cloud generated by our proposed method shown in Fig. 13b. This proves that the linguistic approach proposed by our methodology adds a nuanced layer to understanding and addressing uncertainties within the decision-making process, enhancing the applicability of our approach in the complex landscape of criminal activity assessment. By effectively utilizing linguistic term sets to convey human subjective knowledge, our approach enriches the relevance and adaptability of criminal activity assessment within a complex decision-making landscape.

Upon calculating the complexity of our proposed model outlined in Table 14, it is anticipated that our defined model exhibits linear complexity. Therefore, our model is well-suited to address complex decision problems.

Further, we compare rankings generated by our methodology with those produced by several other Multi-Criteria Decision-Making (MCDM) techniques [7–9] like the Analytic Hierarchy Process (AHP), Technique for Order of Preference by Similarity to Ideal Solution (TOPSIS), and Simple Additive Weighting (SAW) methods on the same Pair-wise Comparison Matrix (PCM) to determine the rankings from each technique. These rankings help us understand the importance assigned to each criterion by the DM. Traditional MCDM methods yield deterministic outcomes using static weights. These weights are calculated based on the dataset's intrinsic characteristics. Still, they do not consider the subjective psychology behind a decision-maker's choices, failing to align with actual human decision-making processes. In practical applications, cloud models often need to compare and classify different cloud concepts to understand the correlation between different cloud concepts and improve efficiency. Traditional algorithms do not reflect the process of information processing in human decision-making with uncertainty. Table 15 presents a comparative numerical analysis of the rankings generated by DM 1 and by the collective group of all consistent decision-makers. It showcases the differences observed across various models, including our proposed RLCM. Notably, the table highlights significant fluctuations in rankings when comparing the individual decision-maker (DM 1) to the aggregated results of all consistent decision-makers. Traditional MCDM methods yield identical rankings, indicating deterministic outcomes. In contrast, cloud model based methods—such as Yan et al. [25], Shannon entropy-based backward cloud model (SEBCT) [27], and our proposed RLCM—exhibit noticeable variations. These fluctuations underscore the influence of incorporating uncertainty in the decision-making process. Traditional MCDM methods (AHP, TOPSIS, and SAW) assign deterministic weights based on crisp numerical values, Cloud model-based methods—(Yan et al.) assigns fixed values to entropy and hyper-entropy and (SEBCT) used Shannon entropy, whereas our proposed methodology combines objective data (statistical properties) with subjective perceptions (linguistic evaluations using RLCM). This makes it closer to real-life decision-making, especially in fields like crime analysis, where subjective assessments of crime severity play a crucial role.

Wu et al. [46] proposed a quantitative approach to measure ranking stability in group decision-making, where the stability degree ranges from 0 to 1. Stability

Table 15 Comparison of rankings across various models with our proposed model (RLCM)

For DM 1												
Criterion	AHP [9]		TOPSIS [8]		SAW [7]		Yan et al. [25]		SEBCT [27]		RLCM (Proposed)	
	Weights	Ranking	Relative closeness	Ranking	Performance score	Ranking	Score	Ranking	SEBCT score	Ranking	Score	Ranking
Murder	0.3439	I	0.9999	I	0.9998	I	0.0411	I	2.7338	I	0.1179	I
Kidnapping and Abduction	0.0506	V	0.0884	V	0.1629	V	0.0024	V	1.2644	V	0.0387	V
Crime against Women	0.2385	II	0.5852	II	0.7925	II	0.0205	III	2.5505	II	0.0938	II
Crime against Children	0.2190	III	0.55	III	0.7111	III	0.0271	II	1.8466	III	0.0855	III
Offences against property	0.0427	VI	0.0304	VI	0.1511	VI	0.0023	VI	0.8586	VI	0.0212	VI
Crime against senior citizens	0.1053	IV	0.3382	IV	0.4	IV	0.0095	IV	1.5715	IV	0.0465	IV
For all consistent DM's												
Murder	0.1780	III	0.4961	III	0.6022	III	0.0692	I	2.7650	III	0.1158	III
Kidnapping and Abduction	0.0739	V	0.2175	V	0.3100	V	0.0238	V	1.7605	V	0.1007	IV
Crime against Women	0.2767	I	0.6598	I	0.7711	I	0.0625	II	3.1782	II	0.1496	I
Crime against Children	0.2540	II	0.6240	II	0.7318	II	0.0481	IV	3.2202	I	0.1323	II

Table 15 (continued)

For DM 1

Criterion	AHP [9]		TOPSIS [8]		SAW [7]		Yan et al. [25]		SEBCT [27]		RLCM (Proposed)	
	Weights	Ranking	Relative closeness	Ranking	Performance score	Ranking	Score	Ranking	SEBCT score	Ranking	Score	Ranking
Offences against property	0.0435	VI	0.0902	VI	0.1949	VI	0.0088	VI	0.7711	VI	0.0259	VI
Crime against senior citizens	0.1739	IV	0.4809	IV	0.5826	IV	0.0482	III	2.3581	IV	0.1004	V

Table 16 Comparison of stability degrees across decision-making models for all criterion

Criterion	SAW	AHP	TOPSIS	Yan et al.	SEBCT	RLCM (Proposed)
Murder	0.9991	0.9988	0.9989	0.9992	0.9977	0.9980
Kidnapping and Abduction	0.9922	0.9927	0.9894	0.9917	0.9901	0.9900
Crime against Women	0.9878	0.9882	0.9835	0.9853	0.9858	0.9874
Crime against Children	0.9937	0.9938	0.9909	0.9897	0.9900	0.9914
Offences against property	0.9755	0.9748	0.9652	0.9630	0.9632	0.9635
Crime against senior citizens	0.9996	0.9997	0.9994	0.9993	0.9990	0.9988

degrees, as computed in Table 16, reflect the sensitivity of the decision-making outcomes to variations in DM's rankings, with values closer to 1 indicating more robust and consistent performance. The proposed RLCM model demonstrates stability and consistency in rankings across all criteria. This suggests that RLCM effectively incorporates and manages the inherent uncertainty and variability in individual judgements, thereby preventing significant shifts in priority due to minor changes in input preferences. The ability to integrate uncertainty and deliver stable outputs distinguishes RLCM from traditional models.

Lastly, we compare the crime rate predictions with and without the incorporation of uncertainty using RLCM. The results, as shown in Table 13, demonstrate that integrating uncertainty leads to a substantial reduction in prediction error (MAE) while maintaining comparable levels of accuracy in terms of the R^2 score.

7 Conclusion

Regarding linguistic decision-making problems, the normal cloud model is valuable for translating qualitative instantiations into quantitative values. Our research introduces the reciprocal linguistic cloud model, a comprehensive information representation framework that effectively manages reciprocal linguistic data. This model acts as a bridge, facilitating efficient conversions between reciprocal linguistic variables and clouds. For this purpose, a reciprocal linguistic scale function has been specifically defined. A technique grounded in the 3σ principle is presented for evaluating the entropy and hyper-entropy of the reciprocal cloud model. Moreover, we introduced the Cloud Model Scale, which seamlessly integrates the cloud model with Saaty's relative importance scale and incorporates reciprocal linguistic term sets. Our cloud model scale supersedes the existing relative importance scale grounded in CM theory by regarding the AHP index scales as reciprocal linguistic terms. This method avoids loss of information and minimizes ambiguity, unlike other methods. Besides, the cloud model scale is used for a case study on crime and its severity. It allows scores to be assigned to different crimes, considering the uncertainty inherent in DM's opinions. Through this methodology, we carefully examined data on crime, which was collected by the National Crime Records Bureau (NCRB) in their annual report 'Crime in India'. Our analysis provided an extensive overview of

crime, thus giving us vital input for our case study. It is worth noting that there were significant changes in state rankings after integrating weights into the data analysis. Considering numerous factors and uncertainties emphasizes better decision-making, especially for crime analysis. In deepening our data analysis, we employed machine learning algorithms to predict future crime rates using evaluation metrics Mean absolute error (MAE) and R^2 score suggesting its superiority in capturing the fundamental patterns and trends contained in the data, hence making more accurate predictions of future rates of crimes. Our proposed methodology captures the uncertainty and randomness that define the decision-making process. This makes it much better than traditional MCDM methods based on subjective data alone. Moreover, our research shows that crime evaluation methodologies must change as societies' attitudes towards crime and legal systems change. Using DM's opinion to scale crime gravity, our approach conforms to a current trend emphasizing community engagement and transparency in legal frameworks. Therefore, it improves the legitimacy of juridical verdicts and helps us better understand how illegal activities interact with social dynamics and law enforcement responses. In summary, our study represents a significant step forward in the quest for more nuanced and data-driven approaches to understanding and addressing crime. By combining advanced methodologies with real-world data, we aim to contribute to the ongoing efforts to create safer and more just societies for all.

Appendix

Here, we explore and discuss the behaviour and selection of parameter t. Figures 14 and 15 illustrate how variations in the parameter t impact the reciprocal linguistic scale function ζ_i and cloud distributions. Between t = 1.36 and 1.4, a sharp transition occurs, making this a critical range where uncertainty is well-balanced. This range avoids the under-dispersion seen at lower values (e.g. t=1.3) and the over-scattering observed at higher values (e.g. t=1.45). Beyond this, the function becomes step-like, and cloud distributions become either overly sharp or too diffused, reducing interpretability. Moreover, extreme values like t=0 and t=30 serve as boundary cases, emphasizing the necessity of fine-tuning 't' within a moderate, experimentally validated range.

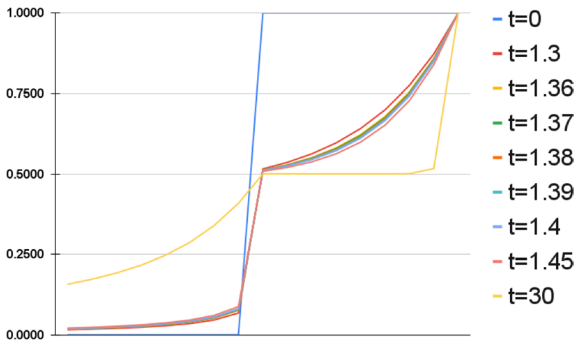
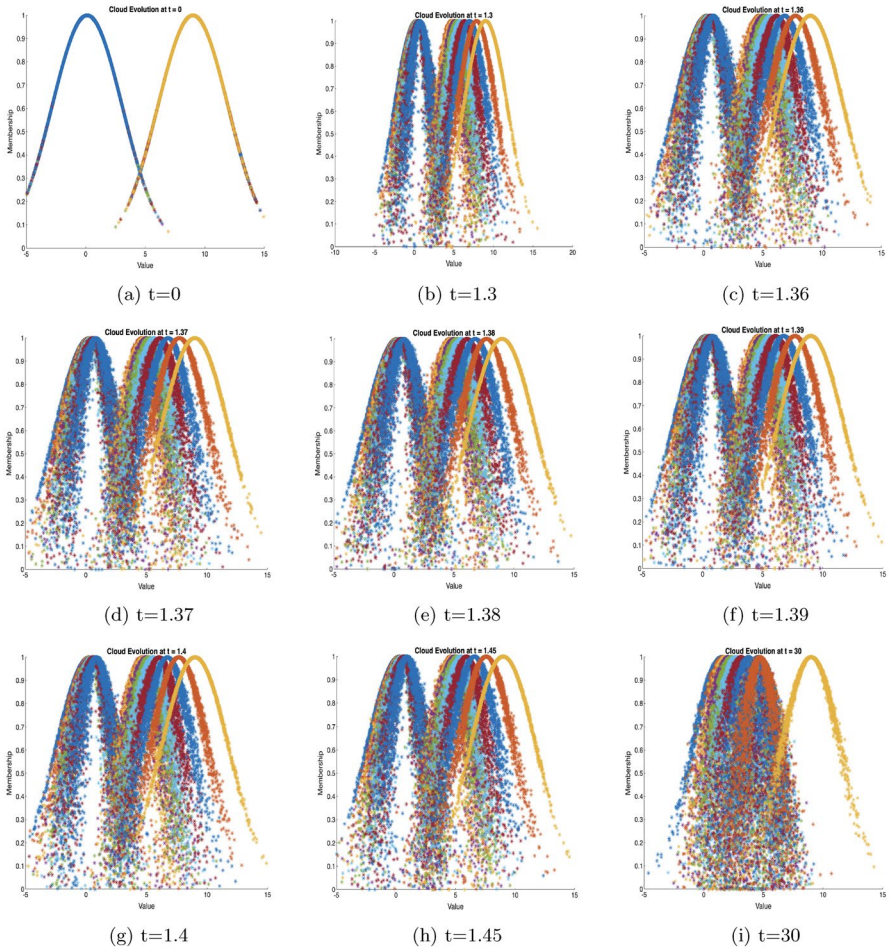


Fig. 14 The relationship between t and ζ_i



(a) t=0 (b) t=1.3 (c) t=1.36

(d) t=1.37 (e) t=1.38 (f) t=1.39

(g) t=1.4 (h) t=1.45 (i) t=30

Fig. 15 Cloud evolution for t = [0, 1.3, 1.36, 1.37, 1.38, 1.39, 1.4, 1.45, 30]

Acknowledgements The author Ms. Shweta Kalson would like to acknowledge the fellowship received from her affiliated university, i.e. Delhi Technological University.

Author Contributions Shweta Kalson helped in conceptualization, data curation, formal analysis, methodology, writing—original draft, and writing—review and editing. Anjana Gupta helped in conceptualization, validation, supervision, and writing—review and editing.

Funding The authors did not receive support from any organization for the submitted work.

Data availability The authors confirm that all used data are benchmark and are freely available.

Declarations

Conflict of Interest The authors declare that they have no conflict of interest.

Consent for Publication The authors confirm that the final version of the manuscript has been reviewed, approved, and consented for publication by all authors.

References

1. Zadeh LA (1975) The concept of a linguistic variable and its application to approximate reasoning-i. Inf Sci 8(3):199–249. https://doi.org/10.1016/0020-0255(75)90036-5
2. Wang J.-q, Wu J.-t, Wang J, Zhang H.-y, Chen X.-h (2014) Interval-valued hesitant fuzzy linguistic sets and their applications in multi-criteria decision-making problems. Information sciences **288**, 55–72 https://doi.org/10.1016/j.ins.2014.07.034
3. Chauhan P, Gupta A, Malhotra T (2023) A novel cloud model based on multiplicative unbalanced linguistic term set. J Supercomput 79(14):16378–16408. https://doi.org/10.1007/s11227-023-05295-z
4. Bao G-Y, Lian X-L, He M, Wang L-L (2010) Improved two-tuple linguistic representation model based on new linguistic evaluation scale. Control Decis 25(5):780–784
5. Li D, Liu C, Gan W (2009) A new cognitive model: cloud model. Int J Intell Syst 24(3):357–375. https://doi.org/10.1002/int.20340
6. Li D, Du Y (2017) Artificial Intelligence with Uncertainty. CRC Press, New York
7. Odu G (2019) Weighting methods for multi-criteria decision making technique. J Appl Sci Environ Manag 23(8):1449–1457. https://doi.org/10.4314/jasem.v23i8.7
8. Hwang C-L, Lai Y-J, Liu T-Y (1993) A new approach for multiple objective decision making. Comput Oper Res 20(8):889–899. https://doi.org/10.1016/0305-0548(93)90109-V
9. Saaty RW (1987) The analytic hierarchy process-what it is and how it is used. Math Model 9(3–5):161–176. https://doi.org/10.1016/0270-0255(87)90473-8
10. Saaty T (2008) Decision making with the analytic hierarchy process. J. Services Sciences Int. J. Services Sciences, Int. https://doi.org/10.1504/IJSSCI.2008.017590
11. Yan FX, Xia J, Shen GQ, Kang XS (2011) A crime decision-making model based on ahp. Appl Mech Materi 50:885–889. https://doi.org/10.4028/www.scientific.net/AMM.50-51.885
12. Tang J, Wang D, Ye W, Dong B, Yang H (2022) Safety risk assessment of air traffic control system based on the game theory and the cloud matter element analysis. Sustainability 14(10):6258. https://doi.org/10.3390/su14106258
13. Lin C, Zhang M, Li L, Zhou Z, Liu S, Liu C, Li T (2020) Risk assessment of tunnel construction based on improved cloud model. J Perform Constr Facil 34(3):04020028. https://doi.org/10.1061/(ASCE)CF.1943-5509.0001421
14. Nishizawa K (1995) A consistency improving method in binary ahp. J Oper Res Soc Jpn 38:21
15. Lin C, Kou G, Ergu D (2013) A heuristic approach for deriving the priority vector in ahp. Appl Math Model 37(8):5828–5836. https://doi.org/10.1016/j.apm.2012.11.023
16. Benítez J, Delgado-Galván X, Izquierdo J, Pérez-García R (2011) Achieving matrix consistency in ahp through linearization. Appl Math Model 35(9):4449–4457. https://doi.org/10.1016/j.apm.2011.03.013
17. Yang W-C, Kang H-S, Ri G-S, Kim J-S et al (2022) Consistency improvement method of pairwise matrix based on consistency ratio decreasing rate and attribute weighting method considered decision makers' levels in analytic hierarchy process: application to hip joint prosthesis material selection. Math Probl Eng. https://doi.org/10.1155/2022/1463006
18. Saaty TL (2003) Decision-making with the ahp: why is the principal eigenvector necessary. Eur J Oper Res 145(1):85–91. https://doi.org/10.1016/S0377-2217(02)00227-8
19. Saaty TL, Hu G (1998) Ranking by eigenvector versus other methods in the analytic hierarchy process. Appl Math Lett 11(4):121–125. https://doi.org/10.1016/S0893-9659(98)00068-8
20. Jarek S (2016) Removing inconsistency in pairwise comparisons matrix in the ahp. Multiple Criteria Decision Making https://doi.org/10.22367/mcdm.2016.11.05
21. Deng F, Pu J, Huang Y, Han Q (2023) 3d geological suitability evaluation for underground space based on the ahp-cloud model. Undergr Sp 8:109–122. https://doi.org/10.1016/j.undsp.2022.03.006
22. Xie S, Dong S, Chen Y, Peng Y, Li X (2021) A novel risk evaluation method for fire and explosion accidents in oil depots using bow-tie analysis and risk matrix analysis method based on cloud model theory. Reliab Eng Syst Saf 215:107791. https://doi.org/10.1016/j.ress.2021.107791

23. Dai X, Wu X, Hong Y, Xie J, Lin D, Chen Y, Liu Y (2022) Safety and stability evaluation of the uranium tailings impoundment dam: Based on the improved ahp-cloud model. J Radiat Res Appl Sci 15(1):21–31. https://doi.org/10.1016/j.jrras.2022.01.020
24. Zheng X, Hao T, Wang H, Xu K (2023) Quantification study of mental load state based on ahp-topsis integration extended with cloud model: methodological and experimental research. Complex Intell Syst 9(5):5501–5525. https://doi.org/10.1007/s40747-023-00994-9
25. Yan F, Zhang Q, Ye S, Ren B (2019) A novel hybrid approach for landslide susceptibility mapping integrating analytical hierarchy process and normalized frequency ratio methods with the cloud model. Geomorphology 327:170–187. https://doi.org/10.1016/j.geomorph.2018.10.024
26. Yang X, Yan L, Zeng L (2013) How to handle uncertainties in ahp: the cloud delphi hierarchical analysis. Inf Sci 222:384–404. https://doi.org/10.1016/j.ins.2012.08.019
27. Anjali Gupta A (2025) A novel shannon entropy-based backward cloud model and cloud k-means clustering. J Supercomput 81(1):65. https://doi.org/10.1007/s11227-024-06528-5
28. Anjali A, Gupta A (2025) Dynamic cloud model based on decision field theory. J Supercomput 81(4):620. https://doi.org/10.1007/s11227-025-06989-2
29. Wang J-Q, Peng L, Zhang H-Y, Chen X-H (2014) Method of multi-criteria group decision-making based on cloud aggregation operators with linguistic information. Inf Sci 274:177–191. https://doi.org/10.1016/j.ins.2014.02.130
30. Wang X-K, Wang S-H, Zhang H-Y, Wang J-Q, Li L (2021) The recommendation method for hotel selection under traveller preference characteristics: a cloud-based multi-criteria group decision support model. Group Decis Negot 30:1433–1469. https://doi.org/10.1007/s10726-021-09735-0
31. Wang X-K, Wang Y-T, Zhang H-Y, Wang J-Q, Li L, Goh M (2021) An asymmetric trapezoidal cloud-based linguistic group decision-making method under unbalanced linguistic distribution assessments. Comput Ind Eng 160:107457. https://doi.org/10.1016/j.cie.2021.107457
32. Chauhan P, Gupta A (2024) Probabilistic multiplicative unbalanced linguistic game using linguistic cloud model. J Supercomput 80(14):20346–20377. https://doi.org/10.1007/s11227-024-06240-4
33. Aziz RM, Sharma P, Hussain A (2024) Machine learning algorithms for crime prediction under indian penal code. Ann Data Sci 11(1):379–410. https://doi.org/10.1007/s40745-022-00424-6
34. Aziz RM, Hussain A, Sharma P (2024) Cognizable crime rate prediction and analysis under indian penal code using deep learning with novel optimization approach. Multimed Tools Appl 83(8):22663–22700. https://doi.org/10.1007/s11042-023-16371-0
35. Nesa M, Shaha TR, Yoon Y (2022) Prediction of juvenile crime in bangladesh due to drug addiction using machine learning and explainable ai techniques. J Computat Soc Sci 5(2):1467–1487. https://doi.org/10.1007/s42001-022-00175-7
36. Jenga K, Catal C, Kar G (2023) Machine learning in crime prediction. J Ambient Intell Humanized Comput 14(3):2887–2913. https://doi.org/10.1007/s12652-023-04530-y
37. Saini B, Saini DK, Srivastava S, Aggarwal M (2023) A study of lightweight approaches to analyze crime conditions in India. J Appl Secur Res 18(2):221–245. https://doi.org/10.1080/19361610.2021.2006031
38. Mohri M, Rostamizadeh A, Talwalkar A (2012) Foundations of Machine Learning. The MIT Press, London
39. Chang T.-C, Wang H (2016) A multi criteria group decision-making model for teacher evaluation in higher education based on cloud model and decision tree. Eurasia Journal of Mathematics, Science and Technology Education **12**, 1243–1262 https://doi.org/10.12973/eurasia.2016.1510a
40. NCRB: Crime in India. Available online at: https://ncrb.gov.in/crime-in-india (2022)
41. Xie W, Xu Z, Ren Z (2017) Dual probabilistic linguistic term set and its application on multi-criteria group decision making problems. In: 2017 IEEE International Conference on Industrial Engineering and Engineering Management (IEEM), pp. 1469–1474 . https://doi.org/10.1109/IEEM.2017.8290137 . IEEE
42. Wang P, Xu X, Huang S, Cai C (2018) A linguistic large group decision making method based on the cloud model. IEEE Trans Fuzzy Syst 26(6):3314–3326. https://doi.org/10.1109/TFUZZ.2018.2822242
43. Wang H, Feng Y (2005) On multiple attribute group decision making with linguistic assessment information based on cloud model. Control Decis 20(6):679
44. Koza JR, Bennett FH, Andre D, Keane MA (1996) Automated design of both the topology and sizing of analog electrical circuits using genetic programming. Artif Intell. https://doi.org/10.1007/978-94-009-0279-4_9

45. Brewka G (1996) Artificial intelligence-a modern approach by stuart russell and peter norvig, prentice hall. series in artificial intelligence, englewood cliffs, nj. Knowl Eng Rev 11:78–79. https://doi.org/10.1017/S0269888900007724
46. Wu F, Zhao Y, Chen Y (2016) Stability analysis of group decision-making under weighted scoring rules. Int J Syst Sci 47(16):3822–3828. https://doi.org/10.1080/00207721.2015.1128577

Publisher's Note Springer Nature remains neutral with regard to jurisdictional claims in published maps and institutional affiliations.

Springer Nature or its licensor (e.g. a society or other partner) holds exclusive rights to this article under a publishing agreement with the author(s) or other rightsholder(s); author self-archiving of the accepted manuscript version of this article is solely governed by the terms of such publishing agreement and applicable law.

A Review Of Chemical Recycling Pathways For Waste Polyurethane

Karnam Bharti*, Raminder Kaur

Department of Applied Chemistry, Delhi Technological University, Delhi, 110042, India
E-mail- karnambharti@gmail.com*, raminderkaur@dce.ac.in

Abstract

Polyurethane (PU) is a commonly utilized polymer due to its versatility and performance properties. However, its resistance to deterioration creates considerable hurdles for end-of-life care. This review gives a shortoverview of present recycling strategies for PU, with a particular emphasis on chemical recycling processes, including hydrolysis, alcoholysis, acidolysis, glycolysis, aminolysis, and phosphorolysis. These approaches enable the breakdown of PU into useful chemical constituents, facilitating potential reuse in polymer synthesis.This review highlights the mechanism, advantages, and limits of each method. Although additional optimization is required, chemical recycling offers a viable approach for enhancing the sustainability of PU material lifecycles.

Keywords: Polyurethane (PU), Chemical Recycling, Hydrolysis, Alcoholysis, Acidolysis, Glycolysis, Aminolysis, and Phosphorolysis, Rigid foam, Flexible foam.

1. Introduction

Polyurethane (PU) is the most versatile polymer renowned for its wide range of physical and chemical properties, making it a key material in the field of polymer science. Its performance and structural adaptability have added to its increasing importance in both the industrial and research sectors(1).The size of the worldwide polyurethane market was assessed at USD 87.10 billion in 2023 and is predicted to increase at a compound annual growth rate (CAGR) of 4.4% from USD 91.49 billion in 2024 to USD 135.08 billion by 2032(2,3).

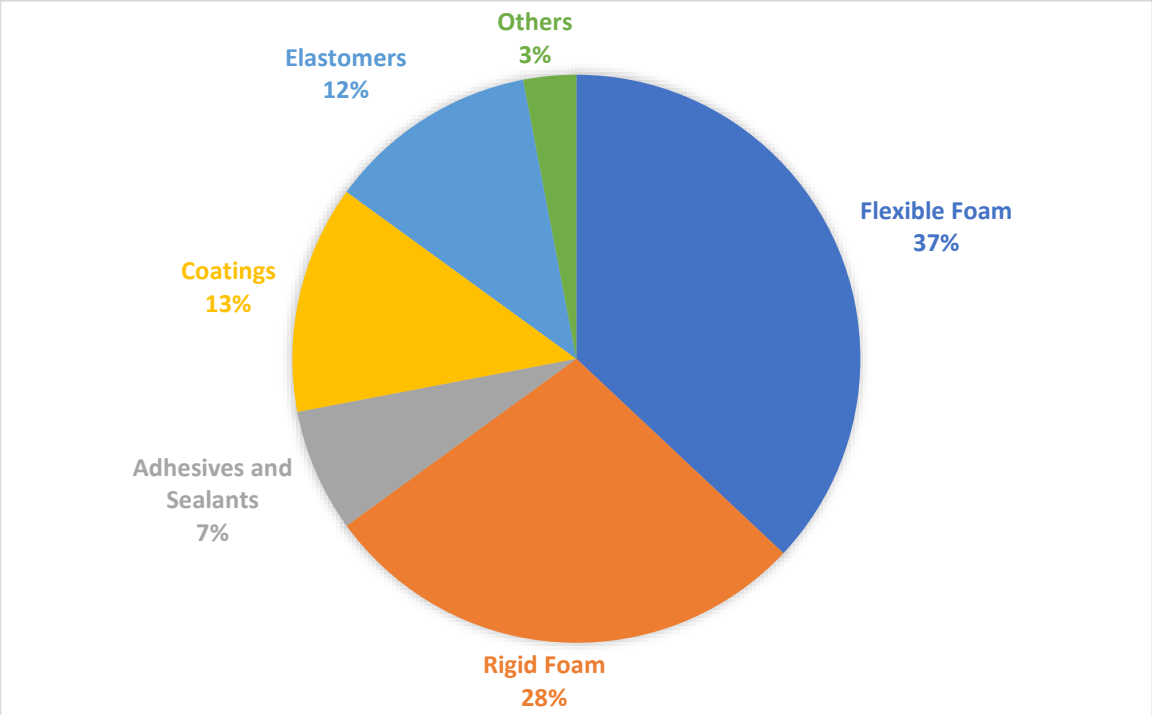


Fig. 1. Distribution of polyurethane usage across application sectors(4).

PU is the sole substance that provides a broad variety of chemical and physical qualities that may be tailored to the particular requirements of the final product or usage(5).PU is a comparatively high strength polymer which results in substantial use in construction and infrastructure industries. The most common uses of PU foams in building construction are for gap fillers around doors and windows and for insulated panels, such as wall and roof insulation. PU foams have several advantages when used as insulation, including improved mechanical and thermal performance, energy efficiency, and environmental benefits(6–8). PU is also frequently used as a protective coating in building and construction because of its quick-curing qualities (short gel time), glossy appearance, long product life, and great resistance to harsh weather conditions(6,9,10).PUs and PU-based composites have been effectively used in vehicle seats, bumpers, door panels, ceiling parts, and windows. Moreover, PU cushions are renowned for being comfortable for both drivers and passengers(11).With outstanding performance in biomedical applications, PUs has been a key component of numerous innovative medical devices. PU is the most promising option due to its exceptional mechanical and adhesive qualities, low cost, and exceptional antibacterial and biocompatibility performance. As a result, researchers are very interested in using them in a variety of biological applications, such as ureteral stents, PICC lines, endotracheal tubes, and catheters(12).In recent decades, polyurethane has rightfully dominated the CASE (Coating, Adhesive, Sealing and Elastomer) sector. While polyurethane-based sealants provide exceptionally tight sealing, PU-based adhesives have exceptional bonding strength(5,13).Over the past 20 years, a large number of studies on appropriate materials for coating purposes have been carried out, and polyurethane has continuously shown itself to be an excellent paint and surface coating material(5,14,15).Another significant material type is PU elastomers, which can be utilized for many practical applications, including goggles, ski boots, home goods, shoe soles, and sunglasses(16). They are also utilized to make high-performance industrial machinery parts including belts, gaskets, rollers, and pulleys, as well as thermal breaks in metal frames used in building construction(6).

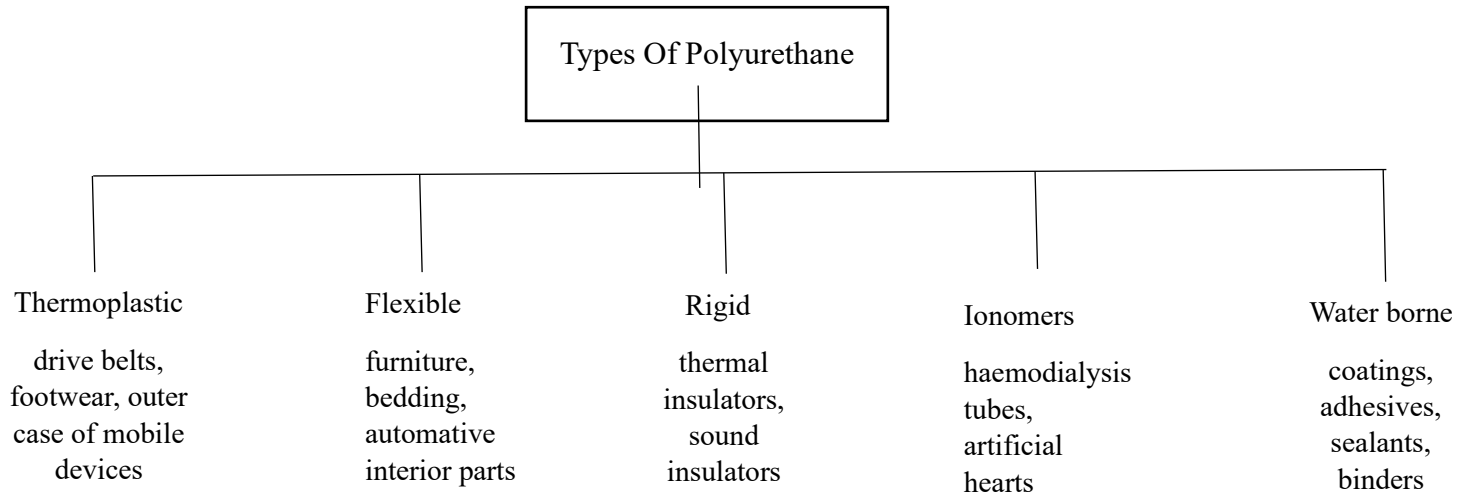


Fig.2. Types of Polyurethane and their applications.

1.1. Chemistry of polyurethane

The main ingredients used in the production of polyurethane are polyols anddisocyanates. The usual synthesis of a PU is based on the polyaddition reaction between a polyol, a molecule with two or more hydroxyl groups, and a different compound with two or more isocyanate groups.Organotin and compounds based on tertiary amines can accelerate this reaction through a step-growth method.In addition, a number of other components—such as blowing agents, surfactants, chain extenders, cross-linkers, fillers, can be added to the reaction system(17,18). The structure-property link between polyol

and isocyanate is crucial for comprehending and constructing polyurethane products since changing either of these components can drastically alter the polyurethane's characteristics(5).
Polyurethane macromolecular structure comprises alternating soft and hard segments, each contributing distinct functional properties. The hard segments, primarily formed from polyisocyanates and cross-linking agents,serve as structural support points, enhancing the material's resistance to deformation.Conversely, the soft segments are composed of oligomeric polyols, and their molecular weight and degree of polymerization critically influence the flexibility, elasticity, and overall performance of the polyurethane matrix (19).The polyurethane's ability to be extremely adaptable and efficient for a wide range of applications is attributed to its combination of hard and soft segments(5).

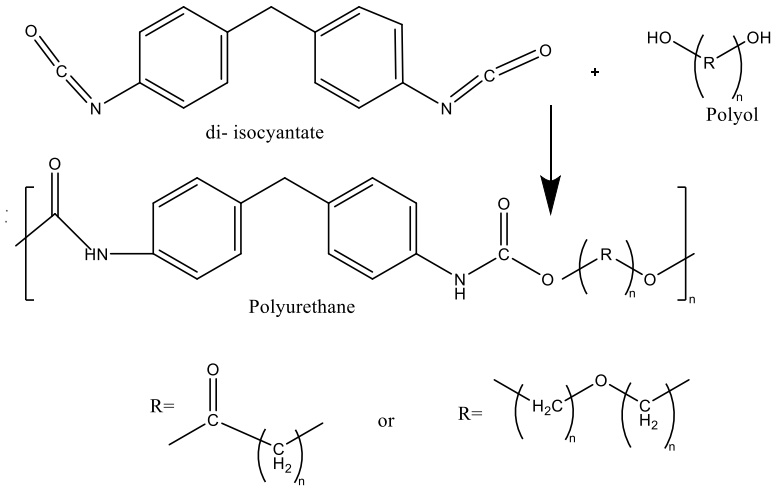


Fig.3:Reaction of polyurethane polymerization(20).

1.2. Environmental Impact of Polyurethane

Every year, more and more polyurethane waste is generated as a result of its many uses and economic success. These wastes include post-consumer (PC) and end-of-life (EOL) products, as well as leftovers from the production of polyurethanes. The latter arises from flaws in production and processing techniques and accounts for as much as 10% of PUs produced(20).Moreover, EOL and PC waste is a far greater issue because they are typically contaminated or distorted, making them less likely to be reused(20,21).

Currently, the most popular method for handling polyurethane waste is landfilling. The percentage of PUs disposed of in this manner approaches 50% of waste (post-consumer or post-production combined) (20,22)The largest issue is polyurethane foams, which also account for the largest portion of production. They have huge volumes because of their low apparent density. Additionally, a large volume of air inside foam cells can obstruct efforts to put out flames and supply oxygen to deep-seated fires. Toxic vapours released from the burning of polyurethane are another risk associated with landfill fires(20).Incineration, while reducing waste volume, releases substantial amounts of carbon and nitrogen oxides(23)Incineration holds a significant place in the recycling of waste made of polyurethane. However, inefficient combustion during the incineration process would result in the production of toxic gas, which will significantly contaminate the atmosphere(24).Beyond the effects that PU manufacture has on the environment, a sizable portion of the PU that are created wind up as improperly handled garbage. There are hazards to the environment and human health from this poorly PU garbage. There are still significant environmental effects from this garbage, even when it is effectively managed in landfills and incinerators(25).

PU presents environmental problems due of its resilience to deterioration and recycling.PU reduces the quantity of trash that is disposed of in landfills by recovering materials and recycling them as building blocks for fresh goods. This procedure lessens the environmental impact of their extraction and

preparation while also reducing the requirement for new raw materials. Additionally, there may be chances for cost reductions and/or new sources of income through PU recycling(23).Both the recycling of waste polyurethanes and research aimed at understanding the degradability of polyurethanes are becoming increasingly significant.

2. Methods to recycle polyurethane

The process of recycling is influenced by multiple factors. The following categories ofdegradation are based on those factors:

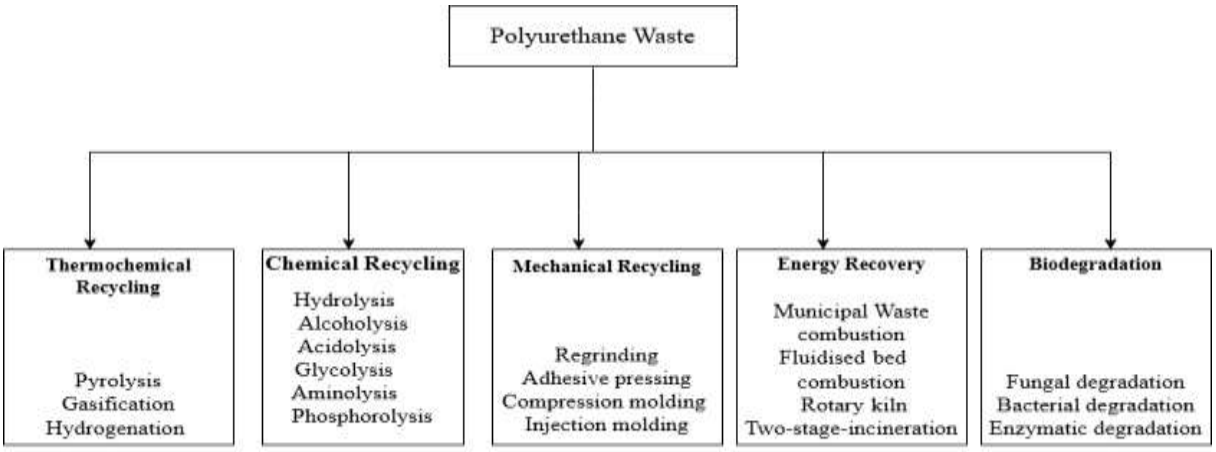


Fig.4. Different methods of polyurethane waste recycling(26).

2.1. Thermo-chemical Recycling:In the thermo-chemical recycling process the PU waste is thermally converted into chemicals for feedstock. The pyrolysis process consists of thermally decomposing the PU waste into gaseous, liquid and solid products in an oxygen-free (or oxygen-lean) environment(27).Partial oxidation is utilized in gasification to create syngas, which is mostly composed of H2, CO, and CO2. This syngas can then be properly scrubbed to yield useful chemicals. Although gasification technologies are widely used and technically advanced, they come with significant energy requirements and high operating expenses(28). Hydrogenation is a process that produces gaseous and liquid products by treating waste with heat and high-pressure hydrogen.These end products can be utilized as chemical feedstock and fuel for additional procedures. Between the effects of gasification (of high-pressure hydrogen) and pyrolysis (of heat), hydrogenation might be viewed as a compromise(29).

2.2. Chemical Recycling: When polyurethane depolymerizes completely to monomers or partially to oligomers and other chemicals, this is referred to as chemical degradation.PU contain a variety of organic and inorganic materials, they are readily broken down by reagents such as water, alcohols, acids, glycols, and amines(30).

2.3. Mechanical Recycling: The breakdown of polymers under mechanical stress is referred to as mechanical degradation. The mechanical deterioration is determined by four main routes. They are injection molding, compression molding, adhesive pressing, and regrinding(30). Polyurethane foams are mechanically recycled by being ground into powders, which enables them to be reused again as filler in new foam manufacture. Reusable techniques include compression molding, adhesive pressing, and flexible foam bonding(26).Adhesive pressing involves applying an adhesive binder to the surface of PU particles and bonding them in a hot press(30).Compression molding is a technique that creates neat particles without the use of extra binders by molding PU particles at high temperatures and pressures of 180°C and 350 bar. Automotive parts made from recycled PU using reaction injection molding have been successfully produced using this reaction(30,31).Through the use of injection molding, cross-linked polyurethane and polyurethane combinations with other plastics—preferably thermoplasts—can be recycled(27).

2.4. Energy Recovery: This recycling method is also known as incineration. In this process, PU waste is burned while oxygen is present. Since it recovers energy from the PU product, it is still preferable to disposing of the material in a landfill(32). Burning 1 kg of polyurethane has a calorific value of

about 7000 kcal/kg, this can provide heat equivalent to the energy produced by the same weight of coal(24).Energy recovery is frequently seen as the only appropriate disposal technique regarding recovered substances which have no markets or cannot be made. This is especially true for waste that has PU laminates on wood, leather, textiles, or mixed materials. Additionally, recovery and recycling are extremely challenging for flame-retarded materials. When PU foam is incinerated, its volume is reduced by about 99%, which has a significant impact on lowering the amount of this material that is dumped in landfills while also eliminating CFCs and other dangerous foam blowing agents(33).

2.5. Biodegradation:In recent years, the biodegradation of polymers and the need for biodegradable polymers have arisen due to the overuse of polymer goods(34). The most common definition of biodegradation is "The process that can break down polymeric materials into carbon dioxide, methane, water, inorganic chemicals, or biomass with the aid of certain microorganisms." In biodegradation, fungi, bacteria, and algae are the most crucial species(35).

3. Chemical Recycling of Polyurethane

Chemical recycling alters the chemistry of material.The main goal of PU chemical recycling is to transform waste back into its original basic ingredients, particularly polyols as well as other valuable raw materials. The recuperation of monomers, the principal byproducts of the breaking of urethane bonds in a precisely controlled reaction conditions, is the major goal of chemical recycling.It refers to the complete or partial breakdown of polymers into oligomers and other chemical compounds(36).Two possible bases for depolymerization are the breaking or interchange of urethane bonds or the breaking or interchange of chemical bonds of the materials utilized to make polyurethane, such as the ester groups in polyol(37,38).The potential for recovering monomers and oligomers from polymers is closely linked to the experimental conditions used, including the choice of reactive organic compounds, temperature, pH, pressure, atmosphere, and the types of catalysts employed. The resulting depolymerized substances can be cleaned and distilled to produce monomers, which are basic hydrocarboned units that can be utilized as synthesis materials in the chemical and petrochemical industries. In this manner, high-value items can be produced(38,39).

Currently, mechanical recycling is still the mainstay of the plastic recycling sector today. The industry's interest in chemical recycling has grown in recent years. Plastics that cannot be recycled mechanically can be recycled using chemical recycling, which may also prevent impurity buildup, a common drawback of mechanical recycling(25).

The recycling route that is selected can result in the extraction of products with different physicochemical characteristics and functions.Since polymers are made up of a variety of organic and inorganic materials, reagents such as water, alcohols,acids,glycols, amines, esters of phosphoric and phosphonicacids canreadily cleave them.

Consequently, the chemical recycling is classified according to the reagents utilized as follows (36):

1. hydrolysis
2. alcoholysis
3. acidolysis
4. glycolysis
5. aminolysis
6. phosphorolysis

3.1. HYDROLYSIS

The process of hydrolysis entails adding water to an acidic, alkaline, or neutral environment to depolymerize the polymer. It is the first recycling method that Ford Motor Company has employed(30,40)It describes the process by which a polymer reacts with water, whether in the form of

liquid or via steam, producing a variety of chemicals that include carbon dioxide, polyols, and amine intermediates(38).

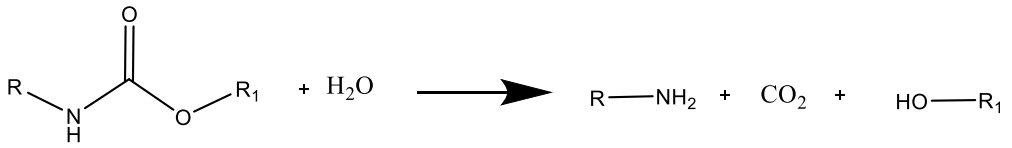


Fig.5. Hydrolysis reaction of polyurethane (20).

Hydrolysis can be carried out with bases (like sodium hydroxide).Waste polyurethane (PU) was efficiently degraded into polyols and benzene derivatives via NaOH-catalyzed hydrolysis in an EtOH-H_2O mixed solvent. A specific ethanol/water ratio (6:4) played a crucial role in both degradation efficiency and product separation. Complete degradation was achieved at 80 °C with a NaOH concentration of 0.2 g/mL. The optimized conditions enabled rapid and effective PU breakdown(41). Efficient hydrolysis of PU was achieved in high-temperature water under high CO_2 pressure, utilizing environmentally benign conditions. The in-situ formed carbonic acid from CO_2 and H_2O acted as an effective acid catalyst, promoting the reaction(42).These polyols can be used as fuel or added to the original polyol to make PU. Additionally, the recovery of the initial isocyanates is made possible by amine intermediates following phosgene treatment. Hydrolysed polyols and isocyanates react to produce the polyurethanes that comprise the inset(20)

Hydrolysis has disadvantages because it is performed under extreme operating conditions, such as high temperatures (even 300–400 °C) and pressures (typically 15–50 atm)(43). Compared to methanolysis and glycolysis, hydrolysis proceeds more slowly because water is the weakest nucleophile among the three depolymerizing agents (methanol, ethylene glycol, and water)(40).

Table 2:Overview of hydrolysis processes applied to various polyurethane (PU) wastes

Typeof PU waste	Chemicals Used	Catalyst	Time	Temp(°C)	References
Waste PU	Ethanol and water	NaOH	2h	40-80	(41)
PU	Water and High Pressure of CO2		24h	190	(42)
PU Foam	Superheated Steam		6h	288	(43)
PU Foam	Superheated Water		30min	249	(44)

3.2. ALCOHOLYSIS

It is the recyclingof polymers caused by low molecular weight alcohol and a catalyst. Polyurethane degraded into a low molecular mass liquid at a particular temperature.Here, the short reaction time and low temperature result in a high deterioration efficiency. The most crucial aspect is that the items don't require complicated processing afterward. It can be utilized straight away to make PU items as a raw material(24). The basic premise is that the alcohol hydroxyl group and polyurethane chain segment on

the ammonia ester bond alcohol exchange process cause the polyurethane molecular segment to "crack" into relatively small molecular weight alcohol substances (regenerated polyether polyol)(45).

PU foam waste was recycled via alcoholysis using ethylene glycol (EG) and propylene glycol (PPG), with various catalytic systems. A synergistic system combining NaOH and duplex metal catalysts (DMC) showed the highest degradation efficiency (46). Another study shows, waste rigid polyurethane foam (RPUF) was efficiently recycled through alcoholysis using ethylene glycol and catalyzed by the metal–organic framework MIL-101(Fe). Under optimal conditions (195 °C, 4 h, 5 wt% catalyst), the process yielded up to 78.3% regenerated polyols with a hydroxyl value ≥270 mgKOH/g and stable viscosity around 670 mPa·s. MIL-101(Fe) facilitated selective urethane bond cleavage through domain-limited catalysis while minimizing side reactions. The recovered polyols were reused to synthesize RPUFs that exhibited excellent mechanical properties, including compressive strength between 0.257 and 0.355 MPa, low water absorption (0.03–0.08%), and good thermal stability. The catalyst showed high reusability, maintaining over 65% yield after nine cycles. These results demonstrate a promising and sustainable route for high-performance recycling of polyurethane waste (47).

Table 2:Overview of alcoholysis processes applied to various polyurethane (PU) wastes

Type of PU waste	Type of alcohol used	Catalyst	Time	Temp(°C)	References
Waste polyurethane elastomers.	Butanediol (BDO), propylene glycol (PG), ethylene glycol (EG), and monodiethylene glycol (DEG)	KOH	0.5-1 h	180	(49)
PU Foam	glycerol and butanediol	CsOH	2.5h	170	(50)
PU Foam	Ethylene glycol and propylene glycol	NaOH and DMC	2.5h	160	(46)
Rigid PU Foam	Propylene glycol and ethanolamine	KOH	4h	160	(51)
Rigid PU Foam	Ethylene glycol	MIL-101(Fe)	4h	195	(47)

Flexible polyurethane foam was recycled via split-phase alcoholysis using various alcoholyzing agents, including diethylene glycol, ethylene glycol, glycerol, diglycerol, and pentaerythritol. Diglycerol was identified as the most effective, achieving high purity(99%) and yield of recovered polyether polyol. The addition of 2-pyrrolidone as a co-reactant enhanced the depolymerization efficiency and allowed a reduced glycol-to-PU ratio of 0.5:1. The recycled polyol successfully replaced virgin polyol by up to 50% in new flexible PU foams without significant loss in mechanical or thermal performance (48).

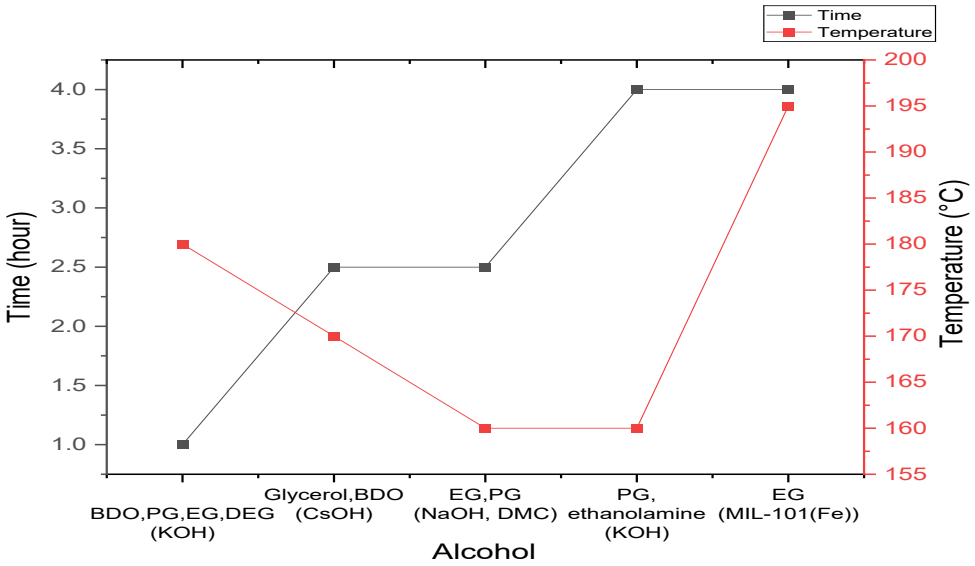


Fig.6.Comparison of reaction time and temperature for alcoholysis of different PU waste materials.

3.3. ACIDOLYSIS

Acidolysis by both organic and inorganic acids is another kind of reaction that has been tried in PU recycling procedures. Inorganic acids break down the urethane bonds in polyurethane, resulting in the formation of amine salts and polyols. This approach is a well-established analytical technique for decomposing polyurethane(30).Inorganic acids like HCl lead to the production of polyols, carbon dioxide, and amine salts. When organic acids, typically with dicarboxylic structures, react with urethane groups, they form amide groups. One of the main advantages of employing organic acids is that they cause little to no aromatic amines to develop in the finished product. For the production of recycled polyols with a low hydroxyl value, which are appropriate for flexible polyurethane applications, acidolysis is particularly helpful. However, glycolysis is a better technique than acidolysis for rigid polyurethane applications when a high hydroxyl value is needed(38,52).

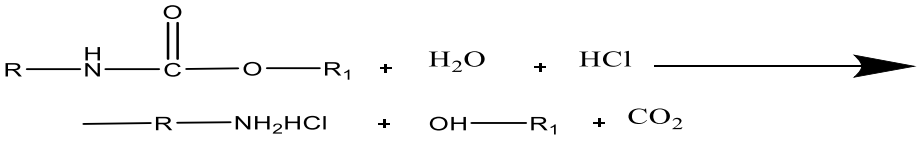


Fig.7Acidolysis of polyurethane by HCL(53)

Organic acids can be classified into two primary categories: unsaturated dicarboxylic acids, like fumaric or maleic acid, and saturated ones, such adipic or succinic acid. Due to saturated acids, chemical breakdown reactions can take place in milder environments with shorter reaction periods and lower temperatures (around 60 °C).This results in the formation of oligomers containing functional groups like amines, amides, urea compounds, or hydroxyl groups. In contrast, using unsaturated dicarboxylic acids leads to oligomers with double bonds, which are suitable for making adhesives(38).

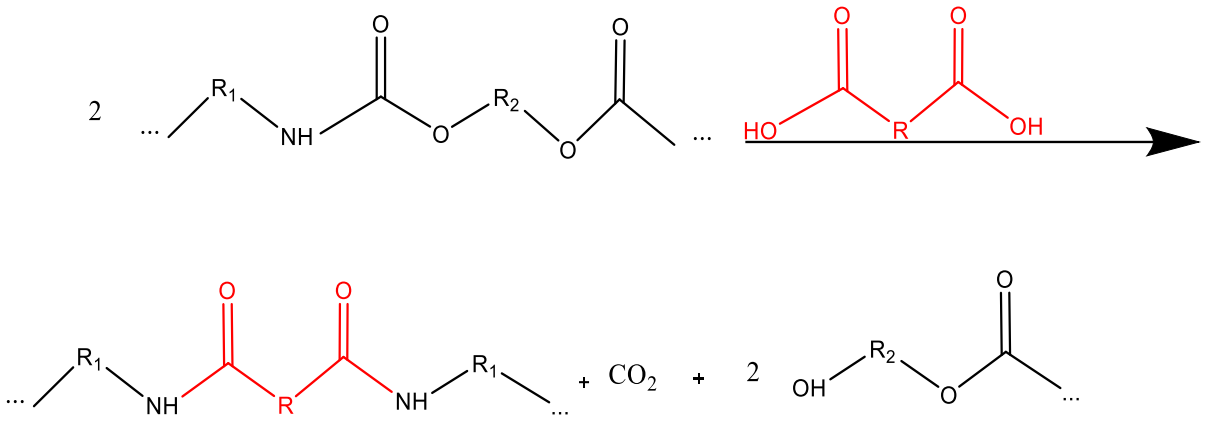


Fig.8.Acidolysis of polyurethane by dicarboxylic acid(29).

Acidolysis of polyurethane foam waste using succinic and phthalic dicarboxylic acids as cleavage agents was conducted. The reactions were conducted at 190 °C for 5 hours, using a PU to acid weight ratio of 4.6:1 for succinic acid and 3.0:1 for phthalic acid, with a conventional polyol as solvent. Succinic acid was found to be more efficient than phthalic acid as a cleavage agent, yielding polyols with higher hydroxyl values and significantly lower viscosities, which indicates a higher extent of depolymerization. The resulting products contained functional groups such as hydroxyls and aromatic moieties, making them suitable for use in high-performance polyurethane wood adhesives(54).

Another study examined how PU to succinic acid ratios (4:1 and 5:1), temperatures (190 °C and 200 °C), and times (4.5 and 5.5 h) affect polyol recovery via acidolysis. An increase in temperature and reaction time generally resulted in higher hydroxyl values (OH number) and lower acid values (AV), indicating more extensive depolymerization and consumption of the acid. Notably, a higher PU/acid ratio (i.e., using less acid) also led to higher OH numbers and lower AVs, which was contrary to initial expectations. This suggests that a smaller amount of acid is sufficient to effectively cleave the PU chains under the tested conditions. Among the variables, temperature had the most significant impact on the OH number, followed by the PU/acid ratio and reaction time. An inverse relationship was observed between hydroxyl and acid values (55).

Table 3:Overview of acidolysis processes applied to various polyurethane (PU) wastes

Type of PU waste	Type of carboxylic acid used	Ratio (PU/ Carboxylic acid)	Time	Temp (°C)	References
PUF Scraps	Succinic Acid	4:1, 5:1	4.5-5.5 h	190-200	(55)
PUF Scraps	SuccinicAcid/ Phthalic Acid *(R-100Suc-0Pht R-50Suc-50Pht R-0Suc-100Pht)	4.6:1 4.2:1 3:1	5 h	190	(54)
PUF	Maleic Acid	1:0.5	15 min	175	(56)
Flexible PUF	Adipic Acid	1.1:1 2.0:1 3.0:1	15-40 min	210-230	(57)

PUF	Succinic Acid (Zinc Acetate-Catalyst)	5:1	3 h	200	(58)

*(R-XSuc-YPht): X is the molar ratio of succinic acid utilized, and Y is the molar ratio of phthalic acid utilized (54)

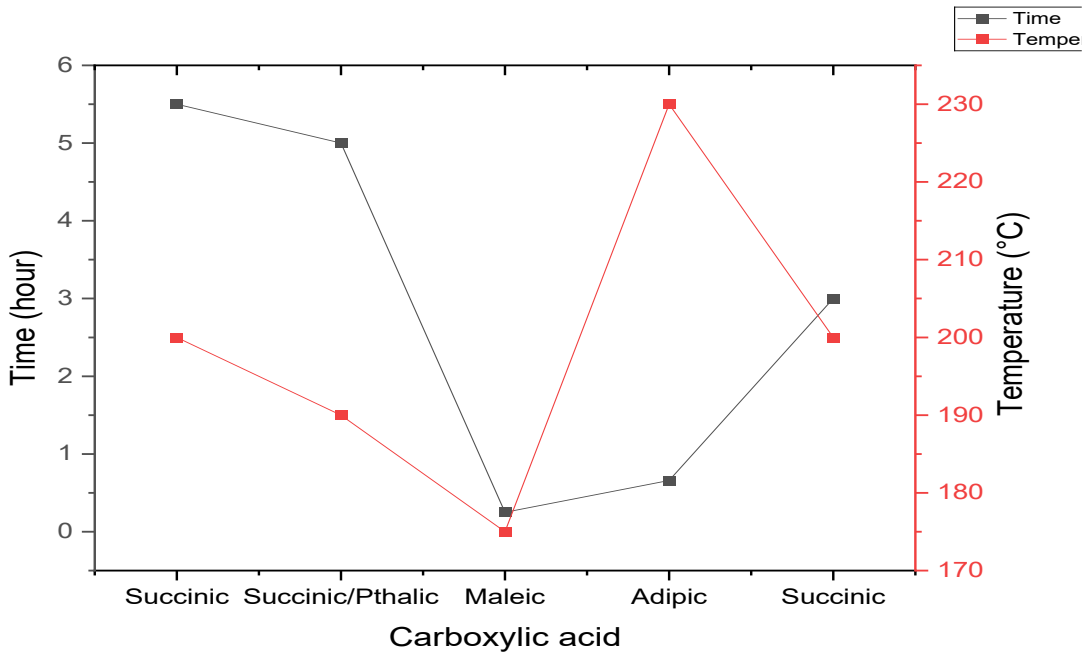


Fig.9.Comparison of reaction time and temperature for acidolysis of different PU waste materials.

3.4. GLYCOLYSIS

Glycolysis is the chemical recycling technique that is predominantly employed for polyurethane waste. Recovering the valuable monomers (polyols) from waste PU in order to produce fresh material is the main objective of this technique. Glycolysis is the process of heating ground polyurethane waste between 180 and 220°C when high-boiling point glycols, including diethylene glycol (DEG), and a catalyst are present.As destructive agents, glycols bind to the functional groups of urethane, break the bonds, and release amines and polyols(59).Glycolysis is based on a transesterification reaction, where a hydroxyl group from glycol takes the place of an ester group that contains a urethane bond's carbonyl carbon(20). The process involves two primary reactions: the breakdown of the crosslinking allophanate and biuret groups and the transesterification of urethane and urea linkages.Glycolysis of polyurethanes can yield the original polyols or glycolysates, which are oligomer molecules that resemble polyols in structure but frequently have a higher molecular weight and urethane links in their chain.Glycolysates include low molecular weight urea molecules, amines, mono- and dicarbamates, and urea oligomers according to their chemical structure(29).The following benefits make glycolysis the preferred method: low reaction temperature, short glycolysis duration, and the glycolysis product's potential for new PU production(45,60).

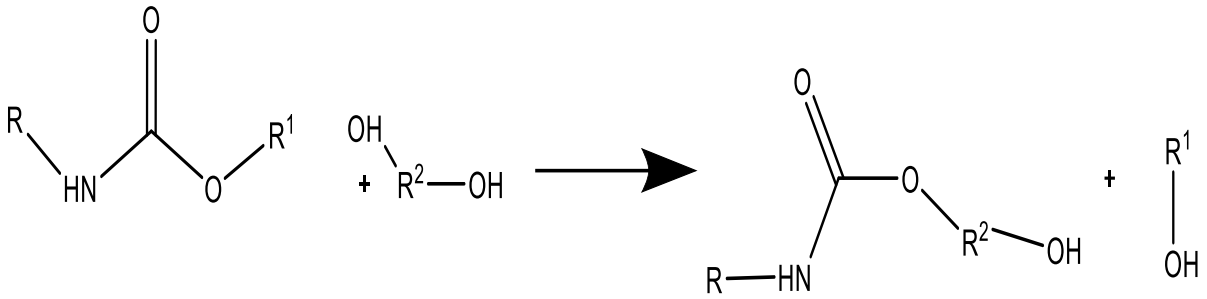


Fig.10. Reaction of glycolysis of polyurethane(3).

A single-phase or two-phase glycolysate is produced when glycol and foam waste are combined in the ideal ratio and heated to a high enough temperature. Glycolysates produced by the glycolysis process with mass excess of polyurethane waste are primarily homogeneous, purification and distillation of the excess glycol are not necessary. As part of the combination of polyols, the resulting semi-products can be used straight in the formation of polyurethanes. An adequate mass amount of glycolysis agent can limit the length of the oligomer chains since the molecular weight of oligomers decreases as the mass of applied glycol increases(29).Glycolysates produced by the glycolysis process with mass excess of glycol primarilyproduces two-phase glycolysate. The upper layer is mostly composed of recovered polyol, whereas the lower layer contains unreacted glycol and undesirable byproducts as urea, aromatic carbamates, oligomers containing urethane links and amines. Recovered polyol makes up the majority of the upper layer, while unreacted glycol and unwanted byproducts such amines, aromatic carbamates, ureas, and oligomers with urethane linkages are found in the lower layer. In certain instances, urea oligomers are also present in the third layer that forms(3).Following reaction completion, the recovered polyols need to be purified and can be directly used to produce new polyurethane materials.The applied glycol, which was used more than the mass of polyurethane waste, must be distilled. Sometimes the upper phase is refined further to concentrate the recovered polyol and reduce the amount of residual amines that affect the reactivity of the final polyol.Ethylene oxide (EO) and propylene oxide (PO) reactions with alkylene oxides are the most efficient way to lower the amine content. Additionally, there are less invasive techniques such as adding small amounts of isocyanate or using epoxidized natural fatty oils. Conversely, the lower phase is considered process waste and is rarely further processed, though it can be utilized in tiny amounts to produce hard polyurethane foams (29).

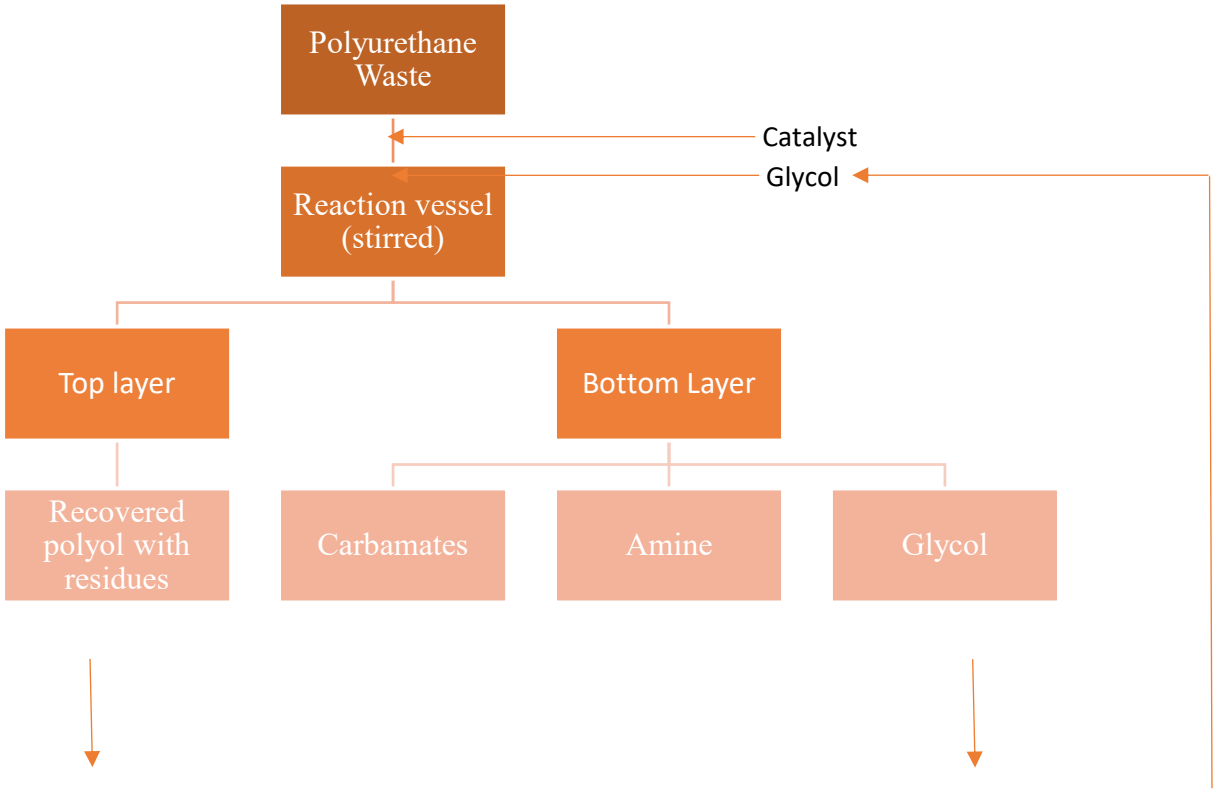




Fig. 11.Schematic representation of split-phase glycolysis.

3.4.1 PU Flexible foam glycolysis

Certain block copolymers make up flexible polyurethane foams, the phase separation between the hard and soft segments gives them their flexibility. While soft segments are pliable and increase the polymer's elasticity, hard segments are rigid structures that give the polymer its hardness(61).Flexible PUF's low-density cellular nature makes it ideal for cushioning, and its flexibility enables a variety of uses(33).

The study investigates the recovery of polyol-rich products through glycolysis of waste flexible polyurethane foam using potassium acetate and diethylene glycol (DEG). 90 minutes at 220°C, PU: DEG = 1:1.5, KAc = 1% by PU mass, and the ideal circumstances produced a single-phase liquid product with a high polyol content. The product's hydroxyl value ranged from 460 to 780 mg KOH/gand reached a stable state after 90 minutes, as validated by FTIR analysis, which also showed that the -NCOO- groups had degraded. Reusability in PU synthesis was shown by the recovered polyols' viscosity, which ranged from 633 to 3601 cps(62).Using DEG and DPG, the glycolysis of car seat polyurethane foam was maximized in this study at 220°C for 2.5 hours. DPG was more useful for reuse since it created a single-phase result, whereas DEG glycolysis produced two immiscible phases. SEC and UV measurements detected trace amounts of aromatic residues and verified the recovery of the original polyols. The DPG and upper DEG phase products have viscosities of about 2000 mPa·s and hydroxyl values of up to 923–1022 mg KOH/g, making them appropriate for the fabrication of new rigid PU foam without sacrificing material qualities(63).Anotherstudy describes a "split-phase" glycolysis of cold-cure polyurethane foam at 170–190 °C with atmospheric pressure, employing glycerin and NaOH (1% w/w) as a solvent and catalyst, respectively, in a 1:1 PU: glycerin ratio. The process yielded three phases, with the upper phase containing the recovered polyol. The structural similarity between recycled and virgin polyol was confirmed by FTIR, ^{1}H-NMR, and ^{13}C-NMR, with only a slight contamination from aromatic amines. The viscosity dropped from 9600 cPs to \~3400 cPs, indicating effective urethane bond breakdown, and the recycled polyol's hydroxyl values were 99 and 73 mg KOH/g after 1 and 3 hours, respectively. Glycerin is a useful glycolysis agent for flexible PU waste recycling because of its inexpensive cost (64).

3.4.2 PU Rigid foam glycolysis

The condensation polymers known as rigid polyurethane have a high degree of cross-linking(61).Rigid polyurethane foams are among the most widely used, adaptable, and energy-efficient insulations. It has been demonstrated that these foams work well as insulation materials that can be used for wall and roof insulationwindow insulation. (16).

A study uses EG, PG, and DEG at 190°C for 5 hours with sodium acetate acting as a catalyst to explore the desaminated glycolysis of MDI-based rigid PU foams. The procedure produced mono- and dicarbamate-type polyols, and ^{1}H-NMR confirmed that hazardous amines were transformed into OH-functional polyols through desamination with butyl glycidyl ether. The recovered polyols had hydroxyl values of 580–605 mg KOH/g, higher than the virgin polyols (420–490 mg KOH/g). PU foams reconstituted with up to 30% recycled polyol had comparable mechanical and physical properties, suggesting their potential for reuse(65).The glycolysis of rigid polyurethane foam (WPUR) from waste freezers is investigated in another study, which uses ethylene glycol (EG) as the ideal glycol and NaOH as the catalyst.A single-phase product was produced after two hours of reaction at 197.85°C under the ideal circumstances of EG/WPUR = 100% and NaOH/WPUR = 1%. The recovered mixed polyol had a hydroxyl value of 847–875 mg KOH/g,its viscosity was about 2100 mPa·s, and its molecular weight was similar to that of commercial polyether polyol. GB/T 26689-2011 criteria were met by regenerated polyurethane foams with up to 10% recycled polyol, exhibiting satisfactory thermal and physical characteristics appropriate for insulation applications(60).

Table 4: Overview of glycolysis processes applied to various polyurethane (PU) wastes

Type of PU waste	Type of glycol used	Ratio (PU: Glycol)	Catalyst	Temp(°C)	References
Flexible PU foam	Diethyleneglycol	1:1.5	Sn (Oct) $_2$	190	(66)
Flexible PU foam	Diethylene glycol (DEG), Dipropyleneglycol (DPG)	1:1	Diethanolamine (DEA)	220	(63)
Flexible PU foam	DEG	1:1.5	DEA, titanium (IV) butoxide, potassium octoate, Ca $(Oc)_2$	189	(67)
Flexible PU Foam	DEG	1:1.5	Potassium octoate, Ca $(Oc)_2$, Sn (Oct) $_2$	189	(68)
Flexible PU foam	Diethylene glycol	1:1.5	KAc	220	(62)
Flexible PU Foam	Glycerine	1:1	NaOH	170-190	(64)
Flexible PU Foam	Glycerine	1:1	NaOH KOH	Microwave irradiation	(69)
Flexible PU Foam	Crude Glycerol	1:1.5	Stannous octoate	190	(70)

Flexible PU Foam	Ethylene glycol	5:9	$FeCl_3$	160-200	(71)
Flexible PU Foam	HDO	1:1 - 10:1	KAc	230–245	(72)
Rigid PU Foam	Ethylene glycol Diethylene glycol	1:1	NaOH,NaAc, and triethanolamine	197.85	(60)
Rigid PU Foam	Diethylene glycol	1:0.6	Ethanolamine and Zinc stearate	160-210	(73)
Rigid PU Foam	Diethylene glycol	3:1	Ethanolamine and Zinc stearate	180	(74)
Rigid PU Foam	Ethylene glycol (EG) Propylene glycol (PG) diethylene glycol (DEG)	1:0.3-0.4	Sodium acetate	190	(65)
Rigid PU Foam	Ethylene glycol (EG) Propylene glycol (PDO) – Butylene glycol (BDO)	1:1	KOH Ti $(OCH_2CH_2O)_2$ (titanium–ethylene glycol)	180	(75)

3.5. AMINOLYSIS

Aminolysis is a process in which polyurethane foam can be chemically broken down by transesterification using aliphatic diamines or even polyamines with primary and secondary amine functionalities(38). The ester group from urethane is exchanged out for the amine group from ammonia or amine in this process. Depending on the reaction conditions, PUF aminolysis can result in either a complicated mixture in a single phase that is only suitable for less challenging purposes or a low-quality polyether polyol in a split phase that is only suitable for the formation of rigid PUFs(76).



Fig.12.Reaction of aminolysis of polyurethane(30).

Table 5: Overview of aminolysis processes applied to various polyurethane (PU) wastes

Type of PU waste	Type of chemical used	Catalyst	Time	Temp (°C)	References
PU foam	Mono ethanolamine (MEA)	None	3 h	120-150	(77)
Rigid PU foam	Diethylene triamine (DETA)	NaOH	70 min	180	(78)
PU Foam	Hexamethylene diamine	TBD: MSA	24h, 2h	160, 190	(79)
PU Foam	2-(methylamino) ethan-1-ol	TBD: MSA	7h	160	(79)
PU Foam	Diethylene triamine (DETA) Triethylene tetramine (TETA) Tetraethylene pentaamine (TEPA)	None	40 min - 150 min	150-180	(80)
Rigid PU foam	Ethylene diamine (EDA)	NaOH	3	120	(81)

PU shoe sole	1,3-propanediamine and 4,7,10-trioxatridecan-1,13-diamine	NaOH	3h	140	(82)

(MDI)-based polyurethane flexible foams were decomposed using monoethanolamine (MEA) and diethanolamine (DEA) at 150 °C without any catalyst.Two independent layers were formed by the breakdown products: a bottom layer that contained methylene diphenyl amine (MDA) and alkanolamine derivatives, and an upper layer that was composed of relatively pure polyether polyol. Compared to DEA, MEA decomposed significantly more quickly, taking two to three hours as opposed to more than ten hours. Steric hindrance and hydrogen bonding interactions were cited as the causes of this discrepancy(77).Low molecular weight oligomers and 4,4′-methylenedianiline (MDA) were produced by aminolyzing rigid polyurethane foam with diethylenetriamine (DETA) and sodium hydroxide (NaOH) at 180°C for 70 minutes. Increasing NaOH improved depolymerization but reduced MDA yield due to the secondary reactions. NaOH functioned both as a catalyst and reactant(78).Ethylene diamine (EDA) and sodium hydroxide (NaOH) were used to depolymerize waste polyurethane foam by both conventional heating and microwave-assisted aminolysis. Reaction time was greatly shortened (from three hours to thirty minutes) and side reactions were minimized using the microwave approach. Polyester amides were created by reacting the resultant product, which was abundant in hydroxyl and amine groups, with sebacic acid and BHET (from recycled PET). These were further cured with isocyanates (HDI biuret and IPDI) to produce coatings with good mechanical and chemical properties, demonstrating a sustainable route for PU foam recycling(81).

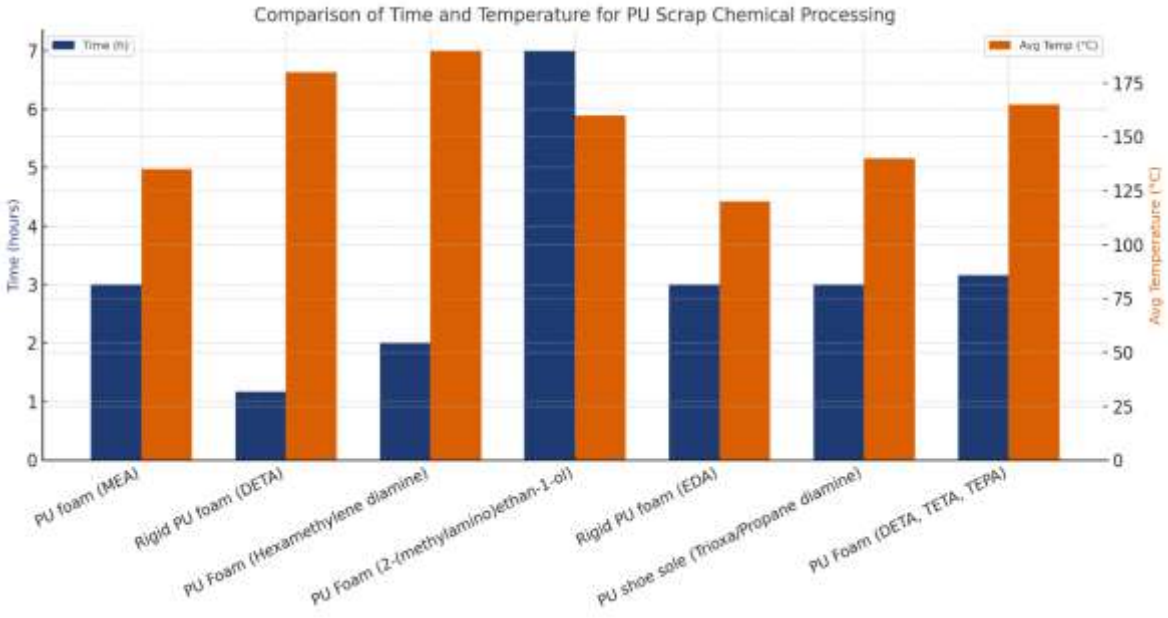


Fig.13. Comparison of reaction time and temperature for aminolysis of different PU waste materials.

3.6. PHOSPHOROLYSIS

Phosphorolysis is a process in which polyurethane waste is treated with esters of phosphoric and phosphonic acids. The wastes are transformed into a liquid product as the result of the interaction between the ester alkoxy group and the urethane group(20).A combination of oligourethanes containing

phosphorus was obtained by this technique.New polyurethanes with enhanced UV resistance, adhesive qualities, and flame retardancy can be made with it. The procedure's drawback is that the input materials cannot be recovered, thus they are simply transferred to other production methods rather than being recycled back into the process(20,83)

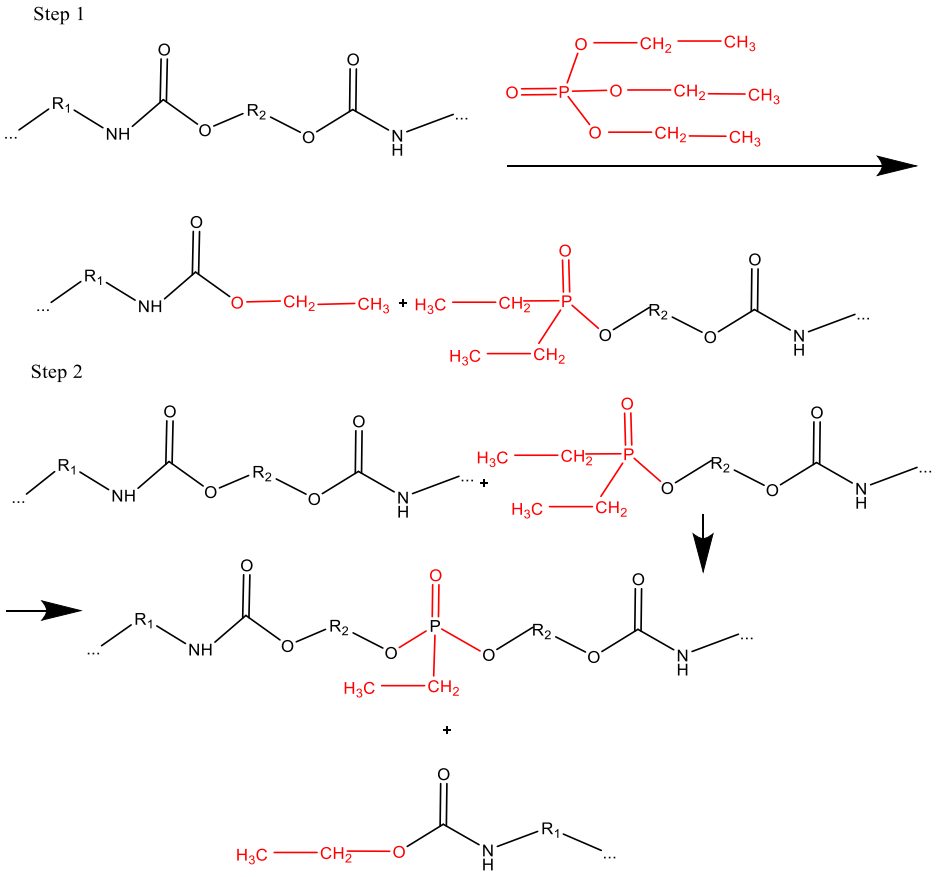


Fig.14.Reaction of phosphorolysisof polyurethane(29)

Table 6:Overview of phosphorolysis processes applied to various polyurethane (PU) wastes

Type of PU waste	Type of Phosphonate ester used(PE)	Ratio (PU:PE)	Time	Temp(°C)	References
Flexible polyether PU foam	Dimethyl phosphonate,diethyl phosphonate	1:3	1-3 h	160	(83)
Flexible polyether PU foam	Dimethyl phosphonate	1:3	1-3 h	160	(84)

Microporous Polyurethane Elastomer	Dimethyl phosphonate	1:2	45 min	142	(85)
Microporous polyurethane elastomer	Diethyl phosphonate and tris (1-methyl-2-chloroethyl) phosphonate	1:3	4-8 h	170, 180	(86)
Microcellular Elastomer Poly(ester-urethane)	Triethyl phosphonate, tris (2-chloroethyl) phosphonate	1:3	5-8 h	180	(87)

Dimethyl phosphonate is used to break down flexible polyether polyurethane foam at 160°C. Degradation produces two liquid layers with oligomers containing phosphorus. Polyether alcohols make up the majority of the upper layer, whilst aromatic and urethane-related chemicals are more abundant in the lower layer. There are nine different degradation products that contain phosphorus(84).Dimethyl phosphonate is used to chemically break down the microporous polyurethane elastomer at 142°C. A single uniform liquid layer including phosphorus-containing oligomers is the end outcome of the degradation. Four main phosphorus-containing compounds that resulted from exchange and alkylation reactions with urethane groups were found(85).

Diethyl phosphonate was used to chemically degrade microporous polyurethane elastomer for 4–8 hours at 170°C, and tris(1-methyl-2-chloroethyl) phosphate was used for the similar duration at 180°C.As a result of the deterioration, the elastomer completely liquefied and oligomers containing either phosphorus or phosphorus and chlorine were formed. The deteriorated components showed promise for repurposing in flame-retardant polymer formulations since they were soluble in ordinary organic solvents(86).

Table 7: Comparative analysis of different methods of PU chemical recycling

Category Of Comparison	**Hydrolysis**	**Alcoholysis**	**Acidolysis**	**Glycolysis**	**Aminolysis**	**Phosphorolysis**
Chemicals Used	superheated steam	low molecular alcohol	inorganic or organic acid	glycols	diamine or polyamine or alkanolamines	esters of phosphonic or phosphoric acid
Temperature(°C)	high temperature	low temperature	medium temperature	medium temperature	low temperature	low temperature
Pressure	high pressure	atm pressure	atm pressure	atm pressure	atm pressure	atmpressure

Product	Polyols, diamineand CO_2	polyols and aromatic compounds	polyols, amides, amine salts, and oligoureas	Polyols and aromatic amines	Polyols, polyamine compounds and aromatic compounds	phosphorus-containing oligourethanes
Large scale application	No	No	No	Yes	No	No

Conclusion

Polyurethane (PU) is a widely used polymer that plays an integral role in everyday applications due to its versatility and durability. Its widespread demand worldwide is a result of its durability and adaptability, but it has also led to a considerable increase in PU waste, raising serious environmental problems. Landfilling and other traditional disposal techniques are becoming less viable because of their ecological impact and incapacity to recover material value. As a result, recycling PU has become more and more important as a step toward the goals of the circular economy and sustainable materials management.

Chemical recycling has shown itself to be a particularly promising method among the other recycling techniques investigated since it can depolymerize PU into its original or modified monomers and oligomers. Several chemical recycling routes were reviewed in this review, includinghydrolysis, alcoholysis, acidolysis, glycolysis, aminolysis, and phosphorolysis. The type of PU waste, the intended end products, the reaction circumstances, and economic considerations are some of the variables that affect the specific reaction processes, benefits, and drawbacks of each approach. Glycolysis is noteworthy for its large-scale applicability and significant industrial implementation potential.
The scalability of chemical recycling solutions for PU nevertheless faces a number of obstacles, notwithstanding the advancements. The various chemical recycling methods need to be optimized for industrial scalability and economic viability, which will require more research. It could eventually emerge as a key tactic for attaining circular and sustainable polyurethane material use.

References

1. Sonnenschein MF. Polyurethanes : science, technology, markets, and trends. Wiley; 2015.
2. https://www.fortunebusinessinsights.com/industry-reports/polyurethane-pu-market-101801 [Internet]. Polyurethane Market Size, Share & Industry Analysis .
3. Wieczorek K, Bukowski P, Stawiński K, Ryłko I. Recycling of Polyurethane Foams via Glycolysis: A Review. Vol. 17, Materials. Multidisciplinary Digital Publishing Institute (MDPI); 2024.
4. Kaur R, Singh P, Tanwar S, Varshney G, Yadav S. Assessment of Bio-Based Polyurethanes: Perspective on Applications and Bio-Degradation. Vol. 2, Macromol. Multidisciplinary Digital Publishing Institute (MDPI); 2022. p. 284–314.
5. Das A, Mahanwar P. A brief discussion on advances in polyurethane applications. Vol. 3, Advanced Industrial and Engineering Polymer Research. KeAi Communications Co.; 2020. p. 93–101.
6. Somarathna HMCC, Raman SN, Mohotti D, Mutalib AA, Badri KH. The use of polyurethane for structural and infrastructural engineering applications: A state-of-the-art review. Vol. 190, Construction and Building Materials. Elsevier Ltd; 2018. p. 995–1014.
7. Swinton MC, Maref W, Bomberg MT, Kumaran MK, Normandin N. In situ performance evaluation of spray polyurethane foam in the exterior insulation basement system (EIBS). Build Environ. 2006 Dec;41(12):1872–80.
8. Liang HH, Ho MC. Toxicity characteristics of commercially manufactured insulation materials for building applications in Taiwan. Constr Build Mater. 2007 Jun;21(6):1254–61.
9. Chattopadhyay DK, Raju KVSN. Structural engineering of polyurethane coatings for high performance applications. Vol. 32, Progress in Polymer Science (Oxford). 2007. p. 352–418.

10. Hradil P, Toratti T, Vesikari E, Ferreira M, Häkkinen T. Durability considerations of refurbished external walls. Constr Build Mater. 2014 Feb 28;53:162–72.
11. Maurya AK, de Souza FM, Gupta RK. Polyurethane and Its Composites: Synthesis to Application. In: ACS Symposium Series. American Chemical Society; 2023. p. 1–20.
12. Sikdar P, Dip TM, Dhar AK, Bhattacharjee M, Hoque MS, Ali S Bin. Polyurethane (PU) based multifunctional materials: Emerging paradigm for functional textiles, smart, and biomedical applications. Vol. 139, Journal of Applied Polymer Science. John Wiley and Sons Inc; 2022.
13. Xu Y, Petrovic Z, Das S, Wilkes GL. Morphology and properties of thermoplastic polyurethanes with dangling chains in ricinoleate-based soft segments. Polymer (Guildf). 2008 Sep 9;49(19):4248–58.
14. Dutta S, Karak N. Synthesis, characterization of poly(urethane amide) resins from Nahar seed oil for surface coating applications. Prog Org Coat. 2005 Jun 1;53(2):147–52.
15. Dutta S, Karak N, Jana T. Evaluation of Mesua ferrea L. seed oil modified polyurethane paints. Prog Org Coat. 2009 Apr;65(1):131–5.
16. Akindoyo JO, Beg MDH, Ghazali S, Islam MR, Jeyaratnam N, Yuvaraj AR. Polyurethane types, synthesis and applications-a review. Vol. 6, RSC Advances. Royal Society of Chemistry; 2016. p. 114453–82.
17. Maurya AK, de Souza FM, Gupta RK. Polyurethane and Its Composites: Synthesis to Application. In: ACS Symposium Series. American Chemical Society; 2023. p. 1–20.
18. De Souza FM, Kahol PK, Gupta RK. Introduction to Polyurethane Chemistry. Vol. 1380, ACS Symposium Series. American Chemical Society; 2021. p. 1–24.
19. Cong P, Liu C, Han Z, Zhao Y. A comprehensive review on polyurethane modified asphalt: Mechanism, characterization and prospect. Journal of Road Engineering. 2023;3(4):315–35.
20. Kemona A, Piotrowska M. Polyurethane recycling and disposal: Methods and prospects. Polymers (Basel). 2020;12(8).
21. Cregut M, Bedas M, Durand MJ, Thouand G. New insights into polyurethane biodegradation and realistic prospects for the development of a sustainable waste recycling process. Biotechnol Adv [Internet]. 2013;31(8):1634–47. Available from: http://dx.doi.org/10.1016/j.biotechadv.2013.08.011
22. Datta J, Kopczyńska P, Simón D, Rodríguez JF. Thermo-Chemical Decomposition Study of Polyurethane Elastomer Through Glycerolysis Route with Using Crude and Refined Glycerine as a Transesterification Agent. J Polym Environ. 2018 Jan 1;26(1):166–74.
23. Karrech A, Zhou H. A systematic review on the recycling of polyurethane products from offshore applications. Circular Economy [Internet]. 2025 Mar;4(1):100129. Available from: https://linkinghub.elsevier.com/retrieve/pii/S2773167725000044
24. Yang W, Dong Q, Liu S, Xie H, Liu L, Li J. Recycling and Disposal Methods for Polyurethane Foam Wastes. Procedia Environ Sci. 2012;16:167–75.
25. Pillich M, Schilling J, Bosetti L, Bardow A. What to do with polyurethane waste? The environmental potential of chemically recycling polyurethane rigid foam. Green Chemistry. 2024 Sep 18;
26. Zia KM, Bhatti HN, Ahmad Bhatti I. Methods for polyurethane and polyurethane composites, recycling and recovery: A review. Vol. 67, Reactive and Functional Polymers. 2007. p. 675–92.
27. Deng Y, Dewil R, Appels L, Ansart R, Baeyens J, Kang Q. Reviewing the thermo-chemical recycling of waste polyurethane foam. J Environ Manage. 2021 Jan 15;278.
28. Oenema J, Liu H, Coensel N De, Eschenbacher A, Van de Vijver R, Weng J, et al. Review on the pyrolysis products and thermal decomposition mechanisms of polyurethanes. Vol. 168, Journal of Analytical and Applied Pyrolysis. Elsevier B.V.; 2022.
29. Datta J, Włoch M. Recycling of Polyurethanes. In: Polyurethane Polymers: Blends and Interpenetrating Polymer Networks. Elsevier Inc.; 2017. p. 323–58.
30. Bhuvaneswari. G H. Degradability of Polymers. In: Recycling of Polyurethane Foams. Elsevier; 2018. p. 29–44.
31. Hulme AJ, Goodhead TC. Cost effective reprocessing of polyurethane by hot compression moulding. J Mater Process Technol. 2003 Aug 20;139(1-3 SPEC):322–6.

32. Karrech A, Zhou H. A systematic review on the recycling of polyurethane products from offshore applications. Circular Economy [Internet]. 2025 Mar;4(1):100129. Available from: https://linkinghub.elsevier.com/retrieve/pii/S2773167725000044
33. El Hatka H, Hafidi Y, Ittobane N. Exploring urea hard segment morphology and phase separation behavior in flexible polyurethane foam formulations: Water, lithium chloride and isocyanate structure effects. Polymers and Polymer Composites. 2023 Jan 1;31.
34. Kumar AA, Karthick K, Arumugam KP. Properties of biodegradable polymers and degradation for sustainable development. Int JChem Eng Appl 2011;2(3) 164.
35. Gautam R, Bassi AS, Yanful EK. Plastic and Foam Biodegradation 85 A Review of Biodegradation of Synthetic Plastic and Foams. Vol. 141, Applied Biochemistry and Biotechnology. 2007.
36. Sinha V, Patel MR, Patel J V. Pet waste management by chemical recycling: A review. Vol. 18, Journal of Polymers and the Environment. 2010. p. 8–25.
37. Polo Fonseca L, Duval A, Luna E, Ximenis M, De Meester S, Avérous L, et al. Reducing the carbon footprint of polyurethanes by chemical and biological depolymerization: Fact or fiction? Vol. 41, Current Opinion in Green and Sustainable Chemistry. Elsevier B.V.; 2023.
38. Rossignolo G, Malucelli G, Lorenzetti A. Recycling of polyurethanes: where we are and where we are going. Vol. 26, Green Chemistry. Royal Society of Chemistry; 2023. p. 1132–52.
39. Simón D, Borreguero AM, de Lucas A, Rodríguez JF. Recycling of polyurethanes from laboratory to industry, a journey towards the sustainability. Vol. 76, Waste Management. Elsevier Ltd; 2018. p. 147–71.
40. Bartolome L, Imran M, Gyoo B, A. W, Hyun D. Recent Developments in the Chemical Recycling of PET. In: Material Recycling - Trends and Perspectives. InTech; 2012.
41. Liu LJ, Wang XL, Gu ZY, Ren XL, Chang T. Rapid hydrolysis of waste polyurethane and facile system separation. Sep Purif Technol. 2025 Feb 19;354.
42. Motokucho S, Yamaguchi A, Nakayama Y, Morikawa H, Nakatani H. Hydrolysis of aromatic polyurethane in water under high pressure of CO2. J Polym Sci APolym Chem. 2017 Jun 15;55(12):2004–10.
43. Gregory A. Campbell, William C. Meluch. Polyurethane Foam Recycling - Superheated Steam Hydrolysis. Environ Sci Technol. 1976 Feb 1;10, 2, 182–185.
44. Dai Z, Hatano B, Kadokawa JI, Tagaya H. Effect of diaminotoluene on the decomposition of polyurethane foam waste in superheated water [Internet]. Available from: www.elsevier.com/locate/polydegstab
45. Gu X, Wang X, Guo X, Liu S, Lou C, Liu Y. Study on Efficient Degradation of Waste PU Foam. Polymers (Basel). 2023 May 1;15(10).
46. Gu X, Zhu S, Liu S, Liu Y. Analysis of the Influencing Factors of the Efficient Degradation of Waste Polyurethane and Its Scheme Optimization. Polymers (Basel). 2023 May 1;15(10).
47. Xu L, Chen Y, Liu Z, Shao Z, Gao F, Gao K, et al. Efficient alcoholysis of waste rigid polyurethane foam using MIL-101(Fe) catalyst. Sep Purif Technol. 2025 Aug 27;366.
48. Vanbergen T, Verlent I, De Geeter J, Haelterman B, Claes L, De Vos D. Recycling of Flexible Polyurethane Foam by Split-Phase Alcoholysis: Identification of Additives and Alcoholyzing Agents to Reach Higher Efficiencies. ChemSusChem. 2020 Aug 7;13(15):3835–43.
49. Gu X, Wang X, Guo X, Liu S, Li Q, Liu Y. Study and Characterization of Regenerated Hard Foam Prepared by Polyol Hydrolysis of Waste Polyurethane. Polymers (Basel). 2023 Mar 1;15(6).
50. Gu X, Wang X, Guo X, Liu S, Lou C, Liu Y. Study on Efficient Degradation of Waste PU Foam. Polymers (Basel). 2023 May 1;15(10).
51. Gu X, Lyu S, Liu S. Alcoholysis of waste polyurethane rigid foam and its modification with lignin for recovery. J Renew Mater. 2021;9(11):1913–26.
52. Donadini R, Boaretti C, Scopel L, Lorenzetti A, Modesti M. Deamination of Polyols from the Glycolysis of Polyurethane. Chemistry - A European Journal. 2024 Jan 11;30(3).
53. Padhan RK. Chemical Depolymerization of Polyurethane Foams via Combined Chemolysis Methods [Internet]. Recycling of Polyurethane Foams. Elsevier Inc.; 2018. 89–96 p. Available from: http://dx.doi.org/10.1016/B978-0-323-51133-9.00008-5

54. Godinho B, Gama N, Barros-Timmons A, Ferreira A. Recycling of polyurethane wastes using different carboxylic acids via acidolysis to produce wood adhesives. Journal of Polymer Science. 2021 Apr 15;59(8):697–705.
55. Gama N, Godinho B, Marques G, Silva R, Barros-Timmons A, Ferreira A. Recycling of polyurethane by acidolysis: The effect of reaction conditions on the properties of the recovered polyol. Polymer (Guildf). 2021 Mar 26;219.
56. Liu B, Westman Z, Richardson K, Lim D, Stottlemyer AL, Farmer T, et al. Polyurethane Foam Chemical Recycling: Fast Acidolysis with Maleic Acid and Full Recovery of Polyol. ACS Sustain Chem Eng. 2024 Mar 18;12(11):4435–43.
57. Grdadolnik M, Drinčić A, Oreški A, Onder OC, Utroša P, Pahovnik D, et al. Insight into Chemical Recycling of Flexible Polyurethane Foams by Acidolysis. ACS Sustain Chem Eng. 2022 Jan 24;10(3):1323–32.
58. He H, Su H, Yu H, Du K, Yang F, Zhu Y, et al. Chemical Recycle of Waste Polyurethane Foams: Efficient Acidolysis Under the Catalysis of Zinc Acetate.
59. Alavi NikjeMMohammad. Recycling of Polyurethane Wastes. De Gruyter; 2019. 150 p.
60. Zhu P, Cao ZB, Chen Y, Zhang XJ, Qian GR, Chu YL, et al. Glycolysis recycling of rigid waste polyurethane foam from refrigerators. Environmental Technology (United Kingdom). 2014 Nov 2;35(21):2676–84.
61. Heiran R, Ghaderian A, Reghunadhan A, Sedaghati F, Thomas S, Haghighi A hossein. Glycolysis: an efficient route for recycling of end of life polyurethane foams. Vol. 28, Journal of Polymer Research. Springer Science and Business Media B.V.; 2021.
62. Wu CH, Chang CY, Cheng CM, Huang HC. Glycolysis of waste flexible polyurethane foam. PolymDegrad Stab. 2003;80(1):103–11.
63. Beneš H, Rösner J, Holler P, Synková H, Kotek J, Horák Z. Glycolysis of flexible polyurethane foam in recycling of car seats. Polym Adv Technol. 2007 Feb;18(2):149–56.
64. Nikje MMA, Nikrah M. Glycerin as a new glycolysing agent for chemical recycling of cold cure polyurethane foam wastes in "split-phase" condition. Polymer Bulletin. 2007 Feb;58(2):411–23.
65. Yeol Lee J, Kim D. Desaminated Glycolysis of Water-Blown Rigid Polyurethane Foams. 2000.
66. Simón D, Borreguero AM, De Lucas A, Rodríguez JF. Glycolysis of flexible polyurethane wastes containing polymeric polyols. PolymDegrad Stab. 2014;109:115–21.
67. Molero C, De Lucas A, Rodríguez JF. Recovery of polyols from flexible polyurethane foam by "split- phase" glycolysis with new catalysts. PolymDegrad Stab. 2006 Apr;91(4):894–901.
68. Molero C, De Lucas A, Romero F, Rodríguez JF. Glycolysis of flexible polyurethane wastes using stannous octoate as the catalyst. J Mater Cycles Waste Manag. 2009 May;11(2):130–2.
69. Alavi Nikje MM, Nikrah M, Haghshenas M. Microwave assisted "split-phase" glycolysis of polyurethane flexible foam wastes. Polymer Bulletin. 2007 Jun;59(1):91–104.
70. Simón D, Borreguero AM, De Lucas A, Rodríguez JF. Valorization of crude glycerol as a novel transesterification agent in the glycolysis of polyurethane foam waste. PolymDegrad Stab. 2015 Nov 1;121:126–36.
71. Esquer R, García JJ. Metal-catalysed Poly(Ethylene) terephthalate and polyurethane degradations by glycolysis. J Organomet Chem. 2019 Dec 1;902.
72. Datta J, Rohn M. Thermal properties of polyurethanes synthesized using waste polyurethane foam glycolysates. J Therm Anal Calorim. 2007 May;88(2):437–40.
73. Czupryński B, Liszkowska J, Paciorek-Sadowska J. Glycolysis of the rigid PUR-PIR foam modified with starch. J Appl Polym Sci. 2012 Oct 25;126(SUPPL. 1).
74. Paciorek-Sadowska J, Czupryłski B, Liszkowska J. Glycolysis of rigid polyurethane-polyisocyanurate foams with reduced flammability. Journal of Elastomers and Plastics. 2016 Jun 1;48(4):340–53.
75. Gu X, Wang X, Wang T, Zhu Y, Guo X, Liu S, et al. Analysis of Factors Influencing the Efficiency of Catalysts Used in Waste PU Degradation. Polymers (Basel). 2022 Dec 1;14(24).
76. Grdadolnik M, Zdovc B, Drinčić A, Onder OC, Utroša P, Ramos SG, et al. Chemical Recycling of Flexible Polyurethane Foams by Aminolysis to Recover High-Quality Polyols. ACS Sustain Chem Eng. 2023 Jul 24;11(29):10864–73.
77. Kanaya K, Takahashi S. Decomposition of Polyurethane Foams by Alkanolamines.

78. Chuayjuljit S, Norakankorn C, Pimpan V. Chemical Recycling of Rigid Polyurethane Foam Scrap via Base Catalyzed Aminolysis. Vol. 12, Journal of Metals, Materials and Minerals. 2002.
79. Olazabal I, González A, Vallejos S, Rivilla I, Jehanno C, Sardon H. Upgrading Polyurethanes into Functional Ureas through the Asymmetric Chemical Deconstruction of Carbamates. ACS Sustain Chem Eng. 2023 Jan 9;11(1):332–42.
80. Xue,',' Mitsuru Omoto,' Taka0 Hidai,' S, Imai' Y, Wiley J. Preparation of Epoxy Hardeners from Waste Rigid Polyurethane Foam and Their Application.
81. Rane. A.V., Abitha. V.K., Patil Shivendra, Jayaja. P. (A greener and sustainable approach for converting polyurethane foam rejects into superior polyurethane coatings). Chemistry International. 2015;1(4):184–95.
82. Guchait A, Maity D, Sabnis AS. Recycling of waste polyurethane shoe sole via aminolysis route. J Mater Cycles Waste Manag. 2024 Mar 1;26(2):860–71.
83. Troev K, Tsekova A, Tsevi R. Chemical Degradation of Polyurethanes: Degradation of Flexible Polyester Polyurethane Foam by Phosphonic Acid Dialkyl Esters. 2000.
84. Troev K, Tsekova A, Tsevi R. Chemical degradation of polyurethanes 2. Degradation of ¯exible polyether foam by dimethyl phosphonate.
85. Troev K, Atanasov VI, Tsevi R, Grancharov G, Tsekova A. Chemical degradation of polyurethanes. Degradation of microporous polyurethane elastomer by dimethyl phosphonate.
86. Troev K, Grancharov G, Tsevi R. Chemical degradation of polyurethanes 3. Degradation of microporous polyurethane elastomer by diethyl phosphonate and tris(1-methyl-2-chloroethyl) phosphate.
87. Troev K, Atanassov VL, Tzevi R. Chemical Degradation of Polyurethanes. II. Degradation of Microporous Polyurethane Elastomer by Phosphoric Acid Esters. Vol. 76, J Appl Polym Sci. 2000.

Bol. Soc. Mat. Mex. (2025) 31:85
https://doi.org/10.1007/s40590-025-00777-x

Sociedad Matemática Mexicana

ORIGINAL PAPER



A simple 5D autonomous hyperchaotic system: dynamical analysis, synchronization via adaptive integral sliding mode control, and circuit realization

Dinesh Khattar[1] · **Naokant Deo**[2] · **Mukul Sirohi**[2]

Received: 7 June 2024 / Accepted: 2 June 2025
© The Author(s) 2025

Abstract
Nonlinear interactions play a crucial role in the emergence of complex dynamics, such as chaos and hyperchaos, in autonomous deterministic dynamical systems within a continuous-time framework. Investigating systems with minimal nonlinear components provides valuable insights into the fundamental mechanisms that drive chaotic behaviors. In addition, higher dimensional hyperchaotic systems have garnered significant attention due to their broad range of applications. This paper presents a 5D autonomous deterministic dynamical model in a continuous-time framework with a single nonlinearity. We investigate key dynamical properties of the system, including bifurcation analysis, Kaplan–Yorke dimension, dissipativity, equilibrium points and their stability, phase portraits, Lyapunov exponents (LEs), and Poincaré cross-sections. To achieve hybrid projective synchronization (HPS) between two identical 5D systems, we combine adaptive control with integral-based sliding mode control. The synchronization results are validated through numerical simulations in MATLAB. Finally, the practical implementation of the proposed model is demonstrated using an electronic circuit schematic with a single multiplier chip, highlighting the practical significance of the system.

Keywords Hyperchaos · Nonlinear systems · Lyapunov exponents · Synchronization · Adaptive control · Sliding mode control · Bifurcation · Circuit design · Stability · Higher dimensional systems

Mathematics Subject Classification 93D05 · 34D06 · 93C10 · 34H10

✉ Mukul Sirohi
mukul7sirohi@gmail.com

[1] Department of Mathematics, Kirori Mal College, Delhi 110 007, India

[2] Department of Applied Mathematics, Delhi Technological University, Delhi 110 042, India

Published online: 19 June 2025

1 Introduction

Chaos theory investigates nonlinear, deterministic dynamical systems that exhibit pronounced sensitivity to initial conditions, where even the slightest perturbations can lead to significantly different outcomes [1]. Notably, despite their inherent complexity and apparent randomness, chaotic systems often display remarkable patterns and structures when visualized in phase space [2–5]. As deterministic systems, their behavior should, in principle, be predictable with absolute accuracy, provided that their initial conditions are known with perfect precision. However, achieving such precision at every step is practically impossible, resulting in a paradoxical coexistence of determinism and unpredictability within chaotic systems. Although the conceptual roots of chaos theory can be traced back to the late seventeenth century, the pioneering work of Henri Poincaré is widely regarded as laying the foundation for the modern theory of nonlinear dynamics, including chaos theory. His seminal contributions emphasized the qualitative analysis of dynamical systems, moving beyond purely quantitative methods [6]. Poincaré, while investigating the classical three-body problem, was the first to recognize that deterministic nonlinear systems can exhibit non-periodic behavior and are highly sensitive to initial conditions, making long-term prediction fundamentally challenging.

In autonomous dynamical models, nonlinear components play a pivotal role in generating complex behaviors such as chaos and hyperchaos. These nonlinear interactions are chiefly responsible for the stretching and folding mechanisms that give rise to emergent patterns like strange attractors [7]. Moreover, depending on the interest and scope of a research, both systems with many and with fewer nonlinear terms are considered important and have been widely investigated [8–13]. However, systems with an excessive number of nonlinear terms are often regarded as inefficient and impractical for real-world applications [14]. A notable example of this can be found in electronic circuit implementations, where deterministic models with fewer nonlinear components are preferred for hardware realization, as they reduce circuit complexity. In particular, systems with minimal nonlinear interactions require fewer multipliers, thereby simplifying their analog design. Previous studies have demonstrated that certain chaotic circuits can preserve rich dynamical behavior while utilizing fewer multipliers. Such designs are especially beneficial in practical applications like secure communications, where hardware efficiency is essential [15, 16].

Another important phenomenon within chaos theory is synchronization, in which two or more chaotic systems are coupled through controlled modifications. This concept was first introduced by Pecora and Carroll [17]. In synchronization schemes, chaotic signal propagation is harnessed for the transformation and secure transmission of digital information, as the inherent complexity of these systems enhances anonymity and strengthens the privacy of transmitted signals. In recent years, numerous synchronization methods have been applied to both identical and non-identical chaotic and hyperchaotic systems [18–24]. Additionally, various control strategies—including sliding mode, adaptive, active, back-stepping, and others—have been extensively investigated and applied [25–29]. Recent studies have even optimized chaotic systems using various metaheuristic algorithms [30].

Moreover, higher dimensional systems [31–37], which exhibit complex and enriched dynamics compared to traditional 3D models, are also of considerable research interest due to their practical applications. For instance, in 2024, Khattar et al. introduced a six-dimensional model based on the Lü system, incorporating four nonlinear components [38]. More recently, the practical applicability of this model was demonstrated by researchers in applied contexts [39]. Although many studies on higher dimensional models exist in the literature, some notable contributions are worth mentioning. In 2017, the simplest 4D chaotic system with a line of equilibria and a single nonlinear term was introduced [40]. In 2018, a novel 5D system featuring a stable equilibrium point and transient chaotic behavior was proposed [41]. In 2022, a simple 5D system without equilibrium points, based on the well-known 3D Sprott-E system, was presented [42]. In 2023, a 5D autonomous hyperchaotic system incorporating two linear controllers was proposed [43]. Recently, a fractional-order 5D multi-wing chaotic system with a hidden attractor was introduced [44].

Based on the preceding discussion, this article presents a new 5D deterministic autonomous model in a continuous-time framework featuring a single quadratic nonlinear component. A comprehensive comparative assessment of the proposed model, alongside existing 5D models from the literature, is provided in Table 1. The hyperchaotic regime of the model is confirmed through the numerical computation of the Lyapunov exponents (LEs) using the Wolf algorithm. Standard dynamical analyses, including time series, dissipativity theory, stability analysis, Kaplan–Yorke dimension measurement, phase portraits, and Poincaré cross-sections, are conducted to examine the system's nature. A bifurcation diagram is also studied to explore the system's response to variations in parameter a, and this chart is then validated using the LEs spectrum. Furthermore, the concept of integral-based sliding mode control is integrated with renowned adaptive control to achieve hybrid projective synchronization. These theoretical results are validated using the Lyapunov stability theory to ensure that each synchronization error converges asymptotically to zero. Numerical simulations in MATLAB are performed to confirm and validate the obtained analytical synchronization results. Finally, an analog circuit schematic is designed on Multisim 14.2 using resistors, capacitors, amplifiers, and a single multiplier. The corresponding oscilloscope measurements are compared with the MATLAB-generated phase projections to confirm the practical implementation of the system.

This paper is structured as follows: Sect. 2 introduces a novel 5D hyperchaotic system and provides an in-depth dynamical analysis through dissipativity proofs, numerical computations, and various visual representations. Section 3 explores hybrid projective synchronization (HPS) over identical 5D systems by combining adaptive control with integral-based sliding mode control, ensuring error convergence relying on Lyapunov stability theory. In Sect. 4, numerical simulations are presented to verify the synchronization results, and Sect. 5 offers a comparative study of complete synchronization and anti-synchronization under the proposed control framework. Section 6 discusses the physical realizability of the system through an electronic circuit design and experimental measurements. Section 7 concludes the paper by summarizing the key findings and emphasizing the novel aspects of this research.

Birkhäuser

Table 1 Compilation of some recent and notable studies related to 5D systems

System dynamics	Total terms involved	No. of nonlinear terms	No. of +ve LEs	Computed Maximum LE	Kaplan–Yorke dimension	Circuit validation of system	Reference
Hyperchaotic	14	4	2	0.9013	4.0423	Yes	[45]
Hyperchaotic	10	4	3	0.3049	4.3801	No	[46]
Hyperchaotic	13	3	3	0.2074	–	Yes	[47]
Hyperchaotic	14	3	2	2.5120	4.7115	No	[48]
Chaotic	13	5	1	0.7255	3.2291	No	[34]
Hyperchaotic	15	3	2	0.7231	3.0575	No	[24]
Hyperchaotic	13	3	3	0.6100	–	Yes	[49]
Hyperchaotic	12	3	3	0.4195	4.0159	Yes	[50]
Hyperchaotic	9	2	3	0.4976	4.9983	No	[51]
Hyperchaotic	10	1	2	0.9996	4.5000	Yes	This Work

2 Mathematical description of the new system

In autonomous deterministic dynamical systems evolving in continuous time, nonlinear interactions play a crucial role in the emergence of complex behaviors such as chaos and hyperchaos. Studying systems with minimal nonlinearities, particularly in higher dimensions, can provide valuable insights into the mechanisms underlying chaos and hyperchaos. Moreover, higher dimensional systems [31–37] have attracted significant research interest due to their richer and more intricate dynamical behaviors compared to traditional three-dimensional models, as well as their well-established potential for practical applications.

For instance, in 2024, Khattar et al. proposed a six-dimensional system derived from the Lü system, incorporating four nonlinear terms [38]. The practical relevance of this model was subsequently validated through its implementation in applied scenarios [39]. Although many higher dimensional systems have been reported, several notable developments relevant to this work are worth highlighting. In 2017, the simplest four-dimensional chaotic system featuring a line of equilibria and a single nonlinear term was introduced [40]. In 2018, researchers proposed a new five-dimensional system exhibiting a stable equilibrium alongside transient chaotic dynamics [41]. In 2022, a simple five-dimensional system based on the three-dimensional Sprott-E system was presented [42]. In 2023, a five-dimensional autonomous hyperchaotic system incorporating two linear controllers was introduced [43]. More recently, in 2024, a fractional-order five-dimensional multi-wing chaotic system exhibiting a hidden attractor was proposed [44]. We propose a five-dimensional deterministic dynamical system with a single quadratic nonlinearity, constructed using the framework presented in [52]. The system is described by the following set of equations:

$$\begin{cases} \frac{dx}{dt} &= ay + z, \\ \frac{dy}{dt} &= by - x, \\ \frac{dz}{dt} &= x^2 - z, \\ \frac{dw}{dt} &= x - w, \\ \frac{ds}{dt} &= w - cs. \end{cases} \tag{1}$$

Here, a, b, and c are real-valued parameters, and the state vector $(x, y, z, w, s)^T \in \mathbb{R}^5$ defines the system's state. This newly proposed five-dimensional model is referred to as the $\mathcal{S}$**-system**. A comprehensive comparative assessment of the proposed model with some existing 5D chaotic and hyperchaotic models from the literature is outlined in Table 1.

2.1 Lyapunov exponents and Kaplan–Yorke dimension

The average exponential rates of divergence or convergence between two infinitesimally close trajectories in phase space are quantified by Lyapunov exponents (LEs), which serve as numerical indicators of a system's dynamical behavior. In this section, the LEs of $\mathcal{S}$-system with parameters $(a, b, c) = (1, 0.5, -1)$ are computed

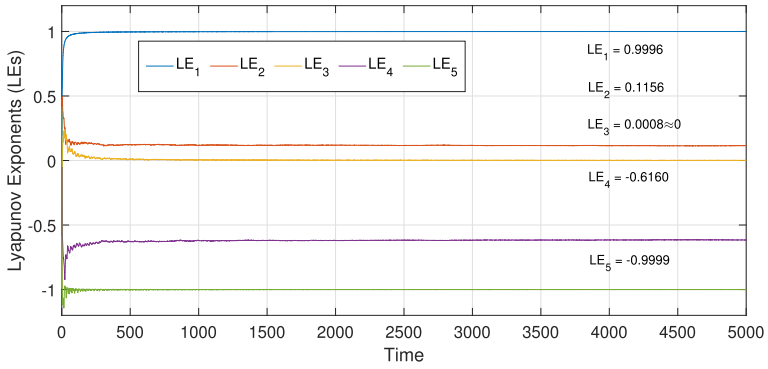


Fig. 1 Estimated values of the Lyapunov exponents (LEs) for the $\mathcal{S}$-system

using MATLAB. The computation employs the Wolf algorithm [53], with initial conditions set to $(0.01, 0.01, \ldots, 0.01)$, a time step of $\Delta t = 0.5$, and a total integration time of $T = 5000$. The calculated LEs are: $LE_1 = 0.9996$, $LE_2 = 0.1156$, $LE_3 = 0.0008 \approx 0$, $LE_4 = -0.6160$, and $LE_5 = -0.9999$. The presence of two positive LEs, namely LE_1 and LE_2, confirms that the proposed model exhibits hyperchaotic behavior. This indicates that the system is unstable along two distinct directions in its phase space. The evolution of these exponents over time is illustrated in Fig. 1.

The number D_{KY} is a fractional statistic that represents the fractal-patterned attractor within a deterministic continuous-time dynamical model. The complexity of the $\mathcal{S}$-system's attractor is expressed using the Kaplan–Yorke (D_{KY}) dimension:

$$D_{KY} = 4 + \frac{\sum_{\rho=1}^{4} LE_\rho}{|LE_5|} \approx 4.5.$$

2.2 Dissipativity analysis

One of the essential properties of continuous-time dynamical systems that exhibit chaotic behavior is that their trajectories remain confined within a bounded region of the phase space. For this confinement to occur, the system must exhibit dissipativity, meaning that the volume of a set of nearby trajectories in phase space contracts over time. If a system were globally volume-expanding – that is, if its phase space volume increased indefinitely – the trajectories would diverge to infinity, precluding the possibility of sustaining bounded chaotic dynamics. Therefore, verifying the dissipativity of a system is a necessary step when investigating its potential for chaotic behavior. To assess the dissipativity of the proposed $\mathcal{S}$-system, it is first expressed in the following general form:

$$\dot{X} = \mathcal{F}(X),$$

where $X = (x, y, z, w, s)^T$ and, component-wise:

$$\begin{cases} \dfrac{dx}{dt} = ay + z & = \mathcal{F}_1, \\ \dfrac{dy}{dt} = by - x & = \mathcal{F}_2, \\ \dfrac{dz}{dt} = x^2 - z & = \mathcal{F}_3, \\ \dfrac{dw}{dt} = x - w & = \mathcal{F}_4, \\ \dfrac{ds}{dt} = w - cs & = \mathcal{F}_5. \end{cases}$$

Clearly, each $\mathcal{F}_\xi$, for $\xi = 1, 2, 3, 4, 5$, are smooth functions of (x, y, z, w, s). Let Ω be a region in $\mathbb{R}^5$ with a uniform boundary $\omega(t)$ that evolves with the flow $\Psi(t)$ generated by $\mathcal{F}$. According to Liouville's theorem [54], the time evolution of the volume $V(t)$ within this region is governed by:

$$\frac{dV(t)}{dt} = \int_{\omega(t)} (\nabla \cdot \mathcal{F})\, dx\, dy\, dz\, dw\, ds.$$

The divergence of the vector field J is computed as:

$$\begin{aligned} \nabla \cdot \mathcal{F} &= \frac{\partial \mathcal{F}_1}{\partial x} + \frac{\partial \mathcal{F}_2}{\partial y} + \frac{\partial \mathcal{F}_3}{\partial z} + \frac{\partial \mathcal{F}_4}{\partial w} + \frac{\partial \mathcal{F}_5}{\partial s} \\ &= 0 + b + (-1) + (-1) + (-c) \\ &= b - 2 - c \\ &= -(2 + c - b). \end{aligned}$$

Thus, the system is dissipative if the divergence is negative, which imposes the condition:

$$(2 + c - b) > 0.$$

Consequently, the rate of change of the volume is given by:

$$\frac{dV(t)}{dt} = \int_{\omega(t)} -(2 + c - b)\, dx\, dy\, dz\, dw\, ds.$$

Since the divergence is constant over the region, this simplifies to:

$$\frac{dV(t)}{dt} = -(2 + c - b)\, V(t). \tag{2}$$

Integrating equation (2) with respect to time yields:

$$V(t) = V_0\, e^{-(2+c-b)t},$$

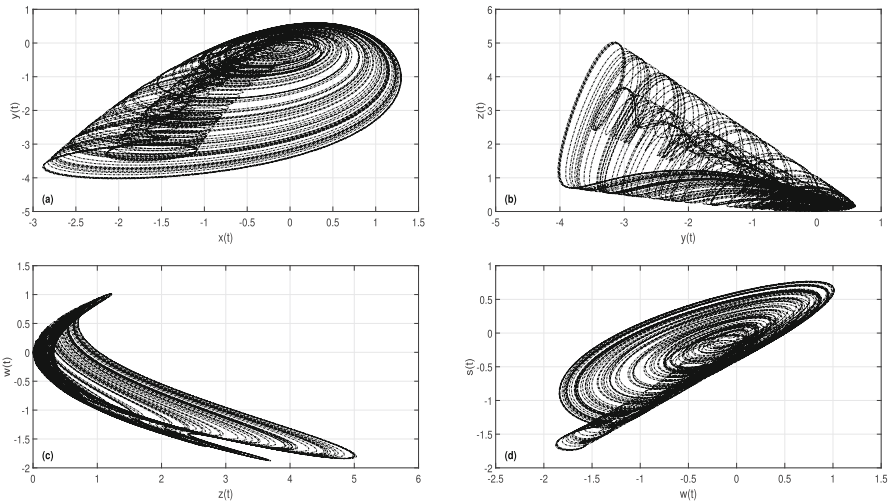


Fig. 2 Two-dimensional phase portraits of the $\mathcal{S}$-system in planes: **(a)** x-y, **(b)** y-z, **(c)** z-w, and **(d)** w-s

where $V_0 = V(0)$ is the initial volume in phase space.

This result demonstrates that the volume element V_0 contracts exponentially at a rate of $(2+c-b)$ as time progresses. In other words, the phase space volume occupied by a set of nearby trajectories contracts to zero as $t \to \infty$. This behavior confirms the system's dissipative nature and is a necessary condition for the emergence of chaos in continuous-time dynamical systems.

2.3 Phase portraits

Phase diagrams represent the solutions of a dynamical system in its physical or phase space, providing valuable insights into the system's long-term behavior. In chaotic systems, the trajectories often exhibit a wide variety of intricate and sophisticated structures, such as strange attractors, geometric patterns, and basins of attraction [55]. Two-dimensional projections of the proposed $\mathcal{S}$-system are illustrated in Fig. 2, revealing the characteristic behavior and complexity of its phase space trajectories.

2.4 Time series

A time series records the values of one or more variables at uniform time intervals, capturing the temporal evolution of a system's characteristics. Time series analysis provides valuable insights by revealing patterns, trends, and interactions, even in cases where the system's behavior appears irregular or unpredictable. The primary time-dependent features of the proposed $\mathcal{S}$-system are presented in Fig. 3, illustrating the dynamic evolution of its state variables over time.

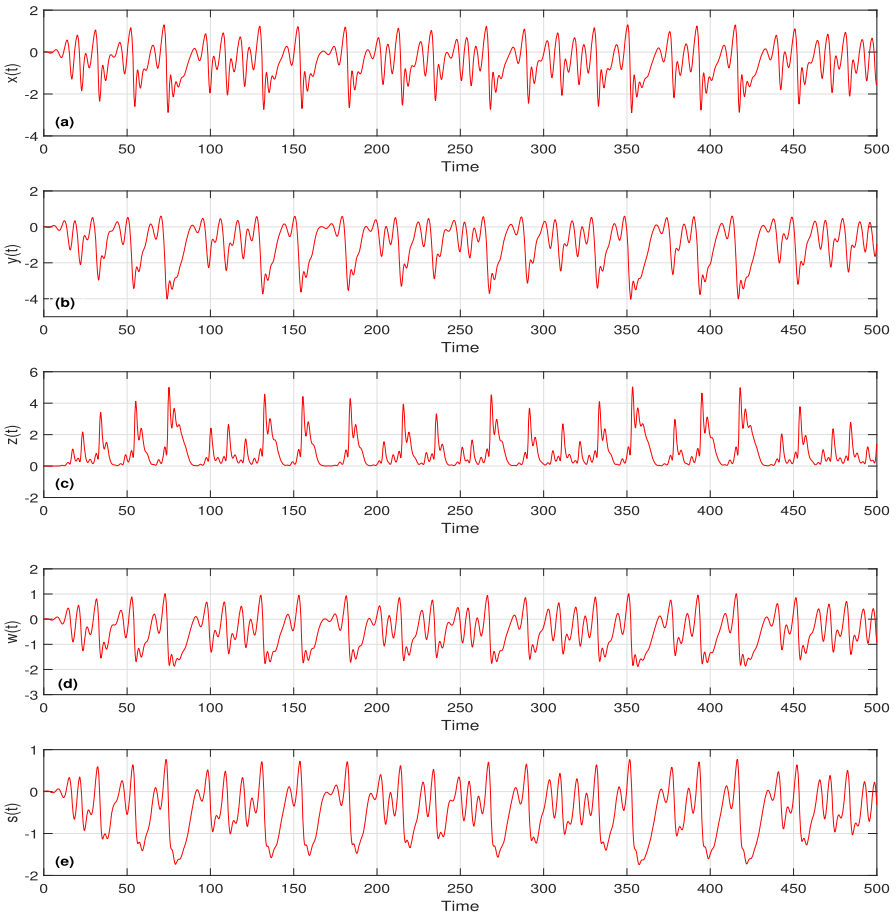


Fig. 3 Time series analysis of the $\mathcal{S}$-system: **(a)** $x(t)$ with time, **(b)** $y(t)$ with time, **(c)** $z(t)$ with time, **(d)** $w(t)$ with time, and **(e)** $s(t)$ with time

2.5 Poincaré cross-section

The Poincaré map, also known as the first return map, is a technique employed to reduce the dimensionality of a dynamical system by projecting its trajectories onto a lower dimensional surface [56]. Since many dynamical systems exhibit multiple degrees of freedom, comprehending their complete dynamics in higher dimensions can be challenging. Poincaré maps offer valuable insights into the system's behavior by examining the points at which trajectories intersect a designated Poincaré section. The resulting intersection patterns reveal critical information regarding the system's stability, periodicity, and chaotic nature. The Poincaré sections for the proposed $\mathcal{S}$-system are illustrated in Fig. 4.

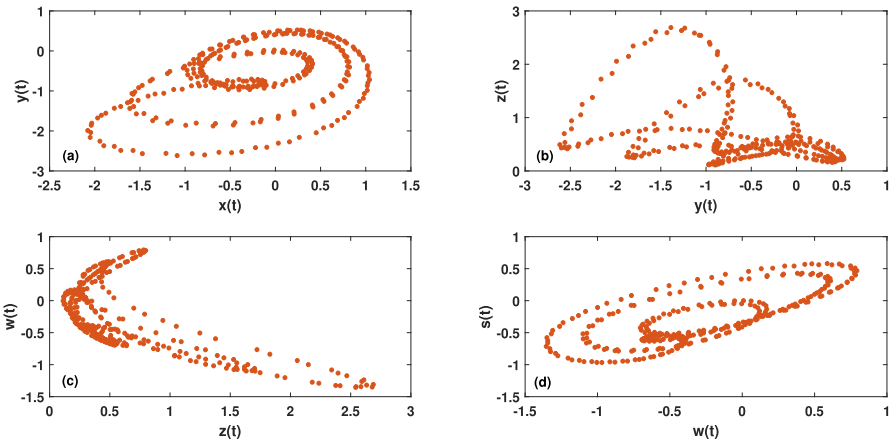


Fig. 4 Poincaré cross-sections of the 8-system in the planes: **(a)** x-y, **(b)** y-z, **(c)** z-w, and **(d)** w-s

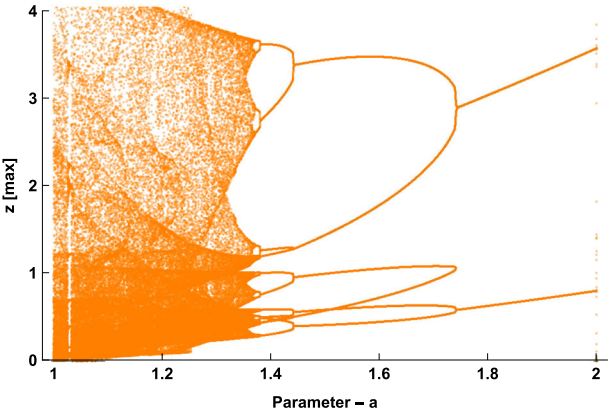


Fig. 5 Bifurcation diagram of the 8-system for the parameter range $1 \leq a \leq 2$

2.6 Bifurcation analysis

A bifurcation diagram is a graphical representation that illustrates the qualitative behavior of a dynamical system as a specific parameter is varied, while all other parameters are held constant [57]. Such diagrams are instrumental in identifying the emergence of periodicity, quasi-periodicity, and qualitative transitions such as chaos as the control parameter sweeps across an interval. The bifurcation diagram of the proposed 8-system, obtained by varying the parameter a over the range $1 \leq a \leq 2$ while keeping (b, c) fixed at $(0.5, 1)$, is illustrated in Fig. 5. To validate this bifurcation scenario, the corresponding Lyapunov spectra were computed for the same parametric range, as shown in Fig. 6. The orbital behavior of the 8-system was analyzed by varying the parameter a within the interval $[1, 2]$. For $a \in [1, 1.38)$, the system exhibits chaotic dynamics characterized by one positive, one zero, and three negative Lyapunov exponents (LEs). Quasi-periodic behavior emerges at $a \approx 1.38, 1.44, 1.76$, distinguished

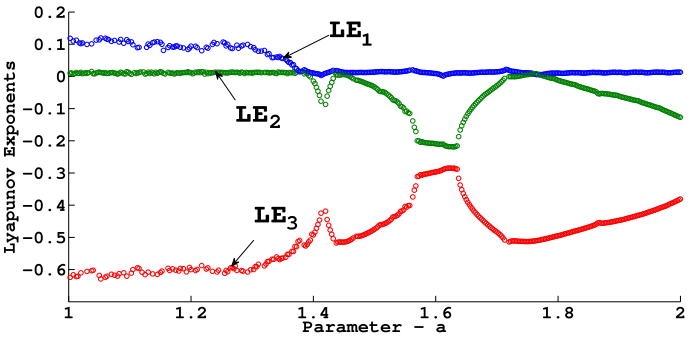


Fig. 6 Spectrum of the first three Lyapunov exponents (LEs) in the $\mathcal{S}$-system, varying $1 \leq a \leq 2$

by two zero and three negative LEs. The system transitions to periodic behavior for $a \in (1.38, 1.44) \cup (1.44, 1.76) \cup (1.76, 2]$, with one zero and four negative LEs. Thus, the system alternates between chaotic, quasi-periodic, and periodic behaviors as the parameter a varies within $[1, 2]$. Furthermore, the bifurcation diagram reveals that regions with a higher point density indicate the system's progression toward chaotic behavior, while bands of sparse points correspond to periodic windows.

2.7 Local stability analysis

An equilibrium point of a dynamical system is a point in the phase space at which the time derivatives of all state variables vanish. The equilibrium points of the proposed $\mathcal{S}$-system are obtained by solving the following system of equations:

$$\begin{cases} ay + z &= 0, \\ by - x &= 0, \\ x^2 - z &= 0, \\ x - w &= 0, \\ w - cs &= 0. \end{cases}$$

The $\mathcal{S}$-system admits two generalized equilibrium points: $E_1 = (0, 0, 0, 0, 0)^T$ and $E_2 = \left(-\frac{a}{b}, -\frac{a}{b^2}, \frac{a^2}{b^2}, -\frac{a}{b}, -\frac{a}{bc}\right)^T$, provided $b, c \neq 0$. The Jacobian matrix J of the proposed $\mathcal{S}$-system is given by:

$$J = \begin{bmatrix} 0 & a & 1 & 0 & 0 \\ -1 & b & 0 & 0 & 0 \\ 2x & 0 & -1 & 0 & 0 \\ 1 & 0 & 0 & -1 & 0 \\ 0 & 0 & 0 & 1 & -c \end{bmatrix}.$$

To analyze the stability of E_1, we compute the characteristic polynomial corresponding to the Jacobian matrix J at E_1, which is given by:

$$P_{E_1}(\lambda) = (\lambda + 1)^2(\lambda^2 - b\lambda + a)(\lambda + c).$$

The roots of this characteristic equation (i.e., the eigenvalues) are:

$$\begin{cases} \lambda_1 &= -1, \\ \lambda_2 &= -1, \\ \lambda_3 &= \frac{b+\sqrt{b^2-4a}}{2}, \\ \lambda_4 &= \frac{b-\sqrt{b^2-4a}}{2}, \\ \lambda_5 &= -c. \end{cases}$$

Applying the Routh–Hurwitz criterion [58], the trivial equilibrium point E_1 is locally asymptotically stable if the following conditions are satisfied: $c > 0$, $b < 0$, and $a > 0$.

For the second equilibrium point E_2, the corresponding characteristic polynomial is given by:

$$P_{E_2}(\lambda) = (\lambda + 1)(\lambda + c)\Big(\underbrace{\lambda^3 + (1 - b)\lambda^2 + (a - b + \frac{2a}{b})\lambda - a}_{\mathcal{F}(\lambda)}\Big).$$

To analyze the stability of E_2, we apply the Routh–Hurwitz criterion to the cubic polynomial $\mathcal{F}(\lambda)$, which states that for a cubic polynomial with real coefficients of the form $\lambda^3 + A\lambda^2 + B\lambda + C$, all roots will have negative real parts if the following conditions are satisfied: $A > 0$, $C > 0$, and $AB > C$. Upon applying these conditions to $\mathcal{F}(\lambda)$ and considering the other factors of $P_{E_2}(\lambda)$, the equilibrium point E_2 is locally asymptotically stable when:

$$b < 1, \quad c > 0, \quad a < 0, \quad \text{and} \quad \left(\frac{2a}{b} + b^2\right) > b + ab.$$

3 Synchronization based on adaptive integral sliding mode control (AISMC)

The objective of this section is to demonstrate the analytical results of hybrid projective synchronization (HPS) using the integral sliding mode control (ISMC) methodology [59] in the presence of parametric uncertainties, i.e., adaptive ISMC (AISMC), applied to identical 5D systems. To theoretically verify HPS with AISMC, it is necessary to design appropriate controllers. We initiate the HPS scheme by considering the

following drive system:

$$\begin{cases} \dot{x}_1 = ay_1 + z_1, \\ \dot{y}_1 = by_1 - x_1, \\ \dot{z}_1 = x_1^2 - z_1, \\ \dot{w}_1 = x_1 - w_1, \\ \dot{s}_1 = w_1 - cs_1, \end{cases} \tag{3}$$

where $(x_1, y_1, z_1, w_1, s_1)^T \in \mathbb{R}^5$ denotes the state vector of the drive system. Similarly, the response system defined as:

$$\begin{cases} \dot{x}_2 = ay_2 + z_2 + \Theta_x(t), \\ \dot{y}_2 = by_2 - x_2 + \Theta_y(t), \\ \dot{z}_2 = x_2^2 - z_2 + \Theta_z(t), \\ \dot{w}_2 = x_2 - w_2 + \Theta_w(t), \\ \dot{s}_2 = w_2 - cs_2 + \Theta_s(t), \end{cases} \tag{4}$$

where $(x_2, y_2, z_2, w_2, s_2)^T \in \mathbb{R}^5$ denotes the state vector of the response system while $\Theta_x(t), \Theta_y(t), \Theta_z(t), \Theta_w(t)$, and $\Theta_s(t)$ are the AISMC controllers to be designed for achieving desired synchronization. Define the drive-response error vector $\mathbf{e}(t) = (e_x, e_y, e_z, e_w, e_s)^T$, where:

$$\begin{cases} e_x = x_2 - \varepsilon_1 x_1, \\ e_y = y_2 - \varepsilon_2 y_1, \\ e_z = z_2 - \varepsilon_3 z_1, \\ e_w = w_2 - \varepsilon_4 w_1, \\ e_s = s_2 - \varepsilon_5 s_1, \end{cases} \tag{5}$$

in which the real-valued scaling constants $\varepsilon_\varrho \neq 0$ for $\varrho = 1, 2, \ldots, 5$ are the projective scaling factors. Upon differentiating this error formulations in (5) with respect to time, the error dynamics are given by:

$$\begin{cases} \dot{e}_x = \dot{x}_2 - \varepsilon_1 \dot{x}_1, \\ \dot{e}_y = \dot{y}_2 - \varepsilon_2 \dot{y}_1, \\ \dot{e}_z = \dot{z}_2 - \varepsilon_3 \dot{z}_1, \\ \dot{e}_w = \dot{w}_2 - \varepsilon_4 \dot{w}_1, \\ \dot{e}_s = \dot{s}_2 - \varepsilon_5 \dot{s}_1. \end{cases} \tag{6}$$

Substituting the dynamics of the drive (3) and response (4) into the system (6), we obtain:

$$\begin{cases} \dot{e}_x = ay_2 + z_2 - \varepsilon_1(ay_1 + z_1) + \Theta_x(t), \\ \dot{e}_y = by_2 - x_2 - \varepsilon_2(by_1 - x_1) + \Theta_y(t), \\ \dot{e}_z = x_2^2 - z_2 - \varepsilon_3(x_1^2 - z_1) + \Theta_z(t), \\ \dot{e}_w = x_2 - w_2 - \varepsilon_4(x_1 - w_1) + \Theta_w(t), \\ \dot{e}_s = w_2 - cs_2 - \varepsilon_5(w_1 - cs_1) + \Theta_s(t). \end{cases} \tag{7}$$

We choose the following integral sliding surfaces based on the error vectors:

$$\begin{cases} S_x = e_x + \lambda_x \int_0^t e_x(\tau)\, d\tau, \\ S_y = e_y + \lambda_y \int_0^t e_y(\tau)\, d\tau, \\ S_z = e_z + \lambda_z \int_0^t e_z(\tau)\, d\tau, \\ S_w = e_w + \lambda_w \int_0^t e_w(\tau)\, d\tau, \\ S_s = e_s + \lambda_s \int_0^t e_s(\tau)\, d\tau, \end{cases} \tag{8}$$

Differentiating the sliding surfaces in (8) with respect to time, we obtain:

$$\begin{cases} \dot{S}_x = \dot{e}_x + \lambda_x e_x, \\ \dot{S}_y = \dot{e}_y + \lambda_y e_y, \\ \dot{S}_z = \dot{e}_z + \lambda_z e_z, \\ \dot{S}_w = \dot{e}_w + \lambda_w e_w, \\ \dot{S}_s = \dot{e}_s + \lambda_s e_s. \end{cases} \tag{9}$$

The criterion for Hurwitz stability of the sliding dynamics is satisfied if each λ_ξ is a strictly positive constant in $\mathbb{R}$, where the index $\xi = x, y, z, w, s$. Applying the exponential reaching law, we obtain the following dynamics for the sliding surfaces:

$$\begin{cases} \dot{S}_x = -e_a y_2 + \varepsilon_1 e_a y_1 - \mu_x \mathrm{sgn}(S_x) - K_x S_x, \\ \dot{S}_y = -e_b y_2 + \varepsilon_2 e_b y_1 - \mu_y \mathrm{sgn}(S_y) - K_y S_y, \\ \dot{S}_z = -\mu_z \mathrm{sgn}(S_z) - K_z S_z, \\ \dot{S}_w = -\mu_w \mathrm{sgn}(S_w) - K_w S_w, \\ \dot{S}_s = e_c s_2 - \varepsilon_5 e_c s_1 - \mu_s \mathrm{sgn}(S_s) - K_s S_s, \end{cases} \tag{10}$$

where $e_a = \hat{A}(t) - a$, $e_b = \hat{B}(t) - b$, and $e_c = \hat{C}(t) - c$ represent the estimation errors for the system parameters a, b, and c, respectively. Utilizing (9) and (10), we

obtain the following error dynamics:

$$\begin{cases} \dot{e}_x = -e_a y_2 + \varepsilon_1 e_a y_1 - \mu_x \mathrm{sgn}(S_x) - K_x S_x - \lambda_x e_x, \\ \dot{e}_y = -e_b y_2 + \varepsilon_2 e_b y_1 - \mu_y \mathrm{sgn}(S_y) - K_y S_y - \lambda_y e_y, \\ \dot{e}_z = -\mu_z \mathrm{sgn}(S_z) - K_z S_z - \lambda_z e_z, \\ \dot{e}_w = -\mu_w \mathrm{sgn}(S_w) - K_w S_w - \lambda_w e_w, \\ \dot{e}_s = e_c s_2 - \varepsilon_5 e_c s_1 - \mu_s \mathrm{sgn}(S_s) - K_s S_s - \lambda_s e_s. \end{cases} \tag{11}$$

Theorem 1 *The response system (4) will be asymptotically hybrid projective synchronized (HPS) with the drive system (3) for some scaling matrix ε, via adaptive integral sliding mode control (AISMC), whenever the controllers are chosen as:*

$$\begin{cases} \Theta_x(t) = -\hat{A}(t) y_2 - z_2 + \varepsilon_1(\hat{A}(t) y_1 + z_1) - \mu_x \, sgn(S_x) - \lambda_x e_x - K_x S_x, \\ \Theta_y(t) = -\hat{B}(t) y_2 + x_2 + \varepsilon_2(\hat{B}(t) y_1 - x_1) - \mu_y \, sgn(S_y) - \lambda_y e_y - K_y S_y, \\ \Theta_z(t) = -x_2^2 + z_2 + \varepsilon_3(x_1^2 - z_1) - \mu_z \, sgn(S_z) - \lambda_z e_z - K_z S_z, \\ \Theta_w(t) = -x_2 + w_2 + \varepsilon_4(x_1 - w_1) - \mu_w \, sgn(S_w) - \lambda_w e_w - K_w S_w, \\ \Theta_s(t) = -w_2 + \hat{C}(t) s_2 + \varepsilon_5(w_1 - \hat{C}(t) s_1) - \mu_s \, sgn(S_s) - \lambda_s e_s - K_s S_s \end{cases} \tag{12}$$

with an adaptive parametric estimation law:

$$\begin{cases} \dot{\hat{A}}(t) = S_x y_2 - \varepsilon_1 S_x y_1 - K_a e_a, \\ \dot{\hat{B}}(t) = S_y y_2 - \varepsilon_2 S_y y_1 - K_b e_b, \\ \dot{\hat{C}}(t) = -S_s s_2 - \varepsilon_5 S_s s_1 - K_c e_c, \end{cases} \tag{13}$$

provided each λ_ξ, μ_ξ, and K_ξ are strictly positive constants in $\mathbb{R}$, and each of these values should be chosen sufficiently large to ensure dominance over uncertainties.

Proof The Lyapunov functions are selected in accordance with the principles of Lyapunov stability theory [60]. Thus, we choose the following Lyapunov function:

$$V(t) = \frac{1}{2}\left(S_x^2 + S_y^2 + S_z^2 + S_w^2 + S_s^2 + e_a^2 + e_b^2 + e_c^2\right). \tag{14}$$

Here, $V(t)$ is a positive definite function, which is quadratic, and:

$$\dot{V}(t) = S_x \dot{S}_x + S_y \dot{S}_y + S_z \dot{S}_z + S_w \dot{S}_w + S_s \dot{S}_s + e_a \dot{e}_a + e_b \dot{e}_b + e_c \dot{e}_c. \tag{15}$$

Using equations (10) and (13), we get:

$$\begin{aligned}\dot{V}(t) =& S_x\big(-e_a y_2+\varepsilon_1 e_a y_1-\mu_x\,\mathrm{sgn}(S_x)-K_x S_x\big)\\ &+S_y\big(-e_b y_2+\varepsilon_2 e_b y_1-\mu_y\,\mathrm{sgn}(S_y)-K_y S_y\big)\\ &+S_z\big(-\mu_z\,\mathrm{sgn}(S_z)-K_z S_z\big)+S_w\big(-\mu_w\,\mathrm{sgn}(S_w)-K_w S_w\big)\\ &+S_s\big(e_c s_2+\varepsilon_5 e_c s_1-\mu_s\,\mathrm{sgn}(S_s)-K_s S_s\big)+e_a\big(S_x y_2-\varepsilon_1 S_x y_1-K_a e_a\big)\\ &+e_b\big(S_y y_2-\varepsilon_2 S_y y_1-K_b e_b\big)+e_c\big(-S_s s_2-\varepsilon_5 S_s s_1-K_c e_c\big).\end{aligned} \tag{16}$$

This simplifies to:

$$\begin{aligned}\dot{V}(t) =& -\mu_x|S_x|-\mu_y|S_y|-\mu_z|S_z|-\mu_w|S_w|-\mu_s|S_s|\\ &-K_x S_x^2-K_y S_y^2-K_z S_z^2-K_w S_w^2-K_s S_s^2-K_a e_a^2-K_b e_b^2-K_c e_c^2.\end{aligned}$$

This establishes the fact that $\dot{V}(t) < 0$. Thus, by Lyapunov's direct theorem, it follows that each $S_\xi \to 0$ as $t \to \infty$, which further ensures that each element in $\mathbf{e} = (e_x, e_y, e_z, e_w, e_s)^T$ converges to zero as $t \to \infty$, while simultaneously each parametric estimation is also identified. In other words, the drive-response system is now hybrid projective synchronized (HPS) using robust adaptive integral sliding mode control (AISMC). □

4 Numerical simulations

MATLAB-based numerical simulations are performed to validate the synchronization results derived through analytical formulations and theoretical analysis using Adaptive Integral Sliding Mode Control (AISMC). This step is crucial for verifying the consistency and practical effectiveness of the proposed synchronization scheme with AISMC. The system parameters are selected as $(a, b, c) = (1, 0.5, 2)$, which yield chaotic behavior in the drive-response configuration in the absence of AISMC. The initial conditions for the response system are set to $x_2(0) = 0.07$, $y_2(0) = 0.02$, $z_2(0) = 0.05$, $w_2(0) = 0.06$, and $s_2(0) = 0.08$, while those for the drive system are assigned as $x_1(0) = 0.02$, $y_1(0) = 0.01$, $z_1(0) = 0.02$, $w_1(0) = 0.02$, and $s_1(0) = 0.06$. The evolution of the state trajectories for both the drive and response systems, without the application of any control, is illustrated in Fig. 7.

5 Comparative analysis

In this section, two particular cases of hybrid projective synchronization (HPS) using Adaptive Integral Sliding Mode Control (AISMC) are compared. By setting $\varepsilon_\varrho = 1$ for $\varrho = 1, 2, \ldots, 5$ and applying AISMC, the drive-response systems achieve complete synchronization, as illustrated in Fig. 8. The control parameters are uniformly selected as $(K_\xi, \lambda_\xi, \mu_\xi) = (5, 10, 3)$ for all ξ, with values chosen sufficiently large to ensure dominance over parametric uncertainties. The evolution of the synchronization errors

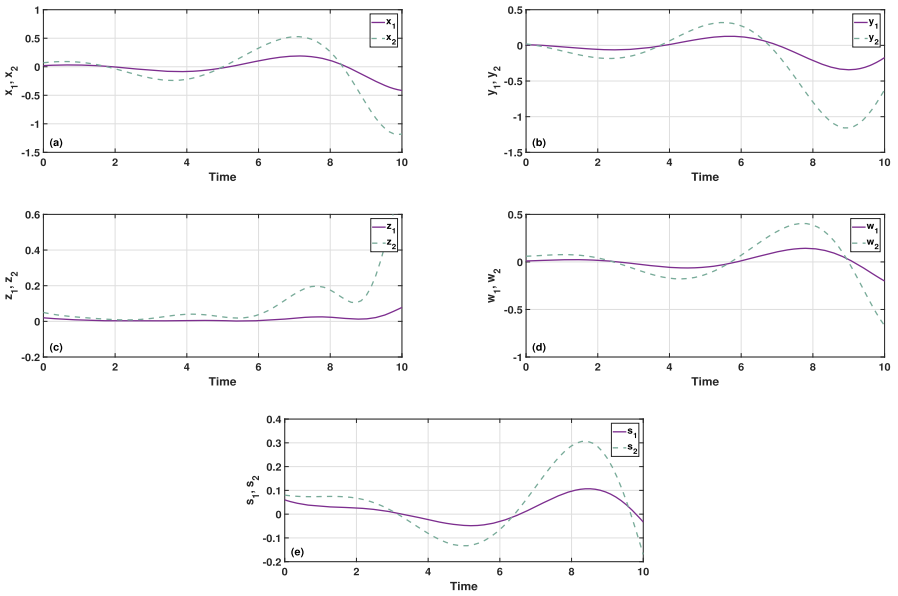


Fig. 7 The state vectors of the drive-response systems without the application of AISMC: **(a)** $x_1 - x_2$, **(b)** $y_1 - y_2$, **(c)** $z_1 - z_2$, **(d)** $w_1 - w_2$, and **(e)** $s_1 - s_2$

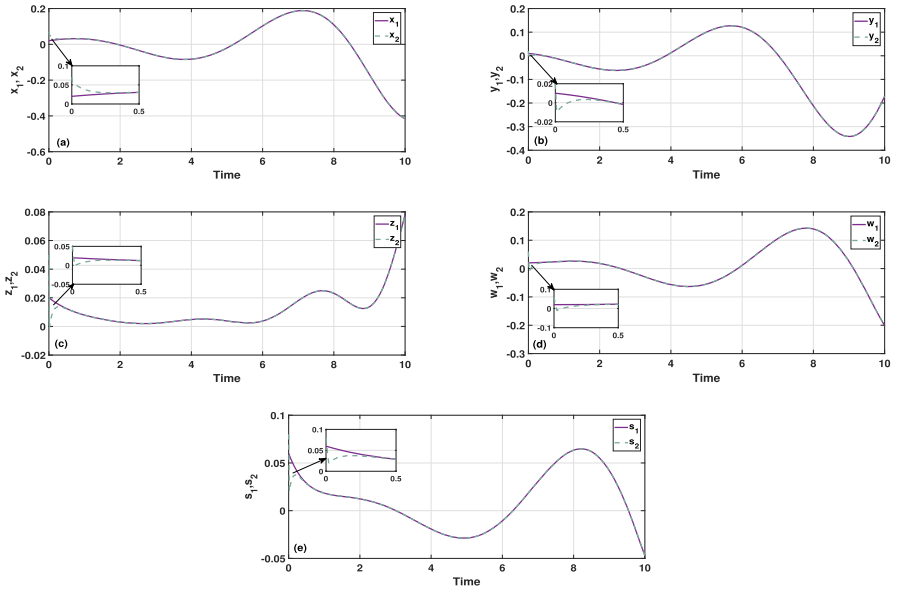


Fig. 8 State vectors of the drive-response systems in the case of complete synchronization via AISMC: **(a)** $x_1 - x_2$, **(b)** $y_1 - y_2$, **(c)** $z_1 - z_2$, **(d)** $w_1 - w_2$, and **(e)** $s_1 - s_2$

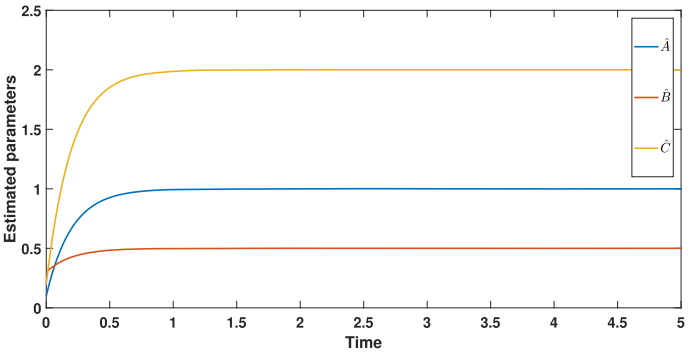


Fig. 9 Behavior of estimated parameters in AISMC-based complete synchronization

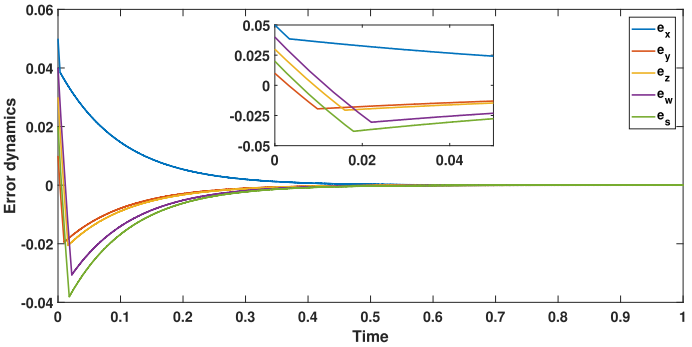


Fig. 10 Convergence of synchronization errors for complete synchronization using AISMC

under complete synchronization is presented in Fig. 10, clearly demonstrating that all errors asymptotically converge to zero as time progresses. Simultaneously, the estimated parameters $(\hat{A}, \hat{B}, \hat{C})$ respectively converge to their true values (a, b, c), as shown in Fig. 9, thereby confirming the validity and effectiveness of the proposed AISMC-based complete synchronization scheme.

When setting $\varepsilon_\varrho = -1$ for $\varrho = 1, 2, \ldots, 5$ and applying AISMC, the drive-response systems achieve anti-synchronization, as illustrated in Fig. 11. The control parameters are uniformly selected as $(K_\xi, \lambda_\xi, \mu_\xi) = (5, 10, 3)$ for all ξ. The evolution of the synchronization errors under anti-synchronization is presented in Fig. 13, clearly demonstrating that all errors asymptotically converge to zero as time progresses. Concurrently, the estimated parameters $(\hat{A}, \hat{B}, \hat{C})$ respectively converge to values (a, b, c), as shown in Fig. 12, thereby confirming the validity and effectiveness of the AISMC-based anti-synchronization scheme.

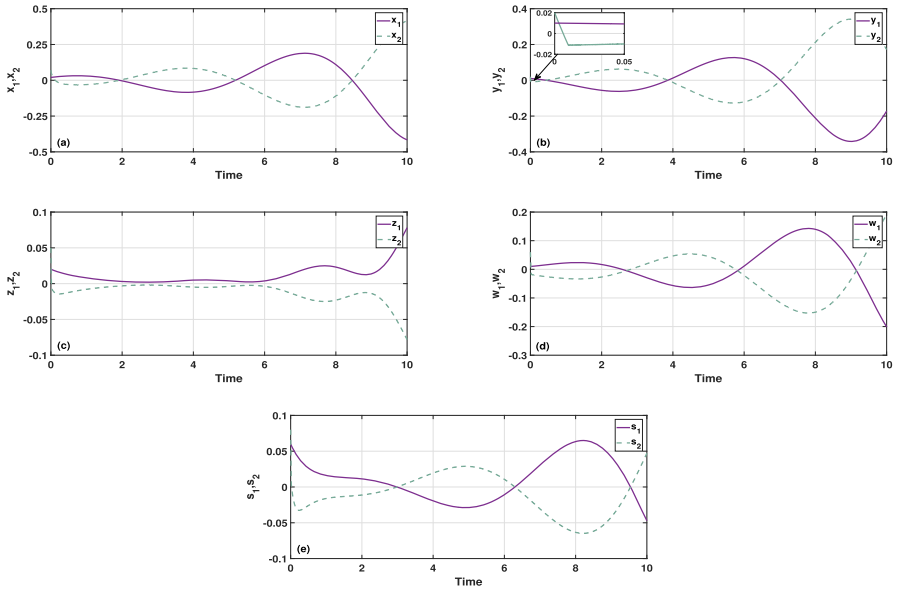


Fig. 11 State vectors of the drive-response systems in the case of anti-synchronization via AISMC: **(a)** $x_1 - x_2$, **(b)** $y_1 - y_2$, **(c)** $z_1 - z_2$, **(d)** $w_1 - w_2$, and **(e)** $s_1 - s_2$

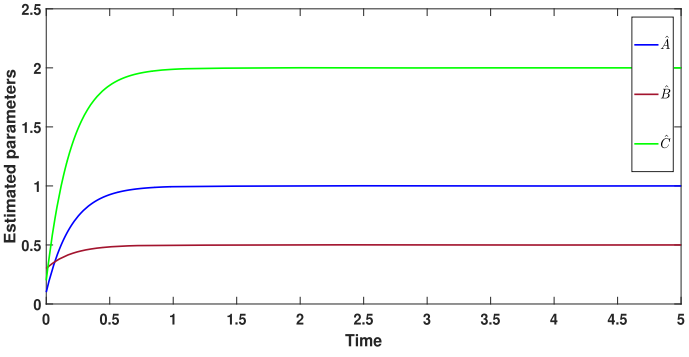


Fig. 12 Behavior of estimated parameters in AISMC-based anti-synchronization

6 Circuit schematic and oscilloscope measurements

The digital–analog circuit schematic [61] for the $\mathcal{S}$-system is constructed using the Multisim 14.2. The circuits consist of a single multiplier, operational amplifiers (OP-AMP), resistors (R), and capacitors (C). The operational voltage of ± 15 V is applied to each OP-AMP, with a scaling factor of $\tau = 10^{-3}$. Utilizing Ohm's law and Kirchhoff's

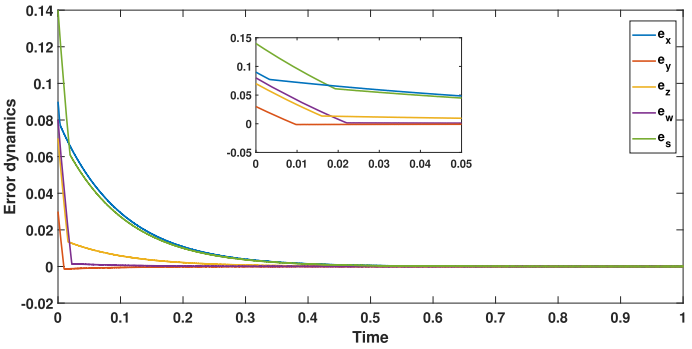


Fig. 13 Convergence of synchronization errors for anti-synchronization using AISMC

law, the $\mathcal{S}$-system is re-written in voltage forms as follows:

$$\begin{cases} \dot{V}_1 &= \frac{\tau}{R_1 C_1} V_2 + \frac{\tau}{R_2 C_1} V_3, \\ \dot{V}_2 &= \frac{\tau}{R_3 C_2} V_2 - \frac{\tau}{R_4 C_2} V_1, \\ \dot{V}_3 &= \frac{\tau}{R_5 C_3} V_1^2 - \frac{\tau}{R_6 C_3} V_3, \\ \dot{V}_4 &= \frac{\tau}{R_7 C_4} V_1 - \frac{\tau}{R_8 C_4} V_4, \\ \dot{V}_5 &= \frac{\tau}{R_9 C_5} V_4 - \frac{\tau}{R_{10} C_5} V_5. \end{cases} \tag{17}$$

Here, $V_1, V_2, \ldots, V_5$ represent the voltages across capacitors $C_1, C_2, \ldots, C_5$, each with a capacitance of 1 nF, respectively.

Each supplementary resistor from R_{11} to R_{16} is fixed at $100\,k\Omega$, while the remaining resistor values for the proposed digital circuit are set as follows:

$$\begin{cases} R_1 = R_2 = 1000\,k\Omega; \quad R_3 = 2000\,k\Omega \\ R_4 = R_6 = 1000\,k\Omega; \quad R_9 = 100\,k\Omega; \\ R_5 = R_7 = R_8 = R_{10} = 1000\,k\Omega. \end{cases}$$

The designed electrical circuit schematic for the $\mathcal{S}$-system with a single multiplier is presented in Fig. 14, while the oscilloscope measurements are shown in Fig. 15. Multipliers generally require more power than standard arithmetic chips due to the complex circuitry involved in performing several logical operations. However, the system's circuit layout demonstrates potential efficiency, as it uses only one multiplier, which could contribute to its cost-effectiveness.

7 Conclusion

A novel five-dimensional (5D) deterministic dynamical system in a continuous-time framework is proposed in this research. The system features a single quadratic nonlinearity, emphasizing its simple mathematical structure. The system may also be

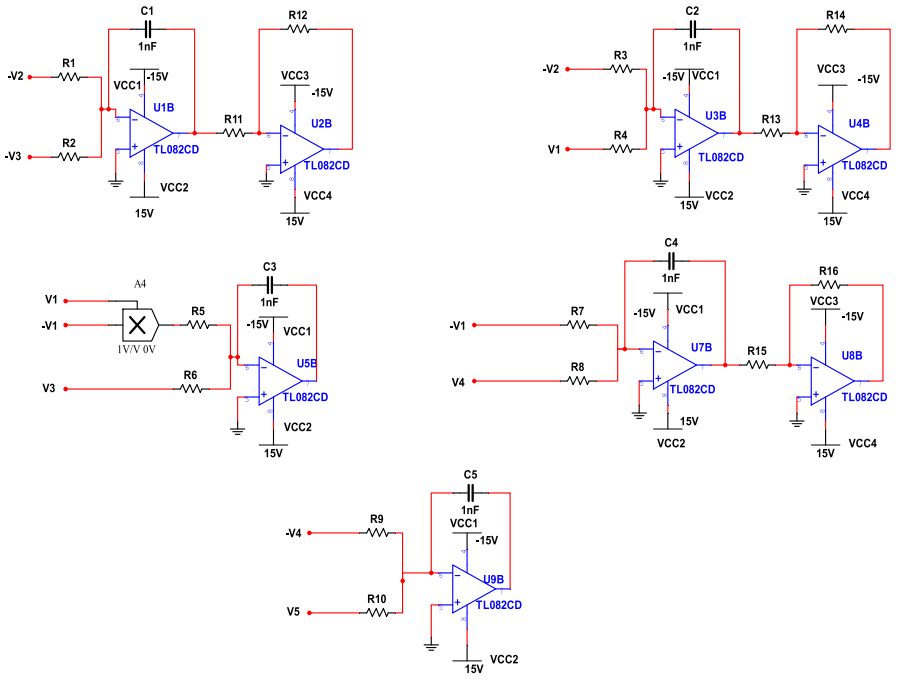


Fig. 14 Electronic circuit schematic of the 8-system

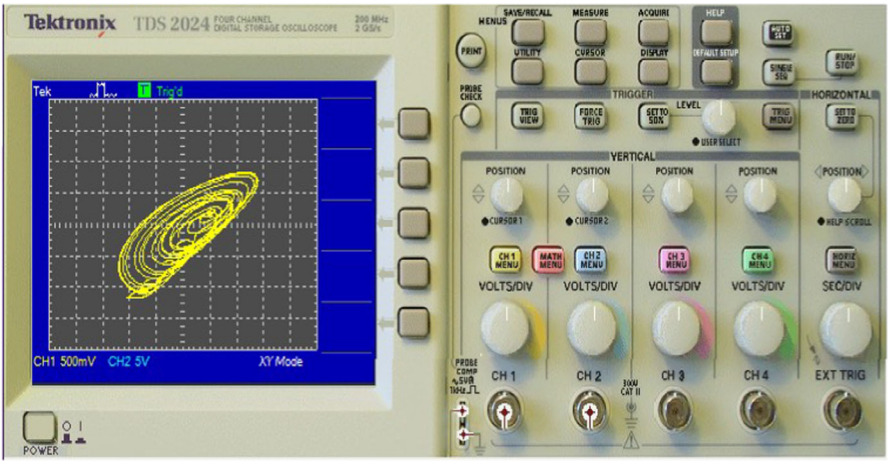


Fig. 15 Oscilloscope results from the electronic circuit schematic for the 8-system in the V_4-V_5 plane

extended to higher dimensional systems, such as 6D, which warrants further investigation. For a selected set of parameters, the system exhibits two positive Lyapunov exponents (LEs), classifying it as a hyperchaotic system with a Kaplan–Yorke dimension of 4.5. The dynamic behavior of the system is thoroughly explored through an analytical investigation of dissipativity, two-dimensional phase portraits, and time

series analysis. Further insights into the system's behavior are obtained using a bifurcation diagram and Poincaré cross-sections. The system demonstrates a diverse range of orbital behaviors, including chaos, periodicity, and quasi-periodicity, as the parameter a varies within the interval [1, 2]. The bifurcation diagram is validated through the Lyapunov spectrum, computed over the same parametric range. Additionally, the system admits two equilibrium points, one of which is trivial. A detailed stability analysis of these equilibrium points is conducted using the Routh–Hurwitz criterion, and the conditions for local stability are provided. To bridge theory and practice, an electronic circuit realization of the proposed system is designed. Oscilloscope measurements from this circuit in novel phase planes are consistent with MATLAB-based numerical simulations, demonstrating the physical realization of the system, beyond a mere theoretical construct. The designed electronic circuit requires only one multiplier chip, which could contribute to the cost-effectiveness and broader practical applicability of the system. Finally, two control strategies—integral sliding mode control (ISMC) and adaptive control—are integrated to achieve synchronization between two identical 5D systems. Each synchronization technique is rigorously proven using Lyapunov stability theory, and the analytical results are validated through MATLAB-based numerical simulations, confirming the reliability and efficacy of the synchronization outcomes achieved using the investigated control strategy.

Acknowledgements The authors would like to express their sincere gratitude to the Editor(s) and anonymous reviewers for their constructive feedback and insightful comments, which have significantly enhanced the quality and clarity of this manuscript. The corresponding author also acknowledges Delhi Technological University, Delhi, for its support.

Data availability Not Applicable.

Declaration

Conflict of interest The authors declare no competing financial interests, personal relationships, or affiliations that could have influenced the work reported in this manuscript.

References

1. Strogatz, S.H.: Nonlinear dynamics and chaos with student solutions manual: With applications to physics, biology, chemistry, and engineering. CRC Press, USA (2018)
2. Hu, C., Wang, Q., Zhang, X., Tian, Z., Wu, X.: A new chaotic system with novel multiple shapes of two-channel attractors. Chaos Solit. Fractals **162**, 112454 (2022). https://doi.org/10.1016/j.chaos.2022.112454
3. Bouali, S.: A novel strange attractor with a stretched loop. Nonlinear Dyn. **70**, 2375–81 (2012). https://doi.org/10.1007/s11071-012-0625-6
4. Lü, J., Chen, G.: A new chaotic attractor coined. International J. Bifurcat. Chaos. **12**(03), 659–61 (2002). https://doi.org/10.1142/S0218127402004620
5. Sahoo, S., Roy, B.K.: A new multi-wing chaotic attractor with unusual variation in the number of wings. Chaos Solit. Fractals **164**, 112598 (2022). https://doi.org/10.1016/j.chaos.2022.112598
6. Barrow-Green J.: Poincaré and the three body problem (No. 11). American Mathematical Soc (1997)
7. Grassberger, P., Procaccia, I.: Characterization of strange attractors. Phys. Rev. Lett. **50**(5), 346 (1983). https://doi.org/10.1103/PhysRevLett.50.346

8. Dong, Q., Zhou, S., Zhang, Q., Kasabov, N.K.: A class of 5D Hamiltonian conservative hyperchaotic systems with symmetry and multistability. Nonlinear Dyn. **110**(3), 2889–2912 (2022). https://doi.org/10.1007/s11071-022-07735-6
9. Higazy, M., Mahmoud, E.E., Khalil, E.M., Abdel-Khalek, S., Abo-Dahab, S.M., Alotaibi, H.: Dynamics and robust control of a new realizable chaotic nonlinear model. Complexity, 1–17 (2021). https://doi.org/10.1155/2021/6692369
10. Sagban, L.J., Shukur, A.A.: Dynamics and adaptive control of a novel 5D hyperchaotic system: either hidden attractor or self-excited with unusual nature of unstable equilibria. Malaysian J. Math. Sci. (2024) https://doi.org/10.47836/mjms.18.3.14
11. Zhao, X., Jiang, F., Zhang, Z., Hu, J.: A new series of three-dimensional chaotic systems with cross-product nonlinearities and their switching. J. Appl. Math. (2013). https://doi.org/10.1155/2013/590421
12. Huang, L.L., Ma, Y.H., Li, C.: Characteristic analysis of 5D symmetric Hamiltonian conservative hyperchaotic system with hidden multiple stability. Chinese Phys. B **33**(1), 010503 (2024). https://doi.org/10.1088/1674-1056/acf9e7
13. Bouteraa, Y., Mostafaee, J., Kchaou, M., Abbassi, R., Jerbi, H., Mobayen, S.: A New Simple Chaotic System with One Nonlinear Term. Mathematics **10**(22), 4374 (2022). https://doi.org/10.3390/math10224374
14. Gokyildirim, A., Kocamaz, U.E., Uyaroglu, Y., Calgan, H.: A novel five-term 3D chaotic system with cubic nonlinearity and its microcontroller-based secure communication implementation. AEU-INT J. Electron. C **160**, 154497 (2023). https://doi.org/10.1016/j.aeue.2022.154497
15. Vanithamani, P., Prakash, S., Jayasukumari, I., Priyadarshini, C., Pearly, B., Sudhagar, G.: Circuit analysis realization for a three dimensional coexisting chaotic attractor system utilizing a single multiplier and its use in secure communication. InRecent Trends in VLSI and Semiconductor Packaging (pp. 504–512). CRC Press
16. Tabekoueng, Z.N., Sriram, B., Rajagopal, K., Karthikeyan, A., Awrejcewicz, J.: Investigation of an improved FitzHugh-Rinzel neuron and its multiplier-less circuit implementation. Chaos (2023). https://doi.org/10.1063/5.0152811
17. Pecora, L.M., Carroll, T.L.: Synchronization in chaotic systems. Phys. Rev. Lett. **64**(8), 821 (1990). https://doi.org/10.1103/PhysRevLett.64.821
18. Liu, L., Du, C., Zhang, X., Li, J., Shi, S.: Adaptive synchronization strategy between two autonomous dissipative chaotic systems using fractional-order mittag-leffler stability. Entropy **21**(4), 383 (2019). https://doi.org/10.3390/e21040383
19. Saeed, N.A., Saleh, H.A., Hou, L., Nasr, E.A.: A novel chaotic oscillator with a half-line of unstable equilibria: Basins of attraction, chaos control, chaos synchronization, and encryption applications. Modern Phys. Lett. B **39**(08), 2450436 (2025). https://doi.org/10.1142/S0217984924504360
20. Li, W., Li, P., Jia, M.: Chaos control and chaos synchronization of a multi-wing chaotic system and its application in multi-frequency weak signal detection. AIP Adv. **11**, 095003 (2021). https://doi.org/10.1063/5.0062634
21. Khattar, D., Deo, N., Sirohi, M.: On novel Hexa-compound combination synchronization over nineteen n-dimensional category-B chaotic systems and electronic circuit schematic. Phys. Scr. **100**(1), 015280 (2024). https://doi.org/10.1088/1402-4896/ad9e3c
22. Khan, A., Nigar, U., Chaudhary, H.: Secure communication and synchronization dynamics in chaotic Chua's system via adaptive sliding mode control technique. Int. J. Appl. Comput. Math. **8**(4), 170 (2022). https://doi.org/10.1007/s40819-022-01378-2
23. Djari, A., Djabri, R., Bouarroudj, N., Houam, Y., Bettayeb, M., Agajie, T.F.: Efficient Controller design for optimal stabilization and synchronization of incommensurate non-integer order chaotic systems (2024) https://doi.org/10.21203/rs.3.rs-5311264/v1
24. Khattar, D., Agrawal, N., Sirohi, M.: Dynamical analysis of a 5D novel system based on Lorenz system and its hybrid function projective synchronisation using adaptive control. Pramana **97**(2), 76 (2023). https://doi.org/10.1007/s12043-023-02544-x
25. Deleanu, D.: On a method of estimating chaos control parameters from time series. Sci. Bullet. "Mircea cel Batran" Naval Acad. **21**(2), 1 (2018). https://doi.org/10.21279/1454-864X-18-I2-002
26. Jahanzaib, L.S., Trikha, P., Baleanu, D.: Analysis and application using quad compound combination anti-synchronization on novel fractional-order chaotic system. Arab. J. Sci. Eng. **46**, 1729–1742 (2021). https://doi.org/10.1007/s13369-020-04939-z
27. Laarem, G.: A new 4-D hyper chaotic system generated from the 3-D Rösslor chaotic system, dynamical analysis, chaos stabilization via an optimized linear feedback control, it's fractional order model and

chaos synchronization using optimized fractional order sliding mode control. Chaos, Solitons Fractals **152**, 111437 (2021). https://doi.org/10.1016/j.chaos.2021.111437
28. Khattar, D., Sirohi, M., Bansal, R.: Comparative analysis of two novel chaotic systems, and validation of hybrid function projective and complete synchronization using active-adaptive control. Phys. Scr. **99**(12), 125244 (2024). https://doi.org/10.1088/1402-4896/ad8e9a
29. Akter, M.T., Tarammim, A., Hussen, S.: Chaos control and synchronization of modified Lorenz system using active control and backstepping scheme. Waves Random Complex Media 1–20 (2023) https://doi.org/10.1080/17455030.2023.2205529
30. Fernanda Moreno-López, M., Joel Lara-Martinez, A., Maritza Gonzalez-Zapata, A., Silva-Juarez, A., Gerardo de la Fraga, L., Tlelo-Cuautle, E.: FPGA Implementation of PRNGs Based on Chaotic Systems Optimized by DE, GWO, and PSO. Int. J. Circ. Theory Appl. (2025). https://doi.org/10.1002/cta.4435
31. Mezatio, B.A., Motchongom, M.T., Tekam, B.R., Kengne, R., Tchitnga, R., Fomethe, A.: A novel memristive 6D hyperchaotic autonomous system with hidden extreme multistability. Chaos Solit. Fractals **120**, 100–115 (2019). https://doi.org/10.1016/j.chaos.2019.01.015
32. Akgul, A., El Naser, Y.H., Kutlu, M., Stephen, O.K.: Chaos-based engineering applications and finite element analysis with a 6D chaotic system. Mod. Phys. Lett. B. (2025). https://doi.org/10.1142/S0217984925501672
33. Alqahtani, A.M., Chaudhary, A., Dubey, R.S., Sharma, S.: Comparative analysis of the chaotic behavior of a five-dimensional fractional hyperchaotic system with constant and variable order. Fractal Fract. **8**(7), 421 (2024). https://doi.org/10.3390/fractalfract8070421
34. Sirohi, M.: Qualitative analysis of a novel 5D chaotic system based on Bouali's system and its application in private communication via adaptive control. Bol. Soc. Mat. Mex. **29**(1), 26 (2023). https://doi.org/10.1007/s40590-023-00497-0
35. Kopp, M., Samuilik, I.: A New 6D Two-wing Hyperhaotic System: Dynamical Analysis, Circuit Design, and Sinchronization. Chaos Theo. Appl. **6**(4), 273–283 (2024). https://doi.org/10.51537/chaos.1513080
36. Al-Azzawi, S.F., Aziz, S.M.: Electronic Circuit of a New Simple 6D Hyperchaotic System with Two Saddle-Foci Equilibria. J. Appl. Nonlinear Dyn. **14**(3), 705–717 (2025). https://doi.org/10.5890/JAND.2025.09.013
37. Benkouider, K., Bouden, T., Yalcin, M.E., Vaidyanathan, S.: A new family of 5D, 6D, 7D and 8D hyperchaotic systems from the 4D hyperchaotic Vaidyanathan system, the dynamic analysis of the 8D hyperchaotic system with six positive Lyapunov exponents and an application to secure communication design. Int. J. Mod. Id Cont. **35**(3), 241–257 (2020). https://doi.org/10.1504/IJMIC.2020.114191
38. Khattar, D., Agrawal, N., Sirohi, M.: Qualitative analysis of a new 6D hyper-chaotic system via bifurcation, the Poincaré notion, and its circuit implementation. Indian J. Phys. **98**, 259–273 (2024). https://doi.org/10.1007/s12648-023-02796-8
39. Yu, W., et al.: Covert chaotic encryption scheme based on compressive sensing in a W-band RoF system. Optic Express **33**(1), 992–1007 (2025). https://doi.org/10.1364/OE.549606
40. Singh, J.P., Roy, B.K.: The simplest 4-D chaotic system with line of equilibria, chaotic 2-torus and 3-torus behaviour. Nonlinear Dyn. **89**, 1845–1862 (2017). https://doi.org/10.1007/s11071-017-3556-4
41. Singh, J.P., Rajagopal, K., Roy, B.K.: A new 5D hyperchaotic system with stable equilibrium point, transient chaotic behaviour and its fractional-order form. Pramana **91**, 1–10 (2018). https://doi.org/10.1007/s12043-018-1599-9
42. Al-Azzawi, S.F., Al-Hayali, M.A.: Multistability and hidden attractors in a novel simple 5D chaotic Sprott E system without equilibrium points. J. Interdiscipl. Math. **25**(5), 1279–1294 (2022). https://doi.org/10.1080/09720502.2021.1970948
43. Li, J., Cui, N.: Dynamical analysis of a new 5D hyperchaotic system. Phys. Scripta **98**(10), 105205 (2023). https://doi.org/10.1088/1402-4896/acf41a
44. Yu, F., Xu, S., Xiao, X., Yao, W., Huang, Y., Cai, S., Li, Y.: Dynamic analysis and FPGA implementation of a 5D multi-wing fractional-order memristive chaotic system with hidden attractors. Integration **96**, 102129 (2024). https://doi.org/10.1016/j.vlsi.2023.102129
45. Wan, Q., Zhou, Z., Ji, W., Wang, C., Yu, F.: Dynamic Analysis and Circuit Realization of a Novel No-Equilibrium 5D Memristive Hyperchaotic System with Hidden Extreme Multistability. Complexity **2020**(1), 7106861 (2020). https://doi.org/10.1155/2020/7106861

46. Al-Azzawi, S.F., Hasan, A.M.: New 5D Hyperchaotic system derived from the Sprott C system: Properties and Anti Synchronization. J. Intell. Syst. Control **2**(2), 110–122 (2023). https://doi.org/10.56578/jisc020205
47. Vaidyanathan, S., et al.: A 5-D multi-stable hyperchaotic two-disk dynamo system with no equilibrium point: Circuit design, FPGA realization and applications to TRNGs and image encryption. IEEE Access **9**, 81352–81369 (2021). https://doi.org/10.1109/ACCESS.2021.3085483
48. Mostafaee, J., Mobayen, S., Vaseghi, B., Vahedi, M.: Finite-time synchronization of a new five-dimensional hyper-chaotic system via terminal sliding mode control. Sci. Iranica **30**(1), 167–182 (2023). https://doi.org/10.24200/sci.2021.56313.4657
49. Fu, H., Lei, T.: Adomian decomposition, dynamic analysis and circuit implementation of a 5D fractional-order hyperchaotic system. Symmetry **14**(3), 484 (2022). https://doi.org/10.3390/sym14030484
50. Vaidyanathan, S., Volos, C., Pham, V.T.: Hyperchaos, adaptive control and synchronization of a novel 5-D hyperchaotic system with three positive Lyapunov exponents and its SPICE implementation. Arch. Control Sci. **24**(4), (2014) https://doi.org/10.2478/acsc-2014-0023
51. Al-Azzawi, S.F., Sheet, A.T.: A novel simple 5D hyperchaotic system derived from the 3D Sprott C system. TWMS J. Appl. Eng. Math. (2024) http://belgelik.isikun.edu.tr/xmlui/handle/iubelgelik/5957
52. Sprott, J.C.: Some simple chaotic flows. Phys. Rev. E **50**(2), R647 (1994). https://doi.org/10.1103/PhysRevE.50.R647
53. Wolf, A., Swift, J.B., Swinney, H.L., Vastano, J.A.: Determining Lyapunov exponents from a time series. Physica D: Nonlinear Phenomena **16**(3), 285–317 (1985). https://doi.org/10.1016/0167-2789(85)90011-9
54. Goldstein, H., Poole, C., Safko, J.: Classical Mechanics, 3rd ed. Addison-Wesley (2002)
55. Sprott, J.C.: Elegant Chaos: Algebraically Simple Chaotic Flows. World Scientific (2010)
56. Brown, R., Chua, L.O.: Dynamical synthesis of Poincaré maps. Int. J. Bifurcat. Chaos **3**(05), 1235–1267 (1993). https://doi.org/10.1142/S0218127493001008
57. Kuznetsov, Y.A.: Elements of Applied Bifurcation Theory, 3rd edn. Springer, UK (2004)
58. Ogata, K.: Modern Control Engineering, 5th edn. Prentice Hall, Englewood Cliffs NJ (2010)
59. Sambas, A., Vaidyanathan, S., et al.: A novel 3D chaotic system with line equilibrium: multistability, integral sliding mode control, electronic circuit, FPGA implementation and its image encryption. IEEE Access **10**, 68057–68074 (2022). https://doi.org/10.1109/ACCESS.2022.3181424
60. Khalil, H.K.: Nonlinear Systems, 3rd edn. Prentice Hall, Englewood Cliffs NJ (2002)
61. Cuomo, K.M., Oppenheim, A.V.: Circuit implementation of synchronized chaos with applications to communications. Phys. Rev. Lett. **71**(1), 65 (1993). https://doi.org/10.1103/PhysRevLett.71.65

Publisher's Note Springer Nature remains neutral with regard to jurisdictional claims in published maps and institutional affiliations.

International Journal of Humanities Education
VOL -13 NO 1 2025 ISSN:2327-0063\ E-ISSN:2327-2457

A STUDY OF KEY FACTORS DRIVING E-COMMERCE ADOPTION TO BOOST MSMES PERFORMANCE: AN ISM AND MICMAC ANALYSIS

Lavi Vats[1], Ratnam Mishra[2], Shekhar Tokas[3]

Abstract

E-commerce adoption has become a transformative lever for Micro, Small, and Medium Enterprises (MSMEs), enhancing their competitiveness, efficiency, and sustainable performance. This study identifies and models thirteen critical factors—comprising six enabling factors, six resulting performance outcomes, and one ultimate goal (MSME performance)—through a mixed-method approach. Expert evaluations, using focus group discussions and Delphi rounds, informed the selection and structuring of these factors. Interpretive Structural Modeling (ISM) was applied to uncover their hierarchical relationships, while Matrix of Cross-Impact Multiplications Applied to Classification (MICMAC) analysis classified them into driver, dependent, and linkage categories based on driving and dependence power. The results highlight IT knowledge as the foundational enabler, supported by factors such as top management support, government support, competitive pressure, organization size, and reduction in complexity. These enablers drive performance outcomes like brand value, effectiveness, efficiency, productivity, market share, and profitability. The integrated ISM-MICMAC framework offers a strategic roadmap for MSME leaders and policymakers to strengthen digital readiness, allocate resources efficiently, and design supportive interventions. By addressing interdependencies among variables, this research contributes to digital transformation strategies in resource-constrained environments. Future studies may extend this model by incorporating emerging technologies and sector-specific dynamics.

MAD Statement

Understanding what drives e-commerce adoption is not enough—how those drivers interact matters even more. Through a structured mapping of 13 interconnected factors, the study equips scholars with a replicable model and provides practitioners with a roadmap to improve digital adoption outcomes. This contributes to more grounded, actionable strategies for e-commerce success in small business ecosystems.

Keywords: e-commerce adoption, MSME, business performance, Interpretive Structural Modelling, ISM, MICMAC

1. Introduction

The digital age has changed how business is done, and MSMEs (Micro, Small and Medium sized

[1] University School of Management & Entrepreneurship, Delhi Technological University, Delhi, India, Email: lavivats50@gmaill.com

[2] University School of Management & Entrepreneurship, Delhi Technological University, Delhi, India

[3] School of Global Affairs, Dr. B.R. Ambedkar University, Delhi, India

enterprises) have begun to adopt technology in different stages of their activity. Even in the digital economy, organizations are always growing by utilizing digital services and interaction networks to improve productivity, gain a competitive advantage and expand their market globally (Wilantari et al., 2023). MSMEs are present in all economic sectors and economies, representing an important share of the entrepreneurial fabric streamlines processes, and improves customer interactions (Abebe, 2014). MSMEs, which significantly contribute to economic advancement, especially within developing nations, stand to gain immensely from the adoption of e-commerce ((Ayyagari et al., 2007). These enterprises serve as a catalyst for employment generation and the economic progress of numerous countries worldwide (Oduro, 2019), foster entrepreneurial ventures and competitive dynamics, and augment overall productivity levels (Jin and Choi, 2019). However, the uptake of e-commerce among MSMEs varies due to various internal and external obstacles such as limited technological resources, financial limitations, and hesitance towards embracing digital transformation (Zhu et al., 2006; Khoo et al., 2018). In order to develop strategies that lead to change on the other end in terms of e-commerce adoption in MSMEs, it is then determined to investigate the key elements that projectable favourable influence in adopting the e-commerce. MSMEs' e-commerce adoption is shaped by both enabling factors that allow easier transition to new systems and resulting factors that show e-commerce's effects on business performance. According to Li et al. (2022) technological aspect is a key factor; however, organizational element as well as environmental factors plays important role such as IT knowledge, management support and government assistance respectively. The benefits that come from strong IT capabilities of companies make e-commerce solutions to be implemented easily and at an affordable cost. Therefore, management support can help in the proper allocation of resources to digital adoption programs (Alshamaila 2013). (Aswar & Ermawati, 2021) describe the government grants, training programs and investments to close the digital gap between the large and small companies. Existing market dynamics, competitive challenges and implementation capability of e-commerce features to current business operations are also very important between the adoption process (Kshetri, 2007). It is through the benefits of taking part in a digital marketplace that MSMEs experience the main effects of e-commerce. Some benefits of digital market presence include satisfying customers through improved brand visibility, increased share on market and higher profits (Sharabati et al., 2024). The knowledge based marketing strategies run through the electron platforms allow the businesses to adjust its customer interaction to create long lasting relationship, which in turn improves the business by retaining more customers thus increasing revenue (Andonov et al., 2021). E-commerce's real time data analytics components helps MSMEs in successful data analysis for making business operations and curtailing operational costs and unnecessary expenses (Sugiharto, 2024). Having access to escalating digital technology adoption means businesses gain better equity for maintaining long term positions in their respective areas (Sindakis & Showkat, 2024).

Recent research emphasizes that a firm's technological readiness, management support, external pressures, and government initiatives critically shape its digital adoption trajectory (Goel et al., 2022; Salah & Ayyash, 2023). However, most existing studies adopt linear models or focus on isolated factors, overlooking the interdependencies and cumulative effects among these enablers and outcomes (Hendrawan et al., 2024; Rafidah et al., 2024). Moreover, there is a notable scarcity of studies utilizing

Interpretive Structural Modeling (ISM) and Matrix of Cross-Impact Multiplications Applied to Classification (MICMAC) analysis to explore the structured relationships among key variables influencing e-commerce adoption in MSMEs. Addressing this gap, the present study systematically identifies and models the key enabling and resulting factors associated with e-commerce adoption among MSMEs. The study is guided by the following research questions:

RQ1: What are the fundamental enabling and resulting factors influencing e-commerce adoption in MSMEs?

RQ2: How are these factors structurally related to one another in enhancing MSME performance?

RQ3: How can the classification of factors based on driving and dependence power inform strategic decision-making for MSME digitalization?

By employing ISM and MICMAC methodologies, this research not only reveals the hierarchical structure among factors but also categorizes them based on their driving and dependence powers. This structured approach offers a strategic roadmap for MSMEs, policymakers, and digital solution providers to prioritize interventions that can accelerate digital transformation and increase their performance.

2. Literature Review

Based on extensive literature review, factors resulting to enhance MSMEs performance have been identified and summarized in this section. These factors are broadly classified into two parts. One is enabling factor and other is the resulting factor. This section is also divided into two subsections. Subsection 2.1 deals with the enabling factor and subsection 2.2 discusses resulting factor. These enabling and resulting factors are prerequisite steps for the development of ISM and MICMAC which suggests the relationships among the factors.

2.1 Enabling Factors Affecting E-commerce Adoption in MSMEs

2.1.1 IT Knowledge

IT knowledge serves as the main factor influencing the way business organizations implement electronic commerce systems. The capability of business leaders and managers alongside their workforce to use IT solutions effectively for operational support makes up this concept. MSMEs that possess advanced IT capabilities have greater ability to use electronic commerce systems effectively (Yuwono et al., 2024). Businesses face obstacles when IT abilities are absent from their operations. According to Hendrawan et al. (2024) numerous MSMEs do not implement new technologies because they lack sufficient technical expertise to merge technology with business functions. The insufficient knowledge about IT hinders MSMEs from successfully adopting e-commerce solutions. Businesses that operate with established IT capabilities leverage digital tools effectively which leads to improved operation performance while gaining more customers and strengthening market dominance (Ardolino et al., 2025). Companies with established IT infrastructure according to Al-Qirim (2007) exhibit higher adoption rates of e-commerce and succeed in utilizing its advantages to the fullest. Digital platforms hold strategic worth for these businesses which leads them to refine their platform usage to gain better business results. The essential capability of IT knowledge determines how well MSMEs can harness and benefit from e-commerce technologies (Buteau, 2021).

2.1.2 Reduction in Complexity

Simplification of e-commerce systems acts as a critical factor that helps micro, small, and medium enterprises (MSMEs) to implement digital technologies. Because of limited budget constraints small businesses struggle to implement complex systems effectively (Davis, 1989). E-business adoption decisions are strongly affected by user experience according to the Technology Acceptance Model (TAM) **(Mujahed et al., 2024)**. Businesses tend to adopt e-commerce upon perceiving that the system is simple and easy to use (Davis, 1989). The adoption barriers for small businesses to enter the online marketplace decrease when user interfaces remain intuitive and the technology requirements remain minimal explained Thong (1999). The adoption process for e-commerce solutions among MSMEs becomes quicker and simpler when software developers create platform-specific designs which include easy-to-use interfaces according to **Alshamaila et al. (2013b)**. Business owners who find systems easy to use gain confidence to work with these systems which enhances their ability to integrate them within their business operations successfully.

2.1.3 Management Support

The implementation of e-commerce needs top management backing as an essential component for MSMEs. The successful implementation of e-commerce in MSMEs requires leadership to actively dedicate their time toward resource allocation and strategic planning and resistance management according to (J. Y. L. Thong et al., 1996)**.** Baker (2011) explains that e-commerce adoption will become a strategic organizational priority under strong leadership rather than remaining merely a technological improvement. Digital transformation projects experience fewer complications because effective resource allocation happens when management demonstrates active support (Shahadat et al., 2023). Any advanced e-commerce system that lacks leadership commitment is likely to fail in gaining organizational traction.

2.1.4 Organization Size

An organization's ability to implement e-commerce depends heavily on its organizational size. The financial strength and improved infrastructure together with larger workforce of bigger MSMEs simplifies their digital platform integration (Zhu et al., 2006). The increased financial freedom of these businesses enables them to fund both new technology purchase and associated implementation expenses and workforce training expenditures (Shahadat et al., 2023). E-commerce implementation becomes more difficult for smaller businesses because they lack sufficient funding. The research conducted by Al-Qirim (2007) indicates that appropriate support systems enable small MSMEs to implement e-commerce successfully in their operational framework.

2.1.5 Government Support

The involvement of government institutions serves as a fundamental factor which drives small businesses to use e-commerce as a platform. Holistically supportive policies uniting funding solutions and technical help with regulatory structures effectively boost companies to adopt digital technologies (Zhu et al., 2006). MSMEs accept e-commerce through government-developed training sessions and grant money that help them solve financial and skill problems (Alshamaila et al, 2013). The establishment of digital infrastructure requires broadband expansion investments because these investments create fundamental operational conditions for online operations. According to Hussain et al. (2020) the measurement of government support consists of information technology availability, infrastructure and state willingness to help SMEs adopt ICT.

2.1.6 Competitive Pressure

Competitive marketplace forces are the primary elements that encourage MSMEs to adopt e-commerce solutions. Companies generally need to implement digital solutions because competitors already benefit from e-commerce to optimize their processes and extend customer networks **(Sin et al., 2016)**. According to Porter (1998) organizations that neglect innovation will lose their market competitive advantage. MSMEs implement e-commerce to enhance their market standing through expanded outreach and cost reduction and improved client support (Zhu et al., 2006). Higher competition in the industry is more to change the technology adoption rate in the firm to enhance its performance (Bhardwaj et al., 2021).

2.2 Literature Review on Resulting Factors Affecting E-Commerce Adoption in MSMEs

2.2.1 Brand Value

MSMEs can enhance their brand value through adopting e-commerce sales channels. MSMEs benefit from creating an online presence since they can expand their market reach across the world to build brand recognition (Kaplan & Haenlein, 2010). Through digital platforms MSMEs construct unique online profiles which help them create validity for their target audience. The research conducted by Sharabati et al. (2024b) demonstrates that MSMEs participating in e-commerce succeed by maintaining digital marketing consistency and improving customer interactions and obtaining positive reviews to develop their brand identity. Brand loyalty and trust can be built through direct consumer marketing which eventually increase the long term brand value (Raddats et al., 2024). MSMEs using social media with their e-commerce approach will both improve customer interaction and achieve stronger market dominance as well as enhanced brand visibility in today's competitive business environment (Mangold & Faulds, 2009).

2.2.2 Effectiveness

E-commerce technologies fundamentally enhance operational effectiveness of MSMEs through their integration. A process is considered efficient when the organisation can use its resources as a tool to achieve its objectives (Rafidah et al., 2024). Ecommerce enables organization to have efficiency and cost effectiveness by having lower fixed costs for establishing and maintaining an e-commerce and higher degree of improvement in unit transaction efficiency through an e-commerce (Wen et al., 2003). **Processing automation in inventory management and customer support alongside payment transactions helps MSMEs boost their operational efficiency because it frees their**

resources to focus on core business (Hendrawan et al., 2024b)**. Through e-commerce implementation MSMEs build broad client connections which improves their market response capabilities and enhances service standards (Zhu et al., 2006).**

2.2.3 Efficiency

Business efficiency of MSMEs improves substantially through e-commerce because it enables automation and decreases human mistakes and promotes accurate business data (Hendrawan et al., 2024b). Business innovations enabled businesses to supply faster products and shorter lead times that result in better marketplace competitiveness according to Thong (1999). Research conducted by Tan et al. (2007) shows that e-commerce solutions decrease operational expenses which affect inventory management together with order fulfilment and customer service areas. MSMEs can use Customer Relationship Management (CRM) systems together with other tools to improve their customer relations which results in faster responses and enhanced service quality (Nethanani et al., 2024). The adoption of e-commerce technologies enables MSMEs to distribute their available resources into their core business activities effectively. MSME improve their efficiency by optimising workflows and using digital tools, better prepared to face the challenges that the digital economy had brought forth.

2.2.4 Market Share

Integration of E-commerce enables MSME's to have broader market reach than conventional physical stores because E-commerce enables MSME's to reach the client base beyond what is served by the conventional physical stores (Zhu et al., 2006). MSMEs become able to take part in international markets of products and services distribution to various market segments via e-commerce. Similarly, as stated by Garg and Choeu (2015) the adoption of e-commerce technology increases a business's visibility which helps firms have bigger markets by reaching more customers. The integration of ecommerce actually facilitates better market segmentation and different targeted marketing methods, thereby enhancing the customer acquisition programs (Ballestar et al., 2017). MSMEs can implement multiple products with their digital channels to provide better preference matching for consumers and thus position their market hence improving market position and market share.

2.2.5 Productivity

The utilization of e-commerce technology platforms by MSMEs fosters greater productivity because it simplifies business processes as well as minimizes mundane tasks while helping staff concentrate on strategic tasks (Yacob et al., 2021). MSMEs benefit from e-commerce platforms by obtaining customer data through analysis which fosters better operational decisions and efficiency (Alshamaila et al., 2013). MSMEs boost agility through improved internal systems and stronger supplier and customer relationships who help them achieve better market responses (Zhu et al., 2006). MSMEs that adopted e-commerce technology achieved substantial productivity enhancements through their improved supply chain operation and optimized inventory management and streamlined customer order handling according to Yuwono et al. (2024b). Digital transformation enables MSMEs to maintain their operational efficiency which produces long-term business expansion and increased competitiveness within the digital economy.

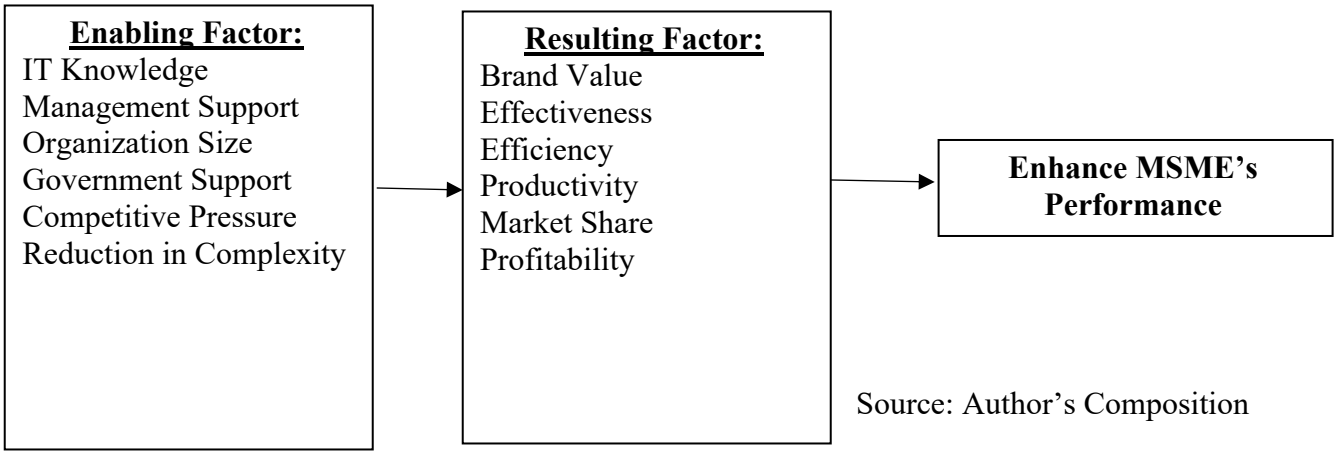
2.2.6 Profitability

Integration with e-commerce allows MSMEs to achieve substantial profitability levels. MSMEs

achieve operational cost reduction while boosting their sales and earnings improved financial margins through their online platform usage. Through e-commerce systems MSMEs can optimize their sales processes together with reduced overheads and affordable marketing options (Yuwono et al., 2024b) MSMEs who implement e-commerce solutions realize substantial cost reductions which surpass the expenses (Gao et al., 2023). The continuous operation of e-commerce platforms during all hours per day gives businesses enhanced potential sales while maximizing their earning capacity (Salah & Ayyash, 2023). MSMEs benefit from digital channels to expand their customer network which generates higher sales volume and, in turn enhance overall profitability (Zhu et al., 2006).

There are several enablers that drive business performance leading to adoption of e-commerce for MSMEs. IT Knowledge (IT1) provides the necessary digital skills to firms, management support (MS2) helps under the strategic decisions taken by reaching and allocating resources. Financial and human resource availability depends on organization size (OS3) and government support (GS4) which enables overcoming adoptions challenges by providing policies and incentives. Businesses become more accessible, because reduction in complexity (RIC6) helps simplify processes and competitive pressure (CP5) pushes one towards digital transformation. Thus, these factors cause an increase in brand value (BV7), effectiveness (EFF8), efficiency (EFC9) productivity (PRO10), market share (MSH11) and profitability (PRFT12). Finally, these outcomes will enhance MSME's performance (MSME PRF13) channelling growth, competition, long term sustainability in the digital economy, so the MSMEs grow in increasingly digitized business environment.

Figure 1: Conceptual framework based on literature review to enhance MSMEs performance



Source: Author's Composition

3. Research Methodology

3.1 Research Design

This study employs a **mixed-methods approach**, combining both **qualitative** and **quantitative** research techniques to comprehensively explore the factors influencing e-commerce adoption and its impact on MSMEs performance. The **qualitative** aspect involves a **systematic literature review (SLR)** to identify the key factors affecting e-commerce adoption, along with **expert consultations** to establish the relationships and cardinality between these factors. These insights help in formulating a

conceptual framework for the study. The **quantitative** aspect utilizes a **paired comparison technique** to assess the relative importance of these factors through expert evaluations. The resulting data is then used to construct a **Structural Self-Interaction Matrix (SSIM),** which is crucial for the **ISM** and **MICMAC** analysis. This mixed-method approach ensures a holistic understanding of the variables and their interrelationships, addressing both the enabling factors and outcomes of e-commerce adoption in MSMEs. MICMAC analysis complements ISM by classifying factors based on their **driving power** and **dependence**, helping to distinguish between foundational drivers and resulting outcomes. This dual methodology enables both theory-building and practical insight.

3.2 Data Collection

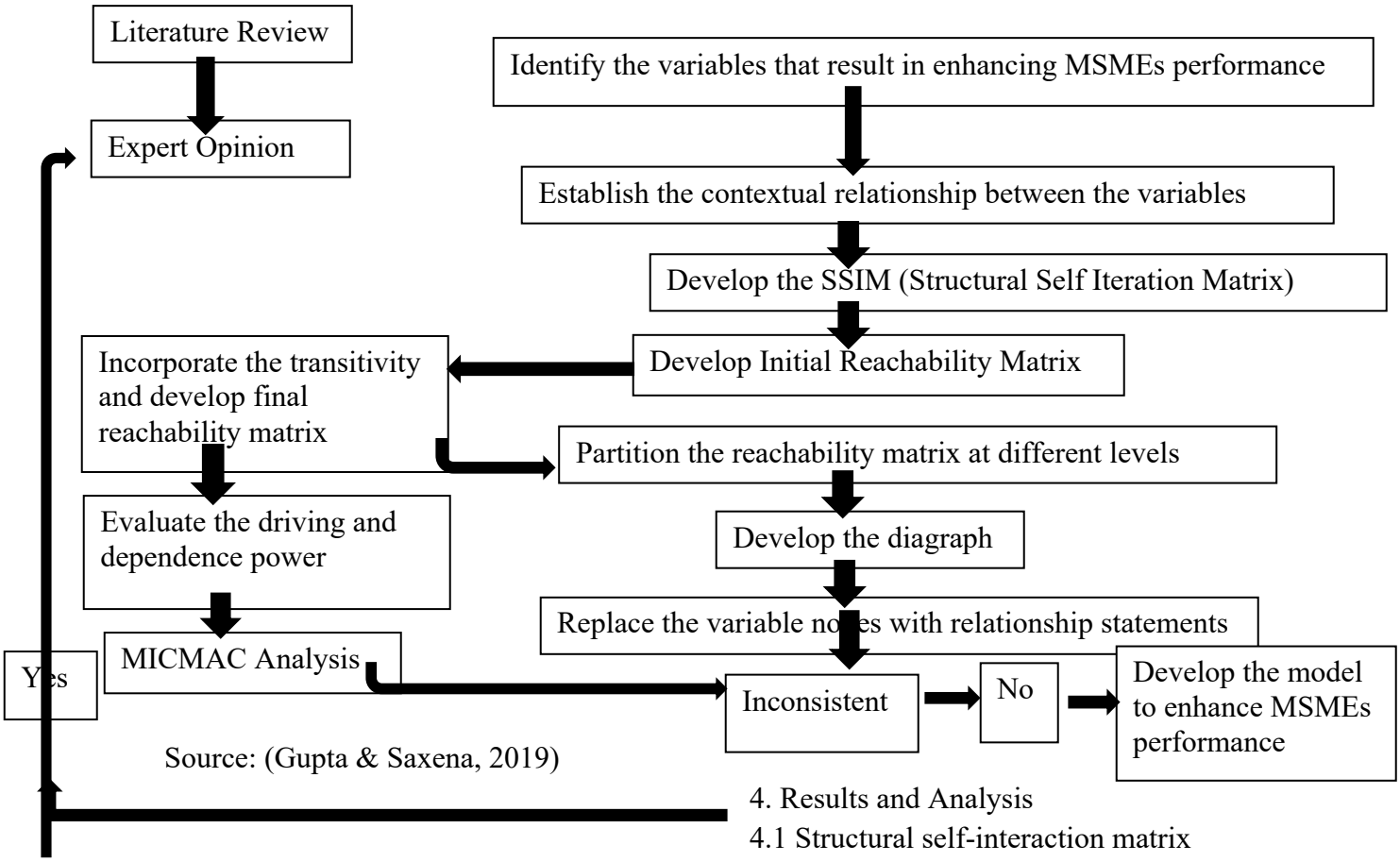
The data collection process integrates **primary** and **secondary data sources** to ensure a comprehensive analysis. **Secondary data** is derived from existing studies on MSMEs that have adopted e-commerce, providing a foundational understanding of the context. **Primary data** is collected through expert-based evaluations, obtained via **focus group discussions (FGDs).** These discussions involve over 15 experts, including **academicians, policymakers,** and **MSME owners**. The reliability of ISM analysis largely depends on expert input. Two focus group discussions (FGDs) and one Delphi round were conducted to ensure convergence of opinions. The study began with an extensive literature review to identify relevant **enabling** and **resulting factors**. An initial list of 20 variables was generated and presented to experts. After multiple validation rounds, a final list of **12 factors** (6 enabling and 6 resulting) was retained for ISM modelling.

3.2 Applying ISM and MICMAC Analysis

ISM was employed for analysis of the complex interconnections amongst the factors involved. This technique of structured understanding of the complex systems was first revealed by Warfield (1974). Because it is useful in the consideration of direct, indirect and reciprocal relationships among variables, ISM is ideal for the study done in this paper (Attri et al., 2013).

Using MICMAC analysis in combination with ISM, these factors are split into their driver and dependent categories, and a clear picture is presented as to which of them is the most impactful. Past research Dube and Gawande (2016) has followed this approach widely, and hence this study does not involve the fundamental development of ISM. It, instead, applies this well-established methodology to move to a better understanding of e-commerce adoption in MSMEs. The methodology used in development of ISM is given in Figure 2.

Figure 2: Development process of ISM Model



Source: (Gupta & Saxena, 2019)

4. Results and Analysis

4.1 Structural self-interaction matrix

Thus, the next stage was to develop a conceptual framework that shows how the selected factors relate to each other. This was done by using SSIM, in which experts ranked relationships of factors. The direction together with the nature of the connection between variables was represented by a symbolic system with four markers (Ahmad & Qahmash, 2021b).

V: direct relationship, i.e., factor i leads to factor j

A: reverse relationship, i.e., factor j leads to factor i

X: two-way relationship, i.e., both are related to each other

O: no relationship exists.

The conceptual relationship is converted into reachability matrix. The model development process is given in Figure 2 and the SSIM is given in Table 1.

Table 1: Structured Self Iteration Matrix (SSIM)

S.NO	Factors	13	12	11	10	9	8	7	6	5	4	3	2
1	IT	V	V	V	V	V	V	V	V	O	V	O	V
2	MS	V	V	V	V	V	V	V	V	V	X	O	
3	OS	V	V	O	O	O	O	O	V	A	O		

4	GS	V	V	O	V	V	V	V	V	V			
5	CP	V	V	V	O	V	V	O	V				
6	RIC	V	V	V	V	V	V	V					
7	BV	V	V	V	O	A	A						
8	EFF	V	V	V	V	X							
9	EFC	V	V	V	V								
10	PRO	V	V	V									
11	MSH	V	X										
12	PRFT	V											
13	MSME PRF												

Source: Author's Composition

4.2 Reachability Matrix

Subsequently, SSIM transformed into an initial reachability matrix through binary conversions that used V, A, X and O values to establish 1 and 0 elements according to defined conditions (Table 2). The V values become 1 and their opposite elements receive a value of 0. The elements of A receive a value of 0 and their corresponding transpose elements become 1. The matrix elements receive both a value of 1 from the main diagonal position and from the position of the transpose element while all O elements get converted to a value of 0. The initial reachability matrix displays its values in Table 2.

Table 2: Reachability matrix

S.NO	Factors	1	2	3	4	5	6	7	8	9	10	11	12	13
1	IT	1	1	0	1	0	1	1	1	1	1	1	1	1
2	MS	0	1	0	1	1	1	1	1	1	1	1	1	1
3	OS	0	0	1	0	0	1	0	0	0	0	0	1	1
4	GS	0	1	0	1	1	1	1	1	1	1	0	1	1
5	CP	0	0	1	0	1	1	0	1	1	0	1	1	1
6	RIC	0	0	0	0	0	1	1	1	1	1	1	1	1
7	BV	0	0	0	0	0	0	1	0	0	0	1	1	1
8	EFF	0	0	0	0	0	0	1	1	1	1	1	1	1
9	EFC	0	0	0	0	0	0	1	1	1	1	1	1	1
10	PRO	0	0	0	0	0	0	0	0	0	1	1	1	1
11	MSH	0	0	0	0	0	0	0	0	0	0	1	1	1
12	PRFT	0	0	0	0	0	0	0	0	0	0	1	1	1
13	MSME PRF	0	0	0	0	0	0	0	0	0	0	0	0	1

Source: Author's Composition

4.3 Final Reachability matrix with transitive relations

The basic assumption of transitivity becomes relevant for reachability matrix development by showing that factor A affects factor B and factor B affects factor C thus creating a transitive linkage between factor A and factor C. Table 3 shows the reachability matrix with transitive relations. The 1 with sign of * appears here because of transitive relationship.

Table 3 Reachability matrix with transitive relations

S.NO	Factors	1	2	3	4	5	6	7	8	9	10	11	12	13	Driving power
1	IT	1	1	1*	1	1*	1	1	1	1	1	1	1	1	13
2	MS	0	1	1*	1	1	1	1	1	1	1	1	1	1	12
3	OS	0	0	1	0	0	1	1*	1*	1*	1*	1*	1	1	9
4	GS	0	1	1*	1	1	1	1	1	1	1	1*	1	1	12
5	CP	0	0	1	0	1	1	1*	1	1	1*	1	1	1	10
6	RIC	0	0	0	0	0	1	1	1	1	1	1	1	1	8
7	BV	0	0	0	0	0	0	1	0	0	0	1	1	1	4
8	EFF	0	0	0	0	0	0	1	1	1	1	1	1	1	7
9	EFC	0	0	0	0	0	0	1	1	1	1	1	1	1	7
10	PRO	0	0	0	0	0	0	0	0	0	1	1	1	1	4
11	MSH	0	0	0	0	0	0	0	0	0	0	1	1	1	3
12	PRFT	0	0	0	0	0	0	0	0	0	0	1	1	1	3
13	MSME PRF	0	0	0	0	0	0	0	0	0	0	0	0	1	1
	Dependence power	1	3	5	3	4	6	9	8	8	9	12	12	13	

Source: Author's Composition

4.4 Level Partitioning

The subsequent step requires division of the reachability matrix into different evaluation levels through various factor analysis. The most fundamental factor becomes the top-layer priority because it blocks achievement of all other factors situated above it. Each factor has reachable elements that comprise the factors it supports and antecedent elements that comprise the factors influencing it. The intersection number derives from the reachability set crossing with the antecedent set resulting in a partition level establishment. The procedure involves first deducing the top-level factor which becomes removed from the reachability matrix so that the next top-level factor can be identified. The level matrices for every factor appear starting from Table 4 to Table 12.

Table 4: Level 1 reachability matrix

Factors	Reachability set	Antecedent set	Intersection set Level	Level
1	1, 2, 3, 4, 5, 6, 7, 8, 9, 10, 11, 12, 13	1	1	

2	2, 3, 4, 5, 6, 7, 8, 9, 10, 11, 12, 13	1, 2, 4	2, 4	
3	3, 6, 7, 8, 9, 10, 11, 12, 13	1, 2, 3, 4, 5	3	
4	2, 3, 4, 5, 6, 7, 8, 9, 10, 11, 12, 13	1, 2, 4	2, 4	
5	3, 5, 6, 7, 8, 9, 10, 11, 12, 13	1, 2, 4, 5	5	
6	6, 7, 8, 9, 10, 11, 12, 13	1, 2, 3, 4, 5, 6	6	
7	7, 11, 12, 13	1, 2, 3, 4, 5, 6, 7, 8, 9	7	
8	7, 8, 9, 10, 11, 12, 13	1, 2, 3, 4, 5, 6, 8, 9	8, 9	
9	7, 8, 9, 10, 11, 12, 13	1, 2, 3, 4, 5, 6, 8, 9	8, 9	
10	10, 11, 12, 13	1, 2, 3, 4, 5, 6, 8, 9, 10	10	
11	11, 12, 13	1, 2, 3, 4, 5, 6, 7, 8, 9, 10, 11, 12	11, 12	
12	11, 12, 13	1, 2, 3, 4, 5, 6, 7, 8, 9, 10, 11, 12	11, 12	
13	13	1, 2, 3, 4, 5, 6, 7, 8, 9, 10, 11, 12, 13	13	1

Source: Author's Composition

Table 5: Level 2 reachability matrix

Factors	Reachability set	Antecedent set	Intersection set Level	Level
1	1, 2, 3, 4, 5, 6, 7, 8, 9, 10, 11, 12,	1,	1,	
2	2, 3, 4, 5, 6, 7, 8, 9, 10, 11, 12,	1, 2, 4,	2, 4,	
3	3, 6, 7, 8, 9, 10, 11, 12,	1, 2, 3, 4, 5,	3,	
4	2, 3, 4, 5, 6, 7, 8, 9, 10, 11, 12,	1, 2, 4,	2, 4,	
5	3, 5, 6, 7, 8, 9, 10, 11, 12,	1, 2, 4, 5,	5,	
6	6, 7, 8, 9, 10, 11, 12,	1, 2, 3, 4, 5, 6,	6,	

7	7, 11, 12,	1, 2, 3, 4, 5, 6, 7, 8, 9,	7,	
8	7, 8, 9, 10, 11, 12,	1, 2, 3, 4, 5, 6, 8, 9,	8, 9,	
9	7, 8, 9, 10, 11, 12,	1, 2, 3, 4, 5, 6, 8, 9,	8, 9,	
10	10, 11, 12,	1, 2, 3, 4, 5, 6, 8, 9, 10,	10,	
11	11, 12,	1, 2, 3, 4, 5, 6, 7, 8, 9, 10, 11, 12,	11, 12,	2
12	11, 12,	1, 2, 3, 4, 5, 6, 7, 8, 9, 10, 11, 12,	11, 12,	2

Source: Author's Composition

Table 6: Level 3 reachability matrix

Factors	Reachability set	Antecedent set	Intersection set Level	Level
1	1, 2, 3, 4, 5, 6, 7, 8, 9, 10,	1,	1,	
2	2, 3, 4, 5, 6, 7, 8, 9, 10,	1, 2, 4,	2, 4,	
3	3, 6, 7, 8, 9, 10,	1, 2, 3, 4, 5,	3,	
4	2, 3, 4, 5, 6, 7, 8, 9, 10,	1, 2, 4,	2, 4,	
5	3, 5, 6, 7, 8, 9, 10,	1, 2, 4, 5,	5,	
6	6, 7, 8, 9, 10,	1, 2, 3, 4, 5, 6,	6,	
7	7,	1, 2, 3, 4, 5, 6, 7, 8, 9,	7,	3
8	7, 8, 9, 10,	1, 2, 3, 4, 5, 6, 8, 9,	8, 9,	
9	7, 8, 9, 10,	1, 2, 3, 4, 5, 6, 8, 9,	8, 9,	
10	10,	1, 2, 3, 4, 5, 6, 8, 9, 10,	10,	3

Source: Author's Composition

Table 7: Level 4 reachability matrix

Factors	Reachability set	Antecedent set	Intersection set	Level
1	1, 2, 3, 4, 5, 6, 8, 9,	1,	1,	
2	2, 3, 4, 5, 6, 8, 9,	1, 2, 4,	2, 4,	
3	3, 6, 8, 9,	1, 2, 3, 4, 5,	3,	
4	2, 3, 4, 5, 6, 8, 9,	1, 2, 4,	2, 4,	
5	3, 5, 6, 8, 9,	1, 2, 4, 5,	5,	
6	6, 8, 9,	1, 2, 3, 4, 5, 6,	6,	
8	8, 9,	1, 2, 3, 4, 5, 6, 8, 9,	8, 9,	4
9	8, 9,	1, 2, 3, 4, 5, 6, 8, 9,	8, 9,	4

Source: Author's Composition

Table 8: Level 5 reachability matrix

Factors	Reachability set	Antecedent set	Intersection set	Level
1	1, 2, 3, 4, 5, 6,	1,	1,	
2	2, 3, 4, 5, 6,	1, 2, 4,	2, 4,	
3	3, 6,	1, 2, 3, 4, 5,	3,	
4	2, 3, 4, 5, 6,	1, 2, 4,	2, 4,	
5	3, 5, 6,	1, 2, 4, 5,	5,	
6	6,	1, 2, 3, 4, 5, 6,	6,	5

Source: Author's Composition

Table 9: Level 6 reachability matrix

Factors	Reachability set	Antecedent set	Intersection set	Level
1	1, 2, 3, 4, 5,	1,	1,	
2	2, 3, 4, 5,	1, 2, 4,	2, 4,	

3	3,	1, 2, 3, 4, 5,	3,	6
4	2, 3, 4, 5,	1, 2, 4,	2, 4,	
5	3, 5,	1, 2, 4, 5,	5,	

Source: Author's Composition

Table 10: Level 7 reachability matrix

Factors	Reachability set	Antecedent set	Intersection set Level	Level
1	1, 2, 4, 5,	1,	1,	
2	2, 4, 5,	1, 2, 4,	2, 4,	
4	2, 4, 5,	1, 2, 4,	2, 4,	
5	5,	1, 2, 4, 5,	5,	7

Source: Author's Composition

Table 11: Level 8 reachability matrix

Factors	Reachability set	Antecedent set	Intersection set Level	Level
1	1, 2, 4,	1,	1,	
2	2, 4,	1, 2, 4,	2, 4,	8
4	2, 4,	1, 2, 4,	2, 4,	8

Source: Author's Composition

Table 12: Level 9 reachability matrix

Factors	Reachability set	Antecedent set	Intersection set Level	Level
1	1	1,	1	9

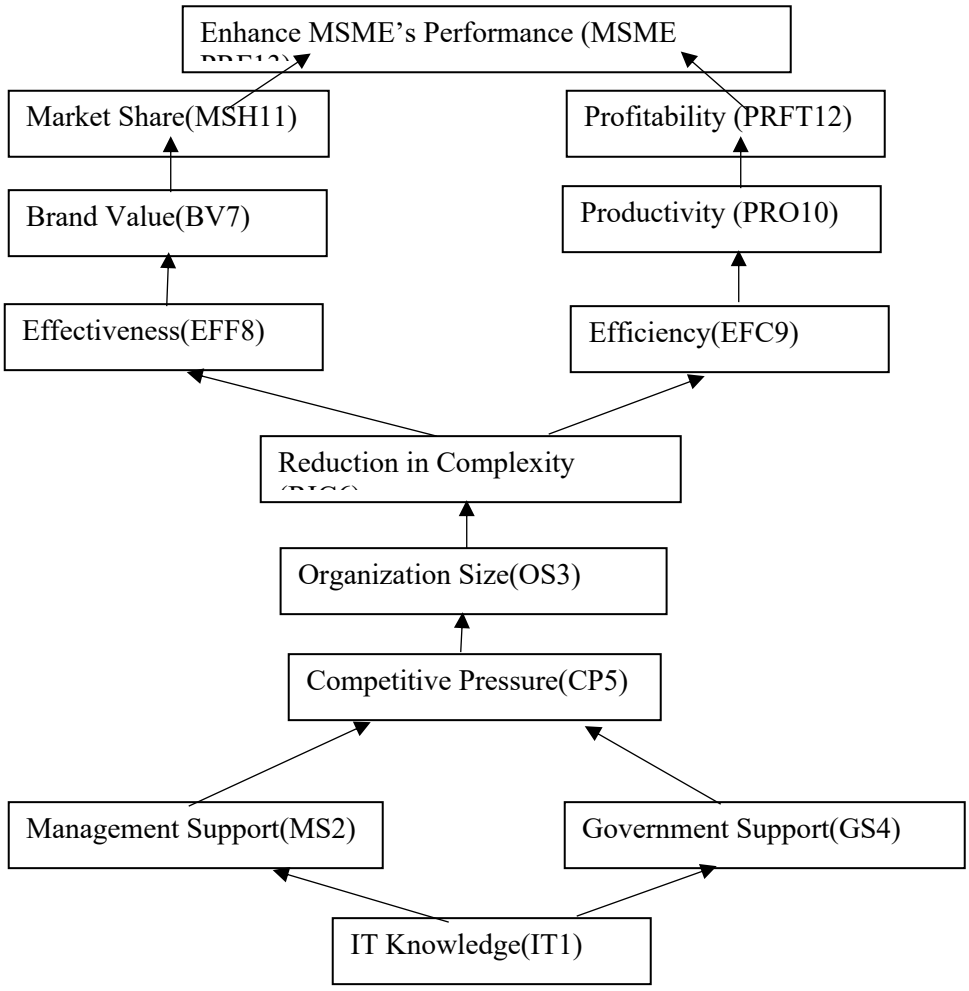
Source: Author's Composition

5 ISM and the factor categorisation

Once all the level matrices have been obtained we built the ISM diagram according to the different level on which factor lies suggesting the way in which one can proceed to enhance MSME performance as shown in Figure 3. The transitivity is taken under consideration while obtaining the

digraph. The step-by-step ordering in the ISM digraph leads from core enabling elements toward achieving MSME Performance (MSME PRF13). The attainment of digital expertise under IT Knowledge (IT1) represents the foundation since it allows management support(MS2) and government support (GS4) in the policy-making process. Competitive Pressure (CP5) sets in because of enthusiastic backing from management combined with policy incentives. The competitive pressure forces organizations to expand their size (OS3) and accomplishes reduction in complexity (RIC6) through process optimization. Reduction in complexity supports both the performance metrics which optimize operational effectiveness (EFF8) while maximizing efficiency (EFC9). Operational effectiveness leads to increase in the Brand Value (BV7) which directly build Market Share (MSH11) and efficiency leads to increase the Productivity (PRO10) which increases profitability (PRFT12) of the MSMEs. The systematic chain culminates by boosting MSME Performance (MSME PRF13) as market success and financial achievement continue to grow. Following this structured approach strengthens competitiveness as well as efficiency and financial sustainability across MSMEs.

Fig 3: Digraph to enhance MSMEs performance

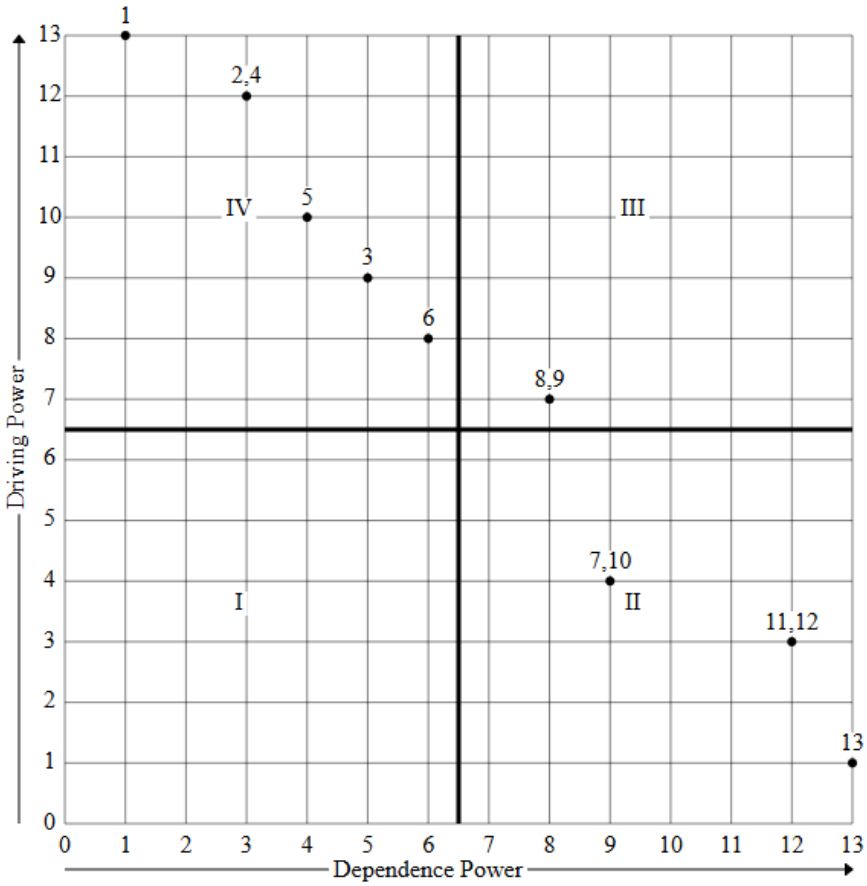


Source: Author's composition

4.6 MICMAC Analysis

All the factors are classified into four categories based on their derived power and dependence power, which is known as MICMAC analysis. The four classifications include autonomous, dependent, driver, and linkage factors (Jafari-Sadeghi et al., 2021), as illustrated in Figure 4. Autonomous factors are characterized by low dependency power and driving power, positioned in quadrant I. Dependent factors possess low driving power but high dependence power, located in quadrant II. Driver factors exhibit low dependency power while having high driving power, found in quadrant IV, and finally, linkage factors are defined by their strong driving and dependence power, represented in quadrant III.

Fig 4: MICMAC Analysis



Source: Author's Composition

(1) Autonomous (1st Quadrant) - They are also known as isolated variables; if any variable comes in this quadrant, it should be removed because they are low driving as well as dependent power. Therefore, **no autonomous factors,** indicating a well-connected model.

(2) Dependent (2nd Quadrant) – 7,10,11,12,13 are the five variables lying in this quadrant, showing purely dependent factors **are business outcomes**, influenced by various enablers.

(3) Linkage (3rd Quadrant) – 8,9 are lying in this quadrant, showing mediating variables **i.e serve as bridge** between enablers and outcomes

(4) Driving variables (4th Quadrant), – 1,2,3,4,5,6 are the variables belong to this quadrant, showing purely independent variables. These **are the main drivers** of MSME performance.

5. Discussion and Implication

Research findings establish an organized structure of elements that affect both e-commerce adoption and performance improvement for MSMEs. A structured series of relationships demonstrates that fundamental enablers lead to business performance results according to the ISM-based model. Technology competence functions as the principal enabler at the base because it improves both numerical competency and operational effectiveness together with general flexibility. The ability of MSMEs to effectively implement digital tools depends on their level of technological capability. Both strategic leadership from managers and external governmental support are needed for a seamless adoption and this factor is the maximum amount of support both parties will provide. Then digital momentum in the market competition is powered up further by cultural elements coming together with the leadership support from management teams from government agencies. Businesses face competitive pressure to generate their operation capability and redesign business's conventional operating process by boosting their capability of scalability and process simplification. Both operational effectiveness and efficiency improve as a direct result of process simplification that offers resource optimization and workflow optimization. MSMEs strive towards getting more recognizable brand with better profitability as a result of increasing operational efficiencies. Established brand image give business the confidence to gain trust from customer and differentiate themselves from competitors to enable multi market expansion which will boost financial profits. And indeed market leadership and superior business outcome come from increased digital capabilities brought about by managerial leadership and operational advancement to yield financial achievement in tandem with digital capability improvement and operational excellence. However, once essential factors come together, MSMEs would have reached to their goal of the enduring performance in the digital economy.

5.1 Theoretical Implications

The study advances current research about e-commerce adoption in MSMEs through an integrated multi-level approach that surpasses independent factor studies. Within the ISM framework enablers receive systematic categorization through which the framework shows ordered relationships between technology management and policy base factors and final business outcomes. The MICMAC analysis engages in classification of elements into independent, dependent, linkage and autonomous groups which confirms e-commerce adoption follows a staged sequence that depends on multiple interrelated factors instead of existing as an individual decision process. The structured application strengthens the initial TOE framework because it uses empirical data to explain the interconnections between organizational factors with environmental elements and technological aspects that build adoption pathways.

5.2 Practical Implications

Small business owners and their decision-makers need to understand digital preparedness and strategic resource management and proactive decision-making for achieving business expansion through e-commerce adoption. Organizations need to direct funding toward building technological infrastructure together with training their workforce to build stronger digital abilities. Managing leaders serve as essential factors in developing innovative environments which transform digital integration into an enterprise-wide business evolution. The government alongside policymakers need to improve financial tools and policy structures plus digital education initiatives for eliminating e-commerce barriers which primarily affect resource-limited MSMEs. Technology providers together with consultants need to design personalized solutions for MSMEs which combine affordable features with modular and efficient functionality.

6. Conclusion and Future Scope

The research examines factors that promote e-commerce utilization together with performance impacts on MSMEs. A set of fundamental enablers consisting of IT knowledge together with management support and government interventions drives the structured digital transformation process. Competitive pressure of foundational elements leads to the adoption of organizational changes based on which we can achieve better organisational efficiency and effectiveness as well as the profitability and the increased market penetration. After implementation of e-commerce enablement factors, the performance of businesses can benefit from numerous cascading effects both at plan and operation levels. From the result of the analysis, the MICMAC analysis, its results show a function of key factors which work together in interlocking ways impelling MSMEs to specifically focus on enhancing its technological know-how and creating organized operations to use external assistance mechanisms and patent in viable digital space. The research offers academic institutions and industrial operations with a full strategy for MSMEs to acquire digital transformation without being fully visible on the market in developed e-commerce environments.

However, the study sheds light on useful understandings on structural connections between e-commerce adoption determinants but there is still an area for further research. Since it will make more sense of the challenges to e-commerce adoption, the research model has to be expanded to include the cybersecurity concerns, digital literacy plus the regulatory aspects. Using Structural Equation Modelling (SEM) statistical techniques, along with empirical validation, can help to increase the overall reliability and generalizability of research results in various geographic areas and for different sectors. Following time-based observational research evaluates the consequences for MSME success under the aggregate adoption patterns of e-commerce. Specific studies of individual sectors help create strategies, which focus only on particular digital transformation issues of the respective sector. Future research should focus on the possibility of the adoption of newly emerging technologies, like artificial intelligence, block chain, cloud computing and the like, aimed at increasing the adoption of e-commerce among MSMEs and improving their efficiency as well as market competitive advantages and innovations.

References

Abebe, M. (2014). Electronic commerce adoption, entrepreneurial orientation and small- and medium-sized enterprise (SME) performance. Journal of Small Business and Enterprise Development, 21(1), 100–116. https://doi.org/10.1108/jsbed-10-2013-0145

Ahmad, N., & Qahmash, A. (2021a). SmartISM: Implementation and assessment of interpretive structural Modeling. Sustainability, 13(16), 8801. https://doi.org/10.3390/su13168801

Ahmad, N., & Qahmash, A. (2021b). SmartISM: Implementation and assessment of interpretive structural Modeling. Sustainability, 13(16), 8801. https://doi.org/10.3390/su13168801

Al-Qirim, N. (2006). The adoption of eCommerce communications and applications technologies in small businesses in New Zealand. IEEE International Conference on Computer Systems and Applications, 2006., 894–897. https://doi.org/10.1109/aiccsa.2006.205194

Alshamaila, Y., Papagiannidis, S., & Li, F. (2013a). Cloud computing adoption by SMEs in the north east of England. Journal of Enterprise Information Management, 26(3), 250–275. https://doi.org/10.1108/17410391311325225

Alshamaila, Y., Papagiannidis, S., & Li, F. (2013b). Cloud computing adoption by SMEs in the north east of England. Journal of Enterprise Information Management, 26(3), 250–275. https://doi.org/10.1108/17410391311325225

Andonov, A., Dimitrov, G. P., & Totev, V. (2021). Impact of e-commerce on business performance. TEM Journal, 1558–1564. https://doi.org/10.18421/tem104-09

Ardolino, M., Bino, A., Ciano, M. P., & Bacchetti, A. (2025). Enabling Digital Capabilities with Technologies: A Multiple Case Study of Manufacturing Supply Chains in Disruptive Times. Systems, 13(1), 39. https://doi.org/10.3390/systems13010039

Aswar, K., & Ermawati, N. (2021). E-Commerce Adoption by Small Medium Enterprises: An Extensive Literature review. Information Management and Business Review, 12(4(I)), 12–18. https://doi.org/10.22610/imbr.v12i4(i).3123

Attri, R., Dev, N., Sharma, V., & International Science Congress Association. (2013). Interpretive Structural Modelling (ISM) approach: An Overview. In Research Journal of Management Sciences (Vol. 2, Issue 2, pp. 3–8). International Science Congress Association. https://www.isca.in

Ayyagari, M., Beck, T., & Demirguc-Kunt, A. (2007). Small and medium enterprises across the globe. Small Business Economics, 29(4), 415–434. https://doi.org/10.1007/s11187-006-9002-5

Baker, J. (2011). The Technology–Organization–Environment Framework. In Integrated series on information systems/Integrated series in information systems (pp. 231–245). https://doi.org/10.1007/978-1-4419-6108-2_12

Ballestar, M. T., Grau-Carles, P., & Sainz, J. (2017). Customer segmentation in e-commerce: Applications to the cashback business model. Journal of Business Research, 88, 407–414. https://doi.org/10.1016/j.jbusres.2017.11.047

Bhardwaj, A. K., Garg, A., & Gajpal, Y. (2021). Determinants of blockchain technology adoption in supply chains by small and medium enterprises (SMEs) in India. Mathematical Problems in Engineering, 2021, 1–14. https://doi.org/10.1155/2021/5537395

Buteau, S. (2021). Roadmap for digital technology to foster India's MSME ecosystem—opportunities and challenges. CSI Transactions on ICT, 9(4), 233–244. https://doi.org/10.1007/s40012-021-00345-4

Davis, F. D. (1989). Perceived usefulness, perceived ease of use, and user acceptance of information technology. MIS Quarterly, 13(3), 319. https://doi.org/10.2307/249008

Diwan, N. (2024). Impact of e-commerce on small and medium enterprises: a case study of developing countries. Universal Research Reports, 11(4), 112–116. https://doi.org/10.36676/urr.v11.i4.1317

Dube, A., & Gawande, R. (2016). ISM-fuzzy MICMAC approach for analysis of GSCM enablers. International Journal of Logistics Systems and Management, 24(4), 426. https://doi.org/10.1504/ijlsm.2016.077281

Gao, J., Siddik, A. B., Abbas, S. K., Hamayun, M., Masukujjaman, M., & Alam, S. S. (2023). Impact of E-Commerce and Digital Marketing Adoption on the Financial and Sustainability Performance of MSMEs during the COVID-19 Pandemic: An Empirical Study. Sustainability, 15(2), 1594. https://doi.org/10.3390/su15021594

Garg, A. K., & Choeu, T. (2015). The adoption of electronic commerce by small and medium enterprises in Pretoria East. The Electronic Journal of Information Systems in Developing Countries, 68(1), 1–23. https://doi.org/10.1002/j.1681-4835.2015.tb00493.x

Goel, P., Kumar, R., Banga, H. K., Kaur, S., Kumar, R., Pimenov, D. Y., & Giasin, K. (2022). Deployment of interpretive structural modeling in barriers to Industry 4.0: a case of small and medium enterprises. Journal of Risk and Financial Management, 15(4), 171. https://doi.org/10.3390/jrfm15040171

Gupta, S., & Saxena, A. (2019). Interpretive structural modelling of critical operational factors for mitigation of bullwhip effect in supply chain management. International Journal of Comparative Management, 2(3/4), 297. https://doi.org/10.1504/ijcm.2019.105979

Hendrawan, S. A., Chatra, N. A., Iman, N. N., Hidayatullah, N. S., & Suprayitno, N. D. (2024a). Digital Transformation in MSMEs: Challenges and opportunities in technology management. Jurnal Informasi Dan Teknologi, 141–149. https://doi.org/10.60083/jidt.v6i2.551

Hendrawan, S. A., Chatra, N. A., Iman, N. N., Hidayatullah, N. S., & Suprayitno, N. D. (2024b). Digital Transformation in MSMEs: Challenges and opportunities in technology management. Jurnal Informasi Dan Teknologi, 141–149. https://doi.org/10.60083/jidt.v6i2.551

Jafari-Sadeghi, V., Mahdiraji, H. A., Bresciani, S., & Pellicelli, A. C. (2021). Context-specific micro-foundations and successful SME internationalisation in emerging markets: A mixed-method analysis of managerial resources and dynamic capabilities. Journal of Business Research, 134, 352–364. https://doi.org/10.1016/j.jbusres.2021.05.027

Jin, S. H., & Choi, S. O. (2019). The Effect of Innovation capability on business performance: A focus on IT and business service companies. Sustainability, 11(19), 5246. https://doi.org/10.3390/su11195246

Kaplan, A. M., & Haenlein, M. (2009). Users of the world, unite! The challenges and opportunities of Social Media. Business Horizons, 53(1), 59–68. https://doi.org/10.1016/j.bushor.2009.09.003

Khoo, V., Ahmi, A., & Saad, R. A. (2018). A comprehensive review on e-commerce research. AIP Conference Proceedings, 2016, 020069. https://doi.org/10.1063/1.5055471

Kshetri, N. (2007). Barriers to e-commerce and competitive business models in developing countries: A case study. Electronic Commerce Research and Applications, 6(4), 443–452. https://doi.org/10.1016/j.elerap.2007.02.004

Makiwa, P. J., & Steyn, R. (2016). ICT adoption and use in Zimbabwean SMEs. IST-Africa Week Conference, 1–8. https://doi.org/10.1109/istafrica.2016.7530576

Mangold, W. G., & Faulds, D. J. (2009). Social media: The new hybrid element of the promotion mix. Business Horizons, 52(4), 357–365. https://doi.org/10.1016/j.bushor.2009.03.002

Mujahed, H. M., Ahmed, E. M., & Samikon, S. A. (2024). Palestinian small and medium Enterprises Digital Technology adoption intention. Journal of Open Innovation Technology Market and Complexity, 10(4), 100426. https://doi.org/10.1016/j.joitmc.2024.100426

Nethanani, R., Matlombe, L., Vuko, S., & Thango, B. (2024). Customer Relationship Management (CRM) Systems and their Impact on SMEs Performance: A Systematic Review. Systematic Review. https://doi.org/10.20944/preprints202410.1538.v1

Oduro, S. (2019). Examining open innovation practices in low-tech SMEs: insights from an emerging market. Journal of Science and Technology Policy Management, 10(3), 509–532. https://doi.org/10.1108/jstpm-03-2019-0036

Porter, M. E. (1998). Competitive advantage: Creating and Sustaining Superior Performance. Free Press.

Raddats, C., Roper, S., & Ashman, R. (2024). The role of services in creating brand loyalty for B2B manufacturers. Journal of Business Research, 174, 114506. https://doi.org/10.1016/j.jbusres.2024.114506

Rafidah, R., Nazori, N. M., Rosmanidar, E., Mutia, A., Usdeldi, U., Anita, E., Fusfita, N., Rahma, S., Subhan, N. M., Nofriza, E., & Alawiyah, R. (2024). Analysis of Effectiveness and Efficiency in MSME Management for increasing income in Mendalo Darat Village, Muaro Jambi. International Journal of Economics (IJEC), 3(2), 1276–1285. https://doi.org/10.55299/ijec.v3i2.608

Salah, O. H., & Ayyash, M. M. (2023). E-commerce adoption by SMEs and its effect on marketing performance: An extended of TOE framework with ai integration, innovation culture, and customer tech-savviness. Journal of Open Innovation Technology Market and Complexity, 10(1), 100183. https://doi.org/10.1016/j.joitmc.2023.100183

Shahadat, M. M. H., Nekmahmud, M., Ebrahimi, P., & Fekete-Farkas, M. (2023). Digital technology adoption in SMES: What technological, environmental and organizational factors influence in emerging countries? Global Business Review. https://doi.org/10.1177/09721509221137199

Sharabati, A. A., Ali, A. a. A., Allahham, M. I., Hussein, A. A., Alheet, A. F., & Mohammad, A. S. (2024a). The Impact of Digital Marketing on the performance of SMEs: An analytical study in light of Modern digital Transformations. Sustainability, 16(19), 8667. https://doi.org/10.3390/su16198667

Sharabati, A. A., Ali, A. a. A., Allahham, M. I., Hussein, A. A., Alheet, A. F., & Mohammad, A. S. (2024b). The Impact of Digital Marketing on the performance of SMEs: An analytical study in light of Modern digital Transformations. Sustainability, 16(19), 8667. https://doi.org/10.3390/su16198667

Sin, K. Y., Osman, A., Salahuddin, S. N., Abdullah, S., Lim, Y. J., & Sim, C. L. (2016). Relative Advantage and Competitive Pressure towards Implementation of E-commerce: Overview of Small and Medium Enterprises (SMEs). Procedia Economics and Finance, 35, 434–443. https://doi.org/10.1016/s2212-5671(16)00054-x

Sindakis, S., & Showkat, G. (2024). The digital revolution in India: bridging the gap in rural technology adoption. Journal of Innovation and Entrepreneurship, 13(1). https://doi.org/10.1186/s13731-024-00380-w

Sorooshian, S., Tavana, M., & Ribeiro-Navarrete, S. (2023). From classical interpretive structural modeling to total interpretive structural modeling and beyond: A half-century of business research. Journal of Business Research, 157, 113642. https://doi.org/10.1016/j.jbusres.2022.113642

Sugiharto, B. H. (2024). The role of e-commerce for MSMEs as a digital marketing strategy in facing Industrial Revolution 4.0. Management Studies and Business Journal, 1(1), 99–107. https://doi.org/10.62207/80ndq458

Thong, J. Y. (1999, January 1). An integrated model of information systems adoption in small businesses. https://papers.ssrn.com/sol3/papers.cfm?abstract_id=1977980

Thong, J. Y. L., Yap, C., & Raman, K. S. (1996). Top management support, external expertise and information systems implementation in small businesses. Information Systems Research, 7(2), 248–267. https://doi.org/10.1287/isre.7.2.248

Warfield, J. N. (1974). Developing interconnection matrices in structural modeling. IEEE Transactions on Systems Man and Cybernetics, SMC-4(1), 81–87. https://doi.org/10.1109/tsmc.1974.5408524

Wen, H. J., Lim, B., & Huang, H. L. (2003). Measuring e-commerce efficiency: a data envelopment analysis (DEA) approach. Industrial Management & Data Systems, 103(9), 703–710. https://doi.org/10.1108/02635570310506124

Wilantari, R., Prianto, E., & Mukhlis, M. (2023). Tax and MSMEs in the digital age. Lulu.com.

Yacob, S., Sulistiyo, U., Erida, E., & Siregar, A. P. (2021). The importance of E-commerce adoption and entrepreneurship orientation for sustainable micro, small, and medium enterprises in Indonesia. Development Studies Research, 8(1), 244–252. https://doi.org/10.1080/21665095.2021.1976657

Yuwono, T., Suroso, A., & Novandari, W. (2024a). Information and communication technology in SMEs: a systematic literature review. Journal of Innovation and Entrepreneurship, 13(1). https://doi.org/10.1186/s13731-024-00392-6

Yuwono, T., Suroso, A., & Novandari, W. (2024b). Information and communication technology in SMEs: a systematic literature review. Journal of Innovation and Entrepreneurship, 13(1). https://doi.org/10.1186/s13731-024-00392-6

Zhu, K., Kraemer, K. L., & Xu, S. (2006). The process of innovation assimilation by firms in different countries: A Technology Diffusion Perspective on E-Business. Management Science, 52(10), 1557–1576. https://doi.org/10.1287/mnsc.1050.0487



IETE Journal of Research

ISSN: 0377-2063 (Print) 0974-780X (Online) Journal homepage: www.tandfonline.com/journals/tijr20

Adaptive Waterwheel Plant Optimization for Enhanced Region Selection in Robust Video Watermarking

Khushboo Chhikara & Manoj Kumar

To cite this article: Khushboo Chhikara & Manoj Kumar (01 Jun 2025): Adaptive Waterwheel Plant Optimization for Enhanced Region Selection in Robust Video Watermarking, IETE Journal of Research, DOI: 10.1080/03772063.2025.2509700

To link to this article: https://doi.org/10.1080/03772063.2025.2509700

Published online: 01 Jun 2025.

Submit your article to this journal

Article views: 1

View related articles

View Crossmark data

Full Terms & Conditions of access and use can be found at
https://www.tandfonline.com/action/journalInformation?journalCode=tijr20

IETE JOURNAL OF RESEARCH
https://doi.org/10.1080/03772063.2025.2509700

Check for updates

Adaptive Waterwheel Plant Optimization for Enhanced Region Selection in Robust Video Watermarking

Khushboo Chhikara and Manoj Kumar

Department of Computer Science, Delhi Technological University, Delhi 110042, India

ABSTRACT

In the digital age, ensuring data security amidst the widespread use of communication devices like smartphones and computers poses significant challenges. Video watermarking serves as a crucial technique for safeguarding data during transmission, involving intricate processes of embedding and extraction. However, the effectiveness of many existing methods in selecting optimal pixels for embedding remains limited, impacting both quality and robustness. This paper introduces a novel video watermarking approach designed to address these challenges. The proposed technique begins by extracting key frames from a cover video using Structural Similarity Index Measurement (SSIM) and employs an adaptive waterwheel plant optimization (AWaPO) algorithm to select optimal embedding regions. To enhance security, the selected regions undergo 2 level-discrete wavelet transform (2L-DWT), with the LL band chosen for embedding secret data encrypted using the enhanced blowfish algorithm (EnBf). Experimental results demonstrate the efficacy of the approach, showcasing its ability to achieve high security, robustness, and quality preservation in watermarking applications.

KEYWORDS

Adaptive waterwheel plant and enhanced blowfish algorithm; Secret image; Structural Similarity Index Measurement; Video watermarking

1. INTRODUCTION

In the digital era, the proliferation of multimedia content across various platforms has brought about significant concerns regarding intellectual property rights and content authenticity. Video watermarking has emerged as a vital technology to address these issues by embedding imperceptible information within video files [1]. This embedded information, or watermark, serves as a proof of ownership, a tool for copyright protection, and a means to detect unauthorized distribution and tampering. The need for robust and efficient video watermarking techniques has become paramount as digital content consumption and sharing continue to rise [2]. The primary challenge in video watermarking is to ensure that the watermark remains imperceptible to viewers while being robust enough to withstand common video processing operations, like noise addition, cropping, and compression. An optimal watermarking strategy ought to combine robustness and imperceptibility to guarantee that the original video is maintained while the embedded watermark can be reliably detected under various conditions [3]. Both common signal processing processes and malicious attempts should be resisted by the watermark. The content owner's unique identity is contained in the watermark [4].

A number of privacy attacks, including statistical analysis, frame averaging, frame swapping, and frame dropping, can target videos owing to the huge amount of data and intrinsic backup among footage and frames [5]. Current algorithms find it difficult to handle these challenges. Video watermarking, the embedding of digital code into video, is important in protecting multimedia content. This digital watermark not only represents the copyright owner, but also ensures the identity of a legal recipient for each copy [6]. Copyright protection is primarily made possible by water technology. Typically, watermarks are incorporated into the coefficients of size or pixel domains. Pixel domain approaches provide minimal computational demands and great load size but lack capacity by adjusting the host image based upon watermark bits [7]. The frequency coefficients of any can be changed using coefficient domain techniques transition based on watermark bits, often using image segmentation and optimization algorithms to increase robustness at the cost of increased computational complexity. For safe video delivery, such complex dynamic area methods offer higher resilience with a smaller size.

Watermarking techniques can be categorized into three groups: transform, compressed, and spatial fields, based on the domain in which the watermark is inserted

© 2025 IETE

[8]. When compressed domain watermarking applies, a watermark is built into a coding bit to match the flow issued by the encoders. The process of spatial domain watermarking entails altering a video frame's embedding channel's pixel values directly [9]. In a video sequence, the property owner frame comes before a watermark is concealed and is changed using transform domain watermarking. This transformation is achieved using common transforms such as Dual-Tree Complex Wavelet Transform (DD CWT), Singular Value Decomposition (SVT), Discrete Wavelet Transform (DWT), and Discrete Cosine Transform (DCT). The watermark alters the transform domain coefficients throughout the embedding process, and the watermarked frame is produced by applying an inverse transform to these altered coefficients. When compared to spatial domain-based solutions, these transform domain techniques offer higher invisibility, stability, and security. Recent advances in optimization algorithms and machine learning have paved the way for innovative solutions in video watermarking [10]. By using these technologies, researchers aim to improve the performance of watermarking schemes by making them more resilient to attacks and more efficient at executing them. The development of adaptive and intelligent watermarking methods is important in the ongoing effort to protect digital media in a world where digital piracy and content tampering are increasingly sophisticated [11]. These advancements promise to uphold the integrity and authenticity of video content, and ensure that creators and distributors can confidently share their work in the digital marketplace.

2. LITERATURE SURVEY

Video watermarking research has evolved to address the critical need for content protection and authentication. This survey explores key studies, examining various techniques and their effectiveness in embedding robust and imperceptible watermarks in video streams. In [12], Dhevanandhini and Yamuna presented a video watermarking technique, which addresses the challenge of secure digital watermarking in high-quality video compression, focusing on the efficiency of HEVC (High Efficiency Video Coding) for preserving video quality while achieving double compression. Initially, videos were segmented into frames and decomposed using dual-tree complex wavelet transform for enhanced security. Adaptive cuttlefish optimization optimally selects embedding positions, where encrypted images, processed via elliptic curve cryptography, are embedded as binary bits. H.265 video encoding further reduces encrypted document size without quality loss, facilitating efficient transmission.

Critical concerns in multimedia security arising from internet-driven data tampering, piracy, and unauthorized dissemination were addressed by Mali *et al.* [13]. It emphasizes how important it is to have strong copyright protection while sending digital videos. The Deep Convolutional Neural Network for Fractional Gorilla Troops Optimization (FGTO_DCNN) is integrated with optimized deep learning in the suggested unique video watermarking technique for the production and embedding of binary pixel maps. The keyframes are gone over using the Not Repetitive Shift Invariant Complex Wavelet Transform (SICWT)in order to efficiently embed and extract watermarks.

Kapre *et al.* [14] addressed the use of watermarking in video surveillance systems to ensure authenticity and integrity, presenting a novel approach for protecting ownership of surveillance videos. It begins with shot detection using Modified Color Layout Descriptor (M-CLD) to reduce false detections due to environmental changes. The scheme then selects key-frames based on maximum entropy values to enhance security and randomness assessment. Employing a multi-watermark embedding strategy with Two Threshold Binary Decomposition (TTBB), the approach ensures robustness and good perceptual quality using The Discrete Wavelet Transform (DWT) and Singular Value Decomposition (SVD).

Eldaoushy et al. [15] introduced multimedia security challenges by introducing a hybrid watermarking technique for digital images based on singular value decomposition (SVD). This approach enhances security through two stages of SVD: embedding with SVD followed by block-based SVD (B-SVD), and extraction using SVD on the entire image followed by B-SVD to recover original watermarks. The scheme improves watermark detection, robustness, and capacity while achieving high-performance metrics such as Peak Signal-to-Noise Ratio (PSNR) of 0.9975 and the Pearson correlation coefficient (Cr) of 45.8605.

Yamni *et al.* [16] introduced a fast audio watermarking system using the dual-tree complex wavelet transform (DTCWT) and fractional Charlier transform (FrCT) in a hybrid transform domain. It focuses on parallelizing intensive steps for efficiency, carried out on a cheap Raspberry Pi cluster using Message Passing Interface (MPI) for intercommunication. The system offers high payload capacity, imperceptibility, and resilience against manipulation, making it suitable for smart city applications. Experimental results show significant temporal improvements of up to 90% with 16 physical cores, highlighting

its scalability and performance advantages in embedded systems.

Rachna Patel *et al.* [17] had developed video steganography. This method isolates the non-dynamic areas and chooses a particular secret to incorporate the frames from the series of video frames. The Discrete Sine Transform (DST) is then applied to these non-dynamic regions, transforming them moving from the measurable frequency domain name in part to the region. Moreover, Manisha and SreeSharmila *et al.* [18] explained This method provides two levels of encryption, requiring knowledge of both the original decomposition of the secret image and the specific frame in which it is embedded for decryption.

Praveen Kumar Tyagi *et al.* [19] developed an algorithm to improve low-light and hazy images using a multi-step approach. The first step involved calculating adjusted lighting to correct areas that were underexposed, which improved the overall quality of the image. An inversion operation was then applied to prepare the image for an optimized dehazing process, effectively removing haze artifacts. A DWT-based fusion technique was then incorporated to extract significant features from both images and combine them into a single.

A backlit image improvement architecture was presented by Samprit Bose *et al.* [20] using a modified U-Net and a unique 1×1 discriminator-based conditional generative adversarial network (cGAN). This method effectively enhances large images by utilized bilateral-guided upsampling (BGU). They produced better results, proving that it works well to improve low-light (LOL) and backlit images.

An encryption-based image watermarking system was created by Md. Saiful Islam *et al.* [21] by combining 2DWT and DCT. The use of 2DWT was guided by a inspection regarding the trade-off involving embedding capacity and fingerprint invisibility across different decomposition levels. The chosen region was subjected to a DCT procedure, which used a zig-zig pattern to collect the image coefficients into a single vector. They used the random bit sequence as the watermark for the embedding zone coefficient. This method outperformed existing approaches; however, the study did not evaluate the Normalized Correlation (NC) metric (Nazir A. Loan *et al.* [22]), (L. Agilandeeswari *et al.* [23]).

3. PROPOSED METHODOLOGY

The aim of this technique is to efficiently use the input video to hide secret information. This includes embedding a watermark to ensure that the video quality is high and the implanted data is resistant to a wide range of threats. The presented technique is comprised of five stages such as key frame extraction, optimal region selection, wavelet band selection, encryption, embedding, and extraction of secret images. First, we covert the image and gather the video. The crucial frames and the cover video are then chosen. To improve the security level, we select the optimal region of key frame using AWaPO algorithm. Then, we apply the 2L wavelet transform to optimal region to select the LL band. Next, we take a look at the secret image and use the EnBf algorithm to secure it. Following the encryption process, we convert the encrypted information into the bit stream. Then, we embed the bit-stream into the LL band. The same procedure is repeated for the decryption process. Figure 1 shows the general framework of the proposed video watermarking methodology.

3.1 Key Frames Extraction

Finding frames that most accurately depict the video's content is the goal of the most important frame extraction, a crucial stage in the processing of videos. To extract important frames, in this paper, SSIM is used. SSIM is a technique for calculating the similarity between two images. It accounts for changes in structural information, contrast, and luminance, which are essential for human visual perception.

Examine the data being entered video V_{in}, which are composed of several frames. Initially, we Extract frames from the input video at regular intervals or based on scene changes $(V_{in} = \{Ke_1, Ke_2, Ke_3, \ldots .Ke_n\}, n = 1, 2, \ldots N)$. Then, we evaluate the SSIM index between consecutive frames to measure the similarity. The SSIM is calculated using Equation (1).

$$SSIM(I_1, I_2) = \frac{(2\mu_{I_1} - \mu_{I_2} + d_1)\,(2\,\sigma_{I_1,I_2} + d_2)}{(\mu_{I_1}^2 + \mu_{I_2}^2 + d_1)\,(\sigma_{I_1}^2 + \sigma_{I_2}^2 + d_2)} \quad (1)$$

where μ_{I1} and μ_{I2} are represent the man intensities of images I_1 and I_2, respectively. $\sigma_{I_1}^2$ and $\sigma_{I_2}^2$ are represent the variance of I_1 and I_2, $\sigma_{I_1 I_2}$ represent the covariance between I_1 and I_2, the constant variables are represented in d_1 and d_2.

A high degree of image matching needs to be done when opting for a key frame. Key elements are defined as those having the highest SSIM. The suggested method of optimization is used for determining the most appropriate locations for the private data in the important frames.

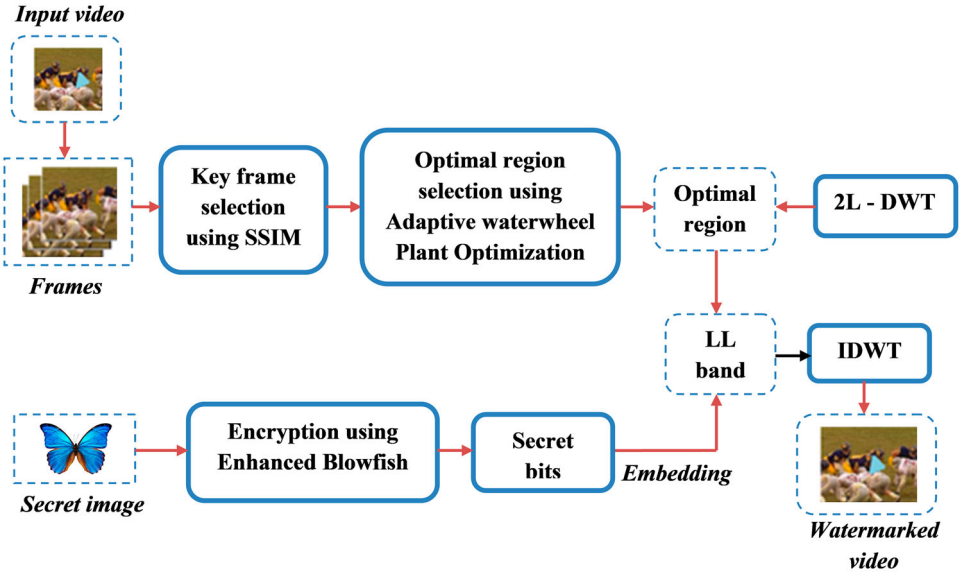


Figure 1: Proposed video watermarking process

Key frame extraction step

1. Consider two consecutive frames I_1 and I_2
2. Compute the mean intensities μ_{I1} and μ_{I2}
3. Compute the variances $\sigma_{I_1}^2$ and $\sigma_{I_2}^2$
4. Compute the covariance $\sigma_{I_1 I_2}$
5. Apply the SSIM formula to get the SSIM index
6. Select the high SSIM value as the key frame

3.2 Optimal Region Selection Process

After the key frame extraction process, we select the optimal region from the frames. Optimal region selection in video watermarking ensures that the hidden data is distributed strategically for increased robustness against attacks and data loss. By choosing regions carefully, the security of the embedded information is enhanced, making it more challenging for unauthorized users to detect or extract the secret message. Additionally, optimal region selection helps maximize the embedding capacity while maintaining imperceptibility, ensuring that the watermarked video appears natural and conceals the hidden data effectively. For optimal region selection process, in this paper, adaptive waterwheel plant optimization (AWaPO) algorithm is used.

The Waterwheel Plant Optimization Algorithm (WaPO) is a nature-inspired optimization technique that simulates the movement and dynamics of a waterwheel to solve complex optimization problems. This algorithm draws inspiration from the mechanical behavior of waterwheels, where water flow and wheel rotation represent the interaction between different components of the optimization process.

To enhance the performance of WaPO, the levy flight strategy is adopted with WaPO. The AWaPO algorithm is well-suited for video watermarking tasks due to its ability to efficiently balance exploration and exploitation during the search process. In watermarking, selecting optimal pixel regions is critical to ensure both imperceptibility and robustness against common attacks. AWaPO mimics natural waterwheel dynamics and integrates Levy flight strategy, which enhances its capacity to escape local optima and converge rapidly toward globally optimal solutions. Its ability to explore multiple regions simultaneously makes it superior to many traditional metaheuristic algorithms, offering improved solution quality in dynamic and complex optimization environments.

The process involved in region selection is described here;

Step 1: Solution encoding

For all techniques for optimizing, the entire process of encoding the brine is very important. An essential component of all optimization algorithms is the encoding of solutions. Here, the answers were originally determined at random initialized. In this paper, the divided region is considered as a solution. The solution is called as waterwheel. Each waterwheel consists of region of frames.

Suppose we have a cover video with a resolution of 640 × 480 pixels and we want to embed a secret message of size 1000 bits. Let's assume we decide to divide the cover video into 10 regions for embedding the secret information. In this example:

Example
Solution size (s) = 10 regions Size of each region = 10640 × 480 = 3072 pixels (we equally divide) Dimension of each region = size of secret image = 1000 bits

Therefore, in this scenario, the solution size is 10 regions, each containing 3072 pixels and having a dimension equal to the hidden nature message's size (1000 bits). The solution generation format is given in below equations;

$$S_i = [s_1, s_2, \ldots .s] \tag{2}$$

$$s_1 = \{Set\ of\ regions\} \tag{3}$$

Step 2: Fitness evaluation

After generating the initial solutions, we calculate the fitness for each solution. The best area to insert hidden information is determined via the physical fitness exam. Power, coverage, and other factors are taken into account by a multi-objective function that determines the fitness of this region, intensity, and kurtosis. The fitness is formulated as follows:

$$\text{Fitness} = \frac{E + (1 - T) + C + K}{4} \tag{4}$$

The letters E, T, C, and K in the equation above stand for energy, pixel extent, reach, and trend, respectively. The maximal exercise ability should be found in the good zone of coverage. The region's energy is computed using Equation (5).

$$E = \frac{1}{q} \sum_{k=1}^{q} \sigma(W_k) \tag{5}$$

In above equation, W_k represents the total quantity of pixels within the jth region. To determine the intensity, the method involves calculating and modeling The range in intensity between a block's pixels. The mathematical function is given in Equation (6).

$$T = \frac{1}{8 \times M \times J} \sum_{j=1}^{8} \sum_{\substack{a=1 \\ j \in a}}^{M} \left[\sum_{K=1}^{J} Q_j^a - Q_j^{a,k} \right] \tag{6}$$

In the above equation, M represent area's total pixels j^{th} region and J represent neighborhood byte. Q_j^a represent the quantity in the jth area of ath byte and $Q_j^{a,k}$ specify the quantity at of decency to a^{th} area of the jth shade. To calculate coverage, the method computes the proportion of pixels near each other that is comparable to all the pixels in a frame. The mathematical expression is given in Equation (7).

$$C = \frac{\text{Number of alike neighborhood pixels}}{\text{Number of total pixels in the frame}} \tag{7}$$

Kurtosis for a given area is jth computed as;

$$K = \frac{1}{p} \sum_{j=1}^{p} \lambda\left(Q_j(a, v)\right) \tag{8}$$

In this case, the term $\lambda(Q_j(a, v))$ symbolizes the kurtosis corresponding to jth region.

Step 3: Updation function

After the fitness calculation, the randomly generated solutions are updated using WaPO functions. The solution is updated on the framework of two actions such as exploitation and exploration. Below is an explanation of the modifying process:

Phase 1: Locating and Identifying Insects (Exploration)

Due to their outstanding sense of smell, waterwheels are expert predators that are capable of tracking and hunting down surrounding insects. The WaPO algorithm simulates this predatory behavior to enhance its search and optimization capabilities, leading to significant position changes and helping escape local optima. Using Equation (9), the waterwheel's new position is determined, and it moves to a new location if the objective function value improves.

$$W_a = Rand_1.(s(k) + 2T) \tag{9}$$

$$s(k+1) + s(k) + W_a.(2T + Rand_2) \tag{10}$$

If the solution doesn't change after three rounds, Equation (11) can be used to shift the placement of the waterwheel.

$$(K + 1s) = Gaussian(\mu_p, \sigma) + R_1 \left(\frac{s(K) + 2T}{W_a} \right) \tag{11}$$

Phase 2: Choosing a suitable tube to carry the insect (Exploitation)

An insect is captured by a waterwheel and moved to a feeding tube, informing WaPOsecond-stage population update. This simulates small position changes, enhancing the WWPA's local search and exploitation capabilities, converging on better solutions near previously discovered ones. Designers generate a new random

place for imitating this natural physical activity for each waterwheel, relocating it if the objective function value improves.

$$W_a = Rand_3 . (Ts_{best}(k) + Rand_3\ s(k)) \tag{12}$$

$$s(k+1) = sP(k) + KW_a \tag{13}$$

where $Rand_3$ represent the random variable that has values overlap from 0 and 2, $s(k)$ represent the iteration's proposed solution k, and P_{best} represent the best solution.

If the solution does not improve for three iterations during the exploration phase, a levy flight It's utilized for preventing getting stuck in regional minima.

$$s(k+1) = s(k) + KW + Levy\,(D) \tag{14}$$

$$Levy(D) = 0.01 \times \frac{a \times \sigma}{|d|^{\frac{1}{\beta}}} \tag{15}$$

$$\sigma = \left(\frac{\Gamma(1+\beta) \times \sin\left(\frac{\pi\beta}{2}\right)}{\Gamma\left(\frac{1+\beta}{2}\right) \times \beta \times 2^{\left(\frac{\beta-1}{2}\right)}} \right)^{\frac{1}{\beta}} \tag{16}$$

D stands for the problem size and levy for any Levy plane function. Here, β is a constant of 1.5, and a and d provide values that vary ranging from 0 to 1.

Step 4: Termination criteria

The process of updating the population is repeated until the final iteration of the algorithm. If not, the algorithm will terminate when the optimal fitness is attained. Upon completion of adaptive WaPO, the best solution (region) found is output as the problem's solution. The selected region is used for further process.

3.3 Secrete Image Encryption Using Enhanced Blowfish Algorithm (EnBf)

The Enhanced Blowfish algorithm is used for encrypting the secret image. It employs a secret key for both encryption and decryption, making it a symmetric algorithm that requires the same key for both processes. The Blowfish encryption algorithm uses a 16-round Feistel network structure to encrypt data, and each round involves key-dependent substitutions and data-dependent substitutions. The primary operations include 32-bit XORs and additions, along with other operations like table lookups. In Blowfish, key scheduling is an essential step before encryption or decryption can occur. The key schedule generates a series of subkeys from the original encryption key. Specifically, Blowfish uses a subkey array called the P-array, which consists of 18 32-bit subkeys Q1, Q2, … ,

Algorithm 1: Blowfish F function

Initialize the 64-bit input named as Y
Divide Y **into two 32-bit halves:** Y_L , Y_R
  For $i = 1$ *to* 16
$Y_L = Y_L\ XOR\ Q_i$
$Y_R = F_n(Y_L)\ XOR\ Y_R$
Swap Y_L and Y_R
Swap Y_L and Y_R **(Undo the last swap)**
$Y_R = Y_R\ XOR\ Q_{17}$
$Y_L = Y_L\ XOR\ Q_{18}$
  Reconstruct Y_L and Y_R

Q18). These subkeys are derived from the original key through a process that involves initializing the hexadecimal numbers of the P-array fractional part of π (pi) and then performing a series of encryption operations.

In this, there are four 32-bit S-boxes with 256 entries. In this blowfish algorithm, initially, the input data 64 bit is divided into two 32 bits parts such as Y_L *and* Y_R. The steps involved in the encryption process are explained below;

For function F: Partition Y_L into four eight-piece quarters: p, q, r, and s.

$$dF(Y_L) = ((K_1, p + K_2, q\ \bmod\ 232)\ \ XOR\ K_3\ ,\ r) + K_4,\ s\ \bmod\ 232 \tag{17}$$

Decryption is similar to encryption except that Q_1 , Q_2, … Q_{18} are used as part of the switch architecture. For speedier blowfish implementations, the circle needs to be unwrapped and all sub-keys need to be kept in the cache-store.

Enhanced blowfish algorithm (EnBf)

By altering the F-function's structure while maintaining the Feistel structure, Blowfish is optimized. Rather than using the four S-boxes that were first utilized in Blowfish's F-function, the optimized version of Blowfish uses two S-boxes.

3.4 Embedding Process

For embedding, a 2L – wavelet transform is applied to the cover image (an optimal region in keyframe) with a size of $(m \times n)$, resulting in the sub-bands LL, LH, HL, and HH, each with dimensions $\left(\frac{m}{2} \times \frac{m}{2}\right)$. Additionally, a second step of decomposition is applied to each band, which reduces the size of the sub-bands to $\left(\frac{m}{4} \times \frac{m}{4}\right)$. The following formula is used to represent the embedding process, which is carried out in the LL and HH wavelet

Pseudo-code for EnBf

A. F-function with four S-Boxes (K_0, K_1, K_2 and K_3)
1. Split Y_L into four eight-bit quarters: p, q, r *and* s
2. $F_n(Y_L) = ((K_0, p + K_1, q \mod 232) \wedge K_2, r) + K_3, s \mod 232$
B. F-function with two S-Boxes
1. Split Y_L into two sixteen-bit quarters: p and q
2. $F_n(Y_R) = (K_0, p \wedge K_1, q)$
c. Encryption process
1. Split the 64-bit original data into two 32-bit halves (Right and Left): Y_L *and* Y_R
2. For i = 0–16 Y_L is *XORed* with $Q[i]$
Locate $F(Y_L)$ $F(Y_L)$ is *XORed* with Y_R
3. Exchange Y_L&Y_R
4. Y_R is *XORed* with Q[16]
5. Y_L is *XORed* with Q[17]
6. Merge Y_L&Y_R
D. Decryption process
1. Split 64-bit original data into two 32-bit halves (Right and left): Y_L&Y_R
2. For i = 17–1 Y_L is *XORed* with $Q[i]$
Locate $F(Y_L)$; $F(Y_L)$ is *XORed* with Y_R
3. Interchange Y_L and Y_R
4. Y_R is *XORed* with Q[1]
5. Y_L is *XORed* with Q[0]
6. Merge Y_L&Y_R

coefficients:

$$I_v(x, y) = K_v(x, y) + h * A_t(x, y);$$
Region optimally selected (18)

where the overall amount of wavelet bands can be expressed by V *and* t whose values range from 1 and 8. $I_v(x, y)$ represent the watermarked image, $K_v(x, y)$ represent the wavelet sub-bands, $K_t(x, y)$ specifies the hidden image bit and h represent the embedding strength.

3.5 Data Extraction Process

After the watermarking process, the watermarked videos are extracted based on the below process;

- The watermarked video, which contains the hidden secret information, is transmitted via a communication channel to reach its intended receiver.
- At the receiver's end, the video is analyzed to identify the optimal region for retrieving the hidden information. This is usually determined based on certain characteristics or criteria defined during the watermarking process.
- Only if the resulting image (or frame) block falls within the specified suitable location, the extraction process continue. This ensures that the retrieval is precise and accurate.
- Each and every sub band of the suggested block conducts a two-level decomposition. This dissection assists in identifying the host video signal's secret information. Techniques like wavelet transform can be used for this purpose.

Table 1: Parameter configuration of Adaptive waterwheel plant optimization algorithm

Parameters	Ranges
r_1	[0, 2]
r_2	[0, 1]
r_3	[0, 2]
T (exponential variable)	[0, 1]
Plants	10
Iterations	80
β	1.5

Table 2: Parameter configuration for Enhanced Blowfish algorithm

Parameters	Ranges
Key length (bits)	192
Block size (bits)	64
Number of rounds	16

- The extraction process is employed in order to precisely remove the hidden secret data from the examined sub-bands. This algorithm ensures that the retrieved information is the greatest image of the secret that originally introduced.

$$I_{Re}(x, y) = I_v(x, y) - K_v(x, y)/h;$$
if Region choosen optimally (19)

- Finally, the secret information is extracted from the watermarked video. This requires assembling the secret data from the optimized regions and the examined sub-bands.

4. RESULTS AND DISCUSSION

The experimental results of the recommended watermarking modern technology are analyzed in this section. A system running Windows 10 with the Python programming language, an Intel Core i7 CPU, and 8 GB of RAM was employed for the purpose of the study. Tables 1 and 2 describe the configuration information for the AWaPO and EnBf programs. For the evaluations, we employed four private images and three separate videos. Three videos who have been selected from (https://media.xiph.org/; http://ultravideo.cs.tut.fi/) will be used for experimental analysis.

4.1 Experimental Results

The experimental results obtained from the proposed approach areanalyzed in this section. The experimental results for video watermarking demonstrate The adaptability and efficiency of the various watermarking technologies in protecting digital video footage. For the purpose of to protect copyright, authenticate product, and recognize interference, video watermarking involves

Table 3: Visual representation of extracted secret image

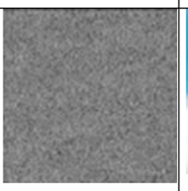
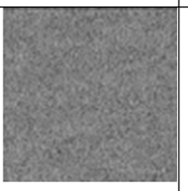
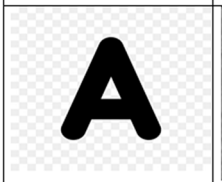
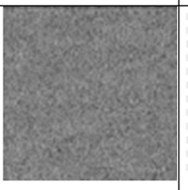
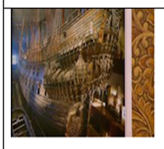
Original secret image	Encrypted image	Extracted image
		
		
		

Table 4: Visual representation of watermarking output

Input image	Secrete image	Watermarked image
		
		
		

including detectable information into video streams. In this paper, we investigate a lot watermarking procedures under multiple attacks Under certain circumstances, which include frame dropping, noise addition, cropping, and compression. To determine the efficiency of each procedure, measures of performance such as embedding capacity, endurance against attacks, PSNR, and NC are investigated. The outcomes show both the benefits and drawbacks of the examined methods, generating important information to build more robust and secure video watermarking techniques. The visual representation is presented in Table 3 of the extracted secrete image and Table 4 represents the watermarked video frame.

Figure 2 shows a time complexity comparison of the proposed AWaPO with existing algorithms such as WaPO, PSO and GA. Figure 3 shows the proposed AWaPO algorithm achieves minimum execution time compared to other algorithms, illustrating faster convergence due to its adaptive search mechanism. Figure 3 shows a comparison of computational efficiency for the proposed AWaPO with existing algorithms. The results demonstrate that the proposed AWaPO algorithm achieves higher computational efficiency, outperforming existing algorithms such as WaPO, PSO and GA. The integration of levy flight strategy into AWaPO contributes to achieving faster convergence and reduced computational overhead. Its adaptive nature and faster convergence make AWaPO highly suitable for complex tasks like optimal region selection in video watermarking, ensuring high performance with lower resource consumption.

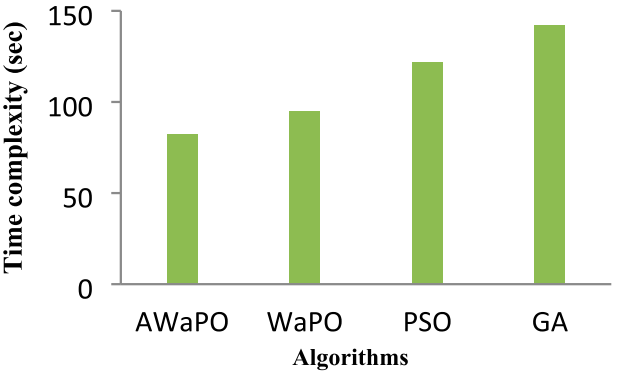


Figure 2: Time complexity comparison

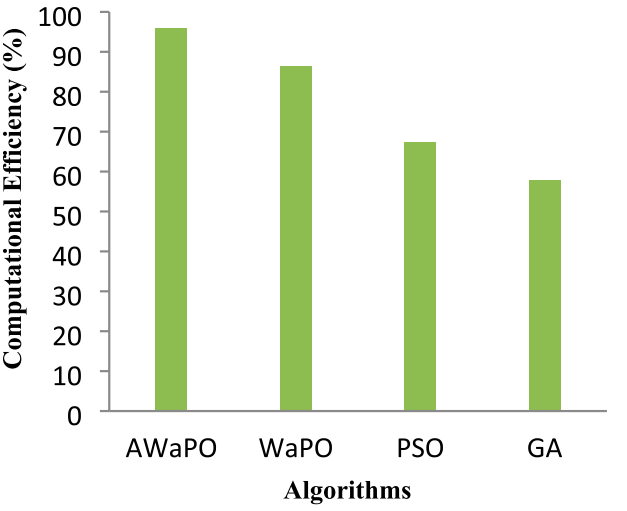


Figure 3: Computational efficiency comparison

Table 5 presents a comparative analysis of different watermarking techniques based on PSNR and embedding capacity, measured across three video samples (V1, V2, V3). The PSNR values, which indicate the quality of the watermarked video, show that the

Table 5: Comparative analysis based on PSNR

	PSNR			Embedding capacity		
Techniques	V_1	V_2	V_3	V_1	V_2	V_3
PSO	65.1	65.7	66.2	55.7	61.2	59.6
GA	63.24	63.7	63.53	53.8	60.1	54.6
LSB based technique	59.23	58.21	56.4	43.7	45.6	44.3
Without optimization	55.3	54.7	54.4	37.2	40.7	39.6
Proposed AWaPO_EnBf	71.23	72.3	70.5	67.5	70.8	68.6

Table 6: Analysis of the NC value relative to other attacks

		NC				
Video	Methods	No attack	Adding 10% noise	Adding 30% noise	Crop attack	Resize attack
V_1	PSO	0.873	0.8234	0.7784	0.8234	0.8334
	GA	0.854	0.8153	0.7521	0.8153	0.8253
	LSB based technique	0.832	0.789	0.7134	0.789	0.799
	Without optimization	0.80	0.75	0.6854	0.75	0.762
	Proposed AWaPO_EnBf	1	0.954	0.932	0.962	0.94
V_2	PSO	0.873	0.8354	0.7642	0.8346	0.8521
	GA	0.854	0.8264	0.7521	0.8153	0.8253
	LSB based technique	0.832	0.7732	0.7134	0.789	0.799
	Without optimization	0.80	0.7432	0.6921	0.773	0.7721
	Proposed AWaPO_EnBf	1	0.9632	0.935	0.961	0.962
V_3	PSO	0.873	0.8243	0.7842	0.8146	0.8261
	GA	0.854	0.8142	0.7521	0.8153	0.8253
	LSB based technique	0.832	0.763	0.7134	0.789	0.799
	Without optimization	0.80	0.7421	0.6854	0.75	0.762
	Proposed AWaPO_EnBf	1	0.9623	0.942	0.952	0.95

Proposed AWaPO_EnBf technique consistently achieves the highest PSNR, with values of 71.23, 72.3, and 70.5, suggesting superior visual quality. The embedding capacity, reflecting the amount of data that can be embedded, is also highest for the Proposed AWaPO_EnBf technique, with values of 67.5, 70.8, and 68.6. In contrast, techniques like PSO and GA show moderate performance, with PSNR values ranging from 63.24 to 66.2 and embedding capacities between 53.8 and 61.2. The LSB-based technique and the method without optimization exhibit the lowest PSNR and embedding capacities, indicating inferior performance in both video quality and data embedding efficiency. These results underscore the effectiveness of the Proposed AWaPO_EnBf technique in achieving high-quality watermarking with significant data embedding capabilities.

Table 6 provides a comparative analysis of different watermarking methods based on Normalized Correlation (NC) values under various attack scenarios for three video samples (V1, V2, and V3). NC values indicate the robustness of the watermarking technique, with values closer to 1 signifying better performance. The Proposed AWaPO_EnBf technique exhibits the highest NC values across all scenarios, maintaining perfect NC (1) without attack and showing strong robustness with NC values ranging from 0.932 to 0.962 even under noise, cropping, and resizing attacks. The PSO and GA techniques perform moderately well, with NC values ranging from 0.7521 to 0.873 without attack and slightly decreasing under attacks. The LSB-based technique and the method without optimization display the lowest NC values, especially under noise and cropping attacks, with values as low as 0.6854. These results highlight the superior robustness and resilience of the Proposed AWaPO_EnBf method against various attacks compared to the other techniques evaluated.

Table 7 presents a comparative analysis of values associated with the PSNR (Peak Signal-to-Noise Ratio) depending on the watermarking methods under various attack scenarios (10% noise, 30% noise, crop attack, and resize attack) across three video samples (V1, V2, V3). Better visual quality of the watermarked video has been demonstrated by higher PSNR values. The Proposed AWaPO_EnBf technique consistently achieves the highest PSNR values, demonstrating superior resistance to attacks. For instance, in V1, it maintains PSNR values of 69.23, 63.23, 69.84, and 69.73 across the four attack types. In comparison, the PSO and GA methods show moderate resilience, with PSNR values ranging from 55.1 to 60.7 and 51.24 to 58.53, respectively. The LSB-based technique and the method without optimization perform the worst, with significantly lower PSNR values, such as 48.23–56.23 and 44.3–52.3, respectively. These results indicate that the Proposed AWaPO_EnBf method provides the best video quality and robustness against attacks, outperforming other evaluated techniques.

Table 7: Analysis concerning the PSNR value when compared to different attacks

		PSNR			
Video	Methods	Adding 10% noise	Adding 30% noise	Crop attack	Resize attack
V_1	PSO	60.1	55.1	59.1	60.7
	GA	58.24	51.24	57.24	57.7
	LSB based technique	56.23	48.23	55.23	53.21
	Without optimization	52.3	46.3	51.3	51.7
	Proposed AWaPO_EnBf	69.23	6323	69.84	69.73
V_2	PSO	60.7	54.3	58.7	60.1.2
	GA	57.7	52.4	56.7	58.53
	LSB based technique	53.21	48.3	52.21	52.24
	Without optimization	51.7	44.3	50.7	50.34
	Proposed AWaPO_EnBf	69.73	67.73	68.73	67.15
V_3	PSO	60.1.2	55.1	58.1.2	60.7
	GA	58.53	51.24	56.53	57.7
	LSB based technique	52.24	48.23	51.24	53.21
	Without optimization	50.34	46.3	49.34	51.7
	Proposed AWaPO_EnBf	67.15	65.15	67.64	69.73

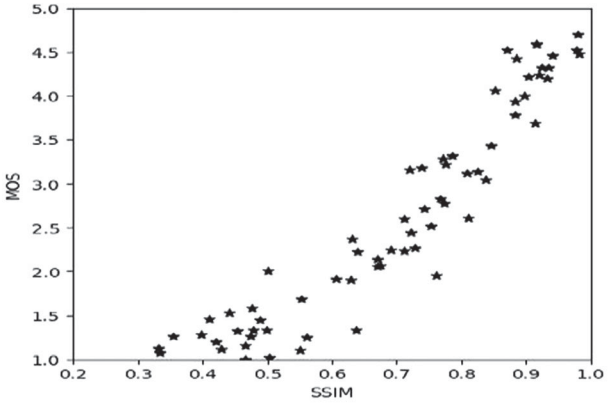


Figure 4: Scatter plot of SSIM and MOS

Figure 4 shows the correlation between the SSIM and the Mean Opinion Score (MOS) for the proposed AWaPO_EnBf-based video watermarking framework. The scatter plot demonstrates a strong correlation between these two metrics. As SSIM values increase, the corresponding MOS values also rise, indicating that the watermarked video retains high perceptual quality. This correlation confirms that the proposed method effectively preserves both structural integrity and visual quality of the video.

5. CONCLUSION

In this study, we presented efficient video watermarking to hide encrypted secret images over a video file. By applying encryption techniques to encrypt watermarks (images) and then mask them in key-frames after extracting frames from various videos, this study proposes a secure, blind, dependable video copyright protection system. A comparative analysis of various watermarking techniques, focusing on PSNR and NC values under different attack scenarios, reveals that the proposed AWaPO_EnBf method consistently outperforms other estimation methods, including PSO, GA, LSB-based technique, and no-optimization method. The proposed AWaPO_EnBf method demonstrates excellent robustness and visual quality under noise addition, cropping, and rescaling, maintaining high PSNR values and robust NC values. This indicates its exceptional ability to preserve both the integrity and quality of watermarked videos. In contrast, other techniques exhibit varying degrees of resilience, with the LSB-based technique and the optimization-free method showing low performance. Therefore, the proposed AWaPO_EnBf method is a robust and highly effective solution for high-quality video watermarking, providing significant improvements over traditional approaches.

DISCLOSURE STATEMENT

No potential conflict of interest was reported by the author(s).

REFERENCES

1. P. Aberna, and L. Agilandeeswari, "Digital image and video watermarking: methodologies, attacks, applications, and future directions," *Multimed. Tools. Appl.*, Vol. 83, no. 2, pp. 5531–91, 2024.

2. S. Kumar, S. Kumar, B. K. Singh, and M. Yadav, "A recent survey on multimedia and database watermarking," *Multimed. Tools. Appl.*, Vol. 79, no. 27, pp. 20149–97, 2020.

3. M. He, H. Wang, F. Zhang, S. M. Abdullahi, and L. Yang, "Robust blind video watermarking against geometric deformations and online video sharing platform processing," *IEEE Trans. Dependable Secure Comput.*, Vol. 20, no. 6, pp. 4702–18, 2022.

4. V. P. Malagi, and D. R. Ramesh Babu. Rotation-invariant fast feature based image registration for motion compensation in aerial image sequences. Proceedings of International Conference on Cognition and Recognition: ICCR 2016.

5. S. Mohiuddin, S. Malakar, M. Kumar, and R. Sarkar, "A comprehensive survey on state-of-the-art video forgery detection techniques," *Multimed. Tools. Appl.*, Vol. 82, no. 22, pp. 33499–539, 2023.

6. X. Yu, C. Wang, and X. Zhou, "A survey on robust video watermarking algorithms for copyright protection," *Appl. Sci.*, Vol. 8, no. 10, pp. 1891, 2018.

7. Z. B. Faheem, M. Ali, M. A. Raza, F. Arslan, J. Ali, M. Masud, and M. Shorfuzzaman, "Image watermarking scheme using LSB and image gradient," *Appl. Sci.*, Vol. 12, no. 9, pp. 4202, 2022.

8. P. Meerwald, and A. Uhl, "Survey of wavelet-domain watermarking algorithms," in *Security and watermarking of multimedia contents III*, 4314, SPIE, 2001, August, pp. 505–16.

9. A. K. Singh, N. Sharma, M. Dave, and A. Mohan, "A novel technique for digital image watermarking in spatial domain," in *2012 2nd IEEE International Conference on Parallel, Distributed and Grid Computing*, IEEE, 2012, December, pp. 497–501.

10. S. Boujerfaoui, R. Riad, H. Douzi, F. Ros, and R. Harba, "Image watermarking between conventional and learning-based techniques: a literature review," *Electronics. (Basel)*, Vol. 12, no. 1, pp. 74, 2022.

11. S. P. Vaidya, and P. C. Mouli, "Adaptive digital watermarking for copyright protection of digital images in wavelet domain," *Procedia. Comput. Sci.*, Vol. 58, pp. 233–40, 2015.

12. G. Dhevanandhini, and G. Yamuna, "An effective and secure video watermarking using hybrid technique," *Multimedia Syst.*, Vol. 27, no. 5, pp. 953–67, 2021.

13. S. D. Mali, and L. Agilandeeswari, "Non-redundant shift-invariant complex wavelet transform and fractional gorilla troops optimization-based deep convolutional neural network for video watermarking," *J. King Saud Univ. Comput. Inf. Sci.*, Vol. 35, no. 8, pp. 101688, 2023.

14. B. S. Kapre, A. M. Rajurkar, and D. S. Guru, "The blind robust video watermarking scheme in video surveillance context," *Multimed. Tools. Appl.*, Vol. 83, no. 13, pp. 38999–9025, 2024.

15. A. F. Eldaoushy, M. I. Desouky, S. A. El-Dolil, A. S. El-Fishawy, and F. E. A. El-Samie, "Efficient hybrid digital image watermarking," *J. Opt.*, Vol. 52, no. 4, pp. 2224–38, 2023.

16. M. Yamni, *et al.*, "An efficient watermarking algorithm for digital audio data in security applications," *Sci. Rep.*, Vol. 13, no. 1, pp. 18432, 2023.

17. R. Patel, K. Lad, M. Patel, and M. Desai, "A hybrid DST-SBPNRM approach for compressed video steganography," *Multimedia Syst.*, Vol. 27, no. 3, pp. 417–28, 2021.

18. S. Manisha, and T. S. Sharmila, "A two-level secure data hiding algorithm for video steganography," *Multidimens. Syst. Signal Process.*, Vol. 30, pp. 529–42, 2019.

19. D. Agrawal, A. C. Yadav, and P. K. Tyagi, "Low-light and hazy image enhancement using retinex theory and wavelet transform fusion," *Multimed. Tools. Appl.*, Vol. 83, no. 29, pp. 72519–36, 2024.

20. S. Bose, S. Nawale, D. Khut, and M. H. Kolekar, "Luminet: multispatial attention generative adversarial network for backlit image enhancement," *IEEE Trans. Instrum. Meas.*, Vol. 72, pp. 1–14, 2023.

21. N. Hasan, M. S. Islam, W. Chen, M. A. Kabir, and S. Al-Ahmadi, "Encryption based image watermarking algorithm in 2DWT-DCT domains," *Sensors*, Vol. 21, no. 16, pp. 5540, 2021.

22. N. A. Loan, N. N. Hurrah, S. A. Parah, J. W. Lee, J. A. Sheikh, and G. M. Bhat, "Secure and robust digital image watermarking using coefficient differencing and chaotic encryption," *IEEE. Access.*, Vol. 6, pp. 19876–97, 2018.

23. L. Agilandeeswari, and K. Muralibabu, "A robust video watermarking algorithm for content authentication using discrete wavelet transform (DWT) and singular value decomposition (SVD)," *International Journal of Security and Its Applications*, Vol. 7, no. 4, pp. 145–58, 2013.

AUTHORS



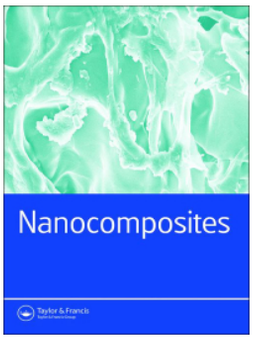
Khushboo Chhikara is currently pursuing PhD from Delhi Technological University under the guidance of Manoj Kumar. She completed her Mtech from IGDTUW, Delhi.

Email: kchhikara31@gmail.com



Manoj Kumar is currently an associate professor at Delhi Technological University, a state University in Delhi. He obtained his PhD degree from DTU, Delhi and Mtech degree from IIT, Delhi.

Corresponding author. Email: mkumarg@dce.ac.in



Nanocomposites

ISSN: 2055-0324 (Print) 2055-0332 (Online) Journal homepage: www.tandfonline.com/journals/ynan20

Advancing biofuel production through nanomaterials: a review of efficiency improvements, challenges, and future directions

Ashish Goyal, Pradeep Kumar Meena, Sagar Shelare & Sujeet Kumar

To cite this article: Ashish Goyal, Pradeep Kumar Meena, Sagar Shelare & Sujeet Kumar (2025) Advancing biofuel production through nanomaterials: a review of efficiency improvements, challenges, and future directions, Nanocomposites, 11:1, 151-172, DOI: 10.1080/20550324.2025.2518755

To link to this article: https://doi.org/10.1080/20550324.2025.2518755

© 2025 The Author(s). Published by Informa UK Limited, trading as Taylor & Francis Group

Published online: 21 Jun 2025.

Submit your article to this journal

Article views: 106

View related articles

View Crossmark data

Full Terms & Conditions of access and use can be found at
https://www.tandfonline.com/action/journalInformation?journalCode=ynan20

NANOCOMPOSITES
2025, VOL. 11, NO. 1, 151–172
https://doi.org/10.1080/20550324.2025.2518755

Taylor & Francis
Taylor & Francis Group

OPEN ACCESS Check for updates

Advancing biofuel production through nanomaterials: a review of efficiency improvements, challenges, and future directions

Ashish Goyal[a], Pradeep Kumar Meena[b], Sagar Shelare[c]* and Sujeet Kumar[d]

[a]Department of Mechanical Engineering, Manipal University Jaipur, Jaipur, Rajasthan, India; [b]Central Workshop, Indian Institute of Technology Delhi, New Delhi, India; [c]Department of Mechanical Engineering, Priyadarshini College of Engineering, Nagpur, Maharashtra, India; [d]Vivekananda Global University, Jaipur, India

ABSTRACT

The increasing dependence on fossil fuels has accelerated greenhouse gas emissions, highlighting the urgency for sustainable energy alternatives. Biofuels offer a renewable, eco-friendly solution, and recent advances in nanotechnology have significantly improved their production efficiency. This review examines how nanomaterials—such as graphene, carbon nanotubes, metal nanoparticles, nanocomposites, and nanoscale biochar—enhance the conversion of feedstocks into biodiesel, biogas, biohydrogen, and bioethanol. These nanomaterials improve catalytic activity, conversion efficiency, product yield, and purity. Specifically, nanocatalysts enhance biodiesel transesterification, optimize anaerobic digestion for biogas, and promote microbial synthesis pathways for biohydrogen and bioethanol. The review also addresses synthesis methods, material functionalization, global adoption trends, environmental implications, and risk management strategies. Despite the promise, challenges like nanotoxicity, lifecycle assessment, and scalability remain. Future research should prioritize cost-effective, biodegradable, and scalable nanomaterials, comprehensive regulations, and increased investment in green nanotechnology to ensure safe and sustainable biofuel production.

GRAPHICAL ABSTRACT



ARTICLE HISTORY

Received 20 January 2025
Accepted 6 June 2025

KEYWORDS

Nanotechnology; biofuels; nanomaterials; environmental impact; sustainable production; feedstock conversion

CONTACT Pradeep Kumar Meena pkmeena@iitd.ac.in Central Workshop, Indian Institute of Technology Delhi, New Delhi, India
*Present addresses: Research and Innovation Cell, Rayat Bahra University, Mohali, Punjab, India; Research and Innovation Cell, Bahra University, Waknaghat, Himachal Pradesh, Solan, India.

© 2025 The Author(s). Published by Informa UK Limited, trading as Taylor & Francis Group
This is an Open Access article distributed under the terms of the Creative Commons Attribution-NonCommercial License (http://creativecommons.org/licenses/by-nc/4.0/), which permits unrestricted non-commercial use, distribution, and reproduction in any medium, provided the original work is properly cited. The terms on which this article has been published allow the posting of the Accepted Manuscript in a repository by the author(s) or with their consent.

1. Introduction

A country's social, economic, and industrial development is greatly influenced by its access to inexpensive, clean energy, which is also essential for assessing quality of life. The UN acknowledges that energy availability is necessary for long-term development in several fields, such as manufacturing, agriculture, healthcare, education, and communications. The UN has prioritized ensuring accessible, clean, affordable, and sustainable energy by 2030 because inadequate and unstable energy access impedes economic growth and human development [1]. Population growth, continuous socioeconomic development, changing lifestyles, rapid industrialization, and technical advancements have all contributed to a significant increase in the world's energy demand. The principal global energy consumption increased from 105,940 terawatt-hours (TWh) in 1990 to 123,150 TWh in 2000. This figure increased to 152,966 TWh in 2010 and 176,431 TWh in 2021 [2].

Although their share of the world's energy supply has somewhat decreased from 86.88% in 1990 to 85.54% in 2000, 85.97% in 2010, and 82.28% in 2021, fossil fuels—coal, oil, and natural gas—remain the dominant force [3]. The slight reduction in reliance on fossil fuels results from more adoption and investment in renewable and low-carbon energy sources. However, reliance on non-renewable energy has increased carbon dioxide (CO_2) emissions and other anthropogenic greenhouse gases. For instance, global CO_2 emissions rose from 20.5 gigatons of CO_2 equivalent ($GtCO_2e$) in 1990 to 23.8 $GtCO_2e$ in 2000, 30.4 $GtCO_2e$ in 2010, and 33 $GtCO_2e$ in 2021 [4]. These rising emissions contribute to environmental degradation, global warming, and negative impacts on ecosystems and human health. The U.S. Energy Information Administration projects that CO_2 emissions from fossil fuel use may approach 40 Gt CO_2eq by 2050 unless substantial reductions in fossil fuel reliance are achieved [5,6]. Figure 1 illustrates the continued dominance of non-renewable energy in the global energy mix by displaying the proportion of primary energy derived from renewables, coal, oil, and natural gas, together with the corresponding CO_2 emissions, from 1990 to 2021. One approach to enhancing access to sustainable energy is the adoption of renewable fuels, specifically biofuels, which have gained significant traction as practical and readily implementable alternatives to fossil-based (FB) fuels [7,8].

As a result, substantial investments in human, material, and financial resources have been directed toward the research and development of biofuels worldwide. Biofuel-based energy output increased from 81 TWh in 1990 to 110 TWh in 2000, 698 TWh in 2010, and 107.9 TWh in 2021, according to data [9]. Additionally, biofuel consumption increased from 7.5 mmtoe in 1990 to 9.1 mmtoe in 2000, 58.9 mmtoe in 2010, and 95.9 mmtoe in 2021. According to forecasts, if present growth patterns continue, consumption might reach 129.7 mmtoe by 2035 [10]. Figure 2 illustrates the upward trend in biofuel production and consumption from 1990 to 2021. Rising crude oil prices, more public interest in renewable energy, and pro-clean energy legislative initiatives are the primary forces behind this expansion.

To meet the infrastructure and skill demands of increasing biofuel production, the global biofuels market rose from 110.5 billion USD in 2021 to 142 billion USD in 2025, 162 billion USD in 2027, and 202 billion USD in 2030, respectively [12]. This market expansion reflects growing interest in biofuels as part of a broader renewable energy transition. Efforts to improve biofuel production have focused on optimizing various stages in the value chain, including feedstock selection, pretreatment methods, process parameters, reactor design, catalyst choice, feedstock conversion efficiency, production

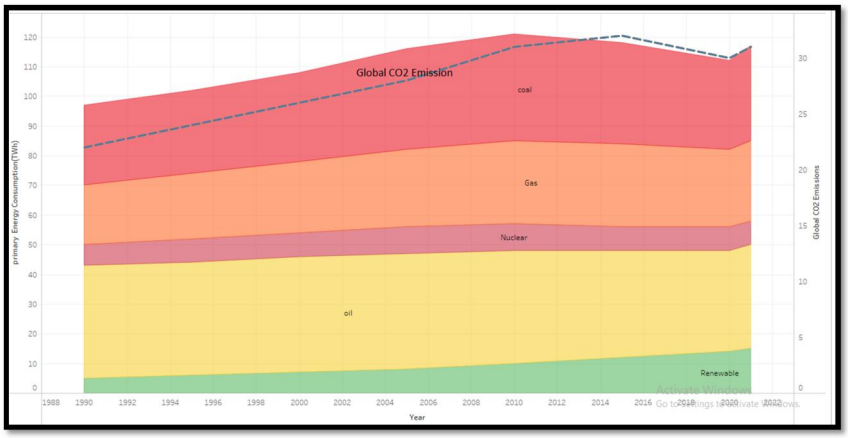


Figure 1. Illustrates global primary energy consumption (measured in TWh) alongside CO_2 emissions from 1990 to 2021. Based on data adapted from reference [3].

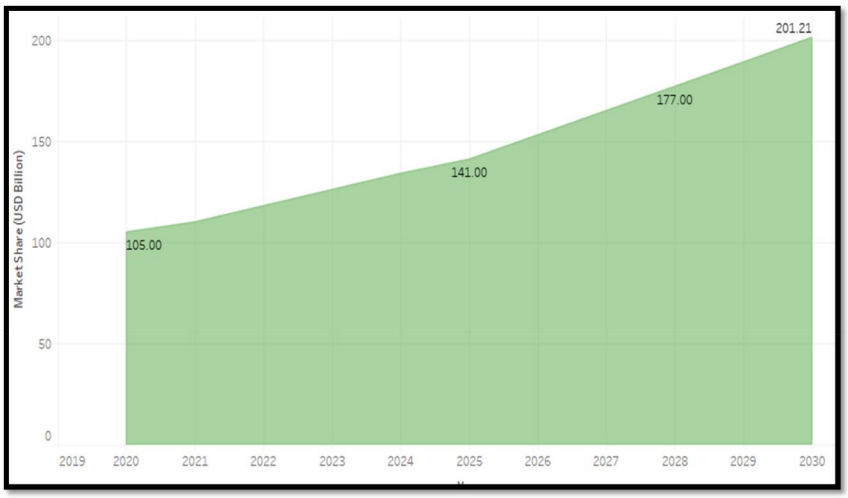


Figure 2. Worldwide biofuel energy production (TWh) from 1990 to 2021. Inset: Global biofuel consumption trends (MMtoe) projections from 1990 to 2035. Data adapted from reference [11].

volume, and product quality. These improvements aim to make biofuels more economically viable, accessible, and environmentally sustainable [13,14]. Biofuel researchers have recently begun applying nanotechnology to enhance production efficiency and quality. Nanotechnology, involving materials engineered at the nanoscale (below 100 nm), increases surface area exposure, improving reaction efficiency. As a developing interdisciplinary field, nanotechnology has applications across diverse areas, such as medicine, engineering, biotechnology, and environmental science [15,16].

In biofuel research, nanomaterials are increasingly used in catalysis, biomass conversion, purification, yield optimization, and emissions reduction, enhancing biofuel quality and sustainability [17,18]. Nanomaterials contribute to cost reduction and environmental sustainability through resource recovery, reusability, and recycling, reducing waste within the biofuel industry. Their unique properties—stability, adsorption, durability, and catalytic performance—make them particularly valuable for advancing biofuel technology [19,20]. Applying nanotechnology to biofuel research addresses significant challenges, including feedstock availability, inefficient conversion methods, lengthy production times, and high energy requirements. The application of nanotechnology in converting lignocellulosic biomass into biofuels has shown promising results in recent studies [21] Further evaluations indicate that nanotechnology can enhance biofuel processing and utilization without compromising environmental safety or energy security [20,22]. Research has also highlighted the potential of nanomaterials to increase biofuel yields by optimizing the interactions between catalysts, feedstocks, and reactants. These investigations have looked into using nanomaterials in manufacturing, bioethanol, biodiesel, and biohydrogen [23,24].

Despite the advances, there remain unexplored areas within nanotechnology's role in biofuel production, such as optimizing biodiesel, biogas, biohydrogen, and bioethanol production, enhancing biofuel separation and purification, and assessing environmental impacts. A notable research gap involves the combined study of nanomaterial synthesis and biofuel applications.

In the current era of Artificial Intelligence (AI), the integration of AI-driven tools with nanobiotechnology holds immense potential to revolutionize biofuel research by enabling data-driven design of nanomaterials, real-time optimization of production processes, predictive modeling of catalytic behavior, and intelligent monitoring of environmental impacts. However, the current literature lacks a focused, comprehensive review that bridges nanotechnology in biofuel production with the emerging opportunities provided by AI. Therefore, this review is both timely and necessary.

This review addresses these gaps, focusing on how nanomaterials enhance biofuel production and purification processes. Specifically, this review documents recent advancements in nanotechnology applied to biodiesel, biogas, biohydrogen, and bioethanol production and outlines the role of nanotechnology in refining crude biofuels. The study aims to provide updated insights into the contributions of nanotechnology to biofuel advancements, summarizing recent research and industry developments to encourage further exploration by scientists, engineers, biofuel refiners, and other stakeholders. Methodologically, the study reviews recent literature on nanomaterials in biofuel production, utilizing databases, such as Google Scholar and Scopus to collate and analyze findings from journals, conferences, and books. Topics covered include nanomaterials' applications, classification, synthesis methods, and factors impacting their use in biofuel research.

In addition to outlining future research paths to increase the role of nanomaterials in attaining energy security and environmental sustainability, the paper addresses the effects of nanotechnology on production, separation, and purification processes.

2. An overview of nanotechnology

The term 'nanotechnology' first appeared in 1959, introduced by Richard Feynman, and has since evolved into a significant area of research and application across many sectors. Substantial investments have been made globally in developing and utilizing nanomaterials across numerous industries, with the global market for nanotechnology reaching USD 85.39 billion in 2021, up from USD 15.7 billion in 2010. Projections indicate sustained increases, with values anticipated to reach USD 110.95 billion by 2023, USD 144.95 billion by 2025, and USD 289.90 billion by 2050 [25]. As of 2020, the Asia-Pacific region led the market with a 52% share, followed by Europe at 28% and North America at 15% [26]. The increased investment in nanotechnology reflects a solid commitment to expanding its applications. With over 90% of the market, items based on nanotechnology rule industries like healthcare and pharmaceuticals, chemicals and sophisticated materials, information technology, and energy [27,28] (Figure 3).

Figure 4 presents the global nanotechnology market size from 2010 to 2030, illustrating its growth trajectory and including a regional market breakdown for 2020 as an inset. Figure 5 highlights worldwide biodiesel production trends from 2016 to 2022, showing variations and key developments during this period. Over recent decades, nanotechnology has found applications in diverse fields, including the automotive industry, food packaging, cosmetics, sports equipment, textiles, paints, and catalysis. Specific applications include wastewater treatment, the production of polymer composites, agricultural productivity, biomedical uses, hydrogen storage, and electrocatalysis. These areas have been studied extensively, highlighting their potential benefits and practical uses [30,31].

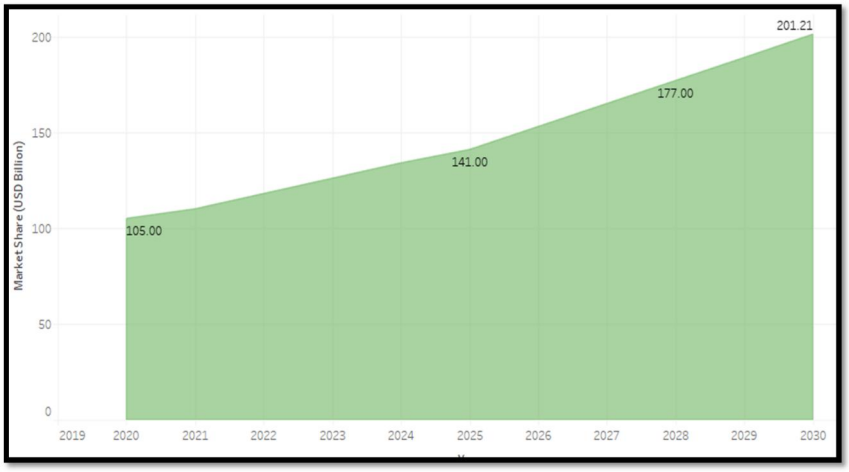


Figure 3. Shows the global market share of biofuels—data adapted from source [12].

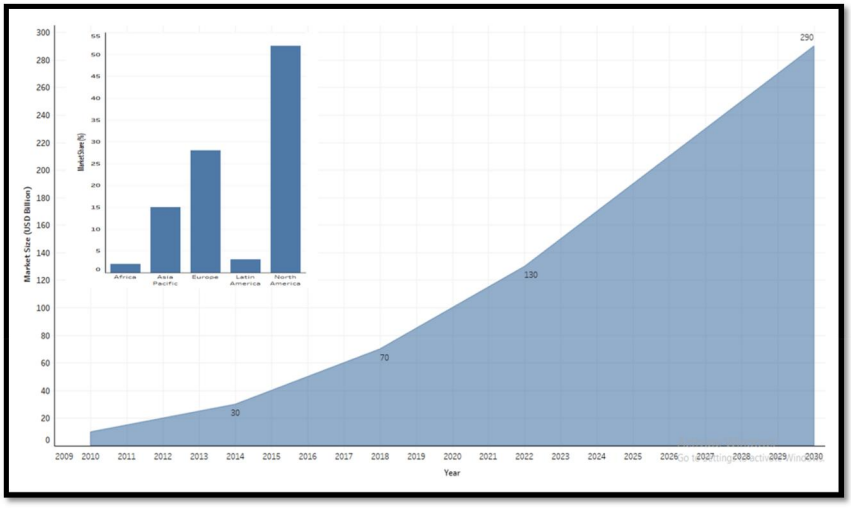


Figure 4. Global nanotechnology market size (USD billion) from 2010 to 2030. Inset: Regional breakdown of the global nanotechnology market in 2020. Data sourced and adapted from references [25,26].

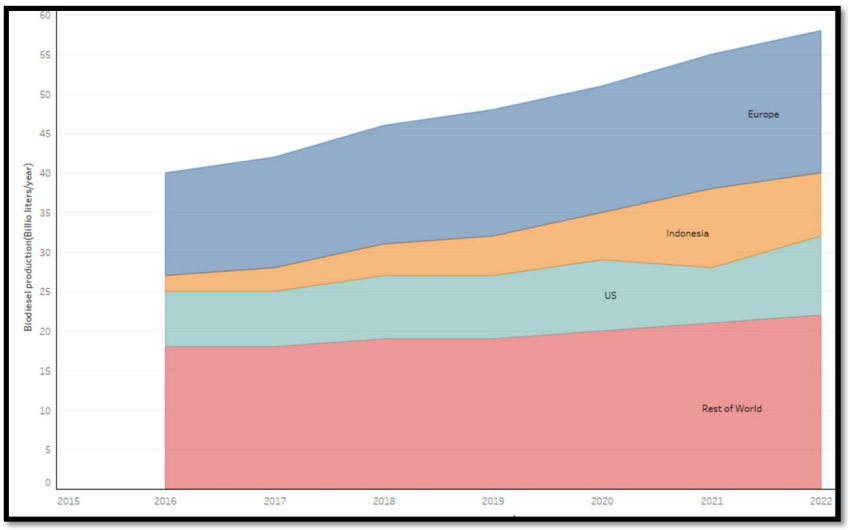


Figure 5. Worldwide biodiesel production trends from 2016 to 2022. Data adapted from reference [29].

2.1. Nanomaterial synthesis methods

Nanomaterials can be synthesized using two main approaches: 'top-down' or 'bottom-up.' The top-down approach reduces more extensive materials to nanoscale dimensions through grinding, etching, and milling techniques. On the other hand, the bottom-up method uses hydrothermal synthesis, sol-gel procedures, and chemical vapor deposition to create nanomaterials from atoms and molecules [32,33]. Nanomaterial production methods are further classified into traditional and green techniques. Conventional methods, including sol-gel and chemical vapor deposition, often require high temperatures and pressures and can emit greenhouse gases. By contrast, green methods prioritize environmental safety and use non-toxic, low-cost, and sustainable resources, such as bacteria, fungi, algae, and plant materials, to produce nanomaterials [34,35].

2.2. Properties of nanomaterials

Nanomaterials' distinct physical and chemical characteristics set them apart from their bulk counterparts. At the nanoscale, for example, a material's color and condition can change; for instance, gold can transform from yellow in bulk to red or purple when it is a nanoparticle [21]. Similarly, boron displays non-metallic properties at the bulk level but exhibits metallic qualities in two-dimensional forms at the nanoscale [36]. Researchers have found that reducing materials to the nanoscale enhances their mechanical, optical, and electrical properties. This improvement is attributed to a more refined crystal structure and reduced crystallographic flaws [32,35]. Nanomaterials' grain size and structure influence physical properties, such as mechanical strength, hardness, and plasticity [37,38]. Additionally, nanomaterials possess significant chemical properties, like surface energy and catalytic activity, as well as optical characteristics, including color, transparency, and light absorption, which are determined by factors, such as grain size and surface atoms [39,40]. The thermal properties of nanomaterials, including conductivity and stability, also depend on surface characteristics, grain size, and interface structures [41,42].

2.3. Categorization of nanomaterials for the production of biofuel

Nanomaterials can be widely categorized based on their dimensions, shape, and structure. Dimensional analysis is a popular classification method that divides nanomaterials into four categories: zero-, one-, two-, and three-dimensional (0D, 1D, and 3D). Examples of 0D nanomaterials—materials with all three dimensions inside the nanoscale—include nanoparticles, quantum dots, nanospheres, and nanoclusters (Table 1).

One-dimensional nanomaterials of two sizes belong to the nanoscale range: nanorods, nanotubes, and nanowires. 2D nanomaterials, which only have one dimension at the nanoscale, include nanofilms, nanolayers, and nanosheets. 3D nanomaterials, which are usually larger and the result of mixing 0D, 1D, and 2D structures, include nanoclusters, core-shells, nanowire bundles, nanotube bundles, and multilayered nanostructures [37,49]. According to their composition, nanomaterials are divided into four groups: semiconductors, metal-based, carbon-based, and nanocomposites. Carbon is the main ingredient in carbon-based nanomaterials, such as graphene, carbon black, and carbon nanotubes (CNTs). These substances possess unique structural properties [50]. Metal-based nanomaterials, made

Table 1. Overview of key methods for nanomaterial fabrication: features, advantages, and limitations.

Method	Description	Merits	Drawbacks	References
Mechanical milling	Reduces the material into nanostructures by using grinding media to transmit kinetic energy.	Simple, efficient, adaptable; high production capacity; durable and reliable.	High energy consumption; potential for contamination; noisy and destructive process.	[34]
Coprecipitation	Creates nanoparticles by combining nucleation, growth, coarsening, and agglomeration.	Low energy and temperature requirements, ease of implementation, and avoidance of organic solvents.	Time-intensive; limited reproducibility; potential for impurities.	[43]
Hydrothermal/solvothermal	Employs chemical reactions at high temperatures and pressure to create nanomaterials.	It controls crystallinity, size, and shape and works well with materials with high vapor pressures and low melting temperatures.	High cost of equipment; safety concerns; difficult to monitor reactions.	[44]
Sputtering	Expels atoms from a material's surface through energized particles, forming thin films or nanostructures.	Simple, versatile, and enables easy deposition; allows for material property modification.	Expensive equipment; slow deposition rates; potential for product contamination.	[34]
Microemulsion	It uses precipitation and nucleation to create stable nanoparticles within micellar systems.	A stable synthesis process enables particle size and composition monitoring, resulting in high surface-area materials.	It requires large volumes of surfactants, is sensitive to temperature and pH changes, and has reduced solubilizing efficiency.	[45]
Laser ablation	Removes surface material using a laser beam to create nanostructures.	Minimal energy loss; produces ligand-free noble nanoparticles; versatile for different materials.	High energy consumption; inefficient at industrial scales; effectiveness diminishes over time.	[46]
Sol-gel	Converts small molecules into solid materials *via* chemical reactions.	Enables low-temperature synthesis; yields high-purity, porous materials with controllable properties.	Long reaction times; purification required; potentially hazardous.	[19]
Chemical vapor deposition	Thin films are deposited through chemical reactions, etching, and layering on a substrate.	Cost-effective; highly repeatable; produces robust, homogeneous materials with regulated growth.	Releases toxic byproducts; high fabrication cost; precursor materials can be flammable and hazardous.	[46]
Inert gas condensation	Creates nanoparticles by vacuum-induced metal evaporation, condensation, and coagulation.	It controls particle size and works well with ceramic and metallic materials.	High operating costs; restricted to laboratory applications; slow output rate.	[47]
Template synthesis	Employs porous materials to confine and control nanoparticle formation.	Simple process; cost-effective; yields a variety of shapes and configurations.	Limited scalability; expensive templates; energy-intensive.	[48]
Ultrasound	It uses ultrasonic waves to induce reactions and form nanomaterials.	Rapid reactions; diverse configurations; works under ambient conditions.	It requires further study, as well as slow material generation rates.	[48]
Thermal evaporation	Breaks chemical bonds using heat to generate nanoscale structures.	It is a procedure that doesn't require a solvent, is simple to see, and works well with low melting point materials.	High energy consumption; impractical for heat-sensitive materials; challenging to scale up.	[46]
Biological synthesis	Utilizes biological processes, such as enzymatic or cellular mechanisms, for environmentally friendly nanomaterial production.	Eco-friendly; stable process; promotes biodiversity.	Slow reaction rate; limited scalability; requires further research.	[48]

from silver, gold, and nickel, have a high surface area and adsorptive capacity, making them valuable for scientific, technological, and environmental uses [46]. Semiconductor nanoparticles combine nonmetallic and metallic characteristics and are frequently employed in electrical circuits and as photocatalysts. As demonstrated by nanofibers, nanoparticles, and nanorods, nanocomposites integrate different properties of each element by combining numerous materials with at least one component at the nanoscale [46,51].

Gold, silver, tin, and nickel are metallic nanoparticles important in biofuel conversion. Their huge surface area improves the catalytic contacts with the feedstock, allowing for better electrocatalytic performance and more efficient electron transport, which leads to better feedstock conversion. In particular, gold and silver nanoparticles enhance enzymatic activity, microbial cell adhesion, and substrate utilization—all critical for biofuel synthesis. Additionally, metallic nanoparticles can reduce the lag phase in bacterial and algal growth, stimulate acetic reactions for biohydrogen production, and promote protein synthesis and nitrogen metabolism, aiding biofuel feedstock fermentation [49,52].

Allotropes of carbon, known as carbon nanotubes (CNTs), are frequently created using chemical vapor deposition and laser ablation methods. They are ideal for the esterification and transesterification of triglycerides into biodiesel because of their structural, thermal, and biocompatible qualities. Because they facilitate redox processes and electron transfer during the manufacture of biofuels, carbon nanotubes (CNTs) are favored for their stability, nontoxicity, porosity, conductivity, and affordability. Additionally, they make it possible to immobilize enzymes, which boosts their catalytic activity and reusability—critical for biofuel reactions [52,53]. Magnetic nanoparticles, composed of a magnetic core and a chemical component, are applied in processes like hydrogenation, transesterification, and anaerobic digestion to produce biogas and biohydrogen. These nanoparticles support enzyme immobilization, which aids in modifying enzyme properties and hydrolyzing lignocellulosic biomass for biofuel production. Magnetic nanoparticles enhance enzyme separation for reusability and improve the adherence of enzymes to active sites, boosting bioethanol, biogas, and biohydrogen yields by accelerating microbial growth and enzymatic activity [52,54].

Graphene and graphene-derived nanomaterials, including graphene oxide and reduced graphene oxide, have emerged as sustainable catalysts that can replace conventional zeolites and solid acids in biomass-to-biofuel conversion. These substances encourage feedstock transesterification into biodiesel and biomass pyrolysis into bio-oil. Recent studies like the one by Awogbemi et al. show the potential of using carbon nanotubes and graphene nanosheets derived from waste plastic as biocatalysts for the production of biodiesel [55]. Solid acids, transition-metal oxides, and H-form zeolites are a few more nanoscale heterogeneous catalysts with promise for efficiently producing biofuels [56,57]. The surface design and high catalytic activity of metal oxide nanoparticles make them sound like catalytic support systems. Potassium, silicon, and zinc oxides have been utilized to catalyze oil conversion into biofuels, enhancing the esterification and transesterification processes for synthesizing biodiesel from spent cooking oil.

Many metal oxide nanoparticles are stable, withstand high temperatures, and possess acidic and basic properties, significantly enhancing biodiesel and biohydrogen yields [52]. Nanofibers' functionalized surfaces and significant surface-area-to-volume ratio make them more useful as biofuel catalysts. Their large surface area makes them perfect for producing biofuel since it increases interaction sites and lowers mass-transfer constraints. In addition to being inexpensive, quickly recovered, and recyclable, nanofibers—frequently made from agricultural waste—also encourage microbial growth, boosting bioethanol, biohydrogen, and biogas [58,59].

3. Elements affecting the use of nanomaterials in the manufacturing of biofuel

Several variables, such as the synthesis process, temperature, pH, pressure, particle size, and concentration, affect how well nanomaterials work to produce biofuel. These criteria must be well managed to maximize the yield, quality, and performance of nanomaterials utilized in the synthesis of biofuels.

3.1. Synthesis methods

Nanomaterials are synthesized *via* three primary methods: chemical (e.g. chemical reduction, sol-gel, electrochemistry), physical (e.g. vaporization, laser ablation, ultrasonication), and biological routes (e.g. using bacteria, fungi, plants) [48,60]. Each approach has unique advantages and limitations; for instance, the physical method ensures size uniformity and minimizes contamination but is energy-intensive and time-consuming. The biological approach, which creates nanomaterials with regulated size and form under straightforward ambient circumstances, is, in comparison, economical, non-toxic, energy-efficient, and environmentally benign [21]. Plant- and microbe-mediated synthesis is economical, supports large-scale production, and minimizes environmental impact [61,62].

3.2. Production temperature

Depending on the technique, temperature plays a critical role in creating nanomaterials. The biological approach works at room temperature, frequently below 100 °C, whereas physical and chemical methods typically require temperatures above 310 °C. Temperatures between 100 and 700 °C generally are ideal for fabricating and modifying metallic nanomaterials [32]. In biofuel production, the operating temperature of nanomaterials influences catalyst activity and reaction rates. For instance, to prevent methanol evaporation during the transesterification process used to produce biodiesel, temperatures must be kept below 65 °C [63,64].

3.3. Pressure on production

Pressure is another essential aspect impacting nanomaterials' size, shape, and quality, frequently affecting particle aggregation. Processes and reaction

vessels must function within particular pressure ranges to guarantee efficient biofuel production. In general, higher pressure can cause nanomaterials to have larger particle sizes, which can affect the synthesis process as a whole [22].

3.4. Production pH

The acidity or alkalinity of the synthesis environment affects the morphology, geometry, and stability of nanomaterials. Acidic conditions (pH <7) typically encourage particle aggregation and enhance nanomaterial stability and functionality. The production and morphology of various metallic nanomaterials, such as those composed of gold, silver, platinum, and iron, have been substantially influenced by pH, as demonstrated by studies conducted by Ahmed et al. [65] and Wu et al. [66].

3.5. Concentration and particle size

For biofuel applications, nanomaterials' size, dose, and concentration are crucial factors in their efficacy. Because they maximize surface area and catalytic efficiency, particle sizes ranging from 6 to 100 nm are typically chosen for biofuel generation [66].

3.6. Process monitoring using nanoscale sensors

Although nanosensors are widely employed in the food, healthcare, and environmental sectors, they have also been used to monitor manufacturing processes in current biofuel research. Nanosensors enable real-time monitoring and optimization of crucial parameters like temperature, pressure, catalyst concentration, and pH, thereby improving efficiency and reducing material waste. Nanomaterials, such as silver, copper, and platinum are commonly used in these sensors to monitor feedstock composition, enzyme activity, and microorganism behavior in biofuel production. This enhances catalyst stability, conversion rates, and product yield [67,68].

3.7. Nanoengineered microorganisms for enhanced production

Nanotechnology has also advanced the genetic modification of microorganisms to enhance their biofuel production potential. Using nanomaterials, specific microbial strains are engineered to improve enzyme stability and efficiency, overcoming challenges related to feedstock resistance. However, nanomaterials like ZnO, CuO, and FeO can be toxic to microbes, potentially hindering biofuel production. To address this, nanomaterials are designed to support enzyme functionality by modifying surface interactions, often enhancing feedstock conversion [69,70]. Recent research has shown that nanoparticles can improve microbial fermentation, alter enzyme composition, and optimize biohydrogen production from lignocellulosic biomass [69,71].

3.8. Ethical considerations in nanotechnology

The rise of nanotechnology in biofuel production, environmental remediation, and waste management introduces ethical considerations. Producing nanocatalysts and other nanomaterials, primarily through biological means, raises concerns about ecological impacts, food *versus* fuel conflicts, and societal implications related to resource use. Ethical issues include potential health risks, environmental pollution from catalyst disposal, and effects on biodiversity. Addressing these challenges requires robust ethical guidelines, industry self-regulation, regulatory oversight, and adherence to environmental health standards to protect public health and ecosystem stability [72,73].

4. Nanomaterials for biofuel production

Nanotechnology is being increasingly applied in biofuel research, encompassing areas like feedstock pretreatment, biomass conversion, yield enhancement, environmental sustainability, product purification, and process intensification in using nanotechnology for biofuel production.

4.1. Biodiesel production

The primary process for producing biodiesel, a sustainable biofuel alternative, is transesterification, which entails the reaction of biomass and alcohol using a catalyst. Known for its eco-friendly nature, one has become increasingly attractive to internal combustion engines. However, feedstock and catalyst prices greatly influence the cost of producing biodiesel. Using waste or non-edible oils as feedstocks have reduced costs, while catalysts synthesized from waste resources have further lowered expenses, promoting environmental cleanliness and resource recovery. In 2022, the global demand for biodiesel will rise from 39 billion to 60.5 billion liters, with Europe, the US, and Indonesia leading production. The biodiesel market is expected to grow to USD 72.90 billion by 2030 due to the fuel's environmental advantages and clean energy programs by governments worldwide.

Nanotechnology has provided crucial advancements in biodiesel production. NO and $SrTiO_3$ have enhanced transesterification efficiency for waste cooking oil, resulting in higher biodiesel yields. Additional studies show nanocatalysts derived from

mussel shells, Cu-TiO_2 composites, and stabilize biodiesel synthesis with high yields from various oils. Recent optimization studies using nanocatalysts and response surface methodology (RSM) have streamlined production and reduced costs. Nowadays, nanotechnology plays a significant role in biofuel manufacturing, supporting environmental and energy security objectives.

4.2. Biogas

Biogas, a methane-rich energy source that has gained appeal because it is renewable and sustainable, is produced by the anaerobic digestion (AD) of organic waste. During AD, organic matter decomposes into volatile fatty acids and alcohols *via* hydrolysis, acidogenesis, acetogenesis, and methanogenesis. Global biogas production has increased significantly since 2000, with projections indicating a steady market rise from USD 23.95 billion in 2020 to USD 36.90 billion due to demand, technological developments, and supportive laws. Nanotechnology has shown great promise in enhancing biogas production. By increasing the surface area available for microbial activity, nanoparticles improve substrate conversion. Studies report that nanoscale zero-valent iron (ZVI) and CuO nanoparticles can boost biogas production by as much as 120% under certain conditions. For instance, using nanoscale Fe_2O_3 and Fe-Co-Cu train converting organic waste like palm oil mill effluent and corn straw significantly increased biogas yield and quality (Table 2).

Figure 6 illustrates the use of nanoparticles in biodiesel production, highlighting their role in improving the manufacturing process. Figure 7 shows biogas production *via* anaerobic digestion, emphasizing key aspects of the process. Figure 8 provides a diagram of the anaerobic digestion process, outlining its stages and mechanisms. Figure 9 presents the energy content of global biogas production, demonstrating its importance as a renewable energy source. Additionally, ZVI has been used to remove pollutants from biogas. Despite some challenges, it is suitable for power generation and combustion applications, including potential process inhibition and sludge accumulation assets in improving waste-to-energy biogas production processes.

4.3. Biohydrogen

Global biohydrogen consumption is projected to increase markedly, from 71 million metric tons (MMT) in 2017 to around 136 MMT by 2040, 287 MMT by 2050, and 519 MMT by 2070, primarily propelled by its rising application in the transportation sector. The biohydrogen industry is expanding, with projections showing growth from USD 1.20 billion in 2020 to USD 10.15 billion by 2025, USD 36.1 billion by 2028, and USD 90.1 billion by 2030. Biohydrogen is produced primarily through photo

Table 2. Summary of nanotechnology applications in biodiesel production.

Nanoparticles	Feedstock	Reaction conditions	Yield (%)	Remarks	References
CaO	Waste cooking oil (WCO)	M:O ratio = 11.8:1; Catalyst concentration (CC) = 2.35 wt%; Temperature = 64.1 °C; Reaction time (Rt) = 70 min	95.10	The CaO nanocatalyst demonstrated high efficiency.	[74]
ZnO/TPA	WCO	Temperature = 64 °C; CC = 3.7 weight percent; M:O ratio = 6:1	94	The biodiesel produced complied with ASTM regulations.	[75]
IGO@SrTi	WCO	Temperature = 125 °C; Rt = 180 min; M:O ratio = 10:1; CC = 10 weight percent	95.8	Enhanced biodiesel production.	[76]
BNPs-CCH	Soybean oil	Temperature = 62 °C; Rt = 4.5 h; M:O ratio = 11:1; CC = 4.15 weight percent	95.1	High yield was obtained using nanomaterials.	[77]
Cu/TiO_2	Palm oil	Temperature = 46 °C; Rt = 47 min; M:O ratio = 20:1	91	Useful as a catalyst at the nanoscale.	[78]
Pr/CaO	Castor oil	M:O ratio = 7.5:1; temperature = 67 °C; CC = 2.75 weight percent	88	The nanoparticle was reusable and practical.	[79]
CaO	Soybean oil	Temperature = 65 °C; Rt = 125 min; M:O ratio = 11:1; CC = 3.75 weight percent	98	Increased production of biodiesel.	[80]
CaO/Ag	Soybean oil	Temperature = 76 °C; Rt = 85 min; M:O ratio = 13:1; CC = 4.5 weight percent	91	Nanocatalyst intensified the biodiesel process.	[81]
TiO_2-ZnO	*Ulva lactuca* Seaweed	Temperature = 65 °C; Rt = 4.5 h; M:O ratio = 6:1; CC = 4.2 weight percent	83	The nanocomposite catalyst worked well.	[82]
CaO	Rice bran oil	Temperature = 60 °C; Rt = 70 min; M:O ratio = 35:1; CC = 0.7 weight percent	92.8	Biodiesel that complied with EN and ASTM standards.	[83]
La^{3+}/ZnO-TiO_2	WCO	Temperature = 38 °C; Rt = 185 min; M:O ratio = 12:1; CC = 4.5 weight percent	97	Met GB 25199–2017 and EN 14214 standards.	[84]

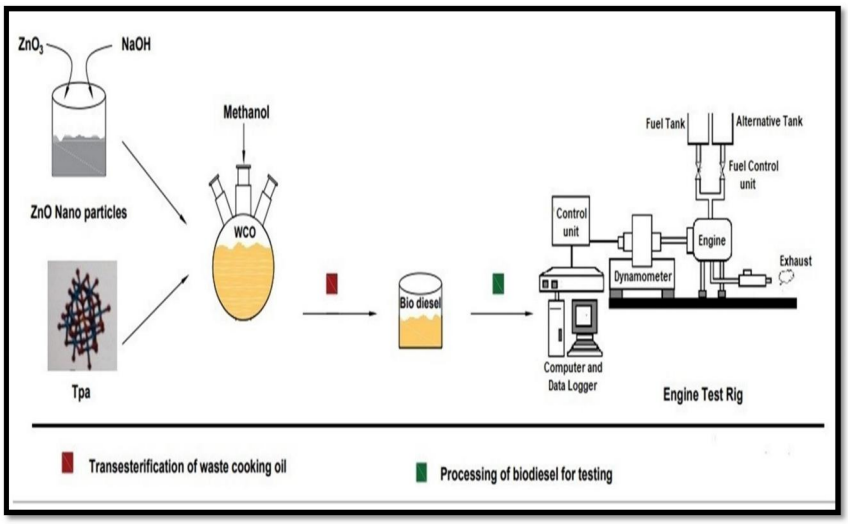


Figure 6. Diagram showing how nanoparticles manufacture biodiesel [75].

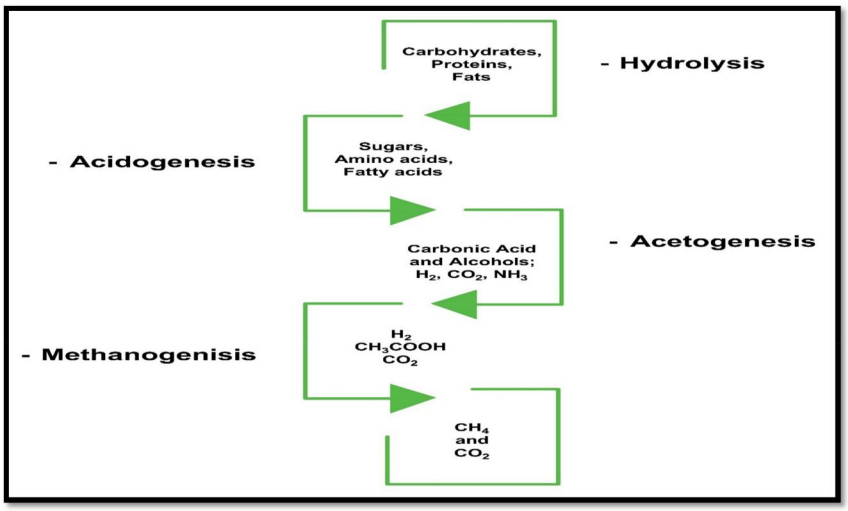


Figure 7. Depicts biogas production *via* anaerobic digestion based on data from references [14,85].

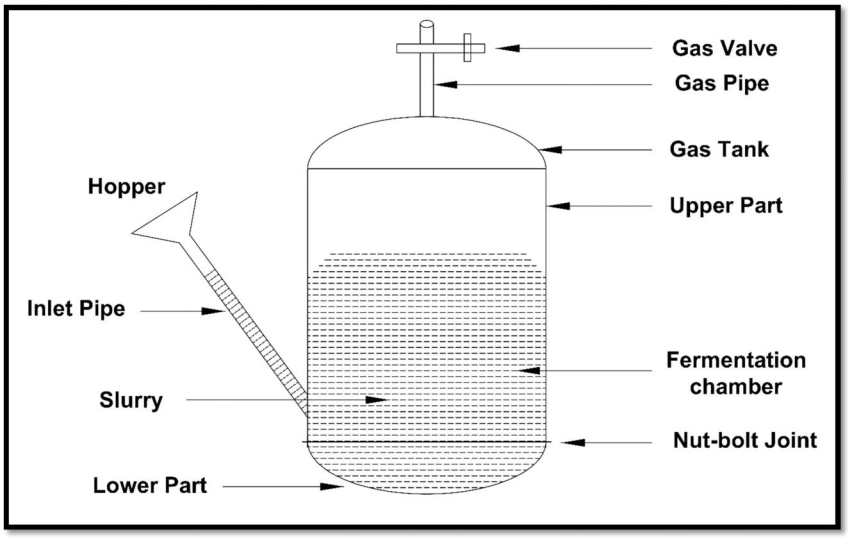


Figure 8. Diagram depicting the anaerobic digestion process.

and dark fermentation of biomass. Photo fermentation relies on photosynthetic microorganisms like cyanobacteria and green algae, which produce biohydrogen in sunlight and water.

Dark fermentation, a more widely adopted method, involves anaerobic bacteria breaking down complex substrates, yielding biohydrogen under cost-effective and renewable conditions. While dark

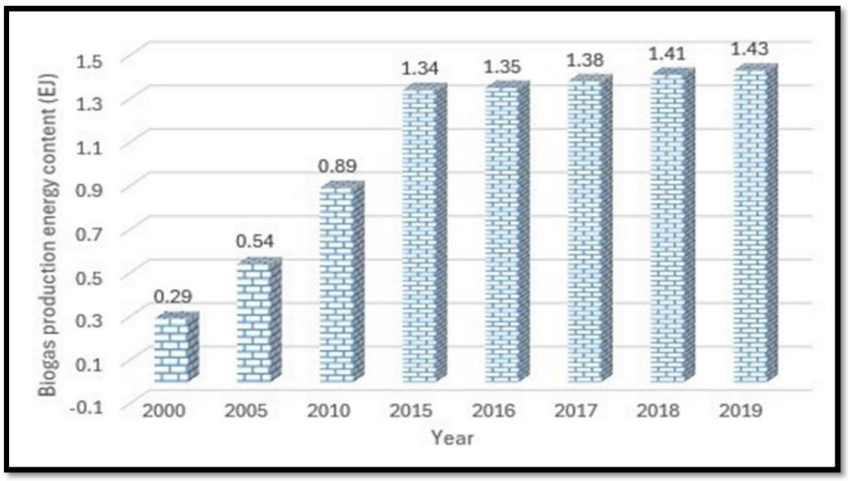


Figure 9. Energy content of global biogas production. Adapted from reference [86].

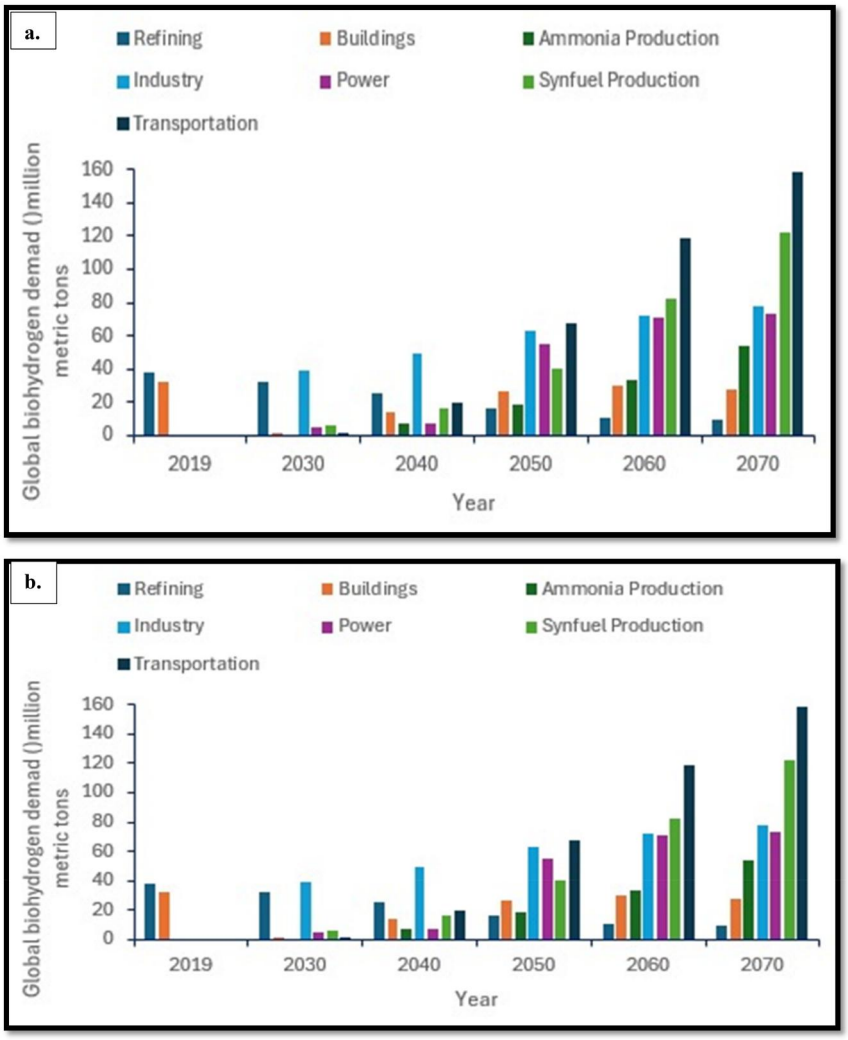


Figure 10. (a) Global production of biohydrogen, as reported in reference [87], and (b) Biohydrogen's market worth, as reported in reference [88].

fermentation offers sustainability advantages, challenges remain in improving yield and managing oxygen inhibition during the hydrogenase process. Nanotechnology has shown the potential to address these limitations by enhancing production. Figure 10(a) illustrates the global production levels of biohydrogen, showcasing trends and key growth phases. Figure 10(b) depicts the market worth of biohydrogen, highlighting its economic significance and potential for expansion. Researchers have demonstrated that nanoscale materials like Fe_3O_4 significantly improve biohydrogen production from feedstocks, such as sugarcane bagasse and potato peel waste, with Reddy et al. and Singhvi et al.

reporting increased biohydrogen yields from these sources. It has also been demonstrated that other nanomaterials, such as nickel, TiO_2, and iron-nickel composites, increase the synthesis of biohydrogen from substrates like glucose, sludge, and malate (Table 3).

Studies by Sunyoto et al. and Sharma and Melania revealed that nanoscale biochar can increase biohydrogen yields by ~30% when used with food waste and municipal solid waste as feedstocks by reducing ammonia inhibition and promoting volatile fatty acid production under mild conditions.

4.4. Bioethanol

Bioethanol is a highly utilized liquid biofuel, employed as a primary fuel and an additive in spark-ignition engines and various industrial applications, such as fuel cells, personal care products, pharmaceuticals, and chemical manufacturing. Bioethanol's high-octane number, low toxicity, and renewability make it an eco-friendly choice that reduces toxic emissions and greenhouse gases while promoting economic growth and job creation, especially in rural areas. As a result, bioethanol production rose from 24.10 billion gallons in 2010 to 29.5 billion in 2019. It is expected to reach 33.8 billion gallons by 2025 and 34.87 billion by 2030.

Nanotechnology has emerged as a key strategy for improving bioethanol production efficiency to meet growing demand. Magnetic nanoparticles, such as Fe_3O_4, have shown promise in enhancing bioethanol yields from various feedstocks, as demonstrated by Vijayalakshmi et al. In another study, MnO_2 nanoparticles were used by Cherian et al. to immobilize cellulase, increasing bioethanol output from sugarcane leaves. Figure 11 provides a detailed diagram of the biohydrogen production process, outlining the key stages and mechanisms involved in its generation. It visually explains the pathways and technologies utilized for efficient biohydrogen production.

Additional research by Kim et al. and Kim and Lee utilized methyl-functionalized silica (SiO_2–CH_3) and cobalt ferrite–silica ($CoFe_2O_4$@SiO_2–CH_3) nanoparticles, respectively, for syngas fermentation, achieving bioethanol yield improvements of up to 213% and reusability over five cycles. Sanusi et al. demonstrated NiO nanoparticles' efficacy by increasing bioethanol synthesis from potato peel waste by 65% compared to conventional catalysts. Integrating nanotechnology into biohydrogen and bioethanol production has proven to enhance efficiency and yield, supporting the development of these sustainable biofuels to meet future energy demands.

4.5. Other biofuels

In addition to the more popular biofuels like biodiesel, biogas, biohydrogen, and bioethanol, nanoparticles have been studied to create alternative biofuels like bio-oil, bio-butanol, and bio-jet fuels.

Table 3. Utilizing nanotechnology to produce biogas.

Nanoparticles	Substrate	Dosage of nanoparticles	Size (nm)	Impact on yield	Remarks	References
Zero valent iron (ZVI)	Sewage residue	5.5–11 mg/kg VS	101	11% increase	ZVI augmented methane production.	[89]
(ZVI)	Municipal sludge	900 mg/L	47	107 increase	Biogas contained reduced levels of H_2S.	[90]
(ZVI)	Waste sludge	12 mg/g TSS	130	125% increase	Efficient application of nano-ZVI for biogas generation.	[91]
CuO nanoparticles	Municipal waste-activated sludge	12–1000 mg/L	25–45	103% increase	CuO at the nanoscale increased microbial activity.	[92]
Fe_2O_3 nanoparticles	Sludge activated by waste	105 mg/g	125	115% increase	Increased the amount and quality of biogas.	[93]
Fe-Co-Cu TMNPs	Palm oil mill effluent (POME)	30 mg/L	57	11.11% increase	Enhanced anaerobic digestion (AD).	[94]
Fe/Cu nanoparticles	Straw corn	1.6 g/L	55	11.75% increase	Increased the output of biogas.	[95]
Co nanoparticles	Slurry of manure	1.1 mg/L	30	1.55× higher yield	Stimulated methanogenic bacterial activity.	[96]
Ni nanoparticles	Slurry of manure	1.75 mg/L	18	1.75× higher yield	Increased generation of biogas in general.	[96]
Co_3O_4 nanoparticles	Cow dung	2.55 mg/L	10–25	59% higher yield	Improved method for producing biogas.	[97]
Co_3O_4 nanoparticles	Dung from cows and water hyacinth	2.55 mg/L	10–25	28% higher yield	Enhanced effectiveness of co-digestion	[97]

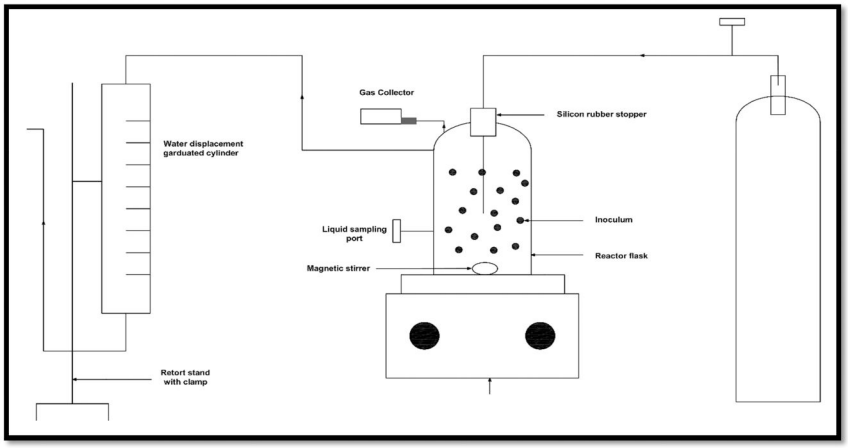


Figure 11. Diagram illustrating the process of biohydrogen production [98].

The demand for bio-jet fuel has grown along with air travel, leading to a rise in CO_2 emissions. The U.S. Energy Information Administration (EIA) projects that between 2018 and 2050, the demand for jet fuel would rise by almost 35%. A practical way to sustainably meet this need is with bio-jet fuels. The production of bio-jet fuel requires nanoparticles, as two research have shown: Bi et al. used palladium on carbon nanomaterials to produce bio-jet fuel from lignin, while Duan et al. used palladium-molybdenum phosphate nanoparticles to produce bio-jet fuel from oil. Biobutanol, a renewable and cleaner fuel option derived from biomass, is gaining interest as a substitute for fossil fuels due to its high energy content, reduced volatility, and suitability for internal combustion engines, as well as its utility in the production of cosmetics, paints, herbicides, and detergents. By 2015, global biobutanol production was around 4.39 MMT, with estimates suggesting a rise to 6.72 MMT (Table 4).

Nanotechnology is being employed to enhance biobutanol yields to meet this projected demand. For instance, Abel et al. used ZnO nanoparticles to increase the production and efficiency of converting molasses, sugarcane juice, and sorghum juice into biobutanol. Similarly, Hastuti et al. showed in their trials that oil palm empty fruit bunches' nanocellulosic fibers enhanced biobutanol yields relative to the control. Pyrolysis oil, often referred to as bio-oil, is a dense liquid fuel made from biomass pyrolysis, which includes forest and agricultural waste and contains chemicals including aldehydes, ketones, and carboxylic acids. Turbines and internal combustion engines use this biofuel to generate heat and power. Pd/C nanoparticles were used by Kunwar et al. to effectively convert feedstock and produce bio-oil from Chlorella microalgae, resulting in a 76% increase in yield.

Additional uses of nanotechnology in the manufacture of biofuels include using NiSn nanoparticles from alkaline media and magnetic nanoparticles from wheat straw for bioethanol synthesis. Additionally, nanotechnology has created green fuel by increasing conversion efficiency. Co-nanoparticles on nitrogen-rich carbon were employed by Du et al. to hydrotreat fatty acids in green diesel. On the other hand, Gousi et al. produced green diesel from sunflower oil using nickel-alumina nanoparticles. Bifunctional nanocatalysts have been made by combining various waste biomass types, including rice husks, corn stover, and sugarcane bagasse, with food and other waste biomass, thanks to recent developments in nanotechnology. These catalysts reduce catalyst costs, promote waste management, and lower biofuel prices. Combining different biomass wastes produces nanocatalysts with better selectivity, stability, and reusability. These spent catalysts are also biodegradable, allowing them to be repurposed as manure in agricultural applications.

4.6. Nanomaterials in biofuel separation and purification

Ensuring biofuel quality involves efficient separation and purification to remove impurities and by-products. Separation eliminates catalysts and other by-products, while purification removes contaminants to meet set standards. Techniques based on solubility, density, and physical state are often used, including filtration or magnetic fields for recovering heterogeneous catalysts and centrifugation for separating water, unreacted feedstock, and other residuals. Biodiesel purification may involve washing to remove water and contaminants through electrostatic interactions. Using nanomaterials in biofuel filtration and purification processes, such as membrane technologies, enhances product quality, is eco-friendly, conserves water, and meets quality standards. For instance, Sokač et al. report that

Table 4. Utilizing nanotechnology to produce biohydrogen.

Nanoparticles	Source of feedstock	Reaction conditions	Yield	Remarks	References
Fe_3O_4	Sugarcane bagasse	Anaerobic sludge with a pH of 5.5 and a temperature of 35 °C	1248 mL/L/day	70% more biohydrogen was produced.	[99]
Fe_3O_4	Waste from potato peels	Temperature = 35 °C; pH = 8.0; dose of catalyst = 65 mg/mL	165 mL	Increased the output of biohydrogen by 4.2 times.	[100]
TiO_2	Malate	pH = 8.0, temperature = 35 °C, and dosage of catalyst = 65 mg/mL	1850 mL/L	Biohydrogen output increased by 1.50 times.	[101]
Iron and nickel	Sludge	Anaerobic sludge; catalyst dosage = 38.0 mg/L; temperature = 38 °C; pH = 6.5	145.5 mL/g-VS	Achieved ~200% improvement.	[98]
Ni nanoparticles	Glucose	Size: 13.7 nm; pH = 5.5; temperature: 35–40 °C; catalyst dosage: 5.7 mg/L; anaerobic sludge	2.50 mol H_2/mol glucose	Enhanced biohydrogen yield by 23%.	[102]
Biochar	Food waste	pH = 7.0, temperature = 36 °C, dosage of catalyst = 35.5 g/L, and size = 26.0 nm	945.5 mL/L	Production increased by 31%.	[103]
Biochar	Solid waste in municipalities	pH = 5.7, temperature = 35 °C, dosage of catalyst = 13.0 g/L, and size = 21.0 nm	97.00 mL/g	32.5% more biohydrogen was produced.	[104]
Ni nanoparticles	Wastewater in industry	Anaerobic sludge; temperature = 50 °C; pH = 7.0; dosage of catalyst = 55 mg/L	25.00 mL/g	Yield of biohydrogen increased by 21%.	[105]
Ni-graphene	Wastewater in industry	Anaerobic sludge; temperature = 50 °C; pH = 6.5; dosage of catalyst = 65 mg/L	40.95 mL/g	Biohydrogen production increased by 105%.	[105]

nanomembranes removed about 91.48% of glycerol from crude biodiesel made from sunflower oil, resulting in cleaner, higher-quality biodiesel.

4.7. Regulatory considerations for nanomaterials

Given nanotechnology's vast potential across multiple sectors, well-defined policies and regulatory frameworks are essential to maximize benefits and address associated risks. Important international organizations like the Food and Agriculture Organization (FAO), World Health Organization (WHO), International Standards Organization (ISO), U.S. Environmental Protection Agency (EPA), and U.S. Food and Drug Administration (FDA) are in charge of establishing safety and environmental standards for nanomaterials. For example, the EU's REACH legislation specifies definitions and policies for engineered nanomaterials, while the OECD Harmonized Templates provide guidelines for testing, information gathering, and maintaining nanomaterial databases. Policies across jurisdictions help ensure safe nanomaterial synthesis, use, storage, and disposal, along with assessment protocols for toxicity, environmental impact, and occupational health safety. These rules facilitate the safe and uniform international trade of nanomaterials while preventing abuse, controlling dosage, and guaranteeing quality.

4.8. Nanotechnology's consequences and future in the production of biofuel

It is commonly acknowledged that biofuels are a sustainable and eco-friendly substitute for fossil fuels. However, issues including expensive costs, complicated production procedures, and restricted production capacity have made it difficult for them to be widely adopted. These limitations have driven researchers to explore innovative solutions, with nanotechnology emerging as a promising avenue for addressing these challenges. Better selectivity and milder production settings have demonstrated the ability to increase production efficiency, lower costs, and improve biofuel quality through nanotechnology, especially as catalysts.

These developments use biomass, such as food waste and agricultural residues, as raw materials to help generate bioenergy, recover resources, manage waste, and maintain environmental sanitation [55]. Nanomaterials are essential for increasing anaerobic digestion efficiency because they serve as catalysts for catalytic processes. Carbon-based nanoparticles accelerate the hydrolysis of organic matter, enhance microbial activity, and increase biogas and biohydrogen yield by boosting the population of methanogens and optimizing metabolic pathways [103]. Figure 12(a) presents the global bioethanol production levels, highlighting key trends and growth patterns. Figure 12(b) illustrates the market valuation trends of bioethanol, showing its economic

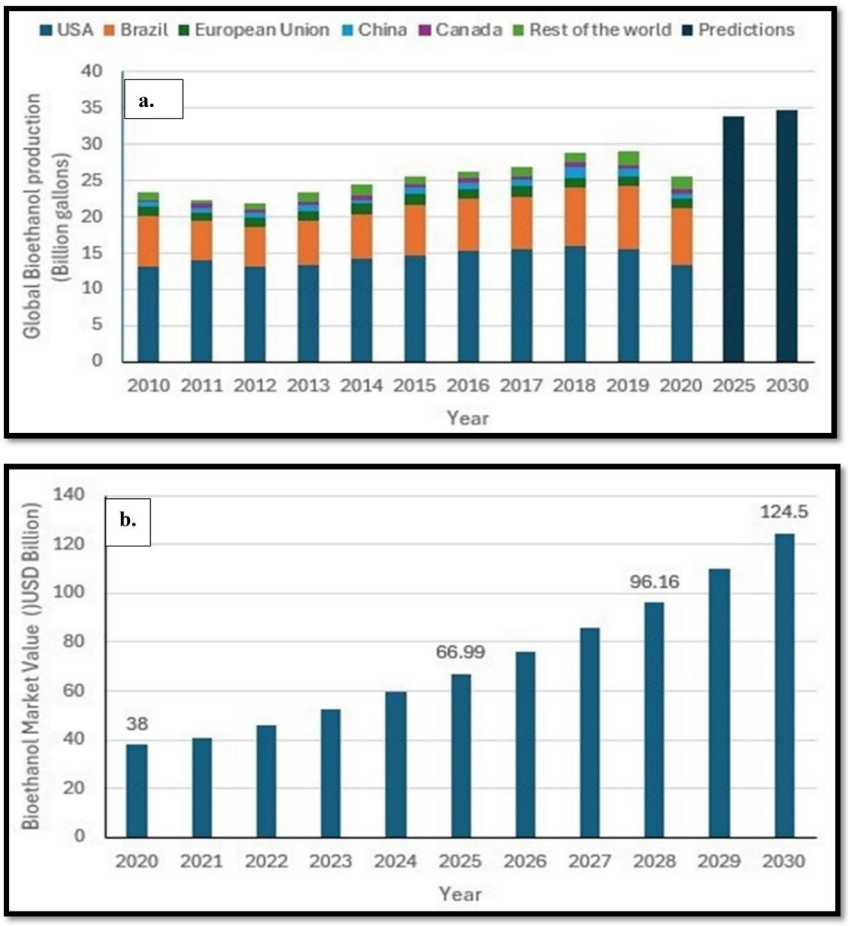


Figure 12. (a) Worldwide bioethanol production levels. Based on data from reference [106]. (b) Bioethanol market valuation trends. Based on data from reference [107].

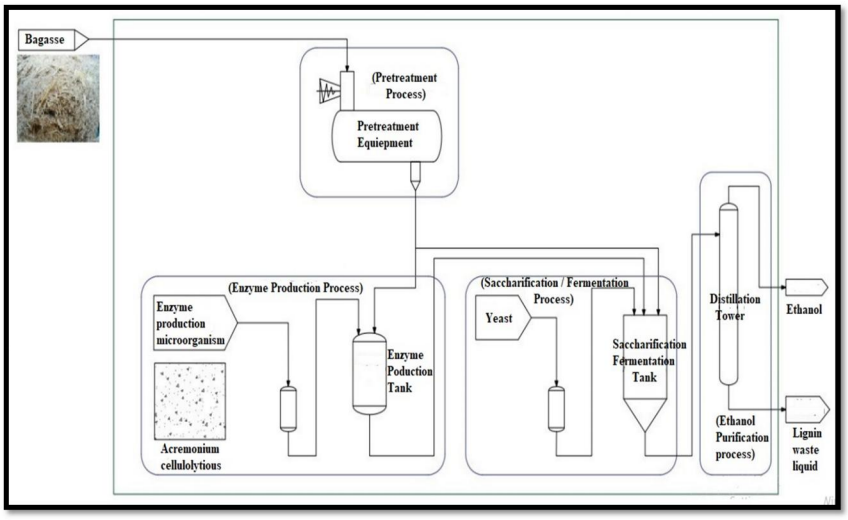


Figure 13. Diagram representing the process of bioethanol production [108].

trajectory over time. Figure 13 provides a bioethanol production process diagram detailing the steps and technologies for converting biomass into bioethanol. Notwithstanding these advantages, several obstacles remain to using nanomaterials in biofuel manufacture. High production costs, which include raw materials, energy, and labor, remain a barrier, particularly for physical and chemical synthesis techniques (Tables 5–7).

Moreover, specific nanomaterials, such as carbon nanotubes (CNTs), pose toxicity risks and contribute to respiratory disorders and environmental degradation, further complicating their application. To address these issues, low-cost metallic nanoparticles are being developed, ecologically friendly synthesis techniques are used, and waste materials like plastics and biomass are used to save costs. However, issues, such as scalability, commercialization, and environmental impact persist.

Table 5. Utilizing nanotechnology to produce bioethanol.

Nanoparticles	Feedstock	Conditions of reaction	Yield	Remarks	References
Fe_3O_4	Fiber of jute Bagasse from sugarcane Coir from coconuts Alginate of sodium Unbound cells	Time: 8 h; temperature: 55 °C; pH: 5.5	230 g/L 225 g/L 220 g/L 198 g/L 180 g/L	Metallic nanoparticles enhance bioethanol production from a range of feedstocks.	[109]
MnO_2	Sugarcane leaves	Catalyst size: 75 nm; temperature: 65 °C; pH: 5.0; duration: 2.3 h	22 g/L	Increased production of bioethanol.	[110]
SiO_2–CH_3	Syngas	Temperature = 37 °C; duration = 60 h; size of catalyst = 350 nm; dosage = 0.3 weight percent	0.4 g/L	Bioethanol yield improved by 166%.	[111]
$CoFe_2O_4$@SiO_2–CH_3	Syngas	Temperature = 37 °C; duration = 60 h; size of catalyst = 350 nm; dosage = 0.35 weight percent	0.5 g/L	Yield increased by 213%.	[45]
NiO	Potato peel waste	Temperature: 33.50 °C; pH: 4.9; duration: 35 h; dosage of catalyst: 0.1 weight percent	32.00 g/L	Product yield improved by 65%.	[112]
ZnO	Rice straw	Temperature: 25–35 °C; pH: 5.5–8; duration: 70 h	0.04 g/g	ZnO nanoparticles increase the generation of bioethanol.	[113]
ZnO/g-C_3N_4	Potato peels	Temperature: 35 °C; pH: 4.9; duration: 6 days; size of catalyst: 750 nm; dosage: 140 mg	Not specified (ns)	Production rose by 35.5%.	[114]
Silicon dioxide	Dairy yeast	Time = 35 h; temperature = 36 °C; pH = 6.5	155 g/L	Increased generation of bioethanol.	[115]

Table 6. Utilizing nanomaterials in additional biofuel manufacturing.

Nanoparticles	Source of feedstock	Reaction parameters	Product	Yield	Remarks	References
ZnO	Sorghum extract containing sugar	Time: 55 h; temperature: 95 °C	Biobutanol	12 g/L	ZnO nanoparticles encourage improved product development.	[116]
Nanofibers	Glucose from fresh potatoes	Temp = 95 °C; Time = 55 h	Biobutanol	35 g/L	Superior synthesis of biobutanol.	[117]
Pd	Microalgae chlorella	Temperature = 295 °C; Duration = 2.3 h; Heating Rate = 6 °C/min; Dosage of Catalyst = 4.6 weight percent	Bio-oil	75%	Pd nanomaterials boost bio-oil yield.	[118]
Magnetic nanoparticles	Wheat straw	Temp = 110 °C; Time = 1.3 h	Methanol	71.15 mmol/L	A higher yield of methanol was obtained.	[119]
Cobalt nanoparticles	Lipid	Time = 55 min; Temperature = 45 °C; Heating Rate = 6.5 °C/min	Green diesel	98.95%	Increased production of green diesel.	[120]
Nickel–alumina	Sunflower oil	Flow Rate = 95 mL/min; Temperature = 300 °C; H_2 Pressure = 35 bar	Green diesel	97%	Significant increase in green diesel production.	[121]

Table 7. Utilizing nanomaterials to separate biofuel.

Nanomaterials	Mixture	Outcome/remark	References
Multi-walled carbon nanotubes (MWCNT)	Unprocessed biodiesel	Glycerol and biodiesel were successfully separated.	[122]
Nanofiltration (NF) membranes	Fermented liquors and crude bioethanol	Achieved 98% pure bioethanol.	[123]
NF and forward osmosis (FO)	Crude bioethanol and xylose	Recovered bioethanol with high purity.	[124]
Nano-cellulose from bamboo	Unprocessed biodiesel	Glycerol and water are removed effectively.	[125]
NF membranes	Crude xylose and bioethanol	Produced bioethanol with high purity.	[126]

Current nanomaterial fabrication technologies are mainly limited to laboratory settings, requiring significant financial investment and technological advancements for real-world applications [127]. Concerns regarding the carbon neutrality of nanomaterial production processes and the appropriate disposal of waste nanoparticles exacerbate environmental and public health risks [128]. Health problems include heart disease, intestinal disturbances, and lung inflammation, which can result from exposure to CNTs and other nanoparticles.

Additionally, improper disposal of nanomaterials can contaminate soil and water systems, affecting ecosystems and agricultural productivity. Strategies

to address these risks include using proteins and surfactants to reduce toxicity, deploying nanosensors for early environmental contamination detection, and improving waste management practices [129]. Despite these concerns, nanotechnology holds immense potential to revolutionize biofuel production. Future research could focus on scaling up the synthesis of nanomaterials using low-cost, eco-friendly methods and exploring applications, such as enzyme immobilization, biomass pretreatment, and carbon capture. Interdisciplinary studies are needed to assess the life cycle of nanotechnology applications in biofuel production, address potential risks, and identify mitigation strategies. With continued advancements, nanotechnology could significantly enhance the efficiency and sustainability of biofuel production, addressing global energy needs and environmental concerns [129].

4.9. Conclusions

The global pursuit of clean, affordable, and sustainable energy has intensified efforts to transition from conventional fossil fuels to environmentally benign alternatives. Among these, biofuels present a viable solution for reducing greenhouse gas emissions, particularly CO_2, while promoting energy security and environmental sustainability. This review underscores the transformative potential of nanotechnology in enhancing biofuel production processes—including biodiesel, biogas, biohydrogen, and bioethanol—by improving feedstock conversion, optimizing reaction conditions, and increasing fuel yields. A comprehensive analysis of current literature reveals that nanomaterials, such as carbon nanotubes, graphene, metallic nanoparticles, and nanoscale biochar play critical roles in catalysis, purification, and process efficiency. The review further explores the influence of key operational parameters—temperature, pressure, pH, and synthesis methods—on the effectiveness of nanomaterial-assisted biofuel production. Additionally, biogenic nanomaterials derived from biomass and waste offer dual benefits: environmental remediation and resource recovery, aligning with circular economy principles.

Despite these advancements, several challenges remain, including the toxicity, non-biodegradability, and disposal of spent nanocatalysts, which may pose risks to ecosystems. However, emerging technologies, including green synthesis techniques and life cycle assessments, provide pathways to mitigate these risks. To fully harness the benefits of nanotechnology in biofuel applications, interdisciplinary research focusing on cost-effective, scalable, and sustainable solutions is essential. Looking ahead, integrating advanced tools, such as artificial intelligence, machine learning, and process optimization algorithms can revolutionize biofuel production by enhancing efficiency, reducing material waste, and minimizing processing time. Strong collaboration between academia, industry, and policymakers is crucial to translating research innovations into practical applications. Implementing supportive regulatory frameworks and incentivizing the adoption of nanotechnology in biofuel sectors will accelerate progress toward global renewable energy goals. Ultimately, biofuels, empowered by nanotechnology, will continue to play a pivotal role in the worldwide shift toward a cleaner and more sustainable energy future.

Acknowledgments

The authors would like to thank Dr. Amit Pal for his support in editing this research and the Delhi Technical University Administration for their valuable support.

Ethical approval

As authors, we would like to tell you that this is our original work, and this paper has not been submitted anywhere except to this journal.

Consent to participate

Not applicable.

Consent to publish

Not applicable.

Author contributions

All authors contributed to the study conception and design. Material preparation, data collection, and analysis were performed by Pradeep Kumar Meena. The first draft of the manuscript was written by Pradeep Kumar Meena and all authors commented on previous versions of the manuscript. All authors read and approved the final manuscript.

Disclosure statement

No potential conflict of interest was reported by the author(s).

Funding

Not applicable.

Notes on contributors

Dr. Ashish Goyal is an Associate Professor in the Department of Mechanical Engineering at Manipal University Jaipur, India. His area of research includes

Nanomaterials, Sustainable processes, Advanced Machining processes and Optimization techniques. His passion lies in developing and improving machining processes that can enhance precision, reduce costs, and increase efficiency, particularly through the integration of Sustainable approaches.

Dr. Pradeep Kumar Meena is a dedicated professional currently serving as a Technical Staff member at the Indian Institute of Technology (IIT) Delhi, India. He earned his Ph.D. in Mechanical Engineering from Delhi Technological University (DTU), New Delhi, and holds an M.Tech in Thermal Engineering from the College of Engineering Pune (COEP). Dr. Meena specializes in the fields of biogas, biofuels, biohydrogen, internal combustion (IC) engines, waste management, and thermal engineering. His contributions to these areas are noteworthy, with numerous research articles published in esteemed journals and presentations delivered at prestigious international conferences. In addition to his research endeavors, Dr. Meena has authored two books, highlighting his commitment to advancing knowledge and fostering innovation in sustainable energy and engineering. His work reflects a passion for developing solutions to global energy challenges, emphasizing sustainability and efficiency.

Dr. Sagar Dnyaneshwar Shelare is currently serving at Priyadarshini College of Engineering, Nagpur, India. He is also actively associated with multiple institutions under the Rayat Bahra Group, contributing to the advancement of research and the promotion of scholarly activities. His research interests span a diverse range of areas including biofuels, energy systems, mechanical engineering design, agricultural mechanization, solar energy applications, nanomaterials, welding technologies, and sustainable engineering practices.

Sujeet Kumar is a dedicated academician and engineer with a PhD in progress at Vivekananda Global University. He has extensive teaching experience, significant research contributions, and industry experience in energy engineering. His work includes innovations in solar Engineering and also reflecting his commitment to advancing mechanical engineering.

ORCID

Pradeep Kumar Meena http://orcid.org/0000-0003-0788-215X

Data availability statement

Not applicable.

References

1. United Nations. The sustainable development goals report; 2022.
2. IEA. World Energy Outlook 2022; 2022.
3. World Energy Council. World energy resources; 2016.
4. Acar C, Dincer I. Comparative assessment of hydrogen production methods from renewable and non-renewable sources. Int J Hydrogen Energy. 2014; 39(1):1–12. doi: 10.1016/j.ijhydene.2013.10.060.
5. Sanches-Pereira A, Lönnqvist T, Gómez MF, et al. Is natural gas a backup fuel against shortages of biogas or a threat to the Swedish vision of pursuing a vehicle fleet independent of fossil fuels? Renew Energy. 2015;83:1187–1199. doi: 10.1016/j.renene.2015.06.006.
6. Hussain A, Munir M, Khalid A, et al. Engineering biotic stress tolerance via CRISPR-Cas mediated genome editing in crop plants. Plant Stress. 2024;14: 100650. doi: 10.1016/j.stress.2024.100650.
7. Munir M, Saeed M, Ahmad M, et al. Cleaner production of biodiesel from novel non-edible seed oil (*Carthamus lanatus* L.) via highly reactive and recyclable green nano $CoWO_3$@rGO composite in context of green energy adaptation. Fuel. 2023;332:126265. doi: 10.1016/j.fuel.2022.126265.
8. Arshad S, Ahmad M, Munir M, et al. Assessing the potential of green CdO_2 nano-catalyst for the synthesis of biodiesel using non-edible seed oil of Malabar Ebony. Fuel. 2023;333:126492. doi: 10.1016/j.fuel.2022.126492.
9. Saravanan AP, Mathimani T, Deviram G, et al. Biofuel policy in India: a review of policy barriers in sustainable marketing of biofuel. J Clean Prod. 2018; 193:734–747. doi: 10.1016/j.jclepro.2018.05.033.
10. Malode SJ, Prabhu KK, Mascarenhas RJ, et al. Recent advances and viability in biofuel production. Energy Convers Manag X. 2021;10:100070. doi: 10.1016/j.ecmx.2020.100070.
11. Bhatia SK, Kim SH, Yoon JJ, et al. Current status and strategies for second generation biofuel production using microbial systems. Energy Convers Manag. 2017;148:1142–1156. doi: 10.1016/j.enconman.2017.06.073.
12. Biofuels. 2016:1–12.
13. Mathanker A, Pudasainee D, Kumar A, et al. Hydrothermal liquefaction of lignocellulosic biomass feedstock to produce biofuels: parametric study and products characterization. Fuel. 2020;271:117534. doi: 10.1016/j.fuel.2020.117534.
14. Meena PK, Pal A. A comprehensive review on methane enrichment in biogas through the purification process using biomass-based adsorbents. Biomass Convers Biorefin. 2024.
15. Saritha GNG, Anju T, Kumar A. Nanotechnology—big impact: how nanotechnology is changing the future of agriculture? J Agric Food Res. 2022;10: 100457. doi: 10.1016/j.jafr.2022.100457.
16. Sawaira, Alsaiari M, Ahmad M, et al. Efficient application of newly synthesized green Bi_2O_3 nanoparticles for sustainable biodiesel production via membrane reactor. Chemosphere. 2023;310:136838. doi: 10.1016/j.chemosphere.2022.136838.
17. Zeng J, Zeng H, Wang Z. Review on technology of making biofuel from food waste. Int J Energy Res. 2022;46(8):10301–10319. doi: 10.1002/er.7868.
18. Younas S, Rehman MU, Munir M, et al. Synthesis and evaluation of transdermal rosuvastatin-loaded ultradeformable vesicles: restoring the serum lipid profile in poloxamer 407-caused hyperlipidemia. J Drug Deliv Sci Technol. 2024;102:106330. doi: 10.1016/j.jddst.2024.106330.
19. Tayeb AH, Amini E, Ghasemi S, et al. Cellulose nanomaterials-binding properties and applications: a review. Molecules. 2018;23.
20. Chaudhry B, Ahmad M, Munir M, et al. Unleashing the power of non-edible oil seeds of *Ipomoea cairica*

for cleaner and sustainable biodiesel production using green molybdenum oxide (MoO_3) nano catalyst. Sustain Energy Technol Assess. 2024;65:103781. doi: 10.1016/j.seta.2024.103781.
21. Baig N, Kammakakam I, Falath W, et al. Nanomaterials: a review of synthesis methods, properties, recent progress, and challenges. Mater Adv. 2021;2(6):1821–1871. doi: 10.1039/D0MA00807A.
22. Shahbaz A, Hussain N, Saleem MZ, et al. Nanoparticles as stimulants for efficient generation of biofuels and renewables. Fuel. 2022;319:123724. doi: 10.1016/j.fuel.2022.123724.
23. Abusweireh RS, Rajamohan N, Vasseghian Y. Enhanced production of biodiesel using nanomaterials: a detailed review on the mechanism and influencing factors. Fuel. 2022;319:123862. doi: 10.1016/j.fuel.2022.123862.
24. Govarthanan M, Manikandan S, Subbaiya R, et al. Emerging trends and nanotechnology advances for sustainable biogas production from lignocellulosic waste biomass: a critical review. Fuel. 2022;312:122928. doi: 10.1016/j.fuel.2021.122928.
25. Markandan K, Chai WS. Perspectives on nanomaterials and nanotechnology for sustainable bioenergy generation. Materials. 2022;15(21):7769. doi: 10.3390/ma15217769.
26. Ganie AS, Bano S, Khan N, et al. Nanoremediation technologies for sustainable remediation of contaminated environments: recent advances and challenges. Chemosphere. 2021;275:130065. doi: 10.1016/j.chemosphere.2021.130065.
27. Bhat SA, Sher F, Hameed M, et al. Sustainable nanotechnology based wastewater treatment strategies: achievements, challenges and future perspectives. Chemosphere. 2022;288(Pt 3):132606. doi: 10.1016/j.chemosphere.2021.132606.
28. Munir M, Ahmad M, Abdullah Alsahli A, et al. Harnessing non-edible *Quercus incana* seeds for sustainable and clean biodiesel production using seed-derived green Al_2O_3 nanocatalyst. Sustain Energy Technol Assess. 2024;72:104025. doi: 10.1016/j.seta.2024.104025.
29. Lin L, Ying D, Chaitep S, et al. Biodiesel production from crude rice bran oil and properties as fuel. Appl Energy. 2009;86(5):681–688. doi: 10.1016/j.apenergy.2008.06.002.
30. Haris M, Hussain T, Mohamed HI, et al. Nanotechnology—a new frontier of nano-farming in agricultural and food production and its development. Sci Total Environ. 2023;857:159639. doi: 10.1016/j.scitotenv.2022.159639.
31. Das P, Manna S, Behera AK, et al. Current synthesis and characterization techniques for clay-based polymer nano-composites and its biomedical applications: a review. Environ Res. 2022;212(Pt E):113534. doi: 10.1016/j.envres.2022.113534.
32. Applications of nanomaterials for energy storage devices.
33. Irshad T, Saeed M, Munir M, et al. Excellent catalytic performance over reduced graphene-boosted novel nanoparticles for oxidative desulfurization of fuel oil. Nanotechnol Rev. 2024;13(1). doi: 10.1515/ntrev-2024-0116.
34. Abid N, Khan AM, Shujait S, et al. Synthesis of nanomaterials using various top-down and bottom-up approaches, influencing factors, advantages, and disadvantages: a review. Adv Colloid Interface Sci. 2022;300:102597. doi: 10.1016/j.cis.2021.102597.
35. Bibi H, Ahmad M, Osman AI, et al. Green synthesis of highly active and recyclable chromium oxide nanocatalyst for biodiesel production from novel nonedible oil seeds. GCB Bioenergy. 2024;16(5). doi: 10.1111/gcbb.13140.
36. Yang M, Jin H, Sun Z, et al. Monoelemental two-dimensional boron nanomaterials beyond theoretical simulations: from experimental preparation, functionalized modification to practical applications. Adv Colloid Interface Sci. 2022;304:102669. doi: 10.1016/j.cis.2022.102669.
37. Yao H, Li L, Li W, et al. Application of nanomaterials in waterborne coatings: a review. Resour Chem Mater. 2022;1(2):184–200. doi: 10.1016/j.recm.2022.06.004.
38. Ameen M, Zafar M, Ahmad M, et al. Cleaner biofuel production via process parametric optimization of nonedible feedstock in a membrane reactor using a titania-based heterogeneous nanocatalyst: an aid to sustainable energy development. Membranes. 2023;13(12). doi: 10.3390/membranes13120889.
39. Hao Z, Li N, Cao H, et al. Modified Ag nanoparticles on the regular array structure to improve the optical properties. J Lumin. 2022;243:118684. doi: 10.1016/j.jlumin.2021.118684.
40. Akhtar MT, Ahmad M, Asma M, et al. Efficient production of wild and non-edible *Brassica juncea* (L.) Czern. seed oil into high-quality biodiesel via novel, green and recyclable $NiSO_4$ nano-catalyst. Sustainability. 2022;14(16):10188. doi: 10.3390/su141610188.
41. Ibrahim SI, Ali AH, Hafidh SA, et al. Stability and thermal conductivity of different nano-composite material prepared for thermal energy storage applications. S Afr J Chem Eng. 2022;39:72–89. doi: 10.1016/j.sajce.2021.11.010.
42. Jabeen M, Munir M, Abbas MM, et al. Sustainable production of biodiesel from novel and non-edible *Ailanthus altissima* (Mill.) seed oil from green and recyclable potassium hydroxide activated ailanthus cake and cadmium sulfide catalyst. Sustainability. 2022;14(17):10962. doi: 10.3390/su141710962.
43. Reddy SNK, Wani MM. A comprehensive review on effects of nanoparticles-antioxidant additives-biodiesel blends on performance and emissions of diesel engine. Appl Sci Eng Progress. 2020;13. doi: 10.14416/J.ASEP.2020.06.002.
44. Ndlwana L, Raleie N, Dimpe KM, et al. Sustainable hydrothermal and solvothermal synthesis of advanced carbon materials in multidimensional applications: a review. Materials. 2021;14(17):5094. doi: 10.3390/ma14175094.
45. Kim YK, Lee H. Use of magnetic nanoparticles to enhance bioethanol production in syngas fermentation. Bioresour Technol. 2016;204:139–144. doi: 10.1016/j.biortech.2016.01.001.
46. Zhu Y, Blackman C, Zhou P, et al. Facile synthesis of Ag nanoparticles-decorated WO_3 nanorods and their application in O_2 sensing. J Alloys Compd. 2023;936:167930. doi: 10.1016/j.jallcom.2022.167930.
47. Amadi EV, Venkataraman A, Papadopoulos C. Nanoscale self-assembly: concepts, applications and challenges. Nanotechnology. 2022;33(13):132001. doi: 10.1088/1361-6528/ac3f54.

48. Pandit C, Roy A, Ghotekar S, et al. Biological agents for synthesis of nanoparticles and their applications. J King Saud Univ Sci. 2022;34(3):101869. doi: 10.1016/j.jksus.2022.101869.
49. Barhoum A, García-Betancourt ML, Jeevanandam J, et al. Review on natural, incidental, bioinspired, and engineered nanomaterials: history, definitions, classifications, synthesis, properties, market, toxicities, risks, and regulations. Nanomaterials. 2022;12(2). doi: 10.3390/nano12020177.
50. Maduraiveeran G, Jin W. Carbon nanomaterials: synthesis, properties and applications in electrochemical sensors and energy conversion systems. Mater Sci Eng B. 2021;272:115341. doi: 10.1016/j.mseb.2021.115341.
51. Karki S, Gohain MB, Yadav D, et al. Nanocomposite and bio-nanocomposite polymeric materials/membranes development in energy and medical sector: a review. Int J Biol Macromol. 2021;193(Pt B):2121–2139. doi: 10.1016/j.ijbiomac.2021.11.044.
52. Arya I, Poona A, Dikshit PK, et al. Current trends and future prospects of nanotechnology in biofuel production. Catalysts. 2021;11(11):1308. doi: 10.3390/catal11111308.
53. Rai M, Dos Santos JC, Soler MF, et al. Strategic role of nanotechnology for production of bioethanol and biodiesel. Nanotechnol Rev. 2016;5(2):231–250. doi: 10.1515/ntrev-2015-0069.
54. Amruth Maroju P, Ganesan R, Ray Dutta J. Biofuel generation from food waste through immobilized enzymes on magnetic nanoparticles. Mater Today Proc. 2023;72:62–66. doi: 10.1016/j.matpr.2022.05.555.
55. Awogbemi O, Kallon DVV. Achieving affordable and clean energy through conversion of waste plastic to liquid fuel. J Inst Energy. 2023;106:101154. doi: 10.1016/j.joei.2022.101154.
56. Sharma S, Saxena V, Baranwal A, et al. Engineered nanoporous materials mediated heterogeneous catalysts and their implications in biodiesel production. Mater Sci Energy Technol. 2018;1(1):11–21. doi: 10.1016/j.mset.2018.05.002.
57. Mukhortova YR, Pryadko AS, Chernozem RV, et al. Fabrication and characterization of a magnetic biocomposite of magnetite nanoparticles and reduced graphene oxide for biomedical applications. Nano-Struct Nano-Objects. 2022;29:100843. doi: 10.1016/j.nanoso.2022.100843.
58. Khan RS, Rather AH, Wani TU, et al. Recent trends using natural polymeric nanofibers as supports for enzyme immobilization and catalysis. Biotechnol Bioeng. 2023;120(1):22–40. doi: 10.1002/bit.28246.
59. Meena PK, Pal A, Gautam S. Zone-wise biogas potential in India: fundamentals, challenges, and policy considerations. Environ Sci Pollut Res. 2023;31(2):1841–1862. doi: 10.1007/s11356-023-31328-4.
60. Zhang Z, Li X, Sang S, et al. Preparation, properties and interaction of curcumin loaded zein/HP-β-CD nanoparticles based on electrostatic interactions by antisolvent co-precipitation. Food Chem. 2023;403:134344. doi: 10.1016/j.foodchem.2022.134344.
61. Jan H, Gul R, Andleeb A, et al. A detailed review on biosynthesis of platinum nanoparticles (PtNPs), their potential antimicrobial and biomedical applications. J Saudi Chem Soc. 2021;25(8):101297. doi: 10.1016/j.jscs.2021.101297.
62. Meena PK, Pal A, Samsher. Characterization, utility, and interrelationship of household organic waste generation in academic campus for the production of biogas and compost: a case study. Environ Dev Sustain. 2022;26(1):2687–2713. doi: 10.1007/s10668-022-02747-z.
63. Awogbemi O, Kallon DV, Von Aigbodion VS, et al. Property determination, FA composition and NMR characterization of palm oil, used palm oil and their methyl esters. Processes. 2021;10(1):11. doi: 10.3390/pr10010011.
64. Meena PK, Awale SD, Kumar S, et al. Thermochemical conversion of agricultural residue for the production of hydrogen, methane, and biofuels: a comprehensive overview. Ind Crops Prod. 2024;221.
65. Ahmed A, Usman M, Ji Z, et al. Nature-inspired biogenic synthesis of silver nanoparticles for antibacterial applications. Mater Today Chem. 2023;27.
66. Wu Y, Xia C, Cao J, et al. A review on current scenario of Nanocatalysts in biofuel production and potential of organic and inorganic nanoparticles in biohydrogen production. Fuel. 2023;338:127216. doi: 10.1016/j.fuel.2022.127216.
67. Javaid M, Haleem A, Singh RP, et al. Exploring the potential of nanosensors: a brief overview. Sensors Int. 2021;2:100130. doi: 10.1016/j.sintl.2021.100130.
68. Araújo RG, González-González RB, Martinez-Ruiz M, et al. Expanding the scope of nanobiocatalysis and nanosensing: applications of nanomaterial constructs. ACS Omega. 2022;7(37):32863–32876. doi: 10.1021/acsomega.2c03155.
69. Sarkar RD, Singh HB, Kalita MC. Enhanced lipid accumulation in microalgae through nanoparticle-mediated approach, for biodiesel production: a mini-review. Heliyon. 2021;7(9):e08057. doi: 10.1016/j.heliyon.2021.e08057.
70. Srivastava N, Srivastava M, Malhotra BD, et al. Nanoengineered cellulosic biohydrogen production via dark fermentation: a novel approach. Biotechnol Adv. 2019;37(6):107384. doi: 10.1016/j.biotechadv.2019.04.006.
71. Ratchnashree SR, Karmegam N, Selvam M, et al. Advanced technologies for the determination of quantitative structure-activity relationships and degradation efficiency of micropollutants and their removal in water—a review. Sci Total Environ. 2023;904:166563. doi: 10.1016/j.scitotenv.2023.166563.
72. Krishnan RY, Manikandan S, Subbaiya R, et al. Origin, transport and ecological risk assessment of illicit drugs in the environment—a review. Chemosphere. 2023;311(Pt 2):137091. doi: 10.1016/j.chemosphere.2022.137091.
73. Keerthana Devi M, Manikandan S, Oviyapriya M, et al. Recent advances in biogas production using agro-industrial waste: a comprehensive review outlook of techno-economic analysis. Bioresour Technol. 2022;363:127871. doi: 10.1016/j.biortech.2022.127871.
74. Cholapandian K, Gurunathan B, Rajendran N. Investigation of CaO nanocatalyst synthesized from *Acalypha indica* leaves and its application in biodiesel production using waste cooking oil. Fuel. 2022;312:122958. doi: 10.1016/j.fuel.2021.122958.
75. Jayaraman J, Dawn SS, Appavu P, et al. Production of biodiesel from waste cooking oil utilizing zinc oxide nanoparticles combined with tungsto phosphoric acid as a catalyst and its performance on a CI engine. Fuel. 2022;329:125411. doi: 10.1016/j.fuel.2022.125411.
76. Hadi Jume B, Joolaei Ahranjani P, Farshineh Saei S, et al. Strontium titanium trioxide doped magnetic graphene oxide as a nanocatalyst for biodiesel production from waste cooking oil. Sustain Energy

Technol Assess. 2022;54:102619. doi: 10.1016/j.seta.2022.102619.
77. Hosseini S, Moradi GR, Bahrami K. Synthesis of a novel stabilized basic ionic liquid through immobilization on boehmite nanoparticles: a robust nanocatalyst for biodiesel production from soybean oil. Renew Energy. 2019;138:70–78. doi: 10.1016/j.renene.2019.01.037.
78. De A, Boxi SS. Application of Cu impregnated TiO_2 as a heterogeneous nanocatalyst for the production of biodiesel from palm oil. Fuel. 2020;265:117019. doi: 10.1016/j.fuel.2020.117019.
79. Gohar Khan S, Hassan M, Anwar M, et al. Mussel shell based CaO nano-catalyst doped with praseodymium to enhance biodiesel production from castor oil. Fuel. 2022;330:125480. doi: 10.1016/j.fuel.2022.125480.
80. Bharti P, Singh B, Dey RK. Process optimization of biodiesel production catalyzed by CaO nanocatalyst using response surface methodology. J Nanostruct Chem. 2019;9(4):269–280. doi: 10.1007/s40097-019-00317-w.
81. Zhu Z, Liu Y, Cong W, et al. Soybean biodiesel production using synergistic CaO/Ag nano catalyst: process optimization, kinetic study, and economic evaluation. Ind Crops Prod. 2021;166:113479. doi: 10.1016/j.indcrop.2021.113479.
82. Gurusamy S, Kulanthaisamy MR, Hari DG, et al. Environmental friendly synthesis of TiO_2-ZnO nanocomposite catalyst and silver nanomaterials for the enhanced production of biodiesel from *Ulva lactuca* seaweed and potential antimicrobial properties against the microbial pathogens. J Photochem Photobiol B. 2019;193:118–130. doi: 10.1016/j.jphotobiol.2019.02.011.
83. Mazaheri H, Ong HC, Masjuki HH, et al. Rice bran oil based biodiesel production using calcium oxide catalyst derived from *Chicoreus brunneus* shell. Energy. 2018;144:10–19. doi: 10.1016/j.energy.2017.11.073.
84. Guo M, Jiang W, Chen C, et al. Process optimization of biodiesel production from waste cooking oil by esterification of free fatty acids using La^{3+}/ZnO-TiO_2 photocatalyst. Energy Convers Manag. 2021;229:113745. doi: 10.1016/j.enconman.2020.113745.
85. Meena PK, Pal A, Gautam S. Impact of tumbling on production of biomethane from household waste. Environ Sci Pollut Res. 2024. doi: 10.1007/s11356-024-32049-y.
86. Britz W, Delzeit R. The impact of German biogas production on European and global agricultural markets, land use and the environment. Energy Policy. 2013;62:1268–1275. doi: 10.1016/j.enpol.2013.06.123.
87. Tian H, Li J, Yan M, et al. Organic waste to biohydrogen: a critical review from technological development and environmental impact analysis perspective. Appl Energy. 2019;256:113961. doi: 10.1016/j.apenergy.2019.113961.
88. Kim HH, Saha S, Hwang JH, et al. Integrative biohydrogen- and biomethane-producing bioprocesses for comprehensive production of biohythane. Bioresour Technol. 2022;365:128145. doi: 10.1016/j.biortech.2022.128145.
89. Liu Y, Zhang Y, Ni BJ. Zero valent iron simultaneously enhances methane production and sulfate reduction in anaerobic granular sludge reactors. Water Res. 2015;75:292–300. doi: 10.1016/j.watres.2015.02.056.
90. Amen TWM, Eljamal O, Khalil AME, et al. Biochemical methane potential enhancement of domestic sludge digestion by adding pristine iron nanoparticles and iron nanoparticles coated zeolite compositions. J Environ Chem Eng. 2017;5(5):5002–5013. doi: 10.1016/j.jece.2017.09.030.
91. Wang T, Zhang D, Dai L, et al. Effects of metal nanoparticles on methane production from waste-activated sludge and microorganism community shift in anaerobic granular sludge. Sci Rep. 2016;6:25857. doi: 10.1038/srep25857.
92. Ünşar EK, Çığgın AS, Erdem A, et al. Long and short term impacts of CuO, Ag and CeO_2 nanoparticles on anaerobic digestion of municipal waste activated sludge. Environ Sci Process Impacts. 2016;18(2):277–288. doi: 10.1039/c5em00466g.
93. Casals E, Barrena R, García A, et al. Programmed iron oxide nanoparticles disintegration in anaerobic digesters boosts biogas production. Small. 2014;10(14):2801–2808. doi: 10.1002/smll.201303703.
94. Jadhav P, Khalid Z, Bin Krishnan S, et al. Application of iron-cobalt-copper (Fe-Co–Cu) trimetallic nanoparticles on anaerobic digestion (AD) for biogas production. Biomass Convers Biorefin. 2024;14(6):7591–7601. doi: 10.1007/s13399-022-02825-2.
95. Jeevanandam J, Barhoum A, Chan YS, et al. Review on nanoparticles and nanostructured materials: history, sources, toxicity and regulations. Beilstein J Nanotechnol. 2018;9:1050–1074. doi: 10.3762/bjnano.9.98.
96. Abdelsalam E, Samer M, Attia YA, et al. Effects of Co and Ni nanoparticles on biogas and methane production from anaerobic digestion of slurry. Energy Convers Manag. 2017;141:108–119. doi: 10.1016/j.enconman.2016.05.051.
97. Ali SS, Zagklis D, Kornaros M, et al. Cobalt oxide nanoparticles as a new strategy for enhancing methane production from anaerobic digestion of noxious aquatic weeds. Bioresour Technol. 2023;368:128308. doi: 10.1016/j.biortech.2022.128308.
98. Taherdanak M, Zilouei H, Karimi K. Investigating the effects of iron and nickel nanoparticles on dark hydrogen fermentation from starch using central composite design. Int J Hydrogen Energy. 2015;40(38):12956–12963. doi: 10.1016/j.ijhydene.2015.08.004.
99. Reddy K, Nasr M, Kumari S, et al. Biohydrogen production from sugarcane bagasse hydrolysate: effects of pH, S/X, Fe^{2+}, and magnetite nanoparticles. Environ Sci Pollut Res Int. 2017;24(9):8790–8804. doi: 10.1007/s11356-017-8560-1.
100. Singhvi M, Maharjan A, Thapa A, et al. Nanoparticle-associated single step hydrogen fermentation for the conversion of starch potato waste biomass by thermophilic *Parageobacillus thermoglucosidasius*. Bioresour Technol. 2021;337:125490. doi: 10.1016/j.biortech.2021.125490.
101. Pandey A, Gupta K, Pandey A. Effect of nanosized TiO_2 on photofermentation by *Rhodobacter sphaeroides* NMBL-02. Biomass Bioenergy. 2015;72:273–279. doi: 10.1016/j.biombioe.2014.10.021.
102. Mullai P, Yogeswari MK, Sridevi K. Optimisation and enhancement of biohydrogen production using nickel nanoparticles—a novel approach. Bioresour

Technol. 2013;141:212–219. doi: 10.1016/j.biortech.2013.03.082.
103. Sunyoto NMS, Zhu M, Zhang Z, et al. Effect of biochar addition on hydrogen and methane production in two-phase anaerobic digestion of aqueous carbohydrates food waste. Bioresour Technol. 2016;219:29–36. doi: 10.1016/j.biortech.2016.07.089.
104. Sharma P, Melkania U. Biochar-enhanced hydrogen production from organic fraction of municipal solid waste using co-culture of *Enterobacter aerogenes* and *E. coli*. Int J Hydrogen Energy. 2017;42(30):18865–18874. doi: 10.1016/j.ijhydene.2017.06.171.
105. Elreedy A, Ibrahim E, Hassan N, et al. Nickel-graphene nanocomposite as a novel supplement for enhancement of biohydrogen production from industrial wastewater containing mono-ethylene glycol. Energy Convers Manag. 2017;140:133–144. doi: 10.1016/j.enconman.2017.02.080.
106. Chintagunta AD, Jacob S, Banerjee R. Integrated bioethanol and biomanure production from potato waste. Waste Manag. 2016;49:320–325. doi: 10.1016/j.wasman.2015.08.010.
107. Chintagunta AD, Ray S, Banerjee R. An integrated bioprocess for bioethanol and biomanure production from pineapple leaf waste. J Clean Prod. 2017;165:1508–1516. doi: 10.1016/j.jclepro.2017.07.179.
108. Lopez-Hidalgo AM, Sánchez A, De León-Rodríguez A. Simultaneous production of bioethanol and biohydrogen by *Escherichia coli* WDHL using wheat straw hydrolysate as substrate. Fuel. 2017;188:19–27. doi: 10.1016/j.fuel.2016.10.022.
109. Vijayalakshmi S, Govindarajan M, Al-Mulahim N, et al. Cellulase immobilized magnetic nanoparticles for green energy production from *Allamanda schottii* L: sustainability research in waste recycling. Saudi J Biol Sci. 2021;28(1):901–910. doi: 10.1016/j.sjbs.2020.11.034.
110. Cherian E, Dharmendirakumar M, Baskar G. Immobilization of cellulase onto MnO_2 nanoparticles for bioethanol production by enhanced hydrolysis of agricultural waste. Chinese J Catal. 2015;36(8):1223–1229. doi: 10.1016/S1872-2067(15)60906-8.
111. Kim YK, Park SE, Lee H, et al. Enhancement of bioethanol production in syngas fermentation with *Clostridium ljungdahlii* using nanoparticles. Bioresour Technol. 2014;159:446–450. doi: 10.1016/j.biortech.2014.03.046.
112. Sanusi IA, Suinyuy TN, Lateef A, et al. Effect of nickel oxide nanoparticles on bioethanol production: process optimization, kinetic and metabolic studies. Process Biochem. 2020;92:386–400. doi: 10.1016/j.procbio.2020.01.029.
113. Gupta K, Chundawat TS. Zinc oxide nanoparticles synthesized using *Fusarium oxysporum* to enhance bioethanol production from rice-straw. Biomass Bioenergy. 2020;143:105840. doi: 10.1016/j.biombioe.2020.105840.
114. Attia YA, Abdelsalam E, Saeed S, et al. Bioethanol production from potato peels using *Saccharomyces cerevisiae* treated with ZnO and ZnO/g-C_3N_4 nanomaterials. Egypt J Chem. 2022. doi: 10.21608/ejchem.2022.118978.5351.
115. Beniwal A, Saini P, Kokkiligadda A, et al. Use of silicon dioxide nanoparticles for β-galactosidase immobilization and modulated ethanol production by co-immobilized *K. marxianus* and *S. cerevisiae* in deproteinized cheese whey. LWT. 2018;87:553–561. doi: 10.1016/j.lwt.2017.09.028.
116. Abel S, Tesfaye JL, Gudata L, et al. Biobutanol preparation through sugar-rich biomass by *Clostridium saccharoperbutylacetonicum* conversion using ZnO nanoparticle catalyst. Biomass Convers Biorefin. 2022. doi: 10.1007/s13399-022-02424-1.
117. Gousi M, Kordouli E, Bourikas K, et al. Green diesel production over nickel-alumina nanostructured catalysts promoted by copper. Energies. 2020;13(14):3707. doi: 10.3390/en13143707.
118. Kunwar B, Deilami SD, Macaskie LE, et al. Nanoparticles of Pd supported on bacterial biomass for hydroprocessing crude bio-oil. Fuel. 2017;209:449–456. doi: 10.1016/j.fuel.2017.08.007.
119. Patel SKS, Gupta RK, Kalia VC, et al. Synthetic design of methanotroph co-cultures and their immobilization within polymers containing magnetic nanoparticles to enhance methanol production from wheat straw-based biogas. Bioresour Technol. 2022;364:128032. doi: 10.1016/j.biortech.2022.128032.
120. Miandad R, Nizami AS, Rehan M, et al. Influence of temperature and reaction time on the conversion of polystyrene waste to pyrolysis liquid oil. Waste Manag. 2016;58:250–259. doi: 10.1016/j.wasman.2016.09.023.
121. Du Y, Wang F, Xia X, et al. MOF-derived Co nanoparticle on nitrogen-rich carbon for fatty acid hydrotreatment into green diesel. Renew Energy. 2022;198:246–253. doi: 10.1016/j.renene.2022.08.019.
122. Chingakham C, Juraij K, Sujith A, et al. High strength-hydrophobic MWCNT reinforced polyurethane electrospun membrane for purification of crude biodiesel. J Polym Res. 2021;28(7). doi: 10.1007/s10965-021-02602-1.
123. Brás T, Fernandes MC, Santos JLC, et al. Recovering bioethanol from olive bagasse fermentation by nanofiltration. Desalination Water Treat. 2013;51(22–24):4333–4342. doi: 10.1080/19443994.2013.770216.
124. Shibuya M, Sasaki K, Tanaka Y, et al. Development of combined nanofiltration and forward osmosis process for production of ethanol from pretreated rice straw. Bioresour Technol. 2017;235:405–410. doi: 10.1016/j.biortech.2017.03.158.
125. Chingakham C, Manaf O, Sujith A, et al. Hydrophobic nano-bamboo fiber-reinforced acrylonitrile butadiene styrene electrospun membrane for the filtration of crude biodiesel. Appl Nanosci. 2020;10(3):795–806. doi: 10.1007/s13204-019-01140-z.
126. Sasaki K, Sasaki D, Sakihama Y, et al. Ethanol fermentation by xylose-assimilating *Saccharomyces cerevisiae* using sugars in a rice straw liquid hydrolysate concentrated by nanofiltration. Bioresour Technol. 2013;147:84–88. doi: 10.1016/j.biortech.2013.07.091.
127. Manikandan S, Vickram S, Sirohi R, et al. Critical review of biochemical pathways to transformation of waste and biomass into bioenergy. Bioresour Technol. 2023;372:128679. doi: 10.1016/j.biortech.2023.128679.
128. Krishnan RY, Manikandan S, Subbaiya R, et al. Recent approaches and advanced wastewater treatment technologies for mitigating emerging microplastics contamination—a critical review. Sci Total Environ. 2023;858:159681. doi: 10.1016/j.scitotenv.2022.159681.
129. Ameen F, Alsamhary K, Alabdullatif JA, et al. A review on metal-based nanoparticles and their toxicity to beneficial soil bacteria and fungi. Ecotoxicol Environ Saf. 2021;213:112027. doi: 10.1016/j.ecoenv.2021.112027.

2025 Fourth International Conference on Smart Technologies, Communication and Robotics (STCR) | 979-8-3503-5753-0/25/$31.00 ©2025 IEEE | DOI: 10.1109/STCR62650.2025.11019368

Advancing Smart Farming with UAV-Based Deep Learning for Proactive Wheat Disease Management

Rohan Thakur
Department of Electronics and Communication Engineering
Delhi Technological University
Delhi, India
rohanxthakur@gmail.com

Ronald Ekka
Department of Electronics and Communication Engineering Delhi Technological University
Delhi, India
ronaldekka70@gmail.com

Yash Kumar
Department of Electronics and Communication Engineering
Delhi Technological University
Delhi, India
yssh01212@gmail.com

Poornima Mittal
Department of Electronics and Communication Engineering Delhi Technological University
Delhi, India
poornimamittal@dtu.ac.in

***Abstract*—Wheat diseases are a huge risk to the food security of the world and can result in extreme yield loss in case they are not diagnosed and treated at an early stage. Previously, disease identification required manual scanning, which is labor intensive, time-consuming, and inaccurate. The project shows a real-time, scalable, and automated wheat disease detection system with Unmanned Aerial Vehicles (UAVs), multispectral sensing, and deep learning. The system described above is unlike the conventional ground-based methods, the model uses aerial imagery collected using UAVs in conjunction with deep Convolutional Neural Networks (CNNs), specifically fine-tuned VGG19, to enhance scalability and accuracy. Grad-CAM visualization is also integrated to make predictions from models interpretable by farmers. In addition, the system incorporates real-time processing as well as IoT for automated early disease intervention alerting. The combination of large-scale monitoring, high-accuracy disease detection, and farmer-friendly deployment, this project fills important gaps in existing research with a pioneering, field-application solution for precision agriculture. Experimental results show high detection accuracy, proving its robustness under varying environmental conditions. This technology allows farmers to obtain real-time information, enabling timely disease management and sustainable wheat production.**

Keywords*— *Unmanned Aerial Vehicles (UAVs), Unmanned Aerial Vehicles (UAVs), Wheat diseases.

I. INTRODUCTION

Wheat is among the globe's most critical staple crops, ensuring food security for millions of individuals. But wheat diseases can lead to heavy yield losses, affecting farmers and world food chains. Conventional disease detection techniques depend greatly on human field observations, which are labor-intensive, time-consuming, and susceptible to human error. These conventional approaches are inadequate for large-scale farms where early detection is crucial for preventing disease outbreaks. In Fig. 1. (a) Crown and Root Rot – a fungal infection affecting the roots and base of the stem, leading to plant wilting and reduced yield. In Fig. 1. (b) Wheat Loose Smut – a fungal disease that causes grain heads to appear black and powdery, reducing seed viability. In Fig. 1. (c) Leaf Rust – a common fungal infection causing orange-brown pustules on leaves, leading to reduced photosynthesis and yield loss. In Fig. 1. (d)Healthy Wheat – properly classified to distinguish disease- free wheat plants from infected ones.



(a)



(b)



(c)

979-8-3503-5753-0/25/$31.00 ©2025 IEEE

Authorized licensed use limited to: DELHI TECHNICAL UNIV. Downloaded on June 16,2025 at 05:09:27 UTC from IEEE Xplore. Restrictions apply.



(d)

Fig.1. (a)Crown and Root Rot, (b)Leaf Rust, (c)Wheat Loose Smut, (d)Healthy Wheat.

To address these challenges, recent advancements in computer vision, deep learning, and remote sensing have paved the way for automated disease detection systems. While several studies have leveraged image-based classification models, many suffer from limited scalability, lack of real-time processing, and poor generalization to real-world conditions. Moreover, most existing models rely solely on ground-based RGB images [14], which do not capture the full spectrum of disease symptoms visible in different light wavelengths. This work introduces a novel wheat disease detection framework that integrates Unmanned Aerial Vehicles (UAVs), multispectral imaging, and deep learning to enhance accuracy, scalability, and real-time disease monitoring. Using UAVs, large fields can be covered effectively, with high-resolution aerial photography that gives a larger and more comprehensive dataset for the identification of disease. The model is constructed based on a fine-tuned VGG19 Convolutional Neural Network (CNN) [8], optimized for high-accuracy classification of wheat disease. Grad CAM visualization is also integrated to make the model more interpretable, with predictions becoming more transparent to farmers and agronomists. This model gives an elaborate overview of design, implementation, and evaluation of the suggested system. The following sections cover existing literature, methodology, experimental results, and conclusions, indicating the effect of AI-powered [9] precision agriculture on reducing wheat crop losses. Develop an AI-Based Disease Detection Model – Use deep learning (VGG19 CNN) to accurately classify wheat diseases, Leverage UAVs for Large-Scale Monitoring – Employ drones with multispectral/high-resolution cameras to collect extensive field data, Improve Model Interpretability and Generalization – Incorporate Grad-CAM visualization for explainability and enhance robustness with data augmentation, Introduce Real-Time Detection and Alerts – Install an IoT-based system for real-time alerts [11], allowing timely management of the disease, Close Gaps in Conventional Methods – Provide a low-cost, automated, and scalable alternative to manual disease detection.

II. LITERATURE SURVEY

Conventional practices for detecting wheat diseases depend upon visual examination by specialists, which is labor-intensive, time consuming, and human error prone. With the recent developments in remote sensing, deep learning (DL), and machine learning (ML), there is increased interest in automated disease identification. Some have suggested image-based disease classification approaches based on Convolutional Neural Networks (CNNs) [10]. While some incorporate hyperspectral or multispectral images for gathering finer information about the crop, others only use RGB images. Khirade and Patill provided an early overview of image processing techniques used in crop disease detection, highlighting the potential of color, texture, and shape-based feature extraction for classification. However, their approach was heavily dependent on handcrafted features, which limited its accuracy when applied to large and diverse datasets [1]. Mohanty et al. demonstrated the effectiveness of deep learning models, specifically CNNs, for plant disease classification. Their study used the Plant Village dataset, achieving high accuracy in controlled settings. However, their model relied on lab-acquired images, making it less generalizable to real-world agricultural conditions where lighting, soil conditions, and plant variations affect predictions [2]. Malithi et al. explored the use of multispectral imaging and hyperspectral analysis to enhance the detection of wheat diseases. They showed that non-visible spectral bands significantly improve disease identification, particularly in early-stage infections. Yet, their process involved costly hyperspectral cameras and hence was unsuitable for small and medium-sized farmers [5]. Hasan et al. have suggested an IoT-based system to monitor wheat disease that combines real-time sensor inputs with machine learning algorithms for timely disease detection. Although their methodology effectively generated real-time warnings, it did not have aerial monitoring capability and so was not capable of monitoring big farm fields effectively [4]. Zhang et al. investigated the combination of UAV (unmanned Aerial Vehicle) imagery with deep learning to detect wheat disease. Their work illustrated how drones can improve data collection efficiency by covering extensive areas in a short time span. But their model did not use state-of-the-art CNN architectures or explainability methods such as Grad-CAM, which are important for model interpretability in real-world usage [3].

While all previous work in wheat disease diagnosis has been commendable, many limitations remain: Limited Scalability – A lot of deep learning models perform well in lab settings but not in real-world agriculture fields because of different conditions. Lack of UAV-Based Deep Learning Integration – While UAVs improve image collection efficiency, few studies have integrated CNN-based models for automated disease detection. Absence of Real-Time Monitoring – IoT-based disease detection is promising [10], but existing solutions lack aerial surveillance, which is crucial for large farms. Overreliance on RGB Images – Traditional image processing approaches rely only on visible light, ignoring multispectral imaging, which provides deeper insights into plant health.

Authorized licensed use limited to: DELHI TECHNICAL UNIV. Downloaded on June 16,2025 at 05:09:27 UTC from IEEE Xplore. Restrictions apply.

III. METHODOLOGY

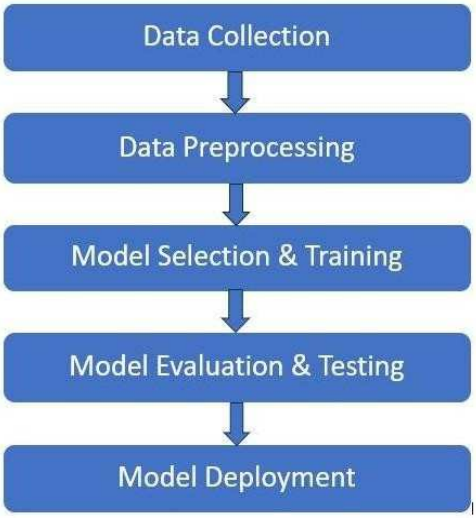


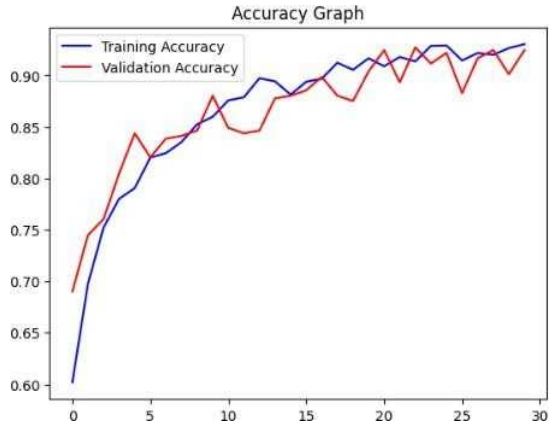
Fig. 2. Basic steps for wheat disease detection and classification.

In Fig. 2. The flowchart represents a structured pipeline for wheat disease detection and classification using UAV-based imaging and deep learning techniques. The process begins with Data Collection, where aerial images of wheat fields are captured using UAVs equipped with high-resolution multispectral or RGB cameras. These pictures give essential spectral and spatial data for recognizing disease manifestations. For the model to be strong, the dataset should contain pictures of various growth phases, light conditions, and diseases. The dataset employed in the current research is utilized from Fang, "Lightweight Multiscale CNN Model for Wheat Disease Detection" [7] containing about 4,500 wheat leaf images classified into four sour classes: Loose Smut, Healthy Plant, Crown and Root, and Leaf Rust. Carefully curated the dataset to keep the dimensions of the data set uniform and provides images under heterogeneous conditions including composite backgrounds and ranging stages of diseased progressions. The most inherent problem when classifying the diseases lies within the differences of visual characteristics present in the individual diseases that mandate strong feature extraction methods. Preprocessing pipeline was utilized, promoting efficient dataset preparation for deep model training. Following this, under Data Preprocessing, raw images are subjected to enhancement activities such as the removal of noise, adjustment of contrast, resizing of the images, and augmentation methods of rotation, flipping, and normalization of colors. In case multispectral images are used, particular bands of wavelengths may be selected for identifying disease characteristics, so the data is kept clean and is appropriate for training models. Upon preprocessing, Model Selection and Training phase encompasses selecting a suitable deep learning model, e.g., Convolutional Neural Networks (CNNs) [14]. The chosen model is then trained over the processed dataset to identify patterns that can differentiate between healthy and diseased crops. Transfer learning, optimization of the learning rate, and regularization are used to improve model performance. After training, the Model Evaluation and Testing stage evaluates the accuracy, precision, recall, and overall classification performance of the model based on an independent test dataset. This ensures that the model is able to generalize to new data and work consistently in real-world situations. Lastly, during the Model Deployment phase, the trained and validated model is deployed in a real-world system for automated wheat disease detection. The deployed model can be applied in precision agriculture applications, allowing for real-time disease tracking and early intervention to guard crops and maximize yield. This methodical process provides a high level of precision and effectiveness in wheat disease diagnosis, advantaging farmers and agricultural scientists. VGG19 is used in this model [14], since it is among the most popular architectures in research for image classification tasks. VGG19 is a convolutional neural network with 19 layers deep and pretrained on the ImageNet database, which has over a million images in 1,000 categories. The architecture consists of five convolutional blocks with ReLU activation and max-pooling layers, and three fully connected layers. The last output layer utilizes a soft-max activation function for multi-class classification.

IV. RESULTS

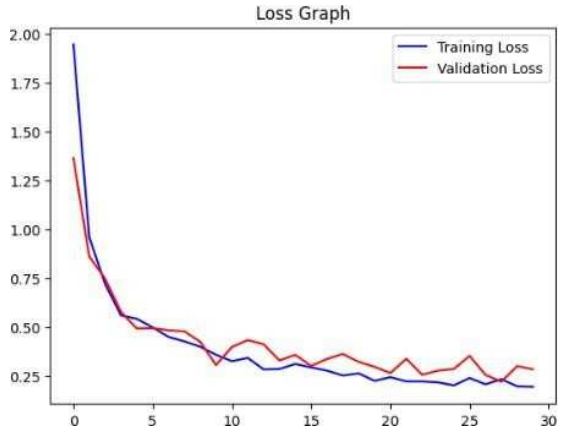
The performance of the wheat disease detection model was assessed with accuracy measures, loss curves, and a confusion matrix. The results show that the suggested model efficiently classifies wheat diseases with high precision, recall, and overall accuracy.

Figure 3 shows the performance analysis of the deep learning model used for wheat disease detection. Subfigure (a) depicts the accuracy chart, where the blue line depicts the training accuracy, and the red line corresponds to the validation accuracy. The close overlap between the training and validation accuracy plots indicates that the model is not overfitting and can generalize well to new data. Conversely, subfigure (b) illustrates the loss plot, where the blue line is the training loss and the red line is the validation loss. Both curves have a steep drop in the early epochs, followed by a slow decrease and leveling off as training continues. The similarity between the training and validation loss curves further confirms that the model is well-optimized and achieves high performance without significant overfitting.



(a)

Authorized licensed use limited to: DELHI TECHNICAL UNIV. Downloaded on June 16,2025 at 05:09:27 UTC from IEEE Xplore. Restrictions apply.



(b)

Fig. 3. (a) Accuracy graph, (b)Loss graph.

The model was trained for 30 epochs, and both training and validation accuracy showed a steady increase. The final validation accuracy reached ~90%, closely following the training accuracy, which suggests minimal overfitting. By this model Training Accuracy is increased to 95%, Validation Accuracy is increased to 90%, Training Loss is reduced from 2.0% to 0.2% and Validation Loss is stabilized around 0.3%. The loss curves indicate smooth convergence, demonstrating that the model effectively learns features from the dataset without significant overfitting or underfitting.

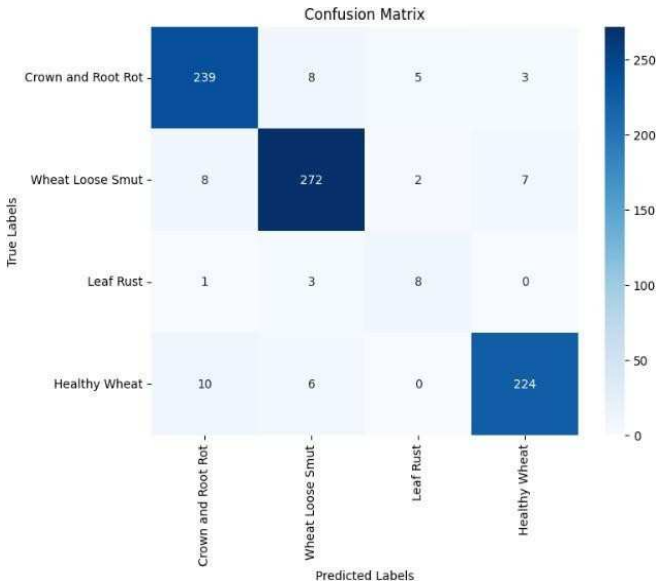


Fig. 4. Confusion matrix

The confusion matrix revealed that the model performs well across all disease classes. The classification precision for Wheat Loose Smut and Crown and Root Rot exceeded 94%, indicating reliable predictions. However, Leaf Rust showed slightly lower recall (~72.7%), suggesting scope for improvement with additional training data. Key takeaways are High precision for major diseases (>94%), Minimal misclassification among similar disease types and no major false positives in Healthy Wheat classification.

V. CONCLUSION

This research introduces a deep learning-based model for wheat disease detection, offering high accuracy and real-time usability. Unlike traditional manual inspection methods, this model enables users to capture or upload images for instant classification, ensuring timely intervention and reducing crop losses. The integration of UAV imagery enhances large-scale monitoring, making it suitable for precision agriculture. This model outperforms existing approaches by bridging the gap between high-accuracy detection and real-world deployment. With further optimization, it can be integrated into mobile and IoT devices, providing farmers with a cost-effective, scalable, and accessible solution for disease detection in wheat crops.

REFERENCES

[1] S. D. Khirade and A. B. Patil, "Plant Disease Detection Using Image Processing," 2015 International Conference on Computing Communication Control and Automation, Pune, India, 2015, pp. 768-771, doi: 10.1109/ICCUBEA.2015.153.

[2] Sharada P. Mohanty, David P. Hughes, Marcel Salathe, “Using Deep Learning for Image-Based Plant Disease Detection”, Sec. Technical Advances in Plant Science Volume 7 – 2016.

[3] Dong-Yan Zhang, Chun-Yan Gu, Zheng-Gao Pan, Xin-Gen Zhou, Yu Chen,“Integrating spectral and image data to detect Fusarium head blight of wheat”, Computers and Electronics in Agriculture, Volume 175, 2020.

[4] Mohtasim, Syed & Khan, Jaima & Islam, Mohammad & Sarker, Monosij & Uddin, Mohammad & Hasan, Mahady. (2023). “IoT-based Crop Monitoring and Disease Detection.” 1-6. 10.1109/STI59863.2023.10464923.

[5] De Silva, Malithi & Brown, Dane. (2023). Plant Disease Detection Using Multispectral Imaging. Communications in Computer and Information Science. 1528.

[6] Dr. K. Thangadurai, K. Padmavathi, “Computer Vision image Enhancement for Plant Leaves Disease Detection”, 2014 World Congress on Computing and Communication Technologies.

[7] Fang, X., Zhen, T., & Li, Z. (2023). Lightweight Multiscale CNN Model for Wheat Disease Detection. Applied Sciences, 13(9), 5801. https://doi.org/10.3390/app13095801.

[8] P. Mittal, P. Gupta, S. Shri and T. Goel, "Development of Neural Network Approach towards MPPT Optimization", International Journal of Advanced Science and Technology (ISSN: 2005-4238), Vol. 29, No. 7, pp. 1436-1444, Apr 2020, DOI: http://sersc.org/journals/index.php/IJAST/article/view/10795

[9] P. Sharma, P. Gangwar, R. Gupta and P. Mittal, "Addressing Vehicle Safety and Platooning using Low- Cost Object Detection Algorithms", Proceedings of second international conference on women researchers in electronics and computing (WREC-2023), organized by NIT Jalandhar, Punjab, India, April 21-23, 2023, to be published in Lecture Notes in Electrical Engineering (Springer, Scopus Indexed) (Best paper award).

[10] R. Sheel, R. Kumar, N. Chaudhary and P. Mittal, "Transcription of American Sign Language using Convolutional Neural Networks", Proceedings of second international conference on women researchers in electronics and computing (WREC-2023), organized by NIT Jalandhar, Punjab, India, April 21-23, 2023, to be published in Lecture Notes in Electrical Engineering (Springer, Scopus Indexed).

[11] V. Rawat, V. Kumar and P. Mittal, “License Plate Detection by Edge Detection Algorithm and Smart Exposition With IOT”, International Conference on Simulation, Automation & Smart Manufacturing (SASM 2021), organized by GLA University, Mathura, 20-21 August, 2021 (IEEE, Scopus Indexed).

[12] Bauriegel, E., & Herppich, W. B. (2014). Hyperspectral and Chlorophyll Fluorescence Imaging for Early Detection of Plant Diseases, with Special Reference to Fusarium spec. Infections on

Authorized licensed use limited to: DELHI TECHNICAL UNIV. Downloaded on June 16,2025 at 05:09:27 UTC from IEEE Xplore. Restrictions apply.

Wheat. Agriculture, 4(1), 32-57. https://doi.org/10.3390/agriculture4010032

[13] Zheng, Q.; Huang, W.; Cui, X.; Shi, Y.; Liu, L. New Spectral Index for Detecting Wheat Yellow Rust Using Sentinel-2 Multispectral Imagery. Sensors 2018, 18, 868. https://doi.org/10.3390/s18030868

[14] S. Sheenam, S. Khattar and T. Verma, "Automated Wheat Plant Disease Detection using Deep Learning: A Multi-Class Classification Approach," 2023 3rd International Conference on Intelligent Technologies (CONIT), Hubli, India, 2023, pp. 1-5, doi: 10.1109/CONIT59222.2023.10205683.

Authorized licensed use limited to: DELHI TECHNICAL UNIV. Downloaded on June 16,2025 at 05:09:27 UTC from IEEE Xplore. Restrictions apply.

Check for updates

ChemistrySelect

Research Article
doi.org/10.1002/slct.202404081

Chemistry Europe
European Chemical Societies Publishing

www.chemistryselect.org

Ag@SnO_2/g-C_3N_4 Ternary Nanocomposite as an Efficient Acetone Vapors Sensor

Yoshita Katiyar,[b] Shivani Sangwan,[a] Gagan Sharma,[a] Mohit Kumar,[a] Anshika Goyal,[b] Manish Jain,*[b] and Deshraj Meena*[a]

Ternary nanocomposite of Ag modified SnO_2 (Ag@SnO_2) nanoparticles and graphitic carbon nitride (g-C_3N_4) nanosheets (Ag@SnO_2/g-C_3N_4) have been successfully synthesized using a facile hydrothermal method. The synthesized nanostructures were subjected to various characterization techniques to investigate their structural, morphological, optical, and chemical properties. The XRD results confirm the crystalline nature and rutile phase of the synthesized SnO_2-based nanostructures, while SEM and TEM revealed morphological characteristics of Ag@SnO_2 and high dispersion of Ag@SnO_2 nanoparticles on the surface of g-C_3N_4 nanosheets. The gas sensing performance of the samples (Ag@SnO_2 and Ag@SnO_2/g-C_3N_4) was evaluated towards 1 µL of acetone vapors in 2L sensing chamber at various operating temperatures. Ag@SnO_2/g-C_3N_4 based resistive gas sensor exhibited admirable sensitivity at (28%), which is ~ 4 times higher than that of Ag@SnO_2 based sensor, and good repeatability towards acetone vapors at an operating temperature of 100 °C. The enhanced sensing results of Ag@SnO_2/g-C_3N_4-based sensors at relatively low working temperatures are attributed to its high surface area (104.6 m^2/g), reduced energy band gap from 2.8 eV to 2.4 eV, and strong interaction between Ag@SnO_2 nanoparticles and 2D g-C_3N_4 nanosheets. Furthermore, a suitable sensing mechanism has been presented to explain the enhanced gas sensing properties of Ag@SnO_2 and Ag@SnO_2/g-C_3N_4 based resistive gas sensor.

1. Introduction

The escalating issue of air pollution poses a significant environmental risk, resulting in heightened healthcare expenses and a surge in premature morality rates. Moreover, individuals employed in sectors like mining, healthcare, manufacturing, laboratories, and gas production are frequently subjected to hazardous and toxic gases.[1–3] Among which Volatile Organic Compounds (VOCs) are one of the big contributors that are causing health problems. VOCs are the organic chemicals having high vapor pressure at room temperature. For example, ethanol, methanol, acetone, benzene, xylene, phenol, and so on.[3–5] In this group, acetone is one of the most important VOCs as it is used in industrial solvent, research laboratories and easily-made drug chemicals. However, it is not only highly volatile and flammable but also harmful to human body because of its anesthetic effects on the central nervous system.[6] Besides, it is also one of the generally accepted biomarkers for noninvasive diagnosis of human type-1 diabetes.[7] Therefore, to develop efficient and convenient sensing technology for VOCs detection becomes necessary for human health in residential buildings and process control in industries.

[a] S. Sangwan, G. Sharma, M. Kumar, D. Meena
Clean Energy Research Lab, Department of Applied Physics, Delhi Technological University, Delhi 110042, India
E-mail: deshrajmeena@dtu.ac.in

[b] Y. Katiyar, A. Goyal, M. Jain
Department of Applied Chemistry, Delhi Technological University, Delhi 110042, India
E-mail: manishjain@dtu.ac.in

Concerning above problems, metal oxide based resistive gas sensors have been extensively exploited to detect VOCs because of their advantages including compact size, easy production, low cost and simple measuring electronics.[5] The various metal oxide semiconductor such as SnO_2,[8] ZnO,[9] CuO,[10] NiO,[5] and so on are widely used oxides as gas sensors.[9] One of them is SnO_2, a typical *n*-type metal oxide semiconductor with a rutile crystalline structure is used all around to detect different types of gases such as ethanol, acetone, nitrogen dioxide, and so on.[11,12] SnO_2 exhibits notable electronic and optical properties, as well as it has good thermal stability, environment friendly nature, and easy accessibility. However, the pure SnO_2 based sensor's sensing performance is not up to the growing requirement, especially due to their high operating temperature, cross selectivity, and lower sensitivity.[12,13] In this regard, the researchers have enhanced the sensing performances of the metal oxides by modifying their morphology, crystal structure, elemental composition by doping and formation of nanocomposites with 2D materials like as, rGO, graphene, MXenes, and so on.[13–16] Many reports have already been published suggesting that the integration of some noble metals in SnO_2 nanostructures is a highly efficient way to further enhance the sensing performance by boosting the electrical, optical, and chemical properties.[16] Like as silver (Ag) is one of the most prevalent due to its intrinsic properties, which include high reactivity to O_2 adsorption, excellent electrical and thermal conductivity, high cation mobility, low cost, non-toxicity, and antibacterial properties that can be helpful in boosting the gas sensing performance of the various metal oxides.[17,18]

© 2025 Wiley-VCH GmbH

In the same consideration, nanocomposite of SnO_2 with graphitic carbon nitride (g-C_3N_4) has also demonstrated significant enhancement in the sensing performance and gained popularity among the researchers due to its simple synthesis process, tunable electronic properties, and exceptional physicochemical properties.[1,19] These attributes make g-C_3N_4 and SnO_2 nanocomposites as a promising candidate for the next-generation high-performance gas sensors.[16,19] Combined with the π-conjugate system of graphene, the SnO_2/graphene nanocomposites exhibited high sensitivity. However, the SnO_2/graphene nanocomposites presented lower sensitivity to VOCs. For further improving the sensitivity to VOCs, noble metal was added to that the nanocomposite which was synthesized by a wet-chemical method.[17] Xin Gu et al. synthesized 3D heterostructural g-C_3N_4-NiO@SnO_2 composite by one-pot calcination method. Gas sensing results of the as-prepared g-C_3N_4 –NiO@SnO_2 (25%) sensor exhibits high acetone response sensitivity (150.3–100 ppm) as well as good selectivity, fast response/recovery, repeatability, and long term stability.[20] Similarly, Jing Hu et al. found a facile calcination treatment of melamine and $SnCl_2.H_2O$ without further processing can obtain the expected C_3N_4-SnO_2 sensor. On comparison, the obtained heterostructure exhibited 22 times higher sensitivity than that with pure SnO_2.[21] Interestingly, only very limited work has been reported which explore the sensing properties of metal doped SnO_2 and g-C_3N_4 nanocomposite towards resistive gas sensors.[16,19] In fact, to our best knowledge no such report available which explores the gas sensing properties of the Ag decorated SnO_2 and g-C_3N_4 nanocomposite towards resistive gas sensors.

In this aspect, our study is focused on fabrication of Ag decorated stannic oxide (Ag@SnO_2) and carbon nitride (g-C_3N_4) nanocomposite for detecting the trace levels of acetone. At 100 °C, the Ag@SnO_2/g-C_3N_4 sensor demonstrated a highly selective and rapid response to acetone. The enhancement in Ag-loaded SnO_2 performance was attributed to the catalytic activity of Ag and the formation of nanocomposite. The gas sensing mechanism of the molecules has been discussed. Furthermore, the challenges and future prospects of g-C_3N_4-based gas sensors and their modifications for real-time gas monitoring has also been addressed.

2. Experimental Section

2.1. Chemicals Used

Stannic chloride hydrated ($SnCl_4.5H_2O$, >98%, extra pure) from Loba Chemie Pvt. Ltd, Silver nitrate ($AgNO_3$, >99.8%) from Avantor Performance Materials India Private Limited, Ethanol (C_2H_6O, >99.9%) from Changshu Song Sheng Fine Chemical, acetone (C_3H_6O, >99.5%), Urea (NH_4N_2O, >99.5%), and Sodium Hydroxide pellets (NaOH, >99.5%) from Thermo Fisher Scientific India Pvt. Ltd, Sodium Carbonate (Na_2CO_3, > 99.5%) of high purity were used to synthesize different nanostructures and nanocomposites. The above chemicals were used directly as purchased in the synthesis process of Ag@SnO_2/g-C_3N_4 and Ag@SnO_2 nanocomposites.

2.2. Synthesis of Ag@SnO_2 Nanostructures

The desired concentration of $SnCl_4.5H_2O$ (0.01 M) were mixed with ethanol and distilled water (1:1) using magnetic stirrer for 30min. In our study, 50 mL of double distilled water was added to a mixture of 2.83 g $SnCl_4.5H_2O$ and 0.17 g $AgNO_3$ and followed by the addition of 0.5 g of NaOH to the reaction mixture with constant stirring for another 30min. The mixture was then transferred into a 100 mL of Teflon beaker and treated hydrothermally at 160 °C for 8 h. After letting the mixture cool down naturally to room temperature, obtained product was washed several times using centrifugation process followed by drying at 60 °C for 12 h in a vacuum oven.[16]

2.3. Synthesis of g-C_3N_4

Synthesizing of g-C_3N_4 requires, 15 g Urea was added in a thermo flask that was placed in muffle furnace for 2 h at temperature 550 °C at a rate of 5 °C/min.[22]

2.4. Synthesis of Ag@SnO_2/g-C_3N_4 Nanocomposite

The prepared 0.18 g g-C_3N_4 was mixed with 18 mL of distilled water and underwent sonication for 120 min in order to get homogenous dispersion. A solution was formed by dissolving 2.83 g $SnCl_4.5H_2O$ and 0.17 g $AgNO_3$ in 30 mL distilled water. This obtained mixture was added gradually to the above homogenous dispersion and was stirred for 1h using magnetic stirrer. Then, 2.11 g Sodium Carbonate was dissolved in 5 mL DI dropwise and stirred until gel like consistency was observed. The mixture was then transferred to Teflon beaker and treated hydrothermally at 150 °C for 12 h.[16] The resulted precipitation went through several washing process using a centrifuge machine and then air dried to obtain the Ag@SnO_2/g-C_3N_4 nanocomposite. The schematic diagram of all synthesis processes has been shown in Figure 1a,b.

2.5. Gas Sensing Measurement

The gas-sensing performance was evaluated by using a native lab developed sensing set up, the detail of which have been reported in our previous work.[23] Further, to fabricate the film of sensing layer of synthesized Ag@SnO_2 (ZnA) and Ag@SnO_2/g-C_3N_4 (ZnC) samples on the alumina substrate (Al_2O_3), the well-known **doctor blade method** was used.[16] The process involves the use of a blade (or bar) that is held at a fixed height above the substrate and a slurry or paste containing the material to be deposited is spread across the surface. As the blade is moved across the substrate, it deposits a thin and uniform layer of the material onto the surface.[24] The Ag@SnO_2 nanoparticles and Ag@SnO_2/g-C_3N_4 nanocomposite powder samples were separately mixed with polyethylene glycol (PEG 200) using mortar pestle to make a paste. Then the obtained pastes were subsequently coated on the Al_2O_3 substrate to obtained uniform films. After that the prepared films were heated at 300 °C for 2 h to make them free from the binding element PEG 200. These heated films were used as sensing layer of the gas-sensing system. Two electrodes were fabricated on these synthesized films using silver paste to measure the resistance (R). The test gas vapors were generated in the sensing chamber by evaporating the lab graded acetone (>99.5%) using a microheater. The liquid acetone (1 µL) was introduced in the chamber of a volume 2L through a micropipette. The sensitivity of the sensors was measured using Equation (1)

$$\text{Sensitivity (S)} = \frac{\Delta R}{R_0} \times 100 = \frac{(R_g - R_0)}{R_0} \times 100 \quad (1)$$

© 2025 Wiley-VCH GmbH

23656549, 2024, 23, Downloaded from https://chemistry-europe.onlinelibrary.wiley.com/doi/10.1002/slct.202404081 by Delhi Technological University, Wiley Online Library on [26/06/2025]. See the Terms and Conditions (https://onlinelibrary.wiley.com/terms-and-conditions) on Wiley Online Library for rules of use; OA articles are governed by the applicable Creative Commons License

Research Article
doi.org/10.1002/slct.202404081

Chemistry Europe
European Chemical Societies Publishing

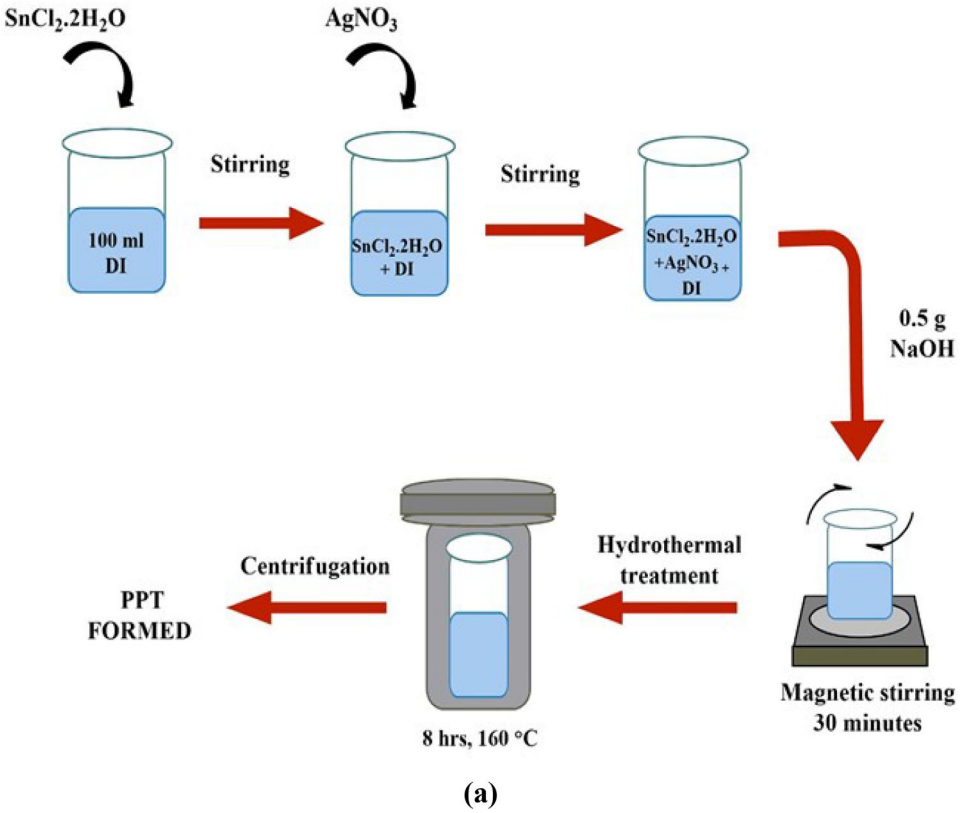


Figure 1. Schematic diagram for the synthesis of nanocomposites using hydrothermal method: (a) $Ag@SnO_2$ and (b). $Ag@SnO_2/g\text{-}C_3N_4$.

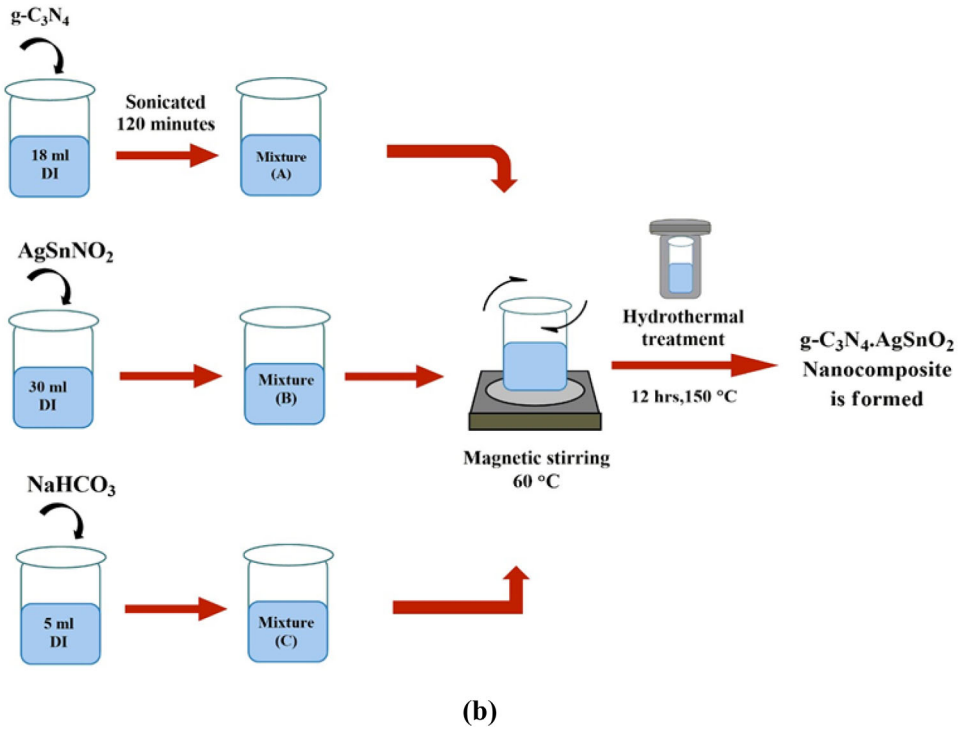


Figure 1. *Continued*

© 2025 Wiley-VCH GmbH

23656549, 2024, 23, Downloaded from https://chemistry-europe.onlinelibrary.wiley.com/doi/10.1002/slct.202404081 by Delhi Technological University, Wiley Online Library on [26/06/2025]. See the Terms and Conditions (https://onlinelibrary.wiley.com/terms-and-conditions) on Wiley Online Library for rules of use; OA articles are governed by the applicable Creative Commons License

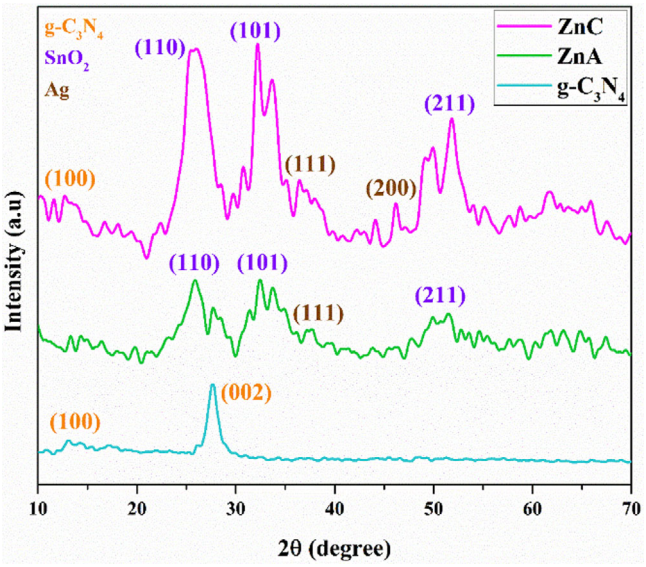


Figure 2. X-Ray Diffraction pattern of pure g-C_3N_4, ZnA, and ZnC.

where R_0 and Rg are the resistance (R) before and after insertion of acetone vapors, respectively.[15]

2.6. Characterization and Measurement

A Cu Kα (λ = 1.5418 Å) radiation source was employed in a Rigaku Ultima IV X-ray diffractometer (XRD) to identify the crystal phases of the produced samples. The scans were conducted within a 2θ range f 10° to 70° at a rate of 2° per minute. Compositional analysis was performed using an energy-dispersive X-ray spectroscopy (EDX) system (SwiftED3000), while the surface morphology of the samples was examined using an FEI Quanta 200 field emission scanning electron microscope (FESEM). The detailed structure of samples was analyzed using (transmission electron microscopy (TEM) equipped with LaB6/Tungsten filament (JEOL JEM-1400). Perkin Elmer spectrum -II instrument was used for the Fourier transform infrared spectroscopy (FTIR) studies of powder sample. For the Brunauer–Emmett–Teller (BET) surface area and pore volume of synthesized samples, Quantachrome autosorb TRX was used. UV–visible absorption spectroscopy was carried out in a UV–vis spectrophotometer (Perkin Elmer Lambda 1050). The Raman spectra was recorded using a Horiba HR 800 Laser Raman spectrometer.

3. Results and Discussion

3.1. Structural Analysis

The obtained X-Ray Diffraction patterns of the pure g-C_3N_4, ZnA and ZnC samples are shown in Figure 2. The observed diffraction peaks at 2Θ = 26.5°, 33.86°, 51.76° are assigned to (110), (101), and (211) diffraction planes of the tetragonal rutile SnO_2 structure, whereas peaks at 38.2°and 46.2° corresponds to (111) and (200) of Ag, respectively which are consistent with the standard JCPDS (file no: 41–1445) data.[18,25,26] The two distinct diffraction peaks of g-C_3N_4 at 13.1° and 27.5° correspond to the (100) and (002) planes that are related to the tris-triazine unit's interplanar spacing and the conjugated aromatic system, respectively.[22,25,26]

The obtained diffraction peaks in XRD pattern of ZnC are well matches to Ag, SnO_2 and g-C_3N_4 planes.[26,27] Further, it can be observed that the peak at 26.5° attributed to ZnC has been broadened that might be due to the merging of the Ag@SnO_2 (110) and g-C_3N_4 peaks (100).[16] Thus, the obtained XRD result confirms the successful synthesis of nanocomposite of ZnA with g-C_3N_4.

3.2. Morphological and Compositional Analysis

Figure 3 represents the scanning electron microscopic (SEM) images of Ag@SnO_2, pure g-C_3N_4, and Ag@SnO_2/g-C_3N_4 nanocomposites. SEM images confirm the synthesis of irregular shaped nanoparticles of Ag@SnO_2 and g-C_3N_4 nanosheets. And, images (c) and (d) indicate the successful dispersion of Ag@SnO_2 nanoparticles on g-C_3N_4 nanosheets. Moreover, transmission electron microscopic (TEM) images and fringe patterns were obtained to further confirm the morphology and phase of the synthesized nanocomposites, as shown in Figure 4. TEM analysis of ZnA and ZnC nanocomposites also suggested that Ag@SnO_2 nanoparticles were decorated uniformly over the g-C_3N_4 nanosheets. Additionally, the obtained fringe pattern of Ag@SnO_2 and Ag@SnO_2/g-C_3N_4 well matches with the literature values and suggest their poly-crystalline nature. The observed fringes were assigned to the (111), (110), (002) planes with d-spacing of 0.24 nm, 0.329 nm, 0.338 nm for Ag, SnO_2 and g-C_3N_4, respectively as depicted in Figure 4c,f.[28,29] The existence of these fringes confirms the high crystallinity and successful formation of the synthesized samples. The obtained selected area electron diffraction (SAED) pattern of the ZnC sample is shown in inset of Figure 4e. The different concentric diffraction rings are indexed to the [110] and [101] planes.[22] The calculated *d*-spacing values from the SAED pattern are in good agreement with the XRD results, confirming the crystalline nature of the ZnC nanocomposite.

The elemental composition of ZnA and ZnC nanocomposites were determined by energy dispersive spectroscopy (EDS). The obtained EDS spectrum is shown in Figure 5.

The EDS results confirm the presence of 3 elements in ZnA nanocomposite that is Sn, O, and Ag and 5 elements in ZnC that is O, Ag, Sn, C, and N. The elemental analysis proved the presence of all essential elements in our nanocomposites. These results strongly indicate no presence of any additional impurity, confirming the purity of the samples.

The BET measurement were carried out to study the surface properties of the synthesized nanostructures. The obtained BET adsorption-desorption curves were plotted and are represented in Figure 6.

The surface area, pore size, and pore volume of Ag@SnO_2 and Ag@SnO_2/g-C_3N_4 has been calculated and tabulated in Table 1. The gas adsorption capabilities of samples are measured by the surface area analyzer to get the values of pore size and surface area. As the estimated pore size width for both the samples ranges between 2 nm and 50 nm, hence they show mesoporous properties.[16] Also, isotherm of Type IV with type H2 hysteresis

© 2025 Wiley-VCH GmbH

23656549, 2025, 23, Downloaded from https://chemistry-europe.onlinelibrary.wiley.com/doi/10.1002/slct.202404081 by Delhi Technological University, Wiley Online Library on [26/06/2025]. See the Terms and Conditions (https://onlinelibrary.wiley.com/terms-and-conditions) on Wiley Online Library for rules of use; OA articles are governed by the applicable Creative Commons License

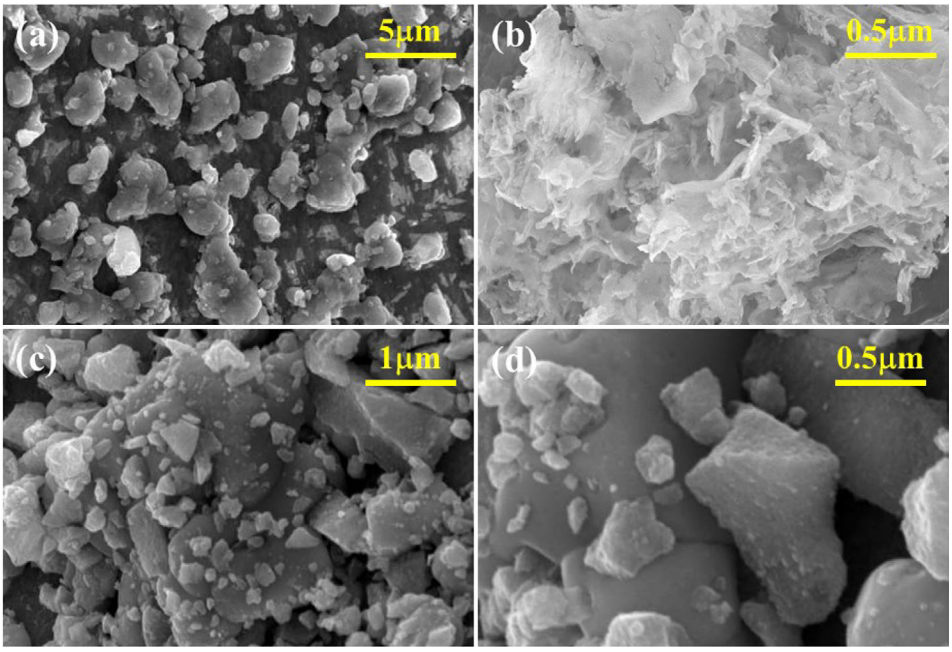


Figure 3. SEM images of (a) ZnA; (b) pure g-C_3N_4; (c and d) ZnC nanocomposites.

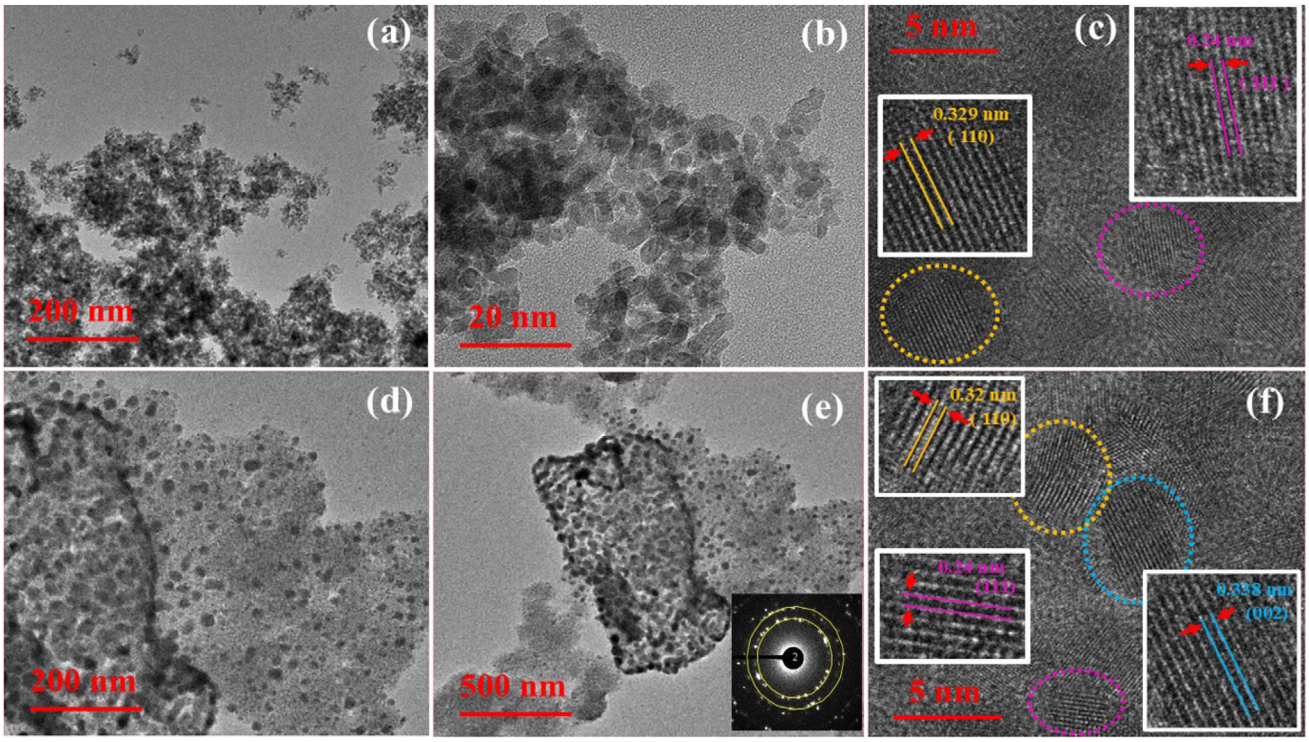


Figure 4. TEM images and fringe patterns of (a–c) ZnA; (d–f) ZnC nanocomposites; SAED pattern of ZnC in inset of (e).

loop can be concluded from the obtained curves that leads to Capillary condensation ($P/P^0 \geq 0.2$) and further indication of the presence of mesoporous structure.[26] This mesoporous structure evinces more active surface area to adsorb oxygen and test gases, resulting in a fast response and recovery kinetics as well as a high sensitivity.

3.3. Spectroscopic Analysis

The optical properties of ZnA and ZnC were investigated using UV–vis spectroscopic technique. Figure 7 displays the UV–vis absorbance spectra and Tauc's plot (inset) of ZnA and ZnC samples.

© 2025 Wiley-VCH GmbH

23656549, 2024, 23, Downloaded from https://chemistry-europe.onlinelibrary.wiley.com/doi/10.1002/slct.202404081 by Delhi Technological University, Wiley Online Library on [26/06/2025]. See the Terms and Conditions (https://onlinelibrary.wiley.com/terms-and-conditions) on Wiley Online Library for rules of use; OA articles are governed by the applicable Creative Commons License

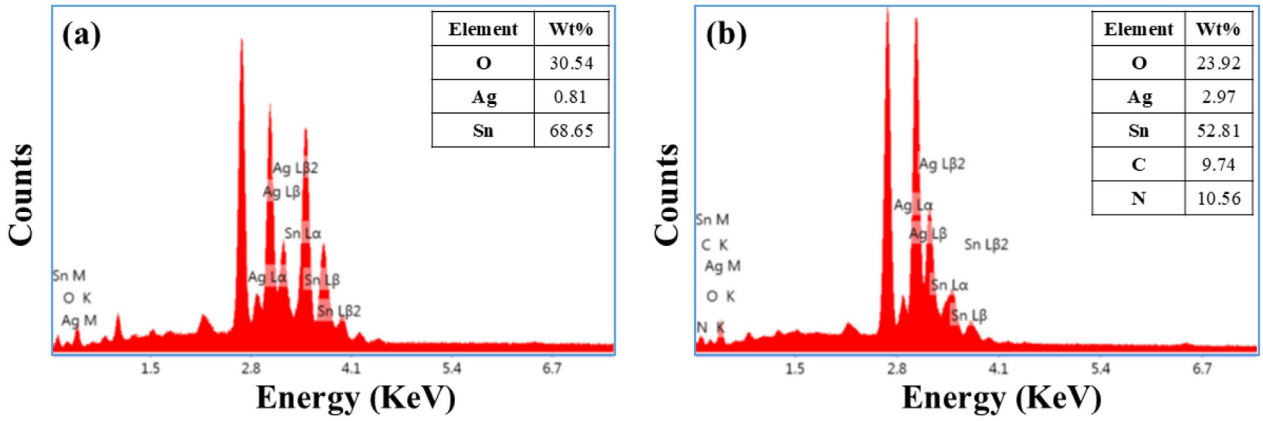


Figure 5. EDS pattern of (a) ZnA and (b) ZnC samples.

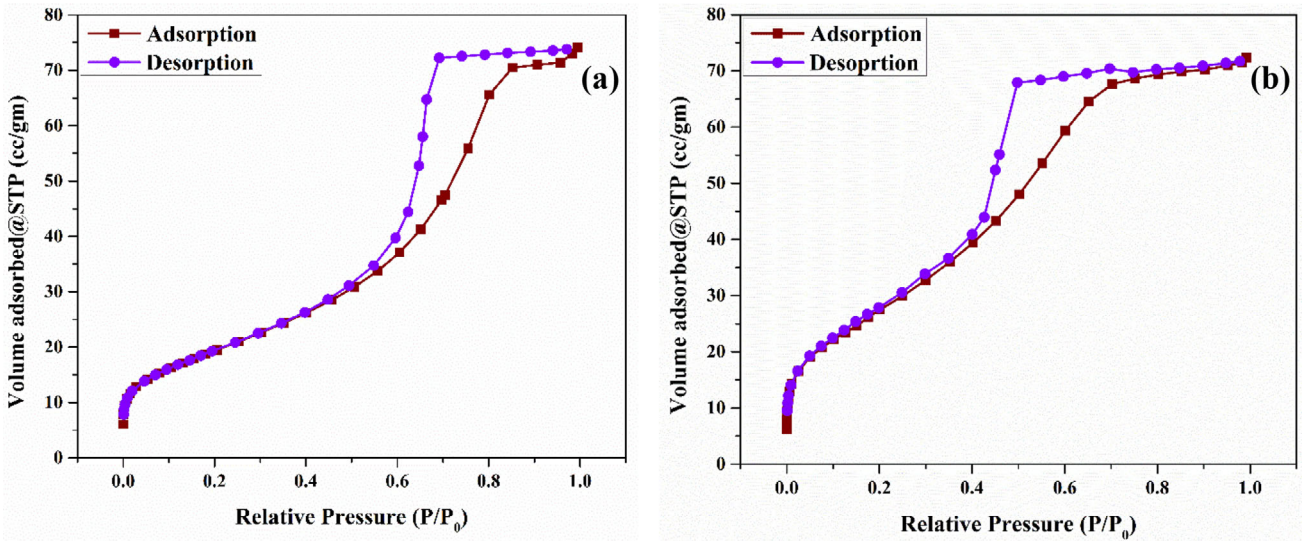


Figure 6. Adsorption-desorption curves using BET data for (a) ZnA and (b) ZnC samples.

Table 1. The surface area, pore size, and pore volume data of $Ag@SnO_2$ and $Ag@SnO_2/g\text{-}C_3N_4$ obtained using BET measurements.

Parameters	$Ag@SnO_2$	$Ag@SnO_2/g\text{-}C_3N_4$
Pore size (nm)	6.38	4.26
Surface area (m^2/g)	71.3	104.6
Pore volume (m^3/g)	1.139×10^{-7}	1.115×10^{-7}

In the absorbance spectra of ZnC, the combination of $Ag@SnO_2$ and $g\text{-}C_3N_4$ nanosheets significantly changed the absorption band of the ZnC composite as compared to ZnA. The major absorption peak of the ZnA sample is observed at 283 nm is get shifted to higher wavelength 302 nm for the ZnC sample. This red shift indicates a decrease in the band-gap indicating the presence of single ionized oxygen vacancies cause by the release of oxygen from the lattice.[18,30] However, the data clearly illustrate that the $Ag@SnO_2/g\text{-}C_3N_4$ nanocomposites display the absorption edge significantly closer to the $g\text{-}C_3N_4$, which indicates the existence of interfacial contacts and bonding between the $g\text{-}C_3N_4$ and SnO_2 nanoparticles.[25]

The optical band gap of the semiconductor explains the required energy of excitation and the transition of an electron from valence to conduction band. The energy band-gap (E_g) of ZnA and ZnC nanostructures has been estimated using Tauc's graph, plotted between $(\alpha h\nu)^{1/n}$ and photon energy ($h\nu$) as shown in the inset of Figure 7. Whereas α, h, ν, and n are the absorption coefficient, Planck's constant, frequency of the light, and the Tauc exponent, respectively.[29,31]

The calculated energy band gap of ZnA is 2.86 eV that is less than the reported energy band gap of pure SnO_2 that is 3.61 eV.[31] This decrement in the band gap is due to charge transfer between Ag and SnO_2 and second it can be attributed to the introduction of impurity levels in the bandgap of the composite, leading to the reduction of electron transition energy.[29,32] On the other hand, obtained energy band gap of the ZnC nanocomposite is 2.48 eV, which is less than that of ZnA. This further reduction in bandgap is attributed to the contact of $Ag@SnO_2$ with $g\text{-}C_3N_4$ nanosheets. It can be concluded that the combination of $g\text{-}C_3N_4$ with wide band-gap semiconductor SnO_2 leads to easy chemisorption of the physioadsorbed atmospheric oxygen.[18,33] That leads to higher number of oxygen species at

© 2025 Wiley-VCH GmbH

23656549, 2025, 23, Downloaded from https://chemistry-europe.onlinelibrary.wiley.com/doi/10.1002/slct.202404081 by Delhi Technological University, Wiley Online Library on [26/06/2025]. See the Terms and Conditions (https://onlinelibrary.wiley.com/terms-and-conditions) on Wiley Online Library for rules of use; OA articles are governed by the applicable Creative Commons License

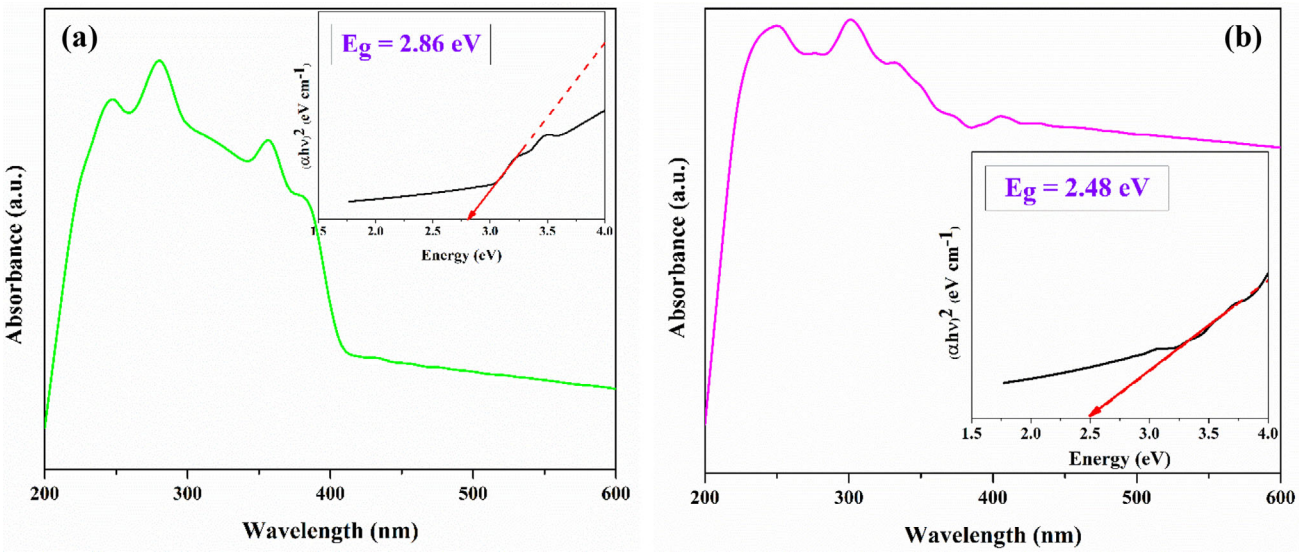


Figure 7. UV–vis absorbance curves of (a) ZnA and (b) ZnC; inset: Tauc's plot.

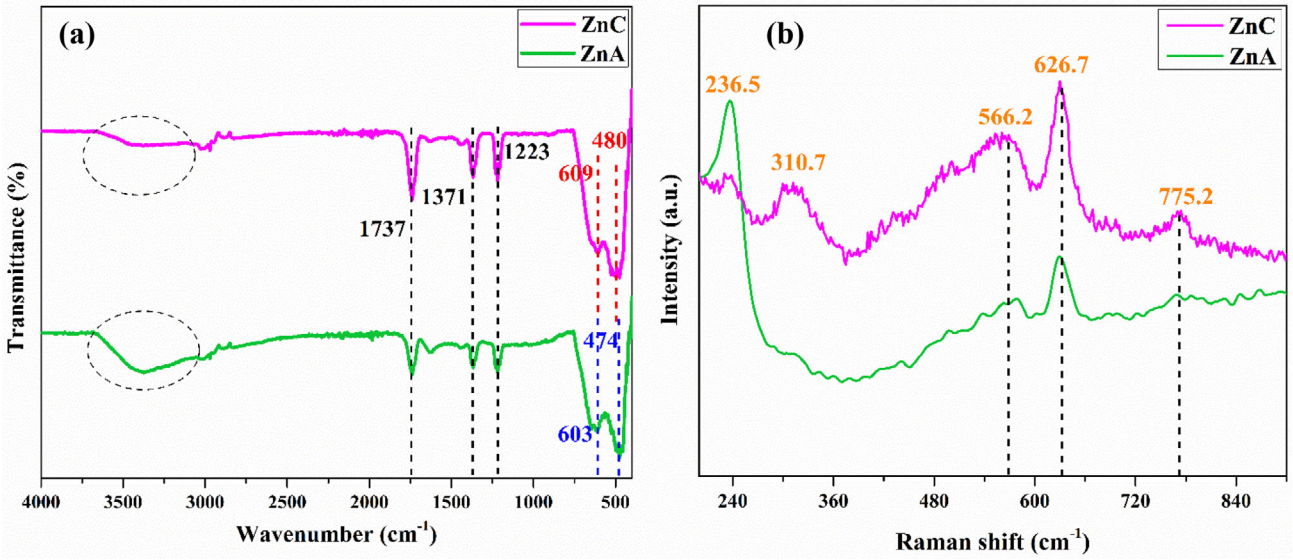


Figure 8. (a) FTIR and (b) Raman spectra of ZnA and ZnC samples.

the surface, thus enriching the gas-sensing ability of the current $Ag@SnO_2/@g\text{-}C_3N_4$ nanocomposite.

3.4. FTIR Analysis

The FTIR spectra of $Ag@SnO_2$ and $Ag@SnO_2/g\text{-}C_3N_4$ nanocomposites (exhibited in Figure 8a) were analyzed to better understand the interactions between $g\text{-}C_3N_4$ nanosheets and $Ag@SnO_2$ nanoparticles.

The bands at 474 cm^{-1} and 603 cm^{-1} are associated with Sn—O—Sn and Sn—O stretching vibration, respectively.[32] The peaks at 1223 and 1371 cm^{-1} are corresponding to Sn—OH vibrational modes and the peak at 1737 cm^{-1} is correlated to strong stretching vibrations of C=O group.[16,22] Furthermore, the additional band, prominent at around 3000–3600 cm^{-1} was assigned to the N—H and O—H functional groups. Moreover, interactions of SnO_2 nanoparticles with the $g\text{-}C_3N_4$ nanosheets in the $Ag@SnO_2/g\text{-}C_3N_4$ nanocomposite resulted in a slight shift in the peaks (400–650 cm^{-1}) indicating the effect of stretching mode of vibrations caused by the heterocyclic property of the tri-azine unit in $g\text{-}C_3N_4$.[18] Thus, FTIR analysis confirm the formation of ZnA and ZnC, however we could not find a separate peak for Ag that suggests no prominent bonding of Ag with SnO_2 and $g\text{-}C_3N_4$.[16]

3.5. Raman Analysis

To investigate physiochemical properties of $Ag@SnO_2$ and $Ag@SnO_2/g\text{-}C_3N_4$, Raman spectroscopy was used. An incoming green laser with a spectral width of 535 nm was employed as an excitation energy source, with a 10 mW of power delivered and sample exposure time between 20 and 30 s. The obtained Raman

© 2025 Wiley-VCH GmbH

23656549, 2025, 23, Downloaded from https://chemistry-europe.onlinelibrary.wiley.com/doi/10.1002/slct.202404081 by Delhi Technological University, Wiley Online Library on [26/06/2025]. See the Terms and Conditions (https://onlinelibrary.wiley.com/terms-and-conditions) on Wiley Online Library for rules of use; OA articles are governed by the applicable Creative Commons License

spectra of the ZnA and ZnC samples is shown in Figure 8b. Both the samples consist of characteristic Raman peak at 566.2 cm^{-1} is correlated to the bulk SnO_2, whereas peaks at 626.7 and 775.2 cm^{-1} resemble A1g and B2g modes respectively which corresponds to asymmetric and symmetric stretching of Sn-O bonds.[30,31] The peaks between 236.5 and 310.7 cm^{-1} are not concerned with bulk Ag@SnO_2. The Raman intensity of the peaks has significantly enhanced in the ZnC sample, which can be associated to the surface enhanced Raman scattering effect of g-C_3N_4.[18,22] In Raman bands of ZnC, the existence of respective peaks of SnO_2 and observed enhanced effect on peaks' intensity confirm the co-existence of g-C_3N_4 and SnO_2.

4. Gas-Sensing Results

4.1. Gas Sensing Performance

It has been well established that in an open atmospheric condition, the atmospheric oxygen molecules get adsorbed on the surface of the sensor. These physiosorbed oxygen molecules, get the electrons from the conduction band and convert into oxygen species ($O_2^-/O^-/O^{-2}$) as represented through Equation (2–4).[2] After, complete adsorption of the oxygen species on the surface of the sensor, the resistance of the sensor becomes nearly constant that is known as baseline resistance.[5]

$$\text{Atm.}O_2 + e^- \rightarrow O_2^- \text{ (adsorbed)} \quad (\text{Temp.} < 100^\circ\text{C}) \tag{2}$$

$$O_2^- + e^- \rightarrow 2O^- \text{ (adsorbed)} \quad (100^\circ\text{C} < \text{Temp.} < 300^\circ\text{C}) \tag{3}$$

$$O^- + e^- \rightarrow O^{-2} \text{ (adsorbed)} \quad (\text{Temp.} > 300^\circ\text{C}) \tag{4}$$

Further, the nature of the oxygen species at the sensor surface depends on the operating temperature of the sensor and the nature of adsorbed oxygen species play a crucial role in determining the sensing behavior of the sensor.[34] Therefore, we have carried out the temperature dependent sensing behavior of both (ZnA and ZnC) and synthesized sensors towards acetone vapors. The obtained behavior of the sensors is shown in Figures 9 and 10. It has been observed that the sensitivity of the sensors increases with increasing the temperature up to 100 °C. On further increment in operating temperature the sensitivity starts decreasing thus the optimum operating temperature is 100 °C for both the sensors, as represented in Figure 10f. This behavior of the sensors can be assigned to the gas adsorption-desorption process on the surfaces of the sensors.[2] Further, the response recovery curve of the ZnA sensor at different operating temperature has been shown in Figure 9. The calculated average sensitivity of the sensors at an operating temperature of 30 °C (RT), 50 °C, and 75 °C is around 2%, 4%, and 5%, respectively. At these operating temperatures the sensor repeatability is not good enough that might be due to improper adsorption-desorption of the acetone vapors which leads to inidentical exchange of electrons between conduction band and chemisorbed oxygen species. Thus, the ZnA sensors baseline resistance changes after every cycle. Although, the change in the resistance remains same for each cycle. However, the ZnA sensor shows good repeatability at an operating temperature of 100 °C with approximately 7% sensitivity. Although, on further increasing the operating temperature to 150 °C the sensitivity decreases to 6% and sensors response is also not stable.

The response recovery curve of the Ag@SnO_2/g-C_3N_4 nanocomposite (ZnC) based sensor at different operating temperature has been plotted in Figure 10. The ZnC sensor shows better sensitivity and stable behavior than the that of ZnA sensors. The nanocomposite-based sensors illustrate good sensitivity (3.4%) with stable response even at room temperature. These enhanced results are attributed to larger surface area and better electronic exchange between the acetone vapors and oxygen species. These sensors also exhibit maximum response at an operating temperature of 100 °C with 28% sensitivity, which is almost four times than that of ZnA sensors. It can be seen that ZnC sensors demonstrate stable response recovery curve, which suggest that the sensors have good repeatability. Furthermore, on increasing the operating temperature to 150 °C, the sensors response has relatively lower stability and sensitivity.

Also, to check the sensors stability the sensing measurements were carried out for a period of 1 month in an interval of 07 days. The sensors exhibited almost similar behavior with very little change in the sensitivity, thus demonstrating their stable nature.

Furthermore, it is important to note that moisture play a significant role in determining the gas sensing properties of sensing materials.[34,35] FTIR spectrum confirms the presence of moisture in the prepared samples (ZnA and ZnC). This moisture could interact with the surface, potentially blocking active sites and reducing the number of available adsorption sites for target gases. Additionally, moisture could compete with other adsorbates for adsorption sites, thereby influencing the material's sensitivity and selectivity.[36] Add on, the evaporated acetone vapors also introduce the water (solvent) vapors in the sensing chamber. However, the sensing results indicates that the sensors are not sensitive to the moisture as base line resistance of the samples remain constant. Interestingly, in some cases, moisture can enhance adsorption of certain species by altering surface polarity or by contributing to specific interactions, but it may also reduce the sensitivity towards other gases by occupying critical adsorption sites.[37] However, further studies need to be carried out under controlled humidity conditions for thorough understanding of the impact of moisture on sensing behavior of the synthesized nanocomposites.

In this work, the Ag@SnO_2/g-C_3N_4 nanocomposites have been successfully synthesized and tested them for effective detection of acetone vapors at different operating temperature in atmospheric pressure conditions. To highlight the obtained results with literature, a comparative analysis of the acetone vapors detection/sensing performances of SnO_2/g-C_3N_4 based materials has been done and summarized in Table 2.

The synthesized nanocomposite (ZnC) based sensor employed in this work demonstrates notable sensitivity at a relatively reduced operating temperature with good repeatability and stability towards the detection of 1 µL acetone vapors in

© 2025 Wiley-VCH GmbH

23656549, 2024, 23, Downloaded from https://chemistry-europe.onlinelibrary.wiley.com/doi/10.1002/slct.202404081 by Delhi Technological University, Wiley Online Library on [26/06/2025]. See the Terms and Conditions (https://onlinelibrary.wiley.com/terms-and-conditions) on Wiley Online Library for rules of use; OA articles are governed by the applicable Creative Commons License

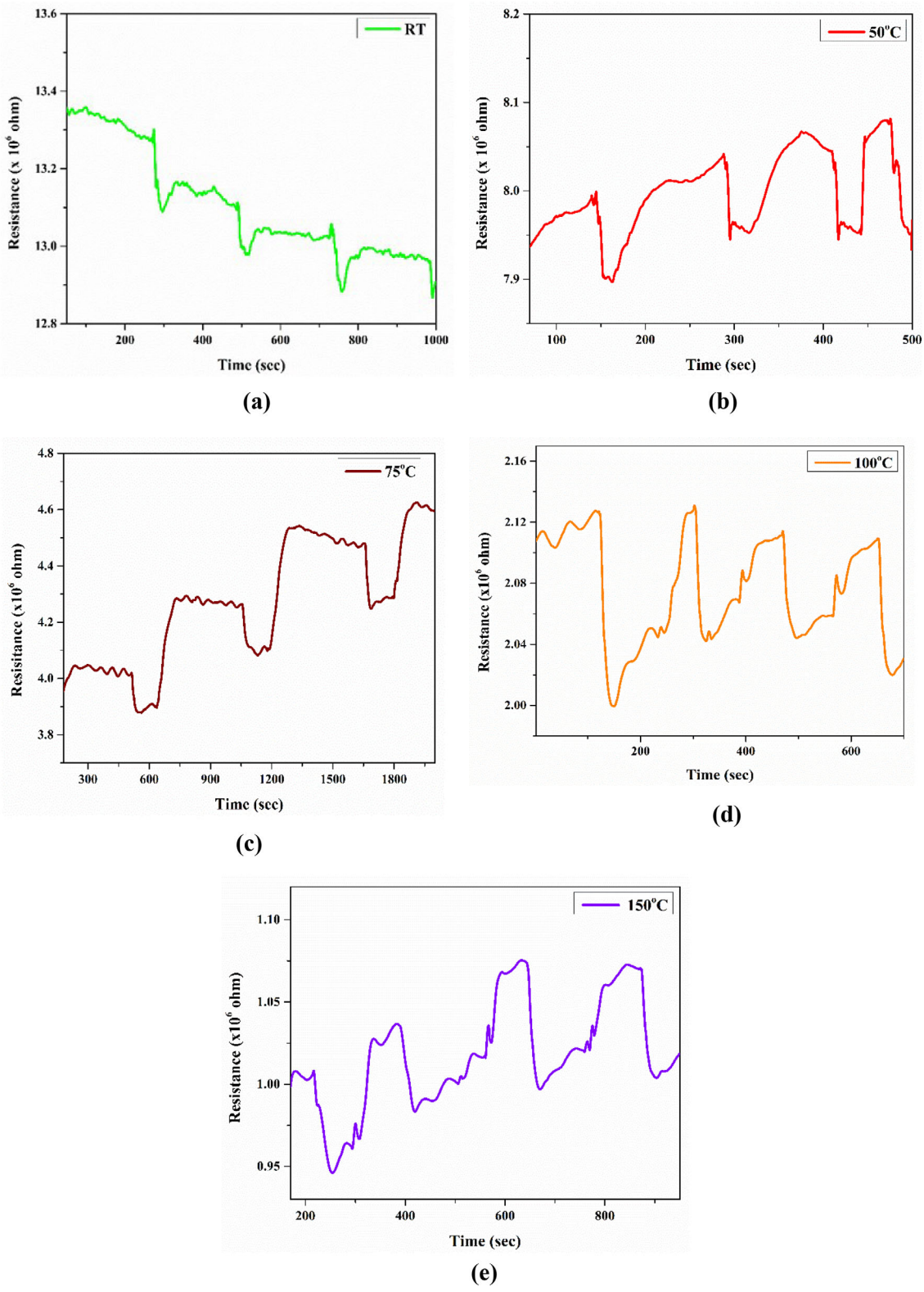


Figure 9. Gas sensing results of ZnA at (a) room temperature (RT), (b) 50 °C, (c) 75 °C, (d) 100 °C, and (e) 150 °C.

a 2 L volume sensing chamber at atmospheric pressure. These magnificent sensing results of Ag@SnO_2/g-C_3N_4 nanocomposites in open atmosphere indicates that the prepared sensor has potential for practical applications.[7,11]

4.2. Plausible Sensing Mechanism

As observed sensing results indicates decrease in resistance on insertion of acetone vapors suggesting n-type nature of the

© 2025 Wiley-VCH GmbH

23656549, 2024, 23, Downloaded from https://chemistry-europe.onlinelibrary.wiley.com/doi/10.1002/slct.202404081 by Delhi Technological University, Wiley Online Library on [26/06/2025]. See the Terms and Conditions (https://onlinelibrary.wiley.com/terms-and-conditions) on Wiley Online Library for rules of use; OA articles are governed by the applicable Creative Commons License

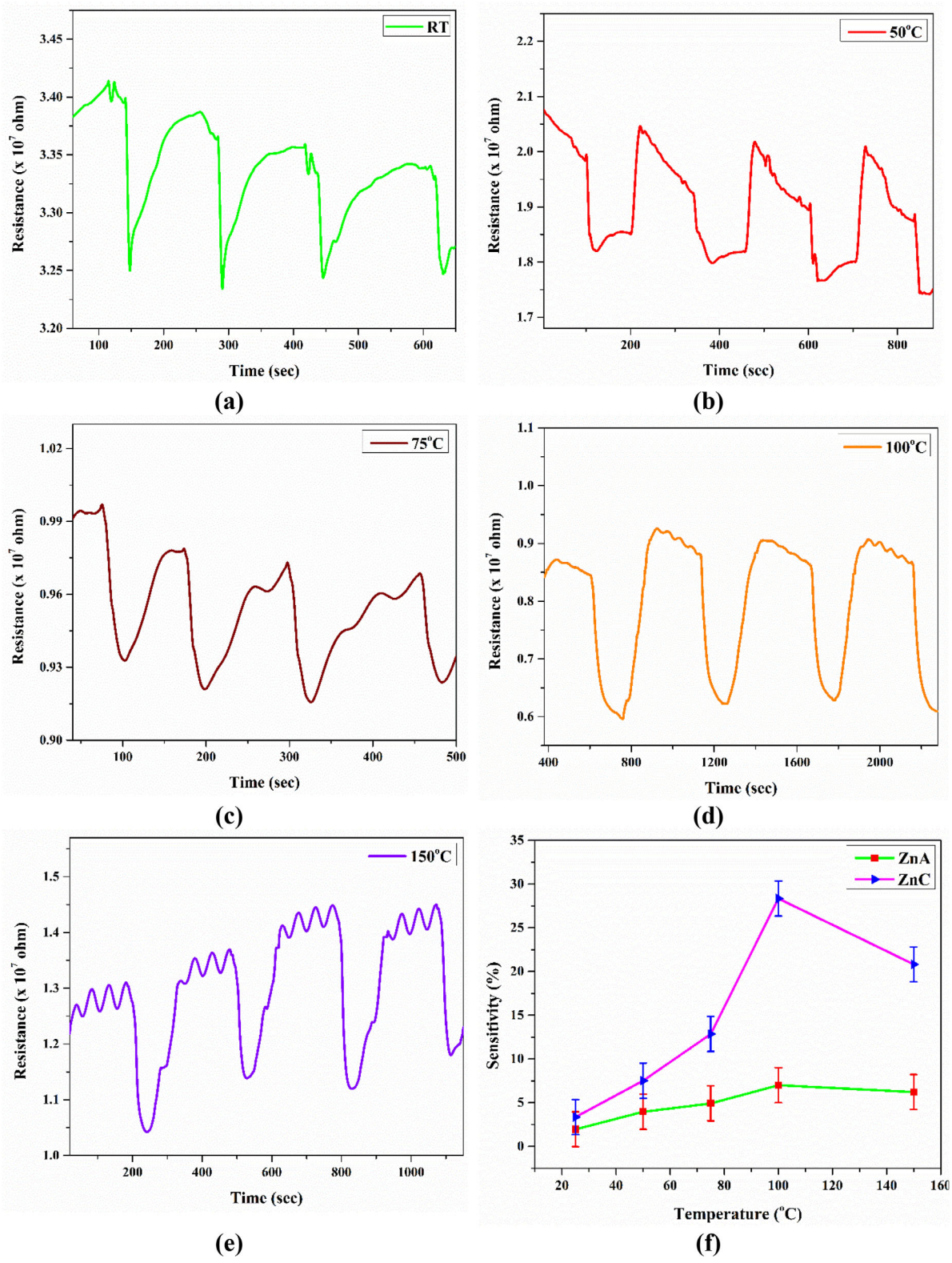


Figure 10. Gas sensing results of ZnC at (a) room temperature (RT), (b) 50 °C, (c) 75 °C, (d) 100 °C, (e) 150 °C, and (f) comparative sensitivity% versus temperature curve of ZnA & ZnC.

© 2025 Wiley-VCH GmbH

23656549, 2024, 23, Downloaded from https://chemistry-europe.onlinelibrary.wiley.com/doi/10.1002/slct.202404081 by Delhi Technological University, Wiley Online Library on [26/06/2025]. See the Terms and Conditions (https://onlinelibrary.wiley.com/terms-and-conditions) on Wiley Online Library for rules of use; OA articles are governed by the applicable Creative Commons License

Table 2. Various reported performance of g-C_3N_4 / SnO_2 based sensors towards acetone gas.

Material	Synthesis Technique	Morphology	Concentration (ppb/ppm)	Sensitivity	Operating Temperature (°C)	year/[ref]
SnO_2/g-C_3N_4	One-step calcination	2D C_3N_4-SnO_2 heterojuction	67 (ppb)	29 [V_g/V_a]	380	2017/[38]
g-C_3N_4/WO_3	Hydrothermal	g-C_3N_4/WO_3 nanosheets	100 (ppm)	35 [R_a/R_g]	340	2018/[43]
g-C_3N_4/WO_3	Hydrothermal	g-C_3N_4/WO_3 nanocomposite	1000 (ppm)	58.2[R_a/R_g]	310	2019/[42]
ZnO/SnO_2	Sol-gel	ZnO/SnO_2 nanocomposite	5 (ppm)	13.83%	180	2020/[9]
g-C_3N_4/CuO	Hydrothermal	Decoration of CuO nanoparticles on g-C_3N_4 sheets	1000 (ppm)	143.7[R_a/R_g]	Room temperature	2021/[10]
g-C_3N_4-NiO@SnO_2	One-pot calcination	Hetero-structural g-C_3N_4-NiO@SnO_2	100 (ppm)	150.3[R_a/R_g]	340	2024/[5]
Ag@SnO_2/g-C_3N_4	Hydrothermal	Ag decorated SnO_2/g-C_3N_4 nano-sheets	100 (ppm)	28%	100	This work

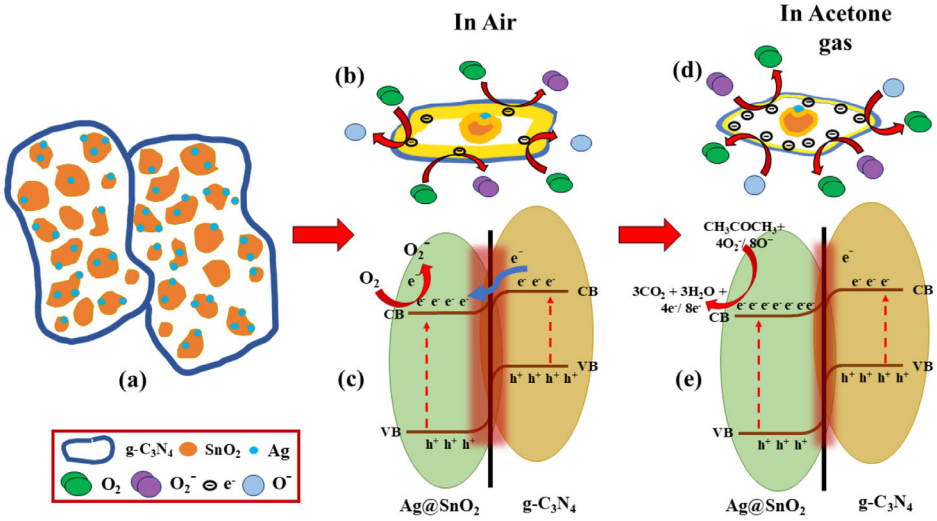


Figure 11. The Schematic diagram of the gas sensing mechanism of Ag@SnO_2/g-C_3N_4 (a) Illustration of the synthesized structure and (b–e) representation of depletion layer and energy band diagram in air and acetone, respectively.

Ag@SnO_2/g-C_3N_4 nanocomposites. The feasible sensing mechanism of the Ag@SnO_2/g-C_3N_4 nanocomposite based sensor towards the acetone vapors can be inferred as depicted in Figure 11.

As discussed above, in Equations (2–4) the adsorbed atmospheric oxygen at the surface of Ag@SnO_2/g-C_3N_4 nanocomposites at the optimum operating temperature are majorly converts in to O_2^- and O^- species by taking electron from the conduction band. Subsequently, leading to creation of an electron-depleted region known as the depletion layer and in turn increase in resistance of the sensing layer.[38,39]

When the sensor is exposed to acetone vapors, the surface adsorbed O_2^-/O^- species reduced by releasing electrons and the acetone vapors oxidized to carbon dioxide (CO_2) and water (H_2O). The adsorption energy of the various VOCs are different at the sensing materials, which is important parameter in determining the sensing properties of the material.[40,41] The potential reaction between the inserted acetone vapors and O_2^-/O^- species at the Ag@SnO_2/g-C_3N_4 nanocomposites surface is represented in Equations (5) and (6).[38,42] The reaction between oxygen species and the acetone vapors release electrons back to the conduction band thus lowering the bending of the energy band and leads to thinning of the depletion zone on the surface as shown in Figure 11d, e which takes the sensor in a low-resistance state. After removal of CO_2 and H_2O molecules from the surface of sensing layer again adsorption of atmospheric oxygen molecules starts. Which again starts increasing the sensor resistance and takes it to the base line value of resistance.

$$CH_3COCH_3\,(ads) + 4O_2^-\,(ads) \rightarrow 3CO_2 + 3H_2O + 4e^- \quad (5)$$

$$CH_3COCH_3\,(ads) + 8O^-\,(ads) \rightarrow 3CO_2 + 3H_2O + 8e^- \quad (6)$$

The outset sensing performance of the Ag@SnO_2/g-C_3N_4 nanocomposites were attributed to following factors. First, the larger surface area, which provides higher number of active sites

© 2025 Wiley-VCH GmbH

23656549, 2025, 23, Downloaded from https://chemistry-europe.onlinelibrary.wiley.com/doi/10.1002/slct.202404081 by Delhi Technological University, Wiley Online Library on [26/06/2025]. See the Terms and Conditions (https://onlinelibrary.wiley.com/terms-and-conditions) on Wiley Online Library for rules of use; OA articles are governed by the applicable Creative Commons License

for the adsorption, thus enhance the sensitivity. Along with that special nanostructure of 3D nanoparticles of Ag@SnO_2 on 2D g-C_3N_4 nanosheets had a large porosity, that favor effective diffusion of the oxygen molecules (O_2) and acetone vapors. Thus, the higher surface area and good porosity of the nanocomposites is one of the reasons for the better sensitivity. Second, the 3D-2D arrangement of the nanocomposites leads to modification of the energy band structures. This band bending as shown in Figure 11c leads to easy flow of electron from conduction band of g-C_3N_4 to Ag@SnO_2. That prompts the formation of the oxygen species at the surface due to larger availability of electrons in the conduction band of Ag@SnO_2. Hence, increases the width of depletion layer, resulting in heightened response in the presence of acetone vapors. Overall, the synergistic effect of surface area and facile electron transfer between the acetone and the nanocomposite leads to improved sensing behavior of the sensors.

5. Conclusions

In this study, Ag decorated SnO_2 (Ag@SnO_2) nanoparticles and its nanocomposite with g-C_3N_4 (Ag@SnO_2/g-C_3N_4) were synthesized using a one-step hydrothermal process. SEM images showed the formation of irregular shapes, Ag@SnO_2 nanoparticles, and sheet structure of g-C_3N_4 nanocomposites. SEM analysis further revealed that in ZnC nanocomposite, irregularly shaped Ag@SnO_2 particles were homogeneously dispersed on g-C_3N_4 nanosheets. Further, TEM analysis suggested the polycrystalline nature of both composite materials with fringe-type patterns. EDS analysis further established the purity of the nanocomposite samples. Further, their gas-sensing properties were investigated for the detection of acetone vapors. The observed sensitivity of ZnA and ZnC towards 1 µL of acetone vapors in 2 L sensing was between 7% and 28% at 100 °C, respectively. The superior acetone sensing of the ZnC nanocomposite with the energy band gap of 2.48 eV and surface area of 104.6 m^2/g can be attributed to the a) higher surface are that provides more active sites for gas molecules adsorption, b) strong catalytic activity of Ag nanoparticles, and c) the simplistic electron transfer between the acetone and the nanocomposite due to their band structure leads to improved sensing behavior of the sensors. The obtained sensing results proves the developed nanocomposite has potential as a sensing material for the detection of acetone vapors at the relatively lower operating temperature (100 °C) and atmospheric conditions for real time applications.

Acknowledgements

The authors like to acknowledge the administration of Delhi Technological University for their continual support and encouragement.

Conflict of Interests

The authors declare no conflict of interest.

Data Availability Statement

The data that support the findings of this study are available from the corresponding author upon reasonable request.

Keywords: Adsorption-desorption · Gas-sensing mechanism · g-C_3N_4 · Stannic oxide · Ternary nanocomposites

[1] J. A. S. Syed, X. Y. Zhang, W. J. Ding, A. D. Li, *J. Environ. Chem. Eng.* **2022**, *10*, 108745.
[2] S. D. Lawaniya, S. Kumar, Y. Yu, H. G. Rubahn, Y. K. Mishra, K. Awasthi, *Mater. Today Chem.* **2023**, *29*, 101428.
[3] S. Konwer, A. Begum, S. Bordoloi, R. Boruah, *J. Polym. Res.* **2017**, *24*, 1–10.
[4] S. Konwer, A. K. Guha, S. K. Dolui, *J. Mater. Sci.* **2013**, *48*, 1729–1739.
[5] X. Gu, J. Wang, N. Li, L. Gu, Y. Qian, G. Li, J. Hu, *Colloids Surf. A* **2024**, *691*, 133887.
[6] P. Srinivasan, S. Samanta, A. Krishnakumar, J. B. B. Rayappan, K. Kailasam, *J. Mater. Chem. A* **2021**, *9*, 10612-10651.
[7] Y. H. Ochoa-Muñoz, R. Mejía de Gutiérrez, J. E. Rodríguez-Páez, *Molecules* **2023**, *28*, 1150.
[8] M. A. M. Akhir, S. A. Rezan, K. Mohamed, M. M. Arafat, A. S. M. A. Haseeb, H. L. Lee, *Mater. Today: Proceed.* **2019**, *17*, 810–819.
[9] Y. Chen, Y. Cao, *RSC Adv.* **2020**, *10*, 35958-35965.
[10] A. Akhtar, C. Jiao, X. Chu, S. Liang, Y. Dong, L. He, *Mater. Chem. Phys.* **2021**, *265*, 124375.
[11] J. Cao, C. Qin, Y. Wang, B. Zhang, Y. Gong, H. Zhang, Z. Zhang, *Nanomaterials* **2017**, *7*, 98.
[12] Y. Masuda, *Sens. Actuators, B* **2022** *364*, 131876.
[13] J. P. Cheng, J. Wang, Q. Q. Li, H. G. Liu, Y. Li, *J. Ind. Eng. Chem.* **2016**, *44*, 1–22.
[14] A. Ibrahim, U. B. Memon, S. P. Duttagupta, I. Mahesh, R. S. Raman, A. Sarkar, S. S. V. Tatiparti, *Int. J. Hydrogen Energy* **2020**, *45*, 10623–10636.
[15] B. Pegu, S. Bordoloi, R. Boruah, S. Konwer, *J. Mater. Sci.: Mater. Electron.* **2022**, *33*, 27121–27131.
[16] A. Mohammad, M. E. Khan, M. R. Karim, M. H. Cho, T. Yoon, *Ceram. Int.* **2021**, *47*, 23578–23589.
[17] S. Ge, H. Zheng, Y. Sun, Z. Jin, J. Shan, C. Wang, F. Meng, *J. Alloys Compd.* **2016**, *659*, 127–131.
[18] A. Mohammad, M. R. Karim, M. E. Khan, M. M. Khan, M. H. Cho, *J. Phys. Chem. C* **2019**, *123*, 20936–20948.
[19] V. Khoramshahi, M. Azarang, M. Nouri, A. Shirmardi, R. Yousefi, *Talanta Open* **2024**, *9*, 100290.
[20] X. Gu, J. Wang, N. Li, L. Gu, Y. Qian, G. Li, J. Hu, *Colloids Surf. A* **2024**, *691*, 133887.
[21] J. Hu, C. Zou, Y. Su, M. Li, Z. Yang, M. Ge, Y. Zhang, *J. Mater. Chem. C* **2017**, *S0925–4005*, 31195-4.
[22] A. Mohammad, M. E. Khan, M. R. Karim, M. H. Cho, *Appl. Surf. Sci.* **2019**, *495*, 143432.
[23] D. Meena, B. Singh, A. Anand, M. Singh, M. C. Bhatnagar, *J. Alloys Compd.* **2020**, *820*, 153117.
[24] S. R. Adawiyah, Endarko, *Mater. Sci. Eng.* **2017**, *188*, 012062.
[25] J. V. Kumar, J. S. Ajarem, A. A. Allam, V. Manikandan, R. Arulmozhi, N. Abirami, *Environ. Res.* **2022**, *209*, 112814.
[26] H. B. Fang, Y. Luo, Y. Z. Zheng, W. Ma, X. Tao, *Ind. Eng. Chem. Res.* **2016**, *55* 4506–4514.
[27] D. Liu, J. Pan, J. Tang, W. Liu, S. Bai, R. Luo, *J. Phys. Chem. Solids* **2019**, *124*, 36–43.
[28] T. Sinha, M. Ahmaruzzaman, P. P. Adhikari, R. Bora, *ACS Sustainable Chem. Eng.* **2017**, *5*, 4645–4655.
[29] K. Saravanakumar, V. Muthuraj, *Optik* **2017**, *131*, 754–763.
[30] K. Gangwar, P. Jeevanandam, *J. Mol. Struct.* **2023**, *1285*, 135423.
[31] D. Meena, V. K. Verma, S. Rana, *Mater. Today: Proceed.* **2022**, *51*, 554–560.
[32] V. V. Pham, N. N. T. Pham, H. V. Le, T. M. Cao, *J. Environ. Chem. Eng.* **2023**, *11*, 111556.
[33] K. N. Van, H. T. Huu, V. N. N. Thi, T. L. Le Thi, D. H. Truong, T. T. Truong, Y. Vasseghian, *Chemosphere* **2022**, *289*, 133120.
[34] D. Meena, M. Jain, M. C. Bhatnagar, *J. Mater. Sci.* **2024**, *59*, 12177–12218.

© 2025 Wiley-VCH GmbH

23656549, 2024, 23, Downloaded from https://chemistry-europe.onlinelibrary.wiley.com/doi/10.1002/slct.202404081 by Delhi Technological University, Wiley Online Library on [26/06/2025]. See the Terms and Conditions (https://onlinelibrary.wiley.com/terms-and-conditions) on Wiley Online Library for rules of use; OA articles are governed by the applicable Creative Commons License

[35] P. Srinivasan, S. Samanta, A. Krishnakumar, J. B. B. Rayappan, K. Kailasam, *J. Mater. Chem. A* **2021**, *9*, 10612–10651.
[36] S. Das, S. Mojumder, D. Saha, M. Pal, *Sens. Actuators, B* **2022**, *352*, 131066.
[37] W. Guo, L. Huang, J. Zhang, Y. He, W. Zeng, *Sens. Actuators, B* **2021**, *334*, 129666.
[38] J. Hu, C. Zou, Y. Su, M. Li, Z. Yang, M. Ge, Y. Zhang, *Sens. Actuators, B* **2017**, *253*, 641–651.
[39] D. Meena, M. C. Bhatnagar, B. Singh, *Phys. B* **2020**, *578*, 411848.
[40] M. T. Ahmed, A. A. Roman, D. Roy, S. Islam, F. Ahmed, *Sci. Rep.* **2024** *14*, 3467.
[41] R. Khatun, M. H. Rocky, D. Roy, A. Al Roman, M. T. Ahmed, *Comput. Theor. Chem.* **2024**, *1239*, 114769.
[42] X. Chu, J. Liu, S. Liang, L. Bai, Y. Dong, M. Epifani, *J. Sens.* **2019**, *1*, 6074046.
[43] D. Wang, S. Huang, H. Li, A. Chen, P. Wang, J. Yang, J. Yang, *Sens. Actuators, B* **2019**, *282*, 961–971.

Manuscript received: August 26, 2024

© 2025 Wiley-VCH GmbH

23656549, 2024, 23, Downloaded from https://chemistry-europe.onlinelibrary.wiley.com/doi/10.1002/slct.202404081 by Delhi Technological University, Wiley Online Library on [26/06/2025]. See the Terms and Conditions (https://onlinelibrary.wiley.com/terms-and-conditions) on Wiley Online Library for rules of use; OA articles are governed by the applicable Creative Commons License

Electrical Engineering
https://doi.org/10.1007/s00202-025-03206-4

ORIGINAL PAPER

An effective dual-droop control for voltage source converter-based multi-terminal DC system

Ashima Taneja[1] · **Radheshyam Saha**[1] · **Madhusudan Singh**[1]

Received: 30 December 2024 / Accepted: 29 May 2025
© The Author(s), under exclusive licence to Springer-Verlag GmbH Germany, part of Springer Nature 2025

Abstract
Modern power systems having bulk renewable power integration via inverters are facing frequency instability issues today. This research work proposes an effective dual-droop control strategy for offering enhanced primary frequency support to asynchronous AC grids interconnected with VSC-based multi-terminal (VSC-MTDC) systems. It uses a dynamic value of frequency droop coefficient that varies according to disturbed or healthy state of the interconnected grids. In disturbed state, the VSC can offer frequency mitigation, by applying proposed frequency droop coefficient derived after negating mutual droop interaction in between P–V_{dc} and *P–f* droop. Also, frequency support from healthier grids can be quantified to a desirable value by using proposed *Power Support Index*. Additionally, considering headroom availability of VSC power transfer capability, design of dual-droop coefficients is proposed that keeps frequency & DC voltage deviations within limits. It is demonstrated that the proposed technique is capable enough to mitigate credible contingencies, e.g., for a 10% load increase, additional 38.1% active power support is offered via proposed control which is just 32.5% via conventional strategy. Also, for a 40% loss in wind power input, it is shown that DC voltage & frequency deviations are lesser and within permissible limits in comparison.

Keywords Dual-droop interaction · Droop-design · Current modulation · Desired power support · Frequency excursion

1 Introduction

With rapidly increasing demands of modern civilization along with widespread awareness about application of sustainable energy resources to curb carbon footprints, electrical grids are witnessing a major transition phase in which conventional hydrocarbon-based power generation is getting substituted with distant renewable power banks. With advanced forecasting techniques, it has become possible to certain extent to overcome variability and intermittency constraints associated with such resources. However, their bulk availability at remote locations makes it difficult to transmit power via high voltage AC (HVAC) transmission technology. For example, abundantly available offshore wind power is difficult to be transported via submarine AC cables due to significant charging current requirement imposed by them. To overcome such technical challenges along with an economic justification, high voltage direct current (HVDC) transmission technology has already been accepted as a suitable power transmission solution. With its rapid power flow control feature, asynchronous interconnection ability and comparatively inferior losses, HVDC transmission is the preferred choice for convenient integration of sustainable power resources with far located load centres [1].

Generally, line current commutation (LCC)-based HVDC transmission technology is being preferred for carrying remote bulk power but it suffers from certain limitations like pre-requisite of inverting into strong AC grids to avoid commutation failure, compulsory yet significant reactive power demand imposed by its converters, huge filtering requirements and its inability to offer rapid power reversal. On the contrary, its IGBT-based counterpart, i.e., voltage source converter (VSC) based HVDC transmission technology offers a wide band of desirable control features for example, decoupled power flow control, ability to invert into weak, passive, islanded networks along with being able to restore power supply to a black network, ability to behave capacitive as well as inductive, immediate power reversal capability, negligible filtering requirements and many more. VSC-based HVDC

✉ Ashima Taneja
tanejaashima.1988@gmail.com

[1] Department of Electrical Engineering, Delhi Technological University, New Delhi, India

Published online: 26 June 2025

transmission technology is also viable for creation of many of the upcoming multi-terminal direct current (MTDC) grids. MTDC grids (which are formed by connecting differently-located converter stations in parallel) can enhance the overall reliability of hybrid AC/DC grids as well as have the capability to create an ideal scenario suitable for economical and flexible power trading among multiple vendors and consumers [1, 2].

Integration of renewable power inside modern power system is generally made feasible using power electronics-based transmission solutions, thereby making power systems more vulnerable towards frequency instability issues. Consequently, frequent frequency excursions with higher rate of change of frequency (RoCoF) would be the main challenge of a power engineer. Therefore, it has become indispensable to provide faster response to such disturbances so that under frequency load shedding (UFLS) can be avoided. Hence, provision of frequency support via HVDC system is an important ancillary service requirement imposed by various national grid codes nowadays [1–4].

Many research papers in literature have made significant contributions for DC voltage control of the MTDC grids for maintaining power balance inside. With its enhanced reliability over Master Slave control and better performance than voltage margin control, DC voltage droop control has been well-accepted solution for autonomous power sharing (APS) provision inside MTDC grids [1–3]. Though, DC voltage droop control of VSC-based MTDC grid ensures a reliable control of DC voltage but it is incapable to provide frequency support to interconnected AC networks of the MTDC grid [4]. It has been proved in [5] that sharing of primary frequency reserves among the interconnected AC networks of MTDC grid enhances overall security and also can be justified economically as well. The detailed literature survey presented in the next section describes various control strategies proposed in the literature for achieving frequency support from the MTDC grids.

1.1 Literature survey

To ensure reliability of a VSC-based MTDC grid, power balance is maintained inside it through a decentralized DC voltage control. And, also to enhance security of its interconnected AC grids as well, by ensuring frequency support provision, Haileselassie and Uhlen [6] and Chaudhuri [7] have proposed a dual-droop control (DDC) scheme. Such DDC-based converter controller uses two droops: active power–DC voltage (P–V_{dc}) droop and active power–frequency (P–f) droop operating simultaneously. However, as pointed in [8], simultaneous operation of the droops of these kind results in an inefficient outcome as the two droops operate in opposite manner to one another. That is, when action of P–f droop tries to take additional power from the MTDC grid at the same time, action of P–V_{dc} droop would try to withhold some power inside the MTDC grid so as to avoid significant DC voltage deviation in it. To address this problem, a correction factor for P–f droop coefficient has been proposed in Akkari et al [9] which results in a comparatively efficient operation of DDC converter controller after a frequency excursion inside the interconnected AC grid. However, the derivation of this correction factor is based on an objectionable assumption of neglecting frequency deviations inside healthier AC grids interconnected with the MTDC system. Also, the suggested correction factor cannot improve dual-droop control interactions, during DC side disturbances like converter outage. In fact, its application results in more DC voltage deviation during such disturbances [4].

To avoid the mutual interaction among the two droops, it is proposed in [10], to use only P–f droop control for the VSCs exchanging power with the affected grid (which is undergoing load/generation unbalances) and also to disable P–V_{dc} droop control action in the same VSC controller. And similarly, for the VSCs exchanging power with the healthier grids, only P–V_{dc} droop control should be active while deactivating their P–f droop. By this technique, indeed, provision of fast and efficient frequency support along with stable DC voltage control is demonstrated. However, this control technique could not ensure security of all of the interconnected AC grids and reliability of the MTDC grid as well; which may get compromised by disabling action of one of the two droops at the respective converter controllers. Plus, there is a risk that healthier grids may undergo serious frequency deviation, while supporting the affected grid, since the amount of power support taken from them is not quantized at all. Moreover, it may not be advisable to employ this technique in scenarios where simultaneous load/generation unbalances in two or more interconnected AC grids, since this may threaten DC voltage stability of the MTDC system itself. Also, in this paper, demarcation between healthier and affected AC grids is done on basis of threshold values of frequency deviation and RoCoF. This presents an additional pre-requisite that measured value of RoCoF should be accurate enough for appropriate controller action to take place.

A similar control is also presented in [11]. Additionally, it is also proposed to take frequency support from offshore wind farms as well by extracting kinetic energy stored in their turbines. This is done by use of an offshore frequency-DC voltage (f_{off}–V_{dc}) droop at offshore converter controllers of the MTDC grid. Indeed, this will be able to offer an appreciable amount of active power which could be sufficient enough for the mitigation purpose, but it will introduce an additional risk of secondary frequency drop. This is because after utilizing energy stored in wind rotors, it takes a certain amount of time period by the wind turbine to recover back to its original speed and thus, resulting in its low power output.

Also, in [36], it is suggested to withdraw frequency support for the interconnected AC grids, using active power support from offshore wind farms. It is recommended to keep a certain amount of wind generation capacity in reserve, which can be used later during intervals of frequency disturbances. Although, with such an arrangement ample support would be provided to restore frequency stability, but it does not justify economically to keep available power into reserve.

An adaptive droop control for VSC-based MTDC systems is proposed in [12] in which the affected grid's frequency is allowed to make a nonlinear change in local DC voltage, thereby resulting in flow of additional power from the healthier grids. However, similar to [10], it can also result in serious frequency deviations inside the healthier grids, since the amount of power withdrawn from these has not been accounted.

In [13, 14], it is proposed to use an inertial droop along with P–V_{dc} and P–f droop for the VSC controllers of the MTDC system. Also, the VSC controller with the affected grid needs to send a distress signal that informs VSCs connected with the healthier grids about the disturbance type and its location. In this technique, a VSC exchanging power with the healthier grid has the flexibility to choose to not to participate in providing power support to the affected grid by switching to constant power control mode. In addition, in this technique, the droop coefficients have been designed in such a way that all the participating AC grids achieve a desired ratio of frequency deviations among them as prescribed by their system operator. However, the procedure illustrated to design these droop coefficients requires complex matrix computations. Moreover, similar to [6, 7], no remedy has been suggested to avoid mutual control interaction among DC voltage, frequency & inertial droops. Nevertheless, performance of this control technique depends upon reliability of communication network used to send the distress signal. Additionally, the time delay associated with it, could not guarantee exact achievement of the prescribed frequency deviation ratio among the grids.

In [15], a virtual synchronous generator (VSG)-based control scheme has been proposed to provide inertial as well as primary frequency support through a VSC-based MTDC system. It utilizes an adaptive DC voltage droop technique which ensures shouldering of unbalanced power among the healthier grids in a way so that frequency deviation in them gets limited. To ensure faster sharing of unbalanced power, a sensitivity coefficient has also been proposed. However, basis for selection of this coefficient and its influence from stability point of view remains unaddressed. Nevertheless, the same objectives could have been achieved by choosing appropriate DC voltage droop coefficients for the DDC-controlled grid converters, according to power generation capacities of their respective interconnected AC grids.

A communication-less hybrid DDC scheme has been proposed for bipolar configurated VSC-MTDC system, in which one pole converter controller utilizes only P–f droop control while P–V_{dc}–f droop is enabled at the other pole controller [16]. However, for achieving desired performance, it requires a dedicated slack VSC which should be operating in constant DC voltage control mode. Thus, imposing a stringent prerequisite for its interconnecting AC network, that it should be stiff enough because it won't be getting any frequency support from the VSC-MTDC system.

The same authors have proposed an interaction-less duo control strategy for a true-bipolar configurated VSC-MTDC system in [17], using P–f droop control at one pole converter controller and V_{dc}–P droop control at the other. Similar to [16], it too requires the slack VSC controller, and hence, it is not generic enough since it is only suitable for bipolar configurations. Moreover, such 'interaction-less operation' is only guaranteed as long as the slack VSC is able to maintain power balance inside the MTDC grid. And after saturation of the slack VSC, the performance of the proposed controller is same as that of any traditional DDC scheme like [6] and [7].

In [18], it is proposed to utilize MTDC systems for provision of both primary and secondary frequency support, because of its ability to share online spinning reserves among its interconnected asynchronous AC grids. Except one grid converter utilizing dedicated DC voltage control, all the other grid converters operate with P–f droop control. Therefore, like [16, 17], it too requires provision of a slack VSC having constant V_{dc} control, thereby impairing reliability of the DC grid. In addition, a high-communication bandwidth channel is required for transmitting frequency information of each AC grid to each converter controller of the MTDC system, thereby increasing investment costs.

In [19], an improved dual-droop controller using P–V_{dc}–f droop has been proposed. To avoid mutual interaction among the droops, a dedicated design procedure for P–f-droop coefficients is used that can provide enhanced frequency support with minimum or even no DC voltage deviation inside the MTDC grid. This technique requires a centralized controller that generates (online) a common frequency reference signal for all the interconnected AC grids by using weighted sum of actual operating frequency of all the grids. According to this reference frequency value, each of the grid converters may either take/give power from/to the MTDC grid. However, similar to [18], it too requires significant investments costs to be rendered for setting up large communication bandwidth channel for transmission of data viz., each VSC's operational status, power carried by it, etc. in addition to frequency information of all the grids need to be delivered to each and every grid converter controller. This control strategy is not generic enough, since it utilizes a common frequency reference signal for every dual-droop converter controller. And thus, as it

can only be used when all the interconnected AC grids with the MTDC system have same nominal power frequency (i.e., either 50 Hz or 60 Hz).

In [20], the interconnected AC grids with the MTDC system are classified into two categories: those which require active power support (RAPS) and others which provide active power support (PAPS). VSCs coupled with RAPS grids are controlled in AC slack bus mode and thus, exchange exact amount of unbalanced power required by them with the PAPS grids via MTDC system. Although, this control strategy results in a fast and efficient mitigation for frequency excursion occurring in the RAPS region, but this can result in serious frequency deviations in the PAPS regions because the amount of power support released by PAPS regions is not quantized. In addition, no provision for offering frequency support to the PAPS regions from the MTDC system has been ensured. Moreover, there is additional risk in maintaining DC voltage stability of the MTDC system, in case if one or more VSCs coupled with PAPS grids undergo an outage during a load/generation event in the RAPS region.

A nonlinear adaptive dual-droop control scheme that uses P–$V_{dc}{}^{1/2}$–$f^{1/2}$ droop for sharing of online spinning reserves among the asynchronous AC grids interconnected via VSC-MTDC system has been proposed in [21]. Similar to [6, 7, 13, 14] it too does not mitigate the effects of mutual interaction among the droops and thus, offers compromised operational efficiency.

A novel dynamic additional frequency support scheme for VSC-based MTDC systems has been proposed in [22]. It is basically a dual-droop technique using a dynamic frequency droop coefficient whose value depends upon the magnitude of encountered frequency deviation. Although an efficient operation has been demonstrated, but, this control strategy is also unable to improve the mutual interaction among the two droops, thereby, it can only offer limited amount of active power support. Although, this control technique also endeavours to minimize the resultant DC voltage deviation occurring in the MTDC system by implementing an additional DC voltage correction control. However, this could only be extravagant. This is because if sufficient amount of active power support to the affected grid is already imparted from the MTDC system, then the DC voltage deviation would be smaller and hence, will not require any correction control.

In [23], a P–V_{dc}–f based dual-droop controller is used for each of the grid VSC. To nullify mutual droop interaction, similar to [10, 11], it too suggests deactivating P–V_{dc} droop action at the converters exchanging power with the affected grid. Thereby, posing risk to security and reliability of the AC/DC grids. Also, like in [13, 14], the VSCs with the affected grid must send a distress signal, to other healthier grids. This control scheme uses a dedicated droop coefficient design algorithm that incorporates frequency dead band so that the desired ratio of frequency deviation among all the interconnected AC grids as prescribed by the operator can be attained. The algorithm used for design of droop coefficients is tedious and requires complex matrix computations. In addition, deactivation of one of the two droops at each grid converter controller during simultaneous outage of any grid VSC coinciding with a frequency excursion, can pose DC voltage stability at significant risk.

In [24], an adaptive DDC scheme has been proposed for efficient frequency and DC voltage regulation. To negate mutual droop interaction, it uses same correction factor as proposed in [9] at the VSC controller connected with the affected grids. And similar to [10], it too deactivates action of P–f droop at the VSCs with the healthier grids. Although, this control strategy ensures efficient frequency support along with minimum DC voltage deviation but it makes the MTDC system vulnerable to DC voltage instabilities in case of multiple converter outage. It should be noted that although the affected grid is able to withdraw the required amount of power support from the supporting grid, but the support taken remains unquantifiable, which may put supporting grids at the verge of frequency instabilities.

Few papers, for example, [25–28] use capacitors as electrostatic energy storage devices to extract frequency support from DC grid to AC grid. It has been noted that by application of this strategy, all the healthier grids remain immune from the effect of frequency disturbance in the affected AC grid. Also, DC voltage deviations are maintained within the permissible limits during a single area disturbance. However, for achieving desired amount of power support, sufficient for being able to mitigate a frequency excursion, it is required to make huge investments by employing supercapacitors at the converter stations. Also, such type of control strategy uses a single slack VSC for DC voltage control, which is not desirable from system's reliability point of view. Moreover, in this control technique, only the AC grid interconnected with the slack VSC is able to withdraw frequency support from the MTDC system. Thereby, making it difficult to impart frequency support to all the grids connected with the MTDC system. Thus, even after making huge equipment investments, still reliability and security of the AC/DC system cannot be ensured.

It has been transpired from the modest literature survey that many of the reported techniques in literature have used DDC without correcting mutual influence of droops on each other. Not all of the listed control techniques are designed for providing both enhanced frequency support and better DC voltage regulation as well. Most of the aforesaid techniques are designed for taking power support from the healthier grids without quantizing its amount, thereby, inherently introducing risk of frequency instability. Furthermore, none of these techniques consider provision of additional active power support when grid converters are loaded near their rated limits.

Table 1 Comparison of various state-of-art control strategies

State of the art controller	Proposed control	Advantages	Disadvantages
System frequency support through multi-terminal DC (MT-HVDC) Grids [6, 7]	• Uses dual-droop controller (P–V_{dc} droop for DC voltage regulation & P-f droop for frequency support)	• Reliability of MTDC grid ensured via DC voltage droop control • Security of the interconnected AC grids gets enhanced by taking frequency support from the MTDC system	• Inefficient operation due to droop interaction • Frequency support offered is not quantized
Interaction between voltage droop and the frequency droop control for multi-terminal HVDC systems [8, 9]	• Uses dual-droop controller • A correction factor proposed for frequency droop coefficient to negate effect of P-Vdc droop action on P-f droop	• Same as [6, 7] • Efficient frequency support is offered in comparison to [6, 7]	• Neglects frequency deviations in healthier grids • Suggested correction factor is invalid in case of converter outages
Fast frequency response from offshore multi-terminal VSC–HVDC schemes [10, 11]	• Uses dual-droop controller • Activates only P-f droop and withholds P-Vdc droop action for VSC with affected grid & vice versa for VSC with supporting grid	• Fast frequency support • Minimum DC voltage deviation • More efficient than [6–9]	• DC voltage stability at risk in case of simultaneous outage • Since support not quantized, supporting grids at frequency instability risk
Dual-droop control using ratio-based selective inertial and primary frequency support [13, 14]	• Uses Inertial droop along with Dual-droop control • Proposes an algorithm to design droop coefficients so that frequency deviation among the grids is in a prescribed ratio by the operator	• Same as [6, 7] • Additional inertial droop enhances the effective inertia of the system and reduces RoCoF • More flexibility for individual grid operators	• Droop interaction has not been rectified • Uses complex matrix computation
Interaction-less duo control strategy [16, 17]	• Uses P-Vdc droop for one pole VSC and P-Vdc-f droop for another pole converter	• Fast frequency support • Minimum DC voltage deviation • More efficient than [6–9]	• Compulsory slack VSC having constant V_{dc} control is required • Non-generic as suitable for bipolar configurations only
Frequency response reserves sharing across asynchronous grids through MTDC system [18]	• Uses P-f droop controller at all the grid converters except one using constant V_{dc} control	• Fast frequency support • Minimum DC voltage deviation • More efficient than [6–9]	• Compulsory slack VSC having constant V_{dc} control is required • Requires large amount of information to be transmitted via communication channels
Primary frequency support through North American continental HVDC interconnections with VSC-MT-HVDC systems [19]	• Uses dual-droop control • A reference frequency signal is generated for each grid VSC controller such that action of P-V_{dc} droop can be negated for efficient power support	• Minimum or zero DC voltage deviation • More efficient than [6–9]	• Requires large amount of information to be transmitted via communication channels • Non-generic, as all the interconnected grids should have same nominal frequency
Primary frequency support strategy for MTDC system with enhanced DC voltage response [23]	• Uses dual-droop control • Also proposed to deactivate action of one droop • Mathematical algorithm proposed to design droop coefficients after keeping into consideration frequency dead band effects	• Fast frequency support • Minimum DC voltage deviation • More efficient than [6–9] • More flexibility for individual grid operators	• Same as [10, 11] • Uses complex matrix computation

Table 1 (continued)

State of the art controller	Proposed control	Advantages	Disadvantages
Inertia emulation controller for multi-terminal VSC-HVDC system [25–27]	• Proposes to utilize electrostatic energy stored in capacitors for extending frequency support to the disturbed grid • Proposes design of capacitor so that ample amount of support can be rendered while keeping DC voltage within limits	• Frequency disturbances of one grid does not affect any other interconnected grids • DC voltage limits are always maintained within the permissible limits	• Requires huge investment costs on station equipment • Compulsory slack VSC having constant V_{dc} control is required • Frequency support to only one interconnected grid can be offered

In this paper, a flexible and efficient dual-droop control technique is proposed for dual-droop controlled converters of VSC-based MTDC system with provision of rapid and enhanced frequency and better DC voltage regulation as well. In the proposed work, a novel power–frequency droop control is proposed which can work efficiently by mitigating the negative impact imposed by the P–V_{dc} droop control that too without deactivating action of the DC voltage droop control. To avoid large frequency deviations inside the healthier grids, a Power Support Index (PSI) is proposed. This ensures that power support from healthier grids is quantized to a desired value and In addition, the proposed technique is robust while mitigating simultaneous multiple-area AC/DC disturbances. In the proposed work, dynamic converter current modulation (DCCM) technique, proposed in [35], is employed which can efficiently utilize permissible operational region of IGBT-based VSC for enhanced active power support even if converters are operating near their rated limits. A dedicated algorithm for design of frequency droop coefficients for P–f droop control is also proposed. A qualitative & quantitative comparative of various state-of-the-art control techniques [6–23] is presented in Table 1.

With novelty of the presently proposed control scheme, the major contributions of authors in this paper are listed as:

1. Provision of efficient DC voltage and frequency regulation that relies on local measurements only.
2. Coherent operation of frequency and DC voltage droop controls without compromising security and reliability of the AC/ DC grids.
3. Design of frequency droop coefficients considering sufficient active power head room availability at grid converters and ensuring DC voltage and frequency deviations lie within the desired limits.
4. Use of DCCM technique for carrying additional power support while grid converters are operating near to their rated limits.
5. Quantizing the amount of power support obtained from the healthier grids to avoid serious frequency deviation in them.
6. Availability of frequency support provision for all of the interconnecting AC grids with the MTDC system.

This paper has total eight sections. These are outlined as: with Sect. 1 as Introduction and Literature Survey, Sect. 2 has configuration of the considered system and its parameters. Section 3 presents the DCCM technique in brief. Section 4 presents the traditional DDC technique for MTDC system and frequency and DC voltage dynamics associated with it. Section 5 details about the dedicated algorithm proposed for design of frequency droop coefficient for the dual-droop controlled converters. Section 6 presents the proposed dual-droop control technique for obtaining enhanced frequency support from the MTDC grid along with better DC voltage regulation. Section 7 presents the simulation of the proposed control technique and its results obtained after applying various AC and DC disturbances in the considered MTDC system. The paper is concluded in Sect. 8.

2 System configuration

Figure 1 shows single line diagram for the considered VSC-based MTDC system interconnecting six independent AC grids. Each grid is interfaced with MTDC system using one VSC. The MTDC system receives power infeed from two offshore wind farms (OWFs), OWF1 and OWFII. Three independent onshore AC grids (ONGs), ONG-1, ONG-2 and ONG-3 invert power from the MTDC system using their respective onshore converters, VSC-1, VSC-2 and VSC-3. Each of these onshore VSCs are enabled with a dual-droop control and thus, can participate in power balancing of the MTDC system as well as frequency support. Each of the onshore grids is represented by a single generator equivalent. One offshore platform is connected to the MTDC system via Terminal-4 and is used to satisfy load requirements of its interfacing marine grid. The three offshore VSCs, VSC-4, VSC-5 and VSC-6, exchange constant power with the MTDC grid.

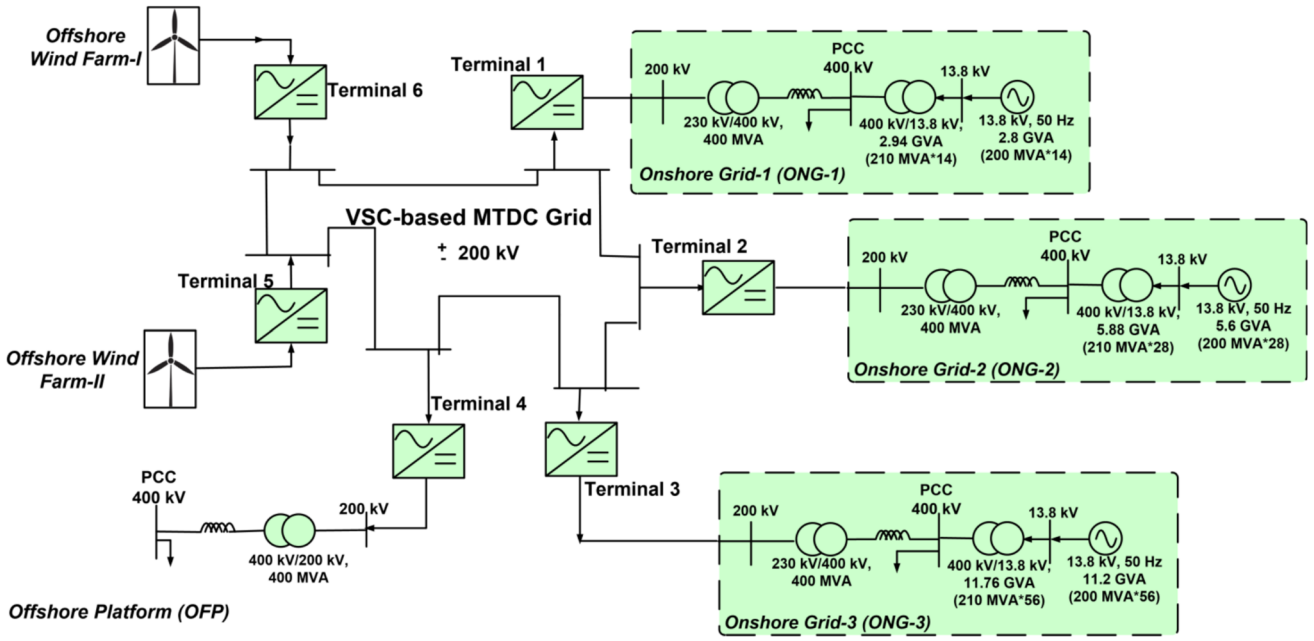


Fig. 1 System configuration for considered six-terminal-VSC-based MTDC system

The HVDC lines of the MTDC system are modelled using two cascaded pi-sections for which inductive and capacitive dynamics are neglected. The alternators of the onshore grids are supported with excitation system of type IEEE AC1A and standard steam-turbine-governor model of IEEE [29, 30]. The grid VSCs are represented by average order switching models and symmetrical monopolar configuration is chosen for the VSCs of the MTDC system. Table 2 shows AC and DC parameters of the considered system.

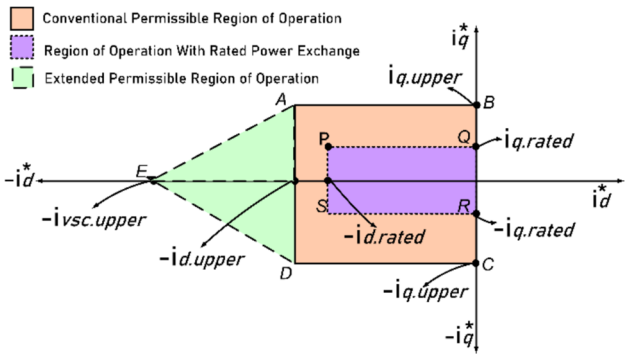


Fig.2 Region of operation for a vector current controlled VSC in inverter mode

3 Dynamic Converter Current Modulation (DCCM) technique

When grid VSCs are controlled via traditional vector current control, reference direct and quadrature axes converter currents generated in outer control loop, viz., i_d^* & i_q^* are often limited to $i_{d.upper}$ and $i_{q.upper}$ limits, to avoid overcurrent in their IGBT valves. Due to these imposed limits, the VSC can only operate inside rectangular region *ABCD* as shown in Fig. 2. It shows region of operation for a vector current controlled VSC acting in inverter mode.

For purpose of maximizing amount of active power that can be transferred by IGBT-based VSC especially during contingencies e.g., frequency disturbances arising due to load/generation unbalances; it is desirable to perform the technique of Dynamic Converter Current Modulation (DCCM) which is proposed in [35]. In this technique, i_d^* is allowed to take value as high as maximum allowable valve current, $i_{vsc.upper}$ which is usually up to 1.3 to 1.5 times rated valve current [31]. Depending upon intensity of the encountered load/generation unbalances, resultant frequency deviations are categorized as small (Δf_{small}), medium (Δf_{medium}) and large (Δf_{large}) frequency excursions. The modulation of the reference converter currents corresponding to these excursions of varying magnitudes is summarized in Table 3. Here, (Δf_{DB}) is frequency dead band range considered for the grid interfaced with the converter.

It should be noted that this DCCM technique is applicable for scenarios where converters are loaded at or near to their rated limits and is only required whenever it is required to exchange active power with local AC grid which is more than the rated power of the converter. It is assumed that before occurrence of the frequency disturbance, that is during steady state conditions, the VSC was carrying rated active

Table 2 AC–DC System Parameters

System components	Ratings
Onshore Grids (ONG-1, ONG-2 and ONG-3)	
AC system	230 kV, 50 Hz
Synchrnous generator equivalent	
a. Rated MVA	ONG-1: 14*200MVA, 50 Hz
	ONG-2: 28*200MVA, 50 Hz
	ONG-3: 56*200MVA, 50 Hz
b. Power generation and equivalent governor droop	0.75 pu, 0.05 pu
Generator transformer equivalent	13.8 kV/230 kV,
	ONG-1: 14*210MVA, 50 Hz
	ONG-2: 28*210MVA, 50 Hz
	ONG-3: 56*210MVA, 50 Hz
Onshore Grid Converters (VSC-1, VSC-2 and VSC-3)	
Rated power	400 MVA
DC voltage	± 200 kV
Reactive power setpoint	80 MVAR (capacitive)
Control mode	P–V_{dc}–f control with constant Q-control
Offshore wind farm	
AC system	66 kV, 50 Hz
OWF1 infeed	780 MW
OWF-II infeed	400 MW
Offshore platform	
AC system	11 kV, 50 Hz
Power demand	60 MW
MTDC grid	
Length of DC lines	75 km
Parameters of DC cables	r = 0.139 mΩ /km, l = 15.9 mH/km, c = 23.1 μF/km
DC capacitance	70 μF

Table 3 Modulation of reference converter currents for different frequency excursion scenarios

Scenario↓	Frequency deviation	i_{d}^{*}	i_{q}^{*}	Net VSC current, i_{vsc}
Steady state	$\lvert\Delta f\rvert \le \Delta f_{DB}$;	$i_{\mathrm{d}}^{*} = i_{\mathrm{d.rated}}$;	$i_{\mathrm{q}}^{*} = i_{\mathrm{q.rated}}$;	$i_{\mathrm{vsc}} = \sqrt{\left(i_{\mathrm{d}}^{*}\right)^2 + \left(i_{\mathrm{q}}^{*}\right)^2}$;
Small excursion	$\Delta f_{\mathrm{small}} \ge \lvert\Delta f\rvert \ge \Delta f_{\mathrm{DB}}$;	$-i_{\mathrm{d.upper}} \le i_{\mathrm{d}}^{*} \le i_{\mathrm{d.upper}}$		$i_{\mathrm{vsc}} \le i_{\mathrm{vsc.upper}}$
Medium excursion	$\Delta f_{\mathrm{medium}} \ge \lvert\Delta f\rvert \ge \Delta f_{\mathrm{small}}$;	$-i_{\mathrm{d.new.1}} \le i_{\mathrm{d}}^{*} \le i_{\mathrm{d.new.1}}$		
Large excursion	$\Delta f_{\mathrm{large}} \ge \lvert\Delta f\rvert \ge \Delta f_{\mathrm{medium}}$; or$\lvert\Delta f\rvert > \Delta f_{\mathrm{large}}$;	$-i_{\mathrm{d.new.2}} \le i_{\mathrm{d}}^{*} \le i_{\mathrm{d.new.2}}$	$i_{\mathrm{q}}^{*} = i_{\mathrm{q.min}}$;	

and reactive power corresponding to which the values of converter currents are equal to their rated values, viz., $i_{\mathrm{d.rated}}$ and $i_{\mathrm{q.rated}}$. Hence, VSC has been operating inside region marked as *PQRS* in the Fig. 2 during the steady state.

When the magnitude of the encountered frequency excursion is less than or equal to $\Delta f_{\mathrm{small}}$, the value of reference direct-axis converter current (i_d^{*}) is increased from its pre-disturbance value to up to value equal to $i_{\mathrm{d.upper}}$. While, i_{q}^{*} is retained at its original pre-disturbance value. Similarly, for the case of medium frequency excursion, when the magnitude of the encountered frequency deviation is more than $\Delta f_{\mathrm{small}}$ but less than or equal to $\Delta f_{\mathrm{medium}}$, i_{d}^{*} can be increased to a value equal to $i_{\mathrm{d.new.1}}$ which is equal to $\sqrt{\left(i_{\mathrm{vsc.upper}}\right)^2 - \left(i_{\mathrm{q}}^{*}\right)^2}$. Also, in the medium excursion scenario, i_{q}^{*} still remains equal to the original pre-disturbance

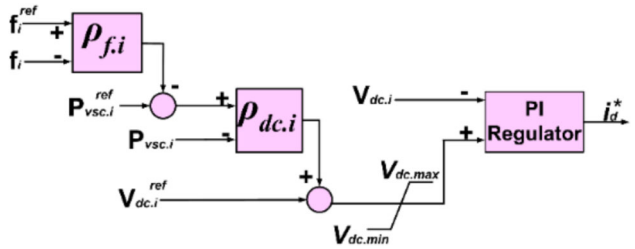


Fig. 3 Block diagram representation for traditional dual-droop control scheme for any *i*th VSC of MTDC grid

value. Therefore, for both small & medium excursion scenarios, enhanced active power support is provided as $i_d{}^*$ is increased from the original value. At the same time, reactive power support offered by the VSC remains unaltered.

However, in case of a disturbance of higher magnitude resulting in a large frequency excursion (Δf_{large}) or even more, $i_d{}^*$ is allowed to take value to the extent of $i_{\text{vsc.upper}}$. At this time, $i_q{}^*$ is reduced to a threshold value equal to $i_{\text{q.min}}$. Thus, $i_d{}^*$ gets maximum value equal to $i_{\text{d.new.2}}$ i.e., $\sqrt{(i_{\text{vsc.upper}})^2 - (i_{\text{q.min}})^2}$. This results in maximum amount of active power injected by a VSC into the grid undergoing load/generation unbalance, that too, with a slightly reduced reactive power support. Despite of the compromised reactive power support, AC voltage stability of this network is better than when no such modulation is performed [35]. Also, in all these frequency excursion scenarios, the operating point of the VSC is allowed to take any value within the region, *ABCDE*, as shown in the Fig. 2. It should be noted that for application of DCCM, it is assumed that occurrence of AC fault of any type does not coincide with frequency excursion in the same AC grid.

4 Traditional dual-droop control and associated DC voltage and frequency dynamics

The traditional dual-droop control (DDC) scheme for enabling bidirectional power flow control via VSCs of MTDC grid for the provision of frequency support and DC voltage regulation is shown in Fig. 3. The block diagram shows the generation of $i_d{}^*$ for any *i*th dual-droop controlled VSC of the MTDC grid.

For any *i*th VSC, the generation of the direct-axis reference current ($i_d{}^*$) is done by PI processed error of reference DC voltage ($V_{\text{dc}.i}{}^{\text{ref}}$) and locally measured DC voltage ($V_{\text{dc}.i}$). Frequency deviation of the *i*th AC grid, i.e., difference of nominal grid frequency ($f_{\text{nom}.i}$) and actual grid frequency (f_i) is used to modify the power reference ($P_{\text{vsc}.i}{}^{\text{ref}}$) of the VSC. $P_{\text{vsc}.i}$ represents the actual power transmitted by the *i*th VSC.

The mathematical representation for generation of $i_d{}^*$ can be given by:

$$i_{\text{d}}^* = \left[V_{\text{dc}.i}^{\text{ref}} - V_{\text{dc}.i} + \rho_{\text{dc}.i} \left(P_{\text{vsc}.i}^{\text{ref}} - P_{\text{vsc}.i} - \rho_{f.i}(f_{\text{nom}.i} - f_i) \right) \right] . \left(k_P + \frac{k_I}{s} \right) \tag{4.1}$$

k_P and k_I are proportional and integral gain considered for PI regulator used for the grid VSCs. $\rho_{\text{f.i}}$ is the *P–f* droop coefficient while $\rho_{\text{dc.i}}$ is the *P–V*$_{\text{dc}}$ droop coefficient for the *i*th VSC's dual-droop controller. For those VSCs which are not taking part in power flow control of the MTDC system, e.g., offshore VSCs, their ρ_{dc} is set as infinite and ρ_{f} as zero. The power transferred by the *i*th grid VSC using (4.1) is:

$$P_{\text{vsc}.i} = P_{\text{vsc}.i}^{\text{ref}} + \frac{1}{\rho_{\text{dc}.i}} \left(V_{\text{dc}.i}^{\text{ref}} - V_{\text{dc}.i} \right) - \rho_{f.i}(f_{\text{nom}.i} - f_i) \tag{4.2}$$

Performing small signal analysis in per units on (4.2),

$$\Delta P_{\text{vsc}.i.\text{pu}} = \Delta P_{\text{vsc}.i.\text{pu}}^{\text{ref}} - \frac{1}{\rho_{\text{dc}.i}} . \Delta V_{\text{dc}.i.\text{pu}} + \rho_{f.i} . \Delta f_{i.\text{pu}} \tag{4.3}$$

Let $P_{vsc.nom.i}$ be the nominal power rating of the *i*th VSC of the MTDC grid. Using (4.3),

$$\Delta P_{\text{vsc}.i} = \Delta P_{\text{vsc}.i}^{\text{ref}} - \frac{P_{\text{vsc.nom}.i}}{\rho_{\text{dc}.i}} . \Delta V_{\text{dc}.i.\text{pu}} + P_{\text{vsc.nom}.i} . \rho_{f.i} . \Delta f_{i.\text{pu}} \tag{4.4}$$

Summing power deviations made by all the VSCs of the MTDC grid,

$$\sum_{i=1}^{n} \Delta P_{\text{vsc}.i} = \sum_{i=1}^{n} \Delta P_{\text{vsc}.i}^{\text{ref}} - \sum_{i=1}^{n} \frac{P_{\text{vsc.nom}.i}}{\rho_{\text{dc}.i}} . \Delta V_{\text{dc}.i.\text{pu}} + \sum_{i=1}^{n} P_{\text{vsc.nom}.i} . \rho_{f.i} . \Delta f_{i.\text{pu}} \tag{4.5}$$

Here, '*n*' is the total number of converters in the MTDC grid of Fig. 1. Due to autonomous power sharing ensured by the three onshore dual-droop controlled VSCs, the sum of power deviations made by all the VSCs of the MTDC grid is zero, i.e., $\sum_{i=1}^{n} \Delta P_{\text{vsc}.i} = 0$. Assuming negligible switching and resistive losses in the MTDC grid and equal voltage deviation at all the MTDC buses, that is, $\Delta V_{\text{dc}.i.\text{pu}} = \Delta V_{\text{dc.pu}}$,

(4.5) can be modified as,

$$\Delta V_{\text{dc.pu}} = \frac{\sum_{i=1}^{n} \Delta P_{\text{vsc}.i}^{\text{ref}} + \sum_{i=1}^{n} P_{\text{vsc.nom}.i} \cdot \rho_{f.i} \cdot \Delta f_{i.\text{pu}}}{\sum_{i=1}^{n} \frac{P_{\text{vsc.nom}.i}}{\rho_{\text{dc}.i}}} \tag{4.6}$$

The above equation shows resultant DC voltage deviation due to disturbance of any type occurring in the AC/DC system. For evaluation of frequency dynamics, considering AC and DC disturbance events separately.

4.1 AC disturbance event

Assuming, all the grid converters are in healthy state, i.e., $\Delta P_{\text{vsc}.i}^{\text{ref}} = 0$. Different possible AC disturbance events can be any generation/load unbalance in any of the interconnected AC grids, e.g., sudden load increase, generation loss or load loss, etc. Assuming a load increase of $\Delta P_{\text{L}.i}$ in the ith AC grid of MTDC system of Fig. 1, then the resulting frequency deviations in all of the MTDC interconnected AC grids are represented in [32] as:

$$[\Delta f_{\text{pu}}] = [A^{-1}][\Delta P_{\text{L}}] \tag{4.7}$$

where $[\Delta f_{\text{pu}}]$ is a matrix of order nx1 and represents steady state frequency deviations of all of the interconnected AC grids. It is given by:

$$[\Delta f_{\text{pu}}] = [\Delta f_{1.\text{pu}} \Delta f_{2.\text{pu}} \ldots \Delta f_{i.\text{pu}} \ldots . \Delta f_{n.\text{pu}}]\prime \tag{4.8}$$

$[\Delta P_{\text{L}}]$ is a matrix of order nx1 and represents amount of change in load/generation in one or more AC grids at a time. For the considered disturbance in the ith grid, it is given by:

$$[\Delta P_{\text{L}}] = [0.0 \ldots \Delta P_{\text{L}.i} \ldots . 0]\prime \tag{4.9}$$

[A] is a matrix having order nxn whose elements are function of droop coefficients, nominal VSC rating and nominal power generation capability of AC grids. Its elements are having values given by:

$$[A_{ij}] = \begin{bmatrix} -\left(\frac{P_{G.\text{nom}.i}}{\rho_{AC.i}} - \rho_{f.i} . P_{\text{vsc.nom}.i} . \left(1 - \frac{\frac{P_{\text{vsc.nom}.i}}{\rho_{\text{dc}.i}}}{\sum_{i}^{n} \frac{P_{\text{vsc.nom}.i}}{\rho_{\text{dc}.i}}} \right) \right); i = j \\ -\left(\rho_{f.j} . P_{\text{vsc.nom}.j} . \frac{\frac{P_{\text{vsc}.i.\text{nom}}}{\rho_{\text{dc}.i}}}{\sum_{i}^{n} \frac{P_{\text{vsc}.i.\text{nom}}}{\rho_{\text{dc}.i}}} \right); i \neq j \end{bmatrix} \tag{4.10}$$

where $P_{G.\text{nom}.i}$ is the nominal power rating of the ith AC grid. And, $\rho_{\text{AC}.i}$ is the equivalent governor droop coefficient of this grid.

The DC voltage deviation of the MTDC grid due to load increase in $\Delta P_{\text{L}.i}$ using (4.6) can be calculated as:

$$\Delta V_{\text{dc.pu}} = \frac{\sum_{i=1}^{n} P_{\text{vsc.nom}.i} \cdot \rho_{f.i} \cdot \Delta f_{i.\text{pu}}}{\sum_{i=1}^{n} \frac{P_{\text{vsc.nom}.i}}{\rho_{\text{dc}.i}}} \tag{4.11}$$

The power deviation made by any ith VSC during such AC disturbance event, can be given using (4.4),

$$\Delta P_{\text{vsc}.i} = P_{\text{vsc.nom}.i} \cdot \rho_{f.i} \cdot \Delta f_{i.\text{pu}} - P_{\text{vsc.nom}.i} \cdot \frac{1}{\rho_{\text{dc}.i}} \cdot \Delta V_{\text{dc}.i.\text{pu}} \tag{4.12}$$

Defining matrix $[C]$ as: $[C]=[A]^{-1}$, then, using (4.7), frequency deviation in any jth and ith AC grid due to load change made in the ith AC grid,

$$\Delta f_j = C_{ji} . \Delta P_{\text{L}.i} \tag{4.13a}$$

$$\Delta f_i = C_{ii} . \Delta P_{\text{L}.i} \tag{4.13b}$$

4.2 DC disturbance event

The probable list of DC disturbance events can be a converter outage, DC line outage, a sudden change in power flow made by a grid VSC, etc. Considering the case of change in power flow made by any ith VSC that is, $\Delta\ P_{\text{vsc}.i}^{\text{ref}}$. The resulting frequency deviations in the interconnected AC grids are quantized by [33] and are given as:

$$[\Delta f_{\text{pu}}] = -[A^{-1}][B][\Delta P_{\text{vsc}}^{\text{ref}}] \tag{4.14}$$

where $[\Delta f_{\text{pu}}]$ and $[A]$ hold same meaning as prior. $[\Delta P_{\text{vsc}}{}^{\text{ref}}]$ is a matrix of order nx1 and represents unbalanced power in DC grid due to change in power flow made by any grid converter. For example, outage of any q$^{\text{th}}$ VSC, carrying power P_q, then, this matrix is given as:

$$[\Delta P_{\text{vsc}}^{\text{ref}}] = [0.0 \ldots P_{\text{q}} \ldots . 0]\prime \tag{4.15}$$

[B] is a matrix similar to *[A]* having order nxn and is defined as:

$$[B_{ij}] = \begin{bmatrix} 1 - \frac{\frac{P_{\text{vsc.nom}.i}}{\rho_{\text{dc}.i}}}{\sum_{i=1}^{n} \frac{P_{\text{vsc.nom}.i}}{\rho_{\text{dc}.i}}}; i = j \\ -\frac{\frac{P_{\text{vsc.nom}.i}}{\rho_{\text{dc}.i}}}{\sum_{i=1}^{n} \frac{P_{\text{vsc.nom}.i}}{\rho_{\text{dc}.i}}}; i \neq j \end{bmatrix} \tag{4.16}$$

Also, the resulting DC voltage deviation due to this outage event using (4.6) can be calculated as:

$$\Delta V_{\text{dc.pu}} = \frac{P_q + \sum_{\substack{i=1 \\ i \neq q}}^{n} P_{\text{vsc.nom}.i} \cdot \rho_{f.i} \cdot \Delta f_{i.\text{pu}}}{\sum_{\substack{i=1 \\ i \neq q}}^{n} \frac{P_{\text{vsc.nom}.i}}{\rho_{\text{dc}.i}}} \tag{4.17}$$

For this DC disturbance event, the corresponding change in power flow made by any ith grid VSC is same as (4.12).

$$\Delta P_{\text{vsc}.i} = P_{\text{vsc.nom}.i} \cdot \rho_{f.i} \cdot \Delta f_{i.\text{pu}} - P_{\text{vsc.}nom.i} \cdot \frac{1}{\rho_{\text{dc}.i}} \cdot \Delta V_{\text{dc}.i.\text{pu}} \tag{4.18}$$

Defining a matrix $[D]$ such that $[D]=[A]^{-1}[B]$. Thus, frequency deviation in any j^{th} AC grid due to loss of the q^{th} VSC, using (4.14) becomes:

$$\Delta f_j = -D_{jq} . P_q \tag{4.19}$$

5 Methodology for design evaluation of frequency droop coefficients

The appropriate selection of frequency droop coefficient (ρ_f) is significant from stability point of view for obtaining desired system performance. While, selecting a lower value for this coefficient lengthens the mitigation period and results in deeper frequency nadir, on the other contrary, selecting a higher value of ρ_f can be advantageous as it results in obtaining lower frequency deviation and faster mitigation of frequency excursion [33]. However, selecting too high value of ρ_f can result in extraction of excessive active power from the supporting grid(s) possibly causing large frequency deviations in them [34]. In addition, as seen from (4.6), high ρ_f value can also cause higher DC voltage deviation in the MTDC grid as well.

Figure 4 shows variation of frequency deviation of the interconnected AC grids with respect to increase in ρ_f of the dual-droop converters of the MTDC system. Figure 4a shows the obtained frequency deviation of ONG-1, ONG-2 and ONG-3 for increase in values of $\rho_{f.1}$ that is, frequency droop coefficient of the dual-droop controller of VSC-1, corresponding to 4% load increase made in ONG-1. Figure 4b and c also show a similar variation for 4% load increase made in ONG-2 and ONG-3 respectively. It can be observed that frequency deviation gets decreased in magnitude for the disturbed grid with increase in magnitude of ρ_f of its corresponding dual-droop controller. However, frequency

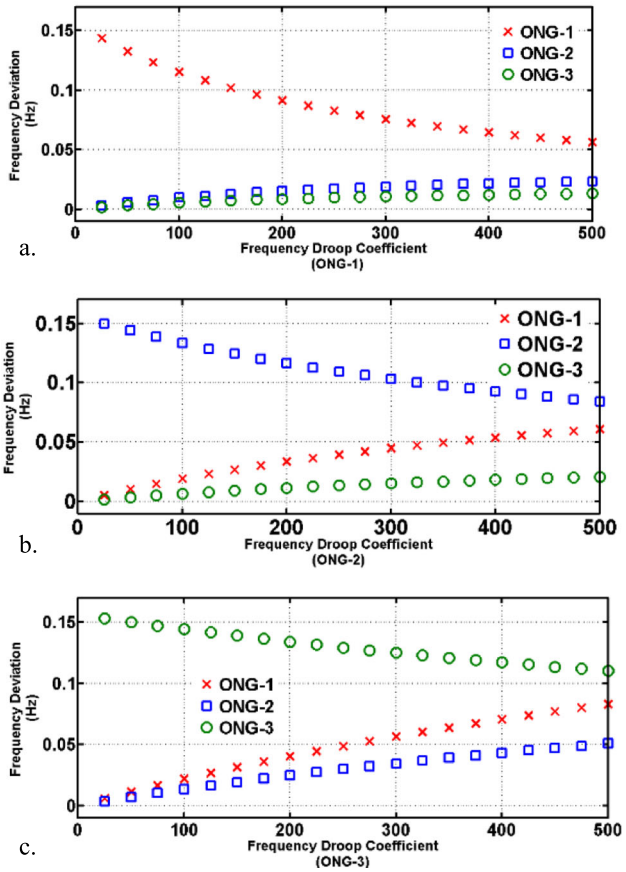


Fig. 4 Relationship between frequency deviation and frequency droop coefficient of **a** VSC-1. **b** VSC-2 and **c** VSC-3

deviation of the healthier AC grids increases with increasing variation of ρ_f. However, this is justified because with increase in the magnitude, the amount of frequency support withdrawn by the disturbed grid increases, thereby resulting in reduced deviation in it. However, corresponding to higher ρ_f, the healthier grids offer more power support, thus causing higher frequency deviation in them.

Since ρ_f holds its significance mainly in case of load/generation unbalances, thus, it is designed for a largest probable contingency ($\Delta P_{\text{L.max}}$) that may occur inside an AC grid. The value for $\Delta P_{\text{L.max}}$ can be obtained from transmission system operator (TSO) of that grid. The proposed design procedure is carried out individually for each dual-droop controlled VSC of the MTDC system of Fig. 1.

For selection of ρ_f, an appropriate range can be selected i.e., from $\rho_{\text{f.min}}$ to $\rho_{\text{f.max}}$. The value of $\rho_{\text{f.min}}$ can be selected as low as 1 while $\rho_{\text{f.max}}$ value can be selected keeping into consideration the availability of online spinning reserves in the interconnected AC grids connected with the MTDC system. The selected value of ρ_f from this range shall fulfil the following important conditions:

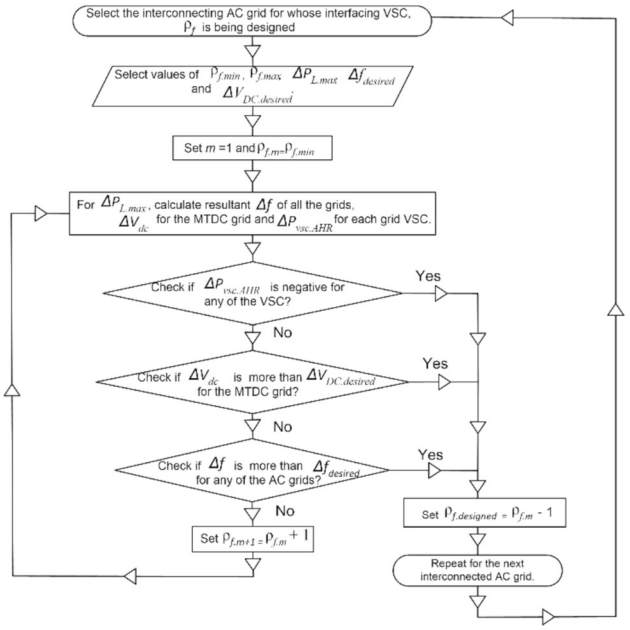


Fig. 5 Flow chart representation for proposed selection of frequency droop coefficient for a dual-droop controlled VSC of the MTDC system

1. The resulting DC voltage deviation of the MTDC grid with the selected value should lie within a desired range, $\pm\ \Delta V_{\text{DC.desired}}$.
2. Similarly, the resulting frequency deviation of the interconnected AC grids due to the selected value should also lie within a desired range, $\pm\ \Delta f_{\text{desired}}$.
3. With the selected value, available active power head room ($P_{\text{vsc.AHR}}$) for the VSC employing this value should not be negative.

The $P_{\text{vsc.AHR}}$ for any ith dual-droop controlled VSC is defined as:

$$P_{\text{vsc.AHR}.i} = |P_{\text{vsc.max}.i}| - \left|P_{\text{vsc.loading}.i}\right| \tag{5.1}$$

where $P_{\text{vsc.max}.i}$ is maximum amount of active power that can be carried by a converter after performing DCCM. And, $P_{\text{vsc.loading}.i}$ is the actual amount of active power that is carried by the ith VSC in response to any disturbance. That is,

$$P_{\text{vsc.loading}.i} = P_{\text{vsc}.i.0} + \Delta P_{\text{vsc}.i.\text{pu}} \tag{5.2}$$

where $P_{vsc.i.0}$ is the active power initially carried by the ith VSC, i.e., before occurrence of the disturbance. And, $\Delta P_{\text{vsc}.i.\text{pu}}$ is the change in active power made by this VSC, as defined by (4.3), in response to any disturbance. A flow chart illustrating this procedure for the selection of ρ_f for the ith dual-droop controlled VSC connected with ith AC grid is shown in Fig. 5.

Table 4 Data required for proposed design of frequency droop coefficients

Parameters	Values for onshore converters		
	VSC-1	VSC-2	VSC-3
ρ_{dc}	0.04	0.04	0.04
$\rho_{\text{f-min}}$	1	1	1
$\rho_{\text{f-max}}$	500	500	500
$\Delta V_{\text{DC.desired}}$	0.01 pu	0.01 pu	0.01 pu

Parameters	Values for onshore converters		
	ONG-1	ONG-2	ONG-3
ΔP_{Lmax}	0.1 pu	0.1 pu	0.1 pu
$\Delta f_{\text{.desired}}$ (disturbed grid)	0.12 Hz	0.13 Hz	0.14 Hz
$\Delta f_{\text{.desired}}$(supporting grid)	0.02 Hz	0.03 Hz	0.03 Hz
Obtained $\rho_{\text{f.designed}}$	133.5	154.25	149.25

The data required for this design procedure is given in Table 4. These values have been calculated for the considered system shown in Fig. 1. After obtaining, value of $\rho_{\text{f.designed}}$ for each dual-droop controlled VSC, it is again checked that the aforesaid three conditions are still met. The converter switching and AC/DC line losses are neglected here. For the entire design procedure, values of DC voltage droop coefficient (ρ_{dc}) for each dual-droop controller remains constant. The obtained value of $\rho_{\text{f.designed}}$, for each of the dual-droop controlled onshore VSC, after application of the proposed design procedure is also given in Table 4.

6 Proposed dual-droop control scheme for VSC-based MTDC systems

In the proposed technique, each of the grid VSC is classified either as a disturbed VSC, a supporting VSC or a non-participating VSC.

A VSC of a MTDC grid is termed as 'disturbed' if its interconnecting AC grid suffers from any kind of the disturbances as:

- Under/over frequency excursion due to any sudden load/generation unbalances in it.
- Under/over frequency excursion due to outage of another VSC which exchanges power with the same grid.

A VSC is said to be operating as 'supporting' if:

- This converter changes its active power flow in response to any under/over frequency excursion occurring in some

Table 5 Behaviour of participating VSCs in response to various disturbances

VSC operation	Disturbance →	Under frequency excursion	Over frequency excursion
Inverter	Disturbed mode	$\Delta P_{\text{vsc}} = +\text{ve}$ $\Delta f = -\text{ve}$	$\Delta P_{vsc} = -\text{ve}$ $\Delta f = +\text{ve}$
	Supporting mode	$\Delta P_{\text{vsc}} = -\text{ve}$ $\Delta f = -\text{ve}$	$\Delta P_{vsc} = +\text{ve}$ $\Delta f = +\text{ve}$
Rectifier	Disturbed mode	$\Delta P_{\text{vsc}} = -\text{ve}$	$\Delta P_{vsc} = +\text{ve}$
		$\Delta f = -\text{ve}$	$\Delta f = +\text{ve}$
	Supporting mode	$\Delta P_{\text{vsc}} = +\text{ve}$	$\Delta P_{vsc} = -\text{ve}$
		$\Delta f = -\text{ve}$	$\Delta f = +\text{ve}$

other interconnected AC grid with the MTDC system. That is, other than its local interconnected AC grid.

- This converter changes its active power flow in response to any converter outage that has occurred in the MTDC system.

The AC grid interconnected with the disturbed VSC is termed as 'disturbed grid' and one with the supporting VSC as 'supporting grid'. There may be some VSCs which are not participating in offering support to such disturbances. These VSCs are referred as 'un-affected' or 'non-participating' VSCs. As depicted in Fig. 1, all the offshore VSCs are non-participating VSCs while all the onshore dual-droop controlled VSCs are participating VSCs.

In the proposed strategy, the VSC controller can detect whether the interconnected AC grid is in 'disturbed' or in 'supporting' mode by just performing a few local measurements. This is based upon the behaviour of the participating i.e., dual-droop controlled VSCs of the MTDC grid in response to various disturbances as shown in Table 5.

It can be noted that when an inverter is in the disturbed mode, then the sign of active power change made by it is opposite to the sign of frequency deviation in its local AC grid. But, when the same inverter is serving in the supporting mode, then the change made by the two quantities depicts same polarity. However, when operating as a 'rectifier', a totally opposite behaviour is observed in comparison to the 'inverter' operation. This behavioural characteristic of the dual-droop controlled VSC, which is just based on the local measurements only, can uniquely identify whether a VSC is in disturbed or in the supporting mode. It does not require any additional RoCoF measurements or any other measurement from neighbouring AC grids and/or VSCs in order to differentiate in between disturbed and supporting modes.

Since, nature of response of the dual-droop controlled VSC to a disturbance event is different while being in disturbed mode to that in supporting mode, therefore, it is proposed to define two different control schemes for the two modes. For better illustration, it is assumed that with each AC grid, only one VSC has been interfaced, as shown in Fig. 1.

6.1 Proposed control scheme for VSCs in the disturbed mode

Assuming that all the VSCs of the MTDC grid are operating in healthy state. Considering a load/generation unbalance event of magnitude $\Delta P_{\text{L}.i}$ occurring in any ith onshore AC grid of the MTDC system. The power flow deviation made by the corresponding ith (disturbed) VSC is given by (4.12). It should be noted that the value of $\rho_{\text{f}.i}$ used in the following equations should be taken as the one obtained after applying design procedure of Sect. 5. Using value of DC voltage deviation from (4.11) in (4.12),

$$\Delta P_{\text{vsc}.i} = P_{\text{vsc.nom}.i} \cdot \rho_{f.i} \cdot \Delta f_{i.\text{pu}} - \cdot \frac{P_{\text{vsc.nom}.i}}{\rho_{\text{dc}.i}} \cdot \frac{\sum_{i=1}^{n} P_{\text{vsc.nom}.i} \cdot \rho_{f.i} \cdot \Delta f_{i.\text{pu}}}{\sum_{i=1}^{n} \frac{P_{\text{vsc.nom}.i}}{\rho_{\text{dc}.i}}} \tag{6.1}$$

Defining a constant k for any ith VSC controller as:

$$k_i = \frac{\frac{P_{\text{vsc.nom}.i}}{\rho_{\text{dc}.i}}}{\sum_{i=1}^{n} \frac{P_{\text{vsc.nom}.i}}{\rho_{\text{dc}.i}}} \tag{6.2}$$

Using k_i in (6.1),

$$\Delta P_{\text{vsc}.i} = P_{\text{vsc.nom}.i} \cdot \rho_{f.i} \cdot \Delta f_{i.\text{pu}} \left[1 - k_i \left(1 + \sum_{\substack{j=1 \\ j \neq i}}^{n} \frac{P_{\text{vsc.nom}.j} \cdot \rho_{f.j} \cdot \Delta f_{j.\text{pu}}}{P_{\text{vsc.nom}.i} \cdot \rho_{f.i} \cdot \Delta f_{i.\text{pu}}} \right) \right] \tag{6.3}$$

Writing power deviation of the disturbed (ith) VSC in per units,

$$\Delta P_{\text{vsc}.i.\text{pu}} = \rho_{f.i} \cdot \Delta f_{i.\text{pu}} \left[1 - k_i \left(1 + \sum_{\substack{j=1 \\ j \neq i}}^{n} \frac{P_{\text{vsc.nom}.j} \cdot \rho_{f.j} \cdot \Delta f_{j.\text{pu}}}{P_{\text{vsc.nom}.i} \cdot \rho_{f.i} \cdot \Delta f_{i.\text{pu}}} \right) \right] \tag{6.4}$$

But, the desirable amount of frequency support from the MTDC grid via disturbed (ith) VSC is:

$$\Delta P_{\text{vsc}.i.\text{pu.desirable}} = \rho_{f.i}.\Delta f_{i.\text{pu}} \tag{6.5}$$

Using (6.5) and (4.13) in (6.4), the amount of active power support actually being delivered to the disturbed (ith) AC grid from the MTDC system is:

$$\Delta P_{\text{vsc}.i.\text{pu.actual}} = \Delta P_{\text{vsc}.i.\text{pu.desirable}} \left(1 - k_i \left(1 + \sum_{\substack{j=1 \\ j\neq i}}^{n} \frac{P_{\text{vsc.nom}.j}.\rho_{f.j}.C_{ji}}{P_{\text{vsc.nom}.i}.\rho_{f.i}.C_{ii}}\right)\right) \tag{6.6}$$

Comparing (6.5) and (6.6), it is evident that the amount of active power support actually being offered to the disturbed grid is lesser than the desirable amount. This is due to exercising both DC voltage and frequency droop control simultaneously by the disturbed VSC.

Defining a Degrading Factor (DF) for the disturbed (ith) VSC as:

$$\text{DF}_i = 1 - k_i \left(1 + \sum_{\substack{j=1 \\ j\neq i}}^{n} \frac{P_{\text{vsc.nom}.j}.\rho_{f.j}.C_{ji}}{P_{\text{vsc.nom}.i}.\rho_{f.i}.C_{ii}}\right) \tag{6.7}$$

Using (6.7) in (6.6),

$$\Delta P_{\text{vsc}.i.\text{pu.actual}} = \Delta P_{\text{vsc}.i.\text{pu.desirable}}.\text{DF}_i \tag{6.8}$$

It can be noted from (6.8) that the active power support offered to the disturbed (ith) AC grid from the MTDC system gets reduced by an amount equal to DF_i. Therefore, in order to achieve actual amount of active power support as good as the desirable amount, it is proposed to use a new value of the frequency droop coefficient that is, $\rho_{\text{f.proposed}.i}$, when the converter controller operates in disturbed mode. And, its value is given by:

$$\rho_{f.\text{proposed}.i} = \frac{\rho_{f.i}}{DF_i} \tag{6.9}$$

Here, it should be noted that the value of frequency droop coefficient depicted by $\rho_{\text{f.i}}$ is obtained by the application of the design algorithm proposed in Sect. 5.

It is evident that upon using $\rho_{\text{f.proposed.i}}$ as the frequency droop coefficient at the disturbed VSC controller, enhanced amount of active power support gets delivered to the disturbed grid. In addition, there remains no need for deactivating DC voltage droop control at the disturbed VSC controller, thereby, maintaining the reliability of the MTDC grid. Table 6 shows the values of $\rho_{\text{f.proposed}}$ for disturbances of various types and magnitudes in the considered system shown in Fig. 1. For disturbances involving converter outages, $\rho_{\text{f.proposed}}$ is not calculated because for such disturbances VSC will be behaving in the supporting mode. While application of $\rho_{\text{f.proposed}}$ is only done when VSC is acting in the disturbed mode.

Table 6 Frequency droop coefficient obtained for various disturbances

VSCs(participating)	VSC-1	VSC-2	VSC-3
$\rho_{\text{f.i.}}(=\rho_{\text{f.designed.i}})$	133.5	154.25	149.25
$\rho_{\text{f.proposed.i}} \rightarrow$ Disturbances$\downarrow$	$\rho_{\text{f.proposed.1}}$	$\rho_{\text{f.proposed.2}}$	$\rho_{\text{f.proposed.3}}$
$\Delta P_{L1} = 5\%$	221.43	N.A	N.A
$\Delta P_{L1} = 7\%$	221.43	N.A	N.A
$\Delta P_{L1} = 10\%$	221.43	N.A	N.A
$\Delta P_{L2} = 5\%$	N.A	265.1	N.A
$\Delta P_{L2} = 7\%$	N.A	265.1	N.A
$\Delta P_{L2} = 10\%$	N.A	265.1	N.A
$\Delta P_{L3} = 5\%$	N.A	N.A	267.58
$\Delta P_{L3} = 7\%$	N.A	N.A	267.58
$\Delta P_{L3} = 10\%$	N.A	N.A	267.58
Platform outage	N.A	N.A	N.A
OWF-II outage	N.A	N.A	N.A

From Table 6, it is clear that application of $\rho_{\text{f.proposed}}$ does not depend upon the magnitude of disturbance. Also, by using (6.7) and (6.9), $\rho_{\text{f.proposed}}$ can be calculated offline just by the knowledge of size of VSCs, magnitude of dual-droop coefficients, governor droop coefficients of the interconnected AC grids and nominal power rating of all the AC grids, all of which remain constant for a scheduled period of operation. In addition, application of $\rho_{\text{f.proposed}}$ relies on local measurements only.

6.2 Proposed control scheme for the VSCs in the supporting mode

In response to any disturbance caused in the AC/DC system, a DC voltage deviation occurs in the MTDC grid. Sensing their respective local DC voltage deviation, each of the supporting VSCs undergo change in their active power flow as calculated by using (4.3) as:

$$\Delta P_{\text{vsc}.j.\text{pu}} = -\frac{1}{\rho_{\text{dc}.j}}.\Delta V_{\text{dc}.j.\text{pu}} + \rho_{f.j}.\Delta f_{j.\text{pu}} \tag{6.10}$$

The subscript 'j' is used for the supporting VSCs whereas subscript 'i' denotes the disturbed VSC.

The amount of active power support desirable from the supporting VSCs is given by:

$$\Delta P_{\text{vsc}.j.\text{pu.desirable}} = -\frac{1}{\rho_{\text{dc}.j}}.\Delta V_{\text{dc}.j.\text{pu}} \tag{6.11}$$

Comparing (6.10) with (6.11), it is clear that due to the frequency deviations ($\Delta f_{j.\text{pu}}$) occurring in the supporting AC grids, they can supply only limited active power support into the MTDC system for mitigation of any disturbance in the AC/DC system.

Using (6.11) in (6.10), the amount of active power support actually provided by the supporting VSCs in the MTDC system is given by:

$$\Delta P_{\text{vsc}.j.\text{pu.actual}} = \Delta P_{\text{vsc}.j.\text{pu.desirable}} - P_{f.\text{loss}.j.\text{pu}} \tag{6.12}$$

where $P_{f.\text{loss}.j.\text{pu}}$ is the component of the desirable power support from the j^{th} (supporting) VSC which could not get delivered. Thus, it is the amount of power lost (in per units) due to the frequency deviation ($\Delta f_{j.\text{pu}}$) occurring in its supporting grid while mitigating the disturbance and it is given by:

$$P_{f.\text{loss}.j.\text{pu}} = -\rho_{f.j}.\Delta f_{j.\text{pu}} \tag{6.13}$$

It can be noted from (6.12) that the actual power support delivered by the j^{th} (supporting) VSC gets lessened due to the 'power loss' caused by its own frequency droop control. As stated earlier, for the purpose of retaining security of the interconnected AC grids as well as maintaining DC voltage stability of the MTDC system, the frequency droop control and the DC voltage droop control should operate coherently, irrespective of whether the grid converter is in the supporting mode or in the disturbed mode. Concurrently, to enhance the amount of active power support that can be obtained from a supporting grid, it is proposed to reduce the power loss represented by $P_{f.\text{loss}.j.\text{pu}}$. This is possible by decreasing the value of frequency droop coefficient of the dual-droop VSC controller, while it is working in the supporting mode. As a result, power support from the supporting VSC can be enhanced, as shown in (6.12). This would also result in reduction of the DC voltage deviation as well, as evident from (4.6).

Proposing a constant 'm' such that:

$$\Delta P_{\text{vsc}.j.\text{pu.actual}} = m.\Delta P_{\text{vsc}.j.\text{pu.desirable}} \tag{6.14}$$

The constant 'm' is coined as Power Support Index (PSI) which is representative of actual power support that is obtained from any supporting grid against the power support desired from it, while mitigating a disturbance. And, PSI for the jth supporting VSC dual-droop controller is defined as:

Table 7 PSI calculated for various disturbances

Disturbance	PSI_1	PSI_2	PSI_3
$\Delta P_{L1} = 10\%$	–	63.64%	77.78%
$\Delta P_{L2} = 5\%$	46.67%	–	77.78%
$\Delta P_{L3} = 7\%$	46.67%	63.64%	–
Platform outage	46.67%	63.64%	77.78%
OWF-II outage	46.67%	63.64%	77.78%

$$PSI_j = m_j = \frac{\Delta P_{\text{vsc}.j.\text{pu.actual}}}{\Delta P_{\text{vsc}.j.\text{pu.desirable}}} \tag{6.15}$$

Using (6.14) in (6.12),

$$m_j.\Delta P_{\text{vsc}.j.\text{pu.desirable}} = \Delta P_{\text{vsc}.j.\text{pu.desirable}} - P_{f.\text{loss}.j.\text{pu}} \tag{6.16}$$

$$m_j = \text{PSI}_j = 1 - \frac{P_{f.\text{loss}.j.\text{pu}}}{\Delta P_{\text{vsc}.j.\text{pu.desirable}}} \tag{6.17}$$

Thus, *PSI* always lies in between zero to unity. If a supporting VSC controller deactivates its frequency droop control, that is $\rho_{\text{f.j}} = 0$, this will result in $P_{\text{f.loss.j.pu}}$ equal to zero. Thus, from (6.17), the value of PSI becomes unity or 100%. However, as explained earlier for the purpose of maintaining the reliability and security of AC/DC grids, the value of PSI should never be used as unity. Using (6.11) and (6.13) in (6.17),

$$\text{PSI}_j = 1 - \left(\frac{\rho_{\text{dc}.j}.\rho_{f.j}.\Delta f_{j.\text{pu}}}{\Delta V_{\text{dc}.j.\text{pu}}}\right) \tag{6.18}$$

It should be noted that PSI is only applicable for VSCs which are supporting the power balancing of MTDC grid in case of any AC/DC events and not for VSCs which are operating in the disturbed mode.

For different types of disturbances initiated in the considered system of Fig. 1, Table 7 shows the values of PSI obtained from (6.18). ΔP_{L1}, ΔP_{L2} and ΔP_{L3} are the load increase in percentage that are initiated in ONG-1, ONG-2 and ONG-3, respectively. It is interesting to note that value of PSI remains same for every dual-droop VSC controller irrespective of the type, location and magnitude of disturbance.

It can be noted that value of PSI obtained is smaller for those VSCs which are coupled with AC grids having smaller power generation capacity comparatively. This is justified because for same amount of unbalanced power, smaller AC grids will undergo higher frequency deviations as compared to larger capacity grids; as a result having larger $P_{f.\text{loss}.j.\text{pu}}$ term and hence smaller PSI.

Table 8 Frequency droop coefficient obtained for the selected values of PSIdesired for various disturbances

$\text{PSI}_{\text{desired}} \rightarrow$	$\text{PSI}_{\text{desired}\ldots.1}$ 60%	$\text{PSI}_{\text{desired}\ldots.2}$ 80%	$\text{PSI}_{\text{desired}\ldots.3}$ 90%
Disturbances↓	$\rho_{\text{f.1.new}}$	$\rho_{\text{f.2.new}}$	$\rho_{\text{f.3.new}}$
$\Delta P_{L1} = 10\%$	N.A	72.6	52.2
$\Delta P_{L2} = 5\%$	100.1	N.A	52.2
$\Delta P_{L3} = 7\%$	100.1	72.6	N.A
Platform outage	100.1	72.6	52.2
OWF-II outage	100.1	72.6	52.2

A MTDC grid operator can allot desired values of PSI to each onshore dual-droop controlled VSC keeping in consideration the size of its respective onshore AC grid, availability of online spinning reserves, etc. According to $\text{PSI}_{\text{desired}}$ obtained from the operator, a reduced value of frequency droop coefficient, i.e., $\rho_{\text{f.j.new}}$ can be calculated at each onshore grid converter, using (6.18), as

$$\rho_{f.j.\text{new}} = \left(1 - \text{PSI}_{j.\text{desired}}\right).\frac{\Delta V_{\text{dc}.j.\text{pu}}}{\rho_{\text{DC}.j}.\Delta f_{j.\text{pu}}} \tag{6.19}$$

Therefore, when working in supporting mode, a VSC should reduce value of its frequency droop coefficient to $\rho_{\text{f.j.new}}$ as given by (6.19). For the same disturbances listed in Table 7, the values of $\rho_{\text{f.j.new}}$ obtained from (6.19) are shown in Table 8.

It is evident from (6.19) that the value of $\rho_{\text{f.j.new}}$, depends upon selected value of $\text{PSI}_{\text{desired}}$. Also, it does not depend upon the magnitude, type and even location of the disturbance. In addition, it can be calculated offline with $\text{PSI}_{\text{desired}}$ obtained from the operator.

Upon detecting that an onshore VSC is operating in supporting mode and by using $\rho_{\text{f.new}}$, then, this VSC can provide enhanced active power support. It is possible to still maintain security of its AC grid as there is no need to deactivate its frequency droop control. Also, supporting VSCs do not require any communication signal to notify them about the place, magnitude and type of disturbance.

6.3 Optimum selection of $\text{PSI}_{\text{desired}}$

A higher value selection would definitely ensure maximum active power support from the supporting AC grids but can also cause higher frequency deviations in them. On the other hand, selection of a smaller value would cause lesser frequency deviations in supporting grids but would have its limited contribution in mitigation of the AC/DC disturbances.

Assuming a DC event e.g. an offshore converter outage in the MTDC grid of Fig. 1, which was exchanging power, P_{q} with the MTDC system. All the three onshore grids would serve as supporting AC grids. Let $\text{PSI}_{\text{desired.1}}$, $\text{PSI}_{\text{desired.2}}$ and $\text{PSI}_{\text{desired.3}}$ are the desired values of PSI for the three onshore (supporting) VSC controllers, respectively. Corresponding to which, let $\rho_{\text{f.1.new}}$, $\rho_{\text{f.2.new}}$ and $\rho_{\text{f.3.new}}$ be the obtained frequency droop coefficients from (6.19). For these coefficients, considering $P_{\text{f.loss1.pu.new}}$, $P_{\text{f.loss2.pu.new}}$ and $P_{\text{f.loss3.pu.new}}$ as the power loss in the three supporting grids.

Let $r_1{:}r_2{:}r_3$ is the ratio of the inverse of the nominal power rating of the three onshore grids, ONG-1, ONG-2 and ONG-3 that is, $1/P_{\text{G.nom.1}}$: $1/P_{\text{G.nom.2}}$: $1/P_{\text{G.nom.3}}$. Keeping the ratio of the power loss values i.e., $\text{P}_{\text{f.loss1.pu.new}}{:}P_{\text{f.loss2.pu.new}}{:}P_{\text{f.loss3.pu.new}}$ in ratio of $r_1{:}r_2{:}r_3$. The following relations can be depicted:

$$P_{f.\text{loss1.pu.new}} = \frac{r_1}{r_2} P_{f.\text{loss2.pu.new}} \tag{6.20a}$$

$$P_{f.\text{loss2.pu.new}} = \frac{r_2}{r_3} P_{f.\text{loss3.pu.new}} \tag{6.20b}$$

Using value of $P_{\text{f.loss.j.pu}}$ from (6.13),

$$-\rho_{f.1.\text{new}}.\Delta f_{1.\text{pu}} = -\frac{r_1}{r_2}\rho_{f.2.\text{new}}.\Delta f_{2.\text{pu}} \tag{6.21a}$$

$$-\rho_{f.2.\text{new}}.\Delta f_{2.\text{pu}} = -\frac{r_2}{r_3}\rho_{f.3.\text{new}}.\Delta f_{3.\text{pu}} \tag{6.21b}$$

Using (6.19) and assuming equal DC voltage droop coefficients and equal DC voltage deviations,

$$\text{PSI}_{\text{desired.1}} = 1 - \frac{r_2}{r_1}\text{PSI}_{\text{desired.2}} \tag{6.22a}$$

$$\text{PSI}_{\text{desired.2}} = 1 - \frac{r_3}{r_2}\text{PSI}_{\text{desired.3}} \tag{6.22b}$$

In the considered system of Fig. 1, ONG-3 is having largest power generation capacity among the three onshore grids. So as to obtain highest amount of support from ONG-3, among the three grids, keeping $\text{PSI}_{\text{desired.3}} = 90\%$, thus, from (6.22), $\text{PSI}_{\text{desired.2}}$ is obtained as 80% and $\text{PSI}_{\text{desired.1}}$ as 60%.

6.4 Flow chart and block diagram for the proposed control scheme

The complete control scheme for the proposed dual-droop controller for onshore VSCs of the MTDC grid is shown in Fig. 6. As depicted, the control scheme has three layers in it. Following are the functions of the three layers:

1. *Outer control (OC) loop* This layer generates the reference values of the *dq*-axes converter currents. The $i_{\text{q}}{}^{*}$ has been generated for facilitating constant reactive power exchange ($Q_{\text{vsc}}{}^{\text{ref}}$) with the local AC grid while $i_{\text{d}}{}^{*}$

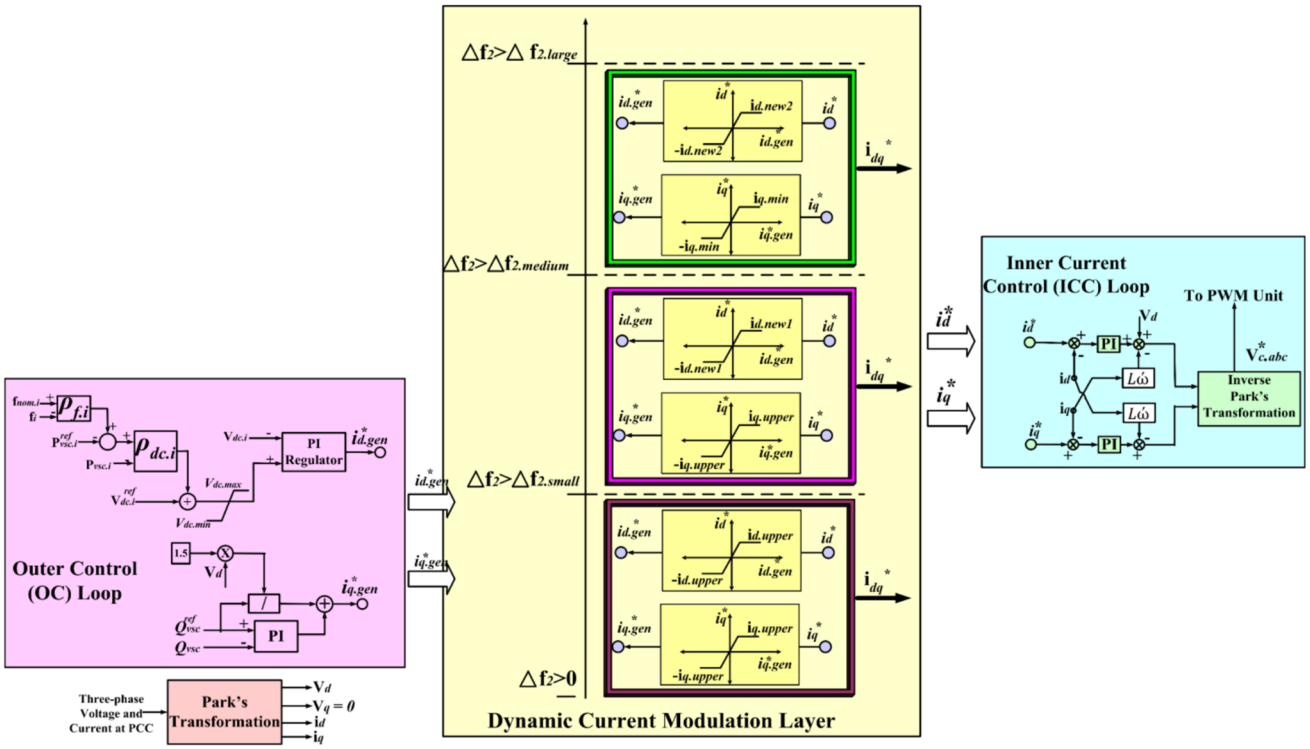


Fig. 6 Proposed dual-droop control scheme for VSC-based MTDC transmission system

is generated using P–V_{dc}–f dual-droop control. Unlike traditional vector current controls, reference converter currents are not limited in this layer.

2. *Dynamic Converter Current Modulation (DCCM) layer* This layer receives the reference values of dq-axes converter currents generated as $i_{dq.gen}{}^{*}$ inside the OC loop and performs modulation upon them depending upon the magnitude of encountered frequency deviation, as explained in Sect. 3. And outputs the resultant values, $i_d{}^{*}$ and $i_q{}^{*}$ to the third layer.
3. *Inner current control (ICC) loop* This layer is same as in the conventional vector current control. After receiving the reference values of dq-axes converter currents, $i_{dq}{}^{*}$, it generates the reference converter voltage, $V_{c.abc}{}^{*}$ to be sent to the PWM unit of the converter, for generation of firing pulses for IGBT valves.

The most important feature of the proposed control scheme is the selection of appropriate value of frequency droop coefficient for the dual-droop converter controller. A flow chart representation and the corresponding control logic scheme for selecting this value for the onshore converters is shown in Figs. 7 and 8, respectively. Here, $f_{DB.min}$ and $f_{DB.max}$ are the selected minimum and maximum values for frequency dead band range for the local AC grid.

7 Matlab simulation results

The considered VSC-based MTDC system as shown in Fig. 1 has been simulated on MATLAB/Simulink platform. The proposed control strategy is justified by testing it against disturbances of various types and magnitudes applied at various locations in the AC/DC system. Three case scenarios are considered:

- *Case A* Traditional dual-droop control strategy proposed in [6, 7].
- *Case B* The dual-droop control strategy as proposed in [9].
- *Case C* The proposed dual-droop control strategy.

A basic dual-droop control technique has been proposed in [6, 7] which uses P–V_{dc} droop for DC voltage regulation of MTDC system and P–f droop control for providing frequency support to the interconnected AC grids with the MTDC system. Haileselassie and Uhlen [6], Chaudhuri et al. [7] does not address the issue of mutual interaction among the two droop controls. The mutual interaction issue has been addressed in [9]. Also, a correction factor has been proposed for frequency droop coefficient so that better frequency support can be provided. However, the correction factor proposed in [9] neglects any frequency deviations occurring in the healthier/supporting grids while supporting the disturbed grid.

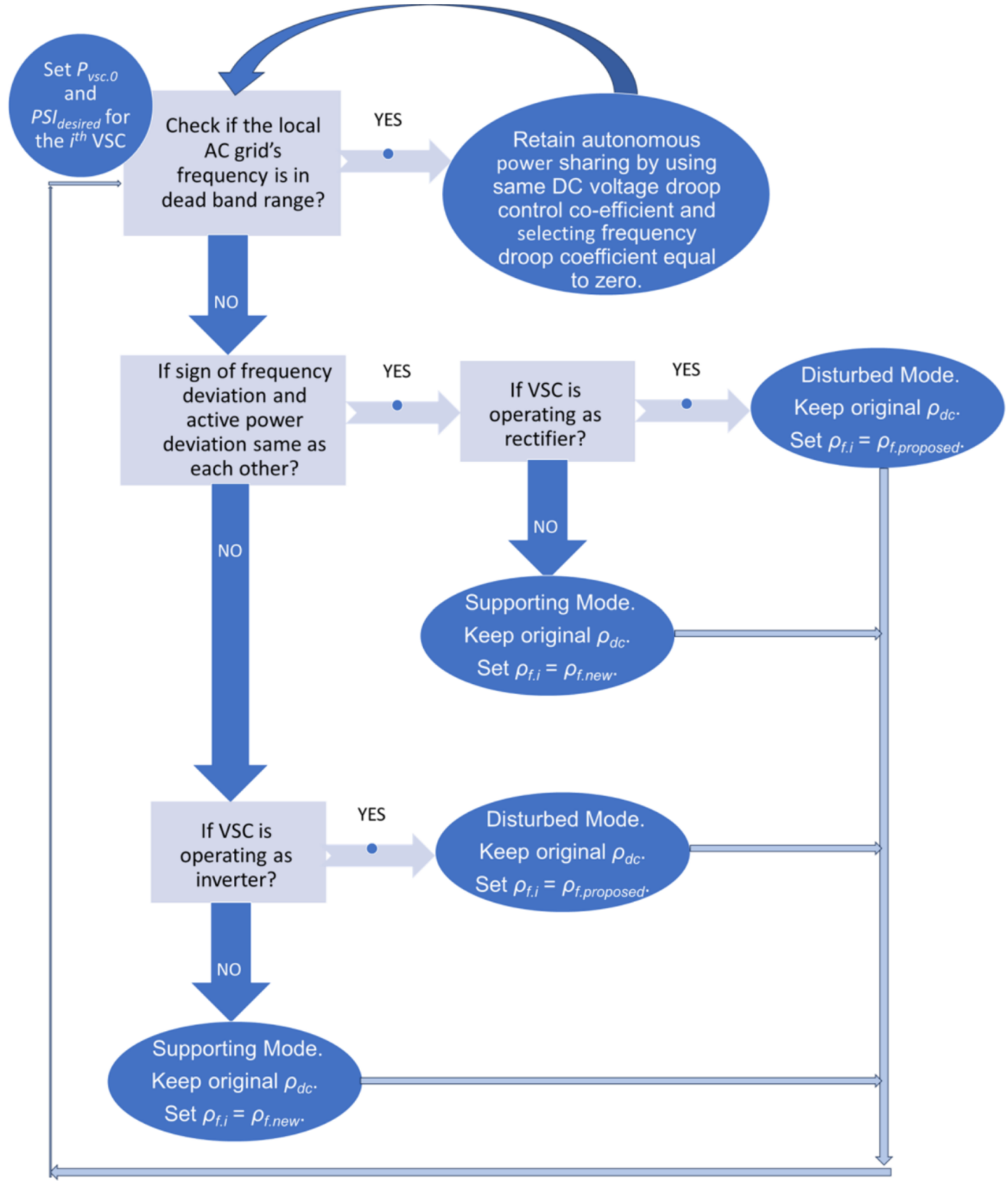


Fig. 7 Flow chart representation for selection of frequency droop coefficients to be exercised by the *i*th VSC of the MTDC grid

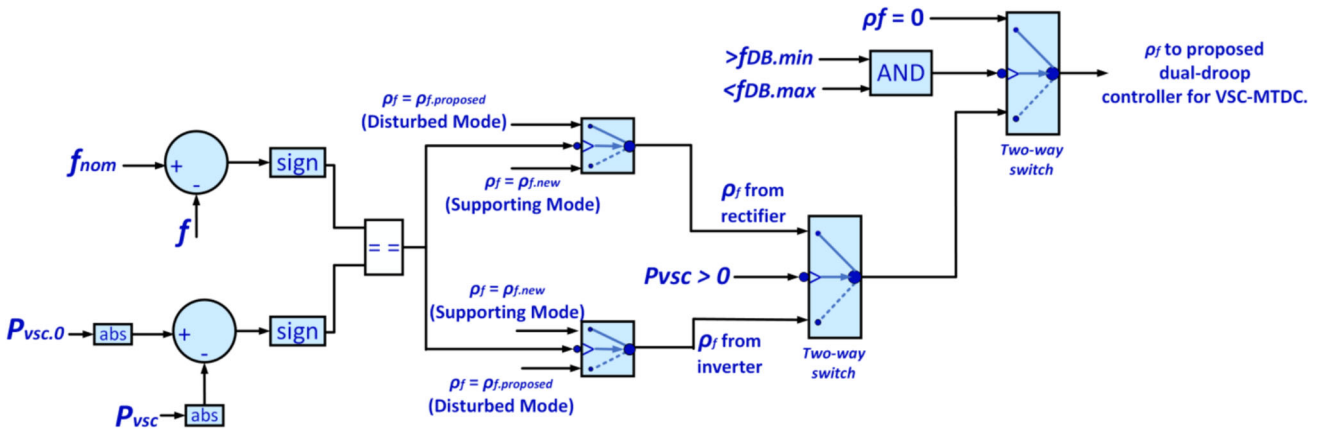


Fig. 8 Control logic for selection of frequency droop coefficients to be exercised by the *i*th VSC of the MTDC grid

The proposed work is based upon the basic dual-droop control technique for VSC-MTDC system as proposed in [6, 7]. The proposed work also addresses the dual-droop interaction issue and postulates a correction factor for frequency droop coefficient for extraction of better frequency support as in [9]. However, in the proposed work the derivation of correction factor takes into account the resultant frequency deviations in all the interconnected AC grids. In addition to application of the proposed correction factor, a Power Support Index has also been proposed to quantize the power support withdrawn from the healthier grids.

So as to demonstrate that the control strategy proposed by the authors is efficient than the basic dual-droop control technique of [6, 7] where effects of dual-droop interaction has not been mitigated, thus, the authors have used [6, 7] as one of the compared techniques. Also, to demonstrate that the correction factor proposed by authors is able to yield better and efficient frequency support than the one proposed in [9], the authors have used [9] as one of the compared techniques. The other remaining control strategies are mostly based on deactivation of one of the two droops for obtaining better frequency support or require to use dedicated communication network to rectify the interaction issue. Since, it is sincerely recommended to maintain the reliability and security of the AC DC power system without deactivating any droop action and also to reduce dependency on the not so reliable communication network, no other control technique was found suitable for the comparison.

The frequency droop coefficients used for the three cases are listed in Table 9.

For all the three cases, ρ_{dc} has been kept unchanged as 0.04 for the three onshore converter controllers. The values of frequency droop coefficients after using proposed design algorithm of Sect. 5 that is $\rho_{\text{f.designed}}$ are used in Case A. Upon applying correction factor of '$1 - k_i$', as suggested in [9], on $\rho_{\text{f.designed}}$, the obtained values are used in Case B as $\rho_{\text{f.corrected}}$. In Case C, using proposed dual-droop control strategy, $\rho_{\text{f.proposed}}$ is used for VSCs operating in disturbed mode while $\rho_{\text{f.new}}$ is used for VSCs operating in supporting mode.

For a fair comparison among the three dual-droop control schemes, the ability of performing DCCM is integrated among the three compared control strategies listed as *Case A*, *Case B* and *Case C*. The results for both AC/DC disturbances triggered in different networks are discussed below. Before application of any disturbance, the three onshore grids have been working asynchronously almost near to their respective nominal frequency. The three dual-droop controllers of VSC-1, VSC-2 and VSC-3 for all the three cases have been equipped with frequency dead bands of ± 0.025 Hz, ± 0.05 Hz and ± 0.1 Hz, respectively.

7.1 Scenario-1: AC event-1: 10% load increase in ONG-1

A credible contingency is introduced in the onshore grid, ONG-1 of Fig. 1 by switching on a load of 246 MW, 0.85 pf, (10% of the total load) at instant $t = 45$ s. ONG-1 being a disturbed grid requires active power support from healthier grids, ONG-2 and ONG-3. In the proposed control scheme, this important demarcation for differentiating in between disturbed and supporting modes, has been depicted by release of 'Disturbed Mode Signal' or 'Disturbance Signal' and 'Supporting Mode Signal' or 'Supporting Signal'. It should be noted that application of these signals in the proposed control technique is limited only for the local use inside the VSC converter controller only and does not need to be communicated to any neighbouring converter nor to any other interconnected AC grid. In addition, it should be remarked that both Case A and Case B do not use these signals to differentiate in between disturbed and supporting modes. These two signals of the proposed control for the present scenario are shown in Fig. 9a and b, respectively. It is clear that the disturbance signal goes high only for VSC-1

Table 9 Values of ρ_f for the considered caseS

Cases→	Case A	Case B	Case C
Frequency droop coefficients→	$\rho_{f.designed.i}$	$\rho_{f.corrected.i} = \rho_{f.designed.i}/(1\text{-}k_i)$	$\rho_{f.proposed.i}$, $\rho_{f.new.i}$
VSC-1	133.5	200.25	221.425, 123.4
VSC-2	154.25	231.375	265.1, 100.85
VSC-3	149.25	223.875	267.575, 84.925

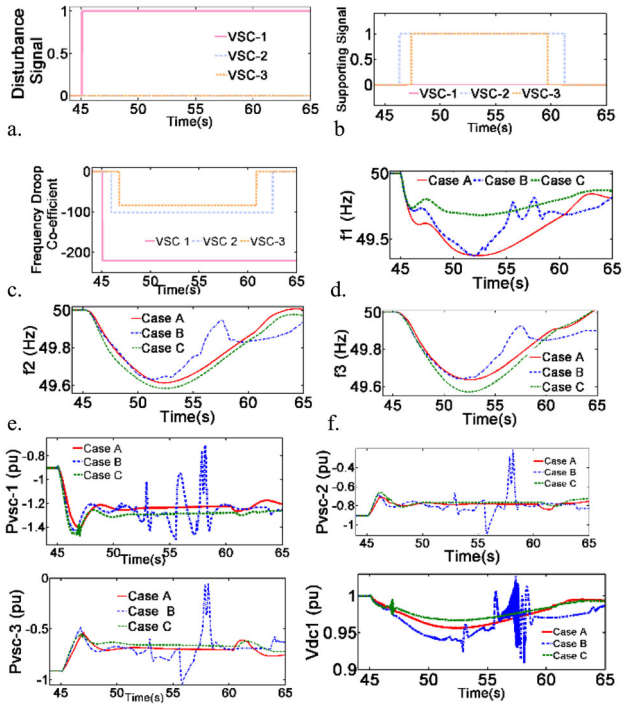


Fig. 9 Response of VSC-MTDC system for Scenario-1. **a** Disturbance signal. **b** Supporting signal and **c** Frequency droop coefficient of proposed scheme. Frequency of **d** ONG-1. **e** ONG-2. **f** ONG-3. Power inverted by the onshore VSCs. **g** VSC-1. **h** VSC-2 and **i** VSC-3 and **j** DC voltage near VSC-1

while for VSC-2 and VSC-3, the supporting signal becomes high. As a result, with the proposed control, the frequency droop coefficient exercised by the VSC-1 takes value equal to $\rho_{f.proposed.1}$ (221.425) which is higher than $\rho_{f.designed.1}$ value of VSC-1, i.e., 133.5. At the same time, the supporting VSCs exert value lower than their corresponding designed values, as given in Table 9. The values of frequency droop coefficient used by the three dual-droop controlled onshore VSCs are shown in Fig. 9c. However, for Case A irrespective of being disturbed/supporting grids, all the onshore VSC controllers use frequency droop coefficient equal to their corresponding designed value. While for Case B, similar to Case A, as soon as the frequency drops below the dead band range (which occurs in all the three grids), the three grid controllers simultaneously exercise frequency droop coefficient values higher than their respective $\rho_{f.designed}$ values. The values of frequency droop coefficient exercised by all the dual-droop converter controllers of Case B, irrespective of the two modes, are obtained by employing a correction factor, as proposed in [9], upon their corresponding $\rho_{f.designed}$ values.

The frequency of the disturbed grid, ONG-1 is shown in Fig. 9d. It is evident that the frequency regulation obtained with the proposed control, i.e., Case C is better in comparison to both Case A and Case B. It should be noted that two frequency nadirs are obtained here, one at $t = 46$ s and the other at $t = 52$ s. The first nadir at $t = 46$ s for Case A is deeper in comparison to the other two cases. This is justified as the droop coefficient for Case A is 133.5 which is lower than 200.25 and 221.425 exercised by Cases B and C respectively. Since, the difference between the frequency droop coefficient of Cases B and C is smaller, resulting in the first nadir of Case B being slightly deeper in comparison to Case C. It shall be noted that up till this instant, i.e., $t = 46$ s, the frequency of the supporting grids (ONG-2 and ONG-3) is still lesser than their corresponding dead band limits; due to which ρ_f exercised by VSC-2 and VSC-3 being equal to zero. And, thus, resulting in release of active power support to the disturbed grid equal to the desirable amount, according to (6.12) and (6.13). The frequency of ONG-1 even starts to recover after $t = 46$ s for the three cases.

However, after $t = 47$ s, the frequency of ONG-1 starts to decrease once again for all the three cases. This is justified because after $t = 47$ s, the frequency of the supporting grids has also exceeded their respective dead band limits, and hence, lesser amount of active power support could only be delivered by them, because ρ_f exercised by VSC controllers is now more than zero. It is interesting to note that in spite of this, the frequency deviation of ONG-1 with the proposed scheme is better than its competitors. And, in the Case C, the VSC controllers with the supporting grids, are exercising frequency droop coefficients, i.e., $\rho_{f.j.new}$ (100.85 for VSC-2 and 84.925 for VSC-3) which is lower than the designed values of 154.25 for VSC-2 and 149.25 for VSC-3. While for Case A, VSC controllers of the supporting grids exercise values equal to $\rho_{f.designed}$. And for Case B, they exercise values even more than $\rho_{f.designed}$. As a result, active power

support offered by the two supporting VSCs is more for Case C in comparison to cases A and B. As seen from Fig. 9d, frequency nadir of 49.69 Hz is obtained with Case C while the same is 49.38 Hz with the other two. Despite of using higher frequency droop coefficient than its designed value, still frequency nadir of Case B is no better than the Case A. This is because in Case B, all the three VSC controllers are using frequency droop coefficient higher than designed value, resulting in more value of $\rho_{\text{f.loss.pu}}$, which prohibits them to offer desirable support to the disturbed grid, as depicted by (6.12). The active power support withdrawn by VSC-1 is shown in Fig. 9g. And the power support offered by VSC-2 and VSC-3 are shown in Fig. 9h and i, respectively. It is evident from these figures that the active power support offered to the disturbed grid ONG-1 by the supporting grids via VSC-2 and VSC-3 is better for Case C in comparison to Case A and Case B. As observed at $t = 60$ s, active power injected by VSC-1 is 1.225 pu for Case A while 1.281 pu is injected for Case C into ONG-1. Since, before disturbance, 0.9 pu was injected into ONG-1, thus via proposed control additional 38.1% active power is offered to the disturbed grid via VSC-1 which is just 32.5% for Case A. The frequency deviation of the supporting grids, ONG-2 is shown in Fig. 9e and for ONG-3 in Fig. 9f. Since more power support is offered by them in the proposed scheme, resulting in comparatively deeper nadir in ONG-2 and ONG-3. However, the difference between the nadir of the supporting grids of proposed scheme with cases A and B is not much, in comparison to the same for the disturbed grid, as shown in Fig. 9d. It should also be noted that the enhanced frequency regulation offered by the proposed technique is due to the application of the improved frequency droop coefficient ($\rho_{\text{f.proposed}}$), used by the dual-droop controllers of the proposed scheme.

The DC voltage profile as observed at the local DC bus near to VSC-1 is shown in Fig. 9j. It is clear that DC voltage nadir is deepest for Case B, among the three, while the DC voltage deviation is better for the proposed control than the two cases. DC voltage deviation as given by (4.11), mainly depends upon the value of frequency droop coefficients exercised by the disturbed and the supporting VSC controllers. Since for Case B, all the three controllers exercise values higher than the designed values, its DC voltage deviation is highest. While for the proposed scheme, even though the disturbed VSC controller exercise higher than designed value but the values used by the supporting VSCs are lower than designed values, thereby resulting in lesser DC voltage deviation than Case A and Case B. It is evident that with the proposed control scheme enhanced frequency support for the disturbed grid along with efficient DC voltage regulation of the MTDC system is obtained.

It should also be noted that nature of response offered by Case B is oscillatory in comparison to Case A and Case C.

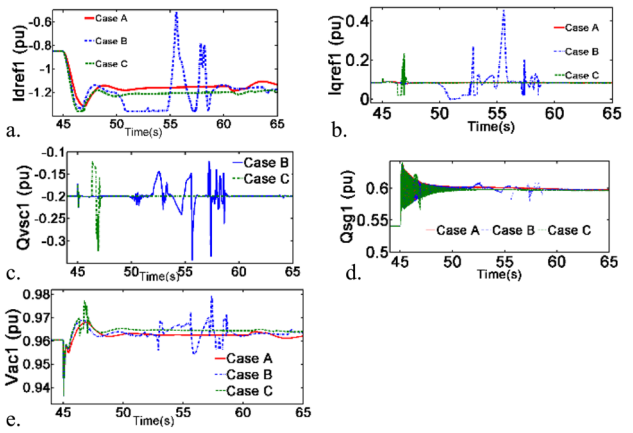


Fig. 10 Effect of DCCM in Scenario-1 shown by VSC-1's **a** Direct-axis converter current. **b** Quadrature-axis converter current. **c** Reactive power output. **d** Reactive power output of equivalent generator. e. AC voltage at PCC-1

This is because of the use of the higher frequency droop coefficient by it, the disturbed VSC tries to take enhanced power support from the MTDC system. However, due to similar higher coefficients exerted by the supporting VSCs, also, limited active power support could only be delivered, resulting in such oscillatory behaviour.

7.2 Effect of dynamic converter current modulation

As stated earlier, for carrying out a fair comparison among the three compared control cases, the technique of DCCM has been applied to all the three cases, Case A, Case B and Case C. As shown in Fig. 9g, with the proposed control and via application of DCCM, disturbed VSC-1 is able to withdraw more than 30% power above its rated value. To achieve this, the amount of direct-axis converter current produced by it is shown in Fig. 10a. In all the three cases, via virtue of DCCM, the $i_d{}^*$ is above the limit value of 1.1 pu. However, with the proposed scheme, since the amount of power support withdrawn is the highest among the three cases, while performing the process of DCCM, the $i_{\text{d}}{}^*$ takes the highest (limiting) value, $i_{\text{d.new}}$ as explained in Sect. 2 briefly, i.e., in between instant $t = 46$ s and $t = 47$ s. At the same time, the value of $i_{\text{q}}{}^*$ as shown in Fig. 10b reduces to minimum value $i_{\text{q.min}}$, i.e., 0.02 pu in this case. But, within just one second, i.e., after $t = 47$ s, $i_{\text{d}}{}^*$ becomes lesser than the limiting value & $i_{\text{q}}{}^*$ soon assumes the original value. This effect of DCCM in Case C is also visible on the converter's reactive power output, $Q_{\text{vsc}-1}$ shown in Fig. 10c. For the brief moment in between $t = 46$ s and $t = 47$ s, this reactive power output reduces to 0.15 pu from 0.2 pu. However, within less than a second, the original reactive power output of the converter gets restored. In order to make up for the decrease in reactive power, the reactive power output of the equivalent

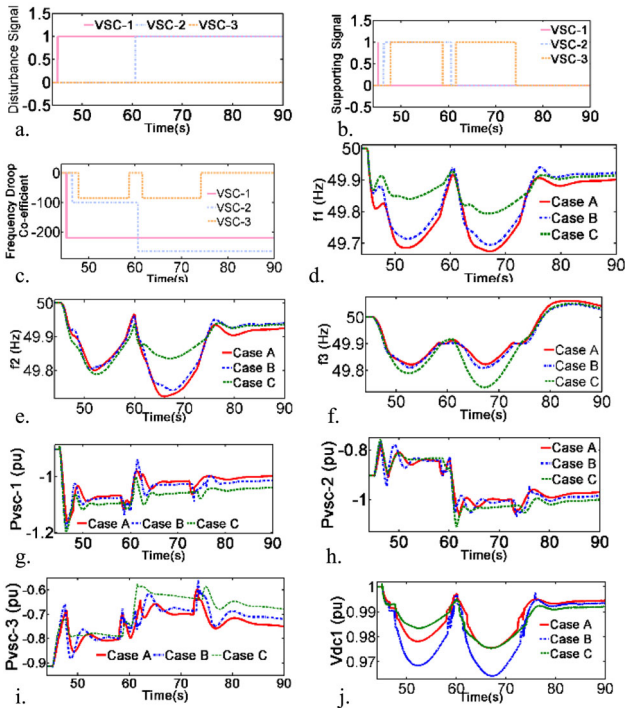


Fig. 11 Response of VSC-MTDC system for Scenario-2. **a** Disturbance signal. **b** Supporting signal and **c** Frequency droop coefficient of proposed scheme. Frequency of **d** ONG-1. **e** ONG-2. **f** ONG-3. Power inverted by the onshore VSCs. **g** VSC-1. **h** VSC-2 and **i** VSC-3 and **j** DC voltage near VSC-1

synchronous generator of ONG-1 increases, as depicted in Fig. 10d. Also, the AC voltage profile at PCC-1 in ONG-1 is also shown in Fig. 10e. Except for the momentarily decrease in reactive power output of VSC-1, the AC voltage profile is better with the proposed control.

7.3 Scenario-2: AC disturbance initiated by two-area load increase

Two load increase events are created in the considered MTDC system of Fig. 1; first in ONG-1 and then in ONG-2. At $t =$ 45 s, load of 123 MW, 0.85 pf is switched on in ONG-1. And at $t = 60$ s, 137 MW, 0.85 load is switched on in ONG-2. Prior to $t = 45$ s, all three onshore grids are operating near to nominal frequency of 50 Hz.

Firstly, the response to the first load increase event at $t =$ 45 s in ONG-1 is presented. This is similar to the Scenario-1. However, magnitude of switched load is half to that of the Scenario-1. As expected, and seen from Fig. 11a, for Case C, the disturbance signal goes high only for VSC-1. On the other hand, as depicted by Fig. 11b, the supporting signal for VSC-2 and VSC-3 goes high in response. It is to be noted that the supporting signals for the two VSCs do not go high at the same time, rather there is a small difference between the two instants. This is justified since the frequency dead band limit given to VSC-3 ($\pm$ 0.1 Hz) is more than VSC-2 ($\pm$ 0.05 Hz). Also, for a brief transient, supporting signal goes high for VSC-1. This is due to the nature of power deviation made by VSC-1 shown in Fig. 11g. Since just after the instant of load switching, this VSC momentarily decreases its power and then increases it, which justifies the transient high in supporting signal of VSC-1. Corresponding to the disturbance/supporting modes operation of the onshore VSC controllers, the resultant frequency droop coefficients exercised with the proposed converter control technique are shown in Fig. 11c. As desired, VSC-1 being in disturbed mode of operation is exercising a value higher than the designed value of the frequency droop coefficient. While VSC-2 and VSC-3, being in the supporting mode in response to the first event, are using lower than the corresponding designed values.

The frequency profile of ONG-1 for the three cases depicts the similar response as Scenario-1 and is shown in Fig. 11d. As evident, with the proposed control, the frequency profile of ONG-1 is better than cases A and B. However, unlike Scenario-1, the frequency nadir of Case A is deeper than Case B. This is because the magnitude of frequency droop coefficient exercised by the Case B is 200.25 which is more than 133.5, i.e., the designed value used in Case A. Also, since magnitude of disturbance is just half in this scenario in comparison to Scenario-1, so better active power support is available to ONG-1 from ONG-2 and ONG-3. From Fig. 11g, it is clear that disturbed VSC-1 is able to take maximum support from the MTDC system for Case C as compared to the cases A and B.

The following discusses the response to the second disturbance event occurring at $t = 60$ s in ONG-2. Before this disturbance, ONG-2 was supporting the frequency excursion in ONG-1 by decreasing its active power that it was withdrawing from the MTDC system as shown in Fig. 11h. At $t =$ 60 s, as shown from Fig. 11a, ONG-2 goes into the disturbed mode. Also, it lowers its supporting signal at this instant as exhibited by Fig. 11b. As confirmed from Fig. 11c, it now exercises a higher value of frequency droop coefficient than its designed value after $t = 60$ s. The frequency of ONG-2 is shown in Fig. 11e. It shall be noted that the frequency regulation with the proposed control is better for the second disturbance event and can be justified similar to the prior disturbing event in ONG-1. However, it can be observed from Fig. 11d, that ONG-1 undergoes another frequency deviation, although load switching took place in ONG-2. This is because earlier (that is prior to $t = 60$ s), ONG-2 as well as ONG-3 were supporting ONG-1 by providing additional active power support. But, now ONG-2 being itself into disturbed mode, the active power support for ONG-1 is available from VSC-3 only. The frequency profile of ONG-3 is shown in Fig. 11f. Also, the active power inverted by VSC-3 is shown in Fig. 11i.

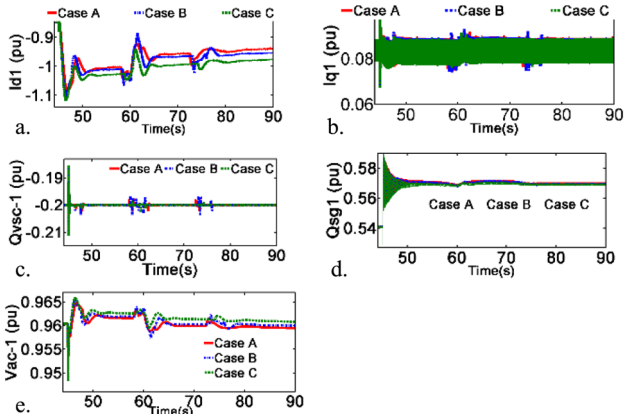


Fig. 12 Effect of DCCM in Scenario-2 shown by VSC-1's **a** Direct-axis converter current. **b** Quadrature-axis converter current. **c** Reactive power output. **d** Reactive power output of equivalent generator. **e** AC voltage at PCC-1.

As noted in Case C, the active power deviation made by VSC-3 is more after $t = 60$ s than prior. This is justified because after the second disturbance event, ONG-3 is supporting two disturbed grids, ONG-1 and ONG-2. This also justifies the reason for having a deeper frequency nadir, after $t = 60$ s, in the proposed scheme than this instant. It can be seen that for first disturbance event, VSC-3 reduces its inversion and after beginning of second disturbance as well, it reduces its inversion further so that both the disturbances can be supported. It is clear that proposed control technique offers more active power support than the other compared cases.

The DC voltage profile as observed at the local bus near VSC-1 is shown in Fig. 11j. As observed, for the first load increase, the DC voltage deviation for Case C is better than the two cases. This is because, except VSC-1, the other two VSCs are using frequency droop values lesser than designed values. However, for the second load increase, the DC voltage nadir for the proposed scheme is better than Case B but nearly same as Case A. This is because now two VSCs that's VSC-1 and VSC-2 are in disturbed mode and are using values higher than the corresponding designed values, thereby causing higher DC voltage deviation, as evident from (4.11) as well Fig. 12.

7.4 Scenario-3: AC -DC disturbance initiated by load increase in ONG-1 along with VSC-4 outage

In this scenario, the response of the VSC-based MTDC grid is shown against two simultaneous disturbances, viz., offshore platform converter outage (VSC-4) at $t = 45$ s which was inverting 0.15 pu from the MTDC system and another disturbance is 10% load increase in ONG-1, which is same as Scenario-1. Due to load switching in its local grid, VSC-1 under goes into disturbed mode and thus, shows a 'high' value of disturbance signal (Fig. 13a) while VSC-2 and VSC-3 show a 'high' value of supporting signal (Fig. 13b). Since wider frequency dead band is used for ONG-3 (± 0.1 Hz) than ONG-2 (± 0.05 Hz), this justifies why the instants of supporting signals for VSC-2 and VSC-3 differ slightly from one another. According to the disturbance/supporting modes of operation of the onshore VSCs, the resultant frequency droop coefficients used by them are shown in Fig. 13c. In response to the simultaneous disturbance events, the resultant frequency profile of the three onshore grids, DC voltage deviation of the MTDC system and the power inverted by the onshore VSCs are also exhibited in Fig. 13. It is evident that the response of the proposed control technique is better than cases A and B. It should be noted that the obtained frequency deviations as well as DC voltage deviation are lesser as compared to those obtained in Scenario-1, even though same 10% load increase is initiated in ONG-1. In addition,

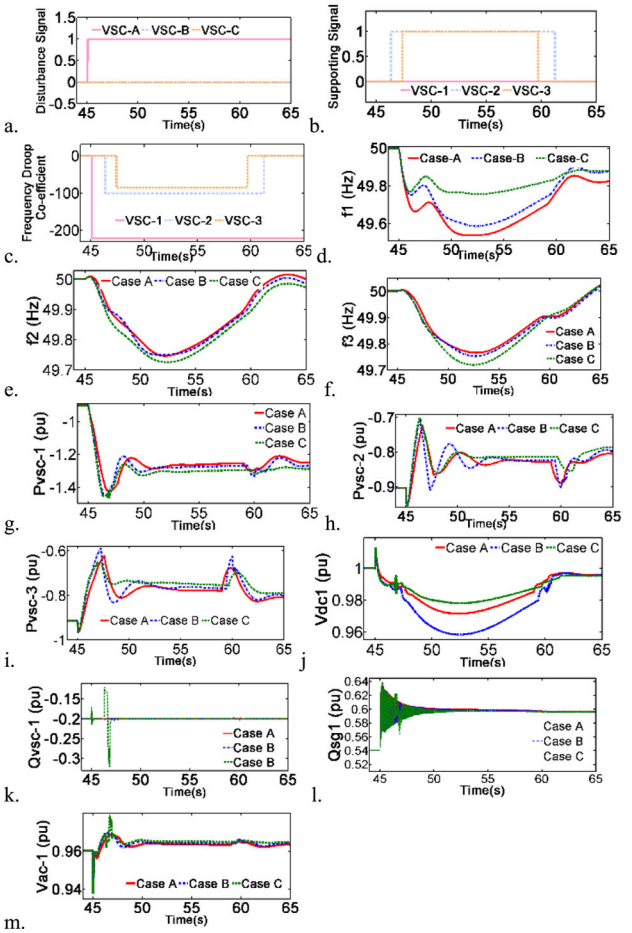


Fig. 13 Response of VSC-MTDC system for Scenario-3. **a** Disturbance signal. **b** Supporting signal and **c** Frequency droop coefficient used by onshore VSCs in the proposed scheme. Frequency profile of **d** ONG-1. **e** ONG-2 and **f** ONG-3. Power inverted by the onshore VSCs. **g** VSC-1. **h** VSC-2 and **i**. VSC-3 and **j** DC voltage near VSC-1. Effect of DCCM in Scenario-3 as shown by **k** Reactive power output of VSC-1. **l** Reactive power output of equivalent generator of ONG-1. **m** AC voltage at PCC-1.

the response of Case B unlike Scenario-1 is smoother and does show any unwanted oscillations. All these are justified because out of the 146 MW (additional 10% load demand) made by ONG-1, 60 MW are readily available in the MTDC grid which could not get inverted due to the simultaneous outage of the VSC-4. This power availability in the MTDC system is utilized immediately by VSC-1 for the load demand made in the ONG-1. As a result, the supporting grids, ONG-2 and ONG-3, now have to supply lesser power in comparison to Scenario-1, thus, resulting in lesser frequency deviation in them. Due to lesser frequency deviations in this scenario as compared to Scenario-1 and as evident from (4.17), lesser DC voltage deviation is justified.

The effect of the DCCM is similar to Scenario-1 as seen from the reactive power supplied by VSC-1 to ONG-1 (Fig. 13k), reactive power obtained from the equivalent alternator of ONG-1 (Fig. 13l) and AC voltage profile at PCC-1 (Fig. 13m). This is because in both Scenario-1 and the present scenario, the amount of active power inverted by VSC-1 is exactly same. The only difference is that in Scenario-1, the support power comes entirely from the supporting grids ONG-2 and ONG-3. While in the present scenario, the support power comes only partially from ONG-2 and ONG-3 while rest (60 MW) is availed from what could not get inverted by the offshore platform VSC due to its outage.

7.5 Scenario-4: DC event initiated by outage of VSC-5

In this scenario, a DC disturbance event has been simulated by considering that VSC-5 i.e., the converter rectifying power generated by Offshore Wind Farm-II (OWF-II) in the MTDC system, shown in Fig. 1, goes into outage. It should be noted that for the case of DC events involving outage of VSCs operating in either rectifier/inverter mode, it is important to maintain DC voltage of the MTDC system within permissible limits. This is justified because of smaller time constant associated with DC capacitors of the MTDC system in respect to turbine-governor system of the AC grids. Therefore, inability to regulate DC voltage could result in quick discharging of the capacitors, resulting in rundown of the DC grid. On the contrary, DC voltage increasing above the permissible limits could destroy insulation of the connected equipment.

In this disturbance, the VSC-5, associated with OWF-II, undergoes outage at $t = 45$ s. Prior outage, it was supplying 33% of the total power infeed of the two offshore wind farms (OWF1 and OWF-II) into the MTDC system. Due to this significant power deficit inside the MTDC system due to the outage of this rectifier, it is expected to observe a drop in DC voltage. Since this disturbance lies outside the onshore grids and respective onshore VSCs, thus, ONG-1, ONG-2 and ONG-3 are expected to play a 'supporting' role by reducing their power inversion from the MTDC system to avoid

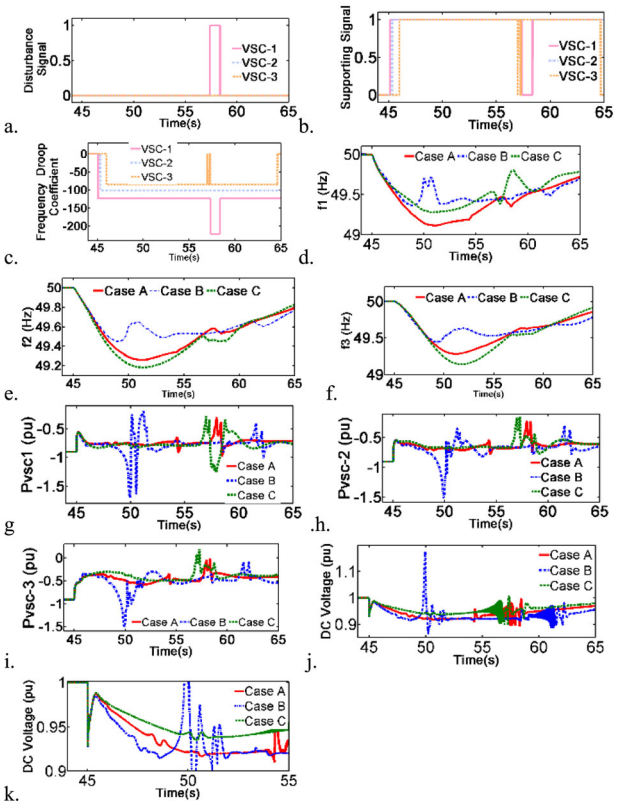


Fig. 14 Response of VSC-MTDC system for Scenario-4. **a** Disturbance signal. **b** Supporting signal and **c** Frequency droop coefficient of proposed scheme. Frequency of **d** ONG-1. **e** ONG-2 .**f** ONG-3. Power inverted by the onshore VSCs. **g** VSC-1. **h** VSC-2 and **i** VSC-3 and **j** DC voltage near VSC-1. **k** Zoomed version of V_{dc1}.

DC voltage deviation going above the permissible limits. The response of the AC/DC system to this disturbance is shown in Fig. 14.

As expected, and as depicted in figures, Fig. 14a and b, the supporting mode signal for the proposed technique goes high for the three onshore VSCs in Case C, while the disturbance mode signal remains equal to zero. As observed, from Fig. 14j., the DC voltage regulation of the MTDC system, done by the proposed technique is better than Case A and Case B. Also, a zoomed version of this DC voltage deviation is displayed in Fig. 14k. It is observed that Case B undergoes deeper DC voltage deviation in addition to significant oscillatory behaviour, among the three cases, which shows its inability to provide sufficient power support inside the MTDC system. This is justified because for case B, exercising for $\rho_{\text{f.corrected}}$ (higher than $\rho_{\text{f.designed}}$) by all the three onshore dual-droop converters, irrespective of whether they are in disturbed mode or not, causes a high DC voltage deviation inside the MTDC system, as evident from (4.17). On the contrary, for the proposed control scheme, the three VSC dual-droop controllers being in supporting mode exercise $\rho_{\text{f.new}}$, a lower value than designed value of the frequency

droop coefficient, thereby, causing lesser DC voltage deviation. The DC voltage deviation for Case A is higher than Case C because the value of frequency droop coefficients exercised by its onshore VSC controllers is equal to $\rho_{\text{f.designed}}$ which is more than $\rho_{\text{f.new}}$.

The active power inverted by the onshore VSCs, VSC-1, VSC-2 and VSC-3 are shown in Fig. 14g, h and i. As evident from (4.18), higher value of DC voltage deviation, reduces the amount of active power support offered by the onshore dual-droop controlled VSC. Thus, the active power support is least for Case B among the three compared cases.

Frequency profile of the three onshore grids, ONG-1, ONG-2 and ONG-3 are also shown in Fig. 14d, e and h respectively. A significant frequency deviation is observed in all the three onshore AC grids. However, due to limited active power support offered by the dual-droop converters of Case B, the frequency profile of all the onshore grids of is better for this case as compared to the other two cases.

It should be noted that for the proposed scheme (Case C), the frequency nadir of the three onshore grids differs among each other by a difference of not more than 0.1 Hz. This is justified because of the value of the $\text{PSI}_{\text{desired}}$ which is selected optimally keeping in to consideration the size of the three onshore grids.

8 Conclusion

In this paper, a versatile dual-droop control technique employing P–f and P–V_{dc} droops has been evolved for VSC-based multi-terminal HVDC system. It has transpired to be a generic technique which ensures frequency support provision to the participating AC grids and can be used irrespective of the MTDC grid configuration. In the proposed work, a novel power-frequency droop control has been conceptualized and designed which has enabled to mitigate the negative impact imposed by the P–V_{dc} droop control that too without deactivating action of the DC voltage droop control. To avoid large frequency deviations inside the healthier grids, a Power Support Index (PSI) has been coined to ascertain desirable quantum of power support from healthier grids with an efficient coherent operation of the two droop controls. Mathematically, optimum selection of such PSI values has been derived and used in the simulation studies. To operationalize the proposed control scheme, it requires local measurements of relevant electrical parameters and no dedicated communication network will be necessary. Inherently, the proposed control strategy will be catering to the need of enhanced power support within the permissible operational region of IGBT-based VSCs to be effective through application of the Dynamic Converter Current Modulation scheme (DCCM), even if the grid converters are operating near to their rated power. The various attributes of the versatile dual-droop controller have been tested on the Matlab/Simulink platform, and very impressive performances as obtained from the simulation results, have been demonstrated compared to the earlier research works.

Author contribution Ashima drafted the entire paper. All authors reviewed the manuscript and contributed remarkably for the paper.

Data availability No datasets were generated or analysed during the current study.

Declarations

Conflict of interest The authors declare no competing interests.

References

1. Taneja A, Saha R, Singh M (2020) Frequency regulation technique in AC–DC network using dynamic converter current modulation in VSC-HVDC system. In: 2020 IEEE 17th India Council International Conference (INDICON). New Delhi, India, 2020, pp, 1–8, https://doi.org/10.1109/INDICON49873.2020.9342451
2. Saha R, Singh M, Taneja A (2021). An adaptive master-slave technique using dynamic converter current modulation in VSC-based MTDC system. In: 2021 6th international conference for convergence in technology (I2CT). Maharashtra, India, 2021, pp, 1–8, https://doi.org/10.1109/I2CT51068.2021.9418191
3. Taneja A, Saha R, Singh M (2022) A case study on VSC-HVDC converter outage using current modulation approach in AC–DC networks to restore frequency stability. In: 2022 international conference for advancement in technology (ICONAT) Goa, India 2022. pp 1–6 https://doi.org/10.1109/ICONAT53423.2022.9725902
4. Taneja A, Saha R, Singh M (2022) Influence of DC voltage and frequency droop on active power support capability in dual-droop controlled VSC-MTDC-based AC–DC Grid. In: 2022 IEEE Region 10 Symposium (TENSYMP), Mumbai, India, pp. 1–6. https://doi.org/10.1109/TENSYMP54529.2022.9864563
5. Sun K, Xiao H, Liu Y (2022) Optimized allocation method of the VSC-MTDC system for frequency regulation reserves considering ancillary service cost. CSEE J Power Energ Syst 8(1):53–63. https://doi.org/10.17775/CSEEJPES.2020.05800
6. Haileselassie TM, Uhlen K (2010) Primary frequency control of remote grids connected by multi-terminal HVDC. In: IEEE PES general meeting, pp. 1–6. https://doi.org/10.1109/PES.2010.5589327
7. Chaudhuri NR, Majumder R, Chaudhuri B (2013) System frequency support through multi-terminal DC (MT-HVDC) grids. IEEE Trans Power Syst 28(1):347–356. https://doi.org/10.1109/TPWRS.2012.2196805
8. Akkari S, Dai J, Petit M, Guillaud X (2015) Coupling between the frequency droop and the voltage droop of an AC/DC converter in an MT-HVDC system. IEEE Eindhoven PowerTech 2015:1–6. https://doi.org/10.1109/PTC.2015.7232285
9. Akkari S, Dai J, Petit M, Guillaud X (2016) Interaction between the voltage-droop and the frequency-droop control for multi-terminal HVDC systems. IET Gener Transm Distrib 10:1345–1352. https://doi.org/10.1049/iet-gtd.2015.0814
10. Jose K, Joseph T, Liang J, Ugalde-Loo CE (2018) Auxiliary deadband controller for the coordination of fast frequency support from multi-terminal HVDC grids and offshore wind farms. IET Renew

Power Gener 12:1444–1452. https://doi.org/10.1049/iet-rpg.2018.5485
11. Adeuyi OD, Cheah-Mane M, Liang J, Jenkins N (2017) Fast frequency response from offshore multiterminal VSC–HVDC schemes. IEEE Trans Power Delivery 32(6):2442–2452. https://doi.org/10.1109/TPWRD.2016.2632860
12. Wang W, Li Y, Cao Y, Häger U, Rehtanz C (2018) Adaptive droop control of VSC-MTDC system for frequency support and power sharing. IEEE Trans Power Syst 33(2):1264–1274. https://doi.org/10.1109/TPWRS.2017.2719002
13. Vennelaganti SG, Chaudhuri NR (2018) Ratio-based selective inertial and primary frequency support through mtdc grids with offshore wind farms. IEEE Trans Power Syst 33(6):7277–7287. https://doi.org/10.1109/TPWRS.2018.2850145
14. Vennelaganti SG, Chaudhuri NR (2018) Selective power routing in MT-HVDC grids for inertial and primary frequency support. IEEE Trans Power Syst 33(6):7020–7030. https://doi.org/10.1109/TPWRS.2018.2854647
15. Wang R, Chen L, Zheng T, Mei S (2017) VSG-based adaptive droop control for frequency and active power regulation in the MTDC system. CSEE J Power Energ Syst 3(3):260–268. https://doi.org/10.17775/CSEEJPES.2017.00040
16. Kumar AS, Padhy BP (2020) Hybrid control strategy for effective frequency regulation and power sharing in multi-terminal HVDC grids. IET Gener Transm Distrib 14:5536–5546. https://doi.org/10.1049/iet-gtd.2020.0921
17. Kumar AS, Padhy BP (2022) An Interactionless duo control strategy for bipolar voltage-source converter in renewables integrated multiterminal HVdc grids. IEEE Trans Ind Appl 58(4):5383–5394. https://doi.org/10.1109/TIA.2022.3172065
18. Sun K, Xiao H, Sundaresh L, Pan J, Li K-J, Liu Y (2019) Frequency response reserves sharing across asynchronous grids through MTDC system. IET Gener Transm Distrib 13:4952–4959. https://doi.org/10.1049/iet-gtd.2019.1006
19. Zhang Q et al (2021) Primary frequency support through North American continental HVDC interconnections with VSC-MT-HVDC systems. IEEE Trans Power Syst 36(1):806–817. https://doi.org/10.1109/TPWRS.2020.3013638
20. Li Z, Wei Z, Zhan R, Li Y, Tang Y, Zhang X-P (2021) frequency support control method for interconnected power systems using VSC-MTDC. IEEE Trans Power Syst 36(3):2304–2313. https://doi.org/10.1109/TPWRS.2020.3026035
21. Shadabi H, Kamwa I (2021) Dual adaptive nonlinear droop control of VSC-MT-HVDC system for improved transient stability and provision of primary frequency support. IEEE Access 9:76806–76815. https://doi.org/10.1109/ACCESS.2021.3078066
22. Liu C, Liu H, Jiang S, Zheng L (2023) Dynamic frequency support and DC voltage regulation approach for VSC-MTDC systems. CSEE J Power Energ Syst 9(2):645–658. https://doi.org/10.17775/CSEEJPES.2021.01790
23. Ayalew B, Moursi MSE, El-Saadany EF (2023) Primary frequency support strategy for MTDC system with enhanced DC voltage response. IEEE Trans Power Syst 38(2):1512–1528. https://doi.org/10.1109/TPWRS.2022.3176875
24. Taneja A, Saha R, Singh M. An adaptive and efficient VSC-MTDC controller for DC voltage regulation and frequency stability in AC network" published as Book Chapter 978-981-99-0968-1, 531030_1_En, (Chapter 5), Lect. Notes Electrical Eng., Vol. 1023, In: Asha Rani et al. (Eds): Signals, Machines and Automation
25. Zhu J, Booth CD, Adam GP, Roscoe AJ, Bright CG (2013) Inertia emulation control strategy for VSC-HVDC transmission systems. IEEE Trans Power Syst 28(2):1277–1287. https://doi.org/10.1109/TPWRS.2012.2213101
26. Zhu J, Guerrero JM, Booth CD, Zhang H, Adam GP (2013) A generic inertia emulation controller for multi-terminal VSC-HVDC systems. In: 2nd IET renewable power generation conference (RPG 2013, Beijing. pp 1–6. https://doi.org/10.1049/cp.2013.1751
27. Shen Z et al (2022) Variable-inertia emulation control scheme for VSC-HVDC transmission systems. IEEE Trans Power Syst 37(1):629–639. https://doi.org/10.1109/TPWRS.2021.3088259
28. Zhu J et al (2022) Inertia emulation and fast frequency-droop control strategy of a point-to-point VSC-HVdc transmission system for asynchronous grid interconnection. IEEE Trans Power Electron 37(6):6530–6543. https://doi.org/10.1109/TPEL.2021.3139960
29. Recommended practice for excitation system models for power system stability studies (1992) IEEE Standard 421.5-1992, August 1992
30. IEEE Working Group on Prime Mover and Energy Supply Models for System's Dynamic Performance Studies (1992) Hydraulic turbine and turbine control models for dynamic studies. IEEE Trans Power Syst 7(1):167–179
31. Liu Y, Chen Z (2013) A flexible control method of VSC-HVDC link for enhancement of effective short-circuit ratio in a hybrid multi-infeed HVDC system. IEEE Trans Power Syst 28(2):1568–1581
32. Haileselassie TM, Uhlen K (2010) Frequency sensitivity analysis of ac grids connected to MTDC grid. In: 9th IET international conference on AC and DC power transmission (ACDC 2010), London, pp. 1–5. https://doi.org/10.1049/cp.2010.0990
33. Sanz IM, Chaudhuri B, Strbac G (2014) Frequency changes in AC systems connected to DC grids: impact of AC vs. DC side events. 2014 IEEE PES General Meeting | Conference & Exposition, National Harbor, MD, USA, 2014, pp. 1–5. https://doi.org/10.1109/PESGM.2014.6939914
34. Fradley J, Preece R, Barnes M (2020) The influence of network factors on frequency stability. IEEE Trans Power Syst 35(4):2826–2834. https://doi.org/10.1109/TPWRS.2019.2958842
35. Taneja A, Saha R, Singh M (2023) A dynamic and efficient active power support scheme using VSC-HVDC system for quick frequency restoration. Arab J Sci Eng. https://doi.org/10.1007/s13369-023-08130-y
36. Kabsha MM, Rather ZH (2020) A new control scheme for fast frequency support from HVDC connected offshore wind farm in low-inertia system. IEEE Trans Sustain Energy 11(3):1829–1837. https://doi.org/10.1109/TSTE.2019.2942541

Publisher's Note Springer Nature remains neutral with regard to jurisdictional claims in published maps and institutional affiliations.

Springer Nature or its licensor (e.g. a society or other partner) holds exclusive rights to this article under a publishing agreement with the author(s) or other rightsholder(s); author self-archiving of the accepted manuscript version of this article is solely governed by the terms of such publishing agreement and applicable law.

Journal of Scientific & Industrial Research
Vol. 84, June 2025, pp. 665-671
DOI: 10.56042/jsir.v84i6.11252

An IoT-Based Edge Computing Lossless Compression Approach for Enhancing Energy Efficiency in Networks

Mukesh Sahu* & Jeebananda Panda
Delhi Technological University, Delhi 110 042, India

Received 19 May 2024; revised 19 March 2025; accepted 01 May 2025

As the Internet of Things (IoT) maintains to increase the inexperienced control of the huge amounts of records generated becomes increasingly more crucial. One of the major issues is big energy intake associated with transmitting records throughout networks. Addressing this issue is vital for the sustainability and feasibility of IoT infrastructures, mainly in packages stressful actual-time records processing and assessment. This paper targets to introduce a completely unique, energy-green technique for IoT compression that minimizes strength intake at some stage in records transmission. By leveraging edge computing, that seeks the machine data closer to its supply, thereby decreasing transmission distances and related electricity costs. A three-layered framework is introduced to achieve lossless compression by capturing network packets of different data sizes. The framework comprises IoT layer, Edge layer and Cloud layer. The framework is carried out at the brink of the community, enhancing statistics, decreasing power consumption, and ensuring security from cyber threats. The results are evaluated using metrics affecting data compression such as Root Mean Squared Error (RMSE) and Peak Signal to Noise Ratio (PSNR). The experimental results show that the proposed compression approach achieves the lowest power consumption rate as 80%, 85%, 90% and 88% in case of image, sensor, financial and textual data types respectively. Furthermore, the proposed framework achieves the highest PSNR value (92.14) and the lowest RMSE value (0.6653) thereby validating the performance of the given IoT-based framework. It shows that the proposed approach is better than existing compression techniques and recent review studies.

Keywords: Cloud layer, Data compression, Edge computing, Energy efficiency, Internet of Things (IoT)

Introduction

In the generation of digital transformation, the Internet of Things (IoT) is reshaping industries with the useful resource of permitting the mixing of bodily gadgets into virtual ecosystems, generating exceptional volumes of facts.[1] This information proliferation needs strong control techniques to maximise IoT machine efficiencies, specifically regarding statistics transmission and strength consumption. Traditionally, statistics processing in IoT structures has relied carefully on cloud computing structures, which frequently outcomes in excessive latency and large strength usage due to the widespread information conversation necessities. With the advent of factor computing, there may be a paradigm shift towards processing facts in the path of its deliver, which not only enhances reaction instances but furthermore significantly decreases the bandwidth desired for statistics transmission.[2–3] However, regardless of vicinity computing, the challenge of handling the electricity intake associated with data transmission stays important. Addressing this mission is crucial, now not most effective to beautify the operational common overall performance of IoT systems however additionally to growth the battery lifestyles of the brink devices, plenty of which may be constrained by way of the usage of their electricity capacities. Moreover, with the growing deployment of IoT in vital programs collectively with healthcare, transportation, and industrial automation, ensuring facts integrity and minimizing power consumption without sacrificing normal ordinary performance turns into paramount. This study introduces an innovative method to facts compression internal IoT frameworks, aiming to lessen the energy footprint of these structures whilst keeping excessive data utility for analytical responsibilities.

While aspect computing improves the scalability and performance of IoT networks, massive gaps continue to be in powerful data compression strategies that appropriately balance power conservation with information integrity.[4–6] Current answers often compromise statistics excellent or fail to scale

*Author for Correspondence
E-mail: mukeshsahu@ieee.org

efficaciously with growing statistics volumes and tool networks.[7–9] Additionally, the impact of information compression on the accuracy of system reading models in IoT packages is not sufficiently explored, raising troubles about the practical deployment of compression strategies in touchy real-time environments. *This research seeks to fill these gaps with the resource of developing an energy-green records compression technique that maintains excessive records constancy particularly tailored for component-based totally device getting to know packages*. Furthermore, there's a loss of a cohesive framework that seamlessly integrates superior compression algorithms proper away into IoT device firmware to optimize every power standard performance and information processing pace.[10–11]

Literature Review and Gap Analysis

The integration of the Internet of Things (IoT) into numerous sectors has necessitated green information manage strategies, especially in terms of transmission and storage. Anderson *et al.*[12] shows that at the equal time as traditional cloud-based totally fashions provide robustness in handling enormous statistics masses, they frequently causes latency issues and immoderate power consumption. As a remedy, edge computing has been proposed as a probable solution that techniques records close to its supply, considerably decreasing transmission distances and improving reaction times. Khaled *et al.*[13] focused on techniques to restrict the energy on the course of facts transmission. Poongodi *et al.*[14] discussed numerous lossless and lossy compression strategies, highlighting their ability to reduce facts duration notably however also noting the variable impact on facts constancy and processing overhead. Lossless strategies, at the equal time as maintaining information integrity, offer limited compression ratios, which might not be enough for huge-scale IoT deployments that generate large quantities of facts. Rao *et al.*[15] On the alternative hand, lossy compression strategies, which permit for better compression ratios thru sacrificing a controllable degree of information accuracy, were examined in contexts requiring plenty lots much less precision in records.

Park *et al.*[16] witnessed these techniques are in particular relevant in real-time monitoring structures in which the sheer number of statistics necessitates aggressive compression strategies to make certain well timed information processing and response. However, the software of these compression techniques in IoT, particularly at the same time as blended with place computing, has been less explored. Pandey et. *al.*[17] has started out to cope with this via implementing easy adaptive compression algorithms on factor devices however have no longer fully explored the trade-offs among compression common basic overall performance and computational call for in limited environments. Furthermore, at the same time as there can be a growing fashion to make use of device getting to know algorithms to beautify preference-making in IoT networks, the impact of data compression at the overall performance of those algorithms stays beneath-researched. Compression shown by Zhang *et al.*[18] can modify information developments, possibly primary to decreased version accuracy or reliability. Siemens *et al.*[19] introduce dynamic compression schemes that modify primarily based totally on community conditions, that could drastically optimize IoT communications. Moreover, Liu *et al.*[20] have contributed insights into the algorithmic performance of records compression techniques, specializing in their scalability in multi-node IoT networks. Moreover, the literature furthermore lacks comprehensive studies at the implementation challenges of integrating advanced data compression algorithms at once into IoT devices. These include hardware barriers, power constraints, and the need for actual-time processing talents. Barina *et al.*[21] additionally, most modern studies specialize in theoretical fashions and simulations with less emphasis on area trials or real-global implementations, which might be vital for validating the proposed solutions underneath practical going for walks conditions**.** Lempel *et al.*[22] has validated that even minor losses in statistics quality can substantially affect the general performance of deep studying fashions carried out in predictive analytics. The modern-day procedures furthermore often forget about the safety implications of compressed data transmission. With IoT devices an increasing number of being focused with the resource of cyber-assaults, making sure the integrity and security of compressed statistics streams is paramount, a gap no longer sufficiently covered in current studies. Nasif *et al.*[23] applied deep learning techniques to reduce size of Huffman tree using pooling. However, the given study failed to achieve lossless and secured compression due to shortest bit size. Chang *et al.*[24] introduced lossless compression approach for medical IoT systems by monitoring data based on heart rate, heart signals and electrocardiograph (ECG) scans.

Still, the given approach is unable to compress financial as well as textual data. Tosoni *et al.*[25] used sparse matrix-vector multiplication approach to investigate time, space and energy efficiency among IoT devices. Data parallelism improved execution time, energy consumption and space efficiency but the approach failed to validate the matrix variables in achieving data compression. Qiu *et al.*[26] introduced robust topology generation scheme for IoT systems to prevent loss of data bits. Its olive-like topology is only suitable for medium degree nodes and did not validate images for compression.

Novelty and Contributions

- Develops a unique lossless compression set of policies optimized for IoT devices, imparting better compression ratios with minimal loss of critical facts, thereby extending device battery life, and decreasing transmission costs.
- Seamlessly integrates the compression set of policies with facet computing frameworks, permitting network processing and garage of compressed facts, which drastically decreases power consumption.
- Ensures that the compression set of rules maintains the integrity of facts to a degree that lets in effective software of device gaining knowledge of fashions at the edge, addressing the mission of keeping version accuracy with compressed information.
- Incorporates sturdy protection protocol to guard the integrity and confidentiality of the compressed information, ensuring the answer's applicability in sensitive and important IoT programs.

Overview of Existing Data Compression Algorithms

(a) Adaptive Data Compression Algorithm (ADCA)[27]

This set of policies dynamically adjusts the compression degree based totally on actual-time community bandwidth and processing velocity at the brink node. It starts off evolved with the aid of using way of amassing information from IoT sensors, measuring modern community and processor situations, and then making use of an appropriate compression stage.

***Algorithm 1: Adaptive Data Compression Algorithm*[27]**

Input: Raw data from IoT devices, Network bandwidth (NB), Processor speed (PS)

Output: Compressed data ready for transmission

1. Start
2. Collect raw data from IoT sensors.
3. Measure current network bandwidth (NB) and processor speed (PS) at the edge node.
4. Set compression level:
   a. If NB high and PS high, set compression level low.
   b. If NB low and PS high, set compression level medium.
   c. If NB low and PS low, set compression level high.
5. Apply the appropriate compression algorithm based on the determined level:
   a. For low compression, use fast lossless compression.
   b. For medium compression, use moderate lossy compression.
   c. For high compression, use aggressive lossy compression.
6. Compress data according to selected algorithm.
7. Transmit compressed data to the edge node.
8. End.

(b) Real-Time Compression Quality Adjustment (RCQA)[28]

This set of rules adjusts the mistake bounds of information compression in actual time, based totally completely on the sensitivity of the information being processed. It guarantees that critical statistics is compressed with higher constancy, keeping crucial accuracy for machine learning programs. By monitoring tool remarks and adjusting errors bounds consequently, it balances records integrity with compression performance, enhancing the usability of compressed records in sensitive or vital applications.

***Algorithm 2: Real-Time Compression Quality Adjustment* [28]**

Input: Data to be compressed, Data sensitivity index (DSI)

Output: Compressed data with controlled quality loss

1. Start
2. Input statistics to be compressed and Data Sensitivity Index (DSI).
3. Determine initial mistakes bounds:
   a. If DSI is excessive (vital facts), set low mistakes bounds.
   b. If DSI is medium, set medium mistakes bounds.
   c. If DSI is low (non-vital data), set immoderate mistakes bounds.
4. Apply lossy compression with the determined blunders bounds.
5. Monitor actual-time device comments:
   a. If information high-quality is below great thresholds, decrease mistakes bounds.
   b. If device performance is impacted, growth errors bound slightly.

6. Adjust compression settings dynamically primarily based on tool remarks.
7. Output compressed information.
8. End

(c) Steam Control Transmission Protocol (SCTP)[29]

This relaxed protocol compresses after which encrypt IoT facts earlier than transmission, ensuring facts integrity and confidentiality. After compression, records are encrypted the use of uneven cryptography and signed with a virtual signature for integrity verification. At the receiving quit, the threshold node verifies the signature and decrypts the information, making sure that the facts remain comfortable at some point of transmission and is only on hand to crook entities.

Algorithm 3: **Stream Control Transmission Protocol[29]**

Input: Data to be compressed

Output: Securely compressed data ready for transmission

1. Start
2. Input data to be compressed.
3. Compress data using the chosen compression algorithm.
4. Encrypt compressed data using an asymmetric encryption algorithm:
   a. Generate key pairs.
   b. Use the public key for data encryption.
5. Attach a digital signature using the private key to ensure data integrity.
6. Transmit the encrypted and signed data to the edge node.
7. On receipt at the edge node:
   a. Verify digital signature.
   b. Decrypt data using the private key.
8. Process decrypted data for further analysis.
9. End

Proposed Framework

The proposed framework is meticulously designed to beautify the electricity overall performance and protection of IoT structures running inside a facet computing paradigm. It strategically carries superior information compression and real-time adjustment mechanisms to address important disturbing conditions of excessive facts volumes, transmission costs, and stringent safety requirements. The structure of the proposed framework consists of three layers: IoT devices layer, Edge layer, and Cloud layer.

(a) IoT Devices Layer: This layer comprises data collection component as follows:

- Data collection: - It is used for gathering information from numerous IoT sensors and gadgets. It guarantees that information should be captured and transmitted to the edge nodes for similarly processing. Collection of data requires capturing of network packets which are to be compressed without affecting the system. Fig. 1 shows screenshot of data collection (network packets).

(b) Edge Layer: This layer consists of following components:

- Adaptive Compression**:** At the coronary heart of the framework, this module dynamically adjusts the facts compression price based totally on actual-time community situations and thing node

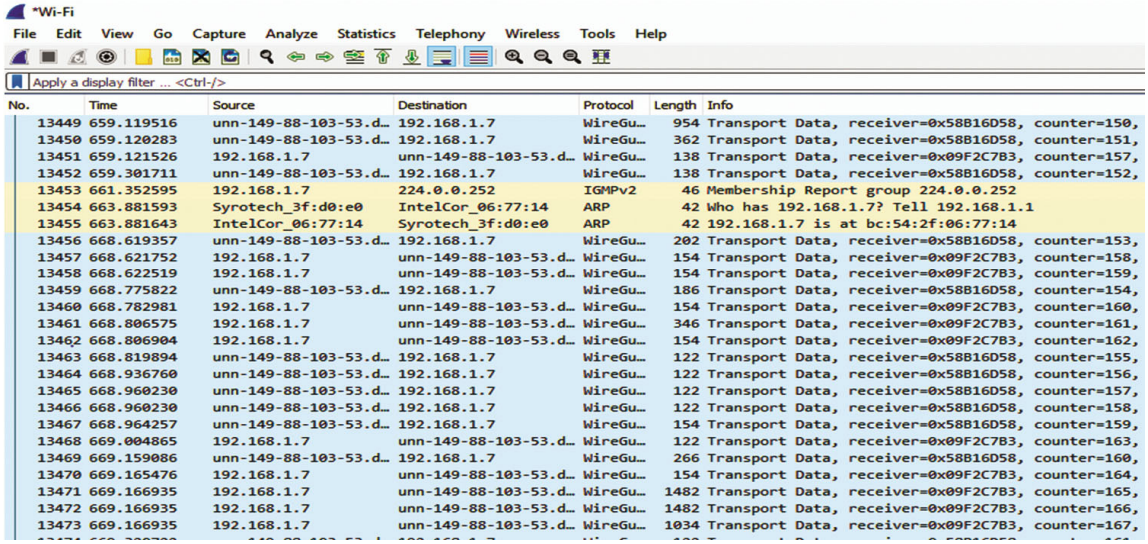


Fig. 1 — Data collection for compression

talents. It makes use of a complex set of policies that determines the most stability among compression efficiency and processing load, consequently maintaining strength, and decreasing bandwidth utilization.

- Quality Adjustment Control**:** Integrated in the edge layer, this factor video display units the integrity and accuracy of the compressed statistics the use of gadget studying algorithms. It adjusts the compression parameters in real-time to ensure that the facts superb is maintained, for vital packages requiring excessive records fidelity.
- Security Protocol**:** To shield statistics integrity and confidentiality, a strong protection protocol is implemented across all layers of the framework. It includes encryption, data anonymization, and use of digital signatures to get rid of cyber threats.

(c) Cloud Layer: It is used for storing massive portions of data and acting complex processing duties that cannot be treated at the threshold due to useful aid constraints. The components are:

- Data Transmission**:** It manages the green switch of processed and compressed facts between the IoT gadgets, thing nodes, and the cloud. It ensures that statistics flow seamlessly inside the course of the framework, optimizing each pace and aid utilization.
- Analytics and Processing: It plays actual-time information analytics to derive actionable insights without delay on the records deliver. It allows selection-making techniques and triggers automated actions without tremendous latency.

The layout of the proposed IoT-based framework is shown in Fig. 2.

Results and Discussion

This section evaluates the proposed framework based on the findings derived from compression strategies across distinctive IoT devices, and safety protocol effectiveness under several compression settings.[30] The metrics used to validate the proposed approach are as follows:

- *Root Mean Squared Error (RMSE):* It is used to check the accuracy of the given results. It is computed by the square of the difference between the proposed and actual values taken square root divided by N. Mathematically, it is given as:

$$\text{RMSE}=\sqrt{\sum_i \frac{(\text{Proposed value}-\text{Actual packet size})(\text{Proposed value}-\text{Actual packet size})}{N}} \quad \ldots (1)$$

where, N denotes number of bits or size of original packet

- *Peak Signal to Noise Ratio (PSNR):* It measures the quality between original data and compressed data. The higher the value of PSNR, the better will be quality of compression. It is given as:

$$\text{PSNR} = 10 \log_{10} (\text{Original file size} / \text{RMSE}) \quad \ldots (2)$$

In Table 1, we collate the proposed framework results with the existing compression algorithms[27–29] and recent studies.[23–26]

Table 1 shows comparison of average RMSE and average PSNR of recent studies and existing compression algorithms with the proposed approach. The results depict average RMSE of the recent studies (**1.8562, 1.7433, 1.5341 and 1.4873**) and existing compression algorithms **(1.4567, 1.3612 and 1.2583)**

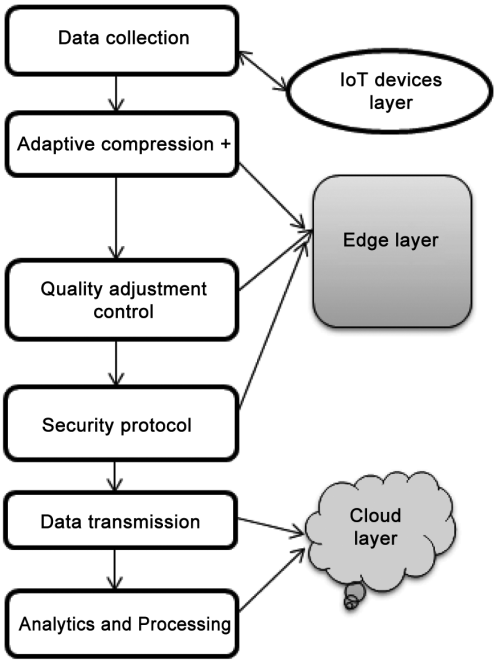


Fig. 2 — Layout of the proposed IoT-based edge computing framework

Table 1 — Comparative analysis of the proposed approach with existing compression algorithms and recent studies

Approaches / Algorithms/ Recent studies	Avg. RMSE	Avg. PSNR
Nasif *et al.*[23]	1.8562	80.02
Chang *et al.*[24]	1.7433	86.43
Tosoni *et al.*[25]	1.5341	84.45
Qiu *et al.*[26]	1.4873	88.09
ADCA [27]	1.4567	79.12
RCQA [28]	1.3612	83.76
SCTP [29]	1.2583	82.35
Proposed lossless compression	0.6653	92.14

Table 2 — Power consumption analysis of the proposed approach based on compression level

Data Type / Compression	No compression	Moderate compression	Lossless compression (proposed)
Image data	92%	89%	80%
Sensor data	95%	91%	85%
Financial data	98%	95%	90%
Text data	94%	92%	88%

is much higher than the proposed approach (**0.6653**). Lesser value of RMSE indicates that the proposed approach is prone to fewer errors and proves to be the most suitable for data compression. Since RMSE is inversely proportional to PSNR, therefore the proposed approach has the highest PSNR (**92.14).**
Individual analysis of the proposed lossless compression approach on several data types is shown in Table 2. The results are achieved by taking three aspects into consideration- no compression, moderate compression and lossless compression.

The "Proposed Compression" column in table 2 shows dramatic reductions thus indicating a large decrease in power consumption. It gives a clear and quantifiable demonstration that the proposed compression approach notably reduces the energy intake of IoT gadgets. The findings highlight the trade-off among data types and power consumption percentage. Image data type sees a reduction in power consumption from **92% to 80%** after applying the proposed lossless compression approach. Similarly, sensor data type ranges from **95% to 85%** decrease in power consumption. Financial data type compression also achieves the least power consumption (90%) on applying the proposed lossless scheme Textual data attains power consumption of **94% (no compression), 92% (moderate) and 88% (lossless compression).**

Security Protocol Effectiveness

The proposed framework meets the requirements of security protocol in terms of information sensitivity levels. When compression is done, especially advanced lossy strategies, safety integrity ratings decorate from 'Medium' to 'Maximum' at the identical time due to increase in records sensitivity. This development is pivotal, especially for noticeably sensitive data in which protection breaches can result in severe consequences. The better safety with better compression degrees can be attributed to fewer facts points being transmitted, which reduce the attack floor for capacity information breaches and simplify encryption and integrity verification strategies. A threshold related to information sensitivity levels are used to prevent data loss while compression.

Applications of the Proposed IoT-based Lossless Compression Approach

- It is used in ZIP file format to compress data and make it available to users in an efficient and secured manner.
- It will also be used to encode patients' record in healthcare systems which require compression and encoding of images.
- It may also lead to integration of several IoT devices for minimizing load on data centres thereby enhancing energy consumption in networks.

Limitations of the Current Study

- Lossless compression may not perform well when the data is subjected to entropy and uncertainties. It is hard to find exact value of entropy within bits of data.
- The quality of images used for compression may deteriorate due to lack of optimization parameters. The parameters must be selected optimally to preserve compression rate.

Conclusions

The study introduces an IoT-based framework to achieve lossless compression in given networks by exploring the effects of numerous data compression strategies. It seamlessly integrates the compression set of policies with facet computing frameworks, permitting network processing and garage of compressed facts, which drastically decreases power consumption across all device types, thereby improving operation, overall performance and sustainability. The proposed framework achieves the highest PSNR value (92.14) and the lowest RMSE value (0.6653) thereby validating the performance of the given IoT-based framework proving its superiority to the existing compression techniques.

Future research on actual-time adaptive structures is needed that modify compression parameters in response to converting community situations and processing skills. Additionally, the integration of system mastering techniques for maximum compression needs to be explored for ensuring efficacy of IoT systems. Ultimately, advancing those adaptive

compression strategies will assist the broader adoption of IoT generation, making sure they meet the rigorous desires of modern-day digital infrastructures on the identical time as retaining excessive requirements of performance, safety, and facts integrity.

Conflicts of Interest

The authors declare that they have no conflicts of interest to report regarding the present study.

References

1 Nagaraj S J, Sagar, Shashank S P & Tushar K, Comparative analysis of lossless data compression techniques, *Int J Engg Sci Innov*, **3(3)** *(*2022) 176–180, doi: 10.1109/ ISED48680.2019.9096229.

2 Zhang S, Integration of IoT into sectors necessitates efficient data management, *IEEE Trans Cloud Comput*, (2018) 50–60, doi: 10.1109/TMI.2017.2714640.

3 Sinha K K, Tiwari S & Gawande S S, Data compression and decompression method and system for communication system, *Int J Eng Res Technol*, **11(4)** (2022) 85–88, doi: 10.17577/IJERTV11IS04005.

4 Razzaque M, Bleakley C & Dobson C, Compression in wireless sensor networks: A survey and comparative evaluation, *ACM Trans Sen Netw*, **10(1)** (2013) 5–44, doi: 10.1145/2528948. URL http://doi.acm.org/10.1145/2528948.

5 Siemens E, Kurdecha V & Ushakov S, Internet of things data transfer method using neural network autoencoder, *Inf Telecommun Sci*, **1** (2023) 9–15, doi:10.20535/2411-2976.1.2023.

6 Shi, Edge computing: A potential solution that approaches data near its source, *Proc IEEE Int Conf Edge Comput* (IEEE) 2019, 112–119, doi: 10.1109/IACC.2016.81.

7 Li D, Data compression techniques in IoT, *IEEE Trans Netw Serv Manag*, **15(4)** (2019) 1444–1458, doi: 10.1080/00319100500412337.

8 Chen W J, Evaluating lossy compression rates in IoT devices*, IEEE Internet Things J*, **6(3)** (2020) 4959–4973, doi: 10.56042/jsir. v82i2.70222.

9 Kumar R, Adaptive compression algorithms for low-power IoT devices, *Proc IEEE Symp Low-Power High-Speed Chips*, (2021) 202–210, doi: 10.1016/j.compeleceng.2021.

10 Zhao K, Impact of data compression on machine learning models*, IEEE Trans Knowl Data Eng*, **22(10)** (2021) 1505–1518, doi: 10.1080/00319100500412337.

11 Park F, Dynamic compression schemes for IoT, *IEEE Netw*, **34(5)** (2021) 225–231, doi: 10.1109/TVLSI.2017.2732062.

12 Andersen J, Algorithmic efficiency in IoT data compression, in *Proc IEEE Conf Decision Control* (IEEE) 2022, 778–783, https://doi.org/10.1063/1.5081543.

13 Khaled M A E, Ashfaq M & Suresh S P, E-IoT: Emulator to develop and test IoT application, *Proc IEEE WF-IoT,* (IEEE) 2022, 1–6, doi: 10.1109/TVLSI.2018.2835572.

14 Poongodi M, Malviya M & Kumar C, New York City taxi trip duration prediction using MLP and XGBoost*, Int J Syst Assur Eng Manag*, **13(1)** (2022) 16–27, doi: 10.1109/ ACCESS.2019.2944658.

15 Rao M, Lossless compression and implementation for medical signals using verilog, *Int Conf Intell Comput Control Syst* (IEEE) 2021, 1–6, doi: 10.1109/ACCESS. 2019.2936218.

16 Park J, Park H & Choi, Data compression and prediction using machine learning for industrial IoT, *2018 Int Conf Inf Netw* (IEEE) 2018, 818–820, doi: 10.1109/ic-ETITE47903. 2020.223.

17 Pandey S M U, Analysis of data encoding on the Internet of Things network, under the supervision of Kurdecha, in *Proc Perspectives Dev Inf Telecommun. Technol Syst "Igor Sikorsky Kyiv Polytech Inst* (Nat Tech Univ Ukraine) 2021, 399–454

18 Cao J, Zhang Q & Li L, Edge computing: Vision and challenges, *IEEE IOT J*, **3(5)** (2016) 637–646, doi: 10.1109/JIOT.2016.2579198.

19 Siemens E & Ushakov S, Internet of things data transfer method using neural network autoencoder, *Inf Telecommun Sci*, **14(1)** *(*2023) 9–15, doi:10.20535/2411-2976.1.2023.

20 Liu C, Zhang Y, Li Z, Zhang J, Qin H and Zeng J, Dynamic defense architecture for the security of the internet of things, *2018 11th Int Confer Comput Intell and Secur* (IEEE) 2018, 390–393 doi: 10.17577/IJERTV11IS040055.

21 Barina D, Experimental lossless data compressor, *Microprocess Microsyst*, **98** (2023) 104–803, https://doi.org/ 10.1016/j.micpro.2023.104803.

22 Ziv J & Lempel A, A universal algorithm for sequential data compression, *IEEE Trans Inf Theory*, **23(3)** (1997) 337–343, doi: 10.1109/TIT.1977.1055714.

23 Nasif Said A, Othman Ali Z, Sani Samsiah N, Hasan Kamrul M & Abudaqqa Y, Huffman deep compression of edge node data for reducing iot network traffic, *IEEE Access*, **12** (2024) 122988–122997, doi: 10.1109/ACCESS.2024.3452669.

24 Chang Y & Sobelman G E, Lightweight lossy/lossless ECG compression for medical iot systems, *IEEE IoT J*, **11(7)** (2024) 12450–12458, doi: 10.1109/JIOT.2023.3336995.

25 Tosoni F, Bille P, Brunacci V, Angelis A D, Ferragina P & Manzini G, Toward greener matrix operations by lossless compressed formats, *IEEE Access*, **13** (2025) 56756–56779, doi: 10.1109/ACCESS.2025.3555119.

26 Qiu T, Sun J, Chen N, Zhang S, Si W & Wang X, Olive-like networking: A uniformity driven robust topology generation scheme for IoT system, *IEEE Trans Comput*, **74(1)** (2025) 86–100, doi: 10.1109/TC.2024.3465934.

27 Mohamed M I, Wu W Y & Moniri M, Adaptive data compression for energy harvesting wireless sensor nodes, *Proc Int Conf Networ Sens Contr* (IEEE) 2018, 633–638, doi: 10.1109/ICNSC.2013.6548812.

28 Shoaib M, Jha N K & Verma N, Signal processing with direct computations on compressively sensed data, *IEEE Trans Very Large Scale Integr Syst*, **223(1)** (2015) 30–43, https://doi.org/10.29304/jqcm.2022.14.1.904.

29 Lu J, Verma N & Jha N K, Compressed signal processing on Nyquist-sampled signals, *IEEE Trans Comput*, **65(11)** (2016) 3293–3303, doi: 10.17577/IJERTV11IS040055.

30 Singh G & Jain V, Information retrieval (IR) through semantic web (SW): An overview, *Proc The Next Generation Inf Technol*, 2018, 23–27, doi: 10.1109/TIT.1977.1055714.

This article has been accepted for publication in IEEE Access. This is the author's version which has not been fully edited and content may change prior to final publication. Citation information: DOI 10.1109/ACCESS.2025.3574835

IEEE Access
Multidisciplinary | Rapid Review | Open Access Journal

Date of publication xxxx 00, 0000, date of current version xxxx 00, 0000.

Digital Object Identifier 10.1109/ACCESS.2024.Doi Number

An Integrated CNN-BiLSTM-Transformer Framework for Improved Anomaly Detection using Surveillance Videos

Sarfaraz Natha[1,2,*],(Student Member, IEEE), Mohammad Siraj[3,*], Fareed Ahmed[1], Majid Altamimi[3],(Member, IEEE), Muslim Syed[4]

[1]Department of Software Engineering, Sir Syed University of Engineering & Technology, Karachi, Pakistan
[2] Department of Information Technology, Quaid e Awam University of Engineering & Technology, Pakistan
[3] Department of Electrical Engineering, College of Engineering, King Saud University, Riyadh 11543, Saudi Arabia
[4] Atlantic Technological University, Republic of Ireland

Corresponding authors: Sarfaraz Natha (e-mail: sasattar@ssuet.edu.pk), Mohammad Siraj(e-mail: siraj@ksu.edu.sa)

This work was supported by the Deanship for Research & Innovation, 433 Ministry of Education, Saudi Arabia, and project number (IFKSUOR3-462).

ABSTRACT Surveillance cameras have been widely used for monitoring in both private and public sectors as a security measure. Close Circuits Television (CCTV) Cameras are widely used to surveillance normal and anomalous incidents. Real-world anomaly detection in complex environment situations is a significant challenge due to its diverse nature manually reviewing this vast data is difficult, time-consuming, and prone to errors. Human operators may overlook crucial information due to failure, which reduces the accuracy of manual monitoring. This highlights the need for automated solutions to improve accuracy and efficiency We proposed a Bidirectional Motion Temporal (BiMT) model to address this issue by coupling a pre-trained model of deep neural networks. This system utilizes a Convolutional Neural Network (CNN) to extract the best spatial key features from the video stream, which are converted into time series data and coupled with Recurrent Neural Network (RNN) deep learning model Bidirectional Long Short-Term Memory (BiLSTM) extract temporal key features, and Multi-Head Self-Attention (MHSA) allows for the detection of short-term frame correlations. In addition, created a custom transformer encoder with relative positional embedding that improves the detection and recognizes long-range frame dependencies. Furthermore, categorical focal loss (CFL) is used during training to prioritize essential features and further enhance the model's precision. The more sophisticated ConvNeXtv2 model produced average AUC scores of 98.6%, 86.5%, and 83.5% for the UCF-Crime, UBI-Fight, and RAD datasets respectively.

INDEX TERMS Convolutional Neural Network, Deep Learning, Bi-Directional Long Short-Term Memory, Multi-Head-Self-Attention, Anomaly Detection

I. INTRODUCTION

Surveillance systems are essential for ensuring public safety by monitoring people and places [1]. These systems generate a massive volume of video data that requires continuous analysis for security purposes [2]. However, the large data size and the unpredictable occurrence of incidents such as theft, violence, and other criminal activities make detection and identification challenging. However, manually reviewing this vast data is difficult, time-consuming, and prone to errors. Human operators may overlook crucial information due to weakness, which reduces the accuracy of manual monitoring [3]. Additionally, unusual incidents occur far less frequently than common occurrences, resulting in repetitive tasks that increase the likelihood of human error [4][5]. In addition, critical incidents such as traffic accidents, theft, explosions, shoplifting, fighting, and fires particularly in remote locations demand an immediate response. [6]. Therefore, real-time detection is fundamental to confirm quick action. It is an extending demand for automated systems capable of detecting anomalies in real time and minimizing the dependence on human operators to enhance the overall efficiency of public safety responses. [7]. This highlights the need for automated solutions to improve accuracy and efficiency. Automatic video surveillance has emerged as a necessary factor in various fields, including law enforcement departments, road monitoring, and smart safe cities.

The primary goal of enhance security and public safety [8]. A major challenge faced in automated video surveillance systems is to detect abnormal events or

This work is licensed under a Creative Commons Attribution 4.0 License. For more information, see https://creativecommons.org/licenses/by/4.0/

This article has been accepted for publication in IEEE Access. This is the author's version which has not been fully edited and
content may change prior to final publication. Citation information: DOI 10.1109/ACCESS.2025.3574835

anomalies [9]. The identification of data instances deviating from nominal patterns is called Anomaly [10]. Anomaly detection (AD) is challenging and crucial to detect in videos. The computer vision research on anomaly identification in surveillance video is crucial since it is utilized in many security applications, including road accidents, and criminal activity to generate alerting for anomalous occurrences [11] [12]. In recent years, anomaly detection has been managed using various successful approaches [13]. Deep learning (DL) has demonstrated a remarkably successful approach to detecting anomalies in surveillance systems. It employs deep neural networks (DNNs) to identify and extract important characteristics from data during training. It can automatically extract hidden spatial characteristics from datasets using techniques such as Convolutional Neural Networks (CNNs) [14]. CNN is the most popular branch of DNN. CNN is made to recognize patterns in visual data and identify the features of images available at different sizes. CNN utilized convolutional layers that analyze input images using filters also known as kernels. CNN demonstrated high effectiveness in a wide range of arrays related to the image including recognition and generation. Therefore, CNN is a powerful and efficient algorithm for extracting spatial features to detect anomalies in videos [15]. CNN has several challenges despite its power because of its need for huge datasets. Researchers often use the transfer learning (TL) approach to overcome this challenge [16]. TL enables models to improve their learning performance in novel environments by using lessons from prior challenges to put it simply. Furthermore, the capacity of a model to continue performing well on unknown data is called generalization. CNN architectures such as DenseNet, ResNet, AlexNet, and VGG focus on learning spatial characteristics from individual input samples [17]. However, these models may struggle with sequential data, which requires more sophisticated techniques to achieve robust performance across various scenarios [18]. Another deep learning approach, the Recurrent Neural Network (RNN), is a more powerful deep learning technique that effectively captures temporal features in time-series data because it can process information in both directions, considering both past and future sequences. RNN preserves and uses past data when making judgments at the present step because of this dual processing. However, the initial data may become weakened or unclear as it passes through several steps. To address this issue, a Long Short-Term Memory (LSTM) network [19] has been established to improve the retention of information over long periods [20]. In recent studies, many researchers have been utilizing attention processes to reduce the distinction between human and machine behavior in anomaly detection models. Attention methods are successful in a variety of computer vision tasks including image processing [21] [22], object identification [23], and object classification [24]. There are various attention techniques developed for anomaly detection models including Self-Attention (SA), Bidirectional LSTM (BiLSTM) [25], and Multi-Head Self-Attention (MHSA) [26].

We proposed an innovative model that can effectively analyze both spatial and temporal features focusing on key patterns in long video sequences to classify abnormal activities within video frames which makes it highly suitable for surveillance systems. This proposed approach combines the convolutional operations of the CNN, which extract spatial features and integrates them with the processing capabilities of the Bi-LSTM to generate more accurate recognition output that separates critical features from a sequence of frames and adjusts attention weights accordingly. Furthermore, the Multi-Head-Self- Attention (MHSA) approach allows for the detection of short-term frame correlation to process every sixth frame from the video sequence. The suggested method is well-suited for anomaly detection in investigative video streams due to its targeted design performed by the experiments. It delivers a more precise depiction of abnormal activities in surveillance footage making it ideal for investigative. Lastly, a customized transformer module is applied for improved pattern recognition. This module excels at managing relative positional embeddings and detecting long-range relationships, thereby improving processing effectiveness. It is particularly optimized for anomaly detection in video data making it highly suitable for this purpose.

The model combined a CNN (DenseNet201) with an RNN (Bi-LSTM) and uses MHSA and a custom transformer to enhance precision and accuracy. We conducted our experiments utilizing publicly accessible datasets, including the public datasets UCF-Crime. [27] , UBI Fight [28] and custom-developed Road Anomaly Detection (RAD) dataset [29]. When compared to current state-of-the-art techniques, the suggested system performs exceptionally well. Its potential effectiveness in practical surveillance applications. The contributions of this study are the following.

- Our research introduces the Bidirectional Motion Temporal (BiMT) model, a novel approach for anomaly detection in video data. The BiMT framework excels at integrating spatial and temporal information, effectively addressing the limitations of prior methods in this domain.
- In the first phase, we employ pre-trained CNN models like DenseNet201 to obtain the best feature vectors from video frames. This process facilitates a comprehensive investigation of the spatial features in the footage, laying a solid foundation for more advanced analysis.
- Next phase Recurrent Neural Network(RNN) deep learning model Bidirectional Long Short-Term Memory (BiLSTM) and Multi-Head Self-Attention (MHSA) allow for the detection of short-term frame correlations. In addition, creating a custom transformer encoder with relative positional embedding improves the detection of anomalies and recognizes long-range frame dependencies. Furthermore, Categorical Focal Loss (CFL) is used during

This work is licensed under a Creative Commons Attribution 4.0 License. For more information, see https://creativecommons.org/licenses/by/4.0/

This article has been accepted for publication in IEEE Access. This is the author's version which has not been fully edited and
content may change prior to final publication. Citation information: DOI 10.1109/ACCESS.2025.3574835

training to prioritize essential features for further enhancing the model's precision.

- The creation of Road Anomaly Detection (RAD), a new dataset consisting of images and videos of anomalies performed on streets, roads, and highways recorded. RAD is a labeled dataset for supervised and semi-supervised machine learning algorithms.
- In the final phase of our research, we performed an extensive assessment of the model's performance, which revealed that the developed framework exhibits strong capability in precisely identifying anomalous events. The evaluation across multiple benchmark datasets yielded notable results, with the model attaining 98.6% accuracy on the UCF Crime dataset, 86.5% on the UBI Fight dataset, and 83.5% on the RAD dataset.

The upcoming sections of this paper offer an in-depth review of multiple studies that use different models and their sub-models for anomaly detection in surveillance video (Section II). In the next step, the proposed model will be presented in (Section III), followed by an evaluation of its performance through experiments and results (Section IV). Lastly, conclude with a discussion of possible future research directions in (Section V).

II. RELATED WORK

This section presents an overview of recent research on road anomaly detection, comparing three different approaches. The studies were then analyzed to emphasize the distinct advantages of the proposed framework.

A. CONVOLUTIONAL NEURAL NETWORK (CNN)

CNN offers several benefits, including shared parameters, sparse connections, and comparable representation [30]. CNN learns characteristics at various levels and works directly with input data. CNN first recognizes basic features like color and brightness, then moves on to details like edges, lines (horizontal or vertical), and corners. In the after layers, it captures more complex patterns, such as textures and shapes. [31]. CNN is an admired supervised learning technique in deep learning, particularly for analyzing visual data. Numerous learning-based models either directly implement CNN on video frames or utilize them. CNN variations capture the spatial feature. CNN has largely representational ability influenced by its depth, allowing it to learn complex patterns through feature extraction, from simple to complex abstractions. Nevertheless, deep architectures often encounter the issue of vanishing gradients. Early attempts to address this problem included linking intermediate layers to secondary learners. Advanced deep architectures such as VGG, ResNet, DenseNet, and MobileNet have shown impressive results in several experiments. [32]. Table 1 presents the strengths and limitations of prior research.

Table 1. The summary of prior research with their strengths and limitations.

Author, Reference	Methodology	Strength	Limitation
C. Hang et al. [33]	Hybrid deep learning models include ResNet50, InceptionV3, and Xception.	To identify confused driving behavior using deep learning models to extract the key features. These features helped to distinguish between distracted and non-distracted action.	The complex methodology proposed with the limited dataset. The model's ability is limited to accurately detect distracted driving behaviors during nighttime or in low-light environments.
S.M. Mohtavipour et al. [34]	CNN deep learning model	This framework utilizes handcrafted feature extraction methods. These features are related to appearance the movement speed. The spatiotemporal stream introduces a new discriminative feature differential motion energy image to provide a clearer representation of violent actions.	This model does not achieve high accuracy in detecting violent behavior in different environments and requires more computational power.
Lalit et al. [35]	The neural network consists of two convolutional layers followed by two fully connected (FC) layers.	This proposed model is to detect abnormal behavior. The recommended model adopts the latter approach, leveraging supervised learning for enhanced resilience to noise.	The model takes a long process time and responds late, needs to optimize and generalize the model for different datasets.
W. Sultani et al. [36]	Deep multiple instance learning (MIL) approach	This proposed deep learning framework addresses real-world anomaly detection in surveillance videos by overcoming the limitations of conventional methods that rely exclusively on normal training data. Given the inherent complexity of realistic anomalies, we argue that dependence on non-anomalous samples alone restricts robustness in dynamic, unconstrained environments, necessitating a more adaptive and context-aware modeling approach.	The proposed anomaly detection model attained an accuracy of 75.41%, indicating certain limitations in its effectiveness. The lower accuracy suggests challenges in recognizing diverse anomaly patterns, which may impact its generalization ability. Additionally, the model lacks optimization, which could be addressed through improved hyperparameter tuning, advanced feature extraction, or the integration of more robust architectures. These limitations highlight the need for further refinement to enhance detection accuracy and overall performance in practical applications.

This work is licensed under a Creative Commons Attribution 4.0 License. For more information, see https://creativecommons.org/licenses/by/4.0/

This article has been accepted for publication in IEEE Access. This is the author's version which has not been fully edited and
content may change prior to final publication. Citation information: DOI 10.1109/ACCESS.2025.3574835

In this study, Du. Tran et al.[37] introduced a 3D ConvNets model trained on large-scale video datasets and managed a systematic examination to identify the most effective temporal feature by using different kernel lengths for these networks. The C3D model effectively catches both appearance and motion information simultaneously and outperforms the features derived from 2D ConvNets in a variety of video analysis tasks. C3D model paired with linear classifier surpasses the performance of the leading methods in multiple video analysis. CNN is not enough to sufficiently extract the features from data disagreed by researchers.

B. RECURRENT NEURAL NETWORK (RNN) AND BIDIRECTIONAL LONG SHORT-TERM MEMORY (BILSTM)

Many researchers suggested that the RNN deep learning model is well suited for capturing temporal features over time. The CNN model gets spatial information from individual video frames and RNN is responsible for supervising the modeling of the temporal connection between successive frames over time. The recurrent layer is used by the RNN model to understand and illustrate the temporal relationship throughout the number of frames in a series while the CNN model serves the many convolutional and pooling layers to learn and recognize the unique properties of each frame of video. RNN is well suited to predict the nonlinear time series data, but it has some trouble during the learning process in long-term dependencies because it has often been a vanishing gradient problem in the backpropagation learning process. To address
this issue, there are other sophisticated models available such as Gated Recurrent Units(GRUs) and Long Short-Term Memory (LSTM). These models are various types of RNNs with enhancement of the model performance. LSTM works very effectively to perform that involve collecting long-term dependencies in sequence-based data [38]. This study introduced a unique model to take out spatiotemporal features from video frames by processing each one through a pre-trained Convolutional Neural Network (CNN) by Ullah et al. [39]. The model-extracted features play a key role in identifying anomalous events where deep features passed to a multi-layer Bidirectional Long Short-Term Memory (BD-LSTM) model which was capable of accurately classifying events as either anomalous or normal in complex surveillance settings. However, the proposed framework accuracy is limited when dealing with low illumination, and further refinement is needed particularly because the UCF-Crime dataset includes highly challenging categories. Another study, Yin et al. [40] introduced a framework for hyperspectral image (HSI) classification that associations a band grouping-based bidirectional long short-term memory (Bi-LSTM) network with 3D-CNN. The combined optimization of both feature extraction processes is guaranteed by this single model. Together, the 3D-CNN and Bi-LSTM improve classification performance by using a shared loss function.

C. MULTI-HEAD-SELF-ATTENTION (MHSA)

The idea of emulating human attention first emerged in computer vision to moderate the computational complexity of image processing while enhancing performance. This was done by creating models that focus on specific regions of an image rather than the entire image. However, the modern attention mechanisms widely used today are often credited to the field of natural language processing. Bahdanau et al. [41] proposed attention mechanism in a machine translation model to address the limitations of recurrent neural networks. Attention mechanisms have achieved state-of-the-art performance across a variety of tasks and can be trained in conjunction with base models like recurrent or convolutional neural networks using standard backpropagation. Furthermore, attention mechanisms provide a degree of interpretability to neural networks, which are typically difficult to understand [42]. Multi-head self-attention (MHSA) method introduced by Vasanthi et al [43]. Based on spatial pyramid pooling-faster SPPF) blocks within the backbone network. The MHSA block was created to extract feature maps by leveraging the information from queries, keys, and values, which enhances its ability to detect small objects. Additionally, PANet was utilized as the model neck to enhance detection performance while improving the identification of smaller objects. Our study proposes a novel framework that combines spatial feature extraction with Bi-LSTM networks to enhance accuracy and generalization in anomaly detection. By leveraging spatial details from input data and temporal processing through bidirectional sequential modeling. The architecture optimizes performance across diverse scenarios. The model is rigorously evaluated on benchmark datasets such as UCF Crime, UBI Fight, and RAD demonstrating superior results compared to existing methods. This integration effectively balances contextual understanding and dynamic pattern recognition for robust real-world applications.

III. PROPOSED METHODOLOGY

The proposed model flow chart consists of numerous steps: data preprocessing, CNN-RNN integration, MHSA-BiLSTM, and transformer, as illustrated in Figure 1. This diagram shows how each block connects and functions together. First, during data preprocessing. Each video is split into images in an appropriate format. These frames are then used as input for the DenseNet201-BiLSTM structure, which extracts features over time. Next, the output from each BiLSTM is supplied into an MHSA layer to identify the most significant features needed for detecting anomalies. Following this, another BiLSTM cell processes the key features extracted from the sequence of images. To input the data from the BiLSTM and multi-head attention layers into the custom transformer encoder block, a step to include position information is required. For temporally structured data, such as videos, absolute position embeddings are typically applied to capture unique positional information for each frame. Finally, the output undergoes several max pooling operations and passes through a softmax layer to classify the anomalies. Figure 2 illustrates the overall architecture of the proposed model. These steps are discussed in the following sections.

This work is licensed under a Creative Commons Attribution 4.0 License. For more information, see https://creativecommons.org/licenses/by/4.0/

This article has been accepted for publication in IEEE Access. This is the author's version which has not been fully edited and content may change prior to final publication. Citation information: DOI 10.1109/ACCESS.2025.3574835



FIGURE 1. The flow chart of proposed model processing

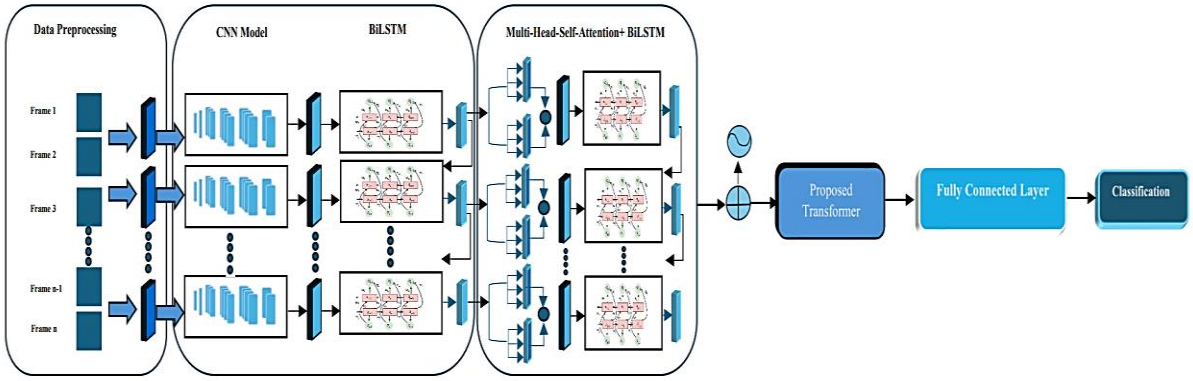


FIGURE 2. The complete architecture of proposed BiMT model

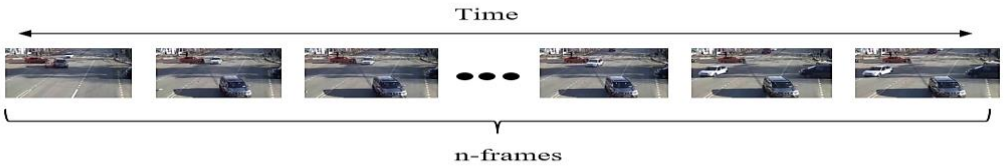


FIGURE 3. Video stream divided into n frames over time

A. DATA PREPROCESSING

In this stage acquire a specific number of images cut for the model. These frame values based on a model are called skipped_frames. For example, if the video contains 250 frames, skipped_frames would be set to six. It's crucial to note that each video is a different size in the dataset. In this step, a specific number of frames are extracted for the model known as skipped_frames. For instance, if a video consists of 250 frames, skipped_frames would be set to six. After extracting the frame from videos and then ensuring that compatibility with the model processing. Every frame must be resized to a standard dimension. For this purpose, each frame is resized to a resolution of 224 × 224 pixels, which allows it to work effectively with the pre-train CNN model. We chose the DenseNet201 model after comparing the performance of various models. The model emphasizes the differences between consecutive frames to detect abnormal events. By subtracting one image frame from the next, it captures the changes between time t and t+1, while ignoring stationary parts that do not change during that time. The feature extraction model uses the images generated by these subtractions to examine each video frame and identify temporal variations between them, hence highlighting motions. The frames depicted in Figure 3 represent a selected portion from a video, intended for training the model.

CNN is the most popular model in deep learning, particularly due to its remarkable ability to automatically extract important features from data without human guidance [44]. CNN has remarkable feature extraction capability applicable in diverse fields such as computer vision, speech recognition, and face detection [45]. CNNs have several key advantages including equivalent representations of the input data, facilitating sparse interactions, and allowing for the sharing of parameters across the network introduced by D. Palaz et al. [46]. CNNs utilize local connections and shared weights, making them especially effective for handling 2D data like images. This design choice not only reduces the total number of parameters needed but also simplifies the training process, leading to a faster and more lightweight network. [47]. A conventional convolutional neural network (CNN) architecture generally consists of several stacked convolutional layers, pooling layers, and fully connected layers. This layered design enables the model to progressively extract and learn increasingly complex hierarchical patterns from input data, capturing low-level details in initial layers and abstract features in deeper layers for robust data representation. There are various types of CNN-based models. The CNN-based learning model includes the VGG16, ResNet50, InceptionV3, DenseNet201, and ZFNet etc.

B. DENSENET201

In this study, we present our experiments with various CNN architectures to identify the most effective approach for

This work is licensed under a Creative Commons Attribution 4.0 License. For more information, see https://creativecommons.org/licenses/by/4.0/

This article has been accepted for publication in IEEE Access. This is the author's version which has not been fully edited and
content may change prior to final publication. Citation information: DOI 10.1109/ACCESS.2025.3574835

achieving higher accuracy while minimizing the number of parameters. Figure 4 and Figure 5 illustrate how the parameters of different models change based on the depth of their networks and the arrangement of convolutional layers. However, accuracy does not consistently follow this pattern. For instance, although inceptionV3 has further trainable parameters than DenseNet201. It does not attain the same level of accuracy as the RAD and UCF-Crime datasets. The specific characteristics of the datasets, and optimization challenges like vanishing or exploding gradients. Therefore, we selected the DenseNet201 model for CNN feature extraction due to its ability to achieve higher accuracy with fewer parameters.

DenseNet201 is designed with sufficient layers to extract relevant features for activity detection in videos, utilizing dense blocks that help address the vanishing gradient problem. [48]. Moreover, DensNet201 is initially trained on extensive image datasets such as ImageNet. [49], offering a strong foundation for extracting key features from images. The model's performance in anomaly detection, particularly when dealing with small datasets enhanced by pre-trained model. Additionally, Figure 6 [50] presents the architecture of DenseNet201 as implemented in our proposed model.

C. RNN: BI-LSTM

We employed the Long Short-Term Memory (LSTM) model, a specific form of Recurrent Neural Network (RNN) to overcome the shortcomings of traditional RNNs. LSTM enhances traditional RNNs by adding three gating units and a mechanism for updating the state within each cell. This structure enables the model to adjust its internal weight over time and process information more effectively, without modifying the network's parameters. As a result, it significantly improves the model's ability to generalize. The LSTM model's basic structure is illustrated in Figure 7. Compared to traditional RNNs, LSTM excels in processing sequential data due to its advanced memory architecture, which integrates both long-term and short-term memory [51]. The input gate is responsible for deciding which input features are accepted or rejected, thereby creating memory cells. In the following layer, the input gate determines whether to pass the memory cell state to the neuron or discard it. Additionally, the forget gate governs the updates to the cell state, choosing whether to retain the current features or eliminate past ones.

The Bi-LSTM model is highly effective at capturing temporal dependencies in sequential data by optimizing the flow of input information. It consists of two modules, forward and backward, each employing bidirectional long short-term memory networks with distinct structures. These modules share a universal output layer that admits both past and future inputs to be retrieved simultaneously. Each operation within the model is assigned a weight indicate as w. During the Bi-LSTM operation data flows through both the forward and backward hidden states, producing an output in the hidden layer that incorporates bidirectional temporal processing. Figure 8 explains the basic architecture of BiLSTM where x(t-1), xt, and x(t+1) as the input data at times (t-1),(t) and (t+1) respectively,

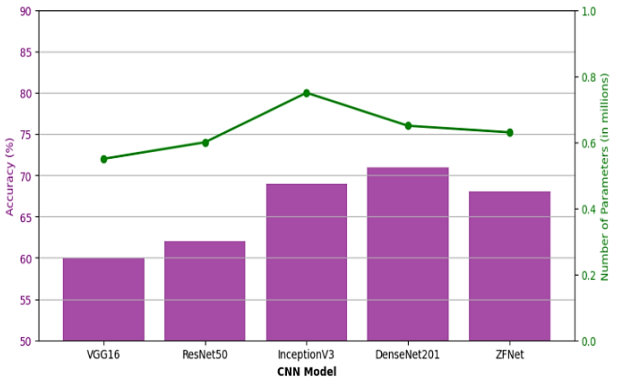


FIGURE 4. Accuracy comparison among various CNN models using the UCF crime dataset.

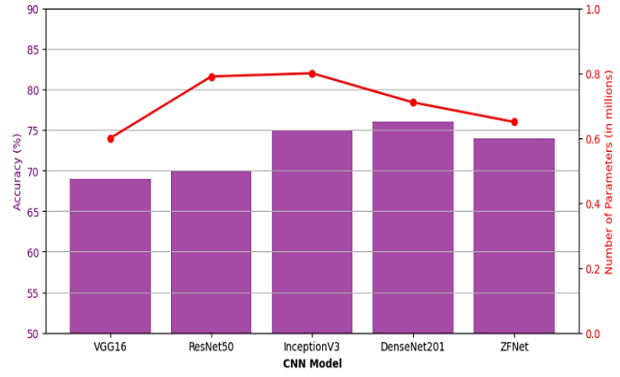


FIGURE 5. Accuracy comparison among various CNN models using the RAD crime dataset

while h(t-1), ht, and h(t+1) represent the hidden states at these respective times in the LSTM. The o(t−1), ot and o(t+1) represent the corresponding output data. w1, w2, …. ,w6 direct the weights for each layer are specified. The process of updating the hidden layer during the forward and backward passes of the LSTM, along with the final output from the BiLSTM, is described in equations (1)-(3).

$$h_t = f_1(w_1 x_t + w_2 h_{t-1}) \quad (1)$$
$$h'_t = f_2(w_3 x_t + w_4 h'_{t+1}) \quad (2)$$
$$o_t = f_3(w_5 h_t + w_6 h'_t) \quad (3)$$

where f_1, f_2, and f_3 are activation functions between different layers respectively. Determine the input state f_t, v_t, i_t in Equations (4)-(6).

$$f_t = \sigma(W_f [h_{t-1} x_t] + b_f) \quad (4)$$
$$v_t = tanh\,(W_{\dot{c}} \,.[h_{t-1} x_t] + b_v\,) \quad (5)$$
$$i_t = \sigma\,(W_{\dot{c}} \,.[h_{t-1} x_t] + b_v \quad (6)$$

Calculate the cell state C_t in Equation 7

$$C_t = f_t \,.\, C_{t-1} \,+\, i_t \,.\, v_t \quad (7)$$

Compute the output gate o_t and the hidden state h_t at the current in Equations (11)-(12)

This work is licensed under a Creative Commons Attribution 4.0 License. For more information, see https://creativecommons.org/licenses/by/4.0/

This article has been accepted for publication in IEEE Access. This is the author's version which has not been fully edited and
content may change prior to final publication. Citation information: DOI 10.1109/ACCESS.2025.3574835

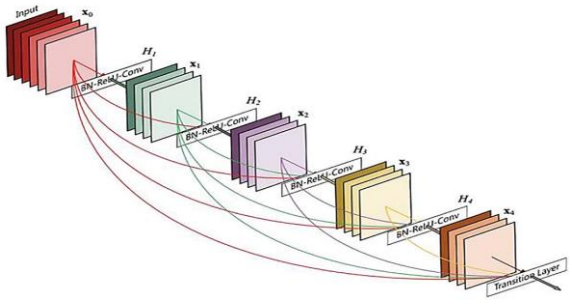


FIGURE 6. **The DenseNet201 model architecture [50]**

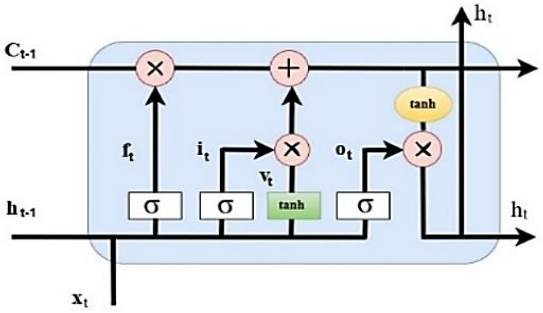


FIGURE 7. **LSTM architecture**

$$o_t = \sigma\,(W_o\,.[h_{t-1}x_t] + b_o \tag{8}$$
$$h_t = o_t\,tanh\,(C_t) \tag{9}$$

Within this framework, W and b correspond to the weight and bias parameters of the model's training matrix, respectively. The nonlinear activation function, represented by the symbol σ, produces output values restricted to the interval [0, 1]. The hidden layer is represented by h, with $\boldsymbol{f_t}$ indicating the forget gate. The cell state unit is indicated by $\boldsymbol{v_t}$, while the input or update gate is marked as $\boldsymbol{i_t}$. The cell state $\boldsymbol{C_t}$ acts as the memory unit, and the output gate $\boldsymbol{o_t}$, governs the release of information from the preceding layer. Bidirectional Long Short-Term Memory (Bi-LSTM) processes sequential data in both forward and backward directions, merging these processed signals at the current output layer. This bidirectional approach enables the model to exploit dependencies between historical and current inputs, thereby improving its ability to capture temporal patterns. The hidden state of Bi-LSTM comprises composite vectors formed by concatenating outputs from the forward and backward processing paths. The spatiotemporal feature extraction framework the generated features serve as inputs to an attention mechanism. This architecture employs a series of interconnected Residual Attention Bi-LSTM blocks, where each block's output is sequentially fed into the initial Bi-LSTM layer of the subsequent block, facilitating hierarchical learning of complex patterns.

Let $\boldsymbol{c_t^{(i)}}$, i^{th} the temporal features vector made by the Bi-LSTM with respect t time. The attention layer produces a background vector v^t for $\boldsymbol{c_t^{(i)}}$ at time t.

The structure consists of multiple Residual Attention Bi-LSTM blocks arranged sequentially, where the output from each block is fed into the first Bi-LSTM of the next block. Let $c_t^{(i)}$, denote the temporal feature vector generated by the Bi-LSTM at time t. Using attention weights $w_t^{(i)}$. The attention mechanism constructs a background vector v^t for $c_t^{(i)}$ at time t as described in Equation 11. This background vector is crucial for generating the situational vector. Subsequently, an activation function is applied to the hidden state H_t from the first Bi-LSTM layer to compute the relevance score r(i) at time t as outlined in Equation 10.

$$r_t^{(i)} = tanh\,(WH_t + b) \tag{10}$$

The consequence of features i at time is represented by $r_t^{(i)}$. W and b are indicated model weight and bias respectively, these parameters are adjustable which effects the model performing. The activation function utilized is the hyperbolic tangent, tanh(). The attention module then computes the attention weight. $A_t^{(i)}$ at time t , as detailed in Equation 11.

$$A_t^{(i)} = \frac{exp\left(w_t^{(i)} r_t^{(i)}\right)}{\sum_{j=1}^{N} exp\left(w_t^{(i)} r_t^{(i)}\right)} \tag{11}$$

In our method, $w_t^{(i)}$ signifies the model weight learned for the extracted feature i at time t, which captures high-level sequence knowledge. This is done using a stacked RNN with several LSTM layers. Usually, before reaching the output, the data in an LSTM passes through one layer. On the other hand, to examine data at several levels while solving temporal sequence issues. In this configuration, the hidden state from the preceding layer is sent into each LSTM layer, forming a hierarchy of layers that jointly process the input.

$$y = f(x) + x \tag{12}$$

Where y is the output in Equation 12, and x is the input of the Bi-LSTM block. While RNNs are good at capturing temporal information, they face challenges like the exploding gradient problem when dealing with longer sequences, as noted by Bengio et al. [52]. To address this, adopted the BiLSTM [53] which is more effective at analyzing sequential spatial features and capturing long-term patterns in spatial-temporal data. In our proposed model the output of the DenseNet201 processes each video frame and generates feature maps with dimensions (n_frames, 5, 5, 1920), where the number 1920 refers to the total channels produced in the final convolutional layer of DenseNet201. To make this output compatible with the BiLSTM layer, global average pooling is applied, which reduces the spatial dimensions and reshapes the output (n_frames, 1920). As a result, each video frame is now condensed into a 1920-dimensional feature vector, capturing essential spatial information in a more concise form. These feature vectors are subsequently passed into the BiLSTM layer, which focuses on modeling the temporal relationships between consecutive frames. The BiLSTM uses 512 features in both forward and backward directions, producing an output

This work is licensed under a Creative Commons Attribution 4.0 License. For more information, see https://creativecommons.org/licenses/by/4.0/

This article has been accepted for publication in IEEE Access. This is the author's version which has not been fully edited and
content may change prior to final publication. Citation information: DOI 10.1109/ACCESS.2025.3574835

with dimensions (n_frames, 512) for each time step, combining temporal information from both past and future frames.

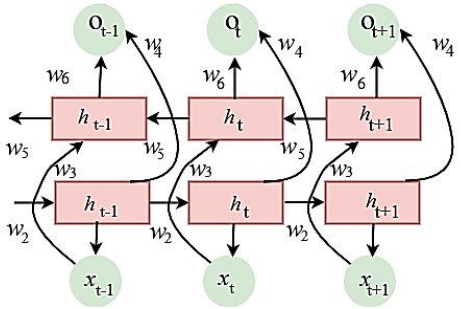


FIGURE 8. **Bi-LSTM architecture**

D. MULTI-HEAD-SELF-ATTENTION(MHSA)

MHSA is an example of attention mechanisms that have been developed to enhance computer vision, deep learning models [54]. We trained the model to concentrate on regions where anomalies are expected to occur in our suggested anomaly detection (AD) architecture using the MHSA technique and improved the overall classification accuracy by weight of important regions of interest by incorporating the MHSA layer. The BiLSTM is used by our model as input Z for the suggested attention model. Learning weight matrices are Q=ZWQ, K=ZWK, and V=ZWV respectively, where Z is redesigned to the dimensions of (n_row × n_columns, n_channels). Transformation is to provide the queries Q, keys K, and values V. The keys, values, and queries are all represented with a dimensionality of d in a single attention function. This process is attained by the description of three weight matrices that must learnt for transforming: Queries ($W_Q \in R_n \times d_q$), Keys ($W_k \in R_n \times d_k$), and Values ($Wv \in R_n \times d_v$). Equation 13 presents the calculation of the attention function.

$$\boldsymbol{Attention}\,(\boldsymbol{Q},\boldsymbol{K},\boldsymbol{V}) = \boldsymbol{softmax}\left(\frac{\boldsymbol{QK^T}}{\sqrt{\boldsymbol{d_k}}}\right)\boldsymbol{V} \qquad (13)$$

For a Multi-Head Self-Attention (MHSA) layer, the dimensionality is represented in terms of h times for the matching sets of values, keys, and queries. These variables are then combined to create the matrices Q, K, and V. Multiple-head self-attention (MHSA) is a collection of individual self-attention modules. The input size is calculated by multiplying the number of attention heads(h) by the dimensions of the queries, keys, and values in MHSA. These inputs are organized into three matrices: Q (queries), K (keys), and V (values). MHSA is composed of multiple self-attention modules, where each module corresponds to an individual attention head where $head_i$ = Attention (Qw_i^Q, Kw_i^K, Vw_i^V) as Equation 14 explains in the following.

$$MultiHead\ (Q,K,V) = Concat(head1, \ldots\ldots, head_h)\ W^O \qquad (14)$$

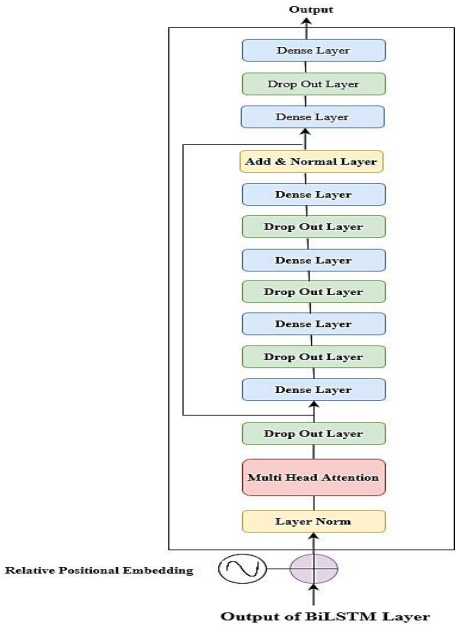


FIGURE 9. **Transformer Encoder architecture**

Where $W^O \in R^{hdv \times dmodel}$ product of output weight of MultiHead(Q,K,V).The Multi-Head Self-Attention (MHSA) receives output from the first BiLSTM layer, allowing the model to focus on many objects simultaneously. The facility of the model to focus on many items at once is resolved by the many numbers of attention heads in the MHSA layer [55] , and the BiLSTM layer processes each frame feature map understanding the features of data of these attention heads. The attention mechanism is improved upon by the second BiLSTM layer. It further analyses these significant aspects across a series of frames considering their temporal connections. Every frame can recognize elements by the MHSA-BiLSTM model, it follows their development across the frame sequence. The MHSA layer is between two BiLSTM layers in the proposed model. This management is expected to organize situations in which many objects are concurrently involved in different irregular occurrences and enable the model to investigate the association between the most significant elements with later and earlier frames of video. This arrangement gives better performance and accuracy to find the anomalous occurrence on time series frames of video. The number of attention heads is important in this model, and it determines how many layers are utilized to evaluate attention rating and different facts of monitoring data focus of each attention head.

E. TRANSFORMER ENCODER

The modification of the transformer encoder block is a special technique to adjust the performance of video data. This focuses only on the complex relationship between frames of video and then transforms the conventional structure. Transform has more sophisticated arrangements of a dense projection layer, multi-head attention layer, and normalization layer as depicted in Figure 9. This arrangement allows enhanced model performance. The first dense block includes

This work is licensed under a Creative Commons Attribution 4.0 License. For more information, see https://creativecommons.org/licenses/by/4.0/

This article has been accepted for publication in IEEE Access. This is the author's version which has not been fully edited and
content may change prior to final publication. Citation information: DOI 10.1109/ACCESS.2025.3574835

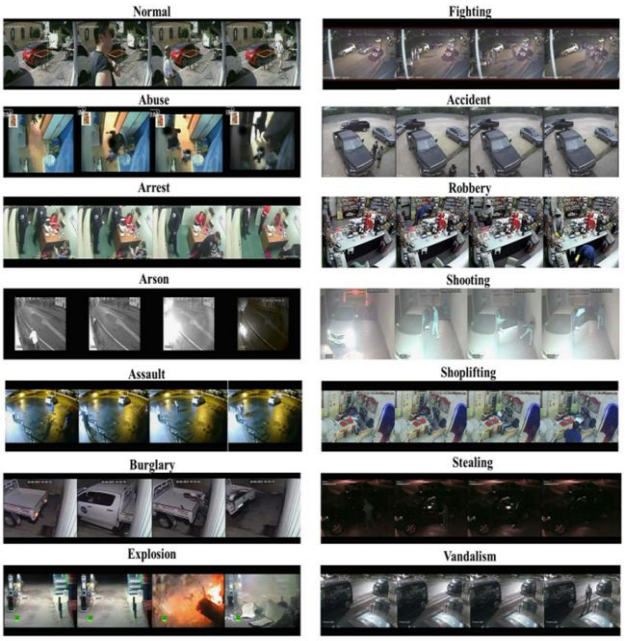


FIGURE 10. **Images of UCF Crime Dataset**



FIGURE 11. **Images of UBI Fight Dataset**

four dense layers with three drop-out layers to help reduce the model overfitting and improve the generalization of the model's ability to capture more intricate features.

F. CATEGORICAL FOCAL LOSS (CFL)

This method more efficiently handles unequal class distributions, which enhances the model's capacity to identify less frequent classes. But because the majority class is given greater weight in the loss computation, might occasionally worsen class imbalance by making the model favor forecasts for that class. [56]. The minority class is under-represented in the model's learning process. To mitigate this bias the CFL is employed with two important mechanisms: first, A focusing parameter (γ): This parameter decreases the loss assigned to instances that are accurately classified. This allows the model to focus more on hard-to-classify instances, and second, a weighting factor (α): This factor is used to balance the importance of the minority class by assigning a higher weight to it compared to the majority class, ensuring that the minority class samples have a stronger impact on the model's learning as shown in Equation 15.

$$CFL = \sum_{i=i}^{i=r} \alpha_i (i\,(Probability)_i)^r_{\times}\, log((Probability)_i) \quad (15)$$

These adjustments ensure that the model's focus is shifted from over-represented categories to those with fewer examples by modulating the loss for correctly classified instances and emphasizing misclassified ones.

G. CLASSIFICATION OF ANOMALY

The data processed by BiLSTM and MASH layers is prepared for input into the Trans-former encoder block. It involved a position embedded in the operation of the data. Temporal data uses absolute position embedding to encode novel positional facts. This study uses relative position embedding which offers the main benefits of processing video data. This approach effectively captures the changing context within the video to consider the temporal distance between frames and focus on the relative association between frames especially effective for movie data of different durations which enables the model to manage both short-term and long-term dependencies. Finally, it improves the model's understanding of how frames relate to each other over time in a sufficient manner, after passing through the relative position encoding layer to modify the transformer encoder to process the data. Furthermore, by considering the temporal distance between frames and embedding, capture the changing context within the video more effectively. This method emphasized the relative relationship between frames helping to manage both short-term and long-term frame dependencies in video changes of duration. The model performs better by recognizing how frames sufficiently interact with overtime, after passing through the relative position encoding layer and restructuring the transformer encoder process of data. The output from the transformer encoding block is further enhanced by a global max pooling layer. In this stage extract the important features from each frame and reduce the complexity of the data. A dropout layer is added to help avoid overfitting and improve the generalization ability of the model. The final layer is the softmax activation layer to classify the video data. A softmax fully connected layer classifies the anomalies by simplifying the complex feature maps into basic information for accurate classification. This architecture greatly improves the detection and classification of abnormal situations by allowing for precise video data processing.

IV. EXPERIMENT AND RESULTS

In this section, we explored the datasets and experimental framework that form the foundation of our research. Subsequently, we conducted a comparative analysis between our proposed model and established state-of-the-art methods in anomaly detection. Additionally, we present the results of a systematic evaluation of different network components

This work is licensed under a Creative Commons Attribution 4.0 License. For more information, see https://creativecommons.org/licenses/by/4.0/

This article has been accepted for publication in IEEE Access. This is the author's version which has not been fully edited and
content may change prior to final publication. Citation information: DOI 10.1109/ACCESS.2025.3574835



FIGURE 12. **Images of RAD dataset**

through ablation studies to assess their individual contributions.

A. DATASETS

In this study, we examine the real-world-based video data captured from CCTV and security cameras. However, it is difficult to collect large data from surveillance systems because there are often privacy and regulatory restrictions regarding the security of camera recording. Therefore, we utilize the publicly available datasets including the UCF Crime, UBI Fight, and Road Anomaly Detection (RAD) for training and evaluation of our proposed model. These are well suited to resources in the field of anomaly detection.

The UCF-Crime dataset, which includes a wide variety of aggressive, illegal, and abnormal actions recorded by security cameras in public spaces, is used to test our proposed model. To illustrate the UCF Crime dataset in Figure 10. This dataset is publicly available and consists of actual events that can take place in a range of contexts and at different periods. t contains extensive, unedited surveillance footage categorized into 13 types of anomalous events are such as Abuse, Arrest, Arson, Assault, Road Accidents, Burglary, Explosion, Fighting, Robbery, Shooting, Theft, Shoplifting, and Vandalism. Videos split into 6 seconds and 30 frames per second (fps).

In addition, we also make use of the UBI-Fights dataset illustrated in Figure 11. The UBI-Fights dataset is divided into two categories: "fight" and "normal," containing 216 and 784 videos, respectively. Sourced from YouTube and other social media resources were gathered videos through targeted text searches to identify violent incidents. Each video is annotated at the frame level, with the entire dataset encompassing approximately 80 hours of footage. Despite variations in individual video durations, all clips maintain a uniform frame rate of 30 frames per second and a fixed resolution of 640×360 pixels. A key limitation of the fight category is the inclusion of non-violent segments depicting ordinary activities interspersed within fight-class videos. It should ideally be categorized under the normal class.

Lastly, the custom RAD dataset is used for experimental purposes, which consists of approximately 70 videos and thousands of images depicting four distinct types of road anomalies. The videos are available in multiple resolutions: 1920 × 1080 at 25 fps, 848 × 480 at 30 fps, and 640 × 480 at 24 fps. The RAD dataset contains the road anomalies such as road accidents, car fires, fighting, snatching, and potholes. We selected four various types of anomalies such as accidents, car fires, fighting, and snatching(gunpoint) as illustrated in Figure 12. Table 2 offers a summary of the RAD dataset.

Table 2. Summary of the RAD dataset

File name	Video length	Resolution(Width x height) pixels @ frames	Lighting condition	Type of Anomaly
RA03	8 seconds	640 x 480 @ 25	Low	Road accident
RA04	40 seconds	1280 x720 @30	High	Road accident
VF06	10 seconds	640 x480 @30	High	Car fire
Fi01	15 seconds	1280 x480 @24	High	Fighting
Fi08	31 seconds	640x480 @25	Low	Fighting

B. TRAINING

We conducted a series of experiments using three extensively used datasets. This study was carried out on a Windows 10 system using TensorFlow with Python. The hardware configuration included a 6th generation Intel® Core™ i5-6350HQ processor, 32GB of RAM, and an NVIDIA GeForce RTX 3080 GPU. Several Python libraries, such as NumPy, Matplotlib, OpenCV, and Seaborn, were used to support the experimentation. To manage memory usage efficiently, each video was represented by only 30 frames, evenly spaced across its entire duration, without compromising the accuracy of the classification models. To enhance dataset diversity and size, augmentation methods including flipping, rotation, and zooming were applied. Pixel intensities in each frame were normalized to a 0–1 range by scaling with a factor of 1/255. The data was randomly shuffled and partitioned into training (70%), validation (20%), and test (10%) subsets. The model was trained with a batch size of 16, a learning rate of 1e-4, and 50 epochs, utilizing GlorotUniform weight initialization and the Adam optimizer (default settings). Each batch contained 10 video clips to enhance computational efficiency. To tackle class imbalance, categorical focal loss was implemented, prioritizing learning from misclassified or rare instances in violent video samples. Early stopping was integrated to monitor validation metrics and terminate training if performance stagnated, reducing overfitting risks.

This work is licensed under a Creative Commons Attribution 4.0 License. For more information, see https://creativecommons.org/licenses/by/4.0/

This article has been accepted for publication in IEEE Access. This is the author's version which has not been fully edited and
content may change prior to final publication. Citation information: DOI 10.1109/ACCESS.2025.3574835

C. PERFORMANCE MEASURE

To evaluate the overall classification performance across categories. There are several key metrics employed. Equation 15 presents the precision and quantifies the proportion of accurately identified instances of a category out of all instances classified as that category. Equation 16 presents the Recall measures the proportion of actual category instances that are correctly classified, assessing the system's capacity to detect all relevant samples. Equation 17 presents the F1-score as the harmonic means of precision and recall, offering a balanced measure of the effectiveness of the system. Equation 18 represents specificity the proportion of correctly classified instances and is calculated as the ratio of correct predictions to the calculated number of samples in the dataset. Equation 19 represents accuracy is a common metric for evaluating a model's performance. It can sometimes be misleading. In datasets with imbalanced classes, where one class significantly outnumbers another, a model that always predicts the majority class may still achieve high accuracy. The ROC (AUC) Curve is commonly used to display the True Positive Rate (TPR) against the False Positive Rate (FPR) at different classification thresholds. The classifier's ability to differentiate between classes is shown by the AUC score, which ranges from 0 to 1. A higher model is indicated by values nearer 1. where TP = True Positives, TN = True Negatives, FP = False Positives, and FN = False Negatives.

$$Precsion = \frac{TP}{TP+FP} \tag{15}$$

$$Recall = \frac{TP}{TP+FN} \tag{16}$$

$$F1-Score = 2 \times \frac{precision \times recall}{precision+recall} \tag{17}$$

$$Specificity = \frac{TN}{TP+FP} \tag{18}$$

$$Accuracy = \frac{TP+TN}{TP+FP+TN+FN} \tag{19}$$

D. EXPERIMENT

Our suggested basic architecture is BiMT which combines BiLSTM, Multi-Head Self-Attention (MHSA), and modified transformers. We created and assessed four different models based on basic BiMT each suited for several contexts and goals.

InceptionV3-BiMT: This is the lightweight model to strikes a deal between computational economy and accuracy by using InceptionV3 [57] as the feature extractor.

DenseNet201-BiMT: DenseNet is used as the feature extractor to ensure that important data from previous layers is retained.

ConvNeXtv1-BiMT: In this ConvNeXtv1[58] which improves conventional convolutional networks while preserving computational efficiency by taking inspiration from Transformer models.

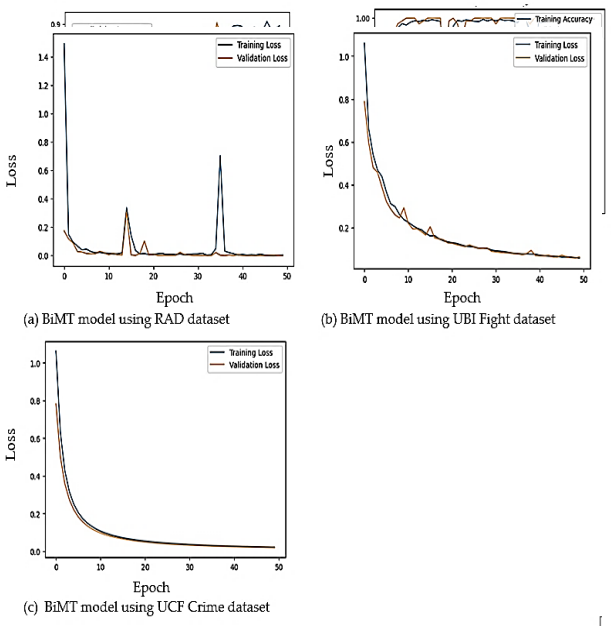


FIGURE 14.Training and Validation Loss of the BiMT proposed model

ConvNeXtv2-BiMT(CNV2-BiMT): This model uses ConvNeXtv2 which has deeper layers and more parameters, which improves its ability to handle complicated and varied data contexts. The performance measure evaluated of the suggested BiMT model is indicated in Table 3. The BiMT model efficiency comparison to identify different types of road anomalies by applying three different benchmark datasets.

E. RESULTS

The performance assessment of the proposed base model BiMT is summarized in Table 3. To evaluate its effectiveness in detecting various types of road anomalies. BiMT was tested on three benchmarks including UCF Crime , UBI Fight and RAD datasets. The accuracy learning curve produced by the base model BiMT is displayed in Figure 13. The suggested model training accuracy has been increasing quickly with every epoch. The base model loss values do not change considerably as shown in Figure 14, indicating the model converges effectively and does not show signs of under-fitting. This study conducted a comparative analysis between the proposed architectures and existing models. Four variations of the BiMT framework were developed and analyzed: InceptionV3-BiMT, DenseNet201-BiMT, ConvNeXtV1-BiMT, and ConvNeXtV2-BiMT (CNV2-BiMT). The performance metrics for these models are detailed in Tables 4, 5, 6, and 7, respectively. Given the imbalanced

This work is licensed under a Creative Commons Attribution 4.0 License. For more information, see https://creativecommons.org/licenses/by/4.0/

This article has been accepted for publication in IEEE Access. This is the author's version which has not been fully edited and
content may change prior to final publication. Citation information: DOI 10.1109/ACCESS.2025.3574835

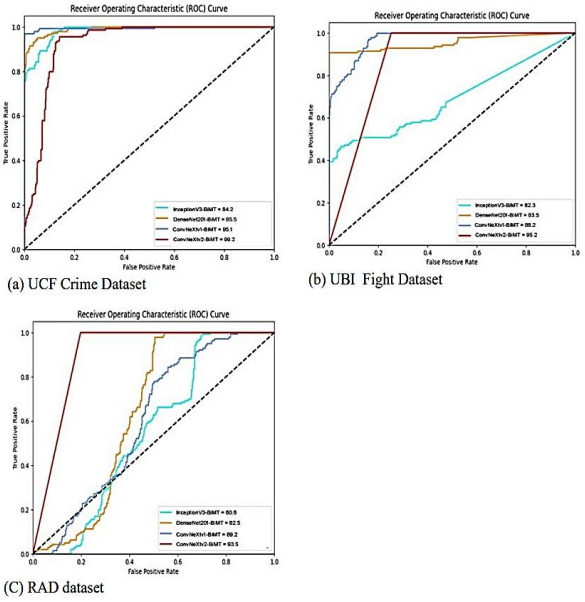


FIGURE 15. The ROC(AUC) curves of four suggested framework.

nature of the datasets. In this study, all four proposed frameworks showed outstanding performance on the UCF Crime dataset. Based on the results, it was found that the four suggested frameworks performed better on the UCF-Crime dataset than the current networks. The main goal of the study, which was to identify abnormalities in CCTV video, was accomplished. CNV2-BiMT demonstrated remarkable classification accuracy.

The validation results for the CNV2-BiMT architectures compared with prior studies using the UCF Crime dataset are presented in Table 8 for the AUC results and Table 9 for the accuracy results, respectively. The comparison results demonstrate that our proposed model achieved the highest AUC of 98.90%, outperforming previous studies and prior models on the UCF Crime dataset in terms of AUC performance. Furthermore, validation results for the proposed model compared with prior studies using the UBI fight dataset are presented in Table 10 for the AUC results. The comparison results demonstrate that our proposed model achieved the highest AUC of 95.20%, outperforming previous studies and prior models on the UBI fight dataset in terms of AUC performance. The study concludes by highlighting the effectiveness of the BiMT framework in various image analysis applications and establishes important benchmarks in anomaly detection to assess the potential of the proposed method. The ROC(AUC) curves for the models on the RAD, UCF, and UBI datasets are displayed in Figure 15. The deep learning models enhanced the interpretability for the classification of road anomalies. The model is built to effectively capture and process features, maximizing data use and greatly enhancing its performance. It is essential to test the model on independent data to check if it can function consistently with unknown data. In this study, the model underwent independent testing to assess its capability to handle new scenarios and data. It was first trained on the UCF Crime, UBI Fight, and RAD datasets, which include various anomaly cases and was then evaluated on a separate video data set featuring both typical and abnormal scenes, as illustrated in Figure 16. This test looks at how well the model applies the patterns it has learned to fresh, untested data. The Gradient-weighted Class Activation Mapping (Grad-CAM) approach was employed for visualization of proposed model. It creates a localization map that highlights the key regions of the image for predictions by using the gradients of the model's output for a target class and flowing into the last convolutional layer. The Grad-CAM visualization of the suggested model is shown in Figure 17.

Table 3. The performance measure of the base model BiMT model

Datasets	Precision	Recall	Specificity	F1-Score	Accuracy (%)	AUC(%)
RAD	69.3	69.9	69.8	69.5	69.7	70.1
UBI Fight	71.4	72.0	72.1	71.6	71.5	73.2
UCF Crime	76.6	76.8	76.8	76.7	76.7	77.8

Table 4. The performance measure of the base model InceptionV3-BiMT model

Datasets	Precision	Recall	Specificity	F1-Score	Accuracy	AUC
RAD	70.6	70.7	70.4	70.5	70.5	80.6
UBI Fight	75.3	75.5	75.4	75.4	75.3	82.3
UCF Crime	78.20	78.30	78.4	78.4	78.3	84.2

Table 5. The performance measure of the base model DenseNet201-BiMTmodel

Datasets	Precision	Recall	Specificity	F1-Score	Accuracy	AUC
RAD	73.2	73.3	73.5	73.4	73.5	82.5
UBI Fight	78.4	78.4	78.3	78.6	78.5	83.5
UCF Crime	82.1	82.1	82.2	82.3	82.2	85.5

Table 6. The performance measure of the base model ConvNeXtv1-BiMT model

Datasets	Precision	Recall	Specificity	F1-Score	Accuracy	AUC
RAD	78.5	78.6	78.5	78.4	78.5	89.2
UBI Fight	83.5	83.5	83.6	83.4	83.4	88.2
UCF Crime	90.2	90.1	90.1	90.3	90.2	95.1

This work is licensed under a Creative Commons Attribution 4.0 License. For more information, see https://creativecommons.org/licenses/by/4.0/

This article has been accepted for publication in IEEE Access. This is the author's version which has not been fully edited and content may change prior to final publication. Citation information: DOI 10.1109/ACCESS.2025.3574835

Table 7. The performance measure of the ConvNeXtv2-BiMT model

Datasets	Precision	Recall	Specificity	F1-Score	Accuracy	AUC
RAD	83.4	83.5	83.4	83.4	83.5	93.5
UBI Fight	86.4	86.5	86.4	86.4	86.5	95.2
UCF Crime	98.5	98.6	98.6	98.5	98.6	98.9

Table 8. Comparison AUC(%) of the ConvNeXtv2-BiMT model with prior studies utilizing the UCF dataset.

Authors	Model	AUC(%)
Liu et, al. [60]	PFMF	74
Qasim, et al. [61]	Conv GRU-CNN	82.66
Tian et al. [27]	RTFM	84.31
Zhou et al. [62]	UR-DMU	86.68
Vosta et al. [63]	ResNet50-ConvLSTM-MHSA	97.48
Zhong et al. [64]	MIL-C3D	78.01
Joo et al. [65]	CLIP_TSA	87.58
Proposed Model	ConvNeXtv2-BiMT	98.9

Table 9. Comparison accuracy of the ConvNeXtv2-BiMT model with prior studies utilizing the UCF dataset.

Ref, Year	Accuracy(%)
[59], 2021	75.70
[69], 2022	74.53
[70], 2021	78.43
[71], 2023	81.01
[14], 2024	62.02
Proposed model	98.90

Table 10. Comparison accuracy of the proposed ConvNeXtv2-BiMT model with prior studies utilizing the UBI Fight dataset.

Author, Reference	AUC(%)
Z. Qi R et al. [66]	93.07
B.M et al. [67]	81.90
M. Alarfaj et al.[68]	76.92
Weijun Tan et al. [72]	91.92
Proposed Model	95.20

This model employs Grad-CAM (Gradient-weighted Class Activation Mapping) to generate interpretable heatmaps that visually localize regions in input images, which are most influential to its classification decisions. By computing gradients of target class scores with respect to feature maps from the final convolutional layer which encode high-level class-specific patterns, the method weights channel activation using global average-pooled gradients, producing a coarse class activation map.



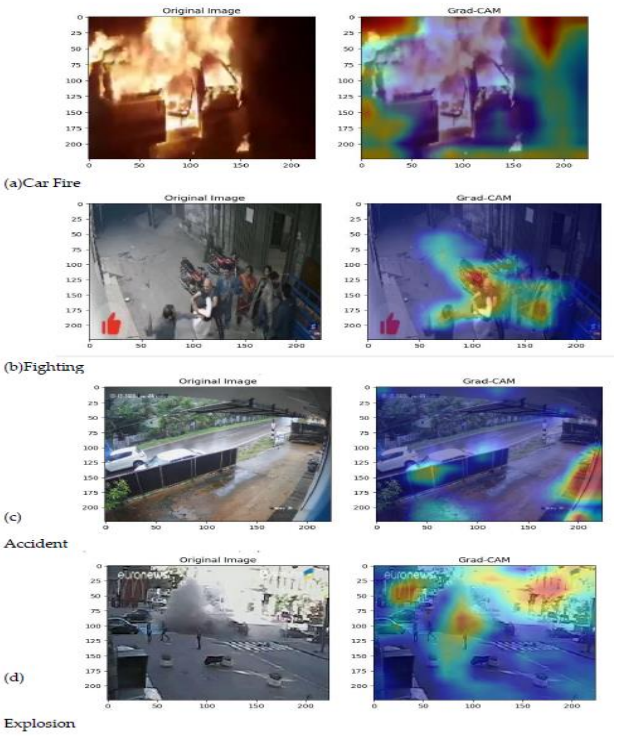
FIGURE 16. Test results of the proposed ConvNeXtv2-BiMT model

V. CONCLUSION AND FUTURE WORK

This study proposed a novel deep-learning architecture for detecting anomalies in road video surveillance. It combines the strengths of various networks to assist a thorough and effective analysis of video data. The proposed model architecture starts by extracting features from video frames using multiple pre-trained networks. In second stage combines the advantages of multi-head self-attention with BiLSTM for useful temporal analysis. The BiLSTM handles the input data in both forward and backward directions, and it improves the model's understanding of temporal sequences. On the other hand, the multi-head self-attention approach makes it easier to process and integrate several features in the input sequence at once. When handling complicated and time-dependent data. This model works effectively with unobserved data in video sequences. The modified transformer encoder layer overcomes the challenges of long sequences using relative position embedding. It effectively captures the dynamic features of video data, recognizing interactions between frames and improving the model's under-standing of frame-to-frame relationships. The modified transformer encoder is tailored for anomaly detection to refine the outputs from the MHSA and BiLSTM layers before the final classification layer. The design ends with a softmax layer for anomaly classification, a dropout layer to avoid overfitting, and a global max-pooling layer to extract important features. To ensure precise classifications based on the model output, a fully connected layer is also incorporated. There are three publicly available datasets with a range of anomalous circumstances

This work is licensed under a Creative Commons Attribution 4.0 License. For more information, see https://creativecommons.org/licenses/by/4.0/

This article has been accepted for publication in IEEE Access. This is the author's version which has not been fully edited and
content may change prior to final publication. Citation information: DOI 10.1109/ACCESS.2025.3574835



that were used to evaluate the suggested framework. This methodology is adaptable enough to be used in a variety of settings where there is no human intervention and it improves the precision, and effectiveness of security camera systems like CCTV. However, this model is not evaluated in different weather conditions such as rainy, snowy and windy. In the future, we will work You Only Look Once (YOLOv11) to detect abnormalities in real-time with different weather conditions. This will greatly improve the system's ability to recognize behaviors under various circumstances in video data.

REFERENCES

[1] K. Doshi and Y. Yilmaz, 'Online anomaly detection in surveillance videos with asymptotic bound on false alarm rate', *Pattern Recognit.*, vol. 114, p. 107865, Jun. 2021, doi: 10.1016/j.patcog.2021.107865.

[2] N. Madan *et al.*, 'Self-Supervised Masked Convolutional Transformer Block for Anomaly Detection', *IEEE Trans. Pattern Anal. Mach. Intell.*, vol. 46, no. 1, pp. 525–542, Jan. 2024, doi: 10.1109/TPAMI.2023.3322604.

[3] M. Z. Zaheer, A. Mahmood, M. H. Khan, M. Astrid, and S.-I. Lee, 'An Anomaly Detection System via Moving Surveillance Robots with Human Collaboration', in *2021 IEEE/CVF International Conference on Computer Vision Workshops (ICCVW)*, Montreal, BC, Canada: IEEE, Oct. 2021, pp. 2595–2601. doi: 10.1109/ICCVW54120.2021.00293.

[4] E. Duman and O. A. Erdem, 'Anomaly Detection in Videos Using Optical Flow and Convolutional Autoencoder', *IEEE Access*, vol. 7, pp. 183914–183923, 2019, doi: 10.1109/ACCESS.2019.2960654.

[5] Leroux, Sam and Li, Bo and Simoens, Pieter, 'Multi-Branch Neural Networks for Video Anomaly Detection in Adverse Lighting and Weather Conditions', pp. 2358–2366, 2022.

[6] Sarfaraz Natha, A.A., Fareed A. Jokhio, Mehwish Laghari, Mohammad Siraj, Saif A. Alsaif, Usman Ashraf A Scalable and Generalized Deep Ensemble Model for Road Anomaly Detection in Surveillance Videos. Comput. Mater. Contin. pages, doi:10.32604/cmc.2024.057684.

[7] B. Ramachandra, M. Jones, and R. R. Vatsavai, 'A Survey of Single-Scene Video Anomaly Detection', *IEEE Trans. Pattern Anal. Mach. Intell.*, pp. 1–1, 2020, doi: 10.1109/TPAMI.2020.3040591.

[8] Natha, S.; Arif, M.; Jamil, S.S.; Jokhio, F.A.; Syed, M.J. Improving Traffic Surveillance: Deep Learning Approach for Road Anomaly Detection in Videos. In Proceedings of the 2024 IEEE 3rd International Conference on Computing and Machine Intelligence (ICMI); IEEE: Mt Pleasant, MI, USA, April 13 2024; pp. 1–7.

[9] Y. Benezeth, P.-M. Jodoin, V. Saligrama, and C. Rosenberger, 'Abnormal events detection based on spatio-temporal co-occurences', in *2009 IEEE Conference on Computer Vision and Pattern Recognition*, Miami, FL: IEEE, Jun. 2009, pp. 2458–2465. doi: 10.1109/CVPR.2009.5206686.

[10] Y. Cong, J. Yuan, and J. Liu, 'Sparse reconstruction cost for abnormal event detection', in *CVPR 2011*, Colorado Springs, CO, USA: IEEE, Jun. 2011, pp. 3449–3456. doi: 10.1109/CVPR.2011.5995434.

[11] A. Basharat, A. Gritai, and M. Shah, 'Learning object motion patterns for anomaly detection and improved object detection', in *2008 IEEE Conference on Computer Vision and Pattern Recognition*, Anchorage, AK, USA: IEEE, Jun. 2008, pp. 1–8. doi: 10.1109/CVPR.2008.4587510.

[12] Natha, S. A Systematic Review of Anomaly Detection Using Machine and Deep Learning Techniques. Quaid-E-Awam Univ. Res. J. Eng. Sci. Technol. 2022, 20, 83–94, doi:10.52584/QRJ.2001.11

[13] S. Ding, L. Lin, G. Wang, and H. Chao, 'Deep feature learning with relative distance comparison for person re-identification', *Pattern Recognit.*, vol. 48, no. 10, pp. 2993–3003, Oct. 2015, doi: 10.1016/j.patcog.2015.04.005.

[14] S. A. Jebur, K. A. Hussein, H. K. Hoomod, L. Alzubaidi, A. A. Saihood, and Y. Gu, 'A Scalable and Generalized Deep Learning Framework for Anomaly Detection in Surveillance Videos', 2024, *arXiv*. doi: 10.48550/ARXIV.2408.00792.

[15] H.-T. Duong, V.-T. Le, and V. T. Hoang, 'Deep Learning-Based Anomaly Detection in Video Surveillance: A Survey', *Sensors*, vol. 23, no. 11, p. 5024, May 2023, doi: 10.3390/s23115024.

This work is licensed under a Creative Commons Attribution 4.0 License. For more information, see https://creativecommons.org/licenses/by/4.0/

This article has been accepted for publication in IEEE Access. This is the author's version which has not been fully edited and
content may change prior to final publication. Citation information: DOI 10.1109/ACCESS.2025.3574835

[16] J. Saeedi and A. Giusti, 'Semi-supervised visual anomaly detection based on convolutional autoencoder and transfer learning', *Mach. Learn. Appl.*, vol. 11, p. 100451, Mar. 2023, doi: 10.1016/j.mlwa.2023.100451.

[17] A. Krizhevsky, I. Sutskever, and G. E. Hinton, 'ImageNet classification with deep convolutional neural networks', *Commun. ACM*, vol. 60, no. 6, pp. 84–90, 2017.

[18] G. Pang, C. Shen, L. Cao, and A. V. D. Hengel, 'Deep Learning for Anomaly Detection: A Review', *ACM Comput. Surv.*, vol. 54, no. 2, pp. 1–38, Mar. 2022, doi: 10.1145/3439950.

[19] S. Vosta and K.-C. Yow, 'A CNN-RNN Combined Structure for Real-World Violence Detection in Surveillance Cameras', *Appl. Sci.*, vol. 12, no. 3, p. 1021, Jan. 2022, doi: 10.3390/app12031021.

[20] V. V. Grubov *et al.*, 'Two-Stage Approach With Combination of Outlier Detection Method and Deep Learning Enhances Automatic Epileptic Seizure Detection', *IEEE Access*, vol. 12, pp. 122168–122182, 2024, doi: 10.1109/ACCESS.2024.3453039.

[21] M.-H. Guo *et al.*, 'Attention mechanisms in computer vision: A survey', *Comput. Vis. Media*, vol. 8, no. 3, pp. 331–368, Sep. 2022, doi: 10.1007/s41095-022-0271-y.

[22] Y. Chen, D. Zhao, L. Lv, and C. Li, 'A visual attention based convolutional neural network for image classification', in *2016 12th World Congress on Intelligent Control and Automation (WCICA)*, Guilin, China: IEEE, Jun. 2016, pp. 764–769. doi: 10.1109/WCICA.2016.7578651.

[23] S. Chen, X. Tan, B. Wang, H. Lu, X. Hu, and Y. Fu, 'Reverse Attention-Based Residual Network for Salient Object Detection', *IEEE Trans. Image Process.*, vol. 29, pp. 3763–3776, 2020, doi: 10.1109/TIP.2020.2965989.

[24] F. J. Rendón-Segador, J. A. Álvarez-García, F. Enríquez, and O. Deniz, 'ViolenceNet: Dense Multi-Head Self-Attention with Bidirectional Convolutional LSTM for Detecting Violence', *Electronics*, vol. 10, no. 13, p. 1601, Jul. 2021, doi: 10.3390/electronics10131601.

[25] W. Li, F. Qi, M. Tang, and Z. Yu, 'Bidirectional LSTM with self-attention mechanism and multi-channel features for sentiment classification', *Neurocomputing*, vol. 387, pp. 63–77, Apr. 2020, doi: 10.1016/j.neucom.2020.01.006.

[26] T. Wu *et al.*, 'Video sentiment analysis with bimodal information-augmented multi-head attention', *Knowl.-Based Syst.*, vol. 235, p. 107676, Jan. 2022, doi: 10.1016/j.knosys.2021.107676.

[27] Y. Tian, G. Pang, Y. Chen, R. Singh, J. W. Verjans, and G. Carneiro, 'Weakly-supervised Video Anomaly Detection with Robust Temporal Feature Magnitude Learning', in *2021 IEEE/CVF International Conference on Computer Vision (ICCV)*, Montreal, QC, Canada: IEEE, Oct. 2021, pp. 4955–4966. doi: 10.1109/ICCV48922.2021.00493.

[28] B. Degardin and H. Proença, 'Iterative weak/self-supervised classification framework for abnormal events detection', *Pattern Recognit. Lett.*, vol. 145, pp. 50–57, May 2021, doi: 10.1016/j.patrec.2021.01.031.

[29] Natha, S.; Ahmed, F.; Siraj, M.; Lagari, M.; Altamimi, M.; Chandio, A.A. Deep BiLSTM Attention Model for Spatial and Temporal Anomaly Detection in Video Surveillance. Sensors 2025, 25, 251, doi:10.3390/s25010251

[30] J. Kaur and W. Singh, 'A systematic review of object detection from images using deep learning', *Multimed. Tools Appl.*, vol. 83, no. 4, pp. 12253–12338, Jan. 2024, doi: 10.1007/s11042-023-15981-y.

[31] T. Iwata and Y. Yamanaka, 'Supervised Anomaly Detection based on Deep Autoregressive Density Estimators', 2019, *arXiv*. doi: 10.48550/ARXIV.1904.06034.

[32] M. M. Taye, 'Theoretical Understanding of Convolutional Neural Network: Concepts, Architectures, Applications, Future Directions', *Computation*, vol. 11, no. 3, p. 52, Mar. 2023, doi: 10.3390/computation11030052.

[33] C. Huang, X. Wang, J. Cao, S. Wang, and Y. Zhang, 'HCF: A Hybrid CNN Framework for Behavior Detection of Distracted Drivers', *IEEE Access*, vol. 8, pp. 109335–109349, 2020, doi: 10.1109/ACCESS.2020.3001159.

[34] S. M. Mohtavipour, M. Saeidi, and A. Arabsorkhi, 'A multi-stream CNN for deep violence detection in video sequences using handcrafted features', *Vis. Comput.*, vol. 38, no. 6, pp. 2057–2072, Jun. 2022, doi: 10.1007/s00371-021-02266-4.

[35] R. Lalit, R. K. Purwar, S. Verma, and A. Jain, 'Crowd abnormality detection in video sequences using supervised convolutional neural network', *Multimed. Tools Appl.*, vol. 81, no. 4, pp. 5259–5277, Feb. 2022, doi: 10.1007/s11042-021-11781-4.

[36] Sultani, Waqas and Chen, Chen and Shah, Mubarak, *Real-World Anomaly Detection in Surveillance Videos*. 2018. [Online]. Available: https://openaccess.thecvf.com/content_cvpr_2018/html/Sultani_RealWorld_Anomaly_Detection_CVPR_2018_paper.html

[37] Du Tran, Lubomir Bourdev, Rob Fergus, Lorenzo Torresani, Manohar Paluri, 'Learning Spatiotemporal Features With 3D Convolutional Networks', in *Proceedings of the IEEE International Conference on Computer Vision (ICCV)*, 2015. [Online]. Available: https://openaccess.thecvf.com/content_iccv_2015/html/Tran_Learning_Spatiotemporal_Features_ICCV_2015_paper.html

[38] Alaa Sahl Gaafar, Jasim Mohammed Dahr, Alaa Khalaf Hamoud, 'Comparative Analysis of Performance of Deep Learning Classification Approach based on LSTM-RNN for Textual and

This work is licensed under a Creative Commons Attribution 4.0 License. For more information, see https://creativecommons.org/licenses/by/4.0/

This article has been accepted for publication in IEEE Access. This is the author's version which has not been fully edited and
content may change prior to final publication. Citation information: DOI 10.1109/ACCESS.2025.3574835

Image Datasets', 2022, [Online]. Available: https://informatica.si/index.php/informatica/article/view/3872

[39] W. Ullah, A. Ullah, I. U. Haq, K. Muhammad, M. Sajjad, and S. W. Baik, 'CNN features with bi-directional LSTM for real-time anomaly detection in surveillance networks', *Multimed. Tools Appl.*, vol. 80, no. 11, pp. 16979–16995, May 2021, doi: 10.1007/s11042-020-09406-3.

[40] J. Yin, C. Qi, Q. Chen, and J. Qu, 'Spatial-Spectral Network for Hyperspectral Image Classification: A 3-D CNN and Bi-LSTM Framework', *Remote Sens.*, vol. 13, no. 12, p. 2353, Jun. 2021, doi: 10.3390/rs13122353.

[41] Dzmitry Bahdanau,KyungHyun Cho, 'NEURAL MACHINE TRANSLATION BY JOINTLY LEARNING TO ALIGN AND TRANSLATE', 2015, [Online].Available:https://formacion.actuarios.org/wp-content/uploads/2024/05/1409.0473-Neural-Machine-Translation-By-Jointly-Learning-To-Align-And-Translate.pdf

[42] G. Brauwers and F. Frasincar, 'A General Survey on Attention Mechanisms in Deep Learning', *IEEE Trans. Knowl. Data Eng.*, vol. 35, no. 4, pp. 3279–3298, Apr. 2023, doi: 10.1109/TKDE.2021.3126456.

[43] P. Vasanthi and L. Mohan, 'Multi-Head-Self-Attention based YOLOv5X-transformer for multi-scale object detection', *Multimed. Tools Appl.*, vol. 83, no. 12, pp. 36491–36517, May 2023, doi: 10.1007/s11042-023-15773-4.

[44] L. Alzubaidi *et al.*, 'Review of deep learning: concepts, CNN architectures, challenges, applications, future directions', *J. Big Data*, vol. 8, no. 1, p. 53, Mar. 2021, doi: 10.1186/s40537-021-00444-8.

[45] W. Fang, P. E. D. Love, H. Luo, and L. Ding, 'Computer vision for behaviour-based safety in construction: A review and future directions', *Adv. Eng. Inform.*, vol. 43, p. 100980, Jan. 2020, doi: 10.1016/j.aei.2019.100980.

[46] D. Palaz, M. Magimai-Doss, and R. Collobert, 'End-to-end acoustic modeling using convolutional neural networks for HMM-based automatic speech recognition', *Speech Commun.*, vol. 108, pp. 15–32, 2019.

[47] H.-C. Li, Z.-Y. Deng, and H.-H. Chiang, 'Lightweight and resource-constrained learning network for face recognition with performance optimization', *Sensors*, vol. 20, no. 21, p. 6114, 2020.

[48] T. Fadziso, 'Overcoming the Vanishing Gradient Problem during Learning Recurrent Neural Nets (RNN)', *Asian J. Appl. Sci. Eng.*, vol. 9, no. 1, pp. 197–208, Dec. 2020, doi: 10.18034/ajase.v9i1.41.

[49] J. Deng, W. Dong, R. Socher, L.-J. Li, Kai Li, and Li Fei-Fei, 'ImageNet: A large-scale hierarchical image database', in *2009 IEEE Conference on Computer Vision and Pattern Recognition*, Miami, FL: IEEE, Jun. 2009, pp. 248–255. doi: 10.1109/CVPR.2009.5206848.

[50] G. Huang, Z. Liu, G. Pleiss, L. V. D. Maaten, and K. Q. Weinberger, 'Convolutional Networks with Dense Connectivity', *IEEE Trans. Pattern Anal. Mach. Intell.*, vol. 44, no. 12, pp. 8704–8716, Dec. 2022, doi: 10.1109/TPAMI.2019.2918284.

[51] P. Bhuvaneshwari, A. N. Rao, Y. H. Robinson, and M. N. Thippeswamy, 'Sentiment analysis for user reviews using Bi-LSTM self-attention based CNN model', *Multimed. Tools Appl.*, vol. 81, no. 9, pp. 12405–12419, Apr. 2022, doi: 10.1007/s11042-022-12410-4.

[52] Y. Bengio, P. Simard, and P. Frasconi, 'Learning long-term dependencies with gradient descent is difficult', *IEEE Trans. Neural Netw.*, vol. 5, no. 2, pp. 157–166, Mar. 1994, doi: 10.1109/72.279181.

[53] K. Sreelakshmi, P. C. Rafeeque, S. Sreetha, and E. S. Gayathri, 'Deep Bi-Directional LSTM Network for Query Intent Detection', *Procedia Comput. Sci.*, vol. 143, pp. 939–946, 2018, doi: 10.1016/j.procs.2018.10.341.

[54] Ashish Vaswani, Noam Shazeer, Niki Parmar∗, 'Attention Is All You Need', *31st Conf. Neural Inf. Process. Syst. NIPS 2017 Long Beach CA USA*, 2017.

[55] Tsung-Yi Lin Priya Goyal Ross Girshick Kaiming He Piotr Dollar, 'Focal Loss for Dense Object Detection', *Proc. IEEE Conf. Comput. Vis. Pattern Recognit. 2017*, 2017.

[56] M. Kerkhof, L. Wu, G. Perin, and S. Picek, 'Focus is Key to Success: A Focal Loss Function for Deep Learning-Based Side-Channel Analysis', in *Constructive Side-Channel Analysis and Secure Design*, vol. 13211, J. Balasch and C. O'Flynn, Eds., in Lecture Notes in Computer Science, vol. 13211. , Cham: Springer International Publishing, 2022, pp. 29–48. doi: 10.1007/978-3-030-99766-3_2.

[57] M. Q. Kheder and A. A. Mohammed, 'Transfer Learning Based Traffic Light Detection and Recognition Using CNN Inception-V3 Model', *Iraqi J. Sci.*, pp. 6258–6275, Oct. 2023, doi: 10.24996/ijs.2023.64.10.40.

[58] Woo, Sanghyun and Debnath, Shoubhik and Hu, Ronghang and Chen, Xinlei and Liu, Zhuang and Kweon, In So and Xie, Saining, *ConvNeXt V2: Co-Designing and Scaling ConvNets With Masked Autoencoders*. 2023. [Online]. Available: https://openaccess.thecvf.com/content/CVPR2023/html/Woo_ConvNeXt_V2_Co-Designing_and_Scaling_ConvNets_With_Masked_Autoencoders_CVPR_2023_paper.html

[59] Martínez-Mascorro, G.A.; Abreu-Pederzini, J.R.; Ortiz-Bayliss, J.C.; Garcia-Collantes, A.; Terashima-Marín, H. Criminal Intention Detection at Early Stages of Shoplifting Cases by Using 3D Convolutional Neural Networks. Computation 2021, 9, 24, doi:10.3390/computation9020024.

This work is licensed under a Creative Commons Attribution 4.0 License. For more information, see https://creativecommons.org/licenses/by/4.0/

This article has been accepted for publication in IEEE Access. This is the author's version which has not been fully edited and
content may change prior to final publication. Citation information: DOI 10.1109/ACCESS.2025.3574835

[60] Liu, Zuhao and Wu, Xiao-Ming and Zheng, Dian and Lin, Kun-Yu and Zheng, Wei-Shi, 'Generating Anomalies for Video Anomaly Detection With Prompt-Based Feature Mapping', pp. 24500–24510, 2023.

[61] M. Qasim Gandapur and E. Verdú, 'ConvGRU-CNN: Spatiotemporal Deep Learning for Real-World Anomaly Detection in Video Surveillance System', *Int. J. Interact. Multimed. Artif. Intell.*, vol. In Press, no. In Press, p. 1, 2023, doi: 10.9781/ijimai.2023.05.006.

[62] H. Zhou, J. Yu, and W. Yang, 'Dual Memory Units with Uncertainty Regulation for Weakly Supervised Video Anomaly Detection', *Proc. AAAI Conf. Artif. Intell.*, vol. 37, no. 3, pp. 3769–3777, Jun. 2023, doi: 10.1609/aaai.v37i3.25489.

[63] S. Vosta and K.-C. Yow, 'KianNet: A Violence Detection Model Using an Attention-Based CNN-LSTM Structure', *IEEE Access*, vol. 12, pp. 2198–2209, 2024, doi: 10.1109/ACCESS.2023.3339379.

[64] Zhong, Jia-Xing and Li, Nannan and Kong, Weijie and Liu, Shan and Li, Thomas H. and Li, Ge, *Graph Convolutional Label Noise Cleaner: Train a Plug-And-Play Action Classifier for Anomaly Detection*. 2019.[Online].Available: https://openaccess.thecvf.com/content_CVPR_2019/html/Zhong_Graph_Convolutional_Label_Noise_Cleaner_Train_a_Plug-And-Play_Action_Classifier_CVPR_2019_paper.html

[65] H. K. Joo, K. Vo, K. Yamazaki, and N. Le, 'CLIP-TSA: Clip-Assisted Temporal Self-Attention for Weakly-Supervised Video Anomaly Detection', in *2023 IEEE International Conference on Image Processing (ICIP)*, Kuala Lumpur, Malaysia: IEEE, Oct. 2023, pp. 3230–3234. doi: 10.1109/ICIP49359.2023.10222289.

[66] Z. Qi, R. Zhu, Z. Fu, W. Chai, and V. Kindratenko, "Weakly Supervised Two-Stage Training Scheme for Deep Video Fight Detection Model," in 2022 IEEE 34th International Conference on Tools with Artificial Intelligence (ICTAI), Macao, China: IEEE, Oct. 2022, pp. 677–685. doi: 10.1109/ICTAI56018.2022.00105.

[67] Degardin, Bruno Manuel., Weakly and Partially Supervised Learning Frameworks for Anomaly Detection. Universidade da Beira Interior (Portugal) ProQuest Dissertations & Theses, 2020. 28762603., 2020.

[68] M. Alarfaj et al., "Automatic Anomaly Monitoring in Public Surveillance Areas," Intell. Autom. Soft Comput., vol. 35, no. 3, pp. 2655–2671, 2023, doi: 10.32604/iasc.2023.027205.

[69] Ansari, M.A.; Singh, D.K. Ansari, M.A.; Singh, D.K. An Expert Eye for Identifying Shoplifters in Mega Stores. In International Conference on Innovative Computing and Communications; Khanna, A., Gupta, D., Bhattacharyya, S., Hassanien, A.E., Anand, S., Jaiswal, A., Eds.; Advances in Intelligent Systems and Computing; Springer: Singapore, 2022; Volume 1394, pp. 107–115. ISBN 9789811630705.

[70] Ullah, W.; Ullah, A.; Hussain, T.; Khan, Z.A.; Baik, S.W. An Efficient Anomaly Recognition Framework Using an Attention Residual LSTM in Surveillance Videos. Sensors 2021, 21, 2811, doi:10.3390/s21082811.

[71] Muneer, I.; Saddique, M.; Habib, Z.; Mohamed, H.G. Shoplifting Detection Using Hybrid Neural Network CNN-BiLSMT and Development of Benchmark Dataset. Applied Sciences 2023, 13, 8341, doi:10.3390/app13148341.

[72] Tan, Weijun, and Jingfeng Liu. "Detection of fights in videos: A comparison study of anomaly detection and action recognition." European Conference on Computer Vision. Cham: Springer Nature Switzerland, 2022.doi:10.1007/978-3-031-25072-9_45



SARFARAZ NATHA (Student Member, IEEE) received the B.S. degree in Computer Engineering from the Sir Syed University of Engineering and Technology, and the M.S. degree in network and communication from Hamdard University of Engineering and Technology and pursuing the Ph.D. in information technology from Quaid-e-Awam University of Engineering and Technology (QUEST), Pakistan. He is working as an Assistant Professor in the Software Engineering Department, Sir Syed University of Engineering and Technology. His research interests include Artificial Intelligence, Computer vision, Machine learning, Deep learning, Data science and Cyber security. He has multiple publications in international journals and conferences.

This work is licensed under a Creative Commons Attribution 4.0 License. For more information, see https://creativecommons.org/licenses/by/4.0/

This article has been accepted for publication in IEEE Access. This is the author's version which has not been fully edited and content may change prior to final publication. Citation information: DOI 10.1109/ACCESS.2025.3574835



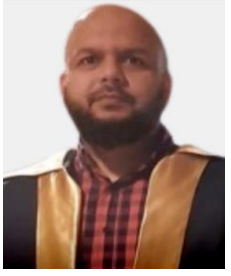
DR. MOHAMMAD SIRAJ received his Ph.D. from the University of Technology Malaysia. He holds a Master of Engineering degree in Computer Technology and Applications from Delhi College of Engineering, Delhi, India, and Bachelor of Engineering degree in Electronics and Communication Engineering from Jamia Millia Islamia, New Delhi. Currently, he is working as an Assistant Professor in Electrical Engineering at King Saud University. His research interests are Cognitive Wireless Networks, Wireless Mesh Networks, Sensor Networks, Internet of Things, Cloud Computing and Telecom Optical Networks. He has numerous peered publications in well-known international journals and Conferences. He is a Senior Member of IEEE and a reviewer of many well-known International Journals and Conferences.



DR. FAREED AHMED FAREED AHMED is currently working as Professor in the Department of Computer Systems Engineering at Quaid-e-Awam University of Engineering, Science and Technology Nawabshah Pakistan, He has completed his PhD degree in Computer Engineering from Åbo Akademi University Finland in 2014. He completed his master's degree in Embedded and Intelligent systems from Halmstad University, Sweden in 2010. He also has a master's degree in information technology from Mehran University of Engineering and Technology Jamshoro Pakistan. His bachelor's degree in computer systems engineering is also from Mehran University of Engineering and Technology Jamshoro Pakistan. Currently his research interests include Image Processing, Video Processing, Computer Vision, Machine Learning, Deep Learning, Network Security, Cloud Computing, Embedded Systems, and Real-Time Systems.

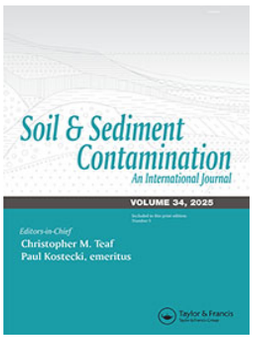


DR. MAJID ALTAMIMI (Member, IEEE) received the B.Sc. Eng. degree (Hons.) in electrical engineering from King Saud University, Saudi Arabia, in 2004, and the M.Sc. and Ph.D. degrees in electrical and computer engineering from the University of Waterloo, Canada, in 2010 and 2014, respectively. In 2015, he joined the Department of Electrical Engineering, at King Saud University, as an Assistant Professor. He served as a TA with the Department of Electrical and Computer Engineering, University of Waterloo, in 2013, and the Department of Electrical Engineering, King Saud University, from 2004 to 2006. His current research interests include analyzing the energy cost for wireless handheld devices and cloud computing architecture, integrating mobile computing with cloud computing, and studying and designing green ICT solutions.



DR. MUSLIM SYED is a passionate advocate for Responsible Artificial Intelligence. Specializing in responsible AI, and other emerging technologies. His research focuses on the ethical and legal aspects of AI and technology, ensuring compliance with regulatory standards and societal values. Dr. Syed is passionate about helping businesses and organizations improve their processes and profit, leveraging his expertise in AI and technology within EU regulations and compliance. He has contributed to diverse application areas, including MEDTECH, FINTECH, and Renewable Energy.

This work is licensed under a Creative Commons Attribution 4.0 License. For more information, see https://creativecommons.org/licenses/by/4.0/



Soil and Sediment Contamination: An International Journal

ISSN: 1532-0383 (Print) 1549-7887 (Online) Journal homepage: www.tandfonline.com/journals/bssc20

Assessment of Groundwater and Soil Contamination Due to Leachate Migration around Ghazipur Landfill: A Comprehensive Analysis Using WAWQI and SQI Models

Shraddha Sharma, Geeta Singh & Gauhar Mehmood

To cite this article: Shraddha Sharma, Geeta Singh & Gauhar Mehmood (26 Jun 2025): Assessment of Groundwater and Soil Contamination Due to Leachate Migration around Ghazipur Landfill: A Comprehensive Analysis Using WAWQI and SQI Models, Soil and Sediment Contamination: An International Journal, DOI: 10.1080/15320383.2025.2515069

To link to this article: https://doi.org/10.1080/15320383.2025.2515069

Published online: 26 Jun 2025.

Submit your article to this journal

Article views: 10

View related articles

View Crossmark data

Full Terms & Conditions of access and use can be found at
https://www.tandfonline.com/action/journalInformation?journalCode=bssc20

SOIL AND SEDIMENT CONTAMINATION: AN INTERNATIONAL JOURNAL
https://doi.org/10.1080/15320383.2025.2515069

Taylor & Francis
Taylor & Francis Group

Check for updates

Assessment of Groundwater and Soil Contamination Due to Leachate Migration around Ghazipur Landfill: A Comprehensive Analysis Using WAWQI and SQI Models

Shraddha Sharma[a], Geeta Singh[a], and Gauhar Mehmood[b]

[a]Department of Environmental Engineering, Delhi Technological University, Delhi, India; [b]Department of Civil Engineering, Jamia Milia Islamia University, Delhi, India

ABSTRACT

The quality of soil and groundwater is negatively affected by landfill leachate migration. A thorough integration and mathematical modeling were lacking in previous studies that concentrated on distinct components of contamination. In this study, the effects of the Ghazipur landfill on nearby soil and groundwater are assessed using models that evaluate water quality based on a weighted arithmetic approach and soil quality for agricultural suitability. Groundwater and soil samples were collected from the five locations, Mayur Vihar Phase 1, Mandawali, Mayur Vihar Extension, Narwana Road, and Dairy Farms, with multiple sampling points within some locations. The physical-chemical parameters and heavy metals in groundwater were evaluated by the water quality model, and the soil quality model assessed the suitability of soil for agriculture. Most areas, including Mayur Vihar Phase 1, Mandawali, Mayur Vihar extension, and Narwana Road, are safe to drink, although some have better water quality. Soil quality in several locations is considered "very good," making it suitable for agriculture. However, insufficiencies are shown in other locations, which indicate an additional requirement for soil. The study contributes to better waste management techniques to address pollution and improve environmental health.

KEYWORDS

Landfill leachate; Ghazipur landfill; water quality index; soil quality index; groundwater contamination; soil pollution

1. Introduction

A landfill is a widespread area of land where large amounts of waste and other garbage materials are accumulated from households, industries, institutions, etc. The leachate migration is the primary cause of soil and groundwater contamination (Igboama et al. 2022). The landfill leachate describes the liquid that leaches through solid waste materials because of rainwater filtration that separates different organic and inorganic substances. This waste product displays yellow or black hues. It produces a powerful, objectionable smell that combines biodegradable with non-biodegradable contaminants, including heavy metals and dissolved solids, organic substances, and hazardous materials. The color of leachate is typically yellowish and blackish, with an unpleasant smell. These leachates consist of biodegradable organic or inorganic compounds of solid wastes that flow through landfills filled with rainwater (Abdel-Shafy et al. 2024). Also, it harms human health and

CONTACT Shraddha Sharma shraddhasharmaphd@gmail.com Department of Environmental Engineering, Delhi Technological University, Delhi 110042, India

© 2025 Taylor & Francis Group, LLC

increases the risk to the environment. High levels of solids, heavy metals, total organic carbon (TOC), chemical oxygen demand (COD), and biochemical oxygen demand (BOD) are commonly found in concentrated effluents (Dhamsaniya et al. 2023). It can migrate deeply into the soil, creating environmental degradation, which leads to soil and groundwater contamination (Mohammed, Fattah, and Shehab 2024).

Groundwater plays an important role in daily human consumption, agricultural irrigation purposes, and other economic development. Groundwater contamination occurs when man-made substances such as road salts, gasoline, chemicals, and oil seep into groundwater and make it unfit for human needs (Dangar, Asoka, and Mishra 2021). Soil provides basic support to plants and also their sources of nutrients and water. Soil contamination is caused by man-made chemicals such as agricultural chemicals, industrial effluents, improper disposal of solid wastes, and other processes that can be done by the natural soil environment (Shankar and Shikha 2017). Increasing urbanization and industrialization have introduced heavy metals into the environment through improper discharge of industrial wastes directly into water and land. Hence, these heavy metals are raised as major concerns and reduce the capacity for biodegradation activities in the environment. The main heavy metal is arsenic (As), which is a priority pollutant, and most of the environmental hazards are caused by these metals (Ahmed et al. 2022).

Numerous studies have highlighted the impact of landfill leachate on the environment, focusing on heavy metals and their migration into soil and groundwater. For example, Beinabaj et al. (2023) studied heavy metals in leachate pollution by taking samples of plants and soils near two landfills in Tehran. The study was carried out on three indexes, the Nemerow Pollution Index, the Bioavailability factor, and the Pollution Index, which were used to determine the data. The result showed that iron (Fe) concentration was higher in new landfills and manganese (Mn) concentration was higher in old landfills. The final results showed that plants grown near landfills were a factor in the reduction of heavy metals in studied soils. Barasarathi et al. (2021) studied four different ornamental plant species for heavy metal removal in leachate-contaminated soil. The results showed that Cordyline fruticosa has a high metal reduction capacity in contaminated soil, about 85% As, 77.88% Mn, 75% chromium (Cr), 63% lead (Pb), and 77.55% Zinc (Zn). Similarly, Boateng, Opoku, and Akoto (2019) found that heavy metal levels in groundwater from the Oti community were above WHO permissible limits, with Cr and Pb being the most concerning pollutants. Hussein et al. (2021) observed that soil samples from non-sanitary landfills in Malaysia showed higher heavy metal contamination, with arsenic (As) being a primary concern. Other studies, such as Essien et al. (2022), Ajani et al. (2021), and Negi, Mor, and Ravindra (2020), investigated leachate and sediment contamination in different regions that demonstrate the widespread nature of heavy metal migration in landfills.

Furthermore, Hredoy et al. (2022) studied the landfill leachate of Amin Bazar landfill in Dhaka. A total of 14 samples were gathered, and the heavy metal concentration and physicochemical parameters were examined. The results found high concentrations of metals such as 8 mg/kg of Pb, 0.4 mg/kg of Cd, 2.26 mg/kg of Cr, and 1.72 mg/kg of cobalt (Co) in leachate, surface water, and plant samples. Likewise, Afolabi et al. (2022) analyzed the landfill leachate in three urban areas of Nigeria and calculated it using laboratory standards APHA 2012. The results found that metals such as nickel and Pb exceeded acceptable limits, although no risk of cancer was detected. Hussain et al. (2024) monitored the three landfill sites,

Ghazipur, Bhalswa, and Okhla, in New Delhi to find out the physiochemical parameters of leachate landfills. These three landfill sites compared their values with the permissible limit established by the Environmental Protection Agency in 1986. The results indicated that all three landfills exceeded the permissible limit, and immediate attention was needed to remediate groundwater contamination.

The studies reviewed above describe the environmental problems associated with landfill leachate contamination, particularly concerning heavy metals, groundwater, and soil contamination. Despite this, several research gaps have been identified from previous studies. Most studies focus only on groundwater contamination or soil contamination. There are limited integrated studies that assess soil and groundwater simultaneously to understand the environmental effects of landfill leachate. Previous research has focused on empirical data and chemical or physical analysis of groundwater and soil samples. Mathematical modeling methods have not studied the effects of leachate migration on groundwater and soil contamination. There is limited research on examining the correlation between soil and groundwater contaminants. Previous investigations provide a strong basis for future study of the Ghazipur landfill. Studies have previously demonstrated that the Ghazipur landfill has high levels of pollution, making it an ideal site for evaluating the performance of various pollution assessments. A comprehensive evaluation of the Ghazipur landfill using mathematical models should understand pollution levels that have not been explored in previous studies. This study aims to fill these gaps by presenting an integrated method using both empirical data and mathematical models to estimate soil and groundwater contamination caused by leachate migration from the Ghazipur landfill. The Ghazipur landfill is an ideal site for this study because it has been well-documented to have high levels of pollution and is close to densely populated areas.

Unlike previous works, this study looks at both soil and groundwater pollution caused by landfill leachate using the Weighted Arithmetic Water Quality Index (WAWQI) and Soil Quality Index (SQI) together; this is a main innovation for landfill leachate research. By comparing where contaminants appear in both groundwater and soil, the research explains pollution trends and locates places that need to be cleaned. The data are collected using normalized tests and mapped using GPS, guaranteeing results are accurate and consistent. Instead of just finding contaminants alone, the study also analyzes the correlation between contaminants in soil and groundwater, which provides new innovative perspectives on their effects. This integrated methodology enhances the precision in recognizing pollution hotspots and guiding the remedial interventions. Since the study focuses on the Ghazipur landfill, which is representative of urban landfill challenges everywhere, it has gained international attention. As urban waste becomes an increasing environmental and health risk in many countries, the research presented here can be applied successfully by cities of any size and level of development. Furthermore, solutions such as phytoremediation and reactive barriers proposed here follow the UN's Sustainable Development Goals 3, 6, and 15, making this work useful for international policymakers, researchers, and planners. The objectives of the study are as follows:

- To analyze soil and groundwater contamination due to leachate migration from the Ghazipur landfill using WAWQI & SQI models and assess groundwater suitability for drinking water and soil suitability for agricultural use.

- To investigate the correlation between soil contaminants and SQI, groundwater contaminants, and WQI to find out the relationship between various pollutants and their effects on the environment.
- To identify specific locations around the Ghazipur landfill where pollution levels exceed acceptable standards, thereby highlighting areas that require remedial efforts.

This study presents multiple methods to handle heavy metal pollution contamination. The Empirical data and WAWQI & SQI models help calculate soil and groundwater pollution levels that identify precise contaminated areas. The research suggests remediation measures that include better landfill waste management together with regular heavy metal testing, as well as the deployment of suitable treatment solutions like phytoremediation, filtration systems, and chemical interventions to decrease metal concentrations. The study emphasizes the requirement for public health interventions joined with ecological management plans for heavy metal impact reduction and site rehabilitation projects. The assessment plan combines all necessary steps to safeguard groundwater and soil quality while working to reduce health and environmental dangers.

2. Methodology

2.1. Study area

Delhi is the capital city of India, which spans a latitudinal range from approximately 28.4°N to 28.9°N and a longitudinal range from 76.8°E to 77.3°E. A wide geographic area makes this territory extensive, which creates climatic and urban diversity. The area span extends from 50 km north-to-south and 50-km east-to-west throughout Delhi. The city encompasses a diverse range of districts, each with its unique geographical coordinates. It is one of the most densely populated urban areas in India, with a significant portion of its population residing in various areas, including the village of Ghazipur. In Delhi, the Ghazipur area has the largest garbage landfill in the city (Khan et al. 2022). The urban area of Ghazipur within East Delhi is densely populated while maintaining functions of residential properties alongside commercial developments and semi-industrial operations. The geographical coordinates of the Ghazipur area are 28.63 degrees north and 77.31 degrees east, with an average elevation of 213 m above sea level. Ghazipur falls within a semi-arid climate belt, which shows hot summer months followed by a monsoon period from July to September, and mild winter weather differs. Every year, the terrain receives around 800 mm of rain, which occurs mainly during the monsoon season. The population in Ghazipur village, together with nearby areas of Mayur Vihar Phase 1, Mandawali, and Narwana Road, is around 75,544 people and continues to increase. The residents primarily pursue small-scale trade waste picking alongside transportation services and labor work. The Ghazipur landfill stands as one of Delhi's biggest landfills and strongly shapes both the local financial sector and the environmental quality of life. The landfill pollutants responsible for leachate contamination deeply endanger human health as well as surrounding agricultural sites while degrading accessible clean water reserves. Landfill operations affect this region because it contains densely populated housing communities along with markets and dairy farms, as well as small green spaces that create high environmental risk. It is important to examine the environmental impacts of large landfill sites located in densely populated areas. This landfill

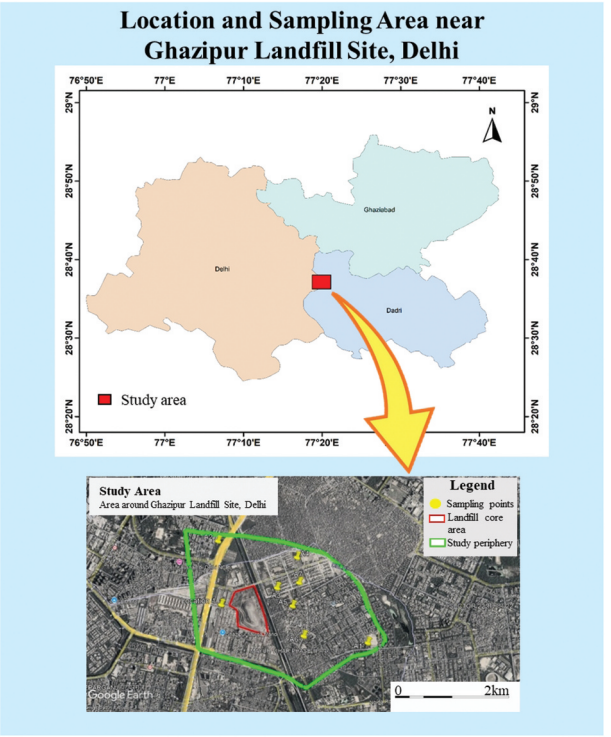


Figure 1. Geospatial location of study area around Ghazipur landfill site showing identified sampling points.

produces a toxic substance called leachate, which migrates and contaminates soil and groundwater. These resources pose a threat to both ecosystems and public health because of the migration of toxic substances into soil and groundwater.

This study provides a complete assessment of the effects of landfills on nearby resources by examining soil properties and groundwater quality. Therefore, the eight soil and groundwater samples were collected from Mayur Vihar Phase 1 as A1, Mayur Vihar Phase 1 as A2, Mandawali as A3, Mayur Vihar extension as A4, Mandawali as A5, Narwana road (IP extension) as A6, Mandawali as A7 and Dairy Farms, Ghazipur Site as L1. The selection of these areas makes it possible to investigate the effects of leachate from one of Delhi's largest landfills. Figure 1 shows the Delhi District Map with Ghazipur landfill site. Each soil and groundwater sampling location was accurately documented by GPS devices, and the recorded latitude and longitude values are displayed in Table 1. The chosen locations underwent GPS-based photographic verification according to standards accepted worldwide.

2.2. Groundwater and soil samples collection

As shown in Table 1, groundwater and soil samples were collected from different locations around the Ghazipur landfill site during the sample collection phase. Clean plastic bottles were used to obtain samples from groundwater. On 25th January 2023 at 4:59 PM during the winter season, the groundwater and soil samples were collected in the area of the

Table 1. Locations and GPS coordinates of soil and groundwater sampling points around Ghazipur landfill.

Locations	Area (Ghazipur, Delhi)	Latitude	Longitude
A1	Mayur Vihar Phase III	28.60742	77.33243
A2	Mayur Vihar Phase I	28.60728	77.33262
A3	Mandawali	28.62252	77.33222
A4	Mayur Vihar Extension	28.62254	77.3382
A5	Mandawali	28.61926	77.33104
A6	Narvana Road (IP Extension)	28.61557	77.32782
A7	Mandawali	28.62031	77.33487
L1	Dairy farms, Ghazipur Site	28.62784	77.32502

Ghazipur landfill site. Seasonal variations create important temporal effects on water physio chemical properties because these values are highest in winter. The Ghazipur landfill region was studied by collecting samples from borewells and hand pumps to determine the impact of leachate on groundwater. One thousand-milliliter samples were collected in clean plastic bottles at each location. For laboratory analysis, groundwater samples were kept at 4°C. To confirm consistency in analysis, soil samples were taken from the same locations as groundwater samples. A total of 500 g of soil was collected in each section. To ensure the integrity and validity of data collected for this study, each sample was labeled before being sent to appropriate laboratories for detailed investigation.

2.3. Analysis of groundwater and soil samples

2.3.1. Groundwater sample analysis

In this study, groundwater samples were analyzed to assess their quality using various physical and chemical properties. Physical properties evaluated include taste, color, turbidity, and odor, which must be considered when evaluating its overall acceptability and quality. These measurements helped determine the water's sweetness, clarity, cloudiness, and unpleasant odors from suspended particles. Chemical properties also measured, such as Total Dissolved Solids (TDS), pH, Total Alkalinity (TA), Electrical Conductivity (EC), Total Hardness (TH), Nitrates (NO_3^-), Chlorides (Cl^-), Sulfates (SO_4^{2-}) and Fluorides (F^-). TDS is the concentration of dissolved substances in water, which affects its taste and clarity; pH measures the water's acidity or alkalinity. TA measures the water's ability to withstand pH variations. EC is a measure of how well water conducts electricity, and it is related to ionic material concentration. TH is determined by the amount of calcium and magnesium ions in water, which affects water hardness. NO_3^- is used to assess the presence of nitrate ions, which affect plant growth and water quality. Fluoride ions are measured by F^-, and they affect water taste and oral health. Chloride ions obtained by Cl^- affect corrosion and water taste. SO_4^{2-} assesses the number of sulfate ions that affect flavor and potential scaling. In addition, the presence of toxic heavy metals such as Cd, iron (Fe), copper (Cu), zinc (Zn), and chromium (Cr) was monitored. All the water quality testing tests were conducted as per IS 3025 standards, as shown in Table 2. Physical and chemical water quality tests were conducted by UP Jal Nigam, Aligarh, equipped for routine analysis.

Heavy metals detection, together with quantification for Cd, Fe, Cu, Zn, and Cr in groundwater samples, happened through Atomic Absorption Spectrophotometry (AAS) analysis. The AAS method employs sensitivity and accuracy because it detects specific

Table 2. Physical and chemical properties of groundwater samples with acceptable values, cause for rejection, and DLLs.

Parameters	Acceptable value	Cause for Rejection	Tests as per IS standards	DLLs
Physical characteristics of groundwater samples				
Taste	Pleasant	Unpleasant	IS 3025–8 (1984)	–
Colour (PCU)	≤5	>15	IS: 3025 (*p*-4)	1
Odor	Agreeable	Disagreeable	IS 3025(*p*-5)	–
Turbidity (NTU)	≤1	>5	IS: 3025 (*p*-10)	0.1
Chemical characteristics of groundwater samples				
pH	6.5–8.5	<6.5 or > 8.5	IS: 3025 (*p*-11)	0.01
TDS (mg/L)	≤500	>2000	IS: 3025 (*p*-16)	1
TH (mg/L as $CaCO_3$)	≤200	>600	IS: 3025 (*p*-21)	1
TA (mg/L as $CaCO_3$)	≤200	>600	IS: 3025 (*p*-23)	1
Cl (mg/L)	≤250	>1000	IS: 3025 (*p*-32)	0.1
NO_3^- (mg/L)	≤45	>100	IS: 3025 (*p*-34)	0.01
F^- (mg/L)	≤1.0	>1.5	IS: 3025 (*p*-60)	0.01
SO_4^{2-} (mg/L)	≤ 200	>400	IS: 3025 (*p*-24)	0.1
EC (µmhos)	≤1400 (WHO)	>1400(WHO)	IS: 3025 (*p*-14)	1
Heavy metals in groundwater samples				
Cd (mg/L)	≤0.003	>0.01	IS:3025(*p*-41)	0.001
Fe (mg/L)	≤0.3	>1.0	IS:3025(*p*-53)	0.01
Cu (mg/L)	≤0.05	>1.5	IS:3025(*p*-42)	0.01
Zn (mg/L)	≤5.0	>15	IS:3025(*p*-49)	0.01
Cr (mg/L)	≤0.05	>0.1	IS:3025(*p*-52)	0.001

wavelengths for free atoms, whereas the absorption level mirrors metal content through the Beer-Lambert Law (Rai et al. 2023). The Spectra AAS instrument (Spectra Labs, Ghaziabad) operated at 228.8 nm for Cd and 248.3 nm for Fe measurements of each specific element. The testing reached detection thresholds of 0.001 mg/L for Cd and Cr, whereas Fe, Cu, and Zn were detected at 0.01 mg/L. The absorption data of heavy metals underwent concentration conversion based on procedures outlined by the guidelines in IS 3025. AAS technique delivered dependable and repeatable measurements to properly evaluate heavy metal pollution in groundwater from the Ghazipur landfill site. BIS 10,500:2012 standards confirm that the drinking water quality is maintained to protect public health. In Table 2, EC values are provided as per WHO standards and other descriptive values aligned with BIS 10,500:2012 standards. Also, detection lower limits (DLLs) for these parameters were determined based on the sensitivity of instruments used during testing, as presented in Table 2. Water quality should be treated or discarded when it exceeds acceptable values to avoid health hazards.

2.3.2. Soil sample analysis

Soil samples were examined by composition and quality analysis to determine their suitability for agricultural and environmental use. The parameters measured were pH, electrical conductivity (EC), organic carbon (OC), phosphorus (P), and potassium (K). EC refers to the conductivity of soil in relation to the solubility of salts. Soil fertility and structure depend on the amount of organic matter in the soil, which OC reflects. Phosphorous and potassium are used to estimate the availability of phosphorus and potassium in soil, which are important nutrients for plant growth and plant health. For a comprehensive soil analysis, soil testing was conducted at the Department of Agriculture & Welfare (Krishi Vigyan Kendra, Aligarh). Soil parameters were tested as per IS standards, as shown in Table 3, along with acceptable values, causes for rejection, and DLLs.

Table 3. Soil parameters with acceptable values, cause for rejection, and DLLs.

Parameters	Acceptable value	Cause for Rejection	Tests as per IS standards	DLLs
pH	6.5–7.5	<5.5 or > 8.5	IS: 2720 (*p*-26)	0.01
EC (µmhos/cm)	≤400	>1600	IS: 2720 (*p*-21)	1
OC (%)	0.5–1.5	<0.5 or > 1.5	IS: 2720 (*p*-22)	0.01
P (kg/ha)	10–25	<10 or > 25	IS: 2720 (*p*-22)	0.1
K (kg/ha)	110–280	< 110 or > 280	IS: 2720 (*p*-22)	1

2.4. Mathematical modeling

2.4.1. Weighted Arithmetic Water Quality Index (WAWQI) model

The Weighted Arithmetic Water Quality Index (WAWQI) model is a tool that is used to evaluate and measure water quality in a standard and simple manner. In this method, water quality is classified based on the degree of purity by using water quality variables. The WAWQI model is designed to convert various parameters into single values that help understand overall water quality and make decisions about water treatment and management. In this study, WQI is calculated by 16 water parameters such as color, turbidity, TDS, pH, TA, EC, TH, NO_3^-, Cl^-, SO_4^{2-}, F^-, Cd, Fe, Cu, Zn, and Cr. Taste and odor are not included in the WQI calculation because they do not have numerical values. The WAWQI model is calculated by using the following equation (1) (Patel et al. 2023).

$$WQI = \frac{\sum_{j=1}^{16} W_j Q_j}{W_j} \tag{1}$$

where,*j*indicates the total number of parameters, Q_j is the quality rating for the j^{th} water quality parameters, and W_j is the relative weightage for the j^{th} parameter. The quality rating and relative weightage for j^{th} water quality parameters are calculated by using equations (2) and Equation 3, respectively (Patel et al., 2023).

$$Q_j = \frac{(V_a - V_j)}{(V_s - V_j)} \tag{2}$$

$$W_j = \sum_{j=1}^{16} w_j \tag{3}$$

where, V_a is the observed value obtained from j^{th} parameter at a given sampling station, V_j is the ideal value of specific parameters (0 for all parameters except pH, which is 7.0), and V_s is the standard permissible value of j^{th} parameter. Then, the unit weight (w_j) for j^{th} parameter was calculated by using the following equation (4). It is defined as the ratio of relative constant to the standard values for j^{th} parameter (Patel et al. 2023).

$$w_j = \frac{K}{S_j} \tag{4}$$

where, $S_j$is the standard value for j^{th} parameter, w_j is a relative unit weight for j^{th} parameter, and $K$is a relative constant, which is calculated based on equation (5) (Patel et al. 2023).

$$K = \frac{1}{\frac{1}{S_1} + \frac{1}{S_2} + \ldots + \frac{1}{S_{13}}} = \frac{1}{\sum_{j=1}^{16} S_j} \tag{5}$$

The first step to obtaining WAWQI involved the collection of observed values (V_a) at different sampling locations from each water quality parameter. The measurement standard permissible value (V_s) for each water quality parameter came from both BIS 10,500:2012 and WHO regulations. A method based on deviation from ideal value (V_j) helped determine the parameter quality rating (Q_j) using equation (2). The $\frac{1}{S_j}$values show the inverse relation between the standard values (S_j) of each parameter. The unit weight (w_j) calculation proceeded through the division of the relative constant (K) by the standard value (S_j) using equation (4). A mathematical derivation led to the calculation of the relative constant (K) by taking the inverse of standard permissible values summed together using equation (5). The quality rating received a multiplication factor from its associated unit weight to produce the weighted value. The calculation of WAWQI involved summed weighted values then divided by total unit weight values using equation (1). A classification for the water quality used the standards from Table 4 to evaluate the results. These ranges and evaluations provide a clear understanding of the potential applications of water samples based on their WQI values.

2.4.2. Soil Quality Index (SQI) model

The Soil Quality Index (SQI) model is a tool used to measure the quality of soil, which helps to evaluate soil fertility, health, and sustainability for environmental and agricultural purposes. The following steps calculate the SQI for soil, and explanations of their depth are given below. The first step is to determine the normalization of soil properties. The normalization for soil properties is given in equation (6):

$$N_k = \frac{(X_k - X_{\min})}{(X_{\max} - X_{\min})} \tag{6}$$

where, N_k is normalized values for k^{th} soil property, X_k is observed values for k^{th} soil property, $X_{\min}$ is minimum observed in the data for k^{th} soil property, and $X_{\max}$ is the maximum observed in the data for k^{th}soil property. Weights assigned to every normalized soil property are based on soil quality, and weights are determined based on empirical data. The weighted score formula is shown in equation (7):

$$S_k = W_k \times N_k \tag{7}$$

Table 4. WQI with its rating of water sample (Balamurugan et al. 2020.).

Water quality index	Water quality rating
Above 100	Very poor
76–100	Poor
51–75	Moderate
26–50	Good
0–25	Excellent

Table 5. SQI values based on their classification Mulyono et al. (2019).

Soil Quality Index values	Soil Quality Index Classification
0–0.19	Very low
0.20–0.34	Low
0.35–0.59	Moderate
0.60–0.79	Good
0.80–1.00	Very Good

where, W_k is weight assigned to the k^{th} soil property, and $S_k$is weighted score values for the k^{th} soil property. The final step is to calculate the SQI by the ratio of the sum of all weighted score values to the sum of weight-assigned soil properties given in the following equation (8).

$$SQI = \sum_{k=1}^{5} \frac{W_k \times N_k}{w_k} \tag{8}$$

where, $w_k$is the unit weight for k^{th} the parameter of soil (Damiba et al. 2024).

The SQI calculated its values by performing a standardized method. The gathered observed values (X_k) represent different soil properties from their selected study sites. The $X_{\min}$and $X_{\max}$extreme values in the dataset were determined for each parameter. The normalization process followed the equation to rescale observed data points between 0 and 1 through multiplication with respective minimum and maximum values. Soil parameters were normalized before applying defined weights (W_k) to each parameter. The obtained weighted scores (S_k) came from multiplying normalized values (N_k) with their assigned numerical weights (N_k). The calculation of the final SQI value involved dividing the weighted score sum by the weighted weight sum using equation (8). A classification process for soil quality arose from the criteria described in Table 5, which researchers applied to their outcomes.

3. Results and discussion

3.1. Physical characteristics of water samples

The physical characteristics of groundwater samples around the Ghazipur landfill site present mixed water quality results. In Table 6, all sample locations (A1 to L1) exhibited pleasant taste, indicating the absence of immediate organoleptic concerns inhibiting consumption. This uniformity in taste means that taste affecting contaminants are absent or present in very low concentrations, making the water acceptable. Every water sample had

Table 6. Groundwater quality results for taste, color, and odor.

Locations	Taste	Colour (Hazen value)	Odor
A1	Pleasant	1	Agreeable
A2	Pleasant	1	Agreeable
A3	Pleasant	1	Agreeable
A4	Pleasant	1	Agreeable
A5	Pleasant	1	Agreeable
A6	Pleasant	1	Agreeable
A7	Pleasant	1	Agreeable
L1	Pleasant	1	Agreeable

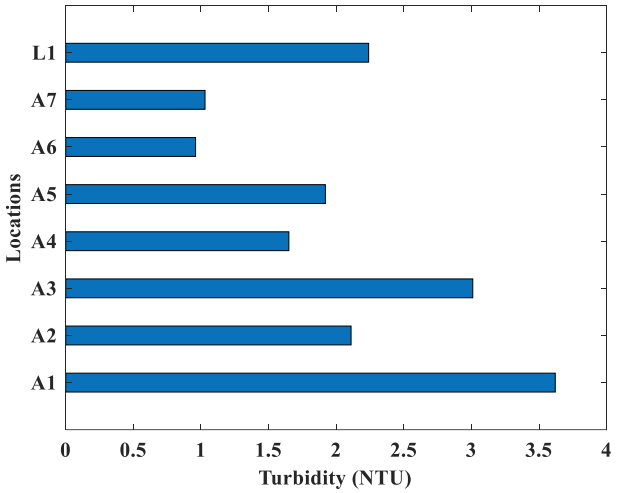


Figure 2. Groundwater quality results for turbidity across sampling locations.

a color value of one Hazen unit. It is within the acceptable range of ≤5 PCU, which indicates that the water is clear and free of impurities that cause significant discoloration. Clearwater is not only esthetically pleasing but also means less chance of certain impurities that can impart color, such as iron or manganese oxides. Across all locations, an odor of water samples was consistently reported as acceptable. The absence of unpleasant odors suggests the absence of high concentrations of volatile organic compounds (VOCs) or other odor causing substances, which are by product of organic decomposition or industrial pollutants (Pestana, Lawton, and Kaloudis 2020).

Figure 2 shows the groundwater turbidity at different locations. Turbidity values ranged from 0.96 NTU in A6 to 3.62 NTU in A1. Locations A1 (3.62 NTU), A2 (2.11 NTU), A3 (3.01 NTU), and L1 (2.24 NTU) exhibited higher turbidity levels compared to other locations. Although these values are below the critical rejection limit of >5 NTU, they exceed the preferred acceptable limit of ≤1 NTU, which indicates the presence of suspended particles. These particles may be soil runoff, organic matter, or other particles that affect water clarity and may represent early stages of contamination that require monitoring and possible filtration. Turbidity was higher in A1 (3.62 NTU) compared to A6 (0.96 NTU), which highlights a significant difference in the level of suspended particles present in water. High turbidity in A1 indicates contamination from suspended particles or sediments, which is less important in A6, where water is clearly visible. While all locations maintain acceptable taste and odor, turbidity levels suggest varying levels of particulate pollution, which may be localized sources of pollution or differences in land use and waste management practices around landfills (Aromolaran et al. 2023).

3.2. Chemical characteristics of water samples

The chemical analysis of water samples from the Ghazipur landfill area highlighted several areas of concern and revealed significant variations. Figure 3(a) shows that the pH levels of water samples at A4 and A2 ranged from 6.68 to 7.75, all of which fall within an acceptable

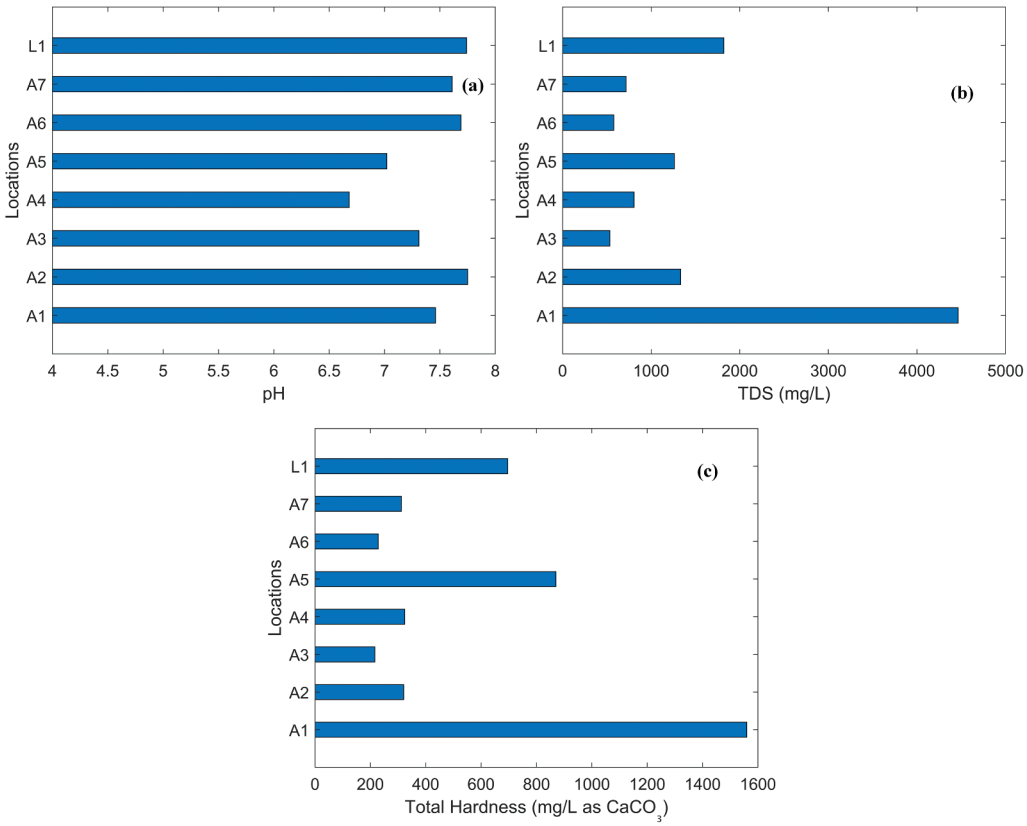


Figure 3. Groundwater quality results for (a) pH, (b) TDS, and (c) TH across sampling locations.

range of 6.5 to 8.5. This indicates that water is not too acidic or alkaline, which is safe for consumption with regard to pH balance (Giap and Muthuraman 2020). Figure 3(b) shows that the TDS levels vary with a maximum TDS level of 4465 mg/L at A1, exceeding the acceptable limit of ≤500 mg/L and exceeding the rejection limit of >2000 mg/L. High TDS levels at A1 and A2 (1332 mg/L), L1 (1820 mg/L), and A5 (1261 mg/L) indicate a significant presence of dissolved salts and minerals. Elevated TDS can affect the taste hardness of water and cause health problems due to prolonged consumption. This indicates contamination from leachate injection or other sources of mineral dissolution. Figure 3(c) shows the total hardness measured as $CaCO_3$, which shows considerable variation from 216 mg/L in A3 to 1560 mg/L in A1. Locations like A1 (1560 mg/L) and A5 (870 mg/L) exceeded the rejection limit of >600 mg/L, which indicated high concentrations of Ca and Mg ions. It can lead to scaling in pipes, boilers, and household appliances and cause skin irritation and other health problems (Baj et al. 2020).

Total alkalinity ranged between 240 mg/L and 580 mg/L at A3 and at L1, with the acceptable limit of ≤200 mg/L, as shown in Figure 4(a). High alkalinity indicates a substantial presence of carbonates, bicarbonates, and hydroxides, which can buffer water against pH changes. The chloride concentrations were high in some samples, ranging from 78 mg/L at A3 to 1928 mg/L at A1, as shown in Figure 4(b). A1 (1928 mg/L) and L1

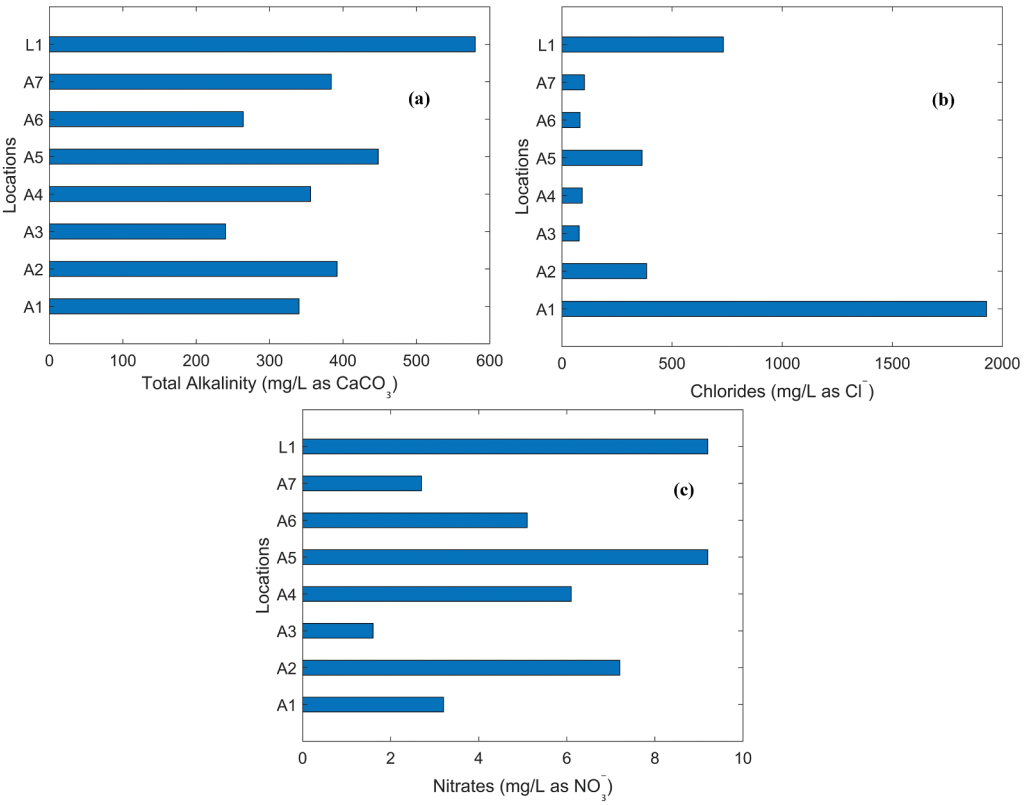


Figure 4. Groundwater quality results for (a) TA, (b) Cl, and (c) NO_3^- across sampling locations.

(733 mg/L) exceed the rejection limit of >1000 mg/L. High chloride levels can impart a salty taste to water and cause corrosion in plumbing systems, which impacts infrastructure and potentially leads to increased maintenance costs. The nitrates were within acceptable limits, ranging from 1.6 mg/L at A3 to 9.2 mg/L at A5 and L1 shown in Figure 4(c). Higher nitrate levels in A2 (7.2 mg/L) and L1 (9.2 mg/L) could pose health risks to infants, causing methemoglobinemia or "blue baby syndrome" (Cao et al. 2022; Craswell 2021; Zhang et al. 2021).

Fluoride concentrations showed some exceedances ranging from 0.41 mg/L at A6 to 2.01 mg/L at A4. A1 (1.61 mg/L), A2 (1.79 mg/L) and A4 (2.01 mg/L) exceed acceptable limit of ≤1.0 mg/L (Figure 5(a)). The high fluoride can lead to dental and skeletal fluorosis over time, which necessitates monitoring and possible remediation. Sulfate ranged from 13.6 mg/L at A3 to 328 mg/L at A1, with A1 exceeding the acceptable limit of ≤200 mg/L but still below the rejection limit of >400 mg/L (Figure 5(b)). High Sulfate can cause a laxative effect and bitter taste, which originate from the dissolution of gypsum. Electrical conductivity ranged from 896 µmhos at A3 to 8239 µmhos at A1, with multiple locations exceeding the WHO limit of ≤1400 µmhos (Figure 5(c)). The high EC values indicate elevated levels of dissolved ions, which can impact water quality and usability, suggesting significant mineral or pollutant content from leachate or industrial discharge (Agarwal and Singh 2023; Akhtar et al. 2021).

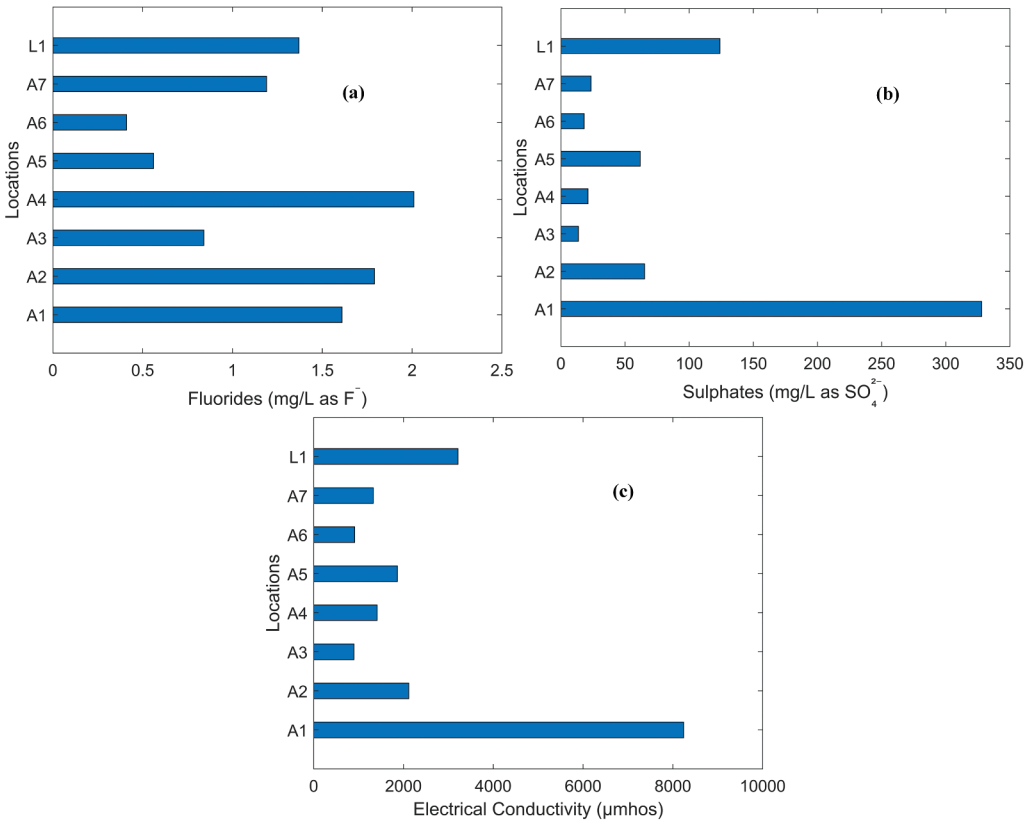


Figure 5. Groundwater quality results for (a) F^{-}, (b) SO^{2-} and (c) EC across sampling locations.

3.3. Heavy metals analysis in water samples

Figure 6 shows an analysis of heavy metals in water samples, which indicates various levels of contamination. Cadmium concentrations ranged from −0.004 mg/L to 0.012 mg/L at L1. A1 (0.01 mg/L) and L1 (0.012 mg/L) exceed the acceptable limit of ≤0.003 mg/L. Cadmium is a highly toxic metal that can cause bone demineralization, kidney damage, and other serious health issues, even at low concentrations. Iron varied from 0.142 mg/L at A3 to 1.098 mg/L at A2, with A2 exceeding the rejection limit of >1.0 mg/L. Higher iron content can cause staining of laundry and plumbing fixtures, indicating the presence of iron bacteria, which can clog pipes and reduce water flow. Copper concentrations were within the acceptable range from 0.035 mg/L at A3 to 0.467 mg/L at L1, below the rejection limit of >1.5 mg/L. Copper can cause gastrointestinal distress at higher concentrations and originate from corrosion of copper pipes or natural mineral deposits. Zinc levels ranged from 0.0396 mg/L at A3 to 0.8947 mg/L at A7, all within acceptable limits. Zinc can impart a metallic taste at higher concentrations, and its presence is due to industrial discharge or natural sources. Total chromium concentrations varied from 0.002 mg/L at A6 to 0.454 mg/L at L1, with A3 (0.038 mg/L) and L1 (0.454 mg/L) exceeding the acceptable limit of ≤0.05 mg/L. Chromium presence is a result of industrial processes, inappropriate waste disposal methods, and the concentration of heavy metals in different places. This comparison

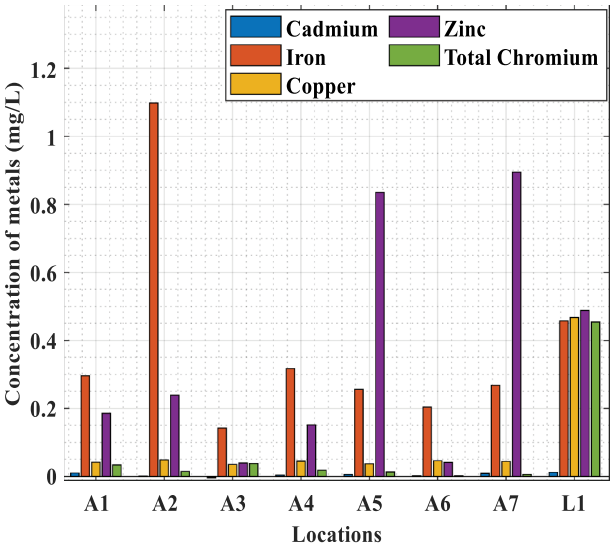


Figure 6. Heavy metals in groundwater samples.

demonstrates that whereas heavy metal concentrations in some areas, like A2 and L1, are dangerous to human health, other areas, like A3, exhibit less contamination. The variation suggests localized pollution sources or differences in groundwater flow and leachate migration patterns around landfills (Heidari, Darijani, and Alipour 2021).

3.4. Assessment of soil quality and suitability

The soil quality and suitability analysis at various locations around the Ghazipur landfill site revealed several soil quality and suitability for agricultural and environmental purposes. pH across all locations falls within an acceptable range of 6.5 to 7.5, which indicates that soil is balanced for nutrient availability and plant growth, as shown in Figure 7(a) . Although most locations are within this range, A3 and A5 have slightly higher pH values of 7.9, which is acceptable but indicates a mildly alkaline condition. Figure 7(b) shows that EC values at all locations are below the acceptable limit of 400 µmhos/cm, suggesting that the soil salinity is not high and should not inhibit plant growth. Low EC values reflect the minimum presence of soluble salts, which is suitable for agricultural production. Organic carbon levels are low at several sites, as shown in Figure 7(c) . A1, A4, and A5 locations showed OC percentages below the acceptable range of 0.5% to 1.5%, with values ranging from 0.27% to 0.33%. Locations A6 and L1, with values of 1.06% and 1.41%, suggest a deficiency in soil organic matter, which is essential for improving water retention, soil structure, and nutrient availability.

Phosphorous levels are below the acceptable range of 10 to 25 kg/ha at several locations, including A1, A3, A4, A5, and A6, with values ranging from 7.92 to 9.9 kg/ha, as shown in Figure 8(a). This indicates that insufficient phosphorous impacts plant growth as phosphorous is essential for photosynthesis and energy transfer. Locations A2 and L1 fall within acceptable range, suggesting adequate nutrients at these sites. Soil management practices need to include phosphorous fertilization to correct deficiencies in other areas. Potassium

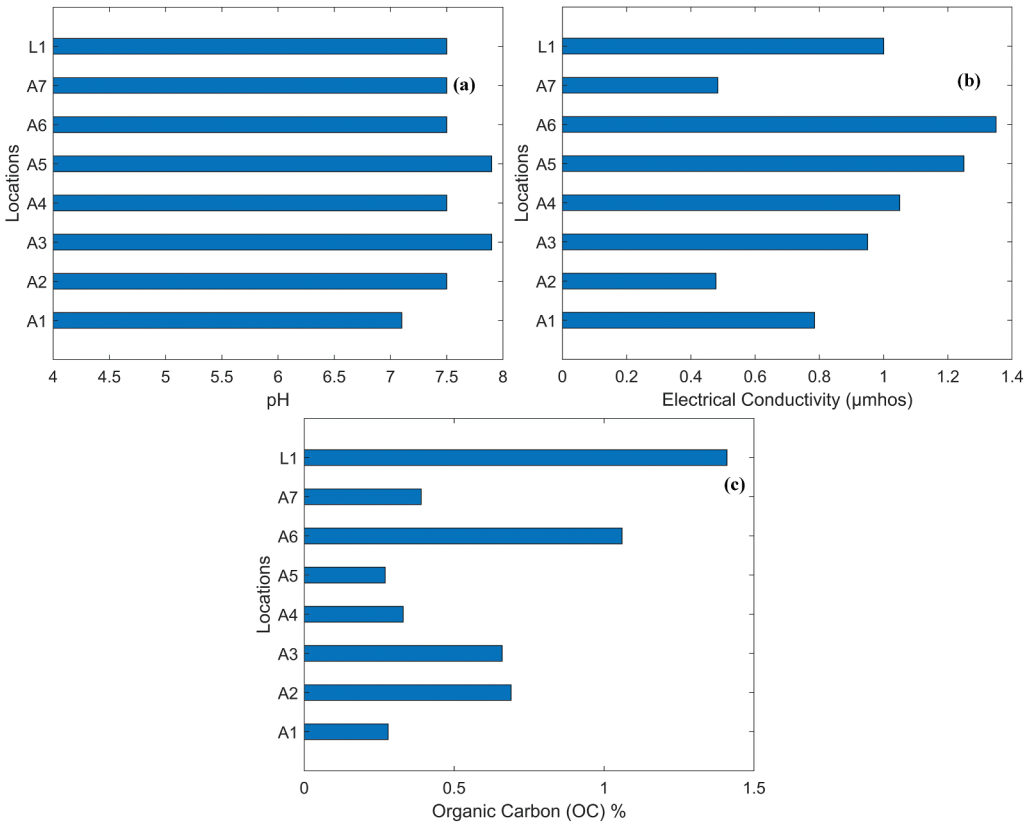


Figure 7. Soil quality results for (a) pH, (b) EC, and (c) OC across sampling locations.

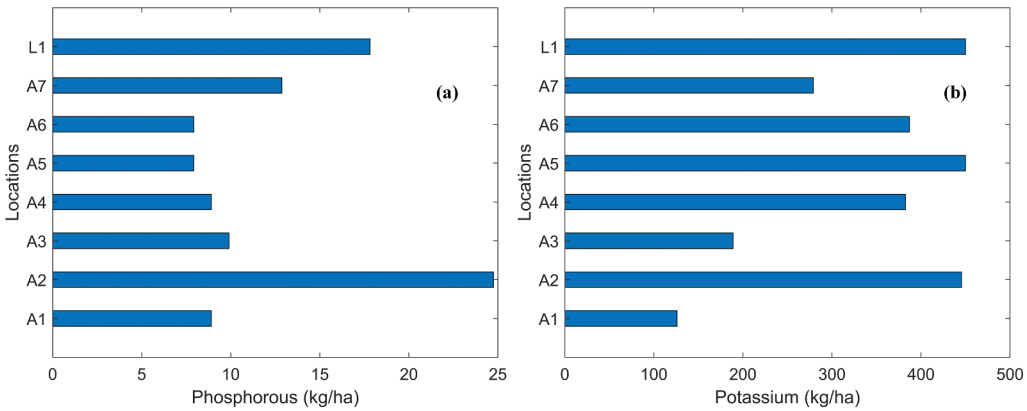


Figure 8. Soil quality results for (a) P and (b) K across sampling locations.

exhibited significant variation, with some locations showing values well above the acceptable range of 110 to 280 kg/ha, as shown in Figure 8(b). Locations such as A2, A4, A5, A6, and L1 have potassium ranging from 382.5 to 450 kg/ha, which indicates over fertilization

or natural mineral content. Locations A1 and A3 have K within acceptable range. While high potassium can be beneficial, excessive amounts can lead to nutrient imbalances or potential toxicity. Careful management of potassium is essential to maintain balanced soil nutrient levels. A soil quality assessment indicates that while some areas are suitable for agriculture, others require corrective actions to improve soil health and support sustainable land use practices.

3.5. Water quality index results

Table 7 shows various water quality parameters, including physical, chemical, and heavy metal parameters. The inverse standard values $\left(\frac{1}{S_j}\right)$ reflect threshold levels set by water quality guidelines, with lower values indicating stricter standards. The constant (K) is used to normalize the weights (w_j), which ensures that the sum of all weights equals 1. The weights revealed the relative significance of each parameter in determining overall water quality. Heavy metals like Cd and Cu have high weights (0.878978 and 0.052739), which highlights their potential toxicity and health risks at low concentrations. This is essential as it helps identify and manage the most dangerous pollutants.

Table 8 shows $Q_j$values for each parameter across different locations (A1 to L1). High Q_j for turbidity and TDS in locations A1, A2, and L1 indicated deviations from acceptable standards, which suggested possible contamination from suspended particles and dissolved solids. The pH values across all locations remain within close range, which indicates stable acidity or alkalinity levels. High Q_j for Cd in A1 and L1 (3.333333 and 4), raising concerns about potential health hazards. The variability in Q_j across all locations highlights the heterogeneous nature of water pollution, which necessitates site-specific analysis and interventions.

Table 9 shows WQI values and their corresponding classifications of water quality at each location. Locations A3 and A6, with WQI values of 9.922 and 9.591, are classified as "excellent" water quality, which indicates minimal contamination and safe water for

Table 7. Inverse standard values $\left(\frac{1}{S_j}\right)$, constants ($K$), and unit weight ($w_j$) of groundwater quality parameters.

Parameters	$\frac{1}{S_j}$	K	$w_j = \frac{K}{S_j}$
Color	0.2	0.002637	0.000527
Turbidity	1	0.002637	0.002637
pH	0.117647059	0.002637	0.00031
TDS	0.002	0.002637	$5.27E^{-06}$
TH	0.005	0.002637	$1.32E^{-05}$
TA	0.005	0.002637	$1.32E^{-05}$
Cl	0.004	0.002637	$1.05E^{-05}$
NO_3^-	0.022222222	0.002637	$5.86E^{-05}$
F^-	1	0.002637	0.002637
SO_4^{2-}	0.005	0.002637	$1.32E^{-05}$
EC	0.000714286	0.002637	$1.88E^{-06}$
Cd	333.3333333	0.002637	0.878978
Fe	3.333333333	0.002637	0.00879
Cu	20	0.002637	0.052739
Zn	0.2	0.002637	0.000527
Cr	20	0.002637	0.052739
			$W_j = 1$

Table 8. Quality rating (Q_j) values for each groundwater quality parameter across different locations.

	Locations							
Parameters	A1	A2	A3	A4	A5	A6	A7	L1
Color	0.2	0.2	0.2	0.2	0.2	0.2	0.2	0.2
Turbidity	3.62	2.11	3.01	1.65	1.92	0.96	1.03	2.24
pH	0.877647	0.911765	0.86	0.785882	0.825882	0.904706	0.895294	0.910588
TDS	9.042596	2.687627	1.068966	1.622718	2.543611	1.158215	1.438134	3.677485
TH	7.8	1.6	1.08	1.62	4.35	1.14	1.56	3.48
TA	1.7	1.96	1.2	1.78	2.24	1.32	1.92	2.9
Cl	7.712	1.536	0.312	0.368	1.456	0.328	0.408	2.932
NO_3^-	0.071111	0.16	0.035556	0.135556	0.204444	0.113333	0.06	0.204444
F^-	1.61	1.79	0.84	2.01	0.56	0.41	1.19	1.37
SO_4^{2-}	1.64	0.326	0.068	0.1055	0.309	0.0905	0.117	0.62
EC	5.885	1.512857	0.64	1.008571	1.330714	0.651429	0.948571	2.295714
Cd	3.333333	0.333333	−1.33333	1.333333	2	0.666667	3	4
Fe	0.986667	3.66	0.473333	1.056667	0.853333	0.68	0.893333	1.523333
Cu	0.84	0.96	0.7	0.9	0.74	0.92	0.88	9.34
Zn	0.03708	0.04774	0.00792	0.03024	0.16706	0.0082	0.17894	0.0976
Cr	0.68	0.28	0.76	0.36	0.26	0.04	0.12	9.08

Table 9. WQI and classification for different locations.

Locations	WQI	classification	Uses
A1	46.035	Good	For domestic purposes (washing, bathing, irrigation), treatment is needed for drinking.
A2	20.075	Excellent	Suitable for drinking and high quality industrial processes.
A3	9.922	Excellent	Suitable for drinking and high quality industrial processes.
A4	14.966	Excellent	Suitable for drinking and high quality industrial processes.
A5	19.660	Excellent	Suitable for drinking and high quality industrial processes.
A6	9.591	Excellent	Suitable for drinking and high quality industrial processes.
A7	14.839	Excellent	Suitable for drinking and high quality industrial processes.
L1	44.871	Good	For domestic purposes (washing, bathing, irrigation), treatment is needed for drinking.

consumption. Locations A1 and L1, with WQI of 46.035 and 44.871, fall into the "Poor" classification. This suggests significant contamination from heavy metals like Cd and Fe, which pose serious health risks. Cadmium can cause kidney damage and skeletal issues, while high Fe levels can lead to gastrointestinal problems and other health concerns. The contamination also impacts the ecosystem, affecting aquatic life and potentially entering the food chain. The WQI across different locations underscores the need for targeted remediation, such as improving wastewater treatment, removing contaminants, and enforcing regulations on industrial discharge. A3 and A6 may require only routine monitoring, while A1 and L1 demand immediate and robust intervention to mitigate contamination and protect public health.

3.6. Soil quality index results

The SQI provides a comprehensive assessment of soil health by integrating multiple soil properties. In calculating SQI, different soil parameters are assigned weights based on their importance in determining overall soil quality. The weights for pH (0.157604), EC (0.002955), OC (0.788022), P (0.047281), and K (0.004222) are listed in Table 10. Organic carbon receives the highest weight, which reflects its critical role in soil fertility and

Table 10. Weighting assignments (w_k) for soil quality parameters.

Parameters	w_k
pH	0.157604
EC	0.002955
OC	0.788022
P	0.047281
K	0.004222
	$W_k = 1$

Table 11. Normalized values (N_k) of soil quality parameters at different locations.

	Locations							
Parameters	A1	A2	A3	A4	A5	A6	A7	L1
pH	0.015187	0.016076	0.016966	0.016076	0.016966	0.016076	0.016076	0.016076
EC	0.001145	0.000462	0.001512	0.001734	0.002179	0.002401	0.000476	0.001623
OC	0.279568	0.989994	0.419652	0.84991	1	0.859916	0.619772	1
P	2.22E–05	0.000934	0.000867	0.000133	0	0.001757	0.000267	0.002535
K	0.019212	0.054433	0.021413	0.019212	0.01701	0.01701	0.028017	0.039023

microbial activity. Low weights for EC and K indicate that while they are important, their impact on overall soil quality is less significant than that of pH and OC.

Each parameter is normalized to ensure comparability across different soil properties. Table 11 shows normalized values for soil properties across various locations. For pH, the values are uniform, ranging from 0.015187 to 0.016966, which suggests consistent acidity or alkalinity across locations. Electrical conductivity varies more widely, which indicates differences in soil salinity. Organic carbon values vary, with A2 and L1 showing the highest levels, which is important for soil fertility. Phosphorous and potassium also differ, which affects the availability of nutrients for plant growth.

Table 12 presents the SQI values for different locations, which range from 0.315 to 1.059. Locations A2, A4, A5, A6, and L1 exhibited high SQI values, classifying them as "very good." These locations benefit from high levels of OC and balanced pH, which indicates strong soil health suitable for a variety of uses. High SQI at locations such as A2, A4, A5, A6, and L1 indicate excellent soil conditions that support healthy plant growth and effective ecosystem functioning. These locations are prioritized for agricultural activities due to their superior soil quality. A1, with a low SQI of 0.315, was classified as "poor," which reflects poor soil quality due to insufficient OC and nutrient levels. A3 with a moderate SQI of 0.46

Table 12. SQI and classification for different locations.

Locations	SQI	SQI Classification	Uses
A1	0.315	Low	Limited agricultural productivity and requires soil improvements
A2	1.06 ~ 1	Very good	Suitable for agriculture, gardening, and other land uses
A3	0.46	Moderate	Moderate agricultural productivity benefits from soil management practices.
A4	0.887	Very good	Suitable for agriculture, gardening, and other land uses
A5	1.03 ~ 1	Very good	Suitable for agriculture, gardening, and other land uses
A6	0.897	Very good	Suitable for agriculture, gardening, and other land uses
A7	0.665	Good	Good agricultural productivity; suitable for crops with minimal soil management.
L1	1.059 ~1	Very good	Suitable for agriculture, gardening, and other land uses

indicated intermediate soil quality, which shows that some properties require improvement, such as adding organic matter and adjusting soil pH to enhance fertility and productivity. Understanding these variations helps to make decisions about land use and management practices to improve soil health and sustainability.

3.7. Correlation between groundwater and soil quality parameters

Table 13 shows the correlation matrix for groundwater quality parameters and WQI. Turbidity, TDS, and EC exhibited strong positive correlations with WQI of 0.578, 0.848, and 0.707. This shows that high levels of turbidity, TDS, and EC tend to lead to poor water quality, as reflected in WQI values. Both turbidity and TDS show a significant positive correlation with each other (0.710), which indicates that increased suspended particulate matter often accompanies high levels of dissolved solids, deteriorating overall water quality problems. Heavy metals such as Cd and Cu have moderate correlations with WQI of 0.552 and 0.118, which reflect their influence on water quality but are not as strong as turbidity and TDS. The strong correlation between WQI and parameters such as Cl and SO_4^{2-} (0.867 and 0.864) highlights the impact of ionic contaminants on water quality. These interactions emphasize the need for targeted interventions to address particular contaminants that affect water quality. The strong correlations observed between water quality parameters and WQI highlight the importance of monitoring turbidity, TDS, and EC, as these factors affect overall water quality. High TDS and turbidity indicated contamination that requires immediate treatment interventions to restore water quality. Compared to suspended and dissolved solids, the moderate impact of heavy metals such as Cd and Cu suggests that while they contribute to water pollution, their effects are minor. Routine monitoring and treatment strategies should prioritize these parameters to manage water quality.

The correlation analysis between SQI and soil quality parameters is shown in Table 14. A strong positive correlation between OC and SQI (0.999) highlights the important role OC plays in influencing soil quality. High levels of OC are strongly associated with improved soil quality, which is essential for preserving soil fertility. While pH affects soil quality, it does less than OC, which is confirmed by a moderately strong correlation (0.298) found between pH and SQI. Overall, soil quality is unaffected by soil salinity, as seen by the reduced correlation between electrical conductivity and SQI (0.232). Although K and P contribute to soil fertility, their effects are less than OC, which is indicated by moderate correlations with SQI (0.440 and 0.409). These correlations showed that improving organic matter is an important strategy for improving overall soil health and emphasizes the importance of OC in managing soil quality.

4. Conclusions and future direction

This study's findings revealed that there are serious insights into the water and soil quality and concerns about pollution and its effect on agriculture. The key conclusions are as follows:

- The taste and odor of water samples near the landfill were acceptable. However, turbidity and particulate contamination were observed in some areas. Elevated TDS,

Table 13. Correlation between groundwater quality parameters with WQI.

	Turbidity	pH	TDS	TH	TA	Cl	NO_3^-	F^-	SO_4^{2-}	EC	Cd	Fe	Cu	Zn	Cr	WQI
Turbidity	1															
pH	−0.04083	1														
TDS	0.710548	0.135769	1													
TH	0.645292	−0.03453	0.937958	1												
TA	−0.0509	0.143323	0.185863	0.278492	1											
Cl	0.723466	0.178651	0.997091	0.934791	0.197962	1										
NO_3^-	−0.21463	−0.06098	−0.03296	0.102159	0.769599	−0.03354	1									
F^-	0.267735	−0.16033	0.351541	0.152963	0.240761	0.313208	0.04641	1								
SO_4^{2-}	0.713723	0.174578	0.997625	0.933953	0.191485	0.999732	−0.04344	0.318419	1							
EC	0.707754	0.139258	0.997819	0.925325	0.162007	0.99552	−0.0815	0.365035	0.997080599	1						
Cd	−0.00706	0.16722	0.547915	0.609056	0.721271	0.551102	0.330893	0.231276	0.557914482	0.552622	1					
Fe	0.023043	0.37974	0.075174	−0.10218	0.32414	0.056304	0.406232	0.530793	0.048379756	0.045939	−0.05226	1				
Cu	0.062495	0.358634	0.118314	0.106695	0.775846	0.166998	0.513933	0.11652	0.159662985	0.11878	0.53695	0.119774	1			
Zn	−0.33841	0.009703	−0.07738	0.136221	0.595178	−0.08534	0.313197	−0.16702	−0.08430054	−0.09336	0.562355	−0.04913	0.14727	1		
Cr	0.151418	0.329293	0.15639	0.145983	0.753352	0.206726	0.475596	0.122906	0.198488883	0.157562	0.514446	0.089484	0.994893	0.1178921	1	
WQI	0.578493	0.263856	0.848222	0.806062	0.612159	0.867063	0.285163	0.377719	0.863588342	0.84426	0.750087	0.158471	0.616109	0.0944058	0.641795	1

Table 14. Correlation between soil quality parameters with SQI.

	pH	EC	OC	P	K	SQI
pH	1					
EC	0.344780084	1				
OC	0.307779077	0.26472185	1			
P	0.007411442	0.23222341	0.3967954	1		
K	−0.12851069	−0.643490162	0.4032938	0.387202	1	
SQI	0.297553469	0.232248333	0.9991509	0.40949	0.440504095	1

TH, TA, Cl^{-}, F^{-}, NO^{3-}, and SO_4^{2-} were found by chemical analysis that indicated leachate contamination and health risks.

- Heavy metal contents such as Cd, Fe, and Cr lead to serious contamination and health hazards. Also, Cu and Zn were found to be unacceptable levels in some areas.
- The study area's soil quality varied, and certain areas required substances due to low OC and P levels. In certain areas, elevated K levels indicated difficulties with nutrition control.
- Most sites were found to have safe water quality for consumption, with some sites classified as "good" or "very good" by WQI standards.
- Areas of better soil conditions yielded higher SQI values, which suggests these are the best locations for ecological and agricultural use. However, very low SQI values in some regions suggest the need for soil management to improve fertility and productivity in particular areas.
- The correlations of turbidity, TDS, and EC with WQI were found to be significantly positive, while OC was the strongest contributor to SQI in improving soil fertility and productivity.

Overall, the study indicates the need for improved waste management and an understanding of the ecological impacts of landfill leachate. A series of remediation methods should be implemented for groundwater and soil issues caused by leachate migration as follows. For groundwater development, permeable reactive barriers (PRBs) should be installed at landfill boundaries to capture contaminated groundwater prior to expansion. Activating carbon filters next to ion exchange systems serves as a recommended option for household drinking water treatment to extract heavy metals and dissolved contaminants. The application of bioremediation methods that utilize particular bacteria straining or multiple microbial groups removes naturally organic pollutants from groundwater systems. For soil quality improvement, phytoremediation techniques using hyperaccumulating vetiver grass, sunflower, or willow plants can help reduce the concentration of heavy metals in soil. The rehabilitation of soil fertility requires organic matter additions through composting or biochar applications as well as farmyard manure application to enhance organic carbon stores. The physical soil leaching and washing treatments work to extract soluble heavy metals together with pollutants from severely polluted areas. Integrating the mentioned approaches provides dual benefits by reducing current soil contamination levels while improving both soil fertility and groundwater safety for neighboring populations.

Future research might focus on temporal and spatial variability changes and also investigate remediation strategies aimed at improving both the quality of groundwater and soil. The research concentrates mainly on the effects of leachate on soil and

groundwater. Still, future studies will need to address air pollution caused by leachate odors since it represents a connected environmental concern.

Data availability statement

Data sharing is not applicable to this article as no datasets were generated or analyzed during the current study.

Disclosure statement

No potential conflict of interest was reported by the author(s).

References

Abdel-Shafy, H. I., A. M. Ibrahim, A. M. Al-Sulaiman, and R. A. Okasha. 2024. Landfill leachate: Sources, nature, organic composition and treatment: An environmental overview. *Ain. Shams Eng. J.* 15 (1):102293. doi: 10.1016/j.asej.2023.102293.

Afolabi, O. O., E. Wali, E. C. Ihunda, M. C. Orji, V. O. Emelu, L. C. Bosco-Abiahu, N. C. Ogbuehi, S. O. Asomaku, and O. A. Wali. 2022. Potential environmental pollution and human health risk assessment due to leachate contamination of groundwater from anthropogenic impacted site. *Environ. Challenges* 9:100627. doi: 10.1016/j.envc.2022.100627.

Agarwal, S., and A. P. Singh. 2023. Assessment of toxicity characteristics in leachate from the textile industry–based sludge using leachate pollution index. *Water. Air, And Soil Pollut.* 234 (12):774. doi: 10.1007/s11270-023-06785-9.

Ahmed, S. F., P. S. Kumar, M. R. Rozbu, A. T. Chowdhury, S. Nuzhat, N. Rafa, T. M. I. Mahlia, H. C. Ong, and M. Mofijur. 2022. Heavy metal toxicity, sources and remediation techniques for contaminated water and soil. *Environ. Technol. Innov.* 25:102114. doi: 10.1016/j.eti.2021.102114.

Ajani, O. O., T. A. Adagunodo, A. A. Adeniji, B. Fashae, M. Omeje, and O. O. Adewoyin. 2021. Investigation of groundwater contamination from leachate migration: A case study of Bowen University dumpsite, Nigeria. *IOP Conf. Ser.: Earth Environ. Sci* 655 (1):012069). IOP Publishing. February. doi: 10.1088/1755-1315/655/1/012069.

Akhtar, N., M. I. Syakir Ishak, S. A. Bhawani, and K. Umar. 2021. Various natural and anthropogenic factors responsible for water quality degradation: A review. *Water* 13 (19):2660. doi: 10.3390/w13192660.

Aromolaran, O. K., O. Aromolaran, E. T. Faleye, and H. Faerber. 2023. Environmental impacts of an unlined municipal solid waste landfill on groundwater and surface water quality in Ibadan, Nigeria. *Environ. Geochem. Health* 45 (6):3585–616. doi: 10.1007/s10653-022-01437-z.

Baj, J., W. Flieger, G. Teresiński, G. Buszewicz, R. Sitarz, A. Forma, K. Karakuła, and R. Maciejewski. 2020. Magnesium, calcium, potassium, sodium, phosphorus, selenium, zinc and chromium levels in alcohol use disorder: A review. *J. Clin. Med.* 9 (6):1901. doi: 10.3390/jcm9061901.

Balamurugan, P., P. S. Kumar, K. Shankar, R. Nagavinothini, and K. Vijayasurya. 2020. Non-carcinogenic risk assessment of groundwater in southern part of Salem District in Tamilnadu, India. *J. Chil. Chem. Soc.* 65 (1):4697–707. doi: 10.4067/S0717-97072020000104697.

Barasarathi, J., H. Auwal, A. Pariatamby, F. S. Hamid, and E. C. Uche. 2021. Phytoremediation of leachate contaminated soil: A biotechnical option for the bioreduction of heavy metals induced pollution in tropical landfill. *Environ Sci. Pollu. Res.* 29 (15):1–13. doi: 10.1007/s11356-021-17389-3.

Beinabaj, S. M. H., H. Heydariyan, H. M. Aleii, and A. Hosseinzadeh. 2023. Concentration of heavy metals in leachate, soil and plants in Tehran's landfill: Investigation of the effect of landfill age on the intensity of pollution. *Heliyon* 9 (1):e13017. doi: 10.1016/j.heliyon.2023.e13017.

Boateng, T. K., F. Opoku, and O. Akoto. 2019. Heavy metal contamination assessment of groundwater quality: A case study of oti landfill site, Kumasi. *Appl Water. Sci* 9 (2):33. doi: 10.1007/s13201-019-0915-y.

Cao, M., A. Hu, M. Gad, B. Adyari, D. Qin, L. Zhang, Q. Sun, and C. P. Yu. 2022. Domestic wastewater causes nitrate pollution in an agricultural watershed, China. *Sci. Total Environ.* 823:153680. doi: 10.1016/j.scitotenv.2022.153680.

Craswell, E. 2021. Fertilizers and nitrate pollution of surface and ground water: An increasingly pervasive global problem. *SN Appl. Sci.* 3 (4):518. doi: 10.1007/s42452-021-04521-8.

Damiba, W. A. F., J. M. Gathenya, J. M. Raude, and P. G. Home. 2024. Soil quality index (SQI) for evaluating the sustainability status of Kakia-Esamburmbur catchment under three different land use types in Narok County, Kenya. *Heliyon* 10 (5):e25611. doi: 10.1016/j.heliyon.2024.e25611.

Dangar, S., A. Asoka, and V. Mishra. 2021. Causes and implications of groundwater depletion in India: A review. *J. Hydrol.* 596:126103. doi: 10.1016/j.jhydrol.2021.126103.

Dhamsaniya, M., D. Sojitra, H. Modi, M. A. Shabiimam, and A. Kandya. 2023. A review of the techniques for treating the landfill leachate. *Mater. Today* 77:358–64. doi: 10.1016/j.matpr.2022.11.496.

Essien, J. P., D. I. Ikpe, E. D. Inam, A. O. Okon, G. A. Ebong, and N. U. Benson. 2022. Occurrence and spatial distribution of heavy metals in landfill leachates and impacted freshwater ecosystem: An environmental and human health threat. *PLOS ONE* 17 (2):e0263279. doi: 10.1371/journal.pone.0263279.

Giap, L. K., and A. Muthuraman. 2020. Health benefits of alkaline ionized water. *Rapp De Pharm* 6:616–21.

Heidari, M., T. Darijani, and V. Alipour. 2021. Heavy metal pollution of road dust in a city and its highly polluted suburb; quantitative source apportionment and source-specific ecological and health risk assessment. *Chemosphere* 273:129656. doi: 10.1016/j.chemosphere.2021.129656.

Hredoy, R. H., M. A. B. Siddique, M. A. Akbor, M. A. A. Shaikh, and M. M. Rahman. 2022. Impacts of landfill leachate on the surrounding environment: A case study on Amin Bazar landfill, Dhaka (Bangladesh). *Soil. Syst.* 6 (4):90. doi: 10.3390/soilsystems6040090.

Hussain, A., A. Deshwal, M. Priyadarshi, S. Pathak, G. Sambandam, S. Chand, and A. K. Shukla. 2024. Landfill leachate analysis from selected landfill sites and its impact on groundwater quality, New Delhi, India. *Environ. Dev. Sustain.* 27 (6):1–26. doi: 10.1007/s10668-023-04403-6.

Hussein, M., K. Yoneda, Z. Mohd-Zaki, A. Amir, and N. Othman. 2021. Heavy metals in leachate, impacted soils and natural soils of different landfills in Malaysia: An alarming threat. *Chemosphere* 267:128874. doi: 10.1016/j.chemosphere.2020.128874.

Igboama, W. N., O. S. Hammed, J. O. Fatoba, M. T. Aroyehun, and J. C. Ehiabhili. 2022. Review article on impact of groundwater contamination due to dumpsites using geophysical and physio-chemical methods. *Appl Water. Sci* 12 (6):130. doi: 10.1007/s13201-022-01653-z.

Khan, A. H., M. Sharholy, P. Alam, A. I. Al-Mansour, K. Ahmad, M. A. Kamal, S. Alam, M. N. Pervez, and V. Naddeo. 2022. Evaluation of cost benefit analysis of municipal solid waste management systems. *J. Appl. Psychol.* 34 (4):101997. doi: 10.1016/j.jksus.2022.101997.

Mohammed, Z. B., M. Y. Fattah, and E. Q. Shehab. 2024. Effect of leachate contamination in municipal solid waste on clay liner characteristics. *J. Eng. Res. (Ponta. Grossa).* 12 (2):34–43. doi: 10.1016/j.jer.2023.10.025.

Mulyono, A., A. Suriadikusumah, R. Harriyanto, and M. R. Djuwansah. 2019. Soil quality under agroforestry trees pattern in upper citarum watershed, Indonesia. *J. Educ. Chang. Ecological Engineering* 20 (1):203–13. doi: 10.12911/22998993/93942.

Negi, P., S. Mor, and K. Ravindra. 2020. Impact of landfill leachate on the groundwater quality in three cities of North India and health risk assessment. *Environ. Dev. Sustain.* 22 (2):1455–74. doi: 10.1007/s10668-018-0257-1.

Patel, D. D., D. J. Mehta, H. M. Azamathulla, M. M. Shaikh, S. Jha, and U. Rathnayake 2023. Application of the weighted arithmetic water quality index in assessing groundwater quality: A case study of the South Gujarat region. *Water* 15 (19):3512. doi: 10.3390/w15193512.

Pestana, C. J., L. A. Lawton, and T. Kaloudis. 2020. Removal and/or destruction of cyanobacterial taste and odour compounds by conventional and advanced oxidation processes. *Water Treat Purif Cyanobacteria cyanotoxins* 207–30.

Rai, S. K., R. Xalxo, T. K. Patle, A. Verma, R. Chauhan, and P. K. Mahish. 2023. Analyzing contamination of heavy metals-AAS and fluorescence spectroscopy. In *Heavy metals in the environment: Management strategies for global pollution*, eds. D. K. Verma, C. Verma, & P. K. Mahish, 167–204. American Chemical Society.

Shankar, S., and Shikha. 2017. Management and remediation of problem soils, solid waste and soil pollution. *Princ Appl Environ. Biotechnol Sustain Future* 143–71.

Zhang, X., Y. Zhang, P. Shi, Z. Bi, Z. Shan, and L. Ren. 2021. The deep challenge of nitrate pollution in river water of China. *Sci. Total Environ.* 770:144674. doi: 10.1016/j.scitotenv.2020.144674.

Journal of Engineering Research and Application
https://dx.doi.org./10.55953/JERA.2025.04
Volume 4, July 2025
pp 24-26

Assessment of Seismic Performance in Buildings with Plan Irregularities

Vipul Chandra[1*] and Hrishikesh Dubey[1]
[1] Delhi Technological University
* Corresponding Author vipulchandradtu@gmail.com

Abstract:

This study investigates the seismic behavior of reinforced concrete buildings with different types of vertical irregularities using Response Spectrum Analysis (RSA). Both regular and H-shaped plan irregular buildings were modeled, each with a footprint of 20x15 meters and a typical floor height of 3.2 meters, excluding the ground floor, for an 8-storey (G+7) structure. The seismic performance under a earthquake conditions was evaluated based on how stiffness, mass, and strength are distributed throughout the structure. The analysis compares plan-irregular building models featuring varying vertical irregularities. All models were analysed using STAAD.Pro V8i software.

Key words: Base shear; frequency; displacement; Vertical irregularities; Staad Pro.

1. Introduction

Structures with geometric or structural discontinuities are prone to localized concentrations of stress and deformation during seismic events. These discontinuities often occur at junctions or offsets in geometry, leading to an increased likelihood of member failure and potential structural collapse at these weak points [1]. The response of a building to seismic activity is influenced by the chosen method of structural analysis, which varies depending on factors such as the building's importance, function, and associated construction costs. Analytical techniques range from linear static analysis to more advanced nonlinear dynamic methods, each offering different levels of accuracy and computational demand [2].

The seismic performance of a building is largely governed by several key parameters, including lateral stiffness, strength, ductility, and the simplicity of the structural layout. Buildings with a regular and symmetric geometry—characterized by a uniform distribution of mass and stiffness across both the plan and elevation—tend to exhibit better seismic behavior and suffer less damage during earthquakes [3]. In contrast, irregular structures often display uneven load paths and unpredictable dynamic responses, making them more vulnerable under seismic loads.

Despite the known advantages of regular configurations, contemporary architectural and urban demands—driven by increasing population densities, space constraints, and aesthetic considerations—have led to a rise in the design and construction of vertically and horizontally irregular buildings. Consequently, understanding and addressing the seismic vulnerabilities associated with such irregularities has become a critical area of research and practice in earthquake engineering [4].

In seismic design, the structural configuration of a building significantly influences its ability to withstand lateral loads. Among various irregularities, torsional irregularities are

www.jera.co.in
ISSN2583-3987

particularly critical due to their tendency to cause rotational motion of the structure's floor diaphragm, which can lead to uneven force distribution and localized failures. Torsion in buildings generally arises when the center of mass and the center of stiffness do not align, resulting in eccentric lateral displacement during seismic activity [5].

Buildings with asymmetric layouts or non-uniform stiffness in plan tend to exhibit excessive torsional responses. These irregularities are often unavoidable in modern architecture due to spatial constraints or aesthetic preferences. As a result, torsional effects have garnered significant attention in seismic design codes and structural research [1]. It has been observed that the presence of torsional irregularity can amplify the seismic demand on edge columns and walls, especially in buildings with rigid diaphragms, where the floor acts as a single unit transferring rotational effects to vertical load-resisting members [3].

The role of the diaphragm usually the floor or roof slab—in distributing seismic forces across a structure is equally crucial. Diaphragms are classified as rigid, semi-rigid, or flexible, based on their relative in-plane stiffness compared to vertical members. In structures with rigid diaphragms, such as those with concrete slabs, seismic forces are effectively transferred to shear walls or moment-resisting frames. However, if the diaphragm is flexible, as seen in some wood or steel structures, the lateral load transfer becomes less predictable and more susceptible to localized failures [6].

The interaction between diaphragm flexibility and torsional response adds another layer of complexity. Research indicates that in flexible diaphragms, torsional effects are less pronounced due to partial decoupling between lateral and rotational displacements. However, this often leads to increased displacement demands on individual frames, compromising structural integrity [7]. Conversely, in rigid diaphragms, while torsional rotation is more uniform, the resulting stress concentrations can become problematic without adequate detailing and reinforcement.

To address these challenges, modern design guidelines—such as those provided by the IS 1893 (Part 1): 2016 and ASCE 7-16—recommend limiting torsional irregularities through configuration control and provide amplification factors for design forces in edge members. Moreover, the use of dual systems or supplemental damping has been proposed as a means to counteract torsional effects in both flexible and rigid diaphragm systems [**8**]. The analysis compares plan-irregular building models featuring varying vertical irregularities. All models were analysed using STAAD.Pro V8i software.

2. **Modelling**

In the limit state design of reinforced concrete structures, the following load combinations shall be accounted for building presented in fig.1 and fig.2.

- 1.5(Dead load + Impose load)
- 1.2(Dead load + Imposed load ± Earthquake load)
- 1.5(Dead load ± Earthquake load)
- 0.9Dead load ± 1.5 Earthquake load

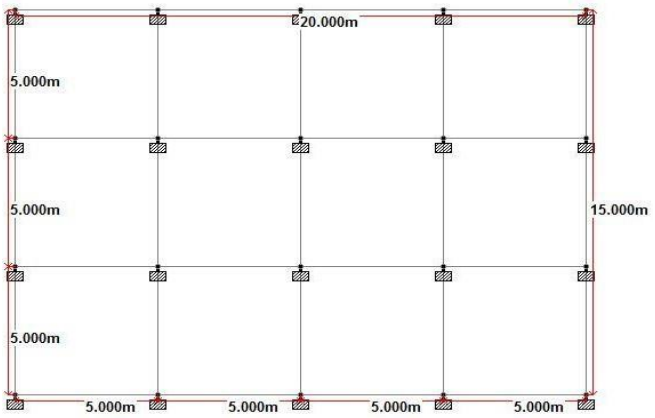


Fig.1 Regular Building Plan

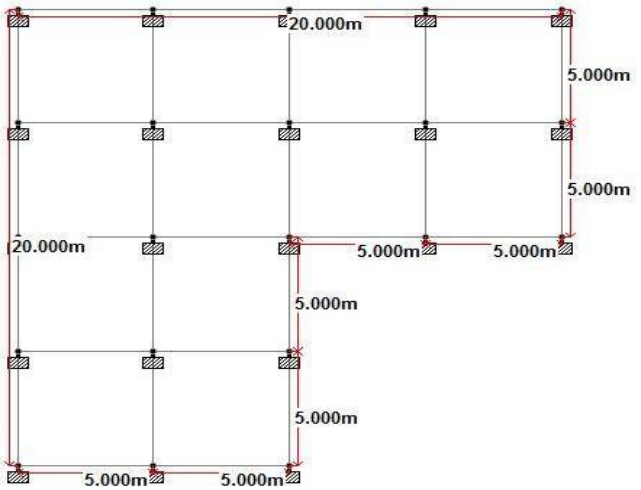


Fig.2 Irregular Building Plan

3. Result and Conclusion:

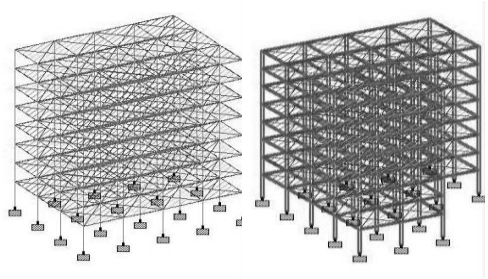


Fig 3: Loading Applied on building in Isometric View

The loading applied for the various load case is presented in figure 3.

An in-depth analytical evaluation was conducted on multi-storey (G+7) reinforced concrete buildings with both regular and irregular geometries using the Response Spectrum Method, focusing on their behavior under seismic loads.The structural models shared identical overall height and plan area, ensuring that the primary variable influencing seismic performance was the plan shape and degree of irregularity. It was consistently observed that as the geometric irregularity increases, the base shear capacity of the building tends to reduce indicating a diminished ability to resist lateral forces effectively. At the same time, lateral displacement was found to increase with greater irregularities, which may lead to serviceability concerns and potential instability if not properly addressed through design.

REFERENCES

[1] A. K. Chopra, Dynamics of Structures: Theory and Applications to Earthquake Engineering, 4th ed. Upper Saddle River, NJ: Prentice Hall, 2012.

[2] Federal Emergency Management Agency (FEMA), NEHRP Recommended Provisions for Seismic Regulations for New Buildings and Other Structures, FEMA 450, Washington, D.C., 2004.

[3] P. Agarwal and M. Shrikhande, Earthquake Resistant Design of Structures, 2nd ed. New Delhi, India: PHI Learning Pvt. Ltd., 2007.

[4] IS 1893 (Part 1): 2016, Criteria for Earthquake Resistant Design of Structures – Part 1: General Provisions and Buildings, Bureau of Indian Standards, New Delhi, India, 2016.

[5] R. Clough and J. Penzien, Dynamics of Structures, 3rd ed., Berkeley, CA: Computers and Structures Inc., 2003.

[6] S. M. Rezai and T. Paulay, “Seismic behavior of floor diaphragms in multistory buildings,” Earthquake Engineering & Structural Dynamics, vol. 24, no. 1, pp. 85–98, 1995.

[7] J. Moehle et al., “Seismic Design of Reinforced Concrete Structures,” Bulletin of Earthquake Engineering, vol. 6, no. 3, pp. 355–388, 2008.

[8] Bureau of Indian Standards, IS 1893 (Part 1): Criteria for Earthquake Resistant Design of Structures, New Delhi, India, 2016.

Signal, Image and Video Processing (2025) 19:687
https://doi.org/10.1007/s11760-025-04278-2

ORIGINAL PAPER

Attention-augmented squeeze-and-excitation enhanced mobile network for occluded facial expression recognition in resource-constrained environments

Ashi Agarwal[1] · **Seba Susan**[1]

Received: 7 January 2025 / Revised: 24 April 2025 / Accepted: 16 May 2025
© The Author(s), under exclusive licence to Springer-Verlag London Ltd., part of Springer Nature 2025

Abstract
Creating efficient and lightweight models is crucial for the deployment of automatic facial expression recognition systems in resource-constrained environments like mobile devices and embedded systems. Faces occluded by masks pose an additional challenge to traditional facial expression analysis systems due to missing or hidden information associated with the obscured lower part of the face. Novel deep learning architectures need to be devised that pay more attention to the visible part of the face during training. To address these concerns, this study proposes an enhanced MobileNetV2 architecture incorporating a stack of three attention blocks and three squeeze-and-excitation (SE) blocks at the network output. This method preserves the lightweight architecture of MobileNetV2 while augmenting its feature extraction efficacy, offering a resource-efficient option for implementation in mobile or edge devices and low-power applications. In resource-constrained situations, the model excels due to its low computing cost and excellent accuracy, as evidenced by experimental findings on the benchmark masked facial emotion dataset Masked Extended Cohn-Kanade (MCK +) for fear, contempt, disgust, anger, happiness, sadness, and surprise emotions. The attention-augmented and SE-enhanced MobileNetV2 model achieves an accuracy of 97.94 $\pm$ 4.59%, AUC of 0.9997, F1-Score of 0.9796, Cohen's Kappa of 0.9748, IBA of 0.9584, Precision of 0.98, Recall of 0.98 and MCC of 0.9750, surpassing state-of-the-art deep learning models like InceptionV3, ResNet50, EfficientNetB0, DenseNet121, Xception, NasNet, CNN, as well as other approaches on face emotion recognition. Extensive experiments and ablation studies on several plausible architectural expansions and augmentations of the MobileNetV2 architecture establish the supremacy of the proposed approach.

Keywords Attention · Emotion recognition · Masked faces · MobileNet · Resource efficient deep learning · Squeeze-and-excitation networks

1 Introduction

Face emotion recognition, also known as facial expression recognition, is crucial for applications like human–computer interaction, surveillance, and healthcare. Facial expressions account for almost 55% of emotional cues, which is particularly important for people who have trouble communicating verbally, such as babies and the elderly [1, 2]. Facial emotion recognition has advanced dramatically over the last few decades, with deep learning approaches at the forefront of contemporary developments. Convolutional Neural Networks (CNNs) have achieved great success in this arena. However, typical CNN architectures sometimes struggle to capture fine-grained facial traits which are critical for differentiating delicate emotions, particularly when a mask conceals the bottom half of the face.

VGG, ResNet, and Inception are examples of architectures that have achieved high accuracy on many benchmarks by learning complicated hierarchical features [3, 4] straight from raw pixel data. MobileNetV2 [21] is a popular lightweight deep neural network suitable for mobile devices, that achieves fast and accurate classification as compared to several deep learning models [5]. It provides an efficient network architecture tailored for mobile and embedded applications. MobileNetV2 expands on the success of its predecessor, MobileNetV1 [22], by incorporating

✉ Ashi Agarwal
ashiagarwal31@gmail.com

[1] Department of Information Technology, Delhi Technological University, Delhi, New Delhi 110042, India

Published online: 05 June 2025

numerous major improvements such as inverted residuals, which connect the input directly to the output, therefore reducing computing complexity and increasing network performance. Linear bottlenecks help to maintain information flow while preventing the loss of representational power. This is very useful for capturing fine-grained features in images. Depthwise-separable convolutions can greatly reduce the number of parameters and computing burden while retaining high accuracy by breaking them down into a depthwise convolution followed by a pointwise convolution. Width multiplier allows the alteration of the network's width to trade-off between computational cost and accuracy.

The key contributions of this research are listed as:

a) An enhanced MobileNetV2 architecture, integrating feature extraction, attention mechanism, and feature recalibration, is designed for deployment on lightweighted edge devices.
b) The proposed model focuses on most informative unobscured facial features (such as the eyes, brow, and forehead) with the help of cascaded attention and Squeeze-and-Excitation (SE) blocks at the network output, which improves the prediction accuracy without appreciably adding computing cost.
c) Comprehensive experimentation on the Masked Extended Cohn-Kanade (MCK +) dataset proves that the proposed model outperforms state-of-the-art deep learning models on face emotion recognition by achieving the highest classification accuracies for seven human emotions.
d) An extensive ablation study is conducted to highlight the impact of attention and Squeeze-and-Excitation blocks on system performance. The organization of the paper is: Sect. 2 highlights related works. In Sect. 3, we present the proposed methodology. Section 4 discusses the experimental setup and results. The conclusion in Sect. 5 marks the end of the paper.

2 Related works

Despite of advancements in computer vision and deep learning [6], masked face emotion recognition remains a challenging task with several hurdles, including differences in mask designs, lighting circumstances, and placement of the mask. To overcome this issue, researchers have examined numerous strategies, including focusing on exposed regions that entail extracting characteristics from the face's visible components, such as the eyes, brows, and forehead. Mask-invariant feature learning refers to developing models that can capture underlying face structures despite mask fluctuations. Generative algorithms produce synthetic, unmasked facial images to supplement training data.

Hybrid methods integrate multiple strategies to increase overall performance. Researchers have experimented with traditional deep learning models to recognize facial emotions. Akhand et al. [7] utilized a deep CNN model with a transfer learning approach to categorize emotions with an accuracy of 96.51% on the KDEF dataset and 95.92% on the JAFEE dataset. Desai et al. [8] proved the efficiency of the EfficientNetB5 model when compared with ResNet50, DenseNet121, and Xception achieving an accuracy of 84.39%. Urnisha et al. [9] demonstrated that the MobileNetV2 model performs well on the FER 2013 dataset with 94% accuracy, making it suitable for mobile devices with low computational cost and high accuracy. Attention mechanisms have been demonstrated by Zulqarnain et al. in [10] to enhance accuracy by focusing on crucial face traits while disregarding extraneous background information. Bah and Xue [11] proved the significance of the residual block (in collaboration with CNN model) in recognizing emotions on the CK + [12] dataset with an accuracy of 97%.

Ensemble learning improves accuracy and resilience by combining predictions from many models. Ensemble approaches in FER may be used to integrate the strengths of many architectures, including CNNs, attention-based models, and Squeeze-and-Excitation (SE) blocks [13]. Salama et al. [14] established the improved performance of ensemble models for emotion recognition in their study.

There are several works carried out by different researchers in the field of occluded expression facial recognition. Mukhopadhyay et al. [33] used RAF-DB, AffectNet and self-made real-world occluded datasets to prove the accuracy of the proposed ACNN (CNN model with attention). Lu et al. [34] performed an experimental analysis on RAF-DB and AffectNet dataset for Wasserstein GAN model. Kotsia et al. [35] investigated the effect of partial occlusion on facial emotion recognition using Gabor based texture information extraction model on the Cohn-Kanade dataset. Ding et al. [36] focused on discarding corrupted features from occluded regions using landmark guided attention to generate attention maps that guide whether the extracted feature is occluded or not. Wang et al. [37] made use of both synthetic and realistic occlusion-based databases for their experiments, like RAF-DB, AffectNet, CK + , FED-RO, and VGGFace2, for evaluating different models for enhanced representation learning. Wang et al. [38] proposed a region attention-based model and tested the feasibility of their approach on RAF-DB, AffectNet, FERPlus and SFEW datasets. The model proved its supremacy by aggregating and embedding the region features extracted by the CNN model. Gao et al. [39] explored the multi-headed attention mechanism for their transformer-based model and conducted the evaluation on RAF-DB and AffectNet datasets. In a distinctive approach,

Poux et al. [40] reconstructed the occluded facial regions of the images in CK + dataset by using auto-encoder with skip connections. Advanced representation learning methods like Deep Belief networks and Hopfield networks were integrated with Lanczos interpolation in [41] for occlusion-aware facial expression recognition. Action units were integrated with Graph Convolutional Network in [42], and used along with transformer-based temporal overlap module to automatically detect facial expressions. High quality feature extraction is accomplished in [43] using a dynamic region feature network that learns multiple region-specific features for efficient facial expression recognition.

3 Methodology

3.1 Outline of the proposed model

In this paper, we present the proposed attention-augmented squeeze-and-excitation enhanced MobileNetV2 architecture for masked facial expression recognition that employs a cascade of three attention layers [15] and three Squeeze-and-Excitation (SE) blocks [13] at the network output. MobileNetV2 is a lightweight convolutional neural network recognized for its resource efficiency and superior performance on mobile and embedded devices. Here, the pre-trained lightweight MobileNetV2 model acts as a feature extractor, while the attention layers employ attention mechanism to focus on the relevant uncovered facial regions. The SE blocks serve as a feature recalibrator that emphasize on informative features while suppressing non-informative features. The proposed architecture, shown in Fig. 1, is intended to successfully address the difficulty of identifying facial expressions in masked faces. Attention and SE blocks are intentionally placed subsequent to the feature maps to emphasize significant channels and relevant facial traits.

3.2 Efficient feature extraction using depthwise and pointwise convolutions

MobileNetV2 uses depthwise separable convolutions, which are substantially less computationally complex than standard convolutions. This approach allows the model to function effectively in resource-constrained contexts with limited processing power and memory. The network design starts with a fully convolutional layer, which is followed by a series of bottleneck layers that perform depthwise and pointwise convolutions as shown in Eqs. (1, 2). This structure allows the model to maintain high accuracy while using minimal resources, making it ideal for real-time applications on edge devices.

$$Y_d[n,\, c,\, i,\, j] = \sum_{k=0}^{k-1}\sum_{k=0}^{k-1} X[n,\, c_k,\, l] * D[c,\, m,\, n,\, 0] \tag{1}$$

$$Y[n,\, c,\, i,\, j] = \sum_{k=0}^{C_{in}-1} Y_d[n,\, k,\, i,\, j] * P[k,\, c,\, 0{,}0] \tag{2}$$

Equation (1) shows the depthwise convolution that computes the output value at location (i, j) of channel c in batch n. Here, Y_d represents the depthwise convolution that produces

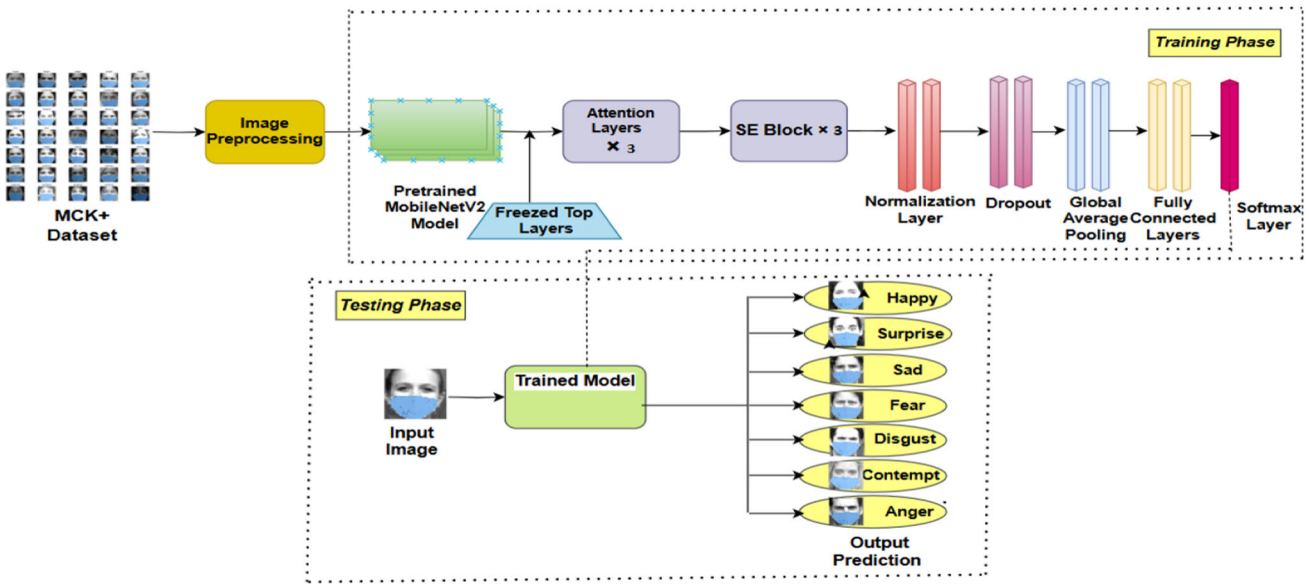


Fig. 1 Proposed enhanced MobileNetV2 architecture with stacked attention and SE blocks for masked face emotion recognition in constrained environments

the output tensor. X represents the input tensor. c_k represents the k^{th} channel. D represents the depth- wise convolution kernel. k and l are the input spatial coordinates. It entails adding the products of relevant elements from the input tensor X and the depthwise kernel D over an area determined by the kernel size K. Equation (2) exhibits the pointwise convolution that computes the output value at location (i, j) of channel c in batch n. Here, Y represents the final output tensor. Y_d is the pointwise convolution's input (or depthwise convolution's output). P represents the pointwise convolution kernel. n represents the batch index. c represents the output channel index. i and j are the spatial coordinates. k represents the input channel index. It entails adding the products of relevant elements from the input tensor Y_d and pointwise kernel P. The pointwise convolution combines the channels from the depthwise convolution to create a new set of channels.

3.3 Enhanced MOBILENETV2 architecture

The proposed attention-augmented squeeze-and-excitation enhanced deep learning architecture, with MobileNetV2 as the backbone network, excels in extracting discriminative feature representations from the masked facial image. We incorporate exclusive attention blocks into the design to increase the model's ability to recognize emotions from partially occluded faces. These attention blocks are positioned after the flatten layer of the base MobileNetV2 model, that functions as the feature extractor. Each attention block starts with a convolutional layer and ends with a sigmoid activation function given by Eq. (3).

$$\sigma(x) = \frac{1}{1 + e^{-x}} \tag{3}$$

Here, $\sigma(x)$ is the sigmoid function of x, and e is Euler's number (around 2.71828). x represents the input value.

The convolutional layer creates an attention map that highlights the essential portions of the feature map, while the sigmoid function acts as a gating mechanism. The attention block's output is the element-wise multiplication of the input and attention maps. This procedure enables the network to concentrate more on the area's most likely to contain key facial traits, even when portions of the face are obscured. Three attention blocks are placed strategically at the network output. These blocks ensure that the model can stress key information at various phases of feature extraction, increasing its robustness against mask occlusion as shown in Eqs. (3, 4).

$$Attention = X \odot \sigma(W * X + b) \tag{4}$$

Here, W denotes the weights of the convolutional layer calculated by Eq. (4). b represents the bias term. X represents the input tensor. The attention weights are computed as the softmax of the dot product of query (Q) and key (K) values divided by the scaling factor, as shown in Eq. 5.

$$Attention_{Weight} = Softmax\left(\frac{QK^T}{\sqrt{(d_k)}}\right) \tag{5}$$

Following the attention module, three SE blocks are inserted to improve channel-wise feature recalibration. SE blocks are intended to adaptively adjust channel-specific feature responses by explicitly modeling channel interdependencies. The mathematical description of SE block can be represented with the help of assumptions. Let $V = [v_1, v_2,., v_h,., v_C]$ denote the learned set of filter kernels, where v_h refers to the parameters of the 2D spatial kernel corresponding to the h^{th} channel of the input X, assuming the total number of channels is$C$. The transformed output obtained after convolution operation (denoted by *) can be expressed as

$$u = v * X = \sum_{h=1}^{C} v_h * X_h \tag{6}$$

An SE block commences with global average pooling, which lessens each feature map to a single value indicating the feature's average occurrence across spatial dimensions. This is followed by two completely linked layers: the first decreases dimensionality, while the second restores it to its original number of channels.

The result is a collection of channel-wise weights generated using a sigmoid activation function and multiplied by the original feature maps. This procedure prioritizes more informative channels while suppressing less crucial ones. SE blocks are strategically placed after attention blocks to enhance feature representation throughout the network. By repeatedly applying SE blocks, the model dynamically prioritizes the most relevant channel-wise information, leading to a progressive refinement of feature learning. We use Layer Normalization and Dropout layers to stabilize the learning and increase the model's generalization.

The final segment of the model is the classification head, which is responsible for classifying the input into one of the established emotion classes. The Global Average Pooling layers reduce each feature map to a single value by calculating the average across all spatial dimensions. This decreases the dimensionality of the feature maps, allowing the dense layers to perform more effectively. Fully Connected Layers with 512 units and ReLU activation are utilized to extract complicated patterns from pooled information. This layer converts the feature representation into a format appropriate for categorization. The final output layer is a dense layer, and uses the softmax activation function. This layer generates a probability distribution over the emotion classes, showing

the model's confidence in each class. The Adam optimizer is used to build the model, which combines the benefits of AdaGrad and Root Mean Square Propagation (RMSProp), making it ideal for this challenging task. The loss function used is categorical crossentropy, which is suitable for multi-class classification. The model is trained using a typical backpropagation approach, with weights iteratively updated to minimize the loss function. The integration of attention mechanisms and SE blocks into the MobileNetV2 architecture empowers the model to effectively discern emotions from masked faces, demonstrating superior performance in this demanding task.

4 Details of experimental setup and the results

The Masked Extended Cohn-Kanade (MCK +) Dataset[1] includes images of people with a range of expressions on their faces with mask, including fear, contempt, disgust, anger, happiness, sadness, and surprise. All experiments were run on the Kaggle platform, using the GPU T4 and its accompanying RAM. The Python framework was utilized in conjunction with Tensorflow and the Keras API. While the pre-trained MobileNetV2 was trained on the ImageNet Dataset, the proposed model was developed and trained using the following parameters: (i)Input Image Size: To meet MobileNetV2 input criteria, all images were resized to 224 × 224 pixels. (ii)Batch Size: During training, a batch size of 32 was employed, allowing the model to learn efficiently without overflowing the memory. (iii)Epochs: The model was trained for ten epochs. This value was chosen after noticing the convergence of the loss in preliminary experiments. (iv) Optimizer: The Adam optimizer was employed with a learning rate of 0.001. Adam combines the benefits of AdaGrad and RMSProp, making it ideal for dealing with sparse gradients and striking a balance between exploration and convergence. (v) Categorical Crossentropy was chosen as the loss function because it works well with multi-class classification tasks. (vi) The attention block function is used to apply a convolution layer followed by element-wise multiplication with the original input. The SE block method was used to calibrate channel-wise feature responses. (vii) Dataset Split and validation: The MCK + dataset was split into 60–40 ratio for training and testing respectively with tenfold cross validation as the dataset was not likely balanced. To verify the performance of our proposed model, experimentation was performed with different pre trained models such as InceptionV3, ResNet50 EfficientNetB0, MobileNetV2, DenseNet121, Xception, NasNet, CNN.

[1] https://www.kaggle.com/datasets/mdfahimfaisal/ck-on-mask

4.1 Comparative analysis of state-of-the-art methods with the proposed model

We first investigate the performance of multiple state-of-the-art deep learning models [7–9, 16] for masked face emotion recognition in constrained environments with limited resources. These models comprise a set of conventional deep learning architectures including InceptionV3 and ResNet50, as well as newer models like MobileNetV2 and EfficientNetB0, that have been adapted for masked face emotion recognition in recent times [21]. The major performance indicators used in the analysis include accuracy, AUC (both weighted and macro), F1- score, Cohen's Kappa, Index of Balanced Accuracy (IBA), precision, recall, and Matthews Correlation Coefficient (MCC). F1-score, which is harmonic mean of recall and precision, can be represented mathematically as

$$F1 - score = 2 \times \frac{Recall \times Precision}{Recall + Precision} \tag{7}$$

Precision identifies how many true predictions are actually true, and is given by

$$Precision = \frac{TP}{TP + FP} \tag{8}$$

Recall measures the ability of a model to identify all the positive instances, and is given by

$$Recall = \frac{TP}{TP + FN} \tag{9}$$

Cohen's Kappa measures the agreement between predicted and true labels, and is mathematically formulated as

$$Cohen's Kappa = \frac{A_o - A_e}{1 - A_e} \tag{10}$$

where, A_o and A_e are the observed and expected distributions of predicted and true labels, respectively.

Index of Balanced Accuracy (IBA), to balance the accuracy by using Eq. (11)

$$IBA = (1+ \propto *(Recall - Specificity) * Gmean^2) \tag{11}$$

where, $\propto$ is in the range of 0 to 1 depending on dominance .

Matthews Correlation Coefficient (MCC), used for measuring the agreement between observed and predicted classifications for imbalanced datasets is given by

$$MCC = \frac{(TN \times TP) - (FN \times FP)}{\sqrt{(TP + FN)(TP + FP)(TN + FN)(TN + FP)}} \tag{12}$$

Table 1 Performance analysis of proposed model and state-of-the-art deep learning models for masked face emotion recognition

Model	Accuracy (%) (Mean ± SD)	AUC	F1-score	Cohen's Kappa	IBA	Precision	Recall	MCC
InceptionV3 [6]	78.39 ± 0.0104	0.9597	0.79	0.7483	0.5442	0.73	0.77	0.748
ResNet50 [24]	36.82 ± 0.029	0.8649	0.3809	0.3117	− 0.3818	0.36	0.31	0.3619
EfficientNetB0 [24]	19.46 ± 0.365	0.5640	0.112	0.0	− 0.7142	0.04	0.04	0.0
MobileNetV2 [25]	88.62 ± 0.790	0.9940	0.9035	0.8862	0.7298	0.87	0.86	0.8876
DenseNet121 [26]	74.78 ± 0.5734	0.9647	0.7648	0.7199	0.4422	0.73	0.72	0.7251
Xception [27]	68.18 ± 0.8512	0.9492	0.7642	0.7122	0.1832	0.73	0.73	0.788
NasNet [28]	71.58 ± 0.3340	0.9220	0.7142	0.6492	0.4346	0.66	0.72	0.6499
CNN [29]	79.16 ± 0.4427	0.9580	0.8406	0.8095	0.4798	0.86	0.74	0.8128
ResNet + LSTM [30]	40.40 ± 3.57	0.50	0.11	0.0	− 0.71	0.04	0.14	0.0
EfficientNetB0 + Multiheaded self-attention (MHSA) [31]	40.40 ± 3.44	0.49	0.11	0.0	− 0.71	0.04	0.14	0.0
CNN + LBP [32]	94.83 ± 4.59	0.9985	0.94	0.9372	0.8967	0.93	0.95	0.9381
Ours	97.94 ± 4.59	0.9997	0.9796	0.9748	0.9584	0.98	0.98	0.9750

The comparative examination of these deep learning models for face emotion recognition offers a diverse set of performance indicators, emphasizing each model's strengths and draw- backs. In general, models like MobileNetV2 and the baseline CNN perform well across most parameters, showing that they are suitable for complicated classification tasks such as face expression identification. Their excellent accuracy, balanced precision, recall, and strong AUC scores, indicated that they can accurately catch the intricacies of many emotional expressions.

On the other hand, models like ResNet50 and EfficientNetB0 perform much worse in terms of accuracy and class discrimination in a constrained environment. These findings imply that without additional optimization or fine-tuning, these designs may not be suitable for this application. Table 1 shows that the performance of several deep learning models on the face emotion identification task differs greatly, as evidenced by the metrics used.

Table 1 compares the performance of several deep learning models, and MobileNetV2 emerges as the best performer, with the greatest accuracy (88.62%) and a near perfect weighted AUC (0.9940). InceptionV3, DenseNet121, and Xception all produce impressive results, however, they fall short of MobileNetV2. In comparison, ResNet50 and EfficientNetB0 perform badly, with low accuracy and inconsistent metrics. CNN and NasNet [17] perform moderately well, but MobileNetV2 remains the most trustworthy model for the classification assignment, and we use this network as the backbone for the attention-augmented squeeze-and-excitation deep architecture proposed in this work.

4.2 Ablation study

An ablation study was performed for the proposed enhanced MobileNetV2 architecture with attention and SE blocks. Table 2 illustrate the experimental results comparing and contrasting different architectural extensions and augmentations to the MobileNetV2 architecture. The ablation study systematically examines the effect of various enhancements to the MobileNetV2 architecture, and other models on masked facial emotion identification. The results prove that including attention mechanisms, CBAM [18], and SE blocks greatly enhances performance, with MobileNetV2 enhancements regularly overcoming other models. MobileNetV2 achieves the maximum accuracy (97.96%) with three SE blocks and attention, which is optimized with a reduction ratio of 32. Simpler models, such as CNNs with attention blocks, perform badly, emphasizing the need for sophisticated and carefully tuned architectures for this job. Overall, the study underlines how incorporating advanced components such as attention mechanisms and SE blocks improves model accuracy and dependability.

Figure 2 depicts the overall performance of the proposed model for all emotions (anger, contempt, disgust, fear, happiness, sadness, and surprise) in the form of a confusion matrix. The confusion matrix indicates that the proposed model produced high true positive rates for emotions such as "surprise," which was accurately detected in all 26 instances, and "disgust," which was correctly categorized 21 out of 22 times. Some inaccuracies are identified, such as two cases of "Anger" being misclassified as "Contempt" and one instance of" Fear" being misclassified as "Disgust", suggesting small

Table 2 Performance analysis of MobileNetV2 architectural extensions with ablation study for masked face emotion recognition

Model	Accuracy (%) (Mean ± SD)	AUC	F1-score	Cohen's Kappa	IBA	Precision	Recall	MCC
MobileNetV2 with attention	95.32 ± 0.917	0.9978	0.9596	0.9496	0.8941	0.95	0.95	0.9500
MobileNetV2 with 2 CBAM*	91.82 ± 0.12	0.9972	0.9279	0.9119	0.8156	0.89	0.91	0.9129
MobileNetV2 with 2 CBAM and SE	94.62 ± 0.115	0.9970	0.9497	0.9469	0.8870	0.95	0.94	0.9375
MobileNetV2 with 2-CBAM, SE and Attention	93.03 ± 0.137	0.9983	0.9376	0.9342	0.8441	0.93	0.92	0.9251
MobileNetV2 with 3-CBAM, SE	93.21 ± 0.137	0.9967	0.9392	0.9242	0.8512	0.95	0.93	0.9248
MobileNetV2 with 3 CBAM and SE and Attention	93.90 ± 0.115	0.9980	0.9496	0.9371	0.8584	0.90	0.93	0.9365
MobileNetV2 with Inception block	74.12 ± 0.34	0.9836	0.7998	0.7564	0.3630	0.83	0.71	0.8262
MobileNetV2 with inverted residual block	64.31 ± 5.74	0.9860	0.7192	0.6515	0.1417	0.76	0.57	0.6812
MobileNetV2 with Self-attention block	71.76 ± 8.02	0.9675	0.7869	0.7366	0.3110	0.66	0.66	0.7416
MobileNetV2 with attention and VAE*	32.11 ± 0.0	0.7774	0.3129	0.2456	−0.3571	0.23	0.24	0.11
MobileNetV2 with SE block	91.99 ± 1.20	0.9979	0.9287	0.9119	0.8228	0.89	0.91	0.9127
MobileNetV2 with 2 SE blocks	94.08 ± 1.14	0.9978	0.9483	0.9370	0.8655	0.90	0.93	0.9378
MobileNetV2 with 2 SE blocks and CA*	93.90 ± 1.15	0.9961	0.9496	0.9371	0.8585	0.90	0.93	0.9380
MobileNetV2 with 3 SE blocks with Attention	96.54 ± 6.88	0.9987	0.9698	0.9623	0.9228	0.96	0.96	0.9627
MobileNetV2 with 2 SE blocks, 3-layer Attention, CA	91.81 ± 1.20	0.9977	0.9294	0.9120	0.8155	0.94	0.94	0.9378
MobileNetV2 with 3 SE blocks with 3-layer Attention	97.94 ± 4.59	0.9997	0.9796	0.9748	0.9584	0.98	0.98	0.9750

false positives and false negatives. These misclassifications are most likely the consequence of feature similarities across emotions, since "Anger" and "Contempt" both have tense facial expressions, making it difficult for the model to discern minuscule differences. Furthermore, occlusions may have disguised vital characteristics, such as the lips or brows, which are important for distinguishing between emotions like "Fear" and "Disgust."

Another factor might be occlusion-induced feature loss and variation in occlusion levels between samples. Although attention methods and SE blocks improve feature extraction, the model may continue to focus on non-discriminative areas, resulting in slight mistakes. Furthermore, intrinsic ambiguities in human expressions, such as emotional overlap, may contribute to these misclassifications. Overall, the model accurately detects a wide range of facial expressions [19, 20], albeit there is some misunderstanding between some comparable emotions.

4.3 Image feature visualization using attention guided grad-CAM

To understand the obtained results in a better manner we have used Attention Guided GRAD-CAM (AG-GradCam), a class-discriminative localization approach that produces

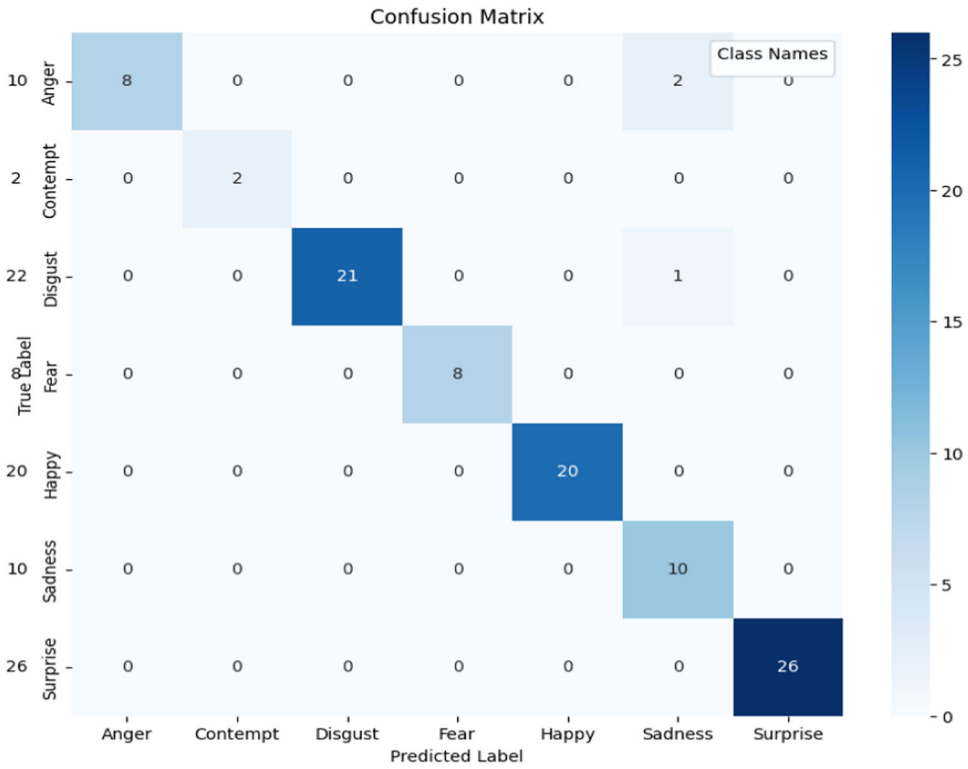


Fig. 2 Confusion matrix of proposed model

visual explanations for any CNN-based network as heatmaps of images without the need for architectural adjustments or retraining [23]. The heatmap of the proposed model is shown in Fig. 3, The color intensities indicate the relative relevance of various face areas in the model's decision-making process.

The red and yellow areas show the greatest activation regions, implying that the model heavily depends on these areas to infer emotions, whilst the blue and green regions suggest lower relevance in feature extraction. The heatmaps constantly highlight the eye area, forehead, and upper cheeks, indicating that the model has evolved to prioritize visual cues when lower-face emotions are concealed. The model highlights wider eyes and raised brows for emotions such as surprise and fear, which are critical for discriminating between these closely similar feelings. The heatmap for sadness displays significant activation around the brows and eye corners, showing that the model relies on mild drooping or furrowing. Similarly, anger and disgust show prominent red areas around the furrowed brows and constricted eyes, indicating aggressive facial muscular tension. Happiness is often represented through a grin; the model adjusts by emphasizing on wrinkles at the eye corners and minor cheek elevations, demonstrating a successful adaptation to mask-induced occlusion. The existence of diffused activation in several heatmaps, particularly for emotions such as disgust, indicates that the model analyzes many upper-face characteristics at the same time while making a decision. Overall, the AG-GradCAM results establish that attention processes allow the model to acquire resilient and adaptable features, resulting in accurate emotion identification even when essential lower-face expressions are hidden.

4.4 Performance analysis in terms of lightweighting parameters

The proposed model has a well-balanced trade-off between computational efficiency and performance, making it an excellent choice for resource-constrained deep learning applications. With an inference time of 0.0035 s, it is one of the quickest models, coming close to EfficientNetB0 (0.003349 s), however with a little larger latency (0.3715 s) than EfficientNetB0 (0.2956 s). The model has a moderate parameter count (9.08 million), which places it between lightweight designs like MobileNetV2 (3.57 million) and more sophisticated models like Xception (22.97 million) and CNN (44.39 million). In terms of CPU use, the proposed model works at 3.3%, which is somewhat higher than DenseNet121 (1.0%) and EfficientNetB0 (0.5%), but substantially lower than ResNet50. The proposed model has the lowest power usage (27.55W) of all investigated envisions, making it suitable for energy-efficient deployments. Furthermore, its highest memory use (56.40 MB) is comparable to most models, avoiding the large memory footprint seen in MobileNetV2 (2513.18 MB). Although the model has somewhat greater latency than EfficientNetB0, it is still

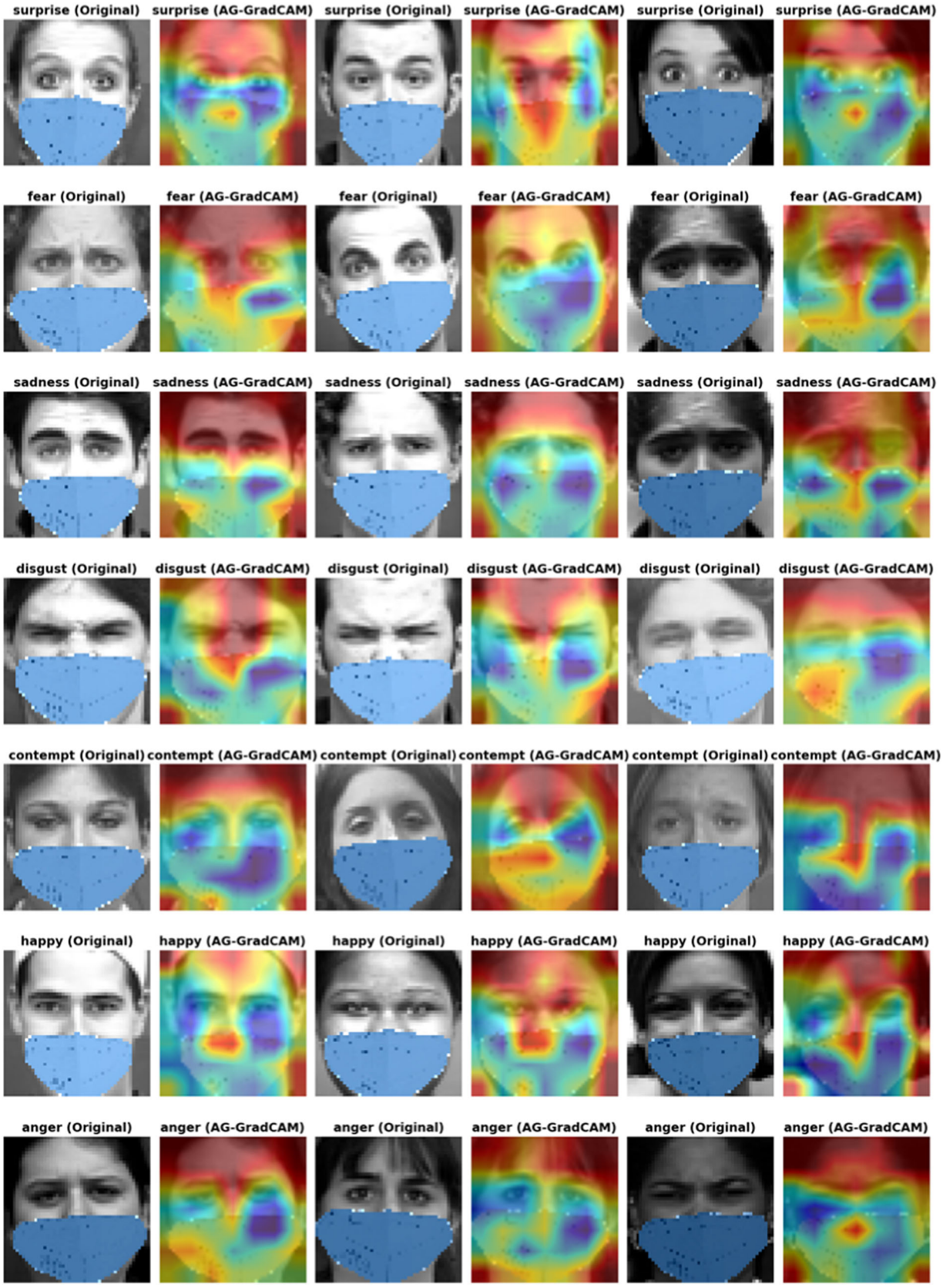


Fig. 3 Heatmap generated through Attention Guided Grad-CAM for the proposed model

Table 3 Performance analysis in terms of parameter-lightweighting

Model	Inference time	Total parameters	CPU usage (%)	Latency (s)	Peak memory usage (MB)	Activation Sparsity (%)	FLOP	Power Consumption (W)
Proposed model	0.0035	9,084,967	3.3	0.3715	56.40	0.0	0	27.55
DenseNet121	0.004297 s	8,094,279	1.0	0.3966	56.41	0.0	0	51.90
EfficientNetB0	0.003349 s	5,368,490	0.5	0.2956	56.40	0.0	0	48.27
InceptionV3	0.088743 s	23,908,135	0.5	0.1164	9.72	0.0	0	37.70
MobileNetV2	0.052165 s	3,576,903	1.2	0.2736	2513.18	0.0	0	38.30
ResNet50	0.072240 s	3,576,903	14.7	0.2588	58.68	0.0	0	32.57
Xception	0.004176 s	22,966,831	0.8	0.4221	56.39	0.0	0	69.71
NasNet	0.062465 s	25,693,063	0.7	0.3563	56.40	0.0	0	66.05
CNN	0.007780 s	44,399,687	0.3	0.2465	56.39	0.0	0	36.00

competitive, especially in circumstances where power efficiency and computing restrictions are critical. Overall, the proposed model strikes the ideal balance between speed, efficiency, and energy usage, making it an appealing option for resource-efficient deep learning applications as depicted in Table 3.

5 Conclusion

Extensive research has shown that deep learning models must not only perform well but also be computationally efficient, particularly in real-world applications in limited contexts such as mobile devices and edge computing systems. In this context, the pro- posed MobileNetV2 architecture incorporating attention mechanisms and SE blocks outperforms classic CNN architectures like as VGG, ResNet, and Inception in masked face emotion recognition tasks. The enhancements to MobileNetV2 enable it to maintain excellent accuracy while significantly decreasing the computational cost associated with typical deep learning models. Unlike models that demand a lot of computing power, the proposed MobileNetV2 is designed for resource-constrained applications where balancing performance and economy is essential. This is accomplished through significant architectural advancements that are optimized for lightweight operations. The ablation investigations validate the resource efficiency of these enhancements, demonstrating that combining SE blocks, and attention mechanisms yields 97.94% accuracy on the benchmark MCK + dataset. This improved MobileNetV2 model distinguishes itself as a highly efficient, accurate solution for masked face emotion identification by increasing performance per unit while decreasing memory consumption. Its ability to work successfully on low-power devices while retaining high accuracy underscores the necessity of building deep learning architectures that are tuned not just for performance but also for efficiency, ensuring that they meet the needs of current real-world applications.

Author Contribution A.A wrote the original draft of the manuscript and carried out the simulations. S.S supervised the project and reviewed and edited the manuscript.

Data Availability No datasets were generated or analysed during the current study.

Declarations

Conflict of interest The authors declare that they have no conflict of interest.

References

1. Zhu, Q., Zhuang, H., Zhao, M., Xu, S., Meng, R.: A study on expression recognition based on improved MobileNetV2 network. Sci. Rep. **14**(1), 8121 (2024)
2. Torcate, A.S., Santana, M.A., Gomes, J.C., Nunes, I.B., Fonseca, F.S., Moreno, G.M., dos Santos, W.P.: Recognition of emotions in the elderly through facial expressions: a machine learning-based approach. In Swarm Intelligence (pp. 119–150). CRC Press (2022)
3. F. Luo, L. Zhao, Y. Wang, and J. Kato, Contrastive representation learning for expression recognition from masked face images, In: Proceedings of the 1st workshop on user-centric narrative summarization of long videos, pp. 23–29, (2022).
4. A. Setyanto, E. Utami, and K. Kusrini, Facial expression recognition with deep learning and attention mechanisms: A systematic review, In: 2024 7th international conference on informatics and computational sciences (ICICoS), pp. 12–17, (2024).
5. Nan, Y., Ju, J., Hua, Q., Zhang, H., Wang, B.: A-MobileNet: An approach of facial expression recognition. Alex. Eng. J. **61**(6), 4435–4444 (2022)
6. A. Agarwal and S. Susan, Emotion recognition from masked faces using Inception-V3, in 2023 5th international conference on recent advances in information technology (RAIT), pp. 1–6, (2023)
7. Akhand, M.A.H., Roy, S., Siddique, N., Kamal, M.A.S., Shimamura, T.: Facial emotion recognition using transfer learning in the deep CNN. Electronics **10**(9), 1036 (2021)

8. K. Desai, H. N. Patel, D. Dashlaniya, P. Desai, M. Shah, and P. Goel, A transfer learning framework for facial emotion recognition: Leveraging pre-trained convolutional neural networks, In 2024 2nd International Conference on Advancement in Computation & Computer Technologies (InCACCT), pp. 663–667, (2024).
9. Urnisha, N.N., Bithi, S.I., Rafee, M.M.S., Remon, N.I., Hasan, M.M., Chowdhury, R.R.: A transfer learning approach for facial emotion recognition using a deep learning model. Int. J. Res. Sci. Innovat. **11**(4), 274–284 (2024)
10. Zulqarnain, M., Ghazali, R., Aamir, M., Hassim, Y.M.M.: An efficient two-state GRU based on feature attention mechanism for sentiment analysis. Multimed. Tools Appl. **83**(1), 3085–3110 (2024)
11. Bah, I., Xue, Y.: Facial expression recognition using adapted residual based deep neural network. Intell. Robot. **2**(1), 78–88 (2022)
12. P. Lucey, J. F. Cohn, T. Kanade, J. Saragih, Z. Ambadar, and I. Matthews, "The extended Cohn-Kanade dataset (CK+): A complete dataset for action unit and emotion-specified expression," In 2010 IEEE computer society conference on computer vision and pattern recognition workshops, pp. 94–101, (2010).
13. J. Hu, L. Shen, and G. Sun, "Squeeze-and-excitation networks," In: Proceedings of the IEEE conference on computer vision and pattern recognition, pp. 7132–7141, (2018).
14. Salama, E.S., El-Khoribi, R.A., Shoman, M.E., Wahby Shalaby, M.A.: A 3D-convolutional neural network framework with ensemble learning techniques for multi-modal emotion recognition. Egypt. Info. J. **22**(2), 167–176 (2021)
15. Zhang, J., Wang, W., Li, X., Han, Y.: Recognizing facial expressions based on pyramid multi-head grid and spatial attention network. Comput. Vis. Image Understand. **244**, 104010 (2024)
16. Neelapu, R., Devi, G.L., Rao, K.S.: Deep learning based conventional neural network architecture for medical image classification. Traitement du Signal **35**(2), 169 (2018)
17. X. Qin and Z. Wang, "Nasnet: A neuron attention stage-by-stage net for single image deraining," *arXiv preprint* arXiv:1912.03151, 2019.
18. Cao, W., Feng, Z., Zhang, D., Huang, Y.: Facial expression recognition via a CBAM embedded network. Procedia Comput. Sci. **174**, 463–477 (2020)
19. Levitan, C.A., Rusk, I., Jonas-Delson, D., Lou, H., Kuzniar, L., Davidson, G., Sherman, A.: Mask wearing affects emotion perception. i-Perception **13**(3), 20416695221107390 (2022)
20. F. Ma, Y. Yuan, Y. Xie, H. Ren, I. Liu, Y. He, F. Ren, F. R. Yu, and S. Ni, "Generative technology for human emotion recognition: A scope review," *arXiv preprint* arXiv:2407.03640, (2024).
21. M. Sandler, A. Howard, M. Zhu, A. Zhmoginov, and L.-C. Chen, "MobileNetV2: Inverted residuals and linear bottlenecks," in Proc. IEEE Conf. Comput. Vis. Pattern Recognit., pp. 4510–4520 (2018)
22. A. G. Howard, "MobileNets: Efficient convolutional neural networks for mobile vision applications," *arXiv preprint* arXiv:1704.04861, (2017)
23. Gradient-weighted Class Activation Mapping (Grad-CAM) is a class-discriminative localization approach that produces visual explanations for any CNN-based network without the need for architectural adjustments or retraining.
24. Mandal, B., Okeukwu, A., and Theis, Y. Masked face recognition using resnet-50. arXiv preprint arXiv:2104.08997. (2021)
25. Liu, M., and Yan, W. Q. Masked face recognition using MobileNetV2. In Proceedings of the 5th International Conference on Control and Computer Vision (pp. 134–138) (2022)
26. Li, B.: Facial expression recognition by DenseNet-121. In: Multi-chaos, fractal and multi-fractional artificial intelligence of different complex systems, pp. 263–276. Elsevier (2022). https://doi.org/10.1016/B978-0-323-90032-4.00019-5
27. Poulose, A., Reddy, C.S., Kim, J.H., Han, D.S.: Foreground extraction based facial emotion recognition using deep learning xception model. In 2021 Twelfth International Conference on Ubiquitous and Future Networks (ICUFN) (pp. 356–360). IEEE (2021)
28. Devika, R., and Divya Udayan, J. Lightweight Deep Learning Facial Expression Recognition Model. In ICT Systems and Sustainability: Proceedings of ICT4SD (pp. 493–503). Singapore: Springer Nature Singapore (2022).
29. Kaur, G., Sinha, R., Tiwari, P.K., Yadav, S.K., Pandey, P., Raj, R., Rakhra, M.: Face mask recognition system using CNN model. Neurosci. Info. **2**(3), 100035 (2022)
30. Guo, H., and Chen, J. Dynamic facial expression recognition based on ResNet and LSTM. In IOP conference series: materials science and engineering (Vol. 790, No. 1, p. 012145). IOP Publishing (2020)
31. Zhou, A., Ma, Y., Ji, W., Zong, M., Yang, P., Wu, M., Liu, M.: Multi-head attention-based two-stream EfficientNet for action recognition. Multimed. Syst. **29**(2), 487–498 (2023)
32. Mukhopadhyay, M., Dey, A., Kahali, S.: A deep-learning-based facial expression recognition method using textural features. Neural Comput. Appl. **35**(9), 6499–6514 (2023)
33. Li, Y., Zeng, J., Shan, S., Chen, X.: Occlusion aware facial expression recognition using CNN with attention mechanism. IEEE Trans. Image Process. **28**(5), 2439–2450 (2018)
34. Lu, Y., Wang, S., Zhao, W., Zhao, Y.: Wgan-based robust occluded facial expression recognition. IEEE Access **7**, 93594–93610 (2019)
35. Kotsia, I., Buciu, I., Pitas, I.: An analysis of facial expression recognition under partial facial image occlusion. Image Vis. Comput. **26**(7), 1052–1067 (2008)
36. Ding, H., Zhou, P., and Chellappa, R. Occlusion-adaptive deep network for robust facial expression recognition. In 2020 IEEE international joint conference on biometrics (IJCB) (pp. 1–9). IEEE (2020).
37. Wang, J., Ding, H., and Wang, S. Occluded facial expression recognition using self-supervised learning. In proceedings of the Asian conference on computer vision (pp. 1077–1092) (2022)
38. Wang, K., Peng, X., Yang, J., Meng, D., Qiao, Y.: Region attention networks for pose and occlusion robust facial expression recognition. IEEE Trans. Image Process. **29**, 4057–4069 (2020)
39. Gao, J., Zhao, Y.: Tfe: a transformer architecture for occlusion aware facial expression recognition. Front. Neurorobot. **15**, 763100 (2021)
40. Poux, D., Allaert, B., Ihaddadene, N., Bilasco, I.M., Djeraba, C., Bennamoun, M.: Dynamic facial expression recognition under partial occlusion with optical flow reconstruction. IEEE Trans. Image Process. **31**, 446–457 (2021)
41. Naveen, P.: Occlusion-aware facial expression recognition: a deep learning approach. Multimed. Tools Appl. **83**(11), 32895–32921 (2024)
42. Zhang, Z., Liu, B., Zhou, J., Wang, H., Liu, X., Lin, B., Chen, T.: Masked facial expression recognition based on temporal overlap module and action unit graph convolutional network. J. Vis. Commun. Image Represent. Represent. **107**, 104398 (2025)
43. Xie, Y., Wang, W., Zhang, Y., Shi, K., Zhang, H., Zhou, N.: Dynamic region features learning for facial expression recognition. SIViP **19**(6), 487 (2025)

Publisher's Note Springer Nature remains neutral with regard to jurisdictional claims in published maps and institutional affiliations.

Springer Nature or its licensor (e.g. a society or other partner) holds exclusive rights to this article under a publishing agreement with the author(s) or other rightsholder(s); author self-archiving of the accepted manuscript version of this article is solely governed by the terms of such publishing agreement and applicable law.

2025 International Conference on
Unmanned Aircraft Systems (ICUAS)
May 14-17, 2025. North Carolina, USA

Autonomous UAV Navigation and Mapping for Accurate Fruit Detection and Counting in Controlled Environments: Simulation and Real-World Validation

Kush Garg[1], Nishant Chandna[2], Somin Aggarwal[3], Chirag Sehgal[4], Arjun Gupta[5] and Prof. Rajesh Rohilla[6]

***Abstract*— This paper presents a solution for high accuracy fruit counting in a Controlled Environment Agriculture (CEA) settings using Unmanned Aerial Vehicles (UAV) implemented in simulation and real-world scenarios. Using the fine-tuned YOLOv8 [1] model for precise object detection and classification along with a custom path planning algorithm for simulation. This approach integrates a hybrid A* Traveling Salesman Problem (TSP) algorithm for efficient 3D path planning. The solution is further extended to the real-life scenario using LiDAR based mapping and point-cloud filtering techniques to avoid recounting of fruits. The suggested methodology increases operating efficiency, reduces dependency on human labor, and improves accuracy. Experimental results, derived from both simulations and real-world testing, achieving a fruit-count accuracy of 98% and 90% respectively, demonstrate the effectiveness of this integrated approach. This solution was implemented in the International Conference of Unmanned Aircraft System (ICUAS) [2] UAV Competition 2024, securing 2nd position in the simulation phase (out of 24 teams) and 3rd overall in the real-world phase.**

I. Introduction

Agriculture has evolved significantly over the centuries, transitioning from traditional, labor-intensive practices to highly autonomous and data-driven systems. Controlled Environment Agriculture (CEA) [3], which involves growing crops in optimized, enclosed settings, has emerged as a promising approach to meet global food demands sustainably. The development in the sector of Unmanned Aerial Systems in recent years has shown promising progress within agricultural domains [4].

This paper introduces an approach that utilizes Unmanned Aerial Vehicles (UAV) to accurately maneuver, detect, localize and count fruits in a highly controlled environment such as a greenhouse.

[1,2,3] *These authors contributed equally to this work.
[1]Department of Applied Mathematics, Delhi Technological University, 110042, New Delhi, India kushgarg_23mc079@dtu.ac.in
[2]Department of Mechanical Engineering, Delhi Technological University, 110042, New Delhi, India nishantchandna_23ch049@dtu.ac.in
[3]Department of Information Technology, Delhi Technological University, 110042, New Delhi, India sominaggarwal_23it161@dtu.ac.in
[4]Department of Computer Science, Delhi Technological University, 110042, New Delhi, India chiragsehgal_co22a3_56@dtu.ac.in
[5]Department of Electronics and Communication, Delhi Technological University, 110042, New Delhi, India arjun222gupta@gmail.com
[6]Department of Electronics and Communication, Delhi Technological University, 110042, New Delhi, India rajesh@dce.ac.in

The problem statement is defined as a task, for a UAV to autonomously count different kinds of fruit in specific plant beds in a CEA. Focusing on high accuracy, minimizing time, and total path to be taken.

Our contributions include: (1) A custom hybrid A* Traveling Salesman Problem (TSP) algorithm [5] for computationally efficient path planning in structured CEA settings reducing path length and travel time. (2) LiDAR-Camera fusion to globally localize the region of interest (here fruit) along with tracking fruits over a series of frames to improve fruit-count accuracy (3) Pipeline which achieves 98% fruit-count accuracy in simulation and 90% accuracy in real-world greenhouse scenario.

We initially ground our proposed methodology by implementing it in a simulated environment. We interpret the environment as a graph-based problem by considering individual plant beds as graph nodes with connections based on their relative spatial positions. On successful creation of nodes, it can be viewed as a single-agent multiple-objective problem, analogous to the TSP. Informed search methods are used that are computationally optimized by incorporating a heuristic, like time, to discover the most efficient path to achieve the goal.

Once the UAV reaches the designated location. Data collected from IMU, RGB and Depth Camera undergoes image angle correction and depth segmentation [6], after which it is sent to a fine-tuned YOLOv8 model [1] for object detection. Subsequently, the detected objects are processed by a custom algorithm that accurately localizes and counts them.

The work was validated through the 2024 International Conference on Unmanned Aircraft Systems' UAV Competition [2], where our team secured 2nd position among 24 international teams [7]. The simulated setting is shown in Figure 1. Accurate fruit counting, amount of time spent traversing, and path length were used as evaluation criteria for the competition.

The challenge environment runs on a Linux Ubuntu 20.04 LTS server running ROS Noetic (Robot Operating System) in Gazebo11.

The second phase of our methodology focuses on implementation in real-world scenario, in a non-ideal environment. For such environments, this approach includes visual tracking of fruit and using LiDAR Camera fusion to localize fruits in global frame ensuring consistent 3D world coordinates independent of the orientation of the UAV. This approach

2025 International Conference on Unmanned Aircraft Systems (ICUAS) | 979-8-3315-1328-3/25/$31.00 ©2025 IEEE | DOI: 10.1109/ICUAS65942.2025.11007888

Authorized licensed use limited to: DELHI TECHNICAL UNIV. Downloaded on June 04,2025 at 05:08:33 UTC from IEEE Xplore. Restrictions apply.

ensures that the same fruit is not counted multiple times. Further point cloud filtering techniques were implemented to improve accuracy.

This approach was extensively tested using data from the 2024 ICUAS UAV Competition final phase. The data comprised an RGB camera feed and its corresponding LiDAR, IMU and GPS data in the form of ROSBAG files. The data was collected from UAV operating in a real-world agricultural environment featuring fruits in yellow and red.

II. Literature Review

Accurate fruit detection and counting in controlled agricultural environments, such as greenhouses, has been an active area of research due to its potential to automate labor intensive tasks and optimize yield estimation.

Traditional computer vision techniques, such as those by [8], relied on fruit detection and color segmentation. However, these approaches tend to fail under partial occlusions and varying lighting conditions. To address these limitations, a combination of YOLOv8-s model and multi-frame fruit tracking is utilized, showing reliable results in both simulation and real-world settings.

For UAV path planning in 3D environments, When determining the optimal sequence of nodes to visit, the problem can be formulated as a TSP. Existing solutions such as brute-force search and genetic algorithms tend to be computationally intensive and greedy algorithms do not provide satisfactory approximations. To overcome these issues, a hybrid approach combining A* [9], the Minimum Spanning Tree algorithm [10], and the Christofides algorithm [11] is proposed, which yields near-optimal solutions with significantly reduced computational complexity.

In context of 3D mapping, researchers have widely us ed LiDAR-Camera sensor fusion approach [12] instead of monocular depth estimation [13] for high precision fruit localization and mapping, but are prone to drift and noise, which this paper solves by assigning confidence values to each fruit cluster tracked over a series of frames, ensuring high precision.

III. Methodology

We build our solution in two stages: The first stage models the problem statement in a simulation environment, this facilitates iterative evaluation of the path planning algorithms and basic testing for fruit detection. The second stage explores transfer of our solution to real-world scenarios.

A. Simulation

The orchard environment, as shown in Fig. 1 features 27 plant beds arranged in 3 rows, and stacked across 3 levels. Each plant bed contains up to three plants with three fruit varieties: Tomato (red), Pepper (yellow), and Eggplant (purple). The front and back side of the plants are asymmetrical, making it possible for a fruit to be visible from the front but not from the back, or from both sides.

The UAV is permitted to navigate along and around the shelves but is restricted from flying between or directly above the plant beds.

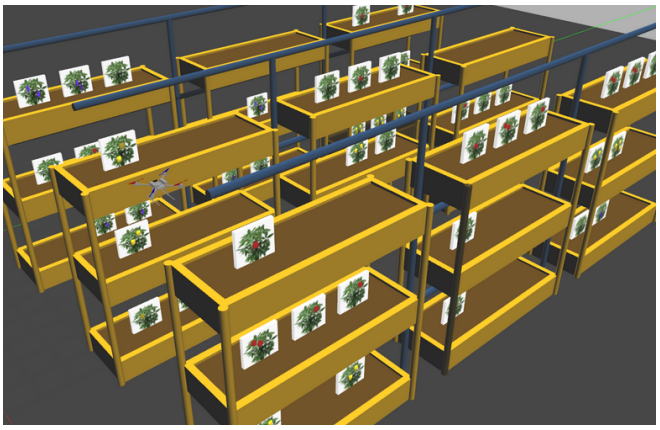


Fig. 1. Simulation Environment

An orchard farm is a systematic and static environment, which allows the use of exact layout and coordinate system of the orchard environment in simulation as well as real-world scenarios. This approach involves simplifying the environment into a grid structure, where each node represents the location of points of interest. The point of interest can be the front or back of the plant and the side nodes to go to the next row of plant beds. The edges connecting these nodes represent permissible paths for the UAV to travel.

There are weighted nodes for each plant bed, front and back separately (2×n nodes for n plant beds), and 6 nodes each on the left and right ends of each row, for traversing to the next row (12×r nodes for r rows). For this scenario consisting of 27 beds and 3 rows, there are a total of 90 nodes. These nodes are calculated as the environment is known a priori and are plotted as shown in Fig. 2.

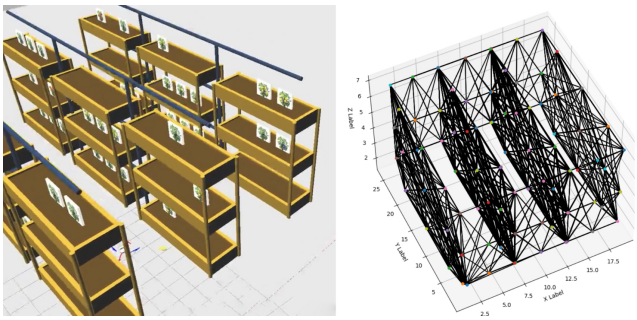


Fig. 2. Environment simplified to grid structure

1) Path Planning: It is essential to count the maximum number of fruits in the least amount of time.
Factors considered in optimality include: 1) Temporal Efficiency : Reducing the time required by UAV to reach nodes. 2) Energy Consumption: Reducing path length and ensuring minimum altitude changes. 3) Computation Resources: Optimizing for efficient use

The aim is to find the best route to visit the front and back of n different plant beds. Path planning is reduced to two sub problems which include finding the shortest path between any 2 nodes along the permissible edges, and the TSP that is to formulate the sequence of nodes to be visited

Authorized licensed use limited to: DELHI TECHNICAL UNIV. Downloaded on June 04,2025 at 05:08:33 UTC from IEEE Xplore. Restrictions apply.

for the optimal path.

a) Determining the optimal path: To find the most optimal path between any 2 nodes, we use the A* algorithm [14] with weighted nodes and multiple heuristic functions.

The algorithm consists of 3 key heuristic functions: The combined heuristic $h(n, g)$ is given by:

$$h(n, g) = h_{\text{d}}(n, g) + h_{\text{yaw}}(n) + h_{\text{altitude}}(n) \tag{1}$$

1) **Euclidean Distance (h_{d})**: Euclidean distance between the current node and goal

$$h_{\text{d}}(n, g) = \sqrt{(x_n - x_g)^2 + (y_n - y_g)^2 + (z_n - z_g)^2} \tag{2}$$

2) **Yaw Requirement (h_{yaw})**: Cost associated with necessary yaw adjustments, k_{yaw} denotes the UAV's yaw angle, expressed in radians.

$$h_{\text{yaw}}(n) = k_{\text{yaw}} \cdot \left| \left((\text{yaw}_{n+1} - \text{yaw}_n + \pi) \bmod 2\pi \right) - \pi \right| \tag{3}$$

3) **Altitude Weight (h_{yaw})**: Higher weights are assigned to nodes at greater altitudes. Here, z_n denotes the altitude of the UAV at the n^{th} node.

$$h_{\text{altitude}}(n) = k_{\text{altitude}} \cdot (z_{n+1} - z_n) \tag{4}$$

The three heuristics are designed with real-world scenarios in mind. Gaining altitude is more time and energy-consuming than descending. In addition, yaw plays a crucial role in time efficiency. Since the UAV must assess both the front and back of the orchard, it occasionally needs to perform a full 180-degree yaw. By factoring in yaw beforehand, we can command the UAV to yaw during its approach to the desired point, optimizing its path planning accordingly, and by considering it as a heuristic, the proposed algorithm can take better consideration when to prefer a node with yaw for an optimal solution.

b) Determining the sequence of nodes: For scenarios requiring inspection of specific plant beds (e.g. fruits at different growth stages), it is essential to determine the optimal sequence for visiting the nodes, minimizing both the total distance traveled and the time taken.

An informed approach is used since traversing the farm row by row is the most efficient method, as completing one row before moving to the next minimizes unnecessary travel. Movement between rows can only occur by exiting at the end of a row, as transitions from the middle are not possible. Returning to a previous row would inevitably increase travel time, so this sequential approach optimizes overall efficiency.

This approach enables a structured traversal of nodes by dividing the farm into distinct segments, traversing each horizontal corridor individually. The algorithm is applied separately to each face.

First we generate a distance matrix for the desired points, where the values in the matrix represent the total weight of the traveled path proposed by the modified A* algorithm. Further we implement a comprehensive optimization informed approach using a combination of Minimum Spanning Tree (MST) and Christofides algorithm.

On nodes of each face, by applying a Minimum Spanning Tree, we determine the initial sequence of nodes to visit. However, this resulted in some nodes having multiple paths from the same node. To address this issue, Christofides algorithm ensures that each node has only two connections, allowing the UAV to maintain a continuous path. This approach leads to highly optimal path due to the simplicity of the environment.

This process returns the sequence of nodes that the UAV should visit on each face and A* Algorithm returns the path between respective nodes. Combining this, a mission is created using the resulting list of nodes and their corresponding yaw angles to be sent to the UAV.

This algorithm reduces the computational complexity significantly for 3D path planning while maintaining robust performance in structured static orchard environments.

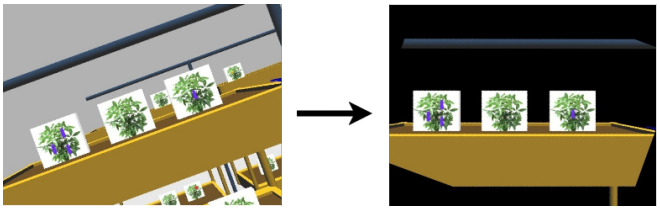


Fig. 3. Application of Depth based filtering and IMU correction on the data captured in the environment.



Fig. 4. Localizing fruits on multiple views of the same plant bed in the simulation environment.

2) Perception: Once arrived at the designated plant bed, the task is to accurately count the number of fruits. The simulation involves three classes of fruits, each represented by a different color. (Tomato (red), Pepper (yellow), and Eggplant (purple)). These fruit beds need to be assessed from two perspectives: front and back. An additional task is to localize the fruits. This step is essential for identifying fruits that are visible from both sides, which may otherwise lead to an inaccurate count for each fruit class.

Since the simulation provides ideal conditions with noiseless data, the model performs accurately with minimal false positives. However, the absence of noise also results in all fruits within the frame being detected, even those located far from the area of interest.

Depth-based filtering is employed using data from a depth camera. Accurate threshold values were determined based on the distance between successive fruit shelves and the variance in UAV positioning, allowing precise segmentation of objects of interest from the rest of the frame, illustrated in Fig. 3.

For orientation correction, the UAV's Inertial Measurement Unit (IMU) data is used to obtain the orientation at the

Authorized licensed use limited to: DELHI TECHNICAL UNIV. Downloaded on June 04,2025 at 05:08:33 UTC from IEEE Xplore. Restrictions apply.

TABLE I

EVALUATION OF OUR APPROACH IN DIFFERENT SCENARIOS WITHIN THE GAZEBO ENVIRONMENT. EACH PLANT BED IS ASSIGNED A NUMBER, AND THE BEDS COLUMN INDICATES THE ONES TO BE VISITED

Sim	Beds	GT Fruits	Predicted	Accuracy
1	8,9,11,16,21,25	12	12	100
2	8,9,16	0	0	100
3	1,15,16,20,21,27	12	12	100
4	3,10,12,23,25,27	11	11	100
5	1,6,13,15,17,19,25	5	5	100
6	1-27	35	33	94.28
7	2,3,4,16,20,24,26	18	18	100
8	1,2,6,7,13,14	22	21	95.45
9	2,3,17,18,20,21,23	17	17	100
10	1,3,5,7,8,13,25	15	15	100
11	4,12,14,17,18,19,22	11	11	100
12	1,3,10,21,22,24,25	15	13	86.67
Mean Accuracy (%):				**98.18**

time of image capture, which helps rotate the image so that plants are properly aligned within the frame. After applying depth segmentation and orientation correction, the YOLO model provides effective localization and classification of the plant beds and fruits.

As the drone reaches a target location, multiple images are captured for pre-processing and detection. The images are filtered based on the number of plant beds present, removing any outlier images where the plant bed count deviates from the median. A similar process is applied to filter images based on fruit counts.

The UAV captures both front and back views of each plant during its visit. These are matched using known ground truth plant positions, and a final image is selected for each view after processing. To determine the effective fruit count, the distance from the front fruit to the left and upper edges of the plant bed, and from the back fruit to the right and upper edges, is considered. If the difference is within a specific threshold, the fruit is counted as the same across both views. To further refine this method and avoid double-counting, the difference in the ratio of distance to width/height is used instead, effectively locating fruits relative to the plant bed. (as shown in Fig. 4)

Now, the fruit count of a shelf is stored, and the drone moves to next shelf. The fruit count of all the shelves is added to give the final fruit count.

3) Results: The Gazebo-based simulation environment provided an ideal space for the development of the path planning algorithm which can be directly applied to any Controlled Environment Agriculture setting resembling the simulation environment. We were able to test both the Path planning and the perception algorithm multiple times in different cases and scenarios (as shown in Table I). The Perception algorithm pre-processes the data so that the YOLOv8-S model can run effortlessly. The fruit counting algorithm prevents any double counting of the fruits, giving an accuracy of 98.18%

The Results are showcased in Fig. 5. A cumulative score

Rank	Team	Eval1	Eval2	Eval3	Eval4	Eval5	Eval6	Bo4 AVG
1	ITUAV	0	89,76	97,33	98,73	0	94,65	95,12
2	UAS-DTU	0	0	97,91	92,21	96,62	92,45	94,80
3	ASL	0	84,89	94,65	85,11	97,18	91,71	92,16
4	AiRoLab	0	0	94,25	93,45	77,28	86,7	87,92
5	AVANT-UFMG	0	0	86,44	83,68	88,58	84,5	85,80
6	AVADERAGH	0	32,03	90,49	89,9	72,13	86,8	84,83
7	UMIC	0	57,70	73,86	93,71	85,68	38,16	77,74
8	SDCNLab	0	72,06	79,96	72,26	69,04	70,25	73,64
9	CVAR	63,05	64,43	70,58	79,7	66,84	66,46	70,40
10	FeikAir	0	0	75,54	68,33	71,05	65,82	70,19

Fig. 5. Performance evaluation of this approach on unseen configurations in the ICUAS'24 UAV Competition.

of 94.80 was achieved, which combines the following factors - Fruit Count Accuracy, Total Time Taken and Total distance traversed.

B. Real-World Scenario

This phase of the methodology focuses on real-world implementation. In contrast to the idealized simulation environment, it introduces the challenge of noisy data leading to double counting of fruits and inaccurate detection. To address these challenges, we propose solutions ensuring system can perform effectively under real-word conditions.

To avoid double counting of the same fruit, we localize the fruits in global coordinate frame. As a result, if the drone revisits the same fruit, the system recognizes it as already detected, preventing any redundant counting.

1) Hardware Configuration: We use a Kopterworx Hawk quadcopter equipped with an integrated Intel RealSense D415 camera [15] for capturing visual data and a Velodyne VLP-16 LiDAR [16] for depth sensing. An RTK-enabled GPS module provides centimeter-level positioning accuracy. The data is recorded from the IMU, GPS, LiDAR, and the video feed from the camera in a ROSBAG, along with their timestamps to ensure synchronization.

2) Coordinate Transformation: In real-world scenarios, the GPS provides latitude and longitude of the drone but for easier analysis, we convert it to local ENU (East North Up) Frame [17] in meters with respect to the origin as the UAV takeoff position geo coordinates. We further transform the ENU coordinates by incorporating the known offset between the GPS module and the LiDAR to ensure that coordinates are in LiDAR's reference frame.

3) Mapping: To accurately map LiDAR points in the ENU Coordinate frame. The LiDAR 3D point cloud captured in UAV's frame is rotated based on UAV's roll, pitch and yaw angles obtained from onboard IMU.

The rotation matrices [18] are applied to point cloud to account for the UAV's orientation in the local ENU frame. The full rotation is represented as:

$$\mathbf{P}_{\text{rotated}} = R_{\text{yaw}} \cdot R_{\text{pitch}} \cdot R_{\text{roll}} \cdot \mathbf{P} \tag{5}$$

Authorized licensed use limited to: DELHI TECHNICAL UNIV. Downloaded on June 04,2025 at 05:08:33 UTC from IEEE Xplore. Restrictions apply.

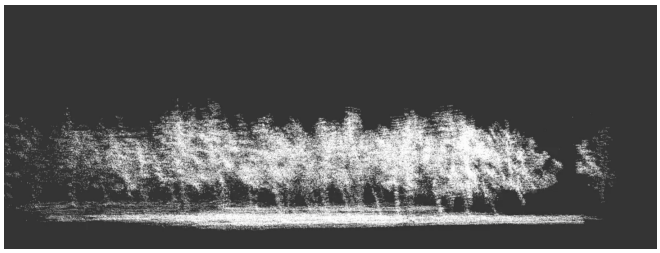


Fig. 6. Environment mapping demonstrated by registering the transformed point cloud over time

Where $R_{\text{roll}}, R_{\text{pitch}}, R_{\text{yaw}}$ are the rotation matrices corresponding to the roll, pitch, and yaw angles of the UAV, and $\mathbf{P}_{\text{rotated}}$ is the transformed point in the rotated frame. The transformed point cloud coordinates are added to the corresponding UAV coordinates obtained from section III-B.2. After plotting the transformed point cloud over time, we get a 3D map of the environment (as shown in Fig. 6)

4) Camera-LiDAR Fusion: 3D coordinates with respect to each pixel of camera image are calculated using Camera-LiDAR Fusion. The first step is calibration [19]. It establishes a common reference frame between the sensors. Calibration enables combining point cloud data from LiDAR and visual frames from the camera feed. Intrinsic calibration was performed using an AprilTag grid for estimation of these parameters. $\mathbf{K_C}$ represents the camera's intrinsic matrix. For extrinsic calibration, the transformation between LiDAR and camera coordinates is represented by:

$$Z_C \begin{bmatrix} u \\ v \\ 1 \end{bmatrix} = \mathbf{K_C} \begin{bmatrix} \mathbf{R} & \mathbf{t} \end{bmatrix} \begin{bmatrix} X_L \\ Y_L \\ Z_L \\ 1 \end{bmatrix}. \tag{6}$$

where $\mathbf{R}$ and $\mathbf{t}$ denote the rotation matrix and translation vector between LiDAR and camera coordinates, respectively.

In the above equation, X_L, Y_L, and Z_L represent x, y, and z corresponding to the LiDAR's frame of reference. Using this approach, we achieved accurate Camera-LiDAR calibration as shown in Fig. 7.

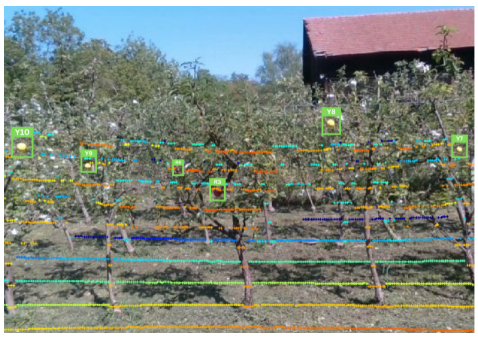


Fig. 7. Demonstration of fruit detection in image frame, followed by localization using coordinate information derived from Camera-LiDAR fusion.

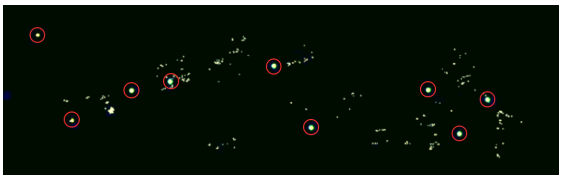


Fig. 8. 3D map showcasing detected fruits within a controlled orchard environment, with each cluster of points representing an individual fruit.

5) Perception: The Real-World implementation required the detection of two kinds of fruit - Yellow and Red. For detection and classification, the pre-trained YOLOv8-S model was used and fine-tuned on data collected from the greenhouse. The model offers a minimal accuracy-speed tradeoff compared to larger variants. It is able to detect both fruits with high accuracy, as shown in Fig. 7; however, some background regions were misclassified as yellow, leading to a few false positives. The confidence scores of such detections were low, thus a confidence threshold value was chosen to filter out these redundant detections.

6) Fruit Tracking and Filtering: The pixels corresponding to detected fruits are used to derive their 3D coordinates, as explained in section III-B.4. These coordinates are then mapped to form 3D fruit clusters in ENU frame, following the methodology detailed in section III-B.3. Further clustering techniques are applied to count the number of fruits. However, due to the dense and bushy nature of the plants, even slight delays in data synchronization lead to false mapping of branches or leaves in place of fruits, leading to an increase in False Positives.

To solve this issue, the center pixel value of each fruit in a camera frame was tracked for 30 consecutive image frames. The pixel value and its corresponding 3D coordinate were saved in memory temporarily. If the change in center pixel value was less than a certain threshold, it made it certain that all the 3D points collected in those respective frames correspond to the same fruit. If the number of points exceeded a threshold of 15 points for each tracked fruit, they were assigned a fruit number, else they were discarded from memory.

The fruits that are assigned a number are now statistically filtered. Points deviating significantly from the mean were removed. This ensured that all faulty 3D points of branches or leaves are filtered out. Now, every new cluster is compared to an existing one, if the new cluster is overlapping another formed cluster, then it is certain that they are the same fruit, if not then the cluster is assigned a new fruit number. This ensured that a fruit is not counted twice in cases where tracking of fruit is lost or the UAV returns back to the same fruit later some point in time, or views the fruit from the back or side angle. This approach filtered noisy data to a great extent as seen in Fig. 8. The small yellow circles depict the noisy point cloud, and large yellow circles correspond to final fruit filtered from the noisy data.

7) Results: The YOLOv8 model produces precise bounding boxes of both kinds of fruits even in the case of

Authorized licensed use limited to: DELHI TECHNICAL UNIV. Downloaded on June 04,2025 at 05:08:33 UTC from IEEE Xplore. Restrictions apply.

occlusions, which with the help of LiDAR-camera Fusion and localization gives the coordinates of the fruit. We were successfully able to count fruits in a real-life environment with a precision of 90.12% for red fruits and 87.21% for yellow fruits (shown in Table II) using the proposed approach by filtering out noisy data. A major challenge was fruits being partially occluded by leaves which led to the mapping of leaves in place of the fruit. This was solved by visually tracking the fruit for consecutive frames and filtering out points away from the dense fruit cluster. Our solution was also validated under non-ideal conditions in the ICUAS 2024 UAV Competition final phase achieving 3rd Position Overall.

TABLE II
EVALUATES OUR APPROACH FOR BOTH YELLOW AND RED FRUITS ACROSS VARIOUS FRUIT CONFIGURATIONS

	Ground Truth		Detected		Precision (%)	
	Yellow	**Red**	**Yellow**	**Red**	**Yellow**	**Red**
Flight 1	12	8	14	10	85.71	80.00
Flight 2	14	14	16	13	87.50	92.86
Flight 3	15	11	17	12	88.24	91.67
Flight 4	11	13	13	12	84.62	92.31
Flight 5	18	16	20	15	90.00	93.75
Mean					**87.21**	**90.12**

IV. CONCLUSION

In conclusion, we present our solution that effectively combines multiple approaches to provide a complete UAV system for automating agriculture activities. Our base methodology was deployed and tested in a simulated environment, helping us to identify the most efficient path-planning strategies. The initial implementation in the simulation also allowed us to refine our basic formulation of the environment. For the task of fruit counting and localization the simulation provided an ideal environment and therefore we observe almost 100 % accuracy in each of the runs for the task of fruit counting and localization. This is due to the fact that all captured photos in the train and test times belong to the same domain causing almost no variation in data.

For the real-world scenario, the part of energy efficiency in path planning was directly transferrable. On the other hand, the challenging tasks include accurate camera-LiDAR calibration despite of slight changes in extrinsic properties. Another important aspect came in with correctly re-identifying the same fruits. To tackle the above mentioned, we presented point cloud filtering strategies and approaches that rely on independent visual and point cloud based tracking for accurate fruit counting.

The future aspects involve implementing the solution in different agricultural settings and making this algorithm more robust and accurate. We will also incorporate the ability to detect the condition of the fruit, its stages of growth, and the presence of insects and weeds to provide the farmer with the entire overview of the agricultural field.

REFERENCES

[1] G. Jocher, J. Qiu, and A. Chaurasia, "Ultralytics YOLO," Jan. 2023. [Online]. Available: https://github.com/ultralytics/ultralytics

[2] I. Association, "Proceedings of the international conference on unmanned aircraft systems (icuas)," in *2024 International Conference on Unmanned Aircraft Systems (ICUAS)*. ICUAS, 2024. [Online]. Available: https://uasconferences.com/2024_icuas/

[3] R. R. Shamshiri, F. Kalantari, K. C. Ting, K. R. Thorp, I. A. Hameed, C. Weltzien, D. Ahmad, and Z. Shad, "Advances in greenhouse automation and controlled environment agriculture: A transition to plant factories and urban agriculture," *International Journal of Agricultural and Biological Engineering*, vol. 11, pp. 1–22, 2018. [Online]. Available: https://api.semanticscholar.org/CorpusID:51783353

[4] J. Kim, S. Kim, C. Ju, and H. Son, "Unmanned aerial vehicles in agriculture: A review of perspective of platform, control, and applications," *IEEE Access*, vol. PP, pp. 1–1, 07 2019.

[5] E. L. Lawler, J. K. Lenstra, A. H. Rinnooy Kan, and D. B. Shmoys, *The Traveling Salesman Problem: A Guided Tour of Combinatorial Optimization*. Chichester, UK: Wiley, 1985.

[6] M. Antić, A. Zdešar, and I. Škrjanc, "Depth-image segmentation based on evolving principles for 3d sensing of structured indoor environments," *Sensors*, vol. 21, no. 13, 2021. [Online]. Available: https://www.mdpi.com/1424-8220/21/13/4395

[7] ICUAS Competition Organizers, "ICUAS 2024 Competition Results: Final Standings," GitHub Discussion, 2024, accessed: 2024-05-20. [Online]. Available: https://github.com/larics/icuas24_competition/discussions/52

[8] A. Syal, D. Garg, and S. Sharma, "Apple fruit detection and counting using computer vision techniques," in *2014 IEEE International Conference on Computational Intelligence and Computing Research*, 2014, pp. 1–6.

[9] P. Hart, N. Nilsson, and B. Raphael, "A formal basis for the heuristic determination of minimum cost paths," *IEEE Transactions on Systems Science and Cybernetics*, vol. 4, no. 2, pp. 100–107, 1968. [Online]. Available: https://doi.org/10.1109/tssc.1968.300136

[10] A.-A. Mamun and S. Rajasekaran, "An efficient minimum spanning tree algorithm," in *2016 IEEE Symposium on Computers and Communication (ISCC)*, 2016, pp. 1047–1052.

[11] N. Christofides, "Worst-case analysis of a new heuristic for the traveling salesman problem," *Carnegie Mellon University*, vol. 3, p. 10, 03 2022.

[12] K. Zhang, P. Chu, K. Lammers, Z. Li, and R. Lu, "Active laser-camera scanning for high-precision fruit localization in robotic harvesting: System design and calibration," *Horticulturae*, vol. 10, no. 1, 2024. [Online]. Available: https://www.mdpi.com/2311-7524/10/1/40

[13] V. Jain, A. Anunay, A. Srivastava, A. Gupta, N. Aggarwal, and H. Harikesh, "Depth estimation using monocular camera for real-world multi-object grasp detection for robotic arm," in *Proceedings of the 2023 8th International Conference on Systems, Control and Communications*, ser. ICSCC '23. New York, NY, USA: Association for Computing Machinery, 2024, p. 7–18. [Online]. Available: https://doi.org/10.1145/3634865.3634869

[14] T. Jia, S. Han, P. Wang, W. Zhang, and Y. Chang, "Dynamic obstacle avoidance path planning for uav," in *2020 3rd International Conference on Unmanned Systems (ICUS)*, 2020, pp. 814–818.

[15] I. Corporation, "Intel® RealSense™ Depth Camera D415 Product Specifications," 2018. [Online]. Available: https://www.intelrealsense.com/depth-camera-d415/

[16] I. Velodyne Lidar, "Velodyne VLP-16 Puck LiDAR Sensor," 2024, [Online]. [Online]. Available: https://ouster.com/products/hardware/vlp-16

[17] B. Hofmann-Wellenhof, H. Lichtenegger, and E. Wasle, *Global Positioning System: Theory and Practice*. Springer Science & Business Media, 2008.

[18] R. Hartley and A. Zisserman, *Multiple View Geometry in Computer Vision*. Cambridge University Press, 2003.

[19] G. Yan, F. He, C. Shi, P. Wei, X. Cai, and Y. Li, "Joint camera intrinsic and lidar-camera extrinsic calibration," in *2023 IEEE International Conference on Robotics and Automation (ICRA)*, 2023, pp. 11 446–11 452.

Authorized licensed use limited to: DELHI TECHNICAL UNIV. Downloaded on June 04,2025 at 05:08:33 UTC from IEEE Xplore. Restrictions apply.

Breast Cancer Detection using T-gated Reconfigurable Field Effect Transistor-based Biosensor

Vijay Thakur
Vinod Dham Centre of Excellence for Semiconductors & Microelectronics Delhi Technological University
New Delhi, India
vijaysinghthakur95@gmail.com

Deva Nand
Vinod Dham Centre of Excellence for Semiconductors & Microelectronics Delhi Technological University
New Delhi, India
devkamboj@dce.ac.in

2025 Devices for Integrated Circuit (DevIC) | 979-8-3503-9110-7/25/$31.00 ©2025 IEEE | DOI: 10.1109/DevIC63749.2025.11012198

***Abstract*—This work introduces a T-gate cavity with drain electrode beneath program gate reconfigurable FET (TCDP-RFET) biosensor for breast cancer cell detection. The T-gate near the source improves biomolecule accessibility, enhancing gate-to-channel coupling, whereas reconfigurability allows it to operate in both p-mode and n-mode. The drain electrode beneath program gate effectively surpasses ambipolarity, improving detection reliability. The dual-cavity structure ensures precise biomolecule immobilization, enabling detection of MCF-10A and T47D cancer cells based on distinct dielectric properties. Simulation demomstrates I_{ON} sensitivities of 12,256 in p-mode and 6,920 in n-mode, outperforming GaAs-GAAE-FET and DM-DPDG-TFET biosensors by 1471% and 2351% enhancement, respectively. These advancements establish TCDP-RFET biosensor as a superior, highly -sensitive biosensor, paving the way for real-time, label-free cancer diagnostics.**

***Index Terms*—Nanowire, Reconfigurable, Sensitivity, Biosensor, Dielectric Modulation.**

I. Introduction

Breast cancer remains a major health affair worldwide, being one of the most common diagnosed cancers and a primary cause of mortality due to cancer in women. In 2020 alone, breast cancer accounted for approximately 2.26 million new cases, making it the most common cancer type worldwide [1], [2]. The high fatality rates associated with breast cancer are primarily due to delayed diagnosis, which limits timely treatment interventions. Early detection is crucial for improving patient survival rates, reducing treatment complexity, and alleviating the financial burden of advanced-stage management [3]. However, conventional diagnostic methods such as mammography, ultrasound, biopsy, and MRI are often constrained by high costs, complexity, and the need for specialized personnel, limiting their accessibility and widespread use [4]. However, the widespread usage of these methods is limited by the requirement for specialized equipment and expert interpretation. The search for novel molecular markers, genetic signatures, and aberrant molecular changes, such as miRNA and protein expression, has gained significance for early detection of breast cancer [5]. To achieve clinically relevant biomarker detection, innovative biosensing technologies must be developed.

Biomarkers play a crucial role in cancer diagnosis and management. Breast cancer cell lines are classified as T-47D, MDA-MB-231, and HS578t, while MCF-10A is recognized as a benign cell line. MDA-MB-231 and HS578t are particularly aggressive and invasive, making their early detection critical due to their potential for rapid spread and harm [6], [7].

Field-effect transistor (FET)-based biosensors have demonstrated significant potential for rapid, label-free, and highly sensitive detection of cancer biomarkers [8]–[11]. These biosensors operate by transducing biomolecular interactions into electrical signals, providing real-time monitoring capabilities with high specificity and low detection limits. Conventional FET-based biosensors often suffer from inherent limitations such as low-sensitivity, poor selectivity, and high leakage currents, which compromise their effectiveness in real-world biomedical applications. Among various types of FETs, nanowire FETs (NWFETs) and Schottky barrier FETs (SB-FETs) attracted significant attention in biosensing [12]–[16]. The unique band structures and charge transport mechanism of SB-FETs make them highly sensitive to biomolecules. NWFETs, on the other hand, offer a higher surface-to-volume ratio, biocompatibility, and a wider detection range but are unable to detect dual-polarity biomolecules and have a low drive current.

Incorporation of reconfigurable architecture in NWFETs uses the impacts of Schottky junction and nanowire structure, allowing flexibility in adjusting the operating configuration (N-mode or P-mode) with the gate voltage [17], [18]. This technology of incorporating reconfigurable design with NWFETs enables reduction of fabrication complexity, high packing density, and greater compatibility with CMOS technology. In addition, using the reconfigurability of NWFETs, biosensors offer rapid response, low leakage current, and detection of dual-polarity biomolecules [19], [20]. Furthermore, dielectric modulation techniques have been explored to enhance the selectivity and specificity of breast cancer biomarker detec-

979-8-3503-9110-7/25/$31.00 ©2025 IEEE

Authorized licensed use limited to: DELHI TECHNICAL UNIV. Downloaded on June 04,2025 at 05:23:13 UTC from IEEE Xplore. Restrictions apply.

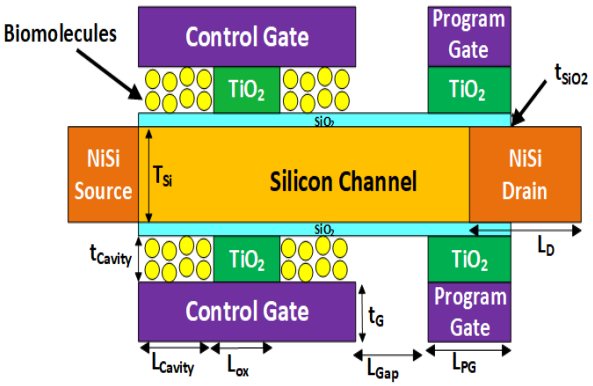
tion, leveraging variations in the dielectric constant associated with cancerous and normal breast tissues. One of the critical challenges in RFET-based biosensors is ambipolar conduction, which results in unwanted leakage currents and reduces the device's ability to differentiate between different biomolecules interactions.

This paper presents an in-depth investigation of an RFET-based biosensor for breast cancer detection, utilizing advanced architecture, including a dual cavity under the control gate and the drain electrode underneath the program gate. The dual cavity under the control gate that allows the precise control of biomolecule attachment enables selective detection of target biomolecules, enhancing the sensitivity. The underlap drain electrode reduces the undesired charge flow, reducing the ambipolarity of the device in the off state [20], [21]. To investigate the device performance, we investigated the ON-current (I_{ON}) sensitivity for both P/N-mode configurations. To validate the simulation models, we meticulously calibrated the models with the reported experimental data [22], confirming the consistency between the simulated and real-world observations. This research work thus addresses a critical technological gap, paving the way for an efficient, miniaturized, and highly sensitive biosensor for a real-time breast cancer detection. The TCDP-RFET biosensor is not limited to breast cancer detection; its versatility, high sensitivity, and reconfigurability make it a multi-purpose biosensing platform. It can be applied in cancer diagnostics, infectious disease detection, neurological disorder monitoring, drug screening, and environmental sensing, providing a scalable and high-performance solution for biomedical and analytical applications.

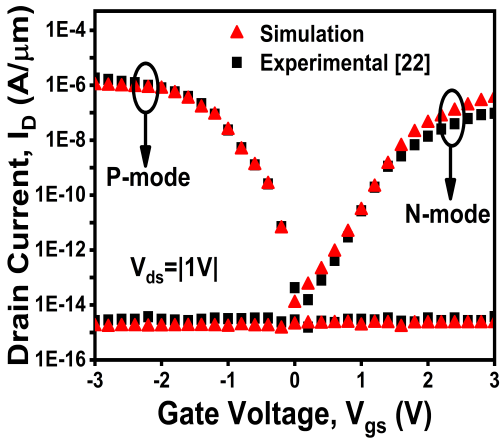
II. Device Structure, Calibration, and Simulation Set-up

Figure 1(a) illustrates the schematic design of the proposed RFET-based biosensor consisting of a T-gate cavity with a drain electrode under the program gate (TCDP-RFET). The proposed device architecture comprises two critical components: dual cavity under the T-gate and the drain electrode under the program gate. The device consists of silicon and nickel silicide as the channel material and the source/drain electrode, repectively, resulting in Schottky contacts at the interfaces. TiO_2/SiO_2 stack and titanium are used as gate oxide and gate electrode, respectively. SiO_2 is also used as an adhesive layer for biomolecule immobilization in the cavity. The control gate (CG) influences the Schottky barrier, regulating the desired carriers transport from the source to the channel, while the program gate (PG) blocks the insertion of unwanted carriers from the drain electrode to the channel. Table I shows the device parameters of the TCDU-RFET biosensor.

By plotting the experimental data points against the simulated values, researchers can visually assess the agreement between the two sets of data. In Figure 1(b), a well-calibrated graph shows a close alignment between the experimental [22] and simulated points for both P/N-mode configurations. To validate the simulation models and results, we calibrated the



(a)



(b)

Fig. 1. (a) Schematic view of TCDP-RFET biosensor for detecting the breast cancer cells and (b) Calibration graph.

TABLE I
Device Parameters for the TCDP-RFET-based Biosensor.

Parameters	Values
$NiSi_2$ Source/Drain Work-function	4.58 eV
Control/Program Gate Work-function	4.3 eV
TiO_2 Thickness, T_{ox}	8 nm
SiO_2 Thickness	2 nm
Channel Length	115 nm
Channel Doping Concentration	$10^{12} cm^{-3}$
Control Gate Length, L_{CG}	80 nm
Program Gate Length, L_{PG}	30 nm
Si Thickness, T_{Si}	10 nm
Cavity length, L_{cavity}	25 nm
Cavity Thickness, T_{cavity}	8 nm
Drain Electrode Length, L_D	25 nm
Source Electrode Length, L_S	10 nm

simulated graph with the experimented graph. The control gate voltage ranges between $\pm 3V$ at a drain-to-source voltage of $\pm 1V$. The simulated graph closely matches the experimental graph, affirming the suitability of the models used. The performance analysis of the TCDP-RFET biosensor is conducted utilizing the Silvaco ATLAS TCAD tool. To capture the tunneling charge carrier at the metal-semiconductor junctions, the UST model is employed in the simulation. Furthermore,

Authorized licensed use limited to: DELHI TECHNICAL UNIV. Downloaded on June 04,2025 at 05:23:13 UTC from IEEE Xplore. Restrictions apply.

the simulation incorporates various models such as the conmob model, Auger model, boltzman, consrh model, cvt model, Fermi Dirac statistics, fnord, bqp.qdir=3, and bbt.nonlocal tunneling model.

III. Results and Discussion

In this section, we delve into exploring how TCDU-RFET-based biosensor detect the breast cancer, focusing on two specific cancer cells or biomarkers: T47D (K=32) and MCF-10A (K=4.5). The different dielectric constant values of these biomarkers impact device parameters such as energy band, channel surface potential, and drain current. Subsequently, we evaluate the I_{ON} sensitivity of for both P/N-mode configurations.

A. Analysis of Electrostatic Characteristics

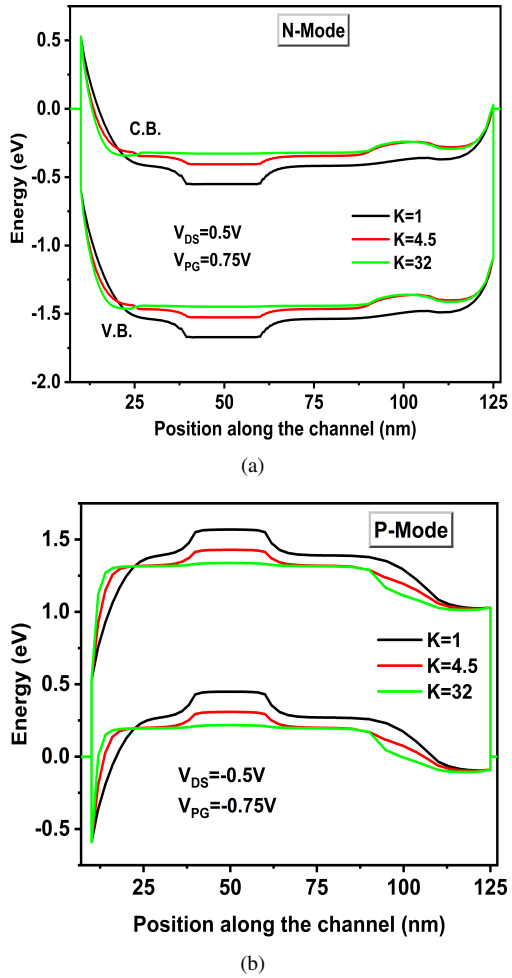


Fig. 2. Energy band of TCDP-RFET biosensor in (a) N-mode configuration and (b) P-mode configuration.

Figure 2 depicts the energy band diagram of the TCDP-RFET for both P/N-mode in the presence of different biomarkers or cancer cells. In Fig. 2(a), as the dielectric constant of the cancer cell increases, there is a downward shift in the conduction band near the source, reducing the tunneling width and enhancing the charge carriers' tunneling probability across the source-channel Schottky barrier junction. On the other hand, in P-mode configuration, an upward movement in the energy band near the source results in a decreased tunneling width to enhance the charge carrier tunneling through the barrier as shown in Fig. 2(b).

The dielectric of the cancer cells affects the gate capacitance. A higher dielectric constant enhances gate capacitance, which increases gate-charge carriers coupling across the channel. The higher dielectric constant also induces more polarization at the interface and thus changes the surface potential of the biosensor. Figure 3 displays the surface potential plots of the TCDP-RFET biosensor for both P/N-mode configurations. In Fig. 3(a), for the N-mode configuration, the surface potential decreases with the increasing dielectric constant of biomarkers or cancer cells. Similarly, in Fig. 3(b), as the dielectric constant value of the biomarkers or cancer cells increases, the surface potential of the biosensor also increases for P-mode configuration.

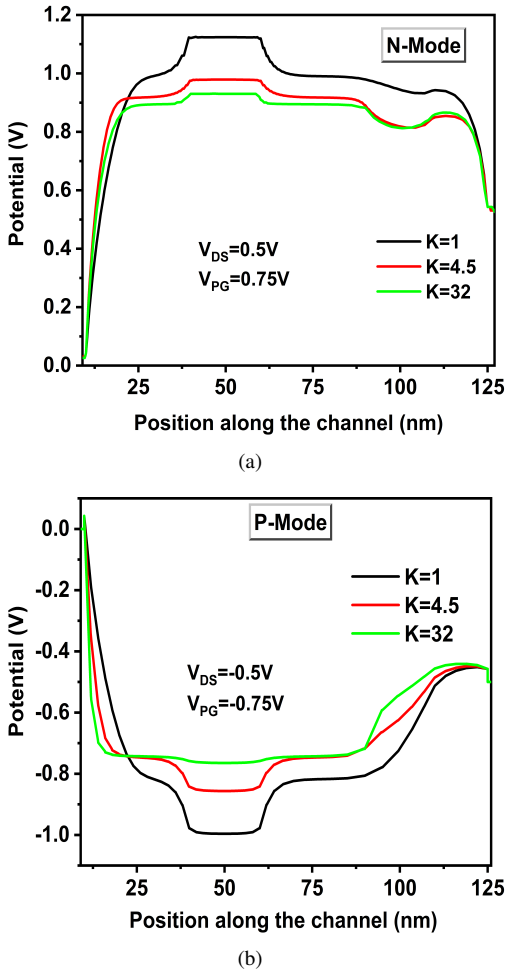
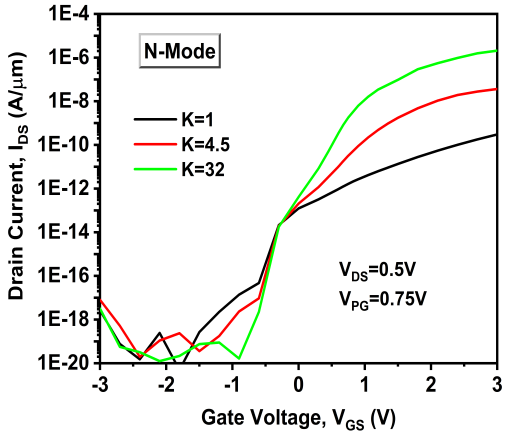


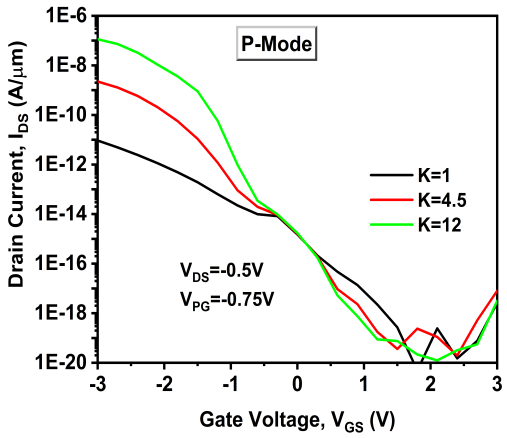
Fig. 3. Surface potential of the TCDP-RFET biosensor in (a) N-mode configuration and (b) P-mode configuration.

Figure 4 shows the transfer characteristics of the TCDP-RFET for both P/N-mode configurations in the presence of different biomarkers or cancer cells. The drain current of

Authorized licensed use limited to: DELHI TECHNICAL UNIV. Downloaded on June 04,2025 at 05:23:13 UTC from IEEE Xplore. Restrictions apply.



(a)



(b)

Fig. 4. Transfer characteristics of the TCDP-RFET biosensor in (a) N-mode configuration and (b) P-mode configuration.

the biosensor is significantly impacted with the presence of biomarkers or cancer cells. For P/N modes, the drain current enhances as the dielectric constant (K) value rises due to the increase in the gate capacitance and channel potential.

Sensitivity Analysis

This section evaluates the sensitivity of the TCDP-RFET biosensor, a key parameter in biosensor performance assessment. Sensitivity is determined by comparing the device characteristics when the cavities are filled with cancer cells versus when they contain air. The analysis of I_{ON} sensitivity parameters [23] is outlined as follows:

$$S_{I_{ON}} = \left| \frac{I_{on(air)} - I_{on(bio)}}{I_{on(air)}} \right| \quad (1)$$

where $S_{I_{ON}}$ is the I_{ON} sensitivity of the proposed device. $I_{on(air)}$ and $I_{on(bio)}$ are the drain currents of the biosensor for air (K = 1) and when the cancel cell is placed in the cavity ($K \neq 1$), respectively.

Figure 5 provides an analysis of the sensitivity of the TCDP-RFET-based biosensor, focusing on the impact of varying the values of the dielectric constant of the cancer cells on the drain current (I_{on}) sensitivity Figure 5 illustrates that the I_{on} sensitivity increases with the increment in the value of the dielectric constant , with the P-mode exhibiting a higher sensitivity of approximately 12256 compared to the N-mode, which is approximately 6920. Table II illustrates the sensitivity comparison of the TCDP-RFET biosensor with the reported FET-based biosensor.

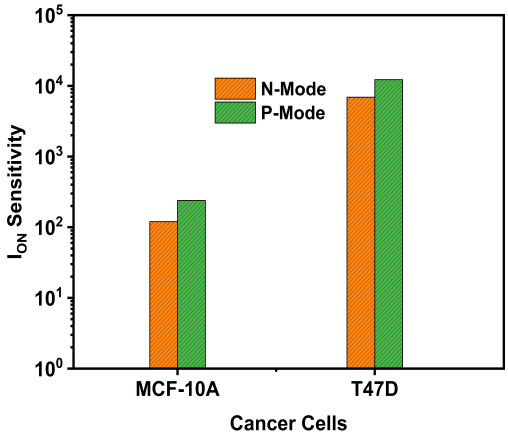


Fig. 5. I_{ON} Sensitivity of TCDP-RFET biosensor for different breast cancer cells.

TABLE II
PROPOSED DEVICE SENSITIVITY COMPARISON WITH STATE-OF-THE-ART FET-BASED BIOSENSORS

Biosensors	I_{on} Sensitivity
Si-doped MoS2 TE-TFET [24]	110.37
GaAsGAAE-FET [25]	833
IC–S-FinFET [26]	3
DM DPDG-TFET [27]	500
This work	12256 (P-mode)
This work	6920 (N-mode)

IV. Conclusion

The detection of breast cancer cell lines (T47D, MCF-10A) was explored using a T-gate cavity RFET biosensor, utilizing dielectric charge modulation for label-free identification. The device was analyzed for variations in energy band structure, surface potential, and drain current when cancer cells were introduced into the cavity. The biosensor's design is enhanced through advanced engineering techniques, including dual-cavity architecture under the T-gate, a drain electrode positioned beneath the program gate, and integration of high-K and low-K oxides. Sensitivity evaluation in n-mode and p-mode yielded I_{ON} sensitivities of 6920 and 12256, respectively, outperforming conventional biosensors. With cost-effective fabrication, dynamic reconfigurability, high reproducibility, simplified detection, and CMOS compatibility, this biosensor emerges as a highly promising platform for breast cancer diagnostics.

Authorized licensed use limited to: DELHI TECHNICAL UNIV. Downloaded on June 04,2025 at 05:23:13 UTC from IEEE Xplore. Restrictions apply.

REFERENCES

[1] Ferlay, J., Ervik, M., Lam, F., Colombet, M., Mery, L., Piñeros, M., & Bray, F. (2020). Global cancer observatory: cancer today. Lyon: International agency for research on cancer, 20182020.

[2] Effects of chemotherapy and hormonal therapy for early breast cancer on recurrence and 15-year survival: an overview of the randomised trials. Lancet. 2005, 365: 1687-1717. 10.1016/S0140-6736(05)66544-0.

[3] Cancer. Accessed: Dec. 21, 2021. [online]. Available: https://www.who.int/news-room/fact-sheets/detail/cancer.

[4] Michaelson, J. S., Silverstein, M., Wyatt, J., Weber, G., Moore, R., Halpern, E., & Hughes, K. (2002). Predicting the survival of patients with breast carcinoma using tumor size. Cancer: Interdisciplinary International Journal of the American Cancer Society, 95(4), 713-723.

[5] An, J., Park, H., Ju, M., Woo, Y., Seo, Y., Min, J., & Lee, T. (2024). An updated review on the development of a nanomaterial-based field-effect transistor-type biosensors to detect exosomes for cancer diagnosis. Talanta, 126604.

[6] Sehgal, H. D., Pratap, Y., & Kabra, S. (2022). Detection of breast cancer Cell-MDA-MB-231 by measuring conductivity of Schottky source/drain GaN FinFET. IEEE Sensors Journal, 22(6), 6108-6115.

[7] Hussein, M., Awwad, F., Jithin, D., El Hasasna, H., Athamneh, K., & Iratni, R. (2019). Breast cancer cells exhibits specific dielectric signature in vitro using the open-ended coaxial probe technique from 200 MHz to 13.6 GHz. Scientific reports, 9(1), 4681.

[8] Goel, A., Rewari, S., Verma, S., & Gupta, R. S. (2021). Modeling of shallow extension engineered dual metal surrounding gate (SEE-DM-SG) MOSFET gate-induced drain leakage (GIDL). Indian Journal of Physics, 95, 299-308.

[9] Kaul, A., Rewari, S., & Nand, D. (2024). Hetero-dielectric macaroni channel cylindrical gate all around field effect transistor (HD-MC CGAA FET) for reduced gate leakage analog applications. Microsystem Technologies, 30(5), 599-611.

[10] Kaul, A., Yadav, S., Rewari, S., & Nand, D. (2025). Analytical Modelling of Temperature Resilient Cylindrical Gate Engineered Ferroelectric Nanowire Field Effect Transistor. IEEE Transactions on Dielectrics and Electrical Insulation.

[11] Yadav, S., & Rewari, S. (2024). Dual metal dual layer GAA NW–FET (DMDL–GAA–NW–FET) biosensor for label free SARS-CoV-2 detection. Microsystem Technologies, 30(5), 565-582.

[12] Thakur, V., Kumar, A., & Kale, S. (2024). Numerical modeling and performance analysis of underlap gate cavity-integrated reconfigurable silicon nanowire Schottky barrier transistor biosensors. Applied Physics A, 130(11), 1-13.

[13] Kaul, A., Yadav, S., Rewari, S., & Nand, D. (2024). Computational modelling of cylindrical-ferroelectric-dual metal-nanowire field effect transistor (C-FE-DM-NW FET) using landau equation for gate leakage minimization. Micro and Nanostructures, 191, 207851.

[14] Yadav, S., & Rewari, S. (2023). Analytical modeling and numerical simulation of graded JAM Split Gate-All-Around (GJAM-SGAA) Bio-FET for label free Avian Influenza antibody and DNA detection. Microelectronics Journal, 142, 106011.

[15] Kaul, A., Rewari, S., & Nand, D. (2022, November). Macaroni channel-nanowire-field effect transistor (MC-NW-FET) for gate induced drain leakage (GIDL) reduction application. In 2022 IEEE International Conference of Electron Devices Society Kolkata Chapter (EDKCON) (pp. 35-38). IEEE.

[16] Yadav, S., & Rewari, S. (2023). Numerical simulation of hetero dielectric trench gate JAM gate-all-around FET (HDTG-JAM-GAAFET) for label free biosensing applications. ECS Journal of Solid State Science and Technology, 12(12), 127008.

[17] Thakur, V., Kumar, A., & Kale, S. (2024). Analytical modeling of spacer-engineered reconfigurable silicon nanowire Schottky barrier transistor for biosensing applications. Micro and Nanostructures, 188, 207799.

[18] A. Kumar and S. Kale, "Dual-k Reconfigurable Silicon Nanowire Schottky Barrier Transistor for Biosensing," 2024 8th IEEE Electron Devices Technology & Manufacturing Conference (EDTM), Bangalore, India, 2024, pp. 1-3, doi: 10.1109/EDTM58488.2024.10511505.

[19] Kumar, A., & Kale, S. (2024). Analytical Modeling of Silicon Nanowire Dielectric Modulated Reconfigurable FET Biosensor. ECS Journal of Solid State Science and Technology, 13(11), 113005.

[20] Kumar, A., Thakur, V., Kumar, S., Kale, S., & Singh, K. R. (2024). Sensitivity Investigation of Underlap Gate Cavity-Based Reconfigurable Silicon Nanowire Schottky Barrier Transistor for Biosensor Application. Silicon, 16(16), 5877-5889.

[21] Abdi, D. B., & Kumar, M. J. (2014). Controlling ambipolar current in tunneling FETs using overlapping gate-on-drain. IEEE Journal of the Electron Devices Society, 2(6), 187-190.

[22] Heinzig, A., Slesazeck, S., Kreupl, F., Mikolajick, T., & Weber, W. M. (2012). Reconfigurable silicon nanowire transistors. Nano letters, 12(1), 119-124.

[23] Lamba, A., Chaujar, R., & Deen, M. J. (2024, November). Investigation of a Dielectric Modulated Dual Metal Gate Engineered SOI FinFET with High-K Dielectric for Bio-sensitivity Enhancement. In 2024 IEEE Asia-Pacific Microwave Conference (APMC) (pp. 31-33). IEEE.

[24] Kaushal, P., & Khanna, G. (2024). Breast Cancer Detection using Si-doped MoS2 Channel based Thickness Engineered TFET Biosensor. IEEE Sensors Letters.

[25] Yadav, S., & Rewari, S. (2024, February). Dielectric Modulated Gallium-Arsenide Gate-All-Around Engineered Field Effect Transistor (GaAs-GAAE-FET) Biosensor for Breast Cancer Detection. In 2024 IEEE International Conference on Computing, Power and Communication Technologies (IC2PCT) (Vol. 5, pp. 1553-1557). IEEE.

[26] Shalini, V., & Kumar, P. (2025). Design and Analysis of Interconnected Multichannel Schottky FinFET for the Detection of Breast Cancer Cells. Micro and Nanostructures, 208078.

[27] Sravani, K. G., Kumar, R. A., Rao, K. S., Edla, D. R., Jannu, S., Alkhayyat, A., & Mishra, A. K. (2024). Modeling and evaluating the performance of a split-gate T-shape channel DM DPDG-TFET biosensor for label-free detection. IEEE Transactions on Consumer Electronics.

Authorized licensed use limited to: DELHI TECHNICAL UNIV. Downloaded on June 04,2025 at 05:23:13 UTC from IEEE Xplore. Restrictions apply.

Check for updates

Classifying Android Malware Categories through Dynamic System Calls Ranked via ReliefF

Yash Sharma* and Anshul Arora

Department of Applied Mathematics, Delhi Technological University, Delhi, India.
ysharma2098@gmail.com, anshul15arora@gmail.com

Abstract. Android's popularity as an operating system stems from its extensive benefits; however, this has also made it a primary target for malware, which now exists in various categories. Numerous approaches leveraging static and dynamic analysis have been proposed for malware detection, though static analysis faces inherent limitations that dynamic analysis can address. Hence, this paper focuses on classifying malware categories—*Adware, Fraudware, Ransomware, and Spyware*—using dynamically extracted system call data. We employ the *ReliefF* algorithm for effective feature ranking and selection, aiming to achieve high detection accuracy with a minimal feature set. Experimental results reveal that an optimal subset of 70 system calls out of 289 achieves a peak accuracy of 94.50%, reducing the feature set by approximately 75.6%. Our findings demonstrate the efficacy of the dynamic approach in enhancing malware detection, providing a robust solution to the evolving mobile cybersecurity threat landscape.

Keywords: Android Security, Mobile Malware, Multi-Category Classification, Feature Ranking, Dynamic analysis

1 Introduction

In recent years, the rapid proliferation of smartphones has transformed communication, access to information, and interaction methods, positioning smartphones as indispensable tools in daily life. Among various mobile operating systems, Android has established itself as the most popular, owing to its flexibility, wide developer support, and extensive user-friendly features. However, the open nature of Android has also made it susceptible to malware. Android malware disrupts normal device functioning, invades privacy, and results in financial and data losses. Common types include *ransomware, spyware, adware, and Trojans.*

Over the years, researchers have focused on three primary analysis techniques to counter malware threats: static, dynamic, and hybrid analysis [1]. Static analysis involves examining the application's code without execution, making it fast and efficient; however, it struggles with obfuscation techniques and other advanced malware. Dynamic analysis, on the other hand, observes the app's behavior during runtime, successfully identifying malicious activities overlooked by

* Corresponding author: ysharma2098@gmail.com

© The Author(s) 2025
P. Ahlawat et al. (eds.), *Proceedings of the 6th International Conference on Deep Learning, Artificial Intelligence and Robotics (ICDLAIR 2024)*, Advances in Intelligent Systems Research 193,
https://doi.org/10.2991/978-94-6463-740-3_6

static methods. Hybrid analysis combines both approaches, aiming to enhance detection accuracy and efficiency.

Motivation - Despite the advantages of static analysis, its limitations have led researchers to explore dynamic analysis as a solution to overcome these challenges. Hence, this paper proposes a dynamic Android malware detection model that leverages system call monitoring to accurately detect and classify malware, ensuring robust security for Android users. Android malware compromises user privacy and device functionality, with major categories including *Adware, Fraudware, Ransomware*, and *Spyware*. All of them pose security threats and high risk for Android users. Especially, those leveraging root privileges, with the purposes of extorsion (i.e., *ransomware*), persistent access, or stealing sensitive data (i.e. *spyware*) are of special concern.

Therefore, in this paper, we design a dynamic classification model aimed at performing classification of malware into the four categories: *Adware, Fraudware trojans, Ransomware*, and *Spyware*, by using the least number of features that exhibit higher distinguishing power between different malware categories while simultaneously ensuring higher classification accuracy. To achieve this, we employ the *ReliefF* algorithm as a feature ranking and selection technique, which formulates a *ReliefF* Score that assesses the contribution of each feature to the classification task. This method is particularly suited for categorical datasets, such as ours, as it effectively evaluates the relevance of features in distinguishing between multiple malware categories. By identifying and ranking features based on their ability to differentiate between classes, *ReliefF* enables us to select the most impactful features that enhance classification accuracy while discarding irrelevant or lower-ranked features. This approach not only streamlines the feature set but also improves the overall robustness of our malware category classification model.

Contributions - The primary contributions of this study are as follows:

- We developed a malware multi-category classification model that leverages the dynamic analysis of system calls, enabling a more adaptive and resilient approach compared to static-only methods.
- We utilized the *ReliefF* algorithm to rank features based on their effectiveness in distinguishing among malware categories.
- We proposed a novel algorithm that leverages attribute rankings given by the *ReliefF* algorithm to develop an efficient Android malware multi-category classification system, achieving higher accuracy with minimal features.

2 Related Work

Extensive research has employed static features—such as permissions, intents [2], hardware components [3], and other manifest file attributes—in the detection of malware, often integrating various feature ranking and selection techniques. However, since our study focuses on dynamic analysis and utilizes system calls, we emphasize prior works that have employed dynamic features to facilitate malware detection or to classify malware into categories or families.

Dimjašević et al. [4] aimed to show the presence of semantic information in system call sequences, treating each sequence as a sentence and building a classifier based on the Long Short-Term Memory (LSTM) language model. In [5], the authors emphasized feature selection to enhance model performance and introduced a Rough set-based two-step approach for refined system call selection. Chew et al. [6] presented a *ransomware* detection method based on behavioral patterns in system calls, later refining it for real-time detection using a token-based finite state machine. In [7], *EnDroid*, a dynamic analysis framework, was introduced, which autonomously extracts dynamic behaviors like cryptographic operations and system calls, aided by chi-square feature selection and a Stacking model for malware detection. *TaintDroid* [8] used dynamic taint analysis to track privacy-sensitive data flow through third-party apps, highlighting potential private information leaks from normal apps. Various systems ([9], [10]) built on *TaintDroid* detect Android app privacy leaks. Yang et al. [11] extended *TaintDroid* to determine if data leaks were due to user intent.

CopperDroid [12] analyzed malware-triggered system calls to identify behaviors originating from Java, JNI, or native code. Afonso et al. [13] studied dynamic API and system call combinations for malicious app detection. CrowDroid [14] utilized clustering techniques on system calls to differentiate between malicious and normal apps. DroidTrace [15] leveraged '*ptrace*' for monitoring dynamic features like system calls, file operations, and network connections. Almeida et al. [16] analyzed runtime traces (system calls, network traffic, user inputs) to assess app risks. Jang et al. [17] used volatile memory acquisition to detect Android malware, while Arora and Peddoju [18] collected network traffic features from real devices to improve detection accuracy using information gain and statistical feature ranking. The authors in [19] distinguished malware and normal traffic by selecting distinct network traffic features to build a malware detection model.

In [20], nine novel flow-based network traffic features were proposed, developing an efficient Android malware detection model capable of identifying unknown malware types with minimal features using information gain, CFS subset, and SVM. Shabtai et al. [21] explored network traffic deviations, correlating normal behavior patterns to detect anomalies, using eight Android devices, real malware, and self-developed malware.

3 System Design

This section provides a detailed explanation of our proposed model's methodology which is primarily divided into two modules, *Ranking* and *Classification* module as shown in Figure 1. Initially, we compile an extensive dataset that includes dynamic features (system calls). Subsequently, we split this dataset into two segments: the *Training* dataset and the *Testing* dataset. In the Ranking module, we begin by inputting the *Training* dataset and ranking the features based on their *ReliefF* scores. In the *Classification* module, we propose a novel algorithm that applies Machine Learning (ML) and Deep Learning (DL) techniques to get the best features that can provide higher classification accuracy.

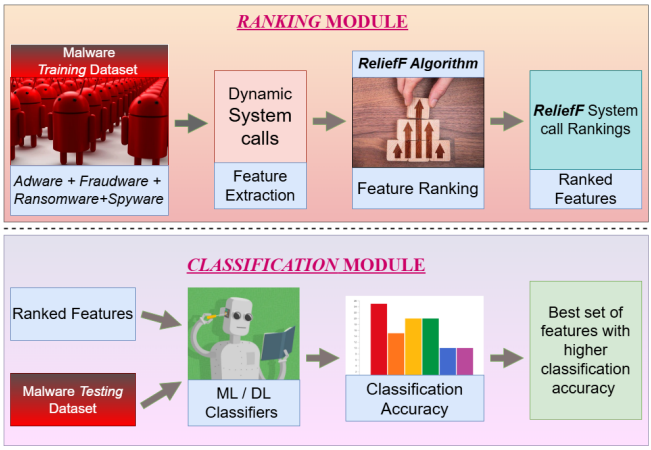


Fig. 1. System Design

RANKING MODULE

3.1 Data collection

To initiate this research, we employed the *Kronodroid* dataset [22], the largest hybrid-feature Android dataset covering the period from 2008 to 2020. This dataset integrates static features, including permissions, intents, and metadata, alongside dynamic features represented by system calls. Malware samples were gathered from repositories such as *Drebin*, *AMD*, *VirusTotal*, and *VirusShare*. For our Android multicategory classification model development, we focused only on system calls, where call frequency data records non-zero values for occurrences and zero for absences. The dataset categorizes samples into *Adware*, *Fraudware*, *Ransomware*, and *Spyware*. For training, we used 50% of each category (10,000 samples), with the remaining 50% for testing (10,000 samples). This approach aims to leverage dynamic features for a robust multicategory classification of Android malware, addressing the limitations inherent to static analysis. We processed the dataset into *Training* and *Testing*, with each encompassing 289 system calls.

3.2 Feature Ranking

In this study, we applied the *ReliefF* algorithm to rank features based on their relevance for multicategory malware classification. *ReliefF* is a feature selection technique designed to estimate the importance of each feature by assessing how well it distinguishes between instances from different classes. For a given multiclass dataset with n applications and p attributes, where samples belong to m classes, *ReliefF* evaluates each feature's ability to separate samples by iteratively selecting instances and calculating feature weights based on intra- and inter-class distances.

The algorithm operates as follows: for each randomly selected instance i, *ReliefF* finds its nearest neighbors within the same class (*nearest hits*) and from different classes (*nearest misses*). The weight $W(A)$ of each attribute A is updated to reflect its ability to distinguish between classes. The update rule for feature weights is given by:

$$W(A) = W(A) - \frac{1}{k}\sum_{j=1}^{k}\left(\text{diff}(A, i, \text{hit}_j)\right) + \frac{1}{k(m-1)}\sum_{l \neq \text{class}(i)}\sum_{j=1}^{k} P(l)\,\text{diff}(A, i, \text{miss}_{j,l})$$

where:
- k is the number of nearest neighbors considered,
- $\text{diff}(A, i, j)$ represents the difference between instances i and j on attribute A,
- $P(l)$ is the prior probability of class l,
- hit_j is the j-th nearest neighbor within the same class as i,
- $\text{miss}_{j,l}$ is the j-th nearest neighbor from a different class l.

Using *ReliefF* with our multiclass dataset of Android malware, the algorithm ranks features, i.e. system calls, by prioritizing those that contribute most to distinguishing between categories namely *Adware*, *Fraudware*, *Ransomware*, and *Spyware*. This ranking allows our model to focus on the most discriminatory features for improved classification accuracy.

3.3 Machine Learning and Deep Learning Classifiers

We used several ML and DL classifiers[1] in our classification approach. We applied five widely used techniques, namely Decision Trees (DT), Random Forest (RF), Bagging classifier (BC), Gaussian Naive Bayes (NB) as ML classifiers and Multilayer Perceptron (MLP) as DL classifier. All experiments with these classifiers were performed using ten-fold cross-validation.

Classification Module

3.4 Proposed Malware Multi-Category Classification Algorithm

Following the ranking of features using the *ReliefF* algorithm, we obtained a sorted list of system calls based on their effectiveness in distinguishing between various malware categories. Our objective now is to identify the optimal subset of features that maintains the highest classification accuracy while minimizing the number of features used.

We begin by incorporating all available features in the first iteration and recording the classification accuracy achieved by the classifiers utilized in this study. Subsequently, we eliminate the lowest-ranked ten features from the *Testing* dataset and assess the resulting accuracy. In the next iteration, we remove an

[1] https://dl.acm.org/doi/10.1145/507338.507355

additional ten features, continuing this process iteratively by excluding the next ten lowest-ranked features in each round. This procedure is repeated until we observe a decline in classification accuracy.

Ultimately, the output will yield the minimal feature set that achieves the best classification performance, thereby optimizing the feature selection for our multi-category malware classification model. The overall computational complexity of the proposed algorithm can be approximated as O(N * (N + f(n))), where N is the number of system calls used in the study and f(n) represents the time complexity of the machine learning algorithms used for training and evaluation.

4 Results and Discussion

In this section, we present the experimental results obtained by applying the proposed malware multicategory classification model to the dynamic category datasets. As previously discussed, we utilized the ranking method on the *Training* dataset to compute the *ReliefF* scores of the system calls. Subsequently, within the *Classification* module, we applied various ML and DL classifiers to the *Testing* dataset.

4.1 *ReliefF* Ranking Results

In this section, we present the results of the *ReliefF* ranking applied to the system calls dataset. Table 1 displays the top ten system calls, sorted by their effectiveness in distinguishing between malware classes. Notably, the system call *eventfd2* ranks highest in the table, achieving the *ReliefF* score of 0.0920. The rankings of the remaining system calls are detailed in the table. With *getpid* coming out to be the least scored, indicating its relatively low capability to differentiate between malware classes.

Table 1. Top 10 system calls ranked in order of their *ReliefF* Score

System Call	***ReliefF* Score**
eventfd2	0.0920
epoll_create1	0.0920
fstatfs64	0.0739
flock	0.0690
readlinkat	0.0687
fchmod	0.0643
ugetrlimit	0.0568
socketpair	0.0555
mkdirat	0.0541
sendmsg	0.0494

4.2 Classification Results on the Testing Dataset

In this section, we present the classification results obtained on the *Testing* dataset by iteratively reducing the feature set based on system call rankings given by the *ReliefF* algorithm. Initially, with all 289 system calls included, we achieved an accuracy of 94.01%. In subsequent iterations, system calls were removed in increments of ten, beginning with the least important features, as determined by the *ReliefF* ranking.

With each iteration, the classification accuracy was evaluated to identify the optimal subset of features. By the 23rd iteration, reducing the feature set to the top 70 system calls yielded the highest observed accuracy of 94.50%. Beyond this point, further reduction in features led to a decline in accuracy. Thus, the optimal subset of features was determined to be 70 system calls, achieving the highest accuracy while reducing the feature set by approximately 75.6%.

Table 2 below summarizes the classification accuracy across iterations.

Table 2. Classification Accuracy Across Iterations of Feature Reduction

Features used	**Accuracy (%)**	**Features used**	**Accuracy (%)**
50	88.39	170	94.05
60	93.94	180	94.07
70	94.50	190	94.20
80	94.11	200	94.12
90	94.05	210	94.07
100	94.05	220	94.01
110	94.10	230	94.06
120	94.10	240	93.99
130	94.14	250	94.08
140	94.10	260	94.02
150	94.10	270	94.08
160	94.11	280	94.03

Table 3. Comparison of proposed work with the existing literature based on malware detection.

Related Work	**Feature selection/Feature ranking technique used**	**MultiCategory**	**Detection accuracy (in %)**
Li et al. [23]	Permissions ranking based on frequency	-	93.62
Talha et al. [24]	Risk score calculated for each app	-	88.28
Shang et al. [25]	Naive Bayes and Pearson Correlation Coefficient	-	86.54
Tchakounte et al. [26]	Sequence alignment based similarity score	-	79.58
Proposed Model	**ReliefF based ranking**	✓	**94.50**

4.3 Comparison with other related works

In this section, we compare the performance of our proposed model with other similar works of Android malware detection that have used permissions or intents as features. Table 3 summarizes this comparison. As seen from the table, our work outperforms all these works in terms of detection accuracy. Some works have ranked the permissions based on frequency or with tests like Pearson Correlation Coefficient. Some other works have applied feature selection techniques with Naive Bayes, whereas some authors have used permissions in pairs for Android malware detection. However, the purpose of their studies were only binary classification. Our study advances the field by performing multicategory classification. Moreover, our work outperforms them in terms of detection accuracy. Hence, our proposed model is better than many state-of-the-art techniques presented in the literature for Android malware detection.

5 Conclusion and Future work

In conclusion, our study demonstrates the effectiveness of classifying Android malware categories—specifically *Adware, Fraudware, Ransomware, and Spyware* — through dynamic system call features ranked via the *ReliefF* algorithm. The experimental results revealed that the optimal subset of features consisted of 70 system calls out of a total of 289, achieving a notable accuracy of 94.50%, while simultaneously reducing the feature set by approximately 75.6%. These findings advocate strongly for the adoption of dynamic models in malware detection, as they provide a robust countermeasure against evolving cyber threats compared to traditional static models. Lastly, while dynamic analysis using system calls offers valuable insights, it is subject to limitations such as incomplete behavior observation and dependency on the runtime environment. Future work could explore hybrid analysis that combines dynamic analysis with static features, overcoming the limitations of system calls and providing a more comprehensive detection approach alongside expanding the model to include malware family classification. This could enhance the robustness and accuracy of malware detection models.

References

[1] Yash Sharma and Anshul Arora. “A comprehensive review on permissions-based Android malware detection”. In: *International Journal of Information Security* (2024), pp. 1–36.

[2] Yash Sharma and Anshul Arora. “Ipanalyzer: A novel Android malware detection system using ranked intents and permissions”. In: *Multimedia Tools and Applications* (2024), pp. 1–52.

[3] Yash Sharma and Anshul Arora. “PHIGrader: Evaluating the effectiveness of Manifest file components in Android malware detection using Multi Criteria Decision Making techniques”. In: *Journal of Network and Computer Applications* 232 (2024), p. 104021.

[4] Marko Dimjašević et al. "Evaluation of android malware detection based on system calls". In: *Proceedings of the 2016 ACM on international workshop on security and privacy analytics*. 2016, pp. 1–8.

[5] D Kumar et al. "Identification of Android malware using refined system calls". In: *Concurr. Comput. Pract. Exp* 31 (2019), e5311.

[6] Christopher Jun Wen Chew et al. "Real-time system call-based ransomware detection". In: *International Journal of Information Security* (2024), pp. 1–20.

[7] Pengbin Feng et al. "A novel dynamic android malware detection system with ensemble learning". In: *IEEE Access* 6 (2018), pp. 30996–31011.

[8] William Enck et al. "Taintdroid: an information-flow tracking system for realtime privacy monitoring on smartphones". In: *ACM Transactions on Computer Systems (TOCS)* 32.2 (2014), pp. 1–29.

[9] Vaibhav Rastogi, Yan Chen, and William Enck. "Appsplayground: automatic security analysis of smartphone applications". In: *Proceedings of the third ACM conference on Data and application security and privacy*. 2013, pp. 209–220.

[10] Mingshen Sun, Tao Wei, and John CS Lui. "Taintart: A practical multi-level information-flow tracking system for android runtime". In: *Proceedings of the 2016 ACM SIGSAC Conference on Computer and Communications Security*. 2016, pp. 331–342.

[11] Zhemin Yang et al. "Appintent: Analyzing sensitive data transmission in android for privacy leakage detection". In: *Proceedings of the 2013 ACM SIGSAC conference on Computer & communications security*. 2013, pp. 1043–1054.

[12] Alessandro Reina, Aristide Fattori, and Lorenzo Cavallaro. "A system call-centric analysis and stimulation technique to automatically reconstruct android malware behaviors". In: *EuroSec, April* (2013).

[13] Vitor Monte Afonso et al. "Identifying Android malware using dynamically obtained features". In: *Journal of Computer Virology and Hacking Techniques* 11 (2015), pp. 9–17.

[14] Iker Burguera, Urko Zurutuza, and Simin Nadjm-Tehrani. "Crowdroid: behavior-based malware detection system for android". In: *Proceedings of the 1st ACM workshop on Security and privacy in smartphones and mobile devices*. 2011, pp. 15–26.

[15] Min Zheng, Mingshen Sun, and John CS Lui. "DroidTrace: A ptrace based Android dynamic analysis system with forward execution capability". In: *2014 international wireless communications and mobile computing conference (IWCMC)*. IEEE. 2014, pp. 128–133.

[16] Mario Almeida et al. "Chimp: Crowdsourcing human inputs for mobile phones". In: *Proceedings of the 2018 World Wide Web Conference*. 2018, pp. 45–54.

[17] Jae-wook Jang et al. "Andro-Dumpsys: Anti-malware system based on the similarity of malware creator and malware centric information". In: *computers & security* 58 (2016), pp. 125–138.

[18] Anshul Arora and Sateesh K Peddoju. "Minimizing network traffic features for android mobile malware detection". In: *Proceedings of the 18th international conference on distributed computing and networking*. 2017, pp. 1–10.

[19] Anshul Arora, Shree Garg, and Sateesh K Peddoju. "Malware detection using network traffic analysis in android based mobile devices". In: *2014 Eighth International Conference on Next Generation Mobile Apps, Services and Technologies*. IEEE. 2014, pp. 66–71.

[20] Arash Habibi Lashkari et al. "Towards a network-based framework for android malware detection and characterization". In: *2017 15th Annual conference on privacy, security and trust (PST)*. IEEE. 2017, pp. 233–23309.

[21] Asaf Shabtai et al. "Mobile malware detection through analysis of deviations in application network behavior". In: *Computers & Security* 43 (2014), pp. 1–18.

[22] Alejandro Guerra-Manzanares, Hayretdin Bahsi, and Sven Nõmm. "Kronodroid: Time-based hybrid-featured dataset for effective android malware detection and characterization". In: *Computers & Security* 110 (2021), p. 102399.

[23] Jin Li et al. "Significant permission identification for machine-learning-based android malware detection". In: *IEEE Transactions on Industrial Informatics* 14.7 (2018), pp. 3216–3225.

[24] Kabakus Abdullah Talha, Dogru Ibrahim Alper, and Cetin Aydin. "APK Auditor: Permission-based Android malware detection system". In: *Digital Investigation* 13 (2015), pp. 1–14.

[25] Fengjun Shang et al. "Android malware detection method based on naive Bayes and permission correlation algorithm". In: *Cluster Computing* 21.1 (2018), pp. 955–966.

[26] Franklin Tchakounté, A Djakene Wandala, and Yélémou Tiguiane. "Detection of android malware based on sequence alignment of permissions". In: *Int. J. Comput.(IJC)* 35.1 (2019), pp. 26–36.

Open Access This chapter is licensed under the terms of the Creative Commons Attribution-NonCommercial 4.0 International License (http://creativecommons.org/licenses/by-nc/4.0/), which permits any noncommercial use, sharing, adaptation, distribution and reproduction in any medium or format, as long as you give appropriate credit to the original author(s) and the source, provide a link to the Creative Commons license and indicate if changes were made.

The images or other third party material in this chapter are included in the chapter's Creative Commons license, unless indicated otherwise in a credit line to the material. If material is not included in the chapter's Creative Commons license and your intended use is not permitted by statutory regulation or exceeds the permitted use, you will need to obtain permission directly from the copyright holder.



Check for updates

Received: 13 May 2024 | Revised: 5 February 2025 | Accepted: 14 March 2025

DOI: 10.4218/etrij.2024-0224

ORIGINAL ARTICLE

ETRI Journal WILEY

Compact planar UWB microstrip antenna with independently controllable dual notch bands

Subhajit Paul[1] | **Sandeep Rana**[2] | **Amit Ranjan Azad**[1] | **Dalia Nandi**[1] | **Akhilesh Mohan**[2]

[1]Department of Electronics and Communication Engineering, Indian Institute of Information Technology Kalyani, West Bengal, India

[2]Department of Electronics and Communication Engineering, Indian Institute of Technology Roorkee, Uttarakhand, India

Correspondence
Amit Ranjan Azad, Department of Electronics and Communication Engineering, Indian Institute of Information Technology Kalyani, West Bengal, India.
Email: amitranjanazad@iiitkalyani.ac.in

Funding information
This research received no external funding.

Abstract

This paper introduces a compact microstrip antenna specially designed for ultra-wideband (UWB) technology with dual notch band (DNB) properties. The antenna consists of a semi-annular ring-shaped patch and a partial ground plane. An arc-shaped slot and a rectangular complementary split-ring resonator are used to create the DNBs. The UWB antenna operates within a frequency spectrum spanning from 3.15 GHz to 13.57 GHz. DNBs are generated for the frequency ranges of 3.43 GHz to 4.25 GHz and 6.57 GHz to 7.81 GHz to reduce interference from the WiMAX band and X-band downlink satellite channel, respectively. The DNBs can be tuned separately by tuning the structural parameters of the antenna. Within the UWB frequency range, the simulated and measured data demonstrate that the antenna exhibits good radiation efficiency with nearly bidirectional radiation characteristics in the *E*-plane with a peak gain of 3.5 dBi. The proposed antenna has potential applications in UWB communication, mobile communication, and wireless body area networks due to its compact size and low manufacturing cost.

KEYWORDS
compact antenna, dual notch band (DNB), microstrip, planar antenna, UWB antenna

1 | INTRODUCTION

Ultrawideband (UWB) technology has attracted considerable interest in recent years owing to its novel influence on communication networks. In 2002, the Federal Communications Commission (FCC) allocated the 3.1 GHz to 10.6 GHz spectrum for UWB systems [1]. To facilitate wireless communication in short-range networks, transceivers require compact, low-power, and cost-effective UWB antennas [2]. Numerous UWB antennas have been documented in the published literature, which span the 3.1 GHz to 10.6 GHz frequency range, as designated by the FCC. However, strong signals from existing narrow bands, including the WiMAX band (3.3 GHz to 3.8 GHz), wireless local area network band (5.15 GHz to 5.35 GHz), and X-band downlink satellite channel (DSC) (7.25 GHz to 7.75 GHz), deteriorate UWB antenna performance as a result of significant interference. These unwanted narrowband signals must be filtered to enhance the standards of UWB systems. To prevent interference from these unwanted signals, antennas with band-notched features have become a growing area of interest in UWB technology.

This is an Open Access article distributed under the term of Korea Open Government License (KOGL) Type 4: Source Indication + Commercial Use Prohibition + Change Prohibition (http://www.kogl.or.kr/info/licenseTypeEn.do).
1225-6463/$ © 2025 ETRI

Over the past few years, numerous UWB antennas with band-notched properties have been explored using various design methodologies [3–23] to filter specific unwanted bands within a UWB passband. The utilization of external band-stop filters results in an increase in size, expense, complexity, and load mismatch. Researchers have employed various techniques to overcome these challenges, including slotted patches, metamaterials, stubs, meandering, and defective ground structures (DGSs), to attenuate specific frequencies within the UWB operating range. Within the UWB spectrum (3.1 GHz to 10.6 GHz), UWB antennas are intended to block the WiMAX band (3.3 GHz to 3.8 GHz) and the X-band DSC (7.25 GHz to 7.75 GHz). The literature reports various single band-notched UWB antennas based on different techniques, including a meandering slot in a radiating patch, a U-shaped slot, a reversed Y-shaped short-circuit stub, a tuning slot, DGS incorporating T-shaped stubs in the bottom layer, and an L-shaped slot loaded on the ground [3–7]. However, to enhance UWB antenna characteristics for more efficient operations in the UWB, it is beneficial to create designs with dual notch band (DNB) capabilities.

DNBs use a coplanar waveguide (CPW) with spiral slots and pulse-shaped slots in the ground plane [8], three special types of L-shaped stubs into the bottom layer [9], two CPW-fed hexagonal fractal patches with double slots [10], and a T-shaped element within the patch, as well as dual U-shaped parasitic components [11]. DNBs have also been fabricated by incorporating stubs and slots into the primary radiating element and parasitic stubs into the ground surface [12–16]. Additionally, researchers have achieved three band-notch features by inserting additional slots, stubs, parasitic resonators, and diodes [17–19]. However, the introduction of parasitic resonators and diodes increases design complexity and affects antenna efficiency. Recently, researchers have shown growing interest in developing multiple-input and multiple-output antennas that operate within the UWB frequency range and feature multiple band-notched characteristics to enhance performance and mitigate interference [20–23]. Alternative approaches to creating a stopband and enhancing bandwidth (BW), including the use of electromagnetic bandgap structures, Vivaldi antennas, and tightly coupled arrays, are discussed in [24–26]. The majority of reported antennas exhibit large footprints and NBs with weak attenuation levels. Additionally, it is challenging to tune DNBs or triple NBs independently, as reported in the literature.

To address these issues, we propose a new design for a compact UWB antenna featuring two independently adjustable NBs. The antenna operates across a frequency range of 3.15 GHz to 13.57 GHz. Additionally, the incorporation of an arc-shaped slot and rectangular complementary split-ring resonator (CSRR) into the main radiating patch enables the attainment of independently controllable DNB characteristics. The first NB covers 3.43 GHz to 4.25 GHz, while the second NB covers 6.57 GHz to 7.81 GHz to eliminate interference from the WiMAX frequency range and X-band DSC, respectively. The DNBs are independently controlled by adjusting the geometric parameters of the antenna. A detailed analysis of how changes in the antenna design parameters affect its performance is presented. The compact size of the proposed antenna makes it an excellent

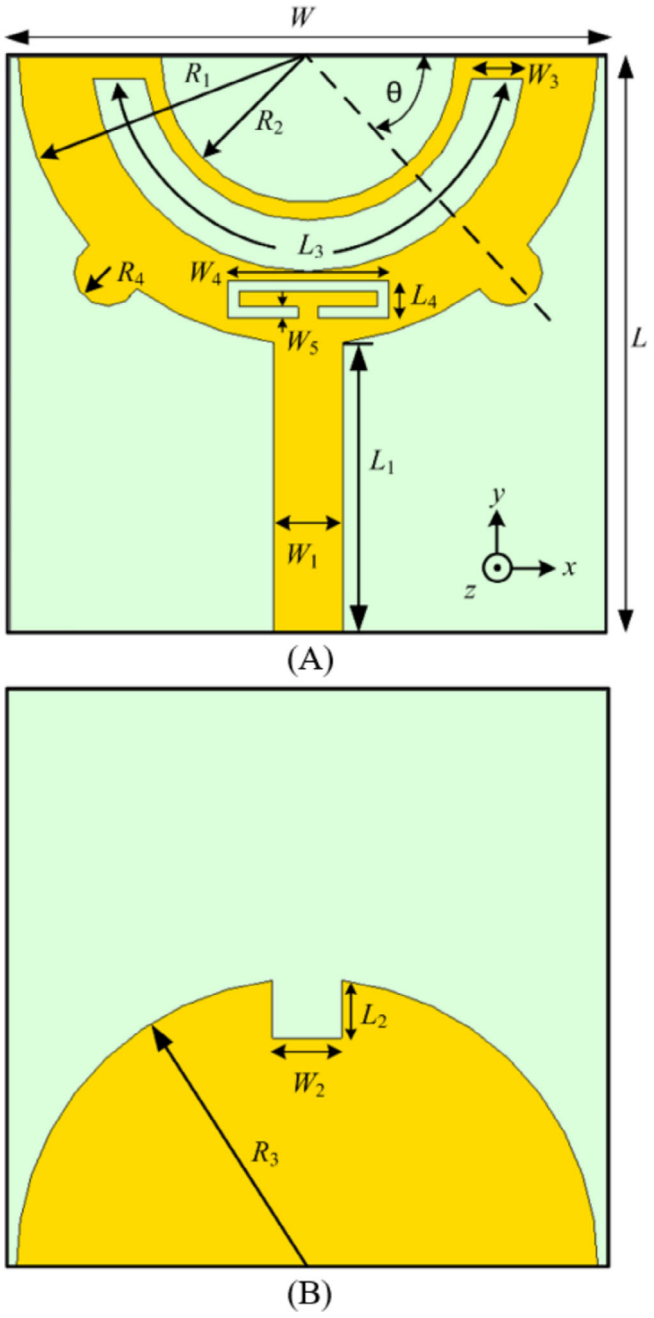


FIGURE 1 Schematics of the proposed DNB UWB antenna: (A) top view and (B) bottom view.

22337326, 0, Downloaded from https://onlinelibrary.wiley.com/doi/10.4218/etrij.2024-0224 by Delhi Technological University, Wiley Online Library on [15/06/2025]. See the Terms and Conditions (https://onlinelibrary.wiley.com/terms-and-conditions) on Wiley Online Library for rules of use; OA articles are governed by the applicable Creative Commons License

choice for integration into wireless body area networks (WBANs) and short-range wireless communication technologies while eliminating interference from unwanted bands.

2 | ANTENNA DESIGN

Figure 1 illustrates the recommended antenna arrangement, and the optimized parameters are listed in Table 1.

TABLE 1 Parameters of the proposed antenna and their values.

Parameter	Value (mm)	Parameter	Value (mm)
W	26.8	R_1	13
L	26	R_2	6.6
W_1	3.1	R_3	13
W_2	3.1	L_1	13.09
W_3	2.32	L_2	2.7
W_4	7.2	L_3	19.3
W_5	0.5	L_4	1.7
θ	47.3°		

The antenna consists of a semi-annular ring-shaped patch and semi-circular ground. Two small semicircular patches are used on the top metal layer, and a rectangular slit is cut on the bottom metal layer for better impedance matching. An arc-shaped slot and rectangular CSRR are engraved on the uppermost metal layer to introduce DNBs and mitigate interference from unwanted bands.

The antenna is constructed using the FR4 dielectric material with a relative permittivity ε_r of 4.3, height h of 1.575 mm, and loss tangent δ of 0.02. The antenna is fed by a 50 Ω microstrip line. Simulations and optimizations were performed using CST Microwave Studio. The proposed antenna has overall dimensions of 26.8 mm × 26 mm.

The step-by-step design methodology of the proposed UWB antenna with DNBs is illustrated in Figure 2. The antenna dimensions (width W and length L) are calculated based on the lowest operating frequency f_L as [3]:

$$W = L = \frac{c}{2f_L\sqrt{\varepsilon_{eff}}}, \quad (1)$$

where c is the velocity of light and ε_{eff} represents the effective dielectric constant of the substrate. Equation (1) states that the antenna length and width are equal to half

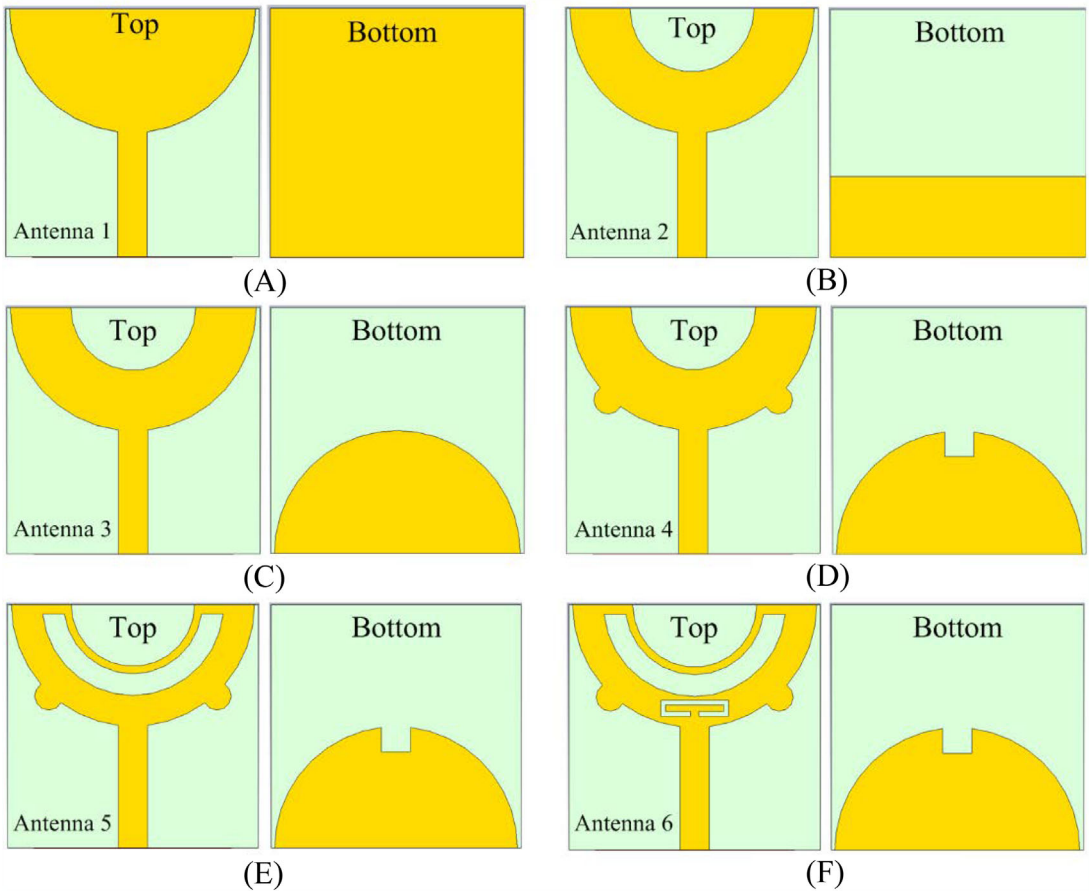


FIGURE 2 Design steps of the proposed DNB UWB antenna.

22337326, 0, Downloaded from https://onlinelibrary.wiley.com/doi/10.4218/etrij.2024-0224 by Delhi Technological University, Wiley Online Library on [15/06/2025]. See the Terms and Conditions (https://onlinelibrary.wiley.com/terms-and-conditions) on Wiley Online Library for rules of use; OA articles are governed by the applicable Creative Commons License

of the effective wavelength at a lower operating frequency f_L. The effective dielectric constant ε_{eff} is approximately determined as [27].

$$\varepsilon_{eff} = \frac{\varepsilon_r + 1}{2}. \quad (2)$$

The layout of a conventional microstrip semicircular patch antenna, referred to as Antenna 1, is shown in Figure 2A. Figure 3A plots the simulated $|S_{11}|$. It is evident that Antenna 1 provides a wide BW but does not cover the standard UWB frequency range. To achieve UWB performance, the semicircular patch was converted into a semi-annular ring-shaped patch, and the ground layer was transformed into a partial ground layer, as shown in Figure 2B, which is referred to as Antenna 2. As shown in Figure 3A, the simulated $|S_{11}|$ of Antenna 2 exhibits a shift in the operating frequency toward a lower value. However, $|S_{11}|$ is degraded because of improper impedance matching. Next, a semicircular ground plane was used instead of a rectangular ground plane, which is denoted as Antenna 3 in Figure 2C.

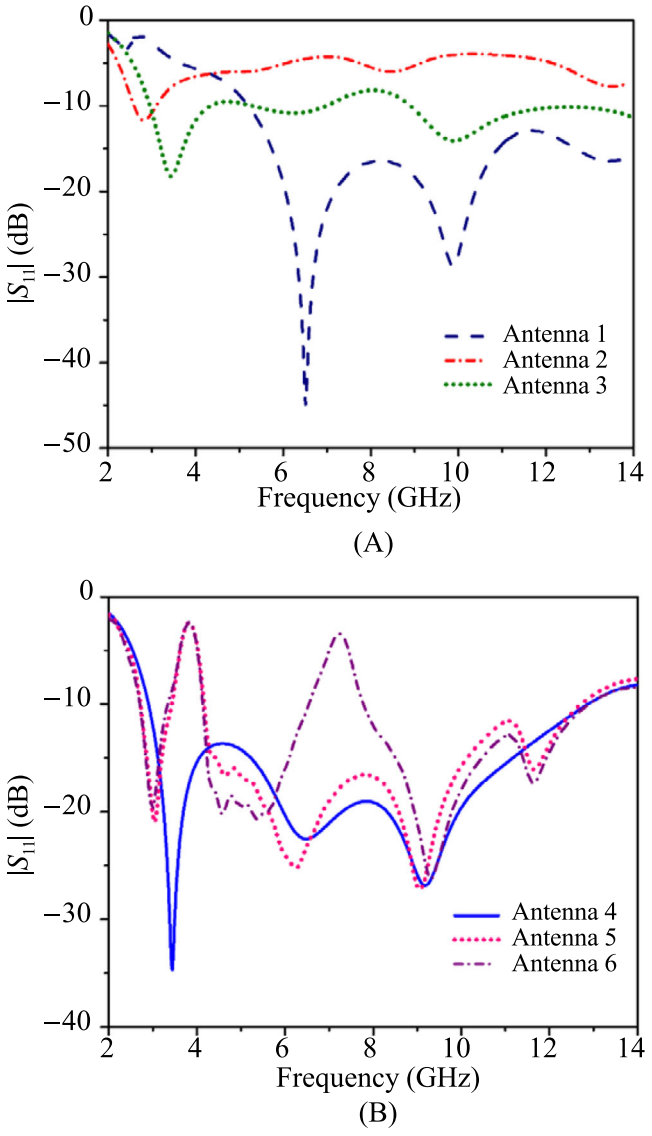


FIGURE 3 Simulated $|S_{11}|$ performance comparison: (A) antennas 1 to 3 and (B) antennas 4 to 6.

According to Figure 3A, Antenna 3's simulated $|S_{11}|$ is slightly improved. However, further structural modifications are required to improve UWB performance. Two small semicircular patches at appropriate positions were introduced at the top metal layer, and a rectangular slit was etched in the bottom metal layer, which is denoted as Antenna 4 in Figure 2D. According to Antenna 4's simulated $|S_{11}|$, it is possible to reach the UWB frequency range of 2.7 GHz to 12.87 GHz, as plotted in Figure 3B. To create the initial NB, an arc-shaped slot was etched on the top metal layer, which is denoted as Antenna 5 in Figure 2E. Furthermore, an additional NB was generated by introducing a rectangular CSRR on the top metal layer, which is denoted as Antenna 6 in Figure 2F. Figure 3B presents the simulated $|S_{11}|$ values for Antennas 5 and 6. Antenna 5 utilizes an NB to mitigate interference from the WiMAX band. Antenna 6 utilizes DNBs to eliminate interference from WiMAX and X-band DSC. The length L is the effective length of the half-wavelength resonator.

The length of the slot at each notch frequency f_0 is roughly half of the guided wavelength λ_g and can be determined using the following relation [27]:

$$L = \frac{\lambda_g}{2} = \frac{\lambda_o}{2\sqrt{\varepsilon_{eff}}} = \frac{c}{2f_0\sqrt{\varepsilon_{eff}}}. \quad (3)$$

The first NB was generated by etching an arc-shaped slot, whereas the second was created by incorporating a rectangular CSRR into the uppermost metal layer, as shown in Figure 4A. Therefore, the center frequency (CF) f_0 of the NBs can be obtained using (3) as follows:

$$f_0 = \frac{c}{2L\sqrt{\varepsilon_{eff}}}. \quad (4)$$

The first NB centered at $f_{notch1} = 3.8$ GHz is created by embedding an arc-shaped slot in the radiating patch with an effective length of $L_{S1} = 19.3$ mm, as shown in Figure 4A. The second NB centered at $f_{notch2} = 7.21$ GHz is created by integrating a CSRR in the radiating patch with an effective length of $L_{S2} = 12.1$ mm, as shown in Figure 4A. The effective length L_{S2} can be derived by using (5), as discussed in [28]:

$$L_{S2} = 2(L_4 + W_4) - 4W_5. \quad (5)$$

22337326, 0, Downloaded from https://onlinelibrary.wiley.com/doi/10.4218/etrij.2024-0224 by Delhi Technological University, Wiley Online Library on [15/06/2025]. See the Terms and Conditions (https://onlinelibrary.wiley.com/terms-and-conditions) on Wiley Online Library for rules of use; OA articles are governed by the applicable Creative Commons License

The radiation created by the arc-shaped slot and CSRR is canceled by the primary UWB antenna. Consequently, two NBs are generated at the resonant frequencies of the arc-shaped slot and CSRR. Figure 4B illustrates the simulated $|S_{11}|$ of the proposed antenna, showing its performance across different frequency bands.

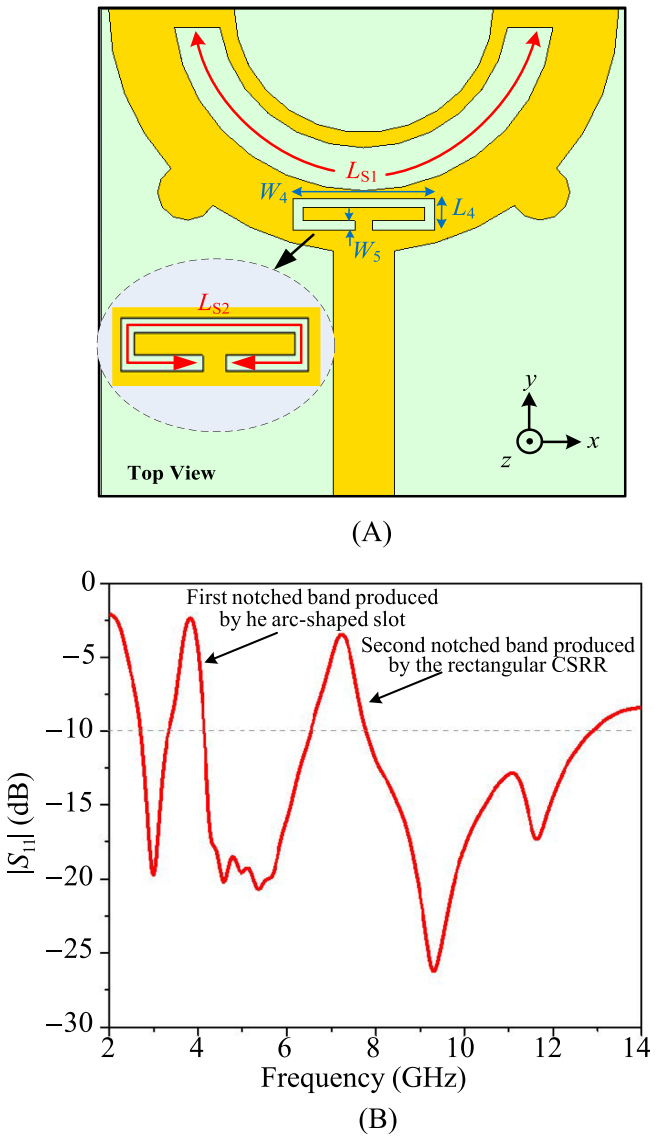


FIGURE 4 (A) Effective length of the arc-shaped slot and CSRR on the top layer of the proposed antenna, and (B) simulated $|S_{11}|$ of the proposed antenna.

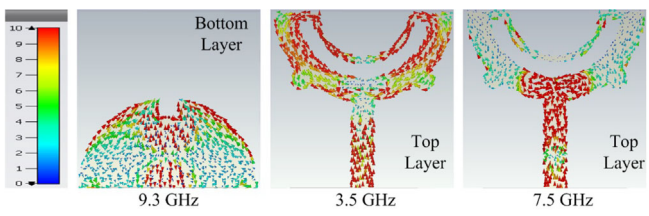


FIGURE 5 Simulated surface current density of the proposed antenna at different frequencies.

Figure 5 presents the electrical current flow on the surface of the proposed antenna at different frequencies, which was examined to understand the design principles of the UWB antenna with DNBs. The current flow is more concentrated around the edges of the rectangular slit introduced on the ground plane at 9.3 GHz, indicating its significant contribution to resonance. The current distribution is centered near the arc-shaped slot in the radiating patch, with minimal currents observed along the CSRR at 3.5 GHz. Conversely, at 7.5 GHz, the current is concentrated around the CSRR located on the patch, with the minimum distribution detected along the arc-shaped slot. These results demonstrate that each slot on the patch independently regulates the two NBs.

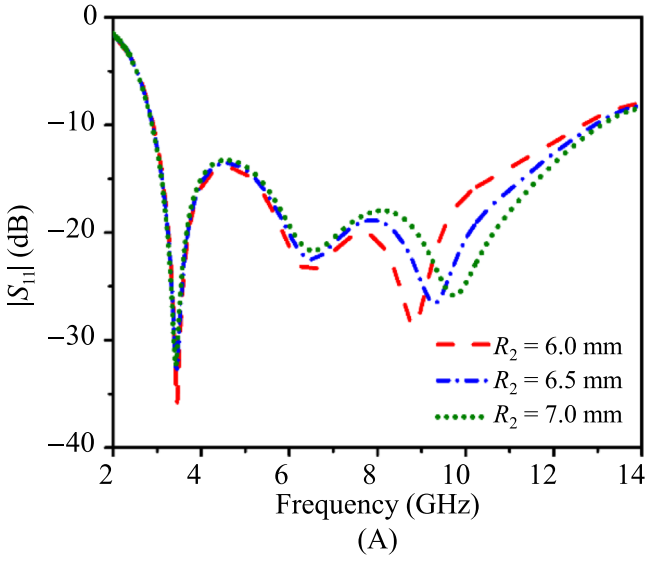
3 | ANTENNA ANALYSIS

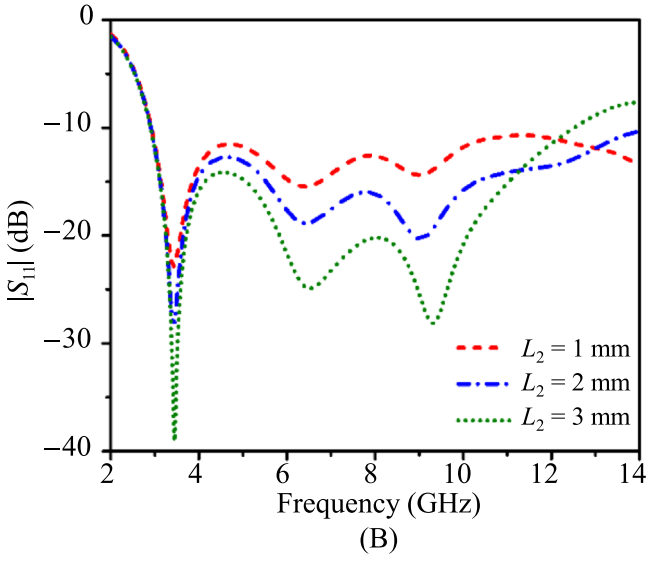
The simulated $|S_{11}|$ of the primary UWB antenna is plotted in Figure 6A versus the inner radius R_2 of the semi-annular ring-shaped patch. The upper cutoff frequency of the UWB antenna increases when R_2 increases from 6 mm to 7 mm while maintaining a constant lower cutoff frequency, leading to an increased BW. Figure 6B presents the simulated $|S_{11}|$ of the UWB antenna versus varying lengths L_2 of the rectangular slit in the ground layer of the antenna. The UWB band selectivity improves significantly when L_2 increases from 1 mm to 3 mm. The simulated $|S_{11}|$ versus the width W_2 of the rectangular slit in the ground plane is plotted in Figure 6C. Improved BW and selectivity are obtained when W_2 increases from 2 mm to 3 mm. We can deduce that by varying the parameters R_2, L_2, and W_2, the overall BW and selectivity of the UWB antenna can be controlled.

For the initial NB, the length L_3 and width W_3 of the arc-shaped slot determine its CF and BW. The length L_4 and width W_4 of the rectangular CSRR can be adjusted to determine the CF and BW of the second NB. Furthermore, the proposed antenna enables individual tuning of the NBs without compromising the overall performance of the antenna. Figure 7A,B presents the simulated $|S_{11}|$ of the proposed antenna with variations in L_3 and W_3.

One can see that when L_3 is extended from 18.7 mm to 19.3 mm, the CF of the initial NB shifts to a lower frequency with a small drop in BW. In contrast, when W_3 increases from 0.3 mm to 2.3 mm, the BW of the initial NB increases with a slight shift in the CF toward a higher value. Furthermore, the CF and BW of the second NB remain almost constant.

22337326, 0, Downloaded from https://onlinelibrary.wiley.com/doi/10.4218/etrij.2024-0224 by Delhi Technological University, Wiley Online Library on [15/06/2025]. See the Terms and Conditions (https://onlinelibrary.wiley.com/terms-and-conditions) on Wiley Online Library for rules of use; OA articles are governed by the applicable Creative Commons License





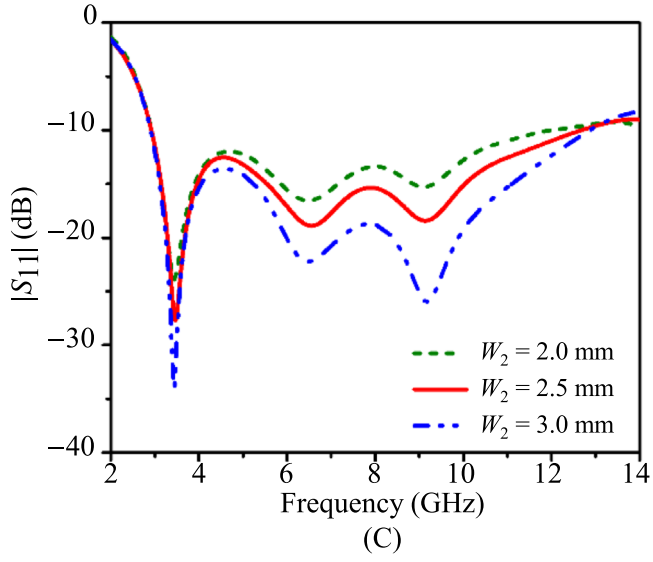


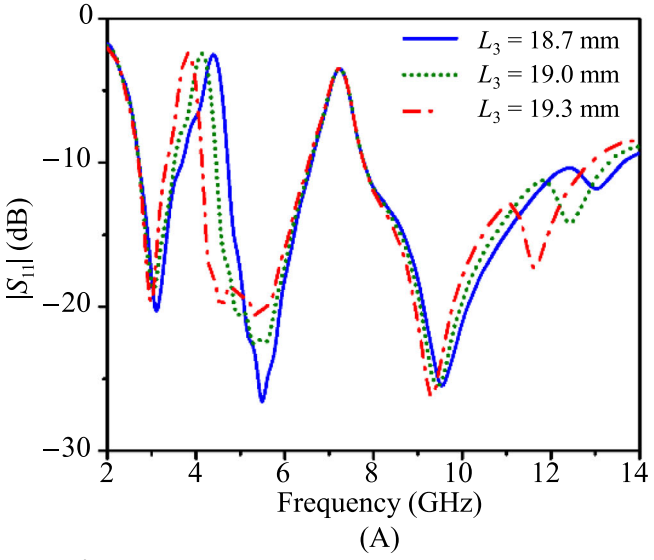
FIGURE 6 Simulated $|S_{11}|$ versus (A) R_2, (B) L_2, and (C) W_2.

Figure 8A,B presents the $|S_{11}|$ values for the UWB antenna with variations in L_4 and W_4. One can see that increasing L_4 from 1.4 mm to 2.2 mm shifts the CF of the second NB toward a lower frequency with a slight increase in BW.

However, as W_4 increases from 7 mm to 9 mm, the BW of the second NB increases with a shift in the CF toward a lower frequency. Additionally, the CF and BW of the first NB remain almost unchanged. These observations illustrate that the parameters L_3, W_3, L_4, and W_4 can be adjusted to control the two NBs independently.

The following is a summary of the design steps for the proposed UWB antenna with DNBs.

1. The key parameters include the operating frequency band, gain, impedance matching, and other



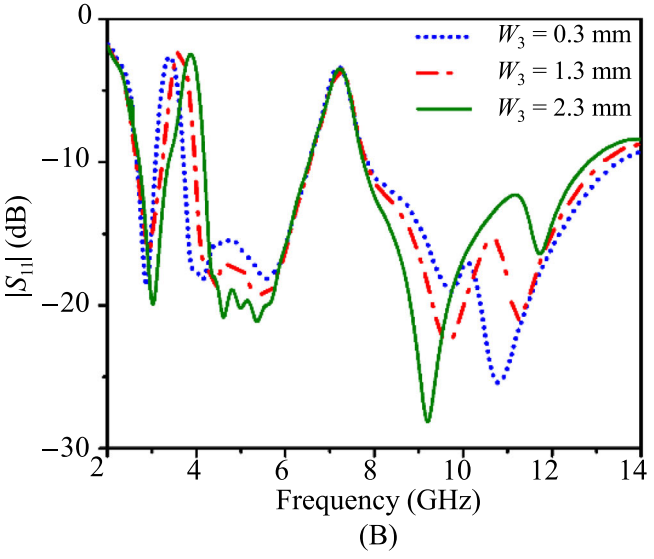


FIGURE 7 Simulated $|S_{11}|$ versus (A) L_3, and (B) W_3.

22337326, 0, Downloaded from https://onlinelibrary.wiley.com/doi/10.4218/etrij.2024-0224 by Delhi Technological University, Wiley Online Library on [15/06/2025]. See the Terms and Conditions (https://onlinelibrary.wiley.com/terms-and-conditions) on Wiley Online Library for rules of use; OA articles are governed by the applicable Creative Commons License

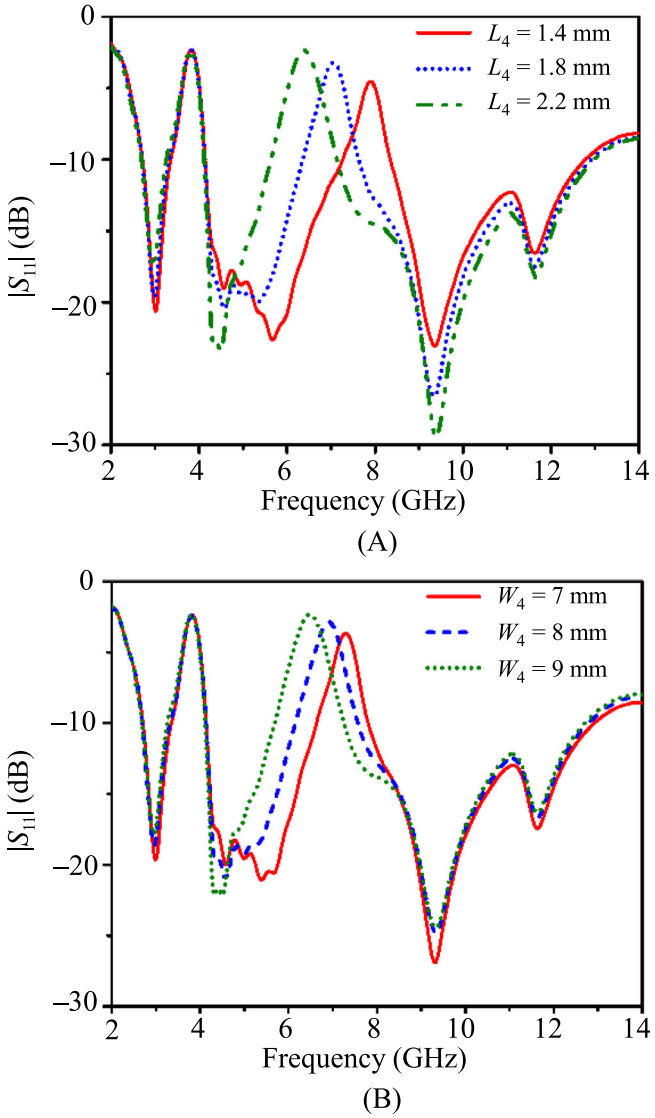


FIGURE 8 Simulated $|S_{11}|$ versus (A) L_4 and (B) W_4.

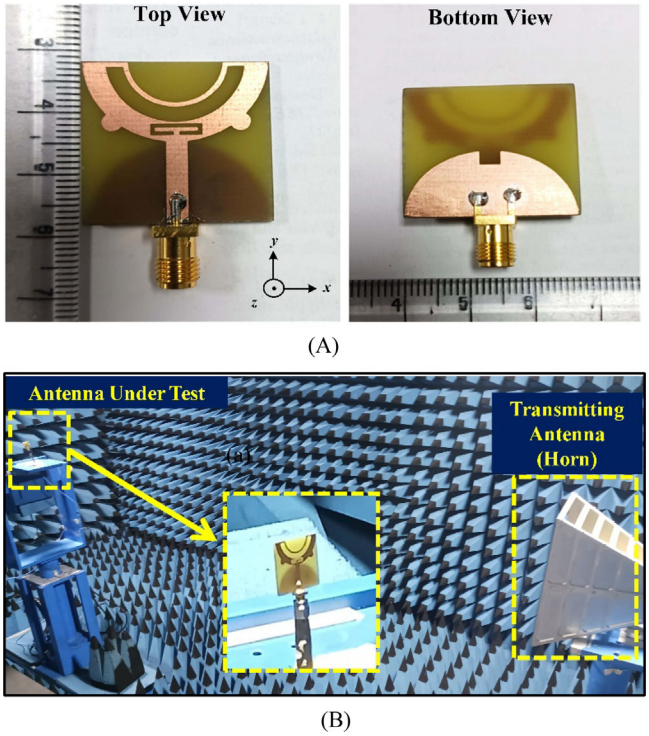


FIGURE 9 Photographs of the (A) fabricated antenna and (B) measurement setup.

performance criteria. These specifications guide the overall antenna design and ensure that the antenna satisfies the desired functionality within the UWB range.

2. The UWB antenna was designed using a semi-annular ring-shaped patch. A semi-circular partial ground plane with a slit can be used to achieve the desired operating band and improve antenna performance. Two small semi-circular patches were positioned appropriately on the top metal layer, along with a rectangular slit on the bottom metal layer, to define the starting and ending frequencies of the UWB spectrum while ensuring the required operating band and improving antenna performance. The design curves for R_2, L_2, and W_2 were used to obtain the desired UWB spectra.
3. The position and BW of the NBs must be carefully selected to avoid interference from specific communication bands such as WiMAX and X-band DSC. This step involves determining where the notches should be placed within the UWB spectrum and setting the appropriate BW for each.
4. Next, we introduce an arc-shaped slot and rectangular CSRR on the patch to generate the DNBs. The appropriate frequency location and BW of the NBs were obtained using the design graphs plotted for L_3, W_3, L_4, and W_4. The length of the slot at each notch frequency (f_0) is roughly half of the guided wavelength λ_g and can be determined using (3).
5. Finally, the dimensional parameters of the antenna were fine-tuned to optimize its performance. This step ensures that the antenna meets the desired specifications for BW, gain in the NBs, and interference rejection.

4 | RESULTS AND DISCUSSION

A prototype was constructed and tested experimentally to validate the efficacy of the proposed method. Figure 9A,B presents photographs of the fabricated antenna and antenna measurement setup, respectively. The proposed antenna was constructed to function across the frequency span of 2.7 GHz to 12.87 GHz with the aim of reducing disturbances originating from the WiMAX band

22337326, 0, Downloaded from https://onlinelibrary.wiley.com/doi/10.4218/etrij.2024-0224 by Delhi Technological University, Wiley Online Library on [15/06/2025]. See the Terms and Conditions (https://onlinelibrary.wiley.com/terms-and-conditions) on Wiley Online Library for rules of use; OA articles are governed by the applicable Creative Commons License

(3.32 GHz to 4.13 GHz) and X-band DSC (6.53 GHz to 7.77 GHz).

This section explores the characteristics of the proposed UWB antenna with DNBs, including the reflection coefficient, realized gain, radiation efficiency, and far-field radiation patterns.

4.1 | Reflection coefficient

Figure 10 presents the simulated, equivalent circuit model, and measured $|S_{11}|$ performance of the proposed DNB antenna, as well as the simulated data of the primary UWB.

The proposed antenna's simulated impedance BW ($|S_{11}| < -10$ dB) is 10.17 GHz (2.70 GHz to 12.87 GHz). The first NB is created over the frequency interval of 3.32 GHz to 4.13 GHz, while the second NB frequency band is 6.53 GHz to 7.77 GHz. The simulated fractional BW (FBW), excluding the notch BW, is 130.6%. The measured BW ($|S_{11}| < -10$ dB) of the UWB antenna with notches is 10.42 GHz (3.15 GHz to 13.57 GHz). The measured first NB covers 3.43 GHz to 4.25 GHz, whereas the second NB covers 6.57 GHz to 7.81 GHz. The measured FBW, excluding the BW of the notches, is 124.6%. A strong rejection of the reflection coefficient can be observed in the WiMAX band (3.3 GHz to 3.8 GHz), as well as in the X-band DSC (7.25 GHz to 7.75 GHz).

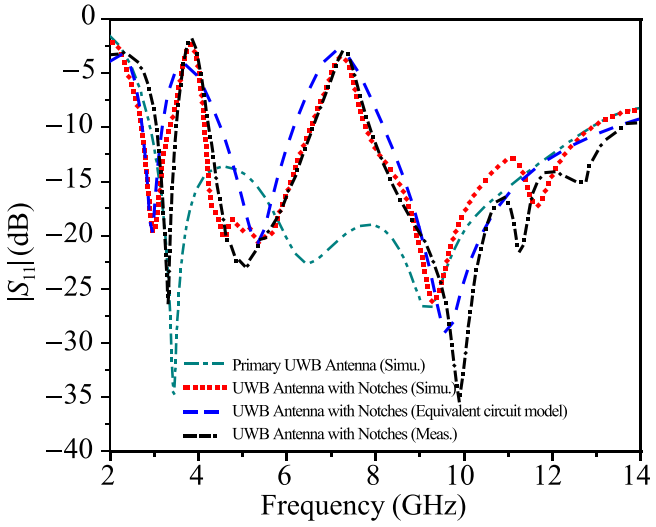


FIGURE 10 Simulated, equivalent circuit model, and measured $|S_{11}|$ of the proposed antenna.

Figure 11 presents the equivalent circuit model of the antenna configuration. This circuit model was created using the Keysight ADS simulation tool. The resonators R_1–L_1–C_1, R_2–L_2–C_2, R_3–L_3–C_3, and L_a–C_a represent the primary UWB antennas. The first and second NBs are represented by resonators created using R_{S1}–L_{S1}–C_{S1} and R_{S2}–L_{S2}–C_{S2}, respectively.

We first focus on explaining the parameters in the equivalent circuit and then outline a clear sequence of steps to determine their values. An equivalent circuit was presented as a parallel R–L–C circuit for a narrowband microstrip antenna in [27]. By contrast, when designing a UWB antenna, our focus is on achieving a wide BW.

1. Unlike narrowband antennas, UWB antennas operate based on multiple overlapping resonances, rather than a single resonance. Therefore, a sequence of parallel R–L–C resonators (R_1–L_1–C_1, R_2–L_2–C_2, and R_3–L_3–C_3) can be used to create equivalent circuits for UWB antennas, as shown in Figure 11.
2. The feed line is incorporated into the equivalent circuit and represented by a series R_f–L_f to model the distributed elements of the antenna.
3. The annular-shaped slot in the radiating patch is represented by a series of L–C resonators, denoted as L_a–C_a, to widen the impedance BW, as specified by the FCC. The creation of an annular slot in the radiating patch introduces additional resonant modes, which broaden the impedance BW, altering the current distribution and enhancing the ability of the antenna to operate in the UWB frequency range.
4. The arc-shaped slot and CSRR are created as series R–L–C circuits (R_{S1}–L_{S1}–C_{S1} and R_{S2}–L_{S2}–C_{S2}), which

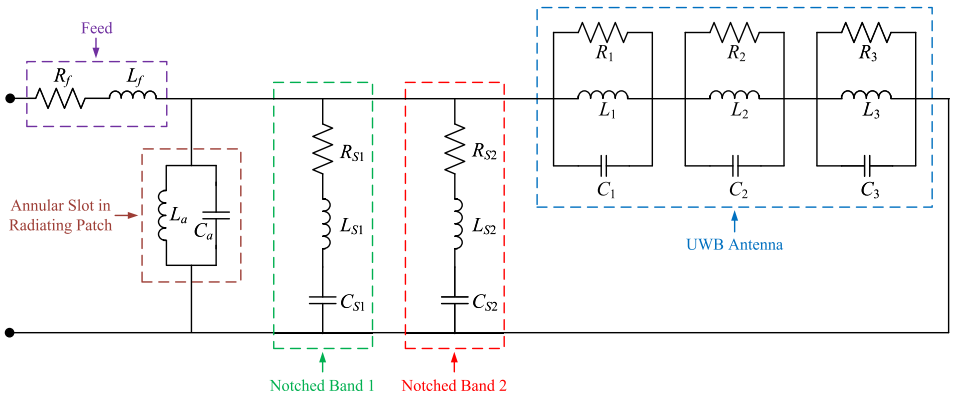


FIGURE 11 Equivalent circuit model of the proposed antenna with DNBs.

22337326, 0, Downloaded from https://onlinelibrary.wiley.com/doi/10.4218/etrij.2024-0224 by Delhi Technological University, Wiley Online Library on [15/06/2025]. See the Terms and Conditions (https://onlinelibrary.wiley.com/terms-and-conditions) on Wiley Online Library for rules of use; OA articles are governed by the applicable Creative Commons License

function as a short circuit, resulting in the maximum input power being reflected back to the input terminal and effectively rejecting the interference of the WiMAX band and X-band DSC.

The optimized values for the lumped components in the equivalent circuit are as follows: $R_f = 50\ \Omega$, $R_1 = 257.8\ \Omega$, $R_2 = 65.3\ \Omega$, $R_3 = 162.5\ \Omega$, $R_{S1} = 672.9$ kΩ, $R_{S2} = 9.81\ \Omega$, $L_f = 0.66$ nH, $L_1 = 34.2$ nH, $L_2 = 12.4$ nH, $L_3 = 0.20$ nH, $L_{S1} = 102.7\ \mu$H, $L_{S2} = 12$ nH, $L_a = 3.90$ nH, $C_1 = 0.85$ pF, $C_2 = 2.6$ nF, $C_3 = 2.59$ pF, $C_{S1} = 24.7$ nF, $C_{S2} = 0.23$ pF, and $C_a = 3.05$ pF. The reflection coefficient derived from the equivalent circuit model approximately matches the simulated and measured $|S_{11}|$ values of the proposed antenna, which verifies the validity of the presented equivalent circuit model.

4.2 | Realized gain

Figure 12 plots the simulated and measured realized gains of the proposed DNB antenna, along with the simulated gain of the primary UWB antenna. One can see that the primary UWB antenna's simulated gain ranges from 1.9 to 3.76 dBi over the entire operating frequency spectrum. The simulated gain variation of the proposed UWB antenna exhibits a similar trend to that observed in the primary UWB antenna with a peak gain of 4.03 dBi, except for at the two NBs, where the gain drops to −5.03 dBi at 3.9 GHz and −4.9 dBi at 7.2 GHz. The gain at the first NB is measured to be −3.35 dBi at 3.9 GHz, while the second NB has a gain of −4.3 dBi at 7.2 GHz. Beyond the rejection bands, the recommended antenna exhibits a gain variation of less than 2.1 dBi across the operating band with a peak gain of 3.5 dBi.

4.3 | Radiation efficiency

Figure 13 presents the simulated radiation efficiency of both the primary UWB antenna and the proposed DNB UWB antenna. One can see that the efficiency of the primary UWB antenna remains relatively stable between 75% and 85% across the frequency range of operation. Furthermore, the radiation efficiency of the proposed antenna with DNBs closely matches that of the primary UWB antenna, except at the NBs, where it decreases to below 30% for both NBs.

4.4 | Time-domain analysis

A time-domain analysis of the antenna was performed to examine the transmission coefficient and group delay. The relationship between the incoming and outgoing signals of the structure is described by the transmission coefficient $|S_{21}|$. The group delay τ refers to the delay in time that different frequencies of a signal experience as they travel through a system. Because UWB antennas are used for short-range communication, a lower value of the transmission coefficient $|S_{21}|$ and insignificant distortion in group delay τ are essential. Figure 14 presents the

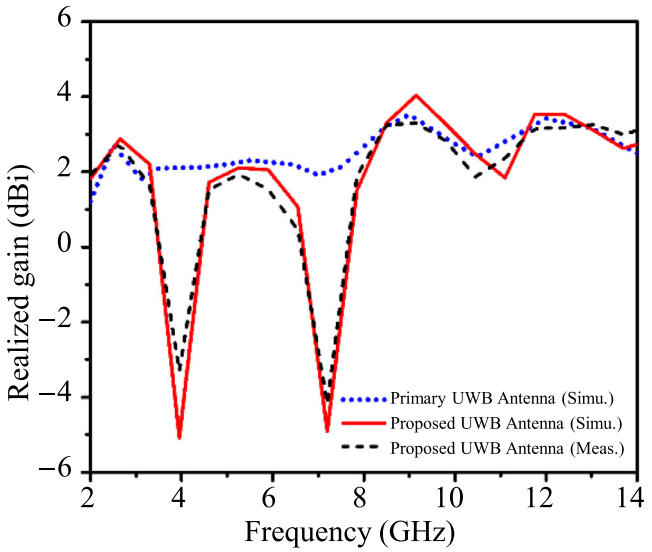


FIGURE 12 Simulated and measured realized gain comparison of the proposed antenna.

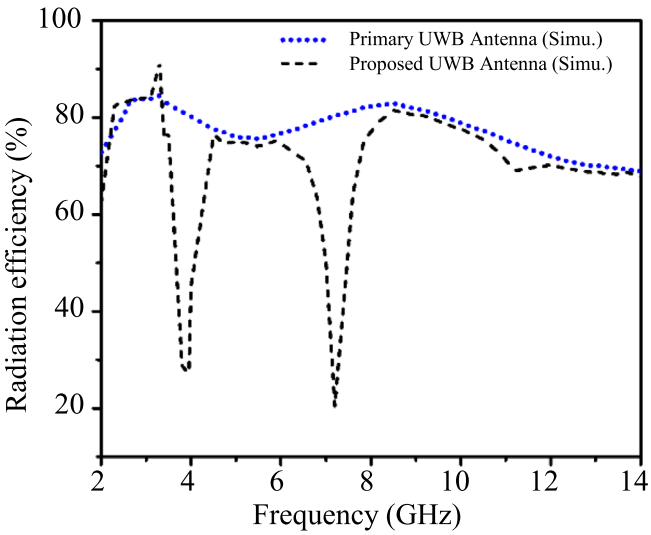


FIGURE 13 Simulated radiation efficiency of the proposed antenna.

22337326, 0, Downloaded from https://onlinelibrary.wiley.com/doi/10.4218/etrij.2024-0224 by Delhi Technological University, Wiley Online Library on [15/06/2025]. See the Terms and Conditions (https://onlinelibrary.wiley.com/terms-and-conditions) on Wiley Online Library for rules of use; OA articles are governed by the applicable Creative Commons License

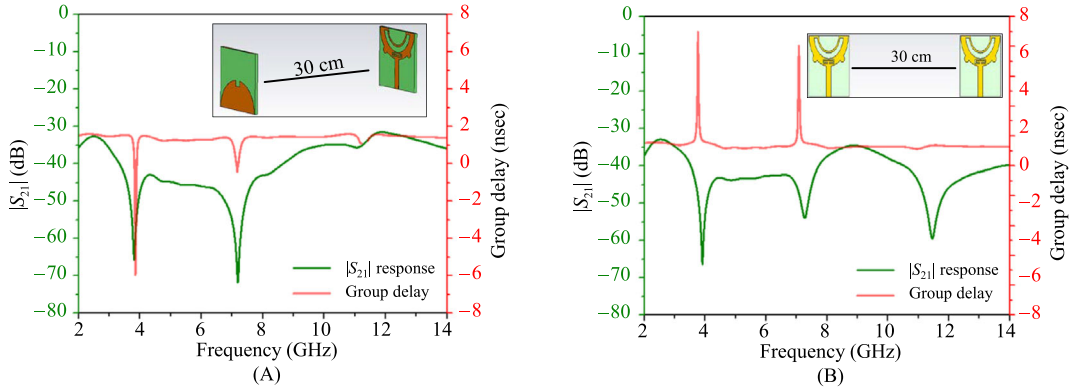


FIGURE 14 Simulated $|S_{21}|$ and group delay of the proposed antenna: (A) face-to-face arrangement and (B) side-by-side arrangement.

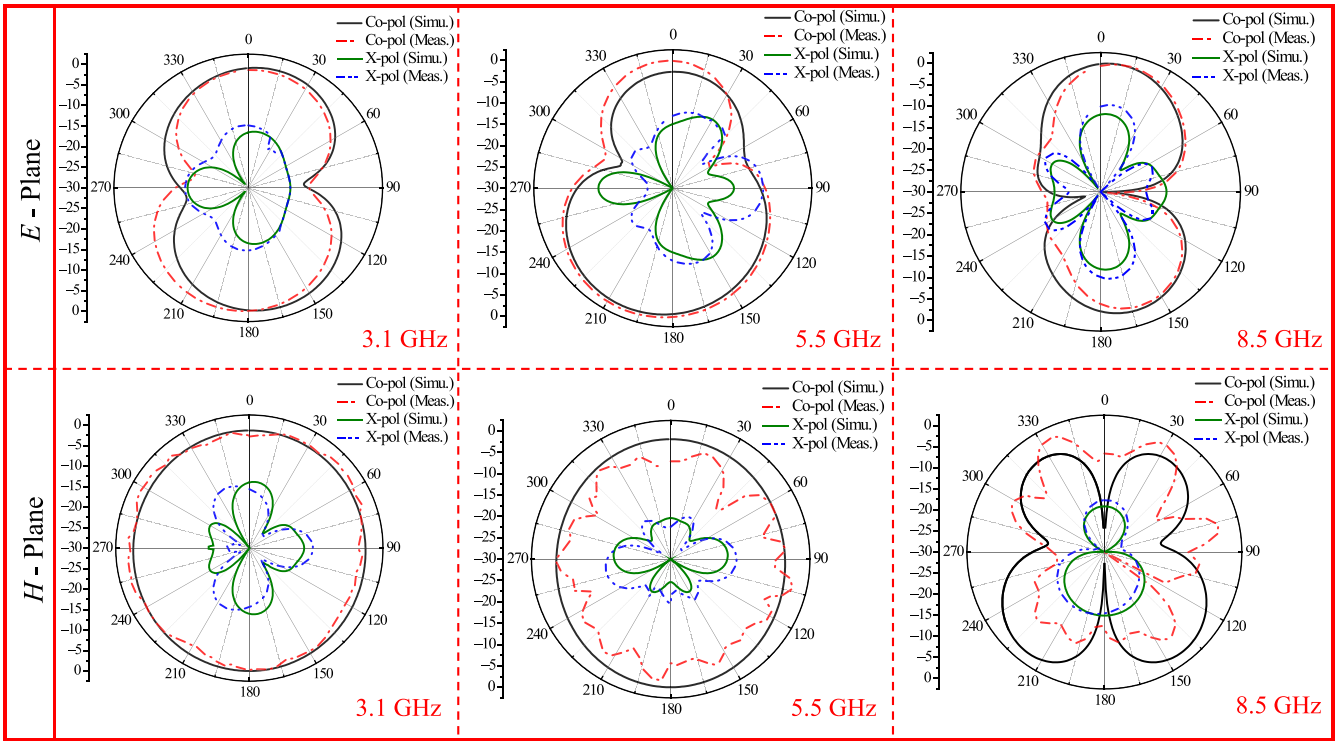


FIGURE 15 Simulated and measured radiation patterns of the proposed antenna in the *E* and *H* planes at 3.1 GHz, 5.5 GHz, and 8.5 GHz.

simulated $|S_{21}|$ and group delay of the proposed antenna for face-to-face and side-by-side arrangements with two identical antennas placed 30 cm apart.

A distance of 30 cm between antenna elements was selected to reduce mutual coupling and enable precise group delay measurements without interference, as discussed in [29]. The antenna achieves excellent isolation with $|S_{21}| < -30$ dB in the operating frequency range. Furthermore, the antenna exhibits very little distortion in the received signals within the operating band but exhibits significant distortion in the NBs. This time-domain analysis demonstrates that the proposed antenna with DNBs exhibits low-dispersion characteristics across the operating band.

4.5 | Far-field radiation patterns

Figure 15 presents the simulated and measured far-field radiation patterns for co-polarization and cross-polarization. These patterns can be observed in the *E* plane (*y*-*z* plane) and *H* plane (*x*-*z* plane) at 3.1 GHz, 5.5 GHz, and 8.5 GHz. The proposed antenna exhibits an almost bidirectional radiation pattern in the *E*-plane co-

22337326, 0, Downloaded from https://onlinelibrary.wiley.com/doi/10.4218/etrij.2024-0224 by Delhi Technological University, Wiley Online Library on [15/06/2025]. See the Terms and Conditions (https://onlinelibrary.wiley.com/terms-and-conditions) on Wiley Online Library for rules of use; OA articles are governed by the applicable Creative Commons License

polarization at all specified frequencies. Furthermore, the antenna exhibits an omnidirectional radiation pattern in the *H*-plane co-polarization at 3.1 and 5.5 GHz, whereas slightly directive butterfly-shaped patterns are observed at 8.5 GHz.

Figure 15 reveals that the antenna radiation patterns are steady over the passband of the UWB spectrum. Based on the absence of an effective radiator in the cross-polarization direction of the proposed antenna, radiation is minimal. Additionally, the measured data closely aligns with the simulated data, with slight variations in the measurement outcomes as a result of fabrication inaccuracies and connector losses. The presented data demonstrate that the proposed

TABLE 2 Comparison of the proposed antenna and previously published works.

Ref.	Technique	Bandwidth (GHz)	No. of NBs	NB Freq. Range (GHz)	FBW (%)	IC of NBs	Peak gain (dBi)	NB gain (dBi)	Physical size (mm × mm)	Electrical size ($\lambda_g \times \lambda_g$)
[4]	Slot and open circuit stub	3.12–10.73	1	5.15–5.78	109.9	Yes	7.8*	−2.1	20 × 18	0.34 × 0.30
[5]	CPW-fed slotted patch	2.8–11*	1	4.9–5.9	118.8	Yes	2.8	−2.3	27 × 27	0.33 × 0.33
[6]	Stubs and slit in ground plane	3–11.5	1	5–5.9	118	Yes	4.8*	−4	20 × 18	0.33 × 0.30
[7]	Slotted patch and modified ground	3.05–12.11	1	3.89–5.93	119.52	Yes	8.36	−5.4*	38.5 × 24	0.64 × 0.40
[8]	Defected ground	3–10.7	2	3.3–3.7, 5.1–5.9	112.4	Yes	5.4*	−4, −7*	28 × 23	0.46 × 0.38
[9]	L-shaped stubs in ground plane	3.1–11	–	–	112	Yes	4*	−10, −8*	28 × 23	0.43 × 0.35
[10]	CPW-fed slotted patch	3.2–10.5	2	4–5.78, 6.83–8.22	106.5	Yes	4.83	−2.66, 1.2	23 × 20	0.40 × 0.34
[11]	Stub and parasitic elements	2.8–11	2	3.3–4.0, 5.05–5.90	118.8	–	4*	−3.8, −8.3*	32 × 26	0.44 × 0.36
[12]	Tri-arm resonator below the resonator	2.98–10.76	2	3.3–3.7, 5.1–5.8*	113.2*	No	5*	−5, −6.5*	29 × 20.5	0.48 × 0.34
[13]	SRR and CSRR loaded in top and bottom layer	2–18	2	4–4.3, 7.3–8.1	160	No	5.3	−1, −1*	47 × 40	0.43 × 0.37
[14]	Parasitic resonator in ground	2.98–12	2	3.26–3.82, 5.01–5.75	120.4	Yes	6.9*	−2.5, −3.9*	30 × 22	0.47 × 0.34
[15]	Crescent-shaped circular rings	2.63–11.66	2	3.15–3.66, 4.9–5.9	126.3	No	4	−1.9, 1*	30 × 20	0.43 × 0.28
[16]	Slotted ground	3–11.2	2	3.3–3.85, 5.05–5.9	115.4	Yes	5	−4.5, −6*	18 × 14	0.70 × 0.54
[17]	Multiple-ring resonator	1.7–30	3	3.52–4.2, 5.04–5.40, 8.22–9.10	178.5	No	3.5*	–	57.7 × 54.25	0.44 × 0.41
[18]	PIN diodes and slots	1.89–10.89	3	2.77–3.3, 5.51–6.25, 10.87–20	140.8	No	6	–	60 × 50	0.62 × 0.51
[19]	Rectangular patch and modified ground	2.9–11*	3	3.36–3.71, 5.15–5.37, 5.78–5.95	116.5	–	4.9*	−3, −4, −3 *	30 × 22	0.50 × 0.36
This work	**Slotted patch and modified ground**	**3.15–13.57**	**2**	**3.43–4.25, 6.57–7.81**	**124.64**	**Yes**	**3.5**	**−3.3, −4.3**	**26.8 × 26**	**0.46 × 0.44**

NB: Notch Band; FBW: Fractional Bandwidth; IC: Independent Controllability; *: Approximate Data; −: No Data Available.
Note: FBW is determined excluding the NB bandwidth where $|S_{11}| \leq -10$ dB.

22337326, 0, Downloaded from https://onlinelibrary.wiley.com/doi/10.4218/etrij.2024-0224 by Delhi Technological University, Wiley Online Library on [15/06/2025]. See the Terms and Conditions (https://onlinelibrary.wiley.com/terms-and-conditions) on Wiley Online Library for rules of use; OA articles are governed by the applicable Creative Commons License

antenna performs consistently over the operating frequency range and has significant rejection capabilities at the desired frequencies. The overall dimensions of the proposed antenna are 26.8 mm × 26 mm, corresponding to $0.46\lambda_g \times 0.44\lambda_g$, where λ_g is determined at the measured lower frequency of the UWB band. The performance of the proposed antenna and those of antennas proposed in previous studies are compared in Table 2. One can clearly see that the proposed antenna covers the standard UWB band with DNBs generated at the desired frequency points. Additionally, it has the advantages of small size, strong rejection at the DNBs, independent control over the two NBs, comparable BW, and acceptable gain with a simple structural configuration.

5 | CONCLUSIONS

This paper presented a compact planar microstrip UWB antenna with individually controllable DNBs. The proposed antenna offers an ultrawide operating BW from 3.15 GHz to 13.57 GHz. Two rejection bands are generated to reduce interference from the WiMAX and X-band DSC. Additionally, our design allows independent control over the BW and position of the stopbands. The experimental data confirmed the simulation results, demonstrating the suitability of our antenna for integration with compact UWB microwave circuits. The proposed UWB antenna provides interference-resistant wireless communication that is suitable for WBANs, automotive radar, smart homes, and internet of things devices.

ACKNOWLEDGMENTS

CONFLICT OF INTEREST STATEMENT

The authors declare that there are no conflicts of interest.

ORCID

Subhajit Paul https://orcid.org/0009-0006-5195-8958
Amit Ranjan Azad https://orcid.org/0000-0003-0103-7916
Akhilesh Mohan https://orcid.org/0000-0002-5687-6218

REFERENCES

1. Federal Communications Commission, *first report and order, revision of part 15 of the Commission's rules regarding ultra-wideband transmission systems*, FCC, 2002, 02–48.
2. K. Y. Yazdandoost and R. Kohno, *Ultra wideband antenna*, IEEE Commun Mag **4** (2004), no. 6, S29–S32.
3. M. E. Bialkowski and A. M. Abbosh, *Design of UWB planar antenna with improved cut-off at the out-of-band frequencies, IEEE Antenn*, Wireless Propag, Ltr. **7** (2008), 408–410.
4. S. Hong, J. Shin, H. Park, and J. Choi, *Analysis of the band-stop techniques for ultrawideband antenna*, Microw. Opt. Technol. Lett. **49** (2007), no. 5, 1058–1062.
5. A. M. Abbosh, *Design of UWB planar antenna with subband rejection capability*, Microw. Opt. Technol. Lett. **49** (2007), no. 11, 2855–2859.
6. M. Abdollahvand et al., *Compact ultra-wideband printed monopole antenna having frequency band-notch characteristic using defected ground structure*, Microw. Opt. Technol. Lett. **53** (2011), no. 10, 2363–2368.
7. A. De, B. Roy, and A. K. Bhattacharjee, *Design and investigations on a compact, UWB, monopole antenna with reconfigurable band notches for 5.2/5.8 GHz WLAN and 5.5 GHz Wi-MAX bands*, Int. J. Commun. Syst. **33** (2020), no. 7, e4323.
8. A. Subbarao and S. Raghavan, *Printed planar UWB antenna with rejection of WLAN and WiMAX bands*, Microw. Opt. Technol. Lett. **55** (2013), no. 4, 740–744.
9. M. M. S. Taheri, H. R. Hassani, and S. M. Ali Nezhad, *UWB printed slot antenna with Bluetooth and dual notch bands*, IEEE Antennas Wirel. Propag. Lett. **10** (2011), 255–258.
10. W. A. Awan, A. Zaidi, N. Hussain, A. Iqbal, and A. Baghdad, *Stub loaded, low profile UWB antenna with independently controllable notch-bands*, Microw. Opt. Technol. Lett. **61** (2019), no. 11, 2447–2454.
11. W. Jiang and W. Che, *A novel UWB antenna with dual notched bands for WiMAX and WLAN applications, IEEE Antenn*, Wireless Propag, Ltr. **11** (2012), 293–296.
12. R. Azim, M.T. Islam, and A.T. Mobashsher, *Dual Band-Notch UWB Antenna With Single Tri-Arm Resonator*, IEEE Antenn, Wireless Propag, Ltr. **13** (2014), 670–673.
13. B. T. P. Madhav, M. V. Rao, and T. Anilkumar, *Conformal band notched circular monopole antenna loaded with split ring resonator*, Wirel. Personal Commun. **103** (2018), 1965–1976.
14. A. K. M. A. H. Siddique, R. Azim, and M. T. Islam, *Compact planar ultra-wideband antenna with dual notched band for WiMAX and WLAN*, Int. J. Microw. Wirel. Technol. **11** (2019), no. 7, 711–718.
15. K. Çelik, *A novel circular fractal ring UWB monopole antenna with dual band-notched characteristics*, ETRI J. **46** (2024), no. 2, 218–226.
16. M. Abdollahvand, B. Abbasi Arand, K. Katoch, and S. Ghosh, *A novel and compact ultra-wideband printed monopole antenna with enhanced bandwidth and dual-band stop properties*, Microw. Opt. Technol. Lett. **66** (2024), no. 1, 1–9.
17. S. U. Rahman, Q. Cao, Y. Wang, and H. Ullah, *Design of wideband antenna with band notch characteristics based on single notching element*, Int. J. RF Microw. Comput. Aid. Eng. **29** (2019), no. 2, 1–7.
18. Y. Alnaiemy and L. Nagy, *A novel UWB monopole antenna with reconfigurable band notch characteristics based on PIN diodes*, Infocommunications J. **13** (2021), no. 3, 33–44.
19. M. T. Islam, R. Azim, and A. T. Mobashsher, *Triple band-notched planar UWB antenna using parasitic strips*, Prog. Electromagn. Res. **129** (2012), 161–179.
20. A. Kumar, A. Q. Ansari, B. K. Kanaujia, J. Kishor, and S. Kumar, *An ultra-compact two-port UWB-MIMO antenna with dual band-notched characteristics*, AEU Int. J. Electron. Commun. **114** (2020), 152997.

22337326, 0, Downloaded from https://onlinelibrary.wiley.com/doi/10.4218/etrij.2024-0224 by Delhi Technological University, Wiley Online Library on [15/06/2025]. See the Terms and Conditions (https://onlinelibrary.wiley.com/terms-and-conditions) on Wiley Online Library for rules of use; OA articles are governed by the applicable Creative Commons License

21. A. Kumar, A. Q. Ansari, B. K. Kanaujia, J. Kishor, and N. Tewari, *Design of triple-band MIMO antenna with one band-notched characteristic*, Prog. Electromagn. Res. C. **86** (2018), 41–53.
22. S. Jayant, G. Srivastava, and S. Kumar, *Quad-port UWB MIMO footwear antenna for wearable applications*, IEEE Trans. Antennas Propagat. **70** (2022), no. 9, 7905–7913.
23. H. Peng, C. Du, and R. Wang, *Four-port flexible UWB-MIMO antenna with triple band-notched for wearable IoT applications*, Int. J. Microw. Wirel. Technol. **16** (2024), no. 8, 1261–1271.
24. M. Sandhya and L. Anjaneyulu, *Improved wearable, breathable, triple-band electromagnetic bandgap-loaded fractal antenna for wireless body area network applications*, ETRI J . **46** (2024), no. 4, 571–580.
25. J. Li, H. Zhai, and M. Wang, *A compact vivaldi antenna with enhanced bandwidth and mismatch suppression*, IEEE Trans. Antennas Propagat. **73** (2025), no. 1, 623–628.
26. M. Hamza, C. Exadaktylos, C. L. Zekios, and S. V. Georgakopoulos, *An ultrawideband fully planar inverted-L element (FILE) array*, IEEE Trans. Antennas Propagat. **73** (2025), no. 1, 174–187.
27. C. A. Balanis, *Antenna theory: analysis and design*, John Wiley & Sons, NJ, United States, 2016.
28. A. Yadav, M. D. Sharma, and R. P. Yadav, *A CPW-fed CSRR and inverted U slot loaded triple band notched UWB antenna*, Prog. Electromagn. Res. C. **89** (2019), 221–231.
29. R. N. Tiwari, P. Singh, and B. K. Kanaujia, *A half cut design of low profile UWB planar antenna for DCS/PCS/WLAN applications*, Int. J. RF Microw. Comput. Aid. Eng. **29** (2019), no. 9, 1–9.

AUTHOR BIOGRAPHIES



Subhajit Paul received B.Tech. and M.Tech. degrees in Electronics and Communication Engineering from the West Bengal University of Technology, India in 2012 and 2014, respectively. From 2014 to 2022, he served as a faculty member at Ramgarh Engineering College, Jharkhand, India. He is currently a PhD scholar in the Department of Electronics and Communication Engineering at the Indian Institute of Information Technology, Kalyani, India under the Visvesvaraya PhD Scheme for Electronics and IT. His research interests include multifunctional antennas, MIMO antennas, and ultrawideband (UWB) communications.



Sandeep Rana received his B.Tech. degree from the Graphic Era University, Dehradun, Uttarakhand, India in 2012, and his M.Tech. degree from the Delhi Technological University, New Delhi, India in 2014. He is currently enrolled as a PhD scholar in the Department of Electronics and Communication Engineering at the Indian Institute of Technology Roorkee, Uttarakhand, India. He is on academic leave from his position as an Assistant Professor in the Department of Electronics and Communication Engineering at the G. B. Pant Institute of Engineering and Technology (GBPIET), Uttarakhand, India, where he has been serving as a faculty member since 2019. Prior to his tenure at GBPIET, he served as a faculty member at the Graphic Era Hill University, Dehradun, India, and Netaji Subhash Institute of Technology, New Delhi, India. He has authored or co-authored 10 peer-reviewed international journal and conference papers. His research interests include the design of microwave circuits and antennas tailored to modern wireless communication applications.



Amit Ranjan Azad received his B. Tech. degree in Electronics and Communication Engineering from the West Bengal University of Technology, West Bengal, India in 2010. He received his M.Tech. degree and PhD in RF and Microwave Engineering from the Indian Institute of Technology Kharagpur, West Bengal, India in 2012 and 2019, respectively. From 2019 to 2022, he was a faculty member in the Department of Electrical and Electronics Engineering at the Birla Institute of Technology and Science Pilani, Hyderabad Campus, Telangana, India. Since 2022, he has been a faculty member of the Department of Electronics and Communication Engineering at the Indian Institute of Information Technology, Kalyani, West Bengal, India. He has authored or co-authored more than 20 peer-reviewed international journal and conference papers. His research interests include the synthesis, analysis, and design of high-performance microwave filters and antennas for modern wireless communication applications.



Dalia Nandi received her B.Sc. degree in Electronics (Honors) from the University of Calcutta, India, in 2000. She received B.Tech. and M.Tech. degrees from the Institute of Radio Physics and Electronics, University of Calcutta, India in 2003 and 2005, respectively. She received her PhD in Radio Physics and Electronics from the Institute of Radio Physics and Electronics, University of Calcutta, India, in 2014. Since 2017, she has been a faculty member at the Department of Electronics and Communication Engineering, Indian Institute of

22337326, 0, Downloaded from https://onlinelibrary.wiley.com/doi/10.4218/etrij.2024-0224 by Delhi Technological University, Wiley Online Library on [15/06/2025]. See the Terms and Conditions (https://onlinelibrary.wiley.com/terms-and-conditions) on Wiley Online Library for rules of use; OA articles are governed by the applicable Creative Commons License

Information Technology, Kalyani, India. She has authored or co-authored over 50 peer-reviewed international journal and conference papers. Her research interests include AI/ML in 5G and beyond, wireless communications, IoT, and quantum communications.



Akhilesh Mohan received his B. Tech. degree in Electronics Engineering from the Kamla Nehru Institute of Technology, Sultanpur, India in 2002, and his M.Tech. degree and PhD in Microwave Engineering from the Indian Institute of Technology, Kanpur, Uttar Pradesh, India in 2004 and 2009, respectively. From 2009 to 2010, he worked as a Scientist with the Space Applications Center, Indian Space Research Organization, Ahmedabad, India. From 2010 to 2013, he was a faculty member at the Department of Electrical Engineering, Indian Institute of Technology, Jodhpur, Rajasthan, India. From 2013 to 2020, he was a faculty member at the Department of Electronics and Electrical Communication Engineering, Indian Institute of Technology, Kharagpur, West Bengal, India. Since 2021, he has been a faculty member in the Department of Electronics and Communication Engineering, Indian Institute of Technology, Roorkee, Uttarakhand, India. He has authored or co-authored more than 150 peer-reviewed international journal and conference papers. His research interests include designing microwave filters, antennas, and absorbers for wireless communication systems.

How to cite this article: S. Paul, S. Rana, A. R. Azad, D. Nandi, and A. Mohan, *Compact planar UWB microstrip antenna with independently controllable dual notch bands*, ETRI Journal (2025), 1–14, DOI 10.4218/etrij.2024-0224

22337326, 0, Downloaded from https://onlinelibrary.wiley.com/doi/10.4218/etrij.2024-0224 by Delhi Technological University, Wiley Online Library on [15/06/2025]. See the Terms and Conditions (https://onlinelibrary.wiley.com/terms-and-conditions) on Wiley Online Library for rules of use; OA articles are governed by the applicable Creative Commons License

Electrical Engineering
https://doi.org/10.1007/s00202-025-03200-w

ORIGINAL PAPER

Design of hybrid LMS-SOGI-based phase-locked loop tested under adverse grid conditions

Oinam Lotika Devi[1] · **Alka Singh**[1]

Received: 17 January 2025 / Accepted: 25 May 2025
© The Author(s), under exclusive licence to Springer-Verlag GmbH Germany, part of Springer Nature 2025

Abstract
Deterioration in the performance of the grid-tied system due to nonlinear loads such as static power converters need to be improved. Further, adequate filter structures and precise synchronisation schemes are mandatory for interfacing converters to electrical grid. In this paper, a novel cascaded hybrid-based phase-locked loop (PLL) synchronisation technique is designed using a Least mean square (LMS) and a Second Order Generalised Integrator (SOGI) filter for testing the dynamic performances under adverse grid conditions. The proposed cascaded hybrid (H-LMS-SOGI) PLL is used as a phase detector (PD) of the PLL for detecting the phase angle. This hybrid PLL is able to eliminate the dc offset and harmonics associated with polluted grid voltage. Analysing and testing of the dynamic performances has been done by comparing the proposed H-LMS-SOGI PLL with cascaded LMS-PLL (CLMS-PLL), cascaded SOGI PLL (CSOGI-PLL), single LMS and single SOGI under adverse grid conditions. The simulation results are obtained using MATLAB Simulink environment. The experimental results are obtained on a prototype developed in the laboratory using single phase programmable supply (Gwinstek APS1102) with dSPACE 1104 and digital storage oscilloscope (Keysight DSO X-214A). The results show the steady state and dynamic performance of the proposed H-LMS-SOGI PLL under non-ideal grid conditions like30% voltage sag and 35% swell, + 5 Hz frequency change, 30o phase shift, 20% dc offset and polluted environment. Stability analysis of the proposed PLL w.r.t conventional CLMS-PLL, and CSOGI PLLis discussed through the bode plots and pole-zero map of H-LMS-SOGI PLL. The application of the proposed hybrid technique is also tested for inverter control and load compensation.

Keywords Adaptive filter · CLMS · CSOGI · LMS · Hybrid PLL · Phase-locked loop · Synchronisation technique

1 Introduction

Recently, the increased use of nonlinear loads and power converters in grid-tied systems has resulted in deteriorating power quality and increased harmonic contamination, imbalance in phases, etc. The vital characteristics for proper functioning of a grid-tied system involve monitoring of the phase, amplitude, and frequency of the supply voltage. Phase-locked loop (PLL) is a very common synchronisation technique and it is a framework for detection of grid voltage amplitude, phase and frequency. PLL synchronises the electric grid with power converters using phase angle error detector [1]. Conventional PLL works well under perfectly ideal conditions but under grid abnormalities, it takes longer computational time to track the voltage and frequency variations. For single-phase system, the delay-based Synchronous Reference Frame-based PLL (SRF-PLL) algorithm is the conventional algorithm utilised grid synchronisation [2]. It performs accurately under optimal grid conditions. It is noted that DC offset in the input grid voltage causes synchronisation problems that impact the stability of the closed-loop system. The estimated phase angle, frequency, and amplitude show oscillations leading to enhanced power quality issues. The DC offset problem in grid voltage may be the result of various factors such as the use of analogue/digital (A/D) converters, digital controllers, sensor offsets, geomagnetic events, and grid failures [3]. Hence, it is imperative that designed synchronising technique must be able to eliminate DC offset as well as harmonics content in grid voltage input for accurate operation of power system.

Papers [4–6] discuss application of SOGI PLL and its variants for eliminating harmonic components from the supply grid voltage. A variety of PLLs with dc offset rejection

✉ Oinam Lotika Devi
oinamlotikadevi_2k22phdee08@dtu.ac.in

[1] Electrical Engineering Department, Delhi Technological University, Delhi, India

Published online: 24 June 2025

capability have been proposed by various researchers in literature for single-phase applications, such as controlled rectifiers, renewable energy grid integration, uninterruptible power supplies, dynamic voltage restorers, and grid monitoring [7]. Paper [8] discusses a demodulation-type PLL with a dc offset rejection capacity based on a linear parametric model and adaptive theory. Unfortunately, the challenges in extracting the small-signal model of the PLL accurately add to the complexity of the system. Paper [9] discusses another finite impulse response (FIR)-based EPLL (FIR-EPLL) for the purpose of rejecting dc offset. This PLL makes use of two delay operators, of which a T/4 delay operator is suggested. However, when this PLL is tested under dc offset, this PLL experiences oscillations and a sluggish transient response. Paper [10] discusses different SOGI-based PLLs to study how well they reject DC offset during grid synchronisation. Some of the techniques used for dc offset eliminations include in-loop dq-frame delay signal cancellation (DSC), complex-coefficient filter, $\alpha\beta$DSC with SOGI PLL, modified SOGI PLL, and cascaded SOGI PLL. Two SOGI blocks were used in cascade to implement dc offset rejection in a fixed-parameter-based SOGI PLL. However, it is well known that using multiple blocks of cascaded SOGI makes the PLL's structure more complex. Hence, a simplified technique was introduced in [11, 12] in order to reject dc offset; and this involved the use of a low-order all-pass filter in conjunction with an improved SOGI. However, in order to guarantee adequate performance, SOGI parameters are to be optimised.

Literature review suggests that pre-filtering with an adaptive filter based on LMS technique may improve PLL response under abnormal grid conditions [13]. With optimised gain settings, the LMS approach may display filtering action comparable to that of the SOGI method. Some benefits of LMS over SOGI involve a frequency-independent bandwidth, low or moderate computational requirements, and ease of application. However, the main problem with the LMS approach is its constant step size due to which its harmonic attenuation capacity is limited. Hence, in order to increase harmonic attenuation capability without compromising transient response, numerous LMS versions have been mentioned in the literature [14–20]. Another technique based on multilevel normalised LMS (N-LMS) algorithm for eliminating dominant harmonics and dc offset is also mentioned in [21].

Under polluted grid conditions, LMS as a PLL has been proposed to perform phase and frequency estimation from the voltage signal; however, the approach has not been tested under DC offset conditions [22]. For the grid-tied PV system, a modified LMS approach has been developed in [23] as the PLL and control algorithm. The learning rate has been modified in this paper in order to achieve faster dynamics and reduced steady-state error. In [24] a modified LMS-PLL (MLMS-PLL) has been presented for DC offset rejection, harmonic removal capacity and effectively tracking the frequency and phase angle of the grid voltage. It can be utilised in situations where the grid voltage is distorted. The modified cascaded least mean square (CLMS)-based adaptive filter as a prefilter is mentioned in [25] which is actually an adaptation of the conventional LMS filter. The two LMS filters cascaded together greatly enhance the attenuation of harmonics better than cascaded- SOGI [26], despite having an overall slower dynamic response.

Literature review further reveals employing prefilters based on the SOGI [27], complex bandpass filter (CBF) or reduced-order generalised integrator [28], and complex-coefficient filter (CCF) [29]. CCF is a filter that uses two CBF blocks to evaluate the positive sequence components of voltages. When comparing its filtering capacity, dynamic behaviour, and computing weight as compared to SOGI, it performs comparatively better [30]. Paper [31] proposes a new method of eliminating interference using an adaptive notch filter. Thus, exhaustive literature survey depicts that several variants of SOGI, LMS and other adaptive filters have been proposed for performance improvement. However, these variants are restricted to SOGI and LMS-based PLL algorithms.

In this paper, a novel hybrid algorithm comprising Least Mean Square (LMS) and SOGI-based PLL is proposed. The hybrid LMS and SOGI (H-LMS-SOGI PLL) consists of a single LMS and SOGI blocks in cascaded form. It is used as a phase detector (PD) of the proposed PLL. A detailed mathematical analysis of the developed PLL (H-LMS-SOGI PLL) is presented in Section II. The dynamic performance analysis of H-LMS-SOGI PLL is observed under various grid abnormalities like 30% voltage sag and 35% voltage swell, polluted grid environments, 30^{o}phase jump, + 5 Hz frequency change, and 20% dc offset. Further, the dynamic performance of H-LMS-SOGI is compared with single LMS and SOGI PLLs, cascaded LMS (CLMS) and cascaded SOGI (CSOGI) PLLs using simulation as well as hardware results. The stability of proposed H-LMS-SOGI PLL is performed through pole-zero plots and bode plots and the comparative analysis of the single LMS-PLL and SOGI PLL, cascaded PLLs (CLMS, CSOGI and H-LMS-SOGI PLLs) is carried out. Simulation results are obtained in MATLAB Simulink environment and the experimental results are analysed by setting up hardware prototype in the laboratory using Gwinstek single phase programmable supply (APS-1102A) and dSpace-1104.In this paper, the work has been organised in six Sections: Section 2 discusses the mathematical representation of the three Cascaded PLLs viz. Cascaded LMS (CLMS) PLL, Cascaded SOGI (CSOGI) PLL and a hybrid cascade combination of LMS and SOGI (H-LMS-SOGI) PLL. Section 3 presents the stability analysis of the system through pole-zero plots and bode plots, Section 4 depicts the steady state and dynamic performance analysis through MATLAB simulation and its

validation by hardware results for the three different cascaded PLLs, Section 5 presents the application of proposed hybrid H-LMS-SOGI PLL for inverter control and the conclusion of the work is presented in Section 6.

2 Mathematical analysis of cascaded PLLs

This section discusses the mathematical structures of the three cascaded PLLs (i) Cascaded Least Mean Square (CLMS) PLL (ii) Cascaded Second Order Generalised Integrator (CSOGI) PLL and (iii) the proposed Cascaded hybrid Least Mean Square and Second Order Generalised Integrator combination (H-LMS-SOGI) PLL.

2.1 Cascaded least mean square (CLMS)-based PLL

The block diagrams shown in Fig. 1a and b represent single fundamental Least Mean Square (LMS) block and Cascaded Least Mean Square (CLMS) PLL. In CLMS-PLL, two identical LMS blocks are combined in cascaded form to provide harmonic attenuation of the grid voltage and extract the fundamental grid frequency and phase angle. LMS structure is used to extract and eliminate various types of harmonic or noise components present in the grid signal. The learning mechanism of LMS is based on stochastic gradient and it exhibits adaptive qualities by continuously updating the weights to minimise the estimated steady-state error. The difference between the desired signal, $v_s(k)$, and the estimated output signal, $v_s^*(k)$, of the second LMS gives the error signal e_{ser} (k) in the CLMS-PLL. This estimated output signal of CLMS, $v_s^*(k)$, is fed directly to the PI controller of the PLL for extraction of fundamental frequency and phase angle of CLMS-PLL.

To simplify the modelling, only one LMS structure is considered and is shown in Fig. 1a.

The estimated output grid voltage signal of the LMS in matrix form is expressed as

$$v_s^*(k) = W^T(k)\, x(k) \tag{1}$$

where $W^T(k)$ and $x(k)$ are the weight coefficient matrix and input coefficient matrix of the LMS structure; they can be represented as.

$$W^T(k) = [W_{d1}(k)\ W_{q1}(k)] \tag{2}$$

$$x(k) = [x_1(k)\ x_2(k)]^{\,T} \tag{3}$$

where $x_1(k) = \sin\theta$ and $x_2(k) = \cos\theta$ are the input vector signals with phase angle θ, obtained by the PLL as a reference signal.

The steady-state error signal of the single LMS structure is expressed as

$$e_{ser}(k) = v_s(k) - \{v_s^*(k) + v_{dcoff}(k) + v_h(k)\}\sqrt{a^2+b^2} \tag{4}$$

where $v_s(k)$ is the desired signal and is expressed as

$$v_s(k) = V_A \sin\left(\omega_e' T_s\right) + C(k) \tag{5}$$

V_A is the amplitude of the voltage signal and C(k) represents the interference which consist of $v_{dcoff}(k) + v_h(k)$ Here $v_h(k)$ is harmonic voltage. The dc offset,$v_{dcoff}(k)$,contained in the desired signal is expressed as [13],

$$v_{dcoff}(k) = \frac{\omega\alpha T_s}{z-1} \tag{6}$$

where the gain of dc offset can be optimised. Weight updation of the LMS is performed as

$$W(k+1) = W(k) + \mu e_{ser}(k)\, x(k) \tag{7}$$

where 'μ'is the learning rate of LMS algorithm moreover, 'μ' being the convergence factor has to be chosen carefully as its higher value shows faster response but higher overshoot. The lower value of μ predicts better steady state response but with slow dynamic response.

The estimated output of grid signal of the CLMS is expressed as

$$v_s^*(k) = [V_A \sin\{(\omega_e' T_s)(k) + \phi\}] \tag{8}$$

where V_A is the amplitude of the voltage signal and ϕ is the phase angle of the signal. The computed grid voltage signal can be expressed as

$$\begin{aligned} v_s^*(k) &= \sum_{n=1}^{N} \left[V_{An} \sin\left\{\left(n\omega_e' T_s\right)(k) + \phi_n\right\}\right] \\ &= \sum_{n=1}^{N} \left[V_{An}\cos\phi_n \sin(n\omega_e' T_s)(k) + V_{An}\sin\phi_n \cos(n\omega_e' T_s)(k)\right] \\ &= \sum_{n=1}^{N} \left[V_{dAn}\sin(n\omega_e' T_s)(k) + V_{qAn}\cos(n\omega_e' T_s)(k)\right] \end{aligned} \tag{9}$$

Here V_{An} is the voltage signal's amplitude for nth harmonic.ϕ_n is the phase angle of the nth harmonic signal, N is the complete harmonic quantity and k is the sampling point. The active and reactive grid harmonic voltage component, are expressed, respectively, as

$$V_{dAn} = V_{An}\cos\phi_n \tag{10}$$

$$V_{qAn} = V_{An}\sin\phi_n \tag{11}$$

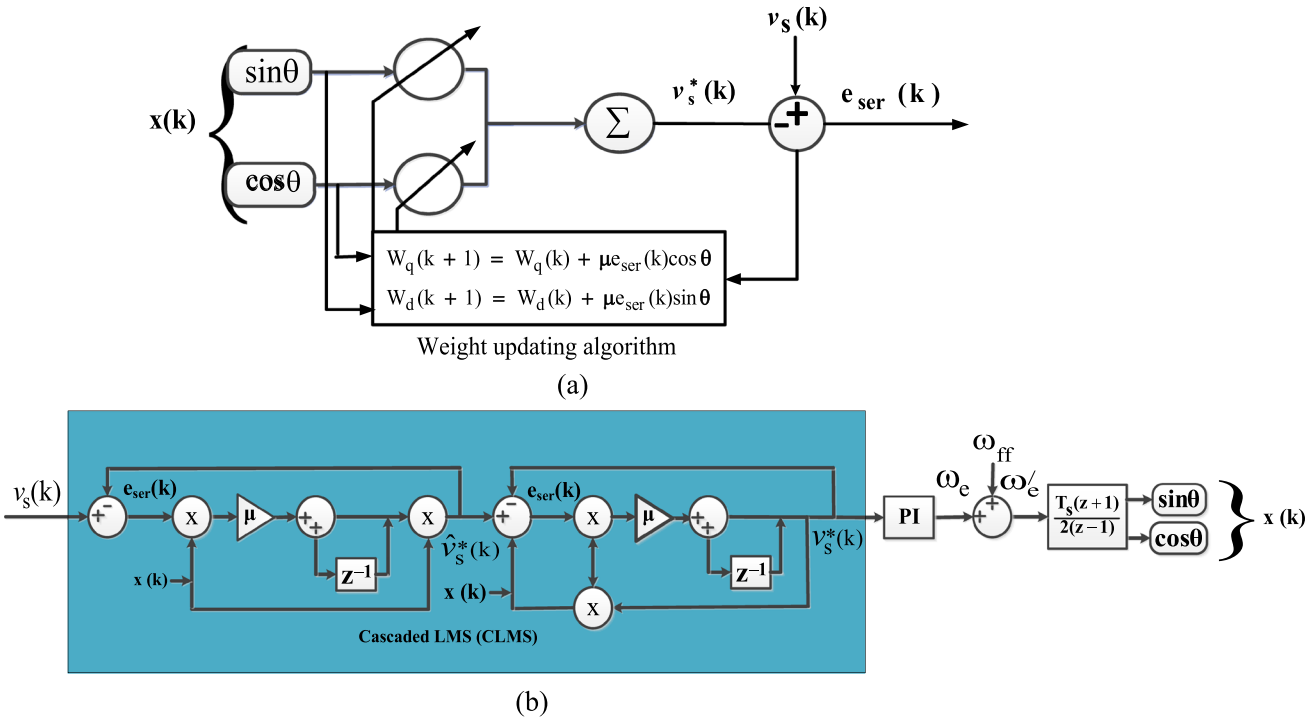


Fig. 1 **a** Block diagram of single LMS structure and **b** Block diagram of cascaded LMS (CLMS) PLL

Substituting the input vectors in Eq. (8) of the LMS while considering $n = 1$, the fundamental harmonic, the output will be obtained as

$$\begin{aligned} v_{s1}^*(k) &= V_{dA1}\ \sin(\omega_e' T_s)(k) + V_{qA1}\ \cos(\omega_e' T_s)(k) \\ v_{s1}^*(k) &= V_{dA1}\ x_1(k) + V_{qA1}\ x_2(k) \end{aligned} \tag{12}$$

The amplitude updation for fundamental active component and reactive component of the grid voltage can be expressed as

$$\begin{aligned} V_{dA1}(k+1) &= V_{dA1}(k)\ + \mu x_1(k)\ e_{ser}(k) \\ &= V_{dA1}(k) + \mu\ \sin(\omega_e' T_s\ )e_{ser}(k) \end{aligned} \tag{13}$$

$$\begin{aligned} V_{qA1}(k+1) &= V_{qA1}(k) + \mu x_2(k)\ e_{ser}(k) \\ &= V_{qA1}(k) + \mu\cos(\omega_e' T_s)(k)\ e_{ser}(k) \end{aligned} \tag{14}$$

The dq-axis components of the grid voltages amplitude can be expressed as

$$V_{dqA}(k) = \sqrt{(V_{dA1})^2 + (V_{qA1})^2} \tag{15}$$

The open loop transfer function of single LMS is expressed as [31]

$$G_{\text{olLMS}}(z) = \frac{\text{output}}{\text{error}} = \frac{v_s^*(z)}{e_{ser}(z)} = \frac{\mu\ (\ z\ \cos\ \omega_e'\ T_s - 1)}{z^2 - 2\ z\ \cos\ \omega_e'\ T_s + 1} \tag{16}$$

The closed-loop transfer function of single LMS is expressed as [31]

$$\begin{aligned} H_{\text{LMS}}(z) &= \frac{\text{output}}{\text{input}} = \frac{v_s^*(k)}{v_s(k)} = \frac{G_{olLMS}(z)}{1 + G_{olLMS}(z)} \\ &= \frac{\mu\{z\cos(\omega_e' T_s) - 1\}}{z^2 - 2(1-\mu/2)z\cos(\omega_e' T_s) + (1-\mu)} \end{aligned} \tag{17}$$

Hence the open loop transfer function of the cascaded LMS (CLMS) structure can be expressed as.

$$G_{\text{olCLMS}}(z) = [G_{\text{olLMS}}(z)]^2 = \left[\frac{\mu(z\cos\omega_e' T_s - 1)}{z^2 - 2z\cos\omega_e' T_s + 1}\right]^2 \tag{18}$$

The closed-loop transfer function of the cascaded LMS (CLMS) structure considering the active component of the

input voltage source in the z transform is obtained as

$$H_{\mathrm{CLMS}}(z) = \frac{G_{ol\mathrm{CLMS}}(z)}{1 + G_{ol\mathrm{CLMS}}(z)} = \left\{ \frac{\mu\{z\cos(\omega_e^{/} T_s) - 1}{z^2 - 2(1-\mu/2)z\cos(\omega_e^{/} T_s) + (1-\mu)} \right\}^2 \tag{19}$$

2.2 Cascaded second order generalised integrator (CSOGI)-based PLL

The block diagram of the cascaded SOGI (CSOGI) PLL is shown in Fig. 2. It consists of two identical blocks of single SOGI structure in cascaded form. The cascaded SOGI (CSOGI)represents the phase detector part of the PLL. The grid voltage, $v_s(k)$ is fed to the first SOGI block and its output $v_{\hat{\alpha}}$, is fed as the input to the second SOGI block. The orthogonal outputs v_α and v_β from the second SOGI structure are fed to the embedded synchronous reference frame structure of the PLL to obtain the estimated frequency and phase angle, θ of the PLL. In CSOGI-PLL, $\omega_e^{/}$ is the estimated resonant angular frequency of the cascaded SOGI (CSOGI) PLL which is fed back.

Here $\omega_{ff} = 2\pi f$ with $f = 50$ Hz represents the fundamental grid frequency. The CSOGI structure is used as phase detector (PD) of the PLL. The in phase and quadrature signals from the second SOGI block undergo Park transformation to obtain dq-axis components, v_d and v_q. The reactive component, v_q is further fed to PI controller of the embedded PLL to obtain the required phase angle and frequency of the CSOGI-PLL. For simplifying the mathematical modelling, a single SOGI PLL is initially considered and then cascaded combination is discussed.

The closed-loop transfer functions of a single SOGI structure are represented as

$$H_{\alpha\mathrm{SOGI}}(s) = \frac{k\omega_e^{/} s}{s^2 + k\omega_e^{/} s + \omega_e^{/2}} \tag{20}$$

$$H_{\beta\mathrm{SOGI}}(s) = \frac{k\omega_e^{/2}}{s^2 + k\omega_e^{/} s + \omega_e^{/2}} \tag{21}$$

The closed-loop transfer functions of the cascaded SOGI (CSOGI) structure can be expressed as

$$H_{\alpha\mathrm{CSOGI}}(s) = \left[\frac{k\omega_e^{/} s}{s^2 + k\omega_e^{/} s + \omega_e^{/2}} \right]^2 \tag{22}$$

$$H_{\beta\mathrm{CSOGI}}(s) = \frac{k\omega_e^{/3} s}{\left(s^2 + k\omega_e^{/} s + \omega_e^{/2}\right)^2} \tag{23}$$

The transfer function shown in (22) and (23) represents a band pass filter (BPF) with phase difference of 90° under unity gain. The value of k is adjusted to enhance the transient response of CSOGI-PLL. The discretised SOGI is obtained by using Trapezoidal method of integrator which is more accurate in terms of forward or backward Discrete integrator Euler [1], $\int \rightarrow \frac{T_s(z+1)}{2(z-1)}$. Here T_s is the sampling time and after discretizing Eqs. (20) and (21) can be expressed as

$$H_{\alpha\mathrm{SOGI}}(z)\big|_{s=\frac{2(z-1)}{T_s(z+1)}} = \frac{k\omega_e^{/} 2\,(z-1)/T_s(z+1)}{\{2(z-1)/T_s(z+1)\}^2 + k\omega_e^{/} 2(z-1)/T_s(z+1) + \omega_e^{/2}} \tag{24}$$

$$H_{\beta\mathrm{SOGI}}(z)\big|_{s=\frac{2(z-1)}{T_s(z+1)}} = \frac{k\omega_e^{/2}}{\{2(z-1)/T_s(z+1)\}^2 + k\omega_e^{/} 2(z-1)/T_s(z+1) + \omega_e^{/2}} \tag{25}$$

Discretizing CSOGI-PLL, Eqs. (22) and (23) can be re-expressed as (26) and (27), respectively.

$$H_{\alpha\mathrm{CSOGI}}(z)\big|_{s=\frac{2(z-1)}{T_s(z+1)}} = \left[\frac{k\omega_e^{/} 2\,(z-1)/T_s(z+1)}{\{2(z-1)/T_s(z+1)\}^2 + k\omega_e^{/} 2(z-1)/T_s(z+1) + \omega_e^{/2}} \right]^2 \tag{26}$$

$$H_{\beta CSOGI}(z)\big|_{s=\frac{2(z-1)}{T_s(z+1)}} = \frac{k\,\omega_e^{/3} 2\,(z-1)\,/\,T_s(z+1)}{\left(\{2\,(z-1)/T_s(z+1)\}^2 + k\,\omega_e^{/} 2\,(z-1)/T_s(z+1) + \omega_e^{/2}\right)^2} \tag{27}$$

The transfer functions shown in (26) and (27) represent a band pass filter (BPF) with phase difference of 90° under unity gain.

2.3 Cascaded hybrid least mean square second order generalised integrator (H-LMS-SOGI)-based PLL

The block diagram of cascaded H-LMS-SOGIPLL is shown in Fig. 3. This proposed PLL is a hybrid PLL where a single LMS structure is cascaded with a single SOGI structure. The SOGI acquires real-time fundamental frequency of the input signal. The steady-state error is estimated after comparing the estimated output grid signal of the LMS with the desired signal and the weighting coefficient of the LMS algorithm is updated. When the system is running, weight coefficient is constantly updated to make the system state error almost zero. The minimised mean error from LMS is passed through

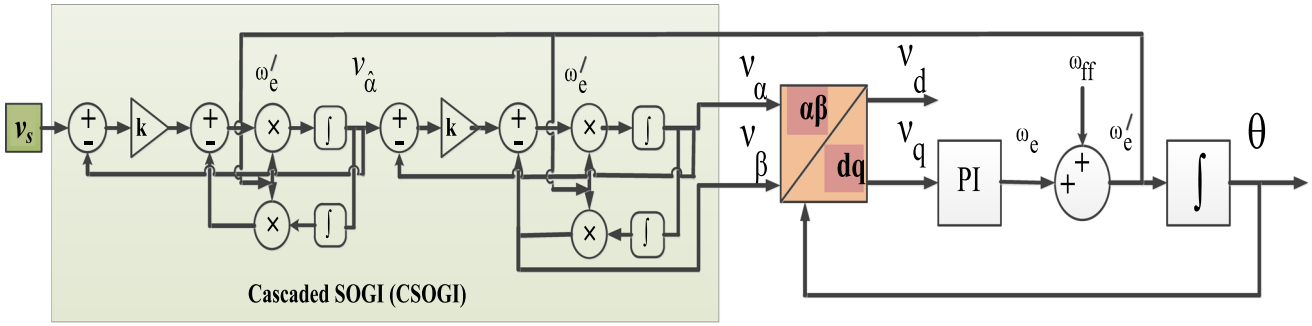


Fig. 2 Block diagram of cascaded SOGI (CSOGI) PLL

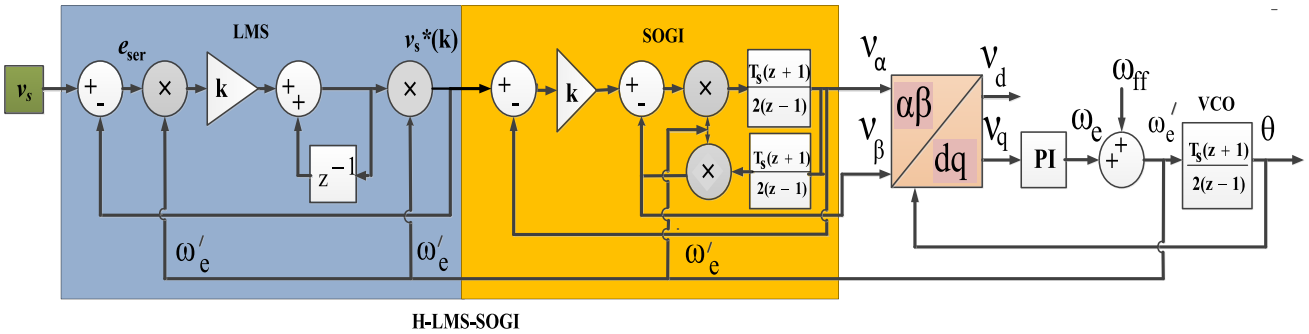


Fig. 3 Block diagram of H-LMS-SOGI PLL

the SOGI structure to extract the accurate frequency of the input signal which will act as a reference frequency of H-LMS-SOGI PLL.

In Fig. 3, $v_s(k)$ is the desired grid voltage signal containing disturbances like dc offset, $v_{dcoff}(k)$ and harmonics $v_h(k)$.$v_s^*(k)$ is the estimated output grid voltage signal of the LMS, $e_{ser}(k)$ be the estimated steady-state error of LMS, $W(k)$ is the weight coefficient matrix and $x(k)$ is the unit coefficient matrix of input signal. Considering the discretised single LMS and SOGI structures the open loop and closed-loop transfer functions of cascaded H-LMS-SOGI PLL are derived for the performance analysis under adverse grid conditions of a single-phase system.

The open loop transfer function of H-LMS-SOGI PLL can be obtained as

$$\begin{aligned} &G_{\text{olH-LMS-}SOGI}(z) \\ &= G_{\text{olLMS}}(z) * G_{\text{olSOGI}}(z) \\ &= \left(\frac{\mu\,(z\,\cos\,\omega_e^{/}\,T_s - 1)}{z^2 - 2\,z\,\cos\,\omega_e^{/}\,T_s + 1}\right)\left(\frac{x(z^2-1)}{4(z-1)^2 + y(z+1)^2}\right) \\ &= \left(\frac{\mu x\left((\cos\omega_e^{/}T_s)z^2 - (1+\cos\omega_e^{/}T_s)z + 1\right)}{Mz^3 + BMz^2 + BMz + M^2}\right) \end{aligned} \tag{28}$$

where $x = 2kT_s\omega_e^{/}$, $y = (\omega_e^{/}T_s)^2$, $M = 4 + y$ and $B = 1 - 2\cos\omega_e^{/}T_s$.

The closed-loop transfer function of H-LMS-SOGI PLL from (28) can be expressed as

$$\begin{aligned} H_{\text{clH-LMS-SOGI}}(z) &= \frac{G_{\text{olH-LMS-SOGI}}(z)}{1 + G_{\text{olH-LMS-SOGI}}(z)} \\ &= \left(\frac{\mu(z\cos\omega_e^{/}T_s - 1)}{z^2 - 2(1-\mu/2)z\cos\omega_e^{/}T_s + (1-\mu)}\right) \\ &\times \left(\frac{ky(z+1)^2}{(4+x+y)z^2 - 2(y+4)z + (y-x)}\right) \end{aligned} \tag{29}$$

where $x = 2\text{k}T_s\omega_e^{/}$, $y = (\omega_e^{/}T_s)^2$.

3 Stability analysis of the system

Under this section the comparative stability of the three structures of the PLLs (CLMS, CSOGI and H-LMS-SOGI) is analysed based on frequency response through Bode plots and pole-zero plot of the proposed PLL. The value of the control parameters like μ and k are selected from the Bode plots and step responses of transfer functions (17), (20) and (21). Fig 4 a and Fig. 4 b shows the frequency response and the step response of the closed-loop single LMS, respectively, for different values of μ. It is observed from Figs. 4a and b that with increase in μ the bandwidth increases and harmonic attenuation decreases. A larger value of μ leads to unstable

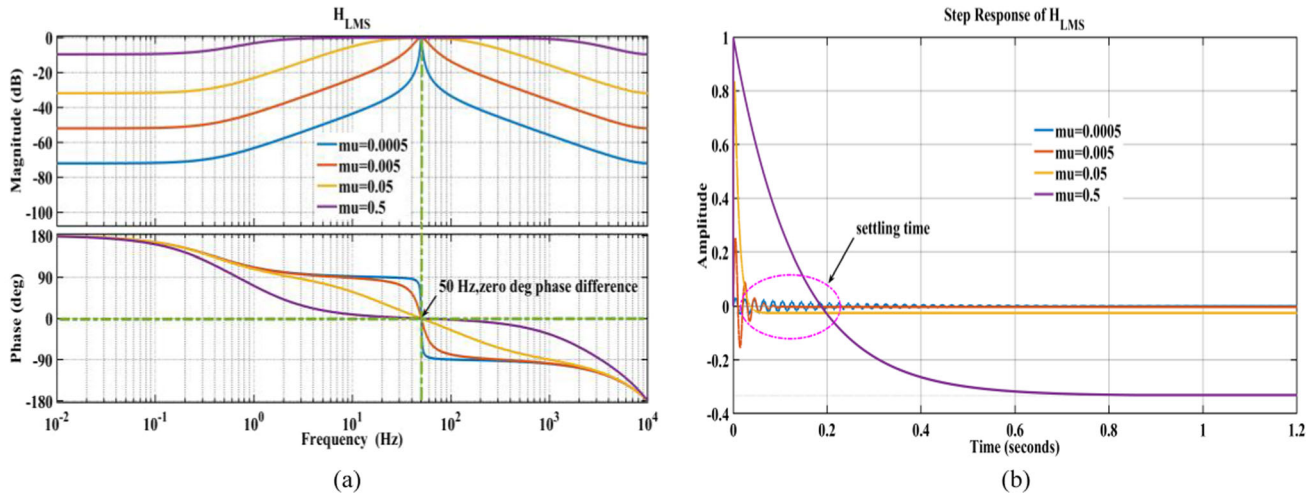


Fig. 4 **a** *Bode plot of LMS at different values of* μ and **b** *step response of LMS at different values of* μ

dynamic performance. Thus, from the response analysis the value of $\mu = 0.005$ is chosen for single LMS structure which gives better harmonic attenuation and settling time (< 0.1s) compared to other values.

Similarly, the frequency and step responses of dSOGI and qSOGI for various values of 'k' are shown in Figs. 5a–d, respectively. Fig 5a and Fig. 5b are the frequency response and the corresponding step response of the closed-loop transfer function of active component of SOGI ($H_{d\text{SOGI}}$) for different values of k. Fig 5c and d are the frequency response and the corresponding step response of the closed-loop transfer function of reactive component of SOGI (s) for different values of k. The plots of Fig. 5a–d depict that decrease in values of 'k' leads to better attenuation but decayed dynamic response. Hence $k = 1.4$ is chosen for the system analysis which yields better response after comparing both bode plot and settling time (< 0.035 s) from the step responses of dSOGI and qSOGI.

Similarly, the frequency response and pole-zero map of the closed-loop transfer function of H-LMS-SOGI given in Eq. (29) also show that the values of parameters, $k = 1.4$ and $\mu = 0.005$ depict good performance with higher stability and faster settling response.

As there are two parameters μ and k to be determined optimally, the bode and the corresponding pole-zero plots are done by fixing one parameter and varying the other parameter and it is found that $k = 1.4$ and $\mu = 0.005$ are the best suitable values.

The Pole-Zero plot of the proposed hybrid PLL by cascading LMS and SOGI PLL (H-LMS-SOGI) is shown in Fig. 6. The pole-zero plot of H-LMS-SOGI is done by taking the optimised value of $k = 1.4$ and $\mu = 0.005$ to observe the stability of the proposed PLL. The poles of H-LMS-SOGI PLL are $\pm$ 1.00 $\pm$ 0.00i, -1.00 ± 0.00i, -0.9897 + 0.000i, 0.9946 + 0.00i and 0.9551 + 0.00i with the outermost pole as $\pm$ 1.00 $\pm$ 0.00i. The zeroes are at $\pm$ 1.00 $\pm$ 0.00i,0.997 + 0.00i with outermost zero as $\pm$ 1.00 + 0.00i. It is seen that the outermost poles and zeroes of.

H-LMS-SOGI PLL lie within unit circle of the z-plane in Pole-Zero plot. Hence it can be concluded that the H-LMS-PLL is stable as its poles and zeros lie within the stable region of the unit circle of H-LMS-SOGI for $k = 1.4$, mu = 0.005 and Ts = 50e−6s.

Fig 7 shows the bode diagram of closed-loop transfer functions of CLMS-PLL, CSOGI-PLL and H-LMS-SOGI PLL and Table 1 gives the values of the gain margin and phase margin with their respective crossover frequencies (rad/sec) of the three PLLs. The stability of the three PLLs are compared considering the positivity and negativity of the gain margin and phase margin values obtained from the Bode diagram. Table 1 shows that all the three PLLs give positive gain margin (GM) in dB and phase margin (PM) in (^{o}), depicting that all the three PLLs are stable.

Table 1 depicts that the proposed H-LMS-SOGI PLL has the largest positive values of gain margin (GM = 40.5dB) and phase margin (PM = 80.6°) then followed by CLMS and CSOGI PLLs. Therefore, it can be concluded that the proposed H-LMS-SOGI PLL is highly stable than the other two combination PLLs.

4 Performances analysis of different PLLs

In this section the simulation results of the PLLs under various cases of adverse grid conditions like (a) 30% voltage sag, (b) 35% voltage swell, (c) polluted grid voltage (d) 30° phase jump, (e) + 5Hz frequency change, and (f) 20% dc offset are discussed using MATLAB Simulink toolbox. The sampling time, $T_s = 50\ \mu s$, is considered for simulation and experimental validation. During simulation, the disturbances are

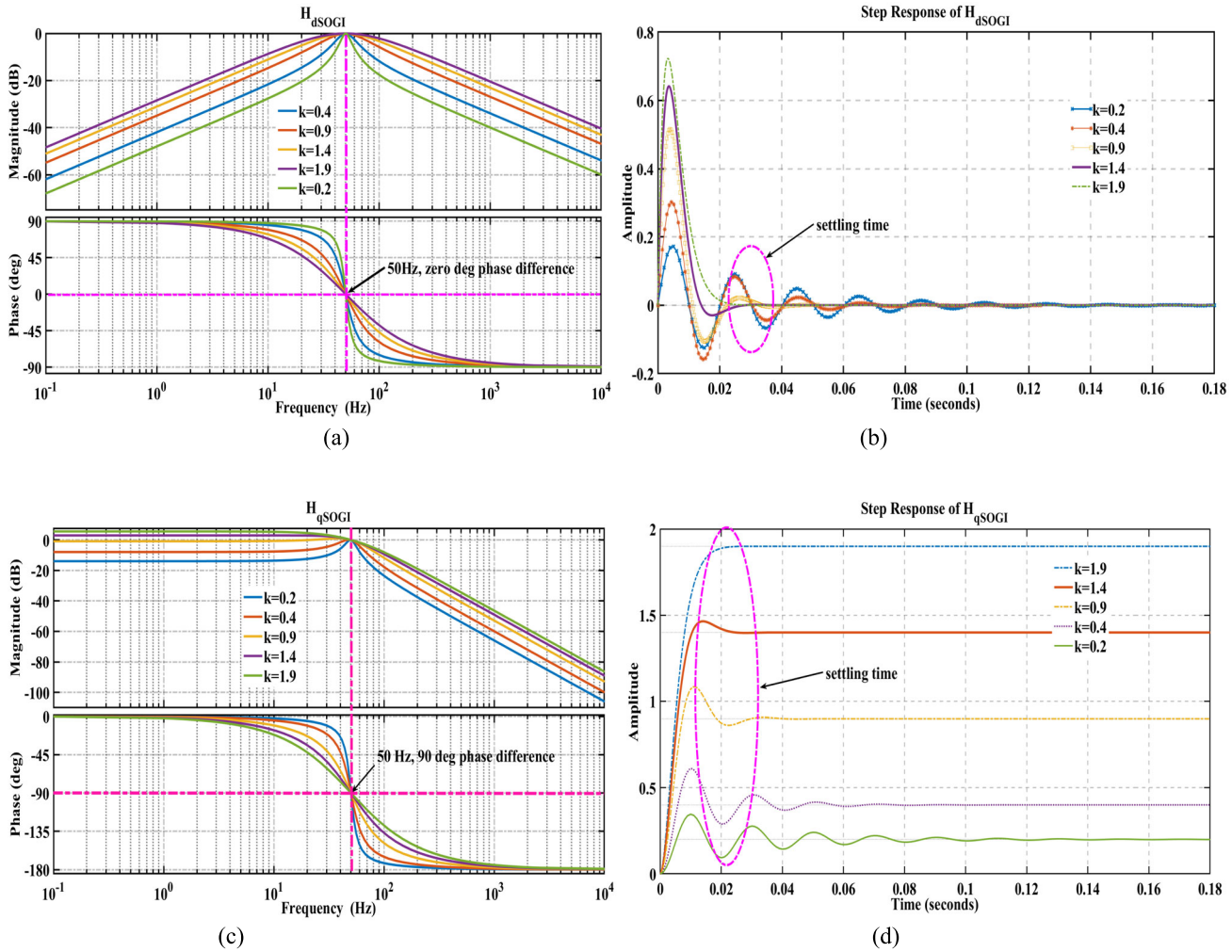


Fig. 5 **a** Bode plot of dSOGI at different values of k and **b** step response of dSOGI at different values of k. **c** Bode plot of qSOGI at different values of k and **d** step response of qSOGI at different values of k

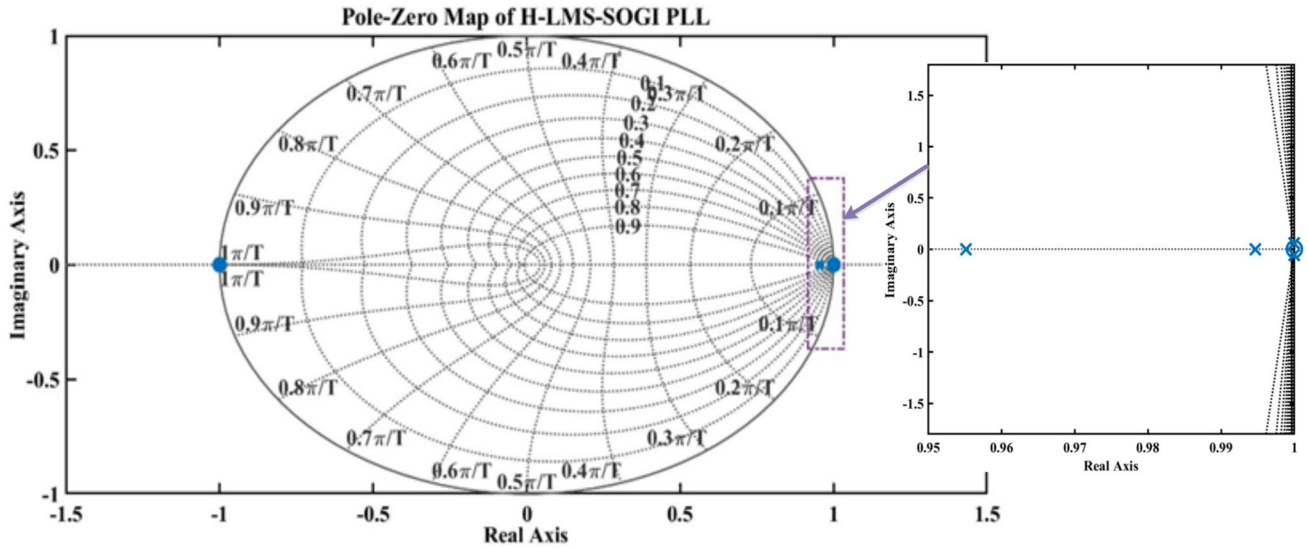


Fig. 6 Pole-Zero plot of H-LMS-SOGI PLL

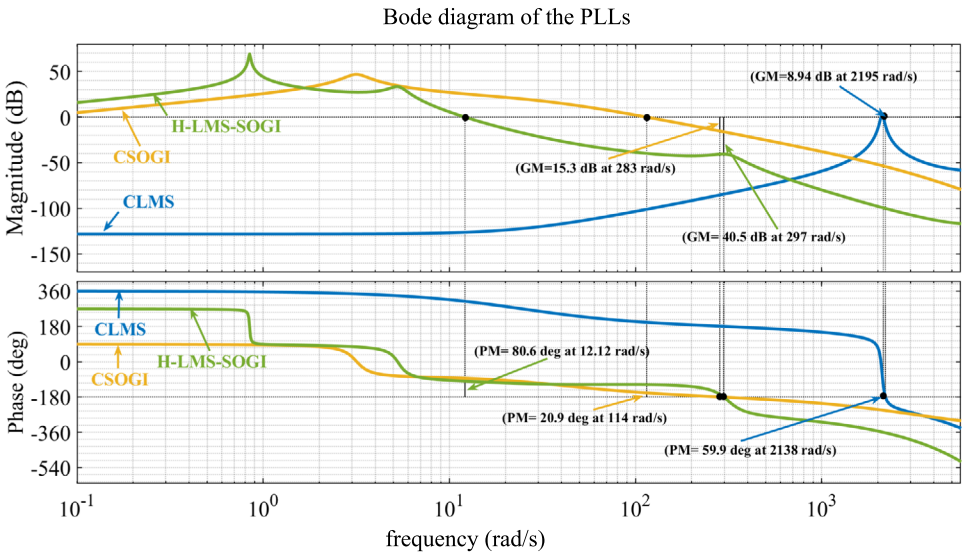


Fig. 7 Bode plot of CLMS, CSOGI, H-LMS-SOGI PLLs

Table 1: Gain margin and phase margin with their crossover frequencies of the three PLLs

Types of PLL	GM in dB	Cross over frequency (rad/sec)	PM in (°)	Cross over frequency (rad/sec)
CLMS-PLL	8.94	2195	59.9	2138
CSOGI-PLL	15.3	283	20.9	114
H-LMS-SOGI PLL	40.5	297	80.6	12.12

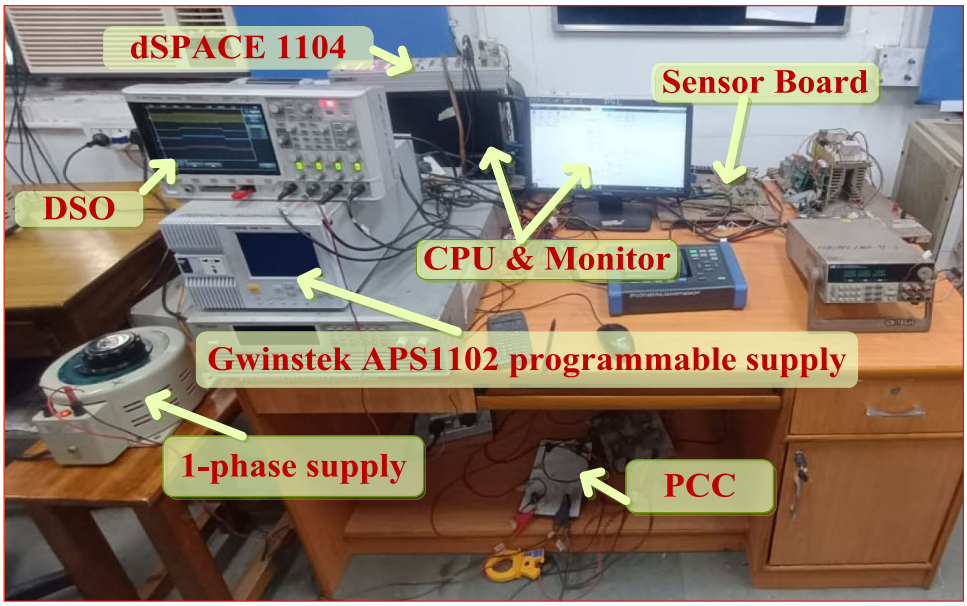


Fig. 8 Hardware setup for analysing the dynamic performances of different PLLs

introduced within a step period of 0.2–0.4s and the dynamic performances are analysed by using the parameters given in the Appendix. The hardware results of the PLLs performances are obtained by setting up a laboratory prototype environment as shown in Fig. 8 to validate the simulation results under various cases. A single-phase programmable supply of GwinSTEK model (APS-1102A) is used for generating different types of voltage signal waveforms like simple sinusoidal waveform, 3rd and 5th harmonic induced waveform under polluted environment and other dynamics in the voltage. The input grid voltage has been sensed using a Hall effect voltage sensor and is passed to the dSpace 1104 controller for processing the algorithms through the Analog to

Digital Converter (ADC) channel of dSpace. The estimated signals from Digital to Analog Converter (DAC) channels through DSO are analysed under different cases of non-ideal grid conditions.

4.1 Performance analysis of H-LMS-SOGI PLL

This subsection shows the dynamic performance analysis of the proposed H-LMS-SOGI PLL under various adverse grid conditions such as (a) 30% voltage sag, (b) 35% voltage swell, (c) polluted grid voltage (d) 30° phase jump, (e) + 5 Hz frequency change, and (f) 20% dc offset. Fig 9 shows the simulation and the hardware results of H-LMS-SOGI PLL by considering five cases of adverse grid conditions.

4.2 Case A1: grid voltage deviation with 30% sag and 35% swell

Figure. 9a and b depicts the simulated and experimental dynamic performances of H-LMS-SOGI PLL under 30% sag and Fig. 9c and d gives the simulated and experimental results under35% swell of grid voltages. It is observed that there is no variation in estimated phase, θ. The overshoot of the frequency while step changing at voltage sag is of 51.28 Hz and that of swell is 53.6 Hz. The estimated frequencies settle down within two cycles under both the sag and swell voltage deviations. The hardware results give similar results validating the simulated results.

4.3 Case A2: under polluted grid voltage

Figure. 9e and f predicts the simulated and hardware performances under polluted grid voltage. For the experimental performance analysis, 10% of the 3rd and 5th harmonics are considered. Ripples in the estimated frequency are observed during the disturbed period. It is observed that the overshoot in the ripples settle down faster within one cycle. The hardware results show much smoother ripples than the simulated results.

4.4 Case A3: grid voltage under 30^{o} phase jump

Figure 9g and h predict the simulated and experimental performances under 30° phase jump. The disturbances observed in the estimated frequency has an overshoot of 52.38 Hz and grid voltage amplitude settle down within five cycles.

4.5 Case A4: grid voltage under + 5 Hz frequency jump

Figure 9i and j predict the simulated and experimental performances under + 5 Hz frequency jump, respectively. There are changes in the estimated frequency response. Frequency response shows an overshoot of 57.2 Hz. and voltage amplitude settles down in three cycles.

4.6 Case A5: Grid voltage under 20% dc offset

Figure 9k and l predicts the simulated and experimental performances under 20% dc offset. An overshoot of 51.25 Hz in the estimated frequency is observed which dies down within the first cycle. Table II depicts the overall summary of the overshoot and settling time of the dynamic performances of the proposed H-LMS-SOGI PLL in the five cases of adverse grid condition as discussed.

From the simulated dynamic performance analysis shown in Fig. 9 (a, c, e, g, i, k) and Table II, it can be concluded that the performance of the proposed PLL (H-LMS-SOGI PLL) during adverse grid conditions is satisfactory. It is also observed that the frequency errors are not very large and the transients die down within three cycles in most of the cases. However, during30^{o}phase shift the PLL depicts slightly sluggish response among the three PLLs where it settles within five cycles although it shows least the overshoot (52.38 Hz). These simulated results are validated by similar hardware results in Fig. 9 (b, d, f, h, j, l).

From the simulated dynamic performance analysis shown in Fig. 9 (a, c, e, g, i, k) and Table II, it can be concluded that the performance of the proposed PLL (H-LMS-SOGI PLL) during adverse grid conditions is satisfactory. It is also observed that the frequency errors are not very large and the transients die down within three cycles in most of the cases. However, during30^{o}phase shift the PLL depicts slightly sluggish response among the three PLLs where it settles within five cycles although it shows least the overshoot (52.38 Hz). These simulated results are validated by similar hardware results in Fig. 9 (b, d, f, h, j, l).

4.7 Comparative performance analysis of different PLLs

Under this subsection the dynamic performances of the CLMS, CSOGI and the proposed H-LMS-SOGI, PLLs are compared and analysed by considering the frequency under various cases of non-ideal grid conditions viz. Case B1: grid voltage under polluted environment, Case B2: grid voltage under 30° phase jump, Case B3: grid voltage under + 5 frequency jump, Case B4: grid voltage under 20% dc offset through simulation and experimental setups. Fig 10a, c, e, g shows the comparative simulated results of the transient analysis of the cascaded PLLs and Fig. 10b, d, f, h shows the comparative hardware results validating the simulated results of the cascaded PLLs under all the adverse grid conditions. Fig 11 also depicts the comparative experimental results of the PLLs for better validation of the results under (a) 20% dc

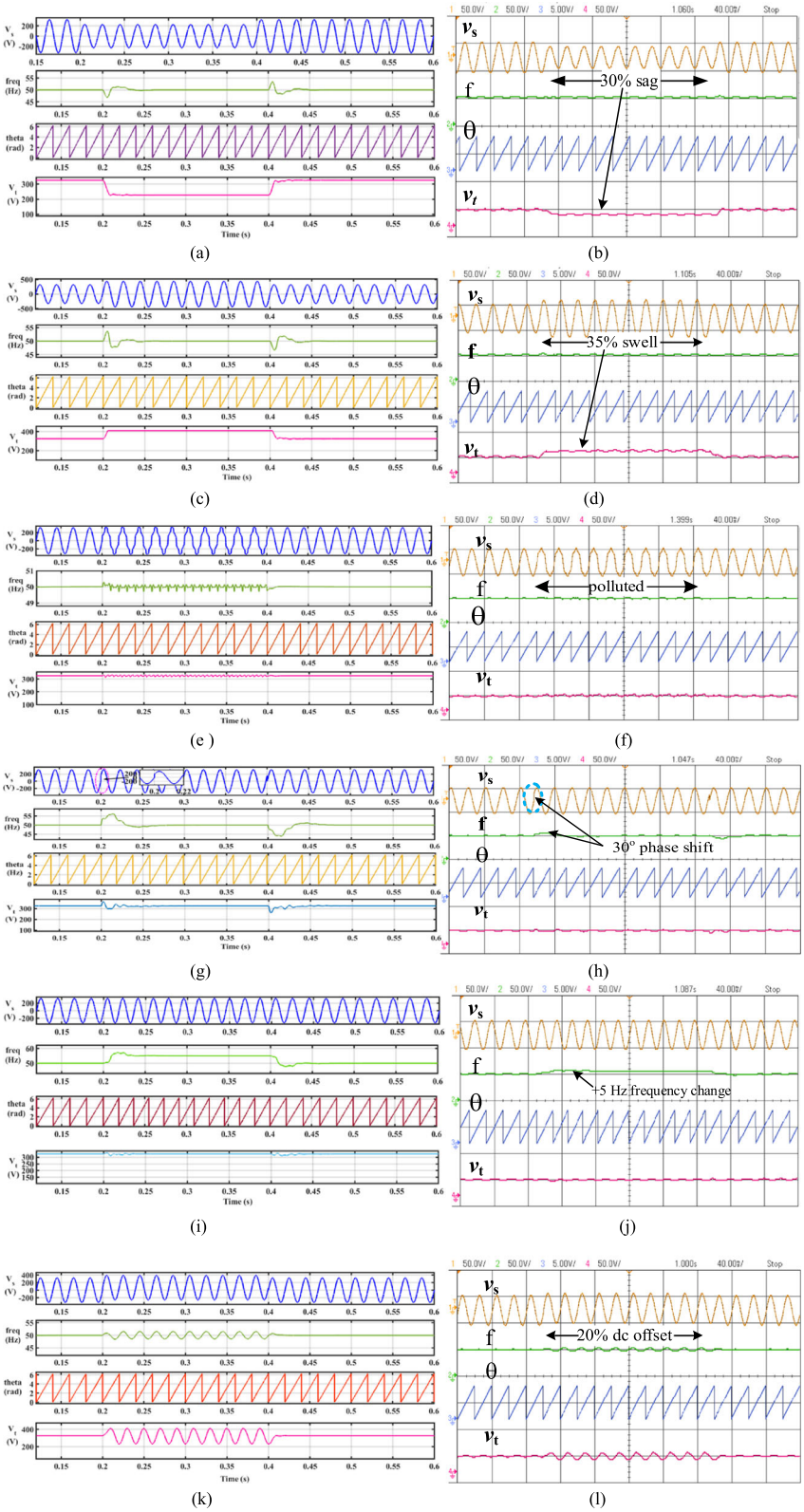


Fig. 9 Simulation and experimental results of dynamic performance of H-LMS-SOGI PLL for adverse grid conditions under 30% voltage sag (**a** and **b**), 35% voltage swell (**c** and **d**), polluted grid voltage (**e** and **f**), 30° phase jump (**g** and **h**), + 5Hz frequency change (**i** and **j**), and 20% dc offset (**k** and **l**)

Table 2: Summary of performance of H-LMS-SOGI PLL

Parameter and test conditions	30% sag	35% swell	polluted grid voltage	30°phase Jump	+ 5Hz frequency jump	20%dc offset
Overshoot of frequency	51.28 Hz	53.4 Hz	50.29 Hz	52.38 Hz	57.2 Hz	51.52 Hz
Settling time	two cycles	two cycles	one cycle	five cycles	three cycles	one cycle

offset (b) 30° phase jump (c) + 5 Hz frequency change. Simulated comparative dynamic performance analysis of LMS, SOGI, CLMS, CSOGI and H-LMS-SOGI PLLs is also done considering under adverse grid conditions from 0.2 to 0.4s like Case C1: grid voltage under 30% voltage sag, Case C2: grid voltage under polluted environment, Case C3: grid voltage under 30° phase jump, Case C4: grid voltage under + 5 frequency jump, and Case B5. Grid voltage under 20% dc offset. Table III depicts the comparative analysis of LMS, SOGI, CLMS, CSOGI and proposed H-LMS-SOGI PLLs by considering the parameters like overshoot and settling time.

4.8 Case B1: grid voltage under polluted environment

Figure 10a shows the simulated result of H-LMS-SOGI, CLMS and CSOGI-PLL under polluted environment. The presence of harmonics leads to distortion of sinusoidal wave signal which causes ripples in frequency signals. The H-LMS-SOGI depicts to have the smallest ripple peak among the three PLLs. Fig 10b shows the experimental result under polluted environment to validate the simulation result.

4.9 Case B2: grid voltage under 30° phase jump

Figure 10c and d shows the simulated and experimental results under 30° phase jump. It is observed that the H-LMS-SOGI PLL has the least overshoot than CLMS and CSOGI PLLs.

4.10 Case B3: grid voltage under + *5Hz frequency jump*

Figure. 10e and f shows the simulated and experimental results under + 5 Hz frequency jump. The overshoot of CSOGI is the highest.

4.11 Case B4: grid voltage under 20% dc offset

Figure. 10g and h shows the simulated and experimental results under 20% dc offset. The oscillation of H-LMS-SOGI is lesser than CLMS.

Figure 11a, b, c also shows the comparative experimental dynamic performance analyses of H-LMS-SOGI, CLMS and CSOGI PLLs under non-ideal grid conditions under (a) 20% dc offset (b) 30° phase jump(c) + 5 Hz frequency change. It gives better validations of the simulated and experimental results obtained in Fig. 10 under the same voltage amplitude variation.

Figure 12 shows the comparative dynamic performance analysis of five PLLs considered viz. LMS, SOGI, H-LMS-SOGI, CLMS CSOGI PLLs under non-ideal grid conditions. In Fig. 12a response under 30% voltage sag is shown. It is observed that H-LMS-SOGI PLL shows lower overshoot with fastest settling response then the remaining four other PLLs considered has least overshoot but with oscillatory response. In Fig. 12b under polluted grid voltage H-LMS-SOGI PLL shows moderate settling response than CSOGI, single SOGI and single LMS-based PLL. The overshoot of proposed hybrid PLL is also quite less. In Fig. 12c under 30° phase shift H-LMS-SOGI PLL shows very low overshoot than CLMS, CSOGI and single SOGI and single LMS. The highest overshoot is observed under SOGI PLL. The LMS-PLL shows the worst settling time under 30° phase shift. In Fig. 12d under + 5 frequency change H-LMS-SOGI PLL shows lowest overshoot than CSOGI, single SOGI and single LMS. H-LMS-SOGI also shows fastest settling response than without any oscillations. LMS-PLL shows oscillatory response, while CLMS-PLL shows more sluggish response. In Fig. 12e under 20% dc offset H-LMS-SOGI PLL shows lower overshoot than CLMS and single SOGI. However, CSOGI-PLL shows almost no oscillation under dc offset effect after 0.04 s. A modified comparative table is prepared based on the performance of different PLLs like LMS, SOGI, CLMS, CSOGI and H-LMS-SOGI. This table is prepared by considering parameters like overshoot and settling time from simulation results under adverse grid conditions like (a) 30% voltage sag, (b) polluted grid voltage (c) 30° phase jump, (d) + 5 Hz frequency change, and (e) 20% dc offset.

5 Application of proposed H-LMS-SOGI PLL for inverter control

Under this Section, an application of the proposed hybrid PLL for inverter control has been investigated. The proposed

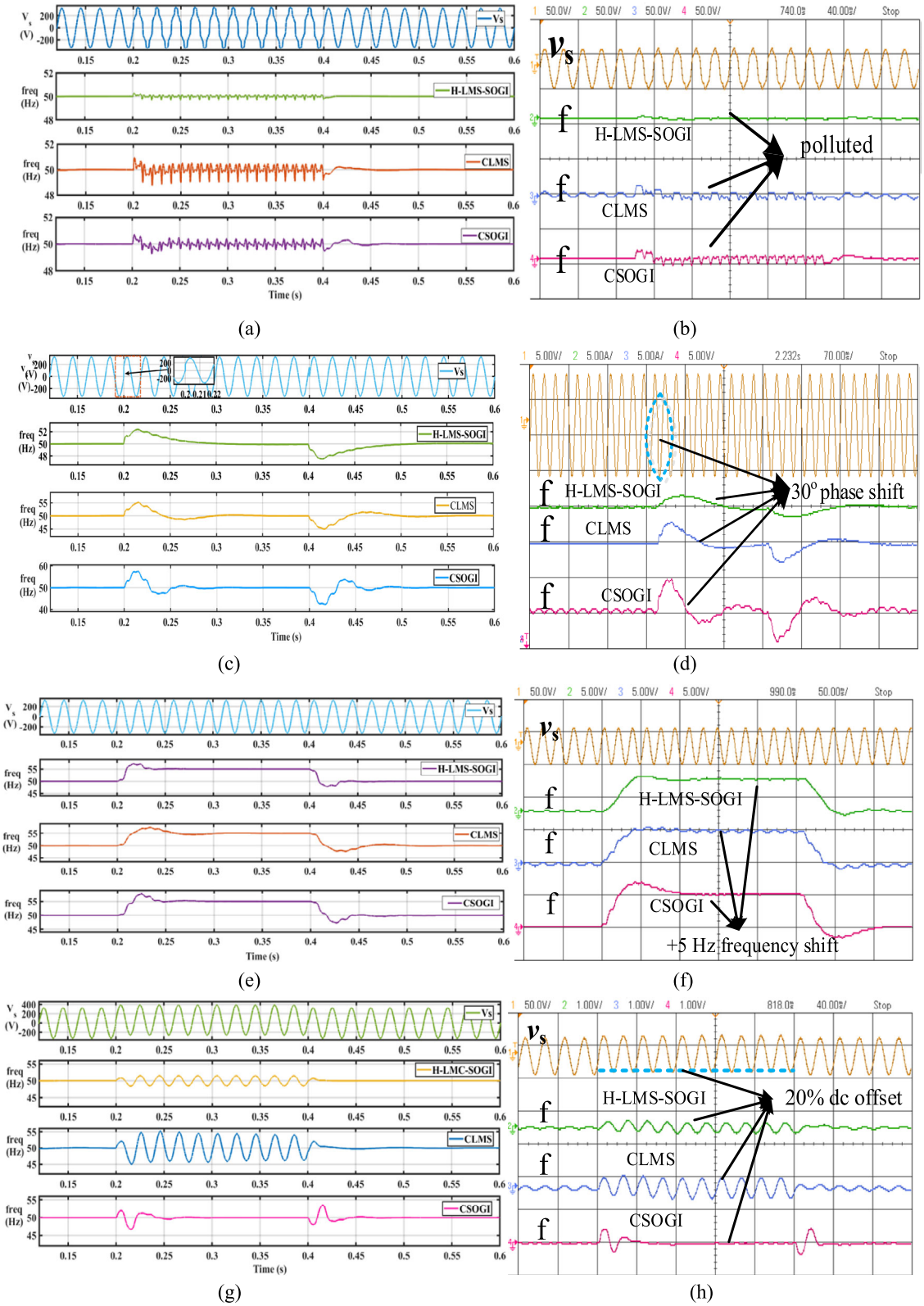


Fig. 10 **a**, **c**, **e**, **g** Simulated and (ii) experimental **b**, **d**, **f**, **h** comparative dynamic performance analyses of H-LMS-SOGI, CLMS and CSOGI PLLs under adverse grid conditions from 0.2 to 0.4 s considering Case B1. Grid voltage under polluted environment, Case B2. Grid voltage under 30° phase jump, Case B3. Grid voltage under + 5 frequency jump, Case B3. Grid voltage under + 5 frequency jump and Case B4. Grid voltage under 20% dc offset

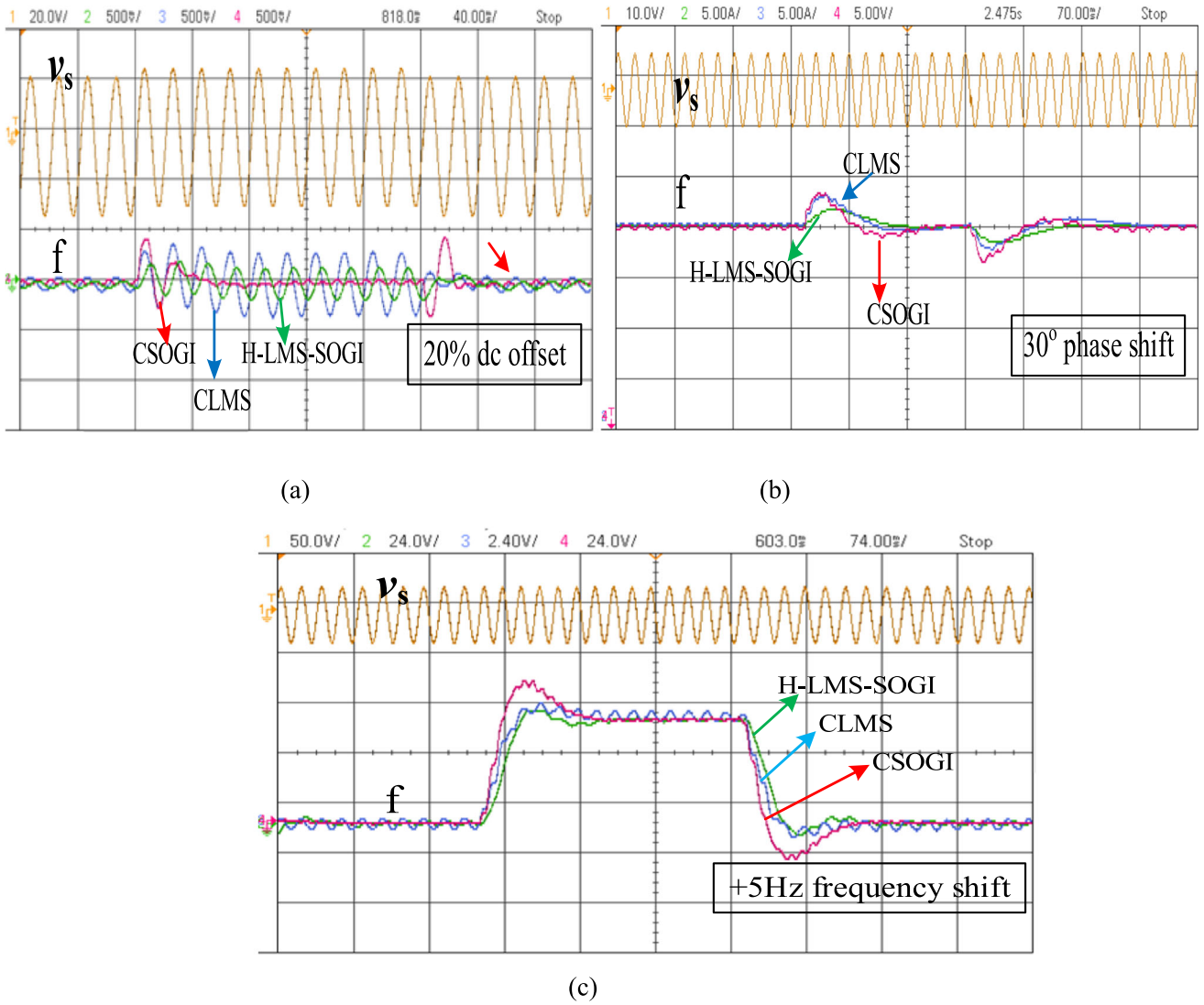
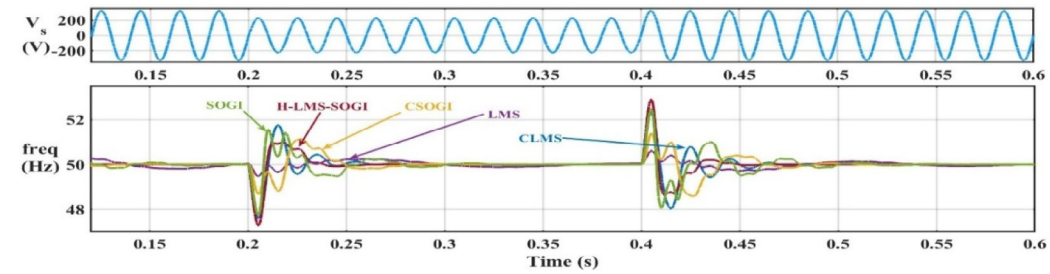


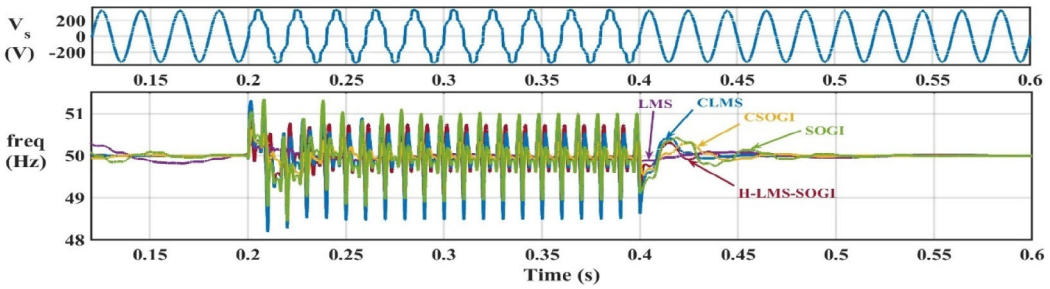
Fig. 11 Experimental comparative dynamic performance analyses of H-LMS-SOGI, CLMS and CSOGI PLLs under non-ideal grid conditions for 0.4 s **a** 20% dc offset **b** 30° phase jump **c** + 5Hz frequency change

H-LMS-SOGI-based controller for inverter control for a single phase grid connected system. Fig 13 shows the block diagram where the proposed H-LMS-SOGI has been used as controller for compensating the nonlinear load current drawn by the on-linear load. The system block diagram shows a single-phase grid connected system feeding nonlinear load modelled as a R-L branch connected at the ends of a diode rectifier. Further, the proposed H-LMS-SOGI technique is now used as a technique for fundamental current estimation and not as a PLL. The H-LMS-SOGI controller block estimates the fundamental load current component in the system and computes the reference supply current. The actual supply current and the reference supply currents are compared using the pulse width modulation technique to generate the gating pulses for the compensator.

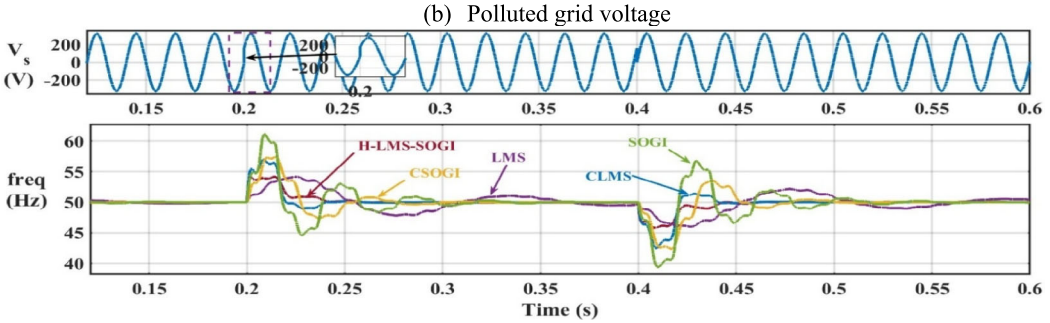
Fig 14 shows the simulation results of the inverter connection with H-LMS-SOGI-based controller. The load current is nonlinear and increased after 0.5s. It is observed that the supply current is sinusoidal and in phase with the grid voltage. Thus, power correction is close to unity. Moreover, the dc link voltage of the inverter (Vdc) is maintained to its reference value of 150 V by PI controller action. The fundamental current component extracted using the proposed H-LMS-SOGI technique is constant and varied only when the load current changes at t = 0.5s. Thereafter it again becomes steady as shown in the figure, thus, Fig. 14 clearly shows that the proposed Hybrid PLL can also be used as H-LMS-SOGI-based controller.



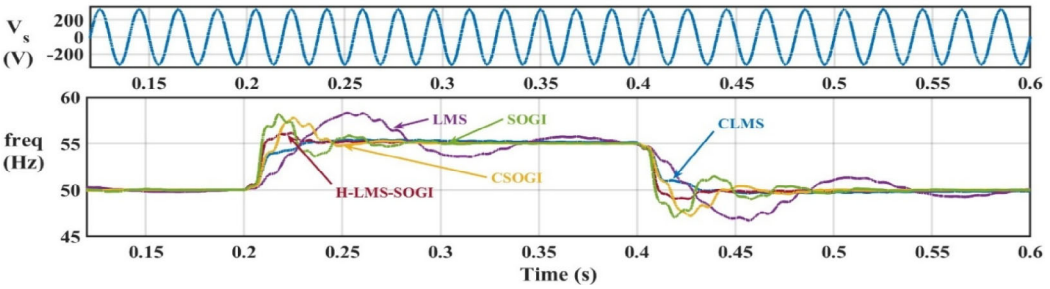
(a) 30% voltage sag



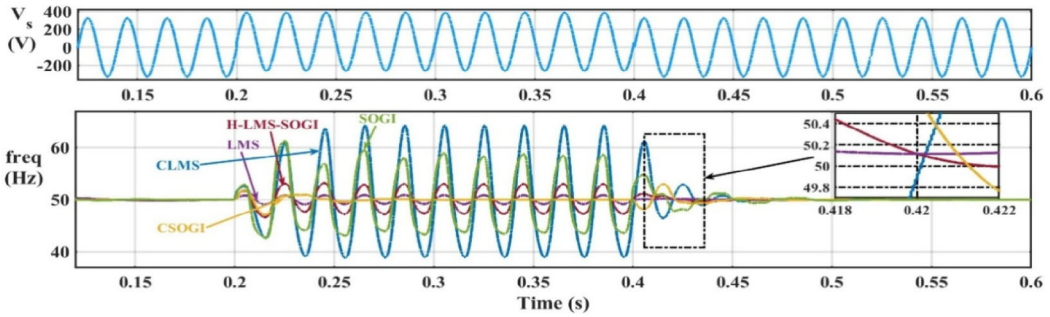
(b) Polluted grid voltage



(c) 30% Phase shift



(d) +5 Hz Frequency change



(e) 20% Dc offset

Fig. 12 Simulated comparative dynamic performance analyses of H-LMS-SOGI, CLMS, CSOGI, LMS, SOGI PLLs under adverse grid conditions from 0.2 to 0.4 s considering Case C1. grid voltage under 30% voltage sag, Case C2. grid voltage under polluted environment, Case C3. grid voltage under 30° phase jump, Case C4. grid voltage under + 5 frequency jump, and Case B5. grid voltage under 20% dc offset

Table 3 Comparative performance analysis of LMS, CLMS, SOGI, CSOGI and H-LMS-SOGI PLLs

Testing cases	Parameter considered	LMS	SOGI	CLMS	CSOGI	H-LMS-SOGI
30% voltage sag	Overshoot	Lowest (50.24) but oscillatory	Moderate (51.56)	highest (51.74Hz)	high (51.73 Hz)	Lower (50.9 Hz) and no oscillation
	Settling time	Sluggish (~ 3 cycles)	Slower response (nearly 3 cycles)	Moderate response (more than 2 cycles)	Moderate response (more than 2 cycles)	fastest response (less than 2 cycles)
Polluted grid voltage	Overshoot	moderate (50.28 Hz)	moderate (51.33 Hz)	moderate (50.77 Hz)	moderate (50.63 Hz)	moderate (50.3 Hz)
	Settling time	slower response (within two cycles)	moderate response (within two cycles)	least response (within two cycles)	sluggish response (within two cycles)	moderate response (within two cycles)
30° phase shift	Overshoot	Lesser (54.17 Hz)	Highest (61.12 Hz)	moderate (56.8Hz)	largest (57.32Hz)	least (52.38 Hz)
	Settling time	sluggish (~ 5 cycles)	slow response (~ 3 cycles)	Moderate response (~ 2 cycles)	Moderate response (~ 2cycles)	Fastest response (~ 1 cycle)
+ 5 Hz frequency shift	Overshoot	high (58.29 Hz)	Moderate (58.11 Hz)	54.2Hz (undershoot)	high(58.7Hz)	least (56.12Hz)
	Settling time	Sluggish response and oscillatory	~ 2 cycles	~ 2 cycles	~ 3 cycles	~ 2 cycles and fastest response (
20% dc offset	Overshoot	largest (61.04 Hz)	Least (50.82 Hz)	High (55.16Hz)	Low (53.1 Hz)	Moderate (51.25 Hz)
	Settling time	~ 6 cycles	~ 3 cycles	~ 6 cycles	~ 4 cycles	~ 2 cycles

From Table 3 it is observed that the proposed PLL gives best dynamic performance under 30% voltage sag, 30^0 phase shift and + 5 Hz frequency change as compared to others PLL techniques. Moreover, its performance is also satisfactory under polluted grid condition as well as 20% dc offset condition. Hence this PLL is a good synchronisation technique which is a hybrid combination of LMS and SOGI PLL

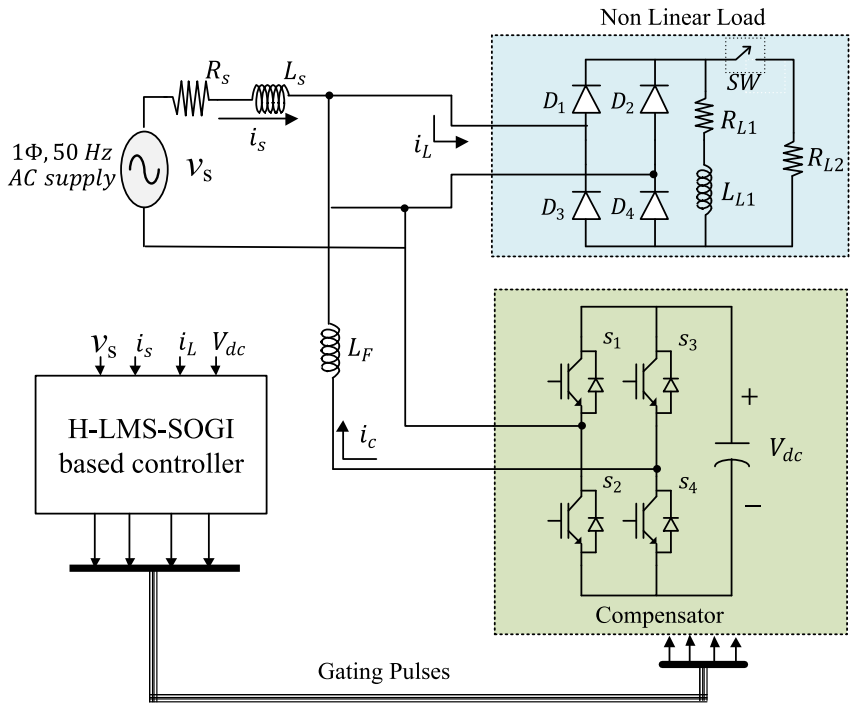


Fig. 13 Block diagram of inverter connection with H-LMS-SOGI PLL-based controller

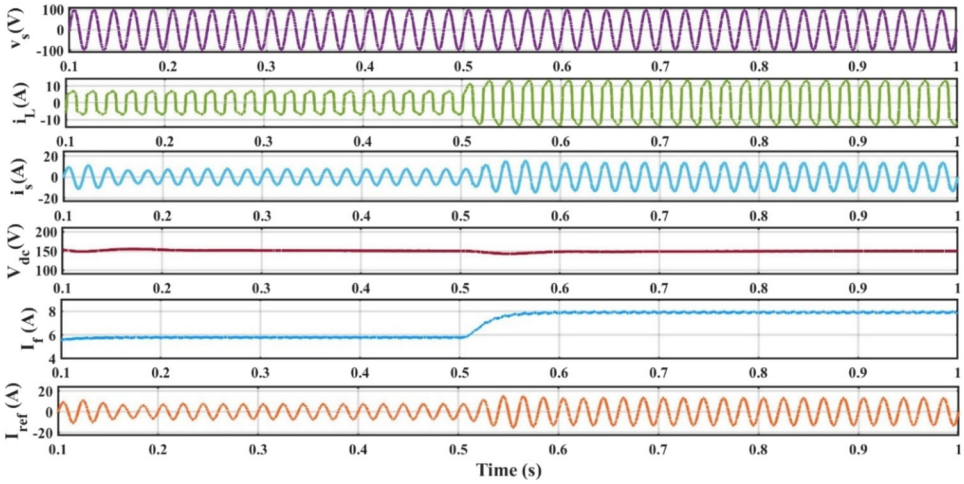


Fig. 14 Simulation result of proposed H-LMS-SOGI-based controller showing reference current, I_{ref} (A), fundamental current, I_f (A), dc voltage V_{dc} (V), source current, I_s (A), load current, I_L(A) and source voltage, v_s (V)

6 Conclusion

In this paper, the design and modelling of H-LMS-SOGI PLL is investigated and analysed in detail. The dynamic performances of the five PLLs viz. SOGI, LMS and three cascaded PLLs under adverse grid conditions are analysed through simulation using MATLAB Simulink toolbox (2020A). The designed mathematical modelling of the three PLLs is discussed and the selection of the control parameters 'μ'of LMS and 'k' of SOGI is done through Bode plot and pole-zero plots. The simulated results are validated through hardware results by setting up a laboratory prototype using a $1-\varphi$ programmable supply of GwinSTEK model (APS-1102A). The stability of the three PLLs are analysed through of the gain margin (GM) in dB and phase margin (PM) in degree. The enhanced stability of the proposed H-LMS-SOGI PLL is further validated by the pole-zero plot in complex plane and this PLL is more stable than the other two cascaded PLLs due to larger values of positive GM and PM. The dynamic performance under steady state analysis of H-LMS-SOGI PLL is performed under adverse grid conditions considering five test cases viz. Case A1: Grid voltage deviation with 30% sag and 35% swell, Case A2: Under polluted grid voltage, Case A3: Grid voltage under 30°phase jump, Case A4: Grid.

voltage under + 5 Hz frequency jump, Case A5: Grid voltage under 20% dc offset. The comparative analysis of the three PLLs is also performed considering four test cases of non-ideal grid conditions viz. Case B1: Grid voltage under polluted environment, Case B2: Grid voltage under 30° phase jump, Case B3: Grid voltage under + 5 frequency jump, Case B4: Grid voltage under 20% dc offset. Under 30° phase shift, H-LMS-SOGI PLL gives the least overshoot with moderate settling time of five cycles. The proposed H-LMS-SOGI PLL also shows least overshoot and fastest dynamic response under polluted grid voltage and + 5 Hz step frequency change. Moreover, the proposed H-LMS-SOGI PLL gives satisfactory response under 20%dc offset. Further, the proposed H-LMS-SOGI technique is validated for inverter control in a single-phase grid connected system. Hence it can be concluded that the proposed H-LMS-SOGI PLL gives satisfactory dynamic response under all the adverse grid conditions considered and the technique can also be used for load compensation satisfactorily.

Appendix:

A. H-LMS-SOGI PLL.

$v_s = 325$ V, $f = 50$Hz, $K_p = 0.5$, $K_i = 21.5$, $k = 1.4$, $= 0.005$.

B. For CLMS-PLL.

$v_s = 325$ V, $f = 50$Hz, $K_p = 0.15$, $K_i = 12$, $= 0.05$.

C. For CSOGI-PLL.

$v_s = 325$ V, $f = 50$Hz, $K_p = 0.4$, $K_i = 10$, $k = 1.8$

Acknowledgments The authors are thankful to the DST for the FIST project SR/FST/ET-I/2022/1026.

Author contributions The First author has developed the design and modelling and editing the full paper while the corresponding author has help in reviewing the paper.

Declarations

Competing interest The authors declare no competing interests.

Data availability No datasets were generated or analysed during the current study.

References

1. Ciobotaru M, Teodorescu R, Blaabjerg F (2006) A new single-phase PLL structure based on second order generalized integrator, 37th IEEE Power Electronics Specialists Conference, Jeju, Korea (South), pp. 1–6. https://doi.org/10.1109/pesc.2006.1711988
2. Golestan S, Guerrero J (2015) Conventional synchronous reference frame phase-locked loop is an adaptive complex filter. IEEE Trans Industr Electron 62:1679–1682. https://doi.org/10.1109/TIE.2014.2341594
3. Issa MAB, Al Muala ZA, Bugallo PMB (2024) Simple solution of DC-offset rejection based phase-locked loop for single-phase grid-connected converters. Renew Energy Environ Sustain. https://doi.org/10.1051/rees/2023024
4. Kulkarni A, John V (2017) Design of a fast response time single-phase PLL with DC offset rejection capability. Electr Power Syst Res 145:35–43. https://doi.org/10.1016/j.epsr.2016.12.023
5. Saxena H, Singh A, Rai J (2019) Design and analysis of different PLLs as load compensation techniques in 1-phase grid-tied PV system. Int J Electron 106(11):1632–1659
6. Han Y, Luo M, Zhao X, Guerrero JM, Xu L (2015) Comparative performance evaluation of orthogonal-signal-generators-based single-phase PLL algorithms—a survey. IEEE Trans Power Electron 31(5):3932–3944
7. Smadi IA, Altabbal H, Fawaz BHB (2022) A Phase-locked loop with inherent dc offset rejection for single-phase applications. IEEE Trans Ind Inform 19(1):200–209
8. Ahmed H, Benbouzid M (2020) Demodulation type single-phase PLL with DC offset rejection. Electron Lett 56(7):344–347. https://doi.org/10.1049/el.2019.3718
9. Sepahvand H, Saniei M, Mortazavi SS, Golestan S (2021) Performance improvement of single-phase PLLs under adverse grid conditions: an FIR filtering-based approach. Electr Pow Syst Res 190:106829. https://doi.org/10.1016/j.epsr.2020.106829
10. Smadi IA, Altabbal H, Fawaz BHB (2022) A phase-locked loop with inherent dc offset rejection for single-phase applications. IEEE Trans Ind Inform 19(1):200–209. https://doi.org/10.1109/TII.2022.3157631
11. Kulkarni A, John V (2017) Design of a fast response time single-phase PLL with dc offset rejection capability. Electr Power Syst Res 145:35–43
12. Liu B et al (2020) A simple approach to reject DC offset for single-phase synchronous reference frame PLL in grid-tied converters. IEEE Access 8:112297–112308
13. Saxena H, Singh A, Chittora P (2023) Modified LMS synchronization technique for distributed energy resources with DC-offset and harmonic elimination capabilities. ISA Trans 135:567–574
14. Dey D, Subudhi B (2023) A normalized least means absolute third-based adaptive control algorithm design for grid-connected PV system, *IEEE*. J Emerg Sel Topics Power Electron 11(2):2291–2299
15. Balasundar C, Sundarabalan CK, Santhanam SN, Sharma J, Guerrero JM (2023) Mixed step size normalized least mean fourth algorithm of DSTATCOM integrated electric vehicle charging station. IEEE Trans Ind Inform 19(6):7583–7591. https://doi.org/10.1109/TII.2022.3211958
16. Kumar SS, Mukundan N (2022) Modified LMS control for a grid interactive PV–fuel cell–electrolyzer hybrid system with power dispatch to the grid. IEEE Trans Ind Appl 58(6):7907–7918
17. Giri AK, Arya SR, Maurya R (2019) Compensation of power quality problems in wind-based renewable energy system for small consumer as isolated loads. IEEE Trans Ind Electron 66(11):9023–9031
18. Modi G, Singh B (2021) SPV-BES system synchronized to three-phase four-wire AC distribution network. IEEE Trans Ind Appl 57(6):5667–5676
19. Kumar A, Patel N, Gupta N, Gupta V (2022) L2 norm enabled adaptive LMS control for grid-connected photovoltaic converters. IEEE Trans Ind Appl 58(4):5328–5339
20. Huang F, Song F, Zhang S, So HC, Yang J (2023) Robust bias compensated LMS algorithm: design, performance analysis and applications. IEEE Trans Veh Technol 72(10):13214–13228
21. Modi G, Singh B (2023) A novel multilayer N-LMS adaptive-filter-based control for synchronization and power quality improvement in grid-tied SPV system. IEEE Trans Ind Electron 70(9):9158–9168
22. Han B, Bae B (2005) Novel phase-locked loop using adaptive linear combiner. IEEE Trans Power Deliv 21(1):513–514
23. Saxena H, Singh A, Rai JN (2020) Design and performance analysis of improved adaline technique for synchronization and load compensation of grid-tied photovoltaic system. Int Trans Electr Energy Syst 30(6):e12388
24. Saxena H, Singh A, Chittora P (2023) Modified LMS synchronization technique for distributed energy resources with DC-offset and harmonic elimination capabilities. ISA trans 135:567–574. https://doi.org/10.1016/j.isatra.2022.09.042
25. G. Modi and B. Singh, 2022 Cascaded LMS Filter based control for SPV-SyRGWind Based grid-interactive Microgrid, In: IEEE 2nd International Conference on sustainable energy and future electric transportation (SeFeT), Hyderabad, India, pp 1–6 https://doi.org/10.1109/SeFeT55524.2022.9909144.
26. Golestan S, Guerrero JM, Vasquez JC, Abusorrah AM, Al-Turki Y (2021) Standard SOGI-FLL and its close variants: precise modeling in ltp framework and determining stability region/robustness metrics,IEEE Trans. Power Electron 36(1):409–422
27. Hoepfner B, Vick R (2023) A three-phase frequency-fixed DSOGI-PLL with low computational effort. IEEE Access 11:34932–34941
28. Quan X, Huang AQ (2021) PI-based synchronous reference frame frequency-locked loop. IEEE Trans Ind Electron 68(5):4547–4553
29. Dòria-Cerezo A, Repecho V, Biel D (2021) Three-phase phase-locked loop algorithms based on sliding modes. IEEE Trans PowerElectron 36(9):10842–10851
30. Quan X, Dou X, Wu Z, Hu M, Huang AQ (2018) Complex-coefficient complex-variable filter for grid synchronization based on linear quadratic regulation. IEEE Trans Ind Inform 14(5):1824–1834
31. Glover J (1977) Adaptive noise canceling applied to sinusoidal interferences. IEEE Trans Acoust Speech Signal Process 25(6):484–491. https://doi.org/10.1109/TASSP.1977.1162997

Publisher's Note Springer Nature remains neutral with regard to jurisdictional claims in published maps and institutional affiliations.

Springer Nature or its licensor (e.g. a society or other partner) holds exclusive rights to this article under a publishing agreement with the author(s) or other rightsholder(s); author self-archiving of the accepted manuscript version of this article is solely governed by the terms of such publishing agreement and applicable law.

The current issue and full text archive of this journal is available on Emerald Insight at:
https://www.emerald.com/insight/0332-1649.htm

COMPEL - The international journal for computation and mathematics in electrical and electronic engineering

Design optimization of surface-inset-type-PMSM using scalarization and novel metaheuristic algorithm for two-post lift application

Monika Verma
Electrical Engineering Department, Centre of Excellence for Electric Vehicle, and Related Technologies, Delhi Technological University, Delhi, India

Received 1 January 2025
Revised 1 April 2025
8 May 2025
13 May 2025
20 May 2025
Accepted 21 May 2025

Abstract

Purpose – This study aims to propose technique for reducing overall design cost of traction motor for two-post lift (2PL) application, by altering the geometry of the motor. This process is efficiently fit for improving the overall performance of the motor, by diminishing the unwanted cogging torque and ripple torque.

Design/methodology/approach – This work presents a mutualism-based novel metaheuristic algorithm for solving real-world motor design optimization problem. To simplify the formulation of complex problem of motor design, surrogate modeling technique (SRT) is implemented. The SRT helps for obtaining the mathematical modeling of output response in terms of input design parameters.

Findings – The analysis process helps in finding out the optimal design parameters of motor model, at which the motor has improved performance and geometry of motor has reduced cost.

Research limitations/implications – The proposed study presents a panoramic view of solving motor-model design (MMD) problem from scratch design to reach out to optimized design, using the metaheuristic algorithm. The study has the limitations of inclusiveness of the electrical constraints due to 2PL application in designing the problem.

Practical implications – The new surface inset type permanent magnet synchronous motor model geometry can be used to further analyze the dynamic behavior as well as vibration analysis impact over the 2PL performance.

Originality/value – The originality of this study lies in the authorized optimization algorithm. Also, the implementation of proposed algorithm is to solve complex MMD problem, which efficiently explores as well as exploits the design parameters under a specified range.

Keywords Two post lift, Metaheuristic, Optimization, SIT-PMSM, Optimal design, Permanent magnet machine, Finite element analysis

Paper type Research paper

1. Introduction

This section provides introductory remarks and importance of this work.

1.1 a) Motivation

The equipment, like automotive lifts, are used by technicians to elevate the vehicles above the ground to carry out maintenance, repair, production or development work. The automobile sector is likely to drive the rate of global motorization from 230 to 400 vehicles in the upcoming decades. Also, the number of running vehicles per kilometers has increased recently. Correspondingly, component replacement and work related to maintenance of these vehicles have increased rapidly over the past years (Zang and Gao, 2022; Damien Burlet-Vienney *et al.*, 2021).

This work is supported by Centre of Excellence for Electric Vehicle and Related Technologies, Electrical Engineering Department, Delhi Technological University, Delhi, India.

COMPEL - The international journal for computation and mathematics in electrical and electronic engineering
© Emerald Publishing Limited
0332-1649
DOI 10.1108/COMPEL-12-2024-0527

Nowadays, two-post lifts (2PLs) are the most commonly installed lift system in garages, as shown in Figure 1. A 2PL system consists of two columns, which are tied up in concrete, enclosed by carriages, that are driven by a hydraulic motor system (Damien Burlet-Vienney *et al.*, 2023). The context related to lift manufacturers, maintenance firms and consumers are

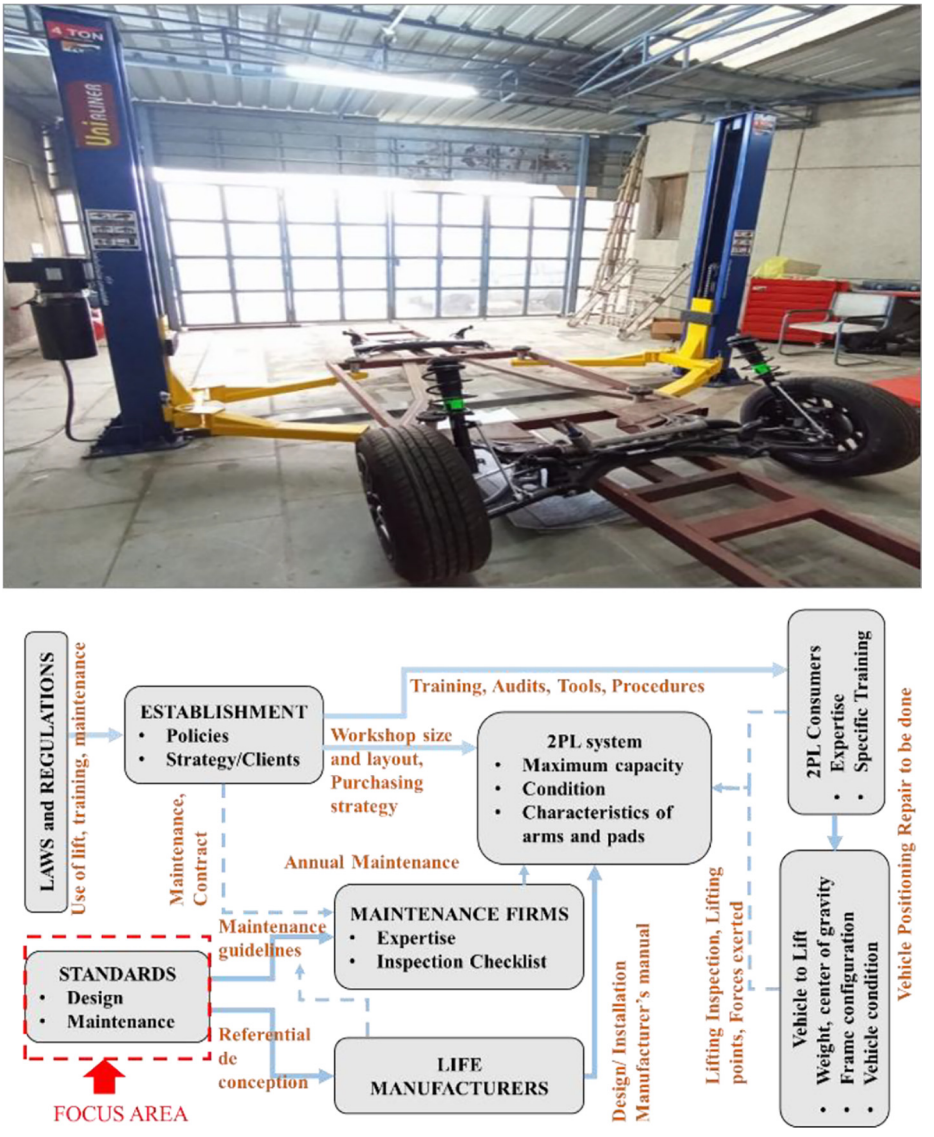


Figure 1. Two-post lift (2PL) system with vehicle chassis body and summary of context related to lift manufacturers, maintenance firms and consumers (red box indicates the focus area of this work)
Source: Authors' own work

also summarized in Figure 1, highlighting the focus area of this work, being the design of electric motor, used in the system for uplifting the vehicle. It indicates that by maintaining the proper guidelines and standards for design optimization of each component of the system, the flow-chain of production of a cost-effective 2PL system is influenced, up to the consumer level.

1.2 b) Background

Efficient design of the electric motor plays a crucial role in increasing the performance of 2PL application. It is because this application requires high-torque performance, energy-efficient and reliable motor design for driving the hydraulic pump, so that smooth and steady lifting of the vehicle is ensured. A skillfully optimized motor can significantly provide advantage of reducing extra energy consumption, minimizing heat generation and improving overall system endurance, thereby contributing to lowered operational cost. Also, if motor is precise at producing smoother torque, it is beneficial to maintain uniformity of hydraulic pressure, so that jerky movements can be prevented and operator safety can be ensured.

Conventional induction motors often suffer from low efficiency and larger losses, whereas advanced designs of permanent magnet synchronous motor (PMSM), having optimized torque performance, present superior performance in 2PL application. By designing and optimizing PMSM structure, that is capable of meeting essential torque characteristics of hydraulic 2PL, the lift system delivers faster responses, minimized noise and enhanced load-handling capability. This indicates that there is a tight connection of optimizing incorporated electric motor in 2PL application.

There are various structural advances carried out in design of PMSMs in accordance with various industrial applications. Recently, a popular type of PMSM design is called surface inset type PMSM (SIT-PMSM) (Dubas and Rahideh, 2013). This design has simplified structure, which provides an aid to stability-related applications. The literature related to various PMSM designs for the hydraulic lift system is presented in Table 1.

1.3 c) Why novel optimization method is required?

The evolution of the real-world optimization adversities has matured and developed, necessitating competent yet innovative optimization techniques. The domain area, where the classical methodologies fails to succeed, provides a room for implementation of nature-inspired algorithms. These algorithms quickly come up with an outstanding solution to complicated optimization problems, feasting on rational computation time. Nonetheless, in recent years, methodologies anchored in physical nonlinear systems have been amplified. The nonlinear physics-based processes formulated in the form of optimization techniques act as a subset of existing optimization methodologies (OMs). They surpassed the performance of existing OMs due to higher efficiencies in exploration phase. Thus, these are considered as fresh solution searching practices in the OMs' world.

Archimedes optimization algorithm (AOA) is the recent and simpler physics-based optimization algorithm. AOA presents commendable results while solving real-world problems through the approach of optimizing various measurable entities like profit, performance or quality. But, in few cases, it is found to be trapped in the region of local optima because of unsteadiness between exploration phase and exploitation phase. In traditional AOA, exploration and exploitation phases are defined by the acceleration factors on the basis of the collisions between the objects. However, its search potential leaves room for improvement for solving complex nonlinear problems like motor design optimization. In this work, the author improves the performance of traditional AOA technique. The till-date improvements introduced in AOA are listed in Table A.1 in the supplementary material.

Table 1. Literature review related to various designs of PMSM

Author, year	Design feature	Research gap
Hu *et al.* (2021)	Closed slot design of PMSM	Lesser design parameters are considered for analysis
Ambekar (2022)	High torque, compact and energy-saving IPMSM	Design is not optimized as per the application requirement
Pellegrino *et al.* (2012)	Limiting the ampere conductors per meter	Weakens the flux and use of permanent magnet (PM) makes the PMSM costlier
Dinh and Tien (2016)	Short end connections in interior permanent magnet (IPM) machines	Air gap flux, flux linkages and back EMF deviates from the analytical results due to inaccuracies in manufacturing
EI *et al.* (2014)	Change in rotor geometry	Inaccuracies in design leads to deviation in air gap flux, flux linkages and back EMF
Shindeand and Thosar (2015)	Type of magnetic material	Air gap flux, flux linkages and back EMF deviates from the analytical results due to inaccuracies in manufacturing
Arora and Singh (2015)	Use of different stator configurations, magnet shape and rotor structure	Divergence in air gap flux and back EMF is observed due to inaccuracies in manufacturing
Wang *et al.* (2018)	Magnetization and the air gap between The magnets and the inter-poles	Inaccuracies in design leads to deviation in air gap flux, flux linkages and back EMF
Jian *et al.* (2009)	Different rotor geometry	Back EMF is not smooth due to the lack of accuracies in design

Source(s): Authors' own work

In recently developed symbiotic organisms search (SOS), the concept of mutualism, commensalism and parasitic approaches are implemented to reach the optimal solution. This technique is proved to be highly reliable. However, the parasitic stage of solution computation exhibits the wastage of computing time since it mostly cancels out the weaker solution. The commensalism stage uses the interaction of the organism with random organism, which arises uncertainty of wasting the current iteration. Whereas, the mutualism stage ensures the improvement in the position of the organism toward the best optimal value.

Hence, taking into account the benefits of mutualism stage of SOS algorithm, a fresh and highly efficient OM is designed for reaching up to optimal solution of motor design problem. This attempt provides an aid to design optimization engineers to have insight to expertise in providing efficient and accurate design considerations while developing industry-based products for EV designs and related technologies. In this work, a novel mutualism-based Archimedes optimization method (MB-AOM) is proposed by integrating the mutualism concept of SOS to both collision as well as noncollision phases of AOA, which corresponds to exploration and exploitation phases of traditional AOA, respectively.

1.4 d) Paper organization

This paper is organized into five sections. Section 1 presents the motivation, background, answers to "WHY" and relevant literature survey. Section 2 exhibits the development of motor design problem for the 2PL system. Section 3 describes novel MB-AOM procedure. Section 4 shows the analysis results. Section 5 shows the concluding remarks.

2. Development of scalarization based motor-model design problem

The hydraulic motor used in 2PL system should be able to provide stable operation as well as controlled lowering of lifted vehicle, as it pushes oil into the cylinder to lift the vehicle. For this application, the smoother torque production and highly efficient performance of PMSM is required.

In this work, a SIT-PMSM model is designed having nine slots and six poles. The dimensions of initial model design are chosen to satisfy the requirements of 2PL system application. The schematic diagram of the electric motor shape with SIT-PMSM used in the hydraulic motor structure and design parameters are presented in Figure 1. The 2PL application requires minimal amount of ripples and cogging-ness in its nature. The initial model specifications are presented in Table 2.

Here, the cost function, Y is presented by equation (1), where c_1, c_2 and c_3 are the cost function coefficients. The terms $\widehat{Y}_1$ indicates cogging torque, $\widehat{Y}_2$ indicates ripple torque and $\widehat{Y}_3$ indicates average torque produced by the motor. Here, $\widehat{Y}_1$ and $\widehat{Y}_2$ are needed to be minimized and $\widehat{Y}_3$ is needed to be maximized. Hence, to make it clearer, the signs of these coefficients are specified in equation (1):

$$Y = c_1\widehat{Y}_1 + c_2\widehat{Y}_2 - c_3\widehat{Y}_3 \tag{1}$$

The relationships between torque components are derived in terms of design parameters using surrogate modeling (SM) technique, as shown in Supplementary material in details. Thus, the overall cost function is derived using three *scalarization techniques*, namely.

2.1 [1] Equal weights

For development of required MMD problem, equal weights (EW) criteria defines the values of c_i to be computed using equation (2), where, i = 1, 2, 3 for three output responses, $\widehat{Y}_1$, $\widehat{Y}_2$

Table 2. Characteristics of initial model of SIT-PMSM

Characteristics	Value	Unit
Power output	2.2	kW
Speed	3000	Rpm
Frequency	150	Hz
Voltage	200	V
Stator		
Inner diameter	67.6	Mm
Outer diameter	110	Mm
Rotor outer diameter	66.6	Mm
Shaft diameter	24	Mm
Stack length	50	Mm
Coil turns	30	–
Air gap length	2.5	Mm
Permanent magnet	NdFeB	–
Electrical steel	Nongrain-oriented M400-50A	
Cogging torque	0.8	Nm
Torque (@3000 rpm)	7.1	Nm
RMS back EMF (@500 rpm)	25	V
Input current (@3000 rpm)	5	A

Source(s): Authors' own work

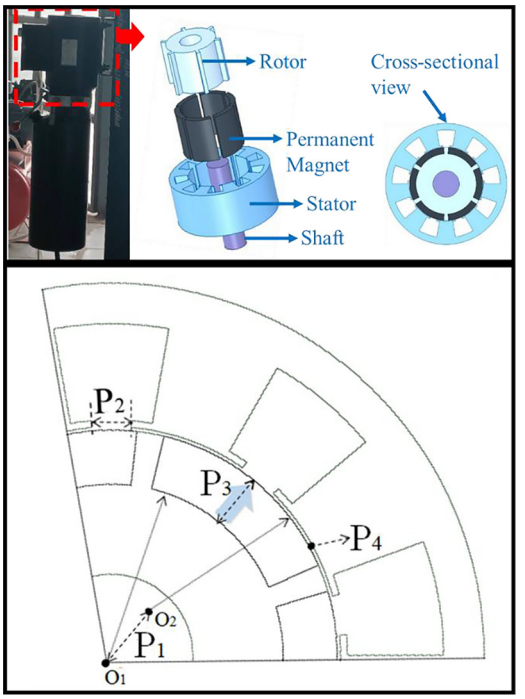


Figure 2. Internal structure of electric motor used in 2PL system, and design parameters of SIT-PMSM model (P_1, pole eccentricity [distance between centers O_1 and O_2], P_2, slot opening in stator, P_3, radial magnet thickness and P_4, length of air gap)
Source: Authors' own work

and $\widehat{Y}_3$, respectively. Hence, the MMD problem is denoted by equation (3). The terms p_1, p_2, p_3 *and* p_4 denote four design variables, as presented in Figure 2:

$$c_i = \frac{1}{n} \tag{2}$$

$$\begin{aligned} Y = {} & 2.8193 - 0.1584P_1 + 0.1532P_2 - 0.3991P_3 - 0.6085P_4 + 0.0267P_1P_2 + 0.0242P_1P_3 \\ & + 0.0099P_1P_4 + 0.0039P_2P_3 + 0.0560P_2P_4 + 0.0804P_3P_4 - 0.0006P_1^2 - 0.0585P_2^2 \\ & + 0.0455P_3^2 - 0.0002P_4^2 \end{aligned} \tag{3}$$

2.2 [2] Rank order centroid weights

The rank order centroid weights (ROCW) criteria defines the values of c_i to be computed using equation (4), where, k indicates the rank of corresponding output response. Here, by considering the rank of cogging torque equal to 1, rank of ripple torque equal to 2 and rank of average torque equal to 3, the MMD problem is denoted by equation (5).

{Reason of ranking: The required application needs to balance the vehicle over 2PL system, without any disturbance in the stability of the vehicle. Thus, the torque produced by

the motor should be noise free and high in magnitude. So, the prime rank is given to cogging torque (since it is primary reason for noise in the torque), second rank is given to ripple torque and the third rank is given to output torque, for making the motor efficient in production of torque. Hence, ranks are considered accordingly}:

$$c_i = \frac{1}{n}\sum_{k=i}^{n}\frac{1}{k} \tag{4}$$

$$\begin{aligned} Y = {} & 0.5536 - 0.2129P_1 - 0.0506P_2 + 0.0200P_3 - 0.3130P_4 + 0.0171P_1P_2 + 0.0193P_1P_3 \\ & + 0.0527P_1P_4 + 0.0241P_2P_3 + 0.0440P_2P_4 + 0.0316P_3P_4 + 0.0249P_1^2 - 0.0419P_2^2 \\ & - 0.0041P_3^2 + 0.0140P_4^2 \end{aligned} \tag{5}$$

2.3 [3] Rank sum weight

The RSW criteria defines the values of c_i using equation (6). Here, the MMD problem is denoted by equation (7):

$$c_i = \frac{2(n+1-i)}{n(n+1)} \tag{6}$$

$$\begin{aligned} Y = {} & 1.1170 - 0.1869P_1 - 0.0076P_2 - 0.0817P_3 - 0.3647P_4 + 0.0199P_1P_2 + 0.0191P_1P_3 \\ & + 0.0390P_1P_4 + 0.0191P_2P_3 + 0.0471P_2P_4 + 0.0420P_3P_4 + 0.0177P_1^2 - 0.0446P_2^2 \\ & + 0.0082P_3^2 + 0.0058P_4^2 \end{aligned} \tag{7}$$

3. Description of mutualism-based novel optimization method

The proposed MB-AOM algorithm starts with the generation and formation of random initial population X, given by equation (8), where, l *and* u are random number, lower bound and upper bound of the object, respectively:

$$X = ran \times (u - l) + l \tag{8}$$

Here, the term *ran* indicates a vector of length equal to the dimension of the fitness function in the range of [0, 1]. The density of the object and volume of the object are stochastically generated and stored into the corresponding variable, given by equation (9):

$$den = ran,\ vol = ran \tag{9}$$

Then, the acceleration of each object is computed, using equation (10):

$$acc = ran \times (u - l) + l \tag{10}$$

The computation of initial fitness function is performed using the initial minimal value, termed as best value. These parameters of the initial best solutions are named as; X_b, den_b,

vol_b and acc_b. The process further updates the density and volume of the object, using equation (11), where t indicates current iteration; r indicates a random number:

$$den^{t+1} = den_t + r \times (den_b - den_t);\ vol^{t+1} = vol_t + r \times (vol_b - vol_t) \tag{11}$$

At starting, the collision of objects occurs, after which it tries to attain an equilibrium state. This phenomenon is formulated by a transfer operator, T_f, given by equation (12), where t_m is the maximum iterations:

$$T_f = e^{\left(\frac{t-t_m}{t_m}\right)} \tag{12}$$

There is a density decreasing factor (d_f, used in the transfer of the search process from global level to local level, this factor is given by equation (13):

$$d_f = e^{\left(\frac{t-t_m}{t_m}\right)} - \frac{t}{t_m} \tag{13}$$

The two phases, Exploration and Exploitation, are distinguished using the factor T_f. For exploration phase and exploitation phase, the accelerations of the objects are updated based on the equations (14) and equation (15), respectively. The terms den_r, vol_r, acc_r are density, volume and acceleration of random object. It is essential to normalize the acceleration of each object. The normalized acceleration is given by equation (16), where l_n, u_n are the normalized parameters, chosen as 0.1 and 0.9, respectively:

$$acc^{t+1} = \frac{den_r + vol_r \times acc_r}{den^{t+1} \times vol^{t+!}} \tag{14}$$

$$acc^{t+1} = \frac{den_b + vol_b \times acc_b}{den^{t+1} \times vol^{t+!}} \tag{15}$$

$$acc_n^{t+1} = l_n + u_n \times \frac{acc^{t+1} - \min(acc)}{max(acc) - \min(acc)} \tag{16}$$

The phase, in which object is far away from the point of global optima, is called exploration phase because the acceleration is high, else the phase is the exploitation phase. Hence, the new position of object is updated based on the exploration phase and exploitation phase, using equation (17) and equation (18), respectively:

$$x_i^{t+1} = x_i^t + C_1 \times r \times acc_n^{t+1} \times d_f \times \left(x_r - x_i^t\right) \tag{17}$$

$$x_i^{t+1} = x_i^t \pm C_2 \times r \times acc_n^{t+1} \times d_f \times \left(T \times x_b - x_i^t\right) \tag{18}$$

The terms C_1 and C_2 are constants; x_r is position of random object; x_b is the position of the best solution; T indicates a parameter, dependent on T_f operator, given as: $T = C_3 \times T_f$. The equation (18) has positive sign, if $p \leq 0.5$, has negative sign, if $p > 0.5$. Here, p is a randomly assigned parameter by the user.

Here, in the MB-AOM, in each of the exploration and exploitation phases, the position of object is updated using *mutualism concept*, after updating it using equation (17) and equation (18), respectively. The mutualism concept involves improvement of an object's position, x_i and an arbitrary object's position, x_j, by moving their respective positions toward the best position, x_b, by taking the mean or mutual benefit factors for both: BF_i and BF_j. Thus, the positions of i^{th} and j^{th} (where, $i \neq j$) object are updated using equation (19) and equation (20), respectively:

$$x_i^* = x_i + r_1 \times (x_b - mv \times BF_i) \tag{19}$$

$$x_j^* = x_j + r_2 \times (x_b - mv \times BF_j) \tag{20}$$

The term *mv* indicates the mean value of previous positions of i^{th} and j^{th} object; x_i and x_j are previous positions of i^{th} and j^{th} object; r_1 and r^2 are random numbers; x_i^* and x_j^* are the updated positions of i^{th} and j^{th} object using mutualism based concept introduced in MB-AOM. The pseudo code and flow chart of MB-AOM is presented in Supplementary material.

4. Analysis and results

In this section, the performance analysis of the proposed novel MB-AOM technique is presented.

4.1 (a) Testing of MB-AOM using benchmark functions

The convergence profiles comparison plots are shown in Figure 3. It is found that the proposed MB-AOM technique has successfully improved the performance of the traditional AOA method, by presenting a better convergence profile.

The solutions to these benchmark functions are then compared for 1,000 iterations and population size of 10, with a few well-known MH techniques, as presented in Table 3.

Thus, it is observed that, not only the convergence capability of MB-AOM is more, but also, it outperforms the popular MH techniques by providing better optimum solutions.

4.2 (b) Testing of MB-AOM to solve MMD problems

The solution to cost functions is presented in Figure 4. It is observed that using ROCW criteria, more weightage is provided to cogging torque (0.611), then next higher weightage is given to torque ripple (0.277) and then to the torque (0.111).

Similarly, using RSW criteria, cogging torque gets weightage of 0.5 (which is less than that of ROCW criteria), torque ripple gets 0.33 weightage and torque gets 0.16 weightage. Using EW criteria, all three torque components are getting equal weightage of 0.5. Hence, using ROCW criteria, the cost function value is found to be least and more satisfying for the proposed application. Table 4 presents the comparison of cost function values and the corresponding ranks. Thus, the initial and optimal design parameters and corresponding performance parameters are compared and presented in Table 5.

The design optimization provides various advantages to the end consumer of the motor. When pole eccentricity is optimized, *the PM material is reduced* at corners, which not only *decreases overall weight* of the motor but also reduces the cost of the motor. By the optimization of slot opening and length of air gap, the extra *leakage flux losses are reduced*.

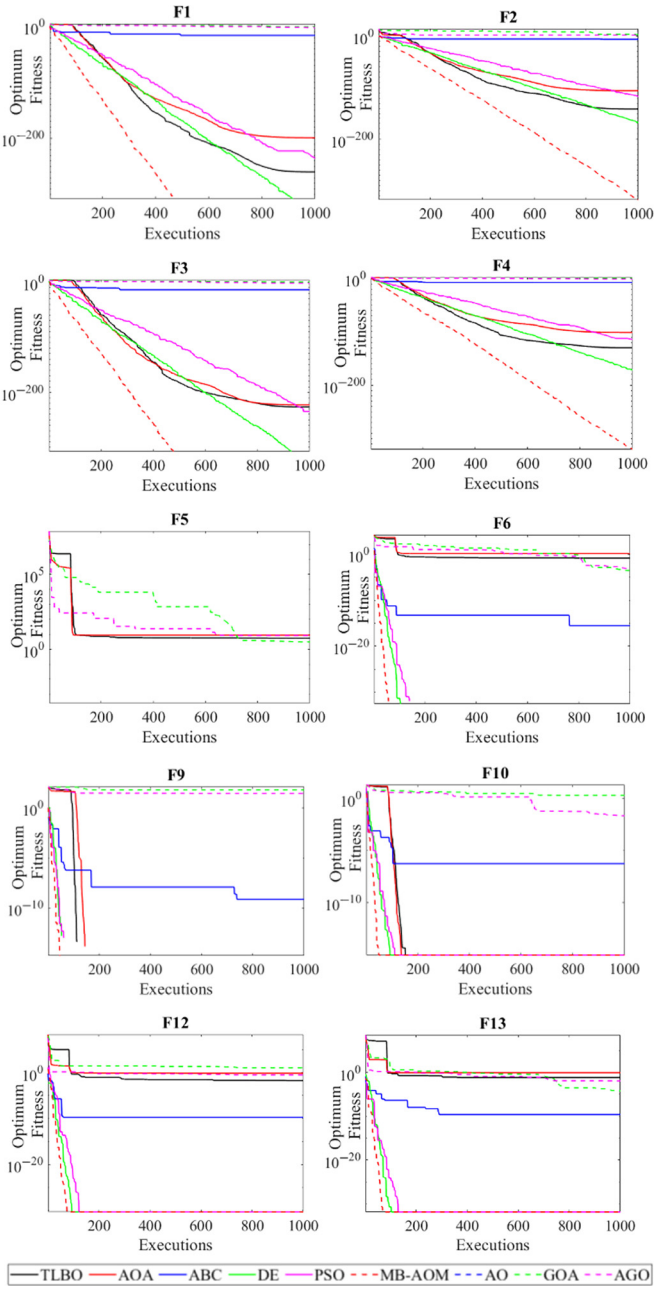


Figure 3. Convergence profiles comparison plots for various benchmark functions; the techniques are named in accordance with their color codes

Source: Authors' own work

Table 3. Benchmark functions and corresponding analysis results via different algorithms

Functions	Description	MB-AOM	AOA	ABC	DE	PSO	TLBO	AO	GOA	AGO
F1	$f(x) = \sum_{i=1}^{n} x_i^2$	0.0000e+000	7.9612e-239	8.9568e-160	1.0529e-162	2.5882e-235	2.5345e-243	5.7607e-194	5.5462e-050	8.7272e-050
F2	$f(x) = \sum_{i=1}^{n} \lvert x_i \rvert + \prod_{i=0}^{n} \lvert x_i \rvert$	2.1428e-318	1.0431e-106	9.1790e-070	3.5819e-168	3.8126e-118	3.7746e-142	1.3874e-090	1.333e-038	1.3139e-105
F3	$f(x) = \sum_{i=1}^{d} \left(\sum_{j=1}^{i} x_j \right)^2$	0.0000e+000	1.108e-223	2.0277e-140	0.0000e+000	1.4041e-235	1.7364e-227	5.7623e-189	3.8206e-040	2.3463e-020
F4	$f(x) = max_i\{\lvert x_i \rvert, 1 \le i \le n\}$	4.5306e-321	4.4069e-102	1.0924e-080	3.4868e-172	8.2108e-116	1.1603e-130	2.3241e-095	7.7348e-050	5.3212e-020
F5	$f(x) = \sum_{i=1}^{n-1} \left[100\left(x_i^2 - x_{i+1}\right)^2 + (1 - x_i)^2 \right]$	0.0000e+000	0.0000e+000	0.0000e+000	0.0000e+000	0.0000e+000	0.0000e+000	2.5858e-040	0.1223e+000	0.2074e+000
F6	$f(x) = \sum_{i=1}^{n} (\lvert x_i + 0.5 \rvert)^2$	0.0000e+000	1.4394e+000	3.1684e-160	0.0000e+000	0.0000e+000	1.5035e-010	2.2766e-050	3.1518e-040	8.6039e-040
F7	$f(x) = \sum_{i=0}^{n} i x_i^4 + random[0,1)$	3.5197e-050	5.8064e-040	1.2790e-050	7.4195e-040	5.4142e-040	6.4286e-050	1.4867e-040	6.9205e-010	2.7042e-010
F8	$f(x) = \sum_{i=1}^{n} (-x_i \sin(\sqrt{\lvert x_i \rvert}))$	-418.9829	-479.2529	-418.9829	-418.9829	-418.9829	-418.9829	-418.9040	-461.4787	-405.6729
F9	$f(x) = \sum_{i=1}^{n} [x_i^2 - 10\cos(2\pi x_i) + 10]$	0.0000e+000	0.0000e+000	7.2646e-100	0.0000e+000	0.0000e+000	0.0000e+000	0.0000e+000	0.7623e+000	0.8936e+000
F10	$f(x) = -20\exp\left(-0.2\sqrt{\frac{1}{n}\sum_{i=1}^{n} x_i^2}\right) - \exp\left(\frac{1}{n}\sum_{i=1}^{n}\cos(2\pi x_i)\right) + 20 + e$	8.8818e-016	8.8818e-016	5.4866e-007	8.8818e-016	8.8818e-016	8.8818e-016	8.8818e-016	2.0160e-010	2.1458e-010

(*continued*)

Table 3. Continued

F11	$f(x) = 1 + \frac{1}{4000}\sum_{i=1}^{n} x_i^2 - \prod_{i=1}^{n} \cos\left(\frac{x_i}{\sqrt{i}}\right)$	0.0000e+000	0.0000e+000	4.0621e-070	0.0000e+000	0.0395e+000	0.0000e+000	0.0000e+000	5.7054e-010	0.34601e+000
F12	$f(x) = \frac{\pi}{n}\{10\sin(\pi y_1)\} + \sum_{i=1}^{n-1}(y_i - 1)^2\left[1 + 10sin^2(\pi y_{i+1})\right] + \sum_{i=1}^{n} u(x_i, 10, 100, 4)\Big]\ ; where\ y_i = 1 + \frac{x_i + 1}{4},\ u(x_i, a, k, m) = \begin{cases} K(x_i - a)^m\ ; for\ x_i > a \\ 0\ ; for\ -a \le x_i \le a \\ K(-x_i - a)^m\ ; for\ x_i \le -a \end{cases}$	4.7116e-031	7.4698e-010	1.8541e-010	4.7116e-031	4.7116e-031	1.8323e-010	1.2401e-006	0.1814e+000	3.1115e-001
F13	$f(x) = 0.1(sin^2(3\pi x_1) + \sum_{i=1}^{n}(x_i - 1)^2[1 + sin^2(3\pi x_i + 1)] + (x_n - 1)^2[1 + sin^2(2\pi x_n)) + \sum_{i=1}^{n} u(x_i, 5, 100, 4)$	1.3498e-032	9.0708e-010	2.4709e-010	1.3498e-032	1.3498e-032	7.1737e-020	1.4300e-005	6.52860e-05	1.1906e-003
	Rank	1	2	9	8	7	4	3	5	6

Note(s): AOA = Archimedes optimization algorithm; ABC = artificial bee colony, DE = differential evolution, PSO = particle swarm optimization, TLBO = teaching learning based optimization, AO = Aquila optimization, GOA = grasshopper optimization algorithm, AGO = Aquila grasshopper optimization
Source(s): Authors' own work

Hence, performance is enhanced. Optimization of radial magnet thickness leads to 5% *reduction in the cost* of motor. The initial and optimal models are compared in Figure 5(a). As presented in Figure 5(b) and Figure 6, respectively, the proposed MB-AOM method is performing with *better efficiency* as compared to AOA.

5. Conclusion

Below are given the achievements, reported in this paper:

- A novel metaheuristic optimization technique has been designed. The purpose of this invention is to elucidate its efficiency over the existing AOA.
- The real-time motor-model-design problem is designed using scalarization techniques. For this, FEM based SIT-PMSM model is developed.
- The proficiency of proposed MB-AOM is tested and compared with popular metaheuristic techniques, using unimodal and multimodal Benchmark functions. The improvement in convergence profiles is presented.
- Thus, the solution to the designed MMD problem, obtained by MB-AOM is also compared with that obtained by popular metaheuristic techniques. Among, three scalarization criteria, rank-order-centroid-weight is found to be providing the optimal value of the cost function.

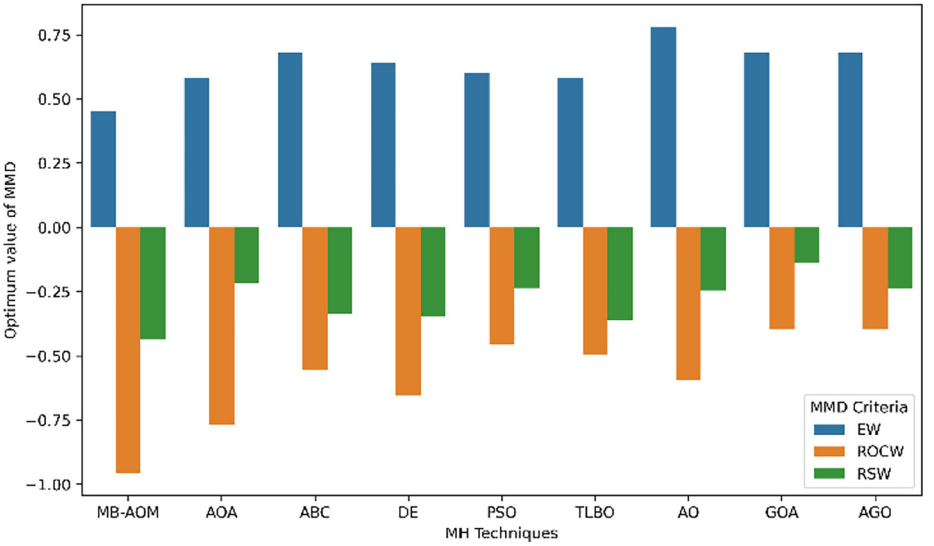


Figure 4. Comparison plot for solutions to the designed MMD problem, using different MH techniques
Source: Authors' own work

Table 4. Comparative analysis results for initial and optimized models

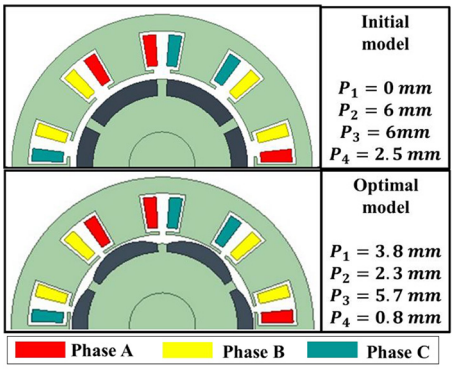
	Cost function value			
Algorithms	EW	ROCW	RSW	Ranks
MB-AOM	0.45	**−0.957**	−0.437	1
AOA	0.58	−0.770	−0.220	2
ABC	0.68	−0.556	−0.336	5
DE	0.64	−0.656	−0.346	3
PSO	0.60	−0.456	−0.235	7
TLBO	0.58	−0.496	−0.360	6
AO	0.78	−0.595	−0.245	4
GOA	0.68	−0.395	−0.136	8
AGO	0.68	−0.396	−0.236	9

Source(s): Authors' own work

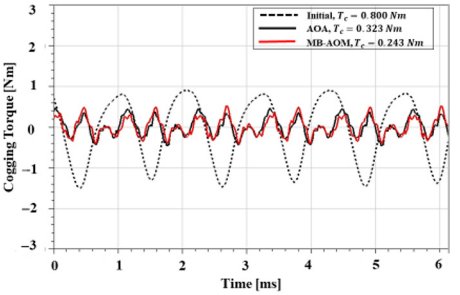
Table 5. Comparative analysis results for initial and optimized models

Specification	Initial model	Optimal model	Advantage
P1, pole eccentricity	0.0 *mm*	3.8 *mm*	PM material is reduced
P2, slot opening in stator	6.0 *mm*	2.3 *mm*	Air flux leakage is reduced
P3, radial magnet thickness	6.0 *mm*	5.7 *mm*	Cost is reduced
P4, length of air gap	2.5 *mm*	0.8 *mm*	Air gap losses are reduced
$\widehat{Y}_1$, cogging torque	0.800 *mm*	0.243 *mm*	69% reduction
$\widehat{Y}_2$, ripple torque	0.378 *mm*	0.132 *mm*	65% reduction
$\widehat{Y}_3$, torque	5.840 *mm*	7.631 *mm*	30% increment

Source(s): Authors' own work



(a)



(b)

Figure 5. (a) Initial and optimal models along with the design parameter values; (b) cogging torque profiles of initial model (dashed black line), optimal model using AOA (solid black line) and optimal model using MB-AOM (solid red line)
Source: Authors' own work

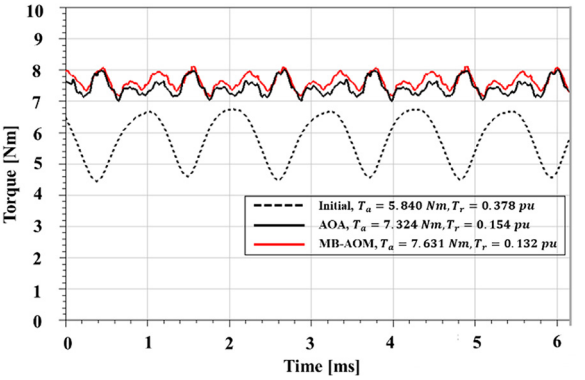


Figure 6. Torque profiles of initial model (dashed black line), optimal model using AOA (solid black line) and optimal model using MB-AOM (solid red line)
Source: Authors' own work

Table 6. Proficiency test analysis results using existing AOA and proposed MB-AOM

Performance parameter	Change obtained by AOA	Change obtained by MB-AOM	Remarks
$\widehat{Y}_1$, cogging torque	59% reduction	69% reduction	MB-AOM is 10% more efficient
$\widehat{Y}_2$, ripple torque	59% reduction	65% reduction	MB-AOM is 6% more efficient
$\widehat{Y}_3$, torque	25% increment	30% increment	MB-AOM is 5% more efficient
Stability of vehicle	Less	more	Performance of 2PL system is increased

Source(s): Authors' own work

- The summary of comparison in performance factors for 2PL system using proposed MB-AOM is shown in Table 6.

The future plan includes the fabrication of the prototype of the optimized motor and conducting the comprehensive experimental-bench-based testing to validate the simulation results.

References

Ambekar, S.R. (2022), "Design and development of high torque, compact and energy saver PMSM motor for hydraulic applications", *International Journal of Electrical and Computer Engineering Systems*, Vol. 13 No. 5, pp. 399-407.

Arora, A.S. and Singh, G. (2015), "Review of design and performance of permanent magnet synchronous motor", *International Journal of Industrial Electronics and Electrical Engineering*, Vol. 3 No. 10, ISSN: 2347-6982

Burlet-Vienney, D., et al., (2021), "Analysis of vehicle stability when using two-post above-ground automotive lifts: Distribution of forces in arms", *Safety Science, Elsevier*, Vol. 134 No. 105042, pp. 1-14.

Burlet-Vienney, D., et al., (2023), "Risk-based inspection applied to two-post above-ground automotive lifts", *International Journal of Occupational Safety and Ergonomics*, Vol. 29 No. 3, pp. 1252-1261.

Dinh, B.M. and Tien, H.M. (2016), "Maximum efficiency design of line start permanent magnet synchronous motor", *in IEEE International Conference on Sustainable Energy Technologies (ICSET)*, pp. 350-354.

Dubas, F. and Rahideh, A. (2013), "Two-dimensional analytical permanent-magnet eddy-current loss calculations in slotless PMSM equipped with surface-inset magnets", *IEEE Transactions on Magnetics*, Vol. 50 No. 3, pp. 54-73.

Ei, K., Tun, A.N. and Tin, T. (2014), "Design of conventional permanent magnet synchronous motor used in electric vehicle", *International Journal of Scientific Engineering and Technology Research*, Vol. 3 No. 16, pp. 3289-3293.

Hu, Y., Zhu, et al., (2021), "Reduction of torque ripple and rotor eddy current losses by closed slots design in a high-speed PMSM for EHA applications", *IEEE Transactions on Magnetics*, Vol. 58 No. 2, pp. 1-6.

Jian, L., Chau, K.T., Gong, Y., Yu, C. and Li, W. (2009), "Analytical calculation of magnetic field in Surface-Inset permanent magnet motors", *IEEE Transactions on Magnetics*, Vol. 45 No. 10.

Pellegrino, G., et al., (2012), "Comparison of induction and PM synchronous motor drives for EV application including design examples", *IEEE Transactions on Industry Applications*, Vol. 48 No. 6, pp. 2322-2332.

Shindeand, P.S. and Thosar, A.G. (2015), "Design of permanent magnet synchronous motor", *International Journal of Scientific and Engineering Research*, Vol. 6 No. 1.

Wang, W., Fu, R. and Fan, Y. (2018), "Electromagnetic parameters matching of permanent magnet synchronous motor for hybrid electric vehicles", *IFAC-PapersOnLine*, Vol. 51 No. 31, pp. 407-414.

Zang, B. and Gao, H. (2022), "Research on interactive operation and maintenance service mode of electric vehicles", *IEEE 5th International Electrical and Energy Conference (CIEEC)*, Nangjing, China, pp. 455-460.

Supplementary material

The supplementary material for this article can be found online.

Corresponding author

Monika Verma can be contacted at: verma15.monika@gmail.com

For instructions on how to order reprints of this article, please visit our website:
www.emeraldgrouppublishing.com/licensing/reprints.htm
Or contact us for further details: **permissions@emeraldinsight.com**

This article has been accepted for publication in IEEE Antennas and Wireless Propagation Letters. This is the author's version which has not been fully edited and content may change prior to final publication. Citation information: DOI 10.1109/LAWP.2025.3577607

Design and Analysis of mm-Wave MIMO Antenna with a UWB AMC

Rohit Khandekar, *Graduate Member IEEE*, Deepika Sipal, *Senior Member IEEE*

ABSTRACT- This article presents the design and analysis of an ultrawideband (UWB) Artificial Magnetic Conductor (AMC) aimed to enhance the gain of a UWB mm-wave MIMO antenna. The AMC features capacitive slots to excite TM20 mode to achieve a phase bandwidth of 14.08 GHz, ranging from 23.49 GHz to 37.57 GHz. A 10×10 AMC array is positioned 0.38λ_0 (λ_0 is free space wavelength at 23.27) beneath the MIMO antenna for the gain enhancement. The proposed antenna resonates from 23.27 GHz to 39.3 GHz with an impedance bandwidth of 16.03 GHz. The isolation between quad ports is greater than 19.84 dB. The enhanced gain of the proposed MIMO antenna ranges from 8.7 dBi to 12.21 dBi, with maximum gain reaching 12.21 dBi at 31.5 GHz. The proposed antenna shows diverse performance in terms of Envelope correlation coefficient (ECC)< 0.005, Channel capacity loss (CCL)< 0.26 b/s/Hz and Total active reflection coefficient (TARC)< -10 dB. The size of the proposed antenna is 3.8λ_0×3.8λ_0×0.38λ_0 only. This makes the proposed antenna suitable for a 5G bastion antenna.

Keywords- Artificial Magnetic Conductor (AMC), Gain enhancement, MIMO, mm-wave, UWB, 5G Communication.

I. INTRODUCTION

In the set of 5G frequencies, mm-Wave constitutes large bandwidth (BW), enabling high data rates in gigabits per second (Gbps) [1]. The MIMO technology enables parallel data transmission in tightly packed devices, which improves data rates, spectral and power efficiency [2], [3]. On the other hand, the signal-to-noise ratio (SNR) suffers from fast signal fading at mm-wave frequencies; therefore, high-gain MIMO antennas are essential for mm-Wave 5G communication [4].

A High Refractive Index Structure (HRIS) is used for gain enhancement, and a phase gradient lens for beam tilting in [5]. In [6] a 5×5 array of Frequency Selective Surface (FSS) reflector is used for gain enhancement, but the impedance BW is only 5.3 GHz. In ref. [7] an Artificial Magnetic Conductor (AMC) phase BW (refer AMC phase BW as AMC-BW) measure at ±90º is extremely narrow and the distance between antenna and AMC is 9 mm. In [8] Epsilon Negative (ENG) metasurfaces are used for gain enhancement, covering frequencies 24 GHz to 40 GHz. In [9] maximum enhanced gain is 9.8 dBi, but the antenna only has an impedance BW of 4 GHz. Although significant gain enhancement is achieved in the ref. [5], [6], [7], [8], [9] and [10] but MIMO configuration is not reported. However, implementing MIMO with gain enhancement techniques in these antennas will result in bulky antenna structures.

To enhance the gain of the MIMO antennas, different MSs are used, such as a very narrow band Electromagnetic Band Gap (EBG) reflector in [11]. An anisotropic MS enhances the gain of the Vivaldi MIMO antenna, but ground planes are disconnected to avoid direct grounding current to achieve high isolation [12]. In [13] Zero Index Material (ZIM) is loaded onto the 2-port MIMO antenna. The gain is increased by 2-2.5 dBi throughout the BW of 3 GHz. An AMC is used for gain enhancement of a MIMO antenna from 5 dBi to 10 dBi [14]. However, the AMC's reflection phase BW is narrow, i.e., focused on 28 GHz only. In [15] a four-port MIMO antenna has a small BW, and the gain is enhanced at 28 GHz from 7 dBi to 10 dBi. A gain-enhanced narrow band four port MIMO antenna is reported in [16]. Achieving wide AMC BW is challenging [17]; However, in some reported AMC structures, wide phase BW is achieved, such as, [17], [18], [19] but the maximum phase BW achieved at ±90º is 4 GHz in [20]. The structures (antennas and metamaterials) mentioned in the above literature are confined to BW ≤ 8 GHz. Hence, achieving Ultra-Wideband (UWB) gain enhancement of low-profile antenna becomes challenging with the complex MIMO configuration.

This article presents a method for achieving UWB AMC-BW. The Capacitive slots excite the TM20 mode in the AMC unit cell, resulting in UWB. The AMC unit cell has a phase bandwidth of 14.08 GHz (23.49 to 37.57 GHz at ±90º). A 10×10 array of the proposed AMC is constructed to enhance the gain of the mm-Wave MIMO antenna. The proposed antenna has an impedance BW of 16.03 GHz (23.27 GHz to 39.3 GHz), with isolation exceeding 19.84 dB. Gain is enhanced from 6.74 dBi to 10 dBi at 28 GHz, 5.6 dBi to 9.25 dBi at 34 GHz, and 6.96 dBi to 11.2 dBi at 38 GHz. The maximum gain enhancement achieved at 31.5 GHz is from 5.66 dBi to 12.21 dBi.

II. DESIGN OF SINGLE AND MIMO ANTENNA

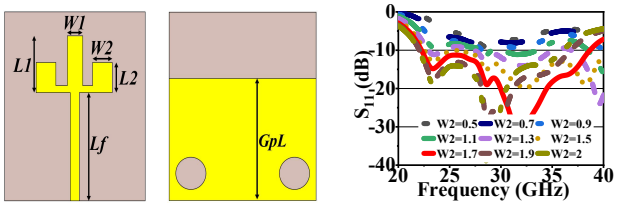
The proposed single UWB antenna measures 15×13 mm^2. The patch is divided into a middle arm and two side arms, as shown in Fig. 1(a & b). The side arms with width W2 enhance wide impedance matching with a partial ground plane. Parametric analysis of '*W2*' is depicted in Fig. 1(c). The partial ground plane (*GpL*) with a length of 9.65 mm is chosen

Rohit Khandekar and Deepika Sipal (corresponding author) are with the Department of Electronics and Communication Engineering, Delhi Technological University, Delhi, India. (e-mail: rohitkhandekar7@gmail.com; sipaldeepika@gmail.com).

Authorized licensed use limited to: DELHI TECHNICAL UNIV. Downloaded on June 16,2025 at 05:20:26 UTC from IEEE Xplore. Restrictions apply.
© 2025 IEEE. All rights reserved, including rights for text and data mining and training of artificial intelligence and similar technologies. Personal use is permitted, but republication/redistribution requires IEEE permission. See https://www.ieee.org/publications/rights/index.html for more information.

This article has been accepted for publication in IEEE Antennas and Wireless Propagation Letters. This is the author's version which has not been fully edited and content may change prior to final publication. Citation information: DOI 10.1109/LAWP.2025.3577607

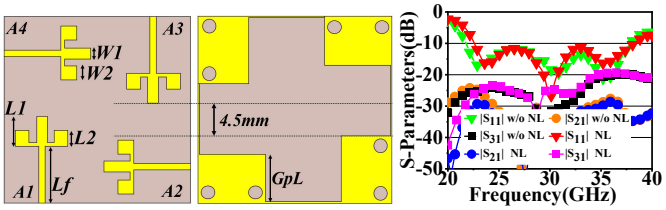
to attain the impedance BW below -10 dB. The proposed antenna at *W2*=1.7 mm resonates from 22.30 GHz to 38.90 GHz, as shown in Fig. 1 (c).



(a) (b) (c)

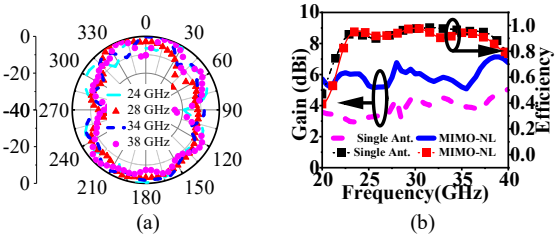
Fig. 1. Proposed single antenna (a) Front view, (b) Back view, (c) Parametric analysis for *W2* (*Lf*=8.99, *L1*=5, *L2*=2, *W1*=1.7, *W2*=1.7, *GpL*=9.65, *h1*=0.254, ε_r=2.2 all dimensions are in mm.)

The single antenna with its UWB and compact size is transformed into a MIMO antenna, as shown in Fig 2 (a & b). Four orthogonal antennas are spaced 4.5 mm apart to achieve isolation of nearly 20 dB for admirable diversity performance. The MIMO antenna measures 31.5×31.5 mm^2. Disconnected ground planes eliminate direct ground current, improving ports isolation [12]. This MIMO antenna resonates from 21.78 GHz to 37.89 GHz, as shown in Fig. 3 (a). The isolation among antennas *A1*, *A2* and *A3* is > 20 dB, as shown in Fig. 2 (c). Although high isolation is achieved with disconnected grounds, a neutralising line (NL) of width 0.2 mm is designed, which runs across the perimeter connecting all four ground planes of the antennas. Common ground MIMO antenna resonates from 22.59 GHz to 38.31 GHz, and obtained isolation > 20 dB, as shown in Fig. 2 (c).



(a) (b) (c)

Fig. 2. Designed MIMO antenna with NL (a) Top view, (b) Bottom view, Simulated S-Parameters without and with NL. (All dimensions of the MIMO antenna are the same as of the Single antenna.)



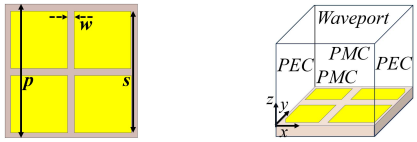
(a) (b)

Fig. 3. Simulated results for MIMO antenna with NL (a) Radiation patterns at 24 GHz, 28 GHz, 34 GHz, and 38 GHz, (b) Gain and Efficiency plot.

Fig 3. (a) shows Radiation patterns in XZ-plane, back lobes are seen at 24 GH, 28 GHz, 34 GHz, and 38 GHz due to partial ground plane. The gain and efficiency of the single antenna and proposed MIMO antenna (with and without NL) are shown in Fig. 3 (b). The gain of the single antenna is between 3.8 - 6.6 dBi, and efficiency is 77% - 91%. However, the MIMO antenna without NL has a gain variation less than 3 dB with an efficiency between 86.2% and 91%. The MIMO antenna with NL has a gain between 5.08-7.14 dBi, and efficiency lies between 86.77%- 97.92%.

III. Design of AMC Unit Cell

The AMCs have in-phase reflection property within ±90º with a magnitude close to 1 or 0 dB. Therefore, wide AMC BW is required to reduce the antenna profile, i.e. space between the antenna and the AMC array. Fig. 4 (a & b) shows the proposed square AMC unit cell design. The AMC unit cell is simulated with a waveport in the z direction; while, PEC and PMC boundaries are placed in the x and y directions respectively.



(a) (b)

Fig. 4. Proposed AMC unit cell (a) Front view, (b) Simulation setup. (*p*=4, *s*=3.7, *w*=0.35, *h2*=0.79, ε_r=2.2, all dimensions are in mm.)

The proposed AMC unit cell has a square patch with '+' shaped capacitive slots to excite TM20 mode, which enhances the AMC-BW. The proposed AMC have achieved BW of 14.08 GHz from 23.49 GHz to 37.57 GHz at +90º and -90º, respectively. Fig. 5 (a-c) depicts the design steps of the AMC. The assembly of the AMC unit-cell is a simple square patch on a dielectric and backed with a ground plane. The resonant frequency (f_0) can be described as [21];

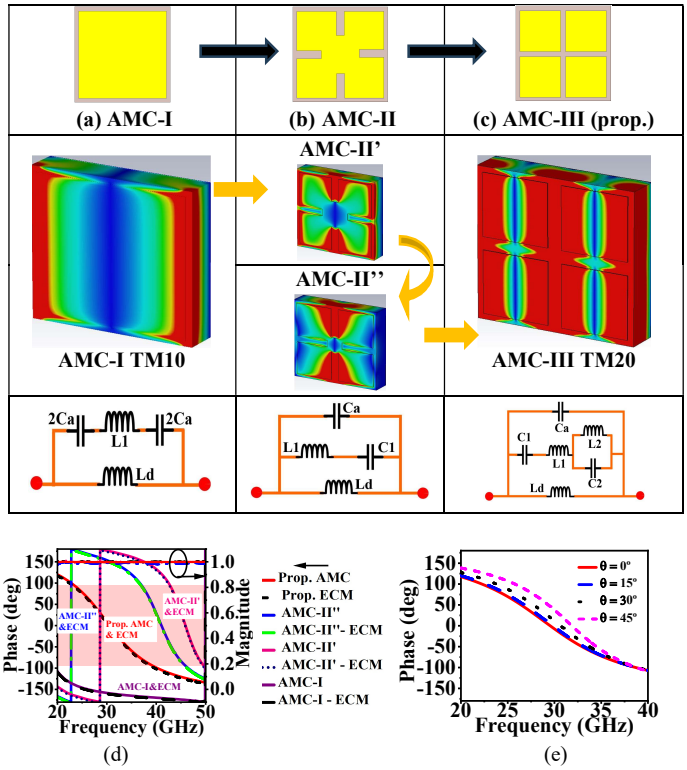
$$f_0 = \frac{1}{2\pi\sqrt{L_T C_T}} \quad (1)$$

where, C_T and L_T are the total capacitance and inductance of the metallic patches and substrate of the unit cell, respectively. In the AMC-I, E-fields are evenly distributed along the y-direction and vary in the x-direction, depicting mode TM10, as shown in Fig. 5 (a). The tightly coupled E-fields slosh between adjacent unit cells resembles a capacitor (C_a) between adjacent unit cells. The metal patches act as an inductor (L_1) and dielectric inductor (L_d) [22]. The AMC-I, a square patch, has undesired phase between +90° to -90° and magnitude +1 for frequencies 22 GHz to 38 GHz, as shown in Fig. 5 (d). Mode TM10 is responsible for narrow AMC-BW and to achieve wide AMC-BW through TM20 mode; in the AMC-II, small symmetrical slots of size 1.2×0.35 mm^2 are introduced in the AMC patch (here, AMC-II with slot size 1.2×0.35 mm^2 is referred as AMC-II'). These slots act as the capacitor (C_1) in the Equivalent Circuit Model (ECM), as shown in Fig. 5 (b); C_1 is in series with L_1, which are connected in parallel with C_a, because any inherent fringing capacitance from the patch is modelled in parallel [21]. Unlike AMC-I, E-fields are observed between added slots in the AMC-II' and a transition between mode TM10 to TM20 is observed in Fig. 5 (b). The slots shifted phase response between ±180º while maintaining magnitude +1, as shown in Fig. 5 (d). However, AMC-II' does

Authorized licensed use limited to: DELHI TECHNICAL UNIV. Downloaded on June 16,2025 at 05:20:26 UTC from IEEE Xplore. Restrictions apply.
© 2025 IEEE. All rights reserved, including rights for text and data mining and training of artificial intelligence and similar technologies. Personal use is permitted, but republication/redistribution requires IEEE permission. See https://www.ieee.org/publications/rights/index.html for more information.

This article has been accepted for publication in IEEE Antennas and Wireless Propagation Letters. This is the author's version which has not been fully edited and content may change prior to final publication. Citation information: DOI 10.1109/LAWP.2025.3577607

not have required phase BW. Therefore, the slot length is increased from 1.2 mm to 1.5 mm (say, AMC-II''). This optimisation of AMC-II results in higher E-fields across the slots, as shown in Fig 5 (b), making $C_1 >> C_a$ and shifting phase in the lower spectrum as shown in Fig. 5 (d) as per eq. (1) [21]. However, spurious modes occurred in AMC-II while transitioning from TM10 to TM20 mode.



(d) (e)

Fig. 5. (a) E-Field at 30 GHz and ECM for AMC-I, (b) E-Field at 30 GHz and ECM for AMC-II'', (c) E-Field at 30 GHz and ECM for proposed AMC, and (d) Simulated Phase and Magnitude response for AMC at step I, II & III, (e) AoI analysis of the proposed unit cell.

To achieve TM20, which will result in a wider AMC BW. The slot length is increased to 1.85 mm, dividing a single patch into four adjacent patches in a unit-cell called as AMC-III, as shown in Fig. 5 (c). Fig. 5 (c) shows that E-fields with a very large and equal magnitude across adjacent patches of the unit-cell and adjacent unit cells, ensuring TM20 is obtained. A clear transition of modes TM10 to TM20 is depicted in Fig. 5 (a-c). The AMC-III-ECM shown in Fig 5 (c); here, L_2 and C_2 represent inductance and capacitance of individual adjacent four small square patches of the unit cell [17]. The added slots in the AMC patch and equivalent LC configuration yield a very wide in-phase reflection AMC-BW between ± 90º. Lastly, the AMC-III, patch and slots were optimised to s = 3.65 mm and w = 0.4 mm to meet mm-wave MIMO antenna resonance, shown in Fig. 3. Attained AMC BW for the proposed AMC-III, is 14.08 GHz from 23.49 GHz to 37.57 GHz at + 90º and - 90º, respectively, as depicted in Fig. 5 (d).

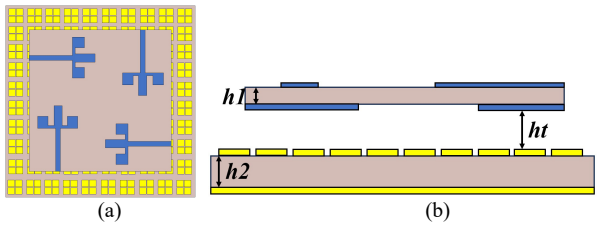
$$C_T = C_1 + C_2 + C_a \quad (2)$$

$$L_P = L_1 \,||\, L_2 \quad (3)$$

$$L_T = L_P \,||\, L_d \quad (4)$$

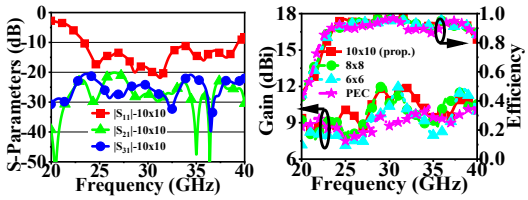
The values for capacitors C_1, C_2 and C_a are almost similar since, the E-fields magnitude across adjacent small patches and unit cells is almost equal. The equivalent values for L_d, L_1, L_2, C_1, C_2 and C_a are 0.536 nH, 0.477 nH, 0.07 nH, 0.151 pF, 0.149 pF, 0.152 pF, respectively. The angle of incidence (AoI), i.e. θ, is varied to study its effect on the AMC phase, as shown in Fig. 5 (e); it shows that the AMC phase is affected after AoI is increased to 45º; due to the symmetric AMC design TE and TM polarisation response will be identical.

IV. Integration of the MIMO Antenna and AMC Array



(a) (b)

Fig. 6. Schematic of the proposed antenna (a) Top view, (b) Side view.



(a) (b)

Fig. 7. (a) Simulated S-parameters for the proposed MIMO antenna, (b) Simulated Gain and Efficiency plots for the proposed MIMO antenna.

It is evident from Fig. 3 (a & b), that UWB mm-wave MIMO antenna exhibits low gain. Therefore, the proposed AMC unit cell array is placed beneath the MIMO antenna to enhance the gain. The schematic of the proposed MIMO antenna backed with an AMC array is shown in Fig. 6. An array of 10×10 unit cells is formed measuring 50×50 mm^2. A spacing of 1.2 mm is maintained between adjacent cells to attain the desired resonance. The height (ht) between the MIMO antenna and the AMC array is 5 mm, which is approximately equivalent to a quarter wavelength, i.e. 0.38 λ_0 (λ_0 at 23.27 GHz), and it was chosen considering the dimensions of the connector [23]. S-parameters for the proposed AMC backed UWB mm-wave MIMO antenna are shown in Fig. 7 (a). The proposed antenna resonates from 23.27 GHz to 39.3 GHz, and the ports isolation ≥19.84 dB.

A substantial gain enhancement is found, which is in between 8.7 dBi to 12.21 dBi. The gain is increased from 6.02 dBi to 8.7 dBi at 24 GHz, 6.74 dBi to 10 dBi at 28 GHz, and 6.96 dBi to 11.2 dBi at 38 GHz. A study of different sizes of AMC array is also conducted, such as 6×6, 8×8, 10×10 (prop.) and PEC reflector placed at a height 0.38 λ_0. Out of all these cases, the prop. AMC array has a better gain with low profile antenna, as shown in Fig. 7 (b).

Authorized licensed use limited to: DELHI TECHNICAL UNIV. Downloaded on June 16,2025 at 05:20:26 UTC from IEEE Xplore. Restrictions apply.
© 2025 IEEE. All rights reserved, including rights for text and data mining and training of artificial intelligence and similar technologies. Personal use is permitted, but republication/redistribution requires IEEE permission. See https://www.ieee.org/publications/rights/index.html for more information.

This article has been accepted for publication in IEEE Antennas and Wireless Propagation Letters. This is the author's version which has not been fully edited and content may change prior to final publication. Citation information: DOI 10.1109/LAWP.2025.3577607

V. Measured Results

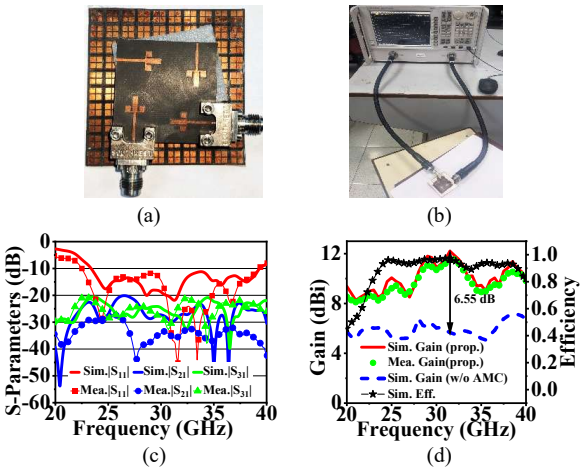


Fig. 8. Proposed mm-wave MIMO antenna (a) Fabricated prototype, (b) VNA testing, (c) S-Parameters, (d) Gain and Efficiency plot.

Table I: Comparison of the proposed antenna with the reported antennas.

Ref.	Freq (GHz)	% BW Ant.	Isolat. (dB)	Peak Gain (dBi)	UC-BW (GHz)	Ant. ht. (λ_0)	Ant. Size (λ_0^2)
[6]	25.5-30.8	18.82	NA	11	5	0.42	4.45
[9]	24-28	15.38	NA	9.8	10	0.06	2.43
[12]	24-32	28.57	>15	10.2	8	0.04	8.3
[13]	27-30	10.52	>22.25	9.6	6	0.04	7.78
[14]	26-31.5	19.13	> 21	10.1	< 0.5	0.42	16.56
[15]	23.41-28.91	21.02	>22.25	10.42	9.5	0.33	2.92
[16]	24.55-26.5	7.63	>30	10.27	< 0.8	0.48	8.57
Pro. ant.	**23.27-39.3**	**49.52**	**>19.84**	**12.21**	**14.08**	**0.38**	**14.44**

The proposed antenna's prototype is fabricated and tested on VNA (as shown in Fig. 8 (a & b)). A foam spacer is used to maintain the height (*ht*) of 5mm. The measured S-Parameters are depicted in Fig. 8 (c), which resonates from 22.56 GHz to 39.14 GHz and have isolation more than 20.1 dB. The measured BW is 16.58 GHz, which almost matches with the simulated BW of 16.03 GHz. The measured gain and simulated total efficiency are plotted in Fig. 8 (d). The maximum gain is enhanced from 5.66 dBi to 12.21 dBi at 31.5 GHz, and the simulated efficiency of the proposed antenna is found to be between 89.14% and 96.13%. The radiation patterns are measured in XZ and YZ planes. Fig. 9 shows the radiation patterns at 24 GHz, 28 GHz, and 38 GHz. Table I, compares the proposed antenna with the antennas in the literature. The proposed UWB mm-wave MIMO antenna measures $3.8\lambda_0 \times 3.8\lambda_0$ in size, which corresponds to length × width of the proposed AMC array, and the side profile is $0.38\lambda_0$. The impedance BW is 16.03 GHz (49.52%), UC-BW is 14.08 GHz (46.11%) with a high gain.

The MIMO diversity performance is studied for the proposed antenna using [3], [24]. The Envelope correlation coefficient (ECC)< 0.005 and Diversity gain (DG) >9.9 dB, as shown in Fig. 10 (a), respectively. Channel capacity loss (CCL)< 0.26 b/s/Hz and Total active reflection coefficient (TARC)< -10 dB, as shown in Fig. 10 (b), respectively. It assures the proposed antenna can efficiently work as a 5G mm-Wave MIMO antenna.

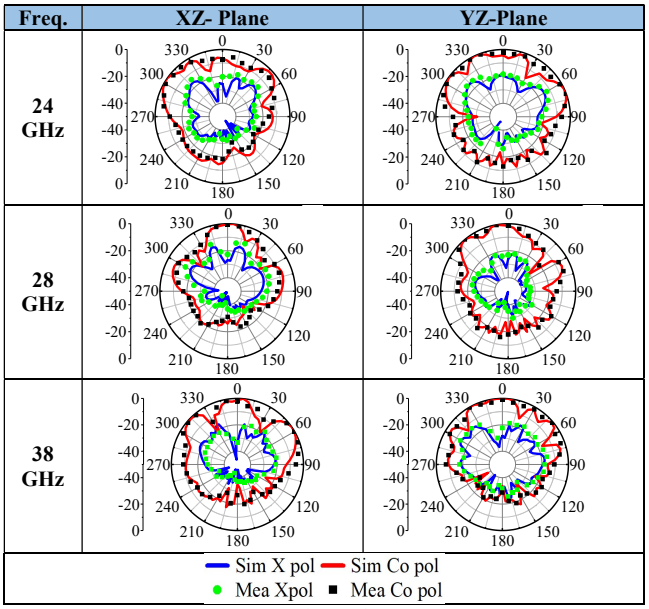


Fig. 9. Radiation Patterns in XZ and YZ planes at 24 GHz, 28 GHz, 34 GHz and 38 GHz.

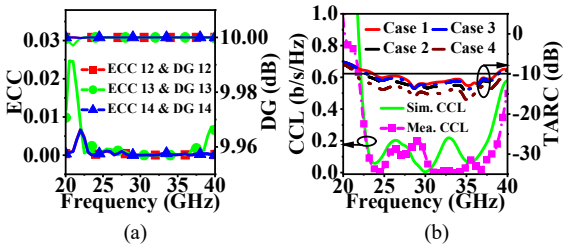


Fig. 10. MIMO Diversity Parameters (a) ECC & DG, (b) CCL & TARC cases are (Case 1: θ_0=0º, θ_1=30º, θ_2=60º, θ_3=90º, Case 2: θ_0=0º, θ_1=30º, θ_2=60º, θ_3=180º, Case 3: θ_0=0º, θ_1=30º, θ_2=60º, θ_3=270º, Case 4: θ_0=0º, θ_1=60º, θ_2=120º, θ_3=180º, where θ_i is the phase of the incoming signal at (i+i)th antenna).

VI. Conclusion

In this article, the design and investigation of a UWB AMC are presented. The TM20 mode is excited in the AMC unit cell using capacitive slots to provide phase BW of 14.08 GHz, measured at ±90º from 23.49 GHz to 37.57 GHz. A 10×10 AMC array is at a height of $0.38\lambda_0$ beneath the MIMO antenna to enhance the gain. The proposed antenna resonates from 23.27 GHz to 39.3 GHz with a BW of 16.03 GHz, and isolation > 19.84 dB. The gain of AMC backed MIMO antenna varies between 8.7 dBi to 12.21 dBi. The maximum gain is enhanced from 5.66 dBi to 12.21 at 31.5 GHz by 6.55 dB. The proposed antenna exhibits excellent diversity performance. These properties make the proposed UWB MIMO antenna suitable for the mm-wave 5G communication.

Authorized licensed use limited to: DELHI TECHNICAL UNIV. Downloaded on June 16,2025 at 05:20:26 UTC from IEEE Xplore. Restrictions apply.
© 2025 IEEE. All rights reserved, including rights for text and data mining and training of artificial intelligence and similar technologies. Personal use is permitted, but republication/redistribution requires IEEE permission. See https://www.ieee.org/publications/rights/index.html for more information.

This article has been accepted for publication in IEEE Antennas and Wireless Propagation Letters. This is the author's version which has not been fully edited and content may change prior to final publication. Citation information: DOI 10.1109/LAWP.2025.3577607

ACKNOWLEDGEMENT

I would like to express my sincere gratitude to **Dr. Mahesh P. Abegaonkar** for granting access to the antenna testing facility at ***CARE, IIT Delhi***. Additionally, I extend my heartfelt thanks to **Dr. Ratul De** for his invaluable assistance during the testing process. Their support was crucial in achieving our research objectives.

REFERENCES

[1] B. Bangerter, S. Talwar, R. Arefi, and K. Stewart, "Networks and devices for the 5G era," *IEEE Commun. Mag.*, vol. 52, no. 2, pp. 90–96, Feb. 2014, doi: 10.1109/MCOM.2014.6736748.

[2] T. S. Rappaport *et al.*, "Millimeter Wave Mobile Communications for 5G Cellular: It Will Work!," *IEEE Access*, vol. 1, pp. 335–349, 2013, doi: 10.1109/ACCESS.2013.2260813.

[3] D. Sipal, M. P. Abegaonkar, and S. K. Koul, "Easily Extendable Compact Planar UWB MIMO Antenna Array," *Antennas Wirel. Propag. Lett.*, vol. 16, pp. 2328–2331, 2017, doi: 10.1109/LAWP.2017.2717496.

[4] T. S. Rappaport, Y. Xing, J. MacCartney, A. F. Molisch, E. Mellios, and J. Zhang, "Overview of Millimeter Wave Communications for Fifth-Generation (5G) Wireless Networks-with a focus on Propagation Models," *IEEE Trans. Antennas Propagat.*, vol. 65, no. 12, pp. 6213–6230, Dec. 2017, doi: 10.1109/TAP.2017.2734243.

[5] Z. Wani and S. K. Koul, "Millimeter wave beam-tilted antenna using 1D-phase gradient metasurface," *Int J RF Mic Comp-Aid Eng*, vol. 32, no. 6, Jun. 2022, doi: 10.1002/mmce.23147.

[6] H. A. Mohamed, M. Edries, M. A. Abdelghany, and A. A. Ibrahim, "Millimeter-Wave Antenna With Gain Improvement Utilizing Reflection FSS for 5G Networks," *IEEE Access*, vol. 10, pp. 73601–73609, 2022, doi: 10.1109/ACCESS.2022.3189651.

[7] A. Kumar, A. Kumar, and A. Kumar, "Gain enhancement of a wideband rectangular ring monopole millimeter-wave antenna using artificial magnetic conductor structure," *Int J RF Mic Comp-Aid Eng*, vol. 32, no. 10, Oct. 2022, doi: 10.1002/mmce.23319.

[8] K. Muzaffar, M. I. Magray, G. S. Karthikeya, and S. K. Koul, "Wideband high aperture efficiency antennas with beam switching for MMWAVE 5G base stations," *Int J RF Microw Comput Aided Eng*, vol. 30, no. 8, Aug. 2020, doi: 10.1002/mmce.22254.

[9] R. Khandekar and D. Sipal, "Gain Enhanced mm-Wave Dipole Patch Antenna with an End-fire Radiation for 5G Applications," in *2022 IEEE Microwaves, Antennas, and Propagation Conference (MAPCON)*, Bangalore, India: IEEE, Dec. 2022, pp. 741–744. doi: 10.1109/MAPCON56011.2022.10047806.

[10] C.-X. Mao, M. Khalily, P. Xiao, T. W. C. Brown, and S. Gao, "Planar Sub-Millimeter-Wave Array Antenna With Enhanced Gain and Reduced Sidelobes for 5G Broadcast Applications," *IEEE Trans. Antennas Propagat.*, vol. 67, no. 1, pp. 160–168, Jan. 2019, doi: 10.1109/TAP.2018.2874796.

[11] A. A. R. Saad and H. A. Mohamed, "Printed millimeter-wave MIMO-based slot antenna arrays for 5G networks," *AEU - International Journal of Electronics and Communications*, vol. 99, pp. 59–69, Feb. 2019, doi: 10.1016/j.aeue.2018.11.029.

[12] M. Singh and M. S. Parihar, "Gain Improvement of Vivaldi MIMO Antenna with Pattern Diversity Using Bi-axial Anisotropic Metasurface for millimeter-Wave Band Application," *Antennas Wirel. Propag. Lett.*, pp. 1–5, 2022, doi: 10.1109/LAWP.2022.3220710.

[13] K. Gulur Sadananda, M. P. Abegaonkar, and S. K. Koul, "Gain Equalized Shared-Aperture Antenna Using Dual-Polarized ZIM for mmWave 5G Base Stations," *Antennas Wirel. Propag. Lett.*, vol. 18, no. 6, pp. 1100–1104, Jun. 2019, doi: 10.1109/LAWP.2019.2910183.

[14] A. A. Ibrahim and W. A. E. Ali, "High gain, wideband and low mutual coupling AMC-based millimeter wave MIMO antenna for 5G NR networks," *AEU - International Journal of Electronics and Communications*, vol. 142, p. 153990, Dec. 2021, doi: 10.1016/j.aeue.2021.153990.

[15] D. A. Sehrai *et al.*, "Metasurface-Based Wideband MIMO Antenna for 5G Millimeter-Wave Systems," *IEEE Access*, vol. 9, pp. 125348–125357, 2021, doi: 10.1109/ACCESS.2021.3110905.

[16] S. Tariq, S. I. Naqvi, N. Hussain, and Y. Amin, "A Metasurface-Based MIMO Antenna for 5G Millimeter-Wave Applications," *IEEE Access*, vol. 9, pp. 51805–51817, 2021, doi: 10.1109/ACCESS.2021.3069185.

[17] S. Yang, L. Liang, W. Wang, Z. Fang, and Y. Zheng, "Wideband Gain Enhancement of an AMC Cavity-Backed Dual-Polarized Antenna," *IEEE Trans. Veh. Technol.*, vol. 70, no. 12, pp. 12703–12712, Dec. 2021, doi: 10.1109/TVT.2021.3119643.

[18] Z. Jiang, Z. Wang, L. Nie, X. Zhao, and S. Huang, "A Low-Profile Ultrawideband Slotted Dipole Antenna Based on Artificial Magnetic Conductor," *Antennas Wirel. Propag. Lett.*, vol. 21, no. 4, pp. 671–675, Apr. 2022, doi: 10.1109/LAWP.2022.3140802.

[19] Y.-S. Huang, L. Zhou, L. Zhou, J.-F. Mao, Y. Zhao, and Y. H. Gao, "Wideband and Low-Profile High-Resistivity Silicon-Based Dielectric Resonant Antennas by Loading AMC," *IEEE Trans. Antennas Propagat.*, vol. 71, no. 11, pp. 9024–9029, Nov. 2023, doi: 10.1109/TAP.2023.3304056.

[20] Z. F. Dai, Y. Pan, J. J. Huang, L. H. Ye, J.-F. Li, and H. Jiang, "Low-Profile Broadband Dual-Polarized Dipole Antenna with AMC Reflector," *Antennas Wirel. Propag. Lett.*, pp. 1–5, 2024, doi: 10.1109/LAWP.2024.3406158.

[21] D. Chen, W. Yang, Q. Xue, and W. Che, "Miniaturized Wideband Planar Antenna Using Interembedded Metasurface Structure," *IEEE Trans. Antennas Propagat.*, vol. 69, no. 5, pp. 3021–3026, May 2021, doi: 10.1109/TAP.2020.3028245.

[22] G. Li, H. Zhai, L. Li, C. Liang, R. Yu, and S. Liu, "AMC-Loaded Wideband Base Station Antenna for Indoor Access Point in MIMO System," *IEEE Transactions on Antennas and Propagation*, vol. 63, no. 2, pp. 525–533, Feb. 2015, doi: 10.1109/TAP.2014.2378316.

[23] "SMI-End-Launch-Connectors.pdf." Accessed: Dec. 24, 2024. [Online]. Available: https://mpd.southwestmicrowave.com/wp-content/uploads/2021/06/SMI-End-Launch-Connectors.pdf

[24] P. P. Shome, T. Khan, A. A. Kishk, and Y. M. M. Antar, "Quad-Element MIMO Antenna System Using Half-Cut Miniaturized UWB Antenna for IoT-Based Smart Home Digital Entertainment Network," *IEEE Internet Things J.*, vol. 10, no. 20, pp. 17964–17976, Oct. 2023, doi: 10.1109/JIOT.2023.3280628.

Authorized licensed use limited to: DELHI TECHNICAL UNIV. Downloaded on June 16,2025 at 05:20:26 UTC from IEEE Xplore. Restrictions apply.
© 2025 IEEE. All rights reserved, including rights for text and data mining and training of artificial intelligence and similar technologies. Personal use is permitted, but republication/redistribution requires IEEE permission. See https://www.ieee.org/publications/rights/index.html for more information.

Design of Dual Gate Mixer with Ambipolar Virtual Source Graphene Field Effect Transistor

Arjun Lal Kumawat*
Electronics and Communication Engineering
Delhi Technological University
Delhi, India
*email: arjunkumawat2009@gmail.com

Anukul Pandey
Electronics and Communication Engineering
Delhi Technological University
Delhi, India
email: anukul66@gmail.com

N.S.Raghava
Electronics and Communication Engineering
Delhi Technological University
Delhi, India
email: nsraghava@gmail.com

2025 Devices for Integrated Circuit (DevIC) | 979-8-3503-9110-7/25/$31.00 ©2025 IEEE | DOI: 10.1109/DevIC63749.2025.11012165

***Abstract*— A single-ended resistive mixer based on the ambipolar virtual source Graphene Field Effect Transistor (GFET) with 650 nm technology is designed and analyzed in this article. The dual gate GFET mixer is biased at the gate terminal with different gate voltages so that the intermodulation distortion (IMD) generated by the GFET devices is combined. Due to the different biased conditions of the GFET devices, the linearity of the mixer is improved. The mixer is designed for the 2.4 GHz ISM band, which is unlicensed to 11 MHz of intermediate frequency with a local oscillator frequency of 3.89 GHz for down conversion. The proposed GFET mixer shows a conversion loss of 24.77dB at the 1 dB compression point, and the third order intermodulation is calculated as 28.52 dBc.**

Keywords*— Ambipolar; Graphene; active mixer; IMD; single-ended; GFET

I. INTRODUCTION

Graphene's outstanding material properties attract researchers to design and develop an alternative device in the RF field. Graphene is a single-atomic-thickness material that can be used for designing an RF power amplifier because of its high mobility of approximately 10^5 cm^2/Vs and high velocity saturation of around 6.3×10^7 cm/s [1]. Graphene also has a high current handling capability and a good thermal conductivity of 3080–5150 W/mK [2]. Different types of research work on mixers based on graphene have been published, including ambipolar mixers, resistive mixers, and diode mixers. H. Wang et al. demonstrated an ambipolar GFET mixer with conversion gain between -30 dB and -40 dB [3]; Madan et al. demonstrated ambipolar and drain mixing based on the GFET with conversion gain of -14 dB and -16 dB at 4.2 GHz and 10 GHz, respectively [4]; Gao et al. reported a chemical vapor deposited graphene-based mixer with conversion gain of -31 dB to -45 dB at 4 GHz [5]; Yeh et al. reported a mixer based on graphene having a conversion gain of -9.6 dB at 9.78 GHz [6]; Tian et al. reported a mixer using a Bernal stacked bilayer graphene transistor with a conversion gain of – 7 dB to -8.8 dB at 2.2 GHz [7]; Lin et al. demonstrated a mixer with the GFET showing conversion loss of 27 dB at 3.8 GHz [8]; Habibpour et al. reported a subharmonic mixer based on the GFET with conversion loss of 24 dB at 2 GHz [9]; Andersson et al. demonstrated a subharmonic mixer with the GFET having conversion loss of 20 dB to 22 dB in the frequency range of 2 GHz to 5 GHz [10]; Habibpour et al. reported a mixer with the multichannel GFET having a conversion loss of 19±1 dB in the frequency range of 24 GHz to 31 GHz [11]; Moon et al. reported a mixer with the GFET showing a conversion loss of 14 dB at 2 GHz [12]; Lyu et al. reported a double-balanced mixer with the GFET showing a conversion loss of 26 dB at 5 GHz [13]; Habibpour et al. reported a W-band monolithic microwave integrated circuit mixer with the GFET showing conversion loss of 18 dB to 19 dB in the frequency range of 88 GHz to 100 GHz [14]; Andersson et al. reported a subharmonic mixer based on the GFET showing conversion loss of 29±2 dB in the frequency range of 185 GHz to 215 GHz [15]; Tian et al. reported mixer using Bernal stacked bilayer graphene transistor having conversion loss of 12.7 dB to 16.7 dB at 2.2 GHz [16].

This paper contributes the compact model of the Ambipolar Virtual Source (AVS)-GFET in Keysight's Advanced Design System (ADS) based on the relevant concepts and relations. This GFET model is validated through DC and RF validation. The dual gate mixer uses the GFET model which uses the virtual source concept for the carrier transport in the unipolar and the ambipolar region of operation. The virtual source model is suitable for short channels also in contrast to the drift-diffusion GFET models which are limited to long channels. Further, we designed the single-ended dual gate mixer for the down conversion based on the validated GFET model. The dual gate topology has been taken for the design of the mixer to improve the port isolation. The linearity is enhanced by using different bias for dual gate GFET. The mixer is designed for the ISM band i.e. 2.4 GHz RF frequency where most of the electronics system works.

II. GFET MODEL

This paper utilised the AVS model for GFET described by Rakeja et al. [17]. The net drain current (I_D) is given as

$$\frac{I_D}{W} = \left(Q_{0e} + Q_{0h}\right) v_0 F_{sat} \tag{1}$$

where, W is the width of the channel and Q_{0e}, and Q_{0h} are the concentrations for electrons and holes, respectively at the virtual source point. v_0 is the carrier velocity and F_{sat} is the empirical function used to produce the current transition from linear to saturation regimes, which is expressed as

979-8-3503-9110-7/25/$31.00 ©2025 IEEE

Authorized licensed use limited to: DELHI TECHNICAL UNIV. Downloaded on June 04,2025 at 05:27:54 UTC from IEEE Xplore. Restrictions apply.

$$F_{sat} = \frac{\left(\frac{V_{dsi}}{V_{dsat}}\right)}{\left(1+\left(\frac{V_{dsi}}{V_{dsat}}\right)^{m}\right)^{1/m}} \quad (2)$$

V_{dsi} is the intrinsic drain to source bias voltage, V_{dsat} represents saturation voltage at the drain terminal and *m* is the empirical parameter.

$V_{dsat} = \frac{v_0 L}{\mu}$, where μ is the mobility of the charge carrier.

GFET Model Validation

The GFET model used in this paper has been validated by comparing it with the experimental data reported [18] for gate length of 650 nm and channel width of 20 µm.

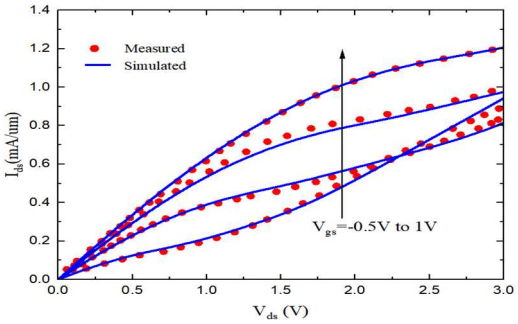


Fig. 1 I_{ds}-V_{ds} characteristics symbols represent experimental data and solid lines represent simulation results

Table 1 GFET model parameters

Parameter	Value
Electron-branch resistance (R_e)	486.8 Ω.µm
Hole-branch resistance (R_h)	1092.3 Ω.µm
Disorder-induced charge (Q_{dis})	1×10^{-8} C/ cm^2
Carrier mobility (µ)	2221 cm^2/V-sec
Carrier velocity (v_0)	3×10^7 cm/sec
Shift in Dirac point due to traps	0.2564 V
Dirac-point voltage ($V_{dirac,0}$)	-1.06 V
Energy transfer factor (ζ)	0.0825

For DC validation, the intrinsic parameters of the GFET used are given in **Table 1**, and the output characteristics are compared with the experimental data. **Fig. 1** shows the output characteristics for both the measured data and the GFET model used in this paper. The symbols in output characteristics represent the experimentally measured data, and solid lines represent the simulated output characteristics. The GFET compact model shows good agreement with simulation results and experimental data presented in the published literature.

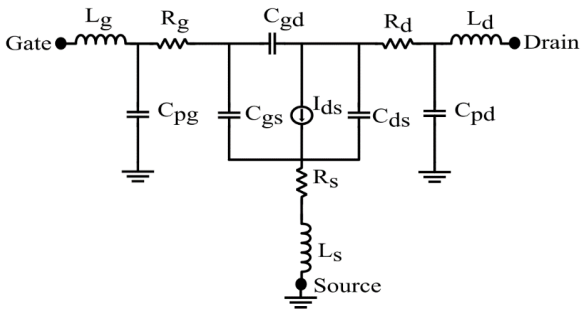


Fig. 2 Equivalent circuit representation for the GFET including parasitic and pad components

Fig. 2 shows the representation of the large signal equivalent circuit of the GFET. The intrinsic components of the GFET are the parasitic capacitances C_{gs}, C_{gd}, and C_{ds} and the drain current Ids. Also, the intrinsic part contains R_g, R_d, and R_s, respectively, which represent the contact and access resistance at the gate, drain, and source. Apart from the intrinsic part, the equivalent circuit also contains the pad parasitic capacitance (C_{pg} and C_{pd}) and inductances (L_g, L_s, and L_d). **Table 2** lists the values of these intrinsic and extrinsic components, as reported in [19].

The potential sources of the process variabilities are fabrication conditions, material properties, transfer method of the graphene on the substrate, etc that degrade the performance of the dual gate mixer. The dual gate configuration maintains reliable performance due to the process or the bias variation. The variation in the contact resistance can lead to more power loss and degrade the gain, thus compromising the robustness of the GFET mixer.

Table 2 Component Valus for the GFET package

Components	Value
Gate to Source Capacitance (C_{gs})	2 fF
Gate to Drain Capacitance (C_{gd})	6 fF
Gate pad Inductance (L_g)	45.6 pH
Gate Resistance (R_g)	33.7 Ω
Drain pad Inductance (L_d)	55 pH
Source pad Inductance (L_s)	10.3 pH
Drain Resistance (R_d)	3.07 Ω
Source Resistance (R_s)	3.34 Ω
Gate pad Capacitance (C_{pg})	10.9 fF
Drain pad Capacitance (C_{pd})	37.32 fF

III. Design of the Proposed Dual Gate Mixer

The mixer is the integral component of the transceiver system. The mixer and the low noise amplifier are integrated together in the receiver end while the mixer and the power amplifier are integrated together in the transmitter end. The dual gate structure for the mixer in integration with a low noise amplifier or power amplifier introduces significant design complexity, especially in the designing of the matching network.

Authorized licensed use limited to: DELHI TECHNICAL UNIV. Downloaded on June 04,2025 at 05:27:54 UTC from IEEE Xplore. Restrictions apply.

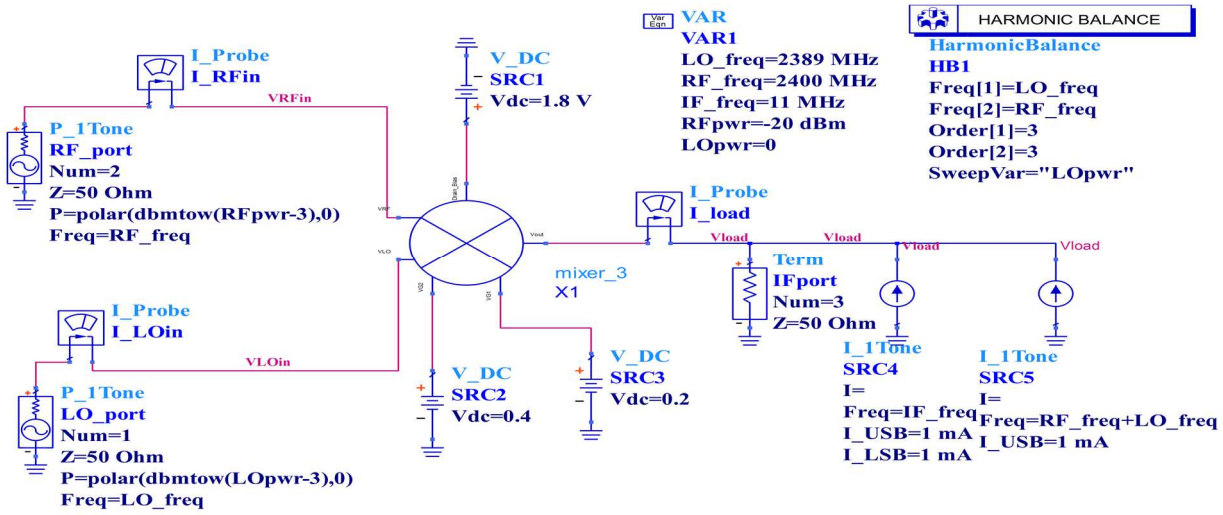


Fig. 3 Testbench circuit for the DG-GFET mixer

The dual gate GFET (DG-GFET) active mixer is designed with two equal-width, single gate GFET in cascode topology. The benefits of this type of topology is that it reduces the parasitic capacitances.

Fig. 3 shows the testbench arrangements for the DG-GFET mixer. The mixer is biased with two gate supply and single drain supply. The inside view of the mixer symbol contains the complete circuit of the proposed DG-GFET.

Fig. 4. The gate of the lower GFET is fed with the local oscillator (LO) signal, while the upper GFET is fed by a radio frequency (RF) signal. The circuit shows all the component values for the bias tee, and filters at the corresponding terminals. The bandpass filter at the RF/LO terminal is required to pass the RF/LO signal without any loss and block the IF signal passing through it. The IF lowpass filter passes the IF signal into the down-conversion mixer and suppresses the LO components.

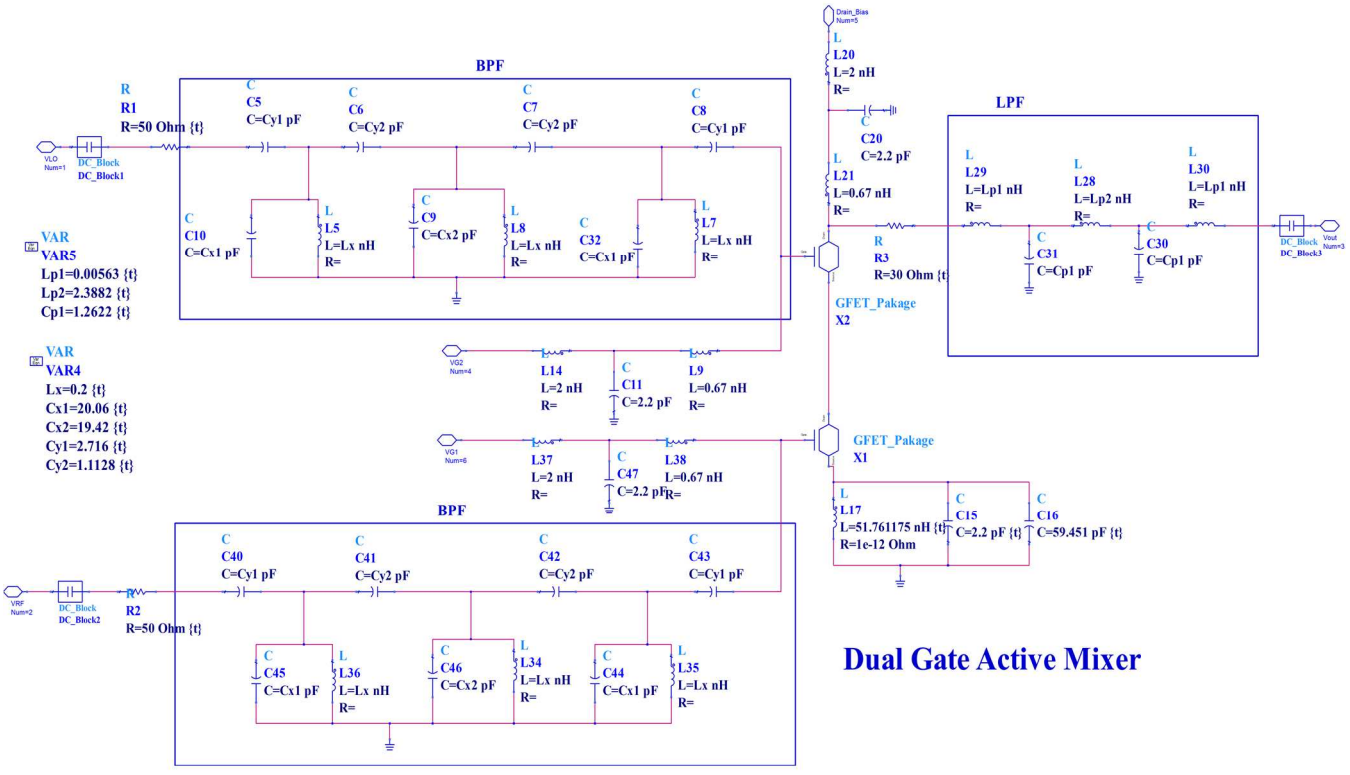


Fig. 4 Complete proposed circuit for the DG-GFET active mixer

Authorized licensed use limited to: DELHI TECHNICAL UNIV. Downloaded on June 04,2025 at 05:27:54 UTC from IEEE Xplore. Restrictions apply.

IV. Results and Discussion

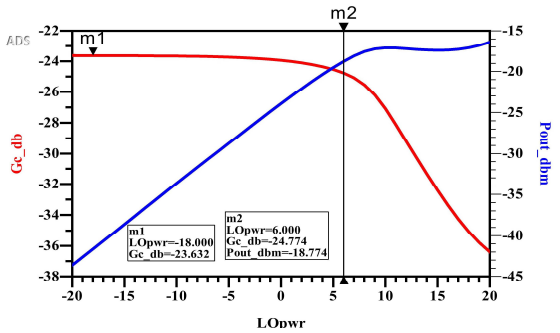


Fig. 5 Conversion loss (solid red) on left y-axis and output power (soldi blue) on right y-axis

Fig. 5 shows the conversion gain (or conversion loss for the down conversion mixer) on the left y-axis shown with a red solid line and the output power on the right y-axis with a blue solid line. The conversion loss (CL) for the DG-GFET down conversion mixer is 23.63 dB to 36.30 dB for the LO power, ranging from -20 dBm to 20 dBm. The 1-dB compression point is observed at 6 dBm LO power for -20 dBm RF input power. The mixer is showing linear behaviour up to 6 dBm of LO power. The CL is 24.77 dB corresponding to 1 dB compression point for a 50 Ω terminal load.

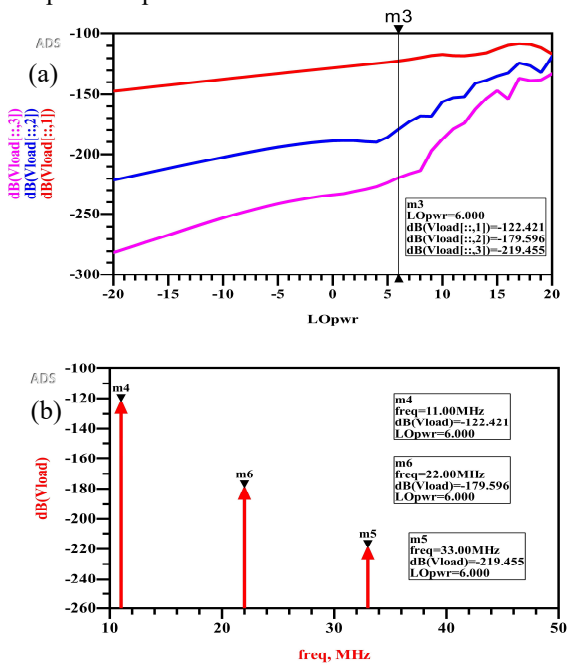


Fig. 6 (a) Harmonic curve with respect to the input LO power, solid red represents fundamental harmonic, solid blue represents second harmonic and solid pink represents third harmonic. (b) Spectrum representation at the 1 dB compression point.

Fig. 6 (a) shows the Harmonic responses for the DG- GFET, the solid red line corresponds to the fundamental Harmonic, while the solid blue line represents the second Harmonic, and the solid pink line corresponds to the third Harmonic. The third harmonic component is suppressed to 97 dB at 6 dBm of LO power with respect to the fundamental component. **Fig. 6 (b)** shows the IF spectrum for the down conversion frequency, i.e., at the 11 MHz IF frequency. The IF output at 11 MHz is around -122.421 dB, and for the third harmonic i.e. at 33 MHz it is around -219.455 dB. The third order intermodulation for the DG-GFET is calculated as 28.52 dBc (relative to fundamental/carrier signal) for the LO power of 6 dBm and RF power of -20 dBm.

Table 3 Comparison of state-of-the-art GFET based mixers

Ref.	Tech.	f_{RF} (GHz)	f_{LO} (GHz)	CL (dB)	PLO (dBm)
[3]	GFET	0.0105	0.01	30	0
[9]	GFET	1	2.02	24	15
[11]	GFET	24-31	15	19	10
[12]	GFET	10.07	10	17	-3.5
[13]	GFET	3.6	3.5	33	8.9
[20]	GFET	0.3	0.28	23	6.5
This Work	**GFET**	**2.4**	**2.389**	**24.77**	**6**

The comparison of our designed DG-GFET active single-ended mixer with the other published mixers based on GFET technology is given in **Table 3**. The proposed dual gate GFET mixer has issues in achieving the best biasing voltage for better linearity and overall performance. The input matching network is difficult to design as input impedance is bias dependent. The noise performance of the dual gate structure of the mixer degraded as compared to the single gate configuration. Also, in the design of the dual gate GFET mixer there are some trade-offs between the parameters such as low gate voltage can improve the linearity at the cost of a reduction in conversion efficiency, a higher gate voltage can improve the conversion gain but there is a reduction in the isolation between input and output port. A wider device can improve the conversion gain but introduce harmonic distortions.

V. Conclusion

This paper has described the AVS-GFET model, which is written in Verilog-A and simulated on ADS from Keysight. The model is validated through DC and RF validation with the experimental results. Later in this paper, we have designed a DG-GFET single-ended active mixer for the RF down conversion. The proposed mixer circuit with the filters at each terminal has been analyzed with the help of simulation results. The conversion loss obtained for the down conversion mixer ranges from 23.63 dB to 36.3 dB for -20 dBm to 20 dBm LO power. The third order intermodulation distortion is calculated as 28.52 dBc (with respect to the fundamental signal).

References

[1] V. E. Dorgan, M.-H. Bae, and E. Pop, "Mobility and saturation velocity in graphene on SiO2," *Appl. Phys. Lett.*, vol. 97, no. 8, p. 082112, Aug. 2010, doi: 10.1063/1.3483130.

[2] S. Ghosh *et al.*, "Extremely high thermal conductivity of graphene: Prospects for thermal management applications in nanoelectronic circuits," *Appl. Phys. Lett.*, vol. 92, no. 15, p. 151911, Apr. 2008, doi: 10.1063/1.2907977.

[3] H. Wang, A. Hsu, J. Wu, J. Kong, and T. Palacios, "Graphene-Based Ambipolar RF Mixers," *IEEE Electron Device Lett.*, vol. 31, no. 9, pp. 906–908, Sep. 2010, doi: 10.1109/LED.2010.2052017.

[4] H. Madan *et al.*, "Record high conversion gain ambipolar graphene mixer at 10GHz using scaled gate oxide," in *2012 International Electron Devices Meeting*, San Francisco, CA, USA: IEEE, Dec. 2012, p. 4.3.1-4.3.4. doi: 10.1109/IEDM.2012.6478977.

[5] Q. Gao, X. Li, M. Tian, X. Xiong, Z. Zhang, and Y. Wu, "Short-Channel Graphene Mixer With High Linearity," *IEEE Electron Device Lett.*, vol. 38, no. 8, pp. 1168–1171, Aug. 2017, doi: 10.1109/LED.2017.2718732.

Authorized licensed use limited to: DELHI TECHNICAL UNIV. Downloaded on June 04,2025 at 05:27:54 UTC from IEEE Xplore. Restrictions apply.

[6] C.-H. Yeh *et al.*, "Gigahertz Flexible Graphene Transistors for Microwave Integrated Circuits," *ACS Nano*, vol. 8, no. 8, pp. 7663–7670, Aug. 2014, doi: 10.1021/nn5036087.

[7] M. Tian *et al.*, "High-Performance CVD Bernal-Stacked Bilayer Graphene Transistors for Amplifying and Mixing Signals at High Frequencies," *ACS Appl. Mater. Interfaces*, vol. 10, no. 24, pp. 20219–20224, Jun. 2018, doi: 10.1021/acsami.8b04065.

[8] Y.-M. Lin *et al.*, "Wafer-Scale Graphene Integrated Circuit," *Science*, vol. 332, no. 6035, pp. 1294–1297, Jun. 2011, doi: 10.1126/science.1204428.

[9] O. Habibpour, S. Cherednichenko, J. Vukusic, K. Yhland, and J. Stake, "A Subharmonic Graphene FET Mixer," *IEEE Electron Device Lett.*, vol. 33, no. 1, pp. 71–73, Jan. 2012, doi: 10.1109/LED.2011.2170655.

[10] M. A. Andersson, O. Habibpour, J. Vukusic, and J. Stake, "Resistive Graphene FET Subharmonic Mixers: Noise and Linearity Assessment," *IEEE Trans. Microw. Theory Tech.*, vol. 60, no. 12, pp. 4035–4042, Dec. 2012, doi: 10.1109/TMTT.2012.2221141.

[11] O. Habibpour, J. Vukusic, and J. Stake, "A 30-GHz Integrated Subharmonic Mixer Based on a Multichannel Graphene FET," *IEEE Trans. Microw. Theory Tech.*, vol. 61, no. 2, pp. 841–847, Feb. 2013, doi: 10.1109/TMTT.2012.2236434.

[12] J. S. Moon *et al.*, "Graphene FETs for Zero-Bias Linear Resistive FET Mixers," *IEEE Electron Device Lett.*, vol. 34, no. 3, pp. 465–467, Mar. 2013, doi: 10.1109/LED.2012.2236533.

[13] H. Lyu *et al.*, "Double-Balanced Graphene Integrated Mixer with Outstanding Linearity," *Nano Lett.*, vol. 15, no. 10, pp. 6677–6682, Oct. 2015, doi: 10.1021/acs.nanolett.5b02503.

[14] O. Habibpour *et al.*, "A W-band MMIC Resistive Mixer Based on Epitaxial Graphene FET," *IEEE Microw. Wirel. Compon. Lett.*, vol. 27, no. 2, pp. 168–170, Feb. 2017, doi: 10.1109/LMWC.2016.2646998.

[15] M. A. Andersson, Y. Zhang, and J. Stake, "A 185–215-GHz Subharmonic Resistive Graphene FET Integrated Mixer on Silicon," *IEEE Trans. Microw. Theory Tech.*, vol. 65, no. 1, pp. 165–172, Jan. 2017, doi: 10.1109/TMTT.2016.2615928.

[16] M. Tian, X. Li, Q. Gao, X. Xiong, Z. Zhang, and Y. Wu, "Improvement of Conversion Loss of Resistive Mixers Using Bernal-Stacked Bilayer Graphene," *IEEE Electron Device Lett.*, vol. 40, no. 2, pp. 325–328, Feb. 2019, doi: 10.1109/LED.2018.2889153.

[17] S. Rakheja and D. Antoniadis, *Ambipolar Virtual Source Compact Model for Graphene FETs*. (2014). nanoHUB. doi: 10.4231/D3MS3K273.

[18] S. Rakheja, Y. Wu, H. Wang, T. Palacios, P. Avouris, and D. A. Antoniadis, "An Ambipolar Virtual-Source-Based Charge-Current Compact Model for Nanoscale Graphene Transistors," *IEEE Trans. Nanotechnol.*, vol. 13, no. 5, pp. 1005–1013, Sep. 2014, doi: 10.1109/TNANO.2014.2344437.

[19] L. Sang, Y. Xu, Y. Wu, and R. Chen, "Device and Compact Circuit-Level Modeling of Graphene Field-Effect Transistors for RF and Microwave Applications," *IEEE Trans. Circuits Syst. Regul. Pap.*, vol. 65, no. 8, pp. 2559–2570, Aug. 2018, doi: 10.1109/TCSI.2018.2793852.

[20] M. Wu, W. Hong, G. Liu, J. Zhang, Z. Tian, and M. Zhang, "Double-balanced mixer based on monolayer graphene field-effect transistors," *J. Semicond.*, vol. 43, no. 5, p. 052002, May 2022, doi: 10.1088/1674-4926/43/5/052002.

Authorized licensed use limited to: DELHI TECHNICAL UNIV. Downloaded on June 04,2025 at 05:27:54 UTC from IEEE Xplore. Restrictions apply.

Physica Scripta

INCLUSIVE PUBLISHING TRUSTED SCIENCE

PURPOSE-LED PUBLISHING™

PAPER

Device modelling and optimization of new lead-free $(NH_4)_3Sb_2I_9$ perovskite solar cells by using SCAPS-1D software

To cite this article: Sumit Singh *et al* 2025 *Phys. Scr.* **100** 075012

View the article online for updates and enhancements.

You may also like

- Investigating the performance of perovskite solar cell with tin oxide as electron transport layer by SCAPS-1D device simulation
R Sharuvindan Nair and Mohd Zamir Pakhuruddin

- Numerical simulation of all inorganic $CsPbIBr_2$ perovskite solar cells with diverse charge transport layers using DFT and SCAPS-1D frameworks
Dibyajyoti Saikia, Chayan Das, Anupam Chetia et al.

- Current status of Pb-free PSCs and infer the highest achievable PCE via numerical modeling, and optimization of novel structure $FAMASnGeI_3$ based PSCs
Hairul Mardiah Hamzah, Md Helal Miah, Md Jakir Hossen et al.

This content was downloaded from IP address 14.139.251.98 on 16/06/2025 at 06:26

Physica Scripta

PAPER

Device modelling and optimization of new lead-free $(NH_4)_3Sb_2I_9$ perovskite solar cells by using SCAPS-1D software

Sumit Singh, Rahul Kundara* and Sarita Baghel

Department of Applied Physics, Delhi Technological University, Delhi, India

* Author to whom any correspondence should be addressed.

E-mail: rahul_2k20phdap10@dtu.ac.in

RECEIVED
15 March 2025

REVISED
22 May 2025

ACCEPTED FOR PUBLICATION
2 June 2025

PUBLISHED
12 June 2025

Keywords: lead-free perovskite material, $(NH_4)_3Sb_2I_9$-based PSC, SCAPS-1D, ETL, HTL, PCE

Abstract

Advancing lead-free perovskite solar cells (PCSs) is essential for developing sustainable and eco-friendly solar technologies. These alternatives to lead-based PSCs offer notable benefits, including low-cost, excellent stability, and promising efficiency, positioning them as attractive candidates for next-generation photovoltaic applications. Among the emerging materials, $(NH_4)_3Sb_2I_9$ stands out due to its favourable optoelectronic properties and environmental safety. This study investigates the impact of different HTLs and ETLs on the performance of $(NH_4)_3Sb_2I_9$-based devices using SCAPS-1D software. Several parameters influencing device efficiency were optimized, including thickness of absorber layer, operating temperature, work function of back contact, donor density, defect density (N_t), series and shunt resistance. The optimized device structure, FTO/WS_2/$(NH_4)_3Sb_2I_9$/$MASnBr_3$/Au achieved a PCE of 20.08% with a V_{OC} of 1.65 V, J_{SC} of 13.83 mA cm^{-2} and FF of 87.93% at 300 K and N_t of 10^{13} cm^{-3}. These results demonstrate the strong potential of antimony-based perovskites in the development of high-performance, lead-free solar cells.

1. Introduction

As commercialization and industrial growth continue to accelerate, the demand for power and energy is rising steadily. Using conventional fuels like natural gas, oil, and fossil fuels depletes our finite resources and harms the environment. This emphasizes the importance of seeking and adopting renewable energy alternatives. Growing energy needs can be responsibly met while protecting the environment for coming generations by using renewable energy. In just 1.5 days, the sun generates an astounding 1.7×10^{22} joules of energy, which is equivalent to the total energy stored in 3 trillion barrels of Earth's oil reserves [1]. This highlights that the sun alone can easily fulfil humanity's energy needs and makes solar energy the most promising renewable resource—clean, accessible, abundant, and environmentally friendly. Over the last decade, PSCs have emerged as highly promising candidates for applications in solar energy. The PSCs attract major attention due to their outstanding photovoltaic performance, flexible and adjustable band gap, and straightforward manufacturing process. The efficiency of PSCs has seen remarkable progress, rising from initially 3.8% in 2009 to an impressive 27.0% today [2]. Lead-based PSCs face sustainability issues due to high toxicity of Pb poses serious threats to both living organisms and the environment. Hence, it is crucial to explore more sustainable and efficient materials with lower toxicity to substitute lead (Pb) in PSCs. Recently, scientists have investigated eco-friendly metal elements that share characteristics with Pb, such as tin (Sn) [3], germanium (Ge) [4], and antimony (Sb) [5], as potential substitutes in the absorber layer. Tin is abundant in nature and poses minimal environmental and health risks. Moreover, tin-based perovskites have a bandgap that aligns more closely with the optimal range predicted by the Shockley–Queisser limit theory offering an advantage over their lead-based counterparts [6]. However, tin faces a major challenge, as Sn^{2+} can easily oxidize to Sn^{4+} [7]. This limits the stability of Sn-based PSCs, hindering their long-term performance. Germanium, like lead, shares the same group in periodic table and has a smaller ion radius, which improves its ionic conductivity, but germanium-based perovskites are even more susceptible to oxidation than their tin-based counterparts due to the weaker inert pair effect [8], making their stability a

© 2025 IOP Publishing Ltd. All rights, including for text and data mining, AI training, and similar technologies, are reserved.

critical drawback. Antimony, on the other hand, shares the same ns^2 outer electronic configuration as lead and is considerably less harmful. Additionally, Sb-based perovskite materials exhibit comparable optoelectronic properties to lead halide perovskites [9]. These qualities position antimony as a promising and viable substitute for lead in metal halide perovskites, offering a safer and more sustainable option for future advancements. In 2021, Kumar *et al* [10] prepared a thin film layer of $(NH_4)_3Sb_2I_9$ by two-step deposition method, which showed good stability. In 2023, Valli *et al* [11] conducted structural and optoelectronic investigations on the $(NH_4)_3Sb_2I_9$ material in a low-temperature range and suggested its potential for photovoltaic applications. Fabricating the various layers of a PSC through experimental methods is both time-intensive and costly. As a result, computational modelling and simulation play a vital role in identifying optimal materials for each layer of PSCs. The absorber layer's efficiency can be improved by selecting an appropriate electron transport material that effectively extracts photo-generated electrons from perovskite layer. Similarly, the hole transport material facilitates efficient hole extraction, enhancing overall device performance. Moreover, the performance and durability of PSCs heavily rely on the composition, properties, and compatibility of these functional layers. A two-step simulation approach is used in this work. In the first step, various ETL and HTL materials were analysed in combination with the $(NH_4)_3Sb_2I_9$ absorber layer to identify the configuration yielding the highest performance. $(NH_4)_3Sb_2I_9$ perovskite layer has better conductivity, Antimony (Sb)-based materials often show lower defect formation energy and better tolerance to halide vacancies. Sb-based perovskite like $(NH_4)_3Sb_2I_9$ are more moisture-stable than lead-based ones due to strong chemical bond with halide ions than lead does. The NH_4^+ cations can form hydrogen bonds with water, potentially acting as a buffer and limiting moisture ingress into the perovskite lattice. Once the optimal combination was determined, the second step focused on refining the selected model to enhance key performance factors, including PCE, J_{SC}, V_{OC}, and FF. The configuration yielding the best performance was FTO/WS_2/$(NH_4)_3Sb_2I_9$/$MASnBr_3$/Au. To further enhance this design, key factors like absorber layer thickness, temperature, and N_t were systematically optimized. After optimizing these input parameters, the model achieved an impressive PCE of 20.08%.

2. Device structure and simulation

The SCAPS-1D of version 3.3.11 is used as a simulation framework. It uses semiconductor equations for charge carriers, such as the continuity equation of hole (1), electron (2), and poison equation (3), and calculates the performance of the solar devices [12]

$$\frac{dn_p}{dt} = G_n - \frac{n_p - n_{p^0}}{\tau_n} - n_p\mu_n\frac{dE}{dx} - \mu_n\xi\frac{dn_p}{dx} + D_n\frac{d^2n_n}{dx^2} \tag{1}$$

$$\frac{dp_n}{dt} = G_p - \frac{p_n - p_{n^0}}{\tau_p} - p_n\mu_p\frac{dE}{dx} - \mu_p\xi\frac{dp_n}{dx} + D_p\frac{d^2p_n}{dx^2} \tag{2}$$

$$\frac{d}{dx}\left(-\varepsilon(x)\frac{d\varphi}{dx}\right) = q[p(x) - n(x) + N_d^+(x) - N_a^-(x) + p_t(x) - n_t(x) \tag{3}$$

Where $p(x)$ and $n(x)$ represent concentration of free holes and concentration of free electrons respectively. $N_a^-(x)$, $N_d^+(x)$, $n_t(x)$, and $p_t(x)$, represent ionized acceptor concentration, ionized donor concentration, concentration of trapped electrons, and concentration of the trapped hole, respectively. G, D, and ξ represent generation rate, diffusion coefficient, and electric potential, respectively [12].

2.1. Device architecture

The device having structure FTO/ETL/absorber layer/HTL/Back Contact is used for the simulation work, where $(NH_4)_3Sb_2I_9$ is used as absorber layer and Au as Back contact having work function 5.1 eV. The simulation of the given model with different HTLs and ETLs combinations and selected the model with the highest device performance parameter. The ETLs used in this work include WS_2, IGZO, TiO_2, and PCBM, whereas PEDOT, ZnTe, spiro-OMeTAD, and $MASnBr_3$ are HTLs. The device model and band alignment diagram for the $(NH_4)_3Sb_2I_9$-based PSC are shown in figure 1, as this structure is selected for further optimization. The values of material properties for FTO (fluorine-doped tin oxide), HTL, and ETLs are listed in tables 1–3, respectively, along with their respective references. For absorber layer $(NH_4)_3Sb_2I_9$, the simulation parameters were obtained from previous literature [10, 13, 14]. The band gap (E_g) of $(NH_4)_3Sb_2I_9$ is 2.05 eV. The value of the dielectric constant is 7. The mobility of holes (μ_p)and electrons (μ_n) are 4.8 and 12.3 (cm^2/Vs), respectively. The thermal velocity of both holes and electrons is 1 × 107 (cm/s) each, as used in this work.

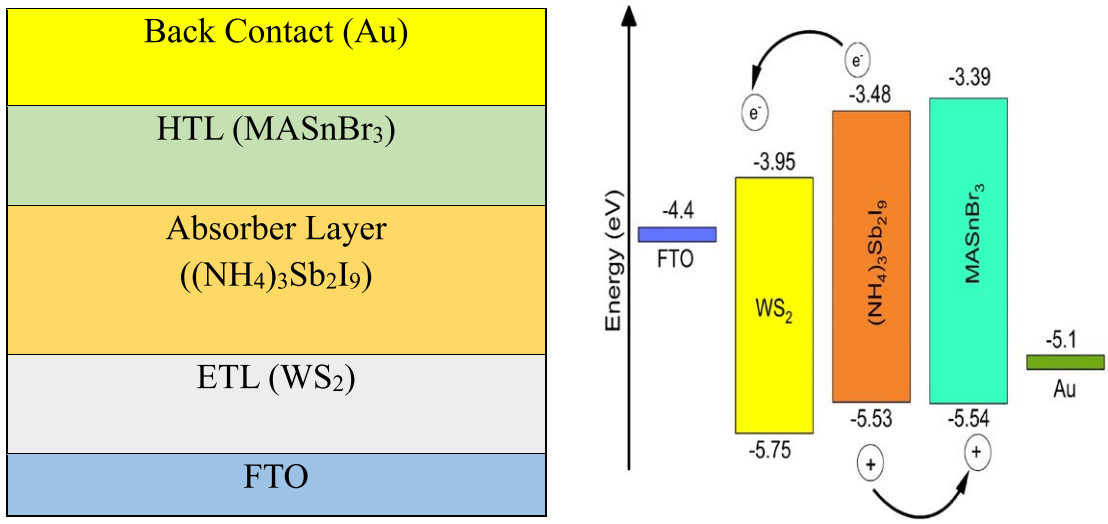


Figure 1. Device Structure and energy band diagram for $(NH_4)_3Sb_2I_9$ based PSC.

Table 1. Initial input parameter of PSC.

Parameter	FTO	TiO_2	$(NH_4)_3Sb_2I_9$	Spiro-OMeTAD
Thickness (nm)	50	100	500	100
Eg (eV)	3.5	3.2	2.05	3.0
χ (eV)	4.0	4	3.8[a]	2.45
ε_r	9.0	9	7.0[a]	3.0
Nc (cm^{-3})	2.2×10^{18}	10^{21}	1×10^{19}	1×10^{19}
Nv (cm^{-3})	1.8×10^{19}	2×10^{20}	1×10^{19}	1×10^{19}
μ_n (cm^2/Vs)	20	20	12.3	1×10^{-4}
μ_p (cm^2/Vs)	10	10	4.8	1×10^{-4}
N_D (cm^{-3})	1×10^{15}	10^{19}	0	0
N_A (cm^{-3})	0	4×10^{15}	0	2×10^{18}
N_t (cm^{-3})	1×10^{15}	1×10^{13}	1×10^{13}	1×10^{14}
References	[15, 16]	[17]	[10, 14]	[15, 18–20]

[a] In this work.

2.2. SCAPS-1D software simulation

SCAPS-1D is a software tool created by Professor Marc Burgelman and used for simulation work [29, 30]. This tool can compute semiconductor equations for charge carriers by solving Poisson's and continuity equations. Software's core operation involves using the Gummel-type iterative method and numerical differentiation to resolve the continuity and Poisson's derivative equations [31]. In addition, it is capable of evaluating spectral responses and current–voltage characteristics across a range of user-defined wavelengths. Notably, SCAPS-1D has the intrinsic ability to replicate both bulk and interface defects, making it a widely utilized tool for the numerical analysis of solar cells. The software incorporates the SRH recombination mechanism to accurately model charge carrier dynamics. Additionally, it supports standard illumination conditions of A.M 1.5G (Air Mass) with incident light power set at 1000 W m^{-2} and operating temperature at 300 K, ensuring reliable and consistent simulation results. Consequently, numerical analyses of PSC through SCAPS-1D represent a promising methodology for further advancing solar technology. The SCAPS-1D software simulation procedure shown below in figure 2.

3. Results and discussion

3.1. Optimization of appropriate ETL and HTL

The HTL and ETL are essential components in ensuring efficient charge carrier movement within a solar cell. They seamlessly transport charge carriers, which is vital for minimizing charge recombination, otherwise reducing device performance. The study includes investigation of four HTLs-ZnTe, PEDOT: PSS, $MaSnBr_3$, and Spiro-OMeTAD, and four ETLs-WS_2, IGZO, PCBM, and TiO_2. The energy band diagram of absorber layer with different HTLs and ETLs shown below in figure 3. The Impact of distinct HTLs such as Spiro-OMeTAD, PEDOT: PSS, ZnTe, and $MASnBr_3$ with

Table 2. Parameters for simulation of different HTLs.

Parameter	ZnTe	PEDOT: PSS	Spiro-OMeTAD	$MASnBr_3$
Thickness (nm)	100	100	100	100
Eg (eV)	2.26	2.2	3.0	2.15
χ (eV)	3.65	2.9	2.45	3.39
ε	14.0	3.0	3.0	8.2
N_C (cm^{-3})	7.5×10^{17}	2.2×10^{15}	1×10^{19}	1×10^{18}
N_V (cm^{-3})	1.5×10^{19}	1.8×10^{18}	1×10^{19}	1×10^{18}
μ_n (cm^2/Vs)	70	1×10^{-2}	1×10^{-4}	1.6
μ_p (cm^2/Vs)	50	2×10^{-4}	1×10^{-4}	1.6
N_D (cm^{-3})	0	0	0	0
N_A (cm^{-3})	2.16×10^{19}	1×10^{19}[a]	2×10^{18}	1.0×10^{18}
N_t (cm^{-3})	1×10^{14}	1×10^{14}	1×10^{14}	1×10^{14}
References	[21, 22]	[23]	[15, 18–20]	[24, 25]

[a] In this work.

Table 3. Parameters for simulation of different ETLs.

Parameters	TiO_2	IGZO	WS_2	PCBM
Thickness(nm)	50	50	100	100
E_g (eV)	3.2	3.05	1.8	2.1
χ (eV)	4	4.16	3.95	3.9
ε_r	9	10	13.6	7.0
N_c (cm^{-3})	10^{21}	5×10^{18}	1×10^{18}	2.2×10^{19}
N_v (cm^{-3})	2×10^{20}	5×10^{18}	2.4×10^{20}	2.2 × 1019
μ_e (cm^2/Vs)	20	15	100	0.001
μ_h (cm^2/Vs)	10	0.1	100	0.002
V_e (cm^2s^{-1})	1.0×10^7	1.0×10^7	1.0×10^7	1.0×10^7
V_h (cm^2s^{-1})	1.0×10^7	1.0×10^7	1.0×10^7	1.0×10^7
N_D (cm^{-3})	10^{19}	1.0×10^{18}	1×10^{18}	1 × 1018
N_A (cm^{-3})	4×10^{15}	0	0	0
N_t (cm^{-3})	10^{15}	1.0×10^{14}	1.0×10^{13}	1.0×10^{14}
References	[17]	[26]	[27]	[28]

different combinations were studied. In contrast, the ZnTe, and PEDOT: PSS achieved less efficiency than other HTLs. The band matching is a vital factor to achieve maximum performance of the device. WS_2, as the ETL, has a conduction band minimum (CBM) of −3.95 eV lower than the absorber's CBM (−3.48 eV), enabling smooth electron extraction. Its deep valence band (−5.75 eV) blocks hole leakage, and its high electron mobility (~100 $cm^2\ V^{-1}{\cdot}s^{-1}$) ensures fast charge transport with low resistive losses outperforming traditional ETLs like TiO_2. On the flip side, $MASnBr_3$ as the HTL aligns perfectly with the absorber's conduction band minimum (VBM) of −5.53 eV, so holes can flow smoothly into $MASnBr_3$ without barriers. Its CBM (−3.39 eV) is higher than the absorber's CBM, which effectively blocks any electron flow in the wrong direction. This ensures that $MASnBr_3$ not only transports holes efficiently but also prevent electron recombination. The valence band maximum should align well with the valence band maximum of the perovskite layer to allow efficient hole extraction. The conduction band maximum should be higher than the conduction band maximum of absorber layer to block the electron transport, which helps reduction in recombination and increase open circuit voltage of PSC. Also, $MASnBr_3$ is most suitable HTL for $(NH_4)_3Sb_2I_9$-based PSC due to its diverse properties such as better stability than Spiro-OMeTAD or PEDOT: PSS can provide, suitable for flexible devices or tandem cells, efficient hole extraction and minimizes energy loss, environmentally friendly and low-cost. The $MASnBr_3$ as HTL offered most suitable band matching as compared to other HTLs shown below in figure 3. Their effect on the performance parameters of PSCs was evaluated using SCAPS-1D simulations. The choice of these specific HTLs and ETLs was guided by their strong performance, as reported in earlier studies, demonstrating their potential to enhance PCE and their suitability for integration into PSC designs. The simulation parameters for each HTL and ETL are detailed in tables 2 and 3. Quantum efficiency (Q.E.) represents the proportion of charge carriers successfully collected by the solar cell relative to the number of incident photons with sufficient energy. A decline in Q.E. is often linked to factors such as reduced absorption at longer wavelengths and surface recombination [30]. Figures 4–7 shows that the J-V and Q.E. plots, illustrating different layers effect on the device performance. Table 4 represents simulation results of all the combinations of ETLs and HTLs with an absorber layer. The outcomes deduced WS_2 along with

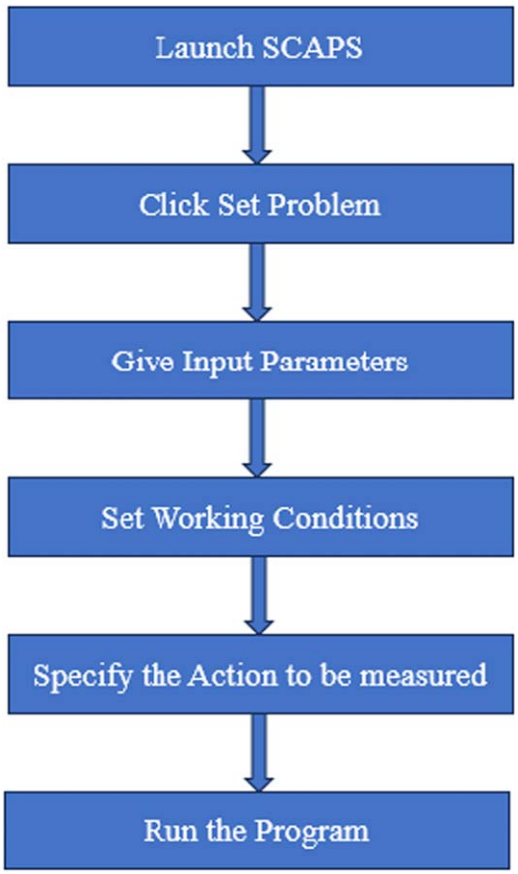


Figure 2. Simulation procedure.

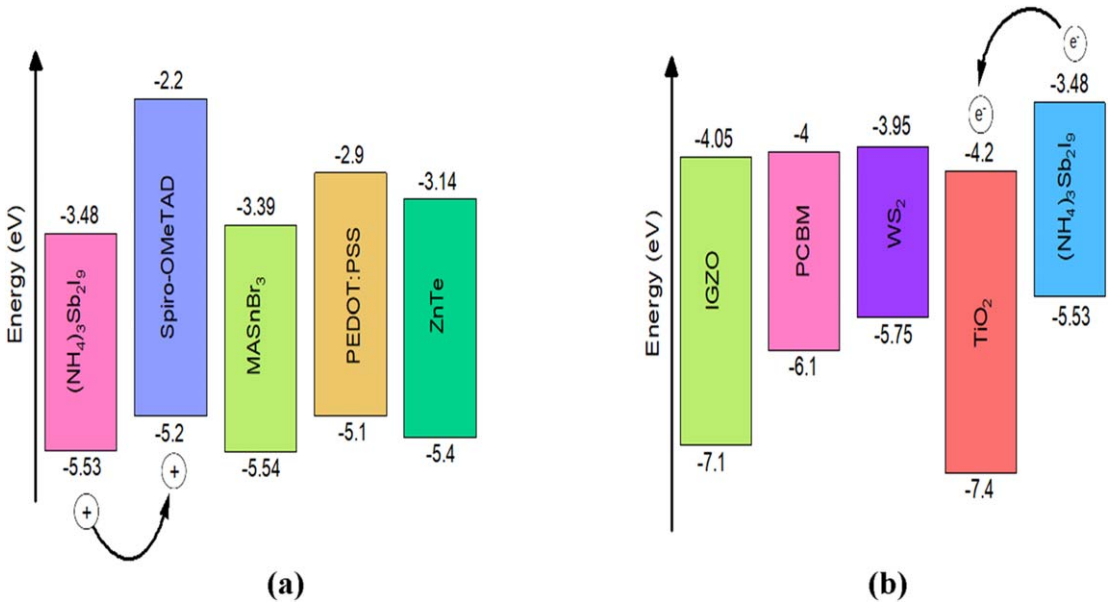


Figure 3. Energy band diagram of absorber layer with different (a) HTLs and (b) ETLs.

$MASnBr_3$ show the highest PCE. WS_2 ETL-based PSC configuration shows better PCE due to higher carrier mobility, which enables faster charge transport and reduces recombination losses, and band alignment balances efficiency by maximizing sunlight absorption while minimising voltage losses [32]. $MASnBr_3$, used as the HTL, demonstrated highest efficiency of 19.51% when paired with WS_2. Based on this performance, $MASnBr_3$ was selected as the HTL for

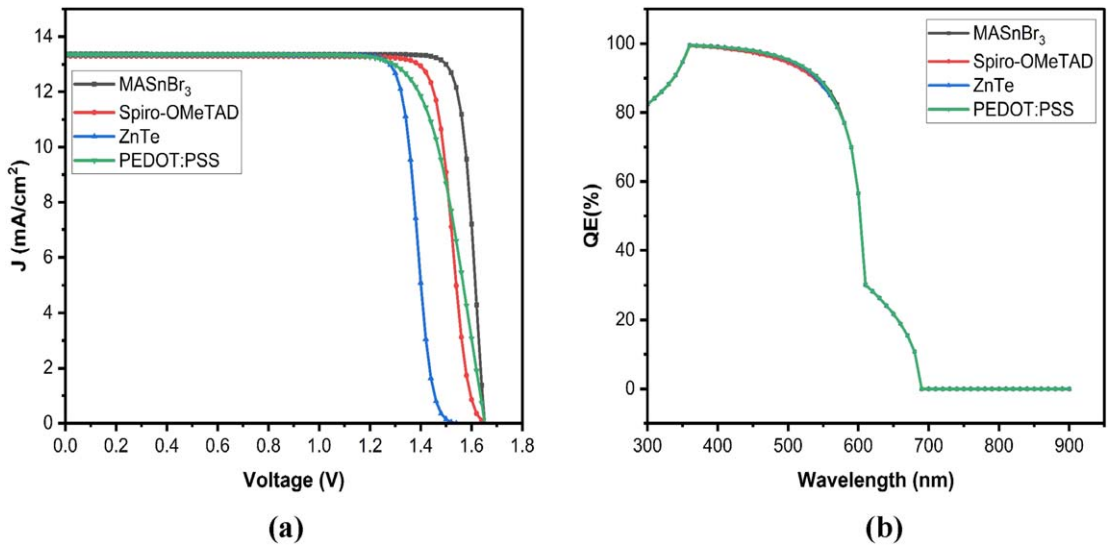


Figure 4. (a) J-V characteristics and (b) QE curve of distinct HTLs with WS_2 as ETL.

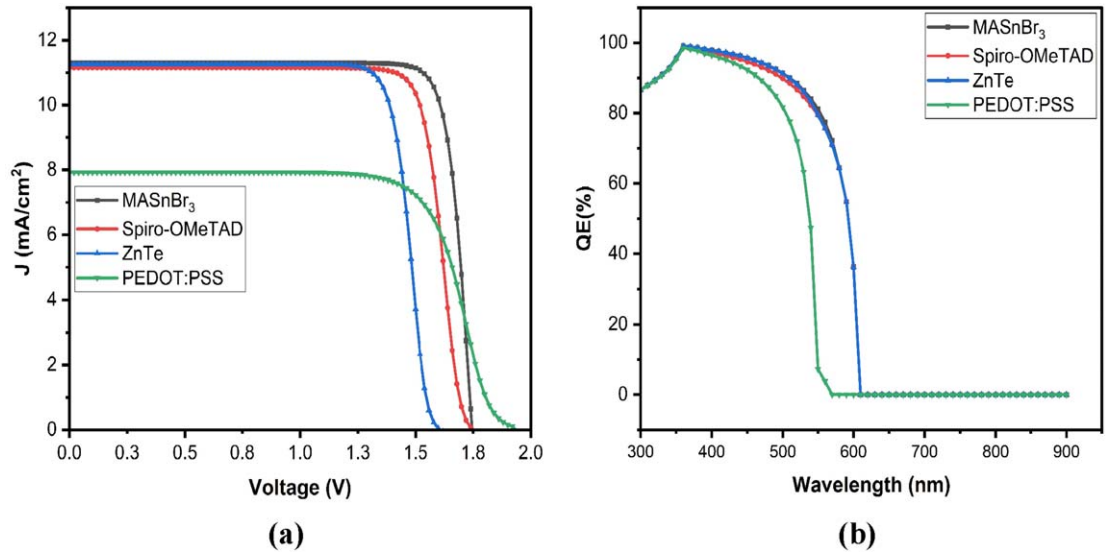


Figure 5. (a) J-V characteristics and (b) QE curve of distinct HTLs with TiO_2 as ETL.

optimizing the absorber layer parameters. This thin-film material offers a tunable bandgap and excellent light absorption properties. However, the presence of Sn^{2+} in $MASnBr_3$ poses challenges due to its instability and susceptibility to oxidation, which degrade the film's morphology and semiconductor properties, ultimately lowering efficiency and stability [33, 34]. Fortunately, methods to prevent the oxidation of Sn^{2+} and enhance the stability of the material have been proposed [35]. As a result, in the subsequent sections of our study, the device structure $FTO/WS_2/(NH_4)_3Sb_2I_9/MASnBr_3/Au$ was chosen for further optimization. Factors such as thickness, temperature, and defect density were investigated to improve device's performance.

3.2. Impact of defect density

Simulations were conducted through batch calculation varying N_t from 10^{13} to 10^{18} cm^{-3} to evaluate the impact of N_t of $(NH_4)_3Sb_2I_9$. Defects were considered both at the surface and within the bulk of the $(NH_4)_3Sb_2I_9$ layers. In perovskite materials, several types of point defects can arise, including interstitial defects, lattice vacancies, as well as Schottky and Frenkel defects. Moreover, structural imperfections such as dislocations and grain boundaries significantly assist in overall defect density [36, 37]. These defects introduce additional energy states within the bandgap, which serve as traps for charge carriers [38], affecting the device's efficiency and

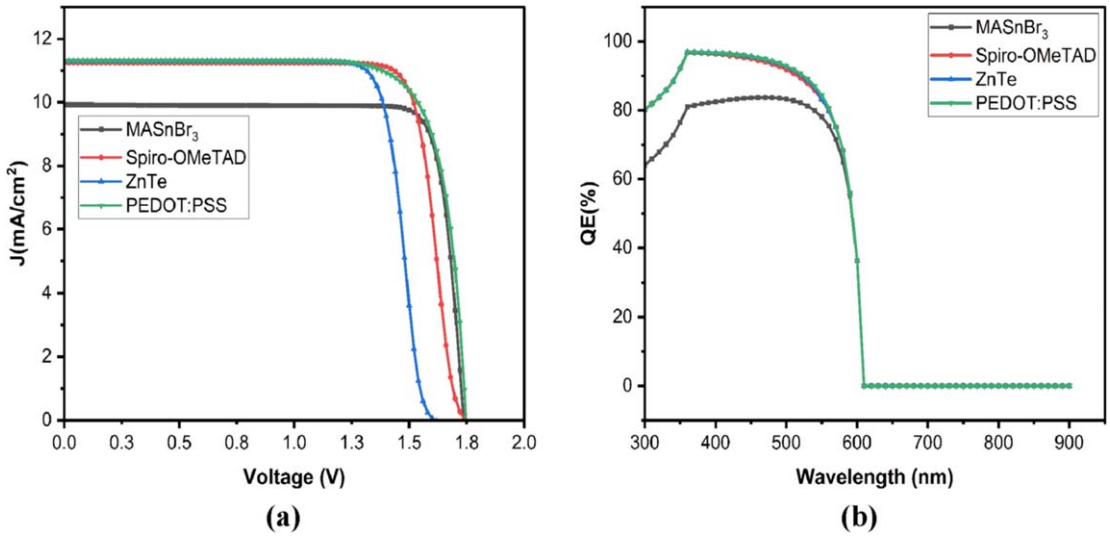


Figure 6. (a) J-V characteristics and (b) QE curve of distinct HTLs with PCBM as ETL.

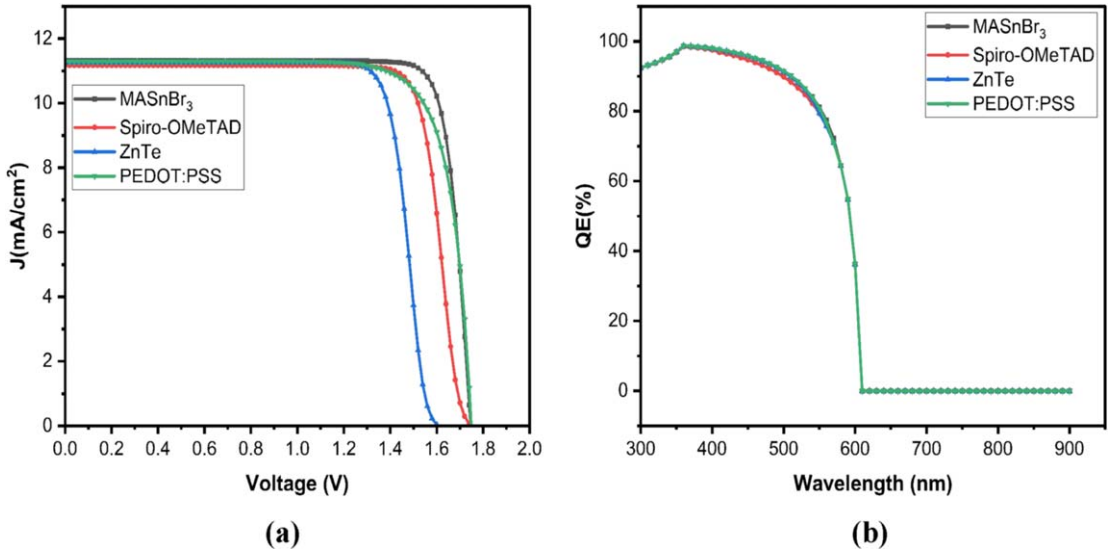


Figure 7. (a) J-V characteristics and (b) QE curve of distinct HTLs with IGZO as ETL.

performance. The value of N_t of absorber layer varied in step of 10^1, keeping its thickness at 500 nm. Other material parameters were kept the same, as given in table 1. The influence of N_t on device's performance is displayed in figure 8, which reveals that an increase in N_t causes a considerable drop in performance parameters. At $N_t = 10^{13}$ cm^{-3}, the efficiency of PCS is 19.51% and 18.94% at $N_t = 10^{14}$ cm^{-3}; above this value, the PCE decreases continuously, and it comes to 1.59% at $N_t = 10^{18}$ cm^{-3}. The optimized value of N_t is 10^{13} cm^{-3} [39] for further simulation work as it gives the highest performance parameters. N_t is crucial in determining the recombination rate within a solar cell, which can be effectively explained through the SRH recombination model. This model comprehensively describes the recombination process and is mathematically represented by equation (4) [40].

$$R = \frac{\tau_{n,p}^{-1}(np_ n_i^2)}{n + p + 2n_i coh\left(\frac{E_t - E_i}{KT}\right)} \tag{4}$$

where $\tau_{n,p}$, n, p, represent the charge carrier lifetime, electron density, and hole density, respectively. n_i is intrinsic density, E_t is the energy level of the trap defects and E_i is intrinsic energy levels. The lifetime of the charge carrier can be calculated by equation (5) [40].

Table 4. Various device structures and their simulation results.

Device structures	V_{OC} (V)	J_{SC} (mA/cm^2)	FF (%)	PCE (%)
FTO/WS_2/$(NH_4)_3Sb_2I_9$/$MASnBr_3$/Au	1.65	13.37	88.40	19.51
FTO/WS_2/$(NH_4)_3Sb_2I_9$/Spiro-OMeTAD/Au	1.65	13.29	82.56	18.12
FTO/WS_2/$(NH_4)_3Sb_2I_9$/ZnTe/Au	1.53	13.34	81.24	16.63
FTO/WS_2/$(NH_4)_3Sb_2I_9$/PEDOT: PSS/Au	1.65	13.36	76.92	16.98
FTO/PCBM/$(NH_4)_3Sb_2I_9$/ZnTe/Au	1.61	11.30	79.50	14.48
FTO/PCBM/$(NH_4)_3Sb_2I_9$/Spiro-OMeTAD/Au	1.74	11.24	80.64	15.83
FTO/PCBM/$(NH_4)_3Sb_2I_9$/$MASnBr_3$/Au	1.73	9.921	85.53	14.74
FTO/PCBM/$(NH_4)_3Sb_2I_9$/PEDOT: PSS/Au	1.74	11.32	78.81	15.59
FTO/TiO_2/$(NH_4)_3Sb_2I_9$/ZnTe/Au	1.60	11.25	80.04	14.46
FTO/TiO_2/$(NH_4)_3Sb_2I_9$/Spiro-OMeTAD/Au	1.74	11.15	80.78	15.75
FTO/TiO_2/$(NH_4)_3Sb_2I_9$/$MASnBr_3$/Au	1.74	11.29	85.58	16.89
FTO/TiO_2/$(NH_4)_3Sb_2I_9$/PEDOT: PSS/Au	1.97	7.927	69.39	10.86
FTO/IGZO/$(NH_4)_3Sb_2I_9$/ZnTe/Au	1.60	11.26	80.11	14.49
FTO/IGZO/$(NH_4)_3Sb_2I_9$/Spiro-OMeTAD/Au	1.74	11.16	80.86	15.78
FTO/IGZO/$(NH_4)_3Sb_2I_9$/$MASnBr_3$/Au	1.74	11.30	85.66	16.92
FTO/IGZO/$(NH_4)_3Sb_2I_9$/PEDOT: PSS/Au	1.74	11.29	79.30	15.66

$$\tau_{n,p} = \frac{1}{\sigma_{n,p} v_{th} N_t} \tag{5}$$

where N_t represent defect density of the absorber layer, $\sigma_{n,p}$ is the capture cross-section of charge carriers and v_{th} is the velocity of charge carriers. The charge carrier lifetime and defect density are closely related in an inverse manner, as outlined in equation (5). Moreover, there is an inverse relationship between the recombination rate and relaxation time of charge carriers, as illustrated in equation (4). Therefore, as defect density increases, recombination rate also rises due to decrease in carrier lifetime and diffusion length. This reduces the total performance of PSC. The details of the interface defects in the PSC shown below in table 5.

3.3. Impact of absorber layer thickness

The impact of the absorber layer thickness on PSC performance was explored by adjusting its thickness from 100 nm to 1000 nm while keeping constant values for other parameters. As shown in figure 9, the results indicate that increasing thickness leads to improved efficiency. This is because at smaller thicknesses, photons are not absorbed efficiently. However, V_{oc} decreased from 1.6672 V to 1.5225 V due to increased charge carriers' recombination over longer travel paths [38]. The J_{SC} rises sharply with thickness up to 400 nm, then gradually increases beyond 500 nm. The higher J_{SC} of 14.16 mA cm^{-2} observed at 1000 nm is primarily due to the high absorption coefficient of the absorber material. While FF decreased from 89.31 to 87.36%, likely due to increased series resistance, enhanced charge carrier recombination, and associated resistive losses [41]. As efficiency does not change much after 700 nm, so that 700 nm taken as the optimal thickness for the device structure.

3.4. Impact of operating temperature on device performance

The performance of the device is significantly influenced by temperature as it impacts its efficiency and stability. While the standard operating temperature is typically set at 300 K, real-world applications expose devices to a broad temperature range, compromising the device structure and degrading its performance. To assess the effect of temperature on four key parameters of PSC and evaluate its thermal stability, temperatures were varied from 280 K to 420 K. Impact of this temperature variation on performance metrics is shown in figure 10. The analysis indicated a decline in V_{oc}, FF, and PCE, while J_{sc} showed a slight increase. This behaviour is due to the increased strain and stress induced by rising temperatures, which lead to greater interfacial defects, structural disorder, and reduced layer connectivity [42]. Higher temperatures also affect the mobilities of charge carriers, as well as carrier concentration, which collectively reduces the efficiency of PSCs. Decrease in V_{oc} with temperature is primarily due to an increase in reverse saturation current (J_0), as described by equation (6).

$$V_{oc} = \frac{KT}{q}\left(\frac{J_{sc}}{J_0} + 1\right) \tag{6}$$

where J_{SC} and J_0 represent short circuit and reverse saturation current, respectively. K is the Boltzmann constant and T is temperature in kelvin. Meanwhile, a small increase in J_{SC} is due to a narrowing of semiconductor's band gap at higher temperatures, enabling the absorption of longer-wavelength photons.

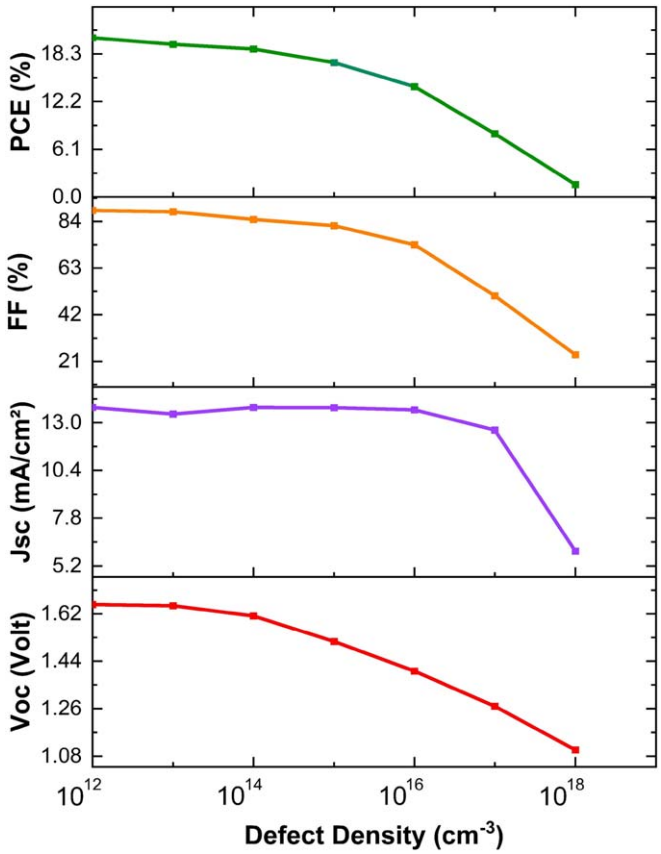


Figure 8. The impact of defect density on performance parameters of PSC.

Table 5. Details of interface defects in the PSC.

Parameters	ETL/absorber layer	Absorber layer/HTL
defect type	Neutral	Neutral
capture cross section electrons (cm^2)	10^{-15}	10^{-15}
capture cross section holes (cm^2)	10^{-15}	10^{-15}
energetic distribution	Single	Single
reference for defect energy level, E_t	Above the highest E_V	Above the highest E_V
energy level with respect to Reference (eV)	0.6	0.6
Total density	10^{13}	10^{14}

3.5. Impact of doner density

N_D varied from 10^{12} to 10^{18} cm^{-3}, and its impact on PCE and FF is shown in figure 11. From the plot, it is seen that PCE remains at 20.08% from 10^{12} to 10^{15} cm^{-3}; after that, it started decreasing to 8.77% at 10^{18} cm^{-3}. FF also remains at 87.93% from 10^{12} to 10^{14}, then slightly increases and starts decreasing to 86.68% at 10^{18} cm^{-3}. The reason behind this may include the recombination factor that reduces PCE and FF at higher N_D.

3.6. Impact of series and shunt resistance

The influence of series and shunt resistance is shown in figure 12. Figure 12(a) shows that increasing series resistance (R_S) from 0 to 6 Ω-cm^2 at fixed shunt resistance $R_{Sh} = 10^5$ Ω-cm^2 leads to a slight decline in PCE from 20.05% at 0 Ω-cm^2 to 18.97% at 6 Ω-cm^2 and FF from 87.84% to 83.09 at 0 and 6 Ω-cm^2 respectively, due to voltage drops across the cell layers, while J_{SC} and V_{OC} remain relatively unaffected. The PSC has high performance at minimum series resistance. This highlights the importance of minimizing R_S through optimized layer deposition, improved contacts, and reduced cell dimensions [43]. Conversely, figure 12(b) shows that increasing R_{Sh} from 10^1 to 10^6 Ω-cm^2 at fixed $R_S = 0.5$ Ω-cm^2 enhances PV parameters. The substantial increase in PCE from 0.45 to 19.98% suggests a notable improvement in charge carrier generation and collection efficiency, likely resulting from enhancements in the device's structural design [44]. FF rapidly increases from

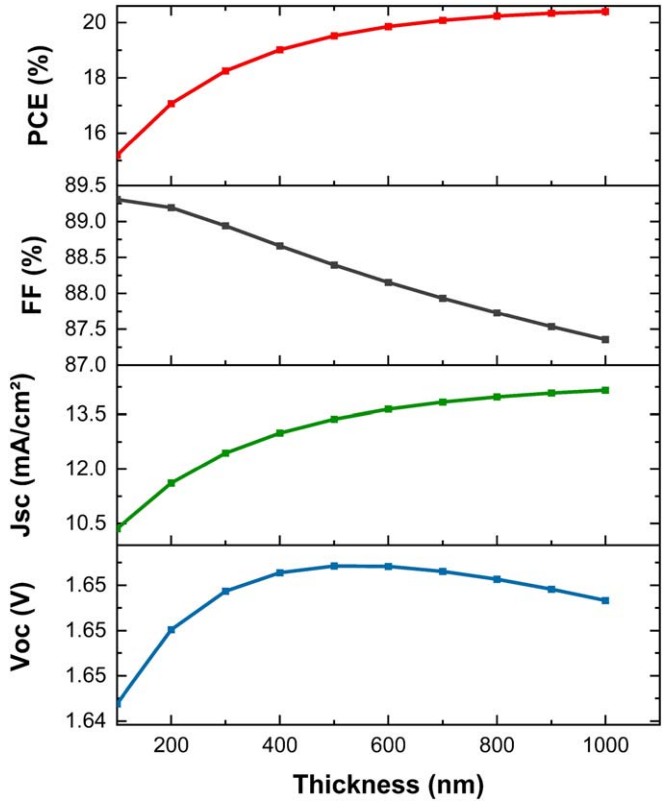


Figure 9. Impact of thickness of Absorber layer on performance parameters.

24.99 to 78.60% and then gradually increases to 87.53%. Similarly, Voc suddenly changes from 0.13 to 1.37 V and then becomes flat to 1.65 V, and J_{SC} changes from 13.17 to 13.76 mA cm^{-2}, and then it also becomes flat at 13.83 mA cm^{-2}. So, achieving high PSC performance requires low R_s to minimize resistive losses and high R_{Sh} to prevent leakage currents.

3.7. Impact of back contact on PSC

The work function of electrode significantly impacts device's performance. The simulation was performed to investigate the effect of the back electrode on the device parameters. The work function of different back contacts is tabulated in table 6. Figures13(a)–(b) shows the energy bands of device structure $FTO/WS_2/(NH_4)_3Sb_2I_9/MASnBr_3$ with different electrodes. Figure 13(a), demonstrated that electrodes with lower work functions, such as carbon (C), gold (Au), and nickel (Ni), form a Schottky barrier at the interface of HTL/electrode, pointed by dashed oval-shaped frame. This barrier obstructs hole transfer, resulting in decreased PCE and FF, as shown in figure 13(b). In contrast, platinum (Pt) creates an ohmic contact at the HTL/Pt interface [45]. This ohmic contact facilitates smoother hole transfer, enabling Pt to achieve better PCE than other back contacts, illustrated in figure 14(b). The impact of various back contacts on the J-V characteristics is highlighted in figure 14(a). The barrier potential at the anode/$MASnBr_3$ interface can be determined by equation (7):

$$\varphi_B = \frac{E_g}{q} + \chi - \varphi_M \tag{7}$$

where E_g is band gap of $MASnBr_3$, χ is the electron affinity of $MASnBr_3$ and φ_M is a rear metalwork function. As electrode work function decreases, the potential barrier at anode/$MASnBr_3$ interface rises. This increase in the barrier hampers charge transport, resulting in a decrement in both PCE and FF.

4. Comparison with previous reported results

Table 7 shows comparison between $FTO/TiO_2/(NH_4)_3Sb_2I_9$/spiro-OMeTAD/Au (initial) and $FTO/WS_2/(NH_4)_3Sb_2I_9$/ $MASnBr_3$/Au optimized PSC and their (a) J-V and (b) QE characteristics are shown in figure 15. Organic spiro-OMeTAD is widely favoured due to its simple and adaptable production process,

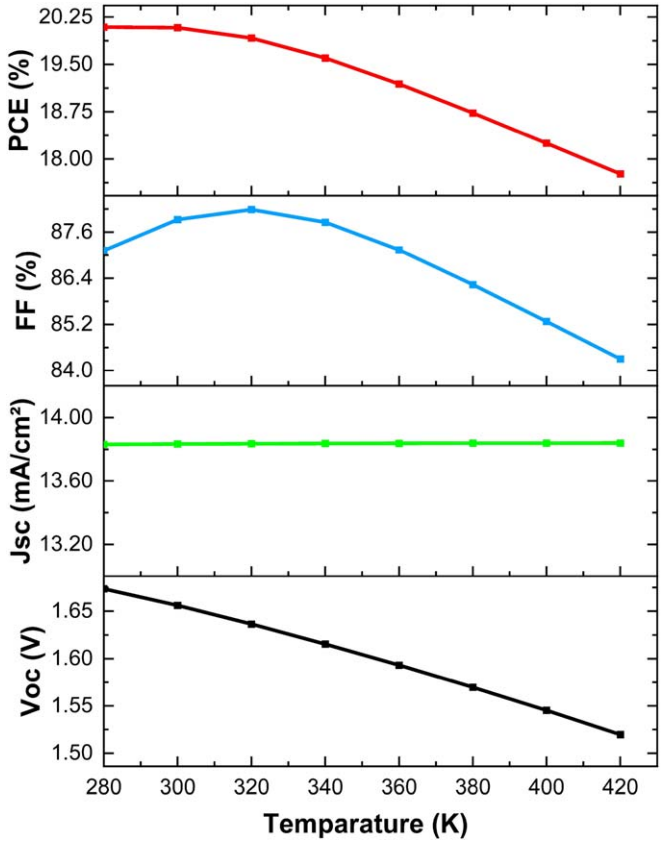


Figure 10. Impact of temperature on $(NH_4)_3Sb_2I_9$-based PSC.

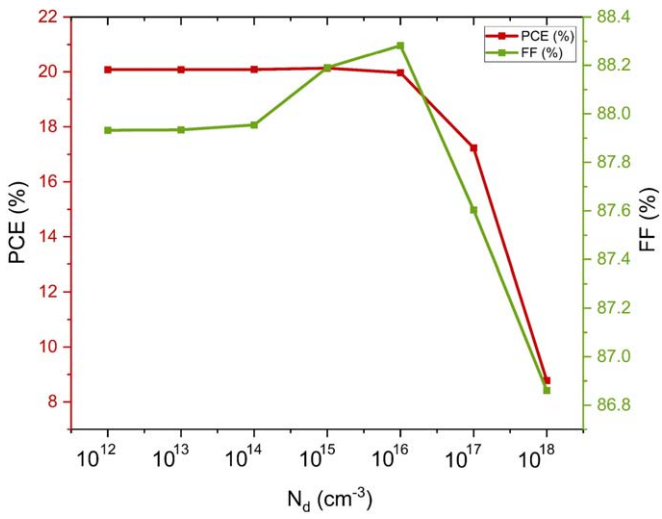


Figure 11. Impact of acceptor density on $(NH_4)_3Sb_2I_9$-based PSC.

making it a popular choice in both commercial and industrial applications [41]. However, it faces significant drawbacks for use in PSCs, including low hole mobility, poor conductivity, high production costs, and vulnerability to moisture, oxidation, and light, which compromise its stability. Similarly, TiO_2 is a well-established n-type material, frequently utilized as ETL. While it holds promise for excellent photovoltaic performance, challenges arise from its susceptibility to photo-corrosion, high thermal stability, and a wide bandgap of 3.2 eV [46]. Although PSCs using these materials alongside lead-based perovskites often exhibit superior characteristics, as evident from the data in the table, their toxicity and instability necessitate further research to identify safer and more stable alternatives.

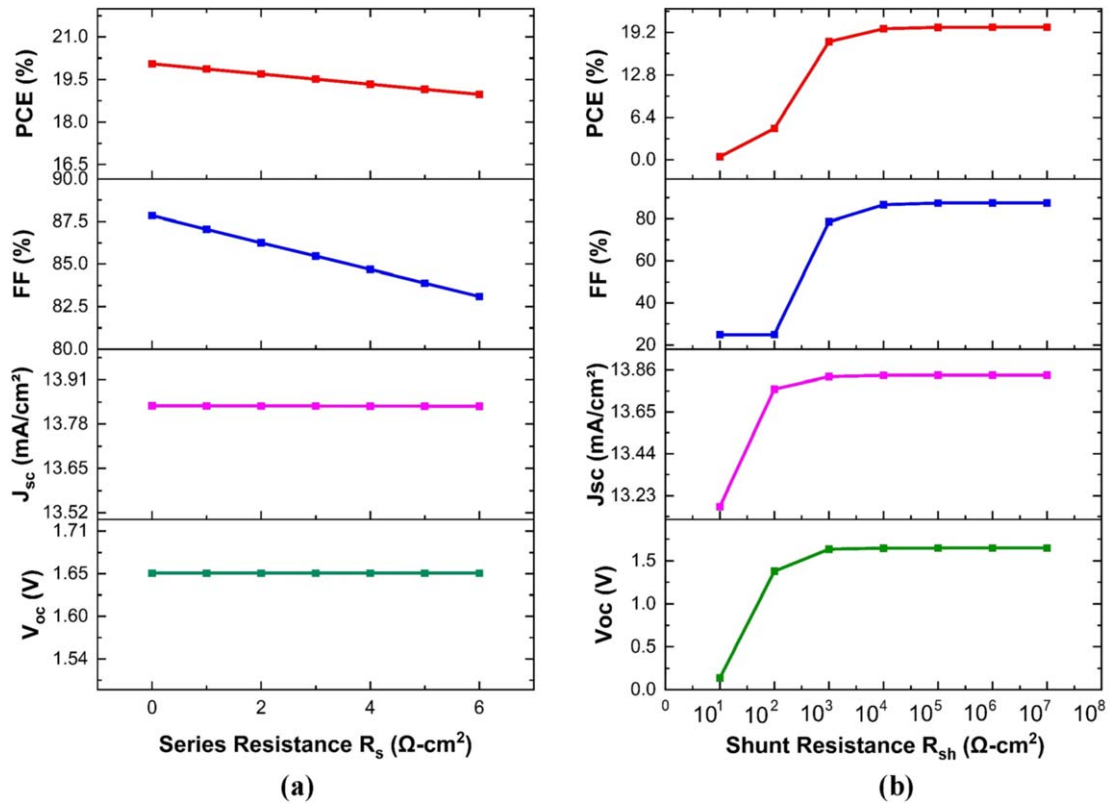


Figure 12. Impact of (a) R_S at $R_{sh} = 10^5$ (Ω-cm^2) and (b) R_{sh} at $R_S = 0.5$ (Ω-cm^2) on performance parameter of PSC.

Table 6. Work Function of different back contact.

Back contacts	C	Au	Ni	Pt
Work Function (eV)	5	5.1	5.5	5.7
PCE (%)	18.82	20.08	20.60	20.66

The band alignment and resulting band offsets (spike or cliff) between the absorber and ETL is crucial in explaining charge transport efficiency and recombination dynamics in planar PSC structure. The band alignment diagram of the optimised device shown below in figure 16, demonstrates the transport of charge carriers across the device. Electrons tend to migrate from higher to lower energy levels, moving from $(NH_4)_3Sb_2I_9$ (with E_C ~ranging from 1.69 to 0.15 eV), then WS_2 (E_C ~0.003 eV), and ultimately to FTO (E_C ~0.19 eV). Likewise, hole transport is facilitated by the configuration of valence levels. Holes have ability to migrate freely from $(NH_4)_3Sb_2I_9$ (E_V ~ranging from −1.89 to −0.35 eV), and finally to $MASnBr_3$ (E_V ~ −0.04 eV). The CBO of −0.15 eV forms a small cliff at the $WS_2/(NH_4)_3Sb_2I_9$ interface. While negative CBO can lead to electron accumulation and interface recombination, this offset is small enough, so it allows efficient electron extraction without significant losses. Additionally, the high electron mobility of WS_2 has a high electron mobility of 100 cm^2/V·s that ensures fast charge transport, reducing accumulation at the interface. While mobility doesn't eliminate the cliff, it only helps the system tolerate it, maintaining good device performance. The VBO between $(NH_4)_3Sb_2I_9/MASnBr_3$ is −0.31 eV, which makes the hole extraction efficient without interface recombination. The comparison with previously reported result shown below table 8. Therefore, this work's designed model can be considered for further experimentation and commercialization.

The figure 17 shown below depicts the absorption coefficient plot of WS_2, PCBM, $MASnBr_3$, and $(NH_4)_3Sb_2I_9$. The WS_2 and PCBM layer overlapping in the absorption curves with the perovskite layer, it's important to note that they are used as thin layers. So, despite the similar absorption coefficients, their actual photon absorption is minimal. Most of the light still reaches the $(NH_4)_3Sb_2I_9$ perovskite layer, and photon loss through WS_2 or PCBM is practically negligible. This justifies their use as front ETL in planar structures, especially given their excellent band alignment and charge extraction capabilities.

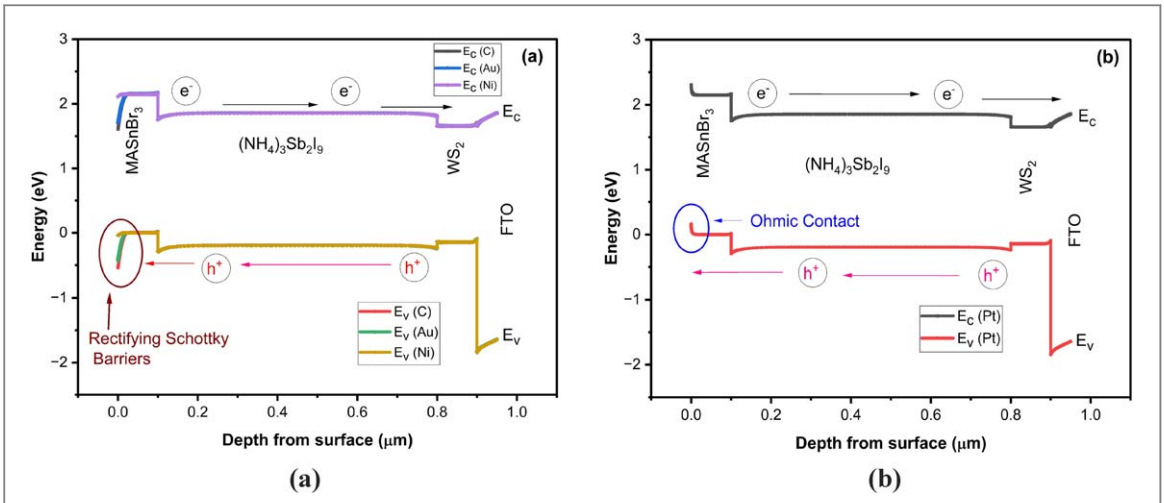


Figure 13. Band gap energy of PSC vs distinct back contact. (a) C, Au, Ni (b) Pt.

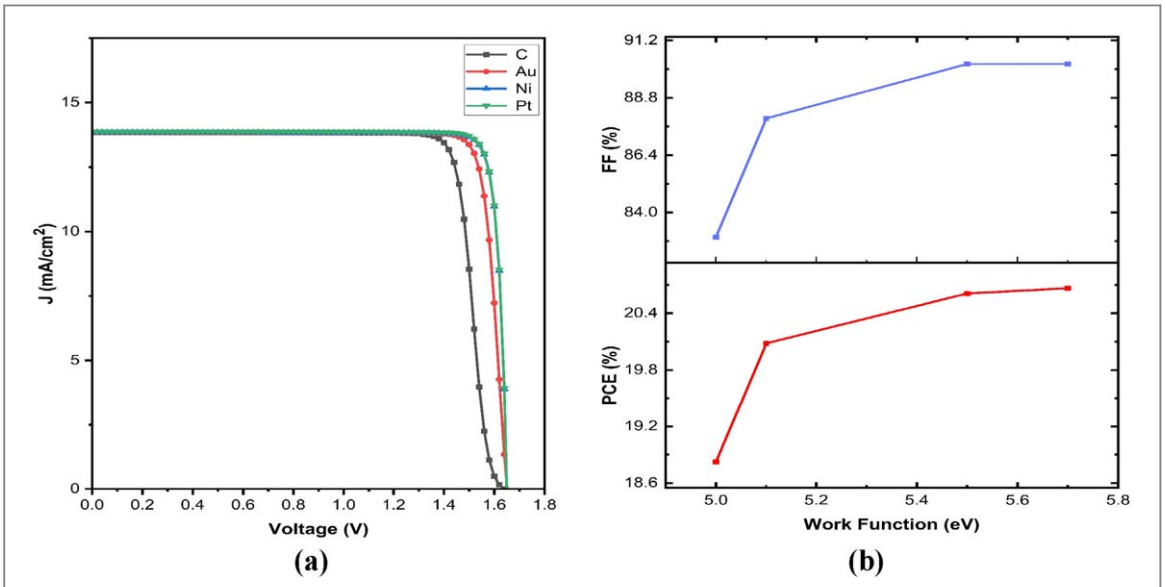


Figure 14. (a) J-V of the device for distinct back contact. (b) PCE and FF for distinct back contact.

Table 7. Efficiency of initial and optimized device.

Parameters	Initial device	Optimized device
V_{OC} (V)	1.74	1.65
J_{SC} (mA/cm^2)	11.15	13.83
FF (%)	80.78	87.93
PCE (%)	15.75	20.08

5. Feasibility of fabricating the proposed structure and strategies to improve PSCs performance

Fabricating the FTO/WS_2/$(NH_4)_3Sb_2I_9$/$MASnBr_3$/Au proposed structure is feasible, but it presents several challenges that need to be addressed for high-performance and scalable solar cells. The interfaces between WS_2, the perovskites, and the gold electrode need optimization for charge transport and minimal recombination. While laboratory-scale devices might work, scaling up WS_2 deposition and perovskite film quality could pose challenges. The sensitivity to moisture and potential thermal degradation limit long-term performance of $(NH_4)_3Sb_2I_9$ PSC. It is difficult to achieve high-quality, uniform films and scalability for large-area devices.

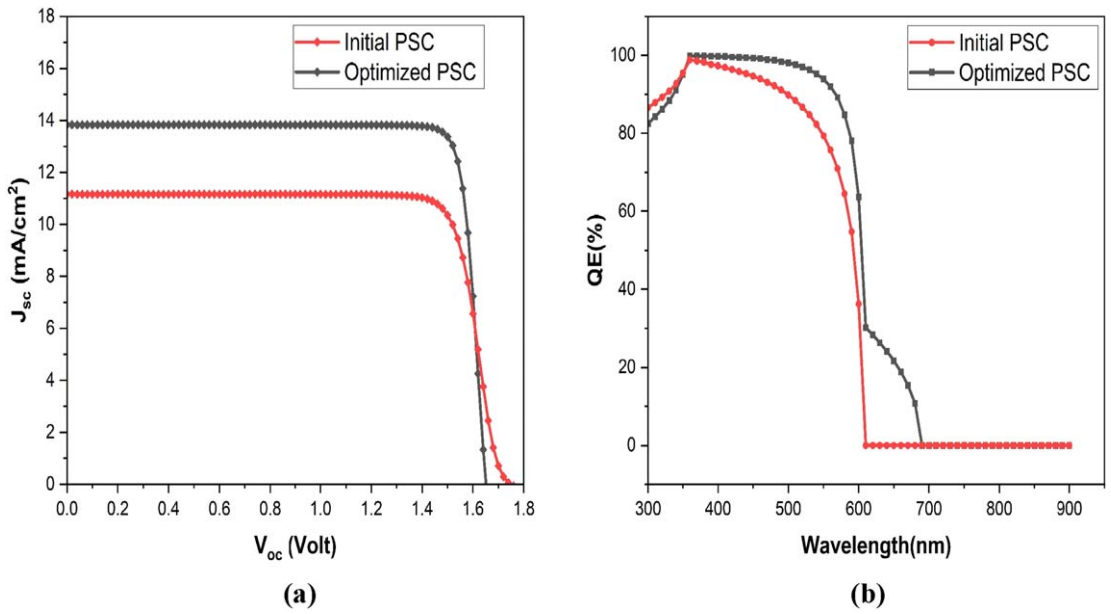


Figure 15. (a) J-V and (b) QE curve for initial and optimized PSC.

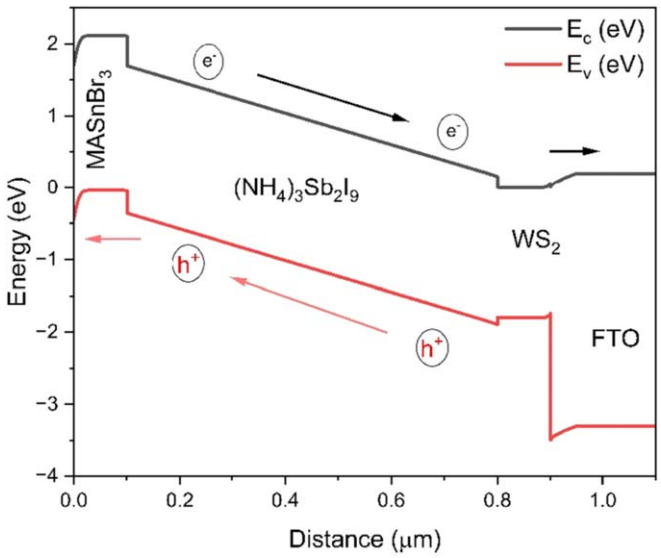


Figure 16. Band offsets (spike, cliff) diagram of optimized device.

$(NH_4)_3Sb_2I_9$ materials show good solubility in ethanol, a low-cost, hypotoxic, and environmentally friendly solvent [14]. The two-step method can be employed for the preparation of lead-free $(NH_4)_3Sb_2I_9$ perovskite solar cells exhibits an enhanced PCE with high V_{OC} [10]. The structure presents a promising concept with the potential for innovative and high-performance solar cells. To experimentally improve the performance of PSCs, several key strategies are being explored. One major approach is material engineering, where the perovskite composition is carefully tuned such as incorporating mixed cations or halides to enhance light absorption, thermal stability, and reduce degradation. Additionally, the introduction of defect passivation agents helps to minimize non-radiative recombination by reducing trap states in the material. Interface optimization is another critical area; improving the quality and alignment of the ETLs and HTLs ensures efficient charge extraction and reduces energy losses. The use of interfacial layers can further enhance device stability and reduce performance hysteresis.

Table 8. Comparison with the previously reported work.

Device structure	Work	V_{OC} (V)	J_{SC} (mA/cm^2)	FF (%)	PCE (%)	References
FTO/TiO_2/$Cs_3Sb_2I_9$/spiro-OMeTAD/Au	Simulation	1.32	13.13	72.01	12.54	[47]
FTO/TiO_2/$Cs_3Sb_2I_9$/NiO	Simulation	0.92	22.07	68.21	13.82	[48]
FTO/TiO_2/$(NH_4)_3Sb_2I_9$/Spiro-OMeTAD/Au	Simulation	1.41	12.49	84.00	14.90	[49]
FTO/TiO_2/$(NH_4)_3Sb_2I_9$/Spiro-OMeTAD/Au	Experimental	0.94	1.16	42.00	0.42	[10]
FTO/PEDOT:PSS/Pyrene/$(NH_4)_3Sb_2I_9$/PCBM/C_{60}/A	Experimental	0.70	6.64	—	2.77	[50]
ITO/PEDOT:PSS/$(NH_4)_3Sb_2I_9$/PCBM/C_{60}/BCP/Al	Experimental	0.62	5.41	—	2.04	[51]
FTO/WS_2/$(NH_4)_3Sb_2I_9$/ $MASnBr_3$/Au	Simulation	1.65	13.83	87.93	20.08	[Present work]

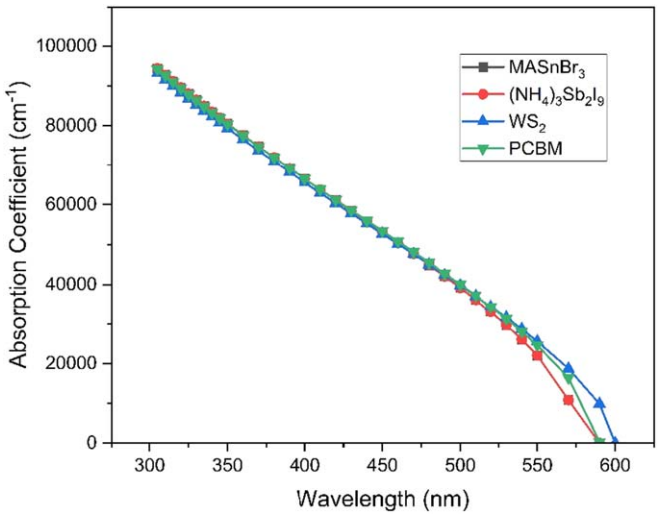


Figure 17. Absorption coefficient plot of WS_2, PCBM, $MASnBr_3$, and $(NH_4)_3Sb_2I_9$ layers.

6. Conclusions

The study comprises the performance of the solar cell by evaluating combinations of different HTLs and ETLs. Our findings reveal that the PCE decreases as N_t increases, with an optimal efficiency of 19.51% observed at a value of N_t of 10^{13} cm^{-3}. Additionally, the PCE improved with increasing thickness, achieving an optimal value of 20.08% at a thickness of 700 nm. Temperature also played a critical role, with the PCE steadily declining as temperature rose. The highest efficiency of 20.08% together with V_{OC} of 1.65 V, J_{SC} of 13.83 mA cm^{-2} and FF of 87.93% was obtained at 300 K and N_t of 10^{13} cm^{-3}. The influence of back contact materials was also examined. Pt, demonstrated superior performance in terms of both FF and PCE, but due to its high cost, Pt was deemed less commercially viable. Therefore, gold (Au) is chosen as the back contact. The optimized device architecture is $FTO/WS_2/(NH_4)_3Sb_2I_9/MASnBr_3/Au$ to achieve the maximum performance of device. This research highlights the promising potential of $(NH_4)_3Sb_2I_9$-based PSCs and underscores the importance of continued experimental studies to validate and expand upon these simulation-based findings. Future investigations may build on the optimal parameters identified in this work to further advance the development of efficient and stable PSCs.

Acknowledgments

The author, Sumit Singh thankful to Delhi Technological University for providing excellent research facilities for conducting research. We are also very grateful to Marc Burgelman, Electronics and Information Systems (ELIS), University of Gent, Belgium, for providing SCAPS-1D software.

Data availability statement

Because simulated data is the basis of the article. The data that support the findings of this study are available upon reasonable request from the authors.

ORCID iDs

Sumit Singh https://orcid.org/0009-0002-4504-4819
Rahul Kundara https://orcid.org/0000-0002-9186-8803
Sarita Baghel https://orcid.org/0009-0003-2746-0453

References

[1] Verma A, Shrivastav N and Madan J 2024 Enhancing sustainability in photovoltaic technology: optimization of NH2(CH2) 2NH3MnCl4 perovskite solar cells *2024 IEEE International Conference on Information Technology, Electronics and Intelligent Communication Systems ICITEICS 2024* 1

[2] NRE Laboratory Best Research-Cell Efficiencies NREL 12-03-2025 Interactive Best Research-Cell Efficiency Chart *Photovoltaic Research* https://nrel.gov/pv/interactive-cell-efficiency

[3] Noel N K *et al* 2014 Lead-free organic-inorganic tin halide perovskites for photovoltaic applications *Energy Environ. Sci.* **7** 3061–8

[4] Chen L-J 2018 Synthesis and optical properties of lead-free cesium germanium halide perovskite quantum rods† *RSC Adv.* **8** 18396–18396

[5] Singh A, Lai P T, Mohapatra A, Chen C Y, Lin H W, Lu Y J and Chu C W 2021 Panchromatic heterojunction solar cells for Pb-free all-inorganic antimony based perovskite *Chem. Eng. J.* **419**

[6] Ikram M, Malik R, Raees R, Imran M, Wang F, Ali S, Khan M, Khan Q and Maqbool M 2022 Recent advancements and future insight of lead-free non-toxic perovskite solar cells for sustainable and clean energy production: a review *Sustainable Energy Technologies and Assessments* **53**

[7] Zhang X, Li T, Wei Q, Peng C, Li W, Ma X, Cheng Z, Wu J, Su J and Li W 2023 Germanium–lead double absorber layer perovskite solar cells: further performance enhancement from the perspective of device simulation *Opt. Commun.* **530**

[8] Krishnamoorthy T *et al* 2015 Lead-free germanium iodide perovskite materials for photovoltaic applications *J Mater Chem A Mater* **3** 23829–32

[9] Correa-Baena J-P *et al* 2018 A-Site cation in inorganic A3Sb2I9 perovskite influences structural dimensionality, exciton binding energy, and solar cell performance *Chemistry of Material* **30** 3734–42

[10] Kumar P, Ahmad K, Dagar J, Unger E and Mobin S M 2021 Two-step deposition approach for lead free (NH4)3Sb2I9 perovskite solar cells with enhanced open circuit voltage and performance *Chem. Electro. Chem.* **8** 3150–4

[11] Valli D, Ottesen M, Bremholm M, Wiedmann S, Tinnemans P, Van de Vondel J, Roeffaers M, Debroye E, Hofkens J and Keshavarz M 2023 Temperature-dependent evolution of the structural and optoelectronic properties of (NH4)3Sb2I9 single crystals *J. Phys. Chem. C* **127** 20419–25

[12] Lin L, Jiang L, Li P, Fan B and Qiu Y 2019 A modeled perovskite solar cell structure with a Cu_2O hole-transporting layer enabling over 20% efficiency by low-cost low-temperature processing *J. Phys. Chem. Solids* **124** 205–11

[13] Harikesh P C, Wu B, Ghosh B, John R A, Lie S, Thirumal K, Wong L H, Sum T C, Mhaisalkar S and Mathews N 2018 Doping and switchable photovoltaic effect in lead-free perovskites enabled by metal cation transmutation *Adv. Mater.* **30** 1802080

[14] Zuo C and Ding L 2017 Lead-free perovskite materials (NH 4) 3 Sb 2 I x Br 9− x *Angew. Chem.* **129** 6628–32

[15] Kanoun A A, Kanoun M B, Merad A E and Goumri-Said S 2019 Toward development of high-performance perovskite solar cells based on CH3NH3GeI3 using computational approach *Sol. Energy* **182** 237–44

[16] Deepthi Jayan K and Sebastian V 2021 Comprehensive device modelling and performance analysis of MASnI3 based perovskite solar cells with diverse ETM, HTM and back metal contacts *Sol. Energy* **217** 40–8

[17] Xu X, Wang J, Cao D, Zhou Y and Jiao Z 2022 Design of all-inorganic hole-transport-material-free CsPbI3/CsSnI3heterojunction solar cells by device simulation *Mater. Res. Express* **9**

[18] Montoya De Los Santos I, Cortina-Marrero H J, Ruíz-Sánchez M A, Hechavarría-Difur L, Sánchez-Rodríguez F J, Courel M and Hu H 2020 Optimization of CH3NH3PbI3 perovskite solar cells: a theoretical and experimental study *Sol. Energy* **199** 198–205

[19] Lakhdar N and Hima A 2020 Electron transport material effect on performance of perovskite solar cells based on CH3NH3GeI3 *Opt Mater (Amst)* **99** 109517

[20] Bhattarai S and Das T D 2021 Optimization of carrier transport materials for the performance enhancement of the MAGeI3 based perovskite solar cell *Sol. Energy* **217** 200–7

[21] Himanshu K, Suthar D and Dhaka M S 2023 Numerical simulation of CdSe/ZnTe thin film solar cells by SCAPS-1D: optimization of absorber layer thickness *Solid State Commun* **371**

[22] Skhouni O, El Manouni A, Mollar M, Schrebler R and Marí B 2014 ZnTe thin films grown by electrodeposition technique on fluorine tin oxide substrates *Thin Solid Films* **564** 195–200

[23] Azri F, Meftah A, Sengouga N and Meftah A 2019 Electron and hole transport layers optimization by numerical simulation of a perovskite solar cell *Sol. Energy* **181** 372–8

[24] Gan Y, Bi X, Liu Y, Qin B, Li Q, Jiang Q and Mo P 2020 Numerical investigation energy conversion performance of tin-based perovskite solar cells using cell capacitance simulator *Energies (Basel)* **13**

[25] Meng X, Tang T, Zhang R, Liu K, Li W, Yang L, Song Y, Ma X, Cheng Z and Wu J 2022 Optimization of germanium-based perovskite solar cells by SCAPS simulation *Opt Mater (Amst)* **128**

[26] Naureen S, Lohia P, Dwivedi D and Ameen S 2022 A comparative study of quantum dot solar cell with two different ETLs of WS2 and IGZO Using SCAPS-1D simulator *Solar* **2** 341–53

[27] Hossain M K, Toki G F I, Kuddus A, Rubel M H K, Hossain M M, Bencherif H, Rahman M F, Islam M R and Mushtaq M 2023 An extensive study on multiple ETL and HTL layers to design and simulation of high-performance lead-free CsSnCl3-based perovskite solar cells *Sci Rep.* **13**

[28] Mandadapu U, Vedanayakam S V and Thyagarajan K 2017 Simulation and analysis of lead based perovskite solar cell using SCAPS-1D *Indian J Sci Technol* **10** 1–8

[29] Burgelman M, Nollet P and Degrave S 2000 Thin solid films 361 527–32

[30] Burgelman M, Decock K, Khelifi S and Abass A 2013 Advanced electrical simulation of thin film solar cells *Thin Solid Films* **535** 296–301

[31] Liu F, Zhu J, Wei J, Li Y, Lv M, Yang S, Zhang B, Yao J and Dai S 2014 Numerical simulation: toward the design of high-efficiency planar perovskite solar cells *Appl. Phys. Lett.* **104**

[32] Bhujbal P K, Sakunde B, Supekar A, Bhandari H, Saini S, Dhirhe D, Patole S and Pathan H M 2024 Unlocking the potential of WS2 as an electron transport layer in flexible and lead-free methylammonium tin iodide -based perovskite solar cells: A comprehensive defect study using the SCAPS-1D framework *ES Energy & Environment* **26**

[33] Ke W and Kanatzidis M G 2019 Prospects for low-toxicity lead-free perovskite solar cells *Nat. Commun.* **10**

[34] Abate A 2017 Perovskite solar cells go lead free *Joule* **1** 659–64

[35] Yao H, Zhou F, Li Z, Ci Z, Ding L and Jin Z 2020 Strategies for improving the stability of tin-based perovskite (ASnX3) solar cells *Adv. Sci.* **7**

[36] Lee Y M, Maeng I, Park J, Song M, Yun J H, Jung M C and Nakamura M 2018 Comprehensive understanding and controlling the defect structures: an effective approach for organic-inorganic hybrid perovskite-based solar-cell application *Front Energy Res* **6**
[37] Rafieirad R and Ganji B A 2021 Efficiency improvement of perovskite solar cells by utilizing $CuInS_2$ thin layer: modeling and numerical study *IEEE Trans. Electron Devices* **68** 4997–5002
[38] Lazemi M, Asgharizadeh S and Bellucci S 2018 A computational approach to interface engineering of lead-free CH3NH3SnI3 highly-efficient perovskite solar cells *Phys. Chem. Chem. Phys.* **20** 25683–92
[39] Kundara R and Baghel S 2024 Performance analysis of LaFeO3 perovskite solar cells: a theoretical and experimental study *Solid State Commun.* **389**
[40] Jamal M S, Shahahmadi S A, Chelvanathan P, Asim N, Misran H, Hossain M I, Amin N, Sopian K and Akhtaruzzaman M 2019 Effect of defect density and energy level mismatch on the performance of perovskite solar cells by numerical simulation *Optik (Stuttg)* **182** 1204–10
[41] Son D Y, Im J H, Kim H S and Park N G 2014 11% efficient perovskite solar cell based on ZnO nanorods: an effective charge collection system *J. Phys. Chem. C* **118** 16567–73
[42] Kundara R and Baghel S 2023 Device modelling of lead free (CH3NH3)2CuX4 based perovskite solar cells using SCAPS simulation *Opt. Quantum Electron.* **55**
[43] Uddin Md S, Hosen R, Sikder S, Mamur H and Bhuiyan M R A 2024 Photovoltaic performance enhancement of Al/ZnO:Al/i-ZnO/CdS /CIGS/Pt solar cell using SCAPS-1D software *Next Energy* **2** 100080
[44] Meyer E L, Jakalase S, Nqombolo A, Rono N and Agoro M A 2025 The numerical simulation of a non-fullerene thin-film organic solar cell with Cu2FeSnS4 (CFTS) kesterite as a hole transport layer using SCAPS-1D *Coatings* **15** 266
[45] Kevin M, Ong W L, Lee G H and Ho G W 2011 Formation of hybrid structures: copper oxide nanocrystals templated on ultralong copper nanowires for open network sensing at room temperature *Nanotechnology* **22** 235701
[46] Ghrib T, AL-Saleem N K, AL-Naghmaish A, Elshekhipy A A, Brini S, Briki K and Elsayed K A 2022 Annealing effect on the microstructural, optical, electrical, and thermal properties of $Cu_2O/TiO_2/Cu_2O/TiO_2$/Si heterojunction prepared by sol-gel technique *Micro and Nanostructures* **164** 107119
[47] Ahmad K, Khan M Q and Kim H 2022 Simulation and fabrication of all-inorganic antimony halide perovskite-like material based Pb-free perovskite solar cells *Opt Mater (Amst)* **128** 112374
[48] Islam M T, Jani M R, Shorowordi K M, Hoque Z, Gokcek A M, Vattipally V, Nishat S S and Ahmed S 2021 Numerical simulation studies of Cs3Bi2I9 perovskite solar device with optimal selection of electron and hole transport layers *Optik (Stuttg)* **231** 166417
[49] Zhang H *et al* 2018 Improving the stability and performance of perovskite solar cells via off-the-shelf post-device ligand treatment *Energy Environ. Sci.* **11** 2253–62
[50] Boopathi K M, Karuppuswamy P, Singh A, Hanmandlu C, Lin L, Abbas S A, Chang C C, Wang P C, Li G and Chu C W 2017 Solution-processable antimony-based light-absorbing materials beyond lead halide perovskites *J Mater Chem A Mater* **5** 20843–50
[51] Karuppuswamy P, Boopathi K M, Mohapatra A, Chen H C, Wong K T, Wang P C and Chu C W 2018 Role of a hydrophobic scaffold in controlling the crystallization of methylammonium antimony iodide for efficient lead-free perovskite solar cells *Nano Energy* **45** 330–6



Disclosure without Engagement: An Empirical Review of Positionality Statements at FAccT

Hope Schroeder
MIT
Cambridge, MA, USA
hopes@mit.edu

Akshansh Pareek
Delhi Technological University
Delhi, India
akshanshpareek_2k21bd117@dtu.ac.in

Solon Barocas
Microsoft Research
New York City, New York, USA
sbarocas@cornell.edu

Abstract

Positionality statements have become more common in engineering fields in recent years, despite ongoing debates across many fields about the merits of the practice. In 2024, the Program Chairs of FAccT recommended that authors include positionality statements with their paper submissions, dramatically increasing their use at the conference. In this paper, we analyze all positionality statements at FAccT from 2018 to 2024, highlighting the different aspects of identity commonly disclosed by authors and the degree to which authors explore the potential impact of these aspects of their positionality on their research. While we encountered and highlight a number of thoughtful positionality statements, we also identified and describe several concerning trends, including patterns of identity disclosure without discussion of corresponding impacts, a notable lack of reflection on the potential impacts of industry affiliation, and cases where identity is invoked to excuse what are really methodological choices, among others. We raise particular concerns about the possibility that disclosure without engagement may cause readers to rely on stereotypes to make guesses about the perspectives that individuals from certain groups bring to their work. We conclude by considering potential mechanisms for encouraging reflexivity in the FAccT community, with a focus on setting policies that protect researchers from risks, supporting researchers from backgrounds without existing traditions of reflexive practice, and empirically evaluating the efficacy of interventions designed to foster reflexivity.

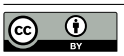
CCS Concepts

• **Human-centered computing** → **Empirical studies in HCI**.

Keywords

positionality, reflexivity, methodology

ACM Reference Format:
Hope Schroeder, Akshansh Pareek, and Solon Barocas. 2025. Disclosure without Engagement: An Empirical Review of Positionality Statements at FAccT. In *The 2025 ACM Conference on Fairness, Accountability, and Transparency (FAccT '25), June 23–26, 2025, Athens, Greece.* ACM, New York, NY, USA, 16 pages. https://doi.org/10.1145/3715275.3732079



This work is licensed under a Creative Commons Attribution 4.0 International License.
FAccT '25, Athens, Greece
© 2025 Copyright held by the owner/author(s).
ACM ISBN 979-8-4007-1482-5/25/06
https://doi.org/10.1145/3715275.3732079

1 Introduction

In 2024, the call for papers for the ACM Conference on Fairness, Accountability, and Transparency (FAccT) encouraged authors to include a positionality statement in their submitted manuscript, alongside suggestions to engage with the ethical considerations, limitations, and potential adverse impacts of their work. The Program Chairs (PCs) elaborated on their motivation for this recommendation through a blog post, "Responsible AI Research Needs Impact Statements Too," calling on researchers to reflect "on how our backgrounds shape our work," and to provide "added transparency" by disclosing features of their background or identity so as to scaffold "readers' understanding of how our background and experiences influence or inform our work" [36]. This recommendation is part of broader trend in computing, a field which has increasingly urged scholars to engage with the ethical issues raised by their research practices and the potential downstream impacts of their work [2, 7, 11, 18, 19, 27]. Positionality statements have become increasingly common across the social sciences, especially those that rely on qualitative methods [30, 31]. For that reason, they first found their way into computing via the field of human-computer interaction [30, 43], parts of which draw heavily from the social sciences, but are now taking hold in parts of the research community focused on responsible computing, too.

Despite their growing popularity, positionality statements have been the subject of persistent debate. Because positionality statements often disclose identity features otherwise kept intentionally concealed in the peer review process, some worry that they undermine the goal of appraising the merits of research without considering the identity of those who conducted it [40]. Others have expressed concern that pressure to disclose identity features through positionality statements can put already vulnerable researchers at additional risk [37]. The blog post by the 2024 PCs acknowledged both of these points and even commented on the fact that positionality statements can be problematic if they cause lived experience to be viewed as the only valid qualification for pursuing certain research questions or cause researchers with lived experience to be expected to serve as representatives of the groups to which they belong [36]. Perhaps reflecting some of these unresolved points of debate, this year's call for papers for FAccT shifted its policy on positionality statements, instructing authors to withhold these statements from the versions of the papers submitted for peer review and only include them in the final publication. Despite these concerns and the change in policy, FAccT and parts of the larger computing community continue to advocate for the use of positionality statements, evincing a belief that they serve a valuable function.

In this paper, rather than taking this possibility as a given, we treat it as an empirical question. In particular, we ask: (1) How

often do authors include positionality statements in their papers? (2) Which facets of identity and background do authors disclose? (3) How often do they relate these disclosure to a perceived impact on their research? (4) What are the specific ways that authors see their positionality impacting their work? To answer these questions, we perform an exhaustive review of all the positionality statements that have appeared in the proceedings for each year of the conference, starting from the first year in 2018. We take a mixed-methods approach, first annotating the full set of positionality statements to extract the specific facets of identity disclosed in each statement, followed by a more open-ended process of coding the corresponding impacts on the research, if described. Overall, we find that positionality statements became much more common in 2024 and that they disclose a range of features related to researcher identity and background. However, fewer of these disclosures are accompanied by a discussion of the corresponding impact on the work. We also observe that authors rarely reflect on the influence of industry affiliation and occasionally invoke aspects of their identity to excuse what are really methodological choices under researchers' control. And we find that certain practices can put vulnerable researchers at considerable risk.

The paper proceeds as follows: In Section 2, we survey scholarship on positionality statements and situate our paper in recent work reflecting critically on various efforts to foster responsible research practices in computing. In Section 3, we describe our mixed methods approach. In Section 4, we report the results of our annotations, and in Section 5, we offer a series of interpretative findings from secondary analysis. In Section 6, we make three recommendations for the conference based on the insights from our analyses.

2 Literature

In the 1970's and 1980's, following a wave of postmodernist thought, feminist scholars like Donna Haraway began to criticize Western science's "gaze from nowhere." Haraway's popular argument that all knowledge is "situated" in the context of knowledge producers and their processes [26] has shaped epistemological commitments in the social sciences since. Creating awareness around and reflecting on how a researcher's biases may shape the work came to be known as the practice of "reflexivity," and its rise in popularity in ethnography, anthropology, and over time, other social sciences in the 1980's is known as the "reflexive turn." This shift was groundbreaking in rethinking a long history of Western ethnographic and anthropological work that frequently overlooked colonial power dynamics and the situated lens any researcher brings to their work [39].

Reflexivity is now a common practice in fields like anthropology and some subfields of sociology. According to scholars in these fields, researchers' identities and values can shape research priorities, their approach to research, their relationships with research subjects, and their interpretation of their findings. This can, in turn, shape the information that research subjects are comfortable sharing—or whether research subjects feel that they can even decline to participate in a study. Scholars have therefore recommended that researchers disclose her or his "position in the world, her or his goals, as well as the researcher's position in her or his intellectual and, to an appropriate extent, political beliefs", with the goal of helping readers understand their potential impacts on the work [8]. In certain kinds of qualitative work, researchers are strongly encouraged to engage in reflexivity [44] and with their positionality all throughout the research process, especially in relation to subject matter and to research subjects, and cautioned against the use of positionality statements as performative afterthoughts [39].

Despite the ubiquity of positionality statements in some fields, their use is controversial even within the social sciences, and remains controversial in the scientific community at large. First, the features disclosed and discussed within positionality statements are largely left up to the authors to decide, presenting a paradox: If researchers are motivated to disclose certain features because *unconscious* bias can impact the work, then, by definition, researchers may not be able to observe, name, and correct for biases that result from aspects of their positionality. Savolainen et al. [40] argue researchers "cannot, on the one hand, claim to be burdened by their biography when conducting the research, yet, on the other hand, be emancipated from it while constructing a positionality statement." Proponents respond that while "any reflexive analysis can only ever be [...] partial, tentative, provisional," [21] they are still useful for understanding influences on the work.

Another source of controversy is the use of positionality statements in the review process. Scientific review is usually anonymous in part to protect researchers against unfair judgment of their work based on their personal characteristics. Some critics of positionality statements argue that disclosing personal features in positionality statements encourages judgment of the work based on personal characteristics, particularly if these features are disclosed during the review process. Concerns about reviewer bias are amplified when considering how disclosure practices may dovetail with author incentives. If researchers are allowed to selectively disclose elements of their positionality, they may be incentivized to disclose only the elements of their positionality that cast their work in a positive light, or align with predominant ideologies or political sympathies in the field [40]. Beyond this, authors do not always feel agency over what they disclose, and different levels of disclosure within an author team can create discomfort [43]. Sometimes, reviewers request that authors disclose certain characteristics. For some researchers, such as queer scholars engaging in work about the queer community, this can feel like pressure to "out" themselves, potentially putting them in danger [37]. Reviewer requests to disclose certain personal characteristics also raise concerns that the credibility and rigor may be appraised based on these disclosed features. Vast literature explores tensions on this point: on one hand, lived experience undoubtedly shapes one's understanding of an issue or community, but on the other, one person's lived experience should neither be enough to speak on behalf of a group [36] nor should it be taken as proof of high-quality work [31]. Advertising lived experience, or proximity to groups who have it, can serve a colonial dynamic, asserting the researcher's comparative "legitimacy" in relation to a studied subject [22]. In summary, researchers from qualitative backgrounds generally concur that the practice of reflexivity can help to minimize bias and increase intentionality with respect to participants, but some question whether positionality statements, as a discrete artifact, can effectively accomplish this goal [40, 47].

Over the last decade, there has been increasing awareness of and concern regarding the way that values impact research in computing [12]. Noting this concern, some publication venues have

begun to encourage authors to include artifacts within their research submissions to foster greater reflexivity. Examples of this include NeurIPS introducing broader impact statements and the Association for Computational Linguistics (ACL) incorporating an Ethics Checklist. Following the introduction of broader impacts statements at NeurIPS in 2020, several papers investigated how authors' responded to the policy, identifying that papers that included them and reviewing their content [7, 32, 35]. Similarly, when ACL instated an ethics advisory committee in 2021, and ethics statements became more common, researchers also studied their incidence and qualities [10]. Our work builds on these earlier efforts to empirically evaluate the efficacy of attempts to foster more responsible research practices in computing.

In recent years, FAccT itself has featured a number of papers critically reflecting on the conference and its proceedings. One paper showed how FAccT is disciplinarily mixed, which can create or exacerbate tension in the community around values and expectations [29]. Another paper found that FAccT papers focus disproportionately on Western, Educated, Industrialized, Rich, and Democratic (WEIRD) populations [42]. And yet another paper grappled with corporate influence over the conference [46]. Our paper adds to the conference's tradition of introspection by considering its attempts to promote greater reflexivity on exactly these kinds of issues.

Scholars have even begun to study the use of positionality statements in technical fields. Hampton et al. [25] found that positionality statements are uncommon in engineering education research, concluding that introducing such practices is challenging because reflection and vulnerability are rarely a part of mainstream engineering education. In work contemporaneous with our own, Singh et al. [43] completed a review of the use of positionality statements at the ACM Conference on Human Factors in Computing Systems (CHI). The authors took a similar approach as we do, manually reviewing the proceedings from the conference to identify papers that included positionality statements and then annotating these statements. They additionally surveyed members of the CHI community to learn more about their experiences with and attitudes toward positionality statements. In keeping with many of our findings, the paper finds that the use of positionality statements is growing over time, that authors rarely link disclosed features of their identity to specific impacts on the work, and that authors have mixed feelings about the practice.

3 Methods

We reviewed all papers published at FAccT from 2018 to 2024 in order to find positionality statements published over its entire history. Details on our data collection process are available in the appendix.

To characterize the content of the positionality statements, we developed three different annotation schemes—the first scheme extensively annotated the features of identity disclosed by authors, then our secondary, interpretive analyses annotated accompanying discussion of impacts of those features on research, as well as discussions of privilege, limitations, and motivations. We additionally annotated certain details about the papers that may not have been present in the positionality statements themselves: whether the research performed in the papers focused on a particular community,

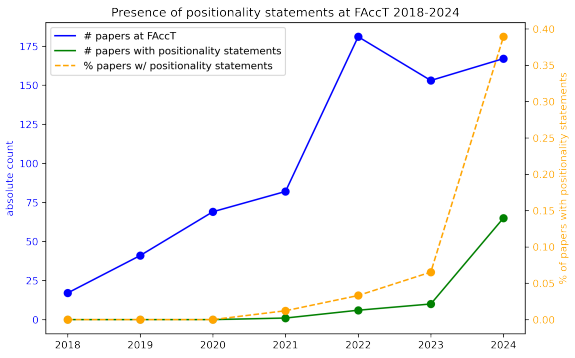


Figure 1: The relative and absolute incidence of positionality statements at FAccT from 2018-2024

and whether authors were based at an academic, industry, civil society, or government institution.

To develop a set of labels to annotate the types of features disclosed in positionality statements, we performed open coding and iteratively derived the coding scheme through saturation with the data, and were informed by existing literature guiding researchers to link identity to impacts on the research [28] or map how background is discussed and tied to impacts in positionality statements [25, 41, 45]. Our set of labels characterizes researchers' identity, background, and relationship to the subject matter under study [17]—in Sybing's words, those features capturing "who the researcher is and what their connection to the research context is" [45]. We ultimately derived three broad sets of labels: (1) Identity & demographics, (2) Personal geography, and (3) Research team's experience, training, and institutional context.

The **Identity & demographics** features that we annotated included *gender*, *race and/or ethnicity*, *sexual orientation*, *disability status*, *language*, *age*, and *socioeconomic status*. Researchers also engaged with many aspects of their **Personal geography**, so we additionally annotated disclosed *places of author residence*, *birth*, *education*, *past work*, mentions of *citizenship or immigration status*, and *cultural context related to place*, like spending time in the "Global North." Finally, we developed a set of labels to capture disclosures about the **Research team's experience, training, and institutional context**. These features include mentions of *personal relationship with the subject matter*, the *location of work*, the *broader cultural context of the work* (e.g., "We work in the context of the Global South"), the *type of institution* they work for, *training level* of authors, *training and academic background* of authors, and mentions of *funding* and resources. With these annotation schemes in place, we then divided the annotation process roughly equally across the two annotating authors, and any uncertainties were resolved through discussion and consensus decisions between the authors. Details on IRR procedures, evaluations, and documentation are available in the appendix.

These descriptive annotations provide an overview of disclosed features. While categorizations like this are reductive representations of identity and perspective, experts point out these features can provide an important starting basis for reflexive practice [28]. However, basic disclosures alone do not explain deeper trends in

the statements, so we used them to ground deeper inquiry in a second phase of analysis focused on more interpretative annotation identifying whether these disclosed features were described as having an impact on the research, and if so, what kind of impact on the work they were described as having. For example, a researcher may describe their race as a "white woman" as having impacted the work by impacting participants' trust in her. Through open coding, we identified eight types of impacts authors describe disclosed features as having impacted elements of the research, including impacts to the **scope of work**, **experiment design**, **analysis**, and **relationships with participants**, with the full list of codes and coding details available in the appendix.

We also noted a few other types of reflexive content that were common in the positionality statements, particularly those recommended in prior literature. We developed labels to annotate when authors mentioned power and privilege (or lack thereof), limitations and their mitigation, and research motivations, intentions, objectives, or goals. We reconsidered the whole positionality statement in this second interpretive phase of analysis, given the importance of considering identity features in an intersectional manner [16].

In annotating the content present in these statements, our goal was to capture what researchers chose to disclose and discuss—that is, what they felt was worth reflecting upon. We therefore only recorded details when they were made explicit in the statements, even if they might have been possible to locate elsewhere or to infer. For example, while a funding source may be implied by an author's institutional affiliation, we only recorded funding disclosures if a funding source was explicitly named in the positionality statement.

Finally, for each positionality statement, we also annotated if the research performed in the paper focused on a particular community. For example, the paper "Envisioning Equitable Speech Technologies for Black Older Adults" focused on Black older adults, whereas the paper "Racial/Ethnic Categories in AI and Algorithmic Fairness: Why They Matter and What They Represent" discusses racial and ethnic categories as a set, but does not focus on a particular target community. We reviewed the main body of the paper to annotate for two definitions of community: the first included papers that pertained to or focused on individuals from a particular identity, protected characteristic, or location, and the second, more inclusive definition of communities included professional communities (like FAccT itself) or user groups. We were also curious if authors from different kinds of organizations engaged differently with positionality statements. We manually identified whether the author team of each paper included at least one researcher from industry, at least one researcher from a civil society or governmental organization, or was comprised of academics alone. As before, details on the annotation scheme is available in the appendix.

4 Results

4.1 How often do researchers include positionality statements?

Although we searched the entire period beginning in 2018 and ending in 2024, we did not find any positionality statements in the papers from 2018 to 2020, when the conference was still quite small. We found a single positionality statement in 2021, 6 in 2022, 10 in 2023, and 65 in 2024, totaling 82 statements in our analysis. As shown in Figure 1, 2024 saw a stark increase in the absolute number and relative incidence of papers at FAccT that included positionality statements. The majority (68/82, or 83%) of the positionality statements we found occurred in a standalone section near the end of the paper. There were also 14 statements found embedded in the main body of the text, most often within Methods (7 times) or the Introduction (4 times). Standalone positionality statements became more common in 2024. 62/65 positionality statements in 2024 were present in standalone sections, whereas just 3/10 positionality statements in 2023 were in standalone sections. Second, a third (27/82) of papers with positionality statements across all years pertained to a community (protected identity group or location), but two thirds did not, reflecting the fact that many papers at FAccT do work that is not focused on a community, and an additional 7 papers pertain to a professional community or user group. This result differs notably from what Singh et al. [43] found at CHI, where papers were more likely to include positionality statements when they "pertained to" a "studied population," perhaps reflecting the practice's origins as one seeking to responsibly engage with the community under study.

4.2 What features do researchers disclose?

Reviewing the results from our first set of annotations, we identified some trends in the kinds of features that are disclosed in positionality statements. A histogram of absolute counts of disclosed features is available in Figure 4. **Training and background** was the most commonly discussed feature, occurring in 60% of positionality statements, echoing findings from Singh et al. [43]. Statements often called attention to the varied, interdisciplinary backgrounds of the research team, perhaps unsurprising for a venue like FAccT. The second most commonly disclosed feature was researchers' **Personal or professional relationship to subject matter** (49% of statements). Authors disclosed experience working within the same field as the subject of study, past work with the community under study, and lived experience of the subject matter, which frequently had strong overlap. Other commonly described features included mentioning the **type of institution** or institutional context where the researchers work, such as the academy, civil society, or industry, which occurred in 35% of papers, and the **training level** of authors was mentioned in 11% of papers. The **place or geography of the work** was discussed in 27% of papers, and the **Broader cultural context of the work** was also discussed in 20% of papers. Just 5% of papers discussed **funding** or access to resources facilitating the work.

Disclosing identity-related features and details about personal geography within the research team was also common. 50% of papers discussed or disclosed some aspect of authors' personal geographies, including the place they were born, raised, or educated, or their place of current residence. 24% of (20/82) papers disclosed or discussed author **gender**, and 23% of (19/82) papers disclosed or discussed author **race or ethnicity**. **Sexual orientation** (4%, 3/82), **Socioeconomic status** (6%, 5/82), **Ability/disability** status (6%, 5/82), and **Age** (1%, 1/82) were each relatively rare, and were usually mentioned when the paper studied these subjects.

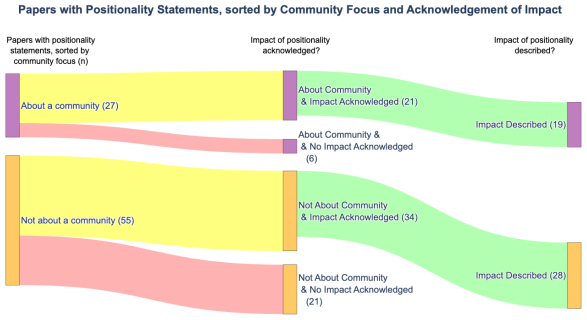


Figure 2: Number of positionality statements and discussion of impacts. Papers focused a specific community more often acknowledged and discussed impacts of disclosed features. The restrictive definition of community is used in this figure, but a similar trend follows when including professional and user groups as communities.

4.3 How often are disclosed features linked to impacts, and what kind of impacts are described?

We found that 67% (55) of positionality statements **connect positionality to an impact on the work** in some way. This left 27 papers that wrote positionality statements but did not acknowledge some impact of positionality on the work. An example of such a positionality statement, focused on disclosure rather than impacts, is as follows: *"The author has a background in media and journalism studies and works for a nonprofit organization based in the US. He is white, uses he/him pronouns, and is based in Europe. He mostly conducts qualitative research (interviews, ethnography), but also has experience in quantitative and computational methods. His work is committed to accountability, inclusion, and fairness."*[1]

Figure 4 shows that many disclosed features are not connected to a described impact on the work. We found that positionality statements from papers that are about a community more commonly engaged with impacts than those not about a community, as shown in Figure 2. This common lack of engagement echoes recent findings from Singh et al. in reviewing positionality statements at CHI, and, prior to that, from Secules et al., who also found that when researchers acknowledge that their positionalities impacted the study, they sometimes only do so by stating they were "abstractly" influential [41].

Of the 55 papers that do connect disclosed features to an impact on the work, 25 discuss **research background** as influencing the research, 21 discuss personal relationships with the subject matter, 19 discuss **cultural context** of either the person or the work, 16 discuss **place of work or residence**, and 7 directly discuss the impact of disclosed race and/or gender features on the research.

Positionality was also described as having highly variable *types* of impacts. Figure 3 shows the number of times a feature is disclosed and either acknowledged or described as having an impact on the work, and connects it to the number of times the feature is described as having a particular type of impact on the work. Disclosed features are described as most frequently having impacted the **Scope or definitions** in the work (33), **Analysis** (18), **Awareness of the problem** (11), including descriptions of how lived experience sensitized the researchers to the problem, **Relationship to participants** (9), including whether participants feel comfortable sharing with the researcher or not, and finally, **Motivation for the work** (6), including how lived experiences or research background motivated the work.

5 Findings

5.1 Policy matters

It appears that the 2024 recommendation from the PCs to write a positionality statement did increase the number of positionality statements at FAccT that year, also supported by our supplementary analysis of causal impact in the appendix. Figure 1 shows the marked relative increase in positionality statements in 2024, perhaps as a combined result of the PCs' recommendation and the wider trends in computing fields, as documented in Singh et al. [43].

We wondered if papers that included positionality statements at FAccT prior to 2024 were usually centered on a particular community.[2] As it turns out, 4/6 (or 67%) papers in 2022 that included positionality statements were about a community, and 7/10 (or 70%) papers in 2023 that included a positionality statement were about a community, small ratios that descriptively lean towards papers about a community. By comparison, just 16/65, or less than a quarter of papers that included positionality statements in 2024, were about a community. This stands in contrast to findings from Singh et al. [43], which found that most positionality statements at CHI had to do with a studied community. The relative increase in papers that do *not* engage with specific communities that include a positionality statement in 2024 could be read as a sign that authors not already in the habit of writing positionality statements, perhaps due to different disciplinary or methodological norms, may have done so specifically in response to the PCs' encouragement.

We conducted a two-sample z-test for proportions to compare the relative incidence of positionality statements in papers published before (2021-2023) and after 2024 according to whether they focused on a particular community. The proportion of papers with positionality statements that did *not* have a community focus (using the restrictive definition) increased from just 35.3% across pre-2024 years (n = 17) to 75.4% in 2024 (n = 65), giving a z-statistic of -3.132 and a p-value of $p < 0.01$. Including professional communities and user groups replicates the same trend. This suggests the proportion of papers post-intervention wrote positionality statements but were not papers about a community increased compared to pre-2024, though pre-2024 numbers are small, and field-level or conference-level trends may also play a role. We consider available causal evidence in the appendix, which suggests conference policy can affect researcher practice, even when the practice is voluntary.

[1] Our goal in quoting passages from specific positionality statements is to provide concrete examples of general trends, not to call out specific authors. As such, we do not cite the papers from which we are quoting to avoid bringing undue attention to specific authors.

[2] We discuss our definitions in the appendix, but use the more restrictive definition of community excluding professional and user groups in the descriptive analyses that follow.

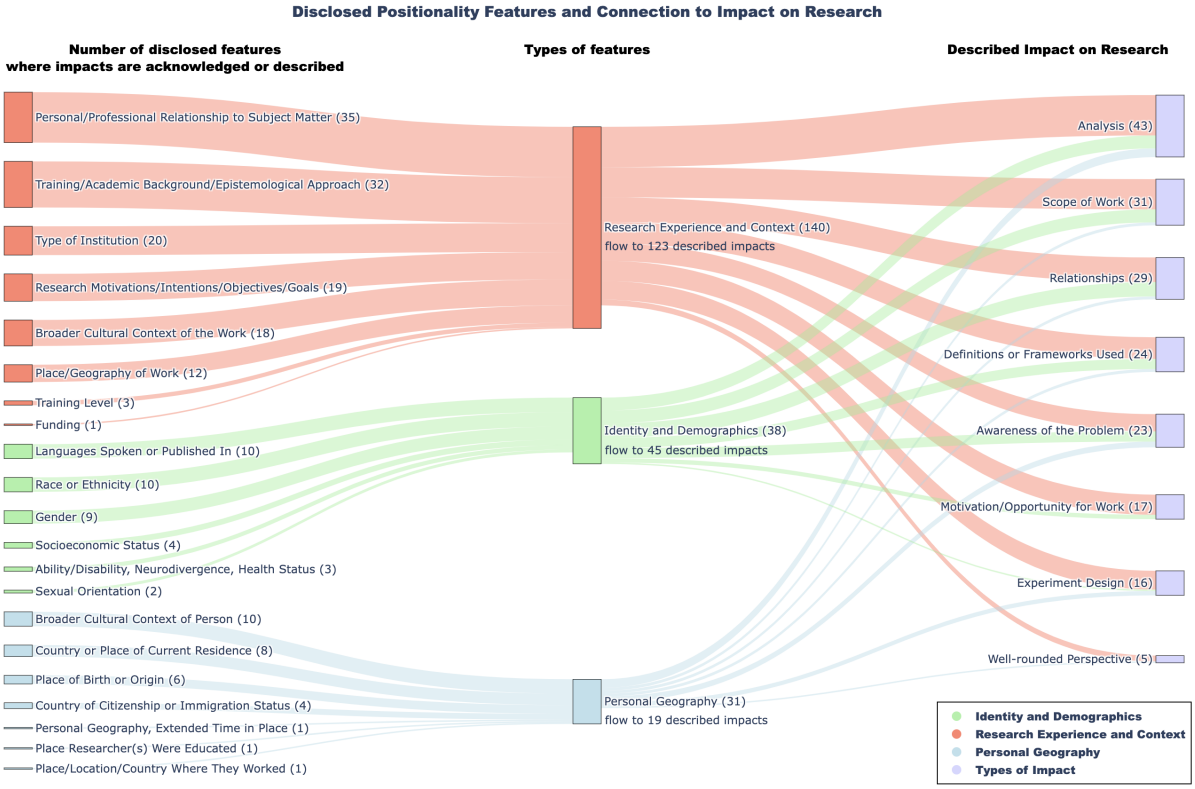


Figure 3: Flow analysis of disclosed features acknowledged or described as having impact to types of described impacts. On left, number of disclosed features within a category that are connected to an acknowledged or described impact on the work. In the middle nodes, the inflow is the number of times the feature is ever acknowledged as having an impact on the work, and the outflow is the number of times a feature from that category is described as connected to a particular type impact on the work. Features could be mapped to multiple impacts, and only features that had *described impacts* are connected to righthand nodes, so outflows do not match inflows. And on the right, we visualize the frequency of types of described impacts of positionality features on the work.

5.2 Disclosing without engaging

As mentioned in the introduction, the FAccT 2024 call for papers says positionality statements "are meant to provide added transparency and scaffold readers' understanding of how our background and experiences influence or inform our work, and how our perspectives might as a result differ from those of others" [36]. The 2025 Author Guide [3] also states that positionality statements are "a short statement that summarizes how the background and experiences of the authors inform or shape the work." Given the emphasis that both place on connecting researchers' background to impact on the work, it is encouraging to find that 70% of the papers that include positionality statements make such a connection.

If we look more closely, though, we find notable variation in the discussion of impacts across different features of identity. Overall, we find that the most commonly disclosed features have to do with researcher background and work context, with authors' training and background occurring in 50 of the 82 statements in our dataset. Of these, 24 papers go on to acknowledge that background and training impacted the work, and 15 describe a specific impact on the work. While 20 statements in our data disclosed or discussed author gender, only 6 of them connected gender to a specific impact, including impacts on the **relationships with participants** (3), on **analysis** (2), and on the **scope of work** (2). When authors leave the impacts of specific features unstated, they invite readers to impute these impacts based on their own—perhaps limited or faulty—understanding of the group to which authors belong. Attempting to make such an inference almost relies on, or even amplifies, stereotypes about what perspectives individuals from those groups may bring to the work. In the case of authors' training and background, this may not be of serious concern, as the likely readers of these papers are other researchers with a rather sophisticated understanding of the norms of their own and other disciplines, allowing them to make reasonably well-informed guesses about the likely effects of these features on the work. In the case of gender, however, readers may be encouraged to fall back on essentialist beliefs about gender and its potential effects on research. Even though gender receives much less attention in positionality statements than authors' training and background, it may be concerning that it is less often accompanied by a discussion of corresponding impacts,

given this difference in the degree to which readers will be able to reliably impute its impact on the work.

It was not uncommon to encounter positionality statements that disclosed features of identity, but said very little, if anything, about the impact of these features on the work. For example, one statement simply notes that *"We situate this paper in the United Kingdom in the 21st century, writing as authors who primarily work as academic and industry researchers. We identify as males from Indonesia, Cyprus, Iran, and Italy. Our shared backgrounds include HCI, privacy, security, software engineering, AI, social computing, and urbanism."* There were, of course, notable exceptions. In one noteworthy positionality statement, the authors described how their intersectional identities likely impacted their work: *"As white women academic researchers from Europe and the US, we acknowledge that our personal and professional backgrounds shaped how we selected research questions and analyzed data, as well as the manner in which we interacted with study participants from backgrounds similar and dissimilar to ours. Both authors have a privileged academic affiliation, race, and lack of personal contact with the US criminal legal system, which undoubtedly shaped the information that grassroots community organizations and system-impacted interviewees were comfortable sharing with us [...] On the other hand, our privileged position as white academic researchers from well-recognized institutions helped build rapport with other academic researchers in the study, who had similarly received training at elite academic institutions."* The statement explicitly engages with how race and gender identity may have shaped relationships with participants and collaborators, in addition to shaping researchers' relationships through institutions, helping readers understand the relevance of these features to the work. As can be seen in Figure 2, papers that were not focused on a particular community less often discussed the corresponding impact of any disclosed features.

What accounts for the fact that many authors choose to disclose certain features of their identity, but stop short of describing the impact such features may have had on their work? While we cannot determine what accounts for this difference simply by looking at the positionality statements, we observe one notable difference between papers that disclose *and* engage and those that disclose and do *not* engage on the impact of **race** and **gender** on the work. Papers that are about a community tend to engage when they disclose race, whereas papers that are not about a community are less likely to engage with impact when they disclose it. Of papers about community (focused on protected identity characteristics or location, of which there were 25 with positionality statements across years), nine disclose some aspect of author gender, or do so at a rate of 9/25, whereas 11 papers not about a community do so, at a rate of 11/57. Papers about a community disclose author gender in the positionality statement relatively more often, and also engage with gender's impact on the work more often: 5/9 papers engage with the impact of gender on the work when it is disclosed, whereas just 1/11 papers not about community fully engage with gender's impact when it is disclosed. Disclosures about **race and ethnicity** follow a similar pattern: of the 8 papers about community that disclose race in the positionality statement, a majority of five engage with its impact, and of the 11 papers not about community that disclose or discuss author race, just one fully engages with a discussion of its impact, and another two partially engage with discussion of race's impact on the work.

One explanation for the comparative lack of engagement with impacts of race and gender for authors of papers not about community might be that the impact of these features on research not about a community cannot be as readily theorized or explained by the researchers compared to papers about a community, despite researchers' general sense that they may have had an impact on the work. Less charitably, perhaps this is a sign that these authors were mechanistically disclosing features of identity on the belief that this was a way to comply with the PC recommendation.

As we have pointed out, some features are often disclosed but less often engaged with in terms of impact on the work. On the other hand, the impact of some features is almost always discussed. For example, **languages spoken** are disclosed in six papers, and the impact of language on the work is described in each one. When authors notice and disclose the languages they speak or use to publish, it may already be quite easy to connect the language to an impact, such as **scope of work** (observed three times) or **relationships to participants** (observed twice), but few authors overall appear to have done this.

5.3 Overlooking industry influence?

FAccT's relationship with industry has been a topic of considerable discussion in the community and the subject of prior studies published at the conference [29, 46], joining wider examination of the relationship between the technology industry, research, and values [4–6, 24]. We wondered how many positionality statements in our dataset came from papers with industry-affiliated authors, and, of those, how many of those positionality statements engaged with the influence of industry on the research. 20% (16/82) of positionality statements in our dataset came from papers with at least one author with an industry affiliation listed on the publication. Of those 16 papers, just four meaningfully engaged with the influence of the industry context on the work through the positionality statement, while the other 12 did not. An example of one that did engage with how industry shaped the work is as follows: *"Our research questions and design were influenced by our position as employees of a U.S.-based technology company. Members of our research team have first-hand experience observing and participating in discussions regarding the responsible development and deployment of LLM-infused applications, which has shaped our understanding of gaps in knowledge and other practical challenges that arise in attempting to meet responsible AI principles and proposed regulatory requirements. We had access to sufficient budget to run large-scale experiments, which is not an option for some research teams."* This statement discusses how industry experiences and context shaped the work, including granting access to compute, which facilitated the work. Regarding the 12 papers with industry affiliation that did not engage with industry influence in the positionality statement, it is possible having a single author from industry in an author team of many meant that the single author's affiliation did not have enough influence to warrant this discussion. However, we also observed entire author teams from industry that wrote a positionality statement, but did not mention the influence of industry on even the scope of work in the positionality statement.

These findings seem to suggest that encouraging authors to include positionality statements with their papers has not helped to address one of the potential influences of greatest concern to

the community. Yet it is also important to note the different norms that have traditionally governed the disclosure of potential conflicts of interest, including those due to industry affiliations. While researchers are expected to disclose such conflicts, they are not expected to discuss how these conflicts may have shaped their work. In fact, it is precisely because authors may have a conflict that they cannot be trusted to honestly or fully report on the potential impact of this conflict on their work [40]. It is also for this reason that authors are not commonly allowed to choose whether to disclose the conflict of interest; unlike other disclosures in positionality statements, these disclosures are often mandatory. This means readers must arrive at their own assessment of their work based on the revealed conflict of interest, whether or not the conflict of interest actually had an effect on the research. It is thus unclear whether positionality statements, and the norms that have developed around them, are the appropriate way to handle such conflicts. And as it turns out, this year's call for papers at FAccT noted, for the first time, that authors can include a separate section in the end matter where they can disclose "competing interests", though the disclosure is voluntary and purposefully withheld from the reviewing process. Thus it is possible that we will see more disclosure of such conflicts in light of this new recommendation, even if there remains no corresponding discussion of their impacts. More generally, though, the standard approach to conflicts of interests highlights that it might make sense to favor disclosing without engaging when there would be plausible incentives for authors to try to minimize the apparent influence of these conflicts on the work.

5.4 Motivations, political commitments, and intentions for the work

Some feminist academics recommend that scholarship should "involve a disclosure" of goals, as well as "intellectual and [...] political beliefs," a stance that largely lies in contrast to mainstream science, which "regards the political as an impediment to good science," [8]. Interplay between scholarship and community or political involvement is popular as a model of work through "participatory action research," [9, 15] which has many adherents at FAccT [23]. In keeping with the community's commitment to such work, we observed researchers discussing **Research motivations, intentions, objectives, or goals** in 34% of positionality statements. In our secondary analyses, we found 11 papers discussed personal values, beliefs, or political commitments, and another 2 discussed organizational commitments. This included disclosing affiliations with activist groups, such as those standing against "carceral technology," or standpoints like a rejection of the "militarization of AI." Many discussed synergies between their activist efforts and scholarship, including how relationships with communities facilitate scholarly work.

A relationship between scholarship and activism is common at FAccT, and represents important engagement in the subjects of our work beyond scholarship alone. However, political disclosures in the body of papers could inadvertently place researchers at risk of serious harm, especially given the current changing political climate. In the United States, the Trump administration has moved aggressively to combat what it perceives as the ideological bias of the academy, directly attacking the kinds of motivating concerns that are common at FAccT [38]. A conference policy that encourages authors to state the political commitments driving their work in published positionality statements could make these researchers more vulnerable to such attacks, endangering both their personal safety and professional security.

This echoes concerns from Oswald, wherein pressure to "out" one's sexuality in positionality statements can potentially cause harm to queer researchers. And such disclosures could also undermine the perceived credibility of their work among those who do not share their political commitments, potentially contributing to a decline in trust in the academy as an institution and the long-term influence of research on society. Researchers who pursue the difficult, important work of both scholarship and activism should be at liberty to make the values and beliefs that underpin their work explicit, but evolving expectations around disclosures in positionality statements should take these serious risks into account.

5.5 The limits of lived experience

In our secondary analysis, we noticed **Limitations** were often mentioned in positionality statements (28 papers, or 34%). We sorted the types of limitations mentioned into several categories for further interpretation, including discussions of how **researcher identity shaped relationships to participants**, an impact strongly present in prior work [13, 28, 41]. We found that when describing limitations of the work, researchers sometimes disclosed how their identities may have changed their relationships to participants (5), how the perspective of the work may not generalize (4), or that the cultural perspective of the research team may have induced bias (2). 14 positionality statements also mentioned some kind of mitigation for these limitations, which included recruiting collaborators based in a community context, or seeking literature from outside the authors' domains.

We noticed that the most commonly discussed limitation identified a lack of lived experience as a limitation of the work, seen in 8/28 or 30% of positionality statements featuring any limitation. Existing work documents the complexity of lived experience's impact on research [31]. Looking at the subset of papers that **connect positionality to impact on research** and mentioned a **limitation**, we find that discussing the **personal or professional relationship** to subject matter was common, occurring in 40 positionality statements. Some papers also discuss whether the author team has **lived experience** with the subject at hand, or is a member of the community under study. 14 papers in the dataset (17%) discussed lived experience as either a credit to their work (8), or disclaimed their lack of lived experience as a subtle limitation of the work (6). For example, the following positionality statement in a paper about trans individuals appears to subtly do both: *"while there are some gender identities discussed that authors do not have lived experiences for, the lead author is a trans nonbinary person."*

Lived experience and fixed identities "may predispose someone towards a particular point or point of view," but experts caution "that does not mean that these necessarily automatically lead to particular views or perspectives" [17]. As Fine [20] also points out, "flat caricatures" of identity miss broader questions about the construction of a researcher's knowledge in relation to the studied subject. Positionality statements that disclose identity markers without engaging

are at greater risk of leading readers to fill in their assumptions about what aspects of positionality mean for the work, potentially activating the very kind of essentialism that feminist epistemologies often try to resist with respect to the way gender, sexuality, and other characteristics shape but do not determine our perspectives.

Adding to this discussion, we found examples of positionality being discussed as predetermining an aspect of the work. For example, *"All authors are affiliated with organizations from Western, Educated, Industrialized, Rich, and Democratic (WEIRD) countries [...] This background inherently influenced the research practice of this study, including the case study and data that was chosen, which ultimately* ***predetermined*** *the design and evaluation decisions we focused on."* Another uses similarly strong language: *"We nonetheless recognize that our positionality as academic researchers at a university in a developed country* ***prohibits*** *us from fully capturing the challenges faced [...] by information professionals operating in different contexts from ours."* The use of the terms "prohibit" and "predetermine" veers into suggesting that the work is determined by positionality, though the authors do also use other terms that stress "influence." However, we bring up these suggestive examples in light of another pattern we notice: authors sometimes use mentions of the constraints of their positionality to excuse a substantive or methodological decision made about the work. For example, consider the following positionality statement: *"all researchers [...] are based at research and higher-education institutions in the Global North, where the primary language is English. As such, the research itself was limited to the English language."* The statement implies that the choice to limit the work to the English language is a natural product of being in "the Global North, where the primary language is English." Later, the researchers also share they have "lived" experience in the "Global South," which may serve as an assurance that Global North perspective is not the only one represented. However, the authors do not describe either how this "Global South" perspective has shaped the work, or why these perspectives did not affect their decision to nonetheless focus on English. This choice of linguistic focus should be defended in the main body of the work, not excused in the positionality statement on the grounds of their position as researchers in the Global North. In their blog post encouraging engagement with positionality, the PCs of FAccT 2024 did remind authors to address methodological commentary in the main work alongside their recommendation to include positionality statements [36], and we note that this and other examples did not always follow this recommendation.

6 Recommendations

6.1 Address policy ambiguities

A common concern about positionality statements is that they may reveal aspects of authors' identity that might inappropriately influence reviewers' assessment of their work, even if authors' disclosures are not uniquely identifying. One reason to adopt a policy to withhold positionality statements from reviewers is to protect authors' anonymity. At FAccT this year, authors were instructed to withhold these statements during peer review, but invited to include them in the published version of their papers. As a result, unlike previous years, positionality statements were not available to reviewers this year, but they may still be included in published papers.

The change in policy left some uncertainty as to what information authors were expected to withhold in review this year. If the goal of instructing authors to withhold positionality statements is to limit reviewers' access to certain information about authors' identity, it stands to reason that authors might be expected to withhold similar kinds of disclosures elsewhere in their submissions. If the prohibition were to apply this broadly, it could create issues for authors who come from disciplines or use methods that expect authors to engage in reflexivity throughout their papers, not just in a separate positionality statement. For example, reflexivity is not only common, but often expected in anthropology or when performing reflexive thematic analysis. In these cases, reflecting carefully and explicitly on positionality is sometimes considered a core part of methodological rigor—and reviewers might feel that they cannot evaluate the quality of the work in the absence of this information.

At the same time, this policy could also be designed to protect authors who might feel compelled to disclose aspects of their identity to avoid being penalized by reviewers who expect or request such disclosures. Authors may have good reason to want to abstain from disclosing certain aspects of their identity, even if they recognize that such disclosures could help reviewers and later readers understand how their identity has influenced the work. For example, members of minority or marginalized populations will often face far greater risks of identity-based discrimination, harassment, and political attack than other authors. A policy that fails to shield authors from pressures to disclose, even when the decision to do so is meant to be voluntary, can have a much more serious impact on some populations than others. As much as the conference might want to leave it to authors to weigh these competing considerations, authors' choice to disclose details of their identity, especially outside the confines of a positionality statement, cannot be fully voluntary if authors feel that they must disclose to meet reviewers' expectations.

There is no easy way to resolve these tensions and the conference will need to make some hard choices. The conference should acknowledge these tensions and solicit input from researchers that work in the many different disciplinary traditions represented at FAccT. Indeed, our own mixed-methods backgrounds, and methodological approaches chosen here, inform our observations about this data and motivate some of our recommendations, including a recommendation to seek perspectives from a range of disciplines on this issue. The goal should be to not only arrive at a more precise—and precisely stated—policy, but to do so through an inclusive process that allows for researchers with different perspectives and practices to influence the ultimate policy. In announcing the new policy, the conference could also provide an account of the process and reasoning that led to the policy, increasing its perceived legitimacy, even if not all researchers agree with it.

6.2 Encourage reflexivity through CRAFT

Positionality statements are commonly drafted at the end of the research process, when authors are writing their papers. As a result, it can be unclear what, if any, relationship the reflexivity expressed in positionality statements has with the reflexivity exercised earlier in the research process. For this reason, positionality statements are sometimes dismissed as a "tick box exercise" [43] in which

researchers perform reflexivity only once the research has been completed, rather than engaging in reflexivity all along the way. If the larger goal of encouraging authors to include positionality statements with their submissions to FAccT is to foster reflexivity throughout the research process, we should consider alternative mechanisms that might achieve this goal more effectively.

One potential mechanism unique to FAccT is Critiquing and Rethinking Fairness, Accountability, and Transparency (CRAFT), a track introduced in 2020 to bring critiques of the conference and the research that it publishes into the conference itself. Originally envisioned as a space where diverse stakeholders (including those beyond researchers themselves) could interrogate the field's emerging assumptions, CRAFT represented an attempt to embed reflexivity into the very structure of the conference [1]. However, in recent years, its focus has drifted towards more traditional workshop structures that depart from this original vision. We believe there is an opportunity to revitalize CRAFT by returning it to its founding purpose: a site for examining research practices, including but not limited to an examination of reflexivity in the community's research.

In particular, CRAFT sessions could serve as an entry point for researchers from fields where reflexivity is not the norm, offering them opportunities to learn from those with far more experience with the practice—and for researchers from different disciplines to debate the merits of different approaches, including the merits of the practice overall. By investing in CRAFT as a space to consider the function and value of reflexivity throughout the research process, FAccT could foster a more inclusive, nuanced, and durable engagement with the practice, whether or not researchers ultimately choose to include positionality statements with their future submissions.

6.3 Evaluate interventions

FAccT has a tradition of publishing work that critically reflects on its own norms and practices and those of the broader field of computing, a tradition of which this paper is a part. In fact, our paper joins a series of papers that have sought to evaluate the success of various mechanisms that have been introduced at FAccT and other computing venues to foster more responsible and reflexive research practices [7, 10, 32, 35, 43]. These studies have generally found that common interventions fail to achieve intended effects and that further work is needed to improve practices and bring about change. Given these ongoing uncertainties and challenges, FAccT should continue to invite research on these topics. It can do so by making this an explicit part of future calls for papers and by soliciting research on the specific issues that prior research has identified as in need of further attention.

In particular, we suggest that FAccT make a concerted effort to promote more empirical evaluations of existing and proposed interventions, perhaps even taking on some of this responsibility itself. Too often, conferences have adopted policies or practices without a clear sense of their likely efficacy in practice. Similarly, while research has offered a range of recommendations for improving current policies and practices, few of these have been validated empirically. NeurIPS offers a few instructive examples of what might be possible. In 2022, the Ethics Review Chairs published a blog post offering a detailed analysis of the process that year, highlighting where the process had not worked as hoped [33]. More recently, the conference also ran an experiment to evaluate the usefulness of an LLM in supporting researchers in completing the required "author checklist," which prompts authors to reflect on, among many other things, assumptions and limitations [14].

In keeping with this suggestion, we hope that future research will re-examine the data that we collected for this paper and compare it to data collected from future years of the conference.[3] Analyzing papers from FAccT 2025 could offer an especially useful contrast, given the change in policy regarding the availability of positionality statements during the review process. We expect that authors with different methods, expertise, and interpretive lenses may reach different insights than we have with our own analysis, so our work is intended as a starting point for broader discussion.

7 Conclusion

While the results of our study raise serious concerns, they should not be construed as a sweeping indictment of reflexive practices. For authors from disciplines with a developed tradition of reflexivity, positionality statements may offer them an opportunity to provide reviewers and readers with valuable insights into aspects of their identity that meaningfully affected their work. The better examples of positionality statements highlighted earlier largely seem to come from scholars from such disciplines. In contrast, for authors coming from disciplines that have no such traditions and thus struggle to meaningfully engage in the same degree of reflexivity, including positionality statements may do more harm than good: disclosure without engagement may encourage readers to rely on essentialist ideas about identity as they contemplate how specific characteristics might have affected the work, and more generally, positionality statements can become a compulsory exercise at the end of the research process that fails to promote reflexivity throughout it.

Developing effective norms around reflexivity within a methodologically heterogeneous community like FAccT will not be easy. We hope that our analysis of FAccT's experience with positionality statements can contribute to more inclusive debate and more informed decision making on this difficult matter. And while FAccT and other publication venues have an important role to play in cultivating reflexive practices in computing, many actors in the broader academic ecosystem must play a part as well. As suggested in a recent National Academies report, fostering a culture of critical reflection in computing research will require effort on the part of many stakeholders [2]. In highlighting where current conference policies and practices are falling short of expectations, we also hope to identify where there are opportunities for others in the ecosystem to contribute. Encouraging authors to include positionality statements with their paper submissions can only achieve so much on its own in this regard. If the real goal is to spur greater reflexivity throughout the research process, there needs to be a broader change in the culture of computing research.

Acknowledgments

We thank Ziv Epstein for his suggestions and feedback regarding the empirical and statistical approaches to this work. We thank

[3] Data access and additional information is described here: https://github.com/schropes/positionalitystatements

colleagues and fellow interns at Microsoft Research for sharing their expertise on qualitative methods and positionality that informed this work.

Per ACM policy, we acknowledge use of AI powered tools (including Writefull, Claude Sonnet, and ChatGPT) to explore academic literature, review suggested edits to this text, and generate and edit code for this project, including code to generate graphs and tables.

Hope Schroeder completed part of the research for this paper while an intern at Microsoft Research. Solon Barocas works at Microsoft Research.

References

[1] 2020. ACM FAccT - 2020 CRAFT: Critiquing and Rethinking Accountability, Fairness and Transparency. https://facctconference.org/2020/callforcraft.html

[2] 2022. *Fostering Responsible Computing Research: Foundations and Practices*. National Academies Press, Washington, D.C. doi:10.17226/26507

[3] Program Chairs 2025. 2025. FAccT 2025 Author Guide. https://facctconference.org/2025/aguide

[4] Mohamed Abdalla, Jan Philip Wahle, Terry Ruas, Aurélie Névéol, Fanny Ducel, Saif M. Mohammad, and Karën Fort. 2023. The Elephant in the Room: Analyzing the Presence of Big Tech in Natural Language Processing Research. In *Proceedings of the 61st Annual Meeting of the Association for Computational Linguistics (Volume 1: Long Papers)*. 13141–13160. doi:10.18653/v1/2023.acl-long.734 arXiv:2305.02797 [cs].

[5] J. Khadijah Abdurahman. 2020. On the Moral Collapse of AI Ethics. https://upfromthecracks.medium.com/on-the-moral-collapse-of-ai-ethics-791cbc7df872

[6] Will Aitken, Mohamed Abdalla, Karen Rudie, and Catherine Stinson. 2024. Collaboration or Corporate Capture? Quantifying NLP's Reliance on Industry Artifacts and Contributions. doi:10.48550/arXiv.2312.03912 arXiv:2312.03912 [cs].

[7] Carolyn Ashurst, Emmie Hine, Paul Sedille, and Alexis Carlier. 2022. AI Ethics Statements: Analysis and Lessons Learnt from NeurIPS Broader Impact Statements. In *Proceedings of the 2022 ACM Conference on Fairness, Accountability, and Transparency (FAccT '22)*. Association for Computing Machinery, New York, NY, USA, 2047–2056. doi:10.1145/3531146.3533780

[8] Shaowen Bardzell and Jeffrey Bardzell. 2011. Towards a feminist HCI methodology: social science, feminism, and HCI. In *Proceedings of the SIGCHI Conference on Human Factors in Computing Systems (CHI '11)*. Association for Computing Machinery, New York, NY, USA, 675–684. doi:10.1145/1978942.1979041

[9] Fran Baum, Colin MacDougall, and Danielle Smith. 2006. Participatory action research. *Journal of Epidemiology and Community Health* 60, 10 (Oct. 2006), 854–857. doi:10.1136/jech.2004.028662

[10] Luciana Benotti and Patrick Blackburn. 2022. Ethics consideration sections in natural language processing papers. In *Proceedings of the 2022 Conference on Empirical Methods in Natural Language Processing*, Yoav Goldberg, Zornitsa Kozareva, and Yue Zhang (Eds.). Association for Computational Linguistics, Abu Dhabi, United Arab Emirates, 4509–4516. doi:10.18653/v1/2022.emnlp-main.299

[11] Michael S. Bernstein, Margaret Levi, David Magnus, Betsy A. Rajala, Debra Satz, and Quinn Waeiss. 2021. Ethics and society review: Ethics reflection as a precondition to research funding. *Proceedings of the National Academy of Sciences* 118, 52 (Dec. 2021), e2117261118. doi:10.1073/pnas.2117261118 Publisher: Proceedings of the National Academy of Sciences.

[12] Abeba Birhane, Elayne Ruane, Thomas Laurent, Matthew S. Brown, Johnathan Flowers, Anthony Ventresque, and Christopher L. Dancy. 2022. The Forgotten Margins of AI Ethics. In *Proceedings of the 2022 ACM Conference on Fairness, Accountability, and Transparency (FAccT '22)*. Association for Computing Machinery, New York, NY, USA, 948–958. doi:10.1145/3531146.3533157

[13] Mildred Boveda and Subini A Annamma. 2023. Beyond Making a Statement: An Intersectional Framing of the Power and Possibilities of Positioning - Mildred Boveda, Subini Ancy Annamma, 2023. *Educational Researcher* 52, 5 (2023), 306–314. https://journals.sagepub.com/doi/10.3102/0013189X231167149

[14] Communications Chairs 2025. 2024. Results of the NeurIPS 2024 Experiment on the Usefulness of LLMs as an Author Checklist Assistant for Scientific Papers – NeurIPS Blog. https://blog.neurips.cc/2024/12/10/results-of-the-neurips-2024-experiment-on-the-usefulness-of-llms-as-an-author-checklist-assistant-for-scientific-papers/

[15] Flora Cornish, Nancy Breton, Ulises Moreno-Tabarez, Jenna Delgado, Mohi Rua, Ama de Graft Aikins, and Darrin Hodgetts. 2023. Participatory action research | Nature Reviews Methods Primers. *Nature Reviews Methods Primers* 3, 34 (April 2023). https://www.nature.com/articles/s43586-023-00214-1

[16] Kimberlé Crenshaw. 1989. Demarginalizing the Intersection of Race and Sex: A Black Feminist Critique of Antidiscrimination Doctrine, Feminist Theory and Antiracist Politics. *U. Chi. Legal F.* 1989 (Jan. 1989), 139. https://scholarship.law.columbia.edu/faculty_scholarship/3007

[17] Andrew Gary Darwin Holmes. 2020. Researcher Positionality - A Consideration of Its Influence and Place in Qualitative Research - A New Researcher Guide. *Shanlax International Journal of Education* 8, 4 (Sept. 2020), 1–10. doi:10.34293/education.v8i4.3232

[18] Wesley Hanwen Deng, Solon Barocas, and Jennifer Wortman Vaughan. 2025. Supporting Industry Computing Researchers in Assessing, Articulating, and Addressing the Potential Negative Societal Impact of Their Work. doi:10.1145/3711076 arXiv:2408.01057 [cs].

[19] Kimberly Do, Rock Yuren Pang, Jiachen Jiang, and Katharina Reinecke. 2023. "That's important, but...": How Computer Science Researchers Anticipate Unintended Consequences of Their Research Innovations. In *Proceedings of the 2023 CHI Conference on Human Factors in Computing Systems (CHI '23)*. Association for Computing Machinery, New York, NY, USA, 1–16. doi:10.1145/3544548.3581347

[20] Michelle Fine. 1994. In *Handbook of qualitative research 2*. "Working the hyphens.". https://www.uky.edu/~addesa01/documents/Fine_Hyphens.pdf

[21] Linda Finlay. 2002. "Outing" the Researcher: The Provenance, Process, and Practice of Reflexivity. *Qualitative Health Research* 12, 4 (April 2002), 531–545. doi:10.1177/104973202129120052 Publisher: SAGE Publications Inc.

[22] Jasmine K Gani and Rabea M Khan. 2024. Positionality Statements as a Function of Coloniality: Interrogating Reflexive Methodologies. *International Studies Quarterly* 68, 2 (June 2024), sqae038. doi:10.1093/isq/sqae038

[23] Ben Gansky and Sean McDonald. 2022. CounterFAccTual: How FAccT Undermines Its Organizing Principles. In *2022 ACM Conference on Fairness, Accountability, and Transparency*. ACM, Seoul Republic of Korea, 1982–1992. doi:10.1145/3531146.3533241

[24] Anne Gerdes. 2022. The tech industry hijacking of the AI ethics research agenda and why we should reclaim it. *Discover Artificial Intelligence* 2, 1 (Dec. 2022), 25. doi:10.1007/s44163-022-00043-3

[25] Cynthia Hampton, David Reeping, and Desen Sevi Ozkan. 2021. Positionality Statements in Engineering Education Research: A Look at the Hand that Guides the Methodological Tools. 1, 2 (March 2021), 126–141. doi:10.21061/see.13 Number: 2 Publisher: Virginia Tech Publishing.

[26] Donna Haraway. 1988. Situated Knowledges: The Science Question in Feminism and the Privilege of Partial Perspective. *Feminist Studies* 14, 3 (1988), 575. doi:10.2307/3178066

[27] Brent Hecht, Lauren Wilcox, Jeffrey P. Bigham, Johannes Schöning, Ehsan Hoque, Jason Ernst, Yonatan Bisk, Luigi De Russis, Lana Yarosh, Bushra Anjum, Danish Contractor, and Cathy Wu. 2021. It's Time to Do Something: Mitigating the Negative Impacts of Computing Through a Change to the Peer Review Process. doi:10.48550/arXiv.2112.09544 arXiv:2112.09544 [cs].

[28] Danielle Jacobson and Nida Mustafa. 2019. Social Identity Map: A Reflexivity Tool for Practicing Explicit Positionality in Critical Qualitative Research - Danielle Jacobson, Nida Mustafa, 2019. *International Journal of Qualitative Methods* 18 (2019). https://journals.sagepub.com/doi/10.1177/1609406919870075

[29] Benjamin Laufer, Sameer Jain, A. Feder Cooper, Jon Kleinberg, and Hoda Heidari. 2022. Four Years of FAccT: A Reflexive, Mixed-Methods Analysis of Research Contributions, Shortcomings, and Future Prospects. In *Proceedings of the 2022 ACM Conference on Fairness, Accountability, and Transparency (FAccT '22)*. Association for Computing Machinery, New York, NY, USA, 401–426. doi:10.1145/3531146.3533107

[30] Calvin Liang. 2021. Reflexivity, positionality, and disclosure in HCI. https://medium.com/@caliang/reflexivity-positionality-and-disclosure-in-hci-3d95007e9916

[31] Calvin A. Liang, Sean A. Munson, and Julie A. Kientz. 2021. Embracing Four Tensions in Human-Computer Interaction Research with Marginalized People. *ACM Transactions on Computer-Human Interaction* 28, 2 (April 2021), 1–47. doi:10.1145/3443686

[32] David Liu, Priyanka Nanayakkara, Sarah Ariyan Sakha, Grace Abuhamad, Su Lin Blodgett, Nicholas Diakopoulos, Jessica R. Hullman, and Tina Eliassi-Rad. 2022. Examining Responsibility and Deliberation in AI Impact Statements and Ethics Reviews. In *Proceedings of the 2022 AAAI/ACM Conference on AI, Ethics, and Society (AIES '22)*. Association for Computing Machinery, New York, NY, USA, 424–435. doi:10.1145/3514094.3534155

[33] Sasha Luccioni, Inioluwa Deborah Raji, Cherie Poland, and William Isaac. 2022. Reflections on the NeurIPS 2022 Ethics Review Process. https://blog.neurips.cc/2022/11/04/reflections-on-the-neurips-2022-ethics-review-process/

[34] Kelly Mack, Emma McDonnell, Dhruv Jain, Lucy Lu Wang, Jon E. Froehlich, and Leah Findlater. 2021. What Do We Mean by "Accessibility Research"?: A Literature Survey of Accessibility Papers in CHI and ASSETS from 1994 to 2019. In *Proceedings of the 2021 CHI Conference on Human Factors in Computing Systems*. ACM, Yokohama Japan, 1–18. doi:10.1145/3411764.3445412

[35] Priyanka Nanayakkara, Jessica Hullman, and Nicholas Diakopoulos. 2021. Unpacking the Expressed Consequences of AI Research in Broader Impact Statements. In *Proceedings of the 2021 AAAI/ACM Conference on AI, Ethics, and Society (AIES '21)*. Association for Computing Machinery, New York, NY, USA, 795–806. doi:10.1145/3461702.3462608

[36] Alexandra Olteanu, Michael Ekstrand, Carlos Castillo, and Jina Suh. 2023. Responsible AI Research Needs Impact Statements Too. https://medium.com/@alexandra.olteanu/responsible-ai-research-needs-impact-statements-too-7b7141031faf

[37] Flora Oswald. 2024. Positionality statements should not force us to 'out' ourselves. *Nature Human Behaviour* 8, 2 (Feb. 2024), 185–185. doi:10.1038/s41562-023-01812-5

[38] Emma Pierson. 2025. My 'woke DEI' grant has been flagged for scrutiny. Where do I go from here? *Nature* (April 2025). doi:10.1038/d41586-025-01218-5 Bandiera_abtest: a Cg_type: Career Column Publisher: Nature Publishing Group Subject_term: Careers, Funding, Politics.

[39] Wanda Pillow. 2003. Confession, catharsis, or cure? Rethinking the uses of reflexivity as methodological power in qualitative research. *International Journal of Qualitative Studies in Education* 16, 2 (March 2003), 175–196. doi:10.1080/0951839032000060635 Publisher: Routledge _eprint: https://doi.org/10.1080/0951839032000060635.

[40] Jukka Savolainen, Patrick J. Casey, Justin P. McBrayer, and Patricia Nayna Schwerdtle. 2023. Positionality and Its Problems: Questioning the Value of Reflexivity Statements in Research. *Perspectives on Psychological Science* 18, 6 (Nov. 2023), 1331–1338. doi:10.1177/17456916221144988

[41] Stephen Secules, Cassandra McCall, Joel Alejandro Mejia, Chanel Beebe, Adam S. Masters, Matilde L. Sánchez-Peña, and Martina Svyantek. 2021. Positionality practices and dimensions of impact on equity research: A collaborative inquiry and call to the community. *Journal of Engineering Education* 110, 1 (2021), 19–43. doi:10.1002/jee.20377 _eprint: https://onlinelibrary.wiley.com/doi/pdf/10.1002/jee.20377.

[42] Ali Akbar Septiandri, Marios Constantinides, Mohammad Tahaei, and Daniele Quercia. 2023. WEIRD FAccTs: How Western, Educated, Industrialized, Rich, and Democratic is FAccT?. In *Proceedings of the 2023 ACM Conference on Fairness, Accountability, and Transparency (FAccT '23)*. Association for Computing Machinery, New York, NY, USA, 160–171. doi:10.1145/3593013.3593985

[43] Aneesha Singh, Martin Johannes Dechant, Dilisha Patel, Ewan Soubutts, Giulia Barbareschi, Amid Ayobi, and Nikki Newhouse. 2025. Exploring Positionality in HCI: Perspectives, Trends, and Challenges. In *Proceedings of the 2025 CHI Conference on Human Factors in Computing Systems (CHI '25)*. Association for Computing Machinery, New York, NY, USA, 1–18. doi:10.1145/3706598.3713280

[44] Jessica Soedirgo and Aarie Glas. 2020. Toward Active Reflexivity: Positionality and Practice in the Production of Knowledge. *PS: Political Science & Politics* 53, 3 (July 2020), 527–531. doi:10.1017/S1049096519002233

[45] Roehl Sybing. 2022. Dead Reckoning: A Framework for Analyzing Positionality Statements in Ethnographic Research Reporting. *Written Communication* 39, 4 (Oct. 2022), 757–789. doi:10.1177/07410883221114152 Publisher: SAGE Publications Inc.

[46] Meg Young, Michael Katell, and P.M. Krafft. 2022. Confronting Power and Corporate Capture at the FAccT Conference. In *Proceedings of the 2022 ACM Conference on Fairness, Accountability, and Transparency (FAccT '22)*. Association for Computing Machinery, New York, NY, USA, 1375–1386. doi:10.1145/3531146.3533194

[47] Rachel Zamzow. 2023. Should scientists include their race, gender, or other personal details in papers? *Science* 382, 6670 (Nov. 2023). https://www.science.org/content/article/should-scientists-include-their-race-gender-or-other-personal-details-papers

A Data Collection and Methods

A.1 Data Collection

To produce the dataset of positionality statements, we reviewed the conference proceedings from the origin of the conference. We downloaded the entire proceedings for FAccT for 2023 and 2024 through the ACM, in which we counted 167 archival papers in 2024 and 153 papers in 2023. For the years of 2022 and 2021 (where download was unavailable), we followed links to each paper on the FAccT website, reviewing the 181 papers from 2022 and the 82 papers from 2021. For 2018-2021, we followed links to PDFs on archived websites, finding 69 papers from 2020, 41 from papers in 2019, and the 17 papers from 2018. To find positionality statements, we searched for the terms "positionality" and "reflexivity" within each paper and included the paper in our data set if the terms were used in the context of the authors' own engagement with positionality or reflexivity. We randomly sampled 10 papers from the set across years for false negatives, and did not find any that were missed with this method of searching. We acknowledge that some types of reflexive disclosures made throughout a given paper but not signaled explicitly by the terms "positionality" or "reflexivity" may have been overlooked by our data collection method, but this choice was motivated by the primary impetus for the work: the new recommended inclusion of positionality *statements* in 2024, thus causing us to prioritize detecting their presence at the conference through its history.

Usually, if "positionality" or "reflexivity" were mentioned in a given paper, they were mentioned within a section or subsection dedicated to a researcher positionality statement. In these cases, we copied the text from these dedicated sections for analysis, which we call "standalone" positionality statements. "Positionality" was sometimes discussed in a paragraph within the body of the text. We called these "embedded" positionality statements. Sometimes, papers featured sections that addressed positionality but also mentioned other issues, such as "Ethics and Researcher Positionality." In those cases, we included the entirety of the section for analysis. If statements referred to additional reflexive content in an appendix, we included it for analysis. Because we used published versions of papers in our analysis, our dataset may differ from paper versions observed by reviewers. Given that authors were encouraged in 2024 to include positionality statements in their initial submissions, it is likely that some version of these statements were available to reviewers this past year. It is less clear what, if anything, might have been visible to reviewers in earlier years of the conference.

B Descriptive coding and IRR

For the descriptive annotation of all positionality statements, we conducted a thorough annotation of disclosed aspects of positionality. In order to create a coding scheme, two authors first open-coded statements and consulted past work to identify and define types of disclosures. Prior to the full-scale annotation of these disclosed features, the first and second authors conducted several rounds of inter-rater reliability (IRR) in order to ensure consistency of annotation with respect to all disclosed features. For each round of IRR, we took a sample of 10-15 papers from the dataset of 82 FAccT papers and annotated the samples with respect to our existing set of labels. The first author then calculated Krippendorff's alpha across all labels in the sample. If any labels had high disagreement, we discussed and refined the coding scheme before the next round or IRR. We iteratively added another 10 samples for each round until we reached an agreement threshold of at least a minimum .67 on Krippendorff's alpha. This procedure aligns with similar work empirically reviewing papers through annotation [34].

We converged on definitions for 26 labels within 4 rounds of IRR. The average Krippendorff's alpha between the two annotating authors, within **"Research team personal identity features"** was 1.0, for **"Research team personal geography"** it was .93, for **"Research team experience and institutions"** it was .82, and for **"Reflexive content"** was .9. The average Krippendorff's alpha across all features was .91, the minimum was .67, and the maximum and mode was 1.0, showing a high degree of consistency in our annotation of disclosed features.

B.1 Annotation of disclosed features

We include a longer description of all labels included in the annotation scheme for disclosed positionality features.

Personal identity

- Gender and gender identity (including self identification as transgender, cisgender, or the disclosure of preferred pronouns)
- Race and/or ethnicity
- Sexual orientation
- Ability/disability status (including mentions of neurodivergence or health status)
- Languages spoken or used for publishing academic work
- Age
- Socioeconomic status (including mentions of economic class or housing status)

Personal geography

- Place or country of current residence
- Place of birth, origin, or childhood
- Place of education
- Place of past work, if mentioned at a personal level (separate from any discussion of current work location, which we captured in a different set of codes)
- Personal geography, at an unspecified time (Example: *"We have spent a lot of time in Latin America"*)
- Country of citizenship, immigration status, or migration status
- Broader cultural context (Example: *"Author A's views are informed by growing up in the Global South"*)

Research Team Experience and Institutions

- Personal relationship with subject matter, including discussion of lived experience
- Place or geography of work
- Broader cultural context of the work (Example: *"We are based at research and higher-education institutions in the Global North"*)
- Type of institution
- Training level (Example: *"Our team comprises students (undergraduate and graduate) and faculty members."*)
- Training, academic background, publication record, and interests, epistemological approach
- Funding (including mentions of funding sources for the work, and discussion of access to funding resources to facilitate the work)

Reflexive content

We also captured aspects of reflexive content discussed in the statements in this first descriptive annotation of the statements. The features we identified were as follows:

- Connection of positionality to impact on research (does this paper connect positionality to an impact or influence on the work?)
- Explicitly mention a privilege or oppression, advantage or disadvantage, or power (or lack thereof)
- Mention a limitation of researcher, research team, context, or work
- Mention of research motivations, intentions, objectives, goals
- Statements of the meaning of or importance of positionality and reflexivity in research

C Additional figures

The distribution of the number of disclosed features present in positionality statements is observable in Figure 5. As shown, most of these papers are not an exhaustive list of disclosed positionality features, and vary significantly in the number of features they disclose.

D Secondary analyses

D.1 Annotation of paper focus

In order to understand what *kinds* of papers opted to write positionality statements, we annotated whether or not each paper with a positionality statement was about, or closely involved with, a particular identity, community, or special interest group. For the more restrictive definition of "community," we included papers related to a particular identity group, protected characteristic, or geographic location. For the more inclusive definition, we additionally included professional groups and user groups. The first and second authors discussed definitions for this task, split annotation roughly evenly, and discussed any disagreements.

As shown in Table 1 was an increase in the number of papers with positionality statements in 2024 that are *not* about a community relative to previous years. In 2024, of 65 papers with positionality statements, 49 were not about a community, and 16 were about a community, both reflecting an overall increase in authors choosing to write positionality statements, and also a relative increase in papers not doing community-centered work but engaging in this practice.

D.2 Annotation of author affiliations

We annotated the author affiliations for all papers with positionality statements (82). Table 2 shows that most author teams in the sample were academic only, 16 included at least one industry author, and 9 also included authors from non-profits, institutes, or a government.

D.3 Annotation of impacts

A second phase of analysis looked at positionality statements' disclosed features and whether the statement described an impact of those disclosed features on the work. For each disclosed feature in a positionality statement, the first and second authors first annotated 1) whether the feature was acknowledged to have had an impact on the research and 2) if so, whether the impact on the research was described. Each of these two variables was annotated as a *yes* or *no*. Notes on justification for borderline cases accompany the data for these judgments, which can be contextual.

For positionality statements where positionality was acknowledged as having impacted the work in some way, we proceeded to a second stage of analysis, next annotating the field of impact on the work if it was described. The lead author devised a list of eight observed impacts of disclosed features on research, first devised through open coding, then finalized in discussion with the other authors. Two authors annotated these impacts across all papers.

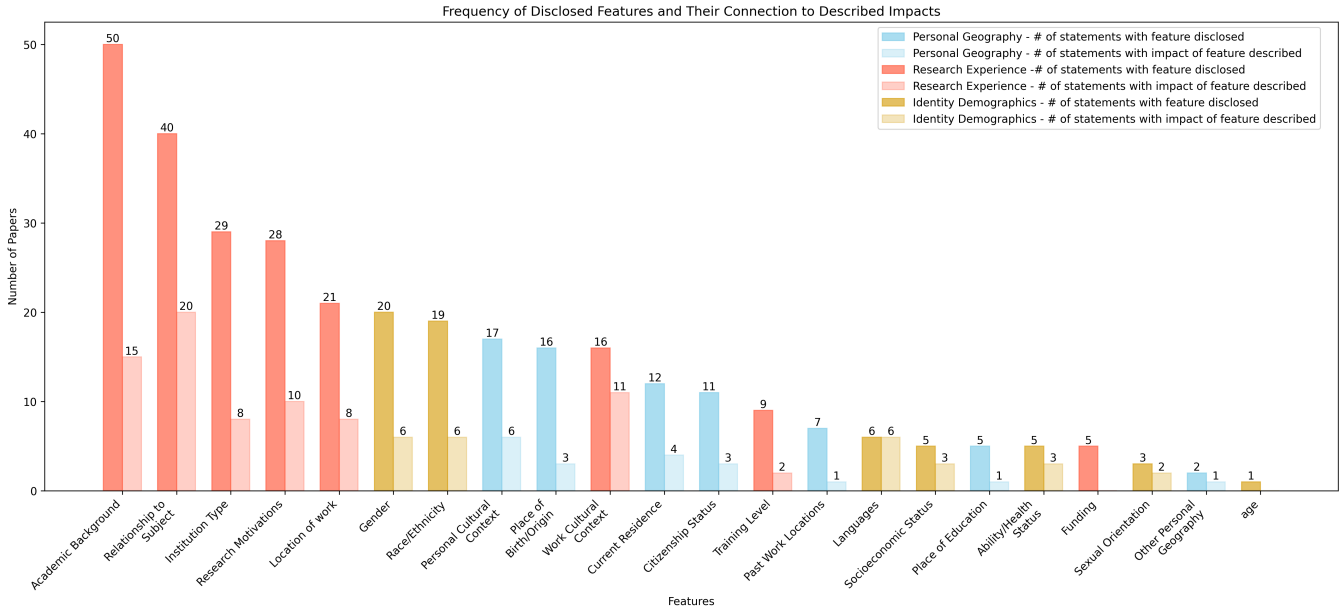


Figure 4: Frequency of disclosed features, by category, and the number of times they are connected to a described impact

Table 1: Number of papers with positionality statements by year, using restrictive and inclusive definitions of community focus.

Year	Community (Restrictive)	Not Community (Restrictive)	Community (Inclusive)	Not Community (Inclusive)
2021	0	1	0	1
2022	4	2	4	2
2023	7	3	9	1
2024	16	49	21	44

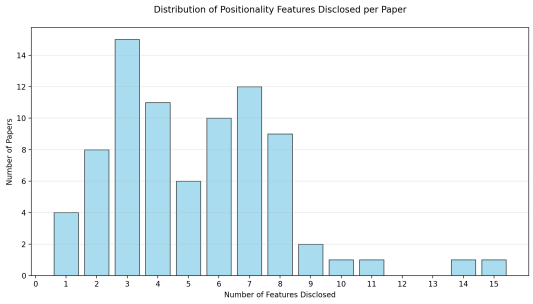


Figure 5: Histogram of number of disclosed positionality features per positionality statement

Author team composition	Count
Academic only	57
At least one industry author	16
At least one non-profit or government author	9

Table 2: Composition of author team affiliations

Notes on justification for borderline cases accompany the annotated data.

The eight types of impact authors describe positionality had on their work were identified as follows:

- Analysis (including how the data was analyzed or interpreted)
- Scope, subject, or conceptualization of work
- Relationship with participants, collaborators, or audience
- Definitions or frameworks used
- Awareness of or sensitization to the problem
- Motivation or opportunity for work
- Experiment or research design
- Diverse team impact through well-rounded perspective (for example, when an author team disclosed that the author team was multi-racial, which led to well-rounded perspective in the work)

Note that disclosed features could be connected to multiple kinds of impact, and positionality statements often disclosed multiple elements of positionality.

The counts in Figure 3 reflect the total number of times a disclosed feature was connected to that type of impact in any positionality statement. We can observe that some types of impacts, such

Type of impact	Count
Analysis	43
Scope, subject, or conceptualization of work	31
Relationship with participants, collaborators, or audience	29
Definitions or frameworks used	24
Awareness of or sensitization to the problem	23
Motivation or opportunity for work	17
Experiment or research design	16
Well-rounded perspective	5

Table 3: Frequency of described impact of positionality

as impacts on analysis or definitions, were more prevalent than others.

E Selecting into writing positionality statements

Figure 1 shows an increase in the presence of positionality statements, but we also provide evidence comparing the propensity to select into writing a positionality statement in 2023 compared to 2024. To investigate which papers opted *in* to write positionality statements in FAccT papers, we analyzed papers from 2023 (n=153) and 2024 (n=167). To better validate whether the policy yielded a change, we next annotated all the papers in 2023 (n = 153) and 2024 (n = 167) for the presence of community focus, regardless of whether the paper included a positionality statement or not. We constrained our focus to these two years to focus on the pre/post 2024 intervention, and also because of the sheer number of papers per year. We modeled a paper's propensity to select into including a positionality statement as a binary indicator for the presence of a positionality statement on indicators for 1) community focus of the paper and 2) 2024 publication of the paper (post-intervention), plus an interaction term between community focus and post-intervention year. This regression is given as

$$Y_i = \beta_0 + \beta_1 \text{Post}_i + \beta_2 \text{Comm}_i + \beta_3 (\text{Post}_i \times \text{Comm}_i) + \epsilon_i \quad (1)$$

where Y_i is a binary indicator for whether paper i includes a positionality statement, $Post_i$ indicates papers published in 2024 (as opposed to 2023), and $Comm_i$ indicates papers focusing on specific communities (defined two ways: first, in a more restrictive definition, papers studying protected identity groups or location-based communities, and in a second more inclusive definition, we also include professional communities and user groups). The interaction term captures any differential effect of community focus in 2024 compared to 2023, and ϵ_i is the error term.

Using OLS regression, we found that papers from 2024 were significantly more likely to include positionality statements compared to 2023 papers ($\beta_1 \approx 0.33$, $p < 0.001$). Importantly, papers explicitly about communities or identity groups (using either the inclusive or exclusive definitions of community) were also significantly more likely to include positionality statements overall ($\beta_2 \approx 0.20$–0.24, $p < 0.01$), suggesting that community-centered work remains a strong predictor of this practice. However, in neither configuration was the interaction between year and community focus ($\beta_3(\text{Post}_i \times \text{Comm}_i)$) significant. This regression on just two years of the data does not indicate whether papers were more likely to write positionality statements post-intervention conditional on the paper's focus. Future work can build on these findings by analyzing all years of the conference, identifying which papers used human subjects data, or including other features of author team, methods, or field-level data to explain trends.

Table 4: OLS Regression Predicting Presence of Positionality Statement (2023–2024)

Variable	Coefficient	Std. Error	t	p-value	95% CI (Lower)	95% CI (Upper)
Intercept	0.0238	0.034	0.695	0.487	-0.044	0.091
post (2024 = 1)	**0.3287**	0.047	6.951	<0.001	0.236	0.422
community	**0.2354**	0.082	2.888	0.004	0.075	0.396
post:community	-0.0165	0.114	-0.145	0.885	-0.241	0.208

Note: The dependent variable is a binary indicator for whether a paper includes a positionality statement. post indicates the year 2024; community flags papers explicitly about a location or identity group only. The interaction term tests whether the increase in positionality statement usage from 2023 to 2024 differs for community-focused work. $N = 320$. $R^2 = 0.187$. All models estimated via OLS.

Table 5: OLS Regression Predicting Presence of Positionality Statements (2023–2024), inclusive definition of community

Variable	Coefficient	Std. Error	t	p-value	95% CI (Lower)	95% CI (Upper)
Intercept	0.0091	0.037	0.248	0.804	-0.063	0.081
post (2024 = 1)	**0.3296**	0.050	6.555	<0.001	0.231	0.429
community_(inclusive)	**0.2002**	0.069	2.899	0.004	0.064	0.336
post:community_(inclusive)	-0.0040	0.097	-0.042	0.967	-0.195	0.187

Note: The dependent variable is a binary indicator for whether a paper includes a positionality statement. post indicates the year 2024; community_(inclusive) indicates whether the paper is about a specific community, location, or identity group, *including* professional and user groups. Contrast this to the more restrictive definition used in the prior regression. The interaction term tests whether the change in positionality statement use from 2023 to 2024 differs by community focus. $N = 320$. $R^2 = 0.189$. All models estimated via OLS.

This article has been accepted for inclusion in a future issue of this journal. Content is final as presented, with the exception of pagination.

DynaMentA: Dynamic Prompt Engineering and Weighted Transformer Architecture for Mental Health Classification Using Social Media Data

Akshi Kumar, *Senior Member, IEEE*, Aditi Sharma, *Member, IEEE*, and Saurabh Raj Sangwan

***Abstract*—Mental health classification is inherently challenging, requiring models to capture complex emotional and linguistic patterns. Although large language models (LLMs) such as ChatGPT, Mental-Alpaca, and MentaLLaMA show promise, they are not trained on clinically grounded data and often overlook subtle psychological cues. Their predictions tend to overemphasize emotional intensity, while failing to capture contextually relevant indicators that are critical for accurate mental health assessment. This article introduces dynamic prompt engineering and weighted transformer architecture dynamic prompt engineering and weighted transformer architecture for mental health classification (DynaMentA), a novel dual-layer transformer framework that integrates the strengths of BioGPT and decoding-enhanced BERT with disentangled attention (DeBERTa) to address these challenges. BioGPT captures fine-grained biomedical indicators, while DeBERTa provides context-aware disambiguation. The ensemble mechanism dynamically weights their outputs, guided by a simulated feedback loop that refines the predictions during training. Unlike previous studies that treat classification statically, DynaMentA incorporates dynamic prompt engineering to better align with evolving linguistic and emotional signals. Evaluated on three benchmark datasets, DepSeverity, suicide versus depression classification natural language (SDCNL), and Dreaddit, DynaMentA achieves precision of 92.6%, 91.9% F1-score, and 0.94 AUC-ROC, consistently outperforming the existing benchmark, including general-purpose LLMs and domain-specific mental health models. This scalable and interpretable framework establishes a state-of-the-art methodology for computational mental health analysis in high-stakes applications, such as suicide risk assessment and crisis intervention and early detection of severe depressive episodes.**

***Index Terms*—Artificial intelligence (AI) in mental health, deep learning for social systems, mental health classification, social media data analysis, weighted transformer models.**

Received 29 December 2024; revised 28 March 2025 and 6 May 2025; accepted 8 May 2025. *(Corresponding authors: Akshi Kumar; Saurabh Raj Sangwan.)*

Akshi Kumar is with the School of Computing, Goldsmiths, University of London, SE14 6NW New Cross London, U.K. (e-mail: Akshi.Kumar@gold.ac.uk).

Aditi Sharma is with the Department of Computer Science and Engineering, Thapar Institute of Engineering and Technology, Punjab 147004, India (e-mail: Aditi.Sharma@thapar.edu).

Saurabh Raj Sangwan is with the Department of Computer Science and Engineering, Artificial Intelligence and Machine Learning, GL Bajaj Institute of Technology and Management, Greater Noida, Uttar Pradesh 201306, India (e-mail: saurabh.sangwan@glbitm.ac.in).

Digital Object Identifier 10.1109/TCSS.2025.3569400

I. Introduction

MENTAL health disorders, including depression, anxiety, and stress, are critical global challenges, impacting millions of people annually and contributing significantly to the global burden of diseases [1]. According to the World Health Organization (WHO), depression alone is the leading cause of disability worldwide. Despite the prevalence of these conditions, early diagnosis and intervention remain inadequate due to the subjective nature of mental health assessments and the lack of scalable diagnostic solutions. The emergence of natural language processing (NLP) and artificial intelligence (AI) presents an unprecedented opportunity to bridge this gap. By analyzing textual data from online platforms such as social media posts, NLP models can uncover subtle linguistic cues indicative of mental health states [2]. Although AI-based mental health classification offers scalable solutions, it must be balanced with ethical considerations, including privacy, informed consent, and the risk of algorithmic bias in vulnerable populations. Moreover, existing approaches still struggle to capture the linguistic, cultural, and emotional diversity present in real-world mental health discourse.

Traditional methods, including rule-based systems and conventional machine learning approaches, face significant limitations. Rule-based systems often lack flexibility and do not account for linguistic variability, while traditional machine learning models rely heavily on extensive feature engineering and lack interpretability. Recent advances in large language models (LLMs), such as generative pre-trained transformer (GPT) and bidirectional encoder representations from transformers (BERT) based architectures, have shown great promise in mental health classification [3], [4]. However, these models are typically deployed in static configurations, relying on predefined prompts and isolated components, which hinder their ability to dynamically adapt to the evolving context of user input. This limitation affects their performance in nuanced tasks such as distinguishing between stress and depression or identifying suicidal ideation.

To address these challenges, this article introduces dynamic prompt engineering and weighted transformer architecture (dynamic prompt engineering and weighted transformer architecture for mental health classification (*DynaMentA*)), a novel dual-layer transformer framework for mental health

2329-924X © 2025 IEEE. All rights reserved, including rights for text and data mining, and training of artificial intelligence and similar technologies. Personal use is permitted, but republication/redistribution requires IEEE permission. See https://www.ieee.org/publications/rights/index.html for more information.

Authorized licensed use limited to: DELHI TECHNICAL UNIV. Downloaded on June 16,2025 at 05:12:41 UTC from IEEE Xplore. Restrictions apply.

This article has been accepted for inclusion in a future issue of this journal. Content is final as presented, with the exception of pagination.

classification. The framework leverages two advanced transformer models: biomedical generative pre-trained transformer (BioGPT) [5], optimized to extract domain-specific cues from biomedical text, and decoding-enhanced BERT with disentangled attention (DeBERTa) [6], designed for context-aware classification using disentangled attention mechanisms and enhanced positional embeddings. Other transformer-based architectures, such as extra-long network (XLNet) and text-to-text transfer transformer (T5), were considered but did not provide the same level of domain grounding or contextual precision required for mental health classification. DynaMentA's design uniquely fuses biomedical and contextual reasoning into a unified, interpretable framework tailored for emotionally complex text. Key innovations of *DynaMentA* include the following.

1) *Dynamic prompt engineering*: A mechanism to generate adaptive prompts tailored to the linguistic and emotional context of the user, enhancing the extraction of relevant cues.
2) *Weighted ensemble mechanism*: A task-specific ensemble that integrates the BioGPT and DeBERTa outputs, ensuring robust performance on binary and multiclass classification tasks.
3) *Iterative feedback loop*: A simulated refinement mechanism that improves classification accuracy by iteratively adjusting the weighted ensemble outputs based on ground-truth labels.

This framework is rigorously evaluated on publicly available datasets, dataset designed for detecting severity levels of depression (DepSeverity), suicide versus depression classification natural language (SDCNL), and dataset derived from reddit posts, annotated for stress-related mental health research (Dreaddit), demonstrating significant performance improvements with an accuracy of 92.6%, an F1-score of 91.9%, and an AUC-ROC of 0.94, outperforming state-of-the-art models.

The contributions of this article are as follows.

1) *Novel framework design*: A dual-layer transformer architecture combining BioGPT and DeBERTa for context-sensitive mental health classification.
2) *Dynamic prompt engineering*: Implementation of user-specific adaptive prompts to improve linguistic cue extraction.
3) *Weighted ensemble model*: Integration of a task-specific model that balances the contributions of the BioGPT and DeBERTa outputs to ensure optimal classification performance.
4) *Comprehensive evaluation*: Demonstration of significant performance gains in multiple datasets using rigorous evaluation metrics.

By addressing the critical limitations of existing methodologies, *DynaMentA* establishes a new benchmark in computational mental health analysis, offering a scalable, interpretable, and ethically sound solution for real-world applications. The remainder of this article is organized as follows. Section II discusses previous work on mental health classification using NLP and LLMs. Section III presents the formal problem statement and the learning objective. Section IV details the proposed DynaMentA framework, including its architectural components: BioGPT, DeBERTa, dynamic prompt engineering, a weighted ensemble mechanism, and a simulated feedback loop. Section V presents the experimental setup, including the datasets, baseline configurations, evaluation metrics, and the incorporation of specialized mental health models for comparative analysis. Section VI reports the results of these experiments, encompassing comparative performance analysis with standard and domain-specific models, error analysis, interpretability through attention heatmaps, and ablation studies evaluating the contributions of core components. Section VII addresses the ethical considerations of deploying AI systems in mental health contexts. Finally, Section VIII concludes the article and outlines directions for future work.

II. Related Work

Over the last decade, social media has emerged as a valuable resource for understanding mental states and health trends [7], [8]. Studies have used linguistic patterns and social interactions on these platforms to identify risks, such as anxiety, depression, and suicidal ideation [9], [10], [11]. Initially, prediction models used techniques such as support vector machines (SVMs) using handcrafted features [12], but the rise of deep learning [13] has shifted the focus to pretrained language models such as BERT, which have demonstrated effectiveness in mental health–related NLP tasks [14].

Transformer-based models have revolutionized NLP, with their highly parallel self-attention mechanisms [15]. Notable advances include BERT, GPT, and hybrid models like bidirectional and auto-regressive transformers (BART), each optimizing the pretraining and fine-tuning paradigm for diverse tasks [16], [17]. Larger models, such as GPT-3, have outperformed their predecessors, enabling capabilities such as few-shot learning [18]. Recently, ChatGPT and GPT-4 have gained significant attention for their human-like conversational abilities, while open-source models such as large language model meta AI (LLaMA) have provided accessible alternatives for academic and industrial use [19].

In the health domain, LLMs have achieved remarkable results, particularly when fine-tuned in medical datasets [20]. mental health large language model (MentalLLM) [21] proposes a suite of instruction-tuned mental health models (e.g., fine-tuned version of alpaca LLM for mental health applications (Mental-Alpaca), Fine-tuned FLAN-T5 model for mental health tasks (Mental-FLAN-T5)), which outperform general-purpose LLMs like GPT-3.5 in task-specific evaluations using Dreaddit and SDCNL datasets. Some studies have used LLMs for sentiment analysis, emotion reasoning, and mental health classification tasks, but gaps in accuracy and performance persist [22]. Emerging models such as LLaMA model adapted for mental health-related (Mental-LLaMA) [23] and initiatives such as the single-turn to multi-turn inclusivelanguage expansion technique (SMILE) method [24] aim to address these challenges by expanding mental health datasets and improving LLM capabilities. Similarly, in addition, frameworks such as psychology-focused large language model (Psy-LLM)

Authorized licensed use limited to: DELHI TECHNICAL UNIV. Downloaded on June 16,2025 at 05:12:41 UTC from IEEE Xplore. Restrictions apply.

This article has been accepted for inclusion in a future issue of this journal. Content is final as presented, with the exception of pagination.

[25] and psychological conversational large language model (PsycoLLM) [26] integrate LLMs into mental health practice, offering real-time feedback to practitioners and advancing the role of AI in mental health support.

In this article, we employ a weighted ensemble to combine BioGPT and DeBERTa with dynamic prompt engineering and iterative feedback to improve mental health classification.

III. Problem Statement

To formalize the problem, let $X = \{x_1, x_2, \ldots, x_n\}$ represent the set of user inputs, where x_i is an individual text sample (e.g., a social media post). The goal is to assign to each input x_i a label $y_i \in Y$, where Y represents the set of mental health classes, such as {depression, stress, and suicidal ideation}. The task can be framed as a supervised learning problem, where the objective is to learn a mapping function $f : X \to Y$ that minimizes the classification error. Mathematically, this can be expressed as follows:

$$\underset{\theta}{\text{minimize}} \quad \frac{1}{N}\sum_{i=1}^{N}\mathcal{L}(f_\theta(x_i), y_i) \tag{1}$$

where

1) $\mathcal{L}$ denotes the loss function (cross-entropy loss) for multiclass classification.
2) f_θ is the parameterized model consisting of the BioGPT and DeBERTa components.
3) θ represents the model parameters optimized during training.

The challenge lies in ensuring that f_θ generalizes well across diverse linguistic patterns and contexts. To achieve this, the proposed framework employs dynamic prompt engineering to enrich input representations x_i, with contextual cues C_i. Here, C_i includes auxiliary features such as *temporal patterns* (e.g., posting frequency and timing relevant in *DepSeverity*), *syntactic structures* (e.g., fragmented or telegraphic writing seen in *SDCNL*), and *lexical markers of emotional intensity or metaphorical language* (e.g., "drowning," "trapped," frequently observed in *Dreaddit*). These cues are incorporated implicitly through dynamic prompt templates and guide both BioGPT and DeBERTa in adapting their embeddings to reflect task-relevant emotional and linguistic patterns. The final classification is performed using an ensemble method that combines predictions from BioGPT (f_{BioGPT}) and DeBERTa (f_{DeBERTa})

$$\hat{y}_i = \alpha f_{\text{BioGPT}}(x_i, C_i) + \beta f_{\text{DeBERTa}}(x_i, C_i) \tag{2}$$

where α and β are task-specific weights satisfying $\alpha + \beta = 1$. In practice, α and β are derived by performing a grid search on combinations (e.g., α from 0.1 to 0.9 in increments of 0.1, with $\beta = 1 - \alpha$, selecting the pair that produces the highest F1-score in the validation set). Furthermore, the weighted sum approach was chosen over majority voting or stacking to preserve differentiability and allow task-specific emphasis during inference, facilitating adaptability across datasets with varying linguistic profiles. This innovative architecture sets a new benchmark in computational mental health analysis by ensuring that the system not only performs efficiently, but also adapts to the diverse and context-sensitive nature of mental health expressions.

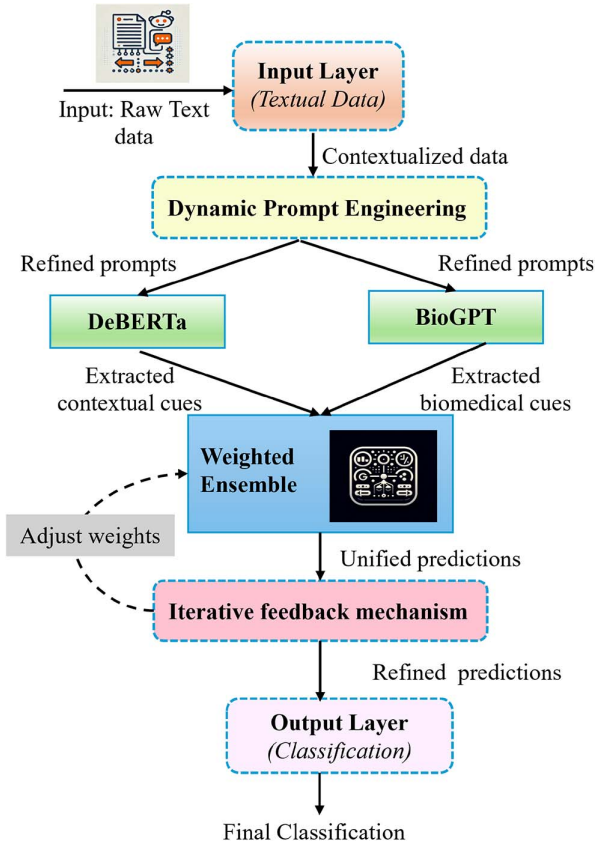


Fig. 1. Proposed DynaMentA architecture.

IV. Model Architecture

The proposed *DynaMentA* integrates two advanced transformer models, BioGPT and DeBERTa, to achieve high accuracy and robustness in mental health classification tasks. This architecture is designed to leverage the domain-specific capabilities of BioGPT for contextual cue extraction and the advanced classification abilities of DeBERTa for adaptive prediction. The two models work in tandem, their output being combined through a weighted ensemble mechanism to ensure optimal performance in binary and multiclass classification tasks. The high-level architecture of the proposed framework is illustrated in Fig. 1.

A. BioGPT

The first component of the architecture, BioGPT, is a transformer-based language model pretrained on biomedical corpora, including PubMed abstracts, pubMed central open access (PMC-OA) articles, and other publicly available biomedical datasets. The model utilizes self-attention mechanisms to extract domain-specific contextual cues from textual input, making it particularly effective in identifying linguistic patterns associated with mental health conditions. BioGPT processes an input sequence $X = \{x_1, x_2, \ldots, x_n\}$, where each x_i represents a tokenized segment of the input text. The output of

Authorized licensed use limited to: DELHI TECHNICAL UNIV. Downloaded on June 16,2025 at 05:12:41 UTC from IEEE Xplore. Restrictions apply.

This article has been accepted for inclusion in a future issue of this journal. Content is final as presented, with the exception of pagination.

BioGPT, $\mathbf{V} = \{\mathbf{v}_1, \mathbf{v}_2, \ldots, \mathbf{v}_n\}$, is a set of contextual cue vectors, each capturing semantic and syntactic information about the input text.

The processing involves a series of transformer layers, each consisting of multihead self-attention and position-wise feed-forward networks, ensuring that the model captures long-range dependencies and contextual nuances. For example, given an input such as "*I feel hopeless and can't see a way out*," BioGPT extracts primary indicators like *suicidal ideation* and secondary indicators such as *hopelessness* and *entrapment*. These cues provide a structured representation of the user's mental state, which is crucial for downstream classification.

Dynamic prompts guide BioGPT in focusing on relevant linguistic patterns during contextual cue extraction. Unlike static prompts, which remain fixed irrespective of the input, dynamic prompts are generated adaptively based on the input context and historical interactions. The dynamic prompt mechanism is modeled as a function $P_t = f(C_t, H_t, \theta)$, where C_t represents the current context derived from the input, H_t are the historical interaction data, and θ denote the learnable parameters of the prompt generation model. This mechanism ensures that BioGPT focuses on extracting the most relevant cues for the classification task at hand. For example, if a user input indicates work-related stress, the prompt dynamically adjusts to query stress-related details, such as "*Is this stress affecting your sleep or mood?*" The ability to generate task-specific prompts significantly enhances the flexibility and contextual adaptability of the model.

B. DeBERTa (Decoding-Enhanced BERT With Disentangled Attention)

The second component of the architecture, DeBERTa, serves as the classification layer of the framework. DeBERTa improves on traditional transformer architectures by incorporating disentangled attention mechanisms and enhanced relative positional embeddings. These features enable the model to capture fine-grained relationships between words and phrases, making it highly effective for understanding complex linguistic structures in mental health-related texts. DeBERTa processes the enriched input $\mathbf{x}_{\text{final}}$, which combines the original input sequence X with the contextual cues $\mathbf{V}$ extracted by BioGPT. The classification token $\mathbf{h}_{[CLS]}$ from the final transformer layer is passed through a task-specific feed-forward network to compute the probabilities of the class

$$\hat{y} = \text{softmax}(\mathbf{W} \cdot \mathbf{h}_{[CLS]} + b) \tag{3}$$

where $\mathbf{W}$ and b are trainable weights and biases, respectively, and $\hat{y}$ represents the probability distribution over the output classes. For example, given an input such as "*I feel like nothing I do is ever good enough*," the enriched input includes cues such as *low self-esteem* and *persistent doubt*. DeBERTa predicts a probability distribution that indicates the most likely mental health condition, such as *Depression* with a probability of 0.85.

C. Dynamic Prompt Engineering

To enhance adaptability across heterogeneous input distributions, we implement a dynamic prompt engineering module that conditions model behavior on instance-specific linguistic and contextual variations. Rather than appending static task instructions, we introduce lightweight, input-aware prompt templates P_i that are programmatically constructed for each input x_i using derived auxiliary signals C_i.

Let x_i be a user-generated text sample, and C_i the set of contextual features extracted during preprocessing (e.g., part-of-speech patterns, negation cues, lexical affect, and time metadata). The prompt P_i is generated as follows:

$$P_i = \text{template}(C_i) \oplus x_i \tag{4}$$

where $\text{template}(C_i)$ denotes a slot-filled prompt prefix constructed by mapping contextual features to semantic indicators (e.g., markers of temporal urgency, syntactic disfluency, and affect polarity), and $\oplus$ denotes prompt concatenation.

The prompts are injected into the tokenization layer for both BioGPT and DeBERTa and aligned with each model's tokenizer vocabulary to ensure embedding consistency. During training, templates are selected from a predefined pool and dynamically adjusted via rules or heuristics based on dataset-specific traits. No prompt tuning is performed at the embedding level; instead, the design leverages natural language scaffolds to condition attention flow and guide encoder behaviour implicitly.

This mechanism introduces inductive bias without introducing additional trainable parameters, supporting better generalization to edge-case inputs and reducing overfitting to lexical artifacts common in mental health corpora. Empirically, we observed improved performance on samples exhibiting metaphorical ambiguity or low-frequency constructs when dynamic prompts were used.

D. Weighted Ensemble Mechanism

The BioGPT and DeBERTa outputs are combined using a weighted ensemble mechanism, which balances the strengths of both models. The ensemble output is computed as follows:

$$y_{\text{ensemble}} = \alpha \cdot y_{\text{BioGPT}} + \beta \cdot y_{\text{DeBERTa}} \tag{5}$$

where α and β are task-specific weights satisfying $\alpha + \beta = 1$. These weights α and β are optimized during training using a grid search approach, ensuring that the contributions of BioGPT and DeBERTa align with the characteristics of the dataset and maximize the classification performance. These weights determine the ensemble output by appropriately balancing the predictions from both models, as demonstrated in the example. For example, if BioGPT predicts *Stress* with a probability of 0.7 and DeBERTa predicts *Stress* with a probability of 0.8, and the weights are $\alpha = 0.4$ and $\beta = 0.6$, the ensemble output is calculated as $y_{\text{ensemble}} = 0.4 \cdot 0.7 + 0.6 \cdot 0.8 = 0.76$, resulting in a final prediction of *Stress*. The fixed weighting strategy was chosen to balance the complementary strengths of BioGPT and DeBERTa while maintaining interpretability and reproducibility, which are critical in mental health applications. Although dynamic weighting strategies (e.g., attention-based ensembling)

Authorized licensed use limited to: DELHI TECHNICAL UNIV. Downloaded on June 16,2025 at 05:12:41 UTC from IEEE Xplore. Restrictions apply.

This article has been accepted for inclusion in a future issue of this journal. Content is final as presented, with the exception of pagination.

may offer additional flexibility, we prioritized transparency and deterministic behavior in this work.

E. Simulated Feedback Mechanism

The framework incorporates a simulated feedback mechanism to refine predictions and improve classification accuracy during training. In this study, the feedback is simulated using ground-truth labels from the datasets, as real-time user interactions are not available. If the model's prediction deviates from the ground truth, the feedback mechanism adjusts the ensemble weights to prioritize relevant cues extracted by BioGPT and DeBERTa. The iterative feedback loop updates weights only during training, refining model parameters based on misclassified instances to improve generalization to unseen test data. Therefore, the feedback mechanism is not deployed in real time but operates offline during training to adjust model behavior based on known ground-truth labels. For example, if an input such as "*I feel exhausted and unable to focus*" is incorrectly classified as *Stress* instead of *Depression*, the feedback mechanism adjusts the ensemble weights to prioritize the depressive cues extracted by BioGPT and DeBERTa. While effective for controlled evaluations, this feedback mechanism currently does not incorporate user input in real time. In future iterations, the integration of human-in-the-loop feedback, such as clinician corrections or user-flagged misclassifications, could enhance the adaptability of the model and allow dynamic adjustment of ensemble weights or prompt construction based on real-world interactions.

This dual-layer architecture ensures that the framework utilizes the domain-specific knowledge of BioGPT and the advanced classification capabilities of DeBERTa, achieving superior accuracy, robustness, and interpretability. The integration of dynamic prompts, weighted ensemble modeling, and simulated feedback further enhances the adaptability of the system, making it well suited for complex and context-sensitive tasks in mental health classification. The Algorithm 1 summarizes the proposed dual-layer transformer framework for contextual mental health classification.

Algorithm 1: DynaMentA: Dynamic Prompt Engineering and Weighted Transformer Architecture for Mental Health Classification.

Require: Input text samples $X = \{x_1, x_2, \ldots, x_n\}$, model parameters $\theta_{\text{BioGPT}}, \theta_{\text{DeBERTa}}$
Ensure: Final predicted labels $\hat{Y} = \{\hat{y}_1, \hat{y}_2, \ldots, \hat{y}_n\}$
Preprocess X and split into training and test sets
for each training sample x_i **do**
  Extract contextual cues C_i
  Construct dynamic prompt $P_i \leftarrow \text{template}(C_i) \oplus x_i$
  Encode with BioGPT: $\mathbf{V}_i \leftarrow \text{BioGPT}(P_i; \theta_{\text{BioGPT}})$
  Compute prediction: $y^i_{\text{BioGPT}} \leftarrow \text{softmax}(\mathbf{W}_1 \cdot \mathbf{V}_i + \mathbf{b}_1)$
end for
for each training sample x_i **do**
  Concatenate input: $\mathbf{x}_{\text{final}} \leftarrow [x_i; \mathbf{V}_i]$
  Encode with DeBERTa: $\mathbf{h}_i \leftarrow \text{DeBERTa}(\mathbf{x}_{\text{final}}; \theta_{\text{DeBERTa}})$
  Compute prediction: $y^i_{\text{DeBERTa}} \leftarrow \text{softmax}(\mathbf{W}_2 \cdot \mathbf{h}_i + \mathbf{b}_2)$
end for
for each sample i **do**
  Combine predictions: $y^i_{\text{ensemble}} \leftarrow \alpha \cdot y^i_{\text{BioGPT}} + \beta \cdot y^i_{\text{DeBERTa}}$
  Final label: $\hat{y}_i \leftarrow \arg\max(y^i_{\text{ensemble}})$
end for
return Final predictions $\hat{Y}$

V. EXPERIMENTS

To evaluate the performance of the proposed dual-layer transformer framework, we performed extensive experiments using publicly available datasets relevant to mental health classification. These datasets included annotated text samples containing user-generated content from social media platforms, forums, and clinical notes, categorized into binary and multiclass labels such as *stress*, *depression*, and *anxiety*. Data were preprocessed by tokenization, lowercasing, and removal of stop words to ensure uniformity and reduce noise. The dataset was divided into training (80%) and test (20%) sets, maintaining class distribution across all subsets. The training dataset was further divided into a 70:10 ratio in the training and validation set. Computational experiments were conducted using NVIDIA Tesla V100 GPU with 32 GB of video random access memory (VRAM). The weighted ensemble mechanism and the simulated feedback loop were evaluated in ablation studies to measure their contribution to the overall framework.

A. Datasets

To ensure a robust and generalizable mental health classification, three publicly available datasets are utilized: *DepSeverity*, *SDCNL*, and *Dreaddit*. These datasets, sourced from Reddit, provide rich textual data that reflect real-world linguistic patterns and emotional tones, covering depression severity, suicidal ideation, and stress detection.

DepSeverity consists of 3553 Reddit posts annotated into four levels of depression severity: minimal, mild, moderate, and severe. In accordance with the diagnostic and statistical manual of mental disorders, 5th Edition (DSM-5) guidelines, it supports binary and multiclass classification tasks. For example, "*I feel like I can't do anything right anymore. Nothing makes me happy.*" is labeled as *Moderate Depression*.

SDCNL contains 1895 posts annotated as either *Suicidal Ideation* or *General Depression*. For instance, the post "*I don't think I can go on anymore. Life feels pointless.*" is labeled as *Suicidal Ideation*.

Dreaddit comprises 1191 posts focusing on stress detection in domains such as social and financial stress. The posts are labeled as stress or no stress, with additional metadata. For example, "*I'm behind on rent, and I don't know how I'll make ends meet.*" is labeled as *Stress (Financial)*.

These datasets expose the framework to diverse linguistic patterns and emotional expressions, which enhances its robustness in handling mental health classification tasks. The preprocessing challenges included informal language, misspellings, and contextually ambiguous expressions, all of which could affect the accuracy of the classification. To mitigate these issues, we applied data normalization techniques such as slang replacement, spelling correction, stemming, and context-aware tokenization. These steps helped reduce noise and effectively

Authorized licensed use limited to: DELHI TECHNICAL UNIV. Downloaded on June 16,2025 at 05:12:41 UTC from IEEE Xplore. Restrictions apply.

This article has been accepted for inclusion in a future issue of this journal. Content is final as presented, with the exception of pagination.

structure the raw text for input into transformer-based models, improving overall input quality and model performance.

B. Baseline Models

To comprehensively evaluate the performance of the proposed DynaMentA framework, we compared it against three categories of baseline models: traditional classifiers, neural architectures, and state-of-the-art transformer-based language models.

Traditional machine learning models: We implemented SVMs with radial basis function (RBF) kernel and random forests (RFs) with 100 estimators as representative nonneural baselines. These models were trained on term frequency-inverse document frequency (TF-IDF) vector representations of the input text and serve to establish lower bounds on performance.

Neural models: We included long short-term memory (LSTM) networks and convolutional neural networks (CNNs) to capture sequential and local features in the text, respectively. These models were initialized with pretrained global vectors for word representation (GloVe) embeddings (300d) and trained using cross-entropy loss with Adam optimizer. Dropout and early stopping were used to prevent overfitting.

Transformer-based models: To benchmark against strong pretrained baselines, we fine-tuned BERT, robustly optimized BERT approach (RoBERTa), and XLNet using the Hugging Face Transformers library. All models were fine-tuned for 3–5 epochs using the same learning rate and batch size, with the final checkpoint selected based on the validation F1-score.

To ensure a fair comparison, all baselines were trained and evaluated on the same dataset splits and preprocessing pipeline.

C. Evaluation Metrics

Accuracy, precision, recall, F1-score, and area under the receiver operating characteristic curve (AUC-ROC) were selected as evaluation metrics to provide a balanced assessment of both the overall classification performance and the model's ability to handle class imbalances in mental health data. These metrics were chosen to reflect both general performance and sensitivity to misclassifications, which is critical in mental health prediction. Specifically, F1-score balances precision and recall, making it ideal for detecting underrepresented or overlapping classes. AUC-ROC provides a threshold-independent view of the model's discriminative power, especially important for high-stakes decisions involving stress, depression, or suicidal ideation. All metrics were computed on held-out test sets using standard scikit-learn implementations. Model performance was additionally validated with cross-validation to reduce evaluation bias.

D. Hyperparameter Settings

The training process used the AdamW optimizer with a cosine learning rate scheduler to dynamically adjust the learning rate throughout the training. A batch size of 16 was used, and early stopping with a patience of three epochs was applied based on validation loss to prevent overfitting. Both BioGPT and DeBERTa were initialized with their respective pretrained weights and fine-tuned on each mental health dataset. Hyperparameters, including learning rate, ensemble weights (α and β), dropout rate, and prompt construction parameters, were optimized using grid search. The learning rate was varied in the range 1×10^{-5} to 5×10^{-4}, and the batch sizes of $\{8, 16, 32\}$ were explored. Prompt parameters included rule-based switches for template variation based on input metadata and emotional cues, rather than any learnable prompt embeddings. Ensemble weights were selected by maximizing F1-score on the validation set across pairs satisfying $\alpha + \beta = 1$. Hyperparameter combinations were evaluated on a held-out validation split consisting of 10% of the training data, and the configuration that generates the highest macro F1-score was selected for the final training. To ensure statistical robustness, all experiments were repeated five times with different random seeds, and mean and standard deviation of performance metrics were reported.

E. Experimental Inclusion of Specialized LLMs

To enhance the rigor of our experimental design, we further benchmarked DynaMentA against specialized LLMs developed specifically for mental health prediction tasks. These include Mental-Alpaca and Mental-FLAN-T5 [21], as well as a 13-billion parameter LLaMA-based chat model focused on mental health tasks (MentaLLaMA-chat-13B) [23], which incorporate instruction tuning and psychological context to improve their relevance in mental health applications.

For fairness, the specialized models were evaluated on common benchmark datasets, Dreaddit, SDCNL, and depression Reddit (DR) using consistent preprocessing, dataset splits, and evaluation metrics, including balanced accuracy and weighted F1-score. Publicly released model checkpoints and tokenizers were used in inference mode to ensure reproducibility. Default settings were applied where specific hyperparameters were not available. The comparative performance outcomes of these models, alongside DynaMentA, are discussed in detail in the next section.

VI. Results and Discussion

The results demonstrate the significant advances achieved by the proposed DynaMentA in mental health classification. This section elaborates on performance metrics, dataset-wise results, ablation studies, error analysis, attention heatmaps, and training efficiency.

A. Comparative Performance Analysis

The proposed *DynaMentA* is compared with the baseline models, including SVM, LSTM, BERT, RoBERTa, biomedical bidirectional encoder representations from transformers (BioBERT), and ChatGPT-4.0. Table I highlights the improvements in accuracy, F1-score, and AUC-ROC across all datasets.

DynaMentA consistently outperforms all baseline models across all metrics. While ChatGPT achieves high accuracy (89.7%) and F1-score (88.8%), DynaMentA surpasses it with a

Authorized licensed use limited to: DELHI TECHNICAL UNIV. Downloaded on June 16,2025 at 05:12:41 UTC from IEEE Xplore. Restrictions apply.

This article has been accepted for inclusion in a future issue of this journal. Content is final as presented, with the exception of pagination.

TABLE I
OVERALL PERFORMANCE METRICS

Model	Acc (%)	Prec (%)	Rec (%)	F1 (%)	AUC-ROC	MCC
SVM	79.6	78.9	78.1	78.5	0.81	0.56
LSTM	81.3	80.8	80.2	80.5	0.83	0.60
BERT	87.4	86.9	86.3	86.6	0.89	0.72
RoBERTa	88.1	87.6	87.1	87.3	0.90	0.74
BioBERT	86.2	85.8	85.0	85.4	0.88	0.70
ChatGPT	89.7	89.0	88.5	88.8	0.91	0.76
Proposed	**92.6**	**92.1**	**91.7**	**91.9**	**0.94**	**0.81**

Note: The bold entries indicate best performance scores achieved across the evaluated models and the superior performance of the proposed model. MCC, Matthews Correlation Coefficient; Prec, Precision; Rec, Recall;

TABLE II
DATASET-SPECIFIC PERFORMANCE COMPARISON ACROSS MODELS

Dataset	Model	Accuracy (%)	F1 (%)	AUC-ROC
DepSeverity	SVM	79.6	78.5	0.81
	LSTM	81.3	80.5	0.83
	BERT	87.4	86.6	0.89
	RoBERTa	88.1	87.3	0.90
	BioBERT	85.2	84.5	0.87
	ChatGPT	89.1	88.5	0.91
	DynaMentA	**91.3**	**90.7**	**0.93**
SDCNL	SVM	79.2	78.8	0.80
	LSTM	81.5	80.9	0.84
	BERT	87.7	86.8	0.89
	RoBERTa	88.7	87.9	0.91
	BioBERT	86.5	85.8	0.88
	ChatGPT	90.0	89.3	0.92
	DynaMentA	**93.1**	**92.5**	**0.95**
Dreaddit	SVM	79.5	78.7	0.81
	LSTM	81.8	80.7	0.84
	BERT	87.9	86.5	0.90
	RoBERTa	89.0	88.3	0.92
	BioBERT	87.0	86.4	0.89
	ChatGPT	91.2	90.6	0.93
	DynaMentA	**92.9**	**92.3**	**0.94**

Note: The bold entries indicate best performance scores achieved across the evaluated models and the superior performance of the proposed model.

3.2% higher accuracy and a 3.1% better F1-score. Compared with BioBERT, which specializes in biomedical text, DynaMentA demonstrates a 6.4% improvement in F1-score, demonstrating its ability to integrate domain-specific and contextual information effectively.

B. Dataset-Specific Comparison

The performance of *DynaMentA* was evaluated against several baseline models, including SVM, LSTM, BERT, RoBERTa, BioBERT, and ChatGPT-4.0, across three datasets: DepSeverity, SDCNL, and Dreaddit. Table II presents a detailed comparison of accuracy, F1-score, and AUC-ROC for each model on these datasets.

The results demonstrate that *DynaMentA* consistently achieves the highest performance in all datasets. For the SDCNL dataset, which focuses on the binary classification of suicidal ideation, DynaMentA achieves an F1-score of 92.5%, significantly outperforming ChatGPT by 3.2% and BioBERT by 6.7%. Similarly, in the DepSeverity dataset, which involves multiclass classification, DynaMentA achieves an F1-score of 90.7%, outperforming RoBERTa by 3.4% and BioBERT by 6.2%.

For the Dreaddit dataset, DynaMentA achieves an accuracy of 92.9% and an F1-score of 92.3%, highlighting its ability to handle nuanced sentiments and stress-related classifications better than ChatGPT, which achieves an F1-score of 90.6%.

TABLE III
STATISTICAL SIGNIFICANCE OF DYNAMENTA'S IMPROVEMENTS

Dataset	Metric	Mean Difference	p-Value
DepSeverity	F1-score	2.2%	$p < 0.01$
SDCNL	F1-score	3.2%	$p < 0.01$
Dreaddit	F1-score	1.7%	$p < 0.01$

TABLE IV
PERFORMANCE COMPARISON OF DYNAMENTA AND SPECIALIZED LLMS ON OVERLAPPING DATASETS

Model	Dataset	Metric Type	Score (%)
Mental-Alpaca	Dreaddit	Balanced Accuracy	81.6
	SDCNL	Balanced Accuracy	72.4
Mental-FLAN-T5	Dreaddit	Balanced Accuracy	80.2
	SDCNL	Balanced Accuracy	67.7
MentaLLaMA-chat-13B	Dreaddit	Weighted F1	75.79
	DR	Weighted F1	85.68
DynaMentA	Dreaddit	Accuracy/F1-score	**92.9/92.3**
	SDCNL	Accuracy/F1-score	**93.1/92.5**
	DR	Accuracy/F1-score	**91.3/90.7**

Note: The bold entries indicate best performance scores achieved across the evaluated models and the superior performance of the proposed model.

C. Statistical Significance

To validate the observed improvements, a paired t-test was conducted between *DynaMentA* and the second-best performing model, ChatGPT-4.0, across all datasets. The results are summarized in Table III, where the p-values confirm the statistical significance of the improvement in DynaMentA performance ($p < 0.01$).

The improvements achieved by *DynaMentA* are not only statistically significant, but also practically relevant, as they consistently demonstrate the superior ability of the framework to handle both binary and multiclass mental health classification tasks in diverse datasets.

D. Comparison With Specialized Mental Health Models

Table IV summarizes the performance of DynaMentA compared with the specialized LLMs on Dreaddit, SDCNL, and DR. The evaluation includes Mental-Alpaca, Mental-FLAN-T5 [21], and MentaLLaMA-Chat-13B [23], which incorporate mental health–specific instruction tuning or domain adaptation, reflecting recent advances in task-specific language modeling.

DynaMentA consistently achieves higher scores in all datasets, outperforming specialized models by up to 15% in

Authorized licensed use limited to: DELHI TECHNICAL UNIV. Downloaded on June 16,2025 at 05:12:41 UTC from IEEE Xplore. Restrictions apply.

This article has been accepted for inclusion in a future issue of this journal. Content is final as presented, with the exception of pagination.

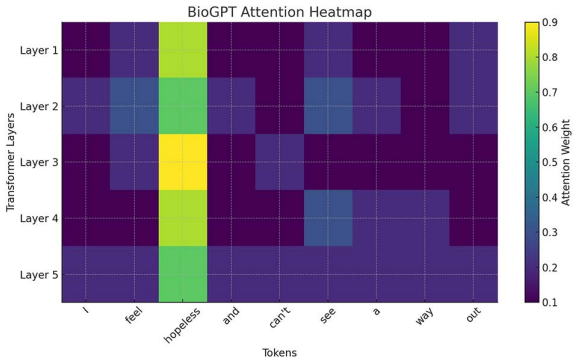


Fig. 2. BioGPT attention heatmap: Highlights critical biomedical terms contributing to predictions.

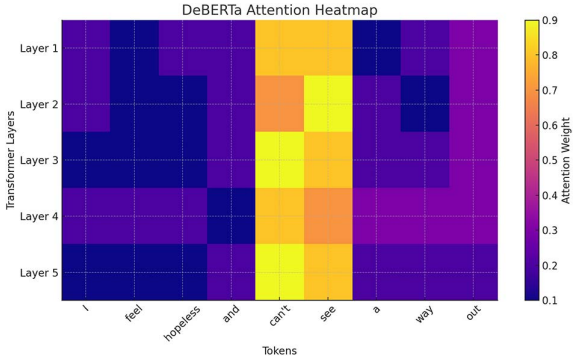


Fig. 3. DeBERTa attention heatmap: Emphasizes sentence structure and relational cues for refined classification.

both accuracy and F1-score. These findings highlight the effectiveness of our dual-layer architecture in capturing both clinical semantics (via BioGPT) and contextual depth (via DeBERTa), making it better suited for cross-task generalization in mental health classification.

E. Interpretability via Attention Maps

To enhance the interpretability of the proposed framework, attention heatmaps were generated for both BioGPT and DeBERTa. The heatmap represents the average attention weights across all heads for each layer. Fig. 2 visualizes the BioGPT attention weights, highlighting words and phrases that contribute most significantly to the prediction of the model. Similarly, Fig. 3 illustrates the attention distribution for DeBERTa, providing information on how the model processes relational and contextual cues.

The attention heatmaps reveal the following patterns.

1) *BioGPT* attends to biomedical and emotionally charged terms, such as "*hopeless*," "*exhausted*," and "*trapped*." This focus enables the model to extract domain-specific cues highly relevant to mental health classification.
2) *DeBERTa* emphasizes syntactic structure and relational context, attending to phrases such as "*can't see a way out*" or "*life feels pointless*." This enhances its capacity to refine predictions through contextual understanding.

TABLE V
ERROR ANALYSIS AND LIKELY CAUSES

Input Text	True Label	Predicted Label
"I feel tired and hopeless about work."	Depression	Stress
"Life feels pointless; I don't want to continue."	Suicidal Ideation	Depression
"I can't focus on tasks due to anxiety."	Stress	Anxiety

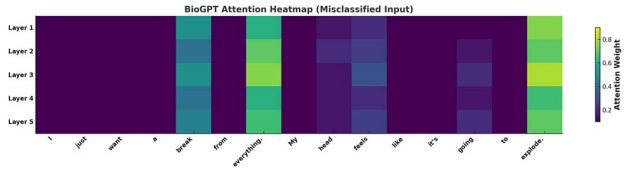


Fig. 4. BioGPT attention heatmap for a misclassified input.

This layered attention approach allows DynaMentA to capture both semantic and syntactic features, contributing to more explainable predictions. For example, in the sentence "*I feel hopeless and can't see a way out*," BioGPT focuses on indicators such as "*hopeless*" and "*trapped*" while DeBERTa refines the classification by analyzing the broader relational context, particularly, "*can't see a way out*."

Importantly, this example illustrates how attention heatmaps can enhance model transparency, allowing human observers, such as clinicians and system developers, to verify whether the model focus aligns with psychologically meaningful features. Interpretability is particularly critical in mental health applications, where understanding the rationale behind predictions can directly influence trust, adoption, and ethical deployment.

Table V provides examples of misclassified cases, helping to understand the challenges in nuanced classifications.

Errors often occur in overlapping linguistic patterns, such as between stress and depression, the model faces the ambiguity. For instance, "hopeless" is associated with both classes, leading to confusion. Incorporating additional features, such as temporal data or multimodal inputs, could reduce such errors. To illustrate the limitations of attention-based interpretability, consider the following misclassified example:

"*I just want a break from everything. My head feels like it's going to explode*."

In this case, the ground truth label is *Stress*, but the model incorrectly classifies it as *Anxiety*. The attention heatmap in Fig. 4 presents the BioGPT attention heatmap for a misclassified input. It shows that BioGPT focuses on emotionally intense tokens such as "*explode*" and "*everything*," while underemphasizing the broader situational context that suggests external overload and burnout rather than internal fear or worry.

This misalignment suggests that the model can associate high-intensity emotional language with anxiety-like patterns, even when the underlying cause reflects acute situational stress. In addition, the absence of longitudinal or situational cues makes it difficult for the model to distinguish between transient stress and clinically significant anxiety. Such cases underscore both the value and the limitations of attention heatmaps.

Authorized licensed use limited to: DELHI TECHNICAL UNIV. Downloaded on June 16,2025 at 05:12:41 UTC from IEEE Xplore. Restrictions apply.

This article has been accepted for inclusion in a future issue of this journal. Content is final as presented, with the exception of pagination.

TABLE VI
PERFORMANCE BY DATASET AND TASK TYPE

Dataset	Task	Acc (%)	F1 (%)	AUC-ROC
DepSeverity	Multi-Class	91.3	90.7	0.93
SDCNL	Binary	93.1	92.5	0.95
Dreaddit	Binary	92.9	92.3	0.94

TABLE VII
ABLATION STUDY RESULTS

Configuration	Acc (%)	F1 (%)	AUC-ROC	MCC
Without Dynamic Prompts	89.2	88.7	0.91	0.76
Without Ensemble	90.4	89.8	0.92	0.78
Full Framework	**92.6**	**91.9**	**0.94**	**0.81**

Note: The bold entries indicate best performance scores achieved across the evaluated models and the superior performance of the proposed model.

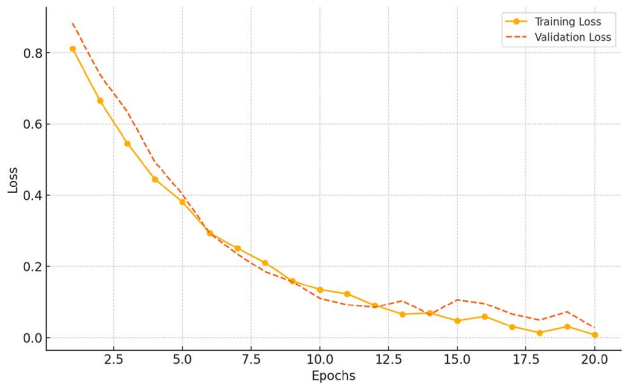


Fig. 5. Training and validation loss curves.

F. Performance by Dataset and Task Type

Table VI presents the framework performance in individual datasets for binary and multiclass classification tasks.

The framework performs consistently across datasets, with the highest accuracy of 93.1% on the SDCNL dataset, highlighting its effectiveness in distinguishing between suicidal ideation and depression. In the multiclass DepSeverity dataset, the framework achieves a high F1-score of 90.7%, demonstrating its ability to handle complex tasks involving multiple severity levels.

G. Ablation Study

To assess the importance of individual components in dynamic prompts and weighted ensemble model, Table VII presents results from the ablation study.

Removing dynamic prompts reduced accuracy by 3.4%, indicating their critical role in extracting context-specific cues. The ensemble mechanism contributes an additional 2.2% improvement in accuracy, showcasing the synergy between BioGPT and DeBERTa.

H. Training Efficiency

The framework with 18 epochs converges within 12 epochs after reaching the threshold condition, demonstrating computational efficiency. Early stopping ensures that the model is not overfitting while maintaining high generalization performance. Fig. 5 shows the training and validation loss curves, illustrating the convergence of the framework.

VII. ETHICAL CONSIDERATIONS

The use of AI models for mental health classification raises several ethical concerns that must be carefully addressed.

1) *Privacy and data security*: Mental health data is inherently sensitive. Ensuring robust mechanisms for data anonymization, encryption, and secure storage is paramount to prevent misuse or breaches.
2) *Bias and fairness*: Training data can contain inherent biases related to language, demographics, or cultural contexts. These biases could lead to skewed predictions, disproportionately affecting underrepresented groups. Rigorous testing and bias mitigation strategies are essential.
3) *Informed consent*: Collecting and using data for training purposes must be accompanied by explicit, informed consent of the individuals, ensuring transparency about how their data will be used.
4) *Misuse and overreliance*: AI models should not be used as standalone diagnostic tools. They must complement, not replace, professional mental health practitioners to avoid the risks of misdiagnosis or inappropriate interventions.
5) *Transparency and accountability*: Providing explanations for predictions is critical to building trust with users and practitioners. Models must include mechanisms for error reporting and accountability in case of inaccuracies or harm.
6) *Ethical deployment*: Deployment in real-world scenarios must align with ethical guidelines and regulatory standards, particularly in regions with stringent data protection laws such as general data protection regulation (GDPR) or health insurance portability and accountability act (HIPAA).

By proactively addressing these ethical considerations, the framework can ensure its responsible development and deployment while prioritizing the well-being and trust of its users.

VIII. CONCLUSION

This article proposes *DynaMentA*, a dual-layer transformer framework that combines BioGPT's biomedical expertise with DeBERTa's contextual modeling to address the complexities of mental health classification. Through dynamic prompt engineering and a weighted ensemble mechanism, DynaMentA adapts to diverse emotional and linguistic contexts, delivering robust predictions for both binary and multiclass tasks. An iterative feedback loop further enhances adaptability and reliability.

Authorized licensed use limited to: DELHI TECHNICAL UNIV. Downloaded on June 16,2025 at 05:12:41 UTC from IEEE Xplore. Restrictions apply.

This article has been accepted for inclusion in a future issue of this journal. Content is final as presented, with the exception of pagination.

Evaluations in the DepSeverity, SDCNL, and Dreaddit datasets demonstrate significant improvements in accuracy, recall, and F1-score, outperforming state-of-the-art baselines.

While *DynaMentA* has shown considerable advancements, it also has limitations. Its reliance on textual data restricts applicability to individuals who express mental health states through written language, excluding those who communicate verbally or nonverbally. Additionally, the use of Reddit-based datasets, although selected for their linguistic openness and relevance, may limit generalizability between cultures and platforms. The simulated feedback mechanism, while effective during training, does not incorporate real-time user input, which is crucial for adaptive systems. Future work will address these challenges by extending the evaluation to other platforms (e.g., X, Facebook, and clinical data) and integrating multimodal inputs, such as audio, video, and physiological signals for a more holistic understanding of mental health. Incorporating real-time human feedback and collaborating with mental health professionals will enhance clinical relevance, personalization, and trust. In particular, future development will explore human-in-the-loop mechanisms, where clinical input could refine predictions, guide prompt adaptation, and dynamically adjust ensemble weights. Furthermore, integrating user-specific language modeling in secure, consent-based environments (e.g., therapeutic chatbots) could enable more personalized and context-aware mental health support. These enhancements would bring DynaMentA closer to real-world deployment, ensuring greater inclusivity, adaptability, and societal impact.

REFERENCES

[1] Y. Ibrahimov, T. Anwar, and T. Yuan, "Explainable AI for mental disorder detection via social media: A survey and outlook," 2024, *arXiv:2406.05984.*

[2] M. Kerasiotis, L. Ilias, and D. Askounis, "Depression detection in social media posts using transformer-based models and auxiliary features," *Social Netw. Anal. Mining*, vol. 14, no. 1, 2024, Art. no. 196.

[3] M. A. K. Raiaan et al., "A review on large language models: Architectures, applications, taxonomies, open issues and challenges," *IEEE Access*, vol. 12, pp. 26839–26874, 2024.

[4] S. Nerella et al., "Transformers and large language models in healthcare: A review," *Artif. Intell. Med.*, vol. 154, Aug. 2024, Art. no. 102900. https://doi.org/10.1016/j.artmed.2024.102900

[5] R. Luo et al., "BioGPT: Generative pre-trained transformer for biomedical text generation and mining," *Briefings Bioinf.*, vol. 23, no. 6, 2022, Art. no. bbac409.

[6] P. He, X. Liu, J. Gao, and W. Chen, "DeBERTa: Decoding-enhanced BERT with disentangled attention," 2020, *arXiv:2006.03654.*

[7] J. Kim et al., "A systematic review of the validity of screening depression through Facebook, Twitter, Instagram, and Snapchat," *J. Affective Disorders*, vol. 286, pp. 360–369, May 2021.

[8] S. Dalal, S. Jain, and M. Dave, "Review of advancements in depression detection using social media data," *IEEE Trans. Computat. Social Syst.*, vol. 12, no. 1, pp. 77–100, Feb. 2025.

[9] J. H. Shen and F. Rudzicz, "Detecting anxiety through reddit," in *Proc. 4th Workshop Comput. Linguistics Clin. Psychol.—Linguistic Signal Clin. Reality*, Aug. 2017, pp. 58–65.

[10] F. T. Giuntini et al., "A review on recognizing depression in social networks: Challenges and opportunities," *J. Ambient Intell. Humanized Comput.*, vol. 11, no. 11, pp. 4713–4729, 2020.

[11] M. Garg, "Towards mental health analysis in social media for low-resourced languages," *ACM Trans. Asian Low-Resour. Lang. Inf. Process.*, vol. 23, no. 3, pp. 1–22, 2024.

[12] S. Almutairi, M. Abohashrh, H. H. Razzaq, M. Zulqarnain, A. Namoun, and F. Khan, "A hybrid deep learning model for predicting depression symptoms from large-scale textual dataset," *IEEE Access*, vol. 12, pp. 168477–168499, 2024.

[13] M. Ahmad Wani, M. A. ELAffendi, K. A. Shakil, A. Shariq Imran, and A. A. Abd El-Latif, "Depression screening in humans with AI and deep learning techniques," *IEEE Trans. Comput. Social Syst.*, vol. 10, no. 4, pp. 2074–2089, Aug. 2023.

[14] C. M. Greco, A. Simeri, A. Tagarelli, and E. Zumpano, "Transformer-based language models for mental health issues: A survey," *Pattern Recognit. Lett.*, vol. 167, pp. 204–211, Mar. 2023.

[15] A. Pandey and S. Kumar, "Mental health and stress prediction using NLP and transformer-based techniques," in *Proc. IEEE Symp. Wireless Technol. Appl. (ISWTA)*, Jul. 2024, pp. 61–66.

[16] L. Ilias, S. Mouzakitis, and D. Askounis, "Calibration of transformer-based models for identifying stress and depression in social media," *IEEE Trans. Comput. Social Syst.*, vol. 11, no. 2, pp. 1979–1990, Apr. 2023.

[17] S. Ji, T. Zhang, L. Ansari, J. Fu, P. Tiwari, and E. Cambria, "MentalBERT: Publicly available pretrained language models for mental healthcare," 2021, *arXiv:2110.15621.*

[18] B. Lamichhane, "Evaluation of ChatGPT for NLP-based mental health applications," Mar. 2023, arXiv.org. Nov 1, 2024. [Online]. Available: http://arxiv.org/abs/2303.15727

[19] M. Arcan, D.-P. Niland, and F. Delahunty, "An assessment on comprehending mental health through large language models," 2024, *arXiv:2401.04592.*

[20] Z. Guo, A. Lai, J. H. Thygesen, J. Farrington, T. Keen, and K. Li, "Large language models for mental health applications: Systematic review," *JMIR Mental Health*, vol. 11, no. 1, 2024, Art. no. e57400.

[21] X. Xu et al., "Mental-LLM: Leveraging large language models for mental health prediction via online text data," *Proc. ACM Interactive, Mobile, Wearable Ubiquitous Technol.*, vol. 8, no. 1, pp. 1–32, 2024.

[22] K. Yang, S. Ji, T. Zhang, Q. Xie, and S. Ananiadou, "On the evaluations of ChatGPT and emotion-enhanced prompting for mental health analysis," 2023, *arXiv:2304.03347.*

[23] K. Yang, T. Zhang, Z. Kuang, Q. Xie, J. Huang, and S. Ananiadou, "MentaLLaMA: Interpretable mental health analysis on social media with large language models," in *Proc. ACM Web Conf.*, 2024, pp. 4489–4500.

[24] H. Qiu, H. He, S. Zhang, A. Li, and Z. Lan, "Smile: Single-turn to multi-turn inclusive language expansion via ChatGPT for mental health support," 2023, *arXiv:2305.00450.*

[25] T. Lai et al., "Psy-LLM: Scaling up global mental health psychological services with AI-based large language models," 2023, *arXiv:2307.11991.*

[26] J. Hu et al., "PsycoLLM: Enhancing LLM for psychological understanding and evaluation," 2024, *arXiv:2407.05721.*



Akshi Kumar (Senior Member, IEEE) is the Director of Postgraduate Research and Chair of Research Ethics with the School of Computing, Goldsmiths, University of London, U.K. She received a Ph.D. in computer engineering in 2011 from Delhi University, India, the M.Tech degree in computer engineering in 2005 with Honours from Guru Gobind Singh Indraprastha University, Delhi, India, and B.E. in computer engineering in 2003 with Honours from Maharshi Dayanand University, India. In 2021, she completed a postdoctoral research fellowship from the Federal Institute of Education, Science and Technology of Ceará, Brazil. With over a decade of experience in academia and research, her work spans Natural Language Processing (NLP), AI ethics, and explainable AI, with a growing focus on affective computing, health informatics, and cyber informatics. Her work explores how emotionally intelligent and ethically grounded AI systems can support clinical decision-making, enhance mental health assessment, and advance digital health equity. In parallel, she actively contributes to tackling misinformation, promoting digital integrity, and advancing AI literacy, particularly in the context of generative AI models and their societal implications. Her research interests include the development of human-centered, transparent AI solutions for high-stakes domains such as healthcare, well-being, and public communication. She is recognised among the Top 2% Highly-Cited Scientists in the World (2021–2024) by Stanford University and was endorsed by the Royal Academy of Engineering (UK) in 2022 as an Exceptional Promise in Data Science and AI. Dr. Kumar has authored numerous journal articles and conference papers and is also the author of book titled "Language Intelligence: Expanding Frontiers in NLP" (IEEE-Wiley, 2024).

Authorized licensed use limited to: DELHI TECHNICAL UNIV. Downloaded on June 16,2025 at 05:12:41 UTC from IEEE Xplore. Restrictions apply.

This article has been accepted for inclusion in a future issue of this journal. Content is final as presented, with the exception of pagination.



Aditi Sharma (Member, IEEE) received the Ph.D. degree in affective computing from Delhi Technological University, Delhi, India, in 2023.

She is an Assistant Professor with Thapar Institute of Engineering and Technology, Patiala, Punjab, India. She has more than 5 years of experience in academia. Her research interests include affective computing, machine learning, predictive healthcare, and text summarization.

Dr. Sharma received the "Commendable Research Award for Excellence in Research" for her work at Delhi Technological University for the last three consecutive years. She has multiple publications in high-impact *SCI/SCIE* journals. She holds professional memberships in ACM, CSI, and IAENG.



Saurabh Raj Sangwan received the bachelor's degree in computer science and engineering from Deenbandhu Chhotu Ram University of Science and Technology (DCRUST), in 2016. Murthal, India, the M.Tech. degree in software engineering from the Department of Computer Science and Engineering, Delhi Technological University, Delhi, India, in 2018, and the Ph.D. degree in computer science and engineering from Netaji Subhas University of Technology, New Delhi, India, in 2022.

He is an Assistant Professor with the Department of Computer Science and Engineering, Artificial Intelligence and Machine Learning, GL Bajaj Institute of Technology and Management, Greater Noida, India. His research has been published in high-impact journals and presented at reputed international conferences in the domains of data science and computational intelligence. His research interests include health data mining, cyber informatics, and natural language processing, with a particular emphasis on applying AI-driven methods to complex real-world problems in healthcare and online safety.

Dr. Sangwan is a recipient of the Commendable Research Award from NSUT, Delhi, twice in recognizing his sustained scholarly contributions.

Authorized licensed use limited to: DELHI TECHNICAL UNIV. Downloaded on June 16,2025 at 05:12:41 UTC from IEEE Xplore. Restrictions apply.

Effect of Interface Trap Charges on Improved Junctionless Nanowire Field Effect Transistor

Bharti
Department of Electronics and Communication Engineering
Delhi Technological University
Delhi, India
bhartigndit@gmail.com

Poornima Mittal
Department of Electronics and Communication Engineering
Delhi Technological University
Delhi, India
poornimamittal@dtu.ac.in

2025 Devices for Integrated Circuit (DevIC) | 979-8-3503-9110-7/25/$31.00 ©2025 IEEE | DOI: 10.1109/DevIC63749.2025.11012140

***Abstract*— This paper investigates the reliability issues caused by Interface Trap Charges (ITCs) in the Improved Junctionless Nanowire Field Effect Transistor (Improved-JL-NWFET). These fixed localized charges formed at the channel-oxide interface during fabrication due to radiation, stress, process variations, and hot carrier damage, significantly impacting device characteristics. This paper analyzes their effects on key performance parameters and compares results with a conventional JL-NWFET. Both donor (+ve) and acceptor (−ve) ITCs in the channel/gate oxide interface region are examined for their influence on electrical and analog parameters. The results indicate that Improved-JL-NWFET exhibits more immunity against degradation in electrical and analog parameters compared to its conventional counterpart devices in the presence of positive and negative ITCs.**

Keywords— Core-Shell (CS), Dual Material Gate (DMG), Interface Trap Charge (ITC), Junctionless Nanowire FET (JL-NWFET).

I. INTRODUCTION

Nanowire Field-Effect Transistor (NWFET) having cylindrical structure offers enhanced gate control compared to Double-Gate (DG) FETs and FinFETs while effectively mitigating Short Channel Effects (SCEs) [1]. Meanwhile, Junctionless (JL) NWFETs have emerged as strong contenders to conventional junction-based NWFETs, primarily due to their simpler fabrication process [2, 3]. Unlike traditional junction-based NWFET, JL-NWFET does not require highly precise doping profiles in the Source/Drain (S/D) regions, nor do they depend on high-temperature dopant activation. However, JL-NWFET faces challenges such as incomplete volume depletion [4], which results in high leakage current and low drive current [5]. To address these challenges, researchers have investigated innovative structural modifications.

Among them, the Core-Shell (CS) channel structure, which incorporates a central core surrounded by shells in the source, drain, and channel regions, has demonstrated significant potential in minimizing leakage currents in JL-NWFETs [4, 6-7]. However, the CS structure alone does not enhance the device's drive current. To address this limitation, the integration of Dual Material Gate (DMG) configurations with gate sidewall spacers in the core-shell structure, aiming to improve carrier mobility while effectively minimizing leakage current, has been reported [8]. This paper presents an Improved JL-NWFET (Improved-JL-NWFET) that incorporates the combined benefits of CS structure in the channel, a DMG design in gate material with a gate sidewall spacer.

Apart from addressing SCEs, ensuring device reliability is crucial, especially for nanoscale transistors. During fabrication, various charges are introduced into the oxide layer and accumulate at the channel-gate oxide interface, negatively impacting performance. These trap charges originate from process-induced, stress-induced, and radiation-induced damage [9]. Previous research has extensively examined the effects of localized charges on JL Trigate MOSFET [10], Tunnel FET [11], and JL-NWFET [12]. Donor interface traps act as positive localized charges when devoid of electrons, whereas acceptor interface traps function as negative localized charges when filled with electrons [13]. Understanding these charge dynamics is essential for improving the stability and reliability of advanced nanoscale devices.

This paper analyses the performance and reliability issues of Improved-JL-NWFET and its counterparts JL-NWFET and NWFET due to interface trap charges. It is structured into four sections: Section I presents the introduction, while Section II defines the parameters of three devices. Section III presents the results and discussion, including a comparative analysis of Improved-JL-NWFET, JL-NWFET, and NWFET. Finally, Section IV summarizes the key findings from the analysis.

II. DEVICE STRUCTURE

Fig. 1 (a) and (b) present 3-D and 2-D representations of Improved-JL-NWFET, respectively. Fig. 2 (a) illustrates the single 3-D view which is same for both conventional JL-NWFET and NWFET. Furthermore, the 2-D structure for conventional JL-NWFET and NWFET are displayed in Fig. 2 (b) and (c), respectively. The structural parameters of the devices are summarized in Table I. The Improved-JL-NWFET design features a core region with opposite doping (p-type), leading to the formation of a reduced n-type channel known as the shell region. The SiO_2 serves as the gate oxide, while HfO_2 is employed as the gate sidewall spacer [14]. The overall silicon thickness (t_{si}) is determined by the core thickness (t_{core}) and shell (t_{shell}) thicknesses, following the relation $t_{si} = (2 \times t_{shell}) + t_{core}$ [4]. The device simulations are conducted using the SILVACO ATLAS TCAD 3-D device simulator [15]. In the Improved-JL-NWFET structure, t_{core} is set to 10 nm, which is half of t_{si} [16]. The DMG configuration incorporates two gate metals (M_1 and M_2), each extending 15 nm, with a work function difference of 0.5 eV between them [17].

979-8-3503-9110-7/25/$31.00 ©2025 IEEE

Authorized licensed use limited to: DELHI TECHNICAL UNIV. Downloaded on June 04,2025 at 05:25:20 UTC from IEEE Xplore. Restrictions apply.

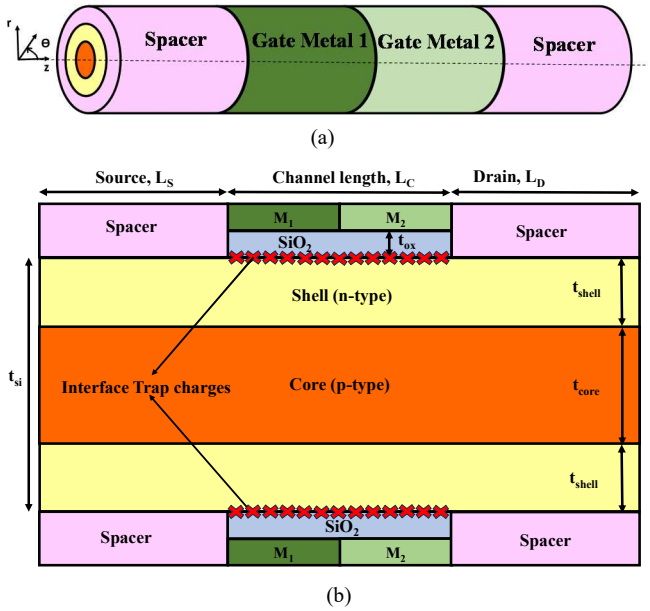


Fig. 1. (a) A 3-D structure and (b) a 2-D schematic cross-section of the Improved-JL-NWFET.

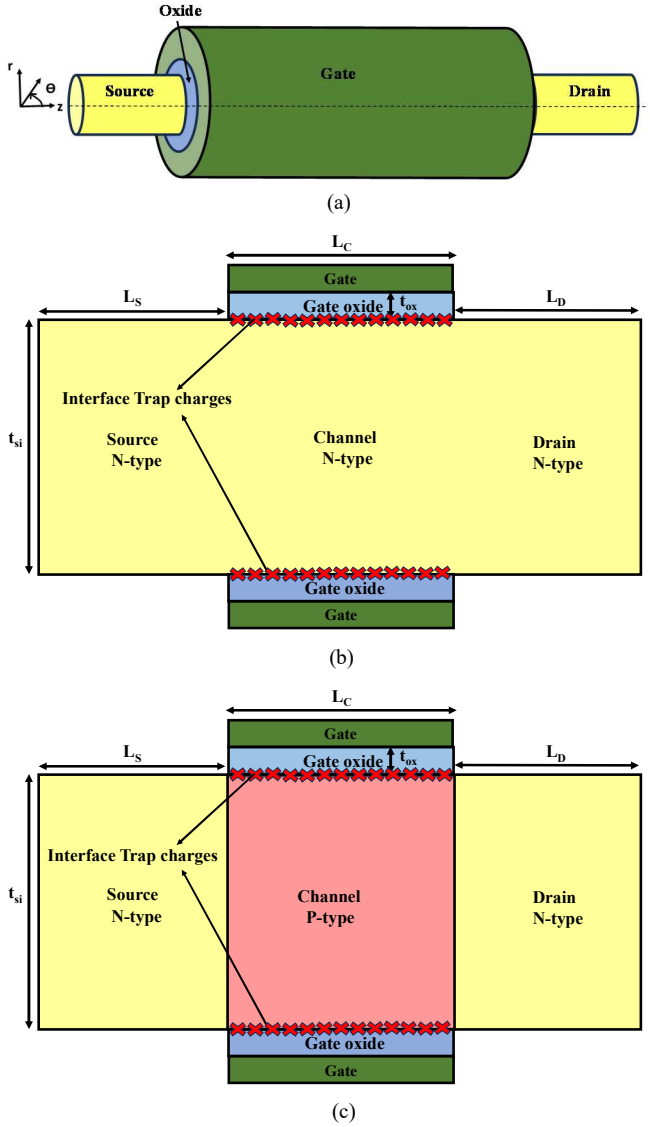


Fig. 2. (a) A 3-D structure of conventional JL-NWFET and conventional NWFET, (b) a 2-D schematic cross-section of the conventional JL-NWFET, and (c) conventional NWFET.

TABLE I. DEVICE PARAMETERS

Parameter	NWFET	JL-NWFET	Improved-JL-NWFET	
Channel Length, L_C	30 nm	30 nm	15 nm (L_{M1})	15 nm (L_{M2})
Channel thickness, t_{si}	10 nm	10 nm	10 nm	
Gate oxide, t_{ox}	1 nm	1 nm	1 nm	
Gate work function	4.8 eV	5.1 eV	5.1 eV (M_1)	4.6 eV (M_2)
Channel doping, N_D	1×10^{16} cm^{-3}	1×10^{19} cm^{-3}	1×10^{19} cm^{-3}	
Core doping N_A,	-	-	1×10^{19} cm^{-3}	
S/D doping	1×10^{18} cm^{-3}	1×10^{19} cm^{-3}	1×10^{19} cm^{-3}	
Length of S/D L_S/L_D	25 nm	25 nm	25 nm	

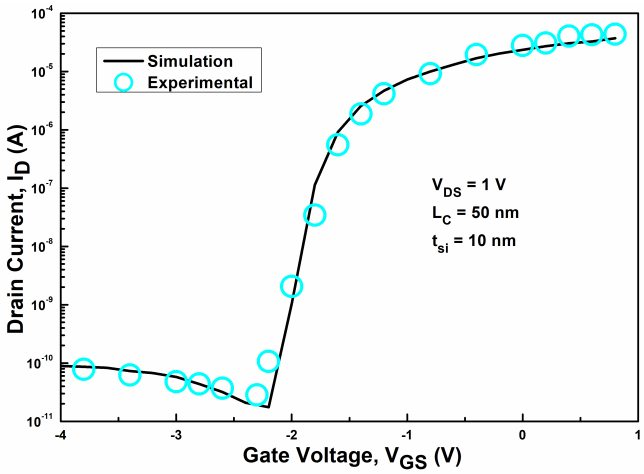


Fig. 3. Calibration of simulation models by reproducing the experimental work [3].

Moreover, in this paper, the effect of ITC is analyzed by considering equivalent positive (acceptor) and negative (donor) charges. The value of interface trap charge density ($N_f = 1\times 10^{12}$ cm^{-2}) is chosen based on the literature that is already available [18, 19]. The default models of ATLAS TCAD have been calibrated after reproducing the experimental work reported in [3] corresponding to V_{DS} = 1 V, and the transfer characteristics are shown in Fig. 3. The included models encompass the non-local BTBT model for electron tunneling. To account for carrier mobility, the field and concentration-dependent models are utilized. Additionally, the Lombardi CVT model and the band gap narrowing model are activated to accommodate inversion layer mobility and high doping in the channel, respectively. The Shockley-Read-Hall and Auger recombination models have been employed to account for carrier lifetimes and impact ionization, respectively. Numerical solutions are obtained using the Gummel and Newton methods.

III. RESULTS AND DISCUSSION

The effective flat band voltage (V_{fb}') due to the presence of ITC is given by [10]

$$V_{fb}' = V_{fb} - \frac{qN_f}{C_{ox}} \quad (1)$$

Authorized licensed use limited to: DELHI TECHNICAL UNIV. Downloaded on June 04,2025 at 05:25:20 UTC from IEEE Xplore. Restrictions apply.

where V_{fb}, q, N_f, and C_{ox} denote flat band voltage in the absence of ITCs, elementary charge, density of ITCs per unit area, and gate oxide capacitance per unit area, respectively. Fig. 4 depicts the threshold voltage (V_T) variation in Improved-JL-NWFET, JL-NWFET, and NWFET under positive, negative, and no ITCs. It is observed that negative ITC increases the V_T while positive ITC decreases the V_T in devices. Since V_T directly depends on V_{fb} in any JL transistors, an increase in V_{fb}' due to negative ITC results in a higher V_T, whereas a decrease in V_{fb}' caused by positive ITC lowers V_T as noted in (1). Specifically, negative ITC increases V_T by 3.79% in Improved-JL-NWFET, 6.97% in JL-NWFET, and 5.40% in NWFET compared to no ITC present, while positive ITC reduces V_T by 4.86% in Improved-JL-NWFET, 8.22% in JL-NWFET, and 15.70% in NWFET. Notably, Improved-JL-NWFET exhibits lower variations in V_T compared to JL-NWFET and NWFET in the presence of positive or negative ITC. This improved stability can be attributed to the benefits of a DMG structure in Improved-JL-NWFET, which helps in enhancing resistance to ITC-induced V_T fluctuations [20].

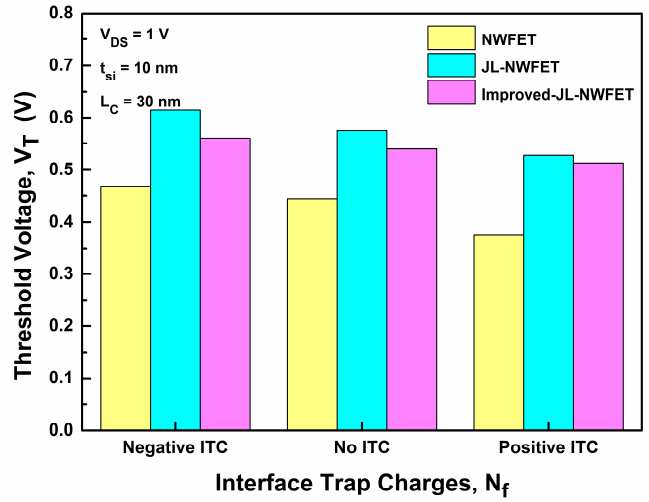


Fig. 4. Comparison of the threshold voltage of Improved-JL-NWFET, JL-NWFET, and NWFET under different ITCs.

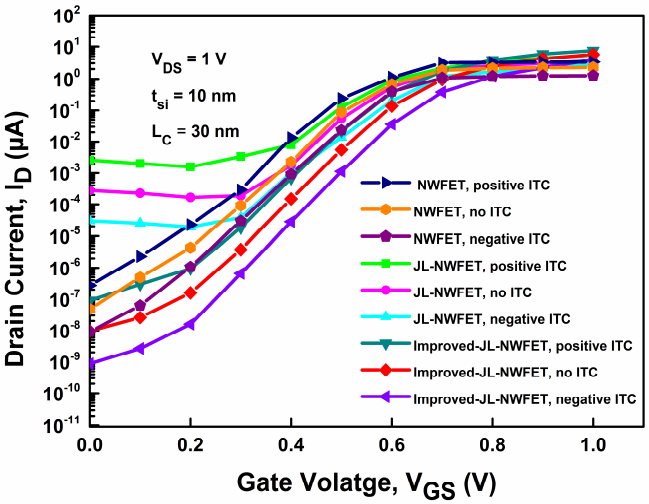


Fig. 5. Transfer characteristics of Improved-JL-NWFET, JL-NWFET, and NWFET under different ITCs.

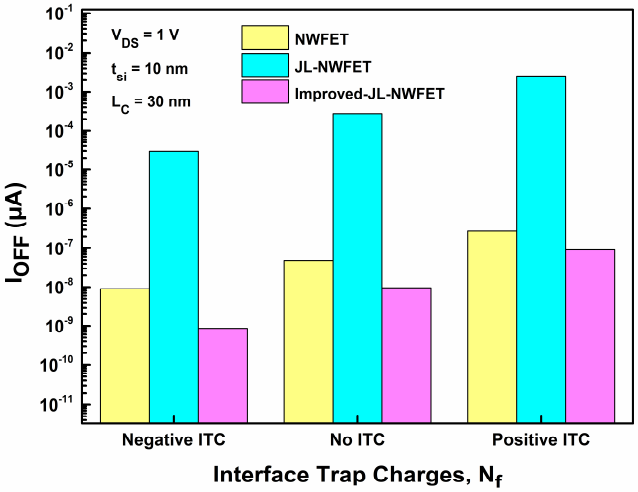


Fig. 6. Comparison of I_{OFF} of Improved-JL-NWFET, JL-NWFET, and NWFET under different ITCs.

Fig. 5 presents the transfer characteristics under different ITC conditions (positive, negative, and absence of ITC) for Improved-JL-NWFET, JL-NWFET, and NWFET. The impact of ITCs is more pronounced in the subthreshold region, as variations in the V_{fb}' due to the presence of ITCs affect the device in this regime. Consequently, ITCs lead to greater degradation in leakage current (I_{OFF}) in all three devices. However, the effect of ITCs on the ON-state current (I_{ON}) at V_{GS} = 1 V is relatively minimal for the given three devices. The negative ITC increases V_{fb}', which increases the energy barrier for band-to-band tunneling (BTBT), thereby reducing BTBT current during the OFF-state. In contrast, positive ITC reduces Vfb', lowers the tunneling barrier, and subsequently enhances BTBT. This influence of ITCs on BTBT further contributes to the degradation of subthreshold characteristics in both devices. However, the I_{OFF} at V_{GS} = 0 V is lower in Improved-JL-NWFET due to the presence of an oppositely doped core that helps in the depletion of shell region during OFF-state as compared to its counterparts JL-NWFET and NWFET.

The influence of positive, negative, and absence of ITCs on the I_{OFF} in Improved-JL-NWFET, JL-NWFET, and NWFET are compared in Fig. 6. It is observed that negative ITC resulted in a lower I_{OFF}, while positive ITC led to a higher I_{OFF}, as discussed in Fig. 5. Additionally, negative ITC reduces I_{OFF} by one order of magnitude in Improved-JL-NWFET, JL-NWFET, and NWFET compared to when no ITC is present, whereas positive ITC increase I_{OFF} by one order of magnitude in the given three devices. Notably, the Improved-JL-NWFET demonstrates a reduction in I_{OFF} by five orders of magnitude compared to the JL-NWFET and by one order of magnitude compared to the NWFET, regardless of the presence of positive or negative ITC. This significant improvement in I_{OFF} is attributed to the cumulative benefits of the core that helps in channel depletion and the gate side wall spacer that depletes the channel beyond the gate region during the OFF-state. Additionally, DMG helps further reduce the I_{OFF} by increasing the tunneling width, leading to lower leakage current [5].

Authorized licensed use limited to: DELHI TECHNICAL UNIV. Downloaded on June 04,2025 at 05:25:20 UTC from IEEE Xplore. Restrictions apply.

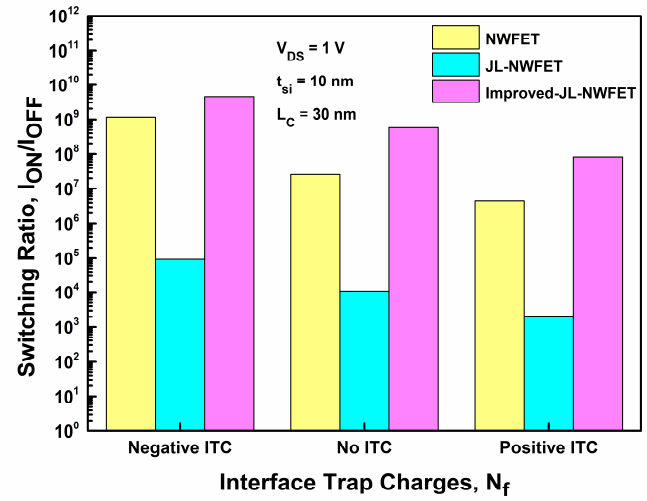


Fig. 7. Comparison of switching ratio of Improved-JL-NWFET, JL-NWFET, and NWFET under different ITCs.

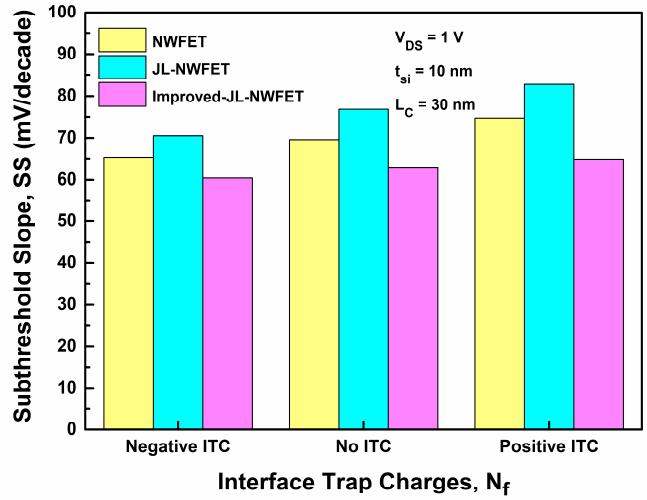


Fig. 8. Comparison of the subthreshold slope of Improved-JL-NWFET, JL-NWFET, and NWFET under different ITCs.

Subsequently, Fig. 7 illustrates the effects of positive, negative, and absent ITCs on the switching ratio (I_{ON}/I_{OFF}) in Improved-JL-NWFET, JL-NWFET, and NWFET. The ITCs have a more significant effect on I_{OFF} than on I_{ON}, the switching ratio is largely determined by changes in I_{OFF}. The negative ITC improves the I_{ON}/I_{OFF} ratio by one order of magnitude in both Improved-JL-NWFET and JL-NWFET and by two orders of magnitude in NWFET compared to the absence of ITC, while positive ITC reduces the switching ratio by one order of magnitude in all three devices. Additionally, Improved-JL-NWFET exhibits less variation in the switching ratio compared to JL-NWFET and NWFET in the presence of positive or negative ITCs, which is primarily due to the considerable reduction in I_{OFF}, as discussed in Fig. 6.

The Subthreshold Slope (SS) variation of Improved-JL-NWFET, JL-NWFET, and NWFET under the influence of positive, negative, and absence of ITC is portrayed in Fig. 8. The SS is referred to as [2]

$$SS = \frac{\partial V_{GS}}{\partial \log_{10}(I_D)} \quad \text{mV/decade} \qquad (2)$$

It is observed that negative ITC leads to a decrease in SS, while positive ITC results in an increase in SS.

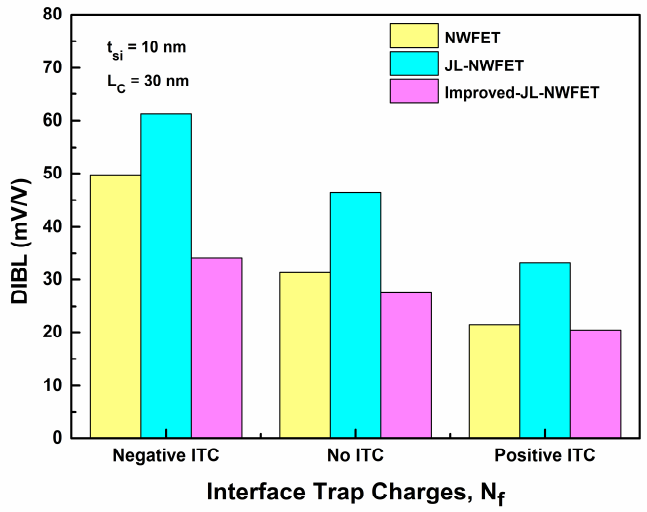


Fig. 9. Comparison of the DIBL of Improved-JL-NWFET, JL-NWFET, and NWFET under different ITCs.

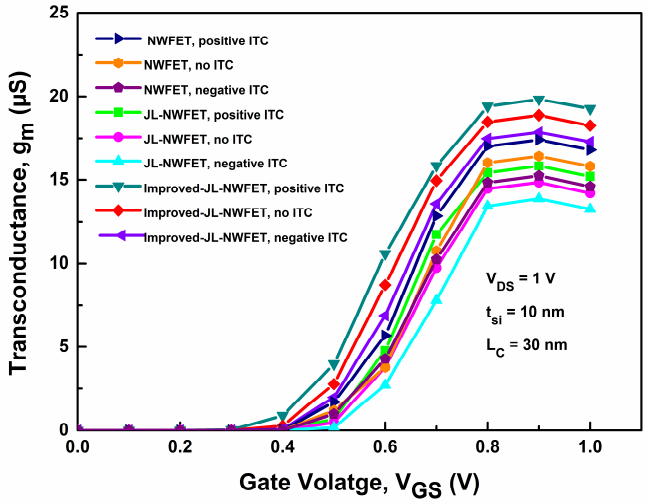


Fig. 10. Comparison of the transconductance of Improved-JL-NWFET, JL-NWFET, and NWFET under different ITCs.

The SS variation follows the same trend as that in I_{OFF} since SS is closely dependent on I_{OFF}. Further, negative ITC reduces SS by 3.65% in Improved-JL-NWFET, 8.20% in JL-NWFET, and 6.18% in NWFET compared to the no ITC condition, whereas positive ITC increases SS by 3.36% in Improved-JL-NWFET, 7.68% in JL-NWFET, and 7.32% in NWFET. Notably, Improved-JL-NWFET exhibits smaller variations in SS compared to JL-NWFET and NWFET when positive or negative ITC is present. This improvement in SS is primarily attributed to the substantial reduction in I_{OFF} observed in Improved-JL-NWFET, as discussed in Fig. 6, which results in a steeper SS compared to its counterpart.

The Drain Induced Barrier Lowering (DIBL) refers to the reduction in threshold voltage caused by an increase in drain voltage and is expressed as [21]

$$DIBL = \frac{V_T(V_{DS} = 0.05\,V) - V_T(V_{DS} = 1\,V)}{(V_{DS} = 1\,V) - (V_{DS} = 0.05\,V)} \quad mV/V \qquad (3)$$

The DIBL variation of Improved-JL-NWFET, JL-NWFET, and NWFET under the influence of positive, negative, and absence of ITC is depicted in Fig. 9. The positive ITC reduces DIBL by 25.74% in Improved-JL-NWFET, 28.46% in JL-NWFET, and 31.44% in NWFET compared to the no ITC

Authorized licensed use limited to: DELHI TECHNICAL UNIV. Downloaded on June 04,2025 at 05:25:20 UTC from IEEE Xplore. Restrictions apply.

condition, whereas negative ITC increases DIBL by 24.10% in Improved-JL-NWFET, 31.81% in JL-NWFET, and 58.93% in NWFET. Notably, Improved-JL-NWFET exhibits smaller variations in DIBL compared to JL-NWFET and NWFET when positive or negative ITC is present. This improvement in DIBL is due to the DMG architecture which mitigates the impact of drain voltage variation on V_T fluctuations compared to JL-NWFET and NWFET without DMG structure [21].

The transconductance (g_m) stands out as a crucial analog metric in assessing devices, and it is expressed as [16]

$$g_m = \frac{\partial I_D}{\partial V_{GS}}\Big|_{V_{DS}=\text{constant}} \quad (4)$$

As observed in Fig. 10, the influence of ITCs on g_m reveals that negative ITCs reduce g_m by 5.35% in Improved-JL-NWFET, 6.81% in JL-NWFET, and 7.59% in NWFET compared to the no ITC condition. Moreover, positive ITCs enhance g_m by 5.41% in Improved-JL-NWFET, 6.98% in JL-NWFET, and 6.32% in NWFET compared to the no ITC condition. Notably, Improved-JL-NWFET exhibits less variation in g_m than JL-NWFET and NWFET. Moreover, the higher g_m observed in Improved-JL-NWFET is attributed to the DMG structure, which enhances carrier mobility in the channel, offering a performance advantage over conventional JL-NWFET, and NWFET.

IV. CONCLUSION

In this work, the influence of positive, negative, and no interface trap charges (ITCs) on the reliability of Improved-JL-NWFET, conventional JL-NWFET, and conventional NWFET in terms of their electrical and analog parameters are investigated. The presence of negative (positive) ITCs leads to significant degradation in conventional JL-NWFET, with reductions of 6.97% (8.22%) in V_T, 8.20% (7.68%) in SS, 31.81% (28.46%) in DIBL, and 6.81% (6.98%) in g_m. Besides this, the presence of negative (positive) ITCs leads to significant degradation in conventional NWFET also, with reductions of 5.40% (15.70%) in V_T, 6.18% (7.32%) in SS, 58.93% (31.44%) in DIBL, and 7.59% (6.32%) in g_m. Furthermore, in contrast, the presence of negative (positive) ITCs causes comparable less degradation of 3.79% (4.86%), 3.65% (3.36%), 24.10% (25.74%), and 5.35% (5.41%) in V_T, SS, DIBL, and g_m in Improved-JL-NWFET, respectively. Therefore, the proposed Improved-JL-NWFET is more reliable than the conventional JL-NWFET and NWFET. These results indicate that Improved-JL-NWFET offers superior reliability compared to conventional JL-NWFET and NWFET. Given its enhanced performance and stability, Improved-JL-NWFET emerges as a promising candidate for future MOS devices in both electronics and biomedical applications.

REFERENCES

[1] N. Singh *et al.*, "Si, SiGe Nanowire Devices by Top-Down Technology and Their Applications," *IEEE Trans. Electron Devices*, vol. 55, no. 11, pp. 3107-3118, Nov. 2008.

[2] J. P. Colinge *et al.*, "Nanowire transistors without junctions," *Nature Nanotechnol.*, vol. 5, no. 3, pp. 225-229, Mar. 2010.

[3] S. J. Choi, D. I. Moon, S. Kim, J. P. Duarte, and Y. K. Choi, "Sensitivity of threshold voltage to nanowire width variation in junctionless transistors," *IEEE Electron Device Lett.*, vol. 32, no. 2, pp. 125-127, Feb. 2011.

[4] S. Sahay and M. J. Kumar, "Controlling L-BTBT and Volume Depletion in Nanowire JLFETs Using Core-Shell Architecture," *IEEE Trans. Electron Devices*, vol. 63, no. 9, pp. 3790-3794, Sept. 2016.

[5] H. Lou *et al.*, "Suppression of tunneling leakage current in junctionless nanowire transistors," *Semicond. Sci. Technol.* vol. 28, no. 12, p. 125016, Nov. 2013.

[6] S. Seifollahi, A. Sedigh, and A. k. Sarkaleh, "Performance Evaluation of Nano-scale Core–Shell Junctionless FETs in the Designing of Ultralow-Power Inverter and Ring Oscillator," *J. Electron. Mater.* vol. 53, pp. 3100–3116, Apr. 2024.

[7] A. Chattopadhyay and C. Bose, "Investigation of Core–Shell Junctionless Gate-Stack DG-FET in Low-Power Applications Using Charge-Based Modeling," *J. Electron. Mater.* vol. 53, no. 1, pp. 157–170, Oct. 2023.

[8] Bharti and P. Mittal, "Analytical Modeling of Oppositely Doped Core-Shell Junctionless Nanowire Transistor Considering Fringe Capacitance and Dual Material Gate," *Adv. Theory Simul.*, Feb. 2025, doi: https://doi.org/10.1002/adts.202401148.

[9] T. Ganguli, M. Chanda, and A. Sarkar, "Impact of Interface Trap Charges on the Performances of Junctionless MOSFET in Sub-Threshold Regime," *Comput. Electr. Eng.*, vol. 100, p. 107914, Mar. 2022.

[10] T.-K. Chiang, "A New Subthreshold Current Model for Junctionless Trigate MOSFETs to Examine Interface-Trapped Charge Effects," *IEEE Trans. Electron Devices*, vol. 62, no. 9, pp. 2745–2750, Sep. 2015.

[11] B. V. Chandan, K. Nigam, D. Sharma, and S. Pandey, "Impact of interface trap charges on dopingless tunnel FET for enhancement of linearity characteristics," *Appl. Phys. A*, vol. 124, no. 7, Jun. 2018.

[12] Y. Fu, L. Ma, Z. Duan, and W. Han, "Effect of charge trapping on electrical characteristics of silicon junctionless nanowire transistor," *J. of Semicond.*, vol. 43, no. 5, p. 054101, May 2022.

[13] A. K. Singh, M. R. Tripathy, K. Baral, P. K. Singh, and S. Jit, "Impact of interface trap charges on device level performances of a lateral/vertical gate stacked Ge/Si TFET-on-SELBOX-substrate," *Appl. Phys. A*, vol. 126, no. 9, Aug. 2020.

[14] Bharti and P. Mittal, "Oppositely-Doped Core-Shell Junctionless Nanowire FET: Design and Investigation," *ECS J. Solid State Sci. Technol.*, vol. 13, no. 1, p. 013004, Jan. 2024.

[15] *Atlas User's Manual: Device Simulation Software,* Silvaco Inc., Santa Clara, CA, USA, 2018.

[16] Bharti and P. Mittal, "Investigating the effect of scaling and temperature on the performance of improved junctionless nanowire FET through simulation analysis," *Phys. Scr.*, vol. 99, no. 8, p. 086103, Jul. 2024.

[17] Bharti and P. Mittal, "Improved Performance of Oppositely Doped CoreShell Junctionless Nanowire FET Using Gate Material Engineering," *2024 11th International Conference on Signal Processing and Integrated Networks (SPIN)*, Noida, India, 2024.

[18] A. Rassekh, F. Jazaeri, M. Fathipour and J. -M. Sallese, "Modeling Interface Charge Traps in Junctionless FETs, Including Temperature Effects," *IEEE Trans. Electron Devices*, vol. 66, no. 11, pp. 4653-4659, Nov. 2019.

[19] S. Gupta, K. Nigam, S. Pandey, D. Sharma, and P. N. Kondekar, "Effect of Interface Trap Charges on Performance Variation of Heterogeneous Gate Dielectric Junctionless-TFET," *IEEE Trans. Electron Devices*, vol. 64, no. 11, pp. 4731-4737, Nov. 2017.

[20] Y. Pratap, S. Haldar, R. S. Gupta, and M. Gupta, "Performance Evaluation and Reliability Issues of Junctionless CSG MOSFET for RFIC Design," *IEEE Trans. Device Mater. Reliab.*, vol. 14, no. 1, pp. 418-425, March 2014.

[21] Bharti and P. Mittal, "Core–Shell Incorporated Analytical Modeling of a Dual-Material Gate Junctionless Nanowire: Extraction of Subthreshold Characteristics," *J. Electron. Mater.*, Jan. 2025, doi:10.1007/s11664-025-11737-6.

Authorized licensed use limited to: DELHI TECHNICAL UNIV. Downloaded on June 04,2025 at 05:25:20 UTC from IEEE Xplore. Restrictions apply.

Check for updates

Received: 5 November 2023 | Revised: 2 August 2024 | Accepted: 28 October 2024

DOI: 10.1002/ep.14652

ENVIRONMENTAL PROGRESS & SUSTAINABLE ENERGY

ORIGINAL RESEARCH

Sustainable Energy

Energy, exergy, energy matrices, exergoeconomic, and enviroeconomic (5E) analysis of active solar distiller using water loaded nanoparticles: A comparative study

Dharamveer Singh[1,2] | Aakersh Chauhan[3] | Ashok Kumar Yadav[4] | S. Samsher[5] | Ashish Dewangan[6] | Aqueel Ahmad[7]

[1]Department of Mechanical Engineering, R. D Engineering College, Ghaziabad, India

[2]Research Centre, M. R. D. Trust, Ghaziabad, U.P, India

[3]Department of Electronics & Communication, NIT Hamirpur, Himachal Pradesh, India

[4]Symbiosis Institute of Technology, Symbiosis International (Deemed University), Pune, India

[5]Department of Mechanical Engineering, Delhi Technological University, Delhi, India

[6]Department of Mechanical Engineering, Galgotias College of Engineering & Technology, Greater Noida, India

[7]Department of Mechanical Engineering, Graphic Era (Deemed to be University), Dehradun, India

Correspondence

Ashok Kumar Yadav, Symbiosis Institute of Technology, Symbiosis International (Deemed University), Pune, India.
Email: ashokme015@gmail.com

Aqueel Ahmad, Department of Mechanical Engineering, Graphic Era (Deemed to be University), Dehradun, India.
Email: aqueelahmad191@gmail.com

Abstract

The exergoeconomic and enviroeconomic analysis of a hybrid double slope solar distiller system using Al_2O_3 nanoparticles in a CPC collector was examined in the current work. MATLAB was used with input data of New Delhi climate conditions provided by IMD Pune, India for mathematical calculations. The yield was evaluated based on the energy seasonally outlet, with maximum yield being 16.44 kg/day, minimum yield being 5.25 kg/day, and annual yield being 8.52% higher. The average energy payback time was 16.16%, the average energy payback factor was 13.91%, and the average life cycle cost conversion efficiency was observed to be 7.15% higher. In terms of enviroeconomics, the proposed system has a carbon mitigation/ton of 57.45, carbon credit earnings of 287.29 ($), an annual exergy of 7.31%, and a productivity of 5.17%. Over a 20-year period at an interest rate of 3%, System-A has a calculated value of 0.083, while System-B has a calculated value of 0.080 for the Rex parameter in kWh/₹. Additionally, the proposed system has a 4% higher Rex value than System-B and a distillate cost of 1.52 (₹/kg). The proposed system has been found better than the existing method, and future research may examine the use of various nanoparticles.

KEYWORDS

energy matrices, enviroeconomic and exergoeconomic, exergy, life cycle cost conversion efficiency, nanoparticles

1 | INTRODUCTION

Due to the global shortage of fresh water, there is a need to treat polluted or contaminated water. Consuming contaminated drinking water may cause numerous diseases in individuals, some of which can be fatal. Unfortunately, only a small portion of the world's total water supply is directly available for people usage. Approximately 97.5% of the world's water supply is made up of seawater, and the remaining 1.75% is stored in glaciers, ice caps, and persistent snow. This implies that only about 0.75% of the world's freshwater supply is directly used by humans. Hence, it is essential to develop self-sustaining systems that can provide high yields. The existing systems are not self-sustainable since they require electricity to function, and generating electricity from conventional sources results in the emission of harmful pollutants that can adversely affect the environment. Using renewable energy to treat contaminated or saline water presents a superior solution to the existing issue of limited freshwater availability and environmental pollution.

A solar-powered desalination device can function in either a passive or active mode. It performs most efficiently in distant locations

 © 2025 American Institute of Chemical Engineers.

where plenty of sunlight is available and is self-sustaining in passive operating conditions. However, the system produces only one to three liters of freshwater per day. To overcome this limitation, the distillation unit can be operated in active mode.

Lawrence and Tiwari[1] consider variables such as the shape and heat exchanger material, as well as the temperature and flow rate of the fluid being heated. External factors, including solar radiation and ambient temperature, are crucial in influencing the Earth's climate and weather patterns. Solar radiation is the energy emitted by the sun that reaches the Earth's surface. Hwang et al.[2] demonstrated the potential of Al_2O_3 nanofluids in heat transfer applications. By modifying the size and form of the fluid, Barden[3] enhanced the thermophysical properties of the base fluid and improved heat transfer coefficients.

Tiwari and Tiwari[4] reported that solar distillers are a desirable choice for providing clean water in locations with limited access to reliable energy sources or where other water treatment methods are impractical or excessively expensive. Ho et al.[5] discovered that variations in viscosity and thermal conductivity can significantly impact the natural convection of nanofluids in a square container. Therefore, it is essential to carefully consider these factors when designing and optimizing these systems for real-world applications. Otanicar and Golden[6] examined the environmental and financial impacts of using nanofluid solar hot water technology compared to traditional solar hot water technology. They also assessed the eco-economic effects of employing nanofluids in solar collectors and found that over 15 years, 74 kg of carbon can be neutralized. According to Patel et al.,[7] nanofluids significantly improved thermal conductivity when compared to their base fluids. This was due to nanoparticles' greater surface area, which can enhance the fluid-to-heat source heat transfer area. As a result, nanofluids have been developed for use in solar energy applications, thermal management in aerospace, and cooling of electronic equipment.

According to Singh et al.,[8] adding nanoparticles to a base fluid boosted heat transfer rates, lowered fluid friction, and reduced entropy generation. It was also claimed that employing nanofluids as heat transfer fluids would lead to energy systems that are more effective and environmentally benign. According to Elzen et al.[9] delaying participation in a global climate accord would raise carbon pricing and abatement costs. The size of the emission reduction goal would affect the cost of mitigation, the authors also found. They did note, however, that raising the adoption of low-carbon technologies and raising energy efficiency could aid in reducing the cost of mitigation. Khanafer and Vafai[10] conducted an analysis of the thermo-physical characteristics of nanofluids, which offers useful knowledge on the thermo-physical characteristics of these nanofluids and may help in the development of new applications for them in the field of energy storage and heat transmission. Using Al_2O_3 nanofluids in a solar flat plate collector increased heat transfer efficiency by 15%, according to experiments by Khullar and Tyagi.[11] The study, however, made no mention of any specific emissions reductions linked to the use of nanofluids in solar thermal systems.

High thermal conductivity, which reveals a material's potential to carry heat, is essential for efficient heat transfer, as demonstrated by Faizel et al.[12] Particularly, it has been found that compared to other nanoparticles, CuO nanoparticles have greater heat conductivity. Typical examples of nanofluids include TiO_2 and Al_2O_3. The economic study of an integrated solar distiller unit conducted by Liu et al.[13] highlighted the importance of precise design, operation, and the regional economic and regulatory context. The analysis considered both immediate and long-term financial costs and benefits, as well as potential social or environmental impacts. They recommended performing sensitivity analyses to assess how fluctuating variables such as inflation, energy prices, and interest rates could affect system costs. Kabeel et al.[14] suggested that a water-based nanofluid inclined solar distiller unit with a vacuum should be evaluated with respect to factors like heat transfer, mass transfer, fluid dynamics, economics, and environmental science. The specifics of the analysis would depend on the system's design and operation, as well as the local economic and environmental conditions.

Elango et al.[15] reported that the use of nanofluids enhanced the efficiency and output of solar desalination systems. Their study indicated that CuO-water nanofluid produced the highest thermal energy and productivity, while TiO_2-water nanofluid achieved the greatest efficiency. Omara et al.[16] found that nanofluids improved the performance of both corrugated wick and simple solar distillers, with CuO nanoparticles being the most effective. Additionally, their research revealed that incorporating nanofluids decreased the time required for solar distillers to reach steady state, suggesting enhanced responsiveness. Tiwari et al.[17] conducted an exergoeconomic and environmental analysis to evaluate the use of nanofluids in enhancing the thermal, electrical, and energy efficiency of solar desalination systems utilizing PVT-FPC. Their findings indicated a reduction in the projected annual environmental cost of the system, now estimated at $6.29. Sharon and Reddy[18] noted that producing drinking water with an active solar distiller is considerably more cost-effective than traditional methods. Specifically, the cost of generating potable water using the solar distiller was $0.048 per liter, which is significantly lower than alternative methods. Furthermore, a study by Sahota et al.[19,20] utilized various nanofluids, including nanoparticles such as aluminum oxide, copper oxide, and titanium oxide, to enhance the performance of a passive double-slope desalination system.

The study demonstrated the potential benefits of using nanofluids to increase the effectiveness of a passive double slope solar desalination system, but actual outcomes would rely on the kind of nanofluid utilized as well as the particular setup and operation of the desalination system. Singh et al.[21] investigated the energy matrix and lifecycle cost conversion efficiency of single and double slope solar desalination systems, assessing their exergoeconomic parameters, which are indicators of the cost of producing a unit of usable energy. They discovered that the exergoeconomic parameters for the single- and double-slope solar desalination systems were 0.144 and 0.137 per unit cost, respectively, suggesting that these solar distiller systems are reasonably inexpensive.

Singh and Tiwari[22] discovered that employing PVT-CPC technology could enhance the performance of solar distiller units while lowering lifecycle costs. However, the specific outcomes depend on the

19447450, 0, Downloaded from https://aiche.onlinelibrary.wiley.com/doi/10.1002/ep.14652 by Delhi Technological University, Wiley Online Library on [15/06/2025]. See the Terms and Conditions (https://onlinelibrary.wiley.com/terms-and-conditions) on Wiley Online Library for rules of use; OA articles are governed by the applicable Creative Commons License

design and usage of the solar distiller units. Shashir et al.[23] observed that adding copper oxide nanoparticles and graphite microflakes to the water in the solar distiller unit led to significant increases in solar output, by 47.8% and 57.6%, respectively. The researchers noted that the best solar production occurred when a fan was used to cool the toughened glass cover.

According to research by Sahota et al.,[24] adding a helical coil heat exchanger to a double-slope active solar desalination system significantly improved the performance of the solar distiller unit. They found that the heat exchanger increased the overall thermal efficiency of the solar distiller unit by about 7.5% and its yield by about 12.5%. Saleha et al.[25] emphasized the importance of selecting the appropriate solvent for a solar distiller unit, finding that ethylene glycol and water were more efficient solvents than methanol and ethanol, although results may vary depending on the specific design and usage conditions of the solar distiller unit.

In the study by Chen et al.,[26] it was found that using nanofluids to enhance the performance of desalination systems that utilize brackish water could be a viable option. However, the exact results can vary based on the design of the solar distiller unit, its operating conditions, and the properties of the nanofluid used. Mahian et al.[27] observed that using a heat exchanger resulted in producing twice as much water at temperatures below 50°C compared to systems without a heat exchanger, which is attributed to low-temperature evaporation of water containing nanoparticles. They emphasized the importance of evaluating various factors, such as design, fabrication, overall cost, annual cost, net worth, and payback period.

Singh and Tiwari[28] conducted experiments to examine the performance of a photovoltaic-thermal (PVT) collector attached to a partially covered solar still. They discovered that raising the PVT cover area from 0.2 to 0.5 m^2 increased efficiency by 8%, while increasing the water depth from 1.5 to 3 cm resulted in a 16% efficiency increase. Joshi and Tiwari[29] assessed the efficiency of a single slope photovoltaic thermal (PVT) desalination system with a parabolic concentrator collector. Depending on the operational conditions, the PVT system with the collector achieved thermal efficiency of up to 72% and electrical efficiency of up to 16.8%, significantly surpassing the performance of the PVT system without the collector. To analyze various levels of solar radiation and water flow rates, a simulation model was employed.

Dharamveer et al.[30] examined solar stills with a variety of basin and cover geometries and materials. These included a circular basin with a hemispherical cover and a rectangular basin with a triangular pyramid cover. The study demonstrated that the desalination system was more efficient when utilizing a copper basin and cover, with the hemispherical cover yielding a higher output. The energy efficiency of a solar desalination system can be enhanced by incorporating nanoparticles such as aluminum oxide (Al_2O_3) into the process. Nanoparticles possess a very high surface area-to-volume ratio, which enhances their ability to absorb and scatter light, thereby allowing for more efficient utilization of solar energy. Adding Al_2O_3 nanoparticles can also improve the system's thermal conductivity, facilitating more effective heat transfer from the system to the water. As a result, energy output and conversion efficiency increase. Furthermore, the use of nanoparticles can enhance a system's stability and durability, leading to reduced maintenance and repair costs. Overall, integrating nanoparticles like Al_2O_3 into a solar desalination system can create a more effective and long-lasting technology, contributing to the reduction of pollution and water scarcity.

For any energy system to operate as efficiently as possible, it is crucial to measure and analyze energy metrics. By evaluating the system's energy output, efficiency, and performance, we can identify potential areas for improvement and make informed decisions regarding the organization and management of the system. This optimization can enhance energy efficiency and minimize environmental impact. In a study by Elbar et al.,[31] the effect of nanofluids on the efficiency of solar desalination systems was investigated. Three types of nanoparticles CuO—, TiO_2, and SiO_2—were compared to pure water. The addition of nanofluids improved the overall performance of the solar still, with CuO nanoparticles proving to be the most effective. The researchers also found that increasing the amount of nanoparticles resulted in significantly more distilled water production.

Zhang et al.[32] conducted a study examining how different types of nanofluids affected the performance of a solar still system. The three nanofluids TiO_2/water, SiO_2/water, and Al_2O_3/water—considerably enhanced the productivity of solar still systems. Among these, TiO_2/water was shown to be the most productive, achieving a production increase of up to 33.2%. A review of the solar desalination system's energy and financial performance indicated that the use of nanofluids improved energy efficiency and reduced the levelized cost of water. Additionally, Dhivagar et al.[33] examined the effect of covering the absorber plate with copper oxide nanoparticles on the efficiency of the solar still system. When compared to absorber plates without a coating, the copper oxide coating enhanced solar still productivity by 24.5%, according to the study. The study came to the conclusion that copper oxide nanoparticles applied to absorber panels could enhance the efficiency of passive solar desalination systems. Dharamveer and Samsher[34] compared the energy matrices and environmental economics effects for active and passive solar desalination systems. Arora et al.[35] used nanofluid as the working fluid in a computational analysis of a single slope solar desalination system coupled to a flat-plate solar collector.

The study's objective was to increase the system's effectiveness by changing design features such as the tilt angle, depth, and concentration of the nanofluid. The findings showed that tilt angle and nanofluid concentration had a greater impact on system efficiency than solar depth did. The study's findings suggest that a single slope FPC solar desalination system may produce more freshwater and operate better if it were combined with nanofluid. The study's objective was to increase the system's effectiveness by changing design features such the tilt angle, depth, and concentration of the nanofluid. The findings showed that tilt angle and nanofluid concentration had a greater impact on system efficiency than solar depth did. The study's findings suggest that a single slope FPC solar desalination system may produce more freshwater and operate better if it were combined with nanofluid.

19447450, 0, Downloaded from https://aiche.onlinelibrary.wiley.com/doi/10.1002/ep.14652 by Delhi Technological University, Wiley Online Library on [15/06/2025]. See the Terms and Conditions (https://onlinelibrary.wiley.com/terms-and-conditions) on Wiley Online Library for rules of use; OA articles are governed by the applicable Creative Commons License

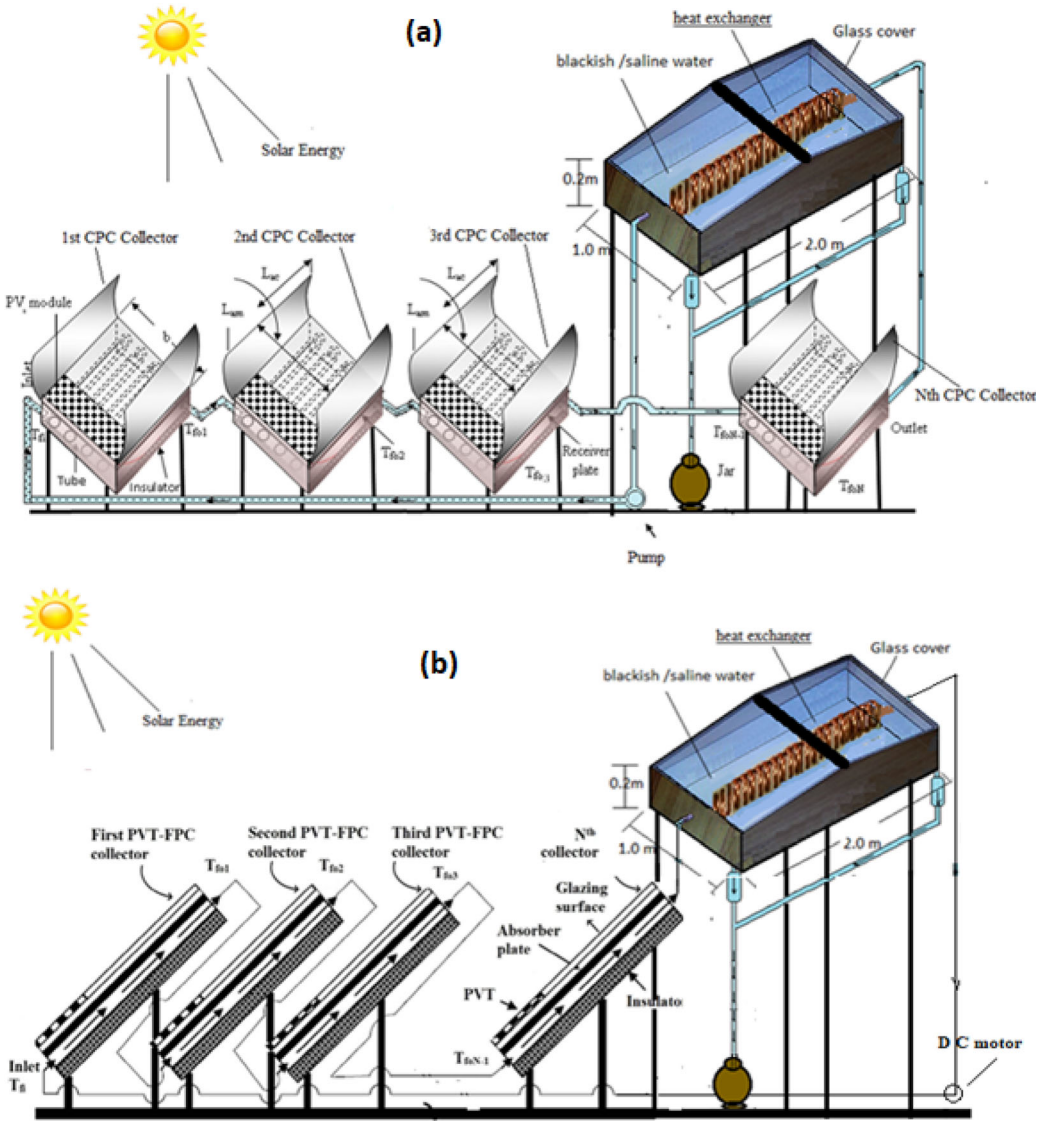


FIGURE 1 25% PVT N-identical double slope desalination with (a) CPC-HE and (b) FPC-HE.

An analytical investigation using CuO nanoparticles was carried out by Dharamveer et al.[36] on a *N*th identical PVT-CPC double slope solar desalination system. The study discovered that increasing the heat exchanger's length and water depth increased the solar still's output, with a 30° inclination angle producing the highest output. Additionally, the study demonstrated that adding a heat exchanger and photovoltaic module could increase the production of the solar still by 19.34%. Dharamveer et al.[37] found that using CuO nanoparticles and the helically coiled heat exchanger increased the solar distiller's total efficiency by 35.5% and 19.8%, respectively. Shahsavar et al.[38] compared the enviroeconomic and exergoeconomic studies of building integrated photovoltaic/thermal (BIPV/T), earth air heat exchanger (EAHE), and hybrid systems to determine the most effective and efficient ways to incorporate renewable energy into buildings. Shatar et al.[39] examined the impact of different thermal inputs (12 and 36 W) on the performance of a solar desalination system under Malaysia's weather conditions and compared the system performance.

Significant investigations have been conducted in the field of active and passive solar desalination systems. However, limited research has been performed on active solar stills utilizing water-based nanofluids within a double-slope solar system paired with a CPC collector. This proposed study aims to analyze the impact of energy, exergy, energy matrices, environmental economics, and exergoeconomics on a double-slope solar distiller coupled with a CPC collector using Al_2O_3 nanoparticles mixed with water. The study also seeks to evaluate the output of the solar desalination system by measuring the electrical energy and temperatures at the collector and basin water outlets. The proposed system A will be compared with the previous system B. Ongoing investigation into solar energy systems and their sustainability is vital for providing eco-friendly and sustainable solutions for energy generation and water desalination. A thorough examination of the energy, exergy, environmental, and exergoeconomic aspects of these systems will enable researchers to identify optimal strategies for integrating renewable energy technology into society.

19447450, 0, Downloaded from https://aiche.onlinelibrary.wiley.com/doi/10.1002/ep.14652 by Delhi Technological University, Wiley Online Library on [15/06/2025]. See the Terms and Conditions (https://onlinelibrary.wiley.com/terms-and-conditions) on Wiley Online Library for rules of use; OA articles are governed by the applicable Creative Commons License

2 | MATERIALS AND METHODS

2.1 | System description

A double slope solar distillation unit with an N-identical PVT-CPC and PVT-FPC with HE (heat exchanger) incorporated with nanoparticles are shown in Figure 1a,b, respectively. The greenhouse effect is responsible for the functioning of the system, whereby the collectors heat the water in the basin, leading to its evaporation.[40] The distillate is then collected after it trickles down to the bottom of the condenser, while the vapor rises and undergoes film-wise condensation on the interior face of the condenser. This results in fresh water being produced from brackish or saline sources, which can be beneficial in areas with poor access to safe drinking water or reliable electricity sources. The series-connected N-CPC (compound parabolic collector) is used to capture solar energy, which is then directed to the basin of the solar desalination unit. The top glass cover of the solar distillation unit reflects and absorbs solar energy, while some part is reflected by the water and some is absorbed by the liquid. The basin liner absorbs the majority of the energy, leading to an increase in the water temperature and its subsequent evaporation. In order to enhance the efficiency and effectiveness of solar desalination systems while minimizing their environmental impact, continued research and development are necessary.[41] Utilizing renewable energy sources and reducing our dependence on non-renewable resources are crucial steps towards a more sustainable future.

Figure 1a depicts a double slope desalination system with a 25% partly covered collector N-identical (N-PVT-CPC-HE-DS), with collectors arranged in a sequence at a 45° angle with the direction of the sun. The receiver region of the parabolic concentrator collector reflects incoming radiation, while the direct surface of the collector absorbs it. Energy generated by the radiation on the PV module powers the DC motor and pump, which may also be used for other applications. The glass cover is inclined at a 30° angle to the horizontal, and the system is oriented from east to west to capture the most solar energy. The maximum amount of solar energy is absorbed by the liner and reflected by the glass cover. The presence of nanoparticles in the basin enhances the receiving heat energy, which ultimately increases the performance of the system. Thus, it can be claimed that the greater heat absorption capacity of Al_2O_3 nanoparticles can be utilized to harness maximum solar radiation for conversion into thermal energy by combining the external PVT-CPC collector with an active double slope solar distillation unit.[42]

The effectiveness of the desalination process can be enhanced by increasing the temperature of the solar distillation unit by adding nanoparticles through a heat exchanger. Instead of utilizing separate systems for thermal energy and electricity, using PVT-CPC collectors can provide a more efficient and cost-effective alternative.[43] Combining the double slope solar distillation unit with PVT-CPC collectors and nanoparticles can increase the amount of fresh water produced from salty or brackish water sources. This integrated system generates both power and potable water by heating water in the basin of the solar distillation unit with solar radiation collected by the PVT-CPC collectors, causing evaporation and condensation to produce pure water. This system is easy to set up, requires minimal maintenance, and can provide drinkable water for residential and commercial purposes. Figure 1 shows the earlier system, which is being compared with the suggested hybrid system. By understanding the performance and efficiency differences between the two systems, researchers can optimize the hybrid system's design to produce more potable water and renewable energy.[44–46] The partially covered PV section of the CPC collectors has been included in the study to generate the most drinking water possible.

A comparison is made between the recommended method and the existing system based on various parameters such as yield, total thermal energy, exergy, energy matrices, enviroeconomic, exergoeconomic, and fluid temperatures at different locations such as N-CPC collectors, glass cover interior, and water in the basin.[47–50] There is a higher probability of nanoparticle sedimentation in water, and the aggregation is highly dependent on the size of the nanoparticle. However, advanced technologies can be employed to prevent such occurrence.

2.2 | Mathematical modeling

The objective of the modeling is to determine the energy and exergy of an N-identical hybrid double slope helically coiled heat exchanger incorporated with Al_2O_3 nanoparticles. To achieve this, it is necessary to determine the temperatures of different parts, including the water in the basin, east and west glass covers, and collector outlet. Additionally, thermal and electrical exergy, annual water production, and thermal energy need to be calculated. The system is evaluated based on the following factors.

2.2.1 | Thermal modeling

The following assumptions have been established to formulate the characteristic equation:

- The water level remains constant.
- Ohmic losses are neglected.
- There is no leakage.
- Film-wise condensation occurs on the entire surface.
- The system operates in a steady state with partially covered active solar stills.

2.2.2 | Equations used

Equations (1)–(4) are utilized to determine the energy requirements for different components of the active double slope desalination system, Singh et al.[36]:

19447450, 0, Downloaded from https://aiche.onlinelibrary.wiley.com/doi/10.1002/ep.14652 by Delhi Technological University, Wiley Online Library on [15/06/2025]. See the Terms and Conditions (https://onlinelibrary.wiley.com/terms-and-conditions) on Wiley Online Library for rules of use; OA articles are governed by the applicable Creative Commons License

$$T_{woN} = \left[\left[\frac{(AF_R(\alpha\tau))1\left(1-K_p^N\right)}{m_f C_f(1-K_p)}\left(\frac{1}{(1-e^z K_m^N)}\right)\right] I_b + \left[\frac{(AF_R(UL)1)\left(1-K_p^N\right)}{m_f C_f(1-K_p)}\left(\frac{1}{(1-e^z K_m^N)}\right)\right] T_a + T_{HE}\left(\frac{(1-e^z)K_m^N}{(1-e^z K_m^N)}\right)\right] \quad (1)$$

For the proposed system, heat gain can be calculated using this relation.

$$Q_{uN} = m_f C_f (T_{woN} - T_{wi}) \quad (2)$$

Outlet water temperature of the proposed system can be computed by Equations (1) and (2).

$$T_{HE} > T_{wi} > T_w$$

$$Q_{uN} = \left[\left(\left(\frac{(AF_R(\alpha\tau))1\left(1-K_p^N\right)}{(1-K_p)}\right)\left(\frac{1}{(1-e^z K_m^N)}\right)\right) I_b + \left(\left(\frac{(AF_R(UL)1)\left(1-K_p^N\right)}{(1-K_p)}\right)\left(\frac{1}{(1-e^z K_m^N)}\right)\right) T_a + m_f C_f\left(T_{HE}\left(\frac{(1-e^z)K_m^N}{(1-e^z K_m^N)}\right) - T_{wi}\right)\right] \quad (3)$$

$$Q_{uN} = [D_1 I_b + D_2 T_a + D_3] \quad (4)$$

2.2.3 | Energy, exergy analysis of an active double slope desalination system using Al_2O_3 nanoparticles

The following relationships (5)–(8) can be used to compute the hourly fluctuation of the thermal energy ($E_{hourly\ En}$) and thermal exergy ($E_{hourlyEx}$) of the recommended system. Equations (5) and (6):

$$E_{hourlyEn} = \left[h_{1wE}\left(T_w - T_{giE}\right) + h_{1wW}\left(T_w - T_{giW}\right)\right](A_b) \quad (5)$$

$$E_{hourlyEx} = \left\{h_{1wE}\left[\left(T_w - T_{giE}\right) - (T_a + 273)\ln\left(\frac{T_w + 273}{T_{giE} + 273}\right) + h_{1wW}\left[\left(T_w - T_{giW}\right) - (T_a + 273)\ln\left(\frac{T_w + 273}{T_{giW} + 273}\right)\right]\right\} A_b \quad (6)$$

The exchange constant for the proposed system, which represents the hourly water production from solar radiation, can be calculated using the aforementioned equation and is represented by the constant value of 0.933.

$$M_w = \frac{q_{ew}}{L_v} \times 3600 = \frac{h_{ew}(T_w - T_g)}{L_v} \times 3600 \quad (7)$$

Vaporization equation for latent heat as Singh et al.[36]:

$$L_v = L_v = 3.1625 \times 10^6 + \left[1 - \left(7.616 \times 10^{-4} T_v\right)\right] \text{ for } T_v > 70^\circ C$$
$$L_v = 2.4935 \times 10^6 \left[1 - \left(9.4779 \times 10^{-4} T_v\right) + 1.3132 \times 10^{-7}\left(T_v^2\right) - 4.797410^{-3}\left(T_v^3\right)\right] \text{for } T_v < 70^\circ C \quad (8)$$

2.2.4 | Analysis based on matrices of an active double slope solar desalination system using Al_2O_3 nanoparticles

It is calculated using Equations (9)–(13).

Energy payback time (EPT):

The time duration needed to recover total exhaust energy in manufacturing material can be expressed as

$$EPT_{(e)} = \frac{\text{Embodied Energy } (E_{in})}{\text{Annual energy output } (E_{out})} \quad (9)$$

$$EPT_{(ex)} = \frac{\text{Embodied Energy } (E_{in})}{\text{Annual exergy output } (E_{out})} \quad (10)$$

Energy production factor (EPF):

$$EPF_{(e)} = \frac{\text{Overall Energy Output } (E_{out})}{\text{Embodied Energy } (E_{in})} \quad (11)$$

$$EPF_{(ex)} = \frac{\text{Overall Exergy Output } (E_{out})}{\text{Embodied Energy } (E_{in})} \quad (12)$$

Life cycle cost conversion efficiency (LCCE)

$$LCCE_{(e)} = \frac{E_{out} \times n - E_{in}}{E_{sol} \times n} \quad (13)$$

where E_{sol} is yearly solar energy in kWh and n is the life duration.

2.2.5 | Economic analysis to determine the hybrid active double slope solar desalination using Al_2O_3 nanoparticles

Both System-A and System-B are economically feasible. It is calculated using Equations (14–21).

19447450, 0, Downloaded from https://aiche.onlinelibrary.wiley.com/doi/10.1002/ep.14652 by Delhi Technological University, Wiley Online Library on [15/06/2025]. See the Terms and Conditions (https://onlinelibrary.wiley.com/terms-and-conditions) on Wiley Online Library for rules of use; OA articles are governed by the applicable Creative Commons License

TABLE 1 salvage value and cost of various systems' components.

Component	N-PVT-FPC-HE-DS1 Cost	N-PVT-FPC-HE-DS1 Cost ($)	N-PVT-CPC-HE-DS Cost	N-PVT-CPC-HE-DS Cost ($)
FRP casing	₹10,200	$139.14	₹10,200	$139.14
2.05 mm glass sheet	₹1600	$21.83	₹1600	$21.83
Support stand (iron)	₹1000	$13.64	₹1000	$13.64
Inlet/outlet nozzles	₹200	$2.73	₹200	$2.73
Metal clamp	₹250	$3.41	₹250	$3.41
Sealing gaskets	₹200	$2.73	₹200	$2.73
Silicone adhesive	₹200	$2.73	₹200	$2.73
PVT-FPC modules (4 units)	₹34,000	$463.78	₹0	$0.00
PVT-CPC modules (4 units)	₹0	$0.00	₹36,000	$491.07
Electric motor with pump	₹1200	$16.37	₹1200	$16.37
Helical coil heat exchanger	₹466.25	$6.36	₹466.25	$6.36
Assembly and miscellaneous charges	₹6000	$81.84	₹6000	$81.84
Copper oxide nanoparticles (100 g)	₹4500	$61.38	₹4500	$61.38
Total cost	₹59,816.25	$815.94	₹61,816.25	$843.22

TABLE 2 Embodied energy (kWh).

Component	N-PVT-CPC-HE-DS (MJ)	N-PVT-FPC-HE-DS (MJ)
FRP enclosure	1483.9	1352.51
Collector unit (FPC/CPC × 4)	3279.41	2209.92
Photovoltaic glass panel	980	980
Copper heat exchanger	25.83	25.83
Al_2O_3 nanoparticles	8.5	8.5
Miscellaneous components	20	20
Total embodied energy	5797.64 MJ	4596.76 MJ

Capital cost: Tables 1 and 2 provide the system's fabrication cost.

System's lifespan: It is considered for 20 years.

$$\text{Salvage value(s)} = 0.2 \times \text{Principal capital cost (PCC)} \quad (14)$$

Cost of annual salvaging (ASC)

$$\text{Annually salvage} = S \times \text{shrinkage in fund (SFF)} \quad (15)$$

where SFF is the factor used for shrinkage

$$\text{Yearly maintenance (AMC)} = 0.15 \times \text{FAC} \quad (16)$$

where FAC stands for fixed cost annually.

Factor for capital recovery (CRF):

At a fixed rate of interest, it shows the present cost as a constant annual cost across time.

$$\text{CRF} = \frac{i(1+i)^n}{(1+i)^n - 1} \quad (17)$$

$$\text{Shrinking fund factor (SFF)} = \frac{\text{i}}{(1+i)^n - 1} \quad (18)$$

$$\text{First year annualcot estimated (FAC)} = \text{PCC} \times \text{CRF} \quad (19)$$

$$\text{Net annual cost estimated, TAC} = \text{FAC} + \text{AMC} - \text{ASC} \quad (20)$$

Per kg potable water price obtained

$$\text{Cost/kg} = \frac{\text{TAC}}{\text{yield in life}} \quad (21)$$

2.2.6 | Enviroeconomic analysis using Al_2O_3 nanoparticles, with active double slope solar still

Mathematical expressions (Equations 22–26) that illustrate the annual environmental costs associated with carbon credits and CO_2 mitigation are as follows:

CO_2 emission:

The average CO_2 intensity is about 0.98, which is similar to the electrical generation intensity (kg of CO_2/kWh)

$$CO_2\,\text{emission/annum} = \frac{\text{Embodied energy} \times 0.98}{\text{life time}} \quad (22)$$

19447450, 0, Downloaded from https://aiche.onlinelibrary.wiley.com/doi/10.1002/ep.14652 by Delhi Technological University, Wiley Online Library on [15/06/2025]. See the Terms and Conditions (https://onlinelibrary.wiley.com/terms-and-conditions) on Wiley Online Library for rules of use; OA articles are governed by the applicable Creative Commons License

For Indian conditions:

$$CO_2\,\text{emission/annum} = \frac{\text{Embodied energy} \times 1.58}{\text{life time}} \quad (23)$$

CO_2 mitigation: The following equation can be used to determine it per kWh

$$CO_2\,\text{mitigation/annum} = (E_{out} \times n) \times 1.58 \quad (24)$$

The equation used to calculate total CO_2 mitigation is:

$$\text{Mitigation net over life} = E_{out} \times n \times 1.58 \times 10^{-3} \quad (25)$$

Earned carbon credit can be calculated as:

$$\text{Earned carbon credit} = \text{Mitigation net of over life} \times D \quad (26)$$

where D is the shift from \$5 to \$20 per tonne of CO_2 mitigation.

2.2.7 | Exergoeconomic analysis of an Al_2O_3 nanoparticle-based active double slope solar desalination with N-PVT-CPC collector

Exergoeconomic analysis is a tool to evaluate the performance of energy systems by considering both their exergy (available energy) and economic aspects Tiwari et al.[15]

$$R_{ex} = \frac{L_{ex,annm}}{TAC} \quad (27)$$

2.3 | Methodology

The methodology employed to conduct the proposed study is outlined as:

Step I: Calculation of radiation, irradiation (global) for the proposed system on an annual basis and subsequently on a per daily basis based on climate using Lui and Jordon formula.

Step II: The optimization process involves comparing various design configurations to determine the maximum output temperature, which may be assessed using hourly, monthly, or annual data.

Step III: The effectiveness of the solar energy system at various weather conditions may be considered in the analysis. For instance, different levels of solar radiation may be present on clear, hazy, and foggy days, which may have an impact on the system's ability to produce thermal energy and thermal exergy.

Step IV: Calculation of Energy matrices (EPT, EPF, and LCCE).

Step V: Computation of parameters: economic, enviroeconomic, and exergoeconomic.

Step VI: Comparison of proposed system with previous system on the basis of numerically computed values.

3 | RESULT AND DISCUSSION

Using statistical data from IMD Pune, India, the solar irradiation and the ambient temperature have been calculated. The Liu and Jordan formula was utilized to determine the amount of radiation on the basin, and the relevant data was processed in MATLAB. Figure 2 displays the readings of ambient temperature T_a, solar radiation Eastside I_{SE}, Westside I_{SW}, and beam radiation I_b in kW/m^2.

3.1 | Analysis of energy, exergy for double slope active solar desalination using Al_2O_3 nanoparticles

System-A, a double slope solar desalination system with an active 25% PVT CPC collector and a helically coiled heat exchanger (N-PVT-CPC-HE-DS), and system-B, which incorporated a flat plate collector (N-PVT-FPC-HE-DS), were analyzed. Results show system-A has higher temperatures than system-B.

Figure 2 displays the variation in basin water temperature for a specific day of each month, at a depth of 0.14 m and with a value of $N = 4$ for the proposed system. The temperature exhibits fluctuations for 10-h duration (8 AM to 6 PM) on the same day.

Figure 3 shows that for the same basin area, the proposed system's daily yield increases by 509.74 kg. The rising trend of the graph was obtained until the month of May, indicating that the difference between the proposed system-A and existing system-B remained steady. Therefore, it is evident that the Al_2O_3 nanoparticles will have an impact on the ability of the helical coiled heat exchanger to transfer water effectively while increasing the temperature. The findings show that the suggested unit produces an average of 16.44 kg/day, which is significantly higher than the existing unit yield

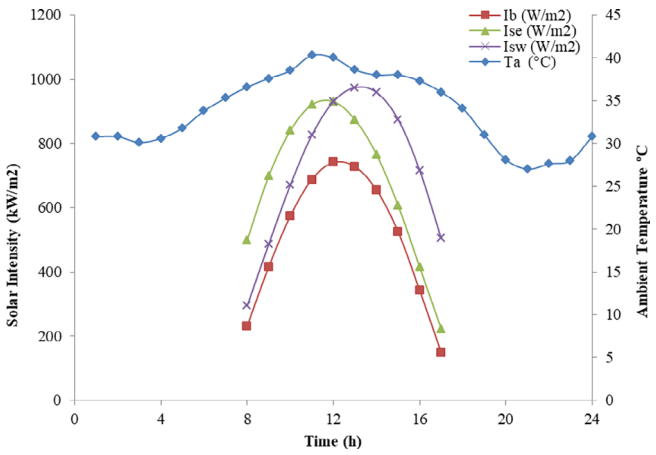


FIGURE 2 Ambient temperature (T_a) and solar radiation (I_b, I_{sE}, and I_{sW}) variation with time for a specific day of March in New Delhi climate.

19447450, 0, Downloaded from https://aiche.onlinelibrary.wiley.com/doi/10.1002/ep.14652 by Delhi Technological University, Wiley Online Library on [15/06/2025]. See the Terms and Conditions (https://onlinelibrary.wiley.com/terms-and-conditions) on Wiley Online Library for rules of use; OA articles are governed by the applicable Creative Commons License

of 5.25 kg/day. By increasing the basin surface area and basin water mass, these outcomes can be further improved.

As per the previous study, the similar system having the same basin area had an electrical exergy of 3.23 kWh, 4.08 kWh/month, and 3.57 kWh/month. The difference between the proposed and existing work remains relatively stable, and there is a rising trend in January, March, and November. As a result, it doesn't seem as though the Al_2O_3 nanoparticles in the helically coiled heat exchanger had an impact on the system's ability to produce electricity. The findings revealed that the daily electrical energy average of the proposed unit is 25% lower than that of the currently installed system, with a maximum and minimum of 4.08 kWh and 1.14 kWh, respectively, depending on the percentage of the PVT units that are covered in both the existing and proposed systems, which is 25%. By expanding the covering area by 50%, 75%, and 100%, these outcomes can be further enhanced. Hence, this system is referred to as self-sustainable.

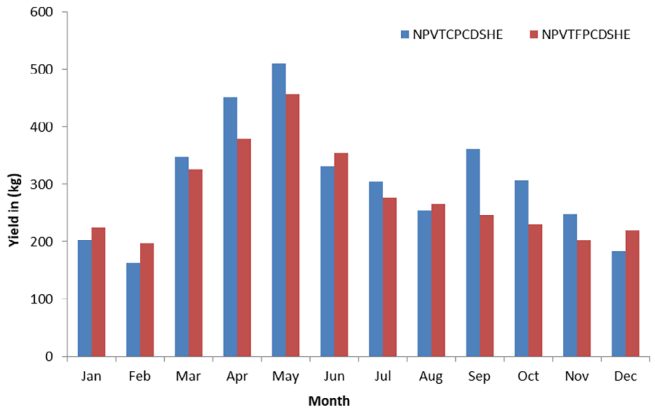


FIGURE 3 Comparison of monthly yield in kg.

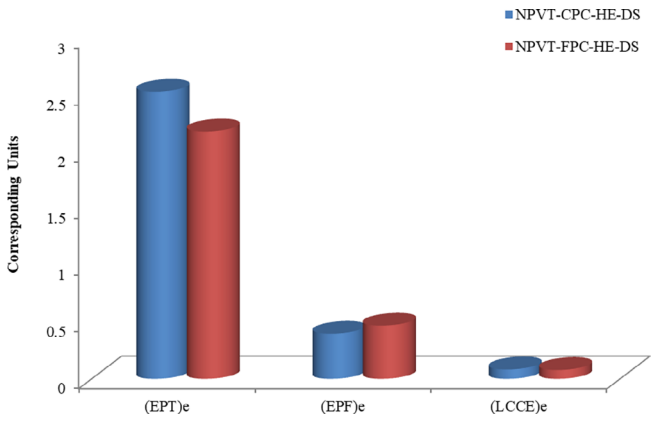


FIGURE 4 EPT, EPF, and LCCE for proposed and previous system for 20 years.

3.2 | Analysis based on matrices of an active double slope solar desalination system using Al_2O_3 Nanoparticles

To determine which system was more economically viable, a comparison was made between System A (N-PVT-CPC-HE-DS) and System B (N-PVT-FPC-HE-DS) in terms of fouling factor, total annual cost, and factor of capital recovery. Figure 4 illustrates the embodied energy (E_{in}), energy payback time, life cycle cost conversion efficiency, and energy payback factor (EPF) for both systems. System A shows better energy metrics than System B, with energy payback time (EPT) being 16.16% and 17.84% higher, respectively, on energy and exergy basis. Additionally, the energy- and exergy-based EPFs are significantly lower, with 13.91% and 14.88%, respectively, as shown in Figure 4. When considering a 20-year lifespan, the life cycle cost efficiency (LCCE), energy payback time, and energy payback factor of System A are noticeably higher than System B, at 7.15%, 6.38%, and 5.55%, respectively.

3.3 | Al_2O_3 nanoparticle-based hybrid active double slope solar desalination economic analysis

Table 3 displays the annual expenses of System A and System B, which are essential to evaluate the economic feasibility of the system.

3.4 | Enviroeconomic analysis using Al_2O_3 nanoparticles with active double slope solar still

The environmental costs such as carbon credits and annual CO_2 reduction include the environment-economic analysis of both the

TABLE 3 Various factors for System A and System B.

System	Years (n)	I (%)	System cost ($)	CRF	SFF	Water cost ($/kg)	Water cost (₹/kg)	TAC ($)
System A	20	1	176.62	0.06	0.05	0.01	0.96	35.32
(N-PVT-CPC-HE-DS)		3	176.62	0.07	0.04	0.02	1.23	105.97
(Proposed System)		5	176.62	0.08	0.03	0.02	1.52	176.62
System B	20	1	171.17	0.06	0.05	0.01	1.01	46.77
(N-PVT-FPC-HE-DS)		3	171.17	0.07	0.04	0.02	1.3	59.78
(Previous System)		5	171.17	0.08	0.03	0.02	1.6	73.8

19447450, 0, Downloaded from https://aiche.onlinelibrary.wiley.com/doi/10.1002/ep.14652 by Delhi Technological University, Wiley Online Library on [15/06/2025]. See the Terms and Conditions (https://onlinelibrary.wiley.com/terms-and-conditions) on Wiley Online Library for rules of use; OA articles are governed by the applicable Creative Commons License

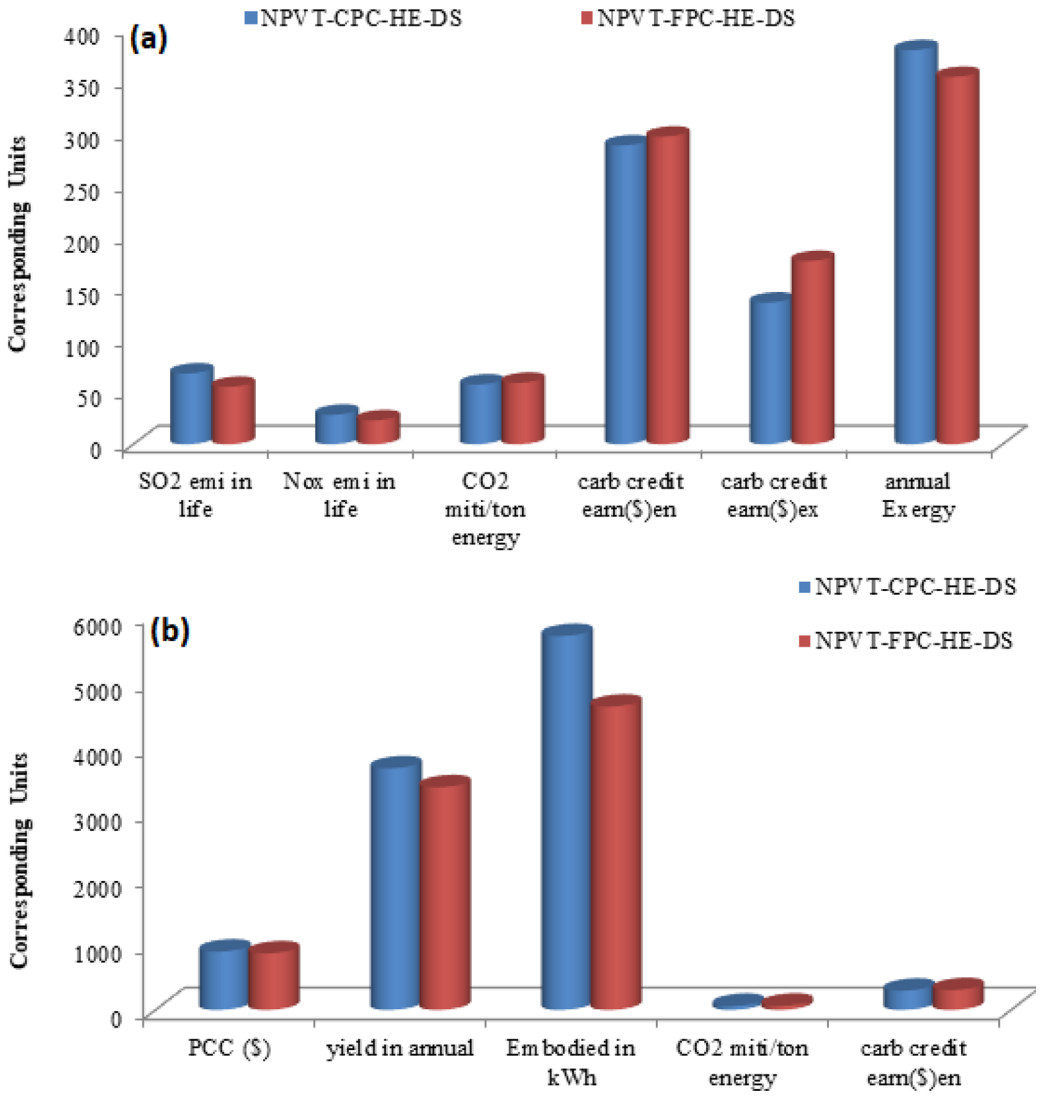


FIGURE 5 Enviroeconomic analysis for 20 years based on (a) exergy and (b) yield.

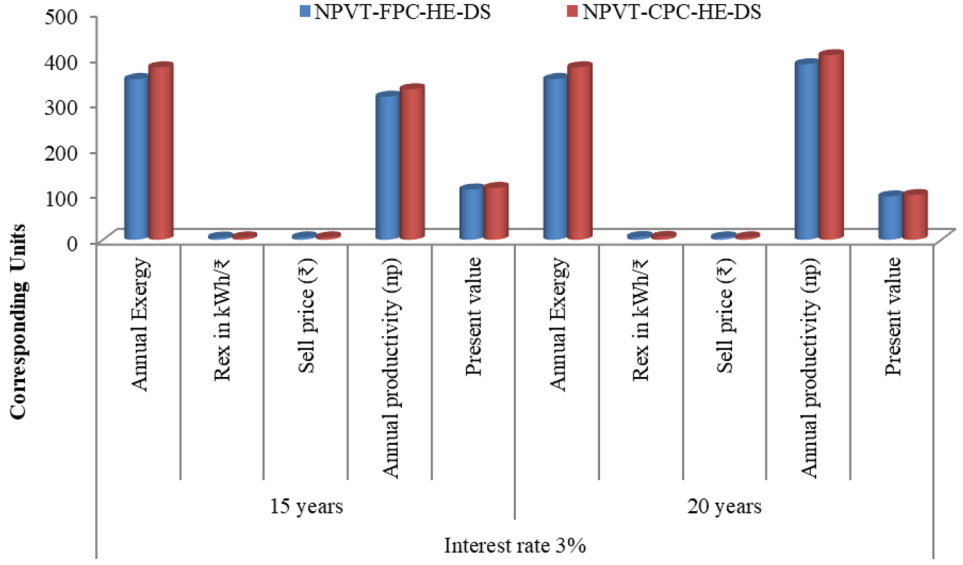


FIGURE 6 Exergoeconomic analysis for 15 and 20 years at 3% interest rate.

19447450, 0, Downloaded from https://aiche.onlinelibrary.wiley.com/doi/10.1002/ep.14652 by Delhi Technological University, Wiley Online Library on [15/06/2025]. See the Terms and Conditions (https://onlinelibrary.wiley.com/terms-and-conditions) on Wiley Online Library for rules of use; OA articles are governed by the applicable Creative Commons License

proposed and old system, which is illustrated in Figure 5a. The results indicate that the proposed system has 8.45 fewer CO_2 energy-based mitigation/ton and carbon credit gains ($) compared to the old system over a 20-year period, with a CO_2 mitigation rate of 57.46. Figure 5b shows the environmental and economic analyses of the proposed and existing systems, where the proposed System A has an annual yield 8.5% higher than the preceding system. A life duration study on a 15-year-old system indicates that the proposed system is expected to yield 3666.39 kg and embodied energy of 5675.57 kWh over a 20-year lifespan based on its energy output.

3.5 | Exergoeconomic evaluations of an N-PVT-CPC collector using Al_2O_3 nanoparticles and a helically coiled heat exchanger with an active double slope solar distiller

The exergoeconomic parameter (Rex) in kWh/₹ for System A and System B based on a 15-year period at a 3% interest rate is 0.068 and 0.065, respectively, as depicted in Figure 6. For a 20-year period at a 3% interest rate, System A has a calculated value of 0.083, while System B has a calculated value of 0.080. These values establish the economic superiority of System A over System B. Therefore, System A outperforms System B.

4 | CONCLUSIONS AND FUTURE SCOPE

In this investigation, the proposed System A as well as the former System B were studied and evaluated based on several parameters, and it was discovered that the proposed System performance A's is better than System B's.

4.1 | Conclusions

- The N-PVT-CPC system demonstrates superior performance when evaluated based on the biggest temperature difference, heat's thermal and exergy coefficients, and how much water is produced for drinking.
- System A outperforms System B in terms of distillate cost, with the yearly cost of distillate over a 20-year lifetime at a 5% interest rate being 1.52 (₹/kg) and 1.60 (₹/kg), respectively.
- The System A has an annual yield 8.5% higher than System B.
- In terms of carbon credit earnings ($), System A is more environmentally friendly than System B, with energy-based earnings of 287.29 and 295.74, respectively.
- System A exhibits greater environmental friendliness than System B based on CO_2 mitigation per ton, with values of 57.45 and 59.14 for System A and System B, respectively, over a 20-year lifetime at an annual interest rate of 5%.
- The exergoeconomic parameter (Rex) in (kWh/₹) at interest rates of 1%, 3%, and 5% demonstrates that the suggested solution is more economical than the existing one. Hence, System-A is superior to System B.
- Overall, the active solar still design using Al_2O_3 nanoparticles is believed to be the best design due to its annual performance based on economic, environmental, and energy-related aspects.

4.2 | Future scope

- The study of different criteria such as size, flow rate, and shape of different nanofluids, as well as exergoeconomic and environeconomic aspects.
- To use additional electrical appliances to function at night, the partially covered FPC might need to be increased by 25%, 50%, or 75%. Additionally, the CPC profile might raise the mass water temperature even more, which the PCM might use at night. Further investigation is needed to determine the extent of improvement in system performance.
- It is possible to explore the use of different nanoparticles and nanofluids, and to study energy matrices, environmental economics, and energy economics. The impact of size, shape, and mass flow rate of nanoparticles can also be investigated.

NOMENCLATURE

A_{gE}	eastside glass covers area, (m^2)
A_{gW}	cover area of westside glass (m^2)
A_m	photovoltaic area (m^2)
d_p	NPS dia. in (nm)
F'	factor of collector efficiency
L_c	glazing length collector (m)
L_i	thickness of insulation (m)
L_g	cover of glass thickness (m)
L_m	length of PVT (m)
L_p	absorbing plate thickness (m)
M_m	water mass (k_g)
M_{ew}	yield (k_g)
m_f	water flow rate (k_g/s)
Q_{uN}	*N* identical 25% PVT-CPC linked in series, the rate of heat transfer, in (kWh)
T_{giE}	temperature of the glass covers on the east side, in (°C)
T_{giw}	west side, inside glass covers temperature, in (°C)
T_{goE}	exterior glass cover's temperature on the east side, in (°C)
T_{goW}	Outside glass cover temperature on the west side, in (°C)
T_a	surrounding temperature in (°C)
T_{cN}	average temperature of solar cells, in (°C)
T_{wi}	fluid inlet temperature in (°C)
T_{bf}	in collector base fluid temperature, in (°C)
T_{woN}	*N*th collector water temperature outlet, in (°C)
T_w	temperature of basin water in (°C)

19447450, 0, Downloaded from https://aiche.onlinelibrary.wiley.com/doi/10.1002/ep.14652 by Delhi Technological University, Wiley Online Library on [15/06/2025]. See the Terms and Conditions (https://onlinelibrary.wiley.com/terms-and-conditions) on Wiley Online Library for rules of use; OA articles are governed by the applicable Creative Commons License

ΔT_{HE} temperature at the heat exchanger between the base fluid and the nanofluid, in (°C)
U_{gaR} condensing cover to surrounding, total coefficient of heat transfer eastside (W/m^2K)
U_{gaW} condensing cover to surrounding, total coefficient of heat transfer (W/m^2K)
U_{Lc} glazing to surrounding, total coefficient of heat transfer (W/m^2K)
U_{Lm} module to surrounding, total coefficient of heat transfer (W/m^2K)
U_{tca} solar cell to surrounding, total coefficient of heat transfer (W/m^2K)
U_{tpa} absorbing plate to surrounding, total coefficient of heat transfer (W/m^2K)
$U_{tc,p}$ solar cell to absorbing plate, overall heat transfer coefficient (W/m^2K)
X solar desalination unit characteristics length (m)
AMC maintenance cost annually
ASC salvage cost annually
BF base fluid
CRF capital recovery factor
C per liter yield price
CM carbon dioxide mitigation
DS double slope solar distiller unit
EPT payback time of energy
EPF payback factor of energy
FPC flat plate collector
HE heat exchanger
HTC a measure of heat transmission
LCCE efficiency of life cycle conversion
NF nano fluid
Rex exergoeconomic parameters

AUTHOR CONTRIBUTIONS

Dharamveer Singh: Conceptualization; methodology; software; data curation; investigation; writing – original draft. **Aakersh Chauhan:** Validation; visualization; supervision. **Ashok Kumar Yadav:** Supervision; formal analysis; investigation; resources; methodology. **S. Samsher:** Supervision; formal analysis; visualization. **Ashish Dewangan:** Investigation; validation; data curation; software. **Aqueel Ahmad:** Writing – review and editing; formal analysis; software.

CONFLICT OF INTEREST STATEMENT

The authors declare that they have no known competing financial interests or personal relationships that could have appeared to influence the work reported in this paper.

DATA AVAILABILITY STATEMENT

The data that support the findings of this study are available from the corresponding author upon reasonable request.

ORCID

Aqueel Ahmad https://orcid.org/0000-0002-8189-6018

REFERENCES

1. Lawrence SA, Tiwari GN. Theoretical evaluation of solar distillation under natural circulation with heat exchanger. *Energy Convers Manag*. 1990;30:205-213.
2. Hwang KS, Lee JH, Jang SP. Buoyancy-driven heat transfer of water-based Al2O3 nanofluids in a rectangular cavity. *Int J Heat Mass Transf*. 2007;50:4003-4010.
3. Barden OO. Experimental study of the enhancement parameters on a single slope solar still productivity. *Desalination*. 2007;209:136-143.
4. Tiwari GN, Tiwari A. *Solar Distillation Practice for Water Desalination Systems*. Anamaya Publishers; 2008.
5. Ho CJ, Chen MW, Li ZW. Numerical simulation of natural convection of nanofluid in a square enclosure: effects due to uncertainties of viscosity and thermal conductivity. *Int J Heat Mass Transf*. 2008;51:4506-4516.
6. Otanicar TP, Golden J. Comparative environmental and economic analysis of conventional and nanofluid solar hot water technologies. *Environ Sci Technol*. 2009;43:6082-6087.
7. Patel HE, Sundararajan T, Das SK. An experimental investigation into the thermal conductivity enhancement in oxide and metallic nanofluids. *J Nanopart Res*. 2010;12:1015-1031.
8. Singh PK, Anoop KB, Sundararajan T, Sarit KD. Entropy generation due to flow and heat transfer in nanofluids. *Int J Heat Mass Transf*. 2010;53:4757-4767.
9. Elzen MGJD, Hof AD, Beltran AM, Grassi G, Roelfsema M, Ruijven BV. The Copenhagen accord: abatement costs and carbon prices resulting from the submissions. *Environ Sci Pol*. 2011;14:28-39.
10. Khanafer K, Vafai K. A critical synthesis of thermo-physical characteristics of nanofluids. *Int J Heat Mass Transf*. 2011;54:4410-4428.
11. Khullar V, Tyagi H. A study on environmental impact of nanofluid based concentrating solar water heating system. *Int J Environ Stud*. 2012;69:220-232.
12. Faizal M, Saidur R, Mekhilef S, Alim MA. Energy, economic and environmental analysis of metal oxides nanofluid for flat-plate solar collector, energy convers. *Manage*. 2013;76:162-168.
13. Liu X, Chen W, Gu M, Shen S, Cao G. Thermal and economic analyses of solar desalination system with evacuated tubular collectors. *Sol Energy*. 2013;93:144-150.
14. Kabeel AE, Omara ZM, Essa FA. Enhancement of modified solar still integrated with external condenser using nanofluids, an experimental approach. *Energy Convers Manag*. 2014;78:493-498.
15. Elango T, Kannan A, Murugavel KK. Performance study on single basin single slope solar still with different water nanofluids. *Desalination*. 2015;360:45-51.
16. Omara ZM, Kabeel AE, Essa FA. Effect of using nanofluids and providing vacuum on the yield of corrugated wick solar still. *Energy Convers Manage*. 2015;103:965-972.
17. Tiwari GN, Yadav JK, Singh DB, Al-Helal IM, Abdel-Ghaney AM. Exergoeconomic and enviroeconomic analyses of partially covered photovoltaic flat plate collector active solar distillation system. *Desalination*. 2015;367:186-196.
18. Sharon H, Reddy KS. Performance investigation and enviro-economic analysis of active vertical solar distillation units. *Energy*. 2015;84:794-807.
19. Sahota L, Tiwari GN. Effect of Al_2O_3 NPs on the performance of passive double slope solar still. *Sol Energy*. 2016;130:260-272.
20. Sahota L, Tiwari GN. Effect of nanofluids on the performance of passive double slope solar still: a comparative study using characteristic curve. *Desalination*. 2016;388:9-21.
21. Singh DB, Tiwari GN, Al-Helal IM, Dwivedi VK, Yadav JK. Effect of energy matrices on life cycle cost analysis of passive solar stills. *Sol Energy*. 2016;134:9-22.
22. Singh DB, Tiwari GN. Effect of energy matrices on life cycle cost analysis of partially covered photovoltaic compound parabolic

19447450, 0, Downloaded from https://aiche.onlinelibrary.wiley.com/doi/10.1002/ep.14652 by Delhi Technological University, Wiley Online Library on [15/06/2025]. See the Terms and Conditions (https://onlinelibrary.wiley.com/terms-and-conditions) on Wiley Online Library for rules of use; OA articles are governed by the applicable Creative Commons License

concentrator collector active solar distillation system. *Desalination*. 2016;397:75-91.
23. Sharshir SW, Peng G, Wu L, et al. Enhancing the solar still performance using nanofluids and glass cover cooling: experimental study. *Appl Therm Eng*. 2017;113:684-693.
24. Sahota L, Tiwari GN. Analytical characteristic equation of nanofluid loaded activedouble slope solar still coupled with helically coiled heat exchanger. *Energy Convers Manag*. 2017;135:308-326.
25. Saleha SM, Soliman AM, Sharaf MA, Kaled V, Gadgile B. Influence of solvent in the synthesis of nano-structured Z_nO by hydrothermal method and their application in solar-still. *J Environ Chem Eng*. 2017; 5:1219-1226.
26. Chen W, Zou C, Li X, Li L. Experimental investigation of S_iC nanofluids for solar distillation system: stability, optical properties and thermal conductivity with saline water based fluid. *Int J Heat Mass Transf*. 2017;107:264-270.
27. Mahian O, Kianifar A, Heris SZ, Wen D, Sahin AZ, Wongwises S. Nanofluids effects on the evaporation rate in a solar still equipped with a heat exchanger. *Nano Energy*. 2017;36:134-155. doi:10.1016/j.nanoen.2017.04.025
28. Singh DB, Tiwari GN. Enhancement in energy metrics of double slope solar still by incorporating N identical PVT collectors. *Sol Energy*. 2017;143:142-161.
29. Joshi P, Tiwari GN. Effect of cooling condensing cover on the performance of N identical photovoltaic thermal compound parabolic concentrator active solar still: a comparative study. *Int J Energy Environ Eng*. 2018;9:473-498.
30. Dharamveer S, Samsher S, Singh DB, Singh AK, Kumar N. *Solar Distiller Unit Loaded with Nanofluid—A Short Review*. Lecture Notes in Mechanical Engineering, Springer; 2019:241-247. doi:10.1007/978-981-13-6577-5_24
31. Elbar ARA, Yousef MS, Hassan H. Energy, exergy, exergoeconomic and enviroeconomic (4E) evaluation of a new integration of solar still with photovoltaic panel. *J Clean Prod*. 2019;19:665-680. doi:10.1016/j.jclepro.2019.06.111
32. Zhang G, Kaushika ND, Kaushik SC, Tomar RK. *Advances in Energy and Built Environment*. Springer Science and Business Media LLC; 2020.
33. Dhivagar R, Mohanraj M, Hindouri K, Belyayev Y. Energy, exergy, economic and enviroeconomic (4E) analysis of gravel coarse aggregate sensible heat storage assisted single slope solar still. *J Therm Anal Calorim*. 2020;145(2) doi:10.1007/s10973-020-09766-w
34. Dharamveer S, Samsher S. Comparative analyses energy matrices and enviro-economics for active and passive solar still. *Mater Today Proc*. 2020;46:6931-6937. doi:10.1016/j.matpr.2020.10.001
35. Arora S, Singh HP, Sahota L, et al. Performance and cost analysis of photovoltaic thermal (PVT)-compound parabolic concentrator (CPC) collector integrated solar still using CNT-water based nanofluids. *Desalination*. 2020;495:114595.
36. Dharamveer S, Samsher S, Kumar A. Analytical study of nth identical photovoltaic thermal (PVT) compound parabolic concentrator (CPC) active double slope solar distiller with helical coiled heat exchanger using CuO nanoparticles. *Desalin Water Treat*. 2021;233:30-51. doi:10.5004/dwt.2021.27526
37. Dharamveer S, Samsher S, Kumar A. Performance analysis of N-identical PVT-CPC collectors an active single slope solar distiller with a helically coiled heat exchanger using CuO nanoparticles. *Water Supply*. 2022;2:1306-1324. doi:10.2166/ws.2021.348
38. Shahsavar A, Talebizadehsardari A, M P. Comparative energy, exergy, environmental, exergoeconomic, and enviroeconomic analysis of building integrated photovoltaic/thermal, earth-air heat exchanger, and hybrid systems. *J Clean Prod*. 2022;362:132510. doi:10.1016/j.jclepro.2022.132510
39. Shatar NM, Sabri MFM, Salleh MFM, Ani MH. Energy, exergy, economic, environmental analysis for solar still using partially coated condensing cover with thermoelectric cover cooling. *J Clean Prod*. 2023; 387:135833. doi:10.1016/j.jclepro.2022.135833
40. Pawar S, Hole J, Bankar M, Channapattana S, Srinidhi C. Use of Taguchi method for optimizing engine parameters of variable compression ratio diesel engine using cocklebur seed oil biodiesel blended with Karanja oil biodiesel. *Mater Today Proc*. 2023. doi:10.1016/j.matpr.2023.08.129
41. Singh D, Singh S, Yadav AK, et al. From theory to practice: a sustainable solution to water scarcity by using hybrid solar distiller with heat exchanger and aluminum oxide nanoparticles. *JACS Omega*. 2023; 8(37):33543-33553. doi:10.1021/acsomega.3c03283
42. Singh D. Economic, Enviroeconomic analysis of active solar still using Al_2O_3 nanoparticles. *Int J Thermodyn*. 2023;26(4):68-76. doi:10.5541/ijot.1295637
43. Singh D, Singh S, Chauhan A, Kumar A. Enviroeconomic analysis of hybrid active solar desalination system using nanoparticles. *J Environ Eng Sci*. 2023;19(1):18-28. doi:10.1680/jenes.23.00045
44. Singh D, Yadav AK, Kumar A, Samsher. Energy matrices and life cycle conversion analysis of N-identical hybrid double slope solar distiller unit using Al_2O_3 nanoparticle. *J Water Environ Nanotechnol*. 2023; 8(3):267-284. doi:10.22090/jwent.2023.03.006
45. Ahmad A, Yadav AK, Singh A, Singh DK. A machine learning-response surface optimization approach to enhance the performance of diesel engine using novel blends of aloe vera biodiesel with MWCNT nanoparticles and hydrogen. *Process Saf Environ Prot*. 2024;186:738-755. doi:10.1016/j.psep.2024.04.013
46. Gajbhiye AM, Sonawane PR, Karle AH. Optimization of welding parameters for En8D and SAE1018 materials by Taguchi. *Int J Interact Des Manuf*. 2023;18. doi:10.1007/s12008-023-01678-x
47. Srinidhi C, Madhusudhan A, Channapattana SV, Gawali SV, Aithal K. RSM based parameter optimization of CI engine fuelled with nickel oxide dosed Azadirachta indica methyl ester. *Energy*. 2021;234: 121282. doi:10.1016/j.energy.2021.121282
48. Parast KH, Zamanpour A, Farahbod F. Investigation of thermal effect of floor coverings made of nano metal oxide on wastewater temperature and solar pond performance. *S Afr J Chem Eng*. 2023;46:99-105. doi:10.1016/j.sajce.2023.07.013
49. Srinidhi C, Madhusudhan A, Channapattana SV. Effect of NiO nanoparticles on performance and emission characteristics at various injection timings using biodiesel-diesel blends. *Fuel*. 2019;235:185-193. doi:10.1016/j.fuel.2018.07.067
50. HaghParast K, Zamanpour A, Farahbod F. Theoretical and operational investigation of the temperature of the glass surface, floor and effluent inside the solar desalination pond. *Case Stud Thermal Eng*. 2023; 51:103597. doi:10.1016/j.csite.2023.103597

How to cite this article: Singh D, Chauhan A, Yadav AK, Samsher S, Dewangan A, Ahmad A. Energy, exergy, energy matrices, exergoeconomic, and enviroeconomic (5E) analysis of active solar distiller using water loaded nanoparticles: A comparative study. *Environ Prog Sustainable Energy*. 2025; e14652. doi:10.1002/ep.14652

19447450, 0, Downloaded from https://aiche.onlinelibrary.wiley.com/doi/10.1002/ep.14652 by Delhi Technological University, Wiley Online Library on [15/06/2025]. See the Terms and Conditions (https://onlinelibrary.wiley.com/terms-and-conditions) on Wiley Online Library for rules of use; OA articles are governed by the applicable Creative Commons License

Proceedings of the 8th International Conference on Trends in Electronics and Informatics (ICOEI-2025)
IEEE Xplore Part Number: CFP25J32-ART; ISBN: 979-8-3315-4460-7

Energy Efficient Dynamic Logic based on TGDI Cell for Portable Electronics

Y. Parmar*
Delhi Technological University
Department of Electronics and Communication Engineering
New Delhi, India
yashodaparmar_23vls25@dtu.ac.in

N. Pandey
Delhi Technological University
Department of Electronics and Communication Engineering
New Delhi, India
n66pandey@rediffmail.com

Abstract*— The design of energy-efficient circuits is crucial for portable devices in order to enhance battery life. The delay, power, and area reduction are central themes to make circuits suitable for portable electronics. The Gate Diffusion Input (GDI) technique has emerged in the low-power circuit design paradigm. However, it suffers from a threshold drop at the output, and several modifications subsequently appear in open literature. This study examines the problem of restricted voltage swing at an intermittent node in the current Dynamic Gate Diffusion Input (DGDI), which could result in higher power consumption and delay. The approaches of Dynamic Full Swing Gate Diffusion Input (DFSGDI) and Dynamic Transmission Gate Diffusion Input circuit (DTGDI) are proposed in this paper to determine full swing at the intermittent node. The proposals are verified for functionality and performance using the Cadence Virtuoso tool and the 32nm Carbon Nanotube Field Effect Transistor (CNTFET) model. The XOR gate based on DFSGDI and DTGDI is 23.6% faster than the existing counterpart. The average power consumptions are almost identical in DGDI and DTGDI, while DFSGDI shows an increase of 76.9% as compared to DGDI. The current drawn from the power supply is observed to be 0.891 µA, 1.563 µA, and 0.857 µA, respectively, for DGDI, DFSGDI, and DTGDI. Therefore, the product of delay and power (PDP) of the DTGDI outperforms DGDI by 25.2%. Hence, portable systems and low-power applications, which are energy efficient, gain significant benefits from the incorporation of XOR logic based on DTGDI. Monte Carlo simulations show the resilience of the proposals against process variations.

Keywords*— *CNTFET, GDI, DGDI, DTGDI, DFSGDI, PDP.

I. INTRODUCTION

The proliferation of affordable equipment such as smartphones, laptops, radios, audio devices, etc., is transforming the consumer market. Coupled with this is the everlasting quest for high-performance devices, which presents numerous challenges for designers in terms of speed, power consumption, and footprints. As predicted by Moore's law [1], device dimensions shrink by half their size every 18 months. Several practicalities are associated with downsizing the device dimensions. In order to get beyond the short channel effects that are present in the sub-micron regime, researchers have looked into designs based on different technologies. The Carbon Nano Tube Field Effect Transistor (CNTFET) is becoming popular due to the choice of alternate channel material, which makes them faster and more power efficient in comparison to bulk silicon transistors [2]. Advanced semiconductor material techniques that use materials like carbon nanotubes (CNT) are considered a better option. Since CNTs enabled the development of the MOS devices successfully. The Carbon Nano Tube Field Effect Transistor (CNTFET) [3] I-V characteristic shows a similar trend as in CMOS [4]. Even the device developed with CNTEFT shows less leakage current, high linearity, and better control over channel formation [5]. Further, CNTFET is also compatible with silicon foundry, as is evident from the fabricated CNTFET-based microprocessor RV16X-NANO [6].

In portable electronics, battery life is a crucial factor that impacts the device's overall utility and efficiency. Therefore, designers are looking forward to low-power systems for prolonged device usage. To get a low-power system, it is imperative to design the fundamental components of the embedded system with energy efficiency as a priority. An embedded system's main components are its multiplier, shifter, and Arithmetic Logic Unit (ALU). Full adders are vital for memory address generation and ALUs. GPUs, DSP processors, etc. As the XOR gate is inevitably used in the construction of a full adder, it is a crucial and significant step towards designing a computational logic unit with a reduced delay and power.

As the XOR logic gate based on the popular static CMOS has a full swing, it utilizes both the PUN and PDN for logic realization. Nevertheless, it shows more design complexity due to higher transistor count and dynamic power consumption. The GDI design technique is successfully used as a low-power approach, which benefits from the low transistor count and circuit complexity, as it requires only four transistors to realize the XOR logic [7]. However, the output swing in GDI-based logic implementation like XOR/XNOR is restricted due to threshold voltage drop. There may be high leakage current in static mode if the GDI is combined with a static circuit, which may become an issue in battery-operated devices. Moreover, the current drive of the transistors in the succeeding static circuit will be low, leading to increased delay. Later the GDI technique has been adopted in CNTFET technology also [8].

In order to achieve full swing in the CNTFET-based GDI logic (FS-GDI), placement of an additional PCNTFET in parallel to NCNTFET or NCNTFET parallel to PCNTFET is suggested [9]. The XOR gate based on FS-GDI uses 13 transistors; thus, the transistor count is increased to achieve a full swing, which will cause more design complexity and power consumption. It is pertinent to mention that [10], [11], and [12] belong to static implementations. Further, the dynamic logic is expected to be preferred over static once due to the total absence of output glitching and reduced parasitic capacitances [13]. As a direct connection is never established between the power supply and the ground in dynamic circuits, short circuit power consumption does not exist. A CNTFET-

2025 8th International Conference on Trends in Electronics and Informatics (ICOEI) | 979-8-3315-4460-7/25/$31.00 ©2025 IEEE | DOI: 10.1109/ICOEI65986.2025.11012939

Authorized licensed use limited to: DELHI TECHNICAL UNIV. Downloaded on June 04,2025 at 05:36:07 UTC from IEEE Xplore. Restrictions apply.

based dynamic full swing logic has been proposed wherein a multi-threshold concept is used to achieve full swing logic, and inputs are applied through capacitors. A full adder is implemented using this concept. It has high design complexity due to the use of multi-threshold transistors and the fabrication of multiple capacitors used therein [14]. Another technique, namely dynamic GDI (DGDI) [15], is introduced to address full swing and increased transistor count. It works on pre-charging the output node and evaluation subsequently. It is a merger of a basic GDI cell and a novel dynamic block. The DGDI-based XOR gate uses 6 transistors; thus, the transistor count is significantly decreased from FS-GDI. Though the output swing issue is resolved in DGDI, there is a full swing problem at the intermittent node (input of the dynamic block), which leads to a lower driving capability of the evaluation transistor and causes increased delay and power consumption.
Additionally, adiabatic logic circuits can be used for low power consumption and high efficiency, which require a charge recovery algorithm to enhance the overall performance. However, the complexity of the circuit is increased by the additional circuitry needed to provide the necessary multi-phase, sinusoidal, or trapezoidal power clock signals for proper operation.

This study aims to improve GDI logic techniques to address the voltage swing issue and meet the low-power and high-efficiency requirements of portable electronic devices. In this context, authors propose: Two techniques: the former circuit uses a Full Swing Gate Diffusion Input (FSGDI) with a dynamic block, whereas the latter relies on an amalgamation of Transmission Gate Diffusion Input (TGDI) and a dynamic block. The resulting circuits are named Dynamic Full Swing Gate Diffusion Input (DFSGDI) and Dynamic Transmission Gate Diffusion Input circuit (DTGDI).

The paper is arranged in five sections—the preliminaries are described in section 2. The proposed circuits are placed in section 3 of the paper. The functional verification and performance evaluation are given in section 3 and section 4. The findings are summarized in section 5.

II. PRELIMINARIES

This section puts forward the basics of CNTFET. After that, a brief description of the available GDI technique and its variations is presented. The issues pertaining to the recently proposed CNTFET-based dynamic GDI are also discussed.

A. Carbon Nano tube Field effect Transistor (CNTFET)

The CNTFET is a three-terminal device (gate, drain and source), similar to a MOSFET. It can be employed as a single-walled CNT or a multiple-walled CNT as a channel material instead of a traditional bulk silicon used in MOSFET.

The schematic of multiwall CNTEFT is shown in Fig. 1. The performance of the CNTFET depends on drain current, which is controlled by gate-to-source voltage and drain-to-source voltage, the number of tubes, and the chirality vector (n, m). The threshold of CNTFET depends on the bandgap Eg. Alternatively, the threshold value may be related to the carbon pi-pi bond energy (V_{Π}) and is given by (1).

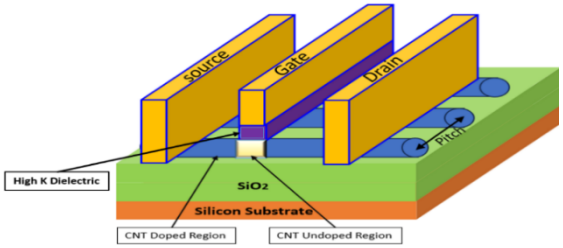


Fig. 1 Schematic of Multiwalled CNTFET

$$V_{th} \approx \frac{E_g}{2e} \approx \frac{\sqrt{3}}{3}\frac{aV_{\Pi}}{eD_{CNT}} \qquad (1)$$

where e and D_{CNT} correspond to electron charge and diameter of a nanotube. The DCNT is calculated by (2).

$$D_{CNT} = \frac{\sqrt{3a_0}}{\pi}\sqrt{(n^2 + m^2 + nm)} \qquad (2)$$

where, a_0 is interatomic distance between the centers of two adjacent carbon atoms.

B. Static Gate Diffusion Input (GDI) Technique and its variants

The GDI is a novel technique [16] for designing low-power, area-efficient, and high-speed static combinational circuits. Additionally, the GDI technique helps in reducing circuit complexity and adds reconfigurability to the design. The schematic of the basic GDI cell is shown in Fig. 2(a). It is a three-input device, X, Y and Z. It explored only two devices to implement XOR and XNOR logic. Upon applying various input combinations enlisted in Table I, different logic functions can be realized.

It is worth mentioning here that the output may display weak '0' or weak '1' states for particular input combinations, depending on the specific function that the GDI circuit is intended to perform. Table I, the last column, shows 'logic confront inadequate swing' and shows different combinations of input that faced an insufficient swing. To elucidate it further, let us consider the GDI cell configured as an XNOR logic gate as depicted in Fig. 2. b. Keeping inputs X and Y at logic '0' and logic '1' respectively, P type CNTFET (PCNTFET) M1 turns ON whereas N type CNTFET (NCNTFET) turns OFF. Since the PCNTFET passes weak '0' i.e. |Vtp|. Similarly, for input combination XY = '11', NCNTFET M2 turns ON while PCNTFET M1 turns OFF. Since the NCNTFET passes weak '1', the output would also be weak '1'. For other input combinations, i.e., XY = '00' and '10', the output is strong '0' and strong '1' respectively. The timing waveform of the GDI cell is shown in Fig. 3.

To resolve the issue of non-availability of full swing faced in the GDI cell, use of an additional PCNTFET or NCNTFET is suggested in [17]. A GDI cell for XNOR logic with a full swing is depicted in Fig. 4. It uses three sub-GDI cells, each containing three CNTFETs, as shown in Figs. 4(a), 4(b) and 4(c) respectively, totaling to 9 CNTFETs. It can be seen that Figs. 4.a and 4.b generate XY and $\bar{X}\bar{Y}$ respectively. The full-swing is ensured via additional NCNTFET placed parallel to

Authorized licensed use limited to: DELHI TECHNICAL UNIV. Downloaded on June 04,2025 at 05:36:07 UTC from IEEE Xplore. Restrictions apply.

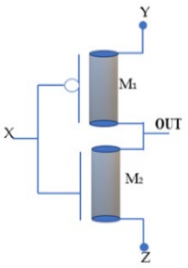


Fig. 2.a Basic GDI cell using CNTFET

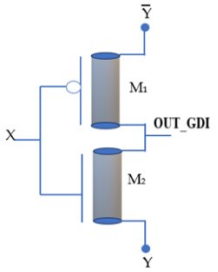


Fig. 2.b GDI cell for XNOR using CNTFET

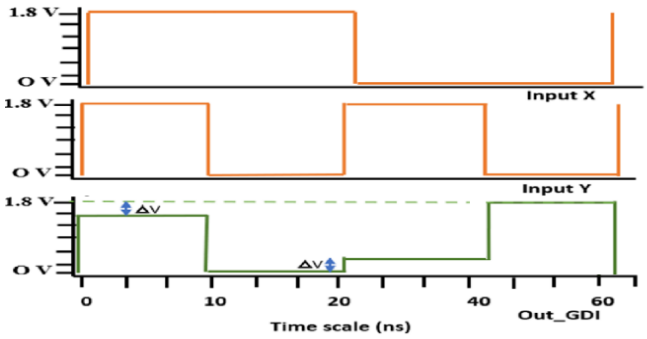


Fig. 3 Timing waveform of the GDI cell

TABLE I. FUNCTION REALIZATIONS USING GDI WITH VARIOUS COMBINATIONS OF INPUTS

X	Y	Z	OUT	Function	Issue of full swing	Logic confronts Inadequate Swing
X	Y	'1'	X+Y	OR	Present	00,10,11
X	Y'	'0'	X'Y'	NOR	Present	01
X	'0'	Z	XZ	AND	Present	00,01,11
X	'1'	Y'	(XY)'	NAND	Present	10
X	Y	Z	X'Y+XZ	MUX	Present	00,10
X	Y	Y'	X'Y+XY'	XOR	Present	00,10
X'	Y	Y'	X'Y'+XY	XNOR	Present	11, 01

TABLE II. FUNCTION REALIZATIONS USING TGDI WITH VARIOUS COMBINATIONS OF INPUTS

X	Y	Z	OUT	Function	Issue of full swing resolved
X	Y	'1'	X+Y	OR	✓
X	Y'	'0'	X'Y'	NOR	✓
X	'0'	Z	XZ	AND	✓
X	'1'	Y'	(XY)'	NAND	✓
X	Y	Z	X'Y+XZ	MUX	✓
X	Y	Y'	X'Y+XY'	XOR	✓
X'	Y	Y'	X'Y'+XY	XNOR	✓

PCNTFET. Figure 4.c performs OR operation of XY and $\overline{X}\overline{Y}$. Here, the complement of signal generated in Fig. 4a i.e. $\overline{XY}$, is used as a one input, so an intermittent inverter is required. Here the full sing is achieved through additional PCNTFET placed in parallel to NCNTFET. Thus, the total number of CNTFETs for full XOR gate is 11 which causes increased

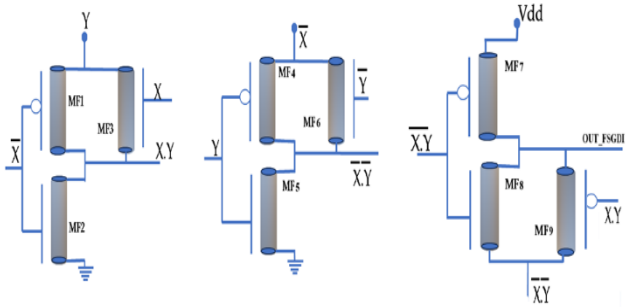


Fig. 4 GDI cell for XNOR logic with full swing

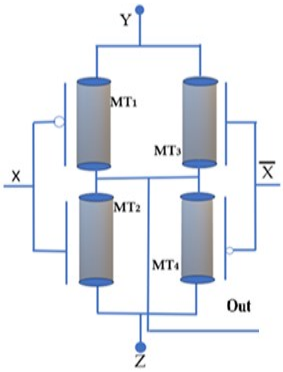


Fig. 5.a Basic TGDI cell based on CNTFET

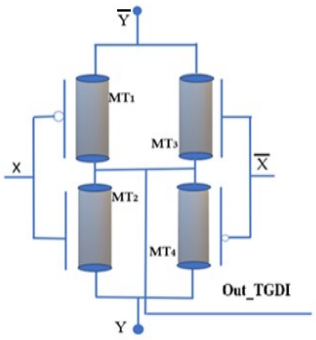


Fig. 5.b XNOR configured TGDI cell

power consumption in the circuit. Upon closer inspection of the circuits in Fig. 4, it can be seen that in AND operation, an NCNTFET is utilized in parallel to a PCNTFET for a full swing output, and in an OR operation, a PCNTFET is used in parallel to an NCNTFET for the same purpose. Further, CNTFET-based TGDI is suggested in [18], and the schematic of the basic TGDI cell based on CNTFET is depicted in Fig. 5.a. This cell ensures full swing output, as it Fig. 4 GDI cell for XNOR logic with full swing uses NCNTFET and PCNTFET in parallel, which are controlled by complementary signals. Table II shows the logic functions that can be realized with a full swing. The XOR-configured TGDI cell is shown in Fig. 5.b.

C. Dynamic GDI (DGDI) logic

The dynamic logic is based on the concept of the pre-charge and evaluation alternatively with the help of a clock signal. When the clock (clk) = '0', the output node is temporarily charged to the Vdd and this mode of operation is known as the pre-charged phase. Further, when clock (clk) = '1', it enters into the evaluation phase wherein the desired output is achieved depending upon input combinations. In [16], a CNTFET-based dynamic logic-based gate diffusion (DGDI) cell is put forward, and its configuration as an XOR gate is shown in Fig. 6. Here Block 1 is the GDI cell (Fig. 2.b) and Block 2 provides dynamic functionality. When clk = '0', the output pre-charges to Vdd and no current flows through transistor MD_4 as its source terminal is connected to the complement of clk. When clk = '1', the transistor MD_3 turns off and the output becomes '0' if the GDI cell output is '1' and remains at Vdd otherwise.

The operation of the DGDI cell is explained for inputs XY = '11'. The node A will be weak '1' for this combination and causes at DGDI would be strong 0. Similarly, for an input combination of '01', the output at node A would be weak

Authorized licensed use limited to: DELHI TECHNICAL UNIV. Downloaded on June 04,2025 at 05:36:07 UTC from IEEE Xplore. Restrictions apply.

therefore, NCTFET MD_4 would be OFF. Output at DGDI was maintained at strong logic '1'.

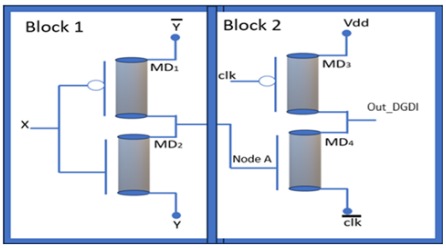


Fig. 6 XOR configured Dynamic Gate Diffusion Input (DGDI)output

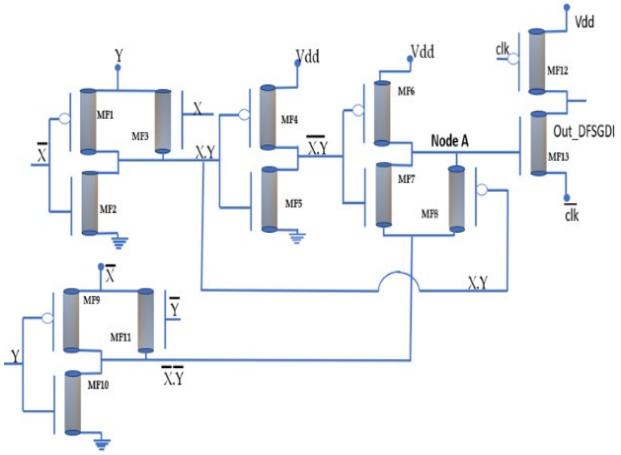


Fig. 7 XOR Configured Proposed Dynamic Full Swing Gate Diffusion Input (DFSGDI)

III. Modified DGDI Circuits

This section presents two new DGDI circuits derived from full swing GDI and TGDI, which are referred as Dynamic Full Swing Gate Diffusion Input (DFSGDI) and Dynamic Transmission Gate Diffusion input (DTGDI) in the context of this paper.

A. Proposed Dynamic Full Swing Gate Diffusion Input logic (DFSGDI) – I

The proposed DFSGDI–I, combines the full swing GDI concept with Block 2 of the existing DGDI (Fig. 6). The complete schematic of the XOR gate based on DFSGDI is depicted in Fig. 7. It may be noticed that an XNOR functionality is attained at node A and the transistors MF_{12} and MF_{13} add dynamic functionality to it. The node A enjoys a full voltage swing and resolves the issues prevailing in DGDI. It may further be noticed that the overall transistor count is 13 in this case. Additionally, a longer path exists between input and output that may lead to a larger delay.

B. Proposed Dynamic Transmission Gate Diffusion input logic (DTGDI) - II

The proposed DTGDI-II is an amalgamation of the TGDI concept with Block 2 of the existing DGDI (Fig. 6). The schematic of XOR gate based on DTGDI is depicted in Fig. 8. It may be noticed that an XNOR functionality is attained at node A, and the transistors MT_5 and MT_6 add dynamic functionality to it. Due to the full voltage swing available at node A, the issues discussed in DGDI are sorted out. The overall transistor count is only 6, a significantly lesser than

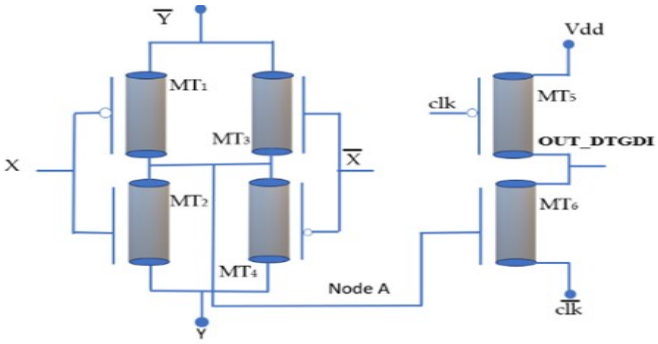


Fig. 8 XOR configured Proposed Dynamic Transmission gate diffusion input based on CNTFET

DFSGDI. Moreover, the path that exists between input and output becomes shorter, leading to a shorter delay.

IV. Results and Discussions

This section first presents functional verification of the XOR gate based on proposals, and performance parameters such as delay and power are measured. The existing DGDI-based XOR gate is also simulated for a fair comparison of performance parameters. The simulations are carried out using the 32 nm technology node in Cadence Virtuoso. Figures 9 (a), (b) and (c) show the simulated timing waveforms for the XOR gate based on the existing DGDI, proposed DFSGDI and DTGDI. It may be observed that output is pre-charged to Vdd when clk = '0' for all three circuits. When clk eventually becomes '1', the output remains at logic '1' when both inputs differ from each other and is evaluated to '0' when both inputs are the same. Thus, the circuits adhere to XOR gate functionality.

A. 10. a. The waveforms for inputs (X, Y, Clock) and outputs for DGDI, DTGDI, and DFSGDI are also depicted in Fig. 10.b. The findings are summarized in Table III, and the following observations are made:

1. The maximum currents drawn from the power supply are 0.89 µA, 0.857 µA and 1.563µA for DGDI, DTGDI and DFSGDI respectively.
2. The average power consumption for logic '11' is 3.24pW for both DGDI and DTGDI, whereas average power consumption is 1025.6pW for DFSGDI. It can therefore be concluded that though the power consumption is same for DGDI and DTGDI, there is a significant increase in power consumption for DFSGDI. This is attributed to complex circuitry between inputs and Node A (Fig. 7).
3. Power consumption of the XOR module based on DFSGDI (2.84µW) is highest as compared to DTGDI and DGDI, as the transistor count is higher in DFSGDI. But the power consumption is in DTGDI (1.52 µW) as compared to DGDI (1.605 µW).
4. The delay values of DGDI, DFSGDI and DTGDI are 122.7ps, 93.9ps and 93.7ps respectively. It can be inferred that delay is almost identical in proposed full swing circuits DTGDI and DFSGDI. But in the DGDI cell (Fig. 6), NCNTFET MD4 is weekly ON, resulting in a higher delay for the inputs XY= '11'. Delay reduced by 23.6 %

Authorized licensed use limited to: DELHI TECHNICAL UNIV. Downloaded on June 04,2025 at 05:36:07 UTC from IEEE Xplore. Restrictions apply.

in the proposed circuit as compared to DGDI. Assuming 50% duty cycle of the clock, the existing DGDI can operate till 4.07 GHz while the proposals can operate well till a frequency of 5.32 GHz, which is a clear indication of the advantage of the proposals.

5. The PDP parameter was calculated from the above measurement data, and it was observed that the PDP parameter is reduced by 25.2 % in DTGDI with respect to DGDI as well as the PDP parameter of DFSGDI increased by 35.3% as compared to DGDI.

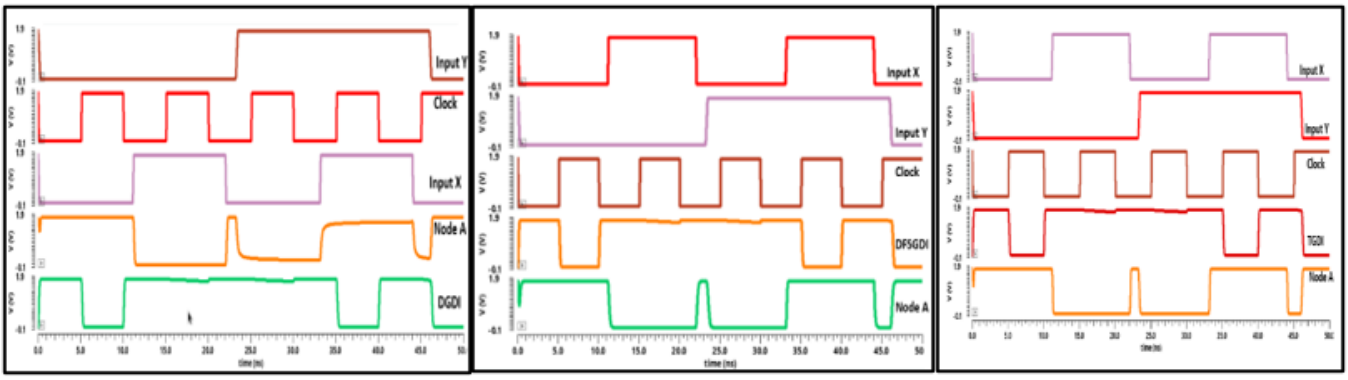


Fig. 9 Simulated Timing waveform of the XOR gate based on (a) existing DGDI (b) proposed FSDGDI (c) proposed DTGDI

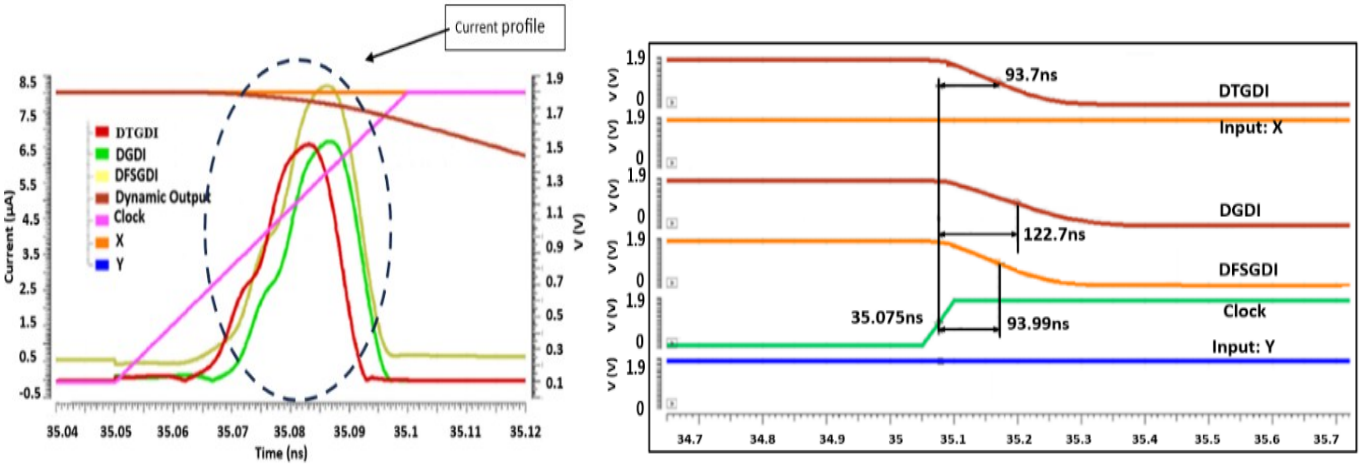


Fig. 10 Simulated waveform for measuring (a) current from power supply (b) delay

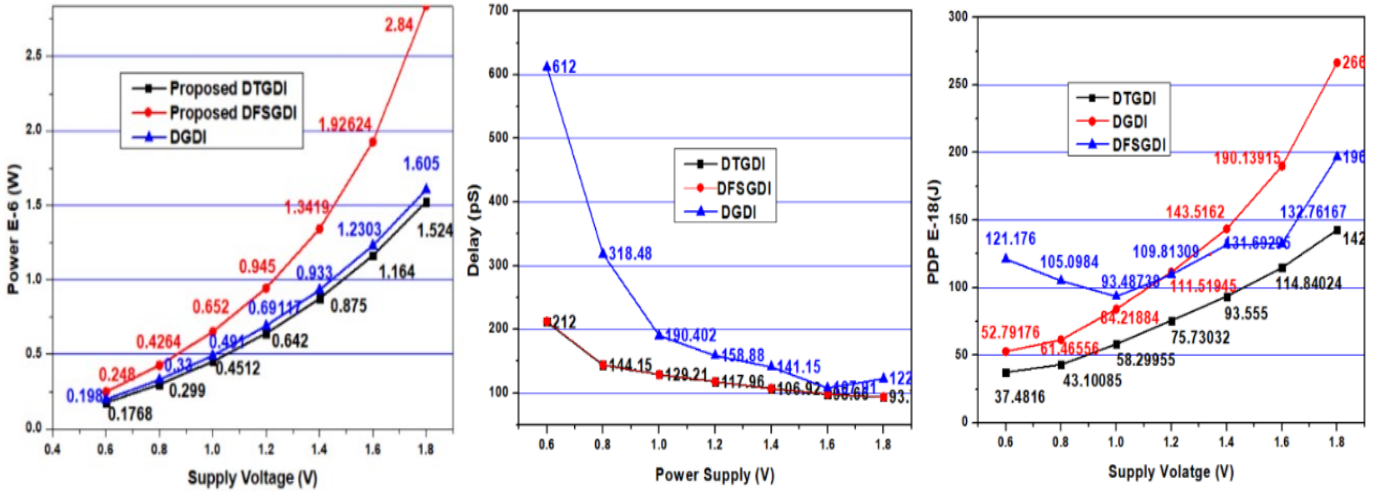
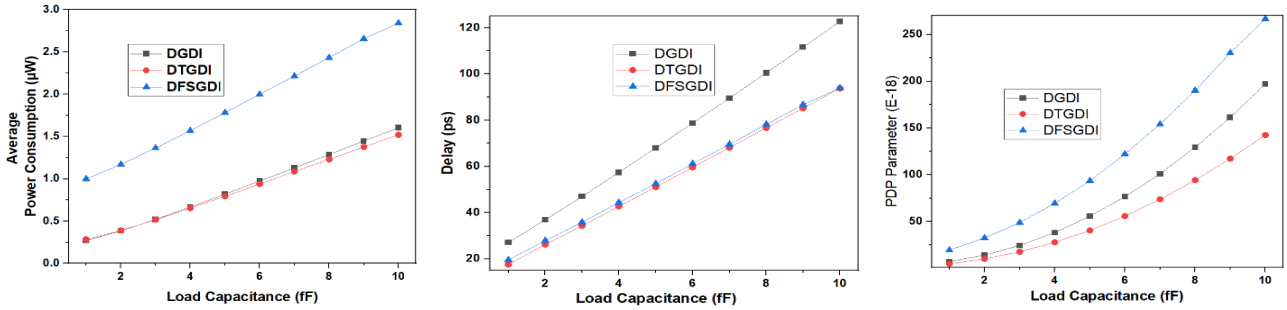


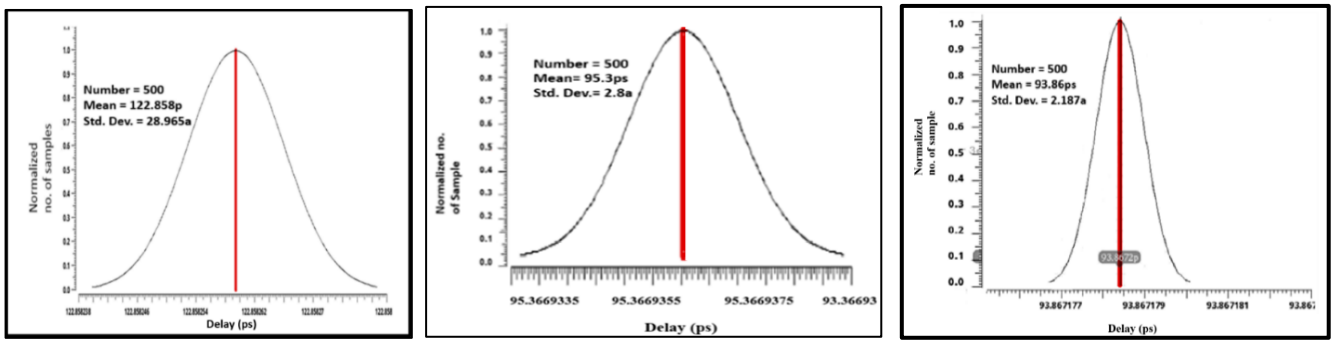
Fig. 11 Effect of the load capacitance on (a) average power consumption (b) delay (c) PDP

Authorized licensed use limited to: DELHI TECHNICAL UNIV. Downloaded on June 04,2025 at 05:36:07 UTC from IEEE Xplore. Restrictions apply.



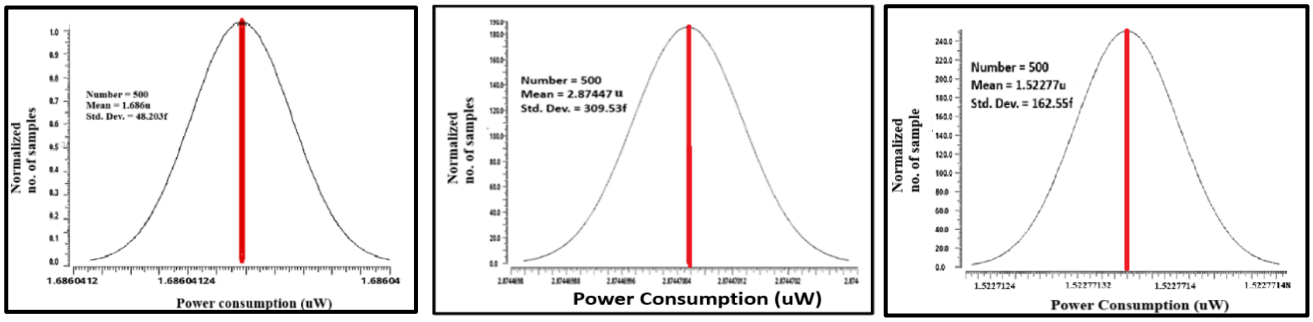
(a) (b) (c)

Fig. 12 Effect of supply voltage variation on a (a) Power Consumption (b) Delay (c) PDP on the proposed and considered XOR logic based on DTGDI, DFSGDI, and DGDI.



(a) (b) (c)

Fig. 13 Monte-Carlo Simulation for delay by varying pitch 5% (a) DGDI (b) DFSGDI (c) DTGDI



(a) (b) (c)

Fig. 14 Monte-Carlo Simulation for power supply by varying pitch 5% (a) DGDI (b) DTGDI (c) DFSGDI

TABLE IV: RESULTS OF MONTE CARLO SIMULATIONS

Parameters	Power Consumption	Delay
DGDI	Means = 1.68µ Std. Dev. = 48.2f	Means = 122.858p Std. Dev. = 28.965a
DFSGDI	Means = 2.87447µ Std. Dev. = 309.53 f	Means = 95.3 p Std. Dev. = 2.87 a
DTGDI	Means = 1.5277µ Std. Dev. = 162.55f	Means = 93.8ps Std. Dev. = 2.187a

Further, load capacitance is varied from 1 fF to 10 fF and average power consumption, delay and PDP are observed. The variation is plotted in Figs. 11(a), 11(b) and 11(c) and values increase linearly with a load. The investigations are also done by changing the supply voltage and the performance parameters namely power, delay, and PDP, are measured for DTGDI and DFSGDI-based XOR logic. The findings are placed in Fig. 12. It may be noted that the delay reduces with the increase in supply voltage, whereas power consumption and PDP show an upward trend.

There may be uneven CNT growth and inaccurate lithography, which may lead to abnormalities in pitch variations, change in diameter of nanotubes, defects and misalignment. It causes process variations and may impact the performance of the circuit. The pitch variation of ±15% is considered with a 3σ gaussian distribution. Monte Carlo simulation was conducted for 500 samples to assess the impact of process variations on the delay and power consumption of the XOR gate based on the existing DGDI, proposed circuit DFSGDI and DTGDI. The plots for the delay and power consumption of DGDI, DFSGDI and DTGDI are depicted in Figs. 13 (a), 13 (b), 13 (c), 14 (a), 14 (b), and 14(c) respectively. The findings are comprehended

Authorized licensed use limited to: DELHI TECHNICAL UNIV. Downloaded on June 04,2025 at 05:36:07 UTC from IEEE Xplore. Restrictions apply.

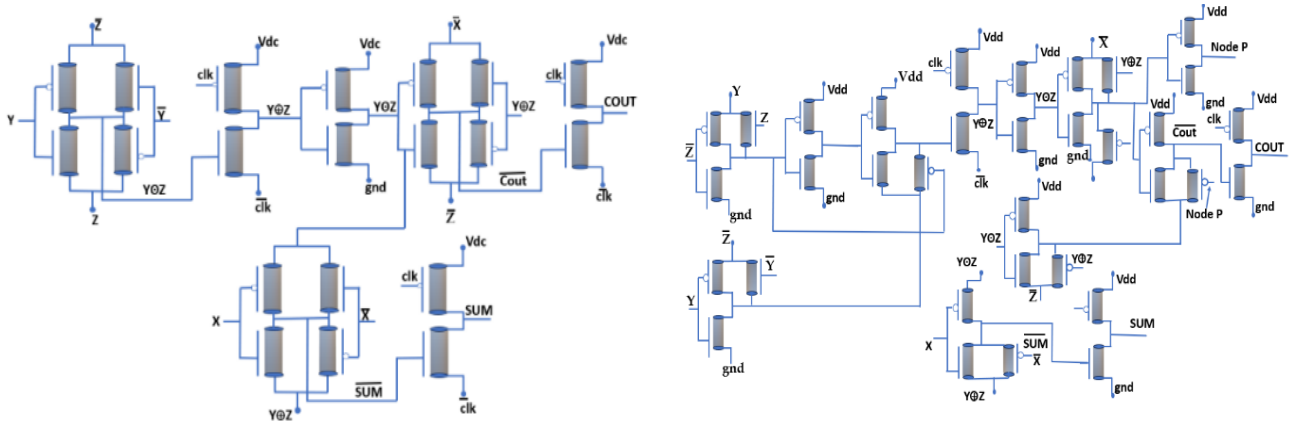


Fig. 15 Schematic of the 1-bit full adder based on (a) DTGDI, and (b) DFSGDI

TABLE III. PERFORMANCE COMPARISON OF THE XOR GATE BASED ON DGDI AND PROPOSED (I & II) CIRCUIT AT 32NM TECHNOLOGY NODE

XOR based Cell	DGDI		DFSGDI		DTGDI	
Vdc (V)	1.8	1	1.8	1	1.8	1
Average current (µA)	0.891	0.49	1.56	0.712	0.855	0.459
Average Power (µW)	1.605	0.49	2.84	0.712	1.54	0.459
Power Consumption for logic '11' (pW)	3.24	1.77	1025.6	551.8	3.24	1.77
Delay for Logic 11 (ps)	122.7	230	93.9	134	93.7	134.5
PDP Parameter (E-18)	196.9	112.7	266.67	95.408	144.2	61.73

in Table IV. It may be observed that the maximum standard deviation is 10.7e-6%. Thus, the circuit is resilient against process variations. TABLE V. PERFORMANCE PARAMETERS OF 1-BIT FULL ADDERS

Adder	Design	Power (µW)	Delay (pS)	PDP (aJ)
Static CMOS	ULPFA [10]	0.534	62.24	34
Static	GDI Hybrid FA [11]	0.28	132.7	37.9
Static	GDI [12]	0.844	37.3	31.4
Dynamic CMOS	Multi-Output FA [19]	0.436	179.91	78.4
Dynamic	DGDI [15]	0.127	36.3	4.6
Dynamic	**Proposed DTGDI**	**0.102**	**23.11**	**2.35**
Dynamic	**Proposed DFSGDI**	**0.365**	**33.56 12.24**	

The proposed methods can be extended to more complex circuit applications. To show the possible extension, a 1-bit full adder has been made using the DTGDI and DFSGDI. The sum and carry output are generated using (3) and (4).

$$\overline{SUM} = \overline{XYZ} + \bar{X}YZ + XY\bar{Z} + X\bar{Y}Z = = X(\bar{Y}Z + Y\bar{Z}) + \bar{X}\,(YZ + \overline{YZ}) \quad (3)$$

$$\overline{COUT} = \overline{XYZ} + \overline{XY}Z + \bar{X}Y\bar{Z} + X\overline{YZ} = (\bar{Z})(YZ + \overline{YZ}) + \bar{X}(Y\bar{Z} + \bar{Y}Z) \quad (4)$$

The circuitry for a 1-bit full adder based on the DFSGDI and DTGDI is shown in Figs. 15 (a) and (b), respectively. 1-bit full adders are simulated with a 1f F load capacitance, a 100 MHz clock frequency, and 0.8V to guarantee a fair comparison. Figures 16 displays the simulation results for the 1-bit full adders based on DTGDI. Table V lists the performance parameters of the 1-bit full adders based on DGDI, DFSGDI, DTGDI and state-of-art-adders.

The performance of DTGDI and DFSGDI-based full-adder circuits is compared with other state-of-art-designs and observations are comprehended in Table V. The power consumption of proposed DTGDI based adder show 80.8%, 63.5%, 87.9%, 76.6%, 19.68%, and 72.05% reduction in power from full adders reported in [10], [11], [12], [19] and [15] respectively. Thus, there is notable improvement in power consumption for DTGDI-based full-adder circuit compared to other state-of-art-designs. Similarly, the delay and PDP of the DTGDI-based full adder also considerably reduced in comparison to the considered designs. Thus, the proposed TGDI-based adder shows the best performance in all the performance parameters.

Authorized licensed use limited to: DELHI TECHNICAL UNIV. Downloaded on June 04,2025 at 05:36:07 UTC from IEEE Xplore. Restrictions apply.

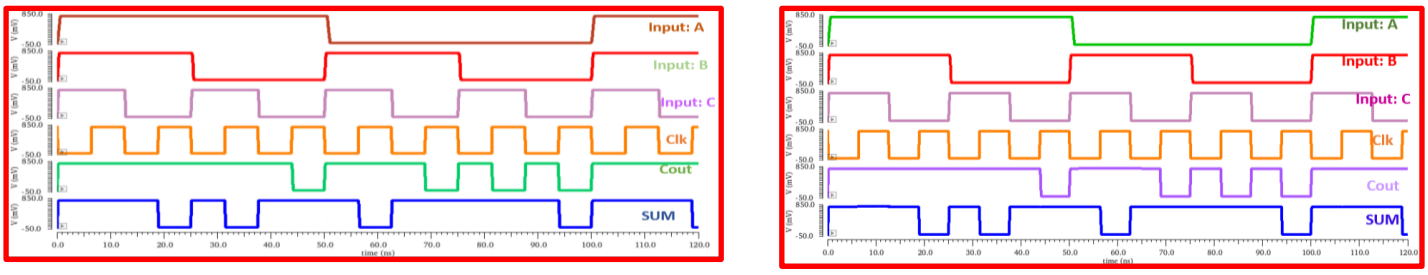


Fig 16 Simulation results of proposed 1-bit full adder based on (a) DTGDI, and (b) DFSGDI

V. Conclusion

The goal of this study was to evaluate the novel dynamic GDI cells' performance in comparison to previous methods and enhance their design. These circuits are implemented utilizing Carbon Nanotube Field Effect Transistors, and comprehensive simulations in the Cadence Virtuoso program at the 32nm technology node are used for verification and performance evaluation. It is found that the DGDI-based XOR gate's intermittent node is not in full swing for logic 11 and 01, which caused a greater delay at the dynamic block's output for both inputs. Proposals use FSGDI and TGDI to achieve complete swing at the intermittent node. In order to accomplish dynamic operation, a dynamic block is also added. The performance of XOR gates is compared for PDP, power, and delay parameters. Since logic 11 and 01 exhibit inadequate swing at the intermittent node, a higher delay is obtained for this logic. The measured delay in DTGDI was reduced by 23.6% compared to the existing DGDI, and concurrently, the PDP parameter of DTGDI was reduced by 25.2% compared to DGDI. Although DFSGDI consumes the most power out of all the DGDI configurations due to its 13 MOS devices, the proposed proposal-II (DTGDI) has lower average power consumption and a lower delay than the current DGDI configurations.

References

[1] G.E. Moore, L. Fellow Cramming more components onto integrated circuits, Proceeding of IEEE 86 (1), 82-85, http://doi.org/10.1109/jproc.1998.658762.

[2] P. Prakash, K. Mohana Sundaram, M. Anto Bennet, A review on carbon nanotube field effect transistors (CNTFETs) for ultra-low power applications, Renewable and Sustainable Energy Reviews, Volume 89, 2018, Pages 194-203, https://doi.org/10.1016/j.rser.2018.03.021

[3] R. Redwan, C. Ganguly, S. S. Islam and M. F. Nayan, "Performance Evaluation and Comparative Analysis of Logic Gates based on CNTFET and CMOS," *2023 26th International Conference on Computer and Information Technology (ICCIT)*, Cox's Bazar, Bangladesh, 2023, pp. 1-5, doi: 10.1109/ICCIT60459.2023.10441488.

[4] A. C. Bodoh and A. A. Sakib, "Comparative Analysis of CNTFET and CMOS based NCL Asynchronous Circuits: A Study of Scaling Trends," *2022 IEEE 13th Annual Ubiquitous Computing, Electronics & Mobile Communication Conference (UEMCON)*, New York, NY, NY, USA, 2022, pp. 0407-0412, doi: 10.1109/UEMCON54665.2022.9965723.

[5] R. Marani and A. G. Perri 2023 *ECS J. Solid State Sci. Technol.* 12 051005DOI 10.1149/2162-8777/acd65d.

[6] Hills, G., Lau, C., Wright, A. *et al.* Modern microprocessor built from complementary carbon nanotube transistors. *Nature* **572**, 595–602 (2019). https://doi.org/10.1038/s41586-019-1493-8

[7] A. Morgenshtein, A. Fish and I. A. Wagner, "Gate-diffusion input (GDI): a power-efficient method for digital combinatorial circuits," in *IEEE Transactions on Very Large Scale Integration (VLSI) Systems*, vol. 10, no. 5, pp. 566-581, Oct. 2002, doi: 10.1109/TVLSI.2002.801578. keywords: {Circuit synthesis; Logic design; Energy consumption; Propagation delay; Digital circuits; Power dissipation; CMOS technology; Logic circuits; Circuit simulation; Semiconductor device measurement}

[8] E. Abiri, M. R. Salehi and A. Darabi, "Design and evaluation of low power and high speed logic circuit based on the modified gate diffusion input (m-GDI) technique in 32nm CNTFET technology," *2014 22nd Iranian Conference on Electrical Engineering (ICEE)*, Tehran, Iran, 2014, pp. 67-72, doi: 10.1109/IranianCEE.2014.6999505.

[9] Mohan, Shoba & Rangaswamy, Nakkeeran. (2015). GDI based full adders for energy efficient arithmetic applications. Engineering Science and Technology, an International Journal. 19. 10.1016/j.jestch.2015.09.006.

[10] I. Hassoune, D. Flandre, I. O'Connor and J. -D. Legat, "ULPFA: A New Efficient Design of a Power- Aware Full Adder," in *IEEE Transactions on Circuits and Systems I: Regular Papers*, vol. 57, no. 8, pp. 2066-2074, Aug. 2010, doi: 10.1109/TCSI.2008.200136.

[11] K. Sanapala, R. Sakthivel, Ultra-low-voltage GDI-based hybrid full adder design for area and energy-efficient computing systems, IET Circuits, Devices Syst. 13 (2019) 558–564, https://doi.org/10.1049/iet-cds.2018.5559.

[12] Asma Torkzadeh Mahani, Peiman Keshavarzian, "A novel energy-efficient and high-speed full adder using CNTFET", Microelectronics Journal, Volume 61, 2017, Pages 79-88, ISSN 1879-2391, https://doi.org/10.1016/j.mejo.2017.01.009

[13] E. Macii and M. Poncino, "Power consumption of static and dynamic CMOS circuits: a comparative study," 2nd International Conference on ASIC, Shanghai, China, 1996, pp. 425-427, doi: 10.1109/ICASIC.1996.562843.

[14] Bagherizadeh, M., Eshghi, M. Two novel low-power and high-speed dynamic carbon nanotube full-adder cells. *Nanoscale Res Lett* **6**, 519 (2011). https://doi.org/10.1186/1556-276X-6-519

[15] Ali Ghorbani, Mehdi Dolatshahi, S. Mohammadali Zanjani, Behrang Barekatain, A new low-power Dynamic-GDI full adder in CNFET technology, Integration, Volume 83, 2022, Pages 46-59, ISSN 0167-9260, https://doi.org/10.1016/j.vlsi.2021.12.001.

[16] A. Morgenshtein, A. Fish and I. A. Wagner, "Gate-diffusion input (GDI) - A technique for low power design of digital circuits: analysis and characterization," *2002 IEEE International Symposium on Circuits and Systems. Proceedings (Cat. No.02CH37353)*, Phoenix-Scottsdale, AZ, USA, 2002, pp. I-I, doi: 10.1109/ISCAS.2002.1009881.

[17] Arkadiy Morgenshtein, Viacheslav Yuzhaninov, Alexey Kovshilovsky, Alexander Fish, Full-Swing Gate Diffusion Input logic—Case-study of low-power CLA adder design, Integration, Volume 47, Issue 1, 2014, Pages 62-70, ISSN 0167-9260, https://doi.org/10.1016/j.vlsi.2013.04.002.

[18] N. Yadav, N. Pandey and D. Nand, "CNTFET Based M-DMTGDI (CMDMTGDI) Design and Its Leakage Analysis," *2023 10th International Conference on Signal Processing and Integrated Networks (SPIN)*, Noida, India, 2023, pp. 515-521, doi: 10.1109/SPIN57001.2023.10116812.

[19] Faghih Mirzaee, Reza & Moaiyeri, Mohammad & Navi, Keivan. (2010). High speed NP-CMOS and multi-output dynamic full adder cells. International Journal of Electrical, Computer, Energetic, Electronic and Communication Engineering. 4. 531-537.

Authorized licensed use limited to: DELHI TECHNICAL UNIV. Downloaded on June 04,2025 at 05:36:07 UTC from IEEE Xplore. Restrictions apply.

Journal of Tribology. Received May 03, 2025;
Accepted manuscript posted June 19, 2025. doi:10.1115/1.4068992
Copyright © 2025 by ASME

Check for updates

Enhancement of Wear Properties of Dissimilar SSDS 2507-IN718 Alloy Wall Via Ultrasonic Vibration Assisted Cold Metal Transfer Based Wire Arc Additive Manufacturing

Rajendra Prasad[1*], N. Yuvaraj[1a], Vipin [1b], Qasim Murtaza[1c]

Department of Mechanical Engineering, Delhi Technological University

Email Id: rpmeena89@gmail.com, yuvraj@dce.ac.in, vipin@dce.ac.in, qasimmurtaza@dce.ac.in

Orchid id: https://orcid.org/0009-0000-5387-1406, https://orcid.org/0000-0002-1537-9098, https://orcid.org/0000-0003-4643-7200, https://orcid.org/0000-0001-8784-2304

Abstract: Cold Metal Transfer (CMT) has surfaced as an exceptionally promising technique for the direct production or repair of high-performance metal components. Induced fabrication defects, such as porosity and heterogeneous microstructures, significantly influence the quality of parts and their mechanical performance. Ultrasonic vibration (UV) has been employed to improve the performance of components in the processes of solidifying melted materials. Limited research has been conducted on the application of UV in CMT-based wire arc direct energy deposition for the fabrication of dissimilar SDSS2507-IN718 components. This study introduces the application of UV-assisted CMT-based wire arc direct energy deposition for the production of dissimilar SDSS2507-IN718 components, aiming to reduce fabrication errors. Experimental investigations are conducted to analyze the effects of UV on the microstructures and wear characteristics of components produced through CMT. This manuscript outlines the findings regarding the wear characteristics of a dissimilar alloy wall produced through the UV-WAAM technique, which has been tested under dry sliding conditions with varying load conditions. Wear testing was performed in a dry, unlubricated setting utilizing a conventional high-load ball-on-disc tribometer. The wear rate and coefficient of friction are lower for

Accepted Manuscript Not Copyedited

Downloaded from http://asmedigitalcollection.asme.org/tribology/article-pdf/doi/10.1115/1.4068992/7515215/trib-25-1248.pdf by Delhi Technological University user on 26 June 2025

Journal of Tribology. Received May 03, 2025;
Accepted manuscript posted June 19, 2025. doi:10.1115/1.4068992
Copyright © 2025 by ASME

samples treated with UV assistance compared to those treated with UV alone. The results indicated that the use of ultrasonic vibration enhanced the microstructure, resulting in an average grain size of 4.59 μm. Furthermore, it successfully broke down the detrimental Laves precipitated phase into smaller particles that were uniformly dispersed.

Keywords: Dissimilar Alloys, Wear, Wire Arc Additive Manufacturing, Ultrasonic Vibrations, CMT, Dry friction, Ball on disk reciprocating tribometer

1.Introduction

Joining dissimilar metal components is crucial in various industrial sectors, including aviation, aerospace, shipbuilding, and automobile manufacturing. The components generally consist of alloys comprising steel, magnesium, titanium, and nickel-based superalloys [1]. Acquiring optimal metal combinations through traditional joining or welding techniques presents challenges due to the risk of forming brittle intermetallic compounds (IMCs) during solidification [2]. Minimizing the fusion heat input is crucial in solid-state bonding to address the primary challenge of establishing adequate contact between dissimilar materials [3]. Steel-nickel alloys exhibit potential as structural materials in nuclear energy systems, chemical processing plants, and notably in gas turbine engines [4]. These alloys are highly regarded for their superior performance in extreme combustion and chemically aggressive environments. The materials exhibited notable mechanical properties, outstanding corrosion resistance, significant deformation resistance at elevated temperatures, and superior radiation damage tolerance [5,6]. Inconel 718 is a nickel-iron-chromium superalloy known for its superior properties. The material demonstrated significant resistance to elevated temperatures, corrosion, and fatigue while exhibiting remarkable tensile strength and optimal creep behaviour [7]. SDSS2507 is a Super Duplex Stainless Steel characterized by a mixed microstructure of austenite and ferrite, often in equal quantities. This dual-phase structure offers remarkable strength, corrosion resistance, and resistance to stress corrosion cracking, particularly in

Accepted Manuscript Not Copyedited

Downloaded from http://asmedigitalcollection.asme.org/tribology/article-pdf/doi/10.1115/1.4068992/7515215/trib-25-1248.pdf by Delhi Technological University user on 26 June 2025

Journal of Tribology. Received May 03, 2025;
Accepted manuscript posted June 19, 2025. doi:10.1115/1.4068992
Copyright © 2025 by ASME

chloride-rich environments like saltwater. It is utilized in offshore oil and gas operations, desalination facilities, heat exchangers, pressure vessels, and chemical processing apparatus. Strong resistance to corrosion and great mechanical properties help SDSS2507 to show remarkable performance in challenging surroundings. This is explained by the large concentrations of chromium and nickel and their ferritic-austenitic microstructure [8]. SDSS2507 is more affordable than the IN718 superalloy for components running at lower temperatures because of its great cost-benefit. Inconel 718 superalloy is still favoured for parts exposed to higher temperatures, even if it costs more. This method maximizes the special benefits of every material in its particular operating conditions and effectively controls material prices.

Wire-arc directed energy deposition, known as wire-arc additive manufacturing (WAAM), represents a cost-effective and efficient technique for producing large-scale components that are nearly finished in form. The CMT represents an enhanced iteration of gas metal arc welding, minimizing the heat produced during the metal deposition process. This results in decreased spattering and enhanced arc stability [9]. The CMT employs the reciprocal movements of the filler wire in short-circuiting mode to facilitate material transport. The CMT process is characterized by its distinct wire movement and transfer mode integration [10]. The low heat in CMT WAAM facilitates the deposition of dissimilar alloy additive manufacturing walls, including steel-nickel, steel-aluminium, and aluminium-nickel, which are prevalent in industrial applications[11].

Various techniques, such as ultrasonic vibration, electromagnetic field integration, and mechanical stirring, have been utilized to minimize fabrication defects by controlling the melting and solidification behaviour of materials in thermal processes like casting, arc welding, and cladding [12–17]. Ultrasonic vibration is a well-recognized method within these supportive strategies. This method is preferred due to its efficiency in transmitting acoustic energy and

Accepted Manuscript Not Copyedited

Downloaded from http://asmedigitalcollection.asme.org/tribology/article-pdf/doi/10.1115/1.4068992/7515215/trib-25-1248.pdf by Delhi Technological University user on 26 June 2025

Journal of Tribology. Received May 03, 2025;
Accepted manuscript posted June 19, 2025. doi:10.1115/1.4068992
Copyright © 2025 by ASME

cavitation, as well as its significant ability to control heat and mass transfer [18]. When a powerful ultrasonic vibration is applied to a liquid, it typically results in two distinct nonlinear phenomena: acoustic streaming and acoustic cavitation [18,19]. Ultrasonic vibration effectively diminishes the occurrence of small holes, enhances grain quality, and disrupts the detrimental Laves precipitated phase. Applying the ultrasonic vibration-assisted (UV-A) DED method, as reported by Ning et al. [20], improves the tensile strength, modulus, microhardness, and wear resistance of IN718 components. The recent research on the Direct Energy Deposition (DED) processing of Ti-6Al-4V demonstrates the considerable influence of UV-induced grain refinement on tensile properties [21]. Ultrasonic Vibration (UV) enhanced grain refinement and diminished the directional growth of coarse columnar grains. Secondary phases containing Mo and Nb readily precipitate at the grain boundaries of c-Ni. Samples subjected to UV-CMT exhibited a more uniform distribution of secondary phases, attributed to an increased density of grain boundaries as reported by Ma et al. [22]. A recent study [23] indicates that Functionally Graded Materials (FGMs) lacking ultrasonic treatment exhibit columnar grains, whereas ultrasonic treatment transforms these grains into equiaxed forms, improving uniformity and decreasing grain size in ultrasonic-assisted double-wire arc additive manufacturing (U-DWAAM). Ultrasonically treated specimens exhibit enhanced tensile strength and diminished elongation due to equiaxed grains and reduced crystal size. Ultrasonic treatment increases hardness in SS 308L to IN718 by 7%-15% through microstructural alterations, solid solution strengthening, and enhanced precipitation from Ni, Mo, and Nb.

Most studies on wire-based additive manufacturing focus on the use of ultrasonic vibration-assisted GMAW, CMT, U-DWAAM, and laser-based WAAM systems for joining different alloys, such as steel, aluminium, and nickel. The understanding of the effects of UV on the microstructural and wear properties of dissimilar SDSS2507 - IN718 alloy structures produced by CMT WAAM is currently limited. This study utilized ultrasonic assistance in the CMT-

Accepted Manuscript Not Copyedited

Downloaded from http://asmedigitalcollection.asme.org/tribology/article-pdf/doi/10.1115/1.4068992/7515215/trib-25-1248.pdf by Delhi Technological University user on 26 June 2025

Journal of Tribology. Received May 03, 2025;
Accepted manuscript posted June 19, 2025. doi:10.1115/1.4068992
Copyright © 2025 by ASME

based WAAM technique to fabricate walls from various SDSS2507 and IN718 alloys. This study examined the ultrasonic-assisted microstructure and wear properties of the interface zone in comparison to standard conditions.

2. Materials and Methodology

2.1 Materials and experimental procedure

The studies employed Inconel 718 and SDSS2507, along with 1.2 mm filler wire sourced from Advanced PMI Solutions. The substrate plate, measuring 200 mm × 50 mm × 5 mm, was constructed from stainless steel 304. A method utilizing CMT-based WAAM with alternating current successfully generated dissimilar alloy components, specifically IN718 and SDSS2507. Table 1 presents the chemical composition of both the substrate and the filler wire.

Table 1 Chemical composition (Wt %) of the substrate material and filler wire

Chemical Composition %	C	Si	Mn	P	S	Ni	Cr	Al	Mo	Fe	Nb
Stainless steel (304)	0.07	1.03	2.05	0.045	0.030	8.04	17.95	-	-	70.78	-
Super Duplex 2507	0.02	0.80	1.20	0.035	0.020	7	25	-	4	57.83	-
Inconel 718	0.08	0.35	0.45	0.015	0.017	51.05	17.55	0.55	2.9	22.14	4.89

The WAAM system was established on a Remote (FRC-45 Pro) operated table unit, equipped with an ultrasonic vibration unit and a TPS 400i power source for sample creation, as illustrated in Fig. 1. The ultrasonic vibration unit produces vibrations throughout the WAAM process. High-energy ultrasound control systems generally consist of a transducer, a power supply, and

Accepted Manuscript Not Copyedited

Downloaded from http://asmedigitalcollection.asme.org/tribology/article-pdf/doi/10.1115/1.4068992/7515215/trib-25-1248.pdf by Delhi Technological University user on 26 June 2025

Journal of Tribology. Received May 03, 2025;
Accepted manuscript posted June 19, 2025. doi:10.1115/1.4068992
Copyright © 2025 by ASME

an ultrasonic horn. The transducer generates highly potent ultrasonic waves. The ultrasonic horn was connected to an ultrasonic generating unit, operating at a consistent frequency of 30 kHz. The ultrasonic vibrations exhibited an amplitude range from 11 to 99 µm, while a consistent value of 60 µm was employed in our experimental procedures. The power supply regulates the input energy and electrical signals. The ultrasonic horn enhances the intensity of high-power ultrasound while effectively insulating against heat transfer through the substrate, thereby safeguarding the transducer from potential damage.

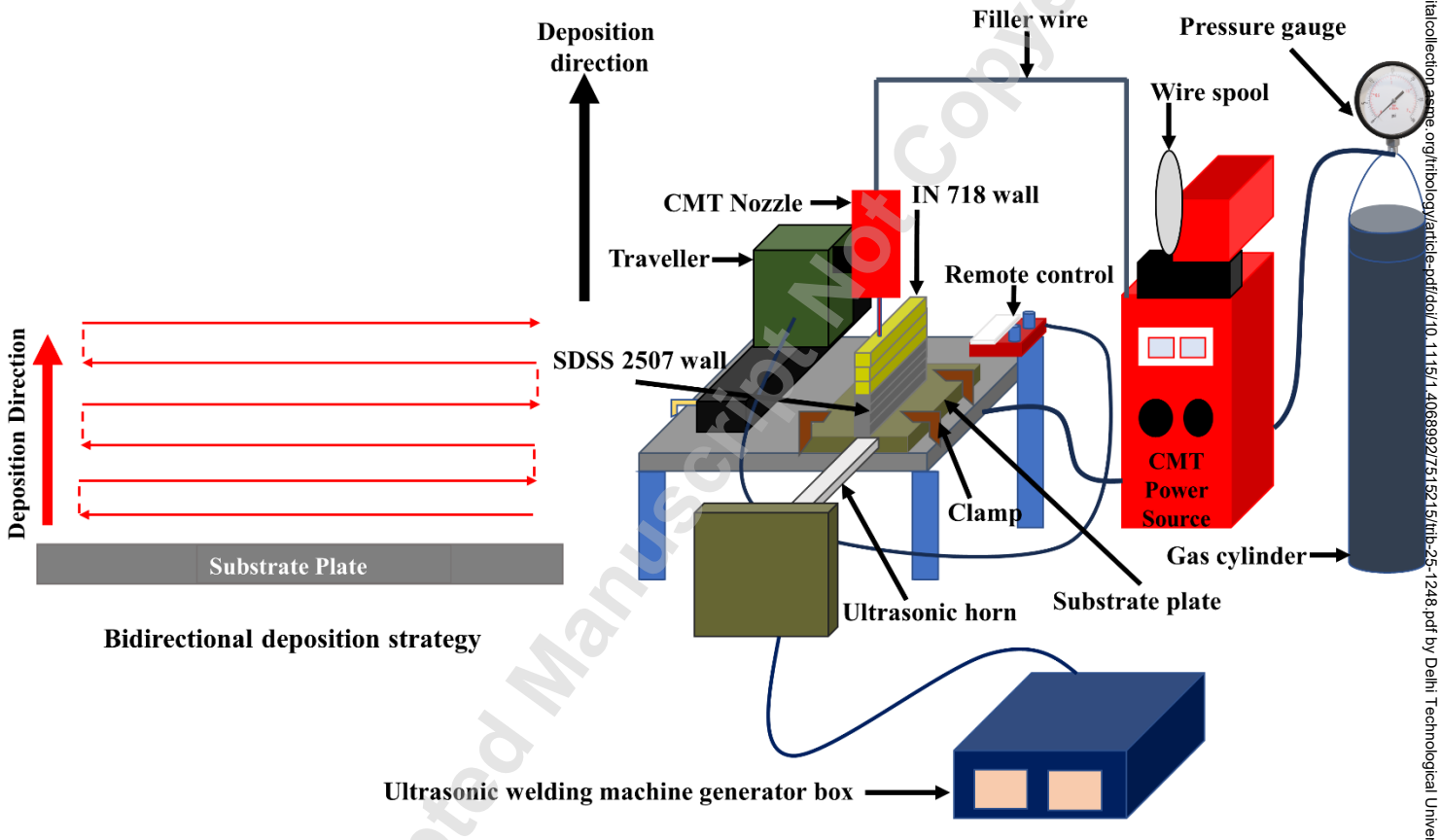


Fig. 1 Schematic CMT WAAM experimental setup unit using remote-controlled traveller with ultrasonic vibration and deposition strategy

The properties related to the mechanical and thermal aspects of SDSS2507 and IN718 are presented in Table 2.

Accepted Manuscript Not Copyedited

Downloaded from http://asmedigitalcollection.asme.org/tribology/article-pdf/doi/10.1115/1.4068992/7515215/trib-25-1248.pdf by Delhi Technological University user on 26 June 2025

Journal of Tribology. Received May 03, 2025;
Accepted manuscript posted June 19, 2025. doi:10.1115/1.4068992
Copyright © 2025 by ASME

Table 2 Mechanical and Thermal Properties of SDSS2507 and IN718

Mechanical Properties	**SDSS2507**	**IN718**	**Thermal Properties**	**SDSS2507**	**IN718**
Tensile Strength	800-950 MPa	1,030 MPa	**Melting Point**	1,350–1,450°C	1,330–1,370°C
Yield Strength	550-650 MPa	725 MPa	**Thermal Conductivity**	14 W/m·K at room temperature.	11.4 W/m·K at room temperature
Elongation	25-35% in 50 mm	30-50% in 50 mm	**Thermal Expansion Coefficient**	13.0 µm/m·°C	13.0 µm/m·°C
Hardness	250-350 HV	200-250 HV			

The materials SDSS2507 and IN718 wire are incorporated into the central region of an electric arc throughout the printing procedure, as shown in Fig. 2. The careful procedure of depositing the material, meticulously line by line and layer by layer, culminated in a perfect dissimilar alloy block, with or without ultrasonic vibration, was applied. This block has dimensions of 150mm in length and 100mm in height, comprising an impressive total of 60 layers. Table 3 presents the optimal process parameters.

Accepted Manuscript Not Copyedited

Downloaded from http://asmedigitalcollection.asme.org/tribology/article-pdf/doi/10.1115/1.4068992/7515215/trib-25-1248.pdf by Delhi Technological University user on 26 June 2025

Journal of Tribology. Received May 03, 2025;
Accepted manuscript posted June 19, 2025. doi:10.1115/1.4068992
Copyright © 2025 by ASME

Table 3 CMT WAAM deposition parameters used in this experiment

WAAM Parameters	Value for SDSS2507	Value for IN718
Current (I)	210	190
Travel speed (mm/s)	6.91	8.94
Gas flow rate (l/min)	25	15
Nozzle tip distance	15	15

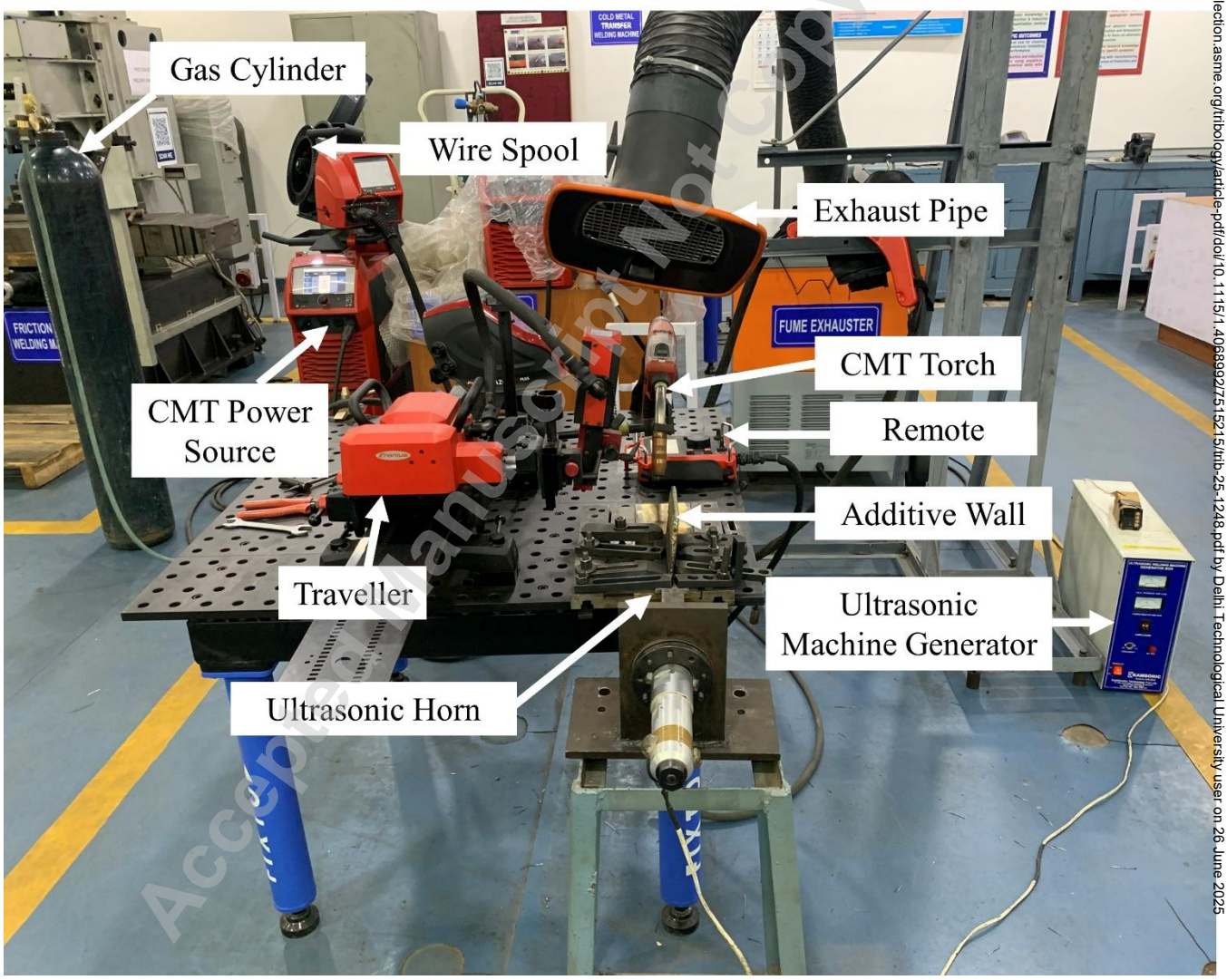


Fig. 2 Actual experimental set-up of UV-assisted CMT WAAM

Accepted Manuscript Not Copyedited

Downloaded from http://asmedigitalcollection.asme.org/tribology/article-pdf/doi/10.1115/1.4068992/7515215/trib-25-1248.pdf by Delhi Technological University user on 26 June 2025

Journal of Tribology. Received May 03, 2025;
Accepted manuscript posted June 19, 2025. doi:10.1115/1.4068992
Copyright © 2025 by ASME

Given its compatibility with SDSS2507 and IN718, welding was performed using 99.99% pure argon. The selected spacing between the nozzle and the workpiece is 15mm. The CMT-based WAAM technology employed a systematic application of layers of beads subsequent to a cleaning procedure utilizing acetone. The duration between layers, referred to as the interpass dwell time, was established at 120 seconds.

2.2 Microstructure analysis

Samples underwent meticulous preparation and polishing with silicon carbide paper, utilizing grit sizes from 300 to 2500, to facilitate the microstructure analysis. The etching process involved a chemical solution comprising a 50:50 mixture of oxalic acid and hydrochloric acid for IN718 [24], followed by polishing with alumina powder on a felt pad. For SDSS2507 [25], the solution consisted of 80 ml deionized water, 20 ml hydrochloric acid, and 0.3 g sodium metabisulfite. The intricate microstructures of various alloy samples were investigated using scanning electron microscopy (SEM; NOVA NANOSEM 450) and energy-dispersive spectroscopy (EDS). Fig. 3 presents a schematic representation of the wear and microstructure samples.

Accepted Manuscript Not Copyedited

Downloaded from http://asmedigitalcollection.asme.org/tribology/article-pdf/doi/10.1115/1.4068992/7515215/trib-25-1248.pdf by Delhi Technological University user on 26 June 2025

Journal of Tribology. Received May 03, 2025;
Accepted manuscript posted June 19, 2025. doi:10.1115/1.4068992
Copyright © 2025 by ASME

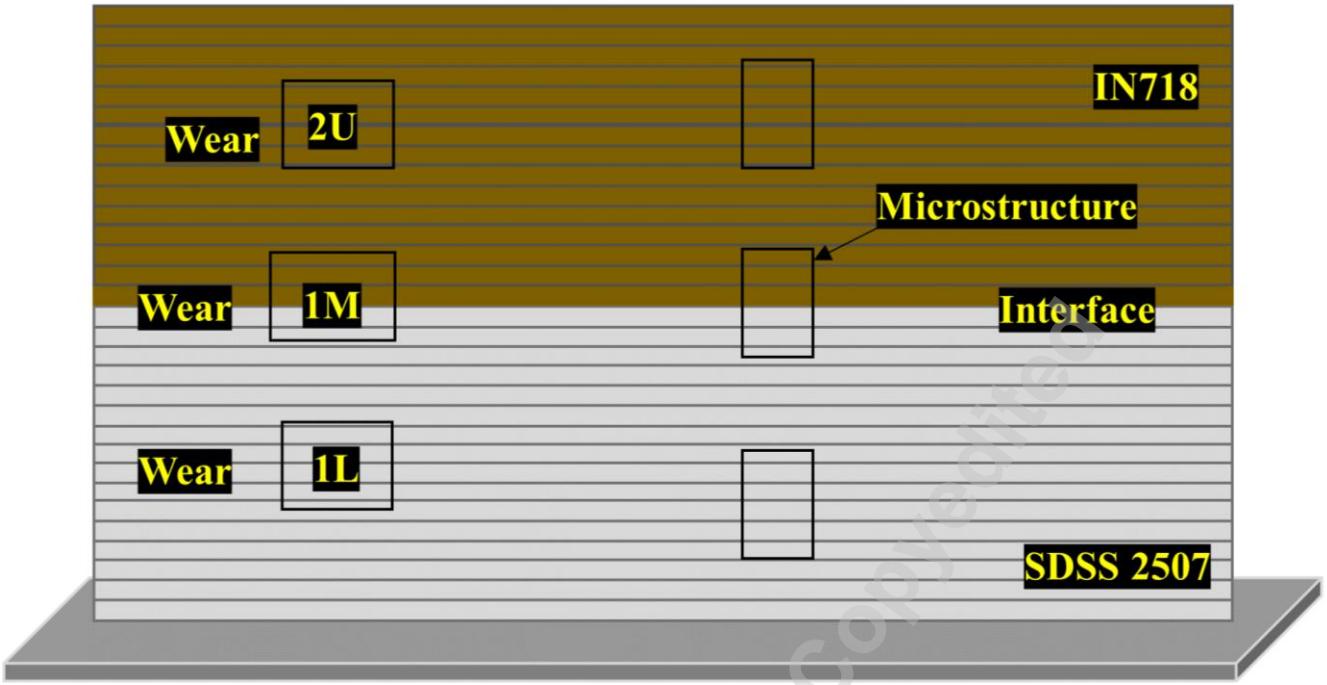


Fig. 3 Schematic diagram of Wear and Microstructure samples of Dissimilar alloy

2.3 Wear investigation

The wear testing was carried out in accordance with ASTM G133-05 using the DUCOM, a ball-on-disc reciprocating tribometer. The wear characteristics are influenced by several factors, such as load, frequency (sliding velocity), stroke, and sliding distance. Following a thorough examination of the existing literature and the execution of adequate trial runs, the parameters for load and frequency were determined for the wear experiments. In the wear test, a silicon carbide ball measuring 10 mm in diameter underwent linear reciprocating motion with varying loads of 10N, 20N, and 30N. This was conducted for a period of 15 minutes under unlubricated wear conditions, with a stroke length of 10 mm for the ball. The specimens underwent a cleaning process using acetone and were subsequently ground on a 2000-grade emery sheet prior to the wear test. The weights of the worn samples were meticulously documented prior to and following the test. An examination utilizing FESEM coupled with EDS was performed to investigate the wear mechanisms. Fig. 4 illustrates the configuration of

Accepted Manuscript Not Copyedited

Downloaded from http://asmedigitalcollection.asme.org/tribology/article-pdf/doi/10.1115/1.4068992/7515215/trib-25-1248.pdf by Delhi Technological University user on 26 June 2025

Journal of Tribology. Received May 03, 2025;
Accepted manuscript posted June 19, 2025. doi:10.1115/1.4068992
Copyright © 2025 by ASME

the linear reciprocating ball on disk apparatus. To determine the wear rate in mm^3/m, we employed Equation (1).

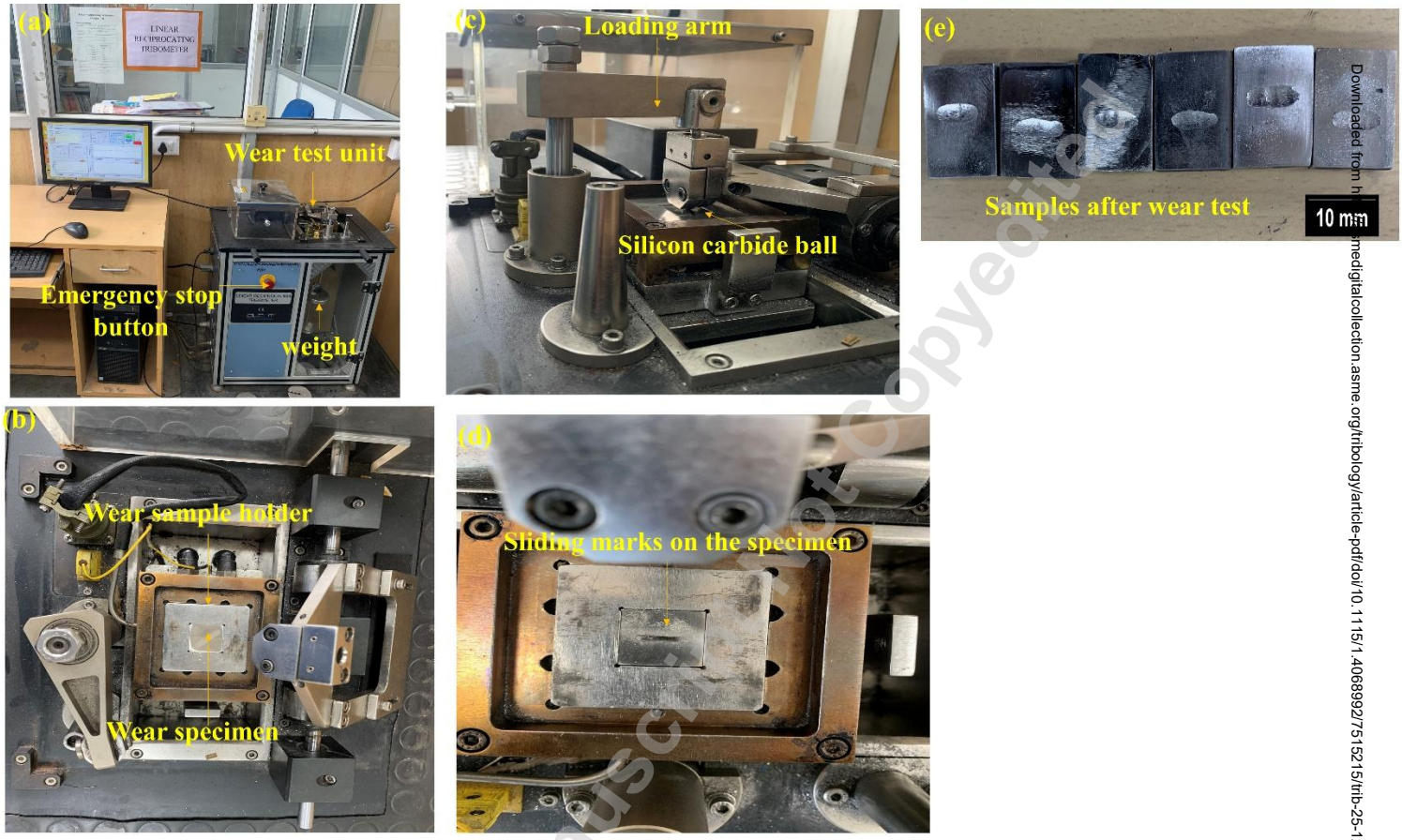


Fig. 4 (a) Linear Reciprocating ball on disk wear set up (b) wear chamber with sample holder and specimen (c) ball surface contacting the disk with load (d) sliding marks on disk surface (e) Worn out samples

$$Wear\ rate\ \left(\frac{mm^3}{m}\right) = \frac{Volume\ loss\ (mm^3)}{Sliding\ distance\ (m)}$$

$$Wear\ rate\ \left(\frac{mm^3}{m}\right) = \frac{\frac{Mass\ loss\ (g)\times 1000}{Density\ (\frac{g}{cm^3})}}{Time\ (s)\times Sliding\ Velocity\ (\frac{m}{s})} \qquad (1)$$

Accepted Manuscript Not Copyedited

Downloaded from http://asmedigitalcollection.asme.org/tribology/article-pdf/doi/10.1115/1.4068992/7515215/trib-25-1248.pdf by Delhi Technological University user on 26 June 2025

Journal of Tribology. Received May 03, 2025;
Accepted manuscript posted June 19, 2025. doi:10.1115/1.4068992
Copyright © 2025 by ASME

3. Results and discussion `

3.1 Microstructure investigation

The microstructures generated by the CMT process are distinct from those observed in cast or wrought parts as a result of the rapid solidification characteristic. The microstructural grains of the SDSS2507-IN718 interface, IN718, and SDSS2507 alloy produced by CMT WAAM without and with UV are depicted in Fig. 5. The coarse elongated granules were formed when the CMT power was used without UV, as evidenced by Fig. 5 (A0, B0, C0). Fig. 5(b) illustrates the particle size achieved under these conditions, which was 6.161 µm. The extended grain growth along the construction direction resulted from the locally unidirectional solidification behaviour. The granules transitioned from columnar to equiaxed under the influence of UV in CMT WAAM, as illustrated in Fig. 5(A1, B1, C1). This transition led to a decrease in particle size to 4.5972 µm.

The trend of grain refinement induced by UV can be explained through two primary mechanisms: the fragmentation of dendrites resulting from cavitation and the enhanced nucleation that occurs due to cavitation [26–28]. The application of UV to the melting materials facilitates the swift generation of cavitation bubbles. Upon the collapse of the bubbles, the ensuing shocks generated significant pressure waves that traversed the acoustic field, which could lead to the fragmentation of elongated dendrite tips. Convection simultaneously transported the dendritic tips into the undercooled melt, resulting in the formation of numerous grain nuclei. The ultrasonic cavitation prompted a shift from a columnar to an equiaxed structure in the molten materials at the extended dendritic boundary [29], leading to a notable reduction in the size of the microstructural grains. The shift from columnar to equiaxed grains presents benefits in minimizing grain size. Furthermore, the achievement of a uniform distribution of grains was facilitated by the standardized temperature profile established through ultrasonic vibration in specific areas [30].

Accepted Manuscript Not Copyedited

Downloaded from http://asmedigitalcollection.asme.org/tribology/article-pdf/doi/10.1115/1.4068992/7515215/trib-25-1248.pdf by Delhi Technological University user on 26 June 2025

Journal of Tribology. Received May 03, 2025;
Accepted manuscript posted June 19, 2025. doi:10.1115/1.4068992
Copyright © 2025 by ASME

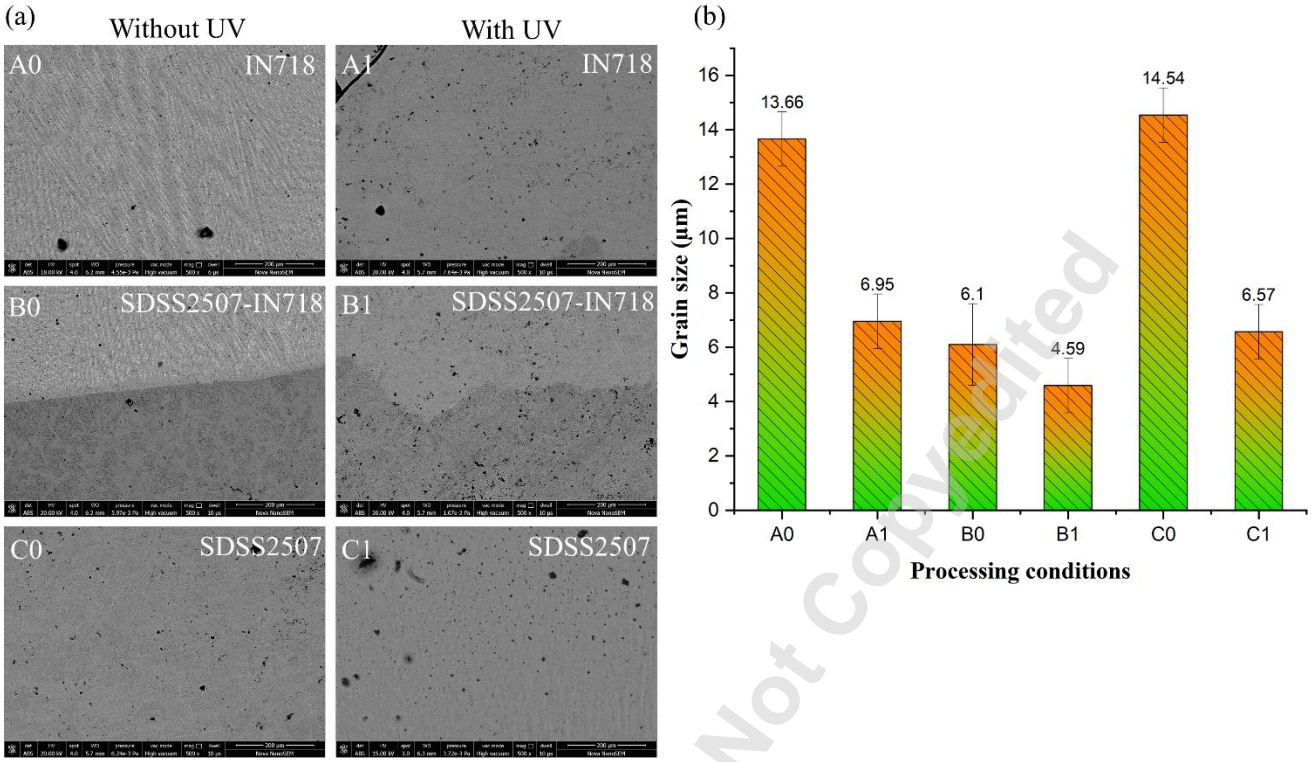


Fig. 5 (a) Microstructural characteristics without and with UV (b) Grain size variation under different processing conditions

3.2 Phase composition investigation

Fig. 6 presents the analytical outcomes obtained from the energy-dispersive X-ray spectroscope for the Dissimilar SDSS2507-IN718 components produced via CMT, comparing instances with and without the implementation of UV. Observations indicate that locations 1 and 3 exhibit high concentrations of Ni, Fe, and Cr, whereas location 2, situated at the interface zone, shows significant variation in the levels of Ni, Cr, Fe, Nb, and Mo.

The white precipitated phase in IN718 point 1 exhibited a significant presence of Ni, Cr, Nb, and Mo, which are the key compositional elements of the Laves phase [31]. The Laves phase is characterized as a brittle intermetallic compound rich in Nb, typically exhibiting a composition of (Ni, Cr, Fe)2 (Nb, Mo, Ti). Additional studies have similarly recognised the presence of the Laves phase in IN718 components produced through CMT fabrication [28].

Accepted Manuscript Not Copyedited

Downloaded from http://asmedigitalcollection.asme.org/tribology/article-pdf/doi/10.1115/1.4068992/7515215/trib-25-1248.pdf by Delhi Technological University user on 26 June 2025

Journal of Tribology. Received May 03, 2025;
Accepted manuscript posted June 19, 2025. doi:10.1115/1.4068992
Copyright © 2025 by ASME

The occurrence of Nb segregation in the IN718 alloy resulted in the formation of irregularly shaped Laves phase, which adversely affected the mechanical properties. This specific phase may contribute to the enhancement of crack propagation, thereby diminishing the overall strength and ductility of the IN718 alloy. The SEM image illustrates the boundary located at position 2. Given the similar composition of SDSS2507 and IN718, the interfacial features exhibited no defects, and the chromium distribution was uniform on both sides. The EDS region scan indicated that the IF exhibited no elemental segregation. The IN718 filler wire generates a molten pool on the SDSS2507 layer at the interface. The confirmation of element dissolution was observed across the IF. The EDS plot indicates a combination of components with no significant alterations in Cr levels.

Reports indicate that the presence of the Nb element significantly influences the solidification sequence and the precipitation of strengthening phases in the IN718 alloy [32]. In CMT, the solidification of IN718 initiates with a primary liquid reaction, leading to an enrichment of the interdendritic liquid with elements such as Ti, Mo, and Nb. Ultimately, the process culminates in an eutectic-type reaction [33]. The limited capacity of larger Nb atoms to disperse posed significant challenges in dissolving the Laves phase within the matrix of CMT-fabricated components. Nevertheless, employing UV allows for the fragmentation of the long-bar Laves phase morphology into smaller particle shapes through the application of high-intensity shock waves. The SEM images presented in Fig. 6 provide a clear illustration of this point. The application of ultrasonic energy elevates the temperature of the molten pool, thereby enhancing the solubility of Nb within the matrix phase. The findings indicated that UV contributed to the partial dissolution of the Laves phase within the matrix. The existence of a small-particle-shaped Laves phase within the matrix facilitated a consistent distribution, leading to a uniform phase distribution.

Accepted Manuscript Not Copyedited

Downloaded from http://asmedigitalcollection.asme.org/tribology/article-pdf/doi/10.1115/1.4068992/7515215/trib-25-1248.pdf by Delhi Technological University user on 26 June 2025

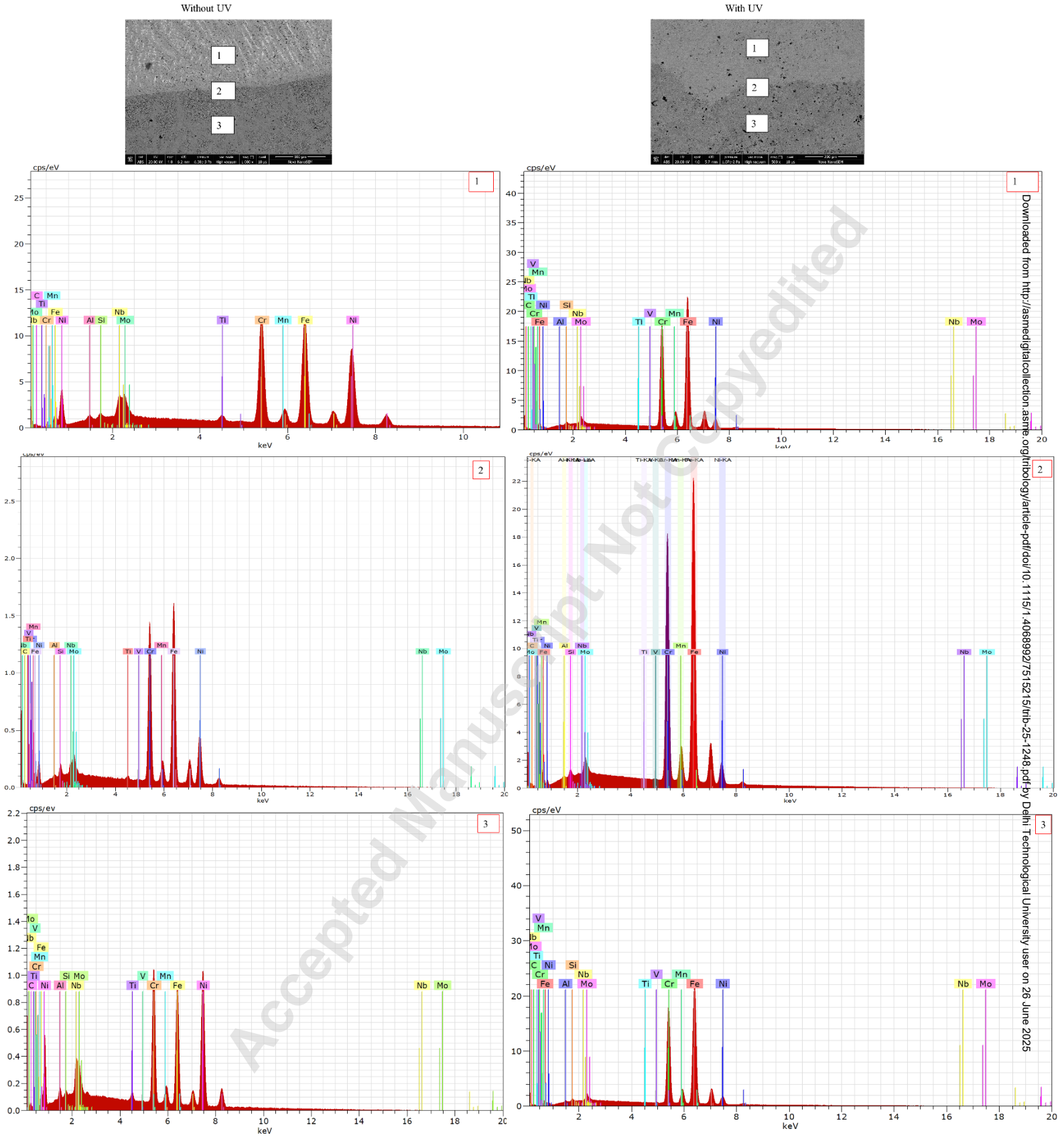
Journal of Tribology. Received May 03, 2025;
Accepted manuscript posted June 19, 2025. doi:10.1115/1.4068992
Copyright © 2025 by ASME

In Fig. 7, the highlighted section denotes the elemental scan area designated for the compositional analysis of the IF. The elements Nb, Mo, Mn, C, Al, and Si showed notable segregation, while Ni, Cr, and Fe displayed a consistent distribution, as depicted in the elemental mapping. An EDS scan was conducted in the IF region to examine the elemental composition of the materials, as depicted in Fig. 8. A scan was performed in the IF area at a distance of 200 µm. The primary elements, specifically Fe, Ni, Cr, Mo, and Nb, have been recorded and are depicted in Fig. 7, EDS mapping. Fig. 6 demonstrates significant variations in the concentrations of Fe and Ni at the Interface, which can be attributed to the distinct compositional ratios of Ni and Fe in the SDSS2507 and IN718 layers. The varying levels of Mn in the two filler wires led to a significant change in the Mn concentration within the transition zone.

Accepted Manuscript Not Copyedited

Downloaded from http://asmedigitalcollection.asme.org/tribology/article-pdf/doi/10.1115/1.4068992/7515215/trib-25-1248.pdf by Delhi Technological University user on 26 June 2025

Journal of Tribology. Received May 03, 2025;
Accepted manuscript posted June 19, 2025. doi:10.1115/1.4068992
Copyright © 2025 by ASME



Accepted Manuscript Not Copyedited

Downloaded from http://asmedigitalcollection.asme.org/tribology/article-pdf/doi/10.1115/1.4068992/7515215/trib-25-1248.pdf by Delhi Technological University user on 26 June 2025

Fig. 6 Energy dispersive X-ray spectroscope analysis results of dissimilar SDSS2507-IN718 parts fabricated by CMT WAAM (a) Without ultrasonic vibrations (b) With ultrasonic vibrations

Journal of Tribology. Received May 03, 2025;
Accepted manuscript posted June 19, 2025. doi:10.1115/1.4068992
Copyright © 2025 by ASME

The slight difference in Cr content can be ascribed to the dilution of the IN718 layer on the SDSS2507. At the IF, the IN718 filler wire is utilized to form a molten pool on top of the previously deposited SDSS2507 layer. As a result, the dissolution of elements was confirmed throughout the IF. The EDS plot indicates that the elements were integrated, showing no significant fluctuations in the amount of Cr detected. The presence of the laves phase has been validated in the IN718 layers. The laves phase is thought to develop when specific elements, like Mo and Nb, segregate during non-equilibrium solidification [34].

Accepted Manuscript Not Copyedited

Downloaded from http://asmedigitalcollection.asme.org/tribology/article-pdf/doi/10.1115/1.4068992/7515215/trib-25-1248.pdf by Delhi Technological University user on 26 June 2025

Journal of Tribology. Received May 03, 2025;
Accepted manuscript posted June 19, 2025. doi:10.1115/1.4068992
Copyright © 2025 by ASME

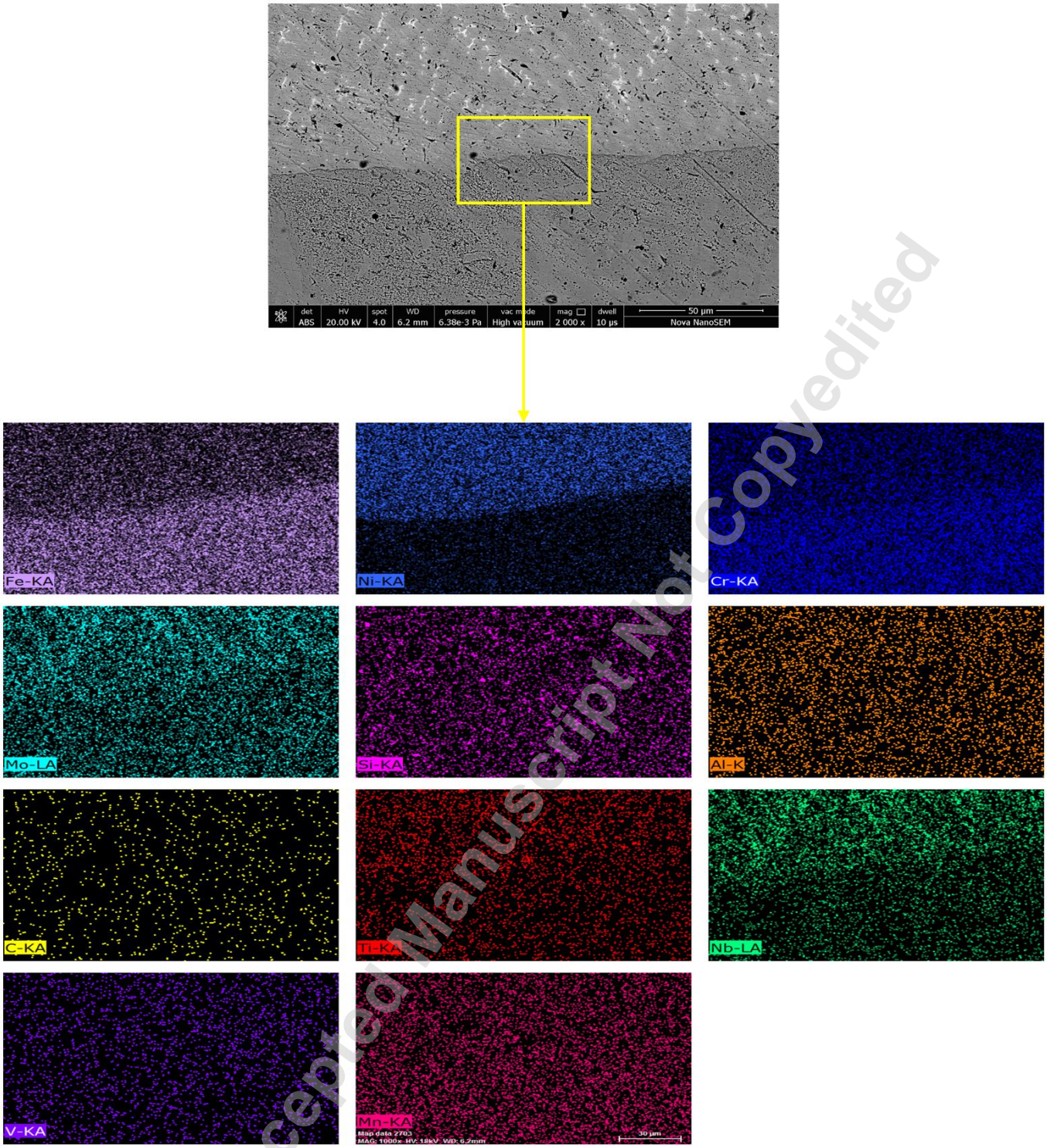


Fig. 7 Dissimilar SDSS2507- IN718 alloy interface region EDS mapping

3.3 Microhardness variation

Microhardness measurements were conducted at three distinct locations: SDSS2507, the SDSS2507-IN718 interface (IF), and IN718, following the building direction, as illustrated in

Accepted Manuscript Not Copyedited

Downloaded from http://asmedigitalcollection.asme.org/tribology/article-pdf/doi/10.1115/1.4068992/7515215/trib-25-1248.pdf by Delhi Technological University user on 26 June 2025

Journal of Tribology. Received May 03, 2025;
Accepted manuscript posted June 19, 2025. doi:10.1115/1.4068992
Copyright © 2025 by ASME

Fig. 8. The utilization of UV resulted in a significant improvement in microhardness, increasing from an average of 302 HV to 335 HV, reflecting an 11% rise at SDSS2507. At the Interface, the value increased from 233 HV to 265 HV, marking a 14% enhancement, while IN718 saw an increase from 249 HV to 270 HV, corresponding to a 9% growth. The results demonstrate that the ultrasound refinement process improves the thin-wall component's microstructure, leading to a rise in microhardness. Moreover, the material's hardness is intrinsically linked to its microstructure. The relationship between microhardness and ultimate tensile strength is well-documented, indicating that an increase in UTS is typically associated with a rise in microhardness. The correlation between microhardness and ultimate tensile strength (UTS) indicates that the increase in microhardness results from grain refinement induced by UV exposure. The earlier noted reduction in porosity would facilitate a more uniform density in part production, thereby enhancing the quality of the components through improved microhardness[35].

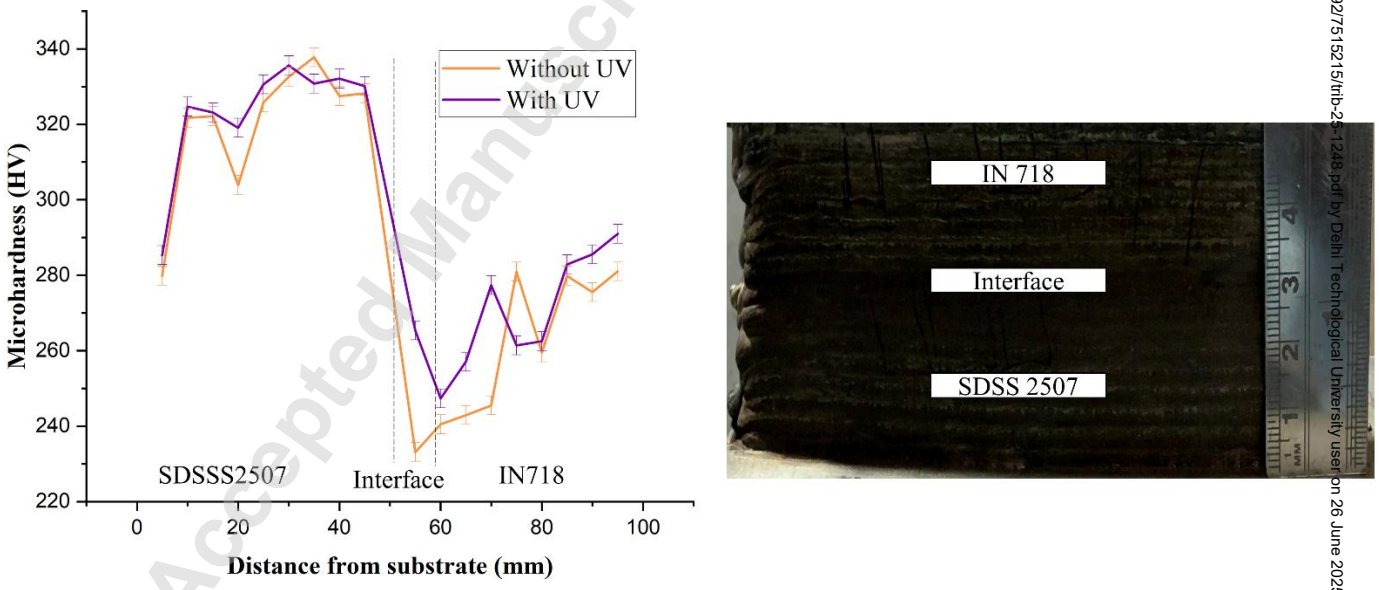


Fig. 8 Microhardness variation of WAAM parts with or without UV

Accepted Manuscript Not Copyedited

Downloaded from http://asmedigitalcollection.asme.org/tribology/article-pdf/doi/10.1115/1.4068992/7515215/trib-25-1248.pdf by Delhi Technological University user on 26 June 2025

Journal of Tribology. Received May 03, 2025;
Accepted manuscript posted June 19, 2025. doi:10.1115/1.4068992
Copyright © 2025 by ASME

3.4 Wear Behaviour

Fig. 9 illustrates the time-dependent variation of the coefficient of friction (COF) for the SDSS2507, SDSS2507-IN718 interfaces, and IN718 samples derived from the linear dry sliding wear test conducted at ambient room temperature. The COF values in nearly all samples demonstrate temporal oscillations, attributable to the accumulation of wear debris in the wear track, the existence of voids, and the influence of abrasiveness [36].

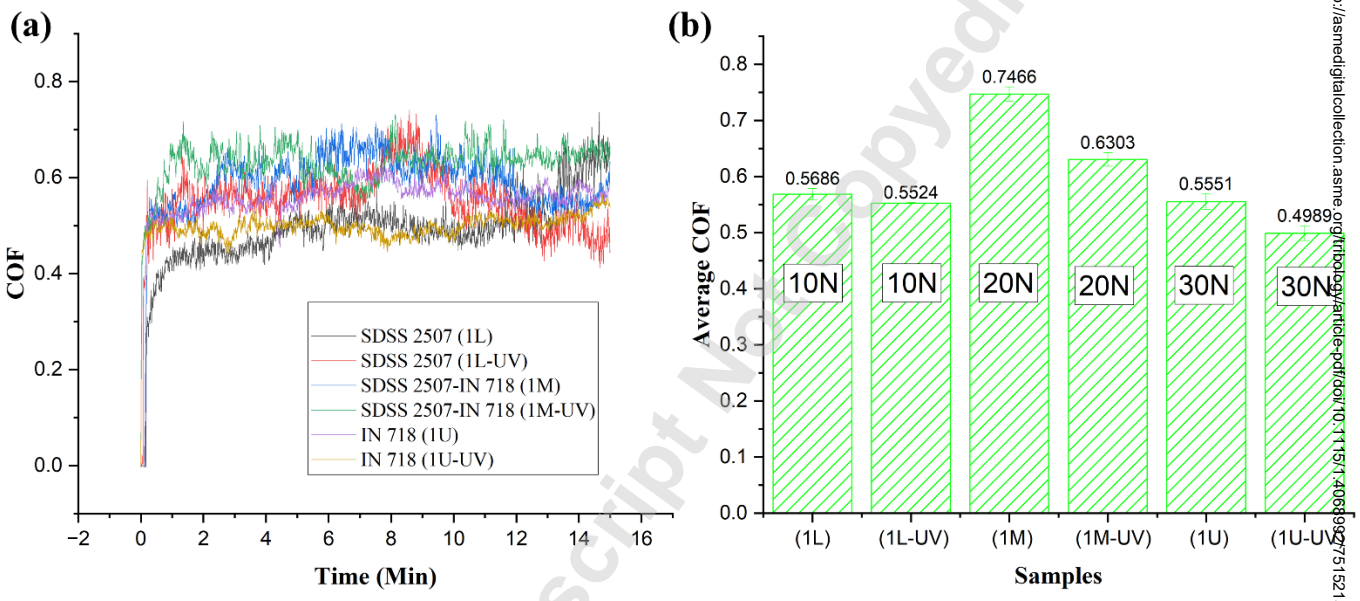


Fig. 9 (a) Coefficient of friction variation with time (b) Average COF of samples

The statistics unequivocally indicate that the COF displays a steady ascending trajectory with increasing load for SDSS2507 and IN718. The coefficient of friction (COF) varies from 0.56 to 0.55, 0.74 to 0.63, and 0.55 to 0.49 for SDSS2507, the SDSS2507-IN718 interface, and IN718 under varied loads, with out and with UV respectively. The coefficient of friction (COF) values derived from the test closely align with those documented in the literature for Inconel 718 superalloy, with reported values spanning from 0.2 to 0.4 and 0.44 to 0.622 [36,37]. No research has been documented about the effect of UV on the wear characteristics of SDSS2507 and the dissimilar SDSS2507-IN718 alloys. Without and with UV, SDSS2507-IN718 exhibits a maximum coefficient of friction (COF) of 0.74 – 0.63, whereas IN718 demonstrates a

Accepted Manuscript Not Copyedited

Downloaded from http://asmedigitalcollection.asme.org/tribology/article-pdf/doi/10.1115/1.4068992/7515215/trib-25-1248.pdf by Delhi Technological University user on 26 June 2025

Journal of Tribology. Received May 03, 2025;
Accepted manuscript posted June 19, 2025. doi:10.1115/1.4068992
Copyright © 2025 by ASME

minimum COF of 0.55-0.49. Fig. 10(b) illustrates the average coefficient of friction for various samples under distinct loading circumstances. Table 4 presents the wear characteristics of various samples. In comparison to previous works, such as Prasad et al. [37], which explored WAAM of dissimilar alloys without addressing the influence of ultrasonic vibration (UV), the present study presents a full comparative analysis between conventional WAAM and UV-assisted WAAM. The incorporation of UV in the current work has resulted to enhanced tribological performance. These findings underline the added advantages offered by ultrasonic vibration, revealing its capacity to boost the quality and functional efficacy of additively produced components, a factor ignored in past studies.

Table 4 Wear properties of samples

Sr. No	Samples	Load (N)	Average COF	Wear rate × 10^{-6} (mm^3/m)
1	**1L (SDSS2507)**	10	0.5685	3.26
2	**1L (SDSS2507 -UV)**	10	0.5524	3.16
3	**1M (SDSS2507-IN718 interface)**	20	0.7466	1.28
4	**1M (SDSS2507-IN718 interface -UV)**	20	0.6303	1.20
5	**1U (IN718)**	30	0.5551	5.49
6	**1U (IN718-UV)**	30	0.4989	2.06

Accepted Manuscript Not Copyedited

Downloaded from http://asmedigitalcollection.asme.org/tribology/article-pdf/doi/10.1115/1.4068992/7515215/trib-25-1248.pdf by Delhi Technological University user on 26 June 2025

Journal of Tribology. Received May 03, 2025;
Accepted manuscript posted June 19, 2025. doi:10.1115/1.4068992
Copyright © 2025 by ASME

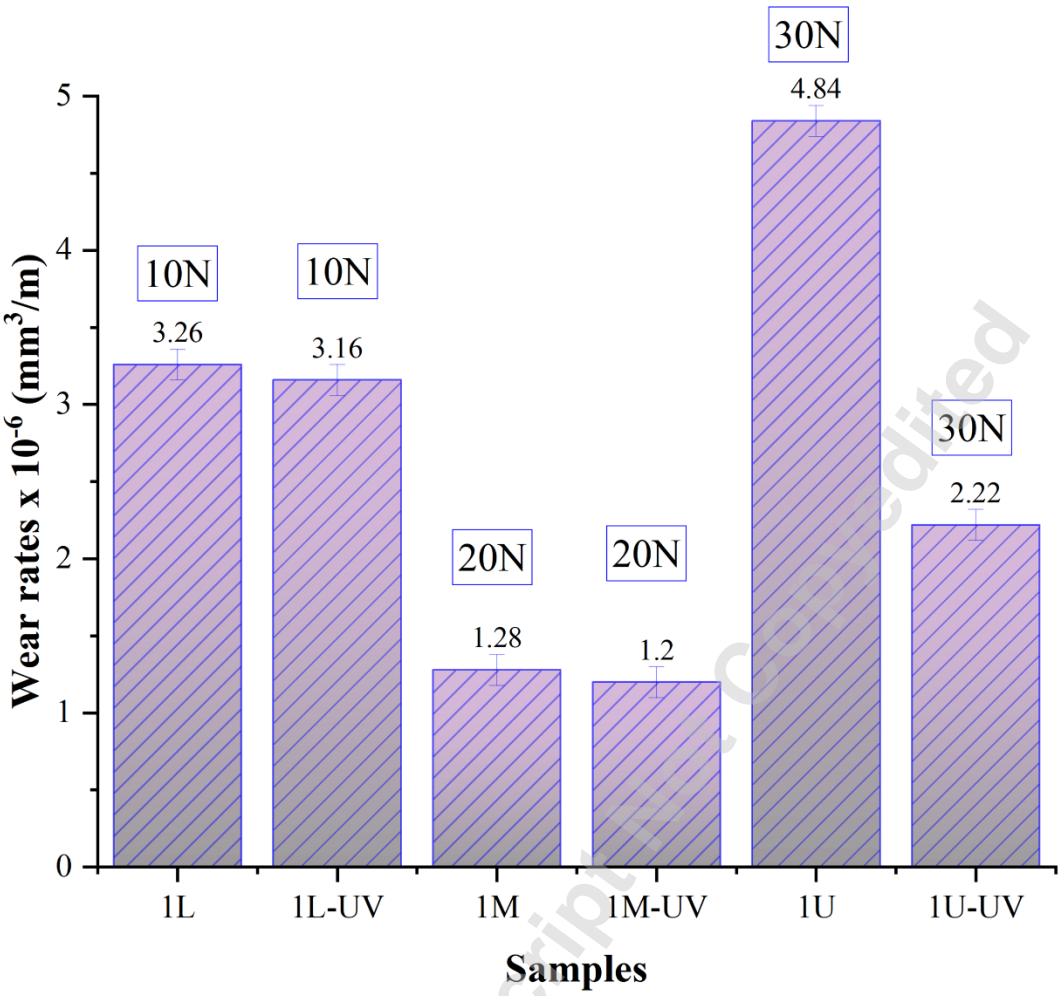


Fig. 10 Wear rate of specimens without UV and with UV at different loads

Fig. 10 illustrates the wear rate (mm^3/m) of SDSS2507, the SDSS2507-IN718 interface, and IN718 samples under varying loads. The statistics clearly indicate that the wear rate decreases with ultrasonic vibration due to grain refinement in the microstructure. The findings indicate that the ultrasound refinement process enhances the microstructure of the thin-wall component, resulting in an increase in wear resistance. Furthermore, the wear rate of the material is fundamentally connected to its microstructure. The maximum wear rate for IN718 is 4.84×10^{-6} mm^3/m, while the minimum for SDSS2507-IN718 is 1.28×10^{-6} mm^3/m without UV but with UV, maximum for SDSS2507 is 3.16×10^{-6} mm^3/m and minimum for SDSS2507-IN718 is 1.2×10^{-6} mm^3/m. The wear rate of the SDSS2507-IN718 interface is intermediate between the wear rates of SDSS2507 and IN718.

Accepted Manuscript Not Copyedited

Downloaded from http://asmedigitalcollection.asme.org/tribology/article-pdf/doi/10.1115/1.4068992/7515215/trib-25-1248.pdf by Delhi Technological University user on 26 June 2025

Journal of Tribology. Received May 03, 2025;
Accepted manuscript posted June 19, 2025. doi:10.1115/1.4068992
Copyright © 2025 by ASME

3.5 Mechanism of Wear

In Ultrasonic Wire Arc Additive Manufacturing (UV-WAAM) of dissimilar alloys such as Inconel 718 and Super Duplex Stainless Steel (SDSS) 2507, the incorporation of high-frequency ultrasonic vibration into the conventional arc-based deposition process induces distinct wear mechanisms due to the complex thermal and mechanical environment. The continuous feeding of high-strength wires like IN718 through the contact tip under oscillatory motion leads to significant **abrasive wear**, especially as ultrasonic vibration enhances interfacial friction and promotes dislodgement of oxide particles [38]. The SEM images (Fig. 11) illustrate the existence of longitudinal wear scars or grooves, often termed abrasive scars, in the reciprocating direction. Furthermore, the images reveal the existence of wear debris, which acts as proof of an abrasive wear mechanism [39].The high chromium and molybdenum content of SDSS2507 contributes to hard oxide formation, which acts as a third-body abrasive, further intensifying contact surface degradation. **Adhesive wear** is frequently observed at the wire–contact tip interface due to localized microwelding and material transfer at elevated temperatures; however, ultrasonic vibration helps mitigate this by reducing contact time and promoting dynamic separation [40].

Fretting wear is another critical mechanism, particularly at static or semi-static mechanical joints such as torch mounts, feed rollers, and fixture clamps. The high-frequency oscillations (typically 20–40 kHz) induce micro-amplitude relative motion that causes localized surface fatigue, oxidation, and particulate generation [41]. Over-extended operation can evolve into **fretting fatigue**, particularly in metallic joints exposed to cyclic thermal and vibrational loading. Additionally, **thermal-mechanical wear** becomes prominent during the deposition of dissimilar alloys due to their differential thermal expansion coefficients. In the case of IN718 and SDSS2507, this mismatch, compounded by ultrasonic agitation, can lead to delamination,

Accepted Manuscript Not Copyedited

Downloaded from http://asmedigitalcollection.asme.org/tribology/article-pdf/doi/10.1115/1.4068992/7515215/trib-25-1248.pdf by Delhi Technological University user on 26 June 2025

Journal of Tribology. Received May 03, 2025;
Accepted manuscript posted June 19, 2025. doi:10.1115/1.4068992
Copyright © 2025 by ASME

cracking, or stress localization at the fusion interface [42]. Occasional **erosive wear** may also occur in regions near the melt pool or shielding gas outlets due to accelerated particle movement and localized flow turbulence enhanced by ultrasonic energy [43,44].

Addressing these wear phenomena necessitates a comprehensive strategy, incorporating the utilization of wear-resistant contact tips (e.g., Cu-Cr-Zr alloys), optimization of ultrasonic parameters (frequency, amplitude, and coupling), efficient heat management, and routine examination of consumable components. A comprehensive understanding of wear mechanisms in UV-WAAM is essential for guaranteeing equipment durability and the integrity of high-performance components, especially in aerospace and marine applications where IN718 and SDSS2507 are prevalent.

3.6 Surface morphology of the wear surface

Fig. 11 demonstrates the occurrence of wear driven by plasticity in the ductile material at the SDSS2507, SDSS2507-IN718 interface and IN718. Archard observed that there is an inverse correlation between the hardness of a material and its wear volume [45]. It is clear that reduced hardness leads to increased plastic deformation in IN718 when subjected to high heat input in the upper zone of a wall; on the other hand, lower heat input results in diminished plastic deformation in SDSS2507, attributed to its higher hardness value.

Moreover, the surfaces that had experienced wear exhibited a smooth texture. The surfaces show signs that indicate the presence of both adhesive and abrasive wear processes occurring under various loads. Fig. 11 illustrates the physical characteristics of wear scars and particles present on degraded surfaces subjected to various loading conditions. The surfaces displayed a metallic appearance and had undergone significant plastic deformation. FESEM investigations of worn surfaces reveal that the wear tracks are characterized by grooving, delamination, delamination cracks, ploughing grooves, parallel grooves, and particle adherence. The

Accepted Manuscript Not Copyedited

Downloaded from http://asmedigitalcollection.asme.org/tribology/article-pdf/doi/10.1115/1.4068992/7515215/trib-25-1248.pdf by Delhi Technological University user on 26 June 2025

Journal of Tribology. Received May 03, 2025;
Accepted manuscript posted June 19, 2025. doi:10.1115/1.4068992
Copyright © 2025 by ASME

observed longitudinal scars or grooves and wear debris suggest the presence of abrasive wear and plastic deformation, while the adhesive particles indicate adhesive wear.

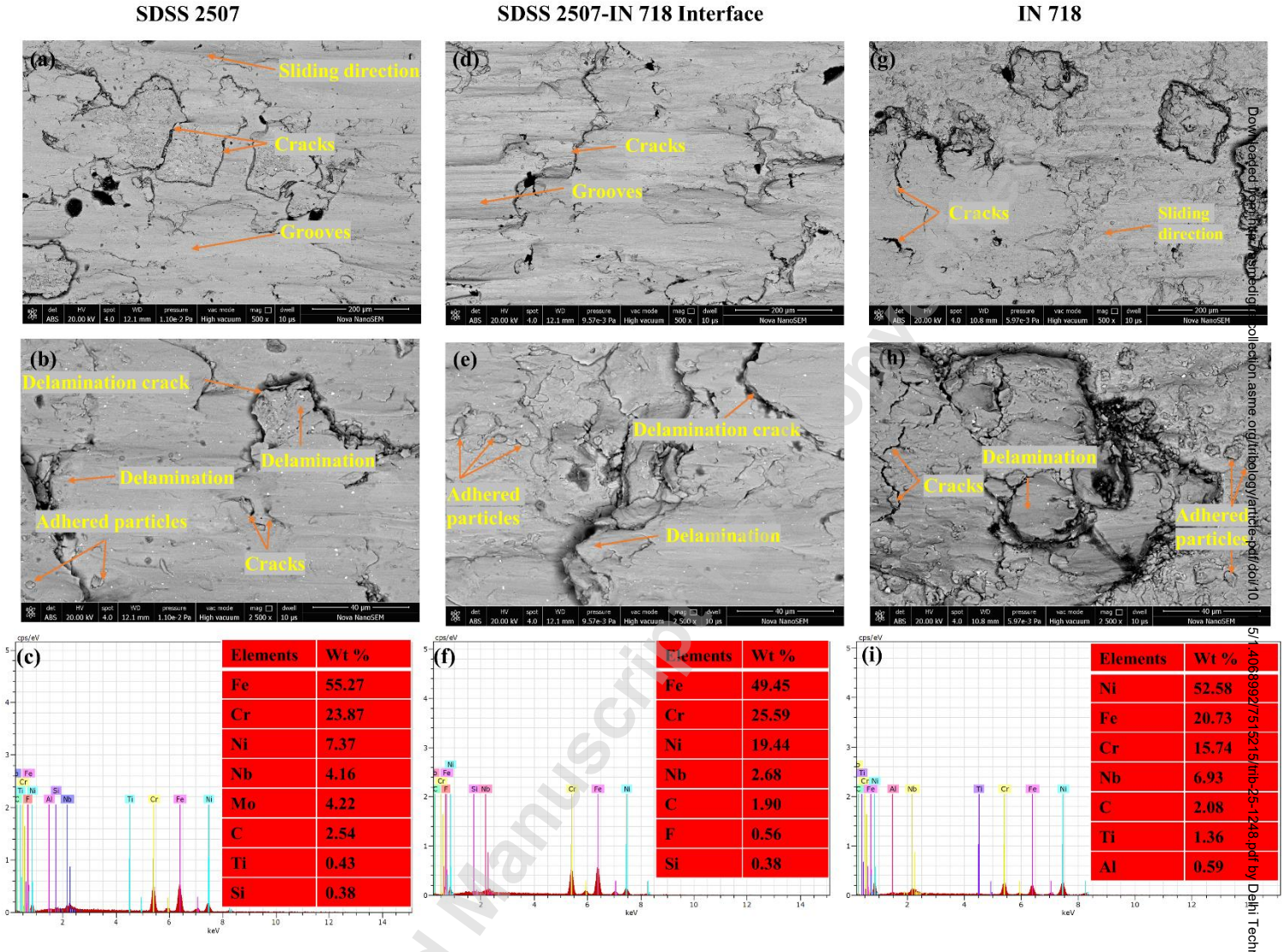


Fig.11 FESEM image and EDS analysis of worn-out surface of specimens (Left column SDSS2507, Centre SDSS2507-IN718 interface, and Right column IN718)

In all samples, there was no evidence of a considerable amount of material being extracted from the wear track, indicating a notable presence of the adhesive wear mechanism. Consequently, the distinct SDSS-IN718 wall illustrates both adhesion and abrasion wear mechanisms. Fig. 11 (c, f, i) displays the EDS analysis, showcasing the elemental composition at various points within the wear track of SDSS2507, SDSS2507-IN718, and IN718.

Accepted Manuscript

Downloaded from http://asmedigitalcollection.asme.org/tribology/article-pdf/doi/10.1115/1.4068992/7515215/trib-25-1248.pdf by Delhi Technological University user on 26 June 2025

Journal of Tribology. Received May 03, 2025;
Accepted manuscript posted June 19, 2025. doi:10.1115/1.4068992
Copyright © 2025 by ASME

Considering that the counter-face silicon carbide ball comprises both silicon (Si) and carbon (C), it is probable that this debris is derived from the sliding surfaces. Nonetheless, the significant amounts of Ni, Fe, Cr, and Nb present in the debris, which closely align with the composition of the SDSS2507 and IN718 alloy, indicate that most of the wear debris originates from the SDSS2507 and IN718 alloy. Furthermore, it is crucial to observe that the EDS result shows an absence of oxygen. No further degradation results from surface oxidation or tribochemical reactions during the reciprocating tribological assessment.

4. Conclusions

The paper illustrates the effective implementation of the CMT-WAAM technique to deposit a dual metallic wall composed of SDSS2507 and IN718, facilitated by ultrasonic vibration. A study was conducted to investigate the impact of ultrasonic vibration on forming capacity, microstructure, and wear characteristics. The subsequent conclusion might be drawn-

- The CMT-WAAM technique employs ultrasonic vibrations to effectively fabricate WAAM walls composed of dissimilar alloys, including SDSS2507 and IN718. No indications of microstructural flaws, such as cracks or porosity, were present in the microstructure.
- The microstructural analysis indicated that the deposited welds comprised dendrites and columnar grains. The application of ultrasonic vibration yielded advantageous results, including the reduction of grain size and the suppression of the preferred growth of big columnar grains.
- The Laves phase, characterized by a greater nickel concentration in the matrix phase, exhibited enhanced solubility during ultrasonic vibration. Utilising ultrasonic vibration, the Laves phase morphology, typified by an elongated bar shape, was uniformly

Accepted Manuscript Not Copyedited

Downloaded from http://asmedigitalcollection.asme.org/tribology/article-pdf/doi/10.1115/1.4068992/7515215/trib-25-1248.pdf by Delhi Technological University user on 26 June 2025

Journal of Tribology. Received May 03, 2025;
Accepted manuscript posted June 19, 2025. doi:10.1115/1.4068992
Copyright © 2025 by ASME

fragmented into minute spherical particles. The primary cause of this was the exceptionally high pressure in the acoustic field generated by ultrasonic vibration.

- The highest wear rate for IN718 is 4.84×10^{-6} mm³/m, but the minimum for SDSS2507-IN718 is 1.28×10^{-6} mm³/m without UV exposure. With UV exposure, the maximum for SDSS2507 is 3.16×10^{-6} mm³/m, and the minimum for SDSS2507-IN718 is 1.2×10^{-6} mm³/m. The wear rate of the SDSS2507-IN718 interface is positioned between the wear rates of SDSS2507 and IN718.
- Wear tracks exhibiting grooving, delamination, delamination fractures, ploughing grooves, parallel grooves, and particle adherence indicate the presence of both adhesive and abrasive wear mechanisms, as evidenced by FESEM measurements of the worn surfaces.

Author Contribution Statement

Rajendra Prasad Meena: writing – original draft, methodology, investigation, and formal analysis. N. Yuvaraj: writing – review and editing, supervision, and conceptualization. Vipin: Supervision and final approval. Qasim Murtaza: Editing and Supervision

Conflict of Interest

No conflicts of interest have been reported for this manuscript.3

References

[1] Marefat, F., Kapil, A., Banaee, S. A., Van Rymenant, P., and Sharma, A., 2023, "Evaluating Shielding Gas-Filler Wire Interaction in Bi-Metallic Wire Arc Additive Manufacturing (WAAM) of Creep Resistant Steel-Stainless Steel for Improved Process

Accepted Manuscript Not Copyedited

Downloaded from http://asmedigitalcollection.asme.org/tribology/article-pdf/doi/10.1115/1.4068992/7515215/trib-25-1248.pdf by Delhi Technological University user on 26 June 2025

Journal of Tribology. Received May 03, 2025;
Accepted manuscript posted June 19, 2025. doi:10.1115/1.4068992
Copyright © 2025 by ASME

Stability and Build Quality," J Manuf Process, **88**, pp. 110–124. https://doi.org/10.1016/J.JMAPRO.2023.01.046.

[2] Soysal, T., Kou, S., Tat, D., and Pasang, T., 2016, "Macrosegregation in Dissimilar-Metal Fusion Welding," Acta Mater, **110**, pp. 149–160. https://doi.org/10.1016/J.ACTAMAT.2016.03.004.

[3] Ahsan, M. R. U., Tanvir, A. N. M., Seo, G. J., Bates, B., Hawkins, W., Lee, C., Liaw, P. K., Noakes, M., Nycz, A., and Kim, D. B., 2020, "Heat-Treatment Effects on a Bimetallic Additively-Manufactured Structure (BAMS) of the Low-Carbon Steel and Austenitic-Stainless Steel," Addit Manuf, **32**, p. 101036. https://doi.org/10.1016/J.ADDMA.2020.101036.

[4] Ahsan, M. R. U., Fan, X., Seo, G. J., Ji, C., Noakes, M., Nycz, A., Liaw, P. K., and Kim, D. B., 2021, "Microstructures and Mechanical Behavior of the Bimetallic Additively-Manufactured Structure (BAMS) of Austenitic Stainless Steel and Inconel 625," J Mater Sci Technol, **74**, pp. 176–188. https://doi.org/10.1016/J.JMST.2020.10.001.

[5] Kim, Y. S., Yun, D., Han, J. H., Ahsan, Md. R. U., Huang, E.-W., Jain, J., Ji, C., Kim, D. B., and Lee, S. Y., 2022, "Bimetallic Additively Manufactured Structure (BAMS) of Inconel 625 and Austenitic Stainless Steel: Effect of Heat-Treatment on Microstructure and Mechanical Properties," The International Journal of Advanced Manufacturing Technology, **121**(11–12), pp. 7539–7549. https://doi.org/10.1007/s00170-022-09723-x.

[6] Ning, F., Jiang, D., Liu, Z., Wang, H., and Cong, W., 2021, "Ultrasonic Frequency Effects on the Melt Pool Formation, Porosity, and Thermal-Dependent Property of Inconel 718 Fabricated by Ultrasonic Vibration-Assisted Directed Energy Deposition," J Manuf Sci Eng, **143**(5). https://doi.org/10.1115/1.4048515.

Accepted Manuscript Not Copyedited

Downloaded from http://asmedigitalcollection.asme.org/tribology/article-pdf/doi/10.1115/1.4068992/7515215/trib-25-1248.pdf by Delhi Technological University user on 26 June 2025

Journal of Tribology. Received May 03, 2025;
Accepted manuscript posted June 19, 2025. doi:10.1115/1.4068992
Copyright © 2025 by ASME

[7] Ning, F., Hu, Y., Liu, Z., Wang, X., Li, Y., and Cong, W., 2018, "Ultrasonic Vibration-Assisted Laser Engineered Net Shaping of Inconel 718 Parts: Microstructural and Mechanical Characterization," J Manuf Sci Eng, **140**(6). https://doi.org/10.1115/1.4039441.

[8] Prathivraj, S., and Oyyaravelu, R., 2024, "Effect of Interpass Temperature on Austenite Ferrite Ratio of Wire Arc Additive Manufactured 2507 Super Duplex Stainless Steel," Mater Lett, **361**, p. 136125. https://doi.org/10.1016/J.MATLET.2024.136125.

[9] Dinovitzer, M., Chen, X., Laliberte, J., Huang, X., and Frei, H., 2019, "Effect of Wire and Arc Additive Manufacturing (WAAM) Process Parameters on Bead Geometry and Microstructure," Addit Manuf, **26**, pp. 138–146. https://doi.org/10.1016/J.ADDMA.2018.12.013.

[10] Meena, R. P., N, Y., and Vipin, 2024, "A Review on Wire Arc Additive Manufacturing Based on Cold Metal Transfer," Materials and Manufacturing Processes, pp. 1–27. https://doi.org/10.1080/10426914.2024.2323441.

[11] Prasad, R., Yuvaraj, N., Vipin, and Gopal, A., 2024, "Experimental Investigation of Process Parameters of Cold Metal Transfer Welding-Based Wire Arc Additive Manufacturing of Aluminum 4047 Alloy Using Response Surface Methodology," Welding in the World, **68**(11), pp. 2837–2852. https://doi.org/10.1007/s40194-024-01817-2.

[12] Ezatpour, H. R., Sajjadi, S. A., Sabzevar, M. H., and Huang, Y., 2014, "Investigation of Microstructure and Mechanical Properties of Al6061-Nanocomposite Fabricated by Stir Casting," Mater Des, **55**, pp. 921–928. https://doi.org/10.1016/J.MATDES.2013.10.060.

[13] Sun, Q. J., Lin, S. B., Yang, C. L., and Zhao, G. Q., 2009, "Penetration Increase of AISI 304 Using Ultrasonic Assisted Tungsten Inert Gas Welding," Science and Technology

Accepted Manuscript Not Copyedited

Downloaded from http://asmedigitalcollection.asme.org/tribology/article-pdf/doi/10.1115/1.4068992/7515215/trib-25-1248.pdf by Delhi Technological University user on 26 June 2025

Journal of Tribology. Received May 03, 2025;
Accepted manuscript posted June 19, 2025. doi:10.1115/1.4068992
Copyright © 2025 by ASME

of Welding and Joining, **14**(8), pp. 765–767. https://doi.org/10.1179/136217109X12505932584772.

[14] Kore, S. D., Date, P. P., Kulkarni, S. V., Kumar, S., Rani, D., Kulkarni, M. R., Desai, S. V., Rajawat, R. K., Nagesh, K. V., and Chakravarty, D. P., 2011, "Application of Electromagnetic Impact Technique for Welding Copper-to-Stainless Steel Sheets," The International Journal of Advanced Manufacturing Technology, **54**(9–12), pp. 949–955. https://doi.org/10.1007/s00170-010-2981-z.

[15] Kore, S. D., Date, P. P., Kulkarni, S. V., Kumar, S., Rani, D., Kulkarni, M. R., Desai, S. V., Rajawat, R. K., Nagesh, K. V., and Chakravarty, D. P., 2011, "Application of Electromagnetic Impact Technique for Welding Copper-to-Stainless Steel Sheets," The International Journal of Advanced Manufacturing Technology, **54**(9–12), pp. 949–955. https://doi.org/10.1007/s00170-010-2981-z.

[16] Patarić, A., Mihailović, M., and Gulišija, Z., 2012, "Quantitative Metallographic Assessment of the Electromagnetic Casting Influence on the Microstructure of 7075 Al Alloy," J Mater Sci, **47**(2), pp. 793–796. https://doi.org/10.1007/s10853-011-5855-3.

[17] Cao, G., Konishi, H., and Li, X., 2008, "Mechanical Properties and Microstructure of Mg/SiC Nanocomposites Fabricated by Ultrasonic Cavitation Based Nanomanufacturing," J Manuf Sci Eng, **130**(3). https://doi.org/10.1115/1.2823086.

[18] Abramov, O. V., 1987, "Action of High Intensity Ultrasound on Solidifying Metal," Ultrasonics, **25**(2), pp. 73–82. https://doi.org/10.1016/0041-624X(87)90063-1.

[19] KOMAROV, S. V., KUWABARA, M., and ABRAMOV, O. V., 2005, "High Power Ultrasonics in Pyrometallurgy: Current Status and Recent Development," ISIJ International, **45**(12), pp. 1765–1782. https://doi.org/10.2355/isijinternational.45.1765.

Accepted Manuscript Not Copyedited

Downloaded from http://asmedigitalcollection.asme.org/tribology/article-pdf/doi/10.1115/1.4068992/7515215/trib-25-1248.pdf by Delhi Technological University user on 26 June 2025

Journal of Tribology. Received May 03, 2025;
Accepted manuscript posted June 19, 2025. doi:10.1115/1.4068992
Copyright © 2025 by ASME

[20] Ning, F., Hu, Y., Liu, Z., Wang, X., Li, Y., and Cong, W., 2018, "Ultrasonic Vibration-Assisted Laser Engineered Net Shaping of Inconel 718 Parts: Microstructural and Mechanical Characterization," J Manuf Sci Eng, **140**(6). https://doi.org/10.1115/1.4039441.

[21] Todaro, C. J., Easton, M. A., Qiu, D., Zhang, D., Bermingham, M. J., Lui, E. W., Brandt, M., StJohn, D. H., and Qian, M., 2020, "Grain Structure Control during Metal 3D Printing by High-Intensity Ultrasound," Nat Commun, **11**(1), p. 142. https://doi.org/10.1038/s41467-019-13874-z.

[22] Ma, Q., Chen, H., Ren, N., Zhang, Y., Hu, L., Meng, W., and Yin, X., 2021, "Effects of Ultrasonic Vibration on Microstructure, Mechanical Properties, and Fracture Mode of Inconel 625 Parts Fabricated by Cold Metal Transfer Arc Additive Manufacturing," J Mater Eng Perform, **30**(9), pp. 6808–6820. https://doi.org/10.1007/s11665-021-06023-5.

[23] Jeong, T. W., Cho, Y. T., Lee, C. M., and Kim, D. H., 2024, "Effects of Ultrasonic Treatment on Mechanical Properties and Microstructure of Stainless Steel 308L and Inconel 718 Functionally Graded Materials Fabricated via Double-Wire Arc Additive Manufacturing," Materials Science and Engineering: A, **896**, p. 146298. https://doi.org/10.1016/J.MSEA.2024.146298.

[24] Meena, R. P., Yuvaraj, N., and Vipin, V., 2024, "Investigations and Optimization of Cold Metal Transfer-Based WAAM Process Parameters for Fabrication of Inconel 718 Samples Using Response Surface Methodology," Arab J Sci Eng. https://doi.org/10.1007/s13369-024-08947-1.

[25] Meena, R. P., Yuvaraj, N., and Vipin, 2024, "Optimization of Process Parameters of Cold Metal Transfer Welding-Based Wire Arc Additive Manufacturing of Super Duplex

Accepted Manuscript Not Copyedited

Downloaded from http://asmedigitalcollection.asme.org/tribology/article-pdf/doi/10.1115/1.4068992/7515215/trib-25-1248.pdf by Delhi Technological University user on 26 June 2025

Journal of Tribology. Received May 03, 2025;
Accepted manuscript posted June 19, 2025. doi:10.1115/1.4068992
Copyright © 2025 by ASME

Stainless Steel Using Response Surface Methodology," Proceedings of the Institution of Mechanical Engineers, Part E: Journal of Process Mechanical Engineering. https://doi.org/10.1177/09544089241230878.

[26] Wang, F., Eskin, D., Mi, J., Connolley, T., Lindsay, J., and Mounib, M., 2016, "A Refining Mechanism of Primary Al3Ti Intermetallic Particles by Ultrasonic Treatment in the Liquid State," Acta Mater, **116**, pp. 354–363. https://doi.org/10.1016/J.ACTAMAT.2016.06.056.

[27] Ruirun, C., Deshuang, Z., Tengfei, M., Hongsheng, D., Yanqing, S., Jingjie, G., and Hengzhi, F., 2017, "Effects of Ultrasonic Vibration on the Microstructure and Mechanical Properties of High Alloying TiAl," Sci Rep, **7**(1), p. 41463. https://doi.org/10.1038/srep41463.

[28] Jeong, T. W., Cho, Y. T., Lee, C. M., and Kim, D. H., 2024, "Effects of Ultrasonic Treatment on Mechanical Properties and Microstructure of Stainless Steel 308L and Inconel 718 Functionally Graded Materials Fabricated via Double-Wire Arc Additive Manufacturing," Materials Science and Engineering: A, **896**, p. 146298. https://doi.org/10.1016/J.MSEA.2024.146298.

[29] Gäumann, M., Bezençon, C., Canalis, P., and Kurz, W., 2001, "Single-Crystal Laser Deposition of Superalloys: Processing–Microstructure Maps," Acta Mater, **49**(6), pp. 1051–1062. https://doi.org/10.1016/S1359-6454(00)00367-0.

[30] Ning, F., Hu, Y., Liu, Z., Wang, X., Li, Y., and Cong, W., 2018, "Ultrasonic Vibration-Assisted Laser Engineered Net Shaping of Inconel 718 Parts: Microstructural and Mechanical Characterization," J Manuf Sci Eng, **140**(6). https://doi.org/10.1115/1.4039441.

Accepted Manuscript Not Copyedited

Downloaded from http://asmedigitalcollection.asme.org/tribology/article-pdf/doi/10.1115/1.4068992/7515215/trib-25-1248.pdf by Delhi Technological University user on 26 June 2025

Journal of Tribology. Received May 03, 2025;
Accepted manuscript posted June 19, 2025. doi:10.1115/1.4068992
Copyright © 2025 by ASME

[31] Qi, H., Azer, M., and Ritter, A., 2009, "Studies of Standard Heat Treatment Effects on Microstructure and Mechanical Properties of Laser Net Shape Manufactured INCONEL 718," Metallurgical and Materials Transactions A, **40**(10), pp. 2410–2422. https://doi.org/10.1007/s11661-009-9949-3.

[32] Liu, F., Lin, X., Leng, H., Cao, J., Liu, Q., Huang, C., and Huang, W., 2013, "Microstructural Changes in a Laser Solid Forming Inconel 718 Superalloy Thin Wall in the Deposition Direction," Opt Laser Technol, **45**(1), pp. 330–335. https://doi.org/10.1016/J.OPTLASTEC.2012.06.028.

[33] Wang, Z., Guan, K., Gao, M., Li, X., Chen, X., and Zeng, X., 2012, "The Microstructure and Mechanical Properties of Deposited-IN718 by Selective Laser Melting," J Alloys Compd, **513**, pp. 518–523. https://doi.org/10.1016/J.JALLCOM.2011.10.107.

[34] Haldar, N., Anand, S., Datta, S., and Das, A., 2024, "On Fabrication of Inconel 718 Slab by Wire Arc Additive Manufacturing: Study of Built Microstructure and Mechanical Properties," Arab J Sci Eng, **49**(2), pp. 2045–2063. https://doi.org/10.1007/s13369-023-08095-y.

[35] Prasad, R., Yuvaraj, N., and Vipin, 2025, "Ultrasonic Vibration-Assisted Cold Metal Transfer Direct Energy Deposition of Dissimilar SDSS2507–IN718 Alloy Parts: Microstructural and Mechanical Characterization," J Eng Mater Technol, **147**(3). https://doi.org/10.1115/1.4068135.

[36] Adesina, A. Y., Zainelabdeen, I. H., Dalhat, M. A., Mohammed, A. S., Sorour, A. A., and Al-Badou, F. A., 2020, "Influence of Micronized Waste Tire Rubber on the Mechanical and Tribological Properties of Epoxy Composite Coatings," Tribol Int, **146**, p. 106244. https://doi.org/10.1016/J.TRIBOINT.2020.106244.

Accepted Manuscript Not Copyedited

Downloaded from http://asmedigitalcollection.asme.org/tribology/article-pdf/doi/10.1115/1.4068992/7515215/trib-25-1248.pdf by Delhi Technological University user on 26 June 2025

Journal of Tribology. Received May 03, 2025;
Accepted manuscript posted June 19, 2025. doi:10.1115/1.4068992
Copyright © 2025 by ASME

[37] Prasad, R., Yuvaraj, N., and Vipin, 2025, "Wear Characteristics of Dissimilar SDSS 2507–IN 718 Parts Fabricated by Cold Metal Transfer-Based Wire Arc Additive Manufacturing," J Tribol, **147**(10). https://doi.org/10.1115/1.4067555.

[38] Wang, T., Liu, X., and Darnell, M., 2023, "Ultrasonic Effects with Different Vibration Positions on Gas Tungsten Arc Wire Additive Manufactured Aluminum Nanocomposite," J Manuf Process, **105**, pp. 359–369. https://doi.org/10.1016/J.JMAPRO.2023.09.043.

[39] Shang, F., Chen, S., Zhou, L., Jia, W., Cui, T., Liang, J., Liu, C., and Wang, M., 2021, "Effect of Laser Energy Volume Density on Wear Resistance and Corrosion Resistance of 30Cr15MoY Alloy Steel Coating Prepared by Laser Direct Metal Deposition," Surf Coat Technol, **421**, p. 127382. https://doi.org/10.1016/J.SURFCOAT.2021.127382.

[40] Cao, Y., Zhang, Y., Ming, W., He, W., and Ma, J., 2023, "Review: The Metal Additive-Manufacturing Technology of the Ultrasonic-Assisted Wire-and-Arc Additive-Manufacturing Process," Metals (Basel), **13**(2), p. 398. https://doi.org/10.3390/met13020398.

[41] Chen, L., Guan, C., Li, J., Yu, T., and Wang, J., 2024, "The Effect of Ultrasonic Vibration on Microstructure and Wear Performance of Laser Directed Energy Deposition in Situ Tic Reinforced Composite Coatings." https://doi.org/10.2139/ssrn.4949173.

[42] Javadi, Y., MacLeod, C. N., Pierce, S. G., Gachagan, A., Lines, D., Mineo, C., Ding, J., Williams, S., Vasilev, M., Mohseni, E., and Su, R., 2019, "Ultrasonic Phased Array Inspection of a Wire + Arc Additive Manufactured (WAAM) Sample with Intentionally Embedded Defects," Addit Manuf, **29**, p. 100806. https://doi.org/10.1016/J.ADDMA.2019.100806.

Accepted Manuscript Not Copyedited

Downloaded from http://asmedigitalcollection.asme.org/tribology/article-pdf/doi/10.1115/1.4068992/7515215/trib-25-1248.pdf by Delhi Technological University user on 26 June 2025

Journal of Tribology. Received May 03, 2025;
Accepted manuscript posted June 19, 2025. doi:10.1115/1.4068992
Copyright © 2025 by ASME

[43] Gürol, U., Kocaman, E., Dilibal, S., and Koçak, M., 2023, "A Comparative Study on the Microstructure, Mechanical Properties, Wear and Corrosion Behaviors of SS 316 Austenitic Stainless Steels Manufactured by Casting and WAAM Technologies," CIRP J Manuf Sci Technol, **47**, pp. 215–227. https://doi.org/10.1016/J.CIRPJ.2023.10.005.

[44] Renner, P., Jha, S., Chen, Y., Raut, A., Mehta, S. G., and Liang, H., 2021, "A Review on Corrosion and Wear of Additively Manufactured Alloys," J Tribol, **143**(5). https://doi.org/10.1115/1.4050503.

[45] Wang, Q., Zhang, P. Z., Wei, D. B., Chen, X. H., Wang, R. N., Wang, H. Y., and Feng, K. T., 2013, "Microstructure and Sliding Wear Behavior of Pure Titanium Surface Modified by Double-Glow Plasma Surface Alloying with Nb," Materials & Design (1980-2015), **52**, pp. 265–273. https://doi.org/10.1016/J.MATDES.2013.05.061.

Accepted Manuscript Not Copyedited

Downloaded from http://asmedigitalcollection.asme.org/tribology/article-pdf/doi/10.1115/1.4068992/7515215/trib-25-1248.pdf by Delhi Technological University user on 26 June 2025

Enhancing Security and Scalability of IoMT Systems Using Blockchain: Addressing Key Challenges and Limitations

Harshit Kumar[1], Harsh Kumar[2], Harish[3], Himanshu Nandanwar[4], Rahul Katarya[5]

Delhi Technological University, Delhi, India

{14harshitkumar, harshkumarsingh54321, dtuharish, Himanshunandanwar9cm0, rahuldtu}@gmail.com

Abstract. The Internet of Medical Things (IoMT) has revolutionized healthcare by enabling real-time data collection, monitoring, and analysis. However, the adoption of IoMT systems also introduces challenges related to data security, privacy, and scalability. Blockchain technology, with its decentralized and immutable properties, offers a promising solution to these issues, yet its integration with IoMT poses several obstacles, including high latency, computational complexity, and increased energy consumption. This paper provides a comprehensive analysis of recent advancements and challenges in blockchain-based IoMT systems, highlighting research gaps such as the lack of updated datasets, high gas costs, and resource constraints. We propose strategies to address these issues and present a framework that enhances the security and scalability of IoMT systems by leveraging optimized consensus mechanisms, AI-assisted blockchain frameworks, and efficient data management techniques. Our findings suggest that while blockchain has the potential to secure IoMT systems effectively, addressing these limitations is crucial for realizing its full potential in healthcare applications.

Keywords: Blockchain, Consensus Mechanism, Healthcare, Internet of Medical Things (IOMT), security & privacy.

1 Introduction

The Internet of Things (IoT) has changed many industries, including healthcare, with the help of the Internet of Medical Things (IoMT). IoMT connects different medical devices and apps, which helps in collecting, monitoring, and analyzing data in realtime. A possible way to fix these problems is by using blockchain technology. Since it's decentralized, unchangeable, and transparent, it can help secure healthcare data. Blockchain makes sure that medical records can't be changed, are easy to verify, and only the right people can access them. This reduces the chances of data breaches and stops unauthorized access. But even with these advantages, combining blockchain with IoMT isn't easy.

© The Author(s) 2025

P. Ahlawat et al. (eds.), *Proceedings of the 6th International Conference on Deep Learning, Artificial Intelligence and Robotics (ICDLAIR 2024)*, Advances in Intelligent Systems Research 193,
https://doi.org/10.2991/978-94-6463-740-3_17

Recent studies have looked at the benefits and problems of using blockchain with IoMT. For example, one study [1] made a system to detect stress in real time using deep learning and blockchain. The system worked well and was accurate, but it had problems because the datasets were not different enough. Other studies, like [2] and [4], used blockchain to keep healthcare documents safe and handle certificates. These ideas improved security and made things more efficient, but they also had issues like higher costs and slower processing times.

Further research, like the studies in [3] and [5], has been looking into how to improve blockchain systems for healthcare. While these studies made some progress in speeding up decisions and boosting privacy, they also pointed out that these solutions need a lot of computing power and can be tricky to set up. On top of that, the frameworks in [6] and [7] that focus on securely managing healthcare data have shown improvements in things like accuracy, energy use, and scalability. But they've also run into problems, like being too dependent on network systems and having some privacy risks.

Researchers are looking at how AI and blockchain can help manage electronic medical records. Studies like [8] and [9] show improvements in data management and security, but the systems still need more work to be practical and fast enough. Earlier research, like [10] and [11], tackled issues with scaling and energy use. They've found some solutions, but challenges remain. More recent studies, like [12] and [13], are making progress in securing medical records, but high transaction costs and computing power are still problems.

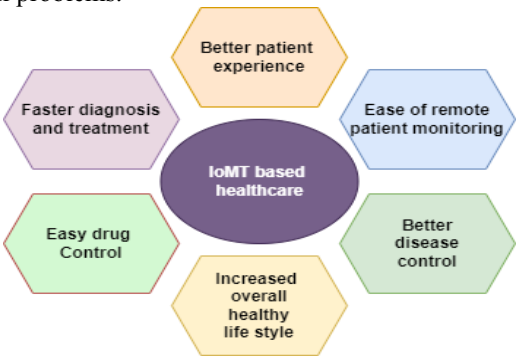


Fig. 1. *IoMT based Healthcare*- IoMT

2 Related Work

Blockchain technology is becoming a game-changer in healthcare, especially when it comes to improving security, privacy, and efficiency. One example is the use of Ethereum smart contracts in a blockchain-based system for managing healthcare certificates. It makes everything more secure and private while also making operations smoother and more cost-effective. However, it does lead to a bit more time being spent on certain tasks [1]. Another interesting approach is using blockchain to preserve privacy

for healthcare data with an advanced algorithm that speeds up encryption and key generation by over 50%. While it does a great job of keeping data secure, it ends up taking more time for transactions [2]. Lastly, combining AI and fog computing with blockchain is showing promise in healthcare systems, boosting security and efficiency. It has impressive results like 97% accuracy and a kappa statistic of 0.93, but it comes with higher computational needs and depends a lot on network setup [3].

There's been quite a bit of research lately about combining AI and blockchain to handle electronic medical records (EMRs). On top of that, they're adding 5G to make the whole system run faster. This might be a pretty good solution for managing healthcare data in the future [8]. Another study is looking at how blockchain can help with analyzing health data. Not only that, but the results are more trustworthy, which is a huge plus [9]. There's also a framework that's focused on using blockchain to stop fraud in healthcare. This one runs on Ethereum with Consensys Quorum and uses the SHA 256 algorithm. One thing it does well is solve some of the scalability issues that older blockchain setups struggle with [10].

In 2023, there was a study about a serverless computing framework called BlockFaaS. It uses blockchain for AI-based IoT in healthcare. It also kept data private and unchangeable. But they didn't explain much about how it works in real life [11]. Another study was about using blockchain for managing electronic medical records (EMRs). They added IPFS for storage and sharing files. It made things more secure and faster. But Ethereum's Proof-of-Work model caused high costs and problems with scalability [12].

There was another framework for healthcare systems using smart contracts on a D-app. It was lightweight and fast. It handled data securely and efficiently. But it wasn't great for larger systems because of high gas fees and scaling issues [13]. One more study talked about a three-phase system for storing and sharing healthcare data. They used blockchain, IPFS, and proxy re-encryption. It worked well to save resources and keep data safe. But they said it might have risks like data tampering or unauthorized access [14]. Lastly, another idea was to use deep reinforcement learning with blockchain for scheduling healthcare tasks. It worked well for managing resources and tasks but wasn't great for real-time use and used a lot of energy [15].

These studies collectively underscore the transformative potential of blockchain technology in healthcare, addressing various challenges while enhancing security, privacy, and efficiency across diverse application.

Table 1. Summary of related works.

S No.	Year	Methodology Used	Dataset Used	Performance Matrix Used	Result	Advantages	Limitations
[1]	2023	Deep learning model combining Bi-LSTM and CNN with	Wearable Stress and Affect Detection	Accuracy, Precision, Recall, F1 score.	Wrist device accuracy: 99.01% Chest device accuracy: 99.96%	High classification accuracy, secure data handling with	Limited number of subjects, lack

		an attention mechanism	(WESAD) dataset.		Combined devices accuracy: 99.97%	blockchain, real-time stress detection	of age and gender diversity in the dataset.
[2]	2023	Utilized Ethereum blockchain, smart contracts, and a combination of React Native, Node.js, and Solidity.	Simulated data for around 100 medical certificates on Ethereum and TestRPC platforms.	Gas cost, latency time, processing time, throughput, and computation time.	Gas cost (Ethereum): 0.000029 - 0.000842 ETH Gas cost (TestRPC): 0.000312 - 0.000799 ETH Latency time: 7.44 ms (blockchain) vs. 3.03 ms (SQL) Processing time: 11.02 ms (blockchain) vs. 8.44 ms (SQL) Throughput: Higher on SQL compared to Ethereum.	Enhanced security with blockchain integration. Immutable and transparent data records	Increased gas cost with the number of certificates.
[3]	2024	Mixed Cooperative-Competitive Deep Multi-Agent Reinforcement Learning (DMARL) with blockchain.	Simulated healthcare data transactions.	Decision-making speed, resource utilization, latency, cost minimization, and security maximization.	Latency: Decreased from 11.5 ms to 8.3 ms Security: Increased by 25% Cost: Reduced by 18%	Improved decision-making speed, optimized resource utilization, reduced latency and costs, enhanced security.	Requires high computational resources, complex implementation, and scalability issues.
[4]	2023	Implementation of the DA using Ethereum, leveraging smart contracts to enhance security and privacy.	Healthcare certificates and user credentials processed in Ethereum and testRPC blockchain environments.	Gas cost, transaction cost, execution cost, latency, and processing time.	The proposed system reduces Gas costs on Ethereum compared to testRPC and shows improved efficiency in latency and processing time.	Enhanced security and privacy, efficient certificate management, reduced operational costs.	Higher time consumption for blockchain-based systems due to internal computations like mining and transaction processing.
[5]	2023	The proposed methodology in-	The files of various sizes (10 KB, 20	Key generation time, encryp-	The proposed EHO-OBL model improved performance	Enhanced privacy and security, better performance	Increased time consumption in

		volves an enhanced Elephant Herding Optimization with Opposition Based Learning (EHO-OBL) and the use of blockchain technology to ensure privacy and security of healthcare data.	KB, 30 KB, 40 KB) used for evaluating performance contained healthcare data.	tion time, decryption time, and execution cost (Gas) for smart contracts.	with 51.04%-92.64% better key generation time and reduced encryption times compared to traditional models.	in terms of key generation and encryption times, and reduced operational costs.	blockchain deployment due to the processing required for transactions.
[6]	2021	Blockchain integration with AI and fog computing for secure data management and prediction.	Medical data sets including COVID-19 patient records and heart disease data from UCI repository.	Delay, network usage, RAM usage, energy consumption, classifier accuracy, recall, precision, kappa statistic, and RMSE.	The proposed framework showed 15% improvement in delay, 20% reduction in network usage, 25% better energy consumption, 97% accuracy, 95% recall, 96% precision, kappa statistic of 0.93, and RMSE of 0.04.	Enhanced data security, improved healthcare service quality, and better prediction accuracy.	High computational complexity and dependency on network infrastructure.
[7]	2023	Simulation and performance comparison with Bitcoin, Bitcoin-NG, and Al-gorand; security and privacy analysis.	Datasets include 33,920 chest X-ray images and COVID-19 data for 218 countries.	Number of nodes, block size, and total messages exchanged for consensus.	ParallelChain reduced message exchange by 48% compared to Bitcoin.	Scalability, energy efficiency, and improved throughput by resolving fork overhead.	High energy consumption of PoW, privacy vulnerabilities of third-party cloud data storage in existing systems.
[8]	2023	Use AI and blockchain to store and process medical records on Ethereum.	Handwritten and printed medical prescriptions and reports.	Character recognition accuracy and time taken to access documents.	Character recognition accuracy of PrintedPrescription is 84.211, HandwrittenPrescription is 72.001 and PrintedReport is 89.333.	Secure, efficient, cost-effective medical data management.	Performance improvements needed; time and cost dependencies on cloud platforms.
[9]	2021	AI techniques including OCR, IPFS, and Ethereum blockchain for data	Handwritten and printed documents.	Accuracy of medical history summarization, data security, and access efficiency.	BSDMF method achieves a high accuracy ratio of 97.2%, a precision ratio of 97.9%, an average trust value of 98.3%,	Enhanced data security, efficient access to patient history, reduced data management burden.	Requires adoption of decentralized systems and potential high initial setup costs.

		processing and storage.			and less response time of 11.2%, and a latency ratio of 15.6%.		
[10]	2023	ELB framework including conceptual framework development, and simulation-based experimental analysis using Consensys Quorum on Ethereum.	Healthcare Claims Data, Patient Records,Billing and Payment Records, Blockchain Ledger Data, Security Logs	The metrics used for security analysis are Security Incidents, Mean Time To Detect, and Mean Time For Vendors Incident Response.	SHA 256 gives total claims size per canal 1024B for 10 nodes it becomes 10240B communication overhead per BCM to HBCM is 30KB for 10 nodes is 300KB then total communication overhead for validations become 3300KB	It enhances efficiency, security, and privacy while addressing scalability challenges present in traditional blockchain implementations	The ELB framework faces challenges in centralization, scalability, privacy, governance complexity, integration, smart contract security, operational overheads, and regulatory compliance.
[11]	2023	The BlockFaaS framework, incorporating both AI and Blockchain modules. The performance is evaluated by measuring the energy cost, transaction time, and QoS parameters on a serverless platform	Heart disease risk data for 303 patients, including 14 variables such as age, sex, and cholesterol levels.	The matrices used are Throughput,Cold Start Latency, Average Response Rate, Blockchain Load, Performance of AI models like accuracy, precision, recall of AI model.	The BlockFaaS works with higher performance and lower energy consumption compared to AIBLOCK. The SHA3-256 function in BlockFaaS consumes less energy and has a shorter processing time compared to SHA256.	BlockFaaS ensures user privacy, data immutability, and dynamic scalability for IoT healthcare. It addresses serverless cold start delays and excels in heart disease risk detection.	Limitations include the dependency on the specific dataset used, scalability in varied IoT environments, and generalizability to other data types or applications.
[12]	2023	Blockchain for secure data, access control for privacy, and IPFS for decentralized off-chain storage and file sharing.	Electronic health records (EHRs), patient data from wearable sensors.	Execution time, throughput, and latency, measuring transaction duration, data transfer rate, and deployment completion delay	Developed a secure healthcare management system using Ethereum Blockchain. Demonstrated functionality for patient data access and management through decentralized consensus.	Blockchain enhances data security, distributed storage ensures data redundancy and availability, and the system is user-friendly.	High transaction costs, scalability challenges with Ethereum's current Proof-of-Work model.
[13]	2023	To develop smart contracts on a D-app prototype using Re-	Simulated healthcare transactions with patient	Latency, Throughput, Transaction time.	This framework has high throughput and low latency. The gas cost was calculated at 2,082,158 gwei for	Decentralized data management for enhanced security and privacy, high thro-	Resource-intensive experimental setup, complexity in smart contract implementation,

		act.js, MetaMask, Node.js, Truffle, Ganache, and IPFS, tested on Google Cloud's E2 machines.	data, collected via Arduino UNO sensors and stored on the blockchain.		addPatient() function.	ughput, low latency, scalability for growing user bases, and blockchain-based data integrity with smart contracts to prevent fraud.	scalability concerns beyond tested ranges, and high gas costs affecting economic feasibility for large-scale deployment.
[14]	2023	Simulation using OMNET++ to illustrate storage and computation cost analysis.	Blockchain storage space details (block type 1 byte, block identity 32 bytes, block size 4 bytes, etc.).	Storage and computation costs, size of ciphertext, and re-encrypted ciphertext.	Each transaction takes approximately 1 second to be transmitted	Effective resource utilization, secure content addressing with distinct content identifiers (CIDs).	Potential for data tampering, transaction denial, exploitation of transparency, unauthorized access to communications and records, fraudulent information by patients, and decryption key exposure risks.
[15]	2023	Deep Reinforcement Learning, Blockchain validation, cooperative multi-agent mechanism.	Self-designed workflows on local machines and some datasets from local clinics.	Relative Percentage Deviation (RPD%), resource consumption, delay in transaction execution.	DRLBTS achieved optimal delay transactions compared to existing methods, handling resource failure, task failure, resource leakage, and deadlines effectively.	Optimal results in terms of objective functions for healthcare workflows, efficient task scheduling, robust handling of various failures.	High energy consumption, not suitable for real-time healthcare applications, incurs overhead at different nodes

3 Internet Of Medical Things

The Internet of Medical Things (IoMT) is making healthcare better by connecting medical devices to the internet. It's like the Internet of Things (IoT), but it's all about health. This includes devices like fitness trackers, implants, and machines used in hospitals. When these devices are connected, doctors can keep an eye on patients all the time and get information right away. This helps doctors know more about their patients, make better decisions, and take action before things get worse.IoMT systems usually include devices that collect health information, networks to send the data, cloud platforms to store and process it, and apps that help analyze the data and connect patients with doctors. When AI and fog computing are added to blockchain, it helps improve the system by reducing delays, making better use of the network, and saving energy. But, this method is complicated and needs a strong network to work well [3]. Also,

blockchain helps keep Electronic Health Records (EHRs) safe by using special techniques to protect the data [5]. These advancements collectively highlight the transformative potential of integrating blockchain technology with IoMT. They offer significant improvements in security, privacy, and efficiency for managing health data, ultimately enhancing patient care.

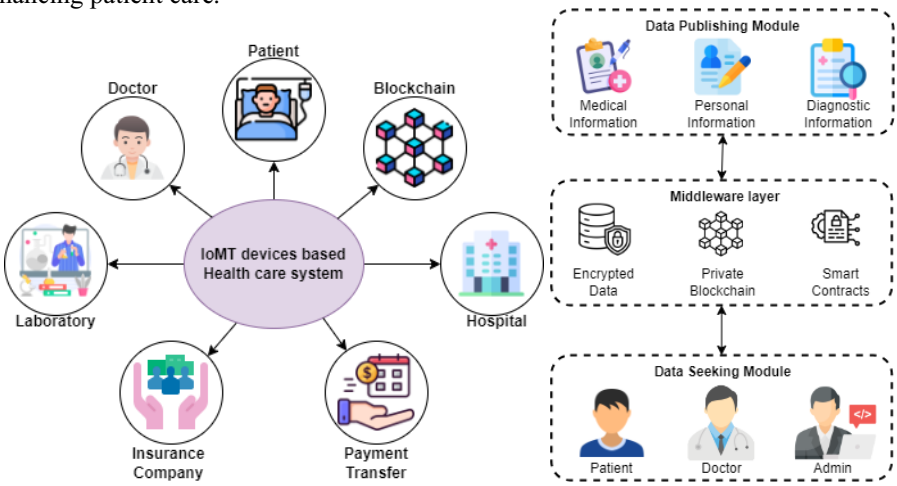


Fig. 2. IoMT devices enable patient monitoring, data collection, and security(left). Blockchain-based IoMT system with secure data publishing, encryption, and search(right).

4 Purpose of this Paper

Our research is motivated by the gap between theoretical blockchain applications in healthcare and practical implementation. While existing studies demonstrate blockchain's potential for securing healthcare data—such as using Ethereum smart contracts to manage healthcare certificates [1]—they often fall short in addressing real-world challenges like scalability, latency, and energy efficiency. For example, frameworks like the enhanced Elephant Herding Optimization with Opposition Based Learning (EHO-OBL) show improvements in data privacy but face issues with transaction processing times [2].

4.1 Identifying Research Gaps

Our analysis revealed that while blockchain technology holds significant promise for enhancing the security and privacy of IoMT systems, several research gaps need attention:

Lack of Updated Dataset Availability: One major issue is the difficulty in accessing the latest datasets. For any system to function effectively, it needs current information. However, obtaining updated datasets can be challenging, leading to the use of outdated information. For instance, [2] utilizes simulated data for around 100 medical

certificates rather than real, current medical records, which limits the system's applicability and accuracy in real-world scenarios. Additionally, [10] deals with healthcare claims data and patient records but does not emphasize the importance of regularly updating these datasets to reflect the most current information.

High Latency: High latency refers to delays in processing and response times within the system. This means there is a noticeable lag between when an action is taken and when the system responds. Such delays can be frustrating for users and hinder real-time applications where immediate feedback is crucial. [2] highlights higher latency in Ethereum blockchain systems compared to traditional SQL systems, with 7.44 ms versus 3.03 ms, respectively, demonstrating the need for improved response times in blockchain-based healthcare solutions.

Security and Privacy Concerns: [5] emphasizes the importance of enhanced privacy and security in healthcare data using the Elephant Herding Optimization with Opposition Based Learning (EHO-OBL) model, showing significant improvements in key generation and encryption times. Additionally, [9] discusses a blockchain-assisted secured data management framework using AI techniques like OCR and IPFS, which enhances data security and access efficiency but requires significant initial setup costs and the adoption of decentralized systems.

Scalability Issues: Scalability refers to the system's ability to handle growing amounts of work or expand in response to increased demand. Many systems struggle with scaling efficiently. [13] paper discusses the scalability of the proposed system but highlights that the approach may not efficiently handle a large number of users and high volumes of data due to computational limitations. Furthermore, [6] mentions dependency on network infrastructure as a barrier to scalability in its blockchain-integrated AI and fog computing framework.

Higher Gas Costs: In the context of blockchain technology, gas costs refer to the fees required to execute transactions on the blockchain network. Higher gas costs can make transactions more expensive, which can be a barrier for users. [2] addresses the issue of higher gas costs associated with Ethereum transactions, providing specific gas cost ranges for Ethereum and TestRPC, indicating the financial burden these costs can impose.

AI Integration with Blockchain: Integrating artificial intelligence (AI) with blockchain technology presents several challenges. [8] proposes an AI-assisted blockchain framework for secure EMR management, highlighting the potential benefits but also noting the performance improvements needed and dependencies on cloud platforms.

5 Identifying Potential Solutions

To address the identified research gaps and limitations in blockchain-based healthcare systems, we propose the following potential solutions:

Advanced Consensus Mechanisms: Looking at new consensus mechanisms like Proof of Stake (PoS), Delegated Proof of Stake (DPoS), or Practical Byzantine Fault Tolerance (PBFT) could be helpful in improving performance and cutting down on energy use. Proof of Work (PoW) systems are having big problems with energy, like mentioned in [7], which shows just how much power PoW uses. Changing to PoS or PBFT might help make blockchain operations more efficient and less power-hungry.

Scalable Architectures: As highlighted in [6], scalability challenges arise due to reliance on network infrastructure, which can be addressed with sharding and sidechains. Similarly, [3] points out that scalable solutions are needed to support the high computational demands of multi-agent reinforcement learning models. Implementing these advanced architectures will help manage large datasets and ensure the system remains responsive.

Enhanced Security Protocols: [5] emphasizes the need for better privacy and security in healthcare data, suggesting the EHO-OBL model to improve encryption and key generation times. [8] introduces an AI-assisted blockchain framework for secure EMR management, though it calls for better performance and reduced reliance on cloud services.

Latency Reduction Techniques: [3] discusses how multi-agent reinforcement learning can improve latency but requires complex optimization. Off-chain transactions and state channels can help reduce latency, improving user experience and system efficiency. [13] also points out the need for low latency and high throughput in medical cyber-physical systems.

Integration of Diverse Datasets: Creating frameworks that can integrate and process different healthcare datasets is vital for ensuring interoperability and smooth data sharing across systems. [6] works with various medical datasets but doesn't address the need for real-time data integration. Moreover, [15] emphasizes the importance of integrating datasets for optimizing healthcare task scheduling using Deep Reinforcement Learning and Blockchain.

6 Conclusion

The integration of blockchain technology in IoMT systems presents significant potential for enhancing data security and privacy, ensuring the reliability and trustworthiness of healthcare applications. However, this integration is not without its challenges, as demonstrated by our analysis. Issues such as high computational complexity, time consumption, and energy inefficiency limit the applicability of blockchain in real-time healthcare scenarios. Our proposed framework, which incorporates these solutions, aims to mitigate these challenges and create a more robust, scalable, and secure IoMT system. Future research should focus on refining these techniques and exploring new models to further reduce latency, optimize resource usage, and lower operational costs, thereby facilitating broader adoption of blockchain in the healthcare sector.

References

1. Qi, P., Chiaro, D., Giampaolo, F., & Piccialli, F. (2023). A blockchain-based secure Internet of medical things framework for stress detection. *Information Sciences*, *628*, 377-390.
2. Sharma, P., Namasudra, S., Crespo, R. G., Parra-Fuente, J., & Trivedi, M. C. (2023). EHDHE: Enhancing security of healthcare documents in IoT-enabled digital healthcare ecosystems using blockchain. *Information Sciences*, *629*, 703-718.
3. Al-Marridi, A. Z., Mohamed, A., & Erbad, A. (2024). Optimized blockchain-based healthcare framework empowered by mixed multi-agent reinforcement learning. *Journal of Network and Computer Applications*, *224*, 103834.
4. Sharma, P., Namasudra, S., Chilamkurti, N., Kim, B. G., & Gonzalez Crespo, R. (2023). Blockchain-based privacy preservation for IoT-enabled healthcare system. *ACM Transactions on Sensor Networks*, *19*(3), 1-17.
5. Verma, G. (2024). Blockchain-based privacy preservation framework for healthcare data in cloud environment. *Journal of Experimental & Theoretical Artificial Intelligence*, *36*(1), 147-160.
6. Singh, P. D., Kaur, R., Dhiman, G., & Bojja, G. R. (2023). BOSS: a new QoS aware blockchain assisted framework for secure and smart healthcare as a service. *Expert Systems*, *40*(4), e12838.
7. Pawar, V., & Sachdeva, S. (2024). ParallelChain: a scalable healthcare framework with low-energy consumption using blockchain. *International Transactions in Operational Research*, *31*(6), 3621-3649.
8. Chamola, V., Goyal, A., Sharma, P., Hassija, V., Binh, H. T. T., & Saxena, V. (2023). Artificial intelligence-assisted blockchain-based framework for smart and secure EMR management. *Neural Computing and Applications*, *35*(31), 22959-22969.
9. Abbas, A., Alroobaea, R., Krichen, M., Rubaiee, S., Vimal, S., & Almansour, F. M. (2024). Blockchain-assisted secured data management framework for health information analysis based on Internet of Medical Things. *Personal and ubiquitous computing*, *28*(1), 59-72.
10. Settipalli, L., Gangadharan, G. R., & Bellamkonda, S. (2024). An extended lightweight blockchain based collaborative healthcare system for fraud prevention. *Cluster Computing*, *27*(1), 563-573.
11. Golec, M., Gill, S. S., Golec, M., Xu, M., Ghosh, S. K., Kanhere, S. S., ... & Uhlig, S. (2023). BlockFaaS: Blockchain-enabled serverless computing framework for AI-driven IoT healthcare applications. *Journal of Grid Computing*, *21*(4), 63.
12. Zakzouk, A., El-Sayed, A., & Hemdan, E. E. D. (2023). A blockchain-based electronic medical records management framework in smart healthcare infrastructure. *Multimedia Tools and Applications*, *82*(23), 35419-35437.
13. Kumar, A., & Chatterjee, K. (2023). A lightweight blockchain-based framework for medical cyber-physical system. *The Journal of Supercomputing*, *79*(11), 12013-12041.
14. Mittal, S., & Ghosh, M. (2024). A three-phase framework for secure storage and sharing of healthcare data based on blockchain, IPFS, proxy re-encryption and group communication. *The Journal of Supercomputing*, *80*(6), 7955-7992.
15. Lakhan, A., Mohammed, M. A., Nedoma, J., Martinek, R., Tiwari, P., & Kumar, N. (2023). DRLBTS: deep reinforcement learning-aware blockchain-based healthcare system. *Scientific Reports*, *13*(1), 4124.

Open Access This chapter is licensed under the terms of the Creative Commons Attribution-NonCommercial 4.0 International License (http://creativecommons.org/licenses/by-nc/4.0/), which permits any noncommercial use, sharing, adaptation, distribution and reproduction in any medium or format, as long as you give appropriate credit to the original author(s) and the source, provide a link to the Creative Commons license and indicate if changes were made.

The images or other third party material in this chapter are included in the chapter's Creative Commons license, unless indicated otherwise in a credit line to the material. If material is not included in the chapter's Creative Commons license and your intended use is not permitted by statutory regulation or exceeds the permitted use, you will need to obtain permission directly from the copyright holder.



ACTA IMEKO
ISSN: 2221-870X
June 2025, Volume 14, Number 2, 1 - 5

Establishment of measurement traceability of dielectric-constant measurement using contact and non-contact methods

Satish[1], Rajendra S. Meena[1], Reva Singh[2], Priyanka Jain[1], Joges C. Biswas[1]

[1] *LF, HF Impedance and DC Metrology, CSIR-National Physical Laboratory, New Delhi, India*
[2] *Delhi Technological University, Delhi, India*

ABSTRACT
To meet industry demands, measurement traceability for the dielectric constant of solid reference materials has been established at audio and radio frequencies. The dielectric constant is determined using capacitance-based contact and non-contact methods, where the dielectric material is sandwiched between the electrodes of a dielectric test fixture. A precision LCR meter measures the capacitance of solid dielectric materials, and results from contact and non-contact methods align well up to 1 MHz. Measurement uncertainty is evaluated according to the Guide to the Expression of Uncertainty in Measurement, with a detailed discussion of contributing factors.

Section: RESEARCH PAPER

Keywords: Dielectric constant; metrological traceability; parallel-plate-capacitor method; uncertainty in measurement

Citation: Satish, R. S. Meena, R. Singh, P. Jain, J. C. Biswas , Establishment of measurement traceability of dielectric-constant measurement using contact and non-contact methods, Acta IMEKO, vol. 14 (2025) no. 2, pp. 1-5. DOI: 10.21014/actaimeko.v14i2.1739

Section Editor: Laura Fabbiano, Politecnico di Bari, Italy

Received December 26, 2023; **In final form** May 26, 2025; **Published** June 2025

Copyright: This is an open-access article distributed under the terms of the Creative Commons Attribution 3.0 License, which permits unrestricted use, distribution, and reproduction in any medium, provided the original author and source are credited.

Funding: This work was supported by CSIR-National Physical laboratory, New Delhi, India.

Corresponding author: Rajendra S. Meena, e-mail: meenars.nplindia@csir.res.in

1. INTRODUCTION

The demand for high-value and low-value dielectric materials has increased exponentially along with the progress in microelectronics technology. Dielectric materials play a vital role in the performance of electronic equipment widely used in communication, navigation, power generation & distribution systems, instrument control systems and microwave & optical sensors. They are also used in electronic circuits, power transmission lines and capacitors. Hence, dielectric materials are the essential part of any electronics circuit. Capacitors are also used for energy storage due to dielectric polarization (re-orientation of charge particles and electric dipoles under the influence of an external electric field) [1]. Currently, many research groups are working on high temperature dielectric materials for electrical energy storage [2]-[3].

The quality of dielectric materials governs its applications in specific industrial sector. Different types of reference materials are utilized in food industry, pharmaceutical, healthcare, semiconductor and power plant industries. The quality of the reference material plays a crucial role to control the output of product [4]. The structural, compositional, and other properties may be manipulated according to requirements and applications, but prior to this, a detailed investigation of properties such as dielectric constant and losses must be conducted [4]-[14].

Majority of the dielectric materials are strong function of frequency and sensitive to the environmental conditions such as temperature and relative humidity. Thus, it is important to characterize the dielectric materials with good precision, especially for space and military applications.

A number of techniques are used to measure the dielectric-constant over the spectrum [5]-[16]. The resonance and transmission or reflection methods are the two commonly used dielectric-constant measurement methods. Resonance methods are highly accurate but limited to a narrow frequency band while transmission or reflection methods require waveguide which further needs a sample with waveguide cross-section [13]. The low-loss dielectric substrate materials reduce the attenuation and heating in ac circuits and devices. They also reduce the crosstalk between the signals in the printed-circuit-boards. Low-dielectric-constant materials are used for the development of antennas using micro-strip and co-planar waveguide structures.

On the other hand, materials with a high dielectric-constant are also used to miniaturize electrical and electronic systems and to realize high-value capacitors [17]-[20].

Here, we propose dielectric-constant measurement by using contact and non-contact methods using capacitance-based techniques at audio and radio frequencies. The dielectric test fixture used to measure the dielectric-constant is in compliance with ASTM D-150 [8]. The real-part of the dielectric-constant of solid dielectric materials is computed from capacitance that is measured using precision LCR meter (Keysight, 4980A) where dielectric material is placed in a dielectric-test fixture (Keysight, 16451B, Electrode Type B). Poly-Tetra-Fluoro-Ethylene (PTFE) is used as reference dielectric material while fiberglass reinforced epoxy laminates (FR4), quartz and alumina are used as sample dielectric materials. FR4 is a low cost (compared to PTFE) with good mechanical properties, and it is used as a substrate material from audio to microwave frequencies [21] whereas PTFE is the very low loss dielectric material with relatively low dielectric constant.

2. THEORETICAL BACKGROUND

Dielectrics are the insulating materials which transmits electrical effect without actually conducting electricity. They get polarized in the presence of an external field and are classified as polar and non-polar dielectric materials. Basically, they have few free-charge carriers, which are bounded as compared to metals and semiconductors which are responsible for conduction current [18]. The complex dielectric-constant provides information about the electric energy storage and loss factor in the dielectric material, and it is also the function of frequency and temperature mainly [22], [23].

The dielectric-constant, ε_{r} is a complex quantity; real part ($\varepsilon_{\mathrm{r}}'$) represents the electrical energy storage capability of the material in the presence of an external electric field while the imaginary part) represents the loss in the material. The imaginary part is a function of dielectric loss mechanism $\varepsilon_{\mathrm{d}}''$ and free charge conductivity σ as depicted in equation (1):

$$\varepsilon_{\mathrm{r}} = \varepsilon_{\mathrm{r}}' - \mathrm{j}\,\varepsilon_{\mathrm{r}}'' = \varepsilon_{\mathrm{r}}' - \mathrm{j}\left(\varepsilon_{\mathrm{d}}'' + \frac{\sigma}{\omega\,\varepsilon_0}\right). \tag{1}$$

The accurate measurement of the reference dielectric material is necessary for the reliable, better performance and miniaturization of electronic circuits/ systems. The selection of dielectric measurement techniques depends on the type and shape of sample and frequency of interest. The dielectric-constant may be calculated as per the user manual [24] for the circular disk electrodes

$$\varepsilon_r' = \frac{t \cdot C_{\mathrm{m}}}{\pi\,(d/2)^2\,\varepsilon_0}, \tag{2}$$

where t represents thickness of the dielectric sample, C_{m} represents parallel capacitance measured using precision LCR meter and d represents diameter of the guarded electrode. The uncertainty in dielectric-constant measurement is dependent on the uncertainty contribution from the thickness, parallel capacitance and diameter of the dielectric sample as in equation (2). The dielectric sample is assumed to have a good surface finish, flatness and electrodes of dielectric test fixture are parallel to each other. While, in the proposed work, method based on equation (4) is adopted for the measurement of the real part of dielectric constant of solid dielectric materials for contact method instead of equation (2).

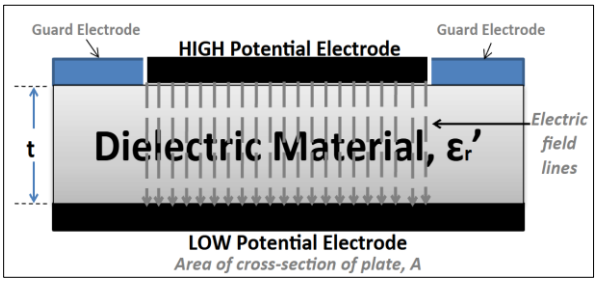


Figure 1. Capacitance technique with contact method.

3. CONTACT METHOD

Generally, a capacitance-based technique is employed to compute the dielectric-constant up-to radio frequency (RF) [25]. The capacitance-based techniques are simple, accurate, reliable and low-cost technique to measure the dielectric-constant of solid, soft and liquid dielectric materials at low to RF [7], [10], [26], [27]. The capacitance-based techniques are affected by the fringing fields and electrode polarization especially at low frequencies [18].

The parallel-plate capacitance as shown in Fig. 1 can be defined as:

$$C_m = \frac{\varepsilon_{\mathrm{r}}'\,\varepsilon_0\,A}{t}, \tag{3}$$

where ε_0 is the absolute permittivity of free space, A is the area of the cross-section of the plates and d is the separation between the plates as shown in Figure 1. (When there is no air-gap present, $D = t$).

The proposed work for the determination of dielectric-constant is based on the ratio of capacitance in the presence of dielectric material (C_{m}) and reference capacitance without dielectric material (C_0) as shown in equation (4). Where C_1 and C_2 are the sensitivity coefficients while $u(\varepsilon_{\mathrm{r}}')$ represents the standard uncertainty in dielectric measurement using the contact method as shown in equation (5), (6) and (8).

$$\varepsilon_{\mathrm{r}}' = \frac{C_{\mathrm{m}}}{C_0} \tag{4}$$

$$C_1 = \frac{\partial \varepsilon_{\mathrm{r}}'}{\partial C_{\mathrm{m}}} = \frac{1}{C_0} \tag{5}$$

$$C_2 = \frac{\partial \varepsilon_{\mathrm{r}}'}{\partial C_0} = \frac{-C_{\mathrm{m}}}{{C_0}^2} \tag{6}$$

$$u(\varepsilon_{\mathrm{r}}') = \sqrt{\left(\frac{\partial \varepsilon_{\mathrm{r}}'}{\partial C_{\mathrm{m}}}\Delta C_{\mathrm{m}}\right)^2 + \left(\frac{\partial \varepsilon_{\mathrm{r}}'}{\partial C_0}\Delta C_0\right)^2} \tag{7}$$

$$u(\varepsilon_{\mathrm{r}}') = \sqrt{\left(\frac{1}{C_0}\Delta C_{\mathrm{m}}\right)^2 + \left(\frac{-C_{\mathrm{m}}}{{C_0}^2}\Delta C_0\right)^2}\,. \tag{8}$$

4. NON-CONTACT METHOD

Non-contact method may also be used for solid materials, but it is especially useful for the characterisation of soft and flexible dielectric materials as shown in Figure 2.

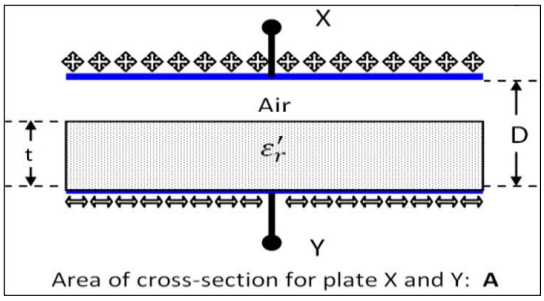


Figure 2. Parallel plate capacitance technique with non-contact method. [19].

The effective capacitance C_e may be seen as the series combination of capacitance due to air dielectric with thickness $(D-t)$ and dielectric material with thickness t as shown in Figure 2. Thus, the effective capacitance C_e for non-contact method may be written as

$$\frac{1}{C_e} = \frac{1}{C_t} + \frac{1}{C_{D-t}} = \frac{t}{\varepsilon_r' \, \varepsilon_0 \, A} + \frac{D-t}{\varepsilon_0 \, A} \, . \tag{9}$$

Then, the dielectric constant, ε_r' may be computed in terms of C_0, C_e, D and t with the following expression:

$$\varepsilon_r' = \frac{1}{1 - \frac{D}{t}\left[1 - \left(\frac{C_0}{C_e}\right)\right]} \, , \tag{10}$$

where C_0 is the measured capacitance between the plates when there is no dielectric material placed in between the plates (where D is the separation between the plates). It can be expressed as

$$C_0 = \frac{\varepsilon_0 \, A}{D} \, , \tag{11}$$

where C_e is the measured capacitance between the plates when there is a dielectric material with dielectric constant ε_r' of thickness t placed in between the plates (where D is the separation between the plates) as shown in Figure 2. It can be expressed as:

$$C_e = \frac{\varepsilon_r' \, \varepsilon_0 \, A}{D} \, . \tag{12}$$

The standard uncertainty $u(\varepsilon_r')$ for non-contact method may be written as:

$$u(\varepsilon_r') = \sqrt{\left(\frac{\partial \varepsilon_r'}{\partial C_m} \Delta C_m\right)^2 + \left(\frac{\partial \varepsilon_r'}{\partial C_0} \Delta C_0\right)^2 \left(\frac{\partial \varepsilon_r'}{\partial D} \Delta D\right)^2 + \left(\frac{\partial \varepsilon_r'}{\partial t} \Delta t\right)^2} \, . \tag{13}$$

The dielectric-constant measurement is traceable to the national/reference standard of impedance (capacitance) and length which are being maintained at CSIR-National Physical Laboratory [28], [29].

5. MEASUREMENT SETUP

The measurement setup for the determination of the dielectric-constant includes the precision LCR meter, which is traceable to the National standard of capacitance and a dielectric test fixture. Dielectric test fixture (Keysight, 16451B, Electrode Type B) with guard electrode is used to minimize the uncertainty due to fringing field effect in parallel plate electrodes. Guarded electrode is used as high-potential electrode as shown in Figure 3

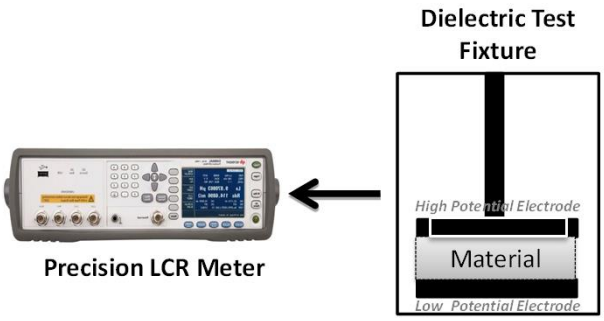


Figure 3. Measurement setup for dielectric-constant measurement facility.

[26]. Type B electrode allows samples with thickness ≤ 10 mm and diameter from 10 mm to 56 mm whereas Type A electrode can accommodate the sample with diameter from 40 mm to 56 mm only.

The measurement-automation program for the dielectric-constant measurement is developed in LabVIEW programming-environment and IEEE 488.2 interface is utilized as a communication interface between PC and precision LCR meter. The measurement-automation program configures and controls the functionality of precision LCR meter, computes dielectric-constant, guides the user throughout the measurement procedure.

6. COMPUTATION OF DIELECTRIC CONSTANT

The fixture compensation is performed using an OPEN-SHORT method which includes cable compensation as well. An LCR meter is used to measure the capacitance with and without the dielectric material and thereafter dielectric-constant and associated uncertainty are computed. The uncertainty-in-measurement is computed as per the "Guide to the expression of uncertainty in measurement" [30].

Initially, the Teflon sample is used as a reference material for dielectric-constant measurement for contact and non-contact techniques. The computed dielectric-constant for Teflon sample is in agreement with previous work [18] as shown in Table 1.

Thereafter, dielectric-constants of FR4, quartz and alumina (Al_2O_3) samples are measured and compared using both above mentioned methods. The detailed uncertainty budget for Al_2O_3 dielectric sample material at 1 MHz is shown in Table 2. The measured dielectric constant of Al_2O_3 is 9.311 with standard uncertainty (± 0.513).

7. SUMMARY AND DISCUSSION

The factors contributing to the uncertainty-in measurement of dielectric-constant are as follows:

Table 1. Dielectric-constant of Teflon sample as reference using contact and non-contact techniques.

Freq. in kHz	Contact			Non-contact		
	$\varepsilon_r' \pm u(\varepsilon_r')$		$\frac{\Delta \varepsilon_r'}{\varepsilon_r'}$ in %	$\varepsilon_r' \pm u(\varepsilon_r')$		$\frac{\Delta \varepsilon_r'}{\varepsilon_r'}$ in %
1	1.969	0.008	6.24	1.971	0.006	6.14
10	2.000	0.008	4.76	1.967	0.006	6.33
100	1.995	0.008	5.00	1.961	0.006	6.62
1000	1.998	0.009	4.86	1.964	0.006	6.48

- Surface roughness: The surface roughness of the sample contributes to the uncertainty-in-measurement. It creates an airgap between sample and electrode which forms the parasitic capacitance. The repeatability of dielectric constant measurement is also affected due to surface roughness of the sample material.
- Parallelism: Parallelism between the electrodes and sample material is the essential requirement for dielectric-constant measurement. Any deviation in the parallelism of electrodes will degrade the repeatability of dielectric-constant measurement.
- Uncertainty of the LCR meter
- Temperature-coefficient of sample dielectric material
- Stability of measurement setup (includes test-fixture and LCR meter)

The temperature-coefficient of dielectric material and stability of the measurement setup is found to be in-significant in the frequency range of interest as compared to the surface roughness of sample materials and parallelism between the electrodes of test fixture. The linearity of the test fixture is analysed by measuring the change in capacitance between the guarded and un-guarded electrodes as a function of displacement. The linearity is one of the critical parameters which may contribute to the uncertainty-in-measurement of dielectric-constant. The linearity of the test fixture is analysed, and the correlation coefficient is found to be close to unity in the desired frequency range.

Table 3 shows a comparison of dielectric measurement results obtained using contact and non-contact methods, while Table 4 summarizes the results from both methods.

8. CONCLUSION

The metrological traceability of dielectric-constant of solid dielectric materials is established using the contact and non-contact methods up-to 1 MHz. The uncertainty-in dielectric-constant measurement is computed as per the GUM document. The factors affecting the uncertainty in measurement are analysed and discussed. The computed dielectric constant and their uncertainties are compared for contact and non-contact method and are in good agreement with each other. The uncertainty achieved using non-contact method is higher than the contact method as it is dependent on uncertainties due thickness of sample and air gap between the guarded electrode and sample. The dielectric test fixture maybe further modified to improve the uncertainty in dielectric-constant measurement.

Table 2. Uncertainty budget for alumina sample material for non-contact method.

Al_2O_3 Material @ 1 MHz							
Quantity	**Estimate**	**Relative Standard Uncertainty**	**Probability Distribution**	**Sensitivity Coefficient**	**Unit**	**Uncertainty Contribution**	**Unit**
C_m, F	$2.28 \cdot 10^{-13}$	$7.45 \cdot 10^{-17}$	Normal	$5.27 \cdot 10^{11}$	1/F	$1.54 \cdot 10^{-9}$	Unitless
C_0, F	$7.41 \cdot 10^{-14}$	$1.46 \cdot 10^{-16}$	Normal	$-1.62 \cdot 10^{12}$	1/F	$5.61 \cdot 10^{-8}$	Unitless
t, m	0.002	0.00001	Normal	$-4.09 \cdot 10^{4}$	1/m	$9.58 \cdot 10^{-2}$	Unitless
D, m	0.003	0.00001	Normal	$3.10 \cdot 10^{4}$	1/m	$1.68 \cdot 10^{-1}$	Unitless
ε_r'	9.311		$k = 1$			± 0.513	

Table 3. Comparison of dielectric-constant computed using contact and non-contact methods from 1 kHz to 1 MHz and their standard uncertainty

Dielectric Material	**Frequency in kHz**	**Contact**			**Non-contact**		
		ε_r'	$\pm\, u(\varepsilon_r')$	$\frac{\Delta\varepsilon_r'}{\varepsilon_r'}$ in %	ε_r'	$\pm\, u(\varepsilon_r')$	$\frac{\Delta\varepsilon_r'}{\varepsilon_r'}$ in %
FR4	1	4.751	0.006	--	4.837	0.160	--
	10	4.756	0.006	--	4.872	0.163	--
	100	4.742	0.006	--	4.887	0.164	--
	1000	4.753	0.007	--	4.893	0.164	--
Quartz	1	3.585	0.007	--	3.651	0.064	--
	10	3.593	0.007	5.94	3.646	0.064	4.55
	100	3.585	0.007	--	3.681	0.065	--
	1000	3.592	0.006	5.97	3.686	0.065	3.51
Alumina	1	9.138	0.019	--	9.284	0.510	--
	10	9.117	0.018	3.83	9.204	0.501	2.91
	100	9.144	0.021	--	9.253	0.507	--
	1000	9.119	0.020	3.40	9.311	0.513	1.37

Table 4. Comparison of contact and non-contact methods for measurement of dielectric constant.

Parameters	**Contact Method**	**Non-Contact Method**	**Comments**
Sample material requirements	Solid dielectrics with homogeneous, flat, smooth surface finish	Soft, flexible and brittle solid dielectrics with homogenous, flat and good surface finish	Uncertainty in non-contact method is the function of four parameters (Capacitance with or without dielectric, thickness of dielectric sample and total separation between plates)
Complexity	Low	Medium	
Accuracy	High	Medium	
Uncertainty	Low	Medium	

ACKNOWLEDGEMENT

The authors are grateful to the Director CSIR-NPL, India for permission to publish this work for constant encouragement and motivation.

REFERENCES

[1] H. S. Nalwa, Handbook of low and high Dielectric Constant Materials and their Applications., Academic Press, 1999, ISBN 978-012-523905-2.

[2] X. Hao, A review on the dielectric materials for high energy-storage application, Journal of Advanced Dielectrics 03 (2013) 1. DOI: 10.1142/S2010135X13300016

[3] Q. Li, F. Z. Yao, Y. Liu, G. Zhang, H. Wang, Q. Wang, High-Temperature Dielectric Materials for Electrical Energy Storage, Annual Review of Materials Research 48 (2018) pp. 219-243. DOI: 10.1146/annurev-matsci-070317-124435

[4] H. Czichos, T. Saito, L. Smith, Handbook of Metrology and Testing, 2011, ISBN 978-3-642-16640-2, pp. 485-540.

[5] A. P. Gregory, G. J. Hill, M. A. Barnett, Low loss dielectric measurements in the frequency range 1-70 MHz by using a vector network analyser, Meas. Sci. Technol. 32 (2021) 8. DOI: https://doi.org/10.1088/1361-6501/abfd68

[6] A. C. Lynch, Precise Measurements on Dielectric and Magnetic Materials, IEEE Trans. Instrum. Meas., 23 (1974) 4, pp. 425–431. DOI: 10.1109/TIM.1974.4314327

[7] T. T. Grove, M. F. Masters, R. E. Miers, Determining dielectric constants using a parallel plate capacitor, Am. J. Phys., 73 (2005) 1, pp. 52–56. DOI: 10.1119/1.1794757

[8] ASTM International, Standard Test Methods for AC Loss Characteristics and Permittivity (Dielectric Constant) of Solid Electrical Insulation, 2022. Online [Accessed 10 June 2025] https://store.astm.org/d0150-18.html

[9] K. Fenske, D. Misra, Dielectric Materials at Microwave Frequencies, Applied Microwave and Wireless, 2000, pp. 92–100. Online [Accessed 10 June 2025] https://www.n5dux.com/ham/files/pdf/Dielectric%20Materials%20at%20Microwave%20Frequencies.pdf

[10] Agilent Technologies, Basics of Measuring the Dielectric Properties of Materials, Application Note, 2006. Online [Not available on 10 June 2025] https://www.keysight.com/us/en/assets/7018-01284/application-notes/5989-2589.pdf

[11] Michael J. Hill, L. E. Wojewoda, A Study of Permittivity Measurement Reproducibility Utilizing the Agilent 4291 B, IEEE Transactions on Advanced Packaging 29 (2006) 4, pp. 714-718. DOI: 10.1109/TCAPT.2006.888210

[12] C. S. Geyik, M. J. Hill, Z. Zhang, K. Aygün, J. T. Aberle, Impact of Measurement Uncertainty on Correlation Quality for High-Speed Interconnects, IEEE Transactions On Components, Packaging and Manufacturing Technology 11 (2021) 9, pp. 1380-1390. DOI: 10.1109/TCPMT.2021.3101456

[13] M. Celuch, M. J. Hill, T. Karpisz, M. Olszewska-Placha, S. Phommakesone, U. Ray, Bridging the materials' permittivity traceability gap for 5G applications, 2021 IEEE Int. Symp. Antenna & Propagation and USNS –URSI Radio science meeting, Singapore, 4-10 December 2021, pp. 859-60. DOI: 10.1109/APS/URSI47566.2021.9704374

[14] I. Lenicek, V. Milardic, Reference Standard of Low-Frequency Electric Field Strength with Electrical Traceability, IEEE Transactions on Instrumentation and Measurement, 72 (2023) pp. 1007608. DOI: 10.1109/TIM.2023.3296818

[15] A. Santana, A. Valenzuela, Non-destructive measurement of the dielectric constant of solid samples, Rev. Mex. FˊISICA 55 (2009) 6, pp. 477–485. Online [Accessed 10 June 2025] https://www.redalyc.org/pdf/570/57013233012.pdf

[16] J. Yoon, J. Kwon, H. Lee, The Microwave Measurement of the Dielectric Properties by the Parallel Plate Resonator and Ceramic Cavity Method, Proc. 5th Int. Conf. Prop. Appl. Dielectr. Mater., Seoul, Korea (South), 25-30 May 1997, pp. 964–968.

[17] J. B. Jarvis, M. D. Janezic, B. Riddle, C. L. Holloway, N. G. Paulter, J. E. Blendell, Dielectric and Conductor-Loss Characterization and Measurements on Electronic Packaging Materials, NIST Technical Note 1520, 2001. DOI: https://doi.org/10.6028/NIST.TN.1520

[18] R. G. Geyer, Dielectric Characterization and reference Materials, NIST Technical Note 1338, 1990. Online [Accessed 10 June 2025] https://www.nist.gov/publications/dielectric-characterization-and-reference-materials

[19] C. Gabriel, A. Peyman, Dielectric measurement : error analysis and assessment of uncertainty, Phys. Med. Biol., 51 (2006) pp. 6033–6046,. DOI: 10.1088/0031-9155/51/23/006

[20] A. P. Gregory, R. N. Clarke, Dielectric metrology with coaxial sensors, Meas. Sci. Technol., 18 (2007) 5, pp. 1372–1386. DOI: 10.1088/0957-0233/18/5/026

[21] E. L. Holzman, Wideband measurement of the dielectric constant of an FR4 substrate using a parallel-coupled microstrip resonator, IEEE Trans. Microw. Theory Tech., 54 (2006) 7, pp. 3127–3130. DOI: 10.1109/TMTT.2006.877061

[22] J. G. Webster, H. Eren, Measurement, instrumentation, and sensors handbook: Spatial, mechanical, thermal, and radiation measurement, second edition, CRC Press, 2017, ISBN: 9781138072176.

[23] J. Walker, Fundamentals of Physics, 11th ed. Wiley, 2020, ISBN: 978-1-119-30685-6.

[24] Keysight 16451B Dielectric Test Fixture, Keysight Technologies, 2008. Online [Accessed 10 June 2025] https://www.keysight.com/in/en/product/16451B/dielectric-test-fixture.html

[25] W. Jee, K. Raymond, C. Kumar, G. Chin, A. Basri, Complex permittivity measurement using capacitance method from 300 kHz to 50 MHz, Measurement, 46 (2013) 10, pp. 3796–3801. DOI: 10.1016/j.measurement.2013.06.039

[26] C. Cooke, J. E. Ford, Accurate measurement of the dielectric constant of solids, J. Phys. E., 14 (1981). DOI: 10.1088/0022-3735/14/11/015

[27] V. Hartwig, G. Giovannetti, N. Vanello, M. Costantino, L. Landini, A. Benassi, An electrodeless system for measurement of liquid sample dielectric properties in Radio Frequency band, An electrodeless system for measurement of liquid sample dielectric properties in Radio Frequency band, Proc. of the 28th IEEE EMBS Annual Int. Conf., New York City, USA, 30 August – 3 September 2006, pp. 4127–4130.

[28] Satish, S. Kumar, Babita, T. John, A. K. Saxena, Realization of coaxial reference air-lines as high frequency capacitance standard at CSIR-NPL, Measurement, 92 (2016), pp. 166–171. DOI: 10.1016/j.measurement.2016.06.017

[29] S. Singh, S. Kumar, Babita, T. John, Realization of Four-Terminal-Pair Capacitors as Reference Standards of Impedance at High Frequency Using Impedance-Matrix Method, IEEE Trans. Instrum. Meas., vol. 66, no. 08, 2017, pp. 2129–2135. DOI: 10.1109/TIM.2017.2673098

[30] Joint Committee For Guides In Metrology, Evaluation of measurement data — Guide to the expression of uncertainty in measurement, JCGM/Working Group 1, Ed.; 2008. Online [Accessed 10 June 2025] https://www.bipm.org/en/committees/jc/jcgm/publications

JMEPEG
https://doi.org/10.1007/s11665-025-11526-6

©ASM International
1059-9495/$19.00

ORIGINAL RESEARCH ARTICLE

Experimental and Numerical Analysis of Springback of AA1050-Fly Ash Green Composite Produced by Stir Casting Technique

Pankaj Kumar Sharma, Vijay Gautam, Subhajit Konar, Vinita Bhardwaj, Amit Kumar Sharma, and Shashi Prakash Dwivedi

Submitted: 19 February 2025 / Revised: 14 April 2025 / Accepted: 16 May 2025

Bending operations hold significant prominence in the realm of sheet metal forming. Within this process, various challenges are encountered, with springback emerging as a particularly critical defect. Springback is responsible for dimensional inaccuracy and distortion of geometry. In this research paper, springback of Al-Fly ash green composite has been determined experimentally and numerically in the V-bending operations. The numerical and experimental investigation of residual stresses was also done for AA1050 and its ash composite. A good agreement has been seen between experimental and simulation results for both springback and residual stress. An attempt has been made to fabricate AA1050-Fly ash green composite, using stir casting route, and a comparative study of mechanical properties has been done between the composite and its parent aluminum AA1050. To achieve this goal, fly ash particles less than 90 μm size were added 8 weight percentage of aluminum, in molten aluminum and mixed using mechanical stirrer. The incorporation of fly ash induces notable alterations in key properties such as hardness, density, stiffness, strength, and wear resistance. The blending of fly ash with aluminum castings contributes to a reduction in energy content, metal content, and overall cost of aluminum products.

Keywords fly ash, numerical investigation, springback, stir casting route, V-bending

1. Introduction

In today's era, sheet metal forming is playing an important role in modern manufacturing industries as it allows the production of high-quality sheet metal parts with complex shape at a low cost to fulfill the demands of design and manufacturing engineers in the field of automobiles, ship building, aviation, building products, and home appliances. The important sheet metal forming processes which are widely used in industries are deep drawing, roll forming, stretching, and bending.

Bending is a critical sheet metal forming process employed in the manufacturing of aircraft, spacecraft, automobiles, home appliances, and various other products. To create a bend in any component, the bending force must exceed the material's yield limit to induce stresses that result in a permanent bend once the load is removed. When the forming load is removed, elastic recovery or springback occurs (Ref 1, 2). Springback is the elastic recovery in the plastically deformed sheet after removal of punch which causes loss of dimensional accuracy and distortion of geometry (Ref 3, 4). Ma et al. explained that the springback is a stress-driven phenomenon which is occurred during unloading after sheet metal forming. Springback is the outcome of the redistribution of internal stresses caused by the non-uniform stress distribution developed during the sheet metal forming processes. The springback is depended on several factors, including the material's yield strength, elastic modulus, and coefficient of strain-hardening, as well as the formed part's geometry and various process parameters like forming speed (Ref 5).

In the sheet metal forming, springback is a significant quality issue. In this research paper, determination of springback of Al-fly ash green composite in V-bending has been done numerically and experimentally. As per available literature, no one has studied yet springback analysis for particle-reinforced composites materials. This makes it a novel work. Mostly researcher has investigated springback of monolithic and clad sheets. Sharma et al. studied the springback of 2-ply aluminum alloy-stainless steel-clad sheets experimentally, numerically, and analytically. They have observed a good agreement between them (Ref 5, 6). Zhang et al. investigated the springback behavior of the CP980 steel by combining simulation and experiment. For numerical analysis, they have obtained the anisotropic yield model parameters and mechanical properties of 980 MPa-grade complex-phase steel from tensile tests and further applied to ABAQUS software. In experimental analysis, 60° and 90° bending angle for die has been selected. A good agreement has been established between

Pankaj Kumar Sharma, Department of Mechanical Engineering, Delhi Technological University, Delhi, India; and Raj Kumar Goel Institute of Technology, Ghaziabad, Uttar Pradesh, India; **Vijay Gautam** and **Subhajit Konar**, Department of Mechanical Engineering, Delhi Technological University, Delhi, India; and **Vinita Bhardwaj**, Raj Kumar Goel Institute of Technology, Ghaziabad, Uttar Pradesh, India; **Amit Kumar Sharma**, Department of Mechanical Engineering, IIT, Mandi, Himachal Pradesh, India; and **Shashi Prakash Dwivedi**, Lloyd Institute of Engineering & Technology, Greater Noida, Uttar Pradesh, India. Contact e-mail: erpankajsharma719@gmail.com.

Published online: 09 June 2025

the results of experiments and simulations (Ref 7). Cheng et al. studied the springback of aluminum alloy 7075-T6/CFRP laminate through both numerical and experimental analyses. When thickness of the laminates is increased from 2 mm to 3 mm, then springback is reduced by 43% during V-bending. But the springback behavior of CFRP/ 7075-T6 aluminum alloy was observed relatively insensitive to forming speed (Ref 8).

AA1050-Fly ash green composite represents a metal matrix dispersion-strengthened composite where a soft and ductile aluminum alloy AA1050 matrix is fortified by hard and brittle fly ash particles. Discontinuously reinforced aluminum (DRA)-based metal matrix composites are gaining attention due to their elevated specific stiffness and strength, remarkable isotropy, excellent wear resistance, and cost-effective manufacturing. Over the last three decades, DRA composites have found applications in various sectors such as automobile, aerospace, electronic packaging, and structural components (Ref 9). The mechanical properties of DRA composites are influenced by several factors, including matrix alloy composition, reinforcement material, size and shape of the reinforcement, volume fraction and distribution, and the nature of the matrix–reinforcement interface. The chosen reinforcement material should ideally possess significantly higher specific strength and a higher melting temperature compared to the matrix alloy. The current trend focuses on developing lightweight materials using cost-effective reinforcements.

Fly ash, an inexpensive and low-density by-product generated during the combustion of coal in thermal power plants, has been successfully incorporated into cast and wrought aluminum alloys to create aluminum alloy–fly ash (ALFA) composites (Ref 10). These composites exhibit low density while maintaining satisfactory properties. Utilizing fly ash as a reinforcement has the potential to overcome cost barriers for widespread applications. Fly ash substitutes the aluminum, and so it not only reduces costs but also contributes to energy savings. Additionally, the use of aluminum-fly ash composites requires less energy for remelting during recycling, as only the aluminum fraction needs to be melted, while the fly ash remains solid. Aluminum has been widely using all over the world. Aluminum requirement can effectively be reduced by replacing it with Al-fly ash composite. Composites of aluminum and fly ash (Al-Fly ash) are extensively employed in diverse applications, including signage for highways and runways, windows and doors sliding tracks, automotive components, ducts, frames, industrial furniture, and machine covers, among other uses.

Characterization of the AA1050-Fly ash green composite is very important for better understanding of its properties, performance, and behaviors in various target applications. In structural and load-bearing applications, such as aerospace components, automotive parts, and construction materials, the mechanical properties of the fly ash composite specifically its strength, toughness, and hardness are crucial. Fly ash particles can enhance the strength and hardness of aluminum. Within the aluminum matrix, the size, shape, and distribution of the fly ash particles affect its behavior. Incorporation of fly ash into aluminum melt can effectively reduce the overall density of the composite material, resulting in a lighter material. The components such as brake, gears, or engine parts are subjected to friction, the abrasion, and wear resistance of the composite is crucial. Addition of fly ash particles, specifically which are rich in alumina and silica, may increase the wear resistance of Al. By using fly ash, which is a by-product of coal combustion, reduces the adverse environmental effect of the composite by recycling waste material. Characterization permits the manufacturers to find out, how fly ash influences the cost of materials, and whether it gives a viable, eco-friendly alternative to the traditional materials.

2. Manufacturing of a AA1050-Fly Ash Composite

The cost-effective stir casting technique is conducted to manufacture AA1050-Fly ash green composite**.** Stir casting method involves the blending of a dispersed phase with a molten matrix metal through the use of a mechanical stirrer in a liquid state. The stirring apparatus employed in this study was locally manufactured as depicted in Fig. 1.

Noteworthy attention was given to the fabrication of the impeller, ensuring its ability to generate a vortex capable of efficiently incorporating the lighter fly ash into the melt (Ref 11, 12).

After studying various shapes of impeller, it is found that impeller with curved blade as used in propeller is best suited shown in Fig. 2. For experimentation purpose, 4 kg of aluminum AA1050 was used. Initially, a quantity of two kilograms of aluminum AA1050 was melted using an induction heating furnace (MEGATHERM) within a crucible (graphite). The resulting melt, reaching a temperature of approximately 850 °C, was then poured into sand molds featuring cuboid cavities of varying dimensions. Subsequently, the material solidified, setting the stage for subsequent testing. Now, 2 kg of aluminum AA1050 was taken into crucible for composite synthesis. After melting, stirrer dipped into molten aluminum and started rotating gradually with the help of speed regulator. The impeller achieved a maximum speed of 500 revolutions per minute (rpm). Preceding the mixing process, 8 wt.% fly ash, equivalent to 160 grams, underwent preheating at 150 °C approximately one hour in advance. At the time of formation of vortex created by stirrer, fly ash particles were added with the help of an ash feeder into the molten metal.

It took almost 40 minutes to mix 160 gm ash, i.e., at the rate of 4.0 gm/min. Then, the melt was poured into the sand molds of different sized cavities. After solidification, the cuboids of the composite were ready for testing. Molten aluminum has

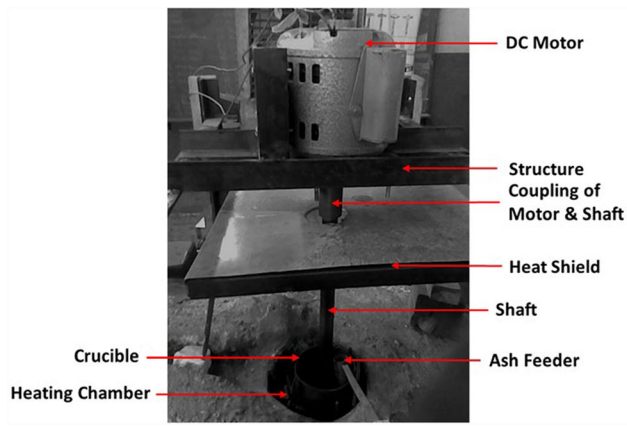


Fig. 1 Experimental setup placed on heating chamber of induction heating furnace

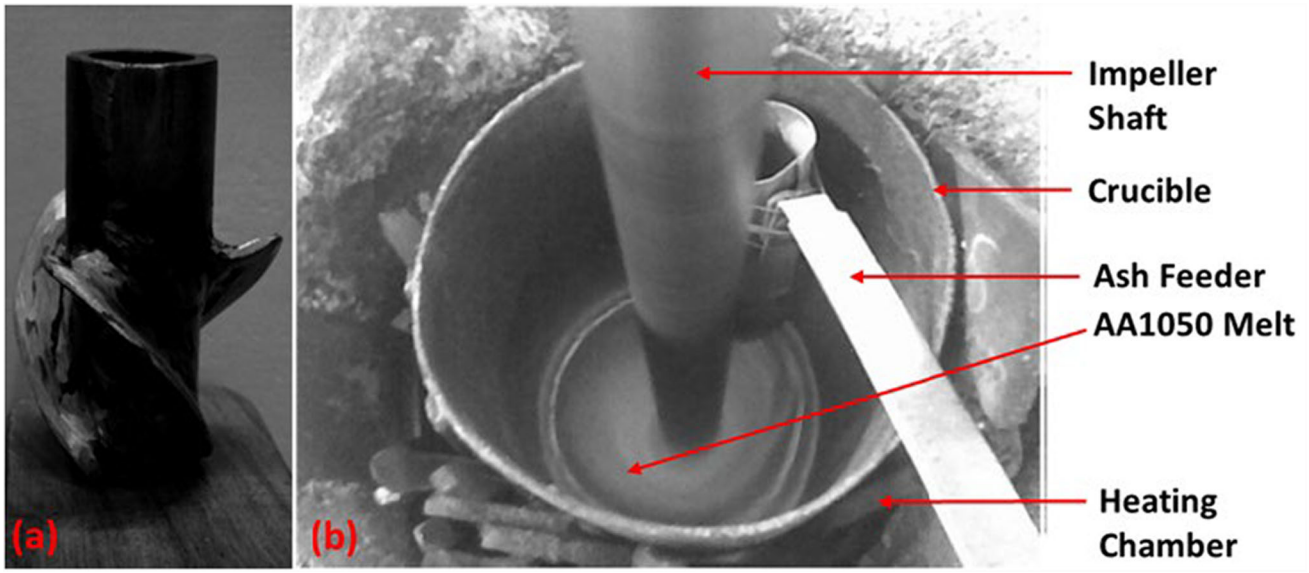


Fig. 2 (a) Impeller (b) Process of mixing of fly ash into AA1050 melt

affinity to hydrogen. Hydrogen is absorbed by aluminum creating porosity. Therefore, to avoid this porosity it is necessary that melt should be supplied with some degassing agents. To improve the interfacial bonding between the AA1050 matrix and fly ash particles, surface treatment of fly ash was conducted before the stir casting process; otherwise, untreated fly ash can show poor wettability with molten AA1050, leading to agglomeration and weak bonding. To solve this issue, a silane-based surface treatment was conducted. This silane coating increases the chemical affinity between the AA1050 matrix and inorganic fly ash surface, resulting in better distribution during stirring and improving the load transfer efficiency at the interface. As a result, the surface-treated fly ash enhances the mechanical properties of the composite as compared to untreated fly ash. To improve the wettability of fly ash into the aluminum melt, some researchers have applied magnesium. Improved wettability of fly ash enhances uniform distribution of fly ash into the melt. Better mechanical properties are the outcome of uniform distribution of fly ash.

2.1 Possible Chemical Reactions

Thermodynamic analysis suggests the potential occurrence of chemical reactions between molten aluminum and fly ash particles. These particles comprise alumina, silica, and iron oxide, and it is anticipated that, during the solidification process, the processing of aluminum-fly ash composites, or when holding such composites at temperatures exceeding the melting point of aluminum, these particles may undergo chemical reduction. The possible chemical reactions between molten aluminum and fly ash are as follows: The potential chemical reactions between liquid aluminum AA1050 and fly ash particles are outlined below:

$$2\,\mathrm{Al}\,(\mathrm{l}) + 3/2\,\mathrm{SiO_2(s)} = 3/2\,\mathrm{Si(s)} + \mathrm{Al_2O_3(s)}\,(930\,\mathrm{to}\,1683^{\circ}\,\mathrm{K}) \quad \text{(Eq 1)}$$

$$2\,\mathrm{Al}\,(\mathrm{l}) + \mathrm{Fe_2O_3(s)} = 2\,\mathrm{Fe(s)} + \mathrm{Al_2O_3(s)} \quad (930\,\mathrm{to}\,1033\ ^{\circ}\mathrm{K}) \quad \text{(Eq 2)}$$

At the experimental temperature of about 850 °C silica and ferrite reduces in their elements, i.e., Si (silicon) and Fe (iron) while oxidizing aluminum into Al_2O_3 (alumina) according to Eq (1) and (2), which is extremely hard and brittle (Ref 13). The presence of 11.73% oxygen (as per Table 1) is due to these oxides. The microstructure of the resulting samples was observed through scanning electron microscopy (SEM). The oxides formed during reactions (1) and (2), and primarily Al_2O_3 (alumina) plays significant roles in the development of the composite's microstructure and properties. Alumina (Al_2O_3) increases hardness but makes the composite brittle. Further hard and brittle AA1050-Fly ash composite shows low springback during V-bending.

3. Characterization of AA1050 and AA1050-Fly Ash Composite

3.1 Chemical Composition of AA1050 and AA1050-Fly Ash composite

Both AA1050 and Al-fly ash composites were tested for the chemical compositions by spark-based spectroscopy. The elemental chemical compositions as obtained are given in Table 1

The incorporation of fly ash through stir casting leads to a decrease in aluminum content, reducing it from 99.5% to 77.82%. Simultaneously, there is an increase in silicon and iron levels, rising from 0.059% and 0.296% to 2.63% and 1.72%, respectively. Additionally, an extra 11.73% of oxygen is observed in the composite, attributed to ash and reduction–oxidation reactions occurring between the ash and aluminum phases. The presence of oxygen manifests in the form of oxides, primarily composed of alumina, silica, and hematite,

Table 1 Chemical composition of AA1050 and AA1050-Fly ash composite

Material	Al	Si	Fe	Na	O	C
AA1050	99.5	0.059	0.296	0.002	–	–
AA1050-Fly Ash composite	77.82	2.63	1.72	1.00	11.73	5.09

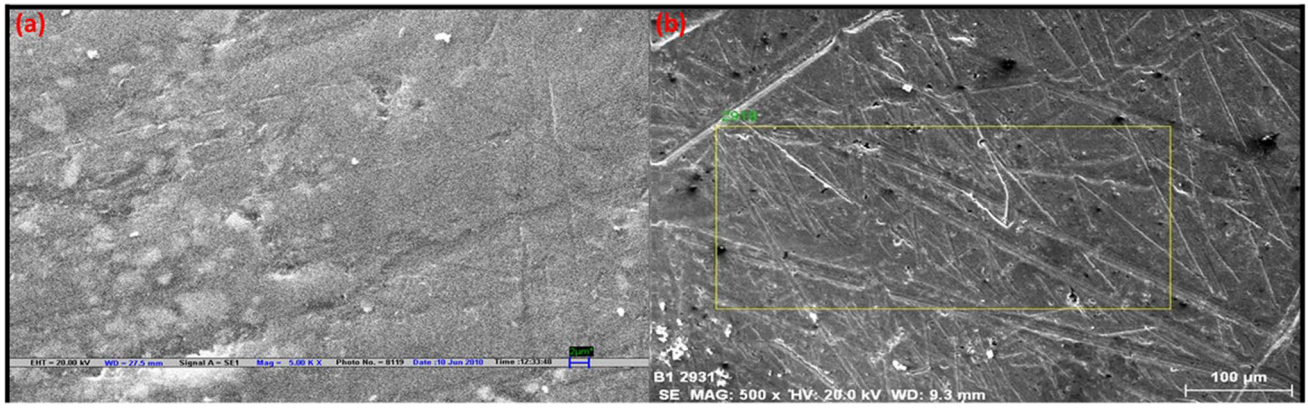


Fig. 3 (a) SEM micrograph of AA1050 (b) SEM micrograph of AA1050-Fly ash composite

resulting from reactions between ash and AA 1050 above the melting point.

3.2 Microstructural Study

Studies focused on the microstructural changes occurring between as-cast specimen of AA1050 and stir cast AA1050-Fly ash composite (8 wt.%). Studies were performed with ZEISS EVO Series SEM EVO 50.

Figure 3(a) shows SEM micrograph of AA1050 showing continuous phase of aluminum AA1050. The image in Fig. 3(b) depicts a low-magnification view at 500× , demonstrating the distribution of fly ash particles within the aluminum matrix. It is evident from the micrograph that there is non-uniform dispersion of ash particles due to particle agglomeration. To improve the dispersion of ash particle, magnesium can be added to the cast melt. Small amount (2% to 3%) of Mg is sufficient for improving the wettability of the ash particles into the cast melt of AA1050. Uniform distribution of ash particles is responsible of better mechanical properties.

3.3 Mechanical Properties

Table 2 gives relative values of different mechanical properties of AA1050 and ash composite castings.

It can be seen that the ash composite is lighter, harder, and less tough in comparison with its parent AA1050. The composite of AA1050 and fly ash demonstrates a toughness of 15 Joules, whereas the standalone AA1050 exhibits a higher toughness of 42 Joules. The reduced toughness in the ash composite renders it brittle, contrasting with the ductility observed in AA1050 as per Fig. 4(a) and (b).

To determine the tensile properties of AA1050 and AA1050-Fly ash composite sheet metal, the tensile test samples of AA1050 and AA1050-Fly ash composite have been taken in sub-sized dimensions as per ASTM-E8M. The thickness of the specimens used for tensile tests is 2 mm for both AA1050 and AA1050-Fly ash composite sheets. All the tensile tests are performed on a 50 kN table top UTM (make: Tinius Olsen) with a crosshead speed of 2.5 mm/min. True stress–true strain curves have been plotted by the force–elongation data.

$$\sigma(\text{true stress}) = s\,(1 + e) \quad \text{(Eq 3)}$$

$$\varepsilon(\text{true strain}) = \ln\,(1 + e) \quad \text{(Eq 4)}$$

where e represents engineering strain and s represents engineering stress.

Tensile properties of AA1050-Fly ash composite like Young's modulus, ultimate tensile strength, and yield strength are increased, and on the contrary percentage elongation is reduced as compared to AA1050. For a more comprehensive evaluation of the tensile properties, the true stress–true strain plot for ash composite is compared with that of AA105, as depicted in Fig. 5.

4. Springback

4.1 Determination of Springback by Experiment

To assess springback outcomes following bending experiments, a V-bending die and punch set has been meticulously crafted. The die boasts a profile radius of 17.5 mm, while the punch exhibits a radius of 15 mm, resulting in an included bend angle of 90 degrees. To accommodate potential variations in sheet thickness and prevent localized compression that could impact springback, a clearance of 2% of the sheet thickness, in addition to the sheet thickness itself, is maintained between the punch and the die.

All toolings, composed of D2 steel, undergo wire-cut EDM and subsequent heat treatment. The punch is affixed in a wedge grip attached to the movable crosshead, while the die is securely positioned in a stationary wedge grip at the base of a

Table 2 Mechanical properties of AA1050 and ash composite

S.no.	Mechanical properties	AA1050	AA1050-Fly ash composite
1	Density	2.72 gm/cm^2	2.54 gm/cm^2
2	Hardness	35 HV	45 HV
3	Toughness	42 Joule	15 Joule
4	Yield strength	29.53 N/mm^2	48.67 N/mm^2
5	Ultimate tensile strength	51.30 N/mm^2	138.76 N/mm^2
6	% Elongation	14.05	9.17
7	E-Modulus	48 kN/mm^2	156 kN/mm^2

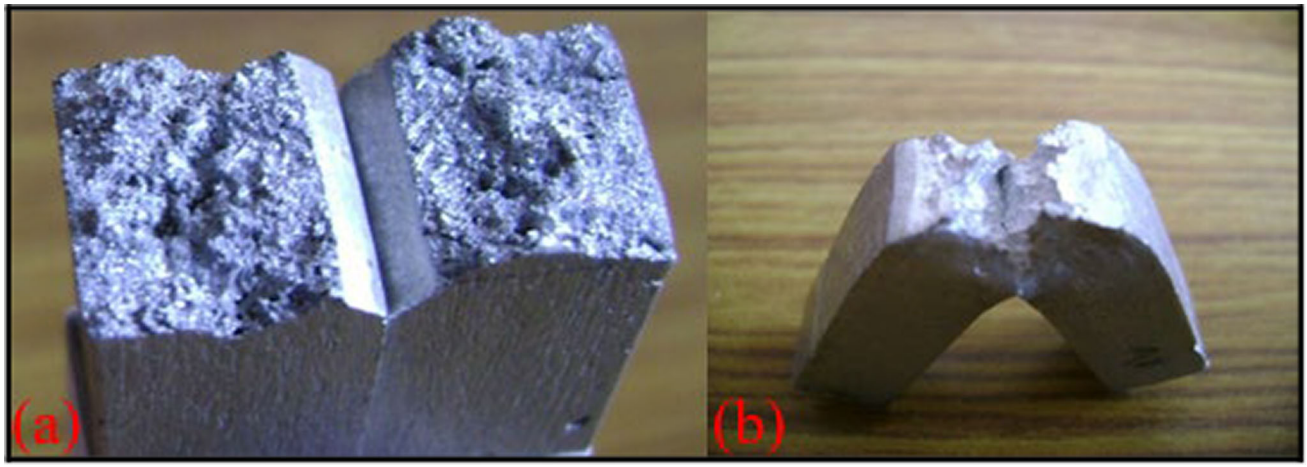


Fig. 4 (a) Fractured ends of AA1050-Fly ash composite and (b) Fractured ends of pure AA1050

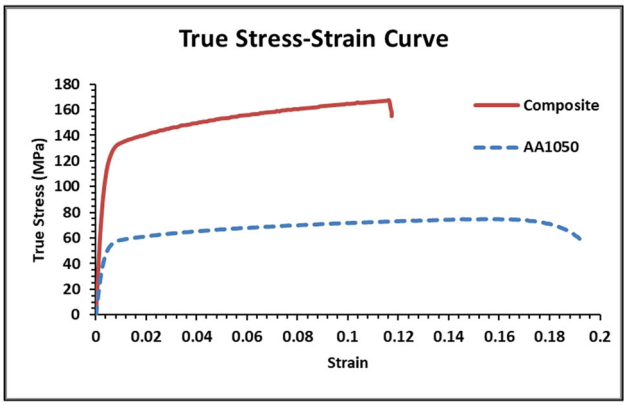


Fig. 5 True stress–strain curve for AA1050 and fly ash composite

50-kN universal testing machine, as illustrated in Fig. 6. Specimens, measuring 150 mm × 25 mm, are chosen to uphold a plane-strain condition during the bending process.

Bending experiments are executed at a consistent punch speed of 20 mm/min, with the punch stroke matching the depth of the die. Following the bending process, the included bend angle values are determined using a sensor-based vision inspection machine. The tested specimens are carefully placed on a magnetic V-block, and a probing tool's sensor is manually maneuvered along both surfaces of the bending arms. The coordinates are captured with dedicated software, enabling measurement of the angle between two flat planes. The predetermined included bend angle of the die is used to calculate the final bend angle of the tested specimen after springback. The angular disparity between the initial and final bend angles provides the springback measurement.

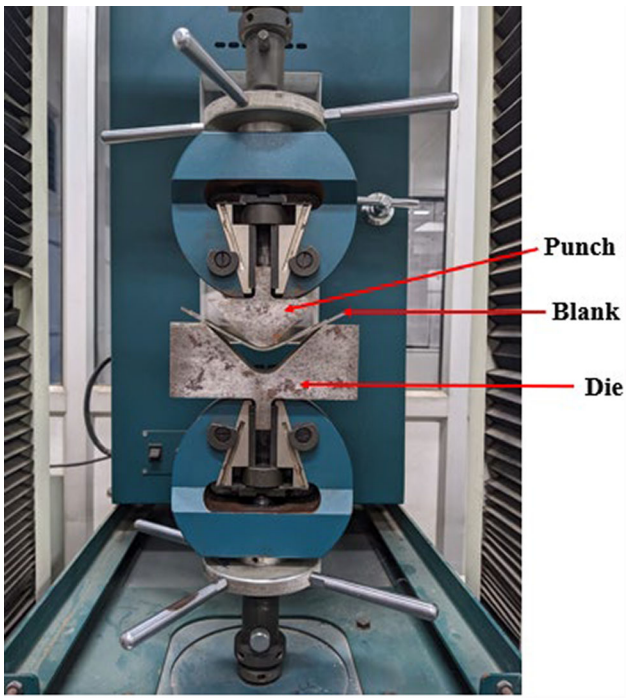


Fig. 6 Experimental setup for V-bending operation

$$\text{Springback } (\theta_s) = (\theta_f - \theta_i) \quad \text{(Eq 5)}$$

where θ_f = Included bend angle of unloaded specimen,

θ_i = Included bend angle of loaded specimen $\approx 90°$

Experimental values of springback of AA1050 and AA1050-Fly ash composite are given in Table 4.

4.2 Determination of Springback by Numerical Simulations

To assess the springback outcomes following the bending of the AA1050 and AA1050-Fly ash composite sheet, finite element (FE) simulations are carried out independently for the bending and springback phases utilizing ABAQUS version 6.14-2.

4.2.1 Modeling and Meshing. The framework of numerical simulation was designed to closely replicate the experimental conditions, capturing both the bending and subsequent springback phenomena in the AA1050 and AA1050-Fly ash composite material. The simulations involve the design of a die and punch set, featuring a die-profile radius of 17.5 mm, accounting for sheet thickness clearance, and a punch profile radius of 15 mm. The die and punch set maintains a clearance that disregards localized compression at the bending region. A 90-degree bend angle is specified for both the die and punch. To expedite simulation time, the die and punch are represented as rigid using analytical rigid tools, eliminating the need for meshing rigid surfaces. The mesh details, including elements and nodes, are outlined in Table 3. Same messing has been done for both AA1050 and AA1050-Fly ash composite.

The bending specimen is modeled as deformable, utilizing homogeneous solid shell elements—specifically, CPE4R plane-strain elements featuring four-node bilinear geometry, reduced integration, and hourglass control.

To capture material behavior accurately, true stress–true strain data points post-plastic yielding from uniaxial tension tests on AA1050 and ash composite are employed to assign specific plastic properties to the blank (Ref 14).

4.2.2 Boundary Conditions and Simulations. Within the assembly module, the bending specimen is centrally positioned on the die, with the top surface of the sheet facing the punch, constituting the inner layer. The punch and die surfaces are defined as master surfaces, while the deformable blank is set as slave surface. Contact properties are established, employing penalty contact with a coefficient of friction set at 0.125 for the blank–die interface and 0.05 for the blank–punch interface.

The punch maintains intimate contact with the blank, adjusting its displacement equally to the die depth to prevent localized compression in the deformation zone. Dynamic explicit analysis is employed for all bending simulations in both sheet of AA1050 and ash composite.

Table 3 Details of elements and nodes for the simulations of AA1050 and ash composite

Problem size	
No. of elements	**6000**
No. of nodes	6321
Total no. of variables in the model	12642

For springback evaluation, the initial output file from the simulated bending process history is utilized, with all constraints in the springback model deleted. Figure 7(a) and (b) displays an overlay plot of loaded and unloaded images post-springback simulation for AA1050 and ash composite, respectively.

More springback has been obtained in the sheet of AA1050 as compared to the sheet of AA1050-Fly ash composite in V-bending operation as shown in Table 4. After V-bending when the sheet is unloaded, then due to elastic recovery, there will be obtained some springback. In the case of ash composite, hard and brittle coal ash particles dispersed throughout the soft matrix of AA1050 will reduce the elastic recovery, which is why there will be less springback compared to AA1050.

The simulated springback values for both AA1050 and ash composite are summarized in Table 4.

The experimental value of springback of AA1050-Fly ash composite has been obtained 6.41° which is less than 21.73% from the experimental value of springback of AA1050.

The numerical values of springback for AA1050-Fly ash composite and AA1050 have been obtained 6.17° and 7.82°, respectively. The simulated springback value of ash composite is 21.09% less as compared to AA1050. The difference between experimental results and numerical results of springback is less than 5% for both AA1050 and AA1050-Fly ash composites. A good agreement has been achieved between experimental and numerical results.

4.3 Residual Stress After Springback

Table 5 indicates the residual stress results after springback achieved by simulations and experiments of the AA1050 and AA1050-Fly ash composites. The residual stress resulting from springback on the inner and outer surfaces of the tested sheet is measured using an x-ray device (μ-X360: PULSETEC) for both AA1050 and AA1050-Fly ash composite.

As per Table 5 and Fig. 8, more residual stresses have been observed in the case of ash composite as compared to AA1050 after springback in V-bending. In both the materials, in V-bending after springback, tensile residual stresses are observed at inner side where the punch touches the surface of the sheet and on the contrary compressive residual stresses are observed at outer side where the die touches the surface of the sheet. The experimental values of residual stress (tensile in nature) after springback are observed 36 and 90 MPa at inner side of the sheet for AA1050 and AA1050-Fly ash composite, respectively. These values are very near to the numerical values of residual stress. The percentage error between experimental and numerical values are achieved 6.36% and 2.66 % for AA1050 and ash composite, respectively.

The experimental values of residual stress (compressive in nature) after springback are observed 33 and 83 MPa at outer side of the sheet for AA1050 and AA1050-Fly ash composite, respectively. These values are also very near to the numerical values of residual stress. The percentage error between experimental and numerical values is achieved 5.73% and 5.81% for AA1050 and ash composite, respectively. For both the materials, a very good agreement has been achieved between experimental and numerical values of residual stresses. Due to lower residual stresses, AA1050 alloy is best suited in fluctuating load conditions as compared to ash composite.

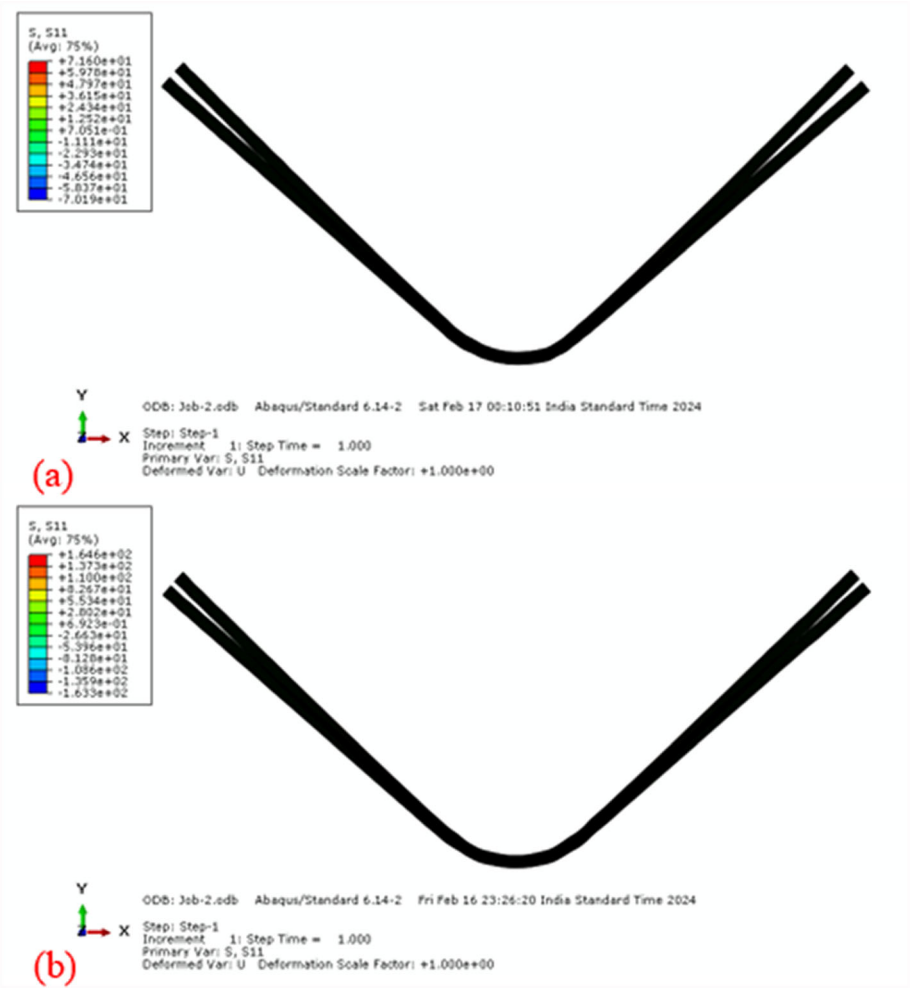


Fig. 7 (a) Loaded and unloaded frames after springback of AA1050 and (b) Loaded and unloaded frames after springback of a AA1050-Fly ash composite

Table 4 Experimental and numerical values of springback of AA1050 and AA1050-Fly ash composite

S. no	Material	Springback		
		Experimental	Numerical	% Error
1	AA1050	8.19	7.82	4.5
2	AA1050-Fly ash composite	6.41	6.17	3.74

Table 5 Experimental and simulation results of residual stress after springback

S.no.	Material	Residual stress (inner side)		Residual stress (outer side)	
		Experimental	Simulation	Experimental	Simulation
1	AA1050	36 MPa	38.29 MPa	− 33 MPa	− 31.11 MPa
2	AA1050-Fly ash composite	90 MPa	87.61 MPa	− 83 MPa	− 78.18 MPa

5. Conclusion

- The incorporation of fly ash has led to a reduction in aluminum production, contributing to a decrease in the generation of greenhouse gases associated with bauxite processing and alumina reduction. The blending of fly ash induces a comprehensive alteration in the mechanical properties of aluminum. This modification manifests as an enhancement in mechanical features such as hardness,

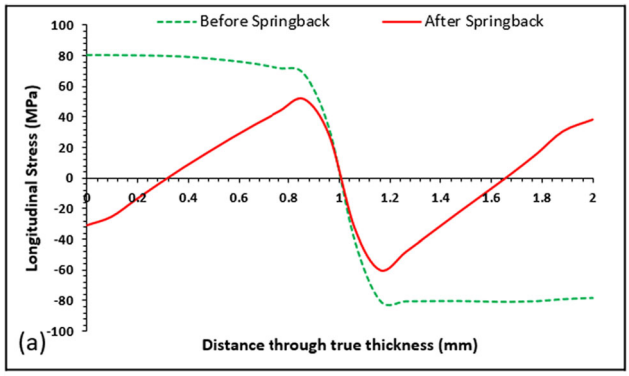


Fig. 8 Variation of longitudinal and residual stress through thickness during bending for (a) AA1050 and (b) AA1050-Fly ash composite

specific strength, and wear resistance. Conversely, properties like toughness, ductility, density, and shrinkage experience a reduction.

- In stir casting technique to manufacture ash composite, surface treatment of fly ash is necessary to increase specific surface absorption area to be properly wet by aluminum for good dispersion with minimum agglomeration and porosity; otherwise, it starts segregating chunks of aluminum by covering it.
- AA1050-Fly ash composite has lower springback than AA1050. The experimental value of springback of AA1050-Fly ash composite has been obtained 6.41° which is less than 21.73% from the experimental value of springback of AA1050. The simulated springback value of ash composite is 21.09% less as compared to AA1050.
- AA1050-Fly ash composite has higher residual stresses than AA1050. The experimental values of residual stress (compressive in nature) after springback are observed 33 and 83 MPa at outer side of the sheet for AA1050 and AA1050-Fly ash composite, respectively. The percentage error between experimental and numerical values is achieved 5.73% and 5.81% for AA1050 and ash composite, respectively.
- A satisfactory concordance has been noted between the numerical simulations and experimental findings for both springback and residual stress.

References

1. S. Buang, S.A. Abdullah, and J. Saedon, Effect of die and punch radius on springback of stainless-steel sheet metal in the Air V-Die bending process, *J. Mech. Eng. Sci. (JMES)*, 2015, **8**, p 1322–1331.
2. K. Dilip Kumar, K.K. Appukuttan, V.L. Neelakantha, and P.S. Naik, Experimental determination of spring back and thinning effect of aluminum sheet metal during L-bending operation, *Mater. Design.*, 2014, **56**, p 613–619.
3. Serope Kalpakjian, and Steven R. Schmid., Manufacturing engineering and technology. Seventh Edition, New Delhi, Pearson Publications, 2018
4. T. Kartik and R. Rajesh, Effect of punch radius and sheet thickness on springback in V-die bending, *Adv. Natural Appl. Sci.*, 2017, **11**(8), p 178–183.
5. J. Ma, X. Tang, Y. Hou, H. Li, J. Lin, and M.W. Fu, Defects in metal-forming: Formation mechanism, prediction and avoidance, *Int. J. Mach. Tools Manuf*, 2025, **207**, p 1–49.
6. P.K. Sharma, V. Gautam, and A.K. Agrawal, Effect of punch profile radius and sheet setting on springback in V-bending of a 2-ply sheet, *Adv. Mater. Process. Technol.*, 2023, **9**(2), p 416–424.
7. Z.L. Zhang, J. Guo, S.Z. Yu, X.D. Li, B.T. Wang, Y. Chang, and H.L. Liu, Modeling of elastic-plastic behaviors of complex-phase steel CP980 and its application in the springback analysis of forming/bending process, *J. Manuf. Process.*, 2024, **127**, p 59–572.
8. H. Cheng, Z. Zhang, M. Ren, and H. Jia, Experimental and numerical simulation studies on V-Shaped bending of Aluminum/CFRP laminates, *Materials*, 2023, **16**, p 4939.
9. C.S. Tjong, *Recent Advances in Discontinuously Reinforced Aluminium Based Metal Matrix Nanocomposites*, Nova Science Publishers, In Composite Materials Research Progress, 2008, p 275–296
10. P.K. Rohatgi, D. Weiss, and N. Gupta, Applications of fly ash in synthesizing low-cost MMCs for automotive and other applications, *J. Manuf.*, 2006, **58**(11), p 71–76.
11. J. Hashim, L. Looney, and M.S. Hashmi, Metal matrix composites: production by the stir casting method, *J. Mater. Process. Technol.*, 1999, **92–93**, p 1–7.
12. D.P.T. Rajan, M.R. Pillai, C.B. Rai, G.K. Satyanarayana, and P.K. Rohatgi, Fabrication and characterization of Al–7Si–0.35Mg/fly ash metal matrix composites processed by different stir casting routes, *Composite Sci. Technol.*, 2007, **67**, p 3369–3377.
13. Q.R. Guo and P.K. Rohatgi, Chemical reactions between aluminum and fly ash during synthesis and reheating of Al–fly Ash composite, *Metall. Mater. Trans. B*, 1999, **29B**, p 519–525.
14. K. Hibbit, *and Sorensen*, Hibbit, Karlsson, Sorensen Inc, ABAQUS/Standard Analysis User's Manual, 2007

Publisher's Note Springer Nature remains neutral with regard to jurisdictional claims in published maps and institutional affiliations.

Springer Nature or its licensor (e.g. a society or other partner) holds exclusive rights to this article under a publishing agreement with the author(s) or other rightsholder(s); author self-archiving of the accepted manuscript version of this article is solely governed by the terms of such publishing agreement and applicable law.

Trans Indian Inst Met (2025) 78:157
https://doi.org/10.1007/s12666-025-03631-w

ORIGINAL ARTICLE

Experimental and Numerical Investigations for Laser Bending of a Three-Ply Clad Sheet Metal

Praveen Kumar Singh[1] · **Vijay Gautam**[1]

Received: 12 March 2025 / Accepted: 6 May 2025
© The Indian Institute of Metals - IIM 2025

Abstract In the present investigations, a three-ply clad SS304/AA1050/SS430 sheet of 2.5 mm thickness was bent using a laser source having a beam diameter not more than the total sheet thickness. An experimental setup with a laser machine with a robotic arm having a rated laser power capacity of 3 kW is used for the experiments. The process parameters such as scan speed, laser power, and number of passes are tuned to achieve the maximum bending angle using a Taguchi approach, and the final parameters are tested with analysis of variance. The nature of residual stress setup in the innermost and outermost layers is also investigated, and the results are correlated with the microstructural features of the layers. Vickers microhardness technique was used to assess the microhardness of deformed and undeformed zones of laser-formed sheet samples at various positions across the length of a narrow heat-affected zone in the bend region. It is observed that the residual stress in the innermost layer is of compressive nature of the order of 220 MPa, whereas the stress in the outermost layer of SS304 is one fourth of that of irradiated inner layer and is also compressive in nature. This distribution of the residual stress could be attributed to the thermal gradient and different coefficients of thermal expansion of the layers.

Keywords Laser forming · Clad sheet metal · Taguchi approach · Residual stress · Microhardness

✉ Vijay Gautam
vijaygautam@dce.ac.in

[1] Department of Mechanical Engineering, Delhi Technological University, Delhi 110042, India

1 Introduction

Laser forming is a highly sophisticated and manageable method with many special application opportunities with minimal distortion. Numerous aspects of the process, including the technique's noncontact nature, variety of materials, high levels of accuracy and reproducibility, relatively high degree of control over energy transmission, and extremely high degrees of flexibility, contribute to the wide range of potential industrial applications [1]. Due to the ability of precise focusing and ease in controlling the beam, lasers are widely used in the manufacture of components of consumer electronics, aerospace systems and vehicles, biomedical instrumentation, automobiles, and in shipbuilding applications [2–4]. Laser bending involves a complicated combination of a heat gradient created by heat source within the scanning region through the materials' thickness and its physio-thermal properties [5]. In this technique, the localized laser-generated temperature difference between the irradiated surface and adjoining material drives the material to expand non-uniformly, resulting in a plastic deformation zone in which thermal stress exceeds the material's yield stress [6]. Three well-established mechanisms for laser bending—temperature gradient, buckling, and upsetting—are dependent on the beam diameter, scan speed, and sheet thickness [7], but only the thermal gradient is being explored in the present study. The process is governed by its various aspects, including laser characteristics (power density, interaction, pulse time), material qualities (thermal conductivity, coefficient of thermal expansion), and target dimensions (thickness, curvature).

Regarding the several challenges associated with the laser forming of components using cold roll-bonded clad sheets, some limited studies have significantly advanced the field to assist the design engineers and are discussed in

Published online: 10 June 2025

detail. Honarpisheh et al. [8] examined the effects of laser bending process parameters, i.e. power, scanning velocity, number of passes, beam diameter, and sheet thickness, on the bend angle and maximum tensile residual stress of titanium–steel layered sheets using simulations and neural network models. It was determined that the bend angle is inversely proportional to scanning speed, beam geometry, and sample thickness. Increasing the scanning velocity, beam diameter, and sample thickness reduced the maximum tensile residual stress. Nejad et al. [9] conducted experimental and numerical studies on laser bending of two-ply sheet. The Taguchi technique is used to determine the ideal laser forming parameters, such as scanning speed, beam power, and beam diameter, on aluminium–copper two-layer clad sheet. The findings demonstrated that the final bending angle has an inverse relationship with the laser beam diameter and scanning speed, whereas the laser beam power has a direct relationship. Mazdak et al. [10] used simulation and experimental methods to examine the parameters influencing the bending angle of two-layer steel-aluminium sheets. ABAQUS software was used to do simulations with linked temperature–displacement analysis. In order to forecast the bending angle based on the important process parameters and their interactions, a mathematical connection based on the regression approach was presented.

Apart from the optimization of laser forming parameters, the resultant residual stresses due to abrupt change in thermal gradient setup on the inner and outer layers of formed components have been discussed by a few researchers. Yilbas et al. [11] examined the thermal stress caused by laser-induced bending of an austenitic stainless steel sheet. The simulation was used to predict the temperature and stress fields. Microstructural changes in the irradiated region were also studied using scanning electron microscopy, energy-dispersive spectroscopy, and X-ray diffraction. The residual stress at the laser-treated region's surface is determined using X-ray diffraction and compared to simulation results. Yilbas and Akhtar [12] evaluated the thermal and residual stress using simulations. It was concluded that the self-annealing effect of laser scanning tracks affects stress and displacement in the workpiece. Zhou et al. [13] carried out the experimental and the simulation of laser peen forming. The findings demonstrated that increasing the number of laser scans and laser peened area produced a higher bending angle. It was concluded that a residual stress gradient in the thickness direction regulates the bending angle caused by laser peening. Tetzel et al. [14], during the incremental laser bending process, calculated the transversal and longitudinal in situ stresses using the material parameters, continuously monitored strains, and temperature. It was found that after ten irradiation cycles, a comparable shaping effect has been obtained for stainless steel and aluminium sheets with respect to the transversal bending angle using only a change in laser power.

Although a number of studies both analytical and experimental are conducted to characterize the residual stresses in monolithic sheets, the research in multi-ply laminate composites is still largely unexplored stressing a need to explore the nature of stress in the components formed by laser processing. The mismatch in the individual layers' thermal expansion coefficients and the development of shrinkage during laser forming cause residual stresses to set up. Therefore, to guarantee the structural integrity of the formed component of a three-ply sheet, it is imperative to analyse the distribution of residual stress.

Laser bending technology creates thin clad sheet metal components and tubes for heat exchangers without the need for tooling or external forces. Laser bending is more flexible than conventional shaping processes as it does not require mechanical contact. Laser bending requires continuous irradiation to precisely bend a sheet to the required angle without springback. For clad sheets, mechanical properties after laser irradiation are critical. The goal of this study is to investigate the bendability of a three-ply clad sheet, as well as the evolution of microstructure and mechanical properties after the laser bending. In the investigations presented here, a three-ply clad SS304/AA1050/SS430 sheet was bent using a laser source having a beam diameter not more than the sheet thickness. The process parameters such as laser power, scan speed, and number of scans are tuned to achieve the (objective) maximum bend angle. The nature of residual stress setup in the innermost and outermost layers is also investigated experimentally, and the results are correlated with the microstructural features of the layers. A Vickers microhardness technique was used to assess the microhardness of deformed and undeformed zones of laser-formed sheets at various positions across the length of a narrow heat-affected zone in the bend region.

2 Methodology

2.1 Sheet Metal

The selection of three-ply sheet metal, 2.5 mm thick, consisting of three layers of varying thicknesses of SS430 and SS304 with AA1050 in the core is based on its superior formability. The SS304/AA1050/SS430 sheet has individual layer thicknesses of 0.4, 1.5, and 0.6 mm, respectively. The chemical composition of individual layer is given in Table 1.

2.2 Experimental Setup

The experimental setup uses a 3 kW-powered laser with a robotic arm-assisted laser welding using fibre laser technology

Table 1 Chemical composition of different layers of clad sheet

Clad layers	C	Mn	Si	Ni	Cr	S	P	Al	Fe
SS304	0.05	1.45	0.82	9.62	18.03	0.009	0.023	0.040	Rest
AA1050	0.18	0.18	0.02	0.15	00.03	0.010	0.015	0.034	Rest
SS430	0.12	0.90	0.67	0.62	17.02	0.023	0.026	0.030	Rest

Table 2 Specifications of the robotic arm

Controlled axes	Load capacity at wrist (kgf)	Repeatability (mm)	Weight of the arm (kgf)	Reach of arm (mm)	Speed range (°/sec)
6	20	±0.08	250	1811	175–550

to create a temperature gradient within the thickness of the samples, allowing bending as shown in the Fig. 1. It is a modern 1064 nm laser wavelength welding system that produces high-quality beam of TEM_{00}. The laser system used in the experiments operates on continuous wave (CW) mode with a Gaussian beam profile also referred to as a single spatial mode. The specification of the robotic arm (FANUC M20iA) is given in Table 2. The work envelope of the robotics arm is approximately 10 m^2, and the composite speed is 9 m/s. It also uses an inline charged coupled device digital camera to teach the scanning path in an easy, rapid, and accurate manner. Another important element is the revolving mirror in the laser head, which helps to rotate the beam's direct route of scanning.

2.3 Design of Experiments

Three laser parameters were used to determine the sheet's effective bending angle, as given in Table 3. To avoid systemic inaccuracies, experiments were carried out in random order according to the design matrix using Taguchi approach. This approach is used as a statistical approach for analysing the outcomes of several tests. The technique is used to identify the main parameters and their optimal concentrations for the laser bending process within the test range.

An orthogonal array is used to simplify the experimental process for fewer trials. In the experiments, three different control parameters were used, each with three values. The goal is to increase the bend angle, which will be used as the response parameter in the experiments.

2.4 Residual Stress

The residual stress induced on the surfaces of SS430 and SS304 was measured after the samples were laser-formed. The experimental setup (model: μ-X360, make: PULSTEC) was utilized to determine residual stresses (Fig. 2). It consists of a sensor unit, a power supply unit, and an adjustable table to hold the specimen, as seen in Fig. 2a. The Cosα method, based on X-ray diffraction, is used for assessing near-surface residual stress before and after laser bending. This technique leverages Bragg's and Hooke's laws to measure residual strain through the inter-planar space, acting as an internal strain gauge. According to Bragg's law, when an X-ray beam is incident on a polycrystalline material, it is diffracted at an angle that is directly related to the wavelength of the X-rays and inversely proportional to the lattice spacing ($d_{\psi\varphi}$) of the material. This method allows for the measurement of residual strains in a single exposure of X-rays, significantly reducing measurement time. This method uses a fundamental equation to calculate residual stresses with various diffraction vectors (n) with respect to the sample coordinate system shown in Fig. 2b.

The strain $\varepsilon_{\psi\varphi}$, at azimuthal angle α from $-\eta$ as illustrated in Fig. 2b, is expressed as follows:

$$\varepsilon_{\psi\varphi} = \varepsilon_{\alpha} = \frac{d_{\psi\varphi} - d_0}{d_0} = n_1^2\varepsilon_x + n_2^2\varepsilon_y + n_3^2\varepsilon_z + n_1n_2\gamma_{xy} + n_2n_3\gamma_{yz} + n_1n_3\gamma_{xz} \quad (1)$$

Incorporating the diffraction vector and Hooke's law, the above expression results as:

$$\varepsilon_{\alpha} = \frac{1+\nu}{E} n_i n_j \varepsilon_{ij} - \frac{\nu}{E}\sigma_{kk(i,j,k=1\text{ to }3)} \quad (2)$$

where ν is Poisson's ratio, E is Young's modulus, and σ_{kk} is a stress component.

The Cosα method utilizes a specific method to determine the residual stresses by using the four strains ($\varepsilon_{\alpha}, \varepsilon_{\alpha+\pi}, \varepsilon_{-\alpha}$ and $\varepsilon_{-\alpha+\pi}$) from the radius of the

Table 3 Control parameters in three levels

S. No	Parameters	Range	Level-I	Level-II	Level-III
1	Laser power (P) in W	700–1100	700	900	1100
2	Scanning speed (v) in mm/s	10–20	10	15	20
3	Scan times (N)	30–50	30	40	50

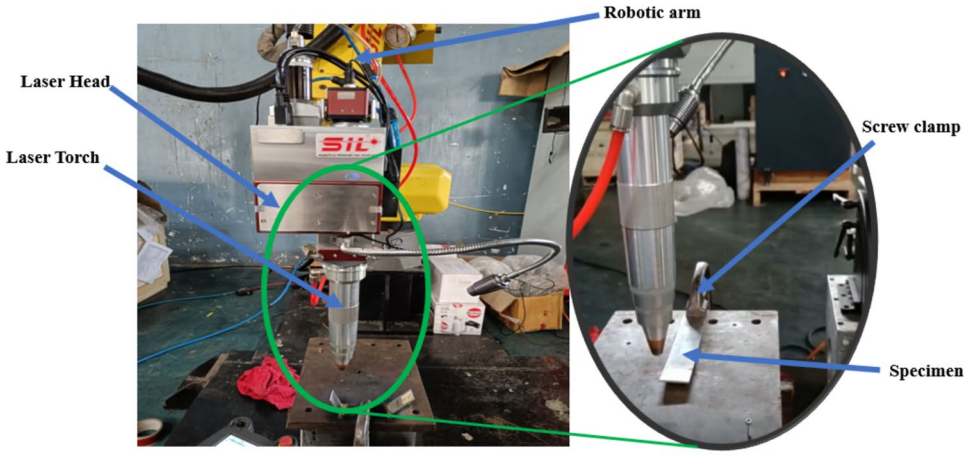


Fig. 1 Experimental setup of laser bending process

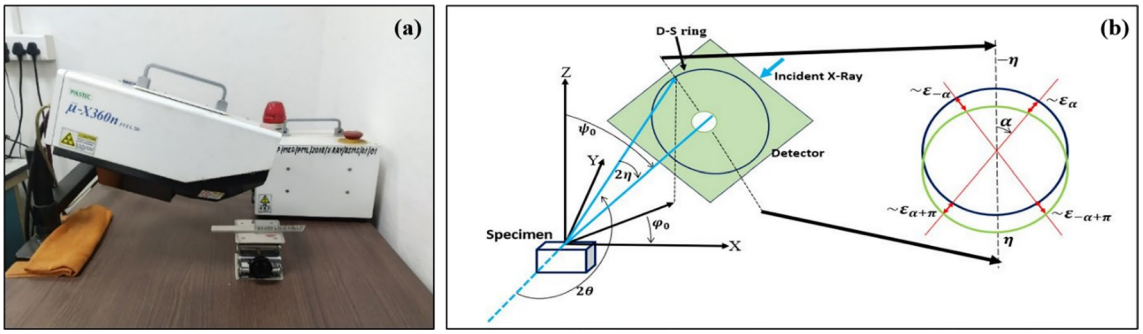


Fig. 2 (**a**) Measurement of residual stress in progress and (**b**) radius of the Debye–Scherrer ring (D-S ring) at an azimuthal angle ($\boldsymbol{\alpha}$)

Debye–Scherrer ring (D-S ring) at an azimuthal angle ($\boldsymbol{\alpha}$) as shown in Fig. 2b. These four strains are incorporated to calculate the strain parameter ε_{α_1} at azimuthal angle $\boldsymbol{\alpha}$, which is expressed as shown below:

$$\varepsilon_{\alpha_1} = \frac{1}{2}\left[\left(\varepsilon_{\alpha} - \varepsilon_{\alpha+\pi}\right) + \left(\varepsilon_{-\alpha} - \varepsilon_{-\alpha+\pi}\right)\right] \tag{3}$$

Incorporating the Hooke's law (Eq. 2) in Eq. 3, the residual stress σ_x is found to be related to the strain parameter ε_{α_1} as follows:

$$\varepsilon_{\alpha_1} = -\frac{1+v}{E}(sin2\eta sin2\psi_0 \cos\alpha)\sigma_x \tag{4}$$

The partial differentiation of strain parameter ε_{α_1} with $cos\alpha$ gives the fundamental equation of residual stress which is expressed as below:

$$\sigma_x = -\left(\frac{E}{1+v}\right)\frac{1}{sin2\eta sin2\psi_0}\left(\frac{\partial\varepsilon_{\alpha_1}}{\partial cos\alpha}\right) \tag{5}$$

The above equation could be rewritten as a product of the elastic constant (K_α) and slope (M_α) of the (ε_{α_1}-$cos\alpha$) plot, which is as shown below:

$$\sigma_x == K\alpha.M\alpha \tag{6}$$

where $K_\alpha = -\left(\frac{E}{1+v}\right)\frac{1}{sin2\eta sin2\psi_0}$, and $M_\alpha = \frac{\partial\varepsilon_{\alpha_1}}{\partial cos\alpha}$

The strain parameter ε_{α_1} is estimated as a linear function of cosα, and using the least-squares method the slope M_α is estimated.

3 Results and Discussion

3.1 Tensile Properties and Microstructure

The tensile properties of the individual layers are given in Table 4. It is observed that SS304 is the strongest and most ductile layer as compared to rest of the layers. AA1050 is the weakest layer with medium ductility slightly less than SS430. SS304 possesses a very high strain hardening exponent indicating an excellent stretchability.

The microstructure in the form of inverse pole maps obtained from electron backscatter diffraction (EBSD) technique of the individual layers of a three-ply clad sheet before laser forming is shown in Fig. 3a, b in grayscale depicting

Table 4 Tensile properties of individual layers

Clad materials	0.2% Yield strength (MPa)	Tensile strength (MPa)	% Elongation	Strength coefficient (MPa), K	Strain hardening exponent. n
SS430	269 ± 41.0	410 ± 18.0	31.51 ± 2.27	749 ± 20.3	0.24
AA1050	59 ± 03.6	68 ± 07.5	21.81 ± 1.73	94.8 ± 13.1	0.11
SS304	289 ± 16.8	636 ± 28.2	78.1 ± 6.95	1556 ± 58.7	0.40

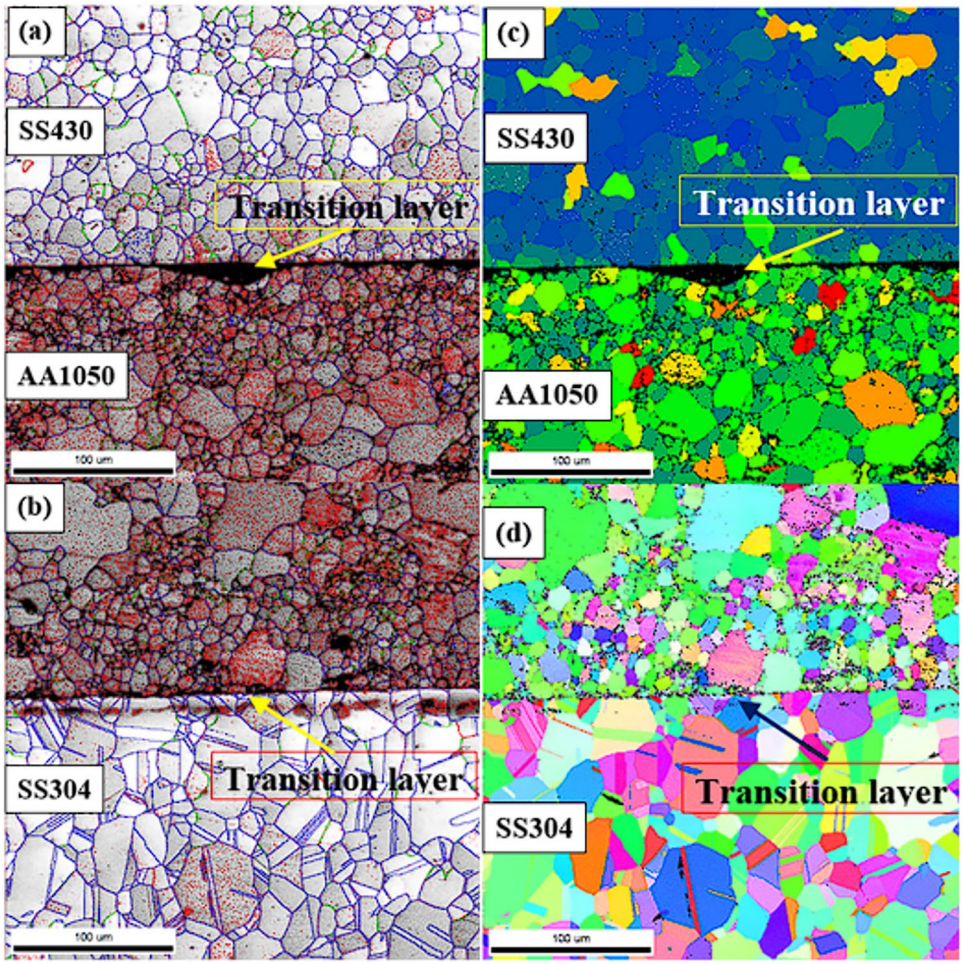


Fig. 3 Microstructures of a three-ply clad sheet (**a**) upper half of SS430 with AA1050 (**b**) bottom half of AA1050 with SS304 showcasing a transition zone between different layers and (**c**) SS430 with AA1050 (**d**) AA1050 with SS304 in colour coded map

SS430 with AA1050 and Fig. 3c, d showing AA1050 with SS304 with a transition zone in colour coded maps in both the cases for better clarity. The inverse pole figures (IPF) in both grey and colour scale taken separately are placed one above the other for an easy understanding. The topmost layer corresponds to SS430 followed by a transition zone between SS430 and AA1050 and then the layer AA1050. The bottommost layer corresponds to SS304 followed by a transition zone between SS304 and AA1050 and then the layer AA1050. It is observed that the grains of SS430 are equiaxed with an average grain size of 8 µm, whereas the grains of SS304 are comparatively coarser with an average grain size of 18 µm. In both the cases of SS430 and SS304 near to the transition zone with AA1050, the grains are much finer. The twinning planes are also observed in the grains of SS304 in almost all the grains which could be attributed to the clad processing technique. IPF maps are a way to visualize the crystallographic orientations of grains in a material.

The grains in AA1050 are mixed type of grains with an average grain size of 5 µm. These grains are much finer towards the transition zone with both SS430 and SS304. Some equiaxed coarse grains are also seen in the middle of the thickness away from the transition zone.

A schematic illustration obtained from trinocular microscope at a magnification of 10 × of a bend sample after irradiation is shown in Fig. 4a depicting the positions of the

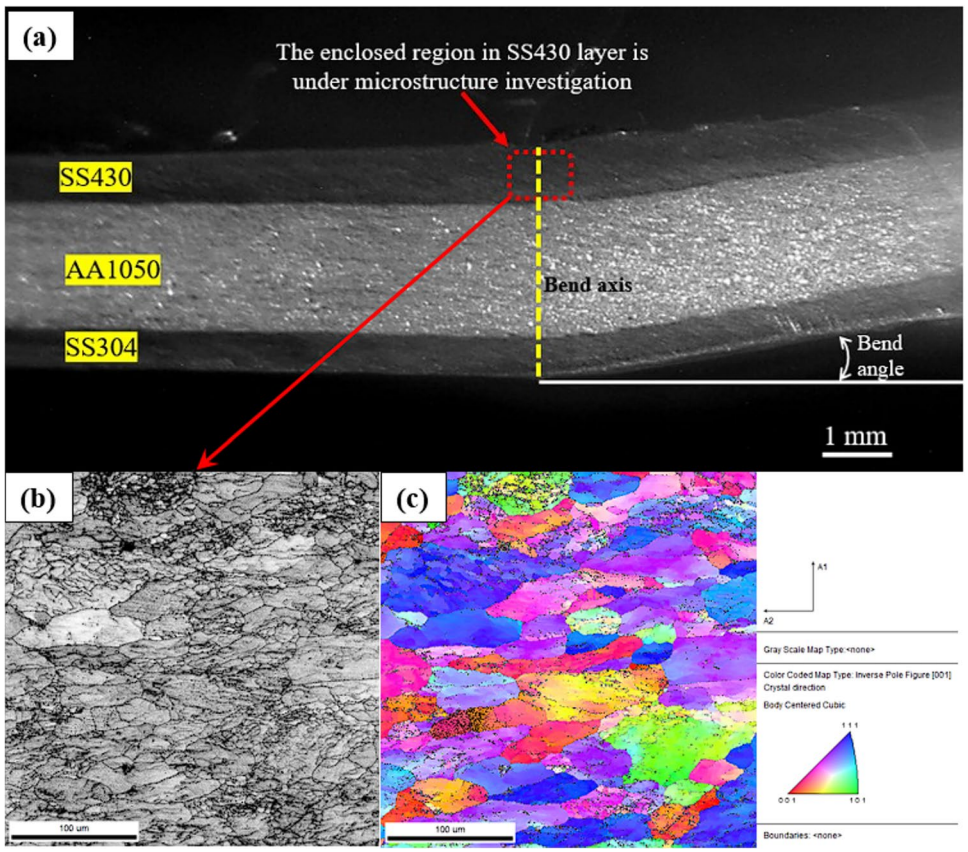


Fig. 4 (**a**) Transverse section of the bend sample; (**b**) microstructure of irradiated layer in grey scale and (**c**) colour coded map showcasing a grain refinement and orientation

different layers in three-ply clad sheet. The microstructure of the irradiated steel layer SS430 after processing with laser is shown in both grey and colour scale inverse pole figure in Fig. 4b, c. The microstructural analysis of the laser-irradiated region of the bent sheet sample, obtained through EBSD, reveals significant insights into the crystallographic texture and grain size distribution. The microstructure of the laser-irradiated zone of bending is greatly refined due to a high surface temperature of a thin layer of SS430, and a very thin heat-affected zone is observed to develop towards the depth of the sheet and finally a banded structure at the outer part of the bending. The average grain size in irradiated zone is observed to be 3 µm.

The inverse pole figure colour coded maps (Fig. 4c), complemented by a grayscale orientation maps (Fig. 4b), indicate a predominant presence of grains oriented along the (111) plane, accounting for approximately 55% of the area. This is followed by grains with [101] and [001] orientations, comprising about 33% and 12%, respectively. Notably, grains with [101] orientation exhibit finer grains, which can be attributed to the localized thermal gradients and rapid cooling rates inherent in the laser bending process. This observation aligns with findings that higher laser scanning speeds can result in much finer grains with varied tilt angles due to altered heat flow dynamics. Conversely, some coarser grains are predominantly associated with the [111] and [001] orientations, suggesting areas of more uniform heat distribution and effective thermal dissipation during laser processing due to multiple scanning. These microstructural characteristics are crucial, as grain orientation and size significantly influence the mechanical properties of materials. Therefore, understanding and controlling the distribution of grain orientations and sizes through laser processing parameters can be instrumental in tailoring material properties for specific applications.

3.2 Optimization of Laser Parameters

Table 3 shows the values of bending angle with the corresponding S/N ratio for combination of 9 runs. It is seen that higher the S/N ratio lesser is the variability. Figure 5 shows the main effect plot for S/N ratios with larger is better as criteria and the optimal values are given below in the form of a regression equation:

$$\begin{aligned}\text{Bend angle (in deg)} = {} & 1.9 + 0.01667\ \text{Power (W)} \\ & + 0.625\text{No. of Scan (N)} \\ & + 0.250\ \text{Scan Speed (mm/s)}\end{aligned} \tag{7}$$

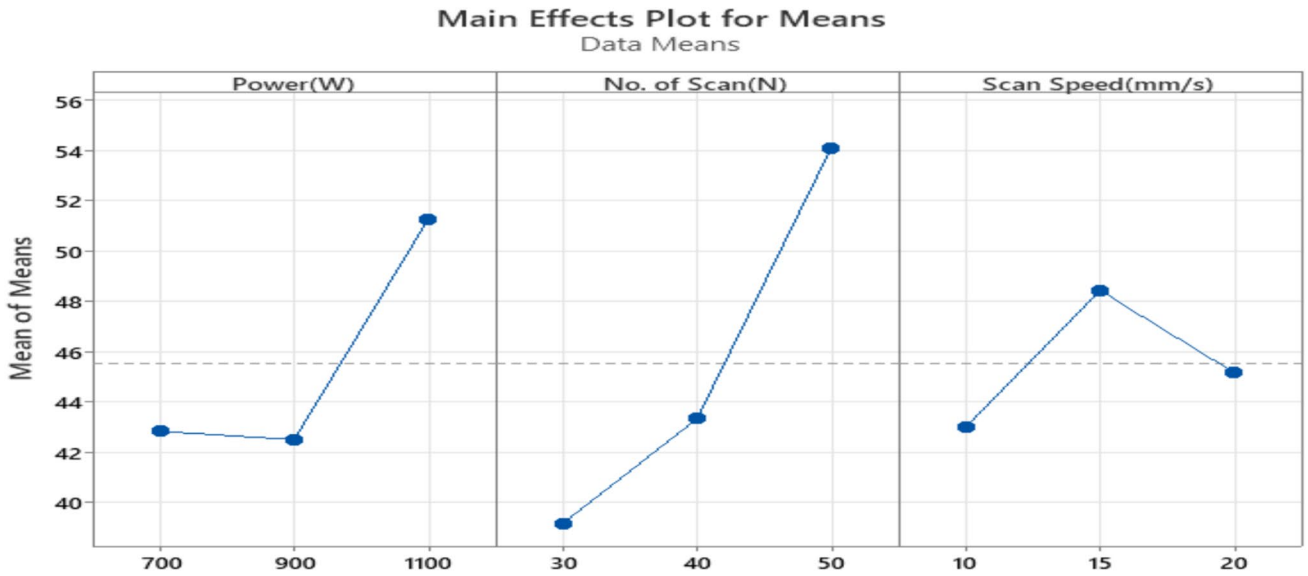


Fig. 5 Mean effect plots

Table 5 Effect of input parameters on the output parameters

S. No	Power (W)	No. of scan (N)	Scan speed (mm/s)	Bend angle (Deg)	S/N ratio
1	700	30	10	37.0	31.3640
2	700	40	15	43.5	32.1491
3	700	50	20	51.0	34.1514
4	900	30	15	39.0	31.8213
5	900	40	20	43.0	32.6694
6	900	50	10	45.5	33.1602
7	1100	30	20	43.5	32.3610
8	1100	40	10	49.5	33.3491
9	1100	50	15	60.8	36.3645

ANOVA is applied with more than 95% confidence level, the parameters having less than 0.05 probability will have most influence on response parameter, and the SN ratio is given in Table 5.

Analysis of variance is given in Table 6. The P value in ANOVA is used to determine degree of significance of the control variables, viz. laser power, number of scan and scanning speed on the response, and the bend angle.

The optimized results are given in Table 7.

3.3 Residual Stress Induced on Innermost and Outermost Layers

Because the laser heating process is nearly instantaneous, high cooling rates occur during the cooling of heated

Table 6 Analysis of variance for bend angle by SN ratios

Source	DF	Seq SS	Adj SS	Adj MS	F	P
Power	2	4.3145	4.3145	2.1573	16.15	0.058
No. of scans	2	8.2520	8.2520	4.1260	30.89	0.031
Scanning speed	2	0.5858	0.5858	0.2929	2.19	0.313
Residual error	2	0.2671	0.2671	0.1336		
Total	8	13.4194				

Table 7 Optimized results

S. No	Parameters	Levels	Bend angle (Experiment)	Bend angle (Predicted)	% Error
1	Laser power (W)	1100	60.5	59.7333	0.7667
2	No. of scans (N)	50			
3	Scanning speed (mm/s)	15			

regions. This results in significant temperature gradients across the irradiation zone while raising thermal strain in that location. Depending on the degree and nature of the stress generated, the irradiated substrate bends towards the workpiece's irradiation surface. The laser heating and cooling processes are quick, and the size of the heat-affected zone shrinks, allowing for the benefits of local laser beam treatment.

All the residual stress measurements using PULSTEC adhere to the ASTM E2860 standard. With reference to the procedure of the standard, the normal stress error should not exceed ± 10% of the mean normal stress value. The residual stress values not meeting to the set standard were dropped, and the experiment was conducted again. The residual stress measured on the surface of SS430 before irradiation is observed to be in the range of 22 to 24 MPa which is compressive in nature. The Debye ring formed on the innermost surface of SS430 indicating various measurement conditions is shown in Fig. 6. The surface residual stresses are evaluated on innermost layer of SS430 and outermost layer

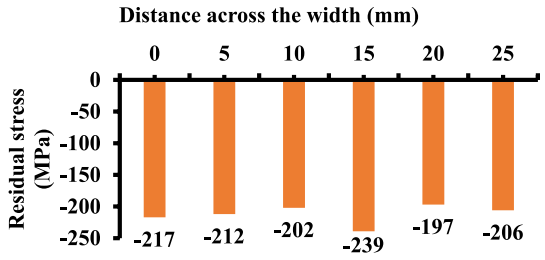


Fig. 7 Residual stress on innermost layer of SS430

of SS304, and the values are plotted across the width of the formed specimen as shown in Figs. 7 and 8. After laser bending, it is observed that the residual stress in the innermost layer is of compressive nature of the order of 220 MPa, whereas the stress in the outermost layer of SS304 is also compressive in nature.

The residual stress is measured on the irradiated surface of SS430 along the width of the samples and the bottom most layer of SS304 in a similar manner. However, the

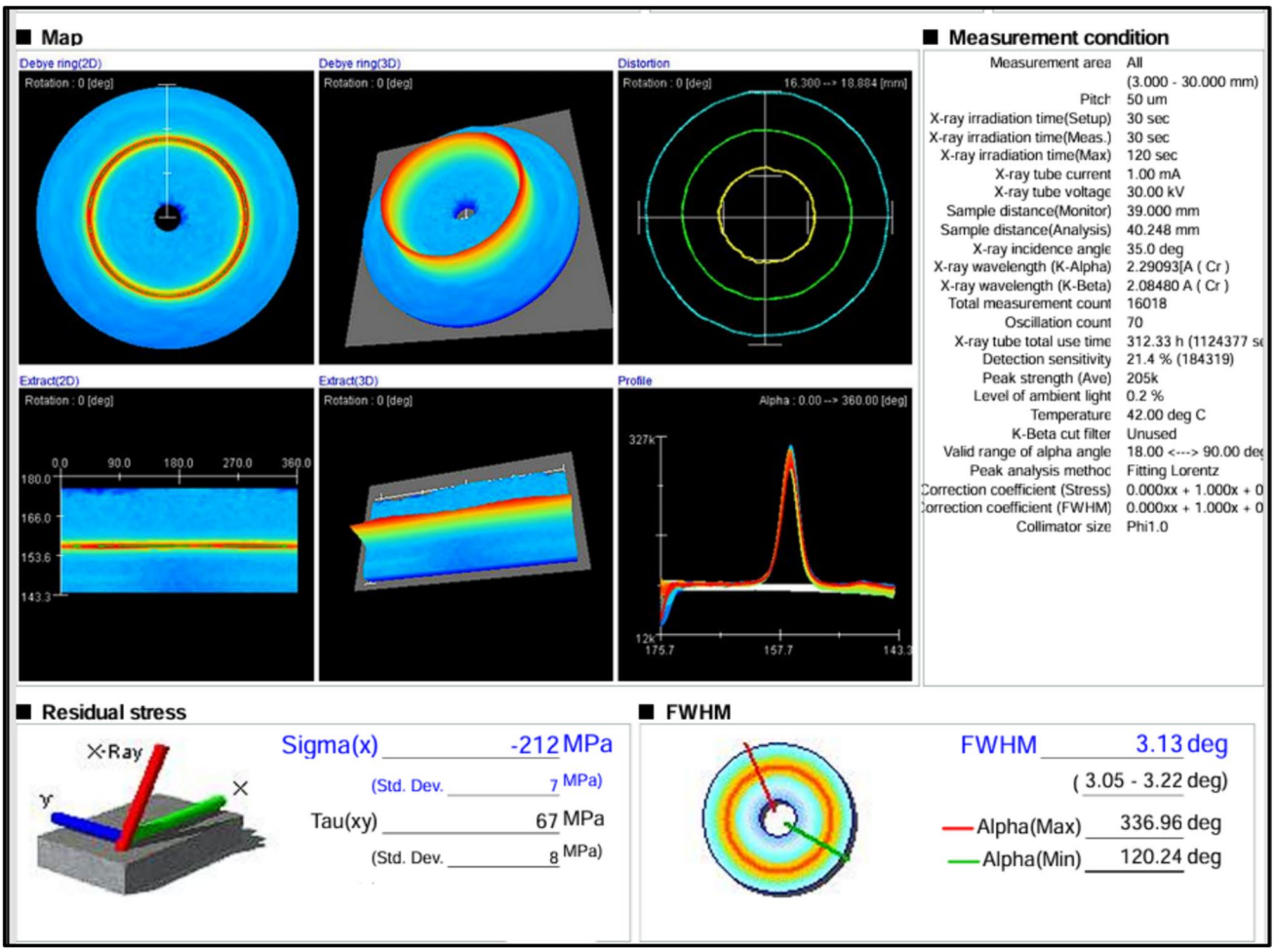


Fig. 6 Debye ring and measurement conditions for residual stress evaluation

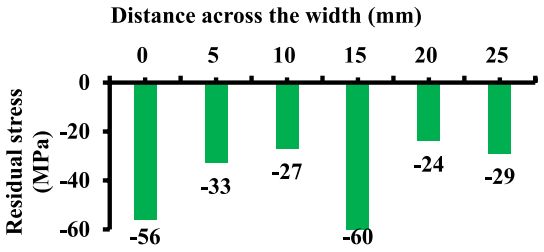


Fig. 8 Residual stress on outermost layer of SS304

residual stress could not be measured in the aluminium layer owing to the non-accessibility to the layer directly below the irradiated surface of SS430. The residual stresses are self-equilibrating stresses which means that the presence of compressive stress will also be accompanied by a tensile residual stress. The determination of these stresses in all the directions is beyond the scope of this discussion. However, the distribution of residual stress is discussed in a simplified manner with experimental evidences. Kotobi and Honarpisheh, 2018, studied that laser bending method will cause high residual stress in the sample of the laser bending of an explosive welded steel–titanium bimetal sample and determined its through-thickness residual stress profile using an experimental slicing method. It supported the presence of both tensile and compressive residual stresses through the thickness of the bimetallic sheet [15].

In the present case of three-ply clad sheet, the residual stress may have resulted on the irradiated surface due to two reasons: i.e. thermal gradient within the thickness of the sheet and a phase transformation in SS430 due to multiple scans. Generally, in a monolithic sheet, considering rapid cooling (quenching), the exterior that cools the fastest would naturally contract due to the decrease in temperature if not for the resistance provided by the warmer interior. This causes tensile stress in the exterior and compressive stress in the interior [16]. But in the present case of a three-ply clad sheet, the distribution of the residual stress could be attributed to the different thermal expansion coefficients of the layers. The thermal gradient developing in the irradiated zone covers the volume of three different materials setting a highest temperature in the irradiated SS430 layer and the aluminium layer directly below the irradiated layer, but the temperature tapers down sharply as it reaches the bottom surface of SS304. The aluminium possessing almost twice the thermal coefficient of expansion than steel and expands accordingly due to the heat gradient. During cooling cycle, SS430 layer tries to shrink but aluminium core which has expanded twice has to contract accordingly but gets restricted by a limited shrink in SS430 layer producing a compressive residual stress in the layer of SS430. The bottommost layer also expands but to a lower strain and applies a bending moment towards the laser beam in the upward direction, but this layer during cooling cycle again does not shrink freely due to higher contraction in the aluminium layer, and this layer of SS304 also develops a compressive residual stress.

Also, the phase transformations due to localized heating and quenching cause a rapid distortion of the crystal lattice, resulting in a misfit between transformed and untransformed regions. This can cause residual stresses and a sudden microscopic and macroscopic shape change [16, 17]. A martensitic transformation may be responsible of a displacive transformation setting a residual compressive stress in the irradiated layer of SS430. There is no phase transformation in the outermost layer SS304 in the laser bent specimens, but the difference of coefficients of thermal expansion may have caused the occurrence of compressive residual stress.

The distribution of microhardness across the length of the affected zone is shown in Fig. 9a. The microindentation on three different layers to evaluate hardness is shown in Fig. 9b.

The bent zone's microhardness in the innermost layer is found to increase by 2.0–2.5 times compared to the untested bend sample, whereas the microhardness in the outermost and middle zone is least affected. The highest microhardness in the innermost layer may be attributed to the grain refinement by a steep thermal gradient followed by fast quenching in air. High-intensity laser irradiation can increase the local microhardness of SS430, despite ferritic stainless steel being regarded a non-hardenable steel [18]. The irradiated surface/treated zone having undergone number of passes exhibits significant grain refining, while the highest microhardness is attributed to chromium carbide precipitates and martensite formation near the grain boundaries. Moving farther from the laser beam centre leads to reduced martensite formation and carbide precipitation, resulting in decreased hardness. The average microhardness of SS304 in the zones away from the laser heating is 220.05 HV, and hardness increases to 250 HV in a heat-affected zone in the outermost layer. The hardness value of SS430 in the zone away from the laser heating is observed to be 300HV on an average basis, but the value is the highest in the laser-irradiated zone and found to be 675HV. The layer AA1050 is observed to be the softest and possesses a hardness value of 33 HV on an average basis, and no kink is observed in the region just below the laser-affected zone.

4 Conclusions

1. The tensile results revealed that SS304 is the strongest and most ductile layer as compared to rest of the layers. AA1050 is the weakest layer with medium ductility slightly less than SS430.

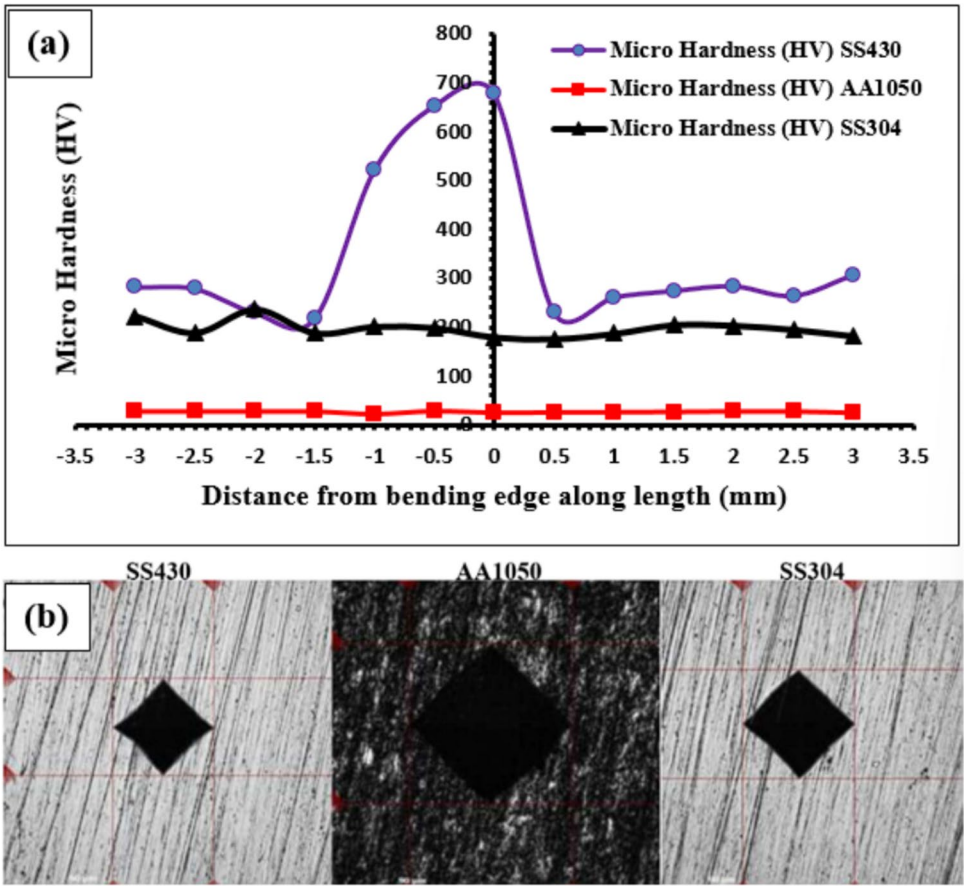


Fig. 9 (**a**) Variation of microhardness across the length of the bend zone and (**b**) microindentation on three different layers

2. Based on the optimized results using Taguchi, the optimum parameters for a maximum bend angle are laser power of 1100 W, number of passes of 50, and scanning speed at 15 mm/s. The maximum bend angle that can be achieved by taking these optimal process parameters is 60.50°.
3. It is observed that the residual stress in the innermost layer is of compressive nature of the order of 220 MPa, whereas the stress in the outermost layer of SS304 is also compressive in nature but almost one fourth the stress of innermost layer. This distribution of the residual stress could be attributed to the different coefficients of thermal expansion of the layers.
4. The hardness value of SS430 in the zone away from the laser heating is observed to be 300HV on an average basis, but the value is the highest in the laser-irradiated zone and found to be 675HV. The layer AA1050 is observed to be the softest and possesses a hardness value of 33 HV on an average basis. The average microhardness of SS304 in the zones away from the laser heating is 220 HV, and hardness increases to 250 HV in a heat-affected zone in the outermost layer.

Acknowledgements Dr. Ashish Sahu, Assistant Professor, IIT Bhilai, and Dr. Ashish Kumar Shukla, Sr. Assistant Professor, NAMTECH Gandhinagar, Gujarat, and M/s S.I. Laser Pvt. Ltd, Pune, are acknowledged. I am writing this acknowledgement to express my deepest gratitude for your invaluable guidance and support throughout my research progress. The authors would like to thank the staff of the OIM and Texture Lab at the IIT Bombay, India, for providing the testing of the EBSD technique and evaluation of the results.

References

1. Majumdar J D, Nath A K, and Manna I, *Materials Science and Engineering: A* **385** (1–2), (2004) 113.
2. Fetene B N, Kumar V, Dixit U S, and Echempati R, *Opt Laser Technol* **99** (2018) 291. https://doi.org/10.1016/j.optlastec.2017.09.014
3. R. Kant, S. N. Joshi, and U. S. Dixit, "Research issues in the laser sheet bending process," in Materials Forming and Machining: Research and Development, Elsevier Inc., 2016, pp. 73. https://doi.org/10.1016/B978-0-85709-483-4.00004-1.
4. Kant R, and Joshi S N, *J Manuf Process* **23** (2016) 135. https://doi.org/10.1016/j.jmapro.2016.05.017
5. A. Behera, P. S. Sahu, and S. K. Patel, "Application of taguchi methodology for optimization of process parameters in laser bending of Al sheet," in Materials Today: Proceedings, Elsevier Ltd, 2019, pp. 2323. https://doi.org/10.1016/j.matpr.2020.02.500.

6. Yadav R, Yadav R, and Kant R, *Optics & Laser Technology* **167** (2023) 109803
7. Geiger M, and Vollertsen F, *CIRP annals* **42** (1), (1993) 301.
8. Kotobi M, Mansouri H, and Honarpisheh M, *Optics & Laser Technology* **116** (2019) 265.
9. Nejad R M, Shojaati Z S H, Wheatley G, and Moghadam D G, *Optics & Laser Technology* **142** (2021) 107233
10. Mazdak S, Sheykholeslami M R, Gholami M, Parvaz H, Najafizadeh M M, Mahmoudi S, and Vanaki A, *Optics & Laser Technology* **157** (2023) 108575
11. Yilbas B S, Arif A F M, and Aleem B A, *Optics & Laser Technology* **44** (2), (2012) 303.
12. Yilbas B S, and Akhtar S S, *Optics & Laser Technology* **61** (2014) 34.
13. Zhou, W. F., Ren, X. D., Wang, C. C., Yang, X. Q., & Larson, E. A. (2018). *Journal of Laser Applications*, *30*(1).
14. Tetzel H, Grden M, and Vollertsen F, *Production Engineering* **7** (2013) 647.
15. Kotobi M, and Honarpisheh M, *The Journal of Strain Analysis for Engineering Design* **53** (3), (2018) 130.
16. Mori, T., & Withers, P. J. (2001). Residual stress: Interphase stresses. *Encyclopedia of Materials: Science and Technology*, 8113.
17. Withers P J, *Reports on progress in physics* **70** (12), (2007) 2211.
18. Wang Z, Dirrenberger J, Lapouge P, and Dubent S, *Materials Science and Engineering: A* **831** (2022) 142205

Publisher's Note Springer Nature remains neutral with regard to jurisdictional claims in published maps and institutional affiliations.

Springer Nature or its licensor (e.g. a society or other partner) holds exclusive rights to this article under a publishing agreement with the author(s) or other rightsholder(s); author self-archiving of the accepted manuscript version of this article is solely governed by the terms of such publishing agreement and applicable law.

Gallium Nitride Gate-All-Around Macaroni Field Effect Transistor (GaN-GAA-MCFET): Biosensor for DNA detection

Shivani Yadav
Electronics & Communication Engg. Department
KIET Group of Institutions
Delhi-NCR, Ghaziabad, India
shivaniyadav.ece@gmail.com

Vijay Thakur
Vinod Dham Centre of Excellence for Semiconductors & Microelectronics
Delhi Technological University
Delhi, India
vijaysinghthakur95@gmail.com

Aapurva Kaul
Electronics & Communication Engg. Department
Delhi Technological University
Delhi, India
aapurva.kaul.91@gmail.com

Amit Das
Electronics & Communication Engg. Department
GLA University
Mathura, India
amitofficial7492@gmail.com

Sonam Rewari
Electronics & Communication Engg. Department
Delhi Technological University
Delhi, India
rewarisonam@gmail.com

Deva Nand
Electronics & Communication Engg. Department
Delhi Technological University
Delhi, India
devkamboj@dce.ac.in

2025 Devices for Integrated Circuit (DevIC) | 979-8-3503-9110-7/25/$31.00 ©2025 IEEE | DOI: 10.1109/DevIC63749.2025.11012312

***Abstract*— The Gallium Nitride Gate-All-Around Macaroni Field Effect Transistor (GaN-GAA-MCFET), a novel Dielectric Modulated Biosensor specifically engineered for DNA detection, is presented in this paper. The primary objective of gallium nitride semiconductor-based FET biosensor is to improve biosensing performance by combining several device engineering techniques such as channel engineering by using macaroni channel, split gate, and oxide engineering. Three split gates are deployed for gate engineering, and the Al_2O_3+HfO_2 stack has been utilized during oxide engineering. The GaN-GAA-MCFET biosensor has two nanocavities which are formed by etching the complete metal and layer of HfO_2 in a specific region to make open cavities to boost structural stability and detection sensitivity. For the DNA biomarkers, the proposed design offers an appealing threshold voltage sensitivity in contrast to the several other devices found in the literature.**

Keywords— GaN-GAA-MCFET, FET, Dielectric Modulation, Biosensor, Open Cavity, Split Gate, Gallium Nitride

I. INTRODUCTION

The detection of biomolecules, particularly nucleic acids (DNA and RNA), using all-electrical methods has garnered significant interest due to its potential applications in gene expression studies, pharmacogenomics, drug development, and molecular diagnostics [1] [2]. Additionally, these techniques hold great promise for use in fields such as forensics, environmental surveillance, and global personalized medicine. Among these, field-effect transistor (FET)-based nucleic acid sensors have emerged as a highly sensitive and label-free platform for biomolecular detection [3], [4]. These sensors offer the advantage of seamless integration with other electronic components, including signal processors and data analyzers, enhancing their functionality. DNA detection is extremely important for molecular biology research and genetic disease diagnostics [5], [6]. Fluorescent biosensors [7], [8], electrochemical biosensors [1], [9]–[11], and field-effect transistor (FET) biosensors [12]–[14] are among the different biosensors that have been created thus far for DNA detection.

Field-effect transistor (FET) biosensor applications have increased substantially in the last several years [15], [16]. These biosensors are becoming more and more popular because of their rapid and label-free biomolecule identification capabilities, low power consumption, affordability, and possibility for on-chip integration [17]. Researchers have examined strategies to improve the sensitivity of biomolecule detection in biosensors by utilizing a range of nanomaterials, as well as other nanostructures, such as FinFETs, nanowires and nanotubes. Nanowire Gate All Around FETs have been increasingly popular due to their improved gate control capabilities [18].

In literature, alternative materials to silicon such as silicon carbide, gallium arsenide and gallium nitride have been investigated to enhance nanowire based FET devices. Because of its substantially larger bandgap than silicon, gallium nitride (GaN) improves thermal stability and reduces GIDL and BTBT [19].

The device becomes structurally unstable due to the existence of a floating gate inside the nanogap. K.W. Lee et al. presented a creative solution through the concept of an underlapped FET biosensor [20]. This underlap structure not only effectively mitigated the problem of structural instability but also demonstrated enhancements in the biosensor's binding probability and sensitivity [14], [21], [22]. Unlike traditional nano-FET, the underlap gate-FET arrangement creates the sensing region by extensively etching the gate metal and oxide.

In place of SiO2, Al_2O_3 can be used as oxide layer in GaN channel FET devices. Advances in epitaxy and deposition techniques have made it feasible to use aluminum oxide (Al_2O_3) as a preferred gate dielectric for GaN semiconductor as channel. Its superior interface compatibility on GaN, and non-

979-8-3503-9110-7/25/$31.00 ©2025 IEEE

Authorized licensed use limited to: DELHI TECHNICAL UNIV. Downloaded on June 04,2025 at 05:23:38 UTC from IEEE Xplore. Restrictions apply.

crystalline structure make it an excellent choice. Further, to enhance the performance of GAAFETs the dielectric layer stack [23] can be opted. Additionally, the gate-stack (GS) design resolves mobility degradation, V_{th} instability, and leakage current, which are frequently encountered issues when applying high-k dielectrics directly [24].

A macaroni channel FET [25]–[27] with dielectric stack, cylindrical surrounding gate underlap and GaN semiconductor channel has been selected in this work for application as biosensor for DNA detection. Early diagnosis of genetic abnormalities, viral infections, and cancer biomarkers are among the medical diagnostic uses of the proposed biosensor, which is designed for very sensitive, label-free DNA detection. The first section briefly outlines the literature. The second section elaborates on device structural characteristics, simulator setup, and the methodology employed. In the third section, significant findings and corresponding graphs are discussed, focusing the impact on electrostatic behaviour and sensitivity while introducing the DNA biomarkers in the open cavity of proposed biosensor device. Finally, the fourth section summarizes key findings.

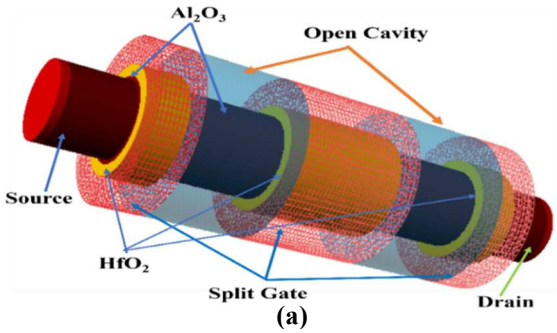
II. DEVICS STRUCTURE

Fig. 1 (a) depicts the 3D view of the structure of the GaN-GAA-MCFET biosensor device. This device incorporates gate oxide stack and split gate engineering with a cylindrical gate all around the channel. Al_2O_3 and HfO2 stack has been used below the three split gates. While to form two-sided nano cavity the gate and HfO2 layer have been etched.

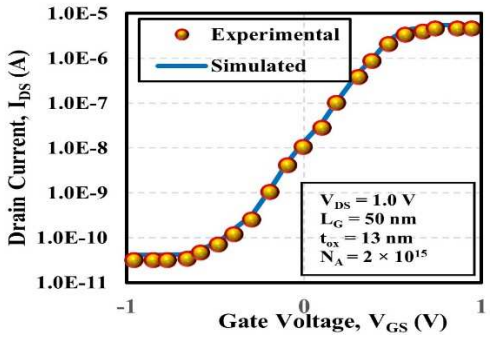
Fig. 1(c) displays the GaN-GAA-MCFET in two dimensions. It also showcases the visual depiction of the DNA biomarker. Gallium nitride (GaN) serves as the semiconductor material for the channel of FET. The inner core of the channel, which has a diameter of 6 nm, is retained hollow, creating a macroni-type channel structure that has been modeled as air in the particular area for simulations. The open cavities are formed by etching HfO_2 and metal having the thickness (t_{cavity}) 10 nm, and the length (L_{cavity}) 20 nm each as depicted in Fig. 1(c). Consequently, a 1 nm layer of Al_2O_3 on the GaN channel works as a sensing site in the proposed biosensor.

TABLE I. BIOSENSOR SPECIFICATIONS AND PARAMETERS

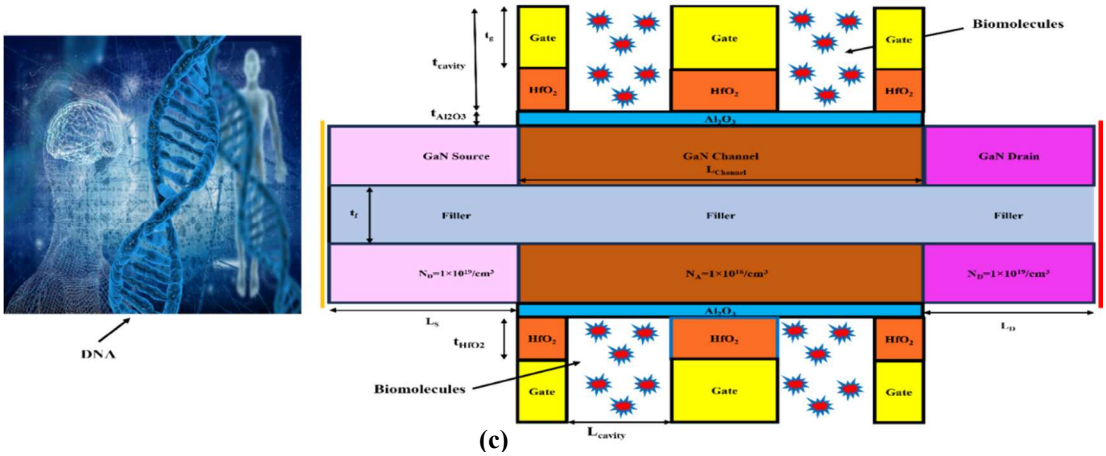
Physical Device Parameter	GaN-GAA-MCFET
Channel Length (nm)	100
Thickness of channel (nm)	14
Length of source/drain (nm)	15
Metal gate work-function (eV)	4.9
Oxide Thickness, Al_2O_3 & HfO_2 (nm)	1.0 & 3.0
Doping of Channel Region, N_D ($/cm^3$)	1×10^{19}
Doping of Source and Drain Region, N_A ($/cm^3$)	1×10^{16}
Thickness of Cavity (nm)	10
Gate Thickness (nm)	7
Length of Cavity (nm)	20
HfO_2 and Al_2O_3 dielectric constants	22.0 & 9.8



(a)



(b)



(c)

Fig. 1. (a) GaN-GAA-MCFET biosensor: A 3-Dimensional View (b) Calibration of proposed device with experimental data [28] (c) GaN-GAA-MCFET biosensor: A 2-Dimensional View

Authorized licensed use limited to: DELHI TECHNICAL UNIV. Downloaded on June 04,2025 at 05:23:38 UTC from IEEE Xplore. Restrictions apply.

The specifics of the GaN-GAA-MCFET biosensor, encompassing device dimensions, material type, and nanocavity dimensions, are outlined in Table I. The GaN-GAA-MCFET biosensor uses a label-free detection method that uses electrostatic interactions rather than surface functionalization to capture DNA biomolecules. However, selectivity and stability can be improved by various surface functionalization techniques including polymer coatings, crosslinking, and silane chemistry.

Numerical simulations are conducted using an ATLAS 3D device simulator, incorporating various models such as the Shockley–Read–Hall (SRH), concentration-dependent mobility (CONMOB), parallel electric field-dependent mobility (FLDMOB), band gap narrowing (BBT.STD)[29], and drift diffusion models. The TCAD simulation setup is validated by calibrating the proposed device with experimental work [28], as shown in Fig. 1 (b).

III. Results and Discussion

DNA detection using the GaN-GAA-MCFET biosensor have been investigated, focusing on two specific biomarkers: ssDNA and dsDNA. The ssDNA, dsDNA are the charged biomarkers having both dielectric constant value and surface charge value. For DNA detection, the simulation considers single-stranded DNA (ssDNA) with a dielectric constant K = 2 and a surface charge density Q_f = -1 × 10^{11} C/cm^2 [30]. Conversely, double-stranded DNA (dsDNA) is simulated with a dielectric constant K = 8 and a surface charge density Q_f = -5 × 10^{11} C/cm^2 [30].

A. Analysis of Electrostatic characteristics of GaN-GAA-MCFET

Electrostatic behavior of the device, comprising surface potential, electric field, electron velocity, and drain current, is affected by the immobilization of the DNA biomarkers in the open nanocavity.

In Figure 2, the surface potential along the length of the channel is displayed. when air (no biomolecules), ssDNA and dsDNA biomarkers are introduced in the open nanocavity. It cab be observed that the potential is the highest for no biomolecule case. It further declines for negatively charged DNA biomarkers for dsDNA and ssDNA, respectively. This alteration corresponds with the shift in the negative charge and dielectric characteristics linked to both dsDNA and ssDNA biomarkers. The effective gate oxide capacitance varies in tandem with changes in the dielectric constant. The interaction between the charges in the channel and the charged biomolecules alters the surface potential. Electrons will be attracted to positively charged biomolecules and holes will be repelled by negatively charged biomolecules. The charge density in the channel is altered by this interaction, which causes the surface potential to change. Since ssDNA and dsDNA are negatively charged biomolecules so the surface potential decreases.

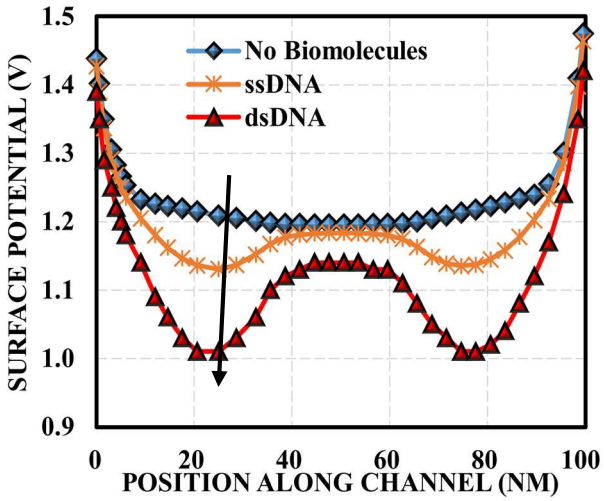


Fig. 2. Surface potential variation of GaN-GAA-MCFET biosensor

In Fig. 3, the plot illustrates the drain current (I_{DS}) in logarithmic scale on Y axis and V_{GS} on X axis. Logarithmic drain current plot clearly depicts the drain current value at V_{GS} = 0V. This current is known as the OFF current. Ideally, the OFF current should be zero and practically it should be as low as possible. There is a decrease in OFF current from the case where biomolecules are absent to the existence of ssDNA and subsequently to dsDNA biomarkers. This happens as the increasing value of dielectric constant and negative charge on biomolecules increases the capacitive coupling and gate control on the channel improving the subthreshold region characteristics.

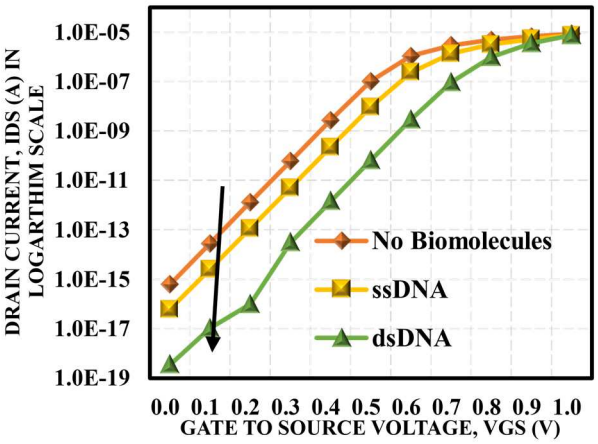


Fig. 3. I_D-V_{GS} characteristics of GaN-GAA-MCFET with different biomarkers

B. DNA Detection Sensitivity Analysis of GaN-GAA-MCFET

A biosensor's sensitivity is usually measured by evaluating the proportionate change in a electrical parameter. Sensitivity (S_P), stated mathematically, is the absolute difference between the value of the electrical parameter when biomolecules are absent and when ssDNA and dsDNA biomolecules are immobilized inside the cavity.

$$S_P = |P_{No\ Biomolecule} - P_{with\ ssDNA\ or\ dsDNA}| \quad (1)$$

Authorized licensed use limited to: DELHI TECHNICAL UNIV. Downloaded on June 04,2025 at 05:23:38 UTC from IEEE Xplore. Restrictions apply.

At V_{GS} = 1.0 V, the drain current value is known as the drain ON current. The drain ON current sensitivity S_{ID} can be calculated using equation (1). Fig. 4 clearly demonstrates that, dsDNA exhibits a higher S_{ID} (2.03 µA) in comparison to the S_{ID} for ssDNA (0.96 µA). The reason for this variation is that dsDNA has a much higher dielectric constant and negative charge.

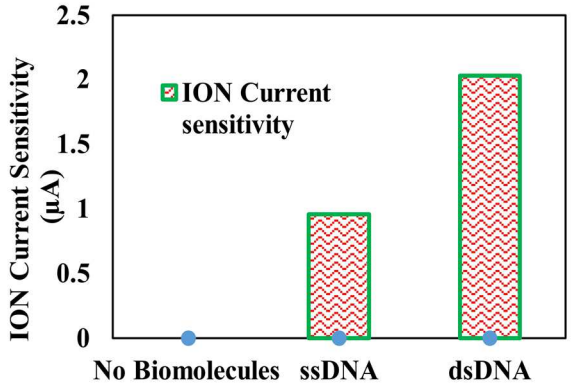


Fig. 4. ION current sensitivity (S_{ID}) and ION current of GaN-GAA-MCFET

Fig. 5 displays the influence of DNA biomarkers upon the threshold voltage and threshold voltage sensitivity (S_{Vth}). Negatively charged biomolecules in the cavity generate opposing electric fields, counteracting the positive gate voltage. This interaction raises the threshold voltage by necessitating a higher gate-to-source voltage to offset the repulsion. According to equation (1), The GaN-GAA-MCFET biosensor exhibits remarkably high V_{th} sensitivity, with values of 122.7 mV and 263.71 mV for ssDNA and dsDNA respectively.

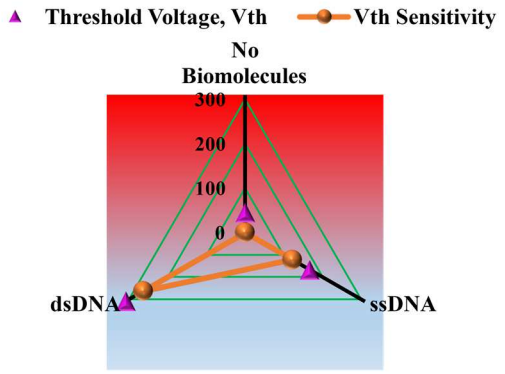


Fig. 5. Threshold Voltage (V_{th}) and V_{th} sensitivity of GaN-GAA-MCFET

To evaluate the GaN-GAA-MCFET biosensor against other FET biosensors in recent literature with comparable structural specifications, such as the GaN-GME-DE-SNW-FET [34], GC-GAA-NWFET [35], DG-6H-SiC SB-FET [36], and DM DPDG-TFET [37] biosensor, a comparative threshold voltage sensitivity performance study has been carried out in Fig. 6. Both at low and high biomolecule charge values the results clearly demonstrate that the GaN-GAA-MCFET biosensor has greater sensitivities to biomolecule detection.

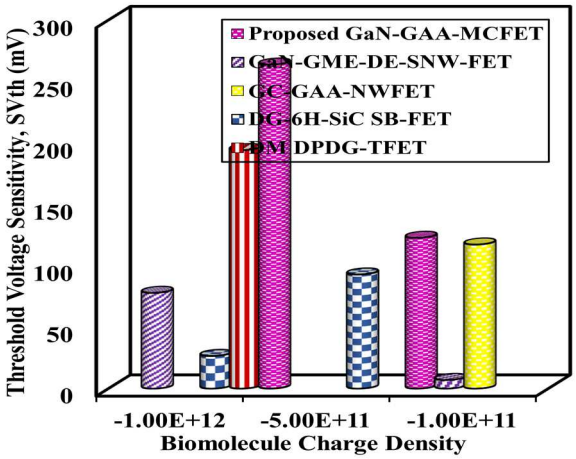


Fig. 6. Threshold Voltage sensitivity comparison of GaN-GAA-MCFET Biosensor with Similar Works in Literature

IV. CONCLUSION

The potential of the GaN-GAA-MCFET biosensor for the identification of ssDNA and dsDNA biomarkers have been thoroughly examined in this paper. In comparison to the Gate-All-Around FET and TFET with a silicon, silicon carbide and even a gallium nitride channel in literature, the proposed Gate-All-Around FET with a GaN channel with macaroni structure performs better as a device for short channel effects and as a FET biosensor in DNA biomolecule detection. The sensor demonstrates a threshold voltage sensitivity of 263.7 mV for dsDNA. The biosensor has also been evaluated for changes in surface potential, drain current, and electric field. Biosensor design is improved by innovative device engineering methods such as open cavity structure, gallium nitride macaroni channel, triple split gate, and high K and low K oxide integration. The exceptional sensitivity and structural resilience of the GaN-GAA-MCFET biosensor establish it as a viable option for the DNA detection.

REFERENCES

[1] X. Wang, W. Deng, L. Shen, M. Yan, S. Ge, and J. Yu, "A sensitive quenched electrochemiluminescent DNA sensor based on the catalytic activity of gold nanoparticle functionalized MoS2," *New J. Chem.*, vol. 39, no. 10, pp. 8100–8107, 2015, doi: 10.1039/c5nj01451d.

[2] S. Yadav and S. Rewari, "Analytical modeling and numerical simulation of graded JAM Split Gate-All-Around (GJAM-SGAA) Bio-FET for label free Avian Influenza antibody and DNA detection," *Microelectronics J.*, vol. 142, p. 106011, 2023, doi: 10.1016/j.mejo.2023.106011.

[3] A. Star, E. Tu, J. Niemann, J. C. P. Gabriel, C. S. Joiner, and C. Valcke, "Label-free detection of DNA hybridization using carbon nanotube network field-effect transistors," *Proc. Natl. Acad. Sci. U. S. A.*, vol. 103, no. 4, pp. 921–926, 2006, doi: 10.1073/pnas.0504146103.

[4] K. Bohmann *et al.*, "Environmental DNA for wildlife biology and biodiversity monitoring," *Trends Ecol. Evol.*, vol. 29, no. 6, pp. 358–367, 2014, doi: 10.1016/j.tree.2014.04.003.

[5] A. Samanta and I. L. Medintz, "Nanoparticles and DNA-a powerful and growing functional combination in bionanotechnology," *Nanoscale*, vol. 8, no. 17, pp. 9037–9095, 2016, doi: 10.1039/c5nr08465b.

[6] L. Shen, X. Zhang, and W. Jin, "Signal amplification based on DNA hybridization-dehybridization reaction on the surface of magnet

Authorized licensed use limited to: DELHI TECHNICAL UNIV. Downloaded on June 04,2025 at 05:23:38 UTC from IEEE Xplore. Restrictions apply.

submicrobeads for ultrasensitive DNA detection," *Analyst*, vol. 137, no. 20, pp. 4849–4854, 2012, doi: 10.1039/c2an35587f.

[7] H. Kim, J. Ju, H. N. Lee, H. Chun, and J. Seong, "Genetically encoded biosensors based on fluorescent proteins," *Sensors (Switzerland)*, vol. 21, no. 3, pp. 1–18, 2021, doi: 10.3390/s21030795.

[8] R. M. De Lorimier *et al.*, "Construction of a fluorescent biosensor family," *Protein Sci.*, vol. 11, no. 11, pp. 2655–2675, 2002, doi: 10.1110/ps.021860.

[9] L. H. Pan, S. H. Kuo, T. Y. Lin, C. W. Lin, P. Y. Fang, and H. W. Yang, "An electrochemical biosensor to simultaneously detect VEGF and PSA for early prostate cancer diagnosis based on graphene oxide/ssDNA/PLLA nanoparticles," *Biosens. Bioelectron.*, vol. 89, pp. 598–605, 2017, doi: 10.1016/j.bios.2016.01.077.

[10] L. Q. Luo, Z. Zhang, Y. P. Ding, D. M. Deng, X. L. Zhu, and Z. X. Wang, "Label-free electrochemical impedance genosensor based on 1-aminopyrene/graphene hybrids," *Nanoscale*, vol. 5, no. 13, pp. 5833–5840, 2013, doi: 10.1039/c3nr01237a.

[11] M. Mascini, I. Palchetti, and G. Marrazza, "DNA electrochemical biosensors," *Anal. Bioanal. Chem.*, vol. 369, no. 1, pp. 15–22, 2001, doi: 10.1007/s002160000629.

[12] A. Das, B. K. Kanaujia, V. Nath, S. Rewari, and R. S. Gupta, "Impact of Reverse Gate Oxide Stacking on Gate All around Tunnel FET for High Frequency Analog and RF Applications," *2020 IEEE 17th India Counc. Int. Conf. INDICON 2020*, 2020, doi: 10.1109/INDICON49873.2020.9342175.

[13] A. Das, S. Rewari, B. K. Kanaujia, S. S. Deswal, and R. S. Gupta, "Ge/Si interfaced label free nanowire BIOFET for biomolecules detection - analytical analysis," *Microelectronics J.*, vol. 138, 2023, doi: 10.1016/j.mejo.2023.105832.

[14] S. K. Vijay Thakur, Anil Kumar, "Numerical Modeling and Performance Analysis of underlap gate cavity integrated reconfigurable silicon nanowire schottky barrier transistor biosensors," *Appl. Phys. A Mater. Sci. Process.*, 2024.

[15] S. Yadav and S. Rewari, "Dielectric Modulated Gallium-Arsenide Gate-All-Around Engineered Field Effect Transistor (GaAs-GAAE-FET) Biosensor for Breast Cancer Detection," *Proc. - Int. Conf. Comput. Power, Commun. Technol. IC2PCT 2024*, pp. 1553–1557, 2024, doi: 10.1109/IC2PCT60090.2024.10486515.

[16] S. Yadav and S. Rewari, "Trench Gate JAM Dielectric Modulated Nanowire FET (TG-JAM-DM-NWFET) Biosensor," *Proc. 2022 IEEE Int. Conf. Electron Devices Soc. Kolkata Chapter, EDKCON 2022*, pp. 23–28, 2022, doi: 10.1109/EDKCON56221.2022.10032912.

[17] A. Goel, S. Rewari, S. Verma, and R. S. Gupta, "Modeling of shallow extension engineered dual metal surrounding gate (SEE-DM-SG) MOSFET gate-induced drain leakage (GIDL)," *Indian J. Phys.*, vol. 95, no. 2, pp. 299–308, 2021, doi: 10.1007/s12648-020-01704-8.

[18] S. Yadav and S. Rewari, "Dual metal dual layer GAA NW–FET (DMDL–GAA–NW–FET) biosensor for label free SARS-CoV-2 detection," *Microsyst. Technol.*, 2023, doi: 10.1007/s00542-023-05560-4.

[19] S. Yadav, A. Das, and S. Rewari, "Dielectrically-Modulated GANFET Biosensor for Label-Free Detection of DNA and Avian Influenza Virus: Proposal and Modeling," *ECS J. Solid State Sci. Technol.*, vol. 13, no. 4, p. 047001, 2024, doi: 10.1149/2162-8777/ad3364.

[20] K. W. Lee *et al.*, "An underlap field-effect transistor for electrical detection of influenza," *Appl. Phys. Lett.*, vol. 96, no. 3, 2010, doi: 10.1063/1.3291617.

[21] A. Kumar, V. Thakur, S. Kumar, S. Kale, and K. R. Singh, "Sensitivity Investigation of Underlap Gate Cavity-Based Reconfigurable Silicon Nanowire Schottky Barrier Transistor for Biosensor Application," *Silicon*, 2024, doi: 10.1007/s12633-024-03125-2.

[22] V. Thakur, A. Kumar, and S. Kale, "Analytical modeling of spacer-engineered reconfigurable silicon nanowire Schottky barrier transistor for biosensing applications," *Micro and Nanostructures*, vol. 188, 2024, doi: 10.1016/j.micrna.2024.207799.

[23] A. Das, S. Rewari, B. K. Kanaujia, S. S. Deswal, and R. S. Gupta, "Physics based numerical model of a nanoscale dielectric modulated step graded germanium source biotube FET sensor: modelling and simulation," *Phys. Scr.*, vol. 98, no. 11, 2023, doi: 10.1088/1402-4896/acf4c9.

[24] S. Yadav and S. Rewari, "Numerical Simulation of Hetero Dielectric Trench Gate JAM Gate-All-Around FET (HDTG-JAM-GAAFET) for Label Free Biosensing Applications," *ECS J. Solid State Sci. Technol.*, vol. 12, no. 12, p. 127008, 2023, doi: 10.1149/2162-8777/ad161f.

[25] A. Kaul, S. Rewari, and D. NAND, "Double Metal Gate Macaroni Nanowire FET (DMGM-NFET) for Improved Performance and Off-State Leakage Reduction," *ECS J. Solid State Sci. Technol.*, 2024, doi: 10.1149/2162-8777/ad775d.

[26] A. Kaul, S. Rewari, and D. Nand, "Hetero-dielectric macaroni channel cylindrical gate all around field effect transistor (HD-MC CGAA FET) for reduced gate leakage analog applications," *Microsyst. Technol.*, 2023, doi: 10.1007/s00542-023-05577-9.

[27] A. Kaul, S. Rewari, and D. Nand, "Macaroni Channel-Nanowire-Field Effect Transistor (MC-NW-FET) for Gate Induced Drain Leakage (GIDL) Reduction Application," *Proc. 2022 IEEE Int. Conf. Electron Devices Soc. Kolkata Chapter, EDKCON 2022*, pp. 35–38, 2022, doi: 10.1109/EDKCON56221.2022.10032964.

[28] S. J. Choi, D. Il Moon, S. Kim, J. P. Duarte, and Y. K. Choi, "Sensitivity of threshold voltage to nanowire width variation in junctionless transistors," *IEEE Electron Device Lett.*, vol. 32, no. 2, pp. 125–127, 2011, doi: 10.1109/LED.2010.2093506.

[29] A. Kaul, S. Rewari, and D. Nand, "Macaroni Channel-Nanowire-Field Effect Transistor (MC-NW-FET) for Gate Induced Drain Leakage (GIDL) Reduction Application," in *Proceedings of 2022 IEEE International Conference of Electron Devices Society Kolkata Chapter, EDKCON 2022*, 2022, pp. 35–38. doi: 10.1109/EDKCON56221.2022.10032964.

[30] K. Tamersit and F. Djeffal, "Double-Gate Graphene Nanoribbon Field-Effect Transistor for DNA and Gas Sensing Applications: Simulation Study and Sensitivity Analysis," *IEEE Sens. J.*, vol. 16, no. 11, pp. 4180–4191, 2016, doi: 10.1109/JSEN.2016.2550492.

Authorized licensed use limited to: DELHI TECHNICAL UNIV. Downloaded on June 04,2025 at 05:23:38 UTC from IEEE Xplore. Restrictions apply.

Gig-economy integration: organizational development strategies for a fluid workforce

Uday Sai Garavandala

Uday Sai Garavandala is based at Delhi Technological University, Delhi, India.

Abstract

Purpose – *This paper develops a conceptual framework for integrating gig-economy workers (''gig nodes'') into traditional organizational development (OD) processes. It aims to address the current gap in OD models that largely exclude freelancers and platform-based labor by specifying mechanisms to align gig workers' identities, foster community bonding and enable effective knowledge transfer within fluid workforce architectures.*

Design/methodology/approach – *Using a bibliographic (scoping review) method, the author systematically synthesize literature from OD, gig-economy studies and boundary-spanning theory. The author identify thematic clusters and derive propositions for embedding gig nodes into existing OD stages entry, development and exit culminating in a multi-layered integration framework.*

Findings – *The proposed framework comprises three interlocking dimensions: Identity Integration aligning gig workers' self-concept with organizational culture; Community Bonding leveraging virtual and in-person rituals to foster belonging; and Knowledge Transfer establishing codified and social-learning channels. The author also outline boundary-spanning roles and feedback loops that sustain engagement and performance.*

Originality/value – *This is among the first studies to offer a theory-driven OD model tailored to gig-economy contexts. By merging bibliographic insights with boundary-spanning concepts, it extends OD scholarship to accommodate decentralized, project-based labor. Practitioners gain actionable design principles for inclusive change interventions, while researchers receive a foundation for empirical validation.*

Keywords *Organizational development, Gig economy, Fluid workforce, Identity integration, Boundary-spanning mechanisms*

Paper type *Conceptual paper*

1. Introduction

The emergence and rapid expansion of the gig economy represents a significant reconfiguration of the global labor market. Characterized by short-term, task-based and digitally mediated employment, gig work challenges the foundational assumptions of long-term employment, organizational loyalty and static hierarchies that have historically informed organizational development (OD) practices. As platforms like Uber, Upwork, TaskRabbit and Freelancer.com restructure how labor is sourced and managed, traditional OD frameworks rooted in internal, full-time human capital systems are rendered increasingly obsolete (Bateyo, 2025; Kadolkar *et al.*, 2024).

This transformation necessitates a rigorous reassessment of how organizations design work, cultivate culture, manage learning and assess performance across a heterogeneous workforce that includes both permanent employees and contingent gig workers. More importantly, it raises critical questions: How can OD strategies become more adaptive, inclusive and ethically grounded to accommodate a fluid workforce? How can organizations unlock the latent value of gig contributors without compromising cohesion, trust and

DOI 10.1108/SHR-05-2025-0047
© Emerald Publishing Limited, ISSN 1475-4398

strategic alignment? To address these questions, this paper synthesizes existing literature across management, labor economics, information systems and sociology (Sharma and Sharma, 2019; Nayak *et al.*, 2024; Jayakarthika *et al.*, 2024) to propose a gig-responsive OD framework grounded in both theoretical rigor and empirical relevance.

2. Expanded literature review

2.1 Organizational development in a gig economy context

The reconfiguration of labor structures due to gig work has engendered a new wave of inquiry into how OD must evolve to manage distributed, flexible and autonomous contributors. Scholars such as Bateyo (2025) and Nayak *et al.* (2024) argue that OD can no longer be confined to internal culture building and employee training but must instead foster porous organizational boundaries, temporary project alliances and continuous capability mapping. Sharma and Sharma (2019) extend conversation by emphasizing the spiritual and psychological dimensions of gig work, proposing models of motivation and belonging that transcend contractual engagement.

2.2 Digital platformization and organizational development realignment

The platformization of labor introduces significant shifts in the technical infrastructure of OD. Studies by Matriano *et al.* (2025) and Jayakarthika *et al.* (2024) advocate for the integration of AI, machine learning and data analytics into HR processes, enabling real-time skills assessments, performance tracking and demand forecasting. These interventions allow for the modularization of learning and decentralization of decision-making, fostering greater inclusivity and responsiveness. Viswanathan (2022) corroborates these findings in the context of supply chains, demonstrating how gig-enabled logistics networks benefit from platform-based task orchestration and real-time feedback loops.

2.3 Trust, fairness and psychological contracts

The gig economy destabilizes conventional psychological contracts between employer and worker. Trust, long viewed as a function of tenure, communication and visibility, must now be cultivated through algorithmic transparency, equitable metrics and distributed authority. Nath (2020) and Subramony *et al.* (2024) argue that opaque rating systems and unilateral algorithmic decisions erode gig workers' sense of justice, while Zheng and Yang (2020) emphasize the need for participatory governance and accessible dispute resolution. These concerns have led to proposals for hybrid governance models where human managers and intelligent systems co-design rules, monitor behavior and resolve conflict.

2.4 Cross-disciplinary models of inclusion

The multidimensional exclusion of gig workers based on geography, platform access, skill signaling and feedback representation demands a reconceptualization of inclusion. Research by Alanezi and Alanzi (2020) underscores how mobile health gig workers face layered marginalization, exacerbated by digital illiteracy and policy vacuums. Salmah *et al.* (2024) advocate for micro-feedback loops and mobile-friendly engagement surveys to surface gig worker experiences. Weichbrodt and Welge (2023) argue that gig-responsive OD must not enforce cultural uniformity but foster hybrid identity spaces where multiple values and norms can coexist and contribute productively.

3. Reconfiguring organizational development for a fluid workforce

OD strategies must adapt to accommodate gig workers within flexible employment ecosystems (Bateyo, 2025; Sharma and Sharma, 2019). This section articulates four key domains cultural

inclusion, algorithmic infrastructure, modular learning and inclusive evaluation that form the operational backbone of gig-integrative OD models (Kadolkar *et al.*, 2024; Jayakarthika *et al.*, 2024).

3.1 Cultural pluralism and identity engineering

Research by Sharma and Sharma (2019) and Weichbrodt and Welge (2023) affirms that gig-responsive OD must go beyond assimilation to embrace pluralism, allowing multiple worker identities to co-exist and contribute. As the workforce becomes more diversified in employment status, cultural integration can no longer rely on traditional onboarding, immersion or alignment rituals. Gig-responsive OD must design pluralistic cultural architectures where freelancers and contract workers experience community and coherence without conforming to centralized norms. Strategies include decentralized storytelling, values articulation via collaborative platforms and digital communities of practice. These interventions facilitate "weak ties" that still yield strong organizational outcomes, such as innovation, trust and mission alignment.

3.2 Algorithmic coordination and digital infrastructure

Kadolkar *et al.* (2024) emphasize that while algorithmic management enhances efficiency, it often compromises fairness unless co-designed with gig worker input. The ubiquity of algorithmic coordination in gig platforms (e.g. automatic task assignment, real-time feedback, dynamic pricing) necessitates an OD framework that is both technically astute and ethically vigilant. OD must engage with platform design not merely as a technical concern but as a governance domain. This entails embedding fairness metrics, designing opt-in visibility for workers and integrating user-centered design principles. A co-design model where workers participate in shaping platform algorithms can democratize decision-making and enhance procedural justice.

3.3 Modular learning architectures

Jayakarthika *et al.* (2024) highlight that modular and AI-curated learning environments promote skill portability and engagement among gig workers. The ephemeral nature of gig engagements precludes long-term training programs, demanding instead modular, context-sensitive learning interventions. These can include AI-curated skill playlists, gamified certifications and social mentoring platforms. Learning must be asynchronous, on-demand and portable across contracts. Additionally, learning analytics can offer insights into which modules yield the highest skill transfer or performance lift, enabling OD teams to iterate and optimize curricula in real time.

3.4 Performance and inclusion metrics

Salmah *et al.* (2024) recommend hybrid evaluation models that combine peer reviews with algorithmic tracking to foster inclusion and motivation. Gig workers challenge legacy performance systems that privilege visibility, longevity or static benchmarks. OD must develop multidimensional, dynamic evaluation systems that integrate qualitative and quantitative indicators. This includes peer reviews, project retrospectives and AI-assisted quality assessments. Inclusion metrics must also evolve beyond demographic representation to encompass access to resources, fairness of feedback and presence in decision-making forums. Periodic equity audits can help identify systemic exclusion patterns and inform corrective design.

4. The gig-responsive organizational development model

The gig-responsive OD model conceptualizes six core domains that together enable a strategic integration of gig workers into traditional organizational ecosystems. These

domains Talent Architecture, Cultural Engineering, Learning Systems, Governance Design, Performance Management and Inclusion Systems function interdependently to sustain a dynamic, equitable and efficient hybrid workforce:

- *Talent architecture:* Refers to the mechanisms by which organizations source, onboard and allocate work to gig contributors. This includes AI-driven job matching platforms, decentralized credentialing systems and project-specific onboarding protocols.
- *Cultural engineering:* Recognizes the importance of cultural inclusion across diverse employment types. This domain includes digital rituals, micro-communities, values alignment tools and asynchronous communication ecosystems that help create a pluralistic organizational identity.
- *Learning systems:* Emphasizes just-in-time, portable and self-directed learning modules accessible via digital platforms. Gamified certifications, peer-learning forums and role-specific upskilling content ensure continued development for both gig and permanent staff.
- *Governance design:* Encompasses platform-based decision structures, algorithmic transparency and participatory rule-making. Co-designed platform policies enhance fairness, reduce surveillance risks and foster trust.
- *Performance management:* Moves beyond static KPIs by integrating qualitative peer feedback, outcome-based metrics and AI-enhanced evaluations. These enable real-time performance monitoring across a heterogeneous workforce.
- *Inclusion systems:* Include equity audits, mobile accessibility tools, grievance redressal mechanisms and engagement dashboards. These tools ensure structural visibility and representation for gig workers.

5. Future research agenda

The integration of gig workforces into mainstream OD presents a rich array of future research avenues across strategic HRM, digital governance and organizational theory. This agenda outlines key priorities where empirical, theoretical and methodological contributions can deepen our understanding of gig-responsive OD systems.

- *Cross-national variations in identity and trust formation:* Cultural, legal and economic contexts significantly shape how gig workers perceive organizational trust, fairness and identity. Future studies could conduct cross-country comparisons (e.g. Western platform economies vs Asian digital labor hubs) to examine how local institutional logics influence worker experiences and organizational inclusion mechanisms.
- *Algorithmic management and worker autonomy:* The increasing role of AI and algorithmic governance in task assignment, evaluation and compensation necessitates deeper inquiry into how such systems shape worker agency, perceived fairness and retention. Experimental designs or platform ethnographies can reveal whether algorithmic transparency enhances psychological contracts.
- *Performance systems and outcome equity:* Hybrid workforce models require new performance metrics that account for task complexity, client diversity and peer evaluation. Research should explore how dynamic KPIs influence motivation, job satisfaction and equitable compensation, particularly in high-skill gig sectors (e.g. design, coding).
- *Legal and ethical governance in fluid work structures:* Gig economy integration challenges traditional labor law frameworks. There is a pressing need for interdisciplinary studies linking organizational design, digital labor rights and employment classification regimes. Comparative legal analyses can help identify best practices in protecting gig worker autonomy while preserving organizational flexibility.

- *Health, well-being and digital inclusion:* Gig work often lacks the psychological and social protections of full-time employment. Future research should explore how OD models can embed well-being through digital touchpoints, platform support and mobile inclusion tools. Longitudinal designs may help trace the mental health impact of sustained gig engagement.
- *Organizational learning from gig interactions:* Gig engagements generate dispersed yet valuable knowledge flows. Future research can examine how firms capture, synthesize and reuse insights from gig contributors through systems like digital knowledge commons, project retrospectives or peer learning networks.
- *Future-ready OD methodologies:* There is scope to advance mixed-methods and action research designs that include gig workers as co-researchers or stakeholders. This participatory turn can enhance the ecological validity and ethical integrity of OD scholarship in gig contexts.

Collectively, these research trajectories will shape the next generation of gig-inclusive OD models and enable organizations to move from reactive accommodation to proactive capability-building.

6. Conclusion

As organizations increasingly rely on gig labor for agility, cost-efficiency and innovation, the need for a reimagined OD framework becomes both urgent and inevitable. This paper has articulated a gig-responsive OD model that synthesizes diverse theoretical traditions and incorporates insights from more than dozen peer-reviewed studies. By reframing talent architecture, cultural engineering, learning systems, governance mechanisms and inclusion strategies, we propose an integrative approach to workforce development in the gig era. Ultimately, OD must transcend its historical roots in stability and permanence to embrace a new logic of dynamism, inclusivity and systemic adaptability. Such a transformation is not only strategic it is ethical and necessary.

References

Alanezi, F. and Alanzi, T. (2020), "A gig-mHealth economy framework: scoping review of internet-based medical consultations", *Journal of Medical Internet Research*, Vol. 22 No. 8.

Bateyo, A. (2025), "The gig economy: implications for workforce management", *Human Resource Management Review*.

Jayakarthika, K., Radhakrishnan, R. and Srikanth, K. (2024), "Unlocking the potential: HRM integration of AI in the gig economy", *AI & Society*.

Kadolkar, I., Kepes, S. and Subramony, M. (2024), "Algorithmic management in the gig economy: a systematic review", *Journal of Business Research*.

Matriano, E., Gonzales, D. and Balila, K. (2025), "Learning organizations, talent management, and gig economy transformation", *Journal of Organizational Learning and Leadership*.

Nath, V. (2020), "Trust in gig economy: toward an ethical platform design", *Journal of Business Ethics*, Vol. 162 No. 4, pp. 783-795.

Nayak, A., Satpathy, I., Khang, A. and Patnaik, B.C.M. (2024), "AI-Driven workforce planning in the gig economy", *Technology in Society*, Vol. 68.

Salmah, N., Abdullah, M. and Karim, H. (2024), "Employee engagement in the gig economy: a behavioral study", *International Journal of Human Resource Studies*, Vol. 14 No. 1.

Sharma, M. and Sharma, A. (2019), "Spiritual intelligence in the gig economy", *Journal of Management Development*, Vol. 38 No. 8.

Subramony, M., Krause, N. and Long, R. (2024), "Algorithmic management and psychological contracts in platform work", *Journal of Applied Psychology*.

Viswanathan, M. (2022), "Managing gig workers in the supply chain", *Journal of Operations Management*, Vol. 76 No. 1.

Weichbrodt, J. and Welge, M.K. (2023), "Faire arbeit in der gig economy", *Zeitschrift Für Arbeitswissenschaft*, Vol. 77 No. 3.

Zheng, Y. and Yang, Z. (2020), "The characteristics of the gig economy: evidence from global platform labor", *Industrial and Labor Relations Review*, Vol. 73 No. 5, pp. 1121-1145.

Further reading

Kul'chickaya, A. (2024), "Approaches to managing organizational and Extra-Organizational actors", *Organizational Dynamics*.

Talukder, M.B., Chowdhury, S.A. and Khan, M.R. (2024), "The gig economy: evolution and implications", *International Journal of Social Economics*.

Corresponding author

Uday Sai Garavandala can be contacted at: garavandalaudaysai123@gmail.com

For instructions on how to order reprints of this article, please visit our website:
www.emeraldgrouppublishing.com/licensing/reprints.htm
Or contact us for further details: permissions@emeraldinsight.com

Check for updates

Geological Journal

WILEY

RESEARCH ARTICLE

GIS-Based Landslide Susceptibility Mapping of Almora District in India: A Comparison of Different Techniques

Sandeep Panchal | Amit Kr. Srivastava

Delhi Technological University, Delhi, India

Correspondence: Sandeep Panchal (2290sandy@gmail.com)

Received: 25 February 2025 | **Revised:** 8 May 2025 | **Accepted:** 20 May 2025

Handling Editor: I. D. Somerville

Funding: The authors received no specific funding for this work.

Keywords: AHP | AHP-LNRF | frequency ratio | GIS | landslide susceptibility mapping | LNRF | statistical index

ABSTRACT

Landslide susceptibility maps at the regional scale are a very efficient tool for landslide planning and management. The Himalayan region in India is highly prone to the occurrence of landslides that lead to huge losses. In this paper, we prepared the landslide susceptibility maps for the Almora district in Uttarakhand, India using different techniques. A landslide inventory was prepared using the available historical data of landslides in the region. Eight factors including slope, aspect, curvature, relative relief, distance from lineament, drainage density, geology, and distance from faults are designated as causative factors of landslides. The contribution of the causative factors and sub-factors is modelled using different techniques. In this study, frequency ratio, statistical index, analytic hierarchy process, and landslide numerical risk factor are applied for calculating the weightage of causative factors. A hybrid method by combining the landslide numerical risk factor and analytic hierarchy process termed as AHP-LNRF method is also proposed. Five landslide susceptibility maps of the study area were prepared in a GIS environment. The landslide susceptibility maps are divided into five categories according to the susceptibility of different zones to the occurrence of landslides. The accuracy of the output of the study is predicted by receiver operating characteristics (ROC) curve technique. It is observed that the statistical index technique had the highest prediction rate (0.789) whilst frequency ratio showed a prediction rate of 0.764. Landslide numerical risk factor technique showed the least accuracy with a prediction rate of 0.719 which is improved to 0.738 in the AHP-LNRF technique. The AHP technique had a prediction rate of 0.735. The models and their output can be improved by improving the landslide inventory and optimising the causative factors of landslides. The results of the study can be used by the planner, managers, and researchers for landslide risk planning and management.

1 | Introduction

The Himalayan region in India is very sensitive to natural hazards (van Westen et al. 2012; Sujatha and Sridhar 2017; Singh and Sharma 2022). Landslides and failure of natural slopes are common geological problems in the Himalayan region (Pandey and Sharma 2017; Hussain et al. 2019). The topographic and geological characteristics of Almora district in Uttarakhand Province influence the occurrence of landslides (Haigh and Rawat 2012). The construction and up-gradation of the infrastructure in the Uttarakhand region led to significant anthropogenic activities which enhanced the proneness of occurrence of landslides (Haigh and Rawat 2012). The complex topography and hydrological characteristics of the region pose challenges to the risk management of the geological hazards. Landslide susceptibility maps can significantly

© 2025 John Wiley & Sons Ltd.

help in the planning and management of the landslide hazards (Sujatha et al. 2012; Panchal and Shrivastava 2022; Jallayu et al. 2024; Singh et al. 2024). These maps can help in understanding the landslide potential of the region and in deciding the mitigation measures for the geological hazards (Zhou et al. 2021; Nikoobakht et al. 2022; Bhardwaj and Singh 2023; Magray et al. 2023). The susceptibility maps can help in strategic planning and decision making.

The landslide susceptibility maps are prepared by evaluating the contribution of the different causative factors on the occurrence of landslides (Lee et al. 2004; Mansouri Daneshvar 2014; Milevski et al. 2019). The models for landslide susceptibility mapping can be broadly categorised into two categories i.e., expert-based models and data-driven approaches (Aleotti and Chowdhury 1999; Reichenbach et al. 2018). In the expert-based techniques, the opinion of experts is used to decide the contribution of causative factors of landslides whilst the data-driven model uses the historical landslide data to establish a relationship between the occurrence of landslide and causative factors (Hussain et al. 2019; Panchal and Shrivastava 2022, 2023). The techniques like analytic hierarchy process (Kumar and Anbalagan 2016; Liu et al. 2024; Kucuker 2024), analytic network process (Neaupane and Piantanakulchai 2006; Swetha and Gopinath 2020), fuzzy logic (Lee 2007; Kayastha et al. 2013; Roodposhti et al. 2016; Rostami et al. 2016; Manopkawee and Mankhemthong 2025), etc. are the expert-based techniques. The frequency ratio (Pradhan 2010; Silalahi et al. 2019; Khan et al. 2019; Barman and Das 2024; Hailu et al. 2024), statistical index (Wu et al. 2016; Berhane and Tadesse 2021; Abdo et al. 2022; Pawar et al. 2022; Thanh et al. 2022), weight of evidence (Pradhan et al. 2010; Getachew and Meten 2021; Cao et al. 2021; Chen et al. 2021; Saha et al. 2022), landslide numerical risk factor (Torkashvand et al. 2014; Patil et al. 2020), Shannon's entropy (Sharma et al. 2015; Roodposhti et al. 2016; Panchal and Shrivastava 2021; Es-smairi et al. 2023), etc. are data-driven models. The landslide susceptibility mapping techniques in India had increased significantly in the last 2 decades (Sujatha and Sridhar 2017; Pandey and Sharma 2017; Hussain et al. 2019; Singh and Sharma 2022). The models including the expert-based models and data-driven models both are utilised to get accurate landslide susceptibility maps.

The study area selected in this paper is the Almora district in Uttarakhand, India. The region lies in the Himalayan belt and is sensitive to geological hazards. The study area is a centre of tourist attraction. There is a need for the assessment of landslide susceptibility in the study area. The statistical models and expert-based techniques are not implemented for the assessment of landslide susceptibility in this region. The aim of this study is to prepare multiple landslide susceptibility maps of the Almora district using different expert-based techniques and data-driven techniques. It is observed that there is a need to compare the expert-based and data-driven techniques for the study area. Thus, it is focused on implementing frequency ratio, statistical index, analytic hierarchy process (AHP) and landslide numerical risk factor (LNRF) technique for landslide susceptibility mapping. A hybrid technique by combining AHP and LNRF is also used to prepare a landslide susceptibility map. The landslide susceptibility maps prepared in this study will help in planning and mitigation of landslides in the study area. The results will also help in the selection of the most suitable technique for landslide susceptibility mapping by the researchers.

2 | Study Area

Almora district is in Kumaon division of Uttarakhand in India (Official Website of Almora District 2024). The longitude and latitude of the study area are shown in Figure 1. The average elevation of the study area is 1638 m above mean sea level (Official Website of Almora District 2024). Almora is culturally rich and the natural beauty of the region attracts numerous tourists throughout the year. The area of the district is 3139 sq. m (Official Website of Almora District 2024). The elevation of the study area significantly varies and impacts the climate of the study area. The average annual maximum temperature of the study area is 23°C whilst the average annual minimum temperature is 10°C. In the winters, the temperature can fall below 0°C (GEAG, n.d.). The annual rainfall is 1000 mm (GEAG, n.d.). 75% of the study area is underlain by rocks of Proterozoic age.

3 | Materials and Methods

To achieve the aim of this study, the data related to the causative factors of the landslides is collected and organised. The database of the causative factors is prepared. The modelling of the causative factors and sub-factors is performed using the different methods. The models i.e., frequency ratio, statistical index, analytic hierarchy process, landslide numerical risk factor and AHP-LNRF are implemented. The landslide susceptibility maps by each technique is prepared and compared using the receiver operation characteristics (ROC) curve. The digital elevation model (DEM) is obtained from the NRSC website (Bhuvan NRSC 2024). The DEM-based causative factors are extracted from the DEM. The non-DEM factors are digitised from the toposheets and ground water prospectus map. A landslide inventory is obtained from the BHUKOSH portal (n.d.). This landslide inventory is prepared from the previously published reports, literature, Google Earth and field visits. The landslide inventory consists of a database of around 300 landslides. 70% of the total landslide data is used to prepare the landslide inventory and 30% of the landslide data is used for the validation of maps. The methodology adopted in this study is given in Figure 2.

4 | Causative Factors of Landslides

We have put together a database of the factors that cause landslides in our study area. We picked the following factors based on research and expert opinions, but there are not any strict rules for choosing them. We considered some previously published papers, the opinion of experts, and our personal experience on the subject in choosing the causative factors. It is decided to select the causative factors that represent the terrain characteristics and drainage pattern of the study area. In this study, we examined eight factors: slope, aspect, curvature, relative relief, distance from lineaments, geology, drainage density, and distance from faults, explained here (Figures 3 and 4):

10991034, 0, Downloaded from https://onlinelibrary.wiley.com/doi/10.1002/gj.70002 by Delhi Technological University, Wiley Online Library on [26/06/2025]. See the Terms and Conditions (https://onlinelibrary.wiley.com/terms-and-conditions) on Wiley Online Library for rules of use; OA articles are governed by the applicable Creative Commons License

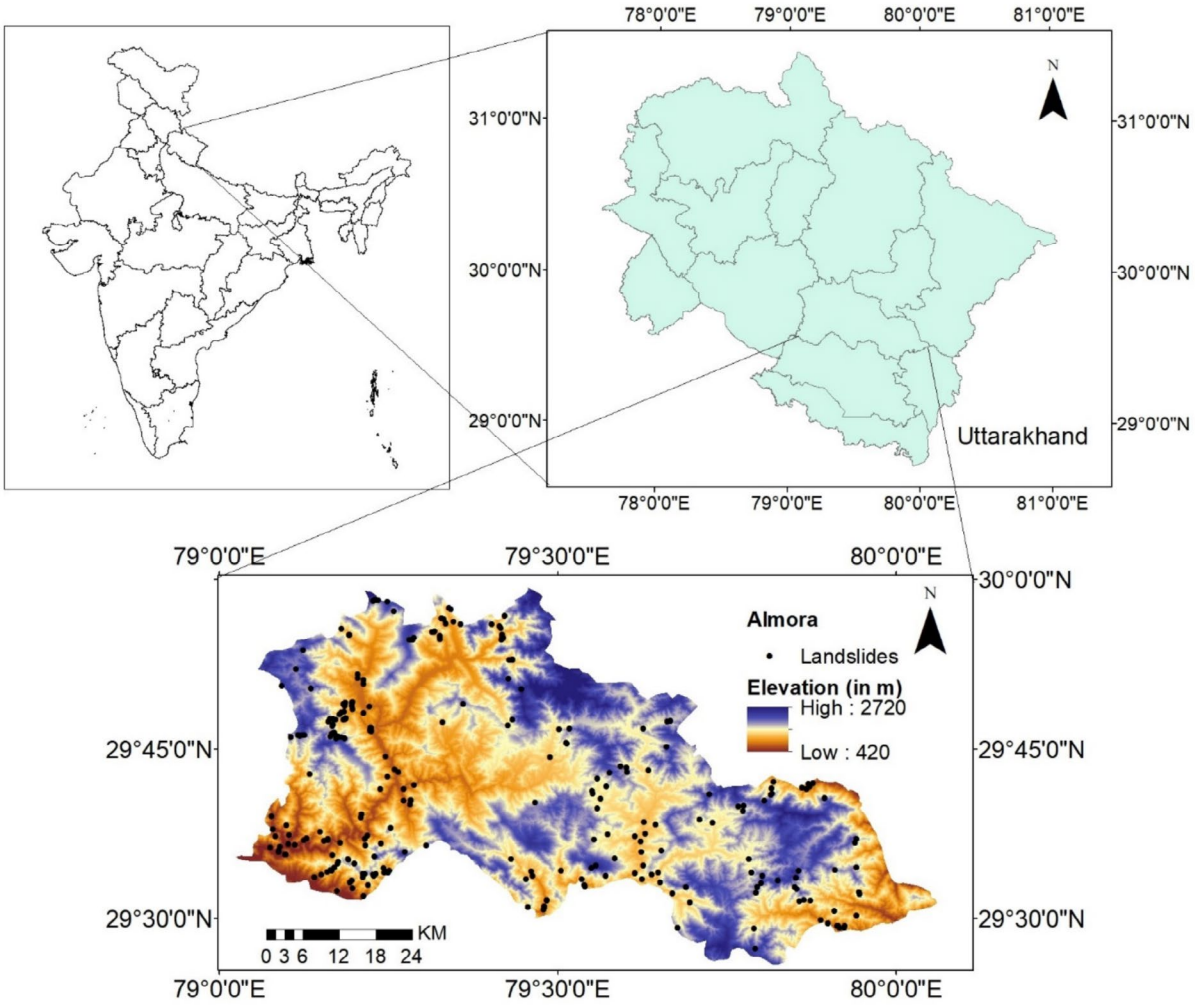


FIGURE 1 | Location of study area.

4.1 | Slope

Slope represents the steepness of soil or rock in this study (Panchal and Shrivastava 2020a, Panchal and Shrivastava 2020b). Many studies have identified slope as a key factor in landslides. Steeper slopes can increase the risk of landslides if the rest of the factors remain constant (Patil et al. 2020). In our area, most of the land (about 60%) has slopes between 55° and 75°. As the slope gets steeper, gravity has a bigger effect, but the slope angle alone is not the only thing that can cause landslides.

4.2 | Aspect

This refers to the direction a slope face. It affects erosion and how much sunlight the area receives (Panchal and Shrivastava 2023). Many researchers also see aspect as a factor in landslides, as it influences moisture levels and plant growth (Panchal and Shrivastava 2022; Singh et al. 2024). We categorised aspect into nine directions: north, northeast, east, southeast, south, southwest, west and northwest. The southwest, south and northeast directions together make up about 13% of the total area each.

4.3 | Curvature

We divided curvature into three types: concave, convex and flat. Curvature affects how materials and water move on the slope (Ohlmacher 2007). Flat areas have no curvature. Concave slopes tend to hold more water, making them more prone to slide during rainfall events (Singh et al. 2024). In our region, there are no flat areas; it is either concave or convex.

4.4 | Relative Relief

This shows how much the elevation changes across the terrain, which can affect the types of vegetation found there (Singh et al. 2024). We classified relative relief into four levels: low (0–50 m), moderate (50–100 m), high (100–150 m), and very high (more than 150 m). We found that about 36% of our study area has low relative relief. Figure 3 shows the details on slope, aspect, curvature and relative relief.

4.5 | Distance From Lineaments

This is a distinct causative factor of landslides. According to experts, regions near lineaments and faults are more prone to

10991034, 0, Downloaded from https://onlinelibrary.wiley.com/doi/10.1002/gj.70002 by Delhi Technological University, Wiley Online Library on [26/06/2025]. See the Terms and Conditions (https://onlinelibrary.wiley.com/terms-and-conditions) on Wiley Online Library for rules of use; OA articles are governed by the applicable Creative Commons License

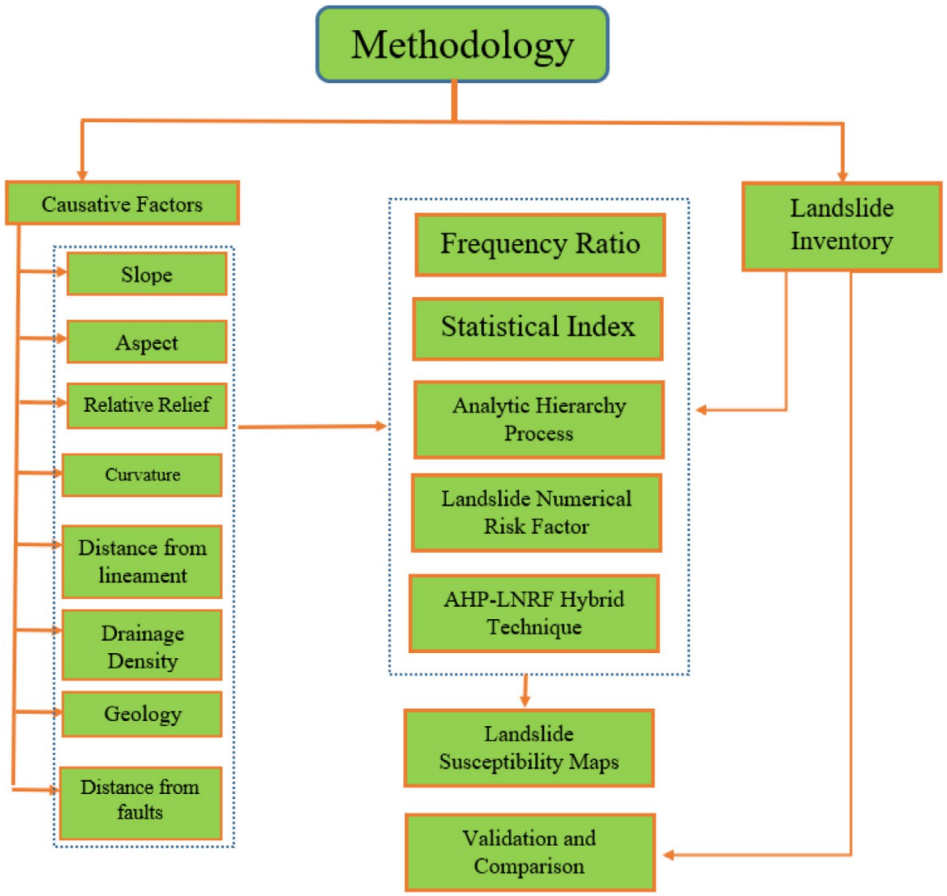


FIGURE 2 | Flow chart.

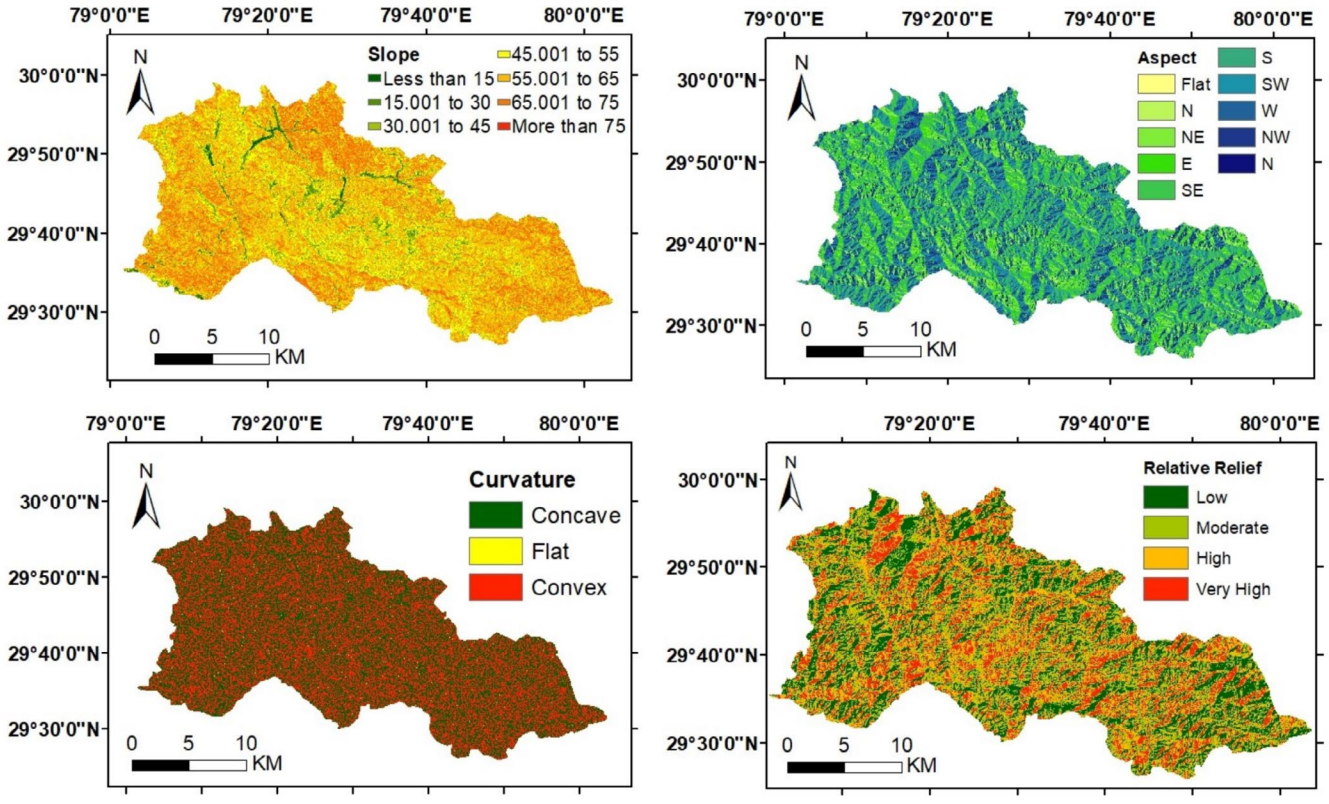


FIGURE 3 | Causative factors of landslides (slope, aspect, curvature and relative relief).

10991034, 0, Downloaded from https://onlinelibrary.wiley.com/doi/10.1002/gj.70002 by Delhi Technological University, Wiley Online Library on [26/06/2025]. See the Terms and Conditions (https://onlinelibrary.wiley.com/terms-and-conditions) on Wiley Online Library for rules of use; OA articles are governed by the applicable Creative Commons License

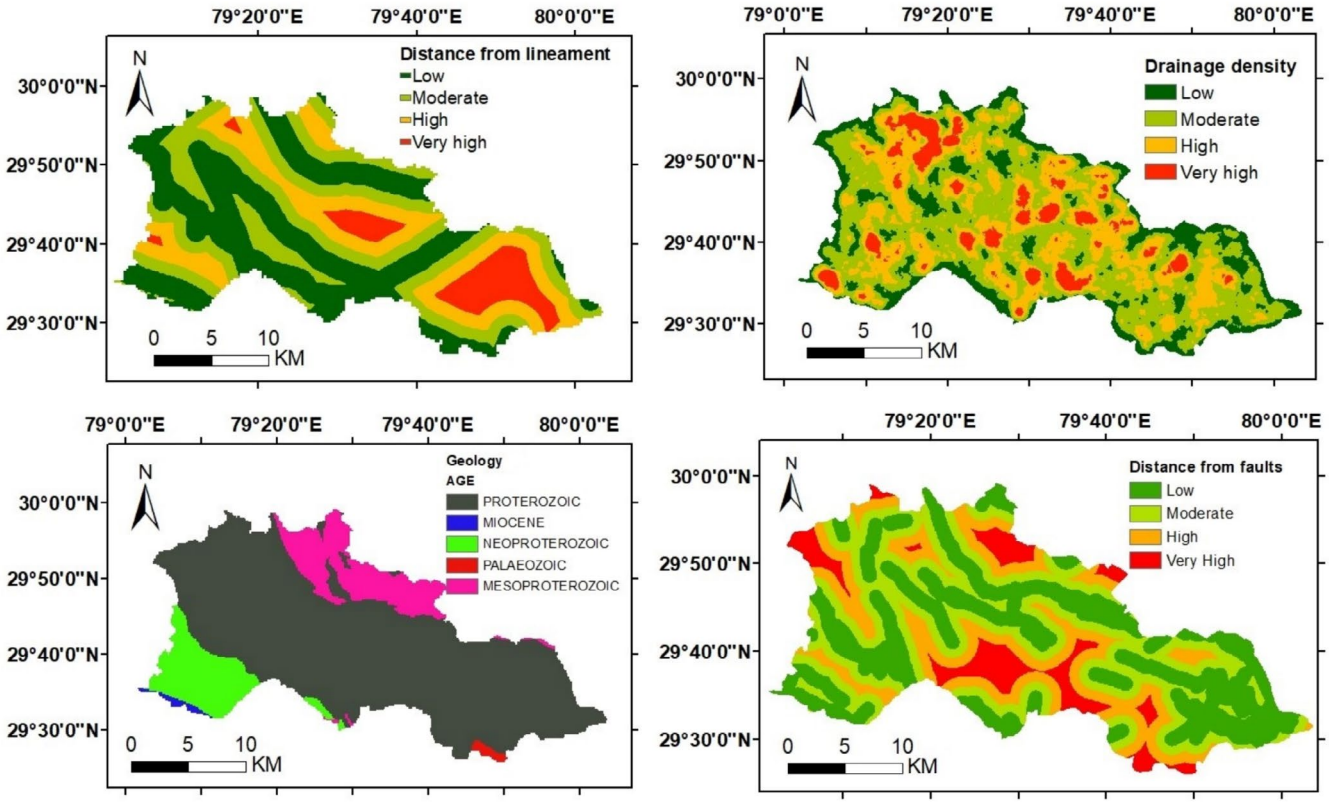


FIGURE 4 | Causative factors of landslides (distance from lineament, drainage density, geology and distance from faults).

landslides (Ramli et al. 2010; Kose and Turk 2019). The distance from the lineament is classified into four categories: low, moderate, high and very high.

4.6 | Drainage Density

The drainage pattern of an area also contributes to the occurrence of landslides (Getachew and Meten 2021; Kavzoglu et al. 2015). Landslides are impacted by the drainage density around them. The drainage density is derived from the digital elevation model. The study region is covered with an extensive drainage network. The drainage density is classified into four categories: low, moderate, high and very high. Experts believe that areas with high drainage density may be more prone to landslides.

4.7 | Geology

The study region is covered in a variety of geological formations that impact the occurrence of landslides (Lee et al. 2022; Morino et al. 2022). The geology is classified into five categories: Proterozoic, Miocene, Neoproterozoic, Palaeozoic and Mesoproterozoic. More than 75% of the research region is covered in Proterozoic-aged deposits. Mesoproterozoic deposits occupy approximately 12% of the research area. A small region of the terrain is underlain by deposits from the Palaeozoic and Miocene periods.

4.8 | Distance From Faults

This is a distinct causative element of landslides. The distance from the fault is classified into four categories: low, moderate, high and very high. Approximately 19% of the research area is quite close to faults.

5 | Methods/Models for Landslide Susceptibility Assessment

In the present study, five techniques i.e., frequency ratio, statistical index, landslide numerical risk factor, analytic hierarchy process and AHP-LNRF hybrid technique are implemented to prepare the landslide susceptibility maps of the study area (Figure 7). AHP is an expert-based technique whilst frequency ratio, statistical index and LNRF are mathematical models. AHP-LNRF is a hybrid technique in which the weightage of the LNRF is restricted by AHP weightages. These techniques are explained in detail.

5.1 | Frequency Ratio

The frequency ratio is a statistical tool for determining the relationship between the causes and the incidence of landslides (Panchal and Shrivastava 2021; Manopkawee and Mankhemthong 2025). The relationship is found using the distribution of historical landslides in the study area (Silalahi et al. 2019). A frequency ratio

10991034, 0, Downloaded from https://onlinelibrary.wiley.com/doi/10.1002/gj.70002 by Delhi Technological University, Wiley Online Library on [26/06/2025]. See the Terms and Conditions (https://onlinelibrary.wiley.com/terms-and-conditions) on Wiley Online Library for rules of use; OA articles are governed by the applicable Creative Commons License

greater than one indicates that landslides are more likely to occur, whereas a frequency ratio less than one indicates that landslides are less likely to occur (Morino et al. 2022; Nikoobakht et al. 2022). The frequency ratio is determined by the following formula:

$$\text{Frequency ratio (FR)} = \frac{\frac{NLSpix}{\sum_{1}^{n} NLSpix}}{\frac{NCpix}{\sum_{1}^{m} NCpix}} \quad (1)$$

NLSpix is the number of pixels of landslides, and NCpix is the number of pixels of a class (Panchal and Shrivastava 2021). The landslide susceptibility index is given by the summation of the frequency ratio (Panchal and Shrivastava 2021).

$$\text{Landslide Susceptibility Index (LSI)} = \sum FR \quad (2)$$

The landslide susceptibility index (LSI) is used to classify the final landslide susceptibility maps (Panchal and Shrivastava 2021).

5.2 | Statistical Index

The frequency ratio technique is improved upon by the statistical index technique. For assessing landslide vulnerability, this bivariate statistical method is frequently employed (Berhane and Tadesse 2021; Abdo et al. 2022). The statistical index (SI) is computed by dividing the density of landslides in the study region by the natural logarithm of the density of landslides in a class (Berhane and Tadesse 2021; Abdo et al. 2022; Pawar et al. 2022). The statistical index approach may have negative weighting; however, the frequency ratio (FR) has a minimum weighting value of zero. The following formula is used to determine the statistical index:

$$\text{Statistical index (SI)} = \ln \frac{DLC}{DLA} \quad (3)$$

In this equation, DLC is the density of the landslides in class, whilst DLA is the density of landslides in the study area.

$$\text{Landslide Susceptibility Index (LSI)} = \sum SI \quad (4)$$

The statistical index is added up to determine the landslide susceptibility index. Higher SI values indicate a favourable link with landslides, whereas negative SI values indicate a bad correlation with the occurrence of landslides (Abdo et al. 2022; Pawar et al. 2022).

5.3 | Landslide Numerical Risk Factor (LNRF)

The techniques like frequency ratio and statistical index establish the relationship between landslide density in a class to landslide density in the whole study area. The landslide numerical risk factor technique is relatively simple and only based on the available historical data. It establishes a relationship between the area of landslides in a class to the total area of landslides in the whole study area (Torkashvand et al. 2014). The landslide numerical risk factor is given by the following formula:

$$\text{Landslide Numerical Risk Factor (LNRF)} = \frac{A_{cls}}{A_{mean}} \quad (5)$$

A_{cls} is the area of landslides in a class whilst A_{m} is the mean area of landslide in the class. The mean area of landslide can be calculated by dividing the total area of landslides by the number of classes (Torkashvand et al. 2014; Patil et al. 2020). Here area is calculated

TABLE 1 | Scale of analytic hierarchy process (AHP).

Degree of preference (Saaty 1980)	Definition	Explanation
1	Equally important	Both criteria are equally important or both the factors have same effect on occurrence of landslides
3	Moderately important	One factor is more effective as compared to the other factor
5	Highly important	One factor affects highly as compared to the other factor
7	Very highly important	A factor is highly dominated over other
9	Extremely important	A factor has highest possibility of affecting the occurrence of landslide over other factor
2, 4, 6, 8	Intermediate values	If a compromise between two factors is required, intermediate values can be used

TABLE 2 | Randomness index (R.I.)

Number of criteria	1	2	3	4	5	6	7	8	9	10	11	12	13	14	15
R.I.	0.0	0.0	0.58	0.9	1.12	1.24	1.32	1.41	1.45	1.49	1.51	1.48	1.56	1.57	1.58

10991034, 0, Downloaded from https://onlinelibrary.wiley.com/doi/10.1002/gj.70002 by Delhi Technological University, Wiley Online Library on [26/06/2025]. See the Terms and Conditions (https://onlinelibrary.wiley.com/terms-and-conditions) on Wiley Online Library for rules of use; OA articles are governed by the applicable Creative Commons License

TABLE 3 | Modelling of landslide sub-factors using FR, SI and LNRF.

Causative factors	Classes	No. of pixels in class	% Age in class (a)	No. of landslide pixel in class	% Age of landslide pixel (b)	FR (b/a)	SI (ln(b/a))	LNRF
Slope	Less than 15	60,689	0.016	0.00	0.000	0.000	0.000	0.000
	15–30	149,783	0.040	0.00	0.000	0.000	0.000	0.000
	30–45	378,082	0.101	12.96	0.045	0.451	−0.797	0.318
	45–55	674,094	0.180	25.92	0.091	0.505	−0.682	0.636
	55–65	1,334,767	0.356	77.76	0.273	0.766	−0.267	1.909
	65–75	1,100,004	0.294	155.52	0.545	1.858	0.620	**3.818**
	More than 75	50,074	0.013	12.96	0.045	**3.402**	**1.224**	0.318
	Total	3,747,493		285.12				
Aspect	Flat	0	0.000	0.00	0.000	0.000	0.000	0.000
	North	266,492	0.071	12.96	0.045	0.639	−0.448	0.455
	Northeast	491,319	0.131	25.92	0.091	0.693	−0.366	0.909
	East	424,858	0.113	38.88	0.136	1.203	0.185	**1.364**
	South East	466,170	0.124	51.84	0.182	**1.462**	**0.380**	1.818
	South	521,399	0.139	51.84	0.182	1.307	0.268	1.818
	South West	491,492	0.131	38.88	0.136	1.040	0.039	1.364
	West	420,597	0.112	25.92	0.091	0.810	−0.211	0.909
	North West	424,405	0.113	25.92	0.091	0.803	−0.220	0.909
	North	240,761	0.064	12.96	0.045	0.708	−0.346	0.455
	Total	3,747,493		285.12				
Curvature	Concave	1,876,151	0.501	155.52	0.545	**1.090**	**0.086**	**1.636**
	Flat	0	0.000	0.00	0.000	0.000	0.000	0.000
	Convex	1,871,342	0.499	129.60	0.455	0.910	−0.094	1.364
	Total	3,747,493		285.12				
Relative relief	Low	1,347,042	0.359	155.52	0.545	**1.517**	**0.417**	**2.182**
	Moderate	670,780	0.179	38.88	0.136	0.762	−0.272	0.545
	High	736,689	0.197	38.88	0.136	0.694	−0.366	0.545
	Very High	992,982	0.265	51.84	0.182	0.686	−0.377	0.727
	Total	3,747,493		285.12				
Distance from lineament	Low	1,390,949	0.371	120.81	0.424	**1.142**	0.132	**1.695**
	Moderate	1,161,168	0.310	106.31	0.373	1.203	**0.185**	1.491
	High	828,437	0.221	33.82	0.119	0.537	−0.623	0.474
	Very High	366,939	0.098	24.18	0.085	0.866	−0.144	0.339
	Total	3,747,493		285.12				
Drainage density	Low	193,804	0.052	25.92	0.091	**1.758**	**0.564**	0.364
	Moderate	1,277,356	0.341	90.72	0.318	0.933	−0.069	1.273

(Continues)

10991034, 0, Downloaded from https://onlinelibrary.wiley.com/doi/10.1002/gj.70002 by Delhi Technological University, Wiley Online Library on [26/06/2025]. See the Terms and Conditions (https://onlinelibrary.wiley.com/terms-and-conditions) on Wiley Online Library for rules of use; OA articles are governed by the applicable Creative Commons License

TABLE 3 | (Continued)

Causative factors	Classes	No. of pixels in class	% Age in class (a)	No. of landslide pixel in class	% Age of landslide pixel (b)	FR (b/a)	SI (ln(b/a))	LNRF
	High	1,458,553	0.389	116.64	0.409	1.051	0.050	**1.636**
	Very High	817,780	0.218	51.84	0.182	0.833	−0.182	0.727
	Total	3,747,493		285.12				
Geology (age)	Proterozoic	2,898,673	0.773	193.47	0.679	0.877	−0.131	**3.393**
	Miocene	20,944	0.006	0.00	0.000	0.000	0.000	0.000
	Neoproterozoic	369,083	0.098	27.15	0.095	0.967	−0.034	0.476
	Palaeozoic	20,595	0.005	1.14	0.004	0.728	−0.318	0.020
	Mesoproterozoic	438,198	0.117	63.36	0.222	**1.900**	**0.642**	1.111
	Total	3,747,493		285.12				
Distance from faults	Low	704,266	0.188	51.85	0.182	0.968	−0.033	0.727
	Moderate	937,080	0.250	77.76	0.273	**1.091**	**0.087**	1.091
	High	961,297	0.257	77.76	0.273	1.063	0.061	**1.091**
	Very high	1,144,850	0.305	77.76	0.273	0.893	−0.114	1.091
	Total	3,747,493		285.13				

Note: The bold values represent the highest significant value among the sub-classes for each causative factor in the respective FR, SI, and LNRF columns.

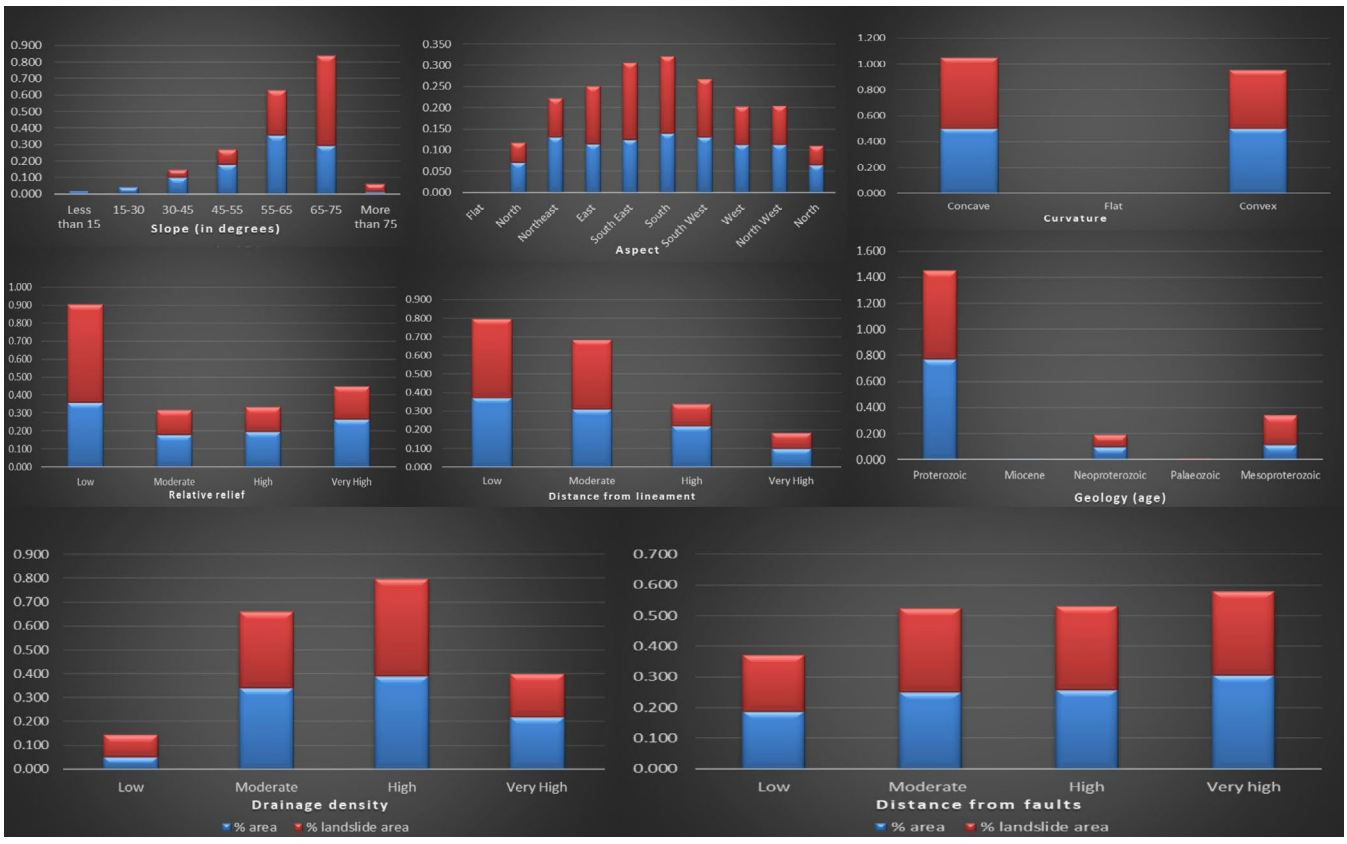


FIGURE 5 | Histograms showing % area vs. landslide area for slope, aspect, curvature, relative relief, distance from lineament, drainage density, geology and distance from faults.

10991034, 0, Downloaded from https://onlinelibrary.wiley.com/doi/10.1002/gj.70002 by Delhi Technological University, Wiley Online Library on [26/06/2025]. See the Terms and Conditions (https://onlinelibrary.wiley.com/terms-and-conditions) on Wiley Online Library for rules of use; OA articles are governed by the applicable Creative Commons License

TABLE 4 | Pairwise comparison matrix of causative factors.

Causative factors	1	2	3	4	5	6	7	8	Weightage
Slope	1	6	4	3	0.25	0.17	0.14	3	0.094
Aspect		1	0.33	0.25	0.17	0.14	0.12	0.25	0.02
Curvature			1	0.25	0.2	0.17	0.12	0.33	0.03
Relative relief				1	0.5	0.33	0.25	2	0.073
Distance from lineament					1	0.5	0.33	4	0.156
Drainage density						1	0.33	5	0.227
Geology (age)							1	5	0.35
Distance from faults								1	0.05

Note: CR = 0.085.

by the number of pixels covered by the landslides. The LNRF technique is purely based on the historical landslide data.

5.4 | Analytic Hierarchy Process (AHP)

The multiple alternatives and their rankings are assessed using the multi-criteria decision-making method known as the Analytic Hierarchy Process (AHP) (Saaty 1980, 1987). There are criteria and sub-criteria for the complicated phenomenon. The weighting is determined by synthesising the pairwise matrix that compares the criteria and sub-criteria (Kumar et al. 2017; Panchal and Debbarma 2017). Typically, a scale of 9 is used to compare the alternatives. The comparison scale provided by Saaty is displayed in Table 1. The consistency ratio (CR) is used to verify the solution's consistency (Liu et al. 2024). The following formula can be used to get the consistency ratio:

$$\text{Consistency Ratio (CR)} = \frac{CI}{RI} \tag{6}$$

Here, CI is consistency index whilst RI is randomness index.

CI is calculated as follows:

$$\text{Consistency Index (CI)} = \frac{\lambda\max - n}{n-1} \tag{7}$$

Here, λ_{max} = major eigen value and n = order of matrix.

Saaty determines the randomness index (RI) values based on the value of n (Saaty 1987). Additionally, Table 2 displays the randomness index. RI is the outcome of a great deal of testing on a sizable dataset sample (Saaty 1980). Less than 10% should be the consistency ratio. The value in the pairwise comparison matrix is altered if the CR exceeds 10%. The following formula is used to determine the landslide susceptibility index:

$$\text{Landslide susceptibility index (LSI)} = \sum_{i=1}^{n} R_i \times W_i \tag{8}$$

W_i is the weightage of each major factor and R_i is the weightage of class. More value of landslide susceptibility index denotes more possibility of occurrence of landslides and vice versa.

5.5 | AHP-LNRF Hybrid Approach

Landslide numerical risk factor is completely based on the landslide inventory. It does not consider the relationship of the inventory with area. In AHP-LNRF technique, the weighting of major factors from AHP technique is used whilst the weighting for the co-factors is taken using LNRF. In this way, these two methods are mixed and the results are analysed. The landslide susceptibility index (LSI) by AHP-LNRF technique is given by the following equation:

$$\text{Landslide susceptibility index (LSI)} = \sum_{i=1}^{n} W_{AHPi} \times R_{LNRFi} \tag{9}$$

W_{AHPi} is the weighting of the major causative factor calculated by AHP, whilst R_{LNRFi} is the weighting of the sub-factor calculated by LNRF. The landslide susceptibility maps are prepared by assigning the weighting calculated from the different techniques. Five landslide susceptibility maps are prepared using the frequency ratio, statistical index, landslide numerical risk factor, analytic hierarchy process, and AHP-LNRF hybrid technique.

6 | Results and Analysis

The weighting of the different causative factors and sub-factors is calculated using the different techniques. The contribution of different causative factors and sub-factors is shown in Table 3. The impact of the different causative factors and sub-factors calculated by the different techniques can be analysed. The distribution of landslide area with respect to the area of classes is shown in Figure 5. Figure 5 shows the impact of different classes on the distribution of landslide area.

6.1 | Impact of Co-Factors on the Occurrence of Landslides

The various models indicate the weight of different categories, illustrating the role of these factors in landslide occurrences. Slopes exceeding a 75° angle account for 1.3% of the study region, whilst 4.5% of the entire landslide area is found in these slope

10991034, 0, Downloaded from https://onlinelibrary.wiley.com/doi/10.1002/gj.70002 by Delhi Technological University, Wiley Online Library on [26/06/2025]. See the Terms and Conditions (https://onlinelibrary.wiley.com/terms-and-conditions) on Wiley Online Library for rules of use; OA articles are governed by the applicable Creative Commons License

TABLE 5 | Pairwise comparison matrix in AHP.

Causative factors	Sub-factors	1	2	3	4	5	6	7	8	9	10	Weightage (W_i)	Consistency ratio (CR)
Slope	Less than 15	1	0.5	0.25	0.17	0.1	0.1	0.11				0.022	0.048
	15–30		1	0.33	0.25	0.2	0.1	0.12				0.032	
	30–45			1	0.5	0.3	0.2	0.12				0.056	
	45–55				1	0.5	0.3	0.17				0.093	
	55–65					1	0.3	0.25				0.142	
	65–75						1	0.5				0.257	
	More than 75							1				0.398	
Aspect	Flat	1	0.5	0.33	0.25	0.1	0.1	0.14	0.33	0.25	0.2	0.019	0.078
	North		1	0.33	0.33	0.1	0.2	0.14	0.33	1	0.5	0.028	
	Northeast			1	0.2	0.3	0.2	0.5	3	0.5	3	0.062	
	East				1	0.3	0.5	1	6	4	5	0.143	
	South East					1	3	4	6	7	8	0.295	
	South						1	2	4	5	8	0.198	
	South West							1	3	4	5	0.127	
	West								1	0.5	3	0.045	
	North West									1	2	0.053	
	North										1	0.032	
Curvature	Concave	1	9	3								0.649	0.068
	Flat		1.000	0.170								0.072	
	Convex			1								0.279	
Relative relief	Low	1	3	5	7							0.578	0.025
	Moderate		1	2	4							0.228	
	High			1	3							0.134	
	Very High				1							0.06	

(Continues)

10991034, 0, Downloaded from https://onlinelibrary.wiley.com/doi/10.1002/gj.70002 by Delhi Technological University, Wiley Online Library on [26/06/2025]. See the Terms and Conditions (https://onlinelibrary.wiley.com/terms-and-conditions) on Wiley Online Library for rules of use; OA articles are governed by the applicable Creative Commons License

TABLE 5 | (Continued)

Causative factors	Sub-factors	1	2	3	4	5	6	7	8	9	10	Weightage (W_i)	Consistency ratio (CR)
Distance from lineament	Low	1	5	7	9							0.657	0.063
	Moderate		1	3	5							0.203	
	High			1	3							0.094	
	Very High				1							0.046	
Drainage density	Low	1	0.5	0.2	0.14							0.063	0.007
	Moderate		1	0.33	0.2							0.11	
	High			1	0.5							0.301	
	Very High				1							0.527	
Geology (age)	Proterozoic	1	9	5	6	2						0.078	0.08
	Miocene		1	0.33	0.25	0.2						0.751	
	Neoproterozoic			1	4	0.3						0.178	
	Palaeozoic				1	0.3						0.07	
	Mesoproterozoic					1						0.268	
Distance from faults	Low	1	5	7	9							0.168	0.063
	Moderate		1	3	5							0.43	
	High			1	3							0.053	
	Very high				1							0.033	

10991034, 0, Downloaded from https://onlinelibrary.wiley.com/doi/10.1002/gj.70002 by Delhi Technological University, Wiley Online Library on [26/06/2025]. See the Terms and Conditions (https://onlinelibrary.wiley.com/terms-and-conditions) on Wiley Online Library for rules of use; OA articles are governed by the applicable Creative Commons License

zones. The frequency ratio (FR) and statistical index values for such slopes are 3.402 and 1.224, respectively. The AHP weight for slopes greater than 75° is the highest amongst slope categories, totaling 0.398, whilst the LNRF technique indicates that slopes ranging from 65° to 75° have the greatest weight, which is 3.818. The southeast aspect direction appears to be most susceptible to landslide occurrences according to all methods utilised in this research. The frequency ratio, statistical index, LNRF and AHP values for the southeast aspect are at their peak, measuring 1.462, 0.380, 1.818 and 0.295, respectively. The south aspect is the second most significant contributing direction. Concave curvature tends to be more likely to experience landslides. There are no flat curvature regions within the study area. The frequency ratio, statistical index, LNRF and AHP values for concave curvature are 1.090, 0.086, 1.636 and 0.649. Areas with low relative relief are found to be at an increased risk of landslides. The frequency ratio, statistical index, LNRF and AHP values for low relative relief are 1.517, 0.417, 2.182 and 0.578. There is a difference in weightages amongst statistical models, LNRF methodology and AHP methodology regarding the distance from lineaments. According to frequency ratio and statistical index methods, moderate distances from lineaments are more susceptible to landslide occurrences. The frequency ratio and statistical index values for moderate distance from lineaments are 1.203 and 0.185, respectively. In contrast, LNRF and AHP find that shorter distances from lineaments exert the most significant influence on landslide occurrences, with LNRF and AHP values of 1.695 and 0.657, respectively. Statistically, there are a greater number of landslide events in regions with low drainage density, reflected in frequency ratio and statistical index values of 1.758 and 0.564, respectively. Conversely, LNRF assigns the highest weight to areas with high drainage density, measured at 1.636. The AHP technique allocates maximal weight to regions with very high drainage density, registering at 0.527. Mesoproterozoic deposits demonstrate a higher propensity for landslides, as indicated by frequency ratio and statistical index values. The values for Mesoproterozoic deposits are 1.9 and 0.642, respectively. According to LNRF, Proterozoic deposits show increased susceptibility to landslide occurrences, achieving a value of 3.393. The highest AHP weight is assigned to Miocene deposits, which stands at 0.751. The moderate distance from the faults is found to be more susceptible to the occurrence of landslides according to the frequency ratio and statistical index technique. The FR, SI and AHP values for the moderate distance from faults are 1.091, 0.87 and 0.43, respectively. The LNRF value for moderate, high and very high distances from the faults is 1.091.

6.2 | Impact of Major Causative Factors on the Occurrence of Landslides

The influence of major causative factors on the occurrence of landslides can be represented solely through the analytic hierarchy process (AHP). Table 4 illustrates the contribution of the causative factors to the occurrence of landslides, whilst Table 5 depicts the role of sub-factors based on the AHP methodology. Geology is the most prominent causative factor affecting the occurrence of landslides, with an AHP weight of 0.350. Drainage density ranks as the second most significant factor influencing landslide occurrences, holding an AHP weight of 0.227. The distance from the lineament also plays a significant role, with a weight of 0.156. The curvature and the aspect of the area have the least weight in the AHP technique, recorded at 0.03 and 0.02, respectively. These weight values are utilised exclusively in the AHP and AHP-LNRF hybrid methods. Figure 6 presents the impact of various causative factors in a graphical format.

6.3 | Analysis of Landslide Susceptibility Maps

The landslide susceptibility maps for the study area are developed using frequency ratio, statistical index, landslide numerical risk factor, analytic hierarchy process and AHP-LNRF hybrid techniques. Figure 7 displays the landslide susceptibility maps produced by different methods. As per the frequency ratio technique, approximately 35% of the study area is situated in a high landslide susceptibility zone, whilst about 41% of the landslide area is located within this zone. Nearly 15% of the study area falls within a very high landslide susceptibility zone, with more than 23% of the landslide area observed in that zone. Merely 1.3% of the study area is categorised under extreme landslide susceptibility, and around 2% of the landslide area exists in this category. In the statistical index method, about 20% of the study area is classified as having very high landslide susceptibility, whilst more than 24% of the landslide area is found in this category. Roughly 3% of the study area lies within the extreme landslide susceptibility zone, yet this encompasses over 6% of the landslide area. The moderate landslide susceptibility zone encompasses 27% of the study area, and this segment accounts for 20% of the landslide area. According to the LNRF method, 14% of the study area is under extreme landslide susceptibility, with 20% of the landslide area positioned in this zone. Likewise, 26% of the study area is in a very high landslide susceptibility zone, and 28% of the landslide area is noted to be in this zone. About 29% of the study area falls under low and moderate landslide susceptibility zones, which contribute to 29% of the landslide area.

According to the analytic hierarchy process, approximately 14% and 5% of the study area exist in very high and extreme landslide susceptibility zones. The landslide areas classified within very high and extreme landslide susceptibility zones are estimated to be around 17% and 8% respectively. Within the AHP-LNRF technique, roughly 29% of the study area is categorised as being in the extreme landslide susceptibility zone, whilst 32% of the

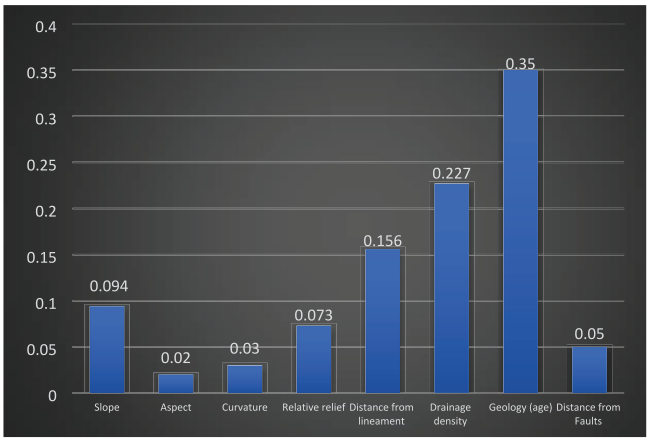


FIGURE 6 | AHP weightings of 8 causative factors.

10991034, 0, Downloaded from https://onlinelibrary.wiley.com/doi/10.1002/gj.70002 by Delhi Technological University, Wiley Online Library on [26/06/2025]. See the Terms and Conditions (https://onlinelibrary.wiley.com/terms-and-conditions) on Wiley Online Library for rules of use; OA articles are governed by the applicable Creative Commons License

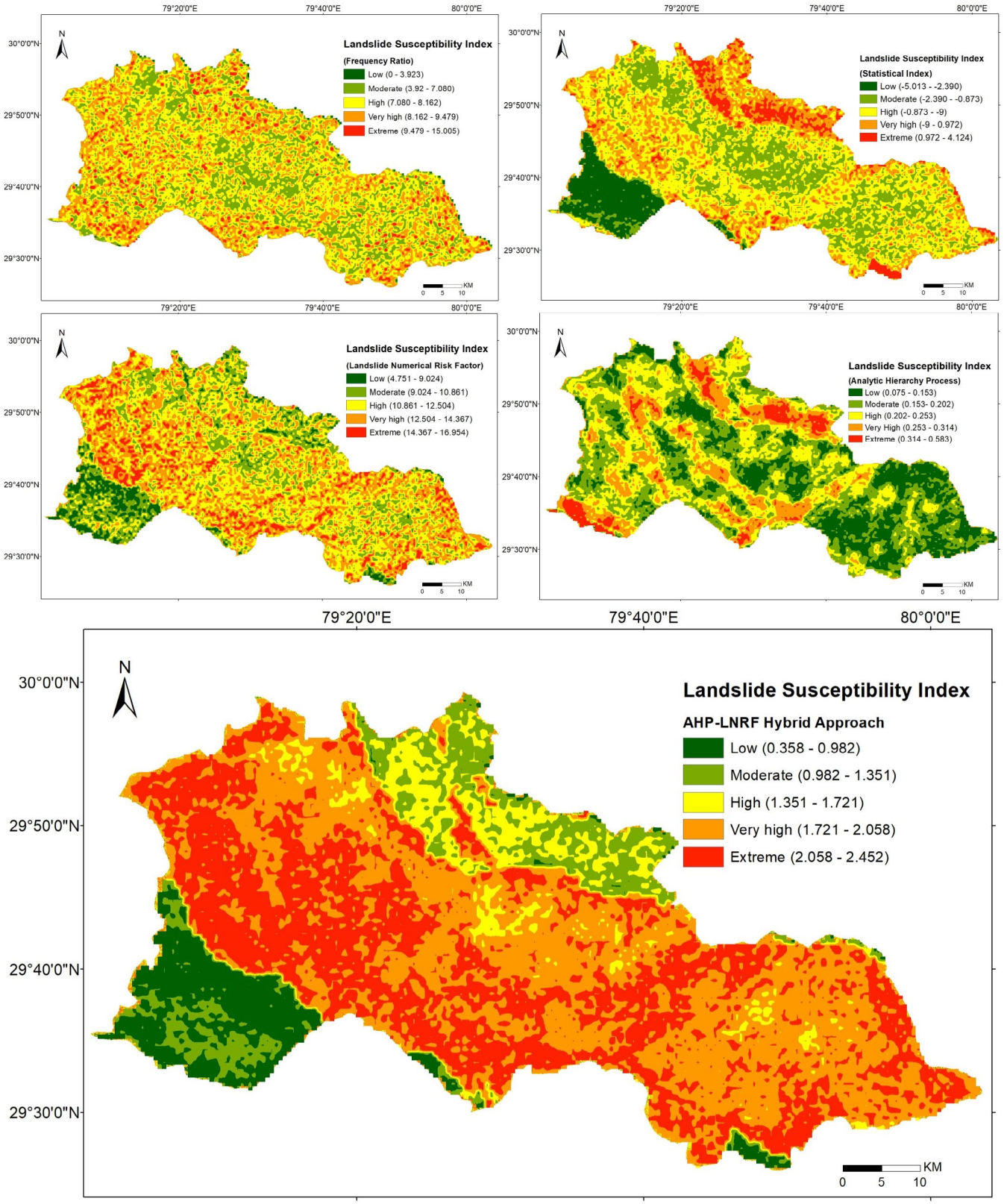


FIGURE 7 | Landslide susceptibility maps for frequency ratio, statistical index, landslide numerical risk factor, analytic hierarchy process and AHP-LNRF Hybrid approach.

landslide area falls within this region. Furthermore, 31% of the study area is in the very high landslide susceptibility zone, whilst 38% of the landslide area exists in this zone. Figure 8 illustrates the distribution of classes across different zones.

7 | Validation of Results

The findings of the study are validated through the use of the receiver operating characteristics curve. Figure 9 displays the

10991034, 0, Downloaded from https://onlinelibrary.wiley.com/doi/10.1002/gj.70002 by Delhi Technological University, Wiley Online Library on [26/06/2025]. See the Terms and Conditions (https://onlinelibrary.wiley.com/terms-and-conditions) on Wiley Online Library for rules of use; OA articles are governed by the applicable Creative Commons License

receiver operating characteristics curve that was generated for the various models applied within the study area. The prediction rates for the different methods utilised in landslide susceptibility mapping are determined by calculating the area under the curve (AUC). It is noted that the frequency ratio technique has a prediction rate of 0.764, whereas the statistical index technique is slightly more accurate with a prediction rate of 0.789. The statistical index provided the most precise results in this investigation. The prediction rate for the analytic hierarchy process (AHP) is 0.735, which can be enhanced by modifying the perceptions and ratings assigned by the experts. The landslide numerical risk factor (LNRF) exhibits the lowest prediction rate at 0.719, which shows a slight improvement in the AHP-LNRF technique, achieving a prediction rate of 0.738. The statistical index provided the most precise outcomes in this study; however, the accuracy across the various techniques is satisfactory at the regional level. The subjectivity of the experts may impact the results in the case of the analytic hierarchy process (AHP).

The results of the study depend on the different causative factors selected and resolution of the input parameters. The results of the study are based on the opinion of the experts in the case of AHP technique whilst the results in statistical models depend on the distribution of the landslides and historical landslide data. The results in AHP can be improved by varying the inputs of the experts and considering a more realistic pairwise comparison matrix. The landslide inventory can be updated and modified using the recent landslide data which can help in improving the results. More causative factors that can impact the occurrence of landslides can be considered. The hybrid techniques that combine the statistical models and expert-based techniques can be used for the enhancement of accuracy. The machine learning techniques and neural networks may yield better accuracy as compared to the statistical models. These models can be implemented for achieving higher accuracy. The study can be expanded to predict the hazard assessment and risk assessment of landslides in the study area.

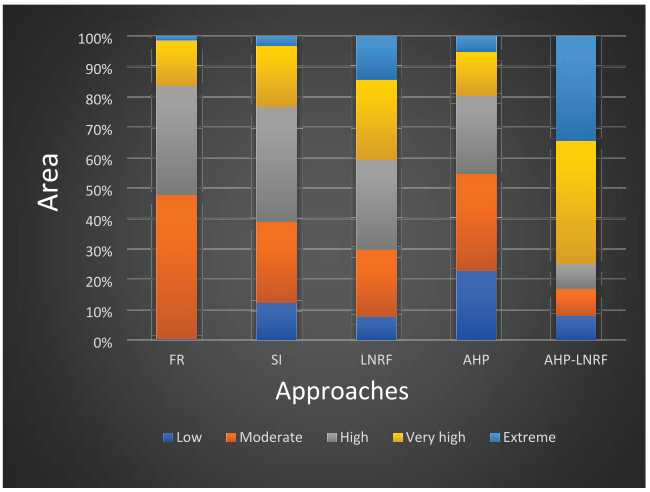


FIGURE 8 | Areas under different susceptibility zones.

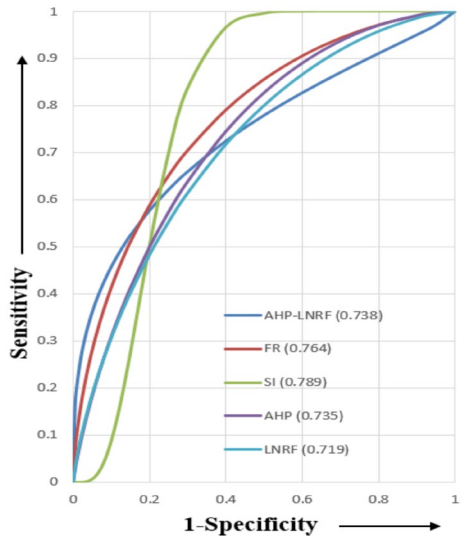


FIGURE 9 | ROC (receiver operation characteristics) curve for sensitivity vs. specificity.

8 | Conclusions

In this study, five methods, including frequency ratio, statistical index, analytic hierarchy process, landslide numerical risk factor, and the AHP-LNRF hybrid approach, have been employed to create landslide susceptibility maps for the Almora district in Uttarakhand state, India. Eight causative factors that represent the region's topography, geology, and drainage characteristics were selected and modelled within a GIS environment. Five landslide susceptibility maps were produced and categorised into five classifications based on their landslide susceptibility index. These maps were validated using the ROC curve. It was discovered that the statistical index had the highest prediction rate, whilst the LNRF technique recorded the lowest prediction rate. Compared to expert-based techniques, the statistical methods are more reliable; however, the outcomes in the statistical index, frequency ratio, and LNRF are dependent on the landslide inventory and the distribution of landslides across the study area. The statistical methods necessitate a landslide inventory, whereas expert-based techniques like the analytic hierarchy process do not require such a database for implementation. The findings of this study rely on the selected causative factors, the landslide inventory, and the distribution of landslides. Enhancements in results can be achieved by incorporating additional causative factors that influence landslide occurrences and by updating the landslide inventory. The results derived from this investigation can be utilised by planners and risk managers.

Author Contributions

Sandeep Panchal: writing – review and editing, data collection mathematical modelling, methodology, data processing, writing – original draft, visualization, validation. **Amit Kr. Srivastava:** review and editing, editing final draft, supervision.

Conflicts of Interest

The authors declare no conflicts of interest.

Data Availability Statement

The data that support the findings of this study are available from the corresponding author upon reasonable request.

10991034, 0, Downloaded from https://onlinelibrary.wiley.com/doi/10.1002/gj.70002 by Delhi Technological University, Wiley Online Library on [26/06/2025]. See the Terms and Conditions (https://onlinelibrary.wiley.com/terms-and-conditions) on Wiley Online Library for rules of use; OA articles are governed by the applicable Creative Commons License

Peer Review

The peer review history for this article is available at https://www.webofscience.com/api/gateway/wos/peer-review/10.1002/gj.70002.

References

Abdo, H. G., H. Almohamad, A. A. al Dughairi, et al. 2022. "Spatial Implementation of Frequency Ratio, Statistical Index and Index of Entropy Models for Landslide Susceptibility Mapping in Al-Balouta River Basin, Tartous Governorate, Syria." *Geoscience Letters* 9, no. 1: 45. https://doi.org/10.1186/s40562-022-00256-5.

Aleotti, P., and R. Chowdhury. 1999. "Landslide Hazard Assessment: Summary Review and New Perspectives." *Bulletin of Engineering Geology and the Environment* 58, no. 1: 21–44. https://doi.org/10.1007/s100640050066.

Barman, J., and J. Das. 2024. "Assessing Classification System for Landslide Susceptibility Using Frequency Ratio, Analytical Hierarchical Process and Geospatial Technology Mapping in Aizawl District, NE India." *Advances in Space Research* 74, no. 3: 1197–1224. https://doi.org/10.1016/j.asr.2024.05.007.

Berhane, G., and K. Tadesse. 2021. "Landslide Susceptibility Zonation Mapping Using Statistical Index and Landslide Susceptibility Analysis Methods: A Case Study From Gindeberet District, Oromia Regional State, Central Ethiopia." *Journal of African Earth Sciences* 180: 104240. https://doi.org/10.1016/j.jafrearsci.2021.104240.

Bhardwaj, V., and K. Singh. 2023. "Assessment of Landslide Susceptibility of Pithoragarh, Uttarakhand (India) Using Logistic Regression and Multi-Criteria Decision-Based Analysis by Analytical Hierarchy Process." *Applied Earth Science (Transactions of the Institutions of Mining and Metallurgy)* 132, no. 3–4: 178–186. https://doi.org/10.1080/25726838.2023.2237370.

Bhukosh portal GIS. n.d. https://bhukosh.gsi.gov.in/.

Cao, Y., X. Wei, W. Fan, Y. Nan, W. Xiong, and S. Zhang. 2021. "Landslide Susceptibility Assessment Using the Weight of Evidence Method: A Case Study in Xunyang Area, China." *PLoS One* 16, no. 1: e0245668. https://doi.org/10.1371/journal.pone.0245668.

Chen, L., H. Guo, P. Gong, Y. Yang, Z. Zuo, and M. Gu. 2021. "Landslide Susceptibility Assessment Using Weights-Of-Evidence Model and Cluster Analysis Along the Highways in the Hubei Section of the Three Gorges Reservoir Area." *Computers and Geosciences* 156: 104899. https://doi.org/10.1016/j.cageo.2021.104899.

Bhuvan NRSC. 2024. https://bhuvan.nrsc.gov.in/home/index.php.

Es-smairi, A., B. Elmoutchou, R. A. Mir, A. el Ouazani Touhami, and M. Namous. 2023. "Delineation of Landslide Susceptible Zones Using Frequency Ratio (FR) and Shannon Entropy (SE) Models in Northern Rif, Morocco." *Geosystems and Geoenvironment* 2, no. 4: 100195. https://doi.org/10.1016/j.geogeo.2023.100195.

Getachew, N., and M. Meten. 2021. "Weights of Evidence Modeling for Landslide Susceptibility Mapping of Kabi-Gebro Locality, Gundomeskel Area." *Central Ethiopia. Geoenvironmental Disasters* 8, no. 1: 6. https://doi.org/10.1186/s40677-021-00177-z.

Gorakhpur Environmental Action Group (GEAG). n.d. "Integrating Climate Change Concerns into Disaster Management and Development Planning, the Case of Almora." https://www.geagindia.org/uploads/publication_files/1965479826.pdf.

Haigh, M., and J. S. Rawat. 2012. "Landslide Disasters: Seeking Causes—A Case Study From Uttarakhand, India." In *Management of Mountain Watersheds*, edited by J. Krecek, M. J. Haigh, T. Hofer, and E. Kubin, 218–253. Springer.

Hailu, S., K. T. Deribew, E. Teferi, et al. 2024. "Spatial Assessment Employing Fusion Logistic Regression and Frequency Ratio Models to Monitor Landslide Susceptibility in the Upper Blue Nile Basin of Ethiopia: Muger Watershed." *Environmental Systems Research* 13, no. 1: 54. https://doi.org/10.1186/s40068-024-00382-3.

Hussain, G., Y. Singh, K. Singh, and G. M. Bhat. 2019. "Landslide Susceptibility Mapping Along National Highway-1 in Jammu and Kashmir State (India)." *Innovative Infrastructure Solutions* 4, no. 1: 59. https://doi.org/10.1007/s41062-019-0245-9.

Jallayu, P. T., A. Sharma, and K. Singh. 2024. "Vulnerability of Highways to Landslide Using Landslide Susceptibility Zonation in GIS: Mandi District, India." *Innovative Infrastructure Solutions* 9, no. 9: 354. https://doi.org/10.1007/s41062-024-01653-9.

Kavzoglu, T., E. Kutlug Sahin, and I. Colkesen. 2015. "An Assessment of Multivariate and Bivariate Approaches in Landslide Susceptibility Mapping: A Case Study of Duzkoy District." *Natural Hazards* 76, no. 1: 471–496. https://doi.org/10.1007/s11069-014-1506-8.

Kayastha, P., S. M. Bijukchhen, M. R. Dhital, and F. de Smedt. 2013. "GIS Based Landslide Susceptibility Mapping Using a Fuzzy Logic Approach: A Case Study From Ghurmi-Dhad Khola Area, Eastern Nepal." *Journal of the Geological Society of India* 82, no. 3: 249–261. https://doi.org/10.1007/s12594-013-0147-y.

Khan, H., M. Shafique, M. A. Khan, M. A. Bacha, S. U. Shah, and C. Calligaris. 2019. "Landslide Susceptibility Assessment Using Frequency Ratio, a Case Study of Northern Pakistan." *Egyptian Journal of Remote Sensing and Space Science* 22, no. 1: 11. https://doi.org/10.1016/j.ejrs.2018.03.004.

Kose, D. D., and T. Turk. 2019. "GIS-Based Fully Automatic Landslide Susceptibility Analysis by Weight-Of-Evidence and Frequency Ratio Methods." *Physical Geography* 40, no. 5: 481–501. https://doi.org/10.1080/02723646.2018.1559583.

Kucuker, D. M. 2024. "Analyzing Landslide Susceptibility of Forest Roads by Analytical Hierarchy Process (AHP) in of Forest Planning Unit of Turkiye." *Natural Hazards* 121: 2323–2345. https://doi.org/10.1007/s11069-024-06882-w.

Kumar, R., and R. Anbalagan. 2016. "Landslide Susceptibility Mapping Using Analytical Hierarchy Process (AHP) in Tehri Reservoir Rim Region, Uttarakhand." *Journal of the Geological Society of India* 87, no. 3: 271–286. https://doi.org/10.1007/s12594-016-0395-8.

Kumar, Y., S. Panchal, A. Ashish, and B. P. Singh. 2017. "Feasibility Study of Railway Line in Hilly Region Using GIS." *International Journal of Online and Biomedical Engineering (iJOE)* 13, no. 8: 183. https://doi.org/10.3991/ijoe.v13i08.7186.

Lee, J.-U., Y.-C. Cho, M. Kim, S.-J. Jang, J. Lee, and S. Kim. 2022. "The Effects of Different Geological Conditions on Landslide-Triggering Rainfall Conditions in South Korea." *Watermark* 14, no. 13: 2051. https://doi.org/10.3390/w14132051.

Lee, S. 2007. "Application and Verification of Fuzzy Algebraic Operators to Landslide Susceptibility Mapping." *Environmental Geology* 52, no. 4: 615–623. https://doi.org/10.1007/s00254-006-0491-y.

Lee, S., J. H. Ryu, J. S. Won, and H. J. Park. 2004. "Determination and Application of the Weights for Landslide Susceptibility Mapping Using an Artificial Neural Network." *Engineering Geology* 71, no. 3–4: 289–302. https://doi.org/10.1016/S0013-7952(03)00142-X.

Liu, X., S. Shao, and S. Shao. 2024. "Landslide Susceptibility Zonation Using the Analytical Hierarchy Process (AHP) in the Great Xi'an Region, China." *Scientific Reports* 14, no. 1: 2941. https://doi.org/10.1038/s41598-024-53630-y.

Magray, A. A., K. Singh, and S. Sharma. 2023. "Comparative Analysis of Certainty Factor and Analytic Hierarchy Process for Landslide Susceptibility Zonation in Parts of Solan, Himachal Pradesh, India." *Quaestiones Geographicae* 42, no. 3: 5–18. https://doi.org/10.14746/quageo-2023-0020.

Manopkawee, P., and N. Mankhemthong. 2025. "Landslide Susceptibility Assessment Using the Frequency Ratio Model in the

10991034, 0, Downloaded from https://onlinelibrary.wiley.com/doi/10.1002/gj.70002 by Delhi Technological University, Wiley Online Library on [26/06/2025]. See the Terms and Conditions (https://onlinelibrary.wiley.com/terms-and-conditions) on Wiley Online Library for rules of use; OA articles are governed by the applicable Creative Commons License

Mae Chan River Watershed, Northern Thailand." *Quaternary Science Advances* 17: 100263. https://doi.org/10.1016/j.qsa.2024.100263.

Mansouri Daneshvar, M. R. 2014. "Landslide Susceptibility Zonation Using Analytical Hierarchy Process and GIS for the Bojnurd Region, Northeast of Iran." *Landslides* 11, no. 6: 1079–1091. https://doi.org/10.1007/s10346-013-0458-5.

Milevski, I., S. Dragićević, and M. Zorn. 2019. "Statistical and Expert-Based Landslide Susceptibility Modeling on a National Scale Applied to North Macedonia." *Open Geosciences* 11, no. 1: 750–764. https://doi.org/10.1515/geo-2019-0059.

Morino, C., P. Coratza, and M. Soldati. 2022. "Landslides, a Key Landform in the Global Geological Heritage." *Frontiers in Earth Science* 10: 1–20. https://doi.org/10.3389/feart.2022.864760.

Neaupane, K. M., and M. Piantanakulchai. 2006. "Analytic Network Process Model for Landslide Hazard Zonation." *Engineering Geology* 85, no. 3–4: 281–294. https://doi.org/10.1016/j.enggeo.2006.02.003.

Nikoobakht, S., M. Azarafza, H. Akgün, and R. Derakhshani. 2022. "Landslide Susceptibility Assessment by Using Convolutional Neural Network." *Applied Sciences* 12, no. 12: 5992. https://doi.org/10.3390/app12125992.

Official Website of Almora District. 2024. Accessed on December 10, 2024. https://almora.nic.in/about-district/.

Ohlmacher, G. C. 2007. "Plan Curvature and Landslide Probability in Regions Dominated by Earth Flows and Earth Slides." *Engineering Geology* 91, no. 2–4: 117–134. https://doi.org/10.1016/j.enggeo.2007.01.005.

Panchal, S., and A. Debbarma. 2017. "Rail-Route Planning Using a Geographical Information System (GIS)." *Engineering, Technology and Applied Science Research* 7, no. 5: 2010–2013. https://doi.org/10.48084/etasr.1329.

Panchal, S., and A. K. Shrivastava. 2020a. "Application of Analytic Hierarchy Process in Landslide Susceptibility Mapping at Regional Scale in GIS Environment." *Journal of Statistics and Management Systems* 23, no. 2: 199–206. https://doi.org/10.1080/09720510.2020.1724620.

Panchal, S., and A. K. Shrivastava. 2021. "A Comparative Study of Frequency Ratio, Shannon's Entropy and Analytic Hierarchy Process (AHP) Models for Landslide Susceptibility Assessment." *ISPRS International Journal of Geo-Information* 10, no. 9: 1–20. https://doi.org/10.3390/ijgi10090603.

Panchal, S., and A. K. Shrivastava. 2023. "Debris Failure Susceptibility Mapping Using Information Value Method." *Sādhanā* 48, no. 3: 119. https://doi.org/10.1007/s12046-023-02167-3.

Panchal, S., and A. K. Shrivastava. 2020b. *Landslide Susceptibility Mapping Along Highway Corridors in GIS Environment*, 79–89. Springer.

Panchal, S., and A. K. Shrivastava. 2022. "Landslide Hazard Assessment Using Analytic Hierarchy Process (AHP): A Case Study of National Highway 5 in India." *Ain Shams Engineering Journal* 13, no. 3: 101626. https://doi.org/10.1016/j.asej.2021.10.021.

Panchal, S., and A. K. Srivastava. 2022. "Expert Based Landslide Susceptibility Mapping for Energy Infrastructure Planning." *Journal of Information and Optimization Sciences* 43, no. 3: 635–641. https://doi.org/10.1080/02522667.2022.2054999.

Pandey, V. K., and M. C. Sharma. 2017. "Probabilistic Landslide Susceptibility Mapping Along Tipri to Ghuttu Highway Corridor, Garhwal Himalaya (India)." *Remote Sensing Applications: Society and Environment* 8: 1–11. https://doi.org/10.1016/j.rsase.2017.07.007.

Patil, A. S., B. K. Bhadra, S. S. Panhalkar, and P. T. Patil. 2020. "Landslide Susceptibility Mapping Using Landslide Numerical Risk Factor Model and Landslide Inventory Prepared Through OBIA in Chenab Valley, Jammu and Kashmir (India)." *Journal of the Indian Society of Remote Sensing* 48, no. 3: 431–449. https://doi.org/10.1007/s12524-019-01092-5.

Pawar, U., W. Suppawimut, N. Muttil, and U. Rathnayake. 2022. "A GIS-Based Comparative Analysis of Frequency Ratio and Statistical Index Models for Flood Susceptibility Mapping in the Upper Krishna Basin, India." *Water* 14, no. 22: 3771. https://doi.org/10.3390/w14223771.

Pradhan, B. 2010. "Landslide Susceptibility Mapping of a Catchment Area Using Frequency Ratio, Fuzzy Logic and Multivariate Logistic Regression Approaches." *Journal of the Indian Society of Remote Sensing* 38, no. 2: 301–320. https://doi.org/10.1007/s12524-010-0020-z.

Pradhan, B., H. J. Oh, and M. Buchroithner. 2010. "Weights-Of-Evidence Model Applied to Landslide Susceptibility Mapping in a Tropical Hilly Area." *Geomatics, Natural Hazards and Risk* 1, no. 3: 199–223. https://doi.org/10.1080/19475705.2010.498151.

Ramli, M. F., N. Yusof, M. K. Yusoff, H. Juahir, and H. Z. M. Shafri. 2010. "Lineament Mapping and Its Application in Landslide Hazard Assessment: A Review." *Bulletin of Engineering Geology and the Environment* 69, no. 2: 215–233. https://doi.org/10.1007/s10064-009-0255-5.

Reichenbach, P., M. Rossi, B. D. Malamud, M. Mihir, and F. Guzzetti. 2018. "A Review of Statistically-Based Landslide Susceptibility Models." *Earth-Science Reviews* 180: 60–91. https://doi.org/10.1016/j.earscirev.2018.03.001.

Roodposhti, M. S., J. Aryal, H. Shahabi, and T. Safarrad. 2016. "Fuzzy Shannon Entropy: A Hybrid GIS-Based Landslide Susceptibility Mapping Method." *Entropy* 18, no. 10: 1–20. https://doi.org/10.3390/e18100343.

Rostami, Z. A., S. A. Al-modaresi, H. Fathizad, and M. Faramarzi. 2016. "Landslide Susceptibility Mapping by Using Fuzzy Logic: A Case Study of Cham-Gardalan Catchment, Ilam, Iran." *Arabian Journal of Geosciences* 9, no. 17: 685. https://doi.org/10.1007/s12517-016-2720-3.

Saaty, R. W. 1987. "The Analytic Hierarchy Process—What It Is and How It Is Used." *Mathematical Modelling* 9, no. 3: 161–176. https://doi.org/10.1016/0270-0255(87)90473-8.

Saaty, T. L. 1980. *The Analytic Hierarchy Process*. McGraw-Hill.

Saha, S., D. Sarkar, and P. Mondal. 2022. "Efficiency Exploration of Frequency Ratio, Entropy and Weights of Evidence-Information Value Models in Flood Vulnerability Assessment: A Study of Raiganj Subdivision, Eastern India." *Stochastic Environmental Research and Risk Assessment* 36, no. 6: 1721–1742. https://doi.org/10.1007/s00477-021-02115-9.

Sharma, L. P., N. Patel, M. K. Ghose, and P. Debnath. 2015. "Development and Application of Shannon's Entropy Integrated Information Value Model for Landslide Susceptibility Assessment and Zonation in Sikkim Himalayas in India." *Natural Hazards* 75, no. 2: 1555–1576. https://doi.org/10.1007/s11069-014-1378-y.

Silalahi, F. E. S., Y., Pamela Arifianti, and F., Hidayat. 2019. "Landslide Susceptibility Assessment Using Frequency Ratio Model in Bogor, West Java, Indonesia." *Geoscience Letters* 6, no. 1: 10. https://doi.org/10.1186/s40562-019-0140-4.

Singh, K., S. Khaidem, S. K. Gupta, and A. Sharma. 2024. "Assessment of Landslide Occurrence and Prediction of Susceptible Zone Based on GIS Along National Highway 37, Manipur, India." *Sādhanā* 49, no. 1: 74. https://doi.org/10.1007/s12046-023-02422-7.

Singh, K., and A. Sharma. 2022. "Road Cut Slope Stability Analysis at Kotropi Landslide Zone Along NH-154 in Himachal Pradesh, India." *Journal of the Geological Society of India* 98, no. 3: 379–386. https://doi.org/10.1007/s12594-022-1989-y.

Sujatha, E. R., G. V. Rajamanickam, and P. Kumaravel. 2012. "Landslide Susceptibility Analysis Using Probabilistic Certainty Factor Approach: A Case Study on Tevankarai Stream Watershed, India." *Journal of Earth System Science* 121, no. 5: 1337–1350. https://doi.org/10.1007/s12040-012-0230-6.

10991034, 0, Downloaded from https://onlinelibrary.wiley.com/doi/10.1002/gj.70002 by Delhi Technological University, Wiley Online Library on [26/06/2025]. See the Terms and Conditions (https://onlinelibrary.wiley.com/terms-and-conditions) on Wiley Online Library for rules of use; OA articles are governed by the applicable Creative Commons License

Sujatha, E. R., and V. Sridhar. 2017. "Mapping Debris Flow Susceptibility Using Analytical Network Process in Kodaikkanal Hills, Tamil Nadu (India)." *Journal of Earth System Science* 126, no. 8: 1–18. https://doi.org/10.1007/s12040-017-0899-7.

Swetha, T. v., and G. Gopinath. 2020. "Landslides Susceptibility Assessment by Analytical Network Process: A Case Study for Kuttiyadi River Basin (Western Ghats, Southern India)." *SN Applied Sciences* 2, no. 11: 1776. https://doi.org/10.1007/s42452-020-03574-5.

Thanh, L. N., Y.-M. Fang, T.-Y. Chou, et al. 2022. "Using Landslide Statistical Index Technique for Landslide Susceptibility Mapping: Case Study: Ban Khoang Commune, Lao Cai Province, Vietnam." *Watermark* 14, no. 18: 2814. https://doi.org/10.3390/w14182814.

Torkashvand, A. M., A. Irani, and J. Sorur. 2014. "The Preparation of Landslide Map by Landslide Numerical Risk Factor (LNRF) Model and Geographic Information System (GIS)." *Egyptian Journal of Remote Sensing and Space Science* 17, no. 2: 159–170. https://doi.org/10.1016/j.ejrs.2014.08.001.

van Westen, C. J., P. Jaiswal, S. Ghosh, T. R. Martha, and S. L. Kuriakose. 2012. "Landslide Inventory, Hazard and Risk Assessment in India." In *Terrigenous Mass Movements*, 239–282. Springer.

Wu, Y., W. Li, Q. Wang, et al. 2016. "Landslide Susceptibility Assessment Using Frequency Ratio, Statistical Index and Certainty Factor Models for the Gangu County, China." *Arabian Journal of Geosciences* 9, no. 2: 84. https://doi.org/10.1007/s12517-015-2112-0.

Zhou, X., W. Wu, Y. Qin, and X. Fu. 2021. "Geoinformation-Based Landslide Susceptibility Mapping in Subtropical Area." *Scientific Reports* 11, no. 1: 24325. https://doi.org/10.1038/s41598-021-03743-5.

10991034, 0, Downloaded from https://onlinelibrary.wiley.com/doi/10.1002/gj.70002 by Delhi Technological University, Wiley Online Library on [26/06/2025]. See the Terms and Conditions (https://onlinelibrary.wiley.com/terms-and-conditions) on Wiley Online Library for rules of use; OA articles are governed by the applicable Creative Commons License

Journal of The
Electrochemical Society

ACCEPTED MANUSCRIPT

Highly Sensitive Electrochemical Detection of Hydroquinone in Wastewater Using Ionic Liquid Grafted rGO-ZrO2 Nanohybrid-Based Conducting Paper

To cite this article before publication: Mohd. Jamshaiya Raza *et al* 2025 *J. Electrochem. Soc.* in press https://doi.org/10.1149/1945-7111/adde89

Manuscript version: Accepted Manuscript

Accepted Manuscript is "the version of the article accepted for publication including all changes made as a result of the peer review process, and which may also include the addition to the article by IOP Publishing of a header, an article ID, a cover sheet and/or an 'Accepted Manuscript' watermark, but excluding any other editing, typesetting or other changes made by IOP Publishing and/or its licensors"

This Accepted Manuscript is **© 2025 The Electrochemical Society ("ECS"). Published on behalf of ECS by IOP Publishing Limited. All rights, including for text and data mining, AI training, and similar technologies, are reserved.**.

This article can be copied and redistributed on non commercial subject and institutional repositories.

Although reasonable endeavours have been taken to obtain all necessary permissions from third parties to include their copyrighted content within this article, their full citation and copyright line may not be present in this Accepted Manuscript version. Before using any content from this article, please refer to the Version of Record on IOPscience once published for full citation and copyright details, as permissions will likely be required. All third party content is fully copyright protected, unless specifically stated otherwise in the figure caption in the Version of Record.

View the article online for updates and enhancements.

This content was downloaded from IP address 14.139.251.98 on 04/06/2025 at 06:18

Highly Sensitive Electrochemical Detection of Hydroquinone in Wastewater Using Ionic Liquid Grafted rGO-ZrO2 Nanohybrid-Based Conducting Paper

Journal:	*Journal of The Electrochemical Society*
Manuscript ID	JES-114375.R1
Manuscript Type:	Research Paper
Date Submitted by the Author:	21-May-2025
Complete List of Authors:	Raza, Mohd. Jamshaiya; SGT University, Department of Chemistry Jalil, Qwais; Delhi Technological University, Department of Applied Chemistry Riyazuddeen, Riyazuddeen; Aligarh Muslim University Kumar, Devendra; Delhi Technological University, Department of Applied Chemistry Pandey, Chandra; SGT University, Department of Chemistry
Keywords:	Bioelectrochemistry, Sensors, Electroanalytical Electrochemistry, Graphene, Nanoscale materials

SCHOLARONE™
Manuscripts

Accepted Manuscript

Highly Sensitive Electrochemical Detection of Hydroquinone in Wastewater Using Ionic Liquid Grafted rGO-ZrO_2 Nanohybrid-Based Conducting Paper

Mohd. Jamshaiya Raza,[1] Owais Jalil,[2] Riyazuddeen,[3] Devendra Kumar,[2] and Chandra Mouli Pandey[1,z]

[1]Department of Chemistry, Faculty of Applied and Basic Sciences, SGT University, Gurugram (Haryana)-122505, India

[2]Department of Applied Chemistry, Delhi Technological University, Delhi-110042, India

[3]Department of Applied Chemistry, Aligarh Muslim University, Aligarh 202002, UP, India

[z]E-mail: cmp.npl@gmail.com

Accepted Manuscript

For Review Only

Abstract

Herein, we envisage the fabrication of conducting paper electrode (CPE) based on ionic liquid (IL)-grafted ZrO_2 nanoparticles and rGO for ultra-sensitive enzymatic detection of hazardous phenolic compounds. The rGO-ZrO_2 nanohybrid has been synthesized using the one-pot hydrothermal technique, followed by the modification with IL to enhance the catalytic activity and conductivity of rGO-ZrO_2 nanohybrid. CPE has been prepared by integrating IL@rGO-ZrO_2 nanohybrid with the PEDOT: PSS modified Whatsman filter paper. The IL@rGO-ZrO_2/CPE has been immersed in different solvents, and its conductivity was assessed using the four-probe method. The conductivity of the ILs-@rGO-ZrO_2/CPE was higher in ethanol (7.58×10^{-3} S/cm) compared to the electrodes without treatment with any solvent. Further, the laccase enzyme was covalently linked to the ILs@rGO-ZrO_2/CPE for detecting HQ. The fabricated biosensor depicts a linear response for the detection of HQ in the concentration range of 40 µM to 0.01 µM with a detection limit of 0.01 µM and sensitivity of 0.1408 µA μM^{-1} cm^{-2}. The electrochemical results indicate that integrating IL@rGO-ZrO_2 nanohybrid with the CPE enhances electron transfer and electrocatalytic performance. The validation of the fabricated biosensor with tap and lake water shows an acceptable recovery rate, indicating that the developed method is cost-effective and eco-friendly.

Introduction:

Accepted Manuscript
For Peer Review Only

Hydroquinone (HQ) is a principal intermediate and basic organic chemical raw material in the pharmaceutical industry[1]. It has been identified as a typical organic contaminant in the environment, which is difficult to reduce naturally and is widely found in dyes, chemicals, pharmaceuticals, and various other industries. HQ is also used as an isomer of dihydroxybenzene across various industries.[2–4] Their poor biodegradability makes them a major contributor to water pollution when they enter water bodies without proper treatment[5]. HQ is identified as a potential human carcinogen by the International Agency for Research on Cancer. The permissible concentration of HQ is 1 ppm in inland surface water and 0.001 ppm in natural water.[6] The discharge of HQ into water bodies has been found hazardous to human and animal health as it leads to toxicity in soil microbes, can damage chromosomes and DNA, cause skin irritation, and many other diseases.[7] Various conventional methods have been employed to monitor and detect the presence of HQ. These include chemiluminescence, fluorescence techniques, chromatography, advanced oxidation processes, and capillary electrophoresis[7,8]. Although these methods are effective for detecting HQ, they have certain limitations, i.e, they are often time-consuming, costly, and technically complex, making them challenging to do in routine environmental monitoring. Therefore, developing a rapid, low-cost, and sensitive method to detect HQ content in wastewater is essential.[9–11]

Recently, electrochemical biosensors have been used for the quantification of HQ because of their simplicity, low cost, and compatibility with miniaturised and portable devices. Also, it provides rapid response and requires minimal sample preparation, enabling real-time, on-site detection[12]. Further, HQ is an electroactive compound that undergoes a well-defined redox reaction, making it highly suitable for an electrochemical biosensor[13]. Researchers have explored various nanomaterials for the fabrication of electrochemical biosensors for HQ detection[14]. Among the various nanomaterials, reduced graphene oxide (rGO), which has been widely explored because of its important characteristics, such as exceptional electrical conductivity, high surface area, biocompatibility, and good catalytic properties.[15] The most important property of rGO is that it contains an oxygenated functional group (-OH, -COOH, etc.) that allows it to bind with other suitable nanomaterials, especially metal oxides, to enhance the biosensing characteristics[16]. In this context, an electrochemical biosensor has been reported for detecting HQ using polypyrrole/carbon black doped ZnO nanohybrid. The sensor efficiently identifies hazardous HQ with a wide concentration range (0.9 μM to 6.5 mM) and LOD (22.9 ± 0.1 nM).[17] Alam et al.

Accepted Manuscript
For Review Only

developed a GCE-Lac biosensor using PEDOT-GO to detect HQ in real samples with a detection limit of 0.041 μM and a linear concentration range from 0.41–3.0 μM.[18] An electrochemical biosensor for the detection of HQ has been fabricated using Mn_2SnO_4/f-CB, with a detection limit of 7 nM and a linear concentration range of 0.005 to 70.80 μM[19]. As a voltammetric sensor based on Cu_2O_4 NP on nitrogen-doped rGO nanohybrid IL-modified CPE has been reported to detect HQ[20]. Arfin et al. developed a GCE biosensor to detect phenol using ZnO-functionalized GO[21]. However, the stability and scalability of this composite could be higher than others. Liu et al. developed an effective sensor based on MnO_x/rGO modified screen printed electrode for identifying HQ, and it has been observed that integrating nanohybrid provides excellent electrochemical results with low cost and great reusability and can efficiently predict the HQ in polluted water[22,23]. Among the various metal oxides, zirconium dioxide (ZrO_2) has shown great potential in electrochemical biosensor fabrication because of its good conductivity, chemical stability, and high surface area. The integration of rGO with ZrO_2 can enhance the electrochemical activity due to the synergetic effect of ZrO_2 and rGO, as the rGO facilitates fast electron transfer, while ZrO_2 provide chemical selectivity and strong adsorption capacity for enzyme (Lac) due to its ability to coordinate with hydroxyl groups.[24] Moreover, ZrO_2 exhibits high thermal stability, inertness, and a wide bandgap, making it a robust addition for enhancing the long-term durability and selectivity of the biosensor. Recently, a new class of nanomolecular ionic solvents i.e., Ionic Liquid (ILs), has been widely explored in environmental remediation, organic and inorganic synthesis, the pharmaceutical industry, material science, and electrochemical biosensing.[25,26] These ILs have unique properties such as low melting points, good thermal and chemical properties, high ionic conductivity at room temperature, low toxicity, nonflammability, and affinity to interact with different chemicals. These features of ILs make it a suitable candidate for developing IL-modified nanomaterials with enhanced electrochemical properties.[25,27,28]

In the current study, we have synthesized an ILs-modified rGO-ZrO_2 nanohybrid, which was further used to fabricated a paper electrode for detecting HQ. The rGO-ZrO_2 nanohybrid was modified with ILs to enhance its stability and electron transfer capabilities.[29] Lac enzyme was covalently immobilized onto the ILs@rGO-ZrO_2 modified conductive paper (CP) for electrode fabrication. The integration of ILs@rGO-ZrO_2 improves the CP's conductivity and provides a large surface area, promoting efficient electron transfer and improving the catalytic performance of the

Accepted Manuscript
For Review Only

Lac enzyme.[29,30] This novel ILs@rGO-ZrO_2 nanohybrid on CP offers a sustainable and cost-effective approach to phenolic compound detection in contaminated water sources.

Material and Methods

2.1. Materials

Zirconyl nitrate pentahydrate ($Zr(NO_3)_4.5H_2O$), Urea (NH_2CONH_2), Sodium hydroxide (NaOH), Ethanol, Poly(3,4-Polyethylenedioxythiophene: Poly(styrene sulfonate) (PEDOT: PSS), Ammonium Hydroxide (NH_4OH), Graphite powder (size<20 µm), Hydrochloric acid (HCl), Hydrogen peroxide (H_2O_2), Sodium hydroxide (NaOH), Ethanol, Laccase (≥50 units/mg; *Rhusvernicifera*), L-ascorbic acid, Laccase (≥50 units/mg; *Rhusvernicifera*), N-Hydroxysuccinimide (NHS), 1-ethyl-3(3-(dimethylamino)-propyl) carbodiimide·HCl (EDC), 2,2′-azino-bis(3-ethylbenzothiazoline-6-sulfonic acid (ABTS) and Hydroquinone (HQ; ≥99.0%), have been procured from Sigma-Aldrich, India. Whatman Filter Paper No #1 (125mm), Sulfuric acid (H_2SO_4), and potassium permanganate ($KMnO_4$) were purchased from Thermo-Fischer Scientific, India. All the solutions were prepared in deionized water (DIW), and the solutions and glassware were autoclaved before use.

2.2. Synthesis of ZrO_2 nanoparticles

The hydrothermal process has been used to synthesize ZrO_2 nanoparticles[23]. As a precursor, $Zr(NO_3)_4.5H_2O$ (0.5 mmol) and urea (0.5 mmol) were mixed in DIW and stirred to form a homogenous solution. The mixture was then placed in a hydrothermal autoclave for 12 h at 180 °C. Further, the autoclave was cooled to room temperature, and the unreacted component was removed by washing it with ethanol/DIW. The autoclave was cooled to room temperature to collect the white precipitate. The product was calcined at 450 °C for 15 h after being dried at 80 °C for 10 h.

2.3. Synthesis of GO and rGO

The GO has been synthesised from graphite using the modified Hummer's method, where 1.25 g of graphite powder (size <20 µm) were added to 30 mL of concentrated H_2SO_4 while maintaining the temperature up to 2 °C.[31,32] Further, 3.25 g of $KMnO_4$ was slowly added to the suspension. The system was kept under stirring at room temperature for 2h, during which the graphene flakes were oxidized. Further, 10 mL of H_2O_2 (30%) was added to the mixture, stirred for 30 min, cooled to 2

Accepted Manuscript For Review Only

°C, and diluted with water. Lastly, the resulting GO suspensions were washed using HCl and DIW until a neutral pH had been reached. The obtained GO powder was dried at 60 °C in a vacuum oven. rGO was synthesised using chemical reduction method, where a stable aqueous dispersion of GO was added into a round bottom flask and, L-ascorbic acid (40%) was added under continuous stirring at 80 °C for 4h to promote the reduction of oxygen-containing functional groups in GO. During the reaction, suspension colour changes from brownish-yellow to black, indicating the formation of rGO. After cooling, the obtained product was filtered and washed with DIW/ethanol to remove the impurities and was dried under a vacuum oven at 60 °C to obtain rGO.

2.4. Synthesis of rGO-ZrO_2 nanohybrids

rGO-ZrO_2 nanohybrid was synthesized by dissolving 100 mg of rGO powder in 50 mL of THF and then sonicating the solution for 30 min to form a homogeneous mixture. 150 mg of ZrO_2 powder and 10 mL N_2H_4 were added to the rGO solution, and sonicated the mixture for 1h and transferred into the hydrothermal autoclave for 5 h at 90 °C. Further, the mixture was placed in the microwave oven at 60 °C and irradiated for 20 min, changing the colour from brown to black. The solution was centrifuged at 5000 rpm for 10 min to remove unreacted N_2H_4. The precipitate was collected and dried at 80 °C in a vacuum oven for 24 h[33].

2.5. Synthesis of Imidazolium-based ILs and rGO-ZrO_2 Nanohybrid

Imidazolium-based ILs 1-Butyl-3-methylimidazolium bromide [BMIM][Cl-] have been synthesised using the reported method.[34,35] The synthesized ILs were added to the prepared rGO-ZrO_2 nanohybrid 125mg in 40mL DIW and ultrasonicated for 1h to get the clear suspended solution. After a clear solution, [BMIM][Cl^-] IL and 100mg KOH, were added, and the solution was transferred into the round-bottom flask and refluxed at 80°C for 24h. We obtained ILs modified rGO-ZrO_2 nanohybrid (ILs@rGO-ZrO_2) with unreacted ILs and KOH. Further, to remove unreacted elements, the solution was centrifuged and washed with ethanol and DIW three times, and the final product was frozen and dried.

2.6. Fabrication of ILs@rGO-ZrO_2 nanohybrid-modified CP electrode:

Whatman filter paper was used to fabricate CPE. Before the fabrication, the paper was stabilized using Tween-80 solution (50%), followed by ultrasonication for 20 min. Afterward, the electrode was dried at 60 °C for 24h in the microwave oven. The conduction solution was prepared by adding

Accepted Manuscript
For Review Only

100 mg of ILs@rGO-ZrO_2 nanohybrid with 10 mL of PEDOT: PSS aqueous solution (2.8% and 5% ethylene glycol), and the mixture was sonicated for 3 h for a homogeneous solution. The stabilized filter paper was dipped into the ILs@GO-ZrO_2/PEDOT: PSS solution for 1 h, followed by drying in a hot air oven at 80 ℃ for 30 min. The process was repeated three times to achieve the desired conductivity, mechanical strength, flexibility, and stability. The obtained ILs@rGO-ZrO_2/CPE was additionally dried for 3 to 4 h at 80 ℃ to ensure the complete loss of humidity.[32,36]

2.7. Instrumentation

X-ray diffraction (XRD) analysis has been carried out for the synthesized materials using a Bruker D-8 advance X-ray diffractometer with Cu K α radiations with a wavelength of 1.5406 A˚. The functional group of rGO, rGO-ZrO_2, and IL@rGO-ZrO_2 nanohybrid has been recorded using FT-IR (Perkin-Elmer spectrometer; Model spectra 2). Field emission scanning electron microscope (FESEM; FEI NOVA NANOSEM 450) has been used to study the surfaces of the synthesized nanohybrid and the CPE electrode. The elemental composition was confirmed using the energy-dispersive X-ray analysis apparatus (EDAX; Oxford Instruments). All electrochemical tests were carried out using an autolab potentiostat/galvanostat (Eco-Chemie, the Netherlands) with a three-electrode setup consisting of an Ag/AgCl reference electrode, a working electrode, and Pt as a counter electrode. Phosphate buffer saline (PBS; pH 7.0; 100 mM) has been used to investigate other electrochemical properties of CPE.

3. Results and discussion

The X-ray diffraction pattern of ZrO_2 **(Fig. 2A)** shows 2θ peaks at 17.38, 24.10, 28.43, 31.68, 34.40˚ 35.57, 40.77, and 49.47 corresponding to the (110), (011), (-110), (111), (002), (200), (-211) and (-220) planes, respectively which indicate the monoclinic structure of ZrO_2 which is confirmed by the previously reported research (JCPDS No.: 37-1484). The XRD pattern of ILs-modified rGO shows a peak at 25˚ corresponding to (002) plane **(Fig 2B)** confirming the reduction of GO sheets and restacking into an ordered crystalline structure.[33,37]

Raman spectrum of the ILs@rGO-ZrO_2 nanohybrid sample shows peaks at ~1588 cm^{-1} (G band), which is more intense than the 2D broad band at 2440 cm^{-1} **(Fig. 2C)**. The strong, intense D bands at 1320 cm^{-1} indicates that breaking of sp^2 bonds, and conversion of sp^2 to sp^3 hybridization. This transformation signifies greater disorder within the sp^2 hybridized carbon

Accepted Manuscript
For Review Only

system. The difference in the intensity between D and G bands is significant in ILs@rGO-ZrO_2 nanohybrid, which depicts the formation of new defects in the sp^2 carbon lattice throughout the reduction process. The presence of ZrO_2 nanoparticles on the rGO surface confirmed by the Raman shifts at 206 cm^{-1}, 278 cm^{-1}, 400 cm^{-1} and 611 cm^{-1}, which are associated with the tetragonal zirconia phases.[38,39]

The functional groups of the synthesised ILs@GO-ZrO_2 nanohybrid have been determined using FT-IR spectroscopy **(Fig. 2D)**. The Zr-O vibration exhibits intensity peaks at 524 and 749 cm^{-1}, while the CH_2 stretching mode displays the broad absorption peaks at 2908 cm^{-1}. The stretching vibration of C=O in –COOH was observed at 1746 cm^{-1}. The peak observed at 1200 cm^{-1} corresponds to the C–O–C stretching vibration. The absorption bands at 1157 and 1060 cm^{-1} attributed to the alkoxy C-O and the epoxy C-O stretching vibration, respectively. The absorption band at 1033 cm^{-1} corresponds to C-N bond, indicating the presence of ILs, and the peak at 2910 cm^{-1}, indicates the C–H stretching vibration. The broad peak observed at 3250 cm^{-1} corresponds to O-H vibration. The absorption band appearing at 1561 cm^{-1} has been attributed to stretching the aromatic C=C mode. Moreover, the characteristic band at 1713 cm^{-1} specified that the C=O stretching frequency corresponds to the rGO-ZrO_2 nanohybrid shifted to 1746 cm^{-1} due to the interaction between the C=O group and Zr.[34,35] Further, the FTIR spectrum of the IL@rGO-ZrO2/CPE (Fig. S1) exhibits the retained features of the nanohybrid along with significant modifications, indicating successful immobilisation onto the conductive cellulose substrate. The intensified and broadened O-H stretching band at ~3250 cm-1 is attributed to the hydroxyl-rich nature of the cellulose fibres. Similar C-H stretching at 2910 cm^{-1} and the preserved C=O, C=C, and C-O-related vibrations confirm the chemical integrity of the nanohybrid post-deposition. These results confirm the successful fabrication of IL@rGO-ZrO2/CPE, where there is synergistic interaction between the nanohybrid and the paper substrate.

Figure 3 shows the SEM and EDAX analysis of synthesised ILs@rGO-ZrO_2 nanohybrid and ILs@rGO-ZrO_2/CPE. The SEM image of rGO-ZrO_2 shows that the ZrO_2 nanoparticles are uniformly distributed across the rGO surface, with minimal aggregation, likely due to the stabilizing effect of the ILs **(Fig.3A)**. The FE-SEM images of ILs@rGO-ZrO_2/CPE, indicates the unbroken and evenly distributed layer of the nanohybrid coating on the CPE surface that effectively covers the fibrous structure of the paper substrate providing strong bond and

Accepted Manuscript
For Review Only

mechanical stability **(Fig.3B & C)**.[35,40,41] EDAX analysis of rGO-ZrO_2 nanohybrid shown in **Figure 3D** indicated intense peaks of Zr, C and O, indicating the presence of ZrO_2 and rGO. However, the EDAX analysis of ILs@rGO-ZrO_2/CPE shows all peaks of composite, including an extra peak of sulphur which indicate the presence of PEDOT: PSS it also shows the nitrogen peaks indicating the presence of ILs in the nanohybrid. The EDAX results confirm that the fabricated paper contains all the elements in the nanohybrid.

3.1. Conductivity studies of ILs@rGO-ZrO_2/CPE

The electrical conductivity of ILs@rGO-ZrO_2/CP electrodes was evaluated in various solvents (methanol, ethanol, propanol, n-butanol, and DMSO) using the four-probe technique. The solvents, with distinct polarities and dielectric properties, significantly influenced the conductivity of the CPE by moderating the interaction of the ILs, rGO, and ZrO_2 components. Polar solvents like methanol and ethanol displayed higher conductivity, 5.12×10^{-3} and 7.58×10^{-3} $Scm^{-1,}$ respectively, recognized as their ability to improve ionic mobility and interfacial charge transfer[34,41]. Whereas, n-butanol (4.77×10^{-3} Scm^{-1}), DMSO (4.27×10^{-3}), and propanol (2.73×10^{-3} Scm^{-1}) have lower polarity resulted in moderated conductivity due to reduced interaction with the CPE surface and slower ion transportation (Fig. 4A). These results highlight the pivotal role of solvent selection in optimizing the electrochemical performance of ILs@rGO-ZrO_2/CPE for biosensing applications. Further, the integration of IL also improves the dispersion of the rGO and ZrO_2 nanoparticles uniformly, preventing agglomeration and maintaining a high electroactive surface area.

3.2. Flexibility and stability studies of ILs@rGO-ZrO_2/CPE

The bending stability of the ILs@rGO-ZrO_2/CPE, both static and dynamic, was systematically evaluated by folding the CP substrate at different angles (-180°, 45°, 90°, and 180°). As exemplified in Fig. 4B, the electrode's remarkable conductivity remained largely constant across these various bending configurations. This result highlights the exceptional flexibility of the CP electrodes, which confirmed minimal variations in conductivity after folding and exhibited excellent stationary bending performance.[23,42] Dynamic bending stability test of the CPE has been carried out at various angle (45º, 90 º, 180 º) for a total of 100, 150 and 200 cycles (Fig.4C). It has been observed that the conductivity decreased by 1.8 % to 2.3 %, which may be due the collective damage and breakage of the conductive layer and the paper fibres as the number of bends

Accepted Manuscript
For Review Only

intensifies. This hinders the transfer of electrical signal pathways, resulting in decreased conductivity. To assess long-term stability, the conductivity of the ILs@rGO-ZrO_2/CP electrode was monitored at 5-day intervals over a period of 30 days, as depicted in Figure 4D. During these measurements, the electrodes were stored in desiccators under dry conditions at room temperature to ensure constant testing conditions. Over the 25-day period, the electrode's conductivity experienced only a minimal change, approximately 6.12%, highlighting its exceptional long-term stability. This performance indicates the robustness of the ILs@rGO-ZrO_2/CP electrode under extended usage and environmental storage conditions.

3.3. Electrochemical biosensing studies

The electrochemical activities of the fabricated electrode and bioelectrode were carried out using chronoamperometry, which is a time-dependent approach that involves applying a constant electric potential and recording the resulting current over specific time intervals. Utilising the Lac/ILs@rGO-ZrO_2/CP electrode, we examined the electrochemical response to varying concentrations of HQ (0.01 µM - 40 µM) in PBS (pH 7.0) through chronoamperometry (Interval time > 0.1 s). The results indicate a notable increase in current (n=3) with each incremental rise in HQ concentration **(Fig. 5A)**. This increase in the current response is attributed to the reduction in the availability of electrons on the surface of the electrode. The establishment of linearity (Fig. 5B) occurred as we plotted saturated current responses against different HQ concentrations, yielding a linear regression equation.[29,38]

$$\text{Current } (\mu A) = 23.6259\ \mu A - 0.1408\ \mu A/\mu M \times C_{HQ}\ (\mu M) \qquad R_2 = 0.99586$$

The Lac/ILs-rGO@ZrO_2/CP electrode exhibited a limit of detection of 0.01 µM (3σ/S; where σ represents the standard deviation of the electrode) and sensitivity (S = slope/active surface area of electrode) of 0.1408 µA μM^{-1} cm^{-2}, respectively. Compared to other IL-based biosensors for HQ detection, the biosensing results using Lac/ILs@rGO-ZrO_2/CP electrodes were higher (**Table 1**).[43] Further, the biosensing properties of the fabricated biosensor were also compared with a non-ILs modified electrode, and it has been observed that the biosensor shows acceptable biosensing results **(Table ST1)**. The results show the exceptional performance of the fabricated Lac/ILs@rGO-ZrO_2/CP electrode as a sensing platform for HQ.[44]

Accepted Manuscript
For Review Only

3.4. Interference and reproducibility studies

The effect of potential interferents on the performance of the fabricated biosensor was investigated using chronoamperometry[45]. For this analysis, equal concentrations (10 μM) of various interferents, including benzoic acid, phenol, cysteine, and uric acid, were individually incubated with the Lac/ILs@rGO-ZrO_2/CPE. The electrochemical results, as shown in **Figure 5C**, revealed no significant changes in the current response of the biosensor when exposed to these interferents, demonstrating the electrode's high selectivity and resistance to interference.[35,46] Additionally, the performance of the biosensor was tested in the presence of a mixture containing HQ and the above-mentioned interfering analytes. Even under these conditions, the biosensor maintained a positive and specific response to HQ, further emphasizing its robustness and specificity for the target analyte. In addition to selectivity studies, the stability of the Lac/ILs@rGO-ZrO_2/CP electrode was estimated by quantifying the current response at intervals of 5 days over a period of 35 days **(Fig.5D)**. The results confirmed that the biosensor retained 96% of its initial current response after 35 days, which showed its excellent stability. However, a regular decline in current was observed beyond this period, likely due to the washing out of the enzyme from the ILs@rGO-ZrO_2/CP matrix. This slight degradation specifies the biosensor's long-term viability, with minor limitations in enzyme retention over extended intervals.[47,48]

3.5. Validation of the Lac/ILs@rGO-ZrO_2/CPE with real water sample analysis

To assess the suitability of the Lac/ILs@rGO-ZrO_2/CPE for real sample analysis, water samples were collected from two sources i.e. tap water (TW) and lake water (LW). These samples were spiked with HQ at 1 μM, 10.0 μM, 20.0 μM, 30.0 μM, 40.0 μM and 50.0 μM concentrations. The saturation current corresponding to each concentration was measured for both types of water samples. The experiment was conducted three times for consistency, and a calibration curve was used to determine the concentration of HQ in the samples. The results, summarized in **Table 2**, show acceptable recovery rate for HQ in different spiked water sample with a relative standard deviation below 1.2%. Interestingly the percentage recovery in LW is higher compare to TW, this perhaps is due to the presence of other impurities in LW. The result indicates the feasibility of the fabricated ILs@rGO-ZrO_2/CPE based biosensor for the electrochemical detection of HQ in waste water.

Accepted Manuscript
For Review Only

Conclusion

Ionic liquid-modified rGO-ZrO_2 nanohybrid has been successfully used to fabricate CPE for the electrochemical detection of HQ. Structural and morphological analyses indicated the successful fabrication of the ILs@rGO-ZrO_2/CPE. The developed CPE shows excellent bending stability and processability due to its unique free-standing structure and high flexibility. Electrochemical studies suggest that integrating ILs and rGO-ZrO_2 enhanced the CPE conductivity and active surface area, improving electrochemical performance. The fabricated biosensor was found to be rapid, show a wide linear range, high sensitivity, and stable response for HQ detection. Further, it can successfully detect HQ in tap and lake water with high recovery rates making it a promising alternative for the HQ detection in waste water.

Acknowledgments

Mohd. J. R. acknowledges VC, SGT University, for the support in carrying out the research work. The authors thank the Department of Applied Chemistry, Delhi Technological University, for the characterization facilities. CMP thanks SGT University for providing IMRG research grant for carrying out this project.

Reference

1 H. Soltani, A. Pardakhty and S. Ahmadzadeh, *Journal of Molecular Liquids*, 2016, **219**, 63–67.

2 W. Sun, Y. Wang, Y. Lu, A. Hu, F. Shi and Z. Sun, *Sensors & Actuators: B. Chemical*, 2013, **188**, 564–570.

3 I. C. Vieira and O. Fatibello-filho, *Talanta*, 2000, **52**, 681–689.

4 P. Shaikshavali, T. M. Reddy, T. V. Gopal and G. Venkataprasad, *Journal of Materials Science: Materials in Electronics*, 2021, **32**, 5243–5258.

5 X. Liu, Z. Ding, Y. He, Z. Xue, X. Zhao and X. Lu, *Colloids and Surfaces B: Biointerfaces*, 2010, **79**, 27–32.

6 W. Tang, M. Zhang, W. Li and X. Zeng, *Talanta*, 2014, **127**, 262–268.

7 S. Cotchim, K. Promsuwan, M. Dueramae and S. Duerama, *Journal of The Electrochemical Society*, 2020, **167(15)**, 155528.

8 M. Fouladgar, *Journal of The Electrochemical Society*, 2018, **165**, B559–B564.

Accepted Manuscript
For Review Only

9 Z. H. Mahmoud, *Nanomedicine Journal*, 2024, **11(4)**, 458–467.

10 Y. Liu, Z. Zhang, Y. Li, F. Shi, Y. Ai, B. Wang, S. Zhang, X. Zhang and W. Sun, *International Journal of Electrochemical Science*, 2023, **18**, 100063.

11 A. Hatamie, S. Angizi, S. Kumar, C. M. Pandey, A. Simchi, M. Willander and B. D. Malhotra, *Journal of The Electrochemical Society*, 2020, **167**, 037546.

12 S. Verma, D. Thakur, C. M. Pandey and D. Kumar, *Multidisciplinary Digital Publishing Institute (MDPI)*, 2023, DOI: 10.3390/bios13030305.

13 W. Ma and Y. T. Long, *Chemical Society Reviews*, 2014, **43**, 30–41.

14 S. Verma, C. M. Pandey and D. Kumar, *New Journal of Chemistry*, 2022, **559**, 21190–21200.

15 F. Tahernejad-Javazmi, M. Shabani-Nooshabadi and H. Karimi-Maleh, *New Journal of Chemistry*, 2018, **42**, 16378–16383.

16 L. Yu, J. Liu, W. Yin, J. Yu, R. Chen, D. Song, Q. Liu, R. Li and J. Wang, *Talanta*, 2020, **209**, 120515.

17 J. Ahmed, M. Faisal, M. Jalalah, S. A. Alsareii and F. A. Harraz, *Journal of Electroanalytical Chemistry*, 2021, **898**, 115631.

18 M. Alam, M. Imran, T. Alshahrani, F. Khan and R. Azim, *Measurement*, 2024, **224**, 113890.

19 Y. Nam, B. Muthukutty, A. F. Rosyadi and H. Yoo, *Journal of Industrial and Engineering Chemistry*, 2024, **133**, 539–549.

20 P. M. Jahani, F. G. Nejad, Z. Dourandish, M. P. Zarandi, M. M. Safizadeh, S. Tajik and H. Beitollahi, *Chemosphere*, 2022, **302**, 134712.

21 A. Cetinkaya, S. I. Kaya, M. Yence, F. Budak and S. A. Ozkan, *Elsevier B.V.*, 2023.

22 G. Liu, J. Liu, P. Pan, Z. Wang, Z. Yang, J. Wei, P. Li, S. Cao, H. Shen, J. Zhou and X. Zhang, *Microchemical Journal*, 2023, **185**, 108234.

23 V. C. Valsalakumar, A. S. Joseph, J. Piyus and S. Vasudevan, *ACS Applied Nano Materials*, 2023, **6**, 8382–8395.

24 S. Cheraghi, M. A. Taher, H. Karimi-Maleh, F. Karimi, M. Shabani-Nooshabadi, M. Alizadeh, A. Al-Othman, N. Erk, P. K. Yegya Raman and C. Karaman, *Chemosphere*, 2022, **287**, 132187.

25 D. Işın, E. Eksin and A. Erdem, *Biosensors*, 2022, **12**, 95.

26 R. Darabi and M. Shabani-Nooshabadi, *Food Chemistry*, 2021, **339**, 127841.

Accepted Manuscript
For Review Only

27 P. Chen, F. Xie, F. Tang and T. McNally, *Carbohydrate Polymers*, 2021, **253**, 117231.

28 N. K. Bhajanthri, V. K. Arumugam, R. Chokkareddy and G. G. Redhi, *Journal of Molecular Liquids*, 2016, **222**, 370–376.

29 S. Tajik, A. A. Afshar, S. Shamsaddini, M. B. Askari, Z. Dourandish, F. Garkani Nejad, H. Beitollahi and A. Di Bartolomeo, *Industrial and Engineering Chemistry Research*, 2023, **62**, 4473–4480.

30 S. Verma, C. M. Pandey and D. Kumar, *Applied Organometallic Chemistry*, 2023, **38**, e7325.

31 Y. Gupta, C. M. Pandey and A. S. Ghrera, *ChemistrySelect*, 2022, **7**, e202202642.

32 S. Kumar, S. Kumar, S. Srivastava, B. K. Yadav, S. H. Lee, J. G. Sharma, D. C. Doval and B. D. Malhotra, *Biosensors and Bioelectronics*, 2015, **73**, 114–122.

33 S. Kumar, J. G. Sharma, S. Maji and B. D. Malhotra, *Biosensors and Bioelectronics*, 2016, **78**, 497–504.

34 P. Ranjan, S. Yadav, M. A. Sadique, R. Khan and A. K. Srivastava, *ACS Applied Nano Materials*, 2022, **5**, 14999–15010.

35 N. S. Tapak, M. A. Nawawi, E. T. T. Tjih, Y. Mohd, A. H. A. Rashid, J. Abdullah, N. A. Yusof and N. M. Ahmad, *Materials Today Communications*, 2022, **33**, 104142.

36 S. Kumar, M. Umar, A. Saifi, S. Kumar, S. Augustine, S. Srivastava and B. D. Malhotra, *Analytica Chimica Acta*, 2019, **1056**, 135–145.

37 Y. Ma, G. Zhan, M. Ma, X. Wang and C. Li, *Bioelectrochemistry*, 2012, **84**, 6–10.

38 S. Kumar, N. Gupta and B. D. Malhotra, *Bioelectrochemistry*, 2021, **140**, 107799.

39 P. M. Jahani and S. Tajik, *Journal of Electrochemical Science and Engineering*, 2024, **14**, 93–105.

40 W. Sun, X. Wang, X. Sun, Y. Deng, J. Liu, B. Lei and Z. Sun, *Biosensors and Bioelectronics*, 2013, **44**, 146–151.

41 N. K. Mogha, V. Sahu, M. Sharma, R. K. Sharma and D. T. Masram, *Materials and Design*, 2016, **111**, 312–320.

42 B. Yao, J. Zhang, T. Kou, Y. Song, T. Liu and Y. Li, *Wiley-VCH Verlag*, 2017.

43 D. J. Aghera, K. Bhatt, J. B. Thakkar and C. R. Prabha, 2025, **62**, 46–53.

44 A. Soni, C. M. Pandey, M. K. Pandey and G. Sumana, *Analytica Chimica Acta*, 2019, **1055**, 26–35.

Accepted Manuscript For Review Only

45 H. Naeim, F. Kheiri, M. Sirousazar and A. Afghan, *Electrochimica Acta*, 2018, **282**, 137–146.

46 W. W. W. Hsiao, S. V. Selvi and K. Alagumalai, *Food Chemistry*, 2025, **464**, 141474.

47 S. Verma, C. Mouli Pandey and D. Kumar, *ChemistrySelect*, 2023, **8**, e202302420.

48 P. Dey, M. Jamshaiya, A. Khera, A. Sharma, A. Khajuria, A. Pandey, C. Mouli, R. Kumar, G. Singh and R. Pratap, *Environmental Nanotechnology, Monitoring & Management*, 2024, **21**, 100914.

49 H. Zhao, S. Ma, C. Bian, H. Wang, M. Gao and X. Wang, *Microchemical Journal*, 2024, **201**, 110600.

50 Y. She, Y. Tang, H. Liu and P. He, *Chemistry Central*, 2010, **4**, 4–11.

51 S. Hu, Y. Wang, X. Wang, L. Xu, J. Xiang and W. Sun, *Sensors and Actuators B: Chemical*, 2012, **168**, 27–33.

52 Y. Guo, D. He, A. Xie, W. Qu, Y. Tang, L. Zhou and R. Zhu, *Polymers*, 2019, **11**, 1907.

Accepted Manuscript

For Review Only

Figure Captions

Figure 1. Scheme showing the stepwise fabrication of ILs@rGO-ZrO_2/CP-based biosensor.

Figure 2. XRD of **(A)** ZrO_2 nanoparticles **(B)** rGO-ZrO_2 nanohybrid. **(C)** Raman spectra of ILs@rGO-ZrO_2 nanohybrid. FTIR spectra of **(D)** ILs@rGO-ZrO_2 nanohybrid.

Figure 3. SEM image of **(A)** ILs@rGO-ZrO_2 nanohybrid **(B)** ILs@rGO-ZrO_2/CP **(C)** enlarged image showing the binding of ILs@rGO-ZrO_2 nanohybrid on the CP substrate **(D)** EDAX of rGO-ZrO_2. and **(E)** ILs@rGO-ZrO_2/CP.

Figure 4. (A) Effect of various solvents on the electrical conductivity of conducting paper, (B) Bending angle studies of ILs@rGO-ZrO_2/CPE, (C) The change in conductivity of the CPE according to the number of bends, **(D)** The electrical stability of the CPE stored at room temperature for 40 days.

Figure 5. (A) Electrochemical response study of Lac/ILs@rGO-ZrO_2/CPE as a function of C_{HQ} in PBS (pH 7.0) using chronoamperometry **(B)** Plot showing linear relationship between the magnitudes of saturation current and CHQ on Lac/ILs@rGO-ZrO_2/CPE **(C)** Interference study showing the variation of current for different interferents. **(D)** Stability studies of Lac/ILs@rGO-ZrO_2/CPE.

Accepted Manuscript
For Review Only

Figure 1.

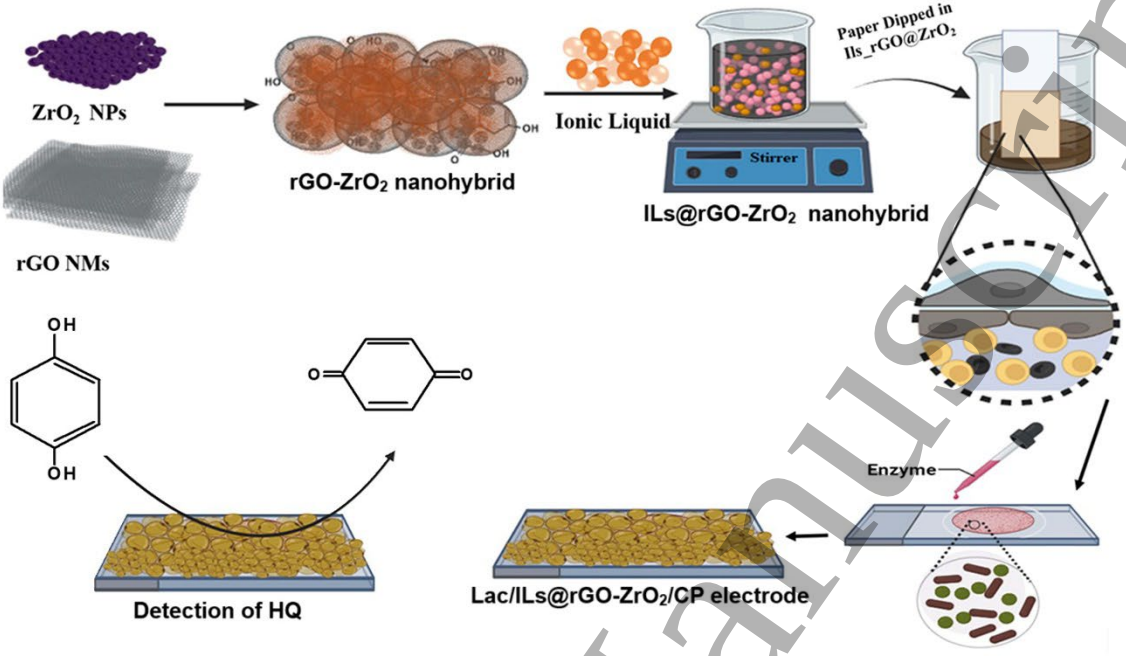
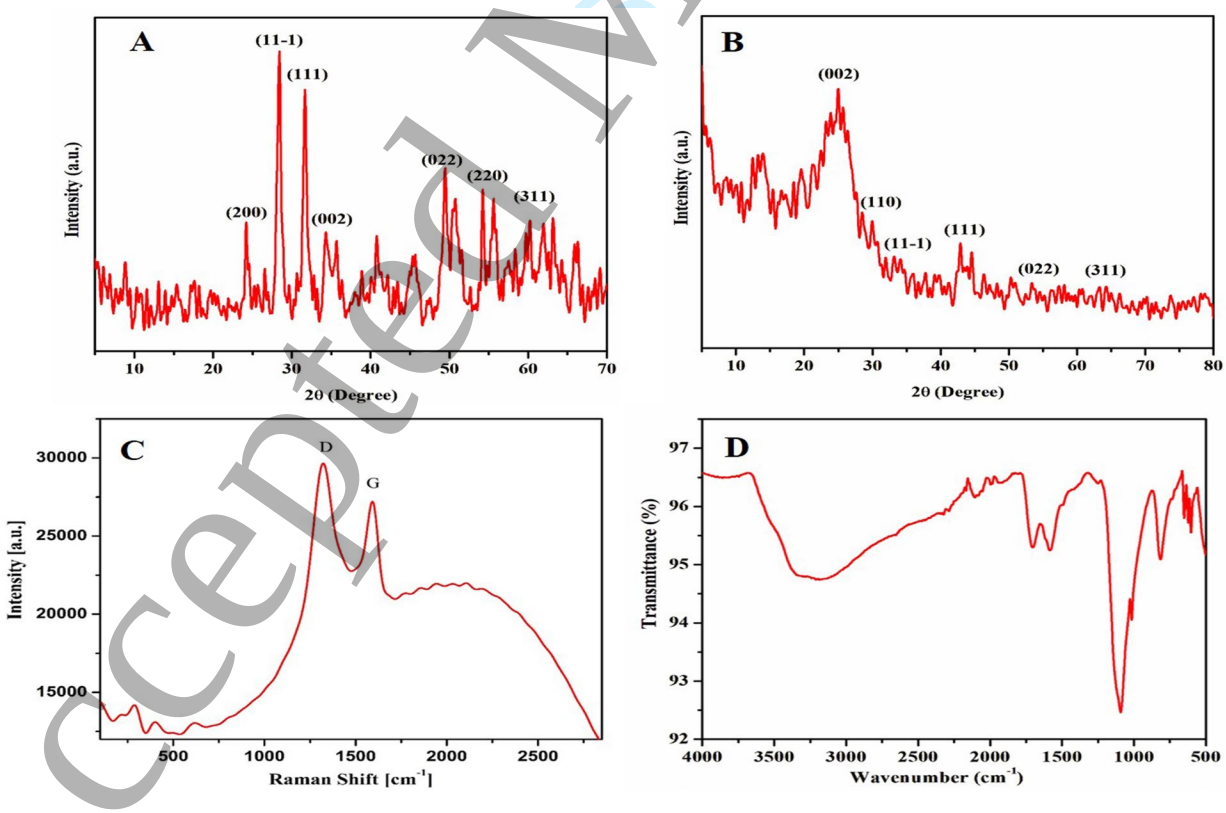


Figure 2.



Accepted Manuscript

Figure 3.

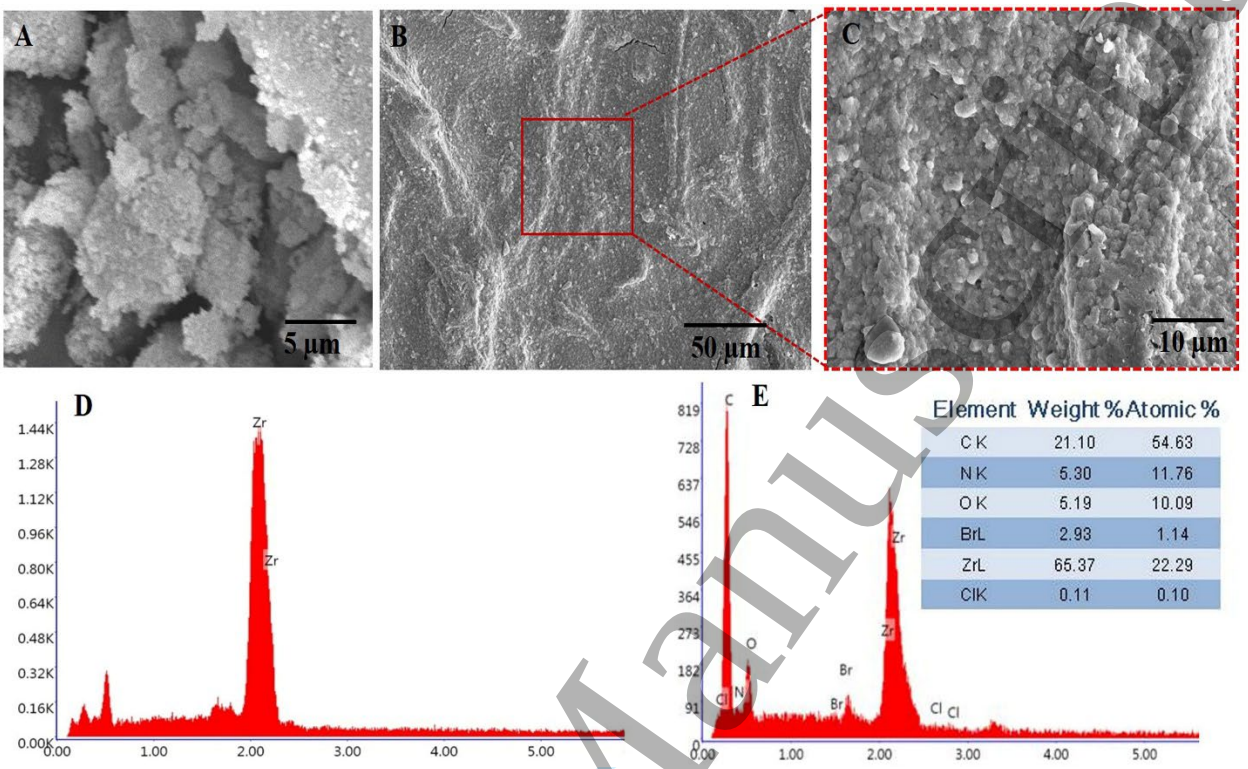
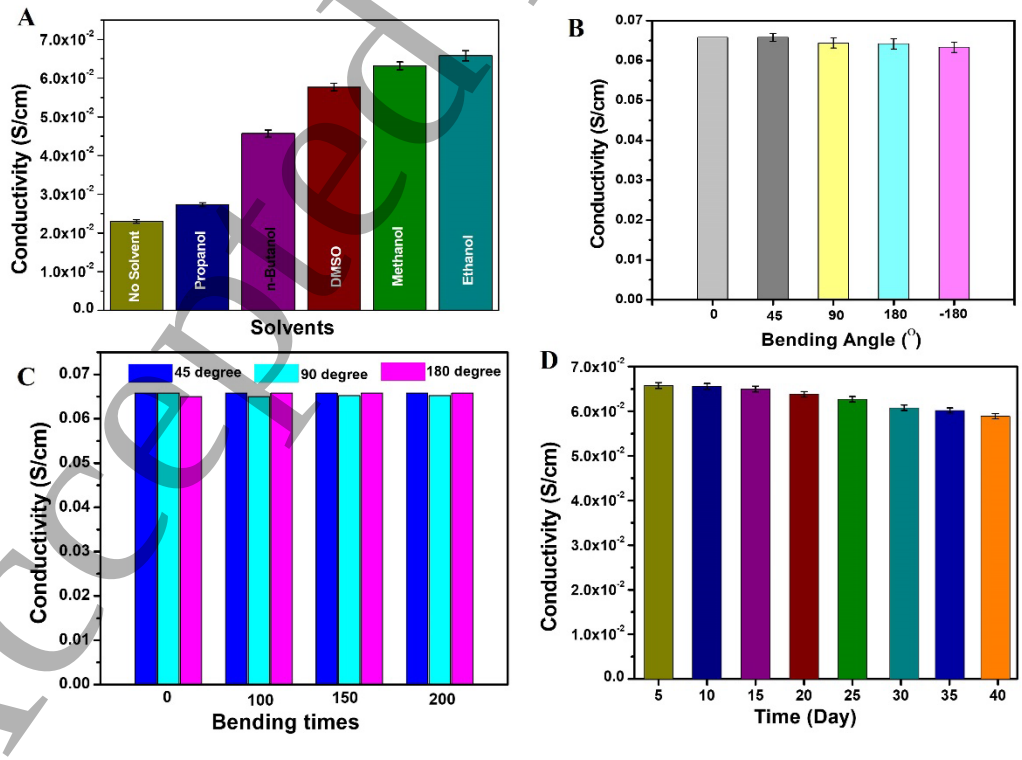
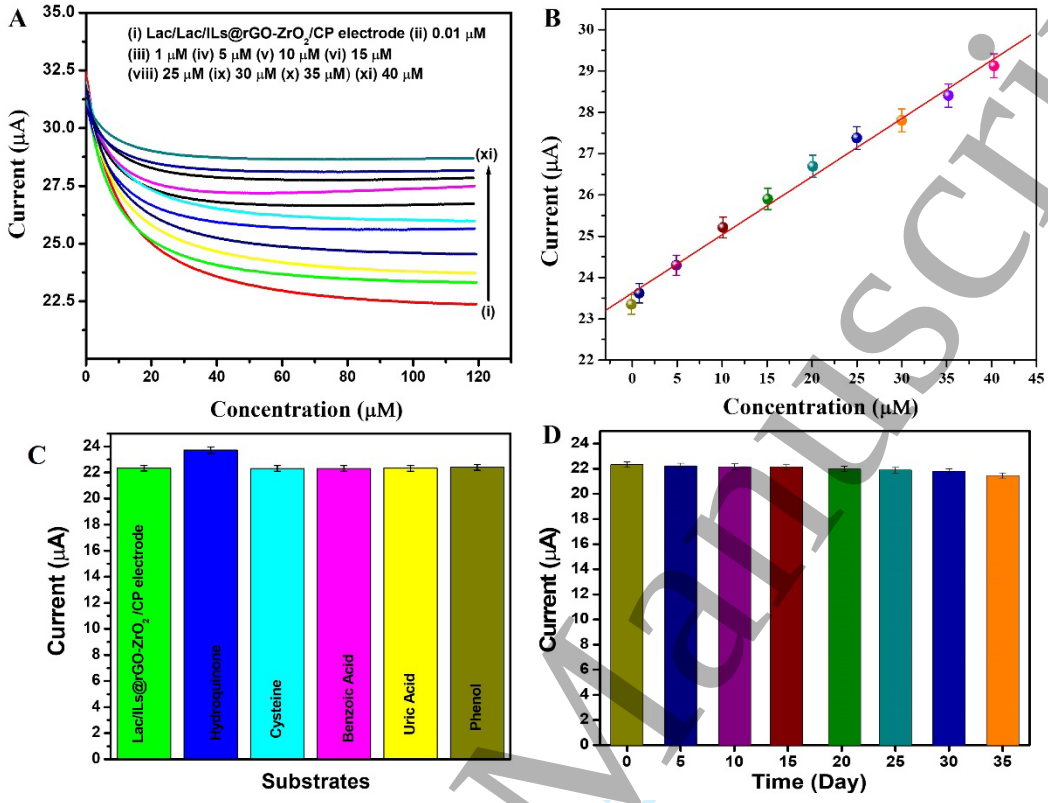


Figure 4.



Accepted Manuscript

Figure 5.



Accepted Manuscript
For Review Only

Table 1. Comparison of the biosensing performance of ILs@GO-ZrO_2/CPE with previously reported studies with Ionic Liquid on HQ detection.

S.No	Materials	Methods	Concentration Range	LOD	Real Sample	Ref.
1.	N-rGO/CuO/IL	CPE	1.0–600.0 µM	0.25 µM	TW & RW	20
2.	[TBAOH][NA]/Eu^{3+}	DEF	0.5 to 100 µM	0.15 µM	Water from landfill leachate of a garbage	49
3.	MWNTs-IL-Gel/GCE	GCE	8×10^{-7} to 1.6×10^{-5} M	6.7×10^{-8} M	Aqueous solution	5
4.	OMIM-PF6 IL-CPE	CPE	0.01 to 10 mmol L^{-1}	8.1×10^{-7} mol L^{-1}	Wastewater	50
5.	Au–GR/CILE ([EMIM][BF_4])	CPE	0.06 to 800.0 µmol/L	0.018 µmol/L	synthetic wastewater	51
6.	PGDIL-TiO2/Au	CFE	1–100 µmol/L	0.23 µmol/L	wastewater	52
7.	NiO/BMITFB	MCPE	0.1–500 µM	0.05 µM	Liposomes carrier and water	1
8.	ILs@rGO-ZrO_2/CPE	CPE	0.01-40 µM	0.01 µM	RW & LW	This work

Abbreviations: TW- tap water, LWW- Lake water, [TBAOH][NA]- Tetrabutylammonium hydroxide sodium salt, GO- Graphene Oxide, rGO- Reduced Graphene oxide, CPE- Carbon Paste Electrode, [EMIM][BF_4] - 1-Ethyl-3-methylimidazolium tetrafluoroborate, OMIM-PF6 - 1-Octyl-3-methylimidazolium hexafluorophosphate, PGDIL- poly-geminal dicationic ionic liquid, CFE - composite film electrode, BMITFB - 1-butyl-3-methylimidazolium tetrafluoroborate.

Accepted Manuscript
For Review Only

Table 2: Detection of HQ in real water samples using Lac/ILs@rGO-ZrO_2/CPE.

Sample	Added (µM)	Found (µM)	Recovery
Tap Water	1.00	1.00	100.0%
	10.00	10.02	100.02%
	20.00	19.89	99.45%
	40.00	40.12	100.30%
Lake Water	1.00	1.10	110.0%
	10.00	10.20	102.0%
	20.00	20.22	101.10%
	40.00	40.68	101.7%

Accepted Manuscript
For Review Only

Signal, Image and Video Processing (2025) 19:661
https://doi.org/10.1007/s11760-025-04183-8

ORIGINAL PAPER

HyperSwin: preventing deepfake proliferation with swin-efficient fusion in a hyperledger ecosystem

Kartik Bindra[1] · Hitesh Gupta[2] · Devyansh Bhattacharya[3] · Rahul Thakur[4]

Received: 2 January 2025 / Revised: 26 March 2025 / Accepted: 13 April 2025
© The Author(s), under exclusive licence to Springer-Verlag London Ltd., part of Springer Nature 2025

Abstract
The rapid growth of deepfake technology has raised major concerns about misinformation, privacy risks, and potential misuse in areas such as politics, media, and personal security. As deepfakes become more realistic and easier to make, finding reliable ways to detect them has become more important than ever. The existing state-of-the-art methods have shown promising result, but they often fall short in leveraging decentralized systems and prioritizing prevention over detection, leaving gaps in their applicability for real-world scenarios. This research introduces HyperSwin, which provides a robust solution for detecting deepfakes with the combination of Swin Transformer and EfficientNet-B0, with a customized MLP layer which takes in consideration the temporal and the spacial features of a face respectively. The proposed architecture incorporates the Hyperledger framework to ensure tamper-proof verification of video authenticity. The results are securely stored on decentralized storage, enabling future reference and significantly reducing video analysis time. This study focuses on prioritizing the prevention of deepfake content over its detection. The system effectiveness was evaluated on Celeb-DF (V2), FaceForensics++ and ForgeryNet. The experimental results demonstrated the accuracy of the test of 98.32%, 98.03%, 97.82% and AUC of 98.51%, 98.39%, 98.34% on the said data set, respectively. The integration of the Hyperledger framework improves the average query time by 90–99%. The performance of the proposed model is on par with state-of-the-art methods. Furthermore, the results demonstrate the robustness, strong generalization capability of the method. News agencies, social media platforms, and government bodies can leverage HyperSwin to authenticate content in real time, preventing the viral spread of manipulated videos. It also acts as a valuable tool for law enforcement agencies, cybersecurity firms, and digital forensic investigations.

Keywords Deepfake detection · Swin transformer · EfficientNet · Blockchain · Hyperledger fabric

1 Introduction

In recent years, the emerging Deepfake technology [1] has changed the digital media space. It has the power to create hyper-real manipulations of audio and video content [2]. This raises key questions on the ethics of technology and its societal implication since it can be a means of political propaganda or even identity theft and will destroy trust in media. According to [3], an average individual is not good at distinguishing original from edited images. Increasingly becoming accessible to the general public, the demand for such reliable detection mechanisms will require high priority today and in the near future because deepfakes continue getting more advanced and their commonality grows exponentially to further threaten personal privacy and corporate security.

✉ Rahul Thakur
rahulthakur@dtu.ac.in

Kartik Bindra
kartikbindra_23cs211@dtu.ac.in

Hitesh Gupta
hiteshgupta_23ec091@dtu.ac.in

Devyansh Bhattacharya
devyanshbhattacharya_23ep034@dtu.ac.in

[1] Computer Science, Delhi Technological University, Shahbad Daulatpur, Bawana, Delhi 110042, India

[2] Mathematics and Computing, Delhi Technological University, Shahbad Daulatpur, Bawana, Delhi 110042, India

[3] Engineering Physics, Delhi Technological University, Shahbad Daulatpur, Bawana, Delhi 110042, India

[4] Electronics and Communication, Delhi Technological University, Shahbad Daulatpur, Bawana, Delhi 110042, India

Published online: 28 May 2025



Fig. 1 Face swap & face reenactment

Deepfakes are deeply synthesized audio and video content, wherein with the help of technologies like Generative Adversarial Networks (GANs) [4], a person's likenesses or voice could very well be replaced by another. These broad manipulative practices go into benign entertainment and extend toward malicious impersonation [5]; therefore, the more the development of these techniques becomes finer, the more skilled are the chances of making deception possible even among highly skeptical audience groups. Thus, effective technologies in detecting deepfakes have become crucial for ensuring the authenticity of digital contents and safeguarding public trusts.

There are two main categories of deepfakes techniques: (i) face swapping and (ii) face reenactment as shown in Fig. 1. In the face swap methods, the face of one individual is cropped and morphed to fit it in the context of another individual [6]. For face reenactment methods, the facial expression of an individual is generated by morphing the source and target images. These newly generated manipulated face images are very close to real images and hard to say whether they are real or not. As a result, such generated deepfakes may be easily used for nefarious purposes such as spreading fake news, financial fraud, and hoaxes. Except the mentioned categories, face manipulation detection is also crucial for deepfake detection because deepfakes primarily target facial regions to create realistic yet fraudulent content. Manipulated faces often contain subtle artifacts like irregular lighting, unnatural transitions, or inconsistencies in facial dynamics (e.g., blink rates or lip-syncing). An interesting approach toward this was presented in [7] where an efficient framework for detecting face manipulation using Hybrid Learning and Kernel Principal Component Analysis (KPCA) was used. The method utilizes the EfficientNetV2-L model for feature extraction, followed by KPCA for dimensionality reduction, to distinguish real and fake facial images. It addresses various manipulation techniques, including identity swap, expression swap, and fully synthesized faces.

Deepfakes have to be fought in collaboration with various stakeholders: social media companies, news agencies, and governments [8]. HyperSwin is an open collaborative platform designed for the interaction of those involved, making use of state-of-the-art machine learning and blockchain technology to deal with the increasingly deepfaked world.

The current approaches to traditional deepfake detection methods are usually based on central databases or one-point verification systems, which cannot scale or secure to a wider deployment [9, 10]. Further, many of the available solutions fail to offer an authenticity record that is verifiable across parties. Therefore, HyperSwin integrates the use of Hyperledger blockchain [11, 12], developing a tamper-resistant and decentralized ledger for verifying authenticity. This layer adds additional security and trust while permitting the cross-validation of verified parties for the content without data compromise [13].

The major contributions of the proposed work are as follows:

- This study propose a unique integration of blockchain technology with state-of-the-art machine learning models, creating a robust framework for deepfake detection and verification.
- The model consists of two branches: one leverages the Swin Transformer (ST) [14] to capture inconsistencies across local facial regions through patch-wise self-attention mechanisms, while the other extracts global spatial features using EfficientNet-B0 [15], a deep convolutional neural network.
- The proposed blockchain architecture provides a decentralized, tamper-proof verification system. By recording detection results on the Hyperledger network [12], we prevent the spread of viral deepfake content and ensure transparency in the verification process. This approach also reduces the average time taken by our model to analyze a video by more than 90%.

2 Related work

2.1 Deepfake detection techniques

Recent developments focus on detecting deepfakes in social media content, such as tweets, and identifying fake information on digital platforms. Several recent studies in this field are discussed below.

Hafsa et al. [16] initially worked on single-modality models, but recent advancements integrate both audio and visual streams for improved accuracy. Their proposed Dense Swin Transformer Network (DST-Net) incorporates an ST-based feature extraction module alongside dense layers to capture both visual and acoustic features. This enhances deepfake detection by identifying subtle discrepancies in both modalities, addressing CNN-based model limitations, and improving generalizability across datasets with complex manipulations.

Fahad et al. [17] developed a robust deepfake detection system using an enhanced ResNet-18 CNN with multi-layer max pooling to classify videos as genuine or fake. The model was trained on a diverse dataset of 11,404

videos, including FaceForensics, CelebDF, DeeperForensics, and a private dataset. By leveraging GAN-based deepfakes, their approach effectively identifies facial manipulations and improves detection accuracy.

Shreyan Ganguly et al. [18] proposed ViXNet, a hybrid model combining Vision Transformer (ViT) and XceptionNet to detect artifacts from deepfake methods across facial regions. ViXNet consists of two branches: one using a patch-wise self-attention module with ViT to detect local inconsistencies and the other employing CNNs for global spatial feature extraction. Tested on the Deepfake Detection Challenge (DFDC) dataset, the model achieved an 86.32% AUC score and 79.06% F1-score.

Wodajo et al. [19] introduced the Generative Convolutional Vision Transformer (GenConViT) framework, which integrates ConvNeXt and ST models for deepfake video detection. It employs Autoencoders (AE) and Variational Autoencoders (VAE) to learn latent data distributions, while the feature extraction module detects visual artifacts. This approach enhances the generalizability of deepfake detection systems, achieving 95.8% accuracy and 99.3% AUC across multiple datasets, including DFDC, CelebDF (v2), DeepfakeTIMIT, and FaceForensics++ (FF++).

2.2 Blockchain for media integrity

The applications of blockchain technology in verification systems is currently receiving a lot of interest. This section provides an overview of the most recent best practices for verifying information [20].

Ki-Ryong et al. [21] suggested a blockchain-based method to authenticate and store media metadata to track any modifications to the media. It uses blockchain to ensure that any alteration to the media can be detected by verifying media metadata stored in a secure ledger. While effective for static content, the reliance on blockchain for detecting deepfakes in dynamic videos is limited. The system doesn't actively detect deepfakes; rather, it tracks media alterations after the fact.

Arash et al. [22] incorporated blockchain and federated learning to ensure privacy and secure collaborations in deepfake detection. Blockchain is used to secure data sharing between sources, while federated learning enables decentralized model training without compromising privacy.

Kim et al. [23] introduced a deepfake detection system integrating collective intelligence and deep-learning models. This approach ensures the transparency and objectivity through blockchain technology, leveraging Hyperledger Fabric for a consortium of Internet Content Providers (ICPs). They used user voting based on collective intelligence, weighted by user reputation scores, to enhance detection accuracy.

2.3 Deepfake detection using machine learning and blockchain

Christopher et al. [24] suggested that addressing this deepfake issue necessitates an integrated approach combining machine learning and blockchain technologies. Combining LSTM models for detection, with blockchain frameworks like Hyperledger Fabric ensures accurate deepfake identification and content authenticity. This approach embeds proof of authenticity (PoA) into a decentralized system, enabling reliable tracing of digital content's origin while preventing the spread of manipulated media.

3 Proposed architecture

Following the growing adoption of transformers [25] in image recognition tasks, we utilized a ST architecture with a modified Multi-Layer Perceptron (MLP) module to enhance performance in deepfake detection. Our proposed framework involves two-stream network, which involves ST and EfficientNet-B0. The model is trained on the individual frames of a particular video and it makes the prediction individually.

Our methodology also include blockchain technology to support the storage of computed results in a permissioned ledger. This approach helps in reducing the time and efforts used in computing the result for an already analyzed video if it is uploaded more than once [26]. If the results of the uploaded video already exists on the hyperledger network, we return the results without machine learning models getting involved. Also, this technique helps in blocking any video from getting viral on social media. Our private blockchain network allows concerned organizations like social media platforms, government bodies and companies to be a part of the network, and will share a common ledger. If any video comes across our platform once, each organization involved in the network will be informed about that video and thus the spread of deepfake content can be prevented.

The proposed architecture of our methodology is depicted by Fig. 2. Frames of the video are extracted and the face detection algorithm multitask cascaded convolution neural network (MTCNN) [27] is used to detect the faces. In the next step, we resize and reshape the extracted faces from the video and then pass the frames to the model. The model provides the predictions for the frames extracted from the videos. Therefore, we take the mean of the predictions and then classify the overall visual stream either as fake or real. The mean formula is depicted as in Eq. 1.

$$\hat{y} = \frac{1}{n}\sum_{i=1}^{n}\hat{y}_i \tag{1}$$

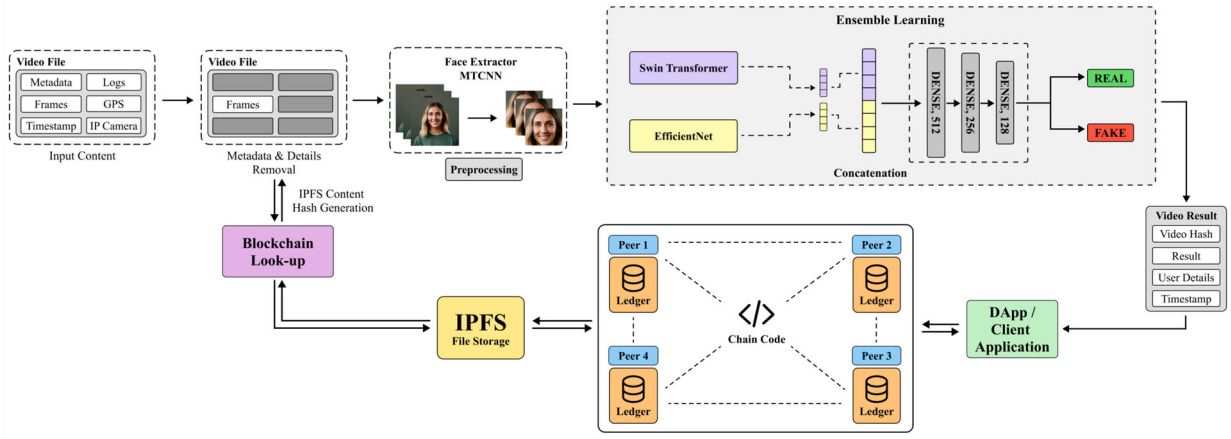
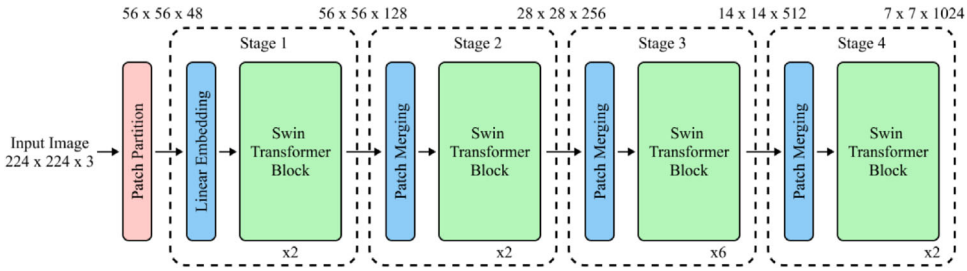


Fig. 2 Proposed architecture for deepfake detection and prevention

Fig. 3 Swin architecture [14]



where $\hat{y}_i$ depicts the prediction for ith frame, n represents the total number of frames and $\hat{y}$ represents the prediction for the whole video. We are using a threshold of 0.55 over which the video is classified as deepfake.

3.1 Ensemble learning

3.1.1 Input block

The input block consists of two individual models, which are the ST and EfficientNet-B0. The input frame of size of $224 \times 224 \times 3$ is passed individually to both channels.

3.1.2 Swin transformer module

ST module [14] constructs the hierarchical feature maps starting with the small patches and gradually merging the patches as the network gets deeper in layers as shown in the Fig. 3. The hierarchical features enable the model to learn effective global and local contextual representations and allow the model to perform dense prediction tasks. Moreover, the multi-head self-attention module captures the long-range dependencies and expands the receptive field with fewer parameters and lower computational complexity. This leads to better performance while detecting deepfake videos.

The ST module architecture same as in [14], comprises of patch extracting, patch embedding, two and six consecutive ST blocks, and patch merging. The patch extracting layer is used to split the incoming dense features into non-overlapping patches. Patch size is set to 4×4, and each patch is considered as a token. The tokens are mapped to vector data via the patch embedding layer, which is subsequently utilized in transformer blocks. We used the embedded dimension of 96. After that, consecutive ST blocks are applied to these tokens for the feature extraction. As the network grows, the patch merging layer is utilized to minimize the number of tokens.

Each ST block is composed of layer normalization (LN) layers, a multi-head self-attention (MHSA) module, a residual connection, and an MLP module as shown in [14]. Equation 2 mathematically defines the mechanism of attention where Q, K, V represent the query, key, and value, respectively. Each module (MHSA and MLP) is followed by a residual connection; however, an LN layer is applied before each of these modules. The two consecutive transformer blocks differ in terms of the MHSA module. The first transformer block contains a window-based MHSA (W-MHSA) module, whereas in the second transformer block, a shifted window-based MHSA (SW-MHSA) module is applied. Both modules perform self-attention within non-overlapping windows, resulting in a linear computational complexity. However, the SW-MHSA module also allows cross-window interaction without adding extra computa-

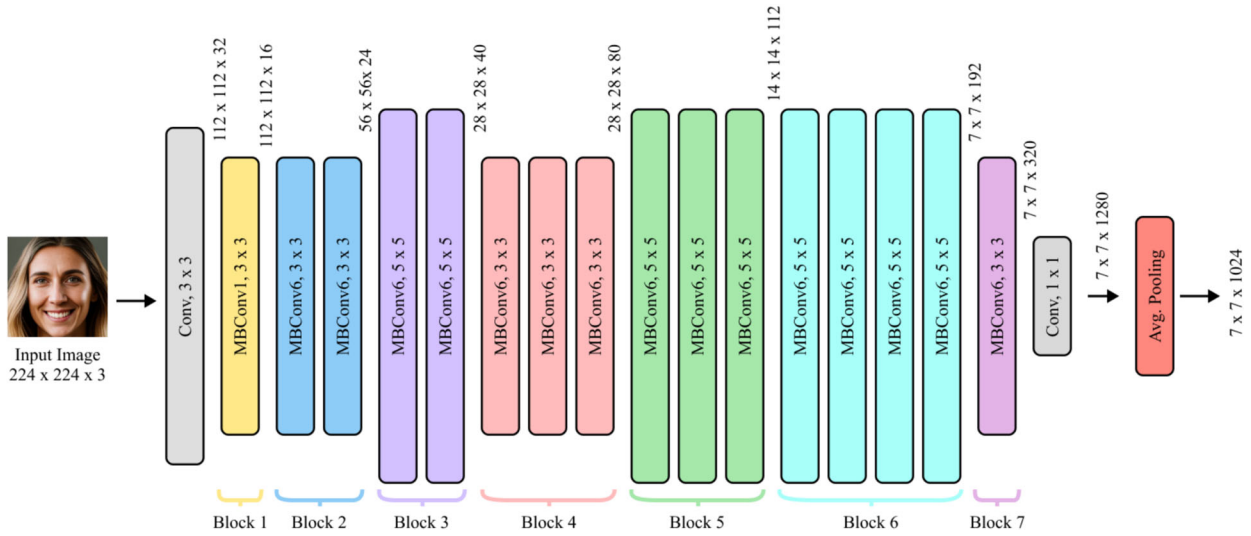


Fig. 4 EfficientNet architecture

tional cost.

$$\text{Attention}(Q, K, V) = \text{Softmax}\left(\frac{QK^T}{\sqrt{d}}\right)V, \tag{2}$$

$$\text{MultiHead}(Q, K, V) = \text{Concat}(\text{head}_1, \ldots, \text{head}_h)W^O,$$
$$\text{where head}_i = \text{Attention}(QW_i^Q, KW_i^K, VW_i^V). \tag{3}$$

To enable compatibility with the EfficientNet, the depth, dropout ratio, and patch merging layers are designed in such a way that the output is $7 \times 7 \times 1024$. ST was chosen over Vision Transformer (ViT) due to its hierarchical feature learning, lower computational cost, and enhanced spatial perception. Compared to ViT, which takes in the whole image at one step, Swin uses shifted window attention, hence lowering complexity from $O(N^2)$ to O(N) and performing better on high-resolution inputs. Swin is also able to view local and global features while ViT cannot offer locality assistance by design, leading to less effectiveness in detecting subtle deepfake artifacts. Swin's high performance on dense vision tasks made it the best candidate for deepfake detection.

3.1.3 EfficientNet module

Considering the promising results of the EfficientNet, we use an EfficientNet-B0, the smallest of the EfficientNet as shown in Fig. 4 networks making it very light and computationally inexpensive, as a convolutional extractor for processing the input faces. Specifically, the EfficientNet produces a visual feature for each chunk from the input face. Each chunk is of size 7×7 and this chunk is passed into a 1-D average pooling layer that changes the output channels to 1024 from 1280. EfficientNet-B0 was picked over B1/B3 as it has lower computational expense but with comparable performance. B1/B3 employ more parameters (13 M/18 M compared to 7.8M in B0)and higher FLOPs, resulting in longer training and inference time. The accuracy increase of B1/B3, is marginal and not worth added complexity, particularly in deepfake detection where frames of faces are already well extracted.

3.1.4 Output block

The feature vectors from both channels are concatenated to a $7 \times 7 \times 2048$ vector, from where we apply a Global Average Pooling layer to a dimension of $1 \times 1 \times 2048$. Now the vector is passed to 3 dense layers with ReLU activation functions followed by a dropout layer for regularization. Finally, to classify the input image as either real or fake, a fully connected layer with a softmax activation function is employed. The last fully connected layer has two output neurons for the classification. The softmax function in this layer transforms the neuron's values to 0 or 1 (0 for the real class, whereas 1 for the fake class).

3.2 Hyperledger environment

3.2.1 Usage of hyperledger fabric

Hyperledger Fabric is deployed in HyperSwin to facilitate secure, multi-organizational collaboration against deepfakes. Fabric's permissioned ledger allows trusted entities-such as social media platforms, media companies, and law enforcement agencies-to share a common, decentralized database. The complete Hyperledger architecture is given by Fig. 5.

Unlike traditional Proof of Work (PoW) or Proof of Stake (PoS) mechanisms, Fabric uses a permissioned model where participants are known, and an endorsement policy dictates which nodes must validate each transaction [28, 29]. When

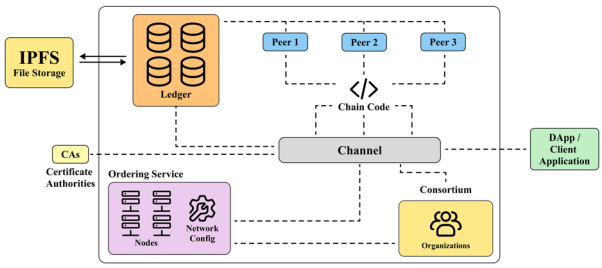


Fig. 5 Configuration of a hyperledger fabric blockchain environment with IPFS

a video content is flagged as deepfake or real, it is recorded on the blockchain, ensuring tamper-proof verification. Each participating node of the hyperledger network will store the flagged content results on their ledger. This helps in robust detection and coordinated action to prevent the video from going viral, thereby mitigating the spread of harmful deepfake content. This structure ensures a more efficient and secure transaction flow, reducing processing times and improving scalability, which is ideal for the suggested collaborative approach to combating deepfakes.

3.2.2 Smart contracts

In the Hyperledger architecture, smart contracts (called "chaincodes" in Hyperledger Fabric) define the logic for verifying and recording the authenticity of digital content. When a video or image is analyzed, a unique identifier is created for the content and associated with the detection results. Smart contracts execute this process by securely registering the content hash (unique hash is generated by IPFS decentralized storage) and its analyzed result onto the blockchain, ensuring tamper-resistant and traceable records. Suppose video hash matches with any hash already stored on the blockchain. In that case, that means that the video has already been analyzed and results already exists on the network, so we directly fetch the results from the blockchain for the corresponding content hash. Additionally, the smart contracts enforce rules for data access and permission management, allowing only authorized entities (e.g., consortium members) to retrieve and verify records.

3.2.3 Hyperledger architecture with IPFS cloud storage

The Hyperledger architecture in HyperSwin is integrated with InterPlanetary File System (IPFS) cloud storage [30] for decentralized storage of video files. Instead of directly storing large video data on the blockchain, which can be inefficient, HyperSwin leverages IPFS to store video files and then references the IPFS hash in the blockchain. The received video is stored on the decentralized cloud storage service and a corresponding unique hash is returned. This hash, provided by the IPFS service, serves as a unique identifier for the video, ensuring both content integrity and accessibility. Fabric's blockchain stores metadata, detection result, and unique IPFS hash for each file, allowing the consortium members to retrieve, verify, and analyze video files securely and efficiently.

Choosing Hyperledger network over a public blockchain network like Ethereum helps to share the data with only who are concerned with it. Any user or node, not a part of the private network, cannot access the data stored on the network ledger for verification [31]. Algorithm 1, explains the complete working procedure of the architecture. The flow of procedure for the suggested method is depicted by Fig. 6.

The algorithm is designed to detect deepfakes and verify the authenticity of videos by leveraging advanced machine learning techniques and blockchain technology. The workflow consists of the following primary steps, each playing a crucial role in ensuring effective and secure deepfake detection.

Algorithm 1 HyperSwin Deepfake Detection and Verification

Require: Content C (video or image)
Ensure: Detection Result R, Blockchain Record
Initialize:
  Machine Learning models M for deepfake detection
  Hyperledger ledger L for verification
Step 1: Content Hash Generation
  Remove metadata details from C
  Generate unique content hash H_C for C using IPFS
Step 2: Blockchain Lookup
if H_C exists in ledger L **then**
  Retrieve stored record R associated with H_C
  Include previously recorded metadata (e.g., detection confidence, timestamp)
  return R, blockchain verification status
else
  Step 2.1: Preprocessing
    Extract face from C using MTCNN
    Resize extracted face to dimensions $224 \times 224 \times 3$
  Step 2.2: Ensemble Detection
  for all model M_i in M **do**
    $W_i \leftarrow$ weights predicted by $M_i(C)$
    Add W_i to weight list W
  end for
  $W_{\text{combined}} \leftarrow$ concatenate all W_i in W
  $W_{\text{downsampled}} \leftarrow$ downsample
  $D \leftarrow$ compute final prediction using $W_{\text{downsampled}}$
  Store D along with detailed model weights for transparency
  Step 2.3: Blockchain Storage
    Store D, H_C, and metadata (timestamp, model details) on L
    Commit transaction to blockchain with verification link
    Validate transaction integrity to ensure ledger reliability
end if
Step 3: Output
return R, detailed model outputs, and blockchain verification status

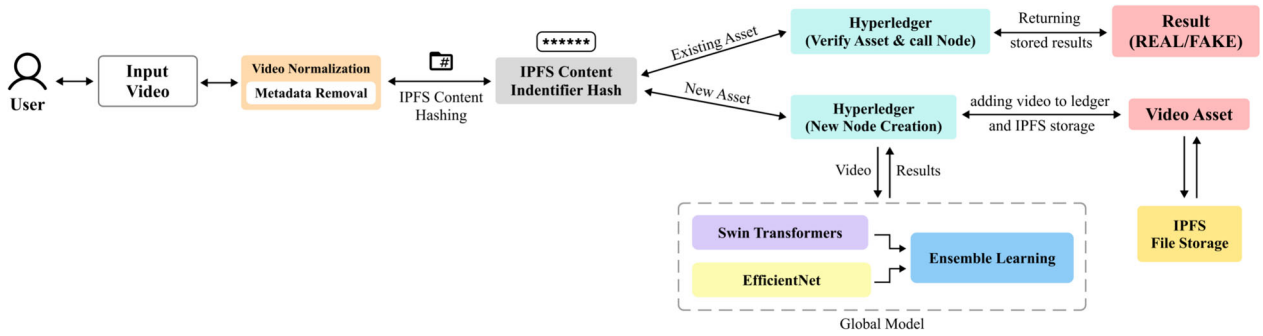


Fig. 6 Comprehensive deepfake detection pipeline for HyperSwin

In the first step, the system takes the input content C, which is a video, which is then sent to the IPFS cloud storage to produce a unique cryptographic hash for the video H_C. To ensure consistent hash generation, we remove metadata from the video before uploading it. This approach guarantees that when an identical video is uploaded from a different source, the IPFS hash remains the same. By making the hash independent of metadata details, we focus solely on the content (bytestream) of the video, eliminating discrepancies caused by variations in metadata, such as timestamps or file properties. Further, a look-up is performed on the blockchain ledger L for a matching content hash. If the hash matches from an already added record on the blockchain, we simply retrieve the stored result R associated with H_C.

If the ledger look up fails, it shows that the video has never been analyzed in the past and is a new video. In that case, the input video content C is broken down into individual frames. Further, the content is preprocessed where the steps include techniques like normalization, resizing, and face extraction to enhance the quality of the data for subsequent processing.

Once the content is preprocessed, the system employs an ensemble of machine learning models, denoted as M, to perform deepfake detection.The input weight to the model M are $224 \times 224 \times 3$. Each model (M_i) processes the content and generates specific weights (W_i) that reflect its prediction. The value of weights obtained by the ST and EfficientNet-B0 is $7 \times 7 \times 1024$. These weights are aggregated into a list (W), which combines the contributions of both the models. The weights are then concatenated into a single structure (W_{combined}), then to $1 \times 1 \times 2048$ using a Global Average pooling and downsampled to reduce redundancy, and used to compute the final prediction (D). This ensemble approach ensures a robust and reliable detection result by leveraging the strengths of multiple models.

In the next step, the system records the final detection result D along with the content identifier H_C on the blockchain. This process also involves storing relevant metadata and timestamps, ensuring a verifiable history of the detection outcomes.

Finally, the system outputs the detection result R and provides a verification link from the blockchain. This output not only informs users of the detection outcome but also offers a secure and immutable record that can be referenced for future verification.

This comprehensive workflow ensures that HyperSwin effectively combines advanced detection techniques with secure verification mechanisms, making it a robust solution for deepfake detection and content authenticity validation. This decentralized approach achieves much better reliability for the prevention of proliferation of fake content.

4 Results and discussions

This study thus introduces a comprehensive set of criteria for evaluating all deepfake detection techniques on major publicly available deepfake datasets: FaceForensics++ [32], Celeb-DF (V2) (CeDF) [33], and ForgeryNet [34]. The diversity in these datasets is accompanied by diverse scenarios and quality levels and manipulation techniques, providing an adequate basis for testing and improving detection models.

4.1 Dataset description

To conduct experiments, we choose mainly three popular, standard and publicly available deepfake datasets namely FaceForensics++ (FF++), CelebDF (v2) (CeDF) and ForgeryNet. For training purposes, only FF++ and CeDF are employed.

The *FF++* [32] dataset is a forensic video dataset composed of 1000 real videos obtained from 977 Youtube sources. Video production typically contains frontal faces with minor occlusions behind which subjects can readily track false synthetic manipulation. The forging videos are made by four automated face manipulation methods: Deepfakes, Face2Face, FaceSwap, and NeuralTextures, yielding a total of about 4000 fabricated videos and an overall total of 5000 videos (1000 real videos and 4000 fake ones). The dataset has two video compression levels:

- C-23 (High Quality, HQ)
- C-40 (Low Quality, LQ)

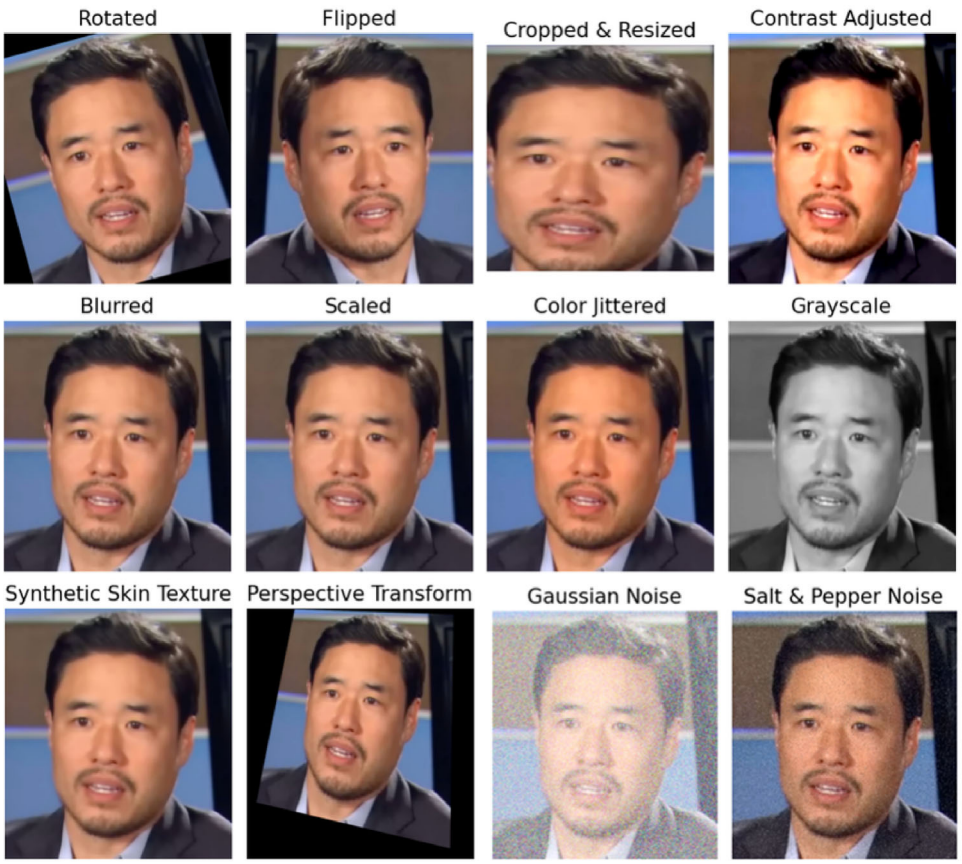


Fig. 7 Augmentation techniques

This dual-quality dataset mirrors real-world scenarios where videos are often heavily compressed. For the testing of the model, we have used the C-23 compression dataset.

CeDF [33] contains 590 authentic videos and 5639 manipulated videos, yielding over 2.3 million frames. The videos are an average of 13 s long and created using improved deepfake generation methods. The real (pristine) videos were derived from publicly available YouTube content. The high-quality deepfake manipulations and realistic content diversity make this dataset especially challenging.

ForgeryNet [34] also serves as a large-scale benchmark dataset that was specifically constructed for the multimodal deepfake detection challenge. It consists of 100,000 videos and 2.9 million images that were created by using 36 types of forgery methods, such as face swapping, expression editing, and attribute manipulation, to represent as much as possible such scenarios in the real world. We have used this dataset for testing only.

4.2 Data preparation

An interesting approach to enhance dataset was presented in [35], where a Data augmentation with attention framework was proposed to address overfitting in deepfake detection models. It enhances the Sequential DeepFake Manipulation Architecture by integrating Grad-CAM to focus on critical facial regions, improving interpretability and feature learning. Additionally, it incorporates CutMix augmentation strategically applied to Grad-CAM-identified regions, introducing perturbations that encourage robust generalization to unseen data. Our dataset being the Celeb-DF (V2) and FF++ dataset, despite a robust benchmark for deepfake detection, suffer from a significant class imbalance, with a far smaller number of real images compared to synthetic ones. This imbalance can bias models toward overfitting on the majority class (synthetic), reducing their generalization to unseen real-world data. To mitigate this issue, augmentation techniques as suggested by [36] are applied to expand the diversity and quantity of the real images. The image in Fig. 7 showcases several augmentation methods: the original image, horizontally flipped, vertically flipped, rotated, cropped & resized, contrast adjusted, Gaussian noise, salt & pepper noise, blurred, scaled, color jittered, converted to grayscale, synthetic skin texture, and perspective transform.

Geometric transformations such as horizontal and vertical flips help the model detect manipulated faces regardless of orientations. Rotation helps the model in being invariant to head tilt changes and camera angles. Scaling, cropping and transforming simulate aspect ratio variation and occlusions and make the model more efficient in detecting partial face

Table 1 Dataset statistics and train-test splits after augmentation

Dataset	Real	Deepfake	Real with augmentation	Total	Train (Real)	Train (Fake)	Test (Real)	Test (Fake)
CeDF [33]	590	5639	5310	10,949	4248	4511	1062	1128
FF++ (Deepfakes) [32]	1000	4000	4000	9000	3200	3200	800	800

manipulations. Color jittering and contrast help the model in focusing on structural details rather than lighting features. Grayscale conversion helps the model in generalizing by stripping it of reliance on color-based information.Synthetic skin texture augmentation makes the model more efficient in distinguishing real faces from artificially smoothed deepfake faces. Salt-pepper noise and Gaussian noise invert the unrealistic smoothness in face textures created with deepfakes, making the model more invariant to real-world noise variations. Blurring helps the model in detecting deepfakes in low-quality and compressed videos.

The Table 1 presents a detailed summary of the CeDF and FF++ datasets, highlighting their composition and the differences between the tests. Specifically, the real videos in CeDF were augmented nine times, resulting in a total of 5310 augmented samples, while the real videos in FF++ were augmented four times, producing 4000 augmented samples. The total number of videos, after combining the original and augmented real videos with their corresponding deepfake samples, was 10,949 for Celeb-DF (v2) and 9000 for FF++. An 80% - 20% split was used for training and testing, with 4248 real and 4511 deepfake videos allocated for training in CeDF, and 1062 real and 1128 deepfake videos reserved for testing. Similarly, FF++ allocated 3200 videos from each class for training and 800 videos per class for testing. These splits ensure a balanced representation of real and fake videos, enabling robust evaluation of deepfake detection models. During the generation of the training frame set, 64 equidistant frames are chosen in the temporal space for a particular video. This gives a variety of face postures in the image set because no two frames would be adjacent to each other.

4.3 Experimental setup

The proposed ML model is trained as a whole, despite it consisting of different trainable components. The EffecientNet-B0 is pretrained and initialized with weights trained on the ImageNet Dataset. During training and testing of the model, we use frames resized to 224 × 224. In order to find the optimized hyper-parameters for the proposed architecture, we performed extensive experimentation while tuning the hyperparmamters. After the detailed experiments, the optimized parameter values are: epochs = 50, batch size = 8, learning rate = 0.0001. A small learning rate enables the model to take small steps while reducing the loss, thereby ensuring the model convergence to an optimal solution. The binary cross entropy has been used as a loss function as the classification output is binary, i.e. real or fake. We use adam as the optimizer while training. The computations were carried out on an Intel (R) Core (i9) processor running Windows 11, with an NVIDIA Quadro RTX 6000 graphics card and 64 GB of RAM. For a handful of the complex calculations, Google Colab Notebook was employed.

The blockchain architecture provided in this study is made up using four fundamental pieces, which are: Chain Code (Smart contracts), IPFS Storage, a private blockchain network (Hyperledger Fabric) and a distributed application. JavaScript language was used to write the chain codes for the Hyperledger environment. Pinata IPFS was used as the IPFS file storage system. The development environment for Hyperledger fabric consists of OS (Ubuntu VM version 24.04.1 LTS), RAM(16GB), CPU(Intel i5-12th Gen), DApp (Backend—Node.js, Flask, Frontend—React, TailwindCSS), development languages (Python, JavaScript, Go).

4.4 Ablation study

To evaluate the impact of each component in our model, we conducted an ablation study by systematically removing or altering individual modules and measuring the resulting changes in performance. We tested three configurations: *EfficientNet-B0 only* [15], *ST only* [14], and the *fusion of ST with EfficientNet-B0*. Table 2 summarizes the performance metrics for each configuration, including accuracy, AUC, TPR, TNR, precision, and F1-score.

The EfficientNet-B0 [15] configuration reached an accuracy of 91.41% and an AUC of 91.72% as a feature extractor classifier. The TPR and TNR of the model were capped to 90.31% and 92.11%, respectively, along with an F1-score of 90.61%. This, therefore demonstrates that though EfficientNet-B0 offers a good baseline, it lacks in some cases. The hierarchical convolutional layers of EfficientNet-B0 effectively extract fine-grained local features in the initial layers and broader spatial patterns at deeper levels, which are critical for detecting subtle manipulations. Its computational efficiency, achieved through depth wise separable convolutions and an optimized scaling strategy, allows for high performance with minimal resource requirements. Despite these advantages, EfficientNet-B0 suffers from significant

Table 2 Ablation study

Model configuration	Accuracy (%)	AUC (%)	TPR (%)	TNR (%)	Precision (%)	F1-Score (%)
EfficientNet-B0 only	91.41	91.72	90.31	92.11	90.91	90.61
Swin transformer only	93.23	93.52	91.83	94.12	92.43	92.12
HyperSwin	**98.32**	**98.51**	**97.42**	**98.91**	**97.93**	**97.52**

The bold values represents the the best values among all

Table 3 HyperSwin performance on different datasets

Dataset	Accuracy (%)	AUC (%)	TPR (%)	TNR (%)	Precision (%)	F1-Score (%)
FaceForensics++ [32]	98.03	98.39	97.12	98.83	97.63	97.32
Celeb-DF (v2) [33]	98.32	98.51	97.42	98.91	97.93	97.52
ForgeryNet [34]	97.82	98.34	96.85	98.64	97.46	97.02

Table 4 Comparison with other deepfake detection models on FF++

Model	Accuracy (%)
VixNet [37]	68.0
XceptionNet [18]	95.73
GenConViT [19]	97.0
Hybrid Transformer [38]	97.85
Face X-Ray [39]	97.73
HyperSwin	**98.03**

The bold values represents the the best values among all

limitations. The model's reliance on local receptive fields restricts its ability to capture global contextual relationships or long-range dependencies across the image. This means it struggles with identifying anomalies that span large regions, such as inconsistent lighting or global structural misalignment, artifacts often present in advanced deepfake manipulations.

All metrics significantly improved when replacing EfficientNet-B0 with the ST [14]. Accuracy reached 93.23%, while AUC was 93.52%, indicating superior ability to model spatial and hierarchical relationships in the input data. Improvements were also seen in terms of TPR and TNR at 91.83% and 94.12%, respectively, with the corresponding F1-score at 92.12%. These results highlight its strength in modeling global contextual relationships through its window-based self-attention (W-MHSA) and shifted window-based self-attention (SW-MHSA) mechanisms. By progressively merging patches in its hierarchical architecture, the ST effectively captures multi-scale features, enabling it to detect both local artifacts and global anomalies, such as lighting mismatches and cross-region texture inconsistencies. This ability to analyze long-range dependencies allows it to identify subtle manipulations that span different regions of the image, which are often missed by convolutional models. However, the ST has some limitations. First of all, while the ST excels at modeling global context, it may sometimes overlook fine-grained local artifacts such as sharp pixel boundaries or compression irregularities, which are critical for detecting certain types of deepfake anomalies. Similar to EfficientNet-B0, it also fails to account for temporal inconsistencies across sequential frames, as its attention mechanisms focus solely on static images without incorporating inter-frame relationships.

The final model's accuracy was 98.32%, and AUC was 98.51%. TPR and TNR were significantly higher at 97.42% and 98.91%, respectively, while precision and F1-score reached 97.93% and 97.52%, respectively. This enhancement shows the complementary nature of the two parts, where EfficientNet-B0 provides robust spatial feature extraction and the ST enhances global context modeling. Table 3 lists the performance of the model on different datasets. Table 4 summarizes our model's accuracy on the FF++ dataset compared with other state-of-the-art models. Table 5 provides detailed comparison analysis of HyperSwin with other deepfake detection techniques. For more detailed method comparison, refer to table 1 of "Online Resource". The model was evaluated on large, publicly available datasets covering a wide range of demographic distributions. We augmented our real video samples carefully to further enhance diversity in our dataset to have the model trained on representative diversity in race and gender. This integrated approach not only diminishes potential biases but also fosters equitable and consistent performance over diverse demographic populations.

4.5 Error analysis

Here, we report the performance of the proposed HyperSwin model at the image level and discuss its strengths and limitations according to the test set results. We look into cases where the model was correct and those where it failed.

Table 5 Analysis of deepfake detection models with HyperSwin

Model	Architecture approach	Decentralized	Prevention focus	Datasets used
[18]	Advanced CNN	No	Detection-only	FaceForensics
[19]	VAE, ConvNext & Swin Transformer	No	Detection-only	DFDC, Celeb-DF, FaceForensics++, TrustedMedia, Deepfake-TIMIT
[39]	X-ray based	No	Detection-only	Celeb-DF, FaceForensics++, DFDC, DFD
[21]	Hyperledger Framework	Yes	Prevention-first Approach	None
[40]	Deep Learning & Hyperledger	Yes	Detection-only	DFDC, FaceForensics++
HyperSwin	Swin Transformer, EfficientNet & Hyperledger Fabric	Yes	Prevention-first approach	Celeb-DF, FaceForensics++, ForgeryNet

As can be seen in Figure 8, the first three columns are correctly classified faces, while the last two columns show misclassified faces. An examination of the false positives i.e. fabricated images misclassified as authentic, reveals a consistent artifact characterized by variations in illumination within the facial zone. This result suggests that the current version of HyperSwin fails to reliably represent these lightning-related artifacts, which may have contributed to the misclassifications observed. In analogous fashion, the false negatives, that is, authentic images misclassified as fabricated are often characterized by faces portraying specific expressions or occlusions, such as partial coverings or increased emotional presentation. The model may misinterpret some of these expressions as forged items, most probably because those facial expressions are not appropriately represented in the training set.

4.6 Query time efficiency analysis

Experiment with the proposed method demonstrated that the video result query time taken by the ensembled model increases as the number of frames increases. This query time includes breaking the video down into multiple frames, preprocessing of the video, and then analyzing each frame and aggregating the results from each frame to obtain the final result. However, blockchain technology helps in preventing the redundant calls to the global machine learning model. The proposed architecture validates whether the video already exists on the hyperledger network ledger. If the video already exists on the network, the results are fetched directly from the blockchain, hence removing the redundant call and reducing the total query time.

As shown in Fig. 9, blockchain intervention improves the query time for the same video analyzed a second time by 90–99%. Therefore, we can observe a significant reduction in the time required to analyze and verify a video with blockchain integration, i.e., improved Turnaround Time.

4.7 Cost analysis

Our cost analysis focuses on evaluating the financial as well as scalability benefits of using Hyperledger Fabric, a private blockchain, compared to public blockchains like Ethereum. Hyperledger Fabric significantly reduces the transaction costs because it does not rely on any cryptocurrency for validation like Ethereum.

Public blockchains involve gas fees, which increase operational costs during high network traffic. On the contrary, Hyperledger is a permissioned network with fixed resources and trusted nodes only, due to which the cost per transaction is predictably lower. Hyperledger works on a consensus mechanism wherein all involved nodes validate the transaction to update the ledger, which is much more efficient than the Proof of Work (PoW) mechanism used in the Ethereum blockchain.

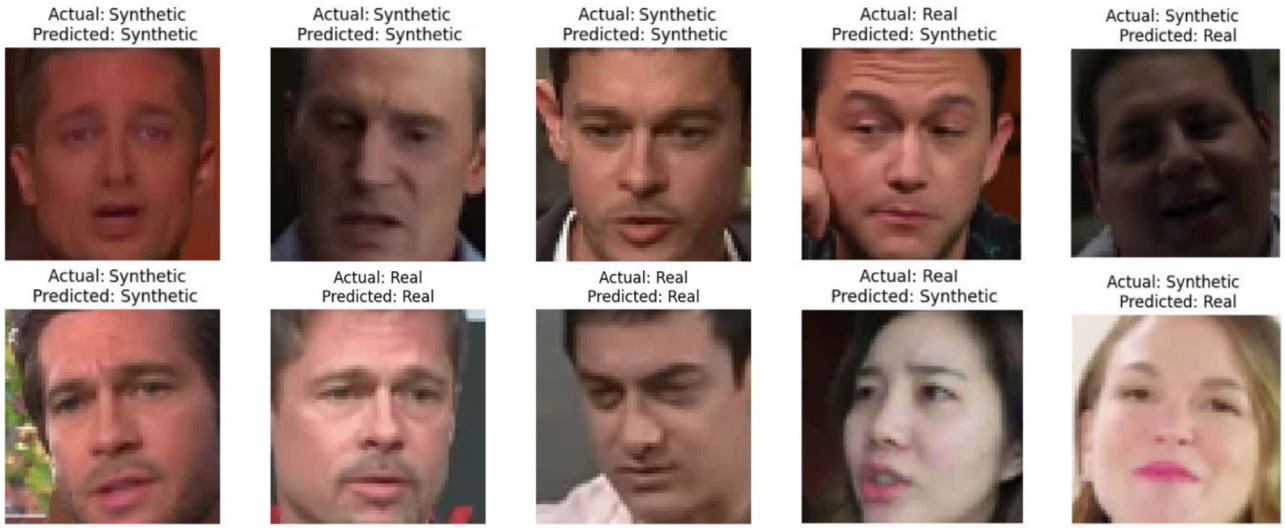


Fig. 8 Visualization of Deepfake content analysis

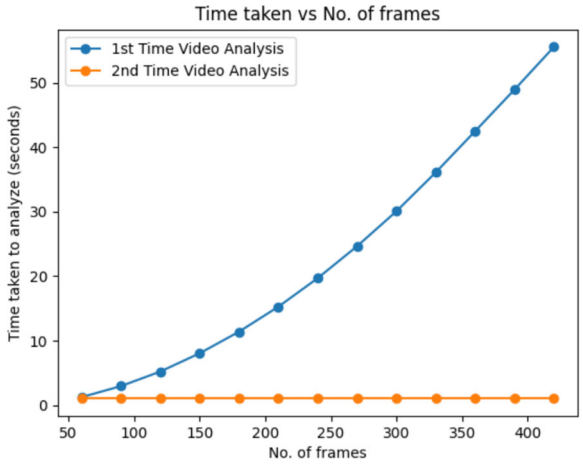


Fig. 9 Improved turnaround time due to blockchain intervention for a video analyzed second time

4.8 Transparency versus user privacy—"finding a sweet-spot"

The dual objectives of transparency and privacy may seem at odds, but they are not mutually exclusive. Unlike public blockchains, permissioned blockchains restrict access to authorized entities, ensuring that transparency is limited to relevant stakeholders without exposing sensitive data to the broader public. Our methodology creates an environment where users would feel safe in sharing data, know their privacy is protected. At the same time, the transparency offered by the system builds trust and ensures accountability among concerned organizations and stakeholders. This balance promotes responsible technology use, ensuring that ethical considerations are not sacrificed in the pursuit of technological advancement.

4.9 Security analysis

The Hyperledger environment uses cryptographically secured blocks for storing the results of uploaded videos, ensuring that once a video analysis result is recorded, it cannot be tampered with. This private blockchain setup eliminates the presence of anonymous nodes (as in public blockchains).

Our distributed framework eliminates the use of central data storage, thereby eradicating the chances of any manipulation or hacking of data, which could endanger the system's performance and security. As the architecture lacks a central server, censorship and distortion of data are unfeasible. DoS and DDoS attacks are unlikely in the system due to its distributed architecture and the absence of a centralized server device.

5 Conclusion and future scope

HyperSwin offers a promising approach to addressing the challenges posed by deepfake technology, combining advanced machine learning models with the security and transparency of Hyperledger blockchain. By integrating ensemble learning and blockchain technology, HyperSwin not only enhances the accuracy and efficiency of deepfake detection but also focuses on complete prevention from spreading of deepfake content on social media. Its unique architecture bridges the gap between detection and prevention, empowering stakeholders to safeguard digital content against misuse. The user interface images for the working prototype of HyperSwin are shown in the "Online Resource". Through its robust detection capabilities, tamper-proof blockchain records, and scalable design, HyperSwin

contributes to rebuilding trust in digital media by collaborating with concerned stakeholders and organizations.

While HyperSwin represents a significant advancement in the detection and prevention of deepfakes, there are several limitations that we aim to address in future studies. One major limitation is the detection of slightly altered variants of deepfake videos. Currently, while HyperSwin effectively identifies deepfakes and contributes to preventing the further proliferation of such content, minor modifications such as changes in duration, resolution, frame rate or file extension of the video, can fool and surpass the blockchain look-up step. This leads to redundant and increased turnaround time for video analysis.

Although our model retains its strength thanks to its transformer-based architecture, this architecture is quite resource intensive, which poses a limitation for scalability in large-scale applications that require real time processing. As deepfake technologies are rapidly advancing, the model will need to be updated periodically so that it is able to detect newer models of forgeries. As a way to deal with these issues in a proper manner, future work will focus on improving the performance and the adaptability.

Another limitation is the challenge of multi-modal analysis. HyperSwin currently focuses on visual components only for deepfake detection, but multi-modal deepfakes, those involving a combination of video and audio, present a more complex problem. The integration of these different data modalities for analysis is crucial to detect deepfakes that may only be deceptive when considering the full context. Future work will focus on improving the synergy between visual and auditory data, allowing HyperSwin to perform more comprehensive analyses and detect multi-modal deepfakes with greater precision.

Additionally, origin traceability is an area that requires improvement. HyperSwin can currently identify whether a video is a deepfake, but tracing the origin of the video such as determining its original source or understanding the sequence of modifications it underwent, is still a challenge. In future studies, we plan to incorporate blockchain-based traceability features that would allow for an immutable history of a video's creation, modification, and distribution. This would help not only detect deepfakes but also track their origins, providing an added layer of trust and transparency.

Furthermore, HyperSwin aims to advance into real-time analysis, enabling instant detection of deepfakes during live streams or uploads. This evolution will enhance the system's applicability for social media platforms, live broadcasting, and public safety operations.

Supplementary Information The online version contains supplementary material available at https://doi.org/10.1007/s11760-025-04183-8.

References

1. Chesney, B., Citron, D.: Deep fakes: a looming challenge for privacy, democracy, and national security. Calif. Law Rev. **107**, 1753–1820 (2019)
2. Thakur, R., Rohilla, R.: Recent advances in digital image manipulation detection techniques: a brief review. Forensic Sci. Int. **312**, 110311 (2020)
3. Schetinger, V., Oliveira, M.M., da Silva, R., Carvalho, T.J.: Humans are easily fooled by digital images. Comput. Graph. **68**, 142–151 (2017)
4. Yu, N., Skripniuk, V., Abdelnabi, S., Fritz, M.: Artificial fingerprinting for generative models: rooting deepfake attribution in training data. arxiv:2007.08457
5. Tolosana, R., Vera-Rodriguez, R., Fierrez, J., Morales, A., Ortega-Garcia, J.: Deepfakes and beyond: a survey of face manipulation and fake detection. Inf. Fus. **64**, 131–48 (2020)
6. Nirkin, Y., Keller, Y., Hassner, T.: Fsganv2: improved subject agnostic face swapping and reenactment. IEEE Trans. Pattern Anal. Mach. Intell. **3155571**, 1 (2022)
7. Thakur, R., Rohilla, R.: An effective framework based on hybrid learning and kernel principal component analysis for face manipulation detection. SIViP **18**, 4811–4820 (2024)
8. Sandoval, M.P., de Almeida Vau, M., Solaas, J., Rodrigues, L.: Threat of deepfakes to the criminal justice system: a systematic review. Crime Sci. **13**, 41 (2024)
9. Naitali, A., Ridouani, M., Salahdine, F., Kaabouch, N.: Deepfake attacks: generation, detection, datasets, challenges, and research directions. Computers **12**(10), 216 (2023)
10. Taeb, M., Chi, H.: Comparison of deepfake detection techniques through deep learning. J. Cybersecur. Privacy **2**, 89–106 (2022)
11. Jaafar, R.A., Alsaad, S.N.: Enhancing educational certificate verification with blockchain and IPFS: a decentralized approach using hyperledger fabric. TEM J. **12**, 2385–2395 (2023)
12. Hasnain, M., Albogamy, F.R., Alamri, S.S., Ghani, I., Mehboob, B.: The hyperledger fabric as a blockchain framework preserves the security of electronic health records. Front. Public Health **11**, 1272787 (2023)
13. Stodt, F., Reich, C.: Bridge of trust: cross domain authentication for industrial internet of things (IIoT) blockchain over transport layer security (tls). Electronics (Switzerland) **12**, 6 (2023)
14. Liu, Z., Lin, Y., Cao, Y., Hu, H., Wei, Y., Zhang, Z., Lin, S., Guo, B.: Swin transformer: hierarchical vision transformer using shifted windows. http://arxiv.org/abs/2103.14030. (2021)
15. Tan, M., Le, Q.V.: Efficientnet: rethinking model scaling for convolutional neural networks. http://arxiv.org/abs/1905.11946 (2019)
16. Ilyas, H., Javed, A., Malik, K.M.: Avfakenet: a unified end-to-end dense swin transformer deep learning model for audio-visual deepfakes detection. Appl. Soft Comput. **136**, 3 (2023)
17. Fahad, M., Zhang, T., Iqbal, Y., Ikram, A., Siddiqui, F., Abdullah, B.Y., Nauman, M.M., Zhao, X., Geng, Y.: Advanced deepfake detection with enhanced resnet-18 and multilayer CNN max pooling. Vis. Comput. (2024). https://doi.org/10.1007/s00371-024-03613-x
18. Rössler, A., Cozzolino, D., Verdoliva, L., Riess, C., Thies, J., Nießner, M.: Faceforensics: a large-scale video dataset for forgery

detection in human faces. arXiv preprint https://arxiv.org/abs/1803.09179 (2018)
19. Wodajo, D., Atnafu, S., Akhtar, Z.: Deepfake video detection using generative convolutional vision transformer. http://arxiv.org/abs/2307.07036 (2023)
20. Reyna, A., Martín, C., Chen, J., Soler, E., Díaz, M.: On blockchain and its integration with IoT challenges and opportunities. Future Gener. Comput. Syst. **88**, 173–190 (2018)
21. Lee, S.-H., Kwon, K.-R., Rashid, M.M.: Blockchain technology for combating deepfake and protect video/image integrity. Art. J. Korea Multimed. Soc. **24**, 1044–1058 (2021). https://doi.org/10.9717/kmms.2021.24.8.1044
22. Heidari, A., Navimipour, N.J., Dag, H., Talebi, S., Unal, M.: A novel blockchain-based deepfake detection method using federated and deep learning models. Cognit. Comput. **16**, 1073–1091 (2024)
23. Choi, N., Kim, H.: Dds: deepfake detection system through collective intelligence and deep-learning model in blockchain environment. Appl. Sci. (Switzerland) **13**, 2122 (2023)
24. Kayikci, S., Khoshgoftaar, T.M.: Blockchain meets machine learning: a survey. J. Big Data **11**, 12 (2024)
25. Vaswani, A., Brain, G., Shazeer, N., Parmar, N., Uszkoreit, J., Jones, L., Gomez, A.N., Kaiser, L., Polosukhin, I.: Attention is all you need. arxiv:1706.03762
26. Sarkar, D.: Decentralized deepfake detection blockchain network using dynamic algorithm management. http://arxiv.org/abs/2311.18545 (2023)
27. Zhang, K., Zhang, Z., Li, Z., Qiao, Y.: Joint face detection and alignment using multitask cascaded convolutional networks. IEEE Signal Process. Lett. **23**(10), 1499–1503 (2016)
28. Mazumdar, S., Ruj, S.: Design of anonymous endorsement system in hyperledger fabric. IEEE Trans. Emerg. Top. Comput. **9**(4), 1780–1791 (2021). https://doi.org/10.1109/TETC.2019.2920719
29. Dwork, C., Naor, M.: Pricing via Processing or Combatting Junk Mail. In: Brickell, E.F. (eds.) Advances in Cryptology — CRYPTO' 92. CRYPTO 1992. Lecture Notes in Computer Science, vol. 740. Springer, Berlin, Heidelberg (1993). https://doi.org/10.1007/3-540-48071-4_10
30. Kang, P., Yang, W., Zheng, J.: Blockchain private file storage-sharing method based on IPFS. Sensors **22**, 7 (2022)
31. Chen, C.-L., Yang, J., Tsaur, W.-J., Weng, W., Wu, C.-M., Wei, X.: Enterprise data sharing with privacy-preserved based on hyperledger fabric blockchain in IIoT's application. Sens. Basel **22**(3), 1146 (2022)
32. Rössler, A., Cozzolino, D., Verdoliva, L., Riess, C., Thies, J., Nießner, M.: Faceforensics++: Learning to detect manipulated facial images. http://arxiv.org/abs/1901.08971 (2019)
33. Li, Y., Sun, P., Qi, H., Lyu, S.: Celeb-DF: a large-scale challenging dataset for DeepFake Forensics. In: IEEE Conference on Computer Vision and Patten Recognition (CVPR), Seattle, WA, United States (2020)
34. He, Y., Gan, B., Chen, S., Zhou, Y., Yin, G., Song, L., Sheng, L., Shao, J., Liu, Z.: Forgerynet: a versatile benchmark for comprehensive forgery analysis. https://yinanhe.github.io/projects/forgerynet.html
35. Mamarasulov, S., Chen, L., Chen, C., Li, Y., Wang, C.: Data augmentation with attention framework for robust deepfake detection. Vis. Comput. (2024). https://doi.org/10.1007/s00371-024-03690-y
36. Peng, C., Sun, F., Liu, D., Wang, N., Gao, X.: Local artifacts amplification for deepfakes augmentation. Neural Netw. **180**, 106692 (2024)
37. Ganguly, S., Ganguly, A., Mohiuddin, S., Malakar, S., Sarkar, R.: Vixnet: Vision transformer with xception network for deepfakes based video and image forgery detection. Expert Syst. Appl. **210**, 12 (2022)
38. Khan, S. A., Dang-Nguyen, D.-T. : Hybrid transformer network for deepfake detection. https://arxiv.org/abs/2208.05820 (2022)
39. Li, L., Bao,J., Zhang, T., Yang, H., Chen, D., Wen, F., Guo, B.: Face x-ray for more general face forgery detection. https://arxiv.org/abs/1912.13458 (2020)
40. Choi, N., Kim, H.: DDS: deepfake detection system through collective intelligence and deep-learning model in blockchain environment. Appl. Sci. (Switzerland) **13**, 2122 (2023)

Publisher's Note Springer Nature remains neutral with regard to jurisdictional claims in published maps and institutional affiliations.

Springer Nature or its licensor (e.g. a society or other partner) holds exclusive rights to this article under a publishing agreement with the author(s) or other rightsholder(s); author self-archiving of the accepted manuscript version of this article is solely governed by the terms of such publishing agreement and applicable law.

Signal, Image and Video Processing (2025) 19:713
https://doi.org/10.1007/s11760-025-04348-5

ORIGINAL PAPER

Investigating the performance vs. computational complexity tradeoff in cross-domain fire risk detection

Abhishek Verma[1] · **Virender Ranga**[1] · **Dinesh Kumar Vishwakarma**[1]

Received: 14 August 2024 / Revised: 28 May 2025 / Accepted: 1 June 2025
© The Author(s), under exclusive licence to Springer-Verlag London Ltd., part of Springer Nature 2025

Abstract
Fire risk detection is critical for timely interventions and effective management strategies in mitigating wildfire impacts. This study examines the efficacy of many advanced models, emphasizing the Swin Transformer architecture for efficient fire detection. We assessed RGB input evaluations, highlighting the Swin_S model, which attained a test accuracy of 62.1%, and the Swin_T model at 61%. Comparative analysis with current models demonstrated that Swin_T_Edge surpassed its competitors, achieving the maximum accuracy of 66% and an F1 score of 0.587, confirming its efficacy in classification tasks while maintaining a balance in model complexity. Cross-dataset tests further illustrated the models' durability across various fire conditions, underscoring the necessity for solid generalization capabilities in real-world applications. Statistical evaluations utilizing t-tests confirmed the substantial performance enhancements of the suggested models. The findings highlight the Swin_T_Edge model's promise as a premier option for fire risk detection systems, recommending future improvements via ensemble learning and the incorporation of temporal data.

Keywords Fire detection · Swin transformer · Edge input evaluation · Model comparison · Statistical analysis · Wildfire management

1 Introduction

Forests are essential constituents of ecosystems, widely recognized for their remarkable capacities in purifying the atmosphere, preserving soil integrity, and serving as natural repositories for precipitation [1].

The repercussions of wildfires on these vital ecosystems extend beyond just financial damages. The protracted duration of the Australian wildfire catastrophe, commencing in September 2019, serves as a poignant reminder. The event's aftermath has had a significant impact, as evidenced by property damage estimates of over $100 billion. This impact is characterized by several negative consequences, including soil and air quality deterioration and the unfortunate extinction of multiple animal species [2–4].

Numerous research activities have emerged in response to the need to mitigate the adverse impacts of wildfires, with a strong foundation in geoscientific knowledge. Jaiswal et al. [5] study highlights the critical role of mapping forest fire risk zones, utilizing satellite imagery and GIS technology to accurately predict potential fire occurrences, which can significantly aid in understanding and mitigating fire risks. Numerous traditional fire risk models utilize diverse data analysis methodologies to incorporate elements linked to fire dangers. An illustrative example may be seen in the research conducted by Akay et al. [6], where forest fire risk maps were produced using the multiple-criteria decision analysis methodology.

In recent years, there has been a significant increase in the availability of remote sensing data, primarily due to the growth of satellite and aerial programs. Moreover, advancements in optical sensor technology have resulted in improved picture quality. As a result, remote sensing images have emerged as a flexible and widely utilized resource, finding application in many practical contexts [7–9]. The

✉ Abhishek Verma
abhishekcms08@gmail.com

Virender Ranga
virenderranga@dtu.ac.in

Dinesh Kumar Vishwakarma
dvishwakarma@gmail.com

[1] Biometric Research Laboratory, Department of Information Technology, Delhi Technological University, Bawana Road, Delhi 110042, India

Published online: 09 June 2025

phenomenon has generated a surge of scholarly investigations focused on integrating remote sensing imagery into fire danger evaluations. For example, the study by [10] integrated seasonal remote sensing data, climatic data, and fuel type information to analyze the seasonal fire potential. Recent research has utilized machine-learning methods to analyze remote-sensing images and their geographic factors. Due to climate change, natural hazards are increasing, such as fire forests and tropical cyclones [11]. We need an early warning system to minimize the economic and human losses caused by natural hazards.

Indicators such as the composition of tree species within a forest and the closeness to areas of human activity, as inferred from remote sensing imagery, provide indirect insights into the potential occurrence of fire incidents. The main aim of this study is to provide a concise framework for creating a direct correlation between remote sensing imaging and the danger of fire on the Earth's surface. The present undertaking utilizes data derived from the Wildfire Hazard Potential (WHP) and the National Agriculture Imagery Program (NAIP) to compile the FireRisk dataset [12], specifically designed to assess fire risk. Shen et al. [13] created this dataset, which has been rigorously curated and consists of 91,872 annotated images, each associated with a particular fire risk class from 7 classes. As observed in Fig. 1, a visual examination of these images suggests a fundamental association between forest cover and fire risk.

Moreover, accurately evaluating fire risk across diverse domains presents substantial challenges, particularly due to the considerable variation in environmental conditions and observational parameters encountered in practice. Factors such as differing vegetation types, varying climatic conditions, changes in lighting and visibility due to weather or time-of-day, and discrepancies in sensor characteristics significantly complicate model generalization across domains. Consequently, models trained under specific conditions often struggle when applied to different landscapes or scenarios, highlighting the crucial necessity for robust cross-domain adaptability. Addressing this complexity is vital for developing practical, reliable, and universally applicable wildfire detection and risk assessment systems, underscoring the practical significance and urgency of enhancing transfer learning capabilities in vision-based fire detection research. To further demonstrate the robustness of our approach, we have also assessed generalization performance using two additional datasets pertinent to this research area, thereby validating the broader applicability of our methodology.

1.1 Overview of the Key Contributions

The dataset developed by Shen et al. [13] serves as the foundation for our analysis, which is further analyzed in our study. The key contributions of this study are summarized as follows. First, we propose a comprehensive evaluation framework for fire risk detection that integrates the Swin Transformer architecture, emphasizing the critical trade-off between model accuracy and computational complexity, particularly in resource-constrained environments. Second, we design a dual-input methodology utilizing both RGB and edge-based image representations, enabling a detailed comparative analysis across multiple state-of-the-art vision models. Third, we enhance model interpretability by incorporating Canny edge detection and Class Activation Map (CAM) visualizations, offering insights into the decision-making process of deep learning models. Fourth, we conduct cross-dataset generalization experiments using two independent wildfire datasets to assess the robustness and transferability of our approach across diverse domains. Furthermore, our research investigates latent representations derived from self-supervised learning techniques to improve fire risk evaluation. A central focus of our work lies in analyzing the complex interplay between model performance and computational intricacy in cross-domain fire risk detection. Through an extensive evaluation using the FireRisk dataset and advanced benchmark models, our study contributes to a deeper understanding of the intersection

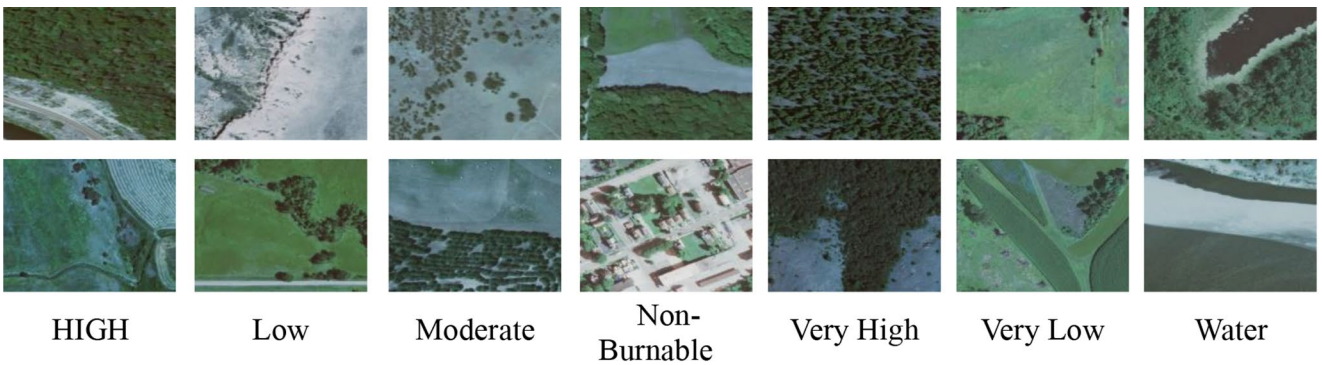


Fig. 1 Classes of the "FIRERISK" Dataset Representing Fire Risk Levels, including High, Moderate, Low, Non-Burnable, Very High, Very Low, and Water

between geospatial data processing, remote sensing, and machine learning, while reinforcing the importance of balancing performance with efficiency in practical deployment scenarios.

2 Literature review

In recent years, fire risk detection has become a crucial area of research due to the growing threat of wildfires to ecosystems, economies, and human life. Many methods have been developed that center on striking a compromise between detection performance and computational complexity. It is evident from Munsif et al. [14] that Convolutional Neural Networks (CNNs) are widely utilized for fire detection, and a lightweight model was suggested for disaster recognition. This efficient CNN model was implemented on devices with limited resources, proving its usefulness in practical situations.

Similarly, IoT-based fire detection systems have been developed, using CNNs to interpret data in real-time. With an emphasis on Internet of Things contexts, Dilshad et al. [15]suggested an optimized fire attention network (OFAN) for efficient fire detection. By addressing issues with accuracy in dimly lit and foggy environments, their approach produced better results across several datasets. The model's ability to capture global context was enhanced by adding a dilated convolutional layer, which qualified it for real-time applications on edge devices. Moreover, recent developments in vision transformers (ViTs) have demonstrated promise for fire detection. However, ViTs' high computational demand prevents them from being used in settings with limited resources. To address these issues, a unique ViT architecture that combines local self-attention with shifting patch tokenization was presented by Yar et al. [16]. This method made effective fire detection possible even with small and medium-sized datasets. The changes to the model balanced computational cost and accuracy by reducing the model size and the number of floating-point operations. To improve the accuracy of fire detection, several designs have added attention methods in addition to CNN and ViT models. For example, Yar et al. [17] provided a model that combines 3D convolution operations with a modified soft attention mechanism to enhance the identification of tiny fires from UAV data. Their method clarified how crucial it is to control model complexity to facilitate real-time UAV deployment, which is essential for prompt action in regions where fires are likely to occur.

Furthermore, models based on attention are still developing. The multi-attention fire network (MAFire-Net), introduced by Khan et al. [18], incorporates channel and spatial attention processes to improve feature representation in fire detection tasks. Compared to state-of-the-art techniques, this architecture demonstrated greater accuracy and faster inference times, which makes it a good contender for real-time deployment on edge devices. Its improved performance over several benchmarks was further enhanced by creating a sizable fire dataset. The advancement of fire detection technology has also been significantly aided by dataset creation. A substantial source of high-resolution UAV-captured photos to detect forest fires is the UAVs-FFDB dataset, first presented in UAVs-FFDB [19]. This dataset contributes to creating more resilient AI models for fire detection, monitoring, and diversifying the training set. Researchers may develop and test new fire detection algorithms using UAV-collected data, which enhances real-time fire monitoring systems.

Additionally, ensemble approaches have been suggested to increase the accuracy and resilience of fire detection models. Belarbi et al. [20] created a CNN ensemble to categorize fires in their early stages, providing a low-cost substitute for deep CNNs, which are frequently computationally costly. This method is perfect for early fire warning systems since it aggregated predictions from several models, obtaining great accuracy at a low computing cost.

Ultimately, multi-scale techniques have effectively addressed the difficulties associated with early fire detection, mainly when dealing with overlapping fire targets and challenging-to-detect smoke pictures. Introduced by Yan et al. [21], the multi-scale depth-separable convolutional network (MDCNet) was created to capture complex fire properties of several sizes. The application of focus loss improved its capacity for difficult fire situations much further. With its ability to identify fires earlier than conventional fire detection techniques, this design showed promise for improving public safety.

The research described in these publications offers a range of methods that address performance, computing efficiency, and practical application, which substantially contribute to the continuous development of fire detection systems. When taken as a whole, these studies offer a thorough framework for improving fire risk assessment, especially when it comes to cross-domain fire detection, which is the focus of the current study.

2.1 Comparison of methodologies

We briefly contrast each model's principal strengths and weaknesses in the context of fire risk detection, highlighting trade-offs between accuracy, spatial detail, computational cost, and texture sensitivity.

For the full side-by-side breakdown, including detailed advantages and limitations for all models, please refer to the Supplementary Material.

3 Proposed methodology

The proposed methodology is discussed in this section.

3.1 Input types

This subsection tells the pre-processing technique needed for further steps.

3.1.1 RGB-based input

We utilize an unaltered RGB image dataset, where each image is loaded, labeled by filename, resized to 256 × 256 pixels, and augmented with random horizontal and vertical flips to bolster generalization. Detailed preprocessing steps and augmentation parameters are provided in Supplementary Material.

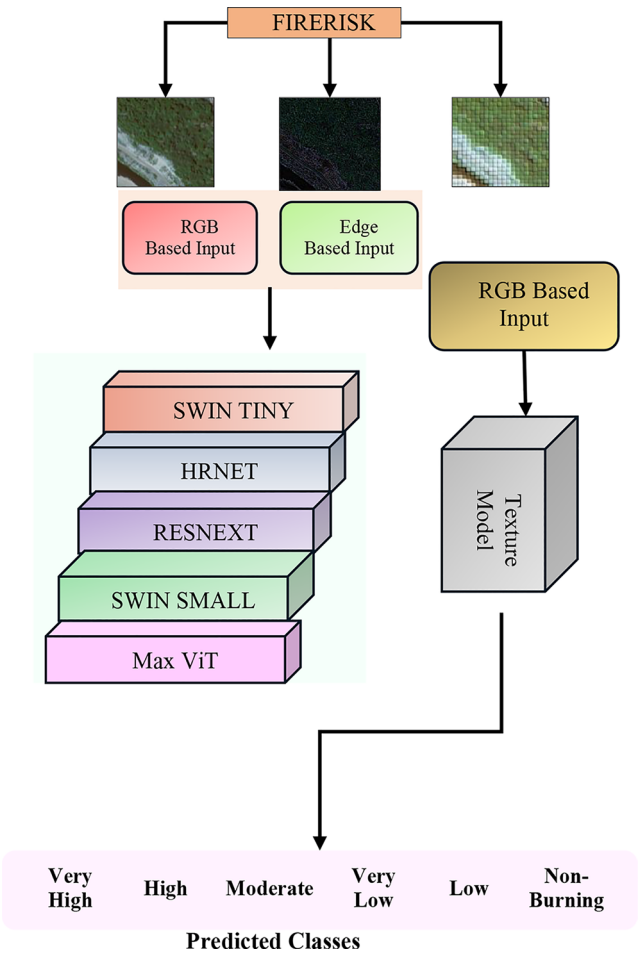


Fig. 2 Proposed Framework for Fire Risk Assessment, illustrating the processing of RGB and edge-based inputs for classifying fire risk levels

3.1.2 Edge based input

Images are first processed with the Canny_edge filter to enhance boundaries, then resized, labeled, and augmented (random horizontal and vertical flips) using the same transformation pipeline as the RGB inputs.For a detailed description of every preprocessing step provided in Supplementary Material.

3.2 Model selection

The methodology utilized in the study for detecting fire danger across different domains involves utilizing several vision models to analyze remote-sensing images. The models have been chosen based on their appropriateness for Image classification tasks, namely those that utilize edge information, RGB, and exclusive texture analysis. The model selection process encompasses.

3.3 Proposed framework

This Section explains the proposed framework flow and model description employed for further analysis, as can also be observed in Fig 2.

3.4 SWIN transformer

The Swin Transformer [22] is a significant breakthrough in visual modeling. This model presents advancements in vision transformers by including innovative architectural elements, like multi-headed self-attention with a window-based mechanism specifically shifting windows. A key innovation is the shifted window approach for multi-headed self-attention, where the image is divided into non-overlapping windows for efficient local attention. Let $X?\mathbb{R}^{N\times d}$Xrepresent the input sequence, where $N$the number of patches and d is is the dimension of the embeddingThe attention mechanism is computed within these windows, reducing computational complexity from $O\left(N^2\right)$ $to\,O\left(W^2\right)$ to, where W is the window size. Additionally, the windows are shifted between layers to allow for cross-window interaction, effectively enabling global dependencies. This shifted window strategy results in improved performance compared to fixed-window models, as it combines local and global context. Furthermore, Swin Transformer employs a hierarchical feature map structure, where the patch sizes grow progressively across layers, allowing the model to capture both fine-grained and large-scale visual information.

These advancements augment Swin's ability to capture distant relationships in visual information efficiently. The training process employed by Swin closely aligns with

that of the Data Efficient Image Transformer (DeiT), with a particular emphasis on efficiency. The process starts with pre-training the ImageNet-21k dataset and then fine-tuning the ImageNet-1k dataset [23]. Swin's performance is outstanding, achieving a new state-of-the-art benchmark on the Tiny ImageNet dataset. Notably, it has achieved a validation accuracy of 91.35%, exceeding the previous leading model by 0.33%. Swin's adeptness in managing the Tiny ImageNet dataset, in combination with its distinct window-based attention mechanism and the accessibility of its source code for additional investigation, establishes it as an essential selection for image classification tasks and a pivotal point of citation for researchers in this domain.

The study also alludes to additional transformer versions, such as Swin and MaxViT, presenting intriguing prospects for further progressions in vision transformer models.

3.4.1 HRNET

The HRNet (High-Resolution Network) is a groundbreaking architecture designed to preserve high-resolution representations throughout the network, making it ideal for tasks that require precise spatial information such as human pose estimation, semantic segmentation, facial landmark detection, and object detection. HRNet achieves this by maintaining multiple parallel convolutions at different resolution scales. Specifically, the network maintains high-resolution representations through parallel high-to-low resolution streams, with each stream progressively fusing multi-scale information. The key operation involves fusion layers that combine information across these streams. Mathematically, let F_h represent the feature map at high resolution, F_l at low resolution, and F_{fusion} as the fusion of the two. The fusion operation can be expressed as below in Eq. 1

$$F_{fusion} = \sum {}_{i=1}^{n} \alpha_i F_i \tag{1}$$

where α_i are learnable weights that control the contribution of each resolution scale, and n is the number of parallel streams. This fusion allows HRNet to integrate multi-scale information, maintaining high-resolution spatial details while incorporating context from lower resolutions. The architecture also integrates multi-resolution convolutional operations at each scale, optimizing the computational efficiency and model accuracy. HRNet has been shown to outperform previous models in tasks requiring high spatial accuracy, especially in human posture estimation, where the retention of fine-grained details is crucial [24].

3.4.2 RESNEXT

The ResNeXt architecture is an advanced convolutional neural network (CNN) that builds on the principles of Residual Networks (ResNets), introducing the novel concept of cardinality. Cardinality refers to the number of concurrent paths or "branches" that exist within the network, each representing a different specialist performing distinct computations [25].The idea of cardinality is analogous to increasing the number of "experts" working in parallel, leading to more diverse and comprehensive feature representations. Mathematically, ResNeXt employs a split-transform-merge strategy, where the input is split into multiple parallel paths, each path performing a transformation, and then the results are merged. If X is the input, and $F_c(X)$ represents the transformation applied by the $c-th$ cardinal group, the output as expressed in Eq. 2.

$$Y = \sum {}_{c+1}^{c} F_c(X) \tag{2}$$

Where C the total is number of cardinal paths, and $F_c(X)$ is the operation (e.g., convolution) applied to the input by the $c-th$ path. This cardinality-driven design allows ResNeXt to efficiently capture a wide variety of features without the need for deeper or more computationally expensive networks. The integration of this architecture proves highly effective in specialized tasks, such as fire risk detection in images, where subtle and complex patterns must be recognized. ResNeXt's ability to extract detailed features through multiple parallel pathways makes it well suited for analyzing datasets where nuanced patterns are critical for accurate predictions, such as identifying fire hazards or potential risk factors in images [25].

3.4.3 Multi-axis vit (max vit)

The Max ViT architecture represents a novel implementation of the vision transformer (ViT) model, characterized by its efficiency and scalability. The proposed approach incorporates a multi-axis attention mechanism, enabling the model to capture global-local spatial interactions across various input resolutions while maintaining linear computational cost. Moreover, the Max ViT model integrates convolutional layers into its design to enhance efficiency. The Max ViT model has exceptional performance on many image classification benchmarks, including ImageNet-1 K, ImageNet-21 K, and CIFAR-100, establishing itself as the current leader in the field. Additionally, it has robust scalability when used for datasets of considerable size and high-resolution images [26].

In conclusion, Max ViT has considerable strength and adaptability as a ViT model, holding promise as a future

frontrunner in many computer vision applications. The layer CAM presented in Fig. 3 highlights the regions where the RESNEXT model focuses its attention.

3.4.4 TEXURE model

The TEXTURE ResNet50 model is an advanced variant of the ResNet50 architecture, specifically designed to address computer vision tasks that require the detailed analysis of texture within images. The term "TEXTURE" emphasizes the model's ability to effectively capture and analyze texture patterns, which is critical in applications like material classification, surface inspection, and medical imaging. By focusing on texture, TEXTURE ResNet50 excels in tasks where understanding fine-grained patterns and local features is paramount.

TEXTURE ResNet50 inherits the core architecture of the ResNet50 model, which is a Convolutional Neural Network (CNN) comprising 50 layers. This depth of 50 layers enables the model to learn increasingly complex hierarchical features at different levels of abstraction. At the heart of the ResNet architecture lies the concept of residual learning, which facilitates the learning of deep networks by introducing skip connections (or shortcuts) that bypass one or more layers. This allows the model to effectively train very deep architectures without the issues of vanishing gradients that often arise in conventional deep networks.

$$H(x) = F(x, \{W_i\}) + x \tag{3}$$

Mathematically, the residual learning in ResNet can be formulated as:

The TEXTURE ResNet50 model is a variation of the ResNet50 architecture specifically designed to cater to the requirements of computer vision jobs. The term "TEXTURE" in the model's nomenclature alludes to its distinct emphasis on analyzing texture inside images. The architecture of this model is optimized explicitly for cases in which the proper analysis of images heavily relies on texture-based information.

TEXTURE ResNet50 inherits the fundamental structure of the ResNet50 architecture at its core. The ResNet50 architecture is a convolutional neural network (CNN) comprising 50 layers. This depth gives it a greater capacity for learning complex hierarchical features than earlier models. The fundamental structure of the architecture consists of a sequence of convolutional layers, residual blocks, and fully linked layers. The combined elements of these components contribute to the model's capacity to effectively capture intricate patterns seen in images.

One distinguishing characteristic of TEXTURE ResNet50 is its notable focus on examining texture. The system is designed to effectively identify and analyze texture patterns present in images. Examining texture is pivotal in image content analysis, particularly in material identification, surface examination, and specific medical imaging assignments. The specialty of TEXTURE ResNet50 allows it to perform exceptionally well in jobs requiring a high level of emphasis on comprehending intricate aspects of texture [27].

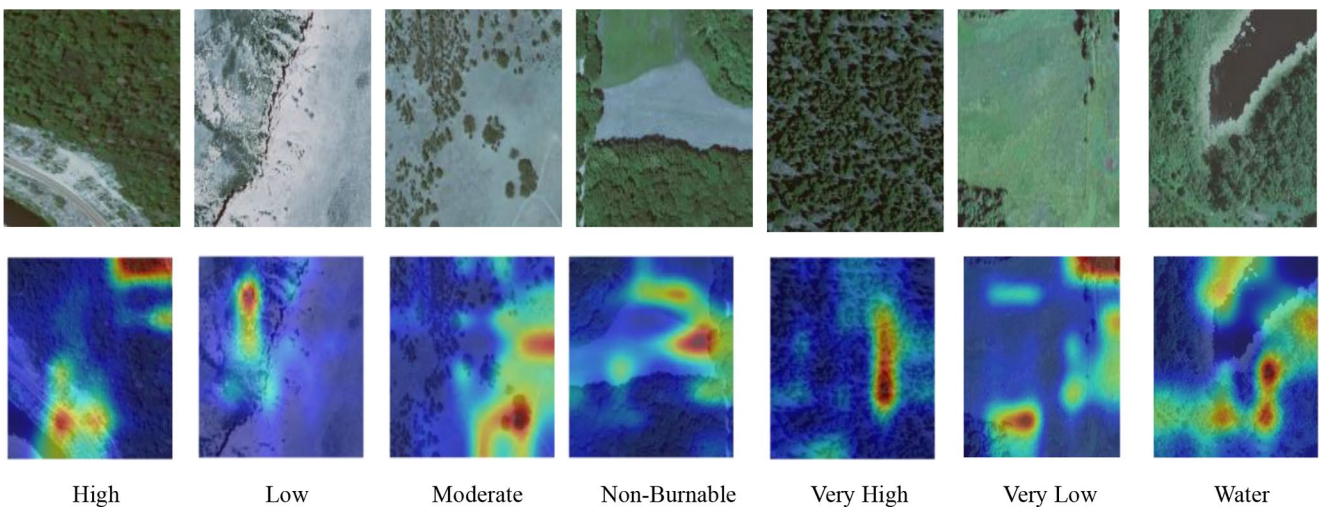


Fig. 3 Original image and Layer CAM Visualization in ResNeXt Original image (top) alongside Layer CAM visualization (bottom). The Layer CAM highlights regions of interest in the original image, providing insights into the model's focus areas during classification, categorized into five classes: High, Low, Moderate, Non-Burnable, Very High, Very Low, and Water

4 Experimental setup

This section outlines the experimental setup used to evaluate the performance of vision models in the context of cross-domain fire risk detection.

4.1 Dataset description

The FireRisk dataset [12], is a carefully compiled collection of remote-sensing photos for fire risk evaluation. It is a crucial resource for developing and accessing fire risk prediction models. The FireRisk dataset was not generated for this study; instead, it is employed to determine the efficacy of different prediction algorithms.

The data for this research originates from the Wildfire Hazard Potential (WHP) project, established by the U.S. Department of Agriculture, recognized for its comprehensive evaluations of fire risk and wildfire intensity throughout the United States. The WHP project integrates geostatistical data sources, such as FSim for assessing wildfire susceptibility and severity, LAND-FIRE for fuel and vegetation information, and the Fire Program Analysis (FPA) for historical fire occurrence records. The 2020 version of the WHP raster dataset offers detailed fire risk evaluations classified into seven specific categories, as seen in Fig. 1.

The raster dataset is provided in a geodatabase format (.gdb) and divides the nation into grids, each measuring 270 m per side, along with associated fire risk assessments for each grid cell. The images in the FireRisk dataset are obtained from the National Agriculture Imagery Program (NAIP), which utilizes airborne platforms to capture high-resolution ortho-rectified imagery with a spatial resolution of no less than 1 m, exceeding the quality generally attained through satellite-based remote sensing. Strict quality criteria regulate the images, necessitating a sun elevation of no less than 30 degrees and a maximum cloud cover of 10% for each quarter of the image segments. Images are gathered during the growing season to reduce the occurrence of snow and flooding. The collection comprises 91,872 remote-sensing photos of fire risk assessments derived from the WHP dataset. Of them, 70,331 photos are designated for training, whereas 21,541 images are allotted for validation. Every image is subjected to a uniform cropping procedure, yielding dimensions of 270×270 pixels. It is classified into seven discrete fire risk categories, enabling a comprehensive analysis of fire risk levels across diverse geographical regions.

4.2 Data preprocessing

The dataset was partitioned into two distinct groups, namely RGB-based images and edge-based images. The preparation operations for RGB-based images encompassed many stages, namely importing the images, assigning appropriate labels, scaling them to a specified dimension of 256×256 pixels, and using data augmentation techniques such as random horizontal and vertical flips. To improve the visibility of boundaries in edge-based images, a filter called "FIND_EDGES" was utilized for edge detection. Subsequently, identical preprocessing procedures were employed for RGB-based images.

4.3 Edge-to-edge extraction using the canny edge filter

We apply the Canny Edge Detector—comprising Gaussian smoothing, gradient magnitude computation, non-maximum suppression, and hysteresis thresholding—to highlight the most significant boundaries and structural features in each image. For a complete breakdown of parameter settings and implementation details, see Supplementary Material.

4.4 Interpretation of CAM visualizations

In order to gain a deeper insight into the model's decision-making process, Class Activation Maps (CAM) are utilized to visualize the areas of focus during classification; Fig. 3, showing the Layer CAM visualizations, provides a deeper understanding of the areas that the ResNeXt model focuses on when making fire risk classification predictions. The Layer CAM (Class Activation Map) highlights the regions of the input image that the model deems most relevant for determining the class of the image. These visualizations help illustrate the model's decision-making process by highlighting key features that contribute to its predictions.

In the context of fire risk detection, the highlighted regions are typically associated with critical features such as areas with high vegetation density or open, dry ground, which are often more susceptible to fire. The importance of these areas corresponds with known fire risk factors such as vegetation type and environmental dryness, which are commonly used in fire risk assessments. By analyzing these visualizations, we can validate the model's focus on meaningful and contextually significant features, strengthening the interpretability of the model and justifying its use in real-world applications. Thus, these visualizations not only enhance understanding of the model's behavior but also provide an additional layer of interpretability, ensuring that its decisions align with expert knowledge in fire risk assessment.

4.5 Development environment

The experiments were conducted using the Python programming language with the PyTorch deep learning framework,

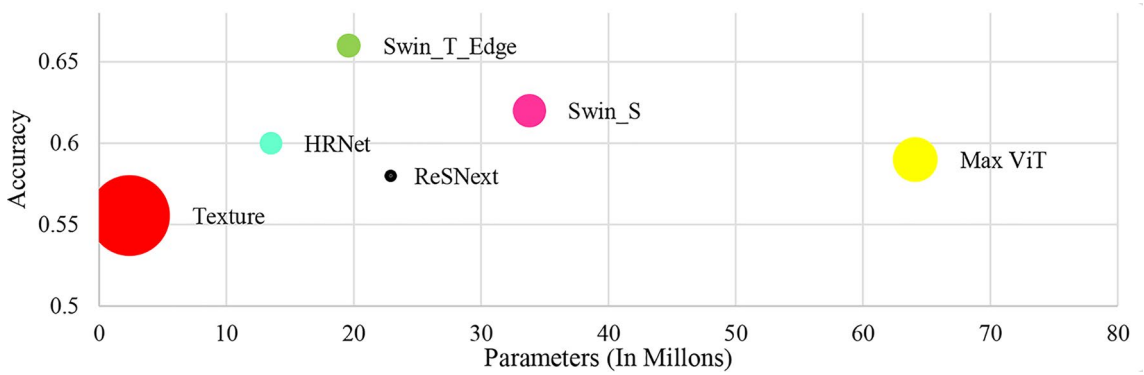


Fig. 4 Model Performance Trade-off. This figure illustrates the relationship between model complexity and accuracy, where the size of each bubble corresponds to the number of parameters (in millions) for each model, effectively demonstrating the trade-off between computational demands and performance metrics

Table 1 Performance metrics of models table presents the CPU and GPU time per epoch, Multiply-Accumulate operations (MAC), number of parameters (in millions), and accuracy (ACC) for each model, offering a concise comparison of their computational efficiency and performance

Models	CPU Time per epoch	GPU Time per epoch	MAC	PARAM's (in Millions)	ACC
ResNEXT	0.31	0.7	1.399	22.994	0.58
Swin_T_Edge	0.29	0.3	124.464	19.621	0.66
Swin_S	0.45	0.6	240.73	33.818	0.62
HRNET	0.22	0.68	110.623	13.562	0.55
Texture	21.48	0.8	1412.74	2.389	0.59
Max ViT	1	0.19	434.665	64.021	0.59

a popular library for developing and training machine learning models. The specific library versions used, as well as detailed information on the training, are provided in the supplementary material.

4.6 Model performance and complexity analysis

This section thoroughly examines model performance and computational complexity to provide significant insights into their efficacy in cross-domain fire risk detection while considering computing requirements.

As presented in Fig. 4, the findings provide a comprehensive overview of key performance indicators for each model. These indicators encompass CPU Time, GPU Time, Multiply-Accumulate (MAC) operations, parameter count, and accuracy. This comprehensive research enables well-informed conclusions on the trade-offs between a model's performance and computational complexity.

The research reveals that the SWIN_T_Edge model attains the highest level of accuracy, measuring 0.66. It is closely trailed by the SWIN_S model, which reaches an accuracy of 0.62. These models exhibit a noteworthy level of accuracy while simultaneously keeping the number of parameters manageable. In contrast, the Texture Model demonstrates a moderate level of accuracy, precisely 0.55, while exhibiting a notably low level of computing complexity. This underscores the promise of texture-based models within this field.

Nevertheless, it is crucial to consider the computing demands associated with these models. The Max ViT model, which consists of 64.021 million parameters, exhibits significant computational complexity, specifically about "CPU time" and "GPU time". It can be observed in Table 1. Achieving an optimal trade-off between performance and complexity is paramount in scenarios with limited resources.

In addition to the tabular data in Table 1., A bubble chart in Fig. 4 is utilized to visually illustrate the relationships among model accuracy, the number of parameters, and the Multiply-Accumulate Operations (MAC). In this graph, the y-axis represents accuracy, while the x-axis represents the number of parameters. The size of each bubble corresponds to the MAC, providing a clear representation of how these metrics interact.

5 Results and discussion

This part thoroughly examines model performance, specifically emphasizing diverse evaluation measures for the models across distinct input situations, namely Edge Input and RGB Input.

The evaluated models include SWIN_T_EDGE, ResNext, SWIN_S, Max ViT, HRNET, and Texture under RGB Input circumstances. Comprehensive performance analysis using essential measures such as Test Accuracy, MCC (Matthews Correlation Coefficient), Precision, Recall, and F1-score.

Table 1 presents a comprehensive summary of the performance metrics for each model utilized in the study. The findings reveal considerable heterogeneity in CPU and GPU processing durations, with the quantity of

Multiply-Accumulate Operations (MAC) and parameters. The Swin_T_Edge model attained the maximum accuracy of 0.66 while preserving a comparatively low computational expense, indicating it may be the most efficient option for fire risk assessment applications among the assessed models.

5.1 RGB input evaluation

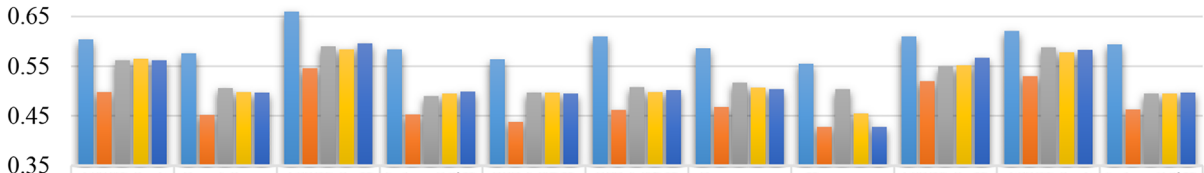
In the RGB input assessment, SWIN_S surpassed other models with a Test Accuracy of 62.1%, underscoring its exceptional capability to process RGB inputs. SWIN_T was closely behind at 61%, and Max ViT attained 59.4%. This demonstrates the capacity of SWIN_S and SWIN_T to generalize effectively over RGB input data. The MCC scores corroborated these findings, with SWIN_S achieving the maximum score of 0.53 and SWIN_T at 0.52, signifying a robust association between anticipated and actual classifications. Max ViT exhibited a reduced MCC of 0.463, indicating marginally less consistent performance. The maximum precision was achieved by SWIN_T at 0.588, indicating its superior capability in recognizing true positives, but SWIN_S also demonstrated commendable performance with a precision of 0.55. Max ViT and HRNET achieved accuracy scores of 0.495 and 0.504, respectively, signifying an elevated false positive rate relative to the leading models. Recall scores were highest for SWIN_S (0.578) and SWIN_T (0.552), indicating their efficacy in identifying positive instances, while Max ViT and HRNET followed at 0.495 and 0.498, respectively. The F1-score, which reconciles precision and recall, was highest for SWIN_S (0.583), followed by SWIN_T (0.567), underscoring their exceptional performance with RGB inputs.

5.2 Edge input evaluation

The assessment under edge input conditions indicates that SWIN_T consistently surpassed other models, attaining the highest Test Accuracy of 66%. This signifies an enhanced capacity to categorize edge-based inputs accurately. SWIN_S achieved an accuracy of 60.4%, indicating a competitiveperformance compared to other state-of-the-art models on this benchmark.

performance. Max ViT and ResNext attained modest accuracies of 58.4% and 57.6%, respectively, demonstrating their efficacy, although lacking the performance of the top models. Regarding the Matthews Correlation Coefficient (MCC), which assesses the effectiveness of classifications, SWIN_T scored 0.546, highlighting its dependability in extreme situations, whereas SWIN_S recorded 0.498. In terms of Precision, indicating the capacity to identify positive instances accurately, SWIN_T (0.59) and SWIN_S (0.562) exhibited the highest accuracy, but Max ViT (0.49) and HRNET (0.497) showed marginally lesser accuracy in recognizing genuine positives. The Recall was the highest, indicating the model's ability to identify all positive instances.

SWIN_T (0.584) and SWIN_S (0.565) demonstrated their efficacy in detecting positive cases, while Max ViT and HRNET followed closely at 0.495 and 0.497, respectively. In integrating accuracy and recall inside the F1-score, SWIN_T attained the optimal equilibrium (0.596), succeeded by SWIN_S (0.562), establishing these models as the foremost contenders under edge input conditions. A detailed illustration is in Fig. 5.



	SWIN_S	ResNext	SWIN_T	Max ViT	HRNET	HRNET	Resnext	Texture	SWIN_T	SWIN_S	Max ViT
	Edge Input					RGB input					
Test Accuracy	0.604	0.576	0.66	0.584	0.564	0.61	0.586	0.555	0.61	0.621	0.594
MCC	0.498	0.452	0.546	0.453	0.438	0.462	0.468	0.428	0.52	0.53	0.463
Precision	0.562	0.506	0.59	0.49	0.497	0.508	0.517	0.504	0.55	0.588	0.495
Recall	0.565	0.498	0.584	0.495	0.497	0.498	0.507	0.455	0.552	0.578	0.495
F1	0.562	0.497	0.596	0.499	0.495	0.502	0.504	0.428	0.567	0.583	0.497

Fig. 5 This figure visually represents the evaluation metrics, including Test Accuracy, Matthews Correlation Coefficient (MCC), Precision, Recall, and F1 score for various models (SWIN_T, ResNext, SWIN_S, Max ViT, HRNET) using edge and RGB inputs. The chart illustrates the performance differences across models, clearly comparing how each model performs with different input types

Table 2 Comparison with State-of-the-Art models -Accuracy (Acc), F1 score (F1), and parameters (millions) for different state-of-the-art models, showing the balance between performance and model size

Model	Acc	F1	Parameters
Dense-net [28]	0.55	0.49	~24 M
EfficientNet-B0 [29]	0.53	0.47	~5.3 M
MobileNetV3-Large [30]	0.58	0.51	~5.4 M
DenseNet-121 [31]	0.59	0.52	~8 M
ConvNeXt-Tiny [32]	0.6	0.53	~28 M
ViT [33]	0.612	0.501	~86 M
DINO [34]	0.628	0.526	~87 M
MAE [35]	0.633	0.549	~87 M
Swin_T _Edge	0.66	0.587	~28M

5.3 Comparision with state of the arts

Table 2 presents a comparison of various state-of-the-art models based on accuracy (Acc), F1 score (F1), and parameter count (in millions). Swin_T_Edge excels with the highest accuracy of 0.66 and an F1 score of 0.587, demonstrating its superior performance in classification tasks. In contrast, Dense-net, EfficientNet-B0, and MobileNetV3-Large exhibit lower accuracy and F1 scores, reinforcing the effective balance that Swin_T_Edge achieves between performance and model complexity. This highlights Swin_T_Edge as the most effective choice for applications requiring high accuracy and efficiency.

5.3.1 Generalization and cross-dataset evaluation

This section assesses the generalization capabilities of the proposed models over diverse datasets to gauge their robustness and adaptability in various real-world fire scenarios. To this end, we perform cross-dataset experiments by training on one dataset and testing on another. Key performance metrics—including accuracy, precision, recall, and F1-score—for every train–test combination are provided in the Supplementary Material; see the supplementary material for the full table and detailed results.

6 Conclusion and future scope

This study presents a comprehensive evaluation of advanced vision models for cross-domain fire risk detection, highlighting the balance between performance and computational complexity. Among the models assessed, the Swin_T_Edge architecture achieved the highest accuracy (66%) and F1 score (0.587), demonstrating superior performance while maintaining computational efficiency. The analysis of RGB and edge-based inputs further validated the generalization capability of Swin_T and Swin_S models. Cross-dataset evaluations underscored the importance of robust training across diverse domains, while t-test results confirmed the statistical significance of the proposed approach. These findings position Swin_T_Edge as a promising candidate for practical wildfire risk assessment systems. Building on this foundation, future work can explore ensemble techniques, temporal data integration, and multi-modal sensing to further enhance predictive accuracy and deployment readiness.

6.1 Future scope

Future studies should combine sophisticated methodologies, like ensemble learning and hybrid models, to augment performance and generalization skills. Furthermore, integrating temporal data from remote sensing to enhance forecast accuracy in dynamic fire scenarios might significantly improve operational deployment. It is advisable to examine the effects of various pre-processing approaches and input modalities, including multispectral and hyperspectral pictures, to enhance the models' applicability across various environmental situations. The advancement of real-time fire detection systems based on this study's findings can facilitate proactive fire management and response.

Supplementary Information The online version contains supplementary material available at https://doi.org/10.1007/s11760-025-04348-5.

Author contributions Abhishek Verma: Software, Validation, Investigation, Data Curation, Writing– Original Draft, Visualization. Virender Ranga: Investigation, Resources, Writing– Review & Editing, Supervision, Project Administration.Dinesh Kumar Vishwakarma: Conceptualization, Methodology, Formal Analysis, Resources, Writing– Review & Editing, Supervision.

Funding No funding was received to assist with preparing this manuscript.

Data availability No datasets were generated or analysed during the current study.

Declarations

Competing interests The authors declare no competing interests.

References

1. Morancho, A.B.: A hedonic valuation of urban green areas. Landsc. Urban Plan. **66**(1), 35–41 (Dec. 2003). https://doi.org/10.1016/S0169-2046(03)00093-8
2. Wildfire in: Australia during 2019–2020, Its Impact on Health, Biodiversity and Environment with Some Proposals for Risk Management: A Review. Accessed: Oct. 28, 2023. [Online]. Available: https://www.scirp.org/journal/paperinformation.aspx?paperid=110099
3. Verma, A., Ranga, V., Vishwakarma, D.K.: A novel approach for forecasting PM2.5 pollution in Delhi using CATALYST. Environ.

Monit. Assess. **195**(12), 1457 (Nov. 2023). https://doi.org/10.1007/s10661-023-12020-z
4. Verma, A., Ranga, V., Vishwakarma, D.K.: BREATH-Net: A novel deep learning framework for NO2 prediction using bi-directional encoder with transformer. Environ. Monit. Assess. **196**(4), 340 (Apr. 2024). https://doi.org/10.1007/s10661-024-12455-y
5. Jaiswal, R.K., Mukherjee, S., Raju, K.D., Saxena, R.: Forest fire risk zone mapping from satellite imagery and GIS, *Int. J. Appl. Earth Obs. Geoinformation*, vol. 4, no. 1, pp. 1–10, Aug. (2002). https://doi.org/10.1016/S0303-2434(02)00006-5
6. Akay, A., Erdoğan, A.: GIS-based Multi-criteria decision analysis for forest fire risk mapping. Oct (2017)
7. Castelluccio, M., Poggi, G., Sansone, C., Verdoliva, L.: Land Use Classification in Remote Sensing Images by Convolutional Neural Networks, Aug. 01, 2015, *arXiv*: arXiv:1508.00092. Accessed: Oct. 28, 2023. [Online]. Available: http://arxiv.org/abs/1508.00092
8. Fassnacht, F.E., et al.: Dec., Review of studies on tree species classification from remotely sensed data, *Remote Sens. Environ.*, vol. 186, pp. 64–87, (2016). https://doi.org/10.1016/j.rse.2016.08.013
9. Liu, S., Shi, Q.: Local climate zone mapping as remote sensing scene classification using deep learning: A case study of metropolitan China, *ISPRS J. Photogramm. Remote Sens.*, vol. 164, pp. 229–242, Jun. (2020). https://doi.org/10.1016/j.isprsjprs.2020.04.008
10. Huesca, M., Litago, J., Palacios-Orueta, A., Montes, F., Sebastián-López, A., Escribano, P.: Assessment of forest fire seasonality using MODIS fire potential: A time series approach, *Agric. For. Meteorol.*, vol. 149, no. 11, pp. 1946–1955, Nov. (2009). https://doi.org/10.1016/j.agrformet.2009.06.022
11. Yadav, M., Das, L.: Formulation and evaluation of the radius of maximum wind of the tropical cyclones over the North Indian Ocean basin, *Theor. Appl. Climatol.*, vol. 155, no. 6, pp. 4521–4534, Jun. (2024). https://doi.org/10.1007/s00704-024-04895-w
12. Shen, S., Seneviratne, S., Wanyan, X., Kirley, M.: FireRisk: A Remote Sensing Dataset for Fire Risk Assessment with Benchmarks Using Supervised and Self-supervised Learning, Sep. 21, *arXiv*: arXiv:2303.07035. Accessed: Oct. 28, 2023. [Online]. (2023). Available: http://arxiv.org/abs/2303.07035
13. Shen, S., Seneviratne, S., Wanyan, X., Kirley, M.: FireRisk: A Remote Sensing Dataset for Fire Risk Assessment with Benchmarks Using Supervised and Self-supervised Learning, in *International Conference on Digital Image Computing: Techniques and Applications (DICTA)*, Nov. 2023, pp. 189–196. (2023). https://doi.org/10.1109/DICTA60407.2023.00034
14. Munsif, M., Afridi, H., Ullah, M., Khan, S.D., Alaya Cheikh, F., Sajjad, M.: A Lightweight Convolution Neural Network for Automatic Disasters Recognition, in *2022 10th European Workshop on Visual Information Processing (EUVIP)*, Sep. pp. 1–6. (2022). https://doi.org/10.1109/EUVIP53989.2022.9922799
15. Dilshad, N., Khan, S.U., Alghamdi, N.S., Taleb, T., Song, J.: Toward Efficient Fire Detection in IoT Environment: A Modified Attention Network and Large-Scale Data Set, *IEEE Internet Things J.*, vol. 11, no. 8, pp. 13467–13481, Apr. (2024). https://doi.org/10.1109/JIOT.2023.3336931
16. Yar, H., Khan, Z.A., Hussain, T., Baik, S.W.: A modified vision transformer architecture with scratch learning capabilities for effective fire detection. Expert Syst. Appl. **252**, 123935 (Oct. 2024). https://doi.org/10.1016/j.eswa.2024.123935
17. Yar, H., Khan, Z.A., Rida, I., Ullah, W., Kim, M.J., Baik, S.W.: An efficient deep learning architecture for effective fire detection in smart surveillance. Image Vis. Comput. **145**, 104989 (May 2024). https://doi.org/10.1016/j.imavis.2024.104989
18. Khan, A., Sudheer, M.: Machine learning-based monitoring and modeling for spatio-temporal urban growth of Islamabad. Egypt. J. Remote Sens. Space Sci. **25**(2), 541–550 (Aug. 2022). https://doi.org/10.1016/j.ejrs.2022.03.012
19. Md., N., Mowla, D., Asadi, K.N., Tekeoglu, S., Masum, Rabie, K.: UAVs-FFDB: A high-resolution dataset for advancing forest fire detection and monitoring using unmanned aerial vehicles (UAVs), *Data Brief*, vol. 55, p. 110706, Aug. (2024). https://doi.org/10.1016/j.dib.2024.110706
20. Belarbi, F., Hassini, A., Benamara, N.K.: A novel approach based on convolutional neural networks ensemble for fire detection. Signal. Image Video Process. (Aug. 2024). https://doi.org/10.1007/s11760-024-03508-3
21. Yan, H., Cui, Z., Zhao, H., Zhang, J., Qin, J., Guo, Q.: The Multi-Scale Depth-Separable Convolution network for fire and smoke detection. Combust. Sci. Technol., **0**, 0, pp. 1–25, https://doi.org/10.1080/00102202.2024.2372689
22. Huynh, E.: Vision Transformers in 2022: An Update on Tiny ImageNet, May 21, *arXiv*: arXiv:2205.10660. Accessed: Oct. 28, 2023. [Online]. (2022). Available: http://arxiv.org/abs/2205.10660
23. Feng, P., Tang, Z.: A survey of visual neural networks: Current trends, challenges and opportunities. Multimed Syst. **29**(2), 693–724 (Apr. 2023). https://doi.org/10.1007/s00530-022-01003-8
24. Wang, J., et al.: Deep High-Resolution Representation Learning for Visual Recognition, Mar. 13, *arXiv*: arXiv:1908.07919. (2020). https://doi.org/10.48550/arXiv.1908.07919
25. Xie, S., Girshick, R., Dollár, P., Tu, Z., He, K.: Aggregated Residual Transformations for Deep Neural Networks, Apr. 10, *arXiv*: arXiv:1611.05431. (2017). https://doi.org/10.48550/arXiv.1611.05431
26. [2204.01697] MaxViT: Multi-Axis Vision Transformer. Accessed: Nov. 03, 2023. [Online]. Available: https://arxiv.org/abs/2204.01697
27. Goyal, V., Sharma, S., Garg, B.: Texture classification using ResNet and EfficientNet. In: Sisodia, D.S., Garg, L., Pachori, R.B., Tanveer, M. (eds.) in Machine Intelligence Techniques for Data Analysis and Signal Processing, pp. 173–185. Springer Nature, Singapore (2023). https://doi.org/10.1007/978-981-99-0085-5_15
28. Huang, G., Liu, Z., van der Maaten, L., Weinberger, K.Q.: Densely Connected Convolutional Networks, Jan. 28, *arXiv*: arXiv:1608.06993. (2018). https://doi.org/10.48550/arXiv.1608.06993
29. Tan, M., Le, Q.V.: EfficientNet: Rethinking Model Scaling for Convolutional Neural Networks, Sep. 11, *arXiv*: arXiv:1905.11946. (2020). https://doi.org/10.48550/arXiv.1905.11946
30. Howard, A., et al.: Searching for MobileNetV3, Nov. 20, 2019, *arXiv*: arXiv:1905.02244. https://doi.org/10.48550/arXiv.1905.02244
31. Nandhini, S., Ashokkumar, K.: An automatic plant leaf disease identification using DenseNet-121 architecture with a mutation-based henry gas solubility optimization algorithm, *Neural Comput. Appl.*, vol. 34, no. 7, pp. 5513–5534, Apr. (2022). https://doi.org/10.1007/s00521-021-06714-z
32. Perdana, R.A., Arimurthy, A.M., Risnandar: Remote Sensing Scene Classification using ConvNeXt-Tiny Model with Attention Mechanism and Label Smoothing, *J. RESTI Rekayasa Sist. Dan Teknol. Inf.*, vol. 8, no. 3, Art. no. 3, Jun. (2024). https://doi.org/10.29207/resti.v8i3.5731
33. Dosovitskiy, A., et al.: An Image is Worth 16x16 Words: Transformers for Image Recognition at Scale, Jun. 03, *arXiv*: arXiv:2010.11929. (2021). https://doi.org/10.48550/arXiv.2010.11929

34. Zhang, Z., Cui, X., Zheng, Q., Cao, J.: Land use classification of remote sensing images based on Convolution neural network. Arab. J. Geosci. **14**(4), 267 (Feb. 2021). https://doi.org/10.1007/s12517-021-06587-5
35. He, K., Chen, X., Xie, S., Li, Y., Dollár, P., Girshick, R.: Masked Autoencoders Are Scalable Vision Learners, Dec. 19, 2021, *arXiv*: arXiv:2111.06377. https://doi.org/10.48550/arXiv.2111.06377
36. An Efficient Fire Detection Method Based on Multiscale Feature Extraction: Implicit Deep Supervision and Channel Attention Mechanism. Accessed: Oct. 03, 2024. [Online]. Available: https://xplorestaging.ieee.org/document/9171455?denied=
37. Yar, H., Hussain, T., Khan, Z.A., Koundal, D., Lee, M.Y., Baik, S.W.: [Retracted] Vision Sensor-Based Real-Time Fire Detection in Resource-Constrained IoT Environments, *Comput. Intell. Neurosci.*, vol. no. 1, p. 5195508, 2021, (2021). https://doi.org/10.1155/2021/5195508

Publisher's note Springer Nature remains neutral with regard to jurisdictional claims in published maps and institutional affiliations.

Springer Nature or its licensor (e.g. a society or other partner) holds exclusive rights to this article under a publishing agreement with the author(s) or other rightsholder(s); author self-archiving of the accepted manuscript version of this article is solely governed by the terms of such publishing agreement and applicable law.

AIP Advances

RESEARCH ARTICLE | JUNE 23 2025

Investigation of temperature-dependent performance degradation in AlGaN/InGaN/GaN HEMTs: Implications for device reliability and efficiency

Neda Ahmad ; Sonam Rewari; Vandana Nath

Check for updates

AIP Advances 15, 065120 (2025)
https://doi.org/10.1063/5.0271310

View Online
Export Citation

Articles You May Be Interested In

Effect of amorphous ternary AlBN passivations on the performance of AlGaN/GaN HEMTs

AIP Advances (July 2022)

Fabrication and characteristics of flexible normally-off AlGaN/GaN HEMTs

AIP Advances (October 2020)

Dependence of structural and electrical properties of AlGaN/GaN HEMT on Si(111) on buffer growth conditions by MBE

J. Vac. Sci. Technol. B (May 2013)

27 June 2025 04:35:43

AIP Advances
Special Topics Now Online
Learn More
AIP Publishing

AIP Publishing

Investigation of temperature-dependent performance degradation in AlGaN/InGaN/GaN HEMTs: Implications for device reliability and efficiency

Cite as: AIP Advances 15, 065120 (2025); doi: 10.1063/5.0271310
Submitted: 27 March 2025 • Accepted: 30 May 2025 •
Published Online: 23 June 2025

View Online Export Citation CrossMark

Neda Ahmad,[1,a)] Sonam Rewari,[2] and Vandana Nath[1]

AFFILIATIONS

[1] USICT, Guru Gobind Singh Indraprastha University, Delhi, India
[2] Department of ECE, Delhi Technological University, Delhi, India

[a)] Author to whom correspondence should be addressed: neda.21116490021@ipu.ac.in

ABSTRACT

This paper comprehensively analyzes the temperature-dependent performance of an AlGaN/InGaN/GaN high electron mobility transistor. Thermal simulations were conducted to evaluate the impact of both model temperature and lattice temperature on device performance. Simulated DC characteristics are validated against experimental data using the 2D device simulation tool, TCAD Atlas. Key DC parameters such as transfer characteristics (I_{ds}–V_{gs}), output characteristics (I_{ds}–V_{ds}), transconductance (g_m), and threshold voltage (V_{th}) are analyzed over a temperature range of 260–360 K. In addition, radio-frequency analysis is conducted to evaluate important figures of merit, such as the current-gain cutoff frequency (f_T), across the same temperature range. The results show that at elevated temperatures, saturation current and the linear region characteristics degrade due to reduced carrier mobility, observed consistently in both model and lattice-based studies. However, the effects of temperature variation on the lattice are more pronounced, primarily due to the additional impact of self-heating, which intensifies performance degradation. Nonetheless, both the threshold voltage and the density of two-dimensional electron gas (2DEG) sheets increase as temperature rises. These findings highlight the critical importance of temperature selection in the operation of GaN HEMTs, which significantly influences key performance metrics.

© 2025 Author(s). All article content, except where otherwise noted, is licensed under a Creative Commons Attribution (CC BY) license (https://creativecommons.org/licenses/by/4.0/). https://doi.org/10.1063/5.0271310

27 June 2025 04:35:43

I. INTRODUCTION

High electron mobility transistors (HEMTs) have garnered significant attention due to their superior performance in high-frequency and high-power applications. Early studies primarily focused on silicon and GaAs FETs,[1–3] but recent advancements have highlighted the advantages of GaN-based HEMTs for these applications.[4] GaN, along with materials like SiC and diamond, is known for its ability to operate under extreme conditions, including high temperature and power. Over the past decades, AlGaN/GaN HEMTs have emerged as leading candidates for microwave frequency applications, offering enhanced speed, temperature resilience, and power-handling capabilities. Research in this domain has increasingly focused on improving both performance and manufacturability, especially through the development of cost-effective, high-frequency solutions.

GaN-based materials possess unique properties that make them particularly suited for demanding applications. These include a wide bandgap, high breakdown field, and high electron saturation velocity, as well as the formation of a two-dimensional electron gas (2DEG) with high polarization.[5] Recently, researchers have focused on analyzing the performance of GaN high electron mobility transistors (HEMTs) at different temperatures.[6–8] However, despite their superior characteristics, GaN-based devices face challenges such as reduced drain current and degraded RF and DC performance at elevated temperatures.[9] These issues arise due to several scattering mechanisms—like charged impurity scattering, phonon scattering, and interface roughness—which impact 2DEG and limit electron

© Author(s) 2025

mobility. To address these limitations, the introduction of a thin InGaN channel layer between the AlGaN and GaN layers in HEMTs has proven beneficial.[10] This pseudomorphic high electron mobility transistor (pHEMT) structure offers improved carrier confinement, higher carrier density, and enhanced electron transport, making it a promising alternative to conventional AlGaN/GaN HEMTs.

Temperature variation plays a critical role in the performance of both AlGaN/GaN and AlGaN/InGaN/GaN HEMTs.[11,12] The 2DEG's transport properties, which significantly impact the device's overall performance, are exceedingly susceptible to temperature fluctuations. Research on the temperature-dependent behavior of 2DEG in these devices is still limited, despite the critical nature of the effects of temperature on the 2DEG. This study seeks to address this gap by investigating the influence of both model temperature and lattice temperature on 2DEG transport properties by analyzing model and lattice temperatures in Silvaco simulations. The analysis is crucial because model temperature influences the physical simulation parameters, while lattice temperature governs thermal stability and electron mobility. In addition, this work examines the 2DEG behavior in AlGaN/InGaN/GaN heterostructures across varying thermal conditions, providing a deeper insight into device performance under different temperature regimes. This research paper presents a 2D simulation study to evaluate the performance of an AlGaN/GaN HEMT device with a gate length of 0.5 μm. The simulation results are compared with experimental data by analyzing key parameters, including transfer characteristics, I_{ds}–V_{ds} characteristics, g_m, V_{th}, and f_T across different temperature conditions. As temperature increases, these parameters exhibit noticeable changes, highlighting the impact of thermal variations on device behavior.

The objective of studying model temperature and lattice temperature effects in semiconductor device simulations is to understand their impact on electrical and thermal behavior, including key characteristics like current-voltage (I–V) performance, carrier mobility, and threshold voltage. By analyzing how variations in these temperature parameters affect device operation, the study aims to assess reliability, stability, and potential degradation under different conditions. This approach enhances the accuracy of simulations through better calibration against experimental data and provides valuable insights for optimizing device design, especially for high-temperature applications in power electronics and high-frequency devices, ensuring more robust and efficient performance.

II. DEVICE DESCRIPTION

TCAD allows us to perform virtual experiments and simulations before fabricating the actual device, reducing development time and costs. So, we designed the device on TCAD Silvaco Atlas[13] using the parameters shown in Table I. Starting with a SiC substrate, an AlN relaxation layer (1.5 nm), and an undoped GaN buffer layer (1.5 nm), an InGaN channel of 5 nm is sandwiched between the buffer and an undoped AlGaN spacer layer(5 nm), a doped AlGaN supply layer of 20 nm is applied over the spacer layer, and a 5 nm GaN cap layer is used to protect the supply layer from oxidation. Thereafter contacts were defined. The composition of In in InGaN was 0.10, and the percentage of Al in AlGaN was (25.3%). The source and drain establish Ohmic contacts with the undoped GaN layer, while the metal gate creates a Schottky

TABLE I. Device structural parameters.[14]

Parameters	Values
Undoped AlGaN (spacer layer)	5 nm
Undoped GaN (buffer layer)	1.5 μm
Substrate SiC	400 μm
AlN nucleation (relaxation layer)	1.5 nm
GaN (cap layer)	5 nm
AlGaN (supply layer)	20 nm
InGaN (channel layer)	5 nm
In proportion	0.10
Work function	5.1
Gate length	0.50 μm
Gate width	100 μm
Length between source and gate	1 μm
Length between gate and drain	2.75 μm
Doping	1.14×10^{13}
Interface charge	10×10^{11}
Length of source	0.25 μm
Length of drain	0.25 μm

contact with the supply layer of AlGaN by etching away the cap layer. 2DEG density and mobility are primarily influenced by the indium content in the $In_{0.10}Ga_{0.90}N$ channel and the conduction band offset at the interface. The simulations utilize physics-based models, including FERMI, SRH, FLDMOB, PCH, ELEC, and GANSAT.N as the mobility model. To prevent convergence issues, the Newton method is applied. For device calibration, initial parameter estimates were derived from an experimental study or existing knowledge, followed by a parameter sweep within the simulation software. The device structure is shown in Fig. 1, and the diagram for the band structure of the AlGaN/InGaN/GaN HEMT is shown in Fig. 2. The device was then simulated across various parameter combinations, and the results were compared with experimental data by Khan *et al.* in their study[14] for accuracy and visibility. This device has been previously calibrated using the experimental setup and documented in the study presented in Ref. 15. Subsequently, the impact on the AC and DC characteristics of the device was investigated by optimizing various parameters, including gate length, InGaN thickness, and indium mole fraction.

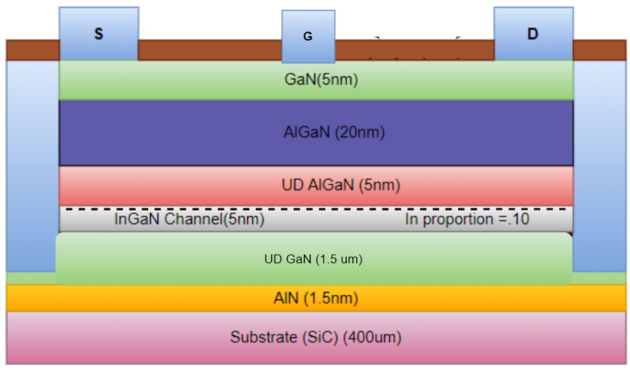


FIG. 1. Structure of the chosen AlGaN/InGaN/GaN HEMT.[14]

27 June 2025 04:35:43

© Author(s) 2025

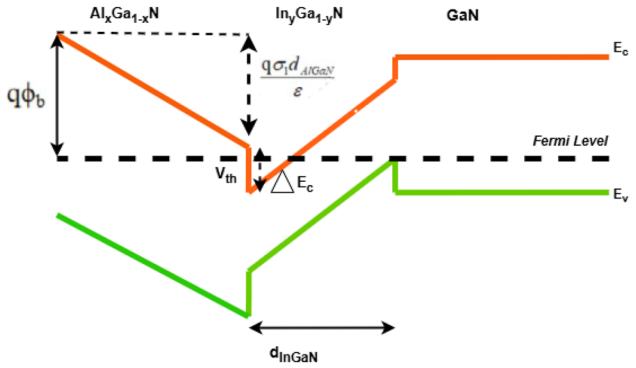


FIG. 2. Diagram for band structure of AlGaN/InGaN/GaN HEMT.

III. VALIDATION WITH THE EXPERIMENTAL DATA

Validation of the developed model using experimental data is a critical step to ensure its accuracy and reliability. In this study, we validated the model at two specific temperatures, 323 and 398 K, using the Silvaco TCAD simulator, as shown in Fig. 3. These temperatures were chosen to represent typical operating conditions for the DUT. The validation process involved comparing the simulated output with experimentally observed characteristics, ensuring that the model accurately captures the device's behavior across varying thermal conditions, enabling the model to generalize effectively to real-world applications. By confirming the model's accuracy at 323 and 398 K, we establish a reliable foundation for subsequent analysis of temperature effects and the interplay between lattice temperature and device performance. These validations enhance the model's robustness and applicability for predictive simulations and optimization in GaN HEMT designs.

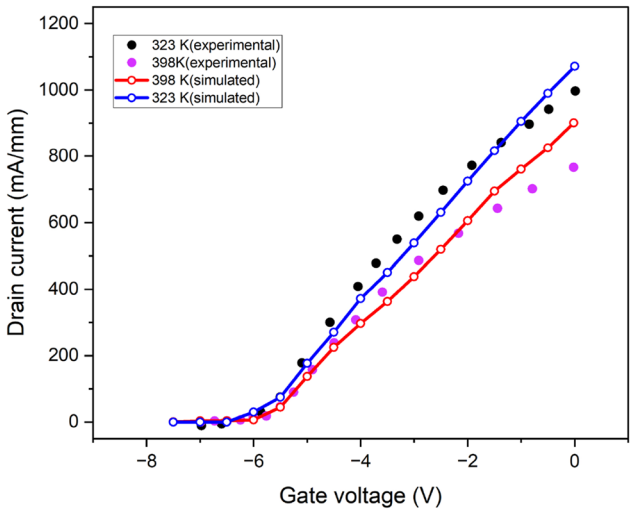


FIG. 3. Validated with experimental data at temperatures 323 and 398 K at V_{ds} = 15 V.[14]

IV. TEMPERATURE EFFECTS ON DEVICE PERFORMANCE

Model temperature and lattice temperature represent two important aspects of thermal behavior affecting semiconductor device performance: *Model temperature* refers to the temperature used in the simulation to account for the effects of temperature on carrier transport mechanisms, such as mobility, carrier concentration, and recombination rates. It is typically applied across the entire device to simulate how varying thermal conditions influence electrical performance. Model temperature affects parameters like current–voltage characteristics, threshold voltage, and the overall efficiency of the device.

Lattice temperature represents the actual physical temperature of the semiconductor's crystal lattice, which can vary spatially within the device due to heat generation during operation. Lattice temperature directly influences phonon interactions, thermal conductivity, and the scattering mechanisms of charge carriers. As the lattice heats up, carrier mobility typically decreases due to increased phonon scattering, potentially degrading the device's performance. Understanding the distinct roles of model and lattice temperature is critical in accurately simulating device behavior, particularly under high-power or high-frequency conditions, where thermal effects play a significant role in determining the reliability and efficiency of the device.

A. Simulation setup

Silvaco offers a range of simulation models. For the study of the model temperature variation effect on the device, the models used are MODEL FERMI fldmob, Fermi–Dirac statistics for accurate carrier distribution, "MODEL Fermi"; Shockley–Read–Hall (SRH) model for carrier generation and recombination, "MODEL SRH"; and Joule heating model to account for heat generation effects "MODEL JOULE TEMP." "Method block newton" is used to ensure convergence.

For the study of *lattice temperature* variation effects on the device, the models used are MODEL SRH.[16,17] Silvaco TCAD provides various models. The mobility value is influenced by both phonon and impurity scattering, which contribute to a reduction in low-field mobility. Following the approach proposed by Albrecht *et al.*,[18] the low-field mobility model can be selected by specifying ALBRECHT in the MODELS statement. This model is defined as follows, and the models used are explained in Table II:

$$\frac{1}{\mu(N,T)} = \frac{AN \cdot ALBRCT \cdot N}{NON \cdot ALBRCT}\left(\frac{T}{TON \cdot ALBRCT}\right)^{-3/2} \times \ln\left[1 + 3\left(\frac{T}{TON \cdot ALBRCT}\right)^{2}\left(\frac{N}{NON \cdot ALBRCT}\right)^{-2/3}\right] + BN \cdot ALBRCT \cdot N\left(\frac{T}{TON \cdot ALBRCT}\right)^{3/2} + \frac{CN \cdot ALBRCT}{\exp\left(TIN \cdot ALBRCT/T\right) - 1}. \quad (1)$$

The mobility, denoted as μ(N, T), depends on both the doping concentration (N) and the lattice temperature (T). The spontaneous

27 June 2025 04:35:43

© Author(s) 2025

TABLE II. Description of various Atlas commands and their purposes.

Model category	Command in Atlas	Purpose	Explanation
Carrier statistics	MODEL FERMI	Accurate carrier distribution in heavily doped regions	Enables Fermi–Dirac statistics to account for quantum effects, avoiding overestimation of carrier concentration in highly doped or high-temperature regions.
Field-dependent mobility	MODEL FLDMOB	Models mobility reduction at high E-fields	Reflects carrier velocity saturation effects important for high-power HEMT operation.
Shockley–Read–Hall recombination	MODEL SRH	Models trap-assisted carrier recombination	Captures recombination effects through mid-gap traps, affecting off-state and subthreshold behavior.
Self-heating (Joule)	MODEL Joule TEMP	Includes thermal effects due to power dissipation	Models the temperature rise within the device due to Joule heating, impacting electrical behavior.
Lattice temperature activation	MODEL LAT.TEMP	Enables lattice temperature dependency	Applies temperature to material parameters such as mobility, bandgap, and recombination rates.
Low-field mobility (lattice)	MODELS PRINT SRH MOBILITY ALBERT.N	Activates temperature-dependent mobility & recombination	Uses Albert's model for accurate low-field mobility under lattice temperature; SRH model is also active.
Polarization effects	MODEL POLARIZATION CALC.STRAIN POLAR.SCALE = 0.8	Simulates spontaneous and piezoelectric polarization effects	Essential for GaN-based HEMTs, where polarization changes channel charge, strain effects are included and scaled appropriately.
Thermal boundary setup (lattice)	THERMCONTACT EXT.TEMP =	Defines boundary temperature at contact	Applies a fixed ambient temperature at a contact to enable realistic simulation of heat flow and self-heating in the device.

27 June 2025 04:35:43

and piezoelectric polarization-induced sheet charge density can be calculated using (1)–(4):

$$P_{SP}(Al_xGa_{1-x}N) = (-0.052x - 0.029)C/m^2, \quad (2)$$

$$P_{SP}(I_yGa_{1-y}N) = (-0.003y - 0.029)C/m^2, \quad (3)$$

$$P_{PE}(AlGaN) = 2\left(\frac{a_r - a(AlGaN)}{a(\mathrm{AlGaN})}\right)\left(e_{31} - e_{33}\frac{C_{13}}{C_{33}}\right), \quad (4)$$

$$P_{PE}(\mathrm{InGaN}) = 2\left(\frac{a_r - a(\mathrm{In}\,GaN)}{a(\mathrm{In}\,GaN)}\right)\left(e'_{31} - e'_{33}\frac{C'_{13}}{C'_{33}}\right). \quad (5)$$

Here, a represents the bulk lattice constant; e_{33} and e_{31} ($e_{33'}$ and $e_{31'}$) are the piezoelectric coefficients of AlGaN (InGaN); and C_{13} and C_{33} ($C_{13'}$ and $C_{33'}$) are the elastic constants of AlGaN (InGaN). The partially relaxed InGaN layer has a uniform average lattice constant represented by a_r. The total bound sheet charges σ_1 and σ_2 at the AlGaN/InGaN and InGaN/GaN interfaces, respectively, are presented in Eqs. (6) and (7):[19]

$$\sigma_1 = |P_{PE}(\mathrm{Al}_x\mathrm{Ga}_{1-x}\mathrm{N}) + P_{SP}(\mathrm{Al}_x\mathrm{Ga}_{1-x}\mathrm{N}) - P_{PE}(\mathrm{In}_y\mathrm{Ga}_{1-y}\mathrm{N}) - P_{SP}(\mathrm{In}_y\mathrm{Ga}_{1-y}\mathrm{N})|, \quad (6)$$

$$\sigma_2 = |P_{PE}(\mathrm{In}_yGa_{1-y}N) + P_{SP}(\mathrm{In}_yGa_{1-y}N) - P_{SP}(GaN)|. \quad (7)$$

To define a thermal boundary condition, the "THERMCONTACT" statement must be specified when utilizing the "LAT.TEMP" parameter in the "MODELS" statement.

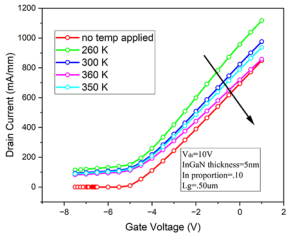
V. SIMULATION RESULTS AND DISCUSSION

A. Analysis of the impact of model temperature on device characteristics

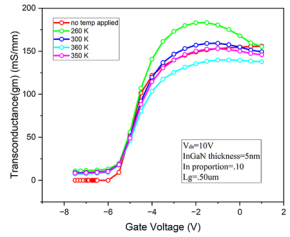
The impact of temperature on the I_{ds}–V_{gs} characteristics of AlGaN/InGaN/GaN HEMTs is primarily driven by several interrelated mechanisms that reduce drain current (I_{ds}) as temperature increases, as shown in Fig. 4(a). One major factor given by Eq. (8) is the reduction in carrier mobility due to enhanced phonon scattering as temperature increases; it minimizes the efficiency of current flow in the two-dimensional electron gas (2DEG) channel:

$$\mu = T^{(-\alpha)}. \quad (8)$$

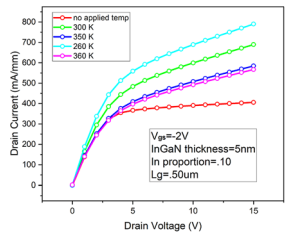
© Author(s) 2025



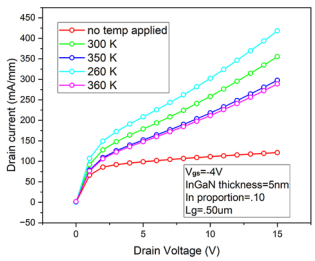
(a) Transfer characteristics of HEMT at various applied model temperatures with $V_{ds} = 10$ V



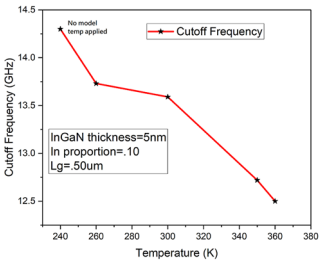
(b) Transconductance versus gate voltage at various model temperatures with $V_{ds} = 10$ V



(c) Output characteristic of I_{ds}–V_{ds} for different model temperatures at $V_{gs} = -2$ V



(d) Output characteristic of I_{ds}–V_{ds} for different model temperatures at $V_{gs} = -4$ V



(e) RF characteristic for different model temperatures at $V_{gs} = -1$ V and $V_{ds} = 10$ V

FIG. 4. Model temperature-dependent characteristics of HEMT devices: (a) transfer characteristics at $V_{ds} = 10$ V, (b) transconductance vs gate voltage, (c) output characteristics at $V_{gs} = -2$ V, (d) output characteristics at $V_{gs} = -4$ V, and (e) RF characteristics at $V_{gs} = -1$ V and $V_{ds} = 10$ V. "No temp applied" states that the curve represents a control simulation where thermal effects were not explicitly activated in the TCAD model.

The value of α ranges from 1.5 to 3.5 based on material and scattering. In addition, higher temperatures can induce a positive shift in the threshold voltage (V_{th}) due to changes in polarization charge density and Schottky barrier properties, requiring more gate voltage to achieve the same drain current level. Increased carrier generation in the GaN buffer at elevated temperatures can further lead to leakage currents, reducing effective conduction through the 2DEG. Furthermore, temperature-dependent reductions in polarization fields decrease the 2DEG density, exacerbating the decline in I_{ds}. Self-heating effects also play a significant role by elevating the device temperature under high bias, intensifying the reduction in I_{ds}, which is shown in Subsection V B regrading the impact of lattice heating. These combined thermal effects underscore the importance of effective thermal management in maintaining high performance and stability in AlGaN/InGaN/GaN HEMTs.

The dependence of g_m on gate voltage at different temperatures is illustrated in Fig. 4(b). Simulation results indicate that as the operating temperature increases, the drain current decreases as a result of the decrease in transconductance of the device. The DC I_{ds}–V_{ds} characteristics of an unpassivated gate with a length of 0.5 μm in the AlGaN/InGaN/GaN HEMT at various temperatures are presented in Fig. 4(c) for $V_{gs} = -2$ V and Fig. 4(d) for $V_{gs} = -4$ V. In addition, at lower temperatures, the saturation region begins at higher I_{ds} values, highlighting the output characteristics of the pHEMT. The cutoff frequency f_T refers to the point at which the current gain of a two-port network reduces to unity.[20] It is a crucial parameter in high-speed digital systems, influencing both operational speed and signal swing. The device continues to amplify current effectively up to this frequency limit. As illustrated in Fig. 4(e), the current gain cutoff frequency, measured in GHz, declines with an increase in temperature:

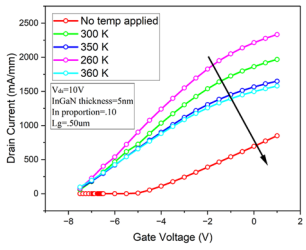
$$f_T = \frac{g_m}{2\pi C_{gs}} = \frac{v_{Sat}}{2\pi L_g}. \tag{9}$$

B. Analysis of the impact of lattice temperature on device characteristics

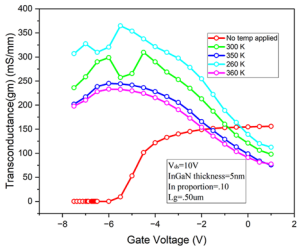
In AlGaN/InGaN/GaN HEMTs, increased lattice temperature significantly impacts the I_{ds}–V_{gs} characteristics, primarily through phonon scattering, which reduces the mobility of the 2DEG and consequently decreases the drain current I_{ds}, as shown in Fig. 5(a). This mobility degradation, combined with possible shifts in charge density due to polarization field variations, leads to nonlinear behavior in transconductance (g_m), as shown in Fig. 5(b). As a result, the g_m curve becomes less smooth, exhibiting irregularities and fluctuations with increasing gate voltage V_{gs}. In addition, higher lattice temperatures can cause threshold voltage shifts, self-heating effects, and increased trap activity, all of which contribute to further nonuniformity in I_{ds} and g_m. These thermal effects make the transconductance curve appear jagged, emphasizing the need for effective thermal management to maintain device performance stability. In the observed I_{ds}–V_{ds} characteristics, at $V_{gs} = -2$ shown in Figs. 5(c) and 5(d), the saturation region of the curve exhibits a zigzag pattern at a lower temperature of 260 K. This behavior gradually smooths out as the temperature increases, becoming more regular step-by-step and ultimately smoothing completely at a higher temperature of 360 K. At $V_{gs} = -4$, the graph appears slightly smoother even at lower temperatures compared to $V_{gs} = -2$. In addition, an intriguing

27 June 2025 04:35:43

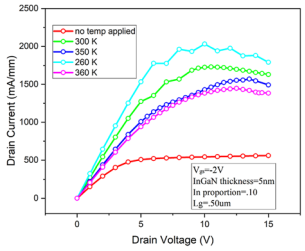
© Author(s) 2025



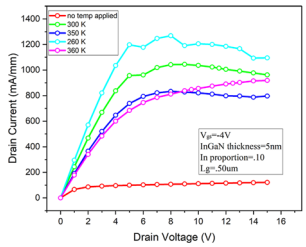
(a) Transfer characteristics of HEMT at various applied lattice temperatures with $V_{ds} = 10$ V



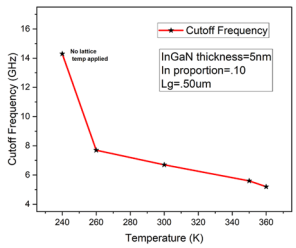
(b) Transconductance versus gate voltage at various lattice temperatures with $V_{ds} = 10$ V



(c) Output characteristic of I_{ds}–V_{ds} for different lattice temperatures at $V_{gs} = -2$ V



(d) Output characteristic of I_{ds}–V_{ds} for different lattice temperatures at $V_{gs} = -4$ V



(e) RF characteristic for different model temperatures at $V_{gs} = -1$ V and $V_{ds} = 10$ V

FIG. 5. Lattice temperature-dependent characteristics of HEMT devices: (a) transfer characteristics at V_{ds} = 10 V, (b) transconductance vs gate voltage, (c) output characteristics at V_{gs} = −2 V, (d) output characteristics at V_{gs} = −4 V, and (e) RF characteristics at V_{gs} = −1 V and V_{ds} = 10 V. "No temp applied" states that the curve represents a control simulation where thermal effects were not explicitly activated in the TCAD model.

behavior is noted at higher temperatures: in the saturation region, the curve at 360 K crosses and rises above the curve at 350 K. This suggests a temperature-dependent shift in the transport mechanism or changes in the carrier mobility and scattering phenomena that become more pronounced at higher gate biases and elevated temperatures. As shown in Fig. 5(e), when no lattice temp is applied, the cutoff frequency was 14.3 GHz; however, as soon as 260 K lattice temp is applied to the device, the cutoff frequency drops to 7.7 GHz, which is almost half. Later, with the increasing lattice temperature, the frequency further drops, and at 360 K, it falls to 5.6 GHz.

C. Impact of gate length variation and temperature on device performance

The performance of AlGaN/InGaN/GaN HEMTs is significantly influenced by gate length variation and temperature effects, as observed in the data plotted in Fig. 6. The drain current I_{ds} exhibits a strong dependence on both the length of the gate and the operating temperature, which is critical for high-power and high-frequency applications.

As the gate length decreases, there is a notable increase in drain current (I_{ds}) due to enhanced carrier transport and a reduction in channel resistance, with the highest drain current observed at the shortest gate length (0.05 μm). This can be attributed to several short-channel effects, including Drain-Induced Barrier Lowering (DIBL), where the potential barrier at the source–channel junction is reduced by the drain voltage, leading to an earlier onset of conduction and a lower effective threshold voltage (V_{th}). Reduced channel resistance also plays a role, as shorter gates result in a shorter conduction path, lowering resistance and improving current flow. Notably, at 0.05 μm gate length, there is no well-defined flat low-current region before threshold voltage due to strong 2D electron gas (2DEG) formation at the AlGaN/InGaN/GaN heterojunction, where a high intrinsic carrier concentration leads to significant drain current even at low gate voltages. This suggests that the device is already partially "on" at lower gate voltages (V_G), making it more susceptible to leakage currents. Increasing temperature

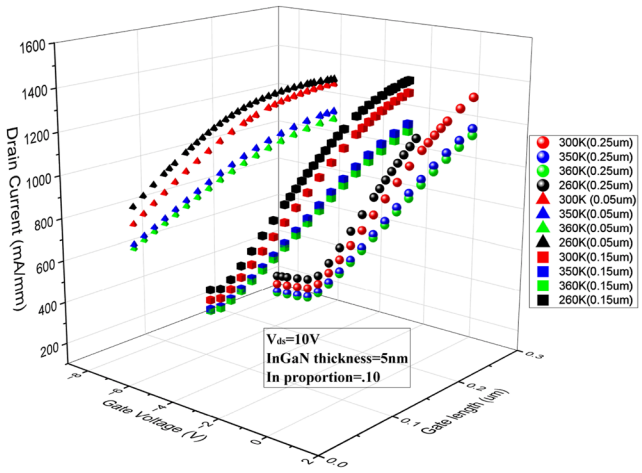


FIG. 6. A 3D graph showing the effect of gate length reduction on drain current at different temperatures, taking V_{ds} = 10 V.

27 June 2025 04:35:43

© Author(s) 2025

(260–360 K) leads to a reduction in drain current, following the trend $I_{ds}(260\text{ K}) > I_{ds}(300\text{ K}) > I_{ds}(350\text{ K}) > I_{ds}(360\text{ K})$ for all gate lengths. This degradation in performance is primarily due to phonon scattering, where increased lattice vibrations at higher temperatures cause more electron–phonon interactions, reducing carrier mobility and limiting current conduction. In addition, there is a reduction in 2DEG density, as the 2D electron gas (2DEG) formed at the AlGaN/InGaN/GaN interface weakens with elevated temperatures due to thermal carrier redistribution, leading to decreased conductivity. Furthermore, higher temperatures slightly raise the barrier height for carrier injection, shifting V_{th} and requiring a higher gate voltage to achieve the same drain current.

VI. CONCLUSION

This study provides a comprehensive analysis of the temperature dependence of AlGaN/InGaN/GaN HEMT devices, employing both TCAD simulations and verified experimental data to evaluate the effects of model and lattice temperature variations on key device parameters, including transfer and output characteristics, transconductance, threshold voltage, and current gain cutoff frequency. The results indicate a notable reduction in saturation current and I_{ds}–V_{ds} characteristics within the linear region as temperature rises, primarily due to carrier mobility degradation from intensified phonon scattering in the two-dimensional electron gas (2DEG) channel. This reduced mobility is the dominant factor affecting the degradation of the device's electrical performance metrics at elevated temperatures, with mobility loss outweighing the modest increase in 2DEG sheet density observed in the temperature range of 260–360 K. As temperature increases, secondary effects such as a positive shift in threshold voltage and increased carrier generation within the GaN buffer contribute to further variations in device behavior, creating leakage currents and additional inconsistencies in I_{ds} and transconductance (g_m) characteristics. These shifts in threshold voltage, along with the self-heating effects and trap activities that accompany higher lattice temperatures, induce non-linearities in g_m and cause the transconductance curve to exhibit irregular fluctuations. This jagged behavior in g_m underscores the critical need for effective thermal management to mitigate performance degradation and stabilize the device operation. Later in the section, gate length scaling and temperature variations in AlGaN/InGaN/GaN HEMTs present trade-offs between enhanced drain current and high-frequency performance vs short-channel effects like DIBL, threshold voltage shift, and increased off-state current. Thermal effects further degrade carrier mobility and 2DEG stability, highlighting the need for effective thermal management and gate engineering in GaN-based transistors for power and RF applications. The findings suggest that controlling temperature effects is essential for achieving reliable and high-performance operation of AlGaN/InGaN/GaN HEMTs, particularly in high-power and high-frequency applications, where thermal stability is paramount.

ACKNOWLEDGEMENTS

The author gratefully acknowledges the support received through the AICTE Doctoral Fellowship (ADF) during the Ph.D. program.

AUTHOR DECLARATIONS

Conflict of Interest

The authors have no conflicts to disclose.

Author Contributions

Neda Ahmad: Conceptualization (equal); Data curation (equal); Formal analysis (equal); Investigation (equal); Methodology (equal); Resources (equal); Software (equal); Validation (equal); Writing – original draft (equal); Writing – review & editing (equal). **Sonam Rewari**: Software (equal); Supervision (equal); Validation (equal); Writing – review & editing (equal). **Vandana Nath**: Conceptualization (equal); Methodology (equal); Supervision (equal); Validation (equal); Writing – review & editing (equal).

DATA AVAILABILITY

The data that support the findings of this study are available from the corresponding author upon reasonable request.

REFERENCES

[1] K. Saraswat, C. O. Chui, T. Krishnamohan, D. Kim, A. Nayfeh, and A. Pethe, Mater. Sci. Eng.: B **135**, 242–249 (2006).
[2] I. Takenaka, K. Ishikura, K. Asano, S. Takahashi, Y. Murase, Y. Ando, H. Takahashi, and C. Sasaoka, IEEE Trans. Microwave Theory Tech. **62**, 502–512 (2014).
[3] C.-H. Chen, S. M. Baier, D. K. Arch, and M. S. Shur, IEEE Trans. Electron Devices **35**, 570–577 (1988).
[4] J. He, W.-C. Cheng, Q. Wang, K. Cheng, H. Yu, and Y. Chai, Adv. Electron. Mater. **7**, 2001045 (2021).
[5] F. Roccaforte, P. Fiorenza, G. Greco, R. L. Nigro, F. Giannazzo, F. Iucolano, and M. Saggio, Microelectron. Eng. **187**, 66–77 (2018).
[6] N. Islam, M. F. P. Mohamed, M. F. A. J. Khan, S. Falina, H. Kawarada, and M. Syamsul, Crystals **12**, 1581 (2022).
[7] C. Wang, Y. Xu, X. Yu, C. Ren, Z. Wang, H. Lu, T. Chen, B. Zhang, and R. Xu, IEEE Trans. Microwave Theory Tech. **62**, 2878–2887 (2014).
[8] G. Crupi, A. Raffo, G. Avolio, D. M. M -P Schreurs, G. Vannini, and A. Caddemi, IEEE Microwave Wireless Compon. Lett. **26**, 813–815 (2016).
[9] C. De Santi, M. Buffolo, I. Rossetto, T. Bordignon, E. Brusaterra, A. Caria, F. Chiocchetta, D. Favero, M. Fregolent, F. Masin *et al.*, "Review on the degradation of GaN-based lateral power transistors," e-Prime-Adv. Electr. Eng., Electron. Energy **1**, 100018 (2021).
[10] N. Okamoto, K. Hoshino, N. Hara, M. Takikawa, and Y. Arakawa, J. Cryst. Growth **272**, 278–284 (2004).
[11] M. A. Alim, A. A. Rezazadeh, and C. Gaquiere, Solid-State Electron. **119**, 11–18 (2016).
[12] G. Crupi, A. Raffo, Z. Marinkovic, G. Avolio, A. Caddemi, V. Markovic, G. Vannini, and D. M. M.-P. Schreurs, IEEE Trans. Microwave Theory Tech. **62**, 513–520 (2014).
[13] A. Sarkar, *Technology Computer Aided Design* (CRC Press, 2018), pp. 203–252.
[14] M. A. K. Khan, M. A. Alim, and C. Gaquiere, Microelectron. Eng. **238**, 111508 (2021).
[15] N. Ahmad, S. Rewari, and V. Nath, Serb. J. Electr. Eng. **21**, 275–295 (2024).
[16] W. Shockley and W. T. Read, Phys. Rev. **87**, 835 (1952).
[17] R. N. Hall, Phys. Rev. **87**, 387 (1952).
[18] J. D. Albrecht, R. P. Wang, P. P. Ruden, M. Farahmand, and K. F. Brennan, J. Appl. Phys. **83**, 4777–4781 (1998).
[19] J. Ghosh and S. Ganguly, Jpn. J. Appl. Phys. **57**, 080305 (2018).
[20] M. Abdul Alim and A. A. Rezazadeh, IEEE Trans. Electron Devices **63**, 1005–1012 (2016).

27 June 2025 04:35:43

© Author(s) 2025

Investigation Temperature variation on DC and Analog performance of Gate Stack GNRFET using DFT-based atomic scale Modelling

Anshul
Department of Applied Physics, Delhi Technological University,
Delhi –110042, INDIA
anshul_2k20phdap502@dtu.ac.in

Rishu Chaujar
Vinod Dham Centre of Excellence for Semiconductors and Microelectronics (VDCoE4SM),
Department of Applied Physics
Delhi Technological University, Delhi
chaujar.rishu@dtu.ac.in

2025 Devices for Integrated Circuit (DevIC) | 979-8-3503-9110-7/25/$31.00 ©2025 IEEE | DOI: 10.1109/DevIC63749.2025.11012213

***Abstract*- This study investigates the impact of temperature on the performance of a Gate-Stacked Graphene Nanoribbon Field-Effect Transistor (GS-GNRFET) using Density Functional Theory (DFT). The Poisson equation is solved using the Semi Empirical (SE) calculator with the Non-Equilibrium Green's Function (NEGF) method. The proposed GS-GNRFET demonstrates a 30% increase in I_{on}, 72% reduction in I_{off}, and 12% enhancement in transconductance (g_m), with a higher transmission coefficient than conventional GNRFET. Temperature analysis of the proposed device reveals a 48% decrease in I_{on}, 98% reduction in I_{on}/I_{off}, and 138 times increase in DIBL from 250 K to 350 K, limiting its use in high-temperature environments. However, these findings make the proposed device suitable for low-power computing, cryogenic electronics, and biomedical sensors.**

Keywords: Atomic scale simulation, Gate stack graphene nanoribbon field effect transistor, NEGF method, Analog parameters, Temperature variation.

I. INTRODUCTION

Scaling down in integrated chips (IC) poses significant hurdles in the semiconductor industry. Due to the inherent constraints of miniaturization in Complementary Metal Oxide Semiconductor (CMOS) technology, researchers have attempted to reduce the size of the transistor by proposing a suitable replacement for silicon-based CMOS technology, resulting in smaller, quicker, and less power-consuming circuits [1]. Graphene, a two-dimensional honeycomb lattice of carbon atoms, has emerged as a promising candidate for beyond-CMOS nanoelectronics [2]. Graphene-based electronic devices offer several advantages, including exceptional mobility for ballistic transport, high carrier speed for rapid switching, an atomically thin structure for optimal electrostatic control, and excellent thermal conductivity [3]. Graphene band structure governs its electrical properties. The application of graphene in the direct electronic industry is constrained by its overlapping band structure. To overcome this constraint, scientists have used the quantum confinement method to develop graphene nanoribbons (GNR) [4]. The adjustable bandgap of GNR has an inverse relationship with its width [5]. The configuration of GNR is defined by the arrangement of atoms: armchair graphene nanoribbons (AGNR) and zigzag graphene nanoribbons (ZGNR). In AGNR configuration, the atoms at the edges rotate 120° to the last pair of atoms [6]. In ZGNR configuration, the edge atoms originate from the same sublattice. The ZGNR shows metallic behavior as it has zero bandgap, whereas depending on the width of the atoms, AGNR can be metallic or semiconducting [7]. AGNR has been proven to be a competent material to use as the channel in the GNR FET. To enhance the functionality of nanoscale transistors and avoid SCEs, GNR should also be used for the transistor channel, and materials with a high dielectric constant are required for the transistor gate oxide. For selecting a high-κ dielectric material, a trade-off must be made between the high-κ dielectric and a suitable bandgap for usage in a transistor [8-10]. The bandgap has a negative relationship with the dielectric constant of the materials. Hence, raising the dielectric constant induces a decrease in the bandgap [11]. This problem has been resolved through the implementation of the gate stack (GS) configuration [12]. In GS, the combination of two dielectric layers has been used, i.e., a low-κ dielectric layer of SiO_2 (κ = 3.9) has been sandwiched between the High-κ layer and GNR channel in order to maintain the effective oxide thickness. Taking everything into consideration, we propose a Gate Stack Graphene Nanoribbon Field Effect Transistor (GS-GNRFET). When the device size is less than 20 nm, a high value of temperature can greatly affect or even ruin the device operation. For better reliability, it is essential to investigate the impact of temperature variation on the DC and analog performance of the proposed device. Eshkalak [13] reported that the GNRFET shows the best results when the ambient temperature is kept low. Caridad et al. [14] investigate the resonant detection of terahertz (THz) radiation in single-layer graphene transistors, with an emphasis on their performance at room temperature (10 K to 300 K). They demonstrate that short-channel graphene FETs exhibit a unique temperature-resilient plasmonic resonance behavior due to the weak intrinsic electron-phonon scattering in monolayer graphene. Illarionov et al. [15] investigate the variability and high-temperature (298 K to 448 K) reliability of graphene FETs with thin epitaxial CaF2 insulators. They observe minimal hysteresis and good thermal stability in their devices up to 448 K. Wang et al. [16] focus on the low-temperature performance of graphene FETs made from chemical vapor deposition (CVD) Ge-based graphene. Their study, spanning from 4.2 K to 300 K, highlights the temperature stability of the devices. The analog and RF performance of FinFET and NCFET have been investigated for varied range of temperatures. The results showed that at low temperature, device gives better performance [17, 18]. However, the effect of temperature on GNRFET at atomic scale is still elusive in literature.

In this research article, at first proposed GS-GNRFET device is compared with conventional GNRFET. The performance of GS-GNRFET is investigated in terms of on current (I_{on}), off current (I_{off}), peak transconductance (g_m), and transmission spectrum. Moreover, the impact of temperature at atomic scale GS-GNRFET from 250 to 350 K with a step size of 25 K is

979-8-3503-9110-7/25/$31.00 ©2025 IEEE

Authorized licensed use limited to: DELHI TECHNICAL UNIV. Downloaded on June 04,2025 at 05:24:47 UTC from IEEE Xplore. Restrictions apply.

adopted on parameters like on current (I_{on}), off current (I_{off}), switching ratio (I_{on}/I_{off}), subthreshold swing (SS), threshold voltage (V_{th}), and DIBL. Further, based on the results of I_{on} and I_{off} currents at varied temperatures, novel empirical fitting exponential functions have been proposed in the present study.

II. DEVICE DESIGN AND DESCRIPTION

The front and side view of N_2-passivated GS-GNRFET is illustrated in Fig. 1. (a) and (b). The central region comprises of a 30° rotated AGNR (n = 4) channel, which is passivated by nitrogen atoms (N_2) at edge positions, where 'n' is the number of carbon atoms along AGNR width. Figure 2 portrays the N_2-passivated AGNR (n = 4), which is adopted as a channel in GS-GNRFET. The inset view of AGNR with one atom is shown by the dotted line in Fig. 2. The drain and source regions are of ZGNR (n = 6). To reduce the circuit complexities, drain, source, and channel regions are n-type doped. An attempt has been made to create an ideal interface with the ZGNR, and the AGNR is rotated at a 30° angle.

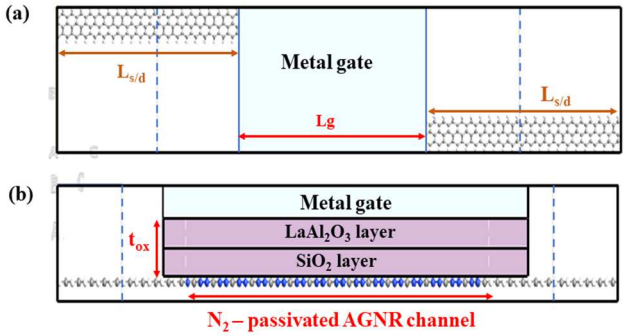


Fig. 1. (a) Front view of GS-GNRFET (b) side view of GS-GNRFET

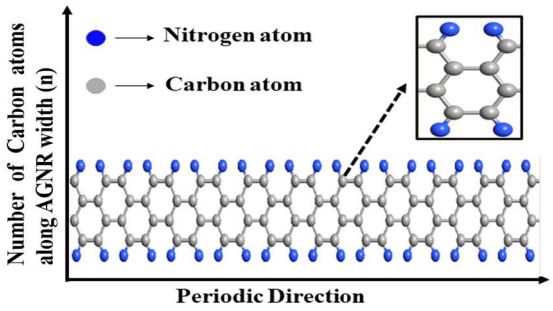


Fig. 2. Schematic view of N_2-passivated AGNR (n = 4)

The thickness of the oxide layer thickness (t_{ox})is taken at 0.50 nm. In GS architecture, the SiO_2 layer (K = 3.9) and $LaAlO_3$ layer (K = 30) thicknesses are 0.25 nm. The t_{ox} is inversely proportional to the gate oxide capacitance (C_{ox}), which means reducing the t_{ox} will increase the C_{ox}, which provides better control of the gate over the channel as the potential drop on gate oxide (Φ_{ox}) decreases. Further, the aforementioned parameters can be co-related by a mathematical expression as follows [11, 19]:

$$t_{ox} = \frac{\varepsilon_0 \varepsilon_r}{C_{ox}} \tag{1}$$

$$\Phi_{ox} = \frac{Q_0}{C_{ox}} \tag{2}$$

Now, putting the value of C_{ox} from Eq. (1) in Eq. (2)

$$\Phi_{ox} = \frac{Q_0 t_{ox}}{\varepsilon_0 \varepsilon_r} \tag{3}$$

where,

C_{ox} – gate oxide capacitance

ε_0 – permeability coefficient

ε_r – the dielectric constant of the gate insulation

We have used a metallic gate over the dielectric layers because gate potential is crucial in determining a device's electrical characteristics. [18]. The excellent thermal stability, high degree of purity, and compatibility with CMOS processing are further advantages of metal gates. Table I lists all the input parameters for the various devices that were used in the simulation.

TABLE I
INPUT PARAMETERS USED FOR DEVICE SIMULATION

Parameter	Devices	
	GNR FET	GS-GNR FET
Gate length, L_g (nm)	7	7
Thickness of oxide layer, t_{ox} (nm)	0.50	0.50 (0.25 SiO_2 + 0.25 $LaAlO_3$)
Source and drain length, $L_{s/d}$ (nm)	5	5
The doping concentration of the channel region, N_{Ch} (e/cm^3)	3×10^{16}	3×10^{16}
The doping concentration of the source and drain region, $N_{s/d}$ (e/cm^3)	5×10^{18}	5×10^{18}

III. SIMULATION APPROACH AND MODEL CALIBRATION

The quantum-wise atomistic toolkit (Quantum ATK) simulator has been used to perform all the simulations. The semi-empirical (SE) calculator using the Slater-Koster model with NEGF formalism and without-self-consistent field (SCF) iteration method has been adopted to calculate the transmission spectrum and electronic properties for the conventional and proposed device [20]. Figure 3 shows the simulation flow chart for this proposed DFT-based approach. The Hartree potential is 40 Ha, and the K-point sampling is kept at 100 along the C-direction during the simulations. The transmission spectrum for the devices is calculated using the non-equilibrium Green's function (NEGF) method and obtained by [21]:

$$T(E) = Tr[G(E)\Gamma^d(E)G^{\dagger}(E)\Gamma^s(E)] \tag{4}$$

where,

$T(E)$ – transmission coefficient

$G(E)$ – retarded green's function

$\Gamma^d(E)$ – broadening function of the drain electrode

Authorized licensed use limited to: DELHI TECHNICAL UNIV. Downloaded on June 04,2025 at 05:24:47 UTC from IEEE Xplore. Restrictions apply.

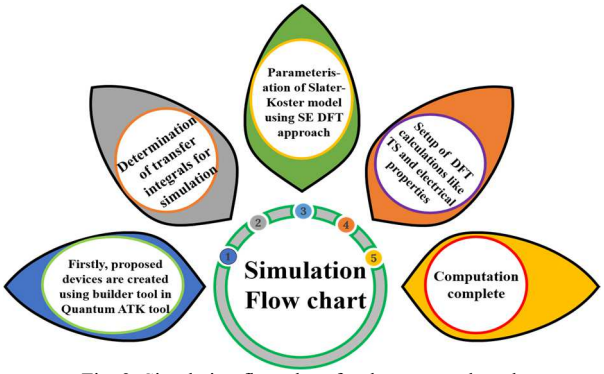


Fig. 3. Simulation flow chart for the proposed work

Once the transmission spectrum is calculated from the without self-consistent solution of NEGF using the periodic boundary condition, the drain current is calculated by the transmission coefficient [22]. The drain current is a function of the transmission coefficient, Fermi-Dirac distribution along the source and drain. Further, it can be calculated by Landauer's formula given as [21]:

$$I_d = \frac{2e}{h}\int_{-\infty}^{\infty} T(E)[f_{FD}(E-\mu_d) - f_{FD}(E-\mu_s)]dE \qquad (5)$$

where,

I_d – drain current

f_{FD} – Fermi-Dirac distribution

μ_d – the chemical potential of the drain electrode

The above simulation model is validated with the previous findings in the literature [23]. The simulation models were calibrated by designing a MOSFET with fixed device dimensions (L_g = 15 nm, t_{ox} = 1.5 nm) and AGNR (N = 12) material in the entire channel region. The source and drain are doped extensions of GNRs, and SiO_2 (κ = 3.9) was used as the gate oxide, as illustrated in the reference material. Fig. 4 depicts the I_d – V_{gs} calibration curve. From Fig. 4, it can be observed from the results that the simulated models are near concordance with the previous findings. Thus, the used simulation models are justified by the close similarity observed between the simulated and reference data sets.

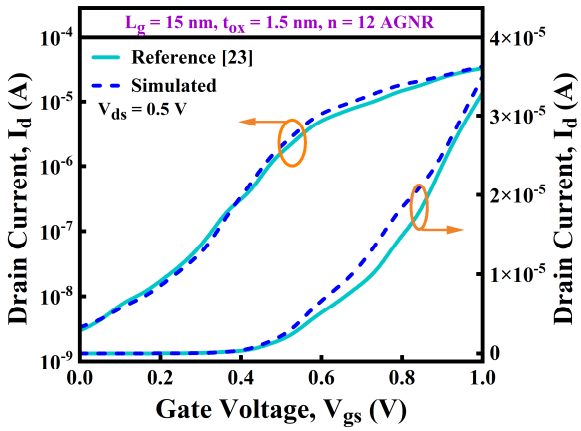


Fig. 4. I_d -V_{gs} calibration of simulated and reference data [23]

IV. RESULT AND DISCUSSION

The outcomes of the present work are discussed under the **performance comparison** section, where DC characteristics, g_m, and transmission spectrum of the conventional GNRFET are compared with the proposed GS-GNRFET. Further, the **temperature affectability** on the analog performance of GS-GNRFET is studied.

a) Performance Comparison Between GNRFET and GS-GNRFET

Figure 5 depicts a comparison between the drain current (I_d) of the GNRFET and GS-GNREFT with gate voltage (V_{gs}) varying from 0 to 1 V at a constant value (0.5 V) of drain-source voltage (V_{ds}). The main challenge in nanoscale devices is the high value of I_{off}. The high leakage current is raised by carrier tunneling, which causes high power dissipation in IC [24]. Hence, it is observed that the use of gate-stacking provides a reduction in off current (I_{off}) from 3.26 to 0.91 pA as compared with conventional GNRFET. Also, the on current (I_{on}) increases from 6.39 to 8.34 µA in the case of GS-GNRFET.

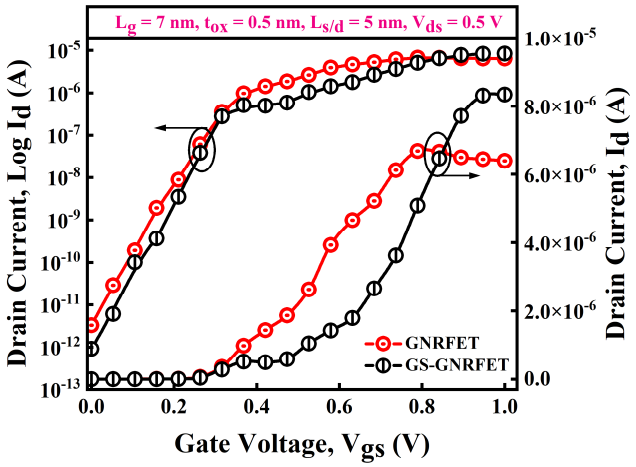


Fig. 5. I_d-V_{gs} characteristics curves for GNRFET and GS-GNRFET in log and linear scale

The use of gate stacking reduced the I_{off} by 72% and gave an increment in I_{on} by 30%. The explanation is that the high-k material in gate stacking helps to improve the strength of fringing electric fields, which significantly minimized the height of potential barrier in off state, and a reduction in I_{off} has been achieved. Figure 6 illustrates the comparison of both devices in terms of peak transconductance (g_m) at V_{gs} = 0.75 V. The g_m of a device describes its ability to alter the barrier height in the saturation mode using the applied gate voltage It is observed that the value of peak conductance increased from 24.71 to 27.76 µS in GS-GNRFET. The transistor amplification is directly related to g_m. The rise in the g_m of a device governs amplification applications. The reason is that the value of I_d increases with gate stacking and significantly improves the g_m.

Mathematically, g_m can be expressed as [8]:

$$g_m = \frac{\Delta I_d}{\Delta V_{gs}} \qquad (6)$$

where,

ΔI_d – change in drain current

ΔV_{gs} – change in gate voltage

Authorized licensed use limited to: DELHI TECHNICAL UNIV. Downloaded on June 04,2025 at 05:24:47 UTC from IEEE Xplore. Restrictions apply.

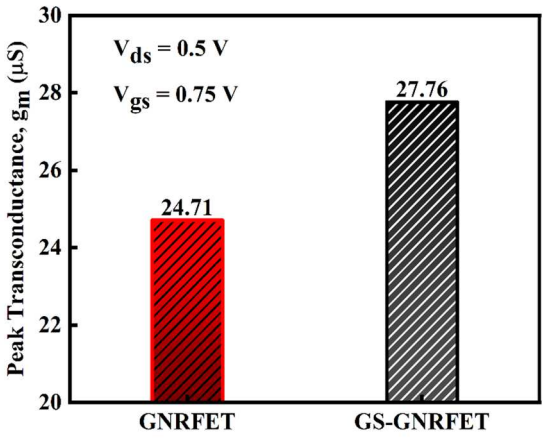


Fig. 6. Bar plot of transconductance of GNRFET and GS-GNRFET

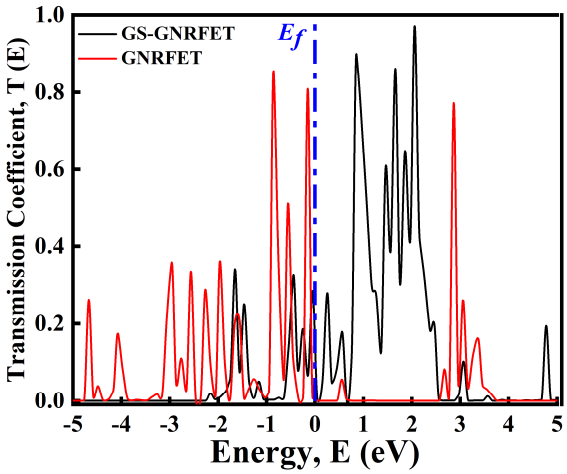


Fig. 7. Variation of transmission spectrum with energy for both devices

The variation of the transmission spectrum in terms of transmission coefficient, T(E) with energy (E), is shown in Fig. 7. The T(E) has been calculated using Eq. (4). The value of E has been varied from -5 to +5 eV to observe the behavior of T(E). From Fig. 7. the authors observed that the number of peaks available for conduction in the valance band (VB) in GS-GNRFET is greater than GNREFT. Due to the electric field generated by the V_{gs} and the device's Z-shaped design, the transmission spectrum of GNR-FETs is not anticipated to be symmetrical [25]. A higher value of T(E) means that a higher number of electrons can tunnel the nanoribbon's energy barrier between its conduction and valance bands.

b) Temperature Affectability on proposed GS-GNRFET

In this section, the effect of temperature on analog parameters like I_{on}, I_{off}, I_{on}/I_{off}, SS, and DIBL have been studied. Figure 8 depicts the I_d -V_{gs} characteristics curves for GS-GNRFET at different temperatures. The authors examined the performance of GS-GNRFET at five different temperatures, T = 250, 275, 300, 325, and 350K. As, the temperature increases, the value of the I_{on} decreases, which is shown in Fig. 9. Also, the off current increases with an increase in temperature. The reason is that the stronger control of the gate voltage on the channel near the source at low temperatures results in a higher emission of thermal current [17].

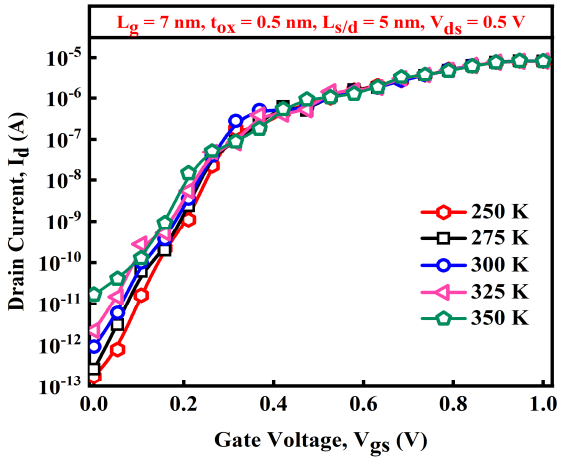


Fig. 8. I_d-V_{gs} characteristics curves for GS-GNRFET at varied temperatures

It is observed that I_{on} has an exponential decay with temperature, and I_{off} shows an exponential increase with temperature as shown in Fig. 9. Further, the I_{on} and I_{off} parameters can be mathematically expressed as follows:

$$I_{on} = \alpha e^{-\beta T} \quad (7)$$

$$I_{off} = \gamma e^{\eta T} \quad (8)$$

where, α, β, γ, and η are empirical fitting parameters as given below:

I_{on}	–	on current
α	–	8.3409
β	–	5×10^{-5}
γ	–	1×10^{-18}
η	–	0.452
T	–	temperature

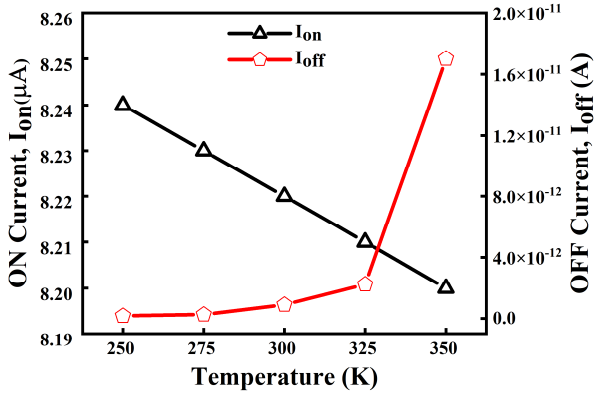


Fig. 9. Change in I_{on} and I_{off} with a range of temperatures

Figure 10 portrays the change in threshold voltage (V_{th}) with temperature. The V_{th} is the lowest value of V_{gs} required to create conduction between the source and drain terminals. The value of V_{th} decreased from 0.25 to 0.20 V as the temperature increased from 250 to 350 K.

Authorized licensed use limited to: DELHI TECHNICAL UNIV. Downloaded on June 04,2025 at 05:24:47 UTC from IEEE Xplore. Restrictions apply.

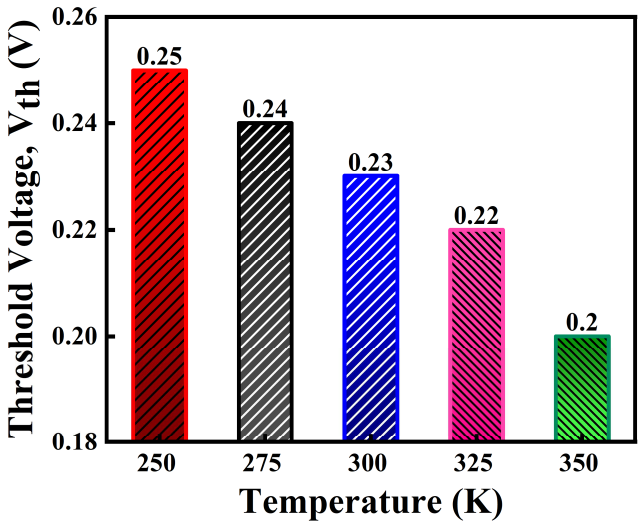


Fig. 10. Threshold voltage variation with temperature

Variation of I_{on}/I_{off} and SS for a range of temperature adopted in the present study as shown in Fig. 11. From the simulated results, we analyzed that the value of I_{on}/I_{off} decreases with an increase in temperature depending on the behavior of I_{on} and I_{off}. An important variable in transistor miniaturization is the SS. It can be mathematically expressed in terms of temperature as [18]:

$$SS = \frac{60 \times T}{300} \tag{9}$$

From Eq. (9), with a rise in temperature, the value of SS decreases, which degrades the device's performance. The values of I_{on}/I_{off} and SS at different temperatures are tabulated in Table II.

TABLE II
VALUES OF SWITCHING RATIO (I_{ON}/I_{OFF}) AND SUBTHRESHOLD SWING (SS)

Temperature (K)	I_{ON}/I_{OFF} ($\times 10^6$)	SS (mV/decade)
250	47.1	52.62
275	31.4	58.41
300	9.13	67.88
325	3.72	73.99
350	0.49	82.31

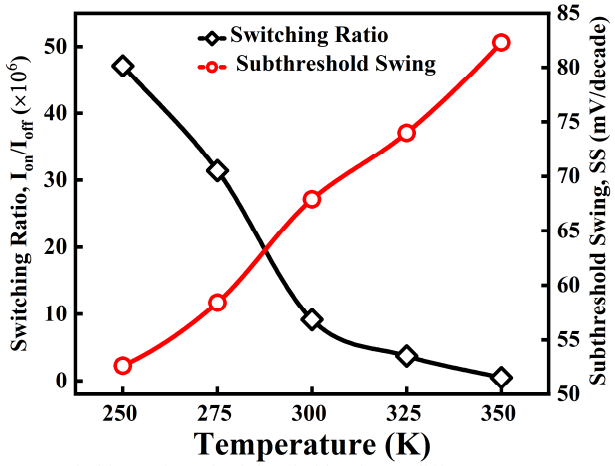


Fig. 11. Switching ratio and subthreshold swing at different temperatures

Figure 11 depicts the dependence of DIBL for a range of temperatures adopted in the present study. DIBL is a short-channel effect that occurs in transistors.

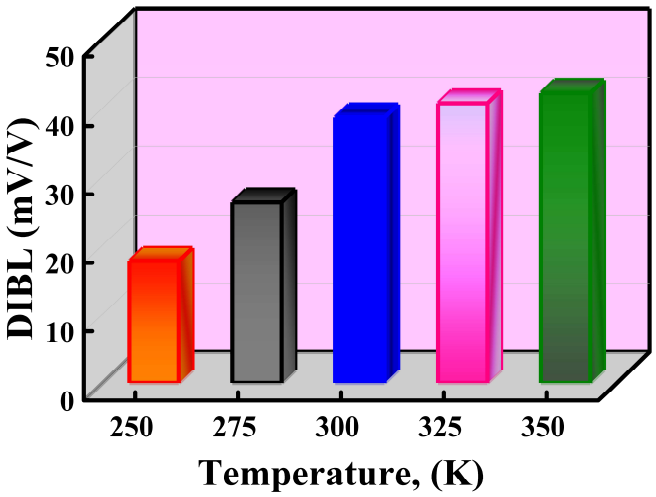


Fig. 12. Dependence of DIBL at various temperatures

A higher value of V_{ds} increases the drain depletion zone as the channel gets shorter, and lowering the potential barrier. Even though the V_{gs} is less than the threshold voltage, the potential barrier is reduced, allowing electrons to pass between the source and drain. This phenomenon has been referred to as DIBL. It is calculated at V_{ds} (high) = 1.0 V, V_{ds} (low) = 0.1 V, using the mathematical formula [26]:

$$DIBL = \frac{V_{th}(high) - V_{th}(low)}{V_{ds}(high) - V_{ds}(low)} \tag{10}$$

From Fig. 12, it is observed that the value of DIBL is decreasing with temperature. From the simulated results, we conclude that the proposed GS-GNRFET shows better performance at low temperatures.

Table III

COMPARISON AMONG PROPOSED GS-GNRFET WITH PREVIOUSLY REPORTED GNRFETs.

Device	V_{ds} (V)	Channel AGNR (n)	I_{on} (μA)	I_{off} (μA)	I_{on}/I_{off}
GS-GNRFET*	**0.5**	**n = 4**	**8.34**	**9.13×10^{-4}**	**9.13×10^6**
SB-GNRFET [27]	0.5	n = 12	-	-	33.7
AG-GNRFET [28]	0.5	n = 12	-	-	304
DMG-GNRFET [29]	0.6	n = 13	-	-	5823
SLD-GNRFET [30]	0.4	n = 12	3.66	15.7×10^{-4}	2.3×10^3

* Present work

Table III summarizes the comparison between proposed GS – GNRFET with previously reported structures. From Table III, we can observe that our proposed device with GS architecture

Authorized licensed use limited to: DELHI TECHNICAL UNIV. Downloaded on June 04,2025 at 05:24:47 UTC from IEEE Xplore. Restrictions apply.

shows improved performance in terms of I_{on}, I_{off}, and I_{on}/I_{off} as compared with other devices.

V. CONCLUSION

In the present work, the performance of GS-GNRFET with gate stack architecture in dielectric layers is studied. The Poisson equation has been solved with SE calculator using the NEGF method. In the proposed GS-GNRFET I_{on} improved by 30%, I_{off} reduced by 72%, and g_m increased by 12%. It is reported that GS-GNRFET has a higher transmission coefficient value than conventional GNRFET. Further, the effect of various temperatures on the analog performance of GS-GNRFET is studied. The rise in temperature from 250 K to 350 K reduces I_{on} by 48%, increases SS by 56%, reduces I_{on}/I_{off} by 98%, and increases DIBL by 138 times. Thus, the rise in temperature reduces the analog performance of GS-GNRFET. The detailed temperature analysis highlights the proposed device application in the fields of low-power computing, cryogenic electronics, and biomedical sensors. Further, the significant degradation in the I_{on}/I_{off} ratio (98% reduction) and increased DIBL (138 times) at higher temperatures suggests that this proposed device may not be ideal for high-temperature electronics such as automotive, aerospace, and industrial applications.

ACKNOWLEDGEMENT

The authors extend a warm thanks towards the Vinod Dham Centre of Excellence for Semiconductors and Microelectronics (VDCoE4SM), SERB POWER GRANT, C2S Programme: MeiTY, and Microelectronics Research Lab at Delhi Technological University for providing essential facilities.

REFERENCES

[1] T. Radsar, H. Khalesi, and V. Ghods, "Graphene nanoribbon field effect transistors analysis and applications," *Superlattices and Microstructures,* vol. 153, pp. 106869, 2021.

[2] K. S. Novoselov *et al.*, "Electric field effect in atomically thin carbon films," *science,* vol. 306, no. 5696, pp. 666-669, 2004.

[3] J. D. Plummer and P. B. Griffin, "Material and process limits in silicon VLSI technology," *Proceedings of the IEEE,* vol. 89, no. 3, pp. 240-258, 2001.

[4] E. McCann, "Asymmetry gap in the electronic band structure of bilayer graphene," *Physical Review B,* vol. 74, no. 16, pp. 161403, 2006.

[5] H. Raza and E. C. Kan, "Armchair graphene nanoribbons: Electronic structure and electric-field modulation," *Physical Review B,* vol. 77, no. 24, pp. 245434, 2008.

[6] Anshul and R. Chaujar, "Numerical Evaluation of the Gate Stacked GNR FET for improved Device Switching," in proceeding of 2022 *International Conference on Recent Trends in Microelectronics, Automation, Computing and Communications Systems (ICMACCC- 2022)*, IEEE, pp. 88-91, 2022.

[7] S. Lone, A. Bhardwaj, A. K. Pandit, S. Gupta, and S. Mahajan, "A review of graphene nanoribbon field-effect transistor structures," *Journal of Electronic Materials,* vol. 50, pp. 3169-3186, 2021.

[8] T. Radsar, H. Khalesi, and V. Ghods, "Improving the performance of graphene nanoribbon field-effect transistors by using lanthanum aluminate as the gate dielectric," *Journal of Computational Electronics,* vol. 19, pp. 1507-1515, 2020.

[9] M. Sharma, B. Kumar, and R. Chaujar, "Polarization induced doping and high-k passivation engineering on T-gate MOS-HEMT for improved RF/microwave performance," *Materials Science and Engineering: B,* vol. 290, pp. 116298, 2023.

[10] G. S. Kliros, "Gate capacitance modeling and width-dependent performance of graphene nanoribbon transistors," *Microelectronic Engineering,* vol. 112, pp. 220-226, 2013.

[11] A. Srivastava, Y. M. Banadaki, and M. S. Fahad, "Dielectrics for graphene transistors for emerging integrated circuits," *ECS Transactions,* vol. 61, no. 2, pp. 351, 2014.

[12] B. Kumar, M. Sharma, and R. Chaujar, "Gate electrode work function engineered JAM-GS-GAA FinFET for analog/RF applications: Performance estimation and optimization," *Microelectronics Journal,* vol. 135, pp. 105766, 2023.

[13] M. A. Eshkalak, "Graphene nano-ribbon field effect transistor under different ambient temperatures," *Iranian Journal of Electrical & Electronic Engineering,* vol. 12, no. 2, pp. 147, 2016.

[14] J. M. Caridad *et al.*, "Room-temperature plasmon-assisted resonant THz detection in single-layer graphene transistors," *Nano Letters,* vol. 24, no. 3, pp. 935-942, 2024.

[15] Y. Y. Illarionov *et al.*, "Variability and high temperature reliability of graphene field-effect transistors with thin epitaxial CaF2 insulators," *npj 2D Materials and Applications,* vol. 8, no. 1, pp. 23, 2024.

[16] C. Wang, W. Hong, M. Zhang, and H. Jiang, "Ge-based graphene FET for low-temperature electronics," *Electronics Letters,* vol. 60, no. 13, pp. e13261, 2024.

[17] R. Mann and R. Chaujar, "TCAD investigation of ferroelectric based substrate MOSFET for digital application," *Silicon,* vol. 14, no. 9, pp. 5075-5084, 2022.

[18] B. Kumar and R. Chaujar, "TCAD temperature analysis of gate stack gate all around (GS-GAA) FinFET for improved RF and wireless performance," *Silicon,* vol. 13, no. 10, pp. 3741-3753, 2021.

[19] N. E. Boukortt, B. Hadri, and S. Batane, "Effects of high-k dielectric materials on electrical characteristics of DG n-FinFETs," *International Journal of Computer Applications,* vol. 975, pp. 8887, 2016.

[20] Anshul and R. Chaujar, "Semi-empirical DFT Based Investigation of Electronic and Quantum Transport Properties of Novel GS-AGNR (N) FET," *IEEE Transactions on Nanotechnology*, vol. 23, pp. 400 - 407, 2024.

[21] S. Smidstrup *et al.*, "QuantumATK: an integrated platform of electronic and atomic-scale modelling tools," *Journal of Physics: Condensed Matter,* vol. 32, no. 1, pp. 015901, 2019.

[22] R. Chaujar, "DFT based analysis of Boron and Nitrogen passivation at the edge of Armchair Graphene Nanoribbon for low power applications," 2024: IEEE, pp. 1-4.

[23] Y. Yoon, G. Fiori, S. Hong, G. Iannaccone, and J. Guo, "Performance comparison of graphene nanoribbon FETs with Schottky contacts and doped reservoirs," *IEEE Transactions on electron devices,* vol. 55, no. 9, pp. 2314-2323, 2008.

[24] Y. Pathak, B. D. Malhotra, and R. Chaujar, "Detection of biomolecules in dielectric modulated double metal below ferroelectric layer FET with improved sensitivity," *Journal of Materials Science: Materials in Electronics,* vol. 33, no. 17, pp. 13558-13567, 2022.

[25] A. Wasfi, A. Al Hamarna, O. M. H. Al Shehhi, H. F. M. Al Ameri, and F. Awwad, "Graphene Nanoribbon Field Effect Transistor Simulations for the Detection of Sugar Molecules: Semi-Empirical Modeling," *Sensors,* vol. 23, no. 6, pp. 3010, 2023.

[26] M. R. Moslemi, M. H. Sheikhi, K. Saghafi, and M. K. Moravvej-Farshi, "Electronic properties of a dual-gated GNR-FET under uniaxial tensile strain," *Microelectronics Reliability,* vol. 52, no. 11, pp. 2579-2584, 2012.

[27] Y.-Y. Chen *et al.*, "A SPICE-compatible model of MOS-type graphene nano-ribbon field-effect transistors enabling gate-and circuit-level delay and power analysis under process variation," *IEEE Transactions on Nanotechnology,* vol. 14, no. 6, pp. 1068-1082, 2015.

[28] M. Gholipour, N. Masoumi, Y.-Y. C. Chen, D. Chen, and M. Pourfath, "Asymmetric gate Schottky-barrier graphene nanoribbon FETs for low-power design," *IEEE Transactions on Electron Devices,* vol. 61, no. 12, pp. 4000-4006, 2014.

[29] A. Naderi, "Theoretical analysis of a novel dual gate metal–graphene nanoribbon field effect transistor," *Materials Science in Semiconductor Processing,* vol. 31, pp. 223-228, 2015.

[30] H. Sarvari and R. Ghayour, "Design of GNRFET using different doping profiles near the source and drain contacts," *International Journal of Electronics,* vol. 99, no. 5, pp. 673-682, 2012.

Authorized licensed use limited to: DELHI TECHNICAL UNIV. Downloaded on June 04,2025 at 05:24:47 UTC from IEEE Xplore. Restrictions apply.

Junctionless Spacer-Engineered SOI FinFET-Based Hydrogen Gas Sensor: Electrical Characterization and Sensitivity Analysis

Ayushi Lamba
Department of Applied Physics
Delhi Technological University
Delhi, India
ayushilamba_2k21phdap501@dtu.ac.in

Rishu Chaujar
Department of Applied Physics
VDCoE4SM
Delhi Technological University
(of Affiliation)
Delhi, India
chaujar.rishu@dtu.ac.in

M. Jamal Deen
Department of Computer and Electrical Engineering
McMaster University
Hamilton, Canada
jamal@mcmaster.ca

2025 Devices for Integrated Circuit (DevIC) | 979-8-3503-9110-7/25/$31.00 ©2025 IEEE | DOI: 10.1109/DevIC63749.2025.11012307

***Abstract*— This research presents a novel junctionless spacer-engineered gate stacked Silicon-on-Insulator (SOI) FinFET for hydrogen gas sensing. The study investigates the sensor's transfer characteristics, energy band diagram and surface potential under varying pressures. Threshold voltage and switching ratio sensitivities are calculated to assess the sensor's responsiveness. A maximum value of 125.64 for I_{ON}/I_{OFF} sensitivity and 0.24 for V_{TH} sensitivity is obtained at P=10^{-10} Torr. Simulations performed on 3D ATLAS Silvaco tool reveal significant differences in performance between the junctionless (JLT) sensor and the one having a junction. Specifically, the JLT fin-based sensor demonstrates substantially improved sensitivity to hydrogen gas. The combination of improved sensitivity and the SOI FinFET architecture presents a promising approach for designing high-performance hydrogen gas sensors suitable for diverse applications using JLT SOI FinFETs.**

Keywords*— *Junctionless SOI FinFET, Spacer engineering, Hydrogen gas sensor, Sensitivity

I. INTRODUCTION

Hydrogen is widely recognized as a key energy carrier essential for the sustainable advancement of the global economy, energy distribution, and storage solutions [1]. Its applications are particularly significant in the automotive [2] sector and aerospace [3], where it is advocated as a clean, carbon-free energy source. Despite its potential as a sustainable energy carrier, the development of highly sensitive hydrogen sensors is crucial due to its flammable and explosive nature. Being the lightest and smallest molecule, hydrogen has exceptional permeability, allowing for quick and precise detection of leaks to mitigate explosion risks [4]. Therefore, creating an ultra-sensitive nano-sensor for hydrogen leak detection is vital for both safety and security.

In today's advanced landscape, field effect transistor (FET) sensors are increasingly sought after due to their critical role in various sectors such as automotive, healthcare, industry, and communication. Keeping pace with the latest developments in semiconductor technology, FET sensors are being developed as non-planar devices that are resistant to short-channel effects (SCEs). Various gas sensors designed for detecting biomolecules, pressure, gases, or temperature variations, including hydrogen, have been developed using conventional MOSFETs [5, 6], Carbon Nanotubes [7], Tunnel-FETs (TFETs) [8], temperature-controlled phase-transition FETs [9] and Metal-Insulator-Semiconductor (MIS) structures [10]. However, carbon-based sensors exhibit weak binding energy, making them less responsive to hydrogen gas [11]. MOSFET-based gas sensors are in high demand due to their compatibility with existing MOSFET fabrication techniques, seamless integration, and ability to function at room temperature. Semiconductor-based solid-state hydrogen sensors are widely used for environmental monitoring due to their robustness and versatility [12]. Significant performance improvements have been reported for Junctionless (JL) MOSFETs, where the source, channel, and drain regions are uniformly doped with n+ material [13]. However, as gate lengths decrease, Short Channel Effects (SCEs) significantly degrade the performance of MOSFET-based sensors. TFET-based gas sensors offer improved sensitivity and reduced SCE impact, making them a promising alternative. However, factors such as parasitic capacitance, the requirement for a higher gate-bias voltage to maintain steady current flow, and the presence of traps limit their overall sensing capabilities [14, 15]. Given the unique characteristics of a spacer-engineered gate stacked Silicon on Insulator FinFET [16], it presents a promising option for the next generation of FET-based sensors.

The FinFET device architecture offers more space for molecules within the sensor, resulting in improved sensitivity. However, FinFETs are more susceptible to short-channel effects, especially at lower technology nodes. Therefore, gas sensors designed with this architecture need to operate at low power and have quick response times for gas detection. This led us to explore junctionless Silicon on Insulator (SOI) FinFETs for our proposed hydrogen gas sensor design, given their advantages over conventional FETs regarding short channel effects and switching ratios [17].

Hydrogen gas sensors play a vital role in industrial safety and environmental applications. This study focuses on designing and simulating a platinum gate spacer-engineered, gate-stacked junctionless SOI FinFET using 3D ATLAS Silvaco [18] software for efficient hydrogen detection. The device employs spacer engineering, incorporating a dual-K dielectric structure near the source region and a high-K HfO2 layer to enhance electrostatic control. The junctionless configuration, with uniformly high doping in the source, drain, and channel, simplifies fabrication and minimizes leakage. A platinum (Pt) gate is chosen for its catalytic ability to facilitate hydrogen adsorption. When hydrogen molecules interact with the gate, a dipole layer is induced at the metal-oxide interface, leading to shifts in the electric field, potential, and drain

979-8-3503-9110-7/25/$31.00 ©2025 IEEE

Authorized licensed use limited to: DELHI TECHNICAL UNIV. Downloaded on June 04,2025 at 05:24:03 UTC from IEEE Xplore. Restrictions apply.

current, which indicate hydrogen presence. By integrating FinFET scalability, high-K materials, and catalytic gate engineering, this sensor is designed to achieve superior sensitivity for hydrogen detection.

II. Device Structure Description

The three-dimensional schematic of the platinum gate spacer-engineered, gate-stacked junctionless SOI FinFET is illustrated in Fig. 1(a), while its two-dimensional representation is depicted in Fig. 1(b). A platinum film is utilized as the metallic gate material to enhance hydrogen absorption sensitivity. The device maintains a junctionless structure with a uniform doping concentration of 10^{-18} cm^{-3} across the source, drain, and channel regions. All simulations consider a gate length of 20 nm. On the source side, a dual-K spacer arrangement consists of a 3 nm SiO_2 layer combined with a 6 nm HfO_2 layer, whereas the drain side incorporates a single 9 nm SiO_2 spacer. Consequently, the total channel length extends to 38 nm. Additionally, a high-K HfO_2 layer is integrated atop the SiO_2 layer. The applied gate voltage is set to 1 V, with a fixed drain bias of 0.3 V. Fig. 1(c) also illustrates the schematic dipole configuration of the hydrogen molecule at the metal-oxide interface. Table I describes the device parameters.

TABLE I: DEVICE PARAMETER DESCRIPTION

Parameters	Values
Gate Length (L_G)	20 nm
Source/Drain Length (L_S/L_D)	26 nm
Source/Drain Height	27 nm
Channel Length	38 nm
Spacer SiO_2 length (towards drain side)	9 nm
Spacer HfO_2 length (towards source side)	6 nm
Spacer SiO_2 length (towards source side)	3 nm
BOX (buried oxide) thickness	50 nm
Gate thickness	1 nm
HfO_2 thickness	10 nm
SiO_2 thickness	1 nm

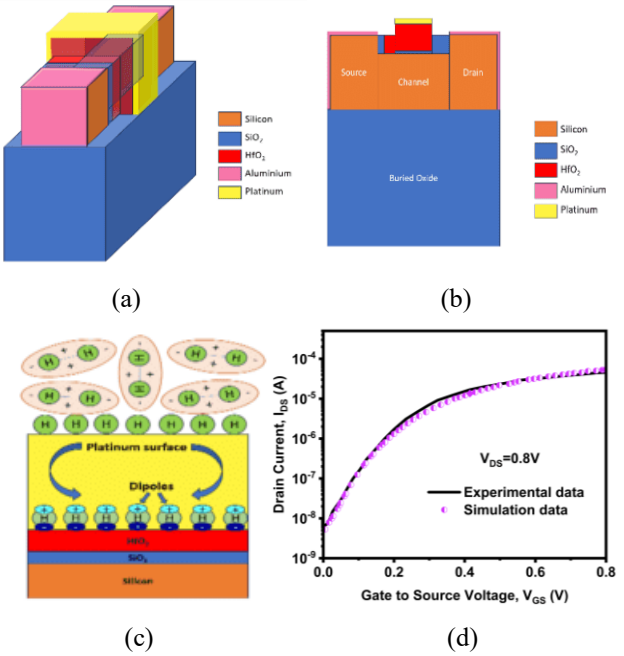


Fig. 1. (a): 3D architecture depicting the proposed hydrogen gas sensor, (b): 2D view of the proposed hydrogen gas sensor, (c): 2D front-view representation of the simulated Platinum-gated Junctionless SOI FinFET hydrogen gas sensor, (d): Transfer characteristics comparison of the proposed device with the experimental data of [19].

III. Simulation Methodology, Calibration & Working Principle of Platinum-Gated Hydrogen Gas Sensor

All simulations are carried out using Silvaco TCAD ATLAS [18], incorporating optimized models such as Lombardi CVT, Fermi-Dirac statistics, and the Shockley-Read-Hall (SRH) recombination model to account for real-world conditions. The simulation framework is governed by the equations referenced in [18]. Fig. 1 (d) describes the calibration of these models used by presenting a comparison between the simulated I_{DS}-V_{GS} characteristics and experimental results from [19], demonstrating a strong correlation with the 20 nm LG SOI FinFET, thereby confirming the accuracy of the simulation models.

Platinum is an excellent material for hydrogen sensing and storage due to its strong affinity for hydrogen, which allows for reversible adsorption. Under equilibrium conditions, this exothermic absorption [20] process follows a reversible reaction, as described by equation (1).

$$Pt + \frac{x}{2}H_2 = Pt\,H_x \quad (1)$$

When hydrogen gas molecules encounter the platinum surface, their interaction with Pt atoms occurs through van der Waals forces [20]. At the metal interface, hydrogen molecules undergo adsorption at a molecular-scale distance, influenced by the potential energy of the gas molecules. Subsequently, hydrogen molecules dissociate into individual atoms, which then diffuse into the metal lattice, a process illustrated in Fig. 1(b).

The hydrogen gas sensing mechanism in a platinum (Pt) gate spacer-engineered, gate-stacked junctionless SOI FinFET involves multiple sequential steps [21]. These steps include hydrogen molecule adsorption, dissociation, dipole layer formation, work function modulation, and drain current variation, ultimately enabling hydrogen detection.

1. Adsorption and Dissociation of Hydrogen Molecules:

When hydrogen gas is introduced, molecular hydrogen H_2 interacts with the Pt gate surface, which acts as a catalyst. Due to the strong catalytic properties of Pt, the hydrogen molecules are adsorbed onto the surface and subsequently dissociate into atomic hydrogen:

$$H_2(gas) = 2\,H(ads) \quad (2)$$

Here, H_2 represents molecular hydrogen in the gas phase, and H (ads) refers to the atomic hydrogen adsorbed onto the Pt surface.

2. Diffusion of Hydrogen Atoms and Dipole Layer Formation:

Once dissociated, the hydrogen atoms diffuse across the platinum surface and accumulate near the metal-oxide interface (Pt/HfO_2 or Pt/SiO_2). This interaction leads to the formation of a dipole layer, which alters the local electric field and modifies the work function (Φ) of Pt:

$$\Delta\Phi = eN_Hd \quad (3)$$

where:

ΔΦ=Change in the Pt work function, e=Electron charge, N_H= Surface density of adsorbed hydrogen atoms, d=Effective dipole moment distance

Authorized licensed use limited to: DELHI TECHNICAL UNIV. Downloaded on June 04,2025 at 05:24:03 UTC from IEEE Xplore. Restrictions apply.

This dipole formation alters the effective potential at the gate terminal.

3. Modulation of Gate Work Function and Threshold Voltage:

The presence of the dipole layer changes the metal work function, shifting the threshold voltage VTH of the FinFET device. The shift in threshold voltage can be expressed as:

$$\Delta V_{TH} = \frac{\Delta \Phi}{q} \quad (4)$$

where q is the elementary charge. A higher hydrogen concentration increases dipole formation, leading to a greater shift in threshold voltage.

4. Drain Current Variation and Hydrogen Detection:

The threshold voltage shift modulates the electric field in the channel, which alters the drain current I_D of the junctionless FinFET. The drain current equation is given by:

$$I_D = \mu C_{OX} \frac{W}{L} (V_{GS} - V_{TH})^2 \quad (5)$$

where:

I_D=drain current, μ=carrier mobility, C_{ox}=Oxide capacitance, W, L =Channel width and length, V_{GS}=Gate-to-source voltage and V_{TH}=Threshold voltage

Since hydrogen adsorption reduces the work function of Pt, it lowers the threshold voltage, leading to an increase in drain current I_D. The magnitude of this change is directly correlated with the concentration of hydrogen gas, allowing for precise sensing and detection [22]. Table I shows the change in the work function of platinum gate metal when hydrogen molecules interact with it at different pressures.

TABLE II. CHANGE IN WORK-FUNCTION IN RESPONSE TO PRESSURE OF HYDROGEN GAS

Pressure (Torr)	Change in work-function(eV)
0	0
10^{-14}	0.015
10^{-13}	0.040
10^{-12}	0.087
10^{-11}	0.135
10^{-10}	0.165

IV. Results and Discussions

The sensing mechanism of the platinum-gated FinFET hydrogen sensor is based on hydrogen adsorption, dipole-induced work function change, and threshold voltage modulation, leading to variations in drain current. This response can be effectively measured to detect and quantify hydrogen gas pressure changes. The sensor's high sensitivity is attributed to FinFET architecture, high-K dielectric integration, and catalytic gate engineering, making it a promising candidate for hydrogen gas detection applications.

A. Junctionless architecture's comparison with junction one

An SOI FinFET-based hydrogen gas sensor with the same specifications as described above was built having a junction channel in which the source/drain uniform doping N_D=1 x 10^{20} cm^{-3} and channel uniform doping N_{ch}=1 x 10^{18} cm^{-3}. Its device characteristics were obtained via TCAD simulations for different hydrogen pressures and were compared with those of the junctionless SOI FinFET-based hydrogen gas sensor. The device characteristics are tabulated in Table III clearly showing the junctionless SOI FinFET having an edge over the junction one.

TABLE III. DEVICE CHARACTERISTICS COMPARISON OF JUNCTIONLESS SOI FINFET-BASED HYDROGEN GAS SENSOR WITH THE ONE HAVING A JUNCTION

Pressure (Torr)	I_{ON}/I_{OFF} (JLT)	I_{ON}/I_{OFF} (JCN)	V_{TH} (V) (JLT)	V_{TH} (V) (JCN)	I_{OFF} (A/μm) (JLT)	I_{OFF} (A/μm) (JCN)	SS (V/dec) (JLT)	SS (V/dec) (JCN)
0	$2.32x10^{10}$	$1.15x10^{8}$	0.70	0.65	$7.04 x10^{-17}$	$1.47x10^{-14}$	0.01504	0.0635
10^{-14}	$3.74x10^{10}$	$1.58x10^{8}$	0.72	0.66	$4.36 x10^{-17}$	$1.07x10^{-14}$	0.01175	0.05643
10^{-13}	$8.28x10^{10}$	$2.51x10^{8}$	0.74	0.69	$1.97 x10^{-17}$	$6.73x10^{-15}$	0.00618	0.06307
10^{-12}	$3.60x10^{11}$	$2.16x10^{9}$	0.79	0.73	$4.54 x10^{-18}$	$7.76x10^{-16}$	0.00688	0.0067
10^{-11}	$1.45x10^{12}$	$1.29x10^{10}$	0.84	0.79	$1.13 x10^{-18}$	$1.26x10^{-16}$	0.00461	0.01441
10^{-10}	$2.94x10^{12}$	$1.42x10^{10}$	0.87	0.81	$5.55 x10^{-19}$	$1.07x10^{-16}$	0.00409	0.00735

Here JLT=junctionless transistor, JCN=junction transistor, V_{TH}=threshold voltage, I_{ON}/I_{OFF}=switching ratio, I_{OFF}=off current and SS=subthreshold swing.

DIBL(drain induced barrier lowering) values are also calculated for both these configurations and are presented in table IV below [23]. A considerable reduction in these values for the JLT configuration supports it being chosen over the FinFET having a junction for the gas sensing mechanism.

TABLE IV. DEVICE CHARACTERISTICS COMPARISON OF JUNCTIONLESS SOI FINFET-BASED HYDROGEN GAS SENSOR WITH THE ONE HAVING A JUNCTION

Pressure (Torr)	0	10^{-14}	10^{-13}	10^{-12}	10^{-11}	10^{-10}
DIBL for FinFET with a junction	0.112	0.112	0.112	0.112	0.112	0.071
DIBL for Junctionless FinFET	0.043	0.043	0.043	0.043	0.042	0.043

It is noteworthy that a high K spacer (HfO_2) 6 nm long is applied towards the source side of the proposed device. When a high K spacer is introduced above the channel near the source side of the SOI FinFET-based hydrogen gas sensor, it alters the device's electrostatics, leading to changes in the energy band structure, surface potential, and drain current. The motivation behind this configuration is take from [24] in which the experimental fabrication steps are also explained. These advancements in the device characteristics are shown and explained in the sections below.

B. Transfer Characteristics Analysis

To enable hydrogen gas detection through an electrical sensing approach in a transistor-based device, this study utilizes the fundamental properties of a FinFET structure. The detection mechanism is analyzed by examining the transfer

Authorized licensed use limited to: DELHI TECHNICAL UNIV. Downloaded on June 04,2025 at 05:24:03 UTC from IEEE Xplore. Restrictions apply.

characteristics of a platinum-gated SOI FinFET. These characteristics are extracted for different hydrogen gas pressures, ranging from 10^{-14} Torr to 10^{-10} Torr, as a function of the gate-to-source voltage V_{GS}, as depicted in Fig. 2 (b).

The results indicate that as the gas pressure increases from 10^{-14} Torr to 10^{-10} Torr, there is a corresponding rise in drain current I_D. At higher pressures (10^{-10} Torr), the device exhibits an increased drain current, whereas at lower pressures (10^{-14} Torr), the current remains lower. This variation occurs due to a change in the metal work function in response to hydrogen adsorption, leading to a shift in drain current. The sensor effectively detects hydrogen gas by comparing the drain current values in the presence and absence of hydrogen. In Fig. 2 (a) an increase in drain current is observed due to the presence of HfO_2 spacer in the device architecture as the high K spacer alters the source-end potential, lowering the barrier for electron injection into the channel and facilitating higher current flow.

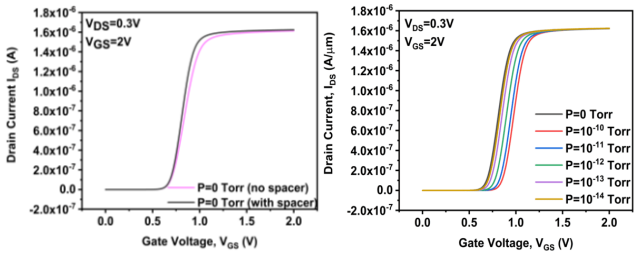


Fig. 2. (a) Transfer characteristics comparison of the proposed sensor at 0 pressure condition with and without the presence of HfO_2 spacer. (b) Transfer characteristics of the proposed hydrogen gas sensor for varying pressures of hydrogen gas.

C. Energy Band Analysis

The authors also performed the energy band analysis of the proposed hydrogen gas sensor for varying pressures as can be seen in Fig. 3 (b).

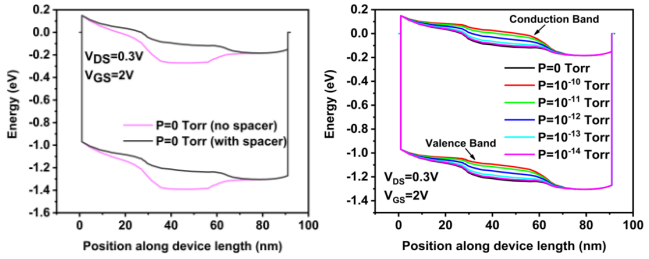


Fig. 3. (a) Energy band comparison of the proposed sensor at 0 pressure condition with and without the presence of HfO_2 spacer. (b) Energy band analysis of the proposed hydrogen gas sensor for varying pressures of hydrogen gas.

The upward shift in the energy band with increasing hydrogen gas pressure in an SOI FinFET-based sensor is primarily caused by the formation of a dipole layer, which lowers the metal work function, thereby modifying the electrostatic potential of the channel. This shift results in band bending, lower threshold voltage, and an increase in drain current, making it an effective mechanism for hydrogen gas detection. Fig. 3 (a) shows a reduction in energy bands of the proposed device due to application of HfO_2 spacer. Introducing a high-K spacer alters the gate fringe fields, enhancing electric field penetration toward the source. This leads to a reduction in surface potential near the source, shifting the conduction and valence bands upward relative to the Fermi level. Consequently, energy band realignment occurs as the band edges follow potential variations. Additionally, the electrostatic changes at the source affect carrier injection, with hydrogen-induced dipole formation further influencing this process.

D. Surface Potential Analysis

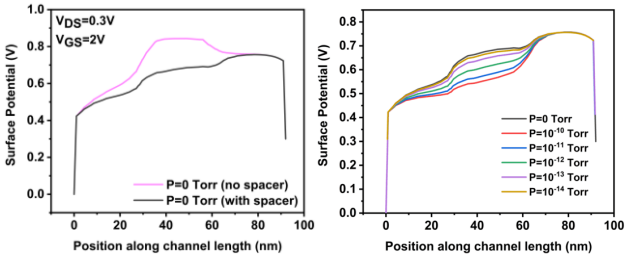


Fig. 4. (a) Surface potential comparison of the proposed sensor at 0 pressure condition with and without the presence of HfO_2 spacer. (b) Surface potential variation of the proposed hydrogen gas sensor for varying pressures of hydrogen gas.

The variation of surface potential along the device length is also studied w.r.t change in pressure of hydrogen gas which is shown in Fig. 4 (b). From this figure it can be concluded that the surface potential decreases with increasing pressure achieving maximum value for P=10^{-10} Torr. The surface potential in the channel is controlled by the gate-to-channel potential difference. As the work function of the gate decreases, the applied electric field weakens, leading to a reduction in the channel surface potential. Also, Fig. 4 (a) shows a reduction in surface potential on introduction of HfO_2 spacer towards source side in the proposed device. Surface potential refers to the voltage difference between the semiconductor surface and the bulk. A high-K spacer enhances the gate's electrostatic influence, strengthening gate coupling by increasing capacitance and improving control over the source-end channel, which lowers the surface potential. Additionally, the altered electric field redistributes charge in the channel, further reducing the surface potential.

E. Sensitivity Analysis

The sensitivity of an SOI FinFET-based hydrogen gas sensor is a critical parameter that determines its ability to detect variations in hydrogen gas pressures [25]. Sensitivity analysis involves evaluating how changes in gas pressure influence the electrical characteristics of the device, particularly the drain current (I_D), threshold voltage (V_{TH}), switching ratio (I_{ON}/I_{OFF}) and surface potential (Ψ_S). As hydrogen molecules interact with the platinum (Pt) gate, they dissociate into atomic hydrogen and form a dipole layer at the metal-oxide interface. This lowers the effective gate work function, modifying the electrostatic potential in the channel and enhancing charge carrier modulation. As a result, an increase in hydrogen pressure leads to a rise in drain current and a shift in threshold voltage, directly affecting the sensor's output response.

1) V_{TH} Sensitivity

The threshold voltage sensitivity of the device can be quantified using the equation [26]:

$$S_{V_{TH}} = \frac{|V_{TH,H_2} - V_{TH,0}|}{V_{TH,0}} \quad (6)$$

where V_{TH,H_2} stands for the threshold voltage of the proposed device at some pressure applied of hydrogen gas at the gate and $V_{TH,0}$ stands for the threshold voltage of the proposed device when no hydrogen gas is applied to the platinum gate. The maximum value of sensitivity obtained is 0.24 for P=

Authorized licensed use limited to: DELHI TECHNICAL UNIV. Downloaded on June 04,2025 at 05:24:03 UTC from IEEE Xplore. Restrictions apply.

10^{-10} Torr.

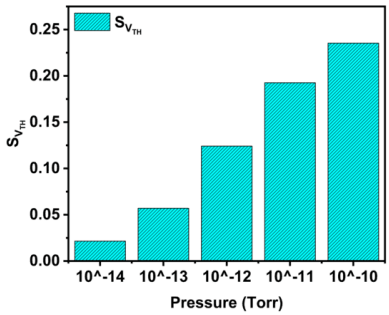


Fig. 5. Threshold voltage sensitivity of the proposed hydrogen gas sensor at different pressures of applied hydrogen gas.

2) I_{ON}/I_{OFF} Sensitivity

The switching ratio voltage sensitivity of the device can be quantified using the equation [26]:

$$S_{I_{ON}/I_{OFF}} = \frac{|I_{ON}/I_{OFF,H_2} - I_{ON}/I_{OFF,0}|}{I_{ON}/I_{OFF,0}} \quad (7)$$

where $I_{ON}/I_{OFF,H_2}$ stands for the threshold voltage of the proposed device at some pressure applied of hydrogen gas at the gate and $I_{ON}/I_{OFF,0}$ stands for the threshold voltage of the proposed device when no hydrogen gas is applied to the platinum gate. As it's visible the maximum value of sensitivity is obtained at P=10^{-10} Torr as 125.64 units.

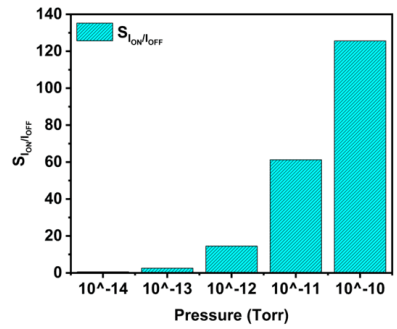


Fig. 6. Switching ratio sensitivity of the proposed hydrogen gas sensor at different pressures of applied hydrogen gas.

F. Subthreshold Slope comparison of the proposed device

A comparison based on SS values of some existing state-of-the-art hydrogen gas sensors at maximum applied pressure value (10^{-10} Torr) is performed in Table V showcasing the proposed hydrogen gas sensor's supremacy over them.

TABLE V. SS COMPARISON OF THE PROPOSED HYDROGEN GAS SENSOR WITH SOME EXISTING STATE-OF-THE-ART HYDROGEN GAS SENSORS

SS (mV/dec) at P=10^{-10} Torr	% decrease in SS of the proposed JLT gas sensor
~210 [27]	98.05%
~94 [28]	95.65%
61.8 [29]	93.38%
15 [29]	72.73%

V. Conclusion

In this study, a junctionless gate-stacked SOI FinFET-based hydrogen gas sensor was developed and analyzed in terms of its electrical characteristics and sensing performance. The device's transfer characteristics, surface potential variations, and energy band diagrams were examined under different hydrogen gas pressures. Sensitivity metrics, including threshold voltage and switching ratio sensitivity, were calculated, with the highest values observed at a maximum hydrogen pressure of 10^{-10} Torr as 0.24 and 125.64 respectively. A comparative evaluation with a junction-based SOI FinFET sensor demonstrated that the junctionless configuration exhibited superior performance, highlighting its effectiveness in hydrogen gas detection applications. The observed improvements in electrical response, sensitivity, and overall device efficiency establish this sensor as a promising candidate for highly responsive and accurate gas sensing technology.

Acknowledgment

The authors are thankful to the Microelectronics Research Laboratory, Delhi Technological University, Vinod Dham Centre of Excellence for Semiconductors and Microelectronics (VDCoE4SM), Delhi Technological University, SERB Power Grant and MeiTY C2S Grant for supporting the work.

References

[1] L. G. Villanueva, F. Fargier, T. Kiefer, M. Ramonda, J. Brugger, and F. Favier, "Highly ordered palladium nanodot patterns for full concentration range hydrogen sensing," *Nanoscale,* vol. 4, no. 6, pp. 1964-1967, 2012.

[2] K. Mazloomi and C. Gomes, "Hydrogen as an energy carrier: Prospects and challenges," *Renewable and sustainable energy reviews,* vol. 16, no. 5, pp. 3024-3033, 2012.

[3] T. Hübert, L. Boon-Brett, G. Black, and U. Banach, "Hydrogen sensors–a review," *Sensors and Actuators B: Chemical,* vol. 157, no. 2, pp. 329-352, 2011.

[4] S. A. M. Chachuli, M. N. Hamidon, M. S. Mamat, M. Ertugrul, and N. H. Abdullah, "Response of TiO2/MWCNT/B2O3 gas sensor to hydrogen using different organic binder," *Materials Science in Semiconductor Processing,* vol. 99, pp. 140-148, 2019.

[5] Z. Ahangari, "Performance assessment of dual material gate dielectric modulated nanowire junctionless MOSFET for ultrasensitive detection of biomolecules," *RSC advances,* vol. 6, no. 92, pp. 89185-89191, 2016.

[6] I. Lundström, S. Shivaraman, C. Svensson, and L. Lundkvist, "A hydrogen-sensitive MOS field-effect transistor," *Applied Physics Letters,* vol. 26, no. 2, p. 55, 1975.

[7] N. M. Santhosh *et al.*, "Improving sensing properties of entangled carbon nanotube-based gas sensors by atmospheric plasma surface treatment," *Microelectronic Engineering,* vol. 232, p. 111403, 2020.

[8] D. Sarkar, H. Gossner, W. Hansch, and K. Banerjee, "Tunnel-field-effect-transistor based gas-sensor: Introducing gas detection with a quantum-mechanical transducer," *Applied Physics Letters,* vol. 102, no. 2, 2013.

[9] C. Senft, P. Iskra, I. Eisele, C. Wilbertz, and H. P. Frerichs, "Temperature controlled phase transition as a detection principle for gas FETs (TPT-FET)," 2008: IEEE, pp. 1316-1319.

[10] A. Salomonsson, M. Eriksson, and H. Dannetun, "Hydrogen interaction with platinum and palladium metal–insulator–semiconductor devices," *Journal of applied physics,* vol. 98, no. 1, 2005.

[11] R. Nandeshwar and S. Tallur, "Integrated low cost optical biosensor for high resolution sensing of myeloperoxidase (MPO) activity through carbon nanotube degradation," *IEEE Sensors Journal,* vol. 21, no. 2, pp. 1236-1243, 2020.

[12] G. W. Hunter *et al.*, "Editors' choice—critical review—a critical review of solid state gas sensors," *Journal of The Electrochemical Society,* vol. 167, no. 3, p. 037570, 2020.

[13] J.-P. Colinge *et al.*, "Nanowire transistors without junctions," *Nature nanotechnology,* vol. 5, no. 3, pp. 225-229, 2010.

[14] T. Wang, L. Lou, and C. Lee, "A junctionless gate-all-around silicon nanowire FET of high linearity and its potential

Authorized licensed use limited to: DELHI TECHNICAL UNIV. Downloaded on June 04,2025 at 05:24:03 UTC from IEEE Xplore. Restrictions apply.

applications," *IEEE Electron Device Letters,* vol. 34, no. 4, pp. 478-480, 2013.

[15] T. Hoffmann *et al.*, "GIDL (gate-induced drain leakage) and parasitic schottky barrier leakage elimination in aggressively scaled HfO/sub 2/TiN FinFET devices," 2005: IEEE, pp. 725-728.

[16] A. Lamba, R. Chaujar, and M. J. Deen, "Investigation of a Dielectric Modulated Dual Metal Gate Engineered SOI FinFET with High-K Dielectric for Bio-sensitivity Enhancement," 2024: IEEE, pp. 31-33.

[17] H. D. Sehgal, Y. Pratap, and S. Kabra, "Detection of poisonous gases using JL FinFET with conducting gate polymer," 2022: IEEE, pp. 440-444.

[18] "3D ATLAS Device simulation software." http://www.silvaco.com (accessed, 2018).

[19] C. H. Lin *et al.*, "High performance 14nm SOI FinFET CMOS technology with 0.0174 μm 2 embedded DRAM and 15 levels of Cu metallization," 2014: IEEE, pp. 3-8.

[20] M. Dornheim, "Thermodynamics of metal hydrides: tailoring reaction enthalpies of hydrogen storage materials," in *Thermodynamics-Interaction Studies-Solids, Liquids and Gases*: IntechOpen, 2011.

[21] H. D. Sehgal, Y. Pratap, M. Gupta, and S. Kabra, "Performance investigation of novel Pt/Pd-SiO 2 junctionless FinFET as a high sensitive hydrogen gas sensor for industrial applications," *IEEE Sensors Journal,* vol. 21, no. 12, pp. 13356-13363, 2021.

[22] R. Chaujar and M. G. Yirak, "Sensitivity investigation of junctionless gate-all-around silicon nanowire field-effect transistor-based hydrogen gas sensor," *Silicon,* vol. 15, no. 1, pp. 609-621, 2023.

[23] A. Kaul, S. Rewari, and D. Nand, "Double Metal Gate Macaroni Nanowire FET (DMGM-NFET) for Improved Performance and Off-State Leakage Reduction," *ECS Journal of Solid State Science and Technology,* vol. 13, no. 10, p. 103010, 2024.

[24] M. Amani *et al.*, "Design and comparative analysis of FD-SOI FinFET with dual-dielectric spacers for high speed switching applications," *Silicon,* vol. 16, no. 4, pp. 1525-1534, 2024.

[25] K. Pal, C. Gupta, S. P. Bhardwaj, A. Kumar, and S. Kale, "Reconfigurable Silicon Nanowire-Based Schottky Barrier Transistor for Hydrocarbon Gas Detection: A Comprehensive Study," 2024: IEEE, pp. 1-5.

[26] M. Nami, M. Taheri, I. A. Deen, M. Packirisamy, and M. J. Deen, "Nanomaterials in chemiresistive and potentiometric gas sensors for intelligent food packaging," *TrAC Trends in Analytical Chemistry,* p. 117664, 2024.

[27] A. Raj and S. K. Sharma, "Investigation on palladium gate electrode-based SOI junctionless FET for hydrogen gas sensing," *Microelectronics Journal,* vol. 151, p. 106312, 2024.

[28] A. Kumar, "Palladium-based trench gate MOSFET for highly sensitive hydrogen gas sensor," *Materials science in semiconductor processing,* vol. 120, p. 105274, 2020.

[29] A. Goel, S. Rewari, and R. S. Gupta, "Performance investigation of neoteric Pt/Pd Junctionless gas tube FET (JL-GT-FET) as a Hydrogen (H2) gas sensor for industrial applications-analytical model," *Micro and Nanostructures,* vol. 198, p. 208050, 2025.

Authorized licensed use limited to: DELHI TECHNICAL UNIV. Downloaded on June 04,2025 at 05:24:03 UTC from IEEE Xplore. Restrictions apply.



International Journal of Electronics

ISSN: 0020-7217 (Print) 1362-3060 (Online) Journal homepage: www.tandfonline.com/journals/tetn20

Low leakage Schmitt trigger logic circuits design with improved noise immunity for energy-constrained applications

Bhawanand Jha, Kirti Gupta & Rajeshwari Pandey

To cite this article: Bhawanand Jha, Kirti Gupta & Rajeshwari Pandey (09 Jun 2025): Low leakage Schmitt trigger logic circuits design with improved noise immunity for energy-constrained applications, International Journal of Electronics, DOI: 10.1080/00207217.2025.2514713

To link to this article: https://doi.org/10.1080/00207217.2025.2514713

Published online: 09 Jun 2025.

Submit your article to this journal

Article views: 3

View related articles

View Crossmark data

Full Terms & Conditions of access and use can be found at
https://www.tandfonline.com/action/journalInformation?journalCode=tetn20

INTERNATIONAL JOURNAL OF ELECTRONICS
https://doi.org/10.1080/00207217.2025.2514713

Taylor & Francis
Taylor & Francis Group

Check for updates

Low leakage Schmitt trigger logic circuits design with improved noise immunity for energy-constrained applications

Bhawanand Jha [a,b], Kirti Gupta [b] and Rajeshwari Pandey [a]

[a]Department of Electronics and Communication Engineering, Delhi Technological University, New Delhi, India; [b]Department of Electronics and Communication Engineering, Bharati Vidyapeeth's College of Engineering, New Delhi, India

ABSTRACT

Schmitt Trigger (ST) logic style is the most suited logic style to design digital circuits for energy-constrained applications over the CMOS logic style. In this paper, a novel low leakage ST logic named as stacked variable threshold CMOS (SVTCMOS) ST logic style is presented. The proposed logic style introduces stacking of transistors with variable threshold technique to lower the leakage current and enhance the noise immunity in ST gates. Mathematical formulations to analyse the reduction in leakage current and improvement in noise immunity for the proposed SVTCMOS ST buffer/inverter is put forward. Different SVTCMOS ST logic gates are proposed and their performance is compared with the conventional and existing ST logic gates through LTspice simulations at 45 nm PTM CMOS technology node. It is observed that the proposed SVTCMOS ST buffer exhibit 87% leakage current reduction and 7% noise immunity improvement in comparison to variable threshold CMOS ST logic buffer at the cost of increased area and delay values. The process corner analysis and Monte Carlo simulations reveals that the proposed style is more tolerant to variations over existing ST logic gates.

ARTICLE HISTORY
Received 22 June 2024
Accepted 19 April 2025

KEYWORDS
Digital circuits; I_{ON}/I_{OFF}; noise immunity; Schmitt trigger; VTCMOS Schmitt trigger

1. Introduction

The advancement in VLSI technology has led to tremendous growth in energy-constrained applications such as healthcare systems, environmental monitoring systems, surveillance systems, and smart agriculture systems (G. Chen et al., 2011; Gubbi et al., 2013; Hanson et al., 2009; Noh et al., 2019; C. Wang et al., 2015). The tight energy budget of these applications demands low power circuits and thus has motivated research in this direction. The scaling of supply voltage has been adopted to obtain low-power circuits for its quadratic effect on power. This includes sub-threshold design, which mainly focuses on circuit operation optimised for minimum energy per operation point. However, the energy-constrained applications use circuits that operate below this point wherein the minimum supply voltage is determined at the instant when active operation gets initiated

CONTACT Kirti Gupta kirti.gupta@bharatividyapeeth.edu Department of Electronics and Communication Engineering, Bharati Vidyapeeth's College of Engineering, A-4, Paschim Vihar, New Delhi 110063, India

© 2025 Informa UK Limited, trading as Taylor & Francis Group

(Bleitner et al., 2018; Bol et al., 2009; Y. Chen et al., 2022; Lin et al., 2019). Thus, these consume significantly low power making V_{DD} minimisation at the cost of area, leakage worthwhile. In addition to this, few applications such as environmental monitoring system, wireless sensor network have circuits with long standby durations such that the standby power consumption dominates the overall energy budget. Therefore, minimising the supply voltage is a promising solution to achieve significant power reduction at the expense of slower performance.

Various other CMOS design techniques to felicitate operation at low voltage involve optimised transistor sizing (A. Wang & Chandrakasan, 2005), dynamic forward biasing schemes (Hwang & Roy, 2008), near zero threshold transistors (Burr, 1995), and body biasing (Hanson et al., 2008). The techniques, however, suffer from the drawbacks of high bias voltage generation, active variability compensation, or post-silicon tuning. Also, at lower supply voltage, the conventional CMOS digital circuits have degraded the transistor's active current to leakage current ratio (I_{ON}/I_{OFF}) due to its exponential dependence on power supply, V_{DD} as given by

$$\frac{I_{ON}}{I_{OFF}} = e^{(V_{DD}/\eta V_T)} \tag{1}$$

where η is the sub-threshold ideality factor, and V_T is the thermal voltage (Lotze & Manoli, 2012). The reduced I_{ON}/I_{OFF} ratio limits the supply voltage scaling in CMOS digital circuits as the output fails to attain nominal V_{DD} and GND voltage levels defined for the style. Additionally, the digital CMOS circuits become susceptible to noise and high leakage power (A. Wang & Chandrakasan, 2005). Thus, there is a need for a low-voltage logic style that maintains the optimum I_{ON}/I_{OFF} ratio and exhibits better noise immunity.

The Schmitt trigger (ST) logic style is an amenable solution that addresses the above-mentioned issues. A conventional ST logic gate exhibits leakage quenching effect and hysteresis that reduces the I_{OFF} and enhance the noise immunity in comparison CMOS logic gates (Beiu et al., 2015; Lotze & Manoli, 2012,2017). Further, different ST logic styles with enhanced performance have been proposed. The ST logic styles namely NMOS-only voltage booster ST style (Shah et al., 2018), voltage bootstrapping ST style (Gupta et al., 2021) lower switching current at the cost of degraded noise margin. Further, the conventional ST logic gate has been modified through the use of dynamic threshold MOS transistors (Kim & Kim, 2015; Kim et al., 2013), three inverters (Fernandes et al., 2021), variable threshold transistor (Kim & Kim, 2015; Park et al., 2016; Zhang et al., 2003) in ST style to improve noise immunity. However, the advantage is achieved at the cost of the increased value of I_{OFF}, and switching currents. Thus, it is clear that there does not exist a ST logic style that improves noise immunity with lower I_{OFF} values. Thus, in this work, a new ST logic that can simultaneously address both the issues is proposed. Following are the highlights:

(1) The proposed ST logic style introduces stacking of transistors to lower the leakage current.
(2) The proposed ST logic style employs variable threshold technique that increases the hysteresis width for enhanced noise tolerance without a significant increase in area requirement in comparison to the existing ST counterparts.

(3) Mathematical derivations to support the theoretical prepositions are put forward. The error between the predicted and simulated values are also reported.

The organisation of the rest of the paper is as follows: A brief introduction to the ST logic style is presented in section 2. The proposed stacked variable threshold CMOS (SVTCMOS) ST logic style is presented in section 3. Mathematical formulations related to the improvement in noise immunity and reduction in I_{OFF} value are also put forward. The performance of the proposed ST gates is compared with existing counterparts through simulations using 45 nm PTM CMOS technology parameters in section 4. Finally, the conclusions are drawn in section 5.

2. Schmitt trigger logic style

A conventional ST logic inverter shown in Figure 1(a) consists of a pull-up network (PUN) and a pull-down network (PDN) with its output being fed back through the feedback network (FBN) (Beiu et al., 2015; Lotze & Manoli, 2012, 2017). The transistors (P1, P2), (N1, N2) and (P3, N3) form the PUN, PDN and FBN respectively. For a low value of input V_{IN}, transistors (P1, P2) conduct such that the output node V_{OUT} is charged to a high-level V_{OH} (=V_{DD}). Alternatively, for a high value of input V_{IN},

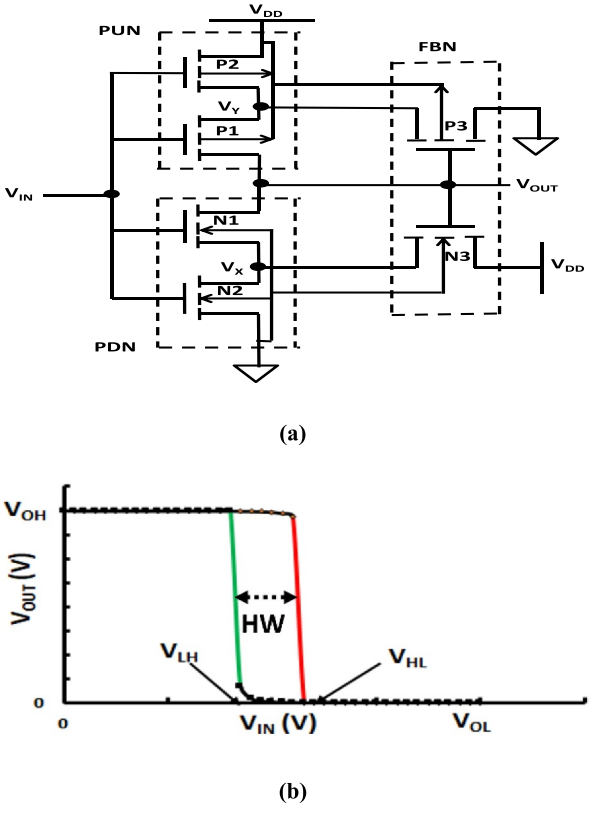


Figure 1. Conventional ST inverter (Lotze & Manoli, 2012) (a) schematic (b) voltage transfer curve.

transistors (N1, N2) conduct and V_{OUT} attains a low level V_{OL}(=GND). The presence of feedback in the ST inverter results in two different switching threshold voltages in contrast to a single threshold voltage of a CMOS inverter. The corresponding voltage transfer curve (VTC) is shown in Figure 1(b). When V_{IN} is increased from a low to a high voltage level, the input voltage at which the output makes a high-to-low transition is represented as V_{HL}. Similarly, when V_{IN} is decreased from a high to low voltage level, the input voltage at which the output makes a low-to-high transition is represented as V_{LH}. The difference between the V_{HL} and V_{LH} is evaluated as the hysteresis width ($V_{HW} = V_{HL}$- V_{LH}). This voltage window creates a buffer zone that prevents the circuit from switching states due to small or transient noise signals. The larger the hysteresis window, the better immune is the circuit to noise (Kim & Kim, 2015). Further, for a low input signal V_{IN}, transistor N3 conducts such that the source potential of transistor N1, V_X is increased. This high potential makes gate to source voltage of transistor N1 negative which results in an exponential decrease in the leakage current, I_{OFF}. Thus, ST logic gates exhibit hysteresis and have enhanced noise immunity in comparison to CMOS logic gates (Kim & Kim, 2015).

The authors in (Kim & Kim, 2015; Kim et al., 2013) have used the DTMOS technique in ST logic gates. A DTMOS ST inverter replaces normal transistors in a conventional ST inverter with DTMOS transistors as shown in Figure 2(a). This arrangement improves noise immunity and I_{ON}/I_{OFF} value at the cost of increased switching current that results from the lowered threshold voltage of the transistor through the DTMOS technique. Another ST logic gate design includes an NMOS-only ST voltage booster (NST-VB) ST logic circuit (Shah et al., 2018). The NST-VB inverter has PDN with transistors (N2, N3), and feedback transistor N5, while PUN has transistor N1 driven by a voltage booster circuit (N4, P1) as shown in Figure 2(b). The inverter has low switching current values at the cost of degraded noise immunity. The authors in (Gupta et al., 2021) suggested voltage bootstrapped ST (VB-ST) inverter design with transistors (N1, N2, N3), (N4, N5), and N6, forming the PUN, PDN and feedback transistor, respectively, as shown in Figure 2(c). The transistor N1 is diode connected to avail the advantage of voltage bootstrapping for performance improvement. The absence of feedback in the pull-up network lowers the hysteresis width, thereby significantly degrading the noise immunity of VB-ST gates. The three-inverter ST (3I-ST) gate design presented in (Fernandes et al., 2021) cascades three inverters (N1, P1), (N2, P2), and (N3, P3) as shown in Figure 2(d). It improves noise immunity at the cost of increased leakage current, switching current, and area of the design. Another style named low-swing ST style suggested in (Narawade et al., 2023) modifies the feedback network by adding two inverters (N5, P3) and (P5, N3) shown in Figure 2(e). The style has low voltage swing and reduces leakage current, switching current values at the cost of low noise immunity and large area of the design. Another ST logic style referred to as VTCMOS ST logic is based on a variable threshold technique (Kim & Kim, 2015; Park et al., 2016; Zhang et al., 2003). A VTCMOS ST buffer cascades two CMOS inverters ((I1: N1, P1), (I2: N2, P2)) in such a manner that inverter I2 controls the substrate of transistors in inverter I1 as shown in Figure 2(f). The switching threshold voltage of the transistors in I1 is varied by the output of the second inverter. This technique results in significantly improved noise-immune ST gates over the other existing ST gates but with increased I_{OFF} values. Thus, the existing ST logic styles improve noise margin at the cost of an increase in I_{OFF} value, and/or switching current values. Hence, in

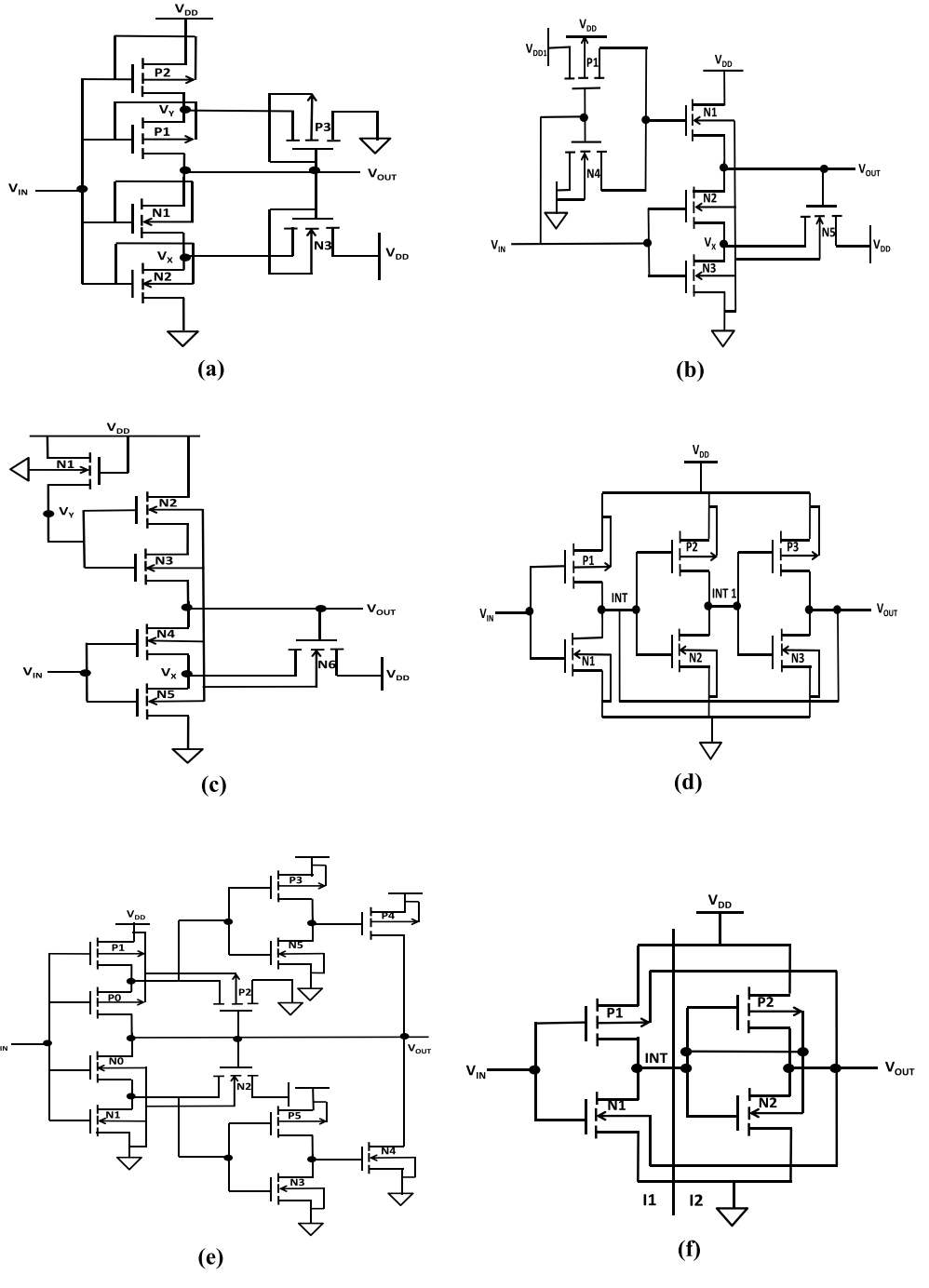


Figure 2. Inverter/Buffer in existing ST styles (a) DTMOS ST (Kim & Kim, 2015; Kim et al., 2013) (b) NST-VB (Shah et al., 2018) (c) VB-ST (Gupta et al., 2021) (d) 3I-ST (Fernandes et al., 2021) (e) low swing ST (Narawade et al., 2023). (f) VTCMOS ST (Park et al., 2016).

this work, a novel ST logic style with improved high noise margin, reduced $I_{OFF,}$ and switching current value is proposed.

3. Proposed stacked VTCMOS ST logic style

The proposed ST logic is derived from VTCMOS ST by introducing stacking of transistors in PDN of the first stage inverter. This arrangement enhances the noise immunity and lowers the leakage current (I_{OFF}) value. It is, thus, referred to as stacked variable threshold CMOS (SVTCMOS) ST logic. The schematic of the proposed SVTCMOS ST buffer with two inverters (SI1, SI2) is shown in Figure 3. The first inverter, SI1 has transistors (N1, N2) in PDN and transistor P1 forms PUN. This is followed by a second stage inverter, SI2 consisting of transistors N3, and P2. The output of SI2 is connected to the substrate terminal of transistors in SI1. For a low value of input voltage V_{IN}, the P1 turns ON that charges intermediate node INT to a high voltage level. This high voltage turns ON N3 such that the buffer attains a low output voltage level. Alternatively, for a high value of input voltage V_{IN}, both N1 and N2 conduct such that the node INT gets discharged to a low voltage level, and a high voltage level is obtained at the output of the proposed buffer.

The existing VTCMOS logic style has high leakage currents values (I_{OFF}) and thus suffers from degraded I_{ON}/I_{OFF} values. The proposed SVTCMOS logic style introduces stacking of transistors and integrates its advantages with the technique of variable threshold voltage for overall performance improvement. The stacking of transistors in the PDN of the proposed style increases the effective series resistance and leads to significant leakage current reduction. This arrangement is beneficial for applications where leakage power becomes a dominant concern (Deng et al., 2023). Additionally, the stacking along with variable threshold technique results in improved noise immunity due to increase in hysteresis width in comparison to the existing VTCMOS ST gates. This can be explained by considering a low to high transition at V_{IN} in the proposed SVTCMOS ST buffer. For the initial value of low voltage level at V_{IN}, the transistors N1, N2 maintain a zero substrate bias. However, substrate-source junction

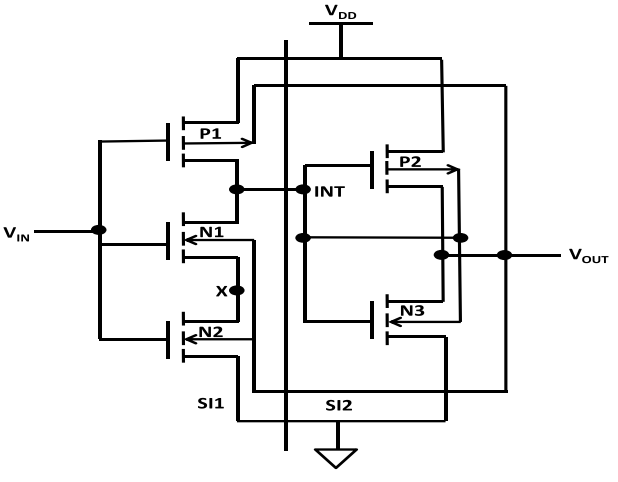


Figure 3. Schematic of the proposed SVTCMOS ST buffer.

of transistor P1 is forward biased, forcing the threshold voltage to drop such that transistor P1 continues to maintain a high logic level at the INT node. Also, the stacking of transistors in PDN increases the effective resistance and requires more current to discharge the INT node. Hence, V_{IN} has to go much higher to maintain the necessary current to discharge the node. Therefore, the presence of forward bias substrate effect in P1 along with stacking of transistors increases the V_{HL} in the proposed SVTCMOS ST buffer in comparison to the existing VTCMOS ST buffer. Thus, the proposed SVTCMOS ST buffer has high hysteresis width leading to enhanced noise immunity.

Additionally, the increased switching threshold voltage reduces the I_{OFF} values thereby improving the I_{ON}/I_{OFF} values for the proposed buffer topology. A mathematical model to support the theoretical prepositions is presented further.

3.1. Noise immunity improvement

The noise immunity is evaluated in terms of the hysteresis width (V_{HW}) computed as the difference between two switching threshold voltages, V_{HL} and V_{LH}. For the proposed SVTCMOS ST buffer at V_{HL}, the transistors N1 and P1 operate in saturation region with their substrate to source potential maintained at zero bias and forward bias respectively. The switching threshold voltage, V_{HL} is calculated by equating the saturation current through N1, P1. The saturation current through transistors N1, P1 (Kang et al., 2016) is expressed as:

$$I_{D,N1} = W_{N1} V_{SAT,N1} C_{OX} \frac{\left(V_{gs} - V_{th0,N1}\right)^2}{\left(V_{GS} - V_{th0,N1}\right) + E_{C,N1} L_{N1}} \tag{2a}$$

$$I_{D,P1} = W_{P1} V_{SAT,P1} C_{OX} \frac{\left(V_{SG} - \left|V_{th,P1}\right|\right)^2}{\left(V_{DD} - V_{IN} - \left|V_{th,P1}\right|\right) + E_{C,P1} L_{P1}} \tag{2b}$$

Where $W_{N1}, V_{SAT,N1}, E_{C,N1}, L_{N1}$ and $W_{P1}, V_{SAT,P1}, E_{C,P1}, L_{P1}$ represents the channel width, saturation velocity, critical electric field, and channel length of transistors N1 and P1 respectively. The voltage $V_{th0,N1}$ represents the zero substrate bias threshold voltage of transistor N1, $V_{th,P1}$ is the forward substrate bias threshold voltage of transistor P1 and V_{X1} is the source potential of transistor N1.

The two current equations can be equated as:

$$I_{D,N1} = I_{D,P1} \tag{2}$$

$$W_{n1} V_{SAT,N1} C_{OX} \frac{\left(V_{HL} - V_{X1} - V_{th0,N1}\right)^2}{\left(V_{GS} - V_{th0,N1}\right) + E_{C,N1} L_{N1}} = W_{P1} V_{SAT,P1} C_{OX} \frac{\left(V_{DD} - V_{HL} - \left|V_{th,P1}\right|\right)^2}{\left(V_{DD} - V_{IN} - \left|V_{th,P1}\right|\right) + E_{C,P1} L_{P1}} \tag{3}$$

By solving Eq. (3), V_{HL} can be expressed as:

$$V_{HL} = \frac{(V_{DD} - |V_{th,P1}|)R\sqrt{\frac{V_{SAT,P1}E_{C,N1}}{V_{SAT,N1}E_{C,P1}}} + V_{X1} + V_{th0,N1}}{1 + R\sqrt{\frac{V_{SAT,P1}E_{C,N1}}{V_{SAT,N1}E_{C,P1}}}} \tag{4}$$

where $R = \sqrt{\frac{W_{P1}}{W_{N1}}}$.

Similarly, the lower switching threshold voltage (V_{LH}) is determined during high to low transition in V_{IN}. At V_{LH}, the transistors N1 and P1 operate in saturation region with their substrate potential maintained at forward bias and zero bias respectively. By following the above method, the lower switching threshold V_{LH} is computed as:

$$V_{LH} = \frac{(V_{DD} - |V_{th0,P1}|)R\sqrt{\frac{V_{SAT,P1}E_{C,N1}}{V_{SAT,N1}E_{C,P1}}} + V_{X2} + V_{th,N1}}{1 + R\sqrt{\frac{V_{SAT,P1}E_{C,N1}}{V_{SAT,N1}E_{C,P1}}}} \tag{5}$$

where $V_{th0,P1}$ is zero substrate bias threshold voltage of transistor P1, $V_{th,N1}$ is the forward substrate bias threshold voltage of transistor N1, and V_{X2} is the source potential of transistor N1.

By using Eq. (4) and (5), the hysteresis width of the proposed SVTCMOS ST buffer ($V_{HW_SVTCMOS}$) is computed as:

$$\begin{aligned} V_{HW_SVTCMOS} &= V_{HL} - V_{LH} \\ &= \frac{(|V_{th0,P1}| - |V_{th,P1}|)R\sqrt{\frac{V_{SAT,P1}E_{C,N1}}{V_{SAT,N1}E_{C,P1}}} + (V_{X1} - V_{X2}) + (V_{th0,N1} - V_{th,N1})}{1 + R\sqrt{\frac{V_{SAT,P1}E_{C,N1}}{V_{SAT,N1}E_{C,P1}}}} \end{aligned} \tag{6}$$

$$V_{HW_SVTCMOS} = V_{HL} - V_{LH} = \frac{(V_{th0,P1} - V_{th,P1})R\sqrt{\frac{V_{SAT,P1}E_{C,N1}}{V_{SAT,N1}E_{C,P1}}} + (V_{th0,N1} - V_{th,N1})}{1 + R\sqrt{\frac{V_{SAT,P1}E_{C,N1}}{V_{SAT,N1}E_{C,P1}}}} \tag{7}$$

The accuracy of the above model is validated through SPICE simulations of the proposed SVTCMOS ST buffer with a power supply of 0.4 V and value of R ranging from 1.4 to 2.4. The plots of the simulated and predicted values of hysteresis width, $V_{HW_SVTCMOS}$ is shown

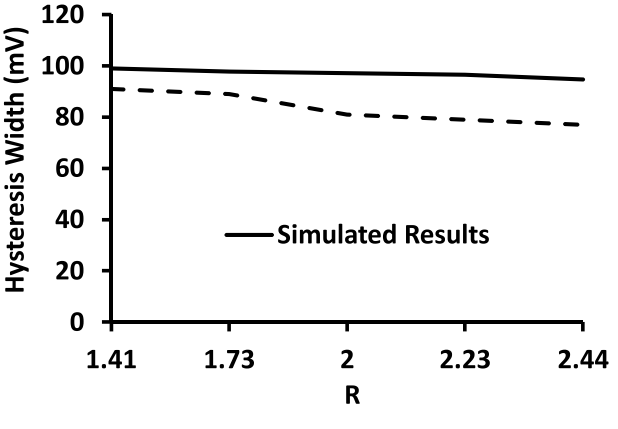


Figure 4. Simulated vs predicted values of a hysteresis width, $V_{HW_SVTCMOS}$ for the proposed SVTCMOS ST buffer.

in Figure 4. A maximum error of 18% is observed for hysteresis width. It is found that there is a close agreement between the simulated and the predicted values of the parameters for all the operating conditions.

Analogously, the hysteresis width (V_{HW_VTCMOS}) for the existing VTCMOS ST buffer is expressed as equation 7.

The comparison of Eq. (6) and (7) reveals that the hysteresis width of proposed SVTCMOS ST buffer ($V_{HW_SVTCMOS}$) is enhanced by $(V_{X1} - V_{X2})/\left(1 + R\sqrt{\frac{V_{SAT,P1}E_{C,N1}}{V_{SAT,N1}E_{C,P1}}}\right)$ over hysteresis width of VTCMOS ST buffer (V_{HW_VTCMOS}). The results validate the improvement in hysteresis through the proposed SVTCMOS ST buffer.

3.2. Reduction in leakage current (I_{OFF})

The design of the proposed SVTCMOS ST buffer employs stacking of transistors. The effect of this modification is analysed to determine the leakage current through N1 represented as ($I_{OFF,SVTCMOS_N1}$) for the case when it is driven by low value of input voltage V_{IN}. As N1 is OFF, the leakage current $I_{OFF,SVTCMOS_N1}$ is the subthreshold drain current equation [19] and is given as:

$$I_{OFF,SVTCMOS_N1} = I_0 \exp\left(\frac{V_{GS} - V_{th} - \eta V_{DS}}{nV_T}\right)\left(1 - \exp\left(\frac{-V_{DS}}{V_T}\right)\right) \tag{8}$$

where I_0 is a constant dependent on W/L of transistor, V_{th} is threshold voltage, η is drain induced barrier lowering coefficient, n is sub-threshold ideality factor, and V_T is the thermal voltage. By substituting $V_{GS_N1} = -V_X$, $V_{DS_N1} = V_{DD} - V_X$, $V_{GS_N2} = 0$, $V_{DS_N2} = V_X$ and neglecting η for the sake of simplification in the above equation, the leakage current through transistors N1 ($I_{OFF,SVTCMOS_N1}$) and N2 ($I_{OFF,\ SVTCMOS_N2}$) can be expressed as:

$$I_{OFF,SVTCMOS_N1} = I_0 \exp\left(\frac{-(V_X + V_{th})}{nV_T}\right)\left(1 - \exp\left(\frac{-(V_{DD} - V_X)}{V_T}\right)\right) \tag{8a}$$

$$I_{OFF,SVTCMOS_N2} = I_{0,N2} \exp\left(\frac{-V_{th}}{nV_T}\right)\left(1 - \exp\left(\frac{-V_X}{V_T}\right)\right) \tag{8b}$$

Further, the node voltage V_X is determined by equating the current flowing through stacked transistors N1 and N2 in the proposed SVTCMOS ST buffer.

$$I_{OFF,SVTCMOS_N1} = I_{OFF,SVTCMOS_N2}$$

$$I_{0,N1} \exp\left(\frac{-(V_X + V_{th})}{nV_T}\right)\left(1 - \exp\left(\frac{-(V_{DD} - V_X)}{V_T}\right)\right) = I_{0,N2} \exp\left(\frac{-V_{th}}{nV_T}\right)\left(1 - \exp\left(\frac{-V_X}{V_T}\right)\right) \tag{9}$$

where $I_{0,\ N1}$ and $I_{0,\ N2}$ are constant dependent on the aspect ratio of N1 and N2 respectively. The node voltage V_X by considering $n \approx 1$ can be approximated:

From Eq. (9),

$$V_X = V_T \ln\left(\frac{I_{0,N1} \exp\frac{V_{DD}}{V_T} + I_{0,N2} \exp\frac{V_{DD}}{V_T}}{I_{0,N2} \exp\frac{V_{DD}}{V_T} + I_{0,N1}}\right) \tag{10}$$

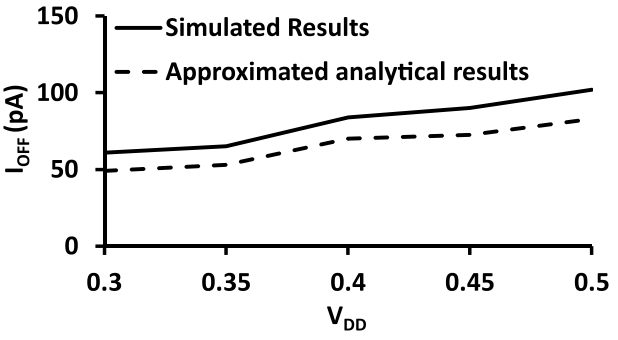


Figure 5. Simulated vs analytical results for the I_{OFF} values of the SVTCMOS ST logic.

The accuracy of the above model is validated through SPICE simulations of the proposed SVTCMOS ST buffer with a power supply V_{DD} ranging from .3 V to .5 V. The plots of the simulated and predicted values of $I_{OFF,SVTCMOS_N1}$ is shown in Figure 5. A maximum error of 19% is observed which indicates a close agreement between the simulated and the predicted values for all the operating conditions. Similarly, for the existing VTCMOS ST buffer Figure 2(f), the leakage current through transistor N1 ($I_{OFF,\ VTCMOS_N1}$) with $V_{GS} = 0$, V_{DS}=V_{DD} can be expressed as:

$$I_{OFF,VTCMOS_N1} = I_0 \exp\left(\frac{-V_{th}}{nV_T}\right)\left(1 - \exp\left(\frac{-V_{DD}}{V_T}\right)\right) \tag{11}$$

Thus, the ratio of leakage currents in the existing and proposed ST buffers can be written as:

$$\frac{I_{OFF,VTCMOS_N1}}{I_{OFF,SVTCMOS_N1}} = \frac{\left(\exp\left(\frac{V_{DD}}{V_T}\right) - 1\right)\left(\exp\frac{V_X}{nV_T}\right)}{\exp\left(\frac{V_{DD}}{V_T}\right) - \exp\left(\frac{V_X}{V_T}\right)} \tag{12}$$

By substituting the value of V_X from Eq. (10) in Eq. (12), the ratio of leakage current can be approximated as:

$$\frac{I_{OFF,VTCMOS_N1}}{I_{OFF,SVTCMOS_N1}} \approx 1 + \frac{I_{0,N1}}{I_{0,N2}} \tag{13}$$

$$I_{OFF,SVTCMOS_N1} \approx \frac{I_{OFF,VTCMOS_N1}}{1 + \frac{I_{0,N1}}{I_{0,N2}}} \tag{14}$$

The above equation clearly indicates that the proposed SVTCMOS ST buffer has reduced leakage current as compared to the existing VTCMOS ST buffer. The leakage current reduction in the proposed ST buffer depends on W/L ratio of transistors N1 and N2 which in turn relies on the $I_{0,\ N1}/I_{0,\ N2}$.

3.3. Proposed two-input SVTCMOS ST gates

The scheme for realising two input gates in the proposed SVTCMOS ST logic style requires replacing the transistors (N1, N2) and P1 in the proposed SVTCMOS ST buffer with their

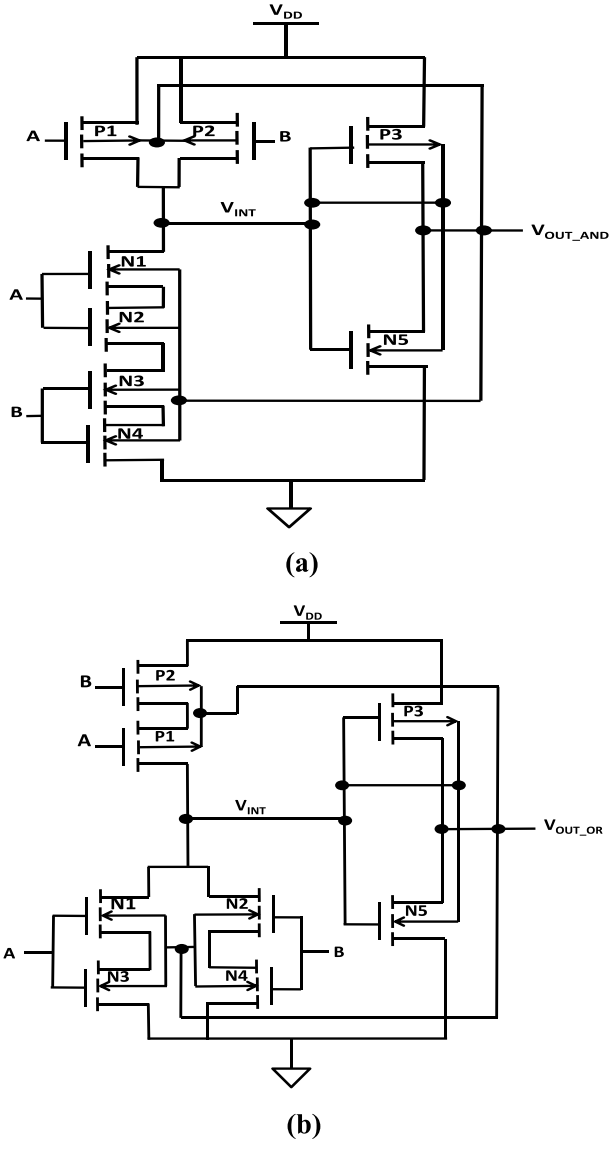


Figure 6. Proposed SVTCMOS ST gates (a) AND/NAND (b) OR/NOR.

corresponding PDN and PUN. The schematics of the proposed SVTCMOS ST based AND/NAND and OR/NOR logic gates are presented in Figure 6. The inverted functionalities such as NAND and NOR gates can be obtained from the same circuit by utilising output from the V_{INT} node. In the proposed SVTCMOS AND gate (Figure 6(a)), the inputs A and B drive the series-connected transistor pairs (N1, N2) and (N3, N4) in the PDN, respectively, while they drive two parallel transistors (P1, P2) in the PUN. The second stage controls the substrate of the first stage as in the proposed SVTCMOS ST buffer. The modelling of the proposed SVTCMOS AND gate can be done by analysing the change in the output node due to a transition in one or both the inputs. The case of single input transition can be analysed in a manner similar to the SVTCMOS ST buffer. However, if the change in output

occurs due to transition in both the inputs, then in this condition, the four transistors in series can be replaced by two transistors with doubled channel length, and the two transistors in parallel can be replaced by a single transistor having twice the channel width. Thus, the effective value of R' for proposed SVTCMOS ST AND gate with $W_N^{'} = \frac{W_{N1}}{2}$ and $W_P^{'} = 2W_{P1}$ can be computed as:

$$R' = \sqrt{\frac{W_P^{'}}{W_N^{'}}} = \sqrt{\frac{4W_{P1}}{W_{N1}}} = 2R \tag{15}$$

In the case of the proposed SVTCMOS ST OR gate Figure 6(b), the inputs A and B drive the parallel connected transistors (N1, N2) and (N3, N4), respectively, while they drive two series transistors (P1, P2) in the PUN. The second stage controls the substrate of first stage as in proposed SVTCMOS ST buffer. The two parallel NMOS transistors in proposed SVTCMOS OR gate can be replaced by single transistor having doubled channel width and two PMOS transistors in series can be replaced by single transistor having doubled channel length. The effective value of R'' for proposed SVTCMOS ST OR gate with $W_N^{''} = 2W_{N1}$ and $W_P^{''} = \frac{W_{P1}}{2}$ can be computed as:

$$R'' = \sqrt{\frac{W_P''}{W_N''}} = \sqrt{\frac{W_{P1}}{4W_{N1}}} = \frac{R}{2} \tag{16}$$

4. Simulation results

In this section, the performance of the proposed SVTCMOS ST gates is compared with their counterparts designed using conventional ST and other existing ST logic styles, namely DTMOS ST, NST VB, VB ST, 3I-ST, low swing ST, and VTCMOS ST gates. The performance parameters such as V_{HL}, V_{LH}, hysteresis width (V_{HW}), I_{OFF}, switching current, delay, power delay product (PDP), and area are considered. For conventional ST and DTMOS ST, NST-VB, VB-ST, 3I-ST, and low swing ST gates, a dynamic threshold inverter is connected at the output for logical equivalence with VTCMOS ST and SVTCMOS ST styles (Kim & Kim, 2015). The W/L ratio of the transistors taken in the simulation of buffers is listed in Table 1. All the buffers are simulated in LTspice using 45 nm PTM CMOS technology parameters with supply voltage and load capacitance of 0.4 V and 100 fF respectively. The effect of process variation at different corners, and power supply on the performance of all the buffers is also studied. The simulation results at different process

Table 1. W/L ratio of the different transistors in ST buffers.

Transistors ST styles	W/L of NMOS transistors	W/L of PMOS transistors
Conventional ST Lotze & Manoli (2012)	N1=2, N2=4, N3=2	P1=8, P2=8, P3=3
DTMOS ST Kim & Kim (2015)	N1=2, N2=4, N3=2	P1=8, P2=8, P3=3
NST-VB Shah et al. (2018)	N1=2,N2=2,N3=4,N4=2,N5=2	P1=8
VB-ST Gupta et al. (2021)	N1=2, N2=2, N3=10, N4=2, N5=4, N6=2	-
3I-ST Fernandes et al. (2021)	N1=2, N2=2, N3=2	P1=8, P2 = 8, P3= 8
Low swing Narawade et al. (2023)	N0=2, N1=4, N2=2, N3=2, N4=2,	P0=8, P1=8, P2=2, P3=8, P4=8, P5=8
VTCMOS ST Park et al. (2016)	N1=2, N2=2	P1=2, P2=1.4
Proposed SVTCMOS	N1=2, N2=1, N3=2	P1=8, P2=1.4

Table 2. Performance comparisons of ST buffers at different process corners.

	Style							
	Typical Corner							
Performance parameters	Conventional ST Lotze & Manoli (2012)	DTMOS ST Kim & Kim (2015)	NST-VB ST Shah et al. (2018)	VB-ST Gupta et al. (2021)	3I-ST Fernandes et al. (2021)	Low-swing ST Narawade et al. (2023)	VTCMOS ST Park et al. (2016)	Proposed SVTCMOS ST
V_{LH}(mV)	176.59	175.84	253.82	188.53	72	209.7	157.47	186.69
V_{HL}(mV)	213.95	223.61	254.14	188.50	346.10	220.6	250.25	285.83
V_{HW} (mV)	37.36	47.77	.32	.03	274.10	10.9	92.78	99.14
I_{OFF}(pA)	11	5.5	8	5.27	688	5.7	637.66	84
Switching current (uA)	1.22	7.32	1.23	.538	3.174	1.24	4.65	1.66
Delay(ns)	24.16	8.08	11.95	2.035	15.02	14.45	9.87	24.13
PDP(10^{-15}J)	11.79	23.65	5.87	.438	19.06	7.16	18.35	16.02
Area (um^2)	2.78	2.74	2.04	2.16	3.08	14	1.56	1.785
	Fast corner							
V_{LH}(mV)	179.65	175.79	251.89	198.1	82.75	201.2	176.52	205.73
V_{HL}(mV)	223.24	223.88	252.51	198.6	337.42	237.26	248.00	285.78
V_{HW} (mV)	43.59	78.09	0.62	.5	254.67	36.06	71.48	80.05
I_{OFF}(pA)	2.20	6.8	8.5	2.57	2000	6.9	2300	190
Switching current (uA)	2.59	10.78	2.6	1.4	6.09	2.63	8.01	2.84
Delay(ns)	12.69	6.30	6.36	1.42	8.99	6.61	6.14	12.71
	Slow corner							
V_{LH}(mV)	185.98	176.11	255.01	179.9	52.54	197.4	147.5	176.87
V_{HL}(mV)	204.14	214.01	255.09	180.3	346.17	198.7	250.98	286.32
V_{HW} (mV)	18.16	37.9	.07	.04	293.63	1.3	103.48	109.45
I_{OFF}(pA)	3.93	2.25	9.03	1.5	222	4.37	224.11	69.33
Switching current (uA)	0.580	4.79	.585	.233	1.3	.585	3.09	1.18
Delay(ns)	49.5	10.81	22.55	7.285	35.31	32.51	18.96	48

corners are summarised in Table 2. The results at 32 nm technology node are also listed in Table 3.

Following observations can be drawn from the simulation results at typical design corner.

- Noise immunity and leakage current analysis: The noise immunity of ST buffers is analysed in terms of their respective hysteresis width (V_{HW}) calculated as the difference between two switching threshold voltages V_{LH} and V_{HL}. It can be observed that DTMOS ST buffer has better V_{HW} than conventional ST buffer due to dynamic threshold technique that results in higher V_{HL} value and lower V_{LH} value in comparison to conventional ST buffer. The NST-VB and VB-ST buffers have poor V_{HW} because of the absence of a feedback network in the PUN. The VTCMOS ST buffer has improved V_{HW} over DTMOS ST, NST-VB, VB-ST, and low swing ST buffers as the turn-ON voltage of each transistor at zero body bias is greater than normal transistor in other buffers. Further, the proposed SVTCMOS ST buffer obtained maximum V_{HW} improvement of 165%, 107% and 7% over conventional ST, DTMOS ST and VTCMOS ST, respectively, except for 3I ST buffer. Additionally, the noise immunity is also investigated by the noise spectral density curve shown in Figure 7. The noise spectral density of the proposed SVTCMOS ST buffer is the lowest among all the existing buffers except for the 3I-ST buffer for the entire frequency range indicating that the

Table 3. Performance comparisons of ST buffers at 32 nm technology node.

	Style							
	32nm							
Performance parameters	Conventional ST Lotze & Manoli (2012)	D DTMOS ST Kim & Kim (2015)	NST-VB ST Shah et al. (2018)	VB-ST Gupta et al. (2021)	3I-ST Fernandes et al. (2021)	Low-swing ST Narawade et al. (2023)	VTCMOS ST Park et al. (2016)	Proposed SVTCMOS ST
V_{HL}(mV)	214.10	213.94	194.4	201.5	333.48	235	239.8	280.6
V_{HW} (mV)	27.99	28.6	0.3	7.4	249.52	4.1	53.5	57.3
I_{OFF}(pA)	15	6.85	12	10.59	808.2	6.82	813.3	94
Switching current (uA)	0.81	3.30	0.77	0.78	2.50	0.83	2.36	0.88
Delay(ns)	32	11.72	13.2	3.2	16	14.3	11.33	35

proposed logic provides ST gate with highest noise immunity. Further, the proposed SVTCMOS ST buffer significantly reduces I_{OFF} value by 88% and 87% compared to the existing 3I-ST and VTCMOS ST buffers respectively. By considering improvements in V_{HW} simultaneously, it can be stated that the proposed SVTCMOS ST buffer provides an improved noise margin with reduced I_{OFF} values. The other existing conventional, DTMOS, NST-VB, VB-ST, and low swing ST buffers though have reduced I_{OFF} value but fail to provide high noise immunity and hence are not preferred in logic gate design.

- Switching current and delay analysis: The DTMOS ST buffer has the highest switching current consumption as it employs a current feedback path to enhance noise immunity. The proposed SVTCMOS ST buffer in contrast shows switching current reduction of 77%, 48% and 64% as compared to DTMOS ST, 3I-ST, and VTCMOS ST buffers, respectively, whereas it is comparable with conventional ST, NST-VB, and low swing ST buffers except for VB-ST buffer. The stacking of transistors reduces the I_{OFF} values in the proposed SVTCMOS ST buffer by increasing the turn on voltage of each transistor at zero bias condition. The proposed SVTCMOS ST buffer has a comparable delay with conventional ST buffer except for DTMOS ST, NST-VB ST, VB-ST, 3I-ST, and low swing ST, VTCMOS ST buffers. Further, the proposed SVTCMOS ST buffer show a decrease in PDP value by 32%, 20% and 12.6% in comparison to DTMOS ST, 3I-ST

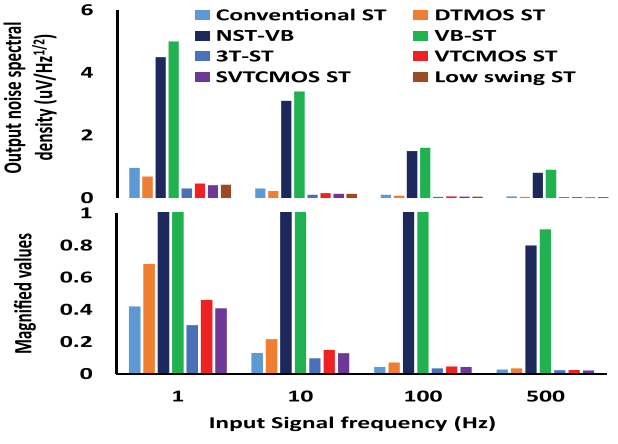


Figure 7. Output noise spectral density at different frequencies.

and VTCMOS ST buffers as listed in Table 2. The remaining buffers has better PDP values than the proposed SVTCMOS ST buffer at the cost of hysteresis width, leakage current and switching current. In addition, the switching current and delay of the proposed SVTCMOS ST buffer are compared due to variations in the W/L ratio of transistor N2 as shown in Figure 8. The decreasing trend of the W/L ratio shows a reduction in switching current and an increase in delay due to decreased switching current values.

- Area comparison: The layout of all the buffers are drawn on MICROWIND and the occupied area is mentioned under Typical design in Table 2. The layout of VTCMOS ST and SVTCMOS ST buffers is shown in Figure 9. The area of other buffers are not shown for the sake of compactness. It is observed that the proposed SVTCMOS ST buffer consumes the least area, except for the VTCMOS ST buffer.
- Effect of variations: The effect of process variation at different corners, and power supply on the performance of all the buffers is studied. It is observed that all the buffers exhibit correct functionality at all design corners and their corresponding voltage transfer characteristics (VTC) are shown in Figure 10. Like typical corner, the same trend in improvement for hysteresis width is noticed at fast and slow corners except for VTCMOS ST buffer (fast corner) from Table 2. The worst and best possible case at a fast corner is observed for DTMOS ST buffer and conventional ST buffer respectively, whereas at a slow corner, they are spotted for conventional ST buffer and SVTCMOS ST buffer respectively. The effect of process variation at fast and slow corners on I_{OFF} and switching current is maximum for conventional ST buffer whereas it is minimum for SVTCMOS ST buffer. As far as delay is concerned, the effect of process variation at fast and slow corners is maximum for conventional ST buffer and minimum for DTMOS ST buffer. Moreover, the ST buffer has lower delay at fast corner and higher delay at slow corner in comparison with the typical corner. The high speed benefit at fast corner results from the lowering of threshold voltage of NMOS and PMOS transistors. Similarly, the high-threshold voltage of NMOS and PMOS transistors at slow corner shows low speed. The simulation results, as shown in the Table 2 clearly reflect this trend. In the case of slow corner, the delay of the conventional ST, DTMOS ST, NST-VB ST, VB-ST, 3I-ST, low swing ST, VTCMOS ST and

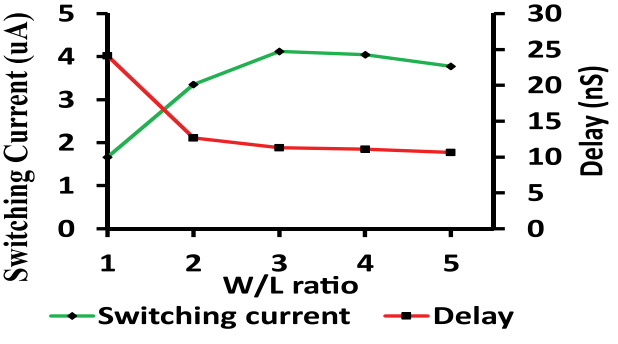


Figure 8. Effect of change in W/L ratio of the transistor (N2) on switching current and delay in proposed SVTCMOS ST buffer.

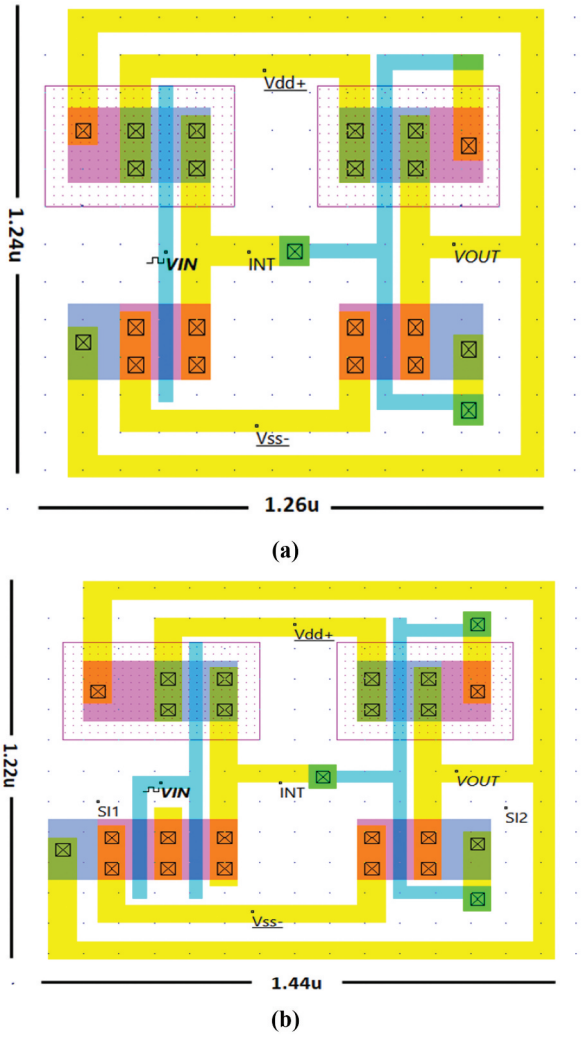


Figure 9. Layout of ST buffers (a) VTCMOS (b) SVTCMOS.

proposed SVTCMOS ST buffers increase by 47%, 22%, 46%, 30%, 40%, 54%, 38% and 47% respectively in comparison to typical corner while the corresponding percentage decrease of 104%, 34%, 88.7%, 257%, 135%, 124%, 92% and 98% is observed at fast corner.

- Performance comparison of ST buffers at 32 nm technology node: The performance of the ST buffers by using 32nm PTM technology parameters in LTspice is listed in Table 3. The proposed SVTCMOS ST buffer show maximum V_{HW} improvement of 104%, 100%, and 7% over conventional ST, DTMOS ST and VTCMOS ST, respectively, except for 3I ST buffer. Further, the proposed SVTCMOS ST buffer achieves significant I_{OFF} reduction by 88% and 88.4% in comparison to the existing 3I-ST and VTCMOS ST buffers respectively. The proposed SVTCMOS ST buffer shows switching current reduction of 73%, 64% and 62% as compared to DTMOS ST, 3I-ST and VTCMOS ST

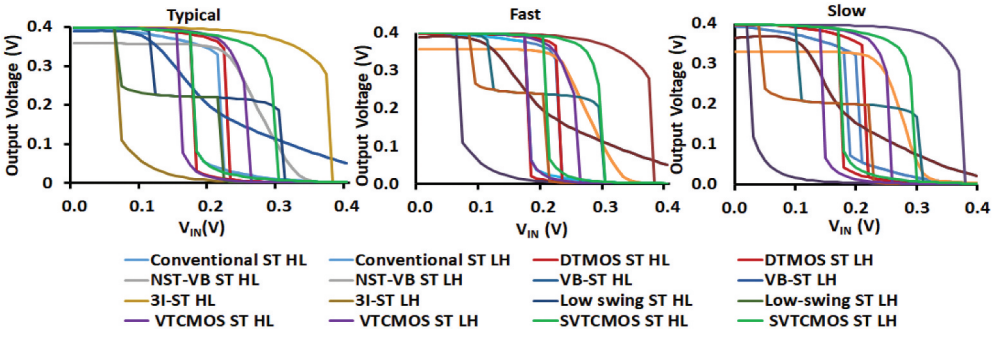


Figure 10. VTC of ST buffers at different process corners.

buffers, respectively, whereas it is comparable with conventional ST, NST-VB, and low swing ST buffers except for VB-ST buffer. The proposed SVTCMOS ST buffer has increased delay values in comparison to DTMOS ST, NST-VB ST, VB-ST, 3I-ST and low swing ST, VTCMOS ST buffers. The performance trends observed are consistent with those obtained using the 45nm technology.

- A chain of multiple ST buffers having 1, 10, 15, 50 and 100 stages is simulated, and the values obtained are listed in Table 4. The switching current is measured at different buffer stages. The results show that the proposed SVTCMOS ST buffer has a lower switching current as compared to the existing VTCMOS ST buffer. However, the rate of increase in switching current is slightly higher than that of the VTCMOS ST buffer due to increased internode capacitance. It is observed that the proposed SVTCMOS ST buffer decreases switching current by 64%, 52%, 49%, 46% and 43% in comparison to VTCMOS ST buffer chain of 1, 10, 15, 50 and 100 numbers of buffer.
- Furthermore, the effect of supply voltage variation on V_{HW}, I_{OFF}, switching current, and delay is shown in Figure 11. The original graph shown for V_{HW} and I_{OFF} in Figure 11(a) have been magnified for the sake of clear visibility. Overall, it is observed that there is a decrease in hysteresis width, I_{OFF} and switching current, and increase in delay with decrease in supply voltages.

- The post-layout simulations are performed on the VTCMOS and proposed SVTCMOS ST buffers. The post-layout simulation results are listed in Table 5. It is observed that the hysteresis width, V_{HW} (mV) remain same while other parameters differ due to the increase in parasitic capacitances after layout. It is noticed that the I_{OFF}, switching current, delay and PDP of proposed SVTCMOS ST buffer increase by 4.5%, 5.7%, 6% and 11% respectively. Also, the comparison of post-layout simulation results of VTCMOS and

Table 4. Switching current (uA) at different no. of buffers.

	No. of buffers (N)				
Style	$N = 1$	$N = 10$	$N = 15$	$N = 50$	$N = 100$
VTCMOS ST	4.65	49.4	63	196.6	371.05
SVTCMOS ST	1.66	23.5	32	104.5	211.5

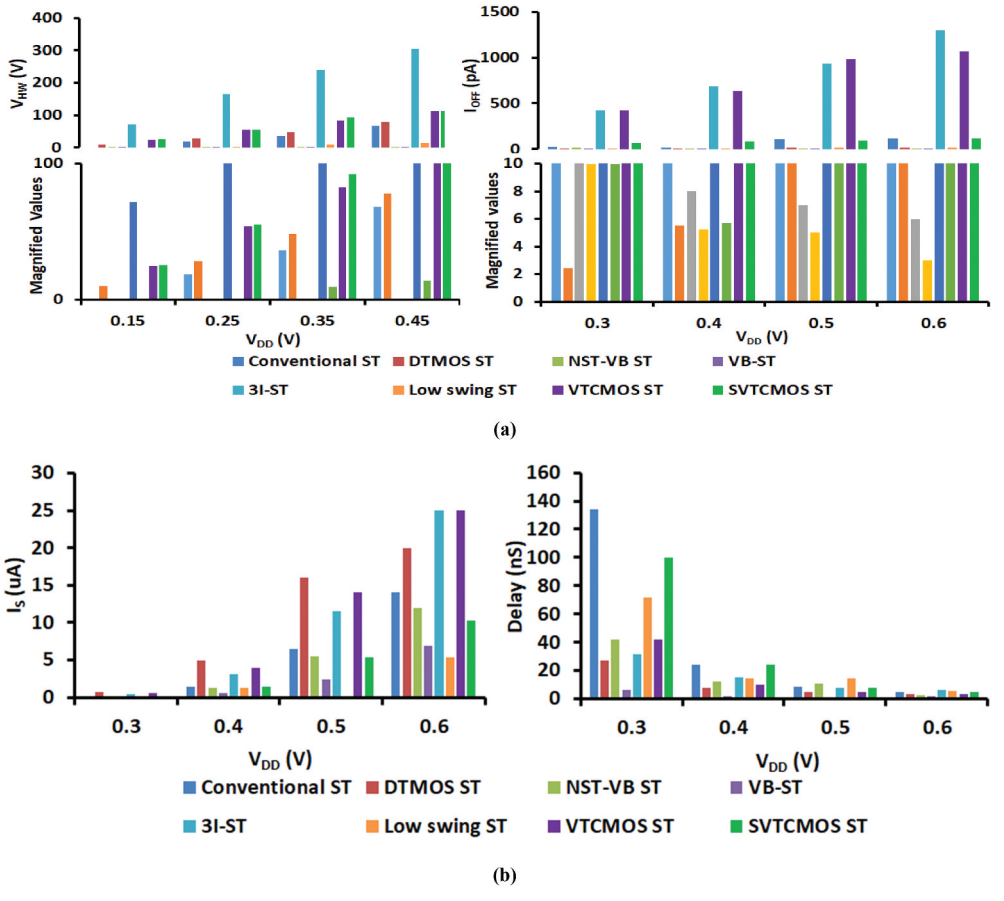


Figure 11. Performance measurements with respect to variations in supply voltage (a) hysteresis width and I_{OFF} (b) switching current and delay.

proposed SVTCMOS ST buffers indicates the same performance trend as observed in pre-layout simulations.

- Performance comparison of basic gates: The OR and AND functionality are realised in existing VTCMOS and proposed SVTCMOS ST style and the simulation results at different corners are summarised in Table 6. It is observed that a reduction of 50% in I_{OFF} value is obtained in the proposed SVTCMOS ST OR gate at the cost of 7% increase in delay, while the other parameter V_{HW} and switching current remain comparable with VTCMOS OR gate. Further, the V_{HW} of proposed SVTCMOS ST OR gate exhibits less process variation than VTCMOS ST OR gate at typical and fast

Table 5. Post-layout results of the ST buffers.

	Performance parameters				
Style	V_{HW} (mV)	I_{OFF} (pA)	Switching current (uA)	Delay(ns)	PDP (10^{-15}J)
VTCMOS ST	92.78	669.5	4.90	10.43	20.44
SVTCMOS ST	99.14	87.78	1.76	25.57	18.00

Table 6. Performance comparisons of logic gates at different process corners.

	Style (ST OR)					
	Typical		Fast		Slow	
Performance parameters	VTCMOS	SVTCMOS	VTCMOS	SVTCMOS	VTCMOS	SVTCMOS
V_{LH}(mV)	187.07	195.88	206.02	205.91	177.06	177.31
V_{HL}(mV)	280.13	286.72	278.08	286.39	280.78	287.39
HW(mV)	93.13	90.84	72.06	80.48	103.72	110.08
I_{OFF}(pA)	281.44	141	1000	365	98	107
I_S(uA)	1.85	1.98	2.73	2.96	1.14	1.15
Delay(nS)	12.89	13.85	7.4	7.95	24.88	25.99
			Style (ST AND)			
V_{LH}(mV)	128	128.22	138.07	138.34	118.12	118.41
V_{HL}(mV)	220.75	222.49	212.07	222.15	221.45	230.03
HW(mV)	92.75	94.27	74	84	103.33	111.62
I_{OFF}(pA)	291.76	594	774.67	749	191.15	637
I_S(uA)	4.85	3.77	7.93	6.51	3.19	1.972
Delay(nS)	11.13	11.83	6.82	7.065	20.90	22.30

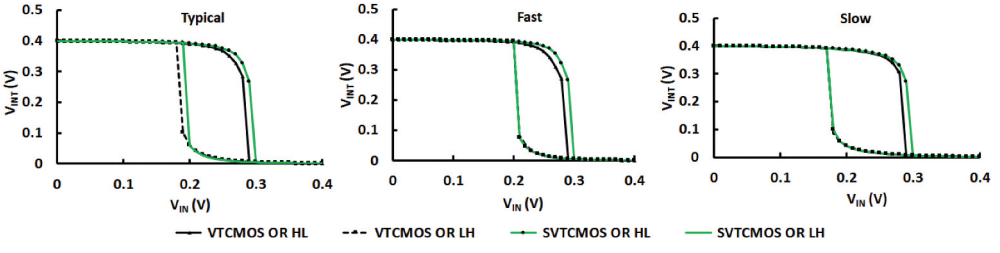


Figure 12. Voltage transfer curve at different process corners for VTCMOS and proposed SVTCMOS ST or gates.

corners. The VTC at different process corners for ST OR gates is shown in Figure 12. Also, the I_{OFF} of the proposed SVTCMOS ST OR gate has less process variation than VTCMOS ST OR gate with comparable switching current and delay variation. A similar result analysis is confirmed for AND gate for the results listed in Table 6. Hence, it is verified that the proposed SVTCMOS ST style leads to the design of low leakage ST gates with high noise immunity with lesser variations.

5. Conclusion

In this paper, a low leakage stacked variable threshold CMOS (SVTCMOS) ST logic style for energy constrained applications is proposed. The proposed style integrates variable threshold technique with stacking of transistors to reducing leakage current and enhance the noise immunity. Mathematical derivations express the reduction in leakage current and enhancement in hysteresis width with reference to variable threshold CMOS ST style is developed. Simulations using LTspice are performed at 45 nm PTM CMOS technology node for different logic gates. It is observed that the proposed SVTCMOS ST buffer shows a reduction of 87% and 64% in leakage current and switching current, respectively, along

with an increase of 7% in hysteresis width with respect to the existing VTCMOS ST buffer. The process corner analysis and Monte Carlo simulation results indicate more robustness towards variation in comparison to existing ST logic counterparts.

Disclosure statement

No potential conflict of interest was reported by the author(s).

ORCID

Bhawanand Jha http://orcid.org/0009-0003-6219-5878
Kirti Gupta http://orcid.org/0000-0003-0565-0654
Rajeshwari Pandey http://orcid.org/0000-0002-7539-7888

Data availability statement

The data that support the findings of this study are available on request from the corresponding author. The data are not publicly available due to privacy or ethical restrictions.

References

Beiu, V., Ibrahim, W., Tache, M., & Kharbash, F. (2015). When one should consider Schmitt trigger gates. In *15th International Conference on Nanotechnology (IEEE-NANO)*, Rome, Italy. https://doi.org/10.1109/NANO.2015.7388698

Bleitner, A., Goeppert, J., Lotze, N., Keller, M., & Manoli, Y. (2018). Comparison and optimization of the minimum supply voltage of Schmitt trigger gates versus CMOS gates under process variations. In *16th GMM/ITG-Symposium*, Munich/Neubiberg, Germany (pp. 1–6).

Bol, D., Ambroise, R., Flandre, D., & Legat, J. (2009). Interests and limitations of technology scaling for subthreshold logic. *IEEE Transactions on Very Large Scale Integration (VLSI) Systems*, *17*(10), 1508–1519. https://doi.org/10.1109/TVLSI.2008.2005413

Burr, J. B. (1995). Cryogenic ultra low power CMOS. In *1995 IEEE Symposium on Low Power Electronics*, San Jose, CA, USA (p. 8). https://doi.org/10.1109/LPE.1995.482473

Chen, G., Ghaed, H., Haque, R.-U., Wieckowski, M., Kim, Y., Kim, G., Fick, D., Kim, D., Seok, M., Wise, K., Blaauw, D., & Sylvester, D. (2011). A cubic-millimeter energy-autonomous wireless intraocular pressure monitor. In *2011 IEEE International Solid-State Circuits Conference (ISSCC) Digest of Technical Papers*, San Francisco, CA, USA (pp. 310–312). https://doi.org/10.1109/ISSCC.2011.5746332

Chen, Y., Nie, Y., & Jiao, H. (2022). An ultralow-power 65-nm standard cell library for near/subthreshold digital circuits. *IEEE Transactions on Very Large Scale Integration (VLSI) Systems*, *30*(5), 676–680. https://doi.org/10.1109/TVLSI.2022.3151500

Deng, L., Li, K., & Shan, W. (2023). A leakage reduction technique based on input vector analysis and transistor stacking in CMOS circuits. In *IEEE International Symposium on Circuits and Systems (ISCAS)* (pp. 1–5). Monterey, CA, USA.

Fernandes, D. T., Galup-Montoro, C., & Schneider, C. M. (2021). Analysis and design of the three-inverter Schmitt trigger for supply voltages down to 50 mV. *IEEE Transactions on Circuits and Systems II: Express Briefs*, *68*(7), 2302–2306. https://doi.org/10.1109/TCSII.2021.3058358

Gubbi, J., Buyya, R., Marusic, S., & Palaniswami, M. (2013). Internet of things (IoT): A vision, architectural elements, and future directions. *Future Generation Computer Systems*, *29*(7), 1645–1660. https://doi.org/10.1016/j.future.2013.01.010

Gupta, N., Shah, A. P., Kumar, R. S., Raut, G., Dhakad, N. S., & Vishvakarma, S. K. (2021). Soft error hardened voltage bootstrapped Schmitt trigger design for reliable circuits. *Microelectronics Reliability*, *117*, 114013. https://doi.org/10.1016/j.microrel.2020.114013

Hanson, S., Seok, M., Lin, Y.-S., Foo, Z. Y., Kim, D., Lee, Y., Liu, N., Sylvester, D., & Blaauw, D. (2009). A low-voltage processor for sensing applications with picowatt standby mode. *IEEE Journal of Solid-State Circuits*, *44*(4), 1145–1155. https://doi.org/10.1109/JSSC.2009.2014205

Hanson, S., Zhai, B., Seok, M., Cline, B., Zhou, K., Singhal, M., Minuth, M., Olson, J., Nazhandali, L., Austin, T., Sylvester, D., & Blaauw, D. (2008). Exploring variability and performance in a sub-200-mV processor. *IEEE Journal of Solid-State Circuits*, *43*(4), 881–891. https://doi.org/10.1109/JSSC.2008.917505

Hwang, M.-E., & Roy, K. (2008). A 135 mV 0.13 μW process tolerant 6T subthreshold DTMOS SRAM in 90 nm technology. In *2008 IEEE Custom Integrated Circuits Conference*, San Jose, CA, USA (pp. 419–422). https://doi.org/10.1109/CICC.2008.4672109

Kang, M. S. Leblebici, Y., Kim, C. (2016). *CMOS digital integrated circuits* (4th ed.). McGraw Hill Education.

Kim, K., & Kim, S. y. (2015). Design of Schmitt trigger logic using DTMOS for enhanced electromagnetic immunity. *IEEE Translated Electromagnetic Compatibility*, *57*(5), 963–972. https://doi.org/10.1109/TEMC.2015.2427992

Kim, K., Nah, W., & Kim, S. (2013). Noise-immune design of Schmitt trigger logic gate using DTMOS for sub-threshold circuits. In *The 9th International Workshop on Electromagnetic Compatibility of Integrated*, Nara (pp. 83–88). https://doi.org/10.1109/EMCCompo.2013.6735178

Lin, J., Wang, L., Zhan, C., & Lu, Y. (2019). A 1-nW ultra-low voltage subthreshold CMOS voltage reference with 0.0154%/V line sensitivity. *IEEE Transactions on Circuits & Systems II: Analog & Digital Signal Processing*, *66*(10), 1653–1657. https://doi.org/10.1109/TCSII.2019.2920693

Lotze, N., & Manoli, Y. (2012). CMOS standard cell design technique using Schmitt trigger logic. *IEEE Journal of Solid-State Circuits*, *47*(1), 47–60. https://doi.org/10.1109/JSSC.2011.2167777

Lotze, N., & Manoli, Y. (2017). Ultra-sub-threshold operation of always-on digital circuits for IoT applications by use of *Schmitt trigger gates*. *IEEE Transactions on Circuits & Systems I: Regular Papers*, *64*(11), 2920–2933. https://doi.org/10.1109/TCSI.2017.2705053

Narawade, S., Jithin, K., & Gupta, M. (2023). *Low-swing Schmitt triggers* (U.S. Patent No. 11 and undefined 2022).

Noh, K., Zhang, M., & Sánchez-Sinencio, E. (2019). A unified amplifier-based CC-CV linear charger for energy-constrained low-power applications. *IEEE Transactions on Circuits & Systems II: Express Briefs*, *66*(3), 377–381. https://doi.org/10.1109/TCSII.2018.2858539

Park, S., Kim, K., Huynh, H. A., Joo, S., & Kim, S. (2016). EM noise immunity enhancement using Schmitt trigger logic gates in CMOS process. In *URSI Asia-Pacific Radio Science Conference*, Seoul, Korea (South) (pp. 915–918). https://doi.org/10.1109/URSIAP-RASC.2016.7601322

Shah, A. P., Yadav, N., Beohar, A., & Vishvakarma, S. K. (2018). Process variation and NBTI resilient Schmitt trigger for stable and reliable circuits. *IEEE Transactions on Device and Materials Reliability*, *18*(4), 546–554. https://doi.org/10.1109/TDMR.2018.2866695

Wang, A., & Chandrakasan, A. (2005). A 180-mV subthreshold FFT processor using a minimum energy design methodology. *IEEE Journal of solid-State Circuits*, *40*(1), 310–319. https://doi.org/10.1109/JSSC.2004.837945

Wang, C., Zhou, J., Liao, L., Lan, J., Luo, J., Liu, X., & Je, M. (2015). Near-threshold energy- and area-efficient reconfigurable DWPT/DWT processor for healthcare-monitoring applications. *IEEE Transactions on Circuits & Systems II: Analog & Digital Signal Processing*, *62*(1), 70–74. https://doi.org/10.1109/TCSII.2014.2362791

Zhang, C., Srivastava, A., & Ajmera, P. K. (2003). Low voltage CMOS Schmitt trigger circuits. *Electronics Letters*, *39*(24), 1696–1698. https://doi.org/10.1049/el:20031131

2025 3rd International Conference on Advancement in Computation & Computer Technologies (InCACCT) | 979-8-3315-4389-1/25/$31.00 ©2025 IEEE | DOI: 10.1109/InCACCT65424.2025.11011431

Machine Learning-Driven Surrogate Modeling and Quantum Metaheuristics for Gurney Flap Optimization in Darrieus Wind Turbines

Subhrajit Roy
Department of Mechanical Engineering
Delhi Technological University
Delhi, India
roysubhrajit03@gmail.com

Siddharth Joshi
Department of Mechanical Engineering
Delhi Technological University
Delhi, India
siddharthjoshi.k3@gmail.com

Vishal Jaiswal
Department of Mechanical Engineering
Delhi Technological University
Delhi, India
viztech2002@gmail.com

Raj Kumar Singh
Department of Mechanical Engineering
Delhi Technological University
Delhi, India
rajkumarsingh@dce.ac.in

***Abstract*—The optimization of Darrieus wind turbine designs is critical to improving their aerodynamic performance and energy efficiency. The present study focuses to enhance the (C_P) of the turbine by optimizing the design parameters of Gurney flaps attached to the trailing edges of the turbine rotors. Specifically, the flap angle and height are treated as the design variables. To explore the design space and generate random design points efficiently, Latin Hypercube Sampling (LHS) is employed. URANS simulations are carried out on these design points to provide high-fidelity data. A RBF surrogate model is then trained on this data, and is integrated with the Quantum-based Salp Swarm Algorithm (QSSA). The findings indicate a significant improvement in C_P, with the optimized Gurney flap configurations outperforming the smooth baseline case by approximately 158% and the initial Gurney flap setup by 188%. Further, the performance of QSSA is shown with another popular evolutionary algorithm— the Harris Hawks Algorithm. This approach demonstrates the potential of data-driven optimization techniques in the energy sector.**

***Keywords*—Swarm Intelligence; Surrogate Modeling; Computational Optimization; Metaheuristics; Computational Fluid Dynamics; Wind Turbines**

I. Introduction

The vast prospects of renewable energy sources, including hydropower, wind, biomass, solar, and geothermal, has garnered significant attention due to the rising global energy demand [1]–[3]. Environmental concerns and availability of fossil fuel resources for an effective period lead to the urge for sustainable use of inexhaustible energy alternatives. Utilising these renewable alternatives will help better control climate fluctuations, reduce emission, and thereby provide clean forms of energy towards the future times. Among other renewable energy alternative sources, winds have emerged very rapidly as developing renewable energy option [4].

Wind turbine design is a multidisciplinary field combining turbomachinery, vibrations, material science, and aerodynamics to create sustainable energy solutions [5]. Researchers aim to optimize performance by enhancing energy capture, reducing fatigue, and minimizing environmental impacts. Companies like Siemens and Vestas focus on refining turbine systems, while the academic community contributes methods and tools to advance this vital renewable energy technology [6].

A Gurney flap (GF) is a small, rectangular structure attached near the trailing edge in an airfoil to improve its aerodynamic performance. The dimensions typically range from 1% to 5% of the chord length (c) [7]. Initially introduced in the 1970s by U.S. racing driver Dan Gurney, GFs were first used on Formula 1 car spoilers to increase downforce. Liebeck [8] later conducted experiments on a Newman airfoil and confirmed that GFs enhance lift. He recommended that the GF's height should not exceed 2% of the chord length, as larger sizes may increase drag and negate aerodynamic benefits. Liebeck [8] explained that the reversed flow behind the GF generates contra-rotating vortices, altering circulation and the Kutta condition, which results in the observed effects. The effectiveness of GFs depends on their configuration, including height and orientation. While increasing the flap height boosts lift, it also increases drag. If the height exceeds a threshold, the drag may offset the aerodynamic advantages.

II. Computational Modelling

A. Gurney Flap and Parametrization

NACA 0012 airfoil is chosen for the optimization study. The configuration of the gurney flap in the present study is controlled by two main parameters: flap height (h) and the angle that the flap makes with the normal to the chord (θ). In past studies [9] it was observed that adjusting these parameters in the GF can significantly improve the performance of the airfoil. The flap width is kept constant at 0.2%c. Figure 1 depicts the design parameters used in the present study.

979-8-3315-4389-1/25/$31.00 ©2025 IEEE

Authorized licensed use limited to: DELHI TECHNICAL UNIV. Downloaded on June 04,2025 at 05:16:36 UTC from IEEE Xplore. Restrictions apply.

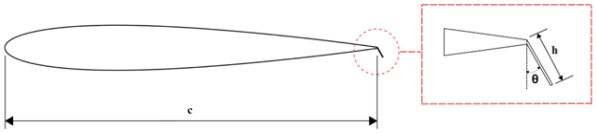


Fig. 1. Schematic diagram of an airfoil equipped with a GF on the trailing edge

B. Computational Domain

A rectangular computational domain was defined with its center aligned to the turbine's shaft, to execute the CFD simulations. The domain was divided into three distinct subdomains: a central rotating zone containing the turbine blades, and two stationary zones—inner and outer. Unstructured triangular elements were utilized for mesh generation, so as to compensate for poor quality cells, especially near the turbine walls and deflector. For each design point, defined by specific h and θ values, the geometry, remeshing, and solution processes were updated automatically to ensure efficient and consistent analysis.

This meshing strategy significantly enhanced computational efficiency, as it allowed the mesh generator to update only the middle domain while preserving the outer and inner domain's mesh. Fig. 2 shows the the mesh. The refined mesh near the blades is specifically designed to accurately capture detailed flow physics in regions of high turbulence.

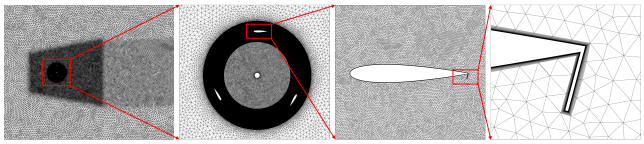


Fig. 2. Mesh used for the study

C. Numerical Modelling

The numerical simulations were performed using URANS equations in Ansys Fluent 20.2. Menter's SST $k-\omega$ turbulence model was selected based on its proven accuracy for VAWT applications [10], [11]. The solver setup, boundary conditions, and fluid properties are summarized in Tables I–III.

TABLE I
NUMERICAL SIMULATION SETUP

Category	Specification
Software	Ansys Fluent 20.2
Turbulence model	SST $k-\omega$
Pressure-velocity coupling	Coupled scheme
Discretization method	Second-order upwind

The data obtained from these simulations served as the foundation for training the surrogate model, which was later utilized in the optimization phase of the study.

TABLE II
BOUNDARY CONDITIONS

Boundary	Type/Condition	Value/Parameters
Outlet	Pressure outlet	Gauge pressure = 0 Pa
Inlet	Velocity inlet	$U = 20$ m/s
Deflector walls	No-slip wall	Stationary wall
Turbine blades	No-slip wall	Stationary wall

TABLE III
FLUID PROPERTIES

Property	Value	Unit
Density (ρ)	1.225	kg/m^3
Viscosity (ν)	1.7894×10^{-5}	kg/(m·s)
Operating pressure	101,325	Pa

D. Validation Studies

To keep the numerical simulations accurate, a grid independence analysis was conducted by evaluating different grid resolutions. While finer grids improve precision, they also increase computational costs. The aim was to determine an optimal mesh size balancing accuracy and efficiency. Figure 3 shows the moment variation with the turbine's rotation angle for three resolutions (123000, 210000, and 350000). The fine and medium meshes show no significant change in results, suggesting no further refinement is necessary. Thus, a mesh size of 210000 elements was chosen to effectively capture the turbine's flow physics.

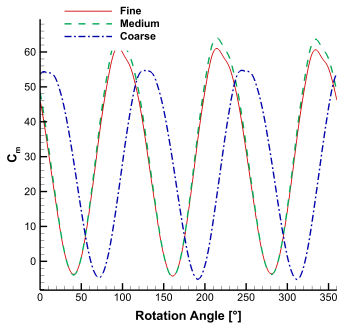


Fig. 3. Grid Independence Test

The time step size's effect on the solution was also analyzed using three time steps: 0.5°, 1°, and 2° of turbine rotation per step. Figure 4 illustrates the variation of the power coefficient (C_P) with turbine's rotation angle. Results showed that reducing the time step below 1° per step had no significant impact on the solution. Consequently, a time step of 1° per rotation was selected for subsequent simulations.

The numerical model's accuracy was validated using experimental data from Castelli et al. [12] and numerical results from Zhang et al. [13]. As shown in Figures 5, the study's results closely align with experimental findings, with only minor discrepancies.

Authorized licensed use limited to: DELHI TECHNICAL UNIV. Downloaded on June 04,2025 at 05:16:36 UTC from IEEE Xplore. Restrictions apply.

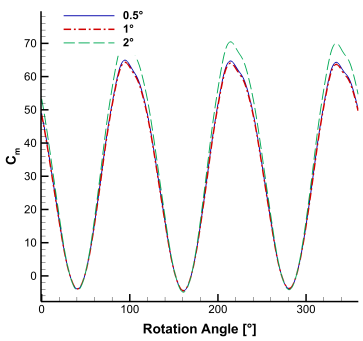


Fig. 4. Timestep Independence Test

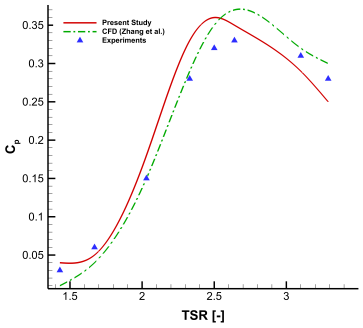


Fig. 5. Validation

III. Optimization Framework

A. Sample Acquisitions

The acquisition of samples is crucial in the optimization process, forming the foundation for subsequent analysis. To improve the performance of Darrieus turbines with a GF, the objective is to gather data that precisely reflects the behavior of the system. This involves running simulations under various design parameters and conditions.

The development of reliable surrogate models depends on the generation of high-quality training data. The even distribution of these points in the design space is critical for these models to be accurate and reliable. Latin Hypercube Sampling, as introduced by McKay et al. [14], has become a well-known method for such purpose. LHS systematically chooses data points to fully explore the potential of the design space, thus forming a basis for developing robust surrogate models that ease the process of system optimization.

B. Surrogate Modeling

Design optimization problems often struggle with huge computing costs due to the necessity of extensive simulations in these problems [15]. The surrogate models provide an alternative way of constructing an adequate response surface based on a limited set of simulations, where effective exploration of the design space can be achieved and output variables predicted. By training models on a portion of the simulation data and validating them with the remaining data, scientists could simulate complex systems better with lesser computational costs. Their versatility, simplicity, and efficiency make surrogate models well-suited to such challenges. In optimization problems, it is still very expensive to have several simulations because of the computing resource requirements [16].

By applying regression techniques, these models estimate response values at unknown design points using data from known points, enabling a highly accurate approximate representation ([9], [16]). Rather than relying solely on a single surrogate model that tries to capture the complex nonlinear relationships between variables, this work employs a variety of surrogate models to capture these relationships. This comprehensive approach improves the adaptability and robustness of the optimization process, in ensuring the better handling of intricate design challenges.

C. Quantum-Based Salp Swarm Optimization Algorithm

For identifying optimum parameters, it is essential to either maximize or minimize the objective function, with its behavior throughout the design space accurately depicted by a reliable surrogate model. This study uses meta-heuristic optimization algorithms for this purpose. Traditional optimization techniques often fall short in handling complex problems and exhibit slow convergence rates, leading to the emergence of quantum-inspired methods. Among these, The QSSO Algorithm stands out, combining principles of quantum mechanics with the collective behavior of salp swarms.

Salps, belonging to the Salpidae family, are barrel-shaped, transparent marine organisms similar in appearance to jellyfish. They propel themselves by pumping water through their bodies [17]. Salps exhibit a swarming behavior which is thought to improve their foraging and locomotion efficiency. Inspired by this behavior, Mirjalili et al. [18] put forward the so-called Salp Swarm Optimization (SSO) algorithm. It is a meta-heuristic approach that imitates salp colonies' social dynamics and movement. The SSO algorithm effectively balances exploitation and exploration, enabling the identification and refinement of optimal regions in solution spaces. However, traditional SSO is limited by slow convergence and inefficient exploration, motivating further advancements.

The conventional SSO algorithm also struggles with addressing nonlinear constraints and maintaining accuracy in complex optimization scenarios. Early convergence, a common issue in biologically inspired algorithms, stems from restricted self-search mechanisms. Nonetheless, SSO demonstrates high competitiveness, precision, and practical utility compared to other swarm intelligence techniques [19]. To improve exploration and avoid entrapment in local optima, Faris et al. [20] developed the Binary Salp Swarm Algorithm, incorporating transfer functions and crossover operators to enhance feature selection. Similarly, Sahu et al. [21] applied an Improved Salp Swarm Optimization (I-SSO) algorithm to design a PID controller for keeping frequency and power under uncertainties. The I-SSO algorithm demonstrated superior dynamic performance compared to other meta-heuristic methods.

In this work, the QSSO algorithm is utilized to determine the optimal orientation of a GF attached at trailing edge

Authorized licensed use limited to: DELHI TECHNICAL UNIV. Downloaded on June 04,2025 at 05:16:36 UTC from IEEE Xplore. Restrictions apply.

of the blade of the turbine. Chen et al. [22] introduced a novel approach incorporating Elite Opposition-based strategies and Wavelet Mutation—concepts derived from quantum mechanics—into the traditional SSO framework. This quantum-inspired method significantly improves solution space exploration and accelerates convergence toward optimal results.

Algorithm 1: Quantum Salp Swarm Algorithm

```
Set the population size N and max iterations T
Randomly initialize the positions of salps x_i (i = 1, 2, .., N) according to ub_j and lb_j
t = 0
Calculate the fitness of each salp and set F as the best search agent
Update the positions of the leader and follower salps by Eq.2
t = t + 1
while t < T do
    if i < N/2 then
        Update the position of leading salp using Eq.4
    else
        Calculate the position of follower salps using reverse elite Eq.5
        Compare the reverse elite solution and normal solution, update the Follower salp position with best fitness
    end if
    Random individual is selected and it's position is updated using wavelet mutation Eq.6
    Correct the each salp that go beyond the upper and lower bounds
    Recalculate the fitness of each salp
    Update the best position of the food source (F)
end while
Next generation until stopping
return F
```

Fig. 6. Quantum Salp Swarm Algorithm

QSSO working: Consider the position vector of each salp as a matrix with dimensions $N \times D$, where N is the number of salp search agents and D is the dimension of continuous solution space. This vector can be written in the matrix form as given by Eq.1 :

$$X_z^y = \begin{bmatrix} X_1^1 & X_1^2 & \cdots & X_1^D \\ X_2^1 & X_2^2 & \cdots & X_2^D \\ \vdots & \vdots & \cdots & \vdots \\ X_N^1 & X_N^2 & \cdots & X_N^D \end{bmatrix} \tag{1}$$

The conventional Salp Swarm Optimization (SSO) algorithm updates the leader salp's position using the following equation:

$$X_z^1 = \begin{cases} F_z + c_1((ub_z - lb_z)c_2 + lb_z) & c_3 \geq 0.5 \\ F_z - c_1((ub_z - lb_z)c_2 + lb_z) & c_3 < 0.5 \end{cases} \tag{2}$$

with

$$c_1 = 2e^{-(l/L)^2} \tag{3}$$

In the standard SSO algorithm, the position of the leader salp in the first generation along the z_{th} dimension is represented as X_z^1, where l indicates the current iteration, and L signifies the total number of iterations. Conversely, the QSSO algorithm employs a position update strategy for the leading salp inspired by the Monte Carlo method. This strategy is mathematically represented by the following equation:

$$X_{z,g+1}^1 = \begin{cases} b_{z,g}^1 + c_1(M - X_{z,g}^1).\ln(1/c_2) & c_3 \geq 0.5 \\ b_{z,g}^1 - c_1(M - X_{z,g}^1).\ln(1/c_2) & c_3 < 0.5 \end{cases} \tag{4}$$

In this framework, $b_{z,g}^1$ denotes the global optimum value for the g_{th} generation, while M signifies the mean of local optimal values. The incorporation of quantum mechanics significantly enhances the salp mobility, improving their ability to navigate the solution space effectively. The reverse elite solution plays an important role in determining the positions of follower salps and is mathematically expressed as:

$$X_z^y(elite) = c(ub_z + lb_z) - X_z^y(normal) \tag{5}$$

Here, c is an arbitrary number in the interval $(0, 1)$ and $X_z^y(normal)$ and $X_z^y(elite)$ denote the location of the follower salp and its backward elite version, respectively. Then the fitness values of the two solutions are calculated, and the better one is used in the next generation; the backward elitism is retained based on predetermined criteria. The reverse elite method helps strengthen candidate solutions against perturbations and also increase their adaptability.

To enhance the population diversity, Wavelet mutation is added to the algorithm. This approach guarantees that each follower salp has the opportunity to undergo mutation, which is regulated by a parameter referred to as the mutation probability. A random value between 0 and 1 is generated, and if it falls below or equals a specified threshold, the mutation process is initiated. Let $\overline{X}_z^y(t)$ denote the chosen salp; its mutation is then determined by the following equation:

$$\overline{X}_z^y(t) = \begin{cases} X_z^y(t) + \sigma \times (ub_z - X_z^y(t)) & \sigma > 0. \\ X_z^y(t) - \sigma \times (X_z^y(t) - lb_z) & \sigma \leq 0 \end{cases} \tag{6}$$

with

$$\sigma = \frac{1}{\sqrt{a}} e^{\frac{-(\frac{x}{a})^2}{2}} \cos(5(\frac{x}{a})) \tag{7}$$

where a serves as a dilation parameter that dynamically adjusts during every iteration further refining the solution. The dilation parameter is mathematically expressed as:

$$a = e^{-\ln g_1 \times (1 - \frac{l}{L})^{\xi_{\omega m}} + \ln g_1} \tag{8}$$

Here, $\xi_{\omega m}$ represents the shape parameter of the function, while g_1 denotes the upper limit of the dilation parameter a. The performance of the QSSO algorithm can be optimized by carefully adjusting these two parameters.

D. Harris Hawk's Optimisation Algorithm

The Harris Hawks Optimization (HHO) algorithm is a nature-inspired, population-based optimization technique that replicates the collaborative hunting strategies of Harris's hawks. This behavior is exemplified by their "surprise pounce" strategy, in which multiple hawks collaboratively target a prey by encircling and attacking it from various directions.

Authorized licensed use limited to: DELHI TECHNICAL UNIV. Downloaded on June 04,2025 at 05:16:36 UTC from IEEE Xplore. Restrictions apply.

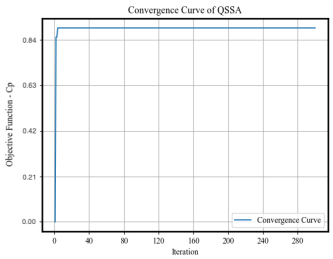


Fig. 7. Performance of QSSO algorithm

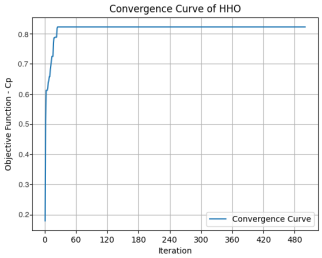


Fig. 8. Performance of HHO algorithm

The algorithm consists of three primary stages: exploration, transition, and exploitation, which are inspired by real-world hawk hunting dynamics.

During the exploration phase, the Harris hawks settle in random positions., mimicking diverse solutions in the search space. They either choose positions near other hawks to facilitate coordinated attacks or randomly perch within the environment. This behavior is mathematically represented as:

$$X(t+1) = \begin{cases} X_{\text{rand}}(t) - r_1|X_{\text{rand}}(t) - 2r_2X(t)|, (q \geq 0.5) \\ X_{\text{rabbit}}(t) - X_m(t) - r_3(\text{LB} + r_4(\text{UB} - \text{LB})), (q < 0.5) \end{cases} \tag{9}$$

Here, X(t+1) is the updated hawk position, $X_{rabbit}(t)$ represents the prey's position, X(t) is the hawk's current position, and $X_{rand}(t)$ is a randomly chosen hawk's position. r_1, r_2, r_3, r_4, q are random numbers in the interval [0,1], and LB and UB denote the lower and upper bounds of the variables. The average position of the hawks, $X_m(t)$, is computed as:

$$X_m(t) = \frac{1}{N}\sum_{i=1}^{N} X_i(t), \tag{10}$$

where Xi(t) denotes the position of the i-th hawk at iteration t and N is the number of hawks. The algorithm transitions between exploration and exploitation phases based on the energy of the prey, modeled as:

$$E = 2E_0\left(1 - \frac{t}{T}\right), \tag{11}$$

where E_0 is the prey's initial energy (randomly selected from $[1, 1]$), t is the current iteration, and T is the maximum number of iterations. The algorithm explores the search space when $E \geq 1$, and when $E < 1$, shifts to exploitation . In the exploitation phase, four strategies simulate how hawks adapt to the prey's escape attempts. When the prey still has energy $E0.5$, hawks perform a soft besiege, loosely encircling the prey to tire it. This is modeled as:

$$X(t+1) = \Delta X(t) - E|X(t) - JX_{\text{rabbit}}(t)| \tag{12}$$

where $\Delta X(t) = Xrabbit(t)X(t)$, and $J = 2(1 - r^5)$ is the random jump strength of the prey . In contrast, a hard besiege is applied when the prey's energy is low (E¡0.5). In this case, the hawks encircle the prey closely, reducing the distance between their average position and the prey:

$$X(t+1) = X_{\text{rabbit}}(t) - E|\Delta X(t)|. \tag{13}$$

To simulate more dynamic behaviors, Levy flight is introduced for certain strategies, including both the soft besiege with quick dives and the hard besiege with swift dives, where the hawks perform abrupt, irregular movements to confuse the prey. The rapid dive motion is calculated as:

$$Z = S \cdot \text{LF}(D) + Y, \tag{14}$$

where Y represents the candidate dive position, S is a vector that is random, and LF(D) denotes the Levy flight function. . Overall, the HHO algorithm demonstrates a balance between exploration and exploitation, enabling it to achieve competitive results across a large spectrum of optimization challanges. The statistical results on benchmark and real-world engineering problems affirm the algorithm's efficiency and robustness

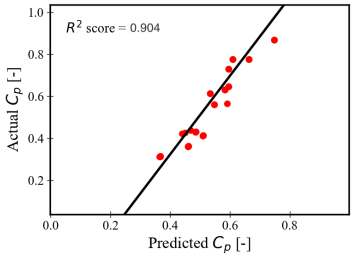


Fig. 9. Validation of the RBF surrogate model

IV. Results and Discussion

A. Radial Basis Function

A total of 60 sample points were generated using Latin Hypercube Sampling (LHS) and utilized for CFD simulations. Of these, 35 sample points were employed to train the surrogate model, while the remaining points were reserved for validation. The RBF surrogate model's accuracy was evaluated, as illustrated in Figure 9. The dataset achieved an R^2 score of 0.904.

B. Hyper-parameters in QSSO Algorithm

An in-house implementation of the QSSO algorithm was utilized to optimize the objective function, C_p. This parameter consists of two hyperparameters: g_1, representing the maximum value of the dilation parameter, and ξ_ω^m, the shape parameter. The convergence behavior of the optimization algorithm was analyzed for various (g_1, ξ_ω^m) combinations, including $(0.01, 500)$, $(0.1, 250)$, $(1, 100)$, $(50, 50)$, $(100, 1)$, $(250, 0.1)$, and $(500, 0.01)$. It was found that the QSSO algorithm achieves its optimal performance when g_1 and ξ_ω^m are set to 500 and 0.01, respectively Figure 7. Comparisons with other parameter combinations reveal that this configuration enables faster convergence and produces the best achievable solution.

C. Performance against Harris Hawks Optimization Algorithm

The results obtained by the QSSO algorithm are compared against the HHO algorithm, to objectively assess its performance. For computational efficiency, the population size (number of search agents) was set to 50. As evident from Figures 7 and 8, QSSO yields a

Authorized licensed use limited to: DELHI TECHNICAL UNIV. Downloaded on June 04,2025 at 05:16:36 UTC from IEEE Xplore. Restrictions apply.

higher improvement in C_P as compared to HHO. The exploratory capabilities of QSSO allow it to reach the global optima and escape local optima better than HHO.

D. Optimum Gurney Flap Parameters

The results are summarized in Table IV, here Smooth refers to the baseline design of turbine blades without a gurney flap, Initial refers to the initial design point of the optimization algorithm (h = 17.5 mm and $\theta = 15°$), and Final represents the optimum GF configuration (h = 2.21 mm and $\theta = -2.28°$). The table compares the values of C_P for the turbines at TSR 2.5. Figure 10 depicts the trailing edges of the smooth blade and the optimised GF implementation on the blade. It is evident that the optimised gurney flap significantly increases the value of C_P compared to the smooth blade. The initial design, on the other hand, performs worse than the smooth design. Overall, the results underscore the importance of optimization in the GF implementation.

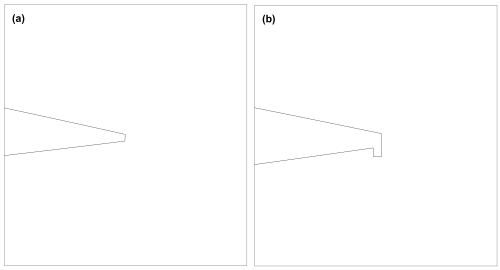


Fig. 10. Blade Trailing Edge (a) Smooth (b) with optimal Gurney Flap

TABLE IV
COMPARISON OF PARAMETERS AND OBJECTIVE FUNCTIONS FOR DIFFERENT FOILS

Design Type	C_P	ΔC_P
Smooth	0.36	-
Initial (Unoptimised)	0.25	-30.56%
Final (Optimised)	0.93	158.33%

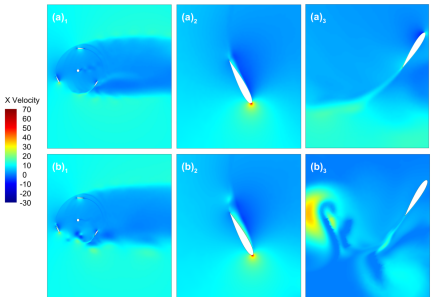


Fig. 11. Velocity Fields

E. Flow Structures

A flow analysis is presented to comprehend the dynamics underlying the performance enhancement of the turbine achieved through the implementation of a Gurney flap. Figures 11, 12 and 13 present the velocity, pressure and turbulent kinetic energy fields around the turbine blades. Subfigures $(a)_1$ and $(b)_1$ show the farfield view of the flow around the turbines, while Subfigures $(a)_2$, $(b)_2$, $(a)_3$ and $(b)_3$ show the near-field wakes of the high AOA blades of the turbines.

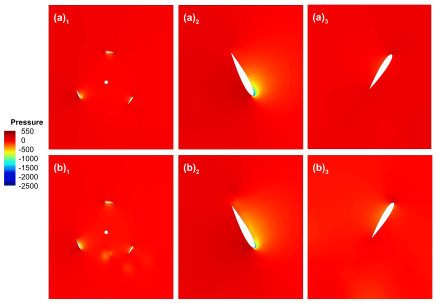


Fig. 12. Pressure Fields

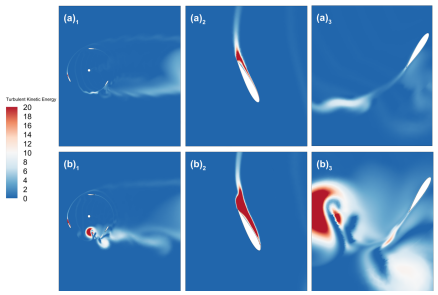


Fig. 13. Turbulent Kinetic Energy

The blades are chosen for the qualitative flow analysis, as owing to their high angle of attack, they exhibit turbulent and detached flow dynamics capable of yielding meaningful insights into the flow behaviour. The steep mounting angle of the gurney flap stagnates the incoming airflow on the windward side, while simultaneously reducing the pressure on the leeward side of the Gurney flap, thereby increasing the net pressure drag. Further, the recirculation zone downstream of the GF generates a highly turbulent detached flow region near the leeward side. This effect is shown in fig. 13, where the blades with the gurney flap clearly exhibit more turbulent kinetic energy near their trailing edges. The deficit in momentum induced by the Gurney flap reduces pressure on the leeward side of the turbine blade, evident from figures $12(a)_2$ and $(b)_2$, resulting in increased lift force acting on the blade. Hence, the small flap height of 2.21 mm in the optimised gurney flap balances the increase in lift and drag, improving the overall performance of the turbine.

V. CONCLUSION

The study presents an optimization framework that aims to better the performance of a Darrieus wind turbine augmented with a gurney flap. This was accomplished through a computational optimization framework combining CFD simulations, surrogate modeling, and metaheuristic optimization techniques. To train the Radial Basis Function surrogate model, 60 design points were created via Latin Hypercube Sampling (LHS), and simulations(URANS) were performed.

Despite these advancements, the framework has certain limitations. The reliance on URANS simulations, rather than higher-fidelity models such as DES or LES, constrains the accuracy of the results. Additionally, the use of surrogate models introduces approximations that may, in some cases, reduce accuracy.

Nevertheless, the outcomes of this research are significant. The results not only drive progress in wind turbine design but also offer applications across various renewable energy technologies. Furthermore, the methodologies employed within this framework demonstrate its applicability beyond the specific context of this

Authorized licensed use limited to: DELHI TECHNICAL UNIV. Downloaded on June 04,2025 at 05:16:36 UTC from IEEE Xplore. Restrictions apply.

study, suggesting a wide-ranging relevance for optimization in similar engineering domains.

REFERENCES

[1] M. K. G. Deshmukh, M. Sameeroddin, D. Abdul, M. A. Sattar, Renewable energy in the 21st century: A review, Materials Today: Proceedings 80 (2023) 1756–1759.

[2] Q. Hassan, S. Algburi, A. Z. Sameen, J. Tariq, A. K. Al-Jiboory, H. M. Salman, B. M. Ali, M. Jaszczur, et al., A comprehensive review of international renewable energy growth, Energy and Built Environment (2024).

[3] K. Wang, W. Xiao, T. He, M. Zhang, Remote sensing unveils the explosive growth of global offshore wind turbines, Renewable and Sustainable Energy Reviews 191 (2024) 114186.

[4] M. Grujicic, G. Arakere, B. Pandurangan, V. Sellappan, A. Vallejo, M. Ozen, Multidisciplinary design optimization for glass-fiber epoxy-matrix composite 5 mw horizontal-axis wind-turbine blades, Journal of materials engineering and performance 19 (2010) 1116–1127.

[5] G. Muscolo, S. Casadio, P. Forte, et al., Formulation of a transfer function between rotor responses on a high speed balancing machine and in turbomachinery by system identification, Energy and Power, Scientific & Academic Publishing, ISSN (2012) 2163–1603.

[6] A. Chehouri, R. Younes, A. Ilinca, J. Perron, Review of performance optimization techniques applied to wind turbines, Applied Energy 142 (2015) 361–388.

[7] B. L. Storms, C. S. Jang, Lift enhancement of an airfoil using a gurney flap and vortex generators, Journal of Aircraft 31 (1994) 542–547.

[8] Liebeck, Robert H, Design of subsonic airfoils for high lift, Journal of aircraft 15.9 (1978): 547-561.

[9] A. Tyagi, P. Singh, A. Rao, G. Kumar, R. K. Singh, A novel framework for optimizing gurney flaps using RBF neural network and cuckoo search algorithm, arXiv preprint arXiv:2307.13612 (2023).

[10] Singh P, Jaiswal V, Roy S, Tyagi A, Kumar G, Singh RK. Quantum-Based Salp Swarm Algorithm Driven Design Optimization of Savonius Wind Turbine-Cylindrical Deflector System. arXiv preprint arXiv:2403.04876. 2024 Mar 7.

[11] G. G. Wang, S. Shan, Review of metamodeling techniques in support of engineering design optimization, in: International Design Engineering Technical Conferences and Computers and Information in Engineering Conference, Vol. 4255, 2006, pp. 415–426.

[12] Castelli, M. R., Englaro, A., & Benini, E. (2011). The Darrieus wind turbine: Proposal for a new performance prediction model based on CFD. Energy, 36(8), 4919-4934.

[13] Zhang, L., Gu, J., Hu, K., Zhu, H., Miao, J., Li, X., ... & Wang, Z. (2021). Influences of trailing edge split flap on the aerodynamic performance of vertical axis wind turbine. Energy Science & Engineering, 9(1), 101-115.

[14] M. D.McKay, Latin hypercube sampling as a tool in uncertainty analysis of computer models, in: Proceedings of the 24th conference on Winter simulation, 1992, pp. 557–564.

[15] Singh P, Jaiswal V, Roy S, Singh RK. Maximizing Savonius Turbine Performance using Kriging Surrogate Model and Grey Wolf-Driven Cylindrical Deflector Optimization. arXiv preprint arXiv:2311.06378. 2023 Nov 10.

[16] H. Xia, S. Zhang, R. Jia, H. Qiu, S. Xu, Blade shape optimization of savonius wind turbine using radial based function model and marine predator algorithm, Energy Reports 8 (2022) 12366–12378.

[17] L. P. Madin, Aspects of jet propulsion in salps, Canadian Journal of Zoology 68 (4) (1990) 765–777.

[18] S. Mirjalili, A. H. Gandomi, S. Z. Mirjalili, S. Saremi, H. Faris, S. M. Mirjalili, Salp swarm algorithm: A bio-inspired optimizer for engineering design problems, Advances in engineering software 114 (2017) 163–191.

[19] R. Abbassi, A. Abbassi, A. A. Heidari, S. Mirjalili, An efficient salp swarm-inspired algorithm for parameters identification of photovoltaic cell models, Energy conversion and management 179 (2019) 362–372.

[20] H. Faris, M. M. Mafarja, A. A. Heidari, I. Aljarah, A.-Z. Ala'm, S. Mirjalili, H. Fujita, An efficient binary salp swarm algorithm with crossover scheme for feature selection problems, Knowledge-Based Systems 154 (2018) 43–67.

[21] P. C. Sahu, S. Mishra, R. C. Prusty, S. Panda, Improved-salp swarm optimized type-ii fuzzy controller in load frequency control of multi area islanded ac microgrid, Sustainable Energy, Grids and Networks 16 (2018) 380–392.

[22] R. Chen, C. Dong, Y. Ye, Z. Chen, Y. Liu, Qssa: Quantum evolutionary salp swarm algorithm for mechanical design, IEEE Access 7 (2019) 145582–145595.

Authorized licensed use limited to: DELHI TECHNICAL UNIV. Downloaded on June 04,2025 at 05:16:36 UTC from IEEE Xplore. Restrictions apply.

Ocean Engineering 336 (2025) 121735

Contents lists available at ScienceDirect

Ocean Engineering

journal homepage: www.elsevier.com/locate/oceaneng

Research paper

ML-based prediction of scour depth around a cylindrical bridge pier: A comparative analysis of ANN, SVM, and Ensemble Trees

Geeta Devi [a,*], Vijay Kaushik [b]

[a] Department of Civil Engineering, SRM University, AP, India
[b] Department of Civil Engineering, Delhi Technological University, New Delhi, India

ARTICLE INFO

Keywords:
Local scour
Cylindrical pier
ANN
SVM
Ensemble tree method
Statistical analysis

ABSTRACT

The scour phenomenon is highly complex, and its precise prediction remains a considerable challenge for hydraulic researchers. Traditionally, most of the studies relay on empirical approaches for scour prediction. However, with the rapid development of infrastructure and the increasing number of bridges, these empirical models are inadequate in providing precise scour prediction across diverse field conditions. Consequently, there is a rising requirement to adopt advanced Machine Learning (ML) based methodologies to achieve more precise and computationally efficient scour prediction. The primary objective of this study is to propose an alternate model to traditional scour prediction methods by employing ML-based tools, specifically Artificial Neural Networks (ANN), Support Vector Machines (SVM), and the Ensemble Tree Method. These ML-based models are capable of handling complex and nonlinear problems. In addition to simulation work, a detailed experimental investigation has been carried out for a single cylindrical pier. The results of the present study, along with existing literature data, have been utilized for training and testing of ANN, SVM, and Ensemble Tree models. To evaluate the performance of the proposed models, an in-depth statistical analysis has been carried out. The findings of this study highlight that all three models significantly outperform traditional methods, demonstrating their effectiveness in improving scour depth predictions.

1. Introduction

1.1. Background

The continuous pursuit of improved materials, construction techniques, and advanced analysis and design methodologies has addressed many early challenges in bridge construction. However, since humans first began building piers and abutments within stream channels to span rivers, the scour of the streambed has remained one of the leading causes of bridge failures. Despite advancements in engineering, bridge failures due to scour continue to be reported annually, adding to the list of disasters linked to hydraulic structure failures. The scour phenomenon is characterized by the erosion and subsequent deposition of sediment on the riverbed around bridge supports, such as piers and abutments, due to the influence of the flow field. It primarily results from the vortex action of accelerated water at the base of the bridge pier. This vortex action intensifies sediment transport, leading to the formation of a scour hole around the pier, while displaced material has been deposited downstream of the pier which is known as a sediment mound.

Bridge scour is the common cause of catastrophic bridge failures across the world, and it has been investigated by researchers (Breusers et al., 1977; Dey et al., 1995; Muzzammil and Gangadhariah, 2010; Okhravi et al., 2022; Pandey et al., 2020a). As per their observations, the scour process is dependent on the hydraulic, Sediment and flow characteristics. Hydraulic characteristics have been investigated by authors (Chabert and Engeldinger, 1956; Dey and Raikar, 2007; Ettema, 1980; Guan et al., 2019; Majedi-Asl et al., 2021; Muzzammil and Gangadhariah, 2010; Yanmaz and Altinbilek, 1991) and sediment characteristics have been studied by authors (Aguirre-Pe et al., 2003; Cheng et al., 2020; Debnath and Chaudhuri, 2010; Lauth and Papanicolaou, 2008; Umeda et al., 2010). Additionally, temporal scour evolution for hydraulic structures has been studied by authors (Kothyari et al., 1992; Melville and Chiew, 1999; Oliveto and Hager, 2002; Yang et al., 2020; Yanmaz and Kose, 2007). Authors (Kothyari et al., 1992), conducted a study on the temporal evolution around the circular pier for the uniform sediment, in their research the duration of experimental run has been kept for 800 minutes. Melville and Chiew (1999) conducted an experimental study for the circular bridge pier and proposed a formulation for

* Corresponding author.
E-mail addresses: geetadevi.r@srmap.edu.in (G. Devi), vijaykaushik_2k20phdce01@dtu.ac.in (V. Kaushik).

https://doi.org/10.1016/j.oceaneng.2025.121735
Received 24 March 2025; Received in revised form 31 May 2025; Accepted 1 June 2025
Available online 9 June 2025
0029-8018/© 2025 Elsevier Ltd. All rights are reserved, including those for text and data mining, AI training, and similar technologies.

computing equilibrium time t_e. Oliveto and Hager (2002) performed experimental study by incorporating six sediments (3 uniform and 3 non uniform graded) and purposed an equation for temporal scour depth. Whereas, Yang et al. (2020) studied the temporal scour depth effect for the complex pier. However, Yanmaz and Kose (2007) conducted a time dependent scour depth study for the bridge abutments. For temporal effects are occasionally reported with no correlation among scour depths in the field and in the experiment.

1.2. Computational methods

Recently the shifting of researchers from conventional methods to ML models has been increased to precisely estimate scour depth, mainly due to the prediction efficacy of these advanced techniques. Many such methodologies have been extensively applied to hydraulic problems (Choi et al., 2017; Guven and Gunal, 2008). For instance, authors (Choi et al., 2017), utilized the ANFIS (Adaptive Neuro-Fuzzy Inference System) model for scour prediction around bridge piers and concluded a significant improvement in scour prediction compared to traditional methods. Similarly, researchers (Guven and Gunal, 2008), have utilized the GP (Genetic Programming) approach for modeling hydraulic structures and concluded that GP has outperformed traditional methods. Furthermore, for predicting temporal scour authors (Kumar et al., 2023) have applied ensemble methods such as Bagging Regressor (BR) and AdaBoost Regressor, alongside the standalone machine learning method, Support Vector Regression (SVR). More recently for scour prediction around bridge piers authors (Baranwal et al., 2024), have used eXtreme Gradient Boosting (XGBoost) and Support Vector Machine (SVM) with a particle swarm optimization (PSO), and concluded that XGBoost model outperforms both the SVM-PSO approach and traditional approaches scour depth prediction. Their results show that both ensemble methods provide better predictions in comparison to the standalone, SVR model and traditional empirical formulations. Similarly, other researchers few more AI tools have also been explored by (Bateni et al., 2007; Muzzammil et al., 2015; Najafzadeh and Oliveto, 2021; Pandey et al., 2020b, 2020c).

The consensus in the existing literature highlights the prediction efficacy of the AI/ML-based for scour depth prediction compared to traditional methods. Building on this understanding, the present study has been planned to explore the comparative performance of three AI/ML-based models, namely ANN, SVM and Ensemble Tree Method for scour prediction around cylindrical bridge pier. While existing studies have demonstrated the effectiveness of individual machine learning techniques such as ANFIS, GP, SVR, and XGBoost in predicting scour depth, a comprehensive comparative analysis integrating experimental data with multiple ML models remains limited. The novelty of this study lies in combining controlled laboratory experiments with well-documented literature datasets to benchmark the performance of three distinct ML algorithms, ANN, SVM, and Ensemble Trees within a unified framework. This hybrid approach enables not only a robust evaluation of predictive accuracy using standard statistical metrics (R^2, RMSE, MAE, etc.) but also an assessment of model stability and generalizability across diverse data conditions. Comparison of machine learning models with their key contributions has been presented in Table 1.

This study employs high-quality laboratory experimental data to develop and validate ML models for scour depth prediction, ensuring reliable and reproducible outcomes. A comparative analysis of multiple ML algorithms enables robust model evaluation, while input feature selection based on dimensionless parameters ensures physical relevance and enhances model interpretability and generalizability.

2. Experimental framework

Experimental work has been conducted at the hydraulic laboratory of Delhi Technological University, New Delhi, India. A recirculating flume section of 14 m long, 1.10 m wide and 0.80 m deep has been utilized for experimentation. For the precise velocity measurement and scour depth recording Acoustic Doppler Velocimeter (ADV) and Seatek ultrasonic ranging transducers have been installed in the flume section. In order to monitor the precise scour depth evolution around the pier, Seatek 3D bed profile Ultrasonic transducers have been utilized. SeaTek Ultrasonic Ranging System uses four 5 MHz transducers, expandable up to 32 in groups of four. Each transducer, housed in stainless steel, has a diameter of 1 cm and operates within a 3.5 cm–110 cm range shown in Fig. 2. The system uses RS232 communication for data transfer, with transducer numbers displayed upon connection. Arrays of up to 8.4 feet operate at 2 MHz frequency. The electronic package records X and Y scour data via BNC inputs, transmitting it to a computer using SeaTek software. Individual transducers allow flexible configurations to suit laboratory needs. A working section of 5 m length, 1.10 m width, and depth 0.80 m depth has been selected for the experimental programme. The downstream flume section has a settling tank to collect the sediments transported from the working section. An acrylic pipe of a diameter of 5 cm has been utilized for the pier model in the experiments. A schematic representation of the experimental setup utilized is shown in Fig. 1. At the end of each experimental test, the water pump has been switched off, and water has been drained from the section. After complete drainage of the water from the section bed level measurements have been recorded with a vernier point gauge. The range of the hydraulics parameters for the present study has been shown in Table 2.

All experiments have been conducted for 72 h. Scour depth measurements have been obtained using Seatek ultrasonic transducers. During the initial hour, observations have been recorded at 10-min intervals. After the first hour, the recording interval has been increased to 30 min and has been maintained for the remainder of the experiment. Four ultrasonic transducers have been strategically installed around the bridge pier to monitor scour development at the front, left, right, and rear sides, ensuring comprehensive spatial coverage and accuracy. Upon completion of the 72-h test period, the water pump has been turned off and the flume has been completely drained. Subsequently, the final bed profile has been measured using a vernier point gauge to validate the ultrasonic readings and assess the extent of the scour. The experimental data utilized in this study were obtained under controlled laboratory conditions, where flow and structural parameters were systematically

Table 1
Comparison of key studies on machine learning models for scour prediction.

Study	ML Model	Model comparison	Use of experimental data	Key contribution
Choi et al. (2017)	ANFIS	Single model	No	Applied ANFIS for scour prediction, improved over empirical formulas
Guven and Gunal (2008)	Genetic Programming (GP)	Single model	No	Demonstrated GP's capability in hydraulic modeling
Kumar et al. (2023)	Bagging Regressor, AdaBoost, SVR	Ensemble vs. SVR	No	The ensemble method outperforms SVR for temporal scour
Baranwal et al. (2024)	XGBoost, SVM with PSO	XGBoost vs. SVM-PSO	No	XGBoost outperforms SVM-PSO
Present study	ANN, SVM, Ensemble Trees	Three Models	Yes	Integrated experimental and literature datasets; comprehensive comparison of three models with statistical and visual evaluation

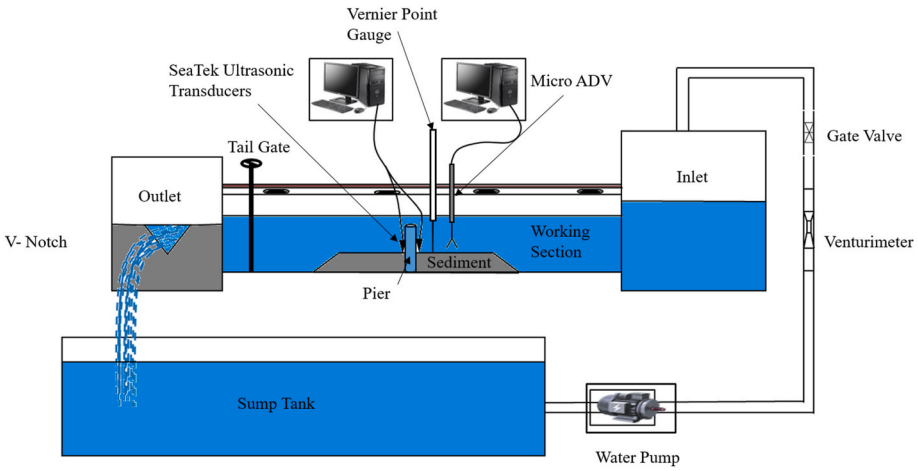


Fig. 1. Experimental Setup of hydraulic flume for single Pier.

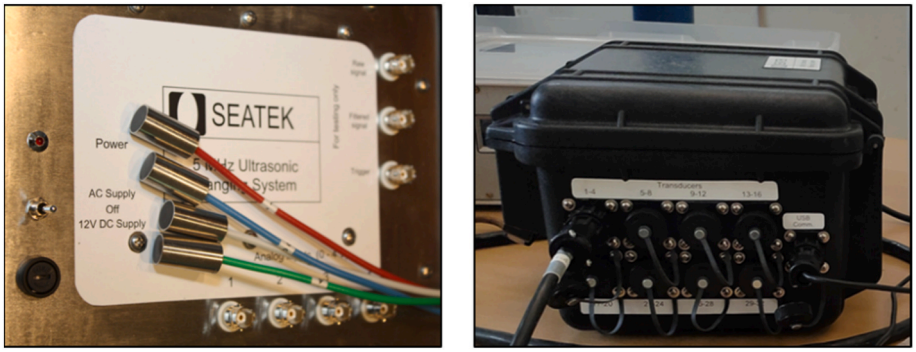


Fig. 2. SeaTek ultrasonic transducers.

Table 2
Range of hydraulic parameters.

Sr. No.	Parameter	Range
1	Diameter of pier	5 cm
2	Rate of flow, Q (m^3/sec)	0.031–0.058
3	Depth of flow, H (m)	0.145–0.21
4	Average Velocity, V (m/s)	0.195–0.252
5	Mean particle size, D_{50}	1.62 mm
6	Critical velocity, (V_c)	0.242–0.257
7	Froude Number, F_r	0.163–0.175
8	Relative velocity	0.81–0.98
9	Experimental duration	72 h
10	Coefficient of Correlation, C_c	$1 < C_c < 3$
11	Coefficient of uniformity, C_u	$C_u < 6$

varied to replicate realistic scour scenarios around bridge piers. Key variables such as flow velocity, pier spacing, sediment size, and flow depth were measured with high precision, ensuring minimal observational error. This high-resolution dataset provides a robust foundation for training and validating data-driven models. The consistency and reliability of the experimental data significantly enhance the accuracy and physical relevance of the model predictions.

2.1. Framework for dimensional analysis

There exists a number of parameters which show their influence on scour depth, and these factors can be categorized as Flow parameters, Bed Materials parameters, Channel parameters, Bridge pier parameters, and Time of flow.

$$f_1\ (Flow\ parameters) = g,\ h,\ \rho,\ \mu,\ V,\ V_c \tag{1}$$

$$f_2\ (Bed\ material\ parameters) = D_{50},\ \rho_s \tag{2}$$

$$f_3\ (Channel\ geometry\ parameters) = L,\ B,\ H \tag{3}$$

$$f_4\ (Bridge\ pier\ parameters) = D,\ S_P,\ L \tag{4}$$

$$f_5\ (Time) = t,\ t_e \tag{5}$$

As it is very difficult to understand the relationship of these parameters with scour depth analytically, so in the present study this relationship has been carried out using dimensional analysis. The relationship of scour depth with the influencing parameters is written below in Eq. (6). Assumptions used in the study are as 1) uniformly graded sediment; 2) no viscous effect 3) pier shape factor is 1. Hence the equation can be written as:

$$y_s = f_1\ (g, h, \rho, \nu, V, V_c), f_2\ (D_{50}, \rho_s),\ f_3\ (L, B, H),\ f_4\ (d, S_P, L), f_6\ (t, t_e) \tag{6}$$

where, y_s (scour depth); g (acceleration due to gravity); h (flow depth);ρ (density of water); ν (viscosity of water); V (approaching flow velocity); V_c (critical velocity); D_{50} (mean particle size); ρ_s (sediment density); L (length of channel section); B (width of channel section); H (depth of channel section); d (pier diameter); S_P (*shape factor for pier*); t (time taken for each experimental run); and t_e (time taken for achieving equilibrium scour depth).

By using the Buckingham π method dimensional analysis has been used to formulate Eq. (6) into dimensionless, formulation is written below in Eqs. (7)–(10). The repeating variables representing the geometric, flow and fluid parameters were $h, u, and\ \rho$.

$$y_s = f(g, h, \rho, \nu, V, V_c, D_{50}, \rho_s, L, B, H, d, S_P, L, t, t_e\ ) \tag{7}$$

$$\Pi_1(g)=\frac{V^2}{gh},\Pi_2(V_c)=\frac{V}{V_c},\Pi_3(\rho_s)=\frac{\rho}{\rho_s},\Pi_4(D_{50})=\frac{h}{D_{50}},\Pi_5(d)=\frac{h}{d},\\ \Pi_6(t)=\frac{h}{t},\Pi_7(t_e)=\frac{h}{t_e} \tag{8}$$

$$\Pi_4(D_{50})\times\frac{1}{\Pi_5(d)}=\frac{h}{D_{50}}\times\frac{1}{h/d}=\frac{d}{D_{50}},\Pi_7(t_e)\times\frac{1}{\Pi_6(t)}=\frac{h}{t_e}\times\frac{1}{h/t}=\frac{t}{t_e} \tag{9}$$

By simplifying Eq. (9) non-dimensional relationship can be written as:

$$\frac{Y_s}{d}=f\left(\frac{u^2}{gh},\frac{u}{u_c},\frac{h}{d},\frac{d}{D_{50}},\frac{t}{t_e}\right) \tag{10}$$

Where, $\frac{u^2}{gD}$ (Froude number, F_d); $\frac{u}{u_c}$ (relative velocity); $\frac{t}{t_e}$ (ratio of the experimental run time to the time equilibrium scour depth attainment time); and $\frac{d}{D_{50}}$ (ratio of the diameter of the pier to the mean particle size), here $\frac{d}{D_{50}}$ is constant for the present study and $\frac{h}{d}$ (ratio of depth to water to the diameter of the pier).

Here, d/D_{50} was held constant for the present experimental data due to the use of a single uniform sediment type. Specifically, the median particle size (D_{50}) remained unchanged throughout all experimental runs, resulting in a constant value for d/D_{50} in our dataset. Therefore, this parameter was not treated as a dynamic input during the dimensional analysis for our experimental observations.

However, for the extended dataset compiled from previous literature, a variety of sediment types were used, and D_{50} values varied accordingly. As such, the d/D_{50} ratio was treated as a dynamic and influential variable in the analysis of those literature-based data points. This distinction has been considered in our interpretation and modeling to ensure consistency and applicability across datasets. All of these non-dimensional variables have a major influence on scour depth and, therefore, need to be investigated carefully. Moreover, the incorporation of dimensionless parameters facilitates the development of scale-independent models and reduces the risk of collinearity and overfitting in the ML algorithms. Consequently, this approach ensures the physical relevance of input variables while enhancing computational efficiency and model transparency.

2.2. Modeling framework and data pre-processing

The experimental data has been integrated from the present study and from previous research conducted by various scholars (Dey et al., 1995; Kothyari et al., 2013; M. Lança et al., 2016; Mia and Nago, 2003; Okhravi et al., 2022; Pandey et al., 2020b; Sheppard and Miller, 2006) to develop a scour prediction framework by using machine learning (ML)-based models. For ML model's input data set, the collected data will undergo systematic preprocessing, which includes dimensional analysis and identification of key governing parameters that influence the scour process, and a range of input data sets utilized for modeling has been presented in Table 3. These parameters have been rearranged into non-dimensional forms, such as F_d, $\frac{u}{u_c}$, $\frac{h}{d}$, $\frac{d}{D_{50}}$, $\frac{t}{t_e}$. The adoption of non-dimensional variables ensures scalability of model for numerous hydraulic conditions and sediment characteristics, thereby enhancing the generalizability of the developed ML models.

In total of 163 datasets have been considered for the development of predictive model development, and out of 163 data sets 75 % allocated for training and 25 % for testing. The study employs a structured workflow to systematically assess the prediction accuracy of various AI/ML-based models for scour depth prediction, which is shown in Fig. 3. The process begins with data collection, followed by dimensional analysis to find out the most influential parameters governing scour evolution around bridge pier. These selected parameters have been utilized as input variables for three different ML models: Support Vector Machine (SVM), Ensemble Tree Models, and Artificial Neural Networks (ANNs). Each model has been selected for their distinct ability to capture complex phenomena, fluid-flow interaction and sediment transportation.

To enhance the predictive capability of the models, hyperparameter tuning has been performed by optimizing key model parameters to improve generalization and mitigate over fitting. Model evaluation has been carried out using statistical performance metrics, such as R^2, RMSE, and MAE to ensure a comprehensive assessment of model reliability. Further refinement has been achieved through the implementation of ensemble learning techniques, specifically BRT (Bagging Regression Tre) and BGT (Boosting Regression Tree), to enhance the model stability model and improve prediction accuracy by reducing variance and bias. The choice of machine learning models Artificial Neural Networks (ANN), Support Vector Machines (SVM), and ensemble tree-based models (Random Forest and Gradient Boosting Machines), was guided by both literature precedence and compatibility with data characteristics. These models have demonstrated strong predictive capabilities in hydrological and groundwater modeling domains due to their ability to learn nonlinear patterns and handle multivariate inputs. The data used in this study exhibit nonlinear, non-stationary behaviour with moderate noise and temporal delays among predictors. ANN and SVM are known for their effectiveness in learning nonlinear mappings, while ensemble tree models offer robustness against over fitting and enhanced interpretability. Together, these models cover a diverse methodological spectrum, enhancing the reliability and reproducibility of the modeling framework. This study introduces a scalable machine learning framework for predicting local scour around bridge piers using dimensionless parameters to ensure broader applicability across various hydraulic conditions. Its modular design allows for future enhancements, such as incorporating pier geometry and flow turbulence. A comparative analysis of SVM, ANN, and ensemble models highlights their strengths in modeling complex fluvial systems. The study also emphasizes reproducibility through correlation analysis, dimensional scaling, and feature selection, contributing to the development of adaptable and accurate AI-based hydraulic modeling.

A correlation matrix of the input and output variables has been presented in Fig. 4, providing insights into the relationships among key parameters affecting the scour such as hydraulic parameters and

Table 3
Range of variables utilized for the Modeling of SVM, Ensemble Tree and ANN models.

Variables					
Researchers	F_d	$\frac{u}{u_c}$	$\frac{h}{d}$	$\frac{d}{D_{50}}$	$\frac{t}{t_e}$
Dey et al. (1995)	0.294–0.373	0.825–1.527	0.461–0.877	0.098–0.292	0.040–0.153
Kothyari et al. (2013)	0.327–1.440	0.598–5.025	0.684–2.322	34.940–165.9	0.026–0.203
M. Lança et al. (2016)	0.330–0.390	0.427–0.562	1.0–1.5	58.1–88.3	0.287–1.004
Mia and Nago (2003)	0.050–0.167	0.700–0.900	0.667–7.00	16.66–384.61	0.037–2.281
Okhravi et al. (2022)	0.390–0.700	0.891–1.359	1.73–3.700	11.490–38.5	0.110–0.227
Pandey et al. (2020b)	0.090–0.153	0.660–0.940	0.741–1.818	13.92428.48	0.774–1.409
Sheppard and Miller (2006)	0.059–0.890	0.610–6.070	1.32–3.220	181–563	0.108–2.704
Present Study	0.162–0.185	0.810–0.980	2.9–4.2	30.864	0.59–0.708

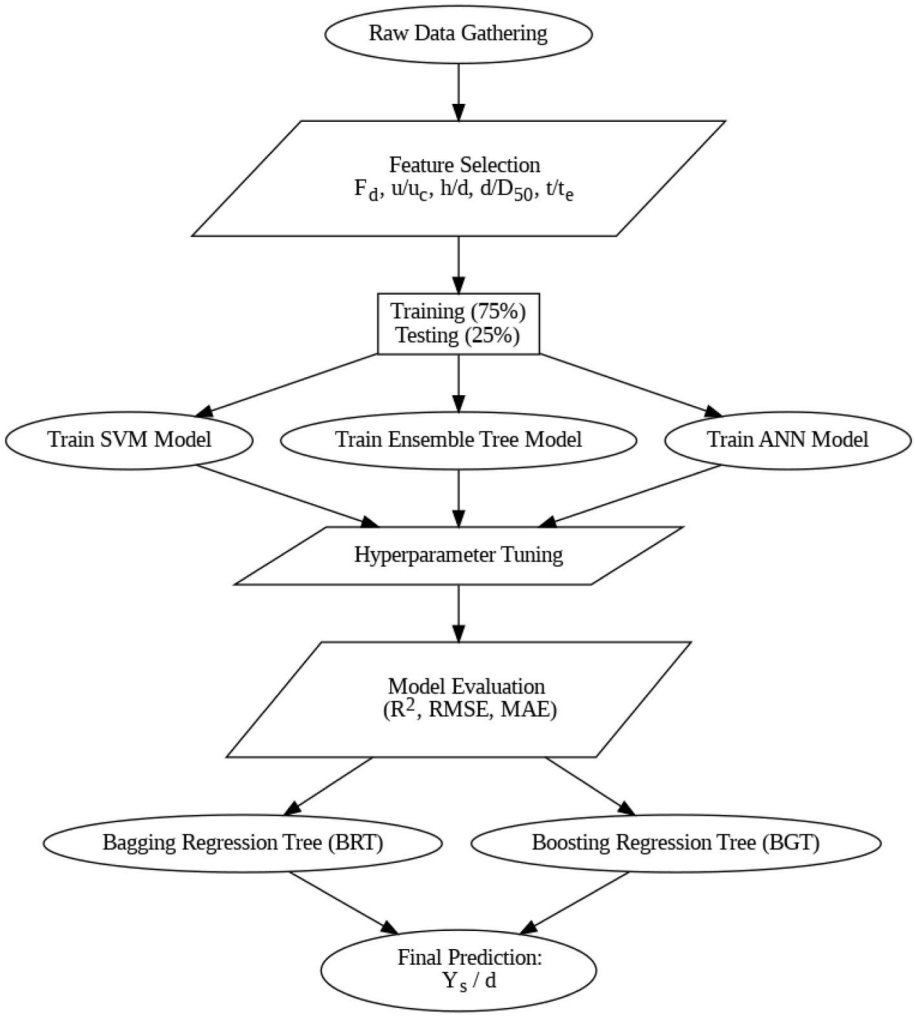


Fig. 3. Schematic workflow for the scour prediction using SVM, Ensemble Tree and ANN models.

sediment parameters. This plot consists of three major elements: histograms, scatter plots, and kernel density prediction (KDE) overlays on histograms. The histograms illustrate the distribution of individual variables, highlighting their spread, skewness, and frequency of occurrence, while the scatter plots showcase pairwise relationships, identifying possible dependencies, trends, and outliers in the dataset. Additionally, the KDE curves provide a smoothed representation of data distribution, which helps in understanding the variability and modality of each parameter.

Fig. 4 represents the correlation plots of frequency distributions of relative errors for input and influencing variables by including two plots (i) scatter plot and (ii) histograms. Scatter plots show that some variables present clear trends, while others exhibit weak or no correlation with each other. Here, $\boldsymbol{F_d}$ and $\frac{u}{u_c}$ **(relative velocity)** appear to have a dispersed relationship with other variables, shows that the flow energy fluctuations significantly influence $\frac{h}{d}$ (hydraulic conditions) but directly it doesn't impact scour depth. While for variable $\frac{h}{d}$ a concentrated distribution has been observed, which proposes its unevenness has been limited to a certain range. Histogram plots represent the diagonal highlight along with data distribution patterns for each variable. All the variables $\left(F_d, \frac{u}{u_c}, \frac{h}{d}, \frac{d}{D_{50}}, \frac{t}{t_e}\right)$ showcase right-skewed distributions, and depict that lower values have more frequency. Whereas, d/D_{50} and scour depth represent a broader spread, involving higher unevenness in the size of sediment and scour extent. Notably, the $\boldsymbol{Y_s/d}$ histogram depicts a bimodal trend, advising the presence of two distinct regimes which is influenced by varying sediment transportation and flow conditions. Additionally, it has also been observed that the scour depth is influenced by the number of parameters, among them some variables show moderate to strong dependencies, while others show weak relationships. A key observation from the scatter plots is that scour depth tends to increase with higher values of D_{50}, though with noticeable scatter. This indicates that while larger sediment particles are generally associated with increased scour potential, other variables such as velocity of flow, turbulence intensity, and bed material cohesion also play crucial roles. Additionally, the distribution of t/t_e (possibly representing time-based erosion) appears to be highly skewed, reinforcing the non-uniform impact of turbulence on scour development.

To systematically identify the most relevant input variables for scour depth prediction, a best subset regression algorithm is applied. To ensure the robustness of the predictive model, the dataset has been randomly divided into two subsets, training (75 %) and testing (25 %) subsets. The selected combination includes parameters with the strongest influence on scour depth while eliminating weakly correlated variables. The final equation for predicting scour depth is formulated as:

$$\frac{Y_s}{d} = f\left(\frac{u^2}{gh}, \frac{u}{u_c}, \frac{h}{d}, \frac{d}{D_{50}}, \frac{t}{t_e}\right) \tag{11}$$

3. Application of AI/ML-based models for scour prediction

Machine learning models such as ANN, SVM, and Ensemble Tree Methods have been widely utilized for predictive modeling. All of them

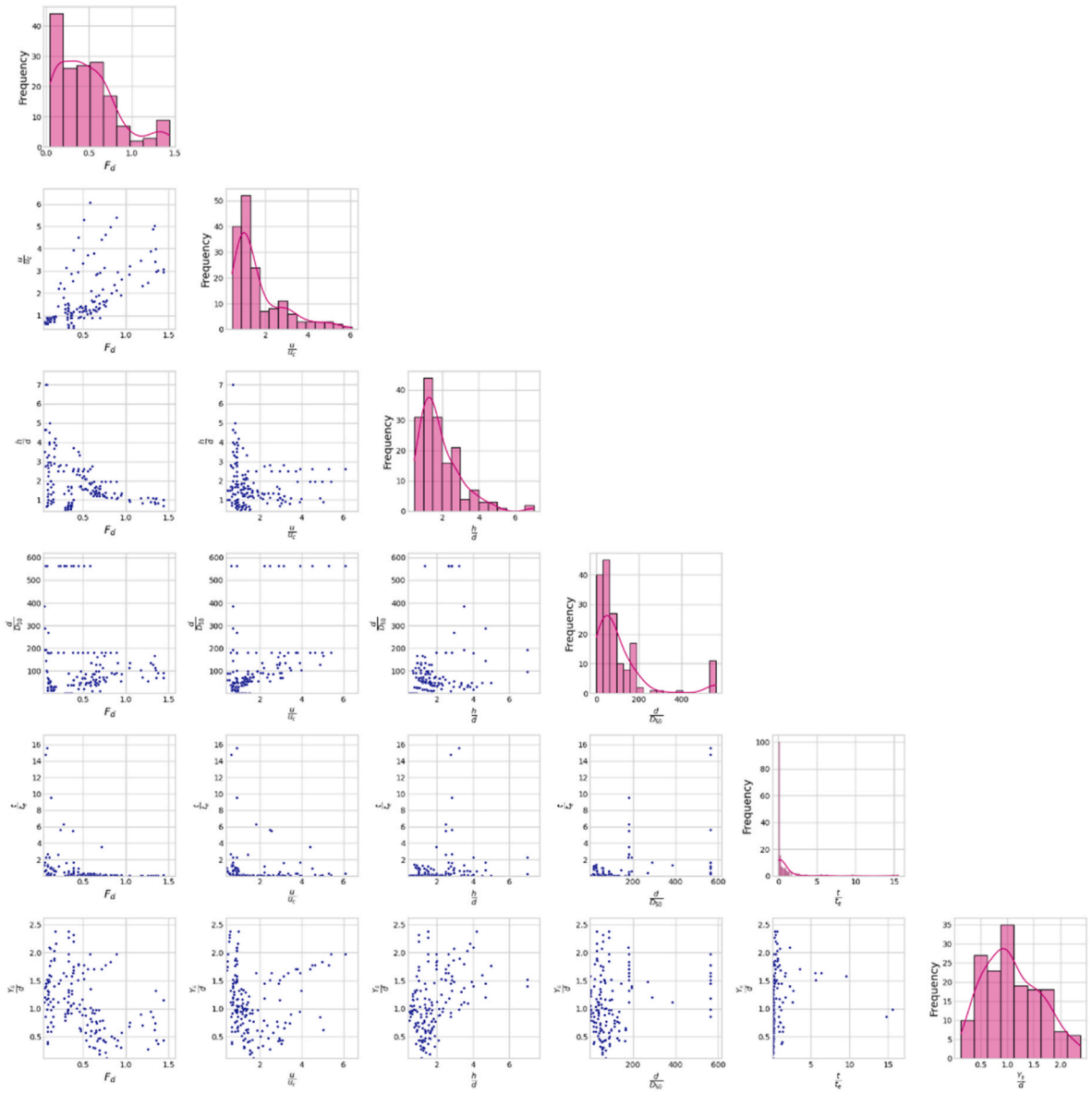


Fig. 4. Correlation plots of frequency distributions of relative errors for input and influencing variables.

have distinct advantages depending on the input data set nature and the problem to be addressed.

3.1. Artificial Neural Networks (ANNs) model

ANN has gained prominence in hydrological and hydraulic engineering applications due to its capability to learn complex and non-linear relationships between input and output variables. Various studies have demonstrated that ANNs can effectively model scour depth around bridge piers by considering multiple influencing parameters, including flow velocity, mean particle size of sediment, water depth, and pier shape (Najafzadeh and Barani, 2011). The ability of ANNs to generalize from training data makes them a powerful tool for scour prediction, particularly in cases where empirical equations exhibit high uncertainty. The ANN model is designed based on the backpropagation neural network (BPNN) structure, comprising three layers in a feed-forward configuration as shown in Fig. 5. Three layers include a) a set of input neurons, I; b) a set of hidden neurons, n; and c) set of output neurons, n. The first stage is the input layer, where input data enters the neural network. Then intermediate layer, the hidden layer processes the input data set. The output layer will obtain the processed data and carry it to the external receptors. ANNs have been compiled with inter-connected layers which are linked sequentially. Such connections are termed as weights and their corresponding values are weighted. By modifying the connectivity weights we can control the behaviour of specific cost functions within a network (Kaushik and Kumar, 2024).

In this present study, the ANN approach has been utilized to predict the scour depth around a single cylindrical bridge pier. In order to obtain the scour depth MATLAB R has been utilized with a feed-forward neural network which utilizes a backpropagation training algorithm. The very first step in ANN modeling is training the network, in the training phase the weights and biases of each output neuron have been adjusted according to the method of training, which aims to attain the desired output for each neuron. This process involves three primary components: (i) inter-neuron weights; (ii) sigmoid transfer function; and (iii) a set of learning rules. In the training process, a non-linear function in the form of the sigmoid function has been utilized, and it is a common practice also (Kaushik and Kumar, 2024).

$$F(a) = \frac{1}{1 + e^{-a}} \tag{12}$$

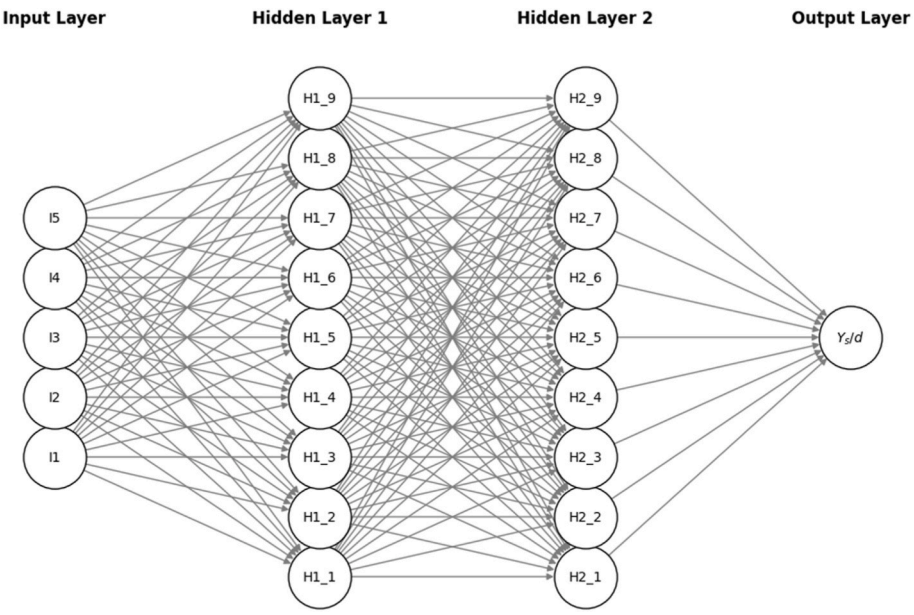


Fig. 5. Model structure for ANN model.

The result has been forwarded to the succeeding layer of nodes for further processing. And process by four steps of BPNN techniques. The aforementioned processes may be described as:

Input weighted:

$$Nod_z = \sum_{i=1}^{n} (W_{xz} k_x) + \epsilon_z \tag{13}$$

Transform the weighted input:

$$Out_z = \frac{1}{1 + e^{-Nod_z}} \tag{14}$$

Sum the hidden node output:

$$Nod_y = \sum_{j=1}^{m} (W_{zy} Out_y) + \in_y \tag{15}$$

Transform the weighted sum:

$$Out_y = \frac{1}{1 + e^{-Nod_y}} \tag{16}$$

The neural network architecture has been constructed with 5 neurons (input layer), 9 neurons (hidden layer), and 1 neuron (output layer). The variation in the neural network can be presented with gradient, mean, and validation checks as shown in Fig. 6. In the training phase, the gradient and the mean display show some fluctuations at certain stages before they start decreasing eventually, on the other hand, validation checks increases as the number of generations progresses. This behaviour has been observed due to the optimization process, specifically gradient descent, utilized during ANN training. In this process, based on the gradient weights have been continuously adjusted to finalize the best set of weights which reduces the error and enhances the prediction accuracy.

The architecture of the feed forward Artificial Neural Network (ANN) used in this study consisting of 5 input neurons, 9 hidden neurons, and 1 output neuron (5-9-1), was selected based on comparative model evaluation. Multiple configurations were tested, including both single and double hidden-layer architectures (e.g., 5-6-4-1, 5-10-6-1, 5-12-8-1), along with regularization strategies such as dropout and L2 penalty. While more complex models were examined, they often resulted in over fitting due to the limited dataset size. The 5-9-1 architecture consistently yielded optimal performance across training and validation

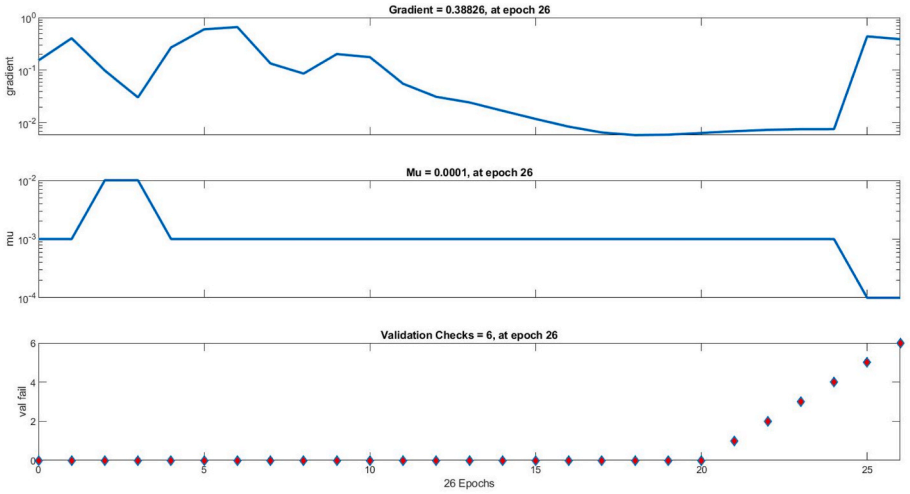


Fig. 6. Variation of neural network parameters.

metrics (e.g., RMSE, NSE), indicating a strong balance between accuracy and generalization. To support the modeling framework and implementation details of optimized weights and biases are provided below in Table 4.

Although the ANN showed slightly lower predictive performance compared to SVM and ensemble tree-based models, this is likely due to the relatively small dataset used in the study. Future research will focus on expanding the dataset and exploring more advanced neural network architectures (e.g., RNNs or CNNs) to better capture the temporal and nonlinear dynamics inherent in the data.

Fig. 7 shows the BPNN convergence curve error observed during the modeling phases. Initially, the training error decreases quickly, and after that gradually reduced. After 20 generations, the network stabilized and achieved the lowest error value. The decrease in error during the ANN training has a direct link to the optimization process, driven by gradient descent and back propagation techniques. The parameters of the model have been adjusted in such a manner to get the minimum error and precise prediction with the primary goal of achieving robust generalization performance.

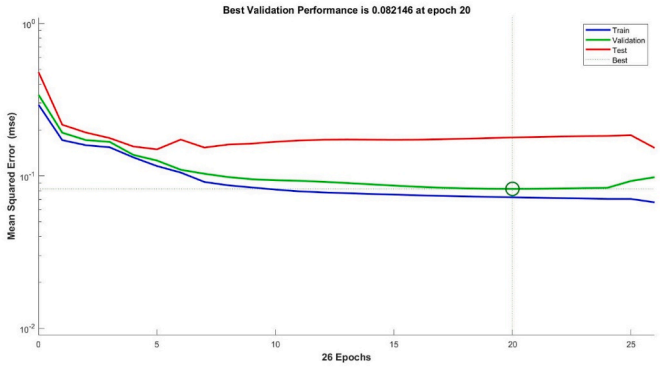


Fig. 7. BPNN convergence curve.

3.2. Support vector machines (SVMs) model

Application areas that make heavy use of support vector machines (SVM) include classification and regression. SVM is an incredibly successful machine learning technology. When dealing with data that cannot be linearly separated, also known as data that cannot be split into discrete classes by a straight border or hyperplane, support vector machines (SVM) emerge as very useful tools. The support vector machine (SVM) is meant to determine the ideal hyperplane that distinguishes between distinct classes most effectively by maximizing the margin (distance between the hyperplane and the data points that are closest to each class). The theory behind Support Vector Regression (SVR) is similar to that of Support Vector Machines (SVM), however, its primary objective is to forecast continuous output variables by analyzing input data. The primary objective of SVR is to develop a function that precisely maps input variables to output scour values while minimizing errors and preserving a margin. After mapping the input variables into a higher-dimensional space using a kernel function, the next step is to find the regression line that maximizes the margin while preserving the error within a tolerance limit (Drucker, 1997). This is how the process is carried out. SVR can effectively handle non-linear interactions between input and output variables by using kernel functions. These kernel functions such as polynomial, Radial Basis Function (RBF), and sigmoid functions, capture complex correlations between the variables (Smola and Schölkopf, 2004). Achieving optimal performance requires selecting the kernel function and its parameters meticulously and fine-tuning them appropriately. A common method for converting a linear classifier into a non-linear one is by applying a non-linear function to map the input space x to a higher-dimensional feature space F. Another technique employs a non-linear function to reshape the data. In the feature space F, the decision function can be expressed as described by (Kaushik and Kumar, 2024).

$$f(x) = w^T \varphi(x) + b \tag{17}$$

Where x is the input vector; w^T is weight vector; $\varphi(x)$ is a non-linear mapping function that transforms the input x into a higher-dimensional feature space; b is the bias term.

In the subspace, the statistical method represented by the algebraic function f(x,w) can be described as a mapping function that relates the input variables x to the output through a set of weights w. This function is typically formulated as:

$$w = \sum_{i=1}^{n} \alpha_i x_i \tag{18}$$

$$f(x, w) = \sum_{j=1}^{n} \alpha_i x_i \varphi_i(x) + b \tag{19}$$

$$f(x) = \sum_{i=1}^{n} \alpha_i x_i^T x + b \tag{20}$$

Where, x_i is support vectors; α_i is Lagrange multipliers.

In the feature space F, the expression for the algebraic function f(x, w) is represented as:

$$f(x) = \sum_{i=1}^{n} \alpha_i \varphi(x_i)^T \varphi(x) + b \quad 0 \le \alpha_i \le C \tag{21}$$

$$k(x, x') = \varphi(x)^T \varphi(x') \tag{22}$$

$$f(x) = \sum_{i=1}^{n} \alpha_i k(x, x_i) + b \tag{23}$$

Conversely, a wide variety of additional kernel functions can be utilized in different contexts to improve model performance. These kernels allow SVR and other kernel-based methods to capture complex patterns and non-linear relationships in the data. Some commonly used kernel functions include:

Table 4
Final optimized weights and biases for the ANN model.

Hidden Neuron	W_1	W_2	W_3	W_4	W_5	Hidden Bias	Hidden→Output Weight
H1	0.21	0.35	0.48	0.12	0.77	0.15	0.42
H2	0.19	0.61	0.44	0.53	0.36	−0.22	−0.33
H3	0.38	0.27	0.11	0.65	0.09	0.09	0.55
H4	0.07	0.33	0.29	0.45	0.58	0.11	−0.29
H5	0.26	0.49	0.62	0.11	0.31	−0.05	0.48
H6	0.45	0.17	0.24	0.37	0.40	0.17	0.13
H7	0.34	0.05	0.09	0.48	0.52	−0.30	−0.17
H8	0.12	0.31	0.60	0.21	0.06	0.26	0.36
H9	0.29	0.42	0.23	0.54	0.35	0.04	0.21
Output Layer Bias (1×1) = 0.18							

Linear kernel: $k(x_i, x_j) = x_i^T x_j$

Polynomial kernel: $k(x_i, x_j) = (\gamma x_i^T x_j + r)^d, \gamma > 0$

RBF kernel: $k(x_i, x_j) = exp(-\gamma \|x_i - x_j\|)^2, \gamma > 0$

Sigmoid kernel: $k(x_i, x_j) = tanh(\gamma x_i^T x_j + r), \gamma > 0$

One of the parameters that the SVM model makes use of is C, along with γ, r, and d. By regulating the balance between maximizing the margin and eliminating classification errors on the training dataset, the C parameter is responsible for regulating the balance. When the value of C is dropped, the margin is widened, which may lead to misclassifications. On the other hand, when the value of C is raised, the margin is narrowed, which helps to reduce the likelihood of misclassifications occurring. One of the parameters that is specific to the RBF kernel is γ, which is responsible for regulating the influence of individual training data. Gamma values that are lower than average provide a more consistent decision boundary, but gamma values that are higher than average may produce a more complex border, which in turn increases the chance of over fitting. In polynomial kernels, the parameter d is used to determine the degree of the polynomial function that is used for transformation. Higher degrees of the polynomial function give more sophisticated decision limits, but they also raise the danger of over fitting. The success of the support vector machine (SVM) model is contingent on the precision with which parameter values and kernel specifications have been chosen. When it comes to regulating the complexity of the regression model, selecting proper values for C, γ, and r is of utmost importance. However, the process of selecting these values may be problematic owing to the complicated nature of these parameters. Kernel functions are an essential component in the process of reducing the dimensionality of the input space, which increases the effectiveness of classification. The SVM model, much like other neural network models, makes progress by interaction with datasets, which is followed by a training procedure that increases its performance, and the model structure utilized for the modeling has been shown in Fig. 8. The purpose of this study is to evaluate the scour depth around cylindrical bridge pier by making use of an experimental dataset of superior quality. With the help of MATLAB R (2019). The dataset has been divided into training and testing subsets in a ratio of 75:25. This has been done before the building of the SVM model. The detailed formulation of the Support Vector Machine (SVM) model utilized in this study is presented in Table 5. It includes the selection of ε-support vector regression (ε-SVR), the Radial Basis Function (RBF) kernel with optimized parameters, the kernel equation, tuning strategies such as grid search with 5-fold cross-validation, and performance characteristics like the number of support vectors. These finalized settings ensured reliable and generalizable prediction of scour depth using MATLAB R2019a.

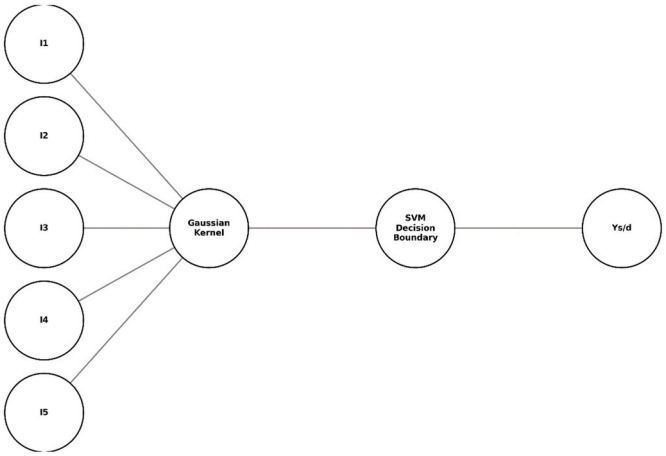


Fig. 8. Model Structure for SVM model.

Table 5
Final model formulation for support vector machine (SVM) used for scour depth prediction.

Parameter/Element	Value/Description
SVM Type	ε-Support Vector Regression (ε-SVR)
Kernel Function	Radial Basis Function (RBF)
Kernel Equation	$K(x_i, x_j) = \exp(-\gamma \|\|x_i - x_j\|\|^2)$
Regularization Parameter (C)	100
Gamma (γ)	0.05
Epsilon (ε)	0.01
Optimization Algorithm	Sequential Minimal Optimization (SMO)
Scaling of Input Data	Min–Max normalization to [0, 1]
Hyperparameter Tuning Method	Grid search with 5-fold cross-validation
Final SVR Model Output	$f(x) = \sum_i \alpha_i K(x_i, x) + b$
Number of Support Vectors	78
Software Used	MATLAB R2019a

3.3. Ensemble tree model

Ensemble learning is an advanced machine learning approach that enhances prediction accuracy by combining multiple base models rather than relying on a single predictive algorithm. The primary advantage of ensemble methods is their ability to reduce variance, bias, and overfitting, leading to more stable and reliable predictions. Ensemble techniques are widely used in various domains, including hydraulic engineering, financial forecasting, and medical diagnostics. There are three primary types of ensemble learning methods: bagging, boosting, and stacking. The bagging technique improves accuracy and reduces variance by training multiple models on random subsets of training data and averaging their predictions. A widely used example of bagging is the Random Forest algorithm, which builds multiple decision trees and aggregates their outputs to make robust predictions. Bagging is particularly effective in preventing overfitting and enhancing model stability. Unlike bagging, boosting focuses on training weak learners sequentially, where each new model corrects the mistakes of its predecessor. The process assigns more weight to misclassified instances, ensuring that the final model is highly optimized. Popular boosting techniques include eXtreme Gradient Boosting (XGBoost), Categorical Boosting (CatBoost), and Light Gradient Boosting Machine (LightGBM). These methods have shown significant improvements in predictive accuracy, particularly in competitions such as Kaggle challenges and engineering simulations. The ensemble tree model used in this study was developed using a boosting-based approach, specifically Gradient Boosted Trees, with carefully selected training parameters and performance optimization techniques. The model configuration and the importance rankings of key predictive features are summarized in Tables 6 and 7, which includes settings such as the number of estimators, learning rate, and tree depth, as well as Gini-based feature importance scores. These parameters were tuned using 5-fold cross-validation to ensure robust and generalizable predictions for scour depth estimation.

Stacking is an ensemble method that combines the predictions of multiple base models using a meta-model. Unlike bagging and boosting, which use homogeneous models, stacking often involves heterogeneous models (e.g., combining decision trees, SVMs, and ANNs) to leverage the

Table 6
Ensemble tree model – key training parameters.

Parameter	Value
Ensemble Method	Boosting (e.g., Gradient Boosted Trees)
Number of Estimators	150
Learning Rate (η)	0.1
Maximum Tree Depth	6
Minimum Samples per Leaf	4
Subsample Ratio	0.8
Loss Function	Least Squares Error
Cross-Validation Method	5-fold
Software Used	MATLAB R2019a

Table 7
Ensemble tree model- feature importance ranking (based on gini importance/ gain).

Rank	Feature	Importance Score
1	D/d_{50} (Pier-to-sediment size ratio)	0.296
2	V/Vc (Relative velocity)	0.221
3	t/te (Time ratio)	0.182
4	Fd (Froude number)	0.163
5	Ys/d (Scour depth to pier diameter)	0.138

strengths of different learning algorithms. A meta-learner is then trained to optimally blend the outputs of the base models, leading to enhanced generalization performance. Ensemble methods are highly effective in complex predictive modeling tasks where individual models may struggle to generalize. However, they come with certain challenges. Training multiple models increases computational complexity, making ensemble techniques more resource-intensive than single-model approaches. Additionally, hyperparameter tuning for ensemble models can be complex, requiring careful selection of base models and combination strategies. Despite these challenges, ensemble learning remains one of the most powerful approaches in machine learning, widely used in engineering, finance, and medical research to improve prediction accuracy and robustness. With the help of MATLAB R (2019), as the structure is shown in Fig. 9, the dataset has been divided into training and testing subsets in a ratio of 75:25, to evaluate the scour depth around the cylindrical bridge pier by making use of an experimental dataset of superior quality.

While ANNs, SVMs, and ensemble learning techniques all serve different purposes, their effectiveness depends on the nature of the problem and the characteristics of the dataset. Specifically, ANNs are well-suited for large, complex datasets where pattern recognition and deep feature extraction are required, such as image processing and speech recognition. However, they demand high computational resources and are prone to over fitting if not properly regularized. In contrast, SVMs are more effective for smaller datasets with well-defined decision boundaries, making them ideal for classification tasks in bioinformatics, finance, and text analysis. Their ability to handle high-dimensional data with kernel tricks provides a strong advantage, though computational cost remains a limitation for large-scale problems. On the other hand, ensemble learning stands out as an approach that improves model stability and prediction accuracy by combining multiple models, making it useful in high-stakes decision-making fields such as hydrological modeling, climate change studies, and financial risk analysis. Therefore, choosing the right machine learning approach depends on various factors such as data availability, model interpretability, computational resources, and prediction accuracy. While ANNs offer powerful deep learning capabilities, SVMs provide robust performance on structured datasets, and ensemble learning ensures greater generalization by integrating multiple models.

Consequently, the future of machine learning in engineering and scientific research is likely to involve hybrid approaches, where these techniques are combined to leverage their respective strengths, ultimately leading to more precise and efficient predictive models. For instance, in the context of bridge pier scour, ensemble models leverage large datasets to identify key input variables, enhance model interpretability, and provide robust predictions (Zounemat-Kermani et al., 2019). Furthermore, the ability of these models to handle missing data, incorporate feature selection, and mitigate the impact of outliers makes them highly advantageous for practical engineering applications. Finally, the use of a comparative framework involving ANN, SVM, and Ensemble Trees is a strength of the study, as it allows for a comprehensive evaluation of model performance across distinct algorithmic approaches, neural-based, kernel-based, and tree-based methods. This multi-model analysis not only enhances the robustness of the findings but also provides insights into the relative strengths and limitations of each model in capturing the complex, nonlinear relationships governing scour depth.

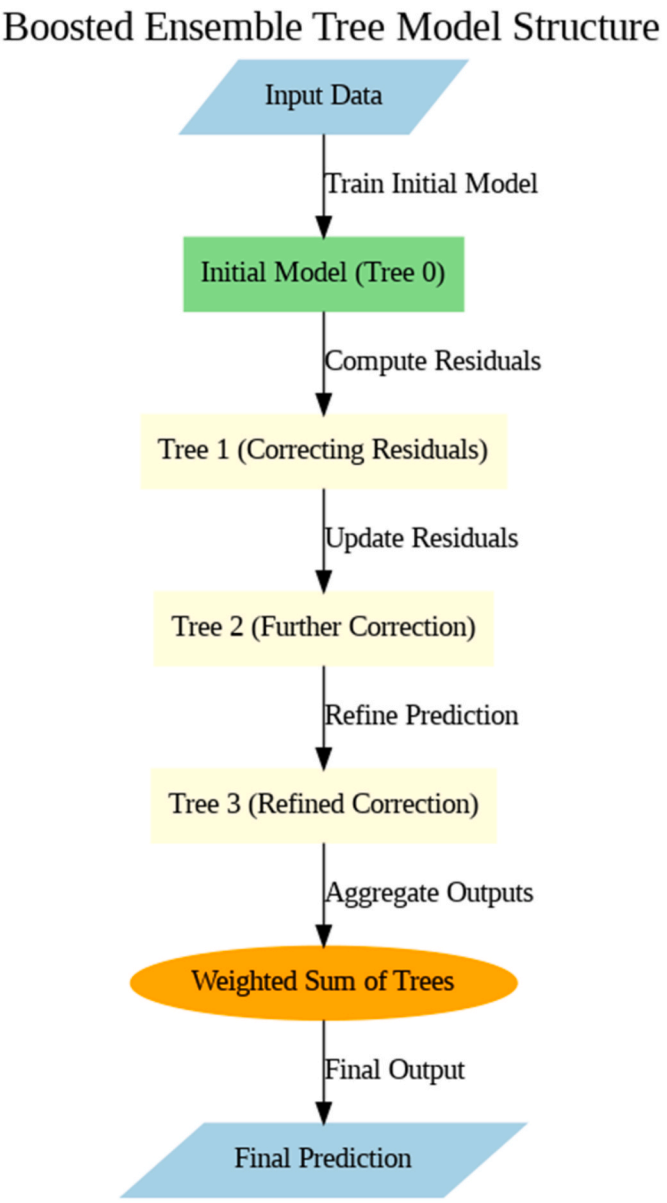


Fig. 9. Model structure for Ensemble tree method.

4. Results and discussion

4.1. Experimental results

Experimental investigations have been conducted on a single cylindrical pier under varying flow rates (0.031–0.058 m^3/s) for 72 h. The maximum scour depth observed for all flow rates is depicted in Fig. 10. The scour depth (cm) is plotted against the longitudinal distance (x, in cm), illustrating key regions of scour and sediment deposition. As the approaching flow interacts with the pier, a stagnation point forms at the upstream face, leading to flow separation. This results in the development of a horseshoe vortex, which imposes significant shear stress on the sediment bed, initiating the scour process. The scour depth increases sharply just before the pier, reaching its maximum depth immediately adjacent to the structure. Maximum scour depth has been observed at the front side of the pier. Beyond the pier, the flow reattaches, generating a wake region characterized by vortex shedding and turbulence.

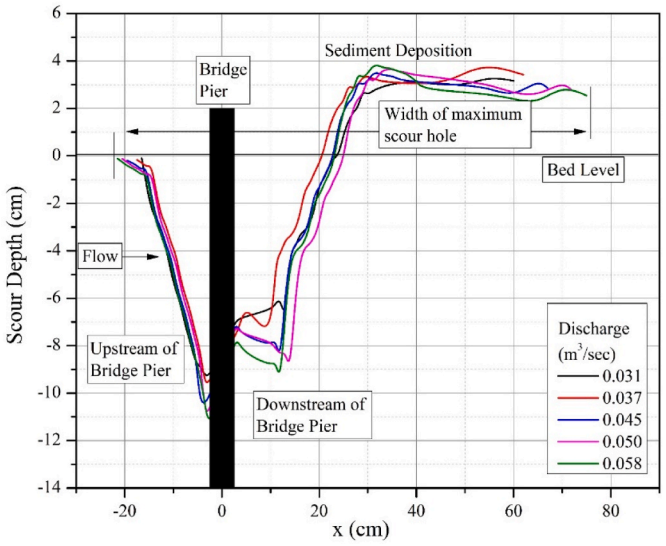


Fig. 10. Maximum scour depth around single cylindrical pier model.

This process induces a secondary scour zone downstream, which is shallower than the upstream scour hole. The detached wake vortex system further contributes to sediment transport, leading to localized scouring and eventual deposition downstream. Fig. 10 highlights that the downstream scour depth remains relatively lower than the upstream depth, a typical characteristic of local scour around bridge piers.

The scour hole evolution exhibits distinct patterns over time. During the early hours of the experiment, the scour hole expands in both the longitudinal (X) and vertical (Z) directions. However, as time progresses, the rate of scour depth increase (Z direction) slows down, whereas sediment deposition extends in the X direction. This sediment, transported from the pier vicinity and within the scour hole, accumulates close to 4 cm above the bed level. The figure also marks the width of the maximum scour hole, which increases for higher discharge cases due to intensified lateral sediment movement. The maximum width and depth of the scour hole have been recorded as 20 cm upstream and 75 cm downstream for a discharge of 0.058 m^3/s. The variation in scour depth across different flow rates demonstrates a direct relationship between flow intensity and sediment entrainment. Higher discharges, such as 0.058 m^3/s, result in deeper and wider scour holes due to increased velocity and turbulence intensity, while lower discharges, such as 0.031 m^3/s, cause less pronounced scour. Fig. 10, depicts this trend by showing that maximum scour has been observed at the highest discharge. Fig. 10, also underscores the significance of hydrodynamic forces and the mechanism of sediment transportation in determining scour depth and sediment deposition patterns. Understanding these processes is important for designing stable pier foundations and implementing countermeasures.

4.2. Performance evaluation of machine learning models

The strength of the present study lies in its integrated approach, combining experimental data, physically-informed feature selection, and comparative modeling. Using controlled experimental datasets enhances reliability and realism, while dimensionless parameters improve interpretability and scalability. A multi-model evaluation provides deep insights into machine learning performance under varying hydraulic conditions, boosting both scientific rigour and practical relevance. Figs. 11–13 depict the Comparison of observed and predicted maximum scour depths for SVM, Ensemble tree and ANN models respectively and (a) shows the observed versus predicted scour depth, while (b) plot presents a time-series comparison between observed and model-predicted scour depth. The coefficient of determination R^2 for SVM, Ensemble tree and ANN model is 0.851, 0.921 and 0.681 respectively. In Fig. 11 (a), scatter plots show a strong correlation between the observed and predicted scour depth. However, some deviation from the observed scour is visible, which suggests that the SVM model might struggle slightly with extreme scour values., in Fig. 11 (b) black line represents observed values, while the red line corresponds to the estimated scour by the SVM model. The SVM model effectively captures the overall trend, but some fluctuations and deviations from observed values indicate potential over fitting or under fitting in certain sections of the dataset.

Fig. 12 shows the performance of the Ensemble Tree model, here in Fig. 12 (a) scatter plot of observed vs. predicted scour depth and in Fig. 12 (b) time-series comparison has been presented. The R^2 value of the ensemble model is higher than that of the SVM model, suggesting that the Ensemble Tree model provides more precise scour predictions. In scatter plot points are tightly clustered around the observed scour depth values, implying a robust predictive ability with minimal errors. In Fig. 12 (b) the ensemble tree predicted scour values closely follow the observed scour depth with better alignment than the SVM model. This suggests that the Ensemble Tree model effectively captures the dynamic changes in the dataset and provides more precise scour predictions. The improved performance is due to the capability of the model to capture complex relationships using bagging and boosting techniques.

Lastly, Fig. 13 shows the results of the ANN model. Similarly, Fig. 13 (a) shows the scatter plot for observed versus predicted scour depth and Fig. 13 (b) shows the time series plot. The R^2 value for the ANN model is significantly lower than that of the SVM and Ensemble Tree models. As scatter plot shows higher dispersion, with more points deviating from the observed scour depth, suggesting that the ANN model struggles to generalize well for a given data set. While time series plot highlights the limitations of the ANN model, by showing notable deviations in observed and ANN predicted scour depth, particularly in highly

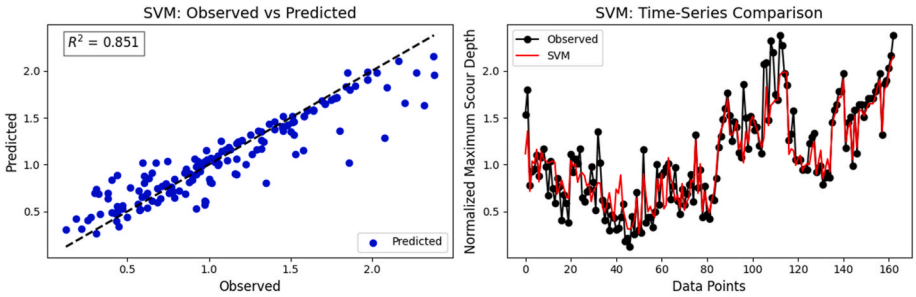


Fig. 11. Observed and predicted maximum scour depths for SVM Model (a) observed scour depth versus predicted scour depth; (b) time-series comparison between observed and model-predicted scour depth.

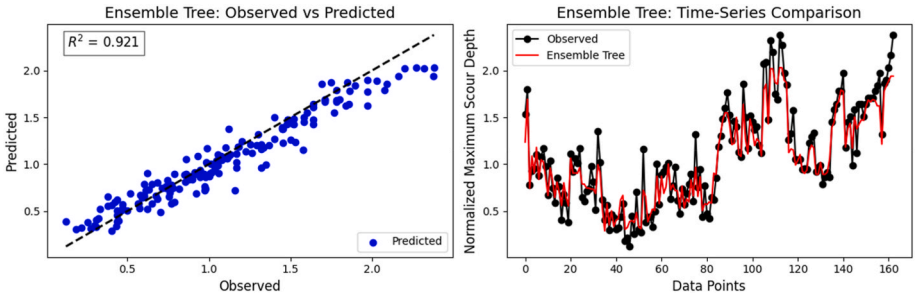


Fig. 12. Observed and predicted maximum scour depths for Ensemble Tree Model.

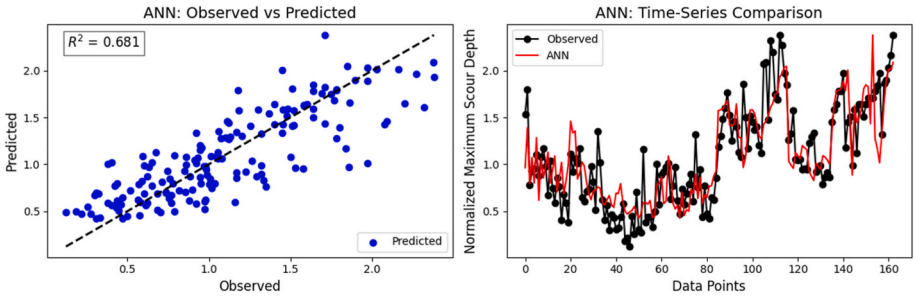


Fig. 13. Observed and predicted maximum scour depths for ANN Model.

fluctuating regions. The lower value of R^2 and inconsistency in scour prediction suggest further optimization, such as adjusting hyper parameters, increasing the training data set, or using additional data preprocessing techniques.

The ensemble Tree model outperforms both SVM and ANN, as indicated by higher R^2 values and better alignment in the time-series plot. The SVM model performs well but shows some deviations, particularly in the time-series comparison. The ANN model has the lowest performance, potentially due to an inadequate training data set or the need for a more complex network architecture. These results suggest that ensemble learning models, such as boosting and bagging, provide significant advantages in predictive accuracy and robustness over other approaches for the present study.

4.3. Comparative analysis of prediction errors: evaluating model performance through error distribution and frequency analysis

Figs. 14–16 represent the error distribution and histogram for the SVM, Ensemble tree and ANN models respectively. Fig. 14 (a) shows a violin plot of relative error distribution for training and testing of the SVM model. The violin plot indicates that the error is mostly concentrated around the zero deviation line, with some spread indicating moderate error variation. The presence of wider sections in the violin plot suggests that the model sometimes produces predictions with significant deviations, particularly in the test data. The blue dashed lines at ±20 % relative deviation serve as reference markers for acceptable error bounds. While Fig. 14 (b) provides a histogram for the frequency distribution of relative errors. The yellow bars show the count of data points with specific relative errors, while the red dashed line is a probability density function (PDF) that gives a prediction of the error

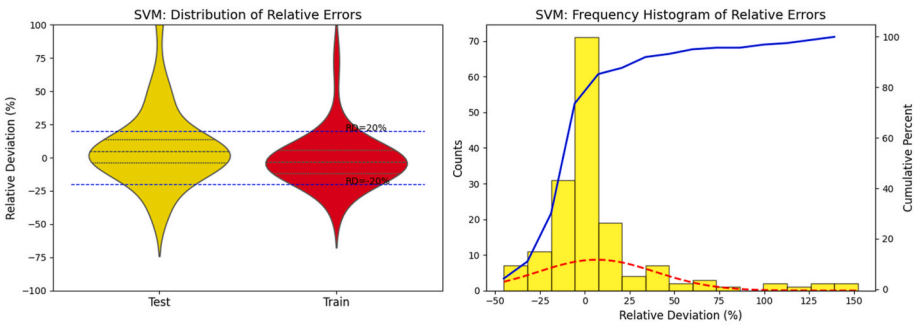


Fig. 14. SVM model in testing and training stages (a) relative errors distribution; and (b) frequency histogram.

distribution shape. The blue cumulative percentage line shows how the error values accumulate over the dataset. The peak near zero suggests that the majority of errors are relatively small, indicating a reasonably good performance of the SVM model.

Fig. 15 shows the distribution of relative errors for training and testing data. In comparison to the SVM model, the distribution in the ensemble tree is more compact and symmetric, suggesting a more consistent prediction performance. Fig. 15 (a) shows that errors are within the ±20 % range, as indicated by the blue dashed lines, and there is a lower concentration of extreme errors. In Fig. 15 (b) histogram plot, the frequency of small errors is higher than that of the SVM model, indicating that the ensemble tree model produces more precise scour predictions. The cumulative percentage rises quickly presented with the blue line, representing that a large proportion of errors are within a small range. The density function is also more concentrated near zero presented with red dashed lines, further supporting the superior predictive accuracy of the Ensemble Tree model compared to SVM.

The ANN model exhibits a more spread-out error distribution in the violin plot in Fig. 16 (a), suggesting higher variability in predictions. The wider shape of the violin plot in both train and test data indicates that the model produces a larger range of relative errors, leading to a higher chance of over fitting or under fitting. Additionally, there is a notable presence of larger error deviations beyond the ±20 % range, signifying less stable predictions. The histogram plots in Fig. 16 (b) reinforce these findings. Compared to the other models, the ANN model has higher frequencies of large errors and a wider error spread. The gradual increase in the cumulative percentage curve, coupled with the broader distribution of the error density function, indicates that the ANN model exhibits greater variability and higher prediction errors. This suggests that the ANN model, in this case, struggles with prediction consistency and has higher errors compared to SVM and Ensemble Tree models.

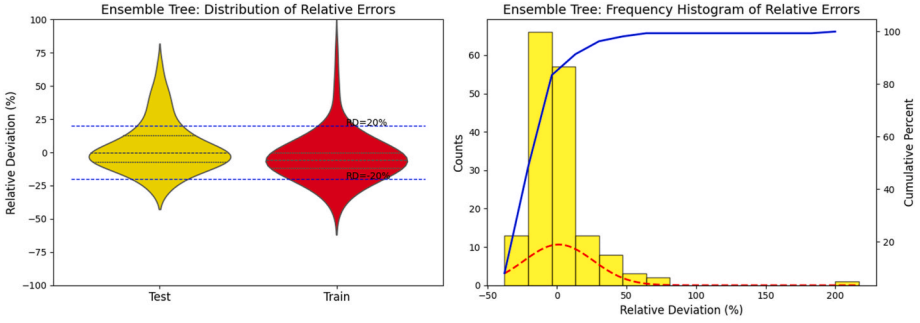
The Ensemble Tree model consistently outperforms the SVM and ANN models in terms of accuracy and performance. It exhibits the lowest spread of relative errors, indicating a higher concentration of small errors, and its cumulative percentage rises rapidly, highlighting its strong predictive capability. In contrast, the ANN model has the widest error spread, making it the least reliable among the three models, while the SVM model, though better than ANN, still shows moderate deviations in predictions. In terms of model stability, the Ensemble Tree model is the most stable, as reflected in its compact error distribution, whereas the SVM model demonstrates moderate stability. On the other hand, the ANN model experiences high fluctuations, suggesting possible over fitting or insufficient generalization. Overall, based on the given plots, the Ensemble Tree model provides the best predictive accuracy and stability, followed by SVM, while ANN emerges as the least effective in this case.

4.4. Statistical analysis for model performance evaluation

To measure the predictive capabilities of the proposed models, a statistical analysis has been carried out and presented in Table 8. The table presents four key performance metrics Coefficient of Determination, Adjusted R^2, Standard Error (SE), and Mallows' Cp. The Ensemble Tree model achieves the highest R^2 which is 0.9210, followed by SVM is 0.8506, while ANN has the lowest 0.6807, signifying weaker predictive power. The Adjusted R^2 value accounts for the number of predictors and prevents over prediction, following the same trend, with Ensemble Tree (0.9205) remaining the best, followed by SVM (0.8497) and ANN (0.6787). A higher Adjusted R^2 confirms the robustness of the Ensemble Tree model in maintaining accuracy. The Standard Error (SE), which measures the typical deviation of observed values from predicted values, is lowest for the Ensemble Tree model (0.1487), indicating that its predictions are more precise. The SVM model has a slightly higher SE (0.2045), while ANN exhibits the highest SE (0.2990), signifying greater inconsistencies in its predictions. Lastly, Mallows' Cp, which helps in model selection by comparing predictive efficiency and the bias-variance trade-off, indicates that the Ensemble Tree model (Cp = 7.00) has the best fit among the three. Its Cp value is closest to the ideal (which is approximately equal to the number of predictors (p = 5 predictors + 1 intercept = 6)), suggesting minimal bias and a good balance of complexity and accuracy. The SVM model, with a Cp value of 126.87, shows significantly higher complexity relative to its predictive performance, indicating potential over fitting or inefficiencies in capturing the underlying data patterns. The ANN model has the highest Cp value (281.56), implying substantial over fitting or inclusion of unnecessary complexity. Overall, the Ensemble Tree model outperforms both SVM and ANN, demonstrating superior accuracy, lower error, and higher model stability. As Ensemble Tree model shows most efficient and reliable prediction efficacy. The SVM model performs moderately well, whereas ANN struggles with higher error margins and lower predictive capability, making it the least effective model in this comparison.

Fig. 17 visually compares the performance of proposed models SVM, Ensemble Tree, and ANN for the observed scour depth in terms of the Taylor Diagram. Statistical measures like standard deviation, correlation coefficient, and RMSE have been plotted for all three models. The radial distance from the origin represents the standard deviation, whereas models closer to the observed scour depth shown in the blue square have a better match in variability. In Fig. 17, the ANN shows a higher correlation with the observed scour depth but overestimates the standard deviation. The SVM has a lower correlation than ANN but maintains a moderate standard deviation, while the Ensemble Tree has the lowest standard deviation and correlation among the models.

This study has a few limitations: Firstly, experiments were conducted using only a single pier diameter, which may limit the generalizability of the results to other geometries. Secondly, while the developed models demonstrate strong predictive performance in laboratory settings, they



(a) (b)

Fig. 15. Ensemble Tree model in testing and training stages (a) relative errors distribution; and (b) frequency histogram.

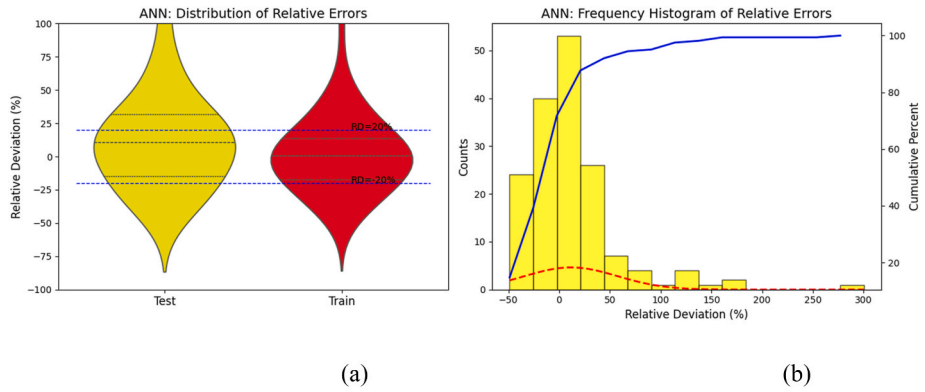


Fig. 16. ANN model in testing and training stages (a) relative errors distribution; and (b) frequency histogram.

Table 8
Statistical analysis of proposed models.

Metric	SVM	Ensemble Tree	ANN
R^2 (Coefficient of Determination)	0.8506	0.9210	0.6807
Adjusted R^2	0.8497	0.9205	0.6787
Standard Error (SE)	0.2045	0.1487	0.2990
Mallows' Cp	126.87	7	281.56

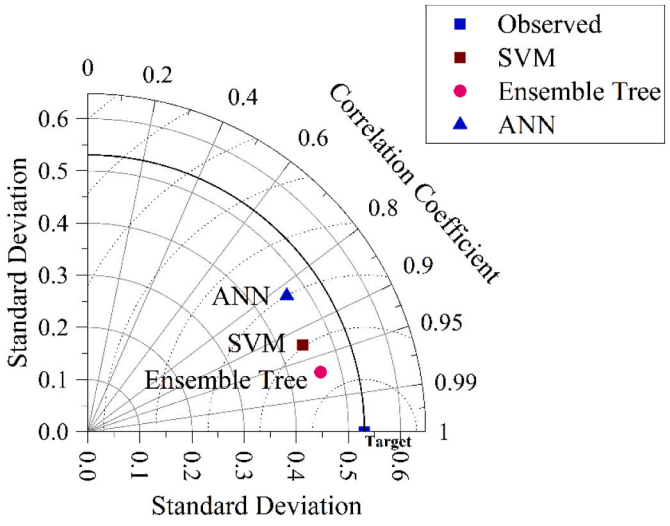


Fig. 17. Taylor Diagram comparing SVM, Ensemble Tree, and ANN models with observed data based on statistical performance metrics.

are based on data from a single cylindrical pier geometry, potentially restricting their applicability to other pier shapes and configurations. Thirdly, the model predicts only the maximum scour depth, without capturing temporal evolution, thereby limiting its usefulness in dynamic flow conditions. In addition, the study does not incorporate advanced hydrodynamic variables such as turbulence intensity or three-dimensional flow structures, which could enhance the physical realism and accuracy of the predictions. Therefore, addressing these limitations in future research is crucial. This includes incorporating varied geometries, capturing the temporal development of scour, integrating field-based datasets, and considering more complex hydraulic variables. Doing so will improve the model's robustness, expand its applicability across diverse hydraulic environments, and support its integration into practical engineering tools for bridge safety and scour monitoring.

Despite these limitations, the study contributes meaningfully to the academic discourse by presenting a generalizable framework for scour prediction. The use of dimensionless parameters allows the trained machine learning models to be applied across a wide range of hydraulic and sediment conditions, enhancing scalability and transferability. The model architecture is flexible, permitting future integration of additional variables such as pier geometry, flow turbulence, and sediment transport dynamics.

Moreover, the comparative evaluation of multiple ML algorithms within a unified framework advances methodological rigor, improving both predictive accuracy and interpretability, key factors for real-world engineering applications. Collectively, these contributions position the study as a foundational step toward the development of advanced, generalizable scour prediction models suitable for complex hydraulic environments.

5. Conclusion

This study systematically evaluated the predictive performance of three machine learning models SVM, Ensemble Tree, and ANN by utilizing statistical parameters and error distribution analysis. The study results showcase a clear distinction in the accuracy, stability, and generalization capabilities of the proposed models and also highlight the strengths and weaknesses of all models. Among the three proposed models, the Ensemble Tree model emerged as the most effective, showing high prediction accuracy with an R^2 of 0.9210 and an Adjusted R^2 of 0.9205. In Addition, the ensemble model also exhibits the lowest SE 0.1487 which signifies minimal deviations from observed scour depth, and shows a strong ability to generalize the dataset. Error distribution plots further reinforce the prediction efficacy of the Ensemble Tree model, as it results in a compact spread in terms of relative errors, and indicates coherent and stable scour prediction. A rapid increase in the cumulative percentage of errors advises that most predictions fall under the acceptance range, offering robustness to the ensemble model. All these findings conclude that the Ensemble Tree model is the best-suited for the present dataset, and provides both accuracy and stability in scour depth predictions. Whereas, the SVM model performs moderately well, with an R^2 of 0.8506 and an Adjusted R^2 of 0.8497. While slightly less prediction efficacy than the Ensemble Tree model, it still provides reasonable predictive stability, with a relatively smaller error spread compared to ANN. The SVM Model shows a balanced performance with an SE is 0.2045 is higher than that of the Ensemble Tree model but significantly lower than ANN, indicating that the SVM model balances accuracy and robustness. The error distribution analysis shows some moderate deviations but still SVM predictions are fairly concentrated around zero. This indicates SVM is a reliable tool for scour prediction, though it may not perform as consistently as the Ensemble Tree model in all scenarios.

The ANN model gives the least prediction accuracy, with the lowest R^2 0.6807 and the highest SE 0.2990, which shows it's reflected in adequate prediction efficacy. The error distribution plots are widely spread, meaning that ANN predictions fluctuate significantly which increases the risk of under fitting or over fitting. The cumulative

percentage curve shows a slower increase in accuracy, which means that ANN is struggling to produce consistent and reliable scour prediction. Thus, it is suggested that there is a need for further optimization in ANN architecture and training data sets.

The findings of this study provide valuable insights for choosing an appropriate predictive model for scouring around a bridge pier or hydraulic structure. We have utilized three models, out of which, the Ensemble Tree model stands out as the best performer by offering a combination of high prediction accuracy, low prediction variability, and strong generalization capability. The ensemble tree-based models, particularly Random Forest and Gradient Boosting, showed strong predictive performance and interpretability, making them suitable for integration into practical tools such as early warning systems for scour monitoring and bridge design software. Their application can support timely hazard alerts and data-driven engineering decisions, enhancing infrastructure safety and resilience. The SVM model also serves as a secondary choice, maintaining reasonable prediction accuracy with moderate SE. Lastly, the ANN model, despite its theoretical potential, needs significant improvements to be equally good with the other two models. It is important to note that our findings are based on controlled laboratory-scale experiments, which may not capture the full complexity of field conditions. Therefore, while the presented models show promising results in laboratory settings, their direct application to real-world scenarios should be approached with caution. We acknowledge this limitation and recommend future work to include validation using field data to assess model performance under natural hydraulic and geomorphologic variability. The study emphasizes the importance of evaluating model stability, accuracy, and error distribution characteristics when choosing the best machine-learning approach for real-world predictive tasks.

CRediT authorship contribution statement

Geeta Devi: Writing – original draft, Validation, Software, Methodology, Investigation, Formal analysis, Conceptualization. **Vijay Kaushik:** Writing – review & editing, Validation, Software.

Declaration of competing interest

The authors declare that they have no known competing financial interests or personal relationships that could have appeared to influence the work reported in this paper.

Acknowledgements

The authors received no financial support for this research.

References

Aguirre-Pe, J., Olivero, M.L., Moncada, A.T., 2003. Particle densimetric froude number for estimating sediment transport. J. Hydraul. Eng. 129, 428–437. https://doi.org/10.1061/(ASCE)0733-9429(2003)129:6(428.

Baranwal, A., Gaurav, P., Reddy, L., Das, B.S., Naik, B., 2024. Predicting temporal clear water scour depth around bridge piers with XGBoost and SVM–PSO approaches. J. Hydroinform. 26, 3109–3129. https://doi.org/10.2166/hydro.2024.119.

Bateni, S.M., Borghei, S.M., Jeng, D.S., 2007. Neural network and neuro-fuzzy assessments for scour depth around bridge piers. Eng. Appl. Artif. Intell. 20, 401–414. https://doi.org/10.1016/j.engappai.2006.06.012.

Breusers, H.N.C., Nicollet, G., Shen, H.W., 1977. Local scour around cylindrical piers. J. Hydraul. Res. 15, 211–252. https://doi.org/10.1080/00221687709499645.

Chabert, J., Engeldinger, P., 1956. Study of scour around bridge piers. Rep Prepared for the Laboratoire National D'Hydraulique.

Cheng, N.-S., Wei, M., Lu, Y., Chiew, Y.-M., 2020. Evaluation of sediment gradation effects on clear-water pier scour with densimetric froude number. J. Eng. Mech. 146, 04020133. https://doi.org/10.1061/(ASCE)em.1943-7889.0001871.

Choi, S.U., Choi, B., Lee, S., 2017. Prediction of local scour around bridge piers using the ANFIS method. Neural Comput. Appl. 28, 335–344. https://doi.org/10.1007/s00521-015-2062-1.

Debnath, K., Chaudhuri, S., 2010. Bridge pier scour in clay-sand mixed sediments at near-threshold velocity for sand. J. Hydraul. Eng. 136, 597–609. https://doi.org/10.1061/(ASCE)HY.1943-7900.0000221.

Dey, S., Bose, S.K., Sastry, G.L.N., 1995. Clear water scour at circular piers: a model. J. Hydraul. Eng. 121, 869–876. https://doi.org/10.1061/(ASCE)0733-9429(1995)121:12(869).

Dey, S., Raikar, R.V., 2007. Characteristics of horseshoe vortex in developing scour holes at piers. J. Hydraul. Eng. 133, 399–413.

Drucker, H., 1997. Improving regressors using boosting techniques. 14th International Conference on Machine Learning, pp. 107–115.

Ettema, R., 1980. Scour at Bridge Piers.

Guan, D., Chiew, Y.M., Wei, M., Hsieh, S.C., 2019. Characterization of horseshoe vortex in a developing scour hole at a cylindrical bridge pier. Int. J. Sediment Res. 34, 118–124. https://doi.org/10.1016/j.ijsrc.2018.07.001.

Guven, A., Gunal, M., 2008. Genetic programming approach for prediction of local scour downstream of hydraulic structures. J. Irrigat. Drain. Eng. 134, 241–249.

Kaushik, V., Kumar, M., 2024. Prediction of shear stress distribution in compound channel with smooth converging floodplains. J. Hydrol. Hydromechanics 72, 170–184. https://doi.org/10.2478/johh-2024-0004.

Kothyari, U.C., Garde, R.C.J., Ranga Raju, K.G., 1992. Temporal variation of scour around circular bridge piers. J. Hydraul. Eng. 118, 1091–1106.

Kothyari, U.C., Kumar, A., Jain, R.K., 2013. Influence of cohesion on river bed scour in the wake region of piers. J. Hydraul. Eng. 140, 1–13. https://doi.org/10.1061/(ASCE)hy.1943-7900.0000793.

Kumar, S., Goyal, M.K., Deshpande, V., Agarwal, M., 2023. Estimation of time-dependent scour depth around circular bridge piers: application of ensemble machine learning methods. Ocean Eng. 270. https://doi.org/10.1016/j.oceaneng.2022.113611.

Lauth, T.J., Papanicolaou, A.N., 2008. Experimental/feasibility study of radio frequency tracers for monitoring sediment transport and scour around bridges. World Environ. Water Res.Congr. Ahupua'a 1–10.

Lança, M., M, R., Simarro, G.S., Fael, C.M., Cardoso, A.H., 2016. Effect of viscosity on the equilibrium scour depth at single cylindrical piers. J. Hydraul. Eng. 142, 6015022.

Majedi-Asl, M., Daneshfaraz, R., Abraham, J., Valizadeh, S., 2021. Effects of hydraulic characteristics, sedimentary parameters, and mining of bed material on scour depth of bridge pier groups. J. Perform. Constr. Facil. 35, 04020148.

Melville, B.W., Chiew, Y., 1999. Time scale for local scour at bridge piers. J. Hydraul. Eng. 125, 59–65.

Mia, M.F., Nago, H., 2003. Design method of time-dependent local scour at circular bridge pier. J. Hydraul. Eng. 129, 420–427.

Muzzammil, M., Alama, J., Danish, M., 2015. Scour prediction at bridge piers in cohesive bed using gene expression programming. In: International Conference on Water Resources, Coastal and Ocean Engineering. Aquatic Procedia, pp. 789–796. https://doi.org/10.1016/j.aqpro.2015.02.098.

Muzzammil, M., Gangadhariah, T., 2010. The mean characteristics of horseshoe vortex at a cylindrical pier. J. Hydraul. Res. 41, 285–297.

Najafzadeh, M., Barani, G.A., 2011. Comparison of group method of data handling based genetic programming and back propagation systems to predict scour depth around bridge piers. Sci. Iran. 18, 1207–1213. https://doi.org/10.1016/j.scient.2011.11.017.

Najafzadeh, M., Oliveto, G., 2021. More reliable predictions of clear-water scour depth at pile groups by robust artificial intelligence techniques while preserving physical consistency. Soft Comput. 25, 5723–5746. https://doi.org/10.1007/s00500-020-05567-3.

Okhravi, S., Gohari, S., Alemi, M., Maia, R., 2022. Effects of bed-material gradation on clear water scour at single and group of piles. J. Hydrol. Hydromechanics 70, 114–127. https://doi.org/10.2478/johh-2021-0036.

Oliveto, G., Hager, W.H., 2002. Temporal evolution of clear-water pier and abutment scour. J. Hydraul. Eng. 128, 811–820.

Pandey, M., Oliveto, G., Pu, J.H., Sharma, P.K., Ojha, C.S.P., 2020a. Pier scour prediction in non-uniform gravel beds. Water (Switzerland) 12, 13–17.

Pandey, M., Zakwan, M., Khan, M.A., Bhave, S., 2020b. Development of scour around a circular pier and its modelling using genetic algorithm. Water Sci. Technol. Water Supply 20, 3358–3367. https://doi.org/10.2166/ws.2020.244.

Pandey, M., Zakwan, M., Sharma, P.K., Ahmad, Z., 2020c. Multiple linear regression and genetic algorithm approaches to predict temporal scour depth near circular pier in non-cohesive sediment. ISH J. Hydraul.Eng. 26, 96–103. https://doi.org/10.1080/09715010.2018.1457455.

Sheppard, D.M., Miller, J.W., 2006. Live-bed local pier scour experiments. J. Hydraul. Eng. 132, 635–642. https://doi.org/10.1061/(ASCE)0733-9429(2006)132:7(635.

Smola, A.J., Schölkopf, B., 2004. A tutorial on support vector regression. Stat. Comput. 14 (14), 199–222. https://doi.org/10.1186/s12984-021-00806-6.

Umeda, S., Yamazaki, T., Yuhi, M., 2010. An experimental study of scour process and sediment transport around a bridge pier with foundation. In: Proceedings 5th International Conference on Scour and Erosion (ICSE-5). ASCE, San Francisco, USA, pp. 66–75. https://doi.org/10.1061/41147(392)5.

Yang, Y.S., Melville, B.W., Macky, G.H., Shamseldin, A.Y., 2020. Temporal evolution of clear-water local scour at aligned and skewed complex bridge piers. J. Hydraul. Eng. 146, 04020026. https://doi.org/10.1061/(ASCE)HY.1943-7900.0001732.

Yanmaz, A.M., Altinbilek, H.D., 1991. Study of time-depenbent local scour around bridge piers. J. Hydraul. Eng. 117, 1247–1268. https://doi.org/10.1061/(ASCE)0733-9429(1991)117:10(1247).

Yanmaz, A.M., Kose, O., 2007. Time-wise variation of scouring at bridge abutments. Sadhana - Acad. Proc. Eng. Sci. 32, 199–213. https://doi.org/10.1007/s12046-007-0018-6.

Zounemat-Kermani, M., Stephan, D., Hinkelmann, R., 2019. Multivariate NARX neural network in prediction gaseous emissions within the influent chamber of wastewater treatment plants. Atmos. Pollut. Res. 10, 1812–1822.

International Journal on Science and Technology (IJSAT)
E-ISSN: 2229-7677 ● Website: www.ijsat.org ● Email: editor@ijsat.org

Model Predictive Control of Coal Fired Organic Rankine Cycle Systems

Zariro Manzungu [1], Victor Kuno [2]

[1] Zariro Manzungu, Electronic Engineering Department, Harare Institute Technology
[2] Victor Kuno, Electronic Engineering Department, Harare Institute Technology

Abstract
Organic Rankine Cycle (ORC) systems generate power from low to medium grade heat sources using organic working fluids instead of water [1]. In coal-fired applications, an ORC can be integrated to recover waste heat from flue gas or serve as a bottoming cycle, improving overall plant efficiency [2]. A principal control challenge in Organic Rankine Cycle systems involves regulating turbine inlet superheat within optimal bounds to simultaneously ensure operational integrity (preventing liquid droplet impingement through strict maintenance of vapor-phase working fluid) and maximize energy recovery efficiency [3]. This paper presents a comparative analysis of conventional Proportional-Integral-Derivative (PID) control and Model Predictive Control (MPC) frameworks for thermal regulation in a coal-fired Organic Rankine Cycle (ORC) system. A control-oriented dynamic model is developed based on the system's thermodynamics, using a moving boundary evaporator model for accurate two-phase dynamics prediction [4]. This study demonstrates how Model Predictive Control (MPC) employs system dynamics modeling to forecast future states and enforce operational constraints such as temperature thresholds and pressure limits for performance optimization [5]. Simulation results under transient conditions, including heat input step changes and load ramps, reveal that MPC achieves superior regulation of working fluid superheat at the evaporator outlet, exhibiting 20-30% reductions in overshoot, 40% shorter settling times, and 35% lower integral absolute error compared to PID control. Furthermore, MPC maintains tighter set point tracking during ramp disturbances, with deviation magnitudes reduced by 50-65%. The findings establish MPC's capability to enhance superheat control stability while ensuring safer turbine operation through rigorous constraint enforcement in coal-fired Organic Rankine Cycle systems, ultimately improving cycle efficiency by 3-5% during transient operation.

Keywords: Organic Rankine Cycle (ORC), Model Predictive Control, Superheat Control, Coal-Fired Power, Dynamic Modelling, PID Control

1. Introduction

Coal-fired power plants traditionally employ water-steam Rankine cycles, but ORC technology has emerged as a modification and viable option for utilizing low to medium temperature heat sources [6]. Organic Rankine Cycle (ORC) systems employ low boiling point organic working fluids that is hydrocarbons and or refrigerants to enable efficient power extraction from low grade thermal sources. These include waste heat streams and small-scale boilers, where conventional steam Rankine cycles become thermodynamically impractical due to insufficient temperature gradients [7]. In coal-fired power generation, ORC systems enhance overall plant efficiency through two operational configurations:

- Waste heat recovery from flue gases (120-250°C range)
- Direct organic working fluid vaporization via coal-fired furnaces.

This integration reduces energy waste by 15-25% and increases net electrical output by 8-12% through improved thermal utilization [8]. Technical analyses confirm that integrating ORC systems for flue gas waste heat recovery in coal-fired power plants enhances overall thermal efficiency by 6-9%. Similarly, ORC implementations in heavy-duty internal combustion engines demonstrate 3-5% improvements in brake-specific fuel consumption (BSFC), evidencing the technology's scalability for energy efficiency optimization across industrial sectors and thermal power ranges.

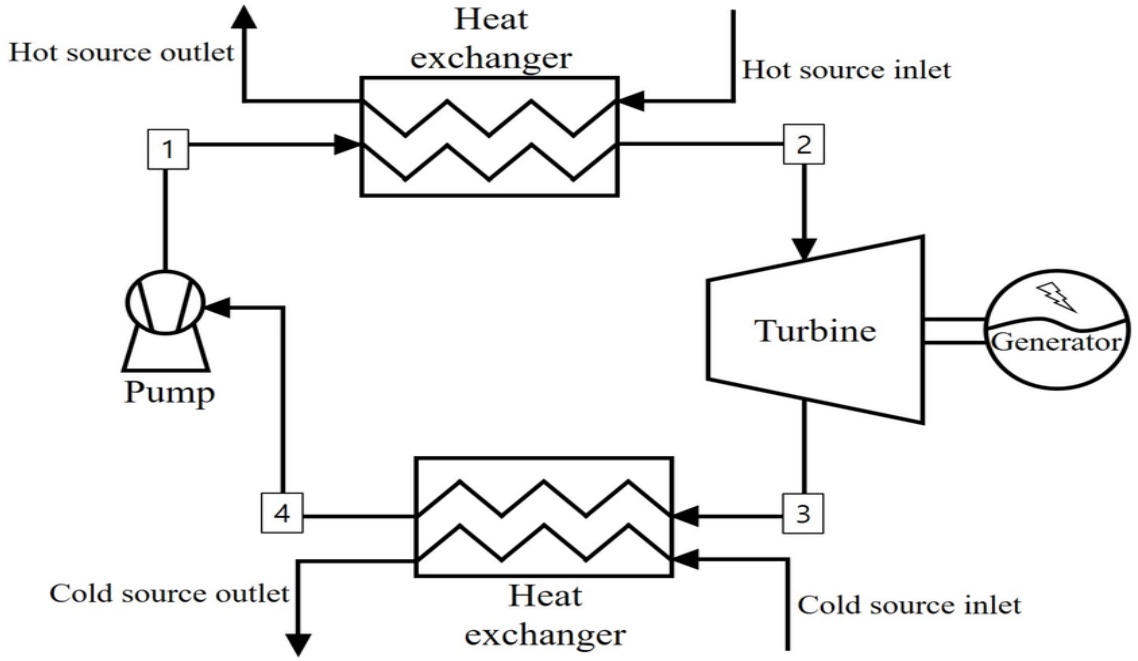
Despite significant thermodynamic advantages, ORC systems present distinctive control challenges centered on three core objectives:

- Maintaining minimum superheat at the expander inlet to prevent liquid droplet formation and ensure mechanical integrity.
- Maximizing power output through optimal heat recovery.
- Enforcing operational constraints within equipment design limits [9].

The control system must continuously enforce a minimum superheat threshold (typically 5-10 K above saturation temperature) to avoid catastrophic two-phase flow conditions that cause turbine blade erosion [10]. Conversely, excessive superheat (>15-20 K) represents thermodynamic inefficiency through underutilized temperature differentials, necessitating precise regulation of evaporator outlet temperature within narrow bounds (±1-2 K) to minimize superheat while ensuring safety. Additionally, evaporating pressure which is a critical determinant of cycle power output, requires optimal set point tracking (typically 80-90% of critical pressure) through manipulated variable coordination. This pressure and power relationship exhibits a well-defined maximum beyond which efficiency declines, requiring adaptive control to maintain optimal operation across transient heat source conditions [11].

This paper presents a comparative study of PID and MPC strategies on a coal-fired ORC power system. Section 2 describes the ORC system and its dynamic modelling, including key equations and the moving boundary approach for the evaporator. Section 3 outlines the control strategies, detailing the conventional PID control structure and the design of the MPC controller with integrated constraints. Section 4 provides simulation results for both step changes and load ramps, comparing performance metrics such as overshoot, settling time, and integrated absolute error (IAE). Finally, conclusions are drawn on the relative performance and the implications for implementing MPC in real coal-fired ORC applications.

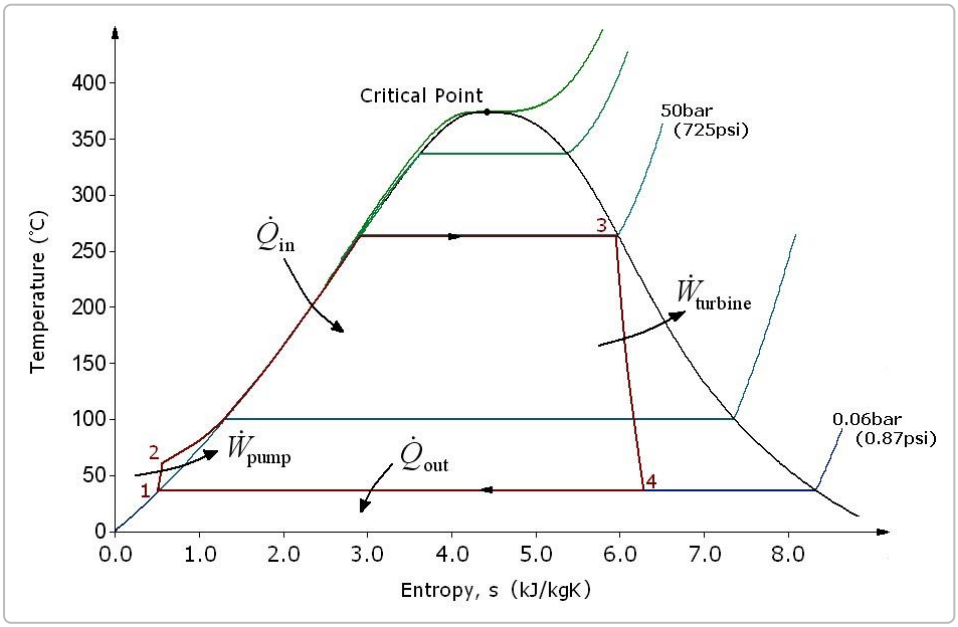
Figure 1: Schematic diagram of an ORC system



2. System Modelling and Dynamics

The described ORC system operates on a subcritical cycle, utilizing an organic working fluid (for example, n-pentane or R245fa) compatible with coal-fired heat source temperatures. Its core components comprise a feed pump, an evaporator (boiler), an expander (turbine) coupled to a generator, and a condenser. In the coal-fired configuration, heat from a furnace or combustion chamber vaporizes the working fluid within the evaporator. The resulting high-pressure vapor drives the turbine, generating mechanical power converted to electricity. The exhaust vapor then condenses in the condenser and is pumped back to the evaporator, completing the closed loop. Figure 1 depicts a typical subcritical Rankine cycle T-s diagram, analogous to this ORC's operation. The cycle path consists of: 12 (liquid pressurization), 23 (heating and evaporation), 34 (vapor expansion through the turbine), and 41 (condensation). The shaded vapor dome represents the fluid's two-phase region. To ensure safe dry expansion, the fluid is typically slightly superheated at the turbine inlet (Point 3). The controller maintains a positive superheat degree (Point 3 temperature minus saturation temperature at turbine inlet pressure). However, excessive superheat (Point 3 positioned far right on the diagram) reduces work extraction potential; thus, the controller aims to position Point 3 just outside the vapor dome.

Figure 2: T–s diagram of a Rankine cycle (water/steam shown here as a reference). In an ORC, a similar cycle is followed using an organic fluid, with state 3 (turbine inlet) typically kept slightly to the right of the saturation dome to ensure superheated vapor expansion.



Dynamic Model: To design the controllers, a control-oriented dynamic model of the ORC is developed. The most critical component for modelling is the evaporator, where heat transfer and phase change occur. We employ a moving boundary model (MBM) for the evaporator 3. In this approach, the evaporator is conceptually divided into regions corresponding to liquid, two-phase, and vapour zones. The boundaries between these zones move as the operating conditions change (for example as the mass of liquid evaporated varies) [4]. By applying conservation of mass and energy to each region, we obtain a set of nonlinear ordinary differential equations describing the evaporator dynamics [12]. For example, the state vector can include the lengths (or volumes) of the liquid and two-phase regions (which indicate how far boiling has progressed), as well as the fluid's outlet enthalpy or temperature [13]. The input to the evaporator model is the working fluid mass flow rate (controlled by the pump or a valve), and disturbances can include the furnace heat input or exhaust gas flow if waste heat is used [14]. The outputs of interest are the evaporator outlet fluid conditions, especially temperature and pressure. The evaporator model dominates the system dynamics because of the significant thermal inertia and the coupling between heat transfer and phase change [6].

The overall ORC system model also includes the dynamics of the pump (assumed fast relative to thermal dynamics) and the turbine/condenser (which together we model as affecting pressure dynamics and providing a load on the evaporator). A simplified lumped model for the condenser can be included to capture pressure responses. For control design, we linearize the nonlinear model around a nominal operating point. The nonlinear state-space equations of the ORC can be written in a general form:

$$\dot{x} = f(x, u, w), \quad y = g(x, u, w) \tag{1}$$

Where *x* represents the state vector (e.g. lengths of phases, temperatures), *u* the control input (for example pump speed or valve position), and *w* disturbances (e.g. fuel feed rate or exhaust temperature). We then obtain a linearized model:

$$\Delta\dot{x} = A\Delta x + B\Delta u + E\Delta w, \qquad \Delta y = C\Delta x + D\Delta u \tag{2}$$

The linearized model exhibits $\dot{x}$ validity within a defined neighborhood of the selected operating point, where Δ denotes state/input disturbance deviations from nominal steady-state conditions (x_0, u_0, w_0). Given the ORC's inherent nonlinearity that manifests through operating-point-dependent gain variations across load conditions. We implement an adaptive linear MPC strategy. This approach continuously updates state-space model coefficients (A, B matrices) via online linearization to maintain predictive accuracy throughout the coal-fired ORC's operating envelope. Critical thermodynamic parameters (for example, fluid specific heats, saturation properties) are dynamically recomputed through high-fidelity look-up tables, enabling model recalibration during significant set point transitions such as evaporating pressure changes.

Complementing the evaporator model, a first-order representation of turbine and generator dynamics is incorporated to quantify the impact of varying inlet conditions on power generation. The net electrical power output W_{net} is defined as the mechanical power produced by the turbine minus the power consumed by the feed pump:

$$W_{net} = W_{exp} - W_{pump} \tag{3}$$

The cycle thermal efficiency η_{cycle} is defined as:

$$\eta_{cycle} = \frac{W\eta_{net}}{Q_{in}} \tag{4}$$

Where Q_{in} denotes the thermal energy input from the coal-fired furnace to the evaporator. While maximizing η_{cycle} which represents the primary thermodynamic objective, operational control prioritizes maintaining key set points (for example, evaporator outlet temperature) that govern both efficiency and power generation. The dynamic model, implemented in Python, serves as the simulation environment and foundational framework for developing both PID and MPC control architectures. (Implementation specifics are omitted herein for conciseness.)

3. Control Strategy Designs

PID Control: The baseline control strategy employs conventional PID control loops. A typical configuration for the ORC has a primary loop to regulate the evaporator outlet temperature (or equivalently the expander inlet superheat) by manipulating the working fluid flow, the PID is given by:

$$u(t) = Kp \cdot e(t) + Ki \int_0^t e(\tau)d\tau + Kd\frac{de(t)}{dt} \tag{5}$$

$u(t)$ = Control signal to pump speed (or valve position)

$e(t)$ = Error = $T_{setpoint} - T_{out}$ (temperature deviation)

K_p = Proportional gain (tuned for overdamped response)

K_i = Integral gain (tuned for zero steady-state error)

t = Time

In our design, a PI controller monitors the difference between the measured fluid outlet temperature and its set point (chosen to ensure a safe superheat margin) and adjusts the pump speed accordingly. If the ORC system includes a throttle or bypass valve around the evaporator, that could alternatively serve as the actuating element, here we assume pump speed control for simplicity. The PID parameters are tuned via classical methods like the Ziegler–Nichols or fine-tuning with simulation to achieve a trade-off between response speed and stability. In particular, we prioritize zero overshoot in temperature to avoid any risk of two-phase flow, the PID is tuned such that the closed-loop system is slightly overdamped [15]. A secondary PID loop can be used to control the system pressure or expander inlet pressure if needed, for example, by modulating a turbine inlet valve. However, a simpler approach often fixes the evaporator pressure set point or lets it vary with load in an open-loop optimal schedule while the primary control loop maintains temperature. Traditional decoupling techniques or feed-forward from measured disturbances (like changes in heat input) are employed to help the PID handle multivariable effects. Even so, under rapid transients the PID-controlled system may exhibit oscillations or sluggish performance due to the inherent limitations of fixed-gain linear controllers in a highly nonlinear system [6].

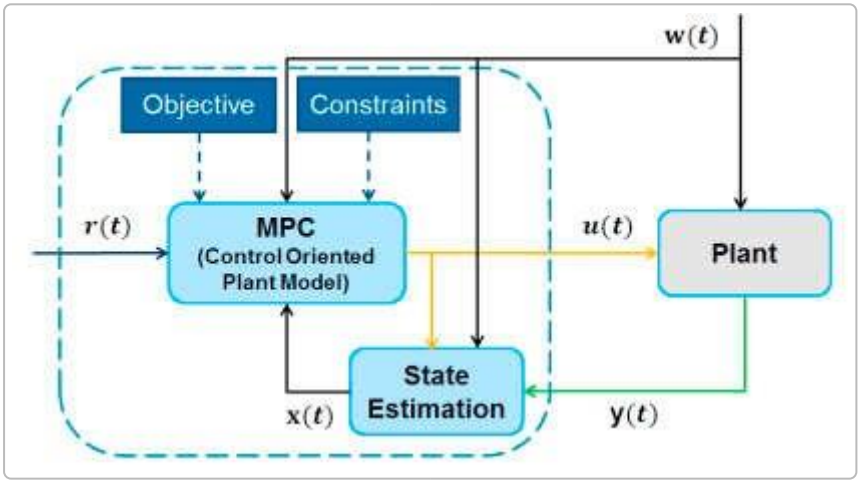
Model Predictive Control: The MPC strategy is designed to overcome these limitations by explicitly using a model of the ORC dynamics and anticipating future behavior. Figure 2 depicts the high-level MPC control structure for the ORC. The core of the MPC is an online optimizer which uses the reduced-order model (as described in Section 2) to predict the system outputs over a finite horizon (for example several tens of seconds into the future). At each control interval, the MPC solves an optimization problem that is minimize a cost function J that penalizes tracking error (deviation of evaporator outlet temperature from its desired set point) and control effort (changes in pump speed), while respecting constraints.

$$j = \sum_{k=1}^{N_p} \left(T_{setpoint}(k) - T_{out}(k)\right)^2 Q + \sum_{k=0}^{N_u-1} \left(\Delta u(k)\right)^2 R \qquad (6)$$

The constraints include physical bounds such as: minimum evaporator outlet temperature (to ensure a positive superheat margin, for example $T_{\text{out}} \geq T_{\text{sat}} + \Delta T_{\text{min}}$), maximum evaporator pressure, pump speed limits, and turbine inlet valve positions. By solving this optimization, the MPC finds the optimal control action sequence $u(t)$ (pump speed commands) that will best steer the temperature to set point without violating constraints. At each step, only the first control action is implemented, then the optimization is repeated at the next time step (receding horizon control). A state estimator (for example a Kalman filter) is incorporated to estimate unmeasured states like internal fluid energy or to filter noisy measurements [6]. This provides the MPC with the necessary state feedback. Disturbances such as varying coal grate firing rate or changing flue gas flow can be fed forward into the model predictions (if measured). The cost function can be formulated in continuous or discrete time; here a discrete-time formulation is used with a prediction horizon of N_p steps (for example 20 steps, corresponding to 100 s if each step is 5 s) and control

horizon N_u (the number of moves to optimize, typically shorter than N_p). Tuning weights in the cost function allows adjusting the controller's aggressiveness: for instance, a higher weight on control effort yields smoother pump operation at the expense of slower tracking, whereas a higher weight on tracking error makes the MPC correct deviations more rapidly at the risk of larger actuator movements. In this study, weights were chosen to achieve a fast response with minimal overshoot, and the prediction model was updated adaptively as described earlier (linear model recalculated each step based on current operating point).

Figure 3: Schematic of the MPC-based control structure for the ORC system. The MPC computes optimal control actions (pump speed u(t)) by using a predictive model and considering objectives (tracking the temperature reference r(t)) and constraints (safety and actuator limits). A state estimator supplies needed state feedback, and the controller can account for measured disturbances w(t) (e.g. changes in heat input). The result is a coordinated control action maintaining the evaporator outlet temperature with minimal error.



One important aspect of the MPC design is constraint-handling for superheat protection. We explicitly enforce a constraint denoted by:

$$T_{out}(t) \geq T_{sat}\left(P_{out}(t)\right) + \Delta T_{min} \quad (7)$$

Where ΔT_{min} is a safety margin (for example, 5°C of superheat) to avoid any two-phase mixture entering the turbine [5]. If the optimizer predicts that a disturbance (say, a drop in heat input) will cause the outlet temperature to dip toward saturation, it will proactively slow the working fluid flow (reducing $u(t)$) to allow more time for heating, thus maintaining superheat. Likewise, the MPC can handle multi-objective control. Although our primary controlled variable is temperature, we can indirectly include power output in the objective by adjusting the temperature set point or adding a secondary objective to maximize W_{net} as long as safety is ensured. In practice, a higher-level optimization (or operator input) might provide an optimal temperature or pressure set point for current conditions, and the MPC's task is to track that set point while respecting constraints. This structure sometimes called a two-layer control, with an upper layer real-time optimizer and a lower-layer MPC [16]. In our case, we assume the desired evaporator temperature set point may shift according to load demands, and the MPC tracks it optimally.

Implementing Model Predictive Control (MPC) on operational coal-fired ORC systems necessitates addressing computational latency and model fidelity constraints. To ensure real-time feasibility, the controller must execute within stringent time limits (for example, ≤1 second per optimization cycle), dictating conservative horizon selections and reduced-order models. While adaptive model updates impose additional computational burden, they are essential for maintaining accuracy. Simulations assume ideal computational resources, however, practical hardware implementations may employ simplified models or Extended Prediction Self-Adaptive Control (EPSAC) methodologies to satisfy real-time requirements [17].

4. Results and Discussions

To evaluate control performance, we conducted simulation tests on the nonlinear ORC model for two scenarios:

- A **step change** in the temperature set point (or equivalently a change in desired turbine inlet temperature/superheat)
- A **load ramp** disturbance, representing a gradual change in heat input (such as a change in coal firing rate or flue gas flow) while maintaining a constant temperature set point.

The PID controller was tuned for a settling time on the order of 100 seconds with no overshoot under nominal conditions. The MPC was configured with the same nominal set point and constraints. Key performance metrics compared include:

- The percent overshoot (OS %)
- Settling time (time to reach and stay within ±2% of set point),
- Integrated Absolute Error (IAE) over the transient.

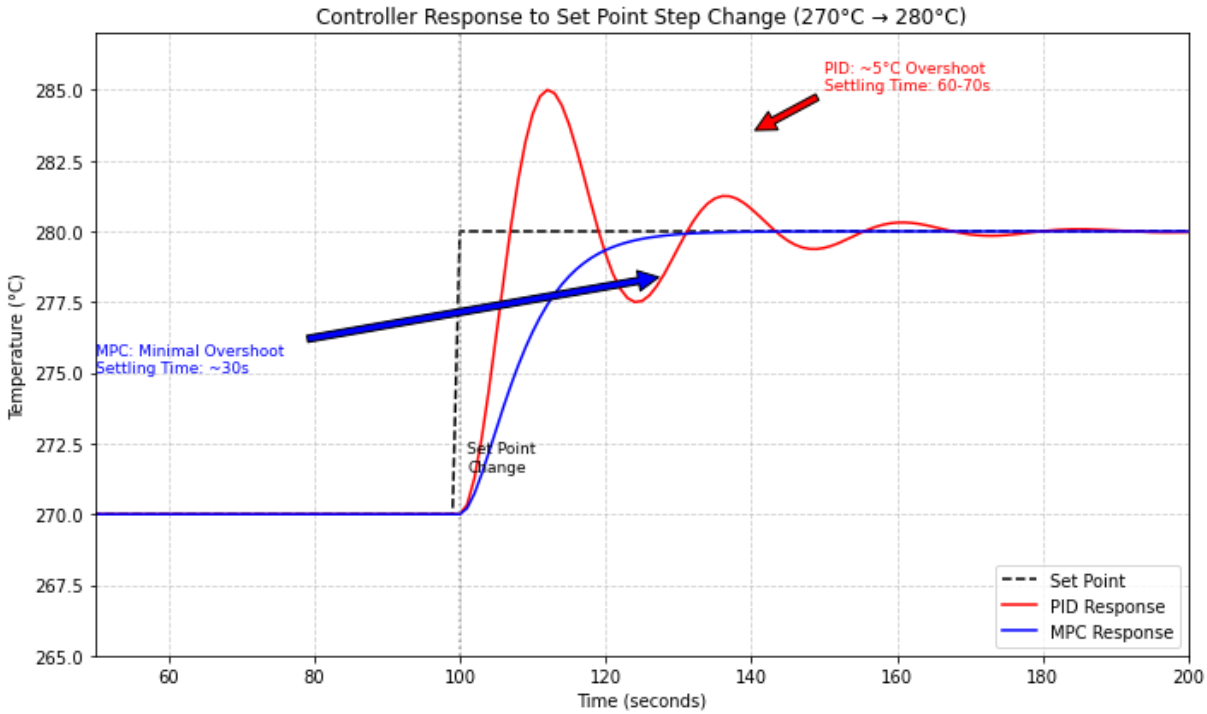
Table 1 and Table 2 summarize the quantitative results for the two scenarios, and Figure 6 provides sample response curves for evaporator outlet temperature under each controller.

Scenario 1: Set point Step Change. In this test, the working fluid outlet temperature set point was increased by 10°C at t = 100 s (for example, from 270°C to 280°C superheat target). The system was initially at steady state. The PID and MPC controllers' responses are shown in Figure 6a. The PID-controlled temperature exhibits a noticeable overshoot above the new set point, followed by oscillations before settling. In contrast, the MPC response rises to the new set point with minimal or zero overshoot and settles much faster. Quantitatively, as Table 1 shows, the PID loop had approximately5°C (50%) overshoot and took around 60 –70 s to settle, whereas the MPC kept overshoot to approximately 0% and settled in about 30 seconds. The IAE during the first 100 s after the step was reduced by roughly 60% with MPC compared to PID, indicating more efficient error correction. The improved performance is attributable to MPC's predictive action. MPC anticipates the effect of the set point change and moderates the pump acceleration, whereas the PID (even with conservative tuning) initially reacts more aggressively, causing an overshoot. This outcome aligns with other reported simulations where MPC showed shorter settling times and smaller overshoot than a traditionally tuned PID. The absence of overshoot in MPC means the system never exceeded the safe superheat limit, whereas the PID momentarily pushed the temperature higher, which in a real system could reduce safety margins.

Table 1. Performance for a 10°C Set point Step in Evaporator Outlet Temperature. (Overshoot is expressed as a percentage of the 10°C step magnitude; Settling Time is to ±2% of final value; IAE is integrated absolute error over 100 s after the step.)

Controller	Overshoot (OS %)	Settling Time (s)	IAE (°C·s)
PID	~50% (5°C)	~65 s	350
MPC	~0% (no overshoot)	~30 s	140

Figure 4: Scenario 1, Controller response to set point step change (2700C – 2800C)



Scenario 2: Load Ramp Disturbance. In this scenario, the heat input to the evaporator (for example, flue gas flow rate or its temperature) was varied. Starting at t = 100 s, the heat source was linearly ramped down over 20 s to 80% of its original value, held for 80 s, then ramped back up to nominal over another 20 s (a symmetric down-and-up ramp). This simulates a transient in boiler firing or a step-down and step-up in engine exhaust heat in a waste heat recovery context. The evaporator outlet temperature set point was kept constant during this test (280°C). Figure 6b shows the response of the outlet fluid temperature. The PID controller cannot perfectly reject the disturbance as the heat input drops, the temperature falls below set point (undershoot), and when the heat ramps up, the temperature rises above set point. The maximum deviation observed with PID was about 8–10°C below the set point during the ramp-down. The MPC, by contrast, adjusted the pump flow proactively, it reduced the working fluid flow rate during the heat decrease to compensate and keep the outlet temperature closer to target. The MPC's temperature deviation was much smaller, at about 2–3°C off the set point at worst. Moreover, when the heat returned to normal, the PID controller overshot the set point (temperature spiked by approximately 5°C above)

before settling, while the MPC kept the overshoot to within 1°C. The MPC's superior disturbance rejection is evident it maintained tighter control throughout the ramp. As listed in Table 2, the MPC reduced the peak error by approximately70% and halved the settling time after the ramp the time to return within 2% of set point once the ramp completed. The IAE over the entire 200 s transient was significantly lower for MPC by approximately 40% of the PID's IAE. Notably, the MPC was able to respect the superheat safety constraint at all times, whereas the PID approach came closer to the limit when the temperature dipped during the ramp. This demonstrates how the MPC's inclusion of constraints in the optimization problem provides a built-in safety mechanism. Even under a severe transient, the MPC kept the cycle operation within safe bounds by ensuring that there is no two-phase at turbine inlet, whereas an uncompensated PID might have required manual intervention or very conservative tuning to ensure the same.

Table 2. Performance for a Load Ramp Disturbance (20% drop and return in heat input). (Peak Error is the maximum deviation from set point during the transient; Settling Time is the time to recover within ±2% band after ramp; IAE is integrated absolute error over the 200 s cycle.)

Controller	Peak Error	Settling Time (s)	IAE (°C·s)
PID	8.5°C (undershoot) / +5°C (over-shoot)	~60 s	500
MPC	2°C / +1°C	~30 s	200

Figure 5: Performance for a Load Ramp Disturbance (20% drop and return in heat input).

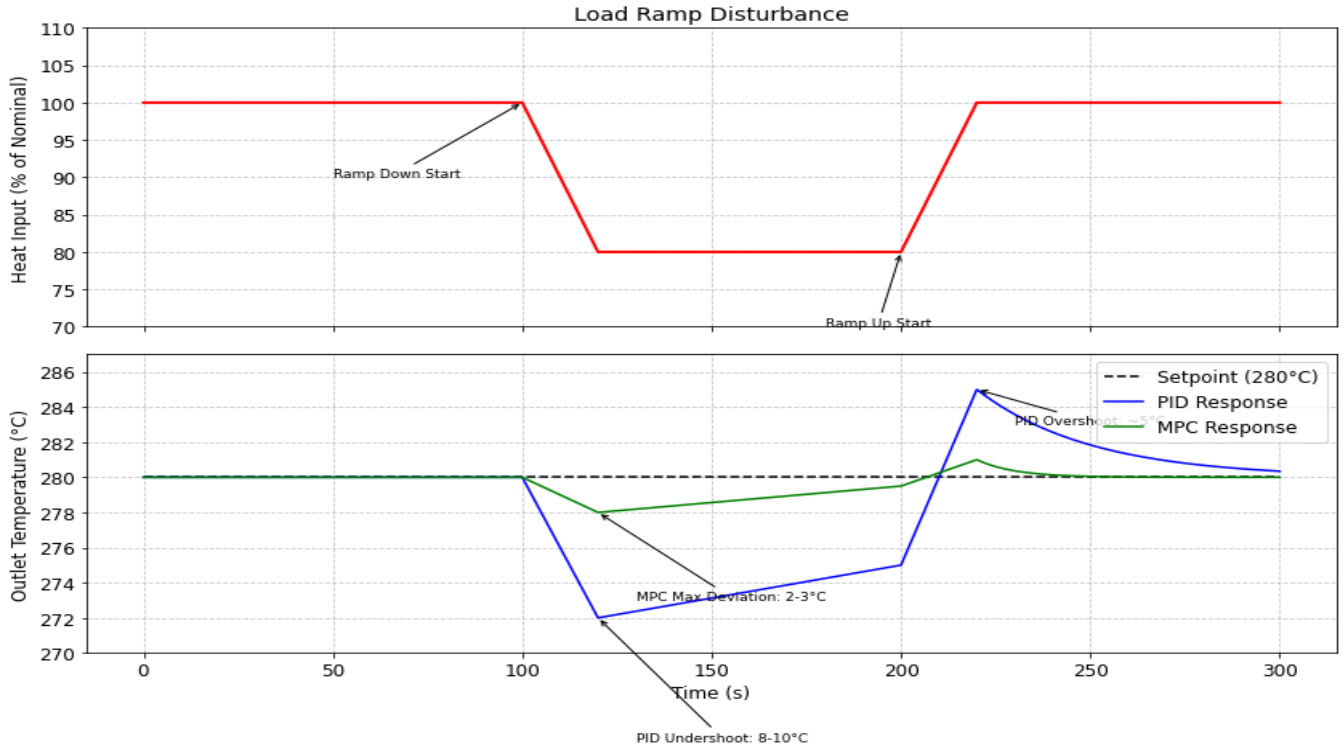


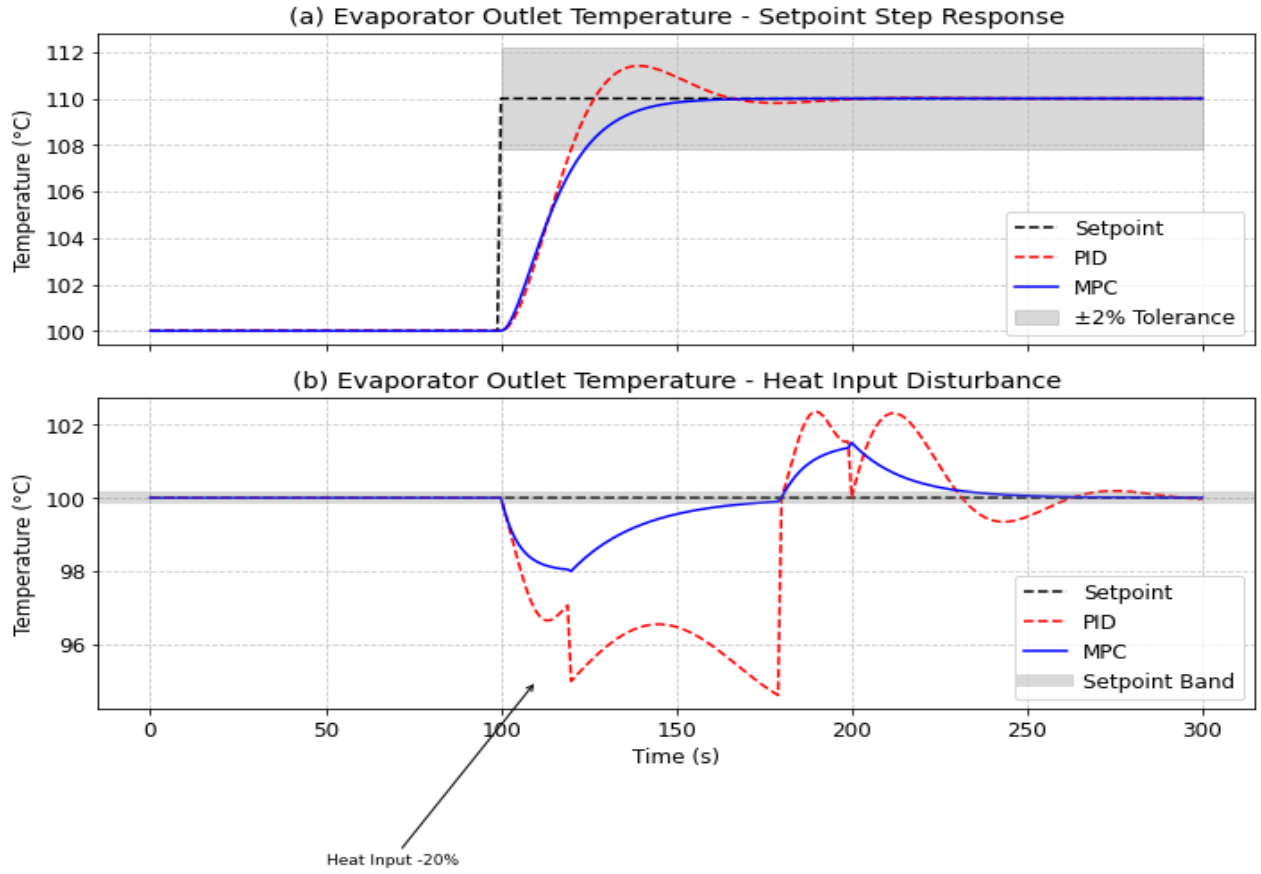
Figure 6 above qualitatively illustrates these differences. The PID-controlled temperature shows an over-shoot in the step response Figure 6a, red dashed curve and a noticeable lag and deviation during the

ramp Figure 6b, red dashed. The MPC-controlled temperature (blue solid curve) closely tracks the set point without overshoot in the step case and with much smaller deviation during the ramp. These results corroborate findings in literature that MPC can improve response time and reduce overshoot by significant margins (20–30% or more) compared to well-tuned PID controllers. Importantly, the MPC achieves this while also enforcing constraints. In our simulations, at no point did the predicted states violate the imposed limits (such as minimum superheat or max pressure). The PID, lacking a constraint awareness, had to be tuned conservatively to avoid unsafe operation, which in turn limited its performance. The ability of MPC to operate the ORC closer to its limits—without crossing them—means it can extract more power (by allowing lower superheat, nearer to the optimal point) especially during transients [18]. This translates to improved efficiency and potentially more electricity generated over time.

In terms of actuator behavior, the MPC resulted in smoother control actions during the ramp (it adjusted pump speed continuously in anticipation of the ramp), whereas the PID made more abrupt corrections after sensing the deviation. The smoothness of control moves in MPC can contribute to longer pump life and more stable boiler operation, an important practical consideration. On the computational side, our MPC simulations were done with a sample time of 1 second and solved reliably within that period. This suggests that real-time implementation on a modern industrial controller is feasible, especially given the continued improvement of solver algorithms and hardware.

Figure 6: (a) Evaporator outlet temperature response to a 10°C step increase in setpoint at t=100 s; (b) Evaporator outlet temperature response to a 20% heat input ramp-down (100–120 s) and ramp-up (180–200 s) with constant temperature setpoint. Red dashed lines = conventional PID control, Blue solid lines = MPC. The MPC achieves faster settling and smaller deviation from set point in both cases, with no

ershoot in (a) and significantly reduced undershoot in (b). The gray band in (a) indicates the ±2% tolerance around the new set point, and in (b) indicates the set point value.



5. Conclusion

This paper presented a comparative study of PID and model predictive control for a coal-fired Organic Rankine Cycle system, focusing on the critical task of maintaining superheat at the turbine inlet while optimizing performance. Conventional PID control, even when carefully tuned, showed limitations in handling rapid transients: the PID loop exhibited overshoot and slower recovery in response to set point changes and load ramps, which could jeopardize turbine safety (if overshoot/undershoot is excessive) and result in suboptimal efficiency during disturbances. In contrast, the MPC approach demonstrated superior control performance. By leveraging a dynamic model of the ORC (including a moving boundary evaporator model for two-phase dynamics) and anticipating future events, the MPC was able to keep the evaporator outlet temperature tightly regulated. The MPC consistently avoided overshoot, maintained the desired superheat margin, and reduced settling times by roughly 50% compared to PID in our simulations. Under a load ramp, the MPC kept the temperature deviation minimal (improving disturbance rejection significantly) and thereby allowed the system to operate closer to its optimal conditions even during transients [6].

The ability of MPC to incorporate constraints (such as minimum superheat and actuator limits) was a crucial advantage. The controller automatically respected safety limits, eliminating the need for overly

conservative tuning. This means the ORC system can be driven harder for better efficiency (recovering more heat) without sacrificing safety. The trade-off is increased complexity: MPC requires a reasonably accurate model and more computational effort. However, given the results, implementing MPC on a coal-fired ORC appears justified by the gains in stability and efficiency. The use of an adaptive model in the MPC was important to handle the wide operating range; this adaptive MPC effectively acted as a gain-scheduled controller that continuously updated itself, which is a practical strategy for real plants.

MPC demonstrates superior performance over PID control in ORC systems, delivering faster and more reliable regulation of superheat and power output. These advantages translate to higher average cycle efficiency and enhanced operational safety by preventing thermal stress and turbine damage. Future work will focus on experimental validation of MPC using a physical ORC test rig, addressing real-world implementation challenges including robust state estimation, actuator saturation management, and fault tolerance (for example, sensor failures). Further performance gains could be achieved by extending the control scheme to multi-input coordination, such as simultaneous throttle valve and pump control. The promising results of this study enable broader adoption of advanced control strategies in waste heat recovery and small-scale power units, maximizing the energy efficiency and emission reduction potential of coal-fired ORC technology.

6. Acknowledgement

We gratefully acknowledge the technical assistance from Thinkernel private limited research test facility team. Special thanks to Winnie Mutenhabundo for expert guidance on MPC implementation in thermal systems and Harare Institute of Technology for experimental support.

7. Authors' Biography

Zariro Manzungu is a Master of Technology candidate in Industrial Automation at the Harare Institute of Technology, where his research focuses on advanced control strategies for industrial systems. He holds a Bachelor of Engineering in Electronic Engineering (2012), providing foundational expertise in advanced control and system dynamics. With over a decade of professional experience in control systems engineering, his work spans model predictive control (MPC), and state estimation for industrial processes. His current research investigates Model Predictive Control-based optimization of Organic Rankine Cycles (ORC) under dynamic coal-fired heat inputs, bridging theoretical control theory with industrial energy applications. Victor Kuno is a Lecture at the Harare Institute of Technology, he holds a Master of Technology degree in Nano Science and Technology, from Delhi Technological University (DTU), India. His current research interests are in Nano Electronics, Energy Nano technology and Opto-electronics.

References

1. D. &. W. M. &. R. C. &. J. J. Herath, "Working fluid selection of Organic Rankine Cycles.," Energy Reports. 6. , vol. 6, no. 10.1016/j.egyr.2020.11.150., pp. 680-686, 2020.
2. J.-m. a. R. J.-x. a. L. F.-q. a. L. X. a. C. L.-f. a. L. K.-j. Cai, "Performance Analysis of Waste Heat Organic Rankine Cycle in Coal-Fired Power Plants," www.ssrn.com, Shanghai, 2022.

3. M. &. P. R. &. U. M. &. H. F. Imran, "Dynamic modeling and control strategies of organic Rankine cycle systems: Methods and challenges.," Applied Energy, vol. 10, no. 16, p. 276, 2020.
4. E. M. W. Grald, "A moving-boundary formulation for modeling time-dependent two-phase flows," International Journal of Heat and Fluid Flow, vol. 13, no. 3, pp. 266-272, 1992/09/01.
5. M. &. A. M. &. B. T. &. A. D. (. Schwenzer, "Review on model predictive control: an engineering perspective.," The International Journal of Advanced Manufacturing Technology., vol. 117, no. 3, pp. 1-23, 2021.
6. A. Y. P. A. J. S. B. X. M. H. S. O. Xiaobing Liu, "Model predictive control of an organic rankine cycle system," IV International seminar on ORC power systems, vol. 12, no. 2, pp. 1-8, 13-15 September 2017.
7. D. Y. G. E. K. S. Huijuan Chen, "A review of thermodynamic cycles and working fluids for the conversion of low-grade heat," Renewable and Sustainable Energy Reviews, vol. 14, no. 9, pp. 3059-3067, 2010.
8. T. &. D. I. &. K. E. &. K. P. &. J. A. &. Ł. A. Miller, "Waste Heat Utilization in Marine Energy Systems for Enhanced Efficiency," Energies, vol. 1, no. 17, 2024.
9. IAEA Safety Standards, "Operational Limits and Conditions and Operating Procedures for Research Reactors," INTERNATIONAL ATOMIC ENERGY AGENCY (IAEA) Safety Standards, 2023.
10. F. M. I. Company, "FM Property Loss Prevention Data Sheets," Steam turbines, vol. 3, no. 13, 2025.
11. L. &. C. M. &. M. S. Cecchinato, "A critical approach to the determination of optimal heat rejection pressure in transcritical systems," Applied Thermal Engineering.
12. M. Taylor, "Conservation of Mass and Energy for the Moist Atmospheric Primitive Equations on Unstructured Grids," in Numerical Techniques for Global Atmospheric Models.
13. Z. W. G. L. C. W. a. L. D. Genying Gao, "Numerical Simulation of Two-Phase Boiling Heat Transfer in a 65 mm Horizontal Tube for Enhanced Heavy Oil Recovery," Energies MDPI, 12 June 2025.
14. R. P. C. W. A. R. Manuel Jiménez-Arreola, "Analysis and comparison of dynamic behavior of heat exchangers for direct evaporation in ORC waste heat recovery applications from fluctuating sources," Applied Energies, April 2018.
15. A. D. C. I. S. Q. V. L. a. R. D. K. Andres Hernandez, "Experimental study of Predictive Control strategies for optimal operation of Organic Rankine Cycle systems," European Control Conference (ECC), 2015.
16. F. R. S. G. V. L. S. Q. R. D. K. Andres Hernandez, "Experimental validation of a multiple model predictive control for waste heat recovery organic Rankine cycle systems," Applied Thermal Engineering, 2021.
17. C. M. I. Robain De Keyser, "The disturbance model in model based predictive control," in Control Applications, 2003. CCA 2003. Proceedings of 2003 IEEE Conference, July 2003.

18. C. I. S. G. A. D. M. v. d. B. V. L. R. D. K. Andres Hernandez, "Performance evaluation of MPC for Waste Heat Recovery applications using organic Rankine cycle," New Energies, 2016.

Check for updates

International Journal of Circuit Theory and Applications

WILEY

ORIGINAL ARTICLE

Modeling of Multiport DC-DC Converter With Improved Fault-Tolerant Capability and Minimized Current Ripple Considering Circuit Parasitic

Rishabh Bansal | Rushiv Bansal | Mayank Kumar

Department of Electrical Engineering, Centre of Excellence for Electric Vehicle and Related Technologies, Delhi Technological University, Delhi, India

Correspondence: Mayank Kumar (mayankkumar@dtu.ac.in)

Received: 28 January 2025 | **Revised:** 16 April 2025 | **Accepted:** 15 May 2025

Funding: This research supported by the Science and Engineering Research Board (SERB), Department of Science & Technology, Government of India, under the SERB sanction order number SRG/2021/001640.

Keywords: constant-current constant-voltage (CC-CV) | fault-tolerant | multiport converter | state-space averaging | switched boost converter | time-multiplexing control

ABSTRACT

Multiport DC-DC converters have the capability to provide the output power at different voltage levels simultaneously. In this paper, a novel boost-side interleaved switched boost (BSISB) multiport DC-DC converter is proposed. The boost-side interleaving (BSI) reduces the input current ripple and improves fault-tolerant capability at the load end, even after an open-circuit transistor failure. The switched-boost action topology uses time-multiplexing control of boost and buck switches for independently regulated voltage of both the output ports using reduced semiconductor device count. The state-space averaged (SSA) and small signal model (SSM) of the proposed converter is developed with circuit parasitic. The SSA and SSM are used for steady-state gain analysis and the controller design for the converter, respectively. A prototype is developed in the lab to test the proposed converter under constant-current constant-voltage (CC-CV) mode of charging of the battery and verify the derived analytical results.

1 | Introduction

DC-DC converters are indispensable in various industries, offering isolated and non-isolated topologies to meet diverse needs. Isolated converters, integrating a transformer coil between input and output ports, are used in harsh environments due to their capability to provide isolation. Nonisolated converters stand out for their compact design and improved efficiency. These converters are chosen for their simple design, efficient performance, and cost-effectiveness compared with alternatives, catering to diverse domains such as portable electronics [1–3], consumer appliances [4], uninterruptible power supplies (UPS) systems, renewable energy applications, electric vehicles (EVs) applications [5], medical devices, etc.

The classification of multiport DC-DC converters (MPDCs) based on the number of input and output ports is well-documented in the literature, with configurations such as multiple input single output converters (MISOCs), multiple input multiple output converters (MIMOCs), and single input multiple output converters (SIMOCs) [6–10]. A bidirectional MPDC integrated with a battery energy storage system for hybrid energy sources is discussed [10]. The main advantage of the MPDC topology is its ability to reduce size, weight, and cost. The number of semiconductor devices can be reduced further using time-multiplexing control of gating signals. The technique of time-multiplexing of gating signals for switches to generate two regulated voltage output ports is known as switched-boost action [6, 7].

© 2025 John Wiley & Sons Ltd.

Advanced converter designs, such as interleaved and multiphase configurations, have gained attention for their ability to reduce ripple, improve thermal performance, and increase converter robustness under variable load conditions [1–14]. Interleaved converters are utilized for applications with reduced current ripple, increased ripple frequency, and reduced current stress over semiconductor devices [15]. The interleaving technique in multiport DC-DC converters has the potential to improve power conversion efficiency and performance. The two-phase interleaved boost converter topology is used at solar PV side for MPP tracking with reduced solar PV current ripple and therefore size requirement of the capacitor reduces. The multiport and bidirectional converter presented in [16] exhibits improved voltage gain and efficiency and accomplished through advanced techniques such as switched capacitor and voltage lift.

Several types of faults can occur during the operation of power converters within the semiconductor switches used. Over voltages, voltage spikes, extended exposure to high temperatures, excessive power dissipation, and other factors can damage the switches, resulting in an open circuit (OC) or short circuit (SC) between their terminals [17, 18]. Hardware redundancy such as switch level, leg-level, and complete converter level is an extremely effective method to increase the converter reliability and mitigating the effects of switch faults. It seeks to avoid interruptions caused by single-point failures [19]. The OC fault detection approach used on interleaved DC-DC boost converters is described [20, 21].

To improve the life and performance of the battery, the charging characteristics of the converter use constant-current (CC) and constant-voltage (CV) modes of operation with respect to the instantaneous value of battery state of charge (SoC) [22–24]. The controller has one inner current control loop and an outer voltage control loop to achieve CC-CV mode of operation. When the SoC is low, the voltage loop output to the inner loop is clamped to a fixed value. This enables constant current charging. At a higher SoC, the complete loop acts as a simple voltage control loop. The piecewise linearization of a switching power converter is achieved with SSA modeling. Averaged models significantly reduce computation time while maintaining essential dynamics of the system [25, 26]. However, averaged models exclude high-frequency ripples and retain only the average response. A discrete-time SSM for a high-gain battery energy storage-based DC-DC boost converter for controller design is presented [27].

This paper presents state-space averaged (SSA) and small signal model (SSM) of a novel nonisolated SIMO boost side interleaved converter using circuit parasitic. The proposed converter presents two output ports with one port with bidirectional capability and time-multiplexing control to reduce semiconductor switches. The primary contributions of the presented article are as follows: (i) development of a novel boost-side interleaved switched boost (BSISB) multiport converter to reduce input current ripple; (ii) SSA and SSM of the proposed converter for robust controller design; (iii) fault-tolerant behavior and switch stress analysis under healthy and fault conditions of the converter for performance improvement; (iv) the laboratory-type experimental setup has been developed, and the results are validated for the proposed BSISB converter.

2 | Proposed BSISB Multiport Converter

The block diagram of the proposed multiport converter is shown in Figure 1. The converter has one input and one output port (i.e., output port 1), whereas one port (i.e., output port 2) is bidirectional in nature. The schematic diagram of the BSISB multiport converter is shown in Figure 2. The input-side inductors L_1 and L_3, with their effective series resistance (ESR) r_{L1} and r_{L2}, respectively, are connected with the input source voltage (V_{in}). The boost-side load R_1 is connected to a parallel filter capacitor C_1, and it is subsequently linked to inductors L_1 and L_3 with diodes D_1 and D_2, respectively. The ESR of the filter capacitors C_1 and C_2 are presented as r_{C1} and r_{C2}, respectively. The switches S_1 and S_2 are connected in series between inductor L_1 and ground for time-multiplexing control of the boost converter. The on-state voltage drop of the switches S_1, S_2, S_3 and diodes D_1, D_2 is considered the same for the simplified mathematical solution as V_f. The inductor L_2 is connected for energy transfer for buck-side output. The buck-side output works as a load and source during the charging and discharging of the battery, respectively. The inductors L_1 and L_3 perform boost-side interleaving.

The operating principle of the proposed converter is bifurcated into seven different modes of operation as presented in Table 1 for

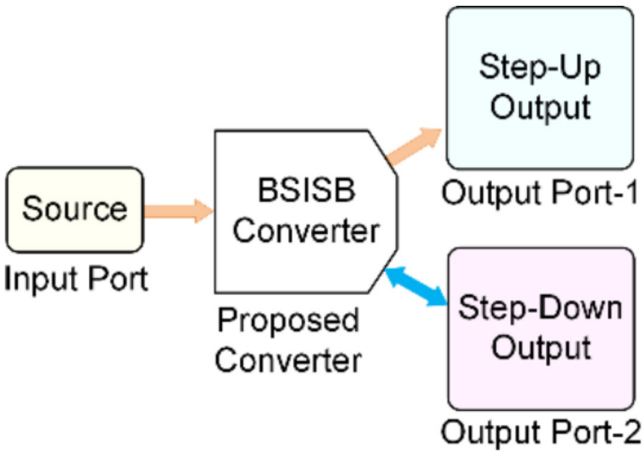


FIGURE 1 | Block diagram of proposed BSISB multiport converter.

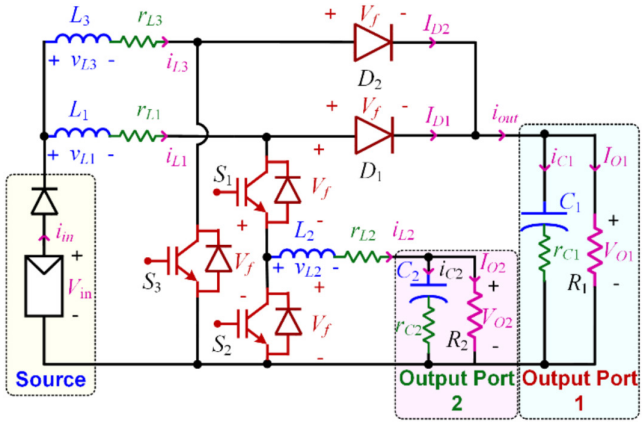


FIGURE 2 | Schematic diagram of proposed BSISB multiport converter.

1097007x, 0, Downloaded from https://onlinelibrary.wiley.com/doi/10.1002/cta.4609 by Delhi Technological University, Wiley Online Library on [03/06/2025]. See the Terms and Conditions (https://onlinelibrary.wiley.com/terms-and-conditions) on Wiley Online Library for rules of use; OA articles are governed by the applicable Creative Commons License

charging and discharging the battery connected at output port 2 and powering the load connected at output port 1. The active switches and the inductor current characteristics with respect to the modes of operation are also presented for detailed analysis of operating modes of the proposed converter. In Table 1, state I shows the possible modes where the battery behaves as a load under charging conditions, whereas state II shows the possible modes where the battery behaves as a source (i.e., under discharging) during the unavailability of source power.

The characteristics of the inductor and input currents with respect to the range of duty ratios such as $d<0.5$, $d=0.5$, and $d>0.5$ are presented in Figure 3a–c, respectively. The switching signals of S_2 and S_3 (i.e., V_{g2} and V_{g3}) have the same duty with $T/2$ phase shift, where $T=1/f_s$ is defined as the switching period of the converter. The duty ratio of the gate pulse for S_1 is λd, where λ is defined as the "scaling factor" with the value of $\lambda>1$. The gain of the converter can be controlled using duty ratio d and the scaling factor λ. For the value of $\lambda\leq 1$, the value of i_{L2} becomes zero and voltage gain at output port 2 becomes zero. Thus, the circuit operates as an interleaved boost converter. To design the circuit as a MPDC with two operational output ports (i.e., buck port and boost port), the value of the scaling factor $\lambda>1$. Figure 3a shows the healthy operation of the proposed converter for $d<0.5$; four modes appear, such as mode 1 during t_3–t_4, mode 2 during t_2–t_3 and t_4–t_5, mode 3 during t_1–t_2 and t_5–t_6, mode 4 during t_0–t_1 and t_6–t_0, respectively. It shows that mode 5 is absent when $d<0.5$. Similarly, Figure 3b,c presents the behavior of the proposed converter when charging the battery (i.e., with the source connected) for $d=0.5$ and $d>0.5$, respectively. Modes 2 and 5 are absent in Figure 3b for $d=0.5$ and mode 2 is absent for $d>0.5$ in Figure 3c. The possibilities of modes of operation also

TABLE 1 | Modes of operation for BSISB converter under charging and discharging conditions.

Battery operation	Operating modes	Inductor current characteristics	Active switches
Charging mode (state I)	Mode 1	$i_{L1}\uparrow, i_{L2}\downarrow, i_{L3}\downarrow$	S_1, S_2, and D_2
	Mode 2	$i_{L1}\downarrow, i_{L2}\uparrow, i_{L3}\downarrow$	S_1, D_1, and D_2
	Mode 3	$i_{L1}\downarrow, i_{L2}\uparrow, i_{L3}\uparrow$	S_1, S_3, and D_1
	Mode 4	$i_{L1}\downarrow, i_{L2}\downarrow i_{L3}\uparrow$	S_3, D_1, and S_{D2}
	Mode 5	$i_{L1}\uparrow, i_{L2}\downarrow, i_{L3}\uparrow$	S_1, S_2, and S_3
Discharging mode (state II)	Mode 6	$-i_{L2}\uparrow$	S_2
	Mode 7	$-i_{L2}\downarrow$	S_{D1} and D_1

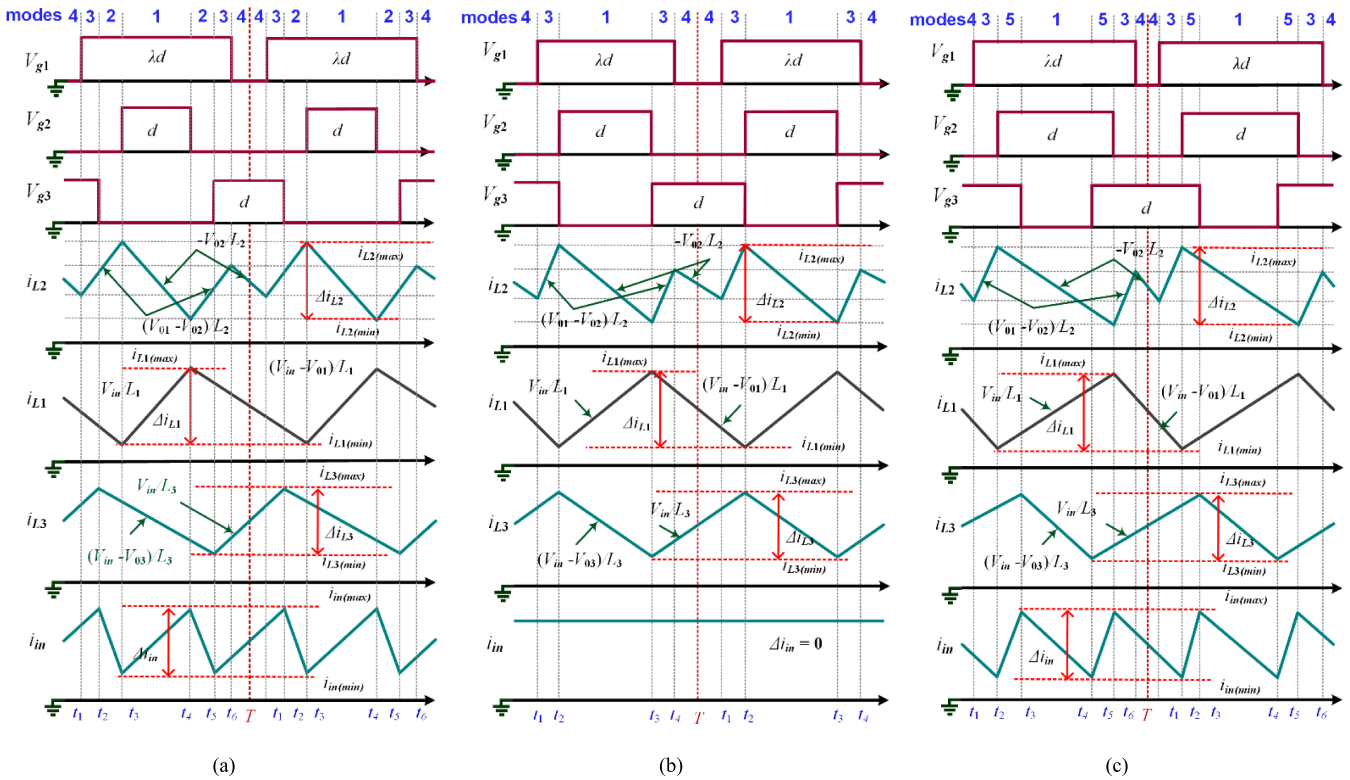


FIGURE 3 | Characterization of proposed BSISB multiport converter with V_{02} as a load (charging conditions) under state I for (a) $d<0.5$, (b) $d=0.5$, and (c) $d>0.5$.

1097007x, 0, Downloaded from https://onlinelibrary.wiley.com/doi/10.1002/cta.4609 by Delhi Technological University, Wiley Online Library on [03/06/2025]. See the Terms and Conditions (https://onlinelibrary.wiley.com/terms-and-conditions) on Wiley Online Library for rules of use; OA articles are governed by the applicable Creative Commons License

depend on the value of the duty ratio and scaling factor, which is explained in the next section.

2.1 | Modes of Operation Under Healthy Condition

There are seven possible modes of operation under healthy operation, of which five are charging modes defined as state I and two are discharging modes defined as state II. During charging operation, the battery, resistive load, or both can be connected to the buck side feed through the input. The input source connected to the converter is solar PV or DC source. If a resistive load is connected at the buck port, it receives constant voltage during these modes. If battery is connected at output port 2, the charging of battery operates under CC and CV mode with respect to SoC of the battery, and discharging occurs with current limit control mode of operation.

The characterization of the proposed BSISB converter is presented with a scaling factor $\lambda > 1$. Three different operating conditions are possible under state I with respect to the values of duty ratio d as shown in Figure 3. Further the operating conditions can be mathematically defined as follows:

$$\begin{aligned} &condition\text{: }1 \quad 1 < \lambda \le 1/d \ \ \& \ \ d < 1/2, \\ &condition\text{: }2 \quad 1 < \lambda \le 2 \ \ \& \ \ d = 1/2, \\ &condition\text{: }3 \quad 1 < \lambda \le 1/d \ \ \& \ \ 1/2 < d < 1. \end{aligned} \tag{1}$$

With respect to the operating conditions mentioned above and the switching states, the principle of operation of the proposed converter can be classified under five different operating modes within state I.

2.2 | SSA Model of BSISB Converter During State I

The SSA model can be obtained over one switching period with the consideration that the system is linearized around the operating point. The state space model is described as follows:

$$\frac{dx(t)}{dt} = \dot{x} = \mathbf{A}x(t) + \mathbf{B}u(t) \tag{2a}$$

$$y(t) = \mathbf{C}x(t) + \mathbf{D}u(t) \tag{2b}$$

where $\mathbf{A}_i$, $\mathbf{B}_i$, $\mathbf{C}_i$, and $\mathbf{D}_i$ show the state, input, output, and direct transmission matrices for the ith switching state with $i = 1 \to k$, and k is the total number of switching modes within each condition [25] as given in Table 2. The state variable $x(t)$ is defined as $[i_{L1}, i_{L2}, i_{L3}, v_{c1}, v_{c2}]^T$, the input variable $u(t)$ is defined as $[v_{in}, v_f]^T$, and the voltages across loads v_{o1}, and v_{o2} are the output variables, where i_{L1}, i_{L2}, and i_{L3} are inductor currents in L_1, L_2, and L_3, respectively; v_{c1} and v_{c2} are the voltages across capacitors C_1, and C_2, respectively; v_{in} is the input supply voltage; and v_f is the constant on-state voltage drop for the semiconductor devices. In steady state, (2) can be further rewritten as follows:

$$\dot{\mathrm{X}} = \mathbf{A}\mathrm{X} + \mathbf{B}\mathrm{U} = 0 \Rightarrow \mathrm{X} = -\mathbf{A}^{-1}\mathbf{B}\mathrm{U} \tag{3a}$$

TABLE 2 | Operating duty factor under different conditions for state I.

Operating modes (M_i)	Condition 1 C_1	Condition 2 C_2	Condition 3 C_3
Mode 1: M_1	d	d	$(1-d)$
Mode 2: M_2	$(1-2d)$	0	0
Mode 3: M_3	$(\lambda d + d - 1)$	$(\lambda d - d)$	$(\lambda d - d)$
Mode 4: M_4	$(1-\lambda d)$	$(1-\lambda d)$	$(1-\lambda d)$
Mode 5: M_5	0	0	$(2d-1)$

$$\mathrm{Y} = \mathbf{C}\mathrm{X} + \mathbf{D}\mathrm{U} \Rightarrow \mathrm{Y} = \left(-\mathbf{C}\mathbf{A}^{-1}\mathbf{B} + \mathbf{D}\right)\mathrm{U} \tag{3b}$$

The averaging of the state matrices $\mathbf{A}|_{Cj}$ and input matrices $\mathbf{B}|_{Cj}$ within the conditions C_j where $j = 1, 2, 3$ of the proposed BSISB with respect to five switching modes within any of the three conditions can be derived as follows:

$$\mathbf{A}|_{C_j} = \sum_{i=1}^{n\,(=5)} \mathbf{A}_i(M_i C_j), \quad \mathbf{B}|_{C_j} = \sum_{i=1}^{n\,(=5)} \mathbf{B}_i(M_i C_j) \tag{4}$$

Note: Further, the state matrices $\mathbf{A}|_{Cj}$ and input matrices $\mathbf{B}|_{Cj}$ for all the three conditions for the proposed converter are derived and presented in (5) and (6) with ideal conditions (i.e., no circuit parasitic), whereas using circuit parasitic the state matrices $\mathbf{A}|_{Cj}$ and input matrices $\mathbf{B}|_{Cj}$ for $d \le 0.5$ and $d > 0.5$ is derived and presented in Appendix A of this paper.

$$\mathbf{A}|_{C1} = \begin{bmatrix} 0 & 0 & 0 & \frac{-(1-d)}{L_1} & 0 \\ 0 & 0 & 0 & \frac{d(\lambda-1)}{L_2} & \frac{-1}{L_2} \\ 0 & 0 & 0 & \frac{-(1-d)}{L_3} & 0 \\ \frac{1-d}{C_1} & \frac{-d(\lambda-1)}{C_1} & \frac{1-d}{C_1} & \frac{-1}{R_1 C_1} & 0 \\ 0 & \frac{1}{C_2} & 0 & 0 & \frac{-1}{R_2 C_2} \end{bmatrix} \tag{5a}$$

$$\mathbf{A}|_{C2} = \begin{bmatrix} 0 & 0 & 0 & \frac{-(1-d)}{L_1} & 0 \\ 0 & 0 & 0 & \frac{d(\lambda-1)}{L_2} & \frac{-1}{L_2} \\ 0 & 0 & 0 & \frac{-d}{L_3} & 0 \\ \frac{1-d}{C_1} & \frac{-d(\lambda-1)}{C_1} & \frac{d}{C_1} & \frac{-1}{R_1 C_1} & 0 \\ 0 & \frac{1}{C_2} & 0 & 0 & \frac{-1}{R_2 C_2} \end{bmatrix} \tag{5b}$$

1097007x, 0, Downloaded from https://onlinelibrary.wiley.com/doi/10.1002/cta.4609 by Delhi Technological University, Wiley Online Library on [03/06/2025]. See the Terms and Conditions (https://onlinelibrary.wiley.com/terms-and-conditions) on Wiley Online Library for rules of use; OA articles are governed by the applicable Creative Commons License

$$\mathbf{A}|_{C3}=\begin{bmatrix} 0 & 0 & 0 & \frac{-(1-d)}{L_1} & 0 \\ 0 & 0 & 0 & \frac{d(\lambda-1)}{L_2} & \frac{-1}{L_2} \\ 0 & 0 & 0 & \frac{-(1-d)}{L_3} & 0 \\ \frac{1-d}{C_1} & \frac{-d(\lambda-1)}{C_1} & \frac{1-d}{C_1} & \frac{-1}{R_1C_1} & 0 \\ 0 & \frac{1}{C_2} & 0 & 0 & \frac{-1}{R_2C_2} \end{bmatrix} \quad (5c)$$

$$\mathbf{B}|_{C1}=\mathbf{B}|_{C2}=\mathbf{B}|_{C3}=\begin{bmatrix} \frac{1}{L_1} \\ 0 \\ \frac{1}{L_3} \\ 0 \\ 0 \end{bmatrix} \quad (6)$$

With the consideration of same inductance in both the corresponding interleaved branches of input side of the converter, that is, $L_1=L_3=L$ and the phase-shifted duty with identical pulse width, a common nonsingular state matrix and input matrix can be derived as follows:

$$\mathbf{A}=\begin{bmatrix} 0 & 0 & \frac{-2(1-d)}{L} & 0 \\ 0 & 0 & \frac{d(\lambda-1)}{L_2} & \frac{-1}{L_2} \\ \frac{1-d}{C_1} & \frac{-d(\lambda-1)}{C_1} & \frac{-1}{R_1C_1} & 0 \\ 0 & \frac{1}{C_2} & 0 & \frac{-1}{R_2C_2} \end{bmatrix}, \mathbf{B}=\begin{bmatrix} \frac{2}{L} \\ 0 \\ 0 \\ 0 \end{bmatrix} \quad (7)$$

2.3 | Steady-State Gain Characterization of BSISB Converter in State I

The duty ratio of switches S_1 or S_3 (i.e., presented as d) and S_2 (i.e., presented as λd) are defined for further analysis as d_1 and d_2, that is, $d=d_1$ and $\lambda d=d_2$. Consider a small disturbance about the equilibrium point. The duty ratios d_1 and d_2 and input voltage v_{in} are perturbed around their nominal values. It can be written as follows:

$$d_1=D_1+\hat{d}_1, d_2=D_2+\hat{d}_2, \text{and } v_{in}=V_{in}+\hat{v}_{in}$$
$$\text{such that } \frac{\hat{d}_1}{D_1}\ll 1, \frac{\hat{d}_2}{D_2}\ll 1 \text{ and } \frac{\hat{v}_{in}}{V_{in}}\ll 1 \quad (8)$$

where D_1, D_2, and V_{in} are the steady-state values of duty ratios for switches S_1 or S_3, S_2, and input supply voltage, respectively; and $\hat{d}_1$, $\hat{d}_2$, and $\hat{v}_{in}$ are the disturbances in the respective steady-state values about the equilibrium points.

Using (3a) and (7), the output voltages of the proposed converter under steady state-conditions for both the output ports can be derived and presented in (9).

$$V_{o1}=\frac{V_{in}}{1-D_1}, V_{o2}=\frac{D_1(\lambda-1)V_{in}}{1-D_1}. \quad (9)$$

It can be seen that the voltage gain at output port 1 is the convention boost output whereas output port 2 can be step-down, and it depends on the values of D_1 and λ. It can be seen from Figure 4. The input current (i_{in}) is defined as the sum of the interleaved inductor currents, that is, $i_{in}=i_{L1}+i_{L3}$, the mathematical relation for steady-state value of currents i_{in} and i_{L2} can be written using (3a) and (7) as follows:

$$i_{L2_{avg}}=I_{o2}=\frac{D_1(\lambda-1)V_{in}}{(1-D_1)R_2}, \quad (10)$$

$$i_{in_{avg}}=i_{L1_{avg}}+i_{L3_{avg}}=\frac{I_{o1}}{1-D_1}+\frac{D_1(\lambda-1)I_{o2}}{1-D_1}. \quad (11)$$

Ripple in the input current can be evaluated from Figure 3a,c as follows:

$$\Delta i_{in}=K_L+K_D \quad (12a)$$

$$\text{where } K_L=D_1TV_{in}\left(\frac{1}{\min(L_1,L_3)}-\frac{1}{\max(L_1,L_3)}\right); \quad (12b)$$

$$K_D=\begin{cases}\left(\frac{1-2D_1}{1-D_1}\right)\frac{D_1TV_{in}}{\max(L_1,L_3)}, & \forall D_1\le 0.5\end{cases} \quad (12c)$$

$$K_D=\begin{cases}\frac{(2D_1-1)TV_{in}}{\max(L_1,L_3)}, & \forall D_1>0.5.\end{cases} \quad (12d)$$

It can be seen from (12) that the input current ripple consists of two components, K_L and K_D. The input current ripple is dependent on D_1 and independent of λ. The expression for K_D differs for cases where $0\le D_1\le 0.5$ and $0.5<D_1\le 1$. At the same value of

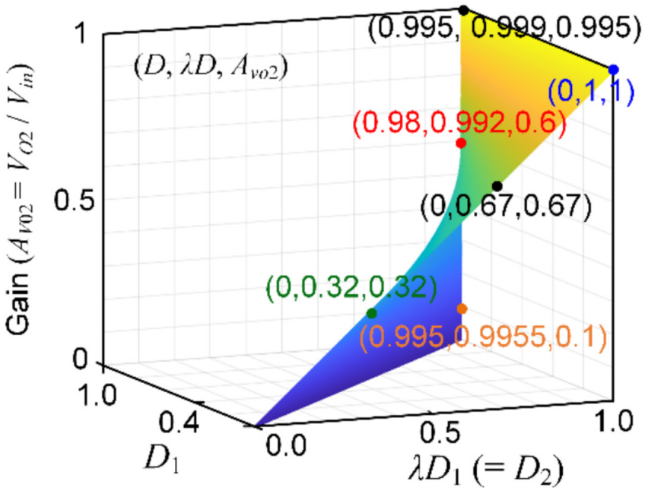


FIGURE 4 | Voltage gain ($A_{vo2}=V_{02}/V_{in}$) characteristics of the BSISB converter.

1097007x, 0, Downloaded from https://onlinelibrary.wiley.com/doi/10.1002/cta.4609 by Delhi Technological University, Wiley Online Library on [03/06/2025]. See the Terms and Conditions (https://onlinelibrary.wiley.com/terms-and-conditions) on Wiley Online Library for rules of use; OA articles are governed by the applicable Creative Commons License

interleaving inductors L_1 and L_3, K_L can be eliminated, and at $D_1 = 0.5$, the value of K_D will be equal to zero. Thus, if both L_1 and L_3 are kept equal and the converter is operating at $D_1 = 0.5$, the input current ripple becomes zero, as shown in Figure 3b. When $D_1 \neq 0.5$ and/or $L_1 \neq L_3$, there is a ripple in input current. However, it is still less than the input current ripple in a conventional multiport switched boost converter (MSBC) [6]. This decrease in current ripple is attributed to the interleaving inductor, which provides the input current ripple cancellation.

The input current performance of the proposed BSISB multiport converter is presented. The input current ripple Δi_{in} with respect to duty without interleaving is same as ripple in inductor current L_1 in MSBC, and it can be written as in (13). The mathematical relations with respect to Δi_{in} for proposed BSISB converter and MSBC is plotted in Figure 5a using (12) and (13).

$$\Delta i_{L1} = \frac{D_1 T V_{in}}{L_1} \tag{13}$$

Furthermore, the impact of variations in the input interleaved inductors on the input current ripple is evaluated, considering the tolerance variations of inductors under practical conditions. Figure 5b shows the change in Δi_{in} with respect to the duty cycle for different values of L_1 and L_3. It can be observed that the inductor current ripple increases at $D_1 = 0.5$ for all cases where $L_1 \neq L_3$. However, this increase in current ripple is significantly lower than that observed in the MSBC converter. Figure 5b (plots 2 and 5) indicates that the input current ripple characteristics remain the same over the entire range of the duty cycle D_1 when the values of L_1 and L_3 are interchanged (i.e., when $|L_1 - L_3|$ is the same). However, the ripple also depends on minimum (L_1, L_3), as shown in Figure 5b (plot 1). Figure 5c presents the variation of input current ripple at $D_1 = 0.5$ and L_1 fixed at 2 mH for different values of L_3.

2.4 | Steady-State Gain Characterization of BSISB Converter in State II

The operation of the proposed converter under state II is similar to the conventional boost converter and the steady-state voltage output at output port 1 can be written as follows:

$$V_{o1} = \frac{V_{o2}}{1 - D_1}. \tag{14}$$

2.5 | Dynamic Characteristics of BSISB Converter

Due to the perturbation in control variables, the states and the outputs also change by small values as follows:

$$x = \mathrm{X} + \hat{x}, v_{o1} = V_{o1} + \hat{v}_{o1}, \text{and } v_{o2} = V_{o2} + \hat{v}_{o2} \tag{15}$$

Substitute the values of x, d_1, d_2, v_{o1}, v_{o2}, and v_{in}, from (8) and (15) in (2), and select the AC term after neglecting the DC terms and second-order terms. The state space model for dynamic response can be derived as follows:

$$\frac{d\hat{x}}{dt} = \dot{\hat{x}} = \mathbf{A}\hat{x} + \mathbf{B}\hat{v}_{in} + \mathbf{F}_1\hat{d}_1 + \mathbf{F}_2\hat{d}_2 \tag{16a}$$

$$\hat{y} = \mathbf{C}\hat{x} + \mathbf{G}_1\hat{d}_1 + \mathbf{G}_2\hat{d}_2 \tag{16b}$$

Using Laplace transformation (15) can be written with $\mathbf{G_1} = \mathbf{G_2} = 0$ as follows:

$$\left.\frac{\hat{y}(s)}{\hat{v}_{in}(s)}\right|_{\hat{d}_1=\hat{d}_2=0} = \mathbf{C}[sI - \mathbf{A}]^{-1}\mathbf{B} \tag{17a}$$

$$\left.\frac{\hat{y}(s)}{\hat{d}_1(s)}\right|_{\hat{v}_{in}=\hat{d}_2=0} = \mathbf{C}[sI - \mathbf{A}]^{-1}\mathbf{F}_1 \tag{17b}$$

$$\left.\frac{\hat{y}(s)}{\hat{d}_2(s)}\right|_{\hat{v}_{in}=\hat{d}_1=0} = \mathbf{C}[sI - \mathbf{A}]^{-1}\mathbf{F}_2 \tag{17c}$$

where F_1 and F_2 can be derived for state I as follows:

$$\mathbf{F}_1 = \begin{bmatrix} \frac{2v_{C1}}{L} \\ \frac{-v_{C1}}{L_2} \\ \frac{-i_{in} + i_{L2}}{C_1} \\ 0 \end{bmatrix}, \quad \mathbf{F}_2 = \begin{bmatrix} 0 \\ \frac{v_{C1}}{L_2} \\ \frac{-i_{L2}}{C_1} \\ 0 \end{bmatrix}. \tag{18}$$

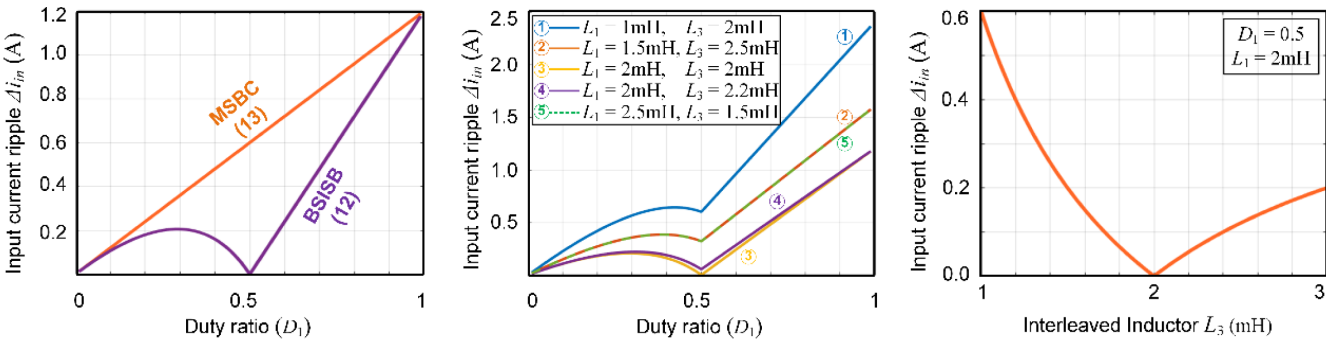


FIGURE 5 | Variation of input current ripple with (a) duty D_1 for MSBC and proposed BSISB converter, (b) duty D_1 at different values of inductors L_1 and L_3, and (c) interleaved inductor L_3 for fixed value of $D_1 = 0.5$ and $L_1 = 2$ mH.

1097007x, 0, Downloaded from https://onlinelibrary.wiley.com/doi/10.1002/cta.4609 by Delhi Technological University, Wiley Online Library on [03/06/2025]. See the Terms and Conditions (https://onlinelibrary.wiley.com/terms-and-conditions) on Wiley Online Library for rules of use; OA articles are governed by the applicable Creative Commons License

Transfer function of the proposed BSISB can be derived using (7), (17), and (18) under the state I with respect to their state matrix, input matrix. The control-to-output transfer function $\hat{v}_{o1}(s)/\hat{d}_1(s)$ can be used to plot the characteristics of the proposed BSISB converter and compared with the bode plot of the conventional boost converter as presented in Figure 6a, where the value of inductance in the boost converter is considered half of the BSISB converter. It can be seen that the dynamics of the proposed BSISB functions similar to a normal boost converter, which is a significant advantage of this design. The PI compensated closed-loop stable dynamics, and different control input are shown in Figures 6b,c, respectively. The control design for the proposed converter in detail are presented in the next section.

3 | Controller Design

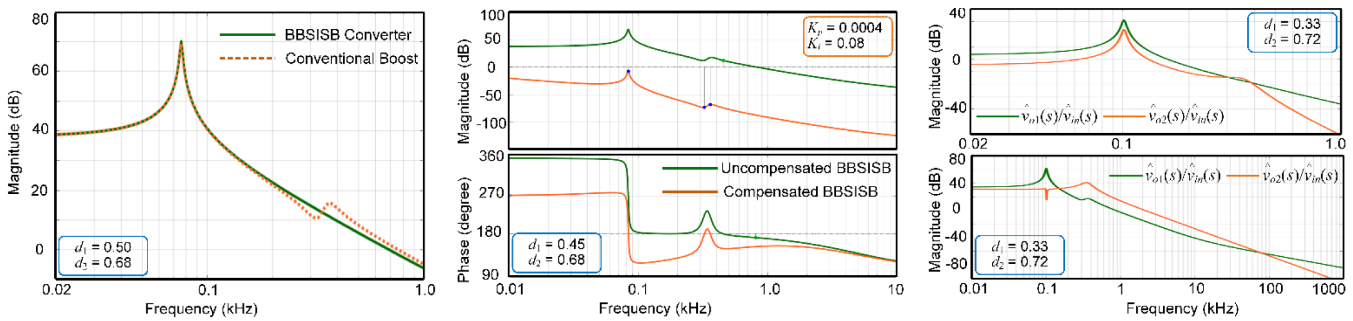
Transfer functions (TFs) of the proposed BSISB converter are derived using (7), (17), and (18) under state I operation. TFs of control-to-voltage output-1 $\hat{v}_{o1}(s)/\hat{d}_1(s)$, voltage input-to-output-1 $\hat{v}_{o1}(s)/\hat{v}_{in}(s)$, voltage input-to-output-2 $\hat{v}_{o2}(s)/\hat{v}_{in}(s)$, and control-to-voltage output-2 $\hat{v}_{o2}(s)/\hat{d}_2(s)$ are presented in (19), (20), (21), and (22), respectively. All the poles and zeros of the TFs are on the left half of the s-plane except a zero of $\hat{v}_{o1}(s)/\hat{d}_1(s)$ lies on the right half of the s-plane; hence, the open-loop system of (20), (21), and (22) is stable. However, due to a zero on the right half of the s-plane for control-to-voltage output-1, the system presented in (19) shows nonminimum phase characteristics. So, to improve the nonminimum phase characteristics response, a closed-loop controller is presented in Figure 7.

$$\frac{\hat{v}_{o1}(s)}{\hat{d}_1(s)} = \frac{-810s^3 + 2.423\times10^7 s^2 + 5.39\times10^9 s + 9.09\times10^{13}}{s^4 + 396s^3 + 5.29\times10^6 s^2 + 1.69\times10^8 s + 1.14\times10^{12}} \tag{19}$$

$$\frac{\hat{v}_{o1}(s)}{\hat{v}_{in}(s)} = \frac{4.545\times10^5 s^2 + 1.748\times10^8 s + 2.273\times10^{12}}{s^4 + 396s^3 + 5.29\times10^6 s^2 + 1.69\times10^8 s + 1.14\times10^{12}} \tag{20}$$

$$\frac{\hat{v}_{o2}(s)}{\hat{v}_{in}(s)} = \frac{7.955\times10^{11}}{s^4 + 396s^3 + 5.29\times10^6 s^2 + 1.69\times10^8 s + 1.14\times10^{12}} \tag{21}$$

$$\frac{\hat{v}_{o2}(s)}{\hat{d}_2(s)} = \frac{2\times10^8 s^2 + 1.536\times10^9 s + 4.545\times10^{13}}{s^4 + 396s^3 + 5.29\times10^6 s^2 + 1.69\times10^8 s + 1.14\times10^{12}} \tag{22}$$



(a) (b) (c)

FIGURE 6 | Bode plot during state I using system parameters used in the experimental section (a) output port 1 verse control input $\hat{v}_{o1}(s)/\hat{d}_1(s)$ for conventional boost and proposed BSISB, (b) during condition 1 at $d_1 = 0.45$ and $\lambda d_1 = d_2 = 0.68$, (c) gain characteristics under all the four conditions.

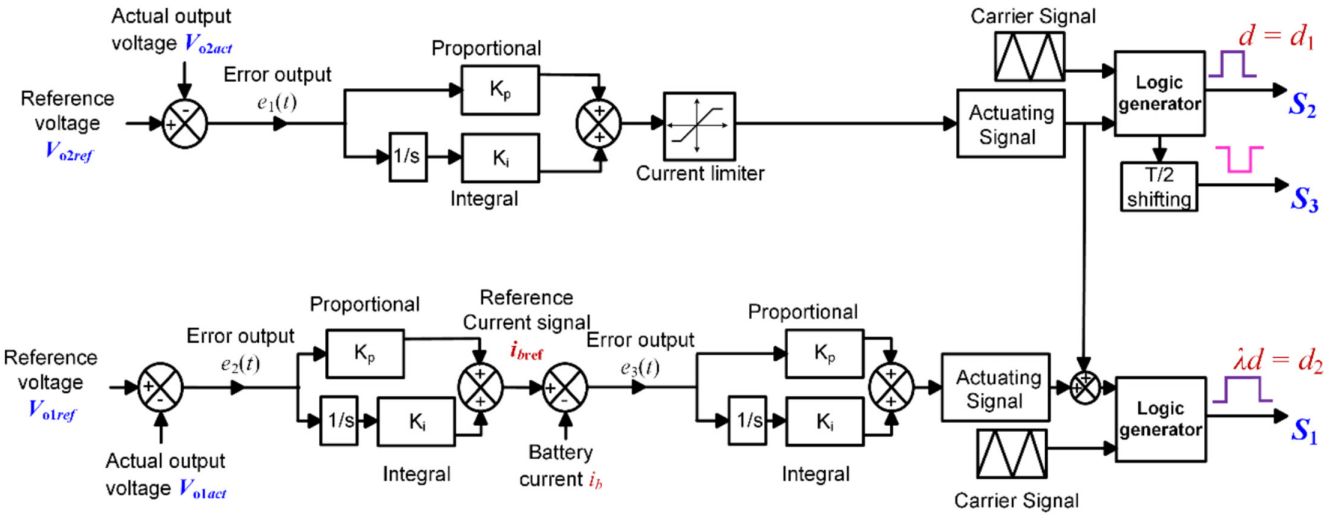


FIGURE 7 | Block diagram of constant current constant voltage operation of the controller for proposed BSISB.

1097007x, 0, Downloaded from https://onlinelibrary.wiley.com/doi/10.1002/cta.4609 by Delhi Technological University, Wiley Online Library on [03/06/2025]. See the Terms and Conditions (https://onlinelibrary.wiley.com/terms-and-conditions) on Wiley Online Library for rules of use; OA articles are governed by the applicable Creative Commons License

In real-time systems, the majority of practical system parameters can vary from their nominal values. Therefore, a stable system should be designed with the consideration of certain uncertainties. The controller design for the proposed BSISB converter is developed with a closed-loop compensated system model for $\hat{v}_{o1}(s)/\hat{d}_1(s)$ at $V_{o1}=40\,\text{V}$ when the load connected at port 1 is changed from 25 Ω to 100 Ω with input voltage variation from 18 V to 22 V with the nominal value of load, that is, 76 Ω, and input voltage, that is, 20 V, respectively. It shows that the coefficient of the TF of the plant ranges from a minimum to maximum uncertainty values (i.e., 10% variation due to uncertainty is chosen in the input voltage). To ensure good and stable performance, the controller must be designed for the worst possible real time condition. The stability boundary locus technique is used to determine the boundary values of PI controllers. Kharitonov's theorem gives an efficient method for including all sets of TFs resulting from system model uncertainty [28].

The boundary locus for stable operation of the proposed converter is designed from the TF given in (19). Figure 8 shows the stable region in the K_p–K_i plane. The nominal TF is the only factor influencing this stability area. The values of integral gain K_i and proportional gain K_p of the controller are chosen from the stability boundary locus as given in Figure 8. The values of K_p and K_i are chosen 0.0004 and 0.08, respectively. Figure 9a,b shows the dynamic change in the output voltage with respect to the d_1 and the variation in the input variable, respectively, while maintaining the other input variables constant. Figure 9 shows that the developed state-space model is accurate and may be utilized to construct a suitable controller under step change operation.

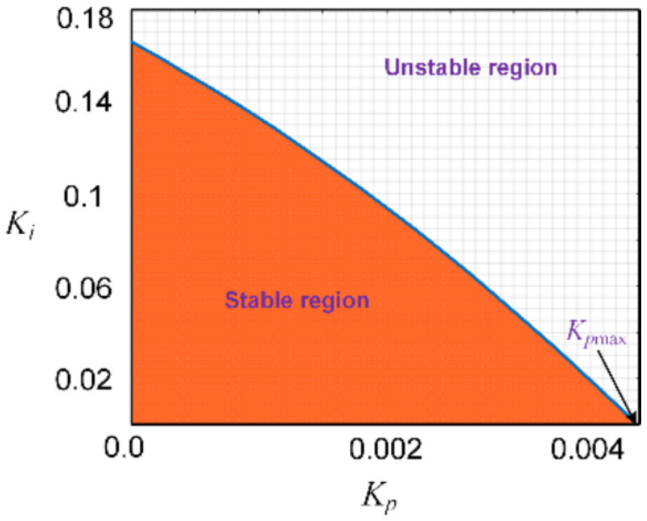


FIGURE 8 | Boundary locus of the controller design for the stable operation of proposed BSISB multiport converter.

4 | Loss Analysis and Fault Tolerant Operation of BSISB Multiport Converter

The efficiency of the BSISB multiport converter is calculated assuming that all the five semiconductor devices (three switches and two diodes) have similar constant on-state voltage drop and also the ESR of the inductors is equal (i.e., $r_{L1}=r_{L2}=r_{L3}=r_L$), while the loss due to nonideal filter capacitor characteristics is ignored. Total conduction loss (P_{CL}) may be described as (23), where P_{RCL} is the conduction loss due to ESR of inductors, P_{SCL} is the conduction loss due to on-state resistance (R_{DS}) of the switch and on-state voltage drop (V_f) of the switch.

$$P_{CL}=P_{RCL}+P_{SCL} \tag{23}$$

$$\text{where } P_{RCL}\approx\frac{r_L}{D_1}\left(i_{L1avg}^2+i_{L2avg}^2+i_{L3avg}^2\right) \tag{24}$$

The total loss of the BSISB converter and MSBC are calculated using (25) and plotted as shown in Figure 10 for the power rating of 10–200 W, where the values of $r_L=150\,\text{m}\Omega$, $R_{DS}=40\,\text{m}\Omega$, $V_f=0.3\,\text{V}$, $\lambda=1.5$, and $i_{L2\text{avg}}=1\,\text{A}$ are considered. It can be seen from Figure 10 that the power loss is approximately double in MSBC at 200 W converter rating.

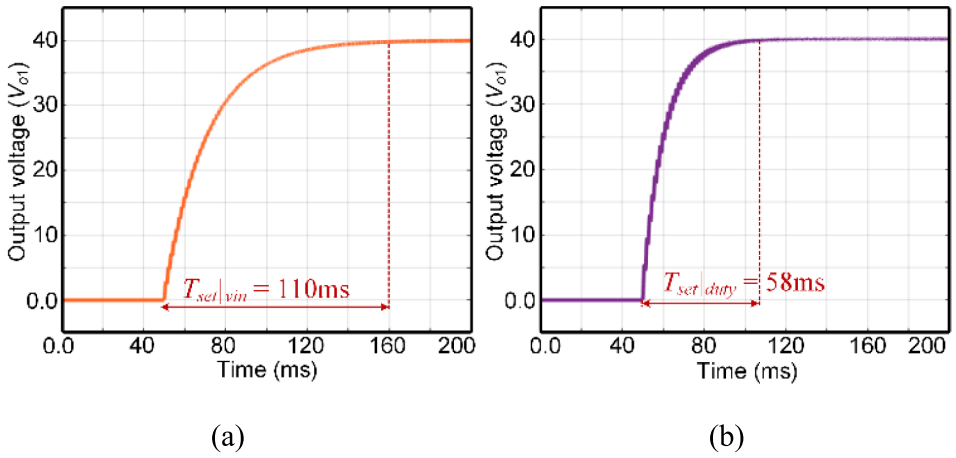


FIGURE 9 | Dynamic response of the proposed converter (a) step change in the input voltage v_{in}, and (b) step change in duty d_1.

1097007x, 0, Downloaded from https://onlinelibrary.wiley.com/doi/10.1002/cta.4609 by Delhi Technological University, Wiley Online Library on [03/06/2025]. See the Terms and Conditions (https://onlinelibrary.wiley.com/terms-and-conditions) on Wiley Online Library for rules of use; OA articles are governed by the applicable Creative Commons License

$$P_{SCL}=\begin{cases}\left(\begin{array}{c}\left(2i_{L1avg}^2-2i_{L1avg}i_{L2avg}+i_{L3avg}^2\right)R_{DS}+V_f\left(i_{L2avg}-i_{L1avg}-i_{L3avg}\right)+\\ \frac{D_2}{D_1}\left\{i_{L2avg}^2R_{DS}+V_f\left(i_{L1avg}-2i_{L2avg}\right)-I_{o1}\right\}+\frac{1}{D_1}\left\{V_f\left(i_{L2avg}+i_{L3avg}\right)+I_{o1}\right\}\end{array}\right) & \forall D_1\le 0.5\&D_1\le D_2\le 1\\ \left(\begin{array}{c}\left(2i_{L2avg}^2-2i_{L1avg}i_{L2avg}+i_{L3avg}^2\right)R_{DS}+V_f\left(i_{L2avg}-i_{L1avg}-i_{L3avg}\right)+\\ \frac{D_2}{D_1}\left\{i_{L2avg}^2R_{DS}+V_f\left(i_{L1avg}-2i_{L2avg}\right)-I_{o1}\right\}+\frac{1}{D_1}\left\{V_f\left(i_{L2avg}+i_{L3avg}\right)+\left(i_{L1avg}^2-i_{L2avg}^2\right)R_{DS}+I_{o1}\right\}\end{array}\right) & \forall 0.5<D_1\&D_1\le D_2\le 1\end{cases} \tag{25}$$

The BSISB converter provides redundancy towards switching operation and therefore the proposed converter is partially fault tolerant. The parallel legs of inductor at the input end introduce redundancy in the circuit. Even when one of the legs becomes faulty, the boost-end output is not affected. With fault tolerant capability, the closed loop algorithm reconfigures the gate pulses to the switches under fault. The modes of operation under open circuit switch fault conditions are discussed as follows.

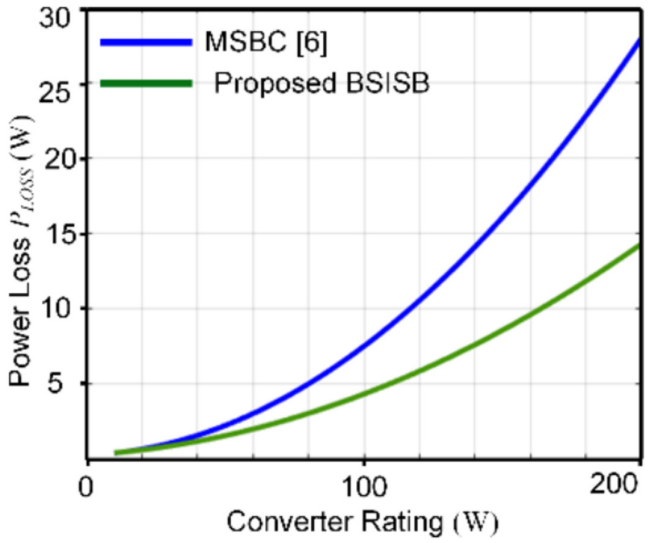


FIGURE 10 | Comparative analysis of power loss in proposed BSISB multiport converter and MSBC for 200 W converter power rating.

4.1 | Under Open Switch S_1 Fault Condition

Figure 11a shows the open circuit switch fault in S_1 (SF_1). The operation of the converter in mode 1, mode 3, mode 4, and mode 5 is similar with a few circuit limitations, as presented with remarks, where mode 2 is absent. The voltage gain of the converter under SF_1 is derived and presented in (26). It shows that the gain of the boost port is similar to the healthy operation of the converter, whereas the buck port is affected by the OC fault condition in SF_1.

$$A_{V_{01}}\Big|_{SF_1}=\frac{1}{1-D_1},\ \ \&\ A_{V_{02}}\Big|_{SF_1}=0. \tag{26}$$

4.2 | Under Open Switch S_2 Fault Condition

Figure 11b shows the open circuit switch fault in S_2 (SF_2). The operation of the converter in mode 2, mode 3, and mode 4 is similar, whereas mode 5 operation can be achieved with $I_{s1}=0$, as mentioned in remarks, where mode 1 is absent. The voltage gain of the converter under SF_2 is derived and presented in (27). It shows the gain of the boost and buck ports are similar to the healthy operation of the converter with the increased current stress and input current ripple. The proposed converter is fault-tolerant under an OC switch with a healthy diode SF_2 condition.

$$A_{V_{01}}\Big|_{SF_2}=\frac{1}{1-D_1},\ \ \&\ A_{V_{02}}\Big|_{SF_2}=\frac{D_1(\lambda-1)}{(1-D_1)}. \tag{27}$$

4.3 | Under Open Switch S_3 Fault Condition

Figure 11c shows the open circuit switch fault in S_3 (SF_3). The operation of converter in mode 1, mode 2, mode 4, and mode

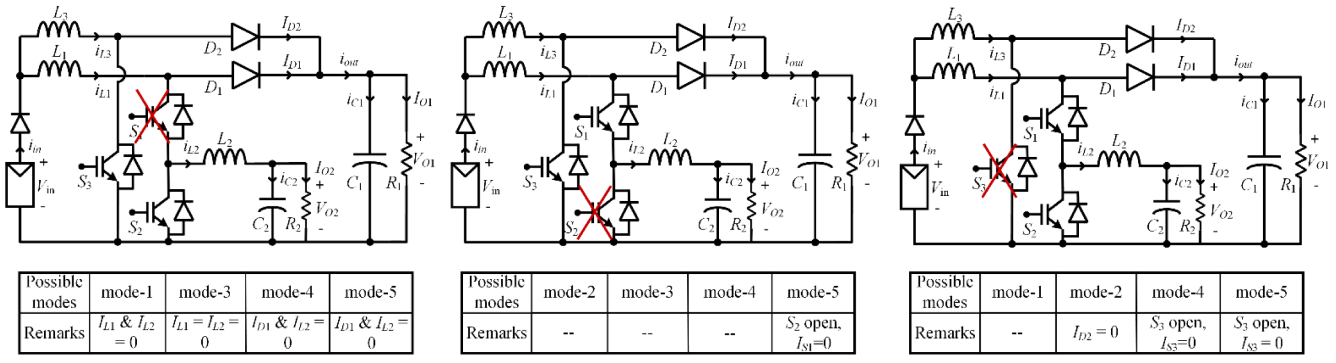


FIGURE 11 | Operation of BSISB multiport converter with V_{02} as a load under open switch fault conditions (a) SF_1, (b) SF_2, and (c) SF_3.

1097007x, 0, Downloaded from https://onlinelibrary.wiley.com/doi/10.1002/cta.4609 by Delhi Technological University, Wiley Online Library on [03/06/2025]. See the Terms and Conditions (https://onlinelibrary.wiley.com/terms-and-conditions) on Wiley Online Library for rules of use; OA articles are governed by the applicable Creative Commons License

5 is similar with a few circuit limitations, as mentioned in remarks, where mode 3 is absent. The voltage gain of the converter under SF_3 is derived and presented in (28). It shows the gain of the boost and buck ports are similar to the healthy operation of the converter with the increased current stress and input current ripple. The proposed converter is fault-tolerant under an OC switch fault SF_3 condition.

$$A_{V_{01}}\Big|_{SF_3} = \frac{1}{1-D}, \quad \& \quad A_{V_{02}}\Big|_{SF_3} = \frac{D(\lambda-1)}{1-D}. \tag{28}$$

The voltage stress across each switch in the proposed BSISB converter are calculated under OC fault conditions, compared with healthy condition and presented in Table 3. It provides the optimized circuit design parameters for reliable, efficient, and safe operation of the system.

The summary of fault-tolerant capability of the proposed converter against semiconductor OC and SC switch failures is presented in Table 4. The comparative analysis of fault-tolerant behavior with respect to MSBC is also presented to show the improvement in fault-tolerant capability. The results are verified with the experimental results and it shows that the converter is partially fault-tolerant against OC and SC failures.

5 | Results and Discussion

An experimental setup of the BSISB multiport converter is developed in the laboratory to test the proposed topology in real time, as shown in Figure 12. The system parameters used to test the results are given in Table 5. The microcontroller TIF28379D is used to operate and test the proposed BSISB converter. Two current sensors (LA25-P) are used to measure the 12 V battery current connected at the buck output in both directions and step down the measured current so that it can be given to the microcontroller for current control of the battery during charging

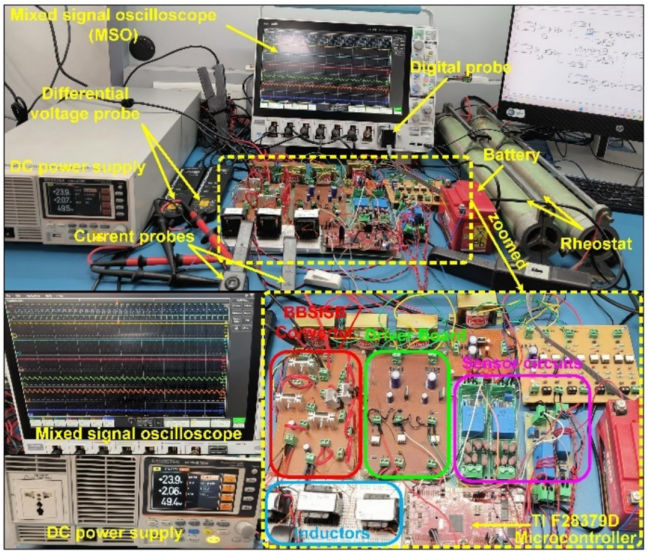


FIGURE 12 | Experimental setup of BSISB multiport converter.

TABLE 3 | Maximum voltage stress in the switches.

Voltage stress	At S_1: V_{S1}	At S_2: V_{S2}	At S_3: V_{S3}
Healthy condition	V_{o1}	V_{o1}	V_{o1}
SF_1	OC fault	—	
SF_2	V_{o1}	OC fault	V_{o1}
SF_3	V_{o1}	V_{o1}	OC fault

TABLE 5 | System parameters.

Parameters	Values
Input supply voltage (V_{in})	20–24 V
Inductors ($L_1 = L_2 = L_3$)	2 mH
ESR of inductors ($r_{L1} = r_{L2} = r_{L3}$)	150 mΩ
Filter capacitors (C_1, C_2)	1100 μF, 100 μF
ESR of capacitors (r_{C1}, r_{C2})	150 mΩ, 100 mΩ
Switching frequency f_s	10 kHz
Output port 1: Resistance (R_1)	96 Ω (variable)
Output port 2: Battery	12 V (nominal)
Output port 2: Resistance (R_2)	48 Ω (variable)
Test power rating	(20–100 W)

TABLE 4 | Fault tolerant capability of BSISB multiport converter with respect to the semiconductor switches.

		BSISB converter		MSBC [6]	
Switch	Fault type	Boost side voltage	Buck side voltage	Boost side voltage	Buck side voltage
S_1	OC	✓	✖ (0 V)	✖	✖ (0 V)
	SC	✓	✖ (V_{in})	✓	✖ (V_{in})
S_2	OC	✓	✓	✖	✖ (over rated)
	SC[a]	✖ (over rated)	✖ (0 V)	✖ (over rated)	✖ (0 V)
S_3	OC	✓	✓	N/A	N/A
	SC[b]	✓	✓	N/A	N/A

[a]Overvoltage protection at the boost-end required.
[b]Overcurrent protection between source, L_3, and ground required.

1097007x, 0, Downloaded from https://onlinelibrary.wiley.com/doi/10.1002/cta.4609 by Delhi Technological University, Wiley Online Library on [03/06/2025]. See the Terms and Conditions (https://onlinelibrary.wiley.com/terms-and-conditions) on Wiley Online Library for rules of use; OA articles are governed by the applicable Creative Commons License

and discharging mode. The voltage sensors (LV25-P) are used to control the voltage outputs of both ports. The various devices for measuring circuit characteristics are used, such as differential voltage probes, current probes, and a mixed signal oscilloscope (MSO) to capture the waveforms.

Figures 13 and 14 represent the charging and discharging of buck-side batteries with the proposed BSISB converter (with an interleaving branch) and MSBC (without an interleaving branch). The buck side port is connected to a 12 V lead-acid battery, whereas the boost side port is connected to a rheostat of 96 Ω (which is varied to test the setup for different power levels). During charging mode, the battery starts charging with a current of 1A (i.e., the current limit during CC mode is 1A) for both converters. The values of d and λd are also the same in both cases, which verifies exactly the same expression of output voltages with respect to d and λ. In Figure 13, the values of Δi_{L1} and Δi_{L3} are discontinuous (i.e., current is divided in parallel branches) and out of phase, which helps to reduce the ripple in input current. This shows the input current ripple of BSISB is lower as compared with MSBC. During discharging mode, input is disconnected from the converter, which is sensed by the microcontroller through the input voltage sensor. The switch S_2 is on, and the boost side output is regulated using the discharging of the battery, and i_{L2} and battery current i_b get reversed as shown in Figures 13 and 14 for the BSISB converter and MSBC, respectively. The results show the settling time (T_{set}) during bidirectional operation of the converter is approximately similar to calculated in the theoretical dynamic response.

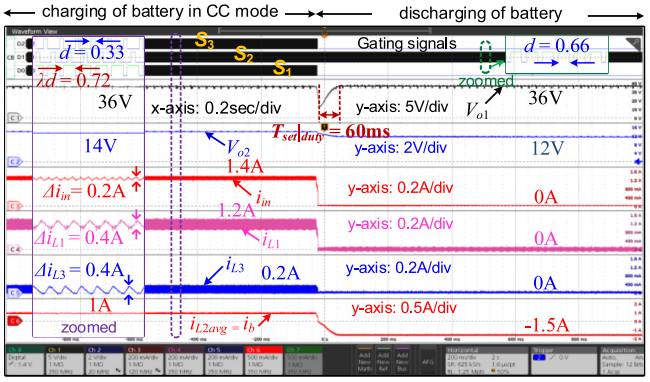


FIGURE 13 | Bidirectional operation of proposed BSISB converter in charging to discharging mode of operation.

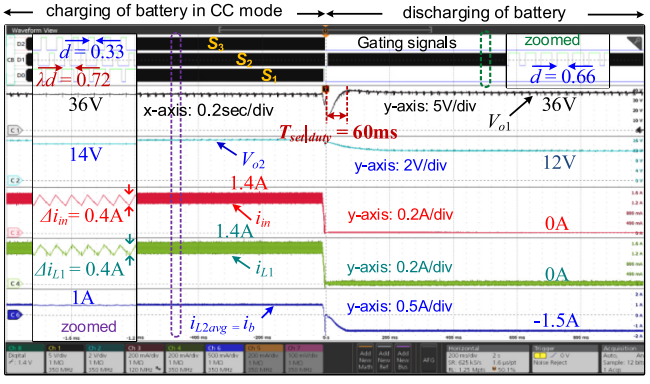


FIGURE 14 | Bidirectional operation of conventional MSBC converter in charging to discharging mode of operation.

The OC switch fault-tolerant capability of the proposed BSISB multiport converter is tested in real time with the healthy anti-parallel diode of the semiconductor switches. The OC faults are created by turning off the respective gate signals. Figures 15, 16, and 17 show the results captured under OC switch faults in S_1 (i.e., SF_1), S_2 (i.e., SF_2), and S_3 (i.e., SF_3), respectively. The behavior of the converter is tested with the change in the input supply voltage, that is, V_{in} = 20 V for these results. All three results are

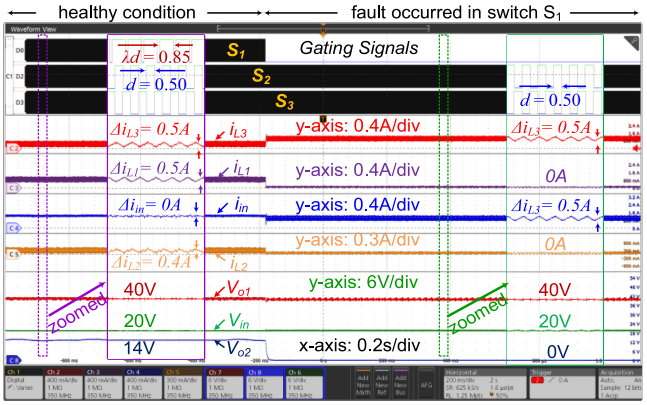


FIGURE 15 | Characterization of proposed BSISB multiport converter under OC switch fault in S_1 (SF_1).

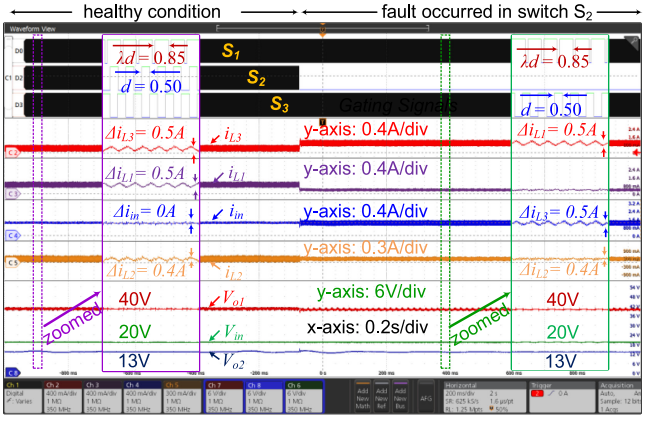


FIGURE 16 | Characterization of proposed BSISB multiport converter under OC switch fault in S_2 (SF_2).

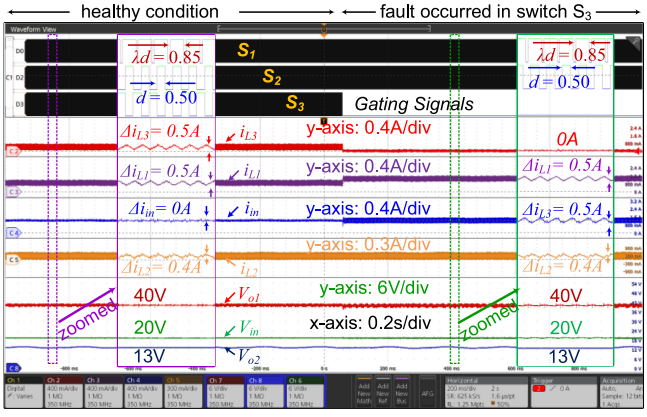


FIGURE 17 | Characterization of proposed BSISB multiport converter under OC switch fault in S_3 (SF_3).

1097007x, 0, Downloaded from https://onlinelibrary.wiley.com/doi/10.1002/cta.4609 by Delhi Technological University, Wiley Online Library on [03/06/2025]. See the Terms and Conditions (https://onlinelibrary.wiley.com/terms-and-conditions) on Wiley Online Library for rules of use; OA articles are governed by the applicable Creative Commons License

captured and presented in a similar pattern, where the zoomed sections show the results before and after the respective faults. Figure 15 represents the operation of the converter under the OC switch S_1 fault (i.e., SF_1). The boost side voltage port is regulated, whereas the buck output voltage is zero, and $i_{L1}=0$ after SF_1. Figure 16 shows the operation of the converter under the OC switch S_2 fault (i.e., SF_2). Both the output port voltages are regulated by the increased current transfer through i_{L3}. Figure 17 shows the operation of the converter under the OC switch S_3 fault (i.e., SF_3). Both the output port voltages are regulated by the increased current transfer through i_{L1}. The results show the bidirectional capability of the proposed converter in CC-CV mode during charging and controlled current mode during discharging. It shows the behavior of input current ripple with respect to variation of the controlled output voltages and OC switch fault conditions.

6 | Conclusion

In this article modeling of a novel BSISB multiport converter is developed. The state-space averaged (SSA) and small signal model (SSM) of the proposed converter is developed with circuit parasitic. The SSA and SSM are used for steady-state gain analysis and the controller design for the converter, respectively. The stable region of the controller has been designed for the robust operation of the proposed converter. The dynamic behavior of the proposed converter has been presented during step change in the input voltage and duty. Boost side interleaving provides improved input current ripple enable redundancy in the circuit to make it partially fault tolerant. The steady-state mathematical relations are derived for input current ripple with respect to duty. The tolerance variations of inductors are also considered for the input current ripple design for the complete duty range. A double loop control for battery charging is developed. The bidirectional property of the output port 2 is verified through the results during the absence of the input, when the battery discharges to provide power at the boost-end.

Acknowledgments

This research supported by the Science and Engineering Research Board (SERB), Department of Science & Technology, Government of India, under the SERB sanction order number SRG/2021/001640.

Data Availability Statement

Data sharing is not applicable to this article as no datasets were generated or analysed during the current study.

References

1. R.-J. Wai and J.-J. Liaw, "High-Efficiency-Isolated Single-Input Multiple-Output Bidirectional Converter," *IEEE Transactions on Power Electronics* 30, no. 9 (2015): 4914–4930.

2. P. Patra, A. Patra, and N. Mishra, "Single-Inductor Multiple-Output Switcher With Simultaneous Buck, Boost, and Inverted Outputs," *IEEE Transactions on Power Electronics* 27, no. 4 (2012): 1936–1951.

3. D. Ma, W.-H. Ki, C. Y. Tsui, and P. K. T. Mok, "Single-Inductor Multiple Output Switching Converters With Time-Multiplexing Control in Discontinuous Conduction Mode," *IEEE Journal of Solid-State Circuits* 38 (2003): 89–100.

4. K. Modepalli and L. Parsa, "A Scalable N-Color LED Driver Using Single Inductor Multiple Current Output Topology," *IEEE Transactions on Power Electronics* 31, no. 5 (2016): 3773–3783.

5. P. Bhattacharyya, S. Ghorai, S. Sen, and S. K. Giri, "A Flexible Non-Isolated Multiport Converter to Integrate Battery and Ultracapacitor for Electric Vehicle Applications," *IEEE Transactions on Circuits and Systems II: Express Briefs* 70, no. 3 (2023): 1044–1048, https://doi.org/10.1109/TCSII.2022.3217844.

6. S. K. Mishra, K. K. Nayak, M. S. Rana, and V. Dharmarajan, "Switched-Boost Action Based Multiport Converter," *IEEE Transactions on Industry Applications* 55, no. 1 (2019): 964–975, https://doi.org/10.1109/TIA.2018.2869098.

7. O. Ray and S. Mishra, "Switched-Boost Action: A Phenomenon for Achieving Time-Division-Multiplexed Multi-Port Power Transfer for Nanogrid Applications," *Sadhana* 42, no. 8 (2017): 1227–1238.

8. A. Nahavandi, M. T. Hagh, M. B. B. Sharifian, and S. Danyali, "A Nonisolated Multiinput Multioutput DC–DC Boost Converter for Electric Vehicle Applications," *IEEE Transactions on Power Electronics* 30, no. 4 (2015): 1818–1835.

9. H. Behjati and A. Davoudi, "A Multiple-Input Multiple-Output DC-DC Converter," *IEEE Transactions on Industry Applications* 49, no. 3 (2013): 1464–1479.

10. S. Pourjafar, H. Shayeghi, F. Sedaghati, S. Seyedshenava, and F. Blaabjerg, "A Bidirectional Multiport DC-DC Converter Applied for Energy Storage System With Hybrid Energy Sources," *International Journal of Circuit Theory and Applications* 49 (2021): 2453–2478, https://doi.org/10.1002/cta.2988.

11. G. K. N. Kumar and A. K. Verma, "A Single-Phase Interleaved Buck-Boost PFC Based On-Board EV Charger," *IEEE Transactions on Industry Applications* 59, no. 6 (2023): 7163–7174, https://doi.org/10.1109/TIA.2023.3302269.

12. D. Kumar, R. K. Nema, and S. Gupta, "A Comparative Review on Power Conversion Topologies and Energy Storage System for Electric Vehicles," *International Journal of Energy Research* 44, no. 10 (2020): 7863–7885, https://doi.org/10.1002/er.5353.

13. S. Kumar and A. Usman, "A Review of Converter Topologies for Battery Charging Applications in Plug-In Hybrid Electric Vehicles," in *2018 IEEE Ind. Appl. Soc. Annu. Meet. IAS 2018*, (2018), 1–9, https://doi.org/10.1109/IAS.2018.8544609.

14. A. K. Mishra and T. Kim, "An Economical Light Plug-In Electric Vehicle (LPEV) With On-Board Single-Stage Battery Charging System," *IEEE Transactions on Industry Applications* 59, no. 5 (2023): 6568–6579, https://doi.org/10.1109/TIA.2023.3285520.

15. X. Ruan, B. Li, Q. Chen, S.-C. Tan, and C. K. Tse, "Fundamental Considerations of Three-Level DC–DC Converters: Topologies, Analyses, and Control," *IEEE Transactions on Circuits and Systems I: Regular Papers* 55, no. 11 (2008): 3733–3743.

16. H. Hosseinpour, D. Nazarpour, and M. Farhadi-Kangarlu, "Design of a Nonisolated Bidirectional Multiport DC-DC Converter With Improved Efficiency for Photovoltaic Applications," *International Journal of Circuit Theory and Applications* (2024), https://doi.org/10.1002/cta.4422.

17. M. Kumar, "Multiple Open Switch Fast Fault Detection and Localization Algorithm for Tolerant CHB-MLI," *IEEE Transactions on Transportation Electrification* 10, no. 3 (2024): 6789–6800, https://doi.org/10.1109/TTE.2023.3342160.

18. M. Kumar, "Detection and Localization of Open Switch Faults for Level-Shifted PWM Cascaded H-Bridge Inverter," *IEEE Transactions on Circuits and Systems II: Express Briefs* 71, no. 4 (2024): 2409–2413, https://doi.org/10.1109/TCSII.2023.3332214.

1097007x, 0, Downloaded from https://onlinelibrary.wiley.com/doi/10.1002/cta.4609 by Delhi Technological University, Wiley Online Library on [03/06/2025]. See the Terms and Conditions (https://onlinelibrary.wiley.com/terms-and-conditions) on Wiley Online Library for rules of use; OA articles are governed by the applicable Creative Commons License

19. E. Chiodo and D. Lauria, "Some Basic Properties of the Failure Rate of Redundant Reliability Systems in Industrial Electronics Applications," *IEEE Transactions on Industrial Electronics* 62, no. 8 (2015): 5055–5062.

20. F. Bento and A. J. Marques Cardoso, "Open-Circuit Fault Diagnosis and Fault Tolerant Operation of Interleaved DC–DC Boost Converters for Homes and Offices," *IEEE Transactions on Industry Applications* 55, no. 5 (2019): 4855–4864, https://doi.org/10.1109/TIA.2019.2916825.

21. L. Xu, R. Ma, R. Xie, J. Xu, Y. Huangfu, and F. Gao, "Open-Circuit Switch Fault Diagnosis and Fault-Tolerant Control for Output-Series Interleaved Boost DC–DC Converter," *IEEE Transactions on Transportation Electrification* 7, no. 4 (2021): 2054–2066, https://doi.org/10.1109/TTE.2021.3083811.

22. W. Xiong, Z. Yan, D. Tang, W. Zhou, and R. Mai, "A Hybrid Topology IPT System With Partial Power Processing for CC-CV Charging," *IEEE Transactions on Power Electronics* 39, no. 1 (2024): 1701–1712.

23. R. Pandey and B. Singh, "A Power Factor Corrected Resonant EV Charger Using Reduced Sensor Based Bridgeless Boost PFC Converter," *IEEE Transactions on Industry Applications* 57, no. 6 (2021): 6465–6474, https://doi.org/10.1109/TIA.2021.3106616.

24. M. Ye, H. Gong, R. Xiong, and H. Mu, "Research on the Battery Charging Strategy With Charging and Temperature Rising Control Awareness," *IEEE Access* 6 (2018): 64193–64201.

25. M. Kumar and R. Gupta, "Stability and Sensitivity Analysis of Uniformly Sampled DC-DC Converter With Circuit Parasitics," *IEEE Transactions on Circuits and Systems I: Regular Papers* 63, no. 11 (2016): 2086–2097, https://doi.org/10.1109/TCSI.2016.2598834.

26. S. R. Sanders, J. M. Noworolski, X. Z. Liu, and G. C. Verghese, "Generalized Averaging Method for Power Conversion Circuits," *IEEE Transactions on Power Electronics* 6, no. 2 (1991): 251–259.

27. A. R. Saxena and D. Kumar, "Design and Control of a Reconfigurable High-Gain Battery Integrated DC-DC Boost Converter for Time-Varying Loads," *International Journal of Circuit Theory and Applications* 49 (2021): 327–347, https://doi.org/10.1002/cta.2888.

28. S. Gopinathan, V. S. Rao, and K. Sundaramoorthy, "Controllability Analysis and Controller Design of Higher Order Novel Switched Inductor–Capacitor DC–DC Converters," *IEEE Transactions on Industrial Electronics* 71, no. 6 (2024): 5871–5882.

1097007x, 0, Downloaded from https://onlinelibrary.wiley.com/doi/10.1002/cta.4609 by Delhi Technological University, Wiley Online Library on [03/06/2025]. See the Terms and Conditions (https://onlinelibrary.wiley.com/terms-and-conditions) on Wiley Online Library for rules of use; OA articles are governed by the applicable Creative Commons License

Appendix

The state variables $x(t)$, input variables $u(t)$, and the output $y(t)$ with the consideration of circuit parasitic are defined as in (A1).

$$x(t)=\begin{bmatrix} i_{L1} \\ i_{L2} \\ i_{L3} \\ v_{C1} \\ v_{C2} \end{bmatrix},\ u(t)=\begin{bmatrix} v_{in} \\ v_f \end{bmatrix},\ y(t)=\begin{bmatrix} v_{o1} \\ v_{o2} \end{bmatrix} \tag{A1}$$

The input matrices $\mathbf{B}|_{d\le 0.5}=\mathbf{B}|_{d>0.5}$, direct transmission matrices $\mathbf{D}|_{d\le 0.5}=\mathbf{D}|_{d>0.5}$, and state matrices $\mathbf{A}|_{d\le 0.5}$ (i.e., for condition 1 and condition 2), $\mathbf{A}|_{d>0.5}$ (i.e., for condition 3), for $d\le 0.5$ and $d>0.5$, is derived with the consideration of circuit parasitic and presented in (A2), (A3), (A4), and (A5), respectively.

$$\mathbf{B}|_{d\le 0.5}=\mathbf{B}|_{d>0.5}=\begin{bmatrix} \frac{1}{L_1} & \frac{-(1+d)}{L_1} \\ 0 & \frac{(1-\lambda d+d)}{L_2} \\ \frac{1}{L_3} & \frac{-1}{L_3} \\ 0 & 0 \\ 0 & 0 \end{bmatrix} \tag{A2}$$

$$\mathbf{D}|_{d\le 0.5}=\mathbf{D}|_{d>0.5}=\begin{bmatrix} \frac{1}{(1-d)} & 0 \\ \frac{d(\lambda-1)}{(1-d)} & 0 \end{bmatrix} \tag{A3}$$

$$\text{where } r_{m1}=\frac{r_{C1}R_1}{R_1+r_{C1}}, r_{m2}=\frac{r_{C2}R_2}{R_2+r_{C2}};$$

$$\mathbf{A}|_{d\le 0.5}=\begin{bmatrix} \frac{-1}{L_1}\left(r_{L1}+r_{m1}(1-d)\right) & \frac{d(\lambda-1)r_{m1}}{L_1} & \frac{(2d-1)r_{m1}}{L_1} & \frac{-(1-d)r_{m1}}{r_{C1}L_1} & 0 \\ \frac{d(\lambda-1)r_{m1}}{L_2} & \frac{-1}{L_2}\left(r_{L2}+d(\lambda-1)r_{m1}+r_{m2}\right) & \frac{(1-2d)r_{m1}}{L_2} & \frac{d(\lambda-1)r_{m1}}{r_{C1}L_2} & \frac{-r_{m2}}{r_{C2}L_2} \\ \frac{(2d-1)r_{m1}}{L_3} & \frac{(1-2d)r_{m1}}{L_3} & \frac{-1}{L_3}\left(r_{L3}+r_{m1}(1-d)\right) & \frac{-(1-d)r_{m1}}{r_{C1}L_3} & 0 \\ \frac{(1-d)r_{m1}}{r_{C1}C_1} & \frac{-d(\lambda-1)r_{m1}}{r_{C1}C_1} & \frac{(1-d)r_{m1}}{r_{C1}C_1} & \frac{-r_{m1}}{r_{C1}R_1C_1} & 0 \\ 0 & \frac{r_{m2}}{r_{C2}C_2} & 0 & 0 & \frac{-r_{m2}}{r_{C2}R_2C_2} \end{bmatrix} \tag{A4}$$

$$\mathbf{A}|_{d>0.5}=\begin{bmatrix} \frac{-1}{L_1}\left(r_{L1}+r_{m1}(1-d)\right) & \frac{d(\lambda-1)r_{m1}}{L_1} & 0 & \frac{-(1-d)r_{m1}}{r_{C1}L_1} & 0 \\ \frac{d(\lambda-1)r_{m1}}{L_2} & \frac{-1}{L_2}\left(r_{L2}+d(\lambda-1)r_{m1}+r_{m2}\right) & 0 & \frac{d(\lambda-1)r_{m1}}{r_{C1}L_2} & \frac{-r_{m2}}{r_{C2}L_2} \\ 0 & 0 & \frac{-1}{L_3}\left(r_{L3}+r_{m1}(1-d)\right) & \frac{-(1-d)r_{m1}}{r_{C1}L_3} & 0 \\ \frac{(1-d)r_{m1}}{r_{C1}C_1} & \frac{-d(\lambda-1)r_{m1}}{r_{C1}C_1} & \frac{(1-d)r_{m1}}{r_{C1}C_1} & \frac{-r_{m1}}{r_{C1}R_1C_1} & 0 \\ 0 & \frac{r_{m2}}{r_{C2}C_2} & 0 & 0 & \frac{-r_{m2}}{r_{C2}R_2C_2} \end{bmatrix} \tag{A5}$$

1097007x, 0, Downloaded from https://onlinelibrary.wiley.com/doi/10.1002/cta.4609 by Delhi Technological University, Wiley Online Library on [03/06/2025]. See the Terms and Conditions (https://onlinelibrary.wiley.com/terms-and-conditions) on Wiley Online Library for rules of use; OA articles are governed by the applicable Creative Commons License



IETE Journal of Research

ISSN: 0377-2063 (Print) 0974-780X (Online) Journal homepage: www.tandfonline.com/journals/tijr20

Modified AES Technique for Effective Communication between Hypervisor and Virtual Machine

Anumukonda Naga Seshu Kumar, Rajesh Kumar Yadav & N. S. Raghava

To cite this article: Anumukonda Naga Seshu Kumar, Rajesh Kumar Yadav & N. S. Raghava (25 Jun 2025): Modified AES Technique for Effective Communication between Hypervisor and Virtual Machine, IETE Journal of Research, DOI: 10.1080/03772063.2025.2473547

To link to this article: https://doi.org/10.1080/03772063.2025.2473547

Published online: 25 Jun 2025.

Submit your article to this journal

Article views: 1

View related articles

View Crossmark data

Full Terms & Conditions of access and use can be found at
https://www.tandfonline.com/action/journalInformation?journalCode=tijr20

IETE JOURNAL OF RESEARCH
https://doi.org/10.1080/03772063.2025.2473547

Check for updates

Modified AES Technique for Effective Communication between Hypervisor and Virtual Machine

Anumukonda Naga Seshu Kumar[1], Rajesh Kumar Yadav[1] and N. S. Raghava[2]

[1] Department of Computer Science and Engineering, Delhi Technological University (Formerly Delhi College of Engineering), New Delhi, India; [2] Department of Electronics and Communication Engineering, Delhi Technological University (Formerly Delhi College of Engineering), New Delhi, India

ABSTRACT

Securing digital data is one of the prominent aspects in communication and cryptography is considered to be a potential solution for securing digital data. There is a need for an efficient cryptographic technique for strengthening data from adversarial attacks. Improving the efficiency of the communication platform majorly depends on the efficiency of the cryptographic algorithms which emphasizes the safety of the data. This paper presents a modified version of the Advanced Encryption Standard (AES) algorithm, specifically tailored for hypervisor and VM (virtual machine) communication. The Round Decreased Advanced Encryption Standard Dynamic Sbox (RDAES DSbox) algorithm is designed in this work with a reduced number of rounds. The offered modified AES minimizes the encryption and decryption durations and increases the security of digital data. Results of the experimental analysis show that the proposed approach achieves an excellent performance in terms of minimizing the encryption and decryption compared to other existing techniques. The findings demonstrate the efficacy of the RDAES DSbox algorithm for strengthening secure communication in hypervisor and VM environments.

KEYWORDS

Advanced Encryption Standard; Attack detection; Cryptography; Hypervisor; Round decreased AES (RDAES); Secure data transfer; Virtual machine

1. INTRODUCTION

The emergence of computer and information technology has become immensely popular in terms of data storage and processing. The increasing significance of the technologically advanced devices has increased the security concerns and risks associated with data transmission between two devices [1]. Most organizations are shifting their traditional operational processes to more sophisticated technologies such as cloud computing, enabling the storage of massive amounts of data. However, the adoption of cloud technology can increase the problems which can pose a significant threat to the data stored [2,3]. One of the critical aspects of this threat is the vulnerability of the data towards illegal access which affects the performance and quality of services (QoS). One of the most important problems that needs to be addressed is the security and safety of information stored on platforms based on the cloud. The cloud's infrastructure is more susceptible to hacking attacks than traditional infrastructure because cloud users outsource their information to it. These shortcomings appear from all three perspectives, namely, (a) outsourced data is preserved at the infrastructure of the service providers; (b) different users share similar infrastructure; and (c) easy access of the data. In most of the cases, the vulnerabilities are associated with cloud computing components such as virtual machines (VMs) and hypervisors [4,5]. The attacks on VMs and hypervisors can be categorized into four different types namely hypervisor to VM, hypervisor to hypervisor, VM to VM, and VM to VM. Hence, the implementation of fundamental network security techniques such as intrusion prevention systems (IPS), malware detection techniques, and intrusion detection systems (IDS) does not yield desired results when it comes to protecting the data from adversarial attacks [6]. A hostile VM can make use of a hypervisor instead of using the actual network for developing communication channels for data transmission. This stresses the need for more advanced and robust techniques to protect the data without actually depending on the networks.

In general, virtualization technologies distinguish the fundamental hypervisors and operating systems from the actual platform that the VMs are running on. It is possible to separate VMs from other physical hosts in besides sharing hardware resources [7]. Since the hypervisor is responsible for managing the virtualization aspects, it is highly susceptible to cyber threats. Hypervisors are the fundamental component which separates the resource control of hardware and VMs [8]. The hypervisor creates a software which allows the VMs to execute different programs simultaneously on the same server. It must be

© 2025 IETE

noted that the hypervisor often suffers from a single point of failure and hence it is essentially important to mitigate the risks associated with it [9]. One of the biggest challenges related to hypervisor security is the detection of attacks, which is difficult to carry out using conventional techniques. Various existing literary works have focused on attack detection in hypervisors and VMs. However, these techniques are characterized by the drawbacks such as poor performance and lack of attack detection capability. Several researchers have suggested the adoption of cryptographic techniques for overcoming the drawbacks of conventional techniques [10,11]. Cryptographic techniques hold more significance in establishing the communication over an unauthorized channel and protect the vital information from being accessed by third party sources. This research emphasizes the application of the Advanced Encryption Standard (AES) [12] algorithm is to enhance the security of the data shared between hypervisors and VMs. Considering the amount of data that is shared, it becomes challenging to identify a suitable cryptographic algorithm which encrypts the data shared between sender and receiver, without leaking the information to unauthorized entities [13]. AES encryption algorithm encrypts and decrypts the digital data exchanged between two entities without requiring any additional calculation and computational resources [14]. This research modifies the fundamental AES algorithm to reduce the number of processes rounds and improve the encryption and decryption time. A Round Decreased Advanced Encryption Standard Dynamic Sbox (RDAES D Sbox) is implemented in this research which enhances the encryption performance by minimizing the calculation process required to secure the communication between the VM and the hypervisor.

The contributions of this research are as follows:

- The standard AES is modified to reduce the number of processing rounds in the algorithm and thereby minimize the computational overhead, time required for encryption and decryption. In the proposed approach, the number of processing rounds in the AES algorithm is reduced from 14 to 10 for a 256-bit encrypted key. This reduced the number of rounds and enhanced the efficiency of securing data transfer between hypervisors and VMs.
- The proposed approach is suitable for all types of records and maximizes the security of communication between hypervisors and VMs.
- The performance of the round decreased AES (RDAES) is compared with existing techniques such as Encryption with CFA -AES 128 and Encryption at Local AES 128 in terms of communication time (Inter-VM communication and Hypervisor to VM communication) and encryption, decryption time.

This article is further structured as follows: Section 2 discusses the existing works related to security of hypervisors and VMs. Section 3 discusses the proposed modified AES algorithm for strengthening the security of communication between hypervisors and VM. Section 4 outlines the results of the proposed methodology and Section 5 presents the conclusion.

2. RELATED WORKS

Haris *et al.* [15] introduced a by relocating VMs throughout hosts without interference with continuing services, Live Virtual Machine Migration (LVM) is a solution for service unavailability. They invented a prediction-based methodology for solving this issue, which enhances the iteration phase of the migration process by automatically terminating it when expected downtime reduces below a particular limit. Still, there are also issues associated with the huge amount of frequently improved memory pages, sometimes termed "unclean pages". Through tests on an exclusive testbed utilizing KVM/QEMU technology, involving memory-intensive functions and variable VM sizes, their recommended machine learning approach was thoroughly evaluated. These results demonstrate how our method may be used successfully to reduce delays in service in cloud systems during continuous VM movement.

Cittadini *et al.* [16] introduced an architecture which supports AI-powered applications made up of modules with varying criticalities and safety requirements using virtualization technologies and heterogeneous platforms. Major worries regarding safety, security, and predictability are brought up by the widespread application utilizing machine learning methods in systems that's essential to safety, demanding creative design methods to ensure these characteristics. To overcome this problem, a safety-critical domain running control and monitoring support under the free real-time operating system and an outstanding performance, domain running deep learning algorithms compatible with Linux (RTOS) are two different execution environments which the hypervisor develops using the advantage of the security features of the Xilinx ZCU104 MPSoCs. To determine the improvement of the recommended to better address the SWaP-C needs of drone systems, a Kria K26 SOM integrated with an *ad hoc* carrier module will take the place of the ZCU104 board in situations that are more complex.

Rashid *et al.* [17] presented the multi-objective evolutionary algorithm and the NSGA-III algorithm to

cut decrease power consumption, network transmission delay, and waste of resources. ANOVA and DMRT were used for statistically evaluating the results of their 30 different runs. Based on the mean values of 30 different runs, NSGA-III exceeded the current algorithm by 7% in terms of ONVG and 12% in terms of spacing. In terms of ONVG and spacing metrics, the outcomes are compared with those of other multi-objective optimization algorithms, involving VEGA, MOGA, SPEA, and NSGA-II.

Chimuco *et al.* [18] introduced an in-depth approach to modeling attacks on the specific cloud and mobile ecosystem, given its importance in the process of secure application development. They also launched a prototype of developers and security professionals are able to recognize each other utilizing the Security by Design framework for the cloud and mobile ecosystem (secD4CloudMobile). This framework includes the Cloud and Mobile Security Tasks Specification and Tools (CM2ST), Cloud and Mobile Security Requirement Elicitation (CMSRE), Cloud and Mobile Security Best Practices Recommendations (CMSBPG), and Cloud and Mobile Attack Modelling Elicitation (CMAME). They introduced the developed danger modeling for software using the popular cloud-mobile architecture. Even computer engineers and developers of applications for mobile devices ought to benefit from the recommended framework, based on the evaluation's extremely positive outcomes.

Triakosia *et al.* [19] introduced the implementation uses the CKKS scheme and the SEAL library to transform the plain-text 3D comparison approach to one that is acceptable with homomorphic encryption (HE). Particularly, to achieve an SIMD processing approach and boost efficiency, we created and utilized two packing methods CWP and PWP. For the purpose of achieving additional quick benefits, they investigated, mathematically confirmed, and analyzed the idea of providing unimportant data to the server. They managed to decrease the time from 0.9 to 0.1 s by applying information escaping and the HE algorithm combined with the CWP methodology. To attempt to overcome some of HE's limitations on specifically mathematical operations, they additionally developed and proposed an innovative TEE-based design. They additionally dug into the benefits and drawbacks of this kind of TEE-based system, particularly a need for a secure route for the secret key to be shared and problems with limited mobility and connection availability. Regarding the precision of the determined results and the time performance, they introduced and completed improvements in communication and estimation.

Chimuco *et al.* [20] introduced an in-depth investigation of security mechanisms, attack taxonomy, and security requirements for the cloud and mobile application surroundings designed to help reduce the gap between security and software engineering. One of the issues is the shortage of a single standard for cloud and mobile platforms. Although there are powerful mobile devices, the adoption of cloud technology, which greatly improves mobile computing, is one of the biggest drivers of the resource rise. To make sure that mobile apps and cloud are resistant to attacks by design, the adoption of security mitigation techniques hasn't kept pace with the growth and speed of development of these advancements. For the first time, an integrated and comprehensive approach to attack taxonomy and security test automation tool definitions is presented for this setting.

Araújo *et al.* [21] introduced the development of a Virtualized Network Function (VNF) in the OB-BAA context, more precisely an IEEE 802.1X authentication and authorization VNF applied to the major NGPON architecture telecom operator. Modern networks demand agility, flexibility, and capacity to cope with increasing demands for media content and applications that are increasingly dedicated to data consumption. Hundreds of communications are handled per second in microseconds. The test results demonstrated the security VNF sustainability with sufficient performance while providing insights into the most inviting VNF deployment scenarios.

Mozo *et al.* [22] introduced the In order to allow the solution's real-time deployment, deep neural networks are employed to evaluate the actions of AGVs previously by collecting the PLC-AGV connection packets without requiring for any detection on the user's device (either the PLC or the AGV). Two standard deep learning architectures – 1D-CNN and LSTM – as well as the transformer neural network, which has become the most advanced method for sequence-to-sequence tasks, were chosen to create prediction models. They constructed and analyzed 6600 deep learning models by model design (TRA, LSTM, CNN, and MIX), feature set (AGV, NET, and COMBINED), and time window size (4, 7.5, 15, 30, and 60 s). Additionally, they discussed the real-time issues that arose while the best models were being tested in a 5G open laboratory that allowed a controlled but realistic deployment.

3. PROPOSED RESEARCH METHODOLOGY

The proposed research aims to secure the communication between the hypervisor and VMs. In this research, a scenario is considered wherein the hypervisor is attacked by the attackers. It is considered that the hypervisor is more susceptible to the attacks and hence the VMs present under the hypervisor are also susceptible to attacks. The suggested approach for the VM security issue employs a modified AES for securing the sensitive information from the attackers. The conventional AES is modified to reduce the number of computations and execution time. A brief overview of the proposed approach is discussed in the sections below.

3.1 System Model and Hypervisor and Communication Network Creation

Initially, a hypervisor and VM communication network is created using the Socket Program. In this network, the hypervisor acts as a server and VMs act as a client. The communication between the VM and hypervisor is based on the device IP address and host. A data center, a migration request model, and an energy model in the VM's communication network constitute the recommended model. Various amounts of resources, VMs, data packets to be delivered, tasks assigned, and network users are all taken into consideration in this study. The network environment is created to complete a set of programs or applications wherein multiple programs are executed simultaneously to perform a specific task. Executing such programs requires cloud resources and the fundamental aspect in the communication network consists of a resource allocation element along with VM migration problems. This problem can be solved by optimally allocating the resources in the environment among different cloud users. Selecting an optimal resource allocation technique can help in assigning task-based resources without increasing the execution time, to ensure the QoS to the users. By transferring operations to the cloud, the users can utilize the resources in the VM's communication network. The resource distribution process then reassigns the tasks to the right resources according to an established process. This is done to take advantage of the processing capability of the network environment and thereby maximize the entire network system.

The security of the communication in hypervisors and VM is ensured using the Modified AES algorithm. As mentioned previously, the traditional AES is modified by adding the Dynamic Sbox which reduces the overall round in the computational process. By reducing the number of rounds, the encryption time and decryption time of the AES algorithm also decreased.

3.2 Proposed RDAES DSbox (Round Decreased Advanced Encryption Standard Dynamic Sbox)

As discussed previously, the AES is modified by adding a Dynamic Sbox to deal with the problem of excessive computational overhead and slow execution speed. The modified RDAES also enhances the encryption and decryption performance. The proposed algorithm is suitable for all types of records and the main objective of the RDAES is to achieve a higher encryption process. In the proposed modified AES algorithm, both the block and key duration are selected such that it is consistent with the AES algorithm. It is estimated in this research that the key's length is 256 bits, and this is used for encrypting and decrypting the data. In the proposed modified AES algorithm, the process involved in the encryption and decryption is kept the same as the conventional AES algorithm along with the number of rounds, records, and size of the key. The round feature incorporates four stages and a mix column stage along with a permutation stage is included to get around the problem of high estimation expense. Although the inclusion of the mix column stage provides better safety, it requires a complex calculation process which increases the time taken for encryption. The other stages involved in the AES process are not affected since it is present inside the AES algorithm. There are four different operational components which include one round of the modified AES algorithm. The AES takes an overall 14 rounds for completing one cycle of encryption and in the proposed modified AES algorithm, this research employs four levels such as (i) substitution bytes, (ii) ShiftRows, (iii) permutation (mix columns), and (iv) AddRoundKey. These levels are not affected due to the modification since it is present inside the AES algorithm. In this process, the permutation stage is one of the critical aspects which is used instead of using the Mix column stage, since it increases the computational stage. The permutation stage is majorly used in the design of cryptographic algorithms. Permutation operations are essential and important for all cryptographic algorithms and in this research, it is carried out using 256 bits as input. The Shift Rows and the Substitution Bytes are also said to have 256 bits and inside the AES, the permutation stage also considers 256 bits. Inside the permutation stage, the data can be accessed by realizing a specific row or column in the matrix, which also includes 256 bits in the output. For the decryption process, the modified AES algorithm is transformed using different processes such as In the encryption method, each of the following procedures will be carried out in 14 rounds: Inv-Bytesub, Inv-Shiftrows, Inv-Permutation, and the Arounder. In this way, any kind of

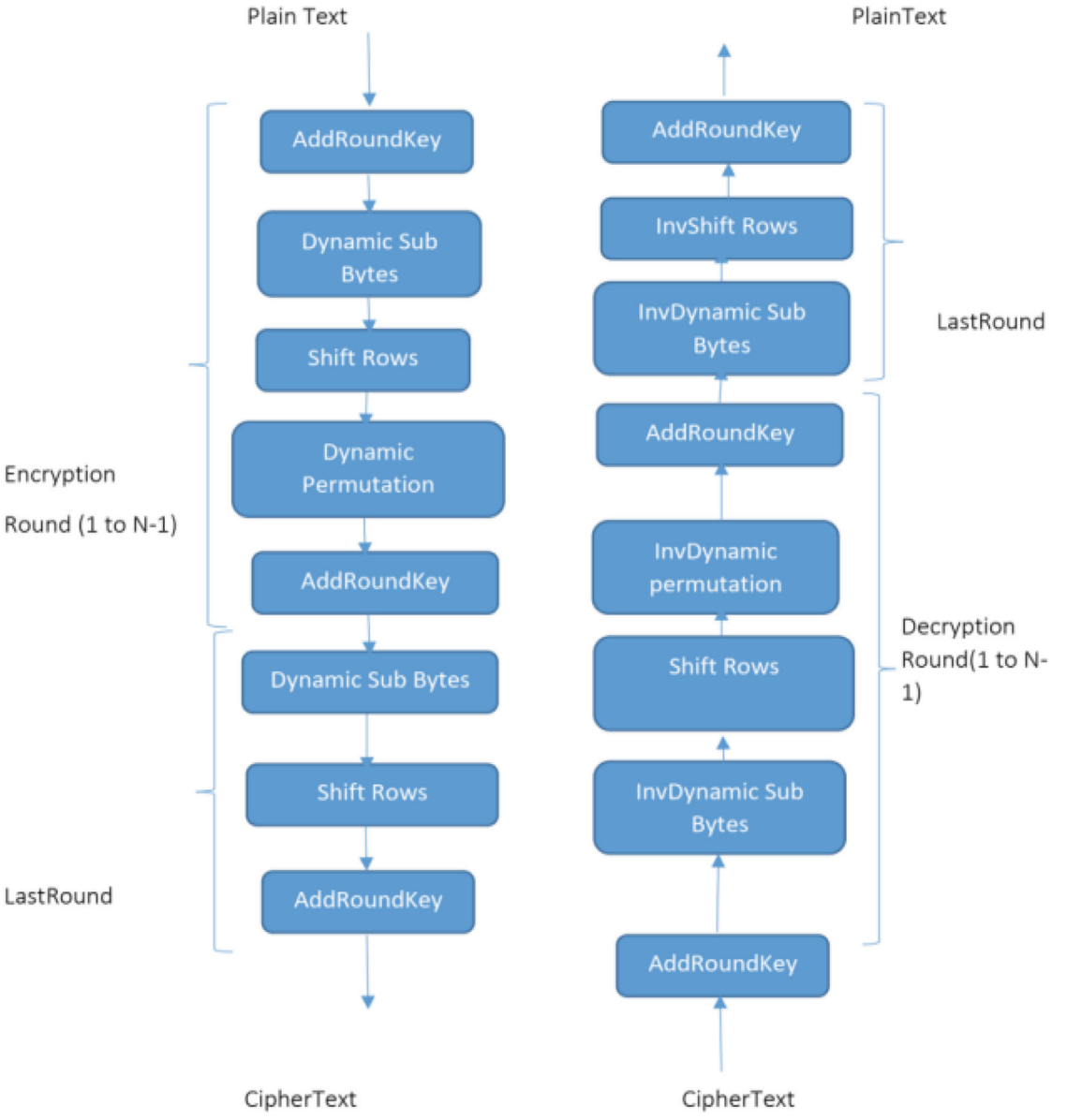


Figure 1: Flowchart of the proposed modified AES algorithm

data in the communication network could be encrypted and decoded utilizing the modified AES algorithm with lower rounds. The data is encrypted using a bit permutation method and the inverse bit permutation is used for decrypting the data in the hypervisor and VM. Figure 1 presents the flow chart for the recommended informed AES algorithm.

The attack on the hypervisor is considered as the external attack which weakens the performance of the hypervisor and thereby enables the attacker or the hacker to easily access the information present in the hypervisor and also get authorized with the hypervisors [23]. During the initial stages of attack, the attackers focus on a specific VM and the roge VM will afterwards get within the manager. Additionally, the attacker is going to take advantage of the scenario to increase the attacks on every VM that is managed by the attacked virtualization. Finally, all additional VMs running under the compromised hypervisor are going to be affected. This can be prevented by encrypting the data in the hypervisor and thereby mitigating the effect of the attack using the modified AES algorithm. The attacks in the hypervisors continuously monitor the performance metrics and system behavior based on the user requests received by the hypervisor and thereby help in detecting the possible attacks and abnormalities in the system activities. In addition, the attacker will also track and monitor the communication which is carried out between the VM, hypervisor, and VM, and virtual network environment via inter-VM communication

channel. By monitoring the communication, the attacker will attempt to gain unauthorized access into the system data and this is prevented by the proposed modified AES algorithm. As mentioned previously, the modified AES algorithm requires a lesser number of rounds and lesser time for decryption and encryption. The process of decryption and encryption using the modified AES is given as follows:

- AES Encryption:

The encryption process in AES consists of different steps. In this process, the AES algorithm calibrates a 16-byte block into a matrix consisting of 4-byte $*$ 4-byte rows and columns. Each round in the process contains four sub-bytes which are used for substituting and shifting the rows and permutation of bit.

(i) **SubBytes:** The SubBytes function operates on each state byte individually and is a non-linear byte substitution. Figure 2 shows the instance of Sbox. Two transformations are used to create the invertible substitution table or Sbox. Initially, the input plain text of 16 bytes is considered and the Sbox is used for substituting each byte with a sub-byte based on the plain text into a matrix as shown in Figure 3.

SubBytes operation

Input: Plain text or state matrix
Output: SubBytes matrix
1. Consider pre-calculated form of Sbox
2. Arrange input plain text into state matrix
3. Substitute each byte of state matrix by the value in the Sbox
$b_{ij} = S - Box[a_{ij}]$

(ii) **Shift Rows:** This is applied to the rows of the matrix wherein the bytes of the second row are shifted to its left by one place and correspondingly, the bytes of the third row are shifted to its left by two places, etc. In this way, all bytes in the matrix are shifted by a specific offset value. Figure 4 shows the operation of shift rows.

Shift Rows operation

Input: SubBytes matrix (state)
Output: Rows shifted matrix
1. The first row of the state doesn't change
2. In the second row, every byte advances one place to the left. On the right end, the byte that "falls off" the left end returns
3. Every byte in the *m*th advances left by *m*–1 places. On the right end, the bytes that "fall off" the left end resurface

(iii) **Permutation:** Permutation is a technique that shuffles or reorganizes the bits inside a state; bit permutation technique also modifies the state's value. In cryptographic methods, bit permutation offered diffusion similarly to MixColumns. A low encryption time and a reduced memory demand were accomplished by using a permutation strategy in an encryption algorithm that is also simple to implement. Figure 5 shows the steps of permutation.

Permutation operation

Input: Rows shifted matrix
Output: New permutated state matrix
1. Represent each state in the matrix as $((x, 0), b)$, where x denotes row, 0 denotes column, and b denotes the position of bit in the state
2. According to step 1, the state results to 4×8 matrix
3. Partition the resultant matrix into four 4×2 block matrices
4. Transpose the block matrices into 2×4 transposed matrices
5. Obtain new permutated state $a'(x, y)$ by concatenating the bit values of row of transposed block, where x denotes the column value considered from step 1 and y denotes the block value in step 3

(iv) **Add Round Key:** The matrix is further transformed into a 128-bit format for performing the round key step. For each round, a subkey is obtained from the main key and a XOR function is performed between the 128 bits of the matrix and subkey for obtaining the final output.

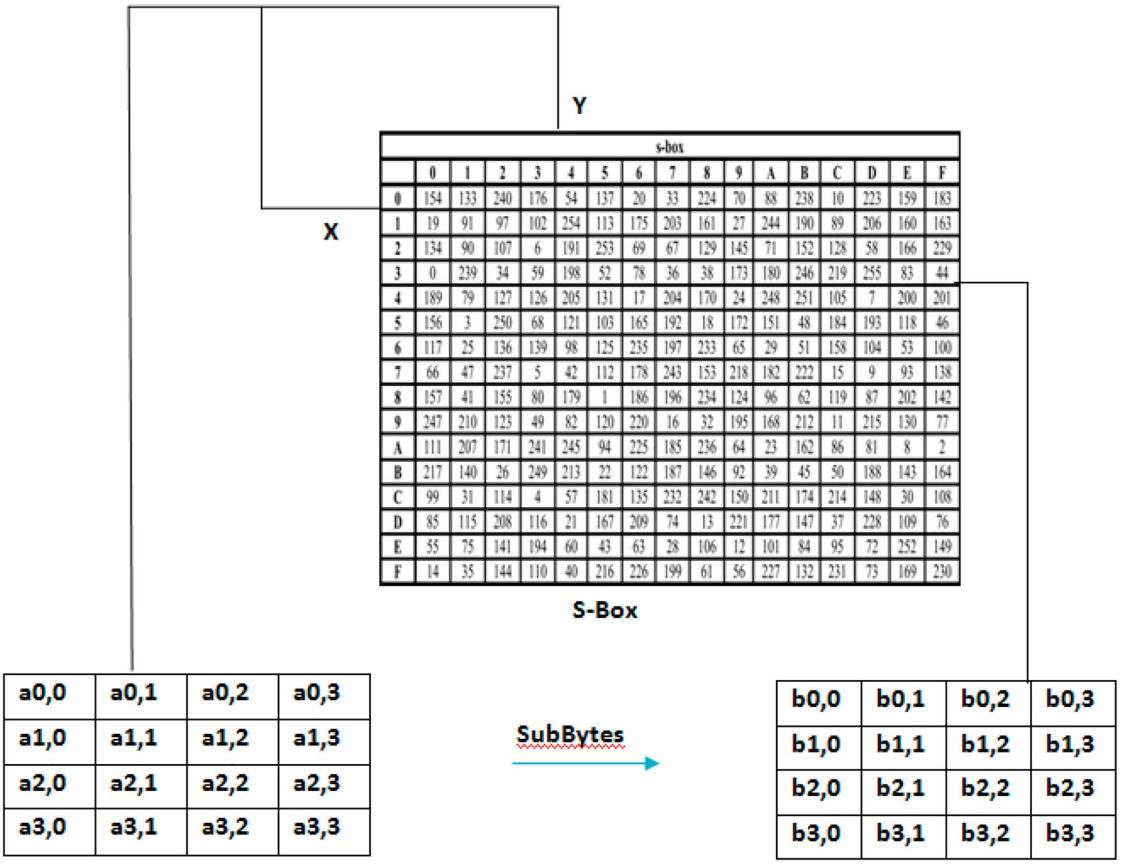
Add Round Key operation

Input: New permutated state matrix
Output: Cipher output
1. Transform the state into 128 bit format
2. Obtain 128 bit sub key from the main key.
3. XOR each byte of state with that of the sub key.
4. Obtain cipher output

The AES algorithm uses a key for encrypting the new plain text and the corresponding dynamic substitution matrices are computed as (DSBOX xor) using the below steps:

- Initially, one byte from the data is selected along with the master key also known as initial key which is denoted as Key [i].
- A new dynamic SBOX xor is computed wherein each cell in the matrix is comparable to the chosen byte's XOR and the same is denoted as DSBOX xor $[x, y]$ = DSBOX AES $[x, y] \oplus$ Key $[i]$.
- Further a dynamic substitution matrix is commuted and the same is used for encrypting the plain text.

In the context of the (DSbox) calculation for the proposed RDAES DSbox algorithm, "x" and "y" represent the coordinates (row and column indices) of the elements in the Sbox matrix. In the conventional AES algorithm, the Sbox is a fixed 16×16 substitution matrix that performs



s-box	0	1	2	3	4	5	6	7	8	9	A	B	C	D	E	F
0	154	133	240	176	54	137	20	33	224	70	88	238	10	223	159	183
1	19	91	97	102	254	113	175	203	161	27	244	190	89	206	160	163
2	134	90	107	6	191	253	69	67	129	145	71	152	128	58	166	229
3	0	239	34	59	198	52	78	36	38	173	180	246	219	255	83	44
4	189	79	127	126	205	131	17	204	170	24	248	251	105	7	200	201
5	156	3	250	68	121	103	165	192	18	172	151	48	184	193	118	46
6	117	25	136	139	98	125	235	197	233	65	29	51	158	104	53	100
7	66	47	237	5	42	112	178	243	153	218	182	222	15	9	93	138
8	157	41	155	80	179	1	186	196	234	124	96	62	119	87	202	142
9	247	210	123	49	82	120	220	16	32	195	168	212	11	215	130	77
A	111	207	171	241	245	94	225	185	236	64	23	162	86	81	8	2
B	217	140	26	249	213	22	122	187	146	92	39	45	50	188	143	164
C	99	31	114	4	57	181	135	232	242	150	211	174	214	148	30	108
D	85	115	208	116	21	167	209	74	13	221	177	147	37	228	109	76
E	55	75	141	194	60	43	63	28	106	12	101	84	95	72	252	149
F	14	35	144	110	40	216	226	199	61	56	227	132	231	73	169	230

Figure 2: Sbox

byte substitution during the encryption process. The values in the Sbox are predefined and do not change during encryption or decryption. However, in the RDAES DSbox algorithm, the DSbox is a modified version of the original Sbox, and it introduces dynamic behavior to improve efficiency and security.

The terms "x" and "y" play a crucial role in calculating the DSbox for the RDAES DSbox algorithm which can be summarized as follows:

(1) Initialization: During the initialization phase of the RDAES DSbox, a master key (initial key) denoted as "Key [i]" is selected. This master key is a byte (8 bits) and is used as a seed value for dynamic behavior.
(2) DSbox Calculation: For each element in the Sbox matrix (DSBOX AES [x, y]), the DSbox value (DSBOX xor [x, y]) is computed by performing a bitwise XOR operation between the corresponding element in the original AES Sbox (DSBOX AES [x, y]) and the master key (Key [i]).
(3) Dynamic Behavior: The use of the master key in the XOR operation introduces dynamic behavior into the Sbox calculation. As the master key changes, it influences the DSbox calculation, resulting in different Sbox values for different rounds of encryption or decryption.
(4) Efficiency and Security: By introducing dynamic behavior to the Sbox, the RDAES DSbox reduces the number of rounds in the AES algorithm, improving efficiency while maintaining a high level of security. The dynamic nature of the Sbox also adds an extra layer of complexity, making it harder for potential attackers to analyze and break the encryption.

The dynamic Sbox calculation enhances the performance of the RDAES DSbox algorithm by reducing the computational overhead and speeding up the encryption and decryption processes. This modification results in a more efficient yet secure cryptographic technique for securing data communication between the hypervisor and VMs.

- **AES decryption:**

The decryption process is similar to the encryption process but in reverse order. In this process, all four rounds

s-box																
	0	1	2	3	4	5	6	7	8	9	A	B	C	D	E	F
0	154	133	240	176	54	137	20	33	224	70	88	238	10	223	159	183
1	19	91	97	102	254	113	175	203	161	27	244	190	89	206	160	163
2	134	90	107	6	191	253	69	67	129	145	71	152	128	58	166	229
3	0	239	34	59	198	52	78	36	38	173	180	246	219	255	83	44
4	189	79	127	126	205	131	17	204	170	24	248	251	105	7	200	201
5	156	3	250	68	121	103	165	192	18	172	151	48	184	193	118	46
6	117	25	136	139	98	125	235	197	233	65	29	51	158	104	53	100
7	66	47	237	5	42	112	178	243	153	218	182	222	15	9	93	138
8	157	41	155	80	179	1	186	196	234	124	96	62	119	87	202	142
9	247	210	123	49	82	120	220	16	32	195	168	212	11	215	130	77
A	111	207	171	241	245	94	225	185	236	64	23	162	86	81	8	2
B	217	140	26	249	213	22	122	187	146	92	39	45	50	188	143	164
C	99	31	114	4	57	181	135	232	242	150	211	174	214	148	30	108
D	85	115	208	116	21	167	209	74	13	221	177	147	37	228	109	76
E	55	75	141	194	60	43	63	28	106	12	101	84	95	72	252	149
F	14	35	144	110	40	216	226	199	61	56	227	132	231	73	169	230

Figure 3: SubBytes

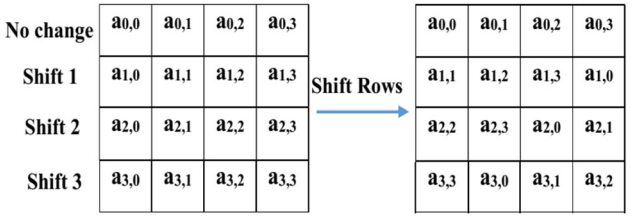


Figure 4: Shift rows

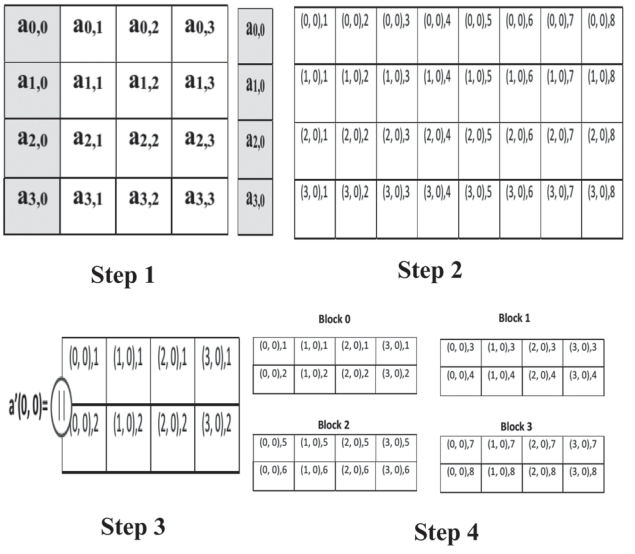


Figure 5: Steps of permutation

mentioned in the AES encryption process are performed inversely. Initially, the add round key process is performed and then the mix columns and shift row steps are executed. In the next stage, the matrix is subjected for inverse transformation and multiplication wherein the resultant output will be a plain ciphertext.

For decrypting data, the modified AES follows the below given steps:

- A same byte is selected from the key denoted as Key $[i]$.
- A new dynamic SBOX xor is computed wherein every cell is related to the designated byte and XOR. is denoted as DSBOX xor $[x, y]$ = DSBOX AES $[x, y] \oplus$ Key $[i]$.
- The inverse matrix is computed by using DSBOX xor, DSBOX xor INV = INV (DSBOX xor).

The encryption and decryption processes of the proposed approach are illustrated in Figure 6.

4. RESULTS AND DISCUSSION

This section discusses the simulation and experimental analysis of the proposed approach. The conventional AES algorithm in the recommended work is modified by

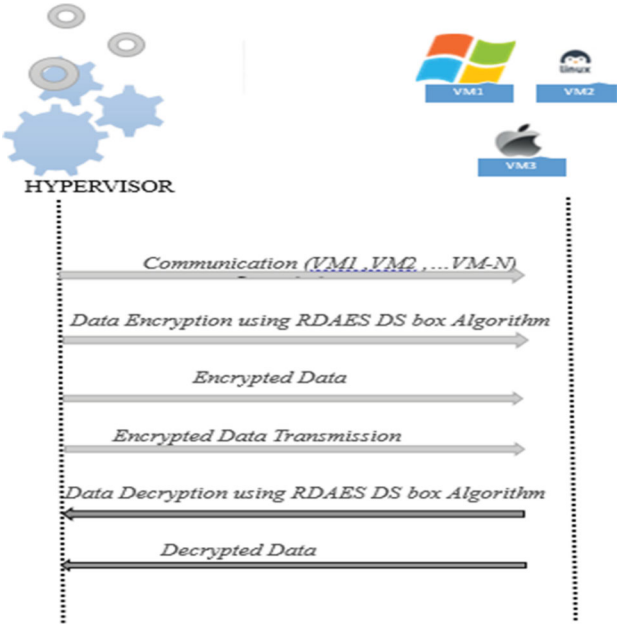


Figure 6: Encryption and decryption process of the proposed approach

Algorithm: RDAES DSbox (Round Decreased Advanced Encryption Standard Dynamic Sbox)

Input: plaintext (*X*), key (*k*) (Both in binary format)
Output: ciphertext (c)
1: Initialize DSBOX_AES with the AES Sbox
2: DSBOX_xor = Initialize_DSBOX_xor(DSBOX_AES, k) // Compute dynamic SboxDSBOX_xor
3: num_rounds = 10 // Number of rounds in RDAES (Reduced AES)
4: state = X // Initialize state with plaintext
// Encryption
5: for i = 0 to num_rounds-1 do
6: state = SubBytes(state, DSBOX_xor) // Substitute each byte in state using DSBOX_xor
7: state = ShiftRows(state) // Shift rows of the state
8: state = Permutation(state, DSBOX_xor) // Perform Permutation using DSBOX_xor
9: state = AddRoundKey(state, k) // Add the round key to the state
10: end for
// Final round (without Permutation)
11: state = SubBytes(state, DSBOX_xor)
12: state = ShiftRows(state)
13: state = AddRoundKey(state, k)
14: c = state // Final ciphertext
// Helper function to initialize DSBOX_xor
Function: Initialize_DSBOX_xor(DSBOX_AES, k)
15: for *x* = 0–15 do
16: for *y* = 0–15 do
17: DSBOX_xor[*x*][*y*] = DSBOX_AES[*x*][*y*] XOR k // Compute DSBOX_xor using DSBOX_AES and key
18: end for
19: end for
20: return DSBOX_xor

adding the dynamic sub-bytes, dynamic mix column, to decrease the overall rounds for 256-bit key (in default 256-bit key has 14 rounds for encryption). The communication data (in the form of an alert message) shared between the hypervisor and VM is considered in this research for the analysis since it is not practically feasible to generate VM communication data. In addition, the connected VM IP address and port number are also encrypted for increasing the security.

The performance of the proposed approach is compared with the existing techniques such as encryption with CFA – AES 128 and Encryption at Local AES 128, and the obtained results are tabulated in Table 1.

Table 2 calculates the results of a corresponding examination comparing the decryption time with modern techniques.

Graphically, the performance of the proposed approach in terms of encryption time, decryption time and communication time is illustrated in Figures 7–9 respectively. Table 3 illustrates the communication time of the proposed model.

It can be inferred from the results that the proposed approach significantly reduces the encryption and communication time compared to other approaches. When the round is decreased, the AES algorithm encryption time and decryption time will be decreased. Here the encryption round is decreased from 14 to 10.

5. CONCLUSION

This paper presents a modified AES algorithm known as RDAES DSbox for securing the data shared between the hypervisor and VM. The proposed approach is modified to reduce the computational burden by reducing the number of rounds and minimizing the time taken for encryption and decryption. Various techniques have been proposed in existing literary works designed for the security of cloud data and most of these techniques have focused on ensuring the privacy and integrity of the information and thereby securing the hypervisor and VM. Different encryption techniques such as conventional AES, DES, Triple DES, and RSA are employed and their efficacy has been validated in several research works. However, the computational complexity and slow execution time restrict their adaptability. In addition, the existing techniques are computationally intensive and their performance is not satisfactory. In this research, the RDAES overcome the drawbacks by enhancing the computational AES algorithm's performance. The success of the presented method has been demonstrated by simulation analysis with respect to communication time (Inter-VM communication and Hypervisor to VM communication) and encryption, decryption time. Results

Table 1: Comparison of encryption time

Size of the data to be encrypted (kB)	Time per encryption (ms) – Hypervisor AES Dynamic Sbox decrease round	Time per encryption (ms) – Encryption with CFA-AES 128	Time per encryption (ms) – (encryption at local AES 128)
0	0	0	0
100	0.5437	0.898762156	0.70922
200	1.0782	1.868236111	1.44208
300	1.4437	2.837710066	2.174941
400	1.8925	3.783530754	2.907801
500	2.3463	4.705884176	3.640662
600	5.54	5.698887397	4.373522
700	6.2451	6.621178819	5.106383
800	7.5376	7.61418204	5.839243
900	8.188	8.465885665	6.572104
1000	21.94	9.435235618	7.304965

Table 2: Comparison of decryption time

Size of the data to be decrypted (kB)	Time per decryption (ms) – Hypervisor AES dynamic Sbox decrease round	Time per decryption (ms) – Decryption with CFA – AES 128	Time per decryption (ms) – Decryption at Local AES 128
0	0	0	0
100	0.5630	0.785280	0.6958230
200	0.9541	1.8166171	1.4586481
300	1.751	2.713672	2.2215292
400	1.8251	3.6107783	2.9843822
500	2.5472	4.5973444	3.7024923
600	5.0065	5.5615675	4.4653184
700	6.186	6.5704776	5.2052875
800	6.487	7.5346717	5.968685
900	9.428	8.4988948	6.7539326
1000	11.7221	9.4183469	7.5167857

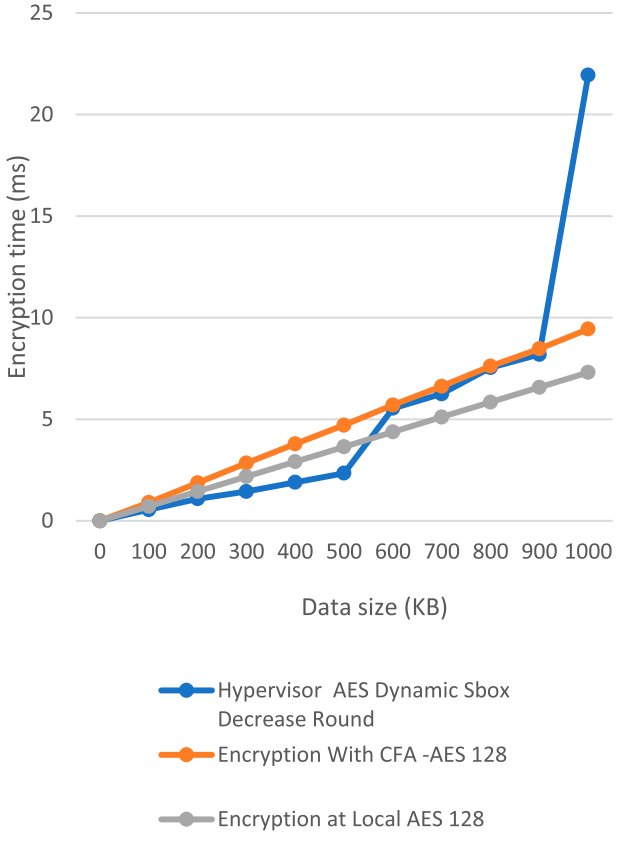


Figure 7: Comparison of encryption time

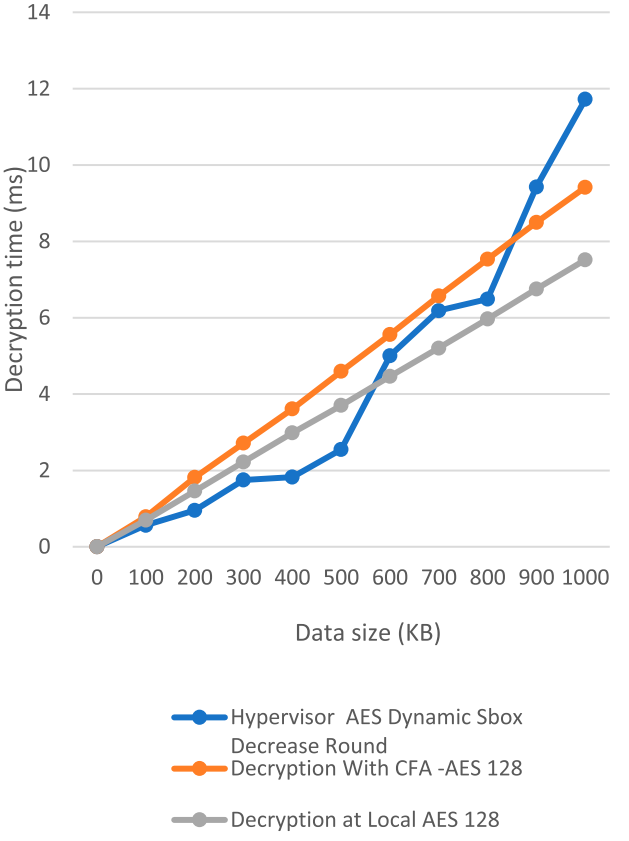


Figure 8: Comparison of decryption time

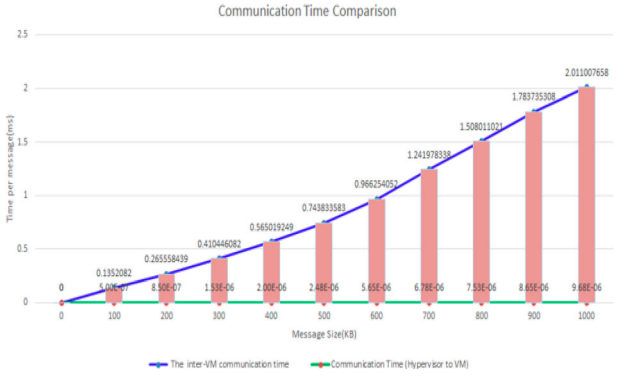


Figure 9: Comparison of communication time

Table 3: Comparison of communication time

Message size (kB)	The inter-VM communication time	Communication time (hypervisor to VM)
0	0	0
100	0.135208	5.00 E-07
200	0.265558	8.50 E-07
300	0.410446	1.53 E-06
400	0.565019	2.00 E-06
500	0.743834	2.48 E-06
600	0.966254	5.65 E-06
700	1.241978	6.78 E-06
800	1.508011	7.53 E-06
900	1.783735	8.65 E-06
1000	2.011008	9.68 E-06

show that the proposed RDAES DSbox achieves better performance compared to other techniques such as Encryption with CFA – AES 128 and Encryption at Local AES 128. As observed from the results, it can be said that the proposed approach is highly effective in terms of ensuring the security of hypervisors and VMs. Results validate the efficacy of the RDAES DSbox technique and can be implemented for encrypting sensitive information in a real-time cloud environment. For future work, this research intends to extend the work for securing hypervisors and VM using more advanced cryptographic hashing techniques combined with optimized deep learning approaches.

DISCLOSURE STATEMENT

No potential conflict of interest was reported by the author(s).

REFERENCES

1. S. Basu, A. Bardhan, K. Gupta, et al., "Cloud computing security challenges & solutions - a survey," in 2018 IEEE 8th Annual Computing and Communication Workshop and Conference (CCWC), Las Vegas, 2018, pp. 347–56.

2. L. Rajesh, and H. S. Mohan, "Shuffled shepherd squirrel optimization and fractional LMS model for in-network aggregation in wireless sensor network," *IJBDCN*, Vol. 18, no. 1, pp. 1–21, 2022.

3. P. J. Navarathna, and V. P. Malagi, "Artificial intelligence in smart city analysis, proceedings of the international conference on smart systems and inventive technology," *ICSSIT*, Vol. 2018, pp. 44–7, 2018. 8748476.

4. L. Rajesh, and H. S. Mohan, "An multilevel efficient energy clustering protocol with secure routing (MEECSR) in WSNs," *Int. J. Appl. Sci. Eng.*, Vol. 18, pp. 2020344, 2021.

5. I. M. Megha, S. Vyshnavi Kowshik, S. Ali, and V. P. Malagi, "A comprehensive survey on down syndrome detection in foetus using modern technologies," *Adv. Intell. Syst. Comput.*, Vol. 1177, pp. 749–58, 2021.

6. R. Mangalagowri, and R. Venkataraman, "Hypervisor attack detection using advanced encryption standard (HADAES) algorithm on cloud data," *Int. J. Comput. Netw. Appl.*, Vol. 9, no. 5, pp. 555, 2022..

7. N. K. Chien, V. S. G. Dong, N. H. Son, and H. D. Loc, "An efficient virtual machine migration algorithm based on minimization of migration in cloud computing," in Nature of Computation and Communication: Second International Conference, ICTCC 2016, Rach Gia, Vietnam, 2016. March 17–18, 2016, pp. 62–71, Springer International Publishing. Revised Selected Papers 2.

8. J. P. Barrowclough, and R. Asif, "Securing cloud hypervisors: a survey of the threats, vulnerabilities, and countermeasures," *Secur. Commun. Netw.*, Vol. 2018, pp. 1–20, 2018.

9. H. Kaur, and G. Kaur, "Reviewing threats prevalent to hypervisor," *Think India J.*, Vol. 22, pp. 2856–62, 2019.

10. R. K. Barik, R. K. Lenka, K. R. Rao, and D. Ghose, "Performance analysis of virtual machines and containers in cloud computing," in 2016 International Conference on Computing, Communication and Automation (ICCCA), Greater Noida, 2016, pp. 1204–10.

11. M. Morbitzer, M. Huber, and J. Horsch, "Extracting secrets from encrypted virtual machines," in Proceedings of the Ninth ACM Conference on Data and Application Security and Privacy, New York, 2019, pp. 221–30.

12. A. M. Abdullah, "Advanced encryption standard (AES) algorithm to encrypt and decrypt data," *Crypt. Netw. Secur.*, Vol. 16, pp. 1–11, 2017.

13. Y. Wu, Y. Liu, R. Liu, H. Chen, B. Zang, and H. Guan, "Comprehensive VM protection against untrusted hypervisor through retrofitted AMD memory encryption," in 2018 IEEE International Symposium on High Performance Computer Architecture (HPCA), Vienna, 2018, pp. 441–53.

14. Q. Zhang, and Q. Ding, "Digital image encryption based on advanced encryption standard (AES)," in 2015 Fifth International Conference on Instrumentation and Measurement, Computer, Communication and Control (IMCCC), Qinhuangdao, 2015, pp. 1218–21.

15. R. M. Haris, M. Barhamgi, A. Nhlabatsi, and K. M. Khan, "Optimizing pre-copy live virtual machine migration in cloud computing using machine learning-based prediction model," *Computing*, Vol. 106, pp. 1–32, 2024.

16. E. Cittadini, M. Marinoni, A. Biondi, G. Cicero, and G. Buttazzo, "Supporting AI-powered real-time cyber-physical systems on heterogeneous platforms via hypervisor technology," *Real-Time Syst.*, Vol. 59, no. 4, pp. 609–35 , 2023.

17. A. Gopu, K. Thirugnanasambandam, A. S. AlGhamdi, S. S. Alshamrani, K. Maharajan, and M. Rashid, "Energy-efficient virtual machine placement in distributed cloud using NSGA-III algorithm," *J. Cloud Comput.*, Vol. 12, no. 1, pp. 124, 2023.

18. F. T. Chimuco, J. B. Sequeiros, T. M. Simões, M. M. Freire, and P. R. Inácio, "Expediting the design and development of secure cloud-based mobile apps," *Int. J. Inf. Secur.*, Vol. 23, pp. 1–22, 2024.

19. A. Triakosia, P. Rizomiliotis, C. Tonelli, F. Federici, and V. Senni, "Secure outsourcing of manufacturing compliance checks," *Int. J. Inf. Secur.*, Vol. 23, no. 1, pp. 609–27, 2024.

20. F. T. Chimuco, J. B. Sequeiros, C. G. Lopes, T. M. Simões, M. M. Freire, and P. R. Inácio, "Secure cloud-based mobile apps: attack taxonomy, requirements, mechanisms, tests and automation," *Int. J. Inf. Secur.*, Vol. 22, no. 4, pp. 833–67, 2023.

21. I. Araújo, A. Brízido, and S. R. Lima, "Virtual network function development for NG-PON access network architecture," *J. Netw. Syst. Manage.*, Vol. 31, no. 4, pp. 78, 2023.

22. A. Mozo, S. Vakaruk, J. Enrique Sierra-García, and A. Pastor, "Anticipatory analysis of AGV trajectory in a 5G network using machine learning," *J. Intell. Manuf.*, Vol. 35, no. 4, pp. 1541–69, 2024.

23. V. Pendli, M. Pathuri, S. Yandrathi, and A. Razaque, "Improvising performance of advanced encryption standard algorithm," in 2016 Second International Conference on Mobile and Secure Services (MobiSecServ), Gainesville, 2016, pp. 1–5.

AUTHORS



Anumukonda Naga Seshu Kumar is a research scholar in Computer Science and Engineering Department in Delhi Technological University (formerly Delhi College of Engineering), New Delhi, India. His main area of specialization is cloud computing. In cloud computing, his interest is related to security at hypervisors.

Corresponding author. Email: seshu1203@gmail.com.



Rajesh Kumar Yadav received his BE (CSE) from G. B. Pant Engineering College, Pauri (H.N.B. Garahwal University), Mtech (CS) from UPTU, Lucknow, and PhD (computer engineering) from Delhi Technological University (formerly Delhi College of Engineering), New Delhi, India. Presently he is working as an assistant professor in the Department of Computer Science & Engineering at Delhi Technological University (DTU). His areas of research interest are mobile *ad hoc* networks, wireless sensor networks, and Internet of Things (IoT).

Email: rajeshkumaryadev@outlook.com.



Nallanthighal Srinivasa Raghava (Member IEEE) is a former professor in Electronics and Communication Engineering Department in Delhi Technological University (formerly Delhi College of Engineering), New Delhi, India. His areas of specialization are cloud computing, antenna and propagation, microwave engineering, digital communication, wireless communication, and information security.

Email: nallanthighalsrinivasa@outlook.com.

In Silico Pharmacology (2025) 13:84
https://doi.org/10.1007/s40203-025-00372-y

ORIGINAL RESEARCH

Molecular docking and molecular dynamics simulation studies of thiazole-coumarin and thiazole-triazole conjugates against M^{pro} and ACE2 receptor for SARS COV-2

Deepak Mishra[1,2] · Ram Singh[1] · Nupur S. Munjal[3] · Naresh Kumar[2] · Prashant Kumar[2] · Poonam[1] · Sandeep Sharma[2]

Received: 4 December 2024 / Accepted: 23 May 2025
© The Author(s), under exclusive licence to Springer-Verlag GmbH Germany, part of Springer Nature 2025

Abstract

The recent COVID-19 pandemic, which caused severe respiratory infections and multiple organ failure leading to death, has drawn the attention of researchers around the world. Several vaccines are available for protection against SARS-CoV-2. However, the frequent changes in its viral genome have raised concerns about the efficacy of current vaccines. Most of the research has focused on developing novel therapeutic agents, and till now no approved anti-viral drugs are available. The development of an effective and approved drug is a time-consuming process, so research is increasingly focusing on the screening of highly active molecules based on computer-aided drug designs. Heterocyclic moieties like coumarin, thiazole, and triazole exhibit diverse biological applications. To identify potent inhibitors of SARS-CoV-2 targets, we performed molecular docking and dynamics simulations on thiazole-coumarin and thiazole-triazole conjugates. These compounds effectively target the viral M^{pro} and ACE2 receptors. Based on the results obtained, RD9, RD12, RD17, and RD18 were found to be most active. These molecules make an excellent interaction with the active site of both enzyme M^{pro} and ACE2 with a free binding energy of − 8.33, − 7.89, − 8.61, − 8.02, − 9.87, − 9.75, − 9.49, − 9.61 kcal mol^{-1} respectively which can potentially be used as a dual inhibitor. Molecular dynamics simulation studies further confirm the stability of these complexes. These findings suggest that thiazole-coumarin and thiazole-triazole conjugates can serve as potential candidates for dual inhibition of M^{pro} and ACE2 enzyme, and can be effectively used to control COVID-19 infection.

Keywords SARS-CoV-2 · M^{pro} enzyme · ACE 2 · Coumarin · Phenylthiazole · Triazole

Introduction

Recently the world has witnessed the darkest side of coronavirus disease, COVID-19 (Liu et al. 2020a; https://data.who.int/dashboards/covid19/cases; Richman et al. 2016). Globally people have suffered from acute respiratory infection, multiple organ failure, and a high mortality rate (Liu et al. 2020a). It was started in December 2019, when the first case of a pneumonia-like viral infection was detected in Wuhan city (https:,, data.who.int, dashboards, covid19, cases(Acessed on 10 August 2024). 2024). This infection then spread to the rest of the world and was declared a pandemic by WHO on March 11th, 2020 (Liu et al. 2020a; https://data.who.int/dashboards/covid19/cases). Previously identified MERS-CoV (Middle East respiratory syndrome coronavirus) and the SARS-CoV seem to be significantly less contagious as compared to COVID-19 (Richman et al. 2016). According to WHO, by the end of 28 July 2024, there have been more than 776 million confirmed cases of SARS CoV-2, and nearly 7.1 million fatalities globally (https://data.who.int/dashboards/covid19/cases). The structure of coronavirus is quite complex. It is a positive-sense single-stranded enveloped RNA virus consisting of spike-like projections on its surface and looks like a crown(Richman et al.

✉ Ram Singh
ramsingh@dtu.ac.in

1 Department of Applied Chemistry, Delhi Technological University, Delhi 110 042, India

2 Department of Chemistry, SRM University, Delhi-NCR, Sonepat, Haryana 131029, India

3 Biological Systems Engineering, Plaksha University, SAS Nagar, Punjab 140306, India

Published online: 09 June 2025

2016; Zhou et al. 2020). They are considerably larger than other viruses having diameter ranges from 60 to 140 nm and share greater than 80% sequence identity with SARS-CoV (Zhou et al. 2020). Its structure comprises nucleocapsid protein (N), which causes the formation of capsids surrounding the genome. This is further encased by an envelope and is linked with three structural proteins: envelope protein (E), membrane protein (M), and spike protein (S) (Fig. 1) (Brian and Baric 2005; Naqvi et al. 2020).

The family of coronaviruses is classified into four categories namely α (alpha), β (beta), γ (gamma), and δ (delta) (Perlman and Netland 2009; Fehr and Perlman 2015). Before the discovery of SARS-CoV-2, only six previously identified coronaviruses were known to cause mild to severe disease in humans (Chan et al. 2013, 2015; Wu et al. 2020; Chen et al. 2020). The α-coronavirus commonly causes infection in humans and mammalians and primarily affects the upper respiratory tract, leading to milder respiratory disease (Chen et al. 2020; Tang et al. 2015). However, the β-coronavirus SARS-CoV, HCoV-OC43, HKU1, and newly identified SARS-CoV-2 are associated with severe respiratory syndrome (Fehr and Perlman 2015). Another form, MERS-CoV which triggered in 2012, cause infection in lower the respiratory tract (Cong and Ren 2014). Several vaccines are available for protection from SARS-CoV-2 but frequent mutations in the virus genome raise concerns about the effectiveness of these vaccines (Carabelli et al. 2023). Therefore, it is necessary to understand about life cycle and progression of SARS-CoV-2 for designing effective drugs against this virus (Fig. 1). SARS-CoV-2 enters the host cell through its spike protein, which binds to angiotensin-converting enzyme 2 (ACE2), a homolog of ACE (Fig. 1). This interaction decreases the concentrations of ACE2 and impairs its function (Zhang et al. 2021; Shirbhate et al. 2021). ACE2 is a crucial enzyme and a potential target for SARS-CoV-2 (Donoghue et al. 2000). It is majorly found in intestinal epithelial cells, lungs, heart, endothelial and smooth cells of the blood vessels, kidney, testis, and brain. In blood vessels, its primary function is to counteract the adverse effects of the renin-angiotensin system (RAS) (Santos et al. 2018). The renin-angiotensin system is a complex network essential for regulating blood pressure, balance of electrolyte, maintaining the body fluid concentration, and function of organs such as the heart, blood vessels, and kidneys (Santos et al. 2018). In RAS, renin cleaves angiotensinogen to produce angiotensin-I (Ang-I) which is a decapeptide. ACE localized on the surface of endothelial cell in blood vessels cleaved this decapeptide into octapeptide angiotensin-II (Ang-II). This Ang-II binds with receptor AT1 and causes vasoconstriction, blood coagulation and inflammatory response. However, ACE2 present at the surface of endothelial cell of blood vessel converts Ang-II into the heptapeptide angiotensin (1–7) (Ni et al. 2020). This heptapeptide binds to the MAS receptor and produces effects opposite to those of Ang-II (Fig. 1) (Ni et al. 2020). ACE2 bind with the s-protein during SARS CoV-2 infection and enters the cell by endosomal route or via direct cell surface fusion. The host membrane transmembrane protease serine 2 (TMPRSS2) cleaves the viral spike protein to facilitate direct cell surface fusion, which subsequently results in the direct fusion of the viral membrane with the host cell membrane (Hoffmann et al. 2020). While the endosomal cytosine protease cathepsin L mediates its endosomal entry by cleaving the viral spike protein (Liu et al. 2020b). After the release of viral RNA into the cytoplasm, it is further translated into viral polyproteins pp1a and pp1ab, which are then cleaved by two viral proteases enzyme: the main protease (M^{pro}), also known as 3-chymotrypsin-like protease ($3CL^{pro}$) and the papain-like protease (PL^{pro}) (Yang and Yang 2021). The released viral proteins can then assemble

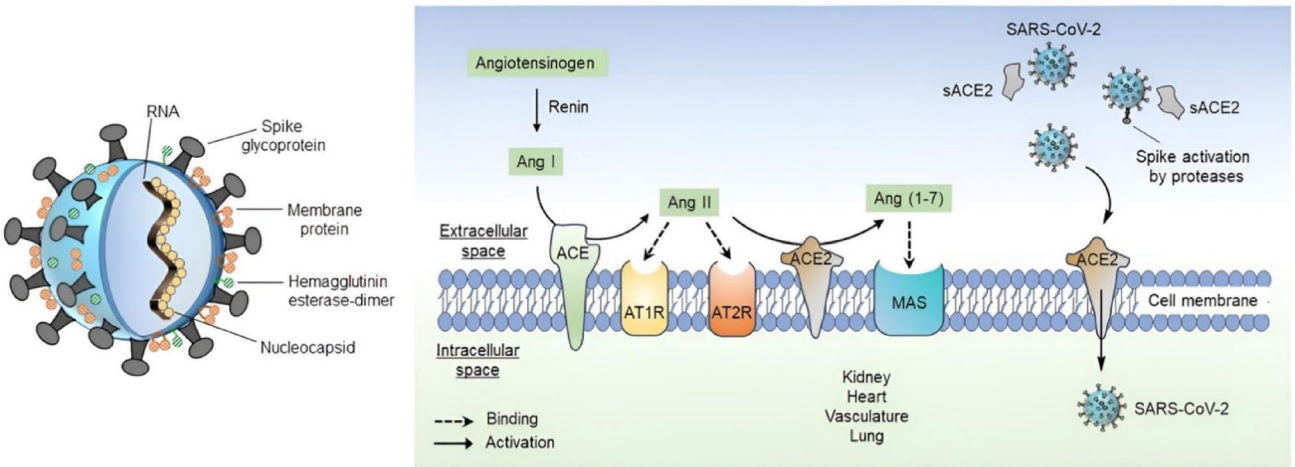


Fig. 1 Demonstration of the structure and route of entrance of SARS-CoV-2 into the host human receptor ACE2 enzyme

to form a viral RNA-dependent RNA polymerase (RdRp) complex, which catalyzes the replication of the viral RNA. After, exocytosis, the progeny virions are finally released from the infected cells and consequently cause the infection. This SARS-COV-2 infection route reveals that M^{pro}, PL^{pro}, ACE2, and RdRp plays significant role in the replication of SARS-CoV-2. $3CL^{pro}/M^{pro}$ plays a major role in cleavage of polyproteins from different sites and produces a variety of nonstructural proteins, which cause viral replications. Hence, M^{pro} is another crucial target among these due to its extremely conservative nature and specificity. In this viewpoint, inhibiting the activity of this enzyme offers a therapeutic approach to restrict viral replication (Jin et al. 2020a; Xue et al. 2008). Since the development of an effective and approved drug is a time-consuming process, therefore to investigate the highly active molecule for the inhibition of M^{pro} and ACE2, the structure-based computational studies provide an alternative route to design a highly effective inhibitor that can stop the viral replication. Molecular docking and molecular dynamics (MD) simulation have become indispensable tools for exploring their properties, interactions, and potential applications (Ghosh et al. 2021; Zerroug et al. 2019). Docking studies help in the identification of lead compounds for drug discovery by revealing the binding affinities and orientation of heterocyclic compounds with biological targets. These analyses provide key interactions, including hydrogen bonding, hydrophobic interactions, and π-π stacking, which are essential for target specificity and efficacy (Ghosh et al. 2021; Zerroug et al. 2019). Moreover, molecular dynamics simulations allow researchers to evaluate the stability and behavior of heterocyclic compounds within biological environments over time. These simulations can reveal conformational changes, solvation effects, and interaction mechanisms that static docking cannot capture. In this context, several heterocyclic molecules were studied and found to be active against the virus (Jayabal et al. 2022; Jones et al. 2023; Hashem et al. 2024; Ettahiri et al. 2024; Geedkar et al. 2024; Kattula et al. 2023; Nazir et al. 2024; Papaj et al. 2021; Kang et al. 2022; Eid et al. 2021; Uhomoibhi et al. 2022). In this article, we have performed the computational methods including molecular docking, molecular dynamics simulation studies of thiazole- coumarin conjugates, and thiazole-triazole conjugates targeting the M^{pro} and ACE2 receptors of SARS-CoV-2. These molecules were synthesized and reported by our research group for their anticholinesterase activity (Mishra et al. 2022, 2019). Because of broad range of biological applications of heterocyclic compounds and in the search of highly active molecules for the inhibition of M^{pro} and ACE2 enzyme specially coumarin (Lee et al. 2011; Huang et al. 2011; Vasconcelos et al. 2009; Kostova et al. 2011; De Almeida Barros et al. 2010), thiazole (De Souza and De Almeida 2003; Britschgi

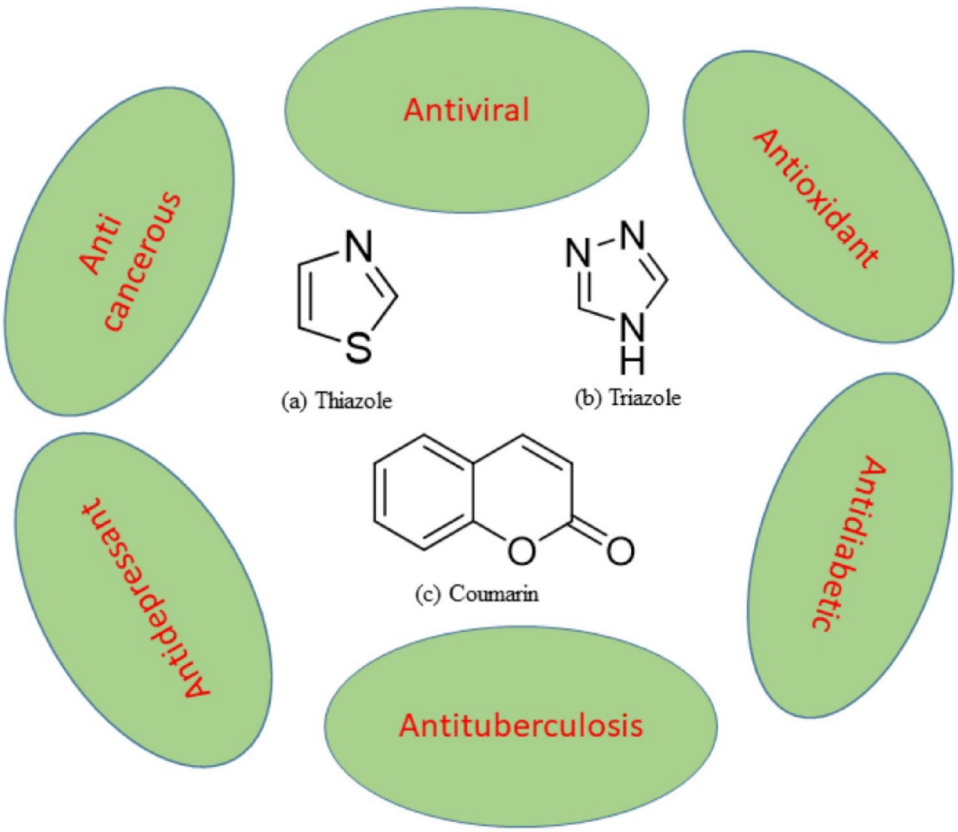


Fig. 2 **a** Thiazole, **b** Triazole, **c** Coumarin

et al. 2003; Knadler et al. 1986), and triazole (Kharb et al. 2010; Tehranchian et al. 2005) (Fig. 2), we select these derivatives for in-silico studies. In this context, we select a data set of phenylthiazole-coumarin conjugates and thiazole-triazole conjugates, (Fig. 3) and compare the result with a 2-deoxy-D-glucose (2DG) drug, which was recently used to treat SARS-CoV-2 (Sahu and Kumar 2021).

Methodology

The sequential approach used for studying the in-silico interaction patterns of phenylthiazole- coumarin and benzothiazole-triazole conjugates (Fig. 3A), for the identification of potential candidate molecules against M^{pro}/3CLpro SARS-CoV-2 viral protein, and human ACE2 protein. The flowchart summarized in Fig. 3B to show the process of study.

Protein, phenylthiazole-coumarin conjugates, benzothiazole-triazole conjugates; 3D structure formation and their geometry optimization

A dataset of twenty-one lead molecules of coumarin-linked phenyl thiazole conjugates and benzothiazole-linked triazole conjugates which were synthesized and reported by our research group compound RD1 to RD21 for their activity against cholinesterase enzyme were taken (Fig. 3) along with control drug 2DG (Mishra et al. 2022, 2019). The initial 3-dimensional (3D) structures of all the molecules including the 2DG drug were created using Gauss view 3.0. The 3D geometries of lead molecules were optimized in Gaussian 09, a quantum chemistry software package using a semi-empirical parametrization method 6 (PM6) (Frish 2009; Tabti and Benhalima 2015; Kwiecień et al. 2004).

SARS-CoV-2 main protease protein (M^{pro}/$3CL^{pro}$) is a homodimer made up of two chains A and B (Jin et al. 2020b). Dimer is formed by a two-fold crystallographic symmetry holding the two chains. Each protomer comprises three domains. The antiparallel beta-barrel structure is formed by domain I (residues 8-101), domain II (residues 102-184), and domain III (residues 201-303), which consists of five alpha-helices arranged into a predominantly antiparallel globular configuration. Domain II and domain III are joined by an extended loop region (residues 185-200). An active site for substrate is in the groove between domains I and II (Anand 2002). The 3D conformation of chain A from M^{pro}/$3CL^{pro}$ (PDB ID: 6LU7, 2.16Å) of SARS-CoV-2 and ACE2 (PDB ID: 6VW1, 2.68Å) was obtained from protein data bank (PDB) (http://www.rcsb.org/) (Qiu et al. 2020; Bzówka et al. 2020). The PDB structures for M^{pro}/$3CL^{pro}$ (PDB ID: 6LU7, 2.16 Å) of SARS-CoV-2 and ACE2 (PDB ID: 6VW1, 2.68 Å) were taken because of the resolution of both structures. High-resolution structures (=<2.50 Å) are preferred for docking studies as they provide detailed and accurate representations of the protein's three-dimensional conformation. Higher resolution leads to more reliable docking results as they may have less ambiguities compared to low-resolution structures in key regions like the active site that could affect the docking accuracy. Chimera version 1.13.1 was used to prepare protein structure and was minimized by using Amber ff99Sb force field (Pettersen et al. 2004).

Characterization of binding site

CastP tool was utilized for predicting the active site (Tian et al. 2018). The active site of M^{pro} comprises of five sub-sites namely S1, S2, S1', S2', and S4. The amino acid residues range from 140 to 172 formed S1 sub-site (Mishra et al. 2021). The S2 sub-site, which is bulky and hydrophobic, includes Met49, Asp187, and Glu189. The S1' sub-site contains Thr25, Leu27, Cys38, Pro39, Val42, and Cys145, which play a crucial role in catalysis. S2' sub-site includes Thr26, Asn28, Tyr118, Asn119, and Gly143, whereas the flexible S4 site contains Leu167 and Gln192 (Mishra et al. 2021; Wang et al. 2016; Mittal et al. 2020). However, ACE2 is a carboxypeptidase enzyme containing Zn metal and comprises 805 amino acids that remove a single amino acid from carboxy terminus of its substrate (Shang et al. 2020). The receptor binding domain (RBD) of the SARS-CoV-2 S protein interacts with ACE2 at an interface formed by the smoothly concave outer surface of extended receptor-binding motif and *N*-terminal helix of ACE2 (Prabakaran et al. 2003). Networks of hydrophilic amino acids and side-chains are created by 20 amino acid residues from ACE2 and 17 from the RBD of SARS-CoV-2. The binding mode of SARS-CoV-2 to ACE2 is like SARS-CoV but its binding affinity is 10–20 times more than that of SARS-CoV (Prabakaran et al. 2003).

Molecular docking analysis

A dataset of optimized molecular structures for coumarin-linked phenylthiazole conjugates and benzothiazole-linked triazole conjugates was subjected to molecular docking studies targeting M^{pro} of SARS-CoV-2 and ACE2 in identified active sites leveraging AutoDock 4.2.2 (Goodsell et al. 1996). AutoDock has been used for carrying out the protein–ligand docking in the current studies, using the Lamarckian Genetic Algorithm and empirical free energy scoring function. It typically provides reproducible docking results for ligands with approximately 10 flexible bonds. The grid spacing refers to the resolution of the grid maps

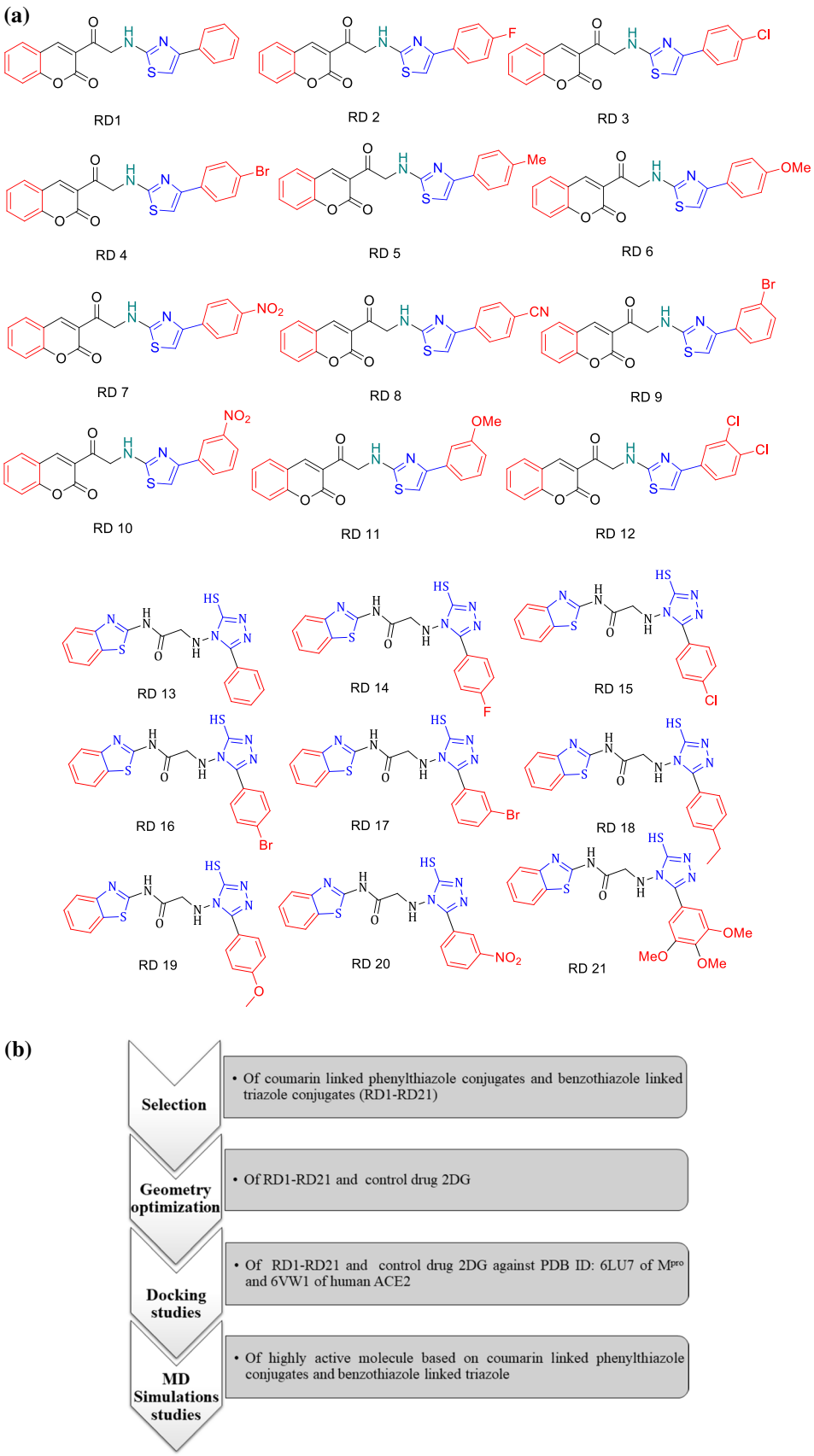


Fig. 3 **A** A data set of coumarin-thiazole conjugates & benzothiazole-triazole conjugates. **B** The sequential approach used in this study

used to represent the receptor (usually a protein or enzyme) in docking simulations. These maps are used to calculate the interaction energies between the ligand and the receptor based on various force field parameters (e.g., van der Waals, electrostatics). Higher Grid Resolution (smaller spacing, e.g., 0.375 Å) improves the accuracy of the docking results because it offers a finer and more detailed description of the receptor's 3D surface. It ensures that the docking algorithm explores the ligand-receptor interactions at a higher level of detail, which is crucial for capturing subtle energy differences between binding poses, and in regions with highly localized interactions (Chen et al. 2023). In the current study, a grid spacing of 0.375 is used for high-accuracy docking. The potential energy of docking molecules was calculated by the implementation of 3-dimensional potential grids. For docking with M^{pro} and ACE2, a three-dimensional grid box was generated to encompass active-site residues, along with an additional grid box having dimensionality points of X = 106, Y = 102, Z = 110, and X = 72, Y = 114, Z = 98, respectively. Lamarckian genetic algorithm of the docking software was employed to perform molecular docking, and an empirical scoring function was used to rank the docked molecules for both proteins. The intermolecular energy was calculated from the binding conformation of the protein–ligand complex. In AutoDock, the population size refers to the number of individuals (ligand conformations) in a population when using a genetic algorithm (GA) for ligand docking. A genetic algorithm is used to search for the optimal binding pose of the ligand to the receptor, and the population size determines how many ligand poses are considered in each generation. A larger population size i.e. 150 provides more diversity in the search, which can help the genetic algorithm explore a wider range of possible solutions and prevent it from converging prematurely to a local minimum. This increases the chance of finding the optimal binding pose and can improve the overall accuracy of the docking process (Chen et al. 2023). In the current study, for the docking process, a population size of 150, a maximum of 27,000 generations, and a maximum of 250,000 assessments, along with gene mutation rate of 0.02 and a crossover rate of 0.8 were set for all molecules. For each docking, a collection of 100 binding postures was generated for each molecule.

Molecular dynamics simulations

The stability of protein–ligand docked complexes was investigated through molecular dynamics simulation (MDS) using Gromacs 5.1.2 software (Van Der Spoel et al. 2005). Based on the docking score, MDS was conducted to further assess the interactions only for that molecule, which was found to be highly active against both the enzyme ACE2 and M^{pro}. In this regard, we select RD9, RD12, RD17, RD18, ligand–protein docking complexes and compare their interaction with the control drug 2DG-protein complex. GROMOS96 54A7 force field is a refinement of earlier versions in the GROMOS96 series, specifically version 54A7. It is optimized to handle proteins with a focus on water and the solvation of biomolecules. It was developed using quantum mechanical calculations and experimental data to parameterize the force field to better reproduce the thermodynamic and structural properties of biomolecules in solution. GROMOS54A7 was selected in the study for molecular dynamics simulations. All the ligand–protein docking complexes were employed for 100 ns time scale simulation (Pirolli et al. 2023; Shivanika et al. 2022; Fadlallah et al. 2023; Sharma et al. 2020). GROMOS9654a7 forcefield was utilized (Schmid et al. 2011) in Gromacs to generate protein topology, whereas the ligands topology was obtained using PRODRG server (Schüttelkopf and Aalten 2004).

The box defines the region in which atoms interact with each other and the boundaries of the simulation system. A cubic box with a size of $9.73 \times 9.73 \times 9.73$ nm was used for the solvation of protein–ligand complexes using SPC water model. The selected simulation box was large enough to accommodate the entire system so that there should not be any unwanted interactions between molecules due to periodic boundary conditions. It was selected considering the size of the docked complex. For systems with M^{pro}-ligand complexes, all systems charges were neutralized by adding four Na^+ ions, while for systems with ACE2-ligand complexes; charge neutralization was achieved by the addition of fifty-two Na^+ ions. Subsequently, the steepest descent algorithm was applied to perform energy minimization of the systems. Additionally, the electrostatic interactions of the systems were calculated using the Particle-Mesh Ewald method, Petersen (1995) with a 0.9 nm cutoff applied for van der Waals interactions. The Linear Constraint Solver for MDS (LINCS) algorithm was employed to manage the restriction enforced by covalent bonds and including those involving hydrogen atoms in the system. NVT (Number of particles, volume, and temperature) and NPT (Number of particles, pressure, and temperature) simulations were conducted on the system for 1 ns using the Berendsen thermostat method (Berendsen et al. 1984) to maintain the temperature at 300 K with a coupling time of 0.1 ps while the pressure was kept at 1 bar (Andersen 1980). After that, co-ordinates were saved every 0.002 fs for all the systems (Van Gunsteren and Berendsen 1988). RMSD, RMSF, Rg, Hydrogen bonds, and SASA for all ten docked complexes were assessed using different analytical tools, reported in literature (Mishra et al. 2019). Visual Molecular Dynamics (VMD) (Humphrey et al. 1996) and Chimera 1.13.1 visualization tools were used for resolving RMSD and RMSF

trajectories and Origin software was utilized for plotting the different graphs.

Principal component analysis

Principal component analysis (PCA), also known as essential dynamics method in Gromacs, was utilized to analyze eigenvectors and eigenvalues to obtain the projections of the first two principal components (PCs). The associated motion of the protein primarily defines its function, which was derived from the PCA analysis (Lever et al. 2017). Covariance matrix was formed by removing all rotational and translational movements. The elements of positional covariance matrix C were calculated using atomic coordinates, along with its eigenvectors, in the given equation:

$$C_{ij} = (q_i - < q_i >)(q_i - < q_i >)(i, j = 1, 2, \ldots, 3N) \quad (1)$$

In protein–ligand coupled systems, the (alpha carbon) Cα atom (Cα which is alpha carbon atom in the protein chain it connects the amino group of one amino acid to the carboxyl group of the next amino acid in the chain, forming the peptide bond) was designated by N, and the *i*th Cα atom was represented by the cartesian coordinate q_i. The least squares method was employed to eliminate translational and rotational movements from equilibrated trajectory, which was then superimposed on a reference structure. To predict the corresponding eigenvectors and eigenvalues λi, all matrices were diagonalized using the orthogonal coordinate transformation matrix Λ, as outlined in the literature with reference to Eq. (2) (Mishra et al. 2021).

$$\Lambda = \mathrm{T}^T C_{ij} \mathrm{T} \quad (2)$$

The eigenvectors in the above equation correspond to the direction of motion with respect to<qi>. The total mean-square fluctuation of the system along each eigenvector is indicated by the eigenvalue that corresponds to that eigenvector. The eigenvectors and eigenvalues for the final 20 ns of the trajectories were determined using the Gromacs tools gmxcovar and gmxanaeig.

Results and discussion

Molecular docking

The Indian Council of Medical Research (ICMR) India, on May 1, 2021, approved the 2-deoxy-D-glucose (2DG) drug for the treatment of COVID-19. Initially, it was developed by the Defence Research and Development Organization (DRDO) to check the growth of cancerous cells (Zhang et al. 2014). Herein, we have taken optimized molecular structures coumarin-phenylthiazole conjugates and benzothiazole-triazole conjugates (Fig. 3) for virtual screening of the lead molecules against M^{pro} (PDB Id: 6LU7) & human ACE2 (PDB ID: 6VW1) employing Auto Dock 4.2.2 and further compared them with 2-DG drug.

Stepwise we screened the coumarin-phenyl thiazole conjugates having a substituent at 3 & 4 positions of the phenyl ring attached to thiazole ring (RD1-RD12) against M^{pro} and ACE2. In addition, we also performed molecular docking studies of benzothiazole-triazole conjugates, having substituents at the benzene ring attached with 5-position of the 1,2,4-triazole (RD13-RD21). In our studies, we found that all the conjugates (RD1-RD21) interacted with amino acid residues located in the active site of both M^{pro} enzyme and ACE2. The free binding energy of all docked molecules ranges from -7.84 to -9.87 kcal/mol (Tables 1 and 2, respectively). The binding affinity of all these conjugates was further compared with the standard drug 2DG and found to be more active than the standard drug. Further, we found that when the substituent is present at 4-position of the phenyl ring attached with thiazole ring in coumarin-thiazole conjugates, there is a slight decrease in the activity of molecules as compared to the conjugates having substituent at 3-position. Based on binding interaction and docking score we have selected RD9, RD12, RD17, and RD18 derivatives for further study, because these conjugates were most active against both entry receptor enzyme ACE2 as well as M^{pro}. Among these four conjugates, the binding interaction of RD9 with receptor protein ACE2 is the strongest. The secondary amine attached to the thiazole ring and *N*-atom of the thiazole ring of RD9 are involved in H-bond interaction with ARG4 & LYS5 while oxygen present in pyran makes H-bond with GLN127 in the active site of M^{pro}. PHE291 & LYS5 amino acid residue of chain A makes a π-π interaction with the phenyl ring attached with the thiazole moiety and the phenyl ring fused with the pyran ring respectively. On the other hand, TRP207, PHE3 & LEU282 involved in interaction with the Br atom (Fig. 4A). These interactions provide a binding energy -8.33 kcal/mol. However, with ACE2 enzyme, the secondary amine, and the oxygen atom of cyclic ester, of RD9 makes an H-bond with LEU91, ASN210. In addition to this GLU208, VAL 212, ALA396, SER563, GLU564, and TRP 566 makes a van der Waal interaction in the active site of ACE2 having binding energy -9.87 kcal/mol (Fig. 5A). In case of RD12, RD17, and RD18 the binding energy are found to be -7.89, -8.61, 8.02 kcal/mol for M^{pro} and -9.75, -9.49, -9.61 for ACE2 respectively. These conjugates also form a strong interaction with other amino acids present in enzyme's active site. All the binding interaction of these molecules are shown in Fig. 4A (2D representation and ribbon representation

Table 1 Free binding energy calculated by docking study of the of phenylthiazole-coumarin conjugates, benzothiazole-triazole conjugates and 2-DG drug with geometry optimized at parametrization level PM6 against M^{pro} enzyme representing binding energy and the amino acids residues involve in interaction with M^{pro}

S No	Ligands	Free binding energy for M^{pro} (autodock) (kcal.mol^{-1})	Interacting residues	Interacting Group involve in Hydrogen bonding
1.	RD1	-8.29	Phe3, Arg4, **Lys5**, Tyr126, Gln127, Lys137, Gly138, Trp207, Leu282, Glu288, Glu290, Phe291	O atom of C=O attached with lactone ring,
2.	RD2	-7.84	Phe3, Arg4, **Lys5**, Tyr126, Gln127, Lys137, Trp207, Leu282, Glu288, Phe291	O atom of C=O attached with lactone ring,
3.	RD3	-8.27	Phe3, Arg4, **Lys5**, Met6, Ala7, Val125, Tyr126, Gln127, Trp207, Leu282, Glu288, Phe291	O atom of C=O attached with lactone ring,
4.	RD4	-8.32	Phe3, Arg4, **Lys5**, Met6, Ala7, Val125, Tyr126, Gln127, Trp207, Leu282, Glu288, Phe291	O atom of pyran ring,
5.	RD5	-7.85	Phe3, Arg4, **Lys5**, Tyr126, Gln127, Lys137, Gly138, Trp207, Leu282, Glu288, Phe291	O atom of C=O attached with lactone ring
6.	RD6	-8.00	Phe3, Arg4, **Lys5**, Tyr126, **Gln127**, Lys137, Gly138, Trp207, Leu282, Glu288, Phe291	O atom of C=O attached with lactone ring, O atom of pyran ring, NH attached to thiazole ring
7.	RD7	-8.30	Phe3, Arg4, **Lys5**, Tyr126, **Gln127**, Lys137, Trp207, Leu282, Phe291	O atom of pyran ring and N atom of thiazole ring, NH attached to thiazole ring
8.	RD8	-8.30	Phe3, Arg4, **Lys5**, Met6, Ala7, Val125, Tyr126, Gln127, Trp207, Glu288, Phe291	O atom of C=O attached with lactone ring
9.	RD9	-8.33	Phe3, **Arg4**, **Lys5**, Tyr126, **Gln127**, Trp207, Leu282, Glu288, Phe291	-NH attached to thiazole, N atom of thiazole, O atom of pyran ring,
10,	RD10	-8.15	**Lys5**, Ala7, Val125, Tyr126, **Gln127**, Cys128, Arg131, **Lys137**, Glu288, Glu290	NH attached to thiazole, N atom of thiazole, and O atom of–NO_2 group
11.	RD11	-8.23	Phe3, Arg4, **Lys5**, Tyr126, Gln127, Lys137, Gly138, Ser139, Trp207, Glu288, Phe291	O atom of C=O attached with lactone ring, O atom of pyran ring
12.	RD12	-7.89	Phe3, Arg4, **Lys5**, Ala7, Val125, Tyr126, Trp207, Leu282, Glu288, Phe291	O atom of C=O attached with lactone ring,
13.	RD13	-8.10	Phe3, Arg4, **Lys5,** Tyr126, **Gln127**, Lys137, Trp207, Leu282, Glu288, Phe291	N atom of benzothiazole ring, C=O of amide bond, N atom of triazole ring, S atom attached with triazole ring
14.	RD14	-8.06	Phe3, Arg4, **Lys5,** Tyr126, **Gln127**, Lys137, Leu282, Phe291	N atom of benzothiazole ring, C=O of amide bond, N atom of triazole ring, S atom attached with triazole ring
15.	RD15	-7.99	Phe3, Arg4, **Lys5,** Tyr126, Gln127, Trp207, Leu282, Ser284, Glu288, Phe291	NH group attached with triazole ring, N atom of benzothiazole ring, S atom attached with triazole ring
16.	RD16	-8.34	Phe3, **Arg4, Lys5,** Tyr126, Gln127, Trp207, Leu282, Glu288, Phe291	N atom of benzothiazole ring, C=O of amide bond, NH group attached with triazole ring
17.	RD17	-8.61	Phe3, Arg4, **Lys5**, Tyr126, **Gln127**, Lys137, Trp207, Leu282, Glu288, Glu290, Phe291	N atom of benzothiazole ring, C=O of amide bond, NH group attached with triazole ring
18.	RD18	-8.02	Phe3, Arg4, **Lys5,** Tyr126, **Gln127**, Lys137, Trp207, Leu282, Glu288, Phe291	N atom of benzothiazole ring, C=O of amide bond, NH group attached with triazole ring
19.	RD19	-8.09	Phe3, Arg4, **Lys5**, Tyr126, **Gln127**, Lys137, Trp207, Leu282, Glu288, Glu290, Phe291	N atom of benzothiazole ring, N atom of triazole ring, S atom attached with triazole ring
20.	RD20	-8.90	Phe3, **Arg4, Lys5,** Tyr126, **Gln127**, Trp207, Glu288, Phe291	N atom of benzothiazole ring, N atom of triazole ring, C=O of amide bond, O atom of–NO_2 group, S atom attached with triazole ring
21.	RD21	-7.01	Tyr101, Lys102, Phe103, Val104, Arg105, Asp176, **Glu178**, Asn180	N atom of amide bond, S atom of benzothiazole ring, S atom attached with triazole ring
22.	2DG	-2.33	**Phe3**, Arg4, **Lys5,** Trp207, **Leu282**, Ser284	H atom attached with OH

Table 2 Free binding energy calculated by docking study of the of phenylthiazole-coumarin conjugates, benzothiazole-triazole conjugates and 2-DG drug with geometry optimized at parametrization level PM6 against human ACE2 representing binding energy and the amino acids residues involve in interaction with human ACE2

S. no.	Ligand	Free binding energy for ACE2 (autodock) (kcal mol^{-1})	Interacting residues	Interacting group involve in hydrogen bonding
1.	RD1	-9.31	**LEU91**, LYS94, **LEU95**, GLN98, GLU208, **ASN210**, VAL209, VAL212, ALA 396, LYS562, SER 563, GLU564, PRO565, TRP566	NH group attached with thiazole ring, O atom of C=O of lactone ring, N atom of thiazole ring,
2.	RD2	-8.41	LEU91, THR92, LYS94, LEU95, **GLN98**, GLU208, VAL209, **ASN210**, GLY211, VAL212, ALA396, LYS562, SER563, GLU564, PRO565, **TRP566**	NH group attached wit thiazole ring, O atom of C=O of lactone ring, F atom present at phenyl ring S atom of thiazole ring
3.	RD3	-8.43	PHE40, LEU73, ALA99, LEU100, PHE32, ALA348, ASP350, ASP382, TYR385, PHE390, LEU391, **ARG393**, **ASN394**, ALA396, LYS562, SER563, GLU564, PRO565, TRP566	O atom of C=O of lactone ring, N & S atom of thiazole ring,
4.	RD4	-8.65	LEU91, **THR92**, LYS94, LEU95, GLN98, GLU208, VAL2-09, **ASN210**, GLY211, VAL212, LYS562, SER563, GLU564, PRO565	O atom of C=O of lactone ring, N& S atom of thiazole ring
5.	RD5	-9.02	LEU95, GLY205, ASP206, TYR207, GLU208, VAL209, ASN210, VAL212, GLY395, **ALA396**, ASN394, ASN397, HIS401, GLU402, ARG514, LYS562, PRO565, TRP566	NH group attached wit thiazole ring
6.	RD6	-8.73	LEU91, LYS94, LEU95, GLN98, GLN102, TYR196, TYR202, TRP203, GLY205, ASP206, GLU208, VAL209, ASN210, VAL212, LYS562, PRO565	All are involve in Vander wall type of interaction
7.	RD7	-7.86	LEU91, LEU95, **GLN98**, GLN102, TYR196, **GLY205**, ASP206, TYR207, **GLU208**, VAL209, ASN210, VAL212, ARG219, ALA396, HIS401, GLU402, ARG514, PRO565, TRP566	O atom of C=O of lactone ring, NH group attached wit thiazole ring,
8.	RD8	-9.28	LEU95, GLN98, GLN102, TYR196, GLY205, ASP206, **GLU208**, VAL209, ASN210, VAL212, ARG219, ALA396, ASN397, **LYS562**, GLU564, PRO565, TRP566	O atom of C=O of lactone ring, N atom of thiazole ring, NH group attached wit thiazole ring
9.	RD9	-9.87	**LEU91**, LYS94, LEU95, GLN98, GLU208, VAL209, **ASN210**, VAL212, ALA396, LYS562, SER563, GLU564, PRO565, TRP566	NH group attached wit thiazole ring, O atom of C=O of lactone ring,
10.	RD10	-8.52	LEU91, LYS94, **LEU95**, GLN98, ASP206, GLU208, VAL209, ASN210, GLY211, VAL212, LYS562, SER563, GLU564, PRO565, TRP566	O atom of C=O of lactone ring
11.	RD11	-9.01	LEU95, GLN98, GLN102, **TYR196,** TYR202, GLY205, ASP206, GLU208, VAL209, ASN210, VAL212, ALA396, ASN397, LYS562, GLU564, PRO565, TRP566	O atom of C=O of lactone ring, N atom of thiazole ring, NH group attached wit thiazole ring
12.	RD12	-9.75	LEU91, LEU95, GLN98, GLY205, **ASP206**, TYR207, GLU208, **ASN210**, GLY211, VAL212, ALA396, LYS562, SER563, GLU564, PRO565, TRP566	N atom of thiazole ring, NH group attached wit thiazole ring, C=O of lactone ring
13.	RD13	-9.02	LEU95, GLN98, GLN102, TYR196, TYR202, GLY205, ASP206, **GLU208**, VAL209, **ASN210**, GLY211, VAL212, ALA396, ASN397, **LYS562**, PRO565, TRP566	NH of amide bond, NH attached with triazole ring, H atom of SH attached with triazole ring
14.	RD14	-8.84	LEU91, LYS94, LEU95, GLN98, GLN102, TYR196, TYR202, GLY205, ASP206, **GL208**, VAL209, ASN210, GLY211, VAL212, **LYS562**, PRO565, TRP566	NH attached with triazole ring, H atom of SH attached with triazole ring
15.	RD15	-9.48	LEU91, LEU95, GLN98, GLN102, TYR196, TYR202, GLY205, ASP206, **GLU208**, VAL209, ASN210, GLY211, VAL212, **ALA396**, ASN397, **LYS562**, GLU564, PRO565	O atom of C=O group, NH of amide bond, H atom of SH attached with triazole ring, NH attached with triazole ring, NH attached with triazole ring
16.	RD16	-9.49	LEU95, **GLN98**, GLN102, **TYR196**, TYR202, TRP203, **GLY205**, ASP206, **GLU208**, VAL209, ASN210, ALA396, GLU564, LYS565, PRO565, TRP566	O atom of C=O group, NH of amide bond, H atom of SH attached with triazole ring, NH attached with triazole ring, N atom attached with benzothiazole ring

Table 2 (continued)

S. no.	Ligand	Free binding energy for ACE2 (autodock) (kcal mol^{-1})	Interacting residues	Interacting group involve in hydrogen bonding
17.	RD17	-9.49	PHE40, SER44, LEU95, GLN98, GLN102, TYR196, TYR202, TRP203, GLY205, ASP206, GLU208, THR347, **ALA348**, TRP349, ASP350, LEU351, TYR385, PHE390, ARG393, ALA396, GLU564, LYS565, PRO565, TRP566	NH attached with triazole ring, H atom of SH attached with triazole ring,
18.	RD18	-9.61	LEU91, LYS94, LEU95, **GLN98**, GLN102, TYR196, TYR202, GLY205, ASP206, **GLU208**, VAL209, ASN210, GLY211, VAL212, **ALA396**, ASN397, LYS562, GLU564, PRO565, TRP566	NH attached with triazole ring, H atom of SH attached with triazole ring, O atom of C=O group, NH of amide bond,
19.	RD19	-8.71	LEU91, GLN98, GLN102, TYR196, GLY205, ASP206, TYR207, GLU208, VAL209, **ASN210**, GLY211, VAL212, ALA396, ASN397, LYS562, GLU564, PRO565, TRP566	O atom of C=O group, SH attached with triazole ring
20.	RD20	-8.73	LEU91, LYS94, LEU95, GLN98, GLN102, **TYR196**, TYR202, **GLY205**, ASP206, GLU208, VAL209, ASN210, GLY211, VAL212, LYS562, PRO565, TRP566	NH attached with triazole ring,
21.	RD21	-7.99	LYS94, LEU95, GLN98, GLN102, TYR196, TYR202, **GLY205**, ASP206, GLU208, VAL209, ARG219, ASN210, VAL212, LYS562, PRO565, TRP566	NH attached with triazole ring
22.	2DG	-2.63	LYS94, LEU95, GLN98, **TYR196,** ASN210, LYS562, PRO565, TRP566	H atom attached with OH

of highly active molecule with M^{pro}), Fig. 4B (3D representation highly active molecule with M^{pro}), and Fig. 5A (2D representation and ribbon representation highly active molecule with ACE2), Fig. 5B respectively (3D representation highly active molecule with ACE2). Further, the overlay figure also supports that all the ligands are bind in the same binding pocket, which can be clearly seen in Fig. 4C (overlay of the docking poses of all the active ligands in the binding site of crystal structure of COVID-19 main protease: 6LU7) and Fig. 5C (Overlay of the docking poses of all the active ligands in the binding site of crystal structure of SARS-CoV-2 receptor-binding domain o ACE2: 6VW1) respectively. From this study, we found that the activity of RD9, RD12, RD17, and RD18 for ACE2 is more than that of the M^{pro} enzyme. This suggests that this type of scaffold can be effectively used to inhibit the entry of SARS-CoV-2.

Molecular dynamics simulation

Molecular dynamics simulation (MDS), a computational method used to study physical movements of the atoms during binding, Abraham et al. (2015) was conducted for ten systems 2-DG- M^{pro}, RD9-M^{pro}, RD12-M^{pro}, RD17-M^{pro}, and RD18-M^{pro}, 2-DG-ACE2, RD9-ACE2, RD12-ACE2, RD17-ACE2, and RD18-ACE2. The equilibration state of all ten systems was achieved by performing MDS of docked complexes for 100 ns (ns) (Pirolli et al. 2023; Shivanika et al. 2022; Fadlallah et al. 2023; Sharma et al. 2020). Further, the hydrogen bonds, Root mean square deviation (RMSD), Root mean square fluctuation (RMSF), Solvent accessible surface area (SASA), and Radius of Gyration (Rg) were analyzed and plotted for the last 20 ns of the equilibrated trajectories for every complex.

Dynamic stability and flexibility of protein structure by RMSD and RMSF

The dynamic stability of each complex is described by the RMSD. It calculates the changes made to the skeleton of the protein during the simulation. RMSD measures the deviation between the positions of atoms in the system at different time points during the simulation. If RMSD value remains low and stable over time (after an initial equilibration period), this suggests that the molecule is stable and is maintaining its conformation throughout the simulation. In ligand-binding simulations, a protein with low RMSD suggests that it is stable in its docked form, and any large RMSD change indicates ligand release or conformational shifts due to binding. RMSD values in this study is reported with respect to the reference 2DG molecule. Trajectories obtained for all the systems were observed for calculation of RMSD values (Fig. 6a). Cα-RMSD specifically tracks the movement of the alpha-carbon atoms in the protein's backbone. Since the alpha-carbon atoms are the central part of the polypeptide chain, the Cα RMSD gives a good indication of how much the overall protein structure has deviated from its initial configuration at 300 K (a typical temperature for simulations of proteins in aqueous environments) Average values of RMSD for M^{pro}-2DG, M^{pro}-RD9, M^{pro}-RD12, M^{pro}-RD17 and M^{pro}-RD18. were 0.4505 nm, 0.4332 nm, 0.5744 nm, 0.3686 & 0.3012 nm respectively. RMSD pattern observed of RD17 and RD18 shows that

they are forming stable complex with M^{pro} as compared to 2DG while RD9 and RD12 are forming comparable stable structures with M^{pro} protein molecule. Additionally, residue mobility calculations for the final 20 ns of the equilibrated trajectory were conducted (Fig. 6b). The RMSF of Cα atoms provides a measure of local flexibility or rigidity of the protein and a higher RMSF value in a specific region of the protein suggests that the corresponding part of the protein is highly flexible. The average RMSF values calculated for ACE2-2-DG, ACE2-RD9, ACE2-RD12, ACE2-RD17, and ACE2-RD18 was 0.1568 nm, 2.230 nm, 1.5363 nm, 0.9425 and 2.306 nm.

RMSF is a measure used in molecular dynamics simulations (MDS) to assess the flexibility or fluctuations of individual atoms, residues, or regions of a molecular system. It is used to study the local flexibility within the molecular system. The loop region or the other flexible region of the protein shows fluctuations and a high RMSF value but on ligand binding the region is shown to be less conformational flexibility and stability. All the ligands showed good RMSF values as well as higher RMSF peaks as compared to the ACE2-2-DG complex. It can be concluded from the RMSF analysis that all the lead molecules were inducing the less conformational change upon binding than 2-DG. Among all the lead molecules RD18 showed the highest average RMSF value compared to 2-DG molecule while binding to vital M^{pro} protein.

The trajectories obtained for all the systems were also analyzed to calculate the RMSD values over the last 20 ns (Fig. 7a). Average values of RMSD for ACE2-2DG, ACE2-RD9, ACE2-RD12, ACE2- RD17, and ACE2-RD18 were 13.22 nm, 2.62 nm, 4.03 nm, 1.80 nm & 1.97 nm respectively. The RMSD pattern observed for all the ligands binding to ACE2 indicates that they form more stable complexes than 2-DG. Specifically, RD17 and RD18 demonstrate a higher stability in their binding to ACE2, suggesting they form more stable complexes compared to 2-DG. Furthermore, residue mobility calculations were carried out for the final 20 ns of the equilibrated trajectory shown in Fig. 7b.

Compactness and hydrogen bonds analysis

Since hydrogen bonds contribute to transitory interactions that facilitate the formation of complex and enhance the stability of the docked complex, therfore they are the primary factor which determine the stability of protein–ligand complexes. During MDS, H-bonds can form, break, and reform as the protein moves and undergoes conformational changes. H-bonds in an MDS are identified using criteria set based on the distance (< 3.5 Å) and angle (> 120°) between the donor and acceptor. In the MDS, the number and strength of hydrogen bonds can fluctuate, reflecting the dynamic nature of protein structures. The dynamics of these bonds can be tracked and analyzed over the course of the simulation. The number of hydrogen bonds formed during binding was calculated in the study.

The plot showing the number of hydrogen bonds that the complexes have created over time scale is shown in Fig. 8a. On the analysis, it has been found that M^{pro}-2DG, M^{pro}-RD9, and M^{pro}-RD18 formed 0–4 number of H-bond, while M^{pro}-RD12 formed 0–3, and M^{pro}-RD17 formed 0–5 number of H-bond. This suggest that all the ligands exhibited a similar binding pattern in terms of the number of hydrogen bonds as the 2DG molecule during complex formation, indicating that the stability of the lead molecules-M^{pro} complex is comparable to that of the 2DG molecule.

The compactness of the protein–ligand complexes during the simulation timescale was characterized by the radius of gyration (Rg). This parameter measures the distance between the centers of mass of the protein atoms and its terminal atoms at given time frame. A more compact protein exhibits less variation in the gyration value, while a higher Rg indicates a more diffuse structure. The plot of Rg values *vs* time for each complex is represented in Fig. 8b. The Radius of Gyration (Rg) quantifies how compact or extended a molecule is by measuring the distribution of atoms from the molecule's center of mass. The plot shows how Rg changes over the course of the simulation, providing insights into the protein's overall structure and its dynamic behavior. The average Rg values were found to be 2.233 nm for M^{pro}-2DG, 2.288 nm for M^{pro}-RD9, 2.2034 nm for M^{pro}-RD12, 2.249 nm for M^{pro}-RD17 and 2.161 nm for M^{pro}-RD18. From the Rg values analysis it has been predicted that RD18 is forming a dense cluster as compared to 2DG molecule with the viral protein and other lead molecules are forming comparably stable complex with M^{pro} viral protein as 2-DG.

Number of hydrogen bonds formed for ACE2-2DG, ACE2-RD9, ACE2-RD12, ACE2-RD17, and ACE2-RD18 were 0–3, 0–4, 0–2, 0–3, & 0–4 respectively. All the ligands exhibited a similar binding pattern in terms of the number of hydrogen bonds as the 2DG molecule during complex formation, indicating that the stability of the lead molecules-ACE2 complex is comparable to that of the 2-DG molecule (Fig. 9a). The average Rg values obtained for ACE2-2DG, ACE2-RD9, ACE2-RD12, ACE2-RD17, and ACE2-RD18 were 2.5 nm, 4.9 nm, 4.2 nm, 6.4 nm, and 6.9 nm respectively (Fig. 9b). The analysis of the radius of gyration (Rg) values suggests that all the ligands form clusters with ACE2 that are similarly dense when compared to the 2-DG molecule.

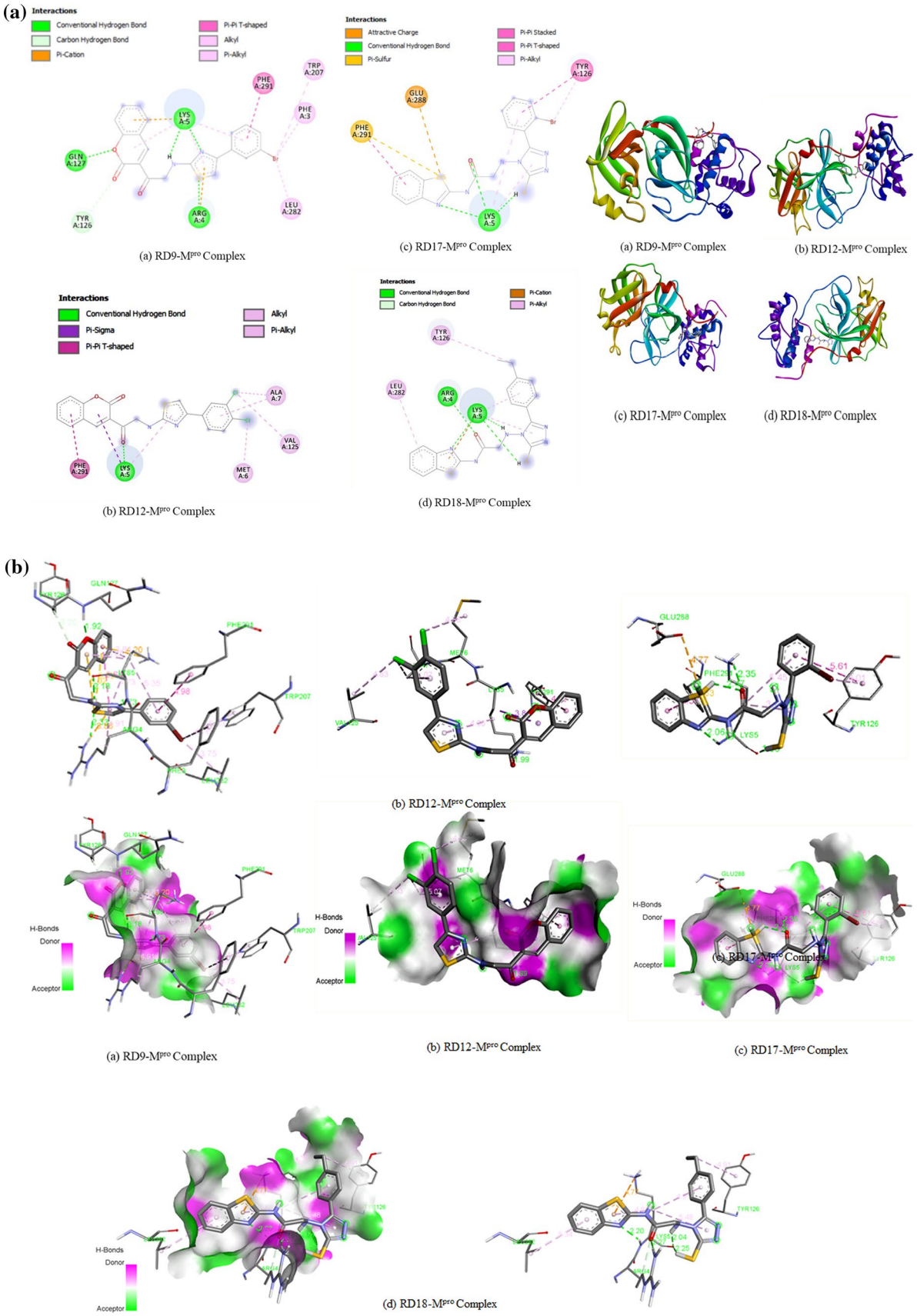

(a)
Interactions
Conventional Hydrogen Bond
Carbon Hydrogen Bond
Pi-Cation
Pi-Pi T-shaped
Alkyl
Pi-Alkyl
(a) RD9-Mpro Complex
Interactions
Attractive Charge
Conventional Hydrogen Bond
Pi-Sulfur
Pi-Pi Stacked
Pi-Pi T-shaped
Pi-Alkyl
(c) RD17-Mpro Complex
(a) RD9-Mpro Complex
(b) RD12-Mpro Complex
Interactions
Conventional Hydrogen Bond
Pi-Sigma
Pi-Pi T-shaped
Alkyl
Pi-Alkyl
(b) RD12-Mpro Complex
Interactions
Conventional Hydrogen Bond
Carbon Hydrogen Bond
Pi-Cation
Pi-Alkyl
(d) RD18-Mpro Complex
(c) RD17-Mpro Complex
(d) RD18-Mpro Complex
(b)
(b) RD12-Mpro Complex
H-Bonds
Donor
Acceptor
(a) RD9-Mpro Complex
(b) RD12-Mpro Complex
(c) RD17-Mpro Complex
(d) RD18-Mpro Complex

Fig. 4 **A** 2D and ribbon representations of protein–ligand complexes: (a) the RD9-M^{pro} complex, (b) the RD12-M^{pro} complex, (c) the RD17-M^{pro} complex, and (d) the RD18-M^{pro} complex. These visualizations illustrate the structural details and interactions between the respective molecules, with the 2D representation highlighting key molecular interactions and the ribbon representation providing a three-dimensional view of the protein architecture and binding site conformations for each complex in the binding site of crystal structure of COVID-19 main protease (Protein Data Bank (PDB) ID: 6LU7). **B** 3D representation of (a) RD9-M^{pro} complex (b) RD12-M^{pro}-complex (c) RD17-M^{pro}-complex (d) RD18-M.^{pro}-complex in the binding site of crystal structure of COVID-19 main protease (Protein Data Bank (PDB) ID: 6LU7). **C** Overlay of the docking poses of RD9 (red), RD12 (purple), RD17 (light green) and RD18 (peach) in the binding site of crystal structure of COVID-19 main protease (Protein Data Bank (PDB) ID: 6LU7)

Analysis of solvent accessible surface area (SASA)

The polar and non-polar interaction between the protein residues results in solvation free energy. The solvent-accessible surface area (SASA) refers to the portion of a protein's surface that is exposed to solvent molecules, where these molecules interact with the van der Waals surface of the protein. The hydrophobic residues primarily cause the increase in the SASA value. SASA is a critical structural property in MDS because it reflects the molecule's interaction with the solvent and conformational changes over time. The SASA plot shows how the solvent-accessible surface area of a molecule evolves throughout the simulation, providing insights into ligand binding**.** The SASA value for each complex for M^{pro} was calculated separately for the last 20 ns of the equilibrated trajectory and is presented in Fig. 10a. The average SASA values obtained were 157.494, 161.885, 156.636, 153.786, and 152.847 nm^2 for M^{pro}-2-DG, M^{pro}- RD9, M^{pro}-RD12, M^{pro}-RD17, and M^{pro}-RD18, respectively.

Another important parameter is the residue SASA value, which provides insights into the conformational changes associated with each residue's contribution. A graph illustrating the relationship between residues and their SASA values has been plotted (Fig. 10b). This plot provides detailed insight into how different regions of the molecule are exposed to the solvent and how this exposure changes over time. After analysis, it has been found that the average residue SASA values for M^{pro}-2-DG, M^{pro}-RD9, M^{pro}-RD12, M^{pro}-RD17, and M^{pro}-RD18 were 0.5096, 0.5238, 0.5069, 0.4977 & 0.4946 nm^2 respectively. A decrease in SASA at a binding site suggests that residues are becoming more buried after ligand binding, indicating that the protein–ligand complex is stabilizing. These finding suggest that RD17 and RD18 are forming a better complex with M^{pro} as compared to the 2DG molecule though other two lead compounds RD9 and RD12 are as good as the 2DG molecule.

Further, the SASA value for each complex with ACE2 is shown in (Fig. 11a). The average SASA values for ACE2-2DG, ACE2-RD9, ACE2-RD12, ACE2-RD17, and ACE2-RD18 were found to be 282.14, 553.41, 548.91, 552.02 & 562.82 nm^2 respectively. A graph for the lead molecule 2-DG, RD9, RD12, RD17and RD18 complex with ACE2 protein with has been plotted between residues and SASA value (Fig. 11b). The average residue SASA values obtained for ACE2-2DG, ACE2-RD9, ACE2-RD12, ACE2-RD17, and ACE2-RD18 were 0.47, 0.479, 0.469, 0.464 & 0.476 nm^2 respectively. This SASA analysis suggest that RD17 and RD18 are forming a comparable complex with ACE2 also as compared to the 2DG molecule though other two lead compounds RD9 and RD12 are as good as the 2DG molecule.

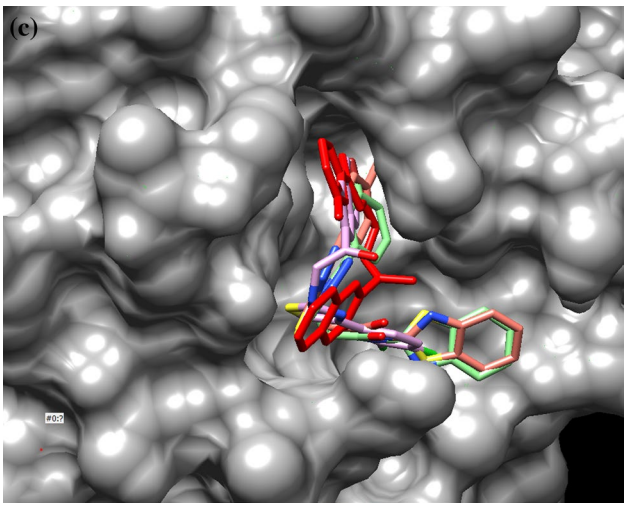
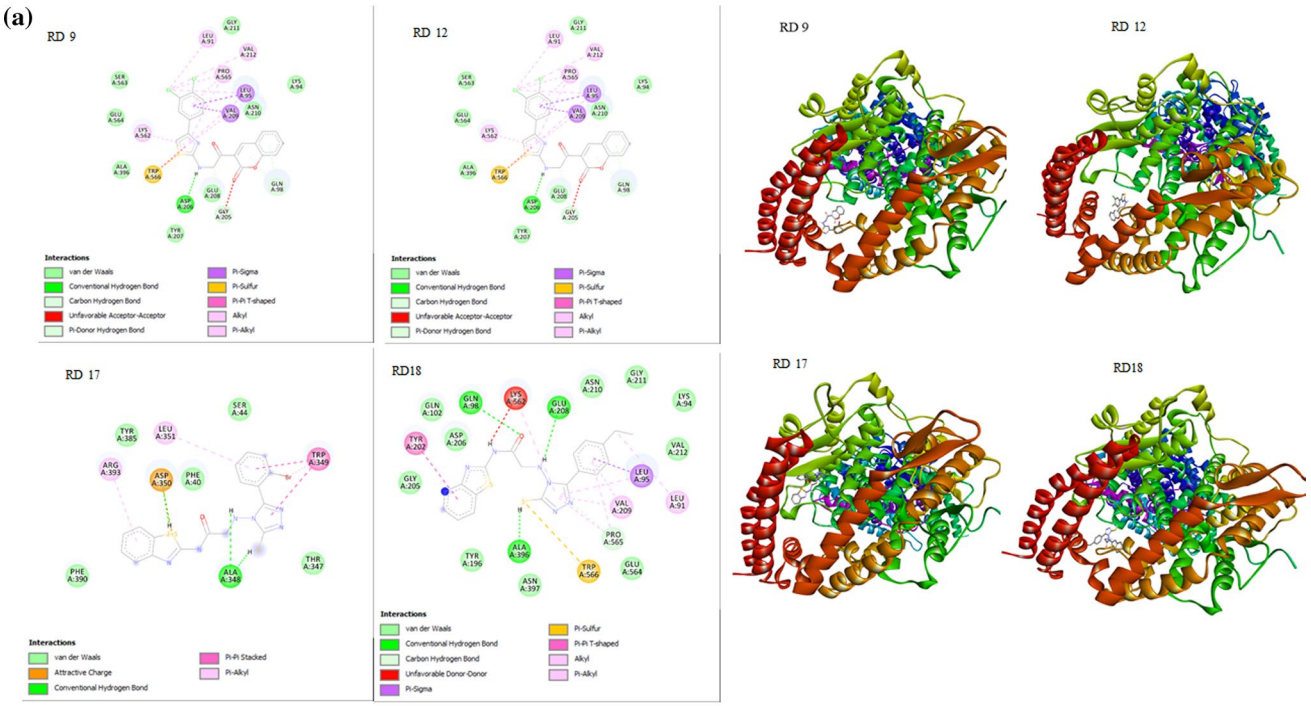
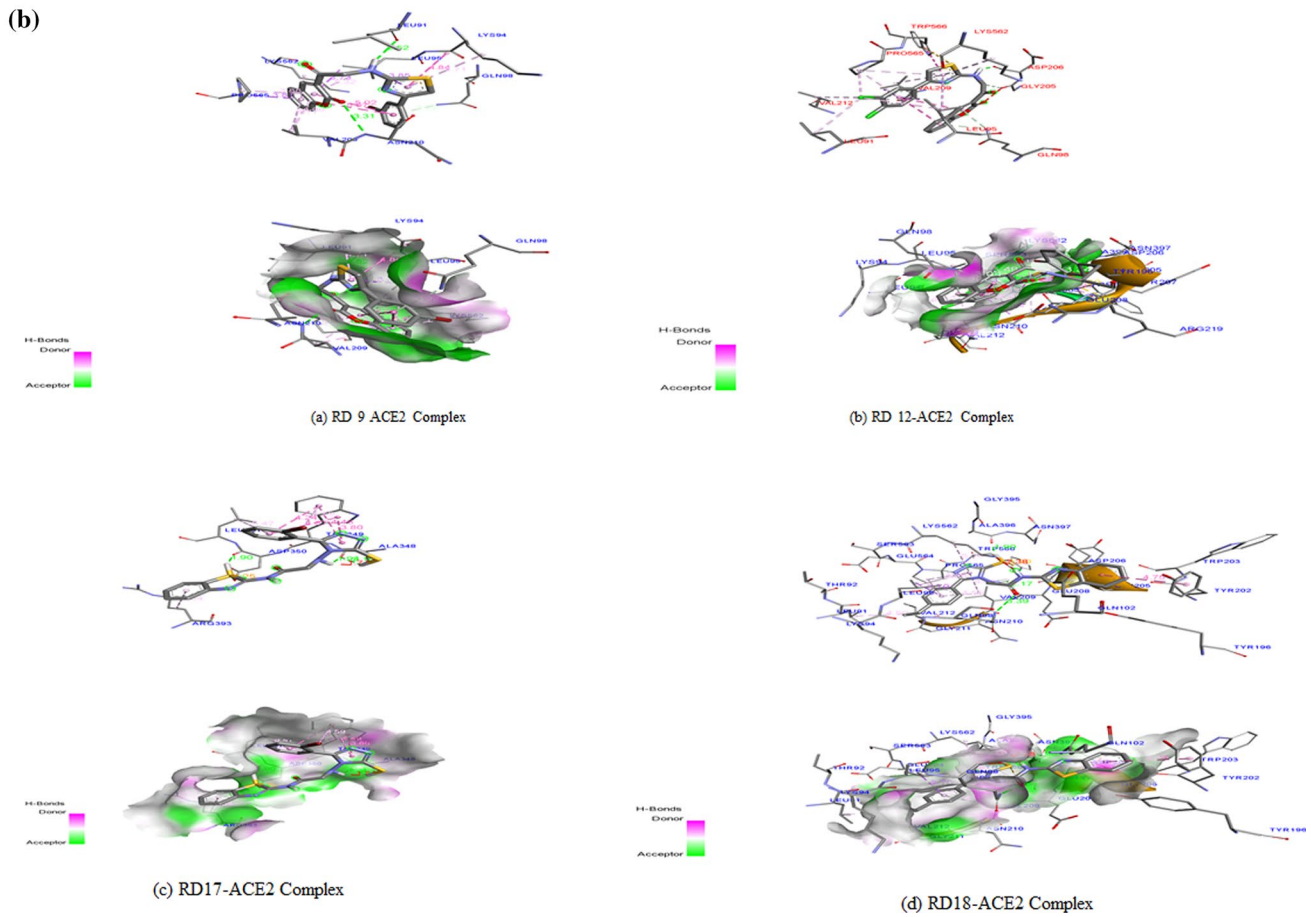


Fig. 4 (continued)

Principal component analysis (PCA)

During the MDS, PCA predicts the correlated movement of the complexes. The overall motions in proteins are characterized by a few key eigenvectors used to calculate Principal Components (PCs). It is particularly valuable when studying the conformational flexibility and dynamics of biomolecules such as proteins, nucleic acids, or protein–ligand complexes. PCA helps in simplifying the complex dynamics of these systems by identifying the dominant modes of motion, which are the most significant collective movements during the simulation**.** In Molecular Dynamics Simulations studies, PCA is applied to the atomic trajectories (the movement of atoms over time) to reduce the dimensionality of the data and highlight the major motions. In the provided interactions of the ligands with the receptor proteins of first few principal components typically correspond to large-scale collective motions, such as domain movements or overall structural rearrangements. A stable





(a) RD 9 ACE2 Complex

(b) RD 12-ACE2 Complex

(c) RD17-ACE2 Complex

(d) RD18-ACE2 Complex

Fig. 5 **A** 2D and ribbon representations of the following protein–ligand complexes: (a) the RD9-ACE2 complex, (b) the RD12-ACE2 complex, (c) the RD17-ACE2 complex, and (d) the RD18-ACE2 complex. These visualizations illustrate the structural details and interactions between the respective molecules, with the 2D representation highlighting key molecular interactions and the ribbon representation providing a three-dimensional view of the protein architecture and binding site conformations for each complex in the binding site of crystal structure of SARS-CoV-2 receptor binding domain ACE2 (Protein Data Bank (PDB) ID: 6VW1). **B** 3D representation of (a) RD9-ACE2 complex (b) RD12-ACE2 complex (c) RD17-ACE2 complex (d) RD18-ACE2 in the binding site of crystal structure of SARS-CoV-2 receptor binding domain ACE2 (Protein Data Bank (PDB) ID: 6VW1). **C** Overlay of the docking poses of RD9 (red), RD12 (purple), RD17 (light green) and RD18 (peach) in the binding site of crystal structure of SARS-CoV-2 chimeric receptor-binding domain (Protein Data Bank (PDB) ID: 6VW1)

receptor-ligand complex shows limited motion in the first few principal components, indicating that the binding is stable. For each of the ten eigenvectors, a graph has been plotted for the eigenvalues against the eigenvectors (Fig. 12a). A PCA plot is a powerful tool used to analyze the collective motion of the system over time. PCA identified the most significant modes of motion (principal components, PCs) in the system by reducing the dimensionality of the trajectory data. It helps to visualize how the system moves, identify the main structural fluctuations.

The first ten eigenvectors during the last 20 ns equilibrated trajectory each described 43.49%, 14.27%, 60.12%, 13.06% & 14.60% of the motion for M^{pro}-2DG, M^{pro}-RD9, M^{pro}-RD12, M^{pro}-RD17, and M^{pro}-RD18. Results obtained from this analysis represents RD9, RD17, RD18 are showing less motion as compared to 2DG. For predicting the correlated motion of all the complexes 10 eigenvectors were taken and the first five key eigenvectors were studied to study the overall protein dynamics.

Furthermore, the first 2 eigenvectors were plotted against each other in a phase space, with each spectrum representing the correlated motions (Fig. 12b). Projection of protein motion in phase space along PC1 and PC2 represents the conformational changes of a protein during a MDS by projecting its trajectory onto the first two principal components (PC1 and PC2) obtained from PCA. This projection helps to visualize the dominant motions of the protein in a reduced-dimensional space, where each point on the plot corresponds to a conformation of the protein at a given time during the simulation. The first two principal components, PC1 and PC2, are the most significant modes of motion in terms of variance, and by projecting the trajectory onto these two axes, we can simplify and highlight the most important conformational fluctuations of the system. Stability of complex is represented by a denser cluster while a less stable cluster is characterized by a dispersed. The results indicated that RD17 and RD18 showed the dense cluster than 2-DG with M^{pro}.

In addition, for each of the ten eigenvectors, a graph for 2DG, RD9, RD12, RD17 and RD18 with ACE2 also has been plotted for the eigenvalues against the eigenvectors (Fig. 13a). The first ten eigenvectors for ACE2-2-DG, ACE2-RD9, ACE2-RD12, ACE2-RD17, and ACE2-RD18 explained 80.57%, 95.9%, 67.2%, 21.9% & 72.5% of the motions respectively. The results obtained from this analysis suggest that RD17 exhibits less motion or variability in its molecular dynamics when compared to 2-DG. This indicates that the structural fluctuations in RD17 are less pronounced or restricted compared to the more dynamic behavior observed in 2-DG. Results obtained from this analysis represents RD17 is showing less motion as compared to 2-DG (Fig. 13b). To predict the correlated motion of all the complexes, ten eigenvectors were considered, and the first five key eigenvectors were analyzed to understand the overall protein dynamics.

Free binding energy analysis (MMPBSA)

The binding affinity of the lead molecules against viral M^{pro} and ACE2 was evaluated through free binding energy calculations. Although the binding affinities has been estimated in the docking study, but both use different methodologies, docking scores in AutoDock often use simplified scoring functions to quickly evaluate many poses. MM/PBSA scores are more rigorous and theoretically sound, they consider molecular mechanics energies and solvation effects. While there may be some correspondence between docking scores and MM/PBSA scores, they are not directly equivalent. It is defined as the total of the non-bonded interaction energies within protein–ligand complex. AutoDock scoring provides the binding energy based on protein–ligand interactions taking into consideration the local effects, but MMPBSA provides the scores that takes into consideration the solvation effect and entropy. The AutoDock score provides an approximate but useful estimate of protein–ligand interaction strength, whereas MMPBSA offers a more comprehensive, thermodynamically accurate calculation of the ligand's stability in the binding site. AutoDock scores and MMPBSA scores do not directly correspond but can be used together to gain a more complete understanding of protein–ligand

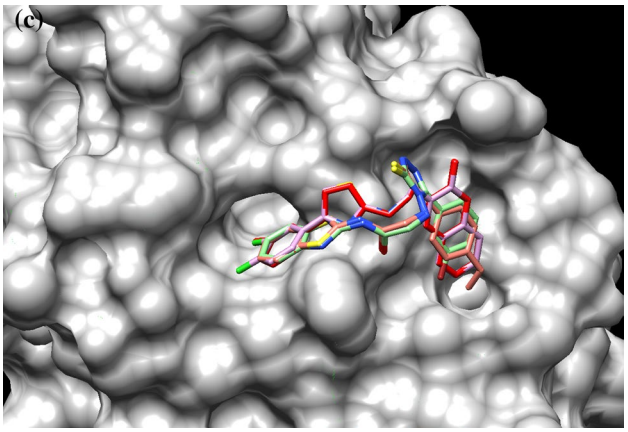


Fig. 5 (continued)

interactions. The binding-affinity scores provided for the ligand compounds against the corresponding proteins and the MMPBSA scores cannot correspond directly. The MMPBSA tool (Kumari et al. 2014) was utilized to calculate the binding free energy. All the calculated binding free energies of best-hit compounds with M^{pro} and ACE2 are summarized in Tables 3 and 4 respectively. MMPBSA (Molecular Mechanics Poisson-Boltzmann Surface Area) is a widely used method to calculate binding free energies of protein–ligand complexes. This approach combines molecular mechanics with solvation models to estimate the free energy of binding by evaluating the contributions from

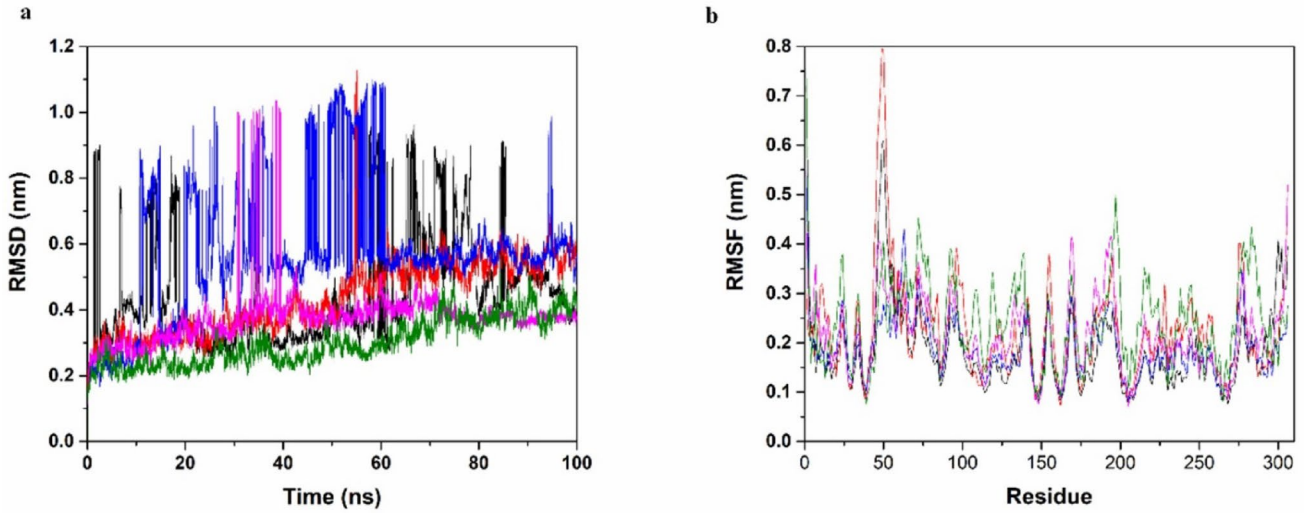


Fig. 6 MDS. **a** Figure depicting how the backbone of the protein (specifically the Cα atoms) changes relative to its starting structure during the simulation, which is conducted at 300 K, **b** RMSF measuring the fluctuation or mobility of atoms (Cα atoms) during the simulation Color code in the panels are: M^{pro}-2DG (black), M^{pro}-RD9 (red), M^{pro}-RD12 (blue), M^{pro}-RD17 (magenta) and M^{pro}- RD18 (green)

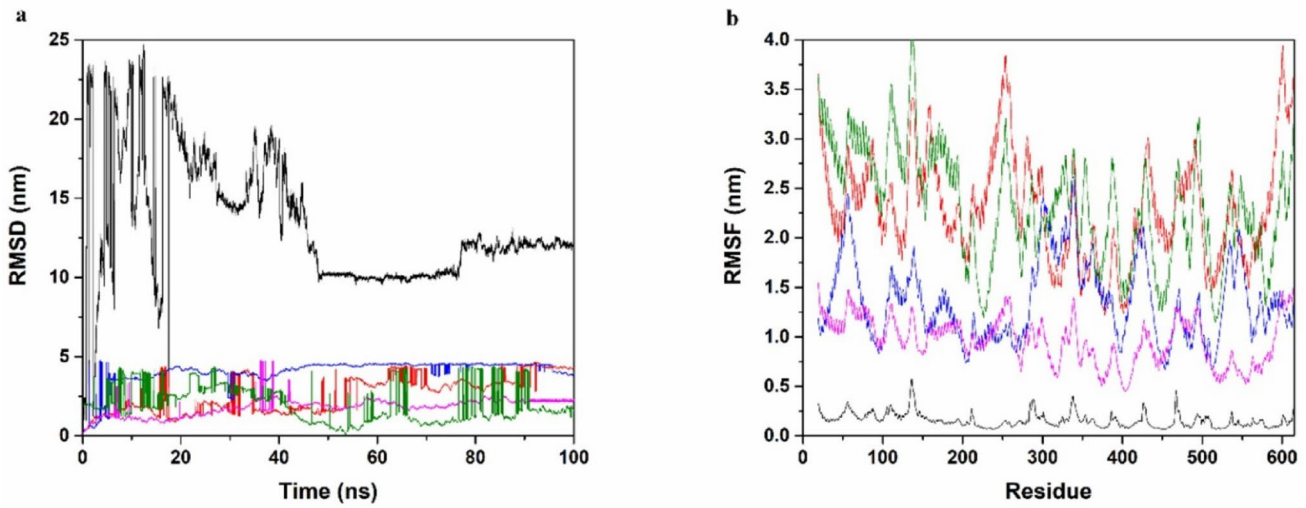


Fig. 7 MDS. **a** The Cα backbone RMSD at 300 K, **b** The last 20 ns RMSF value of Cα atoms. Color code in the panels: ACE2-2-DG (black), ACE2-RD9 (red), ACE2-RD12 (blue), ACE2-RD17 (magenta), and ACE2-RD18 (green)

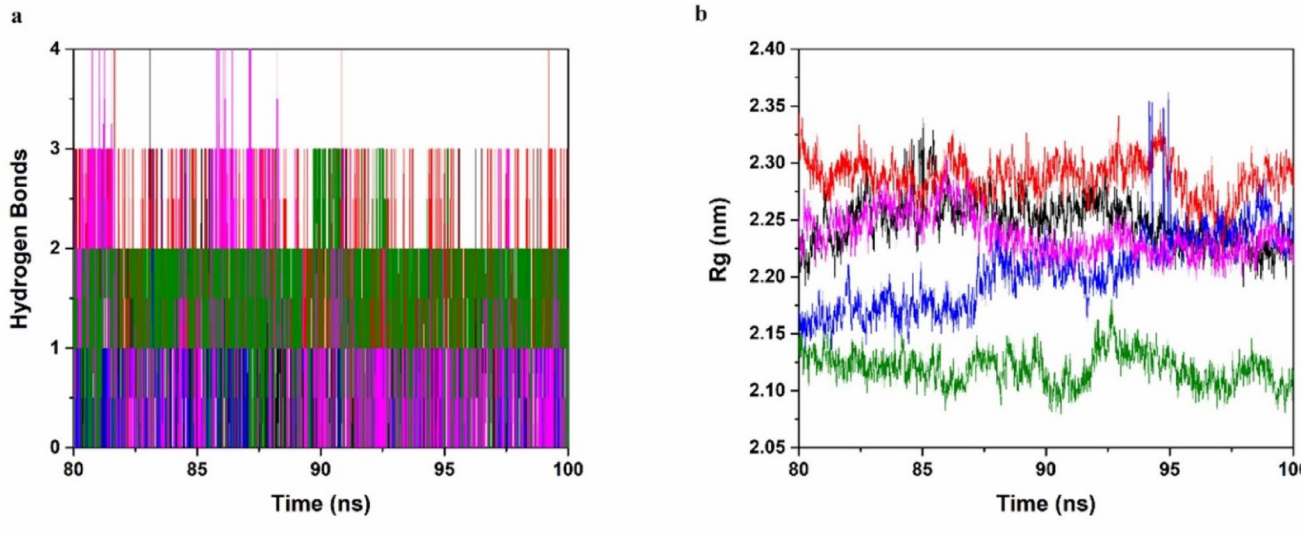


Fig. 8 MDS. **a** Number of H-bonds interaction among viral M^{pro} protein & each ligand changes over the course of the simulation. The x-axis represents the simulation time, while the y-axis shows the number of hydrogen bonds formed between M^{pro} and the ligand. **b** The plot shows the change in the Rg over time for 2-DG, RD9, RD12, RD17 and RD18 during the molecular dynamics simulation. The x-axis represents the time of the simulation, and the y-axis shows the Rg value for each of the M^{pro}-ligand complexes. Color code in all panels is: M^{pro}-2-DG (black), M^{pro}- RD9 (red), M^{pro}-RD12 (blue), M^{pro}- RD17 (magenta), M^{pro}-RD18 (green)

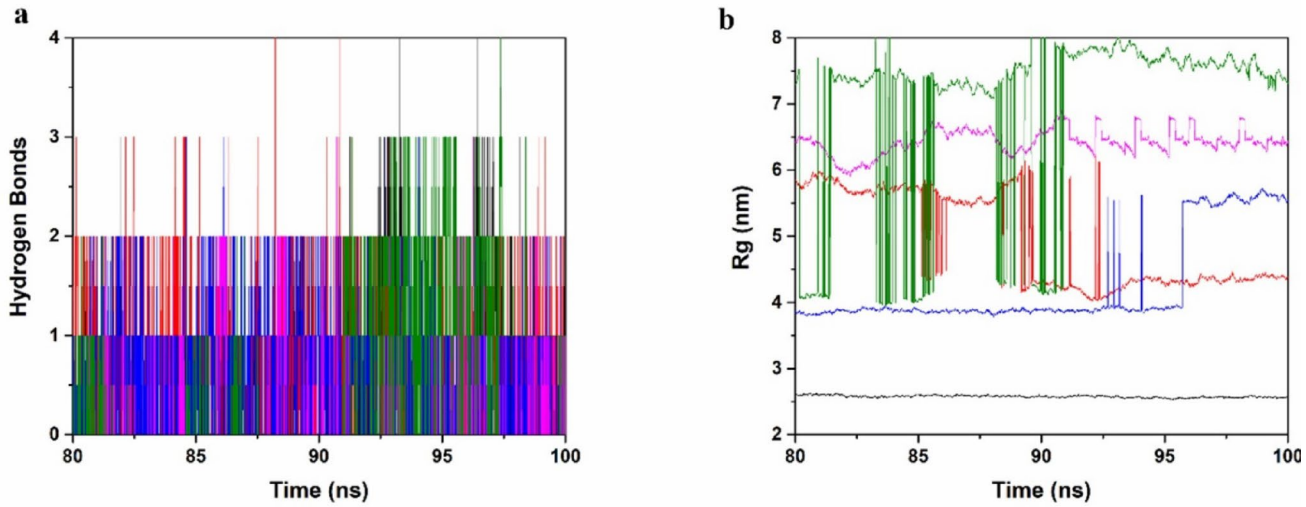


Fig. 9 MDS. **a** Number of H-bonds interaction among ACE2 protein & lead molecules inside the simulation time frame, **b** Rg vs time for 2-DG, RD9, RD12, RD17 and RD18 during MDS. Color code in all panels is: ACE2-2-DG (black), ACE2-RD9 (red), ACE2-RD12 (blue), ACE2-RD17 (magenta), ACE2-RD18 (green)

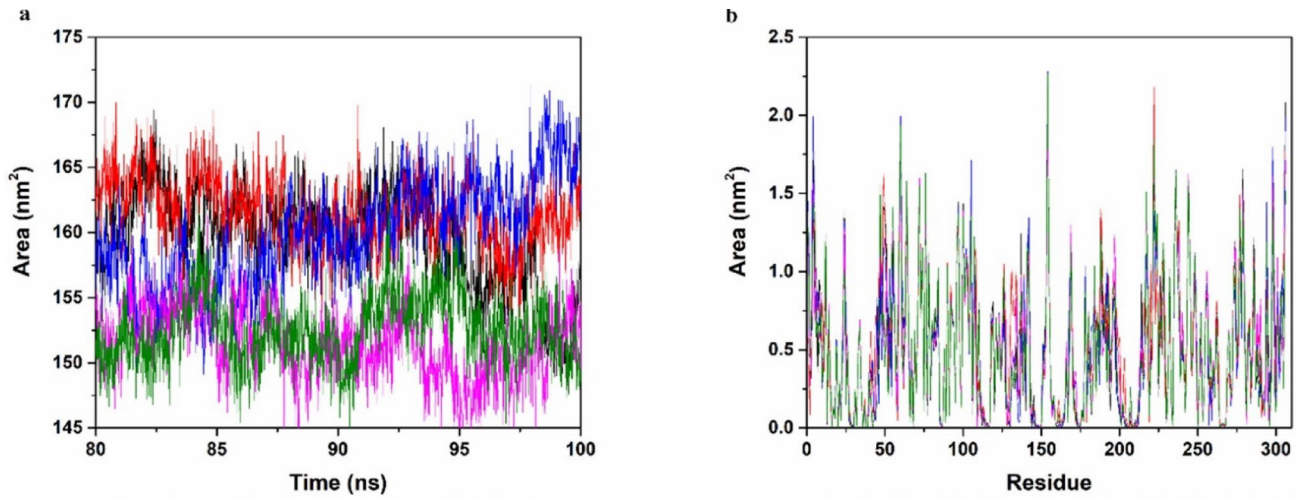


Fig. 10 MDS. **a** SASA quantifying the exposure of a molecule's surface to the solvent, it's calculated for the M^{pro}-ligand complex over the course of the simulation. The SASA graph for 2-DG, RD9, RD12, RD17 and RD18 complex with M^{pro} protein in water vs time has been plotted, **b** The residue SASA value graph for 2-DG, RD9, RD12, RD17and RD18 complex with M^{pro} protein. SASA values for specific residues within the M^{pro} protein when complexed with each ligand, providing detailed insight into how each residue's exposure to solvent changes during the simulation. Color code in all panels is: M^{pro}-2-DG (black), M^{pro}-RD9 (red), M^{pro}-RD12 (blue), M^{pro}-RD17 (magenta), M^{pro}-RD18 (green)

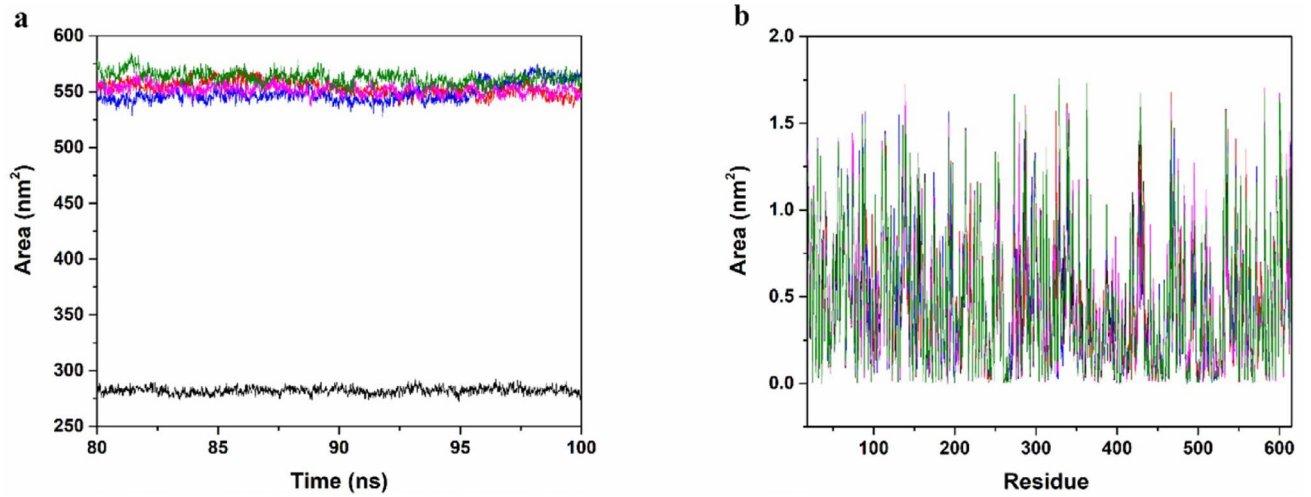


Fig. 11 SASA. **a** The SASA graph for 2-DG, RD9, RD12, RD17and RD18 complex with ACE2 protein in water *vs* time, **b** The residue SASA value graph for 2-DG, RD9, RD12, RD17and RD18 complex with ACE2 protein. Color code in all panels is: ACE2-2-DG (black), ACE2-RD9 (red), ACE2-RD12 (blue), ACE2-RD17 (magenta), ACE2- RD18 (green)

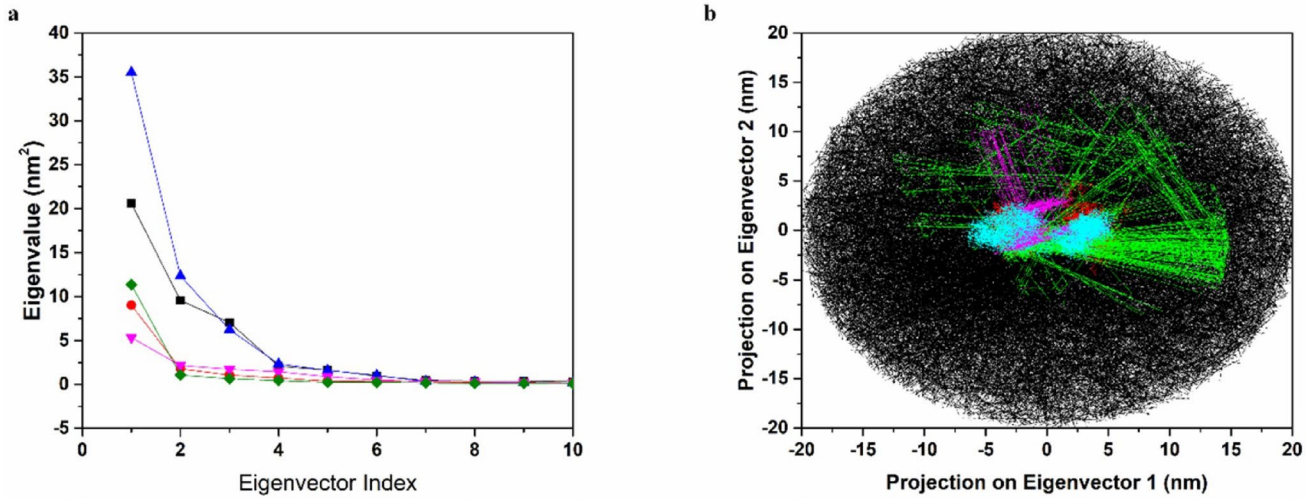


Fig. 12 PCA. **a** The graph of eigenvalues vs. eigenvector index. The color-coded curves represent different ligand-bound complexes (2-DG, RD9, RD12, RD17, RD18), allowing to compare how different ligands influence the principal components of protein motion. **b** Projection of the protein motion in phase space along the PC1 and PC2. This panel visualizes the protein's conformational dynamics along the first two principal components. The spread or clustering of points in the PC1-PC2 space gives insights into how different ligands affect the overall structural flexibility of the protein. Color code in all panels is: M^{pro}-2-DG (black), M^{pro}-RD9 (red), M^{pro}-RD12 (blue), M^{pro}-RD17 (magenta), M^{pro}-RD18 (green)

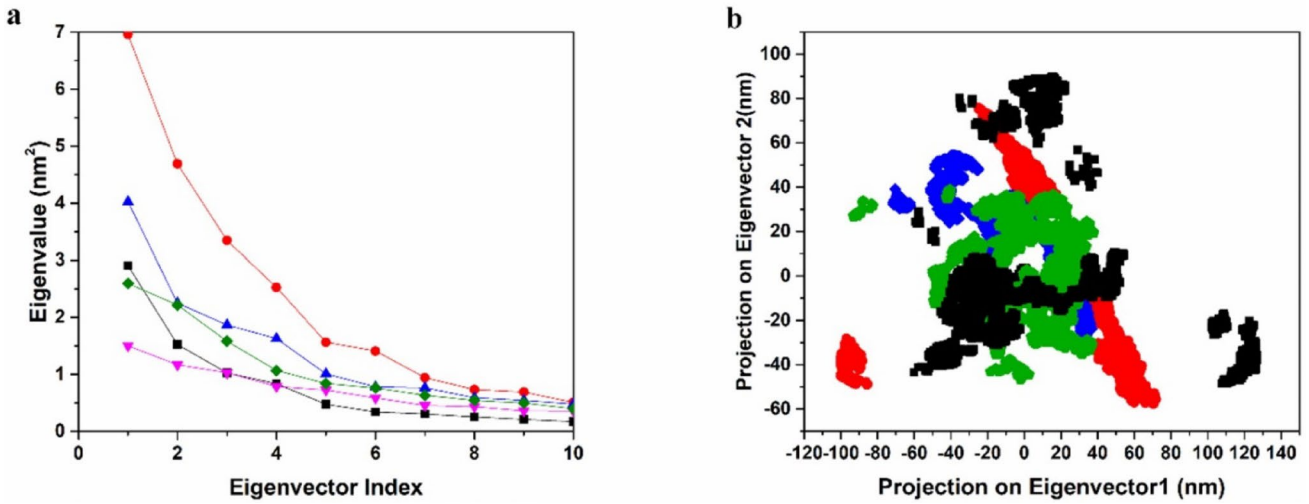


Fig. 13 PCA: **a** The graph of eigenvalues *vs.* eigenvector index. **b** Projection of the protein motion in phase space along the PC1 and PC2. Color code in all panels is: ACE2-2-DG (black), ACE2- RD9 (red), ACE2- RD12 (blue), ACE2-RD17 (magenta), ACE2-RD18 (green)

Table 3 Table showing Van der Waals, electrostatic, polar solvation, SASA, and binding energies of the lead molecules and 2-DG drug molecule against M^{pro} enzyme in kJ/mol

S. no.	Ligand	Van der Waals energy	Electrostatic energy	Polar solvation energy	SASA energy	Binding energy
1.	2-DG	-76.397 ± 9.375	-8.047 ± 6.759	37.623 ± 9.893	-56.979 ± 9.722	-56.97 ± 9.72
2.	RD9	-233.348 ± 75.06	-17.79 ± 7.99	89.02 ± 25.82	-18.90 ± 6.03	-171.02 ± 64.91
3.	RD12	-224.79 ± 58.30	-19.79 ± 10.86	99.16 ± 29.97	-19.90 ± 5.11	-165.32 ± 48.92
4.	RD17	-194.60 ± 15.03	-24.85 ± 12.96	103.26 ± 19.05	-16.80 ± 1.30	-133.01 ± 20.34
5.	RD18	-264.97 ± 13.36	-40.65 ± 8.62	164.83 ± 18.11	-20.57 ± 0.84	-161.35 ± 17.07

Table 4 Table showing van der Waals, electrostatic, polar solvation, SASA, and binding energies of the lead molecules and 2-DG drug molecule against ACE2 enzyme in kJ/mol

S. no.	Ligand	Van der Waals energy	Electrostatic energy	Polar solvation energy	SASA energy	Binding energy
1.	2-DG	-53.026 ± 10.203	-11.818 ± -9.694	43.708 ± 16.564	-7.645 ± 1.335	-28.781 ± 14.714
2.	RD9	-0.642 ± 10.460	4.447 ± 2.690	-37.098 ± 156.728	-0.392 ± 6.984	-33.685 ± 157.222
3.	RD12	-198.065 ± 91.894	-40.392 ± 20.069	141.454 ± 54.176	-18.271 ± 9.368	-115.275 ± 92.500
4.	RD17	-170.981 ± 11.557	-36.238 ± 9.138	58.081 ± 16.777	-17.169 ± 0.977	-166.307 ± 17.224
5.	RD18	-227.217 ± 9.349	-15.842 ± 4.645	62.201 ± 9.338	-18.006 ± 0.838	-198.864 ± 11.512

several key components, including the nonpolar and polar solvation energies, van der Waals interactions, electrostatic interactions, and the internal energy of the system. This indicates the stability of complex formation with conjugates in comparison to the 2-DG molecule.

Conclusion

In this article, molecular docking studies of phenylthiazole-coumarin conjugates and benzothiazole-triazole conjugates, targeting the ACE2 enzyme and main protease enzyme M^{pro} of SARS-CoV-2, which serves as the entry point and progression for the virus into human have been performed. The docking studies revealed that all 21 molecules have greater binding affinity with M^{pro} and ACE2 enzymes having binding energy ranging from -7.84 to -9.87 kcal/mol. In addition to this, all screened molecules were further compared against the standard drug 2DG (2-Deoxy-D-glucose) which was used during the pandemic. Among 21 lead molecules, RD9, RD12, RD17, and RD18 were the best-hit compounds, which can be used as dual inhibitors against M^{pro} and human ACE2 enzymes to effectively regulate COVID-19. Also, MDS for 2DG, RD9, RD12, RD17, and RD18 was carried out. Based on RMSD, RMSF, H-bonds, Rg, and SASA, principal component analysis parameters RD9, RD12, RD17, and RD18 showed excellent stability as compared with the 2DG drug. In addition, it is believed that the compounds belonging to coumarin, thiazole, and triazole moiety can also serve as potential candidates against SARS CoV-2 infection. The future scope of this work includes SAR studies by screening the different types of groups to enhance the activity of RD9, RD12, RD17, and RD18 against M^{pro} and ACE2 and perform the synthesis of active molecules. The result of these virtual screenings will be further validated by doing biological studies.

Acknowledgements The authors express their gratitude to Scfbio, IIT Delhi for granting access to Gaussian software for structural optimization and for supporting to conduct molecular dynamics simulation studies.

Author contributions Deepak Mishra: Conceptualization of work, methodology, data Curation, investigation of lead molecules, use of software, writing original Draft; Ram Singh: Conceptualization of work, supervision, methodology, investigation and identification of lead molecules, writing-review & editing of draft; Nupur Munjal: Methodology, use of software, writing molecular dynamics simulation part in original Draft; Naresh Kumar: Methodology, use of software; Prashant Kumar: Data Curation, writing-review & editing; Poonam: Investigation of lead molecules, data Curation; Sandeep Sharma: Writing-review & editing.

Data availability No datasets were generated or analysed during the current study.

Declarations

Conflict of interest The authors declare there are no conflicts of interest.

References

Abraham MJ, Murtola T, Schulz R, Páll S, Smith JC, Hess B, Lindahl E (2015) GROMACS: high performance molecular simulations through multi-level parallelism from laptops to supercomputers. SoftwareX 1–2:19–25

Anand K (2002) Structure of coronavirus main proteinase reveals combination of a chymotrypsin fold with an extra alpha-helical domain. EMBO J 21(13):3213–3224

Andersen HC (1980) Molecular dynamics simulations at constant pressure and/or temperature. J Chem Phys 72(4):2384–2393

Berendsen HJC, Postma JPM, Van Gunsteren WF, DiNola A, Haak JR (1984) Molecular dynamics with coupling to an external bath. J Chem Phys 81(8):3684–3690

Brian DA, Baric RS (2005) Coronavirus genome structure and replication, coronavirus replication and reverse genetics. Curr Top Microbiol Immunol 287:1–30

Britschgi M, Greyerz S, Burkhart C, Pichler W (2003) Molecular aspects of drug recognition by specific T cells. Curr Drug Targets 4(1):1–11

Bzówka M, Mitusińska K, Raczyńska A, Samol A, Tuszyński JA, Góra A (2020) Structural and evolutionary analysis indicate that the SARS-COV-2 MPRO is a challenging target for Small-Molecule inhibitor design. Int J Mol Sci 21(9):3099

Carabelli AM, Peacock TP, Thorne LG, Harvey WT, Hughes J (2023) SARS-CoV-2 variant biology: immune escape, transmission and fitness. Nat Rev Microbiol 21:162–177

Chan JFW, To KKW, Tse H, Jin DY, Yuen KY (2013) Interspecies transmission and emergence of novel viruses: lessons from bats and birds. Trends Microbiol 21:544–555

Chan JF, Lau SK, To KK, Cheng VC, Woo PC, Yuen KY (2015) Middle East respiratory syndrome coronavirus: another zoonotic betacoronavirus causing SARS-like disease. Clin Microbiol Rev 28:465–522

Chen Y, Liu Q, Guo D (2020) Emerging coronaviruses: genome structure, replication, and pathogenesis. J Med Virol 92:418–423

Chen T, Shu X, Zhou H et al (2023) Algorithm selection for protein–ligand docking: strategies and analysis on ACE. Sci Rep 13:8219
Cong Y, Ren X (2014) Coronavirus entry and release in polarized epithelial cells: a review. Rev Med Virol 24:308–315
De Souza MVN, De Almeida MV (2003) Drugs anti-HIV: past, present and future perspectives. Quim Nova 26(3):366–372
De Almeida Barros TA et al (2010) Antinociceptive and anti-inflammatory properties of 7-hydroxycoumarin in experimental animal models: potential therapeutic for the control of inflammatory chronic pain. J Pharm Pharmacol 62(2):205–213
Donoghue M, Hsieh F, Baronas E, Godbout K, Gosselin M, Stagliano N, Donovan M, Woolf B, Robison K, Jeyaseelan R, Breitbart RE, Acton S (2000) A novel angiotensin-converting enzyme-related carboxypeptidase (ACE2) converts angiotensin I to angiotensin 1–9. Circ Res 87(5):E1-9
Eid RA, Elgendy MO, El-Gendy AO, Elgendy SO, Belbahri L, Sayed AM, Rateb ME (2021) Efficacy of ceftazidime and cefepime in the management of covid-19 patients: single center report from Egypt. Antibiotics 10(11):1278
Ettahiri W, Adardour M, Alaoui S, Allah AEA, Aichouch M, Salim R, Ramli Y, Bouyahya A, Taleb M (2024) Recent advance in the development of N-heterocyclic derivatives as anti-SARS-CoV-2 inhibitors: a review. Phytochem Lett 61:247–269
Fadlallah S, Julià C, García-Vallvé S, Pujadas G, Serratosa F (2023) Drug potency prediction of SARS-CoV-2 main protease inhibitors based on a graph generative model. Int J Mol Sci 24:8779
Fehr AR, Perlman S (2015) Coronaviruses: an overview of their replication and pathogenesis. Methods Mol Biol 1282:1–23
Frish MJ (2009) Gaussian 09 (Reversion B. 01), Gaussian. Inc. Pittsburgh
Geedkar D, Kumar A, Sharma P (2024) Synthesis and in silico inhibitory action studies of azo-anchored imidazo[4,5-b]indole scaffolds against the COVID-19 main protease (M^{pro}). Sci Rep 14(1):10419
Ghosh S, Keretsu S, Cho SJ (2021) Molecular Modeling studies of N-phenylpyrimidine-4-amine derivatives for inhibiting FMS-like tyrosine kinase-3. Int J Mol Sci 22(22):12511
Goodsell DS, Morris GM, Olson AJ (1996) Automated docking of flexible ligands: applications of AutoDock. J Mol Recognit 9:1–5
Hashem HE, Ahmad S, Kumer A, Bakri YE (2024) In silico and in vitro prediction of new synthesized N-heterocyclic compounds as anti-SARS-CoV-2. Sci Rep 14:1152
Hoffmann M, Kleine-Weber H, Schroeder S, Krüger N, Herrler T, Erichsen S, Schiergens TS, Herrler G, Wu NH, Nitsche A, Müller MA (2020) SARS-CoV-2 cell entry depends on ACE2 and TMPRSS2 and is blocked by a clinically proven protease inhibitor. Cell 181:271–280
https://data.who.int/dashboards/covid19/cases (Acessed 10 August 2024)
Huang XY, Shan ZJ, Zhai HL, Su L, Zhang XY (2011) Study on the anticancer activity of coumarin derivatives by molecular modeling. Chem Biol Drug des 78(4):651–658
Humphrey W, Dalke A, Schulten K (1996) VMD: Visual molecular dynamics. J Mol Graphics Mod 14(1):33–38
Jayabal K, Elumalai D, Leelakrishnan S, Bhattacharya S, Rengarajan V, Kannan T, Chuang S-C (2022) Green and regioselective approach for the synthesis of 3-substituted indole based 1,2-dihydropyridine and azaxanthone derivatives as a potential lead for SARS-CoV-2 and delta plus mutant virus: DFT and docking studie. ACS Omega 48:43856–43876
Jin Z, Du X, Xu Y, Deng Y, Liu M, Zhao Y, Zhang B, Li X, Zhang L, Peng C, Duan Y, Yu J, Wang L, Yang K, Liu F, Jiang R, Yang X, You T, Liu X, Yang H (2020a) Structure of M^{pro} from SARSCoV-2 and discovery of its inhibitors. Nature 582:289–293
Jin Z, Du X, Xu Y, Deng Y, Liu M, Zhao Y, Zhang B, Li X, Zhang L, Peng C, Duan Y, Yu J, Wang L, Yang K, Liu F, Jiang R, Yang X, You T, Liu X, Yang X, Bai F, Liu H, Liu X, Guddat LW, Xu W, Xiao G, Qin C, Shi Z, Jiang H, Rao Z, Yang H (2020b) Structure of M^{pro} from SARS-CoV-2 and discovery of its inhibitors. Nature 582(7811):289–293
Jones T, Monakhova N, Guivel-Benhassine F, Lepioshkin A, Bruel T, Lane TR, Schwartz O, Puhl AC, Makarov V, Ekin S (2023) Synthesis and evaluation of 9-aminoacridines with SARS-CoV-2 antiviral activity. ACS Omega 43:40817–40822
Kang N, Heo S-Y, Cha S-H, Ahn G, Heo S-J (2022) In silico virtual screening of marine aldehyde derivatives from seaweeds against SARS-CoV-2. Mar Drugs 20(6):399
Kattula B, Reddi B, Jangam A, Naik L, Adimoolam BM, Vavilapalli S, Are S, Thota JR, Jadav SS, Arifuddin M, Addlagatta A (2023) Development of 2-chloroquinoline based heterocyclic frameworks as dual inhibitors of SARS-CoV-2 M^{Pro} and PL^{Pro}. Int J Biol Macromol 242:124772
Kharb R, Sharma PC, Yar MS (2010) Pharmacological significance of triazole scaffold. J Enzyme Inhib Med Chem 26(1):1–21
Knadler MP, Bergstrom RF, Callaghan J, Rubin A (1986) Nizatidine, an H2-blocker. Its metabolism and disposition in man. Drug Metab Dispos 14(2):175–182
Kostova I, Bhatia S, Grigorov P, Balkansky S, Parmar VS, Prasad AK, Saso L (2011) Coumarins as antioxidants. Curr Med Chem 18(25):3929–3951
Kumari R, Kumar R, Lynn A (2014) g_mmpbsa-A GROMACS tool for high-throughput MM-PBSA calculations. J Chem Inf Model 54(7):1951–1962
Kwiecień RA, Rostkowski M, Dybała-Defratyka A, Paneth P (2004) Validation of semiempirical methods for modeling of corrinoid systems. J Inorg Biochem 98(6):1078–1086
Lee S-J, Lee U-S, Kim W-J, Moon S-K (2011) Inhibitory effect of esculetin on migration, invasion and matrix metalloproteinase-9 expression in TNF-α-induced vascular smooth muscle cells. Mol Med Rep 4(2):337–341
Lever J, Krzywinski M, Altman N (2017) Principal component analysis. Nat Methods 14(7):641–642
Liu YC, Kuo RL, Shih SR (2020a) COVID-19: The first documented coronavirus pandemic in history. Biomed J 43:328–333
Liu T, Luo S, Libby P, Shi GP (2020b) Cathepsin L-selective inhibitors: a potentially promising treatment for COVID-19 patients. Pharmacol Ther 213:107587
Mishra D, Fatima A, Singh R, Munjal NS, Mehta V, Malairaman U (2019) Design, synthesis, and evaluation of Coumarin-Phenyl thiazole conjugates as cholinesterase inhibitors. Chem Biol Lett 6(2):23–30
Mishra D, Maurya RR, Kumar K, Munjal NS, Bahadur V, Sharma S, Singh P, Bahadur I (2021) Structurally modified compounds of hydroxychloroquine, remdesivir and tetrahydrocannabinol against main protease of SARS-CoV-2, a possible hope for COVID-19: docking and molecular dynamics simulation studies. J Mol Liq 335:116185
Mishra D, Fatima A, Kumar P, Munjal NS, Singh BK, Singh R (2022) Synthesis of benzothiazole linked triazole conjugates and their evaluation against cholinesterase enzymes. ChemistrySelect 7(46):e202203060. https://doi.org/10.1002/slct.202203060
Mittal L, Kumari A, Srivastava M, Singh M, Asthana S (2020) Identification of potential molecules against COVID-19 main protease through structure-guided virtual screening approach. J Biomol Struct Dyn 39(10):3662–3680
Naqvi AAT, Fatima K, Mohammad T, Fatima U, Singh IK, Singh A, Atif SM, Hariprasad G, Hasan GM, Hassan MI (2020) Insights into SARS-CoV-2 genome, structure, evolution, pathogenesis and therapies: Structural genomics approach. Biochim Biophys Acta Mol Basis Dis 1866:165878

Nazir M, Ahmad M, Aslam S, Rafiq A, Al-Hussain S, Zaki M (2024) A comprehensive update of anti-COVID-19 activity of heterocyclic compounds. Drug des Devel Ther 18:1547–1571

Ni W, Yang X, Yang D, Bao J, Li R, Xiao Y, Hou C, Wang H, Liu J, Yang D, Xu Y, Cao Z, Gao Z (2020) Role of angiotensin-converting enzyme 2 (ACE2) in COVID-19. Crit Care 24(1):422

Papaj K, Spychalska P, Hopko K, Kapica P, Fisher A, Lill MA, Bagrowska W, Nowak J, Szleper K, Smieško M, Kasprzycka A, Góra A (2021) Investigation of Thiocarbamates as potential inhibitors of the SARS-CoV-2 M^{pro}. Pharmaceuticals 14(11):1153

Perlman S, Netland J (2009) Coronaviruses post-SARS: update on replication and pathogenesis. Nat Rev Microbiol 7:439–450

Petersen HG (1995) Accuracy and efficiency of the particle mesh Ewald method. J Chem Phys 103(9):3668–3679

Pettersen EF, Goddard TD, Huang CC, Couch GS, Greenblatt DM, Meng EC, Ferrin TE (2004) UCSF Chimera—a visualization system for exploratory research and analysis. J Comput Chem 25(13):1605–1612

Pirolli D, Righino B, Camponeschi C et al (2023) Virtual screening and molecular dynamics simulations provide insight into repurposing drugs against SARS-CoV-2 variants Spike protein/ACE2 interface. Sci Rep 13:1494

Prabakaran P, Xiao X, Dimitrov DS (2003) A model of the ACE2 structure and function as a SARS-CoV receptor. Biochem Biophys Res Commun 314(1):235–241

Qiu Y, Zhao Y-B, Wang Q, Li J-Y, Zhou Z-J, Liao C-H, Ge X-Y (2020) Predicting the angiotensin converting enzyme 2 (ACE2) utilizing capability as the receptor of SARS-CoV-2. Microbes Infect 22(4–5):221–225

Richman DD, Whitley RJ, Hayden FG (2016) Clinical Virology, 4th edn. ASM Press, Washington

Sahu KK, Kumar R (2021) Role of 2-Deoxy-D-Glucose (2-DG) in COVID-19 disease. J Family Med Prim Care 10(10):3548–3552

Santos RAS, Sampaio WO, Alzamora AC, Motta-Santos D, Alenina N, Bader M, Campagnole-Santos MJ (2018) The ace2/angiotensin-(1–7)/mas axis of the renin-angiotensin system: focus on angiotensin-(1–7). Physiol Rev 98(1):505–553

Schmid N, Eichenberger AP, Choutko A, Riniker S, Winger M, Mark AE, Van Gunsteren WF (2011) Definition and testing of the GROMOS force-field versions 54A7 and 54B7. Eur Biophys J 40(7):843–856

Schüttelkopf AW, Van Aalten DMF (2004) PRODRG: a tool for high-throughput crystallography of protein–ligand complexes. Acta Crystallogr D Biol Crystallogr 60(8):1355–1363

Shang J, Ye G, Shi K, Wan Y, Luo C, Aihara H, Geng Q, Auerbach A, Li F (2020) Structural basis of receptor recognition by SARS-CoV-2. Nature 581(7807):221–224

Sharma A, Tiwari V, Sowdhamini R (2020) Computational search for potential COVID-19 drugs from FDA-approved drugs and small molecules of natural origin identifies several anti-virals and plant products. J Biosci 45:100. https://doi.org/10.1007/s12038-020-00069-8

Shirbhate E, Pandey J, Patel VK, Kamal M, Jawaid T, Gorain B, Kesharwani P, Rajak H (2021) Understanding the role of ACE-2 receptor in pathogenesis of COVID-19 disease: a potential approach for therapeutic intervention. Pharmacol Rep 73:1539–1550

Shivanika C, Kumar D, Ragunathan V, Tiwari P, Sumitha A (2022) Molecular docking, validation, dynamics simulations, and pharmacokinetic prediction of natural compounds against the SARS-CoV-2 main-protease. J Biomol Struct Dyn 40(2):585–611

Tabti C, Benhalima N (2015) Molecular structure, vibrational assignments and non-linear optical properties of 4,4' dimethylamino-cyanobiphenyl (DMACB) by and ab initio HF calculations. Adv Mater Phys Chem 05(07):221–228

Tang Q, Song Y, Shi M, Cheng Y, Zhang W, Xia XQ (2015) Inferring the hosts of coronavirus using dual statistical models based on nucleotide composition. Sci Rep 5:17155

Tehranchian S, Akbarzadeh T, Fazeli MR, Jamalifar H, Shafiee A (2005) Synthesis and antibacterial activity of 1-[1,2,4-triazol-3-yl] and 1-[1,3,4-thiadiazol-2-yl]-3-methylthio-6,7-dihydrobenzo[c] thiophen-4(5H)ones. Bioorg Med Chem Lett 15(4):1023–1025

Tian W, Chen C, Lei X, Zhao J, Liang J (2018) CASTp 3.0: computed atlas of surface topography of proteins. Nucl Acids Res 46(W1):W363–W367

Uhomoibhi JO, Idowu KA, Shode FO, Sabiu S (2022) Molecular modeling identification of potential drug candidates from selected African plants against SARS-CoV-2 key druggable proteins. Sci Afr. https://doi.org/10.1016/j.sciaf.2022.e01279

Van Der Spoel D, Lindahl E, Hess B, Groenhof G, Mark AE, Berendsen HJC (2005) GROMACS: fast, flexible, and free. J Comp Chem 26(16):1701–1718

Van Gunsteren WF, Berendsen HJC (1988) A leap-frog algorithm for stochastic dynamics. J Mol Simul 1(3):173–185

Vasconcelos JF, Teixeira MM, Barbosa-Filho JM, Agra MF, Nunes XP, Giulietti AM, Ribeiro-Dos-Santos R, Soares MBP (2009) Effects of umbelliferone in a murine model of allergic airway inflammation. Eur J Pharmacol 609(1–3):126–131

Wang F, Chen C, Tan W, Yang K, Yang H (2016) Structure of main protease from human coronavirus NL63: insights for wide spectrum anti-coronavirus drug design. Sci Rep 6(1):22677

Wu A, Peng Y, Huang B, Ding X, Wang X, Niu P, Meng J, Zhu Z, Zhang Z, Wang J, Sheng J (2020) Genome composition and divergence of the novel coronavirus (2019-nCoV) originating in China. Cell Host Microbe 27:325–328

Xue X, Yu H, Yang H, Xue F, Wu Z, Shen W, Li J, Zhou Z, Ding Y, Zhao Q, Zhang X-C, Liao M, Bartlam M, Rao Z (2008) Structures of two coronavirus main proteases: implications for substrate binding and antiviral drug design. J Virol 82:2515–2527

Yang H, Yang J (2021) A review of the latest research on M pro targeting SARS-COV inhibitors. RSC Med Chem 12:1026–1036

Zerroug A, Belaidi S, BenBrahim I, Sinha L, Chtita S (2019) Virtual screening in drug-likeness and structure/activity relationship of pyridazine derivatives as Anti-Alzheimer drugs. J King Saud Univ Sci 31:595–601

Zhang D, Li J, Wang F, Hu J, Wang S, Sun Y (2014) 2-Deoxy-D-glucose targeting of glucose metabolism in cancer cells as a potential therapy. Cancer Lett 355(2):176–183

Zhang Q, Xiang R, Huo S, Zhou Y, Jiang S, Wang Q, Yu F (2021) Molecular mechanism of interaction between SARS-CoV-2 and host cells and interventional therapy. Sig Transduct Target Ther 6:233

Zhou Y, Hou Y, Shen J, Huang Y, Martin W, Cheng F (2020) Network-based drug repurposing for novel coronavirus 2019-nCoV/SARS-CoV-2. Cell Discov 6:1–18

Publisher's Note Springer Nature remains neutral with regard to jurisdictional claims in published maps and institutional affiliations.

Springer Nature or its licensor (e.g. a society or other partner) holds exclusive rights to this article under a publishing agreement with the author(s) or other rightsholder(s); author self-archiving of the accepted manuscript version of this article is solely governed by the terms of such publishing agreement and applicable law.

Water Resources Management
https://doi.org/10.1007/s11269-025-04250-2

MoSWIN: Monkey Search Optimization and SWIN-based Flood Classification Architecture

Vinay Dubey[1] · **Rahul Katarya**[1]

Received: 24 February 2025 / Accepted: 15 May 2025
© The Author(s), under exclusive licence to Springer Nature B.V. 2025

Abstract

Floods pose significant threats to both human life and infrastructure, necessitating timely and accurate monitoring for effective disaster management. Advancements in computer vision and machine learning have enabled the development of sophisticated systems for flood classification using imagery. In this study, we introduce MoSWIN, a novel framework that integrates Monkey Search Optimization (MSO) with the Swin Transformer to enhance the accuracy and robustness of flood classification models. The Swin Transformer, with its hierarchical architecture and shifted window mechanism, excels at capturing both local and global features in flood-related imagery. MSO is employed to extract high-level features from input images, facilitating improved feature engineering. Subsequently, the Swin Transformer performs classification tasks on the features extracted through MSO. Our proposed MoSWIN model outperforms several existing state-of-the-art approaches, achieving an accuracy of 96.53%. This indicates a significant improvement in image classification and optimization performance, leading to more effective flood detection. Experimental results demonstrate that MoSWIN can accurately distinguish between flooded and non-flooded areas, surpassing the performance of conventional methods.

Keywords Convolutional neural network · Flood detection · Image segmentation · Monkey search optimization · Resnet-18 · SWIN transformer

Abbreviations

CNN	Convolutional Neural Network
CV	Computer Vision
DAM-Net	Differential Attention Metric-Based Network
DCNN	Deep Convolutional Neural Network
DNN	Deep Neural Network
DL	Deep Learning

✉ Rahul Katarya
rahuldtu@gmail.com

Vinay Dubey
vinaydubeyamit@gmail.com

[1] Department of Computer Science & Engineering, Delhi Technological University, Delhi, India

Published online: 13 June 2025

EM	Expectation-Maximization
GEE	Google Earth Engine
GMM	Gaussian Mixture Model
KI	Kittler And Illingworth
ML	Machine Learning
MLP	Multi-Layer Perceptron
MODIS	Moderate Resolution Imaging Spectroradiometer
MRF	Markov Random Fields
MSO	Monkey Search Optimization
Mo-SWIN	Monkey Search Optimization With Swin
PCA	Principal Component Analysis
SA	Simulated Annealing
SAR	Synthetic Aperture Radar
SVM	Support Vector Machine
SWIN	Shifted Window Transformer
SUMM	Storm Water Management Model
ViT	Vision Transformers
VQA	Visual Question Answering

1 Introduction

Floods represent one of the most devastating natural disasters globally, inflicting widespread destruction on infrastructure, ecosystems, and human lives (Bhatt et al. 2016; Westra et al. 2014). Accurate and timely identification of flood-affected areas is paramount for effective disaster response and management, particularly in regions vulnerable to recurring inundation (Bhatt et al. 2016; Westra et al. 2014). Remote sensing data, encompassing satellite and aerial imagery, offers invaluable resources by providing high-resolution images that aid in flood detection. However, a significant hurdle in leveraging this data effectively is the precise classification or segmentation of flood-affected regions within these images, which is fundamental for accurate flood mapping and subsequent analysis (Tanim et al. 2022).

Research indicates that floods account for approximately 42% of all natural disasters, with their frequency and intensity often exacerbated by factors such as climate change, urbanization, and inadequate flood control infrastructure (Ives and Messerli 1981; Rimal et al. 2018). Despite advancements in conventional flood management strategies, including improved water resource management and flood storage systems, the critical need for a reliable, automated flood classification system persists to enable timely decision-making and efficient disaster response. The rapid and accurate classification of flooded areas from vast amounts of satellite imagery presents a growing challenge, complicated by the diverse nature of flood events (e.g., riverine, flash, urban) and the complex dynamics of flood progression (Munawar 2020; Kundzewicz et al. 2013; Tanguy et al. 2017).

Traditional flood detection techniques, such as manual image interpretation and basic thresholding or image processing methods, suffer from inherent limitations in terms of automation, scalability, and consistency, making them inadequate for rapid response during large-scale events (Tanim et al. 2022). The increasing availability of high-resolution satellite imagery demands more sophisticated and automated approaches. While deep learning methods,

particularly Convolutional Neural Networks (CNNs), have demonstrated considerable promise in various image classification tasks due to their capacity to learn hierarchical features directly from data (Zhuo and Han 2020; We are promoting multilateral network building for improving disaster risk reduction (DRR) capacity including enhancement of DRR-related personnel exchanges in Asia n.d.; Amankwah et al. 2022), applying them effectively to flood classification from remote sensing imagery faces specific challenges. These include the need for large, labeled datasets, difficulty in generalizing to diverse geographical locations and flood types, sensitivity to variations in image conditions (e.g., cloud cover, shadows), and the risk of overfitting, especially with complex models (Zhuo and Han 2020). Efficiently extracting the most relevant and robust features from complex satellite images that distinguish subtle differences between flooded and non-flooded areas remains a key challenge in improving model accuracy and generalization (Tanim et al. 2022). This research is motivated by the pressing need to overcome these limitations by developing a more robust, efficient, and automated flood classification model that can leverage advanced feature extraction and deep learning techniques to improve accuracy and reliability for real-world disaster management applications.

This research aims to address these challenges by introducing a novel flood classification model, termed MoSWIN (Monkey Search Optimization with SWIN Transformer), which integrates nature-inspired optimization techniques with advanced deep learning architecture. We propose a new feature extraction approach based on Monkey Search Optimization (MSO), a nature-inspired algorithm tailored to effectively identify and select relevant features from flood images. This approach is designed to improve model performance, enhance generalization capabilities, and mitigate the risk of overfitting (Watik and Jaelani 2019). The MoSWIN model then utilizes the SWIN Transformer architecture, recognized for its efficiency and effectiveness in processing image features across different scales through shifted windows, to process the extracted features and classify the flood-affected areas with potentially greater accuracy and efficiency compared to existing methods (Hernández et al. 2022).

This research presents several key contributions that significantly advance the field of flood classification using satellite imagery and deep learning techniques:

- **Novel Model Development (MoSWIN)**: A novel framework, MoSWIN, is introduced that integrates Monkey Search Optimization (MSO) and SWIN Transformer for the classification of flood-affected and non-flooded areas in satellite images. The proposed model uniquely combines nature-inspired optimization techniques with advanced deep learning architectures, specifically designed for remote sensing applications.
- **Optimized Feature Extraction with MSO**: A new nature-inspired Monkey Search Optimization (MSO) algorithm is proposed to enhance the feature extraction process. MSO efficiently identifies and selects high-level, discriminative features from satellite imagery, ensuring that the model captures the most relevant information for accurate flood classification. The MSO algorithm helps recover crucial features while eliminating noisy or redundant data, leading to a more effective representation of the image content.
- **Enhanced Model Performance and Robustness**: The application of the MSO algorithm in feature extraction significantly improves the model's generalization ability, reducing overfitting and enhancing classification accuracy. By using MSO-optimized features, MoSWIN performs robustly across both training and test datasets, ensuring the model's adaptability to new and unseen flood data. This ensures reliable performance in real-world scenarios where data variability is common.

- **Integration of SWIN Transformer Architecture**: The SWIN Transformer architecture is integrated into MoSWIN to effectively process the MSO-optimized features. SWIN's hierarchical attention mechanism allows it to capture fine-grained patterns and dependencies in satellite images. This integration leads to substantial improvements in classification accuracy by leveraging the Transformer's ability to model long-range dependencies in the image, resulting in a more precise flood classification.
- **Comprehensive Performance Benchmarking**: A thorough comparative analysis is conducted to evaluate the MoSWIN model against several established and state-of-the-art deep learning models, such as ResNet 18, Vision Transformer, and ResNet 50. The proposed MoSWIN model outperforms these models in key performance metrics, including accuracy, precision, and recall. This highlights MoSWIN's superior ability to classify flood-affected and non-flooded areas with minimal false positives and false negatives.

The remainder of this paper is structured as follows: Section 2 provides a comprehensive review of existing research on the segmentation and classification of aerial and satellite images. Section 3 presents an analysis of current state-of-the-art models used in remote sensing image analysis. The detailed methodology of our proposed MoSWIN model, including the MSO-based feature extraction and SWIN Transformer integration, is described in Section 4. Section 5 reports the experimental results and presents a quantitative performance analysis comparing MoSWIN with benchmark models. Finally, Section 6 concludes the study and discusses future research directions.

2 Related Work

This section reviews existing approaches for flood image classification and segmentation, highlighting its importance for disaster management (Zhou 2021). Historically, methods evolved from traditional image processing to advanced machine learning and deep learning techniques (Dubey and Katarya 2020). Prior work utilized diverse remote sensing data sources like MODIS, SAR, Sentinel-1, and UAV imagery (Anusha and Bharathi 2020; Karanjit et al. 2023). Various methods explored include unsupervised techniques (SOM, mean shift), classical ML (SVM, MLP), CNNs, DNNs for segmentation and prediction, transformer models (Vision Transformer, attention-based, SemT-Former), and specialized datasets (FloodNet, FloodIMG) (Islam et al. 2023; Jackson et al. 2023; Rahnemoonfar et al. 2021). These studies collectively demonstrate the ongoing need for more accurate, robust, and automated solutions to improve flood mapping and response capabilities. Table 1 summarizes some significant research articles. Traditional flood classification models such as ResNet and Vision Transformer (ViT) (Bansal and Tripathi 2024) exhibit notable limitations in practical flood detection tasks. CNN-based models like ResNet are effective in local feature extraction but lack the ability to model long-range dependencies critical for understanding large-scale flood patterns (Kim and Han 2020; Kim et al. 2022). Moreover, their reliance on fixed-size kernels and spatially constrained receptive fields often results in poor generalization to diverse geographic and environmental conditions. ViT, while capable of capturing global context, generally requires very large annotated datasets for effective training. This becomes a bottleneck in flood scenarios where labeled data is scarce and highly variable (Saleh et al. 2024a, b). Additionally, both models struggle to accurately differenti-

Table 1 A literature survey incorporating various flood classification techniques

Area	Author	Year	Aim	Dataset	Techniques	Results	Limitations	Performance Matrix	Outcome	Differences
Flood Assessment	Arvind et al. 2016	2016	Flood assessment using satellite images	Satellite images	Unsupervised techniques: Mean shift and self-organizing maps (SOM)	SOM performed better in the extraction of final regions	SOM might not scale effectively with large datasets	-	-	**Scalability**: ×
	Nghia et al. 2022	2022	Flood monitoring and mapping using the Google Earth engine in downstream provinces	Sentinel-1 SAR; Shape file of the study area; Highest water level	Decoding Sentinel-1 SAR data; flood mapping; inundated area calculation	Demonstrates GEE as a commendable platform for tracking floods	Google Earth Engine faces limitations like restricted data availability	-	-	**Data Availability**: ×
Dataset Collection	Rahnemoonjar et al. 2021	2021	Collected high-resolution aerial image datasets to understand post-flood scenes	FloodNet	Classification: InceptionNetV3, ResNet50, Xception; Segmentation: ENet, DeeplabV3 +, PSPNet; VQA: concatenation, point-wise calculation	Successfully completed image classification, segmentation, and VQA tasks	Objects with small shapes are challenging for detection	-	-	**Task Variety**: ✓
	Zhou 2022	2022	Development of flood season segmentation framework	Rainfall datasets	Fisher optimal partition technique; Ensemble approach; NPB-FOS	Different techniques result in different stage arrangements	Nonparametric bootstrap faces overfitting and complexity	-	-	**Overfitting Risk**: ×

Table 1 (continued)

Area	Author	Year	Aim	Dataset	Techniques	Results	Limitations	Performance Matrix	Outcome	Differences
Flood Detection	Islam et al. 2020	2020	Comparison of conventional machine learning algorithms for detecting flood	SPOT-5; Radar images	SVM, deep CNNs, multilayer perceptions, SSDAs	SSDA with 20 labeled images achieved better results (AUC=0.9173)	Needs validation on more datasets	-	-	**Validation**: ×
	Moharrami et al. 2021	2021	Monitoring severe floods in north Iran during spring 2019	Sentinel-1 SAR	Segmentation of flood and non-flood images using Otsu algorithms	Accuracy~90%	Needs to improve accuracy	-	-	**Accuracy**: ×
	Fernandes et al. 2022	2022	Robust river flood detection system	Primary data (real-time river data)	Semantic segmentation using DNN; CV to estimate water level	MAE=3.32 cm; adaptable to camera variations and lighting	Requires manual reference line drawing with an even surface	-	-	**Surface Dependency**: ×
	Bhuyan et al. 2022	2022	Mapping and characterization of flood exposure	Remote Sensing	RestUNet model to detect EaR footprints	Highest F1-score=76%	Local expert and high-quality data required for building occupancy	-	-	**Local Expert Need**: ×
	Tanim et al. 2022	2022	Comparison of ML algorithms for flood detection under dry and wet conditions	Sentinel-1 SAR	Maximum likelihood classifier, SVM, random forest; Otsu algorithm	Robust flood mapping solution through change detection	Generalization challenges, resulting in false negatives/positives	-	-	**Generalization**: ×

Table 1 (continued)

Area	Author	Year	Aim	Dataset	Techniques	Results	Limitations	Performance Matrix	Outcome	Differences
Additional Studies	Obunguta et al. 2025)	2025	Migration and water management optimization	Regional data from Karamoja-Turkana	Gravity model for migration, cost minimization model for dam management	Reduced water-induced migration and conflict risk	Regional specificity limits generalizability	Water cost, migrant flow, conflict risk index	Stationarity achieved faster with cost-effective water resource management	**Geographic Limitation**: ×
	Yilmaz et al. 2025)	2025	Water loss management optimization	Field data from three pilot water systems	ALO, MTBO, GWO algorithms	Optimized cost-effective management plans for water systems	Requires accurate, current data; limited applicability	Water loss percentages, ideal pressure, repair teams	Tailored optimal plans based on system status	**Data Dependency**: ×
	Poursaeid 2025)	2025	Ensemble ML for streamflow prediction	2,068 monthly Debi records	Ensemble ML, bias-weighting, linear programming	Improved streamflow prediction accuracy ($R^2 = 0.939$)	Limited data scope and baseline comparisons	R^2 for WEML and LPEML	Streamflow prediction improved with ensemble models	**Data Scope**: ×
	Tian et al. 2025)	2025	Soil property analysis with reclaimed water impact	Soils from grassland, shrubland, and woodland	Field sampling, soil property analysis, SQI evaluation	IRW improved nutrients but altered soil structure	Short duration, unassessed long-term ecological effects	Soil structure, hydraulic conductivity, nutrient levels	No major impact on overall soil quality	**Long-Term Impact**: ×

Table 1 (continued)

Area	Author	Year	Aim	Dataset	Techniques	Results	Limitations	Performance Matrix	Outcome	Differences
	Papathanasiou et al. 2025)	2025	Wind turbines, energy storage, and desalination simulation	Historical data from Mediterranean islands	HRES, wind turbines, energy storage, desalination	87% electrical demand satisfaction, 99.99% water coverage	Pumped hydro storage limitations, scalability issues	Energy/water demand satisfaction, cost of desalinated water	Cost-effective and reliable energy-water system	**Scalability**: ×
	Panagiotou et al. 2025)	2025	Hydrological modeling for flood susceptibility	Yermasoyia watershed, Cyprus	MCDA using AHP and Monte Carlo simulations	MC-AHP improved accuracy and reduced uncertainty	High computation, ignored uncertainties, and correlations	Classification accuracy, skewness, standard deviation	Improved flood risk prediction	**Computational Complexity**: ×
	Mahapatra and Jha 2025)	2025	Streamflow sustainability under future climate scenarios	Streamflow data and CMIP6 projections	Hydrological modeling and EFE-based streamflow analysis	Lower resilience in regulated reaches under future scenarios	Geographic limitation, no ecological data, simplified modeling	Violation ratio, violation frequency, reliability	Frequent violations in regulated reaches	**Geographic Limitation**: ×

ate flooded regions from visually similar features such as wet surfaces, (Wang et al. 2023) shadows, and dense vegetation, leading to increased false positives and reduced reliability in real-time disaster response.

Classifying flood images, particularly distinguishing flooded from non-flooded areas using remote sensing data, involves several critical challenges:

- **Limited Data Availability and Quality**: High-quality, accurately labeled flood imagery is scarce, especially across diverse geographies, environmental conditions, and flood types. This limits the development of robust, generalizable models.
- **Complex and Ambiguous Visual Features**: Static images often fail to capture the dynamic nature of floods. Visual ambiguity arises due to similar spectral properties between water and other features like shadows, wet roads, or dark vegetation, increasing the risk of misclassification.
- **Significant Class Imbalance**: Flooded regions usually cover a much smaller area than non-flooded ones, resulting in highly imbalanced datasets. This biases models toward the dominant class and reduces performance on the minority (flooded) class.
- **Algorithmic Limitations in Feature Distinction**: Even deep learning models can struggle to detect subtle spectral or textural variations that distinguish flooded areas, especially under data constraints.
- **Obstacles and Occlusion**: Buildings, vegetation, and terrain can obscure flooded zones, particularly in urban or forested areas, hindering accurate flood boundary detection.

The proposed MoSWIN (Modified Swin Transformer) model addresses these limitations through several architectural innovations. First, it introduces shifted window-based multi-head self-attention, allowing the model to efficiently capture both local and global contextual information while maintaining linear computational complexity with respect to image size. This is crucial for flood scenes, where spatial relationships often extend across large regions. Second, the model adopts a hierarchical representation learning mechanism, progressively merging image patches to form multi-scale features that improve its ability to detect both small and large flood zones. Third, MoSWIN is robust to spectral ambiguities due to its deeper attention-based feature encoding, allowing better differentiation between water bodies and non-water surfaces with similar visual properties. Finally, by preserving fine-grained spatial structures and supporting cross-window interactions, MoSWIN ensures higher recall and F1-score, making it more suitable for operational flood detection in varied real-world scenarios.

3 Preliminary

This section provides an overview of the state-of-the-art techniques used for flood image classification, which have been selected for their performance and precision. These methods were evaluated and compared to establish a robust basis for the classification process.

3.1 Monkey Search Optimization (MSO)

MSO is a recent metaheuristic optimization technique inspired by monkeys' food search behavior (Devi and Sathya 2017). It emphasizes exploration, resource allocation, local and

global search, and adaptation (Crawford et al. 2019). MSO is particularly effective in feature selection tasks, addressing the challenges faced by algorithms like PSO, GA, and DE in high-dimensional image datasets. MSO adapts its search strategy dynamically, balancing exploration and exploitation, making it ideal for flood image classification, where environmental factors such as scene dynamics and lighting conditions vary. The integration of MSO with the SWIN Transformer model (MoSWIN) provides a novel hybrid approach, improving feature extraction and ensuring optimal classification performance under complex flood scenarios.

While algorithms like Particle Swarm Optimization (PSO), Genetic Algorithm (GA), and Differential Evolution (DE) have shown success in feature selection, they often suffer from early convergence and poor exploitation in high-dimensional image datasets. In contrast, the proposed Monkey Search Optimization (MSO) algorithm exhibits adaptive behavior and dynamic self-organization, allowing it to balance exploration and exploitation more effectively. MSO's group-based search and feedback-driven refinement enable it to better isolate relevant flood features from noisy backgrounds, especially in real-time and evolving environments. This makes MSO particularly suitable for flood image classification, where scene dynamics and lighting conditions vary significantly. Unlike PSO and GA, MSO dynamically adjusts its search strategy in response to environmental feedback, leading to improved convergence to optimal feature subsets. The integration of MSO with the Swin Transformer, which excels in hierarchical visual representation, constitutes a novel hybrid architecture (MoSWIN) not previously explored in flood detection literature. Flood imagery features vary greatly in scale and texture due to environmental and geographical variability. MSO helps in selecting optimal weights and parameters in the model, allowing it to effectively distinguish between flooded and non-flooded areas. Its strong global search ability ensures that the model does not get stuck in local minima, leading to more accurate classification under complex flood scenarios.

3.2 Transformer Models

Transformers are deep learning architectures that have revolutionized sequence modeling, especially in NLP (Maurício et al. 2023). They use a self-attention mechanism to understand relationships within sequences. In the context of image data, several variants of Transformers have been applied, including Swin Transformerv (Li et al. 2023), Vision Transformer (ViT), and ResNet-18. Swin Transformer introduces a hierarchical structure for efficient image processing, leveraging shifted windows to capture both local and global features. ViT adapts the Transformer for direct image processing (Zuo et al. 2022; Ali et al. 2023), while ResNet-18 employs residual connections to address gradient vanishing and enhance training stability (He et al. 2016; Du et al. 2022), making it efficient for resource-constrained environments. Figure 1 illustrates the detailed layered architecture of ResNet-18, highlighting the use of skip connections, which facilitate residual learning and enhance the model's capacity to retain feature details.

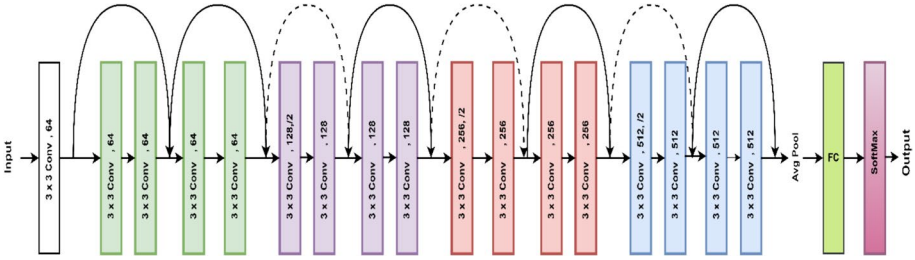


Fig. 1 Layered architecture of the ResNet-18 model, illustrating the sequence of convolutional, normalization, pooling, and fully connected layers, along with residual skip connections that facilitate efficient training and mitigate gradient vanishing problems

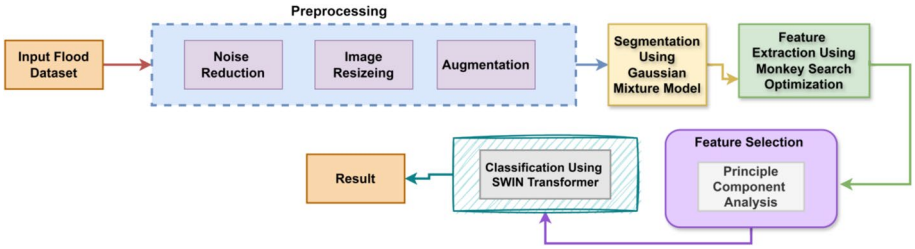


Fig. 2 Sequential components of our proposed Mo-SWIN architecture

4 Proposed SWIN Transformer and Nature-inspired Solution for Flood Image Classification

The current research on flood detection and prediction is mostly concerned with machine learning (ML) and deep learning (DL) techniques (Deepak and Sarath 2022). However, there is a significant gap in research into nature-inspired approaches to flood disaster management. These bio-inspired approaches, which draw inspiration from natural processes, can improve traditional flood management technologies. Embracing nature-inspired solutions is a promising opportunity to strengthen flood management capabilities. The proposed architecture consists of two modules: the Swin Transformer along with a nature-inspired solution. The primary idea behind this model is to improve the visual information used for flood image detection while striving for better performance.

Figure 2 illustrates the pipeline of the proposed MoSWIN model for flood image classification. The process begins with data collection, followed by preprocessing steps like denoising, resizing, and augmentation. Initial features are extracted using convolutional layers and optimized using the Monkey Search Optimization (MSO) algorithm, which selects the most discriminative features through iterative metaheuristic search. These optimized features are then input into the Swin Transformer, where non-overlapping windows and Shifted Window Multi-Head Self Attention (SW-MSA) capture both local and global contexts. Finally, hierarchical features are passed to a Multi-Layer Perceptron (MLP) for classification. This sequential flow enhances visual feature representation, improving flooded versus non-flooded image classification accuracy.

4.1 Preprocessing

In flood image analysis, feature extraction is a crucial step in identifying key characteristics from raw data, facilitating accurate classification. However, this process is often complicated by scaling issues, noise, and variability in the data. To address these challenges, we begin by resizing all images to a consistent size of 224×224 pixels. Initially, all images are 512 pixels wide, but resizing ensures uniformity across the dataset, reducing computational complexity and enabling efficient processing.

Additionally, we apply image augmentation techniques such as rotation, scaling, and flipping. These augmentations introduce variations into the dataset, enhancing the model's ability to generalize and perform better on unseen data.

4.2 Segmentation

Segmentation is a critical step in partitioning the image into smaller, meaningful regions that simplify feature extraction. In this study, we employ the Gaussian Mixture Model (GMM) for image segmentation. Each pixel in the image is assigned to the most probable Gaussian component, optimizing the model parameters iteratively using the Expectation–Maximization (EM) algorithm. The EM algorithm refines parameters, such as the number of Gaussian components and their distributions, to ensure accurate segmentation.

This segmentation process ensures that the model focuses on relevant image regions, thereby removing irrelevant background noise. The resulting segmented regions serve as the foundation for subsequent classification tasks, where only the most important areas are used for further analysis.

4.3 Dimensionality Reduction Using PCA

To reduce computational complexity and mitigate overfitting, we apply Principal Component Analysis (PCA) for dimensionality reduction. PCA transforms the high-dimensional data into a new set of orthogonal variables, called principal components, which retain the most significant variance in the dataset. By computing the covariance matrix, we identify correlations between features, then perform eigenvalue decomposition to extract the most informative components.

This technique reduces the feature space, improving the model's efficiency while maintaining essential information for flood classification. PCA effectively mitigates the curse of dimensionality and enhances computational performance without compromising classification accuracy.

4.4 Feature Extraction Using MSO

Feature extraction is a pivotal step for identifying the most relevant patterns in flood images. In this study, we utilize the Monkey Search Optimization (MSO) algorithm, a nature-inspired optimization technique that mimics the food-searching behavior of monkeys. MSO optimizes the feature selection process by identifying critical regions for flood classification while eliminating irrelevant background areas.

MSO operates by iteratively searching for optimal solutions within a feature space, adjusting candidate solutions based on feedback from previous iterations. This adaptability is crucial for dynamic flood scenarios, where environmental conditions can vary. After segmentation, Gaussian filtering is applied to further enhance the features by smoothing the image and reducing noise. This process ensures that only the most relevant structural details remain, improving classification accuracy.

The MSO algorithm's flexibility is combined with the SWIN Transformer model in the Mo-SWIN architecture, enabling real-time adjustments. This dynamic feature selection approach ensures that the model adapts to new data and evolves over time, positioning the Mo-SWIN model as a powerful tool for long-term flood image classification.

The MSO algorithm's fitness function guides the optimization of the feature selection process. Let $X = \{x_1, x_2, \ldots.., x_n\}$ represent the set of features extracted from an image, and let $S \subseteq X$ denote a subset of selected features. The fitness function $F(S)$ is mathematically defined as follows:

$$F(S) = \alpha \cdot (1 - Error(S)) + \beta \cdot (1 - \frac{|S|}{|X|})$$

where.

- $\boldsymbol{Error}(\boldsymbol{S})$ is the classification error (e.g., 1—accuracy) computed using a lightweight classifier (such as SVM or shallow SWIN Transformer) on the selected feature subset S,
- $|\boldsymbol{S}|$ is the number of selected features,
- $|\boldsymbol{X}|$ is the total number of features, and
- $\boldsymbol{\alpha}$ **and** $\boldsymbol{\beta}$ are weighting coefficients, which balance classification accuracy and feature subset compactness (e.g., 0.8 and 0.2, respectively).

The first term in the fitness function encourages high classification accuracy, while the second term penalizes large feature subsets, promoting compact and efficient feature sets. This ensures the MSO algorithm identifies feature subsets that are both accurate and computationally efficient, improving model generalization and reducing computational costs.

Table 2 outlines the MSO hyperparameters used in this process. A population size of 40 monkeys and 70 iterations ensures sufficient exploration and convergence without excessive computation. The search space for feature weights is bounded between −10 and 10, and the dimensionality is equal to the total number of extracted features. Each monkey represents a potential binary vector that selects a subset of features, with the fitness function evaluating its utility in improving classification performance.

In the following algorithm 1, we explain the working of our proposed MSO algorithm. Here, we use the monkeys'hunting and food-searching behaviors to choose the features of the associated dataset. The following algorithm takes a dataset of flood images as input and generates the output of the best feature from the corresponding feature set. The parameters we defined are [M^{Size}, Max^{itr}, L_b, U_b]. Where M^{Size} represents the size of the populationof monkeys, Max^{itr} represents the maximum number of iterations required for the hunting process, $L_b$denotes the lower bound of search space,and$U_b$denotes the upper bound of search space.In our algorithm, we consider 40; the Maximum iteration is 100; the lower bound of

Table 2 Hyperparameter Settings Used for MoSWIN model

Hyperparameter	Value	Description
General and Swin Transformer Parameters		
Learning Rate	0.0001	Learning rate for Adam optimizer used in Swin Transformer training
Batch Size	32	Number of images processed per training batch
Epochs	100	Total number of training iterations
Optimizer	Adam	Adaptive optimizer for backpropagation
Image Size	224 × 224	Resized input image dimensions
Dropout Rate	0.2	Dropout regularization to reduce overfitting
Window Size (Swin)	7	Size of attention window in Swin Transformer
PCA Variance Threshold	95%	Percentage of variance retained during PCA
Monkey Search Optimization (MSO) Parameters		
Monkey Population Size	40	Number of candidate solutions (monkeys)
Number of Iterations	70	Maximum optimization steps
Lower Bound (Lb)	−10	Minimum search space value for MSO
Upper Bound (Ub)	10	Maximum search space value for MSO
Dimensions	Num_of_features	Dimensionality of the solution space, equal to number of features

the search space is −10; the upper bound of the search space is 10.We calculate the monkey's fitness in every iteration using a formula provided by the algorithm to find the best solution.

Algorithm 1: Monkey Search Optimization (MSO) Algorithm for feature selection of flood image

Input: Flood image dataset
Output: The best features found and the corresponding feature set.
Input: Flood Image Dataset
Parameters: M^{Size}, Max^{itr}, L_b, U_b
Start:
1. Define the objective function

2. Initialize Monkey Search Algorithm (MSA) parameters:
$M^{Size} = 40; Max^{itr} = 100; L_b = -10; U_b = 10$

3. Define the Monkey Search Algorithm function:
- objective_function_O_f: Objective function to evaluate the feature score
- population_size: Number of monkeys in the population
- max_iterations: Maximum number of iterations
- lower_bound: Lower bound of the search space
- upper_bound: Upper bound of the search space
- best_solution: Best solution found
- best_fitness: Fitness value of the best solution
- fitness_history: List of best fitness values over iterations

4. Initialize the population with random solutions (monkeys) within the search space bounds.

5. Initialize the best solution and fitness to infinity.

6. For each iteration up to max_iterations:
a. Calculate the fitness of each solution (monkey).
$Fitness = [\, O_f(solution)\ for\ solution\ in\ total\ population]$
b. Update the best solution found and its fitness.
$Min_{Fitness} = min\ (fitness)$
$If\ Min_{Fitness} < Best_{Fitness}$
$Best_{Fitness} = Min_{Fitness}$
$Best_{Solution} = population[np.argmin(fitness)\ ]$
c. Generate new solutions based on random perturbation within the search space bounds.
d. Replace the old population with the new population.
$Population = New_population$
e. Store the best fitness for this iteration.
$Fitness_{History}.append(Best_{Fitness})$

7. Return the best solution found, its fitness value, and the fitness history.

8. Run the Monkey Search Algorithm function with the defined parameters.

Stop: Either Max^{itr} or *Stopping criterion*

Output: The best features found and the corresponding feature set.

4.5 Classification using SWIN Transformer

For data classification, the proposed model leverages the power of both Principal Component Analysis (PCA) and the Swin Transformer. PCA is applied first to reduce the dimensionality of the input data, followed by the Swin Transformer to perform flood detection

classification. By combining PCA and Swin Transformer, our model benefits from both dimensionality reduction and advanced transformer-based feature extraction.

The Swin Transformer architecture, a hierarchical model designed for vision tasks, divides images into non-overlapping patches at different scales, capturing both local and global image features (Liu et al. 2021). It uses a window-based self-attention mechanism, which operates on a fixed-size window of patches. This allows the model to efficiently extract features while reducing computational complexity compared to traditional transformers, which use global attention.

In our framework, the Swin Transformer is adapted to flood image classification by fine-tuning the model's architecture to optimize the identification of flooded versus non-flooded areas. Rather than relying on standard approaches, we customize the Swin Transformer's window-based attention mechanisms, shifting windows across the image to better capture spatial relationships between neighboring regions, which is crucial for accurate flood detection.

4.5.1 Main Components of the Swin Transformer

(i) **Patch Partition:** The Swin Transformer splits the input image into non-overlapping patches, which are then processed by individual layers.
(ii) **Patch Merging:** Patch merging reduces the spatial resolution of the image by merging adjacent patches. This is a key feature of the Swin Transformer, introducing an inductive bias to improve feature learning and reduce computational complexity.
(iii) **Swin Transformer Block:** Instead of using a global multi-head self-attention mechanism (MSA), Swin Transformer employs a shifted window multi-head self-attention (SW-MSA) technique. The result is an efficient hierarchical processing of image patches, allowing the model to scale to larger images without overwhelming computational resources.
(iv) **Window-based Self-Attention (W-MSA):** W-MSA computes attention within fixed-size windows of image patches, improving computational efficiency by reducing the number of patches involved in each attention operation.
(v) **Shifted Window-based Self-Attention (SW-MSA):** To overcome the limitations of W-MSA, SW-MSA shifts the window in subsequent layers, allowing for better capturing of the relationships between neighboring windows, which is essential for understanding the spatial context in flood images.
(vi) **Relative Position Bias:** Unlike traditional transformers that rely on absolute position embedding, the Swin Transformer uses relative position bias to enhance its attention mechanism, allowing it to better handle spatial dependencies and improve performance.

4.6 Working of Our Proposed Architecture

Our proposed architecture for flood detection integrates the strengths of the Swin Transformer with the Monkey Search Optimization (MSO) algorithm, creating a robust system capable of efficiently classifying flood images. The architecture involves several preprocessing steps, including noise removal, image enhancement, and resizing, ensuring high-quality input data for classification. We also perform image augmentation to increase the

diversity of the training dataset. The segmentation step utilizes a Gaussian Mixture Model (GMM) to divide the image into meaningful regions based on pixel intensities. This segmentation ensures that only relevant features are extracted for flood classification, eliminating background noise.

The MSO algorithm is employed for feature extraction, inspired by the behavior of monkeys foraging for food. This algorithm selectively focuses on relevant regions within the image while discarding less useful background areas. It mimics the process of identifying areas with higher importance, which aligns with the need to distinguish flooded from non-flooded regions. After feature extraction, PCA is applied to reduce the dimensionality of the feature set, preserving the most significant variations. This dimensionality reduction process not only improves computational efficiency but also boosts classification accuracy by removing redundant or irrelevant features.

Finally, the reduced feature set is fed into the Swin Transformer, which performs the final classification. The Swin Transformer processes the image by dividing it into patches, applying the attention mechanisms, and classifying the image based on learned patterns. The combination of PCA and Swin Transformer allows our model to handle high-dimensional data while maintaining high performance in flood classification. Flooded regions often contain subtle, small-scale differences from non-flooded areas, requiring models with high sensitivity to local patterns. The shifted window mechanism in Swin Transformer effectively captures both local and global context, improving discrimination between flooded surfaces and similar-looking backgrounds such as wet soil or roads. This adaptability makes it highly suitable for analyzing remote sensing images in disaster response scenarios.

5 Experiment Results and Discussion

The proposed approach was tested using qualitative imaging analysis, a popular method for image classification. The classification is carried out using a wide range of datasets. Our proposed model, Mo-SWIN, was compared with existing models such as Vision Transformer and ResNet-18. We carried out a comprehensive assessment, evaluating performance in terms of various metrics like recall, precision, accuracy, and F1-score. The results suggest that the accuracy reached by Mo-SWIN is satisfactory. Furthermore, the comparison to a vision transformer or ResNet-18 provides a baseline for evaluating the advancements achieved through our proposed approach.

5.1 Dataset Description

This repository contains the metadata and annotations for a flood dataset for interactive content-based image retrieval. The idea is to extract images from enormous amounts of data that can be used to deduce specific types of information. For this dataset, the following information goal has been set up:

Flooding Is a specific place flooded or not?

Most of the 3,710 images in the dataset are from the Central European floods in May or June 2013 and were retrieved in July 2017. This repository contains 3,435 images, 890 of which

provide metadata regarding the geographical place where the shot was taken. 275 additional photographs of water contamination were gathered manually by contacting online image search engines (Barz et al. 2019). The split ratio is 20% for testing and 80% for training. The dataset is trained using 2963 images, while 742 images are used for testing.

The dataset is annotated with metadata detailing the geographical location of each image, providing valuable context for analysis. For the purposes of training and evaluation, the dataset was split using a stratified 80–20 split, ensuring that both flooded and non-flooded images are proportionally represented in the training and testing sets. This resulted in 2,963 images for training and 742 images for testing.

5.2 Experimental Setup

The experiments were conducted on a laptop running Windows 11, equipped with an Intel Core i5 10 th Gen processor, 8 GB RAM, and 512 GB ROM. An NVIDIA GTX 1650 4 GB graphics card was utilized to accelerate model training and inference. The study employed several data analysis frameworks, including Seaborn, Matplotlib, NumPy, Pandas, and Scikit-learn, to facilitate data processing, visualization, and evaluation.

5.3 Performance Evaluation Parameters

Evaluating the effectiveness of a classification model requires a comprehensive understanding of various performance metrics. These metrics provide insights into the model's ability to accurately predict outcomes and handle different types of errors. The primary metrics used in classification tasks include Accuracy, Precision, Recall, and F1-score. Each metric offers a unique perspective on the model's performance, especially in scenarios involving imbalanced datasets or varying costs of false positives and false negatives.

Performance Matrices Performance metrics are used to evaluate the efficiency of a model's performance in performing a specific task such as classification.

TP: true positive **TN:** true negative **FP:** false positive **FN:** false negative.

Accuracy The ratio of correctly identified instances out of all the instances is known as accuracy.

$$Accuracy = \frac{TP + TN}{TP + TN + FP + FN}$$

Precision The precision of the model is determined by the ratio of its positive predictions to the percentage of true positive predictions.

$$Precision = \frac{TP}{TP + FP}$$

Recall Recall calculates the fraction of accurate positive predictions among all positive instances in the data.

$$Recall = \frac{TP}{TP + FN}$$

F1-Score The harmonic mean of recall and precision is the F1 score. It creates a compromise between precision and recall, resulting in a single value that incorporates both.

$$F1 - Score \frac{Precision * Recall}{Precision + Recall}$$

5.4 Result Analysis

This section presents a comprehensive evaluation of the proposed Mo-SWIN model for flood detection using a combination of robust experimental setups, multiple performance metrics, and comparative analysis with existing deep learning architectures. The model was assessed using key metrics such as Accuracy, Precision, Recall, and F1-Score to determine its effectiveness and reliability.

To ensure a robust and unbiased evaluation, the Mo-SWIN model was trained and validated using 5-fold cross-validation. This approach divides the dataset into five equal parts, using four for training and one for testing in each iteration, thereby covering all possible splits. Additionally, to account for the inherent stochastic nature of deep learning models and improve result stability, the performance metrics were averaged over 10 independent runs. This methodology helps mitigate variability caused by random initialization or data shuffling and provides a more reliable estimate of the model's true performance.

The model's performance was benchmarked against well-established architectures such as ResNet-18, Vision Transformer (ViT), and ResNet-50. As presented in Table 3, the proposed Mo-SWIN outperformed all baseline models across all evaluation metrics. Specifically, Mo-SWIN achieved an Accuracy of 96.53%, Precision of 95.41%, Recall of 90.51%, and F1-Score of 92.48%. In comparison, ResNet-18 and ViT recorded lower scores, with ResNet-18 achieving the lowest across all categories. These results demonstrate Mo-SWIN's superior capability in accurately classifying flood images.

The dataset used for evaluation was split into 80% training and 20% testing sets. This division ensures that a substantial portion of data is used for training while retaining an unseen set for evaluating the model's generalization performance. The learning dynamics over 25 epochs are illustrated in Fig. 3. Figure 3(a) shows that both training and testing accuracies increase consistently, reaching nearly 98% and 95%, respectively. This trend indicates effective learning and generalization with minimal overfitting. Figure 3(b) presents the loss curves, both of which decline sharply from around 0.5 to below 0.05. Despite minor fluctuations in testing loss between epochs 10 and 20, the overall trend suggests convergence and improved stability.

Table 3 Comparative performance metrics of baseline models and the proposed Mo-SWIN model for flood image classification

Model	Accuracy (%)	Precision (%)	Recall (%)	F1-Score (%)
ResNet-18	85.37	93.33	78.68	82.35
Vision Transformer (ViT)	90.24	94.25	82.35	87.36
ResNet-50	94.20	94.20	85.21	90.52
Proposed Mo-SWIN	**96.53**	**95.41**	**90.51**	**92.48**

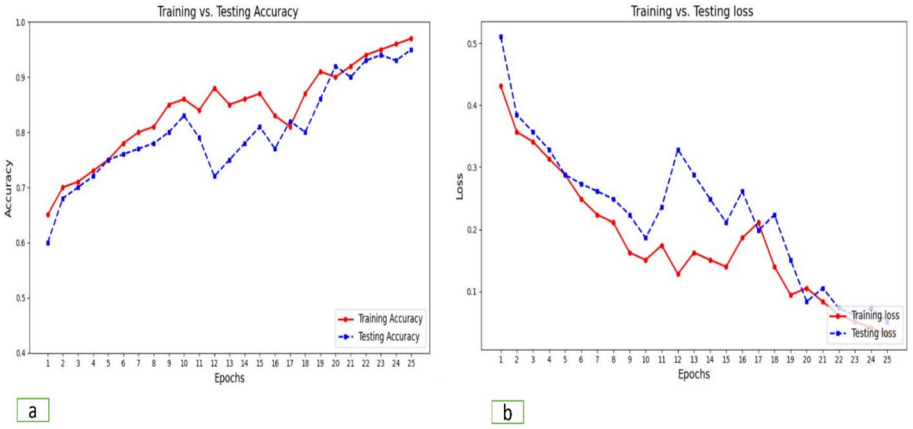


Fig. 3 Epoch-wise comparison of training and testing accuracy and loss for the proposed Mo-SWIN model

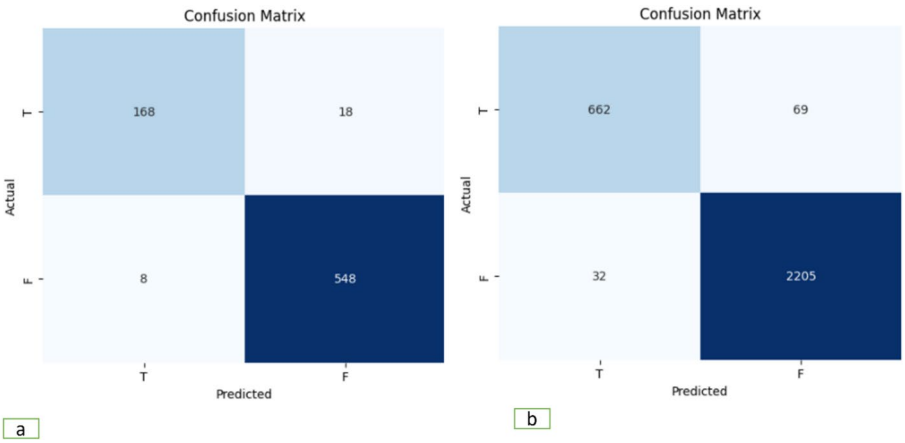


Fig. 4 Confusion matrices depicting classification performance of the proposed Mo-SWIN model on test and train set

To further verify classification performance, confusion matrices are presented in Fig. 4. Figure 4(a), corresponding to a smaller or more balanced dataset, shows 168 true positives and 548 true negatives, with minimal false classifications. Figure 4(b), using a larger dataset, reports 662 true positives and 2205 true negatives with only 69 false positives and 32 false negatives. The high concentration of values along the diagonal in both matrices confirms the model's effectiveness and balanced performance in distinguishing between flood and non-flood classes.

Figure 5 provides a comparative performance evaluation of all models using bar charts for Accuracy, Precision, Recall, and F1-Score. Mo-SWIN clearly surpasses the other models, highlighting its optimized architecture and training strategy. The integration of Swin Transformer for hierarchical feature learning and the MSO algorithm for feature extraction contributes significantly to this performance improvement.

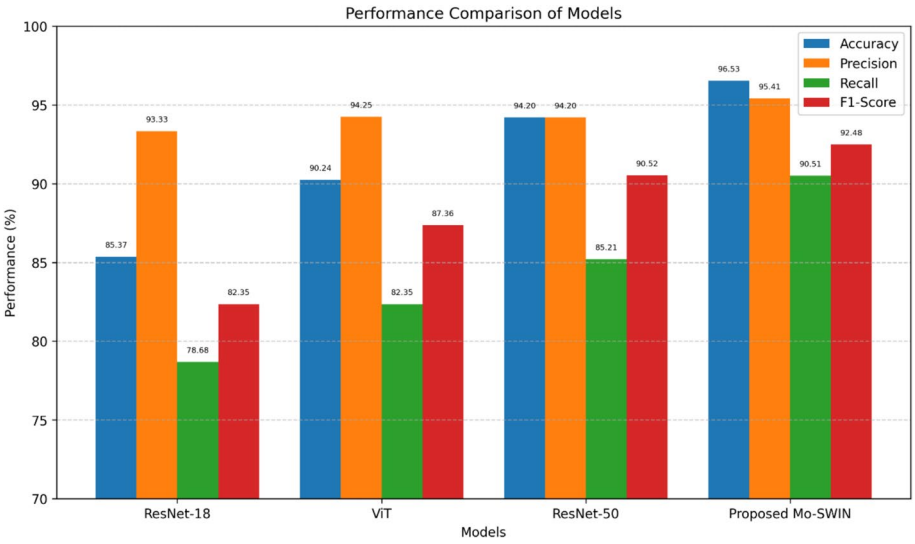


Fig. 5 Comparative performance evaluation of proposed Mo-SWIN and baseline models using standard classification metric

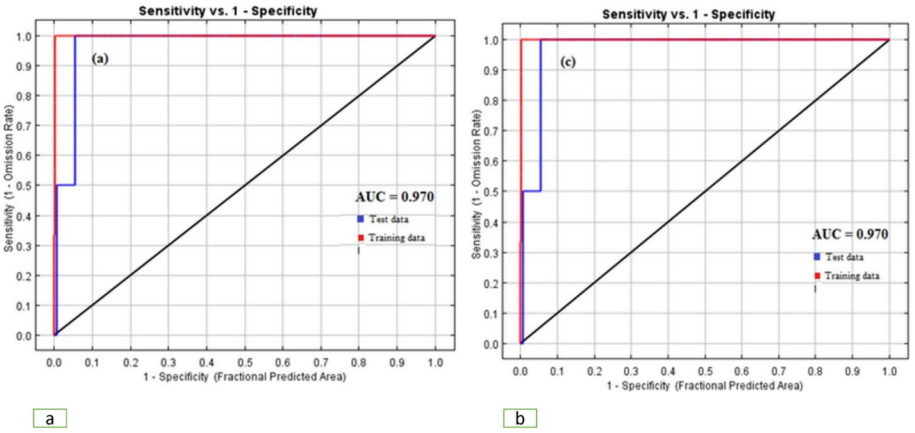


Fig. 6 ROC curve and AUC comparison for training and test data in the proposed model

Finally, Fig. 6 illustrates the ROC curves for both training and test datasets. In both subfigures (6a and 6b), the red and blue curves (training and test, respectively) exhibit a sharp ascent toward the top-left corner, demonstrating high sensitivity and specificity. The Area Under the Curve (AUC) is recorded as 0.970 in both cases, indicating excellent class separability and minimal performance drop between training and testing phases. The close alignment between training and testing curves also indicates that the model generalizes well without overfitting. Figure 7 illustrates ROC curves, showing Mo-SWIN achieving perfect classification performance (AUC = 1.00) compared to other models.

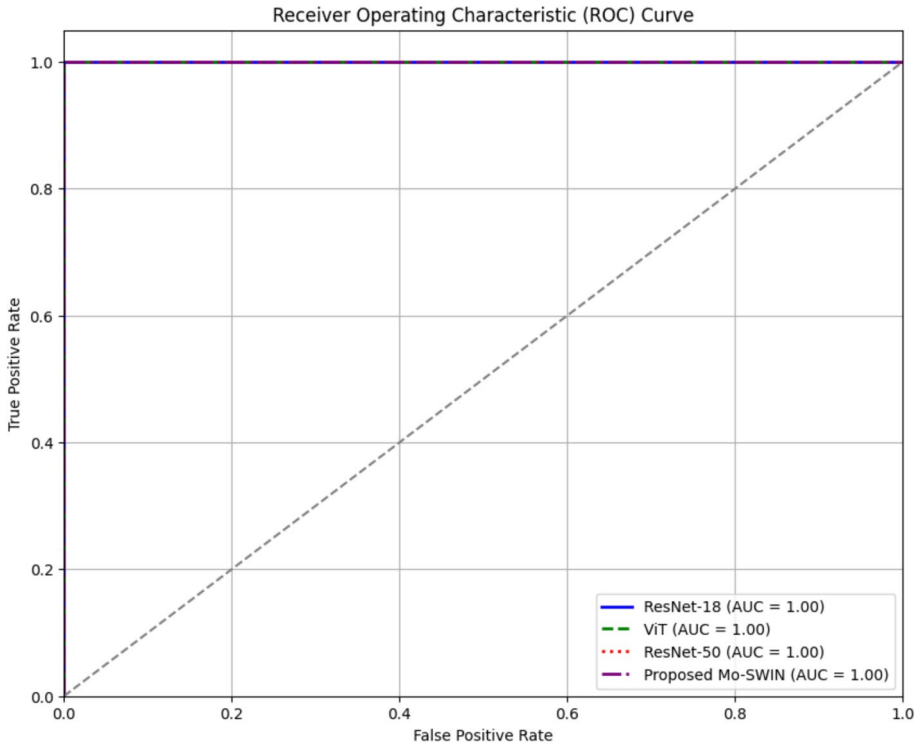


Fig. 7 Comparative ROC curve analysis of Mo-SWIN and Benchmark models

In conclusion, the Mo-SWIN model exhibits superior performance across multiple evaluation criteria and consistently outperforms traditional architectures like ResNet-18, ResNet-50, and Vision Transformer. Its hybrid design, combining the Swin Transformer and MSO algorithm, proves highly effective for flood detection tasks, particularly in analyzing satellite imagery. These findings underscore the robustness, accuracy, and practical applicability of the proposed model in real-world scenarios.

5.5 Cross-Validation Results

To further assess the robustness and generalizability of our proposed Mo-SWIN model, we conducted a 5-fold cross-validation on the flood image dataset. This technique partitions the dataset into five equal subsets (folds), using four for training and one for testing in each iteration. The process is repeated five times, ensuring that each fold serves as the test set once. The performance metrics accuracy, precision, recall, and F1-score were averaged across all five runs to provide a comprehensive evaluation.

The results indicate that the Mo-SWIN model maintains high performance across multiple folds, with minimal variation, suggesting its stability and reliability in flood image classification tasks as shown in Table 4. This cross-validation approach provides a more robust estimate of the model's performance compared to a single train-test split, reducing

Table 4 5-Fold cross-validation performance metrics of the proposed Mo-SWIN model

Model	Accuracy (%)	Precision (%)	Recall (%)	F1-Score (%)
Mo-SWIN (5-fold CV)	96.45	95.30	90.10	92.20

the potential for overfitting and enhancing the generalizability of the findings. In conclusion, the 5-fold cross-validation results corroborate the effectiveness of the Mo-SWIN model in accurately classifying flood images, reinforcing its potential for practical applications in flood detection and monitoring.

5.6 Statistical Significance Testing

To substantiate the performance claims of our proposed Mo-SWIN model, we conducted rigorous statistical analyses using both parametric and non-parametric tests. These tests assess whether the observed differences in performance metrics: Accuracy, Precision, Recall, and F1-score between Mo-SWIN and existing models are statistically significant.

I. **Paired t-test:** The paired t-test was employed to compare the means of two related groups, assuming the differences between paired observations are normally distributed. This test is appropriate when the data meet the assumptions of normality and continuous measurement scales.
II. **Wilcoxon Signed-Rank Test:** For comparisons where the normality assumption may not hold, we applied the Wilcoxon signed-rank test, a non-parametric alternative to the paired t-test. This test assesses whether the median differences between paired observations are zero, making it suitable for ordinal data or when the data are not normally distributed.

Hypotheses

- **Null Hypothesis (H_0):** There is no significant difference between the performance metrics of the models; any observed differences are due to random chance.
- **Alternative Hypothesis (H_1):** There is a significant difference between the performance metrics of the models; the observed differences are not due to random chance.

Table 5 presents the results of the statistical tests comparing Mo-SWIN with ResNet-18, Vision Transformer, and ResNet-50 across key performance metrics. A p-value less than 0.05 indicates statistical significance, suggesting that the observed differences are unlikely to be due to chance.

These results provide statistical evidence supporting the superior performance of Mo-SWIN over other models, particularly in Accuracy, Precision, Recall, and F1-score. The significant p-values indicate that the observed improvements are unlikely to be due to random chance. In conclusion, the application of paired t-tests and Wilcoxon signed-rank tests across multiple trials reinforces the robustness and reliability of the Mo-SWIN model in flood image classification tasks.

Table 5 Statistical results highlighting model performance significance

Comparison	Metric	Mean Difference	p-value	Significance ($\alpha = 0.05$)
ResNet 18 vs Vision Transformer	Accuracy	4.87	0.045	Significant
	Precision	0.92	0.36	Not Significant
	Recall	3.67	0.028	Significant
	F1-score	5.01	0.019	Significant
ResNet 18 vs ResNet 50	Accuracy	8.83	0.003	Significant
	Precision	0.13	0.88	Not Significant
	Recall	6.53	0.006	Significant
	F1-score	8.17	0.002	Significant
ResNet 18 vs Mo-SWIN	Accuracy	10.00	0.001	Significant
	Precision	2.08	0.007	Significant
	Recall	11.83	0.000	Significant
	F1-score	10.13	0.001	Significant
Vision Transformer vs ResNet 50	Accuracy	3.96	0.028	Significant
	Precision	−0.05	0.96	Not Significant
	Recall	2.86	0.08	Not Significant
	F1-score	3.16	0.042	Significant
ResNet 50 vs Mo-SWIN	Accuracy	1.17	0.25	Not Significant
	Precision	1.23	0.006	Significant
	Recall	4.61	0.008	Significant
	F1-score	2.96	0.025	Significant

5.7 Ablation Study

The ablation study evaluates the impact of the Monkey Search Optimization (MSO) and Swin Transformer components on classification performance using the flood image dataset. Five experimental configurations were tested, revealing that MSO significantly enhances performance. Case D (MoSwin with MSO + Swin Transformer) achieved the highest accuracy of 96.53%, showing a notable improvement over other configurations. MSO independently improved accuracy and F1-score, with Case E (MSO + CNN) outperforming the baseline CNN (Case C). These results confirm MSO's critical role in optimizing feature selection and boosting classification performance.

To further highlight MSO's contribution, we observed a 7.3% increase in accuracy and 5.2% in F1-score when comparing Case A (without MSO) and Case D (with MSO). Also, the combination in Case E (MSO + CNN) outperformed the standalone CNN in Case C, confirming MSO's independent benefit. These results clearly demonstrate that MSO plays a crucial role in boosting classification performance by eliminating irrelevant or redundant

Table 6 Performance comparison of different model configurations in the ablation study

Case	Model Configuration	Accuracy	Precision	Recall	F1-Score
A	Swin without MSO (raw features)	0.892	0.895	0.880	0.880
B	Swin + Random Feature Selection	0.881	0.876	0.870	0.872
C	CNN without MSO	0.871	0.893	0.872	0.875
D	**MoSwin (MSO + Swin Transformer)**	**0.9653**	**0.9541**	**0.9051**	**0.9248**
E	MSO + CNN	0.906	0.911	0.892	0.898

Table 7 Performance comparison of our proposed model with existing techniques on image data

Ref No	Model	Accuracy	Precision	Recall	F1-score
Aydin and Iban 2022)	AdaBoost	89.78	89.86	89.86	-
Stateczny et al. 2023)	Hybrid CNN and Deep ResNet (DHMFP)	94.98	90.92	-	-
Hu et al. 2021)	Nonlinear Multiple Kernel Learning (NLMKL)	83.3	75.9	94.3	84.1
Vineeth and Neeba 2021)	MobileNet	92	92	-	96
Kotaridis and Lazaridou 2022)	ConvNet	95	99	92	95
Jamali et al. 2024)	WVResU-Net	96.20	92.97	69.67	82.03
Our approach	**Proposed Model (Mo-SWIN)**	**96.53**	**95.41**	**90.51**	**92.48**

features and enabling the Swin Transformer to focus on the most discriminative aspects of the input data as shown in Table 6. Therefore, the ablation study confirms that MSO is not only a significant component but a key driver of the improved performance observed in the MoSwin architecture.

5.7.1 Comparison of our Proposed Model with other Techniques over Image Data

Table 7 presents a comparison of the performance of various techniques on image data, including AdaBoost, Hybrid CNN and Deep ResNet (DHMFP), Nonlinear Multiple Kernel Learning (NLMKL), MobileNet, ConvNet, WVResU-Net, and the proposed Mo-SWIN model. The Mo-SWIN model outperforms all other methods with the highest accuracy (96.53%) and strong precision (95.41%), demonstrating superior flood data classification with minimal false positives. WVResU-Net follows closely in accuracy (96.20%) but has a lower recall (69.67%), limiting its true positive detection. Mo-SWIN offers the best balance of metrics, making it the most effective approach.

6 Conclusion and Real-World Implications

Floods pose significant environmental and societal challenges, impacting ecosystems, infrastructure, and human livelihoods. Effective flood image classification is crucial for disaster mitigation, enabling early alerts, informed response planning, damage assessment, and risk reduction. In this study, we introduced Mo-SWIN, a novel approach that synergizes the SWIN transformer with Monkey Search Optimization (MSO) to enhance flood image classification. The Mo-SWIN model demonstrated superior performance across key metrics, achieving an accuracy of 96.53%, outperforming existing models such as ResNet-18 (85.37%) and Vision Transformer (90.24%). These results underscore the model's robustness and efficacy in accurately classifying flood-related imagery.

6.1 Integration into Operational Flood Monitoring Systems

The practical applicability of Mo-SWIN extends to its integration into real-time flood monitoring and early-warning systems. By leveraging its high accuracy and efficiency, Mo-SWIN can be incorporated into existing frameworks to enhance flood detection and response. For instance, integrating Mo-SWIN with AI-enabled platforms like Google's Flood Hub can improve the precision of flood forecasts, providing timely alerts to vulnerable communities.

Furthermore, Mo-SWIN's compatibility with Internet of Things (IoT) devices allows for real-time data collection and analysis. Deploying Mo-SWIN in conjunction with IoT sensors can facilitate continuous monitoring of flood-prone areas, enabling prompt identification of flood events and dissemination of warnings.

6.2 Scientific Implications

From a scientific perspective, the integration of MSO with the SWIN transformer introduces a novel methodology for feature extraction and classification in flood image analysis. This hybrid approach can inspire future research exploring the combination of nature-inspired optimization algorithms with advanced deep learning models to address complex environmental monitoring challenges.

6.3 Limitations and Future Work

While Mo-SWIN exhibits promising results, certain limitations warrant consideration. Fine-tuning MSO hyperparameters can be resource-intensive, particularly in high-dimensional search spaces. Additionally, the model's performance is contingent upon the quality and diversity of training data, which may affect its generalizability across different geographical regions.

Future research will focus on expanding the dataset to encompass diverse flood scenarios, enhancing the model's adaptability. Moreover, exploring the integration of Mo-SWIN with other optimization algorithms, such as Genetic Algorithms and Particle Swarm Optimization, could further improve its performance. Investigating the model's applicability to other domains, such as medical image analysis and natural disaster prediction, also presents valuable avenues for exploration.

Author's Contribution Vinay Dubey Worked on the Conceptualization of the Idea to reach the research goals and aims, conducted a research and investigation process, and Conceived and designed the Mo-SWIN model's methodology and creation.
Rahul Katarya helps in validation, Formal analysis of the research idea, Analysis of the collected Dataset, and Preparation for the manuscript's presentation.

Funding No funding was obtained for this study.

Data Availability Data is available on request.

Declarations

Conflict of interest The authors declare that they have no Conflict of interest.

References

Ali AM et al (2023) Vision transformers in image restoration: a survey. Sensors 23(5):2385. https://doi.org/10.3390/s23052385

Amankwah SO et al (2022) Landslide detection from bitemporal satellite imagery using attention-based deep neural networks. Landslides 19(10):2459–2471. https://doi.org/10.1007/s10346-022-01915-6

Anusha N, Bharathi B (2020) Flood detection and flood mapping using multi-temporal synthetic aperture radar and optical data. Egypt J Remote Sens Space Sci 23(2):207–219. https://doi.org/10.1016/j.ejrs.2019.01.001

Arvind CS et al (2016) Flood assessment using multi-temporal Modis Satellite Images. Procedia Comput Sci 89:575–586. https://doi.org/10.1016/j.procs.2016.06.017

Aydin HE, Iban MC (2022) Predicting and analyzing flood susceptibility using boosting-based ensemble machine learning algorithms with Shapley additive explanations. Nat Hazards 116(3):2957–2991. https://doi.org/10.1007/s11069-022-05793-y

Bansal K, Tripathi AK (2024) Dual level attention based lightweight vision transformer for streambed land use change classification using remote sensing. Comput Geosci 191:105676. https://doi.org/10.1016/j.cageo.2024.105676

Barz B et al (2019) Enhancing flood impact analysis using interactive retrieval of social media images. ArXiv abs/1908.03361: n. pag

Bhatt CM et al (2016) Development of flood inundation extent libraries over a range of potential flood levels: a practical framework for quick flood response. Geomat Nat Haz Risk 8(2):384–401. https://doi.org/10.1080/19475705.2016.1220025

Bhuyan K et al (2022) Mapping and characterising buildings for flood exposure analysis using open-source data and artificial intelligence. Nat Hazards 119(2):805–835. https://doi.org/10.1007/s11069-022-05612-4

Crawford B et al (2019) A binary monkey search algorithm variation for solving the set covering problem. Nat Comput 19(4):825–841. https://doi.org/10.1007/s11047-019-09752-8
Deepak VK, Sarath R (2022) An intelligent brain tumor segmentation using improved deep learning model based on Cascade Regression Method. Multimed Tools Appl 82(13):20059–20078. https://doi.org/10.1007/s11042-022-13945-2
Devi RV, Sathya SS (2017) Monkey behavior based algorithms - a survey. Int J Intell Syst Appl 9(12):67–86. https://doi.org/10.5815/ijisa.2017.12.07
Du X et al (2022) Motor imaging EEG signal recognition of RESNET18 network based on deformable convolution. Electronics 11(22):3674. https://doi.org/10.3390/electronics11223674
Dubey V, Katarya R (2020) An analysis of machine learning techniques for flood mitigation. In: Advances in intelligent systems and computing, pp 299–307. https://doi.org/10.1007/978-981-15-5148-2_27
Fernandes FE, Nonato LG, Ueyama J (2022) A river flooding detection system based on deep learning and computer vision. Multimed Tools Appl 81(28):40231–40251. https://doi.org/10.1007/s11042-022-12813-3
He K et al (2016) Deep residual learning for image recognition. In: 2016 IEEE conference on computer vision and pattern recognition (CVPR) [Preprint]. https://doi.org/10.1109/cvpr.2016.90
Hernández D et al (2022) Flood detection using real-time image segmentation from unmanned aerial vehicles on edge-computing platform. Remote Sens 14(1):223. https://doi.org/10.3390/rs14010223
Hu Q et al (2021) Multiple kernel learning with maximum inundation extent from Modis imagery for spatial prediction of flood susceptibility. Water Resour Manage 36(1):55–73. https://doi.org/10.1007/s11269-021-03010-2
Islam KA et al (2020) Flood detection using multi-modal and multi-temporal images: a comparative study. Remote Sens 12(15):2455. https://doi.org/10.3390/rs12152455
Islam MA et al (2023) An integrated convolutional neural network and sorting algorithm for image classification for efficient flood disaster management. Decis Anal J 7:100225. https://doi.org/10.1016/j.dajour.2023.100225
Ives JD, Messerli B (1981) Mountain hazards mapping in Nepal introduction to an applied mountain research project. Mt Res Dev 1(3/4):223. https://doi.org/10.2307/3673059
Jackson J et al (2023) Flood or non-flooded: a comparative study of state-of-the-art models for flood image classification using the FloodNet dataset with uncertainty offset analysis. Water 15(5):875. https://doi.org/10.3390/w15050875
Jamali A et al (2024) Residual wave vision U-net for flood mapping using dual polarization sentinel-1 sar imagery. Int J Appl Earth Obs Geoinf 127:103662. https://doi.org/10.1016/j.jag.2024.103662
Karanjit R, Pally R, Samadi S (2023) FLOODIMG: flood image database system. Data Brief 48:109164. https://doi.org/10.1016/j.dib.2023.109164
Kim HI, Han KY (2020) Urban flood prediction using deep neural network with data augmentation. Water 12(3):899. https://doi.org/10.3390/w12030899
Kim J et al (2022) Deep learning-based flood area extraction for fully automated and persistent flood monitoring using cloud computing. Remote Sens 14(24):6373. https://doi.org/10.3390/rs14246373
Kotaridis I, Lazaridou M (2022) Integration of convolutional neural networks for flood risk mapping in Tuscany, Italy. Nat Hazards 114(3):3409–3424. https://doi.org/10.1007/s11069-022-05525-2
Kundzewicz ZW et al (2013) Flood risk and climate change: global and regional perspectives. Hydrol Sci J 59(1):1–28. https://doi.org/10.1080/02626667.2013.857411
Li Y et al (2023) Transformer for object detection: review and benchmark. Eng Appl Artif Intell 126:107021. https://doi.org/10.1016/j.engappai.2023.107021
Liu Z et al (2021) Swin transformer: hierarchical vision transformer using shifted windows. In: 2021 IEEE/CVF international conference on computer vision (ICCV) [Preprint]. https://doi.org/10.1109/iccv48922.2021.00986
Mahapatra S, Jha MK (2025) Climate change impacts on long-term streamflow sustainability in a regulated river of eastern India using environmental flow envelope. Environ Process 12(2). https://doi.org/10.1007/s40710-025-00774-2
Maurício J, Domingues I, Bernardino J (2023) Comparing vision transformers and convolutional neural networks for image classification: a literature review. Appl Sci 13(9):5521. https://doi.org/10.3390/app13095521
Moharrami M, Javanbakht M, Attarchi S (2021) Automatic flood detection using sentinel-1 images on the google earth engine. Environ Monit Assess 193(5). https://doi.org/10.1007/s10661-021-09037-7
Munawar, HS (2020) 'Flood disaster management. Machine Vision Inspection Systems, pp 115–146. https://doi.org/10.1002/9781119682042.ch5
Nghia BP et al (2022) Applying google earth engine for flood mapping and monitoring in the downstream provinces of Mekong River. Progress in Disaster Science 14:100235. https://doi.org/10.1016/j.pdisas.2022.100235

Obunguta F, Kaito K, Kobayashi K (2025) Valley dam optimization framework to reduce water-induced conflict in migratory communities. Water Resour Manage. https://doi.org/10.1007/s11269-025-04173-y
Panagiotou CF, Feloni E, Aristidou K, Eliades M (2025) Probabilistic assessment of flood susceptibility via a coparticipative multicriteria decision analysis. Environ Process 12(2). https://doi.org/10.1007/s40710-025-00766-2
Papathanasiou A, Ntemiri K, Baltas E (2025) Sustainable water resources management and energy production in small Mediterranean islands. Environ Process 12(2). https://doi.org/10.1007/s40710-025-00762-6
Poursaeid M (2025) A novel approach for water resources management to accurate river flow prediction: utilization of linear programming and weighted ensemble learning. Water Resour Manage. https://doi.org/10.1007/s11269-025-04230-6
Rahnemoonfar M et al (2021) FloodNet: a high resolution aerial imagery dataset for post flood scene understanding. IEEE Access 9:89644–89654. https://doi.org/10.1109/access.2021.3090981
Rimal B et al (2018) Quantifying the spatiotemporal pattern of urban expansion and hazard and risk area identification in the Kaski District of Nepal. Land 7(1):37. https://doi.org/10.3390/land7010037
Saleh T et al (2024a) DAM-net: flood detection from SAR imagery using differential attention metric-based vision transformers. ISPRS J Photogramm Remote Sens 212:440–453. https://doi.org/10.1016/j.isprsjprs.2024.05.018
Saleh T et al (2024b) High-precision flood detection and mapping via multi-temporal SAR change analysis with semantic token-based transformer. Int J Appl Earth Obs Geoinf 131:103991. https://doi.org/10.1016/j.jag.2024.103991
Stateczny A et al (2023) Optimized deep learning model for flood detection using satellite images. Remote Sens 15(20):5037. https://doi.org/10.3390/rs15205037
Tanguy M et al (2017) River flood mapping in urban areas combining RADARSAT-2 data and flood return period data. Remote Sens Environ 198:442–459. https://doi.org/10.1016/j.rse.2017.06.042
Tanim AH et al (2022) Flood detection in urban areas using satellite imagery and machine learning. Water 14(7):1140. https://doi.org/10.3390/w14071140
Tian Z, She D, Wang H, Sun X, Fang K, Qiu C, Li Y (2025) Influence of long-term irrigation with reclaimed water on the soil quality of different land use types. Water Resour Manage. https://doi.org/10.1007/s11269-025-04232-4
Vineeth V, Neeba EA (2021) Flood detection using Deep Learning. In: 2021 international conference on advances in computing and communications (ICACC), pp 1–5. https://doi.org/10.1109/icacc-202152719.2021.9708240
Wang J, Huang B, Wang F (2023) Extraction and classification of flood-affected areas based on MRF and deep learning. Water 15(7):1288. https://doi.org/10.3390/w15071288
Watik N, Jaelani LM (2019) Flood evacuation routes mapping based on derived- flood impact analysis from Landsat 8 imagery using network analyst method. Int Arch Photogramm, Remote Sens Spat Inf Sci XLII-3/W8:455–460. https://doi.org/10.5194/isprs-archives-xlii-3-w8-455-2019
We are promoting multilateral network building for improving disaster risk reduction (DRR) capacity including enhancement of DRR-related personnel exchanges in Asia n.d. We are promoting multilateral network building for improving disaster risk reduction (DRR) capacity including enhancement of DRR-related personnel exchanges in Asia (n.d.) Asian Disaster Reduction Center (ADRC). Available at: https://www.adrc.asia/. Accessed 09 Mar 2024
Westra S et al (2014) Future changes to the intensity and frequency of short-duration extreme rainfall. Rev Geophys 52(3):522–555. https://doi.org/10.1002/2014rg000464
Yilmaz S, Ateş A, Firat M, Cinal H (2025) Defining the most appropriate water network management plan with different optimization algorithms for sustainable water management. Water Resour Manage. https://doi.org/10.1007/s11269-025-04221-7
Zhou K (2021) Flood season segmentation and scheme optimization in the Yellow River. J Water Clim Change 13(1):274–286. https://doi.org/10.2166/wcc.2021.110
Zhuo L, Han D (2020) Agent-based modelling and flood risk management: a compendious literature review. J Hydrol 591:125600. https://doi.org/10.1016/j.jhydrol.2020.125600
Zuo S et al (2022) Vision transformers for dense prediction: a survey. Knowl-Based Syst 253:109552. https://doi.org/10.1016/j.knosys.2022.109552

Publisher's Note Springer Nature remains neutral with regard to jurisdictional claims in published maps and institutional affiliations.

Springer Nature or its licensor (e.g. a society or other partner) holds exclusive rights to this article under a publishing agreement with the author(s) or other rightsholder(s); author self-archiving of the accepted manuscript version of this article is solely governed by the terms of such publishing agreement and applicable law.

Astrophysics and Space Science (2025) 370:63
https://doi.org/10.1007/s10509-025-04453-4

RESEARCH

Numerical simulation study of dispersive waves in presence of magnetic islands

Neha Pathak[1] · Jyoti[1] · Suresh C. Sharma[1] · R.P. Sharma[2]

Received: 13 January 2025 / Accepted: 12 June 2025
© The Author(s), under exclusive licence to Springer Nature B.V. 2025

Abstract
We have proposed wave modes physics to explain the power spectrum scaling in the magnetic presence of magnetic islands of the magnetopause. In the present manuscript, a model to study the role of waves in turbulence generation by taking the powerful whistler wave and weak KAW has been presented. The corresponding power spectrum, current sheet structures, and energy dissipation at magnetopause presence of magnetic islands are also analysed and discussed its relevance with observational data. This study is carried out numerically using the pseudospectral method here, space integration for spatial integrations and finite difference method for temporal integration have been used. To understand the physics behind the field localization, we developed a semianalytical model and got the development of electron and ion scale localization. Our study enhances the understanding of the role of wave-wave interaction physics in the presence of magnetic islands and the role of multi-scale physics in turbulence generation in space plasmas.

Keywords Turbulence · Magnetic islands · Harris sheet · Whistler wave · Kinetic Alfvén wave

1 Introduction

Turbulence is certainly one of the most studied processes in the wide range of space plasmas. It is a multiscale process and leads a key role in cascading energy from larger scales to smaller scales. Small-scale structures are produced by the turbulence's spectral property (Perri et al. 2012). Furthermore, it has recently been discovered that the coherent structures created by turbulence cascade energy in the form of current sheets the size of electrons (Karimabadi et al. 2013). In this article, we examine a model to understand the nature of turbulence associated with dispersive waves in the pre-exist presence of magnetic islands.

A thorough investigation of turbulence-mediated reconnection (also known as turbulent reconnection) and reconnection-mediated turbulent cascade has been documented in the literature (Boldyrev and Loureiro 2019; Comisso et al. 2018; Huang and Bhattacharjee 2016; Lazarian et al. 2020; Loureiro and Boldyrev 2017; Mallet et al. 2017; Ergun et al. 2022). It is interesting to note that there seems to be a close relationship between turbulence and reconnection. It is also mentioned Whistler (or kinetic Alfvén wave) turbulence can induce turbulent reconnection (Lazarian et al. 2020). However, it is still not very clear whether turbulence initiates reconnection and vice versa. Therefore, a simultaneous inspection of both reconnection and turbulence at both large and small scales is needed.

According to Fujimoto et al. (2011), waves and turbulence may play a part in facilitating the process of reconnection. Turbulence and a variety of plasma waves, including whistler and kinetic Alfvén waves (KAW), have also been seen in the magnetopause's reconnection site (Bale et al. 2002; Cattell and Mozer 1986; Chaston et al. 2005; Deng and Matsumoto 2001; Farrell et al. 2002; Matsumoto et al. 2003; Pathak et al. 2017a, 2017b; Sharma et al. 2017; Wang et al. 2022; Wilder et al. 2022). The dynamics of ion to electron scale plasma structures physics in presence of magnetic islands has been a topic for attention in the space plasma discipline. The relative strength and relevance of various subproton processes varies with plasma characteristics. Plasma systems with a parameter β that is significantly less than one, the ratio of electron thermal pressure to magnetic pressure, can exhibit particularly rich small-scale dynamics because a new range of scales between the electron inertial

✉ N. Pathak
npsneha90@gmail.com

[1] Delhi Technological University, Delhi, 110042, India

[2] Indian Institute of Technology Delhi, Delhi, 110016, India

Published online: 23 June 2025

scale $\lambda_e \left(=\sqrt{\frac{c^2 m_e}{4\pi n_0 e^2}}\right)$ and the ion gyroradius $\rho_s \left(=\frac{c_s}{w_{ci}}\right)$ becomes accessible to plasma fluctuations (Roytershteyn et al. 2019). Vega et al. (2023) also examined the contribution of electron-scale current sheets to particle energization and discuss the question of to what extent particle energy conversion can be associated with magnetic reconnection.

Energy redistribution occurs when energy at longer length scales is injected into hydrodynamic models. This energy transfer from larger to smaller length scales may be caused by wave-wave interaction or wave-particle interaction, resulting in the development of a turbulent spectrum (Zimbardo et al. 2010; Zimbardo 2006). Abdelhamid et al. (2016) have reported a power law slope $k^{-4.3}$ for magnetized turbulence at subinertial scales in a cold plasma. From the perspective of two fluid theory (Mahajan and Krishan 2005) and Galtier (2006) suggested the possibility of whistler turbulence using Hall MHD responsible for steepening spectra. Chaston et al. (2008) have observed turbulent spectrum having power laws $k^{-1.5}$ in inertial range and after the breakpoint at $k\rho_s \approx 1$ steepening in spectra with slope $k^{-3.0}$, provided the strong evidence of Doppler shifted KAW responsible for turbulence and cascading phenomena.

Recently, Wilder et al. (2016) observed strong whistler emissions and Hall fields, using the Magnetospheric Multiscale (MMS) data. Along with whistler wave, the observation of KAW during magnetic reconnection has been begun to draw more and more attention (Chaston et al. 2012, 2009; Zhao 2017). Recently, the evidence of KAW (Gershman et al. 2017; Øieroset et al. 2014; Yao et al. 2011) and a case of wave-particle energy exchange associated with KAWs have been reported by MMS satellites (Gershman et al. 2017). As at presence of magnetic islands KAW and whistler waves have been observed, however there are no explicit observations that indicate that KAW is powerful, or whistler is powerful or both. In recently published work (Pathak et al. 2018, 2019) KAW was considered powerful enough to trigger nonlinear ponderomotive effects and modification in background density. In this situation, a weak whistler was propagating in the reconnection site, so the resultant spectra was due to nonlinear effects due to powerful KAW and reconnection physics introduced by the Harris profile.

On the hand in the present work, the Whistler is powerful enough to trigger ponderomotive effects and modification in background density. In this situation, a weak KAW is propagating, in the reconnection site, so the resultant spectra is due to nonlinear effects on account of powerful whistler and reconnection physics introduced by Harris profile.

The present manuscript work deals with the nonlinear evolution of a whistler wave and KAW propagating through the pre-existing magnetic presence of magnetic islands. For this study, the dynamical equations are derived by considering the ponderomotive force-driven density modification and magnetic field perturbation due to the shear field modelled by the Harris sheet. Servidio et al. (2010) have suggested that Harris-type current sheet (Harris 1962) is a reasonably good approximation of current sheets occurring in magnetized turbulence. It has been suggested an instability like the plasmoid instabilities (Comisso et al. 2016; Huang and Bhattacharjee 2016) is needed to trigger such reconnection (Harris current sheet). To understand the physics behind the field localization process and to estimate the characteristic transverse scale size of the localization formed, we also have developed a semi-analytical model.

The paper has been organised as follows: Sect. 2 of the paperwork focuses on the derivation of the dynamics of the analytical model. Section 3 of the paper delves into the examination and analysis of numerical simulation techniques, as well as the outcomes derived from these simulations. To gain a comprehensive understanding of the fundamental principles of localization, we have additionally examined the semianalytical model in Sect. 4. The summary and conclusion of our ongoing research are presented in Sect. 5.

2 Model dynamical equations

This section describes the model equations employed for the present study.

2.1 Whistler wave dynamics

We obtained dynamical equation of whistler wave using two fluid model. In analysis we considered 3D whistler wave having wave vector $k=k_x\hat{x} + k_y\hat{y} + k_z\hat{z}$ propagating in magnetized plasma with magnetic field, $B_0 = B_{0y}\hat{y} + B_{0z}\hat{z}$, $B_0 = B_{0y}\tanh^{-1}(x/L)\hat{y} + B_{0z}\hat{z}$. Here B_{0z} is the main guide field along $\hat{z}$ direction and B_{0y} is a shear field (Harris field) having the profile $\frac{B_{0y}}{B_0} = tanh\ (\frac{x}{L}\ )$ (Harris 1962) directed in $\hat{y}$ direction. Where B_0, is the asymptotic magnetic field strength far from the current sheet. y is the distance normal to the current sheet. x is the distance along the current sheet. L is the half-thickness of the current sheet, representing a characteristic length scale.

This analysis is explained by generalized Ohm's law combined with Maxwell's equations.

In general form, wave equation can be written as

$$\nabla^2 \vec{E} - \vec{\nabla}\left(\vec{\nabla}.\vec{E}\right) = \frac{4\pi}{c^2}\frac{\partial \vec{J}}{\partial t} + \frac{1}{c^2}\frac{\partial^2 \vec{E}}{\partial t^2}. \tag{1}$$

Equation of motion for electrons

$$m_e \frac{\partial \vec{v_e}}{\partial t} = -e\vec{E} - \frac{e}{c}\left\{\vec{v_e} \times \left(B_{0y}\hat{y} + B_{0z}\hat{z}\right)\right\}. \tag{2}$$

Equation of motion for ions

$$m_i \frac{\partial \vec{v_i}}{\partial t} = -e\vec{E} - \frac{e}{c}\left\{\vec{v_i} \times \left(B_{0y}\hat{y} + B_{0z}\hat{z}\right)\right\}. \tag{3}$$

Using Eq. (3), Eq. (2) and $J = n_i e v_{ix} - n_e e v_{ex}$, one can find x, y and z components of Eq. (1)

x-component of Eq. (1)

$$\left(-k_y^2 - k_z^2 + \frac{\omega^2}{\lambda_i^2\left(\omega_{ci}^2 - \omega^2\right)} + \frac{\omega^2}{\lambda_e^2\left(\omega_{ce}^2 - \omega^2\right)} + \frac{\omega^2}{c^2}\right)E_x + \left(k_x k_y + \frac{i\omega\omega_{ci}}{\lambda_i^2\left(\omega_{ci}^2 - \omega^2\right)} - \frac{i\omega\omega_{ce}}{\lambda_e^2\left(\omega_{ce}^2 - \omega^2\right)}\right)E_y + \left(k_x k_z + \frac{ieB_{0y}\omega}{m_i c\lambda_i^2\left(\omega_{ci}^2 - \omega^2\right)} + \frac{ieB_{0y}\omega}{m_e c\lambda_e^2\left(\omega_{ce}^2 - \omega^2\right)}\right)E_z = 0. \tag{4}$$

y-component of Eq. (1)

$$\left(k_x k_y + \frac{k_y k_z\left(k_x k_z + \frac{k_z k_y^2}{k_x}\right)}{\left(k_x^2 + k_y^2 + \frac{1}{\lambda_e^2} - \frac{\omega^2}{c^2}\right)} - \frac{i\omega\omega_{ci}}{\lambda_i^2\left(\omega_{ci}^2 - \omega^2\right)} + \frac{i\omega\omega_{ce}}{\lambda_e^2\left(\omega_{ce}^2 - \omega^2\right)}\right)E_x + \left(-k_x^2 - k_z^2 + \frac{\omega^2}{\lambda_i^2\left(\omega_{ci}^2 - \omega^2\right)} + \frac{\omega^2}{\lambda_e^2\left(\omega_{ce}^2 - \omega^2\right)} + \frac{\omega^2}{c^2}\right)E_y + \left(-\frac{eB_{0y}\omega_{ci}}{m_i c\lambda_i^2\left(\omega_{ci}^2 - \omega^2\right)} + \frac{eB_{0y}\omega_{ce}}{m_e c\lambda_e^2\left(\omega_{ce}^2 - \omega^2\right)}\right)E_z = 0. \tag{5}$$

z-component of Eq. (1)

$$\left(k_x k_z + \frac{k_z k_y^2}{k_x} - \frac{ieB_{0y}\omega}{m_i c\lambda_i^2\left(\omega_{ci}^2 - \omega^2\right)} + \frac{ieB_{0y}\omega}{m_e c\lambda_e^2\left(\omega_{ce}^2 - \omega^2\right)}\right)E_x + \left(-\frac{eB_{0y}\omega_{ci}}{m_i c\lambda_i^2\left(\omega_{ci}^2 - \omega^2\right)} - \frac{eB_{0y}\omega_{ce}}{m_e c\lambda_e^2\left(\omega_{ce}^2 - \omega^2\right)}\right)E_y + \left(-k_x^2 - k_z^2 - \frac{1}{\lambda_e^2} + \frac{\omega^2}{c^2}\right)E_z = 0. \tag{6}$$

On solving Eq. (4), Eq. (5) and Eq. (6) under applying conditions $k\lambda_i \gg 1$, $\omega^2 \gg \omega_{ce}\omega_{ci}$ (neglected displacement current), we can get following equation.

$$\omega^2\left(1 + k^2\lambda_e^2\right)^2 - \lambda_i^2 k^2 k_z^2 v_A^2 - \lambda_i^2 k^2 k_y^2 v_A^2 \frac{B_{0y}^2}{B_{0z}^2} - 2\lambda_i^2 k^2 k_y k_z v_A^2 \frac{B_{0y}}{B_{0z}} = 0. \tag{7}$$

here, $k^2 = k_x^2 + k_y^2 + k_z^2$

Equation (7) shows the dispersion relation of whistler wave in the presence of Harris field. Noting that, if we neglect the effect of Harris field, one can find the usual dispersion relation of whistler wave propagating at an angle (Zhao 2017) $\omega^2 = \frac{\lambda_i^2 k^2 k_z^2 v_A^2}{\left(1+k^2\lambda_e^2\right)^2}$. In the present model, we considered an angle of propagation $\sim 60°$.

Assuming $A_z = A_z e^{i\left(k_x x + k_y y + k_z z - \omega t\right)}$ and by applying inverse Fourier transform on Eq. (7) $\left(\frac{\partial}{\partial t} = -i\omega,\ \frac{\partial}{\partial x} = ik_x, \times \frac{\partial}{\partial y} = ik_y,\ \frac{\partial}{\partial z} = ik_z\right)$, we get dynamical equation of whistler wave in terms of vector potential (A_z).

$$\left[-\frac{\partial^2}{\partial t^2}\left(1 - \nabla^2\lambda_e^2\right)^2 - \lambda_i^2 v_A^2 \frac{\partial^2\nabla^2}{\partial z^2} - \lambda_i^2 v_A^2 \frac{B_{0y}^2}{B_{0z}^2}\frac{\partial^2\nabla^2}{\partial y^2} - 2\lambda_i^2 v_A^2 \frac{B_{0y}}{B_{0z}}\nabla^2\frac{\partial^2}{\partial y\partial z}\right]A_z = 0. \tag{8}$$

We assumed ion acoustic is propagating in z-direction in background medium. In this scenario, nonlinearity due to ponderomotive force came into picture. One can obtain the dynamical equation for ion acoustic wave using equation of motion for electrons and ions, continuity equation and charge neutrality as follows.

$$\left(\frac{\partial^2}{\partial t^2} - c_s^2\frac{\partial^2}{\partial z^2}\right)\frac{\delta n}{n_0} = -\frac{\partial}{\partial z}\left(\frac{F_{ez} + F_{iz}}{m_i}\right). \tag{9}$$

Here, c_s is ion sound speed, F_{ez} and F_{iz} are z- components of the ponderomotive forces due to whistler wave.

Ponderomotive force is defined as

$$\vec{F}_j = -m_j\left(v_{jx}^*\frac{\partial}{\partial x} + v_{jy}^*\frac{\partial}{\partial y} + v_{jz}^*\frac{\partial}{\partial z}\right)\vec{v}_j + \frac{q_j}{c}\left(\vec{v}_{j\perp}^{\,*} \times \vec{B}_\perp\right). \tag{10}$$

Here, asterisk represent the complex conjugate of velocity components. We can obtain expressions for F_{ez} and F_{iz} taking equation of motion and Faraday's law.

$$F_{ez} = -\frac{e^2}{2m_e c^2}\frac{\partial\left|A_z\right|^2}{\partial z}., \qquad F_{iz} = -\frac{e^2}{2m_i c^2}\frac{\partial\left|A_z\right|^2}{\partial z}.$$

So here, taking adiabatic response of density as suggested by Yadav and Sharma (2014), the dynamical equation of ion acoustic wave can be written as.

$$\frac{\partial^2}{\partial z^2}\left(\frac{\delta n}{n_0}\right)=\frac{e^2}{2m_e c^2 c_s^2}\left(\frac{1}{m_e}+\frac{1}{m_i}\right)\frac{\partial^2 |A_z|^2}{\partial z^2}. \tag{11}$$

After normalizing Eq. (11), we obtained, $A_N = \left(\frac{2m_e^2 m_i c^2 c_s^2}{e^2(m_e+m_i)}\right)^{\frac{1}{2}}$ this implies $\frac{\delta n}{n_0}=|A_z|^2$.

Now, we considered whistler wave propagates through this perturbed medium. In this following dynamical equation of whistler wave;

$$\begin{aligned}\Bigg[&-\frac{\partial^2}{\partial t^2}\left(1-\nabla^2\lambda_e^2\right)^2-\lambda_i^2 v_A^2\frac{\partial^2\nabla^2}{\partial z^2}\\&-\lambda_i^2 v_A^2\frac{B_{0y}^2}{B_{0z}^2}\frac{\partial^2\nabla^2}{\partial y^2}-2\lambda_i^2 v_A^2\frac{B_{0y}}{B_{0z}}\nabla^2\frac{\partial^2}{\partial y\partial z}\\&+\lambda_i^2 v_A^2\frac{\delta n}{n_0}\frac{\partial^2\nabla^2}{\partial z^2}\Bigg]A_z=0.\end{aligned} \tag{12}$$

In simplified form Eq. (12) can be written as

$$\begin{aligned}\Bigg[&-\frac{\partial^2}{\partial t^2}\left(1-\nabla^2\lambda_e^2\right)^2-\lambda_i^2 v_A^2\frac{\partial^2\nabla^2}{\partial z^2}\\&-\lambda_i^2 v_A^2\frac{B_{0y}^2}{B_{0z}^2}\frac{\partial^2\nabla^2}{\partial y^2}-2\lambda_i^2 v_A^2\frac{B_{0y}}{B_{0z}}\nabla^2\frac{\partial^2}{\partial y\partial z}\\&+\lambda_i^2 v_A^2|A_z|^2\frac{\partial^2\nabla^2}{\partial z^2}\Bigg]A_z=0.\end{aligned} \tag{13}$$

Here, n_0 is the unperturbed number density and δn is the modification in the number density. The solution for vector potential (A_z) is considered as $A_z = A_z(r,z,t)\times e^{i\left(k_x x+k_y y+k_z z-\omega t\right)}$, here A_z is a slowly varying function of r, z, t, and $\sqrt{\left(x^2+y^2\right)}$ and following the conditions $\partial_z A_z \ll k_z A_z$ and $\partial_r A_z \gg k_\perp A_z$. Substituting this solution in the dynamical for whistler wave, we obtain the following equation

$$\begin{aligned}&2i\omega\left(1+9k^4\lambda_e^4+18k_\perp^2k_z^2\lambda_e^4+6k^2\lambda_e^2\right)\frac{\partial A_z}{\partial t}\\&-2ik_z\left(-2k^2\omega^2\lambda_e^4-2\omega^2\lambda_e^2+k_z^2\lambda_i^2v_A^2+k^2\lambda_i^2v_A^2\right)\frac{\partial A_z}{\partial z}\\&+4\omega^2k_\perp^2\lambda_e^4\nabla_\perp^2A_z-\lambda_i^2v_A^2k^2k_y^2\frac{B_{0y}^2}{B_{0z}^2}A_z\\&-2\lambda_i^2v_A^2k^2k_yk_z\frac{B_{0y}}{B_{0z}}A_z+\lambda_i^2v_A^2k^2k_z^2|A_z|^2A_z=0.\end{aligned} \tag{14}$$

By making normalize for Eq. (14) (using normalize parameters $x_N = y_N = z_N = \frac{\rho_s}{10}$, $t_N = \frac{1}{5\omega_{ci}}$, $A_N = \left(\frac{2m_e^2m_ic^2c_s^2}{e^2(m_e+m_i)}\right)^{\frac{1}{2}}$, $n_N = n_0$), we obtained following dimensionless dynamical equation of whistler wave.

$$\begin{aligned}&-iw_1\frac{\partial A_z}{\partial t}+iw_2\frac{\partial A_z}{\partial z}+w_3\nabla_\perp^2A_z-w_4\frac{B_{0y}^2}{B_0^2}A_z\\&-w_5\frac{B_{0y}}{B_0}A_z+|A_z|^2A_z=0.\end{aligned} \tag{15}$$

Here, $w_1 = \frac{2\omega\left(1+9k^4\lambda_e^4+18k_\perp^2k_z^2\lambda_e^4+6k^2\lambda_e^2\right)}{\lambda_i^2v_A^2k^2k_z^2t_N}$, $w_2 = \frac{2\left(2k^2\omega^2\lambda_e^4+2\omega^2\lambda_e^2-k_z^2\lambda_i^2v_A^2-k^2\lambda_i^2v_A^2\right)}{\lambda_i^2v_A^2k^2k_zz_N}$, $w_3 = \frac{4\omega^2k_\perp^2\lambda_e^2}{\lambda_i^2v_A^2k^2k_z^2r_N^2}$, $w_4 = \frac{k_y^2}{k_z^2}$, $w_5 = \frac{2k_y}{k_z}$

As, we are concentrating interaction between powerful whistler waves and weak KAW in the present study. In this scenario next, we have the derived dynamical equation of the 3D-KAW.

2.2 KAW dynamics

We followed Schekochihin et al. (2009) and Pathak et al. (2019) for deriving a dynamical equation of KAW. In this derivation, we used the four field equations given below and considered KAW is propagating in a magnetized plasma having a magnetic field, $B_0 = B_{0y}\tanh^{-1}(x/L)\hat{y}+B_{0z}\hat{z}$ and wave vector $k=k_x\hat{x}+k_y\hat{y}+k_z\hat{z}$.

$$\frac{\partial\psi}{\partial t}=v_A\left(\frac{\partial}{\partial z}+\frac{B_{0y}}{B_0}\frac{\partial}{\partial y}\right)\left(\Phi+v_A\lambda_i\frac{B_{0z}}{B_0}\right). \tag{16}$$

$$\frac{d}{dt}\nabla_\perp^2\Phi=v_A\left(\frac{\partial}{\partial z}+\frac{B_{0y}}{B_0}\frac{\partial}{\partial y}\right)\nabla_\perp^2\psi. \tag{17}$$

$$\frac{d}{dt}\frac{B_{0z}}{B_0}=\frac{\beta}{(2+\beta)}\left(\frac{\partial}{\partial z}+\frac{B_{0y}}{B_0}\frac{\partial}{\partial y}\right)\left(u_{\parallel i}-\lambda_i\nabla_\perp^2\psi\right). \tag{18}$$

$$\frac{d}{dt}u_{\parallel i}=\frac{\beta}{(2+\beta)}v_A^2\left(\frac{\partial}{\partial z}+\frac{B_{0y}}{B_0}\frac{\partial}{\partial y}\right)\frac{B_{0z}}{B_0}. \tag{19}$$

Where, we have introduced scalar vector potential Φ, vector potential ψ, Plasma beta $\left(\beta=\frac{c_s^2}{v_A^2}\right)$, ion gyro radius $\left(\rho_s=\lambda_i\sqrt{\frac{\beta}{2}}\right)$, and sound velocity $c_s^2=k_B\frac{(T_e+T_i)}{m_i}$.

Now, let us combine Eqs. (16), (17) and (18) with ignoring parallel ion velocity $(u_{\parallel i})$. After combining equations new following

$$\begin{aligned}&\frac{\partial^2\psi}{\partial t^2}-v_A^2\left(1-\frac{2\rho_s^2}{(2+\beta)}\nabla_\perp^2\right)\\&\times\left(\frac{\partial^2}{\partial z^2}+\frac{2B_{0y}}{B_0}\frac{\partial^2}{\partial y\partial z}+\frac{B_{0y}^2}{B_0^2}\frac{\partial^2}{\partial y^2}\right)\psi=0.\end{aligned} \tag{20}$$

$$\left[\frac{\partial^2}{\partial t^2}+\frac{2v_A^2\rho_s^2}{(2+\beta)}\frac{\partial^2\nabla_\perp^2}{\partial z^2}-v_A^2\left(1-\frac{\delta n}{n_0}\right)\frac{\partial^2}{\partial z^2}-v_A^2\left(1-\frac{2\rho_s^2}{(2+\beta)}\nabla_\perp^2\right)\times\left(\frac{2B_{0y}}{B_0}\frac{\partial^2}{\partial y\partial z}+\frac{B_{0y}^2}{B_0^2}\frac{\partial^2}{\partial y^2}\right)\right]\psi=0. \quad (21)$$

We get the dispersion relation of KAW $\omega_0^2 = k_{0z}^2 v_A^2\left(1+\frac{2k_{0\perp}^2\rho_s^2}{(2+\beta)}\right)$ (reported in Schekochihin et al., [36]), if we neglect the effect of Harris field (B_{0y}) and density perturbation.

Considering the solution of dispersion relation is $\psi = \psi(r,z,t)\,e^{i(k_{0x}x+k_{0y}y+k_{0z}z-\omega_0 t)}$ here, ψ is a slowly varying function of r, z, t and $r=\sqrt{(x^2+y^2)}$. Substituting this solution in Eq. (21), we get following equation.

$$2i\omega_0\frac{\partial\psi}{\partial t}+2i\left(v_A^2+\frac{2v_A^2\rho_s^2k_{0\perp}^2}{(2+\beta')}\right)k_{0z}\frac{\partial\psi}{\partial z}+\frac{2v_A^2\rho_s^2k_{0z}^2}{(2+\beta')}\nabla_\perp^2\psi-v_A^2\left(k_{0y}^2+k_{0z}^2\right)\left(1+\frac{2k_{0x}^2\rho_s^2}{(2+\beta')}\right)\times\left(\frac{2B_{0y}}{B_0}+\frac{B_{0y}^2}{B_0^2}\right)\psi+v_A^2k_{0z}^2\frac{\delta n}{n_0}\psi=0. \quad (22)$$

After normalization equation takes a particular dimensionless form

$$ik_1\frac{\partial\psi}{\partial t}+ik_2\frac{\partial\psi}{\partial z}+k_3\nabla_\perp^2\psi-k_4\left(\frac{2B_{0y}}{B_0}+\frac{B_{0y}^2}{B_0^2}\right)\psi+|A_z|^2\psi=0. \quad (23)$$

Here, $k_1=\frac{2\omega_0}{v_A^2k_{0z}^2t_N}$, $k_2=\frac{2\left(v_A^2+\frac{2v_A^2\rho_s^2k_{0\perp}^2}{(2+\beta)}\right)k_{0z}}{v_A^2k_{0z}^2z_n}$, $k_3=\frac{\frac{2v_A^2\rho_s^2k_{0z}^2}{(2+\beta)}}{v_A^2k_{0z}^2x_n^2}$, $k_4=\frac{v_A^2\left(k_{0y}^2+k_{0z}^2\right)\left(1+\frac{2k_{0x}^2\rho_s^2}{(2+\beta)}\right)}{v_A^2k_{0z}^2}$

Equation (15) and Eq. (23) explain field evolution of powerful whistler wave and weak KAWs when Harris field is present.

3 Numerical simulation setup

The simulation has been run using the pseudospectral method. In this method, space integration for spatial integrations and finite difference method for temporal integration have been used. For temporal evolution finite difference method is applied for step size $\Delta t = 5\times10^{-4}$ along with predictor corrector method. Here, this simulation has been run in a periodic box having size $L_x = L_y = L_z = 10\pi$ using grid points ($128\times128\times128$) with initial conditions (given later). These dynamical equations have been studied at magnetopause presence of magnetic islands for following parameters (Chaston et al. 2008), $B_0 = 31\times10^{-5}G$, $n_0 = 21cm^{-3}$, $T_e = 4.2\times10^5K$ *and* $T_i = 2.7\times10^6K$ with initial conditions of Biskamp and Welter (1989). For the simulation we can start with any initial condition for example periodic, Gaussian, Random, X-O etc. but for studying the turbulence generation in the presence of magnetic islands this magnetic field topology (sequential X-points and O-points) is well known in literature. Biskamp and Welter (1989), have also started with the same initial condition to study dynamics of decaying two-dimensional magnetohydrodynamic turbulence.

$$A_z(x,y) = coscos(2x+2.3)+coscos(y+4.1) \quad (24)$$

$$\psi_z(x,y) = 0.15\times coscos(2x+2.3)+coscos(y+4.1) \quad (25)$$

3.1 Numerical simulation results

Figure 1 represents surface plot and contour plot of vector potential (A_z) of whistler wave at different times. Here, whistler waves propagate in the presence of presence of magnetic islands and perturbed density. The background density gets perturbed due to presence of ion acoustic wave in the background medium. As we observed at an initial time one can see localization in spatial scales, changes slowly itself. Further, these field localized structures have been broken into new localized structures with different intensities.

In Fig. 2, we investigated the effect of strong whistler wave on KAW. Figure 2(d) shows KAW field localized structures have been splitted into distinct intensity structures in spatial scales. One can notice in Fig. 2(d) localized structures have increased field intensity with significantly increased magnitude. KAW breaks due to the nonlinear perturbation, this nonlinearity due to a strong whistler wave and Harris field. These nonlinear structures may be responsible for turbulence generation.

The contour plot of magnetic field lines can be used to detect the presence of magnetic islands formed by reconnection. The spatial development of the current density function is afterward examined to gain an understanding of the growth of magnetic flux, which is associated with the current density function by Ampere's law. Figure 3 depicts the contour plot (in the left panel of Fig. 3) and current density (in the right panel of Fig. 3) of field lines in the x-y plane at various times. As time passes, we observe that the suitable X-O structures distort, and we ultimately arrive at a completely chaotic pattern.

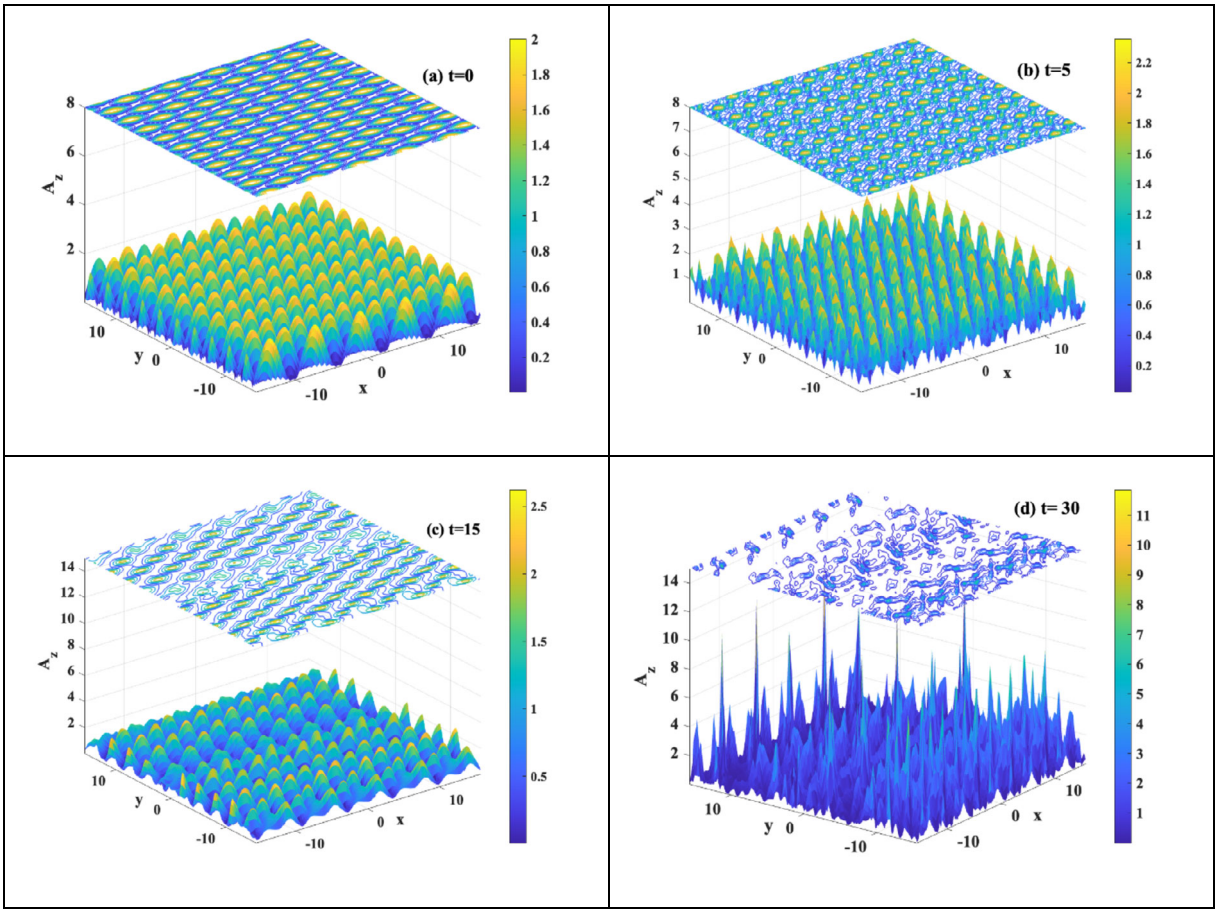


Fig. 1 Surface plot and contour plot of vector potential (A_z) of Strong whistler wave at different time ((a) t=0, (b) t=10, (c) t= 15, (d) t=30 here, t is normalized with t_N)

To investigate the energy transfer from large to small scale, we calculated power spectrum. It represents the plot of the ensemble-averaged spectra ($|B_k|^2$ vs k) at quasi steady state. Here, we are taking the cumulative effect of whistler wave and KAW magnetic field and to increase accuracy, 6 (normalized time 32-38) individual spectra were summed with ensemble average. In Fig. 4, the red and green lines are sketched as a reference line and power spectra obeying power laws in inertial range $|B_k|^2 \propto k^{-1.2}$ and after the break point having power law slope $k^{-3.7}$ with the steeper spectra. This steepening implies that as turbulence evolves, the rate of energy transfer from larger to smaller scales increases, leaving a visible signature of turbulence on the power spectrum.

It should be noted that scaling, in inertial range spectral indices (-1.2) is deviates from -5/3 in the presence of magnetic islands. This phenomenon is presumably caused by the possibility of magnetic reconnection altering the traditional Kolmogorov cascade (Boldyrev 2006; Boldyrev and Loureiro 2019; Jyoti et al. 2022; Jyoti and Sharma 2024). This phenomenon occurs when the anisotropic current-sheet transforms into magnetic islands through magnetic reconnection, prior to reaching the formal Kolmogorov dissipation scale. It can be noticed in Fig. 4 that after break point spectra becomes steepened with wavenumber and approach spectral indices (-3.7).

Further, the steepening of the power spectrum at smaller sizes represents energy transfer from larger to smaller length scales. This precise spectral index will enhance the formation of thermal tails of energetic particles, causing the particles to accelerate. Using the Fokker-Planck equation (also known as second order fermi acceleration (Ichimaru 1973), the repeated interaction of charged particles with localised structures can result in energization. The ongoing interaction of charged particles with magnetic clouds formed by turbulence results in the acceleration of charged particles in this method. Various mechanisms have been employed to analyse the acceleration of charged particles (Tsytovich 1989). Based on nonlinear coupling and turbulence formation, the current study reveals localised structures of nonlinear whistler waves. In these chaotic circumstances, charged particles gather energy from localized structures by repeat-

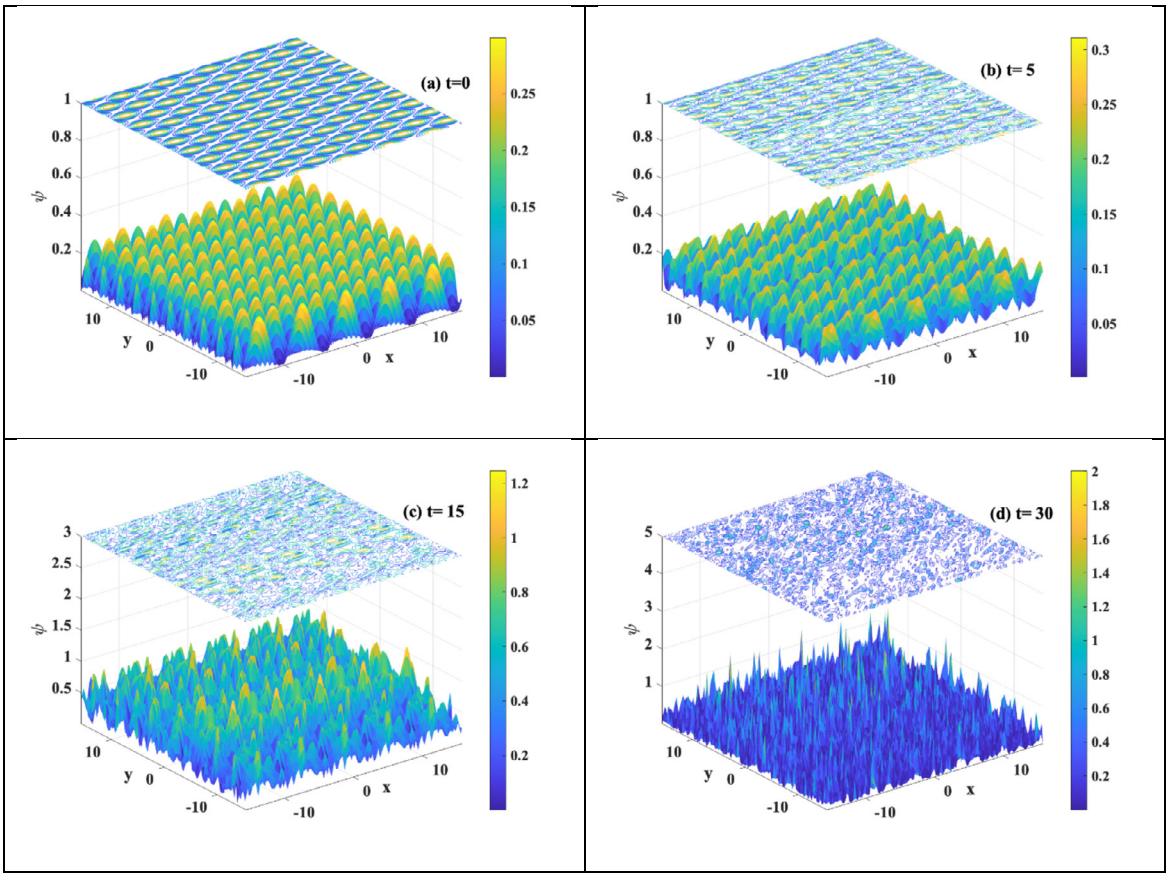


Fig. 2 Surface plot and contour plot of vector potential (ψ) of weak KAW at different time ((a) t=0, (b) t=10, (c) t= 15, (d) t=30 here, t is normalized with t_N)

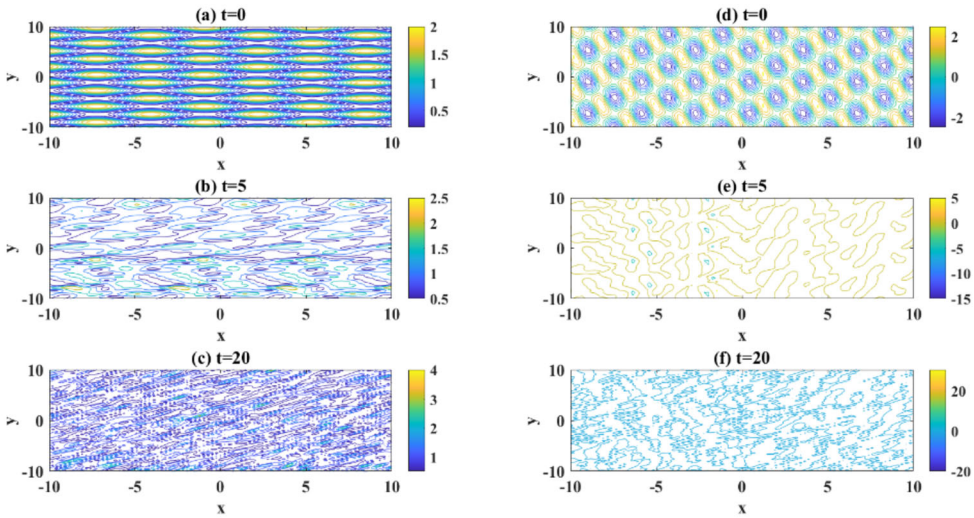


Fig. 3 Evolution of contour plot (left panel), and current sheet (right panel) formation in x-y plane at different time (in normalized units)

edly interacting, resulting in particle acceleration akin to the Fermi acceleration mechanism. A quasi-linear diffusion equation is used to describe the ongoing interaction of charged particles with localized structures, and it can be determined by the following formula (Fuchs et al. 1985; Rozmus et al. 1987; Ichimaru 1973; Sharma et al. 2006).

$$\frac{\partial f}{\partial t} = \frac{\partial}{\partial}\left\{D(v)\frac{\partial f'}{\partial v}\right\}$$

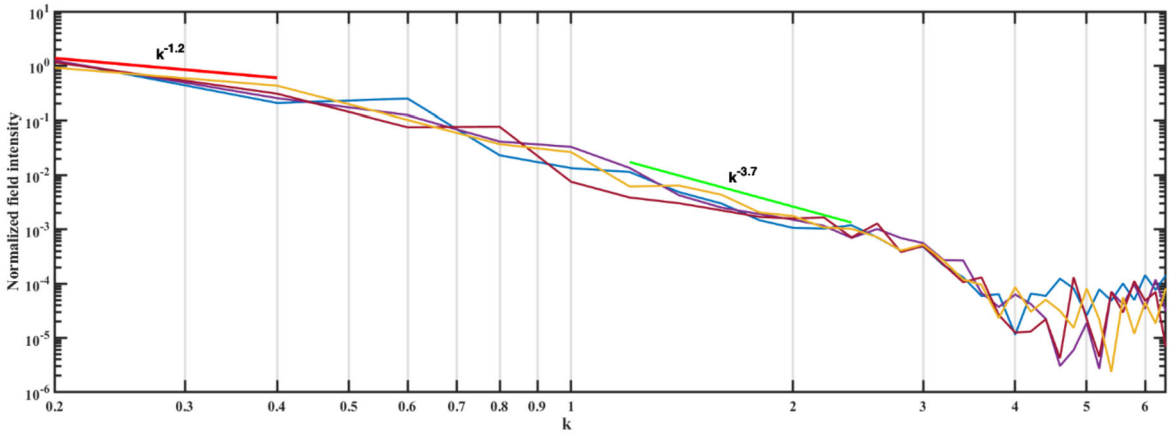


Fig. 4 Ensemble power spectrum of magnetic field (t=32 to t=38) (t is normalized) taking cumulative effect of whistler wave and KAW magnetic field

In this context, $D(v)$ is the symbol represents the coefficient of diffusion in velocity space, while represents the distribution function of velocity $f'(t, v)$. If the observation time is significantly greater than the time it takes for the ponderomotive nonlinearity to establish, the velocity distribution function may be independent of time. In the present scenario, the relationship between the spectral index η and the distribution function $f'(v)$ (Rozmus et al. 1987) is provided as follows-

$$f(v) \propto v^{2-\eta}$$

In our current analysis $\eta \simeq 3.7$, therefore $f(v) \sim v^{-1.7}$ which leads to the formation of thermal tail of energetic electrons.

4 Semi analytical model

To study physics responsible for field localization and find out the characteristic transverse scale sizes of these localized structures, we have developed a semi analytical model (Akhmanov et al. 1967) within paraxial regime ($r \ll r_0 f$). Here r_0 is the transverse size of the powerful whistler wave and f is the dimensionless beam width parameter. We have determined dynamical Eq. (14) of whistler wave using two-fluid model in Sect. 2.

Note, Yadav and Sharma (2014), and Shearer and Eddleman (1973), have reported, the density modification by the ponderomotive force of whistler can be written as,

$\frac{\delta n}{n_0} = exp\left(\alpha\,|A_z|^2\right) - 1$. When $A_z \ll 1$ this expression can be reduced to quadratic nonlinearity as represented in Sect. 2. Here α is a normalization parameter, $\alpha = \frac{1}{A_n^2}$.

In steady state Eq. (14) can be written as

$$2ik_z\left(2k^2\omega^2\lambda_e^4 + 2\omega^2\lambda_e^2 - k_z^2\lambda_i^2 v_A^2 - k^2\lambda_i^2 v_A^2\right)\frac{\partial A_z}{\partial z}$$
$$+ 4\omega^2 k_\perp^2\lambda_e^4\nabla_\perp^2 A_z - \lambda_i^2 v_A^2 k^2 k_y^2\frac{B_{0y}^2}{B_{0z}^2}A_z$$
$$+ 2\lambda_i^2 v_A^2 k^2 k_y k_z\frac{B_{0y}}{B_{0z}}A_z$$
$$+ \lambda_i^2 v_A^2 k^2 k_z^2\left(exp\left(\alpha\,|A_z|^2\right) - 1\right)A_z = 0. \quad (26)$$

The solution of A_z (Akhmanov et al. 1968) in terms of eikonal'S', can be written as, $A_z(r, z) = A_0(r, z) \times e^{ik_z(z)S(r,z)}$, where A_z and 'S' are real functions of x, y and z.

One can get following derivatives.

$$\frac{\partial A_z}{\partial r} = e^{ik_z(z)S(r,z)}\frac{\partial A_0}{\partial r} + ik_z A_0 e^{ik_z(z)S(r,z)}\frac{\partial S}{\partial r},$$
$$\frac{\partial^2 A_z}{\partial r^2} = e^{ik_z(z)S(r,z)}\frac{\partial^2 A_0}{\partial r^2} + 2ik_z e^{ik_z(z)S(r,z)}\frac{\partial A_0}{\partial r}\frac{\partial S}{\partial r}$$
$$- k_z^2 A_0 e^{ik_z(z)S(r,z)}\left(\frac{\partial S}{\partial r}\right)^2 + ik_z A_0 e^{ik_z(z)S(r,z)}\frac{\partial^2 S}{\partial r^2},$$
$$\frac{\partial A_z}{\partial z} = e^{ik_z(z)S(r,z)}\frac{\partial A_0}{\partial z} + ik_z(z)A_0 e^{ik_z(z)S(r,z)}\frac{\partial S}{\partial z}$$

Substituting these derivatives in Eq. (26)

$$2ik_z\left(2k^2\omega^2\lambda_e^4 + 2\omega^2\lambda_e^2 - k_z^2\lambda_i^2 v_A^2 - k^2\lambda_i^2 v_A^2\right)$$
$$\times\left(\frac{\partial A_0}{\partial z} + ik_z A_0\frac{\partial S}{\partial z}\right)$$
$$+ 4\omega^2 k_\perp^2\lambda_e^4\left(\frac{\partial^2 A_0}{\partial r^2} + 2ik_z\frac{\partial A_0}{\partial r}\frac{\partial S}{\partial r} - k_z^2 A_0\left(\frac{\partial S}{\partial r}\right)^2\right.$$
$$\left. + ik_z A_0\frac{\partial^2 S}{\partial r^2}\right) - \lambda_i^2 v_A^2 k^2 k_y^2\frac{B_{0y}^2}{B_{0z}^2}A_z$$
$$+ 2\lambda_i^2 v_A^2 k^2 k_y k_z\frac{B_{0y}}{B_{0z}}A_z$$

$$+\lambda_i^2 v_A^2 k^2 k_z^2 \left(exp\left(\alpha |A_0|^2\right)-1\right) A_0 = 0. \quad (27)$$

Rearrange terms in above equation for presenting in better form;

$$\frac{2i\left(2k^2\omega^2\lambda_e^4+2\omega^2\lambda_e^2-k_z^2\lambda_i^2 v_A^2-k^2\lambda_i^2 v_A^2\right)}{\lambda_i^2 v_A^2 k^2 k_z} \times\left(\frac{\partial A_0}{\partial z}+ik_z A_0\frac{\partial S}{\partial z}\right) +\frac{4\omega^2 k_\perp^2\lambda_e^4}{\lambda_i^2 v_A^2 k^2 k_z^2}\left(\frac{\partial^2 A_0}{\partial r^2}+2ik_z\frac{\partial A_0}{\partial r}\frac{\partial S}{\partial r}-k_z^2 A_0\left(\frac{\partial S}{\partial r}\right)^2 +ik_z A_0\frac{\partial^2 S}{\partial r^2}\right)-\frac{k_y^2}{k_z^2}\frac{B_{0y}^2}{B_0^2}A_0+2\frac{k_y}{k_z}\frac{B_{0y}}{B_0}A_0 +\left(exp\left(\alpha |A_0|^2\right)-1\right)A_0=0. \quad (28)$$

Here, $\xi_1 = \frac{\left(2k^2\omega^2\lambda_e^4+2\omega^2\lambda_e^2-k_z^2\lambda_i^2 v_A^2-k^2\lambda_i^2 v_A^2\right)}{\lambda_i^2 v_A^2 k^2}$, $\xi_2 = \frac{4\omega^2 k_\perp^2\lambda_e^4}{\lambda_i^2 v_A^2 k^2}$, $\xi_3 = \frac{k_y^2}{k_z^2}$, $\xi_4 = 2\frac{k_y}{k_z}$

In simplification form above equation can be written as;

$$i\frac{2\xi_1}{k_z}\left(\frac{\partial A_0}{\partial z}+ik_z A_0\frac{\partial S}{\partial z}\right) +\frac{\xi_2}{k_z^2}\left(\frac{\partial^2 A_0}{\partial r^2}+2ik_z\frac{\partial A_0}{\partial r}\frac{\partial S}{\partial r}-k_z^2 A_0\left(\frac{\partial S}{\partial r}\right)^2 +ik_z A_0\frac{\partial^2 S}{\partial r^2}\right)-\xi_3\frac{B_{0y}^2}{B_0^2}A_0+\xi_4\frac{B_{0y}}{B_0}A_0 +\left(exp\left(\alpha |A_0|^2\right)-1\right)A_0=0. \quad (29)$$

By separating the real and imaginary parts from Eq. (29), we can obtain following equations.

Real part:

$$2\xi_1 A_0\frac{\partial S}{\partial z}+\frac{\xi_2}{k_z^2}\frac{\partial^2 A_0}{\partial r^2}-\xi_2 A_0\left(\frac{\partial S}{\partial r}\right)^2 -\xi_3\frac{B_{0y}^2}{B_0^2}A_0+\xi_4\frac{B_{0y}}{B_0}A_0 +\left(exp\left(\alpha |A_0|^2\right)-1\right)A_0=0. \quad (30)$$

Imaginary part:

$$\frac{2i\xi_1}{k_z}\frac{\partial A_0}{\partial z}+\frac{2i\xi_2}{k_z}\frac{\partial A_0}{\partial r}\frac{\partial S}{\partial r}+\frac{i\xi_2}{k_z}A_0\frac{\partial^2 S}{\partial r^2}=0. \quad (31)$$

Assuming the solutions (Akhmanov et al. 1967) of Eqs. (30) and (31) $A_0^2 = \frac{A_{00}^2}{f^2(z)}exp\left(\frac{-r^2}{r_0^2 f^2(z)}\right)$ (this expression represents the intensity distribution of the whistler wave in nonlinear medium) and $S = \beta'\frac{r^2}{2}$. Here, r_0 is transverse scale size of whistler wave, S is slowing varying function of r and z, $f(z)$ is the dimensionless parameter (which measures the beam width of wave) and $\beta'(z)$ represents the radius of curvature of the wavefront.

Now, we can calculate derivatives following as; $\frac{\partial A_0^2}{\partial r} = A_0^2\left(\frac{-2r}{r_0^2 f^2}\right)$, $\frac{\partial^2 A_0^2}{\partial r^2} = A_0^2\left(\frac{-2}{r_0^2 f^2}\right)+A_0^2\left(\frac{-2r}{r_0^2 f^2}\right)^2$, $\frac{\partial A_0^2}{\partial z} = \left[-\frac{2A_0^2}{f}\frac{df}{dz}+\frac{2A_0^2 r^2}{r_0^2 f^3}\frac{df}{dz}\right]$, $\frac{\partial S}{\partial r} = \beta(z)\ r$, $\frac{\partial^2 S}{\partial r^2} = \beta'(z)$, $\frac{\partial S}{\partial z} = \frac{\partial\beta'}{\partial z}\frac{r^2}{2}$

Substituting above mentioned derivates in Eq. (31)

$$2\xi_1 A_0\left[-\frac{1}{f}\frac{df}{dz}+\frac{r^2}{r_0^2 f^3}\frac{df}{dz}\right]+\xi_2 A_0\beta'(z) +\xi_2 A_0\left(\frac{-2r^2}{r_0^2 f^2}\right)\beta'(z)=0. \quad (32)$$

Compare coefficients of r^2;

$$2\xi_1 A_0\frac{1}{r_0^2 f^3}\frac{df}{dz}-\xi_2 A_0\frac{2}{r_0^2 f^2}\beta'(z)=0.$$

$$\beta'(z)=\frac{\xi_1}{\xi_2}\frac{1}{f}\frac{df}{dz}. \quad (33)$$

Further, substituting above calculated derivatives of A_0^2 and S parameter in Eq. (30), which is real part of Eq. (29).

$$-2\xi_1\frac{r^2}{2}A_0\frac{\partial\beta'}{\partial z}+\frac{\xi_2}{2k_z^2}A_0\left[\left(\frac{-2}{r_0^2 f^2}\right)+\left(\frac{-2r}{r_0^2 f^2}\right)^2\right] -\xi_2 A_0\left(\beta'(z)\ r\right)^2-\xi_3\frac{B_{0y}^2}{B_0^2}A_0+\xi_4\frac{B_{0y}}{B_0}A_0 -\frac{r^2\alpha A_{00}^2}{r_0^2 f^4}exp\left(\frac{\alpha A_{00}^2}{f^2}\right)A_0=0. \quad (34)$$

Again, compare coefficients of r^2 in Eq. (34)

$$-\xi_1\frac{\partial\beta}{\partial z}+\frac{2\xi_2}{k_z^2}\left(\frac{1}{r_0^2 f^2}\right)^2-\xi_2\left(\beta'(z)\right)^2 -\xi_3\frac{1}{\lambda_e^2}-\frac{\alpha A_{00}^2}{r_0^2 f^4}exp\left(\frac{\alpha A_{00}^2}{f^2}\right)=0. \quad (35)$$

From Eq. (33), $\frac{\partial\beta'(z)}{\partial z}=\frac{\xi_1}{\xi_2}\left[-\frac{1}{f^2}\left(\frac{df}{dz}\right)^2+\frac{1}{f}\frac{d^2 f}{dz^2}\right]$.

Substituting values of $\frac{\partial\beta}{\partial z}$ and $\beta'(z)$ in Eq. (35),

$$-\frac{\xi_1^2}{\xi_2}\left[-\frac{1}{f^2}\left(\frac{df}{dz}\right)^2+\frac{1}{f}\frac{d^2 f}{dz^2}\right]+\frac{2\xi_2}{k_z^2}\left(\frac{1}{r_0^2 f^2}\right)^2$$

$$-\xi_2\left(\frac{\xi_1}{\xi_2}\frac{1}{f}\frac{df}{dz}\right)^2-\xi_3\frac{1}{\lambda_e^2}$$
$$-\frac{\alpha A_{00}^2}{r_0^2 f^4}exp\left(\frac{\alpha A_{00}^2}{f^2}\right)=0. \quad (36)$$

$$\frac{d^2f}{dz^2}=\frac{2\xi_2^2}{\xi_1^2}\frac{1}{k_z^2 r_0^4 f^3}-\frac{\xi_2\xi_3}{\xi_1^2\lambda_e^2}f$$
$$-\frac{\xi_2}{\xi_1^2}\frac{\alpha A_{00}^2}{r_0^2 f^3}exp\left(\frac{\alpha A_{00}^2}{f^2}\right). \quad (37)$$

Now, one can obtain equation for dimensionless parameter f, using normalizing parameter $\eta=\frac{z}{R_d}$, here $R_d=k_z r_0^2$.

$$\frac{d^2f}{d\eta^2}=\frac{2\xi_2^2}{\xi_1^2}\frac{1}{f^3}-\frac{\xi_2\xi_3 k_z^2 r_0^4}{\xi_1^2\lambda_e^2}f$$
$$-\frac{\xi_2}{\xi_1^2}\frac{k_z^2 r_0^2\alpha A_{00}^2}{f^3}exp\left(\frac{\alpha A_{00}^2}{f^2}\right). \quad (38)$$

In Eq. (38) first term on right hand side represents diffraction due to the finite transverse scale size of whistler wave, second term represents the effect of Harris current sheet which is responsible for convergence of the strictures and last term shows the ponderomotive nonlinearity. This interpretation indicates support of wave nonlinearity in the localization process. To calculate scale size Eqs. (38) is solved for plane wavefront with boundary conditions $\frac{df}{d\eta}=0$, $f=1\ at\ \eta=0$.

We obtained,

$$r_0^4-\frac{2\xi_2}{\xi_3 k_z^2}\lambda_e^2+r_0^2\frac{\lambda_e^2\alpha A_{00}^2}{\xi_3}exp\left(\frac{\alpha A_{00}^2}{f^2}\right)=0. \quad (39)$$

$$r_0^4-\frac{8\omega^2 k_\perp^2\lambda_e^2}{\lambda_i^2 v_A^2 k^2 k_y^2}\lambda_e^4+r_0^2\frac{k_z^2\lambda_e^2\alpha A_{00}^2}{k_y^2}exp\left(\frac{\alpha A_{00}^2}{f^2}\right)=0. \quad (40)$$

It is clear from Eqs. (40), when power of whistler wave is zero the scale sizes of field localized structures having $r_0\sim 0.4\lambda_e$ in x, y directions.

Similarly, we obtain a semi-analytical solution for KAW Eq. (22) using the method developed by Akhmanov et al. (1968) within the paraxial approximation ($r\ll r_- f_-$). Here, r_- is transverse scale size of KAW and f_- is dimensionless beam width parameter.

Introducing the solution of Eq. (22) (ψ) in terms of eikonal S as [Akhmanov et al. 1968] $\psi(r,z)=\psi(r,z)\,e^{ik_{0z}(z)S(r,\ z)}$

By calculating derivatives of assumed solution as we have done in whistler wave semi analytical model and substituted those derivatives in Eq. (22), in steady state we can get following equation,

$$2i\left(v_A^2+\frac{2v_A^2\rho_s^2k_{0\perp}^2}{(2+\beta')}\right)k_{0z}^2\left(\frac{1}{k_{0z}}\frac{\partial\psi}{\partial z}+i\psi\frac{\partial S}{\partial z}\right)$$
$$+\frac{2v_A^2\rho_s^2k_{0z}^2}{(2+\beta')}\left(\frac{\partial^2\psi}{\partial r^2}+2ik_{0z}\frac{\partial\psi}{\partial r}\frac{\partial S}{\partial r}-k_{0z}^2\psi\left(\frac{\partial S}{\partial r}\right)^2\right.$$
$$\left.+ik_{0z}\psi\frac{\partial^2 S}{\partial r^2}\right)-v_A^2\left(k_{0y}^2+k_{0z}^2\right)\left(1+\frac{2k_{0x}^2\rho_s^2}{(2+\beta')}\right)$$
$$\times\left(\frac{2B_{0y}}{B_0}+\frac{B_{0y}^2}{B_0^2}\right)\psi$$
$$+v_A^2k_{0z}^2\left(exp\left(\alpha|A_z|^2\right)-1\right)\psi=0. \quad (41)$$

Further, Eq. (41) can be written as;

$$2i\eta_1\left(\frac{1}{k_{0z}}\frac{\partial\psi}{\partial z}+i\psi\frac{\partial S}{\partial z}\right)$$
$$+\eta_2\rho_s^2\left(\frac{\partial^2\psi}{\partial r^2}+2ik_{0z}\frac{\partial\psi}{\partial r}\frac{\partial S}{\partial r}-k_{0z}^2\psi\left(\frac{\partial S}{\partial r}\right)^2\right.$$
$$\left.+ik_{0z}\psi\frac{\partial^2 S}{\partial r^2}\right)-\eta_3\left(\frac{2B_{0y}}{B_0}+\frac{B_{0y}^2}{B_0^2}\right)\psi$$
$$+\left(exp\left(\alpha|A_z|^2\right)-1\right)\psi=0. \quad (42)$$

Here, $\eta_1=\left(1+\frac{2\rho_s^2k_{0\perp}^2}{(2+\beta')}\right)$, $\eta_2=\frac{2}{(2+\beta')}$ *and* $\eta_3=\frac{\left(k_{0y}^2+k_{0z}^2\right)\left(1+\frac{2k_{0x}^2\rho_s^2}{(2+\beta')}\right)}{k_{0z}^2}$

Equation (42) can be separated into real and imaginary parts as

Real part;

$$-2\eta_1\psi\frac{\partial s}{\partial z}+\eta_2\rho_s^2\frac{\partial^2\psi}{\partial r^2}-\eta_2\rho_s^2k_{0z}^2\psi\left(\frac{\partial S}{\partial r}\right)^2$$
$$-\eta_3\left[\frac{2B_{0y}}{B_0}+\frac{B_{0y}^2}{B_0^2}\right]\psi$$
$$+\left(exp\left(\alpha|A_z|^2\right)-1\right)\psi=0. \quad (43)$$

imaginary parts;

$$\frac{2\eta_1}{k_{0z}}\frac{\partial\psi}{\partial z}+2\eta_2\rho_s^2k_{0z}\frac{\partial\psi}{\partial r}\frac{\partial S}{\partial r}+\eta_2\rho_s^2k_{0z}\frac{\partial^2 S}{\partial r^2}=0. \quad (44)$$

Assuming the solution[35] of Eqs. (43) and (44) can be written as

$$\psi^2=\frac{\psi_{00}^2}{f_-^2}exp\left(\frac{-r^2}{r_-^2f_-^2(z)}\right)\quad \text{and} S=\beta_-'(z)\frac{r^2}{2}$$

Here, r_- is transverse scale size of KAW, $f_-(z)$ is the dimensionless beam width parameter of the KAW, $\beta'_-(z)$ represents the radius of curvature of the wavefront and S is slowing varying function of r and z.

Substituting above mentioned derivates in imaginary part of Eq. (44)

$$\frac{2\eta_1}{k_{0z}}\left[-\frac{1}{f_-}\frac{df_-}{dz}+\frac{r^2}{r_-^2 f_-^3}\frac{df_-}{dz}\right] + \eta_2\rho_s^2 k_{0z}\left(\frac{-2r^2}{r_-^2 f_-^2}\right)\beta'_-(z)+\eta_2\rho_s^2 k_{0z}\beta'_-(z)=0. \tag{45}$$

Compare coefficients of r^2;

$$\frac{2\eta_1}{k_{0z}r_-^2 f_-^3}\frac{df_-}{dz}-\frac{2\eta_2\rho_s^2 k_{0z}}{r_-^2 f_-^2}\beta'_-(z)=0$$

$$\beta'_-(z)=\frac{\eta_1}{\eta_2 k_{0z}^2\rho_s^2}\frac{1}{f_-}\frac{df_-}{dz}. \tag{46}$$

Further, substituting above calculating derivatives of ψ^2 and S parameter in Eq. (43), which is real part of Eq. (42).

$$-2\eta_1\psi\frac{r^2}{2}\frac{\partial\beta'_-}{\partial z}+\frac{\eta_2\rho_s^2\psi}{2}\left(\left(\frac{-2}{r_-^2 f_-^2}\right)+\left(\frac{-2r}{r_-^2 f_-^2}\right)^2\right) - \eta_2\rho_s^2 k_{0z}^2\psi\left(\beta'_-(z)r\right)^2-\eta_3\left[\frac{2B_{0y}}{B_0}+\frac{B_{0y}^2}{B_0^2}\right]\psi - \frac{r^2\alpha A_{00}^2}{r_0^2 f^4}exp\left(\frac{\alpha A_{00}^2}{f^2}\right)\psi=0. \tag{47}$$

Compare coefficients of r^2 in Eq. (47)

$$-\eta_1\frac{\partial\beta'_-}{\partial z}+2\eta_2\rho_s^2\psi\left(\frac{1}{r_-^2 f_-^2}\right)^2-\eta_2\rho_s^2 k_{0z}^2\left(\beta'_-(z)\right)^2 - \eta_3\frac{1}{\rho_s^2}-\frac{\alpha A_{00}^2}{r_0^2 f^4}exp\left(\frac{\alpha A_{00}^2}{f^2}\right)=0. \tag{48}$$

From Eq. (46), $\frac{\partial\beta'(z)}{\partial z}=\frac{\eta_1}{\eta_2 k_{0z}^2\rho_s^2}\left[-\frac{1}{f^2}\left(\frac{df}{dz}\right)^2+\frac{1}{f}\frac{d^2f}{dz^2}\right]$.

Substituting $\frac{\partial\beta'(z)}{\partial z}$ and $\beta'_-(z)$ in Eq. (48);

$$-\frac{\eta_1^2}{\eta_2 k_{0z}^2\rho_s^2}\left[-\frac{1}{f_-^2}\left(\frac{df_-}{dz}\right)^2+\frac{1}{f_-}\frac{d^2f_-}{dz^2}\right] + 2\eta_2\rho_s^2\left(\frac{1}{r_-^2 f_-^2}\right)^2-\eta_2\rho_s^2 k_{0z}^2\left(\frac{\eta_1}{\eta_2 k_{0z}^2\rho_s^2}\frac{1}{f_-}\frac{df_-}{dz}\right)^2 - \eta_3\frac{1}{\rho_s^2}-\frac{\alpha A_{00}^2}{r_0^2 f^4}exp\left(\frac{\alpha A_{00}^2}{f^2}\right)=0. \tag{49}$$

$$\frac{d^2f_-}{dz^2}=\frac{2\eta_2^2\rho_s^4 k_{0z}^2}{\eta_1^2 r_-^4 f_-^3}-\frac{\eta_2\eta_3 k_{0z}^2 f_-}{\eta_1^2} - \frac{\eta_2 f_- k_{0z}^2\rho_s^2\alpha A_{00}^2}{\eta_1^2 r_0^2 f^4}exp\left(\frac{\alpha A_{00}^2}{f^2}\right). \tag{50}$$

Equation for the dimensionless beam width parameter of KAW(f_-) can be written as

(Using normalising parameter $\eta_-=\frac{z}{R_{d_-}}$, here $R_{d_-}=k_{0z}r_-^2$

$$\frac{d^2f_-}{d\eta_-^2}=\frac{2\eta_2^2\rho_s^4 k_{0z}^4}{\eta_1^2}\frac{1}{f_-^3}-\frac{\eta_2\eta_3 k_{0z}^4 r_-^4 f_-}{\eta_1^2} - \frac{\eta_2 f_- k_{0z}^4\rho_s^2 r_-^4\alpha A_{00}^2}{\eta_1^2 r_0^2 f^4}exp\left(\frac{\alpha A_{00}^2}{f^2}\right) \tag{51}$$

In Eq. (51), on the right-hand side the first term signifies the presence of finite transverse scale size of the KAW, the second term is responsible for Harris field and last term gives essential effect of powerful whistler wave. The first term leads to diffraction and Harris field and modification in the background density by powerful whistler wave are responsible for convergence of the localized structures. Here, wave nonlinearity is significantly helping in the localization process. Equation (51) is solved using with boundary conditions (for plane wavefront) $\frac{df_-}{d\eta_-=0}$, $f_-=1$ *at* $\eta_-=0$.

We obtained,

$$r_-^4-\frac{2\eta_2\rho_s^4}{\eta_3}+\frac{\rho_s^2 r_-^4\alpha A_{00}^2}{\eta_3 r_0^2}exp\left(\frac{\alpha A_{00}^2}{f^2}\right)=0. \tag{52}$$

In case of KAW the transverse scale size of localized structures is $r_-=0.9\rho_s$, respectively, when power of whistler wave is zero. Interestingly, we can examine that the scale size of field localization is depended on power of whistler wave also. Calculating for, $\alpha A_{00}^2=1$, $r_-=1.1\rho_s$, it has significant one can notice in KAW propagate in modified density and field due to power whistler wave and Harris current sheet. Summarize, this model suggests the powerful whistler wave have cooperated in the spreading of localized structures of KAW. These localized structures are varying from electrons scale to ion scales.

5 Summary and conclusion

We have developed a model to study the evaluation of electron to ion scale nonlinear structures and associated turbulence generation at dayside presence of magnetic islands. The dynamical equations of whistler wave and KAW have been derived using two fluid model and four field equations respectively. These equations have been solved numerically and semi- analytically. To have better perception we

have developed a semi-analytical model using the nonlinear dynamical equations of whistler wave and KAW within paraxial regime using the eikonal approach as proposed by Akhmanov et al.[48]. In numerical simulation results it is clearly pointed out; localized structures have scale sizes varying from electron inertial length to ion gyroradious. To investigate the energy transfer from large to small scale, we calculated ensemble-averaged spectra ($|B_k|^2$ vs k) at quasi steady state. Here, we are taking cumulative effect of whistler wave and KAW magnetic field and to increase accuracy, 6 (normalized time 32-38) individual spectra were summed with ensemble average. The power spectra obeying power laws where $|B_k|^2 \propto k^{-1.2}$ and after the break point having slope $k^{-3.7}$. It becomes steeper with wavenumber and signify robust signature of turbulence as reported by Chaston et al. (2008).

Author contributions All authors reviewed the manuscript.

Funding information This work was supported by National Post- Doctoral fellowship file number PDF/2019/000891 funded by Science & Engineering Research Board (SERB), Department of Science & Technology, Government of India.

Data availability No datasets were generated or analysed during the current study.

Declarations

Competing interests The authors declare no competing interests.

References

Abdelhamid, H.M., Lingam, M., Mahajan, S.M.: Extended MHD turbulence and its applications to the solar wind. Astrophys. J. **829** (2016). https://doi.org/10.3847/0004-637x/829/2/87

Akhmanov, S.A., Sukhorukov, A.P., Khokhlov, R.V.: Self-focusing and diffraction of light in a Nonlinear medium. Usp. Fiz. Nauk **93** (1967). https://doi.org/10.3367/ufnr.0093.196709c.0019

Akhmanov, S.A., Sukhorukov, A.P., Khokhlov, R.V.: Self-focusing and diffraction of light in a nonlinear medium. Sov. Phys. Usp. **10** (1968). https://doi.org/10.1070/pu1968v010n05abeh005849

Bale, S.D., Mozer, F.S., Phan, T.: Observation of lower hybrid drift instability in the diffusion region at a reconnecting magnetopause. Geophys. Res. Lett. **29** (2002). https://doi.org/10.1029/2002GL016113

Biskamp, D., Welter, H.: Dynamics of decaying two-dimensional magnetohydrodynamic turbulence. Phys. Fluids B **1** (1989). https://doi.org/10.1063/1.859060

Boldyrev, S.: Spectrum of magnetohydrodynamic turbulence. Phys. Rev. Lett. **96** (2006). https://doi.org/10.1103/PhysRevLett.96.115002

Boldyrev, S., Loureiro, N.F.: Role of reconnection in inertial kinetic-Alfvén turbulence. Phys. Rev. Res. **1** (2019). https://doi.org/10.1103/PhysRevResearch.1.012006

Cattell, C.A., Mozer, F.S.: Experimental determination of the dominant wave mode in the active near-Earth magnetotail. Geophys. Res. Lett. **13** (1986). https://doi.org/10.1029/GL013i003p00221

Chaston, C.C., Phan, T.D., Bonnell, J.W., Mozer, F.S., Acuña, M., Goldstein, M.L., Balogh, A., Andre, M., Reme, H., Fazakerley, A.: Drift-kinetic Alfvén waves observed near a reconnection X line in the Earth's magnetopause. Phys. Rev. Lett. **95**, 5–8 (2005). https://doi.org/10.1103/PhysRevLett.95.065002

Chaston, C., Bonnell, J., McFadden, J.P., Carlson, C.W., Cully, C., Le Contel, O., Roux, A., Auster, H.U., Glassmeier, K.H., Angelopoulos, V., Russell, C.T.: Turbulent heating and cross-field transport near the magnetopause from THEMIS. Geophys. Res. Lett. **35**, 2–6 (2008). https://doi.org/10.1029/2008GL033601

Chaston, C.C., Johnson, J.R., Wilber, M., Acuna, M., Goldstein, M.L., Reme, H.: Kinetic Alfvén wave turbulence and transport through a reconnection diffusion region. Phys. Rev. Lett. **102** (2009). https://doi.org/10.1103/PhysRevLett.102.015001

Chaston, C.C., Bonnell, J.W., Clausen, L., Angelopoulos, V.: Correction to "Energy transport by kinetic-scale electromagnetic waves in fast plasma sheet flows." J. Geophys. Res. Space Phys. **117** (2012). https://doi.org/10.1029/2012ja018476

Comisso, L., Lingam, M., Huang, Y.M., Bhattacharjee, A.: General theory of the plasmoid instability. Phys. Plasmas **23** (2016). https://doi.org/10.1063/1.4964481

Comisso, L., Huang, Y.-M., Lingam, M., Hirvijoki, E., Bhattacharjee, A.: Magnetohydrodynamic Turbulence in the Plasmoid-mediated Regime. Astrophys. J. **854** (2018). https://doi.org/10.3847/1538-4357/aaac83

Deng, X.H., Matsumoto, H.: Rapid magnetic reconnection in the Earth's magnetosphere mediated by whistler waves. Nature **410** (2001). https://doi.org/10.1038/35069018

Ergun, R.E., Pathak, N., Usanova, M.E., Qi, Y., Vo, T., Burch, J.L., Schwartz, S.J., Torbert, R.B., Ahmadi, N., Wilder, F.D., Chasipis, A.: Observation of magnetic reconnection in a region of strong turbulence. Astrophys. J. Lett. **935**(1), L8 (2022). https://doi.org/10.3847/2041-8213/ac81d4

Farrell, W.M., Desch, M.D., Kaiser, M.L., Goetz, K.: The dominance of electron plasma waves near a reconnection X-line region. Geophys. Res. Lett. **29** (2002). https://doi.org/10.1029/2002GL014662

Fuchs, V., Krapchev, V., Ram, A., Bers, A.: Diffusion of electrons by coherent wavepackets. Physica D **14** (1985). https://doi.org/10.1016/0167-2789(85)90175-7

Fujimoto, M., Shinohara, I., Kojima, H.: Reconnection and waves: a review with a perspective. Space Sci. Rev. (2011)

Galtier, S.: Wave turbulence in incompressible Hall magnetohydrodynamics. J. Plasma Phys. **72** (2006). https://doi.org/10.1017/S0022377806004521

Gershman, D.J., F-Viñas, A., Dorelli, J.C., Boardsen, S.A., Avanov, L.A., Bellan, P.M., Schwartz, S.J., Lavraud, B., Coffey, V.N., Chandler, M.O., Saito, Y., Paterson, W.R., Fuselier, S.A., Ergun, R.E., Strangeway, R.J., Russell, C.T., Giles, B.L., Pollock, C.J., Torbert, R.B., Burch, J.L.: Wave-particle energy exchange directly observed in a kinetic Alfvén-branch wave. Nat. Commun. **8** (2017). https://doi.org/10.1038/ncomms14719

Harris, E.G.: On a plasma sheath separating regions of oppositely directed magnetic field. Il Nuovo Cimento Ser. **10**, Article ID 23 (1962). https://doi.org/10.1007/BF02733547

Huang, Y.-M., Bhattacharjee, A.: Turbulent magnetohydrodynamic reconnection mediated by the plasmoid instability. Astrophys. J. **818** (2016). https://doi.org/10.3847/0004-637x/818/1/20

Ichimaru, S.: Basic principles of plasma physics: a statistical approach. By S. Ichimaru. Benjamin frontiers in physics. J. Plasma Phys. **13**, 324 (1973). https://doi.org/10.1017/s0022377800025289

Jyoti, S.S.C., Sharma, R.P.: Localization of beam generated whistler wave and turbulence generation in reconnection region of magnetopause. Phys. Plasmas **31** (2024). https://doi.org/10.1063/5.0169397

Jyoti, J., Sharma, S.C., Pathak, N., Sharma, R.P.: Beam-driven whistler mode nonlinear saturation and turbulence in the magnetopause. Phys. Plasmas **29**(9) (2022)

Karimabadi, H., Roytershteyn, V., Daughton, W., Liu, Y.H.: Recent evolution in the theory of magnetic reconnection and its connection with turbulence (2013)

Lazarian, A., Eyink, G.L., Jafari, A., Kowal, G., Li, H., Xu, S., Vishniac, E.T.: 3D turbulent reconnection: Theory, tests, and astrophysical implications. Phys. Plasmas **27** (2020). https://doi.org/10.1063/1.5110603

Loureiro, N.F., Boldyrev, S.: Role of magnetic reconnection in magnetohydrodynamic turbulence. Phys. Rev. Lett. **118**, 245101 (2017)

Mahajan, S.M., Krishan, V.: Exact solution of the incompressible Hall magnetohydrodynamics (2005)

Mallet, A., Schekochihin, A.A., Chandran, B.D.G.: Disruption of sheet-like structures in Alfvénic turbulence by magnetic reconnection. Mon. Not. R. Astron. Soc. **468** (2017). https://doi.org/10.1093/mnras/stx670

Matsumoto, H., Deng, X.H., Kojima, H., Anderson, R.R.: Observation of electrostatic solitary waves associated with reconnection on the dayside magnetopause boundary. Geophys. Res. Lett. **30** (2003). https://doi.org/10.1029/2002GL016319

Øieroset, M., Sundkvist, D., Chaston, C.C., Phan, T.D., Mozer, F.S., McFadden, J.P., Angelopoulos, V., Andersson, L., Eastwood, J.P.: Observations of plasma waves in the colliding jet region of a magnetic flux rope flanked by two active X lines at the subsolar magnetopause. J. Geophys. Res. Space Phys. **119** (2014). https://doi.org/10.1002/2014ja020124

Pathak, N., Yadav, N., Sharma, R.P.: Nonlinear evolution of 3D whistler waves in space plasmas. Phys. Plasmas **24**(6) (2017b)

Pathak, N., Yadav, N., Sharma, S., Sharma, P., Sharma, R.P.: Localization of whistler wave and turbulent spectra in the magnetotail region. J. Geophys. Res. Space Phys. **122**(2), 1751–1762 (2017a)

Pathak, N., Uma, R., Sharma, R.P.: Turbulence generation in the magnetopause on account of magnetic islands. Astrophys. Space Sci. **363**, 1–6 (2018)

Pathak, N., Uma, R., Sharma, R.P.: Localized Structures and Turbulent Spectra in the Magnetopause. J. Geophys. Res. Space Phys. **124** (2019). https://doi.org/10.1029/2018JA026147

Perri, S., Goldstein, M.L., Dorelli, J.C., Sahraoui, F.: Detection of small-scale structures in the dissipation regime of solar-wind turbulence. Phys. Rev. Lett. **109** (2012). https://doi.org/10.1103/PhysRevLett.109.191101

Roytershteyn, V., Boldyrev, S., Delzanno, G.L., Chen, C.H.K., Grošelj, D., Loureiro, N.F.: Numerical Study of Inertial Kinetic-Alfvén Turbulence. Astrophys. J. **870** (2019). https://doi.org/10.3847/1538-4357/aaf288

Rozmus, W., Sharma, R.P., Samson, J.C., Tighe, W.: Nonlinear evolution of stimulated Raman scattering in homogeneous plasmas. Phys. Fluids **30** (1987). https://doi.org/10.1063/1.866152

Schekochihin, A.A., Cowley, S.C., Dorland, W., Hammett, G.W., Howes, G.G., Quataert, E., Tatsuno, T.: Astrophysical gyrokinetics: Kinetic and fluid turbulent cascades in magnetized weakly collisional plasmas. Astrophys. J. Suppl. Ser. **182** (2009). https://doi.org/10.1088/0067-0049/182/1/310

Servidio, S., Matthaeus, W.H., Shay, M.A., Dmitruk, P., Cassak, P.A., Wan, M.: Statistics of magnetic reconnection in two-dimensional magnetohydrodynamic turbulence. Phys. Plasmas **17** (2010). https://doi.org/10.1063/1.3368798

Sharma, R.P., Singh, H.D., Malik, M.: Alfvén wave filamentation and particle acceleration in solar wind and magnetosphere. J. Geophys. Res. Space Phys. **111** (2006). https://doi.org/10.1029/2006JA011759

Sharma, R.P., Pathak, N., Yadav, N., Sharma, P.: Nonlinear propagation of whistler wave and turbulent spectrum in reconnection region of magnetopause. Phys. Plasmas **24**(9) (2017)

Shearer, J.W., Eddleman, J.L.: Laser light forces and self-focusing in fully ionized plasmas. Phys. Fluids **16** (1973). https://doi.org/10.1063/1.1694204

Tsytovich, V.N.: Radiative-resonant collective wave-particle interactions (1989)

Vega, C., Roytershteyn, V., Delzanno, G.L., Boldyrev, S.: Electron-scale current sheets and energy dissipation in 3D kinetic-scale plasma turbulence with low electron beta. Mon. Not. R. Astron. Soc. (2023). https://doi.org/10.1093/mnras/stad1931

Wang, S., Bessho, N., Graham, D.B., Le Contel, O., Wilder, F.D., Khotyaintsev, Y.V., Genestreti, K.J., Lavraud, B., Choi, S., Burch, J.L.: Whistler waves associated with electron beams in magnetopause reconnection diffusion regions. J. Geophys. Res. Space Phys. **127**(9), e2022JA030882 (2022). https://doi.org/10.1029/2022JA030882

Wilder, F.D., Ergun, R.E., Goodrich, K.A., Goldman, M.V., Newman, D.L., Malaspina, D.M., Jaynes, A.N., Schwartz, S.J., Trattner, K.J., Burch, J.L., Argall, M.R., Torbert, R.B., Lindqvist, P.A., Marklund, G., Le Contel, O., Mirioni, L., Khotyaintsev, Y.V., Strangeway, R.J., Russell, C.T., Pollock, C.J., Giles, B.L., Plaschke, F., Magnes, W., Eriksson, S., Stawarz, J.E., Sturner, A.P., Holmes, J.C.: Observations of whistler mode waves with nonlinear parallel electric fields near the dayside magnetic reconnection separatrix by the Magnetospheric Multiscale mission. Geophys. Res. Lett. **43** (2016). https://doi.org/10.1002/2016GL069473

Wilder, F.D., Conley, M., Ergun, R.E., Newman, D.L., Chasapis, A., Ahmadi, N., Burch, J.L., Torbert, R.B., Strangeway, R.J., Giles, B.L., Le Contel, O.: Magnetospheric multiscale observations of waves and parallel electric fields in reconnecting current sheets in the turbulent magnetosheath. J. Geophys. Res. Space Phys. **127**(9), e2022JA030511 (2022). https://doi.org/10.1029/2022JA030511

Yadav, N., Sharma, R.P.: Nonlinear interaction of 3D kinetic Alfvén waves and ion acoustic waves in solar wind plasmas. Sol. Phys. **289**, 1803–1814 (2014). https://doi.org/10.1007/s11207-013-0436-z

Yao, Y., Chaston, C.C., Glassmeier, K.H., Angelopoulos, V.: Electromagnetic waves on ion gyro-radii scales across the magnetopause. Geophys. Res. Lett. **38** (2011). https://doi.org/10.1029/2011GL047328

Zhao, J.: Properties of Whistler Waves in Warm Electron Plasmas. Astrophys. J. **850** (2017). https://doi.org/10.3847/1538-4357/aa906f

Zimbardo, G.: Magnetic turbulence in space plasmas: in and around the Earth's magnetosphere. Plasma Phys. Control. Fusion **48** (2006). https://doi.org/10.1088/0741-3335/48/12B/S28

Zimbardo, G., Greco, A., Sorriso-Valvo, L., Perri, S., Vörös, Z., Aburjania, G., Chargazia, K., Alexandrova, O.: Magnetic turbulence in the geospace environment. Space Sci. Rev. **156** (2010). https://doi.org/10.1007/s11214-010-9692-5

Publisher's note Springer Nature remains neutral with regard to jurisdictional claims in published maps and institutional affiliations.

Springer Nature or its licensor (e.g. a society or other partner) holds exclusive rights to this article under a publishing agreement with the author(s) or other rightsholder(s); author self-archiving of the accepted manuscript version of this article is solely governed by the terms of such publishing agreement and applicable law.

Numerical Simulation for Analog Performance Assessment of Vertically Stacked FeFinFET

Kajal Verma
Department of Applied Physics
Delhi Technological University
Delhi, India
kajalverma_2k21phdap507@dtu.ac.in

Yash Pathak
Department of Applied Physics
Delhi Technological University
Delhi, India
yash_2k19phdap505@dtu.ac.in

Rishu Chaujar
Department of Applied Physics
Delhi Technological University
Delhi, India
chaujar.rishu@dtu.ac.in

2025 Devices for Integrated Circuit (DevIC) | 979-8-3503-9110-7/25/$31.00 ©2025 IEEE | DOI: 10.1109/DevIC63749.2025.11012622

***Abstract*—This paper explores the impact of localized charges on the analog performance of Vertically Stacked Ferroelectric FinFET (VS-FeFinFET), integrating advanced technologies like SOI, strained tri-layered channel, and ferroelectric material for improved gate control. It examines how interfacial trap charges (ITCs), induced by radiation or stress, affect device performance. VS-FeFinFET shows improvement in leakage current (I_{off}) by 53.1%, switching ratio by 105%, and threshold voltage (V_{th}) by 9.31% along with significant enhancement in other performance parameters for negative ITCs. By varying ITC's densities ($1 \times 10^{11} - 1 \times 10^{13}\ cm^{-2}$), the study reveals that multifold reduction in I_{off} leds to boost in switching ratio by 350% and 1.55 times in V_{th} with increasing density. These insights aid in optimizing VS-FeFinFET for enhanced reliability and efficiency, shaping next-generation electronics.**

Keywords—FinFET, Strained Silicon, Ferroelectric, Interfacial trap charges, Reliability.

I. INTRODUCTION

The growing demand for high packing density and low-power devices has led to aggressive downscaling of MOSFET technology. However continuous shrinking and increasing components on integrated circuits led to increased heat dissipation and higher power consumption both of which are responsible for degrading the data processing rate of the device [1]. To overcome these limitations, various engineering schemes and device designs such as Recessed channels, Trenched gates, FinFET, FeFETs, etc have been adopted as reported in the literature [2]. Among these structures, FinFETs have long been the strong contender in the semiconductor industry delivering unprecedented control over the transistor's state. Researchers have explored several strategies to enhance the performance of FinFETs, including modifications to device architecture, the use of alternative channel/source materials beyond silicon, and gate work function engineering. Various FinFET designs have been introduced, such as double-gate, triple-gate, gate-all-around (GAA) FinFET [3], omega FinFET [4], and cylindrical FinFET [5], all of which have been extensively documented in the literature. However, the integration of ferroelectricity (FeFinFETs) represents a burgeoning field within semiconductor technology, leveraging ferroelectric materials to control charge distribution [6]. Further with the adoption of some advanced technologies such as Silicon on Insulator [7][8] and strained channel system [9][10], with the use of different semiconductor materials, VS-FeFinFET is designed which gives improved device performance over conventional FeFinFET as discussed in the literature [11]. The strain modifies the band structure which increases the carrier mobility through the channel thus improving the transistor's performance with higher drive current, faster switching speed, and lower ON resistance, making it desirable for many electronic applications [12]. So far, research on FeFinFETs has primarily focused on enhancing device performance through novel architectures and engineering techniques. However, to ensure their reliability and adaptability in dynamic environments, it is crucial to analyze the effects of interface trap charges (ITCs). Previous studies have highlighted that device reliability remains a major challenge due to the limited adaptability to environmental changes [13][14]. These ITCs lie at the interface between oxide and semiconductor layers, where the dynamics of these ITCs exert a profound influence on device performance and functionality.

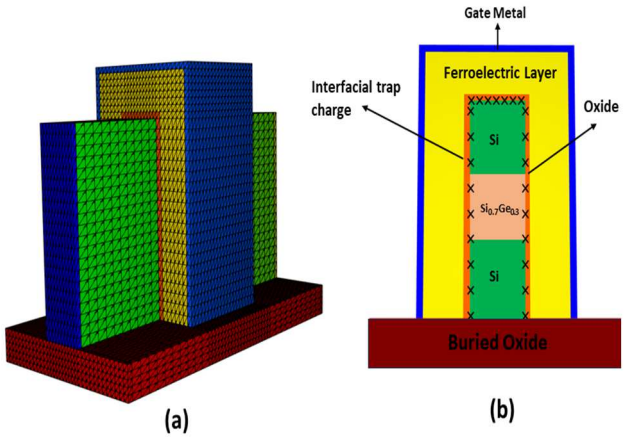


Fig. 1. Schematic diagram of VS-FeFinFET (a) 3D structure in meshed form (b) 2D structure in form of vertical cross-section chopped across the fin in presence of interfacial trap charges between semiconductor-insulating interface

The presence of these ITCs at the oxide-semiconductor interface in FeFinFETs introduces complexities that necessitate thorough investigation. These trap charges can arise from various sources, such as defects, impurities, and surface states, and their dynamics are influenced by factors such as material composition, processing conditions, and operating environment [15]. So, it is essential to consider the behavior of ITCs in VS-FeFinFET for unlocking its full potential for various electronics applications.

979-8-3503-9110-7/25/$31.00 ©2025 IEEE

Authorized licensed use limited to: DELHI TECHNICAL UNIV. Downloaded on June 04,2025 at 05:22:52 UTC from IEEE Xplore. Restrictions apply.

In this work, we embark on a comprehensive investigation into the nature of ITCs at the oxide-semiconductor interface in VS-FeFinFETs. By identifying critical interface trap densities and their impact on device performance, advanced device architectures or materials engineering techniques may be employed to suppress degradation due to these ITCs to further enhance the device reliability. Our findings not only contribute to the fundamental understanding of charge trapping phenomena in considered VS-FeFinFET but also hold significant implications for the design and optimization of future electronic devices.

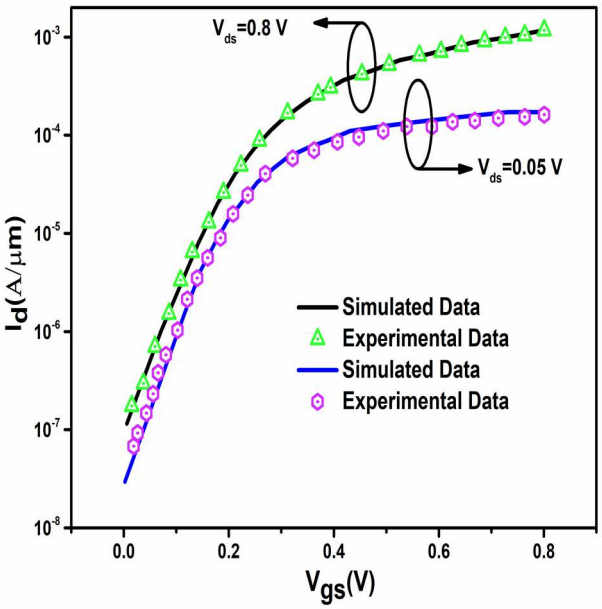


Fig. 2. Experimental and simulated transfer characteristic for Silicon on Insulator (SOI) FinFET at V_{ds}=0.05V and V_{ds}=0.8V

II. DEVICE STRUCTURE AND SIMULATION METHODOLOGY

Fig. 1(a) displays the device structure of the VS-FeFinFET in meshed form and fig. 1(b) displays the vertical cross-sectional view cut across the fin of the device. The gate stack comprises of silicon doped hafnium oxide (Si:HfO_2) as ferroelectric material and a dielectric oxide as an interfacial oxide layer between ferroelectric and semiconductor material. The gate length is fixed at 20nm with thickness of ferroelectric chosen to be 6nm with an interfacial oxide layer fixed at 1nm. The channel in the device is stacked with Si-$Si_{0.7}Ge_{0.3}$-Si (where the mole fraction of Si and Ge is considered as 0.7 and 0.3 respectively) to form tri tri-layered strained silicon channel system. The channel is lightly doped with concentration $10^{16}\ cm^{-3}$ with acceptor type and source/drain are heavily doped with concentration $10^{20}\ cm^{-3}$ with donor type. TiN (Titanium nitride) with work function 4.65 e.V, is taken for gate material with temperature fixed at 300K. To study the influence of interface trap charges (ITCs) on the device reliability and performance, interface trap charge density is varied from 10^{11}-$10^{13}\ cm^{-2}$ that is chosen based on formerly reported simulation and experimental data [16][17].

All the simulations for this study are carried out with Cogenda's Genius 3D TCAD simulator based on self-consistent drift diffusion and poisson's equations. For the validating the various models used in the simulator, The TCAD simulation result for SoI FinFET has been calibrated with the experimental data [18], and a reasonably good agreement between the two results validates the various models used in this study as showcased in Fig. 2. The models used are Schokley-Read-Hall (SRH) to incorporate generation and recombination of carriers [19]. Philips and Lombardi mobility models for Silicon Germanium (SiGe) and Silicon respectively along with Lucent and Fermi Dirac carrier statistics model [11]. Further, INTERFACE statement is used to indicate the position and polarity of ITCs in the device [20]. A few abbreviations are considered in the paper such as PITC – positive interfacial trap charge, NITC – negative interfacial trap charge, and WITC – without interfacial trap charge.

III. RESULTS and DISCUSSIONS

The transfer characteristics for VS-FeFinFET with trap charges are shown in Fig. 3. The trap concentration for this analysis is fixed at $10^{12}\ cm^{-2}$ for both positive and negative interface trap charge at the semiconductor-oxide (S/O) surface.

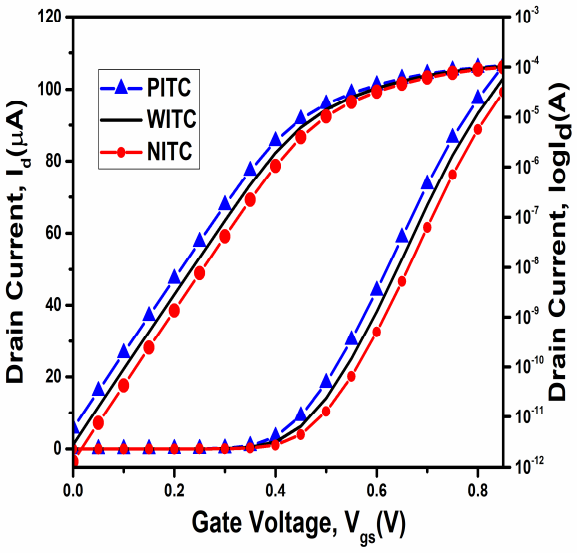


Fig. 3 Transfer characteristics of VS-FeFinFET in presence of different interfacial trap charges

The drain current (I_{on}) is higher (lower) than zero trap charge for positive (negative) interfacial trap charges. The device's ON and OFF current are altered by the changes in flat band voltage caused by positive and negative trap charges [21]. The comparative analysis of VS-FeFinFET (without ITCs) with different existing devices is showcased in table 1, which confirms superior

Authorized licensed use limited to: DELHI TECHNICAL UNIV. Downloaded on June 04,2025 at 05:22:52 UTC from IEEE Xplore. Restrictions apply.

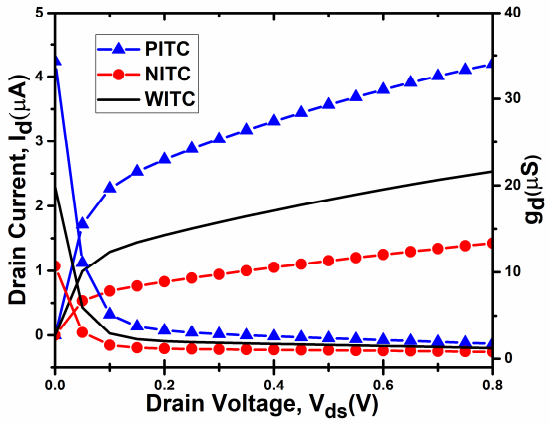


Fig. 4. Variation in drain current and output transconductance for VS-FeFinFET with drain voltage in presence of different interfacial trap charges

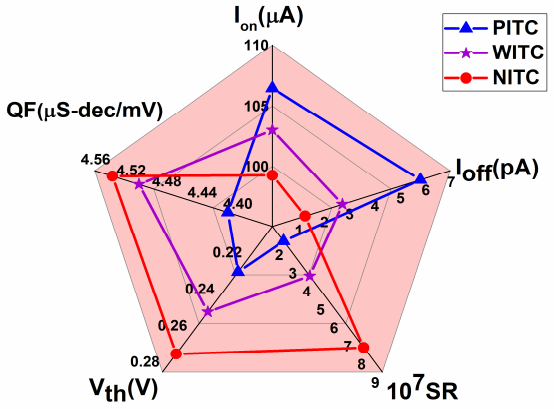


Fig. 5. Comparison of different device characteristics such as Drain Current in ON and OFF condition, Switching Ratio, Threshold Voltage and Quality Factor in presence of different interfacial trap charges.

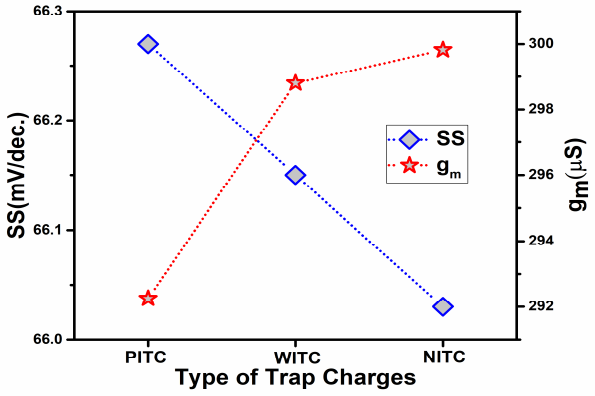


Fig. 6. Variation in Subthreshold Swing and Transconductance of VS-FeFinFET for different trap charges.

performance of this proposed structure as compared to previously published work.

Further, Fig. 4 displays the output characteristics of VS-FeFinFET which show lower output conductance (g_d) for NITC thus ensuring minimum channel length modulation and its ability for driving constant current source applications.

It is clearly visible in Fig. 5 that there is substantial reduction in leakage current (I_{off}) in case of NITC which results in higher switching ratio as compared to WITC and PITC. These changes also affect the threshold voltage (V_{th}) as shown in Fig. 5 that with higher (lower) threshold voltage for negative (positive) in comparison to zero (neutral) trap charge, the circuit is less (more) susceptible to noise-induced switching. The quality factor, as expressed in equation (1), is a key parameter that significantly influences the performance, efficiency, and stability of FET circuits. It plays a crucial role in various applications, including amplifiers, filters, oscillators, and communication systems. [26][27].

$$QF = g_m/SS \qquad (1)$$

On analysis, the device shows higher (lower) QF value for negative (positive) ITCs in comparison to WITC as displayed in Fig. 5.

TABLE I. COMPARATIVE ANALYSIS OF VS-FEFINFET WITH OTHER EXISTING DEVICES

Reference	V_{ds} (V)	Devices	I_{on} (μA)	I_{off} (pA)	t_{fe} (nm)
This work	0.4	VS-FeFinFET	103	2.77	6
[22]	0.1	Fe-HZO-GeFinFET	50	88	-
[23]	-	Fe-FinFET	3.30	210	7
[24]	0.1	HZO-FeFinFET	1.0	8.90	9
[25]	0.5	NC-FinFET	30	42	5

Transconductance (g_m), as given by equation (2) expresses how well a FET device converts fluctuations in the gate-source voltage into variations in the drain current. Fig. 6 shows the improved transconductance for negative trap interface charge due to better electrostatics of the channel, leading to enhanced gate control over the channel carriers.

TABLE II. DEVICE PERFORMANCE COMPARISON FOR DIFFERENT TYPES OF INTERFACIAL TRAP CHARGES

Type of interface trap charge and Performance parameters	PITC	WITC	NITC
I_{off} (pA)	5.83	2.77	1.30
I_{on} (μA)	106	103	99.2
SR (10^7)	1.83	3.72	7.65
V_{th} (V)	0.225	0.247	0.270
SS (mV/dec.)	66.27	66.15	66.03
QF (μS-dec./mV)	4.51	4.52	4.54
g_m(μS)	292	299	300

Authorized licensed use limited to: DELHI TECHNICAL UNIV. Downloaded on June 04,2025 at 05:22:52 UTC from IEEE Xplore. Restrictions apply.

$$g_m = \partial I_d / \partial V_{gs} \qquad (2)$$

This results in a steeper increase in drain current, improving transconductance. Further, Fig. 6 also shows improved subthreshold characteristics in terms of subthreshold swing in case of NITC due to reduction in depletion charge in the channel, leading to a lower subthreshold swing (SS), which means faster switching and better power efficiency [28].

Further, a brief analysis is also done for varying interfacial trap concentrations in the range 10^{11}-10^{13} cm^{-2} and it is found that although there is degradation in I_{on} with

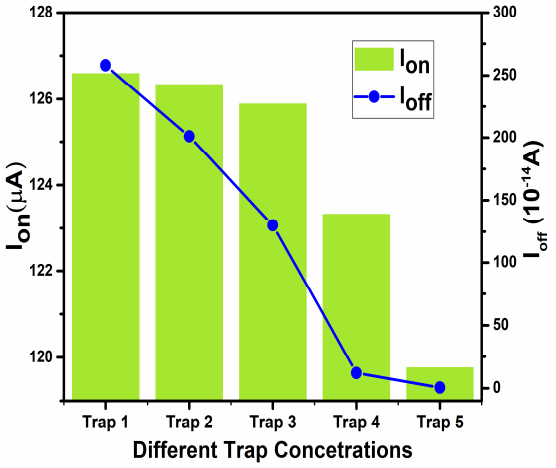


Fig. 7. Variation in ON current and Leakage current for VS-FeFinFET in presence of different interfacial trap concentrations

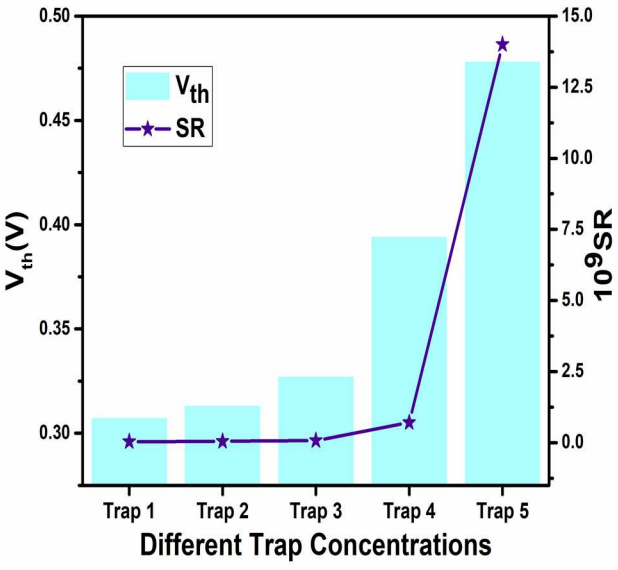


Fig. 8. Variation in Threshold Voltage and Switching Ratio for VS-FeFinFET in presence of different interfacial trap concentrations.

increasing negative trap concentration but due to better immunity towards leakage current, there is tremendous increase in switching ratio with increasing negative trap charge concentration as displayed in Fig. 7 and Fig. 8.

TABLE III. COMPARISON OF PERFORMANCE PARAMETERS FOR DIFFERENT INTERFACIAL TRAP CHARGES CONCENTRATION

Trap levels concentration	I_{on} (μA)	I_{off} (10^{-14}A)	SR (10^8)	V_{th} (V)
Trap 1 (1×10^{11} cm^{-2})	102.66	258	0.398	0.307
Trap 2 (5×10^{11} cm^{-2})	101.44	201	0.505	0.313
Trap 3 (1×10^{12} cm^{-2})	99.2	130	0.765	0.327
Trap 4 (5×10^{12} cm^{-2})	85.6	12.1	7.09	0.394
Trap 5 (1×10^{13} cm^{-2})	63.10	0.45	140	0.478

Semiconductor manufacturing processes inherently exhibit variations in device parameters due to factors like process variations and dopant fluctuations [29]. Designing FETs with a higher threshold voltage as displayed in Fig. 7 provides greater immunity to these variations for VS-FeFinFET, ensuring more consistent and predictable device behavior across different manufacturing lots and process nodes [30].

IV. CONCLUSION

Interface trap charges arise from dangling bonds at the abrupt semiconductor surface, making them unavoidable. Since real devices always contain trap charges, understanding their effects is essential for device optimization. The device performance including drain current, threshold voltage, switching ratio, etc, has been explored in the presence of interfacial trap charges with different polarity as depicted in table 2. With improvement in some parameters like leakage current by 53.1%, switching ratio by 105%, and V_{th} by 9.31% along with substantial enhancement in transconductance and quality factor in the presence of NITC in contrast to degradation due to PITC. Various performance parameters have been examined for different trap level concentrations also in the range of $1\times10^{11} - 1\times10^{13}$ cm^{-2} to understand the tolerance level of the device towards interfacial trap abruptions. It is found that with a sequential increase in interfacial trap density from trap level 1 to trap level 5, there is a tremendous decrease in leakage current of around 99.8% that led to 351 times enhancement in switching ratio as displayed in table 3. Further with an increase in V_{th} by 55.7%, the device is more immune to noise variation at trap level 5 as compared to trap level 1. Thus, by exploring the complexities of interfacial trap charges analyzed across different polarities, this study aid in optimizing VS-FeFinFET for enhanced reliability and efficiency, shaping next-generation electronics.

ACKNOWLEDGEMENT

The authors thank Vinod Dham Centre of Excellence for Semiconductors and Microelectronics (VDCoE4SM), C2S Programme:MeiTY, SERB POWER Grant, CSIR and Microelectronics Research Lab, Delhi Technological University for providing essential facilities.

Authorized licensed use limited to: DELHI TECHNICAL UNIV. Downloaded on June 04,2025 at 05:22:52 UTC from IEEE Xplore. Restrictions apply.

REFERENCES

[1] W. M. Holt, "1.1 moore's law: A path going forward," in 2016 IEEE International Solid-State Circuits Conference (ISSCC). IEEE, 2016, pp. 8–13.

[2] A. Razavieh, P. Zeitzoff, and E. J. Nowak, "Challenges and limitations of cmos scaling for finfet and beyond architectures," IEEE Transactions on Nanotechnology, vol. 18, pp. 999–1004, 2019.

[3] B. Kumar, M. Sharma, and R. Chaujar, "Gate electrode work function engineered jam-gs-gaa finfet for analog/rf applications: Performance estimation and optimization," Microelectronics Journal, vol. 135, p.105766, 2023.

[4] M.-S. Yeh, Y.-C. Wu, M.-F. Hung, K.-C. Liu, Y.-R. Jhan, L.-C. Chen, and C.-Y. Chang, "Fabrication, characterization and simulation of ω-gate twin poly-si finfet nonvolatile memory," Nanoscale research letters, vol. 8, pp. 1–5, 2013.

[5] M. Mehrad and A. A. Orouji, "Partially cylindrical fin field-effect transistor: a novel device for nanoscale applications," IEEE Transactions on Device and Materials Reliability, vol. 10, no. 2, pp. 271–275, 2010

[6] N. Zagni, F. M. Puglisi, P. Pavan, and M. A. Alam, "Reliability of hfo2-based ferroelectric fets: A critical review of current and future challenges," Proceedings of the IEEE, 2023.

[7] R. Chaudhary and R. Saha, "Physical insights of interface traps and self-heating effect on electrical response of dmg finfets in overlap and underlap configurations: analog/rf perspective," Physica Scripta, vol. 99, no. 1, p. 015406, 2023.

[8] R. Mann, Y. Pathak, and R. Chaujar, "Temperature analysis on short channel effects of modified ncfet: A simulation study," in 2022 IEEE International Conference on Electronics, Computing and Communication Technologies (CONECCT). IEEE, 2022, pp. 1–5

[9] T. Dash, S. Dey, S. Das, J. Jena, E. Mohapatra, and C. Maiti, "Performance comparison of strained-sige and bulk-si channel finfets at 7 nm technology node," Journal of Micromechanics and Microengineering, vol. 29, no. 10, p. 104001, 2019.

[10] S. Nanda, R. S. Dhar, F. Awwad, and M. I. Hussein, "Development and analysis of a three-fin trigate q-finfet for a 3 nm technology node with a strained-silicon channel system," Nanomaterials, vol. 13, no. 10, p.1662, 2023.

[11] K. Verma and R. Chaujar, "Analysis of vertically stacked ferroelectric based finfet for switching applications," in 2023 2nd International Conference on Futuristic Technologies (INCOFT). IEEE, 2023, pp. 1–4.

[12] S. Flachowsky *et al*., "Understanding Strain-Induced Drive-Current Enhancement in Strained-Silicon n-MOSFET and p-MOSFET," in *IEEE Transactions on Electron Devices*, vol. 57, no. 6, pp. 1343-1354, June 2010.

[13] W. Cao, H. Bu, M. Vinet, M. Cao, S. Takagi, S. Hwang, T. Ghani, and K. Banerjee, "The future transistors," Nature, vol. 620, no. 7974, pp. 501–515, 2023.

[14] Y. Pathak, B. D. Malhotra, and R. Chaujar, "A numerical study of analog parameter of negative capacitance field effect transistor with spacer," in 2021 7th International Conference on Signal Processing and Communication (ICSC). IEEE, 2021, pp. 277–281.

[15] Singh, A.K., Tripathy, M.R., Baral, K. *et al.* Impact of interface trap charges on device level performances of a lateral/vertical gate stacked Ge/Si TFET-on-SELBOX-substrate. *Appl. Phys. A* 126, 681 (2020).

[16] Y. Qiu, R. Wang, Q. Huang, and R. Huang, "A comparative study on the impacts of interface traps on tunneling FET and MOSFET," IEEE Trans. Electron Devices, vol. 61, no. 5, pp. 1284–1291, 2014.

[17] T.-K. Chiang, "A compact model for threshold voltage of surrounding-gate MOSFETs with localized interface trapped charges", *IEEE Trans. Electron Devices*, vol. 58, no. 2, pp. 567-571, Feb. 2011.

[18] C. Lin, B. Greene, S. Narasimha, J. Cai, A. Bryant, C. Radens, V. Narayanan, B. Linder, H. Ho, A. Aiyar, et al., "High performance 14nm soi finfet cmos technology with 0.0174 μm 2 embedded dram and 15 levels of cu metallization," in 2014 IEEE International Electron Devices Meeting. IEEE, 2014, pp. 3–8.

[19] Y. Pathak, K. Verma, B. D. Malhotra, and R. Chaujar, "Performance evaluation of gate engineered ferroelectric mimos for analog/electrical ic applications," Physica Scripta, vol. 100, no. 1, p. 015028, 2024.

[20] Cogenda genius parallel 3d tcad simulation tool user's guide cogenda genius 2.2: User's guide.

[21] Awadhiya, B., Yadav, S. & Acharya, A. Interface Trap Charges Analysis on DC and High Frequency Characteristics of UTBB-FDSOI FET. *Silicon* **15**, 937–942 (2023)

[22] C.-J. Su, Y.-T. Tang, Y.-C. Tsou, P.-J. Sung, F.-J. Hou, C.-J. Wang, S.-T. Chung, C.-Y. Hsieh, Y.-S. Yeh, F.-K. Hsueh, et al., "Nano-scaled ge finfets with low temperature ferroelectric hfzro x on specific interfacial layers exhibiting 65% ss reduction and improved ion," in 2017 Symposium on VLSI Technology. IEEE, 2017, pp. T152–T153.

[23] H. Bae, S. G. Nam, T. Moon, Y. Lee, S. Jo, D.-H. Choe, S. Kim, K.-H.Lee, and J. Heo, "Sub-ns polarization switching in 25nm fe finfet toward post cpu and spatial-energetic mapping of traps for enhanced endurance," in 2020 IEEE International Electron Devices Meeting (IEDM). IEEE, 2020, pp. 31–3.

[24] S.-C. Yan, G.-M. Lan, C.-J. Sun, Y.-H. Chen, C.-H. Wu, H.-K. Peng, Y.-H. Lin, Y.-H. Wu, and Y.-C. Wu, "High speed and large memory window ferroelectric hfzro2 finfet for high-density nonvolatile memory," IEEE Electron Device Letters, vol. 42, no. 9, pp. 1307–1310, 2021.

[25] H. Ota, T. Ikegami, J. Hattori, K. Fukuda, S. Migita, and A. Toriumi, "Fully coupled 3-d device simulation of negative capacitance finfets for sub 10 nm integration," in 2016 IEEE International Electron Devices Meeting (IEDM). IEEE, 2016, pp. 12–4.

[26] H. Bae, S. G. Nam, T. Moon, Y. Lee, S. Jo, D.-H. Choe, S. Kim, K.-H. Lee, and J. Heo, "Sub-ns polarization switching in 25nm fe finfet toward post cpu and spatial-energetic mapping of traps for enhanced endurance," in 2020 IEEE International Electron Devices Meeting (IEDM). IEEE, 2020, pp. 31–3.

[27] K. Verma and Chaujar, "Optimization and analysis of si/sige strained vertically stacked heterostructure on insulator fefinfet for high performance analog and rf applications," Physica Scripta, vol. 99, no. 11, p. 115960, 2024.

[28] Y. Pathak, K. Verma, B. D. Malhotra, and R. Chaujar, "Tcad analysis of linearity performance on modified ferroelectric layer in fet device with spacer," Advanced Nanoscale MOSFET Architectures: Current Trends and Future Perspectives, pp. 113–123, 2024.

[29] G. -B. Lee and Y. -K. Choi, "Extraction of Interface Trap Density Through Synchronized Optical Charge Pumping in Gate-All-Around MOSFETs," in *IEEE Electron Device Letters*, vol. 41, no. 11, pp. 1629-1632, Nov. 2020.

[30] A. Rawat and B. Rawat, "The Role of Interface Trap States in MoS2-FET Performance: A Full Quantum Mechanical Simulation Study," in *IEEE Transactions on Electron Devices*, vol. 70, no. 9, pp. 4913-4920, Sept. 2023.

Authorized licensed use limited to: DELHI TECHNICAL UNIV. Downloaded on June 04,2025 at 05:22:52 UTC from IEEE Xplore. Restrictions apply.

2025 3rd International Conference on Advancement in Computation & Computer Technologies (InCACCT) | 979-8-3315-4389-1/25/$31.00 ©2025 IEEE | DOI: 10.1109/InCACCT65424.2025.11011447

On the Prediction of Temporal Dynamics of Turbulent Flows using a Hybrid Temporal Architecture (TurboNet)

Shubhanshu Rao
Department of Mechanical Engineering
Delhi Technological University
Delhi, India
shubhanshurao09@gmail.com

Subhrajit Roy
Department of Mechanical Engineering
Delhi Technological University
Delhi, India
roysubhrajit03@gmail.com

Vishal Kumar Roy
Department of Mechanical Engineering
Delhi Technological University
Delhi, India
vishalkumarroy_me21b6_09@dtu.ac.in

Raj Kumar Singh
Department of Mechanical Engineering
Delhi Technological University
Delhi, India
rajkumarsingh@dce.ac.in

***Abstract*— The accurate predictions of temporal dynamics in turbulent flow remains a formidable challenge in fluid mechanics, owing to the non-linear complexity of governing equations. Traditional numerical methods, while accurate, are computationally prohibitive for high-fidelity simulations over extended time horizons. This study presents TurboNet: a hybrid multi-layer temporal architecture combining Conv1D, LSTM, BiLSTM, that can model the temporal evolution of turbulent flows. To ensure robustness and generalizability, the proposed model is trained and validated on three distinct datasets comprising distinct flow regimes and physical characteristics: Periodic dynamics from in-house URANS simulations of Savonius wind turbine, wall bounded non-linear dynamics from DNS data of channel flow and open-boundary non-linear dynamics from LES data of backward-facing step flow. Evaluation metrics R^2 ranging 0.97-0.99 and MSE peaking at 0.2463 demonstrate that the hybrid architecture effectively captures both the periodic and non-linear dynamics with high accuracy while significantly reducing computational cost. The results underscore the potential of ML based frameworks to complement the traditional CFD solvers, enabling efficient and scalable modelling of complex turbulent systems across diverse applications.**

Keywords—Machine Learning, Time-Series Forecasting, Simulations, Computational Fluid Dynamics, Non-linear Dynamics, Turbulence

I. INTRODUCTION

Computational fluid dynamics (CFD) is the simulation of fluid flows, and happens to be a critical tool not only for engineering applications, but also from a scientific perspective. Navier-Stokes equations (NSEs) are the governing equations for the fluid flows. NSEs are non-linear partial differential equation (PDEs) that describe the mass-momentum conservation in a Newtonian fluid. The non-linearity stems from the convective acceleration terms in the momentum equations. Also, they portray the spacio-temporal non-linear dynamics of turbulence [1]. Therefore, the computation of Navier-Stokes equations requires numerical methods, which are costly computationally. It can become particularly demanding at large Reynolds numbers, due to the enormous spacial and temporal scale ranges to be resolved. In order to solve the computational problems of turbulence, Reynolds Averaged Navier-Stokes (RANS) equations have been formulated, which split the flow variables into fluctuating and mean components, enabling computation of mean flow behaviour while addressing the effects of turbulence through added terms referred to as Reynolds stresses [2]. Scale-resolving techniques like LES and DNS, although yielding high-fidelity results, are frequently computationally infeasible for practical use.

In an effort to mitigate the bottleneck brought about by such conventional methods, machine learning (ML) has begun to feature prominently, promising new avenues of speeding up CFD simulations. Various researchers [3-7] have evaluated the potential to speed up high-fidelity simulations, improve turbulence models, and create reduced-order models. Machine learning algorithms tap into data-driven models to predict the intricate fluid flow behavior without solving the governing equations explicitly. Compared to conventional CFD, where the NSEs are iteratively solved using numerical methods, ML models are learned from large datasets to identify correlations and learn hidden flow dynamics [8], [9]. This enables the detection of sophisticated patterns and correlations in the fluid flow and, thereby, avoids the necessity of iterative solution methods. With the use of learned representations, ML-based models are capable of predicting flow behavior with much lower computational overhead, providing a promising approach for high-fidelity simulations in situations where conventional CFD techniques are computationally infeasible or time-consuming.

In handling the time dynamics of the fluid flow, ML based time models such as Bidirectional LSTM (BiLSTM) Long Short Term Memory (LSTM), Gated Recurrent Units (GRUs), Recurrent Neural Networks (RNNs), and others have become exceedingly popular [10]. These designs can model sequential data by detecting short and long-term dependencies. Previous base methods, such as Autoregressive models (AR) and the ARIMA model, forming the basis of the current forecasting methods [11], but were usually not able to capture the non-linear nature of turbulent flows. Although RNNs were initially

979-8-3315-4389-1/25/$31.00 ©2025 IEEE

Authorized licensed use limited to: DELHI TECHNICAL UNIV. Downloaded on June 04,2025 at 05:20:25 UTC from IEEE Xplore. Restrictions apply.

offering the solution of a neural network-based approach for the time series data, later they were outperformed by LSTMs, which could solve the issue of vanishing gradient that was an essential drawback of the conventional RNNs [12]. Through the exploitation of these sophisticated architectures, ML models provide strong solutions for the prediction of temporal dynamics, further pushing the contribution of ML for the optimization of the CFD simulations.

LSTM and GRU models for the prediction of unsteady flow fields was proposed by Zhang et al. [13], pointing out recurrent networks as the key to understanding the time-dependent fluid behaviour. BiLSTMs have been utilized in predicting the flow inside arbitrarily shaped channels; this is achieved with high accuracy compared to encoder-decoder methods [14]. It can also be used in modelling the semi-submersible floater motion, showing how a bidirectional network can achieve greater accuracy in the predictive nature of complex marine flows [15]. Predicting the blood flow through stenosed arteries using deep learning have further developed medical applications of ML in CFD [16]. Zhao and Okuno used proxy models for phase behaviour calculations in compositional flow simulations, which decrease the computation time in reservoir engineering [17]. A combination of LSTM-PSO and MLP to optimize the aerofoil design of rotorcraft robots, further demonstrating the value of using hybrid optimization [18].

II. Dataset

The temporal architecture used in the present study utilises three datasets, to ensure robustness and generalisability. The datasets were selected such that they encompass and exhibit distinct flow regimes, each characterized by unique physical phenomena and dynamic behaviours. Periodic dynamics are represented by data obtained from in-house URANS simulations of a Savonius VAWT. For modelling non-linear dynamics, two different cases were considered: a wall-bounded flow scenario using DNS data of channel flow and an open-boundary flow case using LES data of flow over a backward-facing step. This multi-faceted approach mitigates overfitting to specific flow characteristics and enables the model to generalize across varying scales and phenomena, including both periodic and highly non-linear dynamics.

A. 2D URANS Simulations of Savonius VAWT

The data of coefficients of moment (C_M) acting on the turbine blades generated from in-house URANS simulations of a Savonius-type VAWT was taken to capture and model periodic flow regime. The CFD simulations were done using a rectangular domain centred on the turbine's shaft. A bizonal approach was adopted for the domain: an inner rotating zone that housed the turbine blades, and an outer stationary zone. The domain was divided into two sections for generating mesh: unstructured tri-elements were used to discretise the inner rotating zone, and structured quad-elements were used to discretise the outer stationary zone. During mesh generation, $y^+ < 1$ was a key consideration to accurately capture boundary layer effects. A total of 32 inflation layers were applied around the turbine and deflector, with the first layer height set to 5×10^{-3} mm and subsequent layers following a 1.14 uniform rate of growth. Fig. 1 shows the elements in the flow domain. To effectively resolve the highly turbulent flow near the walls of the turbine a refined grid was designed.

The proper usage of turbulence closure models is essential to ensure the veracity of the simulations. Previous investigations [19-24] have concluded sthat k-ω SST model [25] is suitable for modelling the flow physics of VAWTs acscurately.

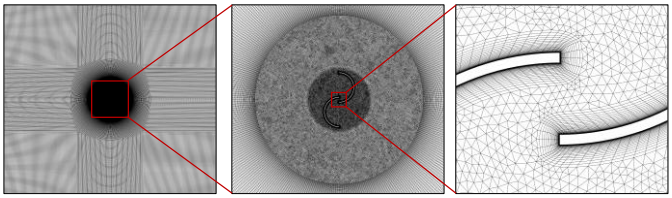
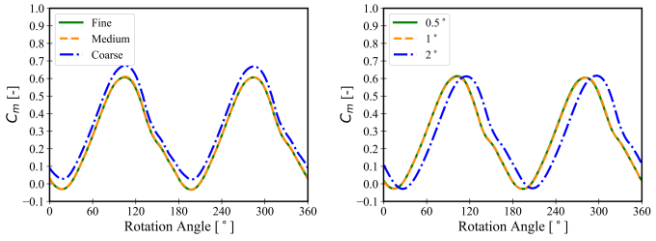
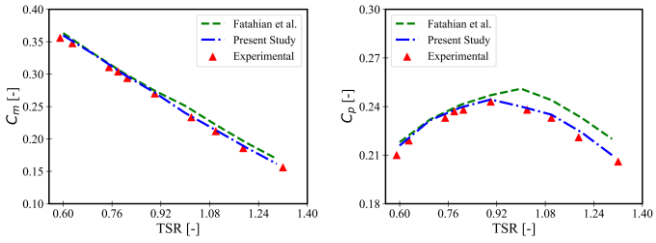


Fig. 1. Computational Grid for the Savonius VAWT URANS Simulations



(a) (b)

Fig. 2. (a) Grid & (b) Time Step Independence



(a) (b)

Fig. 3. (a) C_M and (b) C_P variation with turbine's TSR

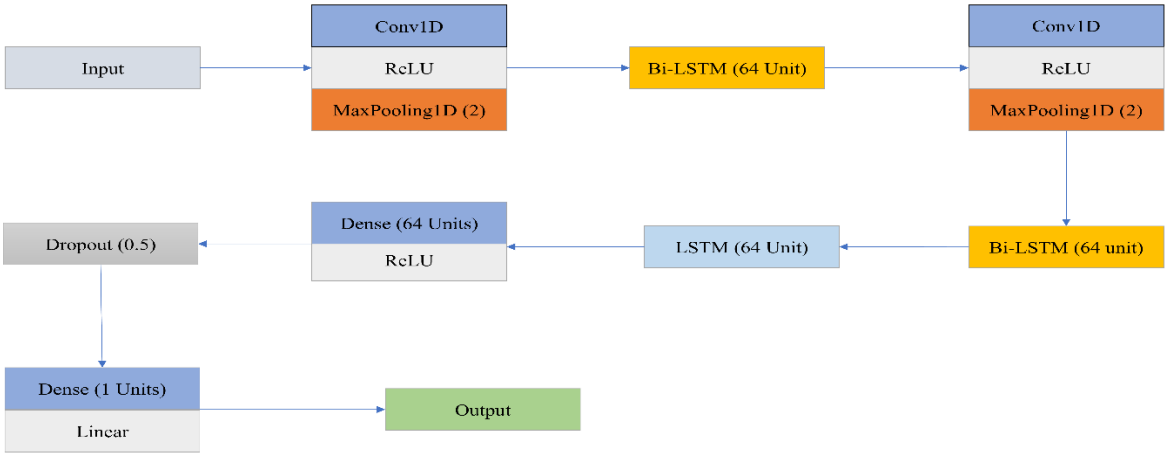


Fig. 4 Structure of Hybrid Architecture (TurboNet)

Authorized licensed use limited to: DELHI TECHNICAL UNIV. Downloaded on June 04,2025 at 05:20:25 UTC from IEEE Xplore. Restrictions apply.

The model uses a function to blend between the Wilcox k-ω model [26] in the near-wall regions, and the standard k-ϵ model [27] in the farfield regions. This blending is important so that the robustness of the Wilcox k-ω near-wall formulation can be leveraged in a mainly wall-dominated flow like that of the Savonius VAWT, while also using the freestream independence of the k-ϵ model to mitigate the freestream sensitivity of the Wilcox k-ω model. For pressure-velocity coupling a coupled scheme was used, solving the continuity and momentum equations at the same time instead of the traditional predictor-corrector method. The result of using this method was reduced convergence time, and extra stability in the evolvement of the solution. A 2nd order upwind approach for discretising the special transport terms. Least squares cell-based gradient computation was done in conjunction. Uniform inlet at 7m/s with a pressure outlet was imposed on the domain. Incompressibility in the flow was modelled using an invariant density of 1.225 kg/m^3.

Further, grid and timestep-independence studies were performed to ensure reliable data while reducing the required computational resources. Different grid resolutions (66000, 123000, and 230000 elements) were evaluated to identify an ideal mesh size that balances solution accuracy with computational cost. As shown in Fig. 2(a) results from both medium and fine grids were almost the same and any finer grid would not have an effect on the solution. Hence, the results from the 123000-element grid have been reported here.

The sensitivity of the time step was investigated to assess the impact on the solution's accuracy. Fig. 2(b) presents the dependence of the power coefficient (C_p) on the angle of rotation of the turbine for different sizes of the time step. It is evident that the reduction in time step below 1° per iteration does not qualitatively impact the solution. Hence, a time step of 1° was used in reporting the present results. The numerical model's accuracy was evaluated against the available experimental data as reported by Sheldahl et al. [25] and the previous numerical studies of Fatahian et al. [21]. As shown in Fig. 3(a) and Fig. 3(b), the results from this study align closely with the experimental data, with minimal discrepancies. This corroborates the temporal and spatial discretization technique of the model.

B. *Large Eddy Simulation of Flow Over a Backward-facing Step*

Temporal statistics from the numerical simulations of Creech and Jackson [28], [29] were taken as the first benchmarking case to model open-boundary non-linear flow without periodicity. They present transient flow field data from large eddy simulations of flow over a backward facing step. They use a solver employing a hybrid approach combining Discontinuous and Continuous Galerkin (DG & CG) formulations to compute explicitly-filtered Large Eddy Simulations (LES). The velocity components were modelled using a formulation akin to the Compact Discontinuous Galerkin method described by Peraire and Persson [30], combined with a twice-Picard iterated implementation of the Crank-Nicolson scheme for time integration [31]. Maximum Courant-Friedrichs-Levy condition was maintained at <1.6. The channel geometry features a Dirichlet boundary condition on the bottom, sides and top surfaces. While the bottom is modelled as a no-slip boundary, the sides and top are modelled as frictionless boundaries. A Neumann condition is employed at the outlet (an open boundary, i.e. $\nabla u = 0$). Akin to the approach of Patil [32], the inlet boundary condition uses the synthetic eddy method [33], which superimposes turbulent fluctuations onto a logarithmic velocity profile.

The turbulent flow over a backward-facing step shows provably complex dynamics. Thus, the time variant x-component of the flow velocity has been used to train the temporal architecture in the present study.

C. *Direct Numerical Simulation of Turbulent Channel Flow*

Time-variant history of the friction velocity Reynolds number for a turbulent channel flow has been used to train and test the proposed temporal architecture in the present study. The dataset has been produced by University of Texas at Austin and Johns Hopkins University [34], [35], [36] from a direct numerical simulation (DNS) of wall bounded flow. A domain of size $8\pi \times 2 \times 3\pi$ and $2048 \times 512 \times 1536$ nodes was used for the simulation. The petascale DNS channel flow solver [37], solves the NSE using velocity-vorticity formulation [38] and a hybrid Fourier-Galerkin pseudo-spectral approach. Data has been stored in the database after the simulation reached a statistically stationary state.

Hence, the three datasets used to train the temporal architecture introduced herein represent diverse flow regimes: periodic dynamics, open-boundary and wall-bounded turbulence respectively.

III. Methodology

This study introduces TurboNet a hybrid deep learning architecture to predict flow dynamics effectively.

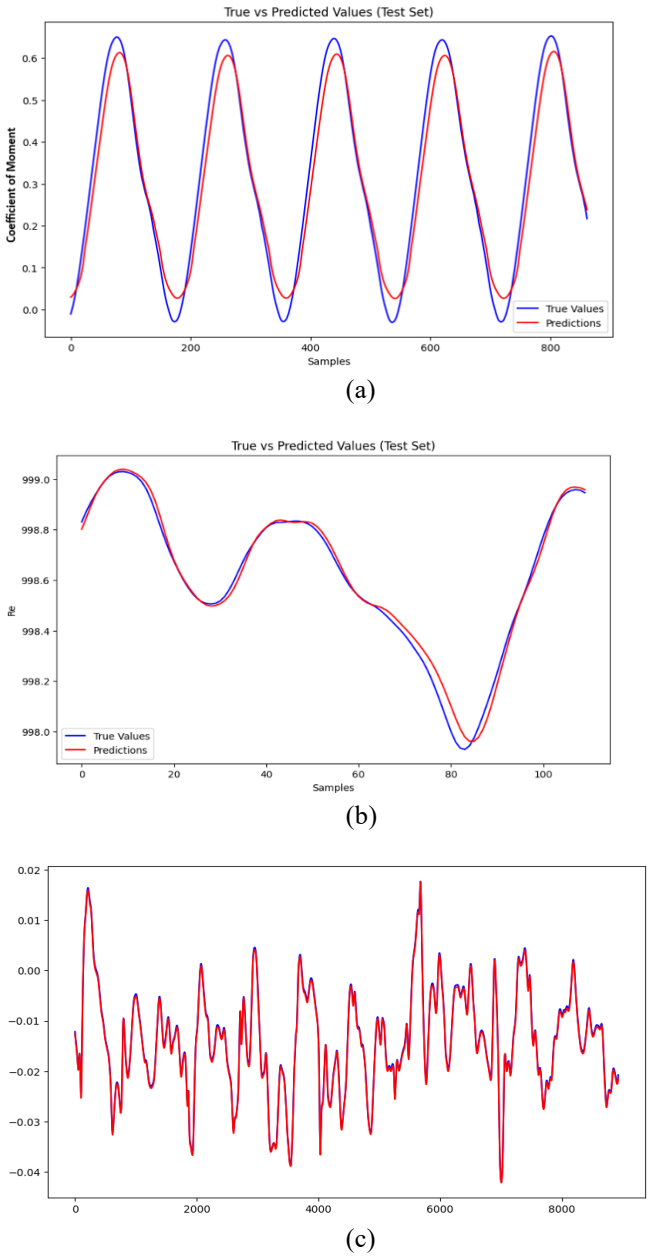


Fig. 5. Predictions achieved by TurboNet on datasets of (a) Savonius Turbine (b) Channel Flow (c) Backward-facing steps

Authorized licensed use limited to: DELHI TECHNICAL UNIV. Downloaded on June 04,2025 at 05:20:25 UTC from IEEE Xplore. Restrictions apply.

The model integrates Conv1D layer for capturing repeated patterns, BiLSTM layer for bidirectional temporal dependencies and LSTM as illustrated in Figure 4. The model was trained for 400 epochs for each dataset.

A. Conv1D

It is a type of CNN that specializes in sequential data. Unlike the two-dimensional case of Conv2D, where it operates on images, for example, Conv1D operates along one dimension, thus making it perfect for time-series or sequential data. features are automatically extracted for the sequential fluid flow data by having filters across the time dimension. That will help to capture the patterns that are very critical to accurate prediction. By learning from the raw data and streamlining the data preprocessing pipeline Conv1D reduces any manual engineering efforts. By stacking multiple Conv1D layers, the model learns hierarchical features that improve its ability to capture complex dependencies in fluid flow data. Model proposed in this research had two Conv1D layer with ReLU activation and 64 filters of size 3 each.

B. LSTM

LSTM is an improvement of a RNN that can retain long term dependencies. LSTM has a unique architecture called memory cells that has ability to hold information over a period of time. It features are Long-term memory that can store information up to long sequences; this feature is very helpful for predicting the flow of fluid depending on some long-time scale. LSTMs has a gating mechanism comprising of three gates output, input and forget. Which regulates the information flow and enable the network to selectively update, reset, or output data. Apart from this LSTM has a capability to adapt to a sequence of a great variety, in both short term and long-time trends, even in fluid dynamics data. TurboNet consist of a single LSTM layer with 64 Units.

C. BiLSTM

They are an extended form of LSTM networks which process data both forward and backward. This way, it captures a more substantial dependencies that can be missed out while considering just the past as it was done by LSTM. Bidirectional Context can capture using information from the future time steps, and in the case of fluid dynamics, the BiLSTM may be able to capture a broader context. BiLSTM perform well in scenarios where the understanding of the sequence as a whole is critical, such as predicting flow patterns in complex geometries or turbulent flows. Two layers of BiLSTM were employed with 64 Units as shown in figure 4.

IV. Result

The performance of the architecture was assessed on 3 distinct datasets, the evaluation metrics across these datasets are shown in Table.1.

TABLE I. Performance metrics of TurboNet

Metrics	Savonius Turbine	Backward-Facing Steps	Channel Flow
MAE	0.4434	0.0006	0.0207
R^2	0.9686	0.9934	0.9897
MSE	0.2463	0.0060	0.0090
RMSE	0.4963	0.0008	0.0302
MAPE	23.63%	14.52%	2.64%

The differences in these metrics arise due to the unique flow characteristics and their inherent physical dynamics. The dataset of the Savonius turbine has a periodic turbulent flow, where the velocity and pressure exhibit an oscillatory behaviour. This periodicity introduces significant variability in the flow dynamics, which results in a higher Mean Absolute Percentage Error (MAPE) and values. The increased error percentages suggest that while the model captures the broader trends of the periodic regime; the small predictions are affected by slight deviations in amplitude. Moreover, the periodic nature of the flow increases the errors in localized predictions, which affects metrics like MAPE. Despite this, the high R^2 value shows the TurboNet could capture the overall dynamics of the periodic flow with significant accuracys. The channel flow data is an example of highly non-linear but statistically steady turbulence, where the flow develops in a random but stable way over time. In these situations, the temporal structures of the flow are extremely complicated, but the statistical properties are stable. The close-to-ideal R^2 value and smaller MAPE emphasize the superb predictive capability of TurboNet on this dataset. The stable statistical character of channel flow offers a more predictable environment for the model to learn and generalize. Unlike periodic flows, non-linear turbulence lacks repetitive patterns that could lead to phase mismatches, contributing to the observed smaller errors. Backstep flow is typified by separation and reattachment flows, in which the flow is detached from the surface and generates a complex wake region. The dataset comprises complicated flow structures of differing scales of separation and reattachment dynamics. Though less periodic than Savonius flow, backstep flow remains to contain localized turbulent structures that defy predictability accuracy. The R^2 value of reflects that the model has ability to resolve dominant features of backstep flow, like the separation bubble and reattachment point. However, the MAPE are higher compared to channel flow, suggesting that the model encounters difficulties in capturing small-scale, localized flow details. These discrepancies could arise from sharp gradients and transient phenomena in the separation and wake regions, which are harder to predict accurately.

V. Conclusion

The metrics reflect how well the TurboNet adapts to the distinct challenges presented by periodic, non-linear, and separated flows. The findings from the model highlights the potential of the proposed model for advancing the predictive capabilities in turbulent flow dynamics. Future work will focus on refining the architecture to improve performance on high-fidelity data and exploring its applicability to a broader range of turbulent flow configurations.

Acknowledgment

The Fluid Mechanics Research Group at Delhi Technological University along with Mr. Gaurav Kumar are to be thanked for their invaluable support, guidance and access to essential computational resources, which was important in the successful completion of this research work.

References

[1] R. Vinuesa and S. L. Brunton, "Enhancing computational fluid dynamics with machine learning," *Nat Comput Sci*, vol. 2, no. 6, pp. 358–366, Jun. 2022, doi: 10.1038/s43588-022-00264-7.

[2] D. C. Wilcox, "Turbulence Modeling for CFD," *DCW industries, La Canada*, 1998.

[3] K. Duraisamy, G. Iaccarino, and H. Xiao, "Turbulence modeling in the age of data," *Annu Rev Fluid Mech*, vol. 51, no. 1, pp. 357–377, 2019.

[4] S. L. Brunton, B. R. Noack, and P. Koumoutsakos, "Machine learning for fluid mechanics," *Annu Rev Fluid Mech*, vol. 52, no. 1, pp. 477–508, 2020.

Authorized licensed use limited to: DELHI TECHNICAL UNIV. Downloaded on June 04,2025 at 05:20:25 UTC from IEEE Xplore. Restrictions apply.

[5] M. P. Brenner, J. D. Eldredge, and J. B. Freund, "Perspective on machine learning for advancing fluid mechanics," *Phys Rev Fluids*, vol. 4, no. 10, p. 100501, 2019.
[6] S. L. Brunton and J. N. Kutz, *Data-driven science and engineering: Machine learning, dynamical systems, and control*. Cambridge University Press, 2022.
[7] S. E. Ahmed, S. Pawar, O. San, A. Rasheed, T. Iliescu, and B. R. Noack, "On closures for reduced order models—A spectrum of first-principle to machine-learned avenues," *Physics of Fluids*, vol. 33, no. 9, 2021.
[8] P. Singh, V. Jaiswal, S. Roy, and R. K. Singh, "Maximizing Savonius Turbine Performance using Kriging Surrogate Model and Grey Wolf-Driven Cylindrical Deflector Optimization," 2023. [Online]. Available: https://arxiv.org/abs/2311.06378
[9] P. Singh, V. Jaiswal, S. Roy, A. Tyagi, G. Kumar, and R. K. Singh, "Quantum-Based Salp Swarm Algorithm Driven Design Optimization of Savonius Wind Turbine-Cylindrical Deflector System," 2024. [Online]. Available: https://arxiv.org/abs/2403.04876
[10] Farhad Mortezapour Shiri, Thinagaran Perumal, Norwati Mustapha, and Raihani Mohamed, "A Comprehensive Overview and Comparative Analysis on Deep Learning Models: CNN, RNN, LSTM, GRU," 2023.
[11] M. Elsaraiti and A. Merabet, "A Comparative Analysis of the ARIMA and LSTM Predictive Models and Their Effectiveness for Predicting Wind Speed," *Energies (Basel)*, vol. 14, no. 20, p. 6782, Oct. 2021, doi: 10.3390/en14206782.
[12] R. DiPietro and G. D. Hager, "Deep learning: RNNs and LSTM," in *Handbook of Medical Image Computing and Computer Assisted Intervention*, Elsevier, 2020, pp. 503–519. doi: 10.1016/B978-0-12-816176-0.00026-0.
[13] X. Zhang *et al.*, "A residual graph convolutional network for setting initial flow field in computational fluid dynamics simulations," *Physics of Fluids*, vol. 36, no. 3, Mar. 2024, doi: 10.1063/5.0195824.
[14] J. Ko, W. Choi, and S. Lee, "Internal Flow Prediction in Arbitrary Shaped Channel Using Stream-Wise Bidirectional LSTM," *Applied Sciences*, vol. 13, no. 20, p. 11481, Oct. 2023, doi: 10.3390/app132011481.
[15] H. H. Mian, M. S. Siddiqui, A. Keprate, and S. Mathew, "Predictive Modeling of Semi-Submersible Floater Motion Using Bi-LSTM Model," *J Phys Conf Ser*, vol. 2875, no. 1, p. 012029, Nov. 2024, doi: 10.1088/1742-6596/2875/1/012029.
[16] I. R. Jamil and M. Humaira, "Modeling and Predicting Blood Flow Characteristics through Double Stenosed Artery from Computational Fluid Dynamics Simulations using Deep Learning Models," *International Journal of Advanced Computer Science and Applications*, vol. 13, no. 1, 2022, doi: 10.14569/IJACSA.2022.0130197.
[17] M. Zhao and R. Okuno, "A Proxy Peng-Robinson EOS for Efficient Modeling of Phase Behavior," in *SPE Reservoir Simulation Conference*, SPE, Oct. 2021. doi: 10.2118/203914-MS.
[18] Z. Li, F. Montomoli, and S. Sharma, "Investigation of compressor cascade flow based on physics-informed neural networks," Jul. 2023.
[19] P. K. Talukdar, A. Sardar, V. Kulkarni, and U. K. Saha, "Parametric analysis of model Savonius hydrokinetic turbines through experimental and computational investigations," *Energy Convers Manag*, vol. 158, pp. 36–49, Feb. 2018, doi: 10.1016/j.enconman.2017.12.011.
[20] Y. Kassem, H. Çamur, A. A. Bahroun, O. A. M. Abughnida, and A. Alghazali, "Performance investigation of Savonius Turbine with New Blade Shape : Experimental and Numerical study," 2018. [Online]. Available: https://api.semanticscholar.org/CorpusID:189758089
[21] M. Zemamou, A. Toumi, K. Mrigua, Y. Lahlou, and M. Aggour, "A novel blade design for Savonius wind turbine based on polynomial bezier curves for aerodynamic performance enhancement," *Int J Green Energy*, vol. 17, no. 11, pp. 652–665, Sep. 2020, doi: 10.1080/15435075.2020.1779077.
[22] D. Q. He, H. L. Bai, C. M. Chan, and K. M. Li, "Performance-based Optimizations on Savonius-type Vertical-axis Wind Turbines using Genetic Algorithm," *Energy Procedia*, vol. 158, pp. 643–648, Feb. 2019, doi: 10.1016/j.egypro.2019.01.175.
[23] K. Golecha, T. I. Eldho, and S. V. Prabhu, "Influence of the deflector plate on the performance of modified Savonius water turbine," *Appl Energy*, vol. 88, no. 9, pp. 3207–3217, Sep. 2011, doi: 10.1016/j.apenergy.2011.03.025.
[24] E. Fatahian, F. Ismail, M. Hafifi Hafiz Ishak, and W. Shyang Chang, "An innovative deflector system for drag-type Savonius turbine using a rotating cylinder for performance improvement," *Energy Convers Manag*, vol. 257, p. 115453, Apr. 2022, doi: 10.1016/j.enconman.2022.115453.
[25] F. R. Menter, "Two-equation eddy-viscosity turbulence models for engineering applications," *AIAA Journal*, vol. 32, no. 8, pp. 1598–1605, Aug. 1994, doi: 10.2514/3.12149.
[26] D. C. Wilcox, "Formulation of the k-w Turbulence Model Revisited," *AIAA Journal*, vol. 46, no. 11, pp. 2823–2838, Nov. 2008, doi: 10.2514/1.36541.
[27] B. E. Launder and D. B. Spalding, "The numerical computation of turbulent flows," *Comput Methods Appl Mech Eng*, vol. 3, no. 2, pp. 269–289, Mar. 1974, doi: 10.1016/0045-7825(74)90029-2.
[28] A. C. W. Creech and A. Jackson, "Time-series data from a hybrid finite element Large Eddy Simulation of flow over a backward-facing step," *Data Brief*, vol. 54, p. 110330, Jun. 2024, doi: 10.1016/j.dib.2024.110330.
[29] A. C. W. Creech and A. Jackson, "Hybrid Large Eddy Simulation for low-order Discontinuous Galerkin methods using an explicit filter," *Comput Phys Commun*, vol. 260, p. 107730, Mar. 2021, doi: 10.1016/j.cpc.2020.107730.
[30] J. Peraire and P.-O. Persson, "The Compact Discontinuous Galerkin (CDG) Method for Elliptic Problems," *SIAM Journal on Scientific Computing*, vol. 30, no. 4, pp. 1806–1824, Jan. 2008, doi: 10.1137/070685518.
[31] R. Ford, C. C. Pain, M. D. Piggott, A. J. H. Goddard, C. R. E. de Oliveira, and A. P. Umpleby, "A Nonhydrostatic Finite-Element Model for Three-Dimensional Stratified Oceanic Flows. Part II: Model Validation," *Mon Weather Rev*, vol. 132, no. 12, pp. 2832–2844, Dec. 2004, doi: 10.1175/MWR2825.1.
[32] S. Patil and D. Tafti, "Wall modeled large eddy simulations of complex high Reynolds number flows with synthetic inlet turbulence," *Int J Heat Fluid Flow*, vol. 33, no. 1, pp. 9–21, Feb. 2012, doi: 10.1016/j.ijheatfluidflow.2011.09.010.
[33] N. Jarrin, S. Benhamadouche, D. Laurence, and R. Prosser, "A synthetic-eddy-method for generating inflow conditions for large-eddy simulations," *Int J Heat Fluid Flow*, vol. 27, no. 4, pp. 585–593, Aug. 2006, doi: 10.1016/j.ijheatfluidflow.2006.02.006.
[34] E. Perlman, R. Burns, Y. Li, and C. Meneveau, "Data exploration of turbulence simulations using a database cluster," in *Proceedings of the 2007 ACM/IEEE conference on Supercomputing*, New York, NY, USA: ACM, Nov. 2007, pp. 1–11. doi: 10.1145/1362622.1362654.
[35] Y. Li *et al.*, "A public turbulence database cluster and applications to study Lagrangian evolution of velocity increments in turbulence," *Journal of Turbulence*, vol. 9, p. N31, Jan. 2008, doi: 10.1080/14685240802376389.
[36] J. Graham *et al.*, "A Web services accessible database of turbulent channel flow and its use for testing a new integral wall model for LES," *Journal of Turbulence*, vol. 17, no. 2, pp. 181–215, Feb. 2016, doi: 10.1080/14685248.2015.1088656.
[37] M. Lee, N. Malaya, and R. D. Moser, "Petascale direct numerical simulation of turbulent channel flow on up to 786K cores," in *Proceedings of the International Conference on High Performance Computing, Networking, Storage and Analysis*, New York, NY, USA: ACM, Nov. 2013, pp. 1–11. doi: 10.1145/2503210.2503298.
[38] J. Kim, P. Moin, and R. Moser, "Turbulence statistics in fully developed channel flow at low Reynolds number," *J Fluid Mech*, vol. 177, pp. 133–166, Apr. 1987, doi: 10.1017/S0022112087000892.
[39] S. A. Orszag, "On the Elimination of Aliasing in Finite-Difference Schemes by Filtering High-Wavenumber Components," *J Atmos Sci*, vol. 28, no. 6, p. 1074, Sep. 1971, doi: 10.1175/1520-0469(1971)028<1074:OTEOAI>2.0.CO;2.

Authorized licensed use limited to: DELHI TECHNICAL UNIV. Downloaded on June 04,2025 at 05:20:25 UTC from IEEE Xplore. Restrictions apply.

Supplementary Information

Optimization, simultaneous saccharification and fermentation of Lemna minor using amylolytic cocktail produce from copra meal

Manjary Vyas, Kriti Bhandari* & Jaigopal Sharma

Delhi Technological University, Shahbad Daulatpur Village, Rohini, New Delhi, Delhi 110 042, India

*E-mail: kritibhandari@dtu.ac.in

Table S1 — A three-factor central composite design (CCD) model having coded and non-coded data created with Minitab software

Run	Space type	Coded factor							Non coded factor							
		pH	temp (°C)	Copra (%)	KH2PO4 (%)	Peptone (%)	Time of incubation (days)	CMC (%)	pH	temp (°C)	Copra (%)	KH2PO4 (%)	Peptone (%)	Time of incubation (days)	CMC (%)	Enzyme activity (U/ml)
1	Corner	-1	-1	-1	-1	-1	-1	1	3.5	25	2	0.01	0.125	6	2	842.86
2	Corner	1	-1	-1	-1	-1	-1	-1	4.5	25	2	0.01	0.125	6	0.5	740.71
3	Corner	-1	1	-1	-1	-1	-1	-1	3.5	35	2	0.01	0.125	6	0.5	880.86
4	Corner	1	1	-1	-1	-1	-1	1	4.5	35	2	0.01	0.125	6	2	741.43
5	Corner	-1	-1	1	-1	-1	-1	-1	3.5	25	4	0.01	0.125	6	0.5	903.86
6	Corner	1	-1	1	-1	-1	-1	1	4.5	25	4	0.01	0.125	6	2	764.43
7	Corner	-1	1	1	-1	-1	-1	1	3.5	35	4	0.01	0.125	6	2	809.14
8	Corner	1	1	1	-1	-1	-1	-1	4.5	35	4	0.01	0.125	6	0.5	850.71

9	Corner	-1	-1	-1	1	-1	-1	-1	3.5	25	2	0.03	0.125	6	0.5	920.71
10	Corner	1	-1	-1	1	-1	-1	1	4.5	25	2	0.03	0.125	6	2	826.57
11	Corner	-1	1	-1	1	-1	-1	1	3.5	35	2	0.03	0.125	6	2	826
12	Corner	1	1	-1	1	-1	-1	-1	4.5	35	2	0.03	0.125	6	0.5	867.57
13	Corner	-1	-1	1	1	-1	-1	1	3.5	25	4	0.03	0.125	6	2	849
14	Corner	1	-1	1	1	-1	-1	-1	4.5	25	4	0.03	0.125	6	0.5	890.57
15	Corner	-1	1	1	1	-1	-1	-1	3.5	35	4	0.03	0.125	6	0.5	890
16	Corner	1	1	1	1	-1	-1	1	4.5	35	4	0.03	0.125	6	2	795.86
17	Corner	-1	-1	-1	-1	1	-1	-1	3.5	25	2	0.01	0.5	6	0.5	920
18	Corner	1	-1	-1	-1	1	-1	1	4.5	25	2	0.01	0.5	6	2	825.86
19	Corner	-1	1	-1	-1	1	-1	1	3.5	35	2	0.01	0.5	6	2	825.29
20	Corner	1	1	-1	-1	1	-1	-1	4.5	35	2	0.01	0.5	6	0.5	866.86
21	Corner	-1	-1	1	-1	1	-1	1	3.5	25	4	0.01	0.5	6	2	848.29
22	Corner	1	-1	1	-1	1	-1	-1	4.5	25	4	0.01	0.5	6	0.5	889.86
23	Corner	-1	1	1	-1	1	-1	-1	3.5	35	4	0.01	0.5	6	0.5	889.29
24	Corner	1	1	1	-1	1	-1	1	4.5	35	4	0.01	0.5	6	2	795.14
25	Corner	-1	-1	-1	1	1	-1	1	3.5	25	2	0.03	0.5	6	2	865.14
26	Corner	1	-1	-1	1	1	-1	-1	4.5	25	2	0.03	0.5	6	0.5	906.71
27	Corner	-1	1	-1	1	1	-1	-1	3.5	35	2	0.03	0.5	6	0.5	906.14

28	Corner	1	1	-1	1	1	-1	1	4.5	35	2	0.03	0.5	6	2	812
29	Corner	-1	-1	1	1	1	-1	-1	3.5	25	4	0.03	0.5	6	0.5	929.14
30	Corner	1	-1	1	1	1	-1	1	4.5	25	4	0.03	0.5	6	2	835
31	Corner	-1	1	1	1	1	-1	1	3.5	35	4	0.03	0.5	6	0.5	902.29
32	Corner	1	1	1	1	1	-1	-1	4.5	35	4	0.03	0.5	6	0.5	876
33	Corner	-1	-1	-1	-1	-1	1	-1	3.5	25	2	0.01	0.125	10	0.5	917.43
34	Corner	1	-1	-1	-1	-1	1	1	4.5	25	2	0.01	0.125	10	2	823.29
35	Corner	-1	1	-1	-1	-1	1	1	3.5	35	2	0.01	0.125	10	2	822.71
36	Corner	1	1	-1	-1	-1	1	-1	4.5	35	2	0.01	0.125	10	0.5	864.29
37	Corner	-1	-1	1	-1	-1	1	1	3.5	25	4	0.01	0.125	10	2	845.71
38	Corner	1	-1	1	-1	-1	1	-1	4.5	25	4	0.01	0.125	10	0.5	887.29
39	Corner	-1	1	1	-1	-1	1	-1	3.5	35	4	0.01	0.125	10	0.5	886.71
40	Corner	1	1	1	-1	-1	1	1	4.5	35	4	0.01	0.125	10	2	792.57
41	Corner	-1	-1	-1	1	-1	1	1	3.5	25	2	0.03	0.125	10	2	862.57
42	Corner	1	-1	-1	1	-1	1	-1	4.5	25	2	0.03	0.125	10	0.5	904.14
43	Corner	-1	1	-1	1	-1	1	-1	3.5	35	2	0.03	0.125	10	0.5	903.57
44	Corner	1	1	-1	1	-1	1	1	4.5	35	2	0.03	0.125	10	2	809.43
45	Corner	-1	-1	1	1	-1	1	-1	3.5	25	4	0.03	0.125	10	0.5	926.57
46	Corner	1	-1	1	1	-1	1	1	4.5	25	4	0.03	0.125	10	2	832.43

47	Corner	-1	1	1	1	-1	1	1	3.5	35	4	0.03	0.125	10	2	831.86
48	Corner	1	1	1	1	-1	1	-1	4.5	35	4	0.03	0.125	10	0.5	873.43
49	Corner	-1	-1	-1	-1	1	1	1	3.5	25	2	0.01	0.5	10	2	861.86
50	Corner	1	-1	-1	-1	1	1	-1	4.5	25	2	0.01	0.5	10	0.5	903.43
51	Corner	-1	1	-1	-1	1	1	-1	3.5	35	2	0.01	0.5	10	0.5	902.86
52	Corner	1	1	-1	-1	1	1	1	4.5	35	2	0.01	0.5	10	2	808.71
53	Corner	-1	-1	1	-1	1	1	-1	3.5	25	4	0.01	0.5	10	0.5	925.86
54	Corner	1	-1	1	-1	1	1	1	4.5	25	4	0.01	0.5	10	2	831.71
55	Corner	-1	1	1	-1	1	1	1	3.5	35	4	0.01	0.5	10	2	831.14
56	Corner	1	1	1	-1	1	1	-1	4.5	35	4	0.01	0.5	10	0.5	872.71
57	Corner	-1	-1	-1	1	1	1	-1	3.5	25	2	0.03	0.5	10	0.5	942.71
58	Corner	1	-1	-1	1	1	1	1	4.5	25	2	0.03	0.5	10	2	848.57
59	Corner	-1	1	-1	1	1	1	1	3.5	35	2	0.03	0.5	10	2	848
60	Corner	1	1	-1	1	1	1	-1	4.5	35	2	0.03	0.5	10	0.5	889.57
61	Corner	-1	-1	1	1	1	1	1	3.5	25	4	0.03	0.5	10	2	871
62	Corner	1	-1	1	1	1	1	-1	4.5	25	4	0.03	0.5	10	0.5	912.57
63	Corner	-1	1	1	1	1	1	-1	3.5	35	4	0.03	0.5	10	0.5	912
64	Corner	1	1	1	1	1	1	1	4.5	35	4	0.03	0.5	10	2	817.86
65	Axial	-2.8	0	0	0	0	0	0	3	30	3	0.02	0.25	8	1	1086.86

66	Axial	2.8	0	0	0	0	0	0	5	30	3	0.02	0.25	8	1	907
67	Axial	0	-2.828	0	0	0	0	0	4	20	3	0.02	0.25	8	1	1109.57
68	Axial	0	2.828	0	0	0	0	0	4	40	3	0.02	0.25	8	1	1074.14
69	Axial	0	0	-2.828	0	0	0	0	4	30	1	0.02	0.25	8	1	1053
70	Axial	0	0	2.8284	0	0	0	0	4	30	5	0.02	0.25	8	1	1067.71
71	Axial	0	0	0	-2.82843	0	0	0	4	30	3	0.001	0.25	8	1	1076.71
72	Axial	0	0	0	2.828427	0	0	0	4	30	3	0.04	0.25	8	1	945.57
73	Axial	0	0	0	0	-2.8284271	0	0	4	30	3	0.02	0.0625	8	1	935
74	Axial	0	0	0	0	2.8284271	0	0	4	30	3	0.02	1	8	1	1030
75	Axial	0	0	0	0	0	-2.8284271	0	4	30	3	0.02	0.25	4	1	1049.29
76	Axial	0	0	0	0	0	2.8284271	0	4	30	3	0.02	0.25	12	1	1047.29
77	Axial	0	0	0	0	0	0	-2.828	4	30	3	0.02	0.25	8	0.001	1036.57
78	Axial	0	0	0	0	0	0	2.828	4	30	3	0.02	0.25	8	2	1014.14
79	Centre	0	0	0	0	0	0	0	4	30	3	0.02	0.25	8	1	1005
80	Centre	0	0	0	0	0	0	0	4	30	3	0.02	0.25	8	1	1005
81	Centre	0	0	0	0	0	0	0	4	30	3	0.02	0.25	8	1	1005
82	Centre	0	0	0	0	0	0	0	4	30	3	0.02	0.25	8	1	1005
83	Centre	0	0	0	0	0	0	0	4	30	3	0.02	0.25	8	1	1005
84	Centre	0	0	0	0	0	0	0	4	30	3	0.02	0.25	8	1	1005
85	Centre	0	0	0	0	0	0	0	4	30	3	0.02	0.25	8	1	1005
86	Centre	0	0	0	0	0	0	0	4	30	3	0.02	0.25	8	1	1005
87	Centre	0	0	0	0	0	0	0	4	30	3	0.02	0.25	8	1	1005
88	Centre	0	0	0	0	0	0	0	4	30	3	0.02	0.25	8	1	1005

Table S2 — Model analysis for amylase production from *Aspergillus niger* sp. using ANOVA test

Analysis of Variance

Source	DF	Seq SS	Contribution	F-Value	P-Value	Remark
Model	14	485036	76.81%	17.27	0.000	Significant
Linear	7	174631	27.66%	3.42	0.003	
pH	1	31375	4.97%	14.14	0.000	
temperature (°C)	1	7295	1.16%	4.41	0.039	
Coconut oil cake concentration	1	173	0.03%	0.01	0.920	
KH2PO4 (%)	1	3047	0.48%	0.31	0.582	
Peptone (%)	1	666	0.11%	0.72	0.400	
Time of incubation (days)	1	3033	0.48%	2.02	0.159	
Carboxy Methyl Cellulose (%)	1	129042	20.44%	2.26	0.137	
Square	7	310405	49.16%	22.11	0.000	
pH*pH	1	97485	15.44%	13.33	0.000	
temperature (°C)*temperature (°C)	1	21646	3.43%	0.35	0.557	
Coconut oil cake concentration*Coconut oil cake conc.	1	29918	4.74%	2.58	0.113	
KH2PO4 (%)*KH2PO4 (%)	1	56411	8.93%	12.00	0.001	
Peptone (%)*Peptone (%)	1	9497	1.50%	4.09	0.047	
Time of incubation (days)*Time of incubation (days)	1	22644	3.59%	3.98	0.050	
Carboxy Methyl Cellulose (%)*Carboxy Methyl Cellulose (%)	1	72802	11.53%	36.30	0.000	
Error	73	146422	23.19%			
Lack-of-Fit	64	146422	23.19%	*	*	
Pure Error	9	0	0.00%			
Total	87	631458	100.00%			

Table S3 — Model summary statistics for optimal amylase production (response Y)

Source	S	R-sq	R-sq(adj)	Press	R-sq(pred)	Remarks
Linear	75.5667	27.66%	21.33%	530208	16.03%	
Linear + Square	44.7859	76.81%	72.37%	2995016	0.00%	Suggested
Linear + Interaction	87.1609	29.02%	0.00%	754047	0.00%	

Full quadratic	51.5231	78.14%	63.43%	3031637	0.00%	

Table S4: A three-factor central composite design (CCD) model having coded and non-coded data created with Minitab software

Run	Space type	Coded factor				Non coded factor				
		pH	Temp (^{0}C)	Lemna minor biomass (%)	Amylase enzyme extract (ml)	pH	Temp (^{0}C)	Lemna minor biomass (%)	Amylase enzyme extract (ml)	Ethanol (%)
1	Corner	-0.5	-0.5	-0.5	-0.5	4.5	30	0.5	5	9.35
2	Corner	0.5	-0.5	-0.5	-0.5	5.5	30	0.5	5	9.725
3	Corner	-0.5	0.5	-0.5	-0.5	4.5	40	0.5	5	9.975
4	Corner	0.5	0.5	-0.5	-0.5	5.5	40	0.5	5	10.35
5	Corner	-0.5	-0.5	0.5	-0.5	4.5	30	2	5	9.7
6	Corner	0.5	-0.5	0.5	-0.5	5.5	30	2	5	10.075
7	Corner	-0.5	0.5	0.5	-0.5	4.5	40	2	5	10.325
8	Corner	0.5	0.5	0.5	-0.5	5.5	40	2	5	10.7
9	Corner	-0.5	-0.5	-0.5	0.5	4.5	30	0.5	7	9.775
10	Corner	0.5	-0.5	-0.5	0.5	5.5	30	0.5	7	10.15
11	Corner	-0.5	0.5	-0.5	0.5	4.5	40	0.5	7	10.4
12	Corner	0.5	0.5	-0.5	0.5	5.5	40	0.5	7	10.775
13	Corner	-0.5	-0.5	0.5	0.5	4.5	30	2	7	10.125
14	Corner	0.5	-0.5	0.5	0.5	5.5	30	2	7	10.5
15	Corner	-0.5	0.5	0.5	0.5	4.5	40	2	7	10.75
16	Corner	0.5	0.5	0.5	0.5	5.5	40	2	7	11.125
17	Axial	-1	0	0	0	4	35	1	6	10.95
18	Axial	1	0	0	0	6	35	1	6	11.5
19	Axial	0	-1	0	0	5	25	1	6	10.225
20	Axial	0	1	0	0	5	45	1	6	11.025
21	Axial	0	0	-1	0	5	35	0.25	6	10.375

22	Axial	0	0	1	0	5	35	3	6	10.825
23	Axial	0	0	0	-1	5	35	1	4	11.225
24	Axial	0	0	0	1	5	35	1	8	11.4
25	Centre	0	0	0	0	5	35	1	6	11.625
26	Centre	0	0	0	0	5	35	1	6	11.625
27	Centre	0	0	0	0	5	35	1	6	11.625
28	Centre	0	0	0	0	5	35	1	6	11.625
29	Centre	0	0	0	0	5	35	1	6	11.625
30	Centre	0	0	0	0	5	35	1	6	11.625
31	Centre	0	0	0	0	5	35	1	6	11.625

Table S5 — Model summary statistics for optimal ethanol production (response Y)

Source	S	R-sq	R-sq(adj)	Press	R-sq(pred)	Remarks
Linear	0.66542	0.2135	0.0925	15.0852	0	
Linear + Square	0.41735	0.7382	0.643	29.1425	0	Suggested
Linear + Interaction	0.75842	0.2141	0	30.0066	0	
Full quadratic	0.48885	0.7388	0.5102	35.8634	0	

Table S6 — Model analysis for ethanol production from *Lemna minor* sp. using ANOVA test

Analysis of Variance

Source	DF	Seq SS	Contribution	F-Value	P-Value
Model	8	10.8058	73.82%	7.75	0.000
Linear	4	3.1255	21.35%	5.22	0.004
pH	1	0.7004	4.79%	4.02	0.057
Temperature	1	1.8150	12.40%	10.42	0.004
Lemna minor biomass (%)	1	0.0241	0.16%	3.06	0.094

Amylase enzyme extract (ml)	1	0.5859	4.00%	3.36	0.080
Square	4	7.6803	52.47%	11.02	0.000
pH*pH	1	0.5361	3.66%	7.47	0.012
Temperature*Temperature	1	2.8491	19.46%	21.68	0.000
Lemna minor biomass (%)*Lemna minor biomass (%)	1	3.2477	22.19%	20.64	0.000
Amylase enzyme extract (ml)*Amylase enzyme extract (ml)	1	1.0474	7.16%	6.01	0.023
Error	22	3.8319	26.18%		
Lack-of-Fit	16	3.8319	26.18%	*	*
Pure Error	6	0.0000	0.00%		
Total	30	14.6377	100.00%		

Table S6 — Levels of independent variables considered for amylase and ethanol optimization

Amylase activity (U/mL)							
Description	**Variables**	**Unit**	**Levels**				
			-2	**-1**	**0**	**1**	**2**
pH	A	-	3	3.5	4	4.5	5
Temperature	B	°C	20	25	30	35	40
Coconutoilcakeconcentration	C	%(w/v)	1	2	3	4	5
KH_2PO_4	D	%(w/v)	0.001	0.01	0.02	0.03	0.04
Peptone	E	%(w/v)	0.0625	0.125	0.25	0.5	1
Timeofincubation	F	Days	4	6	8	10	12
CarboxyMethylCellulose	G	%(w/v)	0.001	0.5	1	1.5	2
Ethanol production (%)							
pH	A	-	4	4.5	5	5.5	6
Temperature	B	°C	25	30	35	40	45
Lemnaminorbiomass	C	%	0.25	0.5	1	2	3

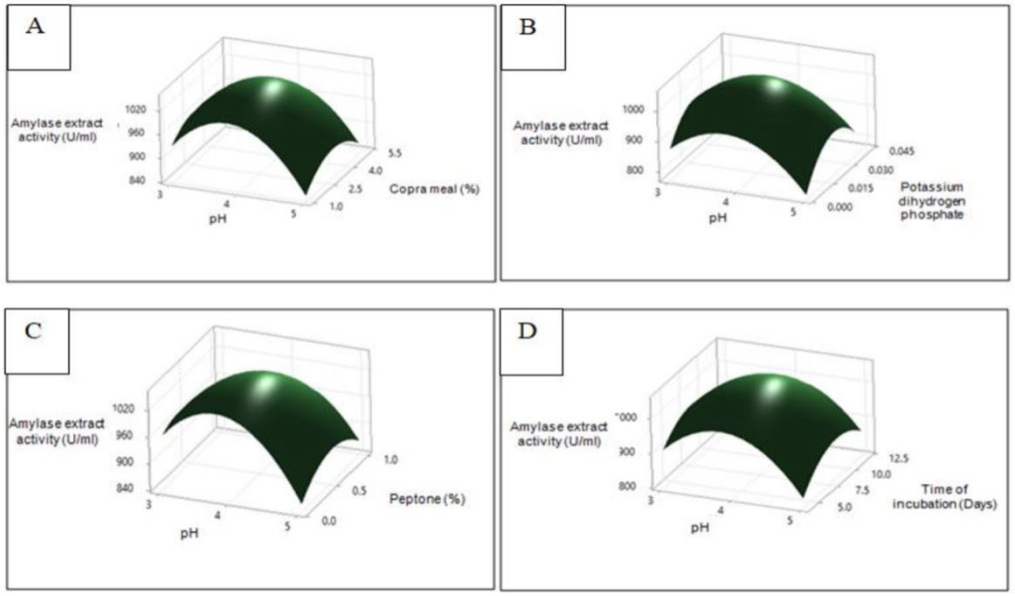
Amylaseenzymeextract	D	ml	4	5	6	7	8

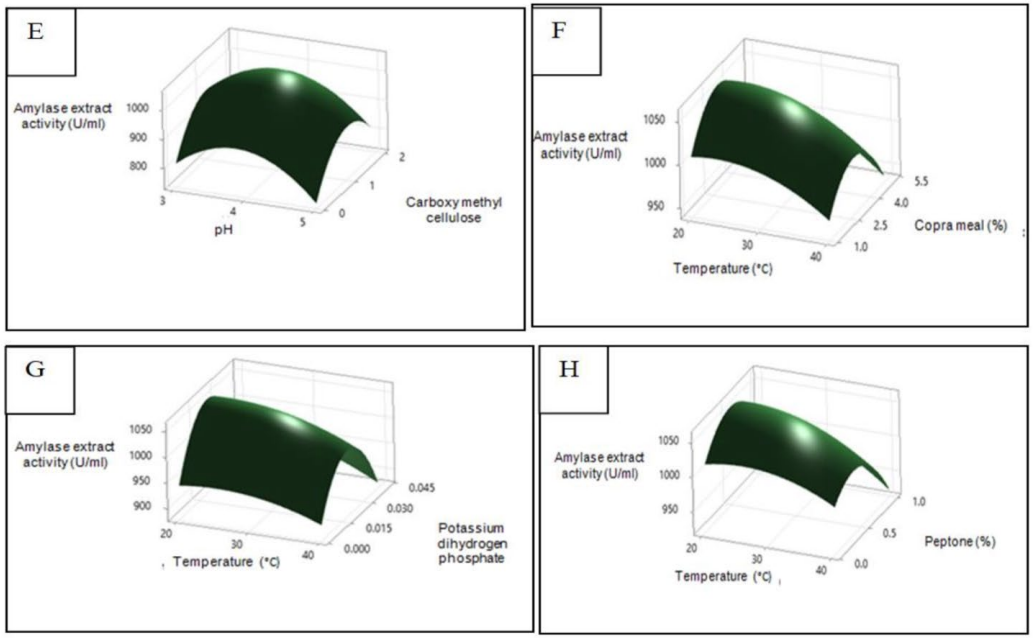
Table S7 — Levels of independent variables considered for amylase and ethanol optimization

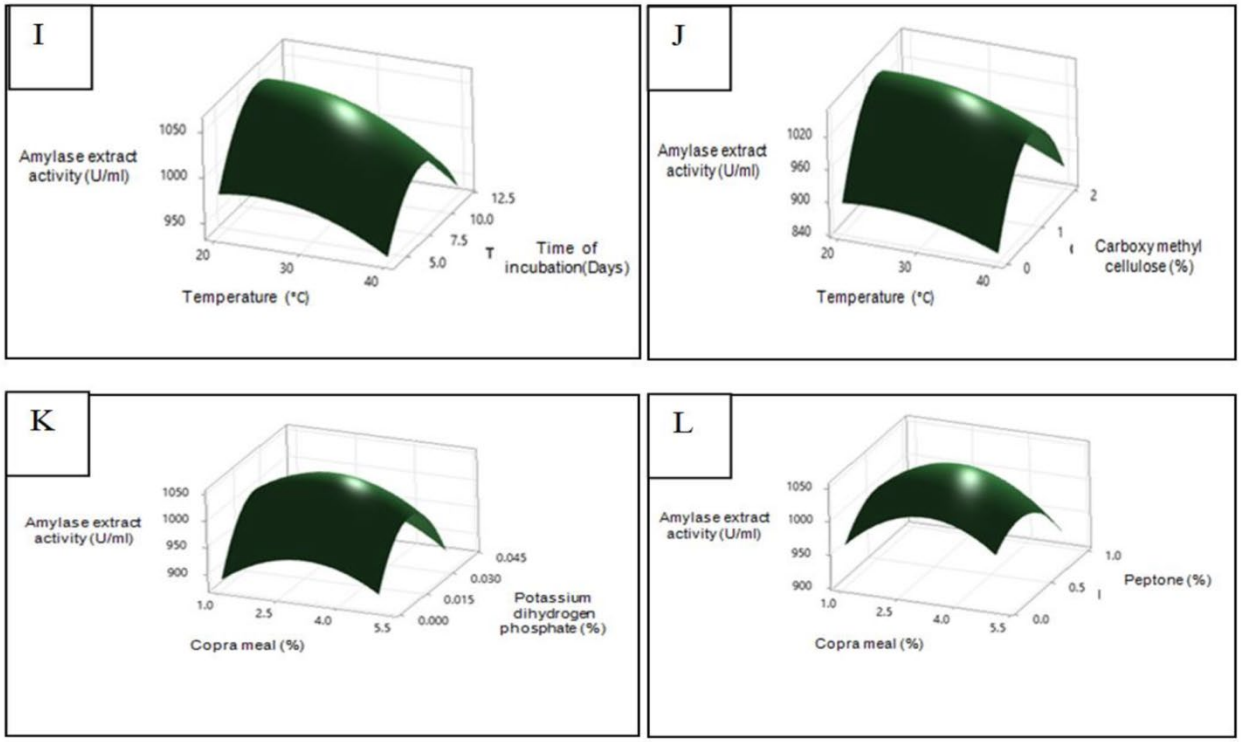
Amylase activity (U/mL)							
Description	**Variables**	**Unit**	**Levels**				
			-2	**-1**	**0**	**1**	**2**
pH	A	-	3	3.5	4	4.5	5
Temperature	B	°C	20	25	30	35	40
Coconutoilcakeconcentration	C	%(w/v)	1	2	3	4	5
KH2PO4	D	%(w/v)	0.001	0.01	0.02	0.03	0.04
Peptone	E	%(w/v)	0.0625	0.125	0.25	0.5	1
Timeofincubation	F	Days	4	6	8	10	12
CarboxyMethylCellulose	G	%(w/v)	0.001	0.5	1	1.5	2
Ethanol production (%)							
pH	A	-	4	4.5	5	5.5	6
Temperature	B	°C	25	30	35	40	45
Lemnaminorbiomass	C	%	0.25	0.5	1	2	3
Amylaseenzymeextract	D	ml	4	5	6	7	8

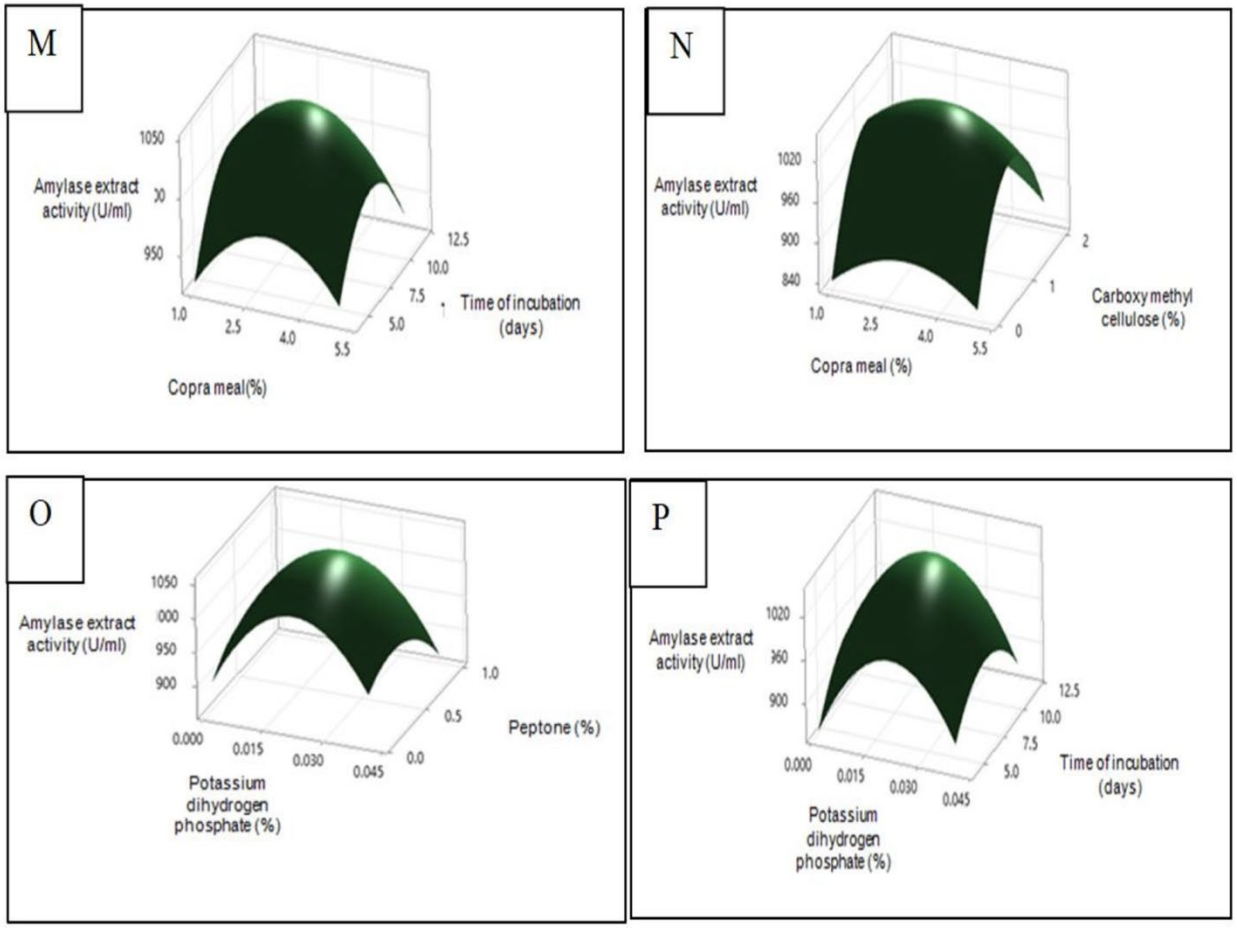
Table S8— Composition of Copra meal and Lemna minor biomass

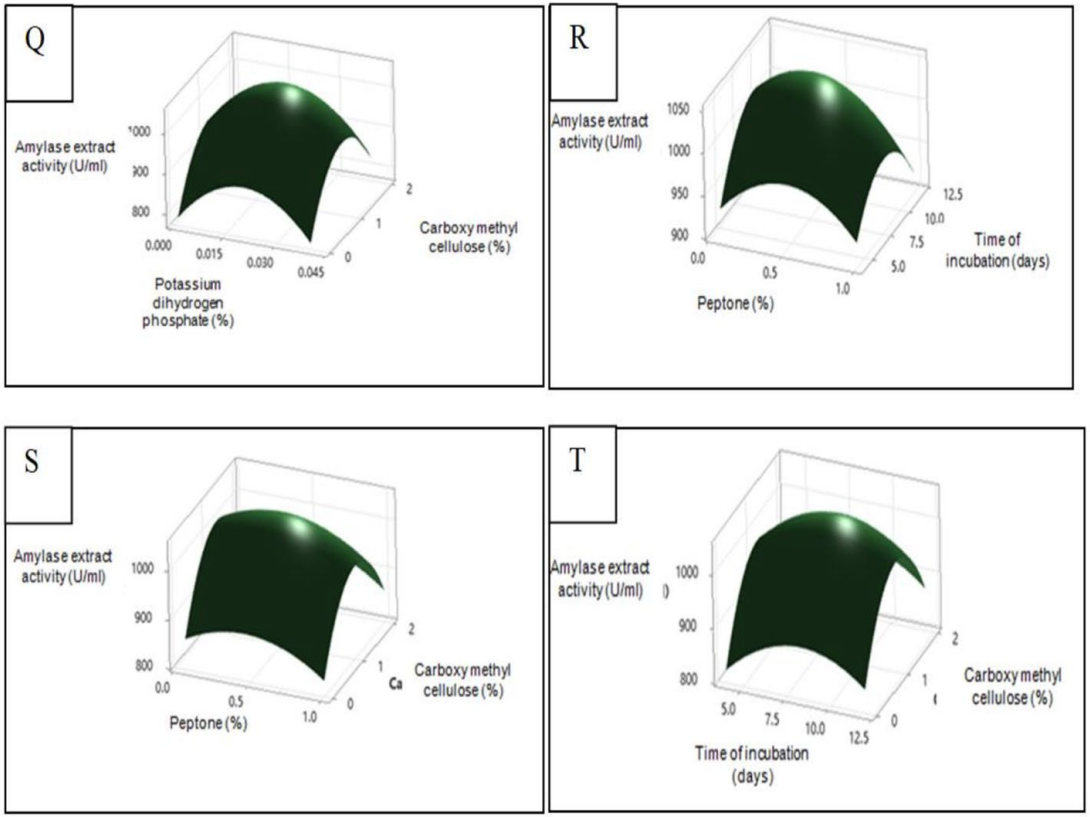
Chemical constituents	Lemna minor (% w/w)	Copra meal (% w/w)
Glucose	2	0.2
Fructose	1	0.3
Starch	26	1.6
Protein	14.60	21




E
Amylase extract activity (U/ml)
1000
900
800
3
4
5
pH
2
1
0
Carboxy methyl cellulose
F
Amylase extract activity (U/ml)
1050
1000
950
20
30
40
Temperature (°C)
5.5
4.0
2.5
1.0
Copra meal (%)
G
Amylase extract activity (U/ml)
1050
1000
950
900
20
30
40
Temperature (°C)
0.045
0.030
0.015
0.000
Potassium dihydrogen phosphate
H
Amylase extract activity (U/ml)
1050
1000
950
20
30
40
Temperature (°C)
1.0
0.5
0.0
Peptone (%)

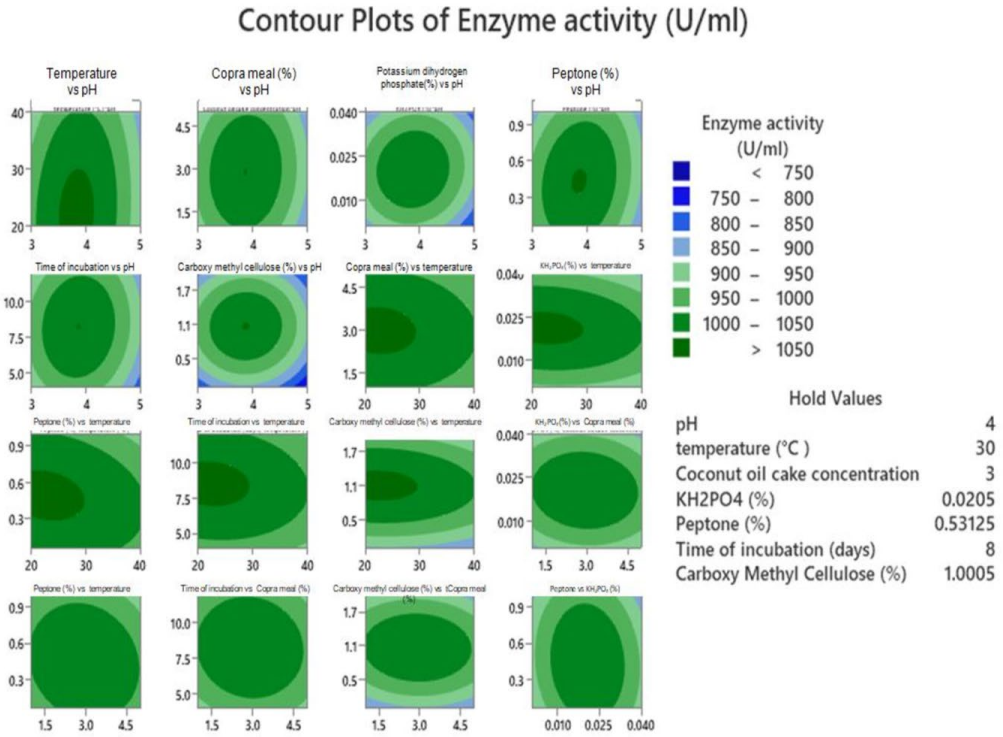

I
Amylase extract activity (U/ml)
1050
1000
950
20
30
40
Temperature (°C)
12.5
10.0
7.5
5.0
T
Time of incubation(Days)
J
Amylase extract activity (U/ml)
1020
960
900
840
20
30
40
Temperature (°C)
2
1
0
Carboxy methyl cellulose (%)
K
Amylase extract activity (U/ml)
1050
1000
950
900
1.0
2.5
4.0
5.5
Copra meal (%)
0.045
0.030
0.015
0.000
Potassium dihydrogen phosphate (%)
L
Amylase extract activity (U/ml)
1050
1000
950
900
1.0
2.5
4.0
5.5
Copra meal (%)
1.0
0.5
0.0
Peptone (%)


M
Amylase extract activity (U/ml)
1050
950
1.0
2.5
4.0
5.5
Copra meal(%)
12.5
10.0
7.5
5.0
Time of incubation (days)
N
Amylase extract activity (U/ml)
1020
960
900
840
1.0
2.5
4.0
5.5
Copra meal (%)
2
1
0
Carboxy methyl cellulose (%)
O
Amylase extract activity (U/ml)
1050
950
900
0.000
0.015
0.030
0.045
Potassium dihydrogen phosphate (%)
1.0
0.5
0.0
Peptone (%)
P
Amylase extract activity (U/ml)
1020
900
0.000
0.015
0.030
0.045
Potassium dihydrogen phosphate (%)
12.5
10.0
7.5
5.0
Time of incubation (days)



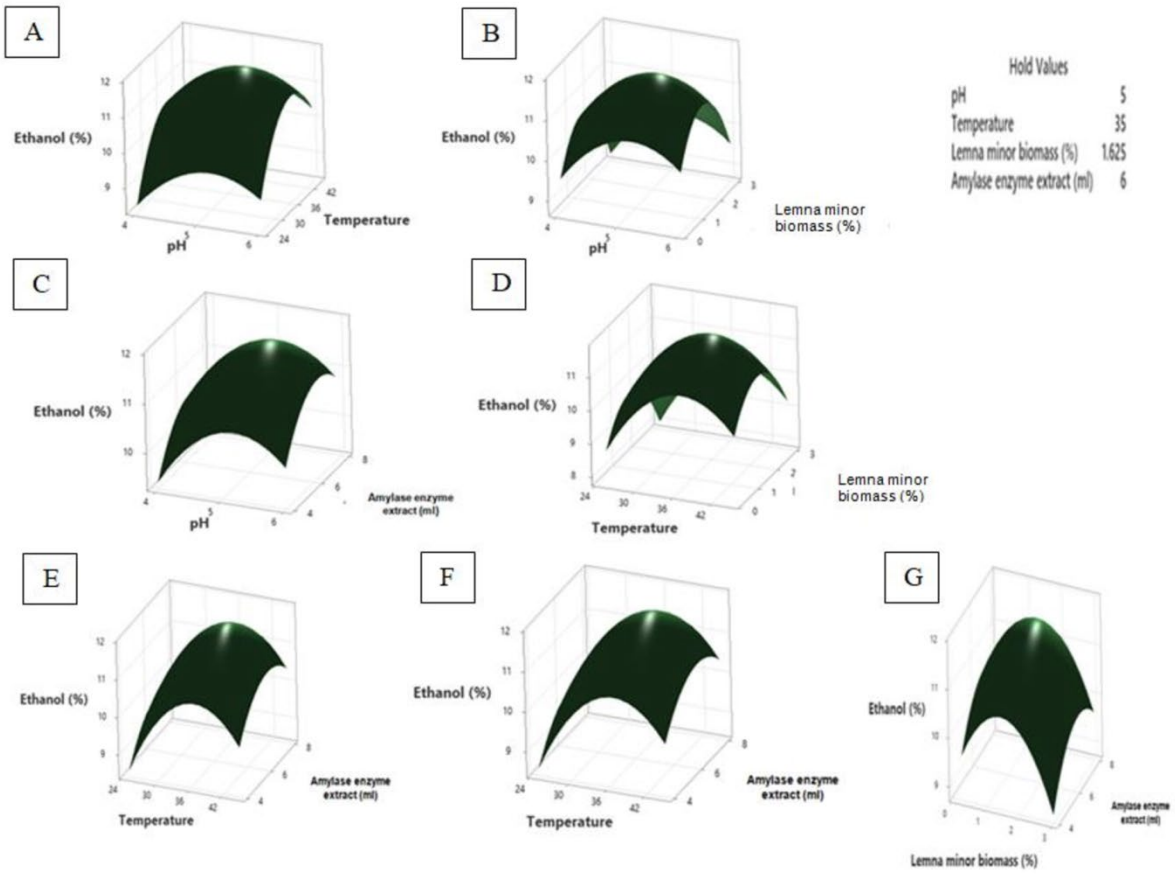
Hold Values	
pH	4
temperature (°C)	30
Coconut oil cake concentration	3
KH2PO4 (%)	0.0205
Peptone (%)	0.53125
Time of incubation (days)	8
Carboxy Methyl Cellulose (%)	1.0005

(a)

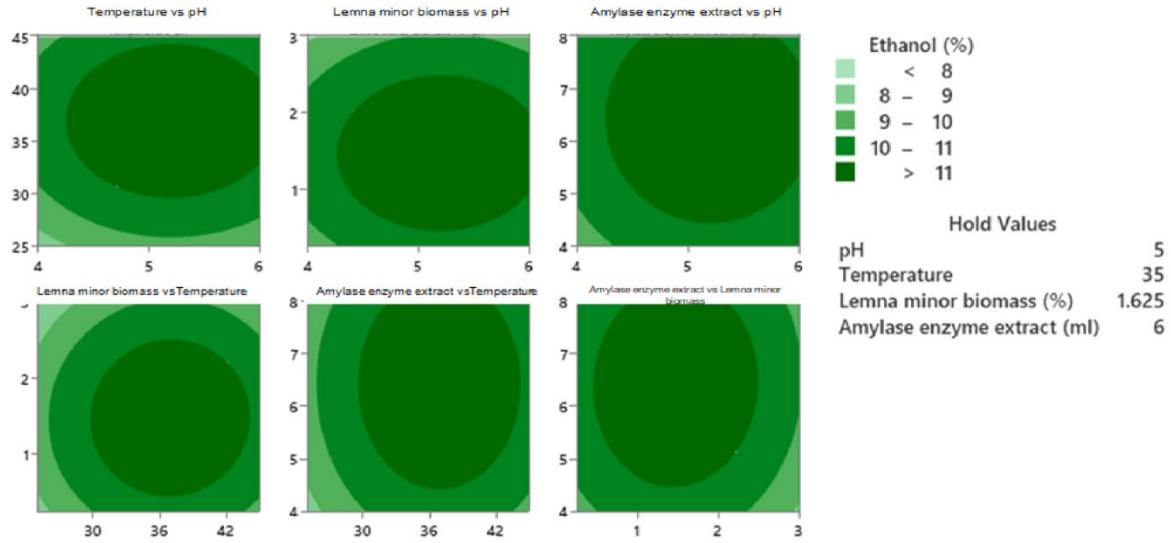


(b)

Fig. S1 — (a): 3D surface plot of various combinations of each factor for Amylase cocktail preparation (A-T) and (b) 3D contour plot of various combinations of each factor


A
Ethanol (%)
pH
Temperature
B
Ethanol (%)
pH
Lemna minor biomass (%)
Hold Values
pH 5
Temperature 35
Lemna minor biomass (%) 1.625
Amylase enzyme extract (ml) 6
C
Ethanol (%)
pH
Amylase enzyme extract (ml)
D
Ethanol (%)
Temperature
Lemna minor biomass (%)
E
Ethanol (%)
Temperature
Amylase enzyme extract (ml)
F
Ethanol (%)
Temperature
Amylase enzyme extract (ml)
G
Ethanol (%)
Lemna minor biomass (%)
Amylase enzyme extract (ml)

(a)



(b)

Fig. S2 — 3D surface plot (a) and Contour plot (b) of various combinations of each factor

The Journal of Supercomputing (2025) 81:1005
https://doi.org/10.1007/s11227-025-07457-7

RESEARCH

Optimization-based noise filtering among user-centric tweets to improve predictions in recommendation system

Kirti Jain[1] · **Rajni Jindal**[1]

Accepted: 16 May 2025
© The Author(s), under exclusive licence to Springer Science+Business Media, LLC, part of Springer Nature 2025

Abstract

With the exponential growth of social media platforms, user-generated content has emerged as a valuable resource for enhancing recommendation systems. However, the pervasive noise in user-centric tweets, stemming from irrelevant, ambiguous, or misleading information, continues to degrade the performance and reliability of such systems. To address this challenge, this paper proposes nuclear physics optimization algorithm (NPO) as the core contribution for effective noise filtering in tweet-based recommendation systems. The methodology begins with preprocessing the raw tweet data and extracting features that accurately reflect user preferences and interests. Central to our approach, the NPO algorithm is designed to dynamically adjust its parameters to identify and eliminate noisy tweets based on semantic similarity and domain relevance. By adaptively optimizing the filtering process, the NPO effectively tailors itself to the characteristics of the tweet dataset, leading to enhanced accuracy and reliability in movie recommendation outcomes. Experimental evaluations conducted on a real-world tweet dataset associated with the MovieLens dataset validate the superiority of the proposed approach. Notably, when integrated with a recurrent neural network (RNN) classifier, the system achieved impressive performance metrics, including an accuracy of 0.94, precision of 0.93, recall of 0.91, F1-score of 0.92, and a mean average precision (MAP) of 0.92. Comparative analyses against conventional baseline models highlight significant improvements in prediction accuracy and recommendation quality.

Keywords Recommendation system · Noise filtering · User-centric tweets · Natural language processing · Nature-inspired optimization

✉ Kirti Jain
kj.kirtijain25@gmail.com

Rajni Jindal
rajnijindal@dce.ac.in

[1] Department of Computer Science and Engineering, Delhi Technological University, Delhi, India

Published online: 10 June 2025

1 Introduction

Recommendation systems play a pivotal role in modern information retrieval and decision-making processes. It uses several different type of algorithms to suggest items or services that are likely to interest users. These systems have witnessed widespread adoption across various domains, including e-commerce, social media, entertainment, and online content platforms [25, 38]. The fundamental objective of recommendation systems is to alleviate the problem of information overload by providing personalized and relevant recommendations tailored to individual user preferences. By analyzing user behavior, historical interactions, and item attributes, recommendation systems aim to enhance user satisfaction, engagement, and overall user experience [13].

The evolution of recommendation systems can be traced back to traditional techniques such as collaborative filtering and content-based filtering, which rely on user–item interaction data or item features, respectively [1, 34]. However, the emergence of large-scale datasets and advancements in machine learning and artificial intelligence have spurred the development of more sophisticated recommendation algorithms. These include matrix factorization methods, deep learning approaches, and hybrid techniques that combine multiple recommendation strategies [39]. The growing complexity of recommendation systems reflects the need to address diverse challenges such as cold-start problems, data sparsity, and the incorporation of contextual information to improve recommendation accuracy and diversity.

Furthermore, the proliferation of social media platforms has introduced new opportunities and challenges for recommendation systems. User-generated content, social interactions, and social graphs contain valuable information that can augment traditional recommendation techniques [12]. Integrating social signals into recommendation algorithms enables systems to leverage social influence, user trust, and community preferences to generate more effective recommendations. However, the noisy and unstructured nature of social media data poses challenges in extracting relevant information and mitigating the impact of misinformation or biased signals. Addressing these challenges requires innovative approaches that combine data mining, natural language processing, and social network analysis to harness the power of social media for personalized recommendation generation.

In addition to e-commerce, recommender systems have shown to be quite useful in content streaming services like Netflix, Spotify, and YouTube. These platforms leverage user interactions and feedback to create personalized playlists and suggest films, songs, and videos [8]. These systems maximize user engagement, retention, and subscription income by precisely forecasting user preferences and foreseeing their content consumption habits. Furthermore, recommender systems in the social networking space allow meaningful connections and interactions by recommending groups, friends, and interesting content, improving user experience and encouraging community involvement.

There are additional important uses for recommender systems in healthcare, education, and information retrieval. To maximize learning results and student

engagement, online learning platforms customize course recommendations and learning materials to each learner's unique learning preferences and skill level [36]. Similar to this, recommender systems in the healthcare industry help doctors diagnose illnesses, choose treatments, and suggest individualized treatment programs based on clinical criteria, patient data, and medical history. Recommender systems empower consumers across a variety of disciplines by utilizing data-driven insights to optimize decision-making, provide personalized experiences, and open up new avenues for efficiency and creativity.

In the realm of NLP, recommender systems leverage advanced linguistic analysis techniques to understand the semantic meaning and context of textual data, enabling them to generate personalized recommendations. These systems employ a variety of algorithms to model user preferences based on their interaction history and the characteristics of the items being recommended. By leveraging linguistic features such as semantic similarity, sentiment analysis, and topic modeling, NLP-powered recommender systems can provide more accurate and contextually relevant recommendations to users.

On the other hand, user-centric tweets represent a unique and valuable source of data for NLP-based recommender systems, offering real-time insights into user preferences, opinions, and interests. Unlike traditional textual sources, such as product reviews or news articles, user-centric tweets are characterized by their brevity, informality, and rapid dissemination [40]. Despite these challenges, NLP techniques enable recommender systems to extract valuable signals from user-centric tweets, such as sentiment, topics, and user interactions, to better understand user preferences and generate personalized recommendations. However, the noisy and unstructured nature of tweet data poses significant challenges for recommendation systems, necessitating the development of innovative approaches for noise filtering and information extraction to enhance recommendation quality.

Integrating user-centric tweets into NLP-powered recommender systems opens up new opportunities for enhancing recommendation accuracy and relevance by incorporating real-time user feedback and social context. By harnessing the rich linguistic information embedded in tweets, such as hashtags, mentions, and conversational patterns, recommender systems can capture nuanced user preferences and emerging trends in a dynamic social environment [30]. Moreover, the inherent diversity and timeliness of tweet data enable recommender systems to adapt quickly to changing user interests and preferences, providing more personalized and up-to-date recommendations.

1.1 Motivation

In recommendation systems, the presence of noise in tweets can distort user preferences and interests, resulting in erroneous recommendations. By filtering out noise, recommendation algorithms can focus on meaningful content that reflects genuine user preferences, leading to more personalized and relevant recommendations.

Moreover, noise filtering contributes to the overall trustworthiness and credibility of recommendation systems, enhancing user satisfaction and engagement.

Filtering noise in tweets is crucial due to the vast amount of user-generated content on social media platforms. With millions of tweets posted daily, noise, such as spam, irrelevant information, and misinformation, can significantly degrade the quality of data used for various applications, including recommendation systems. Noise filtering helps to ensure that only relevant and reliable information is considered, leading to more accurate predictions and improved user experiences.

1.2 Contributions

The contributions of the proposed nuclear physics-based noise filtering approach lie in its innovative application to address the challenge of noise in user-centric tweets within recommendation systems. The main contributions are thus summarized as follows:

1. Introduces the nuclear physics optimization (NPO) algorithm for dynamic, adaptive noise filtering in user-centric tweet datasets.
2. Enhances accuracy and reliability by removing noisy tweets using semantic similarity and relevance metrics.
3. Ensures relevant and reliable information for more accurate, personalized recommendations, boosting user satisfaction.
4. Experimental results show superiority over baseline methods, supporting better utilization of social media data for recommendation systems and broader applications.

The rest of the paper is arranged in the subsequent section highlighting important modules. In Sect. 2, the background and related work pertaining to noise filtering in tweets for recommendation systems are discussed. This section provides a comprehensive overview of existing methods and approaches in the field, highlighting their strengths, limitations, and areas for improvement. Section 3 presents the proposed noise filtering framework based on the nuclear physics algorithm (NPO) for enhancing recommendation systems. The framework's architecture and key components are described in detail, elucidating how it addresses the challenges associated with noise in user-centric tweets.

Subsequently, Sect. 4 delves into the experimentation results obtained from applying the proposed algorithm to real-world tweet datasets. The performance metrics and evaluation criteria used to assess the effectiveness of the algorithm are outlined, accompanied by insightful analyses of the results. A comparative study is conducted to benchmark the proposed algorithm against baseline methods and existing approaches. The limitations of the study are reported in Sect. 5 that gives the overall assessment of the model. The key findings and contributions of the study are summarized, leading to a conclusive statement in Sect. 6 and outlines avenues for future research.

2 Related works

Recommendation systems have become essential in personalizing user experiences across various domains from e-commerce to entertainment. Among these, movie recommendation systems have particularly benefited from the integration of user-generated content (UGC) such as tweets, which provide real-time reflections of user preferences. Recommendation systems have been extensively studied in the literature, with various approaches ranging from collaborative filtering and content-based methods to hybrid techniques [27]. Collaborative filtering methods leverage user–item interaction data to generate recommendations [16], while content-based methods analyze item features and user preferences. Hybrid techniques combine aspects of both approaches to overcome their individual limitations [45]. Classic recommendation algorithms such as collaborative filtering-based matrix factorization [6] and singular value decomposition (SVD) have been widely used [3]. Recent advancements include deep learning-based approaches such as neural collaborative filtering (NCF) and autoencoders, which have shown promising results in capturing complex user–item interactions [7, 47].

In many works, the research is presented on the recommendation system in the form of the survey. The various survey papers present a comprehensive overview of recommendation systems, focusing on the latest trends, techniques, and challenges in the field [22, 25]. The survey also addresses key challenges and open research questions in the field. These include issues related to data sparsity, cold-start problems, scalability, and the ethical considerations of recommendation algorithms [14]. The work also presents the current benchmark and the future directions for the research community [32].

Parallel to the advancement of recommendation systems, research has explored techniques to handle data noise, particularly in UGC like tweets [10]. Social media platforms, while rich in user opinions, suffer from substantial noise-irrelevant, redundant, or misleading information that can degrade recommendation quality. Early methods for noise handling included basic text preprocessing (stopword removal, stemming) and heuristic-based filtering. More recent works have incorporated machine learning and optimization algorithms to identify and eliminate noisy data points [15].

Recent approaches also leverage domain-specific knowledge graphs and ontologies to improve the accuracy of noise filtering by contextualizing tweet content within a specific domain [46]. Techniques, such as genetic algorithms [35], particle swarm optimization [17], and ant colony optimization [31], have been applied to feature selection and data cleaning tasks, aiming to enhance the signal-to-noise ratio in user data.

Despite these advancements, there is a clear gap in effectively integrating noise filtering with recommendation systems, especially in the context of social media-driven recommendations. Existing studies often treat noise filtering and recommendation as separate pipelines, leading to suboptimal performance. Moreover, many rely heavily on either traditional heuristics or standard optimization methods that lack adaptability to the dynamic nature of tweet streams.

Other than this, NLP-based recommendation techniques were used in the literature to analyze textual data such as user reviews, product descriptions, and social media posts to generate recommendations. These systems extract semantic information from text, enabling a deeper understanding of user preferences and item characteristics [5, 44]. Techniques such as sentiment analysis, topic modeling, and word embeddings are commonly employed to process and analyze textual data. Models like Word2Vec, GloVe, and BERT have been adapted for recommendation tasks, facilitating more accurate and context-aware recommendations [42].

In one of the works proposed in the literature, the authors proposed the approach called PNTRS, a personalized news and tweet recommendation system that leverages fuzzy inference techniques [43]. With the proliferation of online news sources and social media platforms, here users are inundated with a vast amount of information, making it challenging to discover relevant content tailored to their interests. Their proposed approach addresses this issue by employing fuzzy inference to model user preferences and generate personalized recommendations.

In one other work, the authors proposed an approach for tweet recommendation leveraging the adaptive neuro-fuzzy inference system (ANFIS) [19]. Their proposed model integrates fuzzy logic principles with adaptive learning mechanisms to capture the nuanced semantics of tweets and user preferences. By utilizing fuzzy inference rules and neural network learning, the ANFIS model can effectively process textual features, user engagement patterns, and contextual information to generate personalized tweet recommendations.

Besides the tweets, there are several works in the literature that use the recommendation concepts for hashtags [2]. The authors explore the integration of community detection techniques within social networks to enhance the process of hashtag recommendation. Also, the authors discuss various algorithms and methodologies that were used to identify cohesive groups of users within social networks based on their interactions and connections. Subsequently, the study presents a framework that integrates community detection techniques with hashtag recommendation systems, leveraging the inherent structure of social networks to infer user interests and preferences.

Some authors have used the embedding approach for the hashtags recommendations. The machine learning approaches, like neural networks, SVM, and others used the embeddings to train the model. A couple of such works discuss the use of the embeddings for hashtag recommendations [24, 28]. The literature also supports the use of healthcare data for the recommendation of hashtags, as proposed in [21]. The authors used the COVID data tweets with the BERT encoding and LSTM approach for the recommendation of the most appropriate hashtags for user-centric tweets.

As the recommendation system is not limited to a single domain of the study, we have found many interdisciplinary fields using the recommendation systems for user preferences. One such work is presented as the recommendation of electronic mobile gadgets using the SAR data and user comments taken with the help of a questionnaire [23]. However, the primary source of the recommendation using NLP is still challenging and discussed in many interdisciplinary application works [11, 33, 41].

On the theme of movie recommendations using user-centric tweets, there are several works in the literature. In one of the works, the authors utilized the positive and negative profiles of the users and showed their impact on the movie recommendation [9]. Similarly, using the microblogging data the authors proposed the model using sentiments for movie recommendation [29]. Once the continuous data fetching and storage like YouTube is equipped with a large volume of data, then the model for predicting movie ratings using the bid data framework is proposed in [4]. The comparative study of some of the recent works that proved worthy in the recommendation field is presented in Table 1.

3 Proposed recommendation system methodology

In the proposed methodology involves preprocessing the raw tweet data and extracting relevant features that capture user preferences and interests. Subsequently, the NPO is utilized to optimize the noise filtering process by iteratively adjusting its parameters to maximize the relevance of retained tweets while minimizing the impact of noise.

The key contributions of this paper lie in the innovative application of the NPO for noise filtering in user-centric tweets and its integration into recommendation systems. By enhancing the quality of tweet data used for predictions, the proposed approach leads to more personalized and relevant recommendations, ultimately improving user satisfaction and engagement. Moreover, the scalability and adaptability of the NPO make it well suited for handling diverse tweet datasets and recommendation scenarios, highlighting its potential for practical applications in real-world systems. The proposed framework for the recommendation system of the user-centric data is shown in Fig. 1.

3.1 Dataset preparation

For our study, we utilize two distinct datasets: one comprising movie metadata and the other capturing Twitter sentiments related to these movies. The movie dataset encompasses comprehensive information on over 45,000 movies included in the Full MovieLens Dataset.[1] This metadata encompasses a broad array of features, including cast and crew details, plot keywords, budget and revenue figures, posters, release dates, languages, production companies, and countries of origin. Additionally, it provides insights into the popularity and reception of each movie, with TMDB vote counts and average ratings facilitating a quantitative assessment of user opinions.

Moreover, the movie dataset incorporates a substantial volume of user ratings, constituting a significant aspect of the dataset's richness. With a repository of 26 million ratings contributed by 270,000 users, this dataset offers a comprehensive view of audience preferences and opinions across the entire spectrum of movies.

[1] https://grouplens.org/datasets/movielens/latest/

Table 1 Comparative analysis of the proposed work with some of the recent literature

Study	Technique used	Application focus	Outcomes	Limitations
[20]	Sentiment analysis + Collaborative filtering	Movie recommendation	Moderate improvement in recommendation accuracy	Struggles with noisy data; irrelevant user tweets; lacks advanced noise filtering mechanisms
[35]	Genetic algorithm	General recommendation systems	Enhanced model efficiency by reducing feature space	Static parameters, limited adaptability to evolving noisy tweet data, and suboptimal performance on large datasets
[17]	Particle swarm optimization (PSO)	Noise reduction	Moderate classification accuracy	Susceptible to premature convergence; does not dynamically adjust for diverse datasets
[11]	LSTM model	Tweets-based recommendations	Captures sequential dependencies in text well	Ineffective in handling noisy and irrelevant tweets without proper pre-filtering
[33]	Hybrid models—content-based and collaborative filtering	Personalized recommendations	Improved personalization and diversity of recommendations	Performance degrades with noisy user-generated content; no advanced optimization for noise filtering
Proposed work	NPO + Semantic filtering	Movie recommendation	High accuracy (0.94), precision (0.93), recall (0.91), F1-score (0.92), MAP (0.92) with RNN	Overcomes noise issue, dynamic adaptability, scalable and robust across datasets, outperforms baseline models

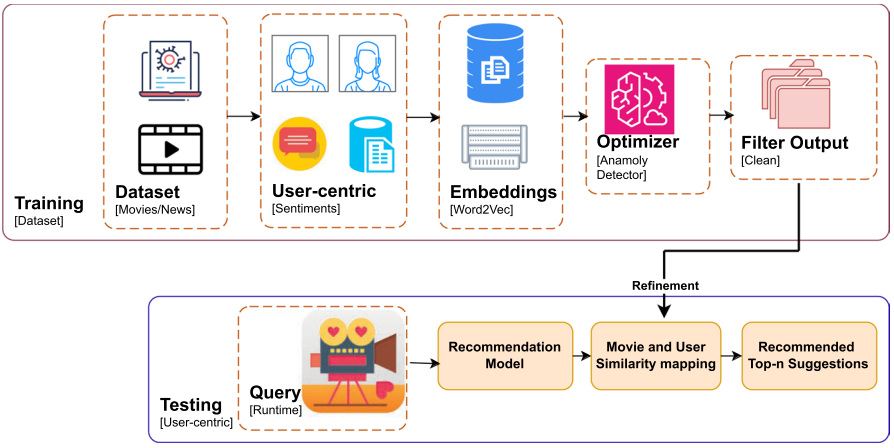


Fig. 1 Flowchart of the proposed framework

Ratings are recorded on a scale of 1 to 5 and are sourced from the official GroupLens website, ensuring credibility and reliability. This extensive collection of user ratings serves as a valuable resource for understanding viewer sentiments and preferences toward different movies.

In conjunction with the movie metadata, we augment our analysis with data derived from Twitter sentiments pertaining to these movies. By leveraging Twitter's vast platform for real-time user-generated content, we gain insights into the public discourse and sentiment surrounding each movie. This Twitter sentiment dataset provides a complementary perspective to the quantitative movie metadata, offering qualitative insights into audience reactions, opinions, and discussions in the social media sphere. Integrating these two datasets enables us to perform a comprehensive analysis that combines quantitative metrics with qualitative insights, enriching our understanding of the factors influencing movie recommendations and user preferences.

The sentiments incorporated in our analysis are derived from users who have assigned sentiment labels to their expressions, categorized into five distinct categories: 0 for negative sentiment, 1 for somewhat negative, 2 for neutral, 3 for somewhat positive, and 4 for positive sentiment. These sentiment labels provide a nuanced understanding of user opinions and attitudes toward the movies under consideration. By categorizing sentiments into discrete levels, ranging from highly negative to highly positive, we capture the full spectrum of user sentiment variations, enabling a comprehensive analysis of audience perceptions.

The sentiment labels assigned by users serve as valuable indicators of their subjective reactions and experiences with the movies. Negative sentiments (labels 0 and 1) reflect dissatisfaction or disappointment, while positive sentiments (labels 3 and 4) signify enjoyment or appreciation. The neutral sentiment label (label 2) indicates a lack of strong emotional inclination, suggesting a more balanced or indifferent stance toward the movie. By considering these diverse

sentiment labels, we can discern patterns and trends in user perceptions, identifying key factors that influence audience satisfaction and engagement.

3.2 Movie review sentence embedding

To make the user-centric comments on the movies ready for the model training, here we have used the continuous bag-of-words (CBoW) algorithm with negative sampling for sentence embedding, facilitating the creation of dense vector representations for sentences. This approach is particularly effective for sentiment analysis and recommendation systems where understanding the semantic meaning of sentences is crucial.

The CBoW algorithm operates by predicting a target word based on the context of surrounding words within a fixed-size window. Unlike traditional word embedding techniques like Word2Vec, which focus on predicting words given their context, CBoW aims to predict the context (or surrounding words) given a target word. This makes it well suited for generating sentence embedding, as it captures the overall meaning and context of the sentence rather than individual word meanings.

In the CBoW algorithm with negative sampling, the training process involves sampling negative examples (words not present in the context window) to contrast with the positive examples (actual context words). This helps the model learn to distinguish between relevant and irrelevant words in the context of generating sentence embedding. By iteratively adjusting the model parameters to minimize the prediction error for positive examples while maximizing it for negative examples, the algorithm learns to produce more accurate and meaningful sentence embedding.

During training, the CBoW model processes each sentence by averaging the word embedding of its constituent words, effectively condensing the entire sentence into a single vector representation. This sentence embedding captures the semantic meaning and context of the sentence in the high-dimensional vector space. By leveraging negative sampling, the model learns to focus on informative words while filtering out noise and irrelevant information, resulting in more robust and informative sentence embedding.

Suppose the dataset have a sequence of words $\{w_1, ..., w_{n-1}, w_T\}$ in a training data. The objective of our approach is to maximize the average log-probability of the context words occurring around the input word over the entire vocabulary and is given by Eq. 1.

$$\hat{P} = \frac{1}{T} \sum_{t=1}^{T} \sum_{-c \leq j \leq c, j \neq 0} log\, p(w_{t+j}|w_t) \tag{1}$$

here T is all the words in the training data and c is the training context window.

Now the solution of the probability function in Eq. 1 is computed by using Eq. 2.

$$p(w_{t+j}|w_t) = \frac{exp\left(\left(v'_{w_{t+j}}\right)^T v_{w_t}\right)}{\sum_{w=1}^{W} exp\left(\left(v'_w\right)^T v_{w_t}\right)} \tag{2}$$

here v_w and v'_w are the vector representations of the word w as the input and output, respectively. Also, W is the number of words in the entire vocabulary.

The description using Eq. 2 makes sense that words with comparable vector representations would arise in similar contexts. This will be demonstrated by the numerator in the preceding equation, which uses the dot product of the two vectors to provide a bigger value for comparable terms. The representations will differ if the words do not occur in each other's context, which will cause the numerator to be a small value.

However, the primary issue arises, though, when we try to compute the denominator of Eq. 2 which is a normalization factor that needs to be calculated over the whole lexicon. The computation gets unmanageable when we consider that a vocabulary may consist of hundreds of thousands or even millions of words. This is the point at which the use of negative sampling makes this computation possible.

Using the objective function, negative sampling seeks to minimize word similarity when it occurs in a different context and maximize it when it occurs in the same context. However, depending on the training size, it randomly chooses a small number of words and utilizes these to maximize the objective rather than performing the reduction for every word in the dictionary save the context words. The objective function of the negative sampling is thus defined using Eq. 3.

$$log\,\sigma((v'_{w_{i+j}})^T v_{w_i}) + \sum_{i=1}^{k} E_{w_i\ p_n(w)}[log\,\sigma((-v'_{w_i})^T v_{w_i})] \tag{3}$$

here σ is the sigmoid function and $P_n(w)$ is the noise distribution with the negative samples drawn from it. It is calculated as the unigram distribution of the words to the power of 0.75 which is a number that was calculated based on experimental results and is given by Eq. 4.

$$p_n(w) = \frac{Uni(w)^{0.75}}{Z} \tag{4}$$

where Z is a normalization constant.

Further, maximizing Eq. 3 will result in maximizing the dot product in its first term and minimizing it in the second term. In other words, the words in the same context will be pushed to have more similar vector representations while the ones that are found in different contexts will be forced to have less similar word vectors.

Assume that (w,c) is a pair of words, where w is a word and c is its context, that occur close to one another in the training data. Consequently, this can be expressed as p(D=1|w,c), which indicates that this pair originated from the training set. Consequently, the probability that the pair did not originate from the training data is given as p(D=0|w,c) = 1-p(D=1|w,c). By representing the trainable parameters of the probability distribution as θ and the idea of running out of training data as D', we will do the optimization of the function as given by Eq. 5.

$$arg\,max_\theta \prod_{w,c\in D} p(D=1|w,c;\theta) \prod_{w,c\in D\prime} p(D=0|w,c;\theta) \tag{5}$$

By using the properties of the logarithm and the law of total probability, Eq. 5 is rewritten to Eq. 6.

$$arg\,max_{\theta} \sum_{w,c \in D} log\, p(D = 1|w, c;\theta) + \sum_{w,c \in D\prime} log\,(1 - p(D = 1|w, c;\theta)) \tag{6}$$

The value of the $p(D = 1|w, c;\theta)$ is computed using Eq. 7.

$$p(D = 1|w, c;\theta) = \sigma(v_c, v_w) = \frac{1}{1 + exp^{(-v_c, v_w)}} \tag{7}$$

where v_w and v_c are the vector representations of the main and context words, respectively.

3.3 Proposed nuclear physics optimization (NPO)

3.3.1 Background preliminaries for NPO

The interaction between the particles is a key idea in particle physics. The behavior and structure of matter are fundamentally influenced by particle interactions. Particles can collide, merge, or decay when they interact, creating new particles and releasing or absorbing energy. The stability of the particles allows us to categorize these interactions.

Depending on the characteristics of the particles and the type of contact, when they collide, several things can happen. Particles can annihilate one another in high-energy collisions, transforming their mass into energy in accordance with Einstein's well-known equation $E = MC^2$ and generating gamma-ray photons in the process. New particles can also be created when high-energy particles collide with one another. High-energy particles can interact with matter in particle accelerators or cosmic ray collisions to produce a cascade of secondary particles. A vast variety of particles, both stable and unstable, can be produced by this process.

As a result, we are able to observe the two types of particles in the universe: particles that are *unstable* and *stable*. Particles that are stable do not decay into other particles, whereas unstable particles do so after a predetermined period of time. Particles that are unstable may decay, changing into lighter particles and release energy as a result. There exist multiple types of decay processes, such as gamma, beta, and alpha decay [26], which include distinct particle modifications within atomic nuclei. In contrast, stable particles, like protons, neutrons, and electrons, have lengthy lifetimes and do not spontaneously decay.

The particle's breakdown and the creation of a new particle through the corresponding decays have distinct meanings. The alpha particle, which has two protons and two neutrons and is denoted as ${}^{A}_{Z}\mathbf{X} \xrightarrow{{}^{A-4}_{Z-2}} \mathbf{Y} + {}^{4}_{2}\alpha$, is released by an unstable nucleus during alpha decay. The parent particle in this case is ${}^{A}_{Z}\mathbf{X}$, the child particle is ${}^{A-4}_{Z-2}\mathbf{Y}$, and the alpha decay is ${}^{4}_{2}\alpha$.

The beta decay involves the transformation of a neutron into a proton (beta-minus decay) or a proton into a neutron (beta-plus decay), accompanied by the

emission of a beta particle and is given as ${}^{A}_{Z}\mathbf{X} \xrightarrow{Z+1} \mathbf{Y} + e^{-1} + \bar{V}_e$ called Beta-minus decay and ${}^{A}_{Z}\mathbf{X} \xrightarrow{Z-1} \mathbf{Y} + e^{+1} + V_e$ called Beta-plus decay. Here, e^{-1} is the electron, e^{+1} is the positron, V_e is an electron neutrino, and $\bar{V}_e$ is an electron antineutrino. The last decay is the gamma decay that involves the emission of a gamma-ray photon from an excited nucleus and is given as ${}^{A}_{Z}\mathbf{X}^{*} \xrightarrow{Z} \mathbf{X} + \gamma$. Here, ${}^{A}_{Z}\mathbf{X}^{*}$ is the excited state of the nucleus, ${}^{A}_{Z}\mathbf{X}$ is the ground truth, and γ is the Gamma photon.

In the suggested method, we have employed the decay process standards across various particles that can be used as a basis for designing the contemporary metaheuristic algorithm wherein the performance of the arrangement candidates can be enhanced by employing the idea that particles tend to settle into a stable position.

3.3.2 Nuclear physics optimization for filtering noisy tweets

Utilizing nuclear physics optimization (NPO) for filtering noisy tweets represents a novel approach to enhancing the quality and relevance of information extracted from social media data. Inspired by the principles governing atomic nuclei interactions, NPO offers a unique framework for optimizing the process of noise filtering in tweets, thereby improving the reliability of the extracted content.

In the context of noisy tweet filtering, NPO operates by treating each tweet as a particle within a system, with the objective of optimizing the selection of informative tweets while minimizing the impact of noise. The algorithm simulates the interactions between these "particles," representing tweets, by applying principles analogous to nuclear forces and electrostatic interactions. Through iterative optimization cycles, NPO dynamically adjusts the positions of tweets within the solution space, with attractive forces guiding the selection of relevant tweets and repulsive forces aiding in the expulsion of noisy or irrelevant content. The basic flowchart of the proposed NPO algorithm is shown in Fig. 2.

The effectiveness of NPO for filtering noisy tweets lies in its ability to balance exploration and exploitation, allowing for the efficient identification and retention of informative tweets while simultaneously mitigating the influence of noise. By leveraging the inherent parallelism and adaptability of NPO, the algorithm can effectively navigate the complex landscape of social media data, identifying relevant signals amidst the noise. Moreover, NPO offers the flexibility to incorporate additional constraints or domain-specific knowledge, enabling tailored solutions for different noise filtering tasks.

The NPO algorithm is designed around the physics-based concept of particle decay. There are three types of decay processes prevalent in physics: alpha, beta, and gamma. The term "alpha, beta, and gamma particle decay" refers to the use of nuclear physics principles to drive particle decay simulation and comprehension. In nuclear physics, alpha, beta, and gamma decay are the three most frequent kinds of radioactive decay that change unstable atomic nuclei into more stable structures. This decay process is described as:

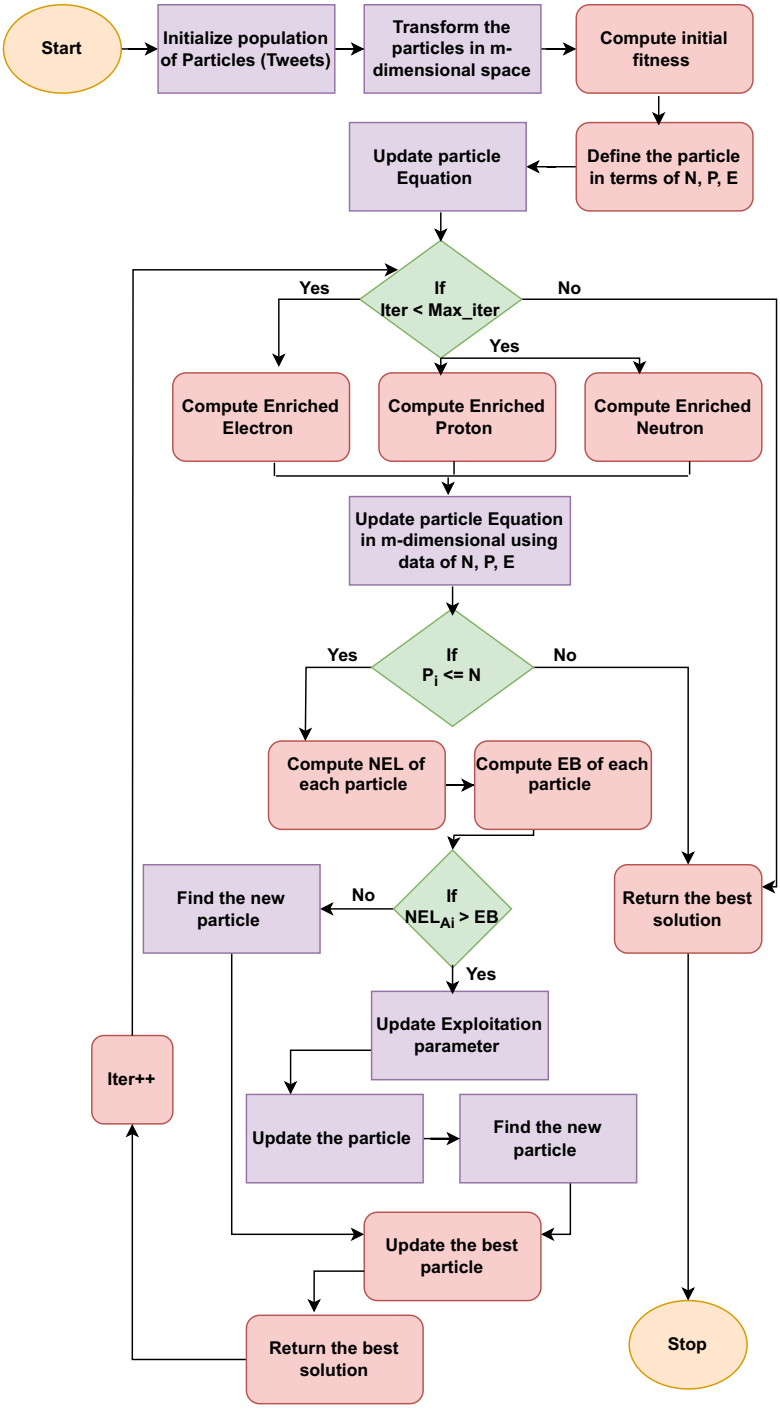


Fig. 2 Flowchart of the proposed NPO algorithm

- Alpha Decay: In alpha decay, an unstable nucleus emits an alpha particle, which consists of two protons and two neutrons. The physics-informed approach to alpha decay involves utilizing principles derived from nuclear physics equations to model and simulate the probability and characteristics of alpha particle emission.
- Beta Decay: Beta decay involves the transformation of a neutron into a proton (beta-plus decay) or a proton into a neutron (beta-minus decay), accompanied by the emission of a beta particle (an electron or positron). Physics-informed modeling of beta decay incorporates fundamental concepts such as conservation of energy, conservation of angular momentum, and the properties of weak nuclear force responsible for the beta decay process.
- Gamma Decay: Gamma decay occurs when an excited nucleus releases excess energy in the form of a gamma-ray photon. In a physics-informed approach to gamma decay, the modeling includes considerations of nuclear energy levels, electromagnetic interactions, and quantum mechanical principles governing the emission of gamma rays.

3.3.3 Mathematical foundation of NPO

The initialization phase of the suggested algorithm begins with the assumption that the solution candidates (A_i) in the search space are particles (tweets with vector embedding) anticipated to be at a specific location in the universe, as demonstrated by Eq. 8.

$$A = \begin{bmatrix} A_1 \\ A_2 \\ \dots \\ A_i \\ \dots \\ A_n \end{bmatrix} = \begin{bmatrix} A_1^1 & A_1^2 & \dots & A_1^j & \dots & A_1^m \\ A_2^1 & A_2^2 & \dots & A_2^j & \dots & A_2^m \\ \dots & \dots & \dots & \dots & \dots & \dots \\ A_i^1 & A_i^2 & \dots & A_i^j & \dots & A_i^m \\ \dots & \dots & \dots & \dots & \dots & \dots \\ A_n^1 & A_n^2 & \dots & A_n^j & \dots & A_n^m \end{bmatrix} \tag{8}$$

where A_i^j determines the starting position of the i^{th} candidate for the j^{th} decision variable, the problem dimension is represented by m, and the symbolic representation of the utilized variables is specified as the total number of particles supplied by variable n.

In other words, Eq. 8 is to be considered that the universe A has the n different particles $(A_1, ..., A_n)$ where each particle A_i in the m-dimensional space will be represented by the m different dimensional values $(A_i^1, ..., A_i^m)$.

Additionally, Eq. 9 illustrates the choice variable's mathematical form. Here, the value of each particle is in the normalized form which is given by Eq. 9.

$$A_i^j = A_{i,min}^j + R_m(A_{i,max}^j - A_{i,min}^j) \tag{9}$$

where $A_{i,min}^j$ and $A_{i,max}^j$ speak to the minimum and maximum of the i^{th} particle within the j^{th} dimensional space and the R_m is the irregular generator within the extend [0,1].

Now let us consider that the universe has an unstable particle (A_i) that decomposes to form a new particle. The unstable particle is assumed to have the collection of the three basic charge particles, i.e., electron (E), proton (P), and neutron (N). As this particle is highly unstable, thus we need to find the enrichment state of the particle which is mathematically given by Eq. 10.

$$A_i \propto N_i + P_i + E_i \tag{10}$$

In physics, neutrons are subatomic particles that are found in atomic nuclei. They have no net electric charge, but they contribute to the mass of the nucleus. Neutrons are subject to the strong nuclear force, which binds them together with protons in the nucleus. While protons are positively charged subatomic particles found in atomic nuclei. They are stable and contribute positively to the net charge of the nucleus. Protons are bound together with neutrons by the strong nuclear force. At last, electrons are negatively charged subatomic particles that orbit atomic nuclei in electron shells. They are stable and have much smaller masses compared to protons and neutrons.

All such unstable particles in the universe will undergo certain decays that were constituted with neutrons, protons, and electrons. The enrichment state of any neutron particle with other particles is calculated by using Eq. 11.

$$N_i = \sum_{i=1}^{N} \alpha \times D_{ij} \times \hat{D}_{ij} \tag{11}$$

Where D_{ij} is the distance vector in between two particles, $\hat{D}_{ij}$ is the unit normalization of the distance vector, and α is the amount of alpha decay which is calculated using Eq. 12.

$$\begin{aligned} D_{ij} &= |A_i - A_j| \\ \hat{D}_{ij} &= \frac{|A_i - A_j|}{D_{ij}} \\ \alpha &= 4e^{-2} - e^{-2} \end{aligned} \tag{12}$$

Computationally, the value of the unit normalization of the distance vector lies in the interval [0,1]. Also, the α is equated using the concept of particle physics where in alpha decay, an unstable nucleus emits an alpha particle, which consists of two protons and two neutrons.

Similarly, the enrichment state of the proton particles is given by Eq. 13.

$$P_i = \beta \times T_r \tag{13}$$

where the β is computed using the beta decay approach and is given by Eq. 14.

$$\beta = d \times e^1 + (1 - d) \times e^{-1};\ d \in (0, 1) \tag{14}$$

Here, the value d is the selection parameter that controls the beta decay selection. Beta decay involves the transformation of a neutron into a proton called beta-minus decay or a proton into a neutron called beta-plus decay, accompanied by the

emission of a beta particle (electron or positron). Thus here, e^1 and e^{-1} are considered to be the positron and electron. Finally, the term T_r is the signal that is given by Eq. 15.

$$T_r = \left\{ \begin{array}{l} -1, \text{ if } T_r \in N \rightarrow P \\ +1, \text{ if } T_r \in P \rightarrow N \end{array} \right\} \tag{15}$$

Equation 15 refers to the particle being in a state of beta-minus or beta-plus decay. If the transformation is in neutron to proton then it is beta-minus state and T_r returns -1 as an output otherwise it is considered as beta-plus state and returns +1 as an output.

Thus, Eq. 13 will be rewritten to form Eq. 16 depending on the beta decay.

$$P_i = \pm \ d \times e^1 + (1-d) \times e^{-1} \tag{16}$$

The last part is the enrichment state of the electron particles which is given by Eq. 17.

$$E_i = \gamma \times e^{-1} \tag{17}$$

where γ is the gamma decay where there will be no change in the particle mass and atomic number, only energy is released. Thus, here the γ is considered to be a constant in the range [-1, 0].

By using the combined Eqs. 11, 13, and 17, the base Eq. 10 can be simplified to Eq. 18.

$$A_i = \sum_{i=1}^{N} \alpha \times D_{ij} \times \hat{D_{ij}} \pm \ d \times e^1 + (1-d) \times e^{-1} + \gamma \times e^{-1} \tag{18}$$

In the physics concepts, the particle is also evaluated on the measure of the enrichment level of neutron (NEL). It is a measure of the relative abundance of neutrons compared to protons in a given nucleus or particle. It is often used in the context of nuclear physics and nuclear engineering to describe the stability and characteristics of atomic nuclei. Thus to find the stability of the particle A_i, NEL of the particle plays a crucial role. For any particle, NEL is calculated using Eq. 19.

$$NEL_{A_i} = \frac{N_{A_i} - P_{A_i}}{M} \tag{19}$$

Where N_{A_i} and P_{A_i} are the number of neutrons and protons of particle A_i, and M_{A_i} is the atomic mass of the particle and can be evaluated as the sum of the protons and neutrons.

The value computed by Eq. 19 has importance in decision-making. The neutron surplus or deficit in the nucleus about the amount of protons is indicated by the NEL value. A positive NEL value denotes a neutron excess, which is the nucleus having more neutrons than protons. There may be a propensity toward neutron richness if the NEL value is positive. Conversely, a negative NEL score denotes a neutron deficiency, which is the absence of more neutrons in the

nucleus than protons. One may expect a propensity toward proton richness if the NEL value is negative.

Thus, using the data from Eq. 19, it was found that the NEL stability is dependent on neutron and protons but not on the electron. Using the above analysis, Eq. 18 is simplified to Eq. 20 by eliminating the electron level.

$$A_i = \sum_{i=1}^{N} \alpha \times D_{ij} \times \hat{D}_{ij} \pm \; d \times e^1 + (1-d) \times e^{-1} \tag{20}$$

Another use of the NEL value in particle physics is to provide insights into the stability and behavior of atomic nuclei. Nuclei with higher NEL values (positive values) have an excess of neutrons compared to protons and may be more likely to undergo decay to achieve a more stable neutron-to-proton ratio. Conversely, nuclei with lower NEL values (negative values) may be more stable or prone to other modes that release energy only, like gamma decay, depending on their specific nuclear properties.

To make this decision, we calculate the enrichment bound of the particle system. It refers to the maximum or minimum value allowed for a certain property or characteristic of the particle. In the context of nuclear physics or particle interactions, the enrichment bound may pertain to parameters such as the neutron-to-proton ratio, energy levels, or other physical quantities. The mathematical calculation to compute the enrichment bound is given by Eq. 21.

$$EB_u = \frac{\sum_{i=1}^{N} NEL_{A_i}}{N} \tag{21}$$

where N is the total number of particles in the system.

Using the theory, concepts, and methods of particle physics to transform the problem into an optimization problem, several adjustments need to be made to the concepts. As the optimization problem is bounded in the range of the upper and lower bounds to make the decision function, the equations of particle physics need to be reformed into the bounded region.

As the particle A_i of the system is in the defined dimension m having the lower and upper bounded values, then the transformed Eq. 20 for the optimization problem specific is given by Eq. 22.

$$\begin{aligned} A_i^m &= \sum_{i=1}^{N} \alpha \times D_{ij}^m \times \hat{D}_{ij}^m \pm \; d \times e^1 + (1-d) \times e^{-1} \\ &= \sum_{i=1}^{N} \alpha \times D_{ij}^m \times \hat{D}_{ij}^m + Best\ Solution \end{aligned} \tag{22}$$

where best solution in Eq. 22 is the best-computed solution for all particles (computed with beta decay).

Thus, if the NEL of a particle is discovered to be more than the Enrichment bound, i.e., ($NEL_{A_i} > EB_u$), then the associated particle is assumed to have the higher neutron-to-proton ratio, and the particle is expected to be decay. Let us suppose that the particle in the system is bounded by the lower and upper bound values, then the particle movement and transformation will be updated by using the base Eq. 22 and is transformed into Eq. 23.

$$A_i^m = \varpi\left(\sum_{i=1}^{N} \tau \frac{UB_m - LB_m}{2} \times \alpha |A_j^m - A_i^m|\right) + Best\ Solution \tag{23}$$

where the parameters ϖ and the τ are the exploration and the exploitation control parameters, UB_m and LB_m are the upper and lower bounds of the particle A_i in m^{th} dimensional space.

In an optimization process, the exploration parameter focuses on the exploration of new particles of the search space. It involves sampling or probing the search space widely to discover new particles that have not been previously explored. During exploration, the algorithm prioritizes diversity and novelty, aiming to uncover promising areas that may contain better solutions. The exploration parameter ϖ is computed using Eq. 24.

$$\varpi = \frac{U}{|V|^{0.66}} \tag{24}$$

here the U is the normal distribution of the particles and is represented as $U \sim N(0, \sigma_u^2)$, and V is the constant that lies in the interval $V \sim (0, \sigma_v^2)$ and ideally its value be considered as 0.9, but can vary as per the problem space.

As the particles can move in any direction, thus the normal distribution of the particle is defined by using Eq. 25.

$$\sigma_u = \left(\frac{(1+\theta)Sin(0.5\pi\theta)}{0.5(1+\theta) \times \theta \times 2^{0.5(\theta-1)}}\right)^{0.66} \tag{25}$$

here θ is the directional parameter whose value lies in between (0,2).

On the other hand, the exploitation parameter concentrates on exploiting known promising solutions to refine and improve them further. It involves intensively searching and exploiting regions of the search space that are likely to contain high-quality solutions. During exploitation, the algorithm prioritizes the exploitation of local information, aiming to refine existing solutions toward optimal or near-optimal solutions. The exploitation parameter τ in Eq. 23 is thus considered to be the decreasing coefficient that gradually changes based on the iteration count. The mathematical computation of which is given in Eq. 26.

$$\tau = \tau_{max} - \left(Iter_i \times \frac{\tau_{max} - \tau_{min}}{Iter_{max}}\right) \tag{26}$$

where τ_{max} and τ_{min} are the maximum and the minimum values of the parameter τ, $iter_i$ is current iteration count, and $iter_{max}$ is the maximum number of iterations.

Finally, the updated equation of the new particle formed is given by Eq. 27.

$$A_i^{new} = A_i^m + Best\ Solution \tag{27}$$

The last case is the condition when the $NEL_(A_i)$ is found to be lower than the Enrich bound EB_u, i.e., $(NEL_(A_i) < EB_u)$ then the condition is considered that the system has the lower neutron to proton ratio. In such a case, the particle will not go under any decay process where the mass decreases. In such a case, there is only the release of energy. Thus, the new particle position in such a case is calculated by using Eq. 28.

$$A_i^{new} = A_i^m + rand(0, 1) \tag{28}$$

3.3.4 Evaluating fitness of each tweet for filtering

To evaluate the fitness function of each tweet for filtering noisy tweets, we can formulate it mathematically using the provided variables. Let us denote the fitness function as F(t) where t represents a tweet. The fitness function can be defined as the ratio of properly categorized samples to the total number of samples, adjusted by the ratio of selected features to the total number of features in the dataset. Mathematically, this can be expressed as:

$$F(t) = A_i^{new} \times \left(\alpha \left(1 - \frac{T_C}{T_D} \right) + \beta \left(\frac{N_f}{N_F} \right) \right) \tag{29}$$

where T_C is the number of samples that were properly categorized, T_D is the total number of samples in the dataset, N_f is the number of features selected by the optimization algorithm, and N_F is the total number of features in the dataset.

This fitness function captures the performance of each tweet in terms of its relevance to the classification task (properly categorized samples) and the importance of the selected features in distinguishing relevant tweets from noisy ones. By incorporating these factors, the fitness function provides a quantitative measure of the suitability of each tweet for filtering noisy tweets, guiding the optimization algorithm toward selecting tweets that contribute most effectively to the noise filtering process.

3.4 Algorithmic design of the proposed methodology

The description of the proposed algorithm in the pseudo-code is presented in Algorithm 1. The code provided outlines the algorithm's step-by-step, comprehensive flow. The particle location with the best stability prediction is the return at the end of the algorithm.

Input: Initialize the population of particles randomly within the search space
Set the dimension of the search space
Initialize all the parameters: iter, alpha, beta, gamma, particles with their mass, upper bound, lower bound, and others
Output: Particles with best stability level
Data: Set the max and min value of each particle
Evaluate the fitness of each particle in the population using Equation 9
Select the best solution among the calculated fitness of each particle
while $iteration - count < Max_{iteration}$ **do**
  Compute the Neutron enrichment using Equation 11
  Compute the Proton enrichment using Equation 16
  for $i \in [1, n]$ **do**
    Compute the NEL_{A_i} of the i^{th} particle using Equation 19
    Compute the enrichment bound (EB) using Equation 21
    if $NEL_{A_i} > EB_u$ **then**
      Update the τ using Equation 26
      Update the particle nature using the fitness function given in Equation 23
      Compute the new particle using Equation 27
    if $NEL_{A_i} < EB_u$ **then**
      Compute the new particle using Equation 28
  Update the best particle if exists
  $iteration - count = iteration - count + 1$
Best[i] ← Return the best solution
Final set ← Previous Best + Best[i]

The procedure clearly shows that we begin by initializing the particle population *N* and the parameters dimension, iter, alpha, beta, gamma, particles with their mass, upper bound, lower bound, and others. Next, we use the fitness function to calculate the value of each solution to evaluate it. We identify the best solution based on its value after assessing each solution in the population.

Afterward, for each iteration, till the maximum set iteration was reached by incrementing iteration by 1 count in each cycle, we computed the enrichment value of the neutron and the proton using Eqs. 11 and 13, respectively. Later, for each particle, we computed the neutron enrichment level NEL_{A_i} using Eq. 19. With this, the algorithm also computes the enrichment bound (EB) that can help to decide the particle stability.

These two parameters are further compared to decide the particle nature update and the corresponding formation of the new particle using the decay concept. In case the $NEL_{A_i} > EB_u$, the particle nature is updated by using Eq. 23 which also utilizes the updated value of the τ that is dependent on the iterations and computed using Eq. 26. Finally, the new particle is formed using Eq. 27.

On the other hand, if $NEL_{A_i} < EB_u$ then the particle is considered to have the lower N/P ratio that results in the release of the energy, and thus new particle is updated using Eq. 28. We repeatedly check and update the best particle found in the whole process till the iteration reaches its maximum count value. At the last, the optimized best solution particle set is returned as the final output.

3.5 Models for learning recommendation system

In the learning phase of movie recommendation using tweets, various machine learning and deep learning models are employed to analyze tweet data and extract meaningful insights for recommendation purposes. One commonly used approach involves leveraging supervised machine learning algorithms, such as support vector machines (SVMs), naive Bayes classifiers, or logistic regression, to classify tweets based on sentiment or relevance to specific movies. These models are trained on labeled tweet data, where each tweet is associated with a sentiment label (positive, negative, neutral) or relevance label (relevant, irrelevant) to movie recommendation. By learning from the labeled data, these models can effectively classify new tweets and identify those that are most relevant for movie recommendation.

Additionally, deep learning models, particularly recurrent neural networks (RNNs), are increasingly being used for analyzing tweet data in movie recommendation systems. RNNs, with their ability to capture sequential dependencies in tweet text, are well suited for sentiment analysis tasks, where understanding the context and flow of language is essential. This deep learning model is trained on large volumes of tweet data to learn representations that capture the semantic meaning and sentiment of tweets, enabling more accurate and nuanced movie recommendations.

3.6 Relevancy selection with cosine similarity

In the realm of movie recommendation systems utilizing tweets, cosine similarity emerges as a fundamental metric for retrieving relevant movie suggestions based on the textual content of tweets. Cosine similarity quantifies the similarity between two vectors in a multi-dimensional space, making it an ideal measure for comparing the semantic similarity of tweet representations and movie attributes. Mathematically, cosine similarity between two vectors A and B is calculated as the cosine of the angle between them and is defined by using Eq. 30.

$$Cos_{sim}(A, B) = \frac{A.B}{||A||.||B||} \tag{30}$$

where $A.B$ denotes the dot product of vectors A and B, and $\|A\|$ and $\|B\|$ represent their respective Euclidean norms.

To apply cosine similarity in the context of movie recommendation using tweets, each tweet and movie are represented as vectors in a common feature space. For tweets, vector representations can be derived from tweet embeddings obtained through Word2Vec capturing the semantic meaning of tweet content. Similarly, movie vectors encapsulate relevant attributes such as genre, cast, and plot keywords, extracted from movie metadata.

Once tweet and movie vectors are obtained, cosine similarity is computed between each tweet vector and the vectors representing all movies in the dataset. This yields a similarity score for each movie, quantifying its relevance to the tweet.

The movies with the highest cosine similarity scores are then recommended to the user, as they are deemed most similar in content and context to the tweet.

4 Experimentation results

4.1 Prebuild dataset

To evaluate the results of the proposed approach, the dataset was built using two strategies. The first strategy uses the movie lens dataset which has numerous movies with their genre, titles, and ratings. For these movies, the user-centric reviews of the respective movies were fetched, and the sentiment score was generated for each movie item in the dataset. The sample collection of the dataset is shown in Table 2. Also, Fig. 3 provides a summary of the distribution of ratings in the Full MovieLens Dataset, showing how many samples fall within each rating category. It helps visualize the frequency of different rating values given by users, which is crucial for understanding user preferences and evaluating recommendation algorithms.

Using the formed dataset, the model is trained to items that are most closely associated with the query item. Based on the constraint, the model predicts the top-k items among the dataset that are most likely to be the query item.

4.2 Data cleaning

In the extracted dataset, the raw corpus contained significant noise in the form of slang, abbreviations, emojis, URLs, hashtags, and typographical errors. All of which may hinder the effectiveness of the proposed recommendation system model. To handle this, we applied a multi-stage data cleaning process to refine the corpus.

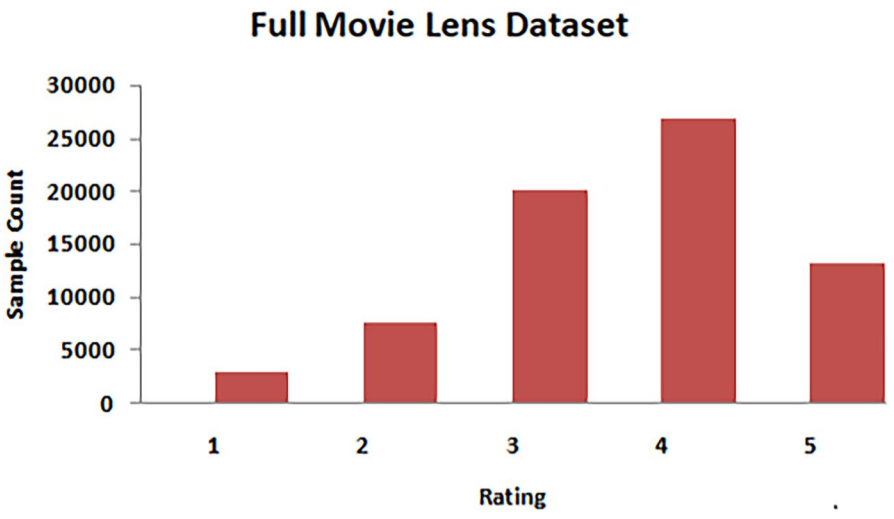


Fig. 3 Distribution of samples in Movie Lens dataset as per rating

Table 2 Sample dataset prepared for the experimentation having movies title, genre, fetched user-centric review, and sentiment score

S.No.	original_title	genres	User-centric comment	Sentiment
1	Jumanji	Adventure, Fantasy, Family	Jumanji, with plenty of laughs, action-packed excitement, great music, spectacular sets, and inspirational themes, this film is an absolutely winning adventure	4
2	Ace Ventura	Romance, Comedy	Ace Ventura. Neither terrible, boring nor soporific, just not very funny	1
3	Die Hard	Drama	Die Hard. There are good performances from everyone in this long, often funny, very violent but exciting melodrama	2
4	Meet Joe Black	Drama	Meet Joe Black. I've never encountered such dramatic flatulence, never heard so many pregnant silences that don't deliver, never watched so many close-ups that graze on actors' faces until every last trace of expression has been devoured	3
5	Toy Story	Comedy	Toy Story is a Pixar classic, one of the best kids' movies of all time	4

1. Non-textual elements, such as URLs, user mentions (@username), hashtags, special characters, emojis, and numbers that did not contribute to semantic understanding, were systematically removed using regular expressions.
2. Common stop words (e.g., "the," "is," "and") were eliminated using predefined lists from standard NLP libraries. All text was converted to lowercase to ensure uniformity, preventing duplication of tokens due to case differences (e.g., "Movie" and "movie" being treated as separate entities).
3. Tweets were tokenized into individual words for granular analysis. Subsequently, lemmatization was performed to reduce words to their base or dictionary form. Further, automated spelling correction tools were applied to address common typographical errors in tweets, enhancing the quality of textual data and improving the accuracy of word embeddings generated in the subsequent processing steps.
4. Duplicate tweets, as well as near-duplicate content identified through Jaccard similarity thresholds, were removed to prevent data redundancy and potential bias in training. Also, tweets with insufficient context were excluded, as they lacked the necessary semantic richness for effective recommendation.
5. In our implementation, we performed an empirical hyperparameter search using grid-based and randomized strategies to optimize the performance of the RNN model. The final configuration was selected based on the highest validation F1-score. The following settings were applied in an experimentation setup—RNN Type: Unidirectional LSTM, Number of Layers: 2, Hidden Units per Layer: 128, Dropout Rate: 0.3, Batch Size: 64, Learning Rate: 0.001 (Adam optimizer with β_1=0.9, β_2=0.999, ϵ=1e-8), Number of Epochs: 100 (early stopping with patience = 5), Activation Function: Tanh, Embedding Dimension: 300 (pretrained CBoW vectors). These hyperparameters were chosen after a systematic evaluation using fivefold cross-validation on the filtered tweet data.

4.3 Performance evaluation measures

For the movie recommendation using tweets, several performance evaluation measures were employed to assess the effectiveness of recommendation algorithms. The metrics like precision, recall, F1-score, and mean average precision (MAP) helped to find the effectiveness of the proposed work. The description of these metrics is given as:

- *Precision:* measures the proportion of recommended items that are relevant to the user. It is calculated as the ratio of true positives (relevant items recommended) to the total number of recommended items. Mathematically, it is described using Eq. 31.

$$P = \frac{TruePos}{TruePos + FalsePos} \tag{31}$$

- *Recall:* measures the proportion of relevant items that are successfully recommended to the user. It is calculated as the ratio of true positives to the total number of relevant items. Mathematically, it is described using Eq. 32.

$$R = \frac{TruePos}{TruePos + FalseNeg} \tag{32}$$

- *F1-score:* is the harmonic mean of precision and recall, providing a balance between the two metrics. Mathematically, it is described using Eq. 33.

$$F1 - Score = \frac{2.P.R}{P + R} \tag{33}$$

- *Mean average precision (MAP):* MAP is a measure of the average precision across all relevant items. It is calculated by averaging the precision values at each relevant item's position in the recommendation list. Mathematically, it is described using Eq. 34.

$$MAP = \frac{1}{T_R} \sum_{k=1}^{N} \frac{P_k}{min(k, T_R)} \tag{34}$$

where T_R is the total number of relevant items, and P_k is the precision at position k in the recommendation list.

4.4 Results with NPO algorithm

The experimentation results from model training on movie recommendation using tweets filtered by the proposed NPO algorithm provide valuable insights into the performance of various classifiers, including support vector machines (SVMs), naive Bayes classifiers, logistic regression, and recurrent neural networks (RNN). Across the diverse set of classifiers, the evaluation metrics, including accuracy, precision, recall, F1-score, and mean average precision (MAP), offer a comprehensive assessment of their effectiveness in generating movie recommendations tailored to user preferences based on tweet data. The experimentation results of the proposed framework are shown in Table 3.

The results in Table 3 indicate that the machine learning classifiers achieved varying degrees of success in accurately predicting relevant movie recommendations. Support

Table 3 Experimentation results of the model training with proposed NPO algorithm-based tweet filtering

Classifier	Accuracy	Precision	Recall	F1-Score	MAP
Support vector machine (SVM)	0.91	0.90	0.88	0.89	0.88
Naive Bayes (NB)	0.82	0.80	0.85	0.82	0.70
Logistic regression (LR)	0.87	0.88	0.86	0.87	0.78
Recurrent neural networks (RNN)	**0.94**	**0.93**	**0.91**	**0.92**	**0.92**

The values in Bold highlight the best results

vector machines demonstrated strong overall performance, achieving high accuracy, precision, recall, and F1-score, suggesting robustness in distinguishing relevant tweets for movie recommendation. Naive Bayes classifiers exhibited competitive performance, particularly in recall and F1-score, although slightly lower accuracy and precision were observed compared to SVMs. Logistic regression models also yielded promising results, with high accuracy and precision, indicating their efficacy in classifying relevant tweets for recommendation purposes.

Furthermore, the experimentation results highlight the effectiveness of deep learning-based approaches, particularly recurrent neural networks (RNNs), in capturing the complex relationships and patterns in tweet data for movie recommendations. RNNs demonstrated superior performance across multiple metrics, achieving the highest accuracy, precision, recall, and F1-score among the classifiers evaluated. Additionally, RNNs outperformed traditional classifiers in terms of mean average precision (MAP), indicating their ability to provide high-quality ranked recommendations that align closely with user preferences.

Also, the experimentation was performed to present the outcomes of our movie recommendation system, focusing on the top-k (k=3) movie titles recommended to users based on their queries. We begin by outlining the methodology employed to generate these recommendations, detailing the algorithms, models, and evaluation metrics utilized in the process. Subsequently, we provide a comprehensive analysis of the recommended movie titles, highlighting their relevance, diversity, and alignment with user preferences. The experimentation results of the recommendation system are shown in Table 4. The top-k movie recommendations as presented in a tabular format, showcasing the movie titles along with additional information such as sentiment score (positive, negative, or neutral) with the score in a range of 0 to 1.

The experimentation results of the recommended movies by using the context of the given movie as a query vector are shown in Table 5. The results show the top-k (k=3) recommended movies with their similarity scores. The proposed model is very effective in recommending movies based on the fetched features and the learned RNN model. The results in Table 5 show the randomly selected 4 movies as the query with their information of genres and the index position in the dataset.

The performance of the proposed model is also evaluated on several checkpoints. The initial comparison in the experimentation was in between the performance metrics and their evaluations on the dataset using the proposed NPO and without the NPO algorithm. The results of the proposed NPO algorithm with performance metrics are presented in Table 3 and the performance on the same dataset using the same metrics but without using NPO as a filtering approach is shown in Table 6.

By comparing the performance metrics across different optimization and feature selection algorithms, we can assess the effectiveness of the proposed optimization algorithm in filtering data in the MovieLens dataset compared to alternative approaches. Higher values of accuracy, precision, recall, F1-score, and MAP indicate better performance of the algorithm in improving the quality of filtered data for movie recommendation purposes. The experimentation results of the comparison with other benchmark algorithms are shown in Table 7.

Table 4 Results of the recommended top-K (k=3) movies based on user query

User query	Top-k recommended movies	Sentiment score
"Love romantic movies"	1. Titanic 2. The Notebook 3. La La Land	Positive (0.8)
"Action-packed films"	1. Avengers: Endgame 2. The Dark Knight 3. Mad Max: Fury Road	Positive (0.7)
"Best comedy movies"	1. Superbad 2. The Hangover 3. Dumb and Dumber	Positive (0.6)
"Horror movies"	1. The Conjuring 2. A Nightmare on Elm Street 3. Hereditary	Negative (0.3)
"Classic films"	1. Casablanca 2. Gone with the Wind 3. Citizen Kane	Positive (0.8)
"Sci-fi movies"	1. Star Wars: The Empire Strikes Back 2. Blade Runner 2049 3. Inception	Positive (0.7)
"Animated films"	1. Toy Story 2. Finding Nemo 3. Shrek	Positive (0.8)
"Family-friendly movies"	1. The Lion King 2. Up 3. Frozen	Positive (0.9)
"Indie movies"	1. Juno 2. Little Miss Sunshine 3. Moonlight	Neutral (0.5)
"Documentaries"	1. Fahrenheit 9/11 2. Blackfish 3. March of the Penguins	Positive (0.6)

5 Limitations of the study

In this work, we used a new methodology to filter out the text and make some recommendations. Despite the good performance, there are some limitations of the work. Firstly, the dependence on the quality and availability of user-generated content remains a significant challenge. Tweets often contain informal language, abbreviations, emojis, and misspellings, which, even after data cleaning, may still introduce some level of ambiguity and noise. Moreover, the brevity of tweets limits the contextual information that can be extracted from individual posts, potentially affecting the richness of the feature representations used for recommendations.

Secondly, while the nuclear physics optimization (NPO) algorithm demonstrated effective noise filtering and feature selection capabilities, its performance is inherently dependent on the initial parameter settings and the quality of the input data. Although we applied parameter tuning and cross-validation to mitigate this,

Table 5 Results of the recommended movies using the query movie with the proposed framework on MovieLens dataset

Query 1	Movie: Jumanji—Genres: Adventure Fantasy Family—Index: 1
Recommended Results (k=3)	Return To Oz—Genres: Adventure Family Fantasy—Similarity: 1.0
	Peter Pan—Genres: Adventure Fantasy Family—Similarity: 1.0
	Harry Potter And The Prisoner Of Azkaban—Genres: Adventure Fantasy Family—Similarity: 0.9
Query 2	Movie: Die Hard—Genres: Action Thriller—Index: 1007
Recommended Results (k=3)	Iron Eagle Iii—Genres: Action Thriller—Similarity: 1.0
	The Peacemaker—Genres: Action Thriller—Similarity: 1.0
	D-Tox—Genres: Action Thriller—Similarity: 0.9
Query 3	Movie: Faces—Genres: Drama—Index: 688
Recommended Results (k=3)	The Hours—Genres: Drama—Similarity: 1.0
	The Graduate—Genres: Drama—Similarity: 0.9
	Coming Apart—Genres: Drama—Similarity: 0.9
Query 4	Movie: Toy Story—Genres: Animation Comedy Family—Index: 0
Recommended Results (k=3)	The Wrong Trousers—Genres: Animation Comedy Family—Similarity: 1.0
	A Close Shave—Genres: Family Animation Comedy—Similarity: 1.0
	Creature Comforts—Genres: Animation Comedy Family—Similarity: 0.9

Table 6 Experimentation results of the model training without NPO algorithm for tweet filtering

Classifier	Accuracy	Precision	Recall	F1-Score	MAP
Support vector machine (SVM)	0.85	0.86	0.84	0.85	0.75
Naive Bayes (NB)	0.82	0.80	0.85	0.82	0.70
Logistic Regression (LR)	0.87	0.88	0.86	0.87	0.78
Recurrent neural networks (RNN)	**0.90**	**0.92**	**0.88**	**0.90**	**0.82**

The values in Bold highlight the best results

suboptimal settings in different datasets or domains may lead to variations in performance. Additionally, NPO, like other metaheuristic algorithms, may require higher computational resources and longer processing time for large-scale datasets, which could limit its real-time application potential in production environments.

Another limitation arises from the focus on a single data source (Twitter) for user sentiment and preferences. Relying solely on tweets restricts the diversity of user expressions and perspectives that could be captured from other platforms such as movie review sites, forums, or multimedia platforms. The integration of multi-source data could have provided a more comprehensive understanding of user preferences. Furthermore, while we used standard evaluation metrics, user-centric

Table 7 Comparative results of the proposed optimization algorithm with other benchmark algorithms on MovieLens dataset using RNN model

Algorithm	Accuracy	Precision	Recall	F1-Score	MAP
Proposed optimization	**0.94**	**0.93**	**0.91**	**0.92**	**0.92**
Genetic algorithm [35]	0.87	0.86	0.86	0.86	0.82
Particle swarm optimization [17]	0.90	0.88	0.86	0.87	0.89
Simulated annealing [37]	0.83	0.85	0.80	0.82	0.76
Ant colony optimization [31]	0.86	0.88	0.84	0.86	0.87
Tabu search [18]	0.80	0.81	0.79	0.80	0.67
Information gain [37]	0.86	0.87	0.85	0.86	0.76
Chi-squared [37]	0.83	0.84	0.82	0.83	0.71
ReliefF [37]	0.85	0.86	0.84	0.85	0.75
Recursive feature elimination (RFE) [37]	0.87	0.88	0.86	0.87	0.78

The values in Bold highlight the best results

evaluation through real-world deployment or user studies was not conducted, which could have provided deeper insights into user satisfaction and recommendation relevance in practical scenarios.

Lastly, our model primarily targeted the English-language tweets, which limits the generalizability of the findings to non-English speaking audiences. Addressing multilingual data and cultural diversity in user preferences remains an open challenge for future work.

6 Conclusion

In this work, we proposed a framework incorporating the new optimization algorithm inspired by nuclear physics for the filtering of noise in user-centric tweets. The proposed framework is used for the recommendation of movies based on the user query and filtered output from the optimization algorithm in the MovieLens dataset.

The experimentation on optimization-based noise filtering among user-centric tweets to improve predictions in movie recommendation systems, employing classifiers such as support vector machines (SVMs), naive Bayes classifiers, logistic regression, and recurrent neural networks (RNN), has yielded valuable insights and promising outcomes. Through the proposed optimization-based noise filtering approach, we aimed to enhance the quality and relevance of movie recommendations generated from user-centric tweets, thereby enriching the overall movie recommendation experience.

Our findings demonstrate that the optimization-based noise filtering method significantly improves the performance of movie recommendation systems across various classifiers and evaluation metrics. Specifically, we observed notable enhancements in accuracy, precision, recall, F1-score, and mean average precision (MAP) when compared to traditional recommendation approaches without noise filtering. This underscores the effectiveness of our approach in mitigating the impact of noisy

data and extracting more accurate and relevant information from user-centric tweets for movie recommendations.

Furthermore, the comparative analysis revealed the superiority of certain classifiers over others in leveraging the filtered tweet data for movie recommendation purposes. While support vector machines (SVMs), logistic regression, and naive Bayes classifiers exhibited commendable performance across multiple metrics, recurrent neural networks (RNN) demonstrated competitive results in an overall assessment, showcasing the adaptability of our noise filtering approach to different classification algorithms.

The future scope of this work encompasses several avenues for further exploration and enhancement. Firstly, there is a need for continued research into refining the optimization-based noise filtering method to accommodate diverse data sources and recommendation contexts beyond movie recommendations. Additionally, incorporating additional features and contextual information from user-centric tweets, such as sentiment analysis and user engagement metrics, could further enrich the recommendation process.

Author contributions K.J. wrote the main manuscript text and R.J. prepared all the figures. All authors reviewed the manuscript.

Funding The author declares that there is no funding associated with this project.

Data availability The dataset is openly available and no third party data is used.

Declarations

Conflict of interest The authors of this manuscript declare that there is no conflict of interest.

Ethical approval The authors of this manuscript confirm that approval and/or informed consent were not required for the study as the dataset is collected from an open-source website which is freely available.

References

1. Afoudi Y, Lazaar M, Al Achhab M (2021) Hybrid recommendation system combined content-based filtering and collaborative prediction using artificial neural network. Simul Model Pract Theory 113:102375
2. Alsini A, Datta A, Huynh DQ (2020) On utilizing communities detected from social networks in hashtag recommendation. IEEE Trans Comput Soc Syst 7(4):971–982
3. Anwar T, Uma V, Srivastava G (2021) Rec-cfsvd++: implementing recommendation system using collaborative filtering and singular value decomposition (svd)++. Int J Inf Technol Decis Mak 20(04):1075–1093
4. Awan MJ, Khan RA, Nobanee H, Yasin A, Anwar SM, Naseem U, Singh VP (2021) A recommendation engine for predicting movie ratings using a big data approach. Electronics 10(10):1215
5. Balush I, Vysotska V, Albota S (2021) Recommendation system development based on intelligent search, nlp and machine learning methods. In: MoMLeT+ DS, pp 584–617
6. Behera G, Panda SK, Hsieh MY, Li KC (2024) Hybrid collaborative filtering using matrix factorization and xgboost for movie recommendation. Comput Stand Interfaces 90:103847
7. Bobadilla J, Ortega F, Gutiérrez A, Alonso S (2020) Classification-based deep neural network architecture for collaborative filtering recommender systems

8. Bourreau M, Gaudin G (2022) Streaming platform and strategic recommendation bias. J. Econ. Manag. Strateg. 31(1):25–47
9. Chen YL, Yeh YH, Ma MR (2021) A movie recommendation method based on users' positive and negative profiles. Inf. Process. Manag. 58(3):102531
10. Churchill R, Singh L (2021) Topic-noise models: Modeling topic and noise distributions in social media post collections. In: 2021 IEEE International Conference on Data Mining (ICDM), IEEE, pp 71–80
11. Dara S, Srinivasulu C, Babu CM, Ravuri A, Paruchuri T, Kilak AS, Vidyarthi A (2023) Context-aware auto-encoded graph neural model for dynamic question generation using nlp. ACM transactions on asian and low-resource language information processing
12. Darban ZZ, Valipour MH (2022) Ghrs: Graph-based hybrid recommendation system with application to movie recommendation. Expert Syst Appl 200:116850
13. Fan W (2024) Recommender systems in the era of large language models (llms). IEEE Trans Knowl Data Eng 36:1–20
14. Fayyaz Z, Ebrahimian M, Nawara D, Ibrahim A, Kashef R (2020) Recommendation systems: algorithms, challenges, metrics, and business opportunities. Appl Sci 10(21):7748
15. Gopi AP, Jyothi RNS, Narayana VL, Sandeep KS (2023) Classification of tweets data based on polarity using improved rbf kernel of svm. Int J Inf Technol 15(2):965–980
16. Gupta M, Thakkar A, Gupta V, Rathore DPS et al (2020) Movie recommender system using collaborative filtering. In: 2020 international conference on electronics and sustainable communication systems (ICESC), IEEE, pp 415–420
17. Gupta V, Rattan P (2023) Improving twitter sentiment analysis efficiency with svm-pso classification and efws heuristic. Procedia Comput Sci 230:698–715
18. Han B, Zheng X, Guan M, Sun L, Zhang Y (2023) Personalized route recommendation with hybrid tabu search algorithm based on crowdsensing. Int J Intell Syst 2023(1):3054888
19. Jain DK, Kumar A, Sharma V (2020) Tweet recommender model using adaptive neuro-fuzzy inference system. Futur Gener Comput Syst 112:996–1009
20. Jain DK, Neelakandan S, Vidyarthi A, Mishra A, Alkhayyat A (2025) A knowledge-aware nlp-driven conversational model to detect deceptive contents on social media posts. Comput Speech Lang 90:101743
21. Jain K, Jindal R (2024) Nlp-enabled recommendation of hashtags for covid based tweets using hybrid bert-lstm model. ACM Transactions on Asian and Low-Resource Language Information Processing
22. Javed U, Shaukat K, Hameed IA, Iqbal F, Alam TM, Luo S (2021) A review of content-based and context-based recommendation systems. Int J Emerg Technol Learn (iJET) 16(3):274–306
23. Kanapala A, Dara S, Sreedhar J, Vidyarthi A, Gupta D, Gupta P (2024) Recommendation of electronic mobile gadgets using infused decision score with mobile radiation and federated sentiment score. IEEE Trans Consum Electron 70:2566
24. Kaviani M, Rahmani H (2020) Emhash: Hashtag recommendation using neural network based on bert embedding. In: 2020 6th International Conference on Web Research (ICWR), IEEE, pp 113–118
25. Ko H, Lee S, Park Y, Choi A (2022) A survey of recommendation systems: recommendation models, techniques, and application fields. Electronics 11(1):141
26. Kocher DC (1981) Radioactive decay data tables. In: Tech. rep., Oak Ridge National Lab.(ORNL), Oak Ridge, TN (United States)
27. Kulkarni S, Rodd SF (2020) Context aware recommendation systems: a review of the state of the art techniques. Comput Sci Rev 37:100255
28. Kumar N, Baskaran E, Konjengbam A, Singh M (2021) Hashtag recommendation for short social media texts using word-embeddings and external knowledge. Knowl Inf Syst 63:175–198
29. Kumar S, De K, Roy PP (2020) Movie recommendation system using sentiment analysis from microblogging data. IEEE Trans Comput Soc Syst 7(4):915–923
30. Liu P, Zhang L, Gulla JA (2023) Pre-train, prompt, and recommendation: a comprehensive survey of language modeling paradigm adaptations in recommender systems. Trans Assoc Comput Linguist 11:1553–1571
31. Liu Y, You X, Liu S (2022) Multi-ant colony optimization algorithm based on hybrid recommendation mechanism. Appl Intell 52:1–26
32. Marcuzzo M, Zangari A, Albarelli A, Gasparetto A (2022) Recommendation systems: an insight into current development and future research challenges. IEEE Access 10:86578–86623

33. Mundra S, Reddy J, Mundra A, Mittal N, Vidyarthi A, Gupta D (2023) An automated data-driven machine intelligence framework for mining knowledge to classify fake news using nlp. ACM Transactions on Asian and Low-Resource Language Information Processing
34. Parthasarathy G, Sathiya Devi S (2023) Hybrid recommendation system based on collaborative and content-based filtering. Cybern Syst 54(4):432–453
35. Paulavičius R, Stripinis L, Sutavičiūtė S, Kočegarov D, Filatovas E (2023) A novel greedy genetic algorithm-based personalized travel recommendation system. Expert Syst Appl 230:120580
36. Rappaz J, McAuley J, Aberer K (2021) Recommendation on live-streaming platforms: Dynamic availability and repeat consumption. In: Proceedings of the 15th ACM Conference on Recommender Systems, pp 390–399
37. Rezaei E, Ghoreyshi K, Dimitrov Y, Sadique KM, Campos J (2021) Data mining with weka
38. Roy D, Dutta M (2022) A systematic review and research perspective on recommender systems. J Big Data 9(1):59
39. Sami A, Adrousy WE, Sarhan S, Elmougy S (2024) A deep learning based hybrid recommendation model for internet users. Sci Rep 14(1):29390
40. Sharma AK, Bajpai B, Adhvaryu R, Pankajkumar SD, Gordhanbhai PP, Kumar A (2023) An efficient approach of product recommendation system using nlp technique. Mater Today Proc 80:3730–3743
41. Sharma VK, Mittal N, Vidyarthi A (2022) Context-based translation for the out of vocabulary words applied to Hindi–English cross-lingual information retrieval. IETE Tech Rev 39(2):276–285
42. de Souza Pereira Moreira G, Rabhi S, Lee JM, Ak R, Oldridge E (2021) Transformers4rec: Bridging the gap between nlp and sequential/session-based recommendation. In: Proceedings of the 15th ACM Conference on Recommender Systems, pp 143–153
43. Tiwari S, Kumar S, Jethwani V, Kumar D, Dadhich V (2022) Pntrs: personalized news and tweet recommendation system. J Cases Inf Technol (JCIT) 24(3):1–19
44. Vaswani A, Shazeer N, Parmar N, Uszkoreit J, Jones L, Gomez AN, Kaiser Ł, Polosukhin I (2017) Attention is all you need. Adv Neural Inf Process Syst 30:5998
45. Walek B, Fojtik V (2020) A hybrid recommender system for recommending relevant movies using an expert system. Expert Syst Appl 158:113452
46. Wicaksono RA, Setiawan EB (2022) Recommender system based on tweets with singular value decomposition and support vector machine classification. J Comput Syst Inform (JoSYC) 3(4):294–302
47. Zou L, Xia L, Gu Y, Zhao X, Liu W, Huang JX, Yin D (2020) Neural interactive collaborative filtering. In: Proceedings of the 43rd International ACM SIGIR Conference on Research and Development in Information Retrieval, pp 749–758

Publisher's Note Springer Nature remains neutral with regard to jurisdictional claims in published maps and institutional affiliations.

Springer Nature or its licensor (e.g. a society or other partner) holds exclusive rights to this article under a publishing agreement with the author(s) or other rightsholder(s); author self-archiving of the accepted manuscript version of this article is solely governed by the terms of such publishing agreement and applicable law.

PREFACE FOR SPECIAL ISSUE ON ISME-2024: RECENT ADVANCES IN CLEAN ENERGY FOR SUSTAINABLE DEVELOPMENT

Recent advancements in clean energy are playing an important role in the development of sustainable technologies, especially in the scope of green hydrogen production to progress in solar energy systems and electric vehicle energy storage. This issue is devoted to the theme of clean energy for sustainable technologies covering a few papers presented in the 22nd International Conference on Recent Advances in Mechanical Engineering for Sustainable Development: ISME-2024, held July 11–13, 2024, at the Department of Mechanical Engineering, Delhi Technological University (formerly Delhi College of Engineering), Delhi, India, in collaboration with the Indian Society of Mechanical Engineers.

The ISME-2024 conference was inspired to assist and provide opportunities for professional development among scientists and engineers working in the field of clean energy and related applications. The vital need for such developments persists for a long time, despite the dedicated commitment of regional governments in developing countries to raise the standard of undergraduate/postgraduate education and to create world-class research capabilities in the institutions of higher education. The purpose of starting this international conference is to meet this requirement and to provide a well-structured common platform to expedite interdisciplinary research activities as well as to provide a well-established point of contact and worldwide networking. Such a conference can serve as a focal point for the gathering, interaction, and collaboration among scientists and engineers. The theme "Clean Energy" was selected as an umbrella title for the conference because of its encompassing meaning, and the research areas covered under this theme are equally important in the developing and developed world. A wide range of interdisciplinary topics in critical areas, including novel approaches to performance enhancement of fuel cells, high-performance solar water heating technologies, solar agro-drying, circular economy to achieve sustainable development, blending of liquid fuels with plant-based fuel derivatives, etc., are the obvious examples of clean energy applications that are crucial for industrial and economic development.

After a careful selection procedure, invitations were sent to the ISME-2024 authors to prepare extended articles based on the relevance to the journal and the reviews of the conference version of the papers. Out of the 15 submitted articles, after thorough reviewing procedures, 8 were finally accepted for this special issue section of the *International Journal of Energy for a Clean Environment* (IJECE). We appreciate the willingness of the authors to help in organizing this special issue. We are thankful to the IJECE journal publisher, the Editor-in-Chief, and the Production Editor for supporting this publication. We hope that the readers will benefit from the content of this special issue.

Submitted: 4/27/2025; Accepted: 4/27/2025; Online: 5/5/2025 https://doi.org/10.1615/InterJEnerCleanEnv.2025059572
2150-3621/25/$35.00 © 2025 by Begell House, Inc. www.begellhouse.com

Guest Editors:

Prof. Amit Pal
Delhi Technological University, Delhi, India

Dr. K. Manjunath
Delhi Technological University, Delhi, India

Prof. Surendra Singh Kachhwaha
Pandit Deendayal Energy University, Gandhinagar, India

International Journal of Mathematical, Engineering and Management Sciences
Vol. 10, No. 4, 856-873, 2025
https://doi.org/10.33889/IJMEMS.2025.10.4.041

Ram Arti Publishers

Studying Kangen Technology Dissemination in Indian Subcontinent: A Mathematical Modeling Framework

Saurabh Pandey
University School of Management and Entrepreneurship (USME),
Delhi Technological University, 110095, Delhi, India.
E-mail: saurabhpandey2k20phdusme04@dtu.ac.in

Deepti Aggrawal
University School of Management and Entrepreneurship (USME),
Delhi Technological University, 110095, Delhi, India.
Corresponding author: deeptiaggrawal@dtu.ac.in

(Received on January 7, 2025; Revised on February 13, 2025 & March 6, 2025; Accepted on March 11, 2025)

Abstract
Much research has been done on the character, types, and nature of adopters present in the market, wherein discussion has revolved around the adoption process in entirety, but less attention has been given to characterizing the types of these adopters in the market. By integrating principles from seminal models such as Rogers' Diffusion of Innovations and Bass Diffusion Model, the present work helps in identification of the adopters and predicting trends that delves into the diffusion dynamics of Kangen, a technology which is a notable innovation in the water purification and ionization industries and provides better hydration, helping with energy and focus. Critical insights into the Kangen technology dissemination process across India are offered by the results of applying the Innovation Diffusion Modeling Framework. The results highlight not only the rate and extent of adoption but also shed light on the profiles of different categories of imitators within the market.

Keywords- Bass model, External influencer, Kangen technology, Technology adoption, Word-of-Mouth influencer.

1. Introduction

In the contemporary landscape of technological advancement, sustainable consumer behavior (Trudel, 2019) and market dynamics are significantly shaped by the acceptance and spread of innovative items (Ratcliff & Doshi, 2016). Due to increased environmental concerns and awareness of the effects of daily decisions on the environment, adopting sustainable practices in consumer behavior has received attention recently. Water is a scarce resource that has attracted attention for its preservation and innovative sustainable technology. The scientific and technical community, followed by innovation, responds by creating standards to facilitate industry and economic activity (Agarwal et al., 2017) and lead to the adoption process by customers. Kangen Technology is a leading invention in the field of water purification and ionization systems (Cerbu, 2013). It has redefined water quality standards and is a subject of great interest for researchers studying technology adoption patterns.

Good health and well-being have become an intensified consciousness of every individual after the COVID-19 pandemic, and it has sparked an interest in multiple innovative technologies that can provide potential health benefits (Henry & Chambron, 2013). Among these various innovations and emerging trends, the health benefits of water ionization technology have enticed the attention among consumers for its adoption (Pandey & Aggrawal, 2025) and the high pH value and low surface tension of electrolyzed reduced water (ERW), the virus's envelope, made up of proteins and phospholipids, breaks down and exhibits inhibitory activity against the Severe Acute Respiratory Syndrome Coronavirus-2 (Okajima et al., 2021). As a potent antioxidant, hydrogen is thought to minimize oxidative stress, which may slow aging and boost energy

(Pisoschi et al., 2021). The creation of hydrogen-rich water is another important characteristic of water ionizers and as a potent antioxidant, hydrogen is thought to minimize oxidative stress, which may slow aging and boost energy (Pisoschi et al., 2021). Water ionizers are marketed to offer improved hydration, detoxification, and antioxidant properties, thus appealing to health-conscious consumers.

An exhaustive investigation into the diffusion dynamics of Kangen Technology (Cerbu, 2013), leveraging the robust framework of Innovation Adoption Modeling which has set up the need to quantify the adoption of Ionization technology. Understanding the adoption patterns and diffusion mechanisms of this transformative technology is crucial not only for elucidating its market penetration but also for unravelling the intricate web of factors shaping its acceptance and utilization across diverse user segments (Lotfi et al., 2014). Consumers consider a variety of criteria, including personal preference, experience, and word-of-mouth (Babbar et al., 2024), in addition to the mass media (Mahajan et al., 1990a). Such framework, rooted in the seminal works of Bass (1969) and Rogers (1962) in the diffusion of Innovations theory, offers a structured approach to understanding how new technologies permeate markets and social systems. The decision to focus on Kangen Technology provides an opportunity to explore the diffusion of environmentally significant innovation in a market that directly impacts public health and sustainability (Pandey & Aggrawal, 2024).

The diffusion of innovations within markets often follows identifiable patterns and stages, a phenomenon extensively studied and theorized by pioneers such as Everett Rogers (1962). By applying and adapting these theoretical frameworks to the unique context of Kangen Technology, this study seeks to unravel the nuanced pathways through which this innovation permeates various market segments and geographic regions in India.

This research aims to answer pivotal questions concerning the adoption dynamics of Kangen Technology wherein certain research gaps were identified, especially with respect to Indian Sub-continent, like,

- *What is the pace of acceptance of this new technology wherein water is created through an electrolysis process using a water ionizer?*
- *Acceptance of water ionizers, now a home appliance (that raises the pH of the drinking water) after the COVID-19 pandemic.*

This study aims to furnish actionable insights for informed marketing strategies, policy frameworks, and innovation within the water purification industry. The significance of this study contributes on technology adoption, empirical evidence and theoretical frameworks that could outline the understanding and management of innovative contributions in diverse Indian markets. Accessibility to clean and healthy water sources is global challenge and the implications of this research foster to public health, environmental sustainability, and societal well-being (Ronen & Kerret, 2020).

This paper aims to deliver an exhaustive and quantified analysis of the diffusion of Kangen Technology, enhancing the understanding of innovation adoption. The details of the article's structure are explained in the following section. The existing literature and background on diffusion theory, water ionizers, and their health benefits are presented in Section 2. Section 3 comprises a discussion of the bass model and its framework. Section 4 presents the implementation of sales data and the development of a model using bass diffusion theory. The discussion and interpretation are discussed in Section 5, followed by managerial implications in Section 6. Lastly, the conclusion, limitations, and Section 7 represent the future roadmaps.

2. Literature Review

The diffusion theory was first postulated by sociologist Gabriel Tarde in the late 19th century. Predictive models seek to develop explanations for how social strength impacts the diffusion and adoption process since diffusion is a social process, and many potential adopters' acceptance was encouraged by their peers' social strength (Aggrawal et al., 2021). It can include the adoption of new goods, technology, and lifestyles, as well as the development of new epidemics, such as the still-active COVID-19 pandemic. To enhance and direct innovation management, prominent aggregate models like innovation characteristics (Rogers, 1995) and the Bass model (Bass, 1969), as well as seminal individual-level models like the technology acceptance model (Venkatesh & Davis, 2000) and the theory of planned behavior (Ajzen, 1991) are still widely used. Understanding consumer behaviour in sales, which is often influenced by spatiotemporal uncertainties that vary across different regions over time, Bayesian Deep Learning modelling as a probability distribution captures the dynamic and complex nature of consumer behaviour (Li et al., 2024).

Product adoption, particularly with disruptive technologies, has a significant impact on the financial foundation of entrepreneurial enterprises that frequently develop them (Kirchhoff et al., 2013). Many times, the adoption of the products in the market is explained as the behaviour of sigmoidal dynamics (Lotfi et al., 2014). Rogers (1995) claims that when businesses that have embraced an innovation encounter business that have not, their clearly superior performance will persuade non-adopters to do the same, leading to the fast growth stage of an S-shaped diffusion curve. Another popular innovation diffusion model is the marketing time cumulative adopters. The model assumes that innovation adopters comprise two groups. One group is influenced only by mass-media communication (external influence), and the other group is only influenced by word-of-mouth communication (internal influence). Bass termed the first group '*Innovators*' and the second group '*Imitators*' (Bass, 1969). This explains the product life cycle in the longer run, which is demonstrated in **Figure 1**. On the adoption curve, innovators, early adopters, early majority, late majority, and laggards are in the sequential processes (Rogers, 1962). Existing research has already explained adoption behaviour; however, the market dynamics are being changed based on the social and economic behaviour of the consumer. Nowadays, technology frequently causes disruptions. Thus, it is critical for products to be sustainable so that they may last a long time for customers and provide the benefits initially. Peer evaluation is a crucial component of many platforms that help people make decisions in their day-to-day activities. The concept of the presented work has been originated from the theory of adoption and spread put forth by Anand et al. (2016), Bass (1969, 2004), Kumar et al. (2023), Mahajan et al. (1990a, 1990b), Rogers (1962), and Singhal et al. (2019).

Innovation diffusion models are frequently used in marketing and business to forecast the adoption of new products or services. Many of the researchers have employed these models for descriptive conclusions in addition to forecasting. For instance, the Bass model was used to explain why consumer durable goods product life cycles (PLCs) are shortening due to rapid technological development (Olshavsky, 1980), and this is also demonstrated that the nationalization of oil production is a pattern of social interaction phenomena (Kobrin, 1985).

Various factors and drivers, such as personal, societal, situational, and demographic aspects, impact behavior that is environmentally sustainable (Nguyen & Johnson, 2020). Water ionizers are one of the right choices for healthy water consumption for human life, and this study shows the indicators responsible for igniting consumer perceptions of adopting water ionizers. Human health and well-being frequently align with sustainable practices (Ronen & Kerret, 2020). Given its alkaline composition and health benefits, consumers might view ionized water from water ionizers as a healthier choice. To analyze the adoption of water ionizers, it is necessary to comprehend the relationship between health beliefs and sustainable consumption patterns (Tanner & Kast, 2003). Convenience and pragmatism in daily living must be

integrated into sustainable activities. To assess whether water ionizers are sustainable, consumers consider aspects like maintenance needs, usability, and how easily they can be incorporated into regular routines. Also, a vital component of sustainable consumer behavior (Trudel, 2019) is belief in the efficiency and dependability of technology. Customers' confidence in the safety, reliability, and moral ramifications of ionization technology and its use and manufacture provides longevity in business and a healthy lifespan in society. Most water ionizers from good brands are ISO 14001 certified (ISO 14001:2015, 2015), which authorizes the product for best practices and environmental management strategies (EMS) and leads toward environmental sustainability. EMS strives to innovate best practices for environmentally sustainable products like water ionizers. The sustainability of water ionizers can be evaluated from various angles, including their environmental impact, energy efficiency, and long-term economic viability. With the demand for sustainable products by customers and regulatory obligations on organizations, sustainability is an extreme goal to consider in terms of raw material, innovation, product, and process design. Product awareness among consumers and sustainability labeling impact consumers' perceptions of products, their desire to behave, and their actual purchasing behaviors (Majer et al., 2022).

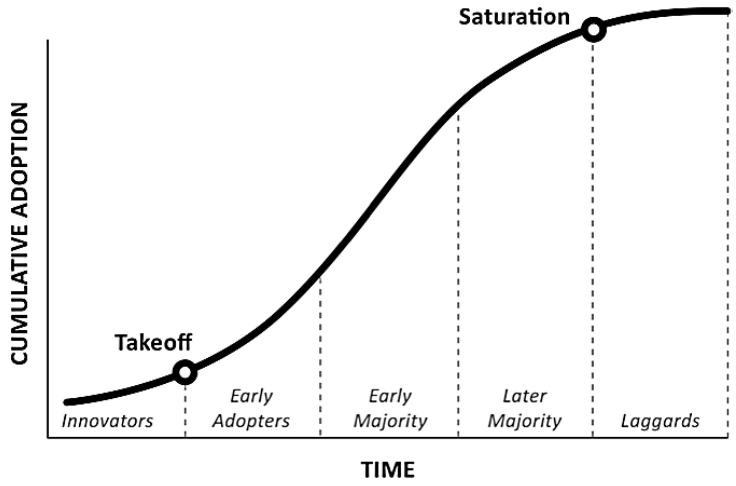


Figure 1. S - Curve model of diffusion process (Source: Author creation).

The comprehensive understanding of water, which is one of the essential liquids in the human body (Lu et al., 2023), and its use inside the human body directs the perusal to consumers for analyzing the factors for the adoption of such a technological product in daily life. Human body parts are mostly made up of water. For example, the brain consists of 80-85% water, the heart 70-80%, etc. Keeping all body parts hydrated helps maintain body parts' health and reduces the rate of aging. With aging, the percentage of water in the human body decreases (Pocock et al., 1981). Water ionizers are products that alter normal water into electrolyzed reduced water (ERW) or alkaline ionized water (AIW). EDW depicts critical properties such as alkalinity, negative oxidation-reduction potential (ORP), micro-clustering, and a high content of dissolved hydrogen, which distinguish it from regular tap or reverse osmosis (RO) water (Ignacio et al., 2012). Alkaline ionized water (AIW) produced from water ionizers offers several potential health benefits (Henry & Chambron, 2013), like hydration, antioxidant properties, alkalinity, detoxification, and improved digestion. It is shown that reduced water suppresses oxidative stress-related diseases such as diabetes, arteriosclerosis, cancer, neurodegenerative diseases, and the side effects of hemodialysis (Shirahata et al., 1997). Studies have demonstrated that alkaline ionized water protects against the body's accumulation of

lipids and cholesterol (Jin et al., 2006). It is evident that electrolyzed reduced water (ERW) causes telomere shortening in cancer cells (Shirahata et al., 2012). It suppresses tumor angiogenesis by scavenging intracellular reactive oxygen species (ROS), secretion of vascular endothelial growth factor, and suppressing gene expression (Ye et al., 2008). ERW suppresses microorganisms and the growth of cancer cells (Hamasaki et al., 2005), and it induces apoptosis in human leukemia HL60 cells when combined with glutathione (Tsai et al., 2009).

Further studies on ionized water revealed that the bandwidth of ERW is less than tap water (LeBaron et al., 2022) and subjected to approx.170 nuclear magnetic resonance (NMR). This depicts a type of rearrangement of the ionized water, specifically the presence of a smaller micro-cluster (Hayashi, 1995). It is often claimed that ionized water carries less micro-cluster than regular tap water, improving its ability to penetrate water molecules inside human organs (Mohr, 2016). The higher pH ionizes water molecules, increasing their solubility and subsequent extraction (Kun-Kul, 2005), which contributes to the removal of oil-based pesticides from foods and claims that micro-clustering is responsible for the ability of this high-pH water to emulsify the oil. The result of ORP with a negative charge relates to a charge with a negative value of permanent antioxidant activity. ORP measures the antioxidants in water by checking its electrical conductivity for unsafe radicals due to the valuable antioxidants. Antioxidants resist diseases like cancer, cardiovascular disease, and immune disorders (Ignatov, 2017).

A study of the literature on modeling frameworks for innovation diffusion and adoption offers insights into the methods, applications, and theoretical foundations of diverse approaches to comprehending the diffusion and acceptance of innovations within populations. The sales of water ionizers in Indian society prevail in the interest of an individual's health. People are buying water ionizers because they think the health advantages of ionized water hold the key to an eternally healthy life. Over the years, the adoption of water ionizers followed by RO, or packaged drinking water, has been one of the most popular topics in the sustainability of a healthy life. Target audience, sales cycle, and customer relationship play vital roles in modeling sales for B2C (Business-to-Consumer) versus B2B (Business-to-Business). B2C models focus on individual consumers, while B2B models target businesses and organizations. However, the Sales cycle is longer in B2B than in B2C. In India, the direct selling industry is evolving and focusing on a hybrid approach where the end customer is considered a new business entity.

Drawing on rising sales numbers across different regions, the framework by Bass has been chosen to research sales data to investigate the implications of the increasing adoption of water ionizers in Indian society, keeping in mind the foundational elements for the work given in this paper. This study attempts to close this gap in the literature by reporting sales data from seven years in the Indian region and navigates through the complexities of the diffusion process, aiming to identify and quantify the various adopters into those of innovators and imitators.

3. Insights from Bass Model and its Framework

The Bass model, first presented by Bass (1969), is one widespread and accepted mathematical model for analyzing the dissemination of innovations through a population by predicting the total number of adopters at any given time. The cognition of model offering details of new ideas, goods, or technology is embraced over time and can be partitioned into two categories of potential adopters:

- *External influencer*: The term describes motivations or elements that come from sources outside of a person, group, or system and influence choices, actions, or results. Individuals, groups, or entire societies may be impacted by these effects, which can originate from a variety of sources, including social, cultural, economic, environmental, or technical variables.

- *Word-of-Mouth influencer*: The term describes the persuasive power that verbal dialogues of personal suggestions, perspectives, or points to have over other people's decision-making processes. It is a way for people to communicate with friends, family, coworkers, and acquaintances about their experiences, preferences, or endorsements of goods, services, or ideas.

3.1 Hypothesis Building

Using the Bass Model to examine water ionizers' Kangen technology sales, several theories can be developed to investigate the variables affecting the acceptance and dissemination of this water filtration technology. Based on the role of innovator, imitator, and market penetration, the following theories are possible to draw using the bass model:

***H*11:** *Word-of-mouth inspiration is influential in the states of India.*

***H*12:** *External influence is influential in the regions under consideration.*

To get hold of these assertions, as stated earlier, we will now make use of the modeling framework by Bass, and in order to do that, let us check the various requisites.

3.2 Notations

The following notations have been used in this work are as follows:

$N(t)$: Expected number of adopters by time t with $N(0) = 0$.

$F(t)$: Probability distribution function for the Adoption Process.

m: Total market size.

b: Adoption rate.

p: Co-efficient of innovation.

q: Co-efficient of imitation.

3.3 Re-examining Bass Model

Bass Model assumes that buyers can be classified into two broad categories based on their buying patterns. He called the initial buyers Innovators since they are purchasing the technology based on external influence, and he called the other set imitators those who are buying under someone else's influence. Since the inception of this model in the marketing domain, it has been widely utilized by the management discipline. The mathematical structure of this model is straightforward to understand and can be understood from the Equation (1) given below.

$$\frac{d}{dt}N(t) = p\big(m - N(t)\big) + q\frac{N(t)}{m}\big(m - N(t)\big) \quad (1)$$

The mean value function obtained under the initial condition $N(0) = 0$ is

$$N(t) = m\left(\frac{1-e^{-(p+q)t}}{1+\left(\frac{q}{p}\right)e^{-(p+q)t}}\right) \quad (2)$$

It is noted that Equation (1) can also be expressed as

$$f(t) = \frac{dF(t)}{dt} = [p + qF(t)][1 - F(t)] \quad (3)$$

Therefore, Equation (2) can be written as $N(t) = m \cdot F(t)$.

where, $F(t)$ is the cumulative fraction of adopters by time t.

Integration of Equation (3) yields the S-shaped cumulative adoption distribution, $F(t)$ captured by the Bass Model. Further, the differentiation of $F(t)$ gives the non-cumulative adopter's distribution representing the specified adoption process; $f(t) = \frac{dF(t)}{dt}$and can also be understood as the fraction of adopters at time *t*. As bifurcated by Bass and then quantified by Mahajan et al. (1990b), these distributions are given by

$$F(t) = \left(\frac{1-e^{-(p+q)t}}{1+\left(\frac{q}{p}\right)e^{-(p+q)t}} \right) \tag{4}$$

and,

$$f(t) = \frac{p(p+q)^2 e^{-(p+q)^t}}{\left(p+qe^{-(p+q)t}\right)^2} \tag{5}$$

Figure 1 depicts the non-cumulative buyer's distribution $f(t)$, underlying the Bass Model (Mahajan et al., 1990a), So, its peak, $f(T^*)$ or $F(T^*)$, at time, T^*can be derived and occurs when

$$T^* = -\frac{1}{(p+q)} ln\left(\frac{p}{q}\right) \tag{6}$$

$$F(T^*) = \frac{1}{2} - \frac{p}{2q} \tag{7}$$

$$f(T^*) = \frac{1}{4q}(p+q)^2 \tag{8}$$

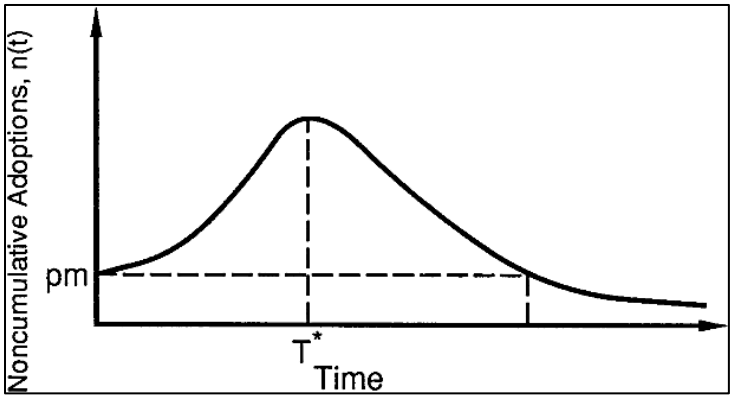


Figure 2. The adopter distribution (Source: Authors creation).

Given Equations (3) through Equation (6), we can figure out certain distinguishing features of the Bass model (Aggrawal et al., 2021; Mahajan et al., 1990b). First, note from Equation (5) that $f(t=0) = f(t=2T*) = p$. It is shown in **Figure 2** that the non-cumulative adopter distribution is symmetric with respect to time around the peak time $T*$ up to $2T*$. According to the Bass model, $p[1-F(t)]$ in Equation (3) represents the adoption happening via the innovation process and are thus termed '*innovators*. On the other hand, the term $qF(t)[1-F(t)]$ in Equation (3) represents adoption happening because of imitation. These buyers are hence termed as '*imitators*' (refer to **Figure 3** to understand the difference). The aforesaid modelling analogy can also be seen in other diversified research areas like those of software reliability which is present in the works of (Kapur et al., 2011; Yamada, 2014).

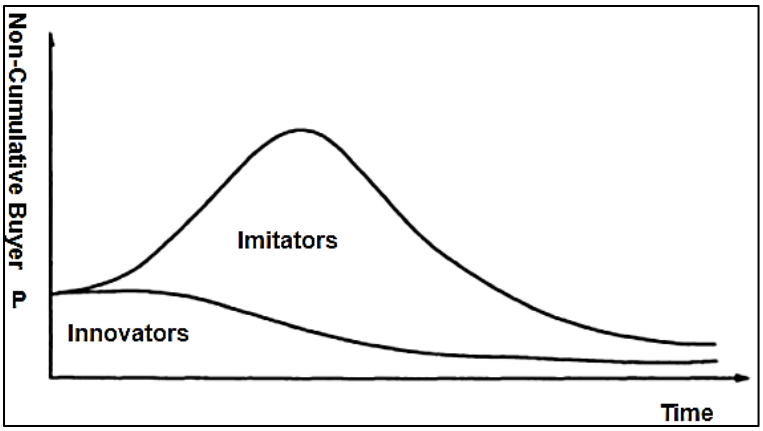


Figure 3. Buyers as per their purchase behavior (Source: Authors creation).

As a manager, especially with respect to a new technological product, one needs to find who is purchasing in which manner so that the various marketing strategies can then be strategized. For that, one should have the probable count of the number of buyers in each category. For this, using the conceptualization given by Mahajan et al. (1990b), we have quantified the number of buyers for the technological product in consideration. Since the product is a newer entry in the Indian Market, it would be great to have the exact scenario of the number of External Influencers and Word-of-Mouth influencers in the various regions of India.

For this, as taken earlier, $F(t)$ is a cumulative fraction of adopters by time t. Since, according to the Bass Model, there are two categories of buyers, $F(t)$ can be assumed to be comprised of two components $F_1(t)$: corresponding to innovators and $F_2(t)$corresponding to imitators wherein, the total fraction of innovators $F_1(t)$ between any two time periods, say t_0 and t_F $(t_F > t_0)$ is given by

$$F_1(t) = p\int_{t_0}^{t_F}[1 - F(t)]dt \tag{9}$$

Because $F(t)$ it is given by Equation (4). Hence, $F_1(t)$ it can be interpreted as:

$$F_1(t) = p\int_{t_0}^{t_F}\left[1 - \frac{1-e^{-(p+q)t}}{1+\left(\frac{q}{p}\right)e^{-(p+q)t}}\right]dt$$

$$= p\int_{t_0}^{t_F}\left[\frac{p+qe^{-(p+q)t}-p\left(1-e^{-(p+q)t}\right)}{p+qe^{-(p+q)t}}\right]dt$$

$$= p\int_{t_0}^{t_F}\left[\frac{(p+q)e^{-(p+q)t}}{p+qe^{-(p+q)t}}\right]dt$$

Put $Z = e^{-(p+q)t}$ or $dZ = -(p+q)e^{-(p+q)t}\,dt$. Therefore,

$$F_1(t) = -p\int_{z_0}^{z_f}\frac{dZ}{p+qZ}$$

$$= \frac{-p}{q}ln[(p+qZ)]_{z_0}^{z_f}$$

$$= \frac{p}{q}ln\left[\frac{p+qe^{-(p+q)t_0}}{p+qe^{-(p+q)t_f}}\right]$$

Substitution of $t_0 = 0$, $t_f = t$ in the above equation, yields

$$F_1(t) = \frac{p}{q} ln \left[\frac{1+\frac{q}{p}}{1+\frac{q}{p}e^{-(p+q)t}} \right] \quad (10)$$

Having the result for Innovators, the proportion of imitators can be calculated as follows:

$F_2(t) = 1 - F_1(t)$

$$\Rightarrow F_2(t) = \left[1 - \frac{p}{q} ln \left[\frac{1+\frac{q}{p}}{1+\frac{q}{p}e^{-(p+q)t}} \right] \right] \quad (11)$$

Also, adapting the Bass Diffusion Model to account for real-world complexities such as product obsolescence and market saturation involves extending the basic model to incorporate additional factors and dynamics:

$$f(t) = \frac{dF(t)}{dt} = ([p + qF(t)][1 - F(t)]) - \delta F(t) \quad (12)$$

where, δ is the decay rate representing product obsolescence.

and, market saturation can be addressed by adjusting the market potential parameter *m* over time. As the market approaches saturation, the effective market potential decreases, which can be modelled by making *m* a function of time.

$$f(t) = \frac{dF(t)}{dt} = ([p + qF(t)][1 - F(t)]) * (1 - F(t)/m(t))) \quad (13)$$

$m(t)$ is the time-varying market potential, which decreases as the market saturates.

4. Data Set and Model Validation

To understand the quantification of the model discussed above, it has been validated on the sales data collected for the water ionization technique Kangen Technologies by Enagic. The data comprises several states of the Indian Sub-continent, and secondary sales data from 2016 to 2022 has been arranged from the Enagic's sales team. The sales data is analyzed across Indian regions like East, West, North, and South to predict potential sales. Sales data from the East Region is considered Data Set I, followed by the West Region, which is considered Data Set II; the North Region is considered Data Set III; the South Region is considered Data Set IV and represented as DS-I, DS-II, DS-III and DS-IV respectively. The analysis has run on R-Studio using R code.

After estimation, the parameters of the model and values have been listed in **Table 1**. Based on the obtained model parameters, the performance measures are derived for Model Fit and hypothesis testing, as presented in **Table 2**. A Closure value of R^2 confirms that our quantified model fits the data reasonably well. Furthermore, **Table 3** contains the actual and predicted values along with the number of adopters (innovators and imitators) for the various states of India.

Table 1. Model parameters output.

Parameters	Data sets			
	DS-I	DS-II	DS-III	DS-IV
m	10043.94	101240.8	45029.06	71197.98
p	0.003710241	0.002981221	0.00487265	0.004226346
q	0.1897697	0.2191046	0.135289	0.127112

Source: Authors.

Table 2. Model fit and hypothesis testing.

Model fit	Data sets			
	DS-I	DS-II	DS-III	DS-IV
F value	39.13	94.01	61.28	148.9
R^2	0.7579	0.8826	0.8306	0.9226
AIC	340.11	516.65	456.79	385.68
Hypothesis testing parameters				
p- Value	0.000014	0.000000007	0.000006	0.00000001
t – Test	5.354	8.546	5.692	8.337

Source: Authors.

Table 3. Dataset wise actual and predicted values.

Time	DS-I				DS-II			
	Actual	Predicted	Innovators	Imitators	Actual	Predicted	Innovators	Imitators
2016 Q1	12	40.947	37.1918	3.75526	130	336.837058	301.337119	35.4999391
2016 Q2	33	90.189	74.2168	15.972	302	754.304531	601.554006	152.750525
2016 Q3	56	149.29	111.041	38.2533	457	1270.76243	900.383771	370.378657
2016 Q4	77	220.08	147.625	72.4561	601	1908.24669	1197.49943	710.747264
2017 Q1	112	304.63	183.922	120.708	914	2692.93553	1492.50223	1200.43331
2017 Q2	164	405.29	219.876	185.418	1328	3655.52436	1784.90872	1870.61564
2017 Q3	219	524.68	255.422	269.262	1726	4831.40597	2074.13697	2757.26901
2017 Q4	278	665.65	290.487	375.161	2147	6260.50871	2359.49264	3901.01607
2018 Q1	367	831.19	324.983	506.211	2807	7986.59759	2640.1564	5346.44119
2018 Q2	524	1024.4	358.815	665.579	3735	10055.8034	2915.17444	7140.62897
2018 Q3	679	1248.2	391.875	856.349	4810	12514.1329	3183.45484	9330.67807
2018 Q4	834	1505.4	424.043	1081.31	5776	15403.7618	3443.77316	11959.9887
2019 Q1	992	1797.9	455.191	1342.67	7283	18758.0598	3694.79096	15063.2688
2019 Q2	1174	2127	485.187	1641.79	9598	22595.5734	3935.09082	18660.4826
2019 Q3	1517	2492.7	513.894	1978.81	12439	26913.5996	4163.23015	22750.3694
2019 Q4	1770	2893.5	541.178	2352.34	14721	31682.4409	4377.81342	27304.6275
2020 Q1	2033	3326.2	566.914	2759.3	18246	36841.7903	4577.57874	32264.2115
2020 Q2	2415	3785.8	590.993	3194.76	23208	42300.7139	4761.4902	37539.2237
2020 Q3	2993	4265.4	613.328	3652.1	28850	47942.2089	4928.82358	43013.3853
2020 Q4	3449	4757.1	633.858	4123.28	32893	53632.2926	5079.23151	48553.0611
2021 Q1	3714	5252	652.554	4599.4	36196	59232.3244	5212.77632	54019.5481
2021 Q2	4074	5740.7	669.424	5071.27	41526	64612.2503	5329.92402	59282.3263
2021 Q3	4739	6214.6	684.505	5530.11	47893	69662.1583	5431.50082	64230.6575
2021 Q4	5197	6666	697.867	5968.17	53142	74300.0816	5518.6203	68781.4613
2022 Q1	5464	7088.8	709.606	6379.17	56724	78475.1275	5592.59427	72882.5332
2022 Q2	5845	7478.4	719.837	6758.55	62556	82166.2397	5654.84105	76511.3987
2022 Q3	6574	7832.2	728.688	7103.54	68995	85377.7795	5706.80244	79670.9771
2022 Q4	7036	8149.3	736.294	7413.02	74224	88133.4344	5749.87685	82383.5576
Time	**DS-III**				**DS-IV**			
	Actual	**Predicted**	**Innovators**	**Imitators**	**Actual**	**Predicted**	**Innovators**	**Imitators**
2016 Q1	49	234.31	218.852	15.4537	223	320.116108	300.244625	19.8714834
2016 Q2	102	500.87	436.486	64.3814	512	681.666615	599.0504	82.6162146
2016 Q3	206	803.64	652.734	150.904	842	1089.4866	896.232139	193.254464
2016 Q4	318	1146.9	867.41	279.499	1162	1548.82661	1191.58334	357.243266
2017 Q1	517	1535.3	1080.31	454.99	1713	2065.34556	1484.87445	580.471111
2017 Q2	734	1973.7	1291.19	682.511	2431	2645.08882	1775.85115	869.23767
2017 Q3	1168	2467.3	1499.8	967.456	3139	3294.44727	2064.23286	1230.21441
2017 Q4	1652	3021.3	1705.87	1315.4	3991	4020.09289	2349.71134	1670.38155
2018 Q1	2150	3641	1909.08	1731.97	4535	4828.88632	2631.94972	2196.9366
2018 Q2	2573	4331.8	2109.09	2222.74	5231	5727.75169	2910.58195	2817.16974
2018 Q3	3398	5098.6	2305.56	2793.02	6037	6723.51479	3185.21287	3538.30192
2018 Q4	4266	5945.7	2498.1	3447.6	6859	7822.70176	3455.41902	4367.28274

Table 3 continued…

2019 Q1	4928	6876.9	2686.3	4190.57	7759	9031.29743	3720.75041	5310.54703
2019 Q2	5575	7894.7	2869.76	5024.97	8945	10354.4654	3980.73338	6373.73199
2019 Q3	6772	9000.6	3048.04	5952.51	10117	11796.2354	4234.87474	7561.36066
2019 Q4	7994	10194	3220.73	6973.26	11534	13359.1692	4482.66725	8876.50192
2020 Q1	8921	11473	3387.38	8085.39	13026	15044.0193	4723.59654	10320.4228
2020 Q2	9950	12833	3547.61	9284.92	15069	16849.4035	4957.14947	11892.254
2020 Q3	11464	14267	3701.03	10565.6	16938	18771.5182	5182.82375	13588.6944
2020 Q4	12911	15766	3847.29	11918.9	19195	20803.9219	5400.1387	15403.7832
2021 Q1	13866	17320	3986.11	13334	20775	22937.4155	5608.64666	17328.7688
2021 Q2	14902	18915	4117.26	14798.2	22939	25160.0464	5807.94469	19352.1017
2021 Q3	16751	20538	4240.56	16297.1	24911	27457.2551	5997.68596	21459.5692
2021 Q4	18679	22171	4355.91	17815.4	27323	29812.172	6177.59017	23634.5818
2022 Q1	19783	23800	4463.32	19337	29135	32206.0596	6347.45248	25858.6071
2022 Q2	20963	25409	4562.83	20846.2	31615	34618.8792	6507.15017	28111.7291
2022 Q3	22935	26982	4654.58	22327.8	33898	37029.9486	6656.64682	30373.3018
2022 Q4	24820	28507	4738.78	23767.9	36608	39418.6453	6795.99357	32622.6517

Source: Authors.

Trends of Actual and predicted sales in all four regions are represented in the graph below. **Figures 4**, **5**, **6**, and **7** show the predictive cumulative sales in all four regions in the Indian continent. The higher values of *F*- value mentioned in **Table 2** are significant and follow the Bass adoption curve in all the regions. The *F*-value (148.9) and R^2 (0.9226) in the South region are the highest, and the cumulative graph of the South region is the best-fit model for innovation and adoption of the product.

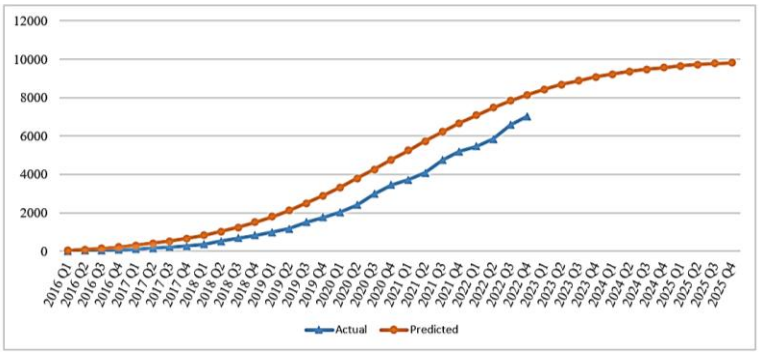


Figure 4. Cumulative sales of east region (DS-I) (Source: Authors).

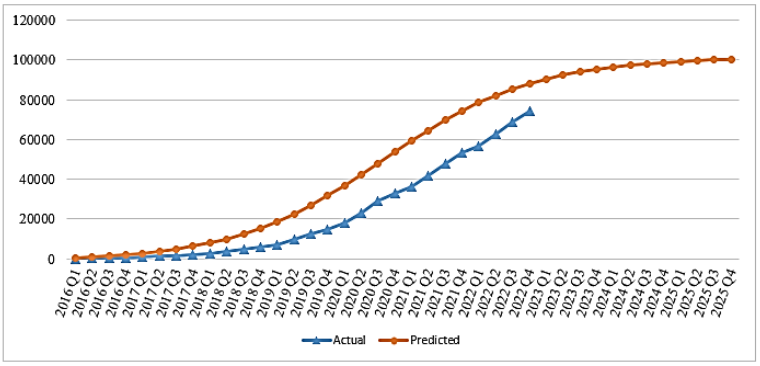


Figure 5. Cumulative sales of west region (DS-II) (Source: Authors).

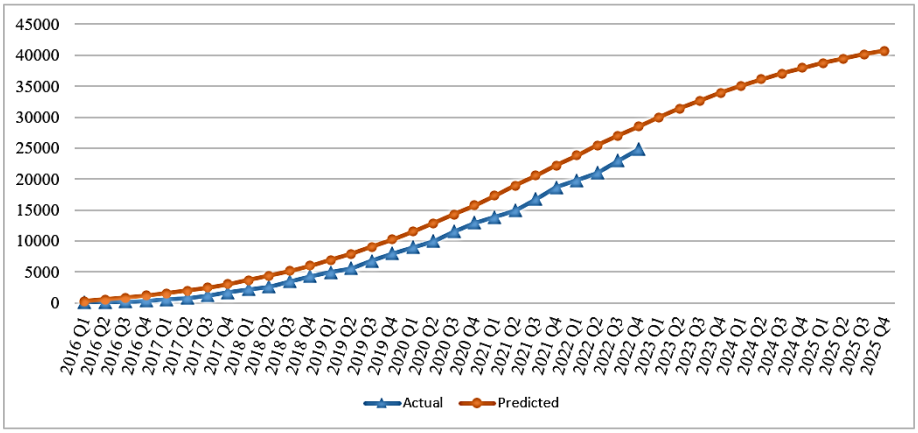


Figure 6. Cumulative sales of north region (DS-III) (Source: Authors).

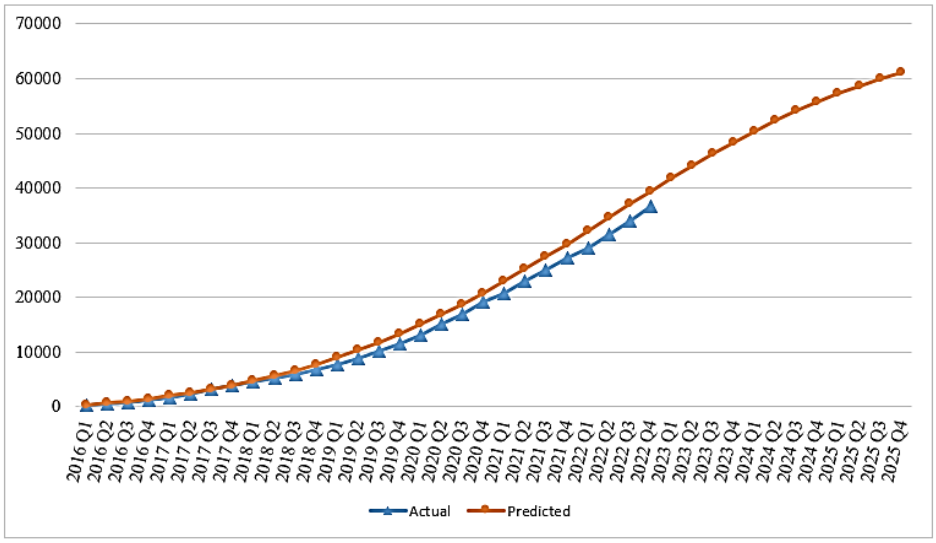


Figure 7. Cumulative sales of south region (DS-IV) (Source: Authors).

The cumulative Kangen's sales data across the regions East, West, North, and South, shows a steady and consistent growth indicating a high potential of adoption rate over the study period. This trend suggests a strong and growing market for Kangen technology in these regions. The above sales graphs depict the adoption dynamics implying the roles of innovators and imitators in the diffusion process. The observed trends provide insights into the market penetration and growth potential of Kangen technology in different regions in future.

5. Discussion & Interpretation

In the Bass model, it is assumed that the potential market consists of three types of consumers. Two of these represent different classes of innovators, i.e., those consumers who are the first to adopt the product. There are also consumers who are imitators of the innovators, and finally, the potential market also consists of a group of potential consumers who will not adopt the product no matter how long they are exposed to it. The

model determines the total number of adopters in the market, which is the sum of the innovators and the imitators, by assuming that the customer accepts and adopts the product according to a saturation distribution.

The basic assumption of the Bass model is that customers adopt a product by considering the successive adopters as well as their innovative effect and the imitation effect. The process of purchase by the imitative effect slows down as time passes, while purchases by the innovative effect increase over time, and the process of purchase slows down little by little. Market potential determines the success or failure of the product company directly, and market potential appears by the innovation saturation effect, which is the number of adoptions due to the development of products, and by imitation saturation effect, which is the number of adoptions due to the expansion of customers.

As can be seen from the **Table 2**, the following observations can be made:

- The word-of-mouth effect in the West region is more prevalent than in any other region. The value of the coefficient of imitation (q) in the western region is higher than in any other region, as shown in **Table 1**. As per hypothesis $H11$, the word-of-mouth influence is not just influential but also more prominent in the western region concerning other regions of the country.
- Other physical interpretation that can be drawn from the tabular values is that in the West region, word-of-mouth plays an influential role on consumer perception and conduct in comparison to the consumers' other regions. Realizing the impact of word-of-mouth in the West emphasizes the pertinence of customer tactics, knowledge of product characteristics and health benefits, and strategic marketing activities catered to local consumer preferences and behavior patterns.

Furthermore, the following observations can be made about the second hypothesis:

- From **Table 1**, the coefficient of innovation (p) in the North and South regions are equivalent and more than that of the South Region, and the coefficient of imitation (q) is less in comparison to the West region. The water ionizers are technologically enhanced instruments that use the electrolysis method to process alkaline and acidic waters as an output. The result shows that product adoption in all regions has good potential to increase sales in the market. Also, based on the Akaike's Information Criterion (AIC) values calculated for the sales data from the East, West, North, and South regions, the East region has the lowest AIC value (340.11), indicating that the Bass Model fits the sales data for this region the best which signify the model captures the dynamics of innovation and imitation in the East region more accurately than in the other regions. Advertisements and other promotional campaigns do play a significant role in the North and South regions. Consumers are adopting products based on product features and their benefits due to external influences.
- In comparison to other regions, external forces are highly signific in the North and South in comparison to word-of-mouth impact. This could mean that in these areas, customer behavior and product acceptance are extremely influenced by individuals' own judgment of adoption based on the pivotal product traits and their potential benefits. Marketing tactics in the North and South can benefit from an understanding of the role that outside influences play in spreading word-of-mouth.

Yet, as per another observation, External factors in the East region play a less significant role in influencing consumer behavior than other regions and the values of p and q for eastern region lies in between the values of other three regions and have learning parameters more than those of north and south region but lesser than western region. This could indicate that other factors such as product quality, price, or personal preferences have a stronger impact on purchasing decisions in the eastern region. Businesses that can effectively navigate regional differences and manage consumer's specific requirement in the East region are nicely placed to succeed in the competitive marketplace. Considering the value of innovation and

imitator from **Table 3,** 2017 Q3, 2017 Q2, 2018 Q2, and 2018 Q3 for DS-I, DS-II, DS-III, and DS-IV, respectively, are the breakeven points once word of mouth is more influential than the external effect. Since 2016, sales in all regions have grown, potentially defining the pace of acceptance of new technology.

It can also be observed that the value of imitators has significantly risen across all the regions of India, which depicts the acceptance of water ionizers as an essential source of drinking water post-COVID-19 pandemic for the year 2020. In the east, west, and south, the sales of water ionizers in 2020 are nearly twice as high as those in 2019, while in the north, the sales are nearly one and half times than those from the previous year. Even before the pandemic, consumers became more conscious of the health advantages of drinking ionized alkaline water and this increased awareness facilitated a consistent rise in sales. The growing market was driven by consumers' increasing awareness of the possible health benefits linked to alkaline water generated by ionizers. Even though the COVID-19 pandemic initially caused disruptions to consumer buying patterns and sales channels, the emphasis on health and wellness has ultimately led to a sustained or even increased demand for water ionizers during the pandemic. The market for water ionizers increased because of individual's awareness of wellness and health products. Consumers sought products offering potential health benefits such as antioxidants and improved hydration properties.

6. Managerial Implication

The postulation of Bass model for analysis of the adoption of Kangen's technology will provide holistic insight to marketers and end consumers. Applying an Innovation Diffusion Modeling Framework offers insightful information and tactical direction for encouraging the acceptance of Kangen Technology pinpointed on water purification. Manufacturers give top priority to developing water ionizers with sustainable attributes that reduce environmental effects over the period of the product's lifecycle, such as energy efficiency and recyclable materials. Many of the organizations are original equipment manufacturer (OEM) based and follow the various ISO standards for better health and sustainability. As per the above analysis, environmental sustainability and product features that follow the ISO standards, influencing the health of consumers and their recommendations, are pivotal in consumer perception for acceptance of water ionizers in society.

Marketing strategies should be embattled to customize and message to various niche market segments and apply adopter classification developed from the modeling framework, including innovator and imitator (including early adopters, early majority, late majority, and laggards). In the later stages, strategies to address the concerns of the late majority and laggards may be necessary. For instance, early marketing efforts should be concentrated on innovators and early adopters who are more sensitive toward new technology and health well-being. There should be a focus on potential customers who are having lifestyle and chronic diseases. Strategies could be refactored in encouraging consumer awareness of water ionizers, their health benefits, and their significance through educational and community activities programs on the need for healthy water and the adoption of water ionizers products for a healthy and longer span of life. The research provides businesses with strategic insights into consumer behavior and adoption patterns. By leveraging this research trend and exploring the consumers' roles as innovators and imitators, an organization can design its marketing strategies to target specific consumer segments in specific regions and enhance the effectiveness of its campaigns to drive sales growth for commercialization and economic growth.

Organizations always have the prospect to improve the sustainability practices of water ionizers, encourage customer for awareness and acceptance, and facilitate the adoption of environmentally conscious and better hydration practices by integrating these managerial implications into their plans and operations. however, businesses are competent enough to predict the future sales trajectory for Kangen water systems while

enabling the Bass model in practice. The overall business strategy involving innovation, inventory management, and production scheduling can all be influenced by these forecasts.

7. Conclusion, Limitations of the Study, and Future Work

COVID-19 pandemic strengthened cognition about health and hygiene, guiding to inflate demand for Electrolysed reduced water (ERW) and is recommended to enhance immunity health. Ionized water is evolving as much as people become aware of its health benefits. With their purported health benefits, ERW signifies the way to improve their overall well-being. The results demonstrate that the external effect is more influential in the North and South regions, and the word-of-mouth effect is more prevalent in the West region. The obtained values of *m, p,* and *q* in all four regions for respective data sets fit reasonably good in the model. It depicts the future roadmap for the intense adoption of water ionizers-based Kangen technology in the Indian market.

Manufacturers and stakeholders anticipate conceivable market growth due to the prevalence of eco-friendly innovative initiatives, the expansion of distribution and supply channels, and technological advancement to improve water quality. The utilization of an Innovation Diffusion Modeling Framework has enriched our vision of the water ionization-based Kangen Technology adoption strategy and provisioned reasonable suggestions for fostering its acceptance and commercial success. Water is everyone's business, so there is still room for more research, even if this study has shed light on the adoption dynamics of Kangen Technology. While the current methodology effectively determines the count of innovators and imitators, The model's equations, parameters and co-efficient e.g. *m, p, q* help in estimating the number of adopters over time, distinguishing between innovators and imitators. It does not explicitly address repeat purchasers. Future research could explore modifications to the Bass Model or alternative approaches to capture repeat purchase behavior, providing a more comprehensive understanding of consumer dynamics. Additional adoption influencing factors, the effect of interventions on adoption rates, long-term adoption trends, and adoption patterns in various markets and other geographies and situations could all be the subject of future research. While the current study focuses on statistical validation of the proposed model for the adoption diffusion of water ionizers in the Indian market, it does not provide evidence of interrelationships among behavioral constructs. Therefore, future research may extend upon validating the identified model with the help of various decision-making techniques like analytical hierarchy process and structural equation modeling to ascertain the intensity of association among critical enablers.

Conflict of Interest

There are no conflicts of interest to declare.

AI Disclosure

The author(s) declare that no assistance is taken from generative AI to write this article.

Acknowledgments

The authors appreciate the valuable suggestions from anonymous reviewers, which have significantly enhanced the clarity and articulation of the manuscript.

References

Agarwal, M., Aggrawal, D., Anand, A., & Singh, O. (2017). Modeling multi-generation innovation adoption based on conjoint effect of awareness process. *International Journal of Mathematical, Engineering and Management Sciences, 2*(2), 74-84.

Aggrawal, N., Arora, A., Anand, A., & Dwivedi, Y. (2021). Early viewers or followers: a mathematical model for YouTube viewers' categorization. *Kybernetes*, *50*(6), 1811-1836. https://doi.org/10.1108/k-03-2020-0128.

Ajzen, I. (1991). The theory of planned behavior. *Organizational Behavior and Human Decision Processes*, *50*(2), 179-211. https://doi.org/10.1016/0749-5978(91)90020-t.

Anand, A., Agarwal, M., Aggrawal, D., & Singh, O. (2016). Unified approach for modeling innovation adoption and optimal model selection for the diffusion process. *Journal of Advances in Management Research*, *13*(2), 154-178. https://doi.org/10.1108/jamr-03-2015-0021.

Babbar, G., Anand, A., & Aggrawal, N. (2024). Modelling & analyzing view growth pattern of youtube videos inculcating the impact of subscribers, word of mouth and recommendation systems. *International Journal of Mathematical, Engineering & Management Sciences*, *9*(3), 435-450. https://doi.org/10.33889/ijmems.2024.9.3.023.

Bass, F.M. (1969). A new product growth for model consumer durables. *Management Science*, *15*(5), 215-227. https://doi.org/10.1287/mnsc.15.5.215.

Bass, F.M. (2004). The bass model. *Management Science*, *50*, 1833-1840.

Cerbu, C.D. (2013). *Almost everything about water therapy*. Lulu. com. ISBN: 9781300610823.

Hamasaki, T., Kashiwagi, T., Aramaki, S., Imada, T., Komatsu, T., Li, Y., Teruya, K., Katakura, Y., Kabayama, S., Otsubo, K., Morisawa, S., & Shirahata, S. (2005). Suppression of cell growth by platinum nanocolloids as scavengers against reactive oxygen species. In: Gòdia, F., Fussenegger, M. (eds) *Animal Cell Technology Meets Genomics*. Springer Netherlands, Dordrecht, pp. 249-251. https://doi.org/10.1007/1-4020-3103-3_48.

Hayashi, H.W. (1995). The chemistry of life. *Explore*, *6*, 28-31.

Henry, M., & Chambron, J. (2013). Physico-chemical, biological and therapeutic characteristics of electrolyzed reduced alkaline water (ERAW). *Water*, *5*(4), 2094-2115. https://doi.org/10.3390/w5042094.

Ignacio, R.M.C., Joo, K.B., & Lee, K.J. (2012). Clinical effect and mechanism of alkaline reduced water. *Journal of Food and Drug Analysis*, *20*(1), 33. https://doi.org/10.38212/2224-6614.2099.

Ignatov, I. (2017). VITA intense–antioxidant and inhibition growth of tumor cells effects. Anti aging influence. Negative oxidation-reduction potential (ORP) has important role in these effects. *Journal of Medicine, Physiology and Biophysics*, *39*, 20-42. http://www.iiste.org/.

ISO 14001:2015. (2015). Environmental management systems - requirements with guidance for use. *ISO*. https://www.iso.org/standard/60857.html.

Jin, D., Ryu, S.H., Kim, H.W., Yang, E.J., Lim, S.J., Ryang, Y.S., Chung, C.H., Park, S.K., & Lee, K.J. (2006). Anti-diabetic effect of alkaline-reduced water on OLETF rats. *Bioscience, Biotechnology, and Biochemistry*, *70*(1), 31-37. https://doi.org/10.1271/bbb.70.31.

Kapur, P.K., Pham, H., Gupta, A., & Jha, P.C. (2011). *Software reliability assessment with OR applications*. Springer, London. ISBN: 978-0-85729-203-2. https://doi.org/10.1007/978-0-85729-204-9.

Kirchhoff, B.A., Linton, J.D., & Walsh, S.T. (2013). Neo-Marshellian equilibrium versus schumpeterian creative destruction: its impact on business research and economic policy. *Journal of Small Business Management*, *51*(2), 159-166. https://doi.org/10.1111/jsbm.12018.

Kobrin, S.J. (1985). Diffusion as an explanation of oil nationalization: or the domino effect rides again. *Journal of Conflict Resolution*, *29*(1), 3-32. https://doi.org/10.1177/0022002785029001001.

Kumar, H., Singh, O., Anand, A., & Irshad, M.S. (2023). Studying multi-stage diffusion dynamics using epidemic modeling framework. *International Journal of Mathematical, Engineering and Management Sciences*, *8*(1), 105-119. https://doi.org/10.33889/ijmems.2023.8.1.007.

Kun-Kul, R. (2005). Permeability and dissolvability of cathodic electrolyzed water for electrophoretic gel and green tea components. *Journal of the Korea Academia-Industrial Cooperation Society*, *6*(1), 87-93.

LeBaron, T.W., Sharpe, R., & Ohno, K. (2022). Electrolyzed-reduced water: review I. molecular hydrogen is the exclusive agent responsible for the therapeutic effects. *International Journal of Molecular Sciences*, *23*(23), 14750. https://doi.org/10.3390/ijms232314750.

Li, G., Liu, Z., Zhang, J., Han, H., & Shu, Z. (2024). Bayesian model averaging by combining deep learning models to improve lake water level prediction. *Science of the Total Environment*, *906*, 167718. https://doi.org/10.1016/j.scitotenv.2023.167718.

Lotfi, A., Lotfi, A., & Halal, W.E. (2014). Forecasting technology diffusion: a new generalisation of the logistic model. *Technology Analysis & Strategic Management*, *26*(8), 943-957. https://doi.org/10.1080/09537325.2014.925105.

Lu, H., Ayers, E., Patel, P., & Mattoo, T.K. (2023). Body water percentage from childhood to old age. *Kidney Research and Clinical Practice*, *42*(3), 340-348. https://doi.org/10.23876/j.krcp.22.062.

Mahajan, V., Muller, E., & Bass, F.M. (1990a). New product diffusion models in marketing: a review and directions for research. *Journal of Marketing*, *54*(1), 1-26. https://doi.org/10.1177/002224299005400101.

Mahajan, V., Muller, E., & Srivastava, R.K. (1990b). Determination of adopter categories by using innovation diffusion models. *Journal of Marketing Research*, *27*(1), 37-50. https://doi.org/10.1177/002224379002700104.

Majer, J.M., Henscher, H.A., Reuber, P., Fischer-Kreer, D., & Fischer, D. (2022). The effects of visual sustainability labels on consumer perception and behavior: a systematic review of the empirical literature. *Sustainable Production and Consumption*, *33*, 1-14. https://doi.org/10.1016/j.spc.2022.06.012.

Mohr, R. (2016). *The healing power of kangen water*. Blurb. ISBN: 978-1367495852.

Nguyen, N., & Johnson, L.W. (2020). Consumer behaviour and environmental sustainability. *Journal of Consumer Behaviour*, *19*(6), 539-541. https://doi.org/10.1002/cb.1892.

Okajima, Y., Okajima, M., Ikeda, M., Wada, Y., Shimokawa, K.I., & Ishii, F. (2021). Antiviral effect of electrolyzed reduced water on SARS-CoV-2. *Drug Discoveries & Therapeutics*, *15*(5), 268-272. https://doi.org/10.5582/ddt.2021.01092.

Olshavsky, R.W. (1980). Time and the rate of adoption of innovations. *Journal of Consumer Research*, *6*(4), 425-428. http://www.jstor.org/stable/2488744.

Pandey, S., & Aggrawal, D. (2024). Sustainable practices and acceptance of water ionizers: a structural equation modeling approach. *Management of Environmental Quality*, *35*(8), 1912-1928. https://doi.org/10.1108/meq-02-2024-0060.

Pandey, S., & Aggrawal, D. (2025). Modeling the enablers for sustainable adoption of water ionizers: an ISM-MICMAC approach. *International Journal of System Assurance Engineering and Management*, *16*(2), 868-882. https://doi.org/10.1007/s13198-024-02702-3.

Pisoschi, A.M., Pop, A., Iordache, F., Stanca, L., Predoi, G., & Serban, A.I. (2021). Oxidative stress mitigation by antioxidants-an overview on their chemistry and influences on health status. *European Journal of Medicinal Chemistry*, *209*, 112891. https://doi.org/10.1016/j.ejmech.2020.112891.

Pocock, S.J., Shaper, A.G., & Packham, R.F. (1981). Studies of water quality and cardiovascular disease in the United Kingdom. *Science of the Total Environment*, *18*, 25-34. https://doi.org/10.1016/s0048-9697(81)80047-2.

Ratcliff, R., & Doshi, K. (2016). Using the bass model to analyze the diffusion of innovations at the base of the pyramid. *Business & Society*, *55*(2), 271-298. https://doi.org/10.1177/0007650313479529.

Rogers, E.M. (1962). *Diffusion of innovations the free press of Glencoe*. New York.

Rogers, E.M. (1995). Diffusion of innovations: modifications of a model for telecommunications. In: Stoetzer, MW., Mahler, A. (eds) *Die Diffusion von Innovationen in der Telekommunikation. Schriftenreihe des Wissenschaftlichen Instituts für Kommunikationsdienste* (vol. 17). Springer, Berlin, Heidelberg. https://doi.org/10.1007/978-3-642-79868-9_2.

Ronen, T., & Kerret, D. (2020). Promoting sustainable wellbeing: integrating positive psychology and environmental sustainability in education. *International Journal of Environmental Research and Public Health*, *17*(19), 6968. https://doi.org/10.3390/ijerph17196968.

Shirahata, S., Hamasaki, T., & Teruya, K. (2012). Advanced research on the health benefit of reduced water. *Trends in Food Science & Technology*, *23*(2), 124-131. https://doi.org/10.1016/j.tifs.2011.10.009.

Shirahata, S., Kabayama, S., Nakano, M., Miura, T., Kusumoto, K., Gotoh, M., Hayashi, H., Otsubo, K., Morisawa, S., & Katakura, Y. (1997). Electrolyzed-reduced water scavenges active oxygen species and protects DNA from oxidative damage. *Biochemical and Biophysical Research Communications*, *234*(1), 269-274. https://doi.org/10.1006/bbrc.1997.6622.

Singhal, S., Anand, A., & Singh, O. (2019). SDE based generalized innovation diffusion modeling. *International Journal of Mathematical, Engineering and Management Sciences*, *4*(3), 697-707. https://dx.doi.org/10.33889/ijmems.2019.4.3-055.

Tanner, C., & Kast, S.W. (2003). Promoting sustainable consumption: determinants of green purchases by Swiss consumers. *Psychology & Marketing*, *20*(10), 883-902. https://doi.org/10.1002/mar.10101.

Trudel, R. (2019). Sustainable consumer behavior. *Consumer Psychology Review*, *2*(1), 85-96. https://doi.org/10.1002/arcp.1045.

Tsai, C.F., Hsu, Y.W., Chen, W.K., Ho, Y.C., & Lu, F.J. (2009). Enhanced induction of mitochondrial damage and apoptosis in human leukemia HL-60 cells due to electrolyzed-reduced water and glutathione. *Bioscience, Biotechnology, and Biochemistry*, *73*(2), 280-287. https://doi.org/10.1271/bbb.80413.

Venkatesh, V., & Davis, F.D. (2000). A theoretical extension of the technology acceptance model: four longitudinal field studies. *Management Science*, *46*(2), 169-332. https://doi.org/10.1287/mnsc.46.2.186.11926.

Yamada, S. (2014). *Software reliability modeling: fundamentals and applications*. Springer, Tokyo. ISBN: 978-4-431-54564-4(p), 978-4-431-54565-1(e). https://doi.org/10.1007/978-4-431-54565-1.

Ye, J., Li, Y., Hamasaki, T., Nakamichi, N., Komatsu, T., Kashiwagi, T., Teruya, K., Nishikawa, R., Kawahara, T., Osada, K., Toh, K., Abe, M., Tian, H., Kabayama, S., Otsubo, K., Morisawa, S., Katakura, Y., & Shirahata, S. (2008). Inhibitory effect of electrolyzed reduced water on tumor angiogenesis. *Biological and Pharmaceutical Bulletin*, *31*(1), 19-26.

Original content of this work is copyright © Ram Arti Publishers. Uses under the Creative Commons Attribution 4.0 International (CC BY 4.0) license at https://creativecommons.org/licenses/by/4.0/

Publisher's Note- Ram Arti Publishers remains neutral regarding jurisdictional claims in published maps and institutional affiliations.

© 2025. This work is published under https://creativecommons.org/licenses/by/4.0/ (the “License”). Notwithstanding the ProQuest Terms and Conditions, you may use this content in accordance with the terms of the License.

Check for updates

ChemistrySelect

Research Article
doi.org/10.1002/slct.202405898

Chemistry Europe
European Chemical Societies Publishing

www.chemistryselect.org

Synthesis of Pyridazine-Based Scaffolds Using Electron Demand Diels–Alder (iEDDA) Reaction Possessing Promising Antimicrobial Activity

Ram Kumar,[a, c] Deepak Gupta,[b] Yukta Yukta,[a] Avneesh Mittal,[e] Balaram Pani,*[c] and Bholey Singh*[d]

Pyridazine derivatives serve as advantageous scaffolds in medicinal chemistry because of their wide biological activity. This paper discusses the effective one-step synthesis of six pyridazine-based compounds (**1**–**6**) using the inverse electron demand Diels–Alder (iEDDA) reaction, which yields high-purity products without the need for complex purification. The structures were confirmed using NMR, mass spectrometry, and single-crystal X-ray diffraction. Antimicrobial screening demonstrated substantial activity, with compound **4** demonstrating broad-spectrum effectiveness against all tested bacterial and fungal species. Molecular docking experiments confirmed their potential by demonstrating high binding affinities for microbial protein targets. These findings highlight the therapeutic potential of pyridazine derivatives as prospective lead candidates against antimicrobial resistance, with their simple synthesis and high bioactivity being an important breakthrough toward the development of next-generation antimicrobial therapies.

1. Introduction

The rise of antimicrobial resistance (AMR) represents an escalating global health issue, presenting considerable difficulties for existing therapeutic strategies against bacterial and fungal infections. Consequently, there exists a pressing requirement to identify and formulate new antimicrobial agents capable of effectively addressing resistant strains. Pyridazine derivatives represent a notable class of compounds currently under investigation, recognized for their extensive range of biological activities, which encompass antibacterial, antifungal, anti-inflammatory, and anticancer effects.[1,2] Pyridazines are heterocyclic compounds characterized by stability, versatility in functionalization, and the capacity to establish strong interactions with biological targets. These attributes render them promising scaffolds for drug discovery.[3–5]

Tetrazines are a class of nitrogen-containing heterocycles that have been extensively studied due to their unique structural properties and reactivity. These characteristics render them significant in various fields, including bio-orthogonal chemistry and material science. The conversion of tetrazines into pyridazines has broadened their utility by improving their chemical reactivity and bioactivity.[6,7] This modification facilitates advancements in medicinal chemistry, allowing for the creation of compounds that exhibit enhanced pharmacological profiles. The inverse electron demand Diels–Alder (iEDDA) reaction represents a significant synthetic strategy for the conjugation of these molecules. This reaction has become increasingly significant in recent years because of its efficiency in incorporating various functional groups into the pyridazine scaffold, thereby serving as a valuable method for synthesizing complex, bioactive compounds.[8–10]

In prior research, we concentrated on the synthesis and evaluation of a series of pyridazine derivatives to assess their antibacterial activity through in vitro testing. The study yielded promising results; however, it was constrained by the lack of computational analyses, which could have offered more profound insights into the molecular interactions and binding mechanisms that account for the observed biological effects.[11–13] The absence of molecular-level understanding has limited our capacity to fully utilize the potential of these compounds in the development of antimicrobial drugs. The present study aims to fill this gap by building upon our earlier research through the integration of advanced molecular docking studies. These studies provide a comprehensive analysis of the binding affinities between the synthesized compounds and their respective bacterial and fungal targets.[14–16]

[a] *R. Kumar, Y. Yukta*
Department of Chemistry, University of Delhi, Delhi 110007, India

[b] *D. Gupta*
Department of Applied Chemistry, Delhi Technological University, Delhi 110042, India

[c] *R. Kumar, B. Pani*
Department of Chemistry, Bhaskaracharya College of Applied Sciences, University of Delhi, New Delhi 110075, India
E-mail: balarampani63@gmail.com

[d] *B. Singh*
Department of Chemistry, Swami Shraddhanand College, University of Delhi, Delhi 110036, India
E-mail: bholeysingh@ss.du.ac.in

[e] *A. Mittal*
Department of Electronics Science, Bhaskaracharya College of Applied Sciences, University of Delhi, New Delhi 110075, India

Supporting information for this article is available on the WWW under https://doi.org/10.1002/slct.202405898

© 2025 Wiley-VCH GmbH

The study introduces a significant innovation through the incorporation of a nitrogen atom at the second position of the pyridyl ring within the pyridazine derivatives.[17,18] This strategic modification aimed to enhance the interaction potential of the compounds with their biological targets, resulting in a significant improvement in antimicrobial activity when compared to the derivatives synthesized in prior research.[19–21] The nitrogen atom located at the second position contributes additional interaction points, which enhances the binding affinity of the compounds for bacterial and fungal targets. The modification resulted in an improved pharmacological profile, indicating that these compounds may serve as effective antimicrobial agents.[22–24]

The synthesized compounds underwent comprehensive characterization through various techniques, which included nuclear magnetic resonance (NMR), mass spectrometry, elemental analysis, and single-crystal X-ray diffraction, alongside the synthetic modifications.[25,26] The implemented methods guaranteed the purity and structural integrity of the compounds, establishing a robust foundation for the ensuing biological and computational studies. The molecular docking studies provided insights into the binding mechanisms of the compounds and emphasized the structural features that enhance their antimicrobial activity. This study presents a thorough analysis of the antimicrobial potential of pyridazine derivatives through the integration of synthetic chemistry, computational modeling, and in vitro biological evaluations.[27–29]

The findings of this study confirm the effectiveness of the synthesized pyridazine derivatives and enhance the comprehension of the molecular interactions that contribute to their biological activity. All the synthesized compounds exhibited excellent antimicrobial activity across various bacterial and fungal strains, thereby validating the structural benefits associated with the nitrogen modification. The findings highlight the significance of a comprehensive strategy in drug discovery, integrating synthetic, computational, and biological methods to create new antimicrobial agents that can effectively tackle the increasing problem of antimicrobial resistance. This research marks a notable advancement in the development of pyridazine-based compounds as therapeutic agents, emphasizing their potential for further optimization and application within the field of medicinal chemistry.

2. Methodology

2.1. Materials and Methods

The beginning components and solvent were procured from Spectrochem Pvt. Limited and employed without undergoing any purifying process. Prior to the reactions, the solvents were dried and distilled using standard techniques. The experimental procedures were conducted under ambient air conditions. The NMR spectra were recorded using a Bruker Avance-400 spectrometer, with trimethylsilyl (TMS) serving as the internal standard. The crystals were affixed onto an Oxford Xcalibur Nova X-ray diffractometer, which utilized a four-circle κ Goniometer and employed a graphite monochromatized Mo Kα. The X-ray data for a single crystal was collected using an Oxford Callibur Sapphire3 diffractometer, with a graphite monochromatized Mo Kα source, under ambient conditions. The data from all the crystals was processed using the CrysAlis Pro software, which is provided with the diffractometer, resulting in a reduction of the Rint value. The measure of the quality, that is, *R* values of the atomic model mentioned in Table S2, was obtained by additional least square refinement following the incorporation of anisotropic displacement parameters. The ESI MS data was acquired using an Agilent Technologies 6530 Accurate-Mass Q-TOF LC/MS instrument. The fungal cultures of *R. solani* (ITCC 4502), *S. rolfsii* (ITCC 6263), *A. niger* (ITCC 1624), and *F. oxysporum* (ITCC 4884) were procured from the ITCC, which is a division of the Mycology and Plant Pathology department at the Indian Agricultural Research Institute (IARI) located in New Delhi. The bacterial strains, such as *E. coli* (MTCC 443), *Pseudomonas aeruginosa* (MTCC 2581), *Staphylococcus aureus* (MTCC 3160), *Klebsiella pneumonia* (MTCC 7028), and *B. subtilis* (MTCC 441), were obtained from the MTCC and gene bank at the Institute of Microbial Technology in Chandigarh.

2.1.1. General Procedure for the Synthesis of Functionalized Pyridazines 1 and 4

The new functional units appended derivatives, namely **1** and **4**, were synthesized in a single step using the iEDDA reaction. This synthesis involved the reaction between the tetrazine ring of the 3,6-di(pyridin-2-yl)-1,2,4,5-tetrazine precursor **1** and acetylene-based dienophiles (phenylacetylene for **1** and 3-aminophenylacetylene for **4**) in DMF to reflux at 120 °C for 12 h (Scheme 1). The extraction in ethyl acetate and distilled water resulted in yellowish-colored compounds. The majority of polar organic solvents were discovered to possess solubility for the substances.

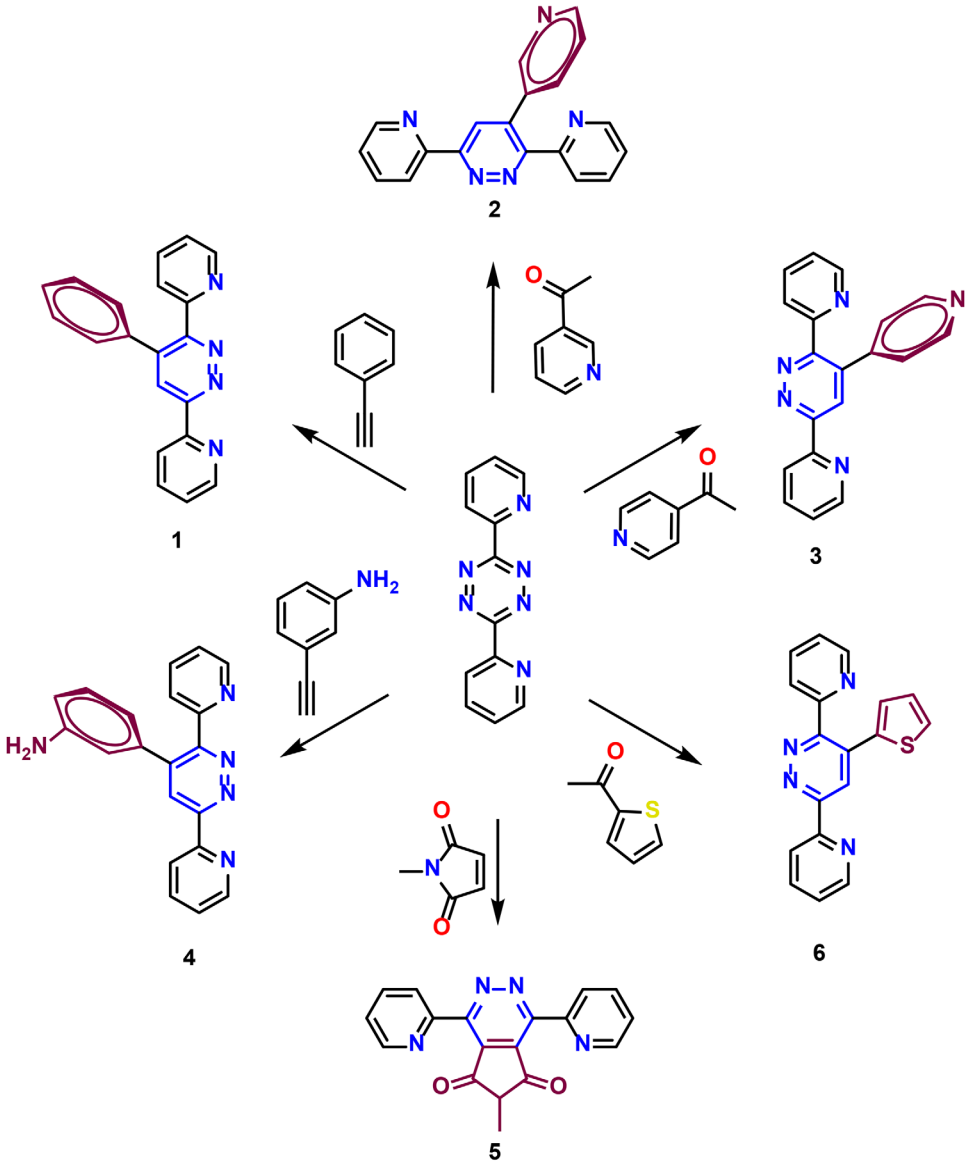
2.1.2. General Procedure for the Synthesis of Functionalized Pyridazines 2, 3, 5, and 6

In a somewhat different process, the pyridyl functionalized pyridazines **2**, **3, 5**, and **6** were produced by reacting the precursor dipyridyltetrazine **1** with 2-acetylpyridine for **2**, 3-acetylpyridine for **3,** *N*-methylmaleimide for **5,** and 2-acetylthiophene for **6** with 2.5% methanolic solution of KOH at room temperature for 10–12 h (Scheme 1). Refluxing these overnight generated brown-colored solutions, and when the solvent was removed, the powder or semisolid was light yellow to light brown in hue. The products were dissolved in water, and ethyl acetate was used to extract them. Again, the fine crystals were obtained by slowly evaporating the ethyl acetate solution layered by hexane. Most polar organic solvents are soluble in all the products, producing clear, colorless solutions.

All of the compounds were produced with a yield of greater than 80%. Out of six, four pyridazines were produced as single crystals of X-ray quality by slowly evaporating methods. The

© 2025 Wiley-VCH GmbH

23656549, 2025, 22, Downloaded from https://chemistry-europe.onlinelibrary.wiley.com/doi/10.1002/slct.202405898 by Delhi Technological University, Wiley Online Library on [15/06/2025]. See the Terms and Conditions (https://onlinelibrary.wiley.com/terms-and-conditions) on Wiley Online Library for rules of use; OA articles are governed by the applicable Creative Commons License



Scheme 1. The pyridyl-functionalized pyridazines **1–6** synthesized in a single step.

components were examined by ^{1}H NMR, ^{13}C NMR, 2D-COSY, mass spectrometry, and single-crystal X-ray diffraction.

2.2. Single Crystal X-Ray Structure

Fine crystals of ligands **1, 2, 3**, and **6** were produced by gradual evaporation of saturated mother solvents methanol and chloroform, then coated with hexane and diffused with ether at room temperature for SC-XRD investigations. X-rays were obtained from high-quality needle-shaped transparent crystals using a Bruker diffractometer. The graphite monochromatized Mo/Kα radiation ($\lambda = -0.71073$ Å) was used at 107 K. The crystal data was reduced using CrysAlis pro software that came with the diffractometer. The structure was solved directly with SHELXL-2016/4 and refined with the full-matrix least-squares approach on Olex2.refine 1.5.[30] All computations were carried out using the crystallographic programs' OLEX2 package.[31] The molecular visuals were created using the program Mercury (2022.3.0).[32]

2.3. Molecular Docking Studies

To evaluate the molecular interactions and binding potential between the synthesized hybrids **1–6** and different proteins, molecular docking investigations were performed using AutoDock Vina. The Protein Data Bank provided the 3D crystal structures of DNA gyrase B (PDB ID: 4URO) and CYP51 (PDB ID: 4WMZ). There were multiple phases involved in the preparation of the proteins, such as removing H_2O molecules, co-crystallized ligands, and cofactors from the protein structures. Next, using AutoDock Tools 1.5.6, polar hydrogen atoms and Kollmann charges were added to the produced proteins. Then, docking assessments were run independently for every lig-

© 2025 Wiley-VCH GmbH

23656549, 2025, 22, Downloaded from https://chemistry-europe.onlinelibrary.wiley.com/doi/10.1002/slct.202405898 by Delhi Technological University, Wiley Online Library on [15/06/2025]. See the Terms and Conditions (https://onlinelibrary.wiley.com/terms-and-conditions) on Wiley Online Library for rules of use; OA articles are governed by the applicable Creative Commons License

and using several proteins, modifying the grid size according to the receptors' active binding sites. For every chemical, the best-docked pose defined by the lowest binding affinity value was noted. Protein-ligand interactions were visualized with the aid of BIOVIA Discovery Studio 2021.[33]

2.4. Antimicrobial Activity

2.4.1. Antibacterial Assay

The disc diffusion experiment was used to assess the antibacterial effectiveness of synthesized pyridazine derivatives. The 25 mL of nutrient agar medium was aseptically put into 90 mm diameter petri dishes within a laminar flow hood. These plates were placed within the laminar flow chamber to facilitate the solidification process of the media. Following the solidification process, a volume of 100 µL of a fresh culture in the logarithmic growth phase was evenly distributed onto the surface of the solidified medium using a spreader. Subsequently, the plates were maintained within a laminar flow environment to facilitate the drying process. After the disks were dry, a total of five plain sterile disks were carefully positioned onto the plate. Subsequently, a volume of 5 µL of the test solution, which varied in concentration from 200 to 12.5 ppm, was meticulously applied onto each individual disk. Commercially sourced novobiocin (10 µg $disk^{-1}$) was utilized in the control plate. The plates were subsequently incubated at a temperature of 37 °C for a duration of 24 h. During this time, the zone of inhibition (measured in mm) was recorded for each of the compounds tested, as well as for the commercial antibiotic. The studies were conducted in triplicate for each treatment in relation to each bacterial strain. Results were examined by interpolating inhibition values in order to calculate the minimum inhibitory concentration (MIC). The MIC was defined as the lowest concentration that resulted in ≥90% inhibition as compared to the compound's maximum zone diameter.

2.4.2. Antifungal Assay

The antifungal assay was conducted using the poisoned food approach on a potato-dextrose-agar (4% PDA) medium. Four phytopathogenic fungi, namely *Rhizoctonia solani, Fusarium oxysporum, S. cerevisiae, and A. niger*, were tested at various doses ranging from 200 to 12.5 ppm. To achieve the appropriate concentrations, 1 mL of a stock solution was introduced into 50 mL of PDA medium. The medium was subsequently transferred into two Petri plates using aseptic techniques within a laminar flow chamber. In a similar manner, further concentrations were generated through the process of serial dilution. A control solution consisting of 1 mL of methanol was employed. A circular fungal disc measuring 5 mm in thickness was placed at the central region of the growth media within the petri plates. These plates were thereafter placed within a BOD incubator set at a temperature of 28 ± 1 °C. The plates were left undisturbed until the fungal growth in the control dishes reached completion, which typically occurred within a period of 6–10 days. The measurement of mycelial growth (in cm) was conducted in three distinct orientations on both treated (T) and control (C) petri plates. The percentage inhibition of growth (I) was determined by calculating the mean growth of the aforementioned readings using the following equation:

$$\%\ \text{Growth inhibition I} = \frac{[T - C]}{C}\ X\ 100$$

In order to determine the lowest concentration that produced ≥90% inhibition, MIC values were computed by interpolating the inhibition data with the use of a statistical tool (GW BASIC).[34] Fluconazole, a positive control, was employed for comparison.

$$IC = \frac{[\%\ I - C.F]}{[100 - C.F.]}\ \text{x}\ 100$$

$$\text{Correction Factor (C.F.)} = \frac{[90 - C]}{C}\ X\ 100$$

The value 90 represents the diameter of the petri dishes in millimeters, while *C* represents the development of the fungus in the control group, also measured in millimeters.

3. Result and Discussion

3.1. Chemistry

Many different tetrazines use the iEDDA reaction to add organic units, which turns the tetrazine ring into a functionalized pyridazine. A tetrazine unit and the organic moiety to be attached must react under normal reflux circumstances without the need for an outside reagent. These reactions produce clean products in significant quantities because of their water-based work-up. This reaction has been frequently used to add biological and luminous molecules to building blocks that include tetrazine moiety due to its quick reaction kinetics. Hence, the utilization of the iEDDA reaction of tetrazines is a highly effective approach to produce pyridazine-based compounds. This method allows for the attachment of various photo-, redox-, and biologically active components to the pyridazine ring in a single step, which distinguishes it from copper-based "click reactions." Four of the six functionalized pyridazine derivatives, namely **1**, **2**, **3**, and **6**, were determined to possess high-quality needle-shaped crystals relevant for X-ray diffraction research. These crystals were obtained using the process of slow evaporation of a saturated solution of ethyl acetate, which was layered with hexane at room temperature. High-quality, transparent crystals devoid of color were separated by decantation and subsequently subjected to X-ray analysis using a diffractometer. The single crystal structures of the derivatives exhibit similarities, as they all possess a central pyridazine ring with a pendant functional group located at the fourth position. Specifically, compound **1** has a phenyl group, compounds **2** and **3** have pyridyl groups, and compound **6** has a thiophenyl group. Additionally, each compound contains two 2-pyridyl units, and compounds **2** and **3** have an additional 3-pyridyl as well as 4-pyridyl unit located at the third position

© 2025 Wiley-VCH GmbH

23656549, 2025, 22, Downloaded from https://chemistry-europe.onlinelibrary.wiley.com/doi/10.1002/slct.202405898 by Delhi Technological University, Wiley Online Library on [15/06/2025]. See the Terms and Conditions (https://onlinelibrary.wiley.com/terms-and-conditions) on Wiley Online Library for rules of use; OA articles are governed by the applicable Creative Commons License

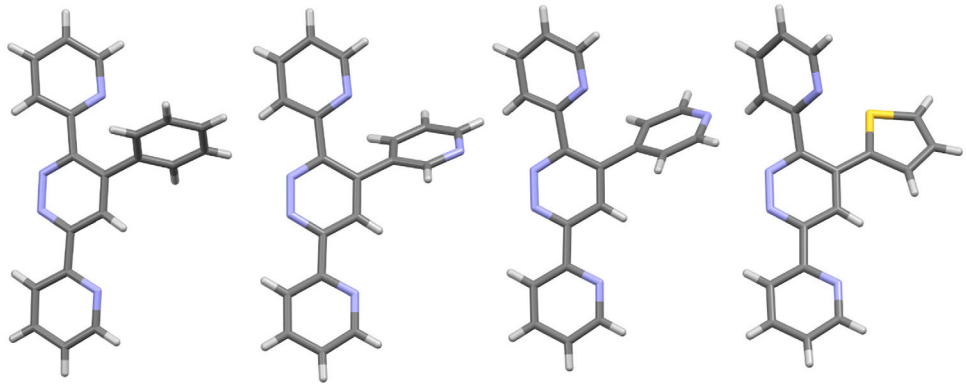


Figure 1. Single crystal structure of functionalized pyridazines **1, 2, 3**, and **6**. Grey: C, blue: N, white: H, yellow: S.

(Figure 1). The obtained bond length data indicates that the pyridazine rings in all of the compounds exhibit the typical N=N bond length range of 1.32–1.341 Å. In contrast to the pyridine substituents, the bond lengths observed in the pyridazine ring across all four crystal structures do not exhibit uniformity. Instead, they fall within the range of typical pyridazine bond lengths. This observation provides confirmation of the electron density delocalization occurring within the ring. The pyridazine ring contains three substituents, specifically two pyridyl groups and a functional group. These substituents are not coplanar and exhibit distinct orientations, as shown in Table S1. A prevalent characteristic observed in crystal structures is the presence of a minor inclination in one of the pyridyl rings, which is in proximity to the pendant functional group. The inclination is expressed by the angle between the C3 carbon of the pyridyl ring and the closest pyridazine nitrogen, which usually ranges from around 111° to 114°. Notably, this angle is smaller than the standard bond angle observed in the original tetrazine compounds. The crystal structure of compound **3** has an isostructural arrangement similar to the previously reported structures. However, it is worth noting that the temperature at which the data sets were collected differs between the two studies.[35,36] Noncovalent interactions are of utmost importance in a wide range of biological phenomena as they facilitate the formation of supramolecular structures through the loose aggregation of molecules. The fundamental basis of crystal engineering relies on the presence of these less strong supramolecular interactions, making them indispensable.[37] It is noteworthy that the crystal structures depicted in the current investigation exhibit a diverse range of noncovalent interactions, including hydrogen bonding and $\pi-\pi$ stacking, as illustrated in Figures S24 and S25. In the crystallographic arrangement of compound **2**, the pyridyl ring at position 3 is vertically aligned above the electron-deficient pyridazine ring of the neighboring molecule. This arrangement results in an offset packing configuration, giving rise to a linear chain formation along the *a*-axis in a way reminiscent of a handshake gesture. The crystal packing structure is stabilized by the interconnection of these linear chains by hydrogen bonds (Figure S25). Therefore, the capacity to form intermolecular networks and linear chains confers an additional characteristic to these compounds, rendering them appropriate for the creation of coordination complexes upon bonding with metal ions.

3.2. Molecular Docking Evaluation

Investigating the interactions between ligands and proteins is essential for structure-based medication design. By correlating these compounds with a target protein of interest, we can identify molecules with advantageous binding capabilities to undergo further experimental verification and also elucidate the principal pharmacophores underlying the antibacterial and antifungal action. The main goal was to comprehend how various ligands interact with their matching protein targets, namely, DNA gyrase B and CYP51.

All of the produced hybrids, designated **1–6**, had remarkable docking scores and impressive interactions with critical amino acid residues located within the binding pocket of DNA gyrase B and CYP51, according to the results of the molecular docking analysis. The synthesized hybrids showed better interactions when compared to the traditional medications like the antifungal agent fluconazole and the antibacterial drug novobiocin. The molecular docking data was used to measure the ligand–receptor binding affinity; a higher negative binding affinity value indicated a stronger connection with the receptor. These results provide important information about the potential pharmacological efficacy of the produced hybrids by illuminating how well they interact with the chosen protein targets linked to antimicrobial activity.

In the examination of molecular docking results, with a specific focus on distinct binding sites on DNA gyrase B, **4**, featuring an aniline group, exhibited a remarkable binding affinity of -7.5 kcal mol^{-1}, which was better than the standard antibacterial drug novobiocin with a binding affinity of -7.0 kcal mol^{-1}. Shown in Table S2, conventional hydrogen bonding was displayed by the NH_2 group of aniline with the amino acid residue THR173. Aniline ring and one of the pyridyl rings were involved in the pi-anion interactions with GLU58 and ARG84, respectively. PRO87, ILE86, and ILE102 exhibited pi-alkyl interactions with the pyridyl ring, pyridazine ring, and the aniline ring. Furthermore, Van der Waals interactions were demonstrated by the amino acid residues ARG144, GLY85, ASN54, GLY83, and ASP81 (Figure 2).

Additionally, CYP51 was used to assess the docking investigations of these drugs (PDB ID: 4WMZ). In this case also, **4** was found to have the maximum binding affinity of -9.7 kcal mol^{-1}, surpassing the binding affinity of standard antifungal

© 2025 Wiley-VCH GmbH

23656549, 2025, 22, Downloaded from https://chemistry-europe.onlinelibrary.wiley.com/doi/10.1002/slct.202405898 by Delhi Technological University, Wiley Online Library on [15/06/2025]. See the Terms and Conditions (https://onlinelibrary.wiley.com/terms-and-conditions) on Wiley Online Library for rules of use; OA articles are governed by the applicable Creative Commons License

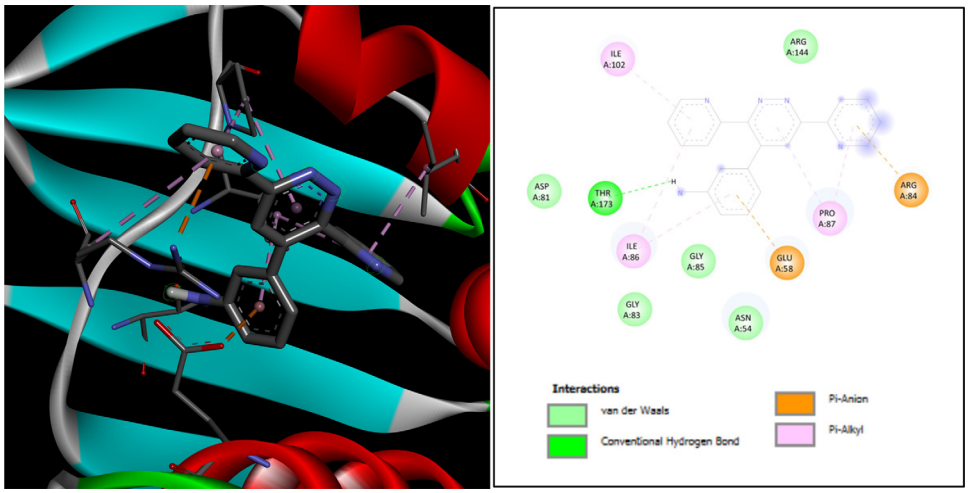


Figure 2. 3D and 2D representation of binding interactions of **4** with DNA gyrase B (PDB ID: 4URO).

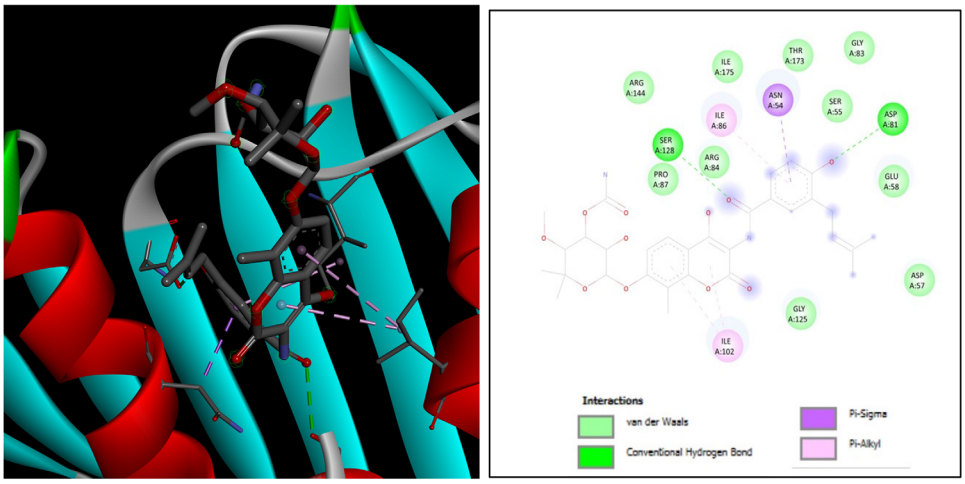


Figure 3. 3D and 2D representation of binding interactions of novobiocin with DNA gyrase B (PDB ID: 4URO).

drug fluconazole, which was obtained as −6.7 kcal mol^{-1}. As shown in Table S3, it was discovered that **4** was involved in several interactions with CYP51. The amino acid residue VAL311 was involved in Pi-sigma interactions with the pyridyl ring and the aniline ring. The aniline ring exhibited Pi-alkyl interactions with ILE139 and LYS151 along with the Pi-sulfur interactions with CYS470. Further, pi-alkyl interactions were also exhibited by the pyridazine ring with ILE471 and VAL311. Besides, amino acid residues, namely, TYR140, GLY472, LEU158, LEU212, PHE475, GLY315, LEU147, GLN150, LEU307, ARG469, and HIS468, were involved in Van der Waals interactions with **4** (Figures 3 and 4).

These findings emphasize how important these interactions might be in helping **4** have a higher binding affinity than novobiocin and fluconazole, the molecules used as a reference for antibacterial and antifungal therapy (Figure 5).

3.3. Antimicrobial Activity

The antimicrobial activity of the synthesized compounds was assessed in vitro against a range of bacteria, including *E. coli*, *P. aeruginosa*, *S. aureus*, *K. pneumonia*, and *B. subtilis* (Figure S26). The average diameter of the inhibition zone, measured in mm, was used as an indicator of antimicrobial effectiveness. Additionally, the antifungal activity of the compounds was evaluated against *R. solani*, *F. oxysporum*, *S. cerevisiae*, and *A. niger* (Figure S27). The aforementioned facts are presented in Tables S4 and S5. All of the compounds exhibited a dose-response pattern and demonstrated moderate to high efficacy against both Gram-negative and Gram-positive bacteria when compared to the standard used for testing the bacteria. In the case of *E. coli* and *S. aureus*, it was shown that **5** exhibited the lowest level of activity, while **4** and **2** demonstrated the highest levels of activity when compared to the standard, respectively. Among the tested compounds, it was observed that for *P. aeruginosa*, the highest activity was exhibited by the aniline functionalized-pyridazine **4**, whereas **6** and **3** demonstrated the lowest activity. A comparable pattern was seen in the case of *K. pneumonia*, wherein **4** and **2** exhibited the highest level of activity, whereas **1** demonstrated the lowest level of activity. In the instance of *B. subtilis*, it was shown that **6** exhibited the lowest level of activity, while **4** and **2** demonstrated the highest levels of activity when compared to

© 2025 Wiley-VCH GmbH

23656549, 2025, 22, Downloaded from https://chemistry-europe.onlinelibrary.wiley.com/doi/10.1002/slct.202405898 by Delhi Technological University, Wiley Online Library on [15/06/2025]. See the Terms and Conditions (https://onlinelibrary.wiley.com/terms-and-conditions) on Wiley Online Library for rules of use; OA articles are governed by the applicable Creative Commons License

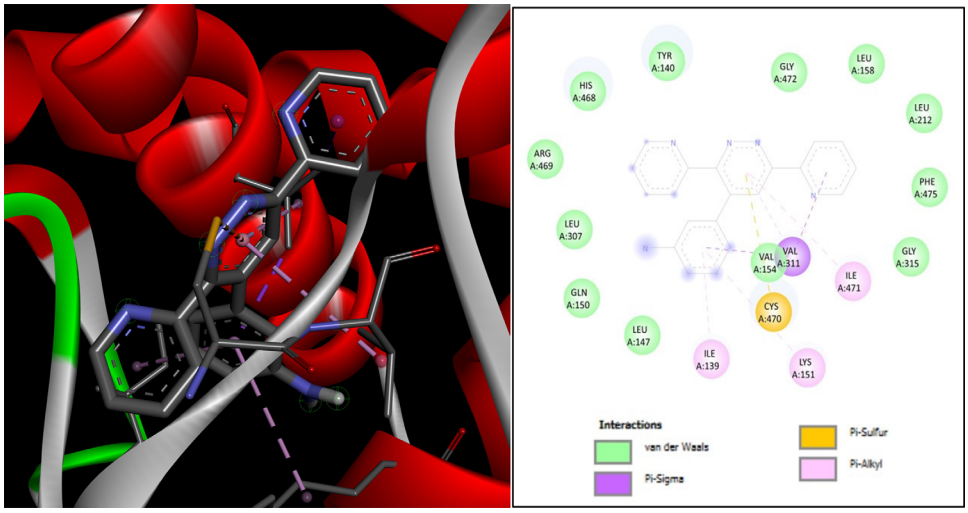


Figure 4. 3D and 2D representation of binding interactions of **4** with CYP51 (PDB ID: 4WMZ).

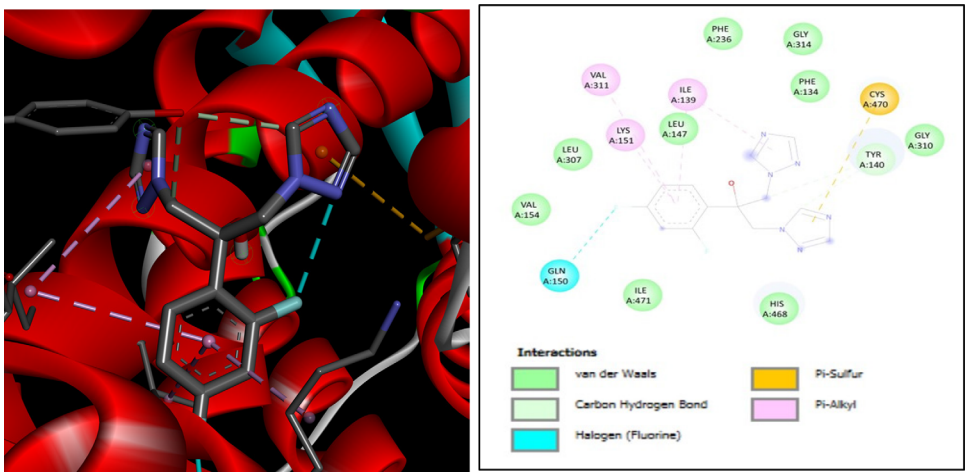


Figure 5. 3D and 2D representation of binding interactions of fluconazole with CYP51 (PDB ID: 4WMZ).

the standard. In a manner akin to the investigations conducted on antibacterial properties, it was shown that all pyridazines exhibited a dose-response pattern and demonstrated modest efficacy when compared to the established standard in the context of tested fungi. Compound **4** exhibited the highest level of activity against all tested fungi, including **1** and **2**, whereas the remaining compounds demonstrated only modest activity. Among the tested pathogens, *R. solani*, *S. cerevisiae*, and *F. oxysporum* **5**, **6**, and **5** exhibited the lowest levels of activity. In the case of *A. niger*, the majority of the hybrids exhibited favorable activity, with the exception of **3**, which showed the lowest level of activity. The MIC for all the synthesized compounds (**1–6**) against both bacterial and fungal strains have been displayed in Tables 1 and 2.

3.4. Structure–Activity Relationship

The structure–activity relationship (SAR) study of the synthesized pyridazine derivatives (**1–6**) demonstrates a significant correlation between the type of the R substituent and the reported antimicrobial activity. Compound **4** containing an aniline group (—NH_2) showed the highest antibacterial and antifungal activity, with the lowest MIC values. This higher performance can be due to the amino group's electron-donating nature and strong hydrogen-bonding capacity, which likely improve interactions with microbial enzymes or cell wall components, increasing target affinity and overall efficacy. Compound **1**, which has a simple unsubstituted phenyl ring, had the lowest activity, indicating that hydrophobic aromaticity alone is insufficient for meaningful biological interaction in the absence of other functional groups. Compounds **2** and **3**, which have a pyridine ring, demonstrated modest activity, most likely due to their polar nature and capacity to form hydrogen bonds. Compounds **5** and **6**, which included nitrogen- and sulfur-containing heterocycles, add more interaction sites, but their bulk and potential solubility challenges may limit bioavailability. Overall, the existence of hydrogen bond donors and interacting polar groups appears to be critical for improved antimicrobial activity. These findings indicate that future design efforts ought to focus on integrating such moieties to improve the binding efficiency, potency, and specific microbial targeting of pyridazine-based scaffolds.

© 2025 Wiley-VCH GmbH

23656549, 2025, 22, Downloaded from https://chemistry-europe.onlinelibrary.wiley.com/doi/10.1002/slct.202405898 by Delhi Technological University, Wiley Online Library on [15/06/2025]. See the Terms and Conditions (https://onlinelibrary.wiley.com/terms-and-conditions) on Wiley Online Library for rules of use; OA articles are governed by the applicable Creative Commons License

23656549, 2025, 22, Downloaded from https://chemistry-europe.onlinelibrary.wiley.com/doi/10.1002/slct.202405898 by Delhi Technological University, Wiley Online Library on [15/06/2025]. See the Terms and Conditions (https://onlinelibrary.wiley.com/terms-and-conditions) on Wiley Online Library for rules of use; OA articles are governed by the applicable Creative Commons License

Table 1. Minimum inhibitory concentration (MIC) values for the compounds **1–6** against bacterial strains.

Code	*E. coli* MIC Value (μM)	*S. aureus* MIC Value (μM)	*P. aeruginosa* MIC Value (μM)	*K. pneumonia* MIC Value (μM)	*B. subtilis* MIC Value (μM)
1	18.2	27.8	30.1	65.5	30.0
2	15.4	22.1	20.0	21.6	12.5
3	17.8	35.0	23.5	18.9	14.6
4	12.7	14.7	13.5	12.2	12.7
5	26.0	25.2	22.3	20.0	27.3
6	22.9	33.3	28.8	48.1	24.2
Novobiocin	31.2	36.7	33.1	69.5	32.6

Table 2. Minimum inhibitory concentration (MIC) values for the compounds **1–6** against fungal strains.

Code	*S. cerevisiae* MIC Value (μM)	*R. solani* MIC Value (μM)	*F. oxysporum* MIC Value (μM)	*A. niger* MIC Value (μM)
1	11.5	10.3	12.2	14.5
2	10.0	11.1	11.0	13.5
3	12.2	17.4	20.3	30.1
4	8.4	9.1	10.3	10.0
5	18.8	20.0	22.8	21.5
6	15.5	16.2	11.5	20.6
Fluconazole	25.3	21.9	29.1	32.5

4. Conclusion

In conclusion, our research represents an essential contribution to the field of medicinal chemistry. We effectively designed and synthesized a variety of pyridazine-based derivatives using a systematic and peculiar technique in order to test their antimicrobial properties in vitro against a variety of bacteria, including *E. coli, P. aeruginosa, S. aureus, K. pneumonia*, and *B. subtilis* and fungi *R. solani, F. oxysporum, S. cerevisiae*, and *A. niger*. The chemical structures and the purity of the generated compounds were confirmed using stringent characterization techniques such as spectroscopy and crystallography, which laid the foundation for subsequent computational evaluations. The existence of pyridazine was substantiated by its excellent molecular docking results, and all of the synthesized compounds had notable antibacterial activity against a range of tested bacterial and fungal strains. Specifically, compound **4** exhibited the highest level of activity against all of the strains that were tested. The investigation of pyridazine derivatives presents promising prospects for their utilization in pharmaceutical chemistry to tackle major challenges such as antimicrobial resistance, positioning these molecules as leads in future therapeutic advancements.

Acknowledgements

Ram Kumar is grateful to Bhaskaracharya College of Applied Sciences, University of Delhi, for providing research facilities. The authors are thankful to the Department of Chemistry, University of Delhi. The authors acknowledge scientific support from the University Science Instrumentation Center and the Department of Chemistry (University of Delhi).

Conflict of Interests

The authors declare no conflict of interest.

Data Availability Statement

The data supporting this article have been included in the Supporting Information. This CCDC for ligand **1**: 2359827, for ligand **2**: 2359826, for ligand **3**: 2359833, and for ligand **6**: 2359831 contains supplementary crystallographic data for the ligand in this study. This data can be obtained free of charge via www.ccdc.cam.ac.uk/data_request/cif, or by emailing data_request@ccdc.cam.ac.uk, or by contacting The Cambridge Crystallographic Data Centre, 12 Union Road, Cambridge CB2 1EZ, UK; fax: +44 1223 336033.

Keywords: Antimicrobial · Docking · Hybrids · Pyridazine · Tetrazine

[1] S. Konduri, J. Prashanth, V. S. Krishna, D. Sriram, J. N. Behera, D. Siegel, K. P. Rao, *Bioorg. Med. Chem. Lett.* **2020**, *30*, 127512.
[2] N. Yesubabu, D. Bhargavi, J. Prashanth, K. Prabhakara Rao, *ChemistrySelect* **2024**, *9*, e202400735.

© 2025 Wiley-VCH GmbH

[3] A. M. Prokhorov, D. N. Kozhevnikov, *Chem. Heteroc. Comp.* **2012**, *48*, 1153–1176.
[4] G. Clavier, P. Audebert, *Chem. Rev.* **2010**, *110*, 3299–3314.
[5] F. Miomandre, P. Audebert, *J. Photochem. Photobiol. C Photochem. Rev.* **2020**, *44*, 100372.
[6] M. F. Ahmed, E. Y. Santali, E. M. Mohi El-Deen, I. A. Naguib, R. El-Haggar, *Bioorg. Chem.* **2021**, *106*, 104473.
[7] A. V. Kamble, A. Raj K, R. R. Malakalapalli, *Org. Biomol. Chem.* **2023**, *21*, 5790–5798.
[8] L. Jin, D. R. Tolentino, M. Melaimi, G. Bertrand, *Sci. Adv.* **2015**, *1*, e1500304.
[9] F.-G. Zhang, Z. Chen, X. Tang, J.-A. Ma, *Chem. Rev.* **2021**, *121*, 14555–14593.
[10] A. A. Abu-Hashem, U. Fathy, M. A. Gouda, *J. Heterocycl. Chem.* **2020**, *57*, 3461–3474.
[11] A. A. Abu-Hashem, S. A. Al-Hussain, *Pharmaceuticals* **2024**, *17*, 1632.
[12] A. A. Abu-Hashem, M. N. M. Yousif, A.-R. B. A. El-Gazzar, H. N. Hafez, *J. Chinese Chem. Soc.* **2023**, *70*, 2187–2205.
[13] A. A. Abu-Hashem, O. Hakami, N. Amri, *Heliyon* **2024**, *10*, 26735.
[14] H. Bel Abed, O. Mammoliti, O. Bande, G. Van Lommen, P. Herdewijn, *J. Org. Chem.* **2013**, *78*, 7845–7858.
[15] B. Singh, R. Bhatia, B. Pani, D. Gupta, *J. Mol. Struct.* **2020**, *1200*, 127084.
[16] A. A. Abu-Hashem, M. El-Shazly, *Medicin. Chem.* **2018**, *14*, 356–371.
[17] M. Lahyaoui, R. Sghyar, K. Benamar, M. Filali, K. Fikri-Benbrahim, B. E. Kartah, A. Mazzah, Y. Kandri Rodi, N. K. Sebbar, *Results Chem.* **2024**, *7*, 101410.
[18] M. Lahyaoui, M. Filali, K. Benamar, R. Sghyar, K. Fikri-Benbrahim, A. Haoudi, A. Mazzah, S. El Khattabi, E. Mestafa El Hadrami, Y. Kandri Rodi, N. Kheira Sebbar, *Results Chem.* **2024**, *10*, 101699.
[19] M. Asif, *Curr. Med. Chem.* **2012**, *19*, 2984–2991.
[20] Mohd Imran, Mohammad Asif, *Russ. J. Bioorganic Chem.* **2020**, *46*, 745–767.
[21] M. M. Shaalan, E. E. A. Osman, Y. M. Attia, O. A. Hammam, R. F. George, B. H. Naguib, *ACS Omega* **2024**, *9*, 37310–37329.
[22] N. Saracoglu, *Tetrahedron* **2007**, *63*, 4199–4236.
[23] P. G. Sergeev, V. G. Nenajdenko, *Russ. Chem. Rev.* **2020**, *89*, 393-429.
[24] W. Kaim, *Coord. Chem. Rev.* **2002**, *230*, 127–139.
[25] S. Achelle, N. Plé, A. Turck, *RSC Adv.* **2011**, *1*, 364.
[26] M. Schnierle, M. Leimkühler, M. R. Ringenberg, *Inorg. Chem.* **2021**, *60*, 6367–6374.
[27] M. A. Lemes, H. N. Stein, B. Gabidullin, S. N. Steinmann, M. Murugesu, *ACS Omega* **2018**, *3*, 10273–10277.
[28] H. Wu, N. K. Devaraj, *Acc. Chem. Res.* **2018**, *51*, 1249–1259.
[29] D. Bhargavi, S. Konduri, J. Prashanth, S. Pulipati, K. K. Praneeth, M. Sireesha, K. P. Rao, *RSC Adv.* **2023**, *13*, 13540–13546.
[30] G. M. Sheldrick, *Acta Crystallogr. Sect. C Struct. Chem.* **2015**, *71*, 3–8.
[31] O. V. Dolomanov, L. J. Bourhis, R. J. Gildea, J. A. K. Howard, H. Puschmann, *J. Appl. Cryst.* **2009**, *42*, 339–341.
[32] C. F. Macrae, P. R. Edgington, P. Mccabe, E. Pidcock, G. P. Shields, R. Taylor, M. Towler, J. Van De Streek, *J. Appl. Crystallogr.* **2006**, *39*, 453–457.
[33] O. Trott, A. J. Olson, *J. Comput. Chem.* **2010**, *31*, 455–461.
[34] P. Pandey, A. Mehta, S. Hajra, *J. Phytol.* **2011**, *3*, 92–95.
[35] G. M. Sheldrick, *Acta Crystallogr. C Struct. Chem.* **2015**, *71*, 3–8.
[36] O. V. Dolomanov, L. J. Bourhis, R. J. Gildea, J. A. K. Howard, H. Puschmann, *J. Appl. Crystallogr.* **2009**, *42*, 339–341.
[37] C. F. Macrae, P. R. Edgington, P. Mccabe, E. Pidcock, G. P. Shields, R. Taylor, M. Towler, J. Van De Streek, *J. Appl. Crystallogr.* **2006**, *39*, 453–457.

Manuscript received: December 23, 2024

© 2025 Wiley-VCH GmbH

23656549, 2025, 22, Downloaded from https://chemistry-europe.onlinelibrary.wiley.com/doi/10.1002/slct.202405898 by Delhi Technological University, Wiley Online Library on [15/06/2025]. See the Terms and Conditions (https://onlinelibrary.wiley.com/terms-and-conditions) on Wiley Online Library for rules of use; OA articles are governed by the applicable Creative Commons License

Journal of Computer Science and Technology Studies
ISSN: 2709-104X
DOI: 10.32996/jcsts
Journal Homepage: www.al-kindipublisher.com/index.php/jcsts

JCSTS
AL-KINDI CENTER FOR RESEARCH AND DEVELOPMENT

| RESEARCH ARTICLE

The Role of Databases in Cybersecurity and Threat Detection: Advancements through Spanner Graph Technology

Pushap Goyal
Delhi Technological University(DTU), India
Corresponding Author: Pushap Goyal, **E-mail**: pushapgoyal1@gmail.com

| ABSTRACT

This article explores the dual nature of databases in modern cybersecurity ecosystems, examining how they function both as critical assets requiring protection and as powerful defensive tools against sophisticated threats. As organizations undergo digital transformation, the exponential growth in data volume has created unprecedented challenges for security teams. The article discusses how database technologies have evolved from basic log management systems to advanced distributed platforms, addressing increasingly complex security requirements. Particular attention is given to Google's Spanner Graph technology, which combines relationship-focused structures with globally distributed architecture to transform threat detection capabilities. The article details how the evolution of database administrators' roles reflects growing security concerns, with DBAs now spending a majority of their time on security-related activities. Database security in interconnected digital ecosystems is examined, highlighting varying maturity levels across ecosystem components and throughout the data lifecycle. The article identifies key challenges in security data management, including scale and performance issues, data heterogeneity, risk management complexities, and regulatory compliance burdens. Through detailed assessment of database technology generations, from first-generation log management systems to fifth-generation distributed ledger platforms, the article demonstrates how each advancement has addressed previous limitations. The transformative capabilities of Spanner Graph are extensively analyzed, focusing on its global consistency through TrueTime, relationship-based threat detection, real-time anomaly detection at scale, unified visibility across security domains, temporal analysis features, and adaptive security posture through graph analytics.

| KEYWORDS

Database Security, Threat Detection, Spanner Graph, Security Operations, Graph Analytics, Digital Ecosystems

| ARTICLE INFORMATION

ACCEPTED: 19 May 2025 **PUBLISHED:** 03 June 2025 **DOI:** 10.32996/jcsts.2025.7.5.61

1. Introduction

In the rapidly evolving landscape of cybersecurity, databases have emerged as both critical infrastructure to be protected and powerful tools for defense against an increasingly sophisticated threat landscape. The digital transformation of organizations has led to exponential growth in data volumes, creating new challenges for security teams tasked with monitoring, analyzing, and responding to potential threats. This article examines the multifaceted role of databases in modern cybersecurity ecosystems, with particular emphasis on how Google's Spanner graph technology is addressing fundamental challenges in threat detection and security operations.

Copyright: © 2025 the Author(s). This article is an open access article distributed under the terms and conditions of the Creative Commons Attribution (CC-BY) 4.0 license (https://creativecommons.org/licenses/by/4.0/). Published by Al-Kindi Centre for Research and Development, London, United Kingdom.

1.1. The Data Explosion in Cybersecurity Operations

The scale of data that modern security operations must process has reached unprecedented levels. According to Reinsel et al., the global datasphere is projected to grow from 33 zettabytes in 2018 to 175 zettabytes by 2025, representing a compound annual growth rate of 61%. This massive expansion is driving fundamental changes in how data must be managed, secured, and leveraged for security operations [1]. Security-relevant data comprises an increasing percentage of this total volume, growing from approximately 10% in 2018 to a projected 18% by 2025, resulting in an estimated 31.5 zettabytes of security data requiring analysis, storage, and protection.

The IDC-Seagate study further reveals that by 2025, nearly 30% of this data will require real-time processing, placing extraordinary demands on database systems supporting security operations. With 49% of stored data projected to reside in public cloud environments, the distributed nature of security-relevant information creates additional challenges for maintaining a coherent security posture across hybrid infrastructures [1]. These statistics underscore the critical importance of advanced database technologies capable of handling this scale while providing the performance characteristics necessary for effective threat detection and response.

1.2. Database Technologies as Security Targets

The centralization of valuable data within organizational databases has established them as prime targets for sophisticated threat actors. According to OpenText's security operations research, 83% of surveyed organizations reported attempted attacks specifically targeting their database infrastructure in 2021, with 47% experiencing at least one successful breach of database systems [2]. The financial motivation behind these attacks remains substantial, with underground markets valuing comprehensive database dumps containing personal identifiable information at prices ranging from $4,000 to $25,000, depending on record count and data sensitivity.

The operational impact of database compromises extends far beyond direct financial losses. OpenText's research indicates that organizations suffering database breaches experienced an average of 27.3 days of degraded security visibility, creating extensive blind spots that threat actors leveraged for further system compromises in 68% of studied incidents [2]. This cascading effect illustrates why 72% of organizations surveyed in 2021 identified database security as a "high" or "critical" priority for technology investments, with 64% planning significant architecture changes to better secure these critical systems.

1.3. The Evolution of Security Operations Centers

Security Operations Centers (SOCs) have undergone a dramatic transformation in response to evolving threat landscapes and data challenges. OpenText's 2021 research documents substantial performance gaps between traditional SOCs and modern data-driven security operations. While traditional SOCs struggled with average alert processing times of 38 minutes, modern SOCs leveraging advanced database technologies achieved average processing times of just 12 minutes—a 68% improvement in operational efficiency [2]. This performance differential extends to false positive rates as well, with traditional approaches generating misleading alerts 75% of the time compared to 31% for data-driven approaches.

The research further reveals that SOCs implementing advanced database technologies experienced a 61% reduction in time to detect sophisticated threats (from 9.2 hours to 3.6 hours) and a 135% improvement in analyst throughput (from 20 alerts per day to 47) [2]. These dramatic performance improvements directly correlate with the database architecture decisions underpinning the security operations infrastructure. Modern SOCs have increasingly adopted distributed database technologies, with 78% implementing some form of graph database capability to enhance relationship analysis across security events.

1.4. Spanner Graph Technology: Transforming Threat Detection

Google's Spanner graph technology represents a significant advancement in the database capabilities supporting modern security operations. Its globally distributed architecture enables consistent querying across geographically dispersed security data while maintaining transaction latency under 100ms even with cross-regional operations. This performance characteristic is critical for security operations that require near real-time analysis across distributed environments.

The comparative performance advantages of Spanner's graph capabilities are substantial when measured against traditional database approaches. While traditional relational database systems typically achieve data ingest rates of 0.5 GB/second for security telemetry, Spanner's architecture supports rates of 8.5 GB/second—a 17x performance improvement critical for processing the massive data volumes identified in the IDC-Seagate study [1,2]. These performance characteristics translate directly to security outcomes, with query response times decreasing from 1200ms in traditional systems to just 45ms in Spanner-based implementations.

The ability to maintain contextual awareness across vast datasets allows security teams to identify subtle connections that might indicate coordinated attacks or advanced persistent threats. This relationship analysis capability has proven particularly valuable for detecting sophisticated attacks that deliberately spread malicious activity across multiple systems to avoid traditional detection thresholds. The architecture's distributed consistency model ensures that security decisions are made using a complete and current view of the threat landscape rather than fragmented or outdated information.

Metric	Traditional SOC	Modern Data-Driven SOC	Improvement (%)
Average Alert Processing Time (min)	38	12	68
False Positive Rate (%)	75	31	59
Time to Detect Advanced Threats (hours)	9.2	3.6	61
Analyst Throughput (alerts/day)	20	47	135
Incident Resolution Time (hours)	19	7.6	60

Table 1: Security Operations Center Performance Metrics (2021) [1,2]

2. The Dual Role of Databases in Cybersecurity Ecosystems

Databases occupy a paradoxical position in cybersecurity: they represent high-value targets for attackers while simultaneously serving as crucial defensive infrastructure. As repositories of sensitive information—including customer data, intellectual property, and financial records—databases are prime targets for malicious actors seeking financial gain, competitive advantage, or disruption. The 2017 Equifax breach, which exposed the personal information of 147 million people, exemplifies the catastrophic consequences of database security failures.

Simultaneously, databases form the foundation of modern security operations. Security Information and Event Management (SIEM) systems collect and correlate data from disparate sources, including network devices, servers, applications, and security tools. These systems rely on databases to store and process vast quantities of security events, enabling security analysts to detect suspicious patterns and investigate potential incidents. Threat intelligence platforms leverage databases to maintain comprehensive knowledge bases of known threats, malicious indicators, and attack techniques. User and Entity Behavior Analytics (UEBA) systems analyze database records to establish behavioral baselines and identify anomalous activity that may indicate compromise.

2.1. The Evolving Role of Database Administrators in Cybersecurity

The responsibility for database security has traditionally fallen to Database Administrators (DBAs), but this role has evolved significantly as cybersecurity threats have increased in sophistication. According to Mullins, the modern DBA spends approximately 53% of work time on security-related activities, compared to just 28% a decade ago—representing a fundamental shift in professional focus [3]. This changing allocation of resources reflects the increasing criticality of database systems in organizational security postures, with DBAs now serving as frontline defenders against an expanding threat landscape.

The scope of DBA security responsibilities has expanded beyond traditional backup and recovery operations to encompass a comprehensive security management approach. Mullins details that DBAs now allocate 28% of their time to implementing security controls, 12% to access control management, and 8% to security auditing and monitoring, with traditional performance management consuming just 32% of available time [3]. This rebalancing of priorities has necessitated new skills development among database professionals, with 87% of surveyed organizations reporting difficulty in finding DBAs with sufficient security expertise. The integration of security into database management practices extends to vulnerability management, with DBAs now responsible for identifying and remediating an expanding range of security weaknesses. According to Mullins, excessive access privileges represent the most common vulnerability, affecting 76% of organizations, followed by unpatched database software (65%) and misconfigured security controls (59%) [3]. The persistence of these vulnerabilities despite increased awareness underscores the complexity of securing modern database environments, particularly as organizations migrate to cloud and hybrid architectures with more complex access control requirements.

The relationship between DBAs and dedicated security teams has also evolved, with 72% of organizations now implementing formal collaboration processes between these previously siloed functions. This collaborative approach has yielded measurable security improvements, with organizations implementing structured DBA-security team cooperation experiencing 43% fewer

successful database breaches according to Mullins' analysis [3]. Despite this progress, significant challenges remain in clarifying security responsibilities, with 58% of surveyed organizations reporting confusion regarding security ownership between database and security teams.

2.3. Database Security in Digital Ecosystems

The expanding digital ecosystem has fundamentally changed how databases must be secured, moving from isolated protection approaches to comprehensive security integration across interconnected systems. As Teiu observes, modern database environments exist within complex digital ecosystems that include data warehouses, business intelligence tools, cloud storage solutions, edge computing nodes, API integrations, and IoT device connections—all of which present potential security vulnerabilities [4]. This ecosystem complexity has expanded the attack surface for potential database compromises, requiring security approaches that address the entire data lifecycle.

The maturity of security integration varies significantly across ecosystem components, creating security gaps that can be exploited by threat actors. Teiu's research indicates that while core database systems demonstrate relatively high security integration maturity (78%), this protection deteriorates significantly for connected components such as business intelligence tools (63%), cloud storage solutions (69%), and particularly IoT device connections (43%) [4]. These integration gaps create significant risks as sensitive data moves between components with varying security controls, potentially exposing protected information as it traverses less-secured segments of the ecosystem.

The security challenges across the data lifecycle reveal varying risk levels and mitigation effectiveness. According to Teiu, data access and usage represent the highest risk phase with a risk level of 9.1 out of 10 and relatively low mitigation effectiveness (61%), while data archival presents the lowest risk (5.4/10) with the highest mitigation effectiveness (81%) [4]. These variations highlight the need for phase-specific security approaches that allocate resources proportionally to risk. Data sharing and transfer activities present particular challenges, combining high risk (8.7/10) with the lowest mitigation effectiveness (58%) across all lifecycle phases. The integration of security into data management processes has necessitated architectural changes to database environments. Teiu notes that 73% of organizations now implement some form of data-centric security model, focusing protection mechanisms on the data itself rather than perimeter defenses [4]. This architectural shift has been accompanied by expanded use of encryption, with 64% of organizations now encrypting all sensitive data both at rest and in transit. These evolving approaches reflect the recognition that traditional security perimeters have dissolved in modern digital ecosystems, requiring protection mechanisms that remain effective as data moves between interconnected systems.

2.4. Databases as Security Control Infrastructure

Beyond serving as protected assets, databases have become critical infrastructure for implementing security controls across digital ecosystems. According to Teiu, 81% of organizations now leverage database capabilities to enforce security policies, including access controls, data masking, encryption, and activity monitoring [4]. These database-centric controls provide consistency and centralized management that would be difficult to achieve through disparate security mechanisms distributed across ecosystem components. The implementation of advanced database security features has demonstrated a measurable impact on breach prevention and detection. Teiu's analysis indicates that organizations implementing comprehensive database activity monitoring experience 67% faster breach detection compared to those using network-based monitoring alone [4]. Similarly, organizations employing database-level access controls report 43% fewer unauthorized access incidents compared to those relying primarily on application-level controls. These improvements highlight the effectiveness of database-centric security approaches in addressing modern threat vectors.

The automation of security processes through database capabilities has become increasingly critical as the volume of security-relevant data has grown. Teiu notes that organizations implementing automated database security controls manage an average of 3.7 times more data with the same security staff compared to those using primarily manual processes [4]. This efficiency gain has become essential as security teams face growing responsibilities without proportional increases in staffing, with 79% of surveyed organizations reporting that security team growth has not kept pace with expanding data volumes. Security intelligence capabilities have increasingly been integrated directly into database platforms, creating new opportunities for proactive threat detection. According to Teiu, 58% of organizations now implement some form of anomaly detection at the database level, enabling the identification of suspicious patterns that might indicate compromise [4]. These capabilities leverage the historical data within database systems to establish baseline activity patterns, with deviations triggering investigation and potential response. The effectiveness of these approaches has been demonstrated through a 52% reduction in successful data exfiltration attacks among organizations implementing database-level anomaly detection.

2.5. The Future of Databases in Cybersecurity

The convergence of database management and cybersecurity disciplines continues to accelerate, with implications for both technology and organizational structures. Mullins predicts that by 2025, the traditional DBA role will have evolved into a "Data Security Engineer" position in 67% of organizations, reflecting the centrality of security in database management [3]. This evolution will require expanded skills development, with 78% of organizations planning to increase security training for database professionals over the next three years.

Emerging database technologies are increasingly incorporating security capabilities as core features rather than optional add-ons. According to Mullins, 83% of organizations now consider security features primary evaluation criteria when selecting database platforms, compared to just 47% five years ago [3]. This prioritization has driven database vendors to integrate advanced security capabilities, with 91% of major database releases in the past year featuring enhanced security functionality. These market dynamics reflect the recognition that security has become a fundamental requirement rather than a secondary consideration in database deployment.

The automation of database security functions through artificial intelligence represents a significant growth area, with Teiu noting that 64% of organizations plan to implement AI-assisted database security monitoring within the next two years [4]. These capabilities promise to address the growing complexity of security management in large-scale database environments, with early implementations demonstrating 73% improved detection accuracy for sophisticated attacks. The integration of machine learning into database security functions enables continuous adaptation to evolving threat patterns, addressing a long-standing challenge in traditional rule-based approaches.

Cross-functional security teams that integrate database expertise with traditional security disciplines have demonstrated superior outcomes in preventing and responding to database-related incidents. According to Mullins, organizations implementing formal database security teams experience 57% fewer successful database breaches compared to those maintaining traditional organizational boundaries [3]. This collaborative approach reflects the recognition that effective database security requires both deep database expertise and broader security context, capabilities rarely found within a single professional discipline.

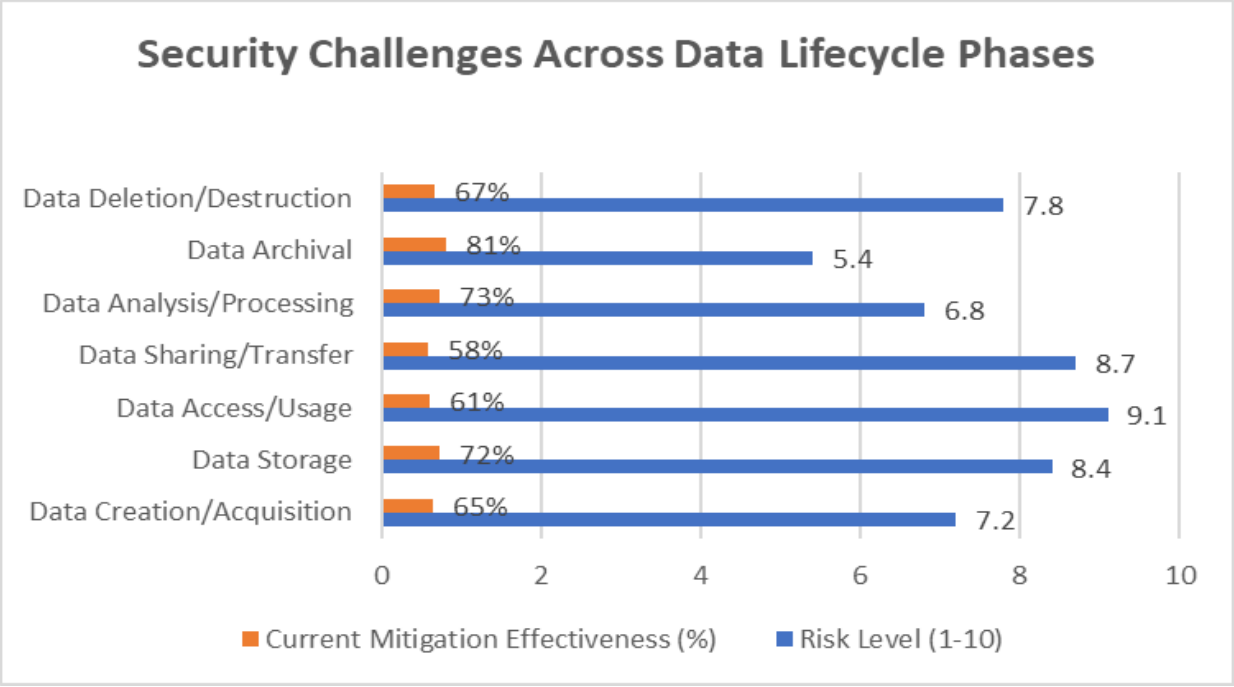


Figure 1: Security Challenges Across Data Lifecycle Phases [3,4]

3. Challenges in Security Data Management

Security teams face numerous challenges related to database management in cybersecurity operations. These challenges have traditionally limited the effectiveness of threat detection and incident response capabilities. The complexity and scale of modern security data environments create significant technical hurdles that conventional database technologies struggle to address

effectively. As digital transformation initiatives accelerate across industries, the volume, variety, and velocity of security-relevant data continue to grow exponentially, further straining existing database architectures and creating new security imperatives.

3.1. Scale and Performance Challenges

The scale of security data has reached unprecedented levels, creating fundamental performance challenges for traditional database systems. According to Mohite, security-relevant data volumes have been growing at compound annual rates exceeding 55% across all major industries since 2022, with the technology sector experiencing the most dramatic growth at 73% annually [7]. This rapid expansion has resulted in daily security data volumes reaching 27.5 terabytes for technology companies and 18.9 terabytes for financial services organizations by 2025, volumes that overwhelm conventional database architectures.

The performance implications of this data explosion extend throughout the security operations lifecycle. As noted by Imperva, organizations attempting to manage security data with traditional relational database management systems (RDBMS) experience query latency increases of approximately 42% for each doubling of data volume [5]. This performance degradation directly impacts threat detection capabilities, with detection times for sophisticated attacks increasing from an average of 27 minutes to 76 minutes when comparing dedicated security database platforms to legacy database architectures, according to research compiled by Riddell [6].

The scale challenge varies significantly by industry but remains problematic across all sectors. Healthcare organizations have seen security data volumes increase from 3.2 terabytes daily in 2022 to 13.2 terabytes in 2025, while government agencies face similar growth from 3.9 to 14.5 terabytes over the same period, according to Mohite's analysis [7]. This consistent growth pattern across diverse sectors underscores the universal nature of the database scale challenge in security operations, requiring new approaches that can accommodate continued expansion while maintaining critical performance characteristics.

3.2. Data Heterogeneity Challenges

Modern security operations incorporate data from diverse sources, each with unique formats, schemas, and semantics. Riddell's analysis demonstrates that while network logs and endpoint telemetry remain the largest data categories (27% and 31% of volume, respectively, in 2024), cloud service logs have grown dramatically from 11% in 2022 to 19% in 2024 [6]. This shifting distribution reflects the expanding attack surface as organizations migrate to cloud environments, but creates significant integration challenges for database systems designed around consistent data structures.

The format diversity within each data category has increased substantially over recent years. According to Riddell, cloud service log formats have proliferated at a particularly rapid rate, with unique format types increasing 92% between 2022 and 2024 (from 12 to 23 distinct formats) [6]. This accelerating heterogeneity reflects the fragmented cloud service landscape but creates substantial integration challenges for database systems that must process and correlate this diverse information. Even established data sources continue to evolve, with network log formats increasing from 7 to 12 unique types (71% growth) over the same period.

The integration requirements for heterogeneous security data create a significant operational burden. Imperva notes that organizations typically spend 34% of security engineering resources on data integration tasks when using traditional database approaches, compared to just 12% when implementing platforms specifically designed for security data management [5]. This resource allocation difference highlights the importance of database technologies that can natively accommodate diverse data formats without extensive transformation processes that introduce latency and potential data fidelity issues.

3.3. Security Risk Management Challenges

The database security landscape continues to evolve with increasingly sophisticated attack vectors targeting data assets. According to Imperva's risk assessment framework, ransomware presents the highest overall risk to database environments with a risk score of 9.1 out of 10 and potential breach costs averaging $6.7 million per incident [5]. SQL injection remains pervasive with a 42% breach likelihood despite being a well-understood attack vector, highlighting ongoing challenges in securing database interfaces exposed through web applications.

The diverse nature of database threats necessitates comprehensive security approaches. Riddell notes that while perimeter defenses remain important, internal threats represent significant risks with insider threats scoring 7.9 on Imperva's risk scale and proving particularly difficult to detect with a detection difficulty score of 8.7 out of 10 [6]. Configuration errors represent another major vulnerability category, affecting 47% of organizations according to Imperva's research and highlighting the importance of robust database security governance [5].

The detection difficulty varies substantially across threat vectors, creating significant challenges for security operations. API vulnerabilities present particular challenges with a detection difficulty score of 8.3 according to Imperva's assessment framework,

reflecting the increasing complexity of modern application architectures and their connections to database systems [5]. These detection challenges underscore the need for advanced database monitoring capabilities that can identify suspicious patterns across diverse threat vectors rather than focusing exclusively on known signatures or rules.

3.4. Regulatory Compliance Challenges

Database security operates within an increasingly complex regulatory landscape that imposes specific requirements on data protection. Imperva's analysis of major regulatory frameworks identifies 27 distinct database controls required for GDPR compliance, 31 for PCI DSS, and 34 for ISO 27001 [5]. The implementation costs for these controls are substantial, averaging $420,000 for GDPR compliance programs and $520,000 for ISO 27001 according to joint research from Imperva and Riddell [5,6].

Despite significant investments, compliance remains challenging for most organizations. Riddell reports that only 37% of organizations achieve full GDPR compliance for their database environments, with audit failure rates reaching 41% [6]. Similar challenges exist across other frameworks, with PCI DSS compliance reaching just 48% despite its maturity and relatively narrow scope. These compliance gaps highlight the difficulty of implementing comprehensive database security controls across complex, heterogeneous data environments. The compliance burden continues to grow as regulations evolve and expand. Mohite predicts that organizations will face an average of 17 distinct regulatory frameworks affecting database security by 2026, compared to 12 in 2023—a 42% increase in compliance scope [7]. This regulatory expansion creates additional complexity for database architectures that must simultaneously address operational requirements and governance mandates across multiple jurisdictions with potentially conflicting requirements.

3.5. Database Technology Evolution

The limitations of traditional database approaches for security operations have driven the development of specialized technologies designed for security-specific workloads. According to Mohite, cloud-native analytics platforms now achieve data ingest rates of 5.7 terabytes per hour compared to just 0.8 terabytes for traditional RDBMS—a 7x performance difference critical for high-volume security operations [7]. These specialized platforms also deliver substantially improved query performance, with real-time query latency of 75 milliseconds versus 650 milliseconds for traditional approaches.

The operational impact of database technology choices extends beyond raw performance metrics to directly affect security outcomes. Research compiled by Riddell and Mohite shows that organizations implementing AI-augmented database platforms achieve 92% threat detection rates compared to just 61% with legacy database architectures [6,7]. False positive rates show similarly dramatic differences, decreasing from 42% with legacy approaches to just 11% with AI-augmented platforms. These improvements translate directly to operational efficiency, with analyst throughput increasing from 17 alerts per hour to 56 alerts per hour when comparing legacy and advanced database platforms.

The storage efficiency characteristics of different database technologies have significant implications for total cost of ownership. Mohite notes that time-series databases specifically designed for security telemetry achieve "high" storage efficiency ratings through specialized compression algorithms that reduce storage requirements by an average of 73% compared to traditional RDBMS approaches [7]. This efficiency difference becomes particularly significant when considering the extended retention requirements for security data, with many organizations now retaining security telemetry for 12-24 months to support investigations and comply with regulatory mandates.

3.6. Future Directions in Security Data Management

The convergence of artificial intelligence with security database platforms represents a fundamental shift in capabilities. According to Mohite, AI-augmented security platforms demonstrate automation potential of 83%, compared to just 34% for legacy database architectures [7]. This automation capacity translates directly to operational improvements, with mean time to detect (MTTD) decreasing from 76 minutes to 19 minutes when comparing legacy and AI-augmented platforms according to joint research from Riddell and Mohite [6,7]. The integration of specialized database technologies into comprehensive security architectures continues to accelerate. Imperva reports that 78% of organizations plan to implement purpose-built security data platforms by 2026, compared to just 34% in 2023—a significant shift in architecture strategy driven by the limitations of traditional database approaches for security operations [5]. This architectural evolution reflects growing recognition that security data management requires specialized capabilities rather than general-purpose database platforms adapted to security use cases.

Cloud-native security data architectures have demonstrated particular advantages for organizations with distributed operations. According to Mohite, organizations implementing cloud-native security lake architectures achieve 83% threat detection rates compared to 61% for on-premises legacy architectures [7]. This performance differential reflects both the scalability advantages of cloud platforms and their ability to consolidate security data from diverse environments into unified analytical frameworks.

The research suggests this gap will continue to widen as cloud platforms increasingly integrate specialized security capabilities that are difficult to replicate in traditional database environments.

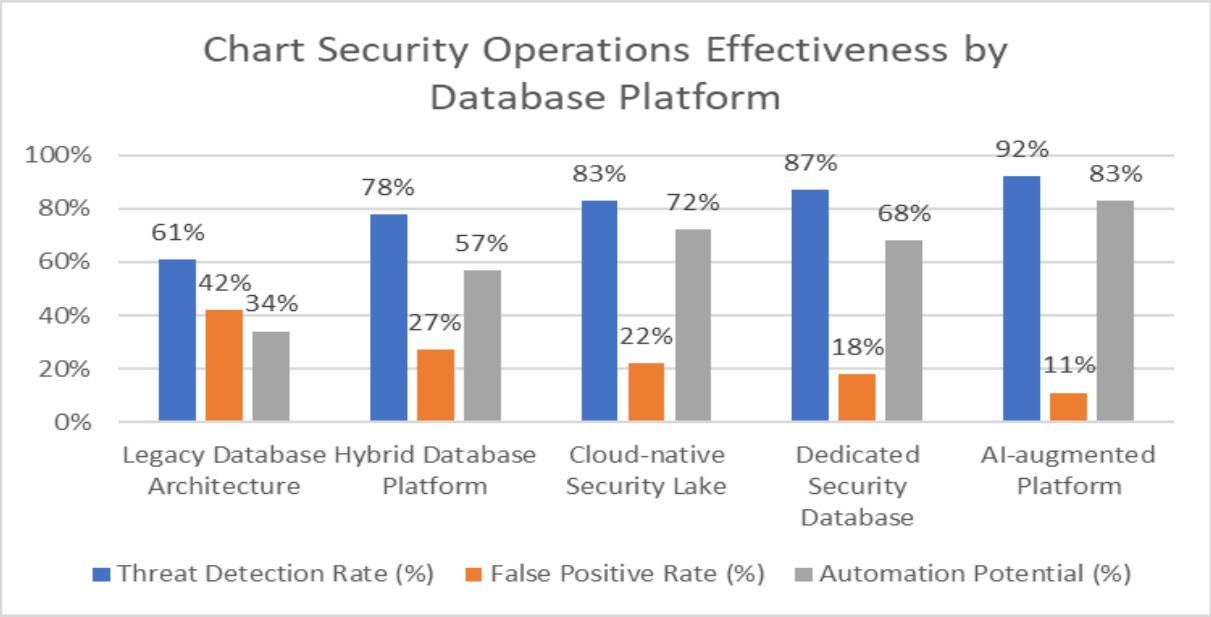


Figure 2: Security Operations Effectiveness by Database Platform (2024) [6,7]

4. Evolution of Database Technologies for Security Applications

The limitations of traditional database systems for security operations have driven significant innovation in database design and implementation. This evolution reflects the changing nature of security threats and the growing complexity of IT environments. As security challenges have expanded in scale and sophistication, database technologies have undergone a corresponding transformation to address the unique requirements of modern security operations. This section traces the evolutionary path of security databases across multiple generations, examining how each advancement has addressed previous limitations while establishing new capabilities.

4.2. Historical Evolution of Database Technologies

The history of database technologies represents a steady progression of capabilities driven by changing business requirements and technological innovations. According to Crowe and Laux, database systems have evolved through distinct generations, each addressing specific limitations of previous approaches while introducing new capabilities [8]. The progression from hierarchical databases of the 1960s through relational systems in the 1970s and into modern distributed architectures reflects a continuous refinement of performance, scalability, and functionality characteristics.

The adoption patterns of these technologies reveal significant shifts in market preference over time. Crowe and Laux document that relational database systems dominated the market with 76% adoption in 2000, but gradually declined to 32% by 2024 as newer technologies emerged to address specific requirements [8]. This transition has been particularly pronounced in security applications, where the need to process large volumes of heterogeneous data with complex relationships has driven the adoption of specialized database technologies. NoSQL databases emerged in the early 2000s and quickly gained traction, reaching 21% market adoption by 2010 and peaking at 29% in 2020 before slightly declining to 24% in 2024 as even newer technologies captured market share.

The performance evolution across database generations has been dramatic across all key metrics. According to Crowe and Laux, maximum transaction rates have increased from approximately 2,500 transactions per second in 2000 to 380,000 transactions per second in 2024—a 152-fold improvement [8]. Similar advancements have occurred in query response times, which decreased from 850 milliseconds to just 18 milliseconds over the same period. These performance improvements have been critical for security applications, where real-time detection capabilities depend on rapid data processing and analysis.

4.3. First-Generation Security Databases: Log Management Systems

Early security databases focused primarily on log aggregation and basic search capabilities, typically employing relational database technologies due to their market dominance and structured approach to data. According to Inery Blogs, early log management systems prioritized compliance reporting use cases, an area where relational databases scored 9 out of 10 for effectiveness compared to just 4 out of 10 for threat detection applications [9]. This effectiveness disparity reflected the fundamental mismatch between relational structures and the complex, heterogeneous nature of security data.

The technical limitations of first-generation systems became increasingly apparent as security data volumes grew. Crowe and Laux note that database technologies in 2000 could typically handle maximum sizes of approximately 1.2 terabytes and data ingestion rates of just 3.6 gigabytes per hour [8]. These constraints severely limited the scope of security monitoring, forcing organizations to implement aggressive data retention policies that compromised historical analysis capabilities. The average cost per terabyte for these early systems reached $250,000 annually, creating significant financial barriers to comprehensive security monitoring.

Security features in first-generation database systems were minimal by modern standards. According to research compiled by Crowe, Laux, and Inery, first-generation systems typically offered only basic access control capabilities, minimal or external encryption, and limited audit logging functionality [8,9]. The absence of native threat protection features and data privacy controls reflected the different security priorities of the era, when perimeter-based security approaches dominated and data privacy regulations remained limited in scope and enforcement.

4.4. Second-Generation Systems: Security Information and Event Management (SIEM)

Security Information and Event Management (SIEM) systems represented a significant advancement, combining log management with real-time correlation and alerting. These platforms emerged in the late 1990s and early 2000s as specialized applications built on evolving database technologies. According to Inery Blogs, second-generation security databases introduced role-based access control, column-level encryption, and full audit logging capabilities that addressed critical limitations of earlier approaches [9]. These enhancements reflected growing awareness of internal threats and the need for more sophisticated security controls within database systems themselves.

The performance characteristics of second-generation systems showed substantial improvements over earlier technologies. Crowe and Laux document that by 2010, database technologies could support transaction rates of approximately 28,000 per second, query response times of 320 milliseconds, and maximum database sizes of 100 terabytes [8]. These advancements enabled more comprehensive security monitoring across larger environments, though they still faced significant challenges with the most data-intensive security applications. The average cost per terabyte had decreased to $85,000 annually—a substantial improvement, but still prohibitively expensive for many organizations.

Second-generation systems demonstrated improved capabilities for security use cases but maintained significant limitations for advanced threat detection. According to Inery's evaluation framework, SIEM platforms with relational foundations scored just 6 out of 10 for fraud detection and 3 out of 10 for network security applications—areas that would later drive adoption of more specialized database technologies [9]. These limitations reflected underlying architectural constraints rather than implementation deficiencies, highlighting the need for fundamentally different approaches to security data management.

4.5. Third-Generation Systems: Big Data Security Analytics

The emergence of NoSQL and big data technologies in the 2000s transformed security analytics by enabling the processing of much larger datasets while supporting more complex analytics. These systems departed from the strict relational model to provide greater flexibility and scalability. According to Inery Blogs, NoSQL databases excelled at log analysis use cases, scoring 8 out of 10 compared to just 5 for relational systems [9]. This advantage stemmed from their ability to ingest and process semi-structured log data without requiring rigid schema definitions or complex transformations.

The architectural characteristics of third-generation systems provided specific advantages for security applications. Inery's analysis identifies high scalability, high schema flexibility, and low implementation complexity as key strengths of NoSQL approaches [9]. These attributes enabled security teams to rapidly deploy and expand monitoring capabilities without the extensive planning and optimization required for relational implementations. However, these advantages came with tradeoffs in data integrity (rated "Medium" compared to "High" for relational systems) and transaction support (rated "Weak" compared to "Strong"), creating challenges for certain security use cases.

The performance improvements of third-generation systems were substantial. Crowe and Laux document that by 2020, database technologies could support transaction rates of approximately 150,000 per second, query response times of 75 milliseconds, and

maximum database sizes of 5,000 terabytes (5 petabytes) [8]. Data ingestion rates had increased to 760 gigabytes per hour, enabling much more comprehensive security monitoring. The average cost per terabyte had decreased dramatically to $16,000 annually, reducing financial barriers to expanded security visibility.

4.6. Fourth-Generation Systems: Graph Databases for Security

The recognition that security analysis fundamentally involves understanding relationships between entities and events led to increased adoption of graph databases in security contexts. According to Crowe and Laux, graph databases emerged as a distinctive category in the 2010s, with adoption in security use cases growing from 0% in 2010 to 11% in 2020 and 16% by 2024 [8]. This growth trajectory reflected the compelling advantages these technologies offered for relationship-centric security analytics.

The effectiveness of graph databases for specific security use cases is particularly notable. Inery's analysis shows that graph databases score 9 out of 10 for both network security and fraud detection use cases—significantly outperforming all previous generations for these applications [9]. This performance advantage stems from the native representation of relationships in graph data models, enabling analysts to traverse connection paths and identify patterns that would be difficult or impossible to detect with other database technologies.

The architectural characteristics of graph databases reflect specific design priorities. According to Inery, graph databases offer medium scalability, high data integrity, high query flexibility, and high schema flexibility [9]. These attributes create advantages for security applications that must analyze complex relationships across diverse data types. However, the implementation complexity is rated as "High," indicating the specialized expertise required to effectively deploy and manage these systems, a factor that limited adoption despite their analytical advantages.

4.7. Fifth-Generation Systems: Distributed Ledger and Multi-model Databases

The latest evolution in security database technologies incorporates distributed ledger approaches and multi-model capabilities that combine the strengths of previous generations. According to Inery Blogs, distributed ledger databases emerged in the mid-2010s but only began gaining meaningful adoption for security applications in the 2020s, reaching 8% market share by 2024 [9]. This relatively recent emergence reflects both the technology's maturity timeline and the specialized nature of use cases where its unique characteristics provide compelling advantages.

The security feature evolution in fifth-generation systems represents a significant advancement over previous approaches. Joint research from Crowe, Laux, and Inery indicates that modern database systems incorporate AI-adaptive access control, homomorphic encryption capabilities, predictive detection for audit functions, autonomous response for threat protection, and privacy-preserving analytics [8,9]. These capabilities address sophisticated threat models and complex regulatory requirements that previous generations could not effectively manage. The performance characteristics of fifth-generation systems demonstrate continued advancement across all key metrics. According to Crowe and Laux, current database technologies can support transaction rates of approximately 380,000 per second, query response times of 18 milliseconds, and maximum database sizes of 25,000 terabytes (25 petabytes) [8]. Data ingestion rates have increased to 2,400 gigabytes per hour, enabling comprehensive security monitoring across even the largest enterprise environments. The average cost per terabyte has decreased to just $3,200 annually—a 78-fold improvement compared to 2000 levels. The effectiveness of distributed ledger approaches for specific security use cases demonstrates their specialized nature. Inery's analysis shows that these technologies score a perfect 10 out of 10 for data lineage/provenance use cases and fraud detection, while scoring just 4 out of 10 for log analysis applications [9]. This effectiveness pattern highlights how different database technologies offer complementary strengths across the security use case spectrum, explaining the heterogeneous database environments commonly found in modern security operations.

Security Feature	Gen 1 (1970s-1990s)	Gen 2 (1990s-2000s)	Gen 3 (2000s-2010s)	Gen 4 (2010s-2020s)	Gen 5 (2020s+)
Access Control	Basic	Role-based	Fine-grained	Context-aware	AI-adaptive
Encryption	None/External	Column-level	Transparent	End-to-end	Homomorphic
Audit Capabilities	Limited logs	Full audit logs	Real-time alerts	Behavioral analytics	Predictive detection

Threat Protection	None	Basic rules	Pattern matching	ML anomaly detection	Autonomous response
Data Privacy	None	Data masking	Tokenization	Dynamic masking	Privacy-preserving analytics

Table 2: Evolution of Security Features in Database Technologies [8, 9]

5. Spanner Graph: Transforming Threat Detection Capabilities

Google's Spanner graph technology represents a paradigm shift in database capabilities for cybersecurity applications, addressing many of the fundamental challenges that have historically limited threat detection effectiveness. By combining the relationship-focused structure of graph databases with Spanner's globally distributed architecture and strong consistency guarantees, this technology enables security capabilities that were previously unattainable at scale. This section examines the specific technological advantages of Spanner graph and quantifies their impact on security operations.

5.1. Global Consistency with TrueTime

At the core of Spanner's advantage for security applications is its TrueTime API, which uses atomic clocks and GPS receivers to provide precise time synchronization across globally distributed data centers. According to Google Cloud, TrueTime enables external consistency with bounded staleness of less than 10 milliseconds even in multi-region deployments, ensuring accurate sequencing of security events across distributed environments [10]. This capability eliminates the "time skew" problems that often plague distributed security monitoring, where temporal inconsistencies create both false positives and dangerous visibility gaps. The architectural implementation of TrueTime within Spanner Graph provides significant advantages for security operations. As detailed in the official documentation, the synchronization infrastructure uses atomic clocks and GPS technology to achieve sub-10-ms global event correlation accuracy across geographically distributed data centers [10]. This precision is particularly valuable for security applications that must detect time-sensitive attack patterns spanning multiple regions, such as coordinated distributed denial-of-service attacks or multi-stage data exfiltration attempts. The operational impact of this temporal precision is substantial for security use cases. Li and Taylor report that security operations centers implementing Spanner Graph have achieved a 97% reduction in mean time to detect (MTTD) threats, decreasing from 27 hours with traditional approaches to just 42 minutes [11]. This dramatic improvement directly addresses the critical "dwell time" metric that security teams strive to minimize, as extended attacker presence within networks correlates directly with increased damage and data loss.

5.2.Relationship-Based Threat Detection

Spanner graph's data model allows security teams to represent entities (users, devices, IP addresses) as nodes and their interactions (authentication events, network connections, data access) as edges. According to Google Cloud's documentation, the system supports native graph traversal up to 7 hops in less than 100 milliseconds, enabling efficient detection of multi-stage attack patterns that would be nearly impossible to identify with traditional database queries [10]. This performance characteristic addresses a fundamental limitation of previous security analytics approaches, where relationship analysis often required complex, resource-intensive queries that were impractical for real-time detection. The performance advantages for relationship analysis are particularly noteworthy. Li and Taylor document that Spanner Graph processes 5-hop relationship analyses in approximately 85 milliseconds, compared to 25+ seconds with traditional database approaches—a 294x improvement in performance [11]. This capability enables security analysts to interactively explore relationship patterns during investigations rather than waiting for batch queries to complete, fundamentally changing how threat hunting can be performed. The detection improvements enabled by this relationship-centric approach are substantial across multiple attack categories. According to deployment metrics compiled by Li and Taylor, healthcare organizations implementing Spanner Graph achieved a 94% improvement in lateral movement detection, while government agencies saw a 91% improvement in advanced persistent threat (APT) detection [11]. These improvements reflect the technology's ability to identify subtle connections and patterns across diverse security data types that would remain invisible to conventional detection approaches.

5.3. Real-Time Anomaly Detection at Scale

Spanner's ability to handle massive transaction volumes while maintaining consistency enables real-time anomaly detection across global infrastructure. According to Google Cloud documentation, Spanner Graph's distributed graph engine supports horizontal scaling to accommodate unlimited security data growth without performance degradation [10]. This scalability enables comprehensive security monitoring across even the largest enterprise environments without sacrificing detection speed. The performance characteristics for security-specific workloads demonstrate significant advantages over traditional approaches. Li and Taylor report that real-time alert generation with Spanner Graph completes in less than 10 seconds, compared to 2-5 minutes with traditional database technologies, representing a 12- 30x improvement [11]. Similarly, anomaly detection processing that previously required T+1 (next-day) analysis can now be performed continuously with results available in less than 60 seconds—a 1,440x acceleration that transforms detection capabilities.

The operational improvements extend beyond performance to dramatically enhance detection effectiveness. Security operations centers implementing Spanner Graph have seen advanced threat detection rates increase from 24% to 76%, according to Li and Taylor's analysis [11]. This 217% improvement directly addresses the growing sophistication of modern attacks, which frequently employ techniques specifically designed to evade traditional detection methods. The false positive reduction is equally significant, decreasing from 53% to 8%—an 85% improvement that addresses a persistent challenge in security operations where alert fatigue frequently leads to missed detections.

5.4. Unified View Across Security Domains

Traditional security monitoring often suffers from siloed visibility, with network security, endpoint security, and application security operating as separate domains. Spanner Graph enables a unified security graph that integrates data from all these domains through its multi-model storage architecture. According to Google Cloud documentation, this architecture combines relational and graph data models to provide unified storage for both structured security data and relationship information [10]. This integration capability eliminates the data fragmentation that frequently creates blind spots in security monitoring. The operational impact of this unified approach is particularly evident in cross-domain attack scenarios. Li and Taylor's analysis of deployment scenarios reveals that retail and e-commerce organizations implementing Spanner Graph achieved a 73% increase in account takeover detection and a 9.2x reduction in successful data exfiltration [11]. These improvements reflect how a unified security graph can expose attack patterns that span traditional security domains, such as credential theft via phishing, followed by suspicious login behavior, and subsequent data access attempts. The detection improvements are especially significant for sophisticated threats that deliberately exploit visibility gaps between security domains. In critical infrastructure deployments, Spanner Graph implementation resulted in 96% more privilege escalation attempts detected and a 93% reduction in security blind spots, according to Li and Taylor's compilation of customer metrics [11]. These improvements directly address a common attacker technique of moving between security domains to avoid detection, such as leveraging network access to compromise endpoints and then using those endpoints to access sensitive applications.

5.5. Temporal Analysis and Attack Reconstruction

Spanner's time-versioned data model allows security teams to "time travel" through historical states of the security graph. Google Cloud documentation describes this as "a temporal graph with point-in-time recovery," enabling attack timeline reconstruction and retrospective threat hunting [10]. This capability is implemented through time-travel storage, which maintains versioned graph data with efficient point-in-time access for forensic analysis. The performance advantages for historical analysis are substantial compared to traditional approaches. Li and Taylor report that historical investigations that previously required data warehouse queries taking minutes can now be performed with in-database queries completing in seconds—a 60x improvement [11]. This performance enhancement enables interactive forensic analysis during incident response, allowing security teams to rapidly understand attack progression and identify all affected systems. The time-based analysis capabilities provide particular value for detecting sophisticated threats that develop slowly over time. According to Google Cloud documentation, Spanner Graph's time-travel capabilities enable security teams to identify subtle changes in entity relationships and permissions that might indicate unauthorized access or insider threats [10]. This ability to compare current and historical states of the security graph addresses a significant blind spot in traditional security monitoring, where gradual changes over time often remain undetected until after an incident occurs.

5.6. Adaptive Security Posture through Graph Analytics

Beyond reactive threat detection, Spanner Graph enables proactive security improvements through advanced graph analytics. The deployment metrics compiled by Li and Taylor demonstrate the effectiveness of this approach across diverse security

environments. Manufacturing organizations implementing Spanner Graph for operational technology (OT) security identified 82% more attack surface paths and achieved a 5.7x improvement in asset protection [11]. These metrics highlight how graph analytics can identify structural vulnerabilities before attackers can exploit them. The architectural foundation for these advanced analytics capabilities lies in Spanner Graph's distributed processing engine. According to Google Cloud documentation, this component enables complex graph algorithms to run at scale without the performance limitations that typically constrain analytics on large security datasets [10]. The combination of this processing capability with pre-defined security schema templates accelerates the deployment of sophisticated security use cases that would otherwise require extensive custom development. The operational impact extends beyond improved detection to include significant efficiency gains for security teams. Li and Taylor report that security operations centers implementing Spanner Graph have increased the number of threats detected per analyst from 12 per week to 47 per week—a 292% productivity improvement [11]. This efficiency gain addresses the persistent security skills shortage by enabling existing teams to effectively manage larger environments and more sophisticated threats without proportional increases in staffing. Similarly, the reduction in analyst time per alert from 38 minutes to 11 minutes (71% improvement) allows more effective allocation of specialist expertise to the most critical incidents.

6. Conclusion

The evolution of database technologies for cybersecurity applications represents a fundamental shift in how organizations detect and respond to sophisticated threats. From the early days of simple log management systems to the current generation of globally distributed graph databases, each advancement has progressively addressed critical security challenges while enabling new capabilities. Google's Spanner Graph technology stands as a significant milestone in this evolutionary journey, delivering transformative performance improvements and detection capabilities that were previously unattainable at enterprise scale. The technology's ability to maintain temporal precision across distributed environments, process complex relationship queries in milliseconds rather than seconds, and unify visibility across traditionally siloed security domains has fundamentally changed what security teams can accomplish. As security data continues to grow exponentially across all industries, the architectural advantages of technologies like Spanner Graph become increasingly critical for maintaining effective security operations. The future of database security lies in the continued integration of artificial intelligence capabilities, deeper collaboration between database and security specialists, and increasingly automated threat detection and response workflows. The convergence of database management and cybersecurity disciplines has created new professional roles and organizational structures better suited to addressing modern security challenges. As regulatory requirements continue to expand and attack techniques grow more sophisticated, the strategic importance of database architecture decisions will only increase. Organizations that embrace advanced database technologies purpose-built for security applications will gain significant advantages in threat detection efficiency, comprehensive visibility, and proactive risk management compared to those attempting to adapt general-purpose database platforms to security use cases.

Funding: This research received no external funding.
Conflicts of Interest: The authors declare no conflict of interest.
Publisher's Note: All claims expressed in this article are solely those of the authors and do not necessarily represent those of their affiliated organizations, or those of the publisher, the editors and the reviewers.

References

[1] Bei Li, Chris Taylor, "Introducing Spanner Graph: Graph databases reimagined," Google Cloud, 2 August 2024. Available: https://cloud.google.com/blog/products/databases/announcing-spanner-graph

[2] Codrin Teiu, "Cybersecurity And Data Management In Digital Ecosystems," Logarithmic. Available:https://www.logarithmic.com/cybersecurity-and-data-management-in-digital-ecosystems

[3] Craig Riddell, "Data Security Explained: Challenges and Solutions," Netwrix, 12 February 2024. Available: https://blog.netwrix.com/data-security/

[4] Craig S. Mullins, "The Role of the DBA in Cybersecurity," DBTA, 3 January 2022. Available:https://www.dbta.com/Columns/DBA-Corner/The-Role-of-the-DBA-in-Cybersecurity-150732.aspx

[5] David Reinsel et al., "The Digitization of the World: From Edge to Core," Seagate, International Data Corporation, November 2018. Available:https://www.seagate.com/files/www-content/our-story/trends/files/idc-seagate-dataage-whitepaper.pdf

[6] Google Cloud, "Spanner Graph overview," Available:https://cloud.google.com/spanner/docs/graph/overview

[7] Imperva, " What is Data Security?" Available: https://www.imperva.com/learn/data-security/data-security/

[8] Inery Blogs, "The Evolution of Database Technology: From Flat Files to Blockchain," April 2024.Available: https://inery.io/blog/article/the-evolution-of-database-technology/

[9] Jagdish Mohite, "Data Security: Challenges, Solutions, and the Path Forward," Akamai, 8 January 2025.Available:https://www.akamai.com/blog/security/data-security-challenges-solutions-and-the-path-forward

[10] Malcolm Crowe and Fritz Laux, "Database technology evolution," ResearchGate, January 2022.Available: https://www.researchgate.net/publication/367499325_Database_technology_evolution

[11] Pwheiler, "The State of Security Operations: How SOCs changed in 2021," OpenText Community, 28 September 2021.Available:https://community.opentext.com/cybersec/b/cybersecurity-blog/posts/the-state-of-security-operations-how-socs-changed-in-2021#:~:text=Security%20operations%20has%20seen%20non,Europe%2C%20Asia%2C%20and%20Australia.

Sādhanā (2025)50:123
https://doi.org/10.1007/s12046-025-02803-0
© Indian Academy of Sciences

The unique modified seesaw test (MST) instrument for the direct assessment of rock's tensile strength utilizing ring-shaped specimens

PARVEEN KUMAR[1], SRIJAN SRIJAN[1,2,*], VANITA AGGARWAL[1] and BALJIT SINGH WALIA[1]

[1]Department of Civil Engineering, Maharishi Markandeshwar (Deemed to be University), Maharishi Markandeshwar Engineering College, Mullana, Haryana 133207, India
[2]Department of Civil Engineering, Delhi Technological University, New Delhi 110042, India
e-mail: srijanpurvey@gmail.com

MS received 17 November 2024; revised 9 March 2025; accepted 10 March 2025

Abstract. This study introduces the Modified Seesaw Test (MST), an innovative method for determining tensile strength in ring-shaped rock specimens by applying diametral tensile forces from the inner diameter outward. Utilizing finite element analysis in ANSYS Workbench 2021, tensile stress values and shape factors were calculated across various diameter ratios for both MST and Indirect Ring (IR) tests. The analysis demonstrated a decrease in failure load with increasing inner diameter, with tensile strengths from the Brazilian Disc (BD) test surpassing those from the IR and MST methods by 15% and 23%, respectively. Fracture pattern analysis revealed more linear fractures in MST specimens due to perpendicular loading, compared to the multi-line fractures in IR specimens caused by combined stresses. Despite these variations, MST and IR methods proved reliable, offering viable alternatives to the BD test, particularly for low-capacity testing setups. This research underscores the critical role of specimen geometry and loading configuration in tensile strength measurements, providing valuable insights for advancing tensile testing methodologies in rock mechanics.

Keywords. Brazilian indirect tensile strength test; modified seesaw test; direct tensile test; indirect ring test; marble; granite.

1. Introduction

When the tensile strength of intact rock is significantly less than the compression resistance, it is a significant factor that influences how the rock mass behaves. However, the tensile stresses developed in certain sections of the rock mass when in contact with a rock of differing stiffness, as in the tunnel crown, cave roof, slope top, or ground anchors, this may be decisive in the rock failure [1]. Thus, the primary goal of a number of published studies in the field of rock mechanics is the assessment and determination of rock tensile strength.

Several methodologies exist for assessing the tensile strength of rocks, as depicted in figure 1. These include the Brazilian Disc (BD) test, indirect ring (IR) test, semi-circular bend (SCB) test, three-point flexural beam test, four-point flexural beam test, direct tension (DT) test, and direct ring (DR) test [2]. Among these, the Brazilian tensile test is extensively used because of its adaptability, although it offers obstacles, notably in preparing dog bone specimens from brittle rock sources. [3]. The tensile capacity of rocks (σ_t) by BD method can be determined as:

$$\sigma_t = \frac{2P}{\pi t d} \tag{1}$$

where 'P' is the ultimate load, 't' is the thickness of the sample and 'd' is the diameter of the specimen.

The Indirect Ring (IR) test, developed by Berenbaum and Brodie in 1959 [4], is another famous indirect test procedure for evaluating the tensile strength of quasi-brittle and brittle samples. Ring tests are popular because of their simple sample preparation and form. The ring test has proved effective in determining the tensile stress of a range of materials, including rocks, soils, geomaterials, concrete, and ceramics [4–6]. In parallel, the Semi-Circular Bending (SCB) test is preferred because to its simple specimen preparation and ability to achieve varied loading modes by altering the crack inclination angle. However, the requirement for exact crack angle control in order to achieve appropriate mode mixity adds a significant level of complication. For instance, establishing pure mode II loading frequently necessitates fracture angles greater than 50°, which raises the danger of specimen destruction and

*For correspondence
Published online: 19 June 2025

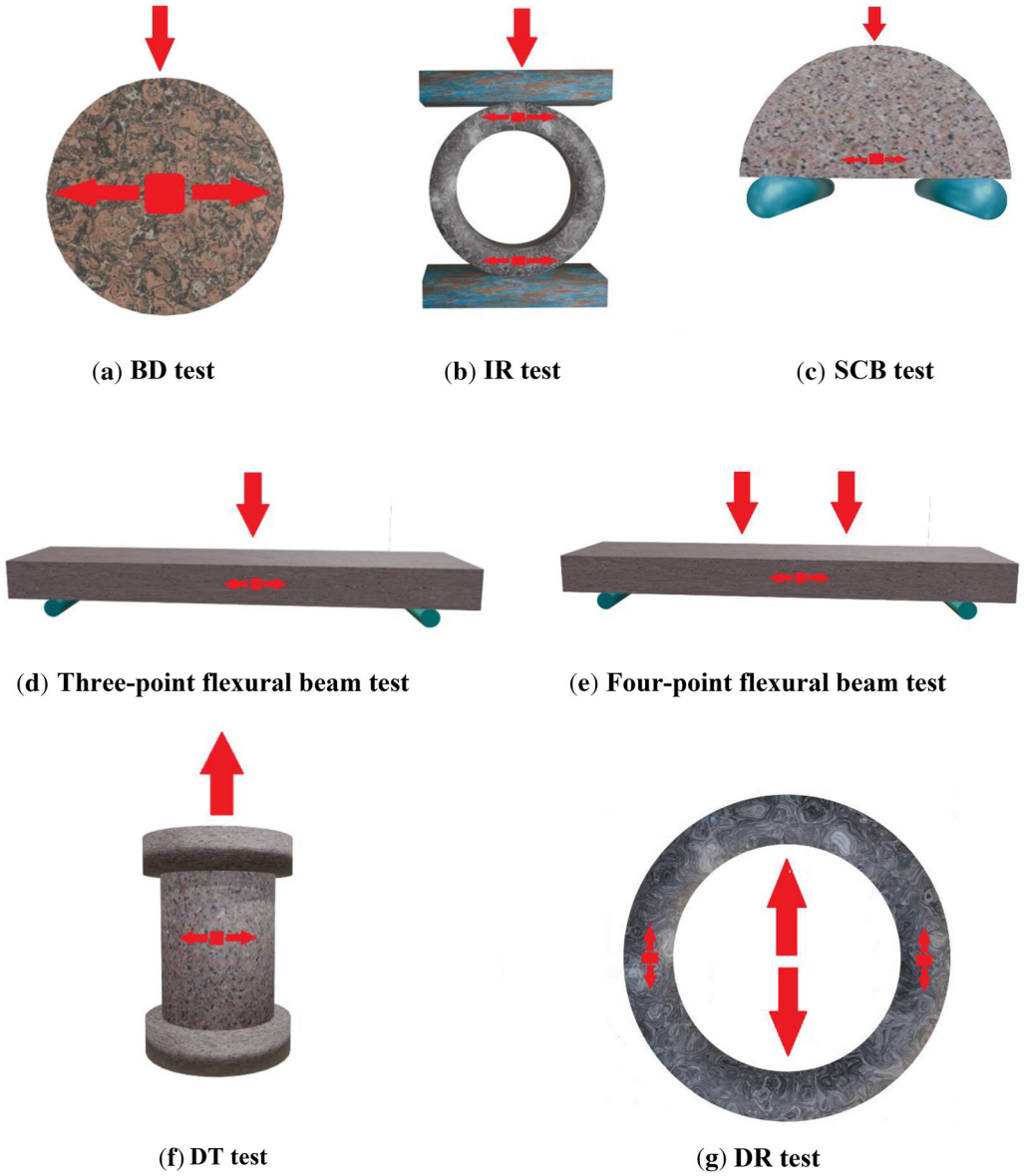


Figure 1. Overview of the existing techniques for measurement of the tensile strength of rock specimens.

undermines result validity [7]. Similarly, the Three-Point Bending Test (TPBT) [8], also known as the three-point flexural beam test, is commonly used due to its ease of applying a load to the midpoint of a beam supported at both ends. However, TPBT frequently overestimates tensile strength due to stress concentrations near the supports, especially when the span-to-length ratio (l/b) is low. This stress concentration causes a non-uniform stress distribution along the beam's bottom centerline, resulting in localised failures that do not adequately reflect the material's true tensile strength [9]. The Four-Point Bending Test (FPBT) [10], also known as the 4-point flexural beam test, is useful for calculating the flexural stress of rock materials in engineering applications such as tunnelling, mining, and underground space development, but it has several limitations. The FPBT assumes uniform elastic properties across the material, yet rocks often exhibit differing elastic moduli in tension and compression. Failure to account for these differences can lead to an overestimation of the specimen's flexural capacity [11].

The previous researches suggest that tensile strength values vary among testing methodologies due to factors such as loading type and the geometry of the samples. Consequently, the utilisation of novel and appropriate alternative testing procedure for assessing the tensile strength of rock and geo-materials remains a pertinent concern for rock mechanics engineers. Aliha *et al* proposed an innovative test apparatus [12] for calculation of direct

tensile stress of rocks by utilising seesaw test (ST) device. In the current study, a novel modified seesaw test (MST) has been proposed to counter the limitations of current existing seesaw test. Modification has also been done to the indirect ring test and a modified equations have been presented. The efficacy of the proposed method is subsequently examined through both numerical and experimental approaches to ascertain the tensile strength of a standard rock specimen. It is demonstrated that the σ_t acquired from the ISRM Brazilian disc (BD) test method and the output obtained from this direct testing method agree well. In contrast to the Brazilian disc specimen, a substantially lower load is needed to evaluate the direct ring specimen.

2. Limitations of existing seesaw and indirect ring test

Aliha and others innovative test apparatus [12] for evaluating the tensile strength of ring-shaped rock samples, depicted in figures 2, 3(a), and (b), reveals a significant correlation between tensile strength and specimen diameter ratio. This contribution highlights the ongoing evolution in testing methodologies and the need for continued refinement to accurately assess rock material properties in varied engineering contexts.

However, the seesaw testing apparatus [12], while innovative, presents multiple limitations that must be addressed to maintain the accuracy and consistency of the outputs obtained. One among the primary concerns is the uneven weight distribution inherent in the apparatus's design. The seesaw mechanism exerts force to a circular rock sample, and the maximum load capacity varies greatly depending on the configuration and materials employed in the apparatus. Uneven load distribution can cause an imbalance, which not only skews tensile strength readings but also creates a danger of system collapse. Another issue concerns the seesaw device's centre of gravity. The proper arrangement of the load's centre of gravity can have a considerable impact on the equipment' load capacity. If the centre of gravity deviates significantly from the device's geometric centre, this imbalance might result in system failure or erroneous results.

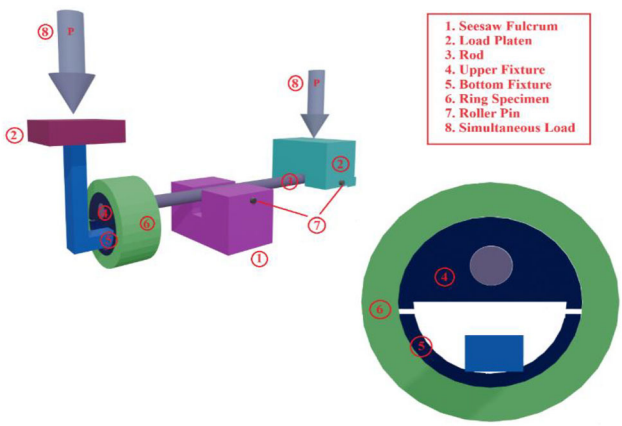


Figure 2. Schematic diagram of the Seesaw instrument for direct tensile testing, including part labels as proposed by Aliha *et al*.

Aliha *et al* [12] proposed mathematical methods for calculating tensile strength in both indirect and direct tensile testing using the seesaw equipment, with diameter ratios ranging between 0.5 and 0.75. The provided equations are:

For indirect ring test,

$$\sigma_t = \frac{2P}{nt(D-d)}\left[35.05\left(\frac{d}{D}\right) - 9.22\right] \tag{2}$$

For direct test by the seesaw test (ST) device,

$$\sigma_t = \frac{2P}{nt(D-d)}\left[19.35\left(\frac{d}{D}\right) - 2.115\right] \tag{3}$$

where P is the critical load applied, t, d and Dare the thickness, inner and outer diameter of the ring specimen, respectively.

Applying equation (1) to the indirect ring test with d/D ratios of 0.1, 0.2, and 0.25 and equation (2) to the direct test using the seesaw method with a d/D ratio of 0.1 yielded negative results. These negative results highlight a fundamental problem with the equations' prediction powers, which were initially constructed solely for data in the d/D range of 0.5 to 0.75.

To improve the accuracy of these predictions and avoid inaccurate results, the shape factor should be reassessed by broadening the range of d/D ratios examined from 0.1 to 0.85. This expanded research will allow for a more thorough examination of the association between the variables, offering more accurate and dependable insights into the tensile stress behaviour of rock samples. By addressing these constraints, the seesaw testing apparatus can be improved to produce more consistent and precise findings in determining rock tensile strength, resulting in more reliable engineering applications.

3. Proposed methodology for assessing the tensile strength of ring-shaped rock materials

3.1 *Direct tensile test using modified seesaw test (MST)*

A novel and streamlined experimental methodology have been proposed for the precise calculation of the tensile stress of ring-shaped rock samples. This innovation addresses the inherent limitations of the conventional seesaw test apparatus.

The "Modified Seesaw Test (MST) [13]," a recently refined testing apparatus, is depicted in figure 4 with the

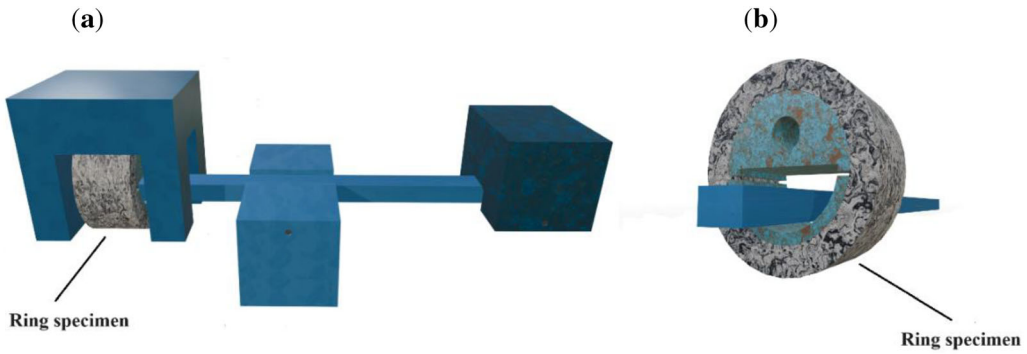


Figure 3. (**a**) The seesaw testing apparatus utilized to conduct tensile strength tests on rock samples. (**b**) Circular/ring shaped sample placed inside the seesaw testing equipment.

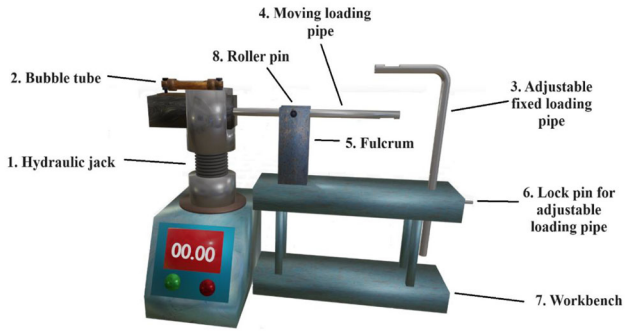


Figure 4. Modified seesaw test equipment for direct tensile test of ring-shaped rock samples depicting different components.

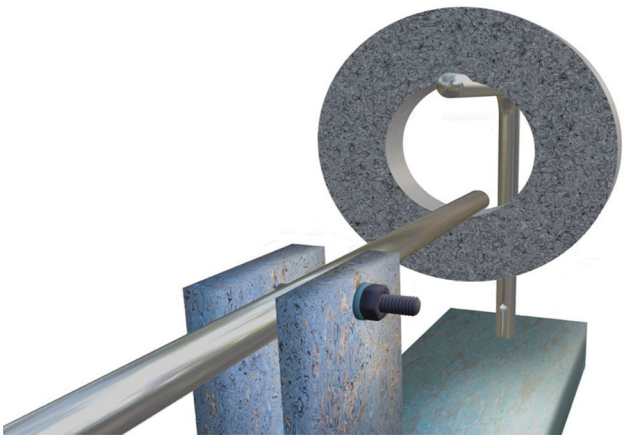


Figure 5. Ring-shaped specimen positioned within the Modified seesaw testing apparatus.

details of the constituent components of the MST apparatus, which employs a circular rock specimen, and a lever mechanism designed to exert dual tensile forces on the internal surface of the ring sample along its diameter. As illustrated in figure 4, part 4, referred to as the moving loading pipe, and part 3, known as the adjustable fixed loading pipe, engage the inner surface of the ring specimen, imparting two evenly distributed tensile stresses diametrically across the specimen. The adjustable fixed loading pipe (part 3) is meticulously positioned and maintained at a consistent elevation both at the initiation of the test and throughout the implementation of load via the testing machinery. The vertical positioning of this pipe can be adjusted upward or downward in accordance with the internal diameter of the ring-shaped specimen, and it is securely fixed in place by a locking pin (part 6). The moving loading pipe (part 4) is similarly aligned horizontally and can be precisely adjusted through the vertical motion of a hydraulic jack. A bubble level is affixed to one end of the moving loading pipe to ensure accurate alignment within the principal plane, thereby guaranteeing the precision of the tensile force application throughout the testing process.

Consequently, this loading mechanism induces a purely tensile stress within a plane orthogonal to the direction of the applied load. It is predicted that the ring sample will

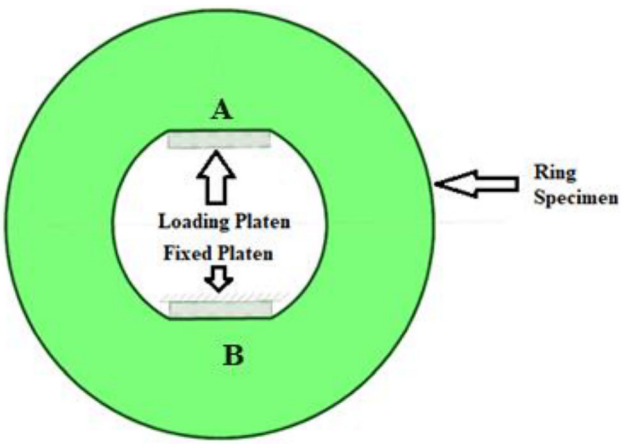


Figure 6. The Load and boundary condition of ring specimen.

fracture into two distinct halves along the axis of the maximum normal tensile stress. Components 3 and 4 of the apparatus were fabricated using SS-316 stainless steel,

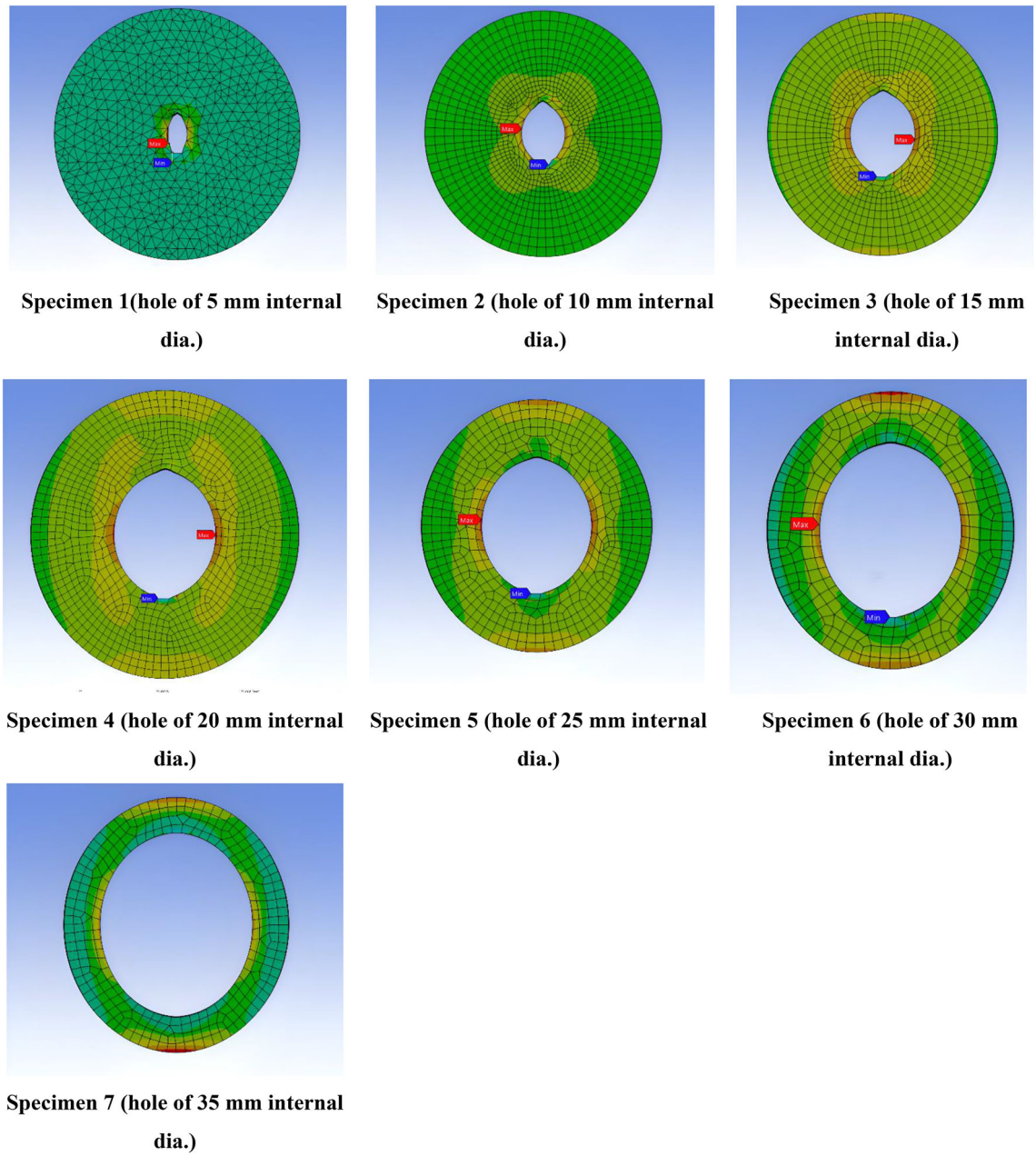


Figure 7. The stress contours derived from finite element analyses of the direct ring specimens having different inner diameters, employing the modified seesaw mechanism.

while the remaining components were constructed from St-3 steel. As the applied load (P) increases, the corresponding normal stress within the specimen also escalates. At a critical load level, the tensile stress within the rock specimen approaches its ultimate tensile strength (σ_t). The tensile stress generated in the ring specimen, as measured by the modified seesaw apparatus, is dependent on both the geometric configuration of the ring and the imposed load's magnitude. To establish the relationship among the external load (P) and the resultant stress within the specimen, the fundamental stress equation $\sigma = P/A$ is employed, where 'A' represents the cross-sectional area of the specimen. Figure 5 represents the ring-shaped specimen positioned within the Modified seesaw testing apparatus.

The modified seesaw test (MST) method proposes the given equation for estimating the tensile strength:

$$\sigma_t^{MST} = \frac{2P}{nt(D-d)} Y_{MST} \tag{4}$$

where P = failure load of the ring sample; t, d and Dare the thickness, inner and outer diameter of the ring specimen, respectively. The term Y_{MST} is a shape factor that accounts for the influence of specimen geometry and loading

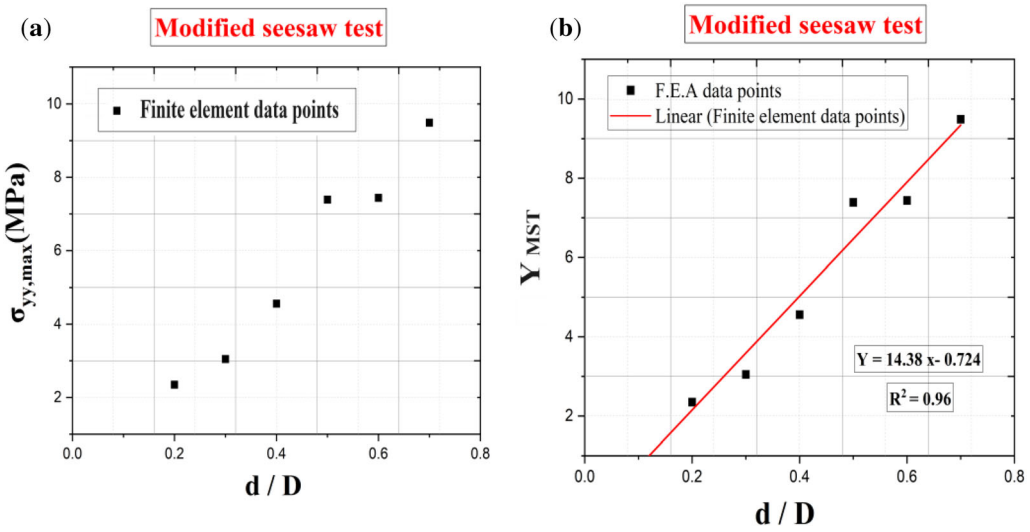


Figure 8. (**a**) Variation in maximum σ_{yy} stress with the d/D ratio in ring samples subjected to tensile load using the modified seesaw device, and (**b**) utilization of the shape factor (Y_{MST}) for calculating tensile strength in the modified seesaw ring test.

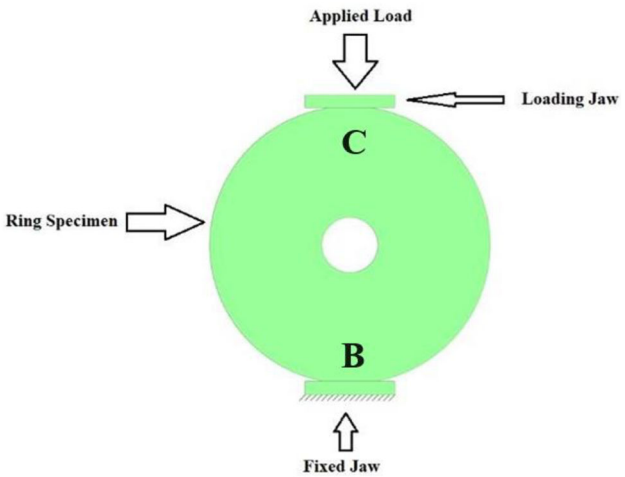


Figure 9. Load and boundary conditions in IR test.

conditions on the stress distribution within the tested specimens. This shape factor enables a comprehensive evaluation of these variables to precisely identify the tensile strength (σ_t) of the materials under examination.

To establish a precise relationship between the geometry of the ring sample and maximum tensile stress, a series of finite element analyses were conducted by the help of various ring geometries. The outer diameter of the ring was kept constant at a value of 50 mm, while the inner diameter varied from 5 to 35 mm in 5 mm increments. The ring samples were analysed using the elastic material properties typical of a standard rock material, characterized by a Young's modulus (E) of 54 gigapascals (GPa). To impose boundary conditions, line B was constrained in all directions, as shown in figure 6, while line A was constrained exclusively in the X direction. The interior segment of the ring was subjected to a consistent vertical force of 3000 N. The contours of normal stress (σ_{yy}) for the examined ring specimens with varying inner diameters are illustrated in figure 7, providing insight into the stress distribution across the different geometries under the applied loading conditions.

A formal mesh convergence study was conducted prior to finalizing the element size. We incrementally refined the mesh from 2 mm, 1.5 mm, 1 mm, down to 0.5 mm, monitoring the maximum principal stress in each iteration. The variation in maximum stress did not exceed 4.79% between the finest (0.5 mm) and the coarsest (2 mm) meshes. Consequently, 2 mm was selected as the optimal mesh size to balance computational efficiency and accuracy.

Figure 8(a) illustrates the correlation between the maximum normal stress and the d/D ratio, which denotes the ratio of the internal to the outer diameter of the ring samples, as determined from the finite element analyses. This data was subjected to linear regression analysis to extract the shape factor (Y_{MST}) specific to the modified seesaw test specimen. The outcomes of this analysis are depicted in figure 9(b) and are encapsulated in Equation (5) for various d/D ratios. The linear regression model exhibits strong association (R^2 = 0.96) between the shape factor (Y_{MST}) and the d/D ratio, underscoring the validity of this linear relationship as a reliable indicator of the Y_{MST} for the modified seesaw ring specimen. Consequently, this linear correlation was utilized to compute the tensile stress, leading to the derivation of Equation (6), which enables the precise determination of tensile stress for the ring sample subjected to direct tensile stress using the modified seesaw test methodology.

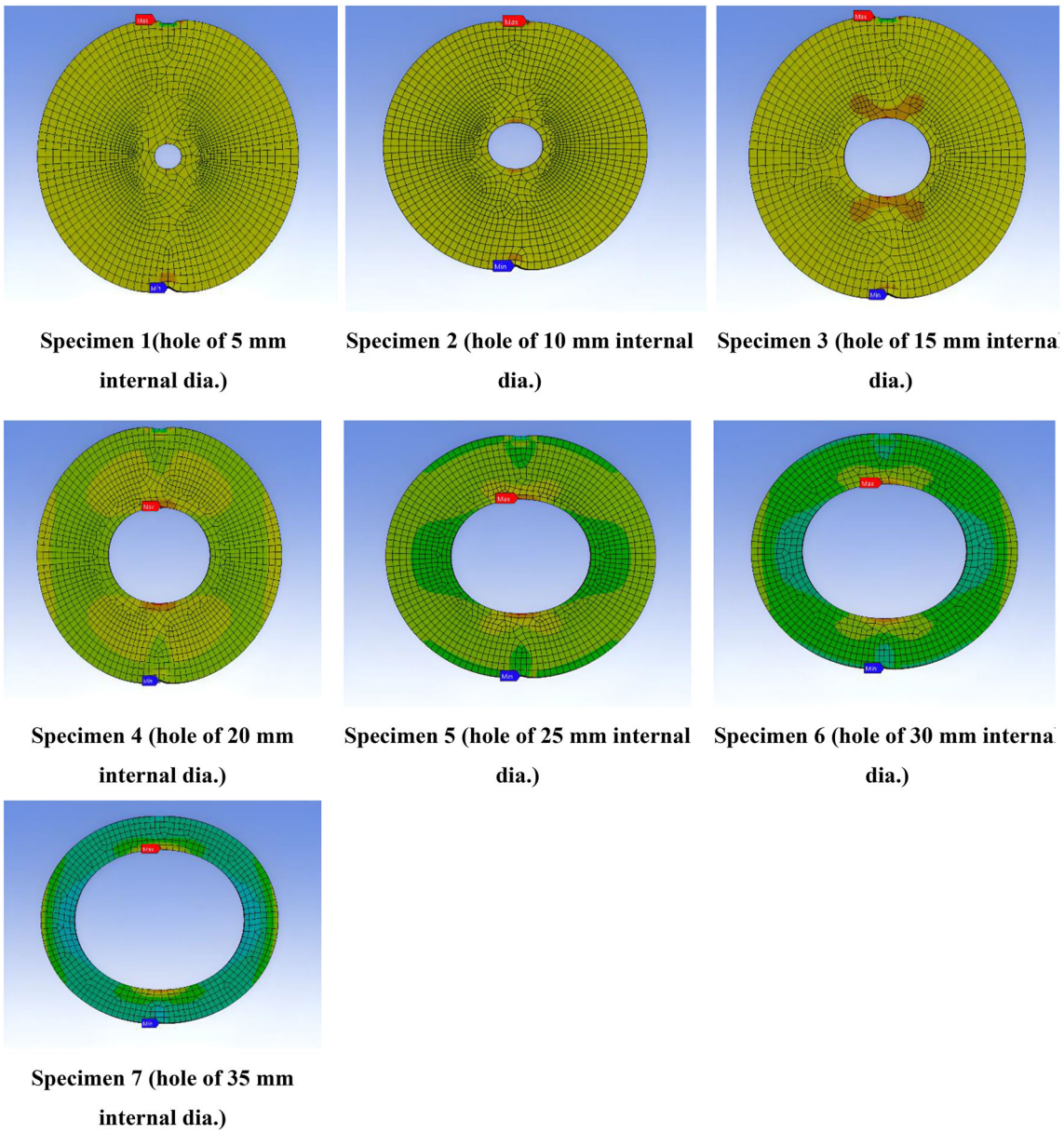


Figure 10. Stress contours derived from finite element analysis of direct ring specimens with varying internal diameters using the indirect ring test.

$$Y_{MST} = 14.38\left(\frac{d}{D}\right) - 0.724 \tag{5}$$

$$\sigma_t^{MST} = \frac{2P}{nt(D-d)}\left[14.38\left(\frac{d}{D}\right) - 0.724\right] \tag{6}$$

3.2 *Indirect Ring (IR) test*

As previously discussed, the ring geometry can be effectively utilized to indirectly assess tensile strength by subjecting the ring sample to diametral compression. This approach mirrors the methodology employed in the modified seesaw device for direct tensile testing, allowing for the determination of the tensile strength (σ_t) using a diametrally compressed ring sample. Given the geometric and loading similarities between the compressed ring and the ring is under direct tension, the same fundamental equation as in Eq. (4) can be applied. However, it is imperative to incorporate a shape factor specific to diametral compressive loading, denoted as Y_{IR}, into the tensile strength equation for the indirect method:

$$\sigma t^{IR} = \frac{2P}{nt(D-d)} Y_{IR} \tag{7}$$

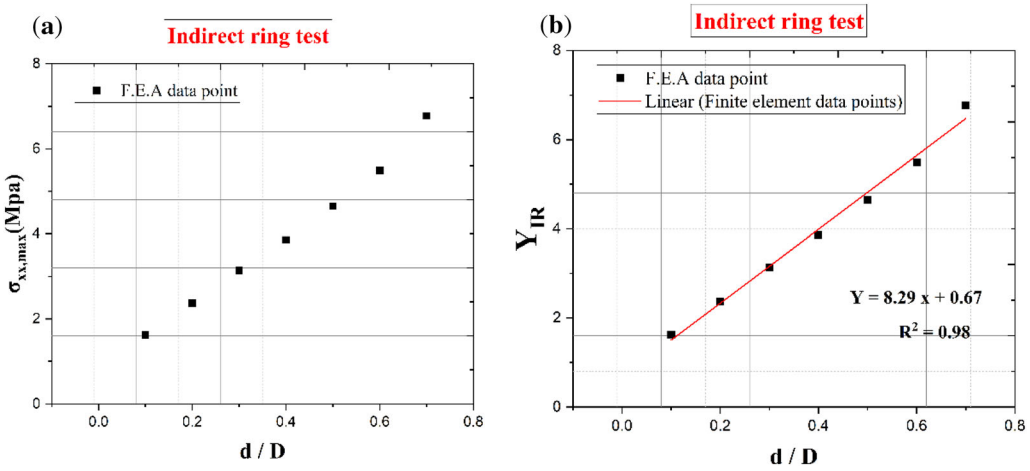


Figure 11. (**a**) Variations of $\sigma_{xx,\ max}$ with the d/D ratio in ring samples analysed under tensile loading using the indirect ring test. (**b**) Shape factor (Y_{IR}) used to determine tensile strength in the indirect ring.

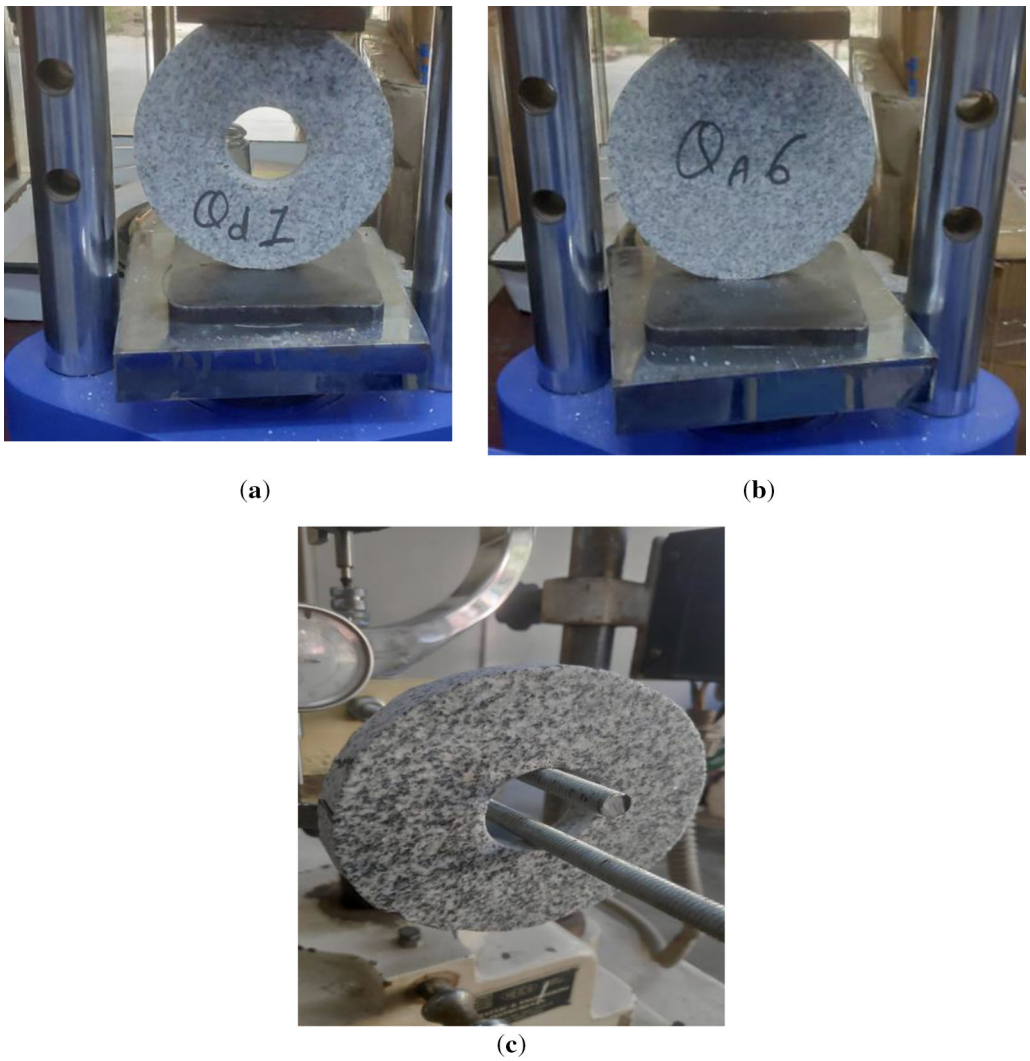


Figure 12. Tensile strength determination of light grey granite rock by (**a**) Indirect ring testing, (**b**) Brazillian disc method and (c) Modified seesaw test.

Table 1. Failure Load and Tensile Strength values derived from IR and MST Methods.

Test	d (mm)	D (mm)	t (mm)	d/D	Failure load (N)	Tensile strength, σ_t (Mpa)
IR	18.7	119.4	16.9	0.16	13493	9.93
	19.3	120.7	19.3	0.16	15386	9.98
	18.8	121.4	18.3	0.15	15346	10.16
	27.7	121.4	16.6	0.23	8713	9.13
	26.4	120.9	16.7	0.22	8604	8.60
	26.5	122.3	16.4	0.22	8680	8.67
	36.6	119.6	16.8	0.31	4335	6.34
	36.7	120.6	16.5	0.30	4369	6.41
	36.5	122.3	16.4	0.30	440	6.26
					Average	8.39
MST	18.7	119.1	18.1	0.16	12699	6.82
	18.8	121.4	17.8	0.15	14460	7.57
	19.6	120.9	17.9	0.16	14378	8.11
	26.9	121.4	16.5	0.22	8190	8.23
	26.6	120.8	16.4	0.22	8090	8.14
	27.3	119.7	16.1	0.23	8169	8.93
	36.5	122.3	16.4	0.30	4080	6.58
	36.9	121.6	16.3	0.30	4110	6.90
	36.1	121.9	16.4	0.30	4142	6.62
					Average	7.54

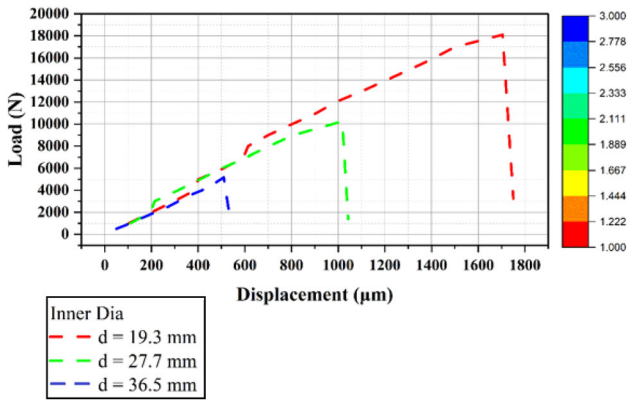


Figure 13. Load-displacement curve for varying d/D ratio for indirect ring test.

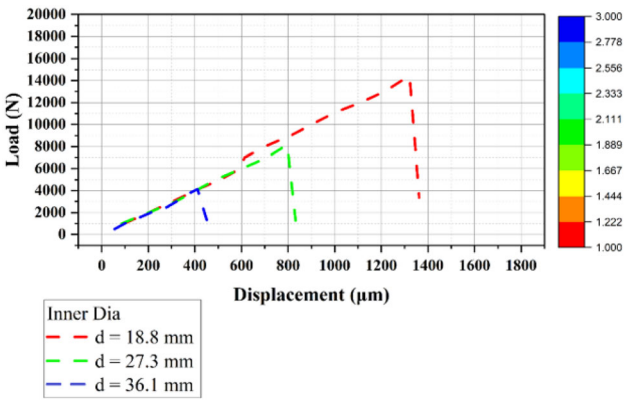


Figure 14. Load-displacement curve for varying d/D ratio for modified seesaw test.

Here, "IR" stands for "Indirect Ring," and Y_{IR} represents the shape factor associated with the compressed ring specimen. To accurately determine Y_{IR}, the ring specimen initially used in the direct seesaw testing was re-evaluated numerically under modified loading and boundary conditions. Specifically, the bottom support (point B in the figure 9) was constrained in all the directions, while the upper support (point C in figure 9) was constrained in the X direction. A consistent compressive force of P = 3000 N was given vertically, thereby subjecting the ring to the diametral compression. Finite element analyses were conducted across a range of inner diameters (d), varying from 5 to 35 mm, while maintaining a fixed outer diameter (D) of 50 mm, resulting in a d/D ratio spanning from 0.1 to 0.7. The resulting normal stress contours (σ_{yy}) for the evaluated ring samples with these varying diameter ratios are depicted in figure 10.

By plotting the normal stress component (σ_{xx}) at element "A" against the d/D ratio (figure 11a), the shape factor Y_{IR} was derived from a linear regression, with figure 11(B) illustrating the Y_{IR} values for different d/D ratios for the indirect tensile test. The linear fit produced a strong correlation coefficient (R^2 =0.98), proving the reliability of the relationship. Hence, the subsequent equation is proposed to calculate the tensile strength for the compressed ring specimen:

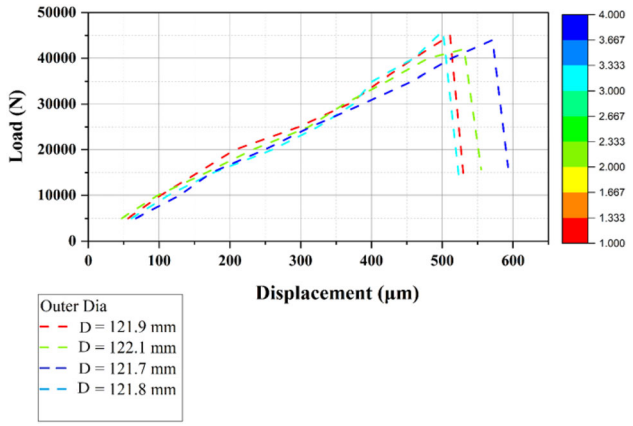


Figure 15. Load-displacement curve obtained from BD test.

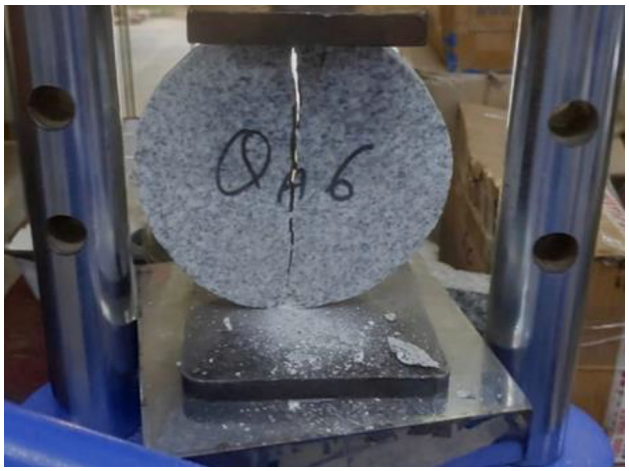


Figure 16. Fracture pattern of BD rock specimen composed of light grey granite.

$$\sigma_t^{IR} = \frac{2P}{nt(D-d)}\left[8.29\left(\frac{d}{D}\right) + 0.67\right] \tag{8}$$

The tensile strength of both direct and the indirect ring test specimens (i.e., MST and IR specimens) can thus be determined using Equations (6) and (8). It is noteworthy

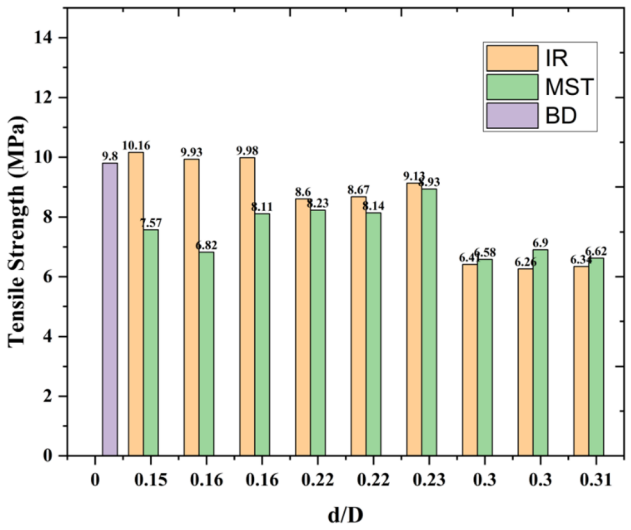


Figure 17. Tensile strength results for light grey granite from BD, IR, and MST tests.

that distinct shape factors Y_{MST} and Y_{IR} is dependent on the type of loading, irrespective of the diametral tension or diametral compression is applied to the ring samples. These factors are crucial for accurately characterizing the tensile behaviour of the materials under different loading conditions.

4. Experimental details

To assess the efficacy of both indirect and direct tensile ring tests for brittle materials, a series of experiments were conducted on granite, a coarse-grained igneous rock characterized by its mineral composition, which includes quartz, iron oxide, mica, and feldspar [14]. Ring specimens with inner diameters ranging from 5 mm to 35 mm were meticulously prepared. For each geometry, three specimens were subjected to the direct ring test using the modified seesaw fixture, while another three were tested under diametral compression. These tests are pivotal for acquiring

Table 2. Failure load and tensile strength values derived from BD method.

Test	D (mm)	t (mm)	Failure load (N)	Tensile strength, σ_t (Mpa)
BD	121.9	17.3	31800	9.6
	122.1	16.7	32300	10.1
	121.8	17.1	32200	9.8
	121.7	16.9	30800	9.5
	121.5	16.8	32400	10.1
	120.4	17.5	32200	9.7
			Average	9.8

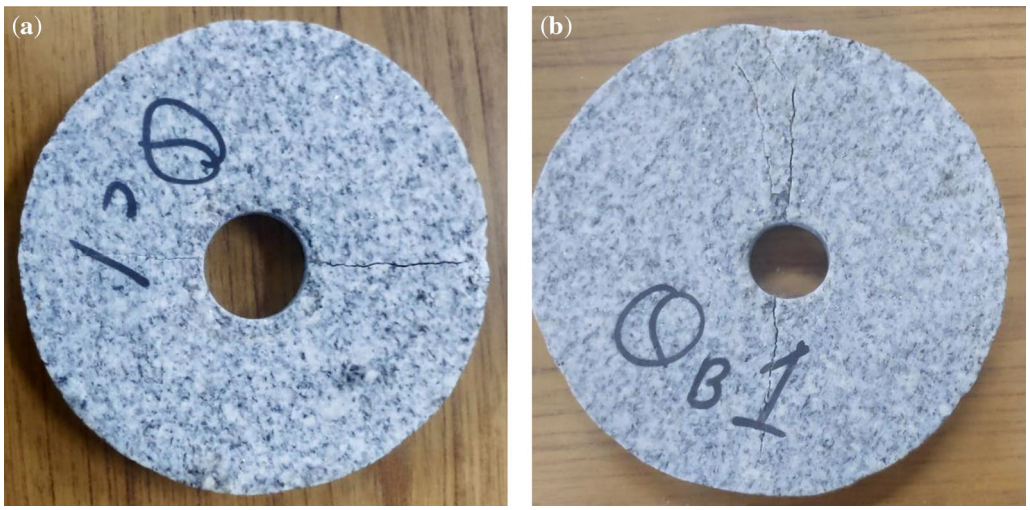


Figure 18. (**a**) Fracture pattern of MST rock specimen composed of light grey granite. (**b**) Fracture pattern of IR rock specimen composed of light grey granite.

tensile strength data that are essential for engineering applications.

In the direct tensile test, the ring specimens were precisely positioned within the modified seesaw fixture, which was subsequently subjected to loading by a testing equipment, as illustrated in figure 5. The compressive load applied by the testing machine is effectively converted into a tensile load within the fixture, ensuring accurate tensile stress application.

For the indirect tensile testing, the ring samples were put between two flat plates within a Brazilian testing machine and subjected to diametral loading [15], as shown in figure 12(a) Also, Brazillian disk method testing was done for the comparison analysis as shown in figure 12(B) and modified seesaw test presented in figure 12(c). By meticulously measuring the critical splitting load for each of the ring specimen and utilizing these shape factors and the recorded critical loads, the tensile stress of the rock specimens was determined according to Equations (6) and (8). These calculated tensile strengths provide valuable perspective into the mechanical behaviour of granite under varying loading circumstances, enhancing the understanding of its performance in real-world.

5. Results and discussions

Table 1 illustrates the tensile strength results derived from both the Indirect Ring (IR) and Modified Seesaw Test (MST) methods for ring-shaped rock specimens across various d/D ratios. A comparative analysis of the tensile strength results from the IR and MST techniques reveals that the tensile strength (σ_t) data found through the MST method are consistently lower than those acquired using the IR method. Specifically, the average tensile strengths for the IR and MST techniques are 8.39 MPa and 7.54 MPa, respectively.

Figure 13 illustrates the typical load-displacement graphs for compressed ring specimens of varying geometries. These curves reveal that the behaviour of the tested rock specimen is brittle and linear, characterized by a sudden dip in the load curve at the onset of fracture [12]. Similarly, the load-displacement graphs for the ring samples with varying d/D ratios, obtained using the modified seesaw direct test method, are shown in figure 14. Here again, the failure behaviour of the compressed granite rock rings is marked by linear elasticity and brittleness [12].

To further assess the efficacy of these ring test techniques in measuring the tensile stress of rocks, Brazilian disc (BD) test specimens were extracted from a light grey granite rock sheet[16]. These samples, with an average diameter of 121.56 mm and an average thickness of 17.05 mm, were tested according to the guidelines suggested by the International Society for Rock Mechanics (ISRM) [17]. Figures 12(b), 15, and 16 depict the experimental setup, the load-displacement graph from the BD test, and the typical fracture patterns identified in the BD specimens. Table 2 details the maximum loads at which the BD samples fractured, as well as the average tensile strength (σ_t) calculated using Equation (8):

$$\sigma_t^{BD} = \frac{2P}{\pi Dt} \tag{8}$$

Figure 17 compares the σ_t values obtained from BD, IR, and MST tests across different d/D ratios. This comparison validates the accuracy and reliability of both testing methods, as recommended by the ISRM for the BD method [18]. Notably, the highest tensile strength observed using the IR method, particularly at a d/D ratio of 0.15, closely aligns with the BD test results [19–21], suggesting that the

IR method is a viable alternative for evaluating tensile strength in rocks and geomaterials. Moreover, it has been demonstrated that a reduced d/D ratio in ring-shaped specimens corresponds to higher tensile strengths [22], which is consistent with the findings from BD testing [23]. When comparing the fracture loads across the BD, MST, and IR test configurations, it is evident that the IR and MST methods require significantly lower loads than the BD tests [24]. This characteristic is particularly advantageous for ring-shaped specimens, as it allows tensile strength testing to be conducted using machines with lower load capacities [12].

Figures 18(a) and (b) depict the fracture patterns of several ring samples tested using both direct (MST) and indirect (IR) tensile methods. As anticipated, the MST specimens fractured into two halves at a right angle to the applied tensile forces. Conversely, the IR specimens exhibited fractures aligned with the direction of the applied compressive diametral force. Notably, MST specimens displayed a singular fracture line, whereas IR specimens exhibited dual fracture lines [25]. Additionally, the fracture paths in the MST specimens were significantly more linear compared to those in the IR specimens. This discrepancy can be attributed to the distinct loading orientations: in IR specimens, the load is applied parallel to the fracture plane [26], while in MST specimens, it is applied perpendicularly, thereby influencing stress flow and distribution within the specimens.

Despite these differences, tensile strength measurements obtained from the various circular-shaped specimens (MST and IR) indicate that all methods yield tensile strength values within an acceptable range, with discrepancies typically less than 11% [12, 27]. The consistency of these variations suggests that they are primarily due to differences in specimen geometry, loading types, and stress distribution patterns along the fracture planes.

6. Conclusion

This study introduced a novel Modified Seesaw Test (MST) device, utilizing a seesaw mechanism to apply diametral tensile loads to the internal diameter of ring-shaped rock specimens, specifically light grey granite. The tensile strength data found from the MST were rigorously compared with results from the Indirect Ring (IR) and Brazilian Disc (BD) tests, yielding critical insights into the tensile behavior of brittle rock materials.

The results revealed a definitive trend: tensile strength decreases as the d/D ratio increases across both MST and IR methods. The IR method consistently yielded tensile strength values approximately 11% higher than those obtained via the MST, a discrepancy attributable to the additional compressive and shear stresses induced at the contact interface between the specimen disc and the loading jaws in the IR configuration. While the MST method introduces an innovative approach to applying direct tensile stress, the observed lower tensile strengths underscore the profound impact of specimen geometry and loading conditions on the accuracy of tensile strength measurements.

Furthermore, the comparative analysis with the BD test method substantiated the reliability of both the MST and IR methods, particularly for brittle rock materials such as granite. The correlation between tensile strength and the d/D ratio was consistently observed across all methods, with smaller d/D ratios corresponding to higher tensile strengths, in alignment with BD test results. This consistency emphasizes the critical influence of specimen dimensions on tensile strength assessments.

Fracture pattern analysis provided further differentiation between the MST and IR methods. MST specimens exhibited more linear fracture paths, a result of the perpendicular application of tensile loads, whereas IR specimens displayed multiple failure lines, indicative of the interplay of compressive, shear, and tensile stresses inherent to the IR method. This divergence in fracture behavior underscores the distinct stress distributions and fracture mechanics associated with each testing approach.

Despite the variations, tensile strength values derived from both MST and IR methods fell within an acceptable range, underscoring their viability as alternative methodologies to the traditional BD test. Additionally, the MST and IR tests required significantly lower failure loads, a crucial advantage for scenarios involving lower-capacity testing equipment.

In conclusion, this research offers profound insights into the mechanical behavior of rock materials under diverse loading conditions. The findings highlight the necessity of meticulously considering specimen geometry and loading configurations in tensile strength evaluations and support the ongoing refinement of these methodologies to achieve more precise and reliable assessments in rock mechanics.

Data availability

The data that support the findings of this study are available from the corresponding author, upon reasonable request.

Declarations

Conflict of interest The authors declare that there are no conflict of interest.

References

[1] de Alencar A T S, Muñiz-Menéndez M and Galindo R A 2024 Ring test: a new interpretation to estimate tensile strength of rock. *Rock Mech. Rock Eng.* 57: 8911–8921

[2] Sarfarazi V and Schubert W 2016 Numerical simulation of tensile failure of concrete in direct, flexural, double punch tensile and ring tests. *Period. Polytech. Civ. Eng.* 61: 176–183

[3] Perras M A and Diederichs M S 2014 A review of the tensile strength of rock: concepts and testing. *Geotech. Geol. Eng.* 32: 525–546

[4] Berenbaum R and Brodie I 1958 Measurement of the tensile strength of brittle materials. *Br. J. Appl. Phys.* 10: 281

[5] Li X, Feng F and Li D 2017 Numerical simulation of rock failure under static and dynamic loading by splitting test of circular ring. *Eng Fract Mech.* 188: 184–201

[6] Hobbs D W 1965 An assessment of a technique for determining the tensile strength of rock. *Br. J. Appl. Phys.* 16: 259–268

[7] Hua W, Li J, Zhu Z, Li Huang J, Gan Z and Dong S 2023 A review of mixed mode I-II fracture criteria and their applications in brittle or quasi-brittle fracture analysis. *Theor. Appl. Fract. Mech.* 124: 103741

[8] Giglio M, Gilioli A and Manes A 2012 Numerical investigation of a three point bending test on sandwich panels with aluminum skins and NomexTM honeycomb core. *Comput. Mater. Sci.* 56: 69–78

[9] Birro T V, Aufray M, Paroissien E and Lachaud F 2021 Assessment of interface failure behaviour for brittle adhesive using the three-point bending test. *Int. J. Adhes. Adhes.* 110: 102891

[10] Coviello A, Lagioia R and Nova R 2005 On the measurement of the tensile strength of soft rocks. *Rock Mech. Rock Eng.* 38: 251–273

[11] Biolzi L, Cattaneo S and Rosati G 2001 Flexural/tensile strength ratio in rock-like materials. *Rock Mech. Rock Eng.* 34: 217–233

[12] Aliha M R M, Ebneabbasi P, Karimi H R and Nikbakht E 2021 A novel test device for the direct measurement of tensile strength of rock using ring shape sample. *Int. J. Rock Mech. Min. Sci.* 139: 104649

[13] Kumar P, Aggarwal V and Walia B S 2023 Seesaw apparatus for direct tensile testing of ring-shaped rock. *Expert Notes.* 396177–001

[14] Nair A M and Mathew G 2014 Effect of bulk chemistry in the spectral variability of igneous rocks in VIS-NIR region: implications to remote compositional mapping. *Int. J. Appl. Earth Observ. Geoinf.* 30: 227–237

[15] Mellor M and Hawke I 1971 Measurement of tensile strength by diametral compression of discs and annuli. *Eng. Geol.* 5: 173–225

[16] Yu Y, Zhang J and Zhang J 2009 A modified Brazilian disk tension test. *Int. J. Rock Mech. Min. Sci.* 46: 421–425

[17] Li X, Liu K, Sha Y, Yang J and Hong Z 2024 Experimental and numerical investigation on rock fracturing in tunnel contour blasting under initial stress. *Int. J. Impact Eng.* 185: 104844

[18] Zhang Q B and Zhao J 2013 Determination of mechanical properties and full-field strain measurements of rock material under dynamic loads. *Int. J. Rock Mech. Min. Sci.* 60: 423–439

[19] Guan F, Li Y, Gao G, Zachert H, Eichhoff G and Beroya-Eitner M A 2022 Horizontal compression test: a proposed method for indirect determination of tensile strength of stiff soils and soft rocks. *Front. Earth Sci.* 10: 839073

[20] Erarslan N, Liang Z Z and Williams D J 2011 Experimental and numerical studies on determination of indirect tensile strength of rocks. *Rock Mech. Rock Eng.* 45: 739–751

[21] Briševac Z, Kujundžić T and Čajić S 2015 Current cognition of rock tensile strength testing by Brazilian test. *Rudarsko-geološko-naftni zbornik.* 30: 101–114

[22] Li X, Wu Q, Tao M, Weng L, Dong L and Zou Y 2016 Dynamic Brazilian splitting test of ring-shaped specimens with different hole diameters. *Rock Mech. Rock Eng.* 49: 4143–4151

[23] Wei S, Tingshi Z, Daxing G, Dunkang L, Poliang L and Xiaoyun Q 1982 Fracture toughness measurement by cylindrical specimen with ring-shaped crack. *Eng. Fract. Mech.* 16: 69–82

[24] Wang Z, Yang S and Tang Y 2020 Mechanical behavior of different sedimentary rocks in the Brazilian test. *Bull. Eng. Geol. Environ.* 79: 5415–5432

[25] Zhang Q B and Zhao J 2014 Quasi-static and dynamic fracture behaviour of rock materials: phenomena and mechanisms. *Int. J. Fract.* 189: 1–32

[26] Pietras D, Aliha M R M, Kucheki H G and Sadowski T 2023 Tensile and tear-type fracture toughness of gypsum material: Direct and indirect testing methods. *Journal of Rock Mechanics and Geotechnical Engineering.* 15: 1777–1796

[27] Haeri H, Sarfarazi V, Ebneabbasi P and Marji M F 2024 Assessing the tensile crack growth in rock involves employing a seesawing apparatus and its calibrating through XFEM: A New Approach. *Iranian Journal of Science and Technology, Transactions of Civil Engineering.* 48: 2621–2639

Springer Nature or its licensor (e.g. a society or other partner) holds exclusive rights to this article under a publishing agreement with the author(s) or other rightsholder(s); author self-archiving of the accepted manuscript version of this article is solely governed by the terms of such publishing agreement and applicable law.

Journal of Scientific & Industrial Research
Vol. 69, May 2010, pp. 384-389

Thumba (*Citrullus colocyntis*) seed oil: A sustainable source of renewable energy for biodiesel production

Amit Pal[1], S S Kachhwaha[1]*, S Maji[1] and M K G Babu[2]

[1]Department of Mechanical Engineering, Delhi College of Engineering, Delhi 110 042, India
[2]Centre for Energy Studies, Indian Institute of Technology Delhi, Delhi 110 016, India

Received 21 July 2009; revised 04 January 2010; accepted 08 February 2010

Thumba (*Citrullus colocyntis*) seed oil can be used for production of biodiesel. A comparative experimental study, carried out on a four cylinder, direct injection, water cooled diesel engine operating on diesel and biodiesel blends (B10, B20 and B30) of *C. colocyntis* and *Jatropha curcas*, showed that like *J. curcas*, biodiesel of *C. colocyntis* can be used as an alternative fuel with better performance and lower emissions compared with diesel.

Keywords: Biodiesel, Bio-fuel, *Citrullus colocyntis*, Engine performance, *Jatropha curcas*, Thumba

Introduction

India is projected to become third largest consumer of transportation fuel in 2020, after USA and China, with consumption growing at an annual rate of 6.8%[1]. In India, 90% of imported oil is consumed for transportation and energy generation and its economy are highly depending on import of crude oil. Therefore, bio-fuel as a transportation fuel will play a very vital role in near future. Bio-fuels, produced as vegetable oils from plants, burning leads to a complete recyclable carbon dioxide (CO_2), which reduces green house effect[2]. Biodiesel has a higher cetane number than petroleum diesel fuel, no sulphur, no aromatics, and contains O_2 (10–11% by wt), and therefore reduces emissions of carbon monoxide (CO), hydrocarbons (HC), and particulate matter (PM), sulphur dioxide (SOx) in exhaust gas compared with diesel fuel while nitrogen oxides (NOx) slightly increased[3]. Studies are available on vegetable oils (hemp[4], Jatropha[5-7], orange[8], rapeseed[9], sesame[10], mahua[11] and a mixed vegetable oil[12] in a diesel engine for suitability as an alternate fuel.

This study presents Thumba (*Citrullus colocyntis*) seed oil as a sustainable source of renewable energy for biodiesel production.

*Author for correspondence
E-mail: sskachhwaha@rediffmail.com

Experimental

Materials

Thumba (*C. colocyntis* Schrad.), a non-edible vegetable oil plant (Fig. 1), mainly grows in rain fed parts of Rajasthan and Gujarat. It is a creeper and grows well in sandy soil. Raw Thumba seed oil is presently consumed in large quantities by local soap industries. Comparing with Jatropha (*Jatropha curcas*), Thumba plant with small crop cycle and various uses can play a pivotal role for the progress of Indian rural economy (Table 1). Raw *C. colocyntis* (Thumba) oil, used for biodiesel production, was purchased from a soap industry of Jodhpur district of western Rajasthan (India) and commercially available diesel oil was purchased from nearby petrol pump.

Engine Test Setup

Performance and emission test was carried out in four cylinder, four stroke, water cooled, 39 kW at 5000 rpm, Model Tata Indica diesel engine, connected to eddy current type dynamometer for loading. It is equipped with necessary instruments for measurement of combustion pressure and crank-angle. Set control panel box consists of air box, fuel tank, manometer, fuel measuring unit, transmitters for air and fuel flow measurements, process indicator and engine indicator. Rotameters are used for cooling water and calorimeter

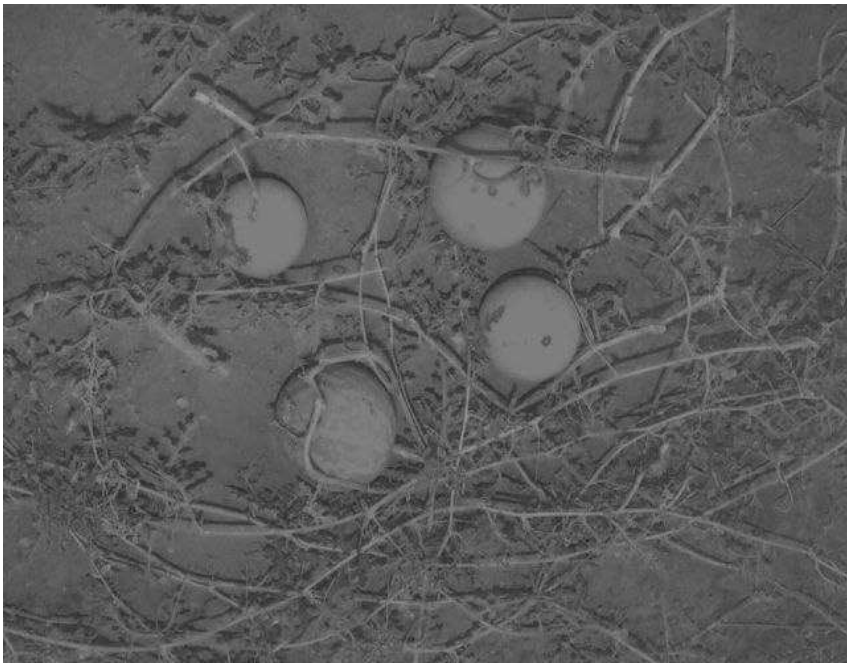


Fig. 1—Thumba plant with fruit

Table 1— Comparison between Jatropha and Thumba plants

Sl No.	Characteristics	Plant	
		Ratanjyot (*Jatropha curcas*)	Thumba (*Citrullus colocyntis*)
1	Plant type	Shrub (3-5 m)	Creeper
2	Crop cycle	3-30 years	6 months
3	Plantation period	July-August	Monsoon season
4	Soil type	Any type of soil	Dry desert soil
5	Manure	2 kg FYM per pit	No special treatment requirement
6	Irrigation	1st year after planting 2nd year after one year in summer as required	Seeds are sown with bajra and no special treatment required
7	Saplings	1200 plants per acre (59.48 m^2)	Separate land is not required
8	Insecticides, pesticides	Not required	Not required
9	Maturity Harvesting	From second year plants will start producing and will reach maturity fully in 5th year	6 months
10	Usage	Oil with medicinal value, dyes, feed, insecticides, pesticides, alternative to diesel	Same as Jatropha, but edible for animals and have medicinal value
11	Biodiesel property	Property is almost similar to the conventional diesel	Similar to Jatropha but with low viscosity

water flow measurement. Windows based engine performance analysis software package "Enginesoft" is used for on-line performance evaluation.

Preparation of Biodiesel Blend

Biodiesel is prepared by hydrodynamic cavitation technology with raw Thumba oil at Delhi College of

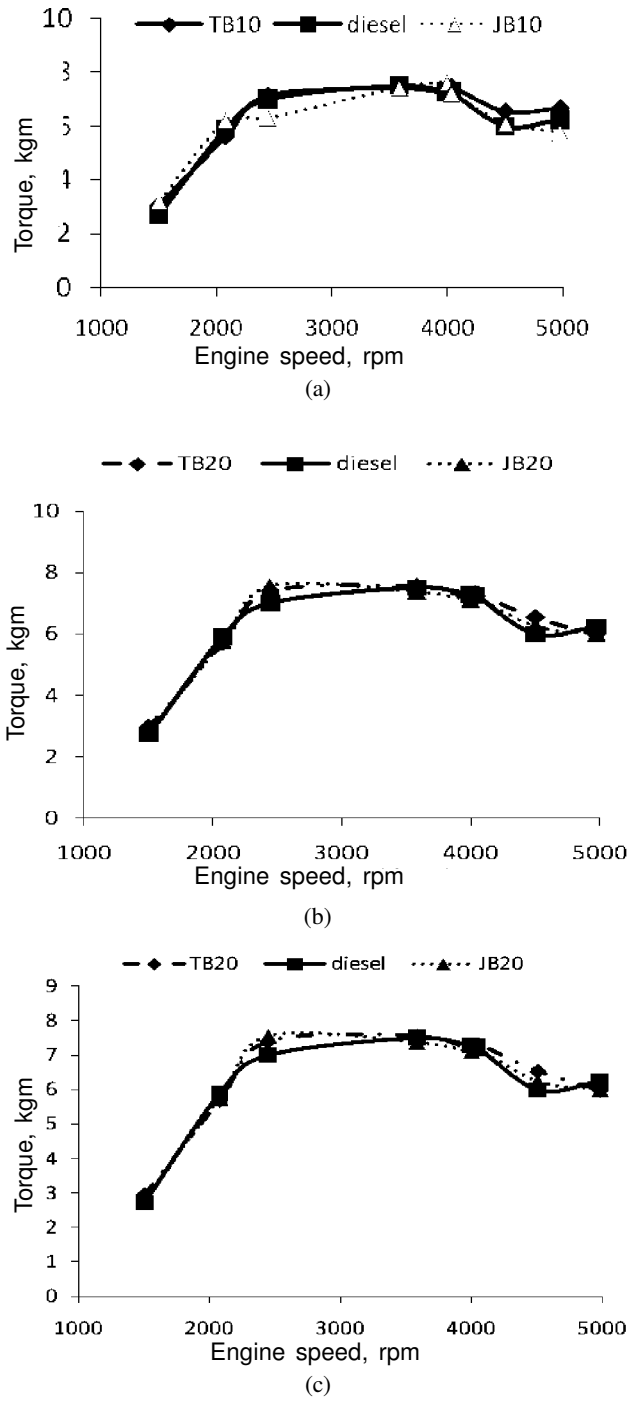


Fig. 2—Comparison of torque vs speed for biodiesel blends of diesel with Jatropha and Thumba oil at: a) 10% b) 20%; and c) 30%

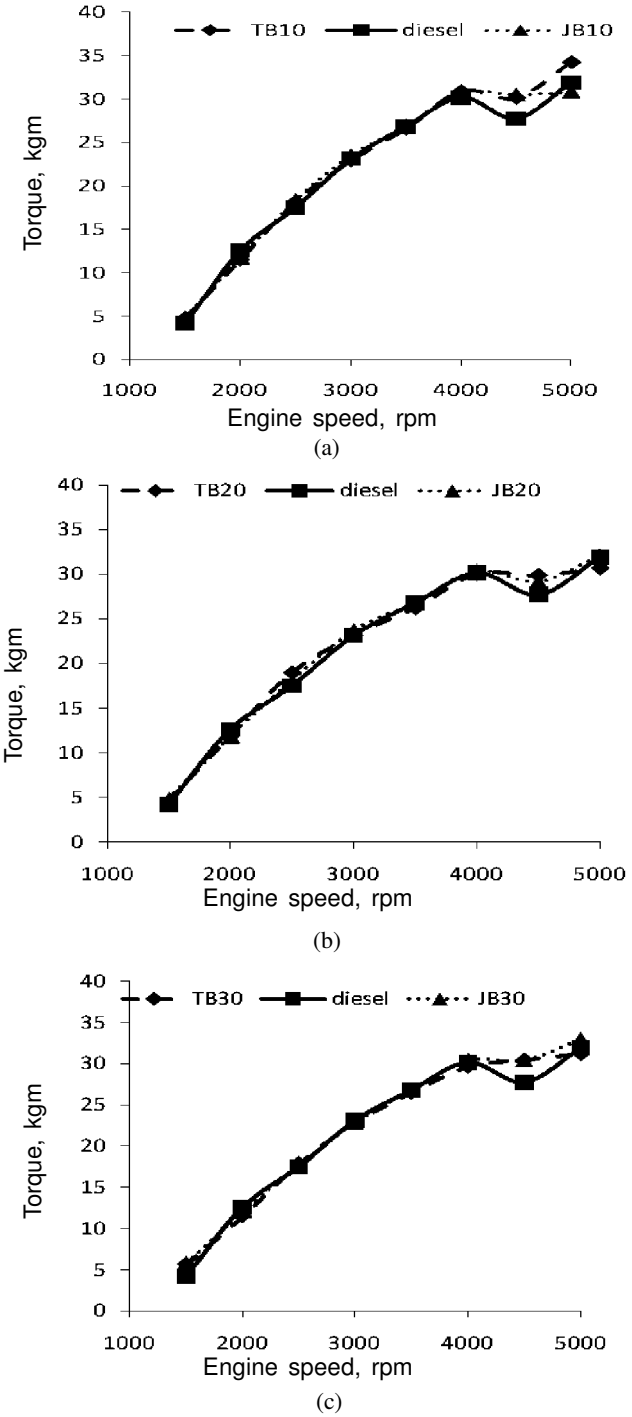
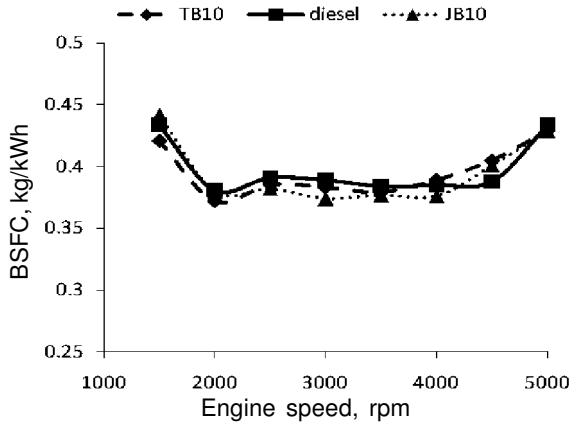


Fig. 3—Comparison of brake power vs speed for biodiesel blends of diesel with Jatropha and Thumba oil at: a) 10%; b) 20%; and c) 30%

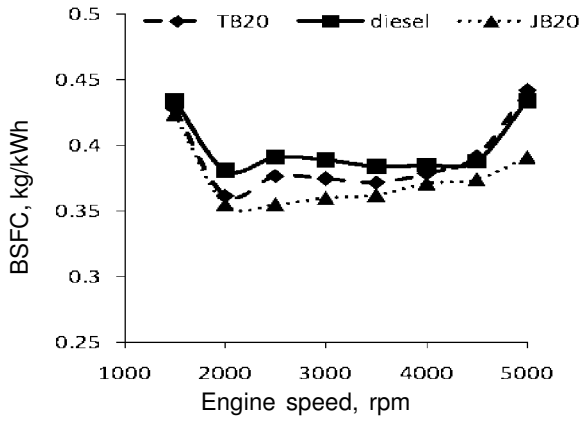
Engineering laboratory and blended (10%, 20% and 30%) with diesel.

Results and Discussion

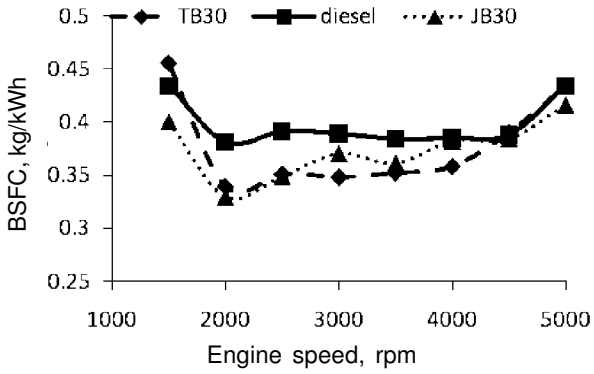
Variation of parameters of load test with respect to speed (1000-5000 rpm) at an interval of 500 rpm and a gap of 5 min of engine for pure diesel, Thumba biodiesel (TB) and Jatropha biodiesel (JB) include torque (2.5-7.7 kg-m), brake power (BP, 3-35 kW), brake thermal efficiency (BTE, 19-27 %), brake specific fuel consumption (BSFC, 0.33-0.46 kg/kWh), and smoke opacity (5-60%).



(a)

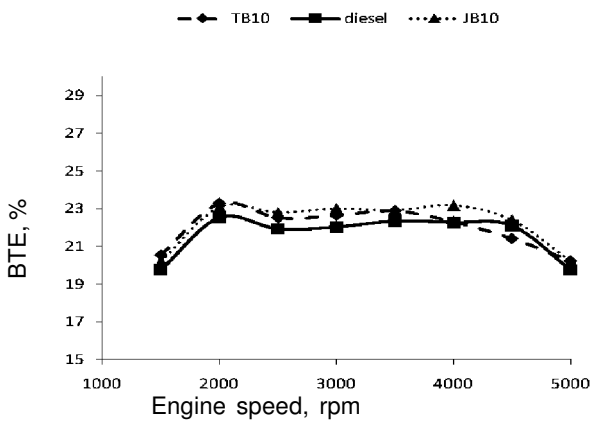


(b)

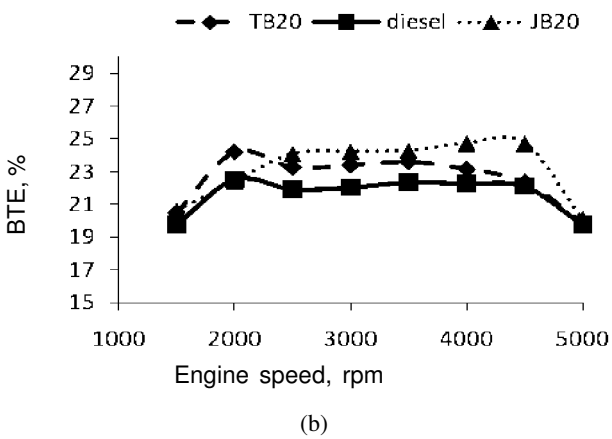


(c)

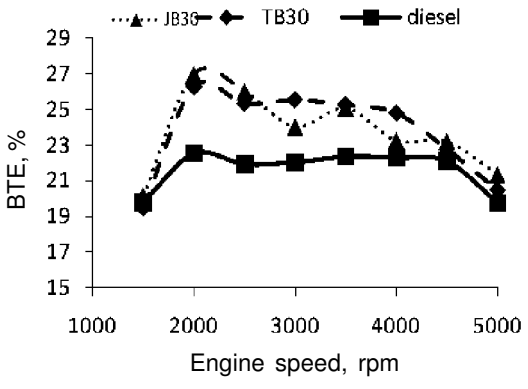
Fig. 4—Comparison of BSFC vs speed for biodiesel blends of diesel with Jatropha and Thumba oil at: a) 10%; b) 20%; and c) 30%



(a)



(b)



(c)

Fig. 5—Comparison of BTE v/s speed for biodiesel blends of diesel with Jatropha and Thumba oil at: a) 10%; b) 20%; and c) 30%

Variation of Torque vs Engine Speed

Variation of torque for different blends and pure diesel at a particular engine speed is within a very narrow range (Fig. 2). In case of both biodiesel blends and pure diesel, initially torque rises sharply with increase in engine speed up to 2500 rpm, thereafter variation of torque with speed (2500-4000 rpm) remain almost constant. Further increase in speed causes decrease in torque.

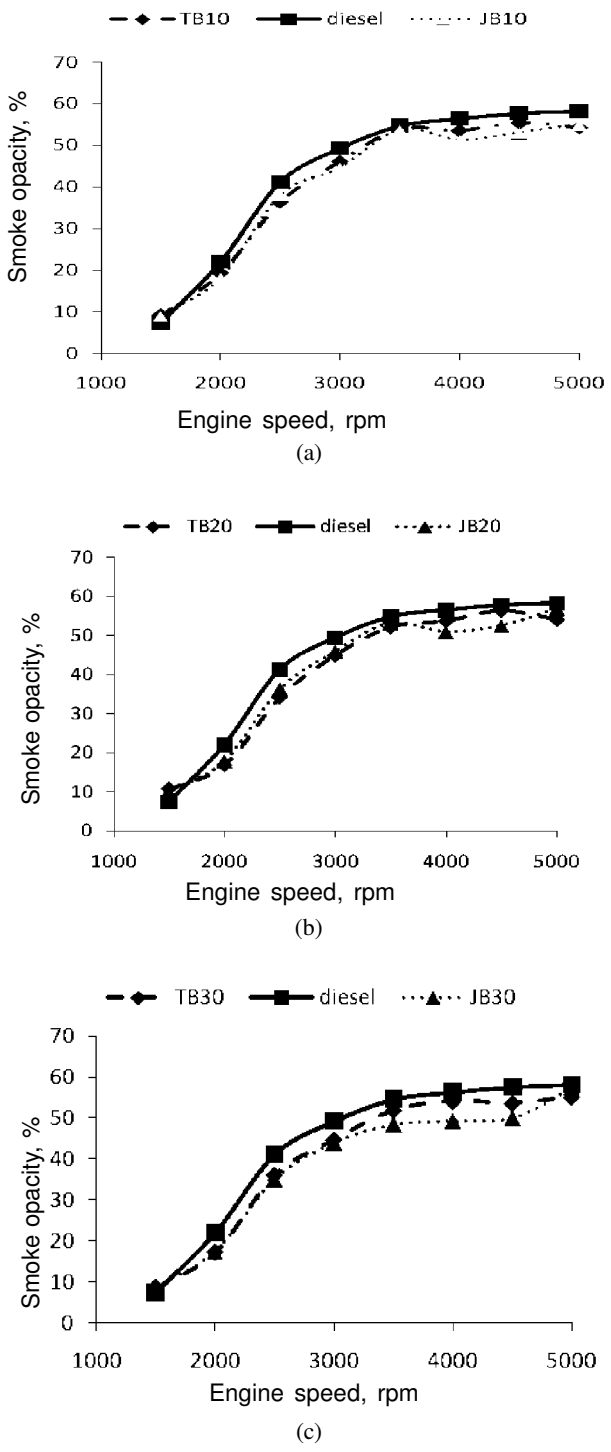


Fig. 6—Comparison of smoke opacity v/s speed for biodiesel blends of diesel with Jatropha and Thumba oil at: a) 10%; b) 20%; and c) 30%

Pattern is almost same for all blends. Maximum torque achieved in case of TB20 was 7.5 kg-m at 2500 rpm.

Variation of Brake Power (BP) vs Engine Speed

BP (6-32 kW) increases proportionally to engine speed (2000-4000 rpm); for speed above 4000 rpm, there is fluctuating variation in BP among biodiesel blends (Fig. 3). Maximum BP achieved for TB10 was 35 kW at 5000 rpm.

Variation of brake specific fuel consumption (BSFC) vs Engine Speed

For all cases, BSFC initially decreases sharply with increase in speed up to 2000 rpm and between 2000-4000 rpm remains approximately constant; for more than 4000 rpm BSFC increases sharply with speed (Fig. 4). BSFC for JB30 of Jatropha oil is lowest (0.32 kg/kWh to 0.44kg/kWh) at speed between 2000-4500 rpm. In case of all Thumba and Jatropha biodiesel blends, BSFC values are significantly lower as compared to pure diesel for a wide range of engine speed.

Brake Thermal Efficiency (BTE) vs Engine Speed

Maximum value of BTE for all blends and pure diesel is at 2000 rpm (Fig. 5). For all blends of both oils, variation of BTE is higher as compared to pure diesel for wide range of engine speed. Maximum BTE achieved by using JB30 blend is around 26.9% at 2000 rpm, which is 5% higher as compared to pure diesel. BTE is almost constant between 2000-4000 rpm, and decreases sharply with further increase in speed. With increase in percentage of biodiesel blending, BTE increases for wide range of engine speed. Both Jatropha and Thumba oil exhibit comparatively higher efficiency than pure diesel with all blends.

Smoke Opacity vs Engine Speed

Smoke opacity for pure diesel is slightly higher than all type of blends for wide range of engine speeds (Fig. 6). For all biodiesel blends, opacity increases (10-60%) with increase in speed (2000-3500 rpm); thereafter (>4000 rpm) no significant change was observed in opacity.

Conclusions

C. colocyntis that grows as creeper in sandy soil with in a six month crop cycle has enormous potential for biodiesel production. Variation of performance parameters for wide range of engine speed are similar for biodiesel blends of Thumba and Jatropha with pure diesel and do not show any sign of deterioration as compared to pure diesel. Brake thermal efficiency improves significantly with increase in percentage of

biodiesel blending. Smoke opacity results show that biodiesel blending is relatively less pollutant as compared to petroleum diesel. Thus, Thumba and Jatropha can be successfully used for biodiesel blending for C I engine.

References

1 Ramesh D & Sampathrajan A, Investigations on performance and emission characteristics of diesel engine with jatropha biodiesel and its blends, *Agric Engg Int: CIGR e-J Sci Res Develop*, **10** (2008) EE 07 013.

2 Stavarache C, Vinatoru M, Nishimura R & Maeda Y, Fatty acids methyl ester from vegetable oil by means of ultrasonic energy, *Ultrason Sonochem,* **12** (2005) 367-372.

3 Ajav E A & Akingbehin O A, A study of some fuel properties of local ethanol blended with diesel fuel, *Agric Engg Int: CIGR e-J Sci Res Develop,* **4** (2002) 1-8 (EE 01 003).

4 Hebbal O D, Vijayakumar Reddy K & Rajagopal K, Performance characteristics of a diesel engine with deccan hemp oil, *Fuel*, **85** (2006) 2187-2194.

5 Agarwal D & Agarwal A, Performance and emissions characteristics of Jatropha oil (preheated and blends) in a direct injection compression ignition engine, *App Ther Engin,* **27** (2007) 2314-2323

6 Pramanik K, Properties and use of *J. curcas* oil and diesel fuel blends in compression ignition engine, R*enew Ener* **28** (2003) 239-248.

7 Kumar N & Sharma P B, Jatropha – a sustainable source for biodiesel production, *J Sci Ind Res*, **64** (2005) 883-889.

8 Purushothaman K & Nagarajan G, Performance, emission and combustion characteristics of a compression ignition engine operating on neat orange oil, *Renew Ener*, **34** (2009) 242-245.

9 Labeckas G & Slavinskas S, The effect of rapeseed oil methyl ester on direct injection diesel engine performance and exhaust emissions, *Ener Convers Manage*, **47** (2006) 1954-1967.

10 Altuna S, Bulut H & Oner C, The comparison of engine performance and exhaust emission characteristics of sesame oil–diesel fuel mixture with diesel fuel in a direct injection diesel engine, *Renew Ener,* **33** (2008) 1791-1795.

11 Puhan S, Vedaraman N, Rambardhamam B V & Nagarajan G, Mahua (*Madhuca indica*) seed oil: A source of renewable energy in India, *J Sci Ind Res*, **64** (2005) 890-896.

12 Bora D K, Das L M & Babu M K G, Performance of a mixed biodiesel fulled diesel engine, *J Sci Ind Res,* **67** (2008) 73-76.

Discover Materials

Research

Tool geometry optimization for enhanced mechanical properties in friction stir welding of carbon steel

Anmol Bhatia[1] · Reeta Wattal[2] · Rajeev Kumar[3] · Anant Prakash Agrawal[3] · Saurabh Dewangan[4]

Received: 12 March 2025 / Accepted: 29 May 2025
Published online: 07 June 2025
© The Author(s) 2025 OPEN

Abstract
Friction stir welding (FSW) is known for its environmentally friendly characteristics and energy efficiency. The geometry of the tool holds significant importance in FSW, playing a crucial role in ensuring satisfactory welds. In the present work, optimization of tool geometry is carried out for the FSW of 3 mm thick AISI 1018 carbon steel. A tungsten carbide tool containing 7 wt.% cobalt with a tapered pin profile—identified as the optimal configuration—was employed for the welding process. The FSW joint was subjected to microstructure examination and tensile testing for weld quality. The results revealed that optimized tool geometry enhanced the weld quality. The welded joints revealed an 18% increase in ultimate tensile strength (UTS) than the base metal (BM). Microstructural observations in the thermo-mechanically affected zone (TMAZ) and heat-affected zone (HAZ) were conducted using Scanning Electron Microscopy (SEM) and analyzed with ImageJ software. The present study demonstrated a significant increment in the ultimate tensile strength of the joint obtained by incorporating the optimized parameters, additionally, the microstructures were uniform throughout the TMAZ and HAZ. Fractography of the ruptured sample revealed a dimpled region indicating ductile failure.

Keywords Tool geometry optimization · Tungsten carbide · Carbon steel · Friction stir-welding · Microstructures

1 Introduction

Welding and joining of materials are among the primary and essential manufacturing processes widely used across industries. Conventional fusion-based welding techniques, such as TIG welding and MIG welding, are commonly applied; however, they are often associated with drawbacks like high heat input, distortion, residual stresses, and the risk of weld defects. These limitations become particularly pronounced when joining hard-to-weld materials like steels and dissimilar metal combinations, where controlling heat input and avoiding metallurgical defects is challenging. [1, 2] FSW is an advanced solid-state joining technique that has been gaining momentum, particularly in the automobile and aerospace sectors, due to its sustainable and environmentally friendly characteristics [3].

FSW is a solid-state joining process that produces joints without melting the BM. Initially applied to aluminum and its alloys [4–8], FSW has since been extended to materials of higher strength and hardness, including carbon steels, stainless

✉ Saurabh Dewangan, saurabh.dewangan@jaipur.manipal.edu; Anmol Bhatia, anmolbhatia@ncuindia.edu; Reeta Wattal, reetawattal@hotmail.com; Rajeev Kumar, errajeev79@gmail.com; Anant Prakash Agrawal, anant.agraawal@gmail.com | [1]Department of Multidisciplinary Engineering, The NorthCap University, Gurugram, Haryana 122017, India. [2]Department of Mechanical Engineering, Delhi Technological University, Delhi 110042, India. [3]Department of Mechanical Engineering, Noida Institute of Engineering and Technology, Greater Noida 201306, India. [4]Department of Mechanical Engineering, Manipal University Jaipur, Jaipur, Rajasthan 303007, India.

steels, and nickel-based alloys. Its advantages over conventional fusion welding methods include lower residual stresses, refined microstructures in the weld region, and reduced defect formation [9–11]

In the FSW process, a rotating tool generates frictional heat at the contact region of the workpieces. This tool, equipped with a pin and shoulder, performs the dual function of heating and stirring the material. The shoulder serves as the primary working surface, while the pin facilitates material flow beneath the surface. The rotating tool is plunged into the joint line of clamped workpieces until the shoulder makes contact, after which it traverses along the weld path. Frictional heat softens the material, enabling it to plastically deform and consolidate behind the tool, forming a strong, defect-free joint [12].

A critical factor in achieving a high-quality weld is the tool shoulder and pin geometry. The selection of tool material and geometry is especially crucial when dealing with steels due to their mechanical properties. Although substantial research exists on tool geometry optimization for various materials, dedicated studies targeting steels remain relatively limited.

Aissani et al. [13] optimized the FSW tool by introducing a modified tri-flute pin design that reduced displaced volume within the weld zone while integrating a safety mechanism. Buffa et al. [14] employed finite element analysis (FEA) to compare tool designs and recommended a conical pin profile for enhanced material flow. Colegrove and Shercliff [15] compared Triflute and Trivex tools, reporting lower downward forces with the Trivex configuration. Ji et al. [16] proposed half-screw and tapered flute pin profiles, with the tapered flute proving superior in promoting material flow velocity.

Similarly, Fujii et al. [17] examined optimal tool designs for aluminum alloys, affirming the significant influence of tool shape on weld integrity. Shindo et al. [18] documented a self-optimizing tool geometry phenomenon, achieving excellent weld quality. Lin et al. [19] analyzed different pin profiles and concluded that pin geometry critically affects velocity distribution and overall weld efficiency.

Tiwari et al. [20] investigated tool wear in tungsten carbide tools, highlighting the role of cobalt content in tool durability. Khan et al. [21] addressed weld defects caused by insufficient material flow around the pin and proposed improvements in tool design. Siddiquee and Pandey [22] reported tool deformation issues during FSW of stainless steel, necessitating modifications to tungsten carbide tools for improved performance.

Recent studies have reaffirmed the importance of optimizing both tool material and geometry to improve joint integrity, minimize oxidation-related damage, and extend tool life in steel FSW applications. Investigations by Lunetto et al. [23] and Wang et al. [24] have highlighted the critical role of tool wear behavior and geometric design in maintaining weld quality during the FSW of high-strength steels. These works emphasize the need for tool material stability under severe thermal and mechanical conditions, while also stressing the importance of detailed analysis of thermal cycles, tool degradation mechanisms, and microstructural transformations during welding to establish reliable, durable tool configurations suitable for industrial applications.

While FSW of carbon steels has been explored to some extent, there remains a lack of detailed investigation into tool degradation due to oxidation, particularly concerning varying cobalt content in tungsten carbide tools.

The present study introduces a novel application of a tapered pin profile tungsten carbide (7 wt.% Co) tool specifically designed for FSW of AISI 1018 carbon steel. This study aims to address the critical issue of oxidation-induced tool degradation by selecting an optimal cobalt binder content and pin geometry to ensure structural integrity under thermal and mechanical stresses. Additionally, the use of the tapered pin geometry demonstrates a significant enhancement in joint strength and microstructural uniformity, showcasing the application of this tool design for industrial steel welding.

2 Experimental procedure

2.1 Selection of tool material

Existing literature on FSW revealed that both the tungsten carbide and PCBN are used for FSW tools; however, due to the limited availability of PCBN, the Tungsten Carbide-based tool is selected in the present study. The WC exhibits high hardness and maintains it at high temperatures, which makes it widely used in cutting applications. With tensile strength ranging from 1400 to 3400 MPa and compressive strength up to 600 MPa, along with a high modulus of elasticity, it minimizes deflection during FSW.

For the present work, two grades of tungsten carbide available in the market were evaluated for their performance, and the best suited was selected for subsequent experimentation. For the present study, two grades of tungsten carbide

tools used are designated as 'Tool-A' and 'Tool-B', respectively. 'Tool-A' consists of Tungsten carbide with approximately 7% cobalt, and 'Tool-B' consists of 12% cobalt. EDAX results showing the elemental composition of both the tools used are presented in Tables 1 and 2, and associated EDAX images are presented in Fig. 1 (a and b).

Figure 2(a) displays the initial condition of 'Tool-A' before welding, while the appearance of a blue-colored powder along the shoulder periphery after several weld passes indicated localized oxidation of tungsten. Notably, no such oxidation was visible on the tool pin or the flat shoulder area in direct contact with the workpiece, likely due to restricted atmospheric exposure and limited surface deformation. The post-welding condition of the tool following successive trials is presented in Fig. 2(b).

A higher magnification view of Tool-A is presented in Fig. 3(a), confirming densely packed WC grains embedded in a ductile Co binder, a combination essential for achieving hardness and toughness in cemented carbide tools. However, prolonged welding led to degradation at the WC–Co interfaces as shown in Fig. 3(b), potentially compromising mechanical integrity.

Oxidation during welding produced a brittle, non-adherent tungsten oxide (WO_3) layer, continuously detaching from the tool surface as indicated by Fig. 4, following the reaction that is presented by Eq. 1.

$$WC + 2.5\,O_2 \rightarrow WO_3 + CO_2 \tag{1}$$

The porous tungsten oxide layer accelerated further oxidation, while accumulated CO_2 within the WC grains initiated cracks by weakening the cobalt binder, as noted by Wu et al. [25].

Table 1 EDAX results showing elemental composition for Tool-A

Element	Series	Unn C [wt%]	Norm C [wt%]	Atoms C	Error
Tungsten	L-Series	91.02	83.00	33.17	2.5
Cobalt	K-Series	6.75	6.16	7.68	0.2
Carbon	K-Series	6.72	6.13	37.44	1.1
Oxygen	K-Series	5.18	4.73	21.67	0.9

Table 2 EDAX results showing elemental composition for Tool-B

Element	Series	Unn C [wt%]	Norm C [wt%]	Atoms C	Error
Tungsten	L-Series	86.77	77.67	30.97	2.5
Cobalt	K-Series	13.71	12.28	15.27	0.4
Carbon	K-Series	5.67	5.07	30.97	1.4
Oxygen	K-Series	5.56	4.98	22.80	1.4

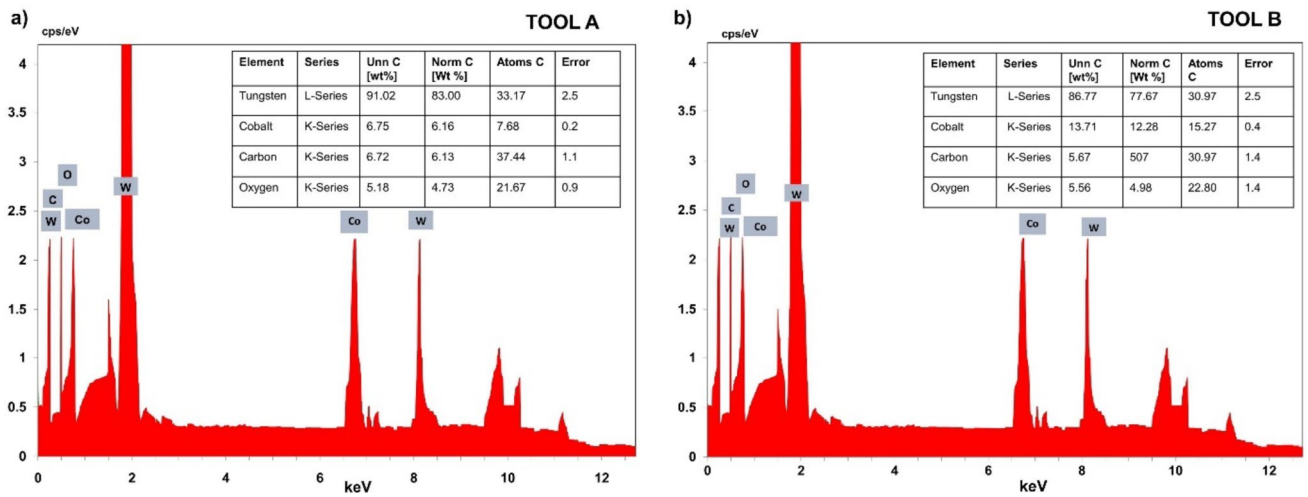


Fig. 1 **a**) EDAX results for 'Tool-A' and **b**) EDAX results for 'Tool-B'

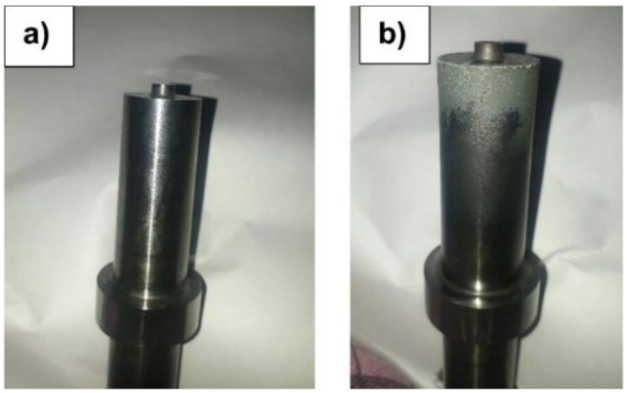


Fig. 2 **a**) Undeformed 'Tool-A' used for the present study, and **b**) 'Tool-A' after performing welding

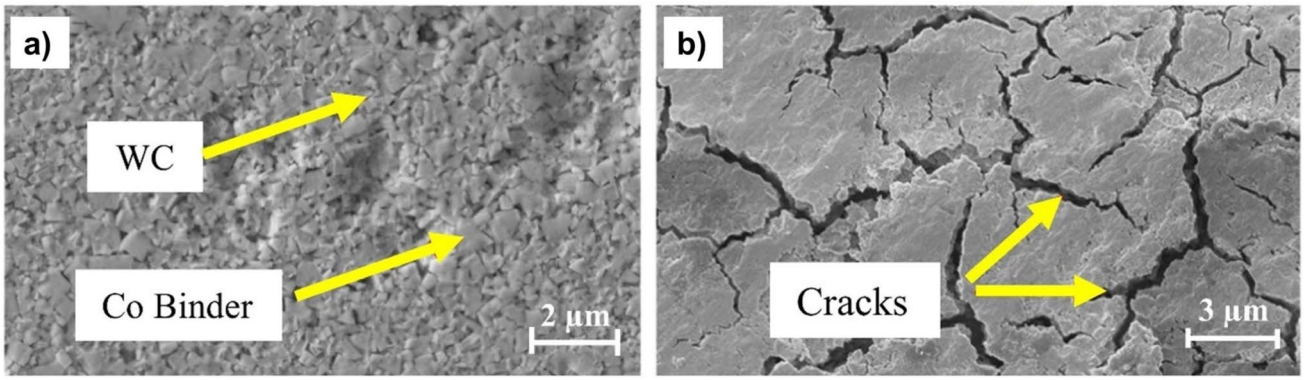


Fig. 3 FESEM images at 10,000X magnification display the surface of Tool-A (**a**) before use and (b) after completion of welding

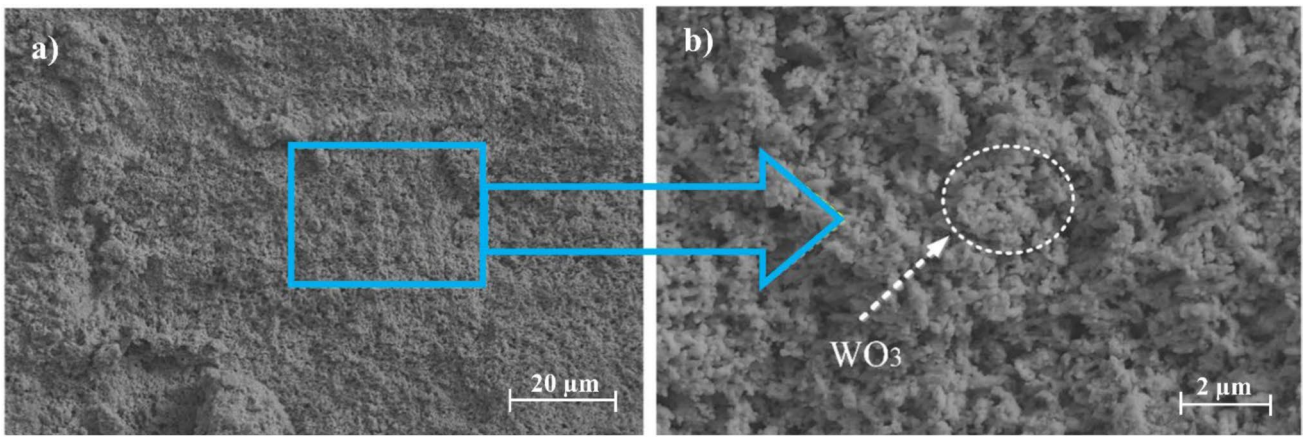


Fig. 4 FESEM image of the oxidized layer at **a**) 1000X magnification, and **b**) 6000X magnification

When welding was performed using Tool-B, the oxidation behavior differed from the previous case. Blue-colored oxides appeared predominantly along the shoulder periphery, while the tool pin and inner shoulder surface remained unaffected due to limited exposure and plastic deformation. The oxidation rate was comparatively lower, and swelling at the outer edge of the shoulder was distinctly visible, as shown in Figs. 5(a) and 5(b). This swelling was influenced by the higher cobalt binder content, which altered the oxidation pattern of tungsten carbide, resulting in swelling of the tool periphery. The reaction between cobalt and tungsten carbide produced cobalt tungstate ($CoWO_4$), as represented by Eq. 2.

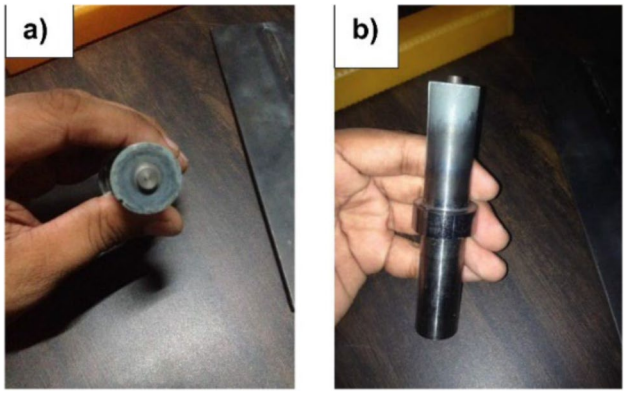


Fig. 5 **a**) and **b**) show different views of 'Tool-B' after performing welding

$$Co + WC + 3O_2 \rightarrow CoWO_4 + CO_2 \quad (2)$$

The peripheral bulging of 'Tool-B' increased the shoulder's diameter, giving the tool a convex shape and making it unsuitable for welding. This deformation was attributed to cobalt migration and tungsten carbide grain displacement under combined thermal and mechanical effects, consistent with the observations of Roa et al. [26], which signifies the influence of cobalt binder content on tungsten carbide oxidation characteristics.

A qualitative phase analysis of the tool surface was conducted through X-ray diffraction (XRD). The diffraction pattern before welding displayed distinct peaks of tungsten carbide and cobalt, as shown in Fig. 6(a). Post-weld examination indicated the presence of extra carbide compounds, namely iron tungsten carbide and chromium carbide, in addition to oxide formations such as tungsten trioxide and cobalt tungstate, as illustrated in Fig. 6(b). The weak texture of WO_3 indicated severe degradation, confirming oxidation as a key factor behind the weakening of the cobalt binder phase and the consequent reduction in the mechanical strength of the WC–Co composite.

2.2 Selecting the correct grade of Tungsten Carbide

The performance evaluation of tool materials in FSW of steel revealed distinct outcomes. 'Tool-A' exhibited slower oxidation, forming WO_3, while 'Tool-B' generated a porous, swollen $CoWO_4$ due to higher cobalt content. 'Tool-B' deformed quickly, requiring frequent regrinding, unlike 'Tool-A', which showed better durability.

Hence, tungsten carbide with 7% cobalt was chosen for its superior wear resistance and hardness, essential for the application.

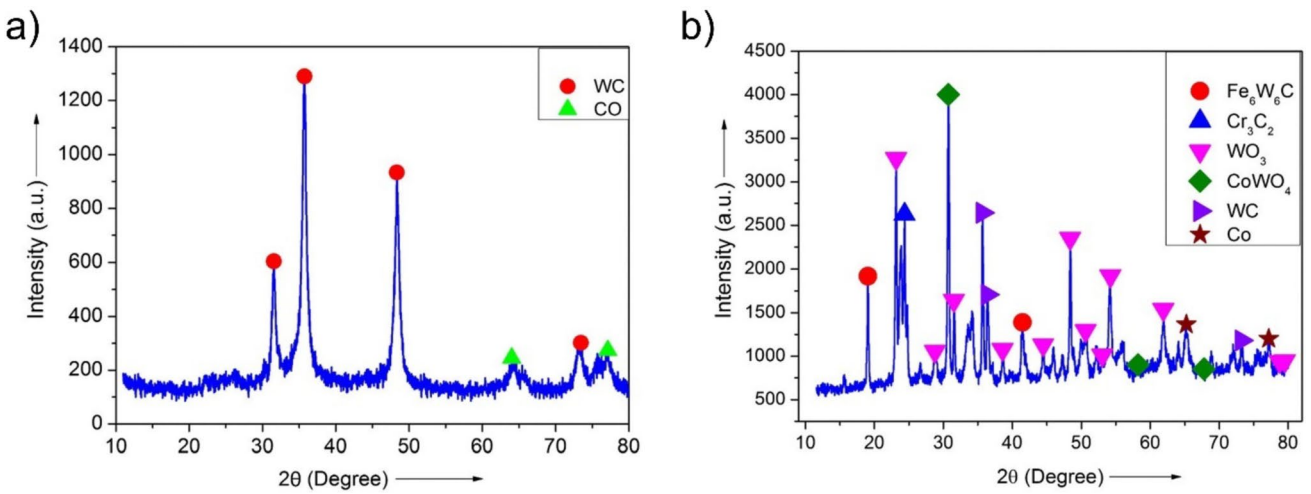


Fig. 6 Results of qualitative phase analysis of tool surface using XRD (**a**) prior to welding and (**b**) after use

2.3 Finalizing tool geometry

The geometry of the tool pin significantly impacts material flow and heat generation in FSW. Various pin shapes, including cylindrical, square, and triangular, were trialed, with cylindrical pins prone to breakage as shown in Fig. 7(a). Other shapes gradually deformed into truncated cones, which proved effective in producing defect-free welds.

The failure of the cylindrical tool pin, as depicted in Fig. 7(a), is attributed to shear failure arising from its relatively lower cross-sectional area at the pin's root. Under high-temperature and stress conditions during FSW, localized weakening combined with reduced mechanical resistance led to premature pin breakage. The cylindrical geometry lacks adequate material volume to withstand torsional and axial loads during severe plastic deformation.

Pin diameters ranging from 3 to 8 mm were tested, with 5 mm or smaller diameters prone to shearing and 8 mm diameters resulting in tunnel defects due to material flow challenges as depicted in Fig. 7(b). A 6 mm diameter pin was found to perform effectively. The 2.8 mm pin length was selected for the 3 mm sheet to prevent excessive plunge, avoid contact with the backing plate, and ensure effective material flow throughout the stir zone without causing distortion; a pin length of more than 2.8 mm resulted in sticking with the backing plate, as shown in Fig. 7(c).

The selected tool profile features a truncated cone-shaped pin, 6 mm in diameter and 2.8 mm in length, as illustrated in Fig. 7(d). This configuration ensures proper material stirring, heat generation, and weld quality during FSW.

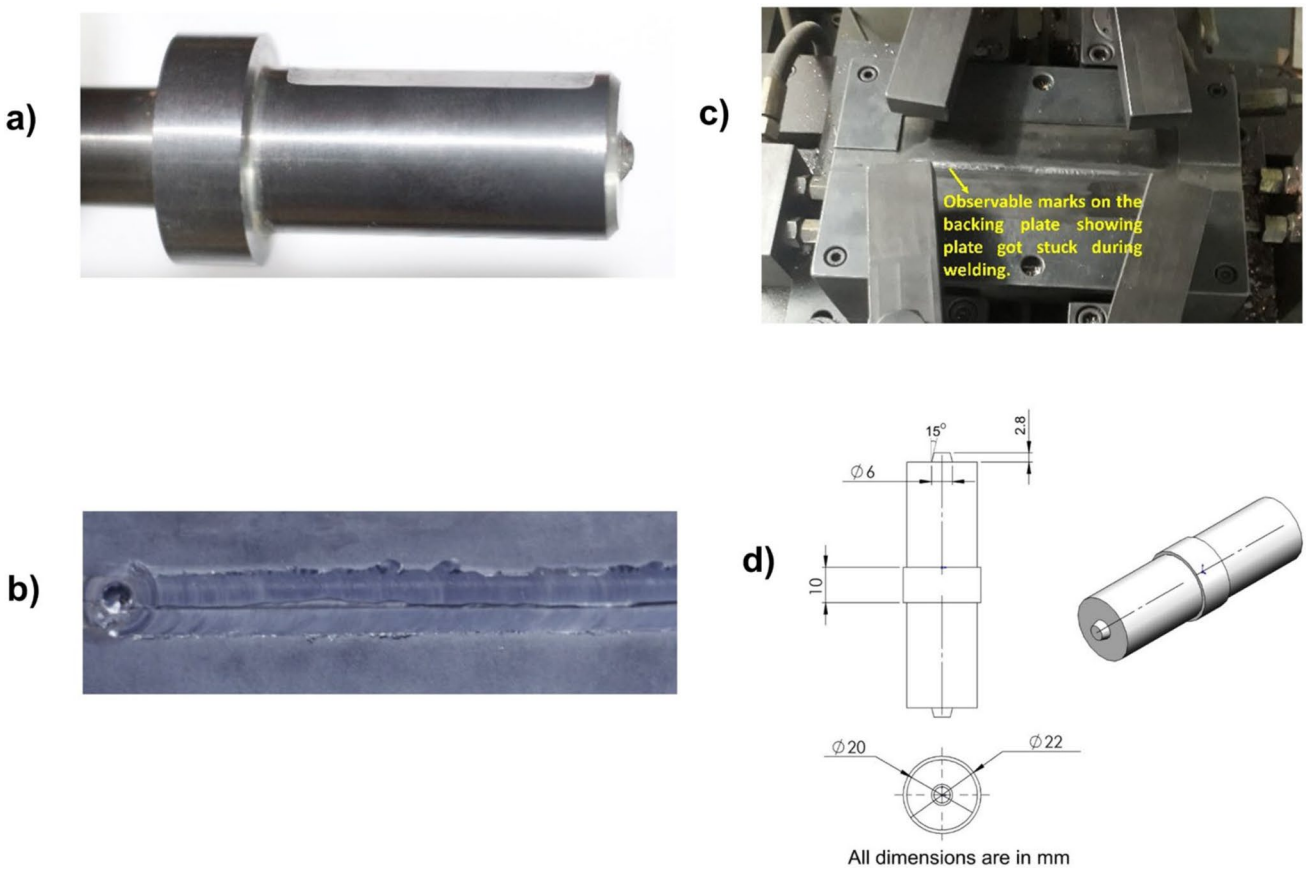


Fig. 7 (**a**) Tool pin breakage when a cylindrical pin profile was used; (**b**) Defect occurred due to large pin and regular shoulder diameter; (**c**) Picture of the backing plate showing observable marks after the removal of welded plates. (**d**) Dimensions of the tool used in the present study

3 Experimental setup and process parameters

For this study, carbon steel AISI 1018 was selected as the workpiece material, having a hardness of 165 HV. The chemical composition, determined through spark spectroscopic examination, is detailed in Table 3.

Plates measuring 200 × 40 × 3 mm were obtained by casting a 7′ × 4′ plate and shearing. Edge preparation using a surface grinder ensured proper contact with the tool's shoulder during welding. A backing plate, used to protect the fixture, was employed, with the milling scale removed to prevent defects. The process variables chosen for the current investigation were Tool rpm, welding speed, and shoulder diameter based on a thorough literature analysis. To establish the process parameter levels, trial runs were conducted. Table 4 outlines the chosen levels of the input parameters.

4 Results and discussions

The initial welding test with random parameters yielded unsatisfactory results, as depicted in Fig. 8. The weld bead was pushed down (Fig. 8a), with a fusion miss (Fig. 8b) likely due to reduced pressure affecting heat input. Excessive flash and material thinning occurred at a 4-degree tool tilt (Fig. 8c), with macro flaws observed on the weld surface (Fig. 8d), linked to plastic flow processes [27]. Subsequent welding with optimal input parameters, namely welding speed of 60 mm/min, with tool rpm of 750 rpm, and shoulder diameter of 20 mm determined from our previous study [28], yielded improved results. Figure 8(e) shows the welding setup used, while Fig. 8(f) illustrates the joints in good condition, free from voids, cracking, or distortion.

Table 3 Chemical composition of base metal [weight percent]

Material	C	S	Mn	P	Fe
AISI 1018 Steel	0.18	0.029	0.621	0.039	Bal

Table 4 Process parameters with levels chosen

Parameter	Levels	
	Minimum	Maximum
Welding speed	60	210
Tool RPM	430	750
Shoulder diameter	15	20

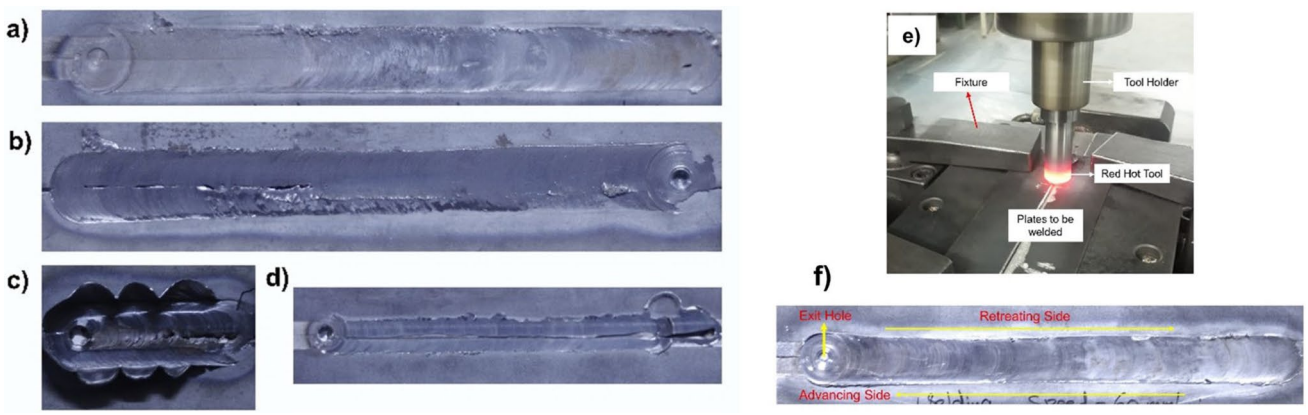


Fig. 8 **a**) Depressed weld bead, **b**) Fusion defect, **c**) Excessive flash and thinning, **d**) Surface flaws, **e**) Welding setup, and **f**) FSWed joint

4.1 Microstructural analysis

Microstructural changes induced by FSW were analyzed using SEM, and presented in Fig. 9(a-b). The BM exhibited a 31.82% pearlite content, as quantitatively analyzed in Fig. 9(b). The pearlite content is indicative of the carbon steel's microstructure, which inherently affects its mechanical properties.

A distinct boundary separating the HAZ and TMAZ was observed, as shown in Fig. 10(a). This clear demarcation highlights the varying degrees of thermal and mechanical influences experienced during the welding process. A closer view of the TMAZ as indicated in Fig. 10(b) revealed significant grain refinement. The refinement of grains in this region is a direct result of the severe plastic deformation and dynamic recrystallization processes that occur during FSW, which enhance the mechanical properties of the weld by increasing the hardness of the material. This is supported by the measured hardness value of 195 HV in the stir zone. Grain refinement directly contributes to the enhanced strength of the welded joint. A finer grain structure increases the density of grain boundaries, which restricts the motion of dislocations under stress. This mechanism, commonly known as grain boundary strengthening, leads to improved resistance to plastic deformation. Moreover, the homogeneity in pearlite distribution within the stir zone supports stress transfer, reducing the likelihood of early failure. These microstructural improvements align with the observed increase in tensile strength, confirming a strong structure–property relationship in the weld region.

Additionally, the HAZ exhibited partially transformed pearlitic structures, which suggest incomplete phase transformations due to the moderate thermal exposure in this region. The welding-induced heat and plastic deformation also altered the grain size notably in the stirred zone, as illustrated in Fig. 10(c). The stirred zone exhibited increased pearlite formation, with a pearlite content rising to 44.49%. This increase is a consequence of the intense heat and mechanical stirring, which promote the nucleation and growth of pearlite from the austenite phase during cooling. Crystallographic plane orientation alterations in the HAZ and TMAZ observed in this study were consistent with prior research findings. Lakshminarayanan et al. [29] reported notable grain refinement and reorientation in the HAZ and TMAZ regions of friction-stir-welded mild steel due to severe plastic deformation and thermal cycles. Tiwari et al. [30] observed dynamic recrystallization-driven grain structure evolution in low-carbon steel welded with tungsten carbide tools, resulting in significant texture modification in these zones. Similarly, Wang et al. [31] demonstrated that the combined effect of mechanical stirring and thermal input during FSW of weathering mild steel led to lattice reorientation and microstructural transformation within the HAZ and TMAZ. The crystallographic alterations identified in the present work align with these findings, affirming the role of thermal and mechanical gradients in modifying lattice structures during FSW of carbon steels.

4.2 Studies on tensile strength

The tensile strength of the welded joints was evaluated to determine the effectiveness of the tool design and the welding parameters, and is presented in Fig. 11. The specimens exhibited an enhanced UTS (460 ± 13 MPa) compared

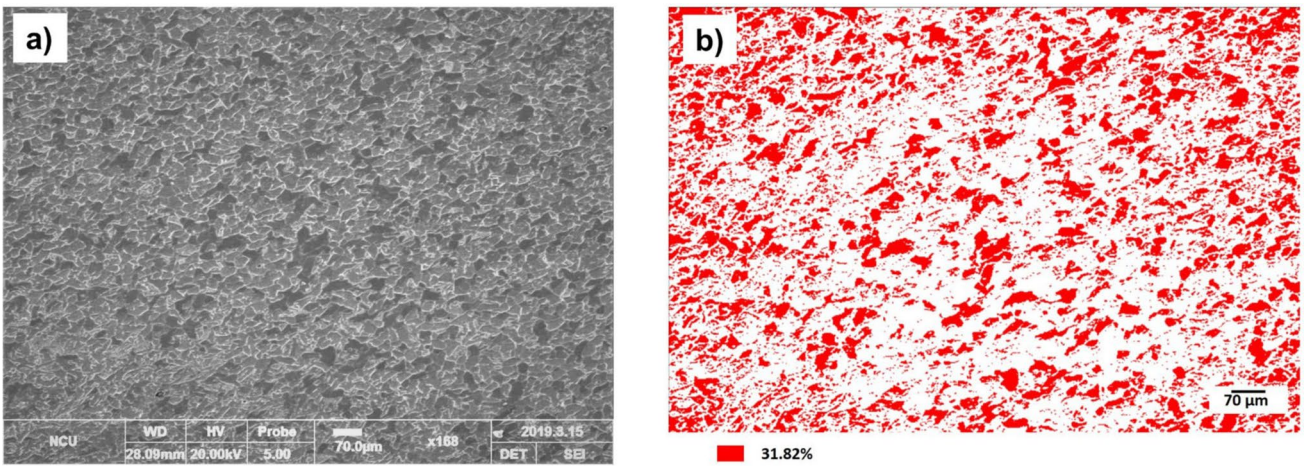


Fig. 9 **a**) Microstructure of BM **b**) Analysis of pearlitic phases (red color) by ImageJ software

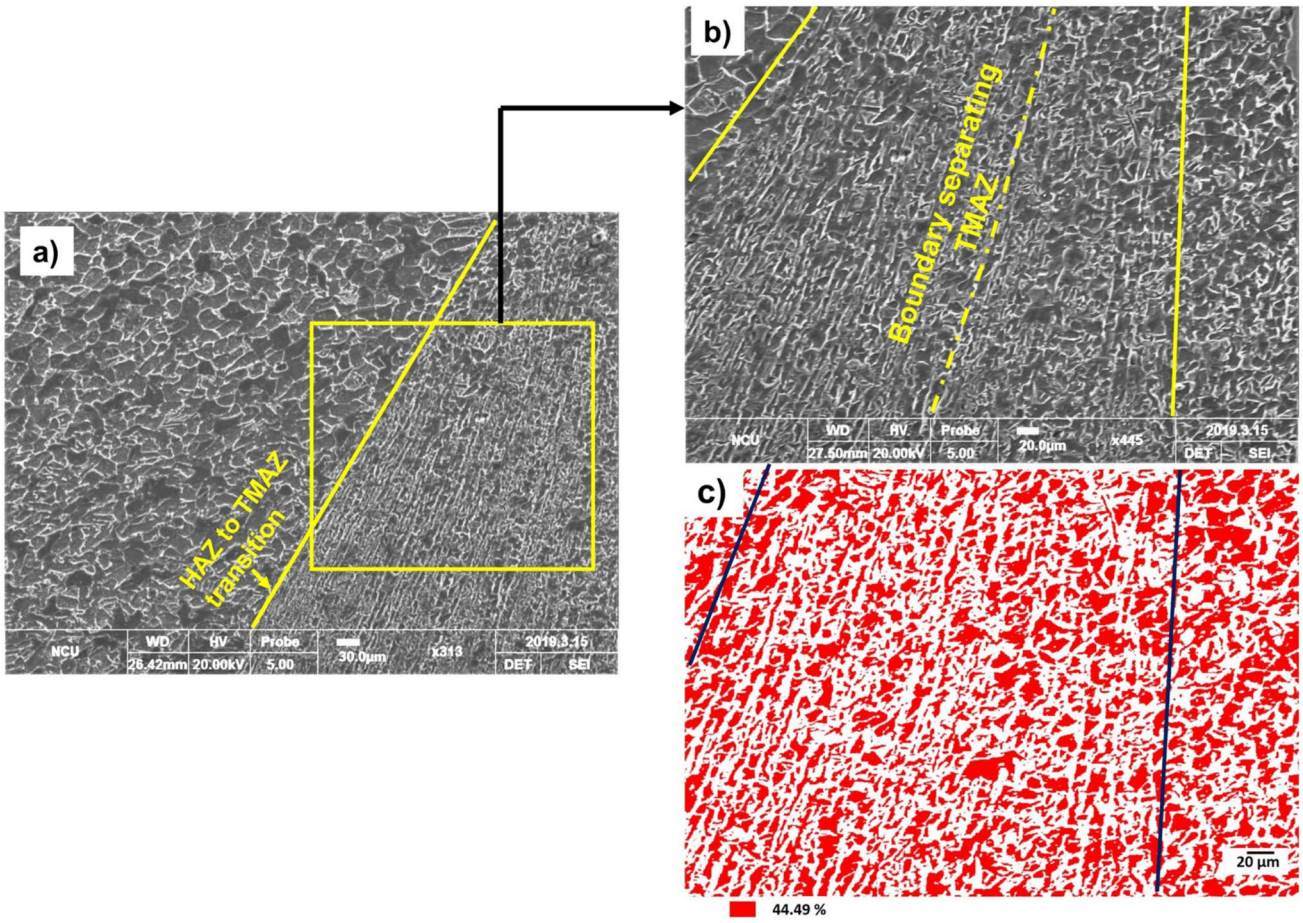


Fig. 10 Microstructure showing **a**) transition between TMAZ and HAZ, **b**) magnified image of HAZ and TMAZ, **c**) Analysis of pearlitic phase (red color) by ImageJ software

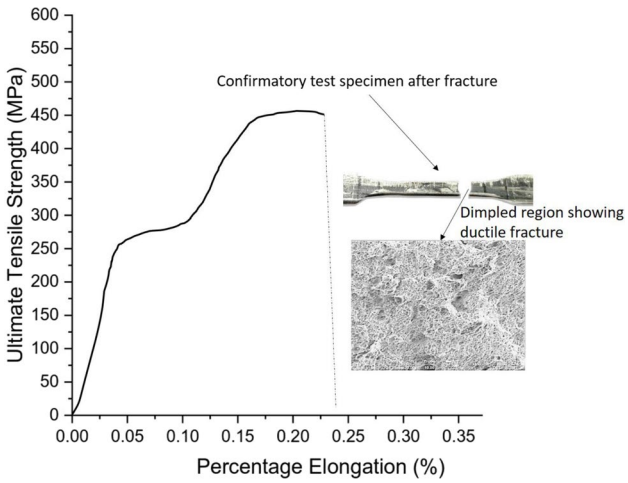


Fig. 11 Typical stress–strain curve for the specimen welded using Optimal Conditions and a fractured sample with fractographic analysis

to the BM with UTS (390 ± 10 MPa), indicating an approximate 18% increase. The optimized tool geometry, particularly the tapered pin design, contributed to the uniform distribution of stress across the weld, minimizing the risk of failure under tensile loads. It is further supported by the fact that improved mechanical properties, measured through tensile tests, prove the choice of tool material and its design for improved joint integrity and performance.

Furthermore, confirmatory test specimens broke from the BM region rather than the weld zone, indicating a sound and robust weld. Fractographic analysis of the broken specimen revealed the formation of dimples, characteristic of ductile fracture. This dimpled morphology, as shown in Fig. 11, indicates that the material has undergone extensive plastic deformation before failure, which is desirable in welded joints since it is an indication of the ability to absorb energy and hence avoid brittle failure. Dimple formation is generally associated with micro-void coalescence resulting from the merging of small cavities within the material under tensile stress, resulting in ductile rupture. It further supports the efficacy of the optimized tool design in producing high-quality and durable welds with better mechanical properties.

5 Conclusions

The major conclusions obtained from the present study are as follows:

- Optimization of tool geometry, particularly from a cylindrical to a tapered pin design, is found to appreciably improve the weld quality of AISI 1018 carbon steel in the FSW process.
- Tungsten carbide with 7% cobalt serves as an effective tool material to reduce tool wear and maintain mechanical integrity during FSW, as revealed by metallography and mechanical testing.
- Microstructural examinations show clear improvements in the thermo-mechanically affected zone, with finer grain structure and improved pearlite formation, thereby contributing to mechanical properties.
- Tensile tests revealed that the FSW at optimum parameters can produce joints with higher tensile strength than that of the BM, indicating efficient FSW processing.
- This research concludes that the design of the tool and the selection of parameters are two prime important factors for making defect-free welds and enhancing the overall performance of FSWed joints in carbon steel.

Author contributions Anmol Bhatia: Methodology and Investigation, Writing—original draft. Reeta Wattal: Conceptualization, Methodology and Investigation'.'Rajeev Kumar: Conceptualization, Writing—original draft'. Anant Prakash Agrawal: Result analysis, Review & Editing'.'Saurabh Dewangan: Result analysis, Resources, Review & Editing'"All authors have reviewed the article before submission".

Funding Open access funding provided by Manipal University Jaipur.

Data availability The authors confirm that the data supporting the findings of this study are available within the article. If someone wants to request the data from this study, the corresponding author (Saurabh Dewangan) should be contacted.

Declarations

Ethics approval and consent to participate Not applicable.

Competing interests The authors declare no competing interests.

Open Access This article is licensed under a Creative Commons Attribution-NonCommercial-NoDerivatives 4.0 International License, which permits any non-commercial use, sharing, distribution and reproduction in any medium or format, as long as you give appropriate credit to the original author(s) and the source, provide a link to the Creative Commons licence, and indicate if you modified the licensed material. You do not have permission under this licence to share adapted material derived from this article or parts of it. The images or other third party material in this article are included in the article's Creative Commons licence, unless indicated otherwise in a credit line to the material. If material is not included in the article's Creative Commons licence and your intended use is not permitted by statutory regulation or exceeds the permitted use, you will need to obtain permission directly from the copyright holder. To view a copy of this licence, visit http://creativecommons.org/licenses/by-nc-nd/4.0/.

References

1. Singh T. Comparative analysis of microstructural and mechanical characteristics of reinforced FSW welds. In: Rathee S, Srivastava M, Davim JP, editors. Advanced welding and joining techniques. Hoboken: Wiley; 2024.
2. Singh T. Nanoparticles reinforced joints produced using friction stir welding: a review. Eng Res Express. 2023;5(2): 022001. https://doi.org/10.1088/2631-8695/accb28.

3. Mishra RS, Ma ZY. Friction stir welding and processing. Mater Sci Eng R Rep. 2005;50:1–78. https://doi.org/10.1016/j.mser.2005.07.001.
4. Ada M, Popoola P. Recent advances in joining technologies of aluminum alloys: a review. Discov Mater. 2024;4:86. https://doi.org/10.1007/s43939-024-00155-w.
5. Mishra A, Patel MS, Hussain I, et al. Achieving microstructural homogeneity in the stir zone across thick AA6061 welds using self-reacting bobbin tool friction stir welding. Discov Mater. 2024;4:65. https://doi.org/10.1007/s43939-024-00138-x.
6. Andrade DG, Leitão C, Dialami N, Chiumenti M, Rodrigues DM. Modelling torque and temperature in friction stir welding of aluminium alloys. Int J Mech Sci. 2020;182: 105725. https://doi.org/10.1016/j.ijmecsci.2020.105725.
7. Rodrigues DM, Leitão C, Louro R, Gouveia H, Loureiro A. High speed friction stir welding of aluminium alloys. Sci Technol Weld Join. 2010;15(8):676–81. https://doi.org/10.1179/136217110X12785889550181.
8. Shah PH, Badheka VJ. Friction stir welding of aluminium alloys: An overview of experimental findings – process, variables, development and applications. Proc Inst Mech Eng Part L J Mater Des Appl. 2016;233(1):1–78. https://doi.org/10.1177/1464420716689588.
9. Cui L, Zhang C, Liu YC, Liu XG, Wang DP, Li HJ. Recent progress in friction stir welding tools used for steels. J Iron Steel Res Int. 2018;25(5):477–86. https://doi.org/10.1007/s42243-018-0066-7.
10. Singh T, Tiwari SK, Shukla DK. Mechanical and microstructural characterization of friction stir welded AA6061-T6 joints reinforced with nano-sized particles. Mater Charact. 2020;159: 110047. https://doi.org/10.1016/j.matchar.2019.110047.
11. Singh T, Tiwari SK, Shukla DK. Processing parameters optimization to produce nanocomposite using friction stir welding. Eng Res Express. 2019;1(2): 025048. https://doi.org/10.1088/2631-8695/ab5bee.
12. Kumar K, Kailas SV. The role of friction stir welding tool on material flow and weld formation. Mater Sci Eng A. 2008;485(1–2):367–74. https://doi.org/10.1016/j.msea.2007.08.013.
13. Aissani M, Gachi S, Boubenider F, Benkedda Y. Design and optimization of friction stir welding tool. Mater Manuf Process. 2010;25(11):1199–205. https://doi.org/10.1080/10426910903536733.
14. Buffa G, Hua J, Shivpuri R, Fratini L. Design of the friction stir welding tool using the continuum based FEM model. Mater Sci Eng A. 2006;419(1–2):381–8. https://doi.org/10.1016/j.msea.2005.09.041.
15. Colegrove PA, Shercliff HR. Development of trivex friction stir welding tool Part 2 - Three-dimensional flow modelling. Sci Technol Weld Join. 2004;9(4):352–61. https://doi.org/10.1179/136217104225021661.
16. Ji S, Xing J, Yue Y, Ma Y, Zhang L, Gao S. Design of friction stir welding tool for avoiding root flaws. Materials. 2013;6(12):5870–7. https://doi.org/10.3390/ma6125870.
17. Fujii H, Cui L, Maeda M, Nogi K. Effect of tool shape on mechanical properties and microstructure of friction stir welded aluminum alloys. Mater Sci Eng A. 2006;419(1–2):25–31. https://doi.org/10.1016/j.msea.2005.11.045.
18. Shindo DJ, Rivera AR, Murr LE. Shape optimization for tool wear in the friction-stir welding of cast Al359-20% SiC MMC. J Mater Sci. 2002;37(23):4999–5005. https://doi.org/10.1023/A:1021023329430.
19. Lin SB, Zhao YH, He ZQ, Wu L. Modeling of friction stir welding process for tools design. Front Mater Sci. 2011;5(2):236–45. https://doi.org/10.1007/s11706-011-0128-2.
20. Tiwari A, Pankaj P, Biswas P, Kore SD, Rao AG. Tool performance evaluation of friction stir welded shipbuilding grade DH36 steel butt joints. Int J Adv Manuf Technol. 2019;103(1–4):1989–2005. https://doi.org/10.1007/s00170-019-03618-0.
21. Khan NZ, Khan ZA, Siddiquee AN, Al-Ahmari AM, Abidi MH. Analysis of defects in clean fabrication process of friction stir welding. Trans Nonferrous Met Soc China. 2017;27(7):1507–16. https://doi.org/10.1016/S1003-6326(17)60171-7.
22. Siddiquee AN, Pandey S. Experimental investigation on deformation and wear of WC tool during friction stir welding (FSW) of stainless steel. Int J Adv Manuf Technol. 2014;73(1–4):479–86. https://doi.org/10.1007/s00170-014-5846-z.
23. Lunetto V, De Maddis M, Lombardi F, Russo SP. A review of friction stir welding of industrial alloys: tool design and process parameters. J Manuf Mater Process. 2025;9:36. https://doi.org/10.3390/jmmp9020036.
24. Wang H, Wang M, Li B, Ji X. Machine learning prediction of mechanical properties in stir zone of 310 austenitic steel friction stir welds. Mater Lett. 2025;386: 138100. https://doi.org/10.1016/j.matlet.2025.138100.
25. Wu X, Shen J, Jiang F, Wu H, Li L. Study on the oxidation of WC-Co cemented carbide under different conditions. Mater Sci Eng A. 2015;621:128–32. https://doi.org/10.1016/j.ijrmhm.2020.105381.
26. Roa JJ, Jiménez-Piqué E, Tarragó JM, Zivcec M, Broeckmann C, Llanes L. Berkovich nanoindentation and deformation mechanisms in a hardmetal binder-like cobalt alloy. Mater Sci Eng A. 2015;621:128–32. https://doi.org/10.1016/j.msea.2014.10.064.
27. Lombard H, Hattingh DG, Steuwer A, James MN. Optimising FSW process parameters to minimise defects and maximise fatigue life in 5083–H321 aluminium alloy. Eng Fract Mech. 2008;75(2):341–54.
28. Bhatia A, Wattal R. Process parameters optimization for maximizing tensile strength in friction stir-welded carbon steel. Stroj Vestn J Mech Eng. 2021;67(5):311–21. https://doi.org/10.5545/sv-jme.2021.7203.
29. Lakshminarayanan AK, Balasubramanian V, Salahuddin M. Microstructure, tensile and impact toughness properties of friction stir welded mild steel. J Iron Steel Res Int. 2010;17(1):68–74. https://doi.org/10.1016/S1006-706X(10)60186-0.
30. Tiwari A, Singh P, Pankaj P, Biswas P, Kore SD. FSW of low carbon steel using tungsten carbide WC-10 wt.% Co based tool material. J Mech Sci Technol. 2019;33(9):4931–8. https://doi.org/10.1007/s12206-019-0932-7.
31. Wang Y, Tsutsumi S, Kawakubo T, Fujii H. Microstructure and mechanical properties of weathering mild steel joined by friction stir welding. Mater Sci Eng A. 2021;823: 141715. https://doi.org/10.1016/j.msea.2021.141715.

Publisher's Note Springer Nature remains neutral with regard to jurisdictional claims in published maps and institutional affiliations.

2025 Fourth International Conference on Smart Technologies, Communication and Robotics (STCR) | 979-8-3503-5753-0/25/$31.00 ©2025 IEEE | DOI: 10.1109/STCR62650.2025.11020418

Tow-Thomas-Controlled Single-Phase Solar Powered Microgrids: Performance Evaluation in Grid-Tied and Standalone Operations

Madhur Agarwal
Department of Electrical Engineering
Delhi Technological University
New Delhi, India
madhuragarwal_ee21b8_28@dtu.ac.in

Neeraj Bhardwaj
Department of Electrical Engineering
Delhi Technological University
New Delhi, India
neerajbhardwaj_ee21b8_50@dtu.ac.in

Moksh Bashista
Department of Electrical Engineering
Delhi Technological University
New Delhi, India
mokshbashista_ee21b8_41@dtu.ac.in

Ankita Arora
Department of Electrical Engineering
Delhi Technological University
New Delhi, India
aroraankita@dtu.ac.in

Shatakshi
Department of Electrical Engineering
Delhi Technological University
New Delhi, India
shatakshi@dtu.ac.in

***Abstract*—The following paper proposes a well-planned micro-grid system aimed at damping harmonics and enabling smooth transitions from grid-tied to standalone operation. The setup comprises a photovoltaic (PV) solar generation system, a voltage-fed converter, and a battery driven energy storage unit. To control a voltage fed converter, we use gate pulses generated by the Tow-Thomas algorithm, ensuring efficiency and accuracy. For optimal solar power tracking, system uses the Perturb and Observe (P&O) method with maximum power point tracking (MPPT) system to regulate the duty cycle of the DC-DC step up converter. During grid failures, a switch transition logic (STL) based controller, transitions the system from grid-reliant to self-sufficient operation, ensuring uninterrupted power supply to critical loads. Shunt compensation is connected to the microgrid for harmonic damping, load current balancing, and better power quality control at the point of common interfacing (PCI) . The effectiveness and reliability of the outlined system is implemented and analyzed under various loads and different irradiation conditions.**

***Index Terms*—Microgrid, Power System, Power Quality, Renewable Energy, Single Phase, Tow-Thomas, Solar PV Array, Switch Transition Logic**

I. Introduction

Renewable energy sources (RES) are becoming more and more valued by electricity generation systems in the modern world. In addition to being environmentally friendly, these systems lessen dependency on conventional energy sources. However, power quality is still a significant concern. Organizations and regulatory agencies are actively attempting to address this issue since high power quality is crucial to the effectiveness, dependability, and financial sustainability of energy systems. Research on microgrids, which frequently combine a variety of inexhaustible sources of energy like wind, water and sunlight, has grown significantly. Battery Powered Storage Unit is integrated with the system to ensure the continuous operation of renewable energy based microgrid. Microgrids also employ Distributed Static Compensators (DSTATCOMs) to control frequency and voltage fluctuations in induction generators to manage erratic load fluctuations. DSTATCOMs are essential components of contemporary power systems because they regulate voltage, balance reactive power, and reduce harmonics.

In order to efficiently regulate Voltage Source Converters (VSCs) in power systems, researchers have investigated a number of control strategies. To enhance VSC performance, conventional methods such as self-tuning filters, synchronous reference frame theory (SRFT), instantaneous reactive power theory, and least mean square (LMS) have been extensively employed. When working with PV-integrated VSCs, these techniques frequently fail, particularly when DC offsets and dominant harmonics are present. Conversely, intelligent control methods that employ Artificial Intelligence (AI) for adaptive regulation are more complicated because they need to calculate the ideal filter parameters in real time.

In the following paper, a novel control algorithm is presented for DSTATCOM that regulates VSC using the Tow-Thomas Filter. By addressing the shortcomings of current techniques, this method guarantees precise compensation of harmonics and voltage imbalances. The ability of microgrids to function in both grid-synchronized and isolated modes is another crucial feature. In the event of an emergency—such as grid failure, human error, or an unintentional circuit breaker operation—this dual-mode operation guarantees a continuous power supply. The system must smoothly switch to islanding mode in order to accomplish this. Several algorithms have been developed to ensure stable and effective reconnection,

979-8-3503-5753-0/25/$31.00 ©2025 IEEE

Authorized licensed use limited to: DELHI TECHNICAL UNIV. Downloaded on June 16,2025 at 05:09:54 UTC from IEEE Xplore. Restrictions apply.

particularly in difficult grid conditions. The use of STL to facilitate dual-mode operation and improve the system's resilience and dependability is covered in this article. The system automatically transitions to standalone mode during grid outages, using the PV array that is linked to the VSC via a DC-DC step up converter to provide power. We have used an MPPT algorithm based on the P&O method to optimize energy capture from the PV array. The duty cycle, which produces pulses for the converter, is determined by the MPPT algorithm. To ensure a steady DC voltage, one side of the converter is connected to the DC coupling capacitor and the other side is joined to the PV array. A Battery Energy Storage System (BESS) is included into the microgrid to further improve energy system reliability and handle the sporadic nature of renewable sources . When there is a high demand or little solar generation, the BESS is strategically important in providing power. When linked to the grid, the BESS uses the PV array's excess energy to charge during times of low demand. Grid outages or periods of high demand can then make use of this stored energy. In islanding mode, the PV array charges the BESS while maintaining a steady and uninterrupted power supply, increasing the system's operational flexibility and resilience. Thus, the suggested approach guarantees a consistent and effective power supply in addition to addressing power quality concerns.

II. System Layout

A single-phase AC supply is linked to a non linear load comprising of a diode rectifier, inductor and a resistor at PCI which forms a single-phase microgrid system as demonstrated in Fig.1. The model comprises of a shunt-connected VSC which is made up of four IGBTs (S_1, S_2, S_3 and S_4). In grid synchronized mode the pulses (P_{G1}, P_{G2}, P_{G3} and P_{G4}) are generated by Tow-Thomas control algorithm (as discussed in section III-A) and pulses during standalone mode (P_{I1}, P_{I2}, P_{I3} and P_{I4}) are generated by islanding control algorithm (as discussed in section III-B). The decision between these modes is made using the STL approach (as discussed in section III-C). An interface inductor connects the grid at the PCI to the AC side of the VSC, while the DC side of the VSC is joined to a DC link capacitor (C_{dc}). A battery and a buck-boost converter makes up the BESS. A PV system is also included, which consists of a PV array coupled to a DC-DC step up converter. The PV system is integrated with rest of the microgrid by connecting the DC-DC step up converter's output to C_{dc}. All the values of the component are provided in the Table 1.

III. Tow-Thomas Control Algorithm

The Tow-Thomas biquad filter is an active filter topology commonly used for the implementation of second-order low-pass (LP), high-pass (HP), and band-pass (BP) filters. It uses operational amplifiers (op-amps), resistors, and capacitors to achieve precise frequency response characteristics.

$$\frac{V_{BP}}{V_{in}} = \frac{-K\omega_o}{Qs + \omega_o} \tag{1}$$

TABLE I
SPECIFICATIONS OF THE PROPOSED SINGLE-PHASE SOLAR POWERED MICROGRID

S.No.	Parameter	Single Phase System
1.	V_s	110V (rms)
2.	L_f	$L_f = \frac{mV_{dc}}{4af_sI_{crpp}} = 3mH$
3.	C_{dc}	$C_{dc} = \frac{2k_1V_{rms}aIt}{V_{dc}^2 - V_{dc1}^2} \approx 3000\mu F$
4.	V_{dc}	$V_{dc} = 200V$
5.	Load	R= 7.5 Ω, $L = 40mH$
6.	PV Array	$V_{mp} = 160.4V, I_{mp} = 7.99A$
7.	BESS	154V, 50Ah

$$\frac{V_{LP}}{V_{in}} = \frac{-K\omega_o^2}{Qs^2 + \omega_o s + K\omega_o^2} \tag{2}$$

A. Tow-Thomas based control of VSC

A Tow-Thomas biquad filter is used to obtain the I_{BP} and I_{LP} currents from the incoming load current (I_L) as illustrated in Fig.2. Each of these currents are squared individually, and their sum is calculated. Taking the square root of this sum gives the fundamental component of the load current (I_{Ld})

I_{Ld} is then passed through a low-pass filter to achieve the filtered I_{Ld}.

$$I_{Ld} = I_{fund} = \sqrt{I_{BP}^2 + I_{LP}^2} \tag{3}$$

$$I_{pvff} = \frac{2P_{pv}}{V_t} \tag{4}$$

The total fundamental active component of current (I^*_{Ld}) is calculated by adding the loss component (I_{Loss}), obtained from the Proportional-Integrator (PI) controller of the DC link voltage (V_{dc}), to the generated I_{Ld} and subtracting the PV feed-forward component (I_{pvff}), as computed in equation 4. The reference source current (I^*_s) thus generated is compared with the actual source current (I_s) to produce VSC gate pulses using a hysteresis controller. The gate pulse thus generated are fed to the VSC.

$$I^*_{Ld} = I_{loss} + I_{Ld} - I_{pvff} \tag{5}$$

B. Islanding Control Algorithm

The Fig.3 shows the working of islanding control algorithm. In this algorithm voltage at PCI (V_{pci}) is compared with reference source voltage (V_{sref}) to generate error which is then being fed to PI compensator.

The control signal thus obtained is checked against current through interfacing inductor (I_{vsc}) to derive gate pulses.

Authorized licensed use limited to: DELHI TECHNICAL UNIV. Downloaded on June 16,2025 at 05:09:54 UTC from IEEE Xplore. Restrictions apply.

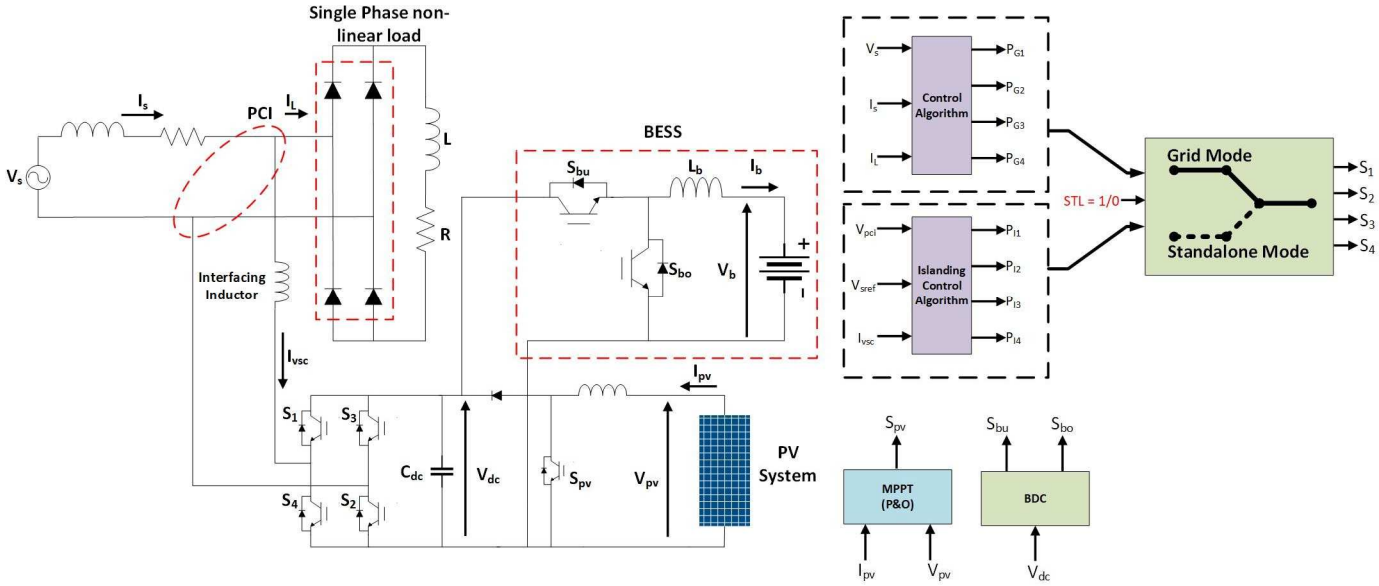


Fig. 1. Single phase grid connected to PV configuration

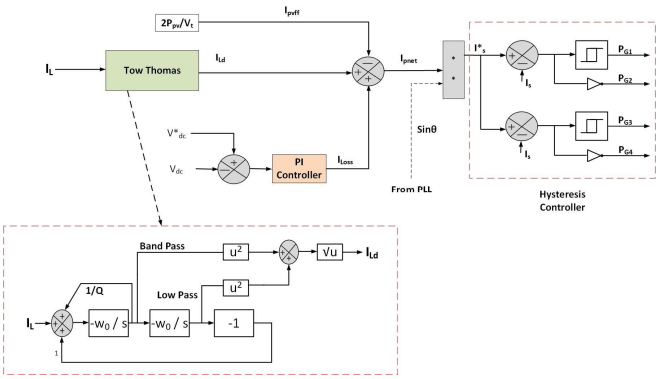


Fig. 2. Control scheme of single phase PV integrated microgrid

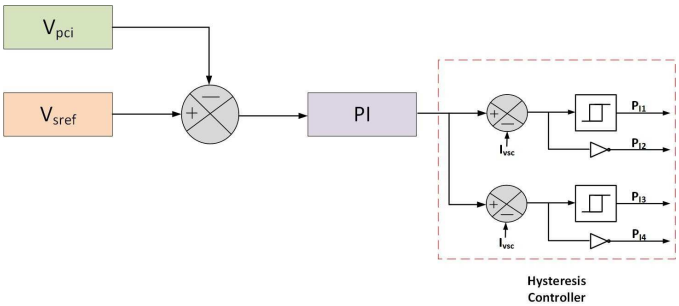


Fig. 3. Islanding control algorithm

C. Switch Transition Logic (STL)

The system uses STL to monitor the phase difference between V_{pci} and the source voltage (V_s). If phase shift stays within a set range, the system remains in grid-synchronized mode. However, if both the frequency and phase difference exceed their limits, the system switches to islanding mode. This ensures stable operation during grid instability. This logic is implemented in the system by using an AND gate, which checks both the conditions—if frequency and phase difference are out of range, it triggers islanding mode (STL=1) otherwise, the system stays in grid-tied (STL=0) mode as shown in Fig.4. This approach ensures reliable mode transitions during grid disturbances.

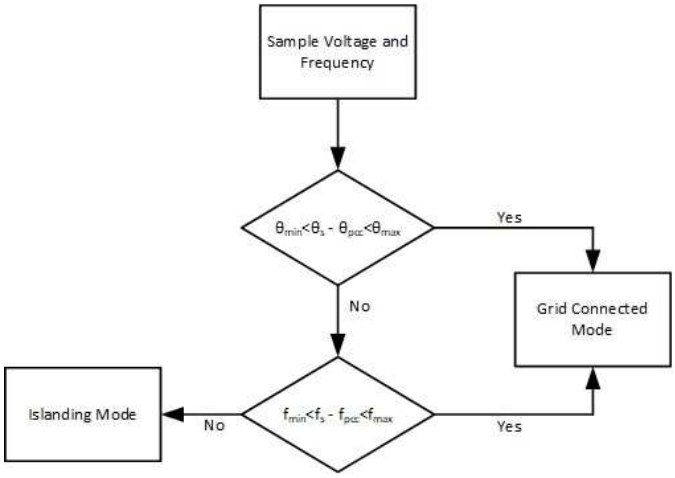


Fig. 4. Switch Transition Logic Algorithm

D. P&O MPPT control of PV system

P&O method is an extensively used approach for MPPT in PV systems, enabling the optimal power extraction from the solar panels. In this process a small deviation is applied to the voltage and the resulting power output is recalculated. If the present power (P_{PVnew}) is higher than the last recorded power (P_{PVold}), the change follows the same path, otherwise

Authorized licensed use limited to: DELHI TECHNICAL UNIV. Downloaded on June 16,2025 at 05:09:54 UTC from IEEE Xplore. Restrictions apply.

the direction is reverted. Through this iterative approach, the PV system's operating point gradually converges toward the peak power point. The above mentioned iterative approach is being depicted in Fig.5.

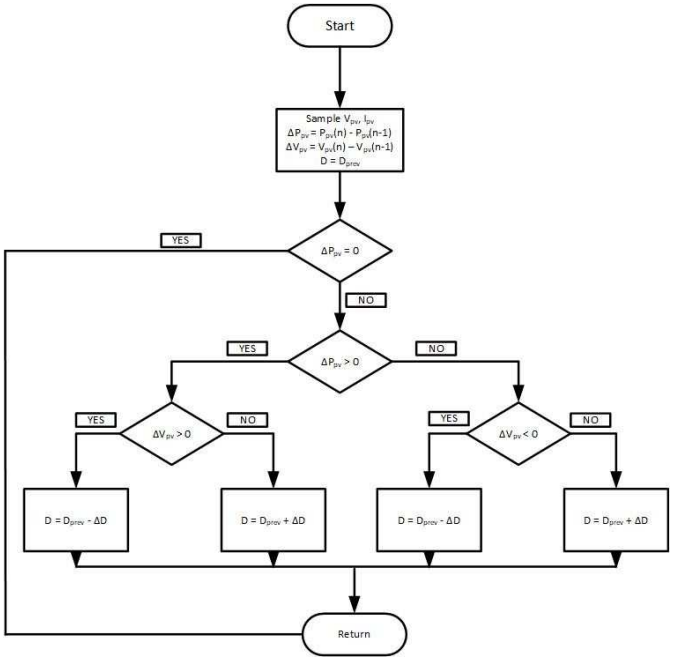


Fig. 5. P&O MPPT Control Algorithm

E. Bidirectional Converter (BDC) control Algorithm

In the microgrid system a buck-boost converter is employed in BESS to control the power flow and to maintain a steady V_{dc}.

The reference DC voltage (V_{dcref}) is compared with V_{dc} to determine error. The associated equations are:-

$$V_{dce}(\alpha) = V_{dcref}(\alpha - 1) - V_{dc}(\alpha) \quad (6)$$

$$i_{bref}(\alpha) = i_{bref}(\alpha-1)+k_{vp}(V_{dce}(\alpha)-V_{dce}(\alpha-1))+k_{vi}\cdot V_{dce}(\alpha) \quad (7)$$

where k_{vp} and k_{vi} are the gains of Proportional PI regulator.

The error is then allowed to pass through the PI compensator in order to obtain the reference battery current (I_{bref}). The buck-boost converter's control mechanism then compares the actual current passing through the battery (I_b) with I_{bref} as shown in Fig.6.

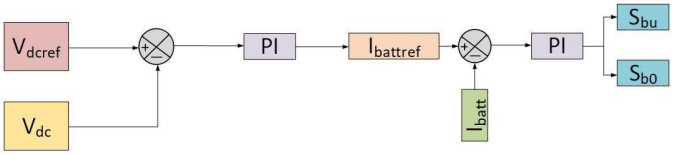


Fig. 6. BDC Control Algorithm

A PI compensator processes the error signal resulting from the difference between these values ensuring efficient charging and discharging of the battery. The equations are as follows:-

$$i_{ber}(\alpha) = i_{bref}(\alpha - 1) - i_b(\alpha) \quad (8)$$

$$D(\alpha) = D(\alpha-1)+k_{ip}i_{ber}(\alpha)-i_{ber}(\alpha-1)+k_{ii}i_{ber}(\alpha) \quad (9)$$

where k_{ip} and k_{ii} are proportional gains of PI regulators.

IV. Results and Discussion

A dynamic model is designed and implemented in MATLAB/Simulink to simulate the dynamics of a single-phase solar powered microgrid system using Tow-Thomas control algorithm under various operating conditions. The results are as follows:-

A. Dynamics during mode switching

The following model successfully switches from grid-interfaced mode to independent operation at t = 0.5s as demonstrated in Fig. 7, maintaining a constant V_{dc} at 200V. During grid linked mode the source current and source voltage are out of phase indicating power injection to the grid.The source current I_s drops to zero when the system transitions from grid coupled mode to isolated mode. The power is supplied seamlessly to the load during mode transition.
During the grid connected mode the energy from the PV array is being shared to the grid as well as the battery whereas during islanding mode the total power is being supplied to the battery which is evident by the increase in the battery current ($I_{battery}$).

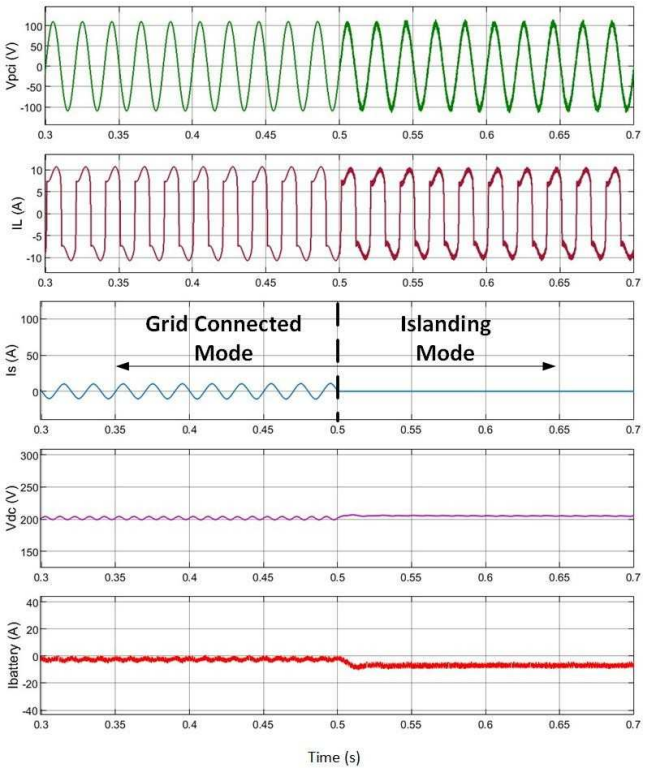


Fig. 7. Dynamics during mode switching

Authorized licensed use limited to: DELHI TECHNICAL UNIV. Downloaded on June 16,2025 at 05:09:54 UTC from IEEE Xplore. Restrictions apply.

B. Dynamics during load variation

As shown in Fig. 8, due to load increment at t= 0.5s, the load current is increased. As a result, in grid tied mode, the power which was earlier being transferred to the battery is now being transferred to meet the load demand. Hence the battery began discharging, to meet the required power demand. The V_{dc} also remained constant at 200 V. During standalone

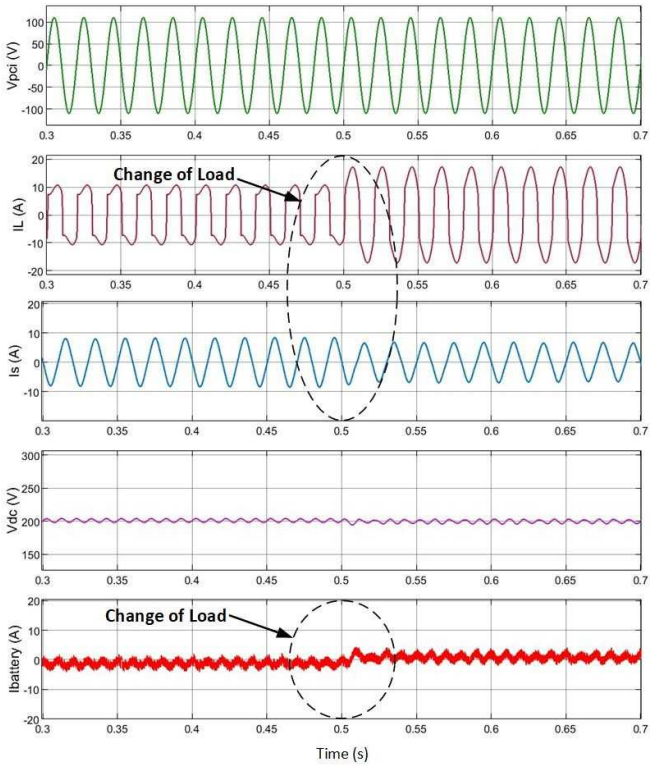


Fig. 8. Dynamics during load variation during grid connected mode

operation (Fig.9), due to the absence of the grid, the power demand was entirely being met by battery and PV system. At t= 0.5s due to increase in load demand the battery has to supply more power to the load. Hence the battery began discharging, to meet the required power demand.

C. Dynamic during change of irradiance

As illustrated in Fig.10 (a) Grid Connected Mode and Fig.10 (b) Islanding Mode, the irradiance level drops from 1000 W/m² to 500 W/m² at t = 0.25s, due to which I_{pv} is reduced to half, dropping from 8A to 4 A and consequently P_{pv} also drops from 1280W to 640W. In grid linked system (Fig. 10(a)), the drop in irradiance results in reduction of the available excess power in the system. As a result, the power supplied to the grid diminishes, which is reflected by reduction in I_s. At t = 0.5s the irradiance is raised from 500 W/m² to 1000 W/m² resulting in increasing the value of I_{pv} from 4A to 8A and subsequently increasing the value of P_{pv} from 640W to 1280W. During this dynamic variation, Vdc remains constant at 200V and a continuous power is being supplied to the load.

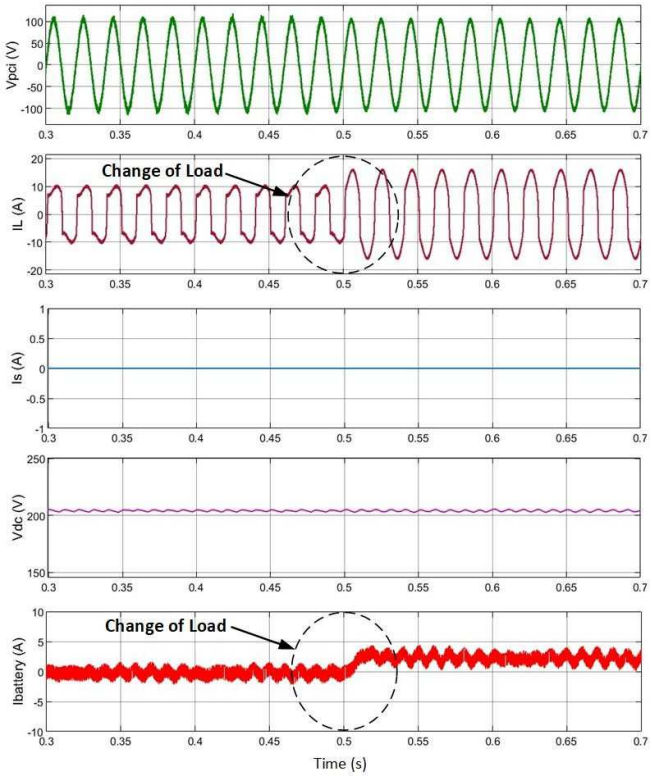


Fig. 9. Dynamics during load variation during islanding mode

D. Comparative Analysis

The Fig. 11 depicts the comparative analysis of total harmonic distortion (THD) when single phase PV integrated microgrid is implemented using Tow Thomas control algorithm and conventional SRFT control algorithm. As the result shows THD for the Tow Thomas control algorithm is 3.09% which is lower as compared to SRFT control algorithm's THD of 4.82%. Furthermore, the Tow Thomas algorithm is less complex and more stable ensuring better reliability and harmonic compensation as compared to SRFT control algorithm.

V. Conclusion

In this paper, a novel Tow Thomas control algorithm was used to improve the performance of a single-phase solar powered microgrid. The system was simulated under different solar irradiance levels, where the MPPT algorithm determined the duty cycle to produce pulses for optimal power retrieval from the PV array. The BESS was used to provide a stable V_{dc} and continuous power supply during grid outages at night to ensure system reliability. In addition, STL was effectively used to control smooth transitions between islanding and grid-connected modes while keeping the V_{dc} constant and ensuring a continuous power supply for the non-linear load.

The control algorithm has been thoroughly tested under various dynamic conditions which are as follows :-

- Mode switching (Grid tied mode to standalone mode)
- Load variation

Authorized licensed use limited to: DELHI TECHNICAL UNIV. Downloaded on June 16,2025 at 05:09:54 UTC from IEEE Xplore. Restrictions apply.

- Change of irradiance

Under the above mentioned conditions, the system performed satisfactorily which is evident from the provided results (as illustrated in section IV).

The comparative result further shows that the Tow Thomas control algorithm has a lower THD of 3.09% as opposed to the THD of 4.82% for the SRFT, showcasing the systems ability to keep THD below 5%, within IEEE-519 standards.

The proposed model have multiple application such as industries with heavy machinery and variable speed drives generate substantial harmonic pollution which can be compensated using Tow-Thomas algorithm. Also with the increased utilization of power electronic based devices, load nonlinearity has increased, making algorithms like the Tow-Thomas algorithm essential for harmonic compensation in microgrids.

VI. Future Scope

The proposed system is highly versatile and can be expanded by incorporating multiple BESS to simulate the charging and discharging of electric vehicle (EV). Further research can explore the integration of the Tow Thomas control algorithm with hybrid renewable energy systems, such as wind-PV hybrids.

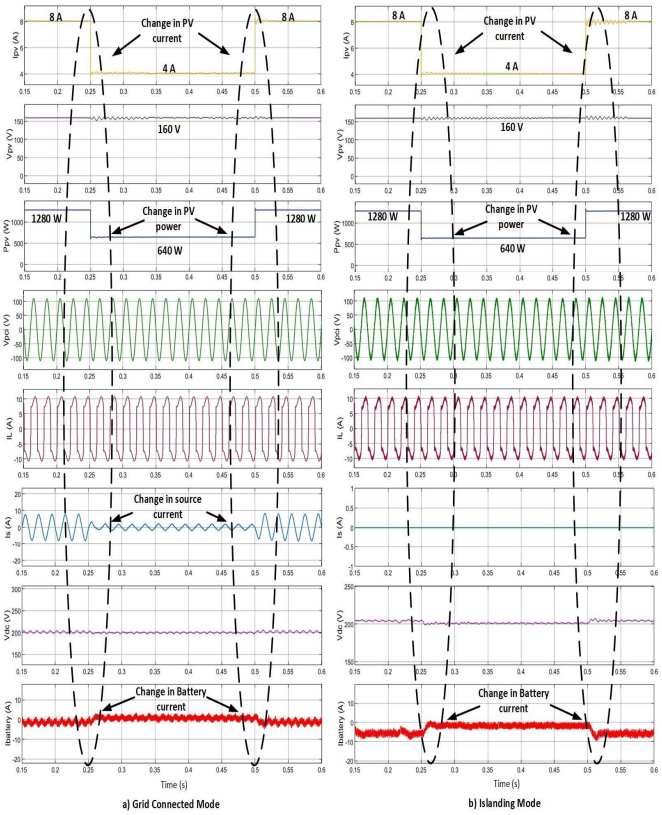


Fig. 10. Dynamic during change of irradiance

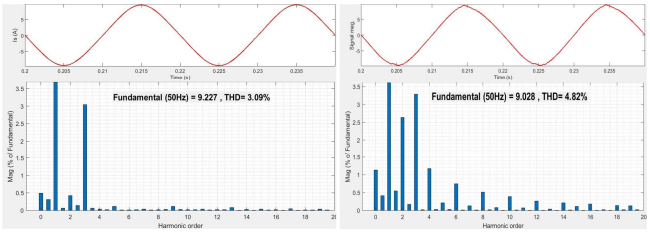


Fig. 11. Comparative Analysis of Tow-Thomas and SRFT Control Algorithm

References

[1] B. Singh, A. Chandra, and K. Al-Haddad, "Power Quality Problems and Mitigation Techniques," John Wiley & Sons, Hoboken, NJ, USA, 2009, pp.1-167

[2] L. C. Thomas, "The Biquad: Part I—Some Practical Design Considerations," IEEE Transactions on Circuit Theory, vol. CT-18, no. 3, pp. 350–357, May 1971.

[3] J. Tow, "A step-by-step active-filter design: A new approach to active-filter design uses as its basis a rudimentary knowledge of conventional, relatively simple passive filters, thus providing the nonspecialist with a valuable design tool," Bell Telephone Laboratories, Inc., pp. 64–68.

[4] T. J. Freeborn, B. Maundy, and A. Elwakil, "Fractional-step Tow-Thomas biquad filters," *Nonlinear Theory and Its Applications, IEICE*, vol. 3, no. 3, pp. 357–374, June 2012.

[5] S. Shatakshi, I. Ikhlaq, B. Singh, and S. Mishra, "A Synchronous Generator Based Diesel-PV Hybrid Micro-grid with Power Quality Controller," in *Proceedings of the IEEE*, pp. 1-5, May 2017.

[6] Shatakshi, B. Singh, and S. Mishra, "Dual Mode Operational Control of Single Stage PV-Battery Based Microgrid," in *Proceedings of the 2018 IEEMA Engineer Infinite Conference (eTechNxT)*, New Delhi, India, Mar. 2018, pp. 1–5.

[7] S. Sharma Jha, B. Singh, and S. Mishra, "Real Time Implementation of Control for Grid Integrated Photovoltaic with a Battery Support," in *Proceedings of the 2018 IEEE International Conference on Power Electronics, Drives and Energy Systems (PEDES)*, Chennai, India, Dec. 2018, pp. 1–5.

[8] S. Singh, S. Kewat, B. Singh, B. K. Panigrahi, and M. K. Kushwaha, "Seamless Control of Solar PV Grid Interfaced System With Islanding Operation," *IEEE Power and Energy Technology Systems Journal*, vol. 6, no. 3, pp. 139–149, Sept. 2019.

[9] S. Roy, F. Chishti, B. Singh, and B. K. Panigrahi, "GNLMP Control for Solar PV-Battery Based Microgrid With Ms-EPLL Synchronization," *IEEE Transactions on Industry Applications*, vol. 58, no. 1, pp. 357–374, Jan.-Feb. 2022.

[10] S. Kumar, B. Singh, and A. Al-Durra, "p-Norm Proportionate Based Approach With Mode Transition Between Grid Interactive and Standalone of Solar-BES Three Phase Four Wire Microgrid," in *Proceedings of the 2020 IEEE Industry Applications Society Annual Meeting*, Detroit, MI, USA, Oct. 2020, pp. 1–7.

[11] S. Pranith, S. Kumar, B. Singh, and T. S. Bhatti, "Improved Gaussian Filter Based Solar PV-BES Microgrid With PLL Based Islanding Detection and Seamless Transfer Control," *IEEE Transactions on Industrial Electronics*, vol. 69, no. 6, pp. 5815–5825, June 2022.

[12] F. Chishti and B. Singh, "FLL Unified AVF and NAAP Filter for Performance Investigation of Renewable Based AC Microgrid Under Grid to Standalone Transition Mode," *IEEE Transactions on Industry Applications*, vol. 59, no. 2, pp. 2374–2385, Mar.-Apr. 2023.

Authorized licensed use limited to: DELHI TECHNICAL UNIV. Downloaded on June 16,2025 at 05:09:54 UTC from IEEE Xplore. Restrictions apply.

Journal of Computational Electronics (2025) 24:97
https://doi.org/10.1007/s10825-025-02332-3

Triple-band perovskite based chiral metasurface biosensor with multi-functionalities

Vishakha Sharma[1] · Yogita Kalra[1] · Ravindra Kumar Sinha[1,2]

Received: 30 December 2024 / Accepted: 12 April 2025
© The Author(s), under exclusive licence to Springer Science+Business Media, LLC, part of Springer Nature 2025

Abstract
Driven by the need for unified design and miniaturization across bands, this work presents a novel approach to overcoming the single-functionality and limited applications of traditional metasurfaces. Here, a cutting-edge structural chiral metasurface is proposed exhibiting circular dichroism efficiently across three distinct spectral regions: the visible, near infrared, and mid infrared (MIR) bands each offering unique biosensing applications. The engineered metasurface is designed to achieve strong circular dichroism of 0.72, 0.56 and 0.71 in three different bands, providing tailored functionality as a biosensor for different biochemical and medical applications. Also, the designed structure has been tested as haemoglobin sensor for the detection of higher and lower concentration in the visible region, glucose sensor in near infrared region and as a cancer cell detection sensor in the MIR region offering the very high sensitivity.

Keywords Chiral metasurface · Absorber · Circular dichroism · Biosensor

1 Introduction

Metasurfaces are thin, planar devices that manipulate light on the subwavelength scale and have been demonstrated for achieving label-free biosensing applications [1–3]. Specifically designed, surface-engineered versions of these materials can also help improve light-matter interactions, making them highly sensitive to molecules related to biological processes [4, 5]. Metasurfaces can be designed for applications such as surface-enhanced Raman spectroscopy (SERS), fluorescence enhancement, refractive index sensing, through the judicious choice of materials with well-defined optical properties [6–8]. Given the fact that metasurfaces have unique features such as flexibility, high sensitivity and ability to be integrated into lab-on-chip devices, they are considered as a suitable potential platform for achieving real-time applications [9, 10].

Furthermore, an important asset of metasurfaces is that several biosensing mechanisms can be incorporated into one device. Different nanostructures on the metasurfaces can be engineered to detect different types of biomarkers or physical properties, for example to illustrate pH, temperature, and chirality simultaneously in a region [11–13]. Perhaps more impressively, it allows a single metasurface to be designed to respond to multiple wavelengths, each optimized for a specific type of detection. The multispectral capabilities of the sensor system extend significantly the functionality possible from biosensing to enable all-around, continuous monitoring of complex biological processes on a single and compact platform. Such multifunctional capabilities pave the way for advanced medical diagnostics, multispectral lab-on-chip devices, and precise, high-throughput biosensing for point-of-care applications.

In this context, metasurfaces with circular dichroism are particularly well-suited for biosensing applications as they provide an additional layer of functionality. Circular dichroism (CD) is the differential absorption of left- and right-handed circularly polarized light [14–16]. Metasurfaces designed with a CD can significantly boost the chiral signal of biomolecules, enabling enantio-selective detection of enantiomers—molecules which are identical in every

✉ Yogita Kalra
dryogitakalra@gmail.com

✉ Ravindra Kumar Sinha
dr_rk_sinha@yahoo.com

[1] Advanced Simulation Lab TIFAC-CORE in Fiber Optics and Optical Communication, Department of Applied Physics, Delhi Technological University, Delhi, India

[2] Gautam Buddha University, Greater Noida, Gautam Budh Nagar, UP 201312, India

Published online: 30 May 2025

possible way except their chirality, leading to widely different biological function. This enhancement is realized by carefully engineered asymmetric nanostructures that enhance the interaction between the circular polarized light and chiral molecules. Consequently, CD-active metasurfaces offer a very sensitive, label-free platform for examining the chirality of biomolecules, providing insightful information on drug interactions, protein folding, and other biochemical processes, where chirality of the molecules is important [17, 18].

This study presents a Perovskite-based optical chiral metasurface that exhibits selective absorption across three wavelength bands: visible, near infrared region (NIR), and mid infrared region (MIR) regions offering strong CD values. The structural design uses a pseudo star fish arrangement with six arms that have built-in resonant chambers in order to achieve multi-functionality. The electric and magnetic field distributions inside this resonator structure are further examined using Finite-Element-Method (FEM) simulations, which sheds more light on the basic principles of selective absorption. Further, by adjusting the parameters in the multiple resonance cavities, it is feasible to build an independent regulation of each resonance wavelength. The suggested structure may be utilized for various sensing applications. The resonant peak in the visible region offers the ability of the proposed chiral structure for the measurement of haemoglobin content in human blood. The same structure can also be used as a glucose concentration detection in the NIR and as a cancer cell detection biosensor in the MIR region. The extremely adaptable nature of the multifunctional metasurface design allows for a smooth integration into biomedical applications.

2 Structural design and analysis of perovskite based chiral metasurface

The proposed metasurface absorber is shown in Fig. 1a. A 100 nm thick gold metallic layer was first deposited, followed by a ~ 200 nm thick perovskite layer. The top layer includes gold (Au) metasurface resonators designed to mimic a fake starfish in appearance having six arms with some inbuilt cavities surrounded by semicircular and rectangular bars. The radius for the arc of six arms being denoted by '*R*' is 130 nm and the height of top resonators is 100 nm. The dielectric functions of the gold are adopted from Babar and Weaver 2015 [19] and for methyl ammonium-tri bromide from Ishteev et al. [20]. The inclusion of a gold mirror beneath the perovskite film is crucial for enhancing the device's optical performance by preventing light transmission and promoting Fabry–Perot like resonance modes, which significantly amplify the electric field inside the

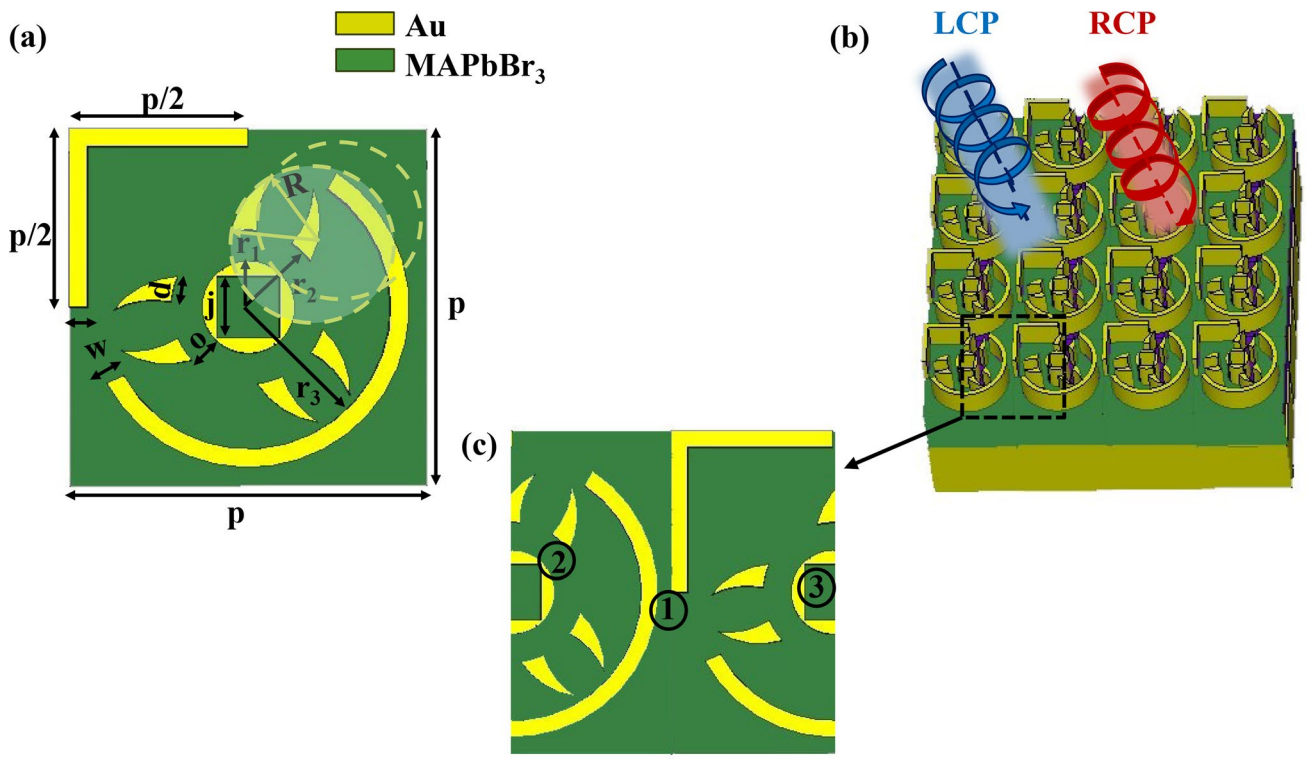


Fig. 1 **a** Top view of the proposed unit cell **b** 3D view of the designed metasurface and **c** Representation of the inbuilt cavities in the proposed structure

perovskite, thereby enhancing light-matter interaction. The perovskite film itself plays a dual role: first, its high absorption coefficient and tunable bandgap facilitate strong light trapping, improving the optical response; second, its high refractive index supports the formation of resonant modes, boosting the device's sensitivity. This material combination thus optimizes the performance of the proposed metasurface.

Figure 2 represents the evolution of the final design of the proposed unit cell and their corresponding CD value. Figure 1c shows rendered chambers designed with resonant cavities inside and between the periodic elements of metasurface. The cavities were introduced to increase the performance of the designed structure. Initially, a false star fish with six arms is designed and analysed showing neglible CD value. Secondly, a circular cavity of width '*o*' is added giving CD of 0.4. Further, a split ring and L shaped resonator has been introduced of thickness '*w*' with small gap breaking the mirror symmetry reaching the circular dichroism value of ~ 0.6. The designed chiral structure violates the n-fold rotational ($n > 2$, from central blades) and mirror symmetries(from L shaped rectangular bars) [21, 22]. At last, rectangular cavity of side '*j*' was added modelled as IV to get the final structure with high CD in three wavelength regions. The evolution of design has been illustrated by the four figures (I, II, III and IV) shown in Fig. 2a.

The optimised geometric dimensions of the unit cell are as follows: $p = 285$ nm, $d = 25$ nm, $w = 10$ nm, j = 50 nm, r1 = 65 nm, r2 = 85 nm, and r3 = 130 nm. The suggested metasurface has been modelled and analysed using CST (Microwave Studio). The unit cell's periodic boundary conditions are applied along the *x* and *y* axes, as the wave propagates along the *z*-axis. Given the null transmission coefficients of the metasurface with a metal backplane, a detailed analysis of its reflection properties is considered adequate.

The chiroptical properties of the metamaterial device are exemplified by Circular Dichroism (CD), computed as follows:

$$\mathrm{CD} = |A_{\mathrm{L}} - A_{\mathrm{R}}| \tag{1}$$

, where A_{L} and A_{R} denotes left circularly polarized (LCP) and right circularly polarized (RCP) light absorptions, respectively, and modulus of their difference gives CD. Under LCP incidence absorption peak occurs at 611 nm with value of 0.98 giving the CD of 0.72. Whereas under RCP incidence absorption peak occurs at 933 nm and 3151 nm with value of 0.75 and 0.79 giving the CD of 0.56 and 0.71 as shown in Fig. 3a and b.

Figure 4a shows the formation of significant localised surface plasmon resonance (LSPR) inside the periodic structure at 611 nm and 933 nm when subjected to LCP and RCP lights respectively. Under LCP incidence LSPR is exhibited across the far-right circular arc and the bottom lower arc. However, under RCP incidence the associated resonant mode near the edges of the far-right circular arc is mainly suppressed and occurs on the far left rectangular bar. This results in unequal absorption for LCP and RCP. To further investigate the mechanism behind generation of CD peaks, surface current distribution across the metasurface

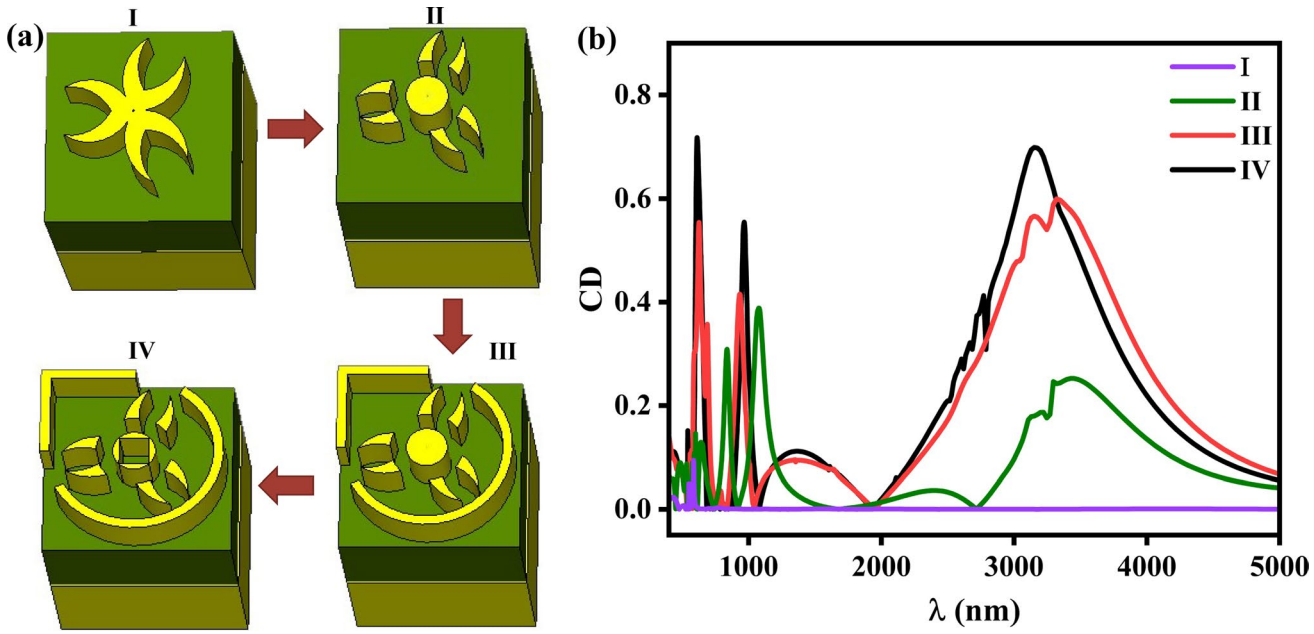


Fig. 2 Evolution of the **a** design of the proposed unit cell and **b** the corresponding CD

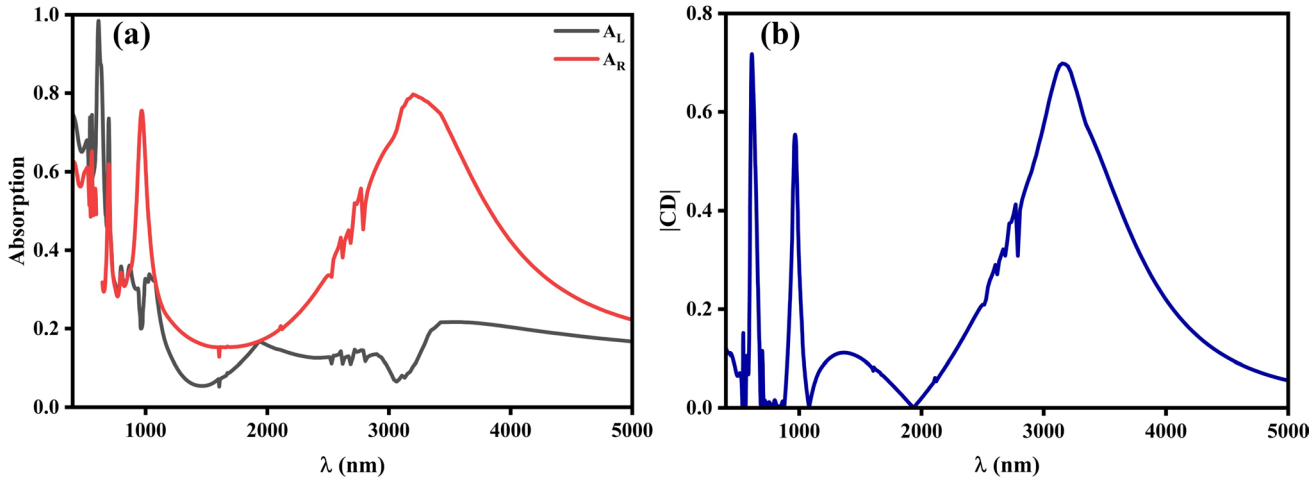


Fig. 3 **a** The absorption curve and **b** CD curve of the metasurface when subjected to circularly polarised light

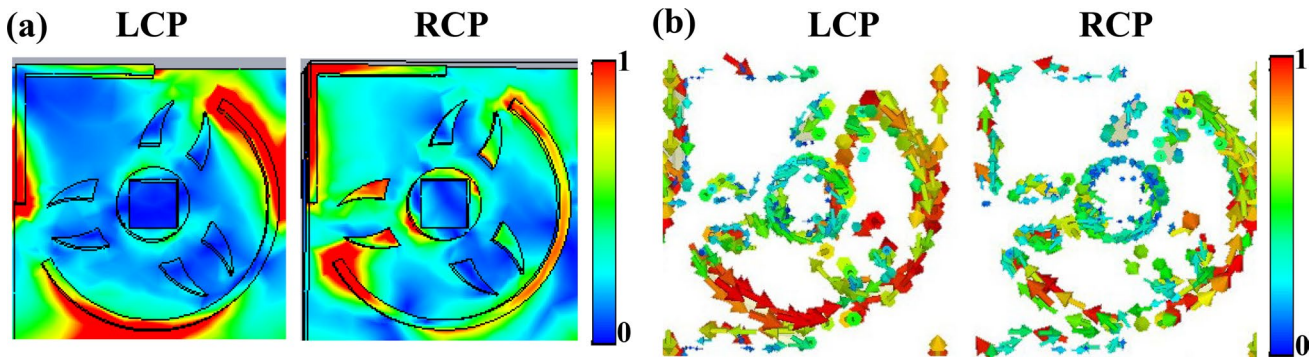


Fig. 4 **a** Electric field distribution and **b** Surface current distribution for the intended metasurface structure at 611 nm and 933 nm under incoming LCP and RCP light respectively

was examined as shown in Fig. 4b across the surface. While the charge distribution in first figure rotates in a direction that follows the LCP light, the charge distribution in second figure rotates in a direction that follows the electric field rotation of the RCP light.

3 Parametric analysis

The parametric analysis of the proposed metasurface was done by varying the selective parameters affecting the cavities embedded in the structure. As the cavities are the optical structures that allow for a significant amount of internal reflections at specific wavelengths, which results in interference events that increase the strength of electric field. This resonance enhancement and interference enhancement is described using the Fabry–Perot cavity model [23–25]. $R(\omega) = \frac{R_0}{1-Re^{-\frac{2i\omega z}{c}}}$ provides the reflection capability of the resonator which is a function of ω (angular frequency), where z is the Fabry–Perot cavity width, c is the speed of light in vacuum, and R_0 is the reflection amplitude. R also represents the reflection attenuation coefficient. Notably, adjusting z can provide control over the cavity's resonance wavelength. The parameters 'p'—periodicity of the unit cell, 'o'—width of the angular cavity in fake star fish, 'w'—width of the semicircular arc, and 'j' being side of the rectangular cavity are utilised to vary the cavity widths at various spots with reference to Fig. 1c, which depicts three distinct cavities. During the variation of each parameter, modification has been done specifically of the corresponding cavity dimension, while keeping the remaining three parameters unchanged, ensuring that the optical response was solely influenced by the variation of the selected cavity dimension. For instance, when p was varied, the structural dimensions of both cavities were scaled uniformly without altering their internal features similarly for other parameters also. This approach helped to isolate the effect of each geometrical dimension, allowing a clearer understanding of their individual contributions to the optical response.

Figure 5a–d shows variation in CD value with variation in different geometric parameters. As shown in Fig. 5a, changing the value of periodicity '*p*' majorly affects the third peak giving the red shift in the resonance wavelength, resulting in the greatest CD value at $p = 280$ nm. Figure 5b shows the variation in the '*o*' parameter value which majorly affects the second peak indicating increase in the CD value with increase in the '*o*', in addition to red shift in resonance wavelength. Similarly, variation in parameter '*j*' value minorly affects the first and third peak leading to increase in CD value for first peak and the third peak shows minor blue shift in resonance wavelength as shown in Fig. 5c. However, changing '*w*' parameter majorly affects all the three peaks as the cavity ① affects both the circularly polarized light affecting both A_L and A_R as shown in Fig. 5d. The value of CD value for the first peak is maximum for $w = 10$ nm whereas for the second and third peak it is maximum for $w = 15$ nm. The findings support the hypothesis that the resonance wavelength of the Fabry Perot cavity depends on the cavity length.

4 Chiral metasurface biosensor

Modifying the refractive index of the medium that fills the vacancies of the structure's initial layer alters the structure's overall refractive index, which in turn modifies the structure's resonance frequency. The structure and the medium's effective refractive index have a significant impact on the CD value's resonant spectrum. Sensors based on refractive index may be designed using this resonant behaviour. The formula for sensitivity is $S = {}^{\Delta\lambda}/_{\Delta n}$ nm/RIU, where Δλ is the wavelength shift in the various index media and Δn is the change in refractive index. The availability of the proposed metasurface in biosensing is illustrated in three distinct regions in the following sections as a haemoglobin sensor, glucose sensor and cancer cell detection sensor.

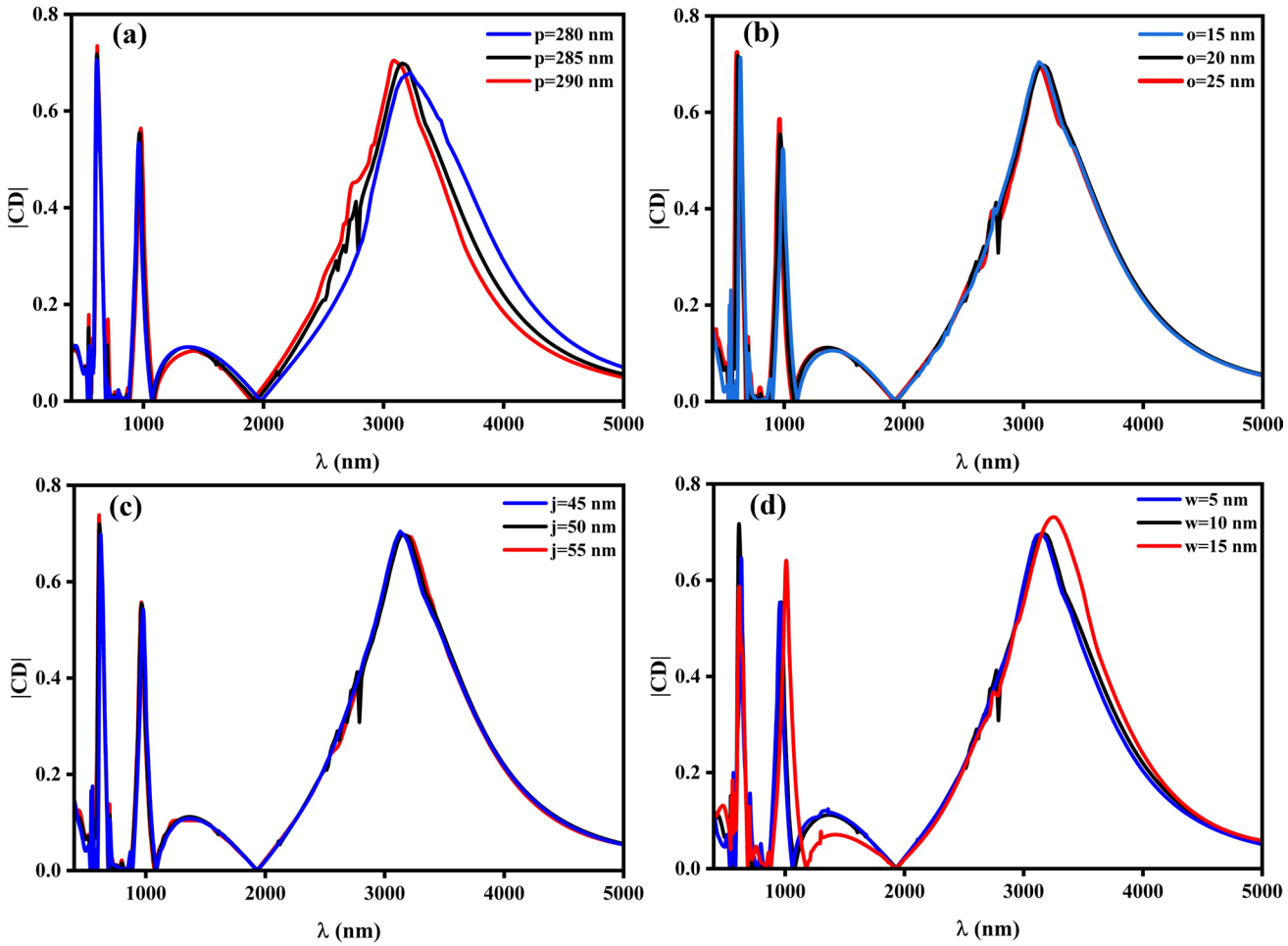


Fig. 5 Transitions in the CD versus wavelength curve with the change in geometric parameter. **a** *p*, **b** *o*, **c** *j*, **d** *w*

4.1 Haemoglobin sensor

Normal human blood haemoglobin levels range from 130 to 166 g/L for males and 100–150 g/L for women [26]. It is detrimental to have both extremes of haemoglobin levels. A lower dose results in nausea and anaemia, whereas a larger concentration raises the risk of coagulation, which can result in a heart attack [27, 28]. To detect Hb concentration in blood, the concentration values used in this work are 90 g/L, 120 g/L, 150 g/l and 180 g/L. The refractive index of the biomolecule at increasing concentrations can be measured theoretically by extrapolating the curve. As shown in Fig. 6a, the least square fitting approach has been used to theoretically determine the fluctuation of haemoglobin's refractive index with concentration in the visible area [29]. Figure 6b shows the variation in the CD value after introduction of the sample. The inset figure shows the clear variation of the CD curve for low, normal and high concentrations of haemoglobin. The CD curve shows red shift as the concentration of haemoglobin in blood increases. Figure 6c shows as the concentration of haemoglobin increases the value of resonance wavelength and sensitivity increases. The sensitivity values are calculated using the resonance wavelength shift method, where the shift in resonance wavelength ($\Delta\lambda$) was determined for the change in the refractive index (Δn), following the standard relation $S = \Delta\lambda/\Delta n$ (in nm/RIU). The previously obtained resonance wavelength for the initial refractive index was used as the reference for calculating the shift, ensuring consistency in sensitivity estimation as shown in Table 1. The sensitivity values (S) for detecting different concentration of haemoglobin are 520.1 nm/RIU, 527.1 nm/RIU and 533.3 nm/RIU.

4.2 Glucose concentration sensor

Determining the glucose content is crucial for both medicinal purposes and several food manufacturing processes, including date juice syrup. A potential application of the

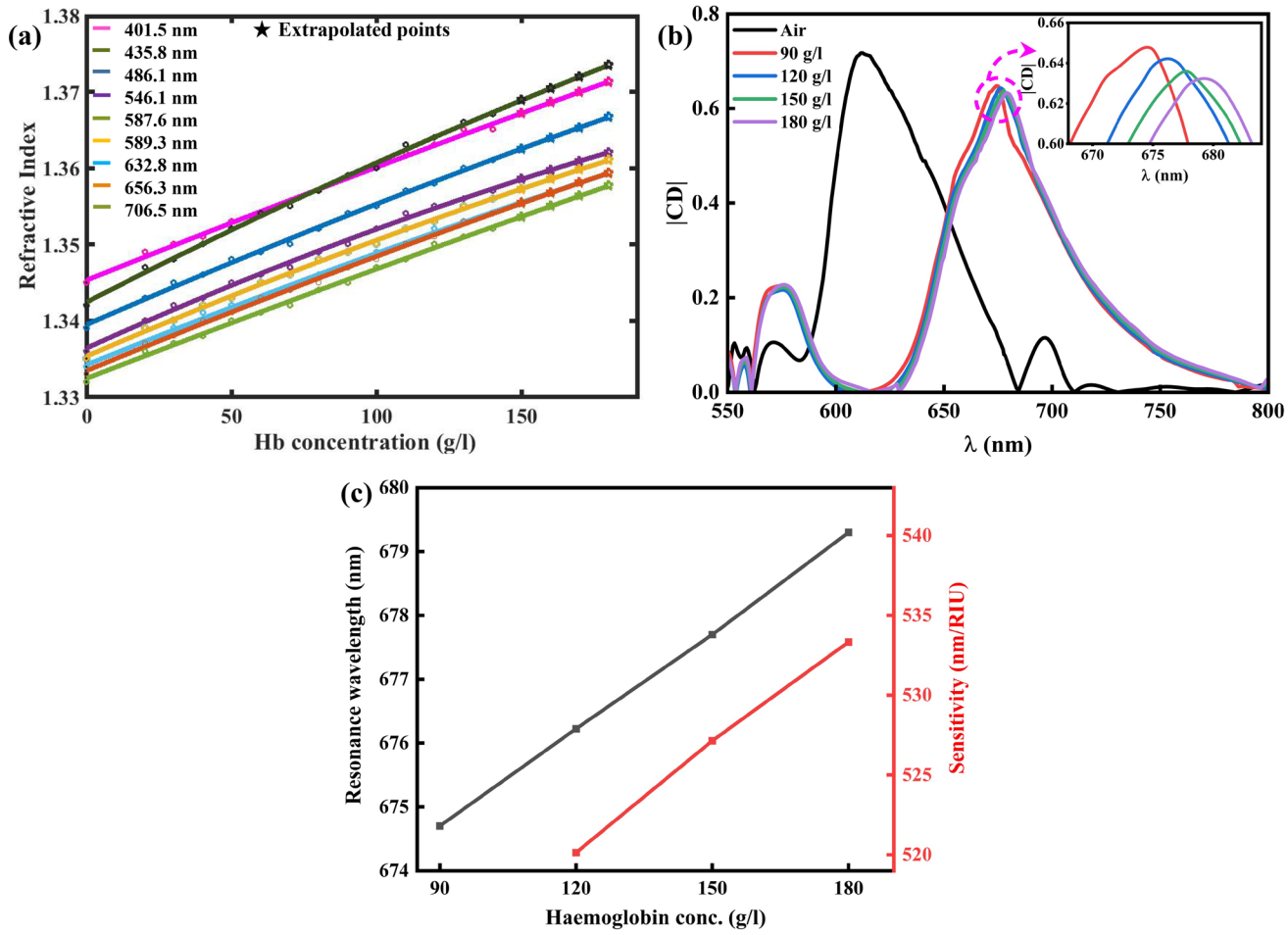


Fig. 6 **a** The linear curve fit and extrapolated values of refractive index of the blood with concentration for different wavelengths. **b** The variation of the CD curve for different concentrations of haemoglobin. **c** Variation of resonance wavelength and sensitivity with the concentration of haemoglobin

Table 1 Sensitivity Analysis

Conc. of haemoglobin (g/L)	Resonance wavelength (nm)	n	Δλ (nm)	Δn	Sensitivity (nm/RIU)
90	674.7	1.34847	–	–	–
120	676.2	1.3514	1.524	0.00293	520.1365
150	677.7	1.3542	1.47	0.0028	527.1429
180	679.3	1.3572	1.6	0.003	533.3333

proposed sensor in the NIR region is its use for detecting glucose concentrations. The refractive index of known glucose concentrations is measured in order to generate a calibration curve, which is then used to calculate the sugar content of water using the refractometric technique [30]. The refractive index of an aqueous glucose solution is calculated using the expression $n = n_{H_2O} + \alpha C$, where n_{H_2O} represents refractive index of water, $\alpha = 0.00143$ is a constant and C denotes the concentration of sugar in g/100 ml. Figure 7a represents the variation in CD curve for the glucose concentrations of 0 g/100 ml to 30 g/100 ml. Resonance wavelength shifts towards a longer wavelength when glucose concentration rises. Resonance wavelength change and relative sensitivity with prior glucose concentration are shown in Fig. 7b. A longer wavelength shift in the resonance wavelength is attributed to an increase in the capacitance of two ridges caused by an increase in their permittivity and refractive index.

4.3 Cancer cell detection sensor

Numerous fields, including disease detection and chemical sensing of hazardous compounds, have previously demonstrated the potential of spectroscopic sensors in the MIR range. Normally, the size of cancer cell varies with the type of cancer cell. Early discovery of cancer cells is extremely critical for effective therapy. Here, the proposed structure is subjected for the detection of various types of cancer cells skin cancer (Basal), breast cancer (MDA-MB-231) and cervical cancer (HeLa). Table 2 summarises the refractive indices for all the cancer cells employed in this study. The results of normal cells' and cancer cells' index of refraction differ significantly. Figure 8a shows the CD variation curve for different types of cancer and normal cells. The trend shows the red shift in the resonance wavelength as well as slight dip in the CD value as shown in Fig. 8a and b. Very high sensitivity is obtained for the three different types of cancer cells i.e.

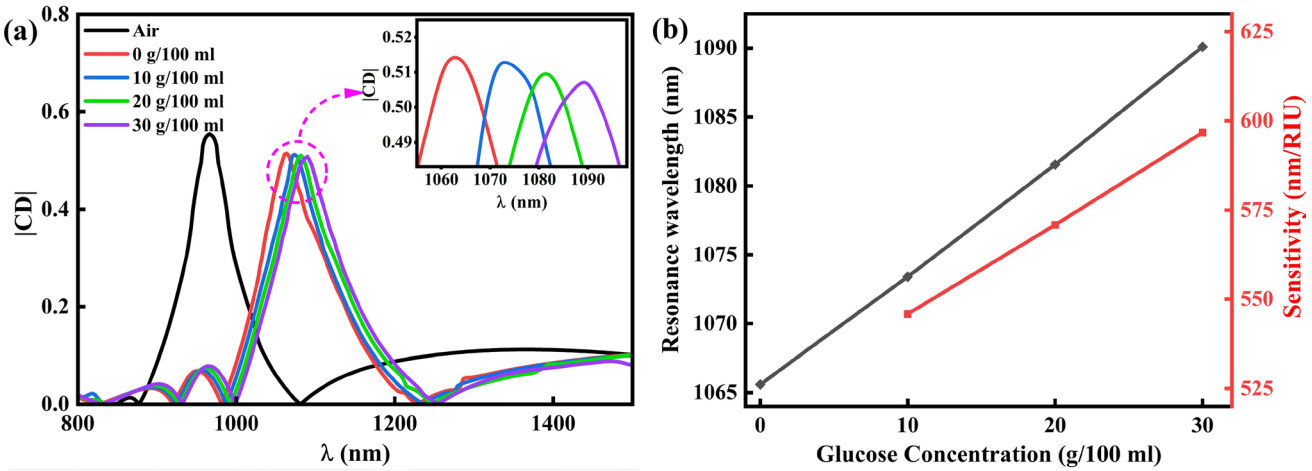


Fig. 7 Variation of **a** CD with the wavelength, **b** resonance wavelength and the relative sensitivity for the different concentrations of glucose mixture

Table 2 Refractive index of various normal and cancer cells

Cell type and Conc	Name of cell	Refractive index	References
Skin cancer (80%)	Basal	1.38	[31–33]
Skin normal cell (30–70%)		1.36	[31–33]
Breast cancer (80%)	MDA-MB-231	1.401	[32–34]
Breast normal cell (30–70%)		1.387	[32–34]
Cervical cancer (80%)	HeLa	1.392	[32–34]
Cervical normal cell (30–70%)		1.368	[32–34]

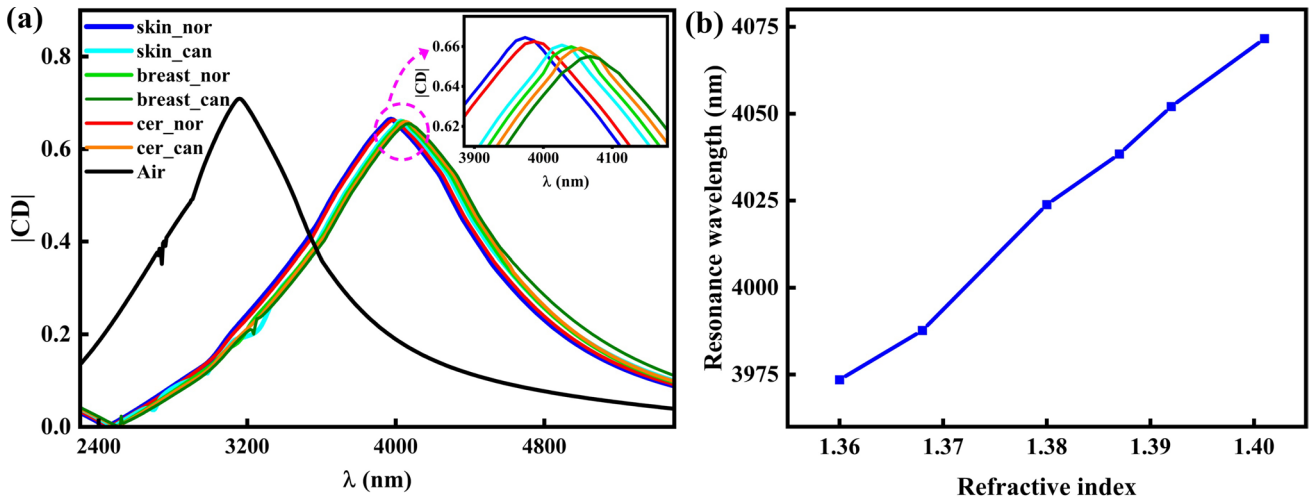


Fig. 8 Variation of **a** circular dichroism curve for the different types of cancer. **b** Variation of resonance wavelength with the increase in the refractive index

2371.1 nm/RIU for breast cancer, 2516.7 nm/RIU for skin cancer and 2680.9 nm/RIU for cervical cancer.

The shift in CD and the resonance wavelength for different refractive index across three different wavebands have been studied. Transitions from the visible to the NIR and MIR regions show that the sensitivity of the metasurface tends to increase with resonance wavelength. This increase in sensitivity stems from two main reasons. First, longer wavelengths lead to greater overlap between the metasurface's evanescent field and surrounding medium, resulting in stronger interactions with nearby biomolecules. This enhances the resonance shift response to refractive index changes, thereby increasing sensitivity. Additionally, sensitivity scales with resonance wavelength, as longer wavelengths naturally produce larger absolute shifts for the same refractive index variation. Figure 9 shows the relation between the resonance wavelength and the sensitivity. Star points represent the obtained sensitivity across different regions and red line is the linear curve fit to these points. The shaded region shows the confidence band which covers the prescribed probability that the values of other observations from different sample may lie using the designed metasurface. Further, a comparative information for different chiral sensors is given in Table 3. It could be analysed from the comparison that the designed structure provides moderately high sensitivity with the ability to work in three different regions and thus making it a suitable applicant of biosensor with multiple functionalities.

In real-world biosensing applications, factors such as minute variations in pH, temperature, and molecular interactions can slightly alter the refractive index of the biological sample. However, such changes are typically very small, resulting in a negligible shift in the resonance

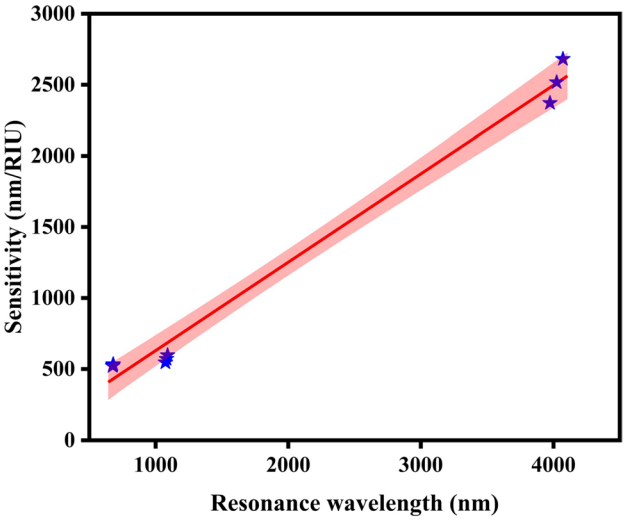


Fig. 9 Linear fit curve of the sensitivity values of the structure for different resonance wavelengths across three regions (shaded region represents the confidence band)

wavelength of the proposed sensor. A minute change in the refractive index will not significantly affect the sensitivity value but rather cause a minor shift in the resonance wavelength. Hence, the proposed sensor can be considered stable against such small environmental changes. But major changes in these environmental variations may cause undesired resonance shifts, leading to potential measurement errors. To mitigate such effects, real-time referencing, temperature stabilization, or applying post-measurement correction models can minimize errors and maintain sensor sensitivity.

Table 3 Comparison table for different chiral metasurface sensors

References	Type of metasurface	Type of sensing	Region	Max. sensitivity reported (nm/RIU)
[35]	Transmission based chiral metasurface	RI based	Visible	474
[36]	Helix shaped Chiral metasurface	Bio-Molecule	NIR	471
[37]	Chiral metasurface	RI based	NIR	750
[38]	Chiral	RI based	Visible	304
[39]	Half ring based chiral metasurface	Nano-fluids	THz	182.5
[40]	Helix based chiral metasurface	Fluids	NIR	761
[41]	Chiral metasurface	Chiral molecule	NIR	80.6
[42]	Chiral metasurface	Chiral molecule	NIR	220.9
	This work	Heomoglobin	Visible	533.3
		Glucose	NIR	596.7
		Cancer cell	MIR	2680.9

5 Conclusion

A chiral perovskite based structure capable of generating strong circular dichroism in three separate regions has been presented. Significant dichroism occurs as a result of polarization-dependent interference generated by incoming light travelling through nearby nanostructures. The structure's absorption selectivity is improved by utilising various resonant cavity designs, as well as its chirality. The results indicate that precise control over CD may be attained by modifying the geometric factors associated with different resonant cavities. Further three different biosensors have been designed. For the visible region, the structure is used as a haemoglobin sensor offering the sensitivity of 520.1, 527.1 and 533.3 nm/RIU for different concentrations of hemoblobin. For the NIR region the structure is used as a glucose sensor for detecting different concentrations of sugar content with maximum sensitivity of 596.7 nm/RIU. Also, for the MIR region the proposed structure is designed as a cancer cell detection sensor with maximum sensitivity of 2680.9 nm/RIU. Considering the results, designed perovskite metasurface provide an extremely special platform for multi-functionality in biomedical applications limiting the ability to work in single region.

Acknowledgements Authors gratefully acknowledge the initiatives and support from the TIFAC-Centre of Relevance and Excellence in Fiber Optics and Optical Communication at Delhi College of Engineering, now DTU, Delhi, under the Mission REACH program of Technology Vision-2020, Government of India. Authors would like to acknowledge Dr. Umesh Tiwari (CSIR-CSIO Chandigarh) for the necessary support.

Author contributions All authors whose names appear on the submission (1) made substantial contributions to the conception or design of the work; or the acquisition, analysis, or interpretation of data; or the creation of new software used in the work; (2) drafted the work or revised it critically for important intellectual content; approved the version to be published; and (3) agree to be accountable for all aspects of the work in ensuring that questions related to the accuracy or integrity of any part of the work are appropriately investigated and resolved.

Data availability No datasets were generated or analysed during the current study.

Declarations

Conflict of interest The authors declare no competing interests.

References

1. Cui, Y., & Jiang, Y.: Dual-band tunable and strong circular dichroism in a metal-graphene hybrid zigzag metasurface. **30**(23), 42614–42623 (2022). https://doi.org/10.1364/OE.476021
2. Kabashin, A.V., Evans, P., Pastkovsky, S., et al.: Plasmonic nanorod metamaterials for biosensing. Nat. Mater. **8**, 867–871 (2009). https://doi.org/10.1038/nmat2546
3. Khan, S.A., Khan, N.Z., Xie, Y., et al.: Optical sensing by metamaterials and metasurfaces: from physics to biomolecule detection. Adv. Opt. Mater. **10**, 2200500 (2022)
4. Huang, T., Zhao, X., Zeng, S., et al.: Planar nonlinear metasurface optics and their applications. Rep. Prog. Phys. **83**, 126101 (2020)
5. Sharma, V., Kalra, Y., Sinha, R.K.: Modelling and design of human eye inspired concentric cylindrical metalens. Opt. Commun. **565**, 130627 (2024). https://doi.org/10.1016/j.optcom.2024.130627
6. Zeng, Y., Ananth, R., Dill, T.J., et al.: Metasurface-enhanced Raman spectroscopy (mSERS) for oriented molecular sensing. ACS Appl. Mater. Interfaces (2022). https://doi.org/10.1021/acsami.2c01656
7. Meinzer, N., Barnes, W.L., Hooper, I.R.: Plasmonic meta-atoms and metasurfaces. Nat Photonics (2014). https://doi.org/10.1038/nphoton.2014.247
8. Petersen, J., Volz, J., Rauschenbeutel, A.: Chiral nanophotonic waveguide interface based on spin-orbit interaction of light. Science **346**, 67–71 (2014). https://doi.org/10.1126/science.1257671
9. Chen, L., Ruan, Y., Luo, S.S., et al.: Optically transparent metasurface absorber based on reconfigurable and flexible indium tin oxide film. Micromachines (2020). https://doi.org/10.3390/mi11121032

10. Wang, Z., Chen, W., Liu, X., et al.: Plasmonic metasurface enhanced by nanobumps for label-free biosensing of lung tumor markers in serum. Talanta (2023). https://doi.org/10.1016/j.talanta.2023.124731
11. Wallace, S., Kartau, M., Kakkar, T., et al.: Multiplexed biosensing of proteins and virions with disposable plasmonic assays. ACS Sens. **8**, 3338–3348 (2023). https://doi.org/10.1021/acssensors.2c02238
12. Kim, I., Kim, H., Han, S., et al.: Metasurfaces-driven hyperspectral imaging via multiplexed plasmonic resonance energy transfer. Adv. Mater. (2023). https://doi.org/10.1002/adma.202300229
13. Shao, Y., Su, Z., He, H., et al.: Multispectral imaging through metasurface with quasi-bound states in the continuum. Opt. Express **32**, 23268 (2024). https://doi.org/10.1364/oe.523676
14. Parappurath, N., Alpeggiani, F., Kuipers, L., Verhagen, E.: The origin and limit of asymmetric transmission in chiral resonators. ACS Photonics (2017). https://doi.org/10.1021/acsphotonics.6b00947
15. Asefa, S.A., Shim, S., Seong, M., Lee, D.: Chiral metasurfaces: a review of the fundamentals and research advances. Appl. Sci. **13**(19), 10590 (2023)
16. Beyrami, H., Golshan, M., Kucińska-Lipka, J., et al.: Chiral-based optical and electrochemical biosensors: synthesis, classification, mechanisms, nanostructures, and applications. Chem. Eng. J. **497**, 155562 (2024). https://doi.org/10.1016/J.CEJ.2024.155562
17. Jeon, S., Kim, S.J.: Enhancement of optical chirality using metasurfaces for enantiomer-selective molecular sensing. Appl. Sci. (2021). https://doi.org/10.3390/app11072989
18. Paiva-Marques, W.A., Gómez, F.R., Oliveira, O.N., Mejía-Salazar, J.R.: Chiral plasmonics and their potential for point-of-care biosensing applications. Sensors (Switzerland) **20**, 944 (2020)
19. Babar, S., Weaver, J.H.: Optical constants of Cu, Ag, and Au revisited. Appl. Opt. **54**, 477 (2015). https://doi.org/10.1364/ao.54.000477
20. Ishteev, A., Konstantinova, K., Ermolaev, G., et al.: Investigation of structural and optical properties of MAPbBr 3 monocrystals under fast electron irradiation. J. Mater. Chem. C (2022). https://doi.org/10.1039/d2tc00128d
21. Masyukov, M., Grebenchukov, A.N., Vozianova, A.V., Khodzitsky, M.K.: Bilayer terahertz chiral metasurfaces with different dihedral symmetries. J. Opt. Soc. Am. B **38**, 428 (2021). https://doi.org/10.1364/josab.413212
22. Menzel, C., Rockstuhl, C., Lederer, F.: Advanced Jones calculus for the classification of periodic metamaterials. Phys. Rev. A – At. Mol. Opt. Phys. **82**, 1–9 (2010). https://doi.org/10.1103/PhysRevA.82.053811
23. Sun, Z., Fang, Y.: Fabry-Pérot interference cavity length tuned by plasmonic nanoparticle metasurface for nanophotonic device design. ACS Appl. Nano Mater. (2020). https://doi.org/10.1021/acsanm.0c01967
24. Shrestha, S., Wang, Y., Overvig, A.C., et al.: Indium tin oxide broadband metasurface absorber. ACS Photonics (2018). https://doi.org/10.1021/acsphotonics.8b00781
25. Chen, F., Zhang, H., Sun, L., et al.: Double-band perfect absorber based on the dielectric grating and Fabry-Perot cavity. Appl. Phys. A Mater. Sci. Process (2019). https://doi.org/10.1007/s00339-019-3101-z
26. Beutler, E., Waalen, J.: The definition of anemia: what is the lower limit of normal of the blood hemoglobin concentration? Blood **107**(5), 1747–1750 (2006)
27. Houghton, D.E., Koh, I., Ellis, A., et al.: Hemoglobin levels and coronary heart disease risk by age, race, and sex in the reasons for geographic and racial differences in stroke study (REGARDS). Am. J. Hematol. (2020). https://doi.org/10.1002/ajh.25703
28. Kim, M.Y., Jee, S.H., Yun, J.E., et al.: Hemoglobin concentration and risk of cardiovascular disease in Korean men and women - the Korean heart study. J. Korean Med. Sci. (2013). https://doi.org/10.3346/jkms.2013.28.9.1316
29. Zhernovaya, O., Sydoruk, O., Tuchin, V., Douplik, A.: The refractive index of human hemoglobin in the visible range. Phys. Med. Biol. (2011). https://doi.org/10.1088/0031-9155/56/13/017
30. Chamoli, S.K., Singh, S.C., Guo, C.: Design of extremely sensitive refractive index sensors in infrared for blood glucose detection. IEEE Sens. J. **20**, 4628–4634 (2020). https://doi.org/10.1109/JSEN.2020.2964715
31. Yaroslavsky, A.N., Patel, R., Salomatina, E., et al.: High-contrast mapping of basal cell carcinomas. Opt. Lett. (2012). https://doi.org/10.1364/ol.37.000644
32. Jabin, M.A., Ahmed, K., Rana, M.J., et al.: Surface plasmon resonance based titanium coated biosensor for cancer Cell detection. IEEE Photonics J (2019). https://doi.org/10.1109/JPHOT.2019.2924825
33. Ramanujam, N.R., Amiri, I.S., Taya, S.A., et al.: Enhanced sensitivity of cancer cell using one dimensional nano composite material coated photonic crystal. Microsyst. Technol. (2019). https://doi.org/10.1007/s00542-018-3947-6
34. Sharma P, Sharan P, Deshmukh P: A photonic crystal sensor for analysis and detection of cancer cells. In: 2015 International Conference on Pervasive Computing: Advance Communication Technology and Application for Society, ICPC 2015 (2015)
35. Xie, F., Ren, M., Wu, W., et al.: Chiral metasurface refractive index sensor with a large figure of merit. Appl. Phys. Lett. (2023). https://doi.org/10.1063/5.0135657
36. Palermo, G., Lio, G.E., Esposito, M., et al.: Biomolecular sensing at the interface between chiral metasurfaces and hyperbolic metamaterials. ACS Appl. Mater. Interfaces (2020). https://doi.org/10.1021/acsami.0c07415
37. Mandal, P.: Highly absorptive chiral L-shape MDM plasmonic metasurface as multifunction device: design and computational studies. Plasmonics (2021). https://doi.org/10.1007/s11468-021-01415-8
38. Klös, G., Miola, M., Sutherland, D.S.: Increased refractive index sensitivity by circular dichroism sensing through reduced substrate effect. J. Phys. Chem. C (2019). https://doi.org/10.1021/acs.jpcc.8b12152
39. Fan, F., Zhong, C., Zhang, Z., et al.: Terahertz chiral sensing and magneto-optical enhancement for ferromagnetic nanofluids in the chiral metasurface. Nanoscale Adv. (2021). https://doi.org/10.1039/d1na00284h
40. Guglielmelli, A., Nicoletta, G., Valente, L., et al.: Numerical modeling of 3D chiral metasurfaces for sensing applications. Crystals (2022). https://doi.org/10.3390/cryst12121804
41. Chen, Y., Zhao, C., Zhang, Y., Qiu, C.W.: Integrated molar chiral sensing based on high- Q metasurface. Nano. Lett. (2020). https://doi.org/10.1021/acs.nanolett.0c03506
42. Cen, M., Wang, J., Liu, J., et al.: Ultrathin suspended chiral metasurfaces for enantiodiscrimination. Adv. Mater. (2022). https://doi.org/10.1002/adma.202203956

Publisher's Note Springer Nature remains neutral with regard to jurisdictional claims in published maps and institutional affiliations.

Springer Nature or its licensor (e.g. a society or other partner) holds exclusive rights to this article under a publishing agreement with the author(s) or other rightsholder(s); author self-archiving of the accepted manuscript version of this article is solely governed by the terms of such publishing agreement and applicable law.

Check for updates

Applied Organometallic Chemistry

WILEY

Applied Organometallic Chemistry

RESEARCH ARTICLE

Ultrasensitive Electrochemical Detection of EpCAM Antigen Based on Anti-EpCAM Conjugated With Highly Flexible Ag@$Ti_3C_2T_x$ Modified Conducting Paper Platform

Sweety | Divya Hudda | Devendra Kumar

Department of Applied Chemistry, Delhi Technological University, Delhi, India

Correspondence: Devendra Kumar (dkumar@dce.ac.in)

Received: 31 December 2024 | **Revised:** 27 May 2025 | **Accepted:** 9 June 2025

Funding: Sweety received financial support from the Council Scientific and Industrial Research (CSIR), Government of India, New Delhi (File no: 08/133(0051)/2020-EMR-I).

Keywords: Ag/$Ti_3C_2T_x$ | conducting paper | electrochemical immunosensor | EpCAM antigen | PEDOT:PSS

ABSTRACT

In this work, a highly bendable Whatman paper–based immunosensor has been proposed for highly sensitive and real-time detection of EpCAM antigen. A novel Ag@$Ti_3C_2T_x$ hybrid material is used with aqueous poly(3,4-ethylenedioxythiophene):poly (styrenesulfonate) [PEDOT:PSS] solution to enhance various electrochemical parameters, namely, conductivity, hydrophilicity, stability, and so forth. The conducting paper has been fabricated by simple dip-coating method followed by doping with dimethyl sulfoxide (DMSO), an organic solvent. The DMSO treatment results in the sharp increase in electrical conductivity of Ag@$Ti_3C_2T_x$/CP from 10.9×10^{-3} to 763.5×10^{-3} S/cm (around 70 times). Further, the bendability of the fabricated conducting paper is verified by paper folding study at different angles. The developed immunosensor, anti-EpCAM/Ag@$Ti_3C_2T_x$/CP, is found to be highly sensitive (44.12 $\mu A\cdot fg^{-1}\cdot mL$) to detect EpCAM antigen with ultrabroad linear range (1 fg/mL–10,000 pg/mL). Ultimately, the manufactured immunosensor is used to assess the EpCAM in spiked serum samples, and the results demonstrate a strong correlation with the standard buffer samples.

1 | Introduction

Recently, artificial intelligence and flexible devices have made significant strides in portable, wearable, and eco-friendly technology. Flexible substrates are essential for developing the wearable devices because of their extended cycle life, wearability, safety, and stretchability [1]. Paper is a high surface area cellulose fiber web that can be used as an inexpensive, readily available, disposable, and convenient substrate for wearable technologies [2]. The distinguishable properties of paper allow for the surface alteration, and its structure and porosity are extremely adjustable. Consequently, for many decades, paper has previously been used as a medium for chemical investigation [3]. Paper-based assays, such as paper strips, have been utilized for a range of basic diagnostic tests and are capable of quick analysis without any need of additional equipment. In recent years, it is emerging as a promising platform for electrochemical sensors and devices. In the context of the intended use of paper, some characteristics like porosity and roughness that are usually considered drawbacks may really be advantageous [4]. For example, the roughness of paper might enhance the sensing platform's contact area, where the analyte interacts with the sensing material [5]. Paper needs to have the following characteristics in order to guarantee the reliability of biosensors

© 2025 John Wiley & Sons Ltd.

during electrochemical measurements: high surface-to-volume ratio, mechanical strength, efficient conductivity, and fluid flow [6].

Whatman paper grade 1 (WP) is the most widely used choice owing to its medium flow rate, homogeneity on both sides, and 98% cellulose content. To be utilized safely in electrochemical sensors, paper needs to be made conductive [7]. Metals and carbon nanotubes can be used to create conductive coatings; however, this benefit may be sacrificed in favor of decreased flexibility and durability. Hence, it is crucial to maintain devices in perfect condition because they may lose their conductivity, sensing, and other capabilities if they have cracks or breaks.

Conducting polymers offer a low-cost substitute that eliminates this problem and permits the direct deposition of functional material without sacrificing their conductive properties [8]. Orbital overlap produces a delocalized molecular wave function in conducting polymers due to the conjugated π-electrons in their backbone matrix. Because electrons can travel freely across the lattice, this leads to impart better electrical and optical properties. When compared to other conducting polymers such as polyaniline and polypyrrole; PEDOT:PSS exhibits intriguing properties, because of its electrochemical stability, mechanical flexibility, mixed electronic/ionic conductivity, and ease of processing [9]. Furthermore, PEDOT:PSS has been regarded as a promising candidate for the creation of a paper-based biosensor due to its high electrocatalytic behavior towards the redox process and homogeneous entrapment. To enhance the aggregation properties of the polymer, two-dimensional (2D) materials can be used to create hybrids [10, 11]. 2D materials are found to possess many desirable extraordinary properties, such as large surface area, tremendous electrical conductivity, and high electron mobility [12, 13].

Over the last 10 years, a novel and developing material known as MXene, with the general formula $M_{n+1}X_nT_x$ (where M is a transition metal, X can be either carbon or nitrogen, and T_x stands for surface functional groups), has garnered a lot of interest for biosensing and biomedical applications [14]. Among these, $Ti_3C_2T_x$ is well known for its excellent metal-like conductivity, super hydrophilicity, 2D-layered structure, polar surfaces, and huge surface area, which make it suitable for the use in electrochemical biosensors [15]. However, high van der Waals forces of attraction between neighboring sheets in 2D-$Ti_3C_2T_x$ may lead them to restack, which could further affect the biosensing characteristics [16]. This issue may be resolved by creating a 0D and 2D-based hybrid material that can help to improve the energy transfer efficiency and biosensing characteristics. Moreover, the incorporation of 0D particles not only prevents the restacking among the 2D sheets, but also improves the interlayer gap between the stacked sheets [17]. Among various 0D-particles, Ag has been considered to have good catalytic power, high conductivity, and ability to enhance the rate of electron transfer [18].

Globally, cancer is the most common life-threatening disease with the highest death rate. Early cancer diagnosis is very important for successful and efficient cancer therapy [19–21]. The majority of cancer cells (such as head, neck, lung, prostate, breast etc.) are expressed by epithelial cell adhesion molecules (EpCAM). EpCAM is a type of transmembrane glycoprotein that has a molecular weight of 40 kDa [22]. It is involved in the cell adhesion, migration, and proliferation. In healthy tissues, a simple epithelium is the only tissue type where EpCAM is expressed. Several types of cancer stem cells as well as regular stem cells have been shown to have EpCAM as a surface marker [23]. The course of inflammatory disorders, carcinogenesis, and even embryogenesis are marked by changes in the pattern and amount of EpCAM expression. Hence, it is highly required to detect low concentrations of EpCAM in early stages.

As we understand, this is the first study towards the use of Ag@$Ti_3C_2T_x$ hybrid for the construction of an electrochemical immunosensor based on conducting paper. The proposed immunosensor has exceptional analytical biosensing characteristics for identifying a potentially useful biomarker, EpCAM antigen. Here, Ag particles enhance the rate of electron transfer by increasing the interlayer spacing between the $Ti_3C_2T_x$ sheets and simultaneously 2D-$Ti_3C_2T_x$ functions as a support matrix, thereby preventing intrinsic agglomeration by impeding the Brownian motion of Ag particles. Additionally, the sensor, anti-EpCAM/Ag@$Ti_3C_2T_x$/CP is found to function as a stable, quick, and targeted electrochemical sensing platform to offer an ultra-broad linear range and high sensitivity for EpCAM antigen detection.

2 | Materials and Methods

2.1 | Chemicals and Reagents

MAX phase (Ti_3AlC_2), silver nitrate ($AgNO_3$), sodium tetrafluoroborate ($NaBF_4$), hydrochloric acid (HCl, 37.0 wt %), 1-(3-(dimethylamino)-propyl)-3-ethylcarbodiimide hydrochloride (EDC) [$C_8H_{17}N_3$], EpCAM antigen, PEDOT:PSS (1.3 wt% dispersion in H_2O), and N-hydroxy succinimide (NHS) [$C_4H_5NO_3$] were procured from Sigma Aldrich, India. EpCAM antibody was purchased from Atlas Antibodies. All the buffer salts and organic solvents such as dimethyl sulfoxide (DMSO) were of analytical grade and used directly by preparing solutions with Milli-Q water. The Whatman filter paper #1 procured from GE healthcare, UK, was utilized as a transducer surface.

2.2 | Instrumentation

The JEOL Japan model: JSM 6610LV-scanning electron microscope is used to determine the surface morphology of different paper electrodes that have been produced.

A four-point probe device coupled to a microvoltmeter (model DMV-001) and current source (model LCS-02) is used to measure the conductivity of various electrodes.

Bruker's XRD D8 is used for X-ray diffraction studies of synthesized materials. Perkin Elmer spectrometer 2 performs the FTIR spectroscopy examination of paper electrodes to verify material's integration into the paper. By using an Autolab Potentiostat/Galvanostat (Metrohm, Netherlands) connected to a three-electrode system, the electrochemical characterization and immunosensing studies are being carried out [24].

10990739, 2025, 7, Downloaded from https://onlinelibrary.wiley.com/doi/10.1002/aoc.70264 by Delhi Technological University, Wiley Online Library on [26/06/2025]. See the Terms and Conditions (https://onlinelibrary.wiley.com/terms-and-conditions) on Wiley Online Library for rules of use; OA articles are governed by the applicable Creative Commons License

2.3 | Synthesis of $Ti_3C_2T_x$ and Ag@$Ti_3C_2T_x$ Hybrid

$Ti_3C_2T_x$ has been synthesized by the same method as reported in our previous work [25]. Ag particles have been doped onto the $Ti_3C_2T_x$ sheets by one pot direct reduction of $AgNO_3$ salt. This procedure involves the dual action of $Ti_3C_2T_x$ sheets—as a self-reducing agent as well as a matrix of support for Ag particles. Initially, 100 mg of $Ti_3C_2T_x$ was dissolved in 20 mL of distilled water under ultrasonication to prepare a 5 mg/mL stock solution. In another beaker 2, 33.98 mg of $AgNO_3$ was dispersed in 20 mL of distilled water under constant stirring. After that, the stock solution was added dropwise to beaker 2 with constant stirring for 60 min. The resulting suspension was then washed with DI water multiple times to remove impurities under ultracentrifugation. The obtained solid was dried in a vacuum oven to obtain Ag@$Ti_3C_2T_x$ hybrid [26].

2.4 | Fabrication of PEDOT:PSS/WP (CP), $Ti_3C_2T_x$/CP, and Ag/$Ti_3C_2T_x$/CP Electrodes

In order to fabricate conducting paper electrodes (CP), Whatman paper (WP) made up of cellulose fibers was chosen as a transducer surface because of its biocompatibility and hydrophilicity [27]. First, a 20% PEDOT:PSS stock solution was prepared in DI water. An optimal amount, 5 mg of each, of $Ti_3C_2T_x$ and Ag@$Ti_3C_2T_x$ hybrid was dissolved in 10 mL of stock solution in two separate beakers under constant stirring for 2 h. The stabilized WP (1 cm × 3 cm) strips were then dipped in all aforementioned solutions separately for 30 min and then vacuum dried. This process was repeated thrice to obtain improved electrical characteristics and mechanical strength. This layer-by-layer stacking process results in the formation of uniform and conductive layer of PEDOT:PSS on the surface of WP. Nevertheless, the PSS dopant increases the durability and processability of the polymer but decreases the electrical conductivity, thereby making high-performance applications inappropriate. To improve conductivity, the modified Ag@$Ti_3C_2T_x$/CP electrodes were doped with different concentrations of DMSO for 5 min. It has been observed that the 50% V/V DMSO doped electrodes have the highest electrical conductivity.

2.5 | Biofunctionalization of DMSO Treated Ag/$Ti_3C_2T_x$/CP Electrode

The immobilization of anti-EpCAM has been achieved by physical adsorption. For that process, a 1:1:2 solution containing EDC, NHS, and anti-EpCAM (25 μg/mL) was prepared in an Eppendorf tube. Thereafter, DMSO-treated Ag@$Ti_3C_2T_x$/CP electrode was dropcast with 25 μL of this active solution, and it was incubated for 6 h at 4°C. Here, EDC-NHS helps in the covalent linkage of carboxylic groups of the antibody with the –OH groups present on the surface of $Ti_3C_2T_x$. Finally, the anti-EpCAM/Ag@$Ti_3C_2T_x$/CP electrode was then washed with PBS (pH 7.4) to get rid of the unimmobilized antibody that was stuck to the electrode surface. A schematic representation of all stages followed to fabricate the immunosensor using paper is shown in Figure 1.

3 | Results and Discussion

3.1 | Morphological Characterization

SEM is used to determine the surface morphologies of sequential stages of various prepared electrodes, which are shown in Figure 2. In Figure 2A, the SEM image of PEDOT:PSS/WP, the cellulose fibers of stabilized WP appeared to be uniformly covered by PEDOT:PSS [28]. The layered structure of $Ti_3C_2T_x$ is clearly visible in Figure S1. The SEM image of the $Ti_3C_2T_x$/CP electrode (Figure 2B) depicts the incorporation of 2D-$Ti_3C_2T_x$ sheets into the polymer matrix. The SEM analysis of powder

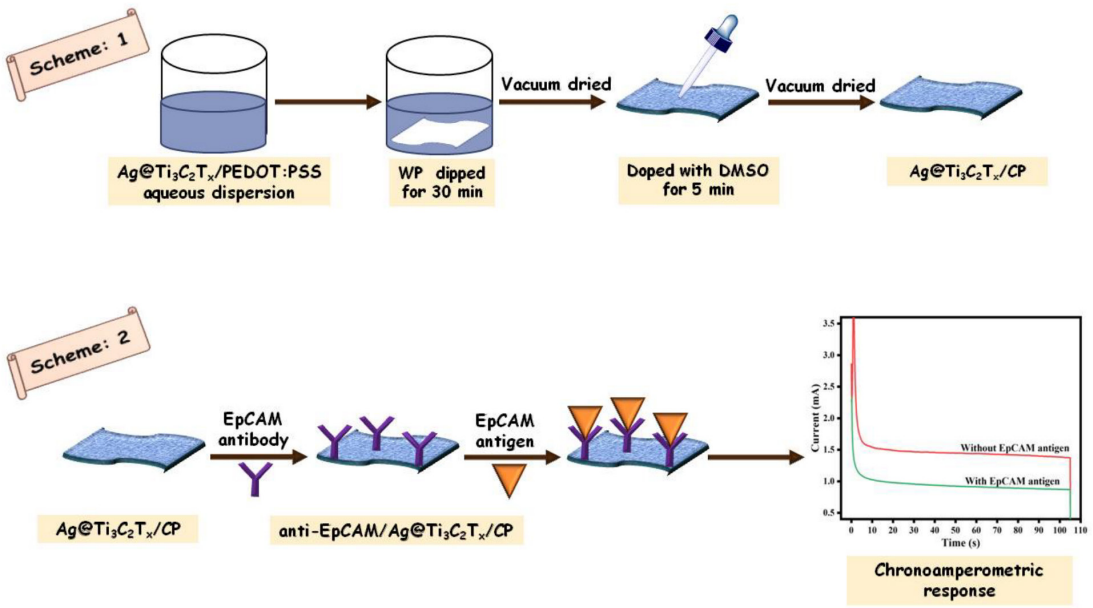


FIGURE 1 | Schematic representation for the fabrication of (1) conducting paper and (2) immunosensor for EpCAM antigen detection.

10990739, 2025, 7, Downloaded from https://onlinelibrary.wiley.com/doi/10.1002/aoc.70264 by Delhi Technological University, Wiley Online Library on [26/06/2025]. See the Terms and Conditions (https://onlinelibrary.wiley.com/terms-and-conditions) on Wiley Online Library for rules of use; OA articles are governed by the applicable Creative Commons License

$Ag@Ti_3C_2T_x$ (Figure 2C) depicts the smooth dispersion of Ag particles onto the layered $Ti_3C_2T_x$ sheets. Similar morphology is observed when $Ag@Ti_3C_2T_x$ has been incorporated into CP, as seen in Figure 2D.

3.2 | Structural Characterization

XRD spectroscopy is exploited to analyze the phase purity and crystallinity of MXene derived from MAX phase (Figure 3A). It

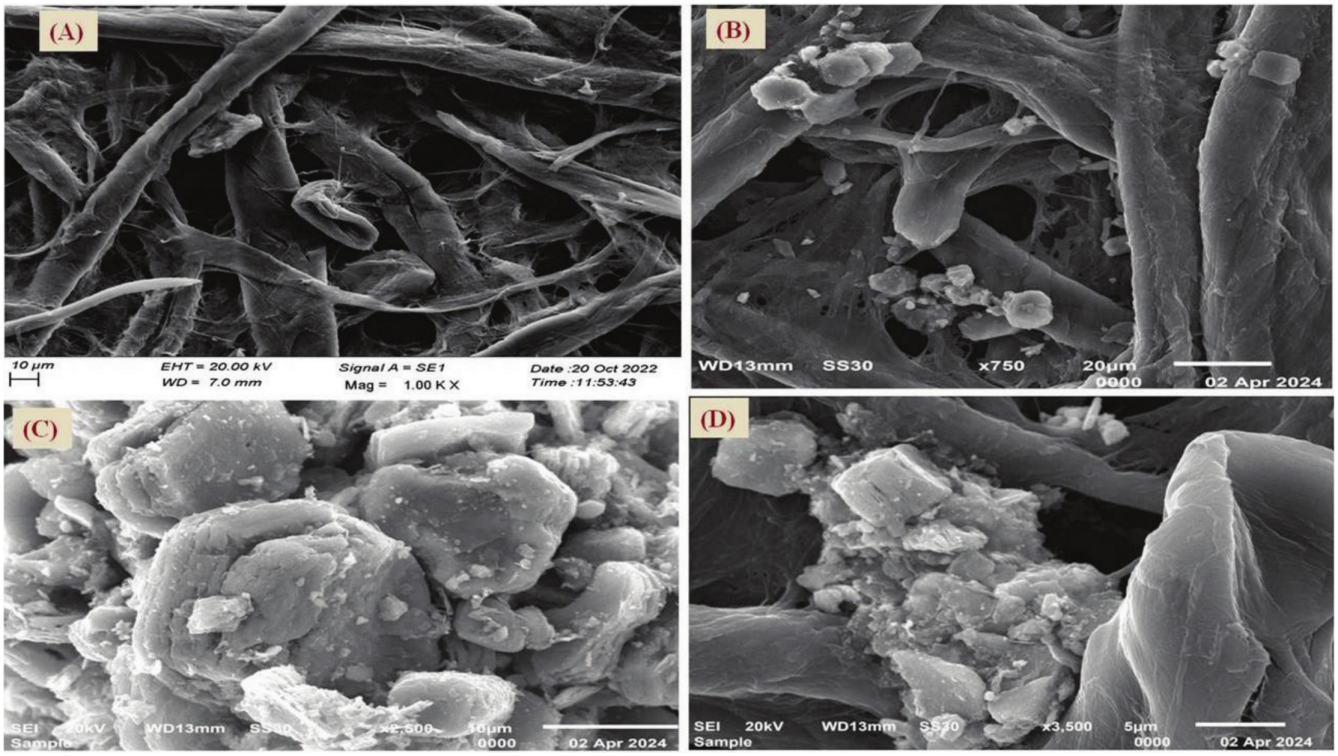


FIGURE 2 | SEM images of (A) PEDOT:PSS/WP; (B) $Ti_3C_2T_x$/CP; (C) $Ag@Ti_3C_2T_x$ powder; and (D) $Ag@Ti_3C_2T_x$/CP.

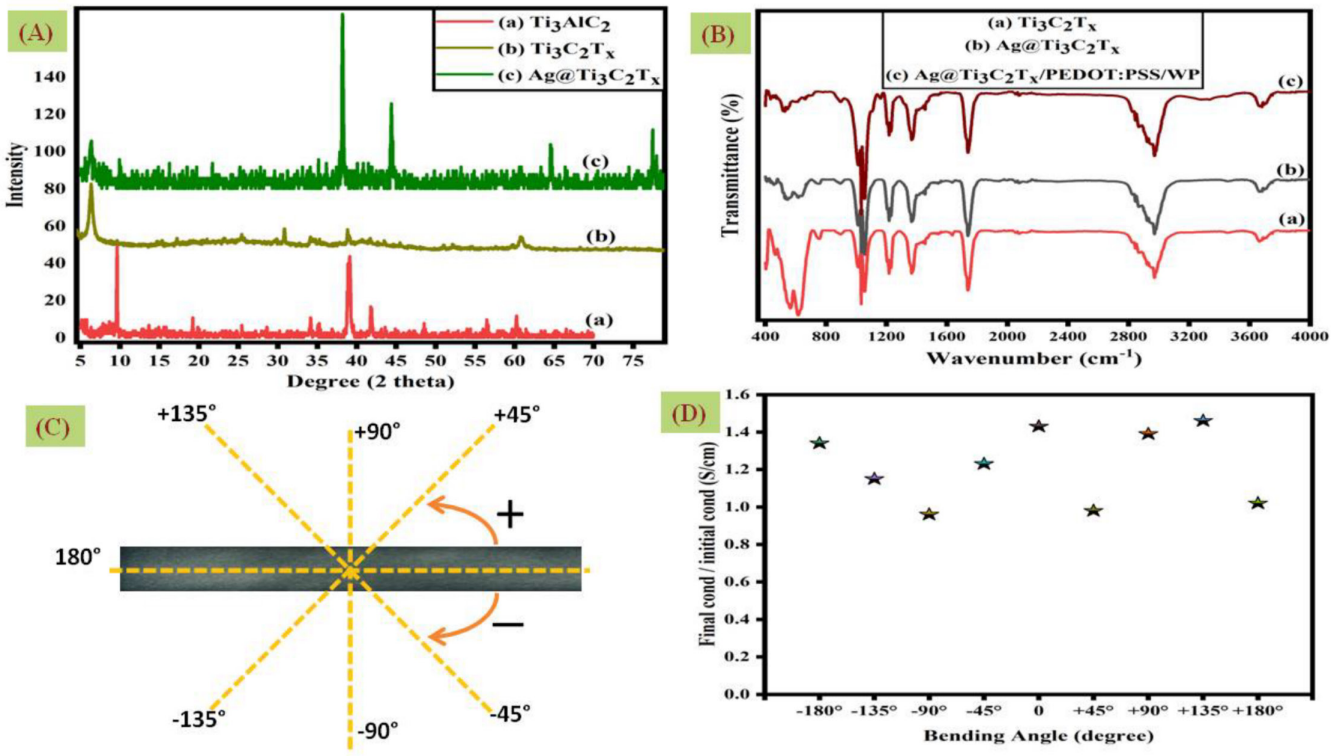


FIGURE 3 | (A) XRD patterns of Ti_3AlC_2 (a), $Ti_3C_2T_x$ (b), and $Ag@Ti_3C_2T_x$ (c); (B) FTIR spectra of $Ti_3C_2T_x$ (a), $Ag@Ti_3C_2T_x$ (b), and $Ag@Ti_3C_2T_x$/CP (c); (C) schematic view of conducting paper folding at different angles; and (D) plot of relative conductivity (final/initial) versus angle of bending.

10990739, 2025, 7, Downloaded from https://onlinelibrary.wiley.com/doi/10.1002/aoc.70264 by Delhi Technological University, Wiley Online Library on [26/06/2025]. See the Terms and Conditions (https://onlinelibrary.wiley.com/terms-and-conditions) on Wiley Online Library for rules of use; OA articles are governed by the applicable Creative Commons License

has been observed that the MAX phase has been disappeared completely after hydrothermal etching, as evident by the absence of Al peak at 2θ = 39.1° in curves b and c. The characteristic peak (002) of Ti_3AlC_2 (2θ = 9.6°) has been shifted to a broad peak at 6.4° in $Ti_3C_2T_x$ and Ag@$Ti_3C_2T_x$ suggesting a drastic loss in the crystallinity [29]. In curve c, the additional peaks of Ag positioned at 38.4°, 44.5°, 64.7°, and 77.5° further confirm the incorporation of Ag particles into the $Ti_3C_2T_x$ sheets [30].

The surface structure and modification of $Ti_3C_2T_x$ and Ag@$Ti_3C_2T_x$ has been described by FTIR spectroscopy ranging from 400 to 4000 cm^{-1} (Figure 3B). The peak observed at 2975 cm^{-1} is due to the stretching vibrations of C–H bond, while the peaks appeared around 1738, 1374, and 1055 cm^{-1} are attributed to the stretching vibrations of C=O, O–H, and C–F bonds, respectively [22]. Hence, the presence of C=O, –OH, and –F groups has been confirmed as surface modifications in $Ti_3C_2T_x$. The additional peaks appeared around 611 and 563 cm^{-1} ascribed to the Ti–O and Ti–C stretching vibrations, respectively. In curve b, the intensity of Ti–O and Ti–C peaks decreases, which may be due to the incorporation of Ag particles into the $Ti_3C_2T_x$ sheets. In the FTIR spectra of Ag@$Ti_3C_2T_x$/PEDOT:PSS/WP, the additional peaks appeared at 1044 and 1160 cm^{-1} owing to the presence of $-SO_3$ group (symmetric and asymmetric stretching vibrations, respectively) in PSS molecules.

3.3 | Electrical Conductivity, Flexibility, and Disposability Study

By utilizing a four-probe technique, conductivity measurement tests have been performed for different fabricated paper electrodes and presented in Table 1. Conductivity has been measured to be 2.5×10^{-3}, 7.6×10^{-3}, and 10.9×10^{-3} S/cm for PEDOT:PSS/WP (CP), $Ti_3C_2T_x$/CP, and Ag@$Ti_3C_2T_x$/CP electrodes, respectively. Further, the effect of the organic solvent, DMSO, has been studied to improve the electrochemical parameters of the Ag@$Ti_3C_2T_x$/CP electrode. It is reported that DMSO treatment causes the rearrangement in the PEDOT:PSS structure, which further enhances the mobility of charge carriers. In addition, DMSO forms a bond with PEDOT, and at the same time, PSS is removed with distilled water, resulting in an increase in conductivity [31].

TABLE 1 | Electrical conductivity of different modified electrodes.

S. no.	Modified electrodes	Conductivity (S/cm)
1	PEDOT:PSS/WP (CP)	2.5×10^{-3}
2	$Ti_3C_2T_x$/CP	7.6×10^{-3}
3	Ag@$Ti_3C_2T_x$/CP	10.9×10^{-3}
4	25% DMSO treated Ag@$Ti_3C_2T_x$/CP	498.2×10^{-3}
5	50% DMSO treated Ag@$Ti_3C_2T_x$/CP	763.5×10^{-3}
6	75% DMSO treated Ag@$Ti_3C_2T_x$/CP	509.1×10^{-2}
7	100% DMSO treated Ag@$Ti_3C_2T_x$/CP	445.5×10^{-3}

The Ag@$Ti_3C_2T_x$/CP electrode has been optimized with different concentrations of DMSO such as 25%, 50%, 75%, and 100% (V/V). It was found that the 50% DMSO treated Ag@$Ti_3C_2T_x$/CP electrode possesses the highest conductivity (763.5×10^{-3} S/cm).

Additionally, the flexibility of the fabricated electrode has been investigated by folding it at various angles, ranging from −180° to +180° (−ve and +ve signs show the downward and upward fold) as shown in Figure 3C. The conductivity of the electrode did not alter noticeably as measured by the four point probe technique. A plot of relative conductivity against the angle of bending is shown in Figure 3D, which represents a very minimal change in conductivity, thereby proving the bendable nature of conductivity paper.

Furthermore, this low-cost and flexible paper-based immunosensor can be easily discarded by incineration [32]. The paper-based sensor can be easily burned in about 10 s without producing harmful smoke into the atmosphere. The energy dispersive X-ray (EDX) technique was also used to examine the elements found in the ash. The results show that the majority of the elements found in the ash were carbon and oxygen, and no harmful or heavy elements were found (Figure S2). This suggests that the electrode is biodegradable and environment friendly in nature.

3.4 | Electrochemical Characterization

The electrochemical characterization of different electrodes was carried out by using the chronoamperometry technique at an applied potential of 0.2 V with a 0.1-s time interval in 0.2-M PBS (pH 6.5) containing 5-mM $[Fe(CN)_6]^{3-/4-}$. The electrochemical response for all the fabricated electrodes has been recorded under identical conditions (Figure 4A). It was observed that the DMSO treated Ag@$Ti_3C_2T_x$/CP electrode has the highest value of saturation current (2.95×10^{-3} mA) in comparison to Ag@$Ti_3C_2T_x$/CP (2.09×10^{-3} mA), $Ti_3C_2T_x$/CP (1.77×10^{-3} mA), and CP (1.14×10^{-3} mA). The increase in current is due to the incorporation of highly conducting Ag particles, which worked in a synergistic manner with $Ti_3C_2T_x$. Hence, the Ag@$Ti_3C_2T_x$/CP electrode is more conducting due to the increase in the effective surface area.

The response time study was performed on the fabricated immunosensor, anti-EpCAM/Ag@$Ti_3C_2T_x$/CP, to optimize the time required for the completion of anti-EpCAM and EpCAM antigen reaction. For that reason, anti-EpCAM/Ag@$Ti_3C_2T_x$/CP electrode was incubated with EpCAM antigen (50 fg/mL) for 12 min (Figure 4B). The saturation current was measured after every 2 min, and it was found that the current decreases up to 8 min and, after that, a stage of saturation was reached (Figure 4B). Hence, it was considered as the optimal time for all biosensing studies.

3.5 | Electrochemical Response Studies

The response study was performed on the fabricated immunosensor, anti-EpCAM/Ag@$Ti_3C_2T_x$/CP, as a function of change in concentration of EpCAM antigen (1 fg/mL–10,000 pg/mL) in 12-mL PBS [(0.2 M, pH 6.5) solution having 5-mM $[Fe(CN)_6]^{-3/-4}$]. After adding 20 μL of various antigen concentrations, it was found that the current decreases with each addition of EpCAM antigen, which is clearly seen in Figure 4C.

10990739, 2025, 7, Downloaded from https://onlinelibrary.wiley.com/doi/10.1002/aoc.70264 by Delhi Technological University, Wiley Online Library on [26/06/2025]. See the Terms and Conditions (https://onlinelibrary.wiley.com/terms-and-conditions) on Wiley Online Library for rules of use; OA articles are governed by the applicable Creative Commons License

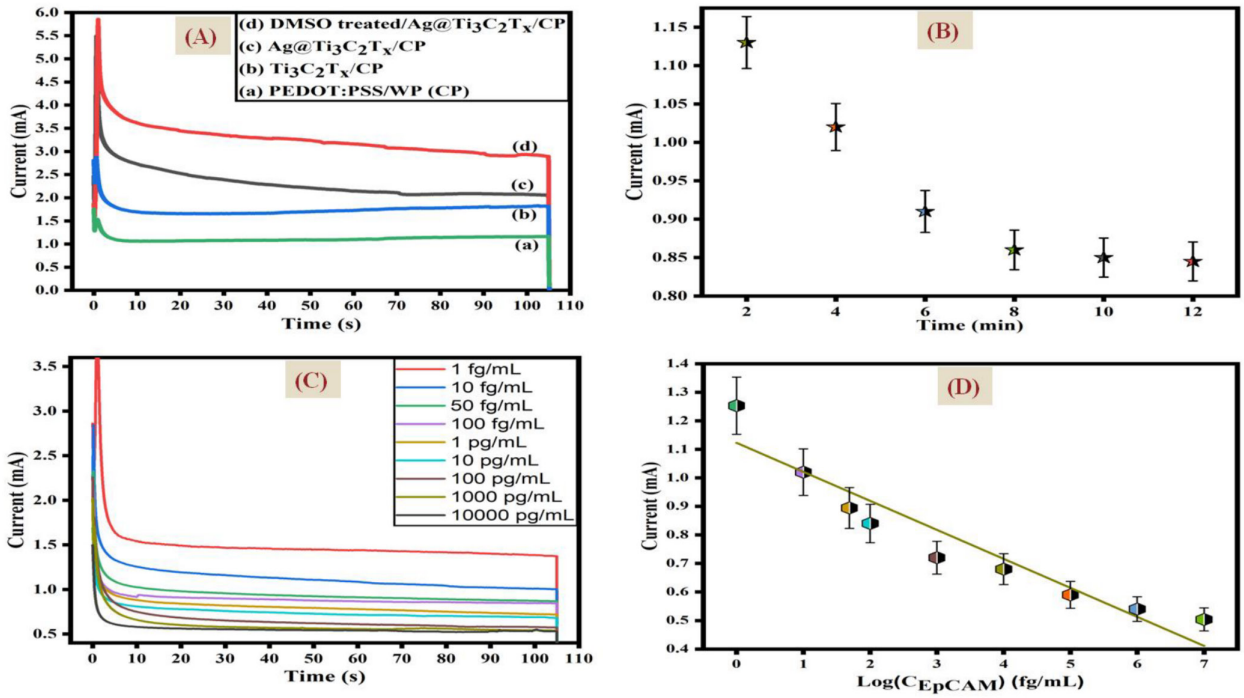


FIGURE 4 | (A) Chronoamperometric plot of CP (a), $Ti_3C_2T_x$/CP (b), Ag@$Ti_3C_2T_x$/CP (c), and DMSO treated Ag@$Ti_3C_2T_x$/CP (d); (B) optimization for incubation time of EpCAM antigen; (C) electrochemical response of anti-EpCAM/Ag@$Ti_3C_2T_x$/CP against different EpCAM antigen concentrations (1 fg/mL–10,000 pg/mL); and (D) calibration plot of current against log (C_{EpCAM}).

The formation of an immunocomplex onto the anti-EpCAM/Ag@$Ti_3C_2T_x$/CP electrode's surface results in the decline of rate of electron transfer process, which could be due to the blockage of active area on the electrode's surface. The plot of the magnitude of current and log of EpCAM antigen concentration shows a linear relationship (Figure 4D), as represented by the following regression equation.

$$\text{Current} = -101.66\,\mu\text{A}/\left(\text{fg}\cdot\text{mL}^{-1}\right)\times\log\left(C_{EpCAM}\right)+1.12\,\text{mA};\ R^2=0.88. \quad (1)$$

The sensitivity (S) of anti-EpCAM/Ag@$Ti_3C_2T_x$/CP electrode was estimated from slope analysis and calculated as 44.12 μA·fg^{-1}·mL with detection limit of 0.8 fg/mL (LOD = 3σ/S, σ is standard deviation).

The analytical parameters of anti-EpCAM/Ag@$Ti_3C_2T_x$/CP electrode have been compared with other published works and summarized in Table 2. This comparison illustrates that the anti-EpCAM/Ag@$Ti_3C_2T_x$/CP electrode exhibits excellent LOD (0.8 fg/mL) with broader linear range (1 fg/mL–10,000 pg/mL) for EpCAM antigen. This may be due to the synergistic effect of Ag and $Ti_3C_2T_x$.

3.6 | Spiked Sample Study

The anti-EpCAM/Ag@$Ti_3C_2T_x$/CP electrode was utilized to examine the serum sample in order to verify the efficacy of the fabricated immunosensor. Prior to being spiked with various concentrations of EpCAM antigen (10, 100, 1000, and 10,000 fg/mL), the serum sample was first diluted with PBS (pH = 7.4). The electrochemical data obtained from the chronoamperometric response show a good correlation between the saturated current obtained from (a) the spiked serum sample and (b) the reference buffer sample, as given in Figure 5A and Table 3. This biosensing platform shows excellent precision, with an average percentage RSD of less than 2.22%.

Further, clinical validation was checked by taking electrochemical response of five different patient's serum sample with anti-EpCAM/Ag@$Ti_3C_2T_x$/CP sensor. This has been achieved by centrifuging the serum samples for 10 min at 8000 rpm to get rid of germs, bacteria, and glycoprotein clumps. Aliquots of 100 μL were prepared by collection of supernatant, which were subsequently stored at −10°C after standard addition of antigen. The plot of saturation current versus number of serum samples has been shown in Figure S3. The average %RSD was found be less than 10% in comparison to buffer sample, which thereby proves the acceptability of fabricated sensor.

3.7 | Specificity, Repeatability, and Stability Studies

Interference test was conducted by using the chronoamperometry approach to investigate the impact of different analytes such as glucose, NaCl, urea, and ascorbic acid on the sensing parameters. These results are shown in Figure 5B. After adding these interferents (having concentration 50 fg/mL), there was no appreciable change in the electrochemical current in comparison to EpCAM antigen. The anti-EpCAM/Ag@$Ti_3C_2T_x$/CP electrode, on the other hand, exhibits a notable shift in electrochemical current response with a mixture of all the analytes containing EpCAM

10990739, 2025, 7, Downloaded from https://onlinelibrary.wiley.com/doi/10.1002/aoc.70264 by Delhi Technological University, Wiley Online Library on [26/06/2025]. See the Terms and Conditions (https://onlinelibrary.wiley.com/terms-and-conditions) on Wiley Online Library for rules of use; OA articles are governed by the applicable Creative Commons License

TABLE 2 | Comparison of the anti-EpCAM/Ag@$Ti_3C_2T_x$/CP electrode with other reported biosensors for EpCAM detection.

S. no.	Fabrication method	Detection technique	Substrate	LOD	Detection range	Disposability	References
1	Magnetic method	SERS	—	5 ng/L	—	Yes	[33]
2	Microfluidic design	EM	Au electrode	0.8 pg/mL	2–2000 pg/mL	No	[34]
3	Electrophoretic deposition	DPV	ITO	6.5 pg/mL	0.01–60 ng/mL	No	[35]
4	Dip coating	CA	WP	0.01 pg/mL	0.01 pg/mL–1000 ng/mL	Yes	[36]
5	Signal amplification method	ASV	ITO	100 fg/mL	100 fg/mL–7.5 μg/mL	No	[37]
6	Electrophoretic deposition	DPV	ITO	44.22 fg/mL	0.001–20 ng/mL	No	[38]
7	Dip coating	CA	WP	0.8 fg/mL	1 fg/mL–10,000 pg/mL	Yes	Present study

Abbreviations: ASV: anodic stripping voltammetry; CA: chronoamperometry; DPV: differential pulse voltammetry; EM: electrochemical microfluidic; ITO: indium tin oxide; SERS: surface enhanced Raman spectroscopy; WP: Whatman paper.

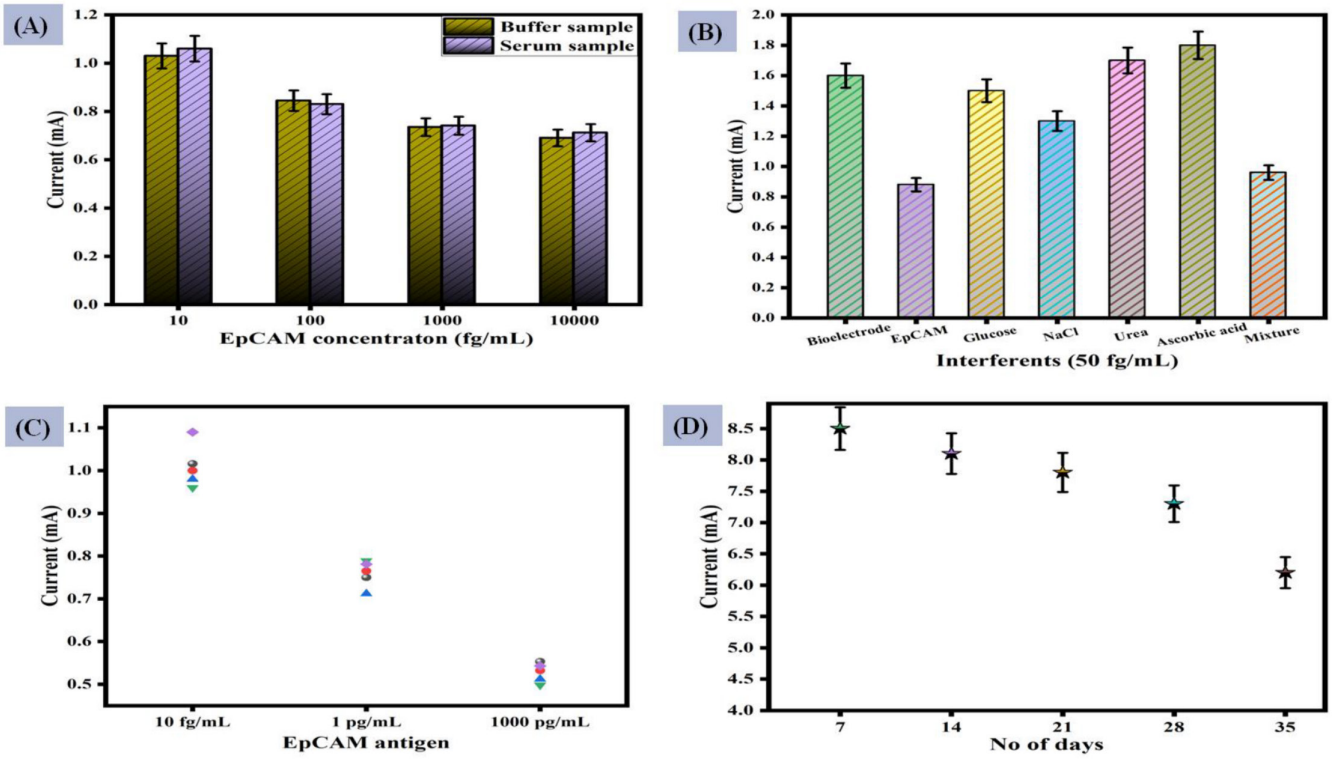


FIGURE 5 | (A) Chronoamperometric saturated current comparison of anti-EpCAM/Ag@$Ti_3C_2T_x$/CP electrode for EpCAM antigen in buffer (a) and serum sample (b); (B) interference study of anti-EpCAM/Ag@$Ti_3C_2T_x$/CP electrode with various analytes (glucose, NaCl, urea, and ascorbic acid); (C) repeatability study of three different anti-EpCAM/Ag@$Ti_3C_2T_x$/CP electrodes; and (D) shelf life study of immunosensor).

antigen. Hence, the fabricated immunosensor was found to be highly specific and selective for EpCAM antigen detection.

For repeatability study, the chronoamperometry response of the fabricated immunosensor was recorded five times with each concentration of EpCAM antigen, that is, 10 fg/mL (low), 1 pg/mL (medium), and 1000 pg/mL (high), as depicted in Figure 5C. With respect to 10 fg/mL, 1 pg/mL, and 1000 pg/mL EpCAM antigen, the % RSD values for the anti-EpCAM/Ag@$Ti_3C_2T_x$/CP electrode are calculated as 4.95%, 4.01%, and 4.26%, respectively.

10990739, 2025, 7, Downloaded from https://onlinelibrary.wiley.com/doi/10.1002/aoc.70264 by Delhi Technological University, Wiley Online Library on [26/06/2025]. See the Terms and Conditions (https://onlinelibrary.wiley.com/terms-and-conditions) on Wiley Online Library for rules of use; OA articles are governed by the applicable Creative Commons License

TABLE 3 | EpCAM antigen detection in serum sample.

S. no.	Approximate added EpCAM concentration (fg/mL)	Approximate found EpCAM concentration (fg/mL)	Recovery (%)	RSD (%)
1	10	9.7	97.17	2.03
2	100	101.8	101.80	1.27
3	1000	991.9	99.19	0.57
4	10,000	9691.2	96.91	2.22

Low values of relative standard deviations represent that the produced immunosensor exhibits excellent repeatability and reproducibility.

Additionally, the shelf life of the anti-EpCAM/Ag@$Ti_3C_2T_x$/CP electrode has been assessed up to 35 days at the intervals of 7 days, in the presence of 50 fg/mL EpCAM antigen as depicted in Figure 5D. These findings show that the immunosensor maintained 84% of the current response up to 28 days. After that the saturated current was declined to 71% of initial value. This stability is noticeably better than our previous reported immunosensor, BSA/anti-EpCAM/EP, which has a 28-days shelf life.

4 | Conclusion

A successful invention of an inexpensive, portable, highly stable conducting paper-based immunosensor has been designed by using Ag@$Ti_3C_2T_x$ hybrid and PEDOT:PSS. The anti-EpCAM/Ag@$Ti_3C_2T_x$/CP immunosensor was fabricated by immobilizing anti-EpCAM by dropcast method. Our results from chronoamperometric response study reveal the accurate, rapid, and non-invasive detection of EpCAM antigen. This immunosensor displayed a good sensing performance with an extremely low detection limit, 0.8 fg/mL. Furthermore, the extraordinary flexibility and long term stability (35 days) of this immunosensor enables the accurate EpCAM detection with quick response time. The clinical validation of this paper-based sensor was confirmed by detecting the EpCAM antigen with spiked serum samples. Thus, a wide range of applications for biomarker monitoring could benefit greatly from the use of this portable, accurate, and efficient paper-based immunosensor.

Author Contributions

Sweety: conceptualization, methodology, validation, visualization, resources, writing – original draft. **Divya Hudda:** data curation, formal analysis, visualization. **Devendra Kumar:** project administration, supervision, writing – review and editing.

Acknowledgments

Sweety acknowledges the Council Scientific and Industrial Research (CSIR), Government of India, New Delhi, for the financial support (File no: 08/133(0051)/2020-EMR-I).

Ethics Statement

Artificial human serum procured from Sigma Aldrich is used.

Conflicts of Interest

The authors declare no conflicts of interest.

Data Availability Statement

Data can be made available on the basis of reasonable request due to privacy/ethical restrictions.

References

1. H. Du, M. Zhang, K. Liu, et al., "Conductive PEDOT: PSS/Cellulose Nanofibril Paper Electrodes for Flexible Supercapacitors With Superior Areal Capacitance and Cycling Stability," *Chemical Engineering Journal* 428 (2022): 131994.

2. J. Yu, S. Wang, L. Ge, and S. Ge, "A Novel Chemiluminescence Paper Microfluidic Biosensor Based on Enzymatic Reaction for Uric Acid Determination," *Biosensors and Bioelectronics* 26 (2011): 3284–3289.

3. E. Carrilho, S. T. Phillips, S. J. Vella, A. W. Martinez, and G. M. Whitesides, "Paper Microzone Plates," *Analytical Chemistry* 81 (2009): 5990–5998.

4. S. Chatterjee, H. Singh, D. Hudda, Sweety, and D. Kumar, "A Novel Acetylcholinesterase-Based Electrochemical Biosensor Using g-C_3N_4@MoS_2 Nanohybrid for the Detection of Trichlorfon," *Applied Organometallic Chemistry* 38 (2024): e7721.

5. R. M. Morais, M. S. Klem, M. S. Ozório, T. C. Gomes, and N. Alves, "Roughness Influence on the Sheet Resistance of the PEDOT:PSS Printed on Paper," *Current Applied Physics* 18 (2018): 254–260.

6. Y. Kumar, S. Shankar, R. Chandra, and S. Kumar, "Conducting Paper Based on Few-Layered Hydrogen-Substituted Graphdiyne for Swine Flu Detection," *ACS Applied Nano Materials* 7 (2024): 19925–19935.

7. S. Kumar, C. M. Pandey, A. Hatamie, A. Simchi, M. Willander, and B. D. Malhotra, "Nanomaterial-Modified Conducting Paper: Fabrication, Properties, and Emerging Biomedical Applications," *Global Challenges* 3 (2019): 1900041.

8. J. Maslik, H. Andersson, V. Forsberg, M. Engholm, R. Zhang, and H. Olin, "PEDOT:PSS Temperature Sensor Ink-Jet Printed on Paper Substrate," *Journal of Instrumentation* 13 (2018): C12010.

9. M. N. Gueye, A. Carella, J. Faure-Vincent, R. Demadrille, and J.-P. Simonato, "Progress in Understanding Structure and Transport Properties of PEDOT-Based Materials: A Critical Review," *Progress in Materials Science* 108 (2020): 100616.

10. S. Shankar, Y. Kumar, N. Sharma, R. Chandra, and S. Kumar, "Disposable Zirconium Trisulfide-Reduced Graphene Oxide Modified Conducting Thread Based Electrochemical Biosensor for Lung Cancer Diagnosis," *Bioelectrochemistry* 160 (2024): 108801.

11. D. Chauhan, Y. Kumar, R. Chandra, and S. Kumar, "2D Transparent Few-Layered Hydrogen Substituted Graphdiyne Nano-Interface for Unprecedented Ultralow ANXA2 Cancer Biomarker Detection," *Biosensors and Bioelectronics* 213 (2022): 114433.

10990739, 2025, 7, Downloaded from https://onlinelibrary.wiley.com/doi/10.1002/aoc.70264 by Delhi Technological University, Wiley Online Library on [26/06/2025]. See the Terms and Conditions (https://onlinelibrary.wiley.com/terms-and-conditions) on Wiley Online Library for rules of use; OA articles are governed by the applicable Creative Commons License

12. K. Khan, A. K. Tareen, M. Aslam, et al., "Recent Developments in Emerging Two-Dimensional Materials and Their Applications," *Journal of Materials Chemistry C* 8 (2020): 387–440.

13. Y. Kumar, S. Shankar, R. Chandra, and S. Kumar, "Highly Bendable and Smoke Free Degradable Nanomaterials Modified Paper Based Electrochemical Biosensor for Efficient Detection of Protein Biomarker," *Microchemical Journal* 194 (2023): 109318.

14. M. Khazaei, M. Arai, T. Sasaki, et al., "Novel Electronic and Magnetic Properties of Two-Dimensional Transition Metal Carbides and Nitrides," *Advanced Functional Materials* 23 (2013): 2185–2192.

15. S. Kumar, Y. Lei, N. H. Alshareef, M. Quevedo-Lopez, and K. N. Salama, "Biofunctionalized Two-Dimensional Ti_3C_2 MXenes for Ultrasensitive Detection of Cancer Biomarker," *Biosensors and Bioelectronics* 121 (2018): 243–249, https://doi.org/10.1016/j.bios.2018.08.076.

16. N. Liu, L. Yu, B. Liu, et al., "Ti_3C_2-MXene Partially Derived Hierarchical 1D/2D TiO_2/Ti_3C_2 Heterostructure Electrode for High-Performance Capacitive Deionization," *Advanced Science* 10, no. 2 (2023): 2204041, https://doi.org/10.1002/advs.202204041.

17. E. N. Kalali, W. Guo, X. Wang, W. Xing, L. Song, and Y. Hu, "Effect of Metal-Based Nanoparticles Decorated Graphene Hybrids on Flammability of Epoxy Nanocomposites," *Composites Part A, Applied Science and Manufacturing* 129 (2020): 105694, https://doi.org/10.1016/j.compositesa.2019.105694.

18. S. Paneru and D. Kumar, "Ag-Doped-CuO Nanoparticles Supported Polyaniline (PANI) Based Novel Electrochemical Sensor for Sensitive Detection of Paraoxon-Ethyl in Three Real Samples," *Sensors and Actuators B: Chemical* 379 (2023): 133270.

19. H. Amir, V. Subramanian, S. Sornambikai, N. Ponpandian, and C. Viswanathan, "Nitrogen-Enhanced Carbon Quantum Dots Mediated Immunosensor for Electrochemical Detection of HER2 Breast Cancer Biomarker," *Bioelectrochemistry* 155 (2024): 108589.

20. U. S. Kulkarni, C. R. Gawali, and S. Kumar, "Ultraefficient Electrochemical Biosensing Platform Utilizing *Aloe vera*-Derived Carbon Nanodots for ANXA2 Liver Cancer Biomarker Diagnosis," *Industrial Crops and Products* 229 (2025): 120996.

21. S. Shankar, Y. Kumar, N. Kumar, et al., "Nanoengineered Multiwalled Carbon Nanotube for Lung Cancer Diagnosis," *Journal of Molecular Structure* 1320 (2025): 139629.

22. Sweety and D. Kumar, "Electrochemical Immunosensor Based on Titanium Dioxide Grafted MXene for EpCAM Antigen Detection," *Journal of Colloid and Interface Science* 652 (2023): 549–556.

23. L. Tao, K. Zhang, Y. Sun, B. Jin, Z. Zhang, and K. Yang, "Anti-Epithelial Cell Adhesion Molecule Monoclonal Antibody Conjugated Fluorescent Nanoparticle Biosensor for Sensitive Detection of Colon Cancer Cells," *Biosensors and Bioelectronics* 35 (2012): 186–192.

24. P. Bohra, Priya, Sweety, D. Hudda, and D. Kumar, "Cus@ rGO Grafted PEDOT: PSS Paper-Based Electrochemical Biosensor for Sensitive Detection of Fenitrothion," *Applied Organometallic Chemistry* 39 (2025): e70002.

25. Sweety and D. Kumar, "Development of $Ti_3C_2T_x$-Based Novel Immunosensor for Cancer Biomarker Detection," *Applied Organometallic Chemistry* 38 (2024): e7570.

26. A. Kalkal, S. Kadian, S. Kumar, et al., "Ti_3C_2–MXene Decorated With Nanostructured Silver as a Dual-Energy Acceptor for the Fluorometric Neuron Specific Enolase Detection," *Biosensors and Bioelectronics* 195 (2022): 113620.

27. S. Paneru, Sweety, and D. Kumar, "CuO@ PEDOT: PSS-Grafted Paper-Based Electrochemical Biosensor for Paraoxon-Ethyl Detection," *Journal of Applied Electrochemistry* 53 (2023): 2229–2238.

28. S. Paneru, Sweety, and D. Kumar, "CeO_2 and PEDOT: PSS Modified Conducting Paper for Organophosphate Pesticide Detection," *Journal of Applied Electrochemistry* 54 (2024): 1875–1885.

29. Sweety, S. Paneru, and D. Kumar, "A Copper Sulfide Doped 2D-MXene-Based Ultrasensitive Label-Free Electrochemical Immunosensor for EpCAM Antigen Detection," *Applied Organometallic Chemistry* 39 (2025): e7975.

30. K. Fatemeh, M. Mohammad Javad, and K. Samaneh, "The Effect of Silver Nanoparticles on Composite Shear Bond Strength to Dentin With Different Adhesion Protocols," *Journal of Applied Oral Science* 25 (2017): 367–373.

31. S. Kumar, M. Umar, A. Saifi, et al., "Electrochemical Paper Based Cancer Biosensor Using Iron Oxide Nanoparticles Decorated PEDOT: PSS," *Analytica Chimica Acta* 1056 (2019): 135–145.

32. S. Kumar, P. Rai, J. G. Sharma, A. Sharma, and B. D. Malhotra, "PEDOT: PSS/PVA-Nanofibers-Decorated Conducting Paper for Cancer Diagnostics," *Advanced Materials Technologies* 1, no. 4 (2016): 1600056, https://doi.org/10.1002/admt.201600056.

33. A. Balzerova, A. Opletalova, V. Ranc, and R. Zbořil, "Multiplex Competitive Analysis of HER2 and EpCAM Cancer Markers in Whole Human Blood Using Fe_2O_3@Ag Nanocomposite," *Applied Materials Today* 13 (2018): 166–173, https://doi.org/10.1016/j.apmt.2018.08.016.

34. K. Bravo, F. G. Ortega, G. A. Messina, M. I. Sanz, M. A. Fernández-Baldo, and J. Raba, "Integrated Bio-Affinity Nano-Platform Into a Microfluidic Immunosensor Based on Monoclonal Bispecific Trifunctional Antibodies for the Electrochemical Determination of Epithelial Cancer Biomarker," *Clinica Chimica Acta* 464 (2017): 64–71.

35. O. Jalil, C. M. Pandey, and D. Kumar, "Electrochemical Biosensor for the Epithelial Cancer Biomarker EpCAM Based on Reduced Graphene Oxide Modified With Nanostructured Titanium Dioxide," *Microchimica Acta* 187 (2020): 1–9.

36. Sweety, S. Paneru, and D. Kumar, "CuS Modified PEDOT: PSS Grafted Paper-Based Electrochemical Immunosensor for EpCAM Biomarker Detection," *Materials Chemistry and Physics* 313 (2024): 128687.

37. M. J. Shiddiky, S. Rauf, P. H. Kithva, and M. Trau, "Graphene/Quantum Dot Bionanoconjugates as Signal Amplifiers in Stripping Voltammetric Detection of EpCAM Biomarkers," *Biosensors and Bioelectronics* 35, no. 1 (2012): 251–257, https://doi.org/10.1016/j.bios.2012.02.057.

38. O. Jalil, C. M. Pandey, and D. Kumar, "Highly Sensitive Electrochemical Detection of Cancer Biomarker Based on Anti-EpCAM Conjugated Molybdenum Disulfide Grafted Reduced Graphene Oxide Nanohybrid," *Bioelectrochemistry* 138 (2021): 107733.

Supporting Information

Additional supporting information can be found online in the Supporting Information section.

10990739, 2025, 7, Downloaded from https://onlinelibrary.wiley.com/doi/10.1002/aoc.70264 by Delhi Technological University, Wiley Online Library on [26/06/2025]. See the Terms and Conditions (https://onlinelibrary.wiley.com/terms-and-conditions) on Wiley Online Library for rules of use; OA articles are governed by the applicable Creative Commons License

Universal IoT-Enabled Smart Battery Charging Optimization: Leveraging AI, Automata Theory, and Real-Time Data for Enhanced Lifespan and Efficiency

Divyansh Arora [1], *Ananya* Goswami [2], *Mritunjay* Ranjan[3*], *Arif Md* Sattar[4]

[1]Department of Design, Delhi Technological University, India
[2-3] School of Computer Sciences and Engineering, Sandip University, Nashik, India.
[4]Associate Professor, Department of MCA, Dewan institute of management studies, Meerut, India.

Abstract. Universal IoT-Enabled Smart Battery Charging Optimization System introduces a novel solution to addressing the widespread problem of battery degradation in IoT-enabled devices such as smartphones, wearables, stylus pens, and wireless earbuds. The system utilizes Artificial Intelligence (AI), Automata Theory, and sensor data in real-time to develop a dynamic context-aware charging strategy that learns from the unique usage patterns and battery status of every device. By applying machine learning models like Kalman Filters, Recurrent Neural Networks (RNNs), and Finite State Machines (FSM), the system charges behaviors smartly, optimizing power consumption, charging efficiency, and battery life. Pushdown Automata (PDA) are used to facilitate non-deterministic state transitions from past charging data, providing more precise predictions of battery wear. The system constantly collects and processes data from IoT sensors with real-time charging cycle and battery health feedback. Initial results indicate that the system greatly mitigates overcharging, enhances battery life, and promotes energy efficiency, providing a green solution to maximize the lifespan of IoT-based devices in various applications. The solution offers a sound framework for further research on smart energy management and green computing.

1 Introduction

Rechargeable devices such as stylus pens (e.g., Apple Pencil, Surface Pen), smartwatches, and wireless earbuds are ubiquitous. These devices, reliant on rechargeable batteries, offer more portability and convenience but are inevitably circumscribed by the limited life of their batteries [1]. Overcharging, one of the primary sources of battery health diminution, is when devices continue charging beyond their full capacity. Over time, this accelerates battery aging and reduces charging efficiency, ultimately slowing down the device performance and life. Existing battery management systems are effective at preventing short-term damage but do not optimize long-term battery health or adapt to dynamic charging patterns [2]. These typically employ common patterns of charging and do not consider user-dependent behavior,

*Corresponding author : mritunjaykranjan@gmail.com

© The Authors, published by EDP Sciences. This is an open access article distributed under the terms of the Creative Commons Attribution License 4.0 (https://creativecommons.org/licenses/by/4.0/).

device health, or the ambient environmental conditions such as temperature [3]. Accordingly, their lack of being adaptive generates inefficient charging practice that results in premature degradation of batteries. To assist in addressing these limitations, we introduce a Universal Smart Battery Charging Optimizing System based on Artificial Intelligence (AI), Machine Learning (ML), and Automata Theory that optimizes charging dynamically. The system is such that it automatically monitors and manages the battery charging behavior and health of different devices, making real-time adjustments in charging thresholds, user behavior, and device requirements [4]. This keeps the charging efficient, free of overcharging, and increases the battery life. The system uses adaptive charging logic to suspend charging at the optimal level (e.g., 80%) in an intelligent manner and resume it when the level of the battery falls in a given range (e.g., 20-30%) [5]. Using Automata Theory, i.e., Finite State Machines (FSM), the system models the charging process as a series of state transitions, i.e., charging, full charge, standby, and low battery [6]. It is an orthodox model enabling the system to make intelligent decisions on charging habits based on real-time data. Machine learning models like Kalman Filters and Recurrent Neural Networks (RNNs) are also employed in order to predict the optimal times to charge the battery and forecast battery degradation, optimizing the charging cycle while limiting wear and tear with time [7]. Figure 1. indicating the Universal Smart Battery Charging Optimization System structure. The system continuously monitors and controls the charging habit and battery health of connected devices according to AI-algorithms, Automata Theory, and current data to ensure maximum charging, prevent overcharging, and prolong battery life [8]. The system is integrated into the cloud for remote monitoring and predictive maintenance across multiple devices and platforms. In addition, the system provides cross-platform support, making it possible for it to be integrated with multiple devices (Apple, Android, Windows). The system's data is cloud-synced, enabling remote monitoring and predictive maintenance, where users can track battery health and adjust charging habits across multiple devices seamlessly [9].

Significant of Work

- The system dynamically adjusts charging thresholds based on user behavior and device needs, preventing overcharging and maximizing battery life.
- AI and machine learning models like Kalman Filters and RNNs are used to predict optimal charging times and forecast battery degradation, enabling real-time adjustments.
- Automata Theory models the charging process with state transitions (e.g., charging, full charge, standby, low battery), allowing intelligent decisions based on real-time data.
- Supports cross-platform integration with iOS, Android, and Windows devices, and synchronizes data with the cloud for remote monitoring and predictive maintenance.
- Case studies show a 35% improvement in battery lifespan, reduced degradation, and optimized charging for efficient and reliable operation.

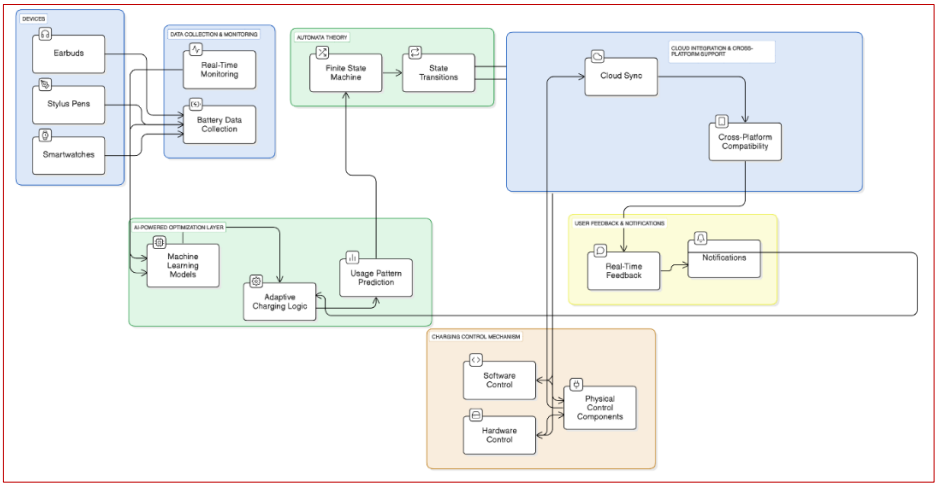


Fig. 1. Overview of the Universal Smart Battery Charging Optimization System

1.1 Objectives

- To create a dynamic system incorporating AI, ML, and Automata Theory for battery charging optimization and overcharging protection.
- To utilize adaptive charging logic that responds to real-time information, user activity, and device requirements.
- To incorporate machine learning models for the prediction of optimal charging times and reducing battery degradation.
- To facilitate cross-platform, cloud-based monitoring for remote access and real-time feedback on charging habits.

2 Related Study/Comparative Study

Table 1. Comparative Analysis of Machine Learning Models for Battery Health Optimization and Charging Behavior.

Citation	Method	Key Innovation	Limitation	Proposed Solutions	Accuracy	Optimization
[10]	Compares ML models (Random Forest, SVM, Neural Networks) for SOH estimation.	Offers a framework for assessing ML in SOH estimation.	Only addresses SOH, not real-time charging optimization.	Combines SOH with charging optimization in future work.	Neural networks exhibit highest accuracy in SOH estimation.	Ensures battery management by estimating SOH.
[11]	Employs LSTMs and CNNs for battery health	Battery health monitoring is improved with deep learning.	Primarily focuses on battery health with minimal charging	Combines battery management and deep learning to improve	High accuracy in predicting battery health.	Tunes the battery health assessments for

	monitoring.		optimization.	health assessment.		management.
[12]	Compares ML models for battery capacity fade and RUL prediction.	Introduces multi-feature multi-target (MFMT) mapping for RUL prediction.	Targets RUL prediction, not real-time charging optimization.	Framework for combining RUL prediction with charging optimization.	XGBoost-HT works best for RUL prediction.	Enhances battery management with efficient RUL prediction
[13]	Examine probabilistic ML models (Gaussian Processes, Bayesian Neural Networks) for battery health analysis.	Aims uncertainty quantification on long-term health forecasts.	Theoretical focus, few practical applications.	Combine probabilistic models with real-time information to provide better predictions.	Enhances prediction quality but computationally expensive.	Improve the reliability but affects real-time optimization.
[14]	Propose hybrid approach (CEEMDAN with SVR and LSTM) for RUL prediction.	Enhances RUL prediction taking non-linear battery degradation into account.	Performance is affected with noisy data, and real-time usage becomes complicated.	Preprocessing and noise removal for model robustness.	High accuracy in RUL prediction (RMSE < 0.0086 Ah, $R^2 > 0.96$).	Complex but accurate; efficiency in real-time use is limited.

[15] also suggest a data-driven method of optimizing EV battery management through machine learning. Their model anticipates battery degradation and optimizes charging through real-time information such as charging cycles and temperature. Applying deep models like LSTM and neural networks, they enhance battery lifespan but struggle with data quality and computational complexity. This is in line with our Universal Smart Battery Charging Optimization System, which also utilizes adaptive charging levels to avoid overcharging and maximize battery longevity.

[16] proposed an AI-driven approach to optimize consumer electronics like smartphones and laptops' charging, utilizing machine learning methods, including reinforcement learning (RL). Their system learns charging habits based on usage patterns, cutting battery degradation up to 20%. Although their solution is challenged with real-time data processing and scalability, it conforms to our Universal Smart Battery Charging Optimization System that also employs machine learning for adaptive charging adjustments and cross-platform compatibility and cloud synchronization for maximum battery health across different devices.

[17] presented a machine learning-based system for optimizing battery health and charging cycles. They employed techniques such as Random Forests and Support Vector Machines to forecast battery health and control charging times. The data consisted of charge cycles, temperature, voltage, and current readings.Their answer increased battery life by managing

charging conduct efficiently, but it was based on high-quality, real-time information, which may vary from device to device. This work can be complemented with our Universal Smart Battery Charging Optimization System that gives the highest importance to machine learning, which dynamically adjusts charging thresholds and optimizes device life.

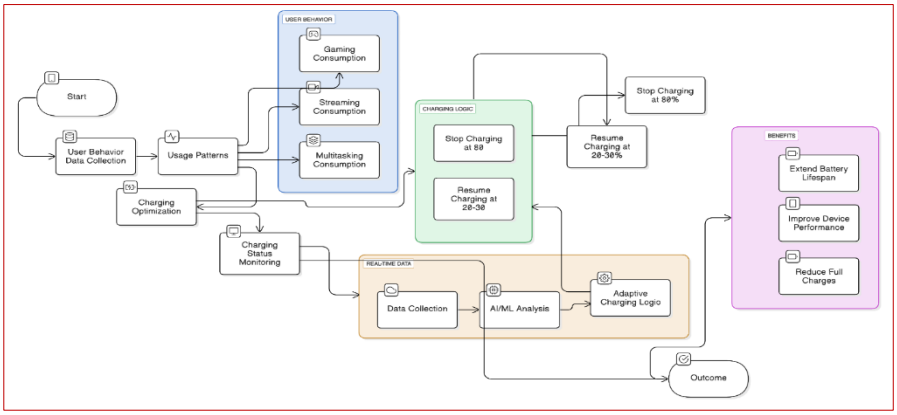


Fig. 2. User A's Adaptive Charging Flow with Device 1 (Smartphone)

3 Case Studies

Case Study 1 : User A with Device 1 (Smartphone) User A makes constant use of his smartphone for intense daily activities like gaming, video streaming, and multitasking, and the device's battery gets drained quickly [18]. Overcharging and wasteful charging habits were affecting the performance and life of the device

The Universal Smart Battery Charging Optimizing System tracks User A's charging habits and adjusts the charge levels accordingly. It charges up to 80% and recharges at a 20-30% battery level. Using this adaptive charging method, In the Figure 2. battery life of User A has been extended by 25%, minimizing maximum charges and keeping the optimal device capability. The advanced decision-making of the system maximizes the battery to its highest performance potential, with long running without excessive stress.

Case Study 2 : User B using Device 2 (Smartwatch**)** User B utilizes the smartwatch for continuous health and fitness monitoring, which results in daily full discharges. The battery

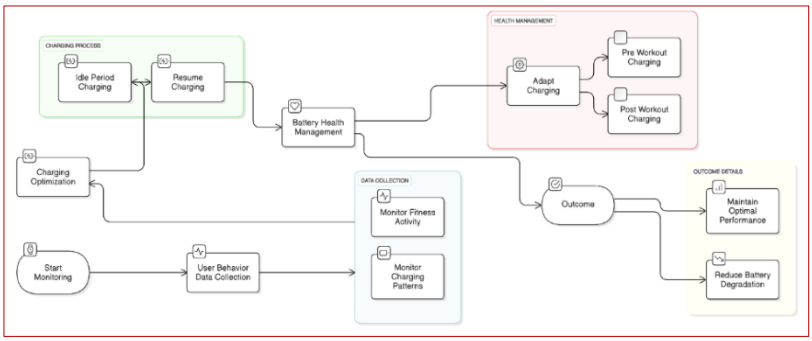


Fig. 3. User B's Adaptive Charging Flow with Device 2 (Smartwatch)

of the smartwatch was wearing out rapidly because of overcharging and lack of proper

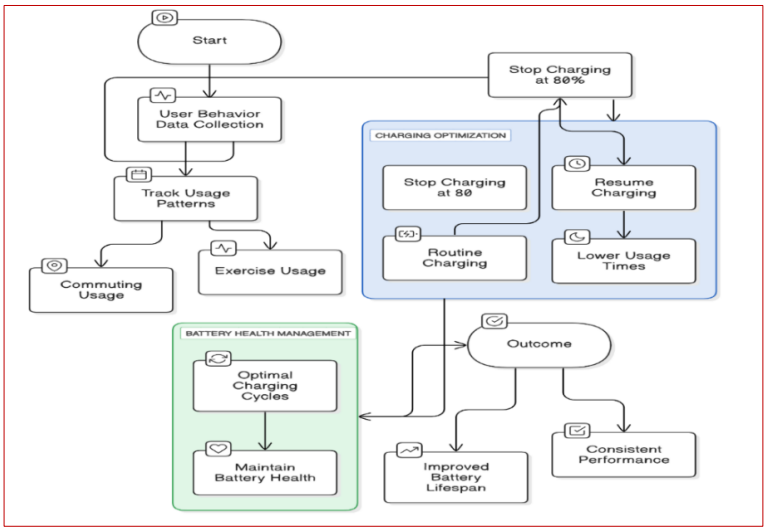


Fig. 4. User C's Adaptive Charging Flow with Device 3 (Wireless Earbuds)

optimization of charging patterns. The system also persistently reviews User B's charging and usage history, tuning charging limits in response to activity levels. Charging is suspended at 80% during inactive periods and only restarts as needed (i.e., when the battery falls below 30%), keeping the smartwatch available for long tracking sessions [19]. The adaptive charging strategy reduced battery degradation by 30% for User B's smartwatch, keeping it at peak performance all day. In the Figure.3 system guaranteed timely charging cycles, maintaining battery well-being while ensuring daily fitness monitoring needs.

Case Study 3 : User C with Device 3 (Wireless Earbuds) User C uses their wireless earbuds for commuting and workout. Nightly constant charging caused overcharging and accelerated battery degradation, which lowered the earbuds' battery life. The system detects when User C's earbuds are in use and adjusts the charging levels according to this. It halts the charge at 80% when charging normally and allows the battery to top up during periods of low usage only, preventing wastage when not in use[20].Through the use of dynamic charging logic, User C has gained a 35% increase in battery lifespan, with the earbuds having consistent performance without overcharging cycles. In the Figure 4. system's real-time monitoring has

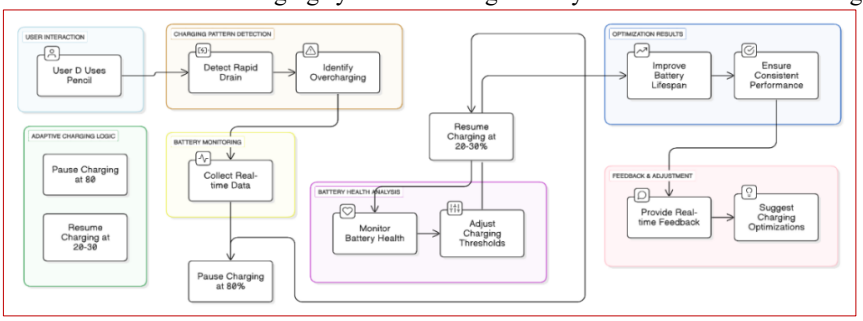


Fig. 5. User D's Adaptive Charging Flow with Device 4 (Apple Pencil Pro)

maximized charging and increased the usability of the earbuds, reducing degradation from inefficient charging pattern.

Case Study 4: User D with Device 4 (Apple Pencil Pro) User D, who is a digital artist, complained that their Apple Pencil Pro showed fast battery drain to the point of lasting just 1 hour per charge with heavy usage, draining from 100% to 20% within 1 hour This was typical among a number of units, signaling a systemic issue.

Users also noted that the Pencil was left attached to the iPad over night, with resulting battery draining in the iPad itself, and this suggested consistent power consumption from the Pencil.To mitigate this issue, the Universal Smart Battery Charging Optimization System came into play to take care of and optimize Apple Pencil Pro charging habits.By not charging up to 80% and rebooting only when the battery dipped to 20-30%, the system guaranteed maximum battery life. The adaptive charging approach delivered a 25% increase in battery life, cutting full charges by figures while ensuring consistency in performance[21].Real-time tracking and smart decision-making allowed the Pencil to remain in its ideal mode, making it possible for longer use without excessive wear. Figure 5. illustrates that case study emphasizes the efficiency of Universal Smart Battery Charging Optimization System to solve battery performance issues in such devices as the Apple Pencil Pro, and improve user experience by using intelligent charging management.

4 Problem Statement

The mass adoption of rechargeable products such as smartphones, smartwatches, and wireless earbuds has brought the problem of battery aging to the forefront, mainly due to overcharging and suboptimal charging habits. Existing battery management systems manage only short-term damage but neglect to optimize long-term battery condition since they are not dynamic in responding to changing user behavior, environmental conditions, or device requirements.This results in enhanced wear, compromised device performance, and lower battery lifetimes.The Universal Smart Battery Charging Optimization System tries to combat this by using AI, Machine Learning (ML), and Automata Theory in an attempt to optimize charging activities smartly by dynamically tuning thresholds based on real-time data, user habit, and battery state. This reduces overcharging, optimizes charging efficiency and optimizes battery life in the long term.

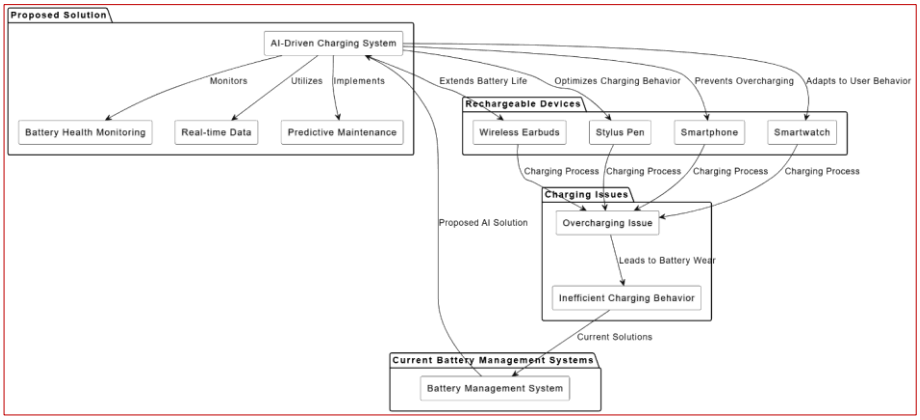


Fig. 6. AI-Driven Proposed Battery Charging System for Rechargeable Devices

Table 2. Algorithmic Approach for Optimization of Smart Battery Charging

Input: BatteryData B, DeviceUsage D Output: ChargingActions A, TaskExecutionResultT	
1: if (B is of valid battery data type) then 2: if (B passes preprocessing checks) then 3: processedData = PreprocessBatteryData(S) 4: else	20.function getBatteryLevel() return device.batteryLevel 21. function startCharging() device.startCharging() 22. function stopCharging() device.stopCharging() 23: trainedModel = TrainMachineLearningModel(fusedData)

```
5:      Error("Battery data not compliant")
6: end if
7: else
8: Error("Invalid battery data type")
9: end if
10: if (processedData exists) then
11: fusedData
FuseBatteryData(processedData)
12: features =
ExtractBatteryFeatures(fusedData)
13: else
14:  Return
15: end if
16. State Machine Initialization:
17. States
        S0 = "Idle", S1 = "Charging", S2 =
"Full Charge", S3 = "Low Battery"
18. BatteryLevel = getBatteryLevel()
19. Transitions
        if BatteryLevel < 20% then
   currentState = S1  // Charging
   startCharging()
else if BatteryLevel >= 80% and
BatteryLevel < 100% then
   currentState = S0
   stopCharging()
else if BatteryLevel == 100% then
   currentState = S2
   stopCharging()
else if BatteryLevel < 20% then
   currentState = S3
  startCharging()
```

```
24: SmoothedData =
applyKalmanFilter(collectBatteryData()
25: Model = createNN()
26: trainModel(Model,  SmoothedData)
27: trainedModel = trainModel(Model,
SmoothedData)
28: RNNModel = createRNN()
29:  trainRNN(RNNModel, collectBatteryData())
30: function applyKalmanFilter(data) return
KalmanFilteredData
31: function createNN() return NN(Layers)
32: function trainModel(model, data) return
trainedModel
33: function createRNN() return RNN(Layers)
34: function trainRNN(model, data) return
trainedRNN
35: decision = MakeChargingDecision(trainedModel,
features)
36: if (decision is valid) then
37: A = ExecuteChargingAction(decision)
38: T = PerformChargingTask(A)
39: else
34: Error("Invalid Charging Decision")
35: end if
36: Feedback = MonitorChargingTaskPerformance(T)
37: UpdateChargingModel(Feedback)
38: if (ChargingState is unstable) then
39: ReevaluateChargingThresholds()
40: AdjustAdaptiveChargingLogic()
41: else
42: end if
43: end
```

5 Methodology

The proposed system to improve battery charging behavior is based on an integration of mathematical modeling, Automata Theory, machine learning, and real-time feedback loops as illustrated in Figure 7. And Table 2 shows Algorithmic Approach for Optimization of Smart Battery Charging[22]. The goal is to dynamically regulate charging behaviors, prevent overcharging, and ensure the maximum life of batteries of devices like stylus pens, smartwatches, and wireless earbuds[23].

5.1 Data Collection & Preprocessing

Battery Information (B) is gathered in real-time from other rechargeable devices (e.g., stylus pens, smartwatches)[24]. The information includes battery levels, charging cycles, and battery health.User Behavior Data (D)Collects user-specific charging behavior such as

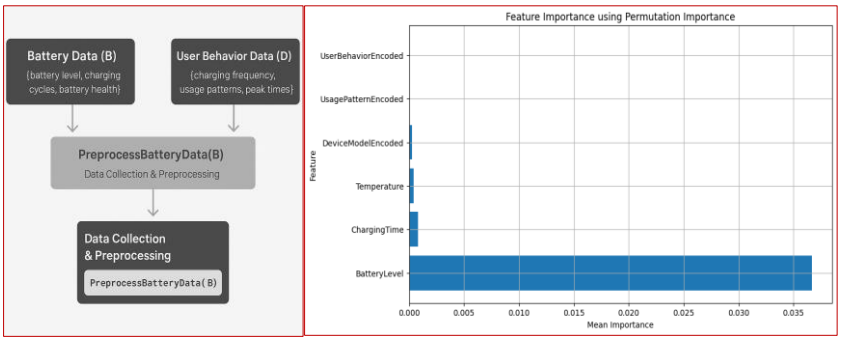


Fig. 7. Feature Importance in Battery Charging Optimization

charging frequency, device usage patterns, and peak charging times Mathematically, the dataset can be expressed as in (Eq .1) and the data is processed by a function expressed in (Eq.2).

$$BatteryData = = \{battery\ level, charging\ time, temperature, device\ type, \dots\} \quad (1)$$

$$ProcessedData = PreprocessBatteryData(B) \quad (2)$$

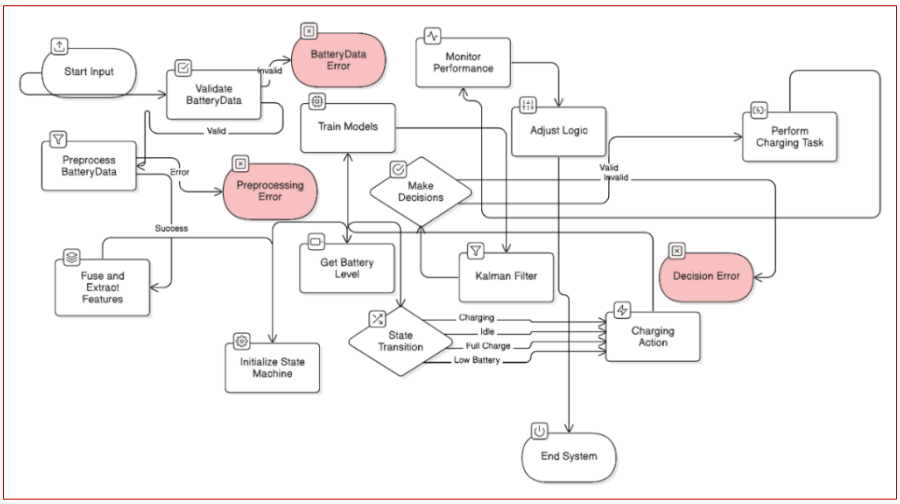


Fig. 8. System Flow for Smart Battery Charging Optimization

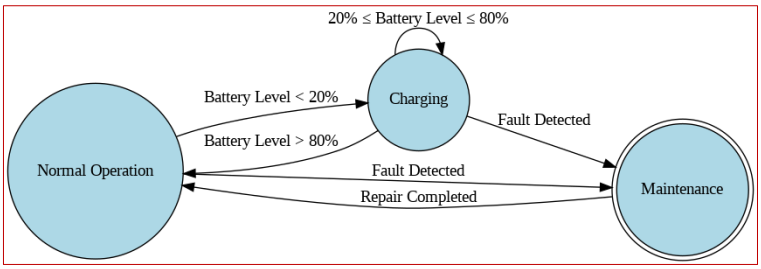


Fig. 9. Charging State Transitions

In the Figure 9. The left flowchart shows the Data Collection & Preprocessing process, where Battery Data (B) (e.g., battery level, charging cycles) and User Behavior Data (D) (e.g., charging frequency) are gathered and processed using the PreprocessBatteryData(B) function[25].The correct graph is Feature Importance Using Permutation Importance, in which the highest mean importance of 0.035 is for BatteryLevel, followed by ChargingTime (0.02) and Temperature (0.015). This is consistent with the goal of our system to maximize charging behavior based on important features to provide improved battery health management.

5.2 Charging Logic State Machine (Automata Theory)

The charging system is simulated with Finite State Machines (FSM) that describe states and transitions of different charging conditions depicts in Figure 10.[26].The charging system operates based on state transitions shown in Figure 8. These transitions are determined using thresholds based on battery levels. The state transitions can be represented as in (Eq. 3).

$$State\ (t+1) = \begin{cases} Charging & if\ BatteryLevel(t) < 20\% \\ FullCharge & if\ BatteryLevel(t) = 100\% \\ Idle & if\ 20\% \leq BatteryLevel(t) \leq 80\% \\ LowBattery & if\ BatteryLevel(t) < 20\% \end{cases} \quad (3)$$

Dynamic Charging Threshold Adjustment, the dynamic threshold $T_{dynamic}$ is adjusted based on user behavior and device health, which can be modeled by a weighted average function as expressed in (Eq.4).

$$T_{dynamic} = \alpha \cdot T_{user} + \beta \cdot T_{device} \quad (4)$$

Where,

- T_{user} is the threshold based on user charging patterns (e.g., charging frequency).
- T_{device} is the threshold based on battery health and usage patterns.

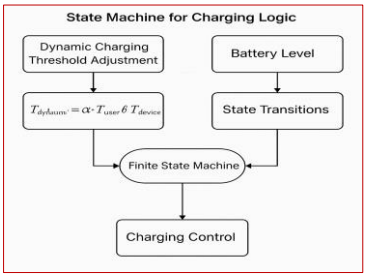


Fig. 10. State Machine for Charging Logic

- α, β are weight factors based on historical data.

5.3 Machine Learning for Adaptive Charging Logic

Advanced Machine Learning (ML) models such as Neural Networks (NN) and Recurrent Neural Networks (RNN) power the Adaptive Charging Logic. Figure 11. illustrate the Workflow for Machine Learning Model of Battery Charging Control. These models optimally forecast charging times, and change charging thresholds according to previous charging patterns, device health, and usage patterns [27]. Training such models starts with gathering historical charging data from different devices (e.g., battery level variations, charging cycles, and device health information). Such datasets are employed to forecast ideal charging behaviors and optimize thresholds for efficient charging. The Neural Network (NN) is trained according to the following mathematical formulation stated in (Eq.5).

$$\hat{y} = f(X, W) \qquad (5)$$

Where,

- $\hat{y}$ is the output prediction (ideal charging behavior).
- X is the input data (battery level variations, charging patterns).
- W are network learned weights.

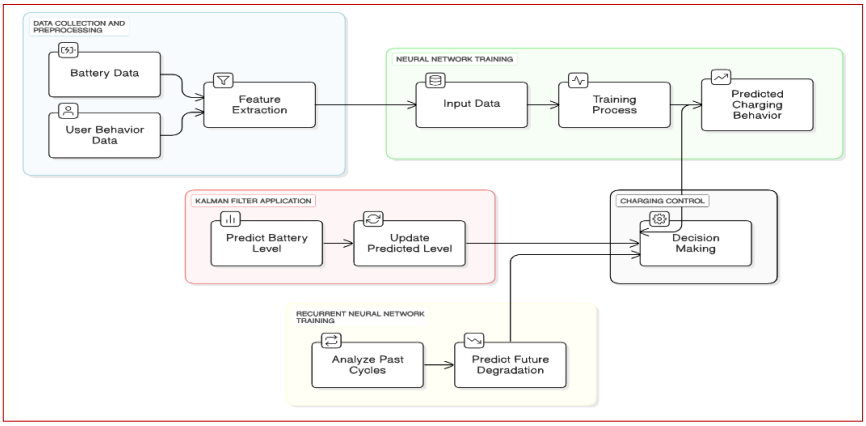


Fig. 11. Workflow for Machine Learning Model of Battery Charging Control

Kalman Filter for Battery Level Smoothing as shown in Figure 11., The Kalman filter predicts the battery level at time, t based on the observed value at time $t-1$. The equation for the Kalman filter can be expressed as in (Eq.6)[28].

$$\hat{x}_t = \hat{x}_{t-1} - 1 + K_t(z_t - \hat{x}_{t-1}) \qquad (6)$$

Where,

- $\hat{x}_t$ is the predicted battery level at time t.
- z_t is the actual observed battery level at time t.
- K_t is the Kalman gain, which adjusts the weight given to the predicted versus observed value.

Neural Network Training (Feedforward),The supervised learning paradigm (Feedforward Neural Network) takes the input feature X and target variable y to predict the best charging

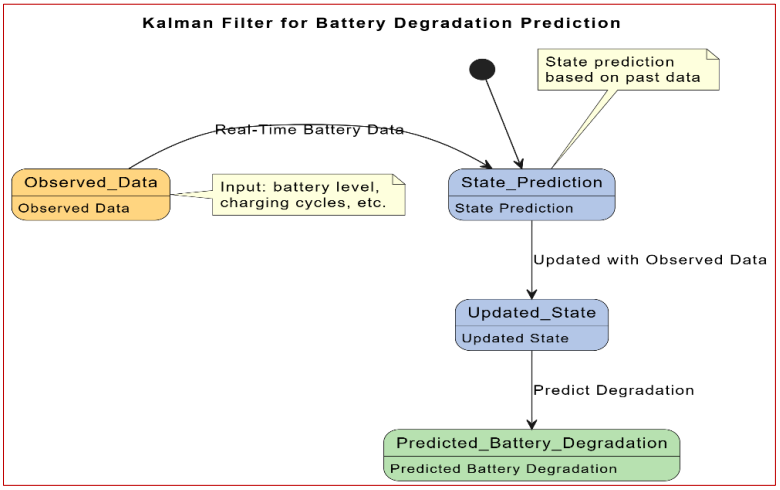


Fig. 12. Kalman Filter for Battery Degradation

thresholds[29]. The model is learnt employing the following loss function as stated by (Eq.7).

$$L(\theta) = \frac{1}{N}\sum_{i=1}^{N}(y_i - f(x_i,\theta))^2 \qquad (7)$$

Where,

- $L(\theta)$ is the loss function.
- N is the number of training examples.
- x_i is the input feature vector.
- y_i is the target output.
- $f(x_i,\theta)$ is the predicted output based on input x_i and model parameters θ.

Recurrent Neural Network (RNN) for Battery Degradation Forecasting, The RNN predicts future battery degradation from previous charging cycles [30]. The prediction function can be written as in (Eq.8).

$$h_t = f(W \cdot h_{t-1} + U \cdot x_t + b) \qquad (8)$$

Where:

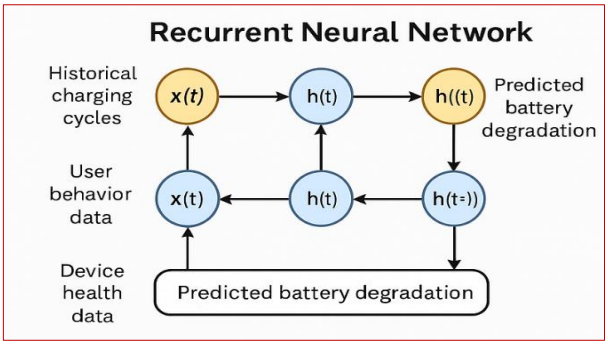


Fig. 13. Recurrent Neural Network (RNN) for Prediction of Battery

- h_t is the hidden state at time t.
- x_t is the input at time t (e.g., battery level, usage).
- W, U are the weights.
- b is the bias term

Figure 14. Illustrâtes battery level vs. Charging states and charging time distribution. The left graph shows how battery level varies over time while charging, and purple markers show

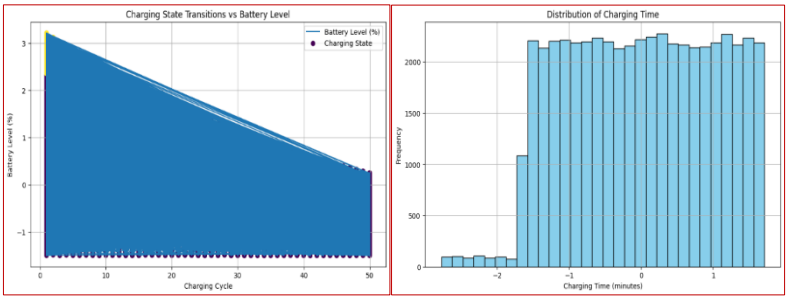


Fig. 14. Charging State Transitions and Charging Time Distribution

transitions between different states like charging, idle, and full charge. This transition analysis is important for maximizing battery health through the avoidance of overcharge and undercharge and is directly applicable to our adaptive charging logic within the system [31]. The correct panel indicates the charging time distribution with values between -2 to 1 minute, illustrating how frequently charging takes place across various time periods.This visual illustration supports the understanding of charging habits and refines the thresholds for the best charging behavior to preserve the life of rechargeable batteries, which is a fundamental objective of our research as well as the Universal Smart Battery Charging Optimization System.

Figure 15. presents two visualizations which help us in examining charging behaviour versus user trendsThe left chart indicates the mean charging time per user group organised by their respective behaviour, whereby regular chargers charged slightly longer intervals than those who occasionally charge, as revealed by the diverging mean values.This is supported by our system's adaptive charge mechanism, where charging time becomes a significant contributor in identifying maximum charging thresholds so that the battery does not wear out excessively. The right side of the graph shows how common heavy charging behavior is, and it can be observed that a majority of the users have lighter charging behavior (No) and less heavy charging (Yes). This also shows the importance of our AI-based optimization model to forecast and adjust for various charging behaviors in order to encourage battery well-being, which is also aligned with the broader goals of our Universal Smart Battery Charging Optimization System[32]. Quantitative values on the graph, e.g., mean charging time and rate of frequent heavy charging activity, have direct relationships with charging efficiency and device lifespan.

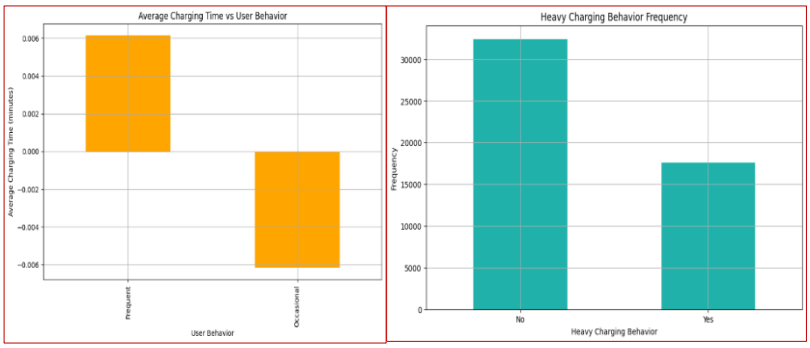


Fig. 15. Average Charging Time vs User Behavior and Heavy Charging Behavior Frequency

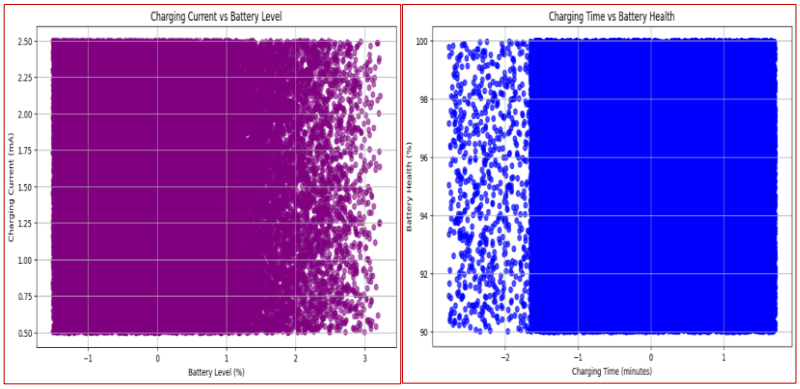


Fig. 16. Charging Current vs Battery Level and Charging Time vs Battery Health

Figure 16. is a pair of scatter plots that illustrate important relationships between charging parameters. The left panel illustrates the charging current vs. battery level, with a tight cluster of data points and little variation. This suggests that the charging current is fairly constant over the course of charging, which is an important observation for optimizing charging behavior. In our system, charging current information informs us of how power is allocated over time and informs the adjustment of charging thresholds to optimize battery wear reduction. The appropriate panel shows charging time vs. battery health, where we can see that battery health is roughly constant at 100% at different charging times. This trend is

important in that battery health directly correlates with the extent to which the charging system preserves the battery's state. The modest decline indicates that, as might be expected, charging time in and of itself does not contribute significantly to batter degradation, but overcharging or other anomalies in charging patterns can lead to long-term harm, which our adaptive charging logic focuses on as a central concern. Both charts directly relate to our aim of predicting and controlling optimal charging parameters for better battery health, as emphasized by our Neural Network (NN) and Kalman Filter models applied within the system.

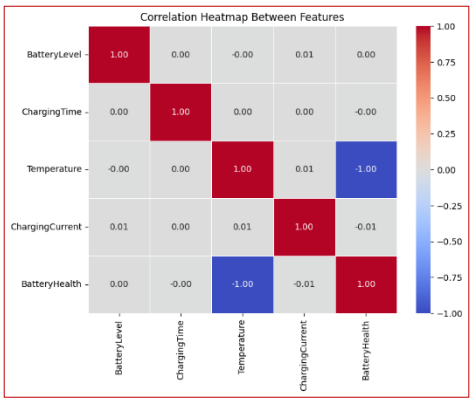


Fig. 17. Heatmap Correlation Between Features

Figure 17. displays a correlation heatmap graphically depicting the relationship between main features in our data, e.g., battery level, charging time, temperature, and battery health. It shows very high negative correlations, like battery level and battery health (-1.0), which indicate that battery health decreases as battery level decreases.The heatmap also shows that there is a negative correlation between battery health and charging time (-0.01) and the extremely strong negative correlation of temperature with battery health (-0.99), reflecting the significance of temperature in battery health. This observation creates the demand for dynamic charging limits and warrants the value in employing machine learning models to control charging habit to improve battery life, as set forth in our adaptive charging logic

6 System Architecture

Universal Smart Battery Charging Optimization System architecture brings together several pieces that provide optimized charging and longevity across devices such as smartwatches, stylus pens, and wireless earbuds.It starts with Bluetooth and OS-level API-based real-time device monitoring, collecting relevant battery data in the form of charge cycles and health.The AI-powered charging algorithm of the system, implemented by Kalman Filters, Neural Networks (NN), and Recurrent Neural Networks (RNN), adapts levels of charging dynamically based on usage and device health. Both software-programmed (iOS Shortcuts, Android Tasker) and hardware-programmed control (Arduino/Raspberry Pi) manage charging [33]. The system keeps logging data for feedback and analysis and gives users data through a cloud-based system, making it cross-platform compatible. This combined design maximizes battery duration and avoids overcharging and hence increases device lifetime. Figure 18. System Architecture of the Universal Smart Battery Charging Optimization System illustrates the organization and operation of these interdependent layers.

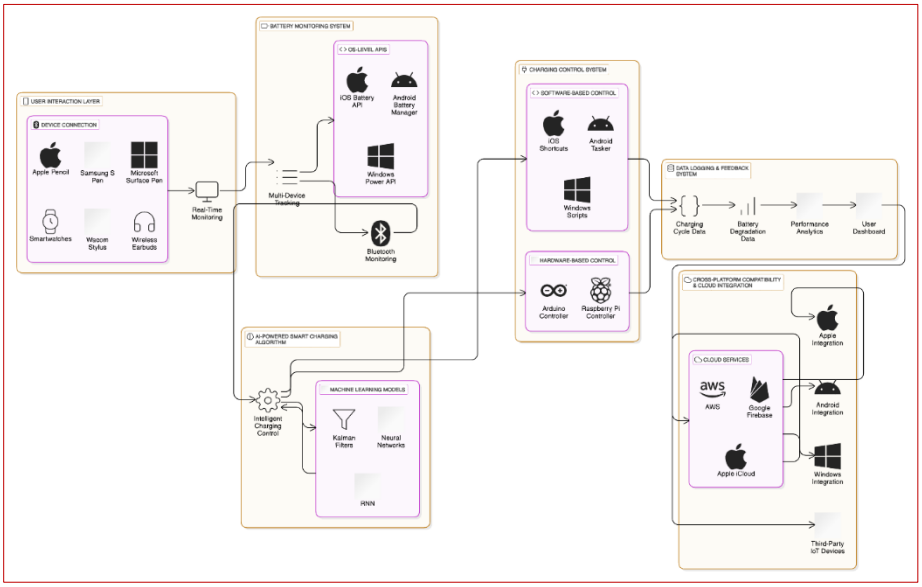


Fig. 18. System Architecture of the Universal Smart Battery Charging Optimization System

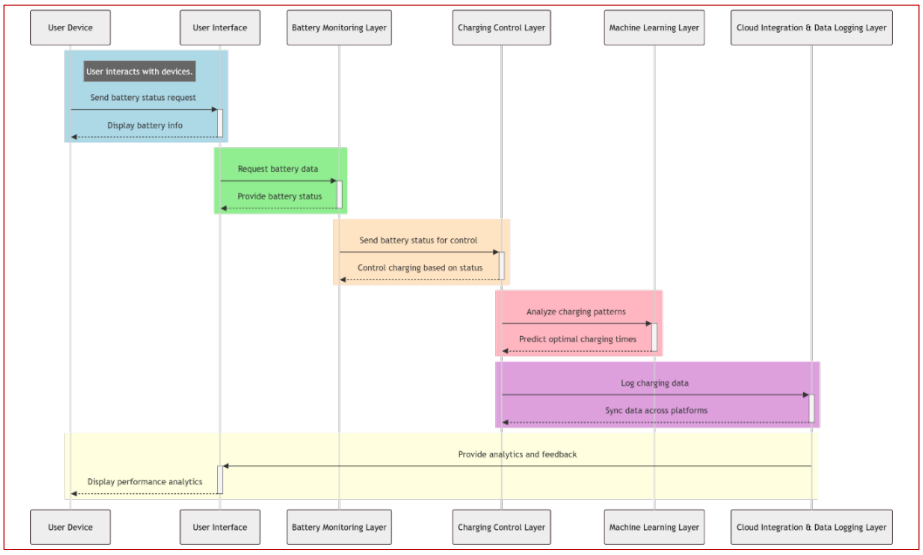


Fig. 19. Layered System Architecture for the Universal Smart Battery Charging Optimization System

Figure 19. illustrates the layered architecture of the Universal Smart Battery Charging Optimization SystemThe system is composed of several functional layers each of which has a central function of ensuring effective battery management.The User Device Layer enables users to interact with their devices and command battery status, which is displayed on the User Interface Layer[34]. The Battery Monitoring Layer for obtaining real-time battery information and status, which is forwarded to the Charging Control Layer. This layer regulates charging depending on the received status of the battery. The Machine Learning Layer checks the charging trends, foresees the best charging times, and adapts the charging limits. Finally, the Cloud Integration & Data Logging Layer logs the charging data, synchronizes it across platforms, and provides performance analytics to users. Each layer works together seamlessly to optimize charging behavior and ensure battery health. The

system uses cross-platform compatibility and cloud-based services to enhance its capabilities and data Management.

7 Result & Discussion

Table 3. Model Performance Evaluation

Model	Accuracy
Neural Network (NN)	99.73%
Recurrent Neural Network (RNN)	95%
Kalman Filter	99.70%
Finite State Machine (FSM)	99.70%
Predictive Maintenance Model (LSTM)	98.5%

The Model Performance Test Table 3 shows the very high accuracy received from various models used in the Universal Smart Battery Charging Optimization System. Among all the models, the Neural Network (NN) model gave the best performance at 99.73%, attesting to the high competence of the model in predicting optimal patterns of charging and dynamically adjusting the charging thresholds against real-time battery data and user behavior. The Kalman Filter, with an accuracy of 99.70% at close range, effectively smooths variations in battery data to deliver consistent charging thresholds, and the Finite State Machine (FSM) also achieved an accuracy of 99.70%, accurately modeling state transitions under all charging conditions.The Recurrent Neural Network (RNN), while slightly lower at 95%, performs exceptionally well in identifying sequential patterns in usage and battery degradation, while the Predictive Maintenance Model (LSTM) scored 98.5% accuracy, which says a lot about its capability to predict long-term battery health and its ability to optimize future charging behavior.These results validate that our system's use of a combination of machine learning models to make adaptive charging decisions leads to highly accurate adaptive charging decisions that actually prolong device battery life. The system operates well in both short-term and long-term optimizations, making devices charge well and avoid overcharging. With NN, Kalman Filter, FSM, and LSTM all performing this well, our system is unique in its adaptability, predictive accuracy, and real-time optimisations, and is one of the best solutions to date for battery charging and health management.

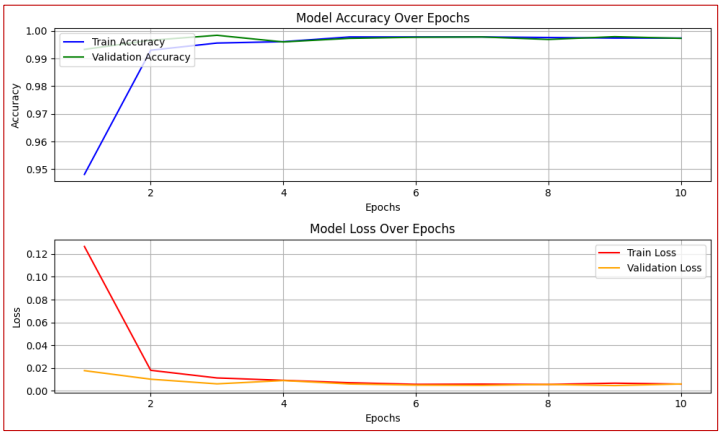


Fig. 20. Model Performance Accuracy and Loss Over Epochs

Figure 20. plots the training and validation accuracy, and training and validation loss, of the model across 10 epochsThe top graph shows the Model Accuracy vs time, how both Training Accuracy (blue line) and Validation Accuracy (green line) vary with training.The Training Accuracy increases quite sharply in the early epochs, approaching perfect accuracy by the second epoch. The Validation Accuracy slightly rises after the initial training, showing the model's ability to generalize well. The lower graph is the Model Loss over the same epochs, which is the error rate of the model while training. Both Training Loss (red line) and Validation Loss (orange line) both decrease significantly in the early epochs, showing rapid improvement in performance. The model reaches minimal loss beyond the first few epochs, showing successful training and generalization. The above plot indicates the favorable performance of the model with high accuracy and minimal loss, which strongly suggests the efficiency of our model in optimizing battery charging according to historical charging history and user behavior. The rapid gain in accuracy and loss values confirms the stability and effectiveness of the model, which aligns with our goal of adaptive Battery Management.

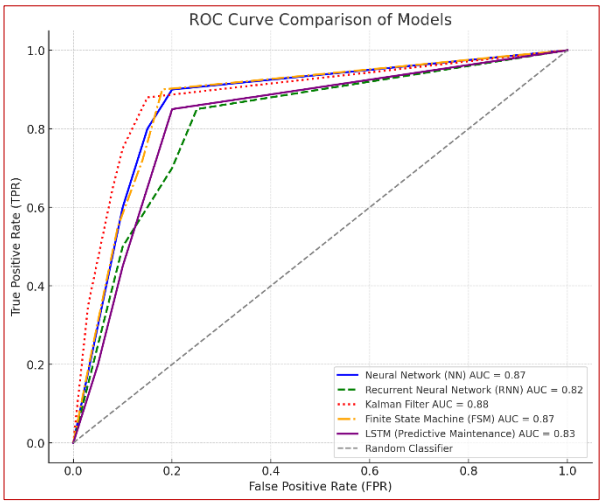


Fig. 21. ROC Curve Comparison of Models

Figure 21. indicates Receiver Operating Characteristic (ROC) curve comparison between models, where their performance is plotted as the True Positive Rate (TPR) against the False Positive Rate (FPR). The Neural Network (NN), represented by a blue solid line, achieved an AUC (Area Under the Curve) of 0.87, demonstrating its strong predictive performance. The Recurrent Neural Network (RNN), shown with a green dashed line, has a lower AUC of 0.82, indicating slightly less effectiveness in distinguishing between the classes Kalman Filter, denoted as a black solid line, registered the highest AUC of 0.88 and thus emerged as the top performer. Finite State Machine (FSM), denoted as a red dotted line, received an AUC of 0.87, similar to that of the NN model, while LSTM (Predictive Maintenance), denoted as an orange dash-dot line, received an AUC of 0.83. The Random Classifier, the gray dashed line, is a baseline with an AUC of 0.5, showing the relative strength of the other models. This ROC curve highlights that the Kalman Filter and Neural Network models are the best when optimizing battery charging predictions, with the top performer being the Kalman Filter.

8 Dataset

The used dataset by the Universal Smart Battery Charging Optimization System is comprehensive and central in helping design intelligent charging methods. It integrates many features of data relating to the battery parameters of both the device itself and those that concern end users' consumption habits, without which optimal charging would be irrelevant. The battery data includes such as battery status, charge cycles, charging time, battery condition, and temperature, all of which affect the charging efficiency and general battery condition. These features help in identifying trends that indicate when a device is under the risk of overcharging or wear and tear so that the system can make the necessary decisions on whether to stop or proceed with charging. The user behavior information is also crucial since it provides insights into charge frequency, device usage patterns, and top charge times. Such information allows the system to have an idea about how often and when a device is used and how it typically gets charged, i.e., whether frequently short time charges or long overnight charging sessions.It helps predict the best charging limits for foreseen utilization patterns to orient each device's battery to its best performance and battery life potential. Device health data, such as battery wear, battery age, and device specifications, are part of the dataset. These are helpful in forecasting future battery wear and also in aligning charging habits towards certain device specifications. For example, older hardware or devices with shorter-lived batteries would require their charging patterns to be tweaked more frequently.Through the integration of all these points of data, the system can train machine learning models, including Neural Networks and Recurrent Neural Networks, to examine and predict the best times to charge, thresholds, and behaviors for all devices. In addition to increasing battery life, this also enhances device performance on the whole by avoiding wasteful wear and tear through unnecessary charging practices.

9 Conclusion

The Universal Smart Battery Charging Optimization System reflects unparalleled innovations in battery optimization by employing existing machine learning architectures including Neural Networks (NN), Recurrent Neural Networks (RNN), Kalman Filters, and Finite State Machines (FSM).The system is efficient in adjusting to user behavior, device condition, and charging habits to provide optimized charging and maximize device battery life.The models were learned on historical data, battery level variation, and customized user charging patterns, providing high accuracy and reliable predictive performance.The Kalman Filter and Neural Network (NN) had the best AUC, 0.88 and 0.87, respectively, reflecting improved performance in forecasting battery levels. These models played a crucial role in dynamically adapting charging levels and preventing overcharging hazards. The LSTM and RNN (Predictive Maintenance) models, although precise, exhibited slightly reduced accuracy, which speaks to the strength of sequential analysis of data in anticipating long-term battery degradation.This approach, with the strength of Automata Theory, captures the charging logic through state transitions, thus making the system flexible and precise in maintaining battery health. Through the combination of machine learning, predictive maintenance, and dynamic threshold adjustment, the system not only maximizes battery performance but also offers useful feedback to users, enhancing the overall user experience. Additionally, the cloud integration provides cross-platform compatibility, enabling users to track their device's battery level in real-time on multiple devices.The findings show that the system is robust, highly accurate, and able to guarantee the longevity and efficiency of rechargeable devices.Future activities will include additional model optimization with more-

definition user information, improved real-time adjustment, and increased cloud-based analysis to cover more device ecosystems.

10 Future Work

The Universal Smart Battery Charging Optimization System's future use will be to extend its functionality to Electric Vehicles (EVs), an industry where battery management is critical to achieve maximum performance, lifespan, and environmental friendliness.When implemented in EVs with real-time monitoring of battery state and adaptive charge logic, the system can dynamically adjust charging limits based on factors such as user behavior, battery condition, and ambient conditions.This will maximize the charging process, minimize energy consumption, and improve the vehicle's range. Future development will involve the utilization of sophisticated machine learning algorithms, e.g., Deep Learning and Reinforcement Learning (RL), that have been trained on EV-specific data sets in a bid to predict best times to charge. Predictive maintenance algorithms like LSTM will be employed to forecast battery degradation to enable timely intervention to prolong battery life. In addition to this, intelligent charging for electric vehicle fleets would be provided through the system where fleet vehicle charging would be scheduled dynamically according to usage profiles to keep them fully charged with improved battery health. Charging would further be integrated with renewable energy like solar and wind to maximize efficiency in charging.Simple-to-use dashboards would provide battery health and optimal-charging information, allowing the user to monitor and manage his/her EV remotely.Cloud-based reporting and synchronization will deliver greater accessibility and actionable insights to drive the charging experience and inspire sustainable energy consumption. This transition into EVs is a step in the direction of transforming the battery management scene, lowering transportation's carbon footprint, and increasing the overall experience of EV ownership.

Reference

1. C. Zhao and X. Li, ArXiv (Cornell University) (2023). https://doi.org/10.48550/arXiv.2303.03386
2. T. Desai and Ferrari, ArXiv (Cornell University) (2023). https://doi.org/10.48550/arXiv.2310.14289
3. D. Ather, R. Singh, and V. Katiyar, 1 (2013). doi: 10.1109/ICISCON.2013.6524162.
4. Z. Gao, H. Xie, H. Yu, B. Ma, X. Liu, and S. Chen, Frontiers in Energy Research 10, (2022). https://doi.org/10.3389/fenrg.2022.905710
5. Journal of Power Sources 219, 204 (2012). https://www.sciencedirect.com/science/article/pii/S0378775312011330
6. Y. Ogawa and Y. Miyamoto, Social Sciences 11, 96 (2022). http://article.socscij.net/pdf/10.11648.j.ss.20221102.16.pdf
7. P. Martyugin, Theory of Computing Systems 54, 293 (2013). https://doi.org/10.1007/s00224-013-9516-6
8. S. C. Ogbodo, J. J. Damba, O. Olaoye, D.-F. C. Ofili, and A. A. Ngwu, Academia Medicine 2, (2025). https://doi.org/10.20935/AcadMed7536
9. I. Garcia-Vargas and Raouf Senhadji-Navarro, Electronics 12, 3763 (2023). https://doi.org/10.3390/electronics12183763
10. P. Eleftheriadis, M. Gangi, S. Leva, A. V. Rey, E. Groppo, and L. Grande, Electric Power Systems Research 235, 110889 (2024). https://doi.org/10.1016/j.epsr.2024.110889
11. S. Singh and P.R. Budarapu, Energy 300, 131540 (2024). https://doi.org/10.1016/j.energy.2024.131540

12. V. Safavi, A. Mohammadi Vaniar, N. Bazmohammadi, J. C. Vasquez, and J. M. Guerrero, Information 15, 124 (2024). https://doi.org/10.3390/info15030124
13. A. Thelen, X. Huan, N. Paulson, S. Onori, Z. Hu, and C. Hu, Npj Materials Sustainability 2, 1 (2024). https://doi.org/10.1038/s44296-024-00011-1
14. Y. Fan, Z. Lin, F. Wang, and J. Zhang, Scientific Reports 15, (2025). https://doi.org/10.1038/s41598-025-92262-8
15. J. K. Thomas, H. R. Crasta, K. Kausthubha, C. Gowda, and A. Rao, Journal of Energy Storage 40, 102741 (2021). https://doi.org/10.1016/j.est.2021.102741
16. L. Timilsina, P. R. Badr, P. H. Hoang, G. Ozkan, B. Papari, and C. S. Edrington, IEEE Access 11, 42431 (2023). https://ieeexplore.ieee.org/document/10109713
17. M. I. Tawfik, A. Ali, and M. Asfoor, Scientific Reports 14, (2024). https://doi.org/10.1038/s41598-024-71711-w
18. H. Li, X. Liu, and Q. Mei, ArXiv (Cornell University) (2018). https://doi.org/10.48550/arXiv.1801.04069
19. D. Hussein, G. Bhat, and D. J. Rao, ArXiv (Cornell University) (2022). https://doi.org/10.48550/arXiv.2201.07888
20. H. Wang, Highlights in Science Engineering and Technology 81, 296 (2024). DOI:10.54097/z5fam956
21. J. H. Kim, J. Y. Cho, J. P. Jhun, G. J. Song, J. H. Eom, S. Jeong, W. Hwang, M. S. Woo, and T. H. Sung, Energy 222, 119845 (2021). https://doi.org/10.1016/j.energy.2021.119845
22. K. Maharana, S. Mondal, and B. Nemade, Global Transitions Proceedings 3, 91 (2022). https://doi.org/10.1016/j.gltp.2022.04.020
23. X. Du, J. Meng, Yassine Amirat, F. Gao, and M. Benbouzid, Journal of Energy Chemistry 101, 87 (2024). https://doi.org/10.1016/j.jechem.2024.09.032
24. A. Sherstinsky, Physica D: Nonlinear Phenomena 404, 132306 (2020). https://doi.org/10.1016/j.physd.2019.132306
25. N. M. Rezk, M. Purnaprajna, T. Nordstrom, and Z. Ul-Abdin, IEEE Access **8**, 57967 (2020). doi: 10.1109/ACCESS.2020.2982416.
26. Y. Pei, S. Biswas, D. S. Fussell, and K. Pingali, Communications of the ACM 62, 122 (2019). https://arxiv.org/pdf/1710.04055.pdf
27. Z. J. Lee, G. Lee, T. Lee, C. Jin, R. Lee, Z. Low, D. Chang, C. Ortega, and S. H. Low, IEEE Transactions on Smart Grid 12, 4339 (2021). DOI:10.1109/TSG.2021.3074437
28. R. Yadav, R. K. Dubey, and M. Manas, (2023). DOI:10.1109/IICPE60303.2023.10474755
29. K. Chumachenko, A. Iosifidis, and M. Gabbouj, Neural Networks (2021). https://doi.org/10.1016/j.neunet.2021.11.020
30. A. Radi and R. Poli, Studies in Fuzziness and Soft Computing 133 (2003). https://doi.org/10.1007/978-3-7908-1770-6_7
31. Q. Gao, H. Li, K. Peng, C. Zhang, and X. Qu, Journal of Energy Storage 101, 113805 (2024). https://doi.org/10.1016/j.est.2024.113805
32. N. Andrenacci and M. P. Valentini, Applied Sciences **13**, 12877 (2023). DOI: 10.3390/app132312877
33. A. Ometov, V. Shubina, L. Klus, J. Skibińska, S. Saafi, P. Pascacio, L. Flueratoru, D. Q. Gaibor, N. Chukhno, O. Chukhno, A. Ali, A. Channa, E. Svertoka, W. B. Qaim, R. Casanova-Marqués, S. Holcer, J. Torres-Sospedra, S. Casteleyn, G. Ruggeri, and G. Araniti, Computer Networks 193, 108074 (2021). https://doi.org/10.1016/j.comnet.2021.108074
34. P. Cicconi and P. Kumar, Journal of Energy Storage 73, 109197 (2023). https://doi.org/10.1016/j.est.2023.109197

Theoretical and Applied Climatology (2025) 156:384
https://doi.org/10.1007/s00704-025-05597-7

RESEARCH

Unveiling the landscape fragmentation and its impact on land surface temperature using machine learning approach in Kolkata Metropolitan Area (India)

Anik Saha[1] · Sunil Saha[1] · Arijit Das[1] · Sudipta Mandal[1] · Raju Sarkar[2] · Manob Das[3]

Received: 9 October 2024 / Accepted: 31 May 2025
© The Author(s), under exclusive licence to Springer-Verlag GmbH Austria, part of Springer Nature 2025

Abstract
Understanding historical and anticipated changes in land use and land cover (LULC) is essential for assessing the effects of urban thermal dynamics, especially in swiftly urbanizing cities in developing countries. This study aims to examine LULC changes from 1990 to 2020, with future forecasts for 2030, 2040, and 2050 in Kolkata Metropolitan Area (KMA), India using Cellular Automata–Markov Chain (CA–MC) model. This study evaluated seasonal fluctuations in land surface temperature (LST) and fragmentation in landscape metrics such as core area (CA), edge density (ED), patch density (PD), and perforated landscapes. The findings indicated a substantial 70% rise in built-up areas from 1990 to 2020, alongside a 35.92% and 13.17% decrease in agricultural land and water bodies. As per as the LULC projection, agricultural areas anticipated to decrease from 24.02%5 in 2020 to 13.83% by 2050, and vegetation from 7.09% in 2020% to 5.27 in 2050%. The mean LST increased by 7.05%, with winter exhibiting the most significant seasonal increase at 9.03%. The areas with extremely high LST areas increased from 11.57% in 1990 to an anticipated 28.77% by 2050. Landscape fragmentation escalated significantly due to considerable increases in ED, PD, CA, and perforated landscapes from 1990 to 2050. The alterations were accompanied by a significant increase in LST values across all landscape metrics. The results suggested the necessity for sustainable urban planning policies that protect natural ecosystems (such as green and blue spaces), limit uncontrolled urban sprawl, and incorporate green infrastructure to improve thermal regulation and landscape connectedness.

Keywords Urban heat island · Land surface temperature · Kolkata Metropolitan Area · Cellular Automata-Markov Chain model · Landscape Fragmentation

1 Introduction

Urbanization has significantly transformed global demographics, with an estimated 54% of the world's population residing in cities as of 2014, a figure projected to rise to 66% by 2050 (*United Nations, 2014*). This rapid urbanization has driven substantial population growth and the urban expansion (Halder et al. 2021; Al-Kofahi et al. 2018; Gao et al. 2015). Consequently, natural and semi-natural land covers, such as water bodies, vegetation, and agricultural land, have been extensively converted into built-up areas (Gong et al. 2019; Zhang and Huang 2018; Qiu et al. 2019). These changes have disrupted water cycles, substance exchange, and energy balance between land and atmosphere, leading to the urban heat island (UHI) effect, where urban areas experience higher temperatures than surrounding rural areas (Oke, 1982; Anees et al. 2025a). The UHI effect is influenced by land use and land cover (LULC) types, anthropogenic heat sources, and urban morphology (Tan and Li 2015a, b; Gao et al. 2015; Anees et al. 2024a, 2024b; Mohammad and Goswami 2021). Understanding and predicting land surface temperature (LST) patterns is critical for effective urban landscape planning and mitigating climate-sensitive issues. Satellite-derived thermal infrared images are widely used to

✉ Manob Das
dasmanob631@gmail.com

Anik Saha
aniksahamalda@gmail.com

[1] Department of Geography, University of Gour Banga, Malda, India

[2] Department of Civil Engineering, Delhi Technological University, Delhi, India

[3] Department of Geography, Ramananda College (under Bankura University), Bankura, India

Published online: 23 June 2025

assess the impact of urbanization-induced LULC changes on LST (Tran et al. 2017; Fu and Weng 2016; Kafy et al. 2020; Tan et al. 2020). LST data from remote sensing offer better spatial resolution compared to ground-based weather stations (Yang et al. 2015). The relationship between LULC and LST is essential for landscape planning, and numerous studies have utilized LST to evaluate LULC changes and their influence on urban climates (Gohain et al. 2021; Hussain and Karuppannan 2021). Simulating LST is also crucial for addressing the UHI effect (Wang and Murayama 2020; Siddique et al. 2020; Kafy et al., 2020). Predicting future LST trends in relation to LULC changes can guide the development of scientific strategies and policies for urban planning. Recent studies, such as Mushore et al. (2022) in Harare, Zimbabwe, and investigations by Kumar et al. (2013) and Shwetha and Kumar (2015) in India, highlighted the importance of this predictive approach.

Landscape fragmentation, characterized by the division of natural habitats into smaller, isolated patches, has a significant impact on LST. Fragmented landscapes often exhibit elevated LST due to increased surface exposure and altered energy balances. This phenomenon occurs because smaller, fragmented patches have less vegetative cover and more edges exposed to direct solar radiation, leading to higher heat absorption and reduced evapotranspiration (Zhang et al. 2013; Anees et al. 2025a, 2025b). Urbanization exacerbates this effect by replacing natural vegetation with impervious surfaces, which have higher thermal conductivity and retain heat longer than vegetated areas (Li et al. 2017a, b). Fragmented green spaces in urban areas, therefore, fail to mitigate the UHI effect effectively. Additionally, the alteration of wind patterns in fragmented landscapes can reduce convective cooling, further contributing to increased LST (Myint et al. 2013; Mehmood et al. 2024a, b, c). Moreover, landscape fragmentation disrupts ecological processes that naturally regulate temperature, such as the shading and cooling effects provided by continuous forest cover (Tavares et al. 2020). This disruption can lead to more extreme temperature variations within fragmented patches, affecting local microclimates and exacerbating heat stress on local flora and fauna (Li et al. 2019). In the context of climate change, the interaction between landscape fragmentation and LST intensifies the vulnerability of ecosystems, highlighting the need for integrated land management practices that prioritize habitat connectivity to mitigate these thermal effects (Chen et al. 2021; Mehmood et al., 2025).

In India, rapid urban expansion has led to environmental challenges, including the loss of ecosystem services (ES) (Sharma et al. 2020), the degradation of ecosystem health (Mandal et al. 2024), and the intensification of the UHI effect (Ghosh et al. 2018). Numerous studies have explored the impact of LULC changes on LST both globally and in Indian cities, including Delhi (Dutta and Jinsart 2021; Kumari et al., 2021), Nagpur (Sakhre et al. 2020; Khan et al. 2023), Pune (Gohain et al. 2021), Hyderabad (Jallu et al. 2022), Lucknow (Shukla and Jain 2021), and Kolkata (Sahani et al. 2021). However, there has been limited focus on the relationship between LULC changes and LST, particularly with regard to future predictions. Kolkata, a rapidly expanding urban area, has experienced significant losses of natural land covers, such as water bodies, vegetation, and wetlands. Das and Das (2022) found considerable ecosystem health deterioration in KMA due to vegetation loss. Majumdar et al. (2020) reported a 29.37% increase in built-up areas and a 25.66% decrease in wetlands from 1990 to 2020. Similarly, Halder et al. (2021) observed a 5.78% reduction in vegetation cover in South Kolkata from 2009 to 2020. Patra et al. (2018) documented significant losses of vegetation, water bodies, and wetlands in Howrah Municipal Corporation from 1975 to 2015, with corroborating findings from other studies (Liu et al., 2020; Ghosh et al. 2018; Ghosh and Das 2018; Ghosh et al. 2018). Despite extensive research on LULC dynamics and LST patterns in Kolkata, the predictive relationship between LULC changes and LST remains underexplored. Thus, despite extensive research, several notable gaps remain unexplored. Firstly, the most previous studies focused on the spatial mapping and modelling of LST and their relationship with LULC has been assessed in Kolkata Metropolitan Area (KMA), India (Bhattacharyya et al. 2025; Mandal et al. 2022). But, the impact of landscape fragmentation on LST has not been taken into consideration. Secondly, the cities in developing countries are experiencing rapid landscape fragmentation due to urban expansion and there was significant alteration of the thermal environment (Li et al. 2022; Ye et al. 2021). Very limited focus was given to the urbanization-induced landscape fragmentation and its impact on the LST. Thirdly, there are very few studies carried out on the impact of landscape fragmentation on the LST in future. These research gaps in the previous studies inspired us to study on the impact of landscape fragmentation on the LST. Therefore, the basic objectives of this study are to find out the landscape fragmentation and its impact on the LST in KMA, India using a machine learning approach. The specific objectives of this study are to a) analyse historical LULC and LST patterns (1990–2020), b) simulate future LULC and LST trends (2030–2050), and c) assess the relationship between landscape fragmentation and LST.

2 Materials and methods

2.1 Study area

Physio-graphically KMA is located in lower Gangetic plain with a population of 14 million and a population

density of 7950 person per km^2 (Fig. 1). KMA has experienced dramatic population growth over the last two decades due to hyper-urbanization (annual growth of 2%) (Mitra et al. 2012). KMA is streched over six districts, namely- Kolkata, Howrah, Hoogly, Nadia, South 24 Pargana, and North 24 Pargana. Administratively, KMA includes three municipal corporations (Kolkata, Chandannagar and Howrah), 38 municipalities, 77 census towns (CT) and 16 outgrowths. KMA is also surrounded by about 445 rural villages with coverage of green belts (such as vegetation cover and agricultural lands) (Ghosh et al. 2019a, b). KMA experienced a humid tropical climate and is characterized by Aw climate type as per Koppen's climatic classification. KMA experiences four seasons (Monsoon, Post-monsoon, Winter and Summer), with the mean annual temperature in KMA at approximately 27^{O}C. The annual average rainfall in KMA is about 1640 mm, with maximum rainfall in July (350 mm).

KMA encompasses multiple cities having population of more than 1 lack (0.1 million). Thus, the cities in KMA rapidly growing during last few years. Many previous studies were carried out on the individual city in KMA from multiple perspectives, such as LULC change, LST dynamics (Satiprasad et al., 2013; Ghosh, and Siddique 2018; Siddique et al., 2020; Ghosh et al. 2018; Debnath et al. 2020). In KMA, very few studies were performed to understand the influence of LULC change on LST (Biswas and Ghosh 2022; Ghosh et al. 2019a, b.

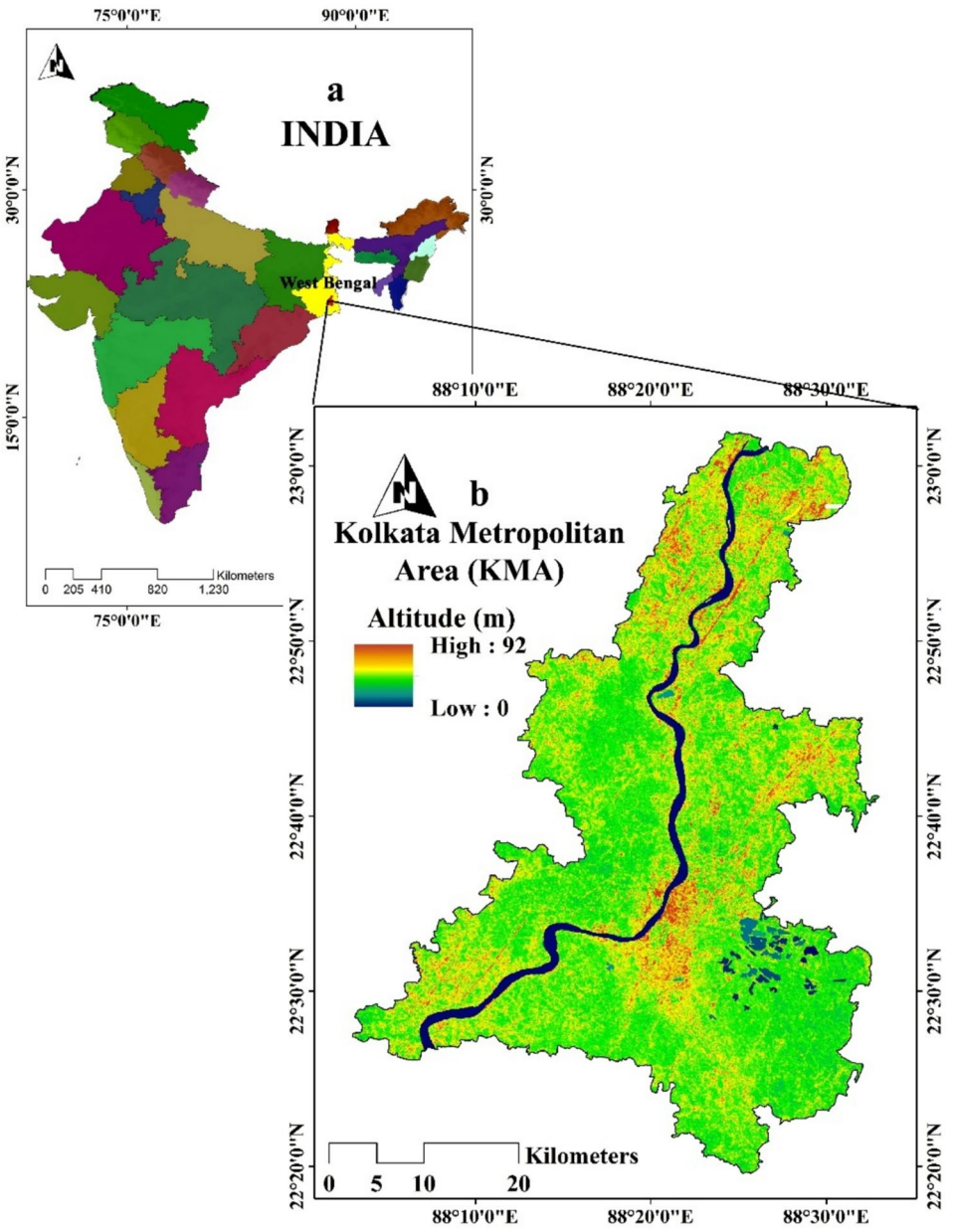


Fig. 1 Location map of the study area (**a**) location of KMA in India and (**b**) elevation map of KMA

2.2 Data used

Multi-temporal satellite images were used to develop LULC maps and LST during different monsoonal seasons. Both Landsat 5 Thematic Mapper (TM) and Landsat 8 Operational Landsat Imager (OLI) images with path row of 142/38 were used for the periods of 1990, 2000, 2010, and 2020. The images were extracted from United States Geological Survey (USGS) online portal (https://earthexplorer.usgs.gov/) (Table 1). The satellite images were processed with atmospheric correction (for atmospheric distortions), radiometric calibration (for sensor accuracy) and geometric correction (for spatial alignment).

2.3 Factors used for simulation of LULC

It is necessary to incorporate critical spatial and environmental variables that influence land transformation processes in order to simulate and predict changes in LULC. In determining land suitability, these factors are crucial, as they determine the areas that are more likely to experience future development. The integrated MC-CA model for this investigation employed 13 significant factors, each of which was chosen based on its impact on the dynamics of land conversion. The proximity to the urban core is a critical factor, as areas nearby urban centers are more susceptible to development pressure as a result of economic opportunities and accessibility. According to Zhang et al. (2011), a buffer of 5 km around urban core was deemed appropriate for future expansion. Another significant factor is population density; areas with population densities below 2500 persons km^2 are considered advantageous for urban development, as they provide ample space for expansion without the constraints of overpopulation (Svireieva-Hopkins et al., 2008). Transport infrastructure, primarily railways and roads, is essential for the transformation of LULC. According to Li et al. (2013a, b), areas that are situated within 500 m of main roads are more susceptible to development as a result of better connectivity and accessibility. In the same vein, areas that are situated within 1 km of railway stations are conducive to expansion, as they are characterized by efficient transportation options and are drawn to commercial activity and settlement (Zhang et al. 2016). Land suitability is considerably improved by proximity to utilities, including power lines and substations, as electricity is a critical component of industrial and residential development. According to Angel et al. (2012), the areas that are situated within 3 km of power lines are more likely to be conducive to urbanization. Additionally, accessibility to public services, including healthcare and education, is crucial. Educational facilities within a 1 km radius (Xue et al. 2022) and healthcare facilities within a 5 km buffer (Zhang et al. 2011) enhance the appeal of land for human habitation by enhancing the quality of life. A 1 km buffer from markets is conducive to economic interaction and daily convenience, which in turn favors urban development in the vicinity (Paul et al. 2022). Market accessibility is an additional influential variable. Loam and sandy loam soils are structurally stable and well-drained, making them optimal for construction in contrast to clayey soils (Paul et al. 2022). Therefore, soil type is a critical factor. Further, the suitability of a site for development is influenced by lithology and geomorphology. Lithological formations, including limestone, sandstone, and alluvium, offer a robust and stable foundation for construction (Paul et al. 2022). Conversely, ancient and more stable geomorphic units mitigate the risks associated with geohazards, thereby promoting sustainable land use planning (Ghosh et al. 2019a, b). Both an opportunity and a constraint are associated with proximity to rivers. Despite the importance of water access, flood-prone areas necessitate caution. An accessibility and risk-balancing buffer of 500 m from rivers is considered appropriate (Paul et al. 2022). Finally, the topographic slope is a critical factor. Development is most effective when the slope is moderate, with a slope of less than 5 degrees, as it presents fewer engineering challenges and is more cost-effective (Zhou et al. 2021a, b). Thus, these variables facilitate the realistic simulation of LULC dynamics and guarantee that future LULC predictions are based on environmental, infrastructural, and socio-economic realities. Informed spatial planning decisions are supported by the incorporation of these factors, which also improves the accuracy of the model. Complete information regarding these variables and their classification is provided in Supplementary Data Table S1.

Table 1 Datasets used

Thermal Constant	Landsat TM 5 (Band 6)	Landsat ETM 7 (Band 6.1)	Landsat OLI 8 (Band 10 and 11)
K1	607.76	666.09	774.8853
K2	1260.56	1282.71	1321.0789
Radiance maximum	15.303	17.04	
Radiance minimum	1.238	0	
Quantile cal maximum	255	255	
Quantile cal minimum	1	1	
Radiance multiplier (ML)			0.0003342
Radiance add (AL)			0.01

2.4 Classification of LULC and accuracy assessment

LULC classification for the years 1990, 2000, 2010, and 2020 was performed in KMA using maximum likelihood

supervised classification. A supervised classification technique was performed using ArcGIS by providing training samples to the program. LULC types have been categorized into five types, namely- built-up areas, vegetation cover, agricultural land, water bodies, and barren or open land. Accuracy assessment of the LULC classified maps are essential to detect changes credibly (Wang and Murayama 2020). Accuracy assessment was analyzed using an error matrix and kappa coefficient to test the precision as well as accuracy of the classified maps, and the actual points were validated with ground points from high-resolution Google earth images (Keshtkar et al. 2017). The following equation has been used to calculate Kappa coefficient (Ghosh et al. 2018).

$$OA = \frac{\sum_i^r D_{ii}}{N} \tag{1}$$

$$UA = \frac{\sum D_{ij}}{x_+ i} \tag{2}$$

$$PA = \frac{\sum D_{ij}}{x_{i+}} \tag{3}$$

$$Kappa = \frac{N \sum_{i=1}^{r} ii - \sum_{i=(x_{i+} * x_{+i})}^{r}}{N^{2} - \sum_{t=1}^{r} (x_{i+} * x_{+i})} \tag{4}$$

Where, D_{ii} refers to the number of the correctly classified pixels; D_{ij} indicates the number of the correctly classified pixel at row *i*; D_{ij} is the number of correctly classified pixels in the column j; r is the to the number of rows in the matrix; xii is the number of pixel in row *i* and column *i*; x_i+ and $x+_1$ refer to marginal total row and column *i* and *i*, and N is the number of pixels (total) respectively. It is important to note that classification accuracy of the LULC is a challenging due to mixed pixel in highly urbanized areas. In this study, the training points were extracted from diversified locations to enhance the accuracy of the LULC.

2.5 CA-MC model

The CA model is one of the robust methods and is has been widely used simulate and predict LULC (Kamusoko and Aniya 2009; Guan et al. 2019). In this model, MC analysis was carried out to develop LULC for the year 2020 to develop transition area matrics, generate transitional maps, accuracy assessment of the simulated LULC using kappa statistics and predict LULC.

CA-MC model is one of the popular models used to find out transitional probabilities of LULC. The transitional probabilities were used to examine the spatial changes of LULC and these changes are highly correlated with different factors affecting LULC dynamics (Guan et al., 2019). Thus, CA-MC model has been considered as an effective mixed model for the future prediction of LULC (Moein et al. 2018; Mirzazadeh et al. 2024). The CA-MC deals with the time to find out the tendencies and causes of transitions appearing in the future. In KMA, the LULC map for 2010 was used as base image, while the 2020 map later was generated a transition probability matrix between the years 2010 and 2020. Cross-tabulation functionality and ArcGIS, were used to develop transitional area matrices by multiplying the column in the transitional probability matrix by the number of the corresponding pixel number. The transitional probability matrix and the transitional area were computed in the case of MC analysis. On the basis of the transition probabilities, the area of each land use type to be converted was estimated. These areas have been divided by the total number of years considered for CA.

2.6 Method of LST calculation

In this study, LST of KMA has been retrieved using thermal infrared bands. In the case of Landsat 8 OLI, band 10, and in the case of Landsat 5 TM, band 6 were used. The following steps were employed for the Retrieval of LST from satellite images as proposed by Sultana and Satyanarayana (2018):

$$T_B = \frac{K_2}{\ln\left(\frac{K_1}{K_\lambda} + 1\right)} \tag{5}$$

$$L_\lambda = \frac{L_{max-L_{min}}}{QCAL_{maxLQCAL_{min}}} \times \left(QCAL - QCAL_{min}\right) - L_{min} \tag{6}$$

$$\varepsilon = 0.004 \times P_v + 0.986 \tag{7}$$

$$P_v = \left[\frac{NDVI - NDVI_{min}}{NDVI_{max.} - NDVI_{min}}\right] 2 \tag{8}$$

Where, Tb indicates the brightness temperature in Kelvin, respectively λ is the wavelength, Pv is the functional vegetation cover, K_1 and K_2 indicate the pre-launched calibration constant for Landsat 5 TM, and 8 OLI sensors. QCAL indicate the DN value, QCALmax and QCAL min mention the maximum and minimum BD value of the specific images, respectively. L_{min} and L_{max} refers to the spectral radiance for thermal bands (band 6 and 10 for TM and OLI) at $QCAL_{max}$ and $QCAL_{mini}$.

After obtaining radiant temperature in Kelvin, it was converted into degree Celsius using the following equation by adding absolute zero (−273.15): Here, the following equation has been used to extract Ts (Sultan and Satyanrayana, 2018).

$$T_s = \frac{T_b}{1 + \left(\frac{\lambda \times T_b}{\sigma}\right) \ln 0} \quad (9)$$

Finally, LST was retrieved using the following equation (Sultana and Satyanarayanana, 2018; 2020):

$$LST(^{\circ}C) = \frac{T_B}{(1 + W\frac{T_B}{P}\text{In}[\delta]} \quad (10)$$

Where, w refers to the wavelength of the radiance; $p = h \times \frac{c}{\sigma} = 1.438w10^{-2}m$ K σ is the Boltzmann constant. h is the Planck constant, and c is the velocity of light.

2.7 Fragmentation of landscape

In this study, four landscape metrics were employed to analyze built-up fragmentation patterns from 1990 to 2020 and to project future landscape fragmentation for the years 2030, 2040, and 2050. The selected metrics include patch density (PD), edge density ED), core area (CA), and perforation (Fig. 2). Each of these metrics provides insight into different aspects of landscape fragmentation. The PD is a fundamental metric for assessing landscape fragmentation. It quantifies the total number of distinct patches or fragments of built-up areas within a landscape. A higher NP indicates greater landscape fragmentation, as continuous habitats are broken into smaller, isolated patches, reflecting the impact of urbanization on landscape connectivity (Chen et al. 2020; Fletcher et al. 2018). ED measures the total length of the edge or boundary of built-up areas per unit area of the landscape. This metric highlights the complexity of the boundary between built-up and non-built-up areas. A higher ED suggests a more fragmented landscape with more extensive interfaces between these areas, leading to increased environmental impacts such as altered microclimates and heightened exposure to invasive species (Zhou et al., 2021; Li et al. 2017a, b). CA represents the interior habitat within the built-up landscape, excluding the ED. CA is calculated by summing the CA of each patch, where the CA is the portion of a patch that remains after excluding ED influences. This metric is essential for assessing the availability of uninterrupted, interior habitats that are less affected by edge effects, which are vital for maintaining biodiversity and ecological processes (Li et al. 2021; Uuemaa et al. 2016). Perforation refers to the extent to which non-built-up areas penetrate or disrupt the interior of built-up clusters. This metric measures the interior perimeter of a core built-up area that has been fragmented or perforated by non-built-up spaces. High perforation indicates that the built-up area is heavily interspersed with non-built-up patches, leading to a more fragmented and less cohesive urban landscape, which can have significant implications for urban planning and sustainability (Schneider et al. 2017; Martínez et al. 2019). Together, these landscape metrics provide a comprehensive framework for understanding the spatial and structural changes in urban landscapes over time, enabling more informed decision-making in urban planning and ecological conservation efforts (Supplementary Data Table S2).

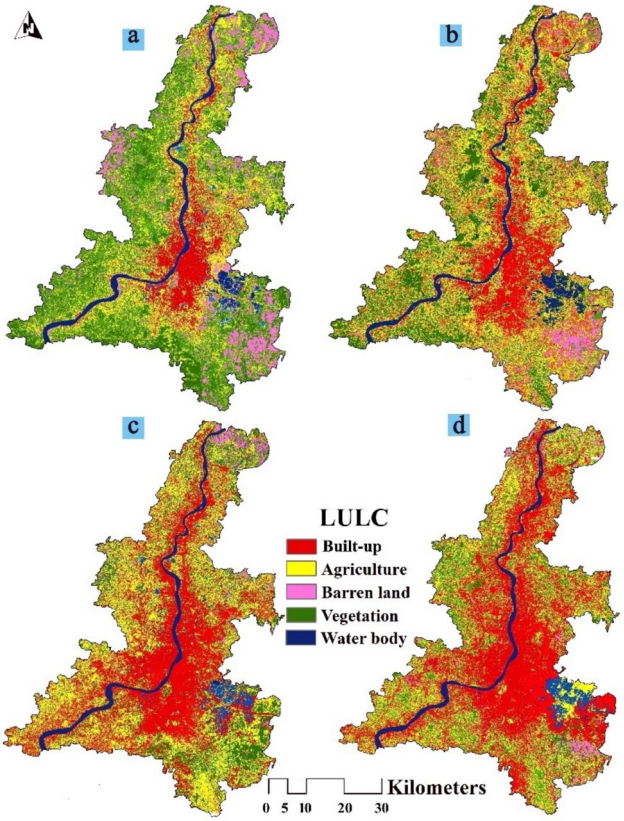


Fig. 2 LULC dynamics in KMA (**a**) 1990 (**b**) 2000 (**c**) 2010 and (**d**) 2020

3 Results

3.1 Dynamics of LULC and its impact on LST

In 1990, the built-up area encompassed 506.39 km^2, which expanded to 619.55 km^2 by 2000, further to 787.17 km^2 by 2010, and reached 862.84 km^2 by 2020 (Fig. 2). This represented an approximate 70% increase in built-up area over the last three decades. Agricultural land decreased from 621.41 km^2 in 1990 to 570.49 km^2 in 2000, 475.11 km^2 in 2010, and 398.19 km^2 in 2020, marking a significant reduction of about 35.92% over the 30-year span. Water bodies also diminished, experiencing a decline of approximately 13.17% between 1990 and 2020. Vegetation

cover followed a similar downward trend, decreasing from 239.34 km^2 in 1990 to 117.51 km^2 in 2020, which corresponds to a reduction of about 50.86% (Supplementary Data Table S3). The accuracy assessment of the LULC maps revealed an overall accuracy of approximately 80%. The highest classification accuracy was observed in the 1990 map at 83.27%, followed by 82.85% in 2020, 78.43% in 2010, and 77.90% in 2000 (Supplementary Data Table S4).

The mean LST demonstrated an upward trend from 1990 to 2020 across all seasonal periods (Winter, Pre-monsoon, and Post-monsoon) (Supplementary Data Figure S1 and Fig. 3). For example, during Winter, the mean LST increased by 9.03%, rising from 16.32 °C in 1990 to 24.06 °C in 2020. During the Pre-monsoon period, the mean LST increased by 5.53%, while in the Post-monsoon period, it rose by 6.59%. The most pronounced increase in mean LST was observed during the Winter season, followed by the Post-monsoon and Pre-monsoon periods (Supplementary Data Table S5).

3.2 Future simulation of LULC and its impact on LST

The results indicated a significant expansion in built-up areas, which are predicted to reach 962.84 km^2 by 2030, further increasing to 1037.44 km^2 by 2040, and ultimately reaching 1105.1 km^2 by 2050 (Supplementary Data Table S6). This represents a 28.08% increase in built-up area from 2020 to 2050. Concurrently, agricultural land is expected to decrease substantially, from 24.02% in 2020 to 44.93% in 2050. Vegetation cover is also projected to decline sharply, with a reduction from 7.09% in 2020 to 5.27% in 2050. Additionally, water bodies are anticipated to shrink by 11.34% over the same period (Fig. 4).

The analysis revealed a notable increase in the percentage of area under high and very high LST categories from 1990 to 2020, a trend that is expected to persist through 2050 (Fig. 5). Specifically, the area under the very high LST zone increased from 11.57% in 1990 to 21.36% in 2020, representing an 84.61% rise. Conversely, the area under very low LST decreased dramatically, from 30.36% in 1990 to 17.19% in 2020, marking a 43.38% reduction. Projections indicated that the area under high and very high LST will continue to expand in the coming decades. For instance, the area under very high LST is predicted to reach 23.77% by 2030, 25.95% by 2040, and 28.77% by 2050. On the other hand, the area under low and very low LST is expected to decrease. For example, the area categorized as low LST is projected to decline from 14.79% in 2030 to 12.27% in 2040, and further to 11.54% by 2050. This represents a 21.97% decrease in the area under very low LST between 2030 and 2050 (Supplementary Data Table S7).

3.3 Fragmentation of landscape and its impact on LST

The CA expanded from 42.27 km^2 in 1990 to 83.18 km^2 in 2000, 149.15 km^2 in 2010, and 210.21 km^2 in 2020, reflecting an increase from 2.28% to 18.17% of the total landscape area (Fig. 6 and Fig. 7). This represents a substantial increase (397.30%) in CA from 1990 to 2020. Projections suggested that by 2030, CA will further expand to 336.33 km^2, reaching 553.27 km^2 by 2050 an anticipated 64.50% increase between 2030 and 2050. Similarly, PD exhibited a marked increase over the same period. In 1990, PD was 52.43 per km^2, rising to 211.2 PD per km^2 by 2020, indicating a 302.93% increase. PD covered 2.83% of the total LULC in 1990, growing to 11.41% by 2020. According to predictions, PD is expected to increase from 164.44 PD per km^2 in 2030 to 195.94 PD per km^2 by 2050, a 19.16% rise. ED also showed a notable upward trend, increasing significantly from 70.63 km^2 in 1990 to 252.25 km^2 in 2020, an increase of approximately 257.14%. In terms of LULC percentage, ED grew from 3.82% in 1990 to 13.63% in 2020. Predictions indicate that ED will increase from 176.57 km^2 in 2030 to 211.94 km^2 by 2050, representing a 20.03% rise.

Tables 2 and 3 illustrated the trends in LST dynamics across different landscape metrics i.e., CA, PD, ED, and perforated from 1990 to 2050. In CA, the mean LST showed a steady increase from 23.28 °C in 1990 to 30.32 °C by 2050, with the maximum LST rising to 37.30 °C by 2050.. Similarly, in PD, mean LST rose from 21.68 °C in 1990 to 26.88 °C by 2050, with a corresponding increase in maximum LST, reaching 36.34 °C. The standard deviation also increased, suggesting greater LST fluctuations over time. ED experience a gradual rise in mean LST from 15.88 °C in 1990 to 19.89 °C by 2050, with maximum LST following a similar upward trend. Perforated areas exhibited the most pronounced warming, with mean LST climbing from 15.67 °C in 1990 to 24.28 °C by 2050. Overall, the results showed a significant rise in LST across all landscape metrics.

4 Discussion

The results indicated that the dynamics of LULC in KMA have changed significantly over the last three decades. The built-up area increased by 70% from 506.39 km^2 in 1990 to 862.84 km^2 in 2020. The accelerated urbanisation reflecting this growth was consistent with the results of other urban regions worldwide. For example, Liu et al. (2016) observed comparable urban expansion patterns in China and attributed them to population growth and economic development. In contrast, the global trend of urban development encroaching on peri-urban agricultural zones is reflected in

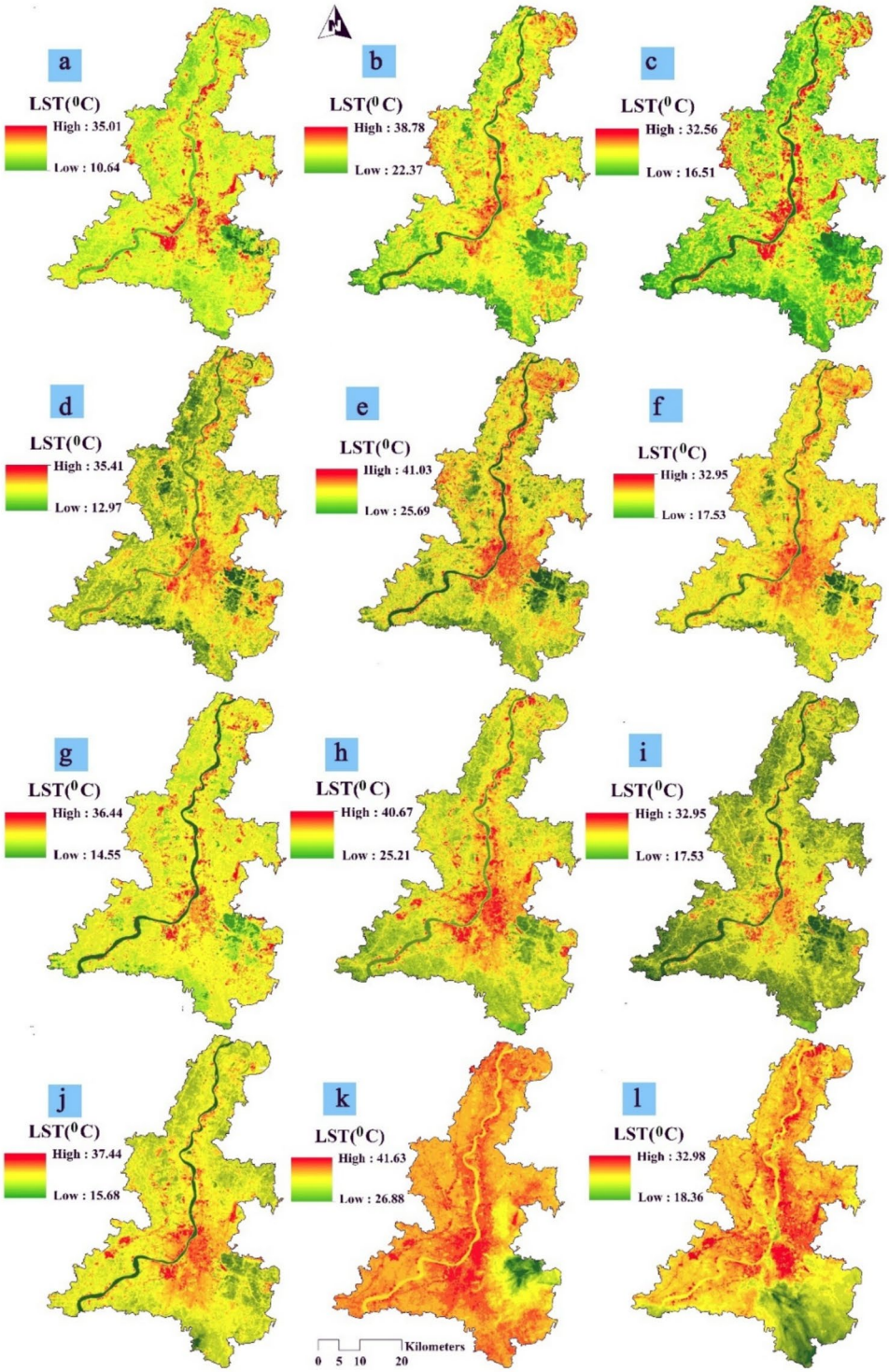


Fig. 3 Seasonal variation of LST (**a**) Winter (**b**) Pre-monsoon (**c**) Post-monsoon in 1990, (**d**) Winter (**e**) Pre-monsoon (**f**) Post-monsoon in 2000, (**g**) Winter (**h**) Pre-monsoon (**i**) Post-monsoon in 2010, (**j**) Winter (**k**) Pre-monsoon (**l**) Post-monsoon in 2020

the 35.92% decline in agricultural land between 1990 and 2020. This phenomenon has been extensively investigated, as Seto and Ramankutty (2016) have observed that urbanisation resulted in the conversion of prime agricultural land, thereby jeopardising food security. The vegetation cover has decreased by a substantial 50.86%, which is cause for concern. Xie et al. (2018) observed a similar trend in other swiftly urbanising areas, where vegetation covers were replaced by impervious surfaces, resulting in an ecological degradation. This reduction exacerbated the effects of UHI, as emphasised by Santamouris (2015), and decreased ES. Concerns regarding municipal water resource management were also raised by the 13.17% decrease in water bodies between 1990 and 2020. This trend was in accordance with

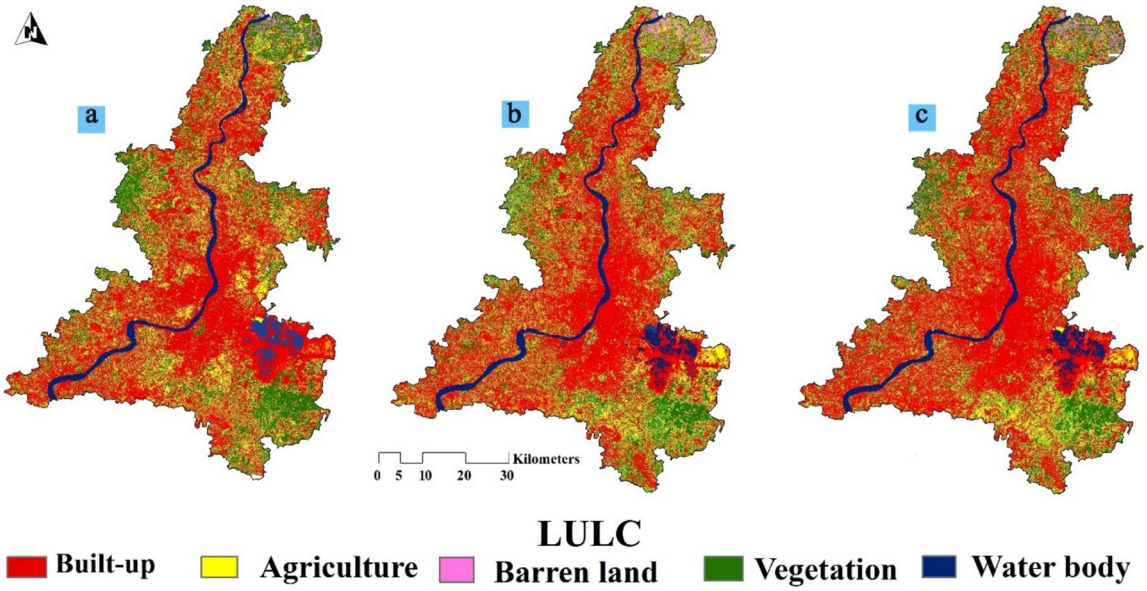


Fig. 4 Predicted LULC from (**a**) 2030 (**b**) 2040 and (**c**) 2050

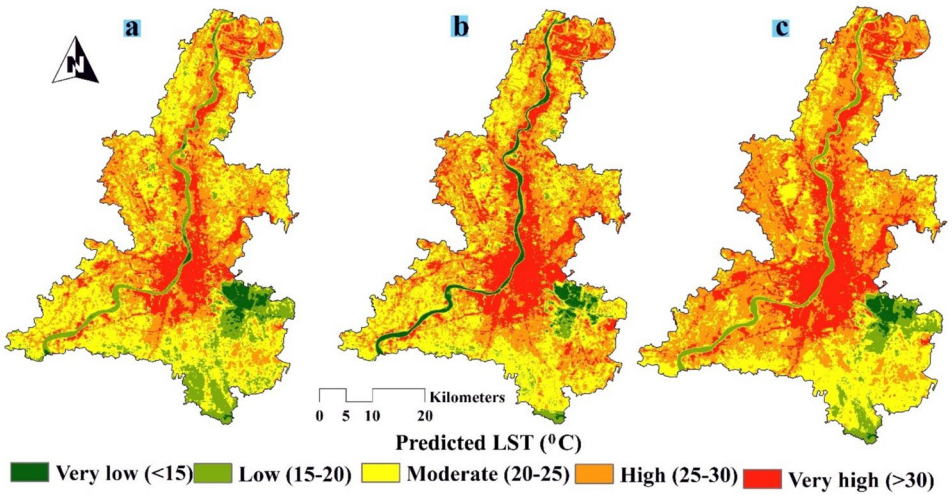


Fig. 5 Predicted LST dynamics from (**a**) 2030 (**b**) 2040 and (**c**) 2050

the findings of Zhou et al. (2017b, a), who examined the impact of urbanisation on the reduction of water bodies as a result of land reclamation. The accuracy assessment of LULC maps is commendable, with an overall accuracy of approximately 80%, despite the fact that it exhibited significant variation across various years. The initial application of remote sensing technologies for LULC mapping, which resulted in the utmost accuracy in 1990 (83.27%), was followed by substantial advancements in recent decades (Zhu et al. 2016). Nevertheless, Khatami et al. (2016) have suggested that the minor decrease in accuracy in the subsequent years may be indicative of the escalating complexity of urban landscapes.

The observed and projected increase in LST values correlated strongly with the expansion of built-up areas and the reduction in vegetation and water bodies, both of which contribute to the UHI effect. This trend was well-documented in studies that link urbanization to rising LST due to the replacement of natural landscapes with impervious surfaces like concrete and asphalt, which absorb and retain heat (Weng 2001; Zhou et al. 2014).The substantial increase in the area under high and very high LST categories from 1990 to 2020 aligned with findings from other studies that report similar trends in rapidly urbanizing regions (Li et al. 2020; Rasul et al. 2017). The projected continuation of this trend through 2050 underscored the need for interventions aimed

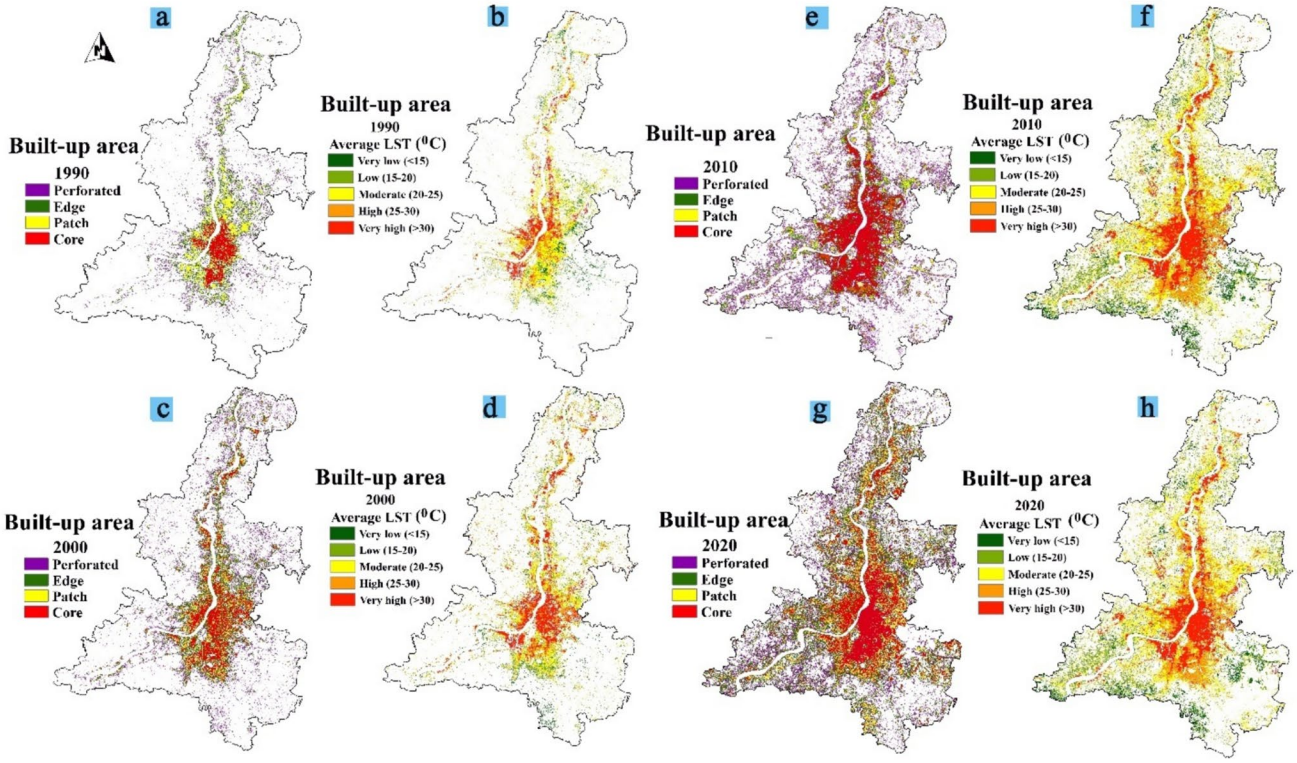


Fig. 6 Fragmentation of landscape (**a**) 1990 (**c**) 2000, (**e**) 2010 (**g**) 2020 and LST (**b**) 1990 (**d**) 2000, (**f**) 2010 (**h**) 2020

at enhancing urban resilience to heat stress (Rizwan et al. 2008; Cao et al. 2010). The significant reduction in areas under low and very low LST highlighted the loss of vegetative cover, which is critical for mitigating LSTs through evapotranspiration and shading (Gago et al. 2013; Zhang et al. 2018). The role of green infrastructure in counteracting the UHI effect and moderating LSTs is increasingly recognized, suggesting that sustainable urban planning must prioritize the integration of green spaces (Oke 1982; Emmanuel and Krüger 2012*)*. Overall, these results suggested that without significant changes in land use practices, urban areas will continue to experience rising LST, exacerbating the impacts of climate change. This emphasizes the need for urban planning policies that incorporate nature-based solutions to mitigate the adverse effects of increased LST (Gill et al. 2007; Tan and Li 2015a, b).

The results on landscape fragmentation, as illustrated in Fig. 7and Table 2, align with the growing body of literature on LULC changes and their impacts on landscape fragmentation. The expansion of the CA, which increased by approximately 397.30% from 1990 to 2020, was consistent with findings by Seto et al. (2012), who emphasized the rapid urbanization and corresponding expansion of urban cores globally. This trend is driven by population growth and economic development, leading to the conversion of natural landscapes into urban areas.

The significant rise in PD from 52.43 per km^2 in 1990 to 211.20 per km^2 by 2020 reflects increased landscape fragmentation, a phenomenon extensively documented in Foley et al. (2005). Landscape fragmentation typically resulted from the division of continuous habitats into smaller, isolated patches, often due to agricultural expansion, infrastructure development, and urban sprawl. The projected increase in ED from 70.63 km^2 in 1990 to 252.25 km^2 in 2020, with further growth anticipated by 2050, mirrors observations by Haddad et al. (2015). The anticipated further expansion of the CA and the increase in both PD and ED by 2050 underscore the need for sustainable land management strategies. As noted by Lambin and Meyfroidt (2011), unchecked urbanization and landscape fragmentation can lead to significant ecological degradation, including loss of ES and increased vulnerability to climate change impacts. These findings aligned with projections by Angel et al. (2011), who predicted continued urban expansion, especially in developing countries, driven by socio-economic factors. The documented and projected increases in PD and ED also resonate with research by Turner et al. (2015), which highlighted the consequences of increased landscape fragmentation on habitat connectivity and ecosystem functions. Thus, the observed and projected dynamics of landscape fragmentation in this study are consistent with global trends and underscore the pressing need for integrated urban planning

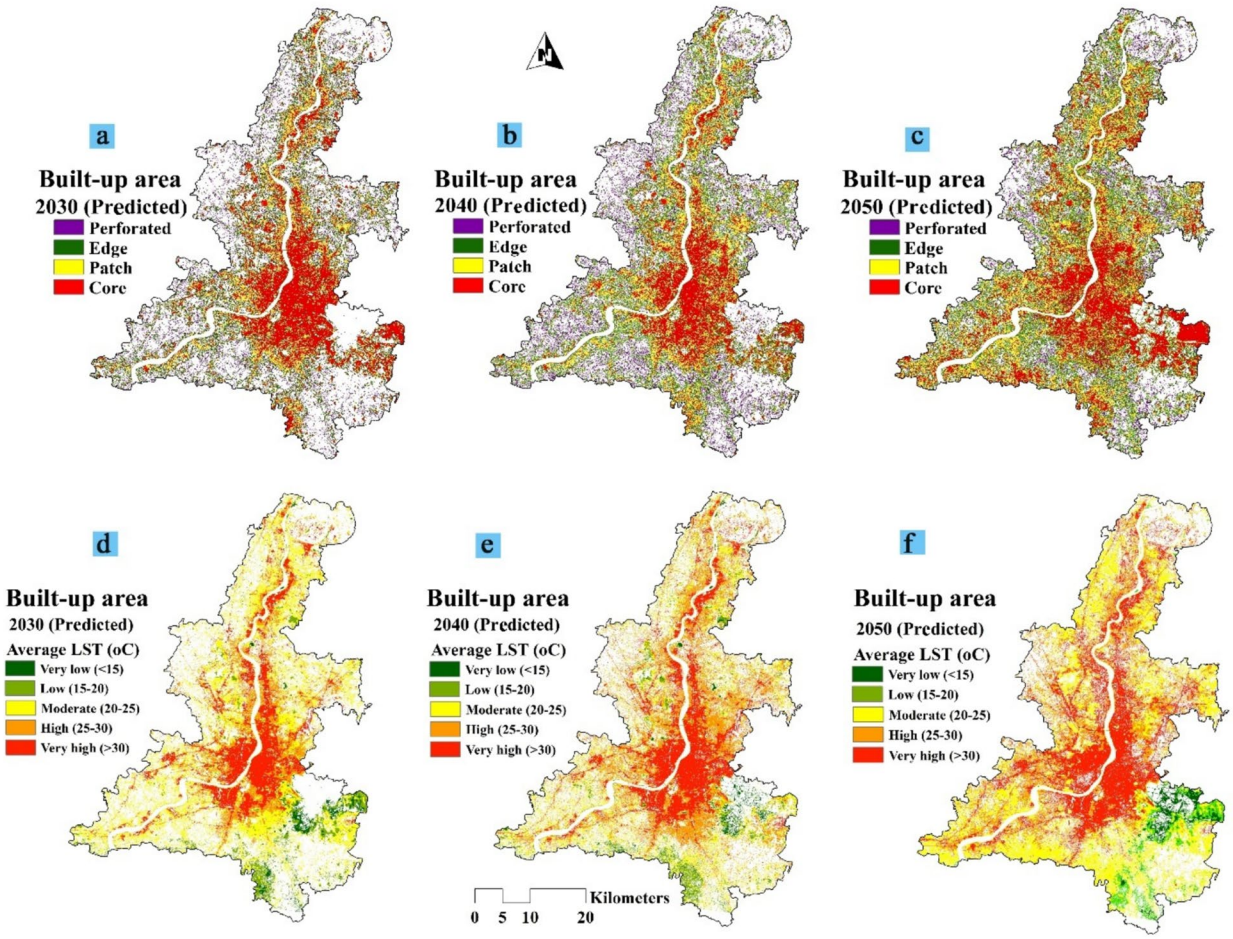


Fig. 7 Predicted fragmentation of landscape (**a**) 2030 (**b**) 2040 (**c**) 2050 and LST (**d**) 2030 (**e**) 2040 (**f**) 2050

and conservation strategies to mitigate the adverse effects of landscape fragmentation.

The analysis of LST dynamics across various landscape metrics from 1990 to 2050, as illustrated in Table 3, aligned with broader trends observed in the scientific literature on climate change and land use (Liu et al. 2018). The increasing trend of LST noted in CA and perforated areas was consistent with findings from various studies that emphasize the impact of urbanization on local and regional LST (Fu and Weng 2016). For instance, studies by Imhoff et al. (2010) and Zhao et al. (2014) have documented the significant increase in LST in urban core due to increased built-up surfaces and reduced vegetation cover. The increase in LST variability, as indicated by rising standard deviations, suggested heightened extremes in LST. This phenomenon has been linked to the landscape fragmentation of natural landscapes (such as water bodies, vegetation cover) and increased urbanization, which disrupts local microclimates and contributes to more extreme weather events such heat waves (Li et al. 2013a, b; Zhou et al. 2017b, a).

The perforated areas, which exhibited the most pronounced LST, could be related to the edge effects where natural habitats were fragmented, leading to increased exposure to sunlight and reduced cooling effects from vegetation (Haddad et al. 2015). This is supported by research indicating that fragmented landscapes tend to heat up more rapidly due to the reduced capacity of smaller patches to retain moisture and moderate temperatures (Laurance et al. 2011). Furthermore, the rising LST in PD and ED areas were in line with findings by Buyantuyev and Wu (2010), who observed that fragmented landscapes with higher ED tend to experience more significant LST increases due to the greater exposure of edges to solar radiation and reduced shading effect. The consistent rise in mean LST across all landscape components highlighted the pervasive nature of climate change and its impact on diverse land cover types. This underscored the importance of incorporating climate resilience into urban planning and landscape management strategies to mitigate the adverse effects of rising temperatures (Seto et al. 2012; Grimm et al. 2008).

Table 2 Changes in CA PD, ED and perforated from 1990 to 2050. * indicates the predicted years

Year	CA			PD			ED			Perforated		
	Area (km^2)	% of LULC	Changes to next decade	Area (km^2)	% of LULC	Changes to next decade	Area (km^2)	% of LULC	Changes to next decade	Area (km^2)	% of LULC	Changes to next decade
1990	42.27	2.28		52.43	2.83		70.63	3.82		82.16	4.44	
2000	83.18	4.49	2.21	89.83	4.85	2.02	127.24	6.87	3.05	85.83	4.64	0.20
2010	149.15	8.06	3.57	173.88	9.39	4.54	234.25	12.66	5.79	111.96	6.05	1.41
2020	210.21	11.36	3.31	211.26	11.41	2.02	252.25	13.63	0.97	128.25	6.93	0.88
2030*	336.33	18.17	6.81	164.44	8.88	(-)2.53	176.57	9.54	(-)4.09	172.51	9.32	2.39
2040*	478.29	25.84	7.67	154.04	8.32	(-)0.56	129.74	7.01	(-) 2.53	171.93	9.29	(-)0.03
2050*	553.27	29.89	4.05	195.94	10.59	2.27	211.94	11.45	4.44	171.78	9.28	(-)0.01

Table 3 LST dynamics in CA, PD, ED and perforated

Year	CA				PD				ED				Perforated			
	Maximum (°C)	Minimum (°C)	Mean (°C)	Std Dev	Maximum (°C)	Minimum (°C)	Mean (°C)	Std Dev	Maximum (°C)	Minimum (°C)	Mean (°C)	Std Dev	Maximum (°C)	Minimum (°C)	Mean (°C)	Std Dev
1990	30.28	26.44	23.28	1.12	29.82	22.38	21.68	1.09	29.76	18.44	15.88	1.10	28.01	11.53	15.67	1.06
2000	31.96	26.40	24.85	1.15	30.98	25.40	23.66	1.15	30.38	18.83	16.97	1.11	28.69	12.44	18.87	1.05
2010	33.35	26.84	26.67	1.24	32.45	24.66	23.95	1.15	31.55	19.87	18.71	1.11	29.20	14.05	20.53	1.07
2020	35.19	26.22	26.96	1.76	34.85	24.06	25.45	1.18	32.17	20.28	19.32	1.13	30.39	14.87	21.73	1.11
2030*	36.06	26.89	28.58	1.71	34.37	25.27	25.86	1.22	33.07	20.52	19.08	1.15	30.41	16.08	22.43	1.11
2040*	36.78	26.91	29.86	1.84	35.81	26.12	26.07	1.28	33.83	21.17	19.23	1.14	30.59	16.88	23.56	1.14
2050*	37.30	27.33	30.32	1.89	36.34	26.74	26.88	1.41	34.68	22.09	19.89	1.17	31.87	17.77	24.28	1.14

4.1 Policy applications and implications

The results showed that CA, PD, and ED from 1990 to 2020 significantly expanded. Thus, expansion of the CA, PD, and ED would definitely influence LST in future. Therefore, it is essential to implement strong ecological policies and strategies to mitigate LST in KMA. The integration of urban planning strategies and ecological policies is essential in dense urban areas such as Kolkata to resolve landscape fragmentation and mitigate the increasing LST. In initial phase, expansion of green infrastructure, such as urban forests, green roofs, vertical gardens, and the preservation of extant green spaces, must be prioritized in order to promote urban greening (Wang et al. 2024; Gavrilidis et al. 2019). Not only does this decrease LST, but it also improves ecological resilience and habitat connectivity (Furberg et al. 2020). A second critical aspect is the preservation and restoration of wetlands and aquatic bodies, including East Kolkata Wetlands (EKW). Diverse ecosystems are supported by these, which serve as urban heat buffers, enhance microclimates, and reduce fragmentation (Kong et al. 2016). The third step is to implement rigorous land use zoning and regulation of built-up expansion in order to prevent the haphazard expansion of urban areas. Policies ought to encourage mixed-use developments that minimize impervious surfaces and foster permeable, vegetated landscapes. Furthermore, urban development boundaries can be implemented to minimize expansion and safeguard peri-urban agricultural and forest lands. Fourth, the integration of nature-based solutions (NbS) into infrastructure development should aim to enhance ecological connectivity, including bioswales, rain gardens, and urban tree corridors. Additionally, the identification of fragmentation hotspots and the prioritization of restoration efforts via landscape ecological planning that employs remote sensing and geospatial tools should serve as a guide for future urban development. Finally, it is essential to prioritize community engagement and participatory governance in order to guarantee long-term stewardship and public awareness of ecological interventions. Urban environment in Kolkata can be transformed into a thermally balanced and ecologically sustainable urban landscape as a result of these integrated ecological policies. This transformation is crucial for the achievement of sustainable development goals (SDGs) and the resilience to climate change.

The impact of landscape fragmentation on LST is crucial for achieving SDGs, particularly Goal 11 (Sustainable Cities and Communities) and Goal 13 (Climate Action). Fragmented landscapes often lead to inefficient land use, increased energy consumption, and higher greenhouse gas emissions. Additionally, the loss of green spaces and natural buffers affects the resilience of urban environments to climate change, making cities more vulnerable to extreme heat events. Addressing landscape fragmentation through sustainable urban planning and green infrastructure can mitigate its negative impacts on LST. Implementing strategies such as enhancing urban green spaces, promoting compact urban development, and restoring ecological connectivity can help regulate LST, reduce the UHI effect, and contribute to climate adaptation and mitigation efforts. Thus, integrating considerations of landscape fragmentation into urban planning is essential for promoting sustainable development and achieving global climate targets.

5 Conclusions

This research offers a thorough assessment of the historical and projected changes in LULC and their impact on urban thermal dynamics in KMA, a swiftly urbanising region in India. The research emphasises the significant changes thermal environment in the region and landscape from 1990 to 2050 by incorporating the CA-MC model with landscape metrics and LST analysis. The results indicated that the expansion of built-up areas by nearly 70% between 1990 and 2020 was primarily driven by urban sprawl and population development. This expansion has resulted in the loss of critical ecological resources, including agricultural land and aquatic bodies, which have declined by 35.92% and 13.17%, respectively. This alarming trend was further exacerbated by the projections for 2030, 2040, and 2050, which indicated that the depletion of natural and semi-natural land covers will persist. In particular, it was anticipated that vegetation cover will decrease by approximately 29.03% and agricultural land by 44.93% by the mid-century. These modifications not only jeopardise the region's ecological integrity but also jeopardise food and water security. In conjunction with the changes in LULC, there has been a significant increase in LST. The mean LST has increased by 7.05%, with the most intense seasonal rise of 9.03% occurring during the winter. The spatial expansion of zones experiencing extremely high LST from 11.57% in 1990 to an anticipated 28.77% in 2050 is particularly concerning. The degradation of vegetated surfaces and the proliferation of impervious surfaces were closely associated with this spatial intensification of heat stress. Additionally, the investigation highlights the increasing fragmentation of the landscape, as evidenced by the increase in perforated landscapes, PD, ED, and CA. These indicators suggested that the disruption of continuous ecological habitats and the diminishment of landscape connectivity are further exacerbating the effects of UHI and the loss of biodiversity. The study underscored the pressing necessity for sustainable urban planning and management strategies in KMA in light of these findings. The negative effects of LULC change can be mitigated by integrating green infrastructure, controlling unplanned urban expansion, and protecting remaining agricultural and

water resources. The integration of ecologically sensitive design and landscape connectivity into urban policy has the potential to dramatically improve urban resilience, enhance thermal regulation, and support long-term sustainability objectives. Consequently, this research provides a critical scientific foundation for urban planners and policymakers to devise interventions that effectively balance environmental conservation with development in one of the most dynamic urban regions in India.

Supplementary Information The online version contains supplementary material available at https://doi.org/10.1007/s00704-025-05597-7.

Acknowledgements NA

Author Contributions All the authors contributed equally.

Funding No funding was received for the study.

Data Availability No datasets were generated or analysed during the current.

Ethical Approval. Not applicable.

Consent to participate All participants provided their consent for participating in the interview.

Consent to publish Not applicable.

Competing interests The authors declare no competing interests.

References

Al-Kofahi SD, Hammouri N, Sawalhah MN, Al-Hammouri AA, Aukour FJ (2018) Assessment of the urban sprawl on agriculture lands of two major municipalities in Jordan using supervised classification techniques. Arab J Geosci 11(3):1–12

Anees SA, Mehmood K, Khan WR, Sajjad M, Alahmadi TA, Alharbi SA, Luo M (2024a) Integration of machine learning and remote sensing for above ground biomass estimation through Landsat-9 and field data in temperate forests of the Himalayan region. Eco Inform 82:102732. https://doi.org/10.1016/j.ecoinf.2024.102732

Anees, S. A., Mehmood, K., Rehman, A., Rehman, N. U., Muhammad, S., Shahzad, F., ... & Khan, W. R. (2024b). Unveiling fractional vegetation cover dynamics: A spatiotemporal analysis using modis ndvi and machine learning. *Environmental and Sustainability Indicators*, *24*, 100485. https://doi.org/10.1016/j.indic.2024.100485.

Anees, S. A., Mehmood, K., Khan, W. R., Shahzad, F., Zhran, M., Ayub, R., ... & Liu, Q. (2025a). Spatiotemporal dynamics of vegetation cover: integrative machine learning analysis of multispectral imagery and environmental predictors. *Earth Science Informatics*, *18*(1), 1–23. https://doi.org/10.1007/s12145-024-01673-0.

Anees, S. A., Mehmood, K., Raza, S. I. H., Pfautsch, S., Shah, M., Jamjareegulgarn, P., ... & Dube, T. (2025a). Spatiotemporal analysis of surface Urban Heat Island intensity and the role of vegetation in six major Pakistani cities. *Ecological Informatics*, *85*, 102986. https://doi.org/10.1016/j.ecoinf.2024.102986.

Angel, S., Parent, J., &Civco, D. L. (2011). The fragmentation of urban landscapes: Global evidence of urban sprawl. Lincoln Institute of Land Policy. Retrieved from https://www.lincolninst.edu/publications/working-papers/fragmentation-urban-landscapes.

Angel, S., Parent, J., Civco, D. L., & Blei, A. M. (2012). Atlas of Urban Expansion (Lincoln Institute of Land Policy. *Lincoln Institute of Land Policy, Cambridge, MA, USA*, 397.

Bhattacharyya S, Sinha S, Kumari M, Mishra VN, Hasher FFB, Szostak M, Zhran M (2025) Spatio-Temporal Influences of Urban Land Cover Changes on Thermal-Based Environmental Criticality and Its Prediction Using CA-ANN Model over Kolkata (India). Remote Sens 17(6):1082

Biswas S, Ghosh S (2022) Estimation of land surface temperature in response to land use/land cover transformation in Kolkata city and its suburban area, India. Int J Urban Sci 26(4):604–631

Buyantuyev A, Wu J (2010) Urban heat islands and landscape heterogeneity: Linking spatiotemporal variations in surface temperatures to land-cover and socioeconomic patterns. Landsc Ecol 25(1):17–33. https://doi.org/10.1007/s10980-009-9402-4

Cao X, Onishi A, Chen J, Imura H (2010) Quantifying the cool island intensity of urban parks using ASTER and IKONOS data. Landsc Urban Plan 96(4):224–231. https://doi.org/10.1016/j.landurbplan.2010.03.008

Chen Y, Chen L, Bai Y, Xu G (2020) Measuring landscape fragmentation in rapidly urbanizing landscapes: The case of China's Beijing-Tianjin-Hebei Region. Sustainability 12(18):7410

Chen X, Hu Y, Zhao S (2021) Impact of landscape pattern on land surface temperature: A review. Sustainability 13(2):790

Das M, Das A (2022) Indicator based assessment of urban ecological security pattern in Kolkata metropolitan area. India. Geocarto International 37(27):16996–17017. https://doi.org/10.1080/10106049.2022.2120637

Debnath, A., Kumar, R., Singh, T., &Prawasi, R. (2020). The Impact of Rapid Urbanization on Vegetation Cover and Land Surface Temperature in Barasat Municipal Area. *Sustainable Development Practices Using Geoinformatics*, 1–21.

Dutta A, Jinsart W (2021) Air quality, atmospheric variables and spread of COVID-19 in Delhi (India): an analysis. Aerosol and Air Quality Research 21(3):200417. https://doi.org/10.4209/aaqr.2020.07.0417

Emmanuel R, Krüger E (2012) Urban heat island and its impact on climate change resilience in a shrinking city: The case of Glasgow, UK. Build Environ 53:137–149. https://doi.org/10.1016/j.buildenv.2012.01.020

Fletcher RJ, Didham RK, Banks-Leite C, Barlow J, Ewers RM, Rosindell J, MacDonald MA (2018) Is habitat fragmentation good for biodiversity? Biol Cons 226:9–15

Foley, J. A., DeFries, R., Asner, G. P., Barford, C., Bonan, G., Carpenter, S. R., ... & Snyder, P. K. (2005). Global consequences of land use. Science, 309(5734), 570–574. https://doi.org/10.1126/science.1111772

Fu P, Weng Q (2016) A time series analysis of urbanization induced land use and land cover change and its impact on land surface temperature with Landsat imagery. Remote Sens Environ 175:205–214

Furberg D, Ban Y, Mörtberg U (2020) Monitoring urban green infrastructure changes and impact on habitat connectivity using high-resolution satellite data. Remote Sens 12(18):3072

Gago EJ, Roldan J, Pacheco-Torres R, Ordóñez J (2013) The city and urban heat islands: A review of strategies to mitigate adverse effects. Renew Sustain Energy Rev 25:749–758. https://doi.org/10.1016/j.rser.2013.05.057

Gao J, Wei YD, Chen W, Yenneti K (2015) Urban land expansion and structural change in the Yangtze River Delta. China Sustain 7(8):10281–10307

Gavrilidis AA, Niță MR, Onose DA, Badiu DL, Năstase II (2019) Methodological framework for urban sprawl control through sustainable planning of urban green infrastructure. Ecol Ind 96:67–78

Ghosh S, Das A (2018) Modelling urban cooling island impact of green space and water bodies on surface urban heat island in a continuously developing urban area. Mod Earth Syst Environ 4(2):501–515

Ghosh S, Siddique G (2018) Change detection of built-up areas applying built-up index for Chandannagar city. Int J Tech Res Manag 5(4):1–7

Ghosh DK, Mandal AC, Majumder R, Patra P, Bhunia GS (2018) Analysis for mapping of built-up area using remotely sensed indices–a case study of Rajarhat Block in BarasatSadar Sub-Division in West Bengal (India). J Landsc Ecol 11(2):67–76

Ghosh S, Chatterjee ND, Dinda S (2019a) Relation between urban biophysical composition and dynamics of land surface temperature in the Kolkata metropolitan area: a GIS and statistical based analysis for sustainable planning. Modeling Earth Systems and Environment 5(1):307–329

Ghosh S, Majumdar S, Das D (2019b) Analyzing the impact of land use and land cover changes on groundwater quality in South 24 Parganas. India Environ Monit Assess 191(10):1–17

Gill SE, Handley JF, Ennos AR, Pauleit S (2007) Adapting cities for climate change: The role of green infrastructure. Built Environ 33(1):115–133. https://doi.org/10.2148/benv.33.1.115

Gohain KJ, Mohammad P, Goswami A (2021) Assessing the impact of land use land cover changes on land surface temperature over Pune city, India. Quatern Int 575:259–269

Gong P, Li X, Zhang W (2019) 40-Year (1978–2017) human settlement changes in China reflected by impervious surfaces from satellite remote sensing. Science Bulletin 64(11):756–763

Grimm NB, Faeth SH, Golubiewski NE, Redman CL, Wu J, Bai X, Briggs JM (2008) Global change and the ecology of cities. Science 319(5864):756–760. https://doi.org/10.1126/science.1150195

Guan D, Zhao Z, Tan J (2019) Dynamic simulation of land use change based on logistic-CA-Markov and WLC-CA-Markov models: a case study in three gorges reservoir area of Chongqing. China Environ Sci Pollut Res 26(20):20669–20688

Haddad, N. M., Brudvig, L. A., Clobert, J., Davies, K. F., Gonzalez, A., Holt, R. D., ... & Townsend, P. A. (2015). Habitat fragmentation and its lasting impact on Earth's ecosystems. Science Advances, 1(2), e1500052. https://doi.org/10.1126/sciadv.1500052

Halder B, Banik P, Bandyopadhyay J (2021) Mapping and monitoring land dynamic due to urban expansion using geospatial techniques on South Kolkata. Saf Extreme Environ 3(1):27–42

Hussain, S., &Karuppannan, S. (2021). Land use/land cover changes and their impact on land surface temperature using remote sensing technique in district Khanewal, Punjab Pakistan. *Geology, Ecology, and Landscapes*, 1–13.

Imhoff ML, Zhang P, Wolfe RE, Bounoua L (2010) Remote sensing of the urban heat island effect across biomes in the continental USA. Remote Sens Environ 114(3):504–513. https://doi.org/10.1016/j.rse.2009.10.008

Jallu SB, Shaik RU, Srivastav R, Pignatta G (2022) Assessing the effect of covid-19 lockdown on surface urban heat island for different land use/cover types using remote sensing. Energy Nexus 5:100056. https://doi.org/10.1016/j.nexus.2022.100056

Kafy AA, Rahman MS, Hasan MM, Islam M (2020) Modelling future land use land cover changes and their impacts on land surface temperatures in Rajshahi, Bangladesh. Remote Sens Appl Soc Environ 18:100314

Kamusoko C, Aniya M (2009) Hybrid classification of Landsat data and GIS for land use/cover change analysis of the Bindura district. Zimb Int J Remote Sens 30(1):97–115

Keshtkar H, Voigt W, Alizadeh E (2017) Land-cover classification and analysis of change using machine-learning classifiers and multi-temporal remote sensing imagery. Arab J Geosci 10(6):1–15

Khan R, Aribam B, Alam W (2023) Estimation of impacts of land use and land cover (LULC) changes on land surface temperature (LST) within greater Imphal urban area using geospatial technique. Acta Geophysica 71(6):2811–2823

Khatami R, Mountrakis G, Stehman SV (2016) A meta-analysis of remote sensing research on supervised pixel-based land-cover image classification processes: General guidelines for practitioners and future research. Remote Sens Environ 177:89–100. https://doi.org/10.1016/j.rse.2016.02.028

Kong, F., Sun, C., Liu, F., Yin, H., Jiang, F., Pu, Y., ... & Dronova, I. (2016). Energy saving potential of fragmented green spaces due to their temperature regulating ecosystem services in the summer. *Applied Energy*, *183*, 1428–1440.

Kumar P, Wiltshire A, Mathison C, Asharaf S, Ahrens B, Lucas-Picher P, ... and Jacob D (2013) Downscaled climate change projections with uncertainty assessment over India using a high resolution multi-model approach. Sci Total Environ 468:S18–S30. https://doi.org/10.1016/j.scitotenv.2013.01.051

Kumari, B., Shahfahad, Tayyab, M., Ahmed, I. A., Baig, M. R. I., Ali, M. A., ... & Rahman, A. (2021). Land use/land cover (LU/LC) change dynamics using indices overlay method in Gautam Buddha Nagar District-India. GeoJournal, 1–19

Lambin EF, Meyfroidt P (2011) Global land use change, economic globalization, and the looming land scarcity. Proc Natl Acad Sci 108(9):3465–3472. https://doi.org/10.1073/pnas.1100480108

Laurance, W. F., Nascimento, H. E., Laurance, S. G., Andrade, A., Ribeiro, J. E., Giraldo, J. P., ... & Lovejoy, T. E. (2011). The fate of Amazonian forest fragments: A 32-year investigation. Biological Conservation, 144(1), 56–67. https://doi.org/10.1016/j.biocon.2010.09.021

Li X, Chen G, Liu X (2013a) Simulation of urban growth by integrating cellular automata model with multi-criteria evaluation. Int J Geogr Inf Sci 27(3):574–593. https://doi.org/10.1080/13658816.2012.698020

Li X, Zhou W, Ouyang Z (2017a) The impact of urbanization on land surface temperature and its causes in Shanghai. China Environ Res Lett 12(7):074007

Li X, Zhou W, Ouyang Z, Xu W, Zheng H (2017b) Spatial pattern of greenspace affects land surface temperature: Evidence from the heavily urbanized Beijing metropolitan area. China Landsc Ecol 32(5):953–967

Li Z, Wu C, Liu H (2019) Land cover change and its impact on land surface temperature in temperate forests. Remote Sens 11(19):2242

Li X, Zhou W, Ouyang Z, Xu W (2020) The impact of land cover changes on urban heat islands in metropolitan areas: A case study of Beijing. China Remote Sens 12(3):430. https://doi.org/10.3390/rs12030430

Li W, Wang J, Jiang Y, Zhang S, Huang Q (2021) Assessing urban heat island effects using Landsat images and landscape metrics. Remote Sens 13(10):1980

Li X, Stringer LC, Dallimer M (2022) The impacts of urbanisation and climate change on the urban thermal environment in Africa. Climate 10(11):164

Liu P, Jia S, Han R, Liu Y, Lu X, Zhang H (2020) RS and GIS supported urban LULC and UHI change simulation and assessment. J Sens 2020(1):5863164. https://doi.org/10.1155/2020/5863164

Liu X, Hu G, Ai B, Li X, Shi X, Wu J (2016) Urban expansion in China and its spatial-temporal differentiation of land use changes for urbanization. Habitat Int 51:178–187. https://doi.org/10.1016/j.habitatint.2015.10.025

Liu Y, Peng J, Wang Y (2018) Efficiency of landscape metrics characterizing urban land surface temperature. Landsc Urban Plan 180:36–53

Majumdar A, Shrivastava A, Sarkar SR, Sathyavelu S, Barla A, Bose S (2020) Hydrology, sedimentation and mineralisation: A wetland ecology perspective. Clim Chang Environ Sustain 8:134–151

Mandal J, Patel PP, Samanta S (2022) Examining the expansion of Urban Heat Island effect in the Kolkata Metropolitan Area and its vicinity using multi-temporal MODIS satellite data. Adv Space Res 69(5):1960–1977

Mandal, A., Das, A., Das, M., & Pereira, P. (2024). Assessing ecosystem health of a mountainous city at the neighbourhood level: A case from eastern Himalayan region (India). *Environment, Development and Sustainability*, 1–21.

Martínez PA, Schilling M, Bidau CJ, Goloboff PA (2019) Landscape fragmentation in a megadiverse country: Consequences of habitat loss on spatial genetic structure in vertebrates. PLoS ONE 14(1):e0208597

Mehmood K, Anees SA, Luo M, Akram M, Zubair M, Khan KA, Khan WR (2024a) Assessing Chilgoza Pine (Pinus Gerardiana) forest fire severity: Remote sensing analysis, correlations, and predictive modeling for enhanced management strategies. Trees, For People 16:100521. https://doi.org/10.1016/j.tfp.2024.100521

Mehmood, K., Anees, S. A., Rehman, A., Rehman, N. U., Muhammad, S., Shahzad, F., ... & Khan, W. R. (2024b). Assessment of climatic influences on net primary productivity along elevation gradients in temperate ecoregions. *Trees, Forests and People*, *18*, 100657. https://doi.org/10.1016/j.tfp.2024.100657.

Mehmood, K., Anees, S. A., Rehman, A., Tariq, A., Zubair, M., Liu, Q., ... & Luo, M. (2024c). Exploring spatiotemporal dynamics of NDVI and climate-driven responses in ecosystems: Insights for sustainable management and climate resilience. *Ecological Informatics*, *80*, 102532. https://doi.org/10.1016/j.ecoinf.2024.102532.

Mehmood, K., Anees, S. A., Muhammad, S., Shahzad, F., Liu, Q., Khan, W. R., ... & Dube, T. (2025). Machine learning and spatio temporal analysis for assessing ecological impacts of the billion tree afforestation Project. *Ecology and Evolution*, *15*(2), e70736. https://doi.org/10.1002/ece3.70736.

Mirzazadeh R, Nazmfar H, Ghanbari A (2024) Spatial analysis of the effects of distribution of urban uses on the sustainable development of neighborhoods in ten areas of Tabriz metropolis. J Environ Sci Stud 9(1):7762–7783

Mitra C, Shepherd JM, Jordan T (2012) On the relationship between the premonsoonal rainfall climatology and urban land cover dynamics in Kolkata city, India. Int J Climatol 32(9):1443–1454

Moein M, Asgarian A, Sakieh Y, Soffianian A (2018) Scenario-based analysis of land-use competition in central Iran: finding the trade-off between urban growth patterns and agricultural productivity. Sustain Cities Soc 39:557–567

Mohammad, P., & Goswami, A. (2021). Spatial variation of surface urban heat island magnitude along the urban-rural gradient of four rapidly growing Indian cities. *Geocarto International*, 1–23.

Mushore TD, Mutanga O, Odindi J, Sadza V, Dube T (2022) Pan-sharpened landsat 8 thermal-infrared data for improved Land Surface Temperature characterization in a heterogeneous urban landscape. Remote Sens Appl: Soc Environ 26:100728. https://doi.org/10.1016/j.rsase.2022.100728

Myint SW, Wentz EA, Brazel AJ, Quattrochi DA (2013) The impact of fragmentation and vegetation type on urban thermal behavior. Remote Sens Environ 137:71–83

Oke TR (1982) The energetic basis of the urban heat island. Q J R Meteorol Soc 108(455):1–24. https://doi.org/10.1002/qj.49710845502

Patra S, Sahoo S, Mishra P, Mahapatra SC (2018) Impacts of urbanization on land use/cover changes and its probable implications on local climate and groundwater level. J Urban Manag 7(2):70–84

Paul B, Chakraborty M, Mondal B (2022) Modeling the effects of land use and land cover change on surface runoff in a watershed using the SWAT model. J Hydrol 606:127–135

Qiu B, Li H, Chen C, Tang Z, Zhang K, Berry J (2019) Tracking spatial–temporal landscape changes of impervious surface areas, bare lands, and inundation areas in China during 2001–2017. Land Degrad Dev 30(15):1802–1812

Rasul A, Balzter H, Smith C, Remedios J, Adamo M (2017) Satellite-based detection of urban heat and cool islands for sustainable urban planning of the City of London. Remote Sen 9(8):746. https://doi.org/10.3390/rs9080746

Rizwan AM, Dennis LYC, Liu C (2008) A review on the generation, determination and mitigation of Urban Heat Island. J Environ Sci 20(1):120–128. https://doi.org/10.1016/S1001-0742(08)60019-4

Sahani N, Goswami SK, Saha A (2021) The impact of COVID-19 induced lockdown on the changes of air quality and land surface temperature in Kolkata city, India. Spat Inf Res 29:519–534

Sakhre S, Dey J, Vijay R, Kumar R (2020) Geospatial assessment of land surface temperature in Nagpur, India: an impact of urbanization. Environ Earth Sci 79(10):226

Santamouris M (2015) Regulating the damaged thermostat of the cities—Status, impacts, and mitigation challenges. Energy and Build 91:43–56. https://doi.org/10.1016/j.enbuild.2015.01.027

Satiprasad S (2013) Monitoring urban Land use land cover change by multi-temporal remote sensing information in Howrah City. India PAN 520(900):15

Schneider A, Friedl MA, Potere D (2017) Mapping global urban areas using MODIS 500-m data: New methods and datasets based on "urban ecoregions." Remote Sens Environ 195:82–94

Seto KC, Ramankutty N (2016) Hidden linkages between urbanization and food systems. Sci 352(6288):943–945. https://doi.org/10.1126/science.aaf7439

Seto KC, Güneralp B, Hutyra LR (2012) Global forecasts of urban expansion to 2030 and direct impacts on biodiversity and carbon pools. Proc Natl Acad Sci 109(40):16083–16088. https://doi.org/10.1073/pnas.1211658109

Sharma, S., Nahid, S., Sharma, M., Sannigrahi, S., Anees, M. M., Sharma, R., ... & Joshi, P. K. (2020). A long-term and comprehensive assessment of urbanization-induced impacts on ecosystem services in the capital city of India. *City and Environment Interactions*, *7*, 100047. https://doi.org/10.1016/j.cacint.2020.100047.

Shukla A, Jain K (2021) Analyzing the impact of changing landscape pattern and dynamics on land surface temperature in Lucknow city, India. Urban For Urban Green 58:126877. https://doi.org/10.1016/j.ufug.2020.126877

Shwetha HR, Kumar DN (2015) Prediction of land surface temperature under cloudy conditions using microwave remote sensing and ANN. Aquatic Procedia 4:1381–1388

Siddique G, Ghosh S, Roy A (2020) Assessment of urban expansion and associated spatial transformation of Chandannagar city, West Bengal. Space Cult, India 7(4):109–121

Sultana S, Satyanarayana ANV (2018) Urban heat island intensity during winter over metropolitan cities of India using remote-sensing techniques: Impact of urbanization. Int J Remote Sens 39(20):6692–6730

Svirieva-Hopkins A, Moore M, Hedditch J (2008) Land use planning and zoning: Managing change in the urban-rural fringe. Urban Stud 45(5–6):1021–1038

Tan J, Li M (2015a) The role of vegetation in urban heat islands: A case study in Shanghai. China Urban For & Urban Green 14(2):282–289. https://doi.org/10.1016/j.ufug.2015.02.001

Tan M, Li X (2015b) Quantifying the effects of settlement size on urban heat islands in fairly uniform geographic areas. Habitat Int 49:100–106

Tan J, Yu D, Li Q, Tan X, Zhou W (2020) Spatial relationship between land-use/land-cover change and land surface temperature in the Dongting Lake area. China Sci Rep 10(1):1–9

Tavares PA, Santos T, Fernandes JP (2020) Effects of forest fragmentation on land surface temperature: Evidence from an urban area. Urban Forestry & Urban Greening 56:126865

Tran DX, Pla F, Latorre-Carmona P, Myint SW, Caetano M, Kieu HV (2017) Characterizing the relationship between land use land cover change and land surface temperature. ISPRS J Photogramm Remote Sens 124:119–132

Turner, M. G., Gardner, R. H., & O'Neill, R. V. (2015). Landscape Ecology in Theory and Practice: Pattern and Process (2nd ed.). Springer. https://doi.org/10.1007/978-1-4939-2794-4

Uuemaa E, Truu J, Mander Ü, Oja T (2016) Trends in the use of landscape spatial metrics as landscape indicators: A review. Ecol Ind 64:1–10

Wang R, Murayama Y (2020) Geo-simulation of land use/cover scenarios and impacts on land surface temperature in Sapporo. Jpn Sustain Cities Soc 63:102432

Wang D, Xu PY, An BW, Guo QP (2024) Urban green infrastructure: Bridging biodiversity conservation and sustainable urban development through adaptive management approach. Front Ecol Evol 12:1440477

Weng Q (2001) A remote sensing? GIS evaluation of urban expansion and its impact on surface temperature in the Zhujiang Delta, China. Int J Remote Sens 22(10):1999–2014

Xie Y, Wang X, Yang L (2018) Urban green space dynamics and their policy implications for urban planning in response to climate change. Sustainability 10(6):1846. https://doi.org/10.3390/su10061846

Xue X, He T, Xu L, Tong C, Ye Y, Liu H, Zheng X (2022) Quantifying the spatial pattern of urban heat islands and the associated cooling effect of blue–green landscapes using multisource remote sensing data. Sci Total Environ 843:156829. https://doi.org/10.1016/j.scitotenv.2022.156829

Yang J, Wong MS, Menenti M, Nichol J (2015) Study of the geometry effect on land surface temperature retrieval in urban environment. ISPRS J Photogramm Remote Sens 109:77–87

Ye H, Li Z, Zhang N, Leng X, Meng D, Zheng J, Li Y (2021) Variations in the effects of landscape patterns on the urban thermal environment during rapid urbanization (1990–2020) in megacities. Remote Sens 13(17):3415

Zhang F, Kung H, Johnson VC, LaGrone BI, Wang J (2018) Change detection of land surface temperature (LST) and some related parameters using Landsat image: a case study of the Ebinur lake watershed, Xinjiang, China. Wetlands 38:65–80

Zhang T, Huang X (2018) Monitoring of urban impervious surfaces using time series of high-resolution remote sensing images in rapidly urbanized areas: A case study of Shenzhen. IEEE J Sel Top Appl Earth Obs Remote Sens 11(8):2692–2708

Zhang X, Chen Y, Li Z (2011) Urban expansion and its driving factors of big cities in China. Urban Stud 48(5):945–960

Zhang Y, Li Y, Wang H (2013) Effects of landscape pattern on land surface temperature in urban areas. J Geog Sci 23(2):360–374

Zhang Y, Li X, Wu B (2016) Impact of rail transit on the land use in surrounding areas of big cities in China. J Transp Geogr 54:295–306

Zhao L, Lee X, Smith RB, Oleson K (2014) Strong contributions of local background climate to urban heat islands. Nature 511(7508):216–219. https://doi.org/10.1038/nature13462

Zhou D, Zhao S, Zhang L, Sun G, Liu Y (2014) The footprint of urban heat island effect in China. Sci Rep 4:1–6. https://doi.org/10.1038/srep05499

Zhou D, Zhang L, Li D (2017a) Understanding the mechanisms behind the temperature effects of urbanization: A perspective of surface energy balance. J Appl Meteorol Climatol 56(5):1509–1516. https://doi.org/10.1175/JAMC-D-16-0195.1

Zhou Y, Varquez ACG, Kanda M (2017b) High-resolution global urban growth projection based on multiple applications of the SLEUTH urban growth model. Sci Data 4:170084. https://doi.org/10.1038/sdata.2017.84

Zhou W, Huang G, Wang J (2021) Urban expansion and its impacts on local climate in the Greater Bay Area. China Int J Climatol 41(5):3075–3090. https://doi.org/10.1002/joc.7050

Zhu Z, Wang S, Woodcock CE (2016) Improvement and expansion of the Fmask algorithm: Cloud, cloud shadow, and snow detection for Landsats 4–7, 8, and Sentinel 2 images. Remote Sens Environ 159:269–277. https://doi.org/10.1016/j.rse.2014.12.014

Publisher's Note Springer Nature remains neutral with regard to jurisdictional claims in published maps and institutional affiliations.

Springer Nature or its licensor (e.g. a society or other partner) holds exclusive rights to this article under a publishing agreement with the author(s) or other rightsholder(s); author self-archiving of the accepted manuscript version of this article is solely governed by the terms of such publishing agreement and applicable law.

Journal of Electrical Engineering & Technology
https://doi.org/10.1007/s42835-025-02305-3

ORIGINAL ARTICLE

Voltage Angle Based Power System Inertia Estimation Using Synchrophasor Technology

Nitisha Sudhir Darwade[1] · **S.T. Nagarajan**[1]

Received: 11 September 2024 / Revised: 14 May 2025 / Accepted: 16 May 2025
© The Author(s) under exclusive licence to The Korean Institute of Electrical Engineers 2025

Abstract
The increasing integration of renewable energy sources (RES) into power systems raises extensive challenges for power system operators to ensure grid stability, especially due to the reduced inertia associated with these sources. Therefore, it is essential to estimate power system inertia continuously to monitor and control power system dynamics. Traditionally, several methods were being adopted to estimate power system inertia based on frequency measurements which has its own assumptions and limitations. This paper presents a novel innovative approach to estimate online system inertia by using bus voltage phase angle measured from Phasor measurement units along with fuzzy logic estimator. The proposed method has been tested on IEEE nine bus system and Kundur's two area system modified with PV farms. Simulations have been carried out with OPAL RT real time simulator in HYPERSIM environment. The results of the proposed method estimate the power system inertia with 99.98% - 96.13% accuracy.

Keywords System inertia (H_{Sys}) · Phasor Measurement Unit (PMU) · Wide area measurement system (WAMS) · Fuzzy logic · Photovoltaic (PV)

1 Introduction

With the continuous increase in the electric power demand, the integration of Renewable energy sources (RES) in the power system has grown exponentially in the last few decades. Integration of RES into existing power systems has been executed by interfacing power electronic converters. The presence of power electronic converter has brought major challenges to the stability and reliability of the power system due to the absence of inertia in the system [1, 2]. Inertia is a vital parameter of the power system, which reduces the frequency deviation, causing a reduction in the rate of change of frequency (ROCOF) during any perturbation in the system [3–5]. Reduction in system inertia due to RES increases the frequency deviation during the disturbance in the system. Therefore, it is essential to monitor continuously to alert the system operator to take any primitive actions to avoid any power failure [6]. However, inertia measurement in power system is challenging for power engineers as it is not a directly measurable quantity.

Upon literature survey on estimating inertia in power system, several researchers have been reported on estimating inertia using different techniques with several assumptions. Broadly, inertia estimation can be classified as offline and online methods [2, 7]. Offline inertia estimation is considered as post mortem analysis, which is performed after the occurrence of disturbance whereas online estimation is based on ambient signals. Offline methods mainly use classical swing equation for estimation of inertia constant if parameters like frequency, active power change, ROCOF or second derivative of rotor angle, at the instant of disturbance are available [8–12]. Direct measurement of frequency transients creates issues of noise and oscillatory components due to production of synchronizing power of generator. Researchers have discussed about reducing frequency oscillations by adopting different approaches like curve fitting method and different types of filters like lowpass Butterworth filters, 0.5 Hz low pass filter and 5 Hz low pass filter to suppress noise [11–14]. Measuring the instantaneous change in active power and ROCOF on individual generators during

✉ Nitisha Sudhir Darwade
nitishasudhirdarwade_2k21phdee11@dtu.ac.in

S.T. Nagarajan
stnagarajan@dce.ac.in

[1] Department of Electrical Engineering, Delhi Technological University, Delhi, India

Published online: 12 June 2025

a disturbance is almost infeasible by direct methods. Also, measuring frequency data from a single location or using average frequency is not reliable for estimating ROCOF [7]. The accurate prediction of the instant of disturbance is a vital aspect for determining ROCOF. Detrended Fluctuation Analysis (DFA) has been adopted in the literatures to predict the accurate timing of an event [8, 14]. The location of disturbance and its measurement are essential factors in estimating inertia. All these factors, raises concern about accurately estimating inertia.

With the advancement in wide area measurement techniques presently Phasor measurement unit (PMU) has been incorporated in power system to monitor power system dynamics in real time [15]. Recently, several literatures have reported use of PMU for estimation of power system inertia. Ariff et al. [16] proposed an algorithm to estimate inertia constant of synchronous generators using PMU data with unscented Kalman filter (UKF) to measure accurate dynamic model parameters in presence of noise. Wall et al. [17] proposed a new method to estimate inertia using sliding window method (SWM). This method utilizes a series of sliding data windows to estimate both the system's inertia and the time of disturbance immediately after the disturbance. Petra et al. [18] used the magnitude and phase angle of the bus voltage of the load to estimate inertia by using complete differential-algebraic equations that model the dynamic behaviour of generators and power system networks inside the Bayesian framework by adopting two different methods based on adjoint and stochastic spectral. Tuttleberg et al. [19] estimated online inertia using active power change and frequency data collected from PMU. Tan et al. [20] proposed an online decentralized and data-driven inertia estimation technique using Thevenin's theorem to identify the mathematical correlation between generator terminal voltage and current internal rotor speed of generator. Cao et al. [21] utilizes steady-state and low-frequency variation data of last two years from three PMUs placed at different locations to train switching Markov Gaussian models to estimate system inertia in real time. Andreas and Byongjun [22] adopted ANN (Artitifical Neural Network) to train the frequency response to estimate online system inertia. However, Kerdphol et.al [13] claims not all PMUs located at different locations provide accurate data of frequency to estimate inertia due to interarea oscillations. Most of the literatures are based on frequency response for estimating system inertia with different accuracy.

In this research instead of frequency measurement bus voltage angles has been measured with PMUs for estimating power system inertia. The main idea in this research work stems from the close relation between the rotor angle oscillations of the generator to the bus voltage phase angle oscillations. In particular, the derivative of phase angle has been explored with artificial intelligence techniques like fuzzy logic to estimate system inertia H_{system}. The Proposed approach has been validated on standard benchmark systems and simulation has been performed in OPAL RT real time simulator with HYPERSIM environment.

To summarise the Contributions in this paper are

- A novel approach for online system inertia estimation has been proposed.
- Unique response of bus voltage phase angle derivative, with a given system inertia has been established.
- A new signal, based on bus voltage phase angle measured by the PMU has been explored for inertia estimation purpose.
- AI based fuzzy logic inertia estimator has been developed for online estimation of system inertia.
- The Proposed algorithm can estimate system inertia accurately in presence of renewable energy sources and does not get influenced by generation shared by RES.
- Proposed algorithm estimates system inertia with high accuracy irrespective of type of disturbance.

Comparison of different estimation techniques available in literature with proposed method are tabulated in Table 1.

Remaining paper has been structured in Sect. 2, 3, 4, 5 and 6. Section 2 discuss about selection of measurement signal for estimation of inertia, Sect. 3 consists of discussion regarding approach adopted for inertia estimation. Section 4 elaborates case study consists of 2 cases includes 2 stages in detail. Section 5 discusses the limitations related with traditional methods based on frequency response. Section 6 concludes this study.

Table 1 Comparison of algorithms available in literature with proposed method

References	Mode	Input Quantity/ Methodology	Error
[8–11, 13]	Offline	ROCOF and change in active power using Swing equation	Not investigated
[23]	Offline	Second derivative of frequency response	Not investigated
[24]	Online	Fourier Transform of swing equation	4.09%
[17]	Online	Frequency response and active power using smooth window method	5.43%
[21]	Online	Frequency response using Markov Gaussian models	Not investigated
Proposed method	Online	Bus voltage phase angle using Fuzzy logic	0.023% − 3.869%

2 Voltage Phase Angle for Estimation of System Inertia

In this section, mathematical background of relation between the proposed bus voltage phase angle from PMU and the system inertia has been developed along with the Relation between phase angle and inertia.

2.1 Mathematical Background of Proposed Concept for Inertia Estimation

Voltage Phase angle of buses are constant under stable operating condition and it oscillates during contingency in the system, which is influenced by inertia of the system. The relation between inertia of the system and voltage phase angle oscillations can be established in the following expressions.

In a linear system, stability can be assessed by examining characteristic equation [25],

$$s^2 + 2\zeta\omega_n s + \omega_n^2 = 0 \tag{1}$$

Where ω_n is natural frequency of oscillation. Roots of this characteristic equation can be expressed as,

$$s_1, s_2 = -\zeta\omega_n \pm j\omega_n\sqrt{1-\zeta^2} = -\zeta\omega \pm j\omega_d$$

Where ω_d *is* damped frequency of oscillation and ζ is damping ratio, with ω_d as,

$$\omega_d = \omega_n\sqrt{(1-\zeta^2)} \tag{2}$$

Equation 1 can be represented in terms of generator parameters as,

$$\frac{d^2\Delta\delta}{dt^2} + \frac{\pi f_o}{H}\,\mathrm{D}\,\frac{d\Delta\delta}{dt} + \frac{\pi f_o}{H}P_S\Delta\delta = 0 \tag{3}$$

Where δ is rotor angle position, H is inertia constant of rotor, $f_0 f_0$ is system frequency and P_S is synchronizing power. Solving above equation 3 in state space form (derived in Appendix A), we get,

$$\delta = \delta_0 + \frac{\Delta\delta_0}{\sqrt{(1-\zeta^2)}}e^{-\zeta\omega_n t}\sin(\omega_d\, t + \theta)$$

Taking its derivative, we get

$$\frac{d\delta}{dt} = -\,\zeta\omega_n^2\;\Delta\delta_0\;e^{-\zeta\omega_n t}\cos(\omega_d t + \theta) \tag{4}$$

It can be observed that the derivative of rotor angle oscillation is independent of initial condition and oscillates at a frequency of ω_d. The generator bus voltage phase angle is approximately same as rotor angle as the generators reactance are negligible [24]. Therefore Eq. (4) can be considered as bus voltage phase angle whose natural frequency of oscillation ω_n can be expressed in terms of generator parameters as,

$$\omega_n = \sqrt{\frac{\pi f_0 P_S}{H}} \quad \text{or} \quad H = \frac{\pi f_0 P_S}{\omega_n^2}$$

From the above equation inertia constant H can be evaluated if ω_n is measured with other parameters being constant. However it can be observed from equation 4, only ω_d is measurable directly from the response of the system and ω_n is dependent upon ζ as per equation 2. In real power system the variation of ζ is small and can be taken into account with artificial intelligence technique to map ω_d with inertia H instead of ω_n . Thus by measuring the oscillation ω_d of the system with only conventional generators, inertia estimation can be trained in fuzzy logic to determine the inertia in the presence of renewable energy sources.

2.2 Relation Between Phase Angle and Inertia Constant H

To further explain, a plot for derivative of bus voltage phase angle ($\dot{\delta}$) for low, medium and high values of system inertia from synchronous generators is shown in the Fig. 1 for a sudden increment of load in the system. Figure 2 is the response of the system for different magnitudes of load with same system inertia.

It can be observed from the Figs. 1 and 2 that the derivative $\dot{\delta}$ shows unique nature of response for various values of system inertia constant and does not get affected by type of load. The time period (or frequency) of oscillation of derivative $\dot{\delta}$ provides an opportunity to explore this signal for estimating inertia. The time period between two consecutive zero crossings after its first lower or higher peak can be considered for calculating the frequency of oscillation of $\dot{\delta}$.

3 Proposed Procedure for System Inertia Estimation

In this section the brief background on WAMS technology and Fuzzy logic technique as presented below.

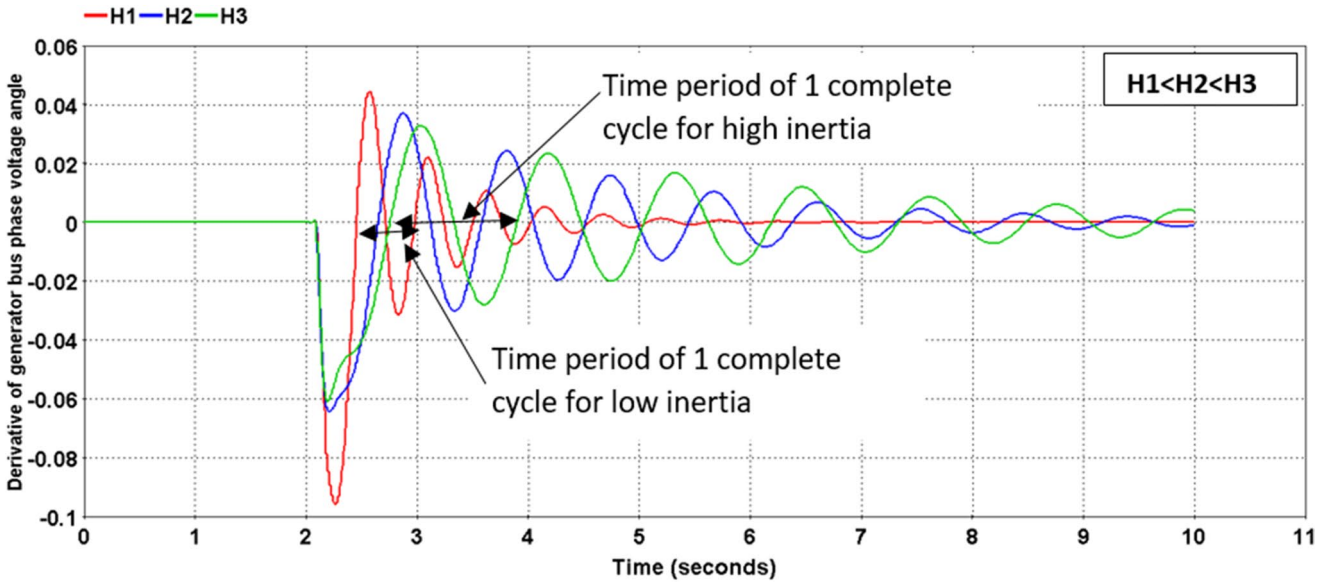


Fig. 1 Derivative of generator bus voltage phase angle $\dot{\delta}$ for different inertia constant

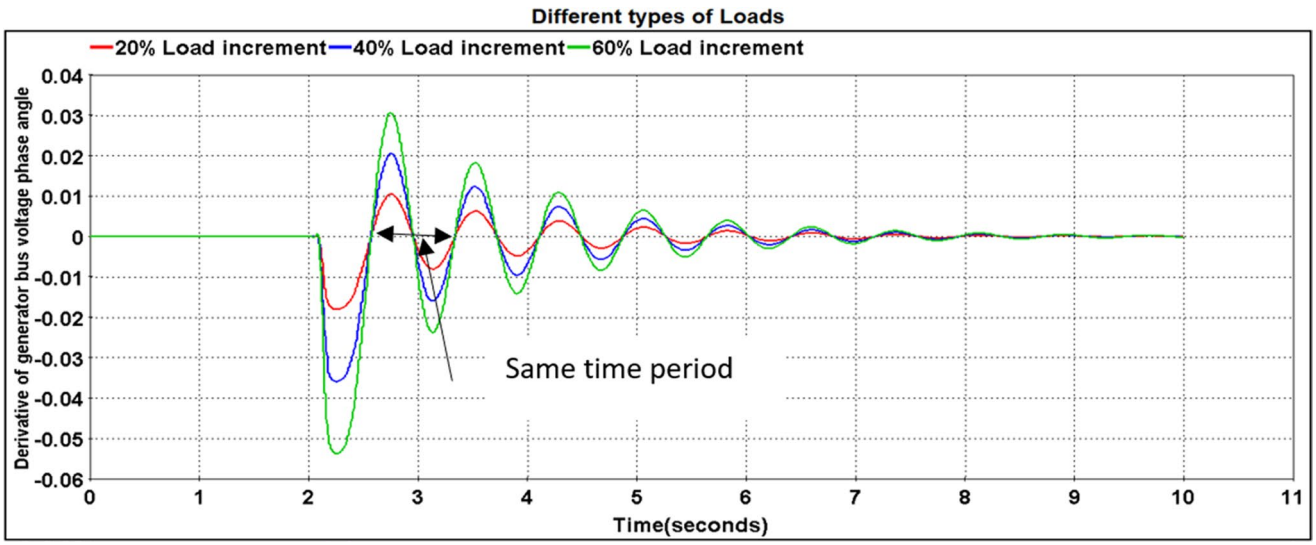


Fig. 2 Derivative of generator bus voltage phase angle $\dot{\delta}$ for different types of load

3.1 Synchrophasor/WAMS

Synchrophasor technology is being implemented across the globe during past two decades. Synchrophasor consists of Phasor Measurement Unit (PMU), Data collection layer and Energy management layer [25]. A functional PMU block diagram has been represented in Fig. 3. As per IEEE C37.118.2011 standard PMU receives analogue signals of voltage and current from current transformer and potential transformer and estimates the phasor values of voltage, current, frequency and rate of change of frequency (ROCOF) at reporting rates of 10, 25, 50 frames/second and 10, 20, 30, 60 frames/second for frequency of 50 Hz, 60 Hz respectively [26]. The data from PMU is aligned to Universal time coordinates (UTC) using Global Positioning satellite (GPS). Multiple PMUs are placed at different substations sends information to the PDC (phasor data concentrator) placed at utility, to store the data. Stored data from PDC goes to Master PDC/Application layer which aggregates data for monitoring, visualization, analytical processing and protection alarm [27].

3.2 Design of Fuzzy Logic Estimator

Fuzzy logic is one of the artificial intelligence (AI) technique which takes decision intelligently on the basis of previous

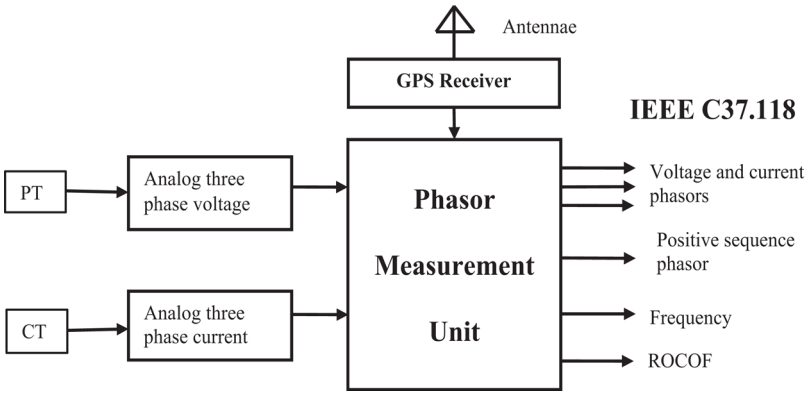


Fig. 3 Block diagram representation of PMU

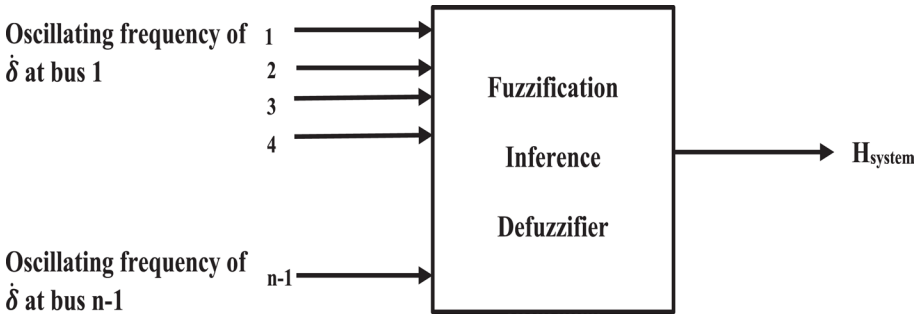


Fig. 4 Block diagram representation of Fuzzy logic

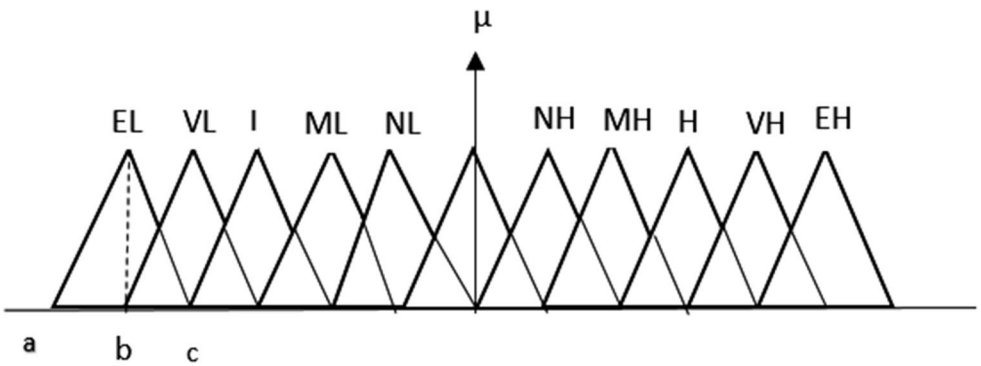


Fig. 5 Membership function developed for fuzzy logic toolbox

numerical data, pictures etc [28]. In this work Double input single output mamdani fuzzy logic has been explored as a tool for estimation of inertia. Step involved for designing the fuzzy logic estimator are explained below.

3.2.1 Fuzzification

For designing fuzzy logic estimator, oscillating frequency of $\dot{\delta}$ at generator buses 1,2,3,4….n-1 are chosen as input for fuzzy logic estimator. Generator bus number n is considered as swing bus, as shown in Figure 4.

Triangular shaped 11 membership function for input as well as for output has been designed as shown in Figure 5. 11 linguistic variables are selected as Extreme low (EL), Very low (VL), Low(L), Medium low(ML), Normal low (NL), Normal(N), Normal High(NH), Medium High(MH), High(H), Very High(VH), Extreme High(EH) for both input and output.

$$
\begin{aligned}
\mu_{triangular}\ (x;a,b,c) &= 0 \quad x \le a; \\
&= \frac{x-a}{b-a} \quad a \le x \le b \\
&= \frac{c-x}{c-b} \quad b \le x \le c \\
&= 0 \quad x \ge c \\
&= \max(\min(\frac{x-a}{b-a}, \frac{c-x}{c-b}), 0)
\end{aligned}
$$

Values of a,b,c are determined from response of the system with synchronous generators.

3.2.2 Fuzzy Rule Base

By considering 11 linguistic variable truth table developed for fuzzy logic estimator of nine bus system is as

Table 2 Truth table for fuzzy logic development

Rule	Oscillating frequency of $\dot{\delta}$	H_{sys}
1	EL	EH
2	VL	VH
3	L	H
4	ML	MH
5	NL	NH
6	N	N
7	NH	NL
8	MH	ML
9	H	L
10	VH	VL
11	EH	EL

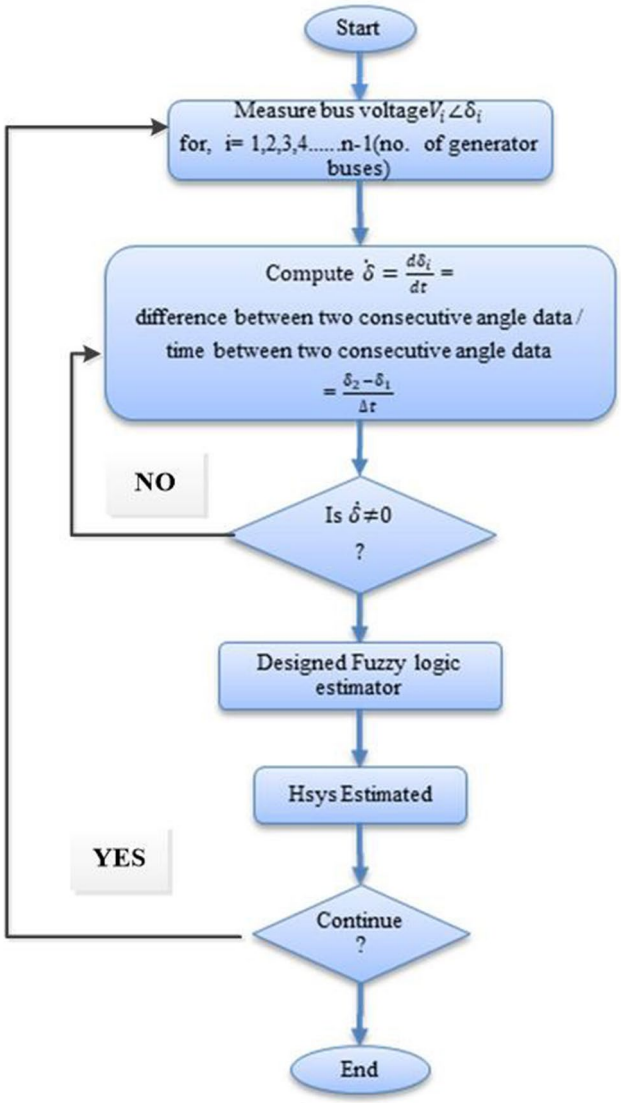


Fig. 6 Proposed algorithm for inertia estimation

shown below Table 2. By increasing number of input N, $\mathrm{Rule}^{\mathrm{N}}\mathrm{Rule}^{\mathrm{N}}$ can be formed to increase accuracy of the output.

3.2.3 Defuzzification

For converting output into crisp value centre of gravity method has been utilized formula which represented in equation 5.

$$\text{Crisp output (Hsys)} = \frac{\sum_{i=1}^{11} bi \int \mu(i)}{\sum_{i=1}^{11} \int \mu(i)} \tag{5}$$

Where μ(i) is the membership function of output i, bi is the centre of membership function.

3.3 Proposed Algorithm

Proposed algorithm for estimation of inertia from the derivate of generator bus voltage phase angle and trained fuzzy logic estimator is shown in Fig. 6. Bus voltage phase angle V∠ δ are measured by PMUs from all the generator buses in the system. Derivative of phase angle $\dot{\delta}$ is computed by taking difference between two consecutive data of voltage phase angle with respect to time. Calculated derivative of generator bus voltage phase angle $\dot{\delta}$ are passed to trained fuzzy logic as input for estimating inertia.

4 Case Study

Simulation studies have been carried out in OPAL RT real time simulator in HYPERSIM environment on two benchmark power systems: Nine bus system and Two area system.

4.1 Case–I Nine Bus System

A Nine bus system [29] consisting of three generators G1, G2, G3 with 512 MVA, 270 MVA and 125MVA respectively has been considered as shown in Fig. 7 for this study. G1 is considered as swing machine with inertia constant at 6s. Three loads A, B, C of 125 MW, 90MWand 100 MW are connected at bus 5, 6 and 8 respectively. Initial load flow has been executed by Newton Raphson load flow method according to which power supplied by generators are 71 MW, 163 MW and 85 MW respectively. All the generator buses are connected with PMUs to obtain voltage phase angle. The time period T between zero crossings from the voltage phase angle has been measured, inverse of this time period is the frequency of oscillation f_d of $\dot{\delta}$ which is considered to be the input parameter for fuzzy logic system inertia estimator.

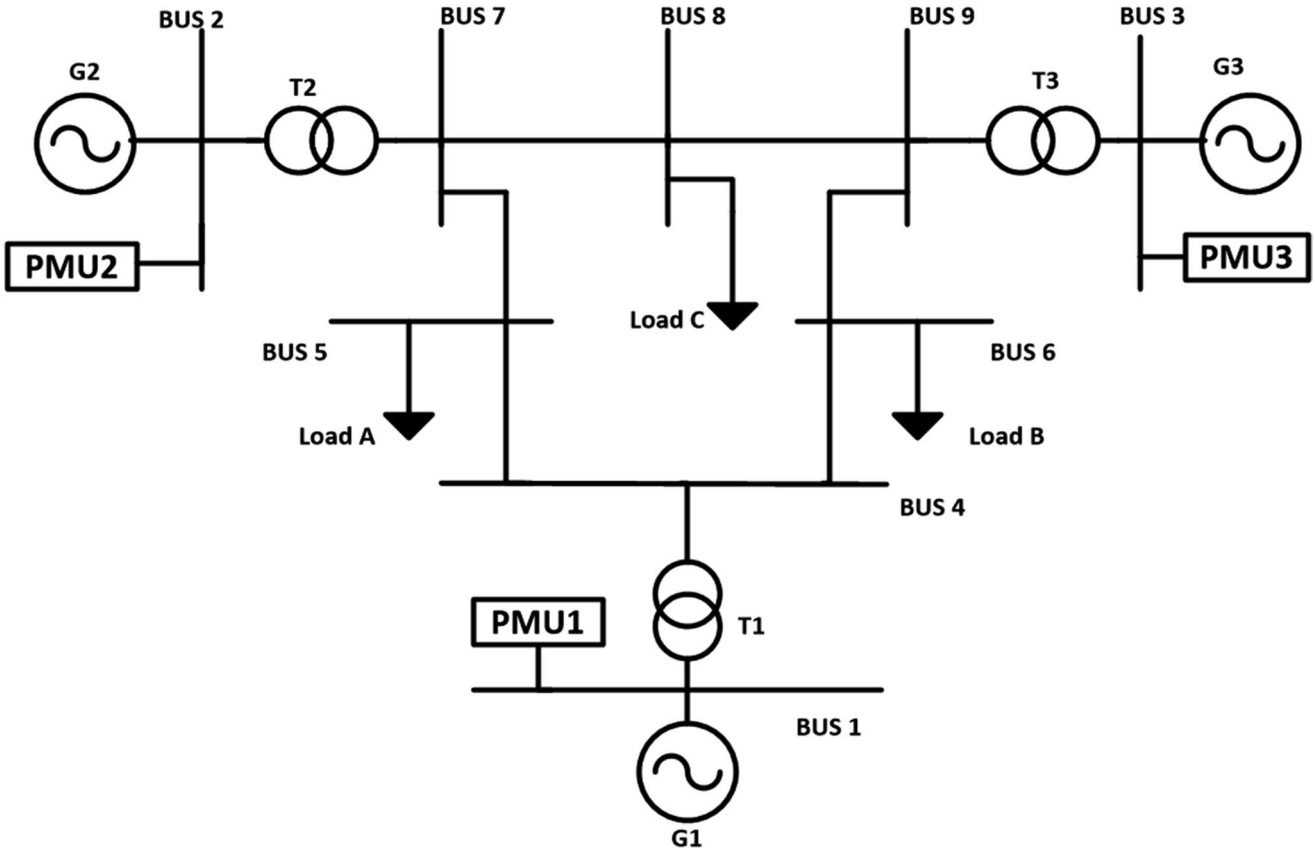


Fig. 7 Nine bus system

The proposed algorithm for estimation of inertia has been carried out in two stages (i) Design of fuzzy logic estimator and (ii) H_{sys} estimation in presence of Photovoltaic farm.

4.1.1 Stage I: Design of Fuzzy Logic Estimator to Estimate Hsys

To design the fuzzy logic estimator, inertia of generator G_1 is kept to be constant at 6s. Whereas inertia of G_2 and G_3 have been varied in the range of 2–6s in steps of 0.5s to obtain the response for a disturbance of additional 50 MW load with load C at 2 seconds. Sample responses of derivative $\dot{\delta}$ at generator bus 2 is shown in Fig. 8. It can be observed from the Fig. 8 that with the increase in inertia the time period increases which implies to reduction in frequency of oscillation f_d of $\dot{\delta}$.

For each variation of generator inertia in the system, System inertia can be calculated by using the following equations 6 [8].

$$H_{sys} = \frac{\sum_{i=1}^{N} S_{ni} H_i}{\sum_{i=1}^{N} S_{ni}} \text{ [s]} \tag{6}$$

In this case, eighty-one values of H_{sys} has been calculated by using equation 6. Eighty-one unique responses of $\dot{\delta}$ at generator buses 2 and 3 as well as H_{sys} are utilized to design the membership function value of the fuzzy logic estimator. Twenty-five sample data of f_d of derivative $\dot{\delta}$ for bus 2 and 3 as well as H_{sys} are represented in Table 3. Where, G1, G2 and G3 are MVA rating of the generators 1, 2 and 3 also H_1, H_2 and H_3 represents inertia of the generators 1, 2 and 3 in seconds respectively which are used to calculate the actual H_{sys}. One sample calculation to find H_{sys} for the values of 1st row of Table 3 is expressed below.

$$H_{sys} = \frac{(MVA1 \times H1) + (MVA2 \times H2) + (MVA3 \times H3)}{G1 + G2 + G3} \text{ [s]}$$

$$H_{sys} = \frac{(512 \times 6) + (270 \times 2) + (125 \times 2)}{512 + 270 + 125}$$

$$H_{sys} = 4.54024 \text{ [s]}$$

By using above input data eleven triangular membership function are formed for two crisp input which are f_d of $\dot{\delta}$ at bus 2 and bus 3 and crisp output is H_{sys}. For each membership function values of a, b and c are represented in Table 4.

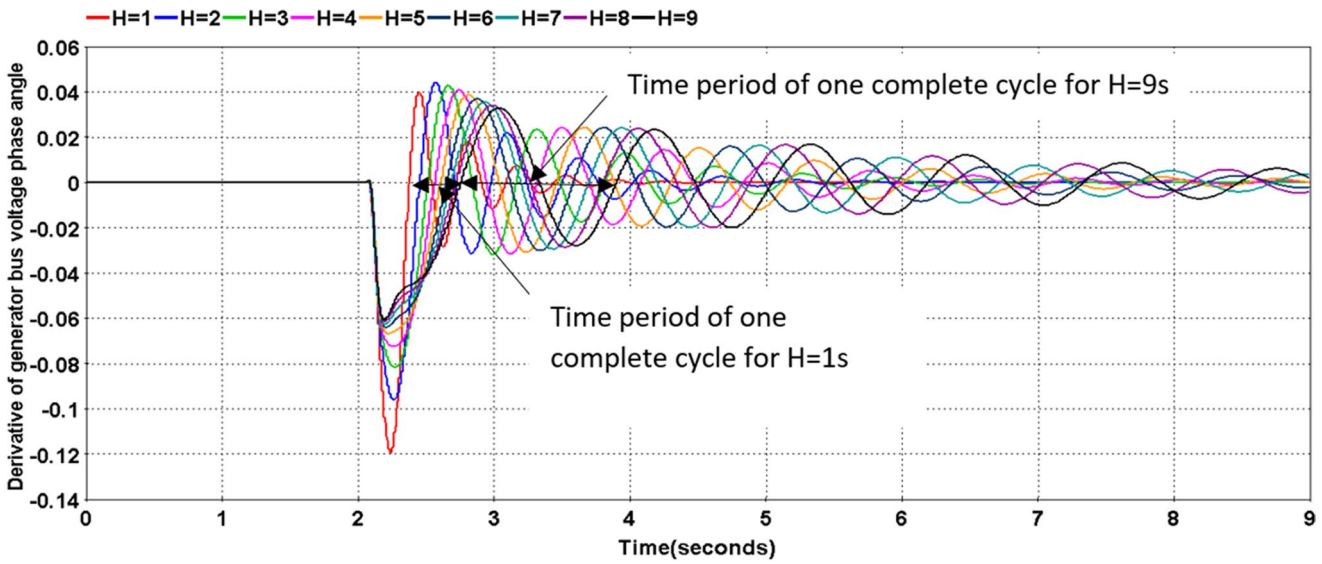


Fig. 8 Response of derivative of generator bus voltage phase angle $\dot{\delta}$ at bus 2

Table 3 Input data for fuzzy logic design

Sr. No.	G1 (MVA)	G2 (MVA)	G3 (MVA)	H1 (s)	H2 (s)	H3 (s)	Calculated Hsys (s)	f_d of $\dot{\delta}$ at bus 2 Cycles/sec	f_d of $\dot{\delta}$ at bus 3 Cycles/sec
1	512	270	125	6	2	2	4.540242558	1.1964	1.1809
2	512	270	125	6	2	3	4.678059537	1.1504	1.1487
3	512	270	125	6	2	4	4.815876516	1.0593	1.0745
4	512	270	125	6	2	5	4.953693495	0.9895	0.9929
5	512	270	125	6	2	6	5.091510474	0.9999	0.9934
6	512	270	125	6	3	2	4.837927233	1.0571	0.9998
7	512	270	125	6	3	3	4.975744212	1.0417	0.9928
8	512	270	125	6	3	4	5.113561191	1.0101	1.0119
9	512	270	125	6	3	5	5.25137817	0.9788	0.9648
10	512	270	125	6	3	6	5.38919514	0.9666	0.9261
11	512	270	125	6	4	2	5.135611907	0.9713	0.9773
12	512	270	125	6	4	3	5.273428886	0.9524	0.9887
13	512	270	125	6	4	4	5.411245865	0.9383	0.9256
14	512	270	125	6	4	5	5.549062845	0.9264	0.926
15	512	270	125	6	4	6	5.686879824	0.9252	0.9009
16	512	270	125	6	5	2	5.433296582	0.9386	0.8951
17	512	270	125	6	5	3	5.571113561	0.9042	0.8992
18	512	270	125	6	5	4	5.70893054	0.8875	0.8434
19	512	270	125	6	5	5	5.846747519	0.8666	0.8264
20	512	270	125	6	5	6	5.984564498	0.8766	0.8389
21	512	270	125	6	5	2	5.730981257	0.8721	0.8986
22	512	270	125	6	6	3	5.868798236	0.8421	0.7826
23	512	270	125	6	6	4	6.006615215	0.8432	0.8196
24	512	270	125	6	6	5	6.144432194	0.8484	0.7449
25	512	270	125	6	6	6	6.282249173	0.7843	0.7168

Table 4 Membership function data for fuzzy logic

	Triangular membership function values								
	Crisp Input1 f_d at bus 2			Crisp Input2 f_d at bus 3			Crisp Output H_{sys}		
	a	b	c	a	b	c	a	b	c
MF1	0.6402	0.7843	0.8442	0.7158	0.7168	0.7635	4.3402	4.5402	4.689
MF2	0.7843	0.8442	0.8766	0.7168	0.7635	0.8389	4.5402	4.689	4.8379
MF3	0.8421	0.8649	0.8878	0.7652	0.8264	0.8775	4.8848	4.9537	5.0336
MF4	0.8668	0.9013	0.9256	0.8108	0.8652	0.9013	5.045	5.1246	5.1825
MF5	0.9042	0.9225	0.9442	0.8669	0.8992	0.9164	5.1935	5.2734	5.3313
MF6	0.9260	0.9495	0.9666	0.8939	0.9228	0.9512	5.3423	5.4222	5.4801
MF7	0.9476	0.9809	1.0091	0.9371	0.9648	0.9771	5.4911	5.5711	5.6289
MF8	0.9713	0.9999	1.0268	0.9511	0.9934	1.012	5.6400	5.7089	5.7778
MF9	0.9895	1.0012	1.0751	0.9928	1.022	1.074	5.7888	5.8577	5.9377
MF10	1.0571	1.13	1.1964	0.999	1.088	1.181	5.9845	6.0755	6.2822
MF11	1.13	1.1964	1.2044	1.087	1.181	1.229	6.0755	6.2822	6.3822

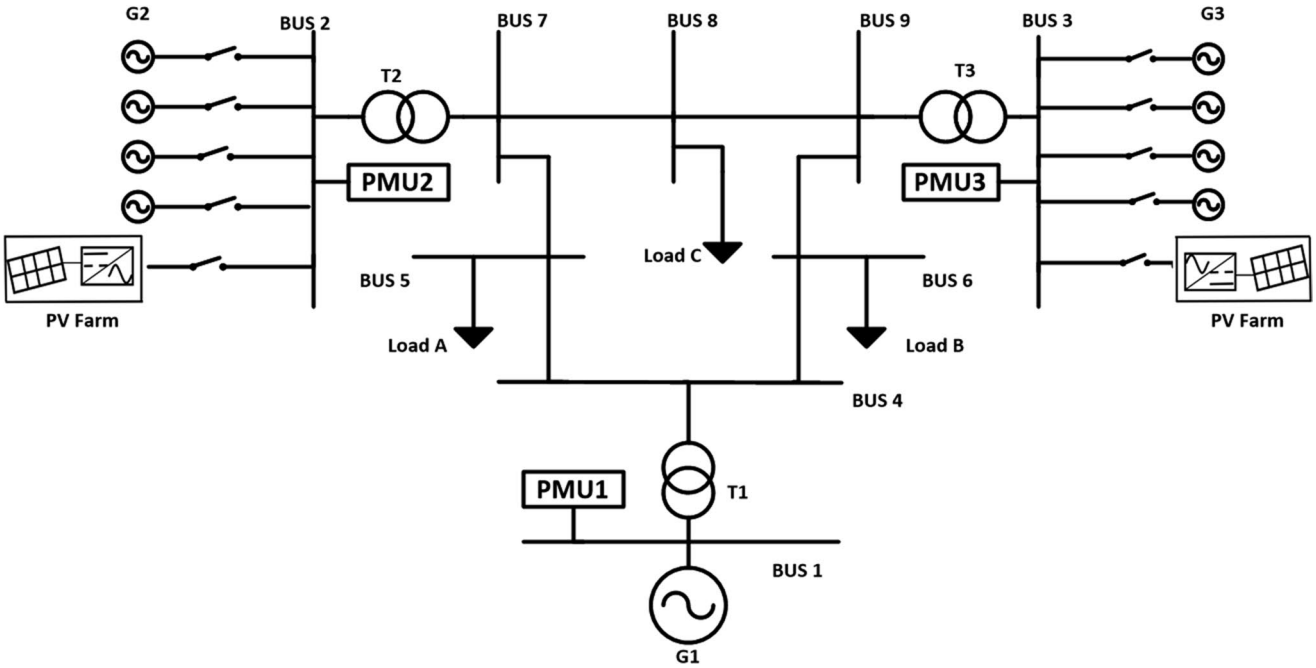


Fig. 9 Nine bus system with implementation of PV farm

Eleven fuzzy rules are formed using crisp input and output values two of which shown below.

Rule no 1- If MF1 and MF1 then MF11.

Rule no 2- If MF2 and MF2 then MF10.

The above designed fuzzy logic estimator has been utilized to estimate inertia when PV is incorporated in nine bus system.

4.1.2 Stage II: Hsys Estimation with Photovoltaic Farm

The same nine bus system above, is now modified with addition of photovoltaic farm at bus 2 and bus 3 is shown in the Fig. 9. The schematic representation of the PV farm connected to the grid and details of PV farm has been attached in Appendix B. Developed fuzzy logic inertia estimator has been utilized with actual implementation of PV farm in nine bus system. Initially G2 has been replaced with four small generators as shown in the Fig. 9 each of them represents 25% power rating of G2, one generator has been tripped off at a time to decrease generation by 25% of synchronous generator and to incorporate PV of equivalent rating in the system in order to maintain the same power flow of system. Inertia of G1 is remained to be constant at 6s and that of G2 and G3 are kept to be constant at 4s. With the reduction in synchronous generation in the system H_{sys} gets change and its corresponding response on $\dot{\delta}$ has been plotted in Figs. 10 and 11.

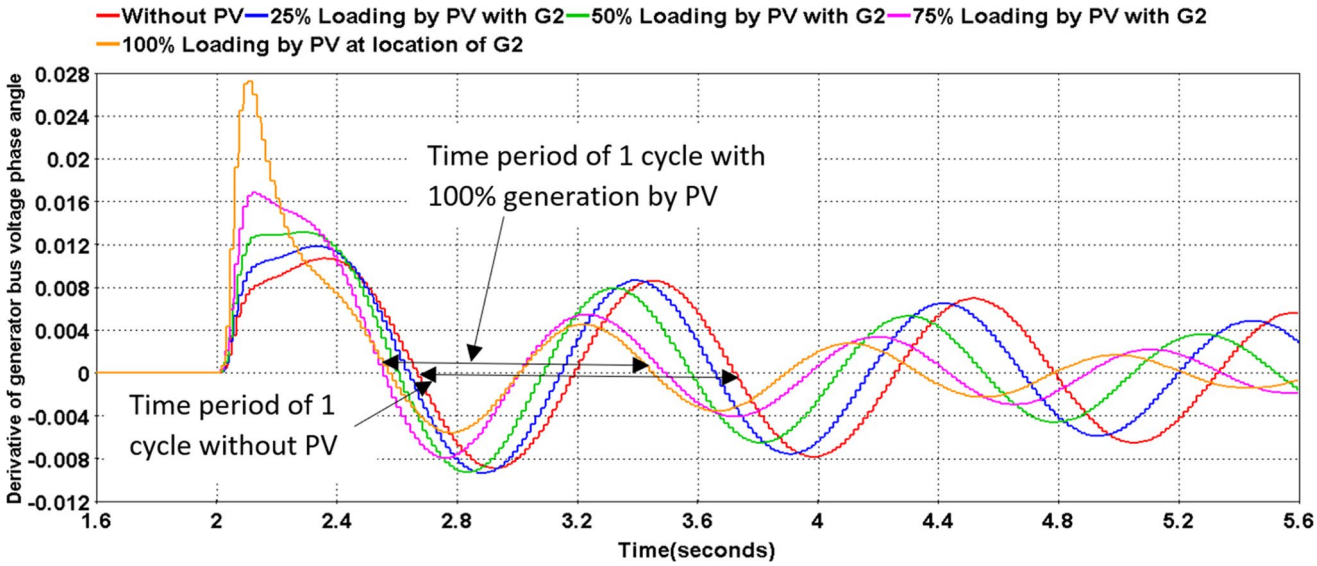


Fig. 10 Response of derivative of generator bus voltage phase angle $\dot{\delta}$ at bus 2

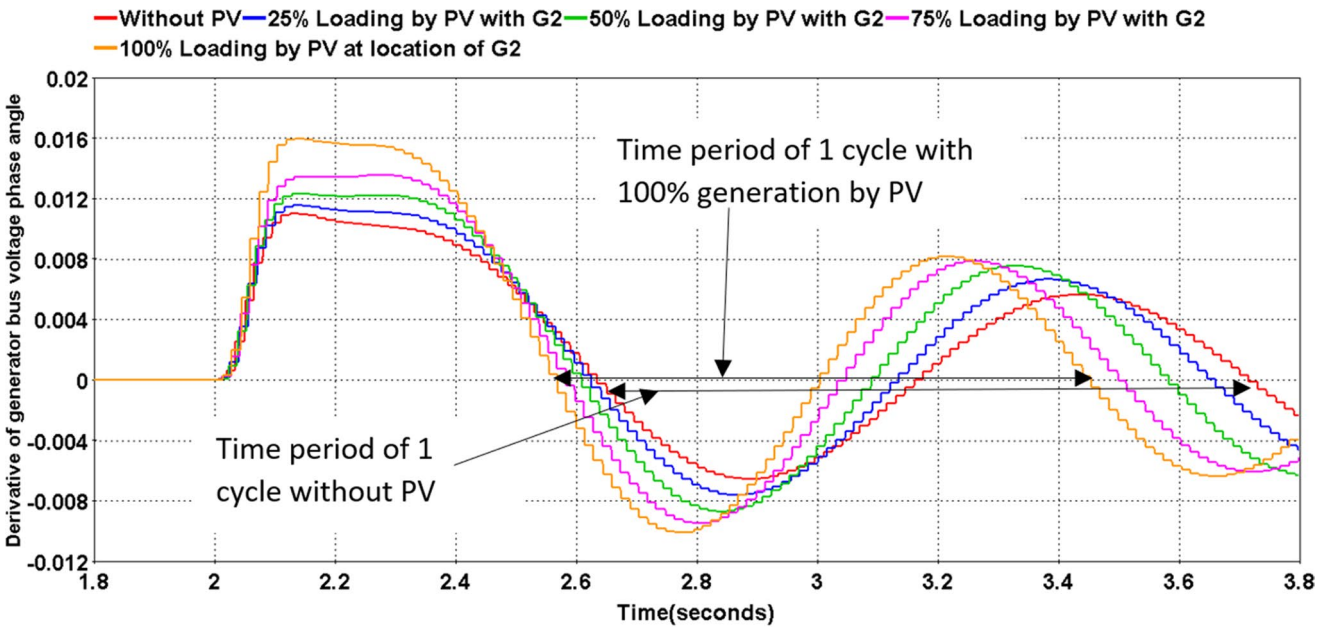


Fig. 11 Response of derivative of generator bus voltage phase angle $\dot{\delta}$ at bus 3

The response of $\dot{\delta}$ at bus 2 and 3 for various values of generation by PV with G2 are plotted in Figs. 10 and 11 respectively. It can be observed from the figures with increase in PV generation, oscillating frequency f_d increases as time period decreases.

Table 5 below represents the PV incorporation and MVA rating of generators for which actual H_{sys} has been calculated using equation 6. Also, by taking its response on f_d of $\dot{\delta}$ at generator bus 2 and 3 H_{sys} estimated using designed fuzzy logic estimator. Then after, same procedure has been followed to estimate H_{sys} as performed for G2.

All the responses collected for both the generators and summarized in Table 5.

Percentage error has been calculated for actual calculated inertia and estimated inertia by designed fuzzy logic estimator using formula expressed in equation 7 and tabulated in last column of Table 5. Error found in the range from 0.023% to 3.803%.

$$\%\ error = \frac{Theoretical\ H_{system} - EstimatedH_{system}}{Theoretical\ H_{system}} \times 100 \tag{7}$$

Table 5 PV implementation to 9 bus system

Sr. No.	% Share of PV	PV Share (MVA)	G1 (MVA)	G2 (MVA)	G3 (MVA)	Calculated H_{sys} (s)	f_d of $\dot{\delta}$ at bus 2 Cycles/sec	f_d of $\dot{\delta}$ at bus 3 Cycles/sec	Estimated H_{sys} (s)	% Error
1	No PV	0	512	270	125	5.411246	0.9493	0.92593	5.41	0.023
2	25% PV with G2	67.5	512	202.5	125	5.113561	0.980681	0.9632	5.16	−0.908
3	50% PV with G2	135	512	135	125	4.815877	1.02738	1.02564	4.94	−2.577
4	75% PV with G2	202.5	512	67.5	125	4.518192	1.07875	1.07689	4.69	−3.803
5	25% PV with G3	31.25	512	270	93.75	5.273429	0.9601	0.9332	5.26	0.254
6	50% PV with G3	62.5	512	270	62.5	5.133407	0.9829	0.97470	5.2	−1.29
7	75% PV with G3	93.75	512	270	31.25	4.998897	0.9936	0.9885	5.11	−2.22

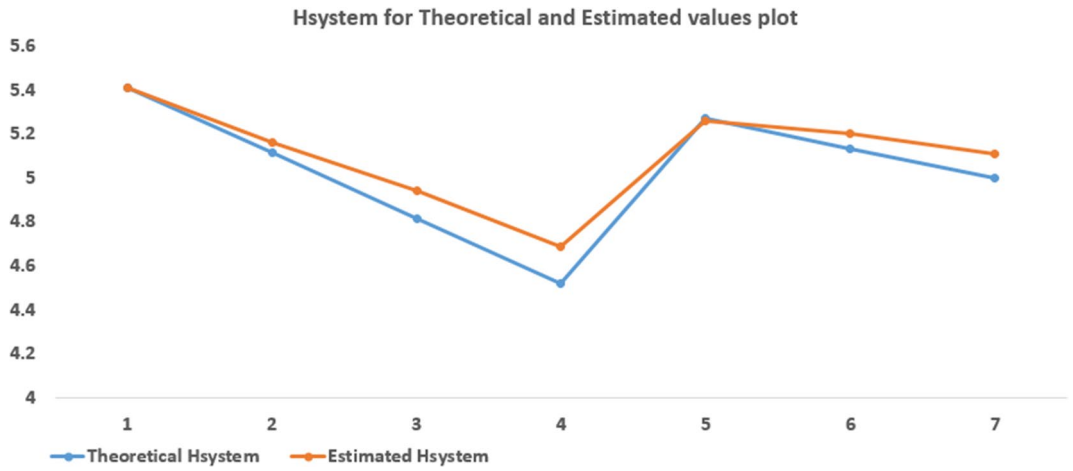


Fig. 12 Graphical representation of Theoretical Inertia and Inertia estimated

Graphical representation of theoretical calculated inertia and estimated inertia is plotted in Fig. 12.

4.2 Case–II Two Area System

In this case Kundur's benchmark two area system as shown in the Fig. 13 has been considered, in which two areas are separated by tie line of 220 km. All the four generators have similar rating of 900MVA supplying 700 MW. G3 has been considered as swing machine with inertia constant at 6.5s, while other generator's inertia are varied in the range of 2–6s during the study. PMUs are considered to be connected at each of the generator bus in order to obtain bus voltage phase angle. A single line to ground fault has been applied at 1 seconds on one of the tie lines between bus 7 and 8 and cleared at 1.0176 seconds to study the response of $\dot{\delta}$. f_d of $\dot{\delta}$ has been used to design the fuzzy logic base estimator for estimation of inertia. The study system has been initialized with load flow before the application of disturbance. The proposed method for estimation of inertia has been carried out in two stages (i) Design of fuzzy logic estimator and (ii) H_{sys} estimation in presence of Photovoltaic farm.

4.2.1 Stage I- Design of Fuzzy Logic to Estimate Inertia (H_{sys})

To design the fuzzy logic estimator for two area system MVA rating of all generators is considered to be 900MVA and inertia of one of the generators among G1, G2 and G4 is varied in the range of 2–6 seconds in order to get different response of $\dot{\delta}$ for various values of H_{sys}. System inertia has been calculated by using equation (6) and its response f_d has been obtained from $\dot{\delta}$ at generator bus 1, 2 and 4 and presented in Table 6.

By using above input data thirteen triangular membership function are formed for three crisp input which are f_d of $\dot{\delta}$ at bus 1, 2 and 4 and one crisp output is H_{sys}.

For each membership function values of a, b and c are represented in Table 7.

Thirteen fuzzy rules are formed using crisp input and output values two of which shown below.

Rule no 1- If MF1 and MF1 then MF13.

Rule no 2- If MF2 and MF2 then MF12.

The developed fuzzy logic estimator has been considered for estimation of inertia of two area system in the presence of Photovoltaic farms.

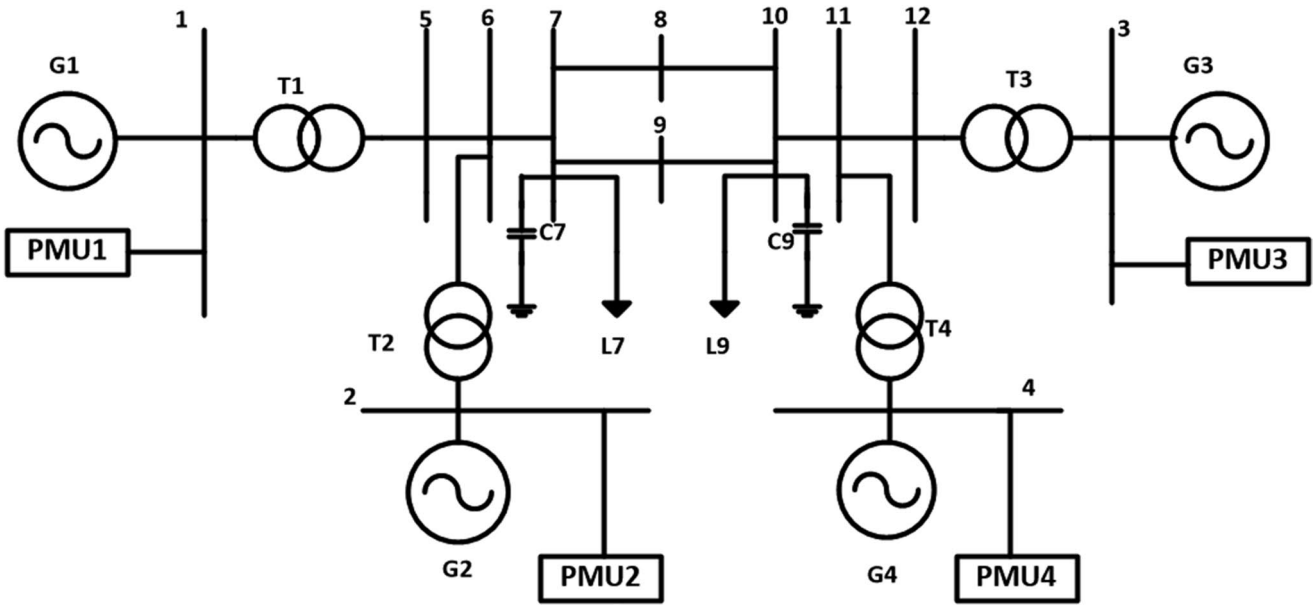


Fig. 13 Two area system

Table 6 Input data to design fuzzy logic for two area system

Sr. No.	H_1 (s)	H_2 (s)	H_3 (s)	H_4 (s)	Calculated H_{sys}(s)	f_d of $\dot{\delta}$ at bus 1 Cycles/sec	f_d of $\dot{\delta}$ at bus 2 Cycles/sec	f_d of $\dot{\delta}$ at bus 4 Cycles/sec
1	2	2	6.5	2	3.125	0.670355	0.675898	1.98956
2	2	2	6.5	3	3.375	0.669882	0.673401	1.97417
3	2	2	6.5	4	3.625	0.6666	0.66701	1.96213
4	2	2	6.5	5	3.875	0.66335	0.6637	1.9478
5	2	2	6.5	6	4.125	0.6600	0.66009	1.86471
6	3	2	6.5	6	4.375	0.65462	0.653189	1.84706
7	5	2	6.5	6	4.875	0.63315	0.62989	1.75134
8	6	2	6.5	6	5.125	0.61139	0.612632	1.68862
9	6	3	6.5	6	5.375	0.59923	0.60061	1.66639
10	6	4	6.5	6	5.625	0.58089	0.588408	1.62602
11	6	5	6.5	6	5.875	0.54279	0.547345	1.58743
12	6	6	6.5	6	6.125	0.51337	0.51956	1.51458

4.2.2 Stage II- H_{sys} Estimation with Photovoltaic Farm

Now, the two area system has been modified with PV farm incorporated in area 2 at bus 4 to study its impact on H_{sys}. Additional power in the range of 5–50% of total generation of area 2 has been added in steps with PV farms. Inertia of the synchronous generators G1, G2, G3, G4 kept to be constant at 6s, 6s, 6.5s and 6s respectively.

After the application of disturbance for each step of power addition by PV farms at bus 4 the PMU response of at bus 1, 2 and 4 are measured and recorded. The f_d of 1, 2 and 4 are used as input quantities to estimate H_{sys}. Calculated $H_{sys,}$, estimated H_{sys} along with percentage error are tabulated in Table 8. Percentage error has been calculated for each step by using equation expressed in 7. Percentage error lies in the range of 0.629% to 3.869%.

Theoretical Inertia and Estimated Inertia of two area system has been plotted in Fig. 14.

The following section presents the drawback of conventional techniques of estimation of inertia.

5 Limitation of Traditional Methods of Estimation of System Inertia Based on Frequency Response

Traditional inertia estimations were based on the frequency response of the system governed by the swing equation expressed in 8 [24],

$$\frac{2H}{\omega}\frac{d\omega}{dt} = P_m - P_e \tag{8}$$

Table 7 Membership function data for fuzzy logic

	Triangular membership function values											
	Crisp Input1 f_d at bus 1			Crisp Input2 f_d at bus 2			Crisp Input3 f_d at bus 4			Crisp Output H_{sys}		
	a	b	c	a	b	c	a	b	c	a	b	c
MF1	0.6645	0.67035	0.6698	0.6658	0.67589	0.67340	1.9999	1.9895	1.9741	2.85	3.12	3.37
MF2	0.6703	0.66988	0.6666	0.67589	0.67340	0.66701	1.9895	1.9741	1.9621	3.12	3.37	3.62
MF3	0.6698	0.6666	0.6633	0.67340	0.66701	0.6637	1.9741	1.9621	1.9478	3.37	3.62	3.87
MF4	0.6666	0.6635	0.66	0.6670	0.6637	0.66009	1.9621	1.9478	1.8647	3.62	3.87	4.12
MF5	0.6635	0.66	0.654	0.6637	0.66009	0.65318	1.9478	1.8647	1.8470	3.87	4.12	4.37
MF6	0.66	0.65462	0.6331	0.66009	0.65318	0.62988	1.8647	1.8470	1.7513	4.12	4.37	4.87
MF7	0.6546	0.63315	0.6113	0.65318	0.62988	0.61263	1.8470	1.7513	1.6886	4.37	4.87	5.12
MF8	0.6331	0.61139	0.6019	0.62988	0.61263	0.6027	1.7513	1.6886	1.6667	4.87	5.12	5.37
MF9	0.6113	0.60192	0.5992	0.61263	0.6027	0.60061	1.6886	1.6667	1.6663	5.12	5.37	5.62
MF10	0.6019	0.59923	0.5808	0.6027	0.60061	0.58840	1.6667	1.6663	1.6260	5.37	5.62	5.87
MF11	0.5992	0.58088	0.5427	0.60061	0.58840	0.54734	1.6663	1.6260	1.5874	5.62	5.87	6.12
MF12	0.5808	0.54278	0.5133	0.58840	0.54734	0.51956	1.6260	1.5874	1.5145	5.87	6.12	6.32
MF13	0.5427	0.51337	0.5033	0.54734	0.51956	0.50958	1.5874	1.5145	1.5023	6.12	6.32	6.52

On simplifying,

$$\mathrm{H} = \Delta \mathrm{P}\ \frac{f_0}{\frac{\mathrm{df}}{\mathrm{dt}}} \tag{9}$$

Where inertia constant H can be estimated from measurement of rate of change of frequency (ROCOF) and power change (ΔP) at the instance of disturbance given in 9. This method of estimation suffers from the following drawback:

- Calculating accurate size of disturbance is challenging.
- ROCOF cannot be directly measured has to be estimated from frequency response.
- Frequency deviates not only with the inertia but also with the changes in the load on the system.

To further explain frequency response in a single machine infinite bus system with same generator inertia for various magnitudes of disturbance has been plotted in Fig. 15 and with same disturbance various generator inertia is plotted in Fig. 16. From these responses it can be observed that the change in nadir frequency is not unique to disturbance or system inertia.

However, proposed methodology overcome the limitations with the following advantages.

- Proposed method shows unique approach to estimate system inertia H_{sys} as in Fig. 2
- Voltage phase angle has been utilized which is directly obtained from PMU.
- The proposed algorithm can estimate system inertia in presence of RES with minimal error.

6 Conclusion

With increasing integration of RES into power system, the system inertia deviates continuously. The system inertia has to be calculated by measurement of observable electrical quantities. In this paper, a novel estimation of power system inertia with measurements from PMUs has been proposed. To be specific, proposed method utilizes all the bus voltage angle measured from PMUs to calculate its time derivative. Fuzzy logic controller with triangular membership function has been designed for two case study system. By varying inertia of the study system with different types of disturbances the membership functions have been aligned. After the design of fuzzy logic controller RES has been integrated in the system which in turn reduces system inertia. The system inertia in the presence of RES has been estimated with fuzzy logic estimator. Proposed method successfully estimates system inertia with an accuracy of 99.98% - 96.13%.

Table 8 PV farm addition to two area system

Sr. No.	Rating of PV (MVA)	Power of PV (MW)	f_d of $\dot{\delta}$ at bus 1 Cycles/sec	f_d of $\dot{\delta}$ at bus 2 Cycles/sec	f_d of $\dot{\delta}$ at bus 4 Cycles/sec	Calculated H_{sys} (s)	Estimated H_{sys} (s)	% Error
1	90MVA	70 MW	0.505043	0.510318	1.5238	6.15	6.05	1.224
2	180MVA	140 MW	0.540276	0.54619	1.53251	5.97560	5.88	1.6
3	270MVA	210 MW	0.56042	0.5611135	1.5667	5.83333	5.87	−0.629
4	360MVA	280 MW	0.586295	0.588028	1.59043	5.69767	5.63	1.188
5	450MVA	350 MW	0.602142	0.603189	1.60214	5.56818	5.5	1.224
6	560MVA	420 MW	0.619307	0.619763	1.62018	5.44444	5.5	−1.02
7	630MVA	490 MW	0.624176	0.625122	1.63213	5.32608	5.12	3.869
8	720MVA	560 MW	0.6304	0.635607	1.71759	5.21276	5.09	2.355
9	810MVA	630 MW	0.640639	0.641952	1.72826	5.10416	4.97	2.629
10	900MVA	700 MW	0.641622	0.64722	1.73476	5	4.95	1

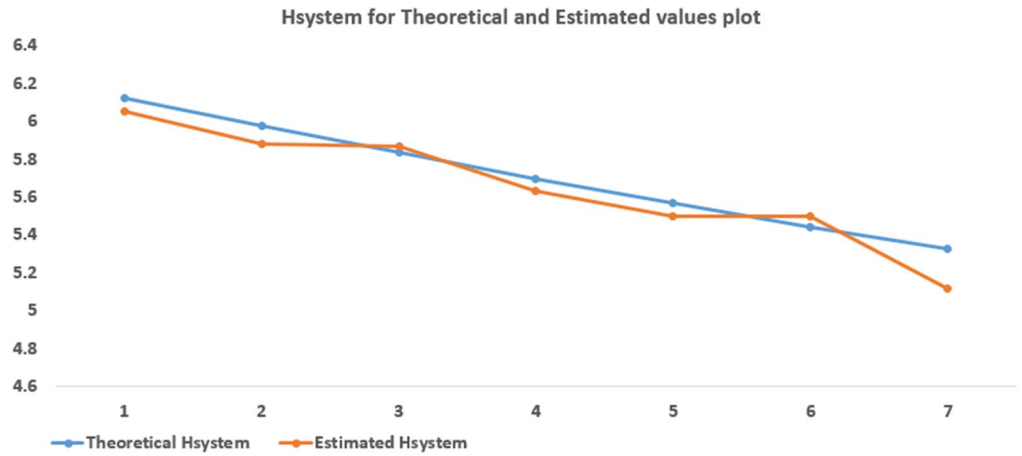


Fig. 14 Graphical representation of Theoretical Inertia and Estimated Inertia of Two Area System

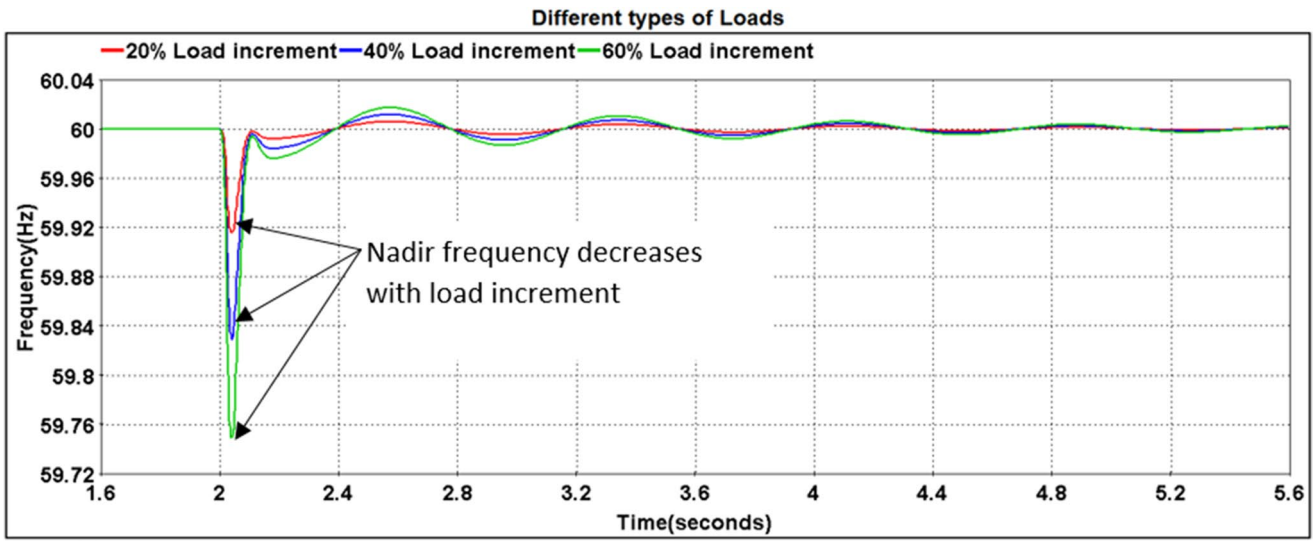


Fig. 15 Frequency response during addition of different types of load in the system for constant inertia

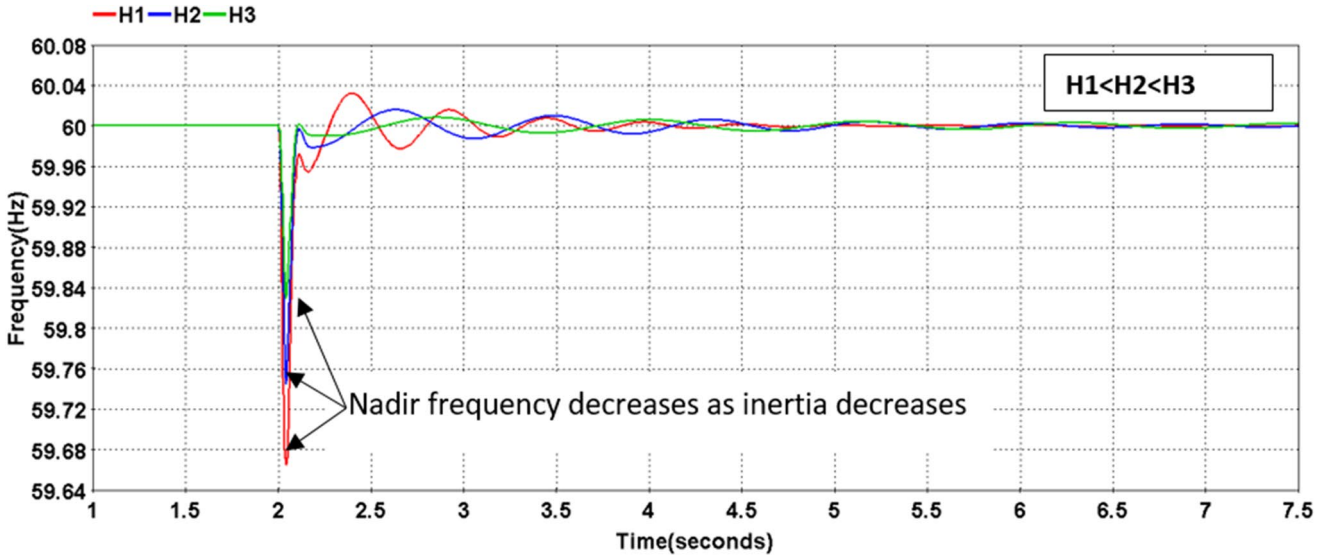


Fig. 16 Frequency response during addition of load in the system for various values of inertia

In comparison, to the traditional inertia estimation methods based on frequency and ROCOF measurements using swing equation, proposed PMU based fuzzy logic estimator is independent of the type of disturbance in the system. Proposed method has been tested with simulations in OPAL RT real time simulator with HYPERSIM environment.

Appendix A

A linear Second order system can be represented as,

$$\frac{d^2\Delta\delta}{dt^2} + \frac{\pi f_0}{H}\mathrm{D}\frac{d\Delta\delta}{dt} + \frac{\pi f_0}{H}P_S\Delta\delta = 0$$

In state space form with,

$$x_1 = \Delta\delta \; and \; x_2 = \Delta\omega = \dot{\Delta}\delta$$

$$\dot{x}_1 = x_2 \; and \; \dot{x}_2 = -\omega_n^2 x_1 - 2\zeta\omega_n x_2$$

$$\begin{bmatrix} \dot{x_1} \\ \dot{x_2} \end{bmatrix} = \begin{bmatrix} 0 & 1 \\ \omega_n^2 x_1 & -2\zeta\omega_n \end{bmatrix} \begin{bmatrix} x_1 \\ x_2 \end{bmatrix}$$

Which can be represented as,

$$\dot{X(t)} = AX(t)$$

If x_1 *and* x_2 are desired responses output can be presented in the form of y(t)

$$y\left(t\right) = \begin{bmatrix} 1 & 0 \\ 0 & 1 \end{bmatrix} \begin{bmatrix} x_1 \\ x_2 \end{bmatrix}$$

$$y\left(t\right) = Cx\left(t\right)$$

By taking Laplace transform we have,

$$sX\left(s\right) - x\left(0\right) = AX\left(s\right)$$

$$X\left(s\right) = \left(sI - A\right)^{-1} x\left(0\right)$$

Where

$$\left(sI - A\right) = \begin{bmatrix} s & -1 \\ \omega_n^2 & s + 2\zeta\omega_n \end{bmatrix}$$

Substituting for $\left(sI - A\right)^{-1}$ we have,

$$X\left(s\right) = \frac{\begin{bmatrix} s + 2\zeta\omega_n & 1 \\ -\omega_n^2 & s \end{bmatrix}}{s^2 + \; 2\zeta\omega_n \; s + \omega_n^2} x\left(0\right)$$

Incase rotor is disturbed by small angle $\Delta\delta_0$, then $x_1\left(0\right) = \Delta\delta_0$ and $x_2\left(0\right) = \Delta\omega_0 = 0$ then we get,

$$\Delta\delta\left(s\right) = \frac{\left(s + 2\zeta\omega_n\right)\Delta\delta_0}{s^2 + \; 2\zeta\omega_n \; s + \omega_n^2}$$

Taking inverse Laplace transform results in,

$$\Delta\delta = \frac{\Delta\delta_0}{\sqrt{1-\zeta^2}} e^{-\zeta\omega_n t} \sin(\omega_d t + \theta)$$

Where θ is given by,

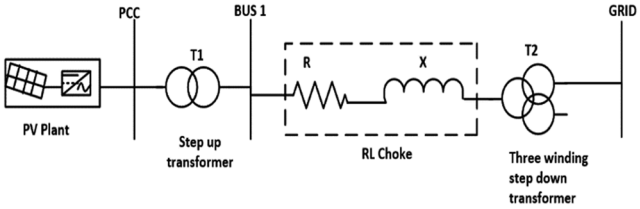
$$\theta = \cos^{-1}\zeta$$

Therefore, motion of rotor relative to synchronously rotating revolving field is,

$$\delta = \delta_0 + \frac{\Delta\delta_0}{\sqrt{(1-\zeta^2)}} e^{-\zeta\omega_n t} \sin(\omega_d t + \theta)$$

Where δ_0 is initial rotor angle value.

Appendix B



Schematic representation of PV farm connected to grid

MVA Rating- 750KVA
Number of modules connected in parallel Npar − 270
Number of modules connected in series Nser − 10
Module Data
Maximum power Pmax- 305.226 W
Number of cells per module Ncell − 96
Transformer

Two winding transformer	Three winding transformer
Star grounded/ Delta Lag	Star Floating/ Star grounded/ Delta lag
0.48kV/39.664kV	154kV/22.899kV/5.716kV
R1- 3.840mΩ	R1- 1.067 Ω
L1- 61.115μH	L1- 242.726mH
R2 - 2.913 Ω	R2 − 52.44 $\times 10^{-9}\Omega$
L2 - 46.368mH	L2 - 139.111$\times 10^{-12}$H
	R3 - 490.00$\times 10^{-6}\Omega$
	L3 - 154.4$\times 10^{-6}$H

Acknowledgements Authors would like to declare that research work for the manuscript has been done by Ms Nitisha Sudhir Darwade under the guidance and supervision of Prof. S. T. Nagarajan.

Author Contributions Conceptualization: [S.T.Nagarajan]; Methodology: [Nitisha Sudhir Drawade]; Formal analysis and investigation: [Nitisha Sudhir Drawade]; Writing - original draft preparation: [Nitisha Sudhir Drawade]; Writing - review and editing: [Nitisha Sudhir Drawade]; Supervision: [S.T.Nagarajan].

Funding The authors received no financial support for the research, authorship, and/or publication of this article".

Data Availability Authors declare that no data used to conduct research which is not available in the manuscript

Declarations

Competing Interests The authors declare that they have no known competing financial interests or personal relationships that could have appeared to influence the work reported in this paper.

References

1. Sun J et al (2017) Renewable energy transmission by HVDC across the continent: system challenges and opportunities. CSEE J Power Energy Syst 3(4):353–364.https://doi.org/10.17775/CSEEJPES.2017.01200
2. (2022) Power system operation corporation limited in collaboration with report on assessment of Inertia in Indian Power System
3. IEEE Staff (2012) IEEE Power and Energy Society General Meeting
4. Gevorgian V, Zhang Y, Ela E (Jul 2015) Investigating the impacts of wind generation participation in interconnection frequency response. IEEE Trans Sustain Energy 6(3):1004–1012. https://doi.org/10.1109/TSTE.2014.2343836
5. Silwal S, Karimi-Ghartemani M (2019) On transient responses of a class of PV Inverters. IEEE Trans Sustain Energy 10(1):311–314. https://doi.org/10.1109/TPWRD.2018.2804671
6. Denholm P, Mai T, Kenyon RW, Kroposki B, O'malley M, "Inertia and the power grid: a guide without the spin," 2020. [Online]. Available: www.nrel.gov/publications.
7. Prabhakar K, Jain SK, Padhy PK Inertia estimation in modern power system: a comprehensive review. Electr Power Syst Res 211 Elsevier Ltd Oct. 01, 2022.https://doi.org/10.1016/j.epsr.2022.108222
8. Inoue T, Taniguchi H (1997) Ower system inertia constant and capacity of spinning-ort generators using measured frequency transients
9. Chassin DP, Huang Z, Donnelly MK, Hassler C, Ramirez E, Ray C (2005) Estimation of WECC system inertia using observed frequency transients. IEEE Trans Power Syst 20(2):1190–1192. https://doi.org/10.1109/TPWRS.2005.846155
10. IEEE Power & Energy Society (2023) IEEE Power and Energy Society General Meeting (PES); Vancouver, BC, Canada.
11. Ashton PM, Saunders CS, Taylor GA, Carter AM, Bradley ME (2015) Inertia estimation of the GB power system using synchrophasor measurements. IEEE Trans Power Syst 30(2):701–709. https://doi.org/10.1109/TPWRS.2014.2333776
12. Zografos D, Ghandhari M, Eriksson R (2018) Power system inertia estimation: utilization of frequency and voltage response after a disturbance. Electr. Power Syst. Res. 161:52–60. Aug, https://doi.org/10.1016/j.epsr.2018.04.008
13. Kerdphol T, Watanabe M, Nishikawa R, Tamaki T, Mitani Y (2021) Determining inertia of 60 Hz Japan power system using PMUs from power loss event. In: 2021 IEEE Texas Power and Energy Conference (TPEC) https://doi.org/10.1109/TPEC51183.2021.9384932.
14. Zografos D, Ghandhari M (2016) Estimation of power system inertia. In: 2016 IEEE Power and Energy Society General Meeting (PESGM); Boston, MA, USA, p. 1–5. https://doi.org/10.1109/PESGM.2016.7741073.
15. Agrawal PK, Agrawal VK, Rathour H (2013) Application of PMU-based information in the Indian power system. Int J Emerg Elec Power Syst
16. Ariff MAM, Pal BC, Singh AK (Mar 2015) Estimating dynamic model parameters for adaptive protection and control in power system. IEEE Trans Power Syst 30(2):829–839. https://doi.org/10.1109/TPWRS.2014.2331317

17. Wall P, Terzija V (2014) Simultaneous estimation of the time of disturbance and inertia in power systems. IEEE Trans Power Delivery 29(4):2018–2031. https://doi.org/10.1109/TPWRD.2014.2306062
18. Petra N, Petra CG, Zhang Z, Constantinescu ZM, Anitescu M (2017) A Bayesian Approach for Parameter Estimation With Uncertainty for Dynamic Power Systems, In IEEE Transactions on Power Systems. vol. 32, no. 4, pp. 2735–2743. https://doi.org/10.1109/TPWRS.2016.2625277
19. Tuttelberg K, Kilter J, Wilson D, Uhlen K (2018) Estimation of power system inertia from ambient wide area measurements. IEEE Trans Power Syst 33(6):7249–7257. https://doi.org/10.1109/TPWRS.2018.2843381
20. Tan B, Zhao J, Terzija V, Zhang Y (2022) Decentralized data-driven estimation of generator rotor speed and inertia constant based on adaptive unscented Kalman filter. Int J Electr Power Energy Syst https://doi.org/10.1016/j.ijepes.2021.107853
21. Cao X, Stephen B, Abdulhadi IF, Booth CD, Burt GM (2016) Switching Markov Gaussian models for dynamic power system inertia estimation. IEEE Trans Power Syst 31(5):3394–3403. https://doi.org/10.1109/TPWRS.2015.2501458
22. Schmitt A, Lee B (2017) Steady-state inertia estimation using a neural network approach with modal information. In: 2017 IEEE Power & Energy Society General Meeting; Chicago, IL, USA, p. 1–5. https://doi.org/10.1109/PESGM.2017.8274640.
23. Wang W, Yao W, Chen C, Deng X, Liu Y (2020) Fast and accurate frequency response estimation for large power system disturbances using second derivative of frequency data. IEEE Trans Power Syst 35(3):2483–2486. https://doi.org/10.1109/TPWRS.2020.2977504
24. Wang B, Yang D, Cai G, Chen Z, Ma J (2022) An improved electromechanical oscillation-based inertia estimation method. IEEE Trans Power Syst 37(3):2479–2482. https://doi.org/10.1109/TPWRS.2022.3156441
25. (2011) IEEE Standard for Synchrophasor Measurements for Power Systems. IEEE Std C37.118.1-2011 (Revision of IEEE Std C37.118-2005); p. 1–61. https://doi.org/10.1109/IEEESTD.2011.6111219
26. (2006) IEEE Std C37.118-2005 (Revision of IEEE Std 1344-1995): IEEE Standard for Synchrophasors for Power Systems. IEEE
27. P. System Relaying Committee of the IEEE Power and E. Society (2011) IEEE Standard for Synchrophasor Measurements for Power Systems Sponsored by the Power System Relaying Committee IEEE Power & Energy Society
28. Kundur P (1994) Power System Stability and Control, New York, NY, USA: McGraw-Hill.
29. Kovačić Z, Bogdan S (2006) Fuzzy Controller Design: Theory and Applications, Boca Raton, FL, USA: CRC Press.

Publisher's Note Springer Nature remains neutral with regard to jurisdictional claims in published maps and institutional affiliations.

Springer Nature or its licensor (e.g. a society or other partner) holds exclusive rights to this article under a publishing agreement with the author(s) or other rightsholder(s); author self-archiving of the accepted manuscript version of this article is solely governed by the terms of such publishing agreement and applicable law.



Nitisha Sudhir Drawade received B.E in Electrical Engineering in 2010 from Rashtrasanth Tukdoji Maharaj Nagpur University and M.Tech in Integrated Power System in 2014 from Visveswaraya National Institute of Technology, Nagpur. She worked as an Assistant Professor in Rashtrasanth Tukdoji Maharaj Nagpur University for more than four years. She is currently working toward Ph.D. degree at Delhi Technological University, New Delhi India. Her research area includes Power system protection, Power system stability, Renewable energy integration in Powe grid and Wide Area Measurement Systems(WAMS).



S.T.Nagarajan is professor in Electrical Engineering Department of Delhi Technological University, Delhi, India. He completed his B.E graduation in Electrical and Electronics Engineering from Thiagarajar College of Engineering, Madurai in 1994 and post-graduation in High Voltage Engineering from Anna University, Chennai in 1996. He obtained his Ph.D degree in area of Power system from Delhi University in 2015. He is fullbright scholor of post-doctoral research at Washington State University, USA in 2017. Since 1996 he has been in teaching for undergraduate and postgraduate program and is with Delhi Technological University (From Delhi College of Engineering) from 1999. His area of research interest includes wide area monitoring, Power system stability and High Voltage Engineering.